JOURNAL
OF THE
PHYSICAL SOCIETY
OF JAPAN

Volume 8

1953

Published by the
PHYSICAL SOCIETY OF JAPAN

JOURNAL OF THE PHYSICAL SOCIETY OF JAPAN Vol. 8, No. 1, JAN.—FEB., 1953

On the "Capture Scattering" of Fast Neutrons

By Tetsuo WAKATSUKI

Department of Physics, Faculty of Science, Osaka University

(Received August 9, 1952)

The differential scattering cross sections of Li-D neutrons were measured for 11 elemens at scattering angle of 90 degrees.

The neutron detector was an ionization chamber connected to an electrometer whose energy sensitivity can be changed to some extent by the change of filling gas and its pressure.

Intensities of scattered neutrons observed with the chamber filled with high pressure methane, whose sensitivity is expected to be nearly constant through the energy region concerned, agreed well with the values calculated from the differential scattering cross sections which were assumed to be equal to $\sigma/2\cdot 1/4\pi$, σ being the total cross sections.

Intensities of scattered neutrons observed with hydrogen filled chamber with greater sensitivity at lower energy side showed 30 to 60% higher values than expected by the same calculation.

These results support the view that (1) half of the total cross section is "capture scattering", and (2) in "capture scattering" process, neutrons are scattered isotropically with less energy than the primary neutrons.

§1. Introduction

It is now generally believed that interaction of fast neutrons can be divided in two kinds of processes, the one, interaction including the formation of compound nucleus and the other, scattering without formation of the compound nucleus.

The relative importance of these two processes depends on the energy of the impinging neutrons. When neutron energy is high enough and the following relation is satisfied

$$\lambdabar=\frac{\lambda}{2\pi}\ll R\,, \qquad (1)$$

where λ is the de Broglie wave length and R is the nuclear radius, the situation becomes very simple and cross sections for both processes σ_c and σ_s become both equall to geometrical cross section of the nucleus, so that

$$\sigma_c=\sigma_s=\pi R^2 \qquad (2)$$

As the total cross section σ is the sum of the two processes

$$\sigma=\sigma_c+\sigma_s=2\pi R^2\,. \qquad (3)$$

In the process of forming compound nucleus, the neutron is captured by nucleus and then particles or photons are emitted. For most cases, reemission of the neutron is predominant and the neutron is supposed to be emitted spherical symmetrically with energy smaller than that of the incident neutron, leaving the nucleus in excited state. In this type of scattering, which will be called as "capture scattering" the probability that the neutron is reemitted without loosing its energy is expected to be very small.

The scattering of fast neutron without the formation of compound nucleus is interpreted as the diffraction of neutron wave and the scattered neutron goes in the forward direction of small angle of the order of $\lambdabar/R$. In this so called "shadow scattering", neutron is scattered without the loss of energy. Elastic scattering occurs in this case.

The view described above is supported by a several experimental evidences. This work was intended to offer further experimental evidences concerning this problem.

That the scattering of fast neutrons seems to consists of isotropic scattering superposed with forward scattering was shown by us, using 3 Mev neutrons[1]. Though σ_c and σ_s were found to be nearly equall for the elements investigated, it can not be regarded as a proof of the idea from which (2) was derived, as 3 Mev energy is not high enough to satisfy the condition (1).

There are two methods to measure σ_c and

15 11 63/Omer

σ_s separately. One is to utilize the difference of the energy of scattered neutrons for both processes. Several authors measured inelastic scattering cross sections using threshold detecters and regarding this as σ_c, the values of σ_s were obtained by taking the difference of σ and σ_c.

Graham and Seaborg²⁾ concluded in this way that the values of σ_c are slightly smaller than $\sigma/2$ for several elements in the case of Ra–Be neutrons. Amaldi et al.³⁾ found that σ_c are almost equal to $\sigma/2$ for 14 Mev neutrons. We must, however, regard the values of σ_c obtained in those experiments as a lower limit of σ_c as the dependence of the detecter on neutron energy may influence the result considerably.

The second method is to utilize the difference of the angular distribution for both processes, not having been used hitherto.

We have tried to obtain the values of σ_c observing the scattered intensity for the scattering angle of 90 degrees, for which angle σ_s is expected to be very small. As the energy of scattered neutrons is different from that of impinging neutrons, it is necessary to know the energy spectrum of scattered neutrons and the dependence of detecter sensitivity on the energy of neutrons to derive σ_c from the observation of scattered intensity.

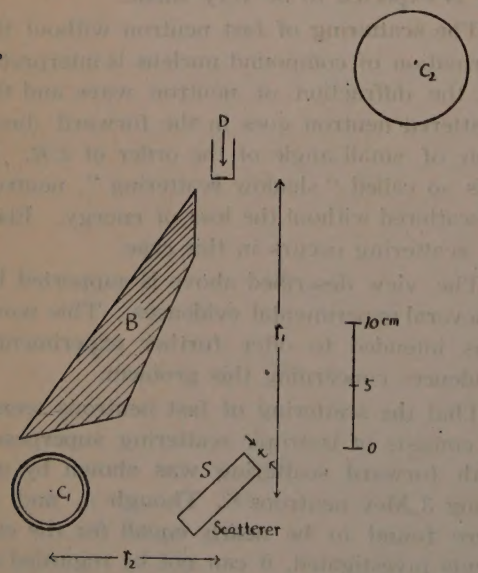

Fig. 1.

The energy spectrum of scattered neutrons can be estimated by the use of Weisskopf's statistical theory. By using neutron detecter with almost constant sensitivity through the energy region concerned, we can calculate the values of σ_c and compare it with $\sigma/2 \cdot 1/4\pi$. Then by comparing the results obtained with the detecter having different energy dependence, it is possible, at least in principle, to test whether the energy spectrum of scattered neutrons expected by the statistical theory is correct or not, or to modify the constants in the statistical theory.

As the neutron source, *Li-D* neutrons were used for which total cross sections and the γ ray intensities following the inelastic scattering were measured already in the previous works⁴⁾⁵⁾.

§ 2. Experimental Arrangements and Procedures

Experimental arrangements are shown in Fig. 1. Fast neutrons scattered by sample S at right angle are detected by ionization chamber C₁. B is a paraffin block to shield the chamber C₁ from direct neutron beams. C₂ is a large volume monitor ionization chamber. Both chambers were connected to electrometers respectively.

Neutron source :

The energy spectrum of *Li-D* neutrons was investigated by Richards⁶⁾ with 1.2 Mev deuterons and by Green and Gibson⁷⁾ with 0.93 Mev deuterons with the similar results. We have produced fast neutrons by bombarding thick metallic lithium by 0.9 Mev (unresolved) deuteron beam, so the energy spectrum similar with those of the above authors may be assumed. For simplicity, the spectrum was assumed to consist of lines as shown in Table 1 in the following discussions.

Table I.

Energy (Mev)	abundance (%)
4	32
8	20
10	8
12	24
14.7	16

Neutron detecter :

The ionization current produced in the high pressure ionization chamber by recoil protons was measured. The effective volume of the ionization chamber C_1 was 5 cm in diameter and 6 cm in length and the filling gas was either 20 atmospheric pressure hydrogen or 42.5 atmospheric pressure methane.

If the dimension of the ionization chamber is large enough compared to the maximum range of recoil protons (R_0), ionization current may be deemed as proportinal to σE, where E is the energy of impinging neutrons. When this condition is not fulfilled, correction factor (k), determined by the dependence of the efficiency of the chamber on neutron energy should be multiplied to σE. As the scattered proton goes for the most part in the forward direction, the situation may be approximated by the simple case of plane electrodes of infinate length spaced D cm apart and perpendicular incidence of fast neutrons onto this plane. Assuming $R \propto E^{2/3}$ and isotropic scattering of neutron in the c–m system, the result is

$$k=1-(1-i)^{2/3}, \qquad (4)$$

Where

$$\left.\begin{aligned} i&=1-\frac{5}{18}\frac{R_0}{D}, && R_0 \leq D \\ \text{or}\quad i&=\frac{D}{R_0}\left\{\frac{5}{2}-\frac{16}{9}\left(\frac{D}{R_0}\right)^{1/4}\right\} && R_0 \geq D. \end{aligned}\right\} \qquad (5)$$

The change of the chamber efficiency with neutron energy for chamber C_1 calculated by (4) and (5) is shown in Fig. 2 in arbitrary scale.

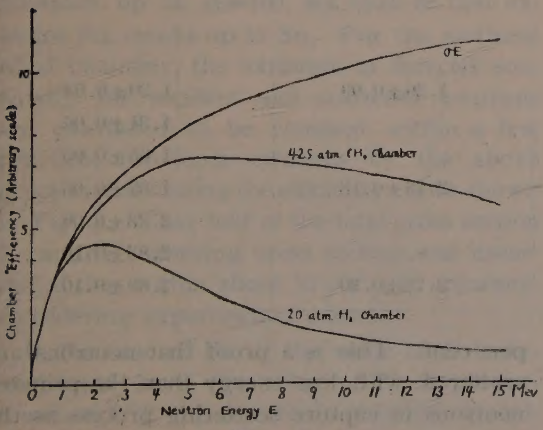

Fig. 2.

From Fig. 2, it is expected that methane filled chamber has nearly flat character over 3 Mev but hydrogen filled chamber has a broad maximum at 2 Mev and decreases steadily with increasing energy.

The results of Fig. 2 were roughly checked by the use of *D-D* neutrons and *Li-D* neutrons.

Scatterers:

The sizes of scatterers were $7.5 \times 10\ \text{cm}^2$ and were placed at angles of 45 degrees to the direction of incident and scattered neutrons. The thicknesses were about 4 cm for most elements.

Procedures:

Let the increase of the ionization current when the scatterer was placed in place be ΔI and the ionization current when the chamber was placed at r cm from the source in the direction of the incident neutrons be I, the following relation holds

$$\Delta I = I N \sigma'(90^\circ)\left(\frac{r}{r_1 r_2}\right)^2 e^{-n\sigma_c\frac{\sqrt{2}}{2}t}, \qquad (6)$$

where N is the total number of atoms in the scatterer, n is the number of atoms per unit area and t, the thickness of the scatterer. r_1 and r_2 are the distances of the scatterer from the source and C_1 respectively. σ' (90°) is related to the differential scattering cross section for scattering angle 90°, $\sigma(90^\circ)$, but is slightly different as the chamber's efficiency is expected to change for primary and scattered neutrons. The exponential factor in (6) is the correction for the diminution of primary neutron intensity in the scatterer.

From equations (2), (3) and (4), $\sigma'(90^\circ)$ can be expressed as

$$\sigma'(90^\circ) = \frac{\Delta I}{I}\frac{1}{N}\left(\frac{r_1 r_2}{r}\right)^2 e^{n\sigma t/2\sqrt{2}} \qquad (7)$$

When the energy spectrum for both incident and scattered neutrons, and the change of detector sensitivity with neutron energy are known, $\sigma(90^\circ)$ can be calculated from (7).

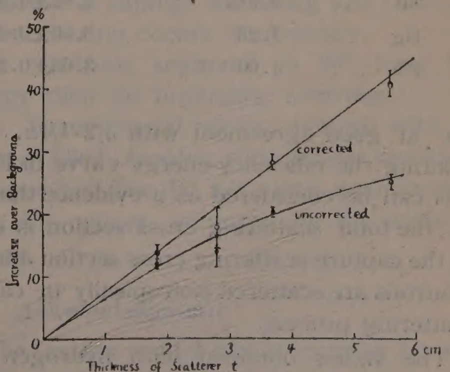

Fig. 3.

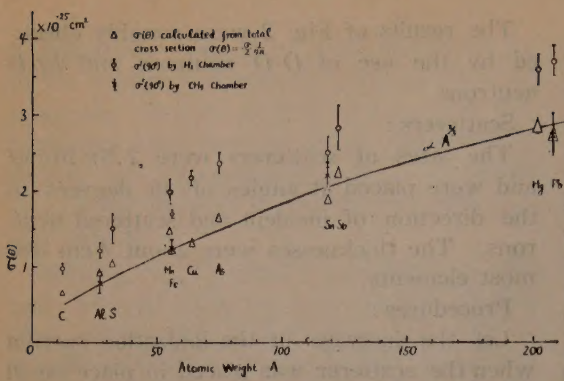

Fig. 4.

§ 3. Results

Fig. 3 shows the increase in ionization current over background when iron scatterers of various thicknesses were placed. It will be seen that the increase ΔI is proportional to the thickness of scatterers after correcting for the decrease of the primary neutron intensities by eq. (6). Therefore, we can derive $\sigma'(90°)$ from eq. (7).

In Table II and Fig. 4, are shown the values of $\sigma'(90°)$ obtained in this way using both hydrogen and methane filled ionization chamber. The last column in the table shows $\sigma/2\cdot 1/4\pi$, which will be equall to $\sigma(90°)$ if the arguement given in § 1 is correct. The values of σ obtained in our previous work[4] was used in the calculation.

§ 4. Discussions

First, we shall estimate the contribution from the shadow scattering precess by the Placzek-Bethe formula[8]

$$\sigma_s(\theta)=[RJ_1(kR\theta)/\theta]^2, \qquad (8)$$

where $\sigma_s(\theta)$ is the differencial scattering cross section due to shadow scattering at θ, k, the wave number and J_1, the Bessel function of the first kind.

Calculation shows that $\sigma_s(90°)$ is 6 to 8% of $\sigma/2\cdot 1/4\pi$ and may be neglected in the following discussions.

Table II

Element	N in 10^{25}	$\sigma'(90°)$ in 10^{-25}cm²		$\frac{\sigma}{2}\frac{1}{4\pi}$ in 10^{-25}cm²
		H_2 chamber	CH_4 chamber	
C	2.36	0.97±0.07		0.65±0.02
Al	1.97	1.21±0.10	0.77±0.12	0.91±0.05
S	0.981	1.51±0.19		1.03±0.05
Mn	1.11	1.99±0.16		1.46±0.04
Fe	1.16	1.69±0.14		
	1.71	1.47±0.26		
	2.33	1.71±0.07		
	3.46	1.67±0.08		
		Mean 1.68±0.05	1.26±0.09	1.20±0.04
Cu	2.14	2.17±0.10		1.31±0.06
As	0.969	2.36±0.14		1.65±0.05
Sn	0.972	2.49±0.21	2.19±0.18	1.87±0.06
Sb	0.915	2.82±0.30		2.23±0.06
Hg	1.23	3.56±0.21		2.83±0.10
Pb	1.00	3.68±0.21	2.72±0.30	2.69±0.10

It is evident from Table II that the values of $\sigma'(90°)$ obtained by methane filled chamber are in good agreement with $\sigma/2\cdot 1/4\pi$. Considering the efficiency-energy curve in Fig. 2. this can be considered as a evidence that half of the total scattering cross section is equall to the capture scattering cross section and that neutrons are scattered isotropically in capture scattering process.

The values obtained with hydrogen filled chamber is greater than $\sigma/2\cdot 1/4\pi$ by 30 to 60 per cent. This is a proof that neutrons are scattered with less energy than the primary neutrons in capture scattering process as the hydrogen filled chamber is more efficient for less energetic neutrons as is clear from Fig.2.

We may discuss the problem quantitatively utilizing Weisskopf's statistical theory.[9] According to Weisskopf, the level density of a nucleus as a function of the excitation energy

E is expressed by the following semi-empirical formula

$$\omega(E)=C\exp[2(E/D)^{1/2}]\,. \qquad (9)$$

The neutrons after capture scattering is expected to have a Maxwellian distribution with mean energy

$$\bar{E}\simeq 2(DE_0)^{1/2}\,, \qquad (10)$$

where E_0 is the energy of primary neutrons.

Heidmann and Bethe[10] calculated the values of D by the analysis of many experimental data from $A\doteqdot 15$ up to 70. The values for Al, S and Fe, for instance, seem to be about 1, 0.69 and 0.32 Mev and these and the values for other elements lie almost on a straight line inversely proportional to A, as are expected by the statistical theory.

We have deduced by the analysis of the gamma-ray intensities resulting from inelastic scattering of *Li-D* neutrons that D is inversely proportional to A up to $A\approx 100$ and for further heavier elements do not decrease but rather increase.[5]

Mean energy of scattered neutrons can be calculated by (10) inserting the values of D as deduced in the above considerations for each energy spectrum of Table I. Assuming the energy dependence of the detector sensitivity we can calculate the ratio of detecter sensitivity for incident and scattered neutrons for each element. In this way, $\sigma(\theta)$ can be calculated from $\sigma'(\theta)$.

As relatively proper values of D can be obtained up to $A\approx 100$, we shall at first examine the results up to Sn. For the methane filled chamber, the variation of detecter sensitivity for incident and scattered neutrons are calculated to be constant within a few per cent for these elements by the above procedure assuming the efficiency curve shown in Fig. 2. That half of the total cross section is capture scattering cross section was ascertained thus within about 10 per cent accuracy, considering experimental errors.

In the case of Pb, if the value of D is extrapolated from the value of Fe as proportional to $1/A$, the detecter sensitivity is calculated to be about 20 per cent smaller for scattered neutrons. If D is taken to be of the same order as Fe, the detecter sensitivity would not change for incident and scattered neutrons. As is evident from Table II, $\sigma'(\theta)$ is in good agreement with $\sigma/2\cdot 1/4\pi$ for methane filled chamber. Therefore, it is considered favorable to take the value of D for Pb to be of the same order as Fe, in agreement with the conclusion of the previous work, so that the arguement stated in § 1 is correct also for Pb.

Next, we shall examine the results obtained by hydrogen filled chamber. In this case, detecter sensitivities are calculated to be 57 and 86% greater for Al and S, 140 to 160% greater for other elements. Experimental results show 30 to 60% larger values than $\sigma/2\cdot 1/4\pi$.

Larger values obtained by hydrogen filled chamber indicate qualitatively that scattered neutrons are evaporated from the nucleus with smaller energies in the capture scattering process, but the quantitative disagreement between calculated and experimental values would need explanation. The reason would partly be due to the uncertainty of the dependency of the detecter sensitivity on neutron energy and partly be due to the application of eq. (10) for this process.

If the assumptions on the energy sensitivities of our neutron detecter is correct and the results are to be interpreted by the statistical theory, the theory must be so modified that the scattered neutron spectrum containes more energetic neutrons than given by eq. (10). This may be explained if the neutrons are scattered without interacting very strongly with nucleons in nucleus, as is suggested by Weisskopf.[11]

§ 5. Conclutions

(1) Differential scattering cross sections at 90° for *Li-D* fast neutrons agree with the values obtained from the total cross sections under the assumptions that half of the total scattering is capture scattering and that capture scattering occurs isotropically.

(2) Neutrons scattered to 90° have less energy than the impinging neutrons.

(3) Experimental results obtained with hydrogen filled chamber with greater sensitivity at lower energies did not agree quantitatively with the values estimated by the statistical theory.

§ 6. Acknowledgment

The author would like to express his gratitude to Prof. S. Kikuchi for his interest

and to Mr. K. Sugimoto for his collaboration during the course of the work.

This work was supported by the grant for the promotion of science from the Ministry of Education.

References

1) T. Wakatsuki and S. Kikuchi: Proc. Phys. Math. Soc. Japan **21** (1939) 656.

2) D. C. Grahame and G. T. Seaborg: Phys. Rev. **53** (1938) 795.

3) E. Amaldi, D. Bocciarelli, B. N. Cacciapuoti and G. C. Trabacchi: Phys. Soc. Cambridge Conference; p. 97 (1947).

4) T. Wakatsuki and K. Sugimoto: Journ. Phys. Soc. Japan **6** (1951) 157.

5) T. Wakatsuki and K. Sugimato: ibid. **7** (1952) 249.

6) H. T. Richards: Phys. Rev. **59** (1941) 796.

7) L. L. Green and W. M.Gibson: Proc. Phys. Soc. **62** (1949) 407.

8) G. Placzek and H. A. Bethe: Phys. Rev. **57** (1940) 1075.

9) V. F. Weissekopf: Phys. Rev. **52** (1937) 295.

10) J. Heidmann and H. A. Bethe: Phys. Rev. **84** (1951) 274.

11) V. F. Weisskopf: Phys. Acta **23** (1950) 187.

JOURNAL OF THE PHYSICAL SOCIETY OF JAPAN Vol. 8, No. 1, JAN.—FEB., 1953

On a Non-linear Approximation of the Interatomic Force in Solid

By Junkichi SOMA* and Masamichi OGI

*Department of Physics, Faculty of Technology,
Department of Physics, Faculty of Science, Hokkaido University, Sapporo

(Received June 25, 1952)

We take new non-linear approximation for the interatomic force in a solid. We calculate the thermal expansion of some materials, and get good agreement with experiment. And it is easily shown that using this non-linear potential conserves type of partition function of linear model.

The interatomic force derived from a Morse function may be written as an approximation in such a from that the force is proportional to the displacement of the atom and its potential is a symmetric type. Then, it is clear that some sorts of phenomena, such as thermal expansion, does not appear. In order to account for these phenomena, the higher orders of the approximation, in which the force includes higher and non-linear terms, must be taken in the consideration. For this purpose trials have been tried by some authors[1]. As one of these trials, we choose the approximation formula expressed by the following equation

$$E_{\text{pot}}=\frac{4a^2D}{\varepsilon^2}(2+\varepsilon x-2\sqrt{1+\varepsilon x}) \qquad (1)$$

where D is the dissociation energy, a is a constant determining the curvature about the minimum point of the curve defined by the

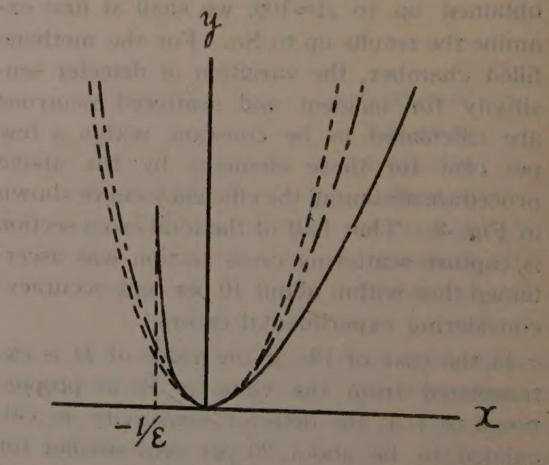

Fig. 1.

--‡--- Linear approx. $y=a^2Dx^2$

—·—·— Morse approx. $y=D(1+e^{-2ax}-2e^{-ax})$

——— Our approx.

$$y=\frac{4a^2D}{\varepsilon^2}(2+\varepsilon x-2\sqrt{1+\varepsilon x})$$

formula and ε is the constant relating to the melting point of the substance, as it will be shown later. Abscissa x is the distance of the atom from the center of force. This curve is shown approximately in Fig. 1.

When $|\varepsilon x|<1$, we can expand Eq. (1)

$$E_{\text{pot}}=\frac{4a^2D}{\varepsilon^2}\left(\frac{1}{4}\varepsilon^2x^2-\frac{1}{8}\varepsilon^3x^3+\cdots\right). \qquad (2)$$

If we take only the first term of expansion (2), it will be a symmetry potential from which the usual linear force can be derived. And the oscillation derived from Eq. (1) is a kind of generalized type of the linear oscillator.

Indeed, the frequency of the oscillation in this potential field is only determined by the first term of the above expansion, that is

$$\nu=\frac{1}{2\pi}\sqrt{\frac{4a^2D}{m}} \qquad (3)$$

where m is the mass of oscillating particle. And it is known that the oscillation in this field has such a nature that the equilibrium position of amplitude shifts gradually, conserving its center of force and frequency constantly2).

Now, put E the total energy of an atom oscillating in this field and $m/2\cdot\varphi(x)$ the kinetic energy of the atom respectively:

$$\frac{m}{2}\varphi(x)=-E_{\text{pot}}+E\,. \qquad (4)$$

It is easily shown that the mean potential energy of an atom in this case is $kT/2$; hence the mean total energy is kT, we get

$$\varphi(x)=\frac{2\cdot4a^2D}{m\varepsilon^2}(2\sqrt{1+\varepsilon x}-\varepsilon x-2)+\frac{2}{m}kT\,. \qquad (5)$$

Taking into account of the fact that the velocity of the atom at the points of maximum amplitude is zero, the maximum amplitude at the given temperature satisfies the equation $\varphi(x)=0$. Solving the above equation, we have

$$x_1=-2\sqrt{\frac{kT}{4a^2D}}+\frac{kT}{4a^2D}\varepsilon\,, \qquad (6)$$

$$x_2=\ 2\sqrt{\frac{kT}{4a^2D}}+\frac{kT}{4a^2D}\varepsilon\,. \qquad (7)$$

According to Eqs. (6), (7) the amount of shift of the equilibrium position of the oscillation is $kT/4a^2D\cdot\varepsilon$, and the atom oscillates with the amplitude $4\sqrt{kT/4a^2D}$ about this equilibrium position.

On the other hand, x is bounded in the following limit, since potential is a real function.

$$1+\varepsilon x\geqq0 \quad \text{or} \quad x\geqq-1/\varepsilon \qquad (8)$$

Eqs. (6), (7) suggest that the amplitude and the abscissa of the equilibrium position of oscillation increase with increasing temperature, but the potential function becomes meaningless in the domain in which x does not satisfy the condition (8). Now, we *assume* that the temperature satisfying the equality in the condition (8) is the melting point T_m. From this assumption we get

$$-2\sqrt{\frac{kT_m}{4a^2D}}+\frac{kT_m}{4a^2D}\varepsilon=-\frac{1}{\varepsilon}\,. \qquad (9)$$

This equation determines the relation between constant ε and melting points T_m, that is

$$\varepsilon^2=\frac{4a^2D}{kT_m}\,. \qquad (10)$$

Taking the average of the coordinate x with respect to time, we get $\bar{x}=kT/4a^2D\cdot\varepsilon$ which express the mean shift of the atom at the given temperature. Thus the volume of a substance consisting of N atoms is $V=Nc(r_0+\bar{x})^3$ at a given temperature, where r_0 is the interatomic distance when each atom rests at the center of force, and c is the constant relating the structure of matter.

Then, the linear thermal expansion coefficient $\beta=1/r_0(d\bar{x}/dT)$ is given by the following expression.

$$\beta=\frac{1}{r_0}\frac{k}{4a^2D}\varepsilon\,. \qquad (11)$$

Substituting the values of melting points T_m, dissociation energies D, interatomic distances r_0 and constants a of the same materials into Eqs. (10), (11), we can compute the numerical values of the thermal expansion coefficients of these materials3). We tabulate these values for the comparison with the experimental ones.

This comparison shows us that the calculated values agree essentially with the experimental ones, especially in the cases of the face centered structure satisfactorily, but the calculated values of two other structures are larger than the experimental ones.

These results which are obtained from one body model, can be easily generalized to the case of crystals with $3N$ degrees of freedom by the parallel treatment with Frenkel's.1)

And it is easily shown by the simple trans-

Table I. Comparison between calculated and experimental values of the thermal expansion coefficient.

Crystal	face centered cubic				body centered cubic				hex.	hex. f.c.
Substance	Cu	Al	Au	Ca	Na	Li	Mo	W	Mg	Co
$\beta_{cal}\times 10^5$	1.43	2.56	1.41	3.08	9.01	7.15	0.774	0.627	3.35	1.29
$\beta_{exp}\times 10^5$	1.62	2.38	1.42	3*	7.05	5.6*	0.549	0.446	2.54	1.23

The tabulated experimental values are taken from the "Landort-Börnstein Tabellen", except two marked by * which are taken from "Shiba's Butsuri Josuhyo".

formation that the partition function Z of this model has the same type in the case of linear oscillator. That is

$$Z=\prod_{i=1}^{3N} Z_i=\prod_{i=1}^{3N}\int e^{-\frac{E_{\text{pot}}}{kT}}dx_i\int e^{-\frac{p_{x_i}^2}{2mkT}}dp_{x_i} \tag{12}$$

where E_{pot} is given by Eq. (1). Put

$$\frac{2}{\varepsilon}(\sqrt{1+\varepsilon x_i}-1)=u_i\,.$$

Then

$$\begin{aligned}Z_{i_{\text{pot}}}&=\int e^{-\frac{4a^2D}{\varepsilon^2kT}(2+\varepsilon x_i-2\sqrt{1+\varepsilon x_i})}dx_i\\ &=\int_{-\infty}^{\infty} e^{-\frac{a^2D}{kT}u_i^2}\left(\frac{\varepsilon}{2}u_i+1\right)du_i\\ &\approx\frac{\varepsilon}{2}\int_{-\infty}^{\infty} e^{-\frac{a^2D}{kT}u_i^2}u_i du_i+\int_{-\infty}^{\infty} e^{-\frac{a^2D}{kT}u_i^2}du_i\,.\end{aligned}$$

Since the integrand of the first integral is an odd function, this integral vanishes. Then

$$Z_{i_{\text{pot}}}=\int_{-\infty}^{\infty} e^{-\frac{a^2D}{kT}u_i^2}du_i\,. \tag{13}$$

This is the same type with the partition function of a linear oscillator model. Therefore, all statistico-thermodynamical relations hold in this non-linear potential model also.

As we have noticed, since this potential becomes meaningless in the domain $x<-1/\varepsilon$, this model is not suitable for discussing the phenomenon such as collision, in which the interaction in the very vicinity predominates. We think, however, that when we discuss the behavior of an atom in a solid which is affected by the resultant force of its all surrounding atoms, this model represents approximately its behavior. Especially this suggests the reasonable mechanism of the thermal expansion.

In conclusion we thank cordially Prof. Y. Ikeda for his kind encouragement.

References

1) For example, Frenkel "Kinetic Theory of Liquids." pp. 136-149.

2) J. Chazy, Comptes Rendus 211, 621 (1940).

3) These data are taken from Tables of Slater's "Introduction to Chemical Physics." (1939).

JOURNAL OF THE PHYSICAL SOCIETY OF JAPAN Vol. 8, No. 1, JAN.—FEB., 1953

Hysteresis Loops of Ceramic Barium Titanate at Higher Frequencies. Part I

By Kyozaburo KAMBE,* Ichiro NAKADA,** and Hidetosi TAKAHASI

Department of Physics, Faculty of Science, University of Tokyo, Tokyo

(Received September 19, 1952)

Field-polarization hysteresis loops of ceramic barium titanate at high frequencies have been observed by a cathode-ray tube. To prevent the temperature rise due to hysteresis loss, pulsed voltage was used. The frequency was increased up to the order of 1 Mc/s, but the loop has not shown any drastic change, except the gradual decrease of the maximum polarization and of the average slope of the loop. The temperature dependence was also examined between the room temperature and about 150°C.

§ 1. Introduction

In the case of ferroelectrics, as barium titanate, two mechanisms must be considered for the variation of polarization. One is the continuous variation of polarization in magnitude and direction within each domain. The other is the sudden change of the direction of the spontaneous polarization by the migration of the domain boundary. In barium titanate, both mechanisms give its permittivity a much greater value than the permittivity of usual non-ferroelectric substances. Especially the latter mechanism makes the permittivity of ferroelectrics strongly dependent on field intensity, and moreover causes the hysteresis phenomenon.

The permittivity of $BaTiO_3$ measured in usual experiments is the one under a weak AC field, and might be regarded as an "initial permittivity". It is reported by von Hippel[1] that the initial permittivity of $BaTiO_3$ ceramics decreases slowly with the increase of frequency up to 10^8 c/s, where it begins to fall off more rapidly. It seems that there is a relaxation in the neighborhood of 10^9 c/s.

However, at present it is not known whether both the two mechanisms described above have comparable contributions to the initial permittivity, or any one of them is predominant. Hence we can arbitrarily assume that the first mechanism is predominant, and the contribution of the second mechanism is negligibly small. Then the observation of the initial permittivity fails to give any information about the second mechanism, and it becomes possible that the second mechanism has a relaxation at a lower frequency than 10^9 c/s. As it means however that the domain boundary ceases to move near that frequency, the hysteresis loop would be affected very much, so that it can be checked by the observation of the frequency dependence of the hysteresis loop. It is the object of the present work to make this observation at frequencies lower than 5×10^6 c/s.

When the migration occurs spasmodically and rapidly, the accompanying sudden change of the polarization causes so called "Barkhausen noise." According to Newton, Ahearn, and McKay[2], the duration of a Barkhausen pulse is of the order of 10^{-6} sec. So far as this observation shows, some change in the loop might be expected at the frequency of the order of 10^6 c/s, though the true nature of the noise is not known.

A distinguishing feature of the present work is the use of the pulse method. To prevent the temperature rise caused by the hysteresis loss, which becomes excessive at higher frequencies, the voltage was applied in a pulsed form, the duty cycle ratio being about one hundredth. In this way the rise of the temperature was cut down to several degrees, and at the same time a well visible loop could be obtained on the cathode-ray tube screen.

The use of the pulse was found, however, to affect the characteristics of the loop considerably. A more detailed study of this effect will be described in Part II.

---

* Now at Tokyo Institute of Technology, Oh-okayama, Tokyo.

** Now at Institute of Industrial Science, University of Tokyo, Chiba.

§2. Experimental Method

Fig. 1 shows schematically the arrangement for the observation of hysteresis loop by pulsed high-frequency voltage. The pulse generator provides periodic pulses of 50 c/s by transforming the AC line voltage, and the high frequency oscillator is modulated by this pulse to oscillate only within the short duration time of the pulse. The high frequency pulse obtained did not have a definite shape, as shown in Fig. 2. The peak amplitude of about 400 V measured across the sample condenser could be attained. The duration of a pulse was about $1\sim2\times10^{-4}$ sec, so that about $10\sim100$ oscillations are contained in each pulse.

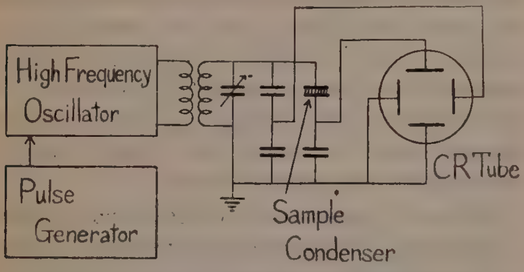

Fig. 1. Circuit diagram for the observation of hysteresis loop by pulsed high frequency.

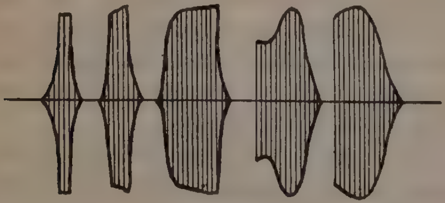

Fig. 2. Various shapes of the high frequency pulse actually used.

Four condensers including the sample condenser were arranged to provide two voltages which are proportional to the voltage and the charge of the sample condenser, and they were indicated on the cathode-ray tube.

To prevent common high-frequency troubles, such as stray capacities or inductances, the condensers and resistances around the sample condenser were connected as close as possible to the terminals of the cathode-ray tube, using thick wires for the leads. Though the cathode-ray tube was not the one specially designed for high-frequency use, we have not met any trouble in our frequency range.

Checks against external influences which would distort the pattern on the screen were performed by substituting the sample condenser in the circuit by an air condenser with low-loss ceramic supports. If the external influences were negligible, a straight line which corresponds to the pure capacity would appear on the screen. In our case the line did not move up to 5 Mc/s, above which a slight change in the inclination and the tendency to become a loop were observed. But these were insignificant for our purpose.

The calibration of voltage and charge was made from the deflection sensitivity of the cathode-ray tube and the capacity of condensers, neglecting stray capacities and inductances, because a rather rough estimation of them seemed to be sufficient for our purpose.

The loops at 10 kc/s, 1 kc/s, and 50 c/s were also observed for the sake of comparison. These voltages were not pulsed.

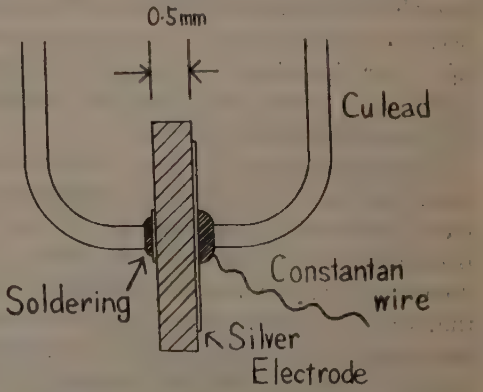

Fig. 3. The sample condenser.

The sample condenser uses a plate of thickness 0.5 mm which is cut out from ceramic $BaTiO_3$ sample, as shown in Fig. 3. The plate has an irregular shape, with the area of $10\sim30\,mm^2$. Silver electrodes are "baked" on it using silver paste, and copper leads are soldered on the electrodes. A constantan wire is soldered on one of the electrodes to form a thermocouple with the copper wire. The shape of the electrodes is nearly circular. One electrode has the diameter of $3\sim5$ mm, and the other has the diameter of $0.5\sim1$ mm. The capacity measured under the weak voltage ranged from 20 to 50 pF for several samples. As the diameter of the electrode is not sufficiently greater than the thickness of the sample plate, the electric field in the sample medium is not sufficiently uniform, so that the results of the measurements described below can be significant only qualitatively.

The sample condenser was immersed in oil to get good electric insulation and uniformity of temperature. In measuring the temperature dependence of the loop, we did not wait the thermal steady state, but all measurements were done while the temperature of the sample condenser was slowly varying. The temperature was first raised from the room temperature to about 150°C, and then lowered again to the room temperature. The cycle required about 5 hours. The heating was made from outside of the oil vessel.

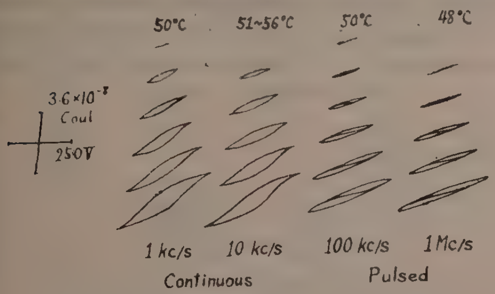

Fig. 4. Hysteresis loops for various frequencies and voltages, at about 50°C. Capacity 21 pF, Dielectric constant about 1000, at 50°C. Thickness 0.48 mm. Area of electrode about 1.1 mm².

§ 3. Results

a) *Dependence on frequency and field intensity*

Fig. 4 shows the sketches of the loops for various frequencies and field intensities, at about 50°C. The loops for 1 kc/s and 10 kc/s continuous voltages are added for comparison. The sample was fairly pure $BaTiO_3$, having the Curie point at about 116°C, and its hysteresis loop did not change appreciably from 40 to 60°C, so that by choosing 50°C we can avoid the trouble, due to hysteresis loss, of holding the sample exactly at one temperature.

The loops at 100 kc/s and 1 Mc/s taken under the pulsed voltages show a characteristic difference from those of 1 kc/s and 10 kc/s. They resemble a distorted ellipse and are more round-tipped than the usual loops. This character is clearly seen in the loops shown in Fig. 8, which use higher voltage. It will be shown in Part II that this difference is largely due to the use of pulsed voltage rather than to the difference in frequency. In short, it is shown there that when we apply a pulsed voltage at 10 kc/s, we have a loop much more like those of 100 kc/s and 1 Mc/s.

In the 100 kc/s and 1 Mc/s loops, pulses are not rectangular, so that only the contour is sketched, which corresponds to the loop for the maximum amplitude of voltage in a pulse.

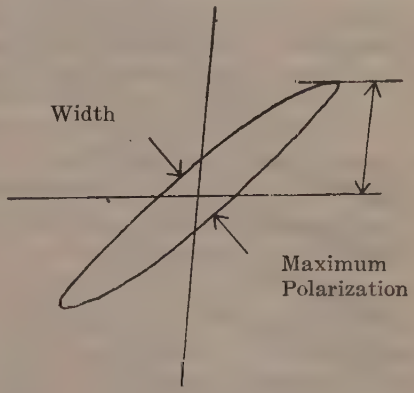

Fig. 5. Two characteristic values of the loop.

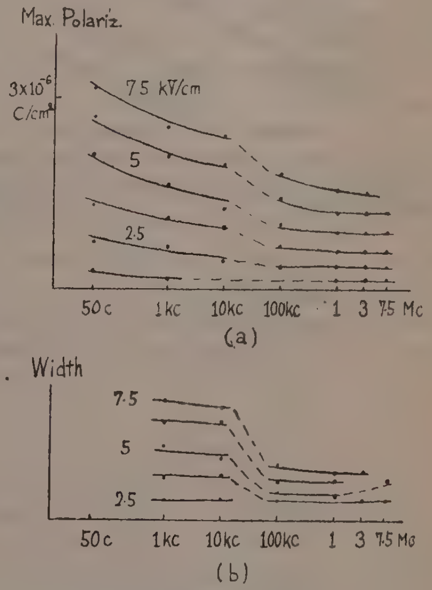

Fig. 6. Dependence on frequency, of a) maximum polarization and b) width. Units of polarization and field intensity show only the order of magnitude.

But it is shown in Part II that this contour does not change with the shape of the pulse. Besides, we have an advantage that we can see a trace of the tips of the loop which is drawn by the varying loop in a pulse. This trace shows the dependence of maximum polarization on the field intensity.

To visualize graphically the variation of the loop, we take two characteristic values of the loop, namely maximum polarization and width. Their definitions are illustrated in Fig. 5. Fig. 6 a) and b) show the dependence of these two values on the frequency and field intensity. A gap between 10 kc/s and 100 kc/s, especially large in the width, is of course a result of the use of pulsed voltage at higher frequncies. The data for 50 c/s and 7.5 Mc/s are added, though they are less reliable.

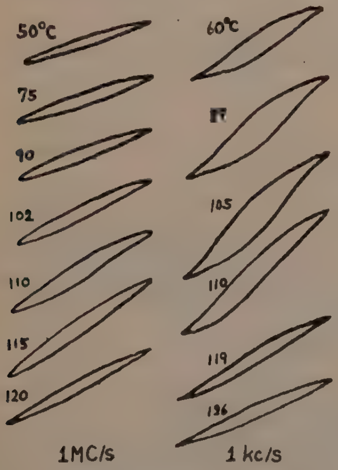

Fig. 7. The variation of the loop with temperature at 1 kc/s and 1 Mc/s. Voltage 300 V (6 kV/cm).

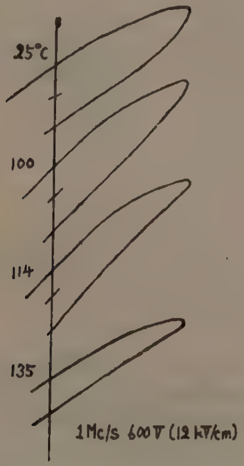

Fig. 8. The variation of the loop with temperature at high voltage.

It is seen that the decrease of maximum polarization with the increase of frequency is much more rapid than the decrease of initial permittivity[1]). It shows that when the frequency becomes higher it becomes difficult for the domain boundary to follow the rapid change of the field intensity. However, the decrease is rather gradual, with no sign of a definite relaxation time. It seems that irreversible migration of domain boundaries still play a principal role in the high-field polarization at frequencies of several megacycles per second.

b) *Dependence on temperature*

Fig. 7 shows the variation of the loop with temperature for 1 kc/s and pulsed 1 Mc/s, under the same field intensity. For 1 Mc/s the loop holds its resemblance to an ellipse. The maximum polarization and width are largest, and the bending of the loop is most distinct, at the temperature several degrees below the Curie point, as in cases of low frequencies. It is seen clearly in Fig. 8 which shows a case of higher voltage.

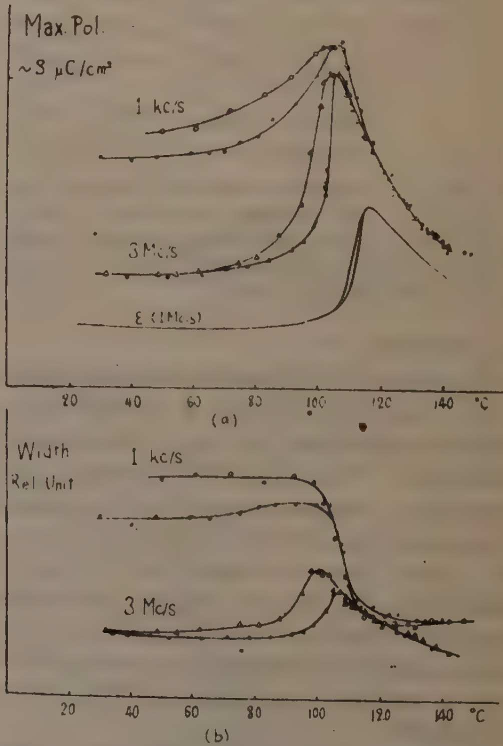

Fig. 9. Comparisons of maximum polarization and width for 1 kc/s and 3 Mc/s. Voltage 300 V (6 kV/cm).

Fig. 9 shows the comparisons between the characteristics of the loop for 1 kc/s and pulsed 3 Mc/s. The 3 Mc/s curves may have been shifted a little to lower temperature, because hysteresis loss would raise the temperature more in the interior of the sample condenser than at the surface. In Fig. 9 a), a capacity curve for the same sample under a weak field is added in the charge scale calculated from $Q=CV$, corresponding to the voltage used for the loops.

For 3 Mc/s the width shows a maximum below the Curie point. It may be related to the fact that ε'' and $\varepsilon''/\varepsilon'$ shows a maximum at the temperature several degrees below the Curie point.1),3) In the neighboring temperature region the difference of maximum polarization between 1 kc/s and 3 Mc/s becomes much smaller than at the room temperature. From these facts and observations of the shape of the loop, it may be concluded that the domain boundary migration becomes easier when the temperature approaches the Curie point from the room temperature.

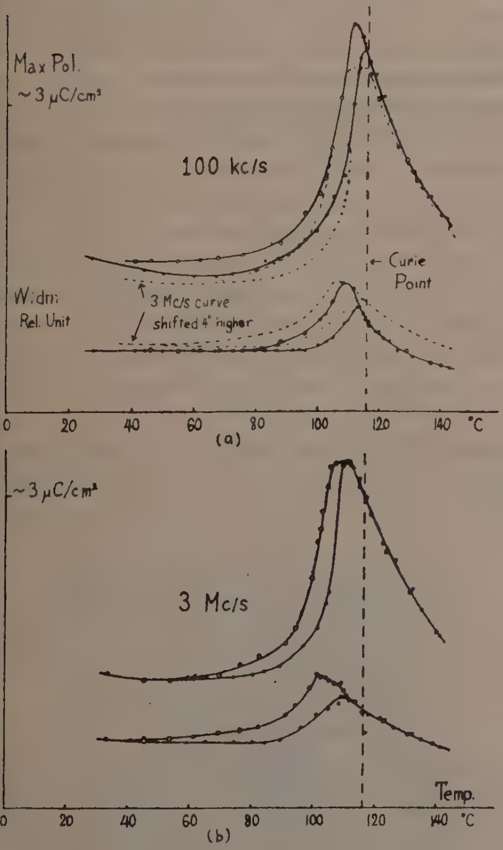

Fig. 10. Comparison between 100 kc/s and 3 Mc/s.

Fig. 10 shows a comparison between 100 kc/s and 3 Mc/s, both pulsed. The 3 Mc/s curve must have been shifted more to lower temperature than 100 kc/s curve, because it seems to be improbable that the maximum polarization is larger for 3 Mc/s than for 100 kc/s at the temperatures several degrees below the Curie point as shown in Fig. 10. When this shift is adjusted, we see that the maximum polarization is larger and the width is smaller for 100 kc/s than for 3 Mc/s in the whole range.

c) *The cubic phase*

In the cubic phase above the Curie point, there is no spontaneous polarization, and accordingly no domains and no hysteresis phenomenon. Nevertheless, as we see in Fig. 7, we have similar loops as those in the room temperature. In the case of pulsed higher frequencies, the width is even larger than that at the room temperature, as we see in Figs. 7, 9, and 10.

However, the essential difference in the loop is known from the trace of the tips of the loop. In the room temperature, the trace indicates that the inclination of the loop increases with the amplitude of applied voltage, whereas in the cubic phase the inclination does not change. In fact, this difference, together with the observations in Part II, ascertains that the loop at the temperature lower than the Curie point is really a hysteresis loop. The difference of maximum polarization and width between 100 kc/s and 3 Mc/s is confirmed in the cubic region by the observations shown in Fig. 11. But their reason is not yet known. It cannot be explained simply by the difference between the temperatures at the surface and the interior of the material.

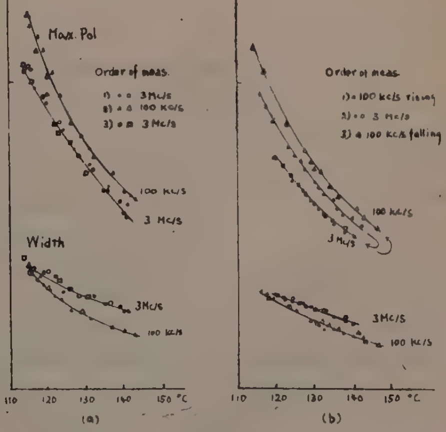

Fig. 11. The check of the difference between 100 kc/s and 3 Mc/s, against the drift of the characteristic values in the course of measurements.

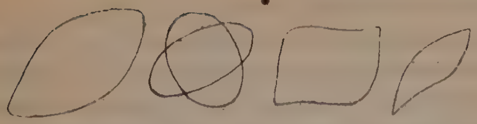

Fig. 12. The irregular patterns obtained by Rochelle salt, when the mechanical vibration is excited. (Pulsed high frequencies.)

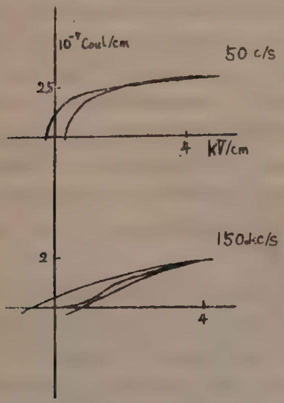

Fig. 13. The loops of Rochelle salt, free from mechanical resonance.

d) *Observations on Rochelle salt*4)

In similar measurements on Rochelle salt, resonant mechanical vibrations could be easily excited in a variety of modes, and showed a loop-pattern that varied irregularly with the frequency as shown in Fig. 12. However, it was possible in one case to find a frequency at which the resonant mechanical vibration was not excited. This is shown in Fig. 13, with the usual 50 c/s loop. The trace of the tips of the loop shows the saturation effect.

The authors wish to express their sincere thanks to Prof. Y. Takagi, and Dr. S. Sawada, who kindly prepared the samples.

References

1) A. von Hippel, Rev. Mod. Phys. **22** (1950) 221.

2) R. R. Newton, A. J. Ahearn, and K. G. McKay, Phys. Rev. **75** (1949) 103.

3) S. Roberts, Phys. Rev. **71** (1947) 890.

4) J. Hablützel, Helv. Phys. Acta, **12** (1939) 489.

JOURNAL OF THE PHYSICAL SOCIETY OF JAPAN Vol. 8, No. 1, JAN.—FEB., 1953

Hysteresis Loops of Ceramic Barium Titanate at Higher Frequencies. Part II

By Kyozaburo KAMBE*

Department of Physics, Faculty of Science,
University of Tokyo, Tokyo

(Received September 19, 1952)

The effect of the use of pulsed voltage on the hysteresis loop was examined using rectangular pulses at the frequency of the order of 10 kc/s. Initial transient phenomena in obtaining a dynamical hysteresis loop was studied using pulses with very small number of swings. The characteristic shape of the loop for pulsed voltage was found to correspond to the initial stage of the loop for continuous voltage. The remanence and its decay could be directly observed oscillographically.

§ 1. Introduction

In Part I we saw that in the observation of hysteresis loops at higher frequencies we can avoid the temperature rise by the use of pulsed voltage. It was found however that the use of pulses may considerably change the characteristics of the loop. The character of the pulse, such as width or shape, was not well defined there. In the present study we have prepared rectangularly pulsed sine voltage, to investigate the effect of the use of pulses in detail. The frequency range is 1 to 100 kc/s, in which we have been able to obtain the voltages both pulsed and not pulsed, and compare the loops under the two conditions.

The method of pulsing which was adopted here afforded us to get very few voltage swings within a pulse, even a fraction of one cycle. Starting from a small fraction, and increasing the number of swings in a pulse, we could investigate how the loop is built up after the application of sine voltage.

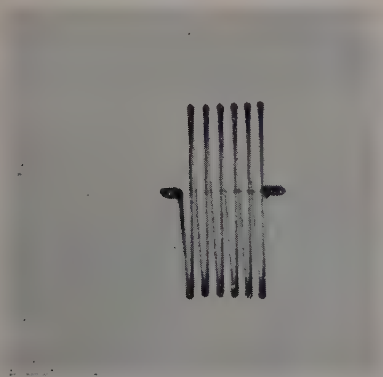

Fig. 1. Rectangularly pulsed sine wave.

By these observations we could find that the loop is really a hysteresis loop and has characteristics that cannot be explained by assuming only the usual high frequency loss.

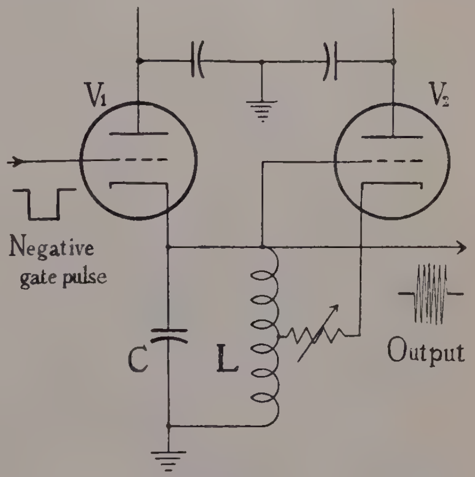

Fig. 2. The oscillator of pulsed sine wave.

§ 2. Experimental Method

To get rectangularly pulsed sine voltage, that is, to get a pulse which consists of a train of sine voltage with constant amplitude as shown in Fig. 1, we used an oscillator illustrated in Fig. 2.**

A rectangular pulse is made up by cutting a portion which has a desired width from the sharp needle-like part of the output of a full-wave rectifier. This pulse has negative sign and is fed into the grid of V_1, which switches off instantaneously the current that is flowing through the coil of the tank circuit. The magnetic energy stored in the coil is released and excites a free oscillation in the tank circuit. The damping of the oscillation is compensated by a proper amount of positive feedback provided by the tube V_2. When the negative pulse ends, V_1 becomes conducting and the oscillation damps out rapidly.

---

* Now at Tokyo Institute of Technology, Oh-okayama, Tokyo

** Cf. B. Chance *et al*, *Waveforms* (Rad. Lab. Ser. *vol.* XIX, Mc-Graw Hill, 1949) p. 140.

The pulse repetition frequency of the negative pulse is 50 c. p. s., halved from the 100 c. p. s. output of the full wave rectifier, and the height, which determines the upper limit of the amplitude of sine voltage, is about 300 V. The width can be varied continuously from zero to about 5×10^{-3} sec.

Each train of sine wave starts always from zero phase, its amplitude being sufficiently constant, and ends at a certain phase that depends on the width of the negative gate pulse. But we could not get sufficiently short rise time and decay time of the gate pulse, so that we could not get rid of the slight deviation from the sine curve at the head and tail of the train, as we see in Fig. 1. The deviation at the head was negligible below 10 kc/s, but a slight "overshoot" at the end was almost always unavoidable when we try to end the train at zero phase.

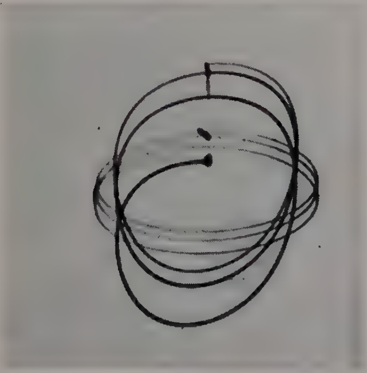

Fig. 3. The loops that we have when we replace the sample condenser by a resistance. The starting point at the center.

The frequency range of sine voltage that we have actually used was from 4 kc/s to 100 kc/s, and in the lower frequencies we used an oxide-cored inductance in the tank circuit of the oscillator. But the use of a core with a closed magnetic circuit considerably distorts the waveform. The distortion is easily found out by substituting the sample condenser in the circuit (Fig. 13) by a suitable resistance and observing the loop. Two examples are shown in Fig. 3. If the shape of the loop resembles well an ellipse, we consider that the waveform is sufficiently pure. We can also observe clearly the deviations at the head and tail of the train by this method. In Fig. 3, the two loops correspond to different frequencies, using the same resistance. One which is very distorted used closed-core inductance. The other shows a distortion at the left end of the first cycle.

As a source of constant sine valtage, a commercial RC-oscillator was used.

Sample condensers had larger capacities than those used in Part I. All measurements were done at 50°C as in Part I.

Other details are almost the same as those of Part I.

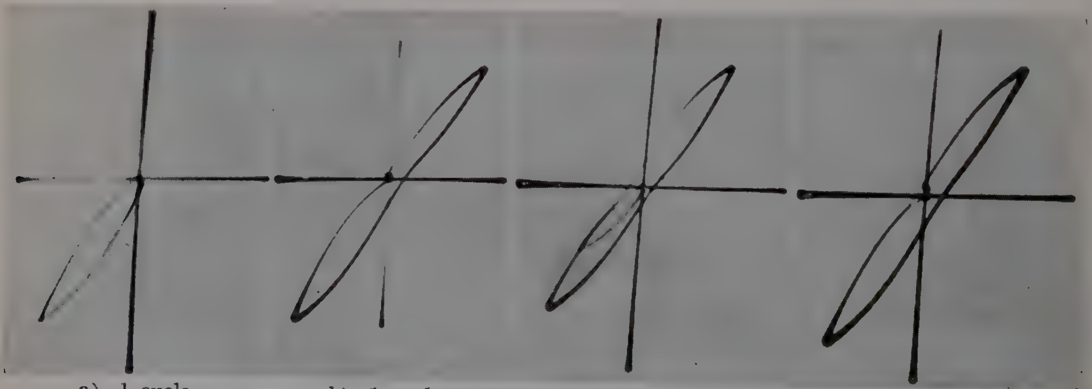

a) ½ cycle b) 1 cycle c) 1½ cycles d) 2 cycles

Fig. 4. Successive variation of the loop corresponding to increasing swing number in a pulse. (4 kc/s, 6 kv/cm)

§ 3. Results

At first we studied how the loop is built up at the initial stage just after the sine voltage is applied. The number of swing in a pulse was increased from ½cycle, holding frequency and amplitude constant. Fig. 4 shows the successive variation of the loop. We see that a closed loop is built up already at about $1\frac{1}{8}$ cycles, and after that exactly the same trace is followed in the succeeding cycles. No appreciable change appears even when the number of swing in a pulse is increased to about 50 cycles. So we see that the initial transient state in the hysteresis loop extends at most to about the first 1/8 cycle.

Of course this is not the absolutely initial state, because the pulse is repeated every 1/50 second, and it is shown below that the after effect does not entirely decay out in the quiescent state between the pulses.

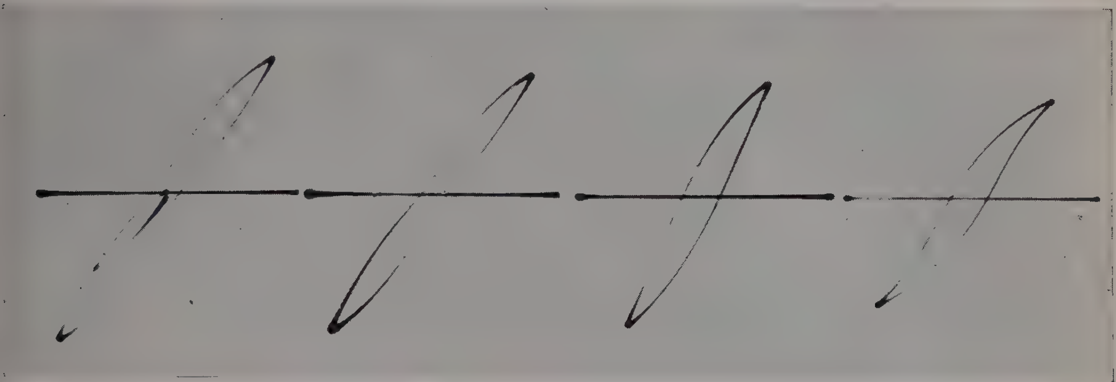

a) Pulse. b) Continuous just applied. c) After one minutes. d) After five minutes.

Fig. 5. Variation of the loop with time after the voltage is switched to the continuous wave.

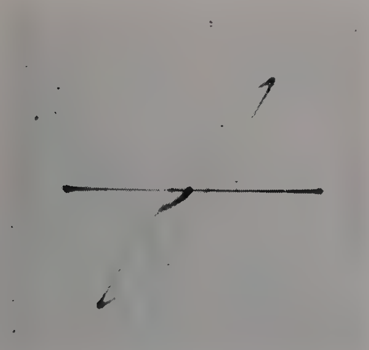

Fig. 6. The loop for pulsed sine wave, several minutes after the voltage is turned from the continuous wave.

However, this existence of quiescent state is sufficient to retain the queer shape of the loop which resembles an airplane propeller. When we switch the voltage to the continuous wave, the loop remains at first the same, as shown in Fig. 5(b), but it changes gradually to the usual form as shown in Fig. 5(d), in 10 to 30 seconds. In a few minutes the loop settles down in a steady state form.

When the voltage is switched back to the pulsed one, the contour of the loop is at first the same as steady state form. Then it returns slowly to the original form as shown in Fig. 6. This process is considerably slower than the former reverse process. Sometimes the loop does not go back completely to the original form, and maintains larger width.

From these observations we can consider that there are two sorts of transient effect in establishing a steady state loop by AC voltage. One proceeds very rapidly and extends only about to first 1/8 cycle. The other proceeds more slowly, changing the loop from the initial form to the usual steady state form, and ends after a few minutes. The latter may be connected with the change of the distribution of ferroelectric domains in the sample. Thus we see that the use of pulsed voltage prevents not only the temperature rise but also the redistribution of the domains.

The initial form of the loop varies by the conditions of preparation of the sample. But the typical form has a narrow part in the middle of the loop as we see in Fig. 4. Fig. 7(a)

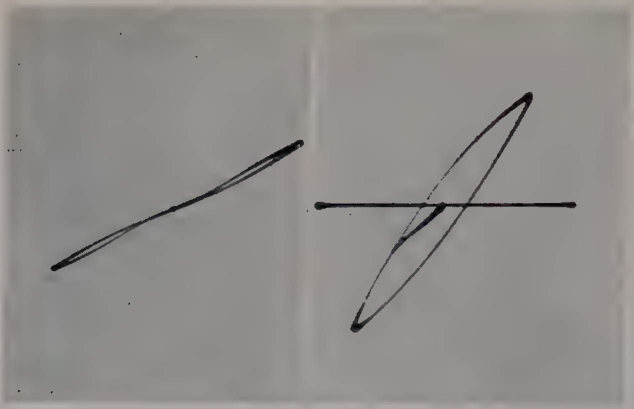

a) b)

Fig. 7. Examples of the loop for pulsed sine voltage.

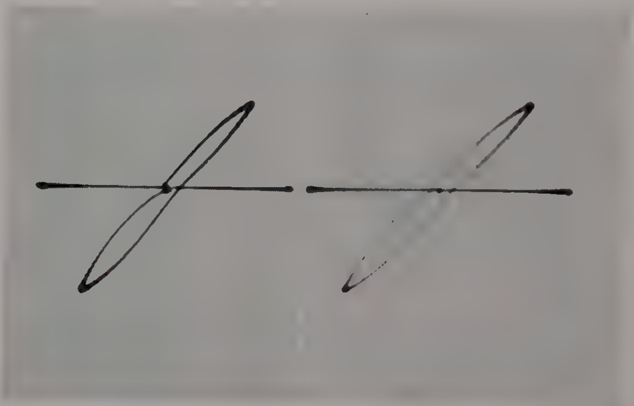

a) 4 kc/s. b) 100 kc/s.

Fig. 8. Comparison of the loops for different frequencies.

shows an example which has very narrow middle part, almost reduced to a line. Whereas Fig. 7 (b) shows an example which has no narrow part.

Comparing the initial form and the steady state form, it was found that, though the shape of the loops is quite different, the difference in the inclination of the loops, that is, in the ratio between field intensity and polarization is comparatively small.

Fig. 8 shows a comparison between the loops for 4 kc/s and 100 kc/s, both pulsed so as to have two cycles in a pulse. We see that there is no dependence on the frequency in this frequency range except the small decrease of the polarization with the increase of frequency. This is the same in the steady state form.

We can vary the form of pulsing from rectangle by varying the form of the negative gate pulse so as to have varying rise time and decay time as shown in Fig. 9. It was found that the contour of the loop, that correspond to the maximum amplitude in each pulse does not depend on the form of pulsing as shown in Fig. 10.

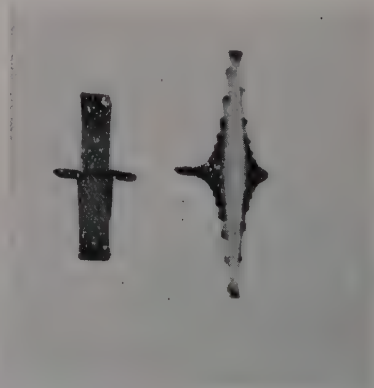

Fig. 9. A rectangular pulse and a pulse with certain rise time and decay time.

§ 4. Discussion

We will consider here the nature of the loops as shown in Fig. 4. Fig. 11 explains

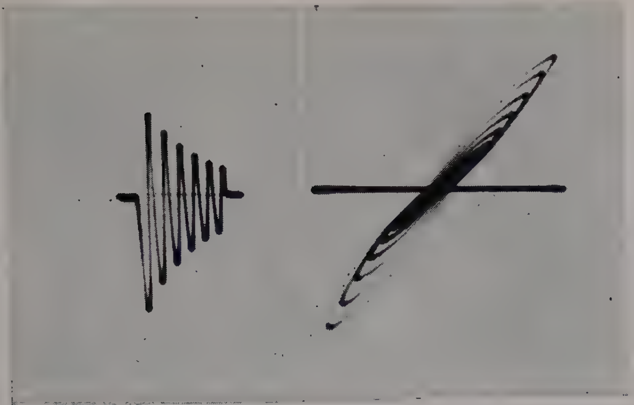

Fig. 10. An example of not rectangular pulse and the loop.

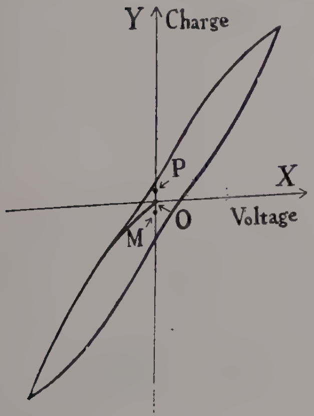

Fig. 11. The sketch of the loop. The relative position of the center M to the starting point O moves with the phase of the end point P.

schematically the characteristics of the loop. The starting point O lies always at the origin of the coordinates on the screen. The end point P on the vertical axis usually does not coincide with O. The center of the loop M also does not coincide with O. The distance PM on the vertical axis is the remanence of the polarization. This remanent polarization decays in the quiescent state between the pulses, and at the starting point of the next pulse its magnitude is diminished to OM.

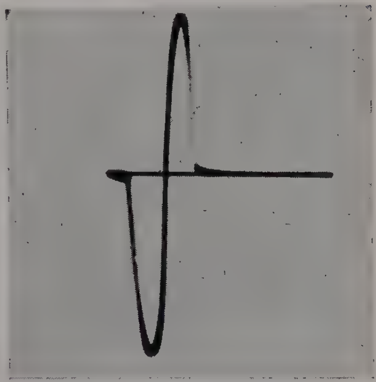

Fig. 12. Variation of polarization with time. We can see the decay of remanence in the quiescent state.

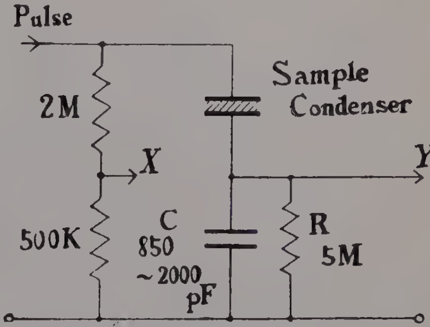

Fig. 13. The circuit around the sample condenser.

Fig. 12 shows the variation of polarization with the time. The remanent polarization decays at first relatively rapidly and then more slowly. The estimation of time constants shows that the first rapid decay may be occurring spontaneously in the sample, and the succeeding slow decay may be due to the decrease of the actual voltage applied to the sample by the discharge of the series condenser C through the leak resistance R. (Fig. 13)

Fig. 14 shows an example which has wide loop and large remanence. The decay of remanance is relatively slow. The steady state form is almost the same as the initial form. We may say that this sample is "dielectrically hard".

When the phase of the end point is changed, OM varies with PM. As O remains always at the origin of the screen, the loop moves up

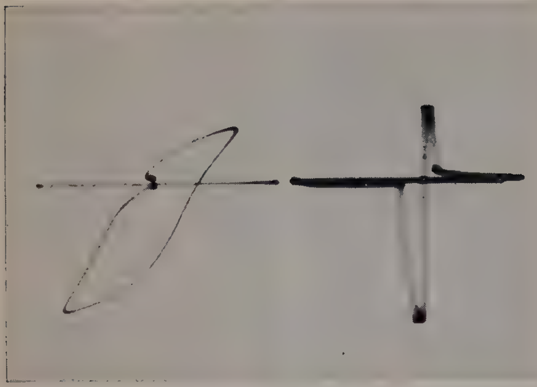

Fig. 14. A sample which shows wide loop and large remanence. Decay of remanence is also slow.

and down as a whole, as shown in Fig. 4. If the sample condenser could be represented by an equivalent circuit of resistance and capacities, a similar loop with the contour of ellipse would be obtained. But the loop would not move with the change of the phase of the end point. So we see that the characteristics of our loop described above can only be explained by the existence of hysteresis and remanence.

Summarizing the results related to Part I, we can say that:

1) The form of the loop under the pulsed voltage is the initial form that the loop takes at the start of applied voltage.

2) Both the initial and the steady state form do not vary very much in the range 10 to 100 kc/s.

3) The loop is almost independent of the width and the shape of the pulse.

The author wishes to express his gratitude to Mr. Hidetosi Takahasi, under whose direction this work was carried out.

JOURNAL OF THE PHYSICAL SOCIETY OF JAPAN Vol. 8, No. 1, JAN.—FEB., 1953

On the Superlattice Formation in Ternary Alloys

By Shoichi MATSUDA

Faculty of Technology, Ibaraki University

(Received October 26, 1951)

The superlattice formations in ternary alloy with body centered cubic lattice are discussed by taking into account the interactions between nearest neighboring atoms as will as those between next nearest neighboring atoms. On the besis of this theory the possibility of the various types of superlattice formations in ternary alloy is inferred. The experimental data on the superlattice formation in Cu-Mn-Al system are discussed from this point of view.

§ 1. Superlattice of A_2BC Type

The superlattice formation in various binary alloys has been hitherto studied in detail under the title of order-disorder transformation. If the number of component elements of the alloy is increased, however, the mode of superlatice formation becomes more complicated than that of simple binary case.[1] A theoretical discussion of the superlattice formation in the case of ternary alloy with component metals A, B and C is now given by taking into account both interaction energies of the nearest neighboring atoms and of the next neighboring neighboring stoms in the metallic lattices. The results thus obtained can reproduce well the manifoldness of the type of superlattices in the ternary alloys. In the following papers alloys of the composition A_2BC with body centered cubic lattice will be considered. In this alloy one possible state of orderd stomic arrangement is as shown in Fig. 1. All A atoms are situated on the lattice points denoted by mark ◉, all B and C atoms on the lattice points denoted by ● and ◉ respectively. Let the lattice points denoted by mark ○ by α sites and the lattice points denoted by ● and ◉ be β and γ sites respectively. Then, if the total

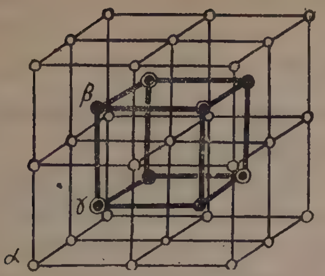

Fig. 1.

number of atoms (total number of lattice points) is N and if the atomic fraction of A etc. is $x_A(=0.5)$ etc., then the number of α sites is $x_A N$ and so forth. In the ordered state, all A atoms are on α sites, all B atoms on β sites, and all C atoms on γ sites. In the state in which unlike atoms interchange their positions the numbers of A stoms on α sites, B atoms on β and C atoms on γ sites decrease with decreasing order of the atomic arrangement. Let the number of A atoms on α sites be $A_\alpha x_A N$ and number of A stoms on β sites be $A_\beta x_B N$ etc., then the nine quatities $A_\alpha \ldots\ldots C_\gamma \ldots\ldots$ defined above are the fractional number of the stoms specified by the capital letters on the sites denoted by the suffix letters. There are following five relations among them:

$$\left.\begin{aligned} A_\alpha+B_\alpha+C_\alpha&=A_\beta+\beta_\beta+C_\beta \\ &=A_\gamma+B_\gamma+C_\gamma=1, \\ A_\alpha x_A+A_\beta x_B+A_\gamma x_C&=x_A, \end{aligned}\right\} \quad (1)$$

$$B_\alpha xA+B_\beta x_B+B_\gamma x_C=x_B. \quad (2)$$

Therefore, four quatities among nine are independent. We take A_α, B_α, B_β and C_γ as independent variables and introduce new parameters S_1 S_2, S_3 and S_4 defined respectively by

$$\left.\begin{aligned} S_1&=\frac{A_\alpha-x_A}{1-x_A} \\ S_3&=\frac{C_\gamma-x_C}{1-x_C} \end{aligned}\right\} \quad \left.\begin{aligned} S_2&=\frac{B_\beta-x_B}{1-x_B} \\ S_4&=\frac{x_B-B_\alpha}{x_B} \end{aligned}\right\} \quad (3)$$

In the ordered state, $A_\alpha=B_\beta=C_\gamma=1$ and $B_\alpha=0$ as mentioned above and hence $S_1=S_2=S_3=S_4=1$. In the disordered state, $A_\alpha=x_A$, $B_\alpha=B_\beta=x_B$ and $C_\gamma=x_c$, for an A atom exists on every lattice point with equal probability x_A, etc. Consequently the relation $S_1=S_2=S_3=S_4=0$ indicates the random distribution of atoms. In the intermediate state of atomic arrangement, the S's take some values between zero and unity. Thus, four parameters define the order of atomic arrangement in the alloy. From Eqs. (1), (2) and (3) A_α etc. can be expressed by S's:

$$A_\alpha=\tfrac{1}{2}(1+S_1) \quad \text{etc.} \quad (4)$$

§ 2. Thermodynamic Functions and Equilibrium Condition

Since the interaction between atoms on the lattice points is due to short distance forces, we shall assume that only the interactions of atoms which are the nearest neighbors as well as the next nearest neighbors to each other can have an appreciable amount. Let V_{AA}, V_{BB} etc. be the potentials between atoms denoted by suffix letters on the nearest neighboring lattice points, and W_{AA}, W_{BB}, W_{CC} etc. those between the atoms on the next nearest neighboring sites. We shall assume they are constant. Now each α site has Z' $(=4)$ nearest neighboring β-sites and Z' γ-sites. As the number of A atoms on α-sites is $A_\alpha x_A N$ and the average number of A atoms on the nearest neighboring β sites is $A_\beta Z'$ and that on the nearest neighboring γ sites is $A_\gamma Z'$, so the average number of nearest neighboring A—A pairs in the alloy is $Q_{AA}^{(1)}=(A_\alpha A_\beta+A_\alpha A_\gamma)Z' x_A N$. The contribution of the nearest neighboring A—A pairs to the potential energy is $V_{AA}\, Q_{AA}^{(1)}$. Thus the potential energy due to the nearest neighboring atoms is given by

$$\begin{aligned} E^{(1)}&=V_{AA}Q_{AA}^{(1)}+V_{BB}Q_{BB}^{(1)}+V_{CC}Q_{CC}^{(1)}+V_{AB}Q_{AB}^{(1)} \\ &\qquad +V_{AC}Q_{AC}^{(1)}+V_{BC}Q_{BC}^{(1)} \\ &=\text{const}+x_Y N\{2V_1A_\alpha(1-A_\alpha)+V_3B_\alpha(1-2B_\alpha) \\ &\quad+(V_1-V_2+V_3)(\tfrac{1}{2}A_\alpha+B_\alpha-2A_\alpha B_\alpha)\} \end{aligned} \quad (5)$$

where

$$x=x_A \qquad Z=2Z'$$

$$\left.\begin{aligned} V_1&=\tfrac{1}{2}(V_{AA}+V_{CC})-V_{AC} \\ V_2&=\tfrac{1}{2}(V_{AA}+V_{BB})-V_{AB} \\ V_3&=\tfrac{1}{2}(V_{BB}+V_{CC})-V_{BC} \end{aligned}\right\} \quad (6)$$

Next, there are $y(=6)$ next neighboring α sites around each α site, y next neighboring γ sites around each β site, and y next neighboring β sites around each γ site. Then, the potential energy arising from the atom pairs on the next nearest neighboring sites is given by

$$\begin{aligned} E^{(2)}&=W_{AA}Q_{AA}^{(2)}+\cdots\cdots+W_{BC}Q_{BC}^{(2)} \\ &=\text{const}+yxN\{W_1(A_\alpha{}^2+A_\beta A_\gamma) \\ &\qquad +W_3(B_\alpha{}^2+B_\beta B_\gamma) \\ &\quad+(W_1-W_2+W_3)(A_\alpha B_\alpha+\tfrac{1}{2}A_\beta B_\beta+\tfrac{1}{2}B_\beta A_\gamma)\} \end{aligned} \quad (7)$$

where, as previously,

$$\left.\begin{aligned} W_1&=\tfrac{1}{2}(W_{AA}+W_{CC})-W_{AC}\\ W_2&=\tfrac{1}{2}(W_{AA}+W_{BB})-W_{AB}\\ W_3&=\tfrac{1}{2}(W_{BB}+W_{CC})-W_{BC}\end{aligned}\right\} \qquad (8)$$

Using (4) and neglecting the constant terms, the configurational energy of alloy can be written as

$$E=E^{(1)}+E^{(2)}=-\sum_{ij\leqq=1}\lambda_{ij}s_is_j \qquad (9)$$

$$\lambda_{11}=\frac{N}{2}\left(\frac{1}{2}ZV_1-\frac{1}{4}gW_1\right)\ \text{etc.} \qquad (10)$$

On the other hand the configurational entropy of the alloy accompanied with this atomic arrangement is

$$\Phi=k\log\Gamma \qquad (11)$$

where Γ is the number of ways of arranging atoms on the lattice point, in the specified manners that is

$$\Gamma=\prod_{A,\alpha}\frac{x_AN;}{A_\alpha x_AN;\ B_\alpha x_AN;\ C_\alpha x_AN;}. \qquad (12)$$

The free energy of the alloy is $F=E-T\Phi$, and the equilibrium atomic arrangement is determined by

$$\frac{\partial E}{\partial S_i}-T\frac{2\Phi}{2S_i}=0 \quad i=1,\ 2,\ 3,\ 4. \qquad (13)$$

§ 3. Condition of the Formation of A_2BC Type Superlattice

The A_2BC type superlattice is formed when all A atoms are on α sites, all B atoms on the β sites and all C atoms on the γ sites. Such state corresponds to the case $S_1=\ldots=S_4=1$. For these values the rates of change of the entropy take following values

$$\lim\frac{\partial\Phi}{\partial S_1}=\lim\frac{\partial\Phi}{\partial S_2}=\lim\frac{\partial\Phi}{\partial S_3}=-\infty$$

$$\lim\frac{\partial\Phi}{\partial S_4}=0.$$

Hence the necessary and sufficient condition for solutions corresponding to A_2BC type superlattice at $T\to0$ is as follows:

$$\lim_{S\to1}\left(\frac{\partial E}{\partial S_1}\right)<0 \quad \lim_{S\to1}\left(\frac{\partial E}{\partial S_2}\right)<0$$

$$\lim_{S\to1}\left(\frac{\partial E}{\partial S_3}\right)<0 \quad \lim_{S\to1}\left(\frac{\partial E}{\partial S_4}\right)=0.$$

With (14) and (10) these relations can be transformed into

$$\left.\begin{aligned} &(3V_1+V_2-V_3)Z-6W_2y>0\\ &-7W_1+6W_2+3W_3>0\\ &W_3-W_1-W_2>0\\ &2(V_1-V_2)Z+(4W_1-W_2)y=0.\end{aligned}\right\} \qquad (14)$$

The above conditions among the interaction potentials must be fulfilled if at all the A_2BC type superlatice formation is to be obtained.

§ 4. Conditions for the Formation of A(BC) Type and $(AB)_3$ C Type

There are two other types of atomic arrangement in the alloy now considered. The one is formed in the case when there is no distinction between β and γ sites. In this case, the numbers of like atoms on β and γ sites are equal to each other, that is $A_\beta=A_\gamma$, $B_\beta=B_\gamma$, and $C_\beta=C_\gamma$. In such a case the following relations are found among S's:

$$S_2=\frac{1}{3}S_1,\quad S_3=\frac{1}{3}(2S_1-S_4),$$

and

$$\frac{\partial\Phi}{\partial S_2}=\frac{\partial\Phi}{\partial S_3}=0.$$

Then, in order that such an atomic arrangement should exist in equilibrium at absolute zero temperature, the following relations deduced from equilibrium condition (13) must be fulfilled:

$$\frac{\partial E}{\partial S_2}=\frac{\partial E}{\partial S_3}=0.$$

In this case the behavior of superlattice formation becomes similar to that of binary alloy which is composed of A and (BC) atoms of equal numbers. The symbol (BC) means that B and C atoms behave as atoms of the same kind.

We shall call such an atomic arrangement the A(BC) type superlattice.

Another type of superlattice arises in the case when there is no distinction between α and β sites, that is, $A_\alpha=A_\beta$, $B_\alpha=B_\beta$ and $C_\alpha=C_\beta$: Then we have the following relations

$$S_2=\frac{1}{3}(S_3-2S_1),\quad S_4=2S_1-S_2,$$

$$\frac{\partial\Phi}{\partial S_1}=0,\quad \frac{\partial\Phi}{\partial S_4}+\frac{2}{3}\frac{\partial\Phi}{2S_2}=0.$$

From (13) we obtain the condition for the formation of such an atomic arrangement in equilibrium state, that is

$$\frac{\partial E}{\partial S_1}=0,\quad \frac{\partial E}{\partial S_2}+\frac{3}{2}\frac{\partial E}{\partial S_4}=0.$$

The behavior of superlattice formation in this case is similar to that of the binary alloy composed of (AB) and C atoms in the compostion of 3 : 1. We shall call such an arrangement the $(AB)_3C$ type.

§ 5. The Behavior of the Superlattice Formation

The superlattice for the case in which the next nearest neighboring interaction vanishes is at first considered. In this case the conditions $W_1=W_2=W_3=0$ are valid. From equilibrium condition (13) we get

$$\frac{\partial E}{\partial S_4}=\frac{\partial E}{\partial S_3}=0 \quad \text{and} \quad \frac{\partial \Phi}{\partial S_2}=\frac{\partial \Phi}{\partial S_3}=0.$$

These are condition for formation of A(BC) type superlattice as decribed in preceding section. The A_2BC type superlattice is not formed.

Next as an example for $W \gtrless 0$ the atomic arrangement is discussed for the alloy having following values of interaction potentials:

$$\left.\begin{aligned} &V_1=V_2=V>0, \quad V_3=0, \\ &W_1=W_2=0, \quad W_3=W. \end{aligned}\right\} \tag{15}$$

These relations mean that the A—B and the A—C atom pairs are more stable than the others on the nearest neighboring lattice points, while the B—C atom pair is the most stable on the next nearest neighboring lattice points. The above value of interaction satisfy the condition (14) of A_2BC type superlattice formation. The equilibrium condition (13) becomes

$$\log\frac{A_\alpha C_\beta}{C_\alpha A_\beta}-\frac{1}{\theta}\left\{2S_1+\frac{9}{8}\eta(S_4-S_2)\right\}=0 \text{ etc.,} \tag{16}$$

where

$$\theta=\frac{kT}{Zx_AV}, \quad \eta=\frac{W}{V}.$$

Eq. (16) has various types of solutions. However, the following three types are of interest, each of which corresponds to one of the above mentioned types of atomic arrangements.

Type I.

$$\left.\begin{aligned} &S_1=S_4=S,\ S_2=S_3=S', \quad \text{and} \\ &\log\frac{(1+S)(1+2S-3S')}{(1+S)^2} \\ &\qquad -\frac{1}{\theta}\left\{2S+\frac{9}{8}\eta(S-S)\right\}=0 \\ &\log\frac{1+3S'}{1+2S-3S'}-\frac{3\eta}{4\theta}(3S'-S)=0. \end{aligned}\right\} \tag{17.1}$$

In this case A_α's are expressed by

$$A_\alpha=\frac{1}{2}(1+S), \quad B_\alpha=C_\alpha=\frac{1}{4}(1-S),$$

$$A_\beta=A_\alpha=\frac{1}{2}(1-S)$$

$$B_\beta=C_\gamma=\frac{1}{4}(1+3S'), \ C_\beta=B_\gamma=\frac{1}{4}(1+2S-3S').$$

Type II. $S_1=S_4=S$, $S_2=S_3=S/3$ and

$$\log\frac{1+S}{1-S}-\left(1+\frac{3}{8}\eta\right)\frac{S}{\theta} \tag{17.2}$$

In this case A_α's are expressed by

$$A_\alpha=\frac{1}{2}(1+S), \quad B_\alpha=C_\alpha=\frac{1}{4}(1-S),$$

$$A_\beta=A_\gamma=\frac{1}{2}(1-S),$$

$$B_\beta=C_\beta=B_\gamma=C_\gamma=\frac{1}{4}(1+S).$$

Type III. $S_1=S_2=S_3=S_4=0$

The solution of type II satisfies the condition for the formation of A(BC) type superlattice in section 5. Therefore the solution of (17.2) represents the behavior of A(BC) type atomic arrangement. If the solution of type III gives the lowest free energy of the alloy, there is no ordered state of atomic arrangement. The behavior of the atomic arangement of three types mentioned above is influenced by the ratio η of the interaction between the next nearest neighboring atoms to that between the nearest neighboring atoms.

(a) $\eta=0$: There is no interaction between atoms on next nearest neighboring lattice points. Both equilibrium conditions (17. I) and (17. II) is reduced into the same equation;

$$\log\frac{1+S}{1-S}-\frac{S}{\theta}=0.$$

This equation agrees with the equilibrium condition in Bragg-William's theory for the A B type superlattice in binary alloy. As stated in section 6 the superlattice of A(BC) type forms alone in accordance with the above equation.

(b) $\eta=1$: Fig. 2 shows the numberical solution of Eqs. (17. I) and (17. II) for $\eta=1$ for various values of parameter (temperature) θ. The curves with suffix letter I are the solutions of type I, which show the behavior of atomic arrangement of A_2BC type superlattice, and the curves with suffix letter II are those of type II (A(BC) type). The line $S=S'=0$ corresponds to the solution of type III.

The free energy for various temperatures is given by

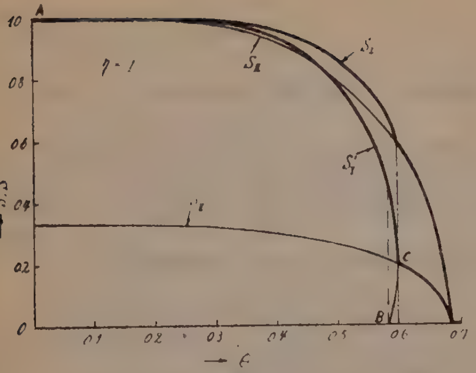

Fig. 2.

$$
\begin{aligned}
\frac{F}{NZx_AV} &= E(S_1S') - \theta\Phi(S_1S') \\
&= \left(\frac{1}{2} + \frac{27}{64}\eta\right)(1-S^2) - \frac{9}{33}\eta(1-SS') \\
&\quad + \frac{27}{64}\eta(1-S'^2) \\
&\quad - \theta\left\{\frac{1}{2}(1+S)\log\frac{1}{2}(1+S)\right. \\
&\qquad + \frac{1}{2}(1-S)\log\frac{1}{4}(1-S) \\
&\qquad + \frac{1}{2}(1-S)\log\frac{1}{2}(1-S) \\
&\qquad + \frac{1}{4}(1+3S')\log\frac{1}{4}(1+3S') \\
&\qquad \left. + \frac{1}{4}(1+2S-3S')\log\frac{1}{4}(1+2S-3S')\right\}
\end{aligned}
\tag{18}
$$

Fig. 3 shows the free energy curves for $\eta=1$. The curve I represents the solution of type I corresponding to AC part in Fig. 2 and I′ is of BC part: the curve II is that of type II and III that of type III. In the temperature range between $\theta=0$ and 0.6 the atomic arrangement of type I (A_2BC) is stable, while type II (A(BC)) is stable between $\theta=0.6$ and 0,687. At $\theta=0,687$ the atomic arrangement becomes random (type III). With temperature change, the mode of atomic arrangement changes discontinuously as shown by thick solid line in Fig. 2.

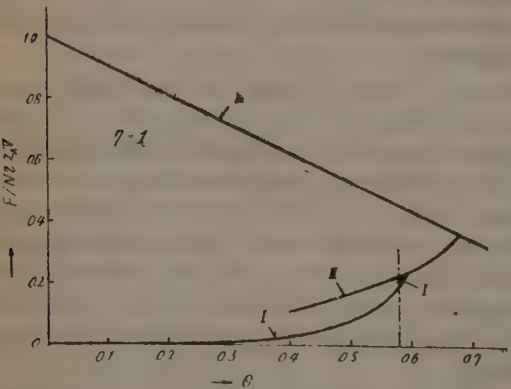

Fig. 3.

(c) $\eta=0.5$: Fig. 4 shows the solution of equilibrium conditions (17. I) and (17. II) for $\eta=0.5$ With decrease of the atomic interaction between next nearest neighboring atoms, the stable range of the existence of the atomic arrangement of A_2BC type decreases. With further decrease of η, such range of A_2BC type becomes narrower, and in limiting case of $\eta=0$ the A_2BC type arrangement vanishes entirely as mentioned in (a).

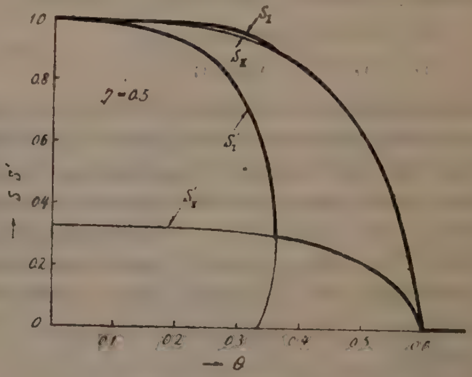

Fig. 4.

(d) $\eta=2$: On the contrary, the increase of η prevents the stable existence of the A (BC) superlattice (type II). Fig. 5 shows the solution of equilibrium conditions (17. I) and (17. II) for the case of $\eta=2$. The thick solid line shows the solution giving stable arrangement of atoms for various temperatures. As

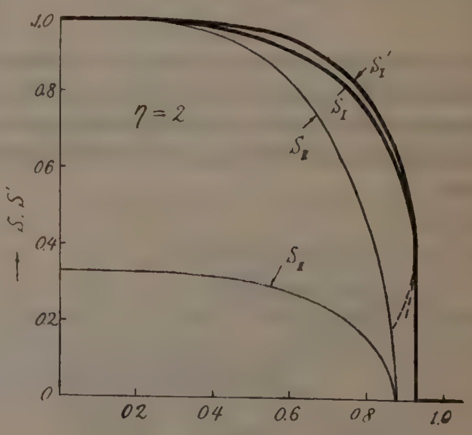

Fig. 5.

shown in the figure the type II does not exist in this case, for the free energy becomes higher than that in the type I. The atomic arrangement of the A_2BC type alone is found in this case.

(e) $\eta<0$: As V is assumed to be positive, W is negative.

Eq. (17. I) becomes

$$\left.\begin{aligned}&\log\frac{(1+S)(1+2S-3S')}{(1-S)^2}\\&\quad-\frac{1}{\theta}\left\{2S+\frac{9}{8}\eta(S-S')\right\}=0\\&\log\frac{1+3S'}{1+2S-3S}+\frac{3}{40}|\eta|(3S'-S)=0.\end{aligned}\right\}\quad(19)$$

In order that the second equation has a solution for positive θ at all, the following relations must be fulfilled:

$$\left.\begin{aligned}&\text{(i)}\quad 3S'-S\leq 0,\\&\qquad\;\; 1+3S'\leq 1+2S-3S',\\\text{or}\;\;&\text{(ii)}\quad 3S'-S\leq 0,\\&\qquad\;\; 1+3S'\geq 1+2S-3S'.\end{aligned}\right\}\quad(20)$$

Both relations are satisfied by $3S'=S$ or $S=S'=0$. The former relation $3S'=S$ is the condition for the formation of the type II and the lattier is for the type III. Accordingly the superlattice formed in this case is of the A(BC) type, and the A_2BC type is not formed. This result is same as that for $\eta=0$. But some difference between these cases will be expected. The present method is not powerful to deal such problem. It may be necessary to discuss by the method which takes short range order into account.

§6. Comparison with Experiment

Some superlattices of body centred cubic type are found experimentally in the ternary alloys[2]. However, the experimental data for the formation of the types of superlattice are not sufficient enough to compare in details with the above theoretical results. Here only some remarks shall be given based on the experimental results in Cu-Al-Mn system. The well known Heusler alloy has the atomic concenteration of 50 Cu : 25 Al : 25 Mn. The experimental results on the superlattice formations of this alloy are given by several authors. The experiment by Bradley and Roders[2] shows that the superlattice of $(Cu\,Mn)_9\,Al_4$ type, in which Cu and Mn atoms behave as if they are of the same kind, is formed in annealed alloy, and A_2BC type (Fig. 1) in the alloy quenched from 800°C. In the former case Al atoms are on γ sites and Cu and Mn atoms are distributed at random on α and β sites in Fig. 1. This structure corresponds to $(AB)_3C$ type discussed in section 5. In the latter case, Cu, Al and Mn atoms lie on α, β and γ sites respectively. In equilibrium state, the superlatice of $Cu_2\,Al\,Mn$ type is supposed to be formed at high temseration and that of $(Cu\,Mn)_3\,Al$ type at room temperature: unfortunately the case of Heusler alloy does not exactly correspond to the case treated in section 4. However, the existence of A_2BC superlattice and that discussed in section 5 may be supported by the above experimental results.

The author express his thanks to Prof. T. Hirone for his kind advice.

References

1) T. Hirone and S. Matsuda: Rikagaku Kenkyujo Iho (Buletine of the physical and chemical Institute) **19** (1940) 931.

2) H. J. Potter: Proc. Phys. Soc. **41** (1929) 135. A. J. Bradley and J. W. Rodgers: Proc. Roy. Soc. **144A** (1934) 340. F. C. Nix and W. Shockley: Rev. Mod. Rhys. **10** (1938) 1.

JOURNAL OF THE PHYSICAL SOCIETY OF JAPAN Vol. 8, No. 1, JAN.—FEB., 1953

Internal Friction of Field-Cooled Ferromagnetic Substances (II) 65-Permalloy and Perminvar*

By Nobuhiko KUNITOMI

The Research Institute for Iron, Steel and Other Metals,
Tôhoku University, Sendai

(Received July 31, 1952)

The magnetostriction, internal friction and Young's modulus have been measured for usually annealed and field-cooled 65-Permalloy and Perminvar. The magnetostriction shows the degree of the effect of field-cooling. The behavior of internal friction of 65-Permalloy shows remarkable difference from that of Ni_3Fe which had previously been observed and explained by the theory considering the rotation of the spontaneous magnetization. It can be explained neither by considering the rotation of the spontaneous magnetization nor by considering the displacement of 180° domain boundaries, so that the other process must be introduced to explain the experimental facts. The internal friction of Perminvar shows intermediate character between Ni_3Fe and 65-Permalloy. It is supposed to be explained by considering both the rotation of the spontaneous magnetization and the other process which is responsible for the internal friction of 65-Permalloy. The change of Young's modulus by the magnetization is consistent with that of internal friction.

§1. Introduction

The magnetic properties of some ferromagnetic substances change remarkably if they are cooled in the longitudinal magnetic field from sufficiently high temperatures. By this treatment, which is usually called field-cooling, the spontaneous magnetization is fixed in the direction close to the applied field, so that the magnetizing process is generally considered to be the displacement of 180° magnetic domain boundaries or the rotation of the spontaneous magnetization from the fixed direction. Recently, the author has derived some theoretical relations¹⁾ between internal friction and magnetization for these two processes. If the magnetizing process is the displacement of 180° domain boundaries, the internal friction Δ is given by

$$\Delta = aJ^2$$

when J is small, where J is the magnetization and a is a constant which is represented by a complicated function of internal stress. This equation shows that Δ vanishes at $J=0$. If, on the contrary, the magnetizing process is the rotation of the spontaneous magnetization, internal friction of the field-cooled substance at demagnetized state should be higher than that of usually annealed one. But, the rate of increase of internal friction with magnetization in the field-cooled substance is less than that in the usual one, so the internal friction of both substances approaches each other with the increase of magnetization. It has been shown from the experimental results that the behavior of the internal friction in Ni_3Fe can be understood by the latter theory based upon the assumption that the magnetizing process is due to the rotation of the spontaneous magnetization. In this paper, internal frictions of 65-Permalloy and Perminvar which are known by the remarkable change of magnetic properties due to the field-cooling have been measured, and their magnetizing processes have been studied by comparing the experimental results with the theoretical conclusions mentioned above.

§2. Experimental Method

The specimen materials used for the measurement were 65-Permalloy (65% Ni, 35% Fe) and Perminvar (50% Ni, 25% Fe, 25% Co). The shape of the specimens is right rectangular bar of 200 mm in length, 8 mm in width and 2 mm in thickness.

---

* This research is carried out under the guidance of Prof. T. Hirone in his research laboratory.

The method of measurement was similar to that developed by Förster and Köster using transversal vibration.[2] In this experiment, the resonant curve of the second overtone vibration (resonant frequency about 840 c.p.s.) was measured for determing the internal friction since the first resonant vibration of the specimen was masked by that of silk fibres which hung the specimen. The detailed method of the measurement is approximately the same as reported in the previous paper,[3] except that the specimen in the form of rectangular bar was used instead of circular cylindrical rod so as to eliminate the beat oscillation, and that the internal friction was calculated from the half-width of resonant curve instead of from the free decay time. Further, Young's modulus was estimated from the resonant frequency. In order to estimate the degree of the effect of the field-cooling, magnetostriction was measured in the same specimens using the optical lever as reported in the previous paper.

§ 3. Results and Discussions

At first, internal stress accumulated in the specimen during their preparation was removed by annealing at 900°C for 2 hours. Thereafter, the specimens were again annealed at 600°C for 1 hr and cooled to the room temperature with the rate of 1°C/min. In one case, the specimens were cooled without applying magnetic field, and in another case, in longitudinal magnetic field of about 100 Oe. The former specimens called "usually annealed specimens" are considered to have uniform directional distribution of the spontaneous magnetization, but the latter called "field-cooled specimens" are considered to have preferrential distribution of the spontaneous magnetization along the direction of the applied field. Since the annealing duration and the cooling rate were made equal for both usually annealed and field-cooled specimens, all of these would have the same atomic arrangement inspite of the effect of superlattice formation.

Magnetostrictions of thus annealed specimens were measured in order to ascertain the effect of field-cooling. The results are shown in Figs. 1 and 2 for 65-Permalloy and Perminvar, respectively. Since the magnetostriction of the field-cooled specimens is about 1/3 or 1/4 of that of usually annealed ones, it may be seen that these are effectively field-cooled. Curve I corresponds to the usually annealed specimens and II to the field-cooled ones.

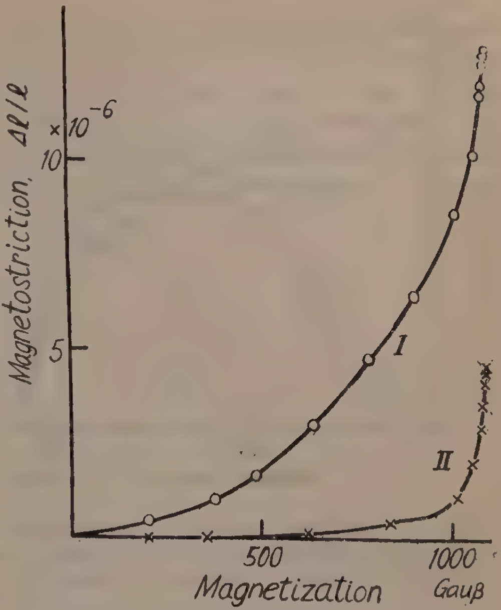

Fig. 1. Magnetostriction of 65-Permalloy. Curves I and II correspond to the usually annealed and field-cooled substances, respectively.

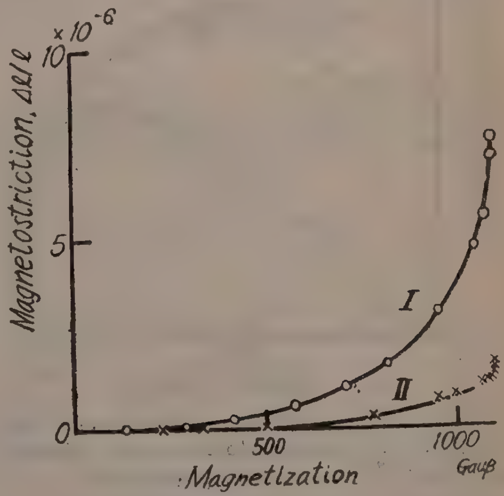

Fig. 2. Magnetostriction of Perminvar. Curves I and II correspond to the usually annealed and field-cooled substances, respectively.

Figs. 3 and 4 show the experimental results of internal friction as functions of magnetization. Internal friction of usually annealed 65-Permalloy (Fig. 3 Curve I) is about 10^{-3} at demagnetized state, but increases rapidly with

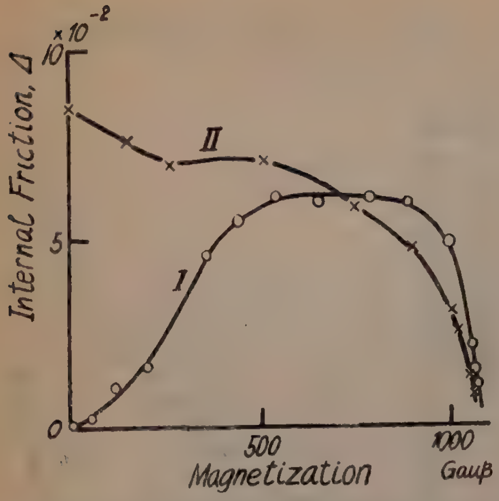

Fig. 3. Internal friction of 65-Permalloy. Curves I and II correspond to the usually annealed and field-cooled substances, respectively.

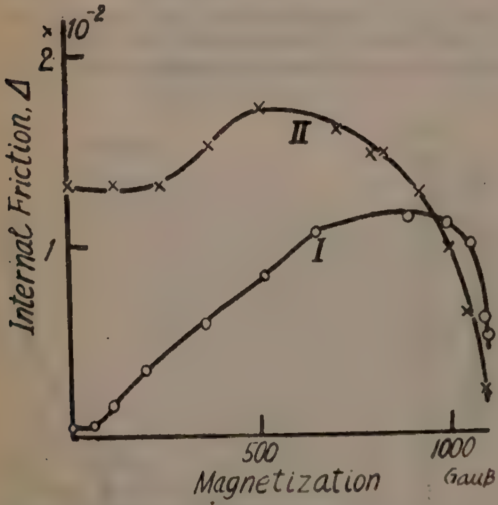

Fig. 4. Internal friction of Perminvar. Curves I and II correspond to the usually annealed and field-cooled substances, respectively.

magnetization. It decreases near the magnetic saturation after passing a maximum. Although internal friction of the completely saturated specimen is expected to be less than that of the demagnetized one, the highest external magnetic field used in this experiment did not exceed 100 Oe, so the internal friction corresponding to the maximum field in Figs. 3 and 4 shows still higher value than the true saturation value.

Previously, the author measured internal friction of Permalloy with the composition of Ni_3Fe under various heat-treatments, and found that the internal friction shows a maximum with the increase of magnetization for every case.[3] This behavior is explained by the theory[4] assuming that the internal friction is caused by the rotation of the spontaneous magnetization. The experimental behavior of usually annealed 65-Permalloy shown by the Curve I in Fig. 3 is similar to that of Ni_3Fe qualitatively. However, the remarkable quantitative difference is found between these substances. As is shown in Table I, the rate of increase of internal friction with magnetization, that is the ratio of the maximum to the demagnetized internal friction, is 5.3 for Ni_3Fe whereas 68 for 65-Permalloy. Such a striking difference suggests that the mechanisms of internal friction in these specimens would be different from each other.

This supposition is supported by the experimental evidence of field-cooled specimens. In the case of Ni_3Fe, internal friction of field-cooled specimen is 1.6 times higher than that of usually annealed one at the demagnetized state, but its rate of increase with magnetization is not so large as that of usually treated one, so that the difference of internal friction between the two specimens becomes the less the higher the magnetization. On the other hand, internal friction of field-cooled 65-Permalloy is very high at the demagnetized state compared with that of usually annealed one (94 times larger as is seen in Table I), and it decreases almost monotonously with the increase of magnetization. Such a behavior cannot be explained even qualitatively by assuming the rotation of the spontaneous magnetization or the displacement of 180° domain boundaries.

Fig. 4 shows the results obtained for

Table I

	$(\Delta_0)_U$	$(\Delta_m)_U$	$(\Delta_0)_F$	$(\Delta_m)_F$	$(\Delta_m/\Delta_0)_U$	$(\Delta_m/\Delta_0)_F$	$(\Delta_0)_F/(\Delta_0)_U$
Ni_3Fe	1.7×10^{-3}	9.0×10^{-3}	2.7×10^{-3}	9.0×10^{-3}	5.3	3.3	1.6
65-Permalloy	0.9 〃	61.0 〃	85.0 〃	70.0 〃	68.0	0.8	94.0
Perminvar	0.4 〃	11.0 〃	13.0 〃	17.0 〃	36.0	1.3	36.0

Perminvar. As is seen from this figure, Perminvar behaves as if it has an intermediate character between 65-Permalloy and Ni_3Fe. This fact is more readily understood from the numerical values of three kinds of ratios tabulated in Table I. In this Table, Δ_0 and Δ_m denote the demagnetized and the maximum internal friction, respectively. The suffices U and F correspond to the usually annealed and the field-cooled specimens, respectively. The values of three kinds of ratios, namely, the ratios of the maximum to the demagnetized internal friction of both usually annealed and field-cooled substances and the ratio of the demagnetized internal friction of usually annealed to that of field-cooled specimens, are shown in the last three columns in Table I. By comparing these three ratios for three substances, we can find that the ratios obtained from the results of Perminvar always show intermediate value between those of Ni_3Fe and 65-Permalloy. In this table, $(\Delta_m/\Delta_0)F$ of 65-Permalloy is below 1.0. It shows the fact that the internal friction of the field-cooled 65-Permalloy decreases nearly monotonously but shows a little maximum having a lower value than the demagnetized internal friction (see Curve II, Fig. 3).

The results described above can be explained as follows: As is seen in the previous paper, internal friction of Ni_3Fe is explained by considering the rotation of spontaneous magnetization by the applied stress. In 65-Permalloy, however, the experimental behavior can be explained neither by considering such a process nor the displacement of 180° domain boundaries. Therefore, it should be concluded that another process might be responsible for the energy dissipation in this case. Although the energy dissipating process due to 90° boundaries in the field-cooled specimen has not yet been studied satisfactorily, it may be expected that it would cause higher internal friction than that due to 180° boundaries, since the applied stress does not affect 180° domain boundary if we consider only magnetostrictive energy. So it might be possible that the internal friction of 65-Permalloy is due to the displacement of the 90° domain boundary. Similarly, internal friction of Perminvar which shows intermediate character might be due to both the displacement of 90° domain boundaries and the rotation of spontaneous magnetization.

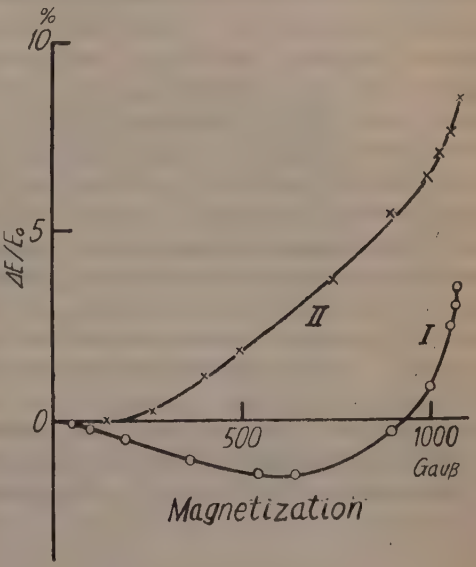

Fig. 5. ΔE-effect of 65-Permalloy. Curves I and II correspond to the usually annealed and field-cooled substances, respectively.

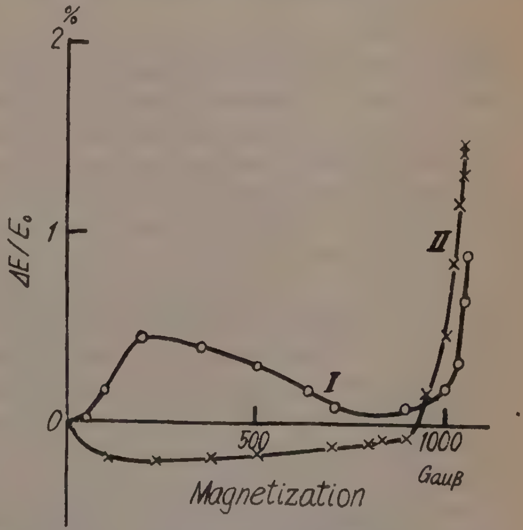

Fig. 6. ΔE-effect of Perminvar. Curves I and II corespond to the usually annealed and field-cooled substances, respectively.

As is shown in Curve I Fig. 5, the Young's modulus of usually annealed 65-Permalloy decreases with the magnetization and increases after showing a minimum. On the other hand, Curve II shows that the Young's modulus of the field-cooled specimen increases monotonously with the magnetization. Such a behavior is in contrast with that of internal friction which shows a maximum in the usually annealed 65-Permalloy and monotonous decrease in the field-cooled one. This contrasting character of the internal friction and Young's modulus is observed for many other substances by other workers.[5] Also, Perminvar shows this contrast as shown in Fig. 6, except in the earlier stage of magnetization in usually annealed specimen in which both the internal friction and Young's modulus increases simultaneously. This fact is explained as follows: The value of the Young's modulus can be separated into two parts, namely, those due to ferromagnetic and non-ferromagnetic origins. Young's modulus of the magnetically saturated specimen does not include ferromagnetic origin. So the contribution of ferromagnetic origins to the Young's modulus for the various stages of magnetization is obtained by the difference of the Young's moduli at various stages and at saturation. Ferromagnetic contributions to the Young's modulus estimated from the curves in Figs. 5 and 6 by using the method mentioned above show the similar behaviors to the curves of Figs. 3 and 4. It shows that the internal friction and the change of the Young's modulus contributed from the ferromagnetic origin are similar characters. Since both characters are determined by the volumes of domains and rotating angles of the spontaneous magnetization by the applied stress, the parallelism of both properties are expected qualitatively. Quantitative comparison of the Young's modulus with internal friction also confirms the existence of the parallelism.

References

1) T. Hirone and N. Kunitomi, J. Phys. Soc. Jap. **7** (1952) 364.
2) F. Förster and W. Köster, Z. Metallkde. **29** (1937) 109.
3) N. Kunitomi, J. Phys. Soc. Jap. **7** (1952) 584.
4) N. Kunitomi, J. Phys. Soc. Jap. **7** (1952) 578.
5) H. J. Williams, R. M. Bozorth and H. Christensen, Phys. Rev. **59** (1941) 1005.
F. J. Beck, J. S. Kouvelities and L. W. McKeehan, Phys. Rev. **84** (1951) 957.

JOURNAL OF THE PHYSICAL SOCIETY OF JAPAN Vol. 8, No. 1, JAN.—FEB., 1953

Atomic Distribution in Binary Solid Solutions
II. Modified Theory for the Case of Nearly Equal Concentrations

By Terutosi MURAKAMI

Institute of Applied Science, Faculty of Engineering,
Kyushu University

(Received July 15, 1952)

In this part, the method described in the preceding part[1] is modified to treat equaly A and B atoms. The chain approximation is employed in the present part, as previously. If the interactions are considered in appropriate manner, the present method gives the same critical temperature as those obtained from Bethe's approximation for most types of lattices. The exceptional cases are the critical temperatures of order-disorder transition in triangular and face-centered cubic lattices. The formulas to express the propagation of order in crystal lattices are obtained in closed forms. And for the cases of simple lattices the formation of the superstructure is discussed.

§1. The Use of Mixed Chain Sums

In the theory described in part I[1], which will be referred as I hereafter, we referred to only one kind of atoms concerning the configurations in the binary descrete systems. And we took account of only the chain configurations connected by the pair of atoms of either of two types, and left the more complicated connections out of considerations. It is evident that such a treatment does not give so good result for the case of two phase separation arising from the tendency of like atoms to aggregate each other as the temperature decreases, since the contribution of the ignored connections becomes important at low temperature, because of the frequent occurrence of tightly connected configurations. And even for the case of order-disorder transition so many configurations other than chain connections are neglected that one can not expect to obtain the good results except for the considerably dilute systems. These situations were already noticed from the simple consideration in I. Then, for the purpose of attaining better approximation method than used in I, we shall equaly treat A and B atoms by considering two types of mixed chain sums, one connected by pairs of unlike atoms (such as $A-B-A-B$ chains) and another by pairs of like atoms (such as $A-A-A-A$ and $B-B-B-B$ chains).

Let us consider the binary system composed of n_a A atoms and n_b B atoms localized at the lattice points of infinite crystal without vacant sites, and denote the concentrations of A and B atoms by x_a and x_b respectively. Then we have

$$N=n_a+n_b\ , \qquad x_a+x_b=1\ ,$$

and

$$\lim_{N\to\infty} n_a/N=x_a\ , \qquad \lim_{N\to\infty} n_b/N=x_b\ ,$$

N being the total number of lattice points. Here the same notation as in I will be used, but the symbols referring to A and B atoms are indicated by subscripts a and b, respectively, and the symbols without subscripts refer to a set of quantities, e.g. m represents a set of numbers m_a and m_b. $\{\boldsymbol{r}_m\}$ stands for a set of coordinates of m_a A atoms and m_b B atoms.

As in I let us define the distribution function $F_m\{\boldsymbol{r}_m\}$ to be proportional to the probability that m atoms occupy the set of lattice points $\{\boldsymbol{r}_m\}$. $F_m\{\boldsymbol{r}_m\}$ is so normalized that

$$\lim_{N\to\infty} N^{-(m_a+m_b)}\mathbf{S}_N\{\boldsymbol{r}_m\}F_m\{\boldsymbol{r}_m\}=1\ . \qquad (1)$$

When $m_a+m_b\ll N$, the probability that the set of lattice points $\{\boldsymbol{r}_m\}$ be occupied by an appropriate set of A and B atoms is equal to $x_a{}^{m_a}x_b{}^{m_b}F_m\{\boldsymbol{r}_m\}$. From the above definition, the pair distribution function which is proportional to the probability that there be an A atom at $\boldsymbol{r}_1$ and a B atom at $\boldsymbol{r}_2$ is given by the following equation, as with I,

$$F_{ab}(\boldsymbol{r}_{1,2})=(N^2/Q_\tau)\mathbf{S}_N\{\boldsymbol{r}_{n-2}\}\exp[-U\{\boldsymbol{r}_n\}/kT], \tag{2}$$

where Q_τ is the configurational partition function defined by

$$Q_\tau=\mathbf{S}_N\{\boldsymbol{r}_n\}\exp[-U\{\boldsymbol{r}_n\}/kT]. \tag{3}$$

$U\{\boldsymbol{r}_n\}$ is the total potential energy of the system at the configuration $\{\boldsymbol{r}_n\}$, and assumed to be, as usual, expressible in the form

$$U\{\boldsymbol{r}_n\}=\sum_{i>j}\varepsilon_{\alpha\beta}(\boldsymbol{r}_{i,j}), \tag{4}$$

$\varepsilon_{\alpha\beta}(\boldsymbol{r}_{i,j})$ being the interaction between an α atom at $\boldsymbol{r}_i$ and a β atom at $\boldsymbol{r}_j$. One may use the convention that the interaction between two atoms overlapping each other is infinity, irrespective of types.

If one introduces the function $f_{\alpha\beta}(\boldsymbol{r})$ defined by

$$f_{\alpha\beta}(\boldsymbol{r}_{i,j})=\exp\{-\varepsilon_{\alpha\beta}(\boldsymbol{r}_{i,j})/kT\}-1, \tag{5}$$

Eq. (2) may be, in the same manner as in I, brought into the form

$$F_{ab}(\boldsymbol{r}_{1,2})=\exp\{-\varepsilon_{ab}(\boldsymbol{r}_{1,2})/kT\}[1+G_{ab}(\boldsymbol{r}_{1,2})], \tag{6}$$

where

$$G_{ab}(\boldsymbol{r}_{1,2})=\sum_{l_a'+l_b'\geq 1}(Z_a/x_a)(Z_b/x_b) \times Z_a^{l'a}Z_b^{l'b}B_{ab,l'}(\boldsymbol{r}_{1,2}), \tag{7}$$

in which Z_a and Z_b are the fugacities of A and B atom, respectively, and $B_{ab,l'}(\boldsymbol{r}_{1,2})$'s are defined by

$$B_{ab,l'}(\boldsymbol{r}_{1,2})=\frac{1}{l_a'!\,l_b'!}\mathbf{S}_N\{\boldsymbol{r}_{l'}\}\sum_{\substack{l'\geqq i>j\geqq 1'\\ l'\geqq k\geqq 1'\\ l'\geqq l\geqq 1'}}\Pi f_{\alpha\beta}(\boldsymbol{r}_{i,j}) \times f_{a\alpha'}(\boldsymbol{r}_{1,k})f_{b\beta'}(\boldsymbol{r}_{2,l}), \tag{8}$$

(sum over all connected products)

where i, j, k and l indicate the atoms which belong to the set $\{\boldsymbol{r}_{l'}\}$.

In order to perform further calculation for (7), we shall, as in I, neglect the other connected products than singly connected, although these more complicated connections are contained in $B_{ab,l'}(\boldsymbol{r}_{1,2})$. At first, we shall define the chain sum $P_{ab,m'}(\boldsymbol{r}_{1,2})$ connected of $(m'+1)$ $f_{\alpha\beta}(\boldsymbol{r})$'s so that

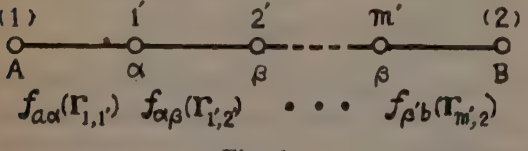
(1)
1'
2'
m'
(2)
A
α
β
β
B
$f_{a\alpha}(\mathbf{r}_{1,1'})$
$f_{\alpha\beta}(\mathbf{r}_{1',2'})$
• • •
$f_{\beta'b}(\mathbf{r}_{m',2})$

Fig. 1.

$$P_{ab,m'}(\boldsymbol{r}_{1,2})=\sum_{(\alpha,\beta)}\mathbf{S}_N\{\boldsymbol{r}_{m'}\}f_{a\alpha}(\boldsymbol{r}_{1,1'}) \times f_{\alpha\beta}(\boldsymbol{r}_{1',2'})\cdots f_{\beta'b}(\boldsymbol{r}_{m',2}), \tag{9}$$

where $\sum_{(\alpha,\beta)}$ means the summation over all possible manners of constructing the distinguishable chain of m_a A atoms and m_b B atoms arranged between the two terminal atoms A at $\boldsymbol{r}_1$ and B at $\boldsymbol{r}_2$ as shown in Fig. 1. There are, however, indistinguishable $(m_a!\,m_b!)$ $P_{ab,m'}(\boldsymbol{r}_{1,2})$'s, which are produced by permutations of identical atoms. Then one obtains as an approximate relation

$$G_{ab}(\boldsymbol{r}_{1,2})\simeq\sum_{m_a'+m_b'\geq 1}x_a^{m_a}x_b^{m_b}P_{ab,m'}(\boldsymbol{r}_{1,2}), \tag{10}$$

analogously with in I. If this approximation is permitted, one obtains, from (10) and (6),

$$F_{ab}(\boldsymbol{r}_{1,2})=\exp\{-\varepsilon_{ab}(\boldsymbol{r}_{1,2})/kT\} \times[1+\sum_{m_a'+m_b'\geq 1}x_a^{m_a}x_b^{m_b}P_{ab,m'}(\boldsymbol{r}_{1,2})], \tag{11}$$

corresponding to Eq. (19) of I.

As mentioned in the previous part, only the difference

$$\Delta\varepsilon(\boldsymbol{r})=\tfrac{1}{2}\{\varepsilon_{aa}(\boldsymbol{r})+\varepsilon_{bb}(\boldsymbol{r})\}-\varepsilon_{ab}(\boldsymbol{r}) \tag{12}$$

is essential for determining atomic distribution. And in I the calculations were performed for the systems in which the interactions vanish except for AA pairs. For the present, we shall consider the following two ways of choosing the interactions so as to be symmetric for A and B. At first, we shall take the choice of the potential energy such that the interactions between like atoms vanish, namely,

$$\varepsilon_{ab}(\boldsymbol{r})=\Delta\varepsilon(\boldsymbol{r}),\quad \varepsilon_{aa}(\boldsymbol{r})=\varepsilon_{bb}(\boldsymbol{r})=0. \tag{13.1}$$

Such a choice may be suitable for the case of two phase separation where the number of AB pairs decreases as the temperature approaches to the transition temperature. Secondly, we may choose as follows:

$$\varepsilon_{ab}(\boldsymbol{r})=0,\quad \varepsilon_{aa}(\boldsymbol{r})=\varepsilon_{bb}(\boldsymbol{r})=\Delta\varepsilon(\boldsymbol{r}). \tag{13.2}$$

This may be suitable for the order-disorder transitions, since the numbers of AA and BB pairs decrease as the temperature approaches to the Curie temperature. For convenience' sake, we shall refer to the interaction energies so chosen that indicated by (13.1) and (13.2) as α-β bonds and α-α bonds, respectively. Thus one obtains from (5)

$$f_{ab}(\boldsymbol{r})=\xi(\boldsymbol{r}),\ f_{aa}(\boldsymbol{r})=f_{bb}(\boldsymbol{r})=0,\ \text{for } \alpha\text{-}\beta \text{ bonds}; \tag{14.1}$$

and

$$f_{ab}(\boldsymbol{r})=0,\ f_{aa}(\boldsymbol{r})=f_{bb}(\boldsymbol{r})=\xi(\boldsymbol{r}),\ \text{for } \alpha\text{-}\alpha \text{ bonds}, \tag{14.2}$$

where

$$\xi(\boldsymbol{r})=\exp\{-\Delta\varepsilon(\boldsymbol{r})/kT\}-1\,, \qquad (15)$$

while in both cases $f(\boldsymbol{r})$ of two atoms overlapping each other is always equal to -1. If we apply (14.1) or (14.2) to the chain sum (9), non-vanishing $f(\boldsymbol{r})$'s may be replaced

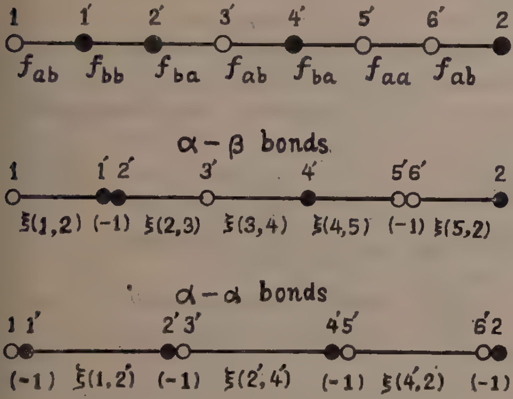

Fig. 2. ○...A atoms, ●...B atoms

by $\xi(\boldsymbol{r})$ or -1. For example, we shall consider the case of $m_a=3$, $m_b=3$. Then we have the connected product as shown in Fig. 2 and the corresponding terms of chain sum is

$$\mathbf{S}_N\{\boldsymbol{r}_{6'}\}f_{ab}(\boldsymbol{r}_{1,1'})f_{bb}(\boldsymbol{r}_{1',2'})f_{ba}(\boldsymbol{r}_{2',3'})$$
$$\times f_{ab}(\boldsymbol{r}_{3',4'})f_{ba}(\boldsymbol{r}_{4',5'})f_{aa}(\boldsymbol{r}_{5',6'})f_{ab}(\boldsymbol{r}_{6',2}). \qquad (16)$$

If one applies Eq. (14) to this lattice sum, Eq. (16) for the case of α-β bonds is reduced to the following form

$$(-)^2\mathbf{S}_N(\boldsymbol{r}_{1',3',4',5'})\xi(\boldsymbol{r}_{1,1'})\xi(\boldsymbol{r}_{1',3'})$$
$$\times\xi(\boldsymbol{r}_{3',4'})\xi(\boldsymbol{r}_{4',5'})\xi(\boldsymbol{r}_{5',2})\,, \qquad (17.1)$$

since the connected pair of like atoms must be overlapped each other not to vanish. And for the case of α-α bonds, we have, from the same as in the case of α-β bonds.

$$(-)^3\mathbf{S}_N(\boldsymbol{r}_{2',4'})\xi(\boldsymbol{r}_{1,2'})\xi(\boldsymbol{r}_{2',4'})\xi(\boldsymbol{r}_{4',2})\,. \qquad (17.2)$$

But, in order to obtain the chain sum $P_{ab,m'}(\boldsymbol{r}_{1,2})$, it must be noticed that one must sum over all distinguishable connections, which are produced by 3 A atoms and 3 B atoms. Thus, in general, the chain sum (9) may be reduced to a simple form by means of the above procedure.

§2. Fourier Transforms of $\xi(\boldsymbol{r})$'s

Corresponding to $g(\boldsymbol{b})$ defined as Eq. (20) of I, we introduce the auxirialy function $g(\boldsymbol{b})$ defined by either

$$g(\boldsymbol{b})=\lim_{N\to\infty}\mathbf{S}_N(\boldsymbol{r})\xi(\boldsymbol{r})\exp\{-2\pi i\boldsymbol{b}\cdot\boldsymbol{r}\}\,, \qquad (18)$$

or

$$\xi(\boldsymbol{r})=\int_0^1\int_0^1\int_0^1 g(\boldsymbol{b})\exp\{2\pi i\boldsymbol{b}\cdot\boldsymbol{r}\}dh_1dh_2dh_3\,, \qquad (19)$$

where $\boldsymbol{r}=l\boldsymbol{a}_1+m\boldsymbol{a}_2+n\boldsymbol{a}_3$ is a translational vector of lattice and $\boldsymbol{b}=h_1\boldsymbol{b}_1+h_2\boldsymbol{b}_2+h_3\boldsymbol{b}_3$ is a reciprocal-space vector. As $\xi(\boldsymbol{r})$ may be written in the same form as that of Fourier integral, one has

$$\lim_{N\to\infty}\mathbf{S}_N\{\boldsymbol{r}_{n'}\}\xi(\boldsymbol{r}_{1,1'})\xi(\boldsymbol{r}_{1',2'})\cdots\xi(\boldsymbol{r}_{n',2})$$
$$=\int\{g(\boldsymbol{b})\}^{n'+1}\exp\{2\pi i\boldsymbol{b}\cdot\boldsymbol{r}_{1,2}\}d\boldsymbol{b}\,, \qquad (20)$$

by the same procedure that used in I, the integration extending over a unit cell of the reciprocal lattice. Then, the (17.1) and (17.2) are written, respectively, as follows

$$(-)^2\int\{g(\boldsymbol{b})\}^5\exp\{2\pi i\boldsymbol{b}\cdot\boldsymbol{r}_{1,2}\}d\boldsymbol{b}$$
$$\text{for } \alpha-\beta \text{ bonds,} \qquad (21.1)$$

$$(-)^3\int\{g(\boldsymbol{b})\}^2\exp\{2\pi i\boldsymbol{b}\cdot\boldsymbol{r}_{1,2}\}d\boldsymbol{b}$$
$$\text{for } \alpha-\alpha \text{ bonds.} \qquad (21.2)$$

It is concluded from (14) and (20) that the lattice sums, which have the same number of the connected pairs of unlike atoms (and then the same number of those of like atoms), gives the same value, provided the two terminal atoms are fixed. Now we shall consider such terms of $\sum_{(\alpha,\beta)}$ in (9) that the number of the connected pairs of unlike atoms in the chain connections, which produced by arranging m_aA and m_bB atoms between A atom at $\boldsymbol{r}_1$ and B atom at $\boldsymbol{r}_2$, must be odd, and we shall denote it by $(2n+1)$ and then the number of the connected pairs of like atoms is (m_a+m_b-2n). These chain connections are obtained in $\binom{m'_a}{n}\binom{m'_b}{n}$ ways by interchange of unlike atoms. Accordingly, the lattice sums made of the above connections, $p^{(n)}_{ab,m'}(\boldsymbol{r}_{1,2})$, are given by

$$p^{(n)}_{ab,m'}(\boldsymbol{r}_{1,2})=(-)^{m'_a+m'_b-2n}\mathbf{S}_N\{\boldsymbol{r}_{2n}\}$$
$$\times\xi(\boldsymbol{r}_{1,i})\cdots\xi(\boldsymbol{r}_{j,2})$$
$$=(-)^{m'_a+m'_b-2n}\int\{g(\boldsymbol{b})\}^{2n+1}$$
$$\times\exp\{2\pi i\boldsymbol{b}\cdot\boldsymbol{r}_{1,2}\}d\boldsymbol{b} \qquad (22.1)$$

for $\alpha-\beta$ bonds, and

$$p^{(n)}_{ab;m'}(\boldsymbol{r}_{1,2})=(-)^{2n+1}\mathbf{S}_N\{\boldsymbol{r}_{m'-2n-1}\}$$
$$\times\xi(\boldsymbol{r}_{1,i})\cdots\xi(\boldsymbol{r}_{j,2})$$
$$=(-)^{2n+1}\int\{g(\boldsymbol{b})\}^{m'_a+m'_b-2n}$$
$$\times\exp\{2\pi i\boldsymbol{b}\cdot\boldsymbol{r}_{1,2}\}d\boldsymbol{b} \qquad (22.2)$$

for $\alpha-\alpha$ bonds, by the same procedure that used in derivation of (17.1) and (17.2) from (16). Accordingly, one may replace the sum $\sum_{(\alpha,\beta)}$ in (9) by the sum $\sum_{(n)}$ over available n, and the chain sum $p_{ab,m'}(\boldsymbol{r}_{1,2})$ may be rewritten as

$$P_{ab,m'}(\boldsymbol{r}_{1,2})=\sum_{(n)}\binom{m'a}{n}\binom{m'b}{n}p^{(n)}_{ab,m'}(\boldsymbol{r}_{1,2}) \quad (23)$$

By means of Eqs. (22) and (23), the pair distribution function given by (11) is written as follows:

$$F_{ab}(\boldsymbol{r}_{1,2})=1-\alpha(\boldsymbol{r}) \quad \text{for } \alpha-\beta \text{ bonds}, \quad (24.1)$$

or

$$F_{ab}(\boldsymbol{r}_{1,2})=1-\beta(\boldsymbol{r}) \quad \text{for } \alpha-\alpha \text{ bonds}, \quad (24.2)$$

where

$$\alpha(\boldsymbol{r})=\xi^2(\boldsymbol{r})-\{1+\xi(\boldsymbol{r})\}\int\frac{g(\boldsymbol{b})\exp\{2\pi i\boldsymbol{b}\cdot\boldsymbol{r}\}}{2-x_a x_b\{1-g^2(\boldsymbol{b})\}}d\boldsymbol{b}, \quad (25.1)$$

and

$$\beta(\boldsymbol{r})=\int\frac{\exp\{2\pi i\boldsymbol{b}\cdot\boldsymbol{r}\}}{\{1-g(\boldsymbol{b})\}[1-x_a x_b\{1-g(\boldsymbol{b})\}]}d\boldsymbol{b}, \quad (25.2)$$

in which $\alpha(\boldsymbol{r})$ and $\beta(\boldsymbol{r})$ are order parameters of some kinds, which may be closely related to the diffuse scattering of X-rays.

§ 3. Propagation of Order in Simple Lattices

All procedures described in the present paper are not necessarily restricted to the nearest neighbor systems. Now we shall, however, confine ourselves to nearest neighbor systems to make further progress. Let the interactions of AA, BB and AB contact be respectively ε_{aa}, ε_{bb} and ε_{ab}. As is well known, if $\varepsilon_{aa}+\varepsilon_{bb}<2\varepsilon_{ab}$ the two-phase separation occurs and if $\varepsilon_{aa}+\varepsilon_{bb}>2\varepsilon_{ab}$ the order-disorder occurs, and we may apply the $\alpha-\beta$ bonds for the former, and $\alpha-\alpha$ bonds for the latter. Here, let us denote $\xi(\boldsymbol{r})$ in (18) for contact neighbor by ξ_0. Then, $g(\boldsymbol{b})$'s are written as Eqs. (29) and (30) of I. Consequently, (25.1) and (25.2) are respectively written as

$$\alpha(\boldsymbol{r})=\xi^2(\boldsymbol{r})-\frac{4\xi_0 x_a x_b}{1-\xi(\boldsymbol{r})}\int\left[\left\{\frac{C_1}{\xi_0}-G(\boldsymbol{b})\right\}^{-1}-\left\{\frac{C_1-1}{\xi_0}-G(\boldsymbol{b})\right\}^{-1}\right]\exp\{2\pi i\boldsymbol{b}\cdot\boldsymbol{r}\}d\boldsymbol{b} \quad (26.1)$$

and

$$\beta(\boldsymbol{r})=\frac{1}{2(1-2x_a x_b)\xi_0}\int\left[\left\{\frac{1}{\xi_0}-G(\boldsymbol{b})\right\}^{-1}-\left\{\frac{C_2}{\xi_0}-G(\boldsymbol{b})\right\}^{-1}\right]\exp\{2\pi i\boldsymbol{b}\cdot\boldsymbol{r}\}d\boldsymbol{b}, \quad (26.2)$$

where

$$C_1=\{(x_a x_b-2)/x_a x_b\}^{1/2}-1,\ C_2=1/2x_a x_b. \quad (27)$$

And $G(\boldsymbol{b})$ is given by one of Eqs. (30) of I.

Next, we shall examine the critical temperature T_c, at which the singular point of the integrand in (26) begins to appear in the analogous manner with in § 4 of I. Thus the values of $\exp\{\Delta\varepsilon/kT_c\}$ obtained from Eq. (26.1) or (26.2) for the case of equal concentrations are given in Table I.

From the above considerations, we see that in most cases the chain-approximation used here gives the same critical temperature that Bethe's approximation gives, provided appropriate bonds are used. It is, however, noteworthy that the calculated values of $\exp\{\Delta\varepsilon/kT_c\}$ for order-disorder transition in the triangular and face-centered lattice deviate remakably from the ones given by Bethe's approximation. These situations are presumably due to the fact that these lattices cannot be decomposed into two equivalent

Table I

Types of Lattices	Two-phase separation $\exp\{\lvert\Delta\varepsilon\rvert/kT_c\}$		Bethe-approximation $\exp\{\lvert\Delta\varepsilon\rvert/kT_c\}$	Order-disorder transition $\exp\{\lvert\Delta\varepsilon\rvert/kT_c\}$	
	$\alpha-\alpha$ chain	$\alpha-\beta$ chain		$\alpha-\alpha$ chain	$\alpha-\beta$ chain
Linear chain	2.00	∞	∞	∞	2.00
Square lattice	1.50	2.00	2.00	2.00	1.50
Triangular	1.33	1.50	1.50	3.00	1.66
Simple cubic	1.33	1.50	1.50	1.50	1.33
Body-centered cubic	1.25	1.33	1.33	1.33	1.25
Face-centered cubic	1.16	1.20	1.20	2.00	1.33

sublattices.

Now we shall consider the dependences of $\alpha(\boldsymbol{r})$ and $\beta(\boldsymbol{r})$ on the temperature and $\boldsymbol{r}$ for the case of simple lattices. At sufficiently high temperature, both $\alpha(\boldsymbol{r})$ and $\beta(\boldsymbol{r})$ vanish, and the pair distribution functions become unity, i.e. atoms are distributed with complete randomness over the whole lattice.

To abbreviate, we shall employ, instead of the temperature, the parameter $\eta_0=-1/\xi_0$, which increases monotonically with temperature from unity at $T=0$ to infinity at $T=\infty$. Then Eqs. (26) become

$$\alpha(\boldsymbol{r})=\eta^{-2}(\boldsymbol{r})+[\eta_0\{1-\eta^{-1}(\boldsymbol{r})\}/4x_a x_b]\cdot[\Phi_1-\Phi_2], \tag{28.1}$$

and

$$\beta(\boldsymbol{r})=\{\eta_0/2(1-2x_a x_b)\}[\Phi_3-\Phi_4], \tag{28.2}$$

where

$$\left.\begin{aligned}\Phi_1&=\int\frac{\exp\{2\pi i\boldsymbol{b}\cdot\boldsymbol{r}\}}{\eta_0-G(\boldsymbol{b})}d\boldsymbol{b},\\ \Phi_2&=\int\frac{\exp\{2\pi i\boldsymbol{b}\cdot\boldsymbol{r}\}}{2\eta_0+G(\boldsymbol{b})}d\boldsymbol{b},\end{aligned}\right\} \tag{29.1}$$

$$\left.\begin{aligned}\Phi_3&=\int\frac{\exp\{2\pi i\boldsymbol{b}\cdot\boldsymbol{r}\}}{\eta_0+G(\boldsymbol{b})}d\boldsymbol{b},\\ \Phi_4&=\int\frac{\exp\{2\pi i\boldsymbol{b}\cdot\boldsymbol{r}\}}{2\eta_0-G(\boldsymbol{b})}d\boldsymbol{b},\end{aligned}\right\} \tag{29.2}$$

and $\eta(\boldsymbol{r})=-1/\xi(\boldsymbol{r})$. For simple cubic lattice, one has

$$G(\boldsymbol{b})=\sum_{i=1}^{3}\cos 2\pi h_i, \tag{30}$$

and one obtains

$$\begin{aligned}\Phi_1&=\int_0^1\!\!\int_0^1\!\!\int_0^1\frac{\exp\{2\pi i(lh_1+mh_2+nh_3)\}}{\eta_0-\cos 2\pi h_1-\cos 2\pi h_2-\cos 2\pi h_3}\\ &\qquad\times dh_1dh_2dh_3\\ &=\int_0^\infty e^{-\eta_0\tau}d\varsigma\int_0^1\!\!\int_0^1\!\!\int_0^1\exp\{2\pi i(lh_1+mh_2+nh_3)\\ &\qquad+2\sum\cos 2\pi h_i\}dh_1dh_2dh_3\\ &=\int_0^\infty I_l(\tau)I_m(\tau)I_n(\tau)e^{-\eta_0\tau}d\tau.\end{aligned} \tag{31}$$

This result was employed by Van Peype[2)] in connection with another problem. One may perform the similar calculations for obtaing

$$\Phi_2=\Phi_4=(-)^{l+m+n}\int I_l(\tau)I_m(\tau)I_n(\tau)e^{-2\eta_0\tau}d\tau, \tag{32}$$

and

$$\Phi_3=(-)^{l+m+n}\int I_l(\tau)I_m(\tau)I_n(\tau)e^{-\eta_0\tau}d\tau, \tag{33}$$

where $I_k(\tau)$ is the Bessel function with pure imaginary argument defined as

$$I_k(\tau)=\sum_{r=0}^{\infty}(\tau/2)^{k+2r}/r!\,(k+r)!. \tag{34}$$

These integral are all positive, and become smaller and smaller as l, m and n increase. And since $|\Phi_1|>|\Phi_2|$ and $|\Phi_3|>|\Phi_4|$, $\alpha(l, m, n)$'s are always positive and monotonically decrease and tend to zero as l, m and n increase, whereas $\beta(l, m, n)$'s decrease in absolute magnitude and is positive or negative according as $(l+m+n)$ is even or odd. Furthermore, we see that these two parameters do not vanish even for large value of l, m and n if the temperature reaches the critical temperature. And the integrals in Eqs. (28) converge for $\eta_0>3$ and diverge for $\eta_0<3$. From the above mentioned, it may be assured that the temperature for $\eta_0=3$ is the critical temperature, as expected previously, at which β approaches to a certain non-vanishing constant at the limit, l, m and $n\to\infty$. This means that the long range order arises at this temperature.

References

1) T. Murakami: J. Phys. Soc. Japan **7** (1952) 549.

2) W. F. Van Paype: Physica, **5** (1938) 465.

Journal of the Physical Society of Japan Vol. 8, No. 1, Jan.—Feb., 1953

Atomic Distribution in Binary Solid Solutions
III. Diffuse Scattering of X-rays by Binary Alloys

By Terutosi Murakami

Institute of Applied Science, Faculty of Engineering,
Kyushu University

(Received July 15, 1952)

The theory of diffuse scattering of X-rays by binary alloys is developed, based on the pair distribution functions of atoms which have been given in the previous parts of this series and which are entirely similar to those appear in the theory of imperfect gases. These distribution functions enable us to perform the theoretical calculation of the distribution of the diffuse intensity of scattered X-rays due to the short range order at the temperature above the critical temperature, and the calculations are carried out both for the case of the order-disorder systems and for the two-phase separation systems. The disk-like shape of the diffuse maxima observed for Cu_3Au is predicted from this theory. And it seems that such anomalous shape does not appear in the case of two-phase separation system.

§ 1. Introduction

The different theories and experiments on the relation between the degree of order and X-ray scattering for two-component alloys have been developed, and especially the problem of propagation of order has brought much interest in this field of research, because this has important significance in the process of formation of the order in crystals. Recently Matsubara¹⁾ obtained the diffuse intensity of X-rays directly from the theory, adopting Zernike's²⁾ statistical method, and illustrated the calculated distribution of diffuse intensity as a function of reciprocal-lattice coordinates for simple cubic lattice. And Fournet³⁾ calculated the intensity of X-rays scattered by gases and liquids, using the statistical theory of fluids developed by Green⁴⁾ and Rodriguez⁵⁾ which is almost identical with Montroll and Mayer's⁶⁾ theory of imperfect gases.

Now we shall attempt to calculate the intensity distribution of scattered X-rays by partially ordered binary alloys as a function of reciprocal-lattice coordinates for the different lattice structures. For this purpose we shall utilize the expressions for the pair distribution functions obtained from the statistical method, given in parts I and II⁷⁾ of this series, which hereafter will be merely referred as I and II, respectively. And this method is favorable to the purpose of calculating the diffuse intensity because the distribution functions are expressed as the Fourier coefficients of certain simple functions. The intensity distribution obtained from our method has similar aspect that given by Matsubara for the order-disorder transition in simple cubic lattice, and in the case of face-centered cubic lattice the calculated intensity distribution has the disk-like diffuse maxima which already have been observed by the experiments on Cu_3Au alloy.⁸⁾⁹⁾¹⁰⁾

§ 2. Atomic Distribution and Scattering of X-rays

It is well known that the intensity of X-rays scattered by a crystal is expressed as follows:

$$I=I_e\sum_i\sum_j f_i f_j \exp\{2\pi i \boldsymbol{b}\cdot\boldsymbol{r}_{i,j}\}\,, \qquad (1)$$

where

$$\boldsymbol{b}=(\boldsymbol{s}-\boldsymbol{s}_0)/\lambda\,, \qquad (2)$$

$$\boldsymbol{r}_{i,j}=\boldsymbol{r}_i-\boldsymbol{r}_j\,, \qquad (3)$$

I_e is the scattering power of X-rays by one free electron, f_i and f_j are so-called atomic structure factors of atoms at the lattice points $\boldsymbol{r}_i$ and $\boldsymbol{r}_j$, respectively, λ is a wave length, and $\boldsymbol{s}_0$ and $\boldsymbol{s}$ are the unit vectors referring to the incident and reflected beams, respectively.

Now let us consider an binary alloy consisting of A and B atoms distributed over N

lattice points and let us denote the concentrations of A and B atoms by x_a and x_b, respectively. In such a system, one has only to consider two-kinds of atomic structure factors f_a and f_b referring to A and B atoms, respectively. The intensity of a scattered beam froma crystal in thermal equilibrium is given as the average values of Eq. (1) over all system of the canonical ensemble, and are given by

$$I=I_e\sum_i^N\sum_j^N<f_if_j>\exp\{2\pi i\boldsymbol{b}\cdot\boldsymbol{r}_{i,j}\}\,,\qquad(4)$$

where $<\ >$ indicates an average. These average values may be written in the following forms, in terms of the distribution function $F_{ab}(\boldsymbol{r}_{i,j})$ defined in the previous parts:

$$<f_if_j>=x_af_a^2+x_bf_b^2-x_ax_b(f_a-f_b)^2F_{ab}(\boldsymbol{r}_{i,j})\quad\text{for } i\neq j,\qquad(5)$$

$$<f_if_j>=(x_af_a+x_bf_b)^2+x_ax_b(f_a-f_b)^2\quad\text{for } i=j.\qquad(6)$$

Then I may be expressed as

$$I=I_e\Big[\sum_{i=j}^N\sum^N\{(x_af_a+x_bf_b)^2+x_ax_b(f_a-f_b)^2\}+\sum_{i\neq j}^N\sum^N\{x_af_a^2+x_bf_b^2-x_ax_b(f_a-f_b)^2\times F_{ab}(\boldsymbol{r}_{i,j})\}\exp\{2\pi i\boldsymbol{b}\cdot\boldsymbol{r}_{i,j}\}\Big]\,.\qquad(7)$$

For brevity, we introduce the parameter $\alpha(\boldsymbol{r})$ defined as

$$F_{ab}(\boldsymbol{r})=1-\alpha(\boldsymbol{r})\,,\qquad(8)$$

which is identical with Eq. (24.1) or Eq. (24.2) of II. For the present one may denote both $\alpha(\boldsymbol{r})$ and $\beta(\boldsymbol{r})$, respectively defined by Eqs. (25·1) and (25.2) of II, by a single symbol $\alpha(\boldsymbol{r})$. Then I becomes

$$I=I_e[(x_af_a+x_bf_b)^2L(\boldsymbol{b})+Nx_ax_b(f_a-f_b)^2\{1+I_D(\boldsymbol{b})\}]\,,\qquad(9)$$

where

$$L(\boldsymbol{b})=\sum_i^N\sum_j^N\exp\{2\pi i\boldsymbol{b}\cdot\boldsymbol{r}_{i,j}\}\,,\qquad(10)$$

and

$$I_D(\boldsymbol{b})=\mathbf{S}'_N(\boldsymbol{r})\alpha(\boldsymbol{r})\exp\{2\pi i\boldsymbol{b}\cdot\boldsymbol{r}\}\,.\qquad(11)$$

In Eq. (9), the first term stands for the crystalline reflection which shows the infinitely strong maxima at the reciprocal-lattice points which satisfy the Laue-Bragg condition, the second term is the uniform background arising from randomness of atomic distribution, and the third term represents the diffuse scattering intensity due to the presence of short-range order. In Eq. (11) $\mathbf{S}'_N(\boldsymbol{r})$ denotes the lattice summation excluding the origin as in the previous parts. Eq. (11) connects the short range order $\alpha(\boldsymbol{r})$ with the diffuse intensity $I_D(\boldsymbol{b})$, and the purpose of the present paper is to investigate this equation in detail.

Now let us calculate $I_D(\boldsymbol{b})$ from Eq. (11), based on the theory of atomic distribution functions developed in part II, in which the order parameter $\alpha(\boldsymbol{r})$ was given by Eq. (26.1) or (26.2).

§ 3. Diffuse Scattering from Partially Ordered System

We shall now consider a nearest neighbor system with equal concentrations, which undergoes the order-disorder transition. For such a system, order parameter $\alpha(\boldsymbol{r})$ defined by Eq. (8) may be obtained from $\beta(\boldsymbol{r})$ of Eq. (26.2) of II:

$$\alpha(\boldsymbol{r})=\frac{1}{\xi_0}\int\left[\left\{\frac{1}{\xi_0}-G(\boldsymbol{b})\right\}^{-1}-\left\{\frac{2}{\xi_0}-G(\boldsymbol{b})\right\}^{-1}\right]e^{2\pi i\boldsymbol{b}\cdot\boldsymbol{r}}d\boldsymbol{b}\,,\qquad(12)$$

where

$$\xi_0=\exp\{-\Delta\varepsilon/kT\}-1\,,\qquad(13)$$

$$\Delta\varepsilon=\frac{1}{2}(\varepsilon_{aa}+\varepsilon_{bb})-\varepsilon_{ab}\,,\qquad(14)$$

ε_{aa}, ε_{bb}, and ε_{ab} are the interaction energies between an AA, a BB and an AB contact, respectively, and $G(\boldsymbol{b})$ is given by one of Eqs. (30) of I. Some of them are of the forms:

$$G(\boldsymbol{b})=\sum_{i=1}^3\cos 2\pi h_i\quad\text{for simple cubic,}\qquad(15.\text{a})$$

$$G(\boldsymbol{b})=4\prod_{i=1}^3\cos 2\pi h_i\quad\text{for body-centered cubic,}\qquad(15.\text{b})$$

and

$$G(\boldsymbol{b})=2\sum_{i>j}^3\cos 2\pi h_i\cos 2\pi h_j\quad\text{for face-centered cubic.}\qquad(15.\text{c})$$

If we introduce $\eta_0=-1/\xi_0$, we obtain, from Eqs. (11) and (12),

$$I_D(\boldsymbol{b})=\mathbf{S}'_N(\boldsymbol{r})\alpha(\boldsymbol{r})e^{2\pi i\boldsymbol{b}\cdot\boldsymbol{r}}=I_D'(\boldsymbol{b})-\alpha_0\,,\qquad(16)$$

where

$$I_D'(\boldsymbol{b})=\eta_0^2/\{\eta_0+G(\boldsymbol{b})\}\{2\eta_0+G(\boldsymbol{b})\}\qquad(17)$$

and

$$\alpha_0=\alpha(0)=\eta_0^2\int\{\eta_0+G(\boldsymbol{b})\}^{-1}\{2\eta_0+G(\boldsymbol{b})\}^{-1}d\boldsymbol{b}.\qquad(18)$$

Using Eqs. (16), (17) and (18), one may rewrite I given by Eq. (9) in the form.

$$I=I_e[(\tfrac{1}{2}f_a+\tfrac{1}{2}f_b)^2L(\boldsymbol{b})+(N/4)(f_a-f_b)^2\times\{(1-\alpha_0)+I_D'(\boldsymbol{b})\}]\,.\qquad(19)$$

In Eq. (19) the term $(1-\alpha_0)$ corresponds to the uniform background, and the term $I_D'(\boldsymbol{b})$ represents the diffuse intensity, and only α_0 and $I_D'(\boldsymbol{b})$ are dependents of the temperature. At extremely high temperature, the crystal is completely disordered state, both of $I_D'(\boldsymbol{b})$ and α_0 may be equal to 1/2, and consequently the intensity of the order of magnitude of $(N/4)\times(f_a-f_b)^2$ may be observed as uniform background. In general it is not easy to calculate α_0 from theory, but we shall not pay attention on this quantity, because it becomes smaller as the temperature decreases. We shall here consider only the diffuse intensity $I_D'(\boldsymbol{b})$ for the different types of lattices.

(I) Simple cubic lattice

In this case $G(\boldsymbol{b})$ is given by Eq. (15.a) and Eq. (17) shows that the diffuse intensity $I_D'(\boldsymbol{b})$ has maximum at the point $h_1=h_2=h_3=1/2$, at which the superstructure reflection appears in the ordered state, and have minima at the crystalline reflections for which h_1, h_2 and h_3 are either 1 or 0. And the maximum of $I_D'(\boldsymbol{b})$ becomes sharp until it attain to infinity at the critical point $(\eta_0=3)$. Figs. 1 shows the contour plots of $I_D(\boldsymbol{b})$ in a plane of reciprocal-lattice of simple cubic lattice at the temperatures $T=1.37T_c$ and $T=1.04T_c$.

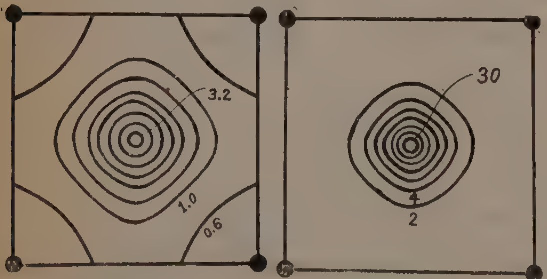

$T=1.37\,T_c$ $T=1.04\,T_c$

Fig. 1. Contour plots of $I_D(h_1, h_2, \frac{1}{2})$ at $T=1.37T_c$ and $T=1.04T_c$ for simple cubic lattice. ● crystalline reflection point.

These figures are in agreement with the ones previously presented by Matsubara[1].

(II) Body-centered cubic lattice

With the same procedure as in the case of simple cubic structure, one obtains the contour plot of $I_D(\boldsymbol{b})$ for body-centered cubic lattice at $T=1.29T_c$ as shown in Fig. 2.

(III) Face-centered cubic lattice

Since most of X-ray measurements of short range order in binary solid solutions have been made in the case of the alloys with face-centered cubic structure such as Cu_3Au. We shall consider the diffuse intensities observed in crystals of this type in detail. And for the present, we shall directly compare the observed intsities with those obtained from our theory. Substituting $G(\boldsymbol{b})$ given by Eq. (15.c) into Eq. (17), one obtains the diffuse intensity $I_D(\boldsymbol{b})$ as shown in Fig. 3. It shows that the diffuse maxima of disk-like shape appear at the positions of superlattice reflection. Fig. 4 gives the calculated distribution of the diffuse intensity in the reciprocal lattice space.

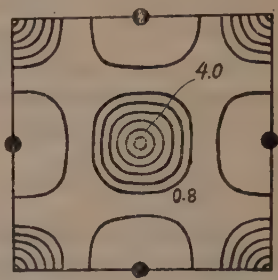

Fig. 2. Contour plot of $I_D(h_1, h_2, 1)$ for body-centered cubic lattice at $T=1.29T_c$. ● crystalline reflections.

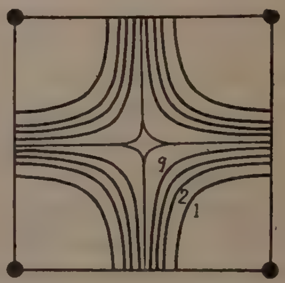

Fig. 3. Contour plot of $I_D(h_1, h_2, 0)$ for face-centered cubic lattice at $T=1.14T_c$. ● crystalline reflections.

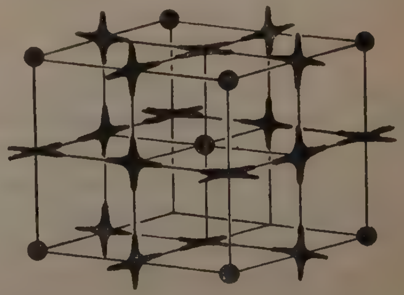

Fig. 4. Distribution of diffuse maxima of scattered intensity by face-centered cubic lattice in three-dimensional reciprocal-lattice space. ● crystalline reflections.

Although the present calculations are confined to the case of equal concentrations, the characteristic features obtained here may be retained for the case of 3:1 alloys such as Cu_3Au.

The results shown in Figs. 3 and 4 are in agreement with the experimental results obtained by Cowley⁸⁾ and other workers. For instance, Fig. 3 shows strong resemblance to the contour plot of the results of Cowley's measurements of the diffuse intensity of X-rays scattered by single crystals of Cu_3Au at 405°C, the transition temperature being 305°C*. Moreover Fig. 4 is of entirely same appearance as the figure which illustrates the distribution of the diffuse intensity from a partially ordered single crystal of Cu_3Au in the reciprocal-lattice space, measured by Guinier and Griffoul.⁹⁾ The same disk-like shape has been found for the relatively sharp super-lattice reflections from single crystals of Cu_3Au for the temperatures below the critical temperature¹⁰⁾¹¹⁾ and also found in the case of the electron diffraction.¹²⁾

§ 4. Diffuse Scattering from Two-Phase Separation Systems

In this section we shall consider the systems which separate into two-phase at the critical temperature. The pair distribution functions for such systems are approximately given by Eqs. (24.1) and (25.1) of II, and for nearest neighbor systems one obtains, from Eqs. (25.1) of II and Eq. (11),

$$I_D(\boldsymbol{b})=I_D'(\boldsymbol{b})+\beta_0-1\,, \tag{20}$$

$$I_D'(\boldsymbol{b})=\frac{\eta_0\{\eta_0+2G(\boldsymbol{b})\}}{\{\eta_0-G(\boldsymbol{b})\}\{2\eta_0+G(\boldsymbol{b})\}}\,, \tag{21}$$

$$\beta_0=\int g(\boldsymbol{b}')g(\boldsymbol{b}'-\boldsymbol{b})\left[1-\frac{4}{\{3-g(\boldsymbol{b})\}\{3+g(\boldsymbol{b})\}}\right]d\boldsymbol{b}\,, \tag{22}$$

and

$$g(\boldsymbol{b})=2\xi_0G(\boldsymbol{b})-1\,, \tag{23}$$

where ξ_0 is defined by Eq. (13), $\eta_0=-1/\xi_0$, and $G(\boldsymbol{b})$ is given by Eq. (15). Then the intensity of reflected X-rays is written as

$$I=I_e[(\tfrac{1}{2}f_a+\tfrac{1}{2}f_b)^2L(\boldsymbol{b})+(N/4)(f_a-f_b)^2 \times\{\beta_0+I_D'(\boldsymbol{b})\}]\,, \tag{24}$$

where β_0 defined by Eq. (22) gives the uniform background and $I_D'(\boldsymbol{b})$ expresses the diffuse intensity.

Since the both of $I_D'(\boldsymbol{b})$ and β_0 are equal to 1/2 at infinitely high temperature, Eq. (24) gives the ordinary Laue-Bragg reflection $(1/4)(f_a+f_a)^2L(\boldsymbol{b})$ and the uniform background $N(f_a-f_b)^2/4$. In general it is not easy to evaluate β_0, but it contributes to the diffuse intensity merely as the uniform background, and we are not interest in this part. Thus, one obtaines, from Eq. (21), the contour plots of $I_D'(\boldsymbol{b})$ as shown in Figs. 5, 6 and 7 for simple cubic, body-centered cubic, and face-centered cubic structures, respectively.

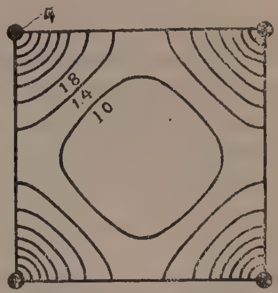

Fig. 5. Intensity of scattered X-rays from simple cubic lattice of two-phase separation type at $T=1.41T_c$. ● crystalline reflections.

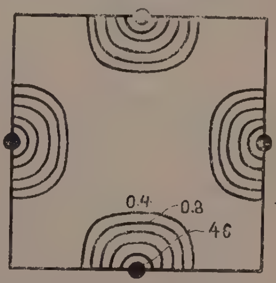

Fig. 6. Intensity of scattered X-rays from body-centered cubic lattice of two-phase separation type at $T=1.29T_c$. ● crystalline reflections.

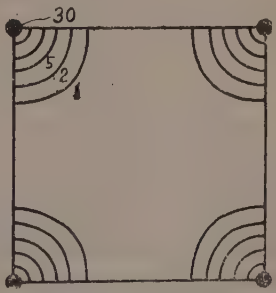

Fig. 7. Intensity of X-rays scattered from face-centered cubic lattice of two-phase separation type at $T=1.03T_c$. ● crystalline reflections.

It will be seen from these figures that for the two-phase separation systems such as

---

* See Fig. 5 of reference 8.

Pt–Au and Ni–Au alloys the maxima of diffuse intensity appear at the crystalline reflections. And these maxima becomes sharp as the temperature decreases, until they are concentrated in the points of crystalline reflection at the critical temperature, while these maxima for the order-disorder systems are concentrated in the point of superlattice reflection. And the disk-like maxima do not appear in two-phase separtion systems irrespective of lattice structure.

The author wishes to express his indebtedness to Dr. S. Ono, who suggested this research, provided valuable discussion and advice during the course of the work, and to Assistant Professor K. Kohra who provided valuable discussion especially for experimental facts.

References

1) T. Matsubara: X-rays, **5** (1949) 102 (in Japanese).
2) F. Zernike: Physica **7** (1940) 565.
3) G. Fournet: C. R. Acad. Sci., Paris **228** (1949) 1421, 1801; **229** (1949) 1071; Acta Cryst. **4** (1951) 293; Thése, Paris (1951).
4) H. S. Green: Proc. Roy. Soc. **A 189** (1947) 103.
5) A. E. Rodriguez: Proc. Roy. Soc. **A 196** (1949) 73.
6) E. W. Montroll & J. E. Mayer: J. Chem. Phys., **8** (1941) 626.
7) T. Murakami: J. Phys. Soc. Japan **7** (1952) 549; **8** (1953) 36.
8) J. M. Cowley: J. Appl. Phys. **21** (1950) 24.
9) A. Guinier & R. Griffoul: Revue de Metallugie **45** (1948) 387.
10) B. Strijk & C. H. MacGillavry: Physica **12** (1946) 129.
11) I. G. Edumunds, R. M. Hinde & H. Lipson: Nature **160** (1947) 305.
12) H. Reather: Acta Cryst. **4** (1951) 70.

JOURNAL OF THE PHYSICAL SOCIETY OF JAPAN Vol. 8, No. 1, JAN.—FEB., 1953

On the Valence Theory of the Methyl Radical

By Takashi ITOH, Kimio OHNO and Masao KOTANI

Department of Physics, Faculty of Science, University of Tokyo, Tokyo, Japan

(Received September 20, 1952)

The electronic structure of the ground state of CH_3 is investigated by the Heitler-London-Slater-Pauling method extended by Voge and Kotani and Siga. The wave functions are constructed without assuming the electron pair bond and taking $(2s)^2(2p)^2$, $(2s)(2p)^3$ and $(2p)^4$ configurations of the carbon atom into account. Assuming a pyramidal model for this radical, seventeen $^2A_1$ states are obtained. The energy matrix for these states is computed by means of the representation matrices of the symmetric group. Solving the secular equation thus obtained for various values of the apex angle, the most stable configuration is found to be slightly nonplanar. The electron pair bond approximation is shown to be fairly good in the cases when $\angle HCH = 120°$ and $109.5°$ (sp^2 and sp^3 hybridization), but it becomes very poor for $\angle HCH = 90°$ (pure p bond).

§1. Introduction

In the Heitler-London-Slater-Pauling (HLSP) theory of molecular structure, the CH bonds are usually discussed by assigning each of them a localized electron pair bond, between the 1*s* orbital of H and some hybridized orbital of C. For example, in the case of the methane molecule, tetrahedral orbitals obtained by the so-called sp^3 hybridization are used to form four bonds with hydrogen atoms. The method of electron pair bonds (e.p.b.) is, however, open to criticism, mainly on the following grounds:

(1) The e.p.b. approximation aims to lower the interatomic energy by choosing orbitals such as to maximize the absolute value of bonding exchange integrals, but it does not duly take the intratomic promotional energies into account.

(2) As a consequence, it is not capable of representing the correspondence to the states of dissociated atoms correctly. For example, according to e.p.b. picture the carbon atom in the methane molecule is in the so-called valence state independently of the C–H distance, which is a certain mixture of various L, S states belonging to $(2s)^2(2p)^2$, $(2s)(2p)^3$ and $(2p)^4$ configurations. However, the due consideration of these intratomic energies is of vital importance to the molecular theory, as Moffitt[1] has emphasized recently.

(3) Even when we adopt the e.p.b. approximation, the choice of the best set of hybridized orbitals is often not without ambiguity. For example, in interpreting the C=C bond of the ethylene, one might assume either tetrahedral orbitals or sp^2 trigonal orbitals plus pure $p\pi$ orbitals.

In order to investigate these problems, it is desirable to calculate the energies and the eigenfunctions of simple hydrocarbons by a more general method which is not subject to the limitation of e.p.b.. For this purpose we proceed as follows.

On the assumption that all ionic structures can be disregarded, let us enumerate all possible configurations obtained by putting four valence electrons of each carbon atom into its four 2-quantum orbitals in different ways. If we take into account all the group-theoretically possible states with proper symmetry of the whole molecule arising from all these configurations, we have a N (say) dimensional subspace of the Hilbert space for our molecule, and the best approximation to the energy and the eigenfunction of the ground state of the molecule will be obtained by solving the N-dimensional secular equation. Since all states describable in terms of e.p.b. are represented by certain ψ-vectors in this subspace, our method is evidently a generalization of the e.p.b. method. Moreover, since our method is invariant against any unitary transformation of the 4 orbitals of the carbon atom, we have no more to worry about the choice of hybridized orbitals. This method shall be called as the generalized Heitler-London method (G.H.L.).

Now, we have already a few works along this line. Voge[2] and Kotani-Siga[3] studied independently the electronic structure of the methane molecule on this method, while Kotani[4] made a preliminary study of the water molecule in a similar way. According to their results, the energy of the ground state is depressed by about 1.3 eV in the case of CH_4 and by about 0.5 eV in the case of H_2O, as compared with the e.p.b. approximation. Although these figures are not very large, there is a partial cancellation between intratomic and interatomic energies; there is a lowering of 2.6 eV of the promotional energy of the C atom in CH_4 resulting from the abandonment of e.p.b. limitation.

In the present paper, similar calculations will be made for CH_3. We assume the triangular pyramidal form for this molecule, and calculate the energy of the molecule in dependence on the apex angle of the pyramid. The reason why we carry out these rather troublesome study is two-fold: Firstly, the bonding power of hybridized orbitals can be studied in dependence on the degree of hybridization and the best degree of hybridization can be found as a function of the apex angle. These studies will throw some light on the nature of e.p.b and hybridization. Secondly, we may hope to determine whether the most stable form of the radical is planar or pyramidal. Although CH_3 is usually regarded as planar, it is not yet confirmed experimentally, and so a more detailed theoretical study of its shape would be of some interest.

§2. Basic Wave Functions

The rectangular coordinate system is taken in such a way that the C nucleus and the three H nuclei H_a, H_b, H_c have coordinates $(0, 0, 0)$, $(R\sin\theta, 0, R\cos\theta)$, $(-\frac{1}{2}R\sin\theta, \frac{1}{2}\sqrt{3}R\sin\theta, R\cos\theta)$, $(-\frac{1}{2}R\sin\theta, -\frac{1}{2}\sqrt{3}R\sin\theta, R\cos\theta)$ respectively, where θ is the angle between each CH bond and the symmetry axis of the radical. The ground state of the radical is $^2A_1$, so that $^2A_1$ part of the energy matrix is to be constructed in the present study. The number of basic $^2A_1$ wave functions may be found as follows. First, we divide the radical into two "zones" C and H_3. The central zone which consists of the single carbon atom, has a spherical symmetry, but its atomic states can be reduced as the representation of C_{3v}. The correspondence is as follows:[5]

$$S = A_1,\quad P = A_2 + E,\quad D = A_1 + 2E,$$
$$S^\circ = A_2,\quad P^\circ = A_1 + E,\quad D^\circ = A_2 + 2E,$$

where S, P, D denote the atomic states of even parity, and $S^\circ, P^\circ, D^\circ$ denote those of odd parity. The H_3 "zone" gives ^2E and $^4A_2$,[6] if all H atoms are in the normal state. Combining these two zones, it is found that each of sp^3 $^3S^\circ$, $^5S^\circ$, $^1P^\circ$, $^3P^\circ$ states of the carbon atom gives rise to one $^2A_1$ state of CH_3, each of s^2p^2 ^1D, ^3P, sp^3 $^1D^\circ$, p^4 ^1D, ^3P two, and sp^3 $^3D^\circ$ three. Thus there are seventeen $^2A_1$ states in all.

The wave functions can be constructed by the method of Serber[7], Yamanouchi[8] and Kotani[3]. First we build up the wave functions of the "zone" H_3. We denote by μ the spin multiplicity of this zone. The orbital functions for each multiplicity are bases of a definite irreducible representation of the symmetric group $\mathfrak{S}_3$. We denote by $U_{\mu;mn}(Q)$ the m, n matrix element for the permutation Q in the irreducible representation corresponding to spin multiplicity μ. Denoting by f_μ the dimension of the representation U_μ, we construct the wave function of H_3 zone

$$\Phi_{\mu;mn} = \sqrt{\frac{f_\mu}{3!}}\sum U_{\mu;mn}(Q)Q\psi_a(6)\psi_b(7)\psi_c(8), \tag{1}$$

where ψ_a, ψ_b, ψ_c denote the 1s orbitals of three hydrogen atoms H_a, H_b, H_c respectively, and 6, 7, 8 denote the positional coordinates of three electrons. The numbering 6, 7, 8 is used for convenience. These wave functions belong to the spin multiplicity μ, since, when permutation Q is applied to electrons, they are transformed by the matrix $U_\mu(Q)$ with respect to the index n. Further, if permutation Q is applied to orbitals, they are transformed by the matrix $U_\mu(Q)$ with respect to the index m. Thus they may also be regarded as the representation of the point group C_{3v}. The explicit forms of $U_\mu(Q)$'s are given in the footnote*, and it can be seen that $\Phi_{\mu;mn}$'s are ^2E for $\mu=2$ and $^4A_2$ for $\mu=4$.

In the same way, we can construct the wave functions of the C "zone"

$$\Phi^{C,\alpha}_{\kappa;kl}=\sqrt{\frac{f_\kappa}{2^{\eta_\alpha}4!}}\sum_P U_{\kappa;kl}(P)P\psi_{\alpha_1}(1)$$
$$\times\psi_{\alpha_2}(2)\psi_{\alpha_3}(3)\psi_{\alpha_4}(4)\ ^{**},\quad(2)$$

where $\alpha_1\alpha_2\alpha_3\alpha_4$ are a set of orbitals taken from the available orbitals $2s$, $2p_x$, $2p_y$ and $2p_z$, and η_α is the number of orbitals in that set which are occupied by two electrons. These functions belong to a definite multiplicity κ, and appropriate linear combinations of them

$$\Phi^{C}_{\kappa\mu;h,l}=\sum_{k,\alpha}c_{\kappa\mu h;k\alpha}\Phi^{C,\alpha}_{\kappa;kl}\qquad(3)$$

will form the bases of irreducible representations of C_{3v}. The coefficients $c_{\kappa\mu h;k\alpha}$ in the above expression can be determined by actually examining the transformation properties of $\Phi^{C,\alpha}_{\kappa;kl}$.

Construction of the $^2A_1$ wave functions of the whole system CH_3 proceeds as follows: We denote by $W_{pq}(S)$ the irreducible representation of the symmetric group $\mathfrak{S}_7$ corresponding to the doublet state. It is given explicitly in Appendix I, and is reduced with respect to the subgroup $\mathfrak{S}_4\times\mathfrak{S}_3$. Thus, for any element of the subgroup $S=PQ(P\in\mathfrak{S}_4, Q\in\mathfrak{S}_3)$,

$$W_{pq}(S)=W_{\kappa\mu km,\lambda\nu ln}(PQ)$$
$$=\delta_{\kappa\lambda}\delta_{\mu\nu}U_{\kappa;kl}(P)U_{\mu;mn}(Q).\quad(4)$$

The doublet functions of CH_3 can be written as

$$\Psi^{\alpha}_{\kappa\mu km,q}=\sqrt{\frac{14}{2^{\eta_\alpha}7!}}\sum W_{\kappa\mu km,q}(S)S\psi_{\alpha_1}(1)$$
$$\times\psi_{\alpha_2}(2)\psi_{\alpha_3}(3)\psi_{\alpha_4}(4)\psi_a(6)\psi_b(7)\psi_c(8).\quad(5)$$

Using the same coefficients $c_{\kappa\mu h;k\alpha}$ as defined above, we finally obtain the $^2A_1$ wave functions of CH_3 by the expression

$$\Psi_{\kappa\mu,q}=\sqrt{\frac{1}{f_\mu}}\sum_{k,\alpha,h}c_{\kappa\mu h;k\alpha}\Psi^{\alpha}_{\kappa\mu kh,q}.\qquad(6)$$

These functions are given explicitly in Appendix II.

The hybridized orbitals used in the e.p.b. function are as follows:

$$\left.\begin{aligned}\psi_1&=\sqrt{1-2\cot^2\theta'}\,\psi_{2z}-\sqrt{2}\cot\theta'\,\psi_{2s}\\ \psi_2&=\sqrt{\tfrac{2}{3}}\,\text{coses}\,\theta'\,\psi_{2\sigma_a}+\sqrt{\tfrac{1}{3}-\tfrac{2}{3}\cot^2\theta'}\,\psi_{2s}\\ \psi_3&=\sqrt{\tfrac{2}{3}}\,\text{cosec}\,\theta'\,\psi_{2\sigma_b}+\sqrt{\tfrac{1}{3}-\tfrac{2}{3}\cot^2\theta'}\,\psi_{2s}\\ \psi_4&=\sqrt{\tfrac{2}{3}}\,\text{cosec}\,\theta'\,\psi_{2\sigma_c}+\sqrt{\tfrac{1}{3}-\tfrac{2}{3}\cot^2\theta'}\,\psi_{2s}\end{aligned}\right\}\quad(7)$$

ψ_2, ψ_3, ψ_4 are equivalent orbitals, with their charge cloud extending along three straight lines which make an angle θ' with the symmetry axis of the radical. For the time being we take the angle θ' equal to θ, i.e. we use the hybridized orbitals whose charge cloud project just to the directions of CH. This choice will be criticized later.

With these hybridized orbitals, the wave function of e.p.b. state can be expressed as a linear combination of the above functions. The coefficients for this linear combination are also given in Appendix II. For details of the method, readers are referred to the paper by Kotani and Siga.³⁾

§ 3. Energy Matrix

The elements of the energy matrix are computed by the formula

$$\int\Psi^{\alpha}_{p,q}H\Psi^{\beta}_{r,q}d\tau=\frac{1}{\sqrt{2^{\eta_\alpha+\eta_\beta}}}\sum_S W_{p,r}(S)$$
$$\times\int(S\Psi^{\alpha})H\Psi^{\beta}d\tau\qquad(8)$$

$$\Psi^{\alpha}=\psi_{\alpha_1}(1)\psi_{\alpha_2}(2)\psi_{\alpha_3}(3)\psi_{\alpha_4}(4)\psi_a(6)\psi_b(7)\psi_c(8)$$
$$\Psi^{\beta}=\psi_{\beta_1}(1)\psi_{\beta_2}(2)\psi_{\beta_3}(3)\psi_{\beta_4}(4)\psi_a(6)\psi_b(7)\psi_c(8).$$

Explicit forms of $W_{p,r}(S)$'s are given in Appendix I.

In constructing these matrix elements, we have neglected the non-orthogonality integrals between atomic orbitals belonging to different atoms, except that we take these integrals into account in the numerical values of the exchange integrals. The result is given in Appendix III. It is true that the non-

---

* The matrices used here are taken in real and orthogonal forms.

$$\mu=2\quad U((12))=\begin{pmatrix}-\frac{1}{2} & \frac{\sqrt{3}}{2}\\ \frac{\sqrt{3}}{2} & \frac{1}{2}\end{pmatrix}\quad U((23))=\begin{pmatrix}1 & 0\\ 0 & -1\end{pmatrix}$$

$$\mu=4\quad U((12))=\ (-1)\qquad U((23))=\ (-1).$$

**

$$\kappa=1\quad U((12))=\begin{pmatrix}1 & 0\\ 0 & -1\end{pmatrix}\quad U((34))=\begin{pmatrix}1 & 0\\ 0 & -1\end{pmatrix}$$

$$U((13))=\begin{pmatrix}-\frac{1}{2} & -\frac{\sqrt{3}}{2}\\ -\frac{\sqrt{3}}{2} & \frac{1}{2}\end{pmatrix}$$

$$\kappa=3\quad U((12))=\begin{pmatrix}-1 & 0 & 0\\ 0 & 1 & 0\\ 0 & 0 & -1\end{pmatrix}\quad U((34))=\begin{pmatrix}-1 & 0 & 0\\ 0 & -1 & 0\\ 0 & 0 & 1\end{pmatrix}$$

$$U((13))=\begin{pmatrix}0 & \sqrt{\frac{1}{2}} & \sqrt{\frac{1}{2}}\\ \sqrt{\frac{1}{2}} & -\frac{1}{2} & \frac{1}{2}\\ \sqrt{\frac{1}{2}} & \frac{1}{2} & -\frac{1}{2}\end{pmatrix}$$

$$\kappa=5\quad U((12))=(-1)\quad U((34))=(-1)\quad U((13))=(-1).$$

orthogonality integrals are often fairly large, and far from being neglegible if taken individually, but according to our experiences in the calculation of molecular energies we obtain rather surprisingly good results by this simplified procedure especially when we use the semi-empirical values for intermolecular integrals. Considering that this "neglect of non-orthogonality" means considerable saving of labour, we have decided to adopt this approximation in the present paper. In this sense our calculation might be regarded as semi-empirical, or "quarter-empirical" at most. The values in eV of atomic and molecular integrals used are as follows:

$F^\circ(s,s)=17.82$ $F^\circ(s,p)=16.07$ $F^\circ(p,p)=14.75$
$G^1(s,p)=2.18$ $F^2(p,p)=0.188$ $I_p-I_s=12.79$

$M_{ss}=0.6333$ $M_{\sigma\sigma}=2.036$
$N_{ss}=2.0$ $N_{\sigma\sigma}=2.25$
$M_{\pi\pi}=-0.0686$ $M_{s\sigma}=1.708$
$N_{\pi\pi}=-0.6$ $N_{s\sigma}=1.69.$

The notations are due to Slater[9] (F, G, I) and Van Vleck and Sherman[10] (M, N). The values of F's, $G^1(s,p)$ and I_p-I_s are taken from Van Vleck's paper.[11] The coulomb integrals $M_{ss}, M_{\sigma\sigma}, M_{\pi\pi}, M_{s\sigma}$ are obtained from Kotani-Amemiya's table[12] by interpolation using the C–H internuclear distance 1.09 Å and the carbon effective charge 3.18. $N_{ss}, N_{\sigma\sigma}, N_{\pi\pi}$ are arithmetical means of Van Vleck's[13] and Penney's[14] $N_{ss}, N_{\sigma\sigma}, N_{\pi\pi}$, and $N_{s\sigma}$ is assumed to be 1.69 following Voge[2]. The coulomb and exchange integrals between hydrogen atoms are denoted by K_{hh} and J_{hh}. They are, as usual, assumed to be 1/10 and 9/10 of the Morse function respectively.

The secular equation is of the seventeenth degree. We have solved it by the iteration method. It was solved for $\theta=90°$ (the plane model), $\theta \doteqdot 80°$ ($\sin^2\theta=0.97$), $\theta \doteqdot 70.5°$ (the tetrahedral model), $\theta=60°$, $\theta \doteqdot 54.7°$ (the right-angled model), and $\theta=45°$.

§ 4. Results of Calculation

The electronic energy of the ground state is given in Table I for various values of θ and illustrated by curves 1 (G.H.L.) and 2 (e.p.b.) in Fig. 1, from which we can see that the methyl radical is most stable at $\theta \doteqdot 80°$, although the plane model is most stable according to the e.p.b. approximation. This was verified further by the calculation of the

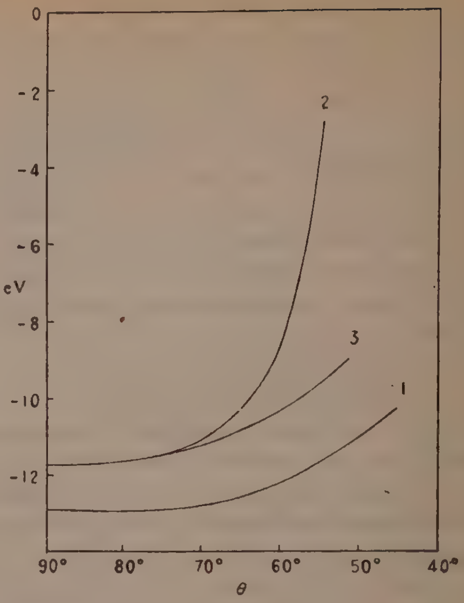

Fig. 1. Electronic Energies of the Ground State of CH_3.
curve 1: G.H.L. method,
curve 2: e.p.b. approximation ($\theta'=\theta$),
curve 3: e.p.b. approximation ($\theta' \neq \theta$).

derivative of the energy with respect to θ. The calculated dissociation energy from the potential minimum 12.97 eV is in fair agreement with one of the semi experimentally determined values 13.12 eV.[15] But there is some uncertainty in the latter value and also there are some questions in our calculation, for example, about the neglect of overlap integrals and of ionic structures and about the choice of the empirical parameters, so the above agreement is fortuitous.

The e.p.b. approximation is fairly good for the plane and tetrahedral models as seen from Table I, but it becomes very poor for the right-angled model. Further, for $\theta<54.7°$ the e.p.b. becomes impossible. But the complete solution changes gradually over the whole region of θ.

The promotional energy of the carbon atom and the wave function of the ground state by G.H.L. method and the e.p.b. approximation are given in Table II and Table III respectively. Here the e.p.b. approximation is not so good even in the plane and tetrahedral models. The contributions of s^2p^2, sp^3 and p^4 configurations of C are shown in Table IV, in which the results for the CH molecule are also given for the sake of comparison.

Table I. Binding Energy (in eV)

θ	G.H.L. method	e.p.b. approx.
90°	12.938	11.729
80°	12.970	11.647
70.5°	12.857	11.175
60°	12.247	8.725
54.7°	11.699	2.811
45°	10.281	—

Table II. Promotional Energy of Carbon Atom (in eV)

θ	G.H.L. method	e.p.b. approx.
90°	4.3	7.2
80°	4.0	7.1
70.5°	3.8	7.0
60°	3.6	7.5
54.7°	3.6	8.5
45°	3.6	—

Table III. Squares of Coefficients of G.H.L. Wave Function (and of e.p.b. Approximation)

No. of the eigenfunction	parent state of the carbon atom	$\theta=90°$	$\theta=80°$	$\theta=70.5°$	$\theta=60°$	$\theta=54.7°$	$\theta=45°$
1	$s^2p^2\,{}^1D$	000 (000)	017 (005)	042 (016)	062 (019)	071 (000)	089 (—)
2	${}^1D$	096 (042)	090 (039)	081 (031)	070 (014)	065 (000)	053 (—)
3	${}^3P$	298 (125)	285 (117)	269 (094)	265 (042)	270 (000)	303 (—)
4	${}^3P$	000 (000)	027 (015)	060 (047)	070 (056)	066 (000)	049 (—)
5	$sp^3\,{}^3P^0$	000 (000)	000 (000)	000 (000)	000 (000)	000 (000)	001 (—)
6	${}^1P^0$	000 (000)	000 (000)	000 (000)	000 (000)	000 (000)	001 (—)
7	${}^3D^0$	000 (000)	017 (015)	049 (063)	085 (167)	102 (250)	123 (—)
8	${}^3D^0$	128 (125)	124 (125)	121 (125)	125 (125)	129 (125)	143 (—)
9	${}^3D^0$	106 (167)	088 (147)	058 (094)	031 (019)	021 (000)	009 (—)
10	${}^1D^0$	000 (000)	003 (005)	007 (021)	012 (056)	013 (083)	014 (—)
11	${}^1D^0$	028 (042)	021 (032)	011 (010)	003 (005)	001 (042)	000 (—)
12	${}^5S^0$	273 (313)	261 (313)	244 (313)	227 (313)	216 (313)	178 (—)
13	${}^3S^0$	009 (021)	005 (012)	001 (000)	000 (058)	000 (188)	001 (—)
14	$p^4\,{}^1D$	000 (000)	002 (005)	004 (016)	007 (019)	008 (000)	009 (—)
15	${}^1D$	015 (042)	013 (039)	011 (031)	008 (014)	007 (000)	005 (—)
16	${}^3P$	048 (125)	043 (117)	034 (094)	025 (042)	022 (000)	016 (—)
17	${}^3P$	000 (000)	003 (015)	007 (047)	009 (056)	009 (000)	007 (—)

Table IV. Contributions of s^2p^2, sp^3 and p^4 configurations (values in parentheses are those of e.p.b. approximation)

	θ	s^2p^2	sp^3	p^4
CH_3	90°	0.39 (0.17)	0.54 (0.67)	0.06 (0.17)
	80°	0.42 (0.18)	0.52 (0.65)	0.06 (0.18)
	70.5°	0.45 (0.19)	0.49 (0.63)	0.06 (0.19)
	60°	0.47 (0.13)	0.48 (0.74)	0.05 (0.13)
	54.7°	0.47 (0.00)	0.48 (1.00)	0.05 (0.00)
	45°	0.49 (—)	0.47 (—)	0.04 (—)
CH_4*		0.41 (0.19)	0.52 (0.63)	0.07 (0.19)

* The figures for CH_4 are the average of two values obtained by Voge[2)] for two different sets of parameters.

§ 5. Discussion

According to the results given in the preceding section, the approximation of e.p.b. is fairly good for the values of θ between 90° and 70.5°, and the energy difference between this approximation and the complete solution is only 1.3 eV at $\theta=80°$ (the most stable configuration). This is equal to the corresponding value in CH_4.

For the promotional energy and the wave function, however, the e.p.b. approximation is not so good, as already pointed out by Voge[2)] and Kotani.[4)] Since the e.p.b. approximation lowers only interatomic energies, and gives too high intratomic energies, it tends to contain too much p^4 configuration and too little s^2p^2 configuration of the carbon atom. This may be clearly seen by Table IV, in which the contributions of s^2p^2, sp^3 and p^4 configurations of the carbon atom are shown, both in our method and by e.p.b. one. In the same table are listed also the results obtained by Voge for the methane molecule, which are very similar to ours for the methyl radical.

As noted in the preceding section, the e.p.b. approximation becomes very poor at the right-angled model. This may be explained as follows: In this case, C–H bonds become pure p-bonds (in the e.p.b. approximation), and so the coefficient of $N_{s\sigma}$ in the expression for the energy of the e.p.b. state vanishes, while this term is about -7 eV for the plane and tetrahedral models. This difference is the main source for the above fact, and this indicates the importance of the s-p hybridization.

Taking these considerations into account, we examined the use of e.p.b. function whose parameter θ' is not equal to θ. Since the bonding power of hybridized orbitals is weakened appreciably with the decrease of θ', the best results within the frame of e.p.b. will be obtained by taking θ' somewhat larger than θ. This is made plausible if we calculate the scalar product

$$\int \Psi^*_{\text{e.p.b.}}(\theta', \theta)\Psi(\theta)dv\,, \qquad (9)$$

in which $\Psi(\theta)$ is the "best" function and $\Psi_{\text{e.p.b.}}(\theta', \theta)$ is the e.p.b. function with hybrization parameter θ', θ indicating the positions of H atoms. From the curve 1 of Fig. 2 which shows this quantity for $\theta \doteqdot 54.7°$ as a function of θ', we can see clearly that $\Psi(\theta)$ resembles more to $\Psi_{\text{e.p.b.}}(\theta', \theta)$ with $\theta'=67°$ than to $\Psi_{\text{e.p.b.}}(\theta, \theta)$. Curve 2 of the same figure represents the absolute value of the binding energy of the state $\Psi_{\text{e.p.b.}}(\theta', \theta)$. These two curves are remarkably similar, and show clearly that θ' should be taken as $\approx 68°$ to obtain the best result, if we adopt the e.p.b. approximation at all.

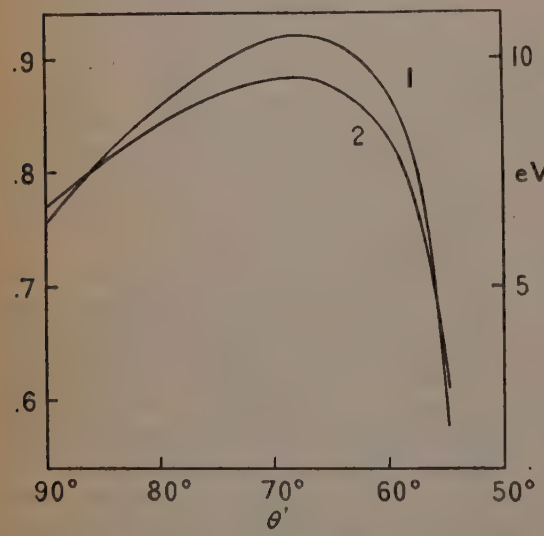

Fig. 2. Scalar Product (9) (curve 1) and the Electronic Energy of the e.p.b. Function $\Psi_{\text{e.p.b.}}(\theta', \theta)$ (curve 2) in the Case of $\theta=54.7°$.

We have made the similar calculations for other values of θ. The best values of θ' for which the scalar product (9) and the binding energy takes the maximum value in absolute magnitude, are functions of θ, and are illustrated by curves 1 and 2 of Fig. 3, respectively. These two curves are also very similar, and show that θ' coincides with θ for $\theta=90°$, and decreases with the decrease of θ but somewhat more showly than the latter.

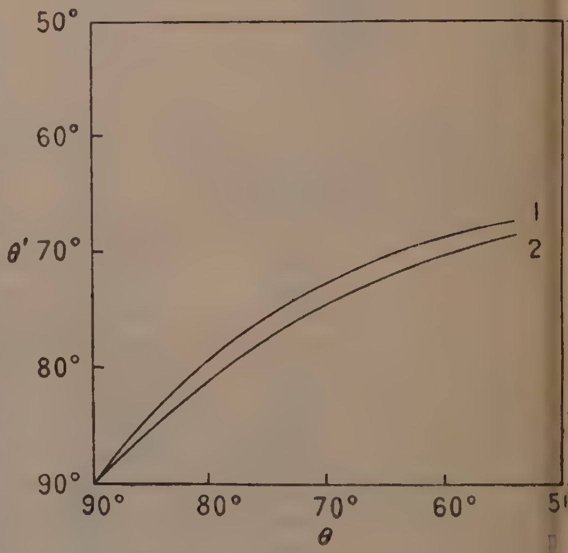

Fig. 3. Best Values of θ'.
Curve 1 shows the value of θ' which maxmizes the scalar product (9).
Curve 2 shows the same quantity which maxmizes the electronic energy of the e.p.b. function.

The maximum values of binding energy of $\Psi_{\text{e.p.b.}}(\theta', \theta)$ are illustlated by curve 3 in Fig. 1 as a function of θ. We can see that it coincides with curve 2($\theta'=\theta$) at $\theta=90°$, but it is as much as 6.8 eV lower than curve 2 at $\theta=54.7°$. Thus the use of $\Psi_{\text{e.p.b.}}(\theta', \theta)$ yields a great stabilization as compared with $\Psi_{\text{e.p.b.}}(\theta, \theta)$ for $\theta<60°$ as was expected.

As to the shape of the methyl radical, there is no definite experimental data at present, but some theoretical presumptions have been made about it. First Penney showed that the plane model is more stable than the tetrahedral model by about 0.7 eV using the e.p.b. approximation.[14] Voge also showed that the plane model is more stable than the right-angled model by 3 eV solving the secular equation of the fourth degree[2]. But these authors did not examined the other models in deail, so their results must not be considered as ontradictory to our result that the most stable onfiguration is slightly non-planar ($\theta=80°$). The recent study of Linnett and Poë indicates hat $\angle$HCH is between 109.5° and 116.5°.[16]) But the double minimum will be not so pronounced as in NH_3, since the potential barrier height is only 1/8 of that in NH_3. Accordingly, the structure of vibrational levels would be rather close to the single minimum case.

APPENDIX I. The Irreducible Representation of $\mathfrak{S}_7$ Corresponding to the Doublet State

The doublet state of seven electron system can be obtained from the singlet state of eight lectron system by removing any one electron from the latter. Thus the irreducible representation f $\mathfrak{S}_7$ corresponding to the doublet state is the same as the irreducible representation of $\mathfrak{S}_8$ corresponding to the singlet state. Now the latter is given explicitly in Serber's paper[17]) and we here emove the fifth electron, for convenience, to obtain the former. Further, in order to reduce it vith respect to $\mathfrak{S}_4\times\mathfrak{S}_3$, we transform it by a transformation T according to $W(S)=T^{-1}U(S)T$, vhere $U(S)$ denotes Serber's matrix and T is given as follows.

$$T=\begin{array}{c|cccccccccccccc}
 & 1211 & 1212 & 1221 & 1222 & 3211 & 3212 & 3411 & 3221 & 3222 & 3421 & 3231 & 3232 & 3431 & 5411 \\
\hline
1 & 0 & 0 & 0 & 0 & 0 & 0 & 0 & 0 & 0 & 0 & 0 & 0 & 0 & 1 \\
2 & 0 & 0 & 0 & 0 & 0 & -\sqrt{\frac{2}{3}} & \sqrt{\frac{1}{3}} & 0 & 0 & 0 & 0 & 0 & 0 & 0 \\
3 & 0 & 0 & 0 & 0 & 0 & 0 & 0 & 0 & 0 & 0 & 0 & \sqrt{\frac{2}{3}} & -\sqrt{\frac{1}{3}} & 0 \\
4 & 0 & 0 & 0 & 0 & 0 & 0 & 0 & 0 & -\sqrt{\frac{2}{3}} & \sqrt{\frac{1}{3}} & 0 & 0 & 0 & 0 \\
5 & 0 & 0 & 0 & 1 & 0 & 0 & 0 & 0 & 0 & 0 & 0 & 0 & 0 & 0 \\
6 & 0 & -1 & 0 & 0 & 0 & 0 & 0 & 0 & 0 & 0 & 0 & 0 & 0 & 0 \\
7 & 0 & 0 & 0 & 0 & 0 & \sqrt{\frac{1}{3}} & \sqrt{\frac{2}{3}} & 0 & 0 & 0 & 0 & 0 & 0 & 0 \\
8 & 0 & 0 & 0 & 0 & 0 & 0 & 0 & 0 & 0 & 0 & 0 & -\sqrt{\frac{1}{3}} & -\sqrt{\frac{2}{3}} & 0 \\
9 & 0 & 0 & 0 & 0 & 0 & 0 & 0 & 0 & \sqrt{\frac{1}{3}} & \sqrt{\frac{2}{3}} & 0 & 0 & 0 & 0 \\
10 & 0 & 0 & 0 & 0 & 1 & 0 & 0 & 0 & 0 & 0 & 0 & 0 & 0 & 0 \\
11 & 0 & 0 & 0 & 0 & 0 & 0 & 0 & 0 & 0 & 0 & -1 & 0 & 0 & 0 \\
12 & 0 & 0 & 0 & 0 & 0 & 0 & 0 & 1 & 0 & 0 & 0 & 0 & 0 & 0 \\
13 & 0 & 0 & -1 & 0 & 0 & 0 & 0 & 0 & 0 & 0 & 0 & 0 & 0 & 0 \\
14 & 1 & 0 & 0 & 0 & 0 & 0 & 0 & 0 & 0 & 0 & 0 & 0 & 0 & 0
\end{array}$$

APPENDIX II. Wave Functions

No. of the Eigenfunction	Parent State of the Carbon Atom	$^2A_1$ Wave Function of CH_3	Coefficient for e.p.b. Wave Function
1	$s^2p^2\ {}^1D$	$\frac{1}{2}\Psi^{xxss}_{1211,q}-\frac{1}{2}\Psi^{yyss}_{1211,q}-\sqrt{\frac{1}{2}}\Psi^{xyss}_{1212,q}$	$-\sqrt{\frac{1}{6}}\sqrt{1-2\cot^2\theta}\cot\theta$
2	〃 ^1D	$\sqrt{\frac{1}{2}}\Psi^{xzss}_{1211,q}+\sqrt{\frac{1}{2}}\Psi^{yzss}_{1212,q}$	$\frac{1}{2}\sqrt{\frac{1}{6}}\sqrt{1-2\cot^2\theta}$
3	〃 ^3P	$\sqrt{\frac{1}{2}}\Psi^{xzss}_{3231,q}+\sqrt{\frac{1}{2}}\Psi^{yzss}_{3232,q}$	$\frac{1}{2}\sqrt{\frac{1}{2}}\sqrt{1-2\cot^2\theta}$
4	〃 ^3P	$-\Psi^{xyss}_{3431,q}$	$-\sqrt{\frac{1}{2}}\sqrt{1-2\cot^2\theta}\cot\theta$
5	$sp^3\ {}^3P^0$	$\frac{1}{2}\Psi^{yyxs}_{3221,q}+\frac{1}{2}\Psi^{zzxs}_{3221,q}+\frac{1}{2}\Psi^{xxys}_{3222,q}+\frac{1}{2}\Psi^{zzys}_{3222,q}$	0
6	〃 $^1P^0$	$\frac{1}{2}\Psi^{yyxs}_{1211,q}+\frac{1}{2}\Psi^{zzxs}_{1211,q}+\frac{1}{2}\Psi^{xxys}_{1212,q}+\frac{1}{2}\Psi^{zzys}_{1212,q}$	0
7	〃 $^3D^0$	$\frac{1}{2}\Psi^{yyxs}_{3221,q}-\frac{1}{2}\Psi^{zzxs}_{3221,q}+\frac{1}{2}\Psi^{xxys}_{3222,q}-\frac{1}{2}\Psi^{zzys}_{3222,q}$	$-\sqrt{\frac{1}{2}}\cot\theta$
8	〃 $^3D^0$	$\frac{1}{2}\Psi^{xxzs}_{3221,q}-\frac{1}{2}\Psi^{yyzs}_{3221,q}-\sqrt{\frac{1}{2}}\Psi^{xyzs}_{3222,q}$	$\frac{1}{2}\sqrt{\frac{1}{2}}$
9	〃 $^3D^0$	$\sqrt{\frac{2}{3}}\Psi^{xyzs}_{3411,q}+\sqrt{\frac{1}{3}}\Psi^{xyzs}_{3431,q}$	$-\sqrt{\frac{1}{6}}(1-2\cot^2\theta)$
10	〃 $^1D^0$	$\frac{1}{2}\Psi^{yyxs}_{1211,q}-\frac{1}{2}\Psi^{zzxs}_{1211,q}+\frac{1}{2}\Psi^{xxys}_{1212,q}-\frac{1}{2}\Psi^{zzys}_{1212,q}$	$\sqrt{\frac{1}{6}}\cot\theta$
11	〃 $^1D^0$	$\frac{1}{2}\Psi^{xxzs}_{1211,q}-\frac{1}{2}\Psi^{yyzs}_{1211,q}-\sqrt{\frac{1}{2}}\Psi^{xyzs}_{1212,q}$	$\frac{1}{2}\sqrt{\frac{1}{6}}(1-4\cot^2\theta)$
12	〃 $^5S^0$	$\Psi^{xyzs}_{5411,q}$	$\frac{\sqrt{5}}{4}$
13	〃 $^3S^0$	$\sqrt{\frac{1}{3}}\Psi^{xyzs}_{3411,q}-\sqrt{\frac{2}{3}}\Psi^{xyzs}_{3431,q}$	$\frac{1}{4}\sqrt{\frac{1}{3}}(1-8\cot^2\theta)$
14	$p^4\ {}^1D$	$\frac{1}{2}\Psi^{xxzz}_{1211,q}-\frac{1}{2}\Psi^{yyzz}_{1211,q}-\sqrt{\frac{1}{2}}\Psi^{xyzz}_{1212,q}$	$\sqrt{\frac{1}{6}}\sqrt{1-2\cot^2\theta}\cot\theta$
15	〃 ^1D	$\sqrt{\frac{1}{2}}\Psi^{yyxz}_{1211,q}+\sqrt{\frac{1}{2}}\Psi^{xxyz}_{1212,q}$	$-\frac{1}{2}\sqrt{\frac{1}{6}}\sqrt{1-2\cot^2\theta}$
16	〃 ^3P	$-\sqrt{\frac{1}{2}}\Psi^{yyxz}_{3221,q}-\sqrt{\frac{1}{2}}\Psi^{xxyz}_{3222,q}$	$-\frac{1}{2}\sqrt{\frac{1}{2}}\sqrt{1-2\cot^2\theta}$
17	〃 ^3P	$\Psi^{zzxy}_{3421,q}$	$\sqrt{\frac{1}{2}}\sqrt{1-2\cot^2\theta}\cot\theta$

APPENDIX III. Energy Matrix

$$H_{1,1}=W(s^2p^2\,{}^1D)-6M_{ss}-3\sin^2\theta M_{\sigma\sigma}-3(1+\cos^2\theta)M_{\pi\pi}+3N_{ss}+\tfrac{3}{2}\sin^2\theta N_{\sigma\sigma}+\tfrac{3}{2}(1+\cos^2\theta)N_{\pi\pi}+3K_{hh}$$

$$H_{2,2}=W(s^2p^2\,{}^1D)-6M_{ss}-\tfrac{3}{2}(1+\cos^2\theta)M_{\sigma\sigma}-\tfrac{3}{2}(2+\sin^2\theta)M_{\pi\pi}+3N_{ss}+\tfrac{3}{4}(1+\cos^2\theta)N_{\sigma\sigma}+\tfrac{3}{4}(2+\sin^2\theta)N_{\pi\pi}+3K_{hh}$$

$$H_{3,3}=W(s^2p^2\,{}^3P)-6M_{ss}-\tfrac{3}{2}(1+\cos^2\theta)M_{\sigma\sigma}-\tfrac{3}{2}(2+\sin^2\theta)M_{\pi\pi}+3N_{ss}-(\tfrac{3}{4}-\tfrac{5}{4}\cos^2\theta)N_{\sigma\sigma}+(\tfrac{7}{4}-\tfrac{5}{4}\cos^2\theta)N_{\pi\pi}+3K_{hh}$$

$$H_{4,4}=W(s^2p^2\,{}^3P)-6M_{ss}-3\sin^2\theta M_{\sigma\sigma}-3(1+\cos^2\theta)M_{\pi\pi}+3N_{ss}-\sin^2\theta N_{\sigma\sigma}-(1+\cos^2\theta)N_{\pi\pi}+3K_{hh}-3J_{hh}$$

$$H_{5,5}=W(sp^3\,{}^3P^0)-3M_{ss}-3M_{\sigma\sigma}-6M_{\pi\pi}+\tfrac{1}{2}N_{ss}+\tfrac{3}{2}\cos^2\theta N_{\sigma\sigma}+(2+\tfrac{3}{2}\sin^2\theta)N_{\pi\pi}+3K_{hh}$$

$$H_{6,6}=W(sp^3\,{}^1P^0)-3M_{ss}-3M_{\sigma\sigma}-6M_{\pi\pi}+\tfrac{3}{2}N_{ss}+\tfrac{3}{2}N_{\sigma\sigma}+3N_{\pi\pi}+3K_{hh}$$

$$H_{7,7}=W(sp^3\,{}^3D^0)-3M_{ss}-3M_{\sigma\sigma}-6M_{\pi\pi}+\tfrac{1}{2}N_{ss}+\tfrac{3}{2}\cos^2\theta N_{\sigma\sigma}+(2+\tfrac{3}{2}\sin^2\theta)N_{\pi\pi}+3K_{hh}$$

$$H_{8,8}=W(sp^3\,{}^3D^0)-3M_{ss}-3M_{\sigma\sigma}-6M_{\pi\pi}+\tfrac{1}{2}N_{ss}+\tfrac{1}{2}(1+2\sin^2\theta)N_{\sigma\sigma}+(2+\cos^2\theta)N_{\pi\pi}+3K_{hh}$$

$$H_{9,9}=W(sp^3\,{}^3D^0)-3M_{ss}-3M_{\sigma\sigma}-6M_{\pi\pi}-N_{ss}-(\tfrac{1}{6}-\tfrac{5}{2}\cos^2\theta)N_{\sigma\sigma}-(\tfrac{1}{3}-\tfrac{5}{2}\sin^2\theta)N_{\pi\pi}+3K_{hh}-3J_{hh}$$

$$H_{10,10}=W(sp^3\,{}^1D^0)-3M_{ss}-3M_{\sigma\sigma}-6M_{\pi\pi}+\tfrac{3}{2}N_{ss}+\tfrac{3}{2}N_{\sigma\sigma}+3N_{\pi\pi}+3K_{hh}$$

$$H_{11,11}=W(sp^3\,{}^1D^0)-3M_{ss}-3M_{\sigma\sigma}-6M_{\pi\pi}+\tfrac{3}{2}N_{ss}+\tfrac{3}{2}N_{\sigma\sigma}+3N_{\pi\pi}+3K_{hh}$$

$$H_{12,12}=W(sp^3\,{}^5S^0)-3M_{ss}-3M_{\sigma\sigma}-6M_{\pi\pi}-\tfrac{3}{4}N_{ss}-\tfrac{3}{4}N_{\sigma\sigma}-\tfrac{3}{2}N_{\pi\pi}+3K_{hh}-3J_{hh}$$

$$H_{13,13}=W(sp^3\,{}^3S^0)-3M_{ss}-3M_{\sigma\sigma}-6M_{\pi\pi}+\tfrac{11}{4}N_{ss}-\tfrac{7}{12}N_{\sigma\sigma}-\tfrac{7}{6}N_{\pi\pi}+3K_{hh}-3J_{hh}$$

$$H_{14,14}=W(p^4\,{}^1D)-3(1+\cos^2\theta)M_{\sigma\sigma}-3(2+\sin^2\theta)M_{\pi\pi}+\tfrac{3}{2}(1+\cos^2\theta)N_{\sigma\sigma}+\tfrac{3}{2}(2+\sin^2\theta)N_{\pi\pi}+3K_{hh}$$

$$H_{15,15}=W(p^4\,{}^1D)-\tfrac{3}{2}(2+\sin^2\theta)M_{\sigma\sigma}-\tfrac{3}{2}(5+\cos^2\theta)M_{\pi\pi}+\tfrac{3}{4}(2+\sin^2\theta)N_{\sigma\sigma}+\tfrac{3}{4}(5+\cos^2\theta)N_{\pi\pi}+3K_{hh}$$

$$H_{16,16}=W(p^4\,{}^3P)-\tfrac{3}{2}(2+\sin^2\theta)M_{\sigma\sigma}-\tfrac{3}{2}(5+\cos^2\theta)M_{\pi\pi}+(\tfrac{1}{2}+\tfrac{1}{4}\sin^2\theta)N_{\sigma\sigma}+(\tfrac{13}{4}+\tfrac{1}{4}\cos^2\theta)N_{\pi\pi}+3K_{hh}$$

$$H_{17,17}=W(p^4\,{}^3P)-3(1+\cos^2\theta)M_{\sigma\sigma}-3(2+\sin^2\theta)M_{\pi\pi}-(1-4\cos^2\theta)N_{\sigma\sigma}-2(1-2\sin^2\theta)N_{\pi\pi}+3K_{hh}-3J_{hh}$$

$$H_{1,14}=H_{2,15}=H_{3,16}=H_{4,17}=G^1(s,p)$$

$$H_{1,4}=H_{14,17}=\sqrt{3}\sin^2\theta(N_{\pi\pi}-N_{\sigma\sigma})$$

$$H_{8,9}=-\sqrt{\tfrac{1}{3}}\sin^2\theta(N_{\pi\pi}-N_{\sigma\sigma})$$

$$H_{8,12}=\sqrt{\tfrac{5}{2}}\sin^2\theta(N_{\pi\pi}-N_{\sigma\sigma})$$

$$H_{8,13}=-\sqrt{\tfrac{1}{6}}\sin^2\theta(N_{\pi\pi}-N_{\sigma\sigma})$$

$$H_{9,11}=-\sin^2\theta(N_{\pi\pi}-N_{\sigma\sigma})$$

$$H_{11,13}=\sqrt{2}\sin^2\theta(N_{\pi\pi}-N_{\sigma\sigma})$$

$$H_{1,3}=H_{2,4}=H_{14,16}=H_{15,17}$$
$$=-\sqrt{3}\sin\theta\cos\theta(N_{\pi\pi}-N_{\sigma\sigma})$$

$$H_{7,11}=H_{8,10}=\sqrt{3}\sin\theta\cos\theta(N_{\pi\pi}-N_{\sigma\sigma})$$

$$H_{3,4}=H_{16,17}=H_{9,10}=-\sin\theta\cos\theta(N_{\pi\pi}-N_{\sigma\sigma})$$

$$H_{7,8}=-2\sin\theta\cos\theta(N_{\pi\pi}-N_{\sigma\sigma})$$

$$H_{7,9}=-\sqrt{\tfrac{1}{3}}\sin\theta\cos\theta(N_{\pi\pi}-N_{\sigma\sigma})$$

$$H_{7,12}=-\sqrt{10}\sin\theta\cos\theta(N_{\pi\pi}-N_{\sigma\sigma})$$

$$H_{7,13}=\sqrt{\tfrac{2}{3}}\sin\theta\cos\theta(N_{\pi\pi}-N_{\sigma\sigma})$$

$$H_{10,13}=-2\sqrt{2}\sin\theta\cos\theta(N_{\pi\pi}-N_{\sigma\sigma})$$

$$H_{2,3}=H_{15,16}=\frac{\sqrt{3}}{2}(\tfrac{3}{2}\sin^2\theta-\cos^2\theta)(N_{\pi\pi}-N_{\sigma\sigma})$$

$$H_{9,12}=\sqrt{\tfrac{5}{6}}(\cos^2\theta-\tfrac{1}{2}\sin^2\theta)(N_{\pi\pi}-N_{\sigma\sigma})$$

$$H_{9,13}=\tfrac{5}{3}\sqrt{\tfrac{1}{2}}(\cos^2\theta-\tfrac{1}{2}\sin^2\theta)(N_{\pi\pi}-N_{\sigma\sigma})$$

$$H_{5,7}=H_{6,10}=3(\tfrac{1}{2}\sin^2\theta-\cos^2\theta)(M_{\pi\pi}-M_{\sigma\sigma}$$
$$-\tfrac{1}{2}N_{\pi\pi}+ +\tfrac{1}{2}N_{\sigma\sigma})$$

$$H_{5,6}=H_{7,10}=-\frac{\sqrt{3}}{2}N_{ss}+\frac{3\sqrt{3}}{4}\sin^2\theta N_{\sigma\sigma}$$
$$+\frac{\sqrt{3}}{2}(\cos^2\theta-\tfrac{1}{2}\sin^2\theta)N_{\pi\pi}$$

$$H_{8,11}=-\frac{\sqrt{3}}{2}N_{ss}+\frac{\sqrt{3}}{2}\cos^2\theta N_{\sigma\sigma}+\frac{\sqrt{3}}{2}\sin^2\theta N_{\pi\pi}$$

$$H_{12,13}=-\frac{\sqrt{15}}{4}N_{ss}+\tfrac{1}{4}\sqrt{\tfrac{5}{3}}N_{\sigma\sigma}+\tfrac{1}{2}\sqrt{\tfrac{5}{3}}N_{\pi\pi}$$

$$H_{1,11}=H_{11,14}=-3\sqrt{2}\cos\theta(M_{s\sigma}-\tfrac{1}{2}N_{s\sigma})$$

$$H_{2,10}=H_{6,15}=H_{10,15}=-H_{2,6}$$
$$=-3\sqrt{\tfrac{1}{2}}\cos\theta(M_{s\sigma}-\tfrac{1}{2}N_{s\sigma})$$

$$H_{3,5}=-H_{3,7}=-3\sqrt{\tfrac{1}{2}}\cos\theta(M_{s\sigma}-\tfrac{5}{6}N_{s\sigma})$$

$$H_{5,16}=H_{7,16}=3\sqrt{\tfrac{1}{2}}\cos\theta(M_{s\sigma}-\tfrac{1}{6}N_{s\sigma})$$

$$H_{4,9}=\sqrt{6}\cos\theta(M_{s\sigma}-\tfrac{4}{3}N_{s\sigma})$$

$$H_{9,17}=\sqrt{6}\cos\theta(M_{s\sigma}+\tfrac{1}{3}N_{s\sigma})$$

$$H_{4,13}=-2\sqrt{3}\cos\theta(M_{s\sigma}-\tfrac{1}{12}N_{s\sigma})$$

$$H_{13,17}=-2\sqrt{3}\cos\theta(M_{s\sigma}-\tfrac{11}{12}N_{s\sigma})$$

$$H_{1,5}=H_{1,7}=H_{2,8}=H_{3,11}=H_{5,14}=H_{10,17}$$
$$=-\sqrt{\tfrac{3}{2}}\sin\theta N_{s\sigma}$$

$$H_{4,6}=H_{4,10}=H_{7,14}=H_{8,15}=H_{11,16}=H_{6,17}$$
$$=\sqrt{\tfrac{3}{2}}\sin\theta N_{s\sigma}$$

$$H_{2,9}=-H_{9,15}=3\sqrt{\tfrac{1}{2}}\sin\theta N_{s\sigma}$$

$$H_{3,8}=-H_{8,16}=-\sqrt{2}\sin\theta N_{s\sigma}$$

$$H_{3,9}=-H_{9,16}=\sqrt{\tfrac{1}{6}}\sin\theta N_{s\sigma}$$

$$H_{3,12}=-H_{12,16}=-\sqrt{5}\sin\theta N_{s\sigma}$$

$$H_{3,13}=-H_{13,16}=-\sqrt{\tfrac{1}{3}}\sin\theta N_{s\sigma}$$

$$H_{4,5}=H_{4,7}=H_{5,17}=-H_{7,17}=-\sqrt{\tfrac{1}{2}}\sin\theta N_{s\sigma}$$

$$H_{1,8}=-H_{8,14}=\sqrt{\tfrac{3}{2}}\cos\theta N_{s\sigma}$$

$$H_{2,5}=H_{5,15}=H_{7,15}=H_{3,10}=-\tfrac{1}{2}\sqrt{\tfrac{3}{2}}\cos\theta N_{s\sigma}$$

$$H_{2,7}=H_{3,6}=H_{6,16}=H_{10,16}=\tfrac{1}{2}\sqrt{\tfrac{3}{2}}\cos\theta N_{s\sigma}$$

$$H_{1,12}=-H_{12,17}=\frac{\sqrt{5}}{2}\cos\theta N_{s\sigma}$$

References

1) W. Moffitt, Proc. Roy. Soc. A **210** (1951) 224.

2) H. H. Voge, J. Chem. Phys. **4** (1936) 581.

3) M. Kotani and M. Siga, Proc. Phys. Math. Soc. Japan, **19** (1937) 471.

4) M. Kotani, Proc. National Acad. Sci. **38** (1952) 547. "Summary of the Conference on Quantum Mechanical Methods in Valence Theory held at Shelter Island".

5) R. S. Mulliken, Phys. Rev. **43** (1933) 279.

6) M. Kotani, Proc. Phys. Math. Soc. Japan, **19** (1937) 460.

7) R. Serber, Phys. Rev. **45** (1934) 461.

8) T. Yamanouchi, Proc. Phys. Math. Soc. Japan, **18** (1936) 623.

9) J. C. Slater, Phys. Rev. **34** (1929) 1293.

10) J. H. Van Vleck and A. Sherman, Revs. Modern Phys. **7** (1935) 167.

11) J. H. Van Vleck, J. Chem. Phys. **2** (1934) 297.

12) M. Kotani and A. Amemiya, Proc. Phys. Math. Soc. Japan **22** (1940) Extra No.

13) J. H. Van Vleck, J. Chem. Phys **2** (1934) 20.

14) W. G. Penney, Trans. Faraday Soc. **31** (1935) 734.

15) H. H. Voge, J. Chem. Phys. **16** (1948) 984. See case (d).

16) J. W. Linnett and A. J. Poë, Trans. Farady Soc. **47** (1951) 1033.

17) R. Serber, J. Chem. Phys. **2** (1934) 697.

JOURNAL OF THE PHYSICAL SOCIETY OF JAPAN Vol. 8, No. 1, JAN.—FEB., 1953

On Verwey-Overbeek's Theory of the Interaction Force between Two Colloidal Particles

Yuichi IKEDA

Kobayasi Institute of Physical Research, Kokubunzi, Tokyo

(Received August 1, 1952)

The theory on the static repulsive force between two charged colloidal particles was established by Verwey and Overbeek (1948). However, as the theory was given in a rather intuitive way, there have been some doubts about its strictness.

In this paper, the expression of the free energy obtained by using V.-O.'s first method is given in a strictly statistical mechanical way; no correction is necessary such as Levine (Proc. Cambridge Phil. Soc. **47** (1951) 217) considered to be.

Two new correction terms are added to V.-O.'s formulae obtained by their second method. One of them is added to cancel the effect that charges still remain on the particle surface when the surface potential is kept constant and the charges of ions vanish. The other is added when the adsorbed ions on the surfaces are kept fixed and the charges of ions vanish, to cancel the effect that the concentrations of ions between two parallel plates are different from the normal concentrations at infinite distance from the plates.

§ 1. Introduction

The theory on the interaction force or the free energy of the colloidal system, where charged particles are immersed in an electrolyte solution, has been considered by Verwey and Overbeek[1,2]. But, on the other hand, Levine[3-9] has given criticism on V.-O.'s theory, and has attempted to revise it. Given in a rather intuitive way, V.-O.'s theory leaves room for some doubts about its strictness, though it is essentially right.

In this paper, we shall consider V.-O.'s theory on the basis of the strict statistical mechanics, and shall give some small corrections at the same time.

§ 2. Electrical Free Energy of the System, where the Charges are Fixed on the Surface of Particles

First of all, we will consider the sysem of two charged particles immersed in an electrolyte solution, where the surface charges are fixed and do not vary with the distance between the particles.

For simplicity, we may assume that the two particles are immersed in an electrolyte solution of volume V and that the surface charge density σ is uniform everywhere on the particles. Furthermore, we will assume that there are m types of ions in the electrolyte solution, N_i of type i, and will put $\sum_{i=1}^{m} N_i = N$, N being the total number of ions. We will number the ions for convenience, and designate the charge of the ith ion as e_i, where $e_1=e_2=\cdots=e_{N_1}$, $e_{N_1+1}=e_{N_1+2}=\cdots=e_{N_1+N_2}$, $\cdots$.

Now we will evaluate the free energy increase F_σ of the system, in the case where the surface charge density changes from 0 to σ. From F_σ we can derive the interaction force between two charged particles. It is easily seen that F_σ can be written as follows:

$$F_\sigma=\sum_{k=1}^{2}\frac{1}{2}\int\varphi_0\sigma dS_k-kT\log\Omega+kT\log\Omega_0\,, \quad (1)$$

$$\Omega=\int\cdots\int\exp(-U/kT)\prod_{i=1}^{N}dv_i\,,$$

$$U=\sum_{i=1}^{N}e_i\varphi(x_i,y_i,z_i)+\sum_{i>k=1}^{N}\frac{e_ie_k}{Dr_{ik}}+U_0\,,$$

$$\Omega_0=\Omega_{(\sigma=0)}\,,$$

where dS_k is the surface element of each particle ($k=1, 2$), the volume integration in the expression of Ω extends over the $3N$-dimensional configuration space of the N ions, U is the energy of the assembly of ions for a given configuration; φ_0 and $\varphi(x_i, y_i, z_i)$ are the electric potential due to σ, on dS_k and at the point e_i possesses, respectively; r_{ik} is the distance between e_i and e_k, D is the dielectric constant of the medium, and U_0 is the energy term due to short range interactions. The first term on the right-hand side of (1) represents the interaction free energy between surface charges, and the other two terms represent the free energy due to ion-ion, ion-surface charge interactions. When $\sigma=0$, F_σ equals zero. In V_k, the inside of the particle k, we will represent the electric potential due to σ as φ_k, the dielectric constant as ε, then we have

$$\Delta\varphi=0 \qquad \text{in } V, \qquad (2)$$

$$\Delta\varphi_k=0 \qquad \text{in } V_k, \qquad (3)$$

$$-\frac{1}{4\pi}\left(D\frac{\partial\varphi_0}{\partial n}-\varepsilon\frac{\partial\varphi_{k0}}{\partial n}\right)=\sigma\,, \qquad \varphi_0=\varphi_{k0}$$

on the surfaces of the particles. (4)

n denotes the direction of the normal at the particle surface, which is drawn from the inside of the particle toward the surrounding solution, and the suffix $_0$ represents the values on the surfaces of particles.

Since φ and φ_0 are proportional to σ, we obtain from (1)

$$\sigma\frac{\partial F_\sigma}{\partial\sigma}=\sum_{k=1}^{2}\sigma\int\varphi_0dS_k+\int\cdots\int\sum_{i=1}^{N}e_i\varphi(x_i,y_i,z_i)$$
$$\exp(-U/kT)\prod_{i=1}^{N}dv_i/\Omega\,. \qquad (5)$$

(5) can be rewritten as follows:

$$\sigma\frac{\partial F_\sigma}{\partial\sigma}=\sum_{i=1}^{N}\int_V\bar{\rho}_i(x_i,y_i,z_i)\,\varphi(x_i,y_i,z_i)dv_i$$
$$+\sigma\sum_{k=1}^{2}\int\varphi_0dS_k$$
$$=\int_V\rho\varphi dv+\sigma\sum_{k=1}^{2}\int\varphi_0dS_k\,, \qquad (6)$$

where

$$\bar{\rho}_i(x_i,y_i,z_i)=e_i\int\cdots\int\exp(-U/kT)dv_1\cdots dv_{i-1}$$
$$\cdot dv_{i+1}\cdots dv_N/\Omega \qquad (7)$$

is the average charge density due to the ith ion at (x_i, y_i, z_i), and

$$\rho(x,y,z)=\sum_{i=1}^{N}\bar{\rho}_i(x,y,z) \qquad (8)$$

is the average charge density at (x, y, z) in the solution.

Here we introduce the average electric potential of this system, and represent it as ψ in V, as ψ_k in V_k. ψ differs from φ, because ψ is dependent not only on σ, but also on the charge distribution of ions. We obtain the following relations for ψ and ψ_k,

$$\rho=-\frac{D}{4\pi}\Delta\psi \qquad \text{in } V, \qquad (9)$$

$$\Delta\psi_k=0 \qquad \text{in } V_k, \qquad (10)$$

$$-\frac{1}{4\pi}\left(D\frac{\partial\psi_0}{\partial n}-\varepsilon\frac{\partial\psi_{k0}}{\partial n}\right)=\sigma\,, \qquad \psi_{k0}=\psi_0$$

on the surfaces of the particles. (11)

Applying Green's theorem in V, we obtain from (2), (6) and (9),

$$\sigma\frac{\partial F_\sigma}{\partial\sigma}=\sigma\sum_{k=1}^{2}\int\varphi_0dS_k-\frac{D}{4\pi}\int_V\varphi\Delta\psi dv$$
$$=\sigma\sum_{k=1}^{2}\int\varphi_0dS_k$$
$$+\sum_{k=1}^{2}\frac{D}{4\pi}\int\left(\varphi_0\frac{\partial\psi_0}{\partial\sigma}-\psi_0\frac{\partial\varphi_0}{\partial n}\right)dS_k\,, \qquad (12)$$

where we may neglect the integral taken on the external surface of V. Similarly, from (3) and (10), we have in V_k

$$\sum_{k=1}^{2}\frac{\varepsilon}{4\pi}\int\left(\varphi_{k0}\frac{\partial\psi_{k0}}{\partial n}-\psi_{k0}\frac{\partial\varphi_{k0}}{\partial n}\right)dS_k=0\,. \qquad (13)$$

Subtracting (13) from (12), and using (4) and (11), we have at once

$$\sigma\frac{\partial F_\sigma}{\partial\sigma}=\sigma\sum_{k=1}^{2}\int\psi_0dS_k\,. \qquad (14)$$

Remembering $F_\sigma=0$ when $\sigma=0$, we integrate (14) and obtain

$$F_\sigma=\sum_{k=1}^{2}\int dS_k\int_0^\sigma \psi_0 d\sigma\,. \tag{15}$$

Though we have just shown the relation (15) in a special case, it is easily seen that (15) is valid in the general case, e. g., in the case where σ is not uniform on the particle surface, or even in the case where the electrolyte solution contains dipolar molecules besides the point charge ions (that is, (15) is valid even when we consider the hydration of colloidal particles, if only the average surface potential ψ_0 is given). It is to be noticed that the condition of electrical neutrality is not necessary for (15) to be derived. This is a strictly statistical mechanical proof of the formula obtained by V.-O.'s first method in the case of fixed σ.

§ 3. Free Energy of the System of the Charged Particles in General

Now we examine the free energy of the system where the surfaces of particles are in equilibrium with the solution.

We assume at first that there are N_i ions of type i ($i=1, 2, \cdots, m$) in an electrolyte solution of volume V, and that the electrical neutrality is satisfied. Then, n ions of type 1 are adsorbed on the surfaces of immersed particles and the chemical equilibrium is established between the surfaces and the bulk of the solution.

The free energy increase $\varDelta F$ by this process can be written as follows:

$$\begin{aligned}\varDelta F&=F_{(n;\,N_1-n,\,N_2,\,\cdots,\,N_m)}-F_{(0;\,N_1,\,N_2,\cdots,\,N_m)}\\&=F_{\sigma(n;\,N_1-n,\,N_2,\,\cdots,\,N_m)}-\int_0^n \mu dn\\&\quad+F_{(0;\,N_1-n,\,N_2,\,\cdots,\,N_m)}-F_{(0;\,N_1,\,N_2,\,\cdots,\,N_m)}\,.\end{aligned} \tag{16}$$

The right-hand side of (16) means the following processes: (i) in the electrolyte solution containing N_i ions of type i (the free energy of this system is $F_{(0;\,N_1,\,N_2,\,\cdots,\,N_m)}$) the charges of n ions of type 1 vanish (the free energy becomes $F_{(0;\,N_1-n,\,N_2,\,\cdots,\,N_m)}$), (ii) then, these discharged ions are adsorbed on the surface of particles (the free energy increases by $-\int_0^n \mu dn$), (iii) and then the discharged ions are again charged up (the free energy increase is given by $F_{\sigma(n;\,N_1-n,\,N_2,\,\cdots,\,N_m)}$); μ is the chemical or non-electrical part of the chemical potential decrease by the adsorption of one ion of type 1 on the particle surface. When $N_1 \gg n$ as usual, we can write

$$F_{(0;\,N_1-n,\,N_2,\,\cdots,\,N_m)}-F_{(0;\,N_1,\,N_2,\,\cdots,\,N_m)}\doteqdot n\int_0^{e_1}\phi_1 de_1\,, \tag{17}$$

following the theory of electrolyte solution, where ϕ_1 is the average electric potential at an ion of type 1 due to all other ions, and is dependent only on N_1/V, N_2/V, $\cdots$, N_m/V, not dependent on n.

In the result, from (15), (16) and (17), $\varDelta F$ is given by

$$\begin{aligned}\varDelta F&=F_{(n;\,N_1-n,\,N_2,\,\cdots,\,N_m)}-F_{(0;\,N_1,\,N_2,\,\cdots,\,N_m)}\\&=\sum_k\int dS_k\int_0^\sigma\psi_0 d\sigma-\int_0^n\mu dn+n\int_0^{e_1}\phi_1 de_1\,.\end{aligned} \tag{18}$$

The general force can be obtained by differentiating $-\varDelta F$ with respect to R where R is a parameter describing the mutual position of two particles. It is to be noticed that the second term and the third on the right-hand side of (18) are functions of n, and do not depend explicitly on R. Then, if the particle surface is in the chemical equilibrium with the bulk of the solution and

$$\partial(\varDelta F)/\partial n=0 \tag{19}$$

exists, the general force $-\partial(\varDelta F)/\partial R$ can be written as follows[8]:

$$-\partial(\varDelta F)/\partial R=-[\partial(\varDelta F)/\partial R]_n=-(\partial F_\sigma/\partial R)_n\,, \tag{20}$$

that is, the force acting between particles can be determined by the mutual position and the surface charge distribution of these particles alone, without knowing the details of equilbrium between the surface and the solution. We have assumed until now that the charges on the particle surface are due to ionic adsorption. However, the above argument is not altered essentially even when the charges are caused by the dissociation of bases on the particle surface.

In a special case, where the surface potential ψ_0 has always a constant value $\bar{\psi}_0$, we have, by substituting (18) into (19),

$$\frac{\partial}{\partial n}\Big(\sum_k\int dS_k\sigma\Big)\bar{\psi}_0-\mu+\int_0^{e_1}\phi_1 de_1=0\,. \tag{21}$$

From (18) and (21), the free energy increase $\varDelta F_\psi$ in this case can be written as follows:

$$\begin{aligned}\varDelta F_\psi&=-\bar{\psi}_0\sum_k\int dS_k\sigma+\sum_k\int dS_k\int_0^\sigma\psi_0 d\sigma\\&=-\sum_k\int dS_k\int_0^{\bar{\psi}_0}\sigma d\psi_0\,.\end{aligned} \tag{22}$$

This is the formula often used by V.-O.

§ 4. Another Formula Describing the Free Energy of the System

Another formula for the free energy of the system, which corresponds to the result obtained by V.-O. using their second method[1)], can be derived as follows.

First, we shall treat the case where the charge is fixed on the surface. We now evaluate the free energy decrease when all ions of the system—ions fixed on the particle, as well as ions in the bulk of the solution—are gradually discharged, and the degree of discharge is represented by λ, decreasing from 1 to 0; this process is similar to the one used by Debye and Hückel, while (15) corresponds to the Güntelberg-Müller's method in the theory of strong electrolytes. Here, we must consider $F_\sigma+F_{el}$, F_{el} being the electrical part of the free energy of the solution; and $F_\sigma+F_{el}$ can be written as follows:

$$F_\sigma+F_{el}=\sum_k\frac{1}{2}\int\varphi_0\sigma dS_k-kT\log\Omega+kT\log\Omega', \tag{23}$$

$$\Omega'=\int\cdots\int\exp(-U_0/kT)\prod_{i=1}^{N-n}dv_i.$$

When all ions are discharged from e_i to λe_i, φ_0, σ and e_i in (23) must be multiplied by λ, so that (23) vanishes when $\lambda=0$. Remembering that $\varphi_0\sigma$ and $U-U_0$ are proportional to λ^2, we transform (23) and have

$$\begin{aligned}F_\sigma+F_{el}&=\int_0^1 d\lambda\frac{\partial}{\partial\lambda}(F_\sigma+F_{el})\\&=\int_0^1 d\lambda\frac{2}{\lambda}\Bigg[\sum_k\int dS_k\frac{\lambda^2\varphi_0\sigma}{2}\\&\quad-\int(U-U_0)\exp(-U/kT)\prod_{i=1}^{N-n}dv_i/\Omega\Bigg]\\&=\int_0^1 d\lambda\frac{2}{\lambda}E_{el(\lambda)},\end{aligned} \tag{24}$$

where $E_{el(\lambda)}$ represents the electrical part of the internal energy of this system. (24) is just the formula from which Levine started[6)]. (Here we may neglect the self-energy term such as Levine considered.) Since (24) as well as (15) is obtained for the same system without any assumption, the dependent part of $\int_0^1 d\lambda(2/\lambda)E_{el}$ on σ must agree with (15).

To describe E_{el} in a convenient form, however, is difficult without any assumption or approximation. But, when we assume the relation of the form

$$\Delta\psi=\lambda f\left(\frac{\lambda\psi}{kT}\right), \tag{25}$$

f being an arbitrary function, and use the thermodynamical relation

$$E_\sigma=F_\sigma-T\frac{\partial F_\sigma}{\partial T}, \tag{26}$$

we can obtain from (15), (25) and (26), the internal energy of this system in the following form,

$$\begin{aligned}E_\sigma&=\frac{1}{2}\int\psi\rho dv+\frac{1}{2}\sum_k\int dS_k\psi_0\sigma\\&=\frac{D}{8\pi}\int_V|\text{grad}\psi|^2dv+\sum_k\frac{\varepsilon}{8\pi}\int_{V_k}|\text{grad}\,\psi_k|^2dv,\end{aligned} \tag{27}$$

and the formula of the free energy in a different form from that of (15);

$$F_\sigma=\int_0^1 d\lambda\frac{2}{\lambda}E_\sigma. \tag{28}$$

Substituting (28) into (16) or (18), we obtain a formula describing the free energy of the general charged system. The proof of (27) and (28) can be carried out in a way analogous to the derivation of Casimir's theorem[10)]. (see **Appendix**) (To the right-hand side of (28), one term is added only when we consider the case of two infinite parallel plates as shown in § **6**.)

Accepting (25) and other uncertain assumptions, Levine added to the right-hand side of (28) a correction term representing a repulsive force[6),7)]. But, no additional term can enter, as we have shown above. Levine gave the relation[6)]

$$\Psi_i(\vec{r})=\psi_i(\vec{r})+\phi_i, \tag{29}$$

where Ψ_i is the average electrostatic potential at an i ion, due to surrounding ions, at position $\vec{r}$ and ϕ_i is the value of Ψ_i in the "interior" or "bulk" of the solution; and then he identified $\psi_i(\vec{r})$ to be ψ without any adequate reason. Thereafter, using the Debye-Hückel's linear approximation equation, Levine derived the additional repulsive force. But, this treatment is very doubtful.

§ 5. The Free Energy of the System Obtained by V.-O.'s Second Method when the Surface Potential is Kept Constant

The free energy of the system when the surface potential is kept constant is given in two different formulae by Verwey-Overbeek[1], which are (22) and

$$\Delta F_\psi=\int_0^1 d\lambda\frac{1}{\lambda}\int[\rho\,\psi]_{\bar{\psi}_0}dv-\sum_k\int dS_k\int_0^{\bar{\psi}_0}\sigma^0 d\psi_0, \tag{30}$$

where the second term on the right-hand side of (30) was overlooked by V.-O.; the suffix $\bar{\psi}_0$ denotes that the integration with respect to λ is taken keeping the surface potential constant, and σ^0 is the surface charge density when $\lambda=0$ in the integration process above. The identity of (22) and (30) was shown by Casimir[10], but he missed the second term on the right-hand side of (30) as he assumed $(\partial\chi/\partial\lambda)_{\lambda=0}=0$ in his notation[5]; $\partial\chi/\partial\lambda$ is not zero in general when $\lambda=0$.

The first term on the right-hand side of (30) was explained by V.-O. assuming a somewhat artificial path of discharging,—the first term corresponds to the work done to discharge all ions from e_i to 0, keeping the surface potential $\bar{\psi}_0$ constant all the time. However, as the surface potential value $\bar{\psi}_0$ still stands at the end of this discharging process, surface charge density remains on the surface when the charges of ions vanish, and σ^0 depends on the distance between the particles[5]; that is, this state cannot be taken as the standard state for the calculation of the free energy. The free energy difference, between the state where the charges of ions vanish keeping the surface potential constant and the state where the charges vanish on the particle surface as well as in the solution, is expressed in the second term on the right-hand side of (30). The electrical part of this free energy difference is $\sum_k\int dS_k\int_0^{\sigma^0}\psi_0 d\sigma$, and the chemical part is $-\sum_k\int dS_k\sigma^0\bar{\psi}_0$, on the assumption of chemical equilibrium between surface and solution; then the total free energy difference is $-\sum_k\int dS_k\int_0^{\bar{\psi}_0}\sigma^0 d\psi_0$. This is the meaning of the second term on the right-hand side of (30).

As the second term vanishes in the case of two parallel infinite plates when the surface potential is kept constant, V.-O.'s calculation carried out for this case[1] does not need any correction.

§ 6. The Free Energy of the Two Parallel Infinite Plates System

If we assume (25), we can derive from (15) a more general formula than (28), which is[5]

$$F_\sigma=\int_{\lambda_0}^1\frac{2}{\lambda}E_\sigma d\lambda+\sum_k\int dS_k\int_0^{\lambda_0\sigma}\psi_0 d\sigma, \tag{31}$$

without any other assumptions (see **Appendix**); in (31) λ_0 is a constant taking an arbitrary value from 0 to 1, and the limiting case $\lambda_0\to0$ is (28).

However, only in the case of two parallel infinite plates system, the second term on the right-hand side of (31) does not vanish when $\lambda_0\to0$, as pointed out by Levine[7,11] and Overbeek[12]. Rewriting (31) for this case, the free energy per unit area is given in the form

$$F_\sigma=\int_{\lambda_0}^1\frac{2}{\lambda}E_\sigma d\lambda+2e_1\int_0^n\lambda_0\psi_{0(\lambda_0,\,n)}dn, \tag{32}$$

where F_σ is the free energy of this system per unit area, and n is the number of the adsorbed ions per unit area.

When λ_0 tends to zero, $\psi_{0(\lambda_0)}$ becomes infinite and $\lim\limits_{\lambda_0\to0}\lambda_0\psi_{0(\lambda_0,\,n)}$ does not vanish assuming the Poisson-Boltzmann equation. It can be easily seen that the electric potential $\psi_{(\lambda_0,\,n)}$ anywhere in the solution becomes equal to $\psi_{0(\lambda_0,\,n)}$ on the surface, when the charges in the solution between the two plates vanish with λ_0. Then, in this case,

$$\lim_{\lambda_0\to0}\lambda_0\psi_{(\lambda_0,\,n)}=\lim_{\lambda_0\to0}\lambda_0\psi_{0(\lambda_0,\,n)}=m\neq0 \tag{33}$$

is obtained. From (33), it is seen that the concentration of ions of type i, anywhere in the solution between the plates, is $\exp(-me_i/kT)$ time larger than the concentration in the bulk of the solution when $\lambda_0\to0$. Then, since m depends on the distance between the particles, the state where λ_0 vanishes cannot be the standard state for the calculation of the free energy, and it is necessary to make the ion concentration of each type between the plates, the same as the respective one in the bulk of the electrolyte solution. Now, it is easily shown that the second term on the right-hand side of (31) is equal to the free energy increase caused by this concentration difference[11]; this term must be added to $\int_0^1(2/\lambda)E_\sigma d\lambda$ for this case.

This is the explanation of the equation

$$F_\sigma=\int_0^1\frac{2}{\lambda}E_\sigma d\lambda+2e_1\int_0^n m\,dn \tag{34}$$

for the parallel plates system when the adsorbed ions are kept fixed.

§ 7. Conclusions

The free energy of the colloidal system—— the system of charged particles immersed in an electrolyte solution—— is derived in a strictly statistical mechanical way. The results contain the formulae derived by Verwey-Overbeek's first method as special cases.

Using treatments analogous to Casimir's[10]), the formulae are rewritten in the forms similar to those of the formulae derived by Verwey-Overbeek's second method, where the relation (25) is assumed but any other assumption is not used. The results are different in some points from those of previous authors. No such correction as Levine[6,7]) proposed is necessary.

The physical explanation of each term of these formulae is satisfactorily given.

In conclusion, the author wishes to express his sincere thanks to Dr. S. Oka for his helpful discussions and encouragements. This work is indebted to the Ministry of Education for the Scientific Research Expenditure.

Appendix

We want to show that if we assume

$$\Delta\psi=\lambda f\left(\frac{\lambda\psi}{kT}\right), \tag{25}$$

we can obtain (27) for E_σ, substituting (15) into (26). When (27) is recognized to be right, the relations (28) or (31) are shown by Levine[5]).

The identity of the two expressions E_σ and E_σ' for the internal energy is now to be shown, where E_σ and E_σ' are described as follows:

$$E_\sigma=\left(1-T\frac{\partial}{\partial T}\right)F_\sigma, \tag{26}$$

$$\begin{aligned}E_\sigma'&=\frac{1}{2}\int_V\psi\rho dv+\frac{1}{2}\sum_k\int dS_k\psi_0\sigma\\&=\frac{D}{8\pi}\int_V|\mathrm{grad}\,\psi|^2dv+\sum_k\frac{\varepsilon}{8\pi}\int_{V_k}|\mathrm{grad}\,\psi_k|^2dv.\end{aligned} \tag{35}$$

Here, the relations (9), (10) and (11) must be remembered.

We can easily derive from (25) the equation

$$\psi\Delta\psi_\sigma=T(\psi_T\Delta\psi_\sigma-\psi_\sigma\Delta\psi_T), \tag{36}$$

where ψ_σ and ψ_T are the partial derivatives of ψ with respect to σ and T, respectively. Substituting (9) into $\frac{1}{2}\int_V\psi\rho dv$ and differentiating with respect to σ, we have

$$\begin{aligned}\frac{\partial}{\partial\sigma}\left[\frac{1}{2}\int_V\psi\rho dv\right]=-\frac{D}{8\pi}\int_V\Big\{\psi_\sigma\Delta\left(1-T\frac{\partial}{\partial T}\right)\psi\\-\left(1-T\frac{\partial}{\partial T}\right)\psi\Delta\psi_\sigma+\psi\Delta\psi_\sigma\Big\}dv,\end{aligned} \tag{37}$$

where the relation (36) is used. Applying Green's theorem, we obtain from (37)

$$\begin{aligned}&\frac{\partial}{\partial\sigma}\left[\frac{1}{2}\int_V\psi\rho dv\right]\\&=-\frac{D}{8\pi}\sum_k\int dS_k\Big\{\frac{\partial\psi_{0\sigma}}{\partial n}\left(1-T\frac{\partial}{\partial T}\right)\psi_0\\&-\psi_{0\sigma}\left(1-T\frac{\partial}{\partial T}\right)\frac{\partial\psi_0}{\partial n}\Big\}.\\&+\frac{D}{8\pi}\cdot\frac{1}{2}\int_V\frac{\partial}{\partial\sigma}\psi|\mathrm{grad}\,|^2dv\\&+\frac{D}{8\pi}\sum_k\int dS_k\psi_0\frac{\partial\psi_{0\sigma}}{\partial n}.\end{aligned} \tag{38}$$

Corresponding to (38), we obtain in V_k

$$\begin{aligned}0&=\frac{\partial}{\partial\sigma}\left[\frac{1}{2}\int_{V_k}\psi_k\rho_k dv\right]\\&=\frac{\varepsilon}{8\pi}\int dS_k\Big\{\frac{\partial\psi_{k0\sigma}}{\partial n}\left(1-T\frac{\partial}{\partial T}\right)\psi_0\\&-\psi_{0\sigma}\left(1-T\frac{\partial}{\partial T}\right)\frac{\partial\psi_{k0}}{\partial n}\Big\}\\&+\frac{\varepsilon}{8\pi}\cdot\frac{1}{2}\int_{V_k}\frac{\partial}{\partial\sigma}|\mathrm{grad}\,\psi_k|^2dv\\&-\frac{\varepsilon}{8\pi}\sum_k\int dS_k\psi_0\frac{\partial\psi_{k0\sigma}}{\partial n},\end{aligned} \tag{39}$$

reminding $\psi_{k0}=\psi_0$ and $\rho_k=0$ in V_k.

We sum up (38) and (39) for each k, and apply (11), then we have

$$\begin{aligned}\frac{\partial}{\partial\sigma}\left[\frac{1}{2}\int_V\psi\rho dv\right]&=\frac{1}{2}\left[\frac{D}{8\pi}\int_V|\mathrm{grad}\,\psi|^2dv\right.\\&\left.+\sum_k\frac{\varepsilon}{8\pi}\int_{V_k}|\mathrm{grad}\,\psi_k|^2dv\right]\\&+\frac{1}{2}\sum_k\int dS_k\Big\{\left(1-T\frac{\partial}{\partial T}\right)\psi_0-\sigma\psi_{0\sigma}-\psi_0\Big\}.\end{aligned} \tag{40}$$

Substituting (40) into $\partial E_\sigma'/\partial\sigma$, we have

$$\frac{\partial}{\partial\sigma}E_\sigma'=\frac{1}{2}\frac{\partial}{\partial\sigma}E_\sigma'+\frac{1}{2}\sum_k\int dS_k\left(1-T\frac{\partial}{\partial T}\right)\psi_0. \tag{41}$$

Then, we obtain

$$\begin{aligned}E_\sigma'&=\left(1-T\frac{\partial}{\partial T}\right)\sum_k\int dS_k\int_0^\sigma{}_0\psi d\sigma\\&=\left(1-T\frac{\partial}{\partial T}\right)F_\sigma=E_\sigma,\end{aligned} \tag{42}$$

this is the required result.

References

1) E. J. W. Verwey & J. Th. G. Overbeek: *Theory of the Stability of Lyophobic Colloids*, Elsevier Pub. Co. Inc. (1948).
2) E. J. W. Verwey & J. Th. G. Overbeek: Trans. Faraday Soc. **42B** (1946) 117.
3) S. Levine: ibid. **42B** (1946) 102.
4) S. Levine: ibid. **44** (1948) 833.
5) S. Levine: Phil. Mag. **41** (1950) 53.
6) S. Levine: Proc. Cambridge Phil. Soc. **47** (1951) 217.
7) S. Levine: ibid. **47** (1951) 230.
8) S. Levine: J. Colloid Sci. **6** (1951) 1.
9) S. Levine: Proc. Phys. Soc. **64A** (1951) 781.
10) H. G. B. Casimir: reference 1, p. 63.
11) S. Levine: Trans. Faraday Soc. **42B** (1946) 128.
12) J. Th. G. Overbeek: ibid. **42B** (1946) 126.

JOURNAL OF THE PHYSICAL SOCIETY OF JAPAN Vol. 8, No. 1, JAN.—FEB., 1953

Probe Measurement for High Frequency Discharge III

By Shoji KOJIMA, Kazuo TAKAYAMA and Akira SHIMAUCHI

Okubo Branch, Tokyo University of Education, Shinjuku, Tokyo

(Received September 19, 1952)

A method to determine the electron temperature and the field strength of high frequency discharge plasmas is given. It is a modified floating double probe method, where the double probe consists of a rod probe and a forked probe. By this method argon discharges in the region between 0.26 and 1.0 mm Hg at 170 Mc/sec have been studied. The electron temperatures and the field strengths were measured as a function of the radius of discharge tubes and compared with theoretical equations. The obtained results were approximately equal to those of direct current discharge.

§ 1. Introduction

The electron temperature and the field strength in the plasma of a direct current gas discharge have been well investigated. But in a high frequency plasma such quantities have not been measured because of lacking in useful methods. It was suggested in the first paper of this series1) that the electron temperature could be determined by a double probe method. Almost same time Johnson and Malter2) found a slightly different double probe method, which was aimed at decaying plasmas of d.c. discharges. Our second paper3) showed the Johnson-Malter's method to be applicable for h.f. discharges. Now we shall describe a method which gives the field strength in addition to the electron temperature4) and the results obtained by the method on the h.f. discharge of argon at about 170 Mc/sec.

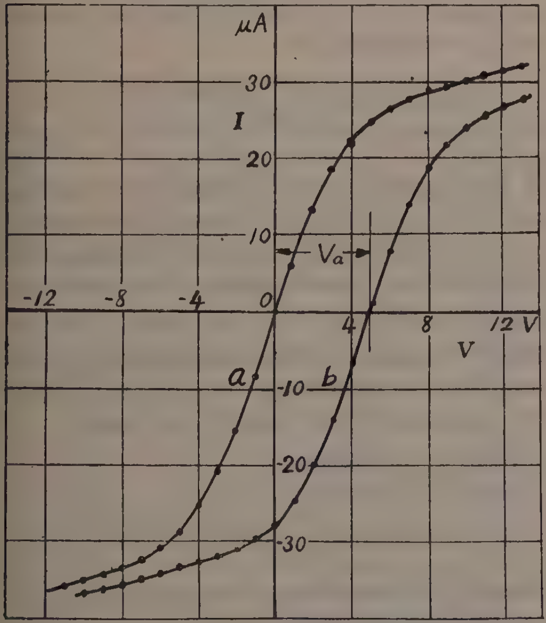

Fig. 1. Double probe current-voltage characteristic. (*a*) with probes 1 and 2, (*b*) with probe 2 and forked probe 3-4 shown in Fig. 2.

§ 2. The Method of Measurements

For the measurement of the electron temperature the floating double probe is usually set perpendicular to the h.f. electric field.3) The curve of the double probe current against voltage applied between the probes has the well known saturation character2) as shown by the curve *a* in Fig. 1. When the double probe is set in the direction of the h.f. field, the characteristic curve is affected by the field. By analysing the curve the determination of the field strength was tried. Experimentally a discharge tube with four probes Nos. 1, 2, 3 and 4 shown in Fig. 2*a* was made and set in the field after such manner as shown in Fig. 2*b*.

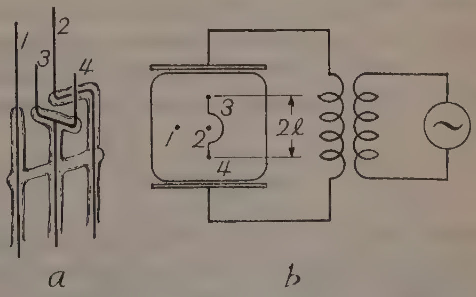

Fig. 2. Shape and arrangement of probes set in the experimental discharge tube.

Two probes P_1 and P_2, which is set perpendicular to the field, formed a usual floating double probe to measure the electron temperature. By h.f. discharges, however, the condition of "floating" was difficult to be produced comparing with the d.c. discharge on account of the effect of stray capacities. In our experiments the probes were arranged in the neutral positions[1], where the characteristic curves were not affected by a touch of hand to the measuring circuit. On such condition the curve *a* in Fig. 1 was obtained by the aid of probes P_1 and P_2. When the probes 2 and 3 were combined they formed a double probe set in the direction of the field. To keep the probes in symmetric position to the neutral plane, probe 4 is introdused. The probes 3 and 4 were interconnected and formed a forked probe P_{34}. The surface area of each of the probe 3 and 4 was a half of the probe 2. The measured characteristic curve of the double probe, which was composed of the probe P_2 and the forked probe P_{34}, is shown by the curve *b* in Fig. 1. This curve is similar to the usual one, but shifted to right by V_a. The reason why the symmetric probes yields an asymmetric character is based on the fact that the floating potential of the forked probe on a slope of potential is approximately determined by one branch at the position of lower potential. We shall give in the next paragraph quantitative treatment on it and describe how V_a depends on the field strength.

§ 3. Theory on the Probe Characteristic Curve

When the potential difference of the probe P_2 from the surrounding plasma is denoted by V_2, which is always negative, the probe current to the plasma, i_2, can be expressed as:[2]

$$i_2=I_e\exp\left(\frac{eV_2}{kT}\right)-I_p\,, \tag{1}$$

where I_e and I_p are the saturation currents carried by electrons and by positive ions respectively, e is the charge of electron, k is Boltzmann constant and T is the electron temperature. Remembering the probes 3 and 4 are kept at the same potential by the short interconnection and in the plasma a uniform field exists, the potential difference of the probes from the surrounding plasma are expressed as:

$$\left.\begin{aligned}V_3&=V_0+\sqrt{2}El\sin\omega t\,,\\ V_4&=V_0-\sqrt{2}El\sin\omega t\,,\end{aligned}\right\} \tag{2}$$

where V_0 is the potential difference between the forked probe and the plasma at the middle position of the forked probe, E is the r.m.s. field strength and $2l$ is the distance between probes 3 and 4 and ω is the angular frequency of h.f. field.

The forked probe current i_{34} is given by i_3+i_4, where

$$i_3=\frac{1}{2}\left\{I_e\exp\left(\frac{eV_3}{kT}\right)-I_p\right\}$$

and i_4 equals to the similar equation except V_3 replaced by V_4, provided that the area of probe 3 and 4 is a half of probe 2, then we obtain:

$$i_{34}=I_e\exp\left(\frac{eV_0}{kT}\right)\cosh\left(\frac{e\sqrt{2}El\sin\omega t}{kT}\right)-I_p\,. \tag{3}$$

Using the relation:

$$\cosh(x\sin\omega t)=\mathrm{I}_0(x)-2\mathrm{I}_2(x)\cos 2\omega t+\cdots\,,$$

where I's are the Bessel function of imaginary argument, i.e. $\mathrm{I}_0(x)=\mathrm{J}_0(ix)$[5], the time average of i_{34} is expressed as:

$$\langle i_{34}\rangle_{\mathrm{Av}}=I_e\exp\left(\frac{eV_0}{kT}\right)\mathrm{I}_0\left(\frac{e\sqrt{2}El}{kT}\right)-I_p\,. \tag{4}$$

If the applied probe voltage between the probe P_2 and the forked probe P_{34} is denoted by V and the probe current flowing from the P_2 to P_{34} through plasma is I, then

$$V=V_2-V_0 \text{ and } I=-\langle i_{34}\rangle_{\mathrm{Av}}=i_2\,. \tag{5}$$

Here V is positive when the probe P_2 is connected to the positive pole of a battery. From the equations (1), (4) and (5) we obtain:

$$\frac{I_p-I}{I_p+I}=\frac{I_p+\langle i_{34}\rangle_{\mathrm{Av}}}{I_p+i_2}=\exp\left(-\frac{eV}{kT}\right)\mathrm{I}_0\left(\frac{e\sqrt{2}El}{kT}\right)\,. \tag{6}$$

Since I_p is obtained from the saturation value of the characteristic curve, we can plot $\log(I_p-I)/(I_p+I)$ against V. The plot yields a straight line whose slope is e/kT. Thus we can determine the electron temperature.

Putting $I=0$, the equation (6) yields:

$$\mathrm{I}_0\left(\frac{e\sqrt{2}El}{kT}\right)=\exp\left(\frac{eV_a}{kT}\right) \tag{7}$$

where V_a is the voltage, at which the characteristic curve is crossing the coordinate axis. This is the relation between the field strength and the shift of the curve. Using the equation (7) we can determine the field strength E by the measurement of V_a.

§ 4. Experimental Procedure

The h.f. power was supplied by a push pull oscillator with the vacuum tube T310, whose rated output was 45 watts for single tube, and introduced to the discharge tubes by a parallel transmission line. Thus the electrodeless discharges were produced at 170 Mc/sec. The measurements with double probe were carried out in a shielding box shown in Fig. 3. The discharge tubes were filled with argon at pressure between 0.26 and 1.0 mm Hg. Some of them, which were sealed by a glass cock, were found to contain a little amount of organic vapours by a spectroscopic analysis. The results with those tubes will be denoted by "impure". A double probe consisted of a rod probe and a forked probe was installed in each discharge tube as shown in Fig. 4. Four tubes with the diameteres of 2.6, 3.4, 5.1 and 5.3 cm were prepared.

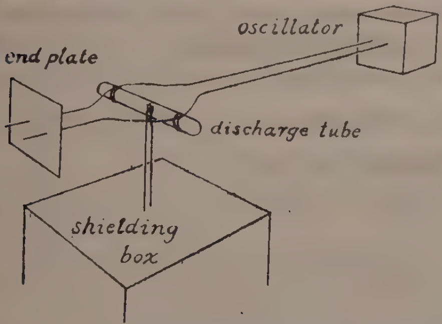

Fig. 3. Schematic diagram of apparatus.

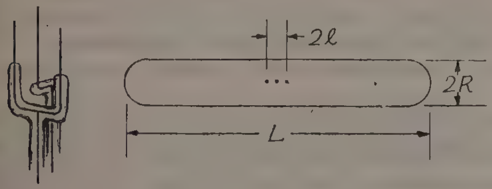

Fig. 4. Discharge tube with forked double probe.

§ 5. Results and Discussion on the Electron Temperature

The electron temperature and the field strength of h.f. plasma are interesting to be compared with d.c. plasma. Theoretically the electron temperature of d.c. plasma was given by Druyvesteyn[6] and by Engel and Steenbeck[7] in the following expression:

$$\left(\frac{eV_i}{kT}\right)^{-1/2}\exp\left(\frac{eV_i}{kT}\right)=1.16\times10^7c^2p^2R^2 \tag{8}$$

where p is the pressure in mm Hg, R is the radius of the discharge tube in cm, V_i is the ionization potential of the gas and c is a constant depending on the kind of gas. For argon gas V_i and c are 15.7 volts and 5.3×10^{-2} (mm Hg cm)$^{-2}$ respectively. As shown by the recent result obtained by Knol[8] this equation agrees well with experiments. Then we should compare our h.f. results with this equation. But in h.f. plasma we could not neglect diffusions in the direction of the axis of discharge tube. This, however, may be corrected by the use of a equivalent radius of the tube, R_e, which was defined by:

$$R_e=2.405\Lambda\,, \tag{9}$$

where Λ is the diffusion length introduced by Brown and MacDonald[4] with the equation:

$$\left(\frac{1}{\Lambda}\right)^2=\left(\frac{\pi}{L}\right)^2+\left(\frac{2.405}{R}\right)^2 \tag{10}$$

L and R being the length and the radius of the cylindrical tube.

The electron temperatures measured with various tubes are given in Fig. 5 as a function of pR_e. In the figure the electron temperatures of d.c. discharges obtained by Knol and by us are also given, and the curve drawn

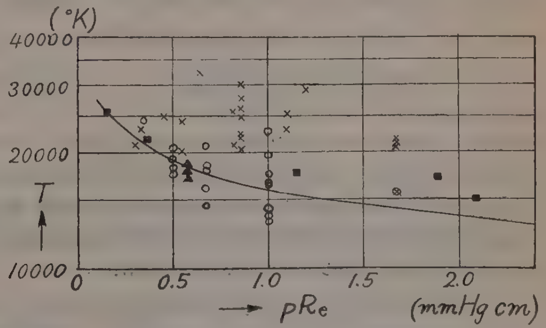

Fig. 5. Electron temperature T as a function of product of gas pressure p and equivalent radius R_e of discharge tube. The experimental values for h.f. and d.c. plasmas of pure and impure argon are inserted as points and the theoretical equation (8) is represented by a curve.
○ h.f. pure; × h.f. impure; ▲ d.c. pure; ■ d.c. measured by Knol[8].

by the equation (8) is shown. It indicates that the electron temperature of h.f. plasma is almost equal to the d.c. plasma.

For a direct comparison of electron temperatures between d.c. and h.f. discharges a long tube equipped with electrodes was filled with argon and mercury vapour as the fluorescent lamp. The obtained electron temperatures of h.f. and d.c. plasmas were 11800° K, and 11900°K respectively. It shows excellent agreement.

§ 6. Results and Discussion on the Field Strength

On the field strength we have not so convenient equation as the electron temperature. If we extend the calculation of Engel and Steenbeck⁷⁾, we can obtain the equation:

$$E=\sqrt{\frac{2\sqrt{\pi}}{3}\frac{2.405}{R}}\sqrt{\frac{kT}{e}V_i}\sqrt{\frac{b_+}{b_e}\frac{V_i+ZV_e}{V_i}}, \tag{11}$$

where b_+ and b_e are mobilities of positive ion and electron, Z is the number of inelastic collisions to ionize and V_e is the mean excitation voltage. This equation contains many quantities which are not well determined.

For simplicity we assume the field strength in the plasma to be equal to the minimum break down field and try to obtain the equation expressing the field strength. Brown and MacDonald⁴⁾ determined the minimum field in the very high frequency region by equating the number of collisions to ionize to the number of collisions to diffuse out of the tube. If this idea is applied for the case where the frequency of the field is smaller than the collision frequency, it yields:

$$E=\frac{4}{\sqrt{3}\pi}\frac{1}{\Lambda}\sqrt{\frac{kT}{e}}V_i, \tag{12}$$

where Λ is the diffusion length given by equation (10). Since this equation does not contain the frequency of the field, it may be applicable for d.c. field too. Both equations (11) and (12) point out the relation:

$$ER_e=\text{const.}\quad\text{or}\quad (E/p)(pR_e)=\text{const.} \tag{13}$$

Putting $T=20000°$ K and $V_i=15.7$ volts, equation (12) yields

$$(E/p)(pR_e)=16.2\ \text{volts}. \tag{14}$$

When we use equation (11) in place of (12), 16.2 volts in equation (14) is multiplied by

$$\frac{\sqrt[4]{\pi^3}}{2\sqrt{2}}\sqrt{\frac{b_+}{b_e}\frac{V_i+ZV_e}{V_i}}.$$

Using the well known expression:

$$\frac{b_+}{b_e}=\sqrt{\frac{m}{M}\frac{T}{T_+}\frac{\lambda_+}{\lambda_e}}$$

where m/M, T/T_+ and λ_e/λ_+ are the ratios of mass, of temperature and of mean free path between the electron and the positive ion, and assuming that $T_+=300°$ K, $\lambda_e/\lambda_+=4$, $Z=9$ and $V_e=11.5$ volts, equation (11) yields

$$(E/p)(pR_e)=3.3\ \text{volts}. \tag{15}$$

These equations have not been verified even in d.c. case, but they will be used tentatively.

The measurements have been carried out with the same tubes which were used for the electron temperature. The obtained results are plotted in Fig. 6. In the figure the field strength E/p is given as a function of pR_e, and equations (14) and (15) are shown by curves. The plots show that the field strength is depend on the purity of gas. This is interesting in comparison with the electron temperature which is almost insensitive for the purity of gas. For the pure argon tubes* the plots are close to the dotted curve which represents equation (15) and for the impure

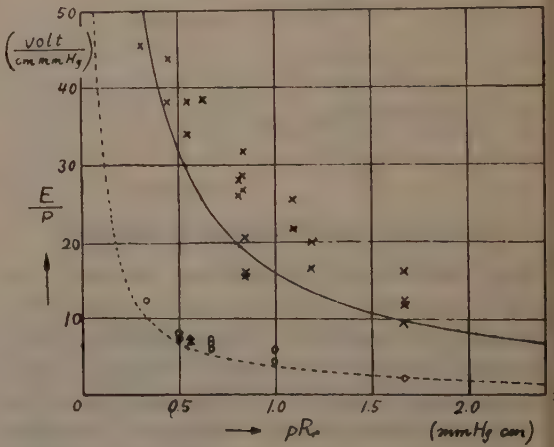

Fig. 6. Field strength E divided by pressure p as a function of product of pressure p and equivalent radius R_e of tube. The experimental values for h.f. and d.c. plasmas of pure and impure argon are inserted as points. The tentative equations (14) and (15) are given by the solid and dotted curves respectively.

○ h.f. pure; × h.f. impure; ▲ d.c. pure.

---

* We have used commertial argon without purification. The word "pure" is used relatively to "impure".

argon tubes the plots are slightly above the solid curve which represents equation (14). These results indicate that the tentative equations are useful.

This study was supported by the Scientific Research Expenditure of the Ministry of Education.

References

1) S. Kojima and K. Takayama: J. Phys. Soc. Japan **4** (1949) 346.

2) E. O. Johnson and L. Malter: Phys. Rev. **76** (1949) 1411; Phys. Rev. **80** (1950) 58.

3) S. Kojima and K. Takayama: J. Phys. Soc. Japan **5** (1950) 357.

4) c.f. Abstract of Annual Meeting of the Institute of Electrical Engineers of Japan, May 1951.

5) E. Jahnke and F. Emde: "Functionentafeln" Leipzig. 1933.

6) M. J. Druyvesteyn: Z. Physik **81** (1933) 571.

7) A. V. Engel and M. Steenbeck: "Electrische Gasentladungen" Berlin 1934 Part II.

8) K. S. Knol: Philips Res. Rep. **6** (1951) 288.

9) S. C. Brown and A. D. MacDonald: Phys. Rev. **76** (1949) 1629.

JOURNAL OF THE PHYSICAL SOCIETY OF JAPAN Vol. 8, No. 1, JAN.—FEB., 1953

Oscillatory Phenomena of Arc in Hot Cathode Discharge Tube (1)

Experimentals (Characteristics of Oscillation)

By Hirosi YOSIMOTO

Department of Physics, Faculty of Science, Okayama University

(Received June 30, 1952)

The oscillatory phenomena are observed in a hot cathode discharge tube like fluorescent lamp. The oscillations occur in the vicinity of the anode, and are the periodical variation of the anode fall accompanied with a sudden ionization. The characteristics of the oscillations depends on the anode conditions as well as the thermoionic emissivity of the cathode.

§ 1. Introduction

Generally in the arc discharge in Hg, rare gas and Hg rare gas mixture the oscillatory phenomena of arc voltage can be observed.

In 1924 Eckart and Compton¹⁾ reported that those are due to the thermoionic emissivity of the cathode. In 1933 Pupp²⁾ reported that in Hg rare gas mixture the oscillations occure at the anode fall. Recently Loh & Dieke³⁾ reported that those occure in the vicinity of anode. Kenty⁴⁾ found that metastable Hg atoms and impure gases influence greatly on the oscillations.

In 1949 the writer⁵⁾ recognized in a hot cathode discharge tube like fluorescent lamp oscillations of the similar nature as those in Hg rare gas mixture. The oscillations are due to the periodic variation of the anode fall and are greatly influenced by thermoionic emission, arc current, gaseous impurity and the construction of the anode.

In this paper there are given the fundamental properties which explain the mechanism of the oscillation.

§ 2. Apparatus

The experimental arrangement is shown in Fig. 1. The discharge tube was the same as the fluorescent lamp in the schematic construction, and it was made of hard glass, 38 mm in dia., and about 40 cm long. The electrodes were constructed with nickel wire and oxide-coated tungsten filament (double spiraled). The arc burned in Hg-A gas mixture and the pressure of A gas was 4 mm. This A gas was purified in Ca arc and its purity was measured to be 99.5% by mass-spectroscopic analysis. Its main impurities were H_2 (0.2%) and H_2O (0.3%).

The arc was obtained from a.c. or d.c.

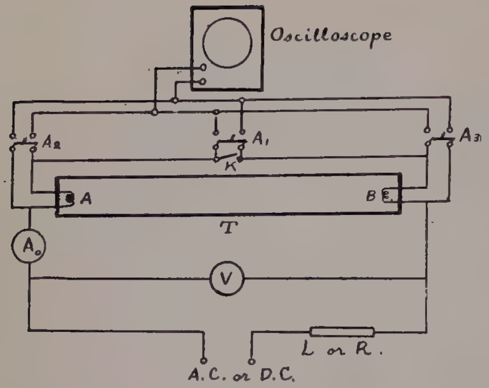

Fig. 1. Diagram of the dischange tube and the circuit.
T: Discharge tube.
A, *B*: Electrodes (oxide-coated tungsten filament).
L: Cocke. *R*: Variable resistance.
A: Ammeter, maximum value 0.5 amp.
K: Starting device (open in working state).

source. And in a.c. discharge the arc was controled by a voltage regulator in series with a chocke *L*, while in d.c. discharge it was maintained by a bank of batteries in series with a variable resistance *R*.

Oscillations in the tube voltage or in the voltage which appeared at electrodes were observed for all values of the current used (from 0.1 amp. to 0.4 amp.) by switches A_1, A_2 or A_3. And they could be studied as a function of the time merely bringing leads directly from the electrodes to the oscillograph.

In this experiment mainly the oscillations in the arc voltage were studied, through the arc current was also oscillatory.

§ 3. Characteristics of Oscillations in Arc Voltage

The oscillatory phenomena are observed in a.c. as well as in d.c. arc discharge in Hg-A gas mixture. The general characteristics of the oscillations are summarised as follows.

(*a*) *Oscillations in A.C. Discharge*

Fig. 2 shows various wave forms of arc voltage in a.c. discharge. The characteristics in two cases, i.e. the quasi-static and the dynamic one are explained as follows.

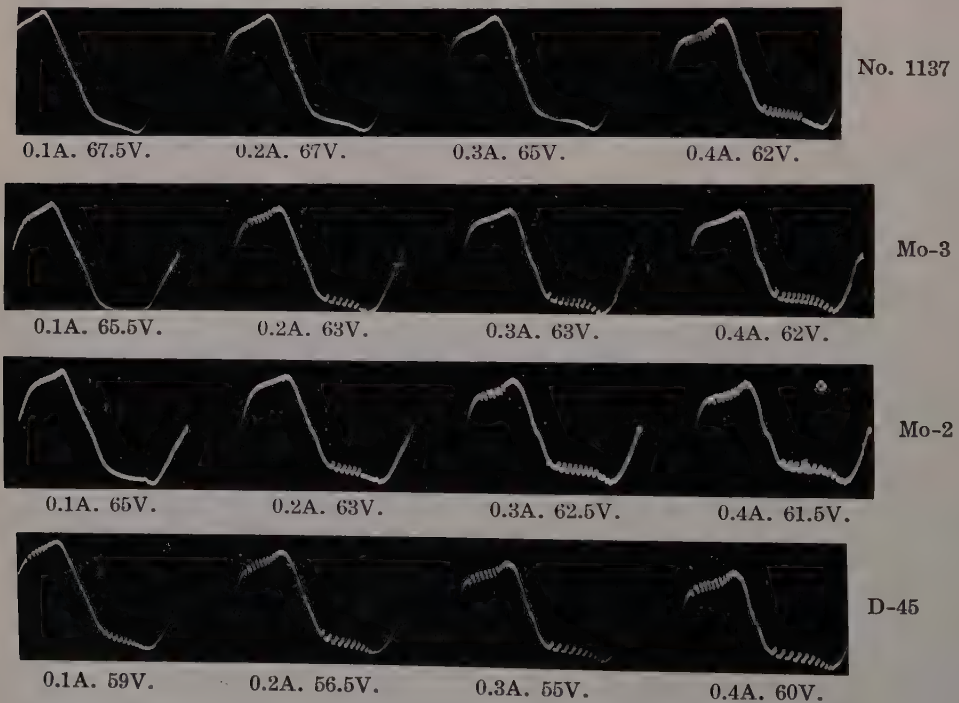

Fig. 2. Various wave forms of arc voltage in a.c. discharge.

"*Quasi-static Characteristics*"

Fig. 3 shows qualitatively the characteristics of the oscillations with respect to the effective values of the arc current. In this case the characteristics were measured at an arbitrary phase in a.c. arc. When the arc current increases, the amplitude increases, while the frequency decreases. Even in the

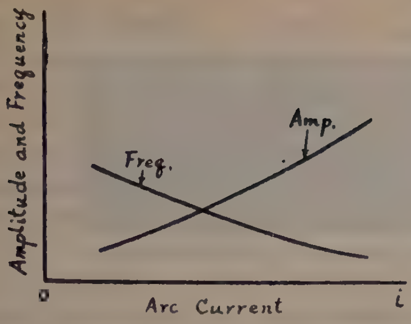

Fig. 3. The quasi-static characteristic of oscillations in a.c.discharge.

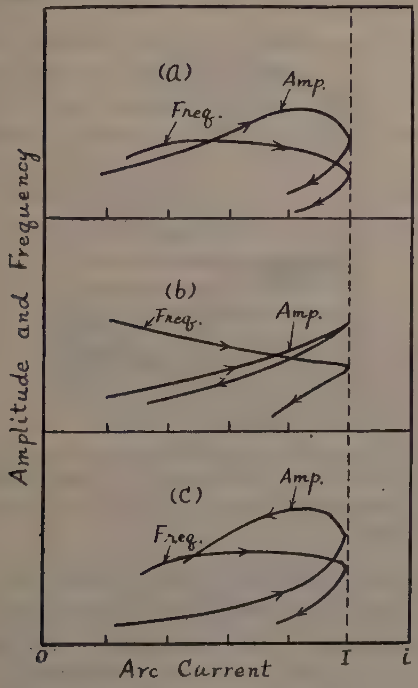

Fig. 4. The dynamic characteristic of oscillations in a.c. discharge.

same discharge tube they differ in each half period in which a certain electrode acts as anode or as cathode.

Next, in the manners of the appearance or the disappearance of the oscillations, there are the following four types. (1) None of the oscillations can be observed, (2) always they are observed and (3) they disappear or (4) appear at a certain value of the current, when the current is decreased gradually. In a discharge tube with a good thermoionic emmision, the oscillations cannot be observed, and, even if they are observed, the frequency is smaller and the amplitude is larger than in that with a smaller emmision.

"Dynamic Characteristics"

Fig. 4 shows the dynamic characteristics of the oscillations. While the frequency monotonously decreases except with the early perod of the half cycle, the amplitude increases at first gradually and decreases via a maximum value, for which there are four types. (1) The maximum amplitude exists in the period of the current increasing, (2) coincides with the maximum current, and (3) exists in the period of the current decreasing. These manners differ from that of the quasi-static characteristics. The oscillatory wave forms are saw-tooth-like as shown in Fig. 5. In these saw-tooth-like voltage the rate of the build-up of the voltage is smaller than that of the decay, so in Fig. 5 the angle θ_1 is larger than θ_2. The former changes with the variation of the arc current, that is, it is greater in the period of the current increasing than in that of the current decreasing, while the latter is nearly independent of the arc current, provided that the external conditions of the circuit remain constant. Fig. 6 shows an example of the observed characteristics, and this characteristic coresponds to the (a) type in Fig. 4.

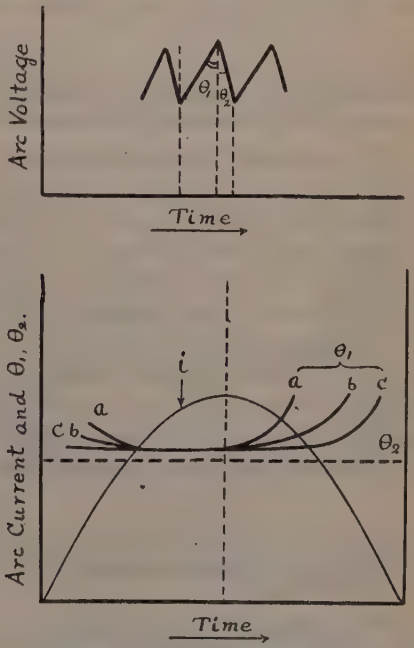

Fig. 5. The manners of the variation of θ_1 and θ_2 in the half cycle period of a.c. discharge. *a*, *b* and *c* represent θ_1 at (*a*), (*b*) and (*c*) type characteristic in Fig. 4.

As show in Fig. 7 the peak of the voltage has a tendency to become flatter according to the decrease of the current after its maximum.

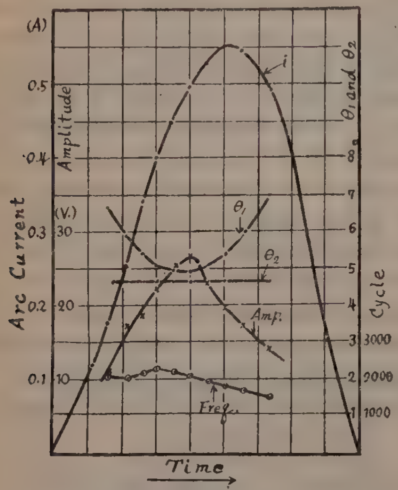

Fig. 6. An example of the obserbed characteristics of arc current and oscillation. (in a case of the effective arc current 0.4 amp.)

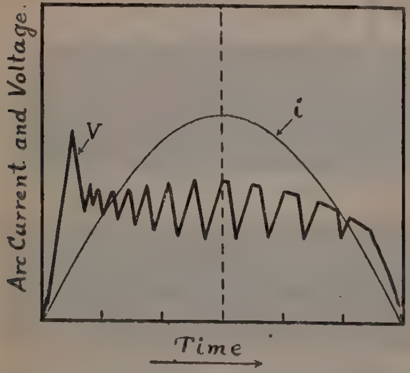

Fig. 7. The schematic manner of oscillatory arc voltage in the half cycle of a.c. discharge.

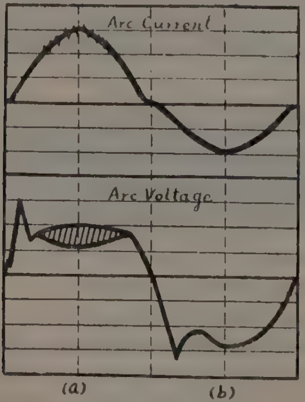

Fig. 8. The wave forms of arc voltage due to the large difference of the thermoionic emissivity.

When one of the two electrodes has no sufficient emission to maitain the arc at a constant cathode drop in the domain of the operation, the wave form of the arc voltage becomes convex as shown in Fig. 8 (b). In such a case the arc is non-oscillatory and even if it is oscillatory, the amplitude is smaller and the frequency is far greater than in the case with good emission.

Generally the reignition voltage[5] is markedly influenced by the thermoionic emissivity of the cathode. From this stand point one can compare the emissivities of the two electrodes. As shown in Fig. 9, it has been often observed that the wave form in each half cycle shows different figure owing to the difference of the emissivity. That is, in this case, in the wave form observed in such a period as the one electrode, which has more ample emission than the other, acts as cathode, the maximum of the amplitude exists in the period of the current increasing, while in the other wave form the maximum exists in the period of the current decreasing.

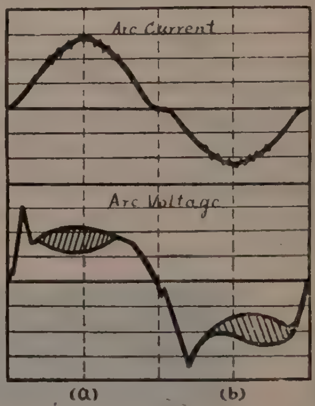

Fig. 9. The wave forms of arc voltage due to the differences of both the thermoionic emissivity and the anode fall.

The example in Fig. 10 shows the wave form in such a case that the one electrode is so super heated that barium is evaporating.

These facts mentioned above denote that both the characteristics and the wave form of the oscillation are intimately related with the thermoionic emission of the cathode.

When some impure gases are added to the discharge tube or freed from the electrodes and the other places, the frequency increases and the amplitude decreases, or the oscilla-

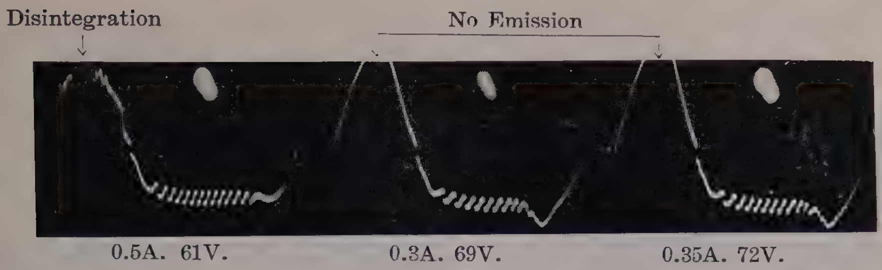

Fig. 10. The wave forms of arc voltage observed when Barium is evaporating in one of the two electrodes.

tions become irregular,

These variations are also observed in the case of the decrease of the argon gas pressure. In this case the temperature of the electrodes becomes higher.

When the pressure of the Hg vapour increases, the oscillations disappear gradually and later reappear. Since in this experiment the anode fall decreases with the increase of the pressure of Hg vapour, such a variation of the oscillations seems to be related directly to the anode fall.

(*b*) *Oscillations in D.C. Discharge*

The arc voltage in d. c. discharge is also oscillatory. Fig. 11 shows an example of the observed d.c. characteristics. The general characteristics of the oscillations are similar to the quasi-static characteristics in a.c. discharge, Fig. 3. That is, when the arc current increases, the amplitude increases, while the frequency decreases.

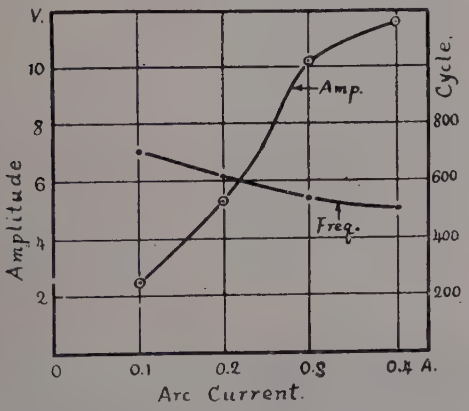

Fig. 11. An example of the characteristics of oscillations in d.c. discharge.

The value of the arc voltage and the mode of the oscillation are influenced by the change of the anode area. Replacing the anode by another one in the Y-shape discharge tube with a common cathode already reported6), it can be observed that the arc voltage and the amplitude decreases and the frequency increases as the anode area is larger. In this case the decrease of the arc voltage should be due to that of the anode fall. Therefore this change of the anode fall may be considered to be the cause of that of the oscillations.

§ 4. Periodic Variation of Potential Difference at Electorode

It has been already reported7) that in a fluorescent lamp the potential differences appear at electrodes. The electrode in this experiment is an oxide-coated tungsten filament. So, when the arc is burning, a potential difference owing to the resistance of the filament should appear at the electrode. The potential difference at the anode is also oscillatory, while, though that at the cathode is oscillatory, only slight ripples are observed. And the former is usually greater than the latter.

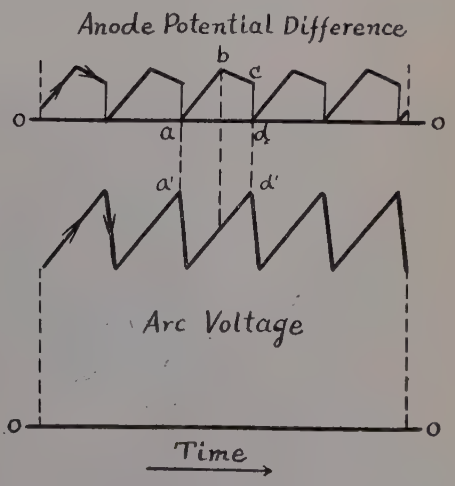

Fig. 12. The wave forms of arc voltage and anode potential difference.

(*a*) *Potential Difference in D.C. Discharge*

The potential difference at the anode is oscillatory and its frequency is the same as that of the oscillations of the arc voltage. In this case it is noteworthy that the potential difference vanishes periodically as shown in Fig. 12 (also refer to Fig. 16). Moreover its vanishing occurs instantaneously and coincides with the instance when the arc voltage becomes maximum.

The potential difference is essentially due to the resistance of the filament. Therefore the variation of the potential difference shows also that of the current fraction which flows into the anode filament. As recognized in Fig. 12, it never changes proportionally to the variation of the arc current. The anode part into which the arc current flows, therefore the anode fall and the potential distribution around the filament change all at the same time in phase. From the modes shown in Fig. 12, one can estimate roughly that the potential distribution and the current change periodically from (1) to (2) state as shown in Fig. 13. At the (2) state the arc current localizes at a part of the anode. In order to change the state from (2) to (1) an abrupt and dense ionization must happen. Thus the oscillation of the potential difference at the anode should be repeated periodically.

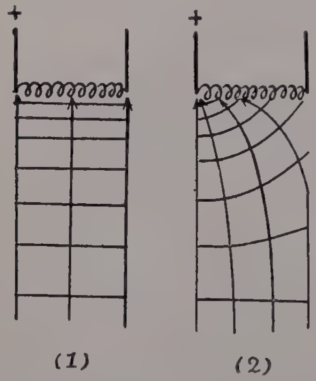

Fig. 13. The manner of the change of potential distribution before the anode.

On the contrary to this, the potential difference at the cathode differs from that at anode, and only slight ripples are observed. They arise owing to the pulsation of the arc current. As has been already reported[7], at the cathode the greater part of the arc current localizes at a fixed small part of the cathode. Therefore the potential difference at the cathode must be proportional to the arc current. And, of course, it should be influenced by the degree of the consumption of barium oxide which changes the flowing point of the current at the cathode.

(*b*) *Potential Difference in A.C. Discharge*

In a.c. dischage the mode of the potential differences at the electrodes are in principle the same as that in d.c. discharge, except its figure is sinusoidal owing to the a.c. current. The frequency of the potential difference at the anode is equal to that of the arc.

In Fig. 14, if the wave from of the arc voltage in the upper side of zero line is that in the period when one electrode (A) acts as cathode, the wave form in the lower side is that in the period when another electrode (B) acts as cathode. The wave form of the potential difference at A electrode differs

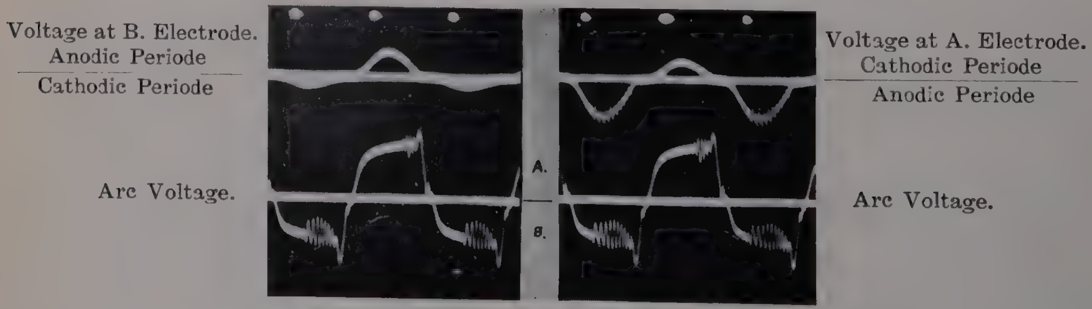

0.4 Amp. 56 Volt.
Potential Difference
at B. Electrode.
Time ⟵

0.4 Amp. 56 Volt
Potential Difference
at A. Electrode.
Time ⟵

Fig. 14. An example of the change of the potential differences at electrodes in a. c. discharge.

markedly from that at B electrode. When the arc is nonoscillatory, the potential difference at the anode is also non-oscillatory. Tables I and II respectively show the values of the various potential differences measured in Fig. 14. From Table I one sees that the emissivity of B electrode is greater than that of A electrode, and also that from Table II the mechanical consumption of the former is smaller than that of the latter, as the positive as well as negative potential differences at electrodes becomes generally greater according to the more consumption of barium oxide[7].

Table I.

Cathode	Reignition Voltage (V)	Arc Voltoge (V)	
A	87.5	69	non oscillation
B	83.0	55	oscillation

Table II.

Electrode	Negative P. D. (V)	Posititve P. D. (V)
A	1.5	3.8
B	0.8	2.1

§ 5. Variations of Oscillations due to Anode Connections

When the connection at the anode is exchanged from one lead to the other, the characteristic of the oscillation changes. Therefore this change is entirely due to the conditions of the anode.

(*a*) *Example in A.C. Discharge*

Fig. 15 shows such an example. In this case the temperature of the filament changed remarkably by the exchange of the anode connection. In one example the one end of the anode filament became super-heated and then the arc became non-oscillatory. In Fig. 15 the connection at B electrode was exchanged and that at A electrode was unchanged. In the half cycle that A electrode acts as anode the variation of the wave form is hardly recognized, but it is striking in the cycle that B electrode acts as anode. These facts denote that the anode temperature has a great influence on the oscillation and, if it becomes greater than a certain value, the arc becomes non-oscillatory.

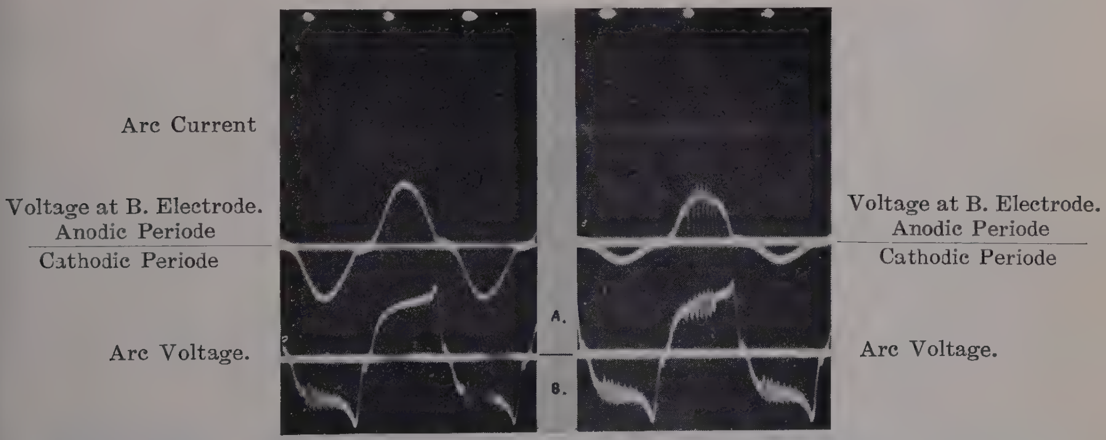

0.35 Amp. 58.2 V
High Temperature Side
Connection at B.
Time ⟵

0.35 Amp. 56.5 V.
Low Temperature Side
Connection at B.
Time ⟵

Fig. 15. An example of the changes of the oscillations due to the exchange of the anode connection in a. c. discharge.

(*b*) *Example in D.C. Discharge*

When the two terminals at the anode are together connected, the oscillation also changes as shown in Fig. 16. Table III

Table III.

Anode Connection	Max. Arc Voltage (V)	Amplitude (V)	Frequency (Cycle)
Normal (B)	44.2	13.8	779
Together (A)	41.8	12.4	920

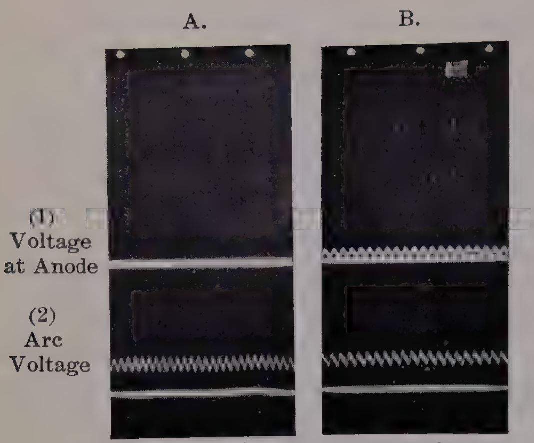

(2) 36.2 Volt. Time ←— Connection: Together.

(2) 37 Volt. Time ←— Connection: Normal.

Fig. 16. An example of the change of the oscillations due to the anode connection in d. c. discharge.

shows the values of arc voltage, amplitude and frequency. In this case the anode drop and the amplitude decrease and the frequency increases, as if the anode area becomes larger.

§ 6. Effects of Auxiliary Arc on the Oscillation

The effect of an auxiliary arc on the oscillation was studied. In a T-shape discharge tube the anode was immersed in the positive column of an auxiliary arc as shown in Fig. 17.

(*a*) *Effects of D.C. Auxiliary Arc*

Fig. 18 shows the oscillations of the main arc in the relation to the auxiliary arc current (also refer to Fig. 19). Table IV shows the values of the frequency, the arc voltage and the potential difference measured in Fig. 18. From these results the oscillations seems to be greatly influenced by the auxiliary arc. Especially the frequency of the main arc is entirely decided by that of the auxiliary arc. For the auxiliary arc below a certain value the former is half of the latter. As shown in Fig. 19, the minimum of the main arc vol-

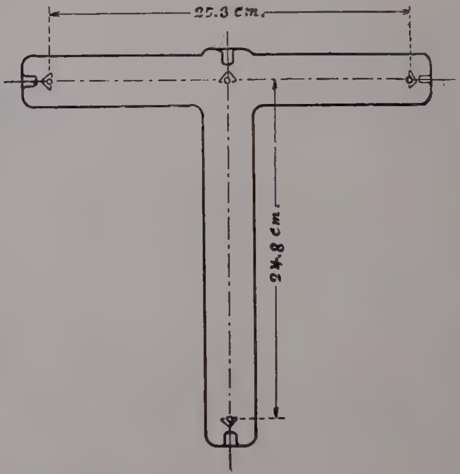

Fig. 17. T-shape discharge tube.

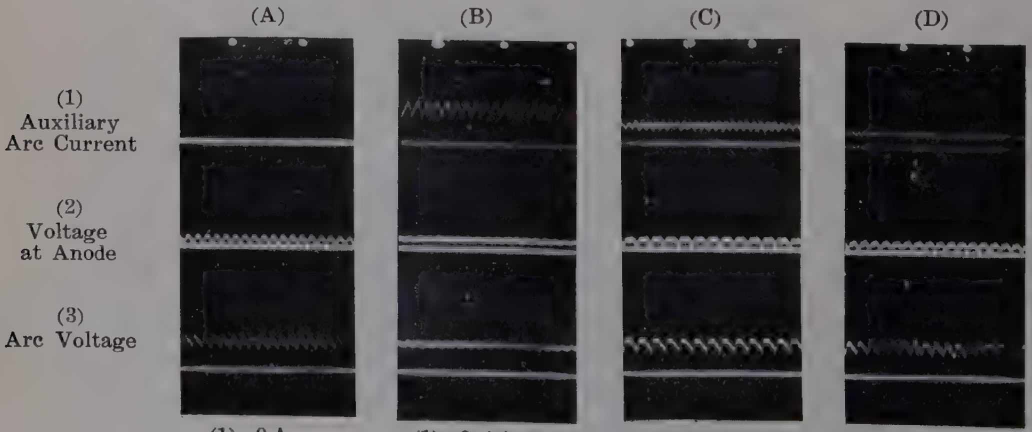

(1) 0 Amp. Time ←— No Auxiliary Arc.

(1) 0.4 Amp. Time ←—

(1) 0.2 Amp. Time ←—

(1) 0.15 Amp. Time ←—

With D. C. Auxiliary Arc.

Main Arc Current: 0.35 Amp.

Fig. 18. The change of the oscillations due to d. c. auxiliary arc.

Table IV.

Auxiliary Arc (A)	Auxil. Arc Freq. (Cycle)	Main Arc Freq. (Cycle)	Main Arc Amplitude (V)	Anode Pottential Diff.	
				Max. Volt. (V)	Min. Volt. (V)
0	0	740	11.9	6.6	0
0.4	684	684	2.4	6.6	5.8
0.2	872	872/2	11.9	6.6	0
0.15	1155	1155/2	11.9	6.6	0

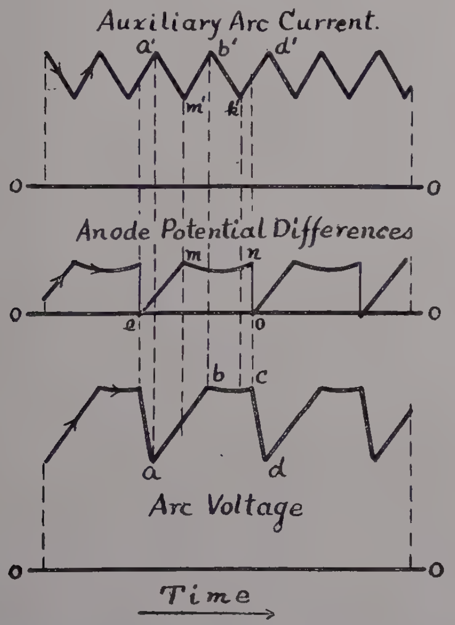

Fig. 19. The oscillations of the main arc and the auxiliary arc.

tage always coincides with the maximum of the auxiliary arc current in phase, but the latter does not always coincide with the former. In this case the rate of the build-up of the main voltage becomes smaller according to the increase of the auxiliary current, while that of the decay remains to be unchanged. Moreover the peaks of the arc voltage become flatter.

For the auxiliary arc above a certain value, the frequency of the main arc coincides with that of the auxiliary one and the main arc voltage decreases notablly and no current's localization at the anode can be observed.

(*b*) *Effects of A.C. Auxiliary Arc*

In this case the effects on the main arc are qualitatively the same as that of the preceding case. Fig. 20 shows an example. Table V gives the values of the arc voltages measured in Fig. 20. From this figure it can be concluded that, if the auxiliary arc is non-

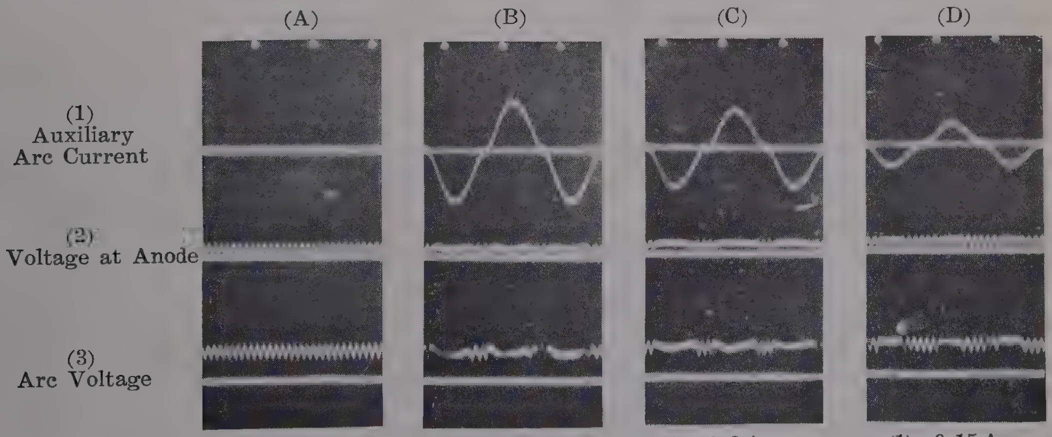

(1) 0 Amp. Time ⟵
(1) 0.4 Amp. Time ⟵
(1) 0.3 Amp. Time ⟵
(1) 0.15 Amp. Time ⟵

No Auxiliary Arc.

With A. C. Auxiliary Arc.

Main Arc Current: 0.35 Amp.

Fig. 20. The change of the oscillations due to the a. c. auxiliary arc.

Table V.

Auxiliary Arc (A)	Max. Auxil. Arc Current (A)	Min. Main Arc Voltage (V)
0.4	0.51	32.7
0.3	0.39	35.6
0.15	0.24	40.4

oscillatory and its current is greater than a certain value, the main arc is also non-oscillatory. According to the increase of the auxiliary arc current, the main arc voltage decreases gradually, that is, the anode fall becomes smaller.

These facts mentioned in this section show not only that the oscillations occur in the anode fall but also that its characteristics may be determined by the amounts of the positive ions around the anode.

§ 7. Conclusion

From the above mentioned results the following subjects can be concluded.

The oscillations are characterized not only by the anode conditions but also by the thermoionic emissivity of the cathode.

The anode conditions determine the anode fall, and in this anode fall there happens a sudden ionization. So the oscillations are presumably due to the alternative occurrences of the ionization and the diffusion of the positive ions.

The thermoionic emissivity of the cathode should act as a regulator of the arc current, therefore it will also characterize the oscillations.

The further discussions about this mechanism will be given in the next paper.

In conclusion the writer wishes to express his sincere appreciation to the Central Research Institute, Hitachi Seisakujo Co. for the permission to perform this research there. And also he wishes to express his sincere thanks to Dr. Y. Toriyama, Dr. H. Hamada and Dr. T. Kambara, of the institute, for their adequate advices and continued interests, and to Mr. M. Sato, Mr. H. Kondo and Mr. M. Takahashi for their helps in the course of this research.

He is also grateful to Dr. B. Arakatu, the President of Konan University, Dr. K. Yamasita, the Professor of Okayama University, and Dr. K. Tanaka, the Professor of Kyoto University, for their kind encouragements.

References

1) C. Eckart & K. T. Compton: Phys. Rev. **24** (1924) 97.

2) W. Pupp: Phys. ZS. **34** (1933) 756.

3) H. Y. Loh & G. H. Dieke: J. O. S. A. **37** (1947) 837.

4) C. Kenty: Phys. Rev. **80** (1950) 95.

5) H. Yosimoto: Hitachi Hyoron **32** (1950) 206. (In Japanese)

6) H. Yosimoto: Report of Phys. Inst. Okayama University. **1** (1951). (In Japanese)

7) H. Yosimoto: Report of Phys. Inst. Okayama University. **2** (1951). (In Japanese)

JOURNAL OF THE PHYSICAL SOCIETY OF JAPAN Vol. 8, No. 1, JAN.—FEB., 1953

Oscillatory Phenomena of Arc in Hot Cathode Discharge Tube (2)

Theoretical (Mechanism of Oscillation)

By Hirosi YOSIMOTO

Department of Physics, Faculty of Science,
Okayama University

(Received June 30, 1952)

In regard to the mechanism of the oscillatory arc in a hot cathode discharge tube like fluorescent lamp, the circumstances was made clear as follows.

The oscillations occur in the following cases. That is, (1). The quantity of the positive ions generated by ionization in the anode fall is greater than that necessary to sustain the arc, and (2) the arc current is smaller than the saturated electron current determined by the cathode temperature.

Accordingly the existence of the excess ions is the cause of the oscillations. Ionization and diffusion occur alternately. Therfore the characteristic of oscillation is determined by the quantity of excess ions. But in this case it is also influenced by the space charge in front of the cathode, that is, by the thermoionic emission of cathode. And generally a fraction of the excess ions will be employed to reduce the anode fall stationarily, if the electron emission becomes to be limited by its saturation value or by the negative space charge in front of the cathode.

§ 1. Introduction

As has been already reported[1)], the oscillatory phenomena are observed in a hot-cathode discharge tube like fluorescent lamp, and the oscillation is the periodical variation of anode fall, and also the characteristics of the oscillations change not only with the anode conditions but also with the thermoionic emissivity of the cathode.

The oscillatory phenomena in a low voltage arc in Hg vapour are given a semi-quantitative theoretical explanation on the basis of the space charge around the filament by Eckart and Compton[2)] in 1924. By their explanation one can learn that the oscillations are influenced by the relative relation between the arc current and the thermoionic emission.

In 1933 Pupp[3)] also studied these phenomena in Hg Argon gas mixture. He artificially supplied positive ions to the anode fall by an auxiliary arc and found that the anode fall changed from positive to negative. Accordingly he concluded that the oscillations should be due to the periodic variation of the quantity of positive ions. Recently Loh and Dieke[4)] as well as Kenty[5)] have also studied the oscillatory phenomena. The cause and the mechanism of oscillations, however, have remained to be clarified.

Now the writer deduces the theory of oscillations from his experimental data of the preceding paper[1)].

§ 2. Mechanism of the Oscillations

From the results reported in the preceding paper[1)], it has become clear that the oscillations in arc discharge are intimately related to the thermoionic emission of the cathode, although they are anodic phenomena. Now the following mechanism about these oscillation can be deduced.

(1) The amounts of the positive ions created by ionization in the anode fall are larger than that required to sustain the arc. That is, excess ions are created around the anode.

(2) Both the anode fall and the excess ions increase according to the increase of the arc current.

(3) As soon as the excess ions arise in the anode fall by a sudden ionization, the anode fall decreases and the arc current increases respectively. The amount of this change in the each case is proportional to that of the excess ions.

(4) The excess ions decrease with time by diffusion or recombination until they become

to vanish. According to this change the anode fall increases and the arc current decreases.

These four conditions show that the existence of the excess ions is the direct cause of the oscillations and that the oscillations are due to the alternative occurrences of ionization and diffusion of positive ions. As already reported⁶⁾, in this study the anode fall is a positive one and moreover is greater than the ionization potential of Hg atom. And the anode fall changes with the arc current, the anode conditions and the pressure of gas. Therefore the amount of the excess ions will also change and the characteristics of the oscillations should be varied.

Now one can explain the general characteristics of the oscillations by the four conditions as follows.

The amplitude of the oscillations shows the amount of the variation of the anode fall and the diffusion time of the excess ions determine the period i.e. the frequency of the oscillations. Therefore, according to the increase of the arc current, the amplitude becomes larger and the frequency becomes smaller, as the amounts of the excess ions increase.

Now, the anode fall V_a (volt) is given as a function of the arc current i (amp,) by an experimental formula⁶⁾,

$$V_a = ai + b, \tag{1}$$

where a and b are a constant depending on the nature of gas, the anode area and the anode temperature. In one of the examples, the values of a and b are respectively 10.5 and 9.8. The number of positive ions N generated by a sudden ionization in front of the anode is given by the relation

$$N = Ki(V_a - V_0), \tag{2}$$

where V_0 is the voltage to cause ionization and K is a constant corresponding to the total ionization power of the electrons. If N_0 is the number of positive ions necessary to maintain the arc and ΔN is that of the excess ions, N is given by the relation

$$N = N_0 + \Delta N\,. \tag{3}$$

Now N_0 is considered to be proportional to the random ion current in the positive column that is proportional to the arc current. So ΔN and N_0 are respectively given from (1), (2) and (3) by the relations

$$\Delta N = Kai^2\,, \tag{4}$$

$$N_0 = K(b - V_0)i\,. \tag{5}$$

The increase of the arc current ΔI and the decrease of the arc voltag ΔV are given by the relations

$$\Delta I = K'\Delta N\,, \tag{6}$$

$$\Delta V = R\Delta I\,, \tag{7}$$

where K' is a constant depending on the nature of gas and R is a constant depending on the resistance or impedance of the external circuit.

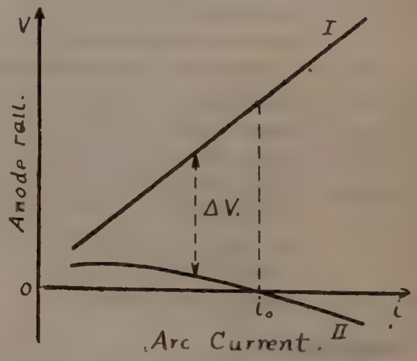

Fig. 1. The relation between the anode fall and the amplitude.

Thus the relation between the anode fall V_a and the amplitude ΔV may be shown qualitatively in Fig. 1. In this figure the curve I shows the upper limit of the anode fall and the curve II the lower limit. So it will be seen that the amplitude of oscillations can be smaller or greater than the anode fall, that is, the anode fall can be positive or negative according to the value of the arc current. And this observed to be the case.

Next, in order to make possible the oscillations to occur freely, the electron emission at the cathode must be so ample that can instantly respond to the increase of current proportional to the amount of excess ions without changing the cathode fall. The electron emission is influenced by the space charge around the cathode. And, as has already been shown⁶⁾, the arc burns in a range of zero-field emission.

Therefore the following cathodic conditions must be added to the preceding four conditions.

(5) If the arc current is larger than the saturated electron current, the oscillations

cannot occur.

(6) If the arc burns in a range of zero-field emission, the oscillations may be able to occur, but in this case they will be influenced by the space charge around the cathode.

That is, when the arc current is greater than the saturated electron current, the increase of electron emission should be due to Shottky-effect, and so the cathode fall must be increased by increasing the input voltage in order to increase the arc current. Therefore in such a case the oscillations cannot occur.

When the arc is burning in a range of zero-field emission, the sign of the space charge around the cathode will be changed from negative to positive according to the increase of arc current.
And Eckart and Compton[2] showed that the oscillations can occur only in the case that the sign of the space charge is positive. The writer also has accepted this picture in this study.

However, so long as the arc burns in the range of zero-field emission, the sign of the space charge can not become positive. If it becomes positive, the current will suddenly increase. So, for the arc current greater than a certain value in the range of zero-field emission, the space charge will be nearly zero to maintain the arc at a constant value, and, as a matter of course, the cathode drop will decrease slightly according to the increase of the arc current. In this circumstance the arc may be immediately influenced by the ions coming from anode side. Thus it may be considered that there is a metastable range in the arc current.

Now in these view points above mentioned, the characteristics of oscillations may be explained as follows.

The relation between the electron current emitted from cathode and the arc current may be shown qualitatively as the full line in Fig. 2. In this figure I_e is the saturated electron current depending on the temperature of cathode and I_0 is the arc current correspond to I_e. Now one may be able to take such an adequate current I_0' that for the current smaller than I_0' the space charge around the cathode becomes negative. Therefore only in the range $I_0 > i > I_0'$ the oscillations may be able to occur. However, if one assume the amount of excess ions to be constant, it will be immediately recongnized that for the current which exists in the region between I_0 and I_u or between I_0' and I_l the increase of arc current does not become to be proportional to the amount of excess ions as shown in Fig. 3 (a). In practice the feature of the increase of current may be shown as *a b c d* in Fig. 3 (b). This is due to that in the range $I_0 > i > I_u$ the arc current cannot exceed I_0, while in the range $I_0' > i > I_l$ a fraction of the excess ions may be used to neutralize the negative space charge and the other fraction to increase the arc current. From this picture one can know that the apparent oscillation region is a little greater than that shown by Eckart and Compton. Therefore the next condition can be deduced.

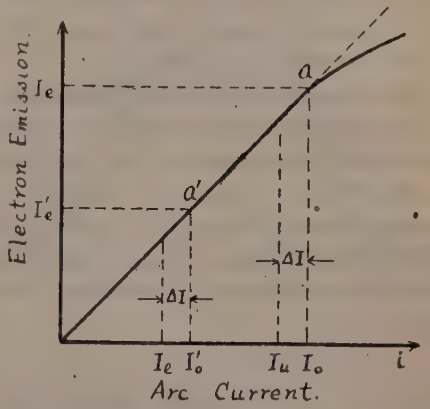

Fig. 2. The relation between the electron current and the electron current emitted from the cathode.

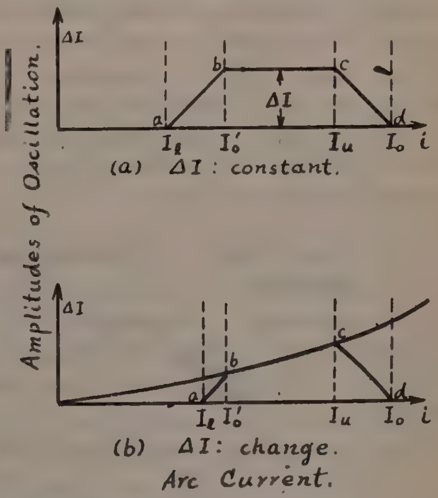

Fig. 3. The oscillatory region and the change of amplitude.

(7) The excess ions are generally composed of two parts of which one participates the oscillations and the other doesn't. And the ratio of them is changed by the relative relation between the arc current and the saturated electron current.

Next, it remains to say the role of the ions, which imparticipates the oscillations, on the arc. About this point the next condition may be deduced.

(8) The non-effective ions to the oscillations make the anode fall to decrease stationarily by a quantity proportional to the number of the ions.

Evidence which supports this picture will be later mentioned. Now, if m is the fraction of the effective ions and n is that of the non-effective ones,

$$\Delta N = m\Delta N + n\Delta N\,. \qquad (8)$$

Therefore the stationary decrease of the anode fall ΔV_n is given by the relation

$$\Delta V_n = RKn\Delta N\,. \qquad (9)$$

By these pictures above mentioned the mechanism of oscillations can be made clear. And this theory fits in a qualitative way much that has been discovered thus far.

Now the writer explains the experimental results reported in the preceding paper by his theory mentioned above.

§ 3. The Chracteristics of Oscillations in A. C. Discharge

As the quasi-static characteristics on a. c. discharge are clear by the above mentioned explanations, now the dynamic ones will be explained.

The arc current i is approximately written by

$$i = I \sin \omega_0 t\,, \qquad (10)$$

where ω_0 is the circular frequency and I is the maximum arc current.

The temperature of cathode will vary periodically with a small amplitude according to the cyclic change of arc current in delayed phase by the heat inertia. The saturated electron curent is determined by the temperature of cathode. Therefore I_0 and I_0' will change in the same phase as the temperature of cathode and may be given by the relations

$$I_0 = I_a + I_m \sin \omega_0(t-\Delta t_0)\,, \qquad (11)$$

and

$$I_0' = I_a' + I_m' \sin \omega_0(t-\Delta t_0)\,, \qquad (12)$$

where I_a and I_a' are constants depending on the arc current and the thermoionic emissivity, I_m and I_m' on the arc current and its frequency, and Δt_0 means the lag of phase.

The increased arc current i' owing to the excess ions is given from Eqs. (4), (6) and (10) by

$$\begin{aligned} i' &= i + \Delta I \\ &= i + KK'ai^2. \end{aligned} \qquad (13)$$

In order to interpret roughly the schematic nature of oscillations, Eq. (13) may be approximately replaced by

$$\begin{aligned} i' &= (I + KK'aI^2)\sin \omega_0 t \\ &\equiv I'\sin \omega_0 t\,. \end{aligned} \qquad (14)$$

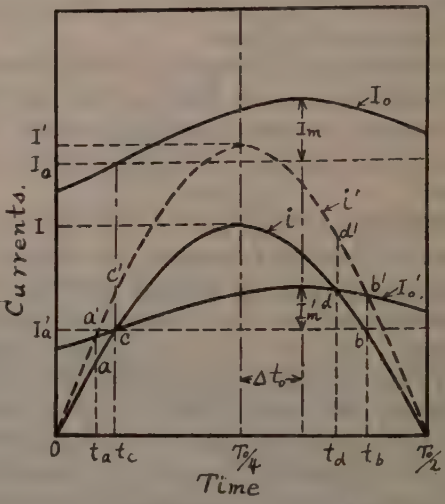

Fig. 4. The manners of i, i′, I₀ and I₀′ in a half cycle of a.c. discharge.

Thus in the half cycle that the electrode acts as cathode I_0, I_0', i and i' are graphically given as shown in Fig. 4. From this figure it will be understood that the oscillations can occur only in the range between t_a and t_b and the non-oscillatory range in the period of the current increasing is smaller than that of the current decreasing. This is observed practically to be the case. Of course, the oscillatory range should be changed by the thermoionic emissivity of cathode. If the electron emission is so surplus that I' is always greater than i', none of the oscillations may be observed in the arc. Practically this is realized by the improvement of thermoionic cathode.

Next, when the oscillations become to be influenced by the negative space charge around the cathode, the situation becomes as shown in Fig. 5 (a). The oscillations can occur in the shaded region. In this region ΔI which determines the amplitude is given from Eqs. (14) and (12) by the relation

$$\begin{aligned}\Delta I &= i' - I_0' \\ &= I' \sin \omega_0 t - I_a' - I_m' \sin \omega_0 (t - \Delta t_0) \\ &= A \sin \omega_0 (t + \Delta t') - I_a' , \qquad (15)\end{aligned}$$

where

$$A = (I'^2 + I_m'^2 - 2I' I_m' \cos \omega_0 \Delta t_0)^{1/2}$$

and

$$\Delta t' = T_{an}^{-1} \frac{I_m' \sin \omega_0 \Delta t_0}{I' - I_m' \cos \omega_0 \Delta t_0} .$$

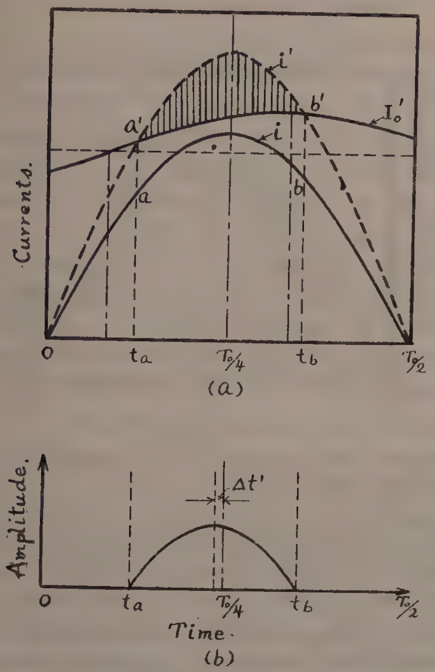

Fig. 5. The oscillation limited by the negative space charge before the cathode.

Accordingly the amplitude are qualitatively shown as in Fig. 5. The maximum of amplitude appears earlier than that of arc current.

On the contorary, when the oscillations become to be restricted by the saturation current of cathode, the situations become as shown in Fig. 6. In this case ΔI is given as follows.

In the ranges $t_a \sim t_c$ and $t_a \sim t_b$ it is shown by Eq. (15). In the ranges $t_c \sim t_e$ and $t_f \sim t_a$ it is given by the relation

$$\Delta I = i' - i = (I' - I) \sin \omega_0 t . \qquad (16)$$

In the range $t_e \sim t_f$ it is given by the relation

$$\Delta I = I_0 - i = I_a - B \sin \omega_0 (t + \Delta t'') , \qquad (17)$$

where

$$B = (I^2 + I_m^2 - 2I I_m \cos \omega_0 \Delta t)^{1/2}$$

and

$$\Delta t'' = T_{an}^{-1} \frac{I_m \sin \omega_0 \Delta t_0}{I - I_m \cos \omega_0 \Delta t_0} .$$

The schematic figure of oscillaions is mainly given by Eqs. (16) and (17), and graphically in Fig. 6 (b). In this case the maximum of amplitude always appear later than that of arc current and its value satisfies at the same time Eqs. (16) and (17). The oscillatory range is greater than that of the preceding case.

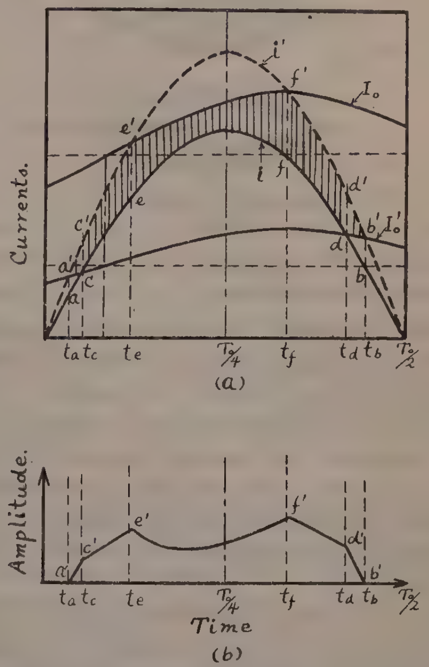

Fig. 6. The oscillation limited by the saturation value of the thermoionic emission.

From these pictures the three types of the dynamic characteristics reported in the preceding paper are rationally explained.

Therefore one can conclude that the electron emission can determine the characteristics of oscillations and also the schematic wave forms.

Now, if the oscillations are not influenced by the electron emission, the maximum of amplitude and that of arc current will occur at the same time. So the oscillatory wave form may be roughly considered as in Fig. 7 (a). Thus in the case of Fig. 5 it will become as in Fig. 7 (c). These schematic features are observed to be the case as shown in Fig. (10) of the preceding paper.

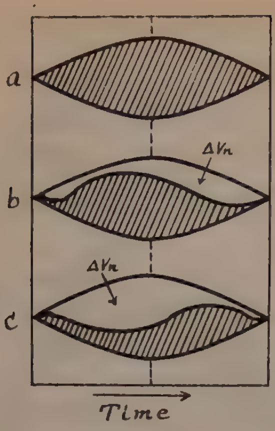

Fig. 7. The schematic wave forms of the oscillatory arc voltage.

When the excess ions are suddenly generated by ionization in the anode fall, the sudden increase of arc current will occur at once. This increase will be, however, influenced by the resistance of external circuit. So the rate of the decrease of voltage will remain constant independent of the change of arc current, if the conditions of external circuit constant.

On the contrary, the diffusion time is influenced not only by the quantity of excess ions but also by the manner of the change of arc current. That is, generally, when the arc current is increasing, the diffusion time becomes smaller than that in the case of constant arc current, as if the quantity of excess ions has become smaller. When the arc current is decreasing, it becomes larger. Therefore the rate of the increase of arc voltage will become to be greater in the period of the current increasing than in that of current decreasing. The frequency is given as the reciprocal of the diffusion time.

Now the diffusion time t_D may be given by the relation

$$t_D = Dm\Delta N - \gamma \frac{dN_0}{dt}, \tag{18}$$

where D and γ are proportional constants. From Eqs. (4), (5) and (10), this equation is given as follows.

$$t_D = KI(m\alpha \sin^2\omega_0 t - \beta \cos \omega_0 t), \tag{19}$$

where $\alpha = DaI$, and $\beta = \gamma(b - V_0)$.

Now, even if one assume that in this equation m is equal to 1, it may not be hindered to interpret the schematic feature of t_D. Eq. (19) will be approximated by the next equation

$$\begin{aligned} t_D &\doteqdot KI(\alpha \sin \omega_0 t - \beta \cos \omega_0 t) \\ &= KIC \sin \omega_0 (t - \Delta t_D), \end{aligned} \tag{20}$$

where

$$C = (\alpha^2 + \beta^2)^{1/2},$$

and

$$\Delta t_D = \frac{1}{\omega_0} T_{an}{}^{-1} \frac{\beta}{\alpha}.$$

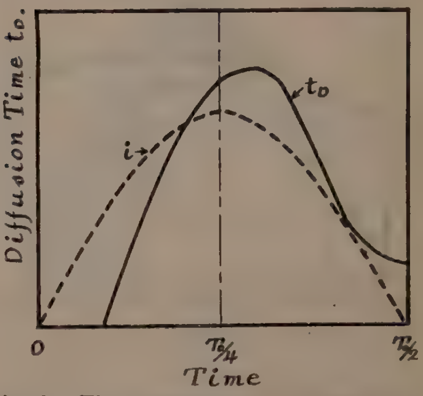

Fig. 8. The manner of the change of the diffusion time t_D.

Fig. 8 shows graphically the manner of t_D given by Eq. (20). From this figure one can know that in the region of oscillation the diffusion time t_D increase monotonously and therefore the frequency decreases likewise. From these considerations, it will be known that the rate of the increase of voltage changes with the arc current as shown in Fig. 5 of the preceding paper.

Next, in the period of the current decreasing, if the positive ions at the anode fall is always the same as that necessary to sustain the arc in spite of the diffusion, the oscillations will not occur. As has been already reported, the peak of voltage has a tendency to become flatter with the decrease of the arc current. Perhaps this phenomenon may be due to the above mentioned mechanism.

Thus the dynamic characteristic in a.c. discharge has been explained by the writer's theory.

§ 4. The Characteristics of Oscillations in Auxiliary Arc

In this case the anode fall shall decrease due to that the random electron current increases owing to the auxiliary arc. Therefore, when the auxiliary current becomes greater than a certain value, the sudden ionization in the anode fall will cease, and the main arc will become non-oscillatory. Of course, the arc voltage will decrease owing to the decrease of the anode fall.

Accordingly, if the auxiliary arc is oscillatory, the oscillation of the main arc will be influenced by the auxiliary arc. That is the frequency of the main arc will be determined by that of the auxiliary arc.

When the auxillary current is smaller than a certain value, the oscillations shall be observed naturally in the main arc, but in this case the diffusion time will be prolonged by the auxiliary arc, as if the quantity of the excess ions has become greater. So the frequency of the main arc will decrease. And, if the auxiliary arc is oscillatory, the main arc voltage will become at least when the auxiliary arc current becomes maximum. However, even if the auxiliary one becomes maximum in the diffusion period of the excess ions, only the diffusion time will be prolonged and the maximum of the auxilary one will not always coincide with the minimum of the main arc voltage. Therefore, if the frequency of the auxiliary arc is greater than that of the main arc without the auxiliary one, the frequency of the main arc f may be considered to be given by the next relation

$$f=f'/n\,,$$

where f' is the frequency of the auxiliary one and n is an integer greater than 1. An example in the case that n is equal to 2 may be considered to be given in Fig. 18 of the preceding paper. Thus by these pictures the experimental results can be understood clearly. This fact is a evidence that supports the diffusion process as a mechanism of anodic oscillation.

§ 5. The Characteristics Influenced by the Anode Conditions

The value of anode fall is determind not only by the arc current but also by the anode area and its construction. Therefore, if the anode area increases, the anode fall will decrease and the amplitude decreases, while the frequency increases. Even if the geometrical area of anode remains constant, the effective area will be changed not only by such the contaminations as oxide film, gaseous impurities and the other substances but also the change of the anode connection.

If the temperature of anode is too high, the Hg vapour pressure around the anode will be lowered and the ionization probability decreases. So the positive ions generated in the anode fall also decrease in quantity. Accordingly in this case the amplitude decreases and the frequency increases. And finally, if none of the excess ions becomes to be generated, the oscillations will cease to occur and the arc becomes non-oscillatory.

§ 6. The Characteristics Influenced by Impure Gases

It has been observed that in the discharge tube used in this study the impure gases are mainly H_2O and H_2. If the discharge tube contains these impure gases, the ionization probability will be decreased by electron capture, inelastic collisions and the destruction of the Hg meta-stable atoms, and the quantity of excess ions generated in the anode fall decreases. Accordingly in the oscillations the amplitude decreases and the frequency increases.

When the impure gases are at random released from the electrode and the other places, the quantity of positive ions changes, the oscillations become irregular, and also the arc becomes unstable.

Of course, the cathode drop increases with the release of impure gases. Accordingly the cathode temperature becomes higher. Eventually, in a.c. discharge, also the anode temperature becomes higher, as the electrode alternately acts as cathode or as anode. So the effects of impure gases on the oscillations are intensified by this increase of anode temperature.

§ 7. The Characteristics Influenced by the Pressures of Argon Gas

As has been already reported[7], the increase of anode temperature becomes remarkable according to the decrease of A gas pressure. So both the density of Hg atoms and that of A atoms will locally decrease in the vicinity of anode, and therefore the probability of ionization will also decrease. This is the reason why the amplitude decreases and the frequency increases according to the decrease of A gas pressure.

§ 8. The Characteristics Influenced by the Vapour Pressure of Hg

When the ambient temperature around discharge tube is increased, the vapour pressure of Hg will also increase. And then the ocillations have a tendency to disapear gradually and to appear again at above a certain tenperature.

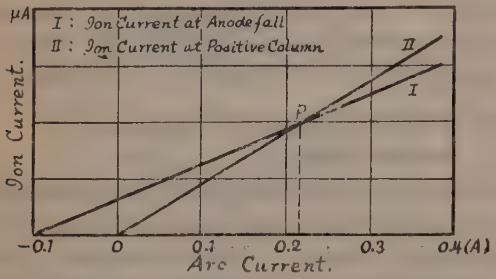

Fig. 9. The chracteristics of the random ion current in the anode fall and the positive column.

As has been already shown⁽⁶⁾, the characteristics between the random ion current and the arc current are represented by a straight line both in the anode fall and in the positive column. And the inclination of the characteristic in the anode fall is smaller than that in the positive column as shown in Fig 9. And according to the increase of Hg vapour pressure the former decreases and the latter increases, therefore the two characteristics will become to intersect one another and moreover the point of intersection will move toward a lower arc current.

From these results one can conclude the following subjects.

The greater the vapour pressure becomes, the smaller the anode fall. Therefore the oscillations gradually become smaller and finally disappear at a certain vapour pressure. But moreover, when the vapour pressure becomes greater than the certain value, the anode fall become too small to maintain the arc. Accordingly again the anode fall increases to supply the positive ions necessary to maintain the arc. Perhaps in this case the excess ions should be generated by ionization, and thus the oscillations become to reappear.

§ 9. Conclusion

Thus the writer could deduce a theory concerning the mechanism of the oscillation in a hot-cathode discharge tube like fluorescent lamp. And by his theory he could explain the oscillations observed in practice. And moreover his theory shows that the anode fall may be freely controlled and therefore the oscillations may be changed as one pleases. And as an application of his theory one can roughly measure the thermoionic emissivity of cathode in a discharge tube like fluorescent lamp.

In conclusion the writer is grateful to Dr. B. Arakatu, the President of Konan University, Dr. K. Yamashita, Dr. K. Asagoe, Dr. K. Umeda of Okayama University and Dr. K. Tanaka of Kyoto University, for their kind encouragement. And his thanks are also due to Mr. M. Sato for his help in the course of this research.

References

(1) H. Yosimoto: J. Phys. soc. Jap. **8** (1953) 59.
(2) C. Eckart and K. T. Compton: Phys. Rev. **24** (1923) 97.
(3) W. Pupp: Phys. ZS. **34** (1933) 756.
(4) H. Y. Loh and G. H. Dieke: J. O. S. A. **37** (1947) 837.
(5) C. Kenty: Phys. Rev. **80** (1950) 95.
(6) H. Yoshimoto: Report of Phys. Inst. Okayama University. **3** (1951) (In Japanese)
(7) H. Yoshimoto; Hitachi Hyoron **32** (1950) 206. (In Japanese)

JOURNAL OF THE PHYSICAL SOCIETY OF JAPAN Vol. 8, No. 1, JAN.—FEB., 1953

The Reflection and Transmission of a Multi-layer Film

By Kôzô ISHIGURO and Toshio KATÔ

Department of Physics, Faculty of Science, University of Tokyo

(Received July 18, 1952)

From the recurrence formula of Weinstein a matrix equation is derived connecting the amplitudes of electric vector of light in the k-th layer with those in the p-th layer of a multi-layer film. The elements of the matrix are expressed as functions of the reflection and transmission of the intermediate film between the media k and p. From this equation, formulas are derived for the transmission and reflection of an arbitrary multi-layer filter as functions of the thickness of the spacing layer. The results are found out to be of the same form as Abelè's equations derived by the consideration of the multiple reflections in the spacing layer. By these equations, the physical meaning of the complicated phase factor of Vašiček's equation is made clear and some new relations of the intensity and phase of the transmitted and reflected light are obtained.

§ 1. Fundamental Formulas

The relation of the electric vector amplitude in the $(p+1)$-th layer and p-th layer (fig. 1) is given by Weinstein's formula[3] as

$$\begin{aligned} 2u_{p+1}X^{+}_{p+1} &= (u_{p+1}+u_p)X_p^{+}\exp(il_p) \\ &\quad +(u_{p+1}-u_p)X_p^{-}\exp(-il_p) \\ 2u_{p+1}X^{-}_{p+1} &= (u_{p+1}-u_p)X_p^{+}\exp(il_p) \\ &\quad +(u_{p+1}+u_p)X_p^{-}\exp(-il_p) \end{aligned} \quad (1)$$

where,

$l_p=(2\pi/\lambda)n_ph_p\cos\varphi_p$

$h_p=$the thickness of the p-th layer

$n_p=$the refractive index of the p-th layer

$\varphi_p=$the angle of refraction (or incidence) in the p-th layer.

In the absorbing layer, n_p and φ_p are complex quantities. The definitions of $X_p^{\pm}$ and u_p will be given in (3) or (4) below.

In the p-th layer of the film, the amplitude at $z=z_p$ of the electric vector parallel to the incident plane is denoted by p_p and the amplitude at $z=z_p$ perpendicular to the incident plane is denoted by S_p.

Then, the electric vectors of the light wave in the p-th layer are represented by $p_p^{\pm}\exp i\tau_p^{\pm}$ and $S_p^{\pm}\exp i\tau_p^{\pm}$ of the both planes of polarization. In the present paper, the following form is adopted for the phase of the light wave*:

$$\begin{aligned} \tau_p^{\pm} &= \omega t-(2\pi/\lambda)n_p\{x\sin\varphi_p\pm(z-z_p)\cos\varphi_p\} \\ &= \tau-(2\pi/\lambda)n_p\{\pm(z-z_p)\cos\varphi_p\} \end{aligned}$$

where $\tau=\omega t-(2\pi/\lambda)n_px\sin\varphi_p$

is a common factor to the every layers.

In the above expressions, the affix $(\pm)$ represents the direction of the wave normal of the light; when the direction of the wave normal makes a sharp angle with the positive z axis, the affix takes $(+)$ sign and when the angle is larger than 90°, the affix is $(-)$ (fig. 1). Also the following quantities are used in (1) for the polarized light:

$$\left.\begin{aligned} X_p^{\pm} &= \pm(p_p^{\pm}\cos\varphi_p\exp i(\tau_p^{\pm}-\tau))_{z=z_p} \\ &= \pm p_p^{\pm}\cos\varphi_p \\ u_p &= m_p/\cos\varphi_p \end{aligned}\right\} \quad (3)$$

when the electric vector is parallel to the incident plane, and

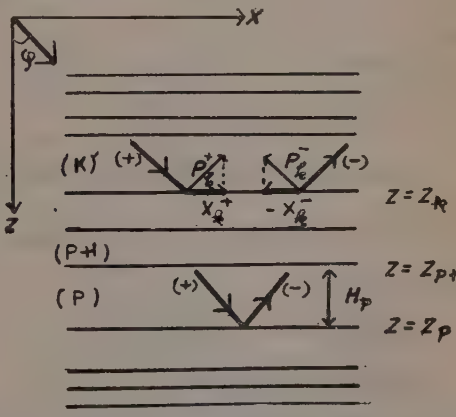

Fig. 1. Notations of multi-layer film (only the parallel comprents of electric vector are presented).

---

* In the paper of Weinstein, $e^{i\omega t}$ is adopted as the phase factor instead of $e^{-i\omega t}$ in the present paper.

$$\left.\begin{aligned} X_p^\pm &= (S_p^\pm \exp i(\tau_p^\pm - \tau))_{z=z_p} \\ &= S_p^\pm \\ u_p &= m_p \cos\varphi_p \end{aligned}\right\} \qquad (4)$$

when the electric vector is perpendicular to the incident plane.

$n_p=\sqrt{\varepsilon_p\mu_p}$ is the refractive index of the p-th layer and ε_p, μ_p are the dielectric constant and the magnetic permiability respectively. $m_p=H_p/E_p$, the ratio of the magnetic vector amplitude to the electric vector amplitude, will be conventionally named as the characteristic admittance[4] and is given by $\sqrt{\varepsilon_p/\mu_p}$ for the light wave in the free space and by $\sqrt{\varepsilon_p/\mu_p}\,(\lambda/n_p)/\lambda_g=\lambda/(\mu_p\lambda_g)$ for TE-wave and by $\sqrt{\varepsilon_p/\mu_p}\,\lambda_g/(\lambda/n_p)=(\varepsilon_p\lambda_g)/\lambda$ for TM-wave in the wave guide, where λ is the free space wave length in the vacuum and λ_g is the guide wave length.[5] In the wave guide, however, only the case $\varphi_p=0$ is considered and λ_g must be used in place of λ/n_p in the equations (1).

Now (1) can be written in the matrix form as

$$\begin{pmatrix} X_{p+1}^+ \\ X_{p+1}^- \end{pmatrix} = W_{p+1,p}\begin{pmatrix} X_p^+ \\ X_p^- \end{pmatrix} \qquad (5)$$

$$\left.\begin{aligned} &= W'_{p+1,p}U_p\begin{pmatrix} X_p^+ \\ X_p^- \end{pmatrix} \\ &= W'_{p+1,p}\begin{pmatrix} X_p'^+ \\ X_p'^- \end{pmatrix} \end{aligned}\right\} \qquad (6)$$

where

$$U_p=\begin{pmatrix} \exp(il_p) & 0 \\ 0 & \exp(-il_p) \end{pmatrix} \qquad (7)$$

$$W'_{p+1,p}=\begin{pmatrix} (u_{p+1}+u_p)/(2u_{p+1}) & (u_{p+1}-u_p)/(2u_{p+1}) \\ (u_{p+1}-u_p)/(2u_{p+1}) & (u_{p+1}+u_p)/(2u_{p+1}) \end{pmatrix}$$

and we note that

$$\left.\begin{aligned} &\det(U_p)=1, \\ &\det(W'_{p+1,p})=u_p/u_{p+1}. \end{aligned}\right\} \qquad (7)'$$

It is clear that $\begin{pmatrix} X_p'^+ \\ X_p'^- \end{pmatrix} = U_p\begin{pmatrix} X_p^+ \\ X_p^- \end{pmatrix}$ corresponds to the amplitudes of the electric vector at the boundary $z=z_{p+1}$, when $X_p^\pm$ is the amplitude at $z=z_p$ by (3) or (4). It follows from (5) that the relation of the electric vector amplitude in the k-th and p-th layer ($k>p$) is given by

$$\begin{aligned} \begin{pmatrix} X_k^+ \\ X_k^- \end{pmatrix} &= W_{k,k-1}W_{k-1,k-2}\cdots W_{p+1,p}\begin{pmatrix} X_p^+ \\ X_p^- \end{pmatrix} \\ &= W_{k,p}\begin{pmatrix} X_p^+ \\ X_p^- \end{pmatrix} \\ &= W'_{k,p}U_p\begin{pmatrix} X_p^+ \\ X_p^- \end{pmatrix} \\ &= W'_{k,p}\begin{pmatrix} X_p'^+ \\ X_p'^- \end{pmatrix} \end{aligned} \qquad (8)$$

where

$$\begin{aligned} \det(W'_{k,p}) &= \det(W_{k,p}) \\ &= \det(W_{k,k-1})(W_{k-1,k-2})\cdots(W_{p+1,p}) \\ &= u_p/u_k \end{aligned} \qquad (9)$$

by virtue of (7′). It is to be remarked that $W_{k,p}$ or $W'_{k,p}$ is a function only of the nature of the medium between the k-th and p-th layers and is independent of the nature of the outer parts of the film.

Now consider the film composed of the $(k-p-1)$ layers between the media k and p both supposed to extend to infinity and denote by

$$\left.\begin{aligned} r_{k,p} &= |r_{k,p}|\exp i\delta_{k,p} \\ t_{k,p} &= |t_{k,p}|\exp i\zeta_{k,p} \end{aligned}\right\} \qquad (10)$$

respectively the amplitude reflection and transmission of this hypothetical film when the light is incident from the side k*. This means that

$$r_{k,p}=X_k^-, \qquad t_{k,p}=X_p'^+$$

if $X_k^+=1$ and $X_p'^-=0$,

so that we have from (8)

$$\begin{pmatrix} 1 \\ r_{k,p} \end{pmatrix} = W'_{k,p}\begin{pmatrix} t_{k,p} \\ 0 \end{pmatrix}. \qquad (11)$$

Similarly let

$$\begin{aligned} r_{p,k} &= |r_{p,k}|\exp i\delta_{p,k} \\ t_{p,k} &= |t_{p,k}|\exp i\zeta_{p,k} \end{aligned}$$

be the reflection and transmission of the same film from the side p. This means that

$$r_{p,k}=X_p'^+, \qquad t_{p,k}=X_k^-$$

---

* In the case of the electric vector parallel to the incident plane, the definition of amplitude transmission given in the present paper differs from the usual one which is defined by $P_p'^+/P_k^+$ instead of $X_p'^+/X_k^+=(\cos\varphi_p P_p'^+)/(\cos\varphi_k P_k^+)$.

if $X_p'^- = 1$ and $X_k^+ = 0$,

and we have as above

$$\begin{pmatrix} 0 \\ t_{p,k} \end{pmatrix} = W'_{k,p} \begin{pmatrix} r_{p,k} \\ 1 \end{pmatrix}. \tag{13}$$

By the four equations (11) and (13), we can express the four matrix elements of $W'_{k,p}$ in terms of $r_{k,p}$, $t_{k,p}$, $r_{p,k}$ and $t_{p,k}$. The result is

$$W'_{k,p} = \begin{pmatrix} 1/t_{kp} & -r_{pk}/t_{kp} \\ r_{kp}/t_{kp} & (t_{kp}t_{pk} - r_{kp}r_{pk})/t_{kp} \end{pmatrix} \tag{14}$$

and (8) becomes

$$\begin{pmatrix} X_k^+ \\ X_k^- \end{pmatrix} = \begin{pmatrix} 1/t_{kp} & -r_{pk}/t_{kp} \\ r_{kp}/t_{kp} & (t_{kp}t_{pk} - r_{kp}r_{pk})/t_{kp} \end{pmatrix} \begin{pmatrix} X'^+_p \\ X'^-_p \end{pmatrix}.$$

It should be noticed that r_{kp}, t_{kp}, r_{pk} and t_{pk} are quantities peculiar to the (kp) film and independent of the nature of the outer parts of the film. Moreover, they are not quite independent of each other, for it follows from the general relation (9) that

$$u_k t_{pk} = u_p t_{kp}. \tag{15}$$

It is clear that the above relations are correct not only for a film composed of several homogeneous layers but also for an inhomogeneous film, for which the refractive index of the film varies continuously in the direction of z axis, for the latter can be regarded as a limiting case of the former.

If u_p and u_k are real, (15) implies that

$$\zeta_{kp} = \zeta_{pk}, \quad T_{kp} = T_{pk} \tag*{(15)$'$}$$

where

$$T_{kp} = (u_p/u_p)|t_{kp}|^2$$
$$T_{pk} = (u_k/u_p)|t_{pk}|^2$$

are the energy transmissions for the incident light from the side k and p respectively.

The energy reflections on the side k and p are defined by

$$R_{kp} = |r_{kp}|^2$$

and

$$R_{pk} = |r_{pk}|^2.$$

§ 2. Properties of Transparent Film

When the film (kp) is transparent, there are further relations among the quantities r_{kp}, t_{kp} etc. In this case the conservation of energy requires that

$$u_k(|X_k^+|^2 - |X_k^-|^2) = u_p(|X_p'^+|^2 - |X_p'^-|^2).$$

Putting (14) into the left-hand side and comparing the coefficients, we obtain

$$(1 - |r_{kp}|^2)/|t_{kp}|^2 = u_p/u_k$$
$$(|t_{kp}t_{pk} - r_{kp}r_{pk}|^2 - |r_{pk}|^2)/|t_{kp}|^2 = u_p/u_k$$
$$(t_{kp}t_{pk} - r_{kp}r_{pk})r^*_{kp}/|t_{kp}|^2 = -r_{pk}/|t_{kp}|^2.$$

From these all and (15), we obtain the following relations which are not independent:6),7)

$$|r_{kp}| = |r_{pk}| \text{ or } R_{kp} = R_{pk}$$
$$1 - |r_{kp}|^2 = (u_p/u_k)|t_{kp}|^2 \text{ or } 1 - R_{kp} = T_{kp}$$
$$r_{kp}t^*_{kp} + r^*_{kp}t_{kp} = 0$$
$$t_{kp}t_{pk} - r_{kp}r_{pk} = t_{kp}/t^*_{kp}. \tag{16}$$

In particular, the third relation implies(7)

$$\delta_{kp} + \delta_{pk} - 2\zeta_{kp} = \pm\pi \tag{17}$$

and hence the fourth relation becomes

$$\begin{aligned} t_{kp}t_{pk} - r_{kp}r_{pk} &= \exp(i2\zeta_{kp}) \\ &= \exp(i(\delta_{kp} + \delta_{pk} \pm \pi)) \end{aligned} \tag{18}$$

By (16), the eq. (14) takes on the simpler form

$$\begin{pmatrix} X_k^+ \\ X_k^- \end{pmatrix} = \begin{pmatrix} 1/t_{kp} & r^*_{kp}/t^*_{kp} \\ r_{kp}/t_{kp} & 1/t^*_{kp} \end{pmatrix} \begin{pmatrix} X'^+_p \\ X'^-_p \end{pmatrix}. \tag{19}$$

In the case of symmetrical film (kp), we have

$$\delta_{kp} = \delta_{pk}$$

and hence the eq. (17) becomes8)

$$\zeta_{kp} = \delta_{kp} \pm (\pi/2). \tag*{(17)$'$}$$

Therefore, the phase difference of the amplitude at $z = z_k$ of the reflected light and the amplitude at $z = z_p$ of the transmitted light of a non-absorbing symmetrical film, such as an ideal Frustrated Total Reflection filter, will be always $\lambda/4$, not being influenced by the thickness of the film.

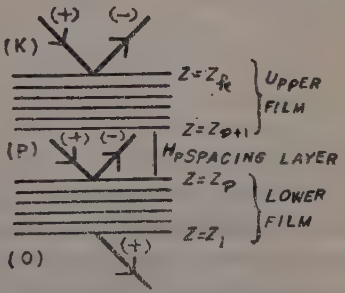

Fig. 2. Multi-layer filter.

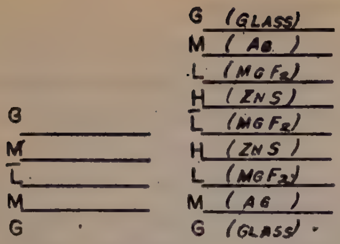

(A) Usual *H. D.* filter.

(B) *H. D.* filter with dielectric multi-layers of $\lambda/4$ thickness.

Fig. 3. Examples of application.

§ 3. Formulas for the Amplitude Reflection and Transmission as Functions of the Thickness of the Spacing Layer

Consider an arbitray intermediate homogeneous layer (say, the p-th layer) of multilayer film $(k, 0)$ and divide the film into three parts: the p-th layer (spacing layer) and the upper and lower parts.

Then it follows from (7) and (8) that

$$\begin{pmatrix} X_k^+ \\ X_k^- \end{pmatrix} = W'_{kp} \begin{pmatrix} X'^+_p \\ X'^-_p \end{pmatrix}$$

$$\begin{pmatrix} X'^+_p \\ X'^-_p \end{pmatrix} = U_p \begin{pmatrix} X_p^+ \\ X_p^- \end{pmatrix}$$

$$\begin{pmatrix} X_p^+ \\ X_p^- \end{pmatrix} = W'_{p0} \begin{pmatrix} X'^+_0 \\ X'^-_0 \end{pmatrix}$$

and

$$\begin{pmatrix} X_k^+ \\ X_k^- \end{pmatrix} = W'_{k0} \begin{pmatrix} X'^+_0 \\ X'^-_0 \end{pmatrix}.$$

Hence, we have

$$W'_{k0} = W'_{kp} U_p W'_{p0}.$$

Putting (14) and (7) and comparing the matrix elements of both side, we obtain

$$r_{k0} = \frac{r_{kp} + (t_{kp}t_{pk} - r_{kp}r_{pk})r_{p0} \exp(-i2l_p)}{1 - r_{pk}r_{p0} \exp(-i2l_p)} \tag{20}$$

$$t_{k0} = \frac{t_{kp}t_{p0} \exp(-il_p)}{1 - r_{pk}r_{p0} \exp(-i2l_p)}. \tag{21}$$

(20) and (21) are the same equations as those derived by F. Abelès from the consideration of the multiple reflections in the p-th layer¹⁾. If we introduce the quantity $\xi \exp i\gamma$ by

$$t_{kp}t_{pk} - r_{kp}r_{pk} = \xi \exp i\gamma \tag{22}$$

with real quantities ξ and γ, (20) is transformed into

$$r_{k0} = \frac{r_{kp} + \xi r_{p0} \exp\{i(\gamma - 2l_p)\}}{1 - r_{pk}r_{p0} \exp(-i2l_p)}. \tag{20$'$}$$

If the upper film of the spacing layer is transparent, if follows from (18) that

$$\left.\begin{aligned} &\xi = 1 \\ &\gamma = 2\zeta_{kp} = \delta_{kp} + \delta_{pk} \pm \pi. \end{aligned}\right\} \tag{23}$$

(20′) with (23) ought to be equivalent to the equation given by the combination of Rouard's and Vasicek's method²⁾. Therefore, the complicated phase factor in the expression of Vasicek,

$$x_1 + x_2 + \ldots + x_{k-1} + \varepsilon_1 + \varepsilon_2 + \ldots \varepsilon_{k-1}$$

is to be equal to $-\gamma$ of the very simple expression (23).

§ 4. Formulas for the Energy Reflection Transmission as Functions of the Thickness of the Spacing Layer

[1] *The case when the upper film of the spacing layer involves absorbing lapers*

It is assumed that the first and last media and the spacing layer are transparent with real u_0, u_p, u_k and l_p.

Then it follows from (20′) and (21) by an elementary calculation that

$$T_{k0} = (u_0/u_k)|t_{k0}|^2 = A/\{1 - \alpha \cos L\} \tag{24}$$

$$\begin{aligned} R_{k0} &= |r_{k0}|^2 \\ &= B\{1 - \eta \cos(L + \beta)\}/\{1 - \alpha \cos L\} \end{aligned} \tag{25}$$

where

$$\begin{aligned} A &= T_{kp}T_{p0}/(1 + R_{pk}R_{p0}) \\ B &= (R_{kp} + \xi^2 R_{p0})/(1 + R_{pk}R_{p0}) \\ \alpha &= 2\sqrt{R_{pk}R_{p0}}/(1 + R_{pk}R_{p0}) \\ L &= 2l_p - \delta_{pk} - \delta_{p0} \\ \beta &= (\delta_{kp} + \delta_{pk} \pm \pi) - \gamma \\ \eta &= 2\xi\sqrt{R_{kp}R_{p0}}/(R_{kp} + R_{p0}) \\ 2l_p &= (4\pi/\lambda) n_p h_p \cos\varphi_p. \end{aligned}$$

[2] *The case when the upper film of the spacing layer is transparent*

In this case, we have by (23)

$$\xi = 1$$

and

$$\beta = 0.$$

This means that the graph of R_{k0} as a function of L is a symmetrical curve with respect to the ordinates at

$$L = g\pi \quad (g = 0,\ 1,\ 2,\ 3, \ldots).$$

Such a symmetry of R_{k0} as the function of the thickness of the spacing layer does not exist for a film such as Hadley-Dennison

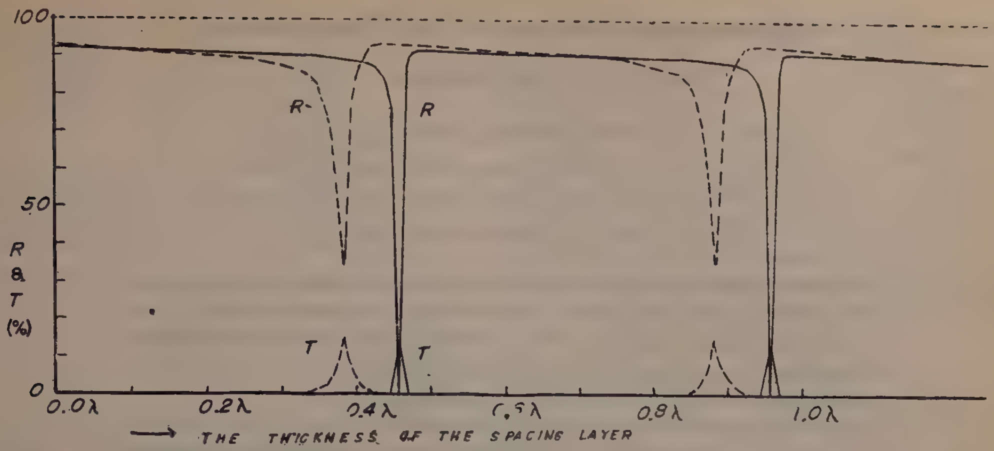

Fig. 4. Energy reflections and transmission of *H-D* filters as the function of the thickness of the spacing layer. Full line $=$*H-D* filter of the constitution $GMLH\bar{L}HLMG$. Broken line $=$*H-D* filter of the constitution $GM\bar{L}MG$ $[(2\pi/\lambda)h_M=0.5]$

filter which involves an absorbing layer in the upper film of the spacing layer.

[3] *The case when the film does not involve any absorbing layer*

In this case, the following relations

$$R_{kp}=R_{pk}$$

$$R_{p0}+T_{p0}=1$$

and

$$R_{kp}+T_{kp}=1$$

are clear from (16) and hence we have

$$B=1-A=(R_{kp}+R_{p0})/(1+R_{kp}R_{p0})$$

$$\alpha=\eta B$$

and

$$R_{k0}=R_{0k}=1-T_{k0} =B\{1-\eta\cos L\}/\{1-\eta B\cos L\}.$$

Moreover, when the film is symmetrical with respect to the spacing layer, it is clear that

$$R_{p0}=R_{pk}=R_{kp} \quad \text{and} \quad \eta=1.$$

Then R_{k0} is given by*

$$R_{k0}=4R_{pk}\sin^2(L/2)/\{(1-R_{pk})^2+4R_{pk}\sin^2(L/2)\}.$$

Hence, by the adequate choice of the thickness of the spacing layer, $R_{k0}=0$ and $T_{k0}=100\%$ can always be realized. This is the one of the favourable natures of F. T. R. filter being compared with H. D. filter.

The application to the special cases will be given in the following paper and here only as the examples of calculation, numerical equations of a usual Hadley-Dennison filter and a generalized H.D. filter with coating of multi-layers of $\lambda/4$ thickness will be shown. It is assumed that the thickness h_M of the silver layer M is $(2\pi/\lambda)h_M=0.5$ and the refractive indices of media G, M, H, L, (fig. 3) are

$$n_G=m_G=1.52,\ n_M=m_M=0.18-i3.64,$$

$$n_L=m_L=1.38,\ n_H=m_H=2.37$$

respectively. Then for the usual H. D. filter of the constitution $G-M-\bar{L}-M-G$ ($\bar{L}$ represents spacing layer),

$$T=\frac{0.00118}{1-0.992\cos(L+84°40')}$$

$$R=\frac{0.912\{1-0.9971\cos(L+85°26')\}}{1-0.9924\cos(L+84°40')}$$

and for the generalized H.D. filter of the constitution

$$G-M-L(\lambda/4)-H(\lambda/4)-\bar{L}-H(\lambda/4)-L(\lambda/4)-M$$

$$T=\frac{0.000174}{1-0.9988\cos(L+29°58')}$$

$$R=\frac{0.908\{1-\cos(L+30°17')\}}{1-0.9988\cos(L+29°58')}$$

are obtained. (Fig. 4)

The work was aided by the Grant for Fundamental Scientific Research.

References

1) F. Abelès: Ann. de Phys. **3** (1948) 516.
2) A. Vasicek: J. de Phys. et Radium **11** (1950) 342.
3) W. Weinstein: J.O.S.A. **37** (1947) 576.
4) B. Salzberg: J.O.S.A. **40** (1950) 465.
5) Slater and Frank: Electromagnetism (1947) p. 136 (McGraw-Hill).
6) F. Abelès: Ann. de Phys. **3** (1948) 518.
7) F. Abelès: C. R. Ac. Sci. **232** (1951) 1415.
8) F. Abelès: C. R. Ac. Sci. **230** (1950) 632.
9) F. Abelès: Ann. de Phys. **5** (1950) 633. (§ 13. Théorèm 3)

---

* This is the same formula which was reported by F. Abelès for the symmetrical film⁹⁾. Hence, the formula of Abelès seems to be correct only in the case of non-absorbing film, though he does not state it explicitly in his paper.

JOURNAL OF THE PHYSICAL SOCIETY OF JAPAN Vol. 8, No. 1, JAN.—FEB., 1953

Experimental Study of the Spectrum of Isotropic Turbulence, III

By Hiroshi SATO

Institute of Industrial Science, University of Tokyo
Chiba City, Japan

(Received September 10, 1952)

In order to clarify the detailed structure of turbulence, measurements were made on the fluctuation of spectral component which is the output of band-pass filter. Using a voltage integrator and a counter-chronograph, two quantities were observed in the so-called isotropic turbulence produced by a grid in a wind-tunnel.

One is the distribution function of amplitude averaged in a certain time interval. Dispersions of distribution under various experimental conditions are computed and compared. The other is the time correlation function of fluctuating output. The magnitude of correlation is not so small even for a time interval of 0.5 second and curves seem to be classified into two groups according to the central frequency.

§1. Introduction

Many fruitful experiments have been undertaken in the isotropic turbulent field which is generated by a grid placed in a wind-tunnel. Decay of turbulent energy, correlation of fluctuating velocities and energy spectrum have been measured by various investigators. The present author also reported some results on the same subject in two previous papers[1][2]. In the latter one, we discussed on the apparatus for determining energy spectrum. For observing the spectral components of low frequency, a serious problem is the fluctuation of filtered output. Mathematically, Fourier transform of arbitrary function is the averaged value in sufficiently long time interval. A band-pass filter is considered to be a device for this transformation. In this case, of course, filtered signal must be read by an output meter with large time constant. If the time constant is not enough, reading of output does not settle. This fact has been one of the greatest sources of error in determining spectrum at its low frequency region. The author thinks, however, this fluctuation may have some physical meaning.

The filtered output averaged in not so long time interval is a slowly varying function of time. In other words, the output corresponds to the number of eddies passed through a hot-wire anemometer in the time interval. Thus we introduce a quantity "spatial configuration of eddies". General wind in this case is considered to be a carrier of turbulence. So, when a certain spectral output is large in a time interval, we say the density of eddy of this size is large in the corresponding spatial range. This configuration depends partly on the characteristics of turbulence generator and partly on the mechanism of energy transference between spectral components of different wave numbers.

Simmons and Salter once reported on the frequency distribution of instantaneous fluctuating velocity[3]. The concept here discussed is different in the point that it is the averaged value in a certain time interval. By constructing a voltage integrator of improved type, we observed the frequency distribution of averaged output and time correlation of it.

§2. Equipment

Measurements were made in a closed wind-tunnel of 60 cm by 60 cm cross-section. A grid as turbulence generator, is made of crossed wooden rods having spacing of 2.5 cm from center to center and breadth of 0.5 cm.

Block diagram of complete electric circuits is shown in Fig. 1. On the bridge, amplifier and band-pass filter, illustrations were given in previous reports. A voltage integrator was newly constructed. The output of filter is amplified and detected to charge a capacitor C through resistor R (Fig. 2). To make voltage rise across C linear, positive feedback is used from C to the cathode of T_4. By

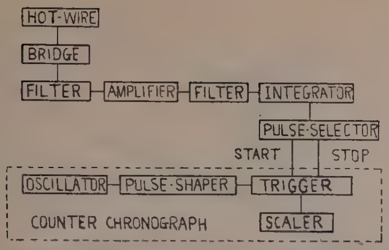

Fig. 1. Block diagram of measuring circuits.

this means, bias voltage from the plate of T_4 and C is maintained constant, independently on the voltage across C. Input is superposed on this bias so the calibration of intergrator is linear as shown in Fig. 3. Capacitor C is followed by a Schmitt trigger for discharging C when the voltage is raised to a certain value. For each discharge, one positive pulse appears at the output terminal. Maximum pulse repetition of 200 per second is obtained by the use of this electronic trigger instead of mechanical relay. Thus the linear integration,

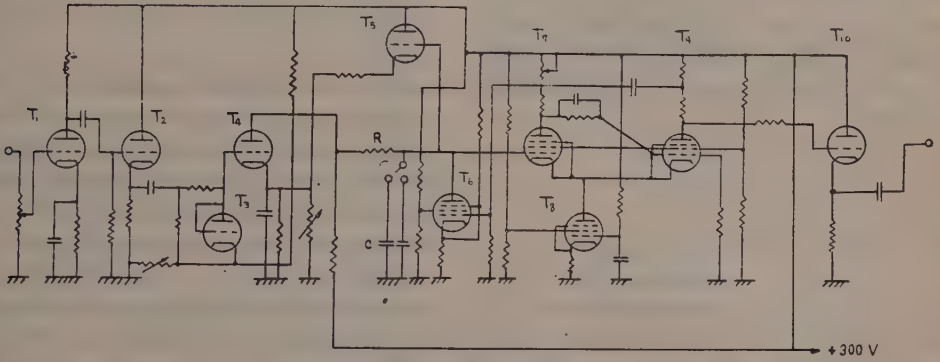

Fig. 2. Voltage integrator.

$$\frac{1}{T}=a+bv$$

is accomplished, where T is the time interval of two adjacent pulses, v is the input voltage and a, b are constants determined by values of circuit elements. It may be noticed here that we deal with $|\overline{u}|$ instead of $\overline{u}^2$, because the linear detection is used in the integrator.

Pulse selector consists of five "flip-flops" and two thyratrons. A thyratron fires with the first pulse from integrator and gives a "start" signal to the next trigger. After a certain pulses from "start", "stop" signal is issued by flip-flop. The number of pulses between "start" and "stop" can be selected in the range from 1 to 32. This device of pulse selection serves for changing the time for averaging.

Time interval of two signals is measured by a counter-chronograph which consists of trigger circuit, oscillator, pulse shaper and scaler. Detailed description of counter-chronograph is given in reference 4. The scaler has nine stage scale-of-two so the maximum counts 512. The frequency of oscillator is chosen according to the time interval to be measured. The probable error of time measurement may be within one percent.

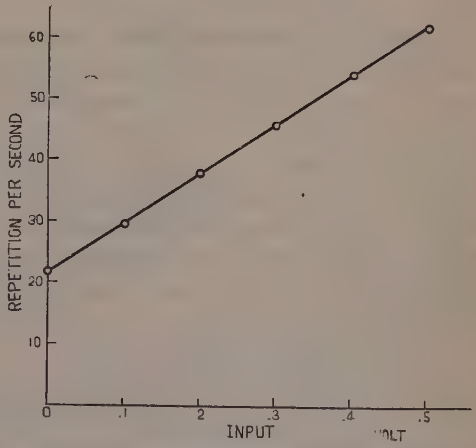

Fig. 3. Characteristics of integrator.

For determining time correlation, pen recording of pulses was also used parallel with counter-chronograph.

§ 3. Distribution Function

By measuring the time interval of pulses and translating it to amplitude, we obtain the distribution function of spectral components. Experiments were made under the condition of wind-speed 10 m/s and central frequencies

37, 140, 550 and 2,500 cps. As a rule, 200 observations were made for random sampling.

In this case, absolute value of amplitude is not important. So the mean value was taken as unity for arranging results. The distribution function has two extreme forms. One is a unit function at mean value ($x=1$) and the other is the right half of normal distribution which has the center at the origin ($x=0$), where x is the non-dimensional amplitude as mentioned above. The former corresponds to the case where the time interval of averaging tends to infinity, while the latter may be the distribution of instantaneous fluctuations.

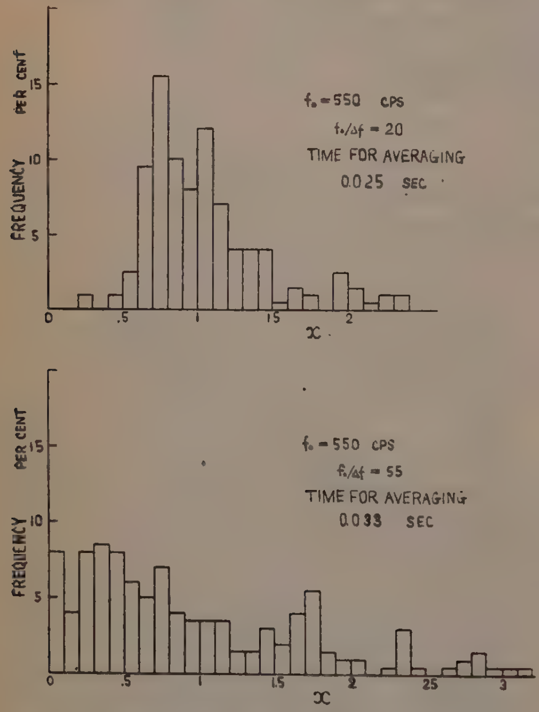

Fig. 4. Distribution for various band breadths.

Typical examples are given in Fig. 4. In this case the parameter of experiment is the band breadth of filter. It is easily seen that the dispersion for narrow band breadth is larger than that for broad one. This fact is clearly shown by calculating standard deviation σ around the axis of $x=1$ (Fig. 5). Points for four central frequencies seem to lie on a single curve when abscissa is taken in the form $f_0/\Delta f$, where f_0 is the central frequency and Δf is the band breadth of filter.

Taking averaging time as a parameter, distribution function is as Fig. 6. Standard deviation σ is plotted against f_0T in Fig. 7. As the measurements were not always performed with constant $f_0/\Delta f$, necessary corrections were made to convert results into the case of $f_0/\Delta f=25$ by using Fig. 5. Corrections were also made for Fig. 5, into $f_0T=10$ using Fig. 7. Though there is no quantity corresponding to f_0 for total energy, it is arranged by assuming $f_0=500$ cps and added in Fig. 7.

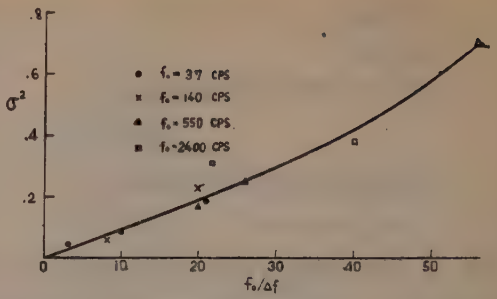

Fig. 5. Standard deviation of distribution around $x=1$ against band breadth, distance from grid 40 cm.

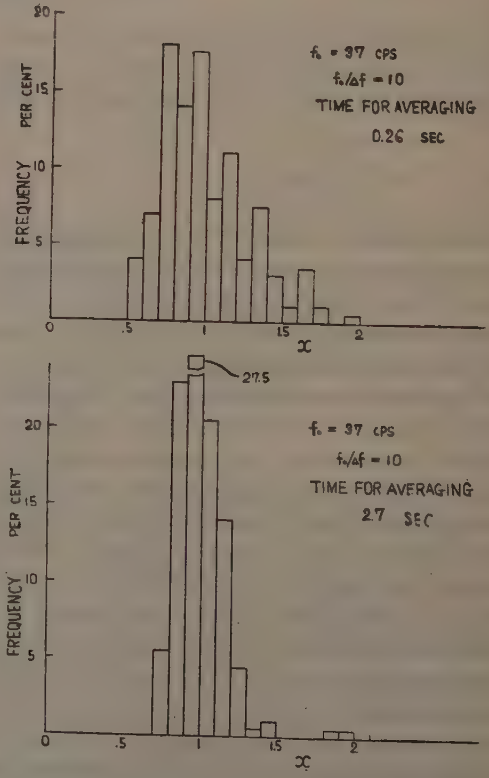

Fig. 6. Distribution for various averaging times.

Observation at various distances from grid are shown in Fig 8. For spectral components, there seems to be no distinct dependence on

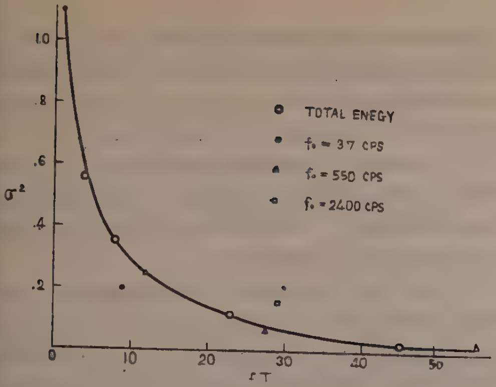

Fig. 7. Standard deviation of distribution around $x=1$, against averaging time, distance from grid 40 cm.

the distance. For total energy, however, dispersion increases as turbulence decays. This factmay be understood by following considerations. The decay of isotropic turbulence is severer at high frequency region than at low frequency, so the representative time of spectrum increases with the distance from grid. The time for averaging which is taken constant throughout decay, is relatively short for the tubulence at large distance from grid. As mentioned above, the short averaging time gives large dispersion.

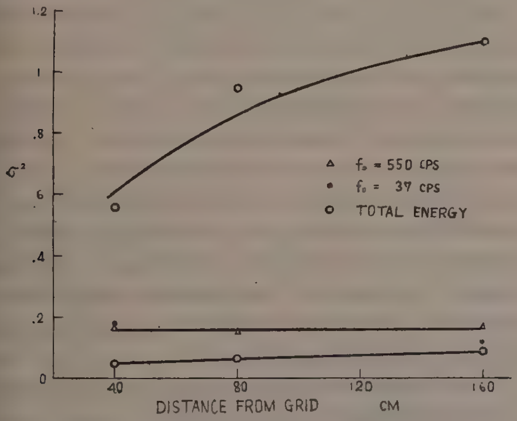

Fig. 8. Standard deviation of distribution against distance from grid.

§ 4. Correlation Coefficient

Another statistical quantity for fluctuating amplitude of spectral component is the time correlation of it which is befind by,

$$R(\xi)=\frac{\sum_i v(t_i)\cdot v(t_i+\xi)}{\sum_i v(t_i)^2}$$

where $R(\xi)$ is the correlation coefficient of time interval ξ and v is the mean value of amplitude in a certain time interval which is short compared with ξ.

By using the relation of integration, above equation becomes,

$$R(\xi)=\frac{\sum_i\left(\frac{1}{T(t_i)}-\left[\frac{1}{T}\right]_{AV}\right)\left(\frac{1}{T(t_i+\xi)}-\left[\frac{1}{T}\right]_{AV}\right)}{\sum_i\left(\frac{1}{T(t_i)}-\left[\frac{1}{T}\right]_{AV}\right)^2}$$

where suffix AV denotes the mean value of total data of sampling.

Measurements were made by two methods, one by a pen recording of pulses and the other by a counter-chronograph. Fig. 9. is a typical example of pulse record. By a random sampling from it we get correlation coefficients. This method is less accurate in measuring pulse interval but the time necessary for recording is shorter. On the contrary, the method by counter-chronograph gives high accuracy in time measurement but nearly an hour is necessary for a sampling of 100. In this case, for large ξ, time interval is taken by a stop-watch and for small ξ, pulse selector is available by the relation,

$$\xi=K\cdot 1\bigg/\left[\frac{1}{T}\right]_{AV},$$

where K is the number of pulses. Time interval between pulses are, of course, not equal, so ξ above obtained is not constant; nevertheless mean value can be observed for $R(\xi)$.

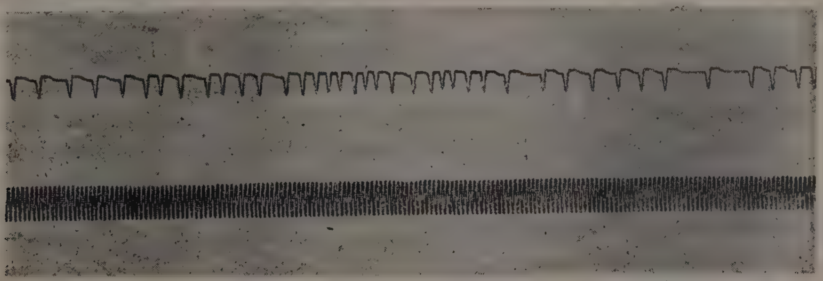

Fig. 9. Record of integrator output, $f_0=140$ cps, $f_0/\Delta f=11$, time mark below is a 50 cps sine wave.

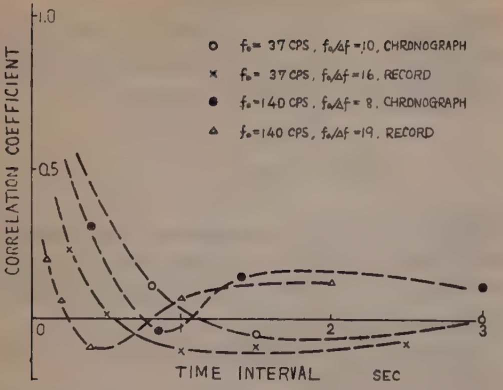

Fig. 10. Time correlation for $f_0=37$ and 140 cps, distance from grid 40 cm — band breadth of filter as parameter.

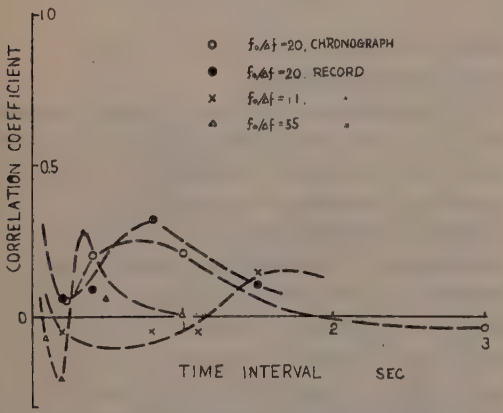

Fig. 11. Time correlation for $f_0=550$ cps, distance from grid 40 cm — band breadth of filter as parameter.

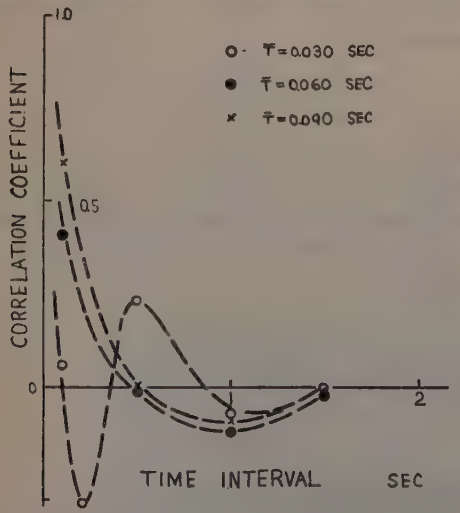

Fig. 12. Time correlation obtained by pulse record, $f_0=550$ cps, $f_0/\Delta f=55$ and distance from grid 40 cm — time for averaging ($\overline{\mathrm{T}}$) as parameter.

Experimental conditions are the same as those of distribution function. The number for sampling is 100 for each ξ and time interval for averaging is nearly ten times of $1/f_0$. Results obtained are shown in Figs. 10–12. Coincidence of results by two methods is satisfactory. From these figures, three facts may be pointed out.

1. For high frequency components, correlation curve has a hump after a sharp fall. The higher the frequency is, the more distinct is this tendency. But the hump disappears for a long averaging time.
2. For low frequency components, correlation decreases to a minus value and gradually tends to zero with increasing time interval. Even in high frequency region this is seen for long averaging time. It is not clear that this tendency relates to the low frequency components or long averaging time.
3. By making the band breadth of filter narrower, correlation curve seems to shift to the ordinate axis without changing its shape.

§ 5. Concluding Remarks

Some statistical quantities were introduced concerning the fluctuating spectral component which is the output of filter. The distribution function of amplitude averaged in a certain interval was observed with three results. The standard deviations for different central frequencies and band breadths lie on a single curve when plotted against Q-value of filter. Under various time intervals for averaging, dispersion seems to be a function of the product of interval and central frequency. Finally, there is no distinct dependence on the distance from grid.

Time correlation measured by two methods can be classified into two groups, one with hump and the other without it. Though the accuracy of correlation measurements is not sufficient for further discussion, these curves may give a suggestion for the mechanism of production of turbulence and energy transference between spectral components.

The author desires to acknowledge his indebtness to Professor I. Tani and Professor H. Kumagai for their valuable advice. His thanks are also due to Mr. Y. Matsubara, to Mr. K. Seimiya and to Miss F. Maeda for their assistance during the course of the work. This resarch has been supported by the financial aid of the Ministry of Education.

References

(1) H. Sato: J. Phys. Soc. Japan **6** (1951) 387-392.

(2) H. Sato: J. Phys. Soc. Japan **7**(1952) 392-396.

(3) L. F. G. Simmons and C. Salter: Proc. Roy Soc. **A145** (1934) 212-238.

(4) W. C. Elmore and M. Sands: Electronics (McGraw-Hill 1949)

JOURNAL OF THE PHYSICAL SOCIETY OF JAPAN Vol. 8, No. 1, JAN.—FEB., 1953

The Evolution of Gas from Nickel Plate

By Tetsuya ARIZUMI and Shun-ichi MAEKAWA

Kobe Kogyo Corporation

(Received April 21, 1952)

The quantitative analyses of gas, evoled from commercial and electrolyticnickel were carried out by means of the micro-gas analyser, whose principle is similar to Prescott and Morrison's apparatus. The main components of the evolved gas were carbon mono-oxide, carbon dioxide, hydrogen, water vapour and nitrogen. The rate of evolution of carbon oxide was found to be determinated by the diffusion of oxygen atoms through metal. A considerably large amount of gas was evolved from the electrolytic nickel, but below 450°C only hydrogen was released, while at higher temperature some other kinds of gas were extracted. The activation energy for degassing of hydrogen were about 5 Kcal/g. atom and 12 Kcal/g. atom for low and high temperature regions respectively. This suggests that there are two mechanisms for the diffusion of hydrogen : one is the normal lattice diffusion and the other is the rift or crystal boundary diffusion.

§ 1. Introduction

When every kind of metal is heated in vacuum, it evolves some amount of gas, whose main components are carbon mono-oxide, carbon dioxide, hydrogen, oxygen, water vapour and nitrogen. These gases are sometimes enclosed in tiny pits or holes, but many of them are occluded in atomic state or in the form of compounds.[1] Atoms of these components diffuse through the metal to surface and there combine together into molecules to evaporate. The present paper concerns on the quantitative analyses of gas, extracted from commercial and electrolytic nickel. The results obtained ndicate that the rate of evolution of carbon oxide from the commercial nickel is determined by the diffusion of oxygen atoms and also that there are two states of occulded hydrogen in the electrolytic nickel.

§ 2. Apparatus

The quantitative analysis of gas was carried out by a microgasanalyser, which is, in principle, similar to Prescott and Morrison's apparatus.[2] The main parts of the apparatus consist of absorption tubes, Toepler pumps, capillary pipets, miniature mercury diffusion pumps, McLeod gauges and so on. The absorption reagents are $Mg(ClO_4)_2$, CuO and liquid air.

The sample to be analysed was heated in a silica tube by a small electric furnace. Among evoled gases, water vapour, carbon dioxide, carbon mono-oxide and hydrogen were analysed and the residual gas was taken as nitrogen.

§ 3. Gas Evoled from Commercial Nickel

Although the total amount and composition of gas extracted from the commercial nickel plate are mainly determined by the history of used material, experimental condition and some other factors, the main components of gas are hydrogen and carbon mono-oxide. To find out the possible temperature dependency of evolved gas, the experiments (1) to determine the composition of gas being evolved at various different temperatures, (2) to determine the rate of gas evolution and (3) to measure the total amount contained in nickel plate, were carried out.

(1) *Gas evolution from commercial nickel*

The nickel plate used in the experiments was the rolled commercial material of 0.12–0.13 mm in thickness. The grease and other contamination were carefully washed by trichlorethylene and then distilled water.

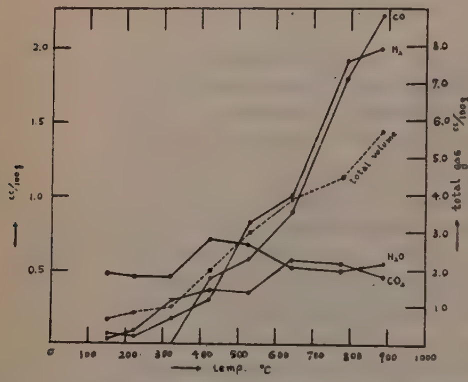

Fig. 1. Evolved gas from commercial Ni plate.

One of analytical results of gas evolved at temperatures from 100° to 900°C for 15 mins. is shown in Fig. 1, in which the total amount of gas is given in cc(NTP) per 100 g nickel. The quantities of carbon mono-oxide and hydrogen increase largely at higher temperature, but those of water vapour and carbon dioxide did not change so much. Although the numerical value for each component gas differs from one sample to other, the general tendency of gas evolution is quite similar to Fig. 1 for all samples. In these experiments each different sample from the same lot was used for each measuring temperature. Fig. 2 is the result obtained for the same sample which was heated successively at higher temperature from 300° to 950°C. In addition, the sample was pre-heated for 3 mins. in vacuum at 850°C, in order to remove the surface-adsorbed gas and surface containimation.

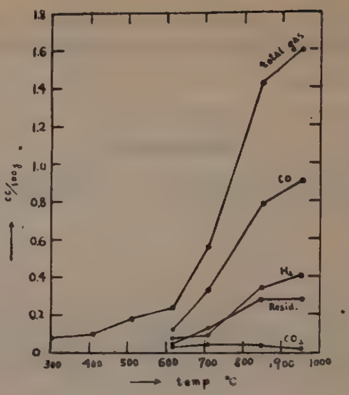

Fig. 2. Evolved gas from Ni plate, previously heated in vacuum.

In the latter case water vapour was not practically detected; even if water vapour was extracted, its amount was so small that it might be adsorbed onto the wall of apparatus. Similarly the quantity of carbon dioxide was usually smaller than that of un-preheated sample and moreover, seemed to have a tendency to decrease at higher temperature.

The velocity of gas evolution is a function of temperature and changes remarkably with time. Fig. 3 is an example for the sample of 0.3 and 0.15 mm in thickness, at a fixed temperature (950°C). The velocity decayed in few mins. to become very small. The

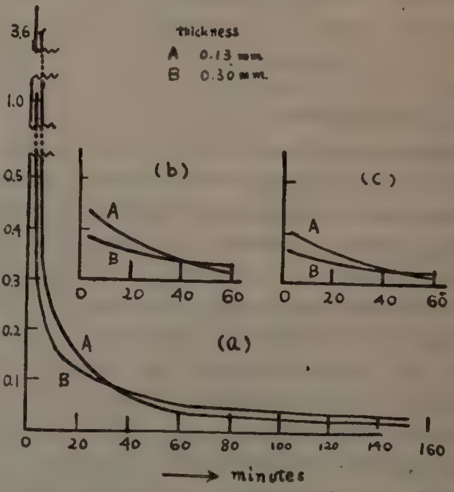

Fig. 3. The evolution velocity of gas at 950°C.

evolution velocity seemed to recover slightly, when the sample was kept at room temperature even in good vacuum for a while. The curves in Fig. 3(b) was obtained 15 hrs after the measurement of (a) had been taken and (c) was likewise at 15 hrs after the case (b).

Table I. Gas from commercial nickel

A % & cc/100 g

	H_2O	CO_2	H_2	CO	Resid
initial	3,(0.14)	15,(0.54)	46,(1.65)	32,(1.16)	4,(0.112)
a	—	1,(0.04)	38,(1.48)	41,(1.59)	20,(0.78)
b	—	—	45,(0.667)	48,(0.712)	7,(0.104)
c	—	—	52,(0.933)	47,(0.844)	1,(0.018)

B % & cc/100 g

	H_2O	CO_2	H_2	CO	Resid
initial	2,(0.02)	13,(0.133)	24,(0.24)	44,(0.451)	17,(0.176)
a	—	1,(0.03)	24,(0.67)	40,(1.11)	35,(0.93)
b	—	1,(0.012)	28,(0.347)	44,(0.546)	27,(0.355)
c	—	—	7,(0.069)	30,(0.295)	63,(0.618)

The recovery of the evolution velocity is observed clearly.

The analysis of the evolved gas in a, b and c are recorded in Table 1. The first raw shows the components of gas, extracted for first 3 mins., which may involve the most part of surface-adsorbed gas, since the sample was only cleaned by trichlorethylene.

(2) *Total amount of gas*

For the purpose of estimating the total gas content in nickel, the sample was heated in vacuum by a tungsten coil to evaporate. The tungsten coil and the glass bulb were previously baked thoroughly. One of results are presented in Table 2 and the commercial nickel always gives the similar result. In the table a considerably large amount of gas was found to be occulded.

Table II. Result of evaporation

	cc/100 g	%
CO_2	19.2	20
H_2	45	47
CO	29	30
Resid.	2.8	3
Total	96	

The rate-determining factor for degassing of nickel is thought to be the diffusion of gas atoms through the metal. Generally the Fick's diffusion law holds for such diffusion process.

$$\frac{\partial c}{\partial t}=K\frac{\partial^2 c}{\partial x^2}$$

Assuming that the concentration of gas atoms in the metal is uniformly constant initially and it is always zero at the suface, the concentration of gas atoms at distance x from the centre of metal plate after t secs is written be

$$c_{xt}=2c_0\sum_{n=1}^{\infty}\frac{(-1)^{n+1}}{\delta_n}\exp\left(-\frac{K\delta_n{}^2 t}{a^2}\right)\cos\left(\frac{\delta_n x}{2}\right) \qquad (1)$$

where,

c_0: initial concentration of gas atoms,
K: diffusivity of gas atoms in metal
$2a$: thickness of metal plate

and

$$\delta_n=\frac{\pi}{2}(2n-1)\,, \qquad n=1,\ 2,\ 3,\ \cdots\ .$$

Thus the total amount of evolved gas during t secs. is

$$Q=\iiint(c_0-c_{xt})\,dxdydz=S\int(c_0-c_{xt})dx \qquad (2)$$

in which S means the total surface area. Neglecting the smaller terms, we obtain

$$Q=\frac{16}{\pi^2}c_0\,aS\left\{1-\exp\left(-\frac{K\pi^2 t}{4a^2}\right)\right\}. \qquad (3)$$

The quantity Q is experimentally determined by the time change of evolved gas at a constant temperature and then the values of c_0 and K are able to be evaluated. The experimental Q-value for oxygen at 890°C are obtained as followed:

$$Q_{30}=1.193\times10^{-5}\ \mathrm{g\cdot atom/cc.Ni}$$
$$Q_{60}=3.32\times10^{-5}\ \mathrm{g\cdot atom/cc.Ni}$$

The subscript means the time in mins. of gas evolution. Substituting these values in Eq. (3), we get

$$c_0=3\times10^{-4}\ \mathrm{g\cdot atom/cc.Ni}$$
$$K=4.7\times10^{-10}\ \mathrm{cm^2/sec}$$

The obtained c_0 agrees nearly with 2.55×10^{-4} g·atom/cc.Ni, derived from the data in

Table 2. The diffusivity constant K for several samples ranges from 1.0 to 3.0×10^{-9} at 950°C and from 4.0 to 10.0×10^{-10} at 900°C. Smithells' K-value for carbon in nickel is 1.8×10^{-8} and for oxygen is 1.5×10^{-10} at 900°C. Our result has the same order as the diffusivity constant of oxygen in nickel. Contrary to Smithells' description, the rate determining factor for the evolution of carbon oxide from nickel seems to be the diffusion process of oxygen atoms in nickel.

§ 4. Hydrogen in Electrolytic Nickel

To study the evolution of hydrogen from nickel, the electrolytic nickel plates were used in the following works.

At first the electrolyte was the solution of nickel sulphate only for avoiding the evolution of other kinds of gas. However the optimum current density for electrolysis is so small that it requires considerably long time to obtain the uniform sample of sufficient thickness. Therefore the solution of nickel sulphate and ammonium chloride, which is well-known electrolyte for the nickel plating, was usually used in the experiments. The gas evolution characteristics was scarcely dependent upon the kind of electrolyte. The current density was 1.0 amp. per dm² at temperature 15–20°C.

(1) *Occulded gas in electrolytic nickel*

According to the evaporation experiments, it was found that the larger amount of gas was occluded in the electrolytic nickel than in the commercial nickel and the most part of it was hydrogen. An example is given in Table 3. The amount of other kind of gas is extremely small below 400°C, but above 500°C considerable amount of other kinds of gas was extracted. Samples Nos. 1, 2, and 3 were the same electrolytic product of thickness of 0.15 mm. The fact that the evolved gas from the electrolytic nickel is not always hydrogen, seems to be rather curious. As seen in Table 3(B), nearly all part of gas is extracted in the first 15 mins., but the rest is evolved very slowly. The comparison of (A) and (B) suggests that a considerable amount of hydrogen remains still in the sample after it was heated at 560°C for 30 mins.

Table III. Gas occluded in electrodeposited Ni

(A)

No. 1	90°C 30 min.	420°C 13 min.	Evaporation	Total
CO_2 %	2	2	3	2.5(3.7cc)
H_2 %	95	97	42	74(121.5cc)
CO %	—	—	42	17.5(29.0cc)
Resid %	3	1	13	6(10.43cc)
Total cc/100g	15.84	79.98	68.8	(164.63)

(B)

	No. 2	No. 3
%, cc/100 g.	560°C, 15 min.	560°C, 30 min.
CO_2	5.5 (6.6)	5 (6.3)
H_2	77 (92.3)	76 (93.3)
CO	3 (3.6)	8 (13.7)
Resid,	14.5 (17.5)	11 (13.7)
Total	(120)	(123.1)

(2) *The rate of evolution of hydrogen*

The above-mentioned results indicate that there are two states of occulusion for hydrogen in nickel: in one state hydrogen is easily extracted at temperature below 450°C, while in the other it is difficult to be evolved even at higher temperature. Fig. 4 shows the time change of logarithms of amount of evolved hydrogen and velocity of its evolution below 420°C for the sample of 0.15 mm in thickness. The similar plot at higher temperature for the same sample, preceedingly heated at 400°C for 2 hrs. in vacuum to remove hydrogen to be released easily, is shown in Fig. 5.

Since the temperature change of slope of the curves in Figs. 4 and 5 corresponds to the variation of the evolution velocity, the following equation holds:

$$\frac{dl_nv}{dt}=A\exp\left(-\frac{E}{RT}\right) \qquad (4)$$

where v, A and E are evolution velocity, a constant and the activation energy for gas evolution respectively. The logarithms of slope of the curves in both preceding figures are plotted against reciprocal temperature ($1/T$°K) in Fig. 6, in which the curves (a) and (b) correspond to these in Figs. 4 and 5

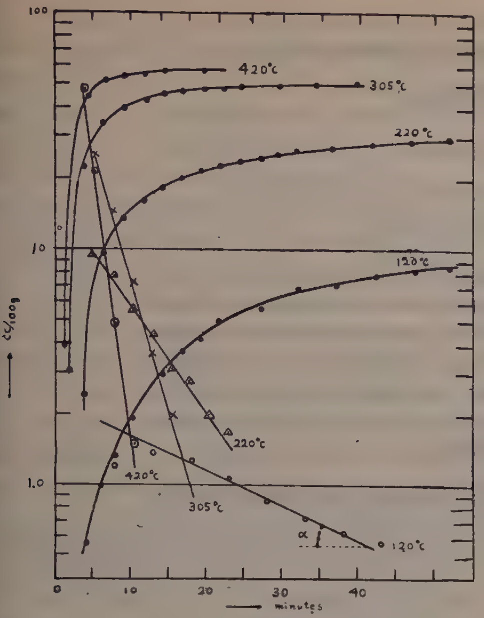

Fig. 4. Evolution of hydrogen from electrolytic Ni at low temperature region.

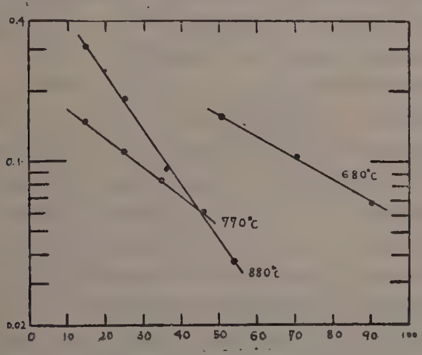

Fig. 5. Velocity of hydrogen evolution at higher temperature.

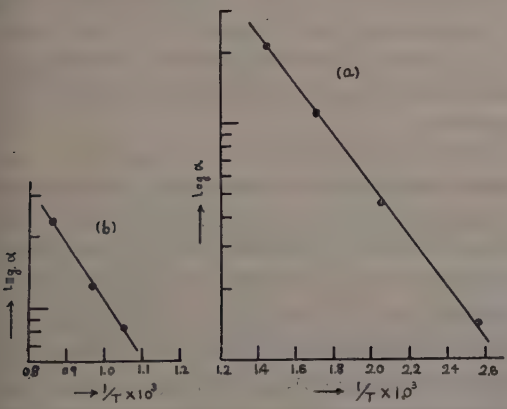

Fig. 6. Activation energy for the evolution of hydrogen.

respectively. Both curves are found to be straight and the activation energy is evaluated to be 4.3 Kcal/g. atom in low temperature range, while 11.5 Kcal/g. atom in higher temperature range. In several other samples the estimated values distribute between 4 and 5 Kcal/g. atom in the former case, while in the latter between 11 ane 12 Kcal/g. atom.

The latter value almost agrees with 12.2 Kcal/g. atom for the energy of lattice diffusion of hydrogen through nickel, described in the previous paper,⁽⁴⁾ but 5 Kcal/g. atom is too low. The possible explanation for such low activation energy may be given in following two ways: Hydrogen in grain boundaries in the electrolysis is evolved through the rift diffusion, or hydrogen atoms diffuse through the distorted structure which is rather common to the electrolytic metal.

§ 5. Summary

The gases evolved from the commercial nickel and electrolytic nickel were studied by micro-gasanalyser in which several kinds of suitable absorption reagents were used.

The gas amount in the commercial nickel was in general about 100 ccs per 100 g. nickel and the main components of gas was carbon oxide and hydrogen. Assuming that the rate of evolution of carbon oxide from nickel is determinated by the diffusion of gas atoms through metal, the diffusivity constant was found to be of the same order as that for oxygen atoms through nickel.

It seems to be possible that there are two mechanisms in the evolution of hydrogen from nickel. For the values of activation energy corresponding to two mechanisms, about 5 Kcal/g. atom and about 12 Kcal/g. atom were obtained respectively.

References

(1) Smithells: Metals and Gas.

(2) C. H. Prescott & T. T. Morrison: Ind. Eng. Chem. Anal. Ed. **11** (1939) 230.

T. Arizumi & S. Maekawa: Kobe Kogyo Tech. Rep. (in Japanese) (1951) No. 10.

(3) Smithells & Ransely: Proc. Roy. Soc. **155** (1936) 195.

(4) E. Stern & H. Eyring: J. Phys Chem. **44** (1940) 955.

JOURNAL OF THE PHYSICAL SOCIETY OF JAPAN Vol. 8, No. 1, JAN.—FEB., 1953

An Electron Diffraction Camera with a Rotating Sector

By Tadashi INO*

Physical Institute, Nagoya University, Nagoya, Japan

(Received September 20, 1952)

An electron diffraction camera provided with a rotating sector was designed, constructed and tested. Though it has no specially original feature, it is simpler compared with that used in the United States and can be constructed at a little expense. A preliminary result was obtained with polystyrene films and was analysed after the method developed by J. Karle and his coworkers. It showed that this equipment was quite satisfactory in its functions.

§1 Introduction

The visual method has been commonly used in the analysis of electron diffraction haloes by gaseous molecules or amorphous substances. Their microphotometer records are almost useless for the analysis, because the atomic term, which givesa background steeply increasing toward the center, is superposed on the molecular term. To get rid of this difficulty, Chr. Finbak[4)] and P. P. Debye[2)] proposed the application of a rotating sector, which, being placed in front of the photographic plate, shuts off a part of diffracted rays so as to make the background uniform and enabled us to take microphotometer records of the diffraction haloes which could be treated quantitatively. This method was developed by Norwegian school[5)6)&15)] and recently refined by workers in the United States,[7)9)–12)&17)] especially J. Karle[9)–12)] and I. Karle, carrying out the plan suggested by P. Debye[2)], determind successfully not only the interatomic distances but also the amplitudes of their thermal vibrations. Therefore the visual method seems to be quite out of date.

The auther constructed a few years ago an electoron diffraction camera provided with a rotating sector and obtained preliminary results. Though his camera has no especially original feature, it is very simpler compared with that used in the United States and can be constructed at a little expense. It is the purpose of this paper to describe the design, contruction, operation of the camera and to give a preliminary result obtained with amorphous polystyrene film.

§2. Design and Construction

Fig. 1a shows the top view of the diffraction unit, which is arranged horizontally on a table. It consists of four parts: electron gun, collimating system, specimen chamber, and camera chamber. The front view of the last two parts is shown in Fig. 1b. The rotating sector is mounted in the camera chamber as shown in Fig. 1c.

The *electron gun* is of a hot cathode type, consisting of a filament (1), a *Trichter*[14)] biasing cup (2) and an anode (3). The position of cathode can be adjusted through the flat ground joint (4) by a cross leader attached on it (not shown in the figure) so that the electron beam passes through a pin hole of diameter 2/100—6/100 mm bored through a piece of platinum plate fixed in the item (5). To facilitate this adjustment, the front of the item (5) is coated with fluorescent materials, so that the beam may be detected on its surface through the window (6). The item (7) is a stop cock which permits shutting off the electron gun from the other parts of the apparatus.

In the *collimating system*, the electron beam passes through two collimating diaphragms of diameter 3 mm and the direction of the beam is precisely controlled by the two pairs of Helmholtz coils (8) so that the electron beam impinges on the center of rotation of the sector by precise control of the voltage impressed across them. The magnetic lens (9) of an iron-encased type focuses the beam on to the photographic plate.

---

* Now at Institute of Polytechnics, Osaka City University, Osaka, Japan

The *specimen chamber* is provided with two specimen holders (10 a) and (10 b) whose camera lengths are about 12 and 30 cm respectively. The position of the specimen is adjusted on a plane normal to the electron beam by the double cone joint shown in the figure. A similar joint (10 c) serves to hold a diaphragm to shut off the stray electrons. The parts 11 a (or 11 b) and 12 a (or 12 b) serve to introduce a liquid air trap and a gas jet into the chamber respectively. In the present experiment, however they are sealed off, for the specimens studied are thin films.

The *sector assembly* consists of a precision ball bearing (13), driving devices (14) and (15), and a ground joint (16), which has a Wilson seal.16) The sector (17) is mounted on the inner race of the ball bearing (13) provided with a pulley. Its outer race is firmly fixed on one end of the strong arm (18). The other end of the arm is fixed on the ground joint (16), so that the sector can be carried up to the position of the diffraction pattern or be removed from by its rotation. The sector is rotated at about 1200 r. p. m. by the power introduced into the vacuum through the Wilson seal and transmitted by a pulley (14) and a fine rubber belt (19). To reduce the magnetic disturbances, the races of the ball bearing are made of phosphor bronze; steel balls, however, were used, since non-magnetic balls of sufficient accuracy were not available. It was proved, however, that the magnetic fields, due to each ball, cancelled out one another inside the race and the disturbance due to the balls was negligible.

Fig. 1 a

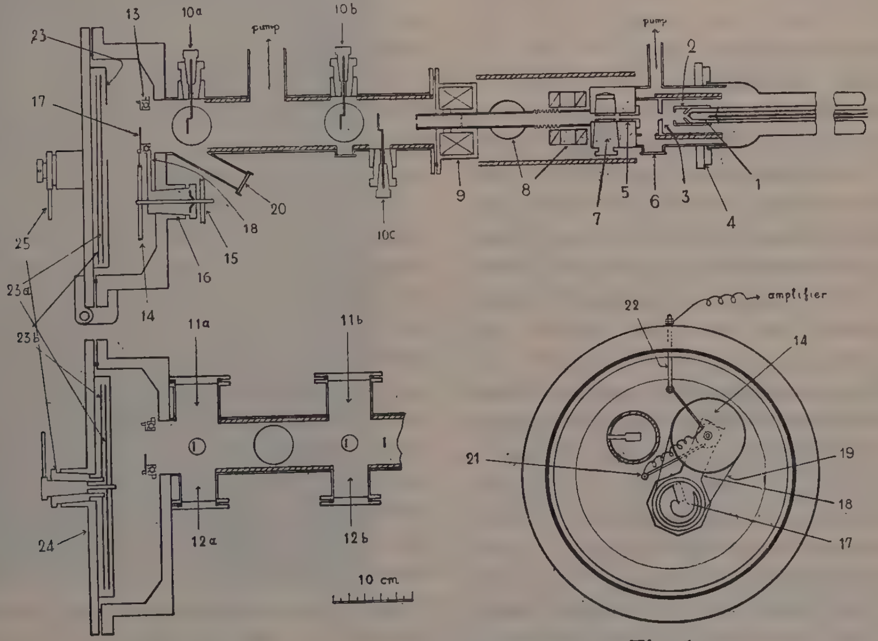

Fig. 1 b

Fig. 1 c

Fig. 1 a and 1 b are the top and the front views of the electron diffraction camera respectively.

Fig. 1 c is the diagram of the interior of camera chamber(the scale shown is 10 cm long).

The *sector* is made of a brass plate of 0.5 mm thickness. We had to cut out the sector by fine files, since no precise cutting machine was available. A precision comparator of a coordinate type was used to draw the curves of sectors, it was however, impossible to draw fine curved directly on the metal plate inhibited by the roughness of its surface. Therefore the curve was first drawn on an alminized glass plate, then the curve was printed on the metal plate by a photographic method. Thus the sectors of the curves $\theta=cr^n$ (n=1, 2 and 3; c being a constant) were prepared. The sectors consist of two separable parts as shown by the dotted line in (17) so that the curve near the center may be filed easily. They are carefully mounted on the inner race of the ball bearing so that the center of the sector and the axis of rotation of the bearing coincide with each other to a precision of better than 0.05 mm. The available range of s, through these sectors, s being $(4\pi \sin \theta/2)/\lambda$, extends from 1 to 32 1/Å, if diffraction photographs are taken with specimen to plate distances of both 12 and 30 cm. The central portion of the sector acts as a beam stop. In order to facilitate the centering of the sector with respect to the electron beam, a fine cross is engraved at its center and a small amount of fluorescent materials is placed in it. When the sector is rotated in its position but not accurately centered with the respect to the beam, a small circular image of fluorescence is observed through the window (20). To carry out an accurate centering, two pairs of Helmholtz coils can be used; but actually it is more convenient to use one of them and for the other degree of freedom the rotation of ground joint (16) is used, which is adjusted precisely by a microscrew (not shown in the figure). The adjusment is carried out under observation by a long focal length microscope through the window (20), and it is completed when the circle converges to a point. When the adjustment is completed, a specimen is placed in its position; then one can observe the diffraction pattern through the sector. If required, it is also possible to see the pattern in its innate state by removing the rotating sector. The Faraday cage (21) shown in Fig. 1 c is used for measuring the current of incident beam. It is supported by a insulated rod attached on the ground joint (16) and its rotation through a certain angle carries the cage up to the position of the primary beam. The beam current can be measured by an amplifier connected to the cage through the insulated vacuum-tight terminal (22).

The *Cassette* is a thin drum (23); it is mounted on the door (24) of the camera chamber and is remountable. In the drum, there are two disks, which may be rotated independently through the double ground joint (25). One of the disks (23 b) near the door, carries three photographic plates of 12×8 cm and the other (23 a) carries a circular window of diameter 8 cm, a rectangular window of 2×8 cm and a fluorescent screen. The former window serves for photographing the diffraction pattern of a test specimen and the latter for recording that of the standard specimen. A pair of photographs of these specimens can be taken on a plate as shown in Fig. 2.

§ 3. Difficulties in the Operation

The first difficulty experienced in the operation of this diffraction unit was the fluctuation in the intensity and the direction of the electron beam. Since the cycle of these fluctuation was 60 per second and the rotation of the sector is about 1200 r. p. m., a stroboscopic phenomenon occurred and a radial pattern was observed near the center of diffraction patterns. This difficulty was avoided by heating the filament of electron gun with a direct current of a battery and by shielding the electron beam carefully from the stray magnetic field. For the latter purpose, the iron cylinders shown as the hatched parts in Fig. 1 a are used.

The second difficulty was the extraneous scattering produced when no specimen was placed in its position. This is considered to be, since the degree of vacuum is about 2×10^{-4} mm Hg (measured by an ionization gauge) in the specimen chamber and the camera, due to the scattering of electrons by the pin hole (5), diaphragms, and walls of the apparatus. To minimize this effect, it is desirable that the stream of electrons emerging from electron gun is so parallel that it hits neither the diaphragms nor the walls. This requirement can be almost satisfied by the use of telefocal Wehnelt cathode; by its proper adjustment the author could reduce the angular divergence of electron beam to about 2×10^{-3} rad.

The third difficulty was the scattering of electrons by the periphery of the hole on which the specimen film was supported. Therefore the holes must be larger than the cross section of the electron beam at the position of the specimen, so that the beam may pass through the holes without hitting their peripheries. Since the diameters of cross sections of the beam were found to be about 0.1 mm and 0.2 mm at the sample positions (10 a) and (10 b) respectively, the holes of 0.3 mm were used for specimen holder. Though this introduced a new technical difficulty in preparing a thin film on such a large hole, it was overcome by an improvement of the technique.

The last difficulty was to give the proper exposure so that the photometry may be performed under the best condition. This difficulty was removed by the use of Faraday cage mentioned in the above section. The adequate exposure time for the hard photographic plate is about 10~30 sec. with an incident beam of 1×10^{-9} amp. in the case of the s^2-sector.

The author experienced no difficulty in the centering of the sector and no trouble with the leakage of the vacuum equipment.

An example of diffraction photographs of polystyrene through the s^3-sector is reproduced in Fig. 2.

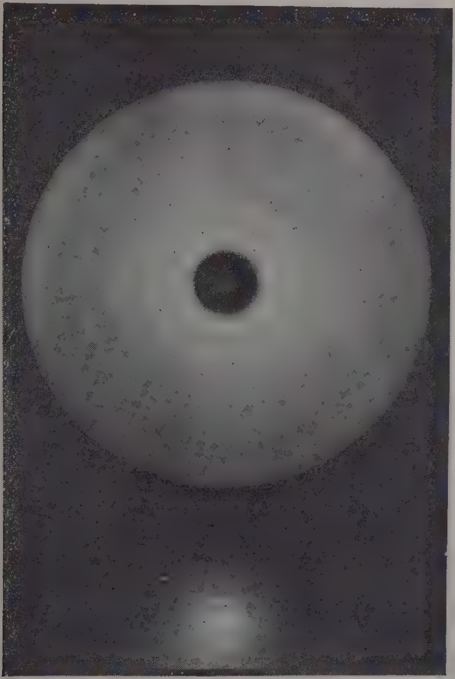

Fig. 2. A typical diffraction photograph of polystyrene film through s^3-sector.

§ 4. Photometry and Calculation

The photometry and the calculation of radial distribution function were carried out after the method developed by J. Karle[10] and his coworkers.

A recording microphotometer of Riken B-type was used, after reconstructing its stage so that the photographic plates can be rotated rapidly about the center of the diffraction pattern while being scanned in order to smooth the irregularities due to graininess in the emulsion. The linearity of electrometer of the microphotometer was calibrated. Some examples of microphotometer traces are reproduced in Fig. 3. The traces were measured by a comparator of a coordinate type as a function of the radius.

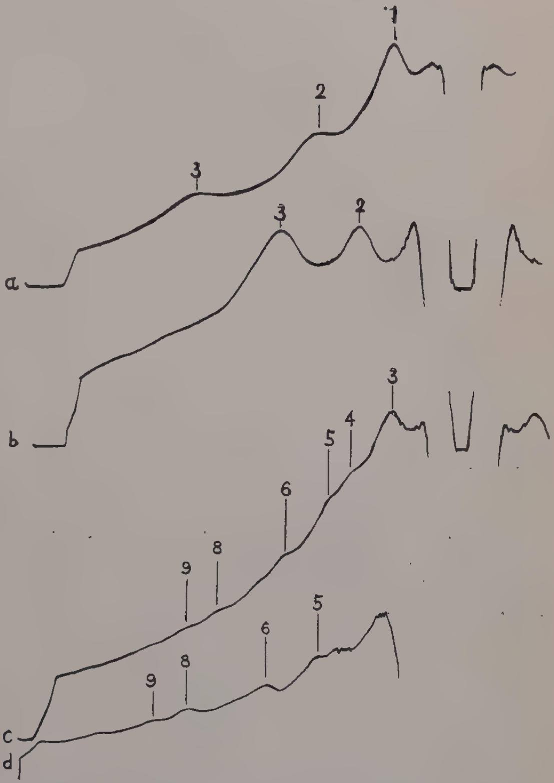

Fig. 3. Typical microphotometer traces of polystyrene. The horizontal scales are not the same.
a. through s-sector with camera length 30 cm.
b. through s^2-sector with camera length 30 cm.
c. through s^2-sector with camera length 12 cm.
d. through s^3-sector with camera length 12 cm.

From the two density versus radius curves corresponding to two different exposures, the calibration curve of electron intensity versus photographic density was obtained. The intensity curve of the diffraction pattern was derived from the density curve by adopting this calibration, For example, the intensity curve derived from the density curve c in Fig. 3 and multiplied by s to accentuate its oscillation is shown in Fig. 4. The smooth background line drawn on this curve through its oscillation was successively refined employing Karle's criterion of positiveness. Then the molecular scattering curve $I_m(s)$ was obtained by dividing the oscillating term by the

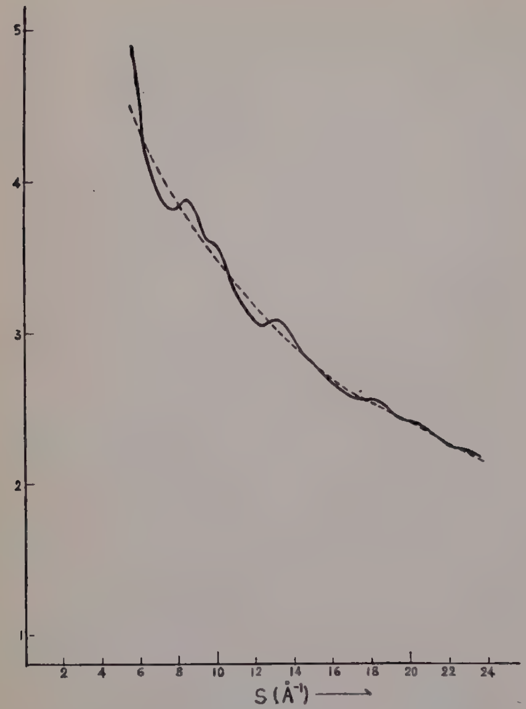

Fig. 4. The intensity curve of polystyrene corresponding to $s^3I(s)$.

The dotted curve is the corrected background line.

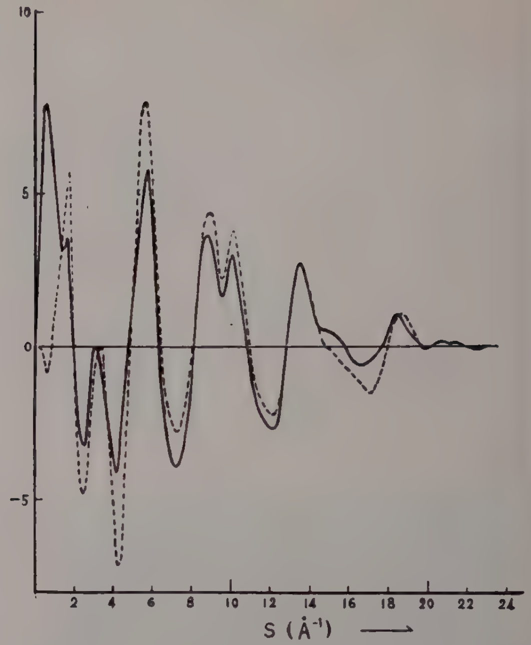

Fig. 5. The modified molecular intensity curves $s\exp(-as^2)\times I_m$, where $a=0.0051$. the dotted curve, uncorrected. (the curve over the region of $s<5$ is substituted for by a theoretical one[8]) the solid curve, corrected.

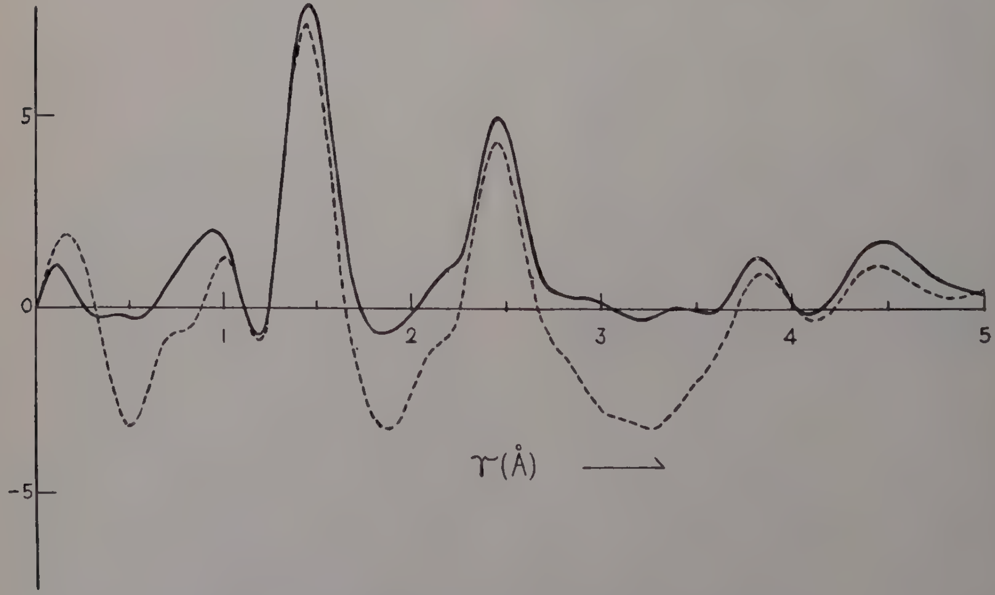

Fig. 6. The radial distrubution curves of polystyrene. the dotted curve, uncorrected curve. the solid curve, corrected curve.

background. Fig. 5 shows such two curves. The dotted one is obtained by using the background line drawn at first, but the curve over the region of $s<5$ is substituted for by a theoretical one.[8] The solid one is obtained by using the refined background line of Fig. 4.

The radial distribution function $f(r)$ is computed from the function $I_m(s)$

$$f(r)=\int_0^{s_{\max}} sI_m(s)\exp(-as^2)\sin(sr)ds \text{ }^{11)}$$

where $s_{\max}$ is the largest value of s available from the photograph (here 24 1/Å) and a is an arbitrary number to avoid the diffraction effect1) (here 0.0051).

This conversion was carried out by the punched card method.13) * Although the details of the procedure are abbreviated here, it is almost the same as that carried out by Karle and his coworkers. The radial distribution curves obtained from the curves in Fig. 5 are shown in Fig. 6.

§ 5. Preliminary Experiment

Polystyrene films were studied by this equipment at first, because it was one of the amorphous substances with comparatively simple structure and it had been studied already well by the visual method by J. Kakinoki.8)

The films were prepared on the clean surface of the water by evaporation from a drop of dilute benzene solution then transferred on to the specimen holder.

The diffraction patterns were always photographed through the s^2– and the s^3–sectors with the camera length of 12 cm and sometimes through the s– and the s^2–sectors with that of 30 cm. The photometer traces of these pattern are shown as c, d, a, and b in Fig. 3 respectively. In Fig. 3 c and 3 d there are observed the ghost patterns near the center. The ghost pattern for $s<5$ is not a positive drawback, for the intensity curve in this range is of little importance for the analysis of haloes and can be easily obtained from a photograph taken with the camera length of 30 cm, if required. The intensity curve from these photometer records and the molecular intensity curves are shown in Fig. 4 and Fig.5 respectively.

The s-values of maxima of Fig. 5 are given in Table I together with those obtained by visual method, for comparison. They coincide well with each other except that the 7th halo in latters is only an inflexion in the present experiment and that the last maximum which has not been observed in the latter is observed here. These facts may prove that the present experiment is more reliable than the experiment with visual method made by well trained experimenters.

Table I. Polystyrene

Max. of halo	s(author)	s(Kakinoki)8)
2	3.05	3.16
3	5.59	5.54
4	8.80	8.64
5	10.03	10.32
6	13.48	13.36
7		15.97
8	18.38	18.32
9	20.42	

The radial distribution functions derived from the dotted curve (uncorrected) and the solid one (corrected) in Fig. 5 are shown in Fig. 6. The remarkable difference between the corrected and uncorrected molecular intensity curves near the origin is due to some incompleteness of the theoretical intensity curve substituted for small s in Fig. 5, though not discussed in detail here.

In the corrected radial distribution curve (solid one) two peaks near $r=1.0$Å and 1.5Å are due to the C–H and the C–C distances of direct bonds respectively and that near $r=2.5$Å is due to the distances intervened by one atom. The peaks which follow are due to the longer atomic distances. The area under the peak of the curve $rf(r)$, not shown here, should be proportional to $\sum_{ij} n_{ij}Z_iZ_j$ where Z_iZ_j is the product of the atomic numbers of atoms separated by the distance r belonging to the peak and n_{ij} is the number of the pair. The ratio of the areas corresponding to the former two peaks is 0.163:1, which is in a good agreement with the theoretical value 0.15:1,8) while the area under the latter one is almost a half of the theoretical value. Although the reason for this discrepancy is not yet cleared up, it may be considered to be due to incompleteness of the correction.

Although the experiment is not yet completed, the author believes that the present diffraction unit operates quite satisfactorily and can furnish far more precise data compared with those obtained by the old visual method.

---

* These punched cards were available at Prof. Morino's laboratory, Chemical Laboratory, Tokyo University.

§ 6. Acknowledgement

The author wishes to express his sincere thanks to Professor R. Uyeda for his kind guidance throughout this work, to Professor J. Kakinoki for his helpful discussion as to the structure of polystyrene and to Professor Y. Morino and Mr. K. Kuchizu for their fine cooperation in the calculation of the Fourier transformation by punched card method. The entire apparatus was constructed by the workshop staff of this Institute, Mr. S. Takahashi and Mr. M. Nonoyama, to whom also his hearty thanks are due.

This work is indebted to the Ministry of Education for the Foundamental Scientific Research Expenditure No. C 4314, 1950.

References

(1) Bragg, W. L. & West, J.: Phil. Mag. **10** (1930) 823.

(2) Debye, P. P.: Phys. Zeits. **40** (1939) 66, 404.

(3) Debye, P.: J. C. P. **9** (1941) 55.

(4) Finbak, Chr.: Avh. Norsk. Vidensk. Akad. Oslo. 1 Math. Nat. Kl, (1937) Nr. 13.

(5) Finbak, Chr., Hassel, O. & Ottar, B.: Arch. Math. Nat. (1941) B.XLIV Nr. 13.

(6) Hassel, O. & Viervall, H.: Acta Chem. Scand. **1** (1947) 149.

(7) Hasting, J. M. & Bauer, S. H.: J. C. P. **18** (1950) 13.

(8) Kakinoki, J.: Sci. Pap. Osaka University, No. 16, 17 (1949).

(9) Karle, I. L. & Karle, J.: J. C. P. **17** (1949) 1052.

(10) Karle, J. & Karle, I. L.: J. C. P. **18** (1950) 957.

(11) Karle, I. L. & Karle, J.: J. C. P. **18** (1950) 963.

(12) Karle, I. L. & Karle, J.: J. C. P. **20** (1952) 63.

(13) Schaffer, P. A., Schomaker, V. & Pauling, L.: J. C. P. **14** (1946) 659.

(14) Steigerwald, K. H.: Optik **5** (1949) 459.

(15) Viervoll, H.: Acta Chem. Scand. **1** (1947) 120.

(16) Wilson, R. R.: Rev. Sci. Inst. **12** (1941) 91.

(17) Yearian, H. J. & Barss, W. M.: J. App. Phys. **19** (1948) 700.

JOURNAL OF THE PHYSICAL SOCIETY OF JAPAN Vol. 8, No. 1, JAN.—FEB., 1953

A Flow-Meter in Vacuum Technique

By Ryozi UYEDA and Yoshikazu SUGIURA*

Physical Institute, Nagoya University, Nagoya, Japan

(Received July 18, 1952)

A direct reading *flow-meter* for the measurement of Q-value in vacuum technique is described. The principle of the meter is to measure the force exerted on a disc placed in a vacuum piping. The kinetic theory shows that the force acting upon the suspending plate, due to the thermal motion of molecules, is stronger than one supposes and this is proved by the experiments. Flow-meters of suspension type are made and tested. The highest sensitivity available is $1\times10^{-3}\mu$Hg. litre/sec per 1 mm. of scale. The application of this meter to measurement of pumping speed, measurement of desorbed gases, vacuum drying and leak detection are described.

§1. Introduction

Several methods(1) are available for the measurement of pressure, P, in vacuum technique. No conventional one, however, is available for the measurement of pumping speed, S, or the so-called Q-value, $Q=PS$. All the methods to measure Q or S, known to date(2), are applicable only to the testing of pumps, but they are not appropriate to vacuum system under their working conditions. Several years ago, one of the authors (*R. U.*)(3) invented a device for this purpose. The principle and mechanism of the device are so simple that it was suspected that the same already appeared in the time of Goede and Knudsen, but we found no such literatures nor informations**. The device, developed in our laboratory, is now called *flow-meter* in our country. It is the purpose of this paper to describe the theory, experiments, an example of design and a few applications of the meter.

§2. Theory

The principle of the meter is only to measure the force, F, exerted on a small disc placed in a vacuum piping. One might suppose, at first, that the force is so weak that its measurement requires impracticable skill; but, actually, it is quite strong even in vacua of the order less than 0.1μHg and can be measured easily. This fact, as described below, is caused by the thermal motion of molecules.

Let us assume the case that a rarefied gas is flowing through a circular pipe of radius a and a small circular disc of radius c is put in the pipe vertically on its axis. If $c\ll a$ and $c\ll\lambda$, λ being the mean free path of gas molecules, the force, F, exerted on the disc by the flow is calculated by the kinetic theory(5). It is given by the formula

$$F=\gamma\alpha\rho\bar{u}\bar{v}\times\pi c^2, \tag{1}$$

where ρ is the density of gas, $\bar{u}$ the mean flow velocity ($\bar{u}\times\pi a^2=S$) and $\bar{v}$ the mean thermal velocity. γ is a constant determined by the nature of reflection of molecules on the disc; $\gamma=2$ if the specular reflection is assumed and $\gamma=1.88$ if the diffuse reflection with conservation of velocities takes place(16). α is another constant; $\alpha=1.00$ for an infinitely extended gas and $\alpha=3\pi/8$ for Knudsen flow ($a\ll\lambda$). Although this formula is derived under the assumption $\bar{v}\gg\bar{u}$, this is well satisfied under usual experimental conditions, because $\bar{v}$ is the order of several hundred meters per second and $\bar{u}$ is the order of several meters per second. Since the thermal velocity is very large, the force turns out quite larger compared with our vague supposition. The formula (1) can be rewritten in the case of Knudsen flow in the form

$$F=3(\pi M/8RT)^{1/2}\gamma Q(c/a)^2, \tag{1'}$$

where R is the gas constant per mol, M the molecular weight of the gas and T the absolute temperature. Eq. (1′) shows that the force is proportional to Q-value independent of the pressure. Therefore, if the force is measured by some appliances, it is directly proportional to Q-value. This is an excellent point of this device.

---

*Now at the Electrotechnical Laboratory, Ministry of Trade and Industry, Tokyo, Japan.

** Estermann & Kane4) used a similar device, but for a different purpose.

On the other band, the force is calculated by hydrodynamics for Poiseuille flow. If the fluid is extended infinitely, it is given by⁽⁷⁾

$$F=16\eta cu, \tag{2}$$

where η is the constant of viscosity and u the flow velocity. When the gas is limited in a pipe, we assumed the form

$$F=\beta\eta c\bar{u}. \tag{2'}$$

This equation shows that the force is proportional to the pumping speed, $S=\pi a^2\bar{u}$ independent of the pressure, because η varies little with the pressure.

§ 3. Experiment

After preliminary experiments by one of the authors (R.U.)⁽³⁾, a detailed measurement was carried out by the other. The latter obtained the empirical formulae⁽⁸⁾

$$F=3(\pi M/8RT)^{1/2}\gamma Q(c/a)^2\{1+k_1(c/a)^2\}$$
$$\text{for Knudsen flow,} \tag{3}$$

where $\gamma=1.8$ and $k_1=1.9$, for $0.2<c/a<0.5$ and

$$F=\beta\eta c\bar{u}\{1+k_2(c/a)\}$$
$$\text{for Poiseuille flow} \tag{4}$$

where $\beta=32$ and $k_2=2.1$ for $0.1<0.3$.

He carried out further an experiment to study the behavior of the force in Knudsen flow and in the intermediate region between Knudseen and Poiseuille flow. His experimental arrangement is shown in Figs. la and b. The force on the disc was measured by the torsion balance shown in Fig. 1b. The pressure was measured by the ionization gauge and the Q-value by the burette⁽⁹⁾ shown in Fig. 1a. The parameters changed in the experiment are pressure, P, Q-value, radius of the disc, c, and the position of the disc. The kind of gas was not varied, only using dry air. If the sensitivity for other gas is required, it can be calculated by eq. (1′) provided the molecular weight is known.

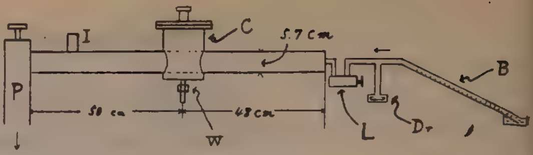

Fig. 1a.

P: Diffusion pump, I: Ionization gauge,
C: Case of the pendulum (see Fig. 1 b),
W: Window (see Fig. 1 b),
L: Variable leak Dr: Drying agent,
B: Burette.

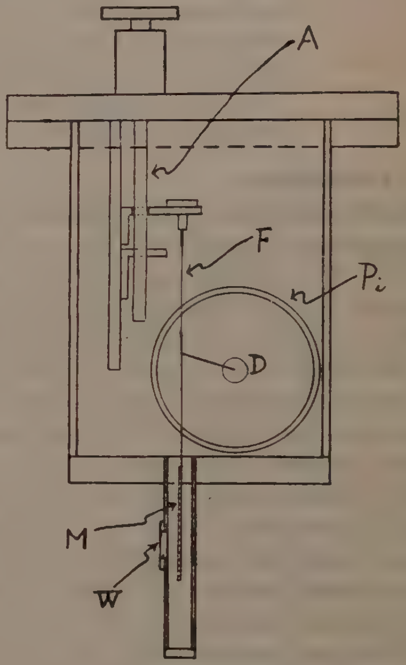

Fig. 1b.

D: Mica disc, F: Tungusten fiber,
Pᵢ: Section of the pipe (shown by dotted lines in Fig. 1 a),
M: Mirror, W: Window,
A: Device to adjust position of the disc.

When the disc is placed on the axis of the pipe, the apparent value of γ, say γ', was calculated by assuming eq. (1′), even in the intermediate region, using experimental values of F, Q, T, c and a. In Fig. 2 the observed value of γ' is plotted against the pressure. It becomes a constant, *i. e.* γ, as the pressure is reduced and the mean value obtained for a small disc is

$$\gamma=1.87. \tag{5}$$

This is in accordance with the latter value mentioned in the previous section. It must be noted that γ' attains a remarkable maximum in the intermediate region. This fact may be correlated with the observations by Knudsen⁽¹⁰⁾ and others⁽¹¹⁾.

If the center of the disc is deviated from the center of the pipe, the force decreases as shown in Fig. 3 where the ratio of forces on deviated and non-deviated disc is plotted against the deviation taking the pipe radius as unity. The curves in Fig. 3 are approximately expressed by

$$F/F_0=1-\kappa(r/a)^2, \qquad (6)$$

where κ is a constant determined by the pressure.

The detailed description of the experiment and discussions will be given in a separate paper(6)

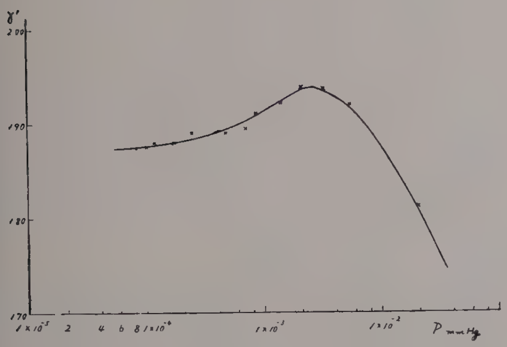

Fig. 2.

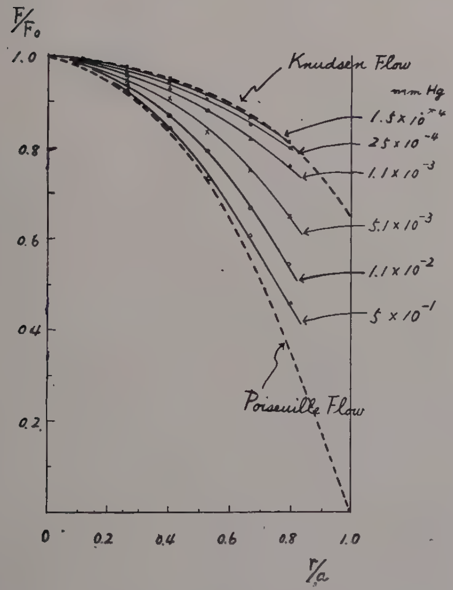

Fig. 3.

———: Formula (6).
........: Theoretical, Poiseuille and Kundsen flow.
○, △, ×: Experiment.

§ 4. Design and Construction

Although several types of flow-meters were designed and tested, the most convenient one designed by Ito(12) in our laboratory is described here. The external feature and the cross section vertical to the axis are shown respectively in Fig. 4a and b. The essential part of the meter is a torsion pendulum shown in the latter figure. Some data of the meter for 50 mm pipe are given in Table I. The suspension is a commercial tungsten fiber and the disc is a mica leaf.

To reduce the disturbing oscillation caused by external oscillations, the geometry of the pendulum is propely arranged. The oil damper is adopted, because it is less expensive than magnetic one. The window is a lens of focal length about 150 mm and a small set of lamp and scale is attached to the case of the meter. The image on the scale is sharp and stable and one can read it with an accuracy of 0.2 mm without difficulty.

The calibration of the meter is carried out by the oil film method devised by one of the authors(13), which is the most convenient for practical purposes. The calibrated value of sensitivity coincides roughly with the theoretical one; the difference between them is less than a few ten per cent. The sensitivity of order $10^{-2}\mu\cdot$l/sec is most commonly used in our laboratory. Even for the sensitivity of the order $10^{-3}\mu\cdot$l/sec, disturbing oscillation does not appear, but the determination of zero point becomes difficult when used for conventional vacuum systems such as vacuum evaporator. The range of scale is 120 mm, if an accurate zero point is required. It can

Table I

No.	Tungsten fiber		Area of mica leaf	Length of arm*	Mass of weight	Period	Sensitivity**
	Length	Diameter					
1	70 mm	35 μ	6× 7mm	17 mm	2.0 gr	3.0 sec	~1 $\mu\cdot$l/sec
2	70	35	18×18	22	2.0	3.0	~1×10^{-1}
3	70	14	18×18	22	1.2	9.5	~1×10^{-2}
4	70	10	18×18	22	1.2	16.	~3×10^{-3}

* Distance between the center of the leaf and the fiber.

** Q-value to produce 1 mm of deflection on the scale placed at 17 cm from the mirror.

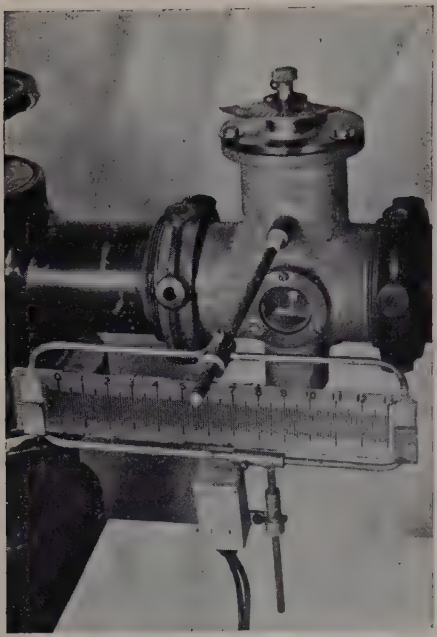

Fig. 4 a.
External feature of N-S-I type flow-meter.

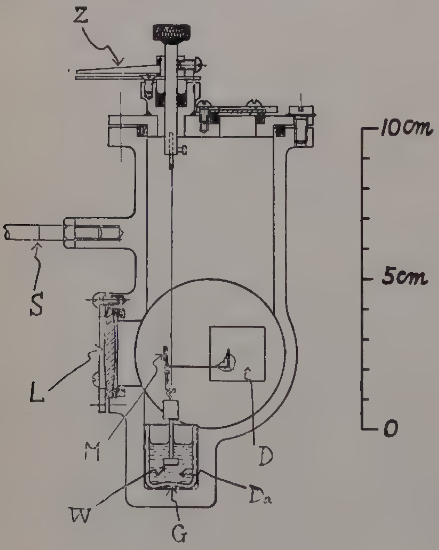

Fig. 4 b.
Z: Zero point indicator, L: Lens (window),
M: Mirror, D: Mica disc, W: Weight,
D_a: Damping oil, G: Glass bottle,
S: Support of the scale (see Fig. 4 a).

be extended, however, by rotating the zero point adjusting device. Sometimes, it is rotated more than 2π to bring the image on the scale.

This meter is very easy to handle and is not destroyed even when the air is admitted suddenly into it. Its reading is nearly proportional to Q-value independent of the pressure. It is constructed with a little expense and no accessory circuit is required.

§ 5. Applications

(a) Testing of pumping speed

It is supposed that the flow-meter is very convenient for the measurement of pumping speed of diffusion pumps when used combined with vacuum gauges. Nakamura* tested many diffusion pumps by this method and proved that the method is actually convenient. In our laboratory the meter is connected to electron diffraction cameras and other equipments. It does not increase the pipe resistance so such and the pumping speed is read at any instant *in situ* the equipment is working. It is useful for adjustment of heater current of diffusion pumps and also for leak detection (see (d)).

(b) Measurement of desorbed gas

It is obvious that the flow-meter is well fitted for the measurement of desorbed gas in a vacuum system. Uchikawa(14) measured in our laboratory the amount of gas desorbed from glass surface when it is baked in a furnace, using a bulb of surface area only *ca.* 350 cm². An example of his results is shown in Figs. 5a and b. In the former figure, the temperature of the furnace and the deflection of the flow-meter are plotted against the time. For every stepwise change of the temperature a large peak of deflection appears. It is remarkable hat a small peak or hump in the deflection corresponds to a small variation in temperature. He assumed the desorbed gas to be water vapor and calculated the amount of desorbed gas at each temperature. A result is shown in the latter figure, where data by Sherwood(15) is also plotted for comparison. Similar measurements were also carried out for glass surfaces of various histories, metal surfaces and rubbers. The authors believe that this is the best method for these purposes.

(c) Vacuum drying

If a flow-meter is applied to an equipment of vacuum drying, its reading should give the rate of dehydration. Its sensitivity is remarkably high, because $1\times10^{-2}\mu\cdot$l/sec corresponds to 1×10^{-8} gr/sec. Flow-meters of pivot type were used by some workers for this purpose in our country. However, the type mentioned in the previous section may be better, and Nakamura is now putting it to a practical test.

---

* K. Nakamura, Tokuda Manufacturing Co., Ltd., Shinagawa-ku, Tokyo, private communication.

(d) Leak detection

The flow-meter, when used as a leak detector, may be inferior to modern leak detectors*, because its sensitivity is the order of $10^{-3}\mu\cdot$l/sec. Since, however, the amount of leak can be read directly, it is used very often in our laboratory and proved to be superior to conventional vacuum gauges.

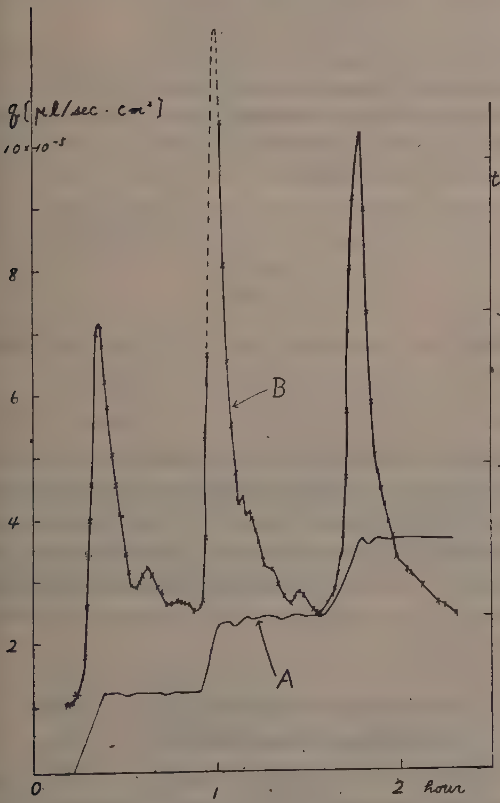

Fig. 5a.
A: Temperature, B: Desorbed gas.

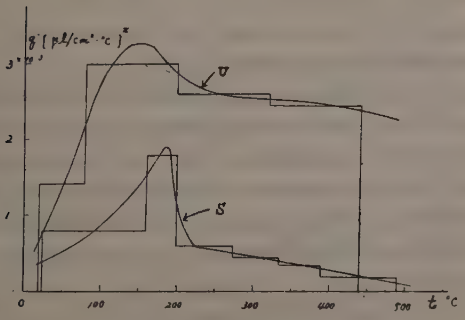

Fig. 5b.
U: Uchikawa, *S*: Sherwood.

It is expected theoretically and proved by experiment that the deflection of flow-meter increrses by 1.6 and 0.5 times when the leakage of air is substituted respectively by CO_2 and H_2 gas. By this procedure virtual and actual leaks are easily separated. It is also advantageous to apply liquid air traps to condense H_2O and CO_2 and let the meter sensitive only to non condensible gases.

In conclution the authors express their sincere thanks to Professor R. Sagane and Doctor H. Seimiya for their encouragements, to Mr. Nakamura for valuable communications, and to members of our laboratory for their helps in many respects. The authors are especially indepted to Mr. S. Takahashi in constructing various types of flow-meters.

This research was helped by research grants of the Ministry of Education.

References

1) S. Dushman: Scientific Foundation of Vacuum Technique (1949) Chapter 6.
2) S. Dushman: *loc. cit.* Chapter 3, § 7.
3) R. Uyeda: J. Appl. Phys. Japan **17** (1948) 136. (in Japanese).
4) I. Estermann & E.D. Kane: J. Appl. Phys. **20** (1949) 608.
5) R. Uyeda & N. Kato: J. Appl. Phys. Japan **17** (1948) 370. (in Japanese).
6) Y. Sugiura: unpublished.
7) H. Lamb: Hydrodynamics (1932) p. 605.
8) Y. Sugiura: Vacuum Technique **1** (1950) No. 2, 7. (in Japanese).
9) B.B. Dayton: Ind. Eng. Chem. **40** (1948) 795.
10) M. Knudsen: Ann. d. Phys. **28** (1909) 75.
11) W. Goede: Ann. d. Phys. **41** (1913) 289. H. Azumi: Bull. Chem. Soc. Japan **12** (1937) 292; **14** (1939) 343. W. G. Pollard & P. D. Present: Phys. Rev. **73** (1948) 762.
12) S. Ito: Vacuum Technique **1** (1950) No. 2, 18. (in Japanese).
13) R. Uyeda: J. Appl. Phys. Japan **17** (1948) 95. (in Japanese).
14) H. Uchikawa: Report of graduate course experiment, Physical Institute, Nagoya University, (1950).
15) R. G. Sherwood: J. Am. Chem. Soc. **40** (1918) 1645.
16) S. Dushman: *loc. cit.* Chapter 6.

---

* According to Dushman(16), leaks of the order $1.4\times10^{-6}\mu\cdot$l/sec can be quite readily detected by the leak detector of mass spectrometer, and other modern detectors seem to have a sensitivity of the order $10^{-4}\mu\cdot$l/sec.

JOURNAL OF THE PHYSICAL SOCIETY OF JAPAN Vol. 8, No. 1, JAN.—FEB., 1953

Failure and Fracture of Metals from the Standpoint of the Stochastic Theory

By Takeo YOKOBORI

Institute of Science and Technology, University of Tokyo

(Received September 2, 1952)

The phenomena of failure and fracture of metals were treated as a Markoff process or chain. In the fundamental types of failure and fracture, the physical meanings of transition probabilities were interpreted and they were found to correspond to the nucleation rate or reaction rate. The following fundamental features were unifiedly interpreted: (1) the dependence of strength on stress velocity or deformation velocity and temperature (2) the dependence of the time for creep fracture on stress and temperature. (3) many features in the endurance limit and the dependence of the number of repeated cycles for fatigue fracture on the stress range (4) the size effect (5) the fluctuation characteristics (6) ductility transition phenomena.

§1. The Stochastic Theory of Failure and Fracture of Metals

The phenomena of failure and fracture of metals were treated as a Markoff process or chain.[1)-2)] Hence, the cumulative probability function $1-p(t)$ is given by

$$dp/dt=-mp \qquad (1)$$

where $m(t)$ is the transition probability, that is, the probability of occurrence of failure or fracture in unit time after the lapse of time t, and in general a function of t, and increases with it under the usual testing conditions. Integrating Eq. (1), we obtain

$$p(t)=\exp\left(-\int_0^t m dt\right). \qquad (2)$$

Since the probability density function q is related so that

$$q=-dp/dt \qquad (3)$$

we obtain the form

$$qdt=m\exp\left(-\int_0^t m dt\right)dt. \qquad (4)$$

Eq. (4) gives the frequency distribution function of time required for failure or fracture. If the value corresponding to the most probable one in Eq. (4) are regarded as the strength, then the strength can be obtained by differentiating Eq. (4) with t and putting to zero, that is,

$$\partial q/\partial t=0. \qquad (5)$$

From Eq. (5) the following form is obtained

$$dm/dt=m^2. \qquad (6)$$

Rigorously, especially when m is constant, the mean value $\bar{t}$ should be taken as follows:

$$\bar{t}=\int_0^\infty tqdt. \qquad (7)$$

When m is constant, Eq. (7) is written in the form

$$\bar{t}=1/m. \qquad (8)$$

When the formula of $m(t)$ and the manner in which stress increases with time are known, the most probable value t_m, and, therefore, the strength can be solved from Eq. (6). On the other hand, when m is constant, the time required for failure or fracture can be given by Eq. (8).

§2. The Physical Interpretation of the Transition Probabilities

Failure and fracture of metals were divided into the following five types. The five types are: (i) yielding (ii) necking (corresponding to ultimate strength) (iii) brittle fracture (iv) creep fracture (v) fatigue fracture. In the cases of (i), (ii) and (iii) strain rate $\dot{\varepsilon}$ is assumed to be kept constant.

(i) Yielding was considered to correspond to the nucleation, the growth, and the movement of a dislocation. For the case in which the moving process[1)] was regarded as rate-determing, the yield stress S_1 was calculated from Eq. (6) in the term of shear stress

$$S_1=\frac{RT}{\alpha_1}\left(\log\dot{\varepsilon}+\frac{\Delta H_1}{RT}+c_1\right)+S_{01}. \qquad (9)$$

For the case in which the nucleation process[2)] was considered as rate-determing, S_1 was calculated as follows:*

$$S_1=C_4[C_0E\dot{\varepsilon}\exp(\Delta f^*/kT)]^{nkT} \qquad (10)$$

in which S_{01} was neglected approximately as compared with S_1.

(ii) Necking was assumed to refer to the formation of a crack nucleus and the beginning of the flow around it in order to smooth out the stress concentration. When the beginning of the flow around the crack was considered as rate-dterming, we get**

$$S_B-S_1=D\varepsilon=D\dot{\varepsilon}t \qquad (11)$$

taking S_1 as the origin of time and assuming in first approximation the linear relation between stress and strain from S_1 to the ultimate strength S_B as shown in Fig. 1. By the similar calculation, we obtain the similar form as Eq. (9) in the term of shear stress:

$$S_B=RT(1/\alpha_1+1/\alpha_2)\left[\log\dot{\varepsilon}+\frac{\Delta H}{RT}+C_B\right]+S_{01} \qquad (12)$$

in which

$$\Delta H=(\Delta H_1/\alpha_1+\Delta H_B/\alpha_B)/(1/\alpha_1+1/\alpha_B)\,,$$

C_B is a constant. For the case in which the nucleation process2) of a crack was taken, we obtained the similar relation as Eq. (10). This relation, however, will be valid only in the case in which S_1 can be neglected as compared with S_B in Fig. 1.

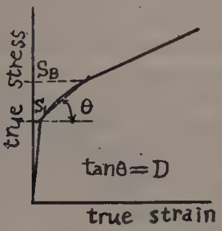

Fig. 1.

(iii) Brittle fracture was considered to refer to the nucleation of a crack and its growth. Each case for the nucleation process2) and for the growth process1) was treated, and the similar relations as Eqs. (9) and (10) were obtained, respectively.

(iv) Creep fracture was divided into the two stages, that is, necking and fracture. In creep m is considered as almost constant. Hence, the time required for fracture was obtained from Eq. (8) for each case of the nucleation process4) of a crack and of its growth process1).

(v) In fatigue, the phenomena were regarded as the problems of a Markoff chain instead of a Markoff process. Fatigue fracture was considered as successive events of the initiation of slip bands, damage and fracture. The initiation of damage5) was interpreted as the nucleation process of a crack nucleus and the occurence of fracture6) was explained as its growth process. In those cases the trainsition probability is not, but, proportional to the nucleation rate or the reaction rate.

§ 3. The Fluctuations of the Strength

The frequency distribution curves*** of failure or fracture stress, S, can be obtained from Eq. (4) when the form of m is known. The calculations were carried out for the case of the reaction rate process as the special case of the nucleation process2). For the case of ordinary nucleation process as rate-determing, the frequency distribution function F can be obtained as follows:****

$$FdX=X^{\delta}\exp(-X^{\delta+1}/\delta+1)dX \qquad (13)$$

in which

$$X=S(L/v)^{1/(\delta+1)} \qquad (14)$$

$$L=(ZkT/h)\exp(-\Delta f^*/kT)C_1^{\delta} \qquad (15)$$

$$\delta=1/nkT \qquad (16)$$

and other notations are the same in the preceding paper2). It is shown with parameter δ as in Fig. 2. It can be seen from

---

* In the case of the initial yielding (loap drop) of annealed iron, the Cottrell-Bilby mechanism3) should be considered. In this case the similar type of equation as Eq. (10) is obtained9) with different parameters. The relation, therefore, such as Eqs. (13), (18) and (19), derived on the basis of Eq. (10) become formally the same in both cases of Cottrell-Bilby mechanism and nucleation process.

** Eq. (11) is a first approximation. The phenomena of necking may be considered as successive events of yielding and necking, and these treatments can be carried out as in reference (6).

*** A. Joffe10) has already called attension to this problem in saying that the frequency distribution curve of the strength of glass has nothing to do with experimental errors.

**** It is interesting to note that Eq. (13) is formally in agreement with Weibull's distribution function1).

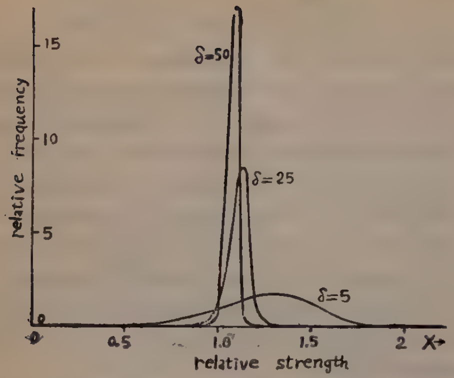

Fig. 2. Frequency distribution of Strength.

Eq. (15) and Fig. 2 that the smaller the specimen volume is, the smaller the $(L/v)^{1/(\delta+1)}$ is, and, therefore, the larger the scatter is. It can also be understood that the frequency distribution curves will be negatively skewed in the case of loading velocity, v, or strain rate, which is higher than ordinary.

The marked characteristics in the fluctuations of the time for creep fracture[4][7] or the number of repeated cycles for fatigue fracture[6][8] can be well interpreted considering the phenomena as the successive events.[6]

§ 4. The Size Effect on the Strength

It is worth to notice that the size effect may be interpreted from the same standpoint used above. For the reaction rate process[1]:

$$S \propto \text{constant} - \log V . \qquad (17)$$

For the nucleation rate process[2]:

$$S \propto V^{-\gamma} \qquad (18)$$

in which V represents the specimen volume.

§ 5. The Ductility Transition Phenomena

The occurrence of so-called 'cold brittleness' was well interpreted[12] on the basis of the stochastic theory. The relation between deformation velocity, V_B, and the absolute temperature for this occurrence was derived as the form:

$$\log V_B = -\frac{Q}{RT} + c_0 . \qquad (19)$$

This interpretation may be more reasonable than that as the change into the momentum transfor mechanism[2].

§ 6. Conclusion

The agreement of the theory with the experiments of the author and in literature was discussed in the author's reports in the references. Much closer approximation to the distribution function might be obtained by taking into considerations statistical distributions of the incubation period (for example, corresponding to S_{01}), ΔH, and α themselves and the variation of Z from specimen to specimen.

In conclusion the author wishes to express his cordial thanks for the active interest taken in these problems by Prof. M. Hirata, without whose valuable suggestions, enlightining discussions and kind encouragement these investigations could not have been accomplished.

References

1) T. Yokobori: J. Phys. Soc. Japan **7** (1952) 122, and in this Jonrnal.
2) T. Yokobori: Ibid. 44.
3) A. H. Cottrell and B. A. Bilby: Proc. Phys. Soc. London, **A 62** (1949) 49.
44.
4) T. Yokobori: J. Phys. Soc. Japan **7** (1952) 48.
5) T. Yokobori: Proceedings of the First Japan National Congress for Applied Mechanics **1** (1951) 97.
6) T. Yokobori: J. Phys. Soc. Japan **8** (1953).
7) T. Yokobori: J. Phys. Soc. Japan **6** (1951) 78.
8) T. Yokobori: Ibid. 81.
9) To be published.
10) A. Joffe: Int. Conf. Phys. II. The Solid State of Matter. Phys. Soc. Lond. (1934) 77.
11) W. Weibull: Ing. Vetenskaps Akad. Handl. **151** (1939).
12) T. Yokobori: J. Phys. Soc. Japan **8** (1953) No. 1.

JOURNAL OF THE PHYSICAL SOCIETY OF JAPAN Vol. 8, No. 1, JAN.—FEB., 1953

Ductility Transition and Cold Brittleness

By Takeo YOKOBORI

Institute of Science and Technology, University of Tokyo

(Received September 2, 1952)

The occurrence of the change of fracture from ductile type to brittle one which is often called 'cold brittleness' is studied from the standpoint of the stochastic theory. In the present paper failure and fracture processes were treated as reaction rate process. The relation between deformation velocity, V_B, and the absolute temperature for brittle fracture was obtained as the form:

$$\log V_B = -\frac{Q}{RT} + c_0 \, .$$

The effect of radius of notch on the transition, the size effect, and the scatter of the brittle strength were also interpreted from the same standpoint. In the case in which the Cottrell-Bilby mechanism for yielding, and nucleation process for brittle fracture, respectively, are regarded as rate-determining, similar results can also be obtained.

§ 1. Introduction

The term 'ductility transition' is used in this paper to mean that the fracture of material such as some steel change from the ductile type to the brittle type with only the absorption of elastic energy. This will occur when temperature is decreased or strain rate is raised to some limit. This type of brittle fracture is often called as 'cold brittleness'. The present paper concerns primarily with the stochastic and physical interpretation of the problems. In the case of notched bars the effect of the stress distribution is not concerned in details.

§ 2. Theoretical Considerations

From the standpoint of the stochastic theory[1)2)], the yield strength S_1 is given by:

$$S_1 = \frac{RT}{\alpha_1}\left(\log \dot{\varepsilon} + \frac{\Delta H_1}{RT} + c_1\right) + S_{01} \, . \qquad (1)$$

where

$c_1 = \log(\alpha_1 E / A_1 RT)$

$A_1 = (Z_1 kT/h) \exp(\Delta\phi_1/R)$

ΔH_1 = the activation energy per g atom for the movement of a dislocation

$\Delta\phi_1$ = increase in entropy

α_1 = unit volume of yielding multiplied by the microscopic stress concentration*

Z_1 = the total number of weak spots available for dislocations

and Hook law is assumed to be obeyed, till yielding the origin of time was taken at S_{01}, and other notations have the usual meanings as in the preceding papers.[2)3)] S_1, S_{01} are denoted in term of shear stress. As to the brittle fracture strength S_2, from the same standpoint, we obtain the similar form:

$$S_2 = \frac{RT}{\alpha_2}(\log \dot{\varepsilon} + \Delta H_2/RT + c_2) + S_{02} \qquad (2)$$

in which $c_2 = \log(\alpha_2 E / A_2 RT)$, $A_2 = (Z_2 kT/h) \times \exp(\Delta\phi_2/R)$, ΔH_2, $\Delta\phi_2$, α_2 and Z_2 correspond to ΔH_1, $\Delta\phi_1$, α_1, and Z_1, respectively. It can be seen from Eqs. (1) and (2) that the yield strength S_1 and the brittle fracture strength S_2 increase linearly as the logarithm of strain rate increases, and S_1/T and S_2/T increase linearly as the reciprocal of the absolute temperature increases.

When α is smaller and $\Delta H/\alpha + S_0$ is larger in yielding that in brittle fracture,*** the brittle fracture strength increases less rapidly than the yield strength with the increase of strain rate or the decrease of temperature as can be seen from Eqs. (1) and (2) and Figs. 1 and 2. In these figures, the origins of $\log \dot{\varepsilon}$ and

---

* The term 'microscopic' was used to distinguish from the macroscopic stress concentration factor such as the notch effect.

** S_2 and S_{02} should be denoted in the term of tensile stress. For comparision with S_1 and S_{01}, however, they were expressed in the term of shear stress in the present paper. See reference (4) as for the agreement of Eq. (2) with experiment.

*** The condition $\Delta H_1/\alpha_1 + S_{01} > \Delta H_2/\alpha_2 + S_{02}$ means that yield stress is greater than brittle fracture stress at absolute zero temperature.

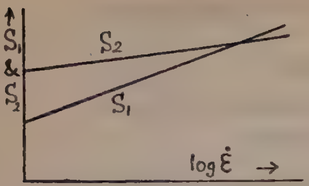

Fig. 1.

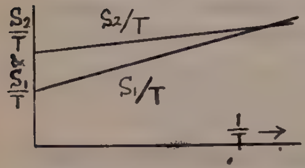

Fig. 2.

$1/T$ were taken at the usual value of them at which S_2 is larger than S_1. Hence, when strain rate increases or temperature decreases, the two straight lines in Figs. 1 and 2 intersect and brittle failure will occur.**** This condition can be obtained putting the right hand side of Eq. (1) equal to that of Eq. (2), that is,

$$\log \dot{\varepsilon} = -\frac{Q}{RT} + c \qquad (3)$$

in which

$$Q = (\Delta H_1/\alpha_1 - \Delta H_2/\alpha_2 + S_{01} - S_{02})/(1/\alpha_1 - 1/\alpha_2)$$

and $c = (c_2/\alpha_2 - c_1\alpha_1)/(1/\alpha_1 - 1/\alpha_2)$.

Q may be expected to be positive.

§ 3. The Effect of Temperature and Deformation Velocity

Since the average elastic strain rate is proportional to[4] deformation velocity V_B, that is, $\dot{\varepsilon} = c_3 V_B$, Eq. (3)' becomes:

$$\log V_B = -(Q/RT) + c_0 \qquad (4)$$

where $c_0 = c - \log c_3$ and c_3 is a constant. Eq. (4) gives the relation between deformation velocity and the absolute temperature for brittle failure, which is in good agreement with experimental results in literature.[5]

§ 4. The Effect of Radius of Notch

The case of notched bar was considered in this section. Under such conditions of testing as determined by Hollomon, the principal effect varying the radius of notch will be to change the rate of strain at the base of the notch without changing the transverse stress. The elastic strain rate at the base of the notch is given by

$$\dot{\varepsilon} = b\dot{\varepsilon}_0 \qquad (8)$$

in which $\dot{\varepsilon}_0$ is the elastic strain rate in the unnotched section, and b is the stress concentration factor. Combining Eqs. (3) and (5), the relation between the stress concentration factor, the temperature and the strain rate ε_0 at which brittle failure occur is given by

$$\log b = -\frac{Q}{RT} + c - \log \dot{\varepsilon}_0 \,. \qquad (6)$$

From the experimental results[6] upon the effect of notch radius, the stress concentration factor for each radius was determined. As can be seen from Fig. 3, the logarithm of b is approximately a linear function of the reciprocal of the absolute temperature in accordance with Eq. (6) except the range of very small radius of notch, where another effect might be predominant.

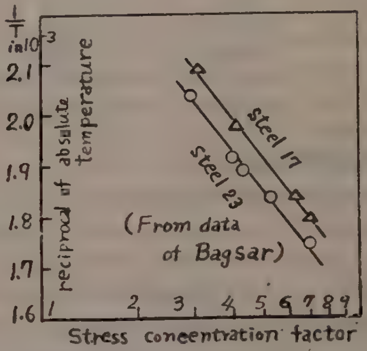

Fig. 3. The effect of radius of notch.

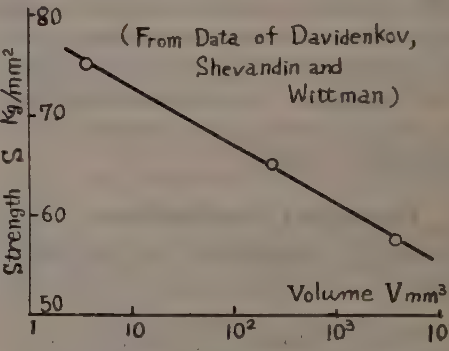

Fig. 4. The size effect on the brittle strength.

When b is constant, Eq. (6) is in good agreement with experments[7].

**** The method of determining the transition temperature from the point of intersection of the two curves of the yield stress and the brittle strength as function of temperature has already been pointed out by A. F. Joffe *et al.*[9]

§ 5. The Effect of the Type of Metal

When $\alpha_1 \geq \alpha_2$ and $\Delta H_1/\alpha_1 + S_{01} \leq \Delta H_2/\alpha_2 + S_{02}$, the two straight lines in Figs. 1 and 2 do not intersect and brittle fracture will not occur. The values of α and ΔH may be considered to depend upon the type of metal, and, therefore, it seems to be understood that the occurrence of ductility transition or cold brittleness depends upon the material.

§ 6. The Size Effect on the Brittle Strength

It is worth to notice that the size effect on the brittle strength can also be interpreted on the basis of the stochastic theory used above. If the density of the weak spots is approximately considered to be the same throughout the section of the specimen, Z is proportional to the volume, V, of the specimen. Hence, from Eq. (1) or (2) the failure strength S can be written in the form:

$$S \propto \text{constant} - \log V \qquad (7)$$

which is also in good agreement with experimental results[8] when S is plotted as a function of the logarithm of V as shown in Fig. 4.

§ 7. The Scatter of the Brittle Strength

It can be seen from Eq. (14) and Fig. 2 (reference (3)) that the smaller the specimen volume is, the smaller the value of Z is, and, therefore, the larger the scatter of the brittle strength is. This is also in good agreement with the experiments[8].

§ 8. Discussion

The interpretation of the ductility transition occurrence introduced in the present paper may be more reasonable than that developed as the change into the momentum transfer mechanism in § 4 of the preceding paper.[3]

When yielding and fracture are treated as successive events, the transition may be considered to correspond to the condition under which the difference between the yield strength and the brittle fracture strength has decreased below some finite value.

If the Cottrell-Bilby mechanism[10] is considered for yielding, and nucleation process[3] is regarded as rate-determining for brittle fracture, the following relations are obtained, respectively:

$$S_1 = S_{01}(C_{11}\dot{\varepsilon})^{nkt} \qquad (8)$$

$$S_2 = S_{02}(C_{22}\dot{\varepsilon})^{lkt}. \qquad (9)$$

The similar type of equations as Eqs. (3), (4) and (6), and, therefore, similar conclutions can be obtained assuming that $n > l$ and S_1 is larger than S_2 at absolute zero temperature.

In conclusion the author wishes to express cordial thanks to Prof. M. Hirata for his kind guidance. Thanks are also due to Dr. J. H. Hollomon for his kindness in sending the author his valuable paper.

References

(1) T. Yokobori: J. Phys. Soc. Japan **8** (1953) No. 1.

(2) T. Yokobori: J. Phys. Soc. Japan **7** (1952) 122.

(3) T. Yokobori: Ibid. 44.

(4) J. H. Hollomon: Trans. Amer. Inst. Min. Met. Engrs. **158** (1944) 298.

(5) F. F. Wittman and V. A. Stepanoff: J. Tech. Phys. U.S.S.R. **9** (1939) 1070.

(6) A. B. Bagsar: Weld. J. (1949) 484.

(7) C. W. MacGregor, N. Grossman and P. R. Sheplar: Weld. Res. Suppl. **12** (1947) 50.

(8) N. Davidenkov, E. Shevandin and F. Wittman: J. Appl Mech. **14** (1947) 63.

(9) A. Joffe, M. W. Kirpitschewa and M. A. Lewitzky: ZS. f. Phys. **22** (1924) 286.

(10) A. H. Cottrell and B. A. Bilby: Proc. Phys. Soc. London. **62**A (1949) 49.

(11) To be published.

JOURNAL OF THE PHYSICAL SOCIETY OF JAPAN Vol. 8, No. 1, JAN.—FEB., 1953

The Half-Life of ThC′

By Takeo HAYASHI,* Yoshihide ISHIZAKI** and Isao KUMABE**

* *Department of Physics, Saikyo University, Kyoto*
** *Department of Physics, University of Kyoto, Kyoto*

(Received October 18, 1952)

The accurate measurement of the half-life of ThC′ was made by the pulse timing circuit method using a G-M counter and a proportional counter. The value of the half-life was found to be $(2.9\pm0.1)\times10^{-7}$ sec. Some details of the pulse timing circuit used are explained in this paper.

§ 1. Introduction

The first direct measurement of the half-life of ThC' was made by Dunworth[1] in 1939. He used the integral method of coincidence counts. This method was repeated with an improved technique by Bradt and Scherrer.[2] Recently owing to the progress of electronics and experimental techniques in the wartime research, the high resolution coincidence circuit and the delay line have become available for such study. By the use of this delayed coincidence method, several workers[3][4][5] obtained the values of the half-life of ThC'. While our present work was carried out by the use of the circuit of other type, which may be called the pulse timing circuit.[6]

The disintegration series between ThB and ThD are shown schematically in the following way:

$$\begin{tikzcd}
 & & \text{ThC}' \arrow[dr, "\alpha"] & \\
\text{ThB} \arrow[r, "\beta"] & \text{ThC} \arrow[ur, "\beta"] \arrow[dr, "\alpha"'] & & \text{ThD} \\
 & & \text{ThC}'' \arrow[ur, "\beta"'] &
\end{tikzcd}$$

In the present work, we could obtain the accurate value of the half-life of ThC′ by measuring the time interval between a beta-emission from ThC and a succeeding alpha-emission from ThC′. This very short time interval could be measured by the use of the pulse timing circuit. The half-life of $(2.9\pm0{\cdot}1)\times10^{-7}$ sec. was obtained by the analysis of experimental data taking into account the measured time-lag inherent to the counter system. In the present paper we describe some details of the whole procedure, especially those of the pulse timing circuit used.

§ 2. Description of the Apparatus

The sample of ThC′ used was the radioactive deposit on a thin aluminium foil, prepared from Thron. This foil was pasted on the inner wall of the end-window proportional counter of flow type with a thin collosion window of 0·18 mg/cm² thick. The end-window G-M counter used had a mica window of 3 mg/cm² thick. Moreover, the window of both counters were set face to each other. So, alpha and beta-particles from the foil were able to penetrate both windows.

The block diagram of our complete circuit is shown in Fig. 1 (A). The circuits from each counter to the third one-shot multivibrators, denoted 3rd M. V. in the diagram, are similar except the linear amplifier, which is inserted immediately after the proportional counter. The delay adjusters in each channels are used in order to obtain the rigorously coincident pulses when the same artificial input pulse applied on the input of the both first M. V.

The output pulses of both third M. V. are fed to the pulse timing circuit, of which details are shown in Fig. 1 (B). When a square pulse, A, with a width of t_A and the other square pulse, B, delayed Δt for the former one, are given to the coincidence circuit in succession, the output pulses from the coincidence tube should be larger in the part of the width where the input two pulses are superposed; the width of the larger height part is to be $t_A-\Delta t$, as shown in Fig. 2. Then, the saw-tooth pulse is generated by the larger height part of the coincidence pulse in the next stage of the circuit, which is so designed that the height of this saw-tooth pulse should be proportional to the width of the coincident pulse. Such saw-tooth pulses, with different heights corresponding to the different delay intervals, are

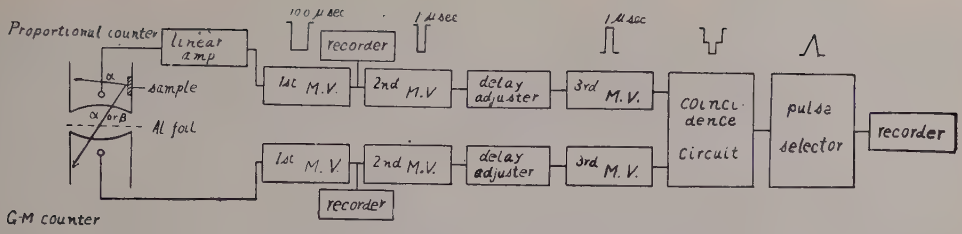

(A) Block diagram of pulse timing circuit

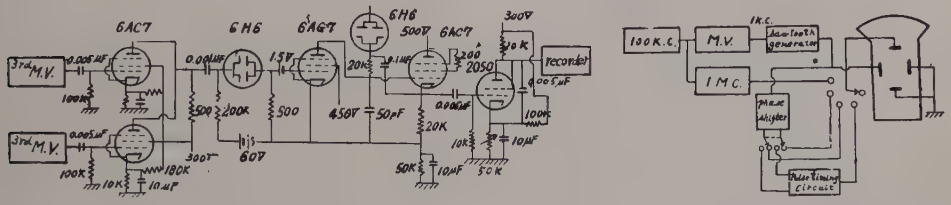

(B) Coincidence circuit and Pulse selector (C) Calibration Circuit

Fig. 1.

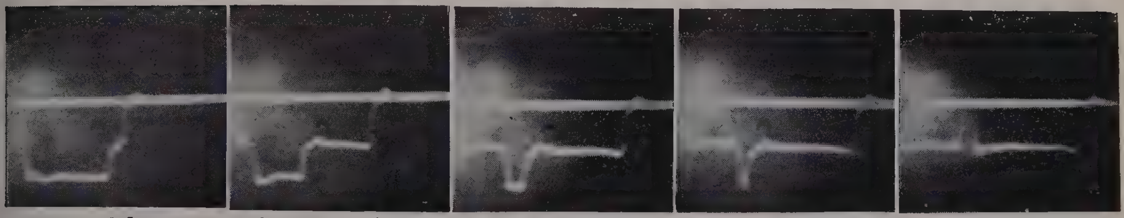

no delay 0.2 μsec delay 0.4 μsec delay 0.5 μsec delay 0.6 μsec delay

Fig. 2.

sent into the discriminator circuit connected to a mechanical recorder. By changing the grid bias of the discriminator tube, we can observe the distribution of the delay time between the two pulses.

While, in order to determine the delay time we used a so-called calibrating circuit shown schematically in Fig. 1 (c). The saw-tooth pulses from the synchroscope circuits, driven by a multivibrator of about 1 k. c., are sent into the x-axis of the cathode-ray tube. Since this multivibrator oscillation is generated by a crystal oscillator of 100 k. c., the time-axis of the cathod-ray tube is synchronized with the 100 k. c. oscillation, while this 100 k. c. oscillation is multiplied synchronously to 1 M. C.. By the application of the 1 M. C. oscillation into the y-axis, the sweeping speed of the time axis can be estimated and found that this speed to be 10 cm per 3 microsec. On the other hand, the saw-tooth pulses for the time axis are given to grids of two phase shifters, each operated by a thyratron with variable and suitable biases respectively. By these phase shifters we can produce pair of pulses with various time intervals, which are easily measured by comparing the positions on the time axis of the known sweep speed. Using these pairs of pulses with known delay time produced by this procedure, we can calibrate precisely the pulse timing circuit.

§ 3. Measurement

Since the counting tube has its "intrinsic" time-lags,[5)7)] estimated to be the order of one tenth of a microsecond, in the measurement of the very short life of radioactive substances some particular precautions must be taken with respect to this point. Therefore, the measurement of the relative time lags between the proportional counter for alpha-particles and the G-M counter was carried out.

The measurement procedure with both counters was as follows: the distribution of the delay time was obtained with and without the aluminium absorber of 6.7 mg/cm² thick between the counters. Without the absorber coincidences of the same α-particles, which penetrate the windows of both counters, were measured in addition to β-α coincidences, while with the absorber enough to stop the α-particles from ThC′, only β-α coincidences were counted. The difference of the coincidence counts with and without the absorber should be α-α coincidences, which give the distribution of the relative time lags of both counters above mentioned. Experimental data obtained are shown in Table I.

Table I

Time interval (μ sec)	−0.15 ~ 0.25	0.25 ~ 0.41	0.41 ~ 0.57	0.57 ~ 0.67	0.67 ~ 0.78	0.78 ~ 0.85
α-α counts	745	3282	2599	734	158	0
β-α counts	739	1504	1685	1647	1246	1222

Table II

Observer	Half-life (10^{-7} sec)	Reference
Dunworth	3±1	(1)
Bradt and Scherrer	2.6±0.4	(2)
Hill	3.0±0.15	(3)
Van Name	2.2±0.1	(4)
Bunyan, Lundby and Walker	3.04±0.04	(5)
Hayashi, Ishizaki and Kumabe	2.9±0.1	Present work

§ 4. Results and Discussion

The values in Table I result into the curves shown in Fig. 3, which are, however, normalized so that the both curves should have equal area above abscissa for the convenience of the following calculation. Using these curves and the formula,

$$\lambda = \{F(A) - F(B)\} \Big/ \int_A^B \{F(t) - P(t)\} dt$$

given by Newton,[8] we could obtain the decay constant of ThC′ to be $\lambda = 2.4 \times 10^6$ sec^{-1}., which corresponds to the half-life $T = 2.9 \times 10^{-7}$ sec. The probable error of this value, mainly caused by the statistics of the counting, was roughly estimated to be 0.1×10^{-7} sec. Moreover, in the present experiment the measurement of the counter time lags was made by using α-particles for both counters, but in practice the G-M counter counted β-rays of ThC. Therefore the difference of the counter time lags for α- and β-rays may cause some experimental error for the final value, but this error seems to be very small comparing to the error above mentioned. In Table II the present value is compared with other values which have been obtained by other workers for the half-life of ThC′. Earlier and more uncertain estimates are omitted.

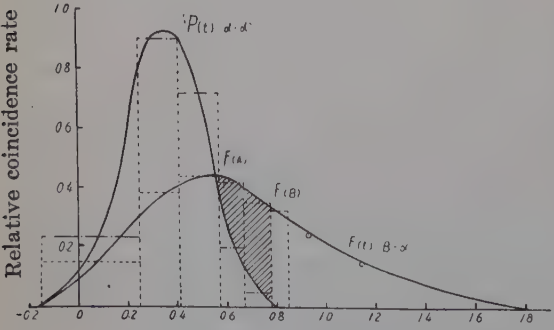

Delay time in μ sec.
Fig. 3.

We should like to thank Prof. K. Kimura and Prof. S. Shimizu of the University of Kyoto for their interest and many helpful suggestions.

References

1) J. V. Dunworth: Nature **144** (1939) 152.
2) H. Bradt and P. Scherrer: Helv. Phys. Acta. **16** (1943) 251.
3) J. M. Hill: Proc. Camb. Phil. Soc. **44** (1948) 440.
4) F. W. Van Name, Jr.: Phys. Rev. **75** (1949) 100.
5) D. E. Bunyan, A. Lundby and D. Walker: Proc. Phys. Soc., London A **62** (1949) 253.
6) H. K. Ticho: Rev. Sci. Inst. **18** (1947) 271.
7) A. R. Lanfer: Rev. Sci. Inst. **21** (1950) 244.
8) T. D. Newton: Phys. Rev. 78 (1950) 490.

JOURNAL OF THE PHYSICAL SOCIETY OF JAPAN Vol. 8, No. 1, JAN.—FEB., 1953

Electron Diffraction Studies on Oxide Films formed on Metals and Alloys
Part 2. Selective Oxidation of Alloys

By Goro HONJO

Tokyo Institute of Technology,
Ohokayama, Meguroku, Tokyo, Japan

(Received May 22, 1952)

Surface oxidation products on various alloys due to varying oxidizing conditions within the range of 300-900°C for temperature and 10^{-4}-760 mmHg. for air pressure are studied by the electron diffraction method. Alloys studied are copper alloys containing 0.3% Be, 0.5% Al, 0.1% Mg, 7% Mn and 7% Ni and that of iron with 13% Al respectively.

The selective oxidation or the phenomenon that the baser component of alloy is oxidized selectively in spite of its much lower content in the mother alloy than the other was found to occur generally in these alloys when the air pressure is sufficiently low and the temperature is high enough. High yield of the secondary electron emission of Be-Cu alloy is concluded to be due to the selective oxidation product BeO having a particular orientation grown on this alloy. An unknown oxide of Ni of a spinel type structure is found on 7% Ni-Cu alloy.

§ 1. Introduction

In the course of studies on the oxidation of alloys at higher temperatures by the electron diffraction method, Miyake[1] has found for some alloys that the surface product consists of the oxide of one of the component metals which is of much lower proportion than the other in the mother alloy. The surface oxide of beryllium- copper containing more than 2% of beryllium and aluminium-copper containing more than 3% of aluminium were identified with beryllium oxide BeO and γ-aluminium trioxide γ-Al_2O_3 respectively. This is the interesting phenomenon known as "*the selective oxidation of alloy*", which has not been investigated throughly as yet.

According to the Miyake's experiment, as the matter of fact, the alloys such as 1% magnesium-copper, 7% manganese-copper, 7% nickel-copper and even beryllium-copper and aluminium-copper, when the content of beryllium and aluminium is smaller than that mentioned above, did not show such phenomena, and the surface products were merely identified with the oxide of copper. The surface oxides formed on 2~15% aluminium-iron were found also to be that of iron. In his experiment the oxidation was carried out throughly in open air, though the oxidizing temperatures were varied. The recent theory on the oxidation of metals and alloys, however, suggests that such phenomena might depend not only on the temperature but also on the air pressure of the oxidation considerably. It is, therefore, desirable to carry on a more extended electron diffraction study of the phenomenon in varied air pressure at various temperatures.

§ 2. General Description of the Experiment

The alloys studied in the present investigation are 0.3% beryllium-copper, 0.5% aluminium-copper, 1% magnesium-copper, 7% manganese-copper, 7% nickel-copper and 13% aluminium-iron. The oxidation is carried out in a quartz tube in which the temperature and pressure are varied respectively within the range of 300~900°C and 10^{-4}~760 mmHg. with the method adopted in the preceding investigation on the oxidation of pure copper by the present author.[2]

It is found that the surface products depend critically on the two conditions of the oxidation. The main experimental results, therefore, except that for 13% aluminium-iron, are summarized in the temperature-pressure diagrams Fig. 1~Fig. 5. In these diagrams the surface products which are identified with the electron diffraction method are represented by various marks, and the conditions of their formation are to be read by the coordinates of the marks; the temperature and the air pressure corresponding to the abscissa and the ordinate respectively. Unless otherwise stated, the specimens are heated up beforehand to the desired temperature in the highest vacuum attainable for our vacuum furnace (about 10^{-4} mmHg.), and then are oxidized at the desired air pressure which is attained by letting in a volume of air into the quartz tube. Therefore, the oxidizing conditions read in these diagrams are those which follows a preheating of a few minutes in the highest vacuum. The numeral attached to each mark indicates the time of oxidation in minutes. Two marks situating in a same point on the diagram correspond to the two different substances formed by a single treatment. Generally in these diagrams the surface products which are identified with the oxides of copper are represented by the marks used in Fig. 1 of the previous paper[2]; plain (○), dotted (⊙) and crossed (⊕) circles corresponding respectively to the three types of cupric oxide CuO and triangle (△) to cuprous oxide Cu_2O. Other marks will be explainted in the following section in which the detailed description and discussion of the results on each alloy are given.

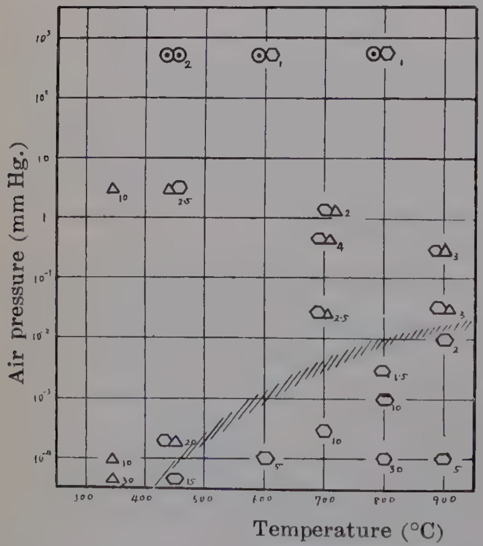

Fig. 1 Temperature pressure diagram for the surface oxidation products on 0.3% Be-Cu.
⬡: BeO, ○, ⊙, ⊕: CuO, △: Cu_2O

§3. Details of the Results and its Discussions

(1) 0.3% Beryllium-Copper

The results on this alloy are summarized in Fig. 1. The surface products at lower air pressures are clearly identified with beryllium oxide BeO (hexagonal, a=2.70 Å, c=4.39 Å) which is represented by hexagon (⬡) in the diagram. It may be seen that at higher temperatures than about 400°C beryllium is selectively oxidized in reduced air pressures in spite of a so small content of it in the alloy. When this alloy is oxidized at higher air pressures from the beginning, as was the case with Miyake's experiment, the surface products are solely identified with cupric oxide. Beryllium oxide appearing at higher pressures in Fig. 1 may be the product in the course of preheating in higher vacuum.

The diffraction rings of beryllium oxide formed in lower air pressures show the arcing which corresponds to a preferred orientation with [00,1] axis perpendicular to the free surface of the specimen and furthermore the intensity distribution in the arcs has generally sharp outer edge at the radius of Debye ring and tails considerably towards the shadow edge of the free surface of the specimen, apparently being due to the refraction effect (Photo. 1). This fact shows that the crystallites of beryllium oxide on these specimens have flat surfaces of (00,1) plane, which are at the same time nearly parallel to the free surface of the specimen.

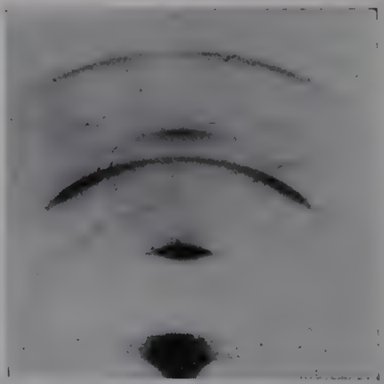

Photo. 1 Electron diffraction pattern due to BeO formed on 0.3% Be-Cu alloy.

It has been well known that the beryllium-copper alloy containing a few percent of beryllium shows a high yield of the secondary electron emission, amounting to 12, after a proper heat treatment in lower air pressures. It is probable that the selective oxidation of beryllium observed in our experiment may take an important part in this high yield. The value of the yield of this alloy beyond that of beryllium oxide itself (4∼5), may be also understood when we assume a higher value of it for the (00,1) plane than the other planes of beryllium oxide.

(2) **0.5% Aluminium-Copper**

The results on this alloy are summarized in Fig. 2. The squares (□) in this diagram represent the products which are identified with γ-aluminium trioxide γ-Al_2O_3. Though the diffraction pattern due to copper aluminate $CuAl_2O_3$ (spinel type, a=8.07 Å), is expected to resemble to that of γ-Al_2O_3 (a=7.90 Å), we can safely say that the products are to be the latter by a precise measurement of the lattice constant on the patterns showing sharper Debye rings. From this diagram it is seen that by the alloy of much lower content of aluminium the selective oxidation of aluminium takes place also in reduced air pressures. In this case, however, the surface products in higher air pressures shows only the pattern of oxides of copper even after the preheating in higher vecuum.

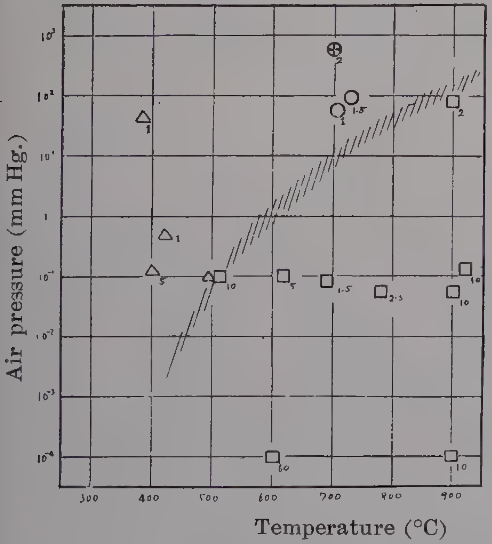

Fig. 2 Temperature pressure diagram for the surface oxidation products on 0.5% Al-Cu.
□: γ-Al_2O_3

(3) **7% Manganese-Copper**

Fig. 3 shows the results on this alloy. The selective oxidation of manganese takes place in reduced air pressures, but the products vary from manganous oxide MnO to manganous manganic oxide Mn_3O_4 (tetragonal, a=5.75 Å, c=9.42 Å) with the variation of air pressure. The former is represented by crossed square (⊠) and the latter, by shaded rectangle (▨). The pattern of MnO often shows characteristic broadening of the rings of different indices which is a similar effect to that was found for magnesium oxide smoke, and be-

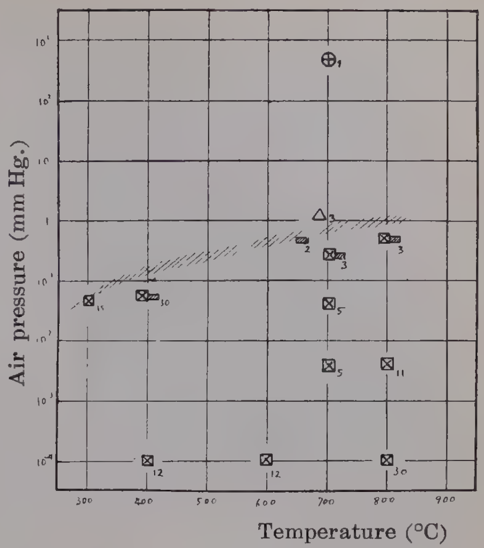

Fig. 3 Temperature pressure diagram for the surface oxidation products on 7% Mn-Cu.
⊠: MnO ▨: Mn_3O_4

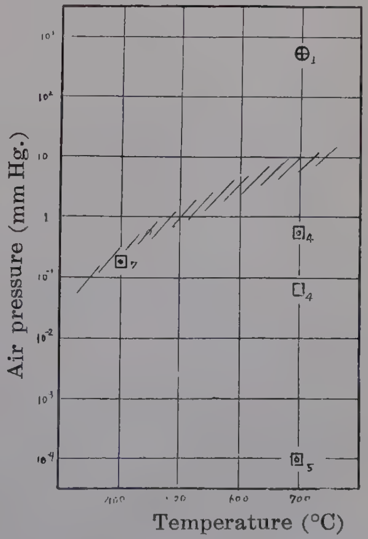

Fig. 4 Temperature pressure diagram for the surface oxidation products on 1% Mg-Cu.
⊡: MgO

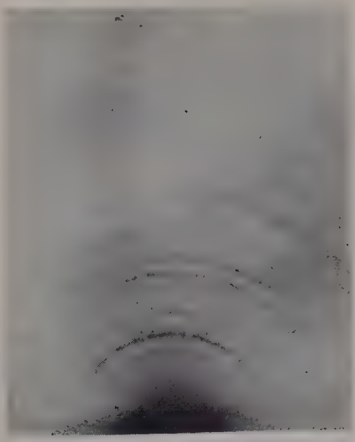

Photo. 2 Electron diffraction pattern due to unknown oxidation product formed on 7% Ni-Cu alloy.

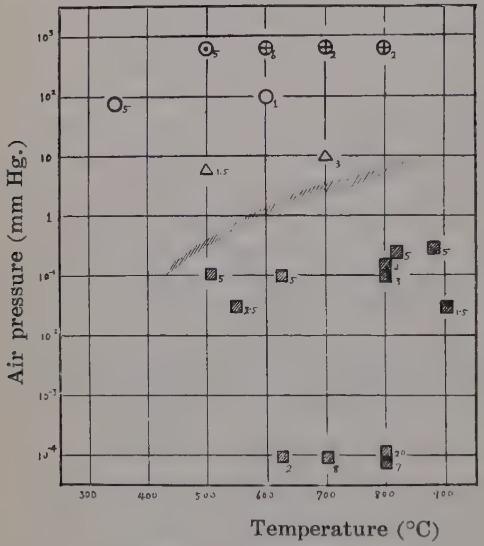

Fig. 5 Temperature pressure diagram for the surface oxidation products on 7% Ni-Cu.
▨: unknown oxide.

ing explained as refraction effect at the surfaces of the smoke particles having clean-cut cubic habit.3) The crystallites in the surface film, therefore, can be concluded to have grown into cubic habit.

(4) **1% Magnesium-Copper**

A few examples listed in Fig. 4, where the surface products identified with magnesium oxide MgO are shown by dotted square (⊡), are sufficient to show the selective oxidation of magnesium in reduced air pressures.

(5) **7% Nickel-Copper**

The surface products formed on this alloy in lower air pressures show always the diffraction pattern represented in Photo. 2, which can not be identified to any known oxides of nickel and copper and are represented in Fig. 5 by shaded square (▨). The observed spacings are tabulated in Table I, together with their estimated intensities. From this data it can be easily seen that the substance is to be of spinal type with lattice constant 8.23 Å. For the spinal type oxide, however, one of its component metal ions should be trivalent which is not capable usually for either component of this alloy and, furthermore, there are known many oxides of copper or nickel of spinel type having the lattice constant near this value. It is, therefore, very much probable that this surface product may due to an impurity in the mother alloy. Specimens cut from blocks of different origins, however, give also the same surface product of the spinal type when they are oxidized in the corresponding conditions. On the other hand, a spectroscopic analysis has proved that there are no impurities in the specimens except a trace of silver which is incapable to be trivalent. Therefore this surface product is supposed to be an unkonwn oxide containing trivalent nickel ion either in the from $CuO.Ni_2O_3$ or $NiO.Ni_2O_3$, since the existence of trivalent nickel ion in solid state has been discusses to be possible. The sharpness of the pattern of this substance indicates the

Table I
Unknown oxide formed on 7% Ni-Cu alloy

index	spacing	intensity	lattice constant
111	4.78	m.	8.30
200	2.29	s.	8.26
311	2.51	v. s.	8.32
222	2.37	v. w.	8.22
400	2.04	s.	8.20
331	1.88	v. w.	8.20
420	1.75	w.	8.26
422	1.67	m.	8.18
333	1.58	s.	8.22
440	1.45	s.	8.24
600	1.38	w.	8.28
622	1.29	w.	8.21
533	1.24	m.	8.20
444	1.18	m.	8.20
			mean 8.235

easiness of the formation of it. In this relation it should be recalled that the velocity of the oxidation of copper increases by adding a small amount of nickel.4)

(6) 13 % Aluminium-Iron

In general the surface products are identified with aluminium trioxide when the alloy is oxidized in lower air pressures and with ferous ferric oxide Fe_3O_4 or α-ferric oxide α-Fe_2O_3 when oxidized in higher air pressures. Even under a same condition of temperature and pressure, however, the surface products are different so erratically from specimen to specimen according to the time of oxidation that the results can not be summarized uniquely in temperature-pressure diagram like as the foregoing alloys. This complexity is proved to be due to the selective oxidation of aluminium and the protective nature of the produced film. The surface of the specimen is covered by the film of γ-Al_2O_3 formed in the period of preheating in higher vacuum. When the following oxidation is not drastic, that is to say, lower in temperature and air pressure and shorter in time, the γ-Al_2O_3 film protects the specimen from the further oxidation. When it is drastic, the film can not protect the specimen from the further oxidation and Fe_3O_4 or Fe_2O_3 is formed on it according to the oxidation pressures. The protective nature of the film depends upon the condition of the formation of the film itself. This is seen from the series of treatment listed in Table II.

Table II

Sample	1st Treatment			Surface Products by the 1st treat.		2nd Treatment			Surface Products after the 2nd treat.	
	Temp. (0°C)	Pressure (mmHg.)	Time (Minute)			Temp. (0°C)	Pressure (mmHg.)	Time (Minute)		
1	900	1×10^{-4}	10	γAl_2O_3	continuos and broad rings showing coherent nature of the oxide film	600	760	20	γAl_2O_3	any change due to 2nd treatment was not appreciated*.
2	900	1×10^{-4}	10	γAl_2O_3		705	760	20	γAl_2O_3	
3	900	1×10^{-4}	10	γAl_2O_3		900	760	20	γAl_2O^3	rings become sharper some of them are doubled.
4	900	1×10^{-4}	5	γAl_2O_3		900	760	5	γAl_2O_3	
5	700	1×10^{-4}	5	γAl_2O_3		900	760	5	γAl_2O_3,αFe_2O_3	spotty pattern
6	600	1×10^{-4}	5	γAl_2O_3		900	760	5	γAl_2O_3,αFe_2O_3	

* Any appreciable change was not detected also by the optical microscope, upto the details of traces of polishing.

§ 4. General Discussion on Selective Oxidation

It is found that in reduced air pressures he selective oxidation of the baser component akes place generally, even by the alloys vhich has shown no such effect in Miyake's xperiment, in which the oxidation was carried ut in open air. The selective oxidation of aloys can be now interpreted as a phenomena lue to the mere fact that the baser component f an alloy is oxidized more rapidly than the obler one. When the supply of the baser netallic ions towards the surface by diffusion s ample enough to consume the oxygen toms attacking the surface of the specimen, nly the oxide of the baser component is ormed. This is the state of affairs in which the surface product is identified plainly with the oxide of baser component, including the case of beryllium-copper and aluminium-copper of Miyake's experiment in open air. The rate of supply of the baser metallic ions to the surface is determined by its content in the mother alloy, its mobility through the oxide film produced and the temperature of the oxidation. The relation seems to account for the fact that the maximum air pressure below which solely the selective oxidation of baser component takes place increases with the temperature. When the supply of oxygen atoms to the surface overcomes that of the baser metallic ions, as the result of increase of the air pressure, the nobler component forms also its oxide. The formation of the oxide of the nobler component, having much lager content in the alloys studied, becomes so abundant for higher air pressures that the oxide of baser component comes to be concealed behind the former for the electron beam. This is the reason why the selective oxidation of the baser component is not found at higher air pressures.

§ 5. Summary

The selective oxidation of the baser component of the alloys, 0.3 % beryllium-copper, 0.5 % aluminium-copper, 1 % magnesium-copper, 7 % manganese-copper, 7 % nickel-copper and 13 % aluminium-iron are found by the electron diffraction method. The crystalline state of the surface oxide on beryllium-copper was discussed in relation to the secondary electron emission of the surface. The crystallites of manganous oxide formed on 7 % manganese-copper are found to grow into cubic habit. The oxidation product on 7 % nickel-copper in lower air pressures is concluded to be an unknown oxide of spinel type including trivalent nickel ion.

In conclusion the author wishes to express his thanks to Prof. S. Miyake for his kind advices and encourragements.

References

(1) S. Miyake: Sc. Pap. I. P. C. R. **29** (1936) p. 167.

(2) G. Honjyo: Jour. of Phys. Soc. Jap. **4** (1949) p. 330.

(3) G. Honjo: Jour. of Phys. Soc. Jap. **2** (1947) p. 133.

J. M. Cowley & A. L. G. Rees: Proc. Phys. Soc. **59** (1947) p. 287.

(4) C. Wagner: Handbuch der Metal Physik, Band I, 2. Teil p. 162 Leipzig, 1940.

JOURNAL OF THE PHYSICAL SOCIETY OF JAPAN Vol. 8, No. 1, JAN.—FEB., 1953

The Application of the Phase Method in Visualizing Ultrasonic Waves

By Yasuo TORIKAI and Katsuo NEGISHI

Institute of Industrial Science, University of Tokyo, Chiba-City

(Received August 12, 1952; received in modified form October 31, 1952)

Ultrasonic waves propagating in a transparent medium can be considered optically as a sort of phase grating. Therefore, the method of phase microscopy may be applied to the image formation of ultrasonic waves. We have studied theoretically and experimentally the application of the phase method in visualizing ultrasonic waves and confirmed the effect of the method for the improvement of the visibility of the image. In the usual Schlieren method for visualizing ultrasonic waves, the zeroth order diffraction image is perfectly screened, while in our method the image receives a proper absorption and phase retardation by the phase plate placed in the diffraction plane. According to the theoretical calculations, the phase retardation for the maxium visibility of the image of progressive waves with the stroboscopic illumination is $\pi/2$ and the optimum absorption varies with the intensity of the waves. In both cases of the usual method and the present phase method, the theoretical curves are compared with the experimental results, showing a considerable agreement between them. Further, the fine structures in the images are seen with the increase of sound intensity.

§1. Introduction

According to Raman and Nath,[1)] the ultrasonic field in a transparent medium can be considered optically as a sort of phase grating in which the refractive index varies sinusoidally in the direction of propagation of the ultrasonic waves, Therefore, it is expected that the method of phase microscopy can be applied to the image formation of ultrasonic waves.

In the usual Schlieren method for visualizing ultrasonic waves, the zeroth order diffraction image is perfectly screened, while in the present phase method the image receives a proper absorption and phase retardation by the phase plate placed in the diffraction plane.

We have studied theoretically and experimentally on the application of the phase method in visualizing the progressive ultrasonic waves and confirmed the effect of the method for the improvement of the visibility of the image. In this paper, we will first discuss the problem theoretically and next describe the experimental procedure, and the results obtained will be compared with the theoretical ones.

§2. Theoretical

The visualizing mathod described in the introduction is principally identical with the method in phase microscopy. Therefore, we will begin with the phase microscopic theory and next extend the theory to the case of the image formation of ultrasonic waves.

In the phase microscope, the object is considered to have a form $f(x_0)$, where x_0 is the coordinate in the object plane, and the phase plate placed in the diffraction plane is assumed to give the phase retardation δ and transmission g only to the zeroth order diffraction image. As was shown by one of the authors before,[2)] the image $F(x)$ formed by a monochromatic plane wave propagating parallel to the optical axis is given by

$$F(x)=C[f(x/M)-Ae^{i\varepsilon}f_0] \qquad (1)$$

where f_0 is the zeroth order term in the Fourier expansion of $f(x_0)$, $Ae^{i\varepsilon}=1-ge^{i\delta}$, M the magnification of the image, and C a constant. Consequently, the intensity distribution in the image plane is

$$|F(x)|^2=|C|^2|f(x/M)-Ae^{i\varepsilon}f_0|^2 \qquad (2)$$

Now, when the object is the progressive ultrasonic wave, $f(x_0)$ becomes a time dependent function as follows:

$$f(x_0,t)=e^{i\frac{2\pi L}{\lambda}\left[\mu_0+\mu\sin 2\pi\left(Nt-\frac{x_0}{\Lambda}\right)\right]}, \qquad (3)$$

where N and Λ are respectively the frequency and the wave length of the ultrasonic wave, λ the wave length of the incident light, μ_0 the refracrive index of the medium when no wave propagates in it, μ the amplitude of the variation of the refractive index of the medium caused by the ultrasonic wave and L is the width of the acoustic field.

The zeroth order term, f_0, in Fourier expansion of eq. (3) developed in the period Λ is given by

$$f_0=e^{i\frac{2\pi L}{\lambda}\mu_0}J_0(v), \qquad (4)$$

where $v=2\pi\mu L/\lambda$ and J_0 represents the zeroth order Bessel function.

By inserting (3) and (4) in (2), the instantaneous intensity in the image plane is given by

$$\begin{aligned}|F(x,t)|^2&=|C|^2\left|e^{iv\sin 2\pi\left(Nt-\frac{x}{M\Lambda}\right)}-Ae^{i\varepsilon}J_0(v)\right|^2\\&=|C|^2\Big[1+A^2J_0^2(v)-2AJ_0(v)\\&\qquad\times\cos\Big\{v\sin 2\pi\Big(Nt-\frac{x}{M\Lambda}\Big)-\varepsilon\Big\}\Big] \qquad (5)\end{aligned}$$

The visual intensity distribution is the time average of the instantaneous distribution and is represented by

$$\begin{aligned}I(x)&=N\int_0^{1/N}|F(x,t)|^2dt\\&=|C|^2[1+A^2J_0^2(v)-2A\cos\varepsilon J_0^2(v)]\\&=|C|^2[1-(1-g^2)J_0^2(v)] \qquad (6)\end{aligned}$$

Namely, the intensity of the image of the homogeneous progressive ultrasonic wave is homogeneous. In this case, the contrast between the image and the dark background is the highest when $g=0$, i.e. in the case of the Schlieren method.

It is in the case of the image formation of progressive waves by the stroboscopic illumination that the phase method is most effectively employed. When the intensity of the incident light varies with time and is represented by $I_0(t)$, the instantaneous intensity of the image is given by

$$\begin{aligned}I(x,t)=|C|^2I_0(t)\Big[1+A^2J_0^2(v)-2AJ_0(v)\\\times\cos\Big\{v\sin 2\pi\Big(Nt-\frac{x}{M\Lambda}\Big)-\varepsilon\Big\}\Big], \qquad (7)\end{aligned}$$

instead of (5).

As a simple case, we assume

$$I_0(t)=1+\sin 2\pi Nt\,. \qquad (8)$$

Inserting it in (7) and averaging with time, we have

$$\begin{aligned}I(x)=|C|^2\Big[1+A^2J_0^2(v)-2A\cos\varepsilon J_0^2(v)\\+2A\sin\varepsilon J_0(v)J_1(v)\cos\frac{2\pi x}{M\Lambda}\Big]. \qquad (9)\end{aligned}$$

That is, the image consists of parallel stripes of bright and dark bands repeated periodically. When the maximum and minimum values of $I(x)$ are designated respectively as $I_{\max}$ and $I_{\min}$, the visibility, V, of the image is defined as follows:

$$V=\frac{I_{\max}-I_{\min}}{I_{\max}+I_{\min}}. \qquad (10)$$

The conditions that the above defined visibility has the maximum value are given by

$$A=\frac{1}{J_0(v)},\quad \cos\varepsilon=J_0(v), \qquad (11)$$

and therefore,

$$g=\frac{\sqrt{1-J_0^2(v)}}{J_0(v)},\qquad \delta=\frac{\pi}{2}+n\pi\ (n\text{ is a integer}).$$

The relations between g and the visibility in case of $\delta=\pi/2$ are shown in Fig. 1 for various values of v.

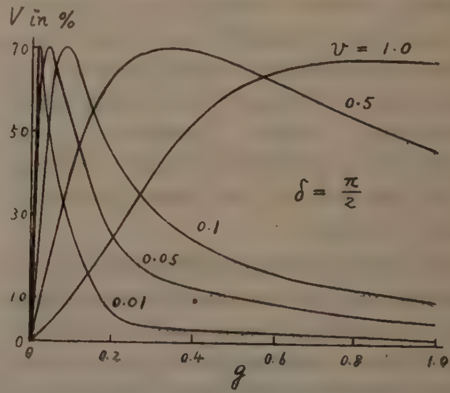

Fig. 1. Relations between g and the visibility in case of $\delta=\pi/2$ for various values of v.

When we use the ultrasonic stroboscope, which we will describe later, as the light source, $I_0(t)$ is not so simple as (8) and is represented by the next form (*cf.* the next section for the details).

$$\begin{aligned}I_0(t)&=KJ_0^2(v_1\sin 2\pi\cdot N/2\cdot t)\\&=K(P_0+P_1\cos 2\pi Nt\\&\qquad+P_2\cos 2\pi\cdot 2Nt+\cdots). \qquad (12)\end{aligned}$$

Substituting (12) in (7) and averaging it with time, we have

$$
\begin{aligned}
I(x)=C'[&P_0\{1+A^2J_0^2(v)-2A\cos\varepsilon J_0^2(v)\}\\
&-P_1 2A\sin\varepsilon J_0(v)J_1(v)\sin\frac{2\pi x}{M\Lambda}\\
&-P_2 2A\cos\varepsilon J_0(v)J_2(v)\cos 2\frac{2\pi x}{M\Lambda}\\
&-P_3 2A\sin\varepsilon J_0(v)J_3(v)\sin 3\frac{2\pi x}{M\Lambda}\\
&-\cdots\cdot],
\end{aligned}
\tag{13}
$$

where C' is a constant.

Using the values used in the experiment described later, the expression in the bracket of eq. (13) is numerically calculated as shown in Fig. 2. In case of the curve (a) of the figure, $g=0.543$ and $\delta=-\pi/2$, therefore $A=1.14$, $A\cos\varepsilon=1$ and $A\sin\varepsilon=-0.543$. Further, the value of v is taken as 0.71 from the conditions (11), using the above values. For the curve (b), $g=0$ and therefore $A=1$, $\varepsilon=0$, using the same value of v and this case corresponds to the Schlieren method. In the above calculations, we used the values of $P_0, P_1, \cdots$ which were obtained from (12) assuming $v_1=2.4048$ (On this point, we will explain the details in the next section). By the comparison between two curves of Fig. 2, it is considered that the phase method is superior in brightness and in visibility to the usual Schlieren method and the periods of bright and dark stripes of both images differ from each other by a factor two. These matters are well verified by the experimental pictures shown later.

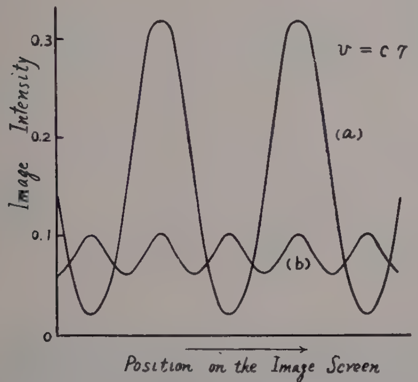

Fig. 2. Image curves of progressive ultrasonic waves by the stroboscopic illumination.
Curve (a): the phase method.
Curve (b): Schlieren method.

§ 3. Experimental Procedure and Results

The apparatus for visualizing ultrasonic waves is schematically shown in Fig. 3. Light from a illuminated slit S is made parallel by lens K, passes through an ultrasonic tank T, and is focussed by a second lens O to its focal plane F in which the diffraction images generated by the ultrasonic wave stand in a row and a bar stop is placed to mask the zeroth order image (in the case of Schlieren method). A third lens O_1 collects the light in the diffracted images and form an image of the cell onto a screen or plate P.

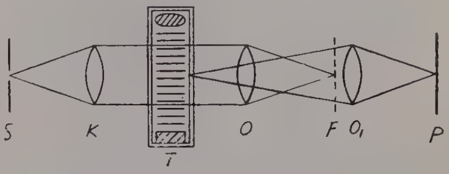

Fig. 3. Apparatus for visualizing ultrasonic waves.

The ultrasonic tank has cemented plate glass windows to allow passage of the incident light. A 2-megacycle X-cut quartz plate mounted in a holder serves as the source of the ultrasonic wave, being placed at one end of the tank. A sound absorbing pad in the opposite end prevents the reflection of sound. The tank is filled with water.

The quartz oscillator plate is driven by an oscillator the output voltage of which can be controlled from zero to several hundred volts. The ultrasonic output or the value of v in eq. (4) can be obtained from the reading of the plate current of the oscillator employing Fig. 4, this figure being obtained by plotting the known values of v found from the diffraction patterns in the plane F (e.g., the zeroth order diffraction spot vanishes for $v=2.4048$.) against the corresponding readings of the plate current.

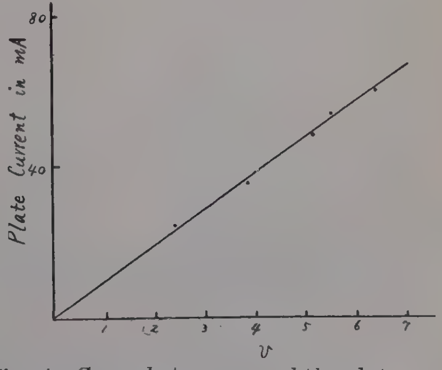

Fig. 4. Curve between v and the plate current of the oscillator.

An example of the image of the amplitude field of ultrasonic waves, obtained by the above apparatus with the continuously illuminating light from the slit S, is shown in Fig. 5. As the light source a low pressure mercury lamp is used. Light from the lamp is focussed on the slit S by a condenser lens. By a filter placed between the lens and the slit only a monochromatic light of 546 mμ in wave length is passed.

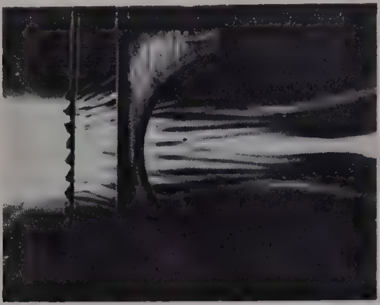

Fig. 5. Image of the ultrasonic wave incident on a combination of a sonic greating and a concave lens by continuous illumination.

Now, in order to obtain the image of the wave-surfaces for applying the phase method, an intermittent light source of equal frequency with the ultrasonic wave is required. For that purpose, the ultrasonic stroboscope developed by Becker[3] etc. as shown in Fig. 6 is used.

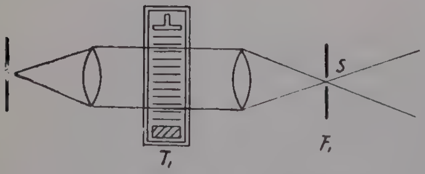

Fig. 6. Ultrasonic stroboscope.

The behaviour of the apparatus is almost similar to the preceding one. The diffraction spectra by the ultrasonic wave in the tank T_1 of the same design with T are produced on the plane F_1. Differing from the preceding case, a 1-megacycle quartz plate is used as the sound source and a reflecting plate is inserted at the opposite end of the tank to obtain 1-megacycle standing ultrasonic waves in it. When only the zeroth order diffraction image is passed through a slit S placed on the plane F_1, the intensity of the light from the slit varies at the frequency of 2-megacycles from the property of the standing ultrasonic wave. Therefore, when the slit S in Fig. 6 is placed at the position of the slit S in Fig. 3 and the optical axis of one system agrees with that of the other system, the image of ultrasonic waves with a stroboscopic illumination can be obtained.

In this case, $I_0(t)$ in (7) is given as (12) in which $N=2$ Mc.

$$I_0(t)=KJ_0^2(v_1\sin 2\pi\cdot N/2\cdot t)$$
$$=K(P_0+P_1\cos 2\pi Nt+P_2\cos 2\pi 2Nt+\cdots) \tag{12}$$

where v_1 is the amplitude of optical phase variation caused by the standing ultrasonic wave and $P_0, P_1, P_2, \cdots$ are the coefficients of Fourier expansion, K being a constant. Assuming $v_1=2.4048$ in (12), we have $J_0(v_1)=0$, and therefore the variation of $I_0(t)$ becomes maximum, this case being optimum as a stroboscope. In this case, a calculation gives

$$P_0=0.3266,\quad P_1=0.4724,\quad P_2=0.1709,$$
$$P_3=0.0275,\quad P_4=0.0024,\quad P_5=0.0001.$$

In the calculation for Fig. 2, the above values are used.

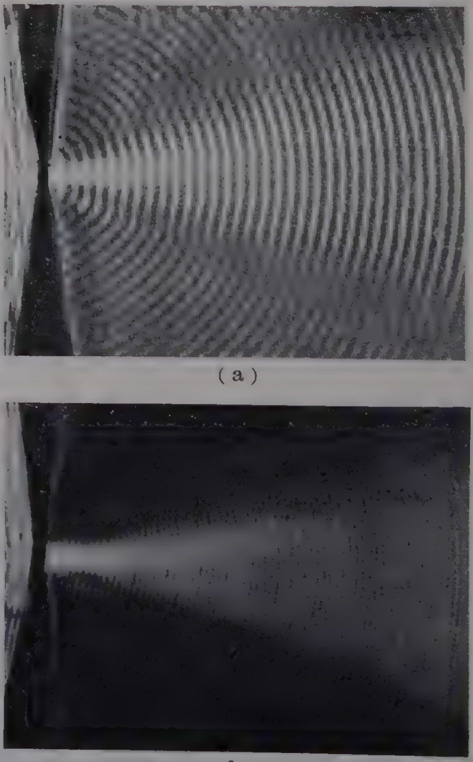

(a)

(b)

Fig. 7. Image of ultrasonic waves passing through a slit with stroboscopic illumination. (a): the phase method. (b): Schlieren method.

In the phase method, the bar stop on the plane F in Fig. 3 must be replaced by a slit shaped phase plate. We used the one specially made by Chiyoda Optic Industrial Co. g and δ of the plate are respectively 0.543 and $-\pi/2$.

The stroboscopic photographs of progressive ultrasonic wave ($v \fallingdotseq 0.7$), obtained by the above described apparatus are shown in Fig. 7 on both cases. It is recognized that the above obtained pictures well verify the result of the preceding theory represented in the curves of Fig. 2.

Next, we show the theoretical curves in Fig. 8 and the image photographs in Fig. 9 obtained for various values of v using the same apparatus and the same phase plate. The two sets of figures coincide with each other at least qualitatively. It is considered from the figures that the fine structure appears in the image of ultrasonic waves with the increase of v. This phenomena appears not only in the case of ultrasonic waves, but also in the image formation in a phase microscope. It seems that no discussion on this point has been performed as yet.

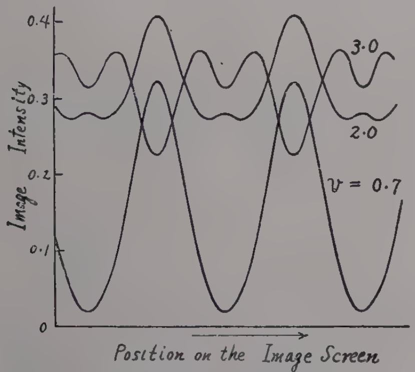

Fig. 8. Theoretical curves of images for various values of v by the phase method.

§ 4. Comparison with the Secondary Interference Method

There is another method for visualizing the wave surfaces of ultrasonic waves than the two methods described above. That is the so-called secondary interference method developed by Hiedemann and others[4]. In this method, neither phase plate nor screening bar is placed in the diffraction plane, but what is obtained on the image screen is the image of an amplitude grating produced at a position behind the ultrasonic cell.

The secondary interference image of progressive ultrasonic waves with stroboscopic illumination was obtained by Bachem[5] and Bergmann[6] and the theoretical calculation on the image was performed by Nomoto.[7] In case of a simple stroboscopic illumination represented by eq. (8), we calculated the maximum visibilities of the images of progressive waves for various values of v by modifying Nomoto's theory and obtained the curve shown in Fig. 10. (We will report shortly the details of this calculation.)

Comparing the figure with Fig. 1, it is considered that the phase method is superior in visibility to the secondary interference method in case of visualizing the progressive ultrasonic waves with stroboscopic illumination, especially for the small value of v.

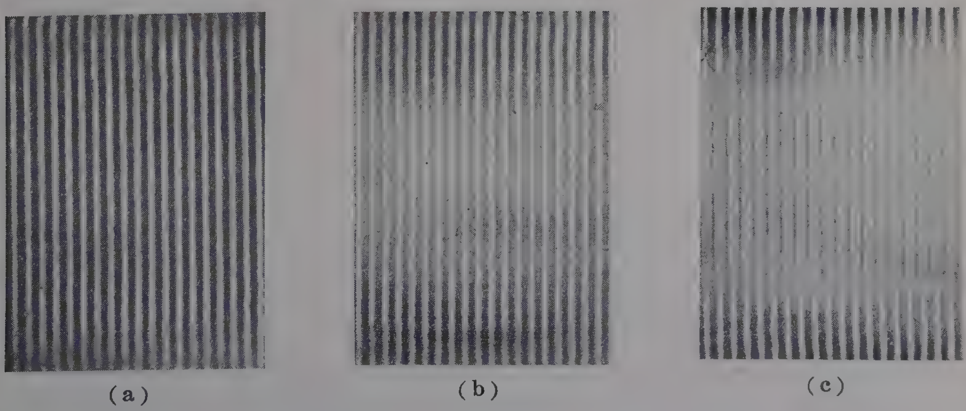
(a) (b) (c)

Fig. 9. Image photographs for various values of v by the phase method.
(a) $v=0.7$ (b) $v=2.0$ (c) $v=3.0$

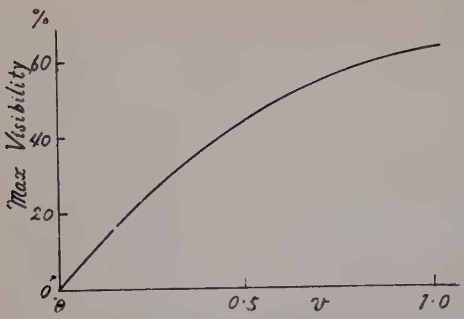

Fig. 10. Curve of v vs the maximum visibility of the image of progressive ultrasonic waves with stroboscopic illumination by the secondary interference method.

§ 5. Note on Heinemann's Paper

Lately, Heinemann[8] reported the application of the phase method in visualizing standing ultrasonic waves by the secondary interference method. It is considered from the photographs obtained by him that the phase method is effectively used only in the case of the image formation of the pure phase grating produced just behind the ultrasonic field. It is shown, however, from our theoretical calculation[9] reported lately that the phase method is not so superior in visibility to the usual Schlieren method in visualizing standing ultrasonic waves and that method should be applied only to the visulization of progressive waves with stroboscopic illumination as shown in the present report.

§ 6. Acknowledgement

We wish to express our sincere thanks to Prof. H. Kubota for his kind interest and support to our work and to Dr. O. Nomoto for his kind advices to us, and to Mr. N. Oikawa at Chiyoda Optic Industrial Co. for the loan of the phase plate.

References

1) C. V. Raman and N. S. Nagendra Nath: Proc. Ind. Acad. Sci. (A) **2** (1935) 406; **3** (1936) 75; **3** (1936) 119.

2) Y. Torikai: J. Phys. Soc. Japan **7** (1952) 330.

3) H. E. R. Becker, W. Hanle und O. Maercks: Phys. Z. **37** (1936) 414.

4) Chr. Bachem, E. Hiedemann und H. R. Asbach: Z. f. Phys. **87** (1934) 734.

5) Chr. Bachem: Z. f. Phys. **87** (1934) 738.

6) L. Bergmann: Sitz.-Ber. Schles. Gesell. f. vaterl. Kultur **108** (1936) 47.

7) O. Nomoto: Proc. Phys.-Math. Soc. Japan **19** (1937) 337.

8) E. Heinemann: Optik **9** (1952) 379.

9) Y. Torikai and K. Negishi: J. Appl. Phys. Japan **21** (1952) 350.

J. PHYS. SOC. JAPAN 8 (1953) 125~126

Some Experimental Studies of the Conductivity and Thermo-electromotive Force of Cs_3Sb Photo-Cathodes

By Toshimichi SAKATA
The Electrical Communication Laboratory

(Received July 18, 1952)

Photoelectric layers of Cs_3Sb produced by reaction of an Sb film with Cs vapour at about 200°C are extremely sensitive photoelectrically. These layers can be considered as an intermetallic compound. It has been well known that the long-wave limit of the external photoelectric effect is in all cases situated at about 0.70μ. In recent years the mechanisms of the emission from Cs_3Sb photo-cathodes have been discussed by various investigators1)→4) independently. But they are not clear at present. The author has carried out following experiments on this subject.

The thermo-electromotive force of these specimens was measured for various temperature difference, keeping the one end of the specimens at constant temperature. The thermo-electromotive force ($\varDelta\theta$) is measured by means of zero method with UX 54 amplifier and the temperature differnce ($\varDelta T$) is measured with two Cu-constantan thermo-junctions.

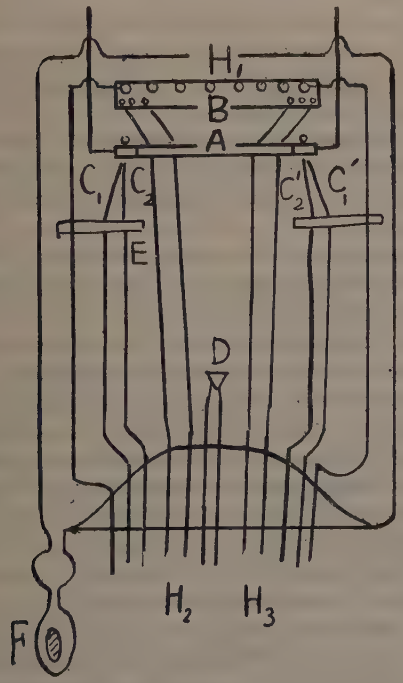

Fig. 1.

It was confirmed that the relation between $\varDelta T$ and $\varDelta\theta$ was linear over the range of $\varDelta T$ from 0° to 30°C. From the gradients of these straight lines, $d\theta/dT$ can be obtained. For this purpose a tube as shown in Fig. 1 was adopted, in which A and B were plain glass plate. The former is of a rectangular form about 5 mm in width and about 25 mm in length. The latter is used for the supporter of uniform heater (H_1) and local heater (H_2, H_3). (C_1, C_2) and (C_1', C_2') are Cu-constantan thermo-junctions, both 0.08 mm in diameter, welded behind the glass plate A. Sb film of adequate thickness was deposited on the surface of A from the anode coil in D. Small mica plate E was used to prevent unfavorable condensing of Sb atoms on the glass wall. Fresh Cs was obtained from another pellet F. The temperature dependency of $d\theta/dT$ is shown in Fig. 2. These curves correspond to twe different specimens (a), (b) as indicated in Fig. 1. In these experimental tubes, thermoelectromotive force has values from 0.3 to 1.1 mV/deg. in the temperature range from 268° to 343°K.

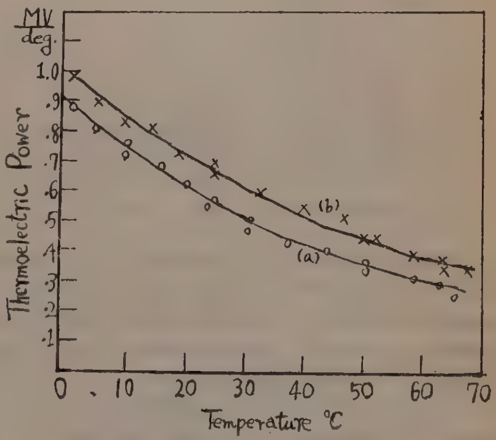

Fig. 2.

Using the familiar relations

$$d\theta/dT = -k/e(2+\log nh^3/2(2\pi mkT)^{3/2}), \quad (1)$$

$$\frac{2(2\pi mkT)^{3/2}}{h^3}e^{\zeta/kT} = n, \quad (2)$$

the following expression may be deduced:

$$d\theta/dT = -(k/e)(2+\zeta/kT). \quad (3)$$

By this formula the chemical potential ζ is calculated for every temperature, of which values are shown in the second column of Table I. Now, since the chemical potential ζ is generally expressed by

$$\zeta = \frac{\varDelta E}{2} - \frac{kT}{2}\log\frac{n_b h^3}{2(2\pi mkT)^{3/2}},$$

the atomic concentration n of impurity centers are estimated at various temperatures. These values were always higher than 10^{20} per cm^3. The activation energies E/2 of their conductivities measured at the same time were respectively 0.24 and 0.27 eV in the wide temperature range. Some of the conductivity data are shown in Fig. 3, where the ordinate is the resistivity in logarithmic scale and the abscissa is the inverse absolute temperature. The curves (a) and (b) among them are the results respectively for the samples (a) and (b) just mentioned. Every curve consists of straight line expressed by

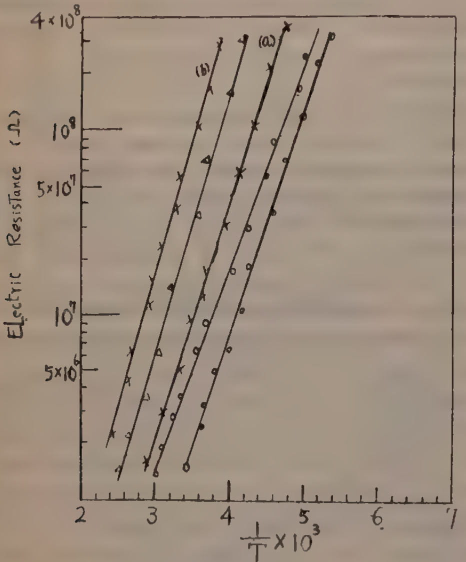

Fig. 3.

$$\rho=\rho_0\exp(\varepsilon/kT)$$

where ε is estimated at about 0.2–0.3 eV. In all cases, the sign of thermo-electromotive force showed the P type of conductivity for Cs_3Sb photo-cathodes.

Table I

Temp.	calculated chemical potentials (eV)		E/2	
	sample (a)	sample (b)	sample (a)	sample (b)
283	0.25	0.28	0.24	0.27
293	0.23	0.26		
303	0.21	0.24		
313	0.18	0.22		
323	0.16	0.20		
333	0.14	0.18		
343		0.17		

At low temperatures, further studies are necessary in order to reach a quantitative results. It appears strange that there is no evidence for such a large concentration of acceptor levels in the optical absorption data. It should be desirable to measure Hall coeffcient for confirmation of these observations.

The author wishes to express his deep thanks to Dr. H. Miyasawa of Tokyo-Shibaura Electric Co. for his active interest in this work and useful suggestions. Thanks are also due to Mr. K. Noga for his discussion.

References

1) P. G. Borzzak: Zhur. Tekh. Fiz. **20** (1950) 923-7. (see chem. Abstract **45** (1951) 437.

2) N. Schaetti and W. Baumgartner: Le Vide **6** (1951) 1041. (see Chem. Abstract **46** (1952) 818.)

3) S. S. Prilezaev: J. Tech. Phys. U.S.R. **9** (1939) 1439.

4) W. Veith: J. Phys. Radium II (1950) 507.

J. Phys. Soc. Japan **8** (1953) 126~128

Directional Dielectric Breakdown in Single Crystals

By Tokuo Suita

Faculty of Eng., Osaka University

(Received July 21, 1952)

The fact that the dielectric breakdown in single crystals follows paths which are oriented in distinct crystallographic directions has been investigated by several authors.1)

For instance, if the applied electric field is in direction of [100] the NaCl single crystal actually breaks down in [110] direction at room temperatures.

The directions of breakdown depend, in general, on temperature, polarity of electrodes, voltage rise and crystal symmetry.

These facts seem to show, that the breakdown in solids is a kind of electronic phenomena.

The magnitude of breakdown strength of NaCl crystals, however, is reported to be independent of their orientation in a uniform electric field.2)

"Low energy criterion" proposed by von Hippel who assumes that the breakdown strength is determined by the accelerating of very slow electrons seems to be consistent with the magnitude effect above mentioned.3)

An alternative "high energy criterion" has been proposed by Fröhlich who postulates that the breakdown field strength corresponds to a field just capable of accelerating the electrons which have already aquired near ionizing velocities.4)

According to Fröhlich's theory the breakdown strength must depend on the orientation of the crystal.

Since every theory of dielectric breakdown has to know how far directional effects enter into

Table 1.

Order of magnitude of directional breakdown voltages F_{100} and F_{110}		Number of pair tests of the given order							
		D. C. field				Impulse field			
		Low temperatures		High temperatures		Low temperatures		High temperatures	
		NaCl (12°C)	KCl (12°C)	NaCl (140°C)	KCl (140°C)	NaCl (30°C)	KCl (55°C)	NaCl (150°C)	KCl (165°C)
$F_{100} < F_{110}$		0	10	3	2	0	8	3	4
$F_{100} > F_{110}$		9	0	5	3	6	2	3	3
$F_{100} = F_{110}$		1	0	1	2	1	1	1	4
Average break-down voltage (KV)	F_{100}	41	48	20	26	23	20	18	19
	F_{110}	38	51	20	26	21	22	18	19

Table 2.

Crystals	Low temperatures		High temperatures	
	Breakdown paths of the sample under a [100] electric field	Order of magnitude of directional breakdown	Breakdown paths of the sample under a [100] electric field	Order of magnitude of directional breakdown
NaCl	[110]	$F_{100}>F_{110}$	[110]	$F_{100}\simeq F_{110}$
KCl	[100]	$F_{100}<F_{110}$	[100] [110]	$F_{100}\simeq F_{110}$

the value of the field strength measured, the author undertook a careful study of the existence of the magnitude effect in KCl and NaCl at room temperatures and about 150°C under a non-uniform field.

The electrode system was chosen to be positive needle and negative plate in which the directional paths are comparatively simple and moreover secondary effects due to ionic space charge and initial electrons appear to be small.

The crystal plates were cut parallel to the (100) and (110) plane of a same crystal block.

They had 1 mm. thickness and 10×10 mm². area.

The needle electrode was changed after each pair test of (100) and (110) crystals.

The experiment was carried out in insulating oil, and the applied voltages were D.C. and impulsive (about $2 \times 40 \mu s$).

Our experimental results of pair tests in KCl and NaCl are summarized in Table 1.

The Table 1 shows as follows:

(1) In NaCl the magnitude of breakdown voltage in [100] is larger than that in [110] at low temperatures, but the two are nearly equal at high temperatures.

(2) In KCl the magnitude of breakdown voltage in [100] is smaller than that in [110] at low temperatures; the order of magnitude is reverse in NaCl and in KCl at low temperatures.

At high temperatures the two directional breakdown voltages in KCl are nearly equal as in NaCl.

(3) The magnitude effect have been observed rather clearly in D.C. than in impulse voltage.

In order to clarify the relation between the directional breakdown voltages and the dominant breakown paths, Table 2 is presented.

We can conclude that at low temperatures the dielectric breakdown actually occurs in the direction of the lowest breakdown strength, but at high temperatures the situation is not so simple.

The existence of the magnitude effect at low temperatures proves "high energy criterion" in this temperature range, but at high temperatures "low energy criterion" is favorable to the non-existence of the magnitude effect.

These results seem to be consistent with our previous experimental results on electron avalanche and time lag, which showed that the number of initial electrons and mutual interaction of avalanches are more important than the magnitude of the avalanche itself at high temperatures.[5)6)]

The difference of order of directional magnitude in NaCl and in KCl is probably due to the difference of formation of ionic space charge and initial electrons.

Further experiments on directional conduction and breakdown in a uniform electric field are in progress.

References

1) L. W. Davisson: Phys. Rev. **70** (1946) 685.
2) A. von Hippel and J. W. Davisson: Phys. Rev. **57** (1940) 156.
3) A. von Hippel and R. S. Alger: Phys. Rev. **76** (1949) 127.
4) H. Fröhlich: Proc. Roy. Soc. A **160** (1937) 230.
5) C. Yamanaka and T. Suita: J.I.E.E. Japan **72** (1952) 276.
6) Y. Inuishi, C. Yamanaka and T. Suita: Tech. Rep. Osaka Univ. **2** (1952) 71.

J. PHYS. SOC. JAPAN **8** (1953) 128

On the Temperature Dependence of Contact Noise

By Yoshio INUISHI

Faculty of Engineering, Osaka University

(Received September 29, 1952)

The author has been engaged[1)] in the unified treatment of various "contact noise", such as noise from current carrying carbon resistors and from semiconductor rectifier biased inversely, and flicker noise. Theories on these noises which hvae been laid foundation by Schottky assume some fluctuating agent that modulates the electron current. The nature of this fluctuating agent must be determined experimentally. From this standpoint we measured the temperature dependence of contact noise for carbon resitors, CuO and Se rectifiers.

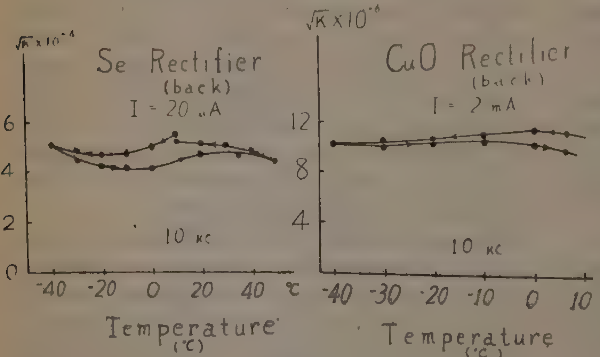

Fig. 1.

A wide band CR-coupled five 6AC7 stage amplifier with attenuator and filter was used and detected by a square law type valve voltmeter. As is well known, the frequncy spectrum of short circuit noise current $<\Delta I^2>_f$ may be represented by

$$<\Delta I^2>_f \fallingdotseq K' I^2 \frac{\Delta f}{f},$$

where I is the mean current, f is the frequency. Keeping I constant, the ambient temperature was varied and K′ at 10 KC was obtained experimentally.

Fig. (1) and (2) shows the releation K vs. temperature for 3 types of samples. From these results we can conclude that "contact noise" from semiconductor rectifier shows no significant dependence on the temperature at 10 KC, but in carbon resistor the noise increases with increasing temperature. These facts may suggest some different fluctuating agent for two types of samples. Both the theory of Du Pré[2)] and that of Richardson[1)3)] predict temperature independence of noise at medium frequency range, if we assume that the mean density of fluctuating agent does not vary with temperature.

Considering above results, the fluctuating agent in the rectifier barrier may be number of ions such as ionized impurity levels and should not be conduction electron number itself which is sensitive to the temperature.

In carbon resistors we found that the noise depends on the pressure of ambient gas,[1)] so the temperature dependence may be ascribed to absorbed gas and water, but further experiment on this point is required.

References

1) Read before annual meeting of Japan. Inst. of Elec. Eng., May, 1951.
2) Du Pré: Phys. Rev. **78** (1950) 615.
3) Richardson, B.S.T.J. **29** (1950) 117.

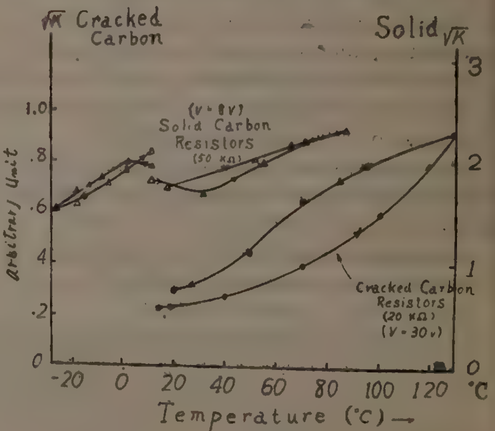

Fig. 2.

J. PHYS. SOC. JAPAN 8 (1953) 129~130

The Transition Structure of the Grain Boundary observed in Soap Bubble Raft

By E. FUKUSHIMA

Department of Physics, Tokyo Metropolitan University, Tokyo

and A. OOKAWA

Department of Physics and Chemistry, Gakushuin University, Mejiro, Tokyo

(Received October 2, 1952)

A transition structure of a grain boundary as an array of dislocations has been proposed by Burgers[1)] and by Bragg[2)] and developed recently by Shockley and Read[3)]. On the other hand, in connection with the grain boundary viscosity, Ke[4)] has pointed out a grain boundary model, in which the transition structure is represented by numerous disordered groups of atoms or diffuse holes.

We formed by the method of Bragg and Nye[5)] the soap bubble model, in which the grain boundaries are observed. Fig. 1 and Fig. 2 represent some of the observed bubble raft, the diameter of the bubble $d \simeq 0.3$ mm. It is recorded the bubble raft in slow motion under external stress, and the photographs are purposely slightly out of focus.

Fig. 1.

In Fig. 1 we can clearly observe the grain boundary constructed of *dislocations in an array.* In the middle part of the boundary, where the boundary is situated symmetrically with the crystallographic orientations of the two grains, we observe the dislocations all on parallel slip planes. While in the lower part of the boundary, where the boundary is situated unsymmetrically, there are two or three sorts of dislocations each on non-parallel slip planes. These affairs correspond to the theoretical expectations shown in Fig. 5 of Shockley-Read's paper[3)].

Fig. 2.

In Fig. 2 we observe a grain boundary constituted of disordered groups of atoms or *diffused holes.* The boundary is evident in the lower part but, when we follow it upwards, it diffuses away into region including many dislocations at random. The photograph is taken at a moment in the process of upwards growth of the grain boundary. At final stage, the whole length of the grain boundary is constituted of diffused holes.

The structure of the grain boundary varies systematically with the angle θ between the crystallographic orientations of the two adjacent grains. It can be observed that, while the boundary with small θ is always constructed of dislocations in an array, the dislocations degenerate into diffused holes for θ greater than about 10°. The details will be published elsewhere.

References

1) J. M. Burgers: Proc. Phys. Soc. London **52** (1940) 23.
2) W. L. Bragg: Proc. Phys. Soc. London **52** (1940) 54.
3) W. Shockley, W. T. Read: Phys. Rev. **78** (1950) 275.
4) T. S. Ke: Phys. Rev. **73** (1948) 267.
5) W. L. Bragg, J. F. Nye: Proc. Roy. Soc. A **190** (1947) 474.

J. PHYS. SOC. JAPAN **8** (1953) 130~131

On the Frequency of the Scintillation Fading of Microwaves

By Osamu TUKIZI

Electrical Communication Laboratory

(Received October 9, 1952)

The theory, developed by the writer1) to account for the scintillation fading of microwaves, predicts that a linear relation, overlooked hitherto, is to hold between the scintillation frequency, ν, and the mean wind speed, $\langle u\rangle$, which is averaged over the whole region of propagation. The aim of the present note is to report results of the analysis worked out for its corroboration upon the basis of data* of a series of propagation tests at the frequency of 4,000 megacycles.

Out of eight runs of propagation tests, four were kept together with the wind velocity measurements, which employed a Marvin-type anemograph attached to a captive balloon, making it possible to read out from recordings the time mean, $\bar{u}$, of the wind velocity at a point near the path of propagation. The time mean, $\bar{u}$, is, if the point of wind observation is properly chosen, supposed to take possibly the place of the spatial mean, $\langle u\rangle$, whose measurement is likely impracticable.

In figures 1 and 2 are shown typical plots of the scintillation frequency, ν, against the mean wind speed, $\bar{u}$, the straight lines being the most probable relations obtained by the method of least squares. Values of the standard deviation, $\Delta\nu$, are also given for each circuit of transmission.

Points of measurement are seen much dispersing in case of the experiment held in the summer of 1951 as compared with the one carried out in March, 1952. This may be attributed to the fact that the roller fading, much severe in summer than in winter, superimposes the records of scintillation and that, at the experiment of March, 1952, an improved anemograph was used, specially designed and constructed to cut off the superposing roller.

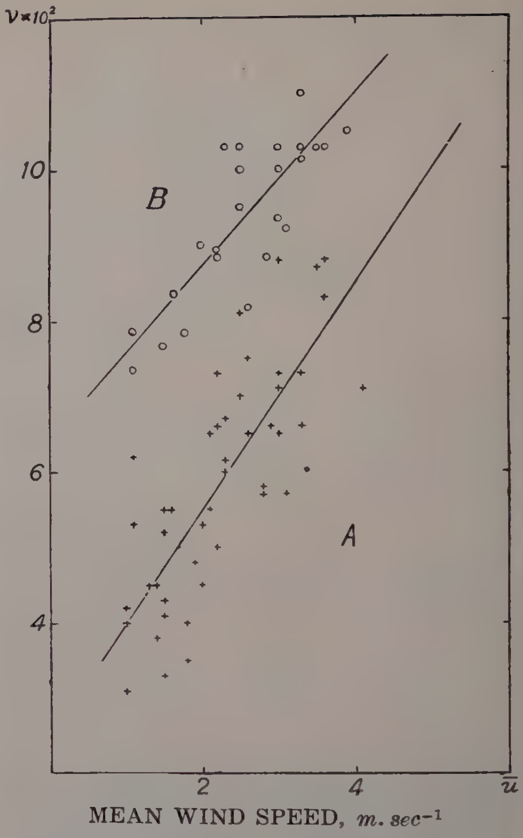

Fig. 1. Experimental relation between ν and $\bar{u}$ as observed July 7~July 27, 1951. Wind velocity measurement at Honjo at an elevation of 200 meters. Computed values of deviation are (A) $\Delta\nu=\pm0.94\times10^{-2}\,\mathrm{sec}^{-1}$ for the Tsukuba-Fujioka circuit and (B) $\Delta\nu=\pm0.59\times10^{-2}\,\mathrm{sec}^{-1}$ for the Tsukuba—Tatebayashi circuit.

It is known to radio scientists that the mean range of the microwave fading, including both scintillation and roller, depends not only on the season but also on the length of transmission-path and on the atmospheric conditions along the path of propagation. Examination of radio records reveals that the signals, transmitted from Tsukuba and received at Tatebayashi and Fujioka simultaneously, both suffer the fading of considerable magnitudes, the ratio of range being of about 3/2, while the waves, transmitted from Kurakake and Futago at slightly different frequencies and received at Ogusu, show unlike types and depths of fading, the ratio of range amounting to about 4. It may be noted that these ratios of fading range are very near to those of standard deviation, *i.e.* 1.6 and 3.8, respectively, in favour

---

* By courtesy of the Radio Wave Section of the Laboratory.

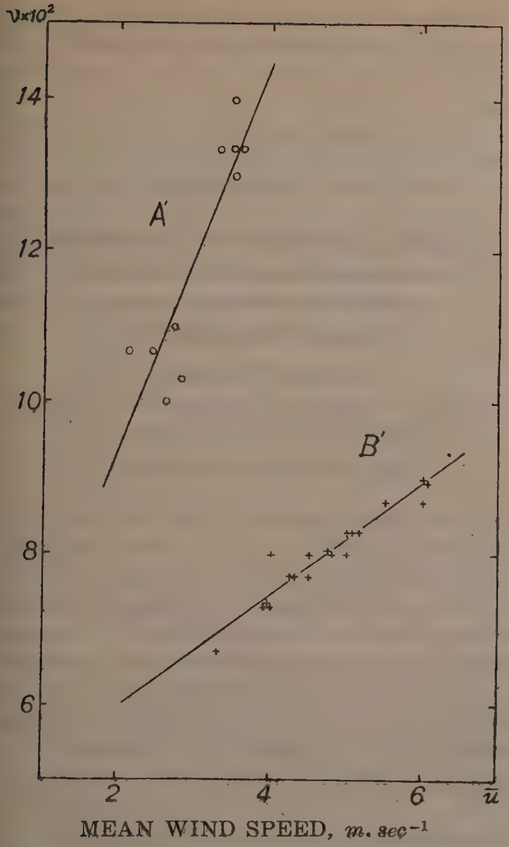

Fig. 2. Experimental relation between ν and $\bar{u}$ as observed March 5~March 31, 1952. Wind velocity measurement at Kugenuma at an elevation of 200 meters. Computed values of deviation are (A′) $\Delta\nu = \pm 0.69 \times 10^{-2}\ \mathrm{sec}^{-1}$ for the Futago—Ogusu circuit and (B′) $\Delta\nu = \pm 0.18 \times 10^{-2}\ \mathrm{sec}^{-1}$ for the Kurakake—Ogusu circuit.

of the interpretation described above.

In fig. 3 is also illustrated another result of analysis, obtained from data of the single transmission-circuit indicated. Averages have been taken, in this case, over each set of frequency values for a given wind velocity, owing to the lack of fine data, particularly, of the latter.

It may be concluded, therefore, that the experimental results stated above appear to support the theoretical prediction that the scintillation frequency be proportional to the mean wind velocity around the path of propagation.

Reference

1) O. Tukizi: To appear in an issue of this Journal.

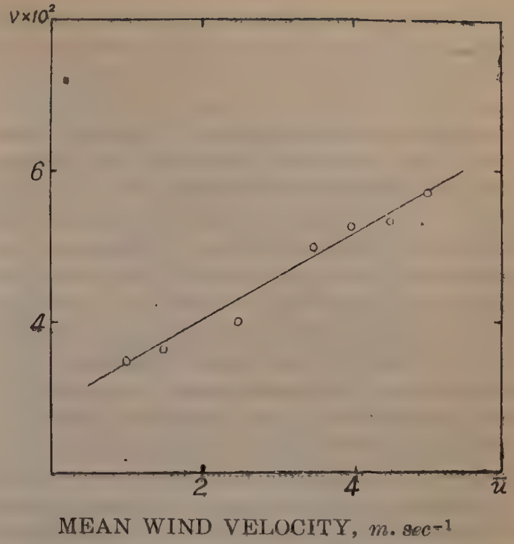

Fig. 3. Experimental relation between ν and $\bar{u}$ based on data of the single transmission-circuit, Oyama-Sodeura, held during Aug. 31~Sept. 16, 1951. Wind observation at Maisaka at a point 300 meters high.

J. Phys. Soc. Japan 8 (1953) 131~132

Length of Coherent Microwaves Generated by an Electronic Oscillator

By Koichi Shimoda

Department of Physics, Faculty of Science, University of Tokyo

(Received Oct. 14, 1952)

It has been generally assumed without any verification that an electronic oscillator would generate an infinite train of coherent waves, if the fluctuation of d.c. supply, temperature variation, and other disturbances were completely removed. We have found that an electronic oscillator such as a klystron does not generate infinitely coherent waves, even if it is operated under constant conditions. A microwave radiation of 8000 Mc from a reflex klystron was found to have a frequency bandwidth of 3±1 kc, and have therefore a coherent length of $10^6 \sim 10^7 \lambda$.

The microwaves were heterodyned with a VHF oscillator which was stabilised with a crystal oscillator controlled by the standard frequency broadcast, JJY. Because the accuracy of the VHF oscillator can be kept equal to the standard frequency, in a short time, it is probably less than one part in 10^8. The ripple of d.c. supply voltage for the klystron was reduced to 4×10^{-5} volts peak-to-peak, so that the frequency modulation caused by the voltage fluctuation might be

40~60 c.p.s. Nevertheless, the beat note of the klystron with the stabilised VHF oscillator was not clear, but the noisy beat was heard. It was also found that the instantaneous frequency, in a convenient means, was almost independent upon the residual fluctuation of the electrode voltage.

We may therefore conclude that such frequency noise of a microwave oscillator is due to the fluctuation of the electron beam. When a resonant cavity is excited by an electron beam through a narrow gap, a concept of electronic admittance is conveniently introduced. Real and imaginary parts of electronic admittance will change with fluctuation of the electron beam. According to this consideration, we may effectively divide the noises of a microwave oscillator into two parts; the one is the amplitude noise or AM noise which is attributed to the fluctuation of electronic conductance and the other is frequency noise or FM noise attributed to the fluctuation of electronic susceptance. The magnitude of FM noise may be estimated in the following.

The number of electrons through the cavity per unit time, $\mathrm{d}N/\mathrm{d}t$, is

$$\frac{\mathrm{d}N}{\mathrm{d}t}=\frac{I}{e},$$

where I is the total beam current. The time constant of the oscillation within the cavity which is excited by the electron beam is $\tau=Q/\omega$, where Q is the loaded Q of the cavity resonator, and ω is the resonant circular frequency. The average number of electrons in a time interval of τ is

$$N=\tau\frac{\mathrm{d}N}{\mathrm{d}t}.$$

And fluctuation by shot effect is $N^{1/2}$. To evaluate these values, we take $I=16$ mA, $Q=200$, and $f=\omega/2\pi=8000$ Mc. Then,

$$\mathrm{d}N/\mathrm{d}t=10^{17}\,\mathrm{sec}^{-1}, \quad \tau=4\times10^{-9}\,\mathrm{sec},$$
$$N=4\times10^{8}, \quad \text{and} \quad N^{1/2}=2\times10^{4}.$$

Because of the shot effect, both the electronic conductance, g, and susceptance, b, will fluctuate, which result in AM and FM noise respectively. The measure of FM noise Δf may be estimated from Δb and electronic tuning range, f_e, which is approximately equal to f/Q. Then we have

$$\Delta f\simeq\left|\frac{\Delta b}{g+jb}\right|f_e\simeq N^{-1/2}\frac{f}{Q}.$$

Using the above values, we have

$$\Delta f\simeq2000\ \text{c.p.s.}$$

This is the same order of magnitude experimentally obtained. Because the frequency fluctuation, Δf, is proportional to $(\omega/Q)^{3/2}$ and $f/\Delta f$ to $\omega^{-1/2}Q^{3/2}$, the higher the frequency, the shorter the coherent length. For example, an oscillator of 10^{12} cycles or 0.3 mm in wavelength might have $f/\Delta f\simeq9\times10^{3}$, if the beam current of 16 mA were possible and Q were proportional to $f^{-1/2}$.

J. Phys. Soc. Japan 8 (1953) 132~133

On the Contribution of the Mutual Perturbation of the Localized Molecular Orbitals to the Charge Distribution

By Kenji NUKASAWA

Research Institute of Applied Electricity, Hokkaido University, Sapporo

(Received October 13, 1952)

In their recent text-book, Syrkin and Dyatkina[1]) have stressed the importance of the contribution of the resonance effect to the increase or decrease in the dipole moment of a molecule when its hydrogen atom has been substituted by various radicals, their discussion having been limited to the qualitative one, however. In this note we shall show that this effect can be treated quantitatively by means of a combination of molecular orbital theory and perturbation theory. Let the molecule under consideration be devided into two parts, A and B. Suppose A and B be separated as far apart as there would be no interaction between them, then the LCAO MO φ_i^A's and φ_i^B's would be localized in A and B respectively. The perturbed MO, when A and B approach each other to the point of the actual distance of the molecule, will be found by a simple extention of the method used by Matsen[2]) who has discussed on the special case where A is phenyl radical and B is an atom having a lone pair which interacts with the π orbitals of A. The vectorial increment of the dipole moment by the electron migration under the perturbation, can be calculated easily from the formula of the perturbed MO's, and amounts to

$$\Delta\mu=\left(\sum_{i}^{\mathrm{vac}}\sum_{j}^{\mathrm{occ}}-\sum_{j}^{\mathrm{vac}}\sum_{i}^{\mathrm{occ}}\right)\frac{\delta_{ji}{}^{2}\boldsymbol{R}_{ji}}{(\varepsilon_j{}^B-\varepsilon_i{}^A)^2}, \qquad (1)$$

neglecting the terms higher than δ^4. In equation (1), δ_{ji} means the perturbing integral

$$\int\varphi_j{}^B\boldsymbol{H}\varphi_i{}^A d\tau,$$

$\varepsilon_j{}^B$ and $\varepsilon_i{}^A$ are the orbital energies of the unperturbed MO, $\varphi_j{}^B$ and $\varphi_i{}^A$, respectively, and $\boldsymbol{R}_{ji}$ is the vector from the centre of the electron cloud of $\varphi_i{}^A$ to that of $\varphi_j{}^B$. The notations *vac* and *occ* have the meaning that the summation should be concerned only with the vacant and occupied levels, respectively.

The increment $\Delta\mu$ was calculated for several molecules which are the products by the condensation of the following molecules: ethylene, formaldehyde, methane, benzene and butadiene. The enery levels of the molecules given in Table I, were calculated by a combination of semi-empirical LCAO MO theory and the experimental knowledge of the ionization energy and the electronic spectra. The δ_{jl}'s were calculated from the LCAO coefficients and the assumption that there exists an interaction only between the nearest atoms, the value of which was taken tentatively as 4 e.v. The LCAO coefficients were estimated from the dipole moment of the radical for C—H or C=O, and from Hueckel's theory for benzene or butadiene. The centre of the electron cloud was taken naturally as the centre of symmetry whenever the latter exists, while in C=O or C—H the former was assumed to be the contact point of Pauling's bond spheres of the two atoms. Butadiene was thought to take the *trans* form, thus having the centre of symmetry.

Table I. Orbital energies (e.v.)[a]

	C_2H_4	HCHO	CH_4	C_6H_6	C_4H_6
ε_1	-10.5^b	-10.9^{bc}	-13.1^b	-12.4	
ε_2	(-2.9)	(-3.9^c)	—	-9.2^b	-9.1^b
ε_3				(-2.9^d)	(-3.1)
ε_4				$(+0.3)$	(-1.9)

a The values in parentheses are of vacant levels.

b These values are ionization energies taken from W. C. Price[3].

c Tentatively assumed that a π electron is involved in the electronic transition, although it would be more reasonable to consider an electron of the oxygen lone pair to be responsible[3][4].

d This level was assumed to be the average height of the lower excited levels, however, taking only singlets into account.

The calculated values of the increment $\Delta\mu$ and the vector sum μ_t, together with the observed value μ_0 in the gas phase, are presented in Table II. The close agreement between μ_t and μ_0 is probably fortuitous in view of the roughness of the approximations which had to be made. Especially the neglect of the induction effect might have compensated the too large electron migration resulting from the incorrect procedure, where we have equated the ε's of vacant levels to the ionization energies instead of to the electron affinities of these levels, the latter being preferable definitely but difficult to be estimated[5]. Nevertheless, Table II shows several interesting features which encourage us to go further. One of these is the prediction of the reverse direction in the moments of toluene and styrene[6]. Another is the success in the quantitative explanation of the difference between the moments of 1-methyl- and 2-methyl-butadiene[7].

Table II. Dipole moments of substituted molecules (e.v.)[a]

Molecules	$CH{=}CH_2$ $\vert$ CHO	$CH{=}CH_2$ $\vert$ CH_3	$CH{=}CH_2$ $\vert$ C_6H_5	CH_3 $\vert$ CHO
$\Delta\mu^b$	$+0.77$	-0.43	-0.36	$+0.62$
μ_t	2.95	0.43	0.36	2.72
μ_0^c	3.04	0.35	<0.2	2.72

Molecules	C_6H_5 $\vert$ CHO	CH_3 $\vert$ C_6H_5	$CH{=}CH{-}C_2H_3$ $\vert$ CH_3	$CH_2{=}C{-}C_2H_3$ $\vert$ CH_3
$\Delta\mu$	$+1.42$	$+0.53$	-0.68	-0.36
μ_t	3.38	0.53	0.68	0.36
μ_0	3.16	0.37	0.68	0.38

a The bond moments of C=O and CH were taken as 2.0 and -0.3, respectively.

b Positive values were given when the net electron cloud migrates from the radicals written above to those below.

c Observed values were taken from the gas values in *Tables of Electric Dipole Moments* (1948), compiled by Wesson in M.I.T., except that of benzaldehyde which was due to Syrkin and Dyatkina[1].

References

1) Syrkin, Dyatkina: *Structure of Molecules* (1946).

2) F. A. Matsen: J. Am. Chem. Soc. **71** (1950) 5243.

3) W. C. Price: Chem. Rev. **41** (1947) 257.

4) H. L. McMurray: J. Chem. Phys. **9** (1941) 231.

5) A. L. Sklar: J. Chem. Phys. **7** (1939) 984.

6) M. M. Otto, H. H. Wenzke: J. Am. Chem. Soc. **57** (1935) 294.

7) N. B. Hannay, C. P. Smyth: J. Am. Chem. Soc. **65** (1943) 1931.

J. PHYS. SOC. JAPAN **8** (1953) 133~134

Microwave Spectrum of Methylamine (I)

By Koichi SHIMODA and Tetsuji NISHIKAWA

Department of Physics, Faculty of Science,
University of Tokyo

(Received November 12, 1952)

We have measured the microwave spectrum of methylamine, CH_3NH_2, by a source modulation spectrograph. The length of the absorption cell used is 5 meters. Twenty four lines with the intensities of about $\alpha=1\sim5\times10^{-7}\,\mathrm{cm}^{-1}$ were observed in the frequency range between 22 and

25 kMc/sec, and their frequencies are listed in Table 1. The accurate frequency measurements

Table 1. Microwave Frequencies of Methylamine Spectrum.

Present Measurement Mc/sec.	Previous Measurement[1] Mc/sec.
22258.35±0.05	22258
22527.93±0.04 22528.21±0.04	22535
22581.49±0.03	22590
22722.62±0.02	22732
22759.22±0.03 22759.63±0.03	
22980.95±0.03 22981.60±0.03	22977
23119.06±0.04	23115
23300.79±0.06	23295
23311.31±0.08	23300
23315.55±0.04	23305
23340.67±0.02 23341.31±0.02	23335
23409.16±0.06	23404
23429.42±0.04	23430
23449.39±0.07 23449.65±0.07 23450.17±0.07	23446
23861.40±0.02	—
24019.01±0.04	24015
24078.75±0.07	24078
24520.75±0.05	24528

were accomplished by a sort of frequency multiplier and an interpolating receiver, accurately controlled by the standard frequency JJY of 4 Mc/sec. Several other lines were detected which were too weak to be accurately measured.

In order to assign these lines and to study the structure and internal rotation of this molecule, we are now constructing a Stark-modulation microwave spectrograph of high sensitivity.

Reference

1) Measured by W. D. Hershberger and J. Turkevitch: from "Molecular Microwave Spectra Tables" P. Kisliuk and C. H. Townes, J. Res. N. B. S. **44** (1950) 611.

J. PHYS. SOC. JAPAN **8** (1952) 134~135

Silicocarbon—Thermal Decomposition Product of Silicone Resin

By Mitio HATOYAMA, Wataru SASAKI
and Zensho ISHII
Electrotechnical Laboratory, Tokyo

(Received November 24, 1952)

Silicone is understood as a resin of special thermal stability. Silicone insulated wire can be used in a circumstance of as high as 300°C. It is, however, decomposed when heated to more than 500°C, the ultimate product of heating in air being SiO_2. Heating in vacuum brings different results. After an hour of heating at 500°C, a sample of silicone resin DC-801 changes itself to a black, hard substance whose resistivity is still very high (more than 10^{12} ohm cm). We propose here to refer to such products of thermal decomposition of Silicones as silicocarbon. As the

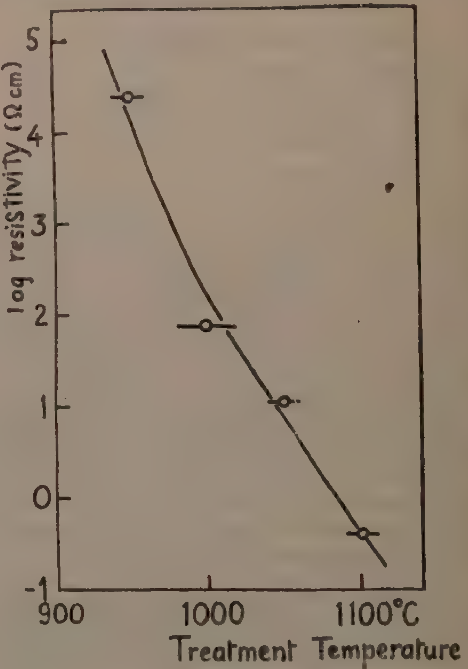

Fig. 1.

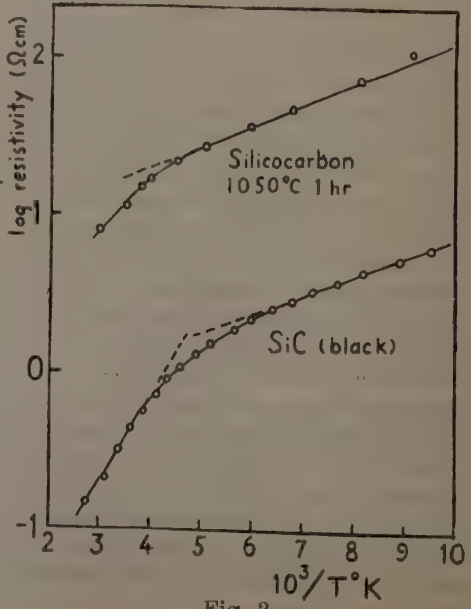

Fig. 2.

temperature of treatment is raised to over 900°C, the resistivity of silicocarbon decreases sharply. The situation is represented in Fig. 1, where the logarithm of the resistivity at room temperature is plotted against the temperature of treatment.

Fig. 2 shows the dependence of the resistivity of a sample heated for an hour at 1050°C on the ambient temperature. The reciprocal of the absolute temperature is taken as the abscissae. For comparison, the resistivity of a sample of black carborundum¹⁾ is also plotted. Both curves have the same slope at lower temperatures and give the activation energy value of 0.054 ev. It was also tried to measure Hall coefficient, but it was too small to be measured, perhaps less than 0.1 cm^3/coul. Neither could it be decided from thermoelectric experiments whether the conductivity is of n- or p-type. One thing we can say is that, when a metal whisker is pressed onto the surface of silicocarbon, p-type thermoelectric voltage is always observed. As for the bulk thermoelectricity, the experiments have shown sometimes p- and sometimes n-type property, the magnitude being always very small. It seems very likely that the conductivity is due to carriers of both types, electrons and holes.

X-ray diffraction experiment of silicocarbon treated at 1050°C have shown rings summarized in Table 1, in addition to intense general backgrounds. Diffraction rings of graphite and carborundum (hexagonal and cubic) are also tabulated²⁾. Some of the silicocarbon rings seem to coincide with those of carborundum and of graphite. This, together with the resistivity-temperature characteristics mentioned above, would at first sight seem to indicate that microcrystalline carborundum is formed as a product of thermal decomposition of Silicone. The situation is, however, not so simple. First, the intense background scattering indicates that the larger part of silicocarbon is still in an amorphous state; hence, if there is microcrystalline carborumdum embedded in an amorphous medium, this material should show the resistance-temperature characteristics of the amorphous medium, not of carborundum. Second, if the conductivity is due to carborundum, there should be a sharp change in intensity of the diffraction rings which might be assigned to carborundum when the treatment temperature is raised, say, from 900° to 1100°C. No such change was observed. It should be added that it seems quite interesting if carborundum is actually formed at such low temperatures.

Table I

Silicocarbon		SiC (cubic and hexagonal forms)		Graphite	
1/d	I	1/d	I	1/d	I
0.30	vs			0.296	1.00
0.38	m	0.386	0.20		
0.40	vs	0.398	1.00		
0.43	s	0.423	0.40		
0.47 ?	w			0.472	0.05
0.49	w	0.500	0.04	0.495	0.10
0.54 ?	vw	0.546	0.02		
0.61	w	0.595	0.04	0.591	0.10
0.65	vs	0.649	0.80		
0.71	m	0.704	0.16		
0.76	s	0.762	0.60		
0.82	m	0.820	0·02	0.815	0.18

vs : very strong
s : strong
m : moderate
w : weak
vw : very weak

References

1) W. Sasaki: J. Phys. Soc. Jap. **7** (1952) 107.

2) J. D. Hanawalt, W. Rinn, L. K. Frevel: Ind. Eng. Chem., Anal. Ed., **10** (1938) 457.

J. Phys. Soc. Japan 8 (1952) 135~136

Spherical Condenser Type Spectrometer

By Yoshiyuki Kobayashi and Gorō Miyamoto

Department of Physics, Faculty of Science, Tokyo University

(Received October 27, 1952)

The spherical condenser was devised by E. M. Purcell¹⁾ as an efficient energy spectrometer of charged particles, and was really shown to be of high efficiency by C. P. Browne and others.²⁾ A spectrometer of this type was also constructed here in order to measure energy spectra of low energy beta-rays and conversion lines due to soft gamma-rays. The instrument is shown schematically in Fig. 1. The radii of the outer and the inner spherical surfaces are 10.5 cm and 9.5 cm respectively. For the convenience of experiments, the outer plate is grounded without any loss in resolving power and available solid angle of the spectrometer. Beause the spectrometer of this type has a good directional focusing, available solid angle might be raised to more than 10 percent of the whole solid angle with irresolution of 1 percent. In our instrument available solid angle is calculated to be about 4 percent. In a preli-

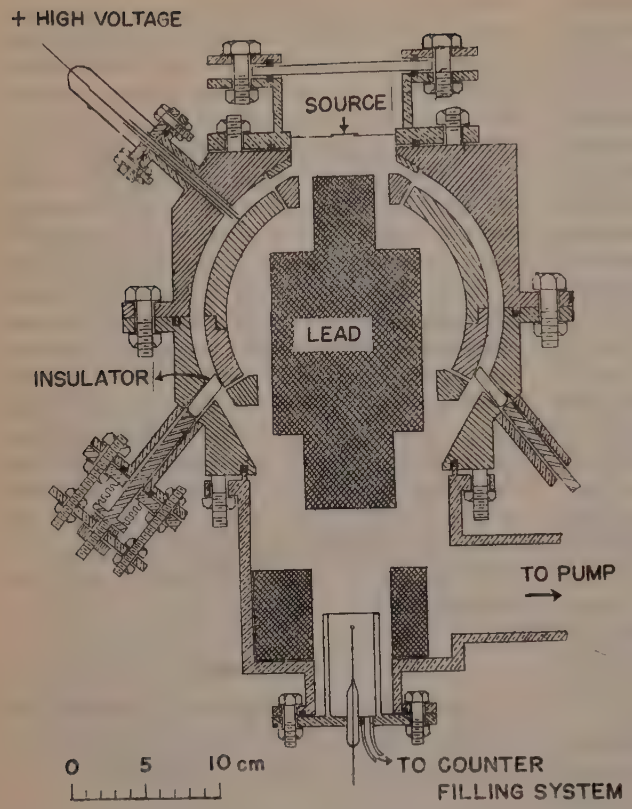

Fig. 1. Vertical section of the spherical condenser type spectrometer. The inner plate is supported by four glass insulators. All slits and shields are grounded.

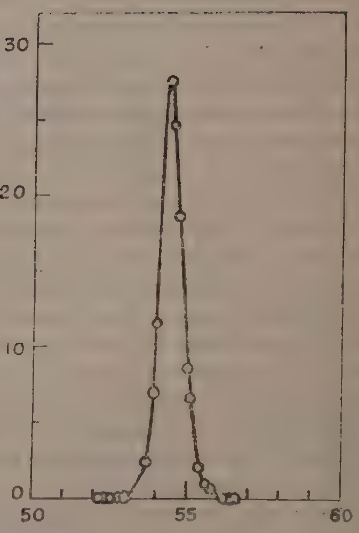

Fig. 2. A line profil of accelerated thermal electrons.

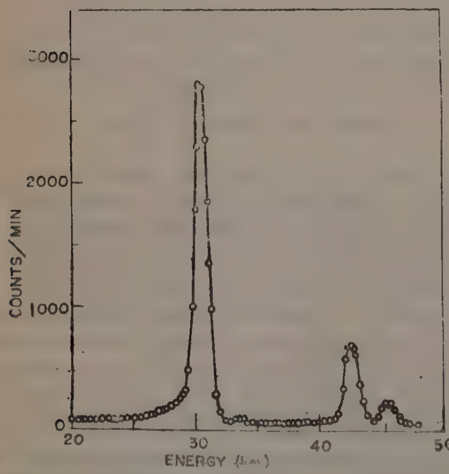

Fig. 3. Conversion line spectrum of RaD.

minary experiment using accelerated thermal electrons, the width at half maximum was measured to be 1.3 percent as illustrated in Fig. 2, and fairly well coincides with the value expected from the sizes of the electron source and the detector. The conversion lines due to the gamma-rays of energy 46.7-kev from RaD was measured for the calibration. The result is shown in Fig. 3. The RaD+E+F collected on platinum ribbon by electrolysis was evaporated on a zapon film of about 30 $\mu g/cm^2$ thickness, and a 20 $\mu g/cm^2$ zapon film was used as the counter-window. Intensity ratios of L, M, N, conversion lines were measured to be $1:0.23\pm0.02:0.06\pm0.005$. The full account of the spectrometer and the results will be soon published.

The authors wish to express their thanks to Mr. G. Iwata for his encouragement and suggertions.

References

1) E. M. Purcell, Phys. Rev. **54** (1938) 818.
2) C. P. Browne, D. S. Craig, and R. M. Williamson: Rev. Sci. Inst. **22** (1951) 952.

Erratum

Effect of Magnetic Field on Precipitation of Ferromagnetic Phase

By Syôhei Miyahara and Tadayasu Mitui

(J. Phys. Soc. Japan **7** (1952) 534)

In Fig. 1 we have erroneously written "$10^{-2}\times$" instead of "$\times 10^3$" as indicated on the ordinate scale.

Un Traitement Statistique de la Résistance à la Rupture du Verre —Sur l'Influence de la Température

Par Nobuzo Terao

(J. Phys. Soc. Japan **7** (1952) 627)

Synopsis line 13 some kcals/mol should be read some 10 kcals/mol.

La graduation de l'ordonnée en Fig. 5 et 6 n'est pas juste. On doit multiplier les valeurs de $\beta(T)$ et $E_0(T)$ par le facteur 5,30.

Page 627, 1ère colonne, ligne 11, au lieu de diffréences, lire différences.

Page 630, 1ère colonne, ligne 3, au lieu de plusieurs kcals/mol, lire plusieurs 10 kcals/mol.

JOURNAL OF THE PHYSICAL SOCIETY OF JAPAN Vol. 8, No. 2, MAR.—APR., 1953

On the Nuclear Interactions of Cosmic Ray Shower Particles in Lead

By Isao KITA and Osamu MINAKAWA

Department of Physics, Kobe University

(Received October 17, 1952)

Using counter controlled cloud chamber in conjunction with hodoscope, nuclear interactions which were caused by secondary shower particles were investigated, and these events classified as high and low energy showers by the inspection of hodoscope pictures. The results show that the multiplicities of the low and the high energy secondary showers are 2.8±0.4 and 3.1±0.4 respectively and from angular distributions of tertiary particles, it is concluded that the mesons are presumably produced multiplily and isotropically in C-system.

§ 1. Introduction

Nuclear interactions of cosmic ray particles have been investigated by many authors using different experimental techniques,[1-12),15-17)] and it has been found that these are very complex events involving various kinds of interactions given rise by nucleons and pi-mesons and others. Hence it is of decisive importance to establish the energy dependences of nuclear interactions for each of them. This work was intended to find some informations about these problems, which were obtained with counter controlled cloud chamber in conjunction with hodoscope. This experiment was performed at Mt. Norikura (alt. 2840 m) in the summer of 1951.

§ 2. Apparatus

The cloud chamber and the counter arrangement are shown in Fig. 1. The inside dimensions of the chamber were 38 cm in diameter and 20 cm in depth and seven lead plates (1 cm thick) were mounted in the chamber. The chamber was filled with 86 cm Hg air saturated by the mixture of alcohol-water. Photographs were taken with a Leica camera at f:4 and illumination was achieved by triggering two argon-mercury filled flash tubes, supplied by 60 μF at 4000 volts, 0.12 second after the expansion.

The counter system contained six trays of counters: A, A*, B, C, D* and E*, as shown in Fig. 1. A five fold concidence $A^{\geq 1}$ $B^{\geq 2}$ $C^{\geq 2}$ was required for the master pulse which triggered an expansion of the chamber. Coincidences between the master pulse and any of the individual counter in trays A*, D* and E* resulted in the flashing of a neon lamp[12)], mounted on a panel located beside the chamber. The neon lights were photographed by the camera together with the cloud chamber picture. Tray E*, located apart 2 meters from the chamber was used as an air shower tray.

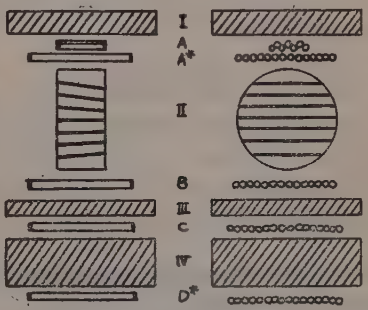

Fig. 1. Diagram of counter and cloud chamber arrangement.

§ 3. Classifications of the Events

The chamber was triggered by the coincidence $A^{\geq 1}$ $B^{\geq 2}$ $C^{\geq 2}$, in order to observe the nuclear interactions produced in lead plate I or II (Fig. 1.). By the inspections of the hodoscope pictures these events are classified as follows:

(a) None or only one counter in tray A* is discharged. This case is interpreted as due to proton passing through plate I without any nuclear interaction and producing penetrating showers in plate II.

(b) Two or more counters in tray A* are discharged.

This is mainly due to a proton or neutron producing a penetrating shower in plate I and the secondary shower particles (most of them are pi-mesons[9,10]) enter the chamber. Hence the nuclear interactions observed may be those produced by these shower particles.

In order to trigger the chamber, at least two shower particles must penetrate plate II with thickness of 5 cm, and the minimum energy of the primary particle responsible to these events is estimated as about 3 Bev, the energy transfered to neutral mesons and nucleons being taken into consideration. When at least one penetrating particle of the shower reached the tray D* which was placed under the lead, 20 cm in thickness, the lower limit of the corresponding shower energy may be about 6 Bev.[10,11]) Therefore all showers were classified as high and low energy events, as follows.

(α) No counter in tray D* is discharged: The energy of the incident particle is about 3–6 Bev and the average is estimated as about 4 Bev, considering the energy spectrum of the primary particles.

(β) One or more counters in tray D* are discharged: The energy is above 6 Bev and the average is about 10 Bev.

From total of 2140 photographs obtained in the experiment, we selected 112 pictures appropriate for our analysis. Among these photographs, 32 were (a)-showers and 102 (b)-showers defined above. All the showers associated with air showers are not considered.

§ 4. Nuclear Interactions produced by Secondary Shower Particles

1. Angular Distribution.

As described above, such showers that discharge two or more counters in tray A* and are classified as (b) consist of secondary shower particles. A large fraction of them being presumably pi-mesons. Some of these pi-mesons produced secondary showers in the chamber and the angular distribution of tertiary particles were investigated.

In Fig. 2. are shown the angular distributions of the shower particles of meson-produced showers separately for high and low energy events, the angle being that between a particle and the shower axis. The curves in Fig. 2, (α) and (β) represent the angular distribution of the low and high energy showers respectively, defined in the proceeding section.

Comparing with the ionization density of incident particles which produce obviously the minimum ionization, only those particles with near-minimum ionization were adopted for our analysis and other heavy tracks were put aside in the present study. Since some of the pictures are not clear enough to discriminate the near-minimum and heavy ionization tracks, some protons of grey tracks[9]) might be contained in the above distribution. It is noted that the distribution for (β) is somewhat sharper than that of (α).

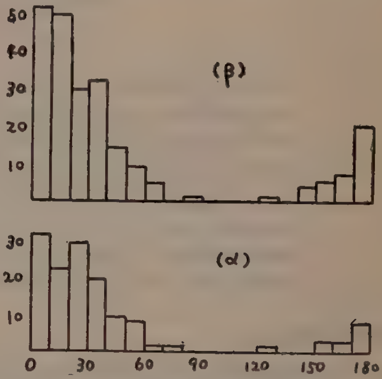

Fig. 2. Angular distributions of the shower particles of meson-produced showers. The curve of (α) is that for lower energy showers and (β) for higher energy showers.

From these distributions, we obtained the mean angle $<\theta>$ and the half maximum angle $\theta_{\frac{1}{2}}$, as follows.

	energy	$<\theta>$	$\theta_{\frac{1}{2}}$
(α)	4 Bev	25°±2°	40°±5°
(β)	10 Bev	22°±2°	30°±5°

If these tertiary particles are assumed to be produced multiplily in meson-nucleon collisions and to emerge isotropically in C-system, the following relations are found among the energy of an incident particle E_π, the half maximum angle $\theta_{\frac{1}{2}}$ and Lorentz factor Γ between C- and L-system.

$$\theta_{\frac{1}{2}}=77^\circ/\Gamma$$

$$E_\pi=\mu(\Gamma^2-2)+\Gamma\sqrt{\Gamma^2-1+\mu^2}\,.$$

E_π is measured in term of proton rest mass and $\mu=m_\pi/m_p=0.15$. For various values of Γ, we obtained the following table.

Table I Relations between the energy of incident particles and $\theta_{\frac{1}{2}}$.

Γ	1.5	2	3	4	
$\theta_{\frac{1}{2}}$	51	39	26	19	deg.
E_π	1.6	3.5	8.9	14	Bev.

Comparing the experimental results with the above table, the agreement between the calculated and observed values of low energy showers is rather satisfactory but that of high energy showers is not so. Considering the large experimental error, however, this descrepancy is not significant and it may conclude that in meson-nucleon collisions below 10 Bev, mesons are produced multiplily and isotropically in C-system.

On the contrary it was reported that the produced mesons are collimated in the two cones for incident mesons for energies above 15 Bev.[6)]

An incident mesons may, however, make plural collisions with a lead nucleus, making the correlation between angles and energies and this effect obscures the above result.

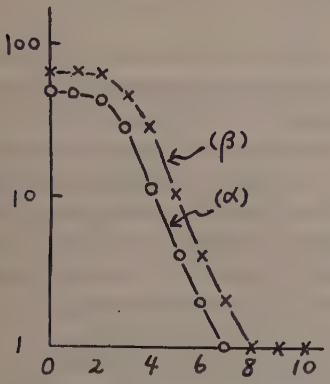

Fig. 3. Integral multiplicity spectra of the shower particles.

2. Multiplicity

Fig. 3. (α) and (β) show the integral multiplicity spectra of the shower particles of low and high energy showers respectively. The average multiplicity is 3.1±0.4 for the high, and 2.8±0.4 for the low energy showers. As shown in the figures, showers of multiplicities 0, 1 and 2 are rare, contrary to the results obtained with nuclear plates. This is because the showers of higher multiplicities have larger probability to be observed due to the selection of coincidence.

Comparing with the results of other experiments, these results give the reasonable values, as follows.

Table II Multiplicities of showers of various energies.

energy(Bev)	multiplicity	material	auther
0.16–1.1	0.4	emulsion	Lock and Yukutieli[16)]
4	2.8±0.4	lead	ours
10	3.1±0.4	lead	〃
30	7±1	gold	Halzler[6)]
60	11±1	gold	〃

A comparision with the number of pi-mesons predicted by Fermi[14)] shows that the multiplicities of this experiment are too high. This difference is attributable partly to the selection of larger showers and partly to the presence of protons among the penetrating ionizing particles. However, the existing uncertainties in the results of this experiment are too large to enable a quantitative camparision to be made.

This work was performed at the laboratory at Mt. Norikura, which was built by courtesy of the Asahi Press, and it was partly supported by the Scientific Research Expenditure of the Department of Education.

References

1) W. W. Brown and A. S. Mckay: Phys. Rev. **77** (1950) 342.
2) W. D. Walker: Phys. Rev. **77** (1950) 686.
3) J. R. Green: Phys. Rev. **80** (1950) 872.
4) B. P. Gregory and J. H. Tinlot: Phys. Rev. **81** (1951) 667, 675.
5) M. B. Gottlieb: Phys. Rev. **82** (1951) 349.
6) A. J. Harlzler: Phys. Rev. **82** (1951) 359.
7) A. Lovati, A. Nura, C. Succi and G. Tagliaferri: Nuovo Comento **8** (1951) 271.
8) C. C. Butler and K. H. Barker: Proc. Phys. Soc. (1949) 64, 4.
9) U. Camerini et al: Phil. Mag. **41** (1949) 1073.
10) U. Camerini et al: Phil. Mag. **42** (1951) 1241.
11) U. Camerini et al: Phil. Mag. **41** (1950) 413.
12) L. Janossy: Cosmic Ray
13) W. Heitler and L. Janossy: Proc. Phys. Soc. **62** (1949) 364, 669.
Hely. Phys. Acta **23** (1950) 417.
14) E. Fermi: Prog. Theor. Phys. **5** (1950) 570.
15) U. Camerini et al: Phil. Mag. **42** (1951) 1261.
16) W. O. Lock and C. Yekutieli: Phil. Mag. **43** (1952) 231.
17) W. O. Walker, N. M. Duller and J. O. Sorrels: Phys. Rev. **86** (1952) 865.

JOURNAL OF THE PHYSICAL SOCIETY OF JAPAN Vol. 8, No. 2, MAR.-APR., 1953

Statistical Theory of Rotational Phase Transition II

By Takehiko OGUCHI

Tokyo Institute of Technology, Oh-okayama, Tokyo

(Received July 28, 1952)

The theory of the rotational phase transitions in the dipolar molecular crystals are discussed. In these crystals, the molecules are under the dipole-dipole interactions between them. The dipole-dipole interactions are simplified as following: the interaction potential between two neighboring molecules along x or y axis is $(J/4)\cos(\omega, \omega')$ and that along z axis is $-(J/2)\cos(\omega, \omega')$, where (ω, ω') is the angle of the orientations of the dipole moments and J is the positive constant. By the cause of such an potential, the dipoles are arranged parallel to each other along z axis and anti-parallel along x and y axis at lower temperatures. The equilibrium state is obtained by solving the non-linear integral equation which is constructed by minimizing the free energy at the stage of the Bethe's approximation and the transition point is determined from the branching point of this integral equation.

§ 1. Introduction

The phase transitions in various molecular crystals have been discussed by many authors since Pauling[1]. Fowler[2] proposed an interesting theory regarding them as cooperative phenomena, but it was a weak point that some vague assumption was included in his theory. Kirkwood[3], along the line of Fowler's treatment, proposed a more rigorous theory at the stage of the Bragg-Williams approximation. Henceforth, various attempts have been performed to improve Kirkwood's theory. From the standpoint of the statistical theory, Chang[4], prior to Kirkwood, had reported a theory applying the Bethe approximation. It was criticized by Nakamura[5], however, that Chang's calculation was wrong in the treatment of the Bethe approximation. In order to proceed with the theory still further, two ways may be considered. One is an improvement of the process of a statistical treatment, along which we have reported in Part I[6] the new theory at the stage of Kikuchi's approximation[7] and have shown that the transition temperature is lowered than that of the former theories, in the two-dimensional square lattice. The other is an improvement of the potential form between the molecules so as to express more closely the situations in a real crystal, because the potential adopted by the former theories is too simple to be suited to a real crystal. Nagamiya[8] studied the properties of the molecular crystals in detail, and divided them into several classes. So a detailed theory must contain a characteristic of them which are remarkable in the potential form chiefly.

Now, we want to take the dipolar molecular crystals. In these crystals, the molecules having rigid dipole moment are under the dipole-dipole interactions between them. A dipole-dipole interaction potential depends on the relative locations in addition to the relative orientations of the dipoles, i.e., it is anisotropic. Unfortunately, however, an anisotropic potential has not been treated by former theories. Accordingly, in this paper, we shall show the method of solving such a problem. This method can be applied not only to the rotational phase transition considered here, but to the various cooperative phenomena in which there is an anisotropic potential.

§ 2. The Fundamental Integral Equation

The rigid dipolar molecules whose dipole moments are $\boldsymbol{\mu}$ respectively, are arranged on a simple cubic lattice. The electrostatic energy between the two molecules separated by a distance $\boldsymbol{r}$ is given by

$$V=(\boldsymbol{\mu}\cdot\text{grad})\frac{(\boldsymbol{\mu}\cdot\boldsymbol{r})}{|\boldsymbol{r}|^3}. \tag{2.1}$$

Let the effective interactions be limited only to those between nearest neighbors. We take the cartesian coordinate coincident with the crystal axes. The interaction energies between the nearest neighboring molecules side by side on the x, y and z axes, whose molecular orientations are $\omega(\theta,\varphi)$ and $\omega'(\theta',\varphi')$ respectively, are

$$V_x(\omega,\omega')=\frac{\mu^2}{d^3}\{\cos(\omega,\omega')-3\sin\theta\sin\theta'\cos\varphi\cos\varphi'\}\,,$$

$$V_y(\omega,\omega')=\frac{\mu^2}{d^3}\{\cos(\omega,\omega')-3\sin\theta\sin\theta'\sin\varphi\sin\varphi'\}\,,$$

$$V_z(\omega,\omega')=\frac{\mu^2}{d^3}\{-2\cos(\omega,\omega')+3\sin\theta\sin\theta'\cos(\varphi-\varphi')\}\,, \quad (2.2)$$

where

$$\cos(\omega,\omega')=\cos\theta\cos\theta'+\sin\theta\sin\theta'\cos(\varphi-\varphi'), \quad (2.3)$$

and (θ,φ) are polar coordinates taking the z axis as a polar axis, and d is a lattice constant. At very low temperatures, all the dipole moments are arranged in one or two directions, for examples, $+z$ and $-z$ axes. The symmetry about the z axis demands that the interaction energies between the molecules on x and y axes, are of the same form, so we take the mean value of them in place of V_x and V_y;

$$V_x=V_y=\frac{\mu^2}{d^3}\left\{\cos(\omega,\omega')-\frac{3}{2}\sin\theta\sin\theta'\cos(\varphi-\varphi')\right\}. \quad (2.2')$$

For the sake of simplifying the calculations, within the limits of preserving a characteristic of the dipolar interaction, we neglect the second terms in (2.2) and (2.2′). The simplifying potential energies are

$$V_x=V_y=\frac{J}{4}\cos(\omega,\omega')\,,$$

$$V_z=-\frac{J}{2}\cos(\omega,\omega')\,, \quad (2.4)$$

where

$$J=\frac{4\mu^2}{d^3}=\text{const.}>0. \quad (2.5)$$

At very low temperatures, the molecules are parallel to each other in z direction and anti-parallel to each other in x and y directions. (See Fig. 1). This is an antiferroelectric arrangement. We notice that in antiferroelectric substances, the dipolar arrangement such as Fig. 2 cannot be realized. This is an important difference between antiferroelectricity and antiferromagnetism.

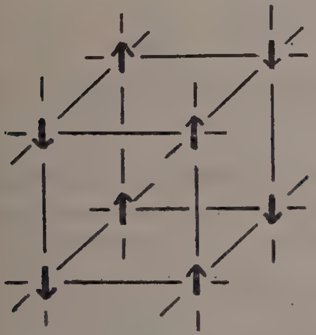

Fig. 1.

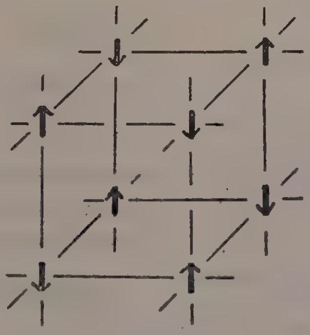

Fig. 2.

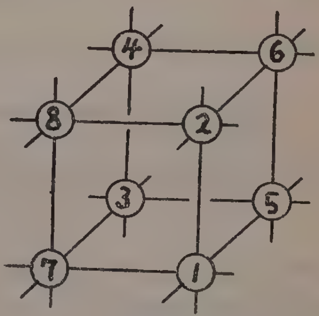

Fig. 3.

We calculate the free energy of the system to the extent of the Bethe approximation. There are several different methods such as those by Chang⁴⁾, Kubo-Hashimura⁹⁾, and Nakamura⁵⁾ respectively, which are regarded as the Bethe approximation in the theory of the rotational phase transition. All of them, however, are for an isotropic potential, so cannot be applied immediately to the anisotropic potential such as (2.4). Thus we use the variational method of the free energy.

As is shown in Fig. 3, the lattice is divided into eight sublattices. Let the probability that the molecular dipole on ith sublattice is in orientation ω_i be denoted by $x_i(\omega_i)$, and the probability of the pair whose end molecular dipoles are in orientations ω_i, ω_j, respectively, be denoted by $y_{ij}(\omega_i,\omega_j)$. These are normalized as follows;

$$\int x_i(\omega_i)d\omega_i=1\,, \quad (2.6a)$$

$$\int y_{ij}(\omega_i,\omega_j)d\omega_j=x_i(\omega_i)\,,$$

$$\int y_{ij}(\omega_i,\omega_j)d\omega_i=x_j(\omega_j)\,, \quad (2.6b)$$

where

$$\int \cdots d\omega_i = \int_0^{2\pi}\int_0^{\pi} \cdots \sin\theta_i d\theta_i d\varphi_i .$$

In order to obtain the configurational entropy, we use a method reforming Kikuchi's one⁷⁾ corresponding to the Bethe approximation in the Ising model of the ferromagnet, so as to be suitable to our system. We must calculate the number of ways of filling the molecules to eight sublattices separately. We use the following notations in the similar way as those in the paper by Kikuchi;

$$x_L(\omega_i) \equiv \prod_{\omega_i} \{x_i(\omega_i)L\}\,! ,$$
$$y_L(\omega_i, \omega_j) \equiv \prod_{\omega_i, \omega_j} \{y_{ij}(\omega_i, \omega_j)L\}! , \qquad (2.7)$$

where L is the number of systems in an ensemble. The number of ways of putting a molecule whose orientation is ω_1, on a (1) sublattice point is calculated referring to Fig. 3, as follows;

$$G_L^{(1)} = \frac{\{x_L(\omega_1)\}^2 \cdot x_L(\omega_2) \cdot x_L(\omega_5) \cdot x_L(\omega_7)}{y_L(\omega_1, \omega_2) \cdot y_L(\omega_1, \omega_5) \cdot y_L(\omega_1, \omega_7) \cdot (L!)^2} . \qquad (2.8)$$

$G_L^{(2)}$ to $G_L^{(8)}$ are obtained in the same ways. Thus the number of ways, G, for one system is given by,

$$\ln G = \frac{1}{L} \ln \prod_{i=1}^{8} G_L^{(i)}$$
$$= \frac{5}{8} N \sum_i \int x_i(\omega_i) \ln x_i(\omega_i) d\omega_i$$
$$- \frac{1}{4} \sum_{(ij)} \iint y_{ij}(\omega_i, \omega_j) \ln y_{ij}(\omega_i, \omega_j) d\omega_i d\omega_j , \qquad (2.9)$$

where $\sum_{(ij)}$ shall mean that the sum is carried out over all pairs (i, j) which are nearest neighbor sublattices in Fig. 3.

The total energy U is given, by utilizing the anisotropic potential (2.4), as

$$U = \frac{N}{4} \sum_{(ij)} \iint V_{ij}(\omega_i, \omega_j) y_{ij}(\omega_i, \omega_j) d\omega_i d\omega_j , \qquad (2.10)$$

where $V_{ij}(\omega_i, \omega_j)$ shall mean $V_x(\omega_i, \omega_j)$, $V_y(\omega_i, \omega_j)$ or $V_z(\omega_i, \omega_j)$ according to whether the pair (i, j) is in the x, y or z directions. Using (2.9) and (2.10), the free energy F is,

$$\frac{F}{NkT} = \frac{1}{4} \sum_{(ij)} \iint \frac{1}{kT} V_{ij}(\omega_i, \omega_j) y_{ij}(\omega_i, \omega_j) d\omega_i d\omega_j$$
$$- \frac{5}{8} \sum_i \int x_i(\omega_i) \ln x_i(\omega_i) d\omega_i$$
$$+ \frac{1}{4} \sum_{(ij)} \iint y_{ij}(\omega_i, \omega_j) \ln y(\omega_i, \omega_j) d\omega_i d\omega_j . \qquad (2.11)$$

We may obtain the equilibrium condition by minimizing the free energy (2.11) under the supplementary condition (2.6). The variational problem, however, is very troublesome in that there are many variational functions and many supplementary conditions between them. So we regard a cube in Fig. 3 composed of eight sublattices as an independent component, so as to make the variational function only one. Let the probability that the eight molecular axes in this cube in orientations $\omega_1, \omega_2, \cdots, \omega_8$, respectively, be denoted by $z(\omega_1, \omega_2, \cdots, \omega_8)$. The relations among x, y and z are

$$x_i(\omega_i) = \int \cdots \int z(\omega_1, \cdots, \omega_8) \prod_{k=1 \neq i}^{8} d\omega_k ,$$
$$y_{ij}(\omega_i, \omega_j) = \int \cdots \int z(\omega_1, \cdots, \omega_8) \prod_{k=1 \neq i, j}^{8} d\omega_k . \qquad (2.12)$$

Using (2.12), we get the free energy (2.11) as following;

$$\frac{8F}{NkT} = 2 \sum_{(ij)} \int \cdots \int \frac{1}{kT} V_{ij}(\omega_i, \omega_j) z \prod_{k=1}^{8} d\omega_k$$
$$-5 \sum_i \int \cdots \int z \ln \left(\int \cdots \int z \prod_{k=1 \neq i}^{8} d\omega_k \right) \prod_{k=1}^{8} d\omega_k$$
$$+2 \sum_{(ij)} \int \cdots \int z \ln \left(\int \cdots \int z \prod_{k=1 \neq i, j}^{8} d\omega_k \right) \prod_{k=1}^{8} d\omega_k . \qquad (2.13)$$

The usual method of indeterminate multiplier gives immediately the first variational equation:

$$2 \sum_{(ij)} \frac{1}{kT} V_{ij}(\omega_i, \omega_j) - 5 \sum_i \ln \int \cdots \int z \prod_{k=1 \neq i}^{8} d\omega_k$$
$$+2 \sum_{(ij)} \ln \int \cdots \int z \prod_{k=1 \neq i, j}^{\infty} d\omega_k = \text{const.} \qquad (2.14)$$

Changing z to x and y using (2.12) again, (2.14) is written as,

$$2 \sum_{(ij)} \frac{1}{kT} V_{ij}(\omega_i, \omega_j) - 5 \sum_i \ln x_i(\omega_i)$$
$$+2 \sum_{(ij)} \ln y_{ij}(\omega_i, \omega_j) = \text{const.} \qquad (2.15)$$

The constant of the right hand side in (2.14) and (2.15) is a multiplier arising from the normalization condition

$$\int \cdots \int z \prod_k d\omega_k = 1 .$$

We have divided the lattice into eight

sublattices in order to simplify the variational problem. But once the variation has been performed, the necessary and sufficient number of the sublattices is four as shown in Fig. 4 to describe our anisotropic system.

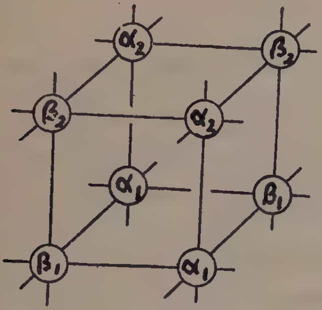

Fig. 4.

Comparing Fig. 3 with Fig. 4, we put

$$(1)=(3)=\alpha_1,\quad (2)=(4)=\alpha_2,$$
$$(5)=(7)=\beta_1,\quad (6)=(8)=\beta_2. \tag{2.16}$$

Thus we obtain from (2.15)

$$\begin{aligned}&y_{\alpha_1\alpha_2}(\alpha_1,\alpha_2)\cdot y_{\beta_1\beta_2}(\beta_1,\beta_2)\{y_{\alpha_1\beta_1}(\alpha_1,\beta_1)\}^2\\ &\quad\cdot\{y_{\alpha_2\beta_2}(\alpha_2,\beta_2)\}^2=\lambda^2\{x_{\alpha_1}(\alpha_1)\cdot x_{\alpha_2}(\alpha_2)\cdot x_{\beta_1}(\beta_1)\\ &\quad\cdot x_{\beta_2}(\beta_2)\}^{5/2}\exp\{K\cos(\alpha_1,\alpha_2)+K\cos(\beta_1,\beta_2)\\ &\quad-K\cos(\alpha_1,\beta_1)-K\cos(\alpha_2,\beta_2)\}\,. \end{aligned}\tag{2.17}$$

where

$$K=J/2kT\,, \tag{2.18}$$

and λ^2 is the constant. The arguments α_1, etc. shall mean ω_{α_1}, etc. (2.17) is the fundamental integral equation. If the potential is not anisotropic, all the y's functions become of the same kind and (2.17) agrees with the ordinary formula of the Bethe approximation.

§ 3. Solutions of the Integral Equation

If we substitute (2.6b) into (2.17), we get the integral equation concerning y. As easily seen,

$$\begin{aligned}y_{\alpha_1\alpha_2}(\alpha_1,\alpha_2)&=\frac{1}{(4\pi)^2}\exp[K\cos(\alpha_1,\alpha_2)]\,,\\ y_{\beta_1\beta_2}(\beta_1,\beta_2)&=\frac{1}{(4\pi)^2}\exp[K\cos(\beta_1,\beta_2)]\,,\\ y_{\alpha_1\beta_1}(\alpha_1,\beta_1)&=\frac{1}{(4\pi)^2}\exp\left[-\frac{K}{2}\cos(\alpha_1,\beta_1)\right],\\ y_{\alpha_2\beta_2}(\alpha_2,\beta_2)&=\frac{1}{(4\pi)^2}\exp\left[-\frac{K}{2}\cos(\alpha_2,\beta_2)\right],\end{aligned}\tag{3.1}$$

are the solutions of (2.17). It may be conjectured from (2.17) that the coefficients in the exponent in $y_{\alpha_1\beta_1}$ and $y_{\alpha_2\beta_2}$ are $-K/2$, but it is automatically obtained as shown in later. Considering from the physical meaning, the solutions (3.2) are the forms of the Boltzmann distributions and the energies of them depend on the angle between the orientations of nearest neighbor molecules, and are independent of the orientations of all other molecules. So they are corresponding to the disordered state. In order to obtain the solutions corresponding to the ordered state, we shall expand $y_{\alpha_1\alpha_2}(\alpha_1,\alpha_2)$ in biaxial spherical harmonics, considering that it should be symmetrical in α_1 and α_2 as following;

$$\begin{aligned}y_{\alpha_1\alpha_2}(\alpha_1,\alpha_2)&=\frac{\mu_1}{(4\pi)^2}\exp[K\cos(\alpha_1,\alpha_2)]\cdot\\ &\cdot[1+c_{10}\{P_1(\alpha_1)+P_1(\alpha_2)\}+c_{20}\{P_2(\alpha_1)\\ &+P_2(\alpha_2)\}+c_{21}P_1(\alpha_1)P_1(\alpha_2)+c_{30}\{(\alpha_1)\\ &+P_3(\alpha_2)\}+c_{31}\{P_1(\alpha_1)P_2(\alpha_2)\\ &+P_2(\alpha_1)P_1(\alpha_2)\}+\cdots]\,,\end{aligned}\tag{3.2)*$$

where $P_n(\alpha_1)$ shall mean the Legendre function $P_n(\cos\theta_{\alpha_1})$ and μ_1 is determined from the normalization condition of $y_{\alpha_1\alpha_2}$ as follows;

$$\mu_1=\frac{1}{H(K)}\left\{1-\frac{1}{3}c_{21}L(K)\cdots\right\}, \tag{3.3}$$

$$H(K)\equiv\sinh K/K\,, \tag{3.4}$$

$$L(K)\equiv H'(K)/H(K)=\coth K-\frac{1}{K}\,, \tag{3.5}$$

where $L(K)$ is the Langevin function. From the consideration of the symmetry, $y_{\beta_1\beta_2}$ should have the form obtained from (3.2) by the transformations

$$\begin{aligned}(\theta_{\alpha_1},\varphi_{\alpha_1})&\to(\pi-\theta_{\beta_1},\pi+\varphi_{\beta_1}),\\ (\theta_{\alpha_2},\varphi_{\alpha_2})&\to(\pi-\theta_{\beta_2},\pi+\varphi_{\beta_2})\,.\end{aligned}\tag{3.6}$$

As $y_{\alpha_1\beta_1}$ and $y_{\alpha_2\beta_2}$ are of the different kind from $y_{\alpha_1\alpha_2}$ and $y_{\beta_1\beta_2}$, we shall eliminate them. We integrate about β_1 and β_2 with the aid of (2.17);

$$\begin{aligned}&\iint y_{\alpha_1\beta_1}(\alpha_1,\beta_1)\cdot y_{\alpha_2\beta_2}(\alpha_2,\beta_2)d\beta_1 d\beta_2\\ &=\lambda\iint\frac{[x_{\alpha_1}(\alpha_1)\cdot x_{\alpha_2}(\alpha_2)\cdot x_{\beta_1}(\beta_1)\cdot x_{\beta_2}(\beta_2)]^{5/4}}{[y_{\alpha_1\alpha_2}(\alpha_1,\alpha_2)\cdot y_{\beta_1\beta_2}(\beta_1,\beta_2)]^{1/2}}\end{aligned}$$

---

* In general, the terms,

$$c_{22}P_1^{\,1}(\alpha_1)P_1^{\,1}(\alpha_2)\cos(\varphi_{\alpha_1}-\varphi_{\alpha_2})$$

and $c_{32}P_2^{\,1}(\alpha_1)P_1^{\,1}(\alpha_2)+P_1^{\,1}(\alpha_1)P_2^{\,1}(\alpha_2)\cos(\varphi_{\alpha_1}-\varphi_{\alpha_2})$ would be added to (3.2), but considering from both sides of (3.7), the coefficients c_{22} and c_{32} in right hand side must be zero, because in the left hand side the terms which contain φ vanish.

$$\times \exp\left[\frac{K}{2}\cos(\alpha_1, \alpha_2)+\frac{K}{2}\cos(\beta_1, \beta_2) -\frac{K}{2}\cos(\alpha_1, \beta_1)-\frac{K}{2}\cos(\alpha_2, \beta_2)\right]d\beta_1 d\beta_2. \tag{3.7}$$

The left hand side reduces to $x_{\alpha_1}(\alpha_1)x_{\alpha_2}(\alpha_2)$ using (2.6b). From (3.2) $x_{\alpha_1}(\alpha_1)$ is explicitly given by

$$\begin{aligned}4\pi x_{\alpha_1}(\alpha_1)=1&+\left[c_{10}\{1+L(K)\}+\frac{2}{5}c_{31}\{L(K)+M(K)\}-\frac{1}{3}c_{10}c_{21}L(K)\{1+L(K)\}\right]P_1(\alpha_1)\\&+\left[c_{20}\{1+M(K)\}+\frac{2}{3}c_{21}L(K)\right]P_2(\alpha_1)\\&+\left[c_{30}\{1+N(K)\}+\frac{3}{5}c_{31}\{L(K)+M(K)\}\right]\times P_3(\alpha_1)\cdots\end{aligned} \tag{3.8}$$

where

$$\begin{aligned}M(K)&\equiv\frac{1}{2}\left\{3\frac{H''(K)}{H(K)}-1\right\},\\ N(K)&\equiv\frac{1}{2}\left\{5\frac{H'''(K)}{H(K)}-3\frac{H'(K)}{H(K)}\right\}.\end{aligned} \tag{3.9}$$

So we have the expression for the left hand side of (3.7) as following;

$$\begin{aligned}\frac{1}{(4\pi)^2}\Big[1&+\Big\{c_{10}(1+L)+\frac{2}{5}c_{31}(L+M)-\frac{1}{3}c_{10}c_{21}L(1+L)\Big\}\{P_1(\alpha_1)+P_1(\alpha_2)\}\\&+\Big\{c_{20}(1+M)+\frac{2}{3}c_{21}L\Big\}\{P_2(\alpha_1)+P_2(\alpha_2)\}\\&+c_{10}^2(1+L)^2P_1(\alpha_1)P_1(\alpha_2)+\Big\{c_{10}c_{20}(1+L)\times(1+M)+\frac{2}{3}c_{10}c_{21}L(1+L)\Big\}\{P_1(\alpha_1)P_2(\alpha_2)+P_2(\alpha_1)P_1(\alpha_2)\}\\&+\Big\{c_{30}(1+N)+\frac{3}{5}c_{31}(L+M)\Big\}\{P_3(\alpha_1)+P_3(\alpha_2)\}\cdots\Big].\end{aligned} \tag{3.10}$$

The right hand side of (3.7) is expanded by the same functions after tedious calculations. The detailed form is not written here, (see reference (10)).

For both sides of (3.7) to be identical, it is necessary and sufficient that the coefficients of the corresponding spherical harmonics of both sides should be identical. From the relation of constant terms,

$$\begin{aligned}\lambda=\frac{1}{4\pi H(K)\cdot H\left(\frac{K}{2}\right)^2}\Big[1&+\frac{1}{24}c_{10}^2\{3+10L(K)-5L(K)^2\}-\frac{1}{3}c_{21}L(K)-\frac{1}{24}c_{10}^2L\left(\frac{K}{2}\right)\\&\times\{3+5L(K)\}^2\cdots\Big].\end{aligned} \tag{3.11}$$

From the coefficients of $P_1(\alpha_1)P_1(\alpha_2)$,

$$\begin{aligned}\frac{1}{2}\left\{1+L\left(\frac{K}{2}\right)^2\right\}c_{21}=\Big[&\frac{1}{8}L\left(\frac{K}{2}\right)\{3+5L(K)\}^2\\&+\frac{1}{16}\left\{1+L\left(\frac{K}{2}\right)^2\right\}\{17+30L(K)+25L(K)^2\}\\&-\{1+L(K)\}^2\Big]c_{10}^3.\end{aligned} \tag{3.12}$$

Considering from (3.12), c_{21} is the order of c_{10}^2. From the similar considerations about the coefficients of $P_2(\alpha_1)+P_2(\alpha_2)$ and $P_1(\alpha_1)P_2(\alpha_2)+P_2(\alpha_1)P_1(\alpha_2)$, c_{20} and c_{31} are the orders of c_{10}^2 and c_{10}^3 respectively. Lastly, the identification of the coefficients of $P_1(\alpha_1)+P_1(\alpha_2)$ reduces to

$$f(K)c_{10}=g(K)c_{10}^3, \tag{3.13}$$

where $f(K)$ and $g(K)$ are the complicated known function of K. One of the solutions of (3.13) is $c_{10}=0$. Since there are no constant terms in the transcendental equation concerning the c's, if we put $c_{10}=0$, c_{20} etc. vanish and the solution (3.2) reduces to (3.1) which corresponds to the disordered state. If c_{10} has non-vanishing real root, c_{20} etc. have also non-zero values. The necessary condition that c_{10} has non-vanishing real root is $f(K)g(K)>0$. If $g(K)$ is the slowly varying function for K and $f(K)$ is the monotonic increasing function and moreover changes the sign at certain point K_c, c_{10} has non-vanishing real roots above K_c and they become imaginary below K_c. Hence K_c may correspond to the transition temperature. The explicit form of $f(K)$ is as follows,

$$f(K)=\frac{1}{4}\left[-1+L(K)+3L\left(\frac{K}{2}\right)+5L(K)L\left(\frac{K}{2}\right)\right]. \tag{3.14}$$

$g(K)$ is always positive near K_c. The solution $f(K_c)=0$ is

$$K_c=0.949\,. \tag{3.15}$$

K_c is one of the branching points of the fundamental integral equation. The solution that $c_{10}=0$, $c_{20}\neq 0$ is also an another branching point. In the latter, the formula corresponding to $f(K)$ has the same form as (3.14) except only L function is substituted by M function, namely:

$$-1+M(K_c')+3M\left(\frac{K_c'}{2}\right)+5M(K_c')\cdot M\left(\frac{K_c'}{2}\right)=0\ , \qquad (3.16)$$

$$K_c'=3.18\ . \qquad (3.17)$$

$L(K)$, $M(K)$, $N(K)$ etc. are the characteristic values corresponding to $n=1, 2, 3$ etc. for the integral equation which has

$$\exp(K\cos(\omega, \omega'))/4\pi H(K)$$

as a kernel and $P_n(\cos\theta)$ as a characteristic function. $P_n(\cos\theta)$ has more zero points as n increases, so that $L(K)>M(K)>N(K)\cdots$. As $L(K)$, $M(K)$, $N(K)$ etc. are the monotonic increasing functions for K, so K_c, K_c', K_c'' for the solution to the formula (3.16) substituted $M(K_c')$ by $N(K_c'')$, are increasing in order. Accordingly, the relation for the free energy *versus* the temperature is schematically shown in Fig. 5. Thus it is concluded that K_c from (3.15) gives the true transition temperature.

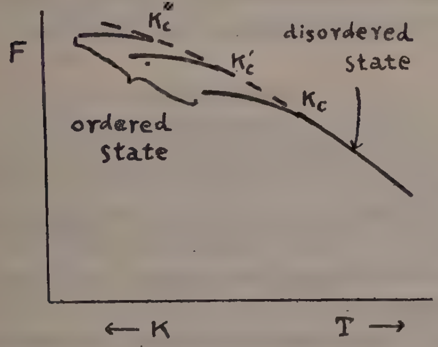

Fig. 5.

The transition temperature from (3.15) is lower than the one for the ordinary isotropic cubic lattice in the Bethe approximation, (in this case, $K_c=0.615$). This is due to the fact that the absolute values of the coefficient of V_x and V_y are half that of V_z. If V_x and V_y are zero (essentially, corresponding to the linear lattice), K_c becomes infinity, i.e. a phase transition does not occur.

§ 4. The Specific Heat

We shall study in this section the behavior of the specific heat at the transition temperature. The average energy is

$$\begin{aligned}U=-\frac{NJ}{4}\Big[&\iint\cos(\alpha_1, \alpha_2)y_{\alpha_1\alpha_2}(\alpha_1, \alpha_2)d\alpha_1 d\alpha_2\\&+\iint\cos(\beta_1, \beta_2)y_{\beta_1\beta_2}(\beta_1, \beta_2)d\beta_1 d\beta_2\\&-\iint\cos(\alpha_1, \beta_1)y_{\alpha_1\beta_1}(\alpha_1, \beta_1)d\alpha_1 d\beta_1\\&-\iint\cos(\alpha_2, \beta_2)y_{\alpha_2\beta_2}(\alpha_2, \beta_2)d\alpha_2 d\beta_2\Big].\end{aligned} \qquad (4.1)$$

We need the explicit form of $y_{\alpha_1\beta_1}$ and $y_{\alpha_2\beta_2}$. To obtain $y_{\alpha_1\beta_1}$, we integrate (3.7) about α_2 and β_2 instead of β_1 and β_2. The result is given by

$$\begin{aligned}y_{\alpha_1\beta_1}(\alpha_1, \beta_1)=&\frac{\mu_3}{(4\pi)^2}\exp\left[-\frac{K}{2}\cos(\alpha_1, \beta_1)\right]\cdot\\&\cdot[1+d_{10}\{P_1(\alpha_1)-P_1(\beta_1)\}+d_{20}\{P_2(\alpha_1)\\&-P_2(\beta_1)\}-d_{21}P_1(\alpha_1)P_1(\beta_1)\cdots]\ ,\end{aligned} \qquad (4.2)$$

where

$$\mu_3=\frac{1}{H\left(\frac{K}{2}\right)}\left[1-\frac{1}{48}c_{10}{}^2L\left(\frac{K}{2}\right)\times\{3+5L(K)\}^2\cdots\right],$$

$$\begin{aligned}d_{10}&=\frac{1}{4}c_{10}\{3+5L(K)\}\ ,\\d_{20}&=-\frac{1}{48}c_{10}{}^2\{3+10L(K)-5L(K)^2\}\\&\quad+\frac{1}{4}c_{20}\{3+5M(K)\}+\frac{5}{6}c_{21}L(K)\ ,\\d_{21}&=\frac{1}{16}c_{10}{}^2\{3+5L(K)\}^2\ ,\end{aligned} \qquad (4.3)$$

and here we calculate up to the terms of order of $c_{10}{}^2$. $y_{\alpha_2\beta_2}$ is obtained by substituting α_1 and β_1 by α_2 and β_2. Thus the average energy is

$$\begin{aligned}U=-\frac{NJ}{2}\Big[&\mu_1\left\{H'(K)+\frac{1}{3}c_{21}H''(K)\right\}\\&+\mu_3\left\{H'\left(\frac{K}{2}\right)+\frac{1}{3}d_{21}H''\left(\frac{K}{2}\right)\right\}\Big].\end{aligned} \qquad (4.4)$$

The average energy is continuous at the transition temperature, so the transition is of second order. The specific heat is

$$\begin{aligned}c_v=\frac{\partial U}{\partial T}=RK^2\frac{\partial}{\partial K}\Big[&\mu_1\left\{H'(K)+\frac{1}{3}c_{21}H''(K)\right\}\\&+\mu_3\left\{H'\left(\frac{K}{2}\right)+\frac{1}{3}d_{21}H''\left(\frac{K}{2}\right)\right\}\Big],\end{aligned} \qquad (4.5)$$

where R is the gas constant. The specific heat just below the transition temperature is

$$c_v(K_c+0)=RK_c^2\Big[-\frac{\frac{1}{3}\cdot dc_{21}/dK\cdot H'(K)+H'(K)}{\{H(K)\}^2}\cdot H'(K)+\frac{H''(K)}{H(K)}+\frac{1}{3}\frac{dc_{21}}{dK}\frac{H''(K)}{H(K)}$$
$$-\frac{1}{2}\frac{\frac{2}{3}\cdot dd_{21}/dK\cdot H'(K/2)+H'(K/2)}{\{H(K/2)\}^2}H'\left(\frac{K}{2}\right)$$
$$+\frac{1}{2}\frac{H''(K/2)}{H(K/2)}+\frac{1}{3}\frac{dd_{21}}{dK}\frac{H''(K/2)}{H(K/2)}\Big]_{K_c} . \quad (4.6)$$

Considering that $dc_{21}/dK=0$ above the transition temperature, the amount of discontinuity of the specific heat at K_c is given by

$$\Delta c_v=-\frac{R}{3}K_c^2\Big[\frac{dc_{21}}{dK}\Big\{\Big(\frac{H'(K)}{H(K)}\Big)^2-\frac{H''(K)}{H(K)}\Big\}$$
$$+\frac{dd_{21}}{dK}\Big\{\Big(\frac{H'(K/2)}{H(K/2)}\Big)^2-\frac{H''(K/2)}{H(K/2)}\Big\}\Big]_{K_c} . \quad (4.7)$$

Putting $K_c=0.949$ into (3.12) etc., we get

$$c_{21}=c_{10}^2 ,$$
$$c_{20}=0.3c_{10}^2 ,$$
$$c_{31}=0.3c_{10}^3 , \quad (\text{at } K=K_c) . \quad (4.8)$$

Substitution of these expressions into (3.13) gives

$$\left(\frac{dc_{10}^2}{dK}\right)_{K_c}=11.68 . \quad (4.9)$$

Using above value we obtain from (4.7),

$$C_v=2.39\,R . \quad (4.10)$$

This value is less than that of the ordinary isotropic Bethe approximation (in the latter, $C_v=2.47R^{5)}$). This is partly due to the fact that the transition temperature is lower than the latter.

Lastly, we shall show that the general expansion (3.2), and (4.2) as a result of it, can be reduced to the factorized forms. If we adopt (3.2) as $y_{\alpha_1\alpha_2}(\alpha_1,\alpha_2)$ and calculate the coefficients of $P_n(\alpha_1)$ up to the terms of order of c_{10}^n, $y_{\alpha_1\beta_1}(\alpha_1,\beta_1)$ can be written as follows;

$$y_{\alpha_1\beta_1}(\alpha_1,\beta_1)=\frac{\mu_3}{(4\pi)^2}\exp\left[-\frac{K}{2}\cos(\alpha_1,\beta_1)\right]$$
$$\cdot[1+d_{10}P_1(\alpha_1)+d_{20}P_2(\alpha_1)+d_{30}P_3(\alpha_1)\cdots]$$
$$\cdot[1-d_{10}P_1(\beta_1)+d_{20}P_2(\beta_1)-d_{30}P_3(\beta_1)\cdots] . \quad (4.11)$$

This is the property of the Bethe approximation which is based on the molecular pairs. In the approximation based on the molecular squares, such a factorized form cannot be obtained without an assumption (compare reference (6)). Transforming (2.17) to the following form,

$$y_{\alpha_1\alpha_2}(\alpha_1,\alpha_2)\cdot y_{\beta_1\beta_2}(\beta_1,\beta_2)$$
$$=\lambda^2\frac{[x_{\alpha_1}(\alpha_1)\cdot x_{\alpha_2}(\alpha_2)\cdot x_{\beta_1}(\beta_1)\cdot x_{\beta_2}(\beta_2)]^{5/2}}{[y_{\alpha_1\beta_1}(\alpha_1,\beta_1)\cdot y_{\alpha_2\beta_2}(\alpha_2,\beta_2)]^2}$$
$$\times\exp[K\cos(\alpha_1,\alpha_2)+K\cos(\beta_1,\beta_2)$$
$$-K\cos(\alpha_1,\beta_1)-K\cos(\alpha_2,\beta_2)] , \quad (4.12)$$

and integrating both sides about β_1 and β_2, we obtain

$$y_{\alpha_1\alpha_2}(\alpha_1,\alpha_2)=\frac{\mu_1}{(4\pi)^3}\exp[-K\cos(\alpha_1,\alpha_2)]$$
$$\cdot[1+c_{10}P_1(\alpha_1)+c_{20}P_2(\alpha_1)+c_{30}P_3(\alpha_1)+\cdots]$$
$$\cdot[1+c_{10}P_1(\alpha_2)+c_{20}P_2(\alpha_2)+c_{30}P_3(\alpha_3)+\cdots]. \quad (4.13)$$

(4·13) shows that $c_{21}=c_{10}^2$ and $c_{10}c_{20}=c_{31}$ and these are consistent with (4.8).

The author is indebted to Professors Y. Takagi and H. Takahashi and R. Kubo and Dr. R. Kikuchi for their continuous interest and encouragement in the progress of this work.

This study was helped by the research grant from the Ministry of Education.

References

1) L. Pauling: Phys. Rev. **36** (1930) 430.
2) R. H. Fowler: Proc. Roy. Soc. **A, 149** (1935) 1.
3) J. G. Kirkwood: J. Chem. Phys. **8** (1940) 205.
4) T. S. Chang: Proc. Camb. Phil. Soc., **33** (1937) 524.
5) T. Nakamura: J. Phys. Soc. Japan **7** (1952) 264.
6) T. Oguchi and Y. Takagi: J. Phys. Soc. Japan, **7** (1952) 145.
7) R. Kikuchi: Phys. Rev., **81** (1951) 988.
8) T. Nagamiya: "*A Collection of Lectures in Physics*," *No. 5, p. 1.*
9) R. Kubo and T. Hashimura: Read at the Meeting of Phys. Soc. Japan at Kyoto, 1949.
10) T. Oguchi: Busseiron Kenkyu (in Japanese), **42** (1951) 36.

JOURNAL OF THE PHYSICAL SOCIETY OF JAPAN Vol. 8, No. 2, MAR.—APR., 1953

A New Type of Striation Observed in Electron-Micrographs of Sericite

By Yoshinobu SEKI

Taihei Mining and Metallurgical Laboratory
Omiya City, Saitama Pref.

(Read October 8, 1951. Received September 27, 1952.)

A series of striae equally spaced was observed in a region of electron-micrograph where two thin rectangular crystal flakes of sericite, a clay mineral, overlapped each other in almost parallel orientation, but with a small rotational angle around their common axis. An interpretation of this striation by hypothesis of double diffraction of electrons caused by rotational overlapping of two crystal flakes was carried out. The possible spacing of the net plane responsible for this diffraction was calculated from the separation of the striation and the small rotational angle of the two flackes. The result did not contradict with that from the electron diffraction photograph of a single flake obtained by a three-stage electron microscope. Thus, this hypothesis has proved itself to work for the interpretation of the present observation.

§ 1. Introduction

A new type of striation observed in an electron-micrograph of sericite, a clay mineral, was already reported by the author1). Its characteristic feature lay in the appearance of a set of equally spaced striae in the region of the microgragh where two distinct crystal flakes overlapped each other in almost parallel orientation.

Mitsuishi *et al.*2) reported similar striations in the electron-micrographs of graphite crystallites. With their micrographs, however, it was not clear whether the patterns were due to such overlapping of the crystal flakes or not. Finch3) suggested that the striations observed with graphite might be interpreted in terms of double diffraction of electrons arising from the rotational slip of the crystallite around its c-axis. Similar consideration was carried out by Green and Weigle4). They named such a pattern the "moiré" pattern. However, they did not present any electron-micrograph showing it. Uyeda5) and Honjo6) are also of opinion that this type of pattern might be interpreted in terms of double diffraction of electrons arising from the above rotational slip or some other causes.

§ 2. Experimental Results

Facts about the striation

Many examples for this type of the striation were obtained in electron-micrographs of sericite. One of them was reproduced in the previous report1) and another is shown in Fig. 1.

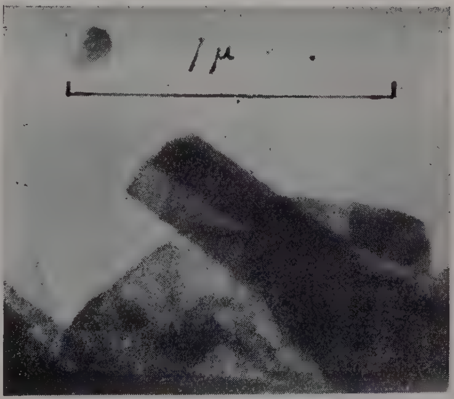

Fig. 1. An electron-micrograph of sericite showing a new type of striation.

The mean separation of striation was measured to be 360Å±35Å with the former micrograph and 230Å±25Å with the present one. The small rotational angle between the two overlapping flakes in each case was measured as the intersectional angle of their long edges. The measured value was 0.013±0.003 in radians with the former micrograph and 0.020±0.002 in radians with the latter.

An electron diffraction analysis of a single flake of sericite

In order to correlate the external from of the sericite crystallite with the positions of its electron diffraction spots and with the spacings of the net planes almost parallel to the incident electrons, the electron diffraction pattern of a single flake of the crystallite and its corresponding electron-micrograph were obtained by means of a three-stage electron microscope. This method of obtaing the diffraction pattern was originally used by Boersch[7),8)]. The diffraction pattern and the electron-micrograph are shown in Figs. 2 and 3, respectively*, being arranged in the manner as to represent their actual geometrical relationships.

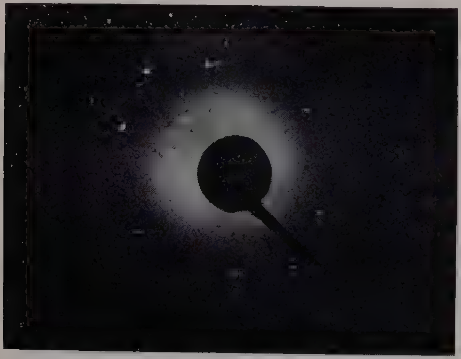

Fig. 2. An electron diffaaction pattern of a single flake of sericite obtained by a three-stage electron microscope using Boersch's method.

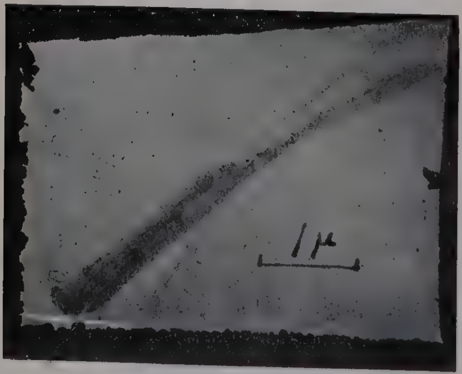

Fig. 3. An electron-micrograph of the crystal flake responsible for the diffraction pattern shown in Fig.2. The field of the object is limited to about $3\mu \times 4\mu$ in area by a movable stop.

Figs. 2 and 3 are arranged in the manner as to represent their actual geometrical relationships.

The clay mineral was identified as sericite by X-ray powder analysis.** The atomic structure of sericite is not clear as yet. However, from many points of view[9)], it is supposed to be very similar to that of muscovite. According to Jackson and West[10)] muscovite cystallizes into a monoclinic structure; a=5.17Å, b=9.02Å c=20.04Å with $\beta=95°30'$. The crystal is well developed parallel to its ab-plane. In this plane, the atomic arrangement is similar to that in the basal plane of hexagonal structure. The electron diffraction analysis of a single flake of sericite showed that the largest of the spacings of the net planes nearly normal to its ab-plane was 4.49Å±0.05Å, and one of the net planes responsible for this value was parallel to the long edge of the crystal flake. If the structure of sericite is assumed to be very similar to that of muscovite as mentioned above and the incident beam is approximately parallel to the c-axis of the crystallite, this plane parallel to the long edge is (110) or (020) plane.

§ 3. A Tentative Interpretation of the Striation

Suppose that two crystal flakes overlap each other in almost parallel orientation, but with an azimuthal rotation of a small angle α. The incident electron beam produces a diffracted and an undiffracted beams by passing through the upper flake (B and A in Figs. 4 and 5). Each of them produces again a diffracted and an undiffracted beams by passing through the lower flake (D and B; C and A in Figs. 4 and 5). The beam which has passed through the two flakes without being diffracted (A) and that diffracted twice by them (D) are almost parallel but are incilined by a small angle ψ to each other as shown in Figs. 4 and 5. The striation under consideration is supposed to be due to the interference between these two beams as shown in Fig. 6. Since α and ψ are very small, the separation s of the striation is calculated to be; $s=d/\alpha$.

By inserting the observed value of the intersectional angle, α, and the mean separation, s, into the above equation, the spacing of the net plane responsible for the striation in the two examples was calculated to be 4.7Å±1.0Å and 4.6Å±0.8Å, respectively.

---

* These two photographs were taken by K. Ito and T. Ito of Nippon Denshi-Kogaku Laboratory.

** The X-ray examination was performed by K. Suzuki of our laboratory.

These values are in accord with that deduced from the electron diffraction analysis of a single flake, 4.49Å±0.05Å, within experimental error.

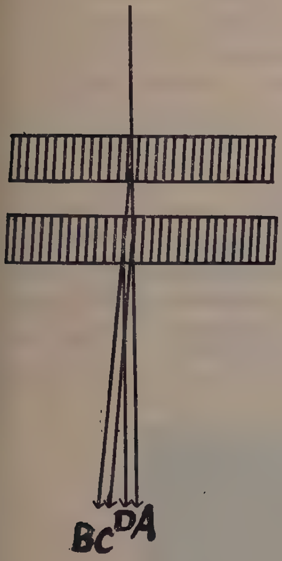

Fig. 4.

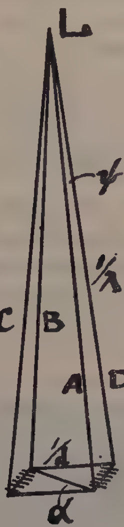

Fig. 5. L is Laue point, α a small rotational angle of two flakes, ψ a small angle between the two beams, A and D.

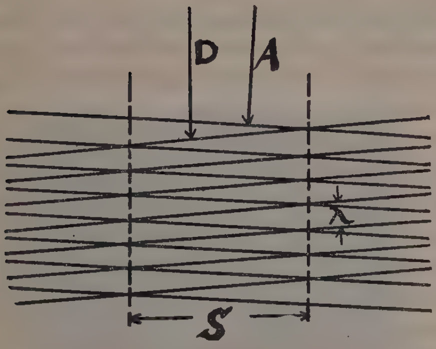

Fig. 6. The parallel lines represent the peaks of the waves.

Since the net planes responsible for the striation should be normal to the direction of the striation as shown in Fig. 5, and since the striae appeared in direction normal to the long edge of the crystal flake in the present examples, the above net plane should be parallel to this long edge. This situation does not contradict with the result of the single flake diffraction analysis that the net plane parallel to the long edge of the flake, whose spacing is 4.49Å±0.05Å, actually exists.

Another set of striae which was observed at a small distance outside the image of the flake in the micrograph represented in the previous note is now supposed to be due to the interference between the other two beams (B and C), diffracted only once by the upper or the lower flake, respectively. These striae might have appeared because of the smallness of the diffraction angle. The defocusing of the micrograph might have an effect for its appearance at such a separated place.

§ 4. Conclusion

The present study has, thus, shown that this new type of striation is interpreted to be due to the overlapping of two thin crystal flakes almost parallel to each other, but with a small angle rotation around their common axis.

Acknowledgements

The author wishes to express his sincere thanks to Prof. R. Uyeda, Nagoya University, and Mr. H. Hagihara, Kobayashi Institute of Physical Research for their encouragement and interest in this work. The author is also indebted to Messers. K. Ito and T. Ito of Nippon Denshi-Kogaku Laboratory for the two photographs taken with their three-stage electron microscope.

References

1) Y. Seki, J. Phys. Soc. Jap. **6** (1951) 534.
2) T. Mitsuishi, H. Nagasaki and R. Uyeda, Proc. Jap. Acad. **127** (1951) 1001.
3) G. I. Finch, private communication to R. Uyeda.
4) T. A. Green and J. Weigle, Helv. Phys. Acta **21** (1948) 217.
5) R. Uyeda, Nippon Buturi Gakkaisi **7** (1952) 146.
6) G. Honjo, Electron-Microscopy, Jap. **2** (1952) 70.
7) H. Boersch, Ann. Physik **27** (1936) 75.
8) M. E. Haine, R. S. Page and R. G. Garfitt, J. Applied Phys. **21** (1950) 173.
9) A. N. Winchell, *Elements of Optical Mineralogy, Part II, Discriptions of Minerals*, 4th ed. Wiley, New York. (1951) p. 369.
10) W. W. Jackson and J. West, Z. Krist. **76** (1931) 211 ; **85** (1933) 160.

JOURNAL OF THE PHYSICAL SOCIETY OF JAPAN Vol. 8, No. 2, MAR.—APR., 1953

Electron Diffraction Investigation of the Actions of Aqueous Heavy Metal Salts on Mineral Surfaces

I. Action of Silver Nitrate and Sulfate on Sphalerite Cleavage Face

By Ryoitiro SATO

Taihei Mining and Metallurgical Laboratory,
Omiya City, Saitama Pref., Japan

(Read April 1, 1951. Received September 27, 1952)

In order, on the one hand, to accumulate data on crystal overgrowth on single crystal surfaces in solid-liquid systems, and, on the other, to elucidate the mechanism involved in activation of sphalerite by heavy metal salts in flotation, electron diffraction investigation has been carried out on the action of silver nitrate and sulfate of comparatively low concentrations upon sphalerite cleavage face. Three kinds of surface products have been revealed: acanthite (Ag_2S), metallic silver, and silver carbonate. It is noteworthy that the produced acanthite crystallites assume a certain epitaxial orientation with respect to the substrate even at room temperatures. In addition, it has been shown that the aging of the surface products in dry atmosphere results in the growth of the acanthite crystallites and the disappearance of the silver.

§ 1. Introduction

Many electron diffraction investigations have been carried out so far on thin layers formed by chemical reactions on various substances.1)2) Most of them, however, are concerned with reactions taking place between solids and gases at comparatively high temperatures, where metal atoms or ions are common to the substrates and the reaction products, as in oxidation or sulfidization of metals, oxidation of minerals, etc. As for reactions taking place between solids and liquids at comparatively low temperatures, electron diffraction has rarely been applied so far to their elucidations, except for electrode phenomena. Accordingly, there are great possibilities that the new kinds of informations on crystal overgrowth on single crystal surfaces would be obtained by the application of electron diffraction method to problems of this field.

In flotation technology it is well recognized that sphalerite (zincblende, ZnS) does not respond to ordinary collectors, unless its surfaces are *activated* by the presence of a low concentration of some heavy metal salts. Although some ambiguities remain, the essential part of the prevailing theory now accepted for the explanation of this phenomenon lies in the interchange of the Zn ions of the mineral surface with the heavy metal ions in the solution, resulting in the formation of the sulfide of the activating metal thereon. If the process proceeds according to the prevailing theory, electro-negative ions (S^{--}) are to be common to the substrate and the product, contrary to the many examples of the chemical reactions cited above. Apart from the above pure physico-chemical interests, the application of electron diffraction method to the elucidation of the mechanism of activation of sulfide minerals is of interest, since, as far as the author's knowledges are concerned, its application in this field has not yet been reported.

If the above interchange of metal ions between substrate and surrounding solution occurs in much larger scale in mineral deposits, this would lead to the formation of *secondary sulfide.*3) In this respect as well, it would be interesting to study these reactions in their initial stages.

From these viewpoints, the author has carried out some electron diffraction investigations on the actions of aqueous heavy metal salts on cleavage face of sphalerite.4)5) The reasons for choosing the cleavage face as the substrate are: with cleavage face of a single crystal electron diffraction method is expected to yield the clearest and most accurate results; and with sphalerite the reactions essential for its flotation in powdered state are supposed to take place on its cleavage face, however minute the particles may be.

The activator commonly used in practice is copper sulfate. However, the electron diffraction investigation of the action of copper sulfate on sphalerite cleavage face by the present author4) has shown that the surface reaction proceeds so slightly, even under intensified conditions, as to yield only diffuse haloes in the diffraction photograph. In what follows the study on the action of silver nitrate and sulfate on sphalerite cleavage face will be reported.

(a) (b)

Fig. 1. Electron diffraction patterns obtained from sphalerite cleavage face soaked in aqueous silver sulfate (50 mg/1, pH 6.4) for 30 min. The photographs were taken after reaction with aqueous potassium ethyl xanthate* (50 mg/1, pH 10.8). Beam is parallel to $[001]_{\mathrm{ZnS}}$ in (a), and $[1\bar{1}0]_{\mathrm{ZnS}}$ in (b). The pattern (a) of the text is shown.

§ 2. Experimental

The sphalerite single crystals used in the present work were yellowish brown and transparent. The silver nitrate ($AgNO_3$) was of analytical grade, and the silver sulfate (Ag_2SO_4) was precipitated from aqueous silver nitrate by addition of concentrated pure sulfuric acid.

The fresh sphalerite cleavage face, about 3×3 mm in size, was soaked in aqueous silver nitrate (or sulfate) of desired concentration and pH value for 30 min. As solvent distilled water was always used. The reaction was always carried out at room temperatures about 15°C. In taking out of the solution, the specimen usually did not expel the solution instantaneously, indicating hydrophilic or poor hydrophobic property. In order to avoid the precipitation of the solute on the surface in drying, it was then rinsed in distilled water. After drying it was inspected by electron diffraction. The camera length of the apparatus was about 30 cm, and the wave length of the electron beam was about 0.065 Å.

Fig. 2. Electron diffraction patterns obtained from sphalerite cleavage face soaked in aqueous silver nitrate (50 mg/1, pH 6.0) for 30 min. The photogragh was taken after reaction with aqueous potassium ethyl xanthate* (50 mg/1, pH 6.4). Beam is parallel to $[001]_{\mathrm{ZnS}}$. The patterns (a) and (b) of the text are shown.

§ 3. Results

The sphalerite cleavage face was soaked in the aqueous silver nitrate or sulfate, the concentration and the pH value being 50 mg/1 ~5 g/1 and 3.0~6.4, respectively, for 30 min. On this surface no change could be detected by naked eye. The diffraction pattern obtained from this specimen was generally composed of three kinds of patterns: (a) the spot pattern due to acanthite (Ag_2S), (b) the Debye-Scherrer rings due to metallic silver, and (c) the arc pattern supposedly due to silver carbonate (Ag_2CO_3). Some of the photographs obtained are reproduced in Figs. 1 and 2. These three kinds of patterns seemed always to appear simultaneously under these experimental conditions. With the increase of the concentration of the solution, the pattern (b) due to metallic silver generally became predominant over the other two. The pH value within the above range seemed not to affect the relative intensities of the three kinds of patterns. Their considerable variations with specimens are most likely ascribed to the uncontrollable surface state of the cleavage face. For silver nitrate and silver sulfate essentially the same pattern was obtained. In most cases the diffraction pattern due to the underlying sphalerite was not observed, except with electrons of larger glancing angle. In the following the three kinds of patterns will be interpreted successively.

---

* The exposure to aqueous potassium ethyl xanthate renders the surface hydrophobic. However, it was confirmed that the electron diffraction pattern remained almost unchanged, except that its contrast became somewhat better and that the pattern (c) became lost.5)

(a). The reaction product responsible for this pattern was identified as acanthite (low temperature modification of Ag_2S) in particular crystalline orientations. Ramsdell[6] showed that acanthite crystallizes in a monoclinic structure, with a=9.47 Å, b=6.92 Å, c=8.28 Å, $\beta=124°$. As he pointed out, this monoclinic lattice can be regarded as a pseudo-orthorhombic lattice, with a=4.74 Å, b=6.92 Å, c=6.87 Å. This unit cell is in good agreement with that analyzed by Palacious and Salvia.[7] Further, this pseudo-orthorhombic lattice can be regarded as a pseudo-cubic lattice, with a=4.74 Å, 4.87 Å, and 4.87 Å.

The feature of the pattern (a) indicates that it is due to a crystal of pseudo-cubic structure, its pseudo-cube face lying parallel to the substrate, with a definite azimuthal orientation. The edge lengths of this pseudo-cube are calculated as

$$a=4.7_0\ \text{Å},\ 4.8_4\ \text{Å, and } 4.8_4\ \text{Å}.$$

These values are in good agreement with those of the pseudo-cube of acanthite within experimental error. By more detailed consideration it is found that the crystalline orientations of the acanthite with respect to the substrate are as follows:

first direction: $(011)_{Ag_2S}//(110)_{ZnS}$,

second direction: $[100]_{Ag_2S} \underset{\text{(almost)}}{//} \begin{cases}[\bar{1}10]_{ZnS} \text{ or} \\ [1\bar{1}0]_{ZnS} .\end{cases}$

If the law of missing spectra found by Ramsdell[6] is taken into account, the acanthite crystal having one of the above orientations is expected to yield the diffraction spots, the positions of which are shown in Fig. 3. However, since the two orientations, as expressed in the "second direction", are expected to be realized simultaneously from consideration of symmetry, the distribution of the spots on the photographic plate is to become symmetrical with respect to the centre line. The expected positions of the spots are in good accordance with those actually observed. The short arcings of the spots in Fig. 1 (b), in which the electron beam is parallel to the $[1\bar{1}0]_{ZnS}$-direction, show that the crystalline orientation has an indefiniteness of about 5° around the $[1\bar{1}0]_{ZnS}$-direction. This arcing was usually symmetrical with respect to the normal to the cleavage face. In Fig. 1 (a), several spots, not corresponding to any of those in Fig. 3 (a), are observed. These extra spots, however, are reasonably explained as coming from the net planes other than those shown in Fig. 3 (a), if the above indefiniteness of the orientation of the crystallites around

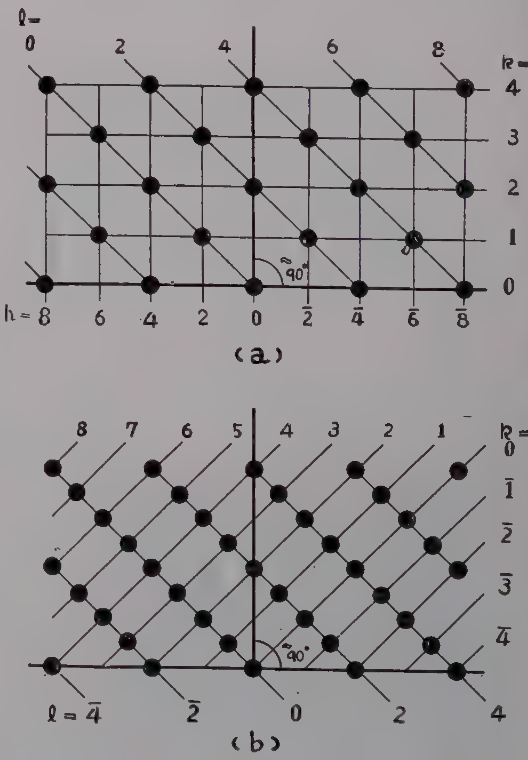

Fig. 3. The positions of the diffraction spots due to the acanthite crystal in the orientation: $(011)_{Ag_2S}//(110)_{ZnS}$, and $[100]_{Ag_2S}//[\bar{1}10]_{ZnS}$. Beam is assumed to be parallel to $[001]_{ZnS}$ in (a), and to $[1\bar{1}0]_{ZnS}$ in (b).

the $[1\bar{1}0]_{ZnS}$-direction is taken into account. The relation of the crystal lattice of acanthite with the atomic arrangement of Zn and S at the interface is shown in Fig. 4. In the figure only one of the two possible orientations is depicted.

The spots were generally elongated towards the shadow edge, implying the refraction effect. This means that the upper surfaces of the crystallites are fairly flat. From the breadth of the spots in the lateral direction the mean size of the coherent crystallites as measured parallel to the substrate is roughly estimated as 30 Å.

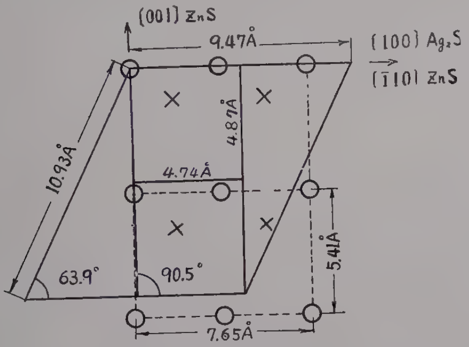

Fig. 4. The relation of the crystal lattice of acanthite with the atomic arrangements of Zn and S at the interface. The orientation of acanthite: $(011)_{Ag_2S}//(110)_{ZnS}$, and $[100]_{Ag_2S}//[\bar{1}10]_{ZnS}$. Circles: Zn. Crosses: S.

(b). The Debye-Scherrer rings (b) were analyzed as due to metallic silver. With some instances it was found that their intensities varied slightly along the circumferences of the rings (Fig. 2). The intensity distribution is consistent with the assumption that the silver crystallites show a weak tendency to be oriented with the $(110)_{Ag}$-plane parallel to the substrate, and otherwise at random. From the breadth of the rings the mean size of the crystallites is roughly estimated as 30 Å or less.

(c). The spacings corresponding to the arcs of the pattern (c) were calculated, and compared with the X-ray ring data given by Hanawalt et al.[8] (Fig. 5). The comparison shows that these arcs are most likely due to silver carbonate (Ag_2CO_3). According to Eldridge,[9] silver carbonate crystallizes in a monoclinic structure, with a=4.83Å, b=9.52Å, c=3.23Å, β=92.7°. In taking account of these values, the net plane tending to lie parallel to the substrate is most likely the $(101)_{Ag_2CO_3}$-plane. From the breadth of the arcs the mean size of the crystallites is roughly estimated as 50Å or more.

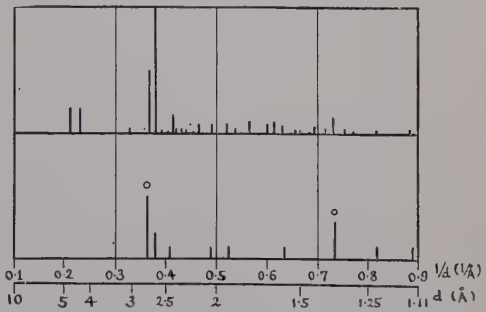

Fig. 5. X-ray Debye-Scherrer ring data[8] of silver carbonate (top) and the analysis of the pattern (c) (bottom). The ring corresponding to the line marked by ○ forms a short arc on the centre line.

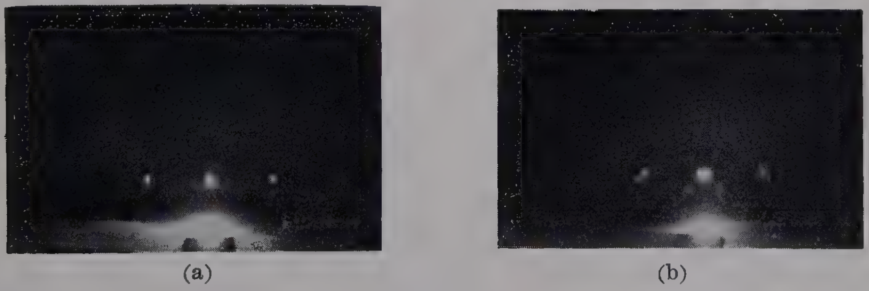
(a)
(b)

Fig. 6. Electron diffraction patterns obtained from sphalerite cleavage face soaked in aqueous silver nitrate (50 mg/1, pH 6.0) for 30 min. The photographs were taken about 300 days after the treatment. Beam is parallel to $[001]_{ZnS}$ in (a), and to $[1\bar{1}0]_{ZnS}$ in (b). The patterns (a) and (c) of the text are shown.

Changes of the reaction products after a long period. The cleavage faces treated with silver nitrate or sulfate as above were kept in a desiccator for about 300 days. The comparison of their electron diffraction photographs (Fig. 6) with those obtained from the cleavage faces immediately after the treatment lead to the results : (1) The spot pattern (a) due to acanthite became sharper, implying the growth of the crystallites. The refraction effect diminished a little, indicating that the upper surfaces of the crystallites became somewhat rougher; (2) The Debye-Scherrer rings (b) due to metallic silver almost disappeared; (3) The arc pattern (c) supposedly due to silver carbonate remained almost unaltered.

§ 4. Discussion

(1) *On acanthite as a reaction product.* The production of acanthite in the present system is well expected from the prevailing theory of the activation of sphalerite according to the equation: $ZnS+2AgNO_3=Ag_2S+Zn(NO_3)_2$, or $ZnS+Ag_2SO_4=Ag_2S+ZnSO_4$. Such reactions taking place on sulfide mineral surfaces are said to be governed by the solubilities of the metal sulfides. The actual observation of acanthite on sphalerite cleavage face shows that this consideration is tenable for the present system, since silver sulfide is less soluble than zinc sulfide.[10)]

According to Lemberg,[11)] acidic solution of silver sulfate reacts with ZnS to form Ag_2S. The present experiment has shown that such reaction is also the case with silver nitrate. Cooke[12)] found that when sphalerite was exposed to concentrated silver nitrate at about 100°C for 50 days, the sphalerite was completely disintegrated, leaving a black powder. This powder was identified by X-ray analysis as argentite (high temperature modification of Ag_2S). However, it is debatable that the product was argentite, since the transformation temperature of acanthite to argentite is about 180°C.[6)]

As to the orientation of the acanthite crystallites on sphalerite cleavage face, it is interesting to note that the formers take almost complete orientation with respect to the latter at temperatures as low as 15°C. In this orientation, as shown in Fig. 4, the misfit of the pseudo-cubic edge length of acanthite (4.74 Å) relative to the atomic distance of sphalerite in the $[\bar{1}10]_{ZnS}$-direction (3.83 Å) is about +23.7 %, and that of another pseudo-cubic edge length (4.87 Å) relative to the atomic distance of sphalerite in the $[001]_{ZnS}$-direction (5.41 Å) is about −10.0 %. The comparatively small misfit of the latter might have induced the present orientation.[13)] More detailed discussion on the orientation relations had better be postponed, until the atomic structure of acanthite will precisely be determined.

The indefiniteness of the orientation of the acanthite crystallites around the $[1\bar{1}0]_{ZnS}$-direction was generally symmetrical with respect to the normal to the sphalerite cleavage face. In most of the cases already studied, where various crystals were deposited onto sphalerite cleavage face,[14)15)] the indefiniteness of their orientations around this direction was asymmetrical with respect to the normal. This is supposed to arise from the asymmetrical atomic arrangement at the cleavage face with respect to the $[1\bar{1}0]_{ZnS}$-direction (see Fig. 4). In the present instance it remains unexplained what role plays this asymmetrical atomic arrangement of the substrate in causing the present symmetrical indefiniteness.

(2) *On metallic silver as a reaction product.* It was already reported that silver nitrate or sulfate reacted with galena (PbS) to precipitate metallic silver.[16)17)] The present result may have shown that these silver salts react also with sphalerite in the same way. Since, however, at least with silver nitrate it tends to decompose on exposure to light or in contact with reducing material to liberate metallic silver, its observation may be ascribed to this cause as well.

Uyeda[18)19)] carried out electron diffraction investigation on thin silver film evaporated onto sphalerite cleavage face. According to him, the silver crystallites are oriented in the same manner as the substrate, when the latter's temperature is above 80-100°C, and at random below this temperature. It is interesting that the silver crystallites in the present case seem easier to be oriented than in his case.

(3) *On silver carbonate as a reaction product.* The precipitation of silver carbonate is probable, since carbon dioxide is usually contained in the solution, and its solubility is much lower than that of silver nitrate or sulfate.

(4) *On the changes of the reaction products*

after a long period. As stated in the proceeding section, the pattern due to the metallic silver almost disappeared after about 300 days. For this, two alternative explanations would be possible. The one is the diffusion of the silver into the interior of the underlying crystal, and another is the combination of the silver with the underlying sphalerite to from acanthite, liberating metallic zinc, which then enters into the interior of the substrate. The diffusion of silver into zinc sulfide was suggested in the studies concerning the structure of luminescent substances.20)** In both of the above explanations, the diffusion of silver through the acanthite produced by the action of silver salt on the sphalerite cleavage face, if any, would accelerate the phenomenon observed. Such diffusion was suggested by Kohlschütter21)** and by Wagner.22)23)**

On the other hand, the pattern due to the acanthite became sharper after the same period, indicating the growth of the crystallites. If the above first explanation is assumed for the disappearance of silver, this growth is to be ascribed to the aggregation of the acanthite crystallites produced by the action of silver salt on the cleavage face. If the second explanation is assumed, it is now to be ascribed to the aggregation of the newly produced acanthite crystallites to those already present on the surface. At the present stage of the study, however, any conclusion on this point may be premature.

Recently Gaudin et al.24) studied the adsorption of silver ion by sphalerite using radioactive silver. According to them, rapid ion exchange occurs at first followed by a slow reaction, to which they assumed several solid-diffusion hypotheses. It should be noticed here that they seem to suppose that the surface product is silver sulfide alone, whereas the present work has shown that besides the sulfide at least metallic silver is formed on the surface. They confirmed the existence of the slow reaction by keeping sphalerite in aqueous silver nitrate overnight. On the contrary, in the present study the changes of the surface state in air for about 300 days have been investigated. Therefore, it may be somewhat impertinent to discuss their result on the basis of the present result. Nevertheless, it may provide an useful key for interpreting their result.

In conclusion the author expresses his sincere thanks to Mr. H. Hagihara for his discussions and encouragement throughout the present work. He is also grateful to the Ministry of Education for the research grant.

References

1) G. P. Thomson and W. Cochrane: *Theory and Practice of Electron Diffraction*, Macmillan and Co., London, 1939.

2) H. Reather: *Ergebnisse der Exakten Naturwissenschaften*, 24. Band, Julius Springer, Berlin, 1951.

3) W. Lindgren: *Mineral Deposits*, MaGraw-Hill Book Co. Inc., 1933, p. 823.

4) R. Sato: *Research Report of Taihei Mining and Metallurgical Laboratory*, No. 1200, 1950, and No. 1250, 1951.

5) R. Sato: *Research Report of Taihei Mining and Metallurgical Laboratory*, No. 1257, 1951.

6) L. S. Ramsdell: Am. Mineral. **28** (1943) 401.

7) J. Palacious and R. Salvia: An. Soc. Espan. Fis. Quim. **29** (1931) 269, cited in Z. Krist., Referatenteil **4** (1933) R. 38.

8) J. D. Hanawalt, H. W. Rinn, and L. K. Frevel : Ind. Eng. Chem., Anal. Ed. **10** (1938) 457.

9) J. E. Eldridge: *Thesis*, 1943, Dartmouth College, cited in J. Donohue and L. Helmholz: J. Am. Chem. Soc. **66** (1944) 295.

10) E. J. Pryor and S. A. Wrobel : Bull. Inst. Mining Met. **60** (1950–51) 201.

11) J. Lemberg: Z. deut. geol. Ges. **46** (1895) 788, cited in J. W. Mellor: *A Comprehensive Treatise on Inorganic and Theoretical Chemistry*, Vol. IV, 1923, p. 606.

12) S. R. B. Cooke: *Advances in Colloid Science*, Vol. III, Interscience Publishers, Inc., New York, 1950.

13) J. H. van der Merwe: Discussions of the Faraday Society, No.5 (Crystal Growth) (1949) 201.

14) M. Kubo and S. Miyake: J. Phys. Soc. Jap. **3** (1948) 114.

15) R. Sato: Unpublished.

16) W. Skey: Chem. News **33** (1876) 35, cited in J. W. Mellor: *A Comprehensive Treatise on Inorganic and Theoretical Chemistry*, Vol. III, 1923, p. 469.

17) J. Lemberg: Z. deut. geol. Ges. **46** (1894)

** These studies dealt with the difusion of silver at much higher temperatures than in the present case. Nevertheless, they might have some relation to the present observation.

793, cited in J. W. Mellor: *A Comprehensive Treatise on Inorganic and Theoretical Chemistry*, Vol. VII, 1927, p. 791.
18) R. Uyeda: Proc. Phys.-Math. Soc. Jap. **22** (1940) 1023.
19) R. Uyeda: Proc. Phys.-Math. Soc. Jap. **24** (1942) 809.
20) N. Riehl: *Physik and Technische Anwendungen der Lumineszenz*, Julius Springer, Berlin, 1941, p. 124; G. R. Fonda: *Preparation and Characteristics of Solid Luminescent Materials*, John Wiley and Sons, Inc., New York, 1948, p. 81.
21) H. W. Kohlschütter: Z. Elektrochem. **38** (1932) 345.
22) C. Wagner: Z. Phys. Chem. **B 21** (1933) 25.
23) C. Wagner: J. Metals **4** (1952) 214.
24) A. M. Gaudin, H. R. Spedden, and M. P. Corriveau: Trans. Am. Inst. Mining Met. Engrs., Mining Eng. **3** (1951) 780.

JOURNAL OF THE PHYSICAL SOCIETY OF JAPAN Vol. 8, No. 2, MAR.—APR., 1953

Crystal Structure of the Ba, Sr and Ca Triple Carbonate

By Jitsuo TERADA

Matsuda Research Laboratory, Tokyo Shibaura Electric Co., Ltd.
Kawasaki, Kanagawa Prefecture, Japan

(Received December 13, 1952)

Crystal structures of the co-precipitated triple carbonates of Ba, Sr and Ca were studied by x-ray powder method using an x-ray Geiger counter spectrometer. There exist three kinds of solid solutions: aragonite type crystal (λ-carbonate), calcite type crystal (β-carbonate) and vaterite type crystal (μ-carbonate); in the $BaCO_3$-$SrCO_3$-$CaCO_3$ system. The phase domains of these three crystal forms are affected some-what by the temperature at which the precipitation is carried out. The triple diagrams are obtained at two stages of precipitation temperatures.

§ 1. Introduction

Recently the intense use of the alkaline earth oxide as the electron emitter of the vacuum tubes has made it necessary to review the virtues of triple oxide coatings instead of the usual barium and strontium double oxide.

Only a few investigators have reported the properties of thermionic emission of the alkaline earth oxide coatings other than (BaSr)O. In 1950 Grey reported the properties of thermionic emission from the BaO-CaO system[1] and in 1951 he studied the thermionic emission contours from the BaO-SrO-CaO system.[2]

It is undoubtedly of importance and interest to correlate the oxide crystal structures with their thermionic emission characteristics. In this paper we have studied the crystal structures of the triple carbonates as a starting-point for the oxide structures.

Survey of Crystal Structures of $CaCO_3$, $BaCO_3$ *and* $SrCO_3$

Calcium carbonate exists in one stable form, β-$CaCO_3$ (calcite) and two unstable forms, λ-$CaCO_3$ (aragonite) and μ-$CaCO_3$ (vaterite) in the ordinary temperature range 0–970°C. Calcite generally results from precipitation at a temperature below 60°C. Aragonite is formed if precipitation is carried out at a temperature approaching the boiling point of water and μ-$CaCO_3$ may be obtained in the same fashion as aragonite except that the temperature is maintained at 60°C.[3]~[5] The structure constants of these three crystal forms of $CaCO_3$ are shown in Table I.

Both barium carbonate and strontium carbonate have a stable aragonite type structure (D_{2h}^{16}—$Pnma$) and the temperature of precipitation has no effect on their crystal forms. These three ortho-rhombic carbonates have the following lattice dimensions.[6]

Table I.

	Name	Symmetry	Space Group	Lattice Dimension	Density	M
β-$CaCO_3$	calcite	rhombohedral	D_{3d}^{6}—$R\bar{3}c$	$a=6{,}36_1$ $\alpha=46°6'$	2,71	2
λ-$CaCO_3$	aragonite	orthorhombic	D_{2h}^{16}—$Pnma$	$a=5{,}72$ $b=4{,}94$ $c=7{,}94$	2,93	4
μ-$CaCO_3$	vaterite	hexagonal	——	$a=4{,}12_0$ $c=8{,}55_6$	2,54	2

Table II.

	$BaCO_3$	$SrCO_3$	$CaCO_3$
a	6,55	6,10	5,72
b	5,26	5,13	4,94
c	8,83	8,42	7,94

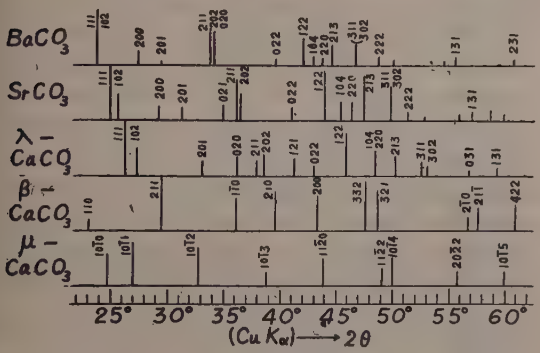

Fig. 1. Powder patterns of single carbonates. μ-$CaCO_3$ pattern is drawn by Gibson, Wyckoff and Merwin's data.

X-ray powder patterns of these single carbonates are also shown in Fig. 1.

§2. Experimental Procedure

The carbonates were prepared from co-precipitation by dropping IN sodium carbonate solution into 1N nitrate solutions of barium, strontium and calcium (the Merck's materials) which had been mixed in the desired molecular proportions. These crystalline powders were then examined by an x-ray Geiger counter spectrometer employing copper K_α radiation.

Crystal forms were exmined carefully in the vicinities of the phase boundaries using the specimens which were made by slow precipitation to avoid the effects of concentrations of the solutions on carbonate crystal forms. Equivalent amounts of dilute solutions (about 1/20 N) of sodium carbonate and nitrate were dropped at the same time from burets into sufficiently large amount of water which was being stirred. As far as our experiments are concerned, we are not able to find any difference in crystal structures between the precipitates made from usual 1*N* solutions and those from the dilute solutions, and the results have been reproduced.

§3. Studies of Double Carbonates

At first we shall describe the studies of three kinds of double carbonates: $(BaSr)CO_3$, $(BaCa)CO_3$ and $(SrCa)CO_3$. Some informations regarding the crystal structure of the triple carbonate will be made clear by these investigations.

(i) *Crystal Structure of the* $BaCO_3$–$SrCO_3$ *System*

The double carbonate of barium and strontium has been used extensively as the cathode material of receiving tubes.

Crystal structure of this system has already been studied by Cork and Gerhard in 1931.7) They found that the co-precipitated $(BaSr)CO_3$ specimen showed only a single intermediate pattern between the patterns of $BaCO_3$ and $SrCO_3$, and that the single pattern of this sort was observed for every co-precipitated specimens, its position with respect to the parents patterns being determined solely by the molecular fractions of the components present. This shows clearly that the metallic barium atoms in the carbonate lattice are replaceable by strontium atoms with a slight accompanying decrease in lattice dimensions or vice versa. They also found a slight deviation from the 'additive law' of Vegard only at each end of the compositions.

(ii) *Crystal Structure of the* $BaCO_3$-$CaCO_3$ *System*

The $BaCO_3$-$CaCO_3$ system offers the most important informations regarding the crystal structure of the carbonate. As is predicted from the lattice dimensions in Table II, the $BaCO_3$-$CaCO_3$ system is the last to form a aragonite type solid solution. In fact the aragonite type solid solution (we may call it as λ-carbonate) appears only in the molecular composition range from 100 % $BaCO_3$ to 20 % fraction of $CaCO_3$, and these λ-solid solutions seem to obey the additive law. Whereas, as reported before,[8)] we get usually the calcite type solid solution (β-carbonate) in this system.

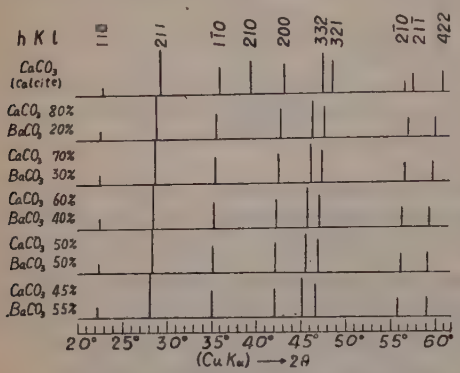

Fig. 2. Powder patterns of β-carbonates in the $BaCO_3$-$CaCO_3$ system.

The β-carbonate is formed in the molecular composition range from 45 to 80 % fraction of $CaCO_3$ in the specimens which are co-precipitated at room temperature (25°~30°C.). On the other hand, when precipitation is carried out at a temperature approaching the boiling point of the solution (90°~105°C.) β-carbonate results over the range from 65 to near 85 % fraction of $CaCO_3$. Powder patterns of β-carbonates are shown in Fig. 2 and they are very similar to that of the calcite except that these β-patterns apparently lack (210) diffraction peak which is a fairly intense line in calcite and dolomite patterns. Presumably ($2\bar{1}0$) peak will also disappear, or those peaks for which $h+k+l=$odd will be extinguished and for those peaks only the oxygen ions contribute to the x-ray scattering in the case of calcite. The data for one of the β-carbonates are illustrated in Table III, and it is seen that the intensities of diffraction peaks almost coincide with those of the calcite pattern.

Table IV shows the bimolecular lattice dimensions of the β-carbonates and in Fig. 3 the volumes of the unit rhombohedra are plotted against molecular compositions. It is readily seen that the volume of unit lattice increases linearly with increasing $BaCO_3$ mol fractions within the limits of experimental

Table III.

The observed x-ray data for one of the β-carbonates: molecular composition is
$BaCO_3 : CaCO_3 = 20 : 80$.

hkl (rhombo. indices)	d	Q(obs.)	Q(cal.)	I(obs.)
110	3, 89	0, 0661	0, 0664	0, 13
211	3, 07$_4$	0, 1058	0, 1060	1, 00
$1\bar{1}0$	2, 50$_5$	0, 1593	0, 1596	0, 27
200	2, 10$_2$	0, 2262	0, 2260	0, 23
332	1, 94$_8$	0, 2640	0, 2644	0, 34
321	1, 89$_6$	0, 2781	0, 2784	0, 24
$21\bar{1}$	1, 60$_7$	0, 3873	0, 3856	0, 15
422	1, 53$_4$	0, 4249	0, 4240	0, 12

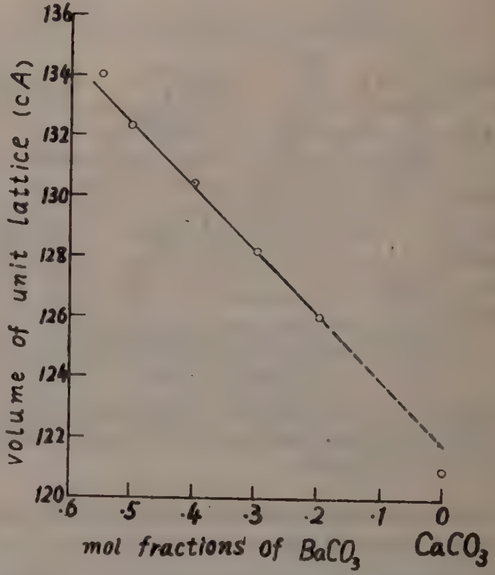

Fig. 3. Relation between the volume of bimolecular unit lattice of β-carbonate and the mol fractions of $BaCO_3$.

Table IV

The bimolecular lattice dimensions of β-carbonates.

molecular composition	a	α
$CaCO_3$ (calcite)	6, 35	46° 3′
$CaCO_3$ 80 % $BaCO_3$ 20 %	6, 48	45°27′
$CaCO_3$ 70 〃 $BaCO_3$ 30 〃	6, 54	45°10′
$CaCO_3$ 60 〃 $BaCO_3$ 40 〃	6, 58	45°13′
$CaCO_3$ 50 〃 $BaCO_3$ 50 〃	6, 64	44°56′
$CaCO_3$ 45 〃 $BaCO_3$ 55 〃	6, 67	44°55′

errors. The disappearance of (210) diffraction peak will be attributed to an extraordinary shrinkage of oxygen ions in carbonate radicals.

A mixed crystalline phase of λ and β-carbonate exists between the λ-phase and β-phase. In this range we obtained only one kind of λ-carbonate whose molecular composition stands at $BaCO_3 : CaCO_3 = 80 : 20$.

The vaterite type solid solution (μ-carbonate) is obtained in the range from 90 to 95 % fraction of $CaCO_3$ in the specimens which are precipitated at room temperature. On both sides of this μ-phase mixed crystalline phases of β and μ-carbonate appear. On the other hand, μ-carbonate does not result solely in the higher temperature specimens, but it is always accompanied with β and λ-carbonate. It seems very interesting from the standpoint of crystallization that in the presence of a little amount of barium ions $CaCO_3$ forms almost pure β-carbonate even at a high temperature near the boiling point of the solution, and at room temperature it forms μ-carbonate. Fig. 4 (a) and (b) show the relation between molecular compositions and the resultant amounts of precipitates in various crystal forms. Fig. 4 (a) shows the result at room temperature and (b) the result at the higher temperature respectively. In these figures the ordinate represents the molecular percentage of the precipitates in various crystal forms, then the sum of the ordinates at any molecular composition always amounts to 100.

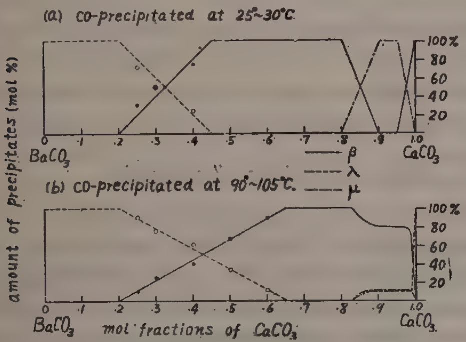

Fig. 4 (a), (b). Variation in crystal forms and the resultant amounts of the precipitates with varying molecular compositions in the $BaCO_3$-$CaCO_3$ system.

In the mixed crystalline phase of λ and β-carbonate the resultant amounts of individual carbonates are calculated from their molecular compositions which are determined from their lattice dimensions using the β-patterns and λ composition of $BaCO_3 : CaCO_3 = 80 : 20$. As to the ($\beta + \mu$) region we reasonably assume a linear change of each resultant amount from the intensity comparison of diffraction peaks. β-carbonate is prevalent even in the ($\lambda + \beta + \mu$) region, which is observed at higher precipitation temperature, the other λ and μ-carbonate both result only a little amount and each of them will amount at most to 10 percent.

(iii) *Crystal Structure of the* $SrCO_3$-$CaCO_3$ *System*

The $SrCO_3$-$CaCO_3$ system is rather a simple case. The lattice dimension of $SrCO_3$ is not so different from that of the aragonite, and λ-carbonate is formed in this system more easily than in the $BaCO_3$-$CaCO_3$ system. However, as is predicted from the crystal forms of $CaCO_3$, β-carbonate must be obtained at least in the specimens which are precipitated at room temperature. Fig. 5 (a) and (b) show the result at room temperature and at the higher precipitation temperature respectively.

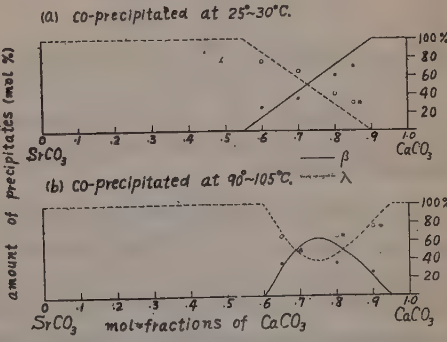

Fig. 5 (a), (b). Variation in crystal forms and the resultant amounts of the precipitates with varying molecular compositions in the $SrCO_3$-$CaCO_3$ system.

λ-carbonate is formed in the molecular composition range from 100 % $SrCO_3$ to 55 % fraction of $CaCO_3$ in the specimens which are precipitated at room temperature. On the other hand, λ-carbonate is formed in two ranges from100 % $SrCO_3$ to 60 % fraction of $CaCO_3$ and from 95 % fraction of $CaCO_3$ to 100 % $CaCO_3$ when precipitation is carried out at higher temperature. β-carbonate is formed in the range from 100 % $CaCO_3$ to near 10 % fraction of $SrCO_3$ at room temperature and the lattice dimension of this sort differs little from that of the calcite. For example, a β-carbonate of mol ratio $SrCO_3 : CaCO_3 = 10 : 90$ has the following lattice dimension: $a = 6{,}42$ $\alpha = 45°32'$. The (210) diffraction peak which is extinguished in β-patterns of $(BaCa)CO_3$ is not extinguished in this case, and no other difference from calcite is conspicuous in powder pattern.

A mixed crystalline region of λ and β-carbonate exists between λ and β-phase in room temperature specimens, and it also exists even in the higher temperatere specimens between two λ-phases. The individual amounts of the precipitates in this region are approximately determined by intensity comparison between (111) diffraction peak of the λ-pattern and (211) peak of the β-pattern which is calibrated by several patterns of standard mixture of $SrCO_3$ and calcite powders. Powder patterns of $SrCO_3$ and aragonite appear superficially very different though they have the same structure, so that two kinds of λ-patterns are obtained in this system: one resembles to $SrCO_3$ and the other to aragonite. Aragonite-like λ-patterns are marked by asterisks in Fig. 5 and the intensity comparison at these points will not be so accurate. The variation in the lattice dimensions of λ-carbonates with varying molecular fractions of the constituents is shown in Fig. 6 for several principal diffraction peaks. These lines for the co-precipitated specimens are, in general, as sharp as those for the pure substances. The observed spacings are seemed to obey the additive law, which is represented by straight lines in the figures, except that a slight deviation occurs near the $SrCO_3$ side. μ-carbonate seldom occurs in this system, but we have experienced once a weak μ-pattern superimposed on β-pattern in a specimen which was precipitated at room temperature from a very concentrated solution of about 8 N and molecular composition of $SrCO_3 : CaCO_3 = 10 : 90$. Specimens of this composition were examined four times from other interest and the results are shown in Table V.

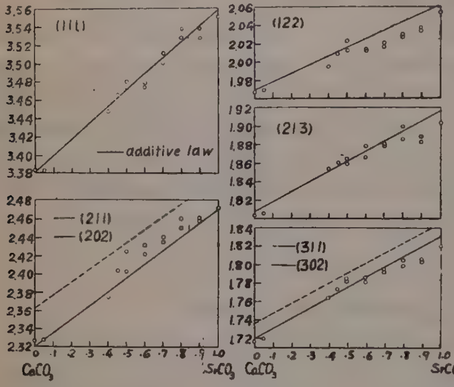

Fig. 6. Variation in the spacings of λ-patterns with varying molecular compositions in the $SrCO_3$-$CaCO_3$ system.

Table V.

No. of specimens	Concentration of solution	pattern
1	1 N	λ
2	1 N	β
3	~1/20 N	β
4	about 8 N	β+μ

In any event, this composition will lie in the neighbourhood of phase boundary at room temperatnre and is in an unstable region. It has already been found experimentally that the least stable phase is generally the first to appear during the primary stages in the crystallization of a very sparingly soluble substance.[4] μ is just the least stable form in the case of $CaCO_3$, then the appearance of μ-carbonate in the specimen precipitated from a very concentrated solution will likely be the case. λ-carbonate of this sort would be resulted by the presence of some contamination such as sulfate ions.[5]

§ 4. Study of Triple Carbonate

On the basis of crystal behaviour of the three kinds of double carbonates, we can easily understand the triple carbonate of barium, strontium and calcium. In all, about 120 co-precipitated specimens were examined and we have found that triple carbonate exists in three crystal forms; λ, β and μ-carbonate. The phase domains are affected somewhat by the temperature at which the precipitation is carried out, as we have seen in the case of double carbonates.

Fig. 7 (a) and (b) show the variation in crystal forms with varying molecular compositions which we have found at room temperature of precipitation (25°~30°C.) and at the higher temperature (90°~105°C.) respectively.

The diagrams are relatively simple except the neighbourhood of $CaCO_3$ apex. β-carbonate exists in an unexpectedly wide range

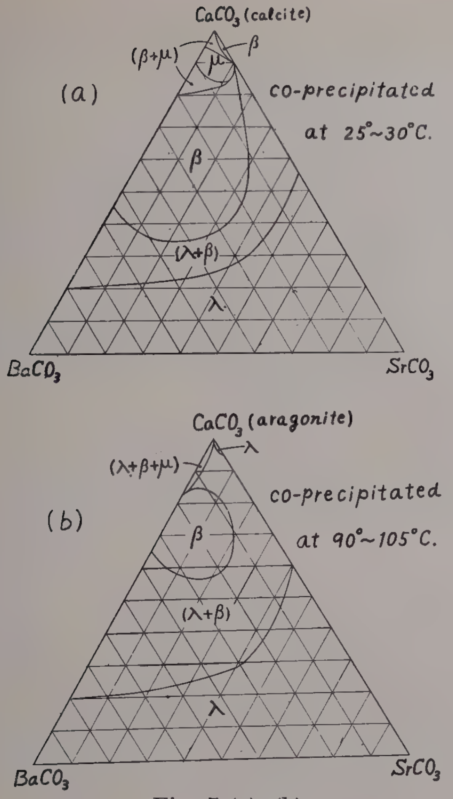

Fig. 7· (a), (b).

even in the higher temperature diagram. Single μ-phase appears in the low temperature diagram but at the higher temperature it exists only in a narrow band accompanied with the other λ and β-carbonate. λ-carbonate which is usually used as a cathode material of vacuum tube appears in a wide range along the $BaCO_3$-$SrCO_3$ side, its single phase extends almost one half of the area of the triple diagrams. Lattice dimensions of several triple carbonates are listed in Table VI. As to a triple β-carbonate, the volume of unit rhombohedron is plotted as a lattice parameter and the volume contours are drawn in Fig. 8. From this figure it is seen that the barium ions extend the volume of calcite-like rhombohedron almost twice as the stromtium ions do. Triple β-carbonate usually lacks (210) diffraction peak or an extraordinarily faint peak is seemed to appear in the x-ray powder pattern. Moreover, in some cases new diffraction peaks which are obtainable in dolomite pattern, such as (221) and $(11\bar{1})$, are seemed to appear, but all of them are very faint and we can say nothing exact about it. The volume contours of λ-carbonates should also be drawn by precise observations, but we are at present not able to do it owing to their relatively low symmetry and only the tendency that the volume of unit lattice decreases with increasing calcium content was recognized. For reference the microphotographs of the carbonates are shown in Fig. 9. λ-carbonate usually appears needle-like in the precipitated specimens and β-carbonate apparently looks rhombohedral appearance. μ-carbonate in our specimens is usually in a very fine crystalline state and looks like a roe. The hexagonal plate appearance of μ-$CaCO_3$, as indicated by literatures,4) was not observed.

Table VI.

Molecular Composition $BaCO_3$: $SrCO_3$: $CaCO_3$	Crystal Form	Lattice Dimension
10:10:80	β	a=6,46 α=45°41′
20:10:70	〃	a=6,52 α=45°24′
10:20:70	〃	a=6,48 α=45°26′
30:10:60	〃	a=6,54 α=45°14′
20:20:60	〃	a=6,55 α=45°28′
50:10:40	〃	a=6,77 α=44°22′
40:20:40	〃	a=6,65 α=45° 5′
30:30:40	〃	a=6,57 α=45° 6′
5: 5:90	μ	a=4,12 c=8,28
5:10:85	〃	a=4,12 c=8,54
55:38: 7	λ	a=6,18 b=5,15 c=8,58
50:35:15	〃	a=6,19 b=5,12 c=8,63

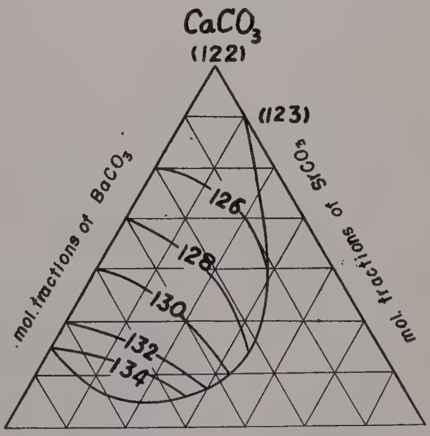

Fig. 8. Volume contours of the triple β-carbonates.

Finally, the system during the precipitation process is not in an equilibrium state as is

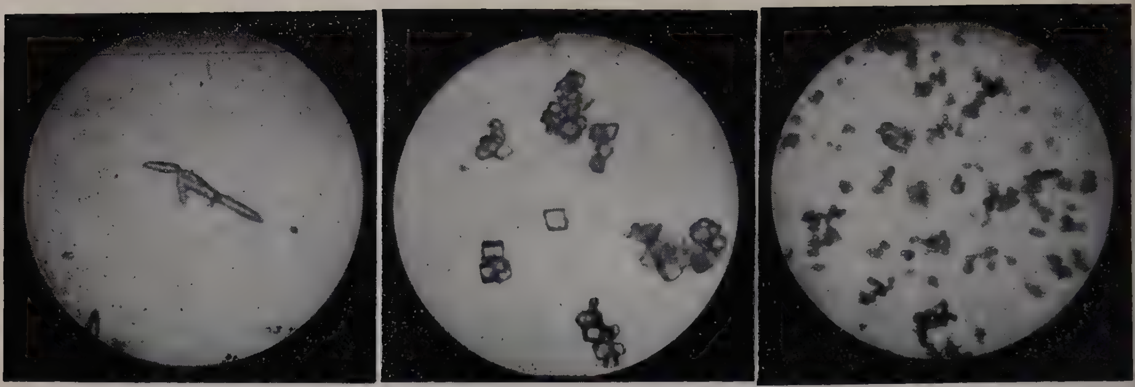

Fig. 9. Microphotographs of the carbonates.

(a)
λ-carbonate
$BaCO_3 : SrCO_3 : CaCO_3$
≒50:35:15 mol %.

(b)
β-carbonate
$BaCO_3 : SrCO_3 : CaCO_3$
≒10:20:70 〃 〃.

(c)
μ-carbonate
$BaCO_3 : SrCO_3 : CaCO_3$
≒5:10:85 〃 〃.

seen in the case of $CaCO_3$. In that case a mixture of two kinds of $CaCO_3$ crystals, such as λ and μ or as β and μ, is obtainable under some conditions. However, as mentioned before, the effect of concentration of nitrate solutions and that of sodium carbonate solution on carbonate crystal forms is negligible in this system and the results are reproducible. The variation in crystal forms depends only on molecular compositions.

§ 5. Conclusions

(1) Three kinds of solid solutions (λ, β and μ-carbonate) are obtained in the $BaCO_3$-$SrCO_3$-$CaCO_3$ system.

(2) In the presence of a little amount of barium ions $CaCO_3$ forms β-carbonate even at a high precipitation temperature, and at a low temperature it forms almost pure μ-carbonate.

(3) A β-carbonate in the $BaCO_3$-$CaCO_3$ system exhibits a typical anomaly compared with the calcite. Its powder pattern always lacks (210) and (2$\bar{1}$0) diffraction peaks and the disappearance of those peaks will be attributed to an extraordinary shrinkage of oxygen ions in carbonate radicals. Triple β-pattern also lacks (210) diffraction peak.

(4) λ-carbonate in the $SrCO_3$-$CaCO_3$ system is seemed to obey the additive law.

(5) Triple λ-carbonate is usually formed in composition range containing below 25 % $CaCO_3$. Its single phase extends almost one half of the area of triple diagram.

(6) Although the system during the precipitation process is not in an equilibrium state, the variation in crystal forms depends only on molecular compositions.

§ 6. Acknowledgment

The author wishes to express his sincere thanks to Mr. S. Niwa who has kindly prepared the carbonate specimens, he is also indebted to Dr. R. Sadanaga for helpful discussions.

References

1) L. E. Grey: Nature **165** (1950) 773.

2) L. E. Grey: Nature **167** (1951) 522.

3) J. Johnston, H. E. Merwin & E. D. Williamson: Amer. J. Sci. [4] **41** (1916) 473.

4) R. E. Gibson, R. W. G. Wyckoff & H. E. Merwin: Amer. J. Sci. **10** (1925) 325.

5) C. E. Imhoff & L. A. Burkardt: Ind. Eng. Chem. **35** (1943) 873.

6) R. W. G. Wyckoff; "The Structure of Crystals" (1948).

7) J. M. Cork & S. L. Gerhard: Amer. Mineral. **16** (1931) 71.

8) J. Terada: J. Phys. Soc. Japan **7** (1952) 432.

JOURNAL OF THE PHYSICAL SOCIETY OF JAPAN Vol. 8, No. 2, MAR.—APR., 1953

The Scattering of Slow Electrons by the Diatomic Molecules
I: General Theory

By Sigeru NAGAHARA

Department of Physics, Faculty of Literature and Science,
Toyama University

(Received October 18, 1952)

A general theory of the scattering of slow electrons by diatomic molecules is formulated. The ellipsoidal coordinates are used, but the separability of the wave equation in these coordinates is not assumed. Explicit expressions for differential and total cross-sections are given, but the numerical evaluation is reserved for a later paper.

§ 1. Introduction

Although the scattering of slow electrons by atoms has been extensively studied theoretically, we have only a few works dealing with the scattering by molecules[1]. This is undoubtedly due to the mathematical complexity of the problem. Firstly, we cannot apply Born's approximation[2], because it is, as generally admitted, least reliable in the low velocity domain; so that we have to solve the Schrödinger equation for the incident electron directly. This problem is fairly simple in the case of atoms on account of the spherical symmetry of the potential field, but in the case of molecules the Schrödinger equation is not separable and the analysis becomes very complicated. Stier and Fisk studied the scattering of slow electrons by the hydrogen melecules but they used such approximate forms for the potential as to enable the separation of variables in elliptic coordinates.

In the present paper we do not assume the separability of the Schrödinger equation and derive a general formula for the cross section. The application of our general theory to the case of the hydrogen molecule will be worked out in the next paper.

In the analysis which follows, we represent the effect of the molecule on the incident electron by a static potential field, so that the exchange effect between the incident and the molecular electrons is not taken into account. Actually it is known that the exchange effect is by no means neglegible in the low energy domain. However, even for the purpose of estimating the contribution of the exchange effect, it appears to us desirable to calculate the scattering by the potential field as accurately as possible.

§ 2. Choice of Units and Coordinates

We use the following atomic units: lengths in units of the Bohr radius $a_H=0.5293$ Å, energies in units of $e^2/a_H=27.204$ eV (twice the ionization energy of the hydrogen atom). Expressed in these units, the Schrödinger equation for the incident electron reads as follows:

$$\left\{-\frac{1}{2}\Delta+\left(V_e-\frac{1}{r_a}-\frac{1}{r_b}\right)\right\}\Psi=E\Psi \quad (1)$$

where V_e denotes the potential energy of the incident electron due to the molecular electronic charge cloud. The two centers are designated by subscripts a and b and their mutual distance by R.

To describe an electron with reference to the two centers, it is convenient to use the following coordinates system:

Prolate spheroidal coordinates, defined by

$$\xi=(r_a+r_b)/R,\ \eta=(r_a-r_b)/R,\ \phi=\phi_a=\phi_b:$$

the domain of these coordinates being $1<\xi<\infty$, $-1<\eta<1$, $0\leq\phi<2\pi$.

Expressed in prolate spheroidal coordinates, the wave equation becomes

$$\begin{aligned} D[\Phi]=\{L_\xi-L_\eta+\kappa^2(\xi^2-\eta^2) \\ -W(\xi,\eta)(\xi^2-\eta^2)\}\Phi=0 \end{aligned} \quad (2)$$

where L_ξ, $W(\xi,\eta)$, κ^2, Φ are defined by

$$\left.\begin{aligned} L_\xi&=\frac{\partial}{\partial\xi}\left\{(\xi^2-1)\frac{\partial}{\partial\xi}\right\}-\frac{m^2}{\xi^2-1} \\ W(\xi,\eta)&=\frac{R^2}{2}\left(-\frac{1}{r_a}-\frac{1}{r_b}+V_e(\xi,\eta)\right) \\ &=\frac{R^2}{2}\left(-\frac{4\xi}{R(\xi^2-\eta^2)}+V_e(\xi,\eta)\right), \\ \kappa^2&=\frac{1}{2}ER^2, \qquad \Psi=\Phi e^{im\varphi} \end{aligned}\right\} \quad (3)$$

§ 3. The Wave Equation

The wave function Φ is expanded in terms of the complete set of orthogonal functions $pe_l^m(\eta)$

$$\Phi_l^m(\xi,\eta)=\sum_j f_{lj}^m(\xi)\, pe_j^m(\eta)\,. \qquad (4)$$

$pe_j^m(\eta)$ is the so-called spheroidal wave function[3] and is defined as the eigenfunction corresponding to the j-th eigenvalue λ_j^m of the equation

$$\{L_\eta+\kappa^2\eta^2\}\, pe_j^m(\eta)=\lambda_j^m\, pe_j^m(\eta)\,, \qquad (5)$$

subject to the boundary conditions that $pe_j^m(\eta)$ is regular at $\eta=\pm1$. The partial differential equation (2) has an infinite set of independent solutions, which are distinguished by l. The choice of these solutions is arbitrary to a large extent. For our scattering problem we require such set of solutions that the incident wave is contained only in one term of the right-side of (4), other terms giving out-going scattered waves only. If we start the numerical integration for $f_{lj}^m(\xi)$ from $\xi=1$, however, we cannot obtain these solutions with prescribed asymptotic forms from the beginning; so that at present we leave the choice of the independent solutions arbitrary, and later we shall carry out the transformation to the required set (see (13) below). It would be sometimes convenient to fix these functions by putting

$$f_{lj}^m(\xi)=\sum_{h=0}^{\infty} c^m_{lj,h}(\xi-1)^{\frac{m}{2}+h}$$

$$c^m_{ll,0}\neq0, \qquad c^m_{lj,0}=0 \quad (l\neq j)$$

If we substitute (4) into (2), we have

$$D[\Phi_l^m(\xi,\eta)]=\sum_j pe_j^m(\eta)\left[\frac{d}{d\xi}\left\{(\xi^2-1)\frac{df_{lj}^m(\xi)}{d\xi}\right\}\right.$$
$$\left.+\left(\kappa^2\xi^2-\frac{m^2}{\xi^2-1}-\lambda_j^m+W(\xi,\eta)\right)f_{lj}^m(\xi)\right]=0. \qquad (6)$$

Multiplying (6) by $pe_l^m(\eta)$ and integrating over the coordinate η, we obtain

$$\frac{d}{d\xi}\left\{(\xi^2-1)\frac{df_{lj}^m(\xi)}{d\xi}\right\}+\left(\kappa^2\xi^2-\frac{m^2}{\xi^2-1}\right.$$
$$\left.-\lambda_j^m\right)f_{lj}^m(\xi)+\sum_{j'}W_{jj'}(\xi)f_{lj'}^m(\xi)=0\,, \qquad (7)$$

where $W_{jj'}$ is defined by

$$W_{jj'}=\frac{1}{N_{jm}}\int pe_j^m(\eta)W(\xi,\eta)\,pe_{j'}^m(\eta)d\eta\,,$$

$$N_{jm}\delta_{jj'}=\int pe_j^m(\eta)\,pe_{j'}^m(\eta)d\eta$$

(6) represent a system of simultaneous differential equations for the infinite number of functions $f_{lj}^m(\xi)$, $j=0,1,2,\ldots$.

Now, the incident plane wave can be expanded in terms of the spheroidal waves as follows:

$$e^{i(kr)}=\sum \varepsilon_m i^l a_{lm}\, pe_l^m(\cos\alpha)\, pe_l^m(\xi)\, pe_l^m(\eta). \qquad (8)$$

It can be shown that the "radial" function $pe_l^m(\xi)$ has the asymptotic form

$$pe_l^m(\xi)\sim\frac{2}{a_{lm}N_{lm}}\frac{\sin(\kappa\xi-\frac{\pi}{2}(l-m))}{\kappa\xi}\,, \qquad (9)$$

$$\varepsilon_0=1,\ \varepsilon_1=\varepsilon_2=\cdots=2$$

for very large values of ξ. (The reader is referred to the Appendix for the proofs of (8) and (9)) Taking this expression into account, we write the asymptotic form of $f_{lj}^m(\xi)$ for $\xi\to\infty$ as follows:

$$f_{lj}^m(\xi)\sim B_{lj}^m\frac{2}{a_j^mN_j^m}\frac{\sin(\kappa\xi-\frac{\pi}{2}j+\delta_{lj}^m)}{\kappa\xi}$$
$$\sim B_{lj}^m\frac{2}{a_{jm}N_{jm}}\left\{e^{-i\delta^m_{lj}}\frac{\sin(\kappa\xi-\frac{\pi}{2}j)}{\kappa\xi}\right.$$
$$\left.+\sin\delta_{lj}^m\frac{e^{i\kappa\xi-\frac{\pi}{2}ij}}{\kappa\xi}\right\}. \qquad (10)$$

Hence, we have

$$\Phi_l^m(\xi,\eta)\sim\sum B_{lj}^m e^{-i\delta^m_{lj}}\left(\frac{2}{a_{jm}N_{jm}}\frac{\sin(\kappa\xi-\frac{\pi}{2}j)}{\kappa\xi}\right.$$
$$\left.\times pe_j^m(\eta)\right)+\sum B_{lj}^m\sin\delta_{lj}^m$$
$$\times\left(\frac{2}{a_{jm}N_{jm}}\frac{e^{i\kappa\xi-\frac{\pi}{2}ij}}{\kappa\xi}pe_j^m(\eta)\right). \qquad (11)$$

We introduce an infinite matrix D_{jl}^m $(j,l=1,2,\cdots)$, which is the inverse of the matrix $B_{lj}^m e^{-i\delta^m_{lj}}$:

$$\sum D_{kl}^m B_{lj}^m e^{-i\delta^m_{lj}}=\delta_{kj} \qquad (12)$$

If we transform our set of solutions Φ_l^m with the matrix D_{jl}^m, we arrive at the set of solutions Φ_j^m with the required asymptotic behaviour:

$$\Phi_j^m(\xi,\eta)=\sum_l D_{jl}^m\Phi_l^m(\xi,\eta)\,. \qquad (13)$$

With the use of (11), (12), the asymptotic form of (13) is found to be as follows:

$$\Phi_j^m(\xi,\eta)\sim\frac{2}{a_{jm}N_{jm}}\frac{\sin(\kappa\xi-\frac{\pi}{2}j)}{\kappa\xi}pe_j^m(\eta)$$
$$+\sum_{j'}\sigma_{jj'}\frac{2}{a_{j'm}N_{j'm}}\frac{e^{i\kappa\xi-\frac{\pi}{2}ij'}}{\kappa\xi}pe_{j'}^m(\eta)\,, \qquad (14)$$

where

$$\sigma_{jj'}{}^{m}=D_{jl}{}^{m}B_{lj'}{}^{m}\sin\delta_{lj'}{}^{m}$$
$$=\frac{1}{2i}\delta_{jj'}-\frac{1}{2i}D_{jl}B_{lj'}e^{-i\delta_{lj'}^{m}}\quad . \tag{15}$$

Considering that the incident wave Ψ^0 is

$$\Psi_0=\sum\varepsilon_m i^j a_{jm}pe_j{}^m(\cos\alpha)pe_j{}^m(\xi)$$
$$\times pe_j{}^m(\eta)\cos m(\varphi-\beta) \tag{16}$$

the wave function Ψ becomes

$$\Psi=\sum\sum\varepsilon_m i^j a_{jm}pe_j{}^m(\cos\alpha)$$
$$\times\Phi_l{}^m(\xi,\eta)\cos m(\varphi-\beta) \tag{17}$$

§ 4. Differential Cross Section and Total Cross Section in Elastic Scattering

From the foregoing results, scattered wave becomes

$$\Psi-\Psi^0=\sum\sum\sum\varepsilon_m i^j a_{jm}pe_j{}^m(\cos\alpha)\sigma_{jj'}{}^m\frac{2}{a_{j'm}N_{j'm}}$$
$$\times\frac{e^{i\kappa\xi-\frac{\pi}{2}ij'}}{\kappa\xi}pe_{j'}{}^m(\eta)\cos m(\varphi-\beta)$$
$$=\frac{e^{i\kappa\xi}}{r}f(\theta,\varphi:\alpha,\beta) \tag{18}$$

where $f(\theta,\varphi:\alpha,\beta)$ is defined by

$$f(\theta,\varphi:\alpha,\beta)=\frac{1}{\kappa}\sum\sum\sum\varepsilon_m i^j a_{jm}pe_j{}^m(\cos\alpha)\sigma_{jj'}{}^m$$
$$\times\frac{2}{a_{j'm}N_{j'm}}e^{-\frac{\pi}{2}ij'}pe_j{}^m(\cos\theta)\cos m(\varphi-\beta) \tag{19}$$

When the orientation of gas molecules is random, the scattering differential cross section observed is obtained by averaging $|f|^2$ with α,β i.e.,

$$Q(\theta,\varphi)=\frac{1}{4\pi}\iint|f|^2\sin\alpha d\alpha d\beta$$
$$=\frac{1}{2\kappa^2}\sum\varepsilon_m a_{jm}{}^2N_{jm}\sigma_{jj'}{}^m\bar{\sigma}_{jj''}{}^m\frac{2}{a_{j'm}N_{j'm}}$$
$$\times\frac{2}{a_{j''m}N_{j''m}}e^{-j'+j''}pe_{j'}{}^m(\cos\theta)pe_{j''}{}^m(\cos\theta) \tag{20}$$

and the total cross section is given by

$$Q=\iint Q(\theta,\varphi)\sin\theta d\theta d\varphi$$
$$=\frac{4\pi}{\kappa^2}\sum\sum\sum\varepsilon_m\frac{a_{jm}{}^2N_{jm}}{a_{j'm}{}^2N_{j'm}}|\sigma_{jj'}{}^m|^2\ . \tag{21}$$

§ 5. Discussion and Conclusion

If the potential V_e takes the form of $(f(\xi)+g(\eta))/(\xi^2-\eta^2)$, non-diagonal term does not appear. If non-diagonal term is neglegible, the results obtained by the author reduce to those obtained by Stier and Fisk.

The main difficulty in carrying out the calculation proposed in this paper is the solution of the simultaneous differential equation and the construction of the inverse matrix $(\sigma_{jj'}{}^m)$. Although the order of this equation and the matrix is infinite, we may obtain good approximation by taking the first several functions only and neglecting the others. We will show in the next paper that by this method our general formulation can be worked out numerically as far as a reasonable approximation for the potential V_e is available.

§ 6. Acknowledgments

I wish to thank Prof. M. Kotani for his much helpful advice and continuous encouragement throughout the research. I should like to thank Hattori-Hōkōkai for financial support.

APPENDIX

Proof of

$$pe_l{}^m(\xi)\sim\frac{2}{a_{lm}N_{lm}}\frac{\sin(\kappa\xi-\frac{\pi}{2}(l-m))}{\kappa\xi}$$

$$e^{i(kr)}=\sum\varepsilon_m i^l a_{lm}pe_l{}^m(\cos\alpha)$$
$$\times pe_l{}^m(\xi)pe_l{}^m(\eta)\cos m(\varphi-\beta)$$

The plane wave $e^{i(kr)}$ can be expanded in the following way:

$$e^{i(kr)}=e^{(ik_x\sin\alpha\sin\beta+ik_y\sin\alpha\sin\beta+ik_z\cos\alpha)r}$$
$$=e^{i\kappa\frac{R}{2}\sqrt{(\xi^2-1)(1-\eta^2)}\sin\alpha\cos(\varphi-\beta)+ik\frac{R}{2}\xi\eta\cos\alpha}$$
$$=e^{i\kappa\xi\eta\cos\alpha}\sum\varepsilon_m i^m J_m(\kappa\sqrt{(\xi^2-1)(1-\eta^2)}$$
$$\times\sin\alpha)\cos m(\varphi-\beta)$$

where

$$\kappa=\tfrac{1}{2}kR,\quad \varepsilon_0=1,\quad \varepsilon_1=\varepsilon_2=\cdots=2\ .$$

The function

$$J_m(\kappa\sqrt{(\xi^2-1)(1-\eta^2)}\sin\alpha)e^{i\kappa\xi\eta\cos\alpha}$$

can be expressed in terms of the functions $pe_l{}^m(\eta)$ and $pe_l{}^m(\xi)$,

$$J_m(\kappa\sqrt{(\xi^2-1)(1-\eta^2)}\sin\alpha)e^{i\kappa\xi\eta\cos\alpha}$$
$$=\sum C_{lm}(\alpha)pe_l{}^m(\xi)pe_l{}^m(\eta)\ . \tag{26}$$

Integrating (26) by $pe_l{}^m(\eta)$ for the coordinate of η, we obtain:

$$C_{lm}(\alpha)pe_l{}^m(\xi)N_{lm}$$
$$=\int J_m(\kappa\sqrt{(\xi^2-1)(1-\eta^2)}\sin\alpha)e^{i\kappa\xi\eta\cos\alpha}pe_l{}^m(\eta)d\eta\ . \tag{27}$$

When we substitute $\cos i\lambda$ for ξ, we obtain:

$$C_{lm}(\alpha)pe_l^m(\cos i\lambda)N_{lm}$$
$$=\int_0^\pi J_m(-i\kappa\sin i\lambda\sin\alpha\sin\mu)$$
$$\times e^{i\kappa\cos i\lambda\cos\alpha\cos\mu}pe_l^m(\cos\mu)\sin\mu d\mu\,. \quad (28)$$

As the right hand term is symmetric with respect to $i\lambda$ and α, $C_{lm}(\alpha)$ can be expressed as follows:

$$C_{lm}(\alpha)=i^{l-m}a_{lm}\,pe_l^m(\cos\alpha) \qquad (29)$$

where a_{lm} is a constant independent of α. Thus, the result follows:

$$e^{i(kr)}=\sum\varepsilon_m i^l a_{lm}pe_l^m(\cos\alpha)pe_l^m(\xi)pe_l^m(\eta)$$
$$\times\cos m(\varphi-\beta)\,.$$

If we substitute (29) in (28), we obtain:

$$N_{lm}a_{lm}pe_l^m(\cos\alpha)pe_l^m(\cos\alpha')$$
$$=i^{-l+m}\int_0^\pi J_m(-i\kappa\sin\alpha\sin\alpha'\sin\mu)$$
$$\times e^{i\kappa\cos\alpha\cos\alpha'\cos\mu}pe_l^m(\cos\mu)\sin\mu d\mu\,. \quad (30)$$

Substituting η for $\cos\mu$ and ξ for $\cos\alpha'$ in the foregoing equation, we obtain:

$$N_{lm}a_{lm}pe_l^m(\cos\alpha)pe_l^m(\xi)$$
$$=i^{-l+m}\int J_m(\kappa\sqrt{(\xi^2-1)(1-\eta^2)}\sin\alpha)$$
$$\times e^{i\kappa\xi\eta\cos\alpha}pe_l^m(\eta)d\eta\,. \qquad (31)$$

If we devide the both hand terms by $\sin^m\alpha$ and taking the limit α zero, we obtain:

$$N_{lm}a_{lm}\gamma_{l0}^m pe_l^m(\xi)=\frac{i^{-l+m}}{2^m m!}\kappa^m(\xi^2-1)^{m/2}$$
$$\times\int(1-\eta^2)^{m/2}e^{i\kappa\xi\eta}pe_l^m(\eta)d\eta \qquad (32)$$

where γ_{l0}^m is defined by

$$pe_l^m(x)=(1-x^2)^{m/2}f(x)=(1-x^2)^{m/2}\sum\gamma_{ls}^m(1-x)^s$$
$$=(1-x^2)^{m/2}(-1)^{l-m}\sum\gamma_{ls}^m(1+x)^s\,.$$

When ξ becomes very large in (32), we obtain:

$$N_{lm}a_{lm}\gamma_{l0}^m pe_l^m(\xi)\sim\frac{i^{-l+m}}{2^m m!}\kappa^m(\xi^2-1)^{m/2}$$
$$\times\frac{2^{m+1}m!\,\gamma_{l0}^m i^{l-m}}{(\kappa\xi)^{m+1}}\sin(\kappa\xi-\tfrac{\pi}{2}l)\,.$$

Thence, we have the required result

$$N_{lm}a_{lm}pe_l^m(\xi)\sim\frac{2\sin(\kappa\xi-\frac{\pi}{2}l)}{\kappa\xi}\,.$$

References

1) Stier: Zeit. f. Physik **76** (1932) 439.
J. B. Fisk: Phys. Rev. **49** (1936) 167.
F. Mott and H. S. W. Massey: "The Theory of Atomic Collisions" (Oxford University Press, London, (1947), second edition.
2) M. Born: Z. Physik **37** (1926) 863.
3) M. Kotani: Proc. Phys.—Math. Soc. Japan, **15** (1933) 30.

JOURNAL OF THE PHYSICAL SOCIETY OF JAPAN Vol. 8, No. 2, MAR.—APR., 1953

Photoelectric Emission and Energy Structure of Cs_3Sb

By Hisao MIYAZAWA

Matsuda Research Laboratory, Tokyo Shibaura Electric Co.,
Kawasaki-shi Kanagawa-ken, Japan

(Received October 6, 1952)

Spectral distributions of the photoelectric yield and energy distributions of the photoelectrons were observed at room temperature, 195°K and 90°K for Cs_3Sb. The facts obtained are as follows: (1) The quantum efficiency Y rises rapidly as $h\nu$ increases above 2ev, and reaches the maximum at $h\nu \sim 3.8$ev, where the magnitude of Y exceeds 10^{-1}. Further, there appears the second maximum at $h\nu \sim 5$ev. (2) For $h\nu \gtrsim 3$ev Y increases with the decrease in temperature in accordance with the relation $(\partial Y/\partial T)/Y \fallingdotseq -10^{-3}$/deg. (3) On the contrary, in the low energy tails at $h\nu \sim 2$ev Y decreases with decreasing temperature, or the photoelectric work function φ shifts with temperature in the form $\partial\varphi/\partial T = -3 \sim 5 \times 10^{-4}$ev/deg. (4) At lower temperatures a minor hump in Y can be seen at $h\nu \sim 2.2$ev. (5) Energy distributions are comparatively temperature-insensitive, but for $h\nu \sim 5$ev, corresponding to the second maximum in Y, there is a growing preponderance of low velocity electrons, which is quite unlike those for smaller $h\nu$.

These results are discussed in terms of a possible energy structure for Cs_3Sb.

§ 1. Introduction

A highly photosensitive "alloy" composed of caesium and antimony was developed by Görlich[1] in an effort to find a more efficient semitransparent photocathode than that of silver-caesium-oxide-caesium well known at the time. Because of its excellent sensitivity in the visible region, especially for blue or daylight, the cathode has been widely utilized in photo-multipliers, television pick-up tubes and many other devices necessitating the conversion of photon energy of several electron volts into electrical one.

In contrast with these applications, very few of the investigations have been concerned with the reason, why the alloy shows such a striking photoelectric effect. A suggestion was proposed[2] that the cathode was not an alloy but an intermetallic compound Cs_3Sb, which showed the properties of a semiconductor. Zworykin and his collaborator have also pointed out in their book[3] that the term "alloy photocathode" is a misnomer and it must be regarded as an intrinsic semiconductor Cs_3Sb. There are, however, no attempts to set up a picture of the electronic energy band structure for Cs_3Sb. In spite of increasing knowledge of electronic processes both in pure ionic and in non-polar semiconductors it appears the work in the field of these intermetallic compounds which show semiconducting properties has been entirely unsatisfactory. At the moment, it may be rather complicated and presumably hazardous to arrive at the complete energy structure from the theoretical view point even though the crystal structure has been strictly determined, while some phenomenological experimental results may suggest a tentative band picture or at least be of help to find a clue to the intrinsic energy band structure.

In the work reported here, measurements of spectral and energy distributions of the photoelectric emission have been made on usually activated Cs_3Sb, as a part of the study obtaining detailed information concerning the electronic energy structure.

§ 2. Experimental Procedures

In order to obtain the correct spectral distribution, a fused quartz phototube like usual commercial type was prepared, since usual glass was opaque for $h\nu > 4$ev. Fig. 1 shows the arrangement of apparatus for the spectral distribution measurements. A high pressure Hg discharge lamp and a ribbon filament tungsten lamp were suitably used as light source L. The output beam from excit slit

S_2 of the monochromator is reflected by a concave spherical mirror M_4 and focused on a thermopile T which indicates the radiant energy, provided a plane mirror M_5 slides out. The light beam can also be focused into the phototube to be measured if M_5 slides in.

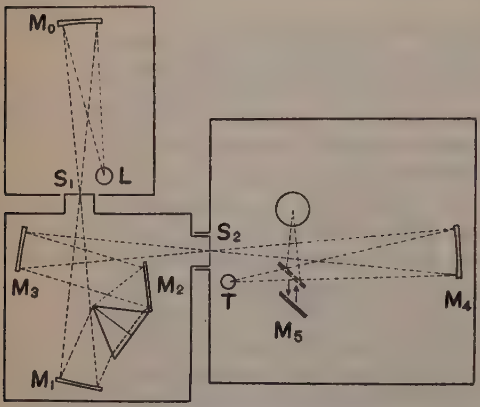

Fig. 1 Arrangement of apparatus.

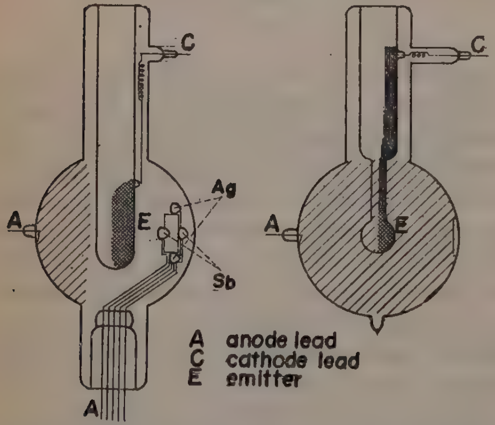

Fig. 2. Typical experimental tubes (a) for measuring temperature effect on spectral distribution of the photoelectric yield and (b) for measuring energy distribution of the photoelectrons. In the latter, Sb film for the emitter preparation has been previously deposited to remove disturbing electrode.

Both absolute sensitivity of T and spectral reflectivity of M_5 have been previously calibrated. This phototube, of which spectral distribution was carefully determined in this way, was used later as the radiant energy indicator instead of the thermopile in all subsequent measurements.

To observe temperature shifts of the quantum efficiency and energy distributions of the photoelectrons, several different types of diodes with central emitters and spherical collectors were prepared. In Fig. 2 two typical tubes are shown. In these cases some absorption losses are not so serious in the results that glass bulbs for germicidal lamp which can transmit more than 60 percent at $h\nu \sim 5$ev are used as spherical collector parts. The measuring arrangements were the same as before except substituting the standard phototube for the thermopile and the test tube for the standard tube respectively. Temperature of the emitter layers was changed by pouring liquid oxygen or dry ice with ethyl ether into Dewar vessel parts of the tubes. It was necessary to evaporate silver base under the emitter layers, otherwise at low temperatures the photocurrents saturate hardly because of poor conductivity of the emitters. Furthermore, in order to obtain reproducible results, it was important to keep strictly the fixed geometry for light incidence so as to illuminate always the definite area of the cathode.

§ 3. Spectral Distribution of the Photoelectric Yield

Spectral quantum efficiency obtained with the fused quartz phototube which serves as a standard in subsequent measurements is

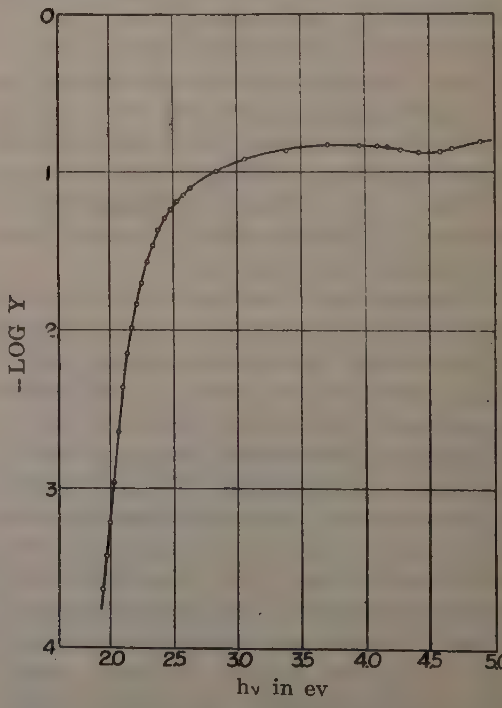

Fig. 3. Spectral distribution of the photoelectric yield Y (in electrons/quantum) for Cs_3Sb in the fused quartz tube.

shown in Fig. 3. The threshold of the Cs_3Sb cathode lies near 1.9ev, and the yield Y increases rapidly until reaching the first maximum at 3.8ev, where the magnitude of Y exceeds 10^{-1}. Since the reflection losses of incident photons by the bulb and the cathode surface are not corrected, true quantum efficiency may be somewhat larger. It may be unreasonable, therefore, to attribute such a large yield merely to the surface effect as in the case of most metals. There is a slight decrease in Y for 4.5ev and appears the second maximum at $h\nu \gtrsim 5$ev. This structure showing two maxima in the spectral distribution has been repeatedly noted by other observers[4] without successful explanation. Though it would be insufficient that the measurements could not be carried out beyond 5ev, an interpretation of this structure would be given in later sections in connection with energy distribution and optical absorption characteristics.

A typical example of temperature effects on Y is seen from Fig. 4, where three curves indicate respectively the sensitivity ratio of a test phototube at 290°K, 195°K and 90°K to the standard one at 290°K. It is seen for $h\nu \gtrsim 3$ev Y increases with the decrease in temperature in accordance with the relation

$$(\partial Y/\partial T)/Y \fallingdotseq -10^{-3}/\text{deg}. \qquad (1)$$

On the other hand, Y decreases in the low energy tails with decreasing temperature. It is then noted that an unexpected minor hump in Y, which is indicated by hatching area, appears without fail at lower temperatures. The photon energy corresponding to the peak of the hump was respectively 2.17ev (5700A) at 195°K and 2.21ev (5600A) at 90°K in all tubes prepared. In addition, cross points A, B, C in spectral sensitivity curves at three different temperatures were excellently reproducible in different tubes and fell in with 4860A, 5060A and 5180A respectively, though the forms and the locations of individual curves were slightly diverse. Rise in sensitivity at low energy tails of the test tube at 290°K to that of the standard one would be probably due to the silver base which might double the optical path of incident photons by reflection because of the decrease in the optical absorption constant, while decrease at higher photon energy should be attributed to the absorption by glass. Structures beyond 6000A were not common to all tubes, and they were not believed to represent intrinsic characteristics for Cs_3Sb. Reducing the data in Fig. 4 to the original spectral distribution Fig. 5 has been obtained. These results have then proved that the low energy tails shift uniformly with temperature

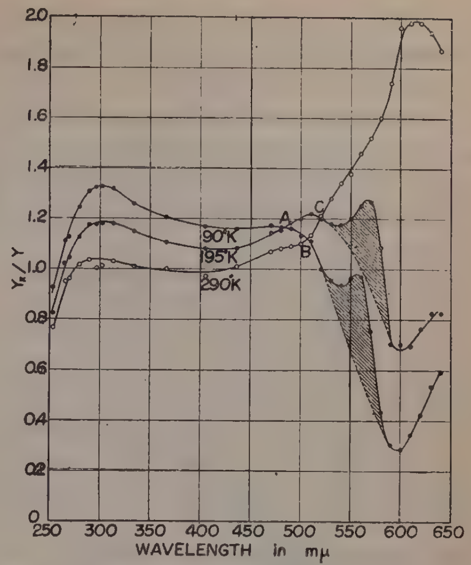

Fig. 4. Spectral sensitivity ratio of a test phototube at three different temperatures to the standard one at 290°K.

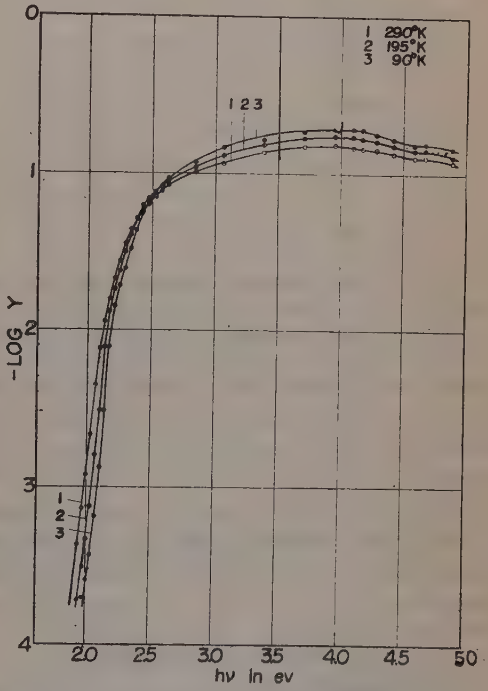

Fig. 5. Dependence of spectral distribution of photoelectric yield on temperature.

as if there is a relation between the photoelectric work function φ and the temperature T which may be expressed by

$$\partial\varphi/\partial T \doteqdot -3\sim5\times10^{-4}\text{ev/deg.} \qquad (2)$$

Enlarging the abscissa in order to make the relation clear, only the low energy tails are given in Fig. 6, where the minor humps at lower temperatures are again indicated by hatching. If the humps were planed away, the relation (2) might be satisfied more distinctly.

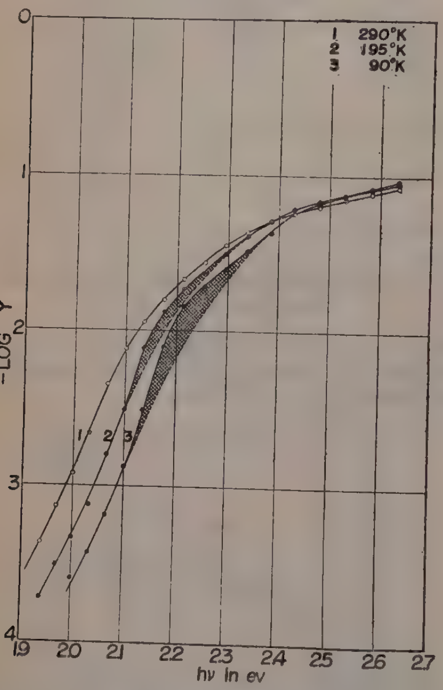

Fig. 6. Temperature displacement of low energy tails of the photoelectric yield. Minor humps at lower temperatures are cross-hatched.

A very similar experimental work has been reported by Schaetti and Baumgartner,⁽⁵⁾ whose data have failed in reaching these relations.

§ 4. Energy Distribution of the Photoelectrons

According to the experimental results in the preceding section, quantum efficiency in the ultraviolet regions shows the temperature effect given by (1), i. e. $(\partial Y/\partial T)/Y \doteqdot -10^{-3}$ /deg. The reason may be ascribed to the following two points: (i) Excited electrons absorbing photon energy may lose their energy by collisions with thermally vibrating lattice before their escape into vacuum. Decrease in temperature will therefore cause the decrease in energy loss of photoelectrons, resulting in the increase in Y. (ii) Probability of photon absorption may be a function of the temperature, where the optical absorption constant may change just like the photoelectric yield.

The first aim of energy distribution measurements was to check which was the case. If the former predominates, the energy distribution of photoelectrons should be fairly sensitive to the temperature. However, the results given in Fig. 7 are inconsistent with this hypothesis. There are no noticeable distinctions between two current-voltage characteristics observed at 290°K and 90°K for $h\nu$=3.387ev, though the emission at 90°K is about twenty percent larger than that at 290°K. Hence the temperature effect in Y in the ultraviolet regions should be accounted for chiefly by the latter reason. Burton has reported⁽⁶⁾ that the spectral distribution parallels the optical absorption constant. It may be then reasonable to assume that, when temperature is lowered, both the photoelectric yield and the absorption constant increase proportionally in these regions. It is desirable to confirm these relations. To our regret, the tubes under test did not permit measurements for confirmation of these observations.

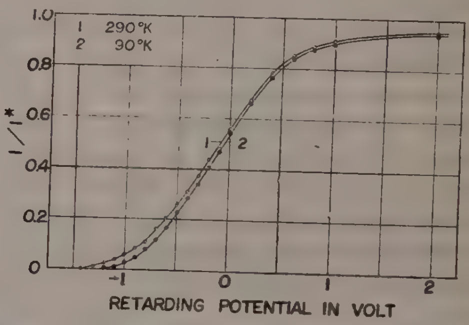

Fig. 7. Current-voltage characteristics at 290°K and 90°K for $h\nu$=3.387ev. The ordinate represented relative current I/I^*, where I^* is saturation photocurrent at V=9.0 volts. $(I^*)_{90°K}/(I^*)_{290°K}$=1.22 in this case. Discrepancy of cut off potential for two curves is due to the displacement of φ as given by (2).

As mentioned above, there is a structure showing two maxima in the spectral distribution and further, there is a parallelism between the spectral distribution and the optical absorption. Since the large quantum yield suggests that the volume photoelectric effect is the case, photoelectrons must be for the most part ascribed to transitions from the full band to the conduction band. As the caesium has one 6*s* valence electron and the antimony is lacking three electrons in 5p shell, the full band in Cs_3Sb may probably be regarded as 5p band and the conduction band as 6s band. Then the structure in spectral distribution and in optical absorption can be expected from the p-band nature usually separated in different ways according to the component of wave number vector **k**, as will be discussed later in more detail.

The second aim of energy distribution measurements was to investigate the phenomena relating to this structure. In Fig. 8, representative curves showing current-voltage characteristics by means of retarding potential techniques are shown. There are no salient phenomena in the energy distributions extending from the threshold to $h\nu \sim 4$ev, but there is a growing preponderance of low energy electrons for $h\nu \gtrsim 4.5$ev as represented by an anomalous curve marked $h\nu = 4.9$ev. It should be remembered now that the former range of photon energy corresponds to the first maximum both in the spectral distribution of the photoelectric yield and in the optical absorption constant, while the latter corresponds to the second maximum. Hence the majority of photoelectrons emitted for $h\nu \sim 5$ev may be due to the excitation from deep energy levels in the occupied p band to those in the vacant s band of the same wave number.

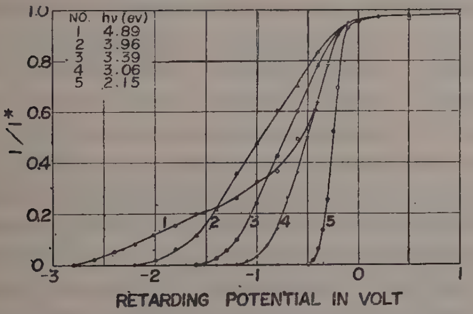

Fig. 8. Current-voltage characteristics at room temperature for several wavelengths. Energy distribution functions should be differentiated from these curves.

§ 5. Remarks on Energy Band Structure

The complete interpretation of these observation in terms of energy level picture for Cs_3Sb is of course too early, but a number of inferences may be drawn with other auxiliary data.

The abrupt rise in the photoelectric yield when $h\nu$ reaches about 1.9ev may be attributed without failure to the emission from an occupied band of electronic energy states with an upper edge 1.9ev below the vacuum level. Temperature effect near the low energy tails of photoelectric emission suggests that this upper edge of the full band deepens with decrease in temperature at the rate about $3 \sim 5 \times 10^{-4}$ev per degree. This rate of the change of energy band edge is in reasonably good agreement with that observed in other materials. In recent years, theoretical treatments on the temperature displacement of energy gap have been given independently by several authors⁷⁾ from a different angle. However, there are too many unknown factors for Cs_3Sb to be compared quantitatively with these theories. The interpretations of a minor hump near the threshold have also been left in abeyance, though its peak has shown quite similar temperature displacement.

As mentioned in the preceding section, this occupied band has been tentatively assumed to be 5p band of antimony. One important feature of the p band is the fact that the $\varepsilon(\mathbf{k})$ curves are able to split, when suitable components of the wave number vector **k** are chosen, in such a way that one curve is concave upward slightly, whereas another curve is concave downward. On the other hand, the upper conduction band has been regarded as 6s band of caesium. The $\varepsilon(\mathbf{k})$ curve for the s band is uniquely concave upward. These are indicated schematically in Fig. 9. The photoelectric emission and the optical absorption may be interpreted with this diagram. Electrons in the occupied p band can be excited vertically to the conductive s band by radiation of frequency ν. As frequency ν increases, the surface photoelectric effect starting at 1.9ev may be soon succeeded by the large volume effect which corresponds to the transition from the state A_1 to the state B_1. Meanwhile the optical absorption ought to begin when $h\nu$ is equal to the energy difference between A_0 and B_0, for which the observation gives 1.6ev. These transitions from P_1 to S should pass through a maximum value and cease by and by, with increasing

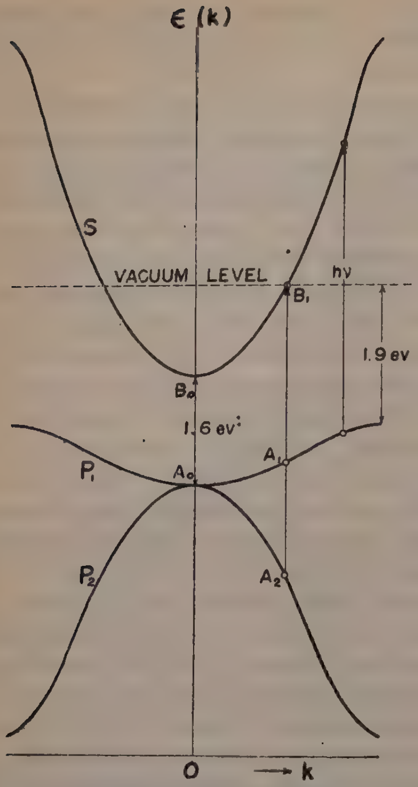

Fig. 9. Schematic diagram showing possible ε(k) curves for Cs_3Sb. The upper is assumed to be empty 6s band and the lower, occupied 5p band.

$h\nu$, because the state density near the top of the occupied band converges to zero. It is reasonable to suppose that the first maximum observed in the spectral quantum yield and in the optical absorption constant is principally due to the electron transitions from P_1 group of the full band to the conduction band S.

Let us consider the case in which $h\nu$ overpasses a critical value $h\nu_0$, corresponding to the energy difference between the states A_2 and B_1. Then P_2 group of the full band can take part in the photoelectric emission, superposing upon the high energy tails of the transitions from P_1 to S. For sufficiently large $h\nu$ the transitions from P_2 to S should overwhelm those from P_1 to S. This may give rise to the structure of the second maximum in spectral distribution of the photoelectric yield and also in optical absorption, just like that in the experimental results. In addition, it is evident that, for an optional frequency ν of radiation, the kinetic energy of photoelectrons owing to the transition from P_2 to S, if possible, is always small compared with that from P_1 to S or from top of the full band. The experimental results that there appears the preponderance of slow photoelectrons for $\nu \gtrsim \nu_0$ are quite consistent with the above view. The data would indicate that $h\nu_0$ ought to be 4.5ev in the present case. Dickey has found[8] that there are interesting anomalies in the energy distribution of photoelectrons from Na and K, which have apparently a strong resemblance to the results described here. But it should be noted that there are fundamental differences between them.

As for the location of lower edge of the conduction band, it requires some auxiliary data such as electrical conductivity. Though the electronic conduction in Cs_3Sb is accompanied by the electrolytic conduction of caesium ions,[9] careful observations have shown that the activation energy $\Delta E/2$ of the electronic conductivity is 0.25～0.30ev,[10] and the order of specific resistivity is about 10 ohm cm. Simple calculations based on these data have proved that the intrinsic conductivity is preferable to the impurity one. There is no evidence of appreciable donor levels from the thermionic emission data.[11] In addition, there appears also no absorption band in the optical absorption data[6] attributed to impurity centers. Recently, however, Sakata has found[12] that the thermo-electromotive force for Cs_3Sb indicates p type and the acceptor concentration must be always larger than 10^{20} cm^{-3}. It is difficult to understand that such a large concentration of acceptor levels does not be accompanied by the corresponding optical absorption, and that what is the origin of the acceptor level. At

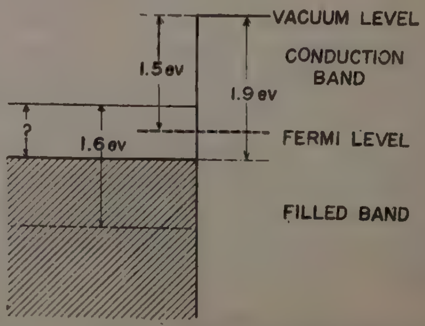

Fig. 10. Tentative energy band diagram for Cs_3Sb.

any rate, it would be premature for the moment to conclude that $\varDelta E$ (0.5~0.6ev) obtained from the electrical conductivity data is the intrinsic energy gap. Unfortunately, measurements at higher temperatures, which are favorable to know the properties of intrinsic semiconductor regardless of impurities, can not be carried out because of the instability of Cs_3Sb.

Fig. 10 represents a tentative energy band picture for Cs_3Sb so far confirmed.

§ 6. Conclusion

In this paper, several photoelectric properties of Cs_3Sb, one of the intermetallic compounds hitherto paid little attention in spite of technical importance, have been described. The discussions given here are only qualitative and alternative aspects, for example, complicated overlapping pictures of two or more energy bands, may be possible. Further satisfactory interpretations of these properties would require quantitative knowledges, as yet unavailable, of crystal structure, band calculation and transition probability.

It should be emphasized that there might be some other substances, like Cs_3Sb under the present investigation, representing borderline cases between metallic alloys and ionic crystals. Such a pursuit has been attempted by Schaetti and Baumgartner,$^{13)}$ who have aimed to obtain highly sensitive photocathodes for visible light.

Study of photoconductivity and some allied phenomena for Cs_3Sb shall be reported in another paper, in which a different view shall be expressed against other authers.$^{14)}$

References

1) P. Görlich: Zeits. f. Phys., **101** (1936) 335.

2) S. Chikazumi *et al.*: Oral presentation to the meeting of Phys. Soc. Japan on October 1944. See also H. Miyazawa, K. Noga, S. Chikazumi and A. Kobayashi: J. Phys. Soc. Japan, **7** (1952) 647.

A. Sommer: Proc. Phys. Soc. (London), **55** (1943) 145, C. A., **37** (1943) 3723. Though Sommer had preceded us to reach the similar conclusion, it had been impossible for us to get the information by the World War II.

That the substance is non-metallic has been pointed out by S. S. Prilezhaev: J. Tech. Phys. U. S. S. R., **9** (1939) 1439.

3) V. K. Zworykin and E. G. Ramberg; "*Photoelectricity*", John Wiley & Sons, New York, 1949, p. 58.

4) V. K. Zworykin and E. G. Ramberg: *loc. cit.*

L. Dunkelman and C. Lock: J. O. S. A., **41** (1951) 802.

V. Schwetzoff and S. Robin: C. R. Acad. Sci. Paris, **233** (1951) 475.

5) N. Schaetti and W. Baumgartner: Helv. Phys. Acta, **24** (1951) 614.

6) J. A. Burton: Phys. Rev., **72** (1947) 531. See also V. K. Zworykin and E. G. Ramberg; *loc. cit.*, p. 59.

7) A. Radkowsky: Phys. Rev., **73** (1948) 749.

J. Bardeen and W. Shockley: Phys. Rev., **80** (1950) 72.

T. Muto and S. Oyama: Prog. Theor. Phys., **5** (1950) 833.

H. Y. Fan: Phys. Rev., **82** (1951) 900.

8) J. Dickey: Phys. Rev., **81** (1951) 612.

9) H. Miyazawa and S. Fukuhara: J. Phys. Soc. Japan, **7** (1952) 645.

10) See references (5) and (12). H. Miyazawa: unpublished.

11) T. Sakata: private communication. Our unpublished data have shown ~1.5ev as the thermionic work function and unusually high Richardson constant.

12) T. Sakata: J. Phys. Soc. Japan, **8** (1953)125.

13) N. Schaetti and W. Baumgartner: Helv. Phys. Acta, **23** (1950) 524, **24** (1951) 609.

14) S. Pakswer and W. O. Reed: J. App. Phys., **22** (1951) 987.

N. S. Khlebnikov and A. E. Melamid: C. A., **43** (1949) 3705 d.

JOURNAL OF THE PHYSICAL SOCIETY OF JAPAN Vol. 8, No. 2, MAR.—APR., 1953

The Faraday Rotation of Waves in a Circular Waveguide

By Hideya GAMO

Department of Physics, University of Tokyo

(Read May 8, 1952, Received September 30, 1952)

Exact solutions of the magnetic rotation of the guided waves in a circular waveguide of infinite length are described, whereby the rotational terms in both magnetization and electric polarization are considered. The normally degenerate modes of the circular guide are separated by the external magnetic field into two partial waves—i.e., the right-handed and left-handed circularly polarized waves, which are neither transverse-electric nor transverse-magnetic but are reduced to the TE- or TM-mode in the limit of vanishing magnetic field. The propagation constant of each partial wave is determined by a transcendental equation derived from the boundary conditions. Curves giving the frequency dependency of the propagation constants for both partial waves are shown for the quasi-TE_{11}-modes, and quasi-TM_{11}-modes for a special value of the coefficients of rotational terms. The dependence of the cutoff frequencies on these coefficients is also obtained. For TM-modes, the cutoff frequencies of both partial waves are found to coincide.

§ 1. Introduction

Lord Rayleigh[1] drew attention to the peculiarity of the magnetic rotation of the plane of polarization arising from the circumstance that the rotation is in the same absolute direction whichever way the light may be travelling, and pointed out the possibility of the one-way transmission of light by making use of the Faraday rotation and of two Nicol prisms at an angle of 45° to each other. This was the first step of the recent development of various one-way systems — for instance, the one-way system composed of two electromechanical transducers treated by E. M. McMillan[2], which may be extended so as to realize the achromatic one-way transmission that is unilateral for all frequencies transmitted.[3]

The microwave analogue of Rayleigh's one-way system, which may find important applications in microwave techniques, can be realized, if we have an element that efficiently rotates the plane of polarization by a static magnetic field. Such an element which violates the reciprocity theorem may be termed a gyrator after Tellegen[4]. Recently, C. L. Hogan[5] published a paper which contains experimental results of the microwave gyrator using ferrites as well as considerations about two types of microwave one-way systems. The author came to consider independently almost the same one-way systems* after McMillan's[6] and Casimir's[7] suggestions. In this connection, we have obtained an exact solution of the equation for the Faraday rotation of waves in an infinite circular waveguide.**

The Faraday effect has been shown to arise from the presence of cross terms in the equations connecting the extensive field quantities $\boldsymbol{B}$ and $\boldsymbol{D}$ to the intensive field quantities $\boldsymbol{H}$ and $\boldsymbol{E}$. Assuming the external magnetic field to be in the z direction, the equations will be written as,

$$\left.\begin{aligned} D_x &= \varepsilon E_x - i\alpha E_y \\ D_y &= \varepsilon E_y + i\alpha E_x \\ D_z &= \varepsilon_z E_z\,, \end{aligned}\right\} \quad (1)$$

$$\left.\begin{aligned} B_x &= \mu H_x - i\kappa H_y \\ B_y &= \mu H_y + i\kappa H_x \\ B_z &= \mu_z H_z\,, \end{aligned}\right\} \quad (2)$$

---

* Incidentally, we remark an interesting property of the one-way system: *the transmission direction of the one-way system can be inverted by changing the sign of the external magnetic field.* It is explained by the fact that due to the general property of the antireciprocity the sign of the gyrator constant, or the transfer constant of the antireciprocal part of the one-way system, is changed by reversing the sense of the external magnetic field.

** After preparation of this paper, the author became aware of a note by H. Suhl and L. R. Walker treating the same subject: Phys. Rev. **86**, (No. 1, 1952) 122.

where the terms in α and κ are characteristic of these field equations. The parameters α and κ depend linearly on the applied magnetic field, and change their signs with the reversal of the latter. The parameter α is responsible for the usual optical Faraday effect which accompanies Zeeman splitting of the absorption lines, while the parameter κ is caused by the rotatory dispersion which accompanies ferromagnetic and paramagnetic absorptions.[8] Although no substance is known to posses both nonvanishing parameters α and κ, we shall consider both of them simultaneously for the sake of generality.

§ 2. The Mathematical Formulation of the Problem

Taking new coordinates

$$\left.\begin{aligned}\xi&=(x+iy)/\sqrt{2}=r\exp(i\theta)/\sqrt{2}\\ \eta&=(x-iy)/\sqrt{2}=r\exp(-i\theta)/\sqrt{2}\,,\end{aligned}\right\}\quad(3)$$

and corresponding field components

$$\left.\begin{aligned}B_\xi&=(B_x+iB_y)/\sqrt{2}\\ B_\eta&=(B_x-iB_y)/\sqrt{2}\,,\ \text{etc.},\end{aligned}\right\}\quad(4)$$

the relations connecting $\boldsymbol{B}$ and $\boldsymbol{D}$ to $\boldsymbol{H}$ and $\boldsymbol{E}$ may be expressed as

$$\left.\begin{aligned}&D_\xi=\varepsilon_\xi E_\xi \quad \text{where} && \varepsilon_\xi=\varepsilon-\alpha\\ &D_\eta=\varepsilon_\eta E_\eta && \varepsilon_\eta=\varepsilon+\alpha\,,\\ &D_z=\varepsilon_z E_z\,,\end{aligned}\right\}\quad(5)$$

$$\left.\begin{aligned}&B_\xi=\mu_\xi H_\xi && \mu_\xi=\mu-\kappa\\ &B_\eta=\mu_\eta H_\eta && \mu_\eta=\mu+\kappa\,.\\ &B_z=\mu_z H_z\,,\end{aligned}\right\}\quad(6)$$

The coefficients of these relations must satisfy the condition due to the passivity of the system or the conservation of energy, that the imaginary parts of ε_ξ, ε_η, ε_z, μ_ξ, μ_η, μ_z be non-negative.

Maxwell's equations, in terms of these quantities, read

$$\left.\begin{aligned}\frac{\partial E_z}{\partial\eta}-\frac{\partial E_\xi}{\partial z}&=\frac{\omega}{c}\mu_\xi H_\xi\\ \frac{\partial E_\eta}{\partial z}-\frac{\partial E_z}{\partial\xi}&=\frac{\omega}{c}\mu_\eta H_\eta\\ \frac{\partial E_\xi}{\partial\xi}-\frac{\partial E_\eta}{\partial\eta}&=\frac{\omega}{c}\mu_z H_z\\ \frac{\partial H_z}{\partial\eta}-\frac{\partial H_\xi}{\partial z}&=-\frac{\omega}{c}\varepsilon_\xi E_\xi\\ \frac{\partial H_\eta}{\partial z}-\frac{\partial H_z}{\partial\xi}&=-\frac{\omega}{c}\varepsilon_\eta E_\eta\\ \frac{\partial H_\xi}{\partial\xi}-\frac{\partial H_\eta}{\partial\eta}&=-\frac{\omega}{c}\varepsilon_z E_z\,,\end{aligned}\right\}\quad(7)$$

with boundary conditions that the tangential components of the electric field vanish at the surface of the circular waveguide $r=r_0$:

$$(E_z)_{r=r_0}=0 \qquad (8)$$

$$(E_\theta)_{r=r_0}=(E_\xi\exp(-i\theta)-E_\eta\exp(i\theta))/\sqrt{2}i=0, \qquad (9)$$

from which the vanishing of the normal components of the magnetic induction

$$(B_r)_{r=r_0}=(B_\xi\exp(-i\theta)+B_\eta\exp(i\theta))/\sqrt{2}=0, \qquad (10)$$

is automatically guaranteed.

§ 3. The Solution

Eliminating ξ, η-components from (7), the equations for the z-components of the fields are obtained:

$$\left.\begin{aligned}&\frac{\partial^2 E_z}{\partial z^2}+\frac{\omega}{c}\frac{\mu_z}{\varepsilon_z}\frac{\varepsilon_\xi\mu_\xi-\varepsilon_\eta\mu_\eta}{\mu_\xi+\mu_\eta}\frac{\partial H_z}{\partial z}+\frac{\omega^2}{c^2}\frac{\varepsilon_\xi+\varepsilon_\eta}{\mu_\xi+\mu_\eta}\mu_\xi\mu_\eta E_z+2\frac{\varepsilon_\xi+\varepsilon_\eta}{\varepsilon_z}\frac{\partial^2 E_z}{\partial\xi\partial\eta}=0\\ &\frac{\partial^2 H_z}{\partial z^2}-\frac{\omega}{c}\frac{\varepsilon_z}{\mu_z}\frac{\varepsilon_\xi\mu_\xi-\varepsilon_\eta\mu_\eta}{\mu_\xi+\mu_\eta}\frac{\partial E_z}{\partial z}+\frac{\omega^2}{c^2}\frac{\mu_\xi+\mu_\eta}{\varepsilon_\xi+\varepsilon_\eta}\varepsilon_\xi\varepsilon_\eta H_z+2\frac{\mu_\xi+\mu_\eta}{\mu_z}\frac{\partial^2 H_z}{\partial\xi\partial\eta}=0\,,\end{aligned}\right\}\quad(11)$$

A few symbols are introduced for convenience, namely:

$$\left.\begin{aligned}\mu&=\frac{\mu_\xi+\mu_\eta}{2} & f&=\frac{\mu_\eta-\mu_\xi}{\mu_\xi+\mu_\eta}=\frac{\kappa}{\mu}\\ \varepsilon&=\frac{\varepsilon_\xi+\varepsilon_\eta}{2} & g&=\frac{\varepsilon_\eta-\varepsilon_\xi}{\varepsilon_\xi+\varepsilon_\eta}=\frac{\alpha}{\varepsilon}\,,\end{aligned}\right\}\quad(12)$$

$$\nu=\omega\sqrt{\varepsilon\mu}/c\,,\qquad \zeta=\sqrt{\mu/\varepsilon}\,. \qquad (13)$$

Since it is convenient to deal with dimensionless quantities νz, $\nu\xi$, $\nu\eta$, we shall take them as new coordinates. The quantities ζH_ξ, ζH_η, ζH_z which have the same dimension as E_ξ, E_η, E_z are also preferable. Hereafter we shall write ξ, η, z in place of $\nu\xi$, $\nu\eta$, νz, and H_ξ, H_η, H_z in place of ζH_ξ, ζH_η, ζH_z. The final equations are

$$\left.\begin{aligned}&\frac{\partial^2 E_z}{\partial z^2}-(f+g)\frac{q}{p}\frac{\partial H_z}{\partial z}+(1-f^2)E_z\\ &\qquad\qquad+\frac{2}{P}\frac{\partial^2 E_z}{\partial\xi\partial\eta}=0\\ &\frac{\partial^2 H_z}{\partial z^2}+(f+g)\frac{p}{q}\frac{\partial E_z}{\partial z}+(1-g^2)H_z\\ &\qquad\qquad+\frac{2}{q}\frac{\partial^2 H_z}{\partial\xi\partial\eta}=0\,,\end{aligned}\right\}\quad(14)$$

where

$$p=\varepsilon_z/\varepsilon\ ,\qquad q=\mu_z/\mu\ . \tag{15}$$

Assuming $E_z=\exp(-wz)T(\xi,\eta)$ and $H_z=KE_z$, and solving with respect to K, we obtain

$$K_1=\frac{1}{2(f+g)w}(b-\sqrt{b^2-4(f+g)^2w^2})\ , \tag{16}$$

$$K_2=\frac{1}{2(f+g)w}(b+\sqrt{b^2-4(f+g)^2w^2})\ , \tag{17}$$

where

$$b=(1-s)w^2+1-g^2-s(1-f^2) \text{ and } s=p/q\ . \tag{18}$$

Putting

$$\left.\begin{aligned}\frac{\partial}{\partial\xi}&=\frac{1}{\sqrt{2}}\exp(-i\theta)\left(\frac{\partial}{\partial r}+\frac{1}{ir}\frac{\partial}{\partial\theta}\right)\\ \frac{\partial}{\partial\eta}&=\frac{1}{\sqrt{2}}\exp(i\theta)\left(\frac{\partial}{\partial r}-\frac{1}{ir}\frac{\partial}{\partial\theta}\right),\end{aligned}\right\} \tag{19}$$

the equations which determine $T(r,\theta)$ become

$$\left.\begin{aligned}&\frac{\partial^2T^{(i)}}{\partial r^2}+\frac{1}{r}\frac{\partial T^{(i)}}{\partial r}+\frac{1}{r^2}\frac{\partial^2T^{(i)}}{\partial\theta^2}+\lambda_i^2T^{(i)}=0\\ &\text{where}\\ &\lambda_i^2=p(w^2+1-f^2)-q(f+g)K_iw\ .\ (i=1,2).\end{aligned}\right\} \tag{20}$$

From above equations, we have

$$E_z^{(i)}=\exp(-wz\mp in\theta)J_n(\lambda_ir)\ ,\ i=1,2. \tag{21}$$

The double signs correspond respectively to the circularly polarized waves of left-handed and right-handed rotations.*

The ξ, η-components of fields are obtained using (5) and (6) as

$$\left.\begin{aligned}E_\xi^{(i)}&=A_\xi^{(i)}\frac{\partial E_z^{(i)}}{\partial\eta}\\ E_\eta^{(i)}&=A_\eta^{(i)}\frac{\partial E_z^{(i)}}{\partial\xi}\\ H_\xi^{(i)}&=C_\xi^{(i)}\frac{\partial E_z^{(i)}}{\partial\eta}\\ H_\eta^{(i)}&=C_\eta^{(i)}\frac{\partial E_z^{(i)}}{\partial\xi}\ ,\end{aligned}\right\} \tag{22}$$

where

$$\left.\begin{aligned}A_\xi^{(i)}&=\{-w-(1-f)K_i\}/\{w^2+(1-f)(1-g)\}\\ A_\eta^{(i)}&=\{-w+(1+f)K_i\}/\{w^2+(1+f)(1+g)\}\\ C_\xi^{(i)}&=\{-wK_i+(1-g)\}/\{w^2+(1-f)(1-g)\}\\ C_\eta^{(i)}&=\{-wK_i-(1-g)\}/\{w^2+(1+f)(1+g)\}.\end{aligned}\right\} \tag{23}$$

Components of fields in polar-coordinates r, which are obtained by using (19) and

$$\left.\begin{aligned}\sqrt{2}E_r&=E_\xi\exp(-i\theta)+E_\eta\exp(i\theta)\\ \sqrt{2}iE_\theta&=E_\xi\exp(-i\theta)-E_\eta\exp(i\theta),\end{aligned}\right\} \tag{24}$$

are

$$\left.\begin{aligned}2E_r^{(i)}&=\{(A_\xi^{(i)}+A_\eta^{(i)})\lambda_iJ_n'(\lambda_ir)\pm n(A_\xi^{(i)}-A_\eta^{(i)})J_n(\lambda_ir)/r\}\exp(-wz\mp in\theta)\\ 2iE_\theta^{(i)}&=\{(A_\xi^{(i)}-A_\eta^{(i)})\lambda_iJ_n'(\lambda_ir)\pm n(A_\xi^{(i)}+A_\eta^{(i)})J_n(\lambda_ir)/r\}\exp(-wz\mp in\theta),\end{aligned}\right\} \tag{25}$$

$$\left.\begin{aligned}2H_r^{(i)}&=\{(C_\xi^{(i)}+C_\eta^{(i)}\lambda_iJ_n'(\lambda_ir)\pm n(C_\xi^{(i)}-C_\eta^{(i)})J_n(\lambda_ir)/r\}\exp(-wz\mp in\theta)\\ 2iH_\theta^{(i)}&=\{(C_\xi^{(i)}-C_\eta^{(i)})\lambda_iJ_n'(\lambda_ir)\pm n(C_\xi^{(i)}+C_\eta^{(i)})J_n(\lambda_ir)/r\}\exp(-wz\mp in\theta).\end{aligned}\right\} \tag{26}$$

The r-, θ-components of the magnetic induction may be derived from

$$B_r=\mu(H_r-ifH_\theta),\quad B_\theta=\mu(H_\theta+ifH_r)\ . \tag{27}$$

Now the boundary conditions (8) and (9) may be satisfied by a superposition of two solutions corresponding to two values of λ_i, namely,

$$E_z=E_z^{(1)}+uE_z^{(2)}=0\ , \tag{28}$$

$$E_\theta=E_\theta^{(1)}+uE_\theta^{(2)}=0\ . \tag{28$'$}$$

Putting (25) in (28) and (28′), we obtain respectively

$$J_n(\lambda_1a)+uJ_n(\lambda_2a)=0, \tag{29}$$

$$\begin{aligned}&(A_\xi^{(1)}-A_\eta^{(1)})\lambda_1J_n'(\lambda_1a)\pm n(A_\xi^{(1)}+A_\eta^{(1)})J_n(\lambda_1a)/a\\ &\qquad+u\{(A_\xi^{(2)}-A_\eta^{(2)})\lambda_2J_n'(\lambda_2a)\pm n(A_\xi^{(2)}+A_\eta^{(2)})J_n(\lambda_2a)/a\}=0.\end{aligned} \tag{29$'$}$$

Thus we obtain the equation for determining the propagation constants for both directions of rotation:

$$A_1\frac{\lambda_1aJ_n'(\lambda_1a)}{J_n(\lambda_1a)}-A_2\frac{\lambda_2aJ_n'(\lambda_2a)}{J_n(\lambda_2a)}\pm nA_3=0, \tag{30}$$

where

$$\left.\begin{aligned}A_1&=2(f+g)^2w^2+(w^2+1-f^2)(b-\sqrt{b^2-4(f+g)^2w^2})\\ A_2&=2(f+g)^2w^2+(w^2+1-f^2)(b+\sqrt{b^2-4(f+g)^2w^2})\\ A_3&=2(fw^2+f^2g-g)\sqrt{b^2-4(f+g)^2w^2}\ ,\end{aligned}\right\} \tag{31}$$

and

---

* These words are used according to the usual convention in optics, meaning the rotation as viewed by the observer.

$$\left.\begin{aligned} \lambda_1{}^2 &= p(w^2+1-f^2)+(q/2) \\ &\qquad \times (b-\sqrt{b^2-4(f+g)^2w^2}) \\ \lambda_2{}^2 &= p(w^2+1-f^2)+(q/2) \\ &\qquad \times (b+\sqrt{b^2-4(f+g)^2w^2}) \\ b &= (1-s)w^2+1-g^2-s(1-f^2)\,, \\ s &= p/q=(\varepsilon_z/\varepsilon)/(\mu_z/\mu), \quad a=r_0\omega\sqrt{\varepsilon\mu}/c\,, \end{aligned}\right\} \tag{32}$$

while the double signs correspond to the circularly polarized waves of left- and right-handed rotations.

The general solution which is the superposition of the solutions corresponding to both directions of rotations may be written as follows :

$$\left.\begin{aligned} E_z &= \textstyle\sum_n\{\alpha_n Z_n{}^-(r,a)\exp(-w^-z+iu\theta)+\beta_n Z_n{}^+(r,a)\exp(-w^+z-in\theta)\} \\ E_r &= (1/2r)\textstyle\sum_n\{\alpha_n R_n{}^-(r,a)\exp(-w^-z+in\theta)+\beta_n R_n{}^+(r,a)\exp(-w^+z-in\theta)\} \\ E_\theta &= (1/2i\theta)\textstyle\sum\{\alpha_n \Theta_n{}^-(r,a)\exp(-w^-z+in\theta)+\beta_n \Theta_n{}^+(r,a)\exp(-w^+Z-in\theta)\}, \end{aligned}\right\} \tag{33}$$

$$\left.\begin{aligned} Z_n{}^+(r,a) &= J_n(\lambda_i{}^+r)/J_n(\lambda_i{}^+a)-J_n(\lambda_i{}^+r)/J_n(\lambda_i{}^+a) \\ R_n{}^+(r,a) &= (A_\xi{}^{(1)}+A_\eta{}^{(1)})\lambda_1{}^+r\,J_n{}'(\lambda_1{}^+r)/J_n(\lambda_1{}^+a)-(A_\xi{}^{(2)}+A_\eta{}^{(2)})\lambda_2{}^+r\,J_n{}'(\lambda_2{}^+r)/J_n(\lambda_2{}^+a) \\ &\quad +n\{(A_\xi{}^{(1)}-A_\eta{}^{(1)})J_n(\lambda_1{}^+r)/J_n(\lambda_1{}^+a)-(A_\xi{}^{(2)}-A_\eta{}^{(2)})\lambda_2{}^+r\,J_n(\lambda_2{}^+r)/J_n(\lambda_2{}^+a)\} \\ \Theta_n{}^+(r,a) &= (A_\xi{}^{(1)}-A_\eta{}^{(1)})\lambda_1{}^+r\,J_n{}'(\lambda_1{}^+r)/J_n(\lambda_1{}^+a)-(A_\xi{}^{(2)}-A_\eta{}^{(2)})\lambda_2{}^+r\,J_n{}'(\lambda_2{}^+r)/J_n(\lambda_2{}^+a) \\ &\quad +n\{(A_\xi{}^{(1)}+A_\eta{}^{(1)})J_n(\lambda_1{}^+r)/J_n(\lambda_1{}^+a)-(A_\xi{}^{(2)}+A_\eta{}^{(2)})\lambda_2{}^+r\,J_n(\lambda_2{}^+r)/J_n(\lambda_2{}^+a)\}\,, \end{aligned}\right\} \tag{34}$$

where the symbols + and − indicate the left-handed and right-handed rotations.

§ 4. Cutoff Frequencies of Quasi-TE- and Quasi-TM-Modes

Using the equations (30)—(32), we shall study how the cutoff frequencies vary by changing the intensity of the external magnetic field. Putting the propagation constant equal to zero in the equation (30), we obtain the equation which determines the cutoff frequencies

$$\sqrt{q(1-g^2)}a\,J_n{}'(\sqrt{q(1-g^2)}a) \mp ng\,J_n(\sqrt{q(1-g^2)}a)=0\,, \tag{35}$$

$$J_n(\sqrt{p(1-f^2)}a)=0\,, \tag{36}$$

where $p=\varepsilon_z/\varepsilon$, $q=\mu_z/\mu$, $a=r_0\omega\sqrt{\varepsilon\mu}/c$, and r_0 is the radius of the wave-guide, and the double signs of (35) correspond to the waves of both rotations.

In the limiting case that f, $g=0$, the first equation reduces to $J_n{}'(\sqrt{q}\,a)=0$, that is, the equation which determines the cutoff frequencies of the transverse-electric modes, and the other reduces to the equation $J_n(\sqrt{p}\,a)=0$, that is, the equation related to the cutoff

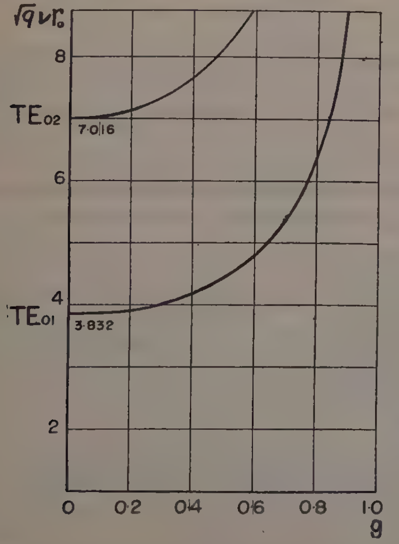

Fig. 1. The cutoff frequencies for quasi-TE$_{0l}$-modes against the parameter $g=\alpha/\varepsilon$. ($\nu=\omega\sqrt{\varepsilon\mu}/c$, r_0: radius of the guide).

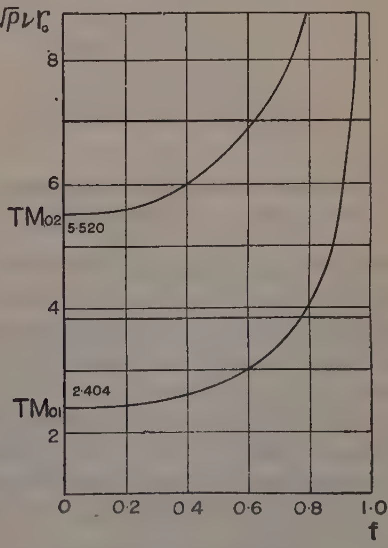

Fig. 2. The cutoff frequencies for quasi-TM$_{0l}$-modes against the parameter $f=\kappa/\mu$. ($\nu=\omega\sqrt{\varepsilon\mu}/c$, r_0: radius of the guide)

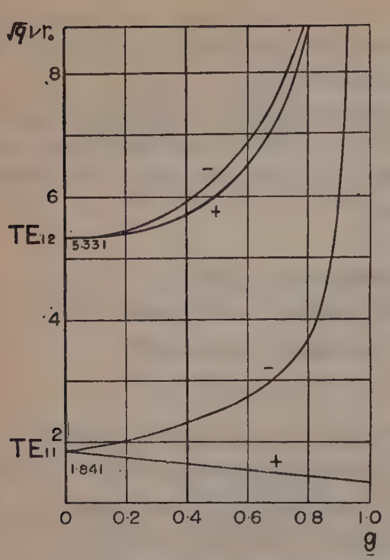

Fig. 3. The cutoff frequencies for quasi-TE$_{1l}$-modes against the parameter g.

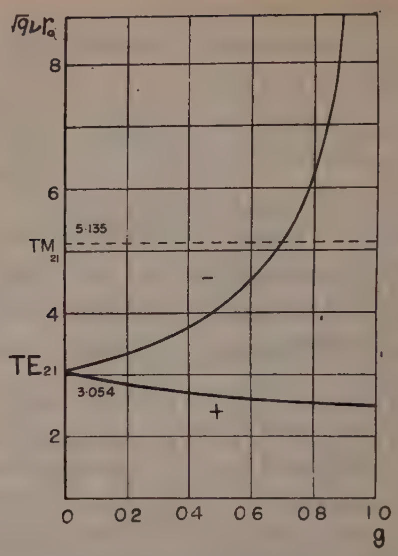

Fig. 5. The cutoff frequencies for quasi-TE$_{21}$-modes against the parameter g.

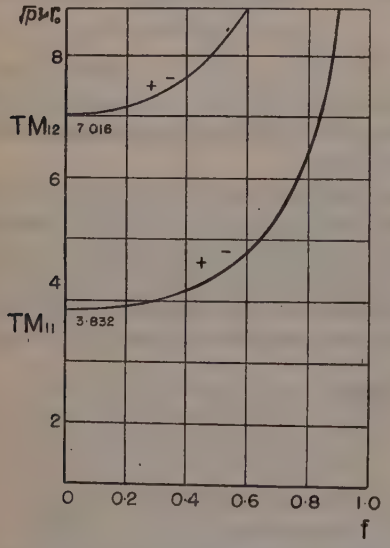

Fig. 4. The cutoff frequencies for quasi-TM$_{1l}$-modes against the parameter f.

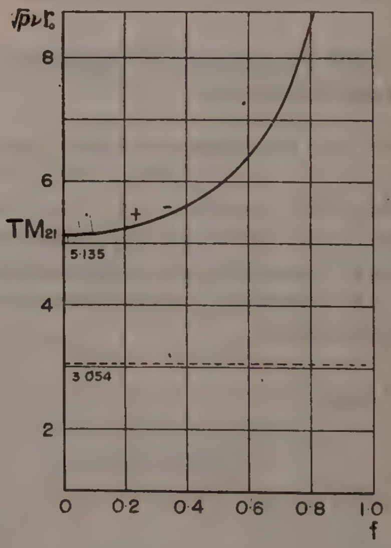

Fig. 6. The cutoff frequencies for quasi-TM$_{21}$-modes against the parameter f.

frequencies of transverse-magnetic modes, so that the two types of modes determined by the equation (35) and (36) belong to the modes corresponding respectively to the TE- and TM-modes. They are, however, neither true transverse-electric nor transverse-magnetic mode, because they have the z-components of both electric and magnetic fields, and they may be called respectively the quasi-TE-mode and quasi-TM-mode.

The cutoff frequencies of several of the lowest modes are calculated, and are shown in figures: Fig. 1 and 2 show the quasi-TE$_{01}$-, TE$_{02}$- and quasi-TM$_{01}$-, TM$_{02}$-modes, and Fig. 3 and 4 show the quasi-TE$_{11}$-, TE$_{12}$-, and the quasi-TM$_{11}$-, TM$_{12}$-modes, and Fig. 5 and 6 show the quasi-TE$_{21}$- and TM$_{21}$-modes.

It is to be remarked that for the quasi-TM-modes, the cutoff frequencies of both partial waves are found to coincide. They are expressed by $a=t_{mn}/\sqrt{p(1-f^2)}$ where t_{mn} is the m-th zero of $J_n(z)$. For the quasi-TE-modes, this coincidence does not occur. The asymmetry between the cutoff behaviors of the quasi-TM-modes and quasi-TE-modes is caused by the boundary conditions, in spite of the symmetry of the wave equations with respect to the electric field and magnetic field.

§ 5. The Amount of Faraday Rotation

The amount of the Faraday rotation per unit length can be evaluated from the difference of the two propagation constants corresponding to the left-handed and right-handed circularly polarized waves. These propagation constants can be calculated from the transcendental equations (30)—(32), where it is noted that the modified Bessel function of the first kind I_n and its derivative I_n' may appear instead of J_n and J_n' because we may have imaginary λ_t. The result of the culculation about a special case that $p=q=1$, $g=0$ and $f=1/2$, is shown in Fig. 7, which shows the propagation constants against the radius of the waveguide multiplied by ν, where two branches belonging to the same quasi-TE- or quasi-TM-mode are seen. The asymptotic lines of the curves in Fig. 7 are given by the propagation constants of plane waves in the free space, because the propagation constants of waves in the limit of the infinite radius approaches the ones of plane waves. The propagation constants of plane waves are easily obtained from (5), and areexp ressed as $\sqrt{(1+f)(1+g)}$ and $\sqrt{(1-f)(1-g)}$ per unit reduced length or, $\omega\sqrt{\mu_\eta\varepsilon_\eta}/c$ and $\omega\sqrt{\varepsilon_\xi\mu_\xi}/c$ per ordinary unit length. Fig. 8 shows the free space Faraday rotation of the limiting cases: the one is the case that f or $g=0$, and the other one is the case that $f=g$. The intermediate cases where $f=cg$ and $c\neq 0,1$ or ∞, lie in the region enclosed by the two limiting cases mentioned above.

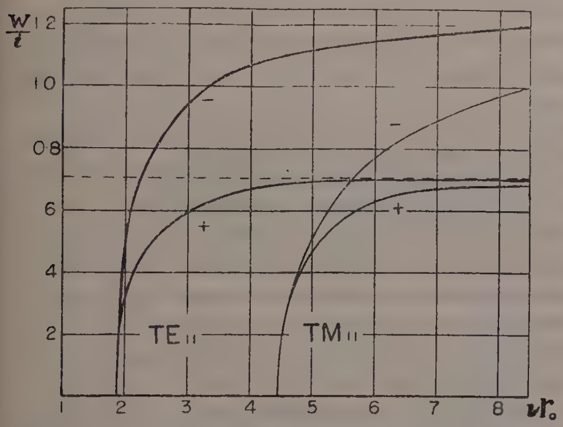

Fig. 7. The propagation constants of circularly polarized waves for $f=0.5$ and $g=0$ against νr_0 ($\nu=\omega\sqrt{\varepsilon\mu}/c$, r_0: radius of the guide)

The Faraday rotation of waves in the circular waveguide is always smaller than the free space Faraday rotation. It is, however, to be expected that the region where Faraday rotation is linearly dependent on the external magnetic field is nearly the same as that for the free space Faraday rotation. In the region of the small values of the parameters f and g, we may evaluate the Faraday rotation by the perturbation method from the wave equations, or by expanding the equation (30).

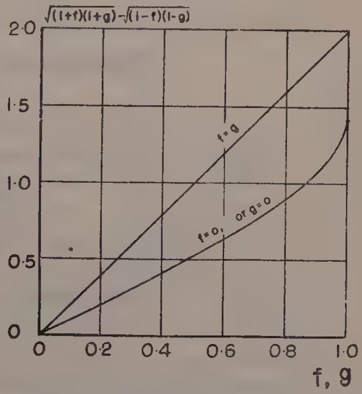

Fig. 8. The Faraday rotation of plane waves in the free space per unit length multipied by ν ($\nu=\omega\sqrt{\varepsilon\mu}/c$).

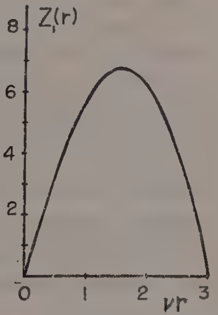

Fig. 9. $Z_1(r)$ in equation (34) for the quasi-TE_{11}-mode at $r_0=3$, $f=1/2$, $g=0$.

The Fig. 9 showing the coefficient of the longitudinal component of the electric field of the quasi-TE_{11}-mode at $a=3$, is supplemented so as to clarify how the quasi-TE_{11}-mode differs from the true TE-mode having no longitudinal component of the electric field.

In conclusion, the author wishes to express his cordial thanks to Prof. Hidetosi Takahasi for his kind guidance and encouragement.

References

1) Rayleigh: Nature **64** (1901) 577-578. Phil. Trans. **176** (1885) 343.

2) E. M. McMillan: J. Acous. Soc. Am. **18** (1946) 344-347.

3) Hideya Gamo: read at the annual meeting of the physical society of Japan October 5, 1951. To be published in the near future.

4) B. D. H. Tellegen: Philips Research Reports **3** (1948) 81-101.

5) C. L. Hogan: Bell System Tech. Jour. **31** (1952) 1-31.

6) E. M. McMillan: J. Acous. Soc. Am. **19** (1947) 922.

7) H. B. G. Casimir: Nuovo Cimento **6** (1949) 227-231.

8) D. Polder: Phil. Mag. **40** (1949) 99-115.

JOURNAL OF THE PHYSICAL SOCIETY OF JAPAN Vol. 8, No. 2, MAR.—APR., 1953

Motion of Electrons in Retarding-Field Tubes under Optimum Receiving Conditions*

By Masaki HIRASHIMA

Research Laboratory, Tokyo-Shibaura Electric Co., Kawasaki City

(Received June 11, 1952)

A description of experiments which were carried out to measure the plate-current distribution in a retarding-field tube of concentric structure, and the energy distribution of electrons flowing into the plate of another experimental tube, both under optimum receiving conditions at the wave lengths of 54 cm and 58 cm respectively, is contained. It is deduced that only a small portion of the plate electrode is effective in contributing to the plate current, and that the mean energy and the increment of energy of electrons gained from the high-frequency fields induced by the incoming wave whose field intensity is estimated to be of the order of 10 mV/m at most are 0.1 eV and approximately 1.2 eV respectively. Approximate calculations, performed on the assumptions that the grid alone is given a superimposed high-frequency voltage, the filament and plate being assumed grounded for high-frequency currents, and that the fields are linear, show that the high-frequency voltage induced on the grid by the incoming wave is about 0.6 volt. The voltage step-up ratio of the receiver under consideration is then calculated to be about 320. The apparent input resistance of the tube is roughly estimated to be of the order of -3.16×10^3 ohms. The equivalent circuit and the condition for generation of self-oscillation are thus derived.

§1. Introduction

The motion of electrons in a retarding-field tube to which only the electrostatic fields were applied was dealt with in the previous paper[1]. In the present paper the case of superimposed high-frequency electric fields is discussed on the assumption that the high-frequency fields are weak in comparison with the static fields. The experimental tube with which the present experiments were carried out is the same except where noted as that reported in the previous paper: The electrode system consists of a filamentary cathode of tungsten, a spiral grid, a mesh plate, and a collecting electrode, all the electrodes being arranged as concentrically as practicably possible. A negative voltage with respect to the cathode is applied to the end plates placed near the extremities of these electrodes, serving as a protector against stray electrons which might disturb the operation of the tube.

---

* Presented at the Fall Meeting of I.E.E. of Japan held in Tokyo, November 2, 1948.

§ 2. Measurements on the Plate-Current Distributions

As is well known, direct-heated filaments have been exclusively used as the cathode of retarding-field tubes (so-called B–K tubes); because an equipotential cathode such as oxide-coated cathode can not be used with good results. It is this fact that has complicated the analysis and behavior of retarding-field tubes. If we take, as usual, the negative end of a filamentary cathode as the reference point, the positive end of the filament is at a higher potential. The virtual cathode to be formed immediately inside of and concentric with the plate may accordingly not be at the same potential, but has a voltage drop corresponding to that along the filament. Besides, the position of the virtual cathode will also shift nearer toward the grid at the positive end than at the negative end. Consequently, unless high-frequency voltages of large amplitude are superimposed on the electrodes, the electrons which are emitted from the portion near the positive end of the filament will be unable to land on the plate which is kept at zero potential (the negative end of the filament). Although an induced current may flow in the plate circuit by virtue of the moving electrons in the grid-plate space, this can not have any d–c component, unless electrons are actually captured by the plate, and hence, according to the conventional theory of detection in retarding-field tubes,[2][3][4] it may not contribute to the sensitivity of the receiver. In order to obtain the current distribution on the plate, the following preliminary experiments were carried out. These experiments were, however, conducted about a year later than those to be described below, and the experimental tube which was employed in these experiments was not the same as that described in the preceding section, thus results obtained gave only a general tendency of the tube behavior. The tube was constructed with a tungsten filament and a spiral grid of the same dimensions as the tube used in the other experiments, with a plate made of six pieces of nickel ring 2 mm long and 7.5 mm in diameter, spaced about 0.5 mm apart with each other, as shown in Fig. 1.[5] From each plate section a welded wire is pulled out respectively through the glass stem to form one line of a Lecher wire system. Each wire was galvanically insulated from the others within the copper pipe, and current measurement to each plate section was possible by the use of a microammeter. These wires were, however, shortcircuited for high-frequency currents by means of condensers (50 pF) at the nearest possible portions to the stem outside the glass bulb, so that these six lead-in wires as a whole were expected to act as one line for high-frequency currents. A weak incoming wave of 54 cm, modulated with a 1000 c/s sinusoidal signal, was received with a doublet antenna attached to the Lecher wires, and the plate current to each section was measured under the optimum

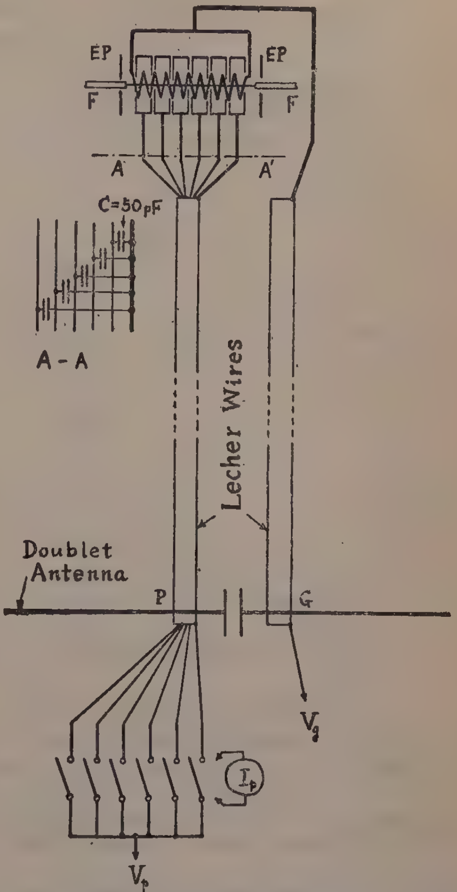

Fig. 1. Experimental set for measuring the plate-current distribution.

receiving condition. The results of the experiments are shown by curve A in Fig. 2, in which No. 5 plate section situated near the negative end of the filament shows the maximum plate current. When the microammeter was replaced with a telephone receiver, the same section gave the maximum signal strength. This reveals that this section contributed the major part to the sensitivity of the receiver. On reversing the polarity of the filament battery, No. 2 section gave the maximum sensitivity.

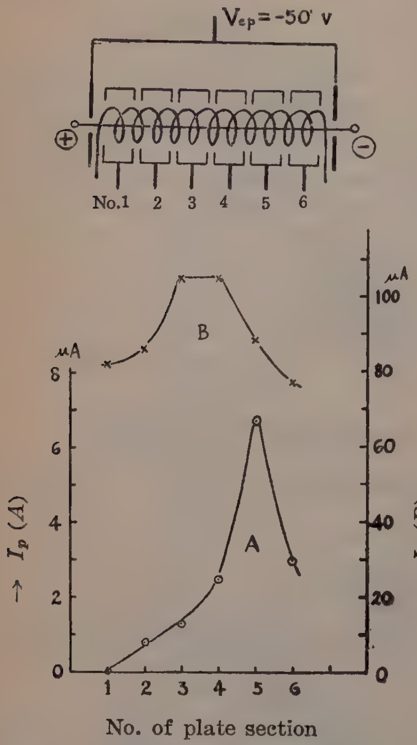

Fig. 2. Plate-current distributions.
A: under the optimum receiving condition ($\lambda=54$ cm);
B: under the optimum self-oscillating condition ($\lambda \doteqdot 54$ cm) without incoming wave.

When only the receiver was adjusted so as to generate the strongest possible oscillation, with the transmitter turned off at the same time, the current distribution curve shown by B in Fig. 2 was obtained. It may be seen from this figure that the current distribution in this case (curve B) shows a more or less flat maximum in the central part and decreases nearly symmetrically toward both ends. This may be explained by assuming that the amplitude of high-frequency voltage was so large that it was able to cover the effect of the voltage drop which would exist along the virtual cathode formed immediately inside of the plate.

The shape of curve A may have resulted from the fact that the filament temperature was not uniform along the wire due to end cooling, the temperature being so low at both ends that ample thermionic emission could not be obtained, and consequently, the initial velocities of thermal electrons were small. If there were no end cooling at all, it would be expected that the current to No. 6 section (or No. 1 section when the polarity of the filament voltage was reversed) would show a maximum value.

Thus, the following experiment was tried in order to compensate for the effect of the voltage drop along the virtual cathode. The six plate sections were given respective voltages equaling those of the parts of the virtual cathode located immediately inside with respect to the negative end of the filament by means of a potentiometer connected across a battery. This arrangement afforded a flexible control on the boundary conditions to which the space charge in the G–P space is made subject. In spite of the fact that the gross plate current increased greatly ($I_p=380\mu A$) compared with the former case ($I_p=14.3\mu A$), the signal strength hereby obtained was far inferior to the case without compensation. The reason for this is unclarified as yet. An explanation lies probably in the inadequate set up of the experimental circuit (such as too high resistances used as the potentiometer, etc.). Business pressure during the war did not permit us to pursue this matter extensively, but it may be almost certain that a very restricted region of the plate is effective in contributing a major part to the sensitivity of a retarding-field tube when used as a receiver.

§ 3. Energy Distribution of Electrons flowing into the Plate

Energy distribution of electrons flowing into the plate under optimum receiving conditions was measured by the retarding field method. Fig. 3 is the diagrammatic representation of the experimental set. The experimental tube is that described in § 1. The weak unmodulated wave of 58 cm, radiated

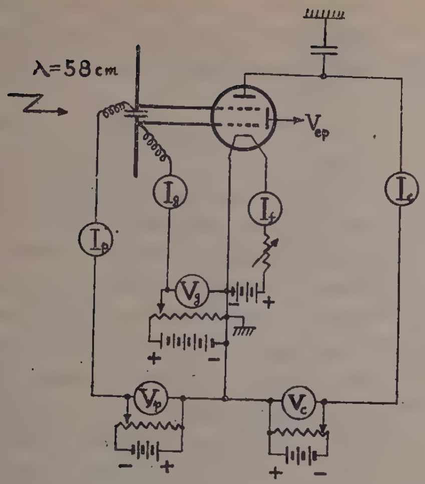

Fig. 3. Means for measuring energy distribution of electrons flowing into the mesh plate.

from a transmitter (not shown in the figure) located at a distance of about 3 meters opposite the receiver, was received with a doublet antenna and was applied to the grid and mesh plate through a Lecher wire system, while negative voltages with respect to the negative end of the filament were applied to the collector (retarding electrode). The field intensity at the receiving doublet antenna was estimated from another experiment to be of the order of a few mV/m to 10 mV/m at most. At each value of the retarding collector voltage V_c the collector currents I_c were measured. The results of the experiment are shown in Fig. 4, in which two cases for $I_f=0.68$A and 0.70A are illustrated (curves I–A and II–A). The results of the measurements are also shown in the figure for the case of no incoming wave with the transmitter turned off (curves I–B and II–B). It may be doubted here that the receiving condition might vary somewhat when the collector voltage V_c was shifted toward the negative value. But this is not the case, because the mesh of the plate is so fine that the Durchgriff (D) of the collector through the mesh plate with respect to the virtual cathode is very small (measured $1/D\approx280$), and the effective voltage on the mesh plate is considered nearly constant irrespective of the values of the retarding collector voltage, as shown clearly in Fig. 5 by the approximate independency of (I_p+I_c) upon V_c. From Figs. 4 and 5 we obtain the transmission coefficient of the mesh plate; $I_c/(I_p+I_c)=25\%$ at $V_c=0$, which is slightly smaller than the value 56%, calculated from the dimensions of the mesh plate. This discrepancy indicates that the deflection of electron trajectories by the grid wire plays a large role, and that the mesh plate potential may be somewhat above the space potential. It should be noted here that the two groups of curves (I and II) must not be compared directly with each other. We must take into consideration the facts that these curves have been obtained under different receiving conditions (i.e., $I_f=0.68$ A and 0.70 A respectively), and that the electrode structure is not a parallel plane but cylindrical, so that only the

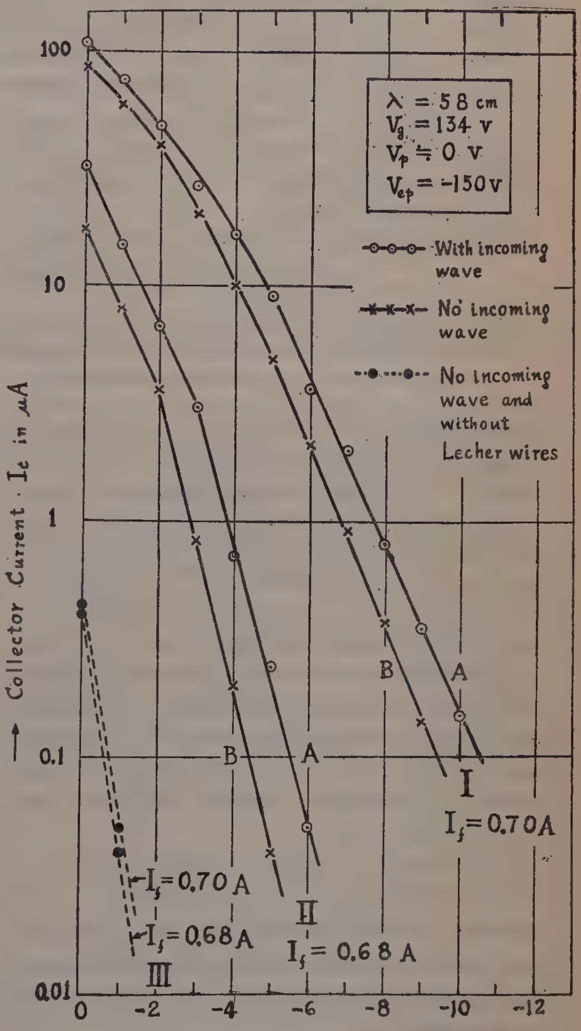

Fig. 4. Relation between collector current and collector voltage, with and without the incoming wave (λ=58 cm).

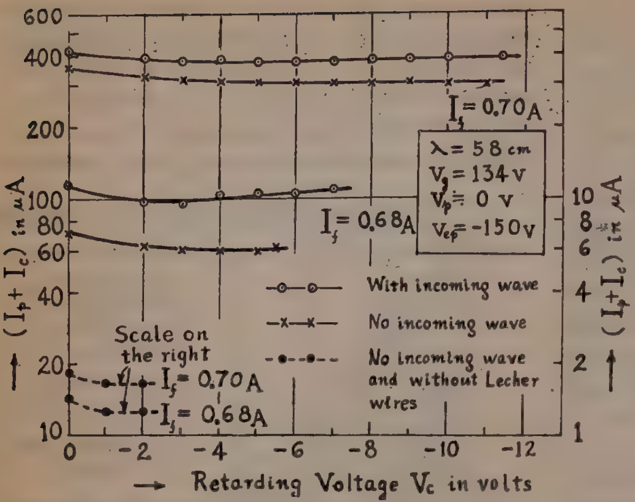

Fig. 5. Experimental verification of approximate constancy of the plate effective voltage independent of the retarding voltage on the collector.

slopes and relative position of the curves belonging to the respective groups must be compared.[6] That these electrons have really gained the energy from the high-frequency fields and are not the so-called "excess-energy electrons" as proposed by E. G. Linder[7] is clearly shown by a group of dotted curves (III) which were obtained with both the Lecher wires and doublet antenna omitted, and without the incoming wave. Fig. 4 shows that the curves run approximately linear except where effects of space charge would appear in the space between the plate and the collector.

The linearity of these curves (I and II) reveals that the energy distribution of the electrons flowing through the mesh plate into the plate-collector space follows closely Maxwell's distribution law, which in this case is expressed by

$$I_c = I_0 \exp(-V_c/\overline{V}) \qquad (1)$$

where I_0 is the saturation current at $V_c=0$, and $\overline{V}$ the mean energy of electrons expressed in electron volts. This is easily calculated from the slope of the curves.

It is also seen from Fig. 4 that the curves (A and B) belonging to the respective groups (I and II) run approximately parallel to each other, the curves (A) shifting toward the larger values of V_c by gaining energy from the incoming wave. Therefore, if we take the difference $\varDelta V_m$ of the voltages corresponding to the intersections of the curves A and B belonging to the respective groups (I and II) with the horizontal line $I_c=0.1\mu$A as an example, it will be equal, as a rough approximation, to the energy increment of electrons gained from the incoming wave. From Fig. 4 we get $\varDelta V_m=1.2$ eV for both groups of curves. These results are summarized in Table I.

It might appear that in the above experiments deflections of electron trajectories by both the grid wire and the mesh plate should be taken into account in obtaining the increment of energy gained by electrons from the incoming wave. Since our considerations concern only the comparison between the two curves (A and B) belonging to the respective groups (I and II), this effect may be neglected in the first approximation, taking into consideration the fact that the curves A and B run nearly parallel to each other; the deflections of electron trajectories by the grid and mesh plate are considered to be similar for both curves belonging to the respective groups. In view of the different conditions under which the results of Table I have been obtained, the similarity of the values of $\varDelta \overline{V}$ and $\varDelta V_m$ for the two groups appears even to

Table I

Curve	Filament Current I_f (Amp)	Mean energy of electrons $\overline{V}$ (eV)	Mean energy of electrons gained from the incoming wave $\varDelta\overline{V}$ (eV)	Increment of electron energy gained from the incoming wave $\varDelta V_m$ (eV)	Incoming wave
I A	0.70	1.24	0.1	1.2	Yes
I B		1.14			No
II A	0.68	0.75	0.1	1.2	Yes
II B		0.65			No

be accidental.

Fig. 4 shows clearly that regeneration in the tube plays a part under optimum receiving conditions. That this is the actual case was confirmed by the following experiment: A resonance circuit tuned to 1000 cycles was inserted in the plate circuit shown in Fig. 3, and the rectified voltage developed across the circuit was fed to a loudspeaker through an amplifier. Keeping the receiver under the same optimum receiving condition as described above, the wave length of the transmitter was finely varied, and a stable beat of 1000 cycles was heard on the speaker. Upon increasing the filament current of the tube under consideration gradually from a small value, self-oscillation was noted, increasing in intensity with the filament current. But with a filament current larger than about 0.70A, an increase in noise was observed when a modulated incoming wave was received with this receiver.

§ 4. Approximate Calculations of the Energies gained by Electrons from the Superimposed High-Frequency Fields

The next step is to calculate the amplitude of the superimposed high-frequency voltage which gives rise to this energy gain of electrons. For a conventional retarding-field tube in which the capacity between the grid and filament is far larger than that between the plate and filament, a basic circuit such as shown in Fig. 6a has usually been adopted in calculations concerning retarding-field tubes. As shown in the figure, the grid is assumed to be grounded for high-frequency currents, and the h.f. voltage is assumed to be applied to the plate.[8)9)] However, for the special tube employed in the experiments described in the preceding section, such a basic circuit as shown in Fig. 6b may be considered more adequate than that shown in Fig. 6a, if we take into consideration the fact that the capacity between the plate and collector is larger than that between the grid and filament. Consequently, it seems more reasonable to assume that the h.f. voltage is superimposed on only the grid, the filament and the plate being assumed grounded. On the basis of the circuit shown in Fig. 6b we will next derive approximate expressions for the energies gained by electrons from the h.f. fields.

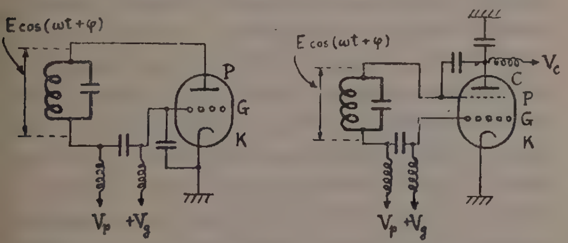

(a) (b)

Fig. 6. Basic circuits of conventional and special retarding-field receivers.

Referring to Fig. 6b, we assume that to the grid is applied a voltage:

$$V_g+E\cos(\omega t+\varphi) \text{ with } V_g \gg E,$$

and to the plate an effective voltage V_p, and we proceed to consider the energy gain of electrons in each inter-electrode space in turn. For the sake of simplicity of calculation, the electrode configuration is assumed to be a parallel plane instead of cylindrical.

a) Energy gained by electrons in a single transit from the cathode to plate through the grid

Let us take a coordinate axis perpendicular to the electrode surfaces, and designate the coordinate of an electron in the G–P space as x when the cathode is taken as the origin, and ξ when the grid is taken as the origin (see Fig. 7), then

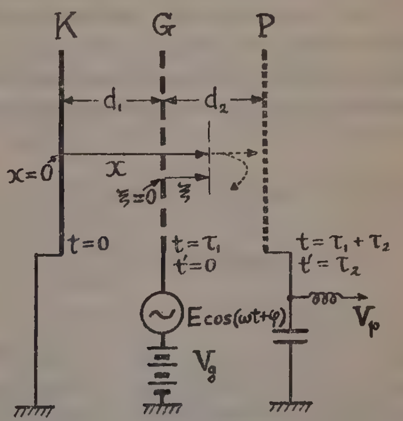

Fig. 7. Illustration of the simplified retarding-field tube under discussion.

$$x=d_1+\xi \tag{2}$$

where d_1 is the distance between the cathode and the grid. If we denote the time taken by the electron to traverse the distances x and ξ by t and t' respectively, then

$$t=t'+\tau_1 \qquad (3)$$

where τ_1 is the transit time of the electron from the cathode to the grid. Denoting the initial velocity at the grid plane ($\xi=0$) of the electron on entering into the G–P space by u_0, and neglecting that at the cathode ($x=0$), the equations of motion of the electron in the G–P space are given by

$$\left.\begin{aligned} \xi&=x-d_1=u_0t'-\frac{\alpha}{2}t'^2 \\ u&=\frac{d\xi}{dt'}=u_0-\alpha t' \end{aligned}\right\} \qquad (4)$$

in which

$$u_0\approx\frac{2d_1}{\tau_1}\left\{1+\frac{k}{2}\cos(\omega\tau_1+\varphi)-\frac{k^2}{8}\cos^2(\omega\tau_1+\varphi)\right\}$$

$$=\frac{2d_1}{\tau_1}\left\{1+\frac{k}{2}\cos\psi-\frac{k^2}{8}\cos^2\psi\right\} \qquad (4a)$$

with the abbreviation $\psi=\omega\tau_1+\varphi$, and α denoting the acceleration:

$$\alpha=\left(\frac{e}{m}\right)\cdot\frac{V_g+E\cos(\omega t+\varphi)-V_p}{d_2}$$

$$\approx\frac{eV_g}{md_2}\{1+k\cos(\omega t'+\psi)\} \qquad (4b)$$

with $k=E/(V_g-V_p)\approx E/V_g\ll 1$, and d_2 the distance between the grid and the plate. e and m are the charge and mass of the electron. By calculating the velocity of the electron at the plate ($\xi=d_2$), and expressing this in electron volts, we obtain as the sum of the energies gained by the electron in the K–G space and the G–P space respectively, the following result:

$$(\varDelta V_1+\varDelta V_2)_1\approx 2E\sin\frac{\omega\tau_2}{2}\cdot\sin\left(\frac{\omega\tau_2}{2}+\psi\right)$$

$$=2E\sin\frac{\omega\tau_2}{2}\cdot\sin\left(\frac{\omega\tau_2}{2}+\omega\tau_1+\varphi\right) \qquad (5)$$

where τ_2 is the transit time of the electron from the grid to the plate. Using the data for τ_1 and τ_2 calculated in the previous paper,[1] we obtain $\omega\tau_1=0.314\pi$ and $\omega\tau_2=1.28\pi$. Hence, Eq. (5) becomes

$$(\varDelta V_1+\varDelta V_2)_1\approx 1.8E\sin(0.954\pi+\varphi). \qquad (5a)$$

This energy gain is represented in Fig. 8 (a) as a function of the phase angle φ at which the electron starts the cathode. It may be seen from this figure that if $V_p=0$, half of the electrons coming into the G–P space might be able to arrive at the plate plane against the retarding field. However, the fact that this can not be the case will be understood in that (I_p+I_e) is very small, as shown in Fig. 5, compared with the current flowing into the G–P space:[1] $I=I_g(1-\alpha)/(1-\eta)=29$ mA for $I_f=0.68$ A and 37 mA for $I_f=0.70$ A, respectively. This may be ascribed, among other things, to (1) the contact difference of potential between the plate and the cathode (the plate potential being about 0.5 volt below the cathode potential); (2) a very small part of the plate electrode is effective in contributing to the operation of the tube due to the voltage drop along the filament, as shown in § 2; (3) the deflection of electron trajectories by the grid wire; and (4) the virtual cathode apparently formed immediately inside of the plate, and etc.

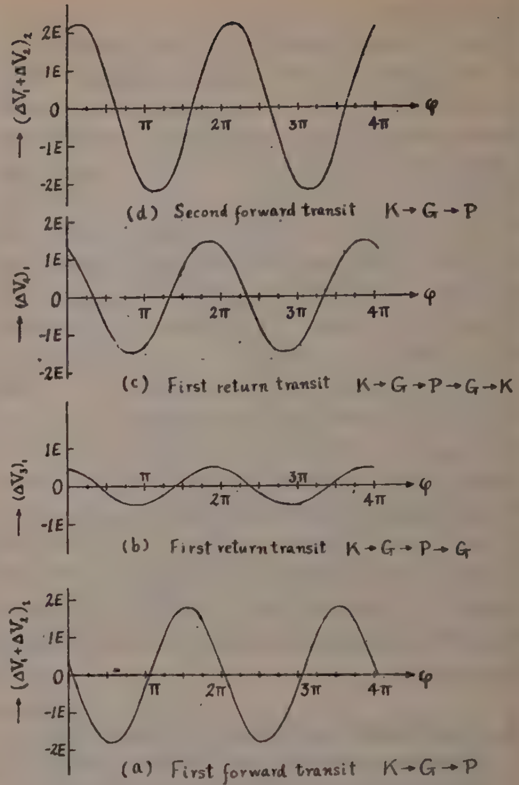

Fig. 8. Energies gained by electrons in various spaces as functions of the phase angle φ at which the electrons leave the cathode.

As described above, in our present calculations an ideal parallel plane electrode system has been assumed in place of the cylindrical one actually used. However, the motion of electrons in the experimental tube would perhaps be similar to that shown schematically in Fig. 9. Due to the deflection of the electrons by the grid wire, the motion of the electrons, which would otherwise be truly radial under the ideal circumstances assumed in the calculations, is given a tangential component. The magnitude of this deflection (θ) varies according to whether the electron passes midway between two grid wires or closer to one of them. The maximum angle of deflection (θ_m) which the electrons undergo in passing through the grid plane is given for the cylindrical electrodes by[10]

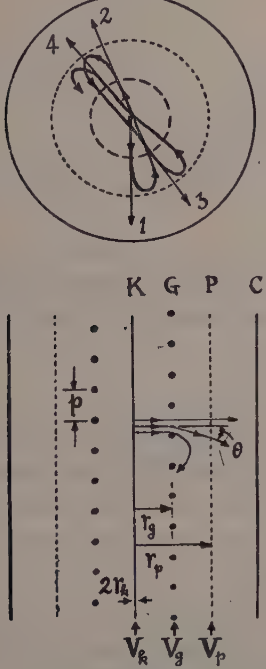

Fig. 9. Deflection of electron trajectories by the grid wire.

$$\tan\theta_m = \frac{p}{4r_g V_g}\left(\frac{V_g - V_k}{\ln\cdot r_g/r_k} + \frac{V_g - V_p}{\ln\cdot r_p/r_g}\right) \qquad (6)$$

where p is the pitch of the grid. The ratio of the current flowing into the plate plane, (I_p+I_c), to that flowing into the G–P space, (I), is then given by

$$(I_p+I_c)/I \approx \frac{1}{\theta_m}\sqrt{\frac{V_p}{V_g}}\,. \qquad (7)$$

On the other hand, as far as the current flowing into the plate plane is concerned, gaining of energy by electrons from the h.f. fields is equivalent to raising the plate potential above the cathode potential by the same amount, assuming a linear field distribution. Let us assume the energy gain to be, for example, 5.5 volts; then the value of V_p in Eq. (7) may be estimated to be about 5 volts, taking the contact difference of potential (-0.5 volt) into consideration. Then $(I_p+I_c)/I \approx 0.6$ for an ideal equipotential cathode.

Thus, the electrons that can jump into the plate plane against the retarding field by gaining energy from the h.f. fields will perhaps be restricted to those which have gained the energies corresponding to those in the neighborhood of the positive peaks of the curve of Fig. 8 (a), almost all electrons being driven back toward the grid again in the G–P space.

b) **Energy gained by electrons returning in the G–P space**

While those electrons which have been given energy from the h.f. fields may enter into the mesh plate against the retarding field, those electrons which have given their energy to the fields will be forced to stop in the inter-electrode space, and driven back toward the grid again, some gaining more energy than they originally had on entering this space. Following the method employed by K. S. Knol, M.J.O. Strutt and A. van der Ziel,[11] with somewhat different boundary conditions in the present case, we next calculate the energy gain of the returning electrons in the G–P space. Referring again to Fig. 7, the equation of motion of an electron in this space is given by

$$\frac{d^2\xi}{dt'^2} = -\frac{e}{m}\cdot\left\{\frac{V_g + E\cos(\omega t'+\psi) - V_p}{d_2}\right\}$$
$$= -\frac{e(V_g - V_p)}{md_2}\{1 + k\cos(\omega t'+\psi)\}. \qquad (8)$$

On integrating Eq. (8) with respect to t', we obtain

$$\frac{d\xi}{dt'} = u_0 - \frac{v_0}{\tau_2}\left[t' + \frac{k}{\omega}\{\sin(\omega t'+\psi) - \sin\psi\}\right] \qquad (9)$$

with

$$\left.\begin{aligned} u_0 &= v_0(1+k\cos\psi)^{1/2} \\ &\approx v_0\left(1 + \frac{k}{2}\cos\psi - \frac{k^2}{8}\cos^2\psi\right) \\ v_0 &= \sqrt{2eV_g/m} = 2d_2/\tau_2 \end{aligned}\right\} \quad (9a)$$

Integrating (9) with respect to t' once more, the following equation is obtained:

$$\xi = u_0 t' - \frac{2d_2}{\tau_2^2}\left[\frac{t'^2}{2} + \frac{k}{\omega^2}\{\cos\psi - \cos(\omega t' + \psi) - \omega t' \sin\psi\}\right]. \quad (10)$$

Putting $\xi = 0$ in this equation, a solution $t' = \tau$ is obtained together with a trivial solution $t' = 0$. As τ is a function of k, it may be put as follows:

$$\tau = 2\tau_2 + C_1 k + C_2 k^2 + \cdots \approx 2\tau_2 + C_1 k + C_2 k^2. \quad (11)$$

From Eqs. (10) and (11) the coefficients C_1 and C_2 are given by

$$C_1 = \frac{1}{\omega^2 \tau_2}\{(\omega\tau_2)^2 \cos\psi + (2\omega\tau_2 - \sin 2\omega\tau_2) \times \sin\psi - (1 - \cos 2\omega\tau_2)\cos\psi\},$$

$$C_2 = -\frac{\tau_2}{4}\cos^2\psi + C_1\left\{\frac{\cos\psi}{2} - \frac{2}{\omega\tau_2}\sin\omega\tau_2 \cdot \cos(\omega\tau_2 + \psi)\right\} - \frac{C_1^2}{2\tau_2}.$$

By substituting (11) into (9) we can calculate the velocity u which would be gained by the returning electron on arriving at the grid plane. The energy thereby gained is given by $m(u^2 - u_0^2)/2$, which when expressed in electron volts runs as follows:

$$(\varDelta V_3)_1 = k V_g \Phi \sin(\omega\tau_2 + \psi) + k^2 V_g \Psi + k^2 V_g \left[\cos 2(\omega\tau_2 + \psi) + \left(\frac{1}{\omega\tau_2}\right) \cdot \left\{\frac{3}{2}\sin 2(\omega\tau_2 + \psi) - \frac{1}{2}\sin 2\psi\right\} - \left(\frac{1}{\omega\tau_2}\right)^2 \cdot \sin 2(\omega\tau_2 + \psi) \cdot \sin 2\omega\tau_2\right] + \cdots. \quad (12)$$

in which

$$\left.\begin{aligned} \Phi &= 4\{(\omega\tau_2)\cos\omega\tau_2 - \sin\omega\tau_2\} \cdot (\omega\tau_2)^{-2} \\ \Psi &= \cos 2\omega\tau_2 - \frac{5}{2}\left(\frac{1}{\omega\tau_2}\right) \cdot \sin 2\omega\tau_2 + 2\left(\frac{1}{\omega\tau_2}\right)^2 (1 - \cos 2\omega\tau_2). \end{aligned}\right\} \quad (13)$$

The functions Φ and Ψ are represented in Fig. 10 as functions of $\omega\tau_2$. If we take only the first term containing k, assuming $k \ll 1$, the following equation is obtained as the energy gain of the returning electron in the G–P space:

$$(\varDelta V_3)_1 \approx k V_g \Phi \sin(\omega\tau_2 + \psi) = E\Phi \sin(\omega\tau_2 + \omega\tau_1 + \varphi). \quad (14)$$

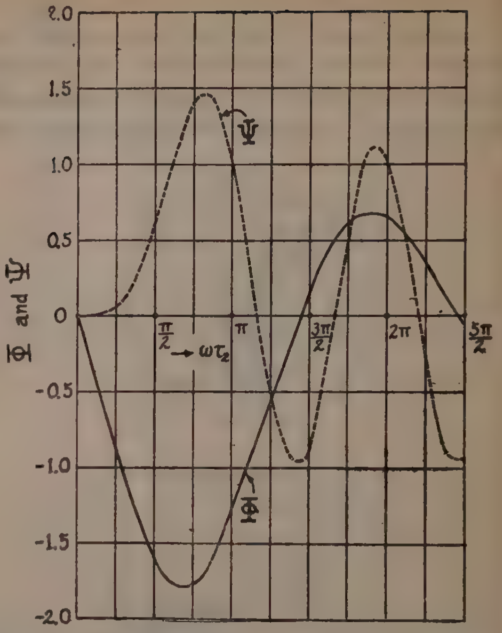

Fig. 10. The functions Φ and Ψ as functions of $\omega\tau_2$.

Since $\omega\tau_2 = 1.28\pi$, we obtain from Fig. 10 $\Phi \approx -0.5$. Hence,

$$(\varDelta V_3)_1 \approx -0.5E\sin(1.594\pi + \varphi). \quad (14a)$$

In Fig. 8 (b) is represented $(\varDelta V_3)_1$, as given by Eq. (14a), as a function of φ, the phase at which the electron leaves the cathode.

c) **Energy gained by electrons in return transit from the plate to the cathode through the grid**

By performing similar calculations to the case (a), we obtain the following result as the energy gained by the electron on arriving at the cathode after completing a single revolution:

$$(\varDelta V_4)_1 \approx E\{\Phi \sin(\omega\tau_2 + \omega\tau_1 + \varphi) - \cos(2\omega\tau_2 + 2\omega\tau_1 + \varphi)\} = E\{-0.5\sin(1.594\pi + \varphi) - \cos(3.188\pi + \varphi)\}. \quad (15)$$

Here the initial velocity of the electron on crossing the grid plane in the reverse direction from the plate to cathode is assumed to be $V_g + (\varDelta V_3)_1$ volts. In Fig. 8 (c) is represented $(\varDelta V_4)_1$ as a function of φ, the phase at which the electron leaves the cathode for the plate.

d) **Energy gained by electrons in the second transit from the cathode to the plate through the grid.**

By repeating again similar calculations to the case (a), and taking the initial velocity $(\Delta V_4)_1$ into consideration, we obtain the following result as the energy gained by the electron in the second transit from the cathode to the plate:

$$\left.\begin{aligned}(\Delta V_1+\Delta V_2)_2 &\approx E\Big\{0 \sin(\omega\tau_2+\omega\tau_1+\varphi)\\ &-\cos(2\omega\tau_2+2\omega\tau_1+\varphi)\\ &+2\sin\left(\frac{5}{2}\omega\tau_2+3\omega\tau_1+\varphi\right)\cdot\sin\frac{\omega\tau_2}{2}\Big\}\\ &=E\{\cos(3.502\pi+\varphi)-0.5\sin(1.594\pi+\varphi)\\ &-\cos(3.188\pi+\varphi)-\cos(4.782\pi+\varphi)\}\,.\end{aligned}\right\} \tag{16}$$

In Fig. 8 (d) is represented $(\Delta V_1+\Delta V_2)_2$ as a function of φ. From this figure it may be seen that the maximum energy gain amounts to about twice the amplitude of the h.f. voltage.

Electrons traversing in a pendulum motion within the tube might gain more than $2E$ volts. However, these electrons are reduced rapidly in number as the revolutions increase and thus, may be neglected to the first approximation.

Thus, it may be estimated that the maximum energy gained from the superimposed h.f. fields by the electrons entering into the plate-collector space is approximately equal to twice the amplitude of the superimposed h.f. voltage on the grid.

Now, assume that the amplitude of the superimposed h.f. voltage E involved in the above calculations be that from self-oscillation set up in the receiver under consideration. If an incoming wave from the transmitter is received with the receiving antenna, and the frequency of this incoming wave is nearly equal to, if not the same as, that of the self-oscillation, this in turn gives rise to an increment of amplitude ΔE in addition to E which is superimposed on the grid. The maximum energy hereby gained by electrons from the incoming wave will be roughly equal to $2\Delta E$.

In view of the fact that the experimental tube with which the experiments described above were carried out was not a parallel plane but a cylindrical structure, the above calculations may be applicable only as the first approximation. With reference to Fig. 2 in the paper[1)] previously published, it is expected that departure from actuality in the K–G space is likely more conspicuous rather than in the G–P space.

§ 5. Voltage Step-Up Ratio of the Receiver

Referring to Fig. 4, the increment of energy gained by electrons from the incoming wave was estimated to be of the order of 1.2 volts. This energy gain of electrons must have resulted from the increment in voltage amplitude (ΔE) due to the incoming wave. Hence $\Delta E \approx 1.2/2 = 0.6\,V$.

On the other hand, the field intensity F at the receiving doublet antenna from the incoming wave was estimated to be of the order of a few mV/m to 10 mV/m at most, this value being obtained from field measurements carried out beforehand. The electromotive force e induced on the doublet antenna may be given by

$$e=\frac{2l}{\pi}F \tag{17}$$

where l is the length of the antenna in m and F in V/m. Assuming, for example, $F=10\,\text{mV/m}$, as a rough approximation, we obtain $e \approx 1.9\,\text{mV}$.

Hence, the voltage step-up ratio of the receiver under consideration is given by

$$\Delta E/e \approx 0.6/1.9\times 10^{-3} = 320\,. \tag{18}$$

This seems to be a reasonable order of magnitude, if we take into consideration the fact that under optimum receiving condition the tube was in a weak self-oscillating condition, the frequency of which being thought to be nearly equal to that of the incoming wave.[12)]

§ 6. Calculation of the Apparent Input Resistance of the Tube and the Equivalent Circuit representing the Optimum Receiving Condition

If we take into consideration the fact that the number of electrons entering into the mesh plate by gaining energy from the superimposed h.f. fields is quite small compared with that of electrons entering the G–P space, it will perhaps be allowable to assume, as the first approximation, that almost all electrons entering the G–P space are caused to return in the same space. Then we can calculate approximately the input (electron) resistance of the tube. Integrating Eq. (12) with respect to φ from $\varphi=0$ to $\varphi=2\pi$ and taking the average over 2π, the mean energy of electrons starting from the cathode at various phases is obtained. By so doing the first and third terms, both containing φ of the first order balance out, and only the second term is left. Let us denote the mean value so obtained by $\overline{V}_e$; if $\overline{V}_e$ is positive, the electrons are given energy from the h.f. fields, and if $\overline{V}_e$ is negative, the fields are given energy by the retarded electrons, and self-oscillation may set in under suitable conditions. The supply or gain of energy $\overline{V}_e$ by the voltage source to or from the tube may be expressed by a positive or negative real admittance $1/\rho$ connected between the grid and plate (or earth). If we denote the h.f. voltage superimposed on the grid by E, then the supplied energy is equal to $E^2/2\rho$. The number of electrons entering the G–P space through the grid openings is given by I/e, where e is the electronic charge and I is the electron current flowing through the grid openings into this space. As the mean energy of any electron is equal to $e\overline{V}_e$, the following equation must hold with reference to Eq. (12):

$$\frac{E^2}{2\rho}=\frac{e\overline{V}_e I}{e}=k^2 I V_g \Psi=\frac{E^2}{V_g}I\Psi\ .$$

From this equation follows:

$$\frac{1}{\rho}=\frac{2I}{V_g}\Psi\ . \tag{19}$$

Since $\Psi \approx -0.8$ for $\omega\tau_2=1.28\pi$ (see Fig. 10), we obtain $\rho \approx -2.4\times10^3$ ohms, taking $I=29$ mA for $I_f=0.68$ A and $V_{g\,\mathrm{mean}}\approx110$ volts in place of $V_g=134$ volts.[1] The fact that ρ is negative in sign indicates that self-oscillation may set in under suitable conditions.

Incidentally, more elaborate calculations than those described above regarding the K–G space lead us to believe that the contribution of the K–G space to the input real admittance is of negligible order in magnitude compared with that of the G–P space.

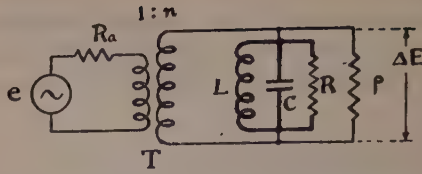

Fig. 11. Equivalent circuit of the receiver under optimum receiving condition.

Thus, the equivalent circuit of the receiver under consideration may be represented as shown in Fig. 11. In this figure R_a denotes the radiation resistance of the doublet antenna (75 ohms), R is the circuit loss, C is the internal capacity (input capacity) of the tube (0.8 pF), and T is an ideal transformer which represents the mismatch taking place in the circuit. The condition for generation of self-oscillation is, therefore, given by

$$\frac{1}{\rho}+\frac{1}{R}+\frac{1}{n^2R_a}\leqq0\ . \tag{20}$$

By taking advantage of the experimental data obtained by H. Lotze[13], the circuit loss R may be estimated to be $R\approx1\times10^4$ ohms, which is thought to be in the right order of magnitude compared with the results obtained by R. Nakamura.[14] Hence, Eq. (20) yields $n^2=41.4$ and $n=6.44$. In view of the fact that the ideal transformer T may be considered as being composed of two transformers: one between the doublet antenna and the Lecher wires, and the other between the Lecher wires and the lead-in wires through the glass stem of the tube, the value of n is considered to be quite reasonable.

That this is in the right order of magnitude is also confirmed by a calculation of the step-up ratio of the induced voltage $\varDelta E$ on the grid, to the voltage induced on the doublet antenna by the incoming wave. This calculation yields the following result:

$$\frac{\varDelta E}{e}=\frac{nZ}{n^2R_a+Z}\approx340 \tag{21}$$

where $Z=\dfrac{\rho R}{\rho+R}\approx-3.16\times10^3$ ohms, the total input resistance of the tube. In view of the approximate calculations performed in estimating the superimposed h.f. voltage amplitude, this result seems to be in exceptionally good agreement with that deduced from the energy distribution measurements ($\approx$320).

In conclusion, the author is greatly indebted to Dr. T. Okabe, whose invaluable suggestions and discussions have resulted in the publication of this paper, and also to Mr. Y. Tanaka for his assistance in calculations and numerous enlightening discussions while the paper was being prepared.

References

1) M. Hirashima: J. Phys. Soc. Japan. **5** (1950) 339.
2) N. Carrara: Proc. I.R.E. **20** (1932) 1615.
3) H. E. Hollmann: Proc. I.R.E. **22** (1934) 630.
4) H. U. Theile: H.F.T.E.A. **50** (1937) 149.
5) W. D. Herschberger: Proc. I.R.E. **24** (1936) 964.
6) S. Sano: J. Inst. Elect. Comm. Eng. Japan. **26** (1942) 764 (in Japanese).
7) E. G. Linder: Proc. I.R.E. **26** (1938) 346.
8) F. W. Gundlach und W. Kleinsteuber: ZS. f. tech. Phys. **22** (1941) 57.
9) W. Kleinsteuber: H.F.T.E.A. **57** (1941) 1.
10) J. L. H. Jonker: Philips Tech. Rev. **5** (1940) 131.
11) K. S. Knol, M. J. O. Strutt and A. van der Ziel: Physica. **5** (1938) 325.
12) B. van der Pol: Phil. Mag. S. 7, **3** (1927) 65.
13) H. Lotze: H.F.T.E.A. **47** (1936) 37.
14) R. Nakamura: J.I.E.E. Japan. **60** (1940) 101 (in Japanese).

JOURNAL OF THE PHYSICAL SOCIETY OF JAPAN Vol. 8, No. 2, MAR.—APR., 1953

On Mechanisms of Mercury Vapour Arc Discharge (I)
Reactive Character of Mercury Arc

By Shoji KIMURA
Hitachi Laboratory, Hitachi Ltd.

(Received August 1, 1952)

By applying an impulsive voltage to the anode of a glass mercury arc rectifier wherein the cathode spot exists, the wave forms of anode voltage, anode current and excitation anode voltage were observed through a high speed oscilloscope or a transient analyser. In consequence it was found that a mercury arc has a characteristic of reactance and it can be explained through the inertia of mercury ions.

§ 1. Introductions

Nowadays there are some reports about the mercury arc of steady state.[1)2)3)4)]

The more the researches on the behavior of the mercury arc in case of steady state become clear the more the researches in case of transient state become important. But any transient characteristic of mercury arc has ever been hardly known. Thus the auther wants to clear the dynamic characteristics of mercury arc.

§ 2. Experimental Procedure

Two kinds of glass mercury arc rectifiers, single anode (100V, 30A rating) and multiple anodes (100V, 30A rating), were used for studying mercury arc. In case of multiple anodes one anode among the three is employed. Multiple anodes have arms but single anode has not.

In order to observe the transient characteristics under application of a high voltage, the circuit is arranged as shown in Fig. 1.

Then the aspect of variation of the arc voltage and the arc current, that is, the voltages across the arc colum and the series resistance in the circuit are observed through a high speed oscilloscope.

Regarding the circuit of Fig. 1 when the excitation anode is ignited, switch S_1 is closed, condenser 0.5μF is charged up and switch S_2 is closed, the sweeping of the time axis of the oscilloscope starts and after a moment the three electrodes gap sparks and an impulsive voltage is given between the electrodes of the rectifier. Since a reactor 17 μH is connected in series with the arc, very high frequency oscillation is restrained and the expected oscillation current flows.

Anode voltage (the voltage between A and C in Fig. 1) and the voltage between B and D are derived by dividing resistances 300 Ω and 100 Ω respectively. The excitation anode voltage (the voltage between E and C in Fig. 1) is applied to the oscilloscope directly. The anode current (equivalent to the voltage be-

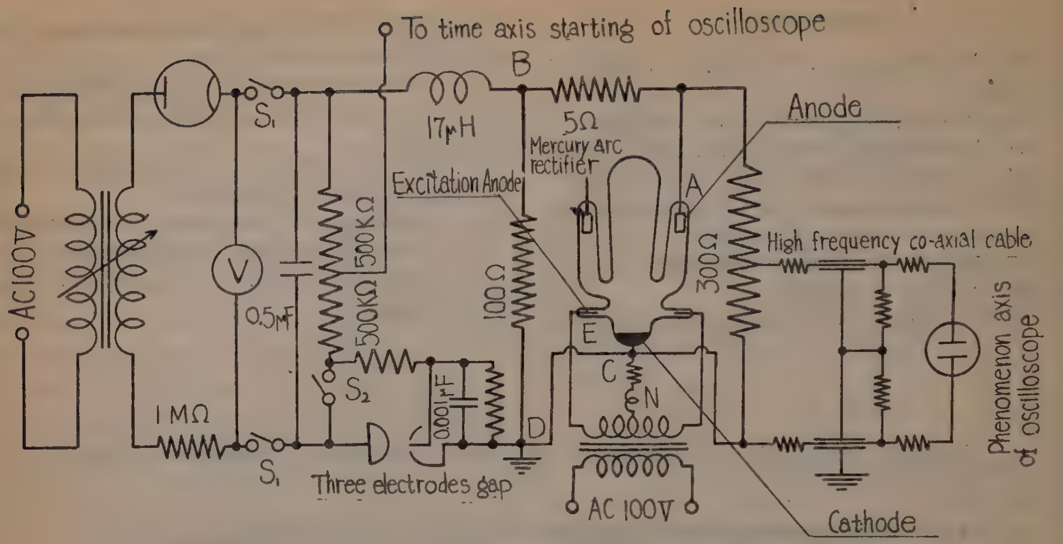

Fig. 1. High voltage phenomena measuring circuit.

tween B and A in Fig. 1) is obtained as a difference of the voltages between B-D and A-C. The applied impulsive voltage is 5kV and the excitation current is 5A. All the circuit condition is arranged to be free from electrical troubles.

A transient analyser is used for the observation of a low impulsive voltage characteristic as shown in Fig. 2. When the discharge tube t_1 discharges, the discharge tube t_2 discharges after a moment and an impulsive current flows in the mercury rectifier at neary the same time as the sweeping of the time axis of oscilloscope starts every cycle. And then the wave form of arc voltage or arc current is obtained as a stationary image on the oscilloscope.

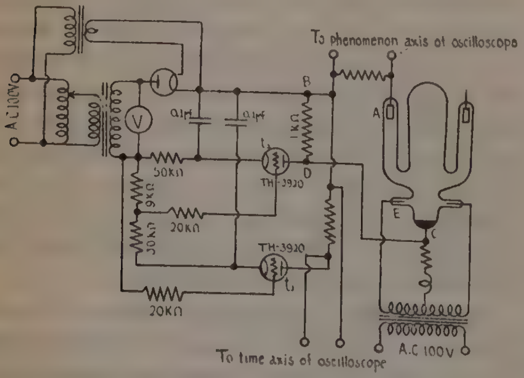

Fig. 2. Transient analyser circuit.

§ 3. Experimental Results

(1) *B-D voltage in Fig. 1 or Fig. 2*

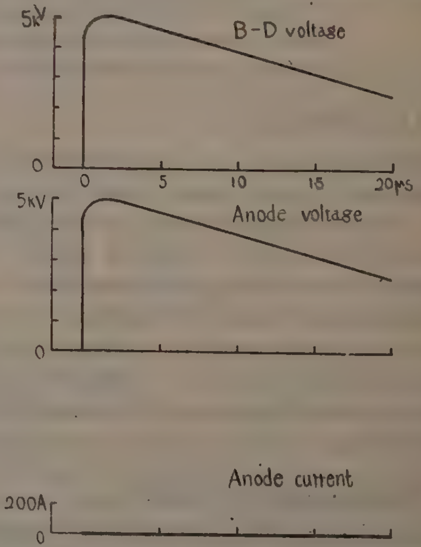

Fig. 3. Negative impulsive characteristic.

In case the cathode spot does not exist or an impulsive voltage is negative, the B-D voltage is completely the same as the source voltage. Fig. 3 shows an example of this case. This fact is proper because a graphite anode can not emit electrons in a normal case. When the cathode spot exists and a positive impulsive voltage is applied, the B-D voltage wave is disturbed, oscillates and turns into a negative voltage taking two different characters as shown in Fig. 4(b)(1) and (2). Just after the impulsive voltage was applied a peak voltage appears in case of the multiple anodes but does not appear in case of the

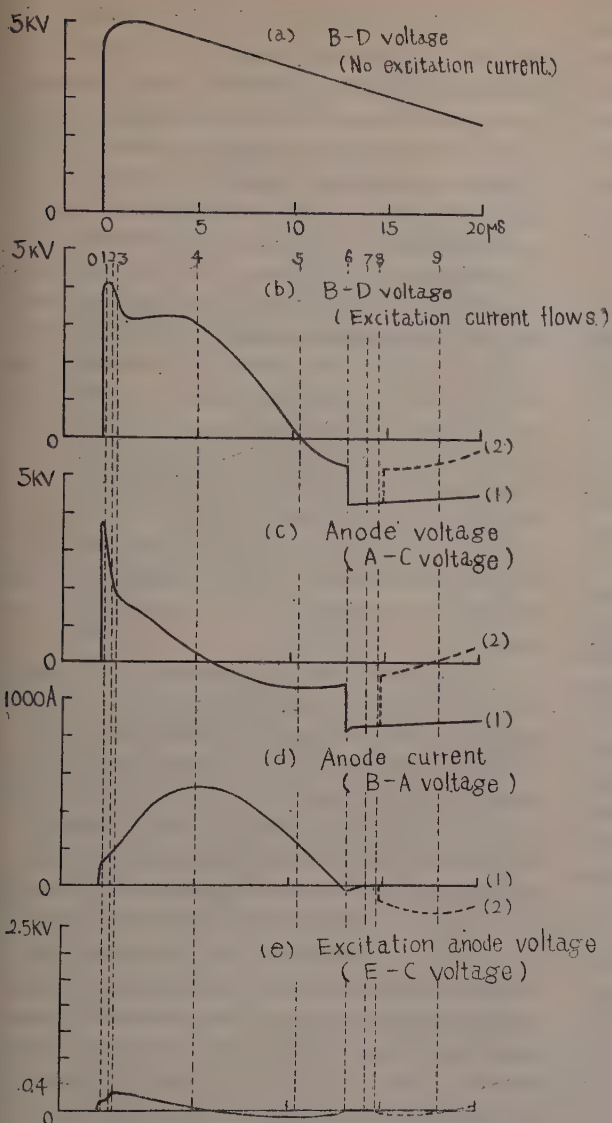

Fig. 4. Positive impulsive characteristic. (Multiple anode)

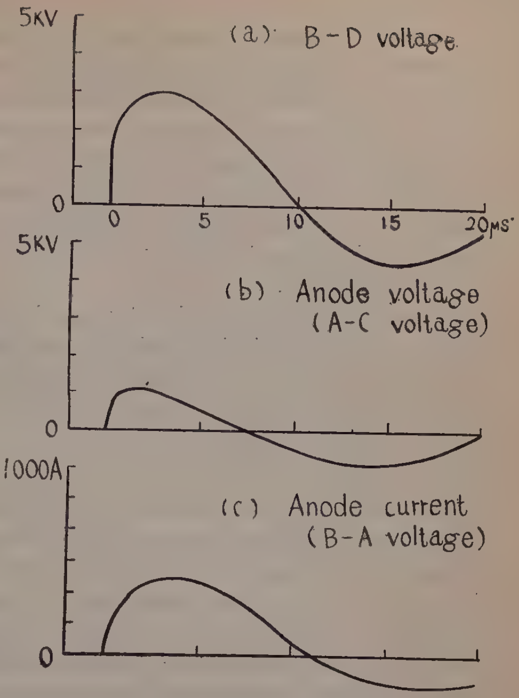

Fig. 5. Positive impulsive characteristic. (Single anode)

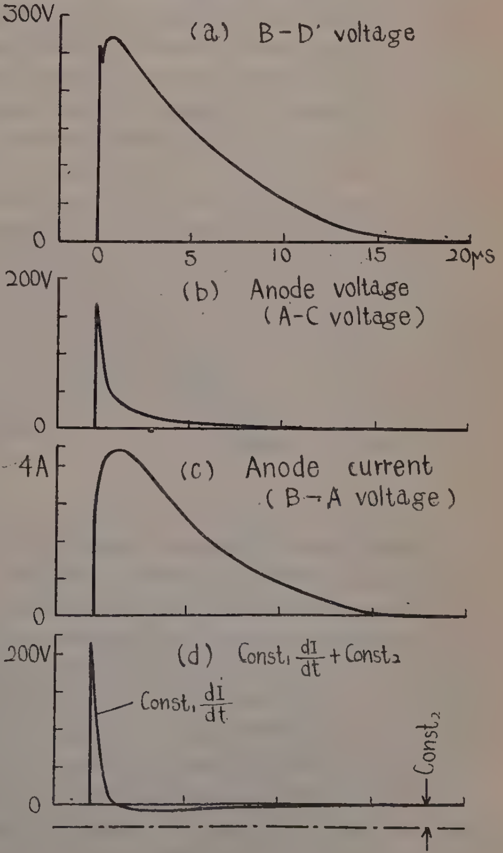

Fig. 6. Positive impulsive characteristic in case of a low voltage.

single anode (Fig. 4(b). Fig. 5(a)).

(2) *Anode voltage (A-C voltage in Fig. 1 or Fig. 2)*

Anode voltage changes in the same way as B-D voltage but the value and the phase relation differ from B-D voltage (Fig. 4(c), Fig. 5(b)). The anode voltage wave takes two forms in its tail of negative parts, that is, Fig. 4(c)(1) and (2). In case of low voltage application a peak voltage appears just after the impulsive voltage was given, but a negative voltage does not appear (Fig. 6(b)(c)).

(3) *Anode current (A-B voltage in Fig. 1 or Fig. 2)*

The anode current varies nearly in sine wave form. The conditions of negative current "to flow or not" have not been known exactly. The auther believes, however, that "flowing" is the case of arc-back, that many electrons emitted from the graphite anode lead to an arc discharge. The instant of zero anode current is later than that of zero anode voltage.

(*4*) *Excitation voltage* (*E C voltage in Fig. 1*)

The wave form of the excitation voltage resembles that of the anode voltage generally, but varies step by step instead of the peak of anode voltage (Fig. 4(e)).

(*5*) *Arc-back*

The impulsive voltage oscillates on account of condenser 0.5μF and reactor 17μH shown in Fig. 1, and no sooner the anode current becomes to zero ampere than positive ions concentrate on the anode surface being attracted by the built up negative anode voltage. Then it is expected in some cases many electrons are emitted from anode surface, that is, an arc-back occours due to the energy of ions concentrated on the anode surface. If the anode current is slight, few ions exist in the discharge space and no arc-back takes place. Through the observations of the bright spots on the anode surface, it is evident that the cases of Fig. 4(b)(1), (c)(1) and (d)(1) are not arc-back and Fig. 4(b)(2), (c)(2) and (d)(2) are arc-back. An arc-back occours almost in every case of single anode as shown in Fig. 5, and yet exact answer for the reason is not found, although the auther considers that it depends upon both the deficiency of the formation of the graphite anode and the high ion density in the discharge space in general.

§ 4. Considerations

(*1*) *Initial state* (*The state 0μs in Fig. 4*)

As only an excitation current flows at the initial state, a positive column and a cathode fall exist but an anode fall does not. And an ion sheath is formed arround the anode surface.

(*2*) *The state just after a voltage was applied* (*The state from 0 to 1 in Fig. 4*)

Just after a voltage was applied, B-D voltage and anode voltage in Fig. 4 increase quickly, and amount to maximum values.

Through this transient period a large number of neutral mercury molecules are ionized, but leave themselves without concentrating into the cathode spot and they permit scarcely anode current to increase and the arc voltage remains nearly equal to B-D voltage.

The excitation arc voltage is about 13V in static state, but in this case becomes higher as shown in Fig. 4(e) under the influence of the voltage of the main arc. Thus it is understood that the excitation anode voltage has the same phase relation as the anode voltage, though the value of the excitation arc voltoge, of course, depends upon the structure of the mercury arc rectifier and the character of the excitation circuit. Because ions run toward the cathode and concentrate in the cathode spot with the lapse of time, many electrons are emitted from the cathode, the electron density increases and the electron temperature decreases in the space.

At this first stage of discharge, it is considered that the increase of current more depends upon the velocity than upon the density of electrons in the neighbourhood of the cathode spot, because the spot area, so the electron density also, can not increase instantly. This seems why the anode current increases rather gradually. A high potential difference is built up the part of arm in case of multiple anodes, but is lost when the influence of electron emission arrives at the part of arm (see Fig. 4(c)). And it does not appear in case of a single anode which has not a narrow part (see Fig. 5(b)).

(*3*) *The moment anode voltage is decreasing quickly* (*The state of 2 in Fig. 4*)

Since many ions are produced in the discharge space and concentrate in the cathode spot, the anode current increases gradually and the anode voltage decreases quickly. On this occasion it is considered that the voltage drops of the part of arm decrease when the influence of electron emission due to the concentration of ions arrives at the arm of the rectifier.

(*4*) *The end of the initial peak voltage* (*The state of 3 Fig. 4*)

After the influence of the electron emission arrives at the part of arm at first, the arc voltage does not vary quickly.

(*5*) *The maximum anode current* (*The state of 4 in Fig. 4*)

According to the concentration of ions in the cathode spot the anode current increases more and more. On the other hand the B-D voltage decreases gradually and the voltage drop across the series resistance increases, thereby the arc voltage decreases. Thus the electric field intensity in the discharge space decreases, the increasing of the anode current stops by and by owing to the decrease of ionization and the anode current amounts to a maximum value notwithstanding that the anode voltage is nearly zero volt. On this occasion B-D voltage is yet positive.

(*6*) *The state of B-D voltage zero volt* (*The state of 5 Fig. 4*)

As the faculty of the electron emission due to the concentrated ions still remains, the positive anode current still continues, but the concentration of ions decreases gradually by diffusion because the ionization does not proceed enough owing to the negative electric field in dischsrge space.

The curcuit including the reactor 17μH as shown in Fig. 1, the B-D voltage oscillates moderately and turns into negative. On this occasion it is considered that there is, as it were, an electric source on cathode surface.

(*7*) *The state after the anode current becomes zero ampere* (*The state from 6 to 7 in Fig. 4*)

Since the electron emission decreases as a result of decrease of the ion current flowing into the cathode spot, the anode current decreases and then becomes zero ampere. When the electron source is lost, electrons flow no longer into anode. At this time the discharge space has still a fairly high negative electric field and many space charges remain. Since the anode has not the faculty of electron emission, only the low diffusion current due to the remained charges flows and the anode voltage becomes nearly equal to the external condenser voltage.

That is, the voltage across the reactance 17μH becomes zero and the negative anode voltage increases instantaneously (see Fig. 4(c)6).

Thereafter the ions are attracted to the anode by the negative anode voltage and then the ion current sets up gradually. But the negative current due to the remained ions is much less than the positive current, and electrons and ions recombine at the wall gradually, and then only the difiusion current from the excitation arc remains as the ion current.

(*8*) *The state of ion current nearly zero ampere or arc-back* (*The state after 7 in Fig.4*)

When only the diffusion current from excitation arc becomes to exist, the negative anode voltage is nearly equal to the voltage across the condenser 0.5μF as shown in Fig. 1. If so sufficient energy that arc-back happens is given to the anode by ions, electrons are emitted from the anode suddenly and a negative arc is produced. Then the negative arc voltage decreases quickly.

(*9*) *The case of a low voltage* (*Fig. 6*)

As in case of a low voltage the change of current is controled not only by the velocities of charges but the densities of charges, that is, the spot area, the rate of change of voltage with current is slight except in its starting transient. Therefore the start is similar to that in case of high voltage, but the wave form in the other time does not change so quickly because the ion densities follow the current to some extent. Thus it does not occour that a positive current flows in spite of a negative arc voltage.

§ 5. Discussions

In order to obtain the equivalent reactance of arc it is assumed that the electric field intensity on the cathode surface is constant and the collision of ions with the neutral molecules can be neglected.

The equation of motion of an ion is expressed by

$$Mx=\tfrac{1}{2}eEt^2, \qquad (1)$$

where M denotes the mass of an ion, that is, 3.3×10^{-22} g,e the electric charge on an ion, that is, 4.7×10^{-10} e.s.u., x the distance from the cathode, E the electric field intensity in e.s.u. and t time in sec. The following considerations are performed about Eq. (1). The greater part of the anode voltage is given in the neighbourhood of the cathode and in the part of arm. The high electric field intensity in the neighbourhood of the cathode, which depends upon the cnocentration of ions, seems to be within about 1 cm by the observation of a very bright light.

If the initial peak voltage in Fig. 4 is considered to depend upon the arm resistance, about 2 kV is given in 1 cm as a result of the applied voltage 4 kV. Therefore the electric field intensity is regarded as about 2000 $\times(1/3)\times10^{-2}$ e.s.u. The time from the start of the motion of an ion till the influence of electron emission appears is estimated approximately as

$$t=\sqrt{\frac{2Mx}{eE}}=0.5\times10^{-6}\ \text{sec}, \qquad (2)$$

where the time of the motion of electrons is disregarded here because it is negligiblly small. This result agrees nearly with the time of the state of 1-2 in Fig. 4. Hereby it is known that the variation of arc voltage or arc current depends upon the motion of ions.

Through above considerations in § 4 it is known that an arc has a reactive character for impulsive current. This relation is expressed dy

$$L\frac{dI}{dt}=V_a, \qquad (3)$$

where I is the anode current, V_a the arc voltage and L the reactance of the arc.

By using the values of dI/dt and V_a at 10μS in Fig. 4(c) and (d),

$$L\doteqdot 7\ \mu\text{H} \qquad (4)$$

is obtained. On this occasion L is considered to depend upon the inertia of ions. The motion of an ion is shown by

$$\frac{\partial Mv}{\partial t}=e\frac{\partial V}{\partial x}\times10^7, \qquad (5)$$

where v (cm/sec) is the velocity of an ion, e the electric charge on an ion, that is, 1.592×10^{-19} coulomb and V the potential (volt). Integrating Eq. (5)

$$\frac{1}{10^7e}\int_0^a\frac{\partial Mv}{\partial t}\partial x=\int_0^a\frac{\partial V}{\partial x}\partial x,$$

that is,

$$\frac{\partial}{\partial t}\frac{1}{10^7e}\int_0^a Mv\partial x=V_a, \qquad (6)$$

where V_a means the arc voltage. Then if the most part of the arc voltage is given near the cathode and v is regarded as nearly constant near the cathode for simplicity, Eq. (6) is simplified as follows:

$$\frac{\partial}{\partial t}\frac{Mav}{10^7e}=V_a. \qquad (7)$$

On this occasion a means the effective arc length having the high electric field intensity. From Eqs. (3) and (7)

$$\frac{\partial}{\partial t}\frac{Mav}{10^7e}=\frac{\partial}{\partial t}LI$$

is obtained. Integrating this equation

$$\frac{Mav}{10^7e}=LI,$$

that is,

$$L=\frac{Mav}{10^7eI}, \qquad (8)$$

when $v=0,\ I=0$ at $t=0$.

And

$$i=Anev, \qquad (9)$$

where i is the ion current, n the ion density, and A is the sectional area of the arc column. Eventually L is obtained as follows.

$$L=\frac{Mai}{10^7e^2AnI}. \qquad (10)$$

If L is dependent only on the velocity of an ion, all of a, A, n and i/I are constant and has the initial values. According to the observation, as well as the probe methode, a, A, n and i/I are regarded as about 1 cm, 0.2 cm^2, 200×10^{11} cm^{-3} and 1/20 respectively.

The value of i/I is estimated from the evapolation quantity of mercury due to the ion current as well known.[5] Therefore

$$L\doteqdot 12\times10^{-6}\text{H} \qquad (11)$$

is obtained. This value is not irrational in comparision with Eq. (4) in spite of rough calculations, hence it seems to be true that L of an arc is dependent to the inertia of ions.

As a matter of fact the increasing of the current depends upon not only the velocity of ions but the ion density too. In such case L is the true reactance but varies more or less with the lapse of time.

The more the rate of the variation of current is small, the more the influence of the increase of ion density becomes evident. In case of the slow variation of arc current as shown in Fig. 6 the increase of the ion density due to ionization is rather much remarkable than the ion velocity.

Next the circuit of Fig. 1 may be replaced with the equivalent circuit as illustrated in Fig. 7, where the reactance 7 μH corresponds to the arc. As switch S_a is closed in the process of the current decreasing, the capacity voltage V_0 is divided by the reactances into reactance voltage V_1 and arc voltage V_2. Then if switch S_a is opend suddenly when the anode current is zero ampere, the arc voltage V_2 changes to V_3, that is, V_0+V_1.

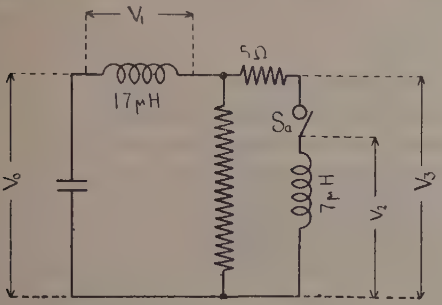

Fig. 7. Explanation figure of an impulsive characteristic.

When S_a is closed the arc voltage takes the value of

$$V_2=\frac{7}{17+7}V_0\fallingdotseq 0.3V_0 .$$

But just when S_a is opened the arc voltage takes the value of

$$V_3=V_0+V_1\fallingdotseq V_0 ,$$

consequently about the thrice peak voltage ought to appear. The experimental data in Fig. 4(c) is supporting this fact.

§ 6. Conclusion

The mercury arc characteristics on an impulsive current were studied experimentaly or theoreticaly. In general a mercury arc has a reactive action for an impulsive current and it is thought to result from the inertia of an ion. And its reactance depends upon the ion density in the neighbourhood of the cathode spot too.

Acknowledgement — The auther wishes to express his sincere thank to Dr. Honda, Dr. Uchida, Dr. Miura, Dr. Kubo and Mr. Hashimoto for their valuable discussion or encouragement.

References

1) I. Langmuir and H. Mott Smith: Tr. G. E. Rev. **27** (1924) 449, 538, 616, 762,810.
2) I. Langmuir: J. Fran. I. 275 Dec. (1932).
3) L. Tonks: Phys. Rev. **51** (1937) 744.
4) L. Tonks: El, Chem. Soc. **72** (1937) 167.
5) A. V. Engel und M. Steenbeck: Elektrische Gasentladungen II (1934) 136.

Journal of the Physical Society of Japan Vol. 8, No. 2, Mar.—Apr., 1953

On Mechanisms of Mercury Vapour Arc Discharge (II)
Structure of Mercury Arc

By Shoji KIMURA

Hitachi Laboratory Hitachi, Ltd.

(Received August 28, 1952)

The research on a mercury arc was performed by movable probes. Through the result of this research the aspect of the distribution of potential, electron temperature, electron density, neutral molecul density and luminous appearance of discharge were made clear. Then the considerations on these quantities were done by dividing the phenomena into the anode fall, the positive column and the distribution of the mercury vapour density. Thus the extensive characteristics of a mercury arc were known.

§ 1. Introduction

There are some experimental or theoretical descriptions about a mercury arc[1)2)]. Wherein the characteristics of an arc are discussed theoretically, or observed experimentally by the probe method applying the gas theorey to analyse the phenomena of the positive column of the arc or glow discharge at a low pressure[3)4)].

Even if the characters of only two or three points in discharge space are known by the probe method, it is not sufficient to discuss about these of the whole discharge space. Therefore some movable probes are used for considering the characters of the various points of mercury arc space.

§ 2. Experimental Apparatus and Method

Since three dimensional measurement is difficult, the symmetrical structure about central axis is used. As shown in Fig. 1 the experimental apparatus is made of a glass cylinder which has a bottom, 26 cm diameter and 40 cm length, and the iron cover on which necessary electrodes, probes etc., are attached. And a special paste is used for maintaing vacuum and the anode current are limited under 20 A for limiting the wall temperature below 40° C. The driving of the cathode spot is limited only in a small glass cylinder which has 1 cm diameter and 0.5 cm length over the mercury cathode pool. Regarding to the probes, the bundle lead wire consisted of nine elemental wires is put in a fine and long glass tube, and these elements are separated at the upper window of the tube.

The active parts of the probe for measurement are Ni-wire segments with 0.5mm diameter and 1 cm length. In Fig. 1 when the coil e is excited, the iron piece f is pulled downwards and the ignition anode h makes contact with mercury pool. When the coil circuit is opened, f moves upwards and the ignition anode is separated from the mercury pool, and then the mercury arc is ignited. When cock g is turned around its axis, the probes P_1, P_2 ··········,P_9, turn too, and the measurement is carried at any position of the probe. On this occasion the measured quantities are the anode currents, the probe currents and the probe voltages.

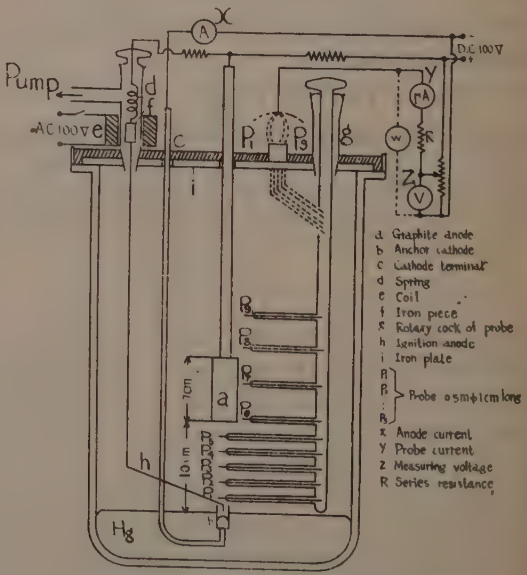

Fig. 1. Measuring apparatus.

§ 3. Observation of Mercury Arc

The transition of mercury arc appearance due to the increase of current are shown in Fig. 2. The cathode spot emits always a very brilliant light at any value of the current as well known. When the anode current is about 3A, the greater part of the discharge space has a faint light, but an especially bright sphere is made under the anode and the side of the anode throws out also more or less bright light than the other parts. If the current becomes 4–5A, the side light disappears. On this occasion if the distance between electrodes is 18 cm, the other bright surface appears on the midway of the arc path. If its distance is 10 cm the above bright surface does not appear. When the current becomes 6A the bright surface disappears and yet the anode bright sphere remains. At about 10A the anode bright sphere disappears and the light in the whole space becomes brilliant gradually. If a comparatively large anode is used the base of anode bright sphere does not cover all anode surface, but the central part of the anode surface.

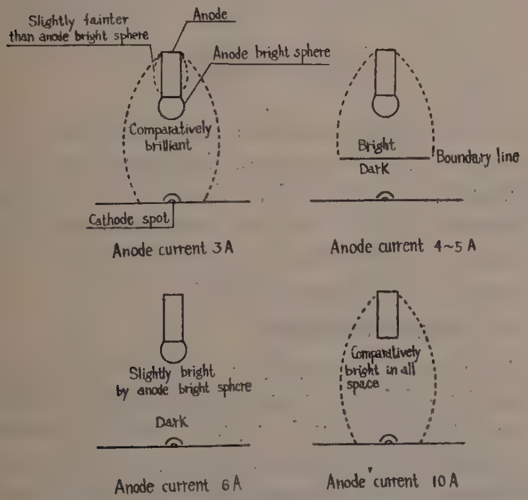

Fig. 2. Observation of mercury arc.

If a round screen is put on the midway of the discharge space, or the cathode spot hides itself behind a kind of obstacle, the anode bright sphere becomes very large as shown in Fig. 3. As the mercury vapour evapolates from the cathode spot and condenses on the wall, the screen or obstacle stops the vapour flowing in the direction of the anode and operates to decrease the vapour density in the vicintiy to the anode. And as the arc path becomes longer the electron density becomes rarer in the vicinity of the anode. When there is the screen or obstacle, the bright sphere becomes much smaller with the rise of the wall temperature but varies slightly with the increase of the current at the same wall temperature. Therefore it is considered that the variation of the bright anode sphere depends upon the vapour density mainly. After all the relation between the bright anode sphere and the current is also attributed to vapour density.

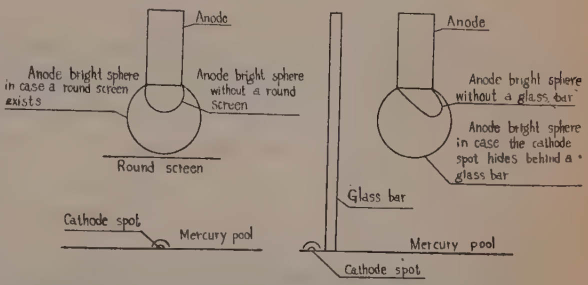
Anode
Anode bright sphere in case a round screen exists
Anode bright sphere without a round screen
Round screen
Cathode spot
Mercury pool
Anode
Anode bright sphere without a glass bar
Anode bright sphere in case the cathode spot hides behind a glass bar
Glass bar
Mercury pool
Cathode spot

Fig. 3. Expansion of anode bright sphere.

The decrease of vapour density is nothing but the deficiency of the space charges and a higher electric field becomes necessary for mainting the current.

§ 4. Electrical Characteristics of Discharge Space

(1) *Potential distributions*

The results of the measurement of the potential distribution are shown in Fig. 4. And from the measured values of space potentials the equipotential lines are drawn. When the current becomes higher, the equipotential lines becomes to rise fairly sharp near the cathode center. Increasing the vapour pressure by raising the wall temperature has been also known to be equal to this phenomenon. After all it is considered that the sharpness of the equipotential lines near the cathode depens upon the vapour density. By the distance between electrodes only the equipotential lines near the anode vary, but these near the cathode do not vary.

(2) *Electron temperatures*

The electron temperatures along the central axis are shown in Fig. 5, where the measured values of probe p_1 near the cathode surface seem to include some errors. It is known from this experiment that the electron tem-

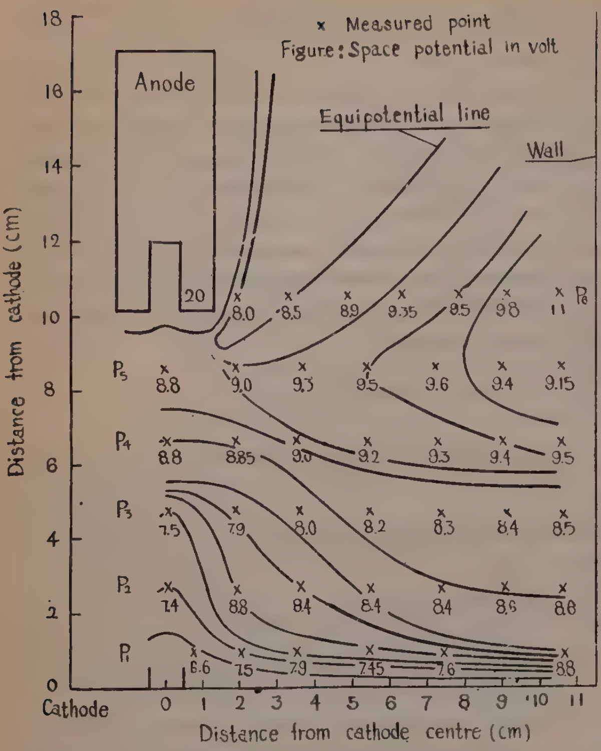

Fig. 4. Potential distribution in case of arc current 5 A and electrodes distance 10 cm.

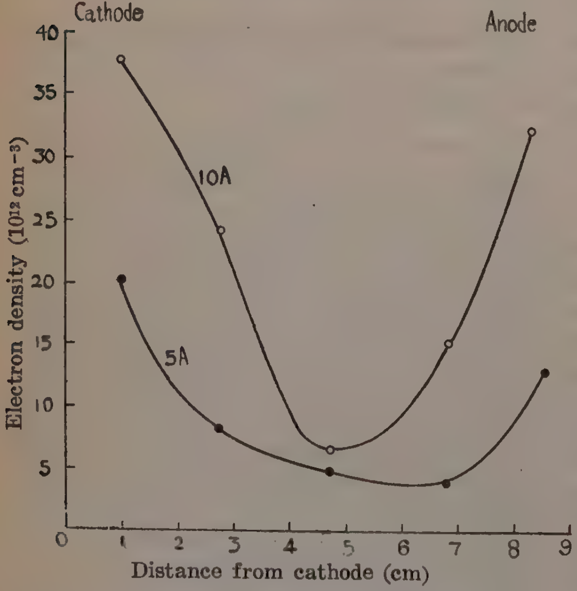

Fig. 6. Electron density along central axis.

perature becomes higher with the decrease of the current and the position of the maximum electron temperature on the midway of arc path approaches toward the cathode with the increase of current.

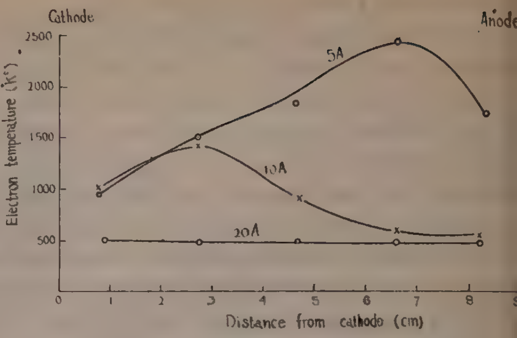

Fig. 5. Electron temperature variation along central axis.

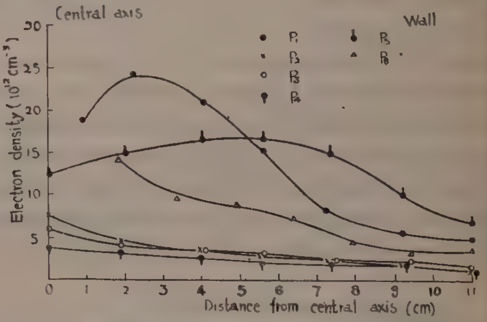

Fig. 7. Electron density from central axis to wall in case of anode current 5 A.

If the current becomes higher, the electron temperature becomes to be more uniform along the central axis. And the more the measured points in the discharge space approach to the wall, the more the electron temperatures become higher.

(*3*) *Electron densities*

The electron density on the central axis has the minimum value on the midway of the arc path as shown in Fig. 6, and increases as the current increases. The electron density becomes lower as the measured points approach to the wall from the central axis. This characteristic is shown in Fig. 7. And when the current is high it is also known that electrons concentrate near the central axis especially. It is interesting that the electron densities of probe p_1 and p_5 are somewhat low in the neighbourhood of the anode and the cathode in Fig. 7.

§ 5. Distribution of Neutral Molecules

(*1*) *Measurement of the mercury vapour densities*

Though various methods have been already used for measuring the densities of neutral molecules,[5] the method of measuring the density of a special point in a discharge space has not ever been tried. The auther succeeded to some extent by the positive probe characteristics.

When the probe potential becomes higher than the space potential, an electron sheath is made round the probe. And the sheath is expected to be fairly thick theoretically.[4] But if the vapour density is fairly high, the electrons which flow into the probe collide with neutral molecules or ions many times, and make new charges or recombine with ions. Therefore in reality the influence of the probe potential does not reach to so far distance.

And then if the thickness of the electron sheath becomes more than the mean free path of electron, somewhat transitions of the positive probe characteristics ought to occour. Ordinarily the probe current is expected to increase sharply by ionization. It is considered that the point 3 of the positive probe characteristic in Fig. 8 is the starting point of ionization and the thickness of the electron sheath is equivalent to the mean free path of neutral molecules. Now in case of a cylindrical probe, if the probe radius, the radius of the electron sheath cylinder, the random electron current and the probe current of the point 3 are represented by r_1, r_2 j_- and j respectively as shown in Fig. 9. there is the following relation

$$\frac{r_2}{r_1}=\frac{j}{j_-} \quad \text{that is,} \quad r_2-r_1=\frac{j-j_-}{j_-}r_1 .$$

And then r_2-r_1, which is equal to the mean free path, is able to be obtained from the known quantities r_1, j and j_-. Since the mean free path is in inverse proportion to the vapour density, after all the vapour density can be obtained.

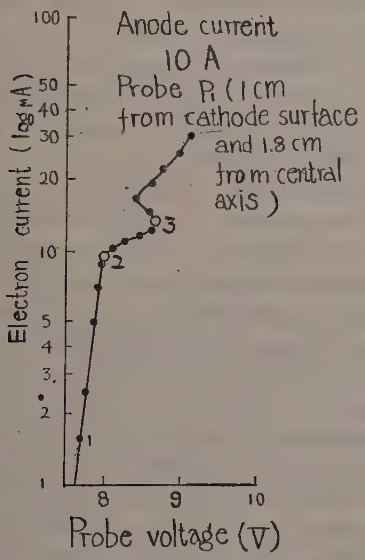

Fig. 8. Positive probe characteristics.

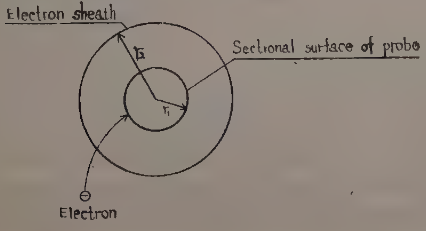

Fig. 9. Electron sheath.

(2) *Distribution of the mercury vapour density*

By the above method $\frac{j}{j-j_-}$, which is proportional to the vapour density, is obtained as shown in Fig 10. The distance between the anode and the cathode is 5 cm in Fig. 10, so the measured points over 5 cm are obtained by the probe P_6 put in the side direction of the anode and apart from the anode. Thus it is found that the vapour density is high in the neighbourhood of the cathode spot and is low in the lower part of the anode and is slightly high in the direction of the anode. Then it is interesting especially that there is a region of very high vapour density on the midway from the cathode to the anode as

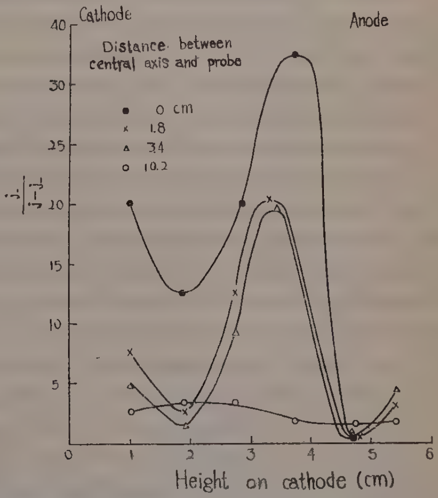

Fig. 10. Vapour density from cathode to unside in case of arc current 10A.

shown in Fig. 10. This feature becomes more remarkable as the current increases. And it is also known that the vapour density is low near the wall and the nonuniformity of the vapour density becomes more remarkable as the current increases.

It is known from the above measurement that the mean free path of electrons is about 2 mm corresponding to the saturation vapour temperature 50–100°C (corresponding saturation vapour density $10^{14}-10^{15}\,\mathrm{cm}^{-3}$) near the anode, and is about 1.2×10^{-2} mm corresponding to the saturation vapour temperature 150–200°C near the cathode.[6] These values are not irrational in comparison with the temperatures of the wall, the anode and the cathode spot, which are said to be about 220–300°C in the spot.[7]

§ 6. Considerations

(1) *Positive column*

As the ions assemble to the cathode spot on account of the electric field, it is known from Poisson's equation that the equipotential lines at the vicinity of the cathode spot are illustrated by Fig. 4. The electrons are shot on all directions from the cathode spot, the electron densities in the space distant from the spot decrease as shown in Fig. 6. On the other side the electron temperature becomes higher since electrons are accelerated by the electric field as shown in Fig. 5. Generally when the vapour density is too high, the electrons can not obtain sufficient energy to ionize the neutral molecules, because the mean free path of electrons is very short. On the contrary when the vapour density is too low, few molecules are ionized because the chances of collision are very rare. Thus the charge density in the neighbourhood of the cathode spot along the central axis is unexpectedly low because of too high vapour densities. And then it is expected that electron densities are rather low on the central axis than the other parts.

For instance curves P_1 and P_5 in Fig. 7 are illustrating this phenomena.

The fact that the electric field on the central axis, especially at the neighbourhood of the cathode, is somewhat weaker than that in the other portion as shown in Fig. 4 is also attributed to this phenomenon.

The relation between the positions of the cathode spot and the forms of the anode bright sphere in Fig. 3 seems to depend upon the distributions of the mercury vapour density. The reason is explained as follows. At first a very brilliant light is seen at the cathode spot, because the electrons emitted from the cathode spot are accelerated by the cathode fall and lose their energies by collisions at the brilliant part. Soon after, they are energized by the electric field again. And when the obtained energy become sufficient to ionize neutral molecules, a violent ionization by collision is set up by those electrons generating many ions and then a brilliant light appears there once more. It is due to the above reason that a brilliant light appears when the vapour density is low and the distance between electrodes is proper, say 18cm. And it is known by a probe method that the potential difference between the cathode spot and the brilliant space is about 10 V which is equal to the effective ionization voltage of the neutral molecules.

The anode bright sphere is also attributed to this phenomenon. And it is thought to be due to the deficiency of the vapour density that the anode bright sphere becomes larger by a kind of obstacle as shown in Fig. 3.

If the vapour density is high, the above special brilliant light does not appear because the resistive action due to collisions balances with the electric field at all parts. Then the whole discharge space becomes brilliant. Various cases of these phenomena are illustrated in Fig. 2.

When the current becomes higher, there exists a negative electric field in the most part of the space. The potential distributions shown in Fig. 11 illustrate this phenomena well.

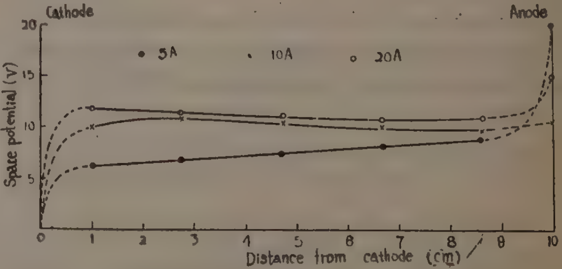

Fig. 11. Potential distribution along central axis.

(2) *Anode fall*

Anode fall exists for supplying the kinetic energy to electrons which is lost on the surface. Since many ions are produced by collision when electrons flow into the anode, in reality some field rich of negative charges seems to exist within the mean free path from the anode.

For instance, even if a probe is inserted in the anode bright sphere, any sharp increase of space potential distinguishable from the other part is not observed.

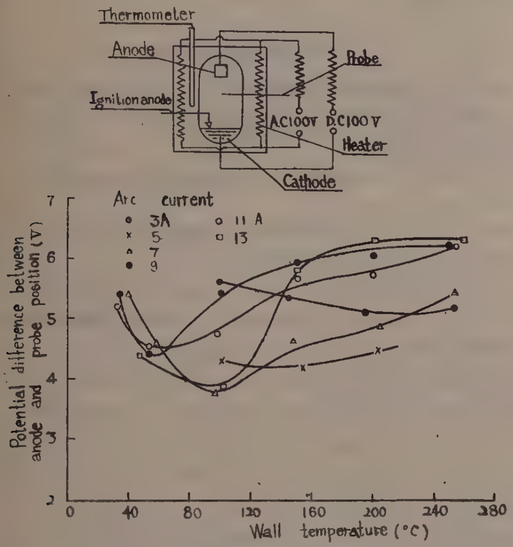

Fig. 12. Potential difference between anode and probe position.

When the electron density increases with the increase of the vapour density, the anode voltage drop decreases by the decrease of the mean free path but the voltage drop across the positive column increases for maintaining some drift velocity of an electron and for supplying the deficiency of electron energy originated in the decrease of the mean free path. Therefore if the vapour density increases by heating the apparatus, the potential difference between the anode and the probe has a minimum value at certain wall temperature as shown in Fig. 12 from the above two effects.

(3) *Relation between charge density and vapour density*

If the temperature of the cathode spot is regarded to be about 300°C as well said, its vapour density is about $4.18\times10^{18}\,\mathrm{cm}^{-3}$, and if the wall temperature is about 40°C, its vapour density is about $10^{14}\,\mathrm{cm}^{-3}$. And then it is believed that there is a variation of the vapour density ranging, $4.18\times10^{14}\,\mathrm{cm}^{-3}$, in the arc space. Though the mercury vapour evaporating from the cathode spot condenses on the wall, the vapour current does not only follow diffusion equation but also shows a delicate variation by the action of charge densities.

In the neighbourhood of the cathode spot the vapour density is estimated as about $10^{16}-10^{18}\,\mathrm{cm}^{-3}$ corresponding to the saturation temperature of the mercury vapour. On the other side the electron density or the ion density in the neighbourhood of the cathode spot is about $10^{13}-10^{14}\,\mathrm{cm}^{-3}$ from Fig. 6. Therefore the vapour current may be considered to follow only diffusion equation in the neighbourhood of the cathode spot. Thus the vapour density decreases in the space depart from the cathode spot as shown in Fig. 10.

It is considered approximately that the ion temperature corresponds to the potential difference in the mean free path. Now this ion temperature is estimated. The vapour density $10^{14}-10^{15}\,\mathrm{cm}^{-3}$ in the neighbourhood of the anode corresponds to the mean free path $10^{-1}-1$ cm and the electric field intensity in the neighbourhood of the anode is about 0.5 volt/cm in case of 10 A as shown in Fig. 11. Therefore the energy that ions are given in the mean free path is about $5\times10^{-2}-5\times10^{-1}$ volt. This value corresponds to the ion temperature $3.5\times10^{2}-3.5\times10^{3}\,{}^\circ\mathrm{K}$. On the other hand as the ion density is $10^{13}-10^{14}\,\mathrm{cm}^{-3}$ and the molecule temperature is about $3.2\times10^{2}-3.7\times10^{2}\,{}^\circ\mathrm{K}$, which corresponds to 50°C~100°C. Therefore the product of temperature and density, which is proportional to the pressure, is about $10^{16}-10^{17}\,{}^\circ\mathrm{K}\cdot\mathrm{cm}^{-3}$ in each case of ions and neutral molecules. Thus the vapour density in the neighbourhood of the anode is thought to be greatly affected by the pressure of ion gas. In addition to this the pressure of electron gas affects its density too. But its effect is not remarkable because electrons give the ionization energy or excitation energy mainly and give only a little kinetic energy to molecules. When the wall temperature is low, the vapour density in the neighbourhood of the anode becomes lower and lower as the ion temperature becomes higher. Next it is considered properly that some kind of force which balances with the pressure of the ion gas in the neighbourhood of the anode ought to exist. This force appears as the large vapour density on the midway of the arc path as shown in Fig. 10 and the force due to this large vapour density balances also with the drift molecular energy from the cathode.

In addition to the above random ion energy the drift ion energy or the anode temperature is also considered to have fairly great effect for the distribution of the vapour density.

§ 7. Conclusion

As a result of several kinds of measurements and considerations on the mercury arc discharge, the following conclusions have been obtained.

(1) The anode bright sphere grows when the mercury vapour density becomes lower.

(2) There is a negative electric field across the positive column on occasion.

(3) There is the part of a low electron density on the midway from cathode to anode.

(4) There is the part of a high electron temperature on the midway from cathode to anode.

(5) There is the part of a high vapour density on the midway from cathode to anode.

(6) A high electron density and a high electric field appear for the side direction at the neighbourhood of the cathode spot.

Acknowledgement — The auther wishes to express his sincere thank to Dr. Honda, Dr. Uchida, Dr. Kubo and Mr. Hashimoto for their valuable discussions and encouragement throughout this work.

References

1) T. J. Killian: Phys. Rev. **35** (1930) 1238.
2) I. Langmuir, H. Mott-Smith: G. E. Rev. **27** (1924) 538.
3) Engel, Steenbeck: Elektrishe Gasentladungen I. II (1934).
4) Loeb: Fundamental Processes of Electrical Discharge in Gases (1939).
5) W. Dällenbach: E. T. Z. **55** (1934) 440.
6) Knoll-Ollendorff-Rompe: Gasedtladungstabellen (1935).
7) M. J. Druyvesteyn, F. M. Penning: Rev. M. Phys. **87** (1940).

JOURNAL OF THE PHYSICAL SOCIETY OF JAPAN Vol. 8, No. 2, MAR.—APR., 1953

On Mechanisms of Mercury Vapour Arc Discharge (III)
Some Characters of Mercury Arc

By Shoji KIMURA
Hitachi Laboratory Hitachi, Ltd.

(Received August 28, 1952)

Various experiments and considerations on the condition of ignition, the arc voltage drop fluctuation due to the motion of the cathode spot, the arc pathes depending upon a baffle inserted in the arc space were performed. And some characters which depended upon the temperatures of some parts of the arc equipment were studied too. As the motion of the cathode spot and the temperatures of the arc equipment have interesting and particular effects on the mercury arc, the relations with those are mentioned in this report.

§ 1. Introduction

The cathode spot drives always on the cathode surface after it is ignited and its driving depends upon the distribution of charge density or vapour density. Therefore it is interesting to consider the aspect of the ignition and the driving of the cathode spot.[1)2)] In addition to these the mercury vapour density increases with the temperature of the arc equipment generally, but decreases in the neighbourhood of a superheated electrode inserted in the discharge space. Thus a mercury arc is affected by the current, the wall temperature, the electrode temperature and the construction of the arc equipment. Therefore a mercury arc is very complicated in comparison with the glow discharge. The auther wishes to describe on those particular characteristics of a mercury arc.

§ 2. Ignition of Mercury Arc

By the apparatus shown in Fig. 1, when the cock S is turned, the ignition anode A_i is separated from the cathode B and an arc current flows between the anode A and the cathode B, that is, the arc starts.

In the figure the ignition anode voltage V is controled with the resistance R_1. The ignition current *mA* in Fig. 1 is read when the ignition anode closes, and is changed with the resistance R_2. The anode voltage means the source voltage E of the anode circuit, and as the anode current the steady arc current is read. When the ignition characteristic depending upon the anode current is obtained, the condenser 2 μF and the resistance R_4 are taken off.

The values of the ignition current and the ignition voltage necessary for various starting conditions are shown in Fig. 2 in case of the anode voltage 100 V. All points shown in the figure satisfy the conditions,

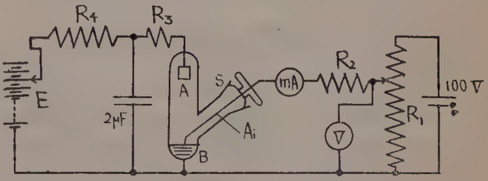

Fig. 1. Ignition circuit of mercury arc.

$$\left.\begin{array}{l}\text{the current} > \text{about } 50\text{ mA}\\ \text{the voltage} > \text{about } 8\text{ V}.\end{array}\right\} \qquad (1)$$

Now taking account of such experimental conclusions the following consideration may be derived. At first an energy is required for the electron emission on the cathode surface, that is,

$$I_+\tfrac{1}{2}m_+v_+^2 = I_+eV_c > K_1, \qquad (2)$$

where m_+ is the mass of an ion, v_+ the velocity of an ion, e the electric charge per ion, K_1 a constant, I_+ the ion current and V_c the voltage between the electrodes as shown in Fig. 1. The emitted electrons produce many ions colliding with many neutral molecules and those ions contribute in turn to the subsequent electron emission. For the ionizing collision a voltage necessary for the acceleration of electrons ought to exist, that is,

$$V_c > K_2, \qquad (3)$$

where K_2 is a constant. Therefore

$$I_+eV_c > I_+eK_2 > K_1, \text{ that is, } I_+ > \frac{K_1}{eK_2}$$

i,e

$$I_+ > K_3$$

is obtained, where K_3 is a constant. As I_-/I_+ is regarded as a constant,

$$I_- > K_4 \qquad (4)$$

is obtained, where I_- is electron current and K_4 a constant.

And then Eqs. (3) and (4) give the limiting values of ignition, and K_2 is about 8 V and K_4 is about 50 mA experimentally. And it is true in reality that an ignition problem is a matter of probability. Thus the condition that the arc is ignited on the same probability ought to be expressed by

$$(V_0 - K_2)(I_- - K_4) = K_5\,, \qquad (5)$$

where K_5 is a constant. In fact this chracter is illustrated in Fig. 2. The ignition probability of the main anode A in Fig. 1 depends upon the anode voltage, the anode current, the ignition anode voltage and the ignition anode current. The relation between the anode voltage and the ignition anode voltage is shown in Fig. 3 where the ignition probability is ½ and the ignition anode current is 50 mA. Fig. 3 shows that the condition of building up the anode arc depends upon the generation of the cathode spot of the ignition

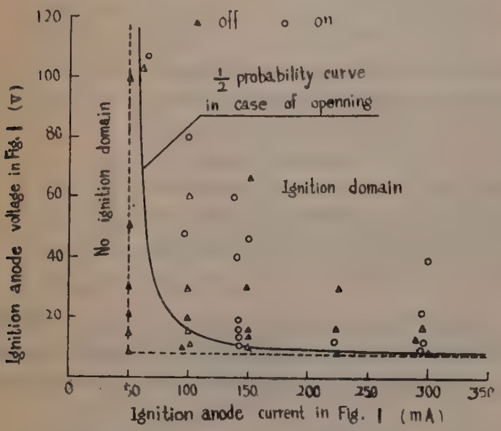

Fig. 2. Ignition characteristics.

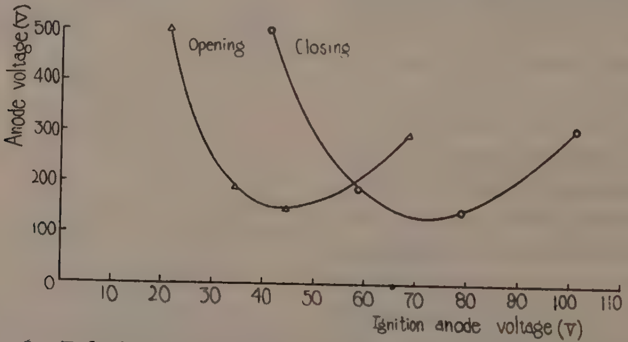

Fig. 3. Relation between anode voltage and ignition voltage.

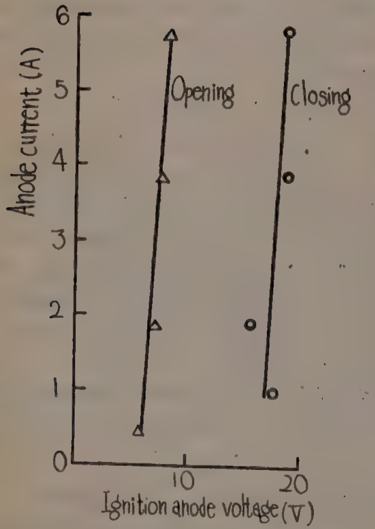

Fig. 4. Relation between anode current and ignition anode voltage.

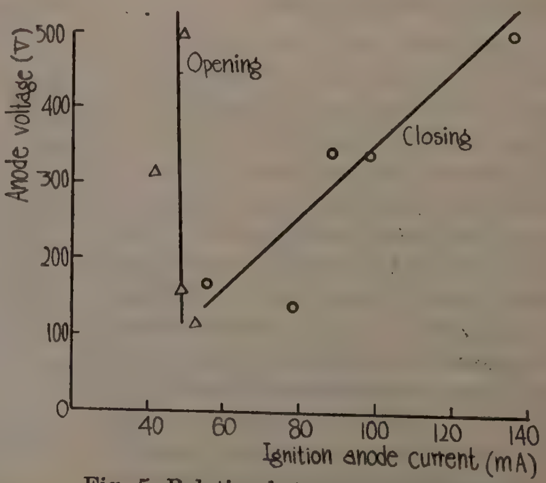

Fig. 5. Relation between anode voltage and ignition anode current.

anode delicately. And it is considered that the anode–ignition anode voltage and the ignition anode–cathode voltage have a relation for the building up of the arc.

The relation between the anode current and the ignition anode voltage is shown in Fig. 4 where the ignition probability is ½, the anode voltage is 90 V and the ignition anode current is 100 mA. The anode current is slightly under the influence of the ignition anode voltage as shown in Fig. 4.

The relation between the anode voltage and the ignition anode current is shown in Fig. 5 where the ignition probability is ½ and the ignition anode voltage is 20 V. The anode voltage is dependent on the ignition anode current in case of closing and is not in case of opening. Though the above results are obtained under a simple electrical circuit condition, various characters are shown under various electrical circuit conditions.

In case of opening, the ignition anode opens and never closes after that. On the contrary in case of closing, the mercury vapour evapolates by the heating at the instant when the ignition anode contacts with the mercury surface. Hence the ignition anode separates again for a moment and the arc starts. But after a moment the ignition anode dips into the pool. So even if the arc of the ignition anode starts in case of closing, the cathode spot is apt to extinct before the anode arc grows enough. This depends upon the fact that the growth of arc is slow unexpectedly because the arc has a reactive character as shown in Part I. If the ignition anode separates from the cathode to a fairly long distance in case of opening or connects with the cathode in case of closing, the ignition anode current is not any longer maintained by the small current or extincts respectively. So the building up of the anode arc must be performed in a short time that the distance between the ignition anode and the cathode is small. Since the building up time of the ignition arc becomes to be short by the increase of the ignition anode voltage, the anode arc becomes easy to build up. This explains the fact that the anode voltage decreases with the increase of the ignition anode voltage in case of the small ignition anode voltage in Fig. 3. If the ignition anode voltage becomes higher, the voltage between the anode and the ignition anode becomes lower. So the higher anode voltage becomes necessary for building up. This shows the characteristic in case of the high ignition anode voltage in Fig. 3. When the anode current is about 0.5～6 A and the anode voltage is constant, the transient anode arc voltage does not go down in the short building up time. So the anode current is considered to be unrelated to the ignition anode voltage as shown in Fig. 4. When the transient ignition anode current becomes higher by the decrease of the series resistance, the voltage between the ignition anode and the cathode becomes higher in the moment of ignition. This has the same meaning as the case of the high ignition anode voltage in Fig. 3. So the characteristic of closing in Fig. 5 may be attributed to this too. It is thought that electrons accumulate in the vicinity of the anode and ions remain in the vicinity of the ignition anode before many electrons are emited by the concentration of ions at the transient state of ignition. On this occasion though the electric field intensity on the cathode surface is high, the region of low or negative electric field intensity is thought to be formed between the anode and the ignition anode. So even if the ignition anode voltage is low in Fig. 5, the above effect is thought to appear. Since the ignition anode is separating from the cathode in case of opening in Fig. 5, the voltage between the ignition anode and the cathode decreases with the increase of current and the above effect does not appear remarkably. But the ignition arc extincts in case of closing before the ignition arc voltage goes down enough. So the above effect is thought to appear remarkably in case of closing.

§ 3. Motion of Cathode Spot

(1) *Cathode spot*

As for the cathode spot the thickness of the dark space is much smaller and only a brilliant spot is able to be observed. The

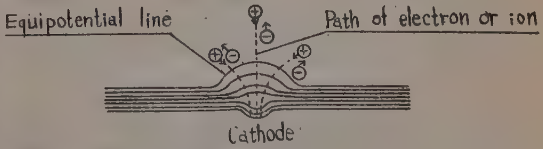

Fig. 6. Equipotential lines in the neighbourhood of the cathode spot.

vicinity of the cathode spot has the convex equipotential surface as shown in Part II, and on the other side it is thought that the very high electric field exists in the dark space of the cathode spot. Therefore the equipotential lines in the neighbourhood of the cathode spot may be considered as shown in Fig. 6. On this occasion the mercury cathode surface of the spot becomes concave by the vapour pressure or the pressure of the ion gas. These equipotential lines form, as it were, a kind of electric lens on the cathode surface. By the operation of this lens many ions concentrate in the cathode spot and make many electrons to emit. These emitted electrons produce also many ions and these ions flow into the cathode spot, and the current is maintained. Then the concentration of ions is affected by the electric field due to the form of the cathode surface. The variations of its form are caused by the pressure of ions and vapour, and is thought to be entirely accidental. Therefore it is expected that the cathode spot moves about on any part of the cathode surface.1) In fact even if there is a kind of obstacle on the cathode surface, the cathode spot takes any position as shown in Fig. 7 and its motion is not limited by the obstacle. When the anode current becomes heavy, it has been known kinematographically by a high speed camera that a group of cathode spots are driving about on the cathode surface. On the contrary when the current decreases the cathode spot extincts because the sufficient ion concentration to emit many electrons does not occour. This limited current is about 4 A at the room temperature 10°C–20°C.

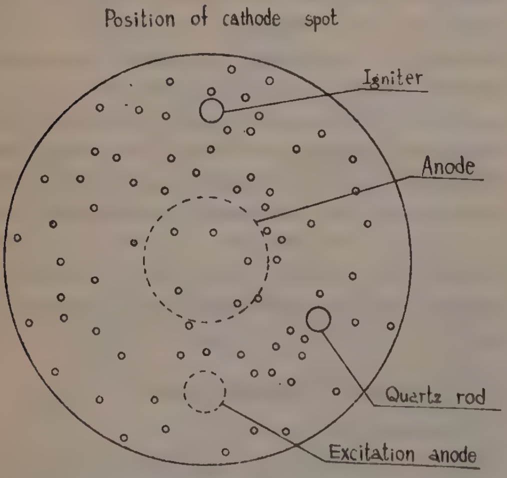

Fig. 7. Position of cathode spot on cathode surface observed every five second where anode current is zero and only excitation anode current exists.

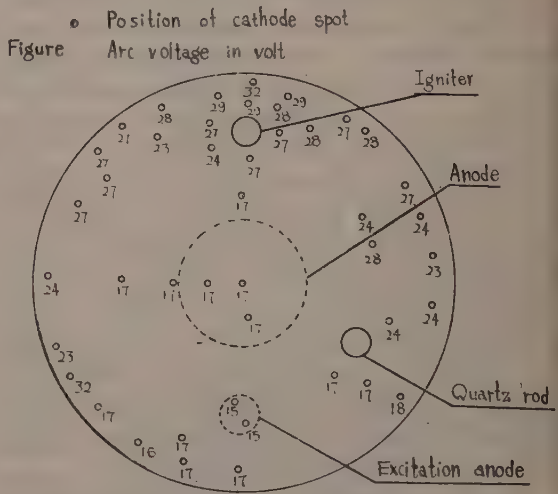

Fig. 8. Position of cathode spot on cathode surface and arc voltage where anode current is zero and only excitation anode current exists.

The structure of the cathode dark space is only known on the outline. Ordinarily it has been said that the current density and the ion current density and the ion current are about 4000 A/cm^2 3) and about 1/10^3 3) of the electron current respectively at the cathode spot. Then the ion current density I_+ is estimated to be about 400 A/cm^2. By using this value, the molecular weight of mercury ($M=200.6$) and the cathode voltage drop($V_c \doteqdot 10$ V), the thickness of the cathode dark space is given as about $d_c \doteqdot 1.7 \times 10^{-5}$ cm from space charge equation. This value is smaller than Smith's experimental value, that is about 10cm^{-3}.4) And then it is concluded that normal space charge equation should'nt be applied for the cathode spot. The difference between these values is thought to depend upon disregarding of the resistance of neutral molecules and applying the equation for the case of a very thin sheath. For instance, in case of a glow discharge there exists a comparatively thick cathode fall and the ionization is performed in its fall. In case of the cathode spot the ionization due to single collision is not considered because the cathode voltage drop is 10 V and about 20 times collisions are performed if the spot temperature is about

300°C as well said. But since mercury molecules have metastable state, the ionization is possible by serial 2 times collisions. And since the cathode fall thickness is very thin, electrons which turn back into the cathode fall by collision must be considered too. These electrons make the cathode fall thickness to be thick.

(2) *Fluctuation of arc voltage*

As the cathode spot moves about on all the cathode surface, the states of the vapour density or the arc path varies from time to time, and them the arc voltage varies always too. For the consideration of this character the positions of the cathode spot and corresponding arc voltages are shown in Fig. 8 in the same way as Fig. 7. And it is known that the arc voltage becomes larger when the cathode spot approaches or hides behind a kind of obstacle. These phenomena may be thought to be due to the deficiency of the vapour density near the anode. The arc voltages are known to fluctuate fairly in case of the free cathode spot as shown in Fig. 9. In case of an anchor cathode the arc voltage is larger than the minimum value in case of the free cathode spot, but does not fluctuate.

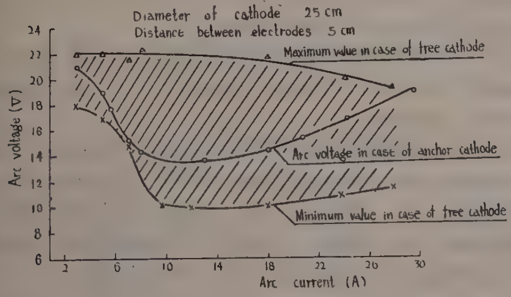

Fig. 9. Fluctuation domain of arc voltage.

§ 4. Arc Voltage

(1) *Arc voltage and vapour density*

The voltage-current curves for various wall temperature are shown in Fig. 10. When the wall temperature, that is, the vapour density increases, the anode fall decreases and the voltage across the positive column increases.

Genellary in case of low vapour density is low and the arc voltage is high, and in case of high vapour density the drift velocity of the charges is low and the arc voltage is high. As the vapour density changes with the arc current, the arc voltage changes with the arc current and the wall temperature, that is, the vapour density as shown in Fig. 10. These characters are particular on the mercury arc.

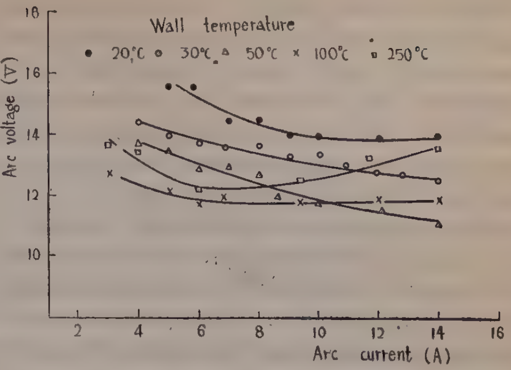

Fig. 10. Arc voltage measured by the same apparatus.

(2) *Effect of anode temperature*

The arc voltage is affected by the anode temperature because the vapour density near the anode depends upon the anode temperature. When S_1 is closed and the ignition anode is operated in the circuit of Fig. 11, the arc current flows into the excitation anode. After the experimental apparatus is heated for a while, S_3 is closed and S_1 is opened, and the arc voltage is measured in a moment while the anode temperature has not yet been elevated. Next after the temperature of the apparatus comes back to the room temperature again, S_2 is closed, the ignition anode is operated, and the apparatus is heated

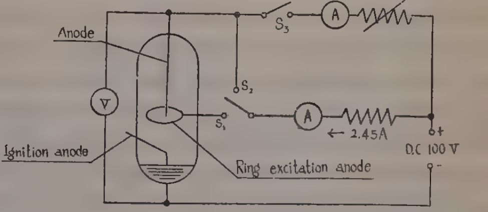

Fig. 11. Arc voltage measuring circuit for knowing the effect of anode temperature.

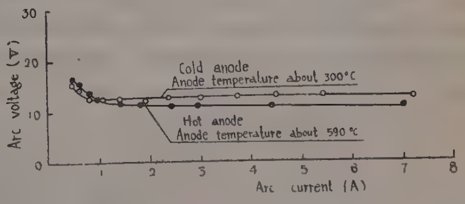

Fig. 12. Effect of anode temperature on arc voltage.

during the same period. Then the temperature of the anode is different from the above state in spite of the same vapour 'distribution condition. At this time S_3 is closed, S_2 is opend and the arc voltage is measured. Thus two kinds of characteristics measured by such methods are shown in Fig. 12. It is known from Fig. 12 that the arc voltage of the hot anode is higher or lower than that of the cold anode as the current is smaller or larger respectively. This phenomenon is thought to occour by the distribution of the vapour density depending upon the anode temperature and to be attributed to the variation of the anode drop.

(3) *Arc voltage of the second anode*

The arc voltage of the second anode inserted in the positave column varies with the vapour density and the main anode current. When the vapour density is low, the electrons which flow into the second anode are accelerated in comparatively long mean free path, and the ionization is performed, and many electrons are produced, and the arc voltage of the second anode becomes lower. When the vapour density is high, the velocities of the electrons is low and a resistive force acts for the motion of electrons, and the arc of the second anode has the resistive characters remarkably but the charge density is high and the second anode voltage varies only a little. When the vapour density is lower, these characters appears more remarkably. For instance, the experiment as shown in Fig. 13 is performed. When cock C in Fig. 13(1) is turned slightly, the arc of the main anode A_1 is ignited. After the front of the anode is heated violently, the front is inserted in the mercury cathode slightly. On this condition the main arc current is maintained even if it is only 0.4 A. Then the arc voltages of the second anode arc measured. These results are shown in Fig. 13(2). The second anode current corresponding to the maximum second anode voltage becomes lower when the vapour density, that is, wall temperature becomes lower.

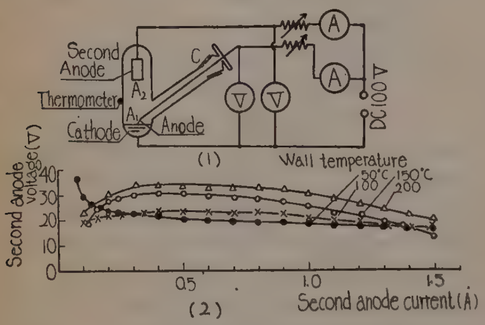

Fig. 13. Arc voltage of second anode.

When the anode current becomes higher, its second anode current becomes higher on account of the increase of the vapour density.

§ 5. Conclusion

The particular characters on the mercury arc are studied and the following conclusions are obtained.

(1) A constant voltage and current are necessary for the starting the mercury arc.

(2) The ignition probability of the mercury arc depends not only upon the ignition anode voltage or current but upon the anode voltage.

(3) The arc path and the arc voltage vary complicately in compliance with the motion of the cathode spot, vapour density and the form of the arc equipment.

(4) The arc voltage of the second anode varies by the vapour density or the main anode current.

Acknowledgement—The auther wishes to express his sincere thank to Dr. Honda, Dr. Uchida, Dr. Miura, Dr. Kubo and Mr. Hashimoto for their valuable discussions and encouragement throughout this work.

References

1) H. V. Bertele: B. J. App. Phys. **3** (1952) 127.

2) C. T. Gallengher: J. App. Phys. **22** (1950) 768.

3) Engel, Steenback: Elektrishe Gasentladungen I. II (1934).

4) C. G. Smith: Phys. Rev. **69** (1946) 96.

JOURNAL OF THE PHYSICAL SOCIETY OF JAPAN Vol. 8, No. 2, MAR.—APR., 1953

Hyperfine Structure of the Spectrum of Mg I

By Kiyoshi MURAKAWA

Institute of Science and Technology, Komaba-machi, Meguro-ku, Tokyo.

(Received November 24, 1952)

Isotope shift (Mg^{26}—Mg^{24}) in the lines Mg I λ4571 (3^1S_0—3^3P_1) and λ2852 (3^1S_0—3^1P_1) was measured. For terms of Mg I isotope shifts that have been measured by various authors are summarized in a diagram (Fig. 4).

§ 1. Introduction

In 1931 the author studied the hyperfine structure (hfs) of some Mg I lines (among them λ4571), using a liquid-air cooled hollow cathode source, and found them to be single¹⁾. The lack of hfs was, as it now seems, due to an insufficient time of exposure. Somewhat later in 1935²⁾, the structure of λ4571 was again studied, using a water-cooled Geisler tube containing argon and magnesium, and the preliminary result was: "the structure is given by—0.029 (2), 0 (20), 0.037 (4), 0.102 (1) cm^{-1}, where numbers in brackets are estimated intensities". This kind of light source was found to give surprisingly sharp lines, and the hfs of λ4571 was later again studied, and the result obtained in 1935 was confirmed except that the component at −0.029 was found to be non-existent and the intensity of the 0.037 component was weaker than the 0.012 component.

The Geisler tube was, however, found to have only about ten hours' life and therefore liquid-air cooled hollow cathode source was again adopted. Unfortunately the investigation was interrupted by the second world war, and was resumed only this year.

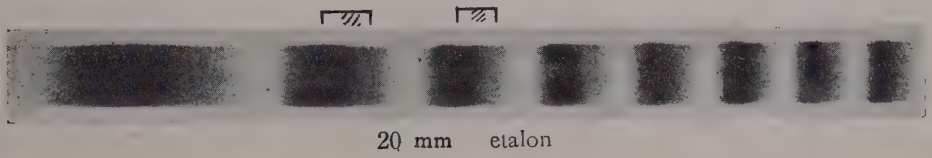

Fig. 1. Enlargement of the interference pattern of Mg I λ4571.

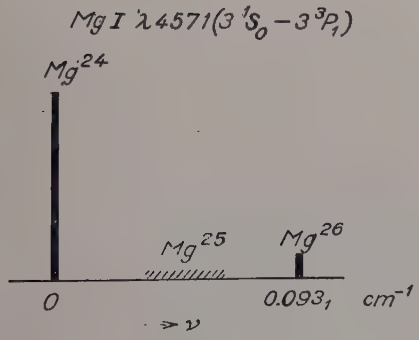

Fig. 2. Hfs of λ4571.

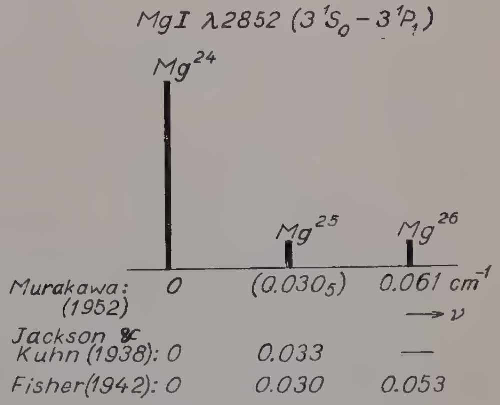
MgI λ2852 ($3^1S_0-3^1P_1$)
Mg^{24}
Mg^{25}
Mg^{26}
Murakawa: (1952) 0 (0.030₅) 0.061 cm⁻¹
→ ν
Jackson & Kuhn (1938): 0 0.033 —
Fisher(1942): 0 0.030 0.053

Fig. 3. Hfs of λ2852.

In the meanwhile Bacher and Sawyer³⁾ measured the isotope shifts in some lines (λ4571 was also included) of Mg I, using a liquid-air cooled hollow cathode source, and Jackson and Kuhn⁴⁾ measured the isotope shift in the resonance line λ2852, using an atomic beam absorption method. Meissner⁵⁾ measured the isotope shifts in the lines $3^1P_1-m^1D_2$ (m=3, 4, 5, 6, 7) and $3^1P_1-n^1S_0$ (n=5, 6), using an atomic beam emission method. Mundie and Meissner⁶⁾ repeated the experiments of Meissner, and Fisher[7] measured the isotope shift in the resonance line λ2852. Crawford and Olson[8] measured the hfs of the green lines ($3^3P_{2,1,0}-4^3S_1$) of Mg I and the resonance lines of Mg II.

§ 2. Experimental Procedure and Result

A liquid-air cooled hollow-cathode discharge tube was used as the light source, and a Fabry-Perot etalon was used in order to examine the hfs. With a discharge current of about 40 milli-amperes λ4571 could be photographed in about one hour. Fig. 1 is a reproduction of the hfs of λ4571 and Fig. 2 represents diagramatically the hfs of λ4571. It is known that the isotopes Mg^{24}, Mg^{25} and Mg^{26} exist in the ratio 7 : 1 : 1 approximately. The measured shift of $Mg^{26}-Mg^{24}$ namely $0.0931 \pm 0.0015\ cm^{-1}$ is to be compared with the previous result of the author $0.102\ cm^{-1}$ and the result of Bacher and Sawyer[3] 0.083 cm^{-1}.

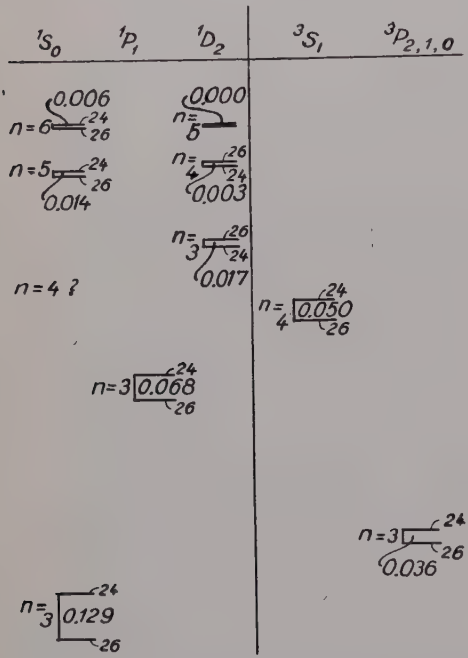

Fig. 4. Diagramatic representation of the isotope shifts in the terms of Mg I. The unit of the shift is cm^{-1}. 24 and 26 mean Mg^{24} and Mg^{26} respectively.

The resonance line λ2852 was found to be reversed on all the plates. However, on some plates that were taken for studying the hfs of other elements which contained magnesium as impurity λ2852 was found to be not reversed, and the hfs was measured, the result being given in Fig. 3. together with the results of other authors.

λ4571 and λ2852 connect the isotope shifts in the singlet and triplet terms of Mg I. Adopting the relative shift of $Mg^{26}-Mg^{24}$ ($0.068\ cm^{-1}$) for the term 3^1P_1 that was determined by Mundie and Meissner[6], all the results of measurements published by various authors can now be summarized in a diagram (Fig. 4). Probably it would have been more adequate to take the origin of the isotope shift at the electron configuration $(3p)^2$, but since in the present experiment the lines λ2783 -2776 ($3s3p\,^3P-3p^{2\,3}P$) were not strong enough to show the Mg^{26}-component clearly, such an attempt has been abandoned in the present work.

It may be remarked that any theoretical calculation[9] of the isotope shift in Mg I terms should take into account the minor details of the perturbation of the $3smd\,^1D_2$ series by the term $3p^{2\,1}D_2$, since the above-mentioned value $0.068\ cm^{-1}$ was determined from the isotope shifts in the series $3^1P_1-m^1D_2$.

Attempts to excite the lines λ2783–2776 strongly are still in progress in this laboratory.

References

1) K. Murakawa: Zeits. f. Physik **72** (1951) 793.

2) K. Murakawa: Proc. Phys.-Math. Soc. Japan **17** (1935) 14.

3) A. E. Bacher and R. A. Sawyer: Phys. Rev. **47** (1936) 587.

4) D. A. Jackson and H. Kuhn: Proc. Roy. Soc. London **A164** (1938) 48.

5) K. W. Meissner: Ann. d. Physik **31** (1938) 505.

6) L. G. Mundie and K. W. Meissner: Phys. Rev. **65** (1944) 265.

7) R. A. Fisher: Rev. Mod. Phys. **14** (1942) 79.

8) M. F. Crawford and N. Olson: Phys. Rev. **76** (1949) 1528.

9) J. P. Vinti: Phys. Rev. **56** (1939) 1120.

JOURNAL OF THE PHYSICAL SOCIETY OF JAPAN Vol. 8, No. 2, MAR.—APR., 1953

Hyperfine Structure of the Spectrum of Tungsten

By Kiyoshi MURAKAWA

Institute of Science and Technology, Komaba-machi, Meguro-ku, Tokyo

(Received December 9, 1952)

The hyperfine structure of the W I spectrum was studied, and the ratio of the distances of the neighbouring components corresponding to the even isotopes $\Delta(184-182)/\Delta(186-184)$ was determined to be 1.206 ± 0.010. Isotope displacement effect in 55 lines of W I and the relative isotope displacement effect in about 29 terms of W I are tabulated. Some odd levels are interpreted as arising from the electron configuration $5d^3 6s^2 6p$.

§ 1. Introduction

The hyperfine structure (hfs) of the spectrum of tungsten was detected for the first time by Grace and More¹⁾ (to be referred to as GM). They interpreted the hfs to be due to the displacement effect of the even isotopes and the splitting due to the nuclear magnetic moment of the odd isotope W^{183}; they suggested that the components that are due to W^{183} are nearly coincident with the components due to W^{182} and W^{184} and suggested that the nuclear spin of W^{183} is 1/2. Kiuti, Hasunuma and Kawada²⁾ (to be referred to as KHK) measured the hfs in many lines of W I and found some lines in which the components due to W^{183} are not coincident with the components due to W^{182} and W^{184}. Kopfermann and Meyer³⁾ (to be referred to as KM) measured the intensities of the hfs of some lines of W I and confirmed the nuclear spin (1/2) of W^{183}. Using enriched isotope W^{183} Fowles⁴⁾ confirmed again the nuclear spin of W^{183} and gave the hfs (due to W^{183}) in some lines of W I. Vreeland and Murakawa⁵⁾ (to be referred to as VM) measured the hfs due to W^{183} in more lines, determined the nuclear magnetic moment of W^{183} and measured the hfs due to the rare isotope W^{180}, using two samples enriched in W^{183} and W^{180} respectively. The present investigation was undertaken, as a continuation of the works of Murakawa and Suwa⁶⁾ about the isotope displacement effect in heavy elements, in order to determine the ratio $\Delta(184-182)/\Delta(186-184)$ more accurately than KM and VM.

§ 2. Experimental Arrangements

Liquid-air cooled hollow cathode discharge tube was used as the light source, and a Fabry-Pérot etalon was used in order to examine the hfs. In the work of VM an aluminium hollow cathode was coated with tungsten oxide, and the strong aluminium hydride band masked the important line λ4269. In the present investigation the hollow cathode was of pure tungsten so that no disturbing band appeared.

Fig. 1 shows some reproductions of the interference patterns of the hfs of W I.

§ 3. Results

Tungsten is known to consist of five isotopes 186 (29.8 %), 184 (30.1 %), 183 (17.3 %), 182 (22.6 %) and 180 (0.2 %). Since in the present experiment only natural tungsten was used, component due to the rare isotope 180 could not be detected, so that we are concerned here only with the four isotopes 186, 184, 183 and 182. KHK found that in the lines λ4269 and λ3817 the components due to W^{183} are not coincident with the components due to W^{182} and W^{184}. In the present experiment the work of KHK was extended, and the positions of the W^{183}-components were measured in λ4269 as shown in Fig. 2 (see also Fig. 1). The term notation published by Laporte and Mack⁷⁾ is used throughout. In the case of λ3817.5 the W^{183}-components were detected but could not be measured accurately. In the case of λ4295 the two components *a* and *b* were not resolved, but the hfs is still suited for determining the ratio $\Delta(184-182)/\Delta(186-184)$. The value of the doublet splitting of W^{183} in the term $d^5s\,{}^7S_3$ (namely about $0.065\,\text{cm}^{-1}$) was taken from the work of VM⁵⁾. The hfs of the three lines given in Fig. 2 allows us to determine the ratio $\Delta(184-182)/\Delta(186-184)$, and we get the value 1.206,

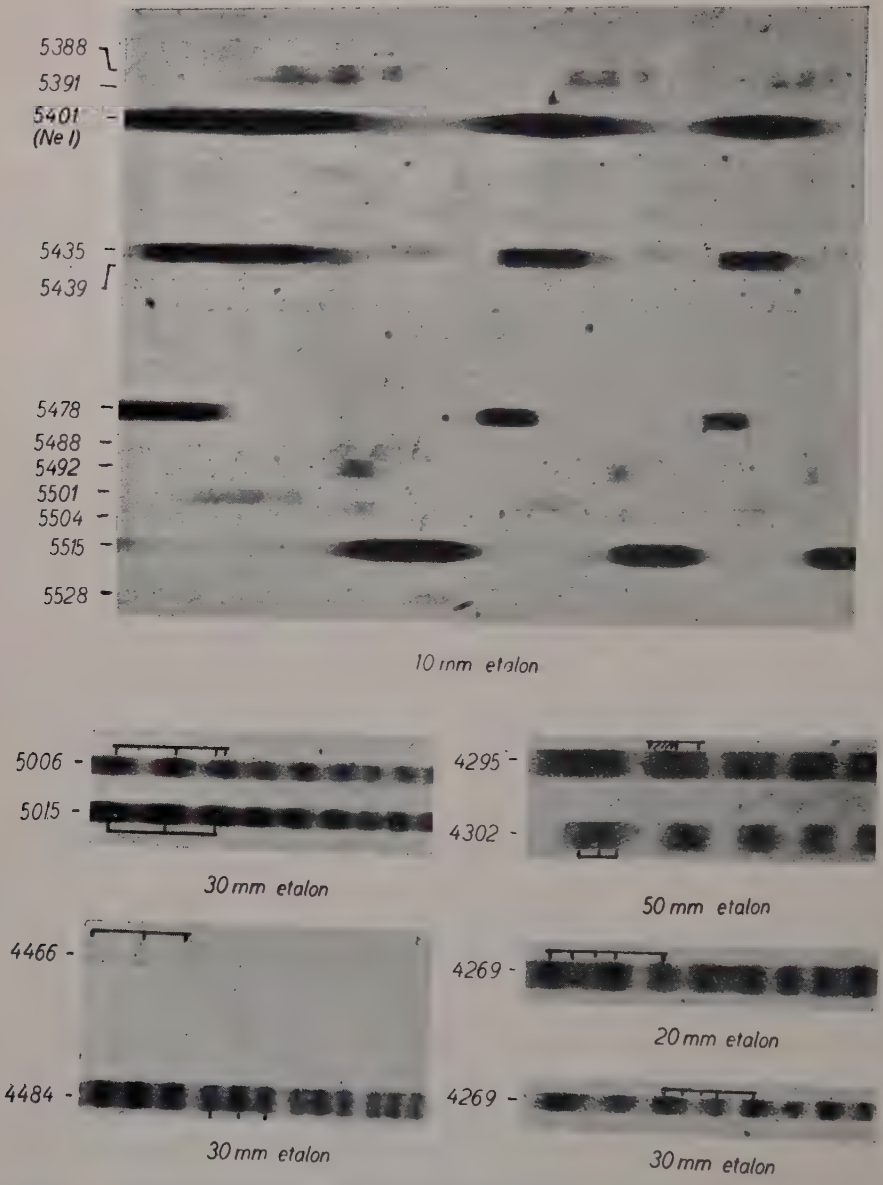

10 mm etalon

30 mm etalon

50 mm etalon

20 mm etalon

30 mm etalon

30 mm etalon

Fig. 1. Enlargement of some interference patterns of the spectrum of W I.

1.19 and 1.21 from the hfs of the lines λ4269, λ3817 and λ4295 respectively. The weighted mean of these is

$$\Delta(184-182)/\Delta(186-184)=1.206\pm0.010.$$

This is to be compared with the value 1.11 given by KM and with the value 1.13 given by VM.

The center of gravity of the W^{183}-components in λ4269 lies just in the middle of the W^{182}- and W^{184}-components. This was assumed to be true in interpreting the hfs of other lines.

In each case of the three lines shown in Fig. 3 the stronger component of W^{183} was resolved from the W^{182}-component, so that the position of the weaker component and that of the W^{184} component could be calculated. The W^{183}-splittings of the terms $^5D_1$ and $^5D_4$ were calculated using the nuclear magnetic moment (0.08 n.m.) of W^{183} published by VM, and the assumption that the $5d^4 6s^2$ configuration is of an LS coupling*. The doublet splitting of the $5d$-electron was assumed to be 4700 cm^{-1}.

---

* This assumption is, however, a very rough approximation.

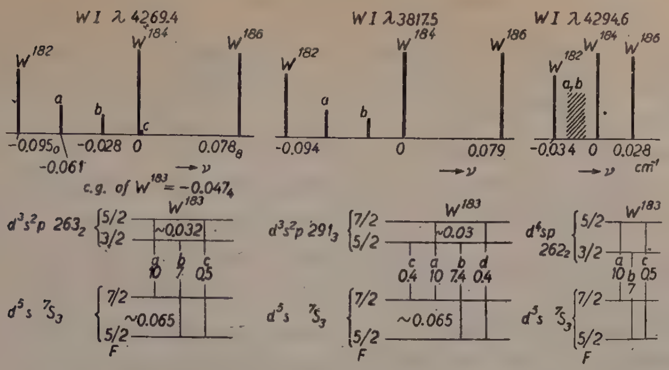

Fig. 2. Hfs of the W I lines λ4269, λ3817 and λ4295.

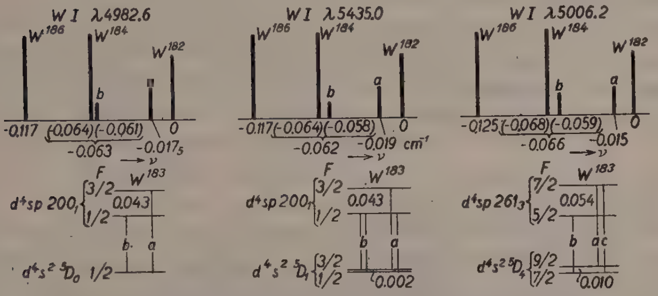

Fig. 3. Hfs of the W I lines λ4983, λ5435 and λ5006.

In lines other than those given in Fig. 2 and Fig. 3 the W^{183}-components were masked by the W^{182}- and W^{184}-components as shown by GM and KM, so that each line gave the impression that it consisted of three components (for example λ4484, see Fig. 1). The hfs of the W I lines measured in the present investigation is given in Table I. In Table II isotope displacement effect in the W I terms that can be derived from Table I is given, where the origin of the displacement is located at the term $5d^56s\,{}^7S_3$, as was done by KM. The term 263_2 has a W^{183}-splitting of about 0.03 cm⁻¹ and a displacement of 0.079 cm⁻¹ between 184 and 186. This can be expected when we assumed an electron configuration $5d^36s^26p$ for the term 263_2. In Table II it was assumed that the odd term with a displacement larger than 0.056 cm⁻¹ between 184 and 186 comes from the configuration $5d^36s^26p$.

The line λ5388 has a wide structure (see Fig. 1), and the final term is given as $5d^56s$ 19_6 by Laporte and Mack[7]. The final term has probably a small isotope displacement effect according to Table II, so that it follows that the displacement effect (186–184) in the initial term 382_6 is of the order of 0.077 cm⁻¹.

Table II. Isotope displacement effect in the W I terms.

Term		$\Delta(182-184)$ (cm⁻¹)	$\Delta(184-186)$ (cm⁻¹)
$5d^46s^2$	${}^5D_0$	0.091	0.076
	${}^5D_1$	0.091	0.076
	${}^5D_2$	0.091	0.076
	${}^5D_3$	0.091	0.076
	${}^5D_4$	0.091	0.076
	09_0	0.085	0.071
$5d^56s$	${}^7S_3$	0	0
$5d^46s6p$	200_1	0.029	0.024
	214_2	0.035	0.029
	214_1	0.038	0.032
	230_3	0.026	0.022
	239_2	0.034	0.028
	247_4	0.029	0.024
	261_3	0.024	0.020
	262_2	0.034	0.028
	266_5	0.030	0.025
	274_3	0.019	0.016
	278_4	0.024	0.020
	287_4	0.031	0.026
	293_2	0.036	0.030
	297_5	0.034	0.028
	305_3	0.038	0.032
Mixture of $5d^46s6p$ and $5d^36s^26p$	277_1	0.050	0.042
	314_4	0.055	0.046
$5d^36s^26p$	263_2	0.095	0.079
	276_2	0.067	0.056
	291_3	0.095	0.079
	291_2	0.072	0.060
	299_3	0.072	0.060

Table I. Hyperfine structure of the spectrum of W I (in unit of cm^{-1})

λ	Combination	182 + a(183)	184 + b(183)	186	Remark†
6012.8	19_6—362_5	−0.064	0	+0.063	
5676.9	17_3—353_2	+0.055§	0	−0.055§	
5648.4	18_3—366_2	+0.065*	0**	−0.055	
5528.0	13_3—314_4	+0.035	0	−0.035	
5514.8	D_2—214_1	+0.0533	0	−0.0459	[GM], [KHK], [KM]
5500.6	$19_5'$—380_4	+0.050	0	−0.053	
5487.8	D_3—230_3	+0.064	0	−0.056	[KHK]
5477.8	09_0—277_1	+0.032	0	−0.029	
5435.0	D_1—200_1	+0.062*	0	−0.055	[KM]
5391.1	D_4—247_4	+0.061	0	−0.052	[KHK]
5388.0	19_6—382_6	−0.082	0	+0.077	[KHK]
5243.0	16_4—354_3	+0.017§	0	−0.017§	
5224.7	D_3—239_2	+0.056	0	−0.048	[KHK], [KM]
5110.4	15_5—346_4	+0.046	0	−0.049	
5069.1	D_2—230_3	+0.058	0	−0.052	[KHK], [KM]
5054.6	D_1—214_2	+0.055	0	−0.052	[KHK]
5053.3	D_1—214_1	+0.051	0	−0.045	[KHK], [KM]
5040.4	13_1—331_2	+0.019§	0	−0.022§	
5015.3	D_3—247_4	+0.0602	0	−0.0530	[KHK], [KM]
5006.2	D_4—261_3	+0.066*	0	−0.059	
4986.9	15_5—351_4	+0.045	0	−0.045	
4982.6	D_0—200_1	+0.063*	0	−0.054	[KM]
4916.2	14_2—353_2	+0.0472	0	−0.0448	
4886.9	D_4—266_5	+0.0615	0	−0.0514	[GM], [KHK], [KM]
4843.8	D_2—239_2	+0.0564	0	−0.0483	[KHK], [KM]
4757.6	S_3—239_2	−0.031*	0**	+0.025	
4680.5	D_3—261_3	+0.058	0	−0.053	[KHK], [KM]
4659.9	D_0—214_1	+0.0527	0	−0.0476	[KHK], [KM]
4643.2	20_2—425_3	+0.050*	0**	−0.041	
4613.3	D_4—278_4	+0.066	0	−0.059	
4504.9	12_4—343_3	+0.051	0	−0.050	
4484.2	D_1—239_2	+0.0544	0	−0.0498	[KHK], [KM]
4466.4	13_3—357_2	+0.071	0	−0.066	
4404.5	14_2—376_3	+0.0781	0	−0.065	
4378.5	D_3—276_2	+0.024	0	−0.021	
4372.5	D_2—261_3	+0.0578	0	−0.0538	
4302.1	S_3—261_3	−0.023	0	+0.020	
4294.6	S_3—262_2	−0.033*	0**	+0.028	
4269.4	S_3—263_2	−0.0950*	0**	+0.0788	[KM]
4244.4	D_4—297_5	+0.0588	0	−0.0483	[KHK]
4171.2	D_3—287_4	+0.060	0	+0.050	
4137.5	D_2—274_3	+0.0625	0	−0.0580	[KHK]
4102.7	D_4—305_3	+0.050	0	−0.044	
4095.7	17_6—414_6	+0.0735	0	−0.0664	
4088.3	D_2—277_1	+0.041	0	−0.035	
4074.4	S_3—274_3	−0.018*	0**	+0.016	
4070.6	D_1—262_2	+0.049	0	−0.045	[KM]
4069.8	$19_5'$—443_6	+0.047	0	−0.049	
4045.6	S_3—276_2	−0.0626	0	+0.596	[KHK], [KM]
4008.8	S_3—278_4	−0.018	0	+0.020	
3965.0	D_4—314_4	+0.033	0	−0.030	
3835.1	D_2—293_2	+0.051	0	−0.048	
3817.5	S_3—291_3	−0.094*	0**	+0.079	
3809.2	S_3—291_2	−0.067	0	+0.064	[KHK]
3707.9	S_3—299_3	−0.069	0	+0.060	

* 182-component only. ** 184-component only.

§ Correlation to the 182- or 186-component uncertain.

† [GM], [KHK] and [KM] mean agreement with GM, KHK, KM respectively within 0.004 cm^{-1}

This means that the term 382_6 arises probably from the configuration $5d^3 6s^2 6p$ also.

References

1) N. S. Grace and K. R. More: Phys. Rev. **45** (1934) 166.

2) M. Kiuti, H. Hasunuma and T. Kawada: Proc. Phys.-Math. Soc. Japan **19** (1937) 1019.

3) H. Kopfermann u. D. Meyer: Zeits. f. Physik **124** (1948) 685.

4) G. R. Fowles: Phys. Rev. **78** (1950)744.

5) J. A. Vreeland and K. Murakawa: Phys. Rev. **83** (1951) 229.

6) K. Murakawa and S. Suwa: Jour. Phys. Soc. Japan **5** (1950) 382; **5** (1950) 429.

7) O. Laporte and J. E. Mack: Phys. Rev. **63** (1943) 246.

JOURNAL OF THE PHYSICAL SOCIETY OF JAPAN Vol. 8, No. 2, MAR.—APR., 1953

Numerical Evaluation of the Intensity Curve of a Multiple-Beam Fizeau Fringe

By Koreo KINOSITA

Department of Physics and Chemistry, Gakushuin University, Mejiro, Tokyo

(Read October 5, 1951; Received October 2, 1952)

Intensity distribution curve of a multiple-beam Fizeau fringe is numerically evaluated for a typical case: normal incidence, R (the reflectivity of silver film)=0.90, θ (the wedge angle)=3×10^{-3} rad., and the order of fringe $t/\frac{\lambda}{2}=6$ in which t represents the thickness of the wedge at the point where the fringe is formed and λ the wave-length of light. The main maximum is about 80% as high as that of the corresponding Fabry-Perot fringe, and is slightly asymmetric. Secondary maxima suggested by Brossel are verified. They are restricted to one side of the main maximum in which the wedge is thicker. The cause of the asymmetry of the main maximum and the origin of secondary maxima are discussed.

§ 1. Introduction

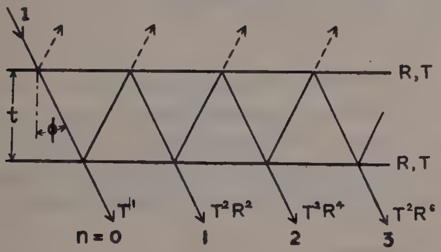

Fig. 1. Multiple-beam interference of equal inclination (Fabry-Perot interferometer).

Multiple-beam interference of *equal inclination*, the typical application of which is the Fabry-Perot interferometer, is familiar to the students of optics. Fig. 1 is a schematic diagram illustrating the principle of this interferometer. The glass-backings are omitted for simplicity. Let the (vector) amplitude of the incident beam be equal to unity. The amplitude A_n of the n-th transmitted beam which has undergone $2n$ times reflections at the surfaces of two parallel, highly reflecting silver films separated by t is given by

$$A_n=TR^n\exp(-in\delta)\,, \tag{1}$$

where

$$\delta=4\pi t\cos\phi/\lambda\,. \tag{2}$$

In these expressions T and R denote the transmission and the reflectivity of the film respectively (both films are assumed to be identical), ϕ the angle of incidence, and λ the wave-length of light. In the derivation of Eq. (1), the phase change at a reflection is assumed to be exactly equal to π, and the phase shift caused by transmission through the film is neglected. When the zero-th, first, $\cdots$, and m-th beams are collected with a lens to form an interference fringe, as is the case in the Fabry-Perot interferometer, the intensity I of the fringe is given by

$$\begin{aligned} I&=\left|\sum_{n=0}^{m}A_n\right|^2\\ &=T^2\frac{(1-R^{(m+1)})^2+4R^{(m+1)}\sin^2(m+1)\delta/2}{(1-R)^2+4R\sin^2\delta/2}\,. \end{aligned} \tag{3}$$

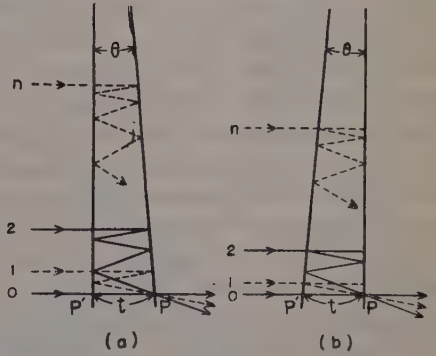

Fig. 2. Multiple-beam interference of equal thickness (Fizeau fringe).

If summed to $n=\infty$, Eq. (3) is reduced to

$$I=T^2/\{(1-R)^2+4R\sin^2\delta/2\}\,, \tag{4}$$

which is the well-known Airy's formula.

Now let us consider the case of the multiple-reflection interference of *equal thickness*

(Fizeau fringes). The most important case is that of normal incidence (Fig. 2). The intensity of the Fizeau fringe at a point P is given by

$$\begin{aligned} I &= |\sum A_n|^2 \\ &= |\sum TR^n \exp(-i\delta_n)|^2 \\ &= T^2\{(\sum R^n \cos\delta_n)^2 + (\sum R^n \sin\delta_n)^2\} \qquad (5) \end{aligned}$$

where A_n represents the amplitude vector of the n-th beam impinging on P after $2n$ times reflections and δ_n its phase lag behind the zero-th beam. Simple calculation* neglecting the fourth power of the wedge angle θ shows that δ_n is given by either Eq. (6) or (7), the former corresponding to the configuration (a) and the latter to (b) of Fig. 2.**

$$\delta_n = \frac{4\pi t}{\lambda}\{n - \tfrac{1}{3}n(n+1)(2n+1)\theta^2\} . \qquad (6)$$

$$\delta_n = \frac{4\pi t}{\lambda}\{n - \tfrac{1}{3}n(2n^2+1)\theta^2\} . \qquad (7)$$

The wedge angle θ which appears in these equations is an experimentally adjustable parameter which determines the number of fringes per cm., X, by the following relation:

$$\theta = X\lambda/2 . \qquad (8)$$

In practice, the convenient range for X is 1~100/cm. The corresponding range for θ is 3×10^{-5}~3×10^{-3} if we assume λ~5,500 Å.

If $\theta \ll 1$ and the reflectivity of both surfaces is so poor that the contribution of the beams other than the zero-th and the first is very small, the second term of the right-hand side of Eq. (6) or (7) can be neglected, and maxima occur at $t/\frac{\lambda}{2} = m$ ($m = 0, 1, 2, \cdots$) where the two beams are in phase. This is the case of the ordinary (two-beam) Fizeau fringe. On the contrary, when the surfaces are highly reflecting, we can no more ignore the contribution of higher order beams, which are *not* in phase with the zero-th at $t/\frac{\lambda}{2} = m$, as is shown in Eq. (6) or (7). If, however, t were small enough, the negative contribution of the second term to the definition of fringe would be very small even for a considerably large value of n (the contribution to I of the beams of very high order is negligible in any way because of the factor R^n in Eq. (5)); then the intensity distribution fixed by Eq. (5) would be like the one given by Eq. (3) or (4). This is the idea of Tolansky who originated the *multiple-beam interferometry.*¹⁾

He grasped the point of the subject, but did not go into the details of the intensity distribution. Brossel's²⁾ and Holden's³⁾ papers in which this subject is discussed in full also leave something vague. This is due to the fact that the analytical evaluation of the summation in Eq. (5) is not practicable. Hereupon the author tried numerical evaluation of the intensity curve for a set of typical values of R, T, θ, and $t/\frac{\lambda}{2}$.

§ 2. Computation

The assumed values of R, T, θ and $t/\frac{\lambda}{2}$ are listed in Table I. The case of normal incidence is considered. These conditions correspond to a typical multiple-beam Fizeau fringe set-up for a microscopic examination.

Table I. Assigned values*** of R, T, θ, and $\frac{t}{\lambda/2}$.

Symbol	Quantity	Assigned to be
R	Reflectivity of silver film	0.90
T	Transmission of silver film	0.02
θ	Wedge angle	3×10^{-3} rad. (X~100/cm.)
$\frac{t}{\lambda/2}$	Order of interference (wedge thickness/half a wave-length)	6

The intensity was computed after Eqs. (5) and (7), taking the summation up to $n=50$. The error due to giving up the summation at $n=50$ is trifling for the present purpose, but its exact evaluation is rather difficult.****

§ 3. Results

The results of intensity calculation are given

---

* Brossel²⁾ showed an ingeneous method of deriving Eq. (7).

** Eq. (6) also represents the phase lag of the n-th beam which impinges on P' after $(2n-1)$ times reflections in the configuration (b), and is useful for the calculation of the reflection fringe. So is Eq. (7) in the configuration (a).

*** The assumed value of R (and T) would be reasonable for $\lambda > 4{,}000$ Å.

**** It is evident that

$$\left|\frac{\Delta I}{I}\right| \leq \left| \left|\sum_{n=0}^{\infty} A_n\right|^2 - \left(\left|\sum_{n=0}^{\infty} A_n\right| \pm \sum_{n=51}^{\infty} |A_n|\right)^2 \right| \Big/ \left|\sum_{n=0}^{\infty} A_n\right|^2$$
$$\sim 2\sum_{n=51}^{\infty} |A_n| \Big/ \left|\sum_{n=0}^{50} A_n\right| .$$

The last expression is easily evaluated, but the upper limit of $|\Delta I/I|$ given by this method is too large to be of practical significance. This will be understood when the reader is referred to Fig. 5.

Table II. Numerical evaluation of the intensity distribution of a multiple-beam Fizeau fringe. $R=0.90$, $(T=0.02)$, $\theta=3\times10^{-3}$ rad. ($X\sim100$/cm.), $t/\frac{\lambda}{2}\sim6$. Normal incidence. Evaluations taking the summation up to $n=10$, 20, 30, 40 and 50. (Numerical values of $J=|\sum R^n \exp(-i\delta_n)|^2$ are given in the table, which give the intensity of fringe I when multiplied by $T^2=0.0004$.)

$t/\frac{\lambda}{2}$	$\overset{10}{\Sigma}$	$\overset{20}{\Sigma}$	$\overset{30}{\Sigma}$	$\overset{40}{\Sigma}$	$\overset{50}{\Sigma}$
5.400	0.13	0.09	0.15	0.14	0.13
5.500	0.47	0.31	0.31	0.31	0.30
5.625	0.25	0.25	0.15	0.13	0.13
5.750	0.53	0.66	0.58	0.79	0.55
5.875	2.77	1.50	1.74	1.71	1.90
5.8875	2.64	2.57	2.34	2.18	2.18
5.900	2.00	3.12	2.70	2.70	2.72
5.9125	1.91	3.11	2.83	3.43	3.40
5.925	3.69	4.74	5.07	5.05	5.09
5.9375	8.12	7.84	6.90	7.04	6.97
5.950	15.26	10.64	10.33	9.99	10.07
5.960	23.37	14.04	14.94	15.24	15.19
5.965	27.81	16.97	18.47	19.04	18.94
5.970	31.54	20.70	22.50	22.84	22.85
5.975	35.99	27.68	29.31	29.10	29.34
5.980	39.11	34.63	35.73	34.30	34.42
5.985	42.02	43.97	42.43	41.71	41.70
5.990	44.43	54.14	50.16	50.07	50.00
5.995	46.10	63.64	57.85	58.42	58.27
6.000	46.95	71.75	67.77	66.83	66.96
6.0025	47.05	74.57	68.56	69.59	69.72
6.005	46.95	76.91	72.61	73.46	73.70
6.0075	46.62	77.37	75.64	76.13	76.47
6.010	46.08	77.23	77.60	77.78	78.00
6.0125	45.33	75.96	78.75	78.43	78.55
6.015	44.05	73.21	78.53	77.84	77.69
6.0175	43.26	70.32	77.45	76.57	76.47
6.020	41.95	66.12	74.72	73.55	73.24
6.0225	40.73	61.59	71.26	70.04	69.71
6.025	38.89	55.70	64.44	63.34	63.09
6.030	35.30	43.74	50.59	50.07	50.17
6.035	31.35	31.78	34.35	34.57	34.85
6.040	27.25	21.27	19.68	20.51	20.64
6.050	19.03	7.64	4.35	4.32	4.23
6.0625	10.28	4.18	7.11	7.17	7.22
6.0675	7.56	4.92	8.39	9.26	9.14
6.070	6.39	5.34	8.36	9.42	9.28
6.075	4.44	5.94	7.03	7.84	7.75
6.0875	1.73	4.92	2.56	1.92	1.96
6.100	1.64	2.80	3.44	4.39	4.31
6.1025	1.46	2.04	3.19	3.98	3.98
6.105	1.59	1.81	3.24	3.73	3.79
6.1125	1.99	1.56	2.51	1.96	2.04
6.115	2.24	1.84	2.32	1.63	1.65
6.1175	2.30	1.99	2.01	1.45	1.39
6.125	2.80	2.31	1.51	1.94	1.90
6.130	2.86	2.28	1.57	2.20	2.32
6.150	2.15	1.07	1.30	1.23	1.25
6.1625	1.26	0.97	1.06	1.27	1.23
6.175	0.60	1.26	1.17	0.94	1.06
6.1875	0.41	1.02	0.78	0.95	0.81
6.200	0.61	0.83	1.06	0.95	1.12
6.225	1.12	1.49	1.20	1.17	1.32
6.250	0.72	0.44	0.71	0.71	0.73
6.375	0.18	0.39	0.34	0.33	0.32
6.500	0.47	0.27	0.30	0.28	0.28
6.600	0.51	0.35	0.36	0.34	0.34

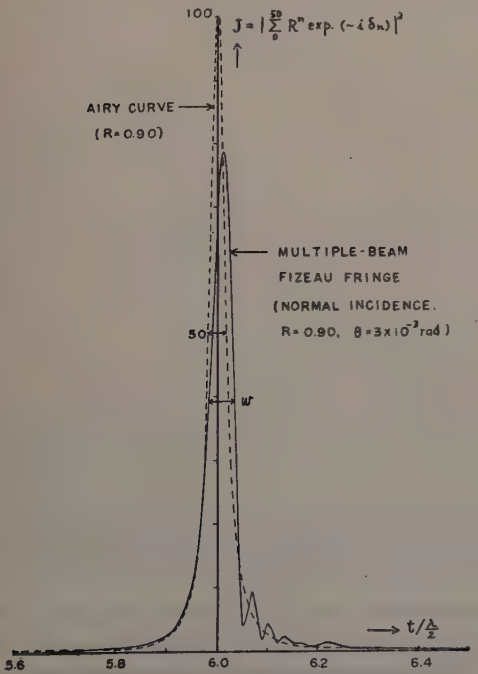

Fig. 3. Intensity curve of multiple-beam Fizeau fringe as compared with corresponding Airy curve.

in Table II and Fig. 3. Figures in Table II give the numerical values of

$$J=|\sum R^n \exp(-i\delta_n)|^2,$$

which shall be called the *reduced intensity* of the fringe, for successive values of $t/\frac{\lambda}{2}$. J multiplied by $T^2=0.0004$ yields the absolute intensity I. Thus the table is useful for different values of T so far as R is fixed at 0.90. Fig. 3 shows the J *vs.* $t/\frac{\lambda}{2}$-curve as compared with the corresponding* Airy curve (Eq. (4), $\delta=4\pi t/\lambda$).

The main intensity maximum of the multiple-beam Fizeau fringe is located at $t/\frac{\lambda}{2}=6.0125$ instead of 6.000 where the maximum should occur when the second term of Eq. (7) is equal to zero, or the Fabry-Perot case, and is about 80% as high as that of the corresponding Airy curve. The fringe falls off a little asymmetrically on the left and right side of the maximum. The half width w is about 0.056 which is 1.6 times as large as that of the corresponding Airy curve. Thus the definition is not much inferior to the Fabry-Perot fringe.

---

* The comparison with the Airy curve is rather formal. In the ordinary Fabry-Perot set-up, the variation of the $\sin^2$ term in Eq. (4) is produced by the variation of ϕ, while t and λ are kept constant. But the same intensity distribution will result with t variable and ϕ, λ constant, because what determines the intensity is a combination of these quantities: $\delta=4\pi t\cos\phi/\lambda$.

The most marked feature is the appearance of the secondary maxima at $t/\frac{\lambda}{2}=6.070$, 6.100, etc. These are restricted to one side of the main maximum in which the wedge is thicker.

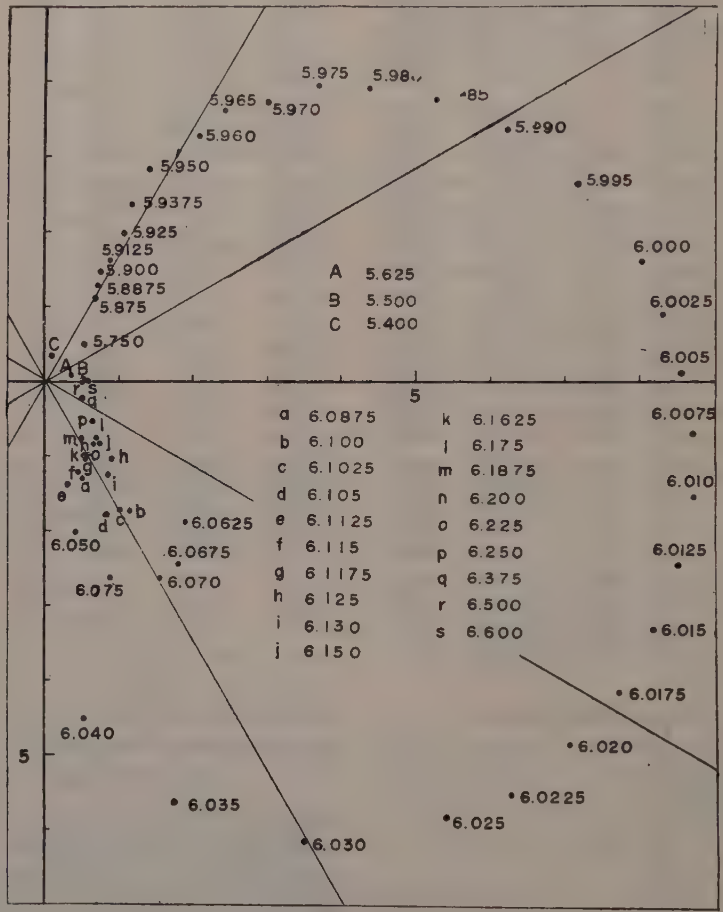

Fig. 4. Reduced resultant amplitudes $S=|\sum R^n \exp(-i\delta_n)|$ for successive values of $t/\frac{\lambda}{2}$ from 5.400 to 6.600.

Brossel[2] suggested that "*If the phase terms* β_n (similar terms with the second term of our Eq. (6) or (7)) *are small, the fringes are asymmetrical. As they become greater, secondary maxima occur in the interference pattern close to the main maximum*", and Holden[3] reported to have verified it experimentally. But no more details have been published so far as the author knows.

§ 4. Discussions

Brossel's discussion on the origin of the secondary maxima which we quoted above is too brief to be clear; it seems desirable to give a fuller explanation on the basis of numerical data.

It might be supposed at first that the secondary maxima have come out because we gave up the summation at $n=50$; it is well known that small sub-maxima do occur in the Fabry-Perot fringe if we give up the summation at a finite value of n (see Eq. (3)). But it can be shown by simple evaluation that the sub-maxima due to this cause are too small to be recognized in the reduced scale of Fig. 3. The secondary maxima discussed here are called into being by those situations which are characteristic to the multiple-beam Fizeau

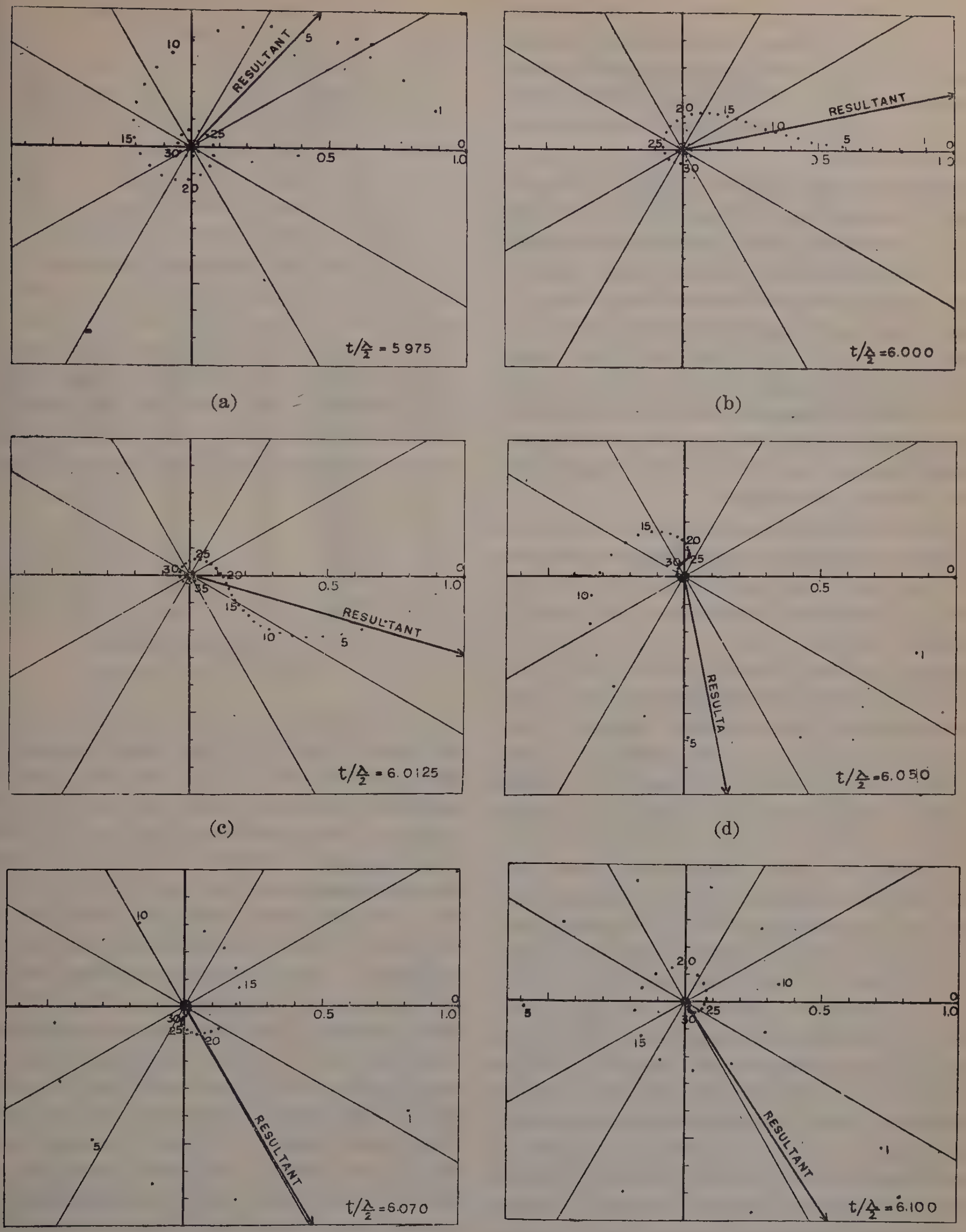

(a) (b) (c) (d) (e) (f)

Fig. 5. Reduced amplitude vectors $\boldsymbol{B}_n$ of successive beams which impinge on the points (a) $t/\frac{\lambda}{2}=5.975$, (b) $t/\frac{\lambda}{2}=6.000$, (c) $t/\frac{\lambda}{2}=6.0125$, (d) $t/\frac{\lambda}{2}=6.050$, (e) $t/\frac{\lambda}{2}=6.070$ and (f) $t/\frac{\lambda}{2}=6.100$.

interference.

For the convenience of discussions we define the *reduced amplitude* of the n-th beam $\boldsymbol{B}_n$ and the *reduced resultant amplitude* $\boldsymbol{S}$ by the following equations, and hereafter we shall treat of the fringe intensity in terms of the reduced intensity J which is equal to $|\boldsymbol{S}|^2$.

$$\boldsymbol{B}_n=\boldsymbol{A}_n/T=R^n \exp(-i\delta_n)\,. \qquad (9)$$

$$S = \sum B_n\,. \qquad (10)$$

In Fig. 4 are plotted the reduced resultant amplitudes for successive values of $t/\frac{\lambda}{2}$ from 5.400 to 6.600. (Only the end points of the radial vectors are plotted in this and following illustrations.)

It is self-evident that what plays the leading part in determining the magnitude and direction of S is the contribution from the beams of lowest orders, the zero-th, first, second, etc. whose (reduced) amplitudes are large in magnitude; and this is the reason why all S's are located in the first and the fourth quadrant. There is, however, another factor which must be taken into account. It is the '*returning*' of the rotation of (reduced) amplitude vector B_n which is to be explained in the following paragraph.

Consider the reduced amplitude vectors of multiply reflected beams which are collected to form the fringe on a point $t/\frac{\lambda}{2} = m + \Delta m$, where m represents an integer (the order of interference) and Δm a (small) fractional number, positive or negative. Fig. 5 (a), (b), (c), (d), (e) and (f) show the distribution of B_n's of successive beams which impinge after multiple reflections on the points $t/\frac{\lambda}{2} = 5.975$, 6.000, 6.0125, 6.050, 6.070 and 6.100 respectively. At $t/\frac{\lambda}{2} = m$ (Fig. 5 (b), $m=6$) where all B_n's would lie in the same direction ($-\delta_n = -2mn\pi$) in the Fabry-Perot case, B_n rotates* monotonously in the positive direction as n increases, owing to the second term of Eq. (7). On the positive side of $t/\frac{\lambda}{2} = m$, or when $\Delta m > 0$, *e.g.* at the points $t/\frac{\lambda}{2} = 6.0125$, 6.050, 6.070 and 6.100 (Fig. 5 (c), (d), (e) and (f)), the reduced amplitude vector B_n which would rotate monotonously in the negative direction if it were not for the second term begins to turn in the opposite direction when n exceeds a certain number r, because the second term grows rapidly with n. This is what we call the '*returning*' of the rotation of (reduced) amplitude vector. Fig. 6 shows the location of the *returning reduced amplitude vector* B_r for successive values of $t/\frac{\lambda}{2}$. On the negative side of $t/\frac{\lambda}{2} = m$, or when $\Delta m < 0$, *e.g.* at $t/\frac{\lambda}{2} = 5.975$ (Fig. 5 (a)), B_n rotates montonously in the positive direction without any *returning*.

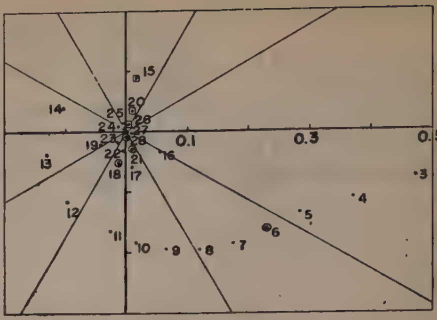

Index to Fig. 6.

No.	$t/\frac{\lambda}{2}$	r	No.	$t/\frac{\lambda}{2}$	r
1	6.000	0	15	6.050	23
2	6.0025	6	16	6.0625	26
3	6.005	7	17	6.0675	27
4	6.0075	9	18	6.070	28
5	6.010	11	19	6.075	29
6	6.0125	12	20	6.0875	31
7	6.015	13	21	6.100	33
8	6.0175	14	22	6.1025	33
9	6.020	15	23	6.105	34
10	6.0225	16	24	6.1125	35
11	6.025	17	25	6.115	35
12	6.030	18	26	6.1175	36
13	6.035	19	27	6.125	37
14	6.040	21	28	6.130	37

Fig. 6. Location of B_r's.
◉: maxima. ▣: minima.

In the neighbourhood of the *returning point* the difference of phase angle of successive B_n's is small, and consequently the sum of these B_n's can make an appreciable contribution to S. As was already mentioned, the magnitude and direction of S is fixed in the main by the location of B_n's of lowest order beams. But if it happens that the direction of the sum of B_n's near the *returning point* coincides with that of the sum of B_n's of lowest order beams, the resultant S will get so much larger; and if the two are in the opposite directions, so much smaller. The former case will produce a maximum in the fringe intensity, and the latter a minimum. The variation of intensity due to this cause superposed on the main variation of intensity which is similar with that in the Fabry-Perot fringe produces the maxima and minima in the intensity distribution curve of the multiple-beam Fizeau fringe.

Now the *returning reduced amplitude vector* B_r itself rotates round and round in the negative direction as Δm (>0) gets larger and larger, as is seen in Fig. 6. In one round there are in general a chance for maximum and a chance for minimum. Thus in the first round a maximum occurs at $t/\frac{\lambda}{2}=6.0125$, which is the main maximum displaced from $t/\frac{\lambda}{2}=6.000$ on account of the *returning effect*, and a minimum at $t/\frac{\lambda}{2}=6.050$. In the second round a maximum takes place at $t/\frac{\lambda}{2}=6.070$, which is the first sub-maximum, and a minimum at $t/\frac{\lambda}{2}=6.0875$; and so on. The cause of the asymmetry of the main maximum and the origin of the secondary maxima which appear on the larger t-side of the main maximum can be explained in this way in terms of the *returning effect*.

---

* Note that the phase angle of B_n is $-\delta_n = -2\pi(m+\Delta m)\{n - \frac{1}{3}n(2n^2+1)\theta^2\}$. For convenience' sake it is treated here dropping the multiples of 2π.

The above considerations can no more be applied when Δm is too large, because in that case the magnitude of B_n's near the *returning point* is so small and their directions so scattered that the *returning* cannot have any marked effect.

It would be possible to detect the secondary maxima as illustrated in Fig. 3 by sensitive experimental technique.

In conclusion the author wishes to express his hearty thanks to his wife Mrs. Tomo Kinosita and to Mr. Koichi Shigenaga who assisted him in numerical computations.

References

1) S. Tolansky: *Multiple-Beam Interferometry of Surfaces and Films*, Oxford, 1948.
2) J. Brossel: *Proc. Phys. Soc.* **59** (1947) 224.
3) J. Holden: *Proc. Phys. Soc.* **62B** (1949) 405.

JOURNAL OF THE PHYSICAL SOCIETY OF JAPAN Vol. 8, No. 2, MAR.—APR., 1953.

Ultraviolet Absorption Spectra of Glasses Containing Ti, and Heavy Metals

By Kikusaburo OSADA

Faculty of Engineering, Nagoya University

(Received September 22, 1952)

The characteristic ultraviolet absorption spectra of glasses with simple compositions were measured to 180 mμ with a small quartz spectrograph. The following results were obtained:

	Ti glass	Tl glass	Pb glass	Bi glass
absorption edge (mμ)	240	290	260	290
absorption maximum (mμ)	—	250	237	250

To investigate, particularly, the mechanism of the absorption maximum at 237 mμ of the Pb glass, spectra of acetate- and of plumbite-solution were measured. And, from the evidence that the spectrum of mixed solution of sodium- and lead-acetate coincides with that of the Pb glass, it may be interpreted that the appearance of the absorption maximum of the Pb glass is due to lead ions bonded weakly unsaturated oxygens in the network of SiO_4.

The variation of luminescence efficiency of them with wave-length of exciting radiations was also measured within the range between 200~300 mμ, and it was found that the luminescence maximum appeared near the corresponding wave-length to the absorption maximum.

§1. Introduction

The constitution of glasses has been investigated by means of X-rays diffraction[1], absorption spectra in visible[2] and in infrared[3] regions, fluorescence spectra[4], refractive index[5], etc. Their characteristic ultraviolet absorption spectra, however, have not yet been measured except ones containing rare earth elements[6], although these are also considered to correlate with their compositions and constitution. Therefore, to investigate the relations between absorption spectra and compositions, some kinds of glasses with simple conpositions were prepared from pure materials, and absorption spectra of thin films of them were measured to 180mμ. And the mechanism of an absorption spectrum of the Pb glass was considered from the evidence that this spectrum coincided with that of mixed solution of sodium- and lead-acetate.

The variation of luminescence efficiency with wave-length of exciting radiations was also measured to find the relations between efficiencies and absorption spectra.

§2. Absorption Spectra

The absorption spectra were measured to 180 mμ with a small quartz spectrogragh, the dispersion of which was 16 mμ/mm at 350 mμ and 1.3 mμ/mm at 200 mμ. Orthochromatic photographic plate supersensitized with liquid paraffine[7] was used and its density was measured with a microphotometer. A hydrogen discharge tube was used for a light source.

a) *Glasses*

Glasses were prepared by melting mixtures of $NaHCO_3$, SiO_2, and metal oxide or carbonate in proportion corresponding to the formula $3Na_2O \cdot 7SiO_2 \cdot M_nO$ (M=Ti, Tl, Pb, or Bi), and absorption spectra of thin films of them several microns thick were measured. The results obtained are shown in Fig. 1,

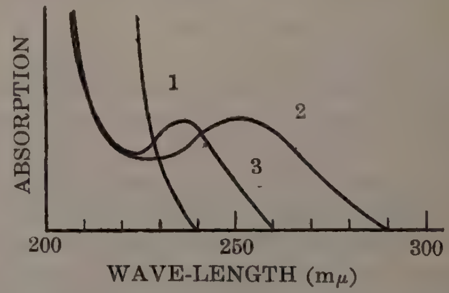

Fig. 1. Absorption spectra of glasses.
(1) Ti glass; (2) Tl- and Bi-glass; (3) Pb glass.

In the Ti glass, an absorption edge appears at 240 mμ. In the Tl-* and the Bi-glass, the edge appears at 290 mμ and a maximum of absorption bands at 250 mμ. In the Pb glass, the edge appears at 260 mμ and a maximum at 237 mμ.

In lead glass ($3K_2O \cdot 7SiO_2 \cdot PbO$, and $3Na_2O \cdot 7B_2O_3 \cdot PbO$) replaced sodium and silicon with potassium and boron, respectively, the spectrum is the same as in the sodium silicate glass.

b) *Acetates and Plumbite in Aqueous Solution*

Solutions were put between two quartz plates holding a thin metal foil 0.01 mm thick and absorption spectra of them in a thin layer were measured. The results obtained are shown in Fig. 2 for acetates and in Fig. 3 for plumbite.

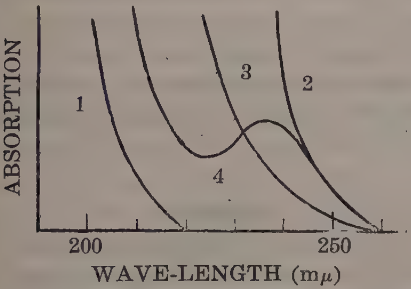

Fig. 2. Absorption spectra of acetate solutions. (1) Sodium acetate; (2) Lead acetate (conc.); (3) Lead acetate (dil.); (4) Mixed solution.

In mixed concentrated solution of sodium- and lead-acetate, an absorption edge appears at 260 mμ and an absorption maximum at 237 mμ. In concentrated solutions of sodium- and of lead-acetate, the edge appears at 220 mμ and 260 mμ, respectively. But in the latter the absorption maximum does not appear at 237 mμ just as in the mixed solution of them, though the transmission increases gradually to the regions of shorter wave-length with decreasing concentration.

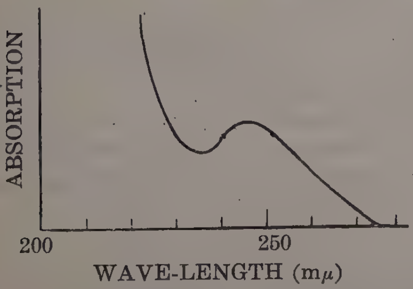

Fig. 3. Absorption spectrum of potassium plumbite solution.

By precipitating $Pb(OH)_2$ from mixed solution of KOH and $Pb(NO_3)_2$ and dissolving that into KOH solution, potassium plumbite solution was prepared. This solution has an absorption edge at 275 mμ and an absorption maximum at 245 mμ.

§ 3. Fluorescence Spectra

When illuminated with ultraviolet radiations, the Ti glass fluoresces emitting a green light and other glass blue ones, but solutions of acetate and of plumbite do not.

The variation of relative luminescence efficiency of glasses with wave-length of exciting radiations was measured within the range between 200~300 mμ by following experiments.

Photographic plate is contacted with celluloid film, over which powdered glass to be measured is spread, and the hydrogen spectrum is photographed on the plate with the same spectrograph. The celluloid film being opaque below 300 mμ, the density of plate in the regions below 300 mμ is proportional to the product of luminescence efficiency of glass and intensity of exciting radiations. On the other hand, the relative intensity of exciting radiations is informed from the density of plate coated with sodium salicylate, instead of powdered glass, since luminescence efficiency of sodium salicylate has been known$^{8)}$. So that the luminescence efficiency of glass is informed from the ratio of density of plate with powdered glass to one with sodium salicylate.

Thus, the relative luminescence efficiency of them was obtained as followed:

In the Tl- and the Bi-glass, the luminescence efficiency is higher within the range between 240~290 mμ, and in the Pb glass, within the range between 210~290 mμ with a maximum near 240 mμ. But in the Ti glass, it is higher below 270 mμ and a maximum does not appear.

§ 4. Discussion

In the glasses containing one of heavy metals, an absorption maximum appears near

---

* This maximum was found after the author's previous paper (J. Phys. Soc. Japan **7** (1952) 332).

250 mμ, but in the Ti glass does not. In the following descriptions, the mechanism of the absorption maximum of the Pb glass will be considered comparing with the spectra of lead compound solutions.

It has been well known from the network theory⁹⁾ of glass that silicate glass consists of a three-dimentional network of SiO_4 tetrahedra, which containes metal ions in interstitial positions. When metal ion is Tl^+, Pb^{++}, or Bi^{+++}, the asymmetry of electrons in non-noble gas configurations of them is thought of as a supplymental condition of glass formation e.g. $Pb_2SiO_4$¹⁰⁾. Therefore, it may be supposed that the appearance of the absorption maximum at 237 mμ of the Pb glass is due to lead ions, which are introduced in the hole of network and exert the attractive force to unsaturated oxygens.

In order to ascertain this assumption, absorption spectra of lead compounds in aqueous solution, that is, lead acetate and plumbite, were examined and compared with that of the Pb glass, since it may be supposed that lead ions bond to oxygens in those solutions.

In solution of plumbite, an absorption maximum appears at 245 mμ. In solutions of lead- and of sodium-acetate, a maximum does not appear, but in mixed solution of them, appears at 237 mμ just as in the Pb glass. So the appearance of this maximum at 237 mμ may be not due to Pb^{++}, nor to $(CH_3COO)^-$, but to lead ions bonded weakly to acetate ions; in mixing those solutions, acetate ions increase in this solution, and the interaction between acetate- and lead-ions may arise from increase of the former.

The spectrum of the Pb glass agrees with that of the mixed solution out acetates. And it may be supposed that the bond system of the former is similar to that of the latter; lead ion is bonded to oxygen, and the oxygen is itself bonded to silicon in the glass and to carbon in the solution, the 2s-2p hybridization of carbon being considered the same as that of the 3s-3p system of silicon¹¹⁾. Therefore, it may be interpreted that the appearance of the absorption maximum at 237 mμ of the Pb glass is due to lead ions bonded weakly to unsaturated oxygens in the network of SiO_4.

The maximum at 250 mμ of the Tl- and the Bi-glass may also originate from thallium- and bismuth-ions bonded weakly to unsaturated oxygens, since thallium- and bismuth-ion have the same electron configuration as lead ion.

In the glasses containing one of heavy metals, the luminescence maximum appears near the corresponding wave-length to the absorption maximum. Accordingly, it may be considered that the heavy metal ions surrounded by (−O−Si) are the centres of fluorescence.

§ 5. Conclusion

When glass contains heavy metal, near 250 mμ appears an absorption maximum originated from the heavy metal ions bonded weakly to unsaturated oxygens in the network of SiO_4. The heavy metal ions are also the centres of fluorescence.

This research was financially supported by the Scientific Research Grant of the Educational Ministry and the Hattori Hôkôkai.

References

1) B. E. Warren: J. App. Phys. **8** (1937) 645; E. Preston: J. Soc. Glass Tech. **26** (1942) 82.

2) S. H. Linwood & W. A. Weyl: J. O. S. A. **32** (1942) 443.

3) J. I. Gerlouin: C. R. Acad. Sci. U. R. S. S. **38** (1943) 126; R. Stair & C. A. Faick: J. Research Natl. Bur. Standards **38** (1947) 95.

4) S. H. Linwood & W. A. Weyl: *ibid.*; R. Tomaschek: Trans. Farady Soc. **35** (1939) 148.

5) K. Fajans & N. J. Kreidl: J. Am. Ceram. Soc. **31** (1948) 105.

6) T. N. Veinberg: Izvest. Akad. Nauk. S. S. S. R. Ser. Fiz. **13** (1949) 203.

7) G. R. Harrison & P. A. Leighton: J. O. S. A. **20** (1930) 313.

8) F. S. Johnson, K. Watanabe & R. Tousey: J. O. S. A. **41** (1951) 702; A. Chevallier & P. Dubouloz: C. R. **194**(1932) 174.

9) B. E. Warren: *ibid.*

10) F. L. Jones & N. J. Kreidl: J. Soc. Glass Tech. **33** (1949) 239.

11) L. Pauling: *The Nature of the Chemical Bond* (1940) p. 84.

JOURNAL OF THE PHYSICAL SOCIETY OF JAPAN Vol. 8, No. 2, MAR.—APR., 1953

On the Fatigue of Ag–Cs Photoelectric Tubes

By Goro KUWABARA

Department of Physics, Faculty of Science, University of Tokyo

(Received November 24, 1952)

The fatigue of Ag-Cs photoelectric tubes was measured for the light of low intensity at room temperature. The results can be explained neither by the hypothesis of de Boer nor by that of Suhrmann. The necessary conditions for obtaining a high accuracy in photoelectric photometry with Ag-Cs phototubes were discussed.

§ 1. Introduction

Photoelectric tubes are generally used for photometry of high accuracy. However, the so-called composite photo-cathode, such as K–H or Ag–Cs is accompanied with the fatigue phenomenon, and without due precautions in using phototubes, this effect would cause systematic errors. The fatigue has been investigated concerning the mechanism of photo-emission, De Boer[1] studied the Ag–Cs phototube with a thick intermediate layer of Cs_2O and developed an idea that the fatigue is caused by decrease of neutral Cs atoms on the surface due to photoionization and poor supply of electrons through the layer to the surface. According to his hypothesis, which is supported also Timofejew[2] and Pakswer[3], the fatigue should depend upon the light intensity or the amount of photocurrent and the anode voltage supplied to the tube, but be independent of the wave length of illuminating light. Suhrmann[4] investigated Naphthalen–Cs, Anthracen–Cs and K–H photocathode at liquid air temperature, and proposed another hypothesis that the fatigue is a sort of excited states. This hypothesis seems to have some relation to the study on photoelectric effects of Alkali-halide by Asmus[5]. However, neither the former nor the latter can completly explain the fatigue of ordinary photo-cathode at room temperature.

We investigated the fatigue of commercial Ag–Cs phototube from a view point of spectral photometry of high precision with little reference to its mechanism.

§ 2. Experimental Arrangement

The investigation on the fatigue phenomenon was carried out with three vacuum Ag–Cs photoelectric tubes of ordinary type. The results on one of them are mainly described in this paper. The other two tubes have also shown the similar behavior qualitatively with regard to the fatigue. The optical arrangement used is shown schematically in Fig. 1. By shifting the prism from A′ to A in Fig. 1, the light from the monochromator 1 (or II) and that from the optical bench can be interchanged with each other smoothly and continuously. Provisions were made in order to maintain the variation of the brightness of three light sources within 0.1 per-cent during the experiment. These three lights from the monochromator I, II and optical bench are adjusted to produce the same image on the same position of the opal glass in front of the phototube under investigation, and the intensity of the light from the bench can be varied according to the inverse square law. The anode voltage supplied to the photo-tube was 100 volts and the photocurrent was amplified with a balanced direct current amplifier with UX–54 electrometer tube. The phototube load resistor was 2×10^{10} or 10^9 ohms, the galvanometer has a short period and sensitivity of 0.75×10^{-9} amp./mm, and the total sensitivity of the amplifier was 1.5×10^{-15} amp./mm or 3×10^{-14} amp/mm. The time constant of the electric circuit including the galvanometer was ca. 2 sec. Most of the

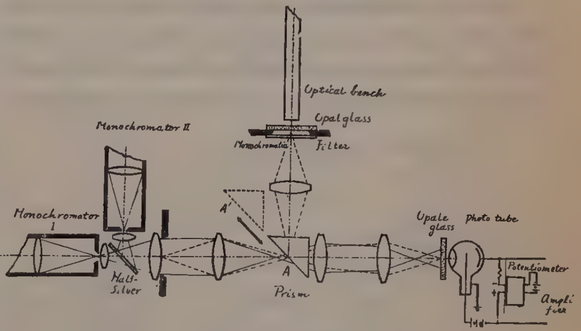

Fig. 1. Optical Arrangement.

potential drop within the load resistor caused by the flow of photocurrent was compensated by the potentiometer inserted in series to the resistor, and not the total photocurrent but the variation or the difference from the steady value was amplified and measured with the galvanometer. The purpose of this investigation being to study the effect of fatigue on the spectral photometry of low light intensity, the light intensity of each monochromatic light was adjusted to produce the photo-current of the same order of 10^{11} amp. and all the experiments were carried out at room temperature.

§ 3. Experimental Results

1. Decay of the Photo-current

The photoelectric tube was illuminated with the light from the monochromator 1 after having been kept in darkness for a long time. Before illumination, the counter voltage, which compensates most of the photo-current had been supplied by the potentiometer, and the galvanometer was shorted with a low resistor in order to avoid the flow of excess current through it. The shunt resistor being cut off at 9 seconds after illumination, the decay of the photo-current was measured. The photo-current decays exponentially with time until the steady state is reached after a few minutes. The current at the initial state was determined by extrapolating those after 9 seconds to zero, and it coincides within the accuracy of 0.3% for each measurement. The results are shown in Fig. 2. The shorter is the wave length of illuminating light, the larger is the amount of fatigue, i.e. the relative decrease of the photo-current to the initial value. When the tube is irradiated with the light of 370 mμ, the fatigue amounts to 10%, but with the light above 600 mμ, the fatigue can not be perceived within the accuracy of 0.1%. The decay constant of the photo-current is nearly the same for various wave-lengths.

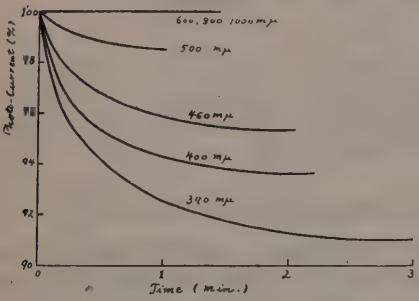

Fig. 2. Decay of Photo-current.

2. The Effects of the Anode Voltage and the Light Intensity.

The anode voltage of the photo-tube being lowered to 50 volts or the light intensity being increased by 5 or 10 times, the amount of fatigue or the relative decrease of the photocurrent remains constant.

3. The Effect of Abrupt Change of the Wave-length of Illuminating Light.

In order to study the response of the photocathode in fatigue to the light of different wave-length, the tube is illuminated with the monochromatic light from the optical bench until the steady state is reached, and then the light from the bench is interchanged with that from the monochromator 1 smoothly and quickly by shifting the prism, and the variation of the photo-current was measured. The

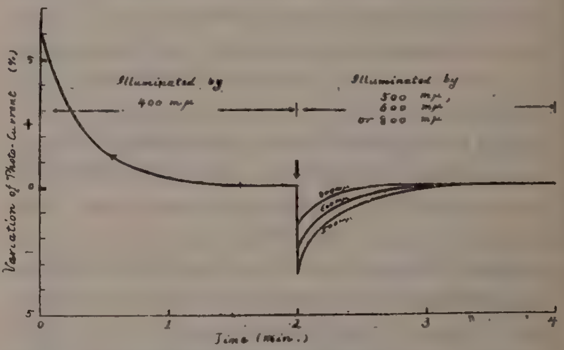

Fig. 3. Variation of Photo-current by Abrupt Change of Illuminating Light.

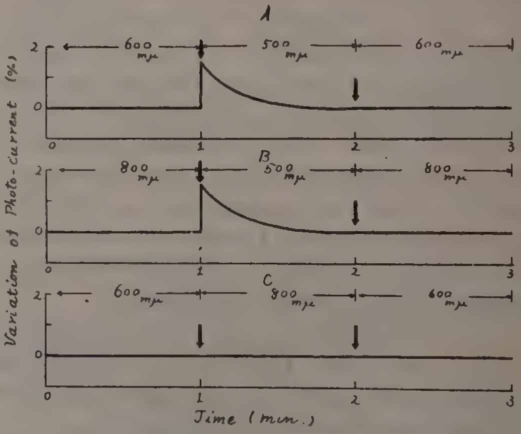

Fig. 4. Variation of Photo-current by Abrupt Change of Illuminating Light.

intensities of the light from the bench and monochromator had been adjusted to give the same steady current. The results were shown in Fig. 3 and 4, and summarized as follows.

(a) When the wave length of these two lights are the same, the photo-current shows no change except the slight disturbance caused by the prism edge, which quickly disappears.

(b) When the photo-tube, which has been brought to fatigue completely by the light between 400 mμ and 500 mμ, is illuminated with the light of wave-length above 600 mμ, the photo-current decreases by a few per cent at the instant of exchange, and then increasing exponentially, attains the steady value after about one minute. This shows that the illumination with violet or blue light diminishes the sensitivity to those light but slightly affects the sensitivity to red or infra-red light and by irradiating with the light of longer wave-length, the sensitivity to violet or blue light recovers quickly.

(c) When the phototube, which has been illuminated by the light above 600 mμ, is suddenly irradiated with the light below 500 mμ, it behaves just as that kept in darkness. This shows that the illumination with yellow, red or infra-red light diminishes the sensitivity neither to the long nor to the short wave-length. The decrease of photo-current for various wave-lengths caused by illuminating with each light for ten minutes is shown in Fig. 5–C, and the decrease of spectral sensitivity due to the illumination with violet light for ten minutes is shown in Fig. 5–D. It is concluded that the decrease of spectral sensitivity by irradiation with violet or blue light is more intense to the shorter wave-length than to the longer.

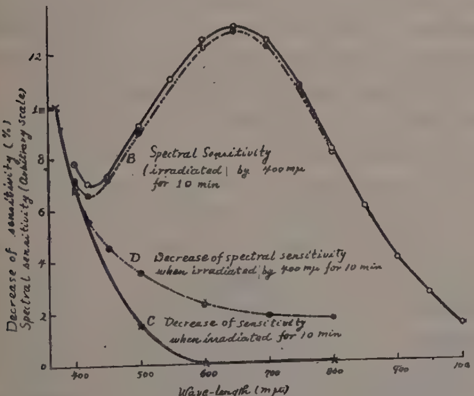

Fig. 5. Variation of Spectral Sensitivity by Illumination.

The spectral sensitivity was measured for the fresh photocathode (Fig. 6–A) and for that brought to fatigue by illuminating with violet light for ten minutes (Fig. 6–B). The spectral sensitivity was calculated from the photo-currents and the spectral intensity distribution of the light source, which was determined by measuring the temperature of the filament. The sensitivity in the fresh state was determined by the method described in (1).

4. Recovery of Fatigue.

The photo-cathode, whose sensitivity was decreased by illuminating with violet light, has been kept in darkness or illuminated with infra-red light for various duration, and its sensitivity to violet light is again measured. The result is shown in Fig. 6. Not only by keeping in darkness but by illuminating with the light above 600 mμ, the photo-tube recovers its sensitivity, and the recovery is more rapid as the intensity of the infra-red light is increased.

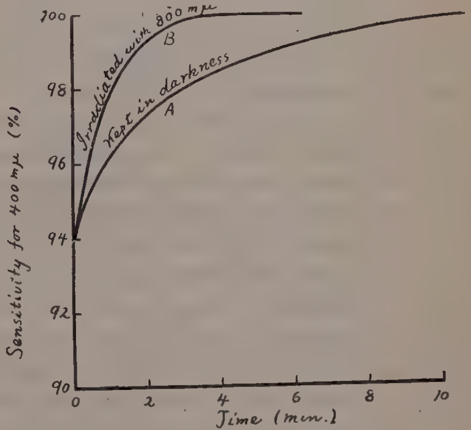

Fig. 6. Recovery of Fatigue.

5. Simultaneous Illumination with Two Lights of Different Wave-length.

The illumination with violet or blue light decreases the sensitivity to the shorter wave-length, while the illumination with red or infra-red light restores the sensitivity of the photo-cathode brought to fatigue.

Above considerations in mind, we will ask for the behavior of the photo-cathode illuminated simultaneously with two lights of different wave-lengths. The photo-current was measured separately for the lights from monochromator I and II, whose intensities were adjusted to give nearly the same photo-current, and then the photo-current caused by simultaneous illumination with these two lights was measured. The results are shown in Tab. 1. The ratios of the currents were measured by the potentiometer and also by the intensity ratios of the lights from the optical bench, which were adjusted to cause the same photo-current for each case.

Table 1. Additivity of Photo-current.
(simultaneous illumination by two lights from monochromator I and II.)
{1−(Photo-current for I plus II)/[(Photo-current for I)+(Photo-current for II)]} ×100(%)

I (mμ) / II (mμ)	400	500	600	800	1000
400	−1.92	−1.24	−0.36	+0.31	+0.11
500		−1.36	−1.03	+0.27	+0.17
600			0.02>	0.02>	0.02>
800				0.02>	0.02>
1000					0.02>

(a) The fatigue caused by illuminating with a composite light. The simultaneous illumination with the light below 500 mμ and that above 600 mμ causes as much fatigue as that corresponding to the shorter wave-length component of the composite light.

(b) The additivity of the photo-current for various wave-lengths. If one of the two components of the composite light is above 600 mμ, the photo-current for the composite light is just the same as the sum of the two photo-currents caused by each component independently.

With regard to the fatigue and the amount of the photo-current, when illuminated simultaneously, the two lights do not interfere with each other so long as one or both components of this composite light are above 600 mμ. If both components are below 500 mμ, the photo-current for composite light is less than the sum of those for each component.

Considering the result described in (2), it is infered that the additivity failure is caused not by the dependence of the relative decrease of photo-current on the light intensity but the non-linearlity of the photo-current for violet or blue light.

The results of the experiments are summarized as follows

(a) The sensitivity of Ag–Cs photo-cathode decreases gradually until the stationary state is reached even by the illumination with the light of low intensity. The shorter is the wave-length of the illuminating light, the more intense is the fatigue caused thereby, and the light above ca. 600 mμ, causes no appreciable fatigue.

(b) The amount of fatigue, that is, the relative decrease of the photo-current depends neither on the anode voltage nor on the light intensity within the intensity range in our experiment.

(c) All the variations of the photo-current can be approximately expressed by the exponential function with nearly the same time constant.

(d) The photo-cathode, whose sensitivity to the short wave-length is diminished by illuminating with violet or blue light, shows little decrease of the sensitivity to the longer wave-length than 600 mμ.

(e) The photo-cathode restores its sensitivity by being kept in darkness or illuminated with red or infra-red light.

(f) When the photo-tube is illuminated simultaneously with two lights of different wave-length, the additivity of the photo-current holds, if the wave-lengths of one or both components are above 600 mμ, however, it does not holds, if both components are below 500 mμ. This shows that, though the linearity of the photo-current is valid for the wave-length above 600 mμ, it is no more valid for the wave-length below 500 mμ.

According to our results, it is difficult to explain the fatigue of ordinary Ag–Cs photo-tube at room temperature by the hypothesis of de Boer or by that of Suhrmann. It can not be ascertained whether the fatigue observed in our experiment is inherent or immaterial to the mechanism of photo-emission. If it is the former case, it may be concluded that the two sensitivity maxima at ca. 380 mμ and at ca. 700 mμ are attributed to the different kinds of photo-emission centers.

§ 4. Necessary Conditions for the Spectral Photometry of High Accuracy

In photo-electric photometry, it is obvious that the photo-tube must be set in the same condition for the two lights to be compared with respect to the optical path, the location of the photo-cathode to be illuminated, the incident angle, the plane of polarization and so forth. To obtain a high accuracy, the linearity of the photo-tube load resistor and the amplifier can not be assumed, and according to our results, even the linearity of the photo-tube is suspicious for violet and blue light. Moreover, though the decrease of the sensitivity is independent upon the intensity of light so long as our experiment covers, it is also suspicious that this relation is valid for a far wider range of the light intensity. Therefore, in the photometry of high accuracy, the photo-tube should be used only as a *zero indicator* which detects only the intensity difference between two lights of the same wave-length.

There have been two devices, in which the above conditions are satisfied. One is that developed by Koana, Murakami *et al*⁽⁶⁾. In order to determine the intensity ratio of two lights, the third light of the same wave-length is introduced as a comparison light, and by a light weakening device, such as the inverse square law or a variable diaphram, which can be calibrated independently, the intensity of comparison light is varied to produce the same amount of photo-current with each of the two lights. Thus the intensity ratio of the two lights to be measured is reduced to that of the comparison light in two cases, which can be accurately determined.

Another is that performed by Hardy⁽⁷⁾ in his self-recording photometer. The light from one light source is splitted into two beams. These two beams, one of which passes through the sample and another passes through the calibrated light weakener, fall on the same phototube alternatively. The transmittance of a sample is measured as a weakening ratio, by which both beams produce the same amount of photo-current.

§ 5. Acknowledgement

The author wishes to express his sincere thanks to Professor Z. Koana for his suggestions and encouragements throughout the work.

References

1) de Boer: Zs. f. Phys. **74** (1932) 604.
2) P. W. Timofejew & N. S. Kondorskaja: Phys. Zs. d. Sowjet. **9** (1936) 983.
3) S. Pakswer: Jour. App. Phys. **18** (1947) 203.
4) R. Suhrmann u. A. Mittmann: Zs. f. Phys. **111** (1938) 137.
5) E. Asmus: Ann. d. Phys. **26** (1936) 73.
6) Z. Koana, T. Murakami u.s.w. Proc. Phys. Math. Soc. Jap. **22** (1940) 940.
6) A. C. Hardy: J.O.S.A. **28** (1938) 360.

JOURNAL OF THE PHYSICAL SOCIETY OF JAPAN Vol. 8, No. 2, MAR.—APR., 1953

Transmission of Ultrasonic Waves through a Plane Plate made of Viscoelastic Material Immersed in a Liquid Medium

By Yasuo TORIKAI

Institute of Industrial Science, University of Tokyo, Chiba-City

(Received October 3, 1952)

The transmission of ultrasonic waves at oblique incidence through a plane plate made of viscoelastic material is theoretically studied. The absorptive properties of the solid medium which have been neglected in the preceding theory are considered. The resulting expression for the transmission is of the same form as in the case of a non-absorptive plate, but the propagation constants of the waves are replaced by complex quantities in the expression. It is shown that when the absorption by the plate is appreciable, the more simple formula can be applied and the formula agrees well with the experimental result. As a note on Srivastava's papers, it is explained that the velocity of rotational waves obtained from the apparent critical angle for rotational waves is always larger than the real value on account of the absorptive property of the solid medium.

§1. Introduction

The transmission of ultrasonic waves at oblique incidence through a plane plate has been studied both theoretically and experimentally by many workers.[1)-13)] In the theoretical treatments up to this time, the sound absorption in the solid medium has been neglected. Among the materials treated, however, there are many ones which have considerably absorptive properties, e.g., ebonite, rubber, gel, and synthetic resin. In these cases, the disregard of the absorptive properties of the plate substances may cause occasionally a considerable error. In the present paper, the author will discuss theoretically the problem, and show the effect of the absorptive property of the plate medium on the transmission. As a result of introducing absorption term, the propagation constants of waves in a viscoelastic medium become complex quantities and especially in case the absorption is appreciable, the expression for the transmission becomes rather simple than in case of non-absorptive material.

Astbury[14)] has discussed the transmission of ultrasonic waves at normal incidence through a viscoelastic plate, and his result is a special case of the present theory.

§2. Nomenclature

ξ, η, ζ = particle displacement in x, y, z, directions
Δ = dilatation
ω = rotation in xy-plane
λ, μ = Lame's elastic constants
ρ_0 = density of liquid medium
ρ = density of plate
$h_0 = p/v_0$
$h = p/v_\Delta$
$k = p/v_\omega$
p = frequency in radians per second
v_0 = velocity of propagation in the liquid
v_Δ = velocity of dilatational waves in solid
v_ω = velocity of rotational waves in solid
θ_0 = incident angle in liquid medium
θ_Δ = angle of refraction of dilatational waves in solid
θ_ω = angle of refraction of rotational waves in solid
$l = h_0 \sin\theta_0 = h \sin\theta_\Delta = k \sin\theta_\omega$
$r_0 = h_0 \cos\theta_0 \quad r = h \cos\theta_\Delta \quad s = k \cos\theta_\omega$

When the absorptive properties of solid medium are considered, the next notations are added.

λ', μ' = voluminal and equivoluminal viscosities
$h = h_1 - ih_2$
$k = k_1 - ik_2$
L_Δ = attenuation in db per cm of dilatational waves in solid
L_ω = attenuation in db per cm of rotational waves in solid
$r = r_1 - ir_2$

$$s=s_1-is_2$$
$$\varepsilon_\Delta=h_2/h_1$$
$$\varepsilon_\omega=k_2/k_1$$

§ 3. Transmission through a Plate Made of Non-Absorptive Material

As the problem of the transmission of ultrasonic waves through a plate made of non-absorptive material has been theoretically investigated by Reissner[4)] and others[5)6)10)13)] already, the outline of the calculation and the resulting expression for the transmission are briefly described in this section and the theory will be extended to the case of viscoelastic medium in the later section.

When a plane plate of thickness d is immersed in liquid medium as shown in Fig. 1, the transmission of ultrasonic waves incident to the plate at angle of incidence, θ_0, is calculated as follows.

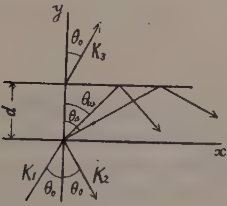

Fig. 1.

Choosing the coordinate axes as shown in Fig. 1, the equations of wave motion in the solid medium are given by (1), being treated as a two-dimensional problem.

$$\left.\begin{aligned}\rho\frac{\partial^2\varDelta}{\partial t^2}&=(\lambda+2\mu)\left(\frac{\partial^2\varDelta}{\partial x^2}+\frac{\partial^2\varDelta}{\partial y^2}\right)\\ \rho\frac{\partial^2\omega}{\partial t^2}&=\mu\left(\frac{\partial^2\omega}{\partial x^2}+\frac{\partial^2\omega}{\partial y^2}\right)\end{aligned}\right\}\quad(1)$$

where

$$\varDelta=\frac{\partial\xi}{\partial x}+\frac{\partial\eta}{\partial y}\,,\qquad 2\omega=\frac{\partial\eta}{\partial x}-\frac{\partial\xi}{\partial y}\,.\qquad(2)$$

Considering the plane waves satisfying (1) and proportional to $\exp(ipt)$, $\varDelta$ and ω are represented by (3), corresponding respectively to the dilatational and rotational waves in the medium.

$$\varDelta=Ae^{i(pt-lx-ry)}\,,\quad 2\omega=Be^{i(pt-lx-sy)}\quad(3)$$

where

$$\left.\begin{aligned}&l^2+r^2=h^2\,, && l^2+s^2=k^2\\ &h^2=\frac{\rho p^2}{\lambda+2\mu}\,, && k^2=\frac{\rho p^2}{\mu}\end{aligned}\right\}\quad(4)$$

In the above expressions, the x-component of propagation constant, l, is common to all waves considered from Snell's law or from the boundary conditions.

When the incident and transmitted waves in the liquid medium are represented respectively by $K_1\exp\{i(pt-lx-r_0y)\}$ and $K_3\exp\{i(pt-lx-r_0y)\}$, the amplitude transmission, K_3/K_1, is represented as follows[4)10)13)]

$$\frac{K_3}{K_1}=\frac{2Ne^{ir_0d}}{2M+i(N^2-M^2+1)}\qquad(5)$$

where

$$\left.\begin{aligned}N&=\frac{f}{\sin rd}+\frac{g}{\sin sd}\\ M&=f\frac{\cos rd}{\sin rd}+g\frac{\cos sd}{\sin sd}\\ f&=\frac{\cos\theta_0}{\rho_0v_0}\frac{\rho v_\Delta}{\cos\theta_\Delta}\cos^2 2\theta_\omega\\ g&=\frac{\cos\theta_0}{\rho_0v_0}\frac{\rho v_\omega}{\cos\theta_\omega}\sin^2 2\theta_\omega\end{aligned}\right\}\quad(6)$$

The same quantity is represented also by another expression as given by[13)]

$$\frac{K_3}{K_1}=\frac{8ie^{ir_0d}(f\sin sd+g\sin rd)}{-8fg+(1+f+g)^2e^{i(r+s)d}-(1+f-g)^2e^{i(r-s)d}+(1-f-g)^2e^{-i(r+s)d}-(1-f+g)^2e^{-i(r-s)d}}\,.\qquad(7)$$

§ 4. Propagation of Elastic Waves in Viscoelastic Medium

In the case of viscoelastic medium, the equations of wave motion, (1), in the non-absorptive medium must be modified. Considering the solid viscosities proportional to the time-rates of changes of strains, the equations of wave motion are represented by[15)16)]

$$\left.\begin{aligned}(\lambda+2\mu)\nabla^2\varDelta+(\lambda'+2\mu')\frac{\partial}{\partial t}\nabla^2\varDelta&=\rho\frac{\partial^2\varDelta}{\partial t^2}\\ \mu\nabla^2\omega+\mu'\frac{\partial}{\partial t}\nabla^2\omega&=\rho\frac{\partial^2\omega}{\partial t^2}\end{aligned}\right\}\quad(8)$$

where $\nabla^2\equiv\partial^2/\partial x^2+\partial^2/\partial y^2$. (cf., appendix, as to the more general case of stress-strain relations in viscoelastic medium.)

Though solutions of (8) proportional to

$\exp(ipt)$ are also given by (3), the expressions in (4) must be modified as follows:

$$\left.\begin{aligned} l^2+r^2=h^2&=\frac{\rho p^2}{\lambda+2\mu+ip(\lambda'+2\mu')} \\ l^2+s^2=k^2&=\frac{\rho p^2}{\mu+ip\mu'}\ . \end{aligned}\right\} \quad (9)$$

Therefore, h, k, r, and s are complex quantities as represented by

$$h=h_1-ih_2,\ k=k_1-ik_2,\ r=r_1-ir_2, \text{ and } s=s_1-is_2\ . \quad (10)$$

Only l is left as real, since, as mensioned in the preceding section, l is common to all waves considered and is real in the wave expressions in liquid medium because of the non-absorptive property of the usually used liquid medium.

It can be verified that h_1, k_1, h_2, and k_2 of eq. (10) are respectively the propagation and attenuation constants of dilatational and rotational waves in the infinitely extended viscoelastic medium just considered. The velocities, v_Δ and v_ω, of dilatational and rotational waves in the same medium are respectively represented by $v_\Delta=p/h_1$ and $v_\omega=p/k_1$ and the attenuations L_Δ and L_ω in db per unit length for both waves are connected with h_2 and k_2 as follows:

$$L_\Delta=8{\cdot}686\,h_2\ ,\quad L_\omega=8{\cdot}686\,k_2\ . \quad (11)$$

From (9) and (10),

$$(h_1-ih_2)^2=\frac{\rho p^2}{\lambda+2\mu+ip(\lambda'+2\mu')} \quad (12a)$$

$$(k_1-ik_2)^2=\frac{\rho p^2}{\mu+ip\mu'} \quad (12b)$$

$$l^2+(r_1-ir_2)^2=(h_1-ih_2)^2 \quad (12c)$$

$$l^2+(s_1-is_2)^2=(k_1-ik_2)^2\ . \quad (12d)$$

From (12a), h_1, h_2, and v_Δ are given by

$$\left.\begin{aligned} h_1^2&=\frac{\rho p^2}{\lambda+2\mu}\left[1-\frac{3}{4}\frac{p^2(\lambda'+2\mu')^2}{(\lambda+2\mu)^2}\cdots\right] \\ h_2^2&=\frac{\rho p^2}{\lambda+2\mu}\frac{1}{4}\frac{p^2(\lambda'+2\mu')^2}{(\lambda+2\mu)^2} \\ &\qquad\times\left[1-\frac{5}{4}\frac{p^2(\lambda'+2\mu')^2}{(\lambda+2\mu)^2}\cdots\right] \\ v_\Delta&=\frac{p}{h_1}=\sqrt{\frac{\lambda+2\mu}{\rho}}\left[1+\frac{3}{8}\frac{p^2(\lambda'+2\mu')^2}{(\lambda+2\mu)^2}\cdots\right] \end{aligned}\right\} \quad (13)$$

Putting $h_2/h_1=\varepsilon_\Delta$,

$$\left.\begin{aligned} \lambda+2\mu&=\frac{\rho p^2}{h_1^2}\frac{1-\varepsilon_\Delta^2}{(1+\varepsilon_\Delta^2)^2} \\ p(\lambda'+2\mu')&=\frac{\rho p^2}{h_1^2}\frac{2\varepsilon_\Delta}{(1+\varepsilon_\Delta^2)^2}\ . \end{aligned}\right\} \quad (14)$$

In practice, ε_Δ is usually less than 0.1 so that h_1, v_Δ, and ε_Δ are approximately given by

$$\left.\begin{aligned} h_1^2&=\frac{\rho p^2}{\lambda+2\mu} \\ v_\Delta&=\sqrt{\frac{\lambda+2\mu}{\rho}} \\ \varepsilon_\Delta&=\frac{1}{2}\frac{p(\lambda'+2\mu')}{\lambda+2\mu}\ . \end{aligned}\right\} \quad (15)$$

From (12b), the similar relations on rotational waves are represented as follows:

$$\left.\begin{aligned} k_1^2&=\frac{\rho p^2}{\mu}\left(1-\frac{3}{4}\frac{p^2\mu'^2}{\mu^2}\cdots\right) \\ k_2^2&=\frac{\rho p^2}{\mu}\frac{1}{4}\frac{p^2\mu'^2}{\mu^2}\left(1-\frac{5}{4}\frac{p^2\mu'^2}{\mu^2}\cdots\right) \\ v_\omega&=\frac{p}{k_1}=\sqrt{\frac{\mu}{\rho}}\left(1+\frac{3}{8}\frac{p^2\mu'^2}{\mu^2}\cdots\right)\ . \end{aligned}\right\} \quad (16)$$

When $k_2/k_1(\equiv\varepsilon_\omega)$ is less than 0.1,

$$k_1^2\doteqdot\frac{\rho p^2}{\mu}\ ,\qquad v_\omega\doteqdot\sqrt{\frac{\mu}{\rho}}\ ,\qquad \varepsilon_\omega=\frac{1}{2}\frac{p\mu'}{\mu}\ . \quad (17)$$

Eqs. (13), (15), (16), and (17) give the values of propagation and attenuation constants and the velocities of harmonic plane elastic waves in the viscoelastic medium in terms of the elastic and viscosity coefficients of the medium.

§ 5. Transmission through a Plate Made of Viscoelastic Medium

Considering the case that the immersed plate in Fig. 1 is made of viscoelastic material, the transmission of ultrasonic waves through the plate can be expressed by the same expression as eq. (6) or (7), but the quantities h, k, r, and s in the equation must be replaced by complex ones given by eq. (10).

r_1, r_2, s_1, and s_2 in eq. (10) are calculated from eqs. (12c) and (12d) as follows:

$$\left.\begin{aligned} r_1^2&=\tfrac{1}{2}[(h_1^2-h_2^2-l^2) \\ &\qquad+\sqrt{(h_1^2-h_2^2-l^2)^2+4h_1^2h_2^2}] \\ r_2^2&=\tfrac{1}{2}[-(h_1^2-h_2^2-l^2) \\ &\qquad+\sqrt{(h_1^2-h_2^2-l^2)^2+4h_1^2h_2^2}] \\ s_1^2&=\tfrac{1}{2}[(k_1^2-k_2^2-l^2) \\ &\qquad+\sqrt{(k_1^2-k_2^2-l^2)^2+4k_1^2k_2^2}] \\ s_2^2&=\tfrac{1}{2}[-(k_1^2-k_2^2-l^2) \\ &\qquad+\sqrt{(k_1^2-k_2^2-l^2)^2+4k_1^2k_2^2}] \end{aligned}\right\} \quad (18)$$

Assuming $h_1^2\gg h_2^2$ and $k_1^2\gg k_2^2$, considering that $l = p/v_0 \cdot \sin\theta_0$ and putting $r_1/h_1 \equiv \mathrm{Re}(\cos\theta_\Delta)$, $r_2/h_1 \equiv \mathrm{Im}(\cos\theta_\Delta)$, $s_1/k_1 \equiv \mathrm{Re}(\cos\theta_\omega)$, and $s_2/k_1 \equiv \mathrm{Im}(\cos\theta_\omega)$, as r_1/h_1, r_2/h_1, s_1/k_1 and s_2/k_1 can be considered respectivelyas the real and imaginary parts of complex quantities $\cos\theta_\Delta$ and $\cos\theta_\omega$, we have the relations:

$$\left.\begin{aligned}
\left(\frac{r_1}{h_1}\right)^2 &= \mathrm{Re}^2(\cos\theta_\Delta) = \frac{1}{2}\left[\left(1-\frac{v_\Delta^2}{v_0^2}\sin^2\theta_0\right) + \sqrt{\left(1-\frac{v_\Delta^2}{v_0^2}\sin^2\theta_0\right)^2 + 4\varepsilon_\Delta^2}\,\right]\\
\left(\frac{r_2}{h_1}\right)^2 &= \mathrm{Im}^2(\cos\theta_\Delta) = \frac{1}{2}\left[-\left(1-\frac{v_\Delta^2}{v_0^2}\sin^2\theta_0\right) + \sqrt{\left(1-\frac{v_\Delta^2}{v_0^2}\sin^2\theta_0\right)^2 + 4\varepsilon_\Delta^2}\,\right]\\
\left(\frac{s_1}{k_1}\right)^2 &= \mathrm{Re}^2(\cos\theta_\omega) = \frac{1}{2}\left[\left(1-\frac{v_\omega^2}{v_0^2}\sin^2\theta_0\right) + \sqrt{\left(1-\frac{v_\omega^2}{v_0^2}\sin^2\theta_0\right)^2 + 4\varepsilon_\omega^2}\,\right]\\
\left(\frac{s_2}{k_1}\right)^2 &= \mathrm{Im}^2(\cos\theta_\omega) = \frac{1}{2}\left[-\left(1-\frac{v_\omega^2}{v_0^2}\sin^2\theta_0\right) + \sqrt{\left(1-\frac{v_\omega^2}{v_0^2}\sin^2\theta_0\right)^2 + 4\varepsilon_\omega^2}\,\right].
\end{aligned}\right\} \quad (19)$$

Four quantities in (19) are plotted as functions of the angle of incidence θ_0 by solid curves in Fig. 2, calculated by assuming the values of the constants: $v_0 = 1468$ m/sec, $v_\Delta = 2780$ m/sec, $v_\omega = 1390$ m/sec, $\varepsilon_\Delta = 0.0041$, and $\varepsilon_\omega = 0.0069$, obtained from the experimental data described later.

In the figure, the broken curves express the same quantities in the case of propagation in non-absorptive medium. It is considered from Fig. 2 or eqs. (19) that the effect of the absorptive properties of medium becomes remarkable at angles of incidence near the critical angles for dilatational and rotational waves.

Strictly speaking, the refractive angles and velocities for dilatational and rotational waves differ from those in the case of non-dissipative plate and moreover, the velocities and attenuation coefficients vary with the angles of refraction as follows.

The wave functions for both wavesare represented respectively by

$$\left.\begin{aligned}
\Delta &= Ae^{i(pt-lx-r_1y)-r_2y}\\
2\omega &= Be^{i(pt-lx-s_1y)-s_2y}
\end{aligned}\right\} \quad (20)$$

from (3) and (10).

From (20), the real angles of refraction, θ_Δ^* and θ_ω^*, the real velocities, v_Δ^* and v_ω^*,

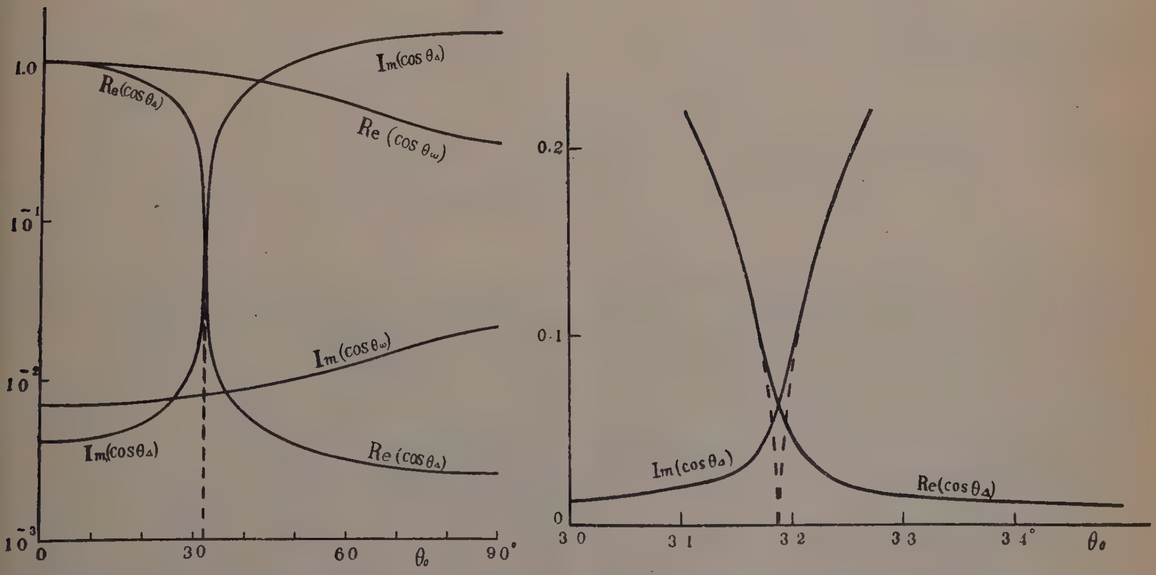

a.   b.

Fig. 2. a. Curves of $\mathrm{Re}(\cos\theta_\Delta)$, $\mathrm{Im}(\cos\theta_\Delta)$, $\mathrm{Re}(\cos\theta_\omega)$, and $\mathrm{Im}(\cos\theta_\omega)$ as functions of angle of incidence θ_0 for a special case of $v_0 = 1468$ m/sec, $v_\Delta = 2780$ m/sec, $v_\omega = 1390$ m/sec, $\varepsilon_\Delta = 0.0041$, and $\varepsilon_\omega = 0.0069$.

b. Curves of $\mathrm{Re}(\cos\theta_\Delta)$ and $\mathrm{Im}(\cos\theta_\Delta)$ near the critical angle of dilatational waves for the same case.

Broken curves show the case of no absorption.

and the real attenuation coefficients h_2^* and k_2^* for both waves are given by

$$\left.\begin{aligned}
\sin\theta_\Delta^* &= \frac{l}{\sqrt{l^2+r_1^2}} = \frac{v_\Delta/v_0\cdot\sin\theta_0}{D_\Delta(\theta_0)}\\
\sin\theta_\omega^* &= \frac{l}{\sqrt{l^2+s_1^2}} = \frac{v_\omega/v_0\cdot\sin\theta_0}{D_\omega(\theta_0)}\\
v_\Delta^* &= \frac{p}{\sqrt{l^2+r_1^2}} = \frac{v_\Delta}{D_\Delta(\theta_0)}\\
v_\omega^* &= \frac{p}{\sqrt{l^2+s_1^2}} = \frac{v_\omega}{D_\omega(\theta_0)}\\
h_2^* &= \frac{h_1h_2}{\sqrt{l^2+r_1^2}} = \frac{h_2}{D_\Delta(\theta_0)}\\
k_2^* &= \frac{k_1k_2}{\sqrt{l^2+s_1^2}} = \frac{k_2}{D_\omega(\theta_0)}
\end{aligned}\right\}\quad(21)$$

where

$$D_\Delta(\theta_0)=\sqrt{\frac{v_\Delta^2}{v_0^2}\sin^2\theta_0+\mathrm{Re}^2(\cos\theta_\Delta)}$$

and

$$D_\omega(\theta_0)=\sqrt{\frac{v_\omega^2}{v_0^2}\sin^2\theta_0+\mathrm{Re}^2(\cos\theta_\omega)}$$

As it is shown from (21) that

$$\frac{v_\Delta^*}{\sin\theta_\Delta^*}=\frac{v_\omega^*}{\sin\theta_\omega^*}=\frac{v_0}{\sin\theta_0}, \qquad (22)$$

it is understood that Snell's law on refraction of waves is strictly correct also in the case of waves refracted into viscoelastic medium in the meaning shown in (22).

Particularly for waves incident normally to that medium, $\theta_\Delta^*=\theta_\omega^*=\theta_0=0$, $v_\Delta^*=v_\Delta$, $v_\omega^*=v_\omega$, $h_2^*=h_2$, and $k_2^*=k_2$, i.e., in this case velocities and attenuation coefficients for both waves agree with those in the infinitely extended same medium.

Now, inserting (10) in (6) and assuming $k_1 \gg k_2$, f and g for the present case are represented as follows:

$$\left.\begin{aligned}
f &= \frac{\rho v_\Delta}{\rho_0 v_0}\,\frac{\cos\theta_0\cos^2 2\theta_\omega}{\mathrm{Re}(\cos\theta_\Delta)-i\,\mathrm{Im}(\cos\theta_\Delta)}\\
g &= 2\frac{\rho v_\omega^2}{\rho_0 v_0^2}\sin 2\theta_0\sin\theta_\omega\\
&\qquad\times[\mathrm{Re}(\cos\theta_\omega)-i\,\mathrm{Im}(\cos\theta_\omega)]
\end{aligned}\right\}\quad(23)$$

By substituting each quantity given by (10) and (23) in (5) or (7), the perfect expression on transmission of plane ultrasonic waves through a plate made of viscoelastic material can be obtained. The form of the expression is the same as the case of non-absorptive plate, but in the present case, f, g, r and s are complex quantities instead of real or pure imaginary ones.

Now, when the sound absorption by the plate immersed in liquid medium is appreciable, the more simple expression can be led from eq. (7) as follows.

The transmission for the present case is represented by

$$\frac{K_3}{K_1}=\frac{4e^{ir_0d}(fe^{is_1d+s_2d}-fe^{-is_1d-s_2d}+ge^{ir_1d+r_2d}-ge^{-ir_1d-r_2d})}{-8fg+(1+f+g)^2e^{i(r_1+s_1)d+(r_2+s_2)d}-(1+f-g)^2e^{i(r_1-s_1)d-(r_2-s_2)d}+(1-f-g)^2e^{-i(r_1+s_1)d-(r_2+s_2)d}-(1-f+g)^3e^{-i(r_1-s_1)d-(r_2-s_2)d}}. \qquad (24)$$

Considering the appreciable absorption by the plate, it can be assumed that $f\exp(is_1d+s_2d) \gg f\exp(-is_1d-s_2d)$ and $g\exp(ir_1d+r_2d) \gg g\exp(-ir_1d-r_2d)$ in the numerator of the right hand side of (24) and in the denominator, the terms except the second term are negligible. Then, eq. (24) is approximately modified as follows:

$$\begin{aligned}
\frac{K_3}{K_1} &= \frac{4e^{ir_0d}(fe^{is_1d+s_2d}+ge^{ir_1d+r_2d})}{(1+f+g)^2e^{i(r_1+s_1)d+(r_2+s_2)d}}\\
&= \frac{4e^{ir_0d}fe^{-ir_1d-r_2d}}{(1+f+g)^2}+\frac{4e^{ir_0d}ge^{-is_1d-s_2d}}{(1+f+g)^2}.
\end{aligned} \qquad (25)$$

It can be verified that the first term in the right hand side of (25) corresponds to the transmission ratio obtained when assumed that only longitudinal waves advancing from the incident surface to the transmitted side without multiple reflections in the plate contribute to the transmission, and the second term to the transmission through rotational waves in the same meaning.

An example of calculation of eq. (25) is shown in Fig. 3, assuming that $\rho_0=1.00$, $\rho=1.18$, $d=0.40$ cm, $v_0=1468$ m/sec, $v_\Delta=2780$ m/sec, $v_\omega=1390$ m/sec, $L_\Delta=8.0$ db/cm, $L_\omega=27$ db/cm and a frequency of ultrasonic waves is ten megacycles per second. In the figure, small circles show an experimental result on a poly-methylmetacrylate plate, 4 mm thick, immersed in water, using ten megacycle ultrasonic waves.* It is seen that at angles of incidence above the critical angle for dilatational waves, 31°52′, the theoretical expression agrees very well with the experimental result, while at angles of incidence below the same angle, the experimental transmissions are appreciably less than the corresponding theoretical ones, but the good agreement on the angles of peaks and troughs in both curves is to be noticed. These lower values of the experimental transmissions seem to be due to the fact that the practically used ultrasonic waves in the experiment are not ideal plane waves but are divergent ones having wave fronts of finite extent. Peaks and troughs of the curves are caused from the interference between two sets of waves represented in eq. (25).

In practice, constants used for the calculations of Figs. 2 and 3 are obtained from the experimental results shown in Fig. 3.

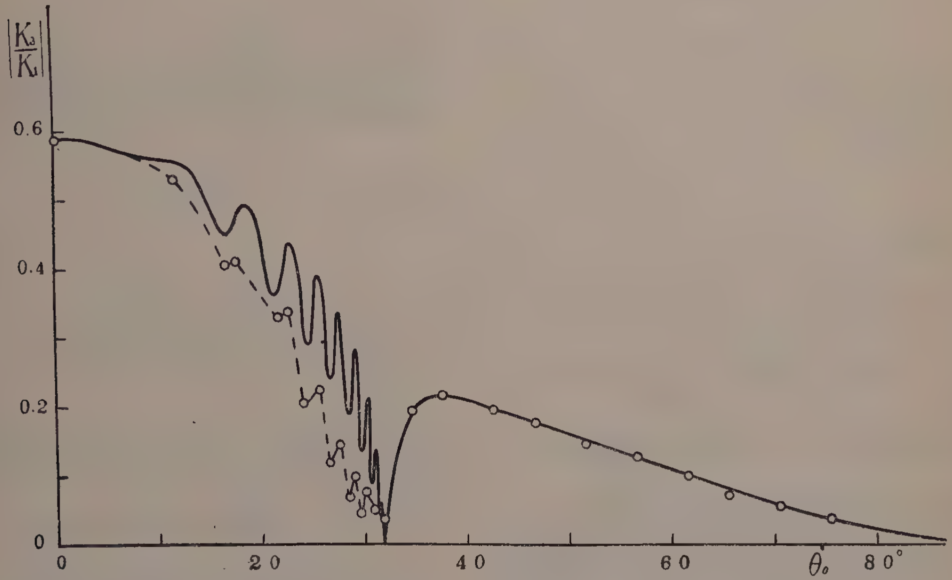

Fig. 3. Theoretical transmission curve for the case of $\rho_0=1.00$, $\rho=1.18$, $d=0.40$ cm, $v_0=1468$ m/sec, $v_\Delta=2780$ m/sec, $v_\omega=1390$ m/sec, $L_\Delta=8.0$ db/cm, $L_\omega=27$ db/cm and ultrasonic frequency of ten megacycles per second.

Small circles show an experimental result on a poly-methylmetacrylate plate immersed in water.

§ 6. Note on Srivastava's Papers

On transmission of ultrasonic waves through a plate made of viscoelastic material, several experimental works have been reported by Srivastava.[11] What seems strange in his papers is that Poisson's ratios are always negative for all samples investigated by him. This is considered to be an important error common to all his papers quoted here. The cause of this error is explained by the author as follows.

Considering the appreciably absorptive properties, especially remarkable for rotational waves, of the samples treated by Srivastava, eq. (25) is assumed to be approximately correct as a formula for transmission of ultrasonic waves in this case. As shown in Fig. 3, the transmission curve represented by (25) has a sharp trough at the critical angle of incidence for dilatational waves, from which the velocity of that waves can be obtained, while the second zero-transmission point does not correspond to the critical angle of incidence for rotational waves in the case of $v_0>v_\omega$ as in Fig. 3, the apparent zero point shifting to a smaller angle of incidence with increase in the absorption for rotational waves in the plate. Thus the determination of the velocity of rotational waves from the second zero-transmission angle becomes impossible. In Fig. 4, using the same values for ρ_0, ρ,

---

* This measurement was made by F. Fujimori.

d, v_0, v_Δ, v_ω, and L_Δ as in Fig. 3, the four curves of transmission ratio near the second zero points corresponding respectively to the four values for L_ω are plotted in logarithmic scale.

The error in Srivastava's papers may occur from overestimating the velocity of rotational waves from the cause above mentioned.

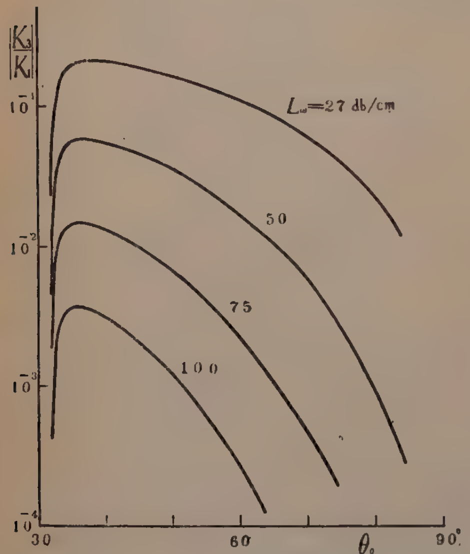

Fig. 4. Four transmission curves near the second zero angles of incidence corresponding respectively to the four values for L_ω, using the same values for ρ_0, ρ, d, v_0, v_Δ, v_ω, and L_Δ as in Fig. 3.

§ 7. Conclusion

The propagation constants of ultrasonic waves in a viscoelastic medium are represented by complex quantities, the real and imaginary parts of which are obtained from viscoelastic constants of the medium and are connected with the velocity and attenuation constants of the waves as shown in eqs. (13), (15), (16), and (17). Using the complex propagation constants, the transmission of ultrasonic waves through an absorbing plate can be expressed by the same formula (5) or (7) as in the case of a non-absorptive plate.

In the case of the appreciably absorptive solid medium, the more simple formula, (25), can be applied and the formula agrees well with the experimental result.

When it is intended to obtain the velocity of rotational waves in viscoelastic solid medium from the transmission curve, it must be noticed that the velocity obtained from the apparent critical angle for rotational waves is always larger than the real value on account of the absorptive property of the solid medium.

In conclusion, the author expresses his sincere thanks to Dr. O. Nomoto for his kind interest to the work.

This study was financially supported by the Scientific Research Grant of the Ministry of Education.

Appendix: Equations of Motion for a Viscoelastic Medium and Propagation Constants. The Most General Case

In this appendix is considered the wave propagation in a viscoelastic medium for the most general case of viscoelastic properties of the medium. For the purpose, the equations of motion and stress-strain relations leading to the wave equations (8) are represented by the tensor representation and next, the generalization of the equations is intended.

The equations of motion and stress-strain relations leading to the wave equations (8) are given by (A.1) and (A.2).[15)16)]

$$\left.\begin{aligned}\partial X_x/\partial x+\partial X_y/\partial y+\partial X_z/\partial z&=\rho\partial^2\xi/\partial t^2\\ \partial X_y/\partial x+\partial Y_y/\partial y+\partial Y_z/\partial z&=\rho\partial^2\eta/\partial t^2\\ \partial X_z/\partial x+\partial Y_z/\partial y+\partial Z_z/\partial z&=\rho\partial^2\zeta/\partial t^2\end{aligned}\right\}\tag{A.1}$$

$$\left.\begin{aligned}X_x&=\lambda\Delta+2\mu\partial\xi/\partial x+\lambda'\partial\Delta/\partial t+2\mu'\partial^2\xi/\partial t\partial x\\ Y_y&=\lambda\Delta+2\mu\partial\eta/\partial y+\lambda'\partial\Delta/\partial t+2\mu'\partial^2\eta/\partial t\partial y\\ Z_z&=\lambda\Delta+2\mu\partial\zeta/\partial z+\lambda'\partial\Delta/\partial t+2\mu'\partial^2\zeta/\partial t\partial z\\ Y_z&=z(\partial\zeta/\partial y+\partial\eta/\partial z)+\mu'\frac{\partial}{\partial t}(\partial\zeta/\partial y+\partial\eta/\partial z)\\ Z_x&=\mu(\partial\xi/\partial z+\partial\zeta/\partial x)+\mu'\frac{\partial}{\partial t}(\partial\xi/\partial z+\partial\zeta/\partial x)\\ X_y&=\mu(\partial\eta/\partial x+\partial\xi/\partial y)+\mu'\frac{\partial}{\partial t}(\partial\eta/\partial x+\partial\xi/\partial y)\end{aligned}\right\}\tag{A.2}$$

Each equation in (A.1) and (A.2) is modified by the tensor representations as follows.

Using the same notations as used in Alfrey's "Mechanical Behavior of High Polymers",[17)] the elements of the stress and strain tensors are represented by

$$\left.\begin{aligned} &\sigma_{11}\equiv X_x \qquad &&\sigma_{12}=\sigma_{21}\equiv X_y \\ &\sigma_{22}\equiv Y_y &&\sigma_{23}=\sigma_{32}\equiv Y_z \\ &\sigma_{33}\equiv Z_z &&\sigma_{31}=\sigma_{13}\equiv X_z \end{aligned}\right\} \quad (A.3)$$

and

$$\varepsilon_{ij}=\frac{1}{2}\left(\frac{\partial\xi_i}{\partial x_j}+\frac{\partial\xi_j}{\partial x_i}\right) . \qquad (A.4)$$

(In the tensor notation the coordinated directions x, y, and z are represented by the symbols x_1, x_2, and x_3, and the displacement components ξ, η, and ζ by ξ_1, ξ_2, and ξ_3.)

Furthermore, by using the deviatoric stress and strain tensors, a very straightforward means of isolating volumetric changes from shape deformations can be obtained.

The deviatoric stress and strain tensors, s_{ij} and e_{ij}, are defined as follows:

$$\left.\begin{aligned} s_{ij}&=\sigma_{ij}-\sigma\delta_{ij} \\ e_{ij}&=\varepsilon_{ij}-\varepsilon\delta_{ij} \end{aligned}\right\} \quad (A.5)$$

where

$$\left.\begin{aligned} \sigma&=\tfrac{1}{3}(\sigma_{11}+\sigma_{22}+\sigma_{33}) \\ \varepsilon&=\tfrac{1}{3}(\varepsilon_{11}+\varepsilon_{22}+\varepsilon_{33}) \end{aligned}\right\} \quad (A.6)$$

and δ_{ij}, the Kronecker Delta, is defined as:

$$\left.\begin{aligned} \delta_{ij}&=0 \qquad (i\neq j) \\ \delta_{ii}&=1 \end{aligned}\right\} \quad (A.7)$$

By the tensor notation mentioned above, eqs. (A.1) and (A.2) are rewritten as follows:

$$\frac{\partial\sigma}{\partial x_i}+\sum_j\frac{\partial s_{ij}}{\partial x_j}=\rho\frac{\partial^2\xi_i}{\partial t^2} \qquad (A.8)$$

$$\left.\begin{aligned} \sigma&=\left[(3\lambda+2\mu)+(3\lambda'+2\mu')\frac{\partial}{\partial t}\right]\varepsilon \\ s_{ij}&=\left[2\mu+2\mu'\frac{\partial}{\partial t}\right]e_{ij} \end{aligned}\right\} \quad (A.9)$$

Substituting (A.9) in (A.8),

$$\left[(3\lambda+2\mu)+(3\lambda'+2\mu')\frac{\partial}{\partial t}\right]\operatorname{grad}\varepsilon + \left(2\mu+2\mu'\frac{\partial}{\partial t}\right)\frac{1}{2}(\operatorname{grad}\varepsilon+\nabla^2\Xi)=\rho\frac{\partial^2\Xi}{\partial t^2} \qquad (A.10)$$

where Ξ is a vector the eomponents of which are represented by ξ_1, ξ_2, and ξ_3.

Writing the divergence of eq. (A.10), the expression for the wave equation of longitudinal waves is obtained as

$$\left[(\lambda+2\mu)+(\lambda'+2\mu')\frac{\partial}{\partial t}\right]\nabla^2\varepsilon=\rho\frac{\partial^2\varepsilon}{\partial t^2} . \qquad (A.11)$$

By writing the rotation of eq. (A.10),

$$\left[\mu+\mu'\frac{\partial}{\partial t}\right]\nabla^2\Omega=\rho\frac{\partial^2\Omega}{\partial t^2} , \qquad (2\Omega=\operatorname{rot}\Xi) \qquad (A.12)$$

corresponding to rotational waves.

Because $3\varepsilon=\Delta$ and the z-component of Ω is ω, (A.11) and (A.12) agree with (8). Namely, eqs. (8) are obtained under the stress-strain relations represented by (A.9).

Most generally, the stress-strain relationships can be represented instead of (A.9) by operator equations given by[18]

$$\mathbf{P}\sigma=\mathbf{Q}\varepsilon , \qquad \mathbf{P}'s_{ij}=\mathbf{Q}'e_{ij} \qquad (A.13)$$

where

$$\left.\begin{aligned} \mathbf{P}&=\frac{\partial^m}{\partial t^m}+p_{m-1}\frac{\partial^{m-1}}{\partial t^{m-1}}+\cdots+p_0 \\ \mathbf{Q}&=q_n\frac{\partial^n}{\partial t^n}+\cdots+q_0 \\ \mathbf{P}'&=\frac{\partial^{m'}}{\partial t^{m'}}+p'_{m'-1}\frac{\partial^{m'-1}}{\partial t^{m'-1}}+\cdots+p_0' \\ \mathbf{Q}'&=q'_{n'}\frac{\partial^{n'}}{\partial t^{n'}}+\cdots+q_0' \end{aligned}\right\} \quad (A.14)$$

and p_m, q_n, $p'_{m'}$ and $q'_{n'}$ are constants, and m, n, m', and n' are integers.

By operating $\mathbf{PP}'$ on both sides of eq. (A.8) and considering eq. (A.13),

$$[\mathbf{P}'\mathbf{Q}+\tfrac{1}{2}\mathbf{PQ}']\operatorname{grad}\varepsilon+\tfrac{1}{2}\mathbf{PQ}'\nabla^2\Xi=\rho\mathbf{PP}'\frac{\partial^2\Xi}{\partial t^2} . \qquad (A.15)$$

Taking divergence of (A.15), we have

$$[\mathbf{P}'\mathbf{Q}+2\mathbf{PQ}']\nabla^2\Delta=3\rho\mathbf{PP}'\frac{\partial^2\Delta}{\partial t^2} . \qquad (A.16)$$

Taking rotation of (A.15), we have

$$\mathbf{PQ}'\nabla^2\omega=2\rho\mathbf{PP}'\frac{\partial^2\omega}{\partial t^2} . \qquad (A.17)$$

Substituting (3) in (A.16) and (A.17),

$$\left.\begin{aligned} l^2+r^2&=\frac{3PP'}{P'Q+2PQ'}\rho p^2\equiv(h_1-ih_2)^2 \\ l^2+s^2&=\frac{2P'}{Q'}\rho p^2\equiv(k_1-ik_2)^2 \end{aligned}\right\} \qquad (A.18)$$

where

$$\left.\begin{aligned} P&=(ip)^m+p_{m-1}(ip)^{m-1}+\cdots+p_0 \\ Q&=q_n(ip)^n+\cdots+q_0 \\ P'&=(ip)^{m'}+p'_{m'-1}(ip)^{m'-1}+\cdots+p_0' \\ Q'&=q'_{n'}(ip)^{n'}+\cdots+q_0' . \end{aligned}\right\} \quad (A.19)$$

From (A.18) the propagation constants for the present case are obtained. Therefore, by using (A.18) instead of (9), the theoretical expression for transmission of ultrasonic waves through a plane plate made of viscoelastic material which has arbitrary stress-strain relations can be obtained in the same way as before.

References

1) R. Bär & A. Walti; Helv. Phys. Acta **7** (1934) 658.
2) Bez-Bardili: Zeits. f. Phys. **96** (1935) 761.
3) A. Walti: Helv. Phys. Acta **11** (1938) 113.
4) H. Reissner: Helv. Phys. Acta **11** (1938) 140.
5) R. Bär: Helv. Phys. Acta **11** (1938) 397.
6) F. Levi & N. S. Nagendra Nath: Helv. Phys. Acta **11** (1938) 408.
7) F. H. Sanders: Can. J. Res. **17A** (1939) 179.
8) J. B. Smythe & R. B. Lindsay: J. Acous. Soc. Am. **16** (1944) 20.
9) W. C. Schneider & C. J. Burton: J. Appl. Phys. **20** (1949) 48.
10) W. T. Thomson: J. Appl. Phys. **21** (1950) 89; **21** (1950) 1215.
11) A. M. Srivastava: Comptes Rendus **22** (1950) 1223; Zeits. f. Phys. **128** (1950) 614; Ind. J. Phys. **25** (1951) 17; J. Acous. Soc. Am. **23** (1951) 553.
12) R. D. Fay & O. V. Fortier: J. Acous. Soc. Am. **23** (1951) 339.
13) Y. Torikai; J. Acous. Soc. Japan **8** (1952) 21.
14) N. F. Astbury: Proc. Roy. Soc. A **196** (1949) 92.
15) N. M. Hosali: Proc. Roy. Soc. **104** (1923) 271.
16) K. Sezawa: Bull. Earthquake Res. Inst. Tokyo **3** (1927) 43.
17) T. Alfrey: *Mechanical Behavior of High Polymers* (Interscience Publishers, Inc., New York, 1948), p. 534.
18) Ditto, p. 537.

JOURNAL OF THE PHYSICAL SOCIETY OF JAPAN Vol. 8, No. 2, MAR.—APR., 1953

On the Detachment of Shock Wave from the Leading Edge of a Finite Wedge*

By Kō TAMADA

Department of Physics, Faculty of Science, University of Kyoto

(Received October 18, 1952)

In this paper is given an approximate analysis of the transition from attached to detached shock wave for the case of a finite wedge. Neglecting the vorticity, the flow behind the shock is expressed approximately by a velocity potential which consists of two parts, one corresponding to a uniform flow and the other to the perturbation flow respectively. The perturbation potential and the shape of the shock wave are determined simultaneously by a fundamental linearized equation in conjunction with appropriate boundary conditions on the shock wave and at the surface of the wedge. They are found to reveal characteristic singularities at the tip of the wedge. Some special treatment is needed for the extreme case of the detachment Mach number. Numerical computations are made for several Mach numbers on the shape of the shock wave and the velocity distributions along the side of the wedge. The drag coefficient of the wedge is also calculated as a function of the Mach number. It may be noticing that the calculated value of the drag coefficient attains its maximum in the midst course of the transition.

§ 1. Introduction

Suppose that a symmetrical wedge of finite length is placed point foremost in a supersonic stream (Fig. 1). When the Mach number M of the oncoming flow is sufficiently large, a shock wave is created at the tip of the wedge (the attached shock wave), and the flow behind the shock is supersonic and uniform in

---

* This paper was presented at the Session of Section II (Fluid Mechanics), the Eighth International Congress on Theoretical and Applied Mechanics, Istanbul, August 1952.

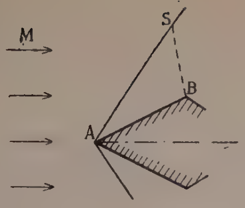

Fig. 1.

the region ABS. (BS is the first Mach wave extending from the endpoint B of the wedge to the shock wave.) The flow in this stage can be analysed completely by the use of the well-known theory of oblique shock waves. Now, if the Mach number M is gradually decreased, the flow speed in the region ABS will first reach the speed of sound at some definite Mach number, M_* say. At lower Mach numbers, the flow behind the shock will become subsonic and must therefore be accelerated to attain to the sonic speed just at the end-point B of the wedge. Thus, in this stage, the flow behind the shock is no more uniform and hence the shock itself will be curved. If M is further reduced, the shock will finally detach from the point of the wedge at a certain Mach number, M_d say.

The steady transit from attached to detached shocks sketched above was first discussed by G. Guderley (**1**) and later on by A. Busemann (**2**). They have given qualitative explanation of the phenomena by observing the flow in the hodograph plane. It is the object of the present paper to obtain some quantitative informations on the problem.

The writer wishes to express his cordial thanks to Professor S. Tomotika for his interest and encouragement throughout this work. The writer's thanks are also due to the Ministry of Education of Japan for a grant in aid for fundamental scientific research.

§2. Analysis of the Field of Flow I

In the present paper, the "critical speed" (which is invariant in passing through the shock wave) is taken as the unit of velocity. Let (x, y) be the rectangular coordinates having the side AB of the wedge as the x-axis (Fig. 2), and let α be the semi-vertex angle of the wedge, and q_u and M be the speed and Mach number of the undisturbed flow respectively.

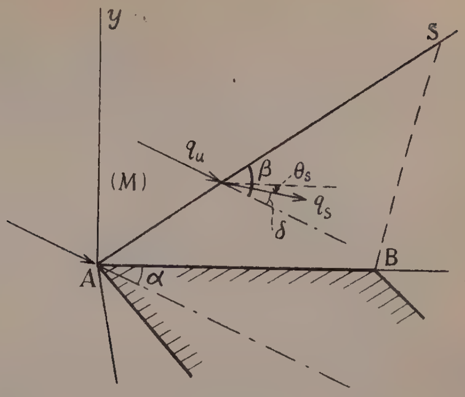

Fig. 2.

Now, even in the transition phase under consideration, the flow in the region ABS is almost uniform, and the entropy change as well as the vorticity in the field of flow may safely be neglected. Therefore the field of flow in question can be expressed approximately by the velocity potential

$$\phi(x, y)=\sigma x+\varepsilon f(x, y)\,, \qquad (1)$$

where ε (assumed to be small) and σ are certain constants. (In later lines, σ will be identified with the velocity just behind the shock wave at the tip A.) The fundamental equation for ϕ is

$$\left.\begin{aligned} 2c^2(\phi_{xx}+\phi_{yy})&=\left(\phi_x\frac{\partial}{\partial x}+\phi_y\frac{\partial}{\partial y}\right)\{(\phi_x)^2+(\phi_y)^2\}\,, \\ 2c^2&=(\gamma+1)-(\gamma-1)\{(\phi_x)^2+(\phi_y)^2\}, \end{aligned}\right\} \qquad (2)$$

where c is the local speed of sound and γ the adiabatic exponent. Substituting (1) in (2) and neglecting the terms of $O(\varepsilon^2)$, we get the equation for f as:

$$f_{xx}+k^{-2}f_{yy}=0\,, \qquad (3)$$

with

$$k^2=(1-\sigma^2)\left\{1-\frac{\gamma-1}{\gamma+1}\sigma^2\right\}^{-1}.$$

Further, if we put

$$\xi=x, \quad \eta=ky\,, \qquad (4)$$

Eq. (3) reduces to the Laplace equation:

$$f_{\xi\xi}+f_{\eta\eta}=0\,. \qquad (5)$$

Next, we consider the boundary conditions. It is evident that along the wedge surface,

$$\phi_y=\phi_\eta=0\,. \qquad (6)$$

At the end-point B of the wedge, the velocity must attain to the local speed of sound so that

$$\phi_x(1,0)=\phi_\xi(1,0)=1\ , \qquad (7)$$

where we have taken, for brevity, the length of the side AB equal to unity. Further, along the shock wave, we impose two "shock-conditions" (as usually done in the isentropic approximation): the first is

$$\left.\begin{aligned}\frac{\gamma+1}{2}M^2\tan(\beta-\delta)&=m\tan\beta+\cot\beta\ ,\\ m&=1+\frac{\gamma-1}{2}M^2\ ,\end{aligned}\right\}\qquad (8)$$

where β and δ are respectively the angle of inclination of the shock wave and the angle of deflection of the velocity, to the direction of the undisturbed flow (Fig. 2). The second is the condition of no slip:

$$q_s\cos(\beta-\delta)=q_u\cos\beta\ , \qquad (9)$$

where q_s is the velocity immediately behind the shock wave and q_u the undisturbed velocity which is related to the Mach number M by

$$q_u^2=\frac{\gamma+1}{2}M^2m^{-1}\ . \qquad (10)$$

We now proceed to find out a solution of (5) satisfying the conditions (6) to (9) approximately. For this purpose, we first consider the solution of the form:

$$f=\Re\zeta^\kappa\ ,\quad \zeta=\xi+i\eta\ , \qquad (11)$$

where κ is a real constant greater than unity. Eq. (11) gives u and v, the x- and y- components of the velocity, in the forms:

$$\left.\begin{aligned}u&=\phi_x=\phi_\xi=\sigma+\varepsilon\kappa\Re\zeta^{\kappa-1}\ ,\\ v&=\phi_y=k\phi_\eta=-\varepsilon k\kappa\Im\zeta^{\kappa-1}\ .\end{aligned}\right\}\qquad (12)$$

It is seen that the condition (6) is already satisfied.

In the next place, we assume, in relation to (11), the shape of the shock wave in the form:

$$y=ax-b\kappa^{-1}x^\kappa,\ \text{or}\ \eta=ka\xi-kb\kappa^{-1}\xi^\kappa, \qquad (13)$$

where a and b are undetermined constants.

The five constants σ, ε, κ, a and b in (1), (11) and (13) will now be determined from the boundary conditions (7), (8) and (9) in the following lines.

First, inserting (13) into (12) and neglecting the terms of the order of ξ^κ, we get the two components u_s and v_s of the velocity immediately behind the shock wave in the forms:

$$u_s\cong\sigma+\varepsilon A\xi^{\kappa-1},\quad v_s\cong\varepsilon B\xi^{\kappa-1} \qquad (14)$$

where

$$\left.\begin{aligned}A&=\kappa(1+k^2a^2)^{\frac{\kappa-1}{2}}\cos\{(\kappa-1)\tan^{-1}(ka)\}\ ,\\ B&=-\kappa k(1+k^2a^2)^{\frac{\kappa-1}{2}}\sin\{(\kappa-1)\tan^{-1}(ka)\}.\end{aligned}\right\}\qquad (14,\mathrm{a})$$

From Eqs. (14) we obtain the results:

$$v_s/u_s=\tan\theta_s\cong\theta_s\cong\varepsilon\sigma^{-1}B\xi^{\kappa-1}\ , \qquad (15)$$

where $\theta_s(=\delta-\alpha)$ is the angle between the x-axis and the velocity vector immediately behind the shock wave. Then, it can be shown from (13) and (15) that along the shock wave,

$$dy/dx=\tan(\beta-\alpha)=a-b\xi^{\kappa-1}\ ,$$

and

$$\left.\begin{aligned}&\left.\begin{aligned}\tan\beta&\cong\lambda\mu^{-1}-b\mu^{-2}\xi^{\kappa-1}\ ,\\ \lambda=\sin\alpha+a\cos\alpha\ ,&\quad \mu=\cos\alpha-a\sin\alpha\ ,\end{aligned}\right\}\\ &\tan(\beta-\delta)\cong a-\{\varepsilon\sigma^{-1}(1+a^2)B+b\}\xi^{\kappa-1}\ .\end{aligned}\right\}\qquad (16)$$

Inserting (16) into the first shock-condition (8), and comparing the constant terms and the terms of the order of $\xi^{\kappa-1}$ on both sides, we obtain the following two equations:

$$\frac{\gamma+1}{2}M^2a\lambda\mu=m\lambda^2+\mu^2\ , \qquad (17)$$

$$\left.\begin{aligned}D_1\varepsilon+D_2b&=0\ ,\\ D_1&=\frac{\gamma+1}{2}M^2(1+a^2)B\lambda^2\mu^2\ ,\\ D_2&=\sigma\left\{\frac{\gamma+1}{2}M^2\lambda^2\mu^2+\mu^2-m\lambda^2\right\}\ .\end{aligned}\right\}\qquad (18)$$

Also, we have, from (14) and (15),

$$\left.\begin{aligned}\sin\delta&=\sin(\alpha+\theta_s)\cong\sin\alpha+(\varepsilon\sigma^{-1}B\cos\alpha)\xi^{\kappa-1},\\ \cos\delta&=\cos(\alpha+\theta_s)\cong\cos\alpha-(\varepsilon\sigma^{-1}B\sin\alpha)\xi^{\kappa-1},\\ q_s&=(u_s^2+v_s^2)^{1/2}\cong\sigma+\varepsilon A\xi^{\kappa-1}\ .\end{aligned}\right\}\qquad (19)$$

Inserting these results in the second shock-condition (9), and equating the constant terms and the terms of the order of $\xi^{\kappa-1}$ on both sides just as in obtaining (17) and (18), we get the further two relations:

$$\sigma=\mu q_u\ , \qquad (20)$$

$$\left.\begin{aligned}E_1\varepsilon+E_2b&=0\ ,\\ E_1=-\mu(A+aB)\ ,&\quad E_2=\sigma\sin\alpha\ .\end{aligned}\right\}\qquad (21)$$

Finally, the condition (7) gives the equation:

$$\sigma+\varepsilon\kappa=1\ . \qquad (22)$$

We are now able to determine the five unknowns a, σ. κ, ε and b in question by the five equations (17) to (22). First, we calculate the value of a from (17) for given values of

α and M. Then, σ is at once evaluated by (20) combined with (10). It may be remarked here that the relations (17) and (20) (hence a and σ) are really identical with those for the case of an infinite wedge. We next observe Eqs. (18) and (21). Since they are linear homogeneous equation in ε and b, it is necessary, for non-trivial solution, that

$$D_1E_2-D_2E_1=0\ ,$$

from which we obtain, after some reductions, the equation for determining the characteristic exponent κ as:

$$k\tan\{(\kappa-1)\tan^{-1}(ka)\}=\frac{\frac{\gamma+1}{2}M^2\lambda^2\mu^2+\mu^2-m\lambda^2}{\frac{\gamma+1}{2}M^2\lambda^3\mu+a(\mu^2-m\lambda^2)}\ . \tag{23}$$

Knowing the value of κ from (23), it is easy to calculate the corresponding values of ε and b from (22) in conjunction with either of Eqs. (18) and (21).

Thus, once we have obtained the values of a, σ, κ, ε and b, we are ready to calculate the velocity distribution by (12), the shape of shock wave by (13), and so forth, However, the discussions on these matters will be postponed to § 4.

Now, as will be seen presently (Fig. 4), the value of κ goes to unity as M approaches to M_d, the detachment Mach number. This means clearly that the mode of approximation used in the preceding analysis becomes improper, and especially when $M=M_d$, the solution obtained above becomes invalid. Therefore, in the next section, we seek for an alternative form of solution for the extreme case $M=M_d$.

§ 3. Analysis of the Field of Flow II

In case when $M=M_d$, it is more convenient to use the "shock polar" (i.e., the relation between M, q_s and δ) in place of (8), as the first shock-condition. The equation of the shock polar is usually expressed as:

$$(n-q_u\bar{u})\bar{v}^2=(q_u-\bar{u})^2(q_u\bar{u}-1)\ , \tag{24}$$

with

$$n=1+M^2m^{-1}\ ,\quad \bar{u}=q_s\cos\delta\ ,\quad \bar{v}=q_s\sin\delta\ .$$

(This is easily obtained by eliminating β from (8) and (9).) Fig. 3 (relating to Fig. 2) shows the shock polar for the extreme case $M=M_d$ under consideration. As is seen from the figure, the shock polar just touches the u_s-axis when $M=M_d$ at the point A ($u_s=\sigma$, $v_s=0$: image point of the state at the tip A of the wedge). Therefore, if we expand both sides of Eq. (24) in power series of $u_s-\sigma$ and v_s, we get, after some calculations,

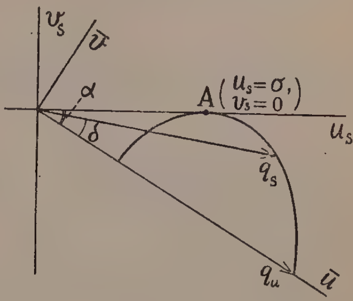

Fig. 3.

$$\left.\begin{aligned}&v_s\cong\omega(u_s-\sigma)^2,\\ &\omega=\frac{3q_u\sigma\cos\alpha-n+\gamma(1-n)\cos^2\alpha}{q_u\{2+\sigma^2+q_u^2+2\gamma(1-n)\sigma q_u^{-1}\cos\alpha\}\sin\alpha}\,.\end{aligned}\right\} \tag{25}$$

with

$$(n-q_u\sigma\cos\alpha)(\sigma\sin\alpha)^2=(q_u-\sigma\cos\alpha)^2(q_u\sigma\cos\alpha-1)\ , \tag{26}$$

$$\sigma(2n-3\sigma q_u\cos\alpha)\sin^2\alpha=(q_u-\sigma\cos\alpha)(q_u^2+2-3q_u\sigma\cos\alpha)\cos\alpha\ . \tag{27}$$

Eq. (25) describes the shock polar in the vicinity of the point A, and will be used below as the first shock-condition.

Now, it is suggested from (25) that the appropriate form of the velocity potential ϕ in the present case will be

$$\left.\begin{aligned}&\phi=\sigma\xi+\varepsilon f(\xi,\eta)\ ,\\ &f=\Re[\zeta\{\log(h\zeta)\}^{-1}]\ ,\quad \zeta=\xi+i\eta\ ,\end{aligned}\right\} \tag{28}$$

where ε (assumed to be small) and h are unknown constants. Eqs. (28) gives the velocity components u and v as:

$$\left.\begin{aligned}&u=\phi_\xi\cong\sigma+\varepsilon\{\log(h\sqrt{\xi^2+\eta^2})\}^{-1},\\ &v=k\phi_\eta\cong k\varepsilon\{\log(h\sqrt{\xi^2+\eta^2})\}^{-2}\tan^{-1}(\eta/\xi).\end{aligned}\right\} \tag{29}$$

Next we assume, corresponding to (28), the shape of shock wave in the following form:

$$y=ax+bx\{\log(hx)\}^{-1}\ ,$$
$$\text{or}\quad \eta=ka\xi+kb\xi\{\log(h\xi)\}^{-1}. \tag{30}$$

From (29) and (30), the velocity components u_s and v_s immediately behind the shock wave are expressed as:

$$\left.\begin{aligned}&u_s\cong\sigma+\varepsilon\{\log(h\xi)\}^{-1},\\ &v_s\cong k\varepsilon\{\log(h\xi)\}^{-2}\tan^{-1}(ka)\ .\end{aligned}\right\} \tag{31}$$

Then, introducing Eqs. (31) into the first shock-condition (25), and comparing the expressions on both sides, we get at once the equation for ε in the form:

$$\varepsilon = k\omega^{-1}\tan^{-1}(ka). \qquad (32)$$

On the other hand, if we insert the following relations (which are easily obtained from (31)):

$$\left.\begin{aligned} \delta &= \alpha + \theta_s \cong \alpha\,, \\ \tan\beta &\cong \lambda\mu^{-1} + b\mu^{-2}\{\log(h\xi)\}^{-1}\,, \\ q_s &\cong \sigma + \varepsilon\{\log(h\xi)\}^{-1} \end{aligned}\right\} \quad (33)$$

into the second shock-condition (9), and equate the constant terms and the coefficients of $\{\log(h\xi)\}^{-1}$ on both sides, we obtain the following two equations:

$$\sigma = \mu q_u\,, \qquad (34)$$

$$-\sigma^2 b \sin\alpha' = \mu^2 q_u \varepsilon\,. \qquad (35)$$

Finally, the condition (7) that the velocity at the end-point B ($\xi=1$, $\eta=0$) must be sonic furnishes one more equation:

$$\sigma + \varepsilon(\log h)^{-1} = 1\,. \qquad (36)$$

Eqs. (26), (27) and (34) determine the values of $M(=M_d)$, σ and a, while ε, b and h can be calculated from (32), (35) and (36).

§ 4. Numerical Discussions

The writer has carried out numerical calculation for the case when the semi-apex angle α of the wedge is equal to 20°. Fig. 4 shows the calculated values of the parameters a, σ, κ, ε and b in the first analysis (§ 2) as functions of M. It is to be noted here that as $M \to M_d$, the value of κ approaches to unity, the prohibited value. Thus, when $M \to M_d$, we must turn to the second analysis (§ 3), where the calculated values of the parameters are $M=1.84005$, $\sigma=0.93224$, $a=0.99625$, $\varepsilon=-0.11473$, $b=0.21552$ and $h=0.18394$.

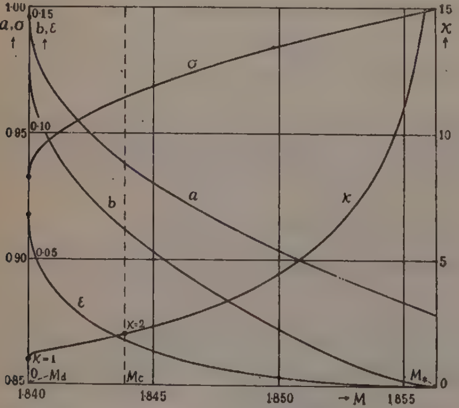

Fig. 4. $\alpha=20°$, $M_*=1.8563$, $M_c=1.8439$, $M_d=1.8400$

In Fig, 5 are shown, for several values of M, the velocity distributions along the side AB of the wedge, as well as the shapes of the shock wave relative to the straight shock for $M=M_*$,

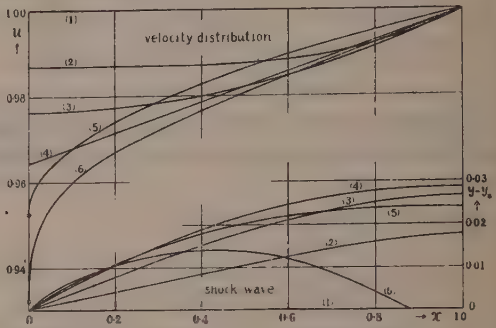

Fig. 5. $y_* = y(M_*) = 0.8787x$

(1) $M = M_* = 1.8563$, $\kappa = \infty$,
(2) $M = 1.8508$, $\kappa = 5$,
(3) $M = 1.8471$, $\kappa = 3$,
(4) $M = M_c = 1.8439$, $\kappa = 2$,
(5) $M = 1.8416$, $\kappa = 1.5$,
(6) $M = M_d = 1.8400$, (§ 3).

It will be seen clearly from this figure that the velocity gradient as well as the curvature of the shock wave at the tip A of the wedge are zero for $M > M_c$, finite for $M = M_c$, and infinite for $M < M_c$. The state for $M = M_c$ ($\kappa=2$) corresponds to Busemann's "Crocco point". It is interesting to note that the said transition may be regarded as "preperation" for the detachment of the shock wave.

§ 5. Pressure Distribution and Drag Coefficient

We define, as usual, the pressure coefficient C_p in the form:

$$C_p = \frac{2}{\gamma M^2}\left(\frac{p}{p_u} - 1\right), \qquad (37)$$

where p_u and p are respectively the pressures in the undisturbed flow and in the flow behind the shock wave. Denoting by P_A the pressure at the point A of the wedge behind the shock wave, the theory of oblique shock waves gives the pressure ratio p_A/p_u:

$$\frac{p_A}{p_u} = \frac{\lambda - s^2 a\mu}{a\mu - s^2\lambda}\,, \qquad s^2 = \frac{\gamma-1}{\gamma+1}\,. \qquad (38)$$

Also, Bernoulli's theorem gives the result:

$$\frac{p}{p_A}=\frac{p}{p_*}\frac{p_*}{p_A}=\left\{\frac{1-s^2q^2}{1-s^2\sigma^2}\right\}^{\frac{\gamma}{\gamma-1}}, \qquad (39)$$

p_* being the pressure corresponding to the critical speed.

Now, according to the preceding analysis, the velocity on the side AB of the wedge is given by

$$q=u=\sigma+\varepsilon g(x)\,,$$
$$g(x)=\left.\begin{cases}\kappa x^{\kappa-1}\,, & M_*>M>M_a\\ \{\log(hx)\}^{-1}\,. & M=M_a\end{cases}\right\} \qquad (40)$$

Inserting (40) into (39), we get the equation giving the pressure distribution on the surface of the wedge:

$$\frac{p}{p_A}\cong 1-\frac{2\gamma}{\gamma+1}\frac{\varepsilon\sigma}{1-s^2\sigma^2}g(x)\,. \qquad (41)$$

Further, from (37) to (41), we obtain a formula for the drag coefficient C_D of the wedge defined as:

$$C_D=\frac{2\int_0^1 C_p \sin\alpha dx}{2\sin\alpha}=\int_0^1 C_p dx \qquad (42)$$

in the form:

$$\left.\begin{aligned}&C_D=\frac{2}{\gamma M^2}\left(K\frac{p_A}{p_u}-1\right),\\ &K=\begin{cases}1-2(\gamma+1)^{-1}\varepsilon\sigma(1-s^2\sigma^2)^{-1}, \\ \qquad\qquad\qquad\qquad M_*>M>M_a\\ 1-2(\gamma+1)^{-1}\varepsilon\sigma(1-s^2\sigma^2)^{-1}\\ \qquad\times\int_0^1\{\log(hx)\}^{-1}dx\,. \quad M=M_a\end{cases}\end{aligned}\right\} \qquad (43)$$

Fig. 6 shows the calculated values of C_D for the case $\alpha=20°$. It will be seen that the curve of C_D for the case of an infinite wedge has a vertical tangent at $M=M_a$, while in the case of a finite wedge it represents a maximum between M_* and M_a. Also, the figure suggests that the curve of C_D for a finite wedge seems to have smooth continuation in the region of detached shock wave, as has been predicted by Busemann (2).

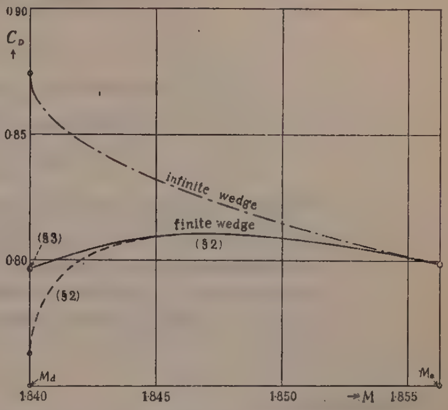

Fig. 6.

References

1) G. Guderley: Tech. Rep. No. F-TR-2168-ND, Air Materiel Command (Wright Field), 1947.

2) A. Busemann: N.A.C.A. Tech. Note No. 1858.

JOURNAL OF THE PHYSICAL SOCIETY OF JAPAN Vol. 8, No. 2, MAR.—APR., 1953

A Note on Cross Mach Lines in Simple Waves in the Plane Supersonic Flow

By Zirō HASIMOTO
Department of Mathematics and Physics,
Ritumeikan University, Kyoto

(Received November 29, 1952)

Explicit representation of cross Mach lines in simple waves has already been obtained for the case of polytropic gases. In the present paper, a more general expression is deduced without restriction to any special type of gases. It is also shown that the distribution of the stream function along a cross Mach line can be expressed in a very simple form.

§1. Introduction

In the interaction problem of simple waves in the two-dimensional, steady, irrotational and isentropic flow of a perfect gas moving at a supersonic velocity, we sometimes encounter with characteristic initial value problems for a certain partial differential equation of hyperbolic type. For instance, in order to study theoretically the structure of a jet of gas issuing from a plane nozzle at a uniform supersonic velocity, we must solve interaction problem of two simple waves starting from two rims of the nozzle. In this case, if the partial differential equation for the stream function is taken as the basis of the theory, the first step for solving the problem is to search for the solution in a characteristic quadrangle under a prescribed value of the stream function along two adjacent sides of the region, each of which is respectively a cross Mach line in each simple wave. However, it is difficult in general to solve analytically such an interaction problem for the case of polytropic gases. Thus we are compelled to use some approximate methods. As a method frequently used in many cases, there is one which repalces the true relation of changes of state by an approximate one to be convenient for the theoretical analysis. This is equivalent to supposing a hypothetical gas obeying the approximate relation of changes of state, and therefore such a theory is called the theory of hypothetical gases.

For polytropic gases, explicit representations for cross Mach lines and streamlines have already been obtained.[1] The present paper shows that if a certain function is introduced for the case of arbitrary gases, general representations for cross Mach lines in simple waves and the value of the stream function along any cross Mach line can be obtained in simple forms which are convenient in the theory of hypothetical gases. The practical application of the results to interaction problems of simple waves will be reported in a later paper.

§2. The Function χ and the Variable τ

Consider a two-dimensional, steady, irrotational and isentropic flow of a perfect gas. As usual, let q denote the magnitude of the flow velocity vector, θ the angle between the velocity vector and a fixed direction along which the x-axis is chosen, ρ the density of gas, ρ_0 the density at some standard point, and c the local velocity of sound. Now, we define a function χ as follows:

$$\chi=\left\{\frac{\rho_0 q^2}{\rho}\frac{d}{dq}\left(\frac{\rho_0}{\rho q}\right)\right\}^{\frac{1}{4}}. \tag{1}$$

The importance of this function has originally been emphasized by Imai.[2] Indeed, it will be seen that the function is very usefull for the analytical treatment of simple waves.

Taking account of the definition of the velocity of sound $c^2=dp/d\rho$ as well as Bernoulli's equation in differential form $qdq+\rho^{-1}dp=0$, χ is expressed in the form:

$$\chi=\left(\frac{\rho_0}{\rho}\right)^{\frac{1}{2}}\left(\frac{q^2}{c^2}-1\right)^{\frac{1}{4}}, \tag{2}$$

or introducing the Mach angle A defined as

$$\sin A=\frac{c}{q}, \tag{3}$$

we can write χ in the form:

$$\chi=\left(\frac{\rho_0}{\rho}\right)^{\frac{1}{2}}\cot^{\frac{1}{2}}A. \qquad (4)$$

When the characteristic relation of gas $p=p(\rho)$ between pressure and density is assigned, the function χ is expressed as a function of q.

Here we introduce a variable τ in place of q by the relation

$$\tau=\int_{q_*}^{q}\frac{\rho\chi^2}{\rho_0 q}\,dq=\int_{q_*}^{q}\left(\frac{1}{c^2}-\frac{1}{q^2}\right)^{\frac{1}{2}}dq, \qquad (5)$$

where q_* is a constant. Then the function χ can be considered as a function of τ. It is well-known that in the τ, θ-plane the equations $\tau\pm\theta=$constant express the characteristics of the fundamental equation for the stream function of the flow.

§ 3. Cross Mach Lines in Simple Waves

As is well-known, the region of a simple wave consists of two families of Mach lines; the Mach lines of one family are straight lines, along each of which the state of flow remains constant, while those of the other family are non-straight Mach lines, called cross Mach lines, all of which map onto a single characteristics in the hodograph τ, θ-plane.

Now, we call the characteristics $\tau\mp\theta=$constant in the hodograph plane Γ_+-, Γ_--characteristics, and the corresponding simple waves in the physical x, y-plane Γ_+-, Γ_--simple waves, i.e.,

$$\Gamma_+\text{-wave}: \quad \tau-\theta=\text{constant}, \qquad (6)$$

$$\Gamma_-\text{-wave}: \quad \tau+\theta=\text{constant}. \qquad (7)$$

Further, in a Γ_--wave (or Γ_+-wave) we denote by C_+ (or C_-) the straight Mach line and by C_- (or C_+) the cross Mach lines. In the following, we consider, without loss of generality, only the case of Γ_--waves.

Denoting by ω the angle which a straight Mach line C_+ in a Γ_--wave makes with the positive direction of the y-axis, the coordinates x, y of any point P in the region of the wave can be expressed by

$$x=a(\sigma)-r\sin\omega(\sigma),\quad y=b(\sigma)+r\cos\omega(\sigma), \qquad (8)$$

where $a(\sigma)$, $b(\sigma)$ and $\omega(\sigma)$ are arbitrary functions of a parameter σ, and r is the distance of the point P(x, y) measured from an initial curve $x=a$, $y=b$ along a straight Mach line $\sigma=$constant passing through the point P, as shown in Fig. 1. When all the straight Mach lines issue from a fixed point, i.e., when $a=$constant, $b=$constant, the wave is called a "centred simple wave".

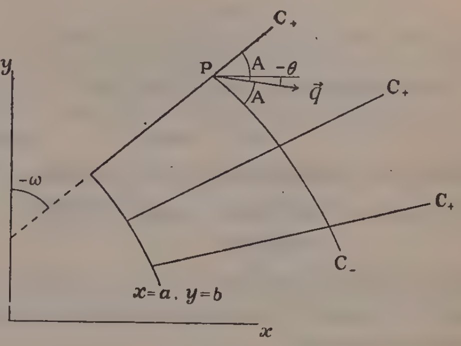

Fig. 1.

Now we assume that ω varies monotonously with σ. Then we can take ω as a parameter in place of σ. Between ω, θ and A there exists a relation

$$\omega=\theta+A-\pi/2 \text{ for } \Gamma_-\text{-wave}. \qquad (9)$$

In order to obtain the representation of the cross Mach lines we assume that the initial curve $x=a$, $y=b$ is a given cross Mach line. Then, the differential equation for any cross Mach line C_-:

$$\frac{dy}{dx}=\tan(\theta-A),$$

can be reduced to

$$\frac{dr}{r}=-\cot 2A\,d\omega. \qquad (10)$$

For polytropic gases, this equation has already ben integrated. However. it is shown that a more general representation of cross Mach lines is possible, without restriction to any type of gases.

Along any cross Mach line in a simple wave we obtain

$$\rho c r\chi=\text{constant}, \qquad (11)$$

where r is the distance of any point measured along a straight Mach line from an initial given cross Mach line.

This statement can be proved as follows. Taking into account the definition of the velocity of sound and Bernoulli's equation in differential form, we get from (3)

$$\frac{dc}{c}=-\sin^2 A\frac{d\rho}{\rho}+\cot A\,dA.$$

And from (4) we get

$$\frac{d\chi}{\chi}=-\frac{1}{2}\frac{d\rho}{\rho}-\frac{dA}{\sin 2A}.$$

Then, from these two relations we have

$$d\log(\rho c\chi)=\frac{1}{2}\cos 2A\frac{d\rho}{\rho}+\cot 2A\,dA\,. \tag{12}$$

But, from Eqs. (9), (7) and (5) we obtain

$$d\omega-dA=d\theta=-d\tau=\frac{1}{2}\sin 2A\frac{d\rho}{\rho}$$

$$\text{for } \Gamma_{-}\text{-wave.} \tag{13}$$

Hence, from Eqs. (12) and (13) it follows

$$\begin{aligned} d\log(\rho c\chi) &= \cot 2A(d\omega-dA)+\cot 2A\,dA \\ &= \cot 2A\,d\omega. \end{aligned}$$

Since the right-hand side of this equation is equal to $-d\log r$ from Eq. (10), the above equation becomes

$$d\log(\rho c r\chi)=0.$$

Therefore, any cross Mach line C_- in a Γ_--wave is represented by $\rho c r\chi$=constant. The same result holds for the case of the cross Mach lines in a Γ_+-simple wave.

§ 4. The Value of the Stream Function along a Cross Mach Line

The formula for the streamlines in a simple wave can be obtained by integration of the equation:

$$\frac{dy}{dx}=\tan\theta\,. \tag{14}$$

Now, we choose a streamline for the initial curve: $x=a$, $y=b$, and we denote by r the distance of any point measured from this initial streamline along the straight Mach line C_+ passing through the point. Then, as in § 3, Eq. (14) reduces to

$$\frac{dr}{r}=-\cot A\,d\omega\,. \tag{15}$$

For polytropic gases, this equation can be integrated, yielding explicitly the distance r as a function of ω.¹⁾ However, without restriction to any special type of gases, through integration of Eq. (15) in the same way as in § 3 we get

$$\rho c r=\text{constant.} \tag{16}$$

This relation is obvious intuitively from the well-known fact that the normel component of the velocity of gas across a straight Mach line is equal to the local velocity of sound.

Next, we proceed to the determination of the stream function in a simple wave. From the above expression for the streamlines it follows that, denoting by Ψ_0 the value of the stream function along a certain given curve, the stream function Ψ at any point P in a simple wave is expressed by

$$\Psi=\Psi_0+\rho c r\,, \tag{17}$$

where r is the distance of the point P from the given curve measured along a straight Mach line passing through the point P and the value of Ψ_0 is to be taken at the point of intersection of the given curve and the straight Mach line through P. When the given curve is a streamline, Ψ_0 is of course constant. When it is a cross Mach line, it follows from the relation (11) and (17) that the value of Ψ along any cross Mach line is obtained in the form:

$$\Psi=\Psi_i+\frac{k}{\chi}, \tag{18}$$

in which Ψ_i is the value of Ψ along a given initial cross Mach line and k is constant along each cross Mach line. Here, also it must be noted that the value of Ψ_i on the right-hand side of relation (18) is to be taken at the point of intersection of the given initial cross Mach line and the straight Mach line passing through the point P under consideration.

In particular, when a centred simple wave is concerned, the value of Ψ along any cross Mach line in its field can be expressed by

$$\Psi=\Psi_C+\frac{k}{\chi}, \tag{19}$$

in which Ψ_C denotes the value of Ψ at the centre C, and k is constant along each cross Mach line. Inversely, if the values of Ψ along a cross Mach line in a simple wave can be written in the form (19), then the simple wave has a centre. For, provided it has no centre, it may be possible to draw a streamline CQ along which $\Psi=\Psi_C$=constant and a cross Mach line CR, and a straight Mach line PQR as shown in Fig. 2. Let $\overline{PQ}=r$, $\overline{PR}=r'$. Then we have from the expression of cross Mach lines

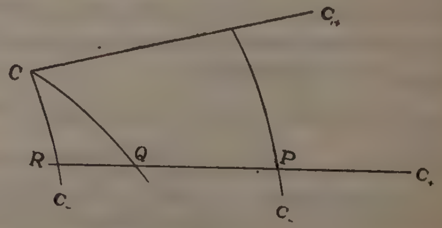

Fig. 2.

$$\rho c r' \chi = \text{constant} = k' \text{ say,}$$

and also from (19) we get

$$\frac{k}{\chi} = \rho c r.$$

But, it must be $k=k'$ by the condition on the straight Mach line passing through the point C. Thus, it must be $r=r'$ which is however impossible in general.

In conclusion, the author wishes to express his hearty thanks to Prof. S. Tomotika for his incessant encouragement throughout this work, and also to the Ministry of Education for grant in aid.

References

1) R. Courant and K. O. Friedrichs, "Supersonic Flow and Shock Waves", Interscience Publishers, New York (1948), Section 110, Chapter IV B.

2) I. Imai, Ooyōsugaku-Rikigaku **1** (1947) 147. (in Japanese).

JOURNAL OF THE PHYSICAL SOCIETY OF JAPAN Vol. 8, No. 2, MAR.—APR., 1953

On the Limiting Line in a Simple Wave

By Zirō HASIMOTO

Department of Mathematics and Physics,
Ritumeikan University, Kyoto

(Received November 29, 1952)

A few discussions are made on the condition in the neighbourhood of an envelope formed by the straight Mach lines in a simple wave, obtaining the result that at the envelope, which may be called a "limiting line" as in the case of ordinary flows other than simple waves, the cross Mach lines have a cusp and the distribution of the stream function along the cross Mach lines takes an extremum.

§1. Introduction

In the theory of hodograph method for treating two-dimensional, steady, irrotational, isentropic, supersonic flow of a perfect gas, much are well established about the singular behaviours of the mapping between the physical and the hodograph planes.[1] For instance, the mapping of the hodograph u, v-plane into the physical x, y-plane forms a fold in the x, y-plane if $J=\partial(x,y)/\partial(u,v)$ vanishes along a critical curve in the u, v-plane; here J denotes the Jacobian of the function $x=x(u,v)$, $y=y(u,v)$ deduced from the solution of the linear hodograph equation for the stream function. The edge of the fold in the x, y-plane, called a limiting line, is an envelope of one family of Mach lines and at the same time it is a locus of cusps of the other family of Mach lines. Moreover, at the critical curve in the u, v-plane along which $J=0$ the images of streamlines are tangential to the characteristics of the hodograph equation.

However, the above statement cannot be applied to the case of simple waves. In this case, the Jacobian J vanishes identically throughout the whole region of a simple wave, which is mapped on to a single curve, namely, one of the characteristics in the u, v-plane. Thus, the usual method of predicting the occurrence and the location of a limiting line cannot be used in the case of simple waves.

Since the occurrence of a limiting line, though physically impossible in the actual flow, seems occasionally be related to the occurrence of a shock wave, it will be of practical importance to settle the condition in the neighbourhood of a limiting line for the case of simple waves.

In the present paper it is shown that, in a simple wave the cross Mach lines have a cusp on the limiting line, which is an envelope of the straight Mach lines and also the distribution of the stream function along any cross Mach line takes an extremum there. Apparently these facts have never been proved so far, although they might be inferred from those of the limiting line in ordinary flows. Making use of the above character of the stream function we can predict the occurrence of a limiting line from the stream function expressed as a function of a characteristic variable. A practical application of the present result will be given in the present writer's later paper dealing with the occurrence of limiting lines in plane gas jets.

§ 2. Expression for the Limiting Line in a Simple Wave

Consider simple waves in two-dimensional, steady, irrotational, isentropic, supersonic flow of a perfect gas. As is well known, the region of a simple wave is covered with two families of Mach lines: (a) the straight Mach lines along each of which the state of flow remains constant, and (b) the curved Mach lines, called cross Mach lines, which are mapped on to the same characteristic of the hodograph equation. So, it would be quite natural to suppose that the possible limiting line in a simple wave is an envelope of the straight Mach lines. As will be shown in the following lines, it can be simply expressed by making use of the analytical representation of simple waves.

The rectangular coordinates x, y of any point P (x, y) in the field of a simple wave can be expressed in the form[2)]

$$x=a(\sigma)-r\sin\omega(\sigma)\,,\quad y=b(\sigma)+r\cos\omega(\sigma).$$

Here, $x=a(\sigma)$, $y=b(\sigma)$ represents an initially given curve expressed with a parameter σ, r measures the distance of the point P from this initial curve along the straight Mach line passing through it, and $\omega(\sigma)$ as a function of σ is the angle between the straight Mach line and the y-axis. In what follows, we assume that the parameter σ can be replaced by ω itself, i.e., we confine ourselves to the simple waves described by

$$x=a(\omega)-r\sin\omega,\quad y=b(\omega)+r\cos\omega. \qquad (1)$$

Eliminating r between these two equations, the family of straight Mach lines can be expressed in the form $f(x, y, \omega)=0$. Hence, from two equations $f=0$ and $\partial f/\partial\omega=0$ we obtain the parametric representation of the envelope, say $\mathcal{E}$, of straight Mach lines. It can be expressed by (1) with

$$r=a_\omega\cos\omega+b_\omega\sin\omega. \qquad (2)$$

§ 3. Behaviour of Cross Mach Lines at the Limiting Line $\mathcal{E}$

We call a simple wave a Γ_+-wave or a Γ_--wave according as its image in the hodograph plane belongs to the characteristics of one kind or to those of the other[2)]. Here we consider, without loss of generality, only the case of a Γ_--wave defined as

$$\tau+\theta=\text{constant},$$

where θ denotes the angle between the velocity vector, $\vec{q}$, and the positive x-axis, and τ is a variable introduced in place of q such that[3)]

$$\tau=\int_{q_*}^{q}\left(\frac{1}{c^2}-\frac{1}{q^2}\right)^{\frac{1}{2}}dq\,,$$

c being the local velocity of sound and q_* a certain constant. $\tau+\theta$ and $\tau-\theta$ are the characteristic variables in the hodograph plane. Between ω, θ and the Mach angle, A, there exists a relation

$$\omega=\theta+A-\frac{\pi}{2}\quad\text{for}\quad\Gamma_-\text{-wave}\,. \qquad (3)$$

Further, we denote by C_+ the straight Mach lines and by C_- the cross Mach lines in a Γ_--wave, see Fig. 1.

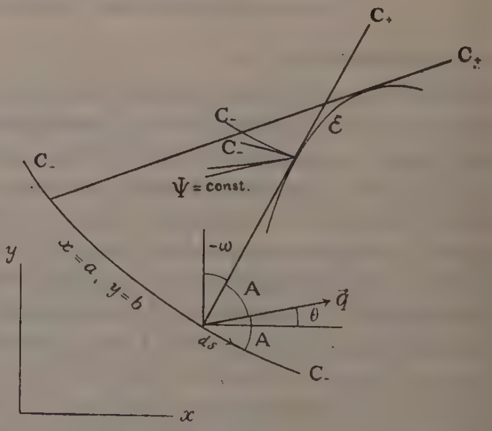

Fig. 1

Then we can prove that, *in a simple wave, the cross Mach lines have a cusp at the limiting line.*

Now suppose that the initial curve $x=a(\omega)$, $y=b(\omega)$ is a prescribed cross Mach line in a Γ_--wave. Then, as shown in the preceding paper[3)], any cross Mach line C_- can be expressed by equations (1), provided that

$$\left.\begin{aligned} &\rho c r \chi = \text{constant along } C_- \\ \text{with} \quad &\chi = \left(\frac{\rho_0}{\rho}\right)^{\frac{1}{2}} \cot^{\frac{1}{2}} A \,, \end{aligned}\right\} \quad (4)$$

where ρ is the density of the gas and ρ_0 is a constant. Taking into consideration the following relations as proved in the preceding paper,

$$d \log (\rho c \chi) = -d \log r = \cot 2A \, d\omega \,,$$

we find, from (1) and (4), that

$$\left.\begin{aligned} dx &= da - \frac{\sin(2A-\omega)}{\sin 2A} r\, d\omega \,, \\ dy &= db - \frac{\cos(2A-\omega)}{\sin 2A} r\, d\omega \end{aligned}\right\} \quad (5)$$

along a cross Mach line C_-. Since $x=a$, $y=b$ is a cross Mach line, we have

$$db = -da \tan(A-\theta) \,. \qquad (6)$$

But, by virtue of (2), (3) and (6), we obtain

$$r\, d\omega = \frac{\sin 2A}{\sin(2A-\omega)} da = \frac{\sin 2A}{\cos(2A-\omega)} db \text{ at } \varepsilon, \qquad (7)$$

and insertion of these equations into (5) gives ultimately

$$(dx, dy)_{\text{along } C_-} = 0 \text{ at } \varepsilon \,. \qquad (8)$$

Thus, the statement that the cross Mach lines have a cusp at ε has been proved.

§ 3. Condition for the Stream Function at the Limiting Line

In the hodograph method for treating simple waves, the stream function is conveniently expressed by its distribution along the cross Mach lines. In the present section we search for the condition for the stream function along the cross Mach lines valid at the limiting line, whereby we can predict vice versa the occurrence of the limiting line.

As in § 3, we suppose that $x=a$, $y=b$ is an initially prescribed cross Mach line, and that along it the stream function, Ψ, equals Ψ_0 as a function of ω. Then, the value of Ψ along any cross Mach line can be expressed in the form[3]:

$$\Psi = \Psi_0 + \frac{k}{\chi} \,, \qquad (9)$$

with χ as defined in the preceding section, where k is a constant along each cross Mach line.

Then we can prove that *the distribution of the stream function along the cross Mach lines takes an extremum at the limiting line* ε.

Denote by s the arc length measured along the initial cross Mach line. Since, at any point the component of velocity normal to C_- equals the local velocity of sound, c, we obtain

$$\frac{d\Psi_0}{ds} = \frac{d\Psi_0}{d\omega}\frac{d\omega}{ds} = -\rho c \,. \qquad (10)$$

And, along $x=a$, $y=b$, we have

$$ds = da \cos(A-\theta) - db \sin(A-\theta) \,, \qquad (11)$$

(see Fig. 1), which reduces, by (3) and (7), to

$$ds = \frac{r\, d\omega}{\sin 2A} \quad \text{at } \varepsilon. \qquad (12)$$

By differentiating Eq. (9) with respect to ω and taking account of (4), (10) and (12), we have

$$(d\Psi)_{\text{along } C_-} = -\rho c r \left(\frac{d\omega}{\sin 2A} + \frac{d\chi}{\chi} \right) \quad \text{at } \varepsilon. \qquad (13)$$

Since, however, as shown in the preceding paper[3], the following relations hold

$$d\omega - dA = \frac{1}{2} \sin 2A \frac{d\rho}{\rho} \,,$$

$$\frac{d\chi}{\chi} = -\frac{1}{2}\frac{d\rho}{\rho} - \frac{dA}{\sin 2A} \,,$$

the right-hand side of (13) vanishes. Hence, we have ultimately

$$(d\Psi)_{\text{along } C_-} = 0 \quad \text{at } \varepsilon, \qquad (14)$$

and our statement has thus been proved.

Incidentally, since

$$d\tau = \frac{d\tau}{d\chi}\frac{d\chi}{d\omega} d\omega = -\frac{\chi}{\sin 2A}\frac{d\tau}{d\chi} d\omega \,,$$

we find that

$$\left(\frac{d\Psi}{d\tau}\right)_{\text{along } \tau+\theta=\text{constant}} = 0 \quad \text{at } \varepsilon. \qquad (15)$$

Here, a few words should be added about the Jacobian $J = \partial(x,y)/\partial(u,v)$. If we use the characteristic variables ξ, η defined as

$$\xi = \tau - \theta \,, \quad \eta = \tau + \theta \,,$$

a Γ_--simple wave is represented by $\eta =$ constant in the hodograph plane and in this case the stream function can be expressed as a function of ξ only, and accordingly the condition (15) at the limiting line is expressed as

$$\left(\frac{d\Psi}{d\xi}\right)_{\text{along } \eta=\text{constant}} = 0 \quad \text{at } \varepsilon. \qquad (16)$$

On the other hand, the Jacobian J is expressed, in general, in the form

$$J=\frac{\partial(x,y)}{\partial(u,v)}=-\frac{4}{\rho^2 q^4}\left(\frac{q^2}{c^2}-1\right)\Psi_\xi\Psi_\eta . \quad (17)$$

From this relation we see that, in ordinary flows other than simple waves Ψ_ξ or Ψ_η vanishes at the image of the limiting line, whilst in a simple wave one of them vanishes identically and accordingly J itself too vanishes identically, and the remaining one vanishes at the image of the limiting line when the stream function has been expressed by its distribution along the cross Mach lines.

In conclusion, the author wishes to express his cordial thanks to Prof. S. Tomotika for his incessant encouragement throughout this work. The author's thanks are also due to the Ministry of Education for a grant in aid for fundamental scientific research.

References

1) R. Courant and K. O. Friedrichs: "Supersonic Flow and Shock Waves", Interscience Publishers, New York (1948), Section 30, Chapter II.

2) R. Conrant and K. O. Friedrichs: Sections 108 and 109, Chapter IV B.

3) Z. Hasimoto: Jour. Phys. Soc. Japan, **8** (1953) 248.

JOURNAL OF THE PHYSICAL SOCIETY OF JAPAN Vol. 8, No. 2, MAR.—APR., 1953

A Spherical Obstacle in the Flow of a Viscous Fluid through a Tube

By Shōichi WAKIYA

Faculty of Engineering, Niigata University, Nagaoka

(Received December 6, 1952)

The Poiseuille flow through a circular tube as affected by the presence of a fixed spherical obstacle with its center on the axis of the tube is considered on the basis of the Stokes approximation. Expressions for the resultant force acting on the sphere and for the pressure difference which must be added to maintain the total flux through the tube at the value corresponding to the case of absence of the obstacle are obtained correctly to $(a/r_0)^5$, where a and r_0 are the radii of the sphere and the tube respectively. If terms of the order of $(a/r_0)^2$ can be neglected, the magnitude of the resistance is shown to be equal to that of a sphere moving with a constant velocity along the axis of a tube, which was first obtained by Ladenburg.

§ 1. Introduction

The effect of boundary walls on the motion of an obstacle in a viscous fluid has been considered in various cases, on the basis of the Stokes or Oseen approximation. In particular, this problem was systematically dealt with by Faxén1) for the case of a sphere moving with a constant velocity. It seems that his method may also be very useful to find out the effect of a spherical obstacle on the flow of a viscous fluid bounded by a fixed wall.

In this paper, the steady flow of a viscous fluid past a sphere in a straight tube of circular cross section will be dealt with using Faxén's procedure, with special consideration of the blocking effect of the sphere. Besides, the total resistance of the sphere will be discussed in comparison with the case in which a sphere moves with a constant velocity along the axis of the tube; the latter problem was first considered by Ladenburg2) and later by Faxén3).

§ 2. Solution of the Differential Equations

We shall consider only the case that a fixed sphere has its center on the axis of an infinitely long straight tube having a circular cross section and that the steady motion of a viscous incompressible fluid can be described approximately by the Stokes equations of motion.

If we make use of the cylindrical coordinates (r, z, φ) having the center of the sphere as the origin and the axis of the tube as the z-axis, equations of motion and of continuity are reduced to

$$\frac{\partial p}{\partial r}=\mu\left(\Delta-\frac{1}{r^2}\right)v_r, \quad \frac{\partial p}{\partial z}=\mu\Delta v_z, \tag{1}$$

with

$$\Delta=\frac{\partial^2}{\partial r^2}+\frac{1}{r}\frac{\partial}{\partial r}+\frac{\partial^2}{\partial z^2},$$

and

$$\frac{\partial}{\partial r}(rv_r)+\frac{\partial}{\partial z}(rv_z)=0 \tag{2}$$

respectively, where μ is the coefficient of viscosity, p is the pressure, and v_r, v_z are the r, z components of the velocity.

Now suppose that the undisturbed flow through the tube should be Poiseuille's flow with the pressure distribution:

$$p_0=-4\mu Uz/r_0^2+\text{const};$$

then the following conditions must be satisfied

$$v_z=v_0=U(1-r^2/r_0^2), \quad v_r=0 \quad \text{for} \quad z=\pm\infty, \tag{3}$$

$$v_z=v_r=0 \quad \text{for} \quad R=\sqrt{r^2+z^2}=a, \tag{4}$$

$$v_z=v_r=0 \quad \text{for} \quad r=r_0, \tag{5}$$

where U is a constant having the dimensions of velocity and a, r_0 are the radii of the sphere and the tube respectively.

We shall, as usual, adopt the method of successive approximation. In the first place, omitting the boundary condition (5), we obtain the state produced by the reflection of Poiseuille's flow on the sphere:

$$\left.\begin{aligned}
v_{1z}&=-2\left(\frac{A}{R}-\frac{B}{R^3}-4\frac{D}{R^5}\right)+\left(\frac{A}{R}-\frac{3B-4C}{R^3}\right.\\
&\qquad\left.-40\frac{D}{R}\right)\frac{r^2}{R^2}-5\left(\frac{C}{R^3}-7\frac{D}{R^5}\right)\frac{r^4}{R^4},\\
v_{1r}&=-\frac{zr}{R^2}\left\{\left(\frac{A}{R}-3\frac{B}{R^3}-20\frac{D}{R^5}\right)\right.\\
&\qquad\left.-5\left(\frac{C}{R^3}-7\frac{D}{R^5}\right)\frac{r^2}{R^2}\right\},\\
p_1&=-2\mu\left(\frac{A}{R}+2\frac{C}{R^3}-5\frac{C}{R^3}\frac{r^2}{R^2}\right)\frac{z}{R^2},
\end{aligned}\right\} \tag{6}$$

where

$$\left.\begin{aligned}
A&=\frac{3}{4}aU\left(1-\frac{2}{3}\frac{a^2}{r_0^2}\right),\\
B&=\frac{1}{4}a^3U\left(1-4\frac{a^2}{r_0^2}\right),\\
C&=\frac{7}{8}a^3U\frac{a^2}{r_0^2},\\
D&=\frac{1}{8}a^5U\frac{a^2}{r_0^2}.
\end{aligned}\right\} \tag{7}$$

The flow as given by (6) vanishes at infinity and satisfies the condition (4) by the addition of Poiseuille's flow v_0.

The next step is to find the state produced by the reflection of the flow (6) on the inner surface of the tube. For this purpose, we shall alter (6) to integral forms such that

$$\left.\begin{aligned}
v_{1z}&=-\frac{2}{\pi}\int_0^\infty[g(\lambda)K_0(\lambda r)+f(\lambda)\lambda rK_1(\lambda r)]\\
&\qquad\times\cos\lambda z d\lambda,\\
v_{1r}&=\frac{2}{\pi}\int_0^\infty[f(\lambda)\lambda rK_0(\lambda r)\\
&\qquad+\{2f(\lambda)+g(\lambda)\}K_1(\lambda r)]\sin\lambda z d\lambda,\\
p_1&=\mu\frac{4}{\pi}\int_0^\infty f(\lambda)\lambda K_0(\lambda r)\sin\lambda z d\lambda,
\end{aligned}\right\} \tag{8}$$

where

$$f(\lambda)=-A+\frac{C}{3}\lambda^2, \quad g(\lambda)=2A+B\lambda^2-\frac{D}{3}\lambda^4, \tag{9}$$

and K_n, I_n are the modified Bessel functions of the nth order.

In analogy to (8) it will readily be seen that

$$\left.\begin{aligned}
v_{2z}&=\frac{2}{\pi}\int_0^\infty[G(\lambda)I_0(\lambda r)-F(\lambda)\lambda rI_1(\lambda r)]\cos\lambda z d\lambda,\\
v_{2r}&=-\frac{2}{\pi}\int_0^\infty[F(\lambda)\lambda rI_0(\lambda r)\\
&\qquad-\{2F(\lambda)+G(\lambda)\}I_1(\lambda r)]\sin\lambda z d\lambda,\\
p_2&=-\mu\frac{4}{\pi}\int_0^\infty F(\lambda)\lambda I_0(\lambda r)\sin\lambda z d\lambda
\end{aligned}\right\} \tag{10}$$

are another solutions of the equations (1) and (2). In order that (10) may satisfy the condition (5) by the addition of (6), we should have

$$\begin{aligned}
F(\lambda)&=f(\lambda)\frac{K_0(\lambda r_0)}{I_0(\lambda r_0)}\\
&\qquad-\frac{1}{\Delta}\left\{f(\lambda)\frac{I_1(\lambda r_0)}{I_0(\lambda r_0)}+\frac{2f(\lambda)+g(\lambda)}{\lambda r_0}\right\},
\end{aligned}$$

$$\left.\begin{aligned} G(\lambda)=g(\lambda)&\frac{K_0(\lambda r_0)}{I_0(\lambda r_0)} \\ &-\frac{1}{\varDelta}\left\{g(\lambda)\frac{I_1(\lambda r_0)}{I_0(\lambda r_0)}+f(\lambda)\lambda r_0\right\}, \end{aligned}\right\} \tag{11}$$

where

$$\varDelta=2I_0(\lambda r_0)I_1(\lambda r_0)-\lambda r_0\{[I_0(\lambda r_0)]^2-[I_1(\lambda r_0)]^2\}.$$

With these values of $F(\lambda)$ and $G(\lambda)$, our integrals converge and the flow (v_{2z}, v_{2r}) tends to zero at infinity. Therefore (10) with (11) is the reflected state looked for.

Thus, for the first step of successive approximation, we have

$$\left.\begin{aligned} v_z&=c(v_{1z}+v_{2z})+v_0, \\ v_r&=c(v_{1r}+v_{2r}), \\ p&=c(p_1+p_2)+p_0 \end{aligned}\right\} \tag{12}$$

as the solution of our problem. The constant c can be determined by the condition that the mean velocity on the sphere becomes zero; thus

$$c=\frac{U\left(1-\dfrac{2}{3}\dfrac{a^2}{r_0^2}\right)}{\dfrac{4}{3}\dfrac{A}{a}-\dfrac{1}{c}\left\{(v_{2z})_0+\dfrac{a^2}{6\mu}\left(\dfrac{\partial p_2}{\partial z}\right)_0\right\}}, \tag{13}$$

where suffix zero denotes that the value at the origin should be taken.

The flow (12) exactly satisfies the conditions on the wall and at infinity, but only approximately the condition on the surface of the sphere. If we use (6) and (10), the value of c is correct to the order of $(a/r_0)^5$.

Finally, calculating the values of the integrals in (13) numerically, we have the expression:

$$c=\frac{1-(2/3)\xi^2}{\{1-(2/3)\xi^2\}-(2.104\,\xi-3.49\,\xi^3+2.50\,\xi^5)} \tag{14}$$

keeping terms up to ξ^6, where $\xi=a/r_0$.

§ 3. Blocking Effect of the Sphere

It may be interesting to consider about the pressure at infinity. Clearly we have $(p_1)_{z\to\infty}=0$, and from (10) and (11)

$$(p_2)_{z\to\infty}=\lim_{z\to\infty}\mu\frac{4}{\pi}\int_0^\infty c\left\{-A\frac{\lambda^2 I_1(\lambda r_0)}{\varDelta I_0(\lambda r_0)}I_0(\lambda r)+(B+\tfrac{2}{3}C)\frac{\lambda^3}{r_0\varDelta}I_0(\lambda r)\right\}\frac{\sin\lambda z}{\lambda}d\lambda.$$

$\{\lambda_2 I_1(\lambda r_0)/\varDelta I_0(\lambda r_0)\}I_0(\lambda r)$ and $(\lambda^3/\varDelta)I_0(\lambda r)$ are continuous functions of λ which are monotonous or at most have a maximum, so that applying Dirichlet's integral theorem we have

$$(p_2)_{z\to\infty}=-8\mu\left\{\frac{A}{r_0^2}-\frac{2}{r_0^4}(B+\tfrac{2}{3}C)\right\}c. \tag{15}$$

Hence, in order to maintain the total flux through the tube in the presence of a spherical obstacle at the value corresponding to the Poiseuille flow v_0, additional pressure difference $\varDelta p$ must be added such that

$$\begin{aligned} \varDelta p&=-2(p_2)_{z\to\infty} \\ &=8\mu\frac{U}{r_0}\frac{(3/2)\xi-2\xi^3+(5/3)\xi^5}{1-2.104\xi+2.09\xi^3-1.11\xi^3} \end{aligned} \tag{16}$$

at the both ends of the (practically infinitely long) tube.

The values of $\varDelta p/(\mu U/r_0)$ corresponding to some values of $\xi=a/r_0$ are shown in the fifth column of Table I.

Table I

$\dfrac{a}{r_0}$	c	$\dfrac{W}{6\pi\mu aU}$	$c'=\dfrac{W'}{6\pi\mu aU}$	$\dfrac{\varDelta p}{\mu U/r_0}$
0.1	1.26	1.25	1.26	1.50
0.2	1.68	1.63	1.68	3.80
0.3	2.37	2.23	2.36	7.60
0.4	3.56	3.18	3.54	13.9
0.5	5.8	4.8	5.6	25.

§ 4. Force Acting on the Sphere

The total resistance of the sphere takes the direction of the z-axis and becomes

$$\begin{aligned} W&=8\pi\mu Ac \\ &=\frac{6\pi\mu aU\{1-(2/3)\xi^2\}}{1-2.104\xi+2.09\xi^3-1.11\xi^5}. \end{aligned} \tag{17}$$

If we put

$$A=\frac{3}{4}aU,\quad B=\frac{1}{4}a^3U,\quad C=D=0 \tag{18}$$

in place of (7), we have Ladenburg's case mentioned before. The total resistance in his case is therefore easily given by

$$\begin{aligned} W'&=6\pi\mu aUc' \\ &=\frac{6\pi\mu aU}{1-2.104\xi+2.09\xi^3-0.95\xi^5}. \end{aligned} \tag{19}$$

In Table I are shown some values of c, $W/6\pi\mu aU$ and c'.

If terms of the order of $(a/r_0)^2$ are neglected, the expression (7) is equal to (18). We have therefore under the same approximation

$$\frac{W}{6\pi\mu aU}=\frac{W'}{6\pi\mu aU}=1+2.1\frac{a}{r_0},$$

which seems to be more accurate than the formula given by Ladenburg[2]: $1+2.4\,a/r_0$. The expression (19) coincides completely with the one obtained by Faxén[3] for the same case, taking the Oseen approximation as the basis, if the Reynolds number is taken equal to zero in his result.

In conclusion the author wishes to express his sincere thanks to Professor I. Imai of the Tokyo University for his kind guidance throughout this work.

References

1) H. Faxén: Ann. d. Phys. **68** (1922) 89, and his other papers.
2) R. Ladenburg: Ann. d. Phys. **23** (1907) 447.
3) H. Faxén: Arkiv for mat., astr. och fys. **17** (1923).

JOURNAL OF THE PHYSICAL SOCIETY OF JAPAN Vol. 8, No. 2, MAR.—APR., 1953

On the Subsonic Flow of a Compressible Fluid past a Prolate Spheroid

By Kinzō HIDA

Department of Applied Physics, Faculty of Engineering, Naniwa University

(Received December 8, 1952)

The steady irrotational subsonic flow of a compressible fluid past a prolate spheroid is discussed by Janzen-Rayleigh's method and the velocity potential correct to M^2 is given in elliptic coordinates, where M is the Mach number for the undisturbed flow at infinity. Numerical discussions are made for two cases in which $t=0.9$ and 0.1, t being the thickness-ratio of the body. In the former case the velocity distribution on the surface of the body is shown, while in the latter only the maximum velocity at the end of the minor-axis of the spheroid is given. The so-called critical Mach number, M_{crit}, at which the maximum fluid velocity in the field of flow first becomes equal to the local sound velocity, is also calculated in both cases and is found to be $M_{\text{crit}}=0.615$ and 0.972 respectively. In Appendix some numerical values of Legendre's spherical functions $P_n(z)$ and $Q_n(z)$ ($n=1\sim13$) are tabulated for various values of z ranging from 1.01 to 2.

§1. Introduction and Summary

So far the subsonic flow of a compressible fluid past three-dimensional obstacles has been discussed only in a few cases. The flows past slender bodies have been dealt with by the use of the linear theory due orignally to Prandtl and Glauert, while those past blunt-nosed thick bodies like sphere and Rankine ovoid have been discussed by using the M^2-expansion method (Janzen-Rayleigh's method).[1][2][3]

In this paper the axially symmetrical flow of a compressible fluid past a prolate spheroid is investigated by applying the M^2-expansion method under the assumption that the flow is irrotational and isentropic and the velocity potential correct to M^2 is obtained, where M is the Mach number of the undisturbed uniform flow at infinity. Especially the velocity distribution on the surface of the spheroid is evaluated numerically in two cases in which the thickness-ratio, t, of the body is equal to 0.9 and 0.1 respectively. For thicker one various formulae are expanded in power series of the eccentricity, e, of the body, and the results are shown in Fig. 1. For the thinner one, however, only the maximum velocity at the end of the minor-axis of the body is given.

The so-called critical Mach number, M_{crit}, at which the maximum fluid velocity in the field of flow first attains the local sound

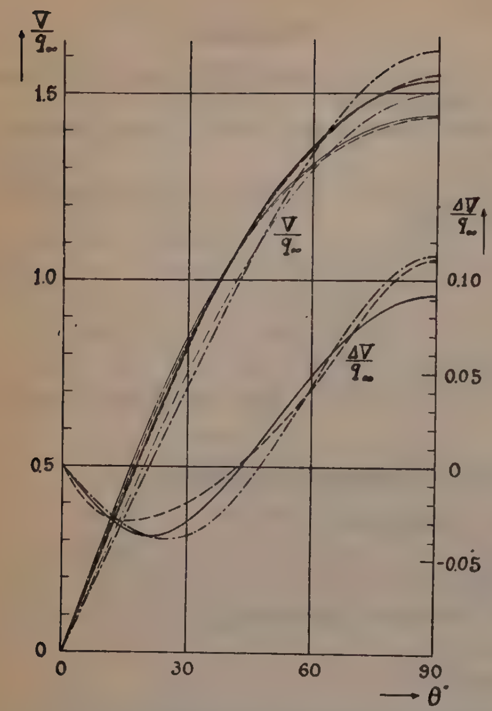

Fig. 1. Velocity distributions, V/q_∞, on the surface of various bodies and the compressibility effect, $\Delta V/q_\infty$, for surface velocity at $M=0.6$, both being plotted against the angle θ between the radius vector through the point under consideration and the x-axis.

━━━━	at $M=0.6$	Prolate spheroid with $t=0.9$ (Author).
────	at $M=0$	
━ ━ ━ ━	at $M=0.6$	Rankine ovoid with $t=0.9$ (Hasimoto[3]).
─ ─ ─ ─	at $M=0$	
━·━·━	at $M=0.6$	Sphere (first approximation) (Tamada[2]).
─·─·─	at $M=0$	

velocity, is determined in both cases, obtaining the results that $M_{\mathrm{crit}}=0.615$ for the thicker spheroid and $M_{\mathrm{crit}}=0.972$ for the thinner one.

In Appendix some numerical values of Legendre's spherical functions $P_n(z)$ and $Q_n(z)$ ($\eta=1\sim13$) are tabulated for various values of z ranging from 1.01 to 2.

Recently we have become aware that the same problem was studied by Schmieden and Kawalki[4]. They found the second approximate solution for the stream function ψ by using the linear theory, but numerical discussion was made only for the maximum velocity.

§ 2. Fundamental Equation

The equation for the velocity potential Φ can be written, in cylindrical coordinates (x, ω), as:

$$\left(\frac{\partial^2}{\partial x^2}+\frac{\partial^2}{\partial\tilde{\omega}^2}+\frac{1}{\tilde{\omega}}\frac{\partial}{\partial\tilde{\omega}}\right)\Phi \cdot$$
$$=-\frac{1}{\rho}\left(\frac{\partial\rho}{\partial x}\frac{\partial\Phi}{\partial x}+\frac{\partial\rho}{\partial\tilde{\omega}}\frac{\partial\Phi}{\partial\tilde{\omega}}\right), \quad (1)$$

where ρ is the density of the gas and for the isentropic flow it is connected with the fluid velocity q by the relation:

$$\frac{\rho}{\rho_\infty}=\left\{1-\frac{\gamma-1}{2}M^2\left(\frac{q^2}{q_\infty{}^2}-1\right)\right\}^{\frac{1}{\gamma-1}}. \quad (2)$$

Here γ denotes the ratio of specific heats of the gas and the suffix ∞ refers to values at infinity.

Transforming $(x, \tilde{\omega})$ into the elliptic coordinates (ζ, μ) by the formulae

$$x=k\mu\zeta\,, \quad \tilde{\omega}=k(1-\mu^2)^{1/2}(\zeta^2-1)^{1/2}$$

and assuming that Φ and q can be expanded in power series of M^2 as

$$\Phi=\Phi_0+\Phi_1M^2+\cdots, \quad q^2=q_0{}^2+q_1{}^2M^2+\cdots, \quad (3)$$

we have

$$\left.\begin{aligned} q_0{}^2&=\frac{1}{k^2(\zeta^2-\mu^2)}\left\{(1-\mu^2)\left(\frac{\partial\Phi_0}{\partial\mu}\right)^2\right.\\ &\qquad\left.+(\zeta^2-1)\left(\frac{\partial\Phi_0}{\partial\zeta}\right)^2\right\},\\ q_1{}^2&=\frac{1}{k^2(\zeta^2-\mu^2)}\left\{(1-\mu^2)\left(\frac{\partial\Phi_0}{\partial\mu}\right)\left(\frac{\partial\Phi_1}{\partial\mu}\right)\right.\\ &\qquad\left.+(\zeta^2-1)\left(\frac{\partial\Phi_0}{\partial\zeta}\right)\left(\frac{\partial\Phi_1}{\partial\zeta}\right)\right\}. \end{aligned}\right\} \quad (4)$$

Substituting (3) and (4) in (1) and comparing the coefficients of the same powers of M we have

$$\left.\begin{aligned} \bar{\Delta}\Phi_1&=0\,,\\ \bar{\Delta}\Phi_1&=\frac{1}{2q_\infty{}^2}\left\{(1-\mu^2)\frac{\partial\Phi_0}{\partial\mu}\frac{\partial q_0{}^2}{\partial\mu}\right.\\ &\qquad\left.+(\zeta^2-1)\frac{\partial\Phi_0}{\partial\zeta}\frac{\partial q_0{}^2}{\partial\zeta}\right\}, \end{aligned}\right\} \quad (5)$$

with

$$\bar{\Delta}\equiv\frac{\partial}{\partial\mu}\left\{(1-\mu^2)\frac{\partial}{\partial\mu}\right\}+\frac{\partial}{\partial\zeta}\left\{(\zeta^2-1)\frac{\partial}{\partial\zeta}\right\}. \quad (6)$$

The first equation in (5) is the fundamental equation for an incompressible fluid and for the axially symmetrical flow past a prolate spheroid its solution is easily seen to be given by

$$\Phi_0=q_\infty kP_1(\mu)\{P_1(\zeta)+AQ_1(\zeta)\}, \quad (7)$$

with

$$A=-\frac{1}{Q_1'(\zeta_0)}, \tag{8}$$

where P_n and Q_n are Legendre's spherical functions of the first and second kinds respectively, and k, ζ_0 relate with the half-lengths a, b of the axes of the spheroid as

$$\zeta_0=\frac{a}{\sqrt{a^2-b^2}}=\frac{1}{e}, \quad k=\frac{a}{\zeta_0}=ae, \tag{9}$$

e being the eccentricity.

Substituting (7) in (5), we get, after some reductions,

$$\begin{aligned}\frac{\bar{\Delta}\Phi_1}{q_\infty k}=&A\left\{\frac{\mu(5\mu^2-3)}{\zeta^2-\mu^2}+4\,\frac{\mu^3(\mu^2-1)}{(\zeta^2-\mu^2)^2}\right\}+A^2\left[\left\{\frac{\mu(5\mu^2-3)}{\zeta^2-\mu^2}+4\,\frac{\mu^3(\mu^2-1)}{(\zeta^2-\mu^2)^2}\right\}\log\frac{\zeta+1}{\zeta-1}+\left\{\frac{4\mu\zeta(1-2\mu^2)}{(\zeta^2-\mu^2)^2}\right.\right.\\&\left.\left.-\frac{2\mu\zeta}{\zeta^2-\mu^2}+\frac{2\mu\zeta}{\zeta^2-1}\right\}\right]+A^3\left[\left\{\frac{\mu(5\mu^2-3)}{4(\zeta^2-\mu^2)}+\frac{\mu^3(\mu^2-1)}{(\zeta^2-\mu^2)^2}\right\}\left(\log\frac{\zeta+1}{\zeta-1}\right)^2+\left\{\frac{2\mu\zeta(1-2\mu^2)}{(\zeta^2-\mu^2)^2}\right.\right.\\&\left.-\frac{\mu\zeta}{\zeta^2-\mu^2}+\frac{\mu\zeta}{\zeta^2-1}\right\}\log\frac{\zeta+1}{\zeta-1}+\left(4\mu^3-\frac{\mu}{1-\mu^2}\right)\frac{1}{(\zeta^2-\mu^2)^2}+\left(\mu+\frac{\mu}{1-\mu^2}\right)\frac{1}{\zeta^2-\mu^2}\\&\left.+\left(-\mu+\frac{\mu}{1-\mu^2}\right)\frac{1}{(\zeta^2-1)^2}-\left(\mu+\frac{\mu}{1-\mu^2}\right)\frac{1}{\zeta^2-1}\right].\end{aligned} \tag{10}$$

§ 3. Application of Poggi's Method of Integration

We now proceed to solve equation (10) of Poisson's type subject to suitable boundary conditions. For this purpose we shall make use of Poggi's device[5], and consider the right-hand side of (10) as representing the continuous distribution of sources and sinks in an incompressible fluid flow.

After some elementary calculations we easily find that subject to the boundary conditions

$$\text{(i)} \qquad \phi=0 \qquad \text{at infinity},$$

$$\text{(ii)} \qquad \frac{\partial\phi}{\partial\zeta}=0 \qquad \text{at } \zeta=\zeta_0,$$

the appropriate solution of the differential equation:

$$\bar{\Delta}\phi=f(\mu,\zeta) \tag{11}$$

is given by

$$\begin{aligned}-2\phi=\sum_{n=0}^{\infty}(2n+1)P_n(\mu)\Big[&Q_n(\zeta)\int_{-1}^{1}P_n(\mu_1)d\mu_1\int_{\zeta_0}^{\zeta}P_n(\zeta_1)f(\mu_1,\zeta_1)d\zeta_1\\&+P_n(\zeta)\int_{-1}^{1}P_n(\mu_1)d\mu_1\int_{\zeta}^{\infty}Q_n(\zeta_1)f(\mu_1,\zeta_1)d\zeta_1\\&-Q_n(\zeta)\frac{P_n'(\zeta_0)}{Q_n'(\zeta_0)}\int_{-1}^{1}P_n(\mu_1)d\mu_1\int_{\zeta_0}^{\infty}Q_n(\zeta_1)f(\mu_1,\zeta_1)d\zeta_1\Big].\end{aligned} \tag{12}$$

Thus, carrying out rather tedious calculations we obtain the solution of equation (10) in the form:

$$\frac{\Phi_1}{q_\infty k}=A\Phi_1'+A^2\Phi_1''+A^3\Phi_1''', \tag{13}$$

where

$$\Phi_1'=-\frac{\mu^3}{2(\zeta^2-\mu^2)}+\frac{\zeta_0^2\mu}{2(\zeta^2-\mu^2)}+\zeta_0L(\mu,\zeta;\zeta_0), \tag{14a}$$

$$\begin{aligned}\Phi_1''=&\frac{\mu\zeta}{\zeta^2-\mu^2}-\mu\left\{1+\frac{\mu^2}{2(\zeta^2-\mu^2)}\right\}\log\frac{\zeta+1}{\zeta-1}+\frac{\mu\zeta}{4}\left(\log\frac{\zeta+1}{\zeta-1}\right)^2-\frac{\mu\zeta_0}{\zeta^2-\mu^2}\left\{1-\frac{\zeta_0}{2}\log\frac{\zeta_0+1}{\zeta_0-1}\right\}\\&-\mu\frac{Q_1(\zeta)}{Q_1'(\zeta_0)}\left\{\frac{1}{4}\left(\log\frac{\zeta_0+1}{\zeta_0-1}\right)^2-\frac{\zeta_0}{\zeta_0^2-1}\log\frac{\zeta_0+1}{\zeta_0-1}+\frac{1}{\zeta_0^2-1}\right\}+\left\{\frac{1}{\zeta_0^2-1}+2\zeta_0Q_1'(\zeta_0)\right\}L(\mu,\zeta;\zeta_0),\end{aligned} \tag{14b}$$

$$\Phi_1'''=\frac{1}{24}\mu\zeta\left(\log\frac{\zeta+1}{\zeta-1}\right)^3-\frac{1}{8}\left(\frac{\mu^3}{\zeta^2-\mu^2}+2\mu\right)\left(\log\frac{\zeta+1}{\zeta-1}\right)^2+\frac{1}{2}\frac{\mu\zeta}{\zeta^2-\mu^2}\log\frac{\zeta+1}{\zeta-1}-\frac{\mu}{4(\zeta^2-1)}$$

$$+\frac{1}{8}\zeta_0\log\frac{\zeta_0+1}{\zeta_0-1}\left(\zeta_0\log\frac{\zeta_0+1}{\zeta_0-1}-4\right)\frac{\mu}{\zeta^2-\mu^2}+\mu\frac{Q_1(\zeta)}{Q_1'(\zeta_0)}\left\{-\frac{\zeta_0}{2(\zeta_0^2-1)^2}\right.$$
$$\left.-\frac{1}{2(\zeta^2-1)}\left(\log\frac{\zeta_0+1}{\zeta_0-1}\right)+\frac{1}{4}\frac{\zeta_0}{\zeta_0^2-1}\left(\log\frac{\zeta_0+1}{\zeta_0-1}\right)^2-\frac{1}{24}\left(\log\frac{\zeta_0+1}{\zeta_0-1}\right)^3\right\}$$
$$+\left\{\frac{\zeta_0}{4}\left(\log\frac{\zeta_0+1}{\zeta_0-1}\right)^2-\left(\frac{1}{2}\frac{1}{\zeta_0^2-1}+1\right)\log\frac{\zeta_0+1}{\zeta_0-1}+\frac{\zeta_0}{\zeta_0^2-1}\right\}L(\mu,\zeta;\zeta_0)+\psi(\mu,\zeta;\zeta_0)\,. \tag{14c}$$

Here, for convenience's sake, we have put

$$L(\mu,\zeta;\zeta_0)=\sum_{m=0}^{\infty}(4m+3)P_{2m+1}(\mu)Q_{2m+1}(\zeta)\frac{Q_{2m+1}(\zeta_0)}{Q'_{2m+1}(\zeta_0)}\,, \tag{15}$$

$$2\psi(\mu,\zeta;\zeta_0)=\sum_{m=0}^{\infty}(4m+3)P_{2m+1}(\mu)\left\{Q_{2m+1}(\zeta)\int_{\zeta_0}^{\zeta}\frac{P_{2m+1}(\zeta_1)Q'_{2m+1}(\zeta_1)}{\zeta_1(\zeta_1^2-1)}d\zeta_1\right.$$
$$\left.+P_{2m+1}(\zeta)\int_{\zeta}^{\infty}\frac{Q_{2m+1}(\zeta_1)Q'_{2m+1}(\zeta_1)}{\zeta_1(\zeta_1^2-1)}d\zeta_1-Q_{2m+1}(\zeta)\frac{P'_{2m+1}(\zeta_0)}{Q'_{2m+1}(\zeta_0)}\int_{\zeta_0}^{\infty}\frac{Q_{2m+1}(\zeta_1)Q'_{2m+1}(\zeta_1)}{\zeta_1(\zeta_1^2-1)}d\zeta_1\right\}$$
$$-2\sum_{m=0}^{\infty}(4m+3)P_{2m+1}(\mu)\left\{Q_{2m+1}(\zeta)\int_{\zeta_0}^{\zeta}\frac{P_{2m+1}(\zeta_1)Q_{2m+1}(\zeta_1)}{(\zeta_1^2-1)^2}d\zeta_1\right.$$
$$\left.+P_{2m+1}(\zeta)\int_{\zeta}^{\infty}\frac{Q^2_{2m+1}(\zeta_1)}{(\zeta_1^2-1)^2}d\zeta_1-Q_{2m+1}(\zeta)\frac{P'_{2m+1}(\zeta_0)}{Q'_{2m+1}(\zeta_0)}\int_{\zeta_0}^{\infty}\frac{Q^2_{2m+1}(\zeta_1)}{(\zeta_1^2-1)}d\zeta_1\right\}\,. \tag{16}$$

In particular, the velocity distribution on the surface of the body is given, correct to the order of M^2, by

$$\frac{V(\mu)}{q_\infty}=\frac{(1-\mu^2)^{1/2}}{q_\infty k(\zeta_0^2-\mu^2)^{1/2}}\left(\frac{\partial\Phi}{\partial\mu}\right)_{\zeta=\zeta_0}=V_0+V_1M^2\,, \tag{17}$$

where

$$\left.\begin{aligned}
V_0&=\frac{(1-\mu^2)^{1/2}}{(\zeta_0^2-\mu^2)^{1/2}}\frac{Q_0'(\zeta_0)}{Q_1'(\zeta_0)}\,,\\
V_1&=\frac{(1-\mu^2)^{1/2}}{(\zeta_0^2-\mu^2)^{1/2}}\left\{A\left(\frac{\partial\Phi_1'}{\partial\mu}\right)_{\zeta=\zeta_0}+A^2\left(\frac{\partial\Phi_1''}{\partial\mu}\right)_{\zeta=\zeta_0}+A^3\left(\frac{\partial\Phi_1'''}{\partial\mu}\right)_{\zeta=\zeta_0}\right\}\\
&=-\frac{Q_0'(\zeta_0)}{\{Q_1'(\zeta_0)\}^3}\frac{1}{(\zeta_0^2-\mu^2)^{1/2}}\left[\frac{(1-\mu^2)^{1/2}}{6Q_1'(\zeta_0)}\left\{\frac{1}{4}\left(\log\frac{\zeta_0+1}{\zeta_0-1}\right)^3-\frac{3\zeta_0}{2(\zeta_0^2-1)}\left(\log\frac{\zeta_0+1}{\zeta_0-1}\right)^2\right.\right.\\
&\left.\left.\quad+\left(\frac{15}{4}+\frac{3}{\zeta_0^2-1}\right)\log\frac{\zeta_0+1}{\zeta_0-1}+\frac{3\zeta_0(7-5\zeta_0^2)}{2(\zeta_0^2-1)^2}\right\}-\frac{Q_0'}{4\zeta_0}L^*(\mu,\zeta_0)+\frac{1}{4}N(\mu,\zeta_0)\right],
\end{aligned}\right\} \tag{18}$$

with

$$L^*(\mu,\zeta_0)=-(1-\mu^2)^{1/2}\frac{\partial L(\mu,\zeta_0)}{\partial\mu}=-(1-\mu^2)^{1/2}\sum_{m=0}^{\infty}(4m+3)P'_{2m+1}(\mu)\frac{Q^2_{2m+1}(\zeta_0)}{Q'_{2m+1}(\zeta_0)}\,, \tag{19}$$

$$N(\mu,\zeta_0)=-(1-\mu^2)^{1/2}\sum_{m=0}^{\infty}(4m+3)\frac{P'_{2m+1}(\mu)}{Q'_{2m+1}(\zeta_0)}\int_{\zeta_0}^{\infty}\frac{(\zeta_1^2+1)}{\zeta_1^2(\zeta_1^2-1)^2}Q^2_{2m+1}(\zeta_1)d\zeta_1\,. \tag{20}$$

The summation of two infinite series in (19) and (20) seems to be almost intractable, and therefore recourse must be had to numerical calculations. In the following sections we shall consider two typical cases in which the thickness-ratio of the spheroid is equal to 0.9 and 0.1 respectively.

§ 4. Case of a Thick Spheroid for which $t=0.9$

In the first place we shall consider the case of a thick prolate spheroid whose thickness-ratio is nearly equal to unity. In this case, the spheroid does not differ much from a sphere in shape and the eccentricity e, is fairly small. Therefore we are able to expand various terms in (19) and (20) into power series in e. Thus, we obtain

$$L^*(\mu,\zeta_0)=\frac{P_1^1(\mu)}{2}\left(e\qquad-\frac{12}{175}e^5-\frac{184}{2625}e^7-\frac{20964}{336875}e^9\right)$$

$$
\begin{aligned}
&+\frac{P_3{}^1(\mu)}{10}\left(e^3+\frac{5}{9}e^5+\frac{25}{81}e^7+\frac{6065}{34749}e^9\right)\\
&+\frac{4P_5{}^1(\mu)}{189}\left(e^5+\frac{14}{13}e^7+\frac{791}{845}e^9\right)\\
&+\frac{2P_7{}^1(\mu)}{429}\left(e^7+\frac{27}{17}e^9\right)\\
&+\frac{64P_9{}^1(\mu)}{60775}\left(e^9\right)+0(e^{11})\,, \qquad (21)
\end{aligned}
$$

$$
\begin{aligned}
N(\mu,\zeta_0)=&\frac{P_1{}^1(\mu)}{14}e^4\left(1+\frac{31}{15}e^2+\frac{4277}{1925}e^4+\frac{988\,627}{375\,375}e^6+\frac{105\,238\,223}{39\,414\,375}e^8\right)\\
&+\frac{P_3{}^1(\mu)}{110}e^6\left(1+\frac{322}{117}e^2+\frac{149\,711}{34\,749}e^4+\frac{9\,851\,884}{1\,772\,199}e^6\right)\\
&+\frac{P_5{}^1(\mu)}{2\,835}e^8\left(1+\frac{739}{221}e^2+\frac{343\,190}{54\,587}e^4\right)\\
&+\frac{2P_7{}^1(\mu)}{8\,151}e^{10}\left(1+\frac{464}{119}e^2\right)\\
&+\frac{64P_9{}^1(\mu)}{1\,397\,825}e^{12}+0(e^{14})\,. \qquad (22)
\end{aligned}
$$

The series for $N(\mu,\zeta_0)$ can also be rewritten in an alternative form as:

$$
\begin{aligned}
N(\mu,\zeta_0)=&\frac{1+e^2}{2(1-e^2)}e^3L(\mu,\zeta_0)\\
&-\frac{5P_1{}^1(\mu)}{28}e^4\left(1+\frac{148}{75}e^2+\frac{16\,472}{9\,625}e^4+\frac{2\,733\,452}{1\,876\,875}e^6+\frac{247\,638\,848}{197\,071\,875}e^8\right)\\
&-\frac{9P_3{}^1(\mu)}{220}e^6\left(1+\frac{2\,645}{1\,053}e^2+\frac{1\,007\,741}{312\,741}e^4+\frac{56\,380\,735}{15\,949\,791}e^6\right)\\
&-\frac{26P_5{}^1(\mu)}{2\,835}e^8\left(1+\frac{8\,722}{2\,873}e^2+\frac{3\,481\,289}{709\,631}e^4\right)\\
&-\frac{17P_7{}^1(\mu)}{8\,151}e^{10}\left(1+\frac{7\,185}{2\,023}e^2\right)\\
&-\frac{672P_9{}^1(\mu)}{1\,397\,825}e^{12}+0(e^{14})\,. \qquad (23)
\end{aligned}
$$

In these formulae $P_{2m+1}{}^1(\mu)$ denotes the associated Legendre function.

In case when $t=0.9$, we have

$$e=0.43589,$$

and the velocity distribution on the surface of the body is given by

$$
\begin{aligned}
\frac{V(\mu)}{q_\infty}=&\frac{1}{(1-0.19\,\mu^2)^{1/2}}[1.4403P_1{}^1(\mu)\\
&+M^2\{0.1499P_1{}^1(\mu)-0.0753P_3{}^1(\mu)\\
&-0.0033P_5{}^1(\mu)-0.0001P_7{}^1(\mu)\}]\,.
\end{aligned}
$$

Figure 1 shows the velocity distribution for the case with $M=0$ (incompressible flow) and $M=0.6$ with the difference between these two values. In this figure are also shown for comparison the velocity distributions for the cases of a sphere[2)] and a Rankine ovoid whose thikness-ratio is 0.9.[3)]

In the limiting case $e\to 0$, we get, from (17), (18) and (21),

$$
\begin{aligned}
\frac{V(\mu)}{q_\infty}=&\frac{3}{2}P_1{}^1(\mu)+\left\{\frac{7}{40}P_1{}^1(\mu)\right.\\
&\left.-\frac{81}{880}P_3{}^1(\mu)\right\}M^2+\cdots
\end{aligned}
$$

and it is seen that, as should be expected, this result is in accord with the known result for a sphere[2)].

The critical velocity q_* in the field of flow, which is defined as that value equal to the local sound velocity, is connected with the Mach number M by the relation

$$\left(\frac{q_*}{q}\right)^2=\frac{(\gamma-1)M^2+2}{(\gamma+1)M^2}\,,$$

and it is easy to calculate the so-called critical Mach number M_{crit} graphically, since it is plausible that the maximum fluid velocity appears at the end of minor-axis of the spheroid. For present case, taking the fluid to be air for which $\gamma=1.405$, we get $M_{\text{crit}}=0.615$. It will be of some interest to compare this value with the corresponding one for a sphere, which, to the first approximation is given by $M_{\text{crit}}=0.587$[2].

§ 5. Case of a Thin Spheroid for which $t=0.1$

The thinner the spheroid is, the nearer ζ_0 tends to unity, so that the evaluation of the series in (19) becomes difficult. Therefore only the maximum velocity at the end of minor-axis of the spheroid has been calculated. When ζ_0 is nearly equal to unity, the series in (19) becomes poorly convergent, but fortunately it turns out to be an alternating series at the point $\mu=0$ under consideration and we can apply Euler's summation formula:[6]

$$\sum_{n=0}^{\infty}(-1)^n a_n=\sum_{n=0}^{\infty}\frac{1}{2^{n+1}}\varDelta^n a_0\,,$$

where

$$\varDelta^0 a_k=a_k,\quad \varDelta^n a_{k+1}-\varDelta^n a_k=\varDelta^{n+1}a_k\,.$$

For evaluating the definite integral in (20) the range of integration may be conveniently divided into two parts, one is the integral from ζ_0 to a certain appropriate value, say 2, and the other from 2 to infinity. The latter integral can be evaluated without difficulty, since, the integrand can be expanded in series of $1/\zeta_1$, but the former can only be calculated by numerical integration, by calculating the values of the integrand at various points by the use of Euler's summation formula. For the prolate spheroid for which $t=0.1$, we have

$$\zeta_0=1.005078,\quad L^*(0,\ \zeta_0)=0.04126.$$

Thus, dividing the range of integration (ζ_0, 2) into appropriate twelve parts, all of wnich are not however necessarily equal, and approximating the curve of the integrand by suitable parabolas in each part, we get, after some laborious numerical integrations,

$$N(0,\ \zeta_0)=-3.02,$$

with the relative error less than 1%.

Thus we get finally the expression for the velocity at the end of the minor-axis of the spheroid in the form:

$$\frac{V(0)}{q_\infty}=1.02071+0.00462\,M^2+\cdots\,.$$

In this case, the critical Mach number is found to be

$$M_{\text{crit}}=0.972,$$

which may be compared with the value, $M_{\text{crit}}=0.962$, which has been obtained for the same body from the linear theory. (This value has been reestimated by the present author from Sears's note.[7]) A rather large difference between these two values seems to be due to the difference in the nature of convergence of the two methods.

Acknowledgements

The author wishes to express his cordial thanks to Prof. S. Tomotika for his continual encouragement throughout this work and for his kind inspection of the manuscript. The author's thanks are also due to Dr. K. Tamada and other members in the research group on hydrodynamics of a compressible fluid in the University of Kyoto, for their useful discussions and suggestions.

Finally, the author is indebted to the Ministry of Education for a grant in aid for fundamental scientific research.

APPENDIX

Numerical values of $P_n(z)$ and $Q_n(z)$

In order to perform numerical calculations in § 5 in the text it has been necessary to know numerical values of $Q_{2m+1}(z)$ for the range $1.00<z\leqq 2$. Thus we have calculated beforehand such numerical values together with those of $P_{2m+1}(z)$ because of the want of any available tables for this purpose.

To find values of $P_n(z)$ and $Q_n(z)$ of higher degrees, use has been made of the recurrence formulae:

$$\left.\begin{aligned}P_{n+1}(z)&=zP_n(z)+\frac{n}{n+1}\{zP_n(z)-P_{n-1}(z)\},\\ Q_{n+1}(z)&=zQ_n(z)+\frac{n}{n+1}\{zQ_n(z)-Q_{n-1}(z)\},\end{aligned}\right\}\qquad\text{(A 1)}$$

with

$$P_0(z)=1\,,\qquad Q_0(z)=\frac{1}{2}\log\frac{z+1}{z-1}\,,\qquad\text{(A 2)}$$

and the calculated values have been occasionally examined by the well-known Lommel's relation:

$$P_n(z)Q_{n-1}(z)-P_{n-1}(z)Q_n(z)=\frac{1}{n}\,.\qquad\text{(A 3)}$$

It may be added here that numerical values of $P_n'(z)$ and $Q_n'(z)$ can be conveniently calculated, when necessary, by using the other recurrence formulae:

$$\left.\begin{aligned}(z^2-1)P_n'(z)&=nzP_n(z)-nP_{n-1}(z)\,,\\(z^2-1)Q_n'(z)&=nzQ_n(z)-nQ_{n-1}(z)\,.\end{aligned}\right\}\quad(\text{A }4)$$

Table I. Numerical Values of $P_n(z)$ $(P_0(z)=1)$.

$z=P_1$	P_2	P_3	P_4	P_5	P_6	P_7	P_8	P_9	P_{10}	P_{11}	P_{12}	P_{13}
✓(100/99)	1.01515	1.03042	1.05095	1.07691	1.10849	1.14592	1.18950	1.23956	1.29648	1.36069	1.43269	1.51304
✓(75/74)	1.02027	1.04075	1.06837	1.10341	1.14624	1.19729	1.25707	1.32620	1.40538	1.49544	1.59729	1.71199
✓(36/35)	1.04286	1.08663	1.14643	1.22354	1.31962	1.43674	1.57743	1.74476	1.94238	2.17463	2.44665	2.76449
1.01	1.03015	1.06075	1.10227	1.15532	1.22071	1.29943	1.39268	1.50187	1.62867	1·77505	1.94324	2.13587
1.02	1.06060	1.12302	1.20914	1.32157	1.46371	1.63992	1.85559	2.11741	2.43350	2.81377	3.27022	3.81733
1.03	1.09135	1.18682	1.32073	1.49917	1.73033	2.02487	2.39649	2.86263	3.44532	4.17236	5.07872	6.20837
1.04	1.12240	1.25126	1.43713	1.68858	2.02195	2.45790	3.02370	3.75509	4.69873	5.91539	7.48418	9.50800
1.05	1.15375	1.31906	1.55846	1.89025	2.34001	2.94280	3.74613	4.81401	6.23243	8.11681	10.62203	13.95588
1.06	1.18540	1.38754	1.68484	2.10464	2.68598	3.48357	4.57336	6.06038	8.08958	10.86093	11.65034	19.83868
1.07	1.21735	1.45761	1.81636	3.33222	3.06140	4.08440	5.51560	7.51707	10.31816	14.24348	19.75270	27.49715
1.08	1.24960	1.52928	1.95314	2.57348	3.46787	4.74972	6.58380	9.20897	12.97139	18.37286	26.14138	37.33407
1.09	1.28215	1.60257	2.09529	2.82891	3.90703	5.48416	7.78960	11.16311	16.10817	23.37134	34.06082	49.82316
1.10	1.31500	1.67750	2.24294	3.09902	4.38057	6.29258	9.14544	13·40879	19.79348	29.37649	43.79142	65.51893
1.125	1.39844	1.87207	2.63681	3.84188	5.72655	8.67134	13.28039	20.51297	31.89412	49.85172		
1.15	1.48375	2.07719	3.06753	4.68803	7.32766	11.63148	18.66867	30.21341	49.21449			
1.175	1.57094	2.29309	3.53696	5.64619	9.21537	15.26967	25.57754	43.19489	73.41280			
1.20	1.66000	2.52000	4.04700	6.72552	11.42364	19.69368	34.31508	60.27536				
1.25	1.84375	3.00781	5.19678	9.28650	16.95091	31.39048	58.73938					
1.30	2.03500	3.54250	6.53294	12.45307	24.23571	47.83787						
1.35	2.23375	4.12594	8.07221	16.31473	33.65212	70.38661						
1.40	2.44000	4.76000	9.83200	20.96864	45.62618							
1.45	2.65375	5.44656	11.83034	26.51994	60.64022							
1.50	2.87500	6.18750	14.08594	33.08203								
1.60	3.34000	7.84000	19.44700	49.73536								
1.70	3.83500	9.73250	26.07794									
1.80	4.36000	11.88000	34.15200									
1.90	4.91500	14.29750	43.85294									
2.00	5.50000	17.00000	55.37500									

Table II. Numerical Values of $Q_n(z)$.

z	Q_0	Q_1	Q_2	Q_3	Q_4	Q_5	Q_6	Q_7	Q_8	Q_9	Q_{10}	Q_{11}	Q_{12}	Q_{13}
$\sqrt{(100/99)}$	2.99322	2.00830	1.53102	1.22568	1.00749	0.84207	0.71200	0.60717	0.52118	0.44970	0.38967	0.33885	0.29554	0.25842
$\sqrt{(75/74)}$	2.84854	1.86772	1.39618	1.59749	0.88640	0.72828	0.60550	0.50783	0.42879	0.36398	0.31031	0.26551	0.22786	0.19607
$\sqrt{(36/35)}$	2.47789	1.51304	1.06281	0.78778	0.60106	0.46704	0.36750	0.29186	0.23343	0.18776	0.15171	0.12305	0.10012	0.08168
1.01	2.65165	1.67817	1.21660	0.92916	0.72985	0.58353	0.47230	0.38573	0.31271	0.26230	0.21786	0.18162	0.15189	0.12736
1.02	2·30756	1.35371	0.91740	0.65710	0.48488	0.36456	0.27766	0.21348	0.16533	0.12878	0.10078	0.07917	0.06240	0.04932
1.03	2.10730	1.17052	0.75480	0.51539	0.36290	0.26050	0.18949	0.13919	0.10300	0.07667	0.05734	0.04306	0.03244	0.02451
1.04	1.96591	1.04455	0.64654	0.42430	0.28733	0.19843	0.13891	0.09821	0.06996	0.05013	0.03610	0.02610	0.01893	0.01377
1.05	1.85679	0.94963	0.56727	0.35963	0.23538	0.15715	0·10638	0.07273	0.05011	0.03473	0.02419	0.01692	0.01187	0.00835
1.06	1.76806	0.87414	0.50586	0.31092	0.19736	0.12783	0.08395	0.05569	0.03723	0.02504	0.01693	0.01149	0.00782	0.00534
1.07	1.69340	0.81194	0.45647	0.27274	0.16835	0.10605	0.06774	0.04372	0.02843	0.01860	0.01223	0.00808	0.00535	0.00356
1.08	1.62905	0.75937	0.41566	0.24194	0.14552	0.08934	0.05562	0.03499	0.02218	0.01415	0.00907	0.00584	0.00377	0.00244
1.09	1.57255	0.71408	0.38125	0.21655	0.12713	0.07619	0.04631	0.02844	0.01760	0.01096	0.00686	0.00431	0.00272	0.00172
1.10	1.52226	0.67449	0.35177	0.19526	0.11204	0.06564	0·03901	0.02342	0.01417	0.00863	0.00528	0.00325	0.00200	0.00124
1.125	1.41661	0.59368	0.29354	0.15459	0.08420	0.04683	0.02642	0.01507	0.00866	0.00501	0.00291	0.00170		
1.15	1.33129	0.53099	0.25031	0.12576	0.06537	0.03470	0.01869	0.01017	0.00558	0.00308	0.00171			
1.175	1.26000	0.48050	0.21688	0.10439	0.05199	0.02645	0.01366	0.00712	0.00375	0.00198	0.00105			
1.20	1.19895	0.43874	0.19025	0.08801	0.04214	0.02061	0.01023	0.00513	0.00259	0.00132				
1.25	1.09861	0.37327	0.15057	0.06484	0.02891	0.01317	0.00609	0.00284	0.00134					
1.30	1.01844	0.32397	0.12253	0.04949	0.02070	0.00885	0.00384	0.00168						
1.35	0.95212	0.28536	0.10180	0.03880	0.01532	0.00618	0.00253	0.00105						
1.40	0.89588	0.25423	0.08595	0.03105	0.01162	0.00445	0.00173							
1.45	0.84730	0.22858	0.07352	0.02528	0.00900	0.00328	0.00121							
1.50	0.80472	0.20708	0.06357	0.02087	0.00710	0.00247								
1.60	0.73317	0.17307	0.04878	0.01471	0.00460	0.00147								
1.70	0.67496	0.14744	0.03848	0.01075	0.00311									
1.80	0.62638	0.12749	0.03102	0.00808	0.00218									
1.90	0.58504	0.11157	0.02545	0.00621	0.00157									
2.00	0.54931	0.09861	0.02118	0.00487	0.00116									

References

1) C. Kaplan: N. A. C. A. Tech. Note, No. 762 (1940).

2) K. Tamada: Proc. Phys.-Math. Soc. Japan **21** (1939) 743.

3) H. Hasimoto: J. Phys. Soc. Japan **6** (1951) 175.

4) C. Schmieden and K. H. Kawalki: N.A.C.A. Tech. Memo. No. 1233 (1949).

5) L. Poggi: L'Aerotecnica **12** (1932) 1579.

6) K. Knopp: *Theory and application of infinite series*. Second ed. (1947) 262.

7) W. R. Sears: Quart. App. Math. **4** (1946) 89.

JOURNAL OF THE PHYSICAL SOCIETY OF JAPAN Vol. 8, No. 2, MAR.—APR., 1953

Fatigue Fracture from the Standpoint of the Stochastic Theory

By Takeo YOKOBORI

Institute of Science and Technology, University of Tokyo

(Received July 18, 1952)

In the previous paper the author studied the statistical aspects of fatigue fracture. In this paper as a fundamental case experiments were carried out under the reversed tension and compression fatigue test. From the results the fluctuations of the number of repeated cycles to fracture were found to have marked characteristics, which are basic features of fatigue fracture. Theoretically the problems were treated as successive events such as of damage and fracture from the standpoint of the stochastic theory, and the theory is in good agreement with these experiments. Attempt has been made to interprete the physical meaning of the transition probability from the standpoint of rate process theory, and it seems to be understood as the reaction rate.

§ 1. Introduction

The author previously published the statistical theory of fatigue fracture,1) and showed that the fluctuations of the number of cycles sustained to fracture (fatigue life) have marked characteristics. In the present paper as a fundamental case experiments were carried out under the reversed tension and compression test, in which stress distribution is uniform and theoretical treatment is easier than in bending or torsion, Theoretically the problems were treated as successive events such as of damage and fracture from the standpoint of the stochastic theory.

§ 2. Experiments

The material used is mild steel with composition as shown in Table I, and annealed an hour at 850°C. From this material specimens were machined to have the same dimension and the same surface finish condition as possible. The dimensions of specimen are shown in Fig. 1. Tests were carried out with Haigh's uniform tension and compression fatigue testing machine, under the pure reversed stress (no mean stress).

Table 1. Composition of Specimen (%)

C	S_i	M_n	P	S	C_r	C_u
0.19	0.18	0.47	0.013	0.007	0.16	0.25

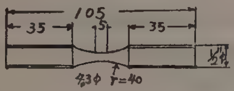

Fig. 1.

Experiment I: The tests were carried out upon the specimens with the same coarse paper finish. The frequency distribution curves of the number of repeated cycles to fracture are shown in Figs. 2, 3 and 4 corresponding to the constant stress range of 25.4, 24.3 and 22 kg/mm² respectively. For each series of test the number of specimens tested were 80∼102.

Experiment II: The tests were carried out upon the specimens with the same 0000 emery paper finish. The number of specimens were thirty, and the stress range was 24.3 kg/mm². The frequency distribution curve of the fatigue life is shown in Fig. 5.

Since the logarithms of the variable are found to obey approximately normal distribution in Figs. 2, 3 and 4, the upper and lower confidence limits of 90 per cent of the average number $\overline{N}$, of cycles to fracture can be obtained by this transformation. By this method $13\times10^4 \geqq \overline{N} \geqq 9.4\times10^4$ for the case of experiment II (Fig. 5), and $4.2\times10^4 \geqq \overline{N} \geqq 3.3\times10^4$ for the case of the same stress range but poorer surface finish (Fig. 3).

From experiment I and II and the previous experiments it can be understood that the frequency distribution curve of fatigue life has the following characteristics:

(a) It has the positive skewness.

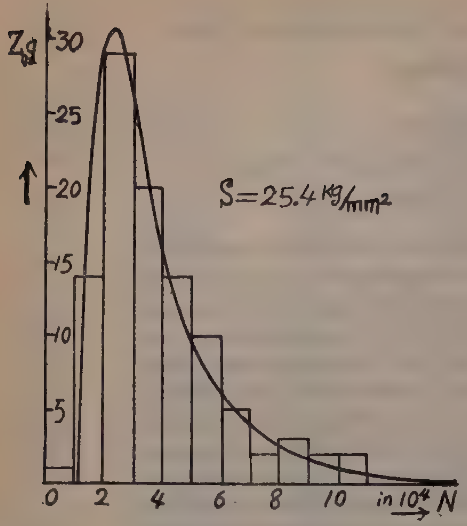

Fig. 2. Frequency distribution curve of the number of cycles to fracture.

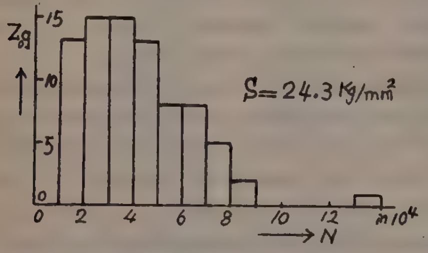

Fig. 3. Frequency distribution curve of the number of cycles to fracture.

(b) The width of scatter increases rapidly with the increase of stress range.

(c) It becomes almost the same curve if the scale of the number of repeated cycles are chosen suitably.

(d) The width of scatter is larger in well surface finished specimens than in poorer ones.

§ 3. The Stochastic Theory of Fatigue Fracture

It has been known by experiments[1][2][3] that in fatigue fracture process at first slip bands appear (as fatigue layer at last saturating in the case of non-uniform stress distribution such as bending or torsion), and then damage occurs, and at last fracture follows in the specimen. The author divided the whole process into the three stages. The three stages are:

i. From the instant of application of stress to the initiation of slip bands.

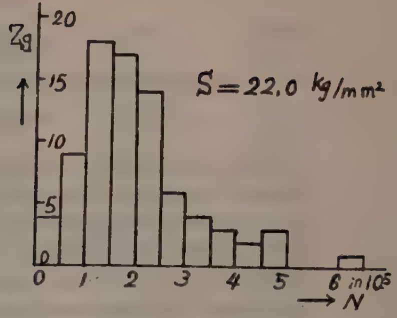

Fig. 4. Frequency distribution curve of the number of cycles to fracture.

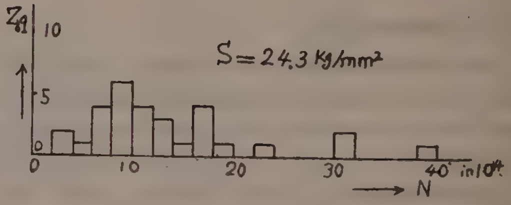

Fig. 5. Frequency distribution curve of the number of cycles to fracture.
(The effect of surface finish)

ii. From the initiation of slip bands to the beginning of damage.

iii. From the beginning of damage to fracture.

The average number of cycles $\bar{N}_s$ corresponding to the first stage may be considered much smaller than those of the second and the third from the experimental data.[1][2] Hence, the origin of the number of repeated cycles were measured from $\bar{N}_s$ without appreciable error. The fracture phenomena were taken as successive events of occurring of damage and fracture from the standpoint of stochastic theory.

If we denote

m_0=the probability of occurrence of damage in unit cycle

m=the probability of occurrence of fracture in unit cycle

and m_0 and m are almost independent of repeated cycles, then the probability of fracture occurrence between N and $N+dN$

after N repeated cycles assumes the form

$$qdN = mm_0/m_0 - m[\exp(-mN) - \exp(-m_0N)]dN. \quad (1)$$

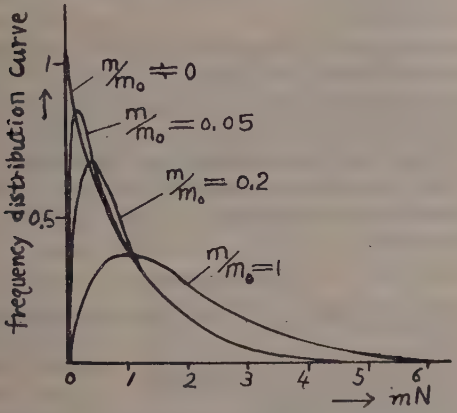

Fig. 6. Frequency distribution curves of the number of cycles to fracture (calculated). The effect of m/m_0.

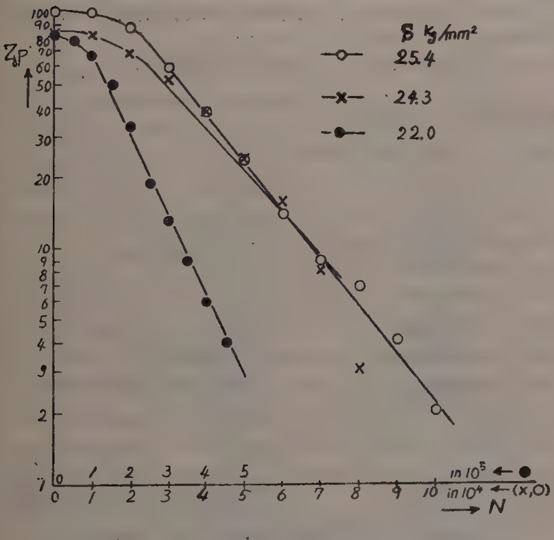

Fig. 7. The probability that the number of cycles to fracture will have a larger value than N.

On the other hand, it may be considered from the experiments that damage line–the relation between stress range and the number of repeated cycles to damage–lies very near the lower boundary[3)4)] of the scatter band of fracture curve, so-called "*N-S* curve", and the width of scatter of damag line seems to be much smaller[2)] than that of fracture line. Consequently, m may be said to be much smaller than m_0. The frequency distribution curves calculated from Eq. (1) are shown in Fig. 6 for various values of m/m_0. Chi-square method was used to test the fitness of these calculated curves to the experimental results. For example, the correctness of fit of the calculated curve with the value $m/m_0=0.2$ was checked for the observed results shown in Fig. 1 as follows. Table 2 gives the values observed and calculated. If the classes 1 to 2 and 6 to 11 are pooled, the degrees of freedom are 5−2=3. Then $\chi^2=1.031$ gives $P\{\chi^2 \geqq 1.031\} \doteqdot 0.8$. The agreement is very satisfactory. It can be understood that the frequency distribution curves do not assume the form $m\exp[-mN]$ exactly, but have the parts in which m apparently increases when assumed as a single events.*

Table 2

	N 10^4	Calculated values	Observed values
1	0.5	0	1
2	1.5	15	14
3	2.5	30	29
4	3.5	20	20
5	4.5	12	14
6	5.5	7	10
7	6.5	5	5
8	7.5	3.5	2
9	8.5	2.5	3
10	9.5	1.5	2
11	10.5	1	2

When m is far smaller than m_0 so that the second term in parentheses of Eq. (3) can be neglected, Eq. (1) corresponds to the curve with the parameter $m/m_0 \doteqdot 0$ in Fig. 6. In this case, from Fig. 7 plotted by the same method as applied in the previous paper,[1)] it can be seen that m is almost constant value over the most range of N concerned as assumed. In this case $\overline{N}$ is equal to m.

§ 4. Physical Interpretation of the Transition Probability

The initiation of damage seems to be understood as the nucleation process[5)] of crack nucleus and the nucleation rate seems to correspond to m_0, that is,[5)]**

$$m_0 = A_0 \exp\left\{-\left(\Delta f^* - \alpha S + \frac{\beta}{S^4}\right)\Big/ kT\right\}, \quad (2)$$

in which S represents tensile stress range.

---

* m may be expected to increase gradually with increase of N also by the increase of stress in the manner as shown in the reference (1).

** In reference (5). m_0 and A_0 are denoted by the letters, m and A, respectively.

On the other hand, the occurrence of fracture seems to be reaction rate process,⁽⁶⁾ that is, the growth process of a crack nucleus. If fracture are assumed to occur when a pair of atoms more are separated after a crack nucleus of a critical size⁽⁷⁾ has been nucleated, then we can written the transition probability as the form⁽⁶⁾:

$$A_f \exp(-\Delta F/kT) \exp(\alpha_f S/kT)\,, \qquad (3)$$

in which ΔF is the free energy of activation, and A_f is a constant. When the logarithms of m determined from Fig. 7 are plotted against each stress range, roughly linear relations are obtained between them as shown in Fig. 8, which is predicted by the formula (1). Since the density of the weak spots as the origins of crack nucleus may be said to be much larger than that of the nucleated crack with a critical size, A_0 may be considered to be much larger than A_f. Hence, when the difference of other factor in Eq. (2) and the formula (3) are not so conspicuously, m_0 may be larger than m, which is in agreement with experiments.

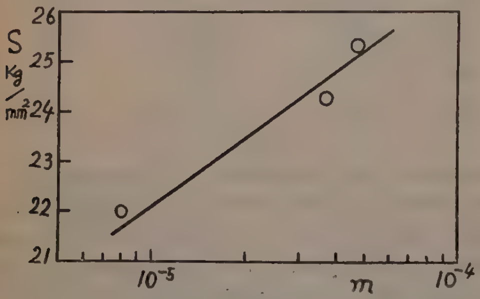

Fig. 8. The relation between m and stress range S.

Since α_f contains the stress concentration factor of the weak spots associated with rate process, α_f should be larger in coarse finished specimens than in well finished ones. Therefore, in well finished specimens m is smaller, that is, $\bar{N}$ and the scatter of N are are larger than in poor finished ones, which is qualitatively in good agreement with this experiment.

In conclusion the author wishes to express sincere thanks to Prof. M. Hirata for his encouragement, Prof. K. Ômori for his kind advice and communication, and for Prof. F. Nakanisi for his kindness for this work.

This work was supported by the Scientific Research Expenditure of the Ministry of Education.

References

1) T. Yokobori: J. Phys. Soc. Japan, **6** (1951) 81.

2) H. B. Wishart and S. W. Lyon: Trans. Am. Soc. Metals, **25** (1937) 690

3) To be published.

4) J. B. Johnson and T. T. Oberg: Metals & Alloys **9** (1938) 259.

5) T. Yokobori: Proceedings of the First Japan National Congress for Applied Mechanics **1** (1951) 97.

6) T. Yokobori: J. Phys. Soc. Japan **7** (1952) 122.

7) T. Yokobori: Ibid. **7** (1952) 44.

Errata to Reference (1), (6) and (7)

Vol.	P.	Col.	Line	Should be read	
6	84	left	1	are	area
6	85	right	12	$\sqrt{ydy}$	ydy
6	86	right	16	Kchle	Kohle
7	44	left	22	Yielding the	Yielding, the
7	44	left	40	racius	radius
7	45	left	3	proceis	process
7	45	left	4	$1-P$	$1-p$
7	45	left	31	relaxatio	relaxation
7	45	right	16	invelving	involving
7	46	left	3	Zener	Zener and Hollomon
7	46	left	24	speciment	specimen
7	46	right	9	q	Q
7	46	right	Fig. 2	S	x
7	46	right	Fig. 2	q	Q
7	47	right	28	Zener,	Zener and J.H. Hollomon,
7	122	right	35	$-dz/dt$	$-dZ/dt$
7	122	right	43	$\exp[v\exp(\Delta H/kT)]$	$\log[v\exp(\Delta H/kT)]$ +const.

Errata to Reference (5)

P.	Col.	Line	should be read	
97	left	25	the rate of cracks	the rate of nucleation of cracks in unit cycle
98	left	22	$\frac{1}{2}\sigma_{wb}(1+2\cos 2\varphi)$	$\frac{1}{2}\sigma_{wb}(1+\cos 2\varphi)$

J. PHYS. SOC. JAPAN 8 (1953) 269~270

The change of the refractive index of semi-conducting film irradiated by intense light

By Kozo ISHIGURO

Department of Physics, Faculty of General Education, University of Tokyo, Komaba, Tokyo

(Received November 14, 1952)

The difference of the optical path length in a semi-conducting film deposited on a glass substrate and in an air layer of equal thickness can be determined easily from the shift of interference fringes formed with a double slit interferometer of Rayleigh-Röwe type.[1] In the course of such measurements by the writer, it was found that there occured some additional shift of the interference fringes when the film was irradiated with intense white light of an incandescent tungsten lamp (500 watt). The shift occured usually in the direction indicating an increase of the refractive index of the film. As the same effect was also observed by irradiation with quartz mercury lamp (of high pressure type, 250 watt), this phenomenon can not be attributed to the effect of the temperature rise of the film by absorption of the energy of the incident light and may be a more essential optical property of semi-conducting materials.

Fig. 1 shows the effect observed with films of Germanium, Cadmium sulfide and Zinc sulfide. These films were prepared by evaporation in a vaccum of the order 1×10^{-4} mmHg. The thicknesses of them were determined by the multiple beam interference method of Tolansky,[2] and were 0.375 μ(Ge), 0.300 μ(ZnS) and 2.31 μ(CdS). The additional Ag film to cause the multiple reflections for the measurement of thickness was evaporated on the specimen after the effect of the irradiation of light had been observed.

Neglecting the multiple reflections within the film for the first approximation, the amount of the change of the refractive index of the film by the irradiation of light was obtained from the observed shift of the fringes by the following equations,

$$l(n-1)=\lambda\Delta$$

or

$$l\delta n=\lambda\delta\Delta$$

and hence, $\delta n/n=(1-1/n)\delta\Delta/\Delta$.

Here n is the refractive index of the film and $\lambda\Delta$ the difference of the optical path length in the film and in the air layer of equal thickness, λ being the wave length in air, while δn and $\lambda\delta\Delta$ are their changes caused by the irradiation of light. In Fig. 1, $\delta n/n$ in percentage are given for different conditions of irradiation. The wave length used in the observation was always $\lambda=0.59\,\mu$ and the refractive indices of Ge, CdS and

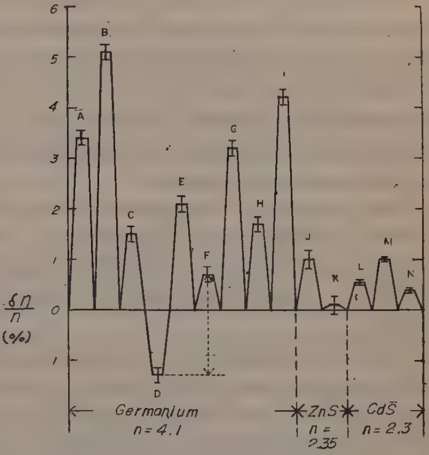

Fig. 1. The change of the refractive indices of Ge, ZnS and CdS by irradiation of intense light.

The conditions of irradiation for cases given in Fig. 1.

When not specially remarked, the light is projected from the air side of the film. The intensities of the tungsten lamp and the mercury lamp on the surface of the film were 10 watt/cm² and 5 watt/cm² respectively by rough estimation.

- (A) Tungsten lamp (projected from the air side of the film).
- (B) Tungsten lamp (projected from the glass side of the film).
- (C) Tungsten lamp with an infra-red cut-off filter by which the longer wave lengths than 7000 A are cut off.
- (D) Nichrom wire heater, by which the mercury thermometer placed at the position of the film was warmed up to indicate 80°C.
- (E) Tungsten lamp from behind the unheated nichrom wire heater.
- (F) Simultaneous action of the tungsten lamp and the nichrom wire heater.
- (G) Quartz mercury lamp of high presure type.
- (H) Quartz mercury lamp with a ultra violet cut-off filter by which the shorter wave lengths than 3800 A are cut off.
- (I) Quartz mercury lamp (projected from the glass side of the film).
- (J) Quartz mercury lamp.
- (K) Quartz mercury lamp with ultra violet cut-off filter.
- (L) Tungsten lamp.
- (M) Quartz mercury lamp.
- (N) Quartz mercury lamp with a green filter which transmitts only $\lambda=5461$A of mercury.

ZnS were assumed to be 4.1, 2.3 and 2.35 respectively.

The results of the present experiments are summed up as follows:

(1) The refractive index of a semi-conducting film increases usually by the irradiation of light.

(2) In general, the effect is larger for the irradiation from the glass substrate side than for the irradiation from the air side of film. (Compare (A) and (B), (G) and (I) in Fig. 1)

(3) The time lag is very large and is of the order of serveral tenth seconds.

(4) The change of the refractive index of ZnS which is transparent in region of visible rays is caused by the irradiation of light of shorter wave length than 3800 A. (Compare (J) and (K))

(5) While the irradiations with tungsten lamp and with mercury lamp cause effect of the same order for Ge film, for which the absorption edge lies in region of infra-red ((A) and (G)), the same mercury lamp exhibits about 2 times larger effect than the tungsten lamp for CdS film of which the absorption is observed only for the shorter wave length region than 5000 A ((L) and (M)).

(6) The heating with a nichrom wire heater causes the shift of the fringes in the opposite direction, as if the refraction index of the film decreased. From this fact it may be concluded that the shift of the fringes by irradiation is not due to temperature rise of the film (D).

(7) Simultaneous effect of the nichrom wire heater and the tungsten lamp is almost equal to the algebraic sum of the independent effects of the nichrom wire heater and the tungsten lamp. ((E)+(D)=(F))

The results of the more quantitative measurements of these effects will be reported in future. The writer wishes to thank Dr. G. Kuwabara for his several helpful suggestions. The study was aided by the Grant in Aid for Fundamental Scientific Research.

References

1) F. Kohlausch: "Praktische Physik" (B. G. Teubner, Berlin, 1935) p. 398.
K. Ishiguro: J. Phys. Soc. Japan 5 (1950) 187.

2) S. Tolansky: "Multiple-beam interferometry of surface and film".
(Oxford university press 1948)

J. PHYS. SOC. JAPAN 8 (1953) 270~271

Fine and Hyper-fine Structure of Paramagnetic Resonance Spectra in Several Diluted Manganese Salts

By Izuo HAYASHI and Kazuo ÔNO

Institute of Science and Technology, University of Tokyo

(Received November 19, 1952)

Fine and hyperfine structure of the paramagnetic resonance spectra in diluted manganese salts have been studied by several authers. Bleaney and Ingram1) have studied on diluted $MnSiF_6 \cdot 6H_2O$ and $Mn(NH_4)_2(SO_4)_2 \cdot 6H_2O$ whose theory being developed by Abragam and Pryce2). Schneider and England3) have made measurements on diluted MnS and solution of Mn^{++}, and Tinkham and others4) on solution of Mn^{++}.

We have observed these structures in some other manganese salts, and some results on manganese acetate have been reported5), which has a typical fine structure in rhombic crystalline field.

The spectrum has been analysed in terms of the usual Hamiltonian

$$H=g\beta \boldsymbol{HS}+D\{S_z^2-\tfrac{1}{3}S(S+1)\}+E(S_x^2-S_y^2)$$
$$+F(a)+AS_zI_z+B(S_xI_x+S_yI_y)$$

where the notations are the same with Bleaney and Ingram. Values of D, E, A and B are shown in Table for five kinds of diluted manganese salts, in which signs of A and B can not be determined by our measurements, but we assumed that these values are negative.

Results for $Mn(NH_4)_2(SO_4)_2 \cdot 6H_2O$ and $MnSiF_6 \cdot 6H_2O$ agree with Bleaney and Ingram except that A and B in $MnSiF_6 \cdot 6H_2O$ are smaller than results of Bleaney and Ingram at room temperature by about 4%, the difference being above experimental error. Values of A in Mn^{++} solutions obtained by Schneider and England (98 gauss)3), and Tinkham, Weinstein and Kip4) (95 gauss) coincide with our values in $Mn(NH_4)_2 \cdot (SO_4)_2 \cdot 6H_2O$, $MnSiF_6 \cdot 6H_2O$ and $MnSO_4 \cdot 7H_2O$ crystals, but these are different from that in $Mn(CH_3COO)_2 \cdot 3H_2O$. The value of A for diluted MnS (phosphorescent ZnS) obtained by England and Schneider6)3) is 68 gauss, and agrees with our result. The hyperfine structure is nearly isotropic for all cases.

For salts studied by us, the g value is 2.000 ± 0.005 and isotropic within experimental error.

In manganese acetate [$Zn(CH_3COO)_2 \cdot 3H_2O$], the z and x directions of the crystalline field are respectively c and b axes of the crystal symmetry. In manganese sulphate, [$MgSO_4 \cdot 7H_2O$, rhombic, $a{:}b{:}c=0.9901{:}1{:}0.5709$7)], an unit cell

Table

	D (gauss)	E (gauss)	A (gauss)	B (gauss)	a (gauss)
$Mn(CH_3COO)_2\cdot 3H_2O$	252	27	−89.8	−90.8	—
$Mn(NH_4)_2(SO_4)_2\cdot 6H_2O$	256	≈80	−97.5	—	5
$MnSiF_6\cdot 6H_2O$	−183	0	−96.1	−95.0	8
$MnSO_4\cdot 7H_2O$	428	~0	−94.7	—	—
MnS (powder)	~0	~0	−69.0	—	—

contains four ions and direction cosines of the z-directions to a, b and c axes are (0.282, 0.952, 0.122) (0.282, 0.952, −0.122) (−0.282, 0.952, 0.122) (−0.282, 0.952, −0.122). The crystalline field in this case is very nearly axially symmetric.

Salts were diluted with Zn ions with an exception of $MnSO_4\cdot 7H_2O$, which was diluted with Mg ions. The wave length of microwaves was 3.0 cm and measurements were done at room temperature. The magnetic field was modulated by a small amount with 2.5 KC, and the crystal detector out-put was amplified and detected by a phase sensitive detector. The magnetic field was calibrated by proton resonance.

The authors are indebted to Assist. Prof. K. Oshima of our institute for offering us samples of manganese activated fluorescent ZnS, and they express their thanks to Prof. H. Kumagai for his encouragements and discussions.

References

1) B. Bleaney and D. J. E. Ingram: Proc. Roy. Soc. **A 205** (1951) 336.

2) A. Abragam and M. H. L. Pryce: Proc. Roy. Soc. **A 205** (1951) 135.

3) E. E. Schneider and T. S. England: Physica **17** (1951) 221.

4) M. Tinkham, R. Weinstein and A. F. Kip: Phys. Rev. **84** (1951) 848.

5) H. Kumagai, K. Ôno, I. Hayashi and K. Kambe: Phys. Rev. **87** (1952) 374.

6) T. S. England and E. E. Schneider: Nature **166** (1950) 437.

7) P. Groth: *Chemische Crystallographie*, 2 teil, p. 428.

J. PHYS. SOC. JAPAN **8** (1953) 271~272

Diffusion accompanied with Absorption of the Langmuir Type

By Hiroshi FUJITA

Department of Fisheries, Faculty of Agriculture, Kyoto University, Maizuru, Japan

(Received November 20, 1952)

In a recent paper3) the author showed that the unidimensional diffusion equation with a concentration-dependent diffusion coefficient, $D(C)$, of the form

$$D(C)=\frac{D(0)}{(1-\lambda C)^2} \quad (\lambda\geqq 0) \qquad (1)$$

can be integrated formally in a semi-infinite medium under the conditions that the medium is initially free from diffusing substance and its surface is maintained at a constant concentration throughout the process. This form of the concentration dependence of $D(C)$ is interesting not only theoretically but also practically, since it gives a $D-C$ plot resembling rather closely the types which are often observed in many polymer-solvent systems. In fact, it was shown in the paper3) that the $D-C$ data obtained by Crank and Park,2) and later by Park,4) for the system polystyrene-chloroform can be well represented by equation (1). The purpose of the present paper is to consider in what case this type of the concentration dependence is expected to be obtained in a polymer-solvent system.

It is generally considered that when a solvent is allowed to penetrate into a high-polymeric solid, the solvent molecules diffuse freely along capillaries within the solid and are concomitantly absorbed into the meshes of the polymer network to be immobilized there. Taking, for example, one-dimensional case, this process may be represented by the equation of diffusion with absorption of the form

$$\frac{\partial C}{\partial t}=K\frac{\partial^2 C}{\partial x^2}-\frac{\partial S}{\partial t}, \qquad (2)$$

where x is the distance measured in the direction of diffusion, t is the time, C is the over-all concentration of solvent free to diffuse, and S is the over-all concentration of solvent absorbed; K is the diffusion coefficient of freely diffusing solvent and is assumed here to be constant. When the rate of absorption is much greater than that of free diffusion (this condition is usually realized), C and S are connected by a relationship called the isotherm. If an isotherm of the Langmuir type governs the process of absorption, the following equation should hold:

$$S=\frac{C}{\alpha+\beta C}, \qquad (3)$$

where α and β are constants dependent on conditions of the system concerned. According to Crank's paper[1)] concerning the mathematical theory of dyeing process of fibers, in some cases it may be sufficiently accurate to neglect the term $\partial C/\partial t$ completely and to write equation (2) in the form

$$\frac{\partial S}{\partial t}=K\frac{\partial^2 C}{\partial x^2}\,. \qquad (4)$$

Solving equation (3) for C, and inserting the resultant equation into equation (4), there results an equation of the form

$$\frac{\partial S}{\partial t}=\frac{\partial}{\partial x}\left[\frac{K\alpha}{(1-\beta S)^2}\frac{\partial S}{\partial x}\right], \qquad (5)$$

which is the equation of simple diffusion when the diffusion coefficient has the form given by equation (1). Thus, so far as the neglect of the term $\partial C/\partial t$ in equation (2) is permitted, diffusion with absorption of the Langmuir type may be represented as simple diffusion with the concentration-dependent diffusion coefficient of the form of equation (1). It may be inferred on this basis that the strongly concentration-dependent diffusion coefficients found in Crank and Park's work[2)] for the polystyrene-chloroform system were resulted from a strong absorbing power of polystyrene to chloroform. It is interesting to note that the special form of the diffusion coefficient given by equation (1) has a correlation to the well-known Langmuir type of absorption isotherm.

Literature Cited

1) J. Crank: Phil. Mag. **39** (1948) 140.
2) J. Crank and G. S. Park: Trans. Faraday Soc. **45** (1949) 240.
3) H. Fujita: Textile Research J. **22** (12) (1952) (in press).
4) G. S. Park: Trans. Faraday Soc. **46** (1950) 684.

J. PHYS. SOC. JAPAN 8 (1953) 272~273

Some Experimental Studies of the Conductivity and Thermo-electromotive Force of Cs_3Sb Photo-Cathodes II

By Toshimichi SAKATA
The Electrical Communication Laboratory

(Received December 10, 1952)

As mentioned in the previous report[1)], the sign of thermo-electromotive force (T.E.M.F.) showed the P-type semiconductivity for Cs_3Sb photo-cathodes in the temperature range from 283° to 343°K. In order to confirm further quantitative results, the measurements have been extended towards somewhat lower temperature ranges.

The measurements of the T.E.M.F. in the range of the low temperatures were performed with the well known method, using the UX-54A amplifier. A great precaution was paid to avoid unavailable small leakage current (~10^{-12} ampere).

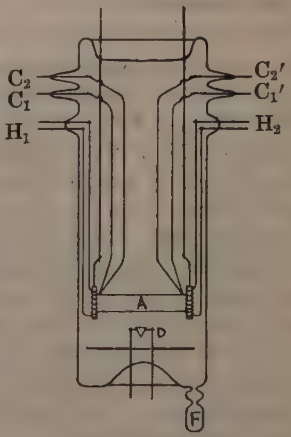

Fig. 1.

A: a plain glass plate of rectangular form, 10mm in width and 30mm in length.
H_1, H_2: local heaters.
C, C′: Cu-constantan thermo-junctions, both 0.025mm in diameter, attached to behind the plate A.
D: evaporation cup of Sb.
F: Cs pellet.

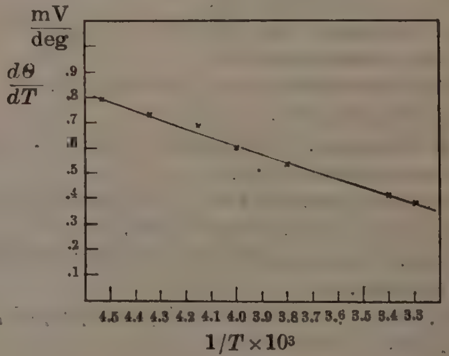

Fig. 2.

The construction of experimental vacuum tube shown in Fig. 1 was nearly the same as described in the previous paper[1)], except that the tube form was changed for the convenience of cooling. A typical example of the temperature dependency of $d\theta/dT$ is shown in Fig. 2. In all cases, the sign of T.E.M.F. showed the P-type, and the magnitude ranged from 0.37 to 0.80 mV/deg in the temperature range from 303°K to 221°K. The chemical potential ζ_s', evaluated from the equation

$$d\Theta/dT=-\left(\frac{k}{e}\right)\left(2+\frac{\zeta}{kT}\right),$$

had values of 0.17–0.21 eV.

The activation energy $\varDelta E/2$ of the conductivity measured simultaneously were 0.20 eV. in the same temperature range (Fig. 3). Using the relation

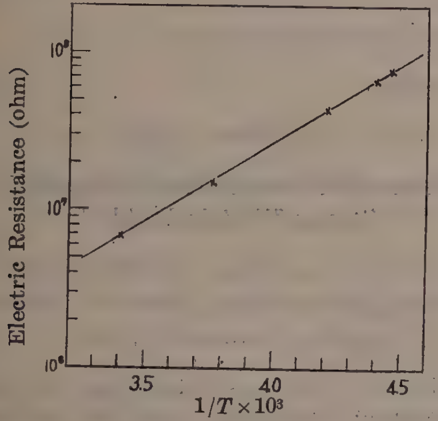

Fig. 3.

$$\zeta=\frac{\varDelta E}{2}-\frac{kT}{2}\log\frac{n_b h^3}{2(2\pi mkT)^{3/2}},$$

the atomic concentration n_b of acceptors was estimated at various temperatures as shown in Table I.

Table I.

Temp (°K)	T.E.M.F. $d\Theta/dT$ (mV/deg)	ζ (eV)	n_b (1/cm³)	$\frac{\varDelta E}{2}$ (eV)
303	0.39	0.17_0	$>1.3\times10^{19}$	0.20
293	0.42	0.17_3	〃	〃
283	0.45	0.17_6	〃	〃
273	0.50	0.18_3	〃	〃
263	0.54	0.18_7	〃	〃
253	0.59	0.19_3	〃	〃
243	0.65	0.19_9	〃	〃
233	0.71	0.20	〃	〃
223	0.78	0.21	〃	〃

Borzyak[2)] has found that the conduction in the dark is due to the positive holes unless excess Cs is introduced. Therefore, acceptor levels in the present case are probably related to the stoichiometric excess of Sb. It would be reasonable that there is no appreciable discrepancy between the magnitude of T.E.M.F. and the activity. It is insufficient to draw further conclusions as to the electronic state of the substance only from the T.E.M.F. data. The author is intending to undertake the experiments on the Hall effect and the optical properties of this substance.

The author expresses his sincerest gratitude to Dr. H. Miyasawa of Tokyo-Shibaura Electric Company for his helpful guidance and discussions throughout this work.

References

1) T. Sakata: Journ. Phys. Soc. Jap. **8** No. 1 (1953) 236.

2) P. G. Borzyak: Zhur. Tekh. Fiz **20** (1950) 923. (See Chem. Abstract **45** (1951) 437)

J. PHYS. SOC. JAPAN **8** (1953) 273~274

Auger and Conversion Lines from RaD

By Yoshiyuki KOBAYASHI and Gorō MIYAMOTO

Department of Physics, Faculty of Science,
University of Tokyo

(Received December 12, 1952)

With a view to studying conversion lines and beta-rays of RaD, the low energy portion of the spectrum was examined using the spherical condenser type spectrometer[1)]. A source of RaD with its daughters was prepared by electrolysis and by evaporation in a high vacuum. The source backing and the counter-window were zapon films of about 30 and 20 μg/cm² thickness respectively. The spectrum was measured from 3 to 50 kev, and the result below 22 kev is shown in Fig. 1. In order to eliminate contributions from RaE and polonium, a source of RaE+Po prepared by the similar procedures was also examined under the same conditions, and we could not find any line below 50 kev. The intensity of

Table 1. Classification of the observed lines.

Observed lines or bumps (kev)	X-rays or γ-rays corresponding to the observed lines		
	Radiations	Energy (kev)	Transitions
7.0, 7.5, 8.1	L_{α_1} [a)]	10.8	L_{III}—M_V
9.2, 9.7, 10.3	L_{β_1} [b)]	13.0	L_{II}—M_{IV}
	L_{β_2}	13.0	L_{III}—N_V
	L_{β_3}	13.3	L_I—M_{III}
	L_{β_4}	12.7	L_I—M_{II}
8.7	L_{β_4} ?	12.7	L_I—M_{II}
11.5~12.5	L_{γ_1} [c)]	15.3	L_{II}—N_{IV}
12.5~13.5	$L_{\gamma_2}, \ldots, \gamma_6$?	15.6~16.3	
5.5~6.6	L_l	9.4	L_{III}—M_I
11.0	γ-ray	27.4 ?	
4 ~ 5.1 ?	γ-ray	7 ~ 8	
14.5~16 ?			

a), *b*) See reference 2).

c) S. G. Cohen and A. A. Jaffe: Phys. Rev. **86** (1952) 800.

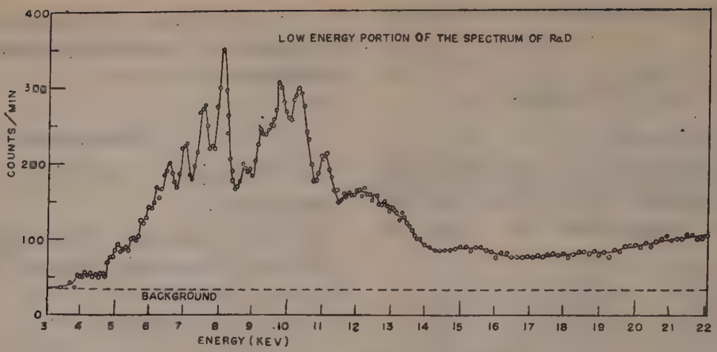

Fig. 1. Spectrum of RaD.

the L_1 conversion line due to the 46.7 kev gamma-ray was 2700 counts per minute.

Many lines were fouud below 14 kev, and most of them could be explained as Auger electrons. The observed lines and plausible origins of them are tabulated in Table 1. We can see in the table that there are much more vacancies in the L_{III} shell of bismuth than expected from ionization following internal conversion in RaD decay, and there must exist $L_{III}-L_I$ transition as pointed out by Salgueiro and Valadares from the study of X-reys2). The line at 11.0 kev can hardly be attributed to Auger electrons. If we assume it to be a L_1 conversion line, there might be a gamma-ray of the energy 27.4 kev. Since efficiency of the counter drops rapidly with energy below 6 kev, we cannot draw definite conclusions concerning this part of the spectrum, But a bump from 4 to 5.1 kev may be considered to be conversion lines due to the gamma-ray of the energy 7~8 kev reported by several authors3)4).

We could not find any line between 14 and 30 kev. The upper limit to intensities of lines in this region, relative to the L_1 conversion line will be about 1 per cent5).

On account of the existence of Auger electrons, we could not obtain any result about the primary beta-ray.

Details will be reported later.

References

1) Y. Kobayashi and G. Miyamoto: Journ. Phys. Soc. Jap. **8** (1952) 135.

2) L. Salgueiro and M. Valadares: Portugaliae Physica **3** (1949) 21.

3) S. T. Tsien: Phys. Rev. **69** (1946) 38.

4) S. C. Curran, J. Angus, and A. L. Cockroft: Phil. Mag. **40** (1949) 36.

5) L. Cranberg: Phys. Rev. **77** (1950) 155.

J. Phys. Soc. Japan **8** (1953) 274~277

Electronic Conductivities of Solids in Strong Electric Fields I

By Chiyoe Yamanaka and Tokuo Suita
Faculty of Engineering, Osaka University

(Received November 27, 1952)

It is one of the most interesting subjects in researches of insulation to study the prebreakdown phenomena of solids. We have reported on some behaviours of prebreakdown currents in solids1)2)3). In order to clarify the intrinsically electronic currents, we are now studying the pulse conduction of solids in strong electric fields.

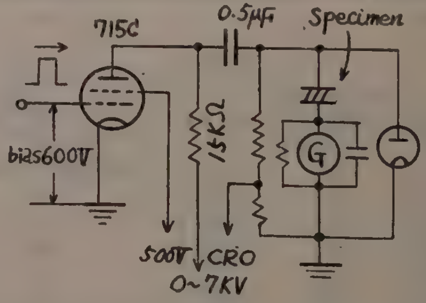

Fig. 1. The Measuring apparatus.

Our measuring apparatus are shown in Fig. 1. The pulser was constructed in the same way as the rader system. The properties of pulser were as follows, the pulse form: rectangular square pulse, the maximum pulse height: 7 KV, the pulse duration: 4~1000 μ sec, the pulse repetition: 10~100 cycles per sec. Applying the pulses of slow repetition rate to the specimens, we could measure the mean current by a galvanometer. To exclude the charging or absorbed currents we inserted a parallel resistance with the specimens.

The specimens were, polar crystals (single crystals of KCl, NaCl, KBr and some other mixed ionic crystals) and amorphous solids (soda lime glasses). The former were bored at the centers provided with electric guard rings. Their electrodes were prepared by sputtering of silver. The latter were in the form of bubbles blown from small tubes with mercury electrodes.

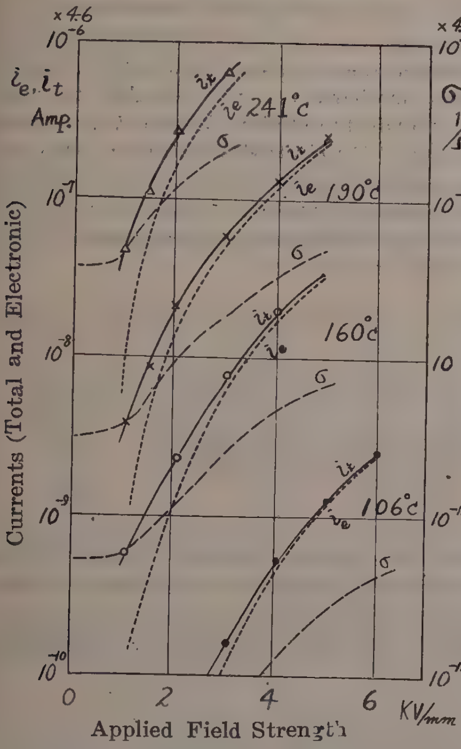

Fig. 2. The deviation from the ohm's law in strong D.C. field in KCl.

Fig. 2 shows the deviations from the Ohm's law in strong D.C. fields in KCl. The full lines are the observed total currents. The broken lines are the conductivities. The dotted lines are the electronic current components which are estimated from these deviations. In the D.C. fields the deviation began to appear at the field strength 1-2 KV/mm. At the higher temperatures these deviations appeared at the lower fields. In Fig. 3, 4 and 5 we can see the behaviours of the pulsed currents in KCl at various fields strengths and temperatures. At the lower temperatures when we applied the longer pulse, the more dominant influence of the ionic space charges seemed to exist and distort the internal fields. But at the higher temperatures we could not notice the ionic space charge effect in the current curves even in the D.C. field. When we used the shoter pulse than 10 μ sec duration we could measure the current in the ionic space charge free conditions. In KCl, the current-field curve seems to show the field emission type that was proposed by Schottky and Frenkel⁴⁾. But the applying external field is tenth smaller than that the theoretical relation

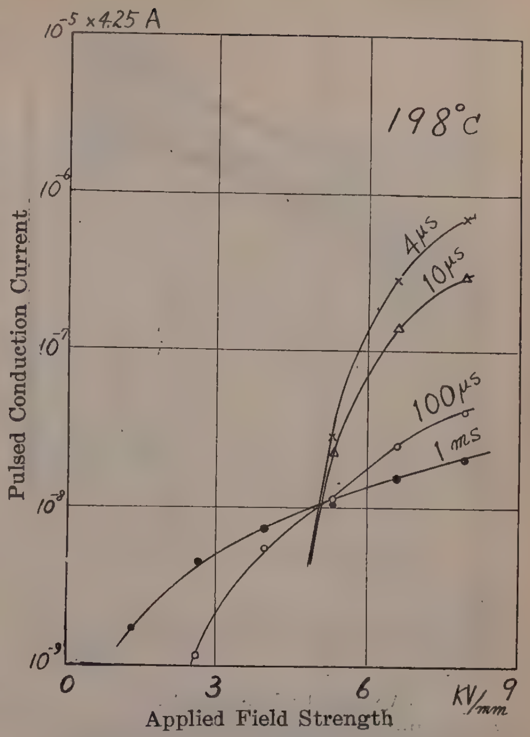

Fig. 3. Pulsed conduction current in KCl at 198°C.

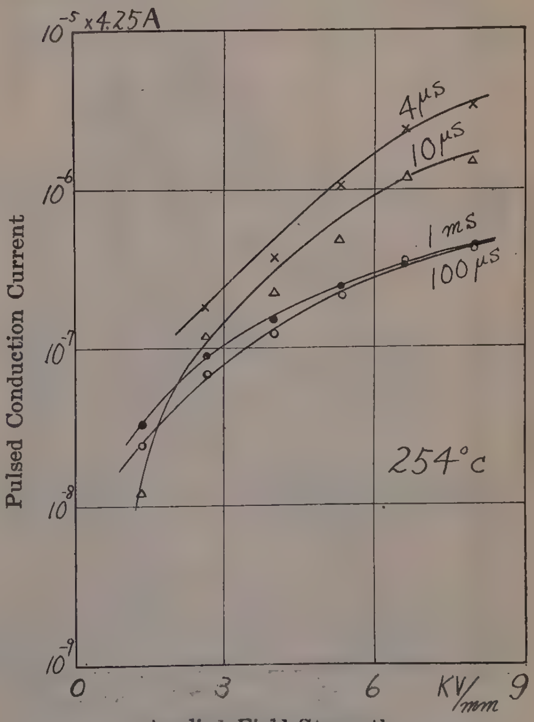

Fig. 4. Pulsed conduction current in KCl at 254°C.

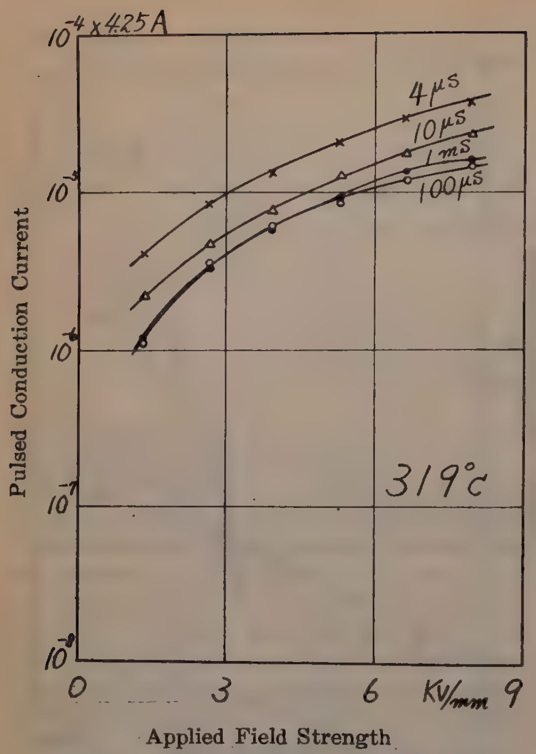

Fig. 5. Pulsed Conduction Current in KCl at 319°C.

predicts. So it may be concluded that these emission electrons contribute to produce the partial electron avalanches which may be absorbed or trapped on the way to the anode.

In Fig. 6 we show the current-voltage curve of the amorphous solid, glass. These results were not so simple that we could not decide whether the emission theory or the Fröhlich's[6] impurity dominant mechanism would be able to more clearly explain the affairs. In Fig. 7 we can see the effects of the electrodes distances. The distances became longer, the stronger trapping effects appeared. The table I shows the ionization path ($\Lambda=1/\alpha$) of glass at room temperatures that are derived from Fig. 7.

Table 1. Ionization path of electron in glass ($\Lambda=1/\alpha$)

Applied Field	Voltage Type	$\Lambda\times10^{-3}$cm
50 KV/mm	4 sec pulse	1.30
30 KV/mm	4 sec pulse	2.61
50 KV/mm	D. C.	4.56
30 KV/mm	D. C.	5.48

From the results mentioned above for the prebreakdown phenomena in these kinds of solids, we cannot neglect the effect of the various space charges as well as the partial electron multiplica-

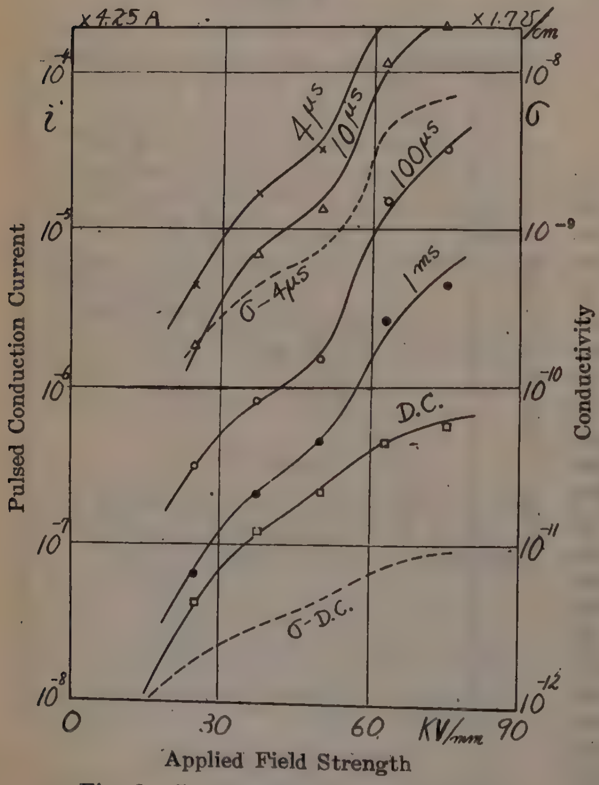

Fig. 6. Conductivity of glass at room temperature.

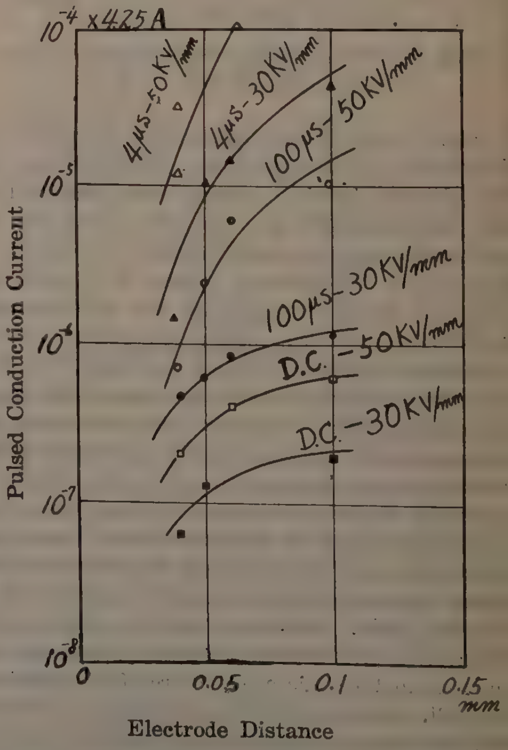

Fig. 7. The Effect of Electrode Distance in Conduction current of glass.

tion at the internal barriers which may be initiated by the emitted electrons.

References

1) C. Yamanaka & T. Suita: J. Phys. Soc. Japan **6** (1951) 194.
2) C. Yamanaka & T. Suita: J. Phys. Soc. Japan **7** (1952) 225.
3) Y. Inuishi, C. Yamanaka & T. Suita: Tech. Rep. Osaka Univ. **2** (1952) 71.
4) Frenkel: J. Tech. Phys. U.S.S.R. **6** (1938) 685.
5) H. Frohlich: Proc. Roy. Soc. **188** (1947) 521.

J. Phys. Soc. Japan 8 (1953) 277~278

Electron Avalanche in Liquids at Strong Electric Fields

By Chiyoe Yamanaka and Tokuo Suita
Faculty of Engineering, Osaka University

(Received November 27, 1952)

We have reported the prebreakdown phenomena1)2) in solids in strong electric fields. Recently we have been studying the prebreakdown phenomena in liquids. The aims of these researches are to study the liquid-breakdown mechanism and to apply the analized informations to the non-disrupting test of practical insulators5).

Under D.C. strong field, the passing currents in liquids are also pulsive. At these junctures, using a pulse amplifier and an electronic counter, the distributions of pulses which were composed of multiplicated electrons could be measured. The electrodes were two steel balls (diameter 10 mm) and needle-plate.

The speciemens were mineral oil, toluene and carbon tetrachloride. The mineral oils were carefully treated and degassed.

In Fig. 1, 2 and 3 we show the pulse distributions of these specimens between the sphere gaps at the room temperatures. The ordinates of the distributions are the frequencies of the pulses which are formed of more than n electrons and the abscissas are the magnitudes of avalanches. The upper half straight lines of them seems to obey the Furry's distribution and mean the successive impact ionizations. The inclinations of these lines show the average magnitudes of the electron avalanches. Another lower flat portions indicate the existence of the intermittent pulses which have definite magnitudes and almost regular repetition rate. These pulses may be

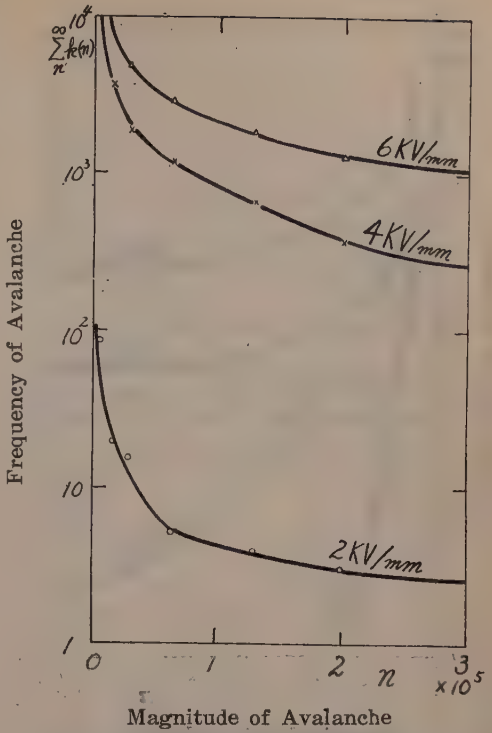

Fig. 1. Avalanche distribution in mineral oil at room temperature between the sphere gap 1 mm.

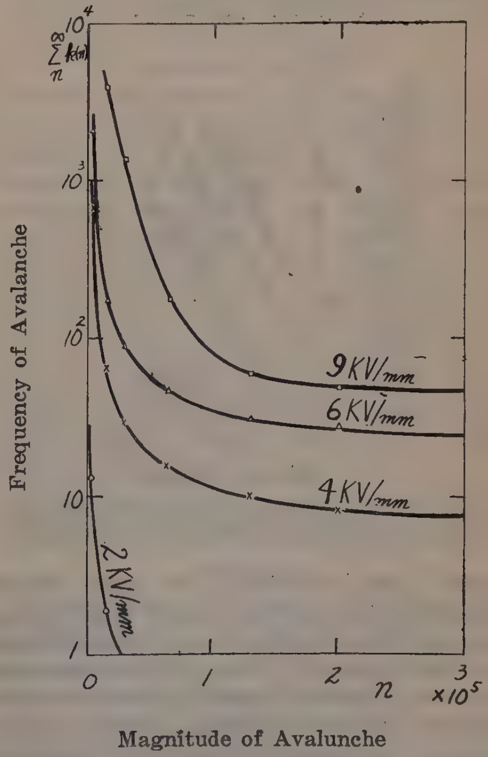

Fig. 2. Avalanche distribution in toluene at room temperature between the sphere gap 1 mm.

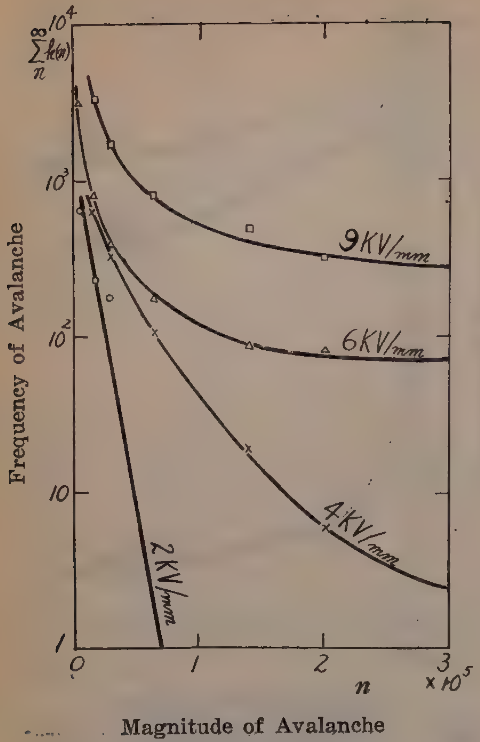

Fig. 3. Avalanche distribution in carbon tetrachloride at room temperature between the sphere gap 1 mm.

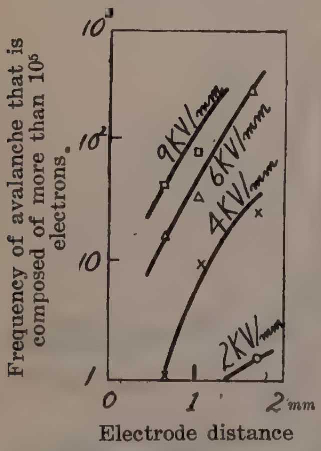

Fig. 4. The influence of electrode distance in the distribution of avalanche in toluene.

caused by the sweeping of the space charges produced by the positive ions and negative ones which are formed of the electron-attachments to the liquid molecules. These intermittent pulse effect were more dominant in the shoter electrode-distances. As for the influence of the electrode distance, the longer distance in a given field strength were arranged, the more numerous electrons in an avalanche appeared. Fig. 4 shows these behaviours in toluene. These effects are also seen in the experimental results of conduction currents. Making a comparison between these liquids, the pulses of mineral oil were rather steady and large in magnitude, in the cases of toluene and carbon tetrachloride they were respectively small and intermediate. In Fig. 5, we show the results of needle-plate electrodes in the mineral oil. We could notice a polarity effect in the distribution of avalanches.

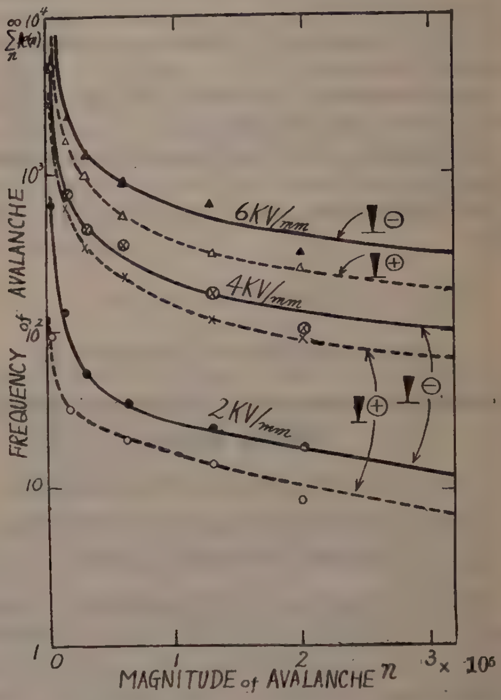

Fig. 5. The Polarity effect in the distribution of Avalanches in Mineral oil.

These experimental results manifest the existence of the electron avalanches in liquids for the decisive cause of the breakdown in the strong field. The lowest limit field strength of the avalanche in these liquids is 2-4 KV/mm. The critical avalanche size that produces the breakdown in liquids is hundred times smaller (10^5) than that in solids[3][4] (10^7).

References

1) C. Yamanaka and T. Suita: J. Phys. Soc. Japan **6** (1951) 194.

2) C. Yamanaka and T. Suita: J. Phys. Soc. Japan **7** (1952) 225.

3) Y. Inuishi, C. Yamanaka and T. Suita: Tech. Rep. Osaka Univ. **2** (1952) 71.

4) C. Yamanaka and T. Suita: Jour. I. E. E. Japan **72** (1952) 276.

5) C. Yamanaka and T. Suita: Read before the annual meeting of I.E.E. Japan **1** (1952) 17.

J. PHYS. SOC. JAPAN 8 (1953) 279

Color-centers of KCl·KBr mixed crystals in visible region

By Sei-ichi KONDO and Masaru MATSUMOTO
Laboratory of Physical Chemistry,
Osaka Liberal Arts University

(Received December 1, 1952)

Several investigations have recently been reported on the color-centers of alkali halides containing cation impurites in dilute concentrations1)2), and on those of alkali halide mixed crystals whose common ion is positive3).

In the present paper mixed crystals of which common ion is cation are treated. That is, potassium chloride and potassium bromide form the mixed crystal system of the "Rückenlose Reihe" crystallizing easily to single transparent one in all molal proportions. The ionic distances between nearest cation and anion of this mixed crystal measured by X-rays are known to change almost linearly proportional to the molal concentrations and obey the Vegard's rule4). In such complete mixed crystal the component anions have commonly been considered to distribute almost statistically on the lattice points. But futher considerations such as made by Durham5) may lead to the assumption that the ions are displaced a little from their geometrical lattice points, owing to their differences in ionic radii, and this may be the same to the neighboring sites of the vacancies. The crystals for the present observation were prepared by ordinary cooling method mixing each halide of high purity, and its ionic distances were determined with single crystals used for the measurement of absorption bands by the X-ray back reflection method for (800) plane. The crystals were colored by X-ray irradiation of 40 K. V. and 4 m.a. about 3 hours at room temperature

The representative absorption curves are illustrated in Fig. 1. Although the curves of Br ion rich crystals are relatively flat, they are very smooth and couldn't be resolved into different peaks. These features may show, either that there are few types of the negative ion single vacancies in this mixed crystals in which common ion is positive, or that these impurity anions at the second or more neighboring sites of the vacancy don't play so important parts to the energy state of the trapped electron as the ions of first nearest neighboring sites do in the case of cation impurities. If not, these curves might have several peaks or be deformed somewhat.

The wave length of the absorption peaks were carefully determined and compared with their interionic distances in Fig. 2. The irregular point of the curve is of about 0.11 molal fraction of potassium bromide. From this figure we may assume that Br ions may be apt to locate around the cations surrounding the negative vacany owing to its weaker binding force to the potassium ion than Cl ions, so that small quantities of Br ion may almost flock together around the vacancies, and push cations toward the vacany site. This may result in the decrease of the radii of the negative single vacancies in spite of the increase of the mean ionic distances, and this might cause the decrease of the wave length of the absorption maximum if the mollwo's relation6) hold for such a case.

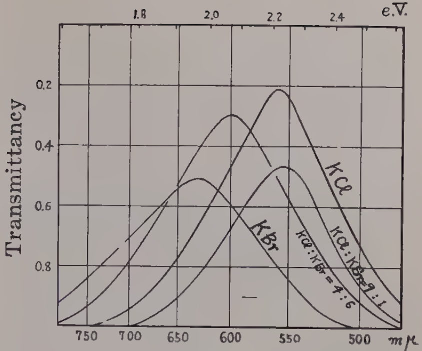

Fig. 1. Wave length vs transmittance I/I_0 of F-bands of KCl-KBr mixed crystals colored by X-rays at room temperature.

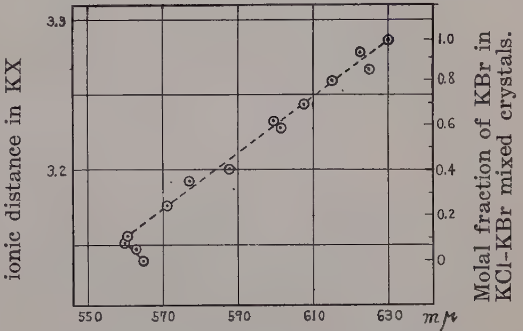

Fig. 2. Relation between wave lengths of absorption maximum of F-bands of X-rayed KCl-KBr mixed crystals and their ionic distances between cation and anion.

We thank Dr. Shigeru Fujita of Osaka university for the amplifier techniques.

References

1) E. Burstein, J. J. Oberly, B. W. Henvis, and M. White: Phys. Rev. **86** (1952) 225-6.
2) S. Kondo and T. Suita: J. Phys. Soc. Japan **5** (1950) 200.
3) S. Kondo: to be published.
4) L. Vegard: Z. Phys. **5** (1921) 17.
5) G. S. Durham and J. A. Hawkins: J. Chem. Phys. **19** (1951) 149.
6) E. Mollwo: Gött, Nachr. Math.-Phys. KL., (1931) 97 and 236.

J. Phys. Soc. Japan 8 (1953) 280~282

On the Dynamical Behaviour of the Grain Boundary in Bubble Raft under Shear Stress

By E. Fukushima

Department of Physics, Tokyo Metropolitan University, Tokyo

and A. Ookawa

Department of Physics and Chemistry, Gakushuin Uuiversity, Mejiro, Tokyo

(Received December 20, 1952)

As was reported in the previous note[1], the grain boundary observed in the soap bubble raft can be classified in respect to the statical transition structure into three types. The grain boundary of type A is constituted of the disordered groups of atoms or the diffused holes, the grain boundary of type B is constituted of the dislocations all on parallel slip planes, and the grain boundary of type C is constituted of two or three sorts of dislocations each on non-parallel slip planes.

Here is reported on the dynamical behaviour of the grain boundary under shear stress, the diameter of the bubbles being about 1 *mm*. Each type of the grain boundary according to the above statical classification acts in discriminatively different manner. It deserves noting that the grain boundary of type C has characteristics similar to that of type A as well as to that of type B.

Fig. 1 shows the grain boundary of type A between two grains, (*a*) before and (*b*) after relative displacement of the grains amounting to about 5 *mm*. The location of the grain boundary is stationary. This is the viscous flow along the nearly straight boundary and corresponds to the mechanisms suggested by Kê[2] and Mott[3]. In the course of relative displacement of the two grains, the bubbles on the grain boundary are ob served to change frequently their allignance from one grain to another grain. When the grain boundary is not straight, it can be observed the generation of new dislocations at turning points of the boundary (see under right in (*b*)) as well as the recrystallization of hump portion of one grain to another grain such as to effect a straight boundary.

Fig. 2 shows the grain boundary of type B, (*a*) before and (*b*) after relative displacement of the two grains amounting to about 1.5 *mm*. From the general view it is clear that the grain boundary changes its location and that the dislocations displace themselves in perfect cooperation. The displacement of the boundary is unlimited so long as the interaction between the frame and the nearby dislocation can be negligible. The behaviour is expected to correspond to the suggestion by Bragg[4] and by Read-Shockley[5] and to the observation in bubble raft by Lomer-Nye[6] and that on zinc crystal by Washburn-Parker[7].

The symmetrical grain boundary of type C is shown in Fig. 3, (*a*) before and (*b*) after relative displacement of about 0.5 *mm* between the two grains. On application of the shearing stress,

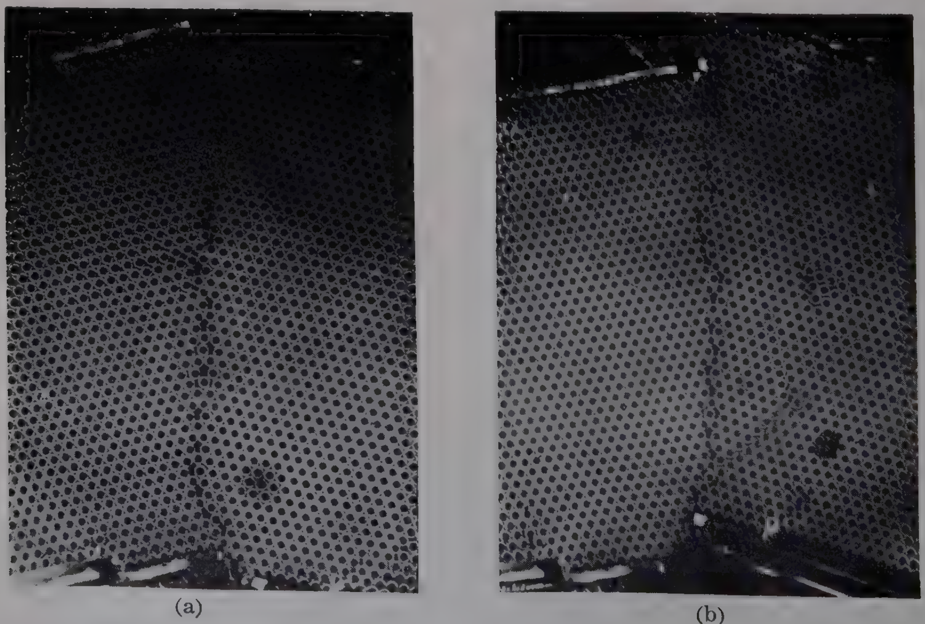

(a) (b)

Fig. 1.

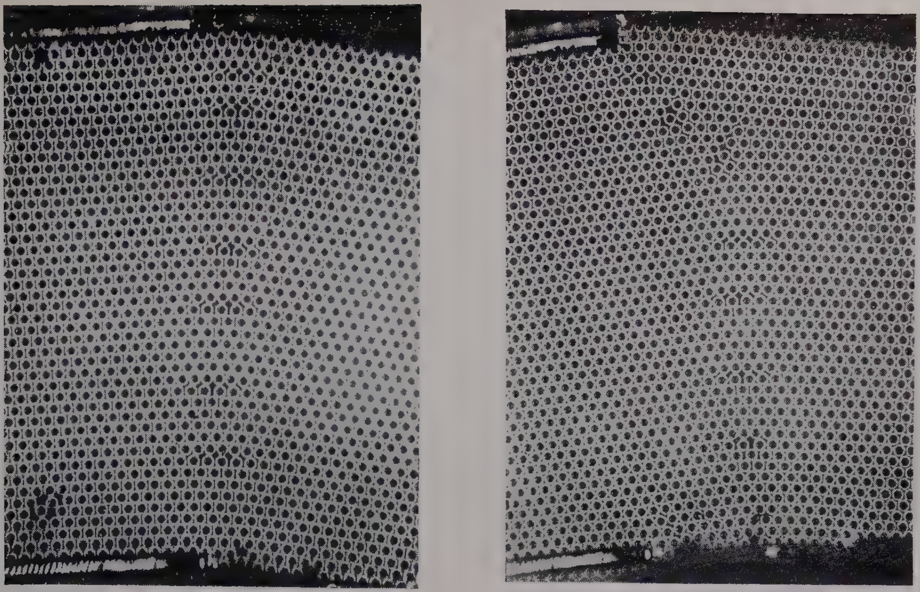
(a) (b)

Fig. 2.

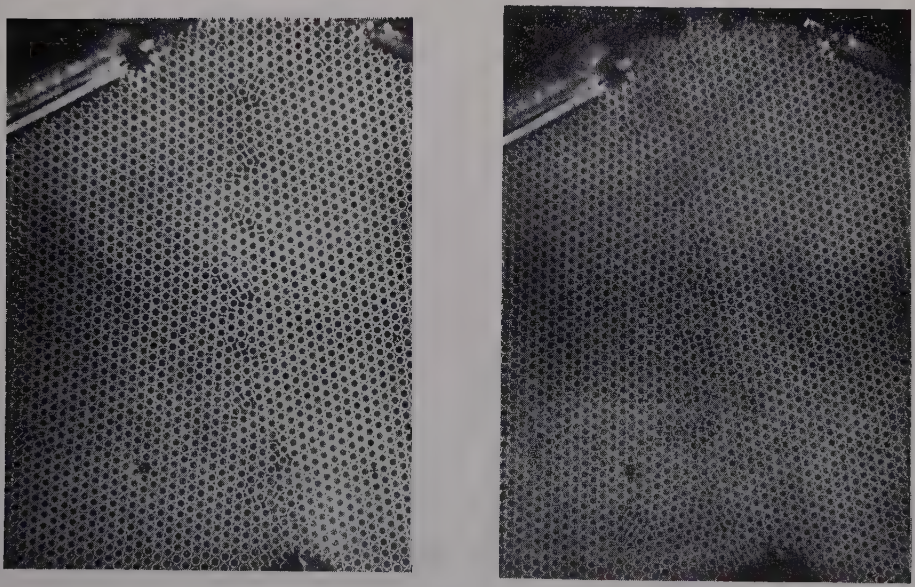
(a) (b)

Fig. 3.

the boundary displaces itself in similar way to that of type B until pair dislocations each on non-parallel slip planes come in distance shorter than a minimum spacing, the amount of displacement of the boundary the larger the greater the average spacing of the dislocations constituting the boundary. Then we observe that further displacement of the boundary is only realized accompanying such an alternation of the nature of the constituent dislocations as to change one dislocation on a specified slip plane to that on another non-parallel slip plane. The alternating nature of the dislocations can be favourably explained by dislocation reaction between the constituent dislocations and other moving dislocations of the third sort with characteristic slip plane nearly parallel to the grain boundary. As an effect of the new dislocations traversing along the grain boundary, we have the relative displacement of the two grains along the grain boundary rather similar to the viscous flow of the boundary of type A. The latter effect is predominant when the average spacing of the constituent dislocations is small.

The details are in preparation for publication in this Journal.

References

1) E. Fukushima, A. Ookawa: J. Phys. Soc. Japan **8** (1953) 129.
2) T. S. Kê: Phys. Rev. **73** (1948) 267.
3) N. F. Mott: Proc. Phys. Soc. London **60** (1948) 391.
4) W. L. Bragg: Proc. Phys. Soc. London **52** (1940) 54.
5) W. T. Read, W. Shockley: Phys. Rev. **78** (1950) 275.
6) W. M. Lomer, J. F. Nye: Proc. Roy. Soc. **A 212** (1952) 576.
7) J. Washburn, E. R. Parker: J. Metals **4** (1952) 1076.

Errata

An Electron Diffraction Camera with a Rotating Sector

By Tadashi Ino

J. Phys. Soc. Jap. **8** (1953) 92-98

p. 92 left column				
	line 6	givesa	should be read	gives a
	21	P. Debye[2]	〃	P. Debye[3]
p. 93 left column under Fig. 1				
	line 7	curved	〃	curves
p. 94 left column				
	line 17	with the	〃	with
	line 26	adjusment	〃	adjustment
p. 95 right column under Fig. 3				
	line 7	calibration,	〃	calibration.

JOURNAL OF THE PHYSICAL SOCIETY OF JAPAN Vol. 8, No. 3, MAY—JUNE, 1953

Proton Magnetic Resonance Absorption in Cetyl Alcohol

By Shoji KOJIMA and Shizuko OGAWA*

Tokyo University of Education

(Received January 9, 1953)

The line shape of the proton absorption in cetyl alcohol was studied with an autodyne receiver between room temperature and the melting point. The second moment was calculated from recorded derivative curves. The obtained second moment had a hysteresis effect. When the temperature was raised from room temperature, the second moment was almost constant of about 18.5 gauss^2 and it decreased abruptly to the value of 8 gauss^2 near the melting point. When the temperature was lowered from the melting point the second moment kept a small value till the transition point and then increased. The large second moment seems to be arisen from the monoclinic state and the small second moment from the hexagonal state. It was observed that the resonance line had a fine structure at its center.

§ 1. Introduction

Measurements of nuclear magnetic resonance absorptions give nuclear g-values. In these cases the resonance field of the interesting nucleus consists of the applied magnetic field and the perturbing field, which is mainly produced by other nuclei in the molecule. Since this perturbing field broadens or splits the resonance line, the analysis of the line shape gives some indications concerning molecular structure[1]. It is also known that the width of the absorption line in solids is strongly affected by molecular motion in the crystal lattice[2].

On cetyl alcohol it is reported to show anormalies on dielectric properties and on specific heat[3]. These are considered to be caused by molecular rotation. We have tried to verify this consideration by the method of proton resonance. A preliminary experiment carried out with a super-regenerative oscillator yielded change of the hight of the absorption line, but gave little information about its shape[4].

In the present paper are described the results of an investigation by an autodyne oscillator[5] and lock-in amplifier method, which yields the derivative of lines precisely.

§ 2. Apparatus and Experimental Procedure

The observation of the nuclear magnetic resonance absorption is taken by the variation of the resistive part in the oscillator coil in which the sample is inserted, and this variation occurs at a resonance between the oscillator frequency and the transition frequency which is a function of static magnetic field applied to the sample.

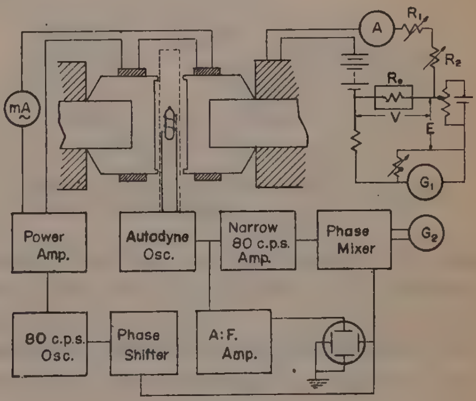

Fig. 1. The block diagram of the apparatus.

The block diagram of the apparatus is shown in Fig. 1. The oscillator used was of an autodyne type which could be worked at 8 mc/s in low power level. The signal picked up from the anode circuit of the oscillator was introduced to a narrow band amplifier[6] and detected by a phase sensitive detector[7], whose output was recorded on a bromide paper with the galvanometer G_2 and light beam. The field modulation was supplied by a tuning-fork oscillator of the frequency of 80 c/s. The narrow band amplifier of this frequency was made with the circuit of negative feedback of twin-T in two stages and its band width was about 3 c/s. The circuit are shown in Fig. 2. Since the modulation anplitude was kept to be much smaller than the breadth of the line, the record yielded the derivative of the absorption curve, from which the second moment was calculated. As a monitor the anode voltage of the oscillator was observed by an oscilloscope with an audio frequency amplifier of two stages. The oscillator coil was shielded by a cylindrical copper tube to be eliminated the level shift which produced by an induction of static field variation.

---

* Now Ochanomizu Women's University.

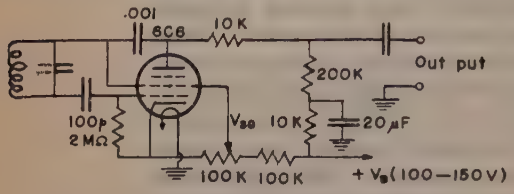

Fig. 2. a. The autodyne oscillator.

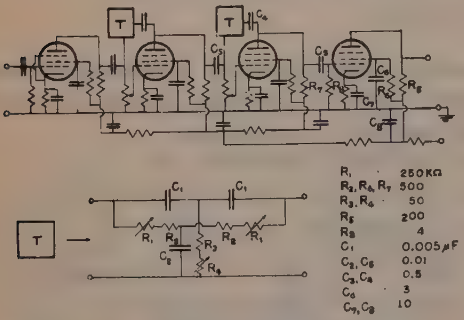

Fig. 2. b. The narrow band amplifier and twin-*T*.

The temperature of the sampie was varied from the room temperature to above the melting point by hot air brown into the above mentioned shielding pipe from a heater, whose temperature was controlled. The heating or cooling of the sample was carried out with the rate of about two degrees per hour and the sweep of the absorption line with a time of about fifteen minutes. Thus the temperature gradient in the sample was suppressed and the saturation effect was avoided. The temperature of the sample was measured by a thermojunction enclosed in a capillary tube. The sample was about 1 gram and enclosed in thin glass envelope.

The electro-magnet excited by the current of about 1 ampere from storage batteries of 70 volts yielded the field strength of 1500 gauss.

The pole pieces, which were 9.5 cm in diameter and shimmed by the method of Rose[5], were set in parallel with the aide of three spacers. The magnetic field was controlled with two resistors R_1 and R_2. One of which, R_2, was equipped with a worm gear for fine adjustments. The current of the magnet was recorded with the galvanometer G_1 by a balanced method. The voltage across the standard manganin resistor R_0, which was immersed in water, being free from the temperature change, was approximately compensated by the electromotive force E given by a battery. These are shown in the block diagram. The output of phase sensitive detector and this field variation were recorded automatically on a bromide paper with two galvanometers G_1 and G_2 simultaneously.

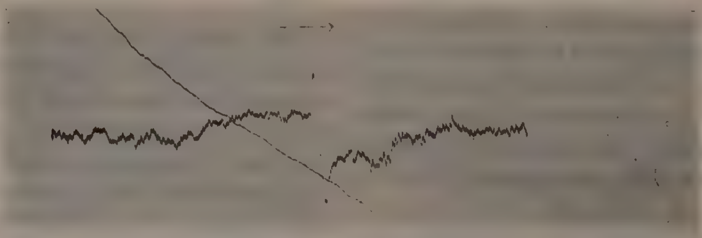

Fig. 3. A photographic paper recorded at room temperature. The line across indicates the field change.

The field homogeneity was tested with the proton resonance in a dilute solution of nickel nitrate about 1 cm³. The distance between minimum and maximum of the derivative curve of absorption line was less than 0.06 gauss. It suggests that the field inhomogeneity is less than this value.

For the determination of the thermal behavior of the sample the thermal curve had been measured. The sample of about 1 gr. enclosed in a thin walled glass tube was immersed in a water bath, which temperature was raised or lowered between 38°C and 52°C with constant speed during over one or two hours run. The temperatures of the sample and water were measured with two thermo-junctions respectively. The results are shown in Fig. 4.

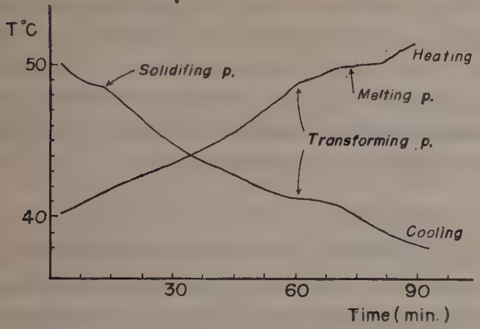

Fig. 4. The thermal curve. The variation with time of the temperature of cetyl alcohol immersed in a water bath which temperature was raised or lowered between 38°C and 52°C.

§ 3. Results of the Experiments

At each experiment the temperature of the sample was varied from the room temperature to slightly above the melting point and then lowered to the initial temperature. One experiment yielded a series of resonance line derivatives corresponding to various temperatures. One series of the measurements is reproduced in Fig. 5. The absorption line at 30°C had a broad width of about 20 gauss and a fine structure in its center*. Till the transition point is reached this width remained constant and then decreased to abont 10 gauss. Above the melting point the line became very sharp as usual liquid. When the temperature was decreased, the absorption line at 46°C had a narrow width which was smaller than that of the previous case. This narrow width remained till the transition point and then gradually increased untill it reached to the broad width of the beginning. This behaviour is more clearly shown by a curve of the second moment of the line, which is reproduced in Fig. 6. The second moment was about 18.5 gauss^2 at 30°C and remains till the transition point. When the temperature was decreased it was $5\sim6$ gauss^2 between the freezing point and transition point.

The thermal curve was taken to determine the melting, freezing and transition points. When the temperature was raised, a little anomaly was observed at 48°C. This point seems to be a transition point. The melting point was obtained as 49.5°C. When the temperature was lowered, the clear edge corresponding to the freezing point was appeared at 48.5°C. On further cooling at about 41°C appeared a hump which was accepted with a transition point. If this figure is compared with Fig. 6, it is seen that these thermal points correspond to the points which show

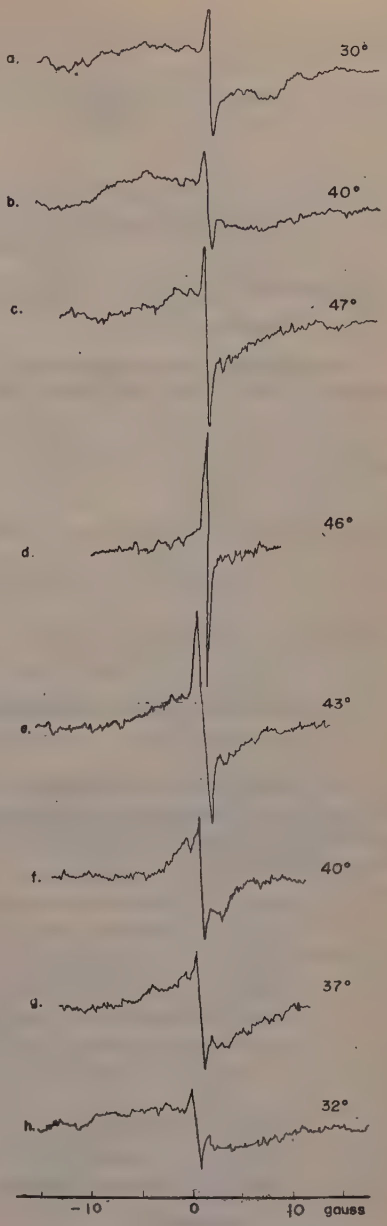

Fig. 5. Resonance line derivatives for cetyl alcohol, illustrating the hysteresis curve.
a.b.c. Increasing Temperature
d.e.f.g.h. Decreasing Temperature

---

* Such fine structure was observed by Andrew in paraffin and interpreted by him to be caused by the rotation of end groupe in the molecule. The present paper does not touch this problem.

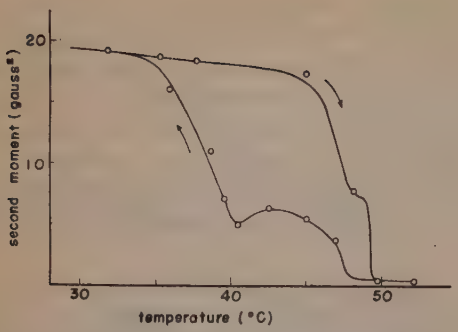

Fig. 6. The variation with temperature of the second moment of the resonance line.

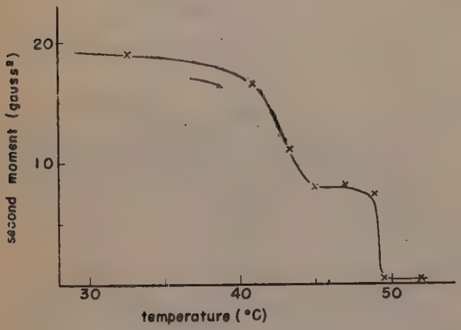

Fig. 7. The variation with temperature of the second moment. Temperature of the sample was raised several hours later from the preceding measurement.

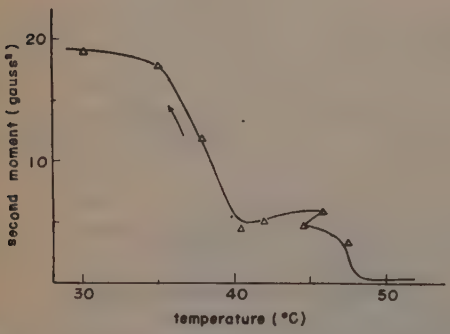

Fig. 8. The variation of the second moment. Temperature was again raised somewhat in the cooling process.

the variations in the second moment curve.

In the experiments mentioned above the sample was reserved at the room temperature during a few days or at 0°C during the night. When the successive experiment was started with short interval such as several hours, the variation of the second moment did not show the same character. In this case the second moment began to decrease far under the transition point as shown in Fig. 7. When the sample was cooled till a certain temperature which laid in the region between the freezing point and the transition point and kept at that temperature, the second moment grew gradually for a few days. When it was cooled till that temperature and again raised, the second moment did not decreased but increased as shown in Fig. 8.

§ 4. Discussion

Cetyl alcohol, n-C$_{16}$H$_{33}$OH, is known to be dimorphous like other members of the normal primary alcohol series. These structual forms are monoclinic one with chains inclined to the base of the cell and hexagonal one with parallel chained normal to the base of the unit cell.

The hexagonal structure results from rotation of the molecule about their chain length. Therefore it is expected from Andrew's discussion about paraffins that the second moment of the hexagonal form is about one-third of that of monoclinic one. The obtained second moment of about 18 gauss^2 seems to correspond to monoclinic form and the value between 4 and 7 gauss^2 to hexagonal form. In the present experiments the hexagonal form appeared not only in the cooling process as the case of paraffin which was found by Andrew, but also in the heating process, even if the region is very narrow.

Recently Hoffman and Smith[9] have concluded the existence of one more form beside monoclinic and hexagonal ones in some long primary alcohols from the measurement of dielectric constant. The minimum at 40°C of the curve of the second moment shown in Fig. 6 may be interpreted as due to this third form, because this form is known by the X-ray diffraction experiment[10] to have slightly larger spacing than hexagonal form so long as we assume the molecular rotation in both the third and hexagonal forms. If the third form is non-rotating state as suggested by Hoffman and Smith, this interpretation, however, will be unlikely.

Finally authors are indebted to Dr. Kakiuchi of Institute of Science and Technology, University of Tokyo who prepared a pure sample and gave the valuable discussion.

References

1) H. S. Gutowsky and G. E. Pake: J. Chem. Phys. **18** (1950) 162.

2) E. R. Andrew: J. Chem. Phys. **18** (1950) 607.

3) K. Sano and Y. Kakiuchi: J. Phys. Soc. Japan **4** (1949) 178; Y. Kakiuchi, T. Sakurai and T. Suzuki: J. Phys. Soc. Japan **5** (1950) 369; Y. Kakiuchi, H. Komatsu and S. Kyoya: J. Phys. Soc. Japan **6** (1951) 321.

4) S. Kojima and S. Ogawa: Science of Light **1** (1951) 101.

5) K. Sano: Proc. J. Phys. Soc. Japan **6** (1951) 228.

6) M. I. T. Radiation Laboratory Series. Pd. 18.

7) N. A. Schuster: Rev. Sci. Inst. **22** (1951) 254.

8) M. E. Rose: Phys. Rev. **53** (1938) 715.

9) J. D. Hoffman and C. P. Smith: J.A.C.S. **71** (1949) 431.

10) D. G. Kolp and F. S. Lutton: J.A.C.S. **73** (1951) 5593.

JOURNAL OF THE PHYSICAL SOCIETY OF JAPAN Vol. 8, No. 3, MAY—JUNE, 1953

Nuclear Magnetic Resonance Experiment on the Single Crystals of $K_2HgCl_4 \cdot H_2O$ and $K_2SnCl_4 \cdot H_2O$. Part I

By Junkichi ITOH, Riichiro KUSAKA, Yukio YAMAGATA, Ryoiti KIRIYAMA, Hideko IBAMOTO, Teinosuke KANDA* and Yoshika MASUDA*

Department of Physics and Department of Chemistry, Osaka University

(Received January 9, 1953)

Proton magnetic resonances of water molecules in the single crystals of $K_2HgCl_4H_2O$ and $K_2SnCl_4H_2O$ were observed, and the distance and the direction of proton-proton line in each of water molecules in the unit cell were determined. The absorption lines are generally composed of four component lines, of which the separation varies with the direction of the externally applied magnetic field. These results are fairly well explained with the Pake's formula for two-proton system and by the fact that there are two different p-p directions in these crystals. The p-p distance in a water molecule determined in this experiment is 1.607 Å, and the angles between the a-axis and p-p lines which lie on the plane parallel to the c-plane are ±21.4° for Hg-salt, and 1.62 Å and ±39.5° respectively for Sn-salt.

Each component line has further fine structures when the external field is applied to some particular directions. This cannot be explained by the assumption of two-spin system only, but understood by introducing the assumption of four-spin system.

§1. Introduction

Application of nuclear magnetic resonance absorption to the investigation of hydrated crystals was first developed by Pake1). He and Gutowsky2) further advanced this method generally to the structural investigation of crystals and obtained fruitful results. On the other hand, Bloembergen3) investigated proton resonance in paramagnetic crystal and Poulis4) in paramagnetic and antiferromagnetic crystals. All these investigations are based upon the magnetic dipole-dipole interactions between nuclei, sometimes between nuclei and paramagnetic ions.

Pake's first experiment1) on the single crystal of $CaSO_4 \cdot 2H_2O$ showed the splitting of resonance line into four components varying with the direction of externally applied magnetic field, and he calculated both the number of component lines and the dependence of their splitting on the direction of applied field by treating the magnetic dipole-dipole interaction between two protons within a water molecule as a perturbation. The formula for the separation of component lines for two proton system is represented as follows:

---

* Now in Department of Physics, Kobe University.

$$\Delta H = \pm \tfrac{3}{2}\mu r^{-3}(3\cos^2\theta - 1) \qquad (1)$$

where μ is the proton moment, r is the distance between two protons, θ is the angle between p-p direction and the external field, and ΔH is the difference of the resonance field for two proton system from the resonance field for free proton. In the present paper, it will be described that this formula is well applied to the interpretation of our experiments on the single crystals of $K_2HgCl_4\cdot H_2O$ and $K_2SnCl_4\cdot H_2O$, and the values r and the angles between the p-p direction and the a-axis will be calculated by measuring ΔH for several directions of the applied field.

Each component line has the finite width caused by the magnetic dipole interactions with the more distant nuclei in the crystal than the partner proton, and in Pake's case the shape of each component line is almost symmetric about its maximum, but in our case it is asymmetric and sometimes shows further fine structure. This asymmetry is due to the relatively strong influence of protons in the adjacent water molecules. We shall discuss this fine structure in the succeeding paper.

§ 2. The Crystal Structures of $K_2HgCl_4\cdot H_2O$ and $K_2SnCl_4\cdot H_2O$

According to the crystal structure analysis of $K_2HgCl_4\cdot H_2O$[5], the dimension of the unit cell is $a=8.27$, $b=11.63$, $c=8.89$ kX, it contains four formula units and the space group is V_h^9-Pbam. Positions of Hg, K and Cl ions are determined precisely, but the position of water molecule is somewhat uncertain. Figs. 1-a show the projection of the unit cell on the c-plane and its perspective.

Owing to the smallness of X-ray scattering power of water molecule compared with those of the other heavier atoms, the position of the oxygen atom and needles to say the hydrogen atom can not be located in the crystal lattice precisely. However, it is expected from some considerations of the crystal structure and the appearance of the packing of these atoms or ions and the temperature and frequency dependences of the dielectric behaviours[6] that the water molecules have a definite direction of their proton-proton lines and the adjacent two water molecules in the same channel along the c-axis in the lattice may be oriented so as to cancel their electric dipole moments with each other at room temperature.

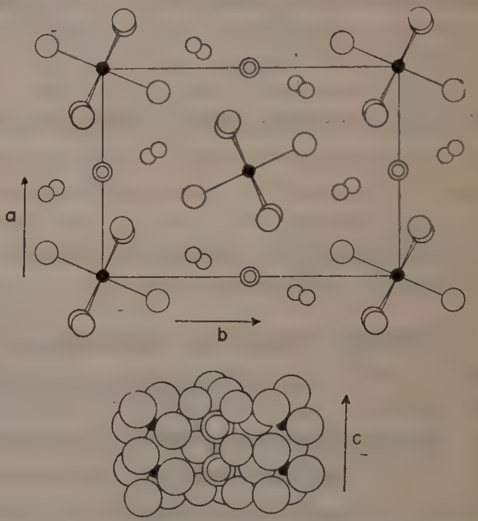

Fig. 1. a. Projection of the unit cell of $K_2HgCl_4\cdot H_2O$ single crystal on the c-plane and the perspective of the unit cell.

● Hg, ○ Cl, ○ K, ◎ H_2O

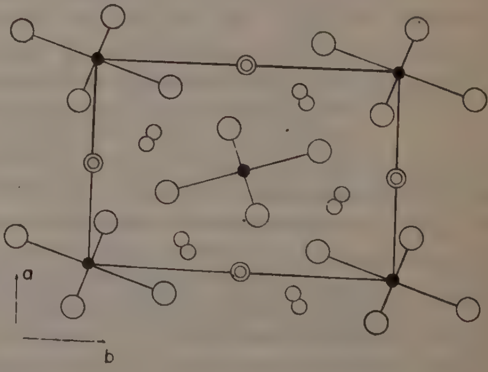

Fig. 1. b. Projection of the unit cell of $K_2SnCl_4\cdot H_2O$ single crystal on the c-plane.

● Sn, ○ Cl, ○ K, ◎ H_2O.

The crystal structure of $K_2SnCl_4\cdot H_2O$ is very similar to that of $K_2HgCl_4\cdot H_2O$[7]. The unit cell dimension is $a=8.21$, $b=12.05$, and $c=9.10$ kX and the cell contains four formula unit. It resembles the mercury salt in consisting of chains of tin-chloride octahedra. These run parallel to the c-axis and the water molecules lie in the channel which are composed between those chains. However, the possible space group of the tin salt is

$V_h^{16}-Pbnm$ which differs from that of the mercury salt. It would seem worthwhile to ascertain whether these two salts really have different space groups or not[8]. Fig. 1-b shows the projection of the unit cell on the *c*-plane. As to the position and the orientation of the water molecule, the quite similar consideration may be deduced as in the case of the mercury salt.

§ 3 Experimental Procedure

The block diagram of the whole detecting system is shown in Fig. 2. The detector is an autodyne type detector[9]. The oscillator coil involves the sample which is rotatable around the axis of the coil. Volume of the single crystals in our experiment was about 5 to 10 cc. In the experiments measuring the separation, the amplified detector signals are directly fed to Y-axis of an oscilloscope while the X-axis is fed by the modulation voltage of the magnetic field. The separation of the absorption peaks appeared on the oscilloscope screen when large modulation voltage was used was measured directly or by the photograph of the figure. In these experiments the frequency which is about 9.3 mc/sec, and the static magnetic field which is perpendicular to the axis of the coil were kept constant at appropriate values, and the amplitude of the modulation field was made considerably larger than the maximum separation of the component lines. The photographs of the figures on the oscilloscope screen for the single crystal of $K_2HgCl_4 \cdot H_2O$ are reproduced in Fig. 3, where the crystal was rotated around the *c*-axis. By the method mentioned above, we can hardly determine the shapes of the individual component lines. To do this, the modulation amplitude was reduced to much smaller value than the half width of the individual lines, and after amplified with a resonance amplifier, the audio output was detected by a phase-sensitive detector. The static magnetic field was swept very slowly through the resonance position, while the r-f was kept constant, and at the same time the dc. output of the phase sensitive detector which shows the derivative of the resonance curve was recorded by a recording milliammeter. In this case, the oscillation intensity was weakened enough to avoid the deformation of the line shape caused by the saturation effect.

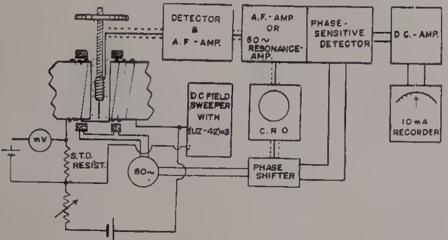

Fig. 2. Block diagram of the whole detecting system.

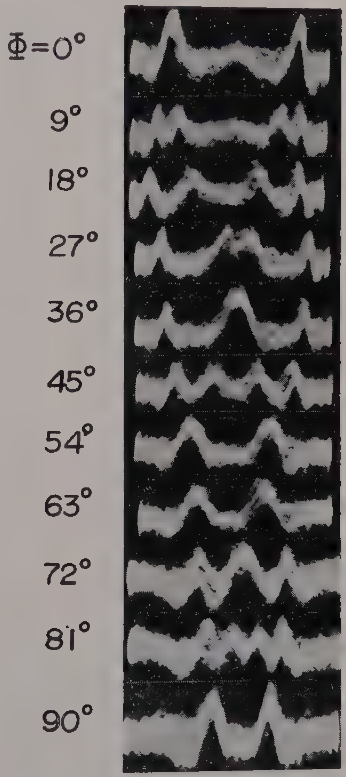

Fig. 3. Photograghs of the figures on the oscilloscope screen in the case of $K_2HgCl_4 \cdot H_2O$ single crystal. In this case, the crystal is rotated around its *c*-axis which is perpendicular to the external field. $\varPhi$ is the angle between the external field and the *a*-axis.

The current through the magnet was measured by a simple potentiometric device, and the relation between the current and the value of the magnetic field was determined by measuring the proton resonance in liquid water at the frequencies coincided with the harmonics of 500 kc or 110 kc quartz oscillator. The current marks are recorded simultaneously on the recording milliammeter chart, as the sweep of the current was not uniform enough. One scale division of the current mark corresponds to about 0.08 gauss, so that the separation of the resonance peaks or the width of each peak can be determined fairly accurately.

§ 4. Results and Discussions

In the formula (1) for the separation of the resonance lines in two proton system, $\cos\theta$ can be written as $\cos\delta\cos(\Phi-\Phi_0)$ where the angles θ, δ, Φ, and Φ_0 which are defined as illustrated in Fig. 4 have the following meaning:

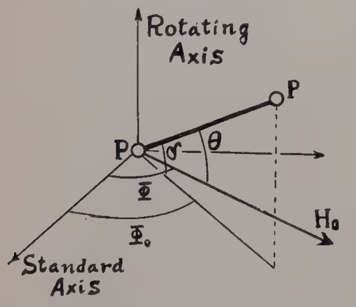

Fig. 4. Figure showing the definition of the angles θ, δ, Φ, and Φ_0.

θ: the angle between the static magnetic field and the direction of the p-p line,

$\frac{\pi}{2}-\delta$: the angle between the axis of rotation (which is always perpendicular to the static field) and the p-p line. In the case when the crystal is rotated around the *c*-axis, $\frac{\pi}{2}-\delta$ is the angle between the p-p line and the *c*-axis.

Φ: the angle between the static field and the definite direction in the plane which is perpendicular to the axis of rotation. In the case when the crystal is rotated around the *c*-axis, Φ is chosen as the angle between the static field and the *a*-axis.

Φ_0: the angle between the projection of the p-p direction on the plane which is perpendicular to the axis of rotation and the definite direction on the same plane. In the case when the crystal is rotated around the *c*-axis, Φ_0 is the angle between the projection of p-p line on the *c*-plane and the *a*-axis.

Then (1) becomes

$$\Delta H=\pm\tfrac{3}{2}\mu r^{-3}\{3\cos^2\delta\cos^2(\Phi-\Phi_0)-1\} \quad (2)$$

I. Single crystal of $K_2HgCl_4\cdot H_2O$.

The results for the case when the external field was rotated in the *c*-plane were already shown in Fig. 3. The relative line separations were determined from Fig. 3 and some more similar experiments, while the absolute value of the separation was determined either from the separation of lines on the recording milliammeter or from the value of the current change corresponding to the variation of field strength so as to shift one peak to the position of the other peak of the pair on the oscilloscope screen.

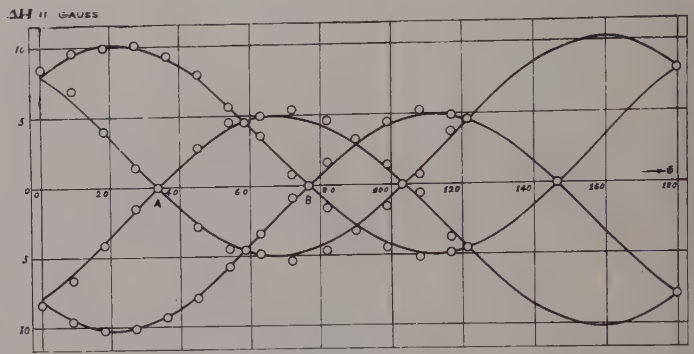

Fig. 5. ΔH as a function of the angle Φ, the angle between the external field and the *a*-axis, for the single crystal of $K_2HgCl_4\cdot H_2O$. Experimental values are indicated by the circles, while the curves are the calculated ones using the equation (2) with the values $\Phi_0=\pm21.4°$, $\delta=0$ and $6\mu r^{-3}=20.15$ gauss.

Fig. 5 shows the separation of the lines from their center of gravity as a function of the angle Φ between the applied magnetic field and the *a*-axis. The curves are composed of four similar sine curves differing only in phases, and these are symmetric about the *a*- or the *b*-axis. These results indicate that there are two directions for p-p lines in this crystal and they have symmetry of mirror reflection with respect to the *a*- or the *b*-plane. Thus, the angles Φ_0 for these two p-p directions differ only in sign with the same absolute values and the values of r for these two groups should be the same. The angle Φ_0 is equal to the angle of maximum separation, or, is equal to the half of the difference of the angles A and B denoted in Fig. 5. The value obtained from Fig. 5 is ±(21.4±0.5°) for each group respectively. Next, the angle δ can be determined from the difference of the angles giving the maximum separation and the zero splitting or from the difference of two angles giving zero splitting in one curve. The angle between the direction for maximum splitting and that for zero splitting is determined to be 54.7±0.5° for both groups.

Thus the value of the angle δ is calculated to be zero, within the error of 0.5°. This means that each p-p line is perpendicular to the *c*-axis. These results were made sure by the experiments in which the static field was rotated in the *b*-plane or the static field was rotated in a plane perpendicular to one of the p-p lines. In the former case only two peaks were observed in any direction of the static field and in the latter case the separation of one group was always constant.

Next, we determined the p-p distance for the proton pair forming two proton system which corresponds to the pair in one water molecule, by measuring the absolute value of the line separation. In the formula (2), putting $\delta=0$, the maximum separation is given by $3\mu r^{-3}$ and from the measured value of the maximum value of ΔH which is 20.15/2 gauss, p-p distance was determined to be 1.607Å.

Fig. 6 shows one of the derivative curves of a component line drawn on the recording milliammeter chart, together with its integrated curve. This corresponds to the case when the external field is directed parallel to the *c*-axis and since in this case both of two groups of the proton pairs are perpendicular to the static field, only two resonance peaks are observed. Each peak shows remarkable structures. Though for the other directions of the external field there are many cases when the fine structure is less remarkable than in the case shown in Fig. 6, the shape of each peak is more or less asymmetric about its maximum. In Pake's experiment on gypsum[1)], each component line appeared to have a simple symmetric shape and could be interpreted by the consideration that the absorption system is pure "two proton system" composed of the two protons in a water molecule, and the other nuclei located more distantly act only to broaden each line of two proton resonance symmetrically. In our case, however, since two water molecules located adjacently along the *c*-axis are considerably close with each other, the system does not behave as pure two proton system but more probably as a four proton system. The details of the calculation and the discussion about four proton system will be described in the succeeding paper.

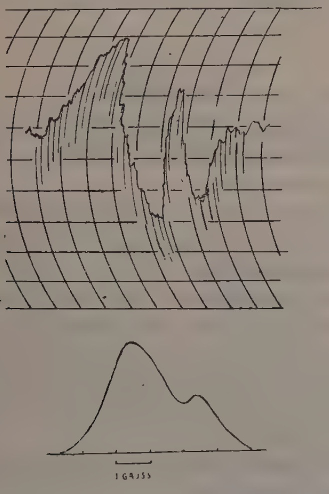

Fig. 6. Observed derivative curve on the recording milliammeter chart and its integrated absorption curve for $K_2HgCl_4\cdot H_2O$, in the case when the static field is parallel to the *c*-axis. Current marks are shown on the derivative curve.

Since the water molecules may begin to rotate when the temperature of the crystal is made high, we made the resonance experiment at various temperature. As this crystal changes its structure at about 80°C, the highest temperature used was just below this. The anhydration temperature is more higher than 80°C. Neither the separation of pair lines nor the width of the component peaks change even at the highest temperature. This suggest that the water molecules do not begin to rotate, even partially, below 70°C.

The value of Φ_0, which is $\pm 21°$, is interpreted roughly by the following simple consideration. The configuration of ions around one water molecule is roughly a parallelpiped formed by four chlorine and four potassium ions located alternatively at the corners. It may be the case that positively charged proton is attracted in the direction of negatively charged chlorine ions. The angle between the line joining two chlorine ions located at the diagonal corner in the plane perpendicular to the *c*-axis and the *a*-axis is about 19°, calculated from the X-ray analysis data. This angle is very near the observed angle of p-p direction with respect to the *a*-axis. Of course, this consideration is only approximate, since for the calculation of the electric field around water molecule more neighbors must be taken into consideration. However, this consideration suggests the qualitative

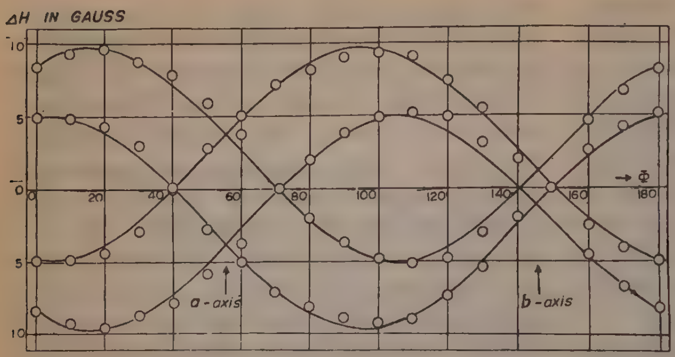

Fig. 7. ΔH as a function of Φ for the single crystal of Sn-salt. In this case, the angle Φ is the one between the external field and the intersection of the c-plane and the (110) plane, which is the natural crystal surface. The direction of this intersection makes an angle of 55.6° with the a-axis. Also the direction of the a- and b-axes are indicated in the figure. Circular marks represent the experimental points while the curves are the calculated ones using the equation (2) with the values $\Phi_0=\pm16.1°$, $\delta=0$ and $6\mu r^{-3}=19.65$ gauss.

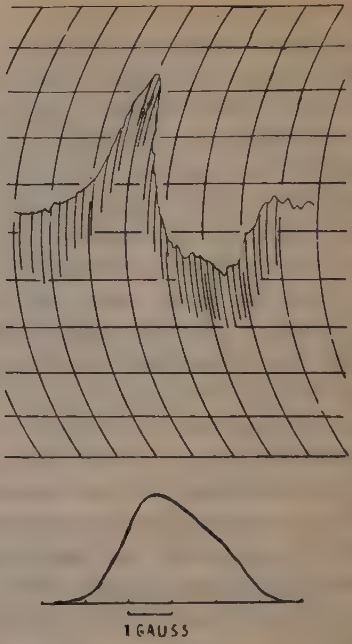

Fig. 8. Observed derivative curve and its integrated absorption curve for Sn salt, when the external field is directed along the c-axis. Current marks are shown on the derivative curve.

existence of O–H····Cl bond.

The observed p-p distance, 1.607Å, is a little larger than that in the case of free H_2O molecule¹⁰⁾, suggesting also the effect of the attraction of the surrounding chlorine ions.

2. Single crystal of $K_2SnCl_4 \cdot H_2O$.

In the first place, the external field was rotated in the c-plane. The line separations are shown in Fig. 7. From this figure, the angles between p-p lines and the a-axis and also the p-p distance were calculated to be ±39.5° and 1.62Å respectively. Fig. 8 shows the derivative curve in the case when the static field is directed to the c-axis and its integrated curve. Though remarkable fine structure is not observed, still the peak is strongly asymmetric about its maximum. The interpretation of line shape by the consideration of four spin system will be described in the succeeding paper.

Since in this case two more chlorine ions lie considerably near the water molecule, the effect of these two must be taken into consideration for the calculation of the electric field around the water molecule. The calculated directions of maximum attraction are about ±34° which coincide approximately with the experimental values.

References

1) G. E. Pake: J. Chem. Phys. **16** (1948) 327.

2) H. S. Gutowsky and G. E. Pake: J. Chem. Phys. **18** (1950) 162.

3) N. Bloembergen: Physica. **16** (1950) 95.

4) N. J. Poulis and G. E. G. Hardeman: Physica. **18** (1952) 201.

5) C. M. MacGillavry, J. H. de Wilde and J. M. Bijvoet: Z. Krist. **100** (1938) 212.

(6) R. Kiriyama and H. Ibamoto: Presented to the second congress of international union of crystallography, 1951. The full report will be published shortly.

7) H. Brasseur and A. de Rassenfosse: Z. Krist. **101** (1939) 389.

8) R. W. G. Wyckoff: *Crystal structure*, vol. 2 (1951). Interscience Pub. N. Y.

9) N. J. Hopkins: Rev. Sci. Instr. **20** (1949) 401.

10) G. Herzberg: *Infrared and Raman spectra of polyatomic molecules* (1945).

JOURNAL OF THE PHYSICAL SOCIETY OF JAPAN Vol. 8, No. 3, MAY—JUNE, 1953

Nuclear Magnetic Resonance Experiment on the Single Crystals of $K_2HgCl_4 \cdot H_2O$ and $K_2SnCl_4 \cdot H_2O$.

II. The resonance absorption due to four proton system and the revised determination of their crystal structures

By Junkichi ITOH, Riichiro KUSAKA, Yukio YAMAGATA,
Ryoiti KIRIYAMA and Hideko IBAMOTO

Department of Physics and Department of Chemistry, Osaka University

(Received January 9, 1953)

The energy levels and the transition probabilities are calculated for four proton interaction. The result of calculation is applied to the case of the single crystals of $K_2HgCl_4 \cdot H_2O$ and $K_2SnCl_4 \cdot H_2O$. Ten absorption lines are expected from the theoretical calculation, of which each five form a group. Since in general cases the separations between the lines belonging to one of these groups are small compared to the separation between these groups as a whole, the expected resonance figure roughly coincides with the case of two proton resonance. But the shapes of resonance peaks have further fine structures. The observed fine structures were analysed by the theoretical consideration, and it is shown that the agreement between the theory and the experiment is satisfactory, if we take the distance of main protons to be 1.607 Å and the distance between the proton-proton lines for adjacent water molecules which are parallel with each other to be 3.60 Å in the case of Hg-salt and 1.62 Å and 3.90 Å respectively in the case of Sn-salt. From these results, the positions of the oxygen atoms in the crystal lattice may be determined with a few assumptions, and the probable space group of $K_2SnCl_4 \cdot H_2O$ will be $V_h{}^9 - Pbam$ which is identical to that of $K_2HgCl_4 \cdot H_2O$ contrary to the previous X-ray determination.

§ 1. Introduction

In the preceding paper[1], we described the experimental results of the proton resonance by the single crystals of $K_2HgCl_4 \cdot H_2O$ and $K_2SnCl_4 \cdot H_2O$. It will be referred as A throughout in this paper. It was shown in A that the positions of the proton resonance lines coincide with Pake's formula[2] for two proton system, while the individual absorption lines have further fine structures. These fine structures are due to the interaction of protons belonging to the neighboring water molecule, forming a four proton system. The details of calculation of four proton resonance and the comparison with the experimental results will be shown in this paper.

Three proton resonance was treated by Andrew and Bersohn[3] and the experiments on three proton system were performed by Gutowsky et. al.,[4] by Kakiuchi et. al.[5] and by Richards and Smiths[6]. Calculation of four proton resonance was done by Tomita in connection with the problem of solid methane[7]. Lately, by a private communication which was received after our work had been completed, we knew that Bersohn* treated this problem more completely in connection with solid methane and ammonium chloride[8]. But since their calculations are not applicable directly in our case, we shall describe our calculation in some details, though some parts of calculation overlap with theirs. The experimental investigation on four proton system was performed by Gutowsky et. al.[4] using some powdered crystals, but the detailed analysis has not yet been done.

A brief report of our investigation was already published in J. Chem. Phys.[9]

§ 2. The Calculation of the Energy Levels and the Transition Probabilities in a Four Proton System**

---

* We want to express our thanks to Dr. R. Bersohn for sending to J.I. a part of his manuscript befor the publication.

** In the course of our calculation, we received some valuable discussions from Dr. K. Tomita, to whom we express our gratitudes.

We take a system which consists of four protons. It is assumed that no spin-dependent external force except that of the applied magnetic field acts on the system. Also it is assumed that these four protons are fixed rigidly in the crystal lattice. Then the Hamiltonian for this four proton system is given in the following form:

$$H=H_m+\mathfrak{H}\,, \tag{1}$$

where H_m means the part of the Hamiltonian due to the applied magnetic field and $\mathfrak{H}$ means that of mutual interactions between four protons. Let the individual spin vectors of the four protons be $\mathbf{s}_1$, $\mathbf{s}_2$, $\mathbf{s}_3$ and $\mathbf{s}_4$, the applied field be $\mathbf{H}$, the vector joining the proton i and the j be $\mathbf{r}_{ij}$, its magnitude be r_{ij}, and the proton moment be μ. Then

$$H_m=2\mu\mathbf{H}(\mathbf{s}_1+\mathbf{s}_2+\mathbf{s}_3+\mathbf{s}_4) \tag{2}$$

and

$$\mathfrak{H}=\sum_{i>j}\mathfrak{H}_{ij} \tag{3}$$

where

$$\mathfrak{H}_{ij}=4\mu^2 r_{ij}^{-3}\left[\mathbf{s}_i\,\mathbf{s}_j-\frac{(\mathbf{s}_i\mathbf{r}_{ij})\,(\mathbf{s}_j\mathbf{r}_{ij})}{r_{ij}^2}\right]. \tag{4}$$

As the basic representation of the states of the four proton system without the mutual interactions, we take $(I_1,\ I_2,\ I,\ m)$ representation where $\mathbf{I}_1=\mathbf{s}_1+\mathbf{s}_2$, $\mathbf{I}_2=\mathbf{s}_3+\mathbf{s}_4$, $\mathbf{I}=\mathbf{I}_1+\mathbf{I}_2$ and m is the z-component of $\mathbf{I}$. The z-axis is taken in the direction of the applied magnetic field. Then H_m is decided by the value of m and the eigen-values W_m of H_m are given by

$$W_m=2\mu Hm\,, \tag{5}$$

in which the values of m are one of the integers from $+2$ to -2. Since the magnitude of I_1 or I_2 is either one of 1, 0, or -1 and $I=I_1+I_2$, I_1+I_2-1, ... $|I_1-I_2|$, there are sixteen states, in which two are non-degenerate, two are fourfold degenerate and one is sixfold degenerate. Actually, however, the sixtet state splits in two triplets.

By the interaction between protons, which are assumed to be much smaller than H_m, these degeneracies are generally resolved. For the calculation of the energy levels, we should compute matrix elements of $\mathfrak{H}$ with respect to these zero order states. Now, $\mathfrak{H}_{ij}$ can be transformed to a more convenient form, which was given by Van Vleck[10]. Apart from the terms which are independent of the value of spins, $\mathfrak{H}_{ij}$ can be expressed as

$$\mathfrak{H}_{ij}=A_{ij}[\mathbf{s}_i\mathbf{s}_j-3m_im_j]\,, \tag{6}$$

where

$$A_{ij}=2\mu^2r_{ij}^{-3}(3\cos^2\theta_{ij}-1)\,, \tag{7}$$

θ_{ij} being the angle between $\mathbf{r}_{ij}$ and $\mathbf{H}$.

The representation of $\mathfrak{H}$ with respect to $(I_1,\ I_2,\ I,\ m)$ bases can be devided to six sub-matrices, non-diagonal terms between the different sub-matrices being zero. They are given in Table 1, where

$$\left.\begin{aligned}a&=A_{12}+A_{34}\\ b&=A_{13}+A_{14}+A_{23}+A_{24}\\ c&=A_{13}+A_{14}-A_{23}-A_{24}\\ d&=A_{13}-A_{14}+A_{23}-A_{24}\\ e&=A_{13}-A_{14}-A_{23}+A_{24}\,.\end{aligned}\right\} \tag{8}$$

By using these matrix elements, the secular equations can be constructed and the eigenvalues of the energies will be computed by solving them. In general cases, it is impossible to obtain analytical expression of the whole solutions, though, of course, they can be solved by the numerical computations. Some of the solutions for energies, however, are obtainable analytically; those are

$$\left.\begin{aligned}&W_1=4\mu H-\frac{a}{2}-\frac{b}{2} && \text{(from } A \text{ of Table 1)}\\ &W_{16}=-4\mu H-\frac{a}{2}-\frac{b}{2} && \text{(from } F \text{ of Table 1)}\\ &W_9=0 &&\\ &\left.\begin{aligned}&W_6=\frac{a+b}{4}+\frac{1}{4}\sqrt{(a+b)^2+2(2a-b)^2+6e^2}\\ &W_{10}=\frac{a+b}{4}-\frac{1}{4}\sqrt{(a+b)^2+2(2a-b)^2+6e^2}\end{aligned}\right\} && \text{(from } C \text{ of Table 1)}\end{aligned}\right\} \tag{9}$$

The suffices of W's in these expressions are rather arbitrary, but, in some cases, they represent the order in energy magnitudes, the level having smaller number having higher energy. The other equations are not solved analytically in general case. But in some special cases, they are easily soluble.

First, when $A_{12}=A_{34}$, $A_{13}=A_{24}$ and $A_{14}=A_{23}$,

Table 1.

Matrix elements of $\mathfrak{H}$ with respect to (I_1, I_2, I, m) representation.

(Since all matrices are symmetric, only half of the non-diagonal elements are shown)

	(1,1,2,2)
(1,1,2,2)	$-(a+b)/2$

Singlet (A)

	(1,1,2,1)	(1,1,1,1)	(1,0,1,1)	(0,1,1,1)
(1,1,2,1)	$(a+b)/4$	$-3(A_{12}\quad A_{34})/4$	$-3d/4\sqrt{2}$	$-3c/4\sqrt{2}$
(1,1,1,1)		$(a-b)/4$	$-d/4\sqrt{2}$	$c/4\sqrt{2}$
(1,0,1,1)			$-A_{12}/2$	$e/4$
(0,1,1,1)				$-A_{34}/2$

Quartet (B)

	(1,1,0,0)	(1,1,2,0)	(0,0,0,0)
(1,1,0,0)	0	$-(2a-b)/2\sqrt{2}$	0
(1,1,2,0)		$(a+b)/2$	$-3e/2\sqrt{6}$
(0,0,0,0)			0

Triplet (C)

	(1,0,1,0)	(0,1,1,0)	(1,1,1,0)
(1,0,1,0)	A_{12}	$-e/2$	$d/2\sqrt{2}$
(0,1,1,0)		A_{34}	$-c/2\sqrt{2}$
(1,1,1,0)			$-(a-b)/2$

Triplet (D)

	(1,1,2,−1)	(1,1,1,−1)	(1,0,1,−1)	(0,1,1,−1)
(1,1,2,−1)	$(a+b)/4$	$3(A_{12}-A_{34})/4$	$3d/4\sqrt{2}$	$3c/4\sqrt{2}$
(1,1,1,−1)		$(a-b)/4$	$-d/4\sqrt{2}$	$c/4\sqrt{2}$
(1,0,1,−1)			$-A_{12}/2$	$e/4$
(0,1,1,−1)				$-A_{34}/2$

Quartet (E)

	(1,1,2,−2)
(1,1,2,−2)	$-(a+b)/2$

Singlet (F)

c and d become zero. In this case, the equations derived from (B), (D) and (E) are easily solved and the results are given by

$$\left.\begin{aligned} W_2&=2\mu H+\tfrac{1}{4}(a+b)\\ W_3&=2\mu H+\tfrac{1}{4}(a-b)\\ W_4&=2\mu H-\tfrac{1}{4}(a-e)\\ W_5&=2\mu H-\tfrac{1}{4}(a+e) \end{aligned}\right\}\text{(from } B \text{ of Table 1)}$$

$$\left.\begin{aligned} W_7&=\tfrac{1}{2}(a+e)\\ W_8&=\tfrac{1}{2}(a-e)\\ W_{11}&=-\tfrac{1}{2}(a-b) \end{aligned}\right\}\text{(from } D \text{ of Table 1)}$$

$$\left.\begin{aligned} W_{12}&=-2\mu H+\tfrac{1}{4}(a+b)\\ W_{13}&=-2\mu H+\tfrac{1}{4}(a-b)\\ W_{14}&=-2\mu H-\tfrac{1}{4}(a-e)\\ W_{15}&=-2\mu H-\tfrac{1}{4}(a+e) \end{aligned}\right\}\text{(from } E \text{ of Table 1)} \tag{10}$$

Since the nuclear resonance absorption lines correspond to the transitions satisfying the selection rules $\Delta m=\pm 1$, we computed the values of $h\nu$ of the resonance radiation from the above expressions for W's. Experimentally, however, we observed the separations of the absorption lines in magnetic field strength, the frequency of the radio-wave being kept constant. Therefore, transforming the separation in energy to the separation in magnetic field strength, we finally obtained the expressions for the resonance fields corresponding to the frequency ν.

$$H=H^{*}\pm\begin{cases}3/2(P_{12}+P_{13}+P_{14})\\ 3/2(P_{12}+P_{13}-P_{14})\\ 3/2(P_{12}-P_{13}+P_{14})\\ 3/2\sqrt{(P_{12}^{2}+P_{13}^{2}+P_{14}^{2})-\tfrac{2}{3}(P_{12}P_{13}+P_{12}P_{14}+P_{13}P_{14})}\\ 3/2(P_{12}-P_{13}-P_{14})\end{cases} \tag{11}$$

where H^{*} is the Zeeman field for free proton corresponding to the frequency ν, or is equal to $h\nu/2\mu$ and $P_{ij}=\mu r_{ij}^{-3}(3\cos^{2}\theta_{ij}-1)$. In the experiment to be described in the following sections, the conditions $A_{12}=A_{34}$ and $A_{13}=A_{24}$ are always fulfilled, since $\boldsymbol{r}_{12}$ and $\boldsymbol{r}_{34}$ are parallel with each other and $\boldsymbol{r}_{13}$ and $\boldsymbol{r}_{24}$ are also parallel. But, the condition $A_{14}=A_{23}$ is not always fulfilled. This condition is fulfilled only when $\boldsymbol{H}$ lies on either one of the bisector planes of $\boldsymbol{r}_{14}$ and $\boldsymbol{r}_{23}$. However, in our experimental case, $\boldsymbol{r}_{12}(//\boldsymbol{r}_{34})$ is much smaller than the other p-p distances and except when $\theta_{12}(=\theta_{34})$ is near 55°, $A_{12}(=A_{34})$ is larger than the other A_{ij}'s. In this case, the secular equations can be solved with good approximation and the results of the solutions are

$$H=H^{*}\pm\left[\;3/2P_{12}\begin{cases}+3/4(2P_{13}+P_{14}+P_{23})\\ +3/4(2P_{13}-P_{14}-P_{23})\\ -3/4(2P_{13}-P_{14}-P_{23})\\ -1/4(2P_{13}+P_{14}+P_{23})\\ -3/4(2P_{13}+P_{14}+P_{23})\end{cases}\right]\begin{array}{c}(1)\\ (1/2)\\ (1/2)\\ (3/2)\\ (1/2)\end{array} \tag{12}$$

In this expression, the terms $\pm 3/2P_{12}$ represent two proton resonance lines as discussed by Pake[2]. In the case when P_{12} is the same order as the other P_{ij}'s, the ten component lines overlap with each other and this is uninteresting case for four proton interaction.

The transition probabilities, or the intensities of the component lines are proportional to the square of the matrix elements of I_x with respect to the states concerning the transition. In the case when $A_{12}=A_{34}$, $A_{13}=A_{24}$ and A_{12} is much larger than the other A_{ij}'s, the transition probabilities can be culculated easily. The results for the relative probabilities, are shown in the last brackets of the expression (12).

The results obtained in (12) will be compared with the experimental results in the following sections.

§ 3. Discussion of the Experiment on $K_2HgCl_4\cdot H_2O$

As shown in *A*, there exist two types of water molecules in the single crystal of this salt. One type of water molecules has their p-p directions parallel to a line which is perpendicular to the *c*-axis and makes an angle of +21° with respect to the *a*-axis, while the other type has p-p direction which is perpendicular to the *c*-axis and makes an angle of −21° to the *a*-axis. Considering the crystal symmetry, it is concluded that, of the four water molecules in a unit cell, two which situate on a line parallel to the *c*-axis have the same p-p direction and the dipole moments of these two water molecules direct oppositely with each other along the *c*-axis. The part of the lattice which contains these water molecules and the surrounding ions is shown in Fig. 1. The configuration of ions around the other type of water molecules is just the gliding reflection with respect to the *b*-plane. Then protons belonging to these two water molecules of either one of two type can be considered as forming a four proton system, since the distance of one of the proton belonging to these water molecules and those not belonging to them are considerably larger than the distance between these four protons. The effects of protons and other ions outside the four proton group upon the four proton resonance lines may be considered to broaden them by a small amount.

Now, as shown in *A*, the resonance absorption lines can be considered roughly as two proton resonances. By the effect of four proton interaction, fine structures in each of the absorption lines were produced. This implies that the distances between the main

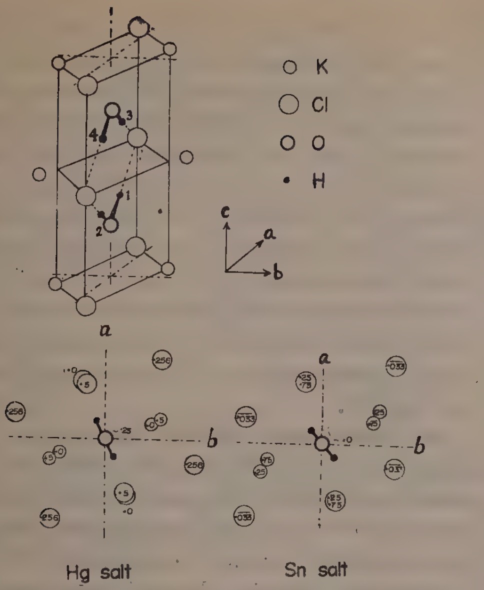

Fig. 1. Two water molecules which form a four proton system and their environment in the lattice for $K_2HgCl_4 \cdot H_2O$, and the projection diagrams on tne c-plane for Hg- and Sn-salts. Positions of protons are determined by A and also by this paper. The configuration of ions around the other two water molecules is just the mirror reflection of that shown in this figure with respect of the b-plane.

proton are much smaller than those between other pairs in four proton system. If we denote proton 1 to proton 4 as shown in Fig. 1, this means that the proton distance between 1 and 2, or, r_{12}, and that between 3 and 4, or, r_{34}, are smaller than r_{13}, r_{14}, r_{23} and r_{24}. Moreover, as mentioned above, $\boldsymbol{r}_{12}$ is parallel to $\boldsymbol{r}_{34}$, and $\boldsymbol{r}_{13}$ is parallel to $\boldsymbol{r}_{24}$. This case of four proton system is just the case which was discussed already in Section 2, and we may analyse the experimental results with the theoretical formula described above.

Since two types of four proton systems differ only in the angle with respect to the a-axis, we may consider only one of them. For any direction of the static field, there exist ten absorption lines in general. But they can be devided into two groups, generally well separated, one having the value $+3/2P_{12}$ and the other having the value $-3/2P_{12}$ in (12). Then for one group of lines, the center of gravity of them coincided with $+3/2P_{12}$ and for the other group it coincides with $-3/2P_{12}$, Except when θ_{12}, the angle between $\boldsymbol{r}_{12}$ and $\boldsymbol{H}$, is near 55°, these two groups separate well with each other. Since in the case when H lies in the c-plane the separation due to the terms containing r_{13}, r_{14}, r_{23} and r_{24} is not large and each group of five lines forms a single line with a slight asymmetric distribution with respect to its maximum. The center of gravity of absorption peak and its maximum does not differ appreciably. Therefore r_{12} $(=r_{34})$ can be decided with sufficient accuracy from visually measured angular distribution curve of resonance lines already shown in A. After detailed analysis of four proton interaction, center of gravity of individual group will be determined later and further discussions will be postponed until there. r_{12} determined from the maximum separation 20.15 gauss is equal to 1.607Å as shown in A.

Now, the effect of four proton interaction is most clearly demonstrated in the absorption lines when the direction of the magnetic field is coincided with the c-axis. The detail of the absorption line shape was shown in Fig. 6 of A. In this case, two types of four proton systems locate in the similar situation and the absorption lines corresponding to both groups coincide completely with each other. It can be seen from that figure that each of two well separated peaks consists at least with two partially overlapping lines. Actually, by the theoretical consideration, it consists of five lines. To compare the experimental curve with the theoretical one, one should compute the effect of other nuclei not belonging to the four proton system on the absorption line width. It is not clear how the external nuclei affect on the width of the individual lines in four proton resonance. Here we simply assumed that each component ten lines in four proton resonance have the same shape and width. The Gaussian shape is assumed and the width was determined so as to have the mean of the second moments for four individual protons by the dipolar interaction acted externally from the surrounding nuclei. The second moment $\langle \Delta H^2 \rangle_{Av}$ was calculated using the formula of Van Vleck$^{10)}$. This assumption of Gaussion shape is only approximate, since the effects of nearest protons which lie up and down the four proton group are predominant in $\langle \Delta H^2 \rangle_{Av}$ and the broadening effect of single line by them may not be symmetrical. But for the discussion given below, probably it will be sufficient to assume Gaussian distribution. To thus calculated second moment, that due to the field inhomogeneity which was determined by the water resonance width (0.06 gauss[2]) was added. In this calculation the value of r_{13} should be known. Using the value of r_{12} given above and assuming an appropriate value for r_{13}, the effects of surrounding protons are easily calculable. Also assuming the positions of water molecules and surrounding ions predicted by X-ray analysis[11]), the effects of surrounding ions other than protons can be calculated.

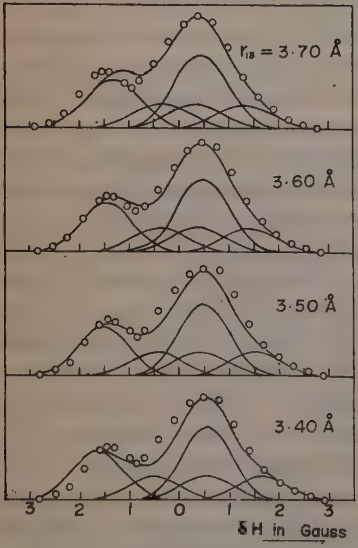

Fig. 2. The theoretical resonance curves for $K_2HgCl_4 \cdot H_2O$ in the case when the static field is parallel to the c-axis, corresponding to various values of r_{13} indicated in the figures. δH is the value of the static field strength measured from the value of the higher one of two resonance fields for two proton system. The experimental plots are written with circular marks. Only one peak at the higher field strength is shown.

Now, by the value of r_{12} given above and various values of r_{13} assumed appropriately, positions of ten lines due to four proton interaction were calculated by (12). Then Gaussian type component absorption peaks corresponding to the above calculated second moment are drawn at these positions with the intensities shown in (12) and also their summation curves are constructed in Fig. 2. Since it is sufficient to compare the experimental data with the theoretical curve for either one of the five components, only one group at the higher field is shown in the figure. In this figure the experimental plots already shown in A are also reproduced by circular marks with the intensities to coincide with the calculated curve at the maximum. The theoretical curves are drawn for various values of r_{13}. Best fit with the experimental plots is obtained when r_{13}=3.60Å, perhaps within the error of ±0.05Å. In Fig. 3 complete absorption curve is drawn for the case of r_{12}=1.607Å and r_{13}=3.60Å together with the experimental plots. The agreement seems satisfactory.

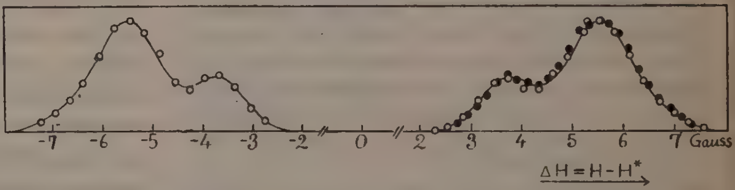

Fig. 3. The complete absorption curve in the case when the static field is parallel to the c-axis. Circular marks are the experimental plots.

The calculation of the positions of resonance lines due to four proton interaction and also their widths in the second moment was performed for various directions of the static magnetic field, and was compared with the experimental results. In all figures described in the following, the calculated curves and the experimental plots are made to coincide at the maximum. First, the case when the field is parallel to $\boldsymbol{r}_{12}$ was considered. The calculated absorption curve by using the values of r_{12} and r_{13} obtained above and the experimental plots are shown in Fig. 4. In this case also the agreement is satisfactory,

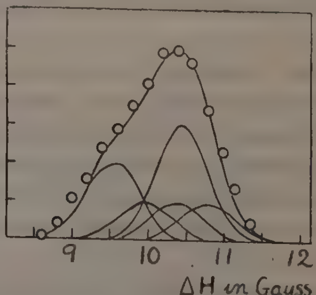

Fig. 4. The calculated curves (individual components and their summation) and the experimental plots for $K_2HgCl_4 \cdot H_2O$ in the case when the static field is parallel to the main p-p direction (r_{12}). Only one half at the higher side in field strength is shown.

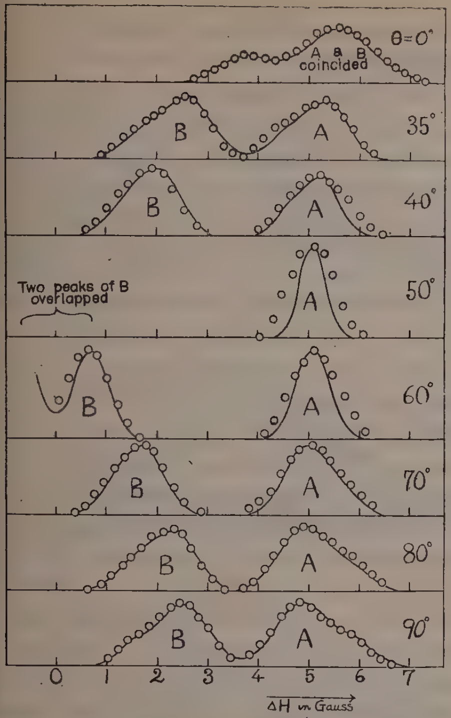

Fig. 5. The calculated curves and the experimental plots for $K_2HgCl_4 \cdot H_2O$ in the case when the static field is rotated in a plane perpendicular to one of the main p-p directions (r_{12}). The peaks due to the four proton system which has r_{12} perpendicular to the static field are denoted as A, while the peaks due to the other system are denoted as B. Only one half at the higher side in field strength is shown. θ is the angle between the static field and the *c*-axis. The height of each peak is represented in arbitrary unit.

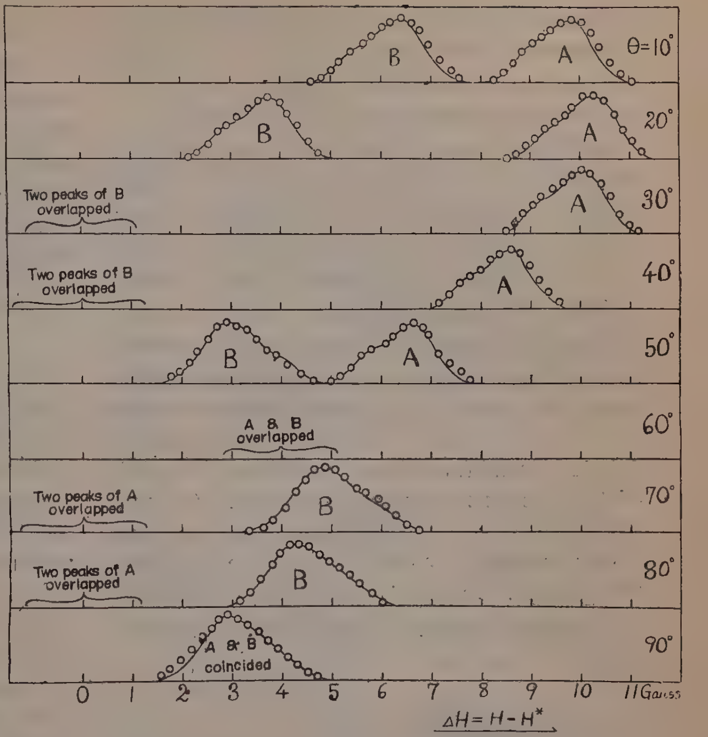

Fig. 6. The calculated curves and the experimental plots for $K_2HgCl_4 \cdot H_2O$ in the case when the static field is rotated in the *c*-plane. Peaks due to two four-proton systems are denoted as A and B respectively. Only half of the total curve is shown. θ is the angle between the static field and the *a*-axis. The height of each peak is represented in arbitrary unit.

indicating that the value of r_{12} determined from visual measurement on the oscilloscope screen corresponds to the real one. This implies that visually determined position of absorption line corresponds to the center of gravity of it rather than to the maximum of it. Notwithstanding that visually determined position corresponds to either the maximum or the center of gravity, the agreement between the theoretical and the experimental results in Fig. 4 indicates that the values $r_{12}=1.607$ and $r_{13}=3.60$Å are the actual ones.

Next, the theoretical and the experimental results are compared in the case when the direction of the static field is rotated in a plane perpendicular to one of $\boldsymbol{r}_{12}$ vectors in two four proton system. In this case, the positions of the absonption lines differ slightly with the calculated positions, though the observed line sharps are quite similar to the calculated ones. However, since it was very difficult to cut the single crystal in the desired shape and moreover the value of angle 21° may by in error within ±0.3°, these discrepancies may due to the fact that the magnetic field did not lie actually in the desired plane. Since the direction of the *c*-axis is definite, we assumed that, due to the slight error in the angle between p-p direction and the *a*-axis or/and due to the slight error in cutting of the crystal, the plane in which the static field was rotated is distorted about few degrees with respect to the desired plane. To fit the theoretical curve with the experimental one, this angle of discrepancy was taken as 1.5°, the *c*-axis lying on the plane of rotation. In Fig. 5 the theoretical curves are drawn with this assumption, together with the experimental plots. The agreement seems satisfactory. Owing to the fact that there are two types of four proton systems, the observed curves are complicated in some cases by the overlapping of different groups of the absorption lines. Some remarks are given in the interpretation of the figure.

In Fig. 6, some curves are given when the magnetic field is rotated in the c-plane. Again, overlapping of the different groups occurs, but the agreement between the theoretical and the experimental results seems satisfactory also in this case.

From the result of the X-ray analysis[11], the distance between the neighboring water molecules which align along the c-axis in a unit cell is roughly estimated about $c/2$, or 4.45Å. From the above mentioned analysis of the proton resonance experiment, the configuration of water molecules shown in Fig. 7 was deduced for each one of the four proton groups. In a water molecule, considering the potential energy, slight deformation in the configuration from the free molecule may occur more easily in deforming the bond angle ∠HOH than streching O–H distances[13]. Therefore, we may assume that O–H distance given in the literature[13] (0.957Å) does not change and the bond angle ∠HOH (105°) increases slightly in this crystal. Then the distance from the oxygen atom of the water molecule to the H–H line which is denoted as h in Fig. 7, becomes 0.515Å, and in this case, the bond angle of ∠HOH will be 115°. Therefore, the O–O′ distance which corresponds to that of the adjacent water molecules in the unit cell becomes 4.63Å, larger than $c/2$ which is predicted by the X-ray analysis. From these considerations, it may be concluded that the probable parameter of the oxygen atom of the water molecule of this crystal is $z=0.23$ instead of the approximate value of $z=1/4$ determimed by the original X-ray analysis[11].

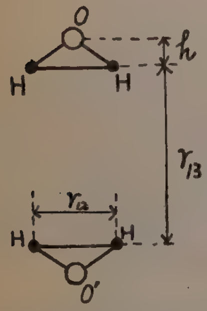

Fig. 7. Configuration of two water molecules forming a four proton system in the plane containing O and H atoms. h is the distance between the oxygen atom and the p-p direction in a water molecule.

§ 4. Discussion of the Experiments on $K_2SnCl_4 \cdot H_2O$

Since the crystal structure[14] of $K_2SnCl_4 \cdot H_2O$ (see Fig. 1) is similar to that of the Hg-salt[11], we shall discuss the results of the former crystal briefly. In the Sn-salt, r_{12} which was determined in A and checked by more detailed analysis is 1.62Å, slightly larger than that in the case of the Hg-salt. r_{13} can be determined by the shape of the absorption peak in the case when the static field is parallel to the c-axis. As shown in A, fine structure in each one of peaks is less

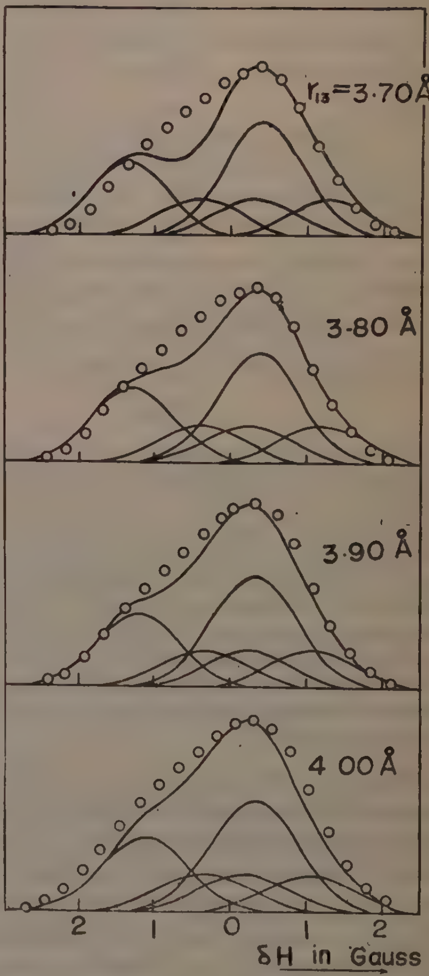

Fig. 8. The calculated curves for $K_2SnCl_4 \cdot H_2O$ in the case when the static field is parallel to the c-axis, corresponding to various values of r_{13} indicated in the figures. The experimental plots are written with circular marks. Only one peak at the higher field strength is shown. δH has the same meaning as illustrated in Fig. 2.

predominant in the Sn-salt than in the Hg-salt. So, we cannot determine r_{13} as accurate as in the case of the Hg-salt. In Fig. 8, the calculated distribution curves are compared with the experimental one just as in the case of the Hg-salt. Most probable value for r_{13} is 3.90Å, though the fit is not so satisfactry as in the case of the Hg-salt. Shapes of some absorption curves are calculated and were compared with the experimental data, but more definite conclusion about the value of r_{13} was not obtainable.

The distances between the neighbouring water molecules aligned on a line parallel to the c-axis in the unit cell are predicted by the X-ray analysis as $c/2=4.56$Å. Just as in the case of the Hg-salt, the O–O′ distance of the adjacent water molecules in the Sn-salt may be computed. From the abovementioned results, it is obtained that the O–O′ distance where the two proton lines are each other inside of it is 4.91Å and the bond angle of ∠HOH is about 115°. This O–O′ distance is somewhat longer than that determined from the X-ray analysis. However, the position of the oxygen atom in the unit cell of space group V_h^{16}–$Pbnm$ determined by X-ray analysis for this crystal is a parameter-free, special position[15], namely this position is not movable in accordance with the operation of this space group. Whereupon, it becomes necessary to choose a new space group to avoid this contradiction. The most probable one is V_h^{9}–$Pbnm$ identical with that of the Hg-salt. According to this space group, the atomic positions of $K_2SnCl_4\cdot H_2O$ are revised as follows:

4 Sn on 4(e) with $z=0.25$
4 Cl_{I} on 4(g) with $x=0.21$, $y=-0.05$
4 Cl_{II} on 4(h) with $x=0.21$, $y=-0.05$
8 Cl_{III} on 8(i) with $x=0.02$, $y=0.25$, $z=0.217$
4 K_{I} on 4(g) with $x=0.40$, $y=0.127$
4 K_{II} on 4(h) with $x=0.34$, $y=0.20$
4 O on 4(f) with $z=0.22$

By the nuclear magnetic experiment alone, it is not clear which of two alternatives for the position of the oxygen atomwhich correspond to upward and downward displacements from the position $c/2$ is the actual case. But, it may be probable that the case of downward displacement is the actual one in conformity with the electrostatic effect of the surrounding ions. In the above expression, this case was chosen.

Owing to the weaker X-ray scattering power of oxygen atom than the other heavier atoms, its position is not clearly decided by the X-ray analysis and it will be unable to recognize which space group is the actual one from the X-ray experiment alone. The analysis of the nuclear magnetic resonance experiment discussed above is probably more accurate for the decision of the position of the oxygen atom, and the space group is more clearly determined by the present experiment.

References

1) J. Itoh, R. Kusaka, Y. Yamagata, R. Kiriyama, H. Ibamoto, T. Kanda and Y. Masuda: J. Phys. Soc. Japan. **8** (1953) 287.

2) G. E. Pake: J. Chem. Phys. **16** (1948) 327.

3) E. R. Andrew and R. Bersohn: J. Chem. Phys. **18** (1950) 159.

4) H. S. Gutowsky, G. B. Kistiakowsky, G. E. Pake, E. M. Purcell: J. Chem. Phys. **17** (1949) 930.
H. S. Gutowsky and G. E. Pake: J. Chem. Phys. **18** (1950) 162.

5) Y. Kakiuchi, S. Shono, H. Komatsu and K. Kigoshi: J. Chem. Phys. **19** (1951) 1069. J. Phys. Soc. Japan. **7** (1952) 108.

6) Richards and Smiths: Trans. Far. Soc. **47** (1951) 1261.

7) K. Tomita: Busseiron-Kenkyu (in Japanese), **46** (1952) 142. Phys. Rev. **89** (1953) 429.

8) R. Bersohn: Private communication (to be published in J. Chem. Phys.)

9) J. Itoh, R. Kusaka, Y. Yamagata, R. Kiriyama and H. Ibamoto: J. Chem. Phys. **20** (1952) 1503.

10) J. H. Van Vleck: Phys. Rev. **74** (1948) 1168.

11) McGillavry, de Wilde and Bijvoet: Z. Krist. **100** (1938) 212.

12) G. Herzberg: *Infrared and Raman spectra of polyatomic molecules.* (1945) 170.

13) G. Herzberg: loc. cit. 489.

14) H. Brasseur and A. de Rassenfosse: Z. Krist. **101** (1939) 389.

15) R. W. G. Wyckoff (*Crystal structure*, vol. 2, 1951) suggested that the space group of the Sn-salt may be doubtful, and stated that further experiment on this point is expected.

Journal of the Physical Society of Japan Vol. 8, No. 3, May—June, 1953

Mathematical Formulations of Physical Quantities for *j-j*-coupling Nuclear Shell Model

By Sadaaki Yanagawa

Department of Applied Physics, Faculty of Engineering, University of Tokyo

(Received January 31, 1953)

Fractional parentage coefficients defined by G. Racah[1] for nuclear *j-j*-coupling wave functions $((j)^2, j:(j)^3)$, $((j)^3, j:(j)^4)$ and $((j)^4, j:(j)^5)$ (maximum T only) for $j=3/2$ and $j=5/2$ are calculated by group theoretical method[2]. Using these coefficients formulae are derived for the matrix elements of operators generally defined such as $T_0^{(p)}(S^{(k)}\cdot L^{(k)})$ or $T_0^{(p)}S_0^{(0)}L_0^{(k)}$ in a nuclear configuration consisted of several closed shells and one unfilled shell, in terms of the basic two body integrals.

Introduction

In treating the nuclear structure, it may not be well known that whether the *j-j*-coupling shell model is applicable or not, and also the mathematical formulation for them have not yet been given in sufficiently manner.

But it may be considered that the Racah's result in L-S-coupling case is the most complete method, as they need no assumptions on nucleons such as Mayer's independent particle model and so on. In this connection the same method in our case will give us the most sufficient formulations.

In the course of our investigation, B. H. Flowers'[3][4] paper has been published. In this paper we can find the same procedure as we have done. But there are many details different from them, and values of coefficients and $U^{(k)}$ are necessary to calculate the matrix element of operators in the configuration consisted of closed shells and one unfilled shell (§ 2, 3). So we will tabulate them as simple as possible avoiding duplication with Flowers'.

The $2l+1$ orbital components of single nucleon wave function l are invariant under the group of unitary transformations $U(2l+1)$ with odd dimensions. While invariance under the sub-group of $2l+1$ dimensional rotation group $B(l)$ in L-S-coupling shell model introduces the necessary reduction scheme as follows···

$$U(2l+1)\longrightarrow B(l)\longrightarrow (G(2),\ \text{if}\ \ l=3)\longrightarrow L(B(1)).$$

But, in *j-j*-coupling shell model one can not adopt this scheme because of the invariance under the group of unitary transformations $U(2j+1)$ with even dimensions for $2j+1$ components of single nucleon wave function l_j. The sub-group corresponding to $B(l)$ in L-S-coupling is "symplectic" group $C((2j+1)1/2)$ in *j-j*-coupling case. We can construct symplectic group as the fundamental irreducible representation $[10\cdots]$ of $U(2j+1)$ corresponds to the fundamental irreducible representation $(10\cdots)$ of $C((2j+1)1/2)$. Further we can construct 3 dimensional rotation group $B(1)$ as the fundamental representation $(10\cdots)$ of $C((2j+1)/2)$ corresponds to the irreducible representation J of $B(1)$.

Thus we adopt the reduction scheme in this paper as follows;

$$U(2j+1)\longrightarrow C((2j+1)1/2)\longrightarrow B(1).$$

In § 1, in order to reduce to one nucleon or two nucleons system, fractional parentage coefficients (hereafter we denote c.f.p.) have been calculated by group theoretical method for above-mentioned values and tabulated in the form of Jahn's paper[5].

In § 2, general theory for obtaining matrix elements of interaction operator Q have included, in the quantum state of nucleons system

$$\psi(\gamma TM_T JM_J)$$

as J. P. Elliott[6] expanded in L-S-coupling shell model. The operator $Q=\sum_{i>j} Q(ij)$ (only two body interaction assumed) is generally the products of scalar parts of tensor operators each operates only on one part; T, S and L part, of the eigen-function. Namely $Q(ij)$ has a next form

$$Q(ij)=T_0^{(p)}(ij)(S^{(k)}(ij)\cdot L^{(k)}(ij))$$
$$\text{or}\ \ T_0^{(p)}(ij)S_0^{(0)}(ij)L_0^{(k)}(ij).$$

In § 3, an example of obtaining matrix

elements of some interaction operators have been shown.

§ 1

In Flowers' paper we can find the same classification of states as our scheme demands. Then we have omitted the table of classification of states completely and we have only tabulated necessary equations and reduction formulae for obtaining c.f.p.. Notations used here are those of Racah's, Jahn's and so on.

$\boxed{j=3/2}$

$n=1$

[1]=(10)=(3/2)

$n=2$

[1]×[1]=[11]+[2]
(10)×(10)=(00)+(11)+(20)
[2]=(20)=(1)+(3)
[11]=(11)+(00)
(11)=(2)

$n=3$

[2]×[1]=[3]+[21]
[11]×[1]=[21]+[111]
(20)×(10)=(30)+(21)+(10)
(11)×(10)=(21)×(10)
[3]=(30)=(3/2)+(5/2)+(9/2)
[21]=(21)+(10)
[111]=(10)=(3/2)
(21)=(1/2)+(5/2)+(7/2)

$n=4$

[3]×[1]=[4]+[31]
[21×[1]=[31]+[22]+[211]
[111]×[1]=[211]+[1111]
(30)×(10)=(40)+(31)+(20)
(21)×(10)=(31)+(22)+(20)+(11)
[4]=(40)=(0)+(2)+(3)+(4)+(6)
[31]=(31)+(20)
[22]=(22)+(11)+(00)
[211]=(20)+(11)
[1111]=(00)
(31)=(1)+(2)+(3)+(4)+(5)
(22)=(2)+(4)

The unit operator $u_q^{(k)}$ introduced by G. Racah ($k=0, 1, 2, 3, \ldots$; $q=k, k-1, \ldots, -k$) is defined as follows,

$$(jm|u_q^{(k)}|jm')=(-)^{j+m}V(jjk:mm'q)$$

which vanishes when k is larger than $2j$ from the triangular condition of j, j and k. For every value of k, there are $2k+1$ matrices of this kind with $2j+1$ rows and columns, this gives a total of $(2j+1)^2$ matrices for each j. In virtue of the linearly independencies of these $(2j+1)^2$ matrices with dimension $2j+1$, they form the full linear group of $2j+1$ dimension and its unitary sub-group $U(2j+1)$. Further the tensors $u_q^{(k)}$ of odd degree are the infinitesimal operators of a sub-group of the group $U(2j+1)$. It is easy to see that this group is the symplectic group, which leaves invariant the anti-symmetric bilinear form

$$\sum_{i=1}^{(2j+1)/2} x^i y^{-i} - x^{-i} y^i .$$

For a system of n nucleons we can define a set of $u_q^{(k)}(i)$ ($i=1, 2, \ldots, n$) each operating on one nucleon and we can construct the symmetrical tensor

$$U_q^{(k)} = \sum_{i=1}^{n} u_q^{(k)}(i)$$

operating on the whole system. It is evident that the $U_q^{(k)}$ also satisfies the structure relation in the meaning of Lie group. In the course of calculation of c.f.p., the matrix $U_q^{(k)}$ plays a great important role. Then we tabulated the values of so-called double-barred $U^{(k)}$ matrices when k is odd ($k=3$) and even ($k=2$), necessary enough to get c.f.p..

$$((00)0\|U^{(3)}\|(00)0)=\|0\|$$
$$((11)2\|U^{(3)}\|(11)2)=\|-\sqrt{2}\|$$

$((20)J\|U^{(3)}\|(20)J')$

J \ J'	1	3
1	0	$2\sqrt{\frac{3}{5}}$
3	$2\sqrt{\frac{3}{5}}$	$2\sqrt{\frac{3}{10}}$

$([11](C)J\|U^{(2)}\|[11](C')J')$

(C)		(00)	(11)
(C)	J' \ J	0	2
(00)	0	0	1
(11)	2	1	0

$([2](20)J\|U^{(2)}\|[2](20)J')$

J \ J'	1	3
1	$-\frac{2\sqrt{6}}{5}$	$\frac{\sqrt{21}}{5}$
3	$\frac{\sqrt{21}}{5}$	$\frac{2\sqrt{21}}{5}$

$U_q^{(3)}$ is an infinitesimal operator of $C(2)$, and from this fact the relation

$$((C)J\|U^{(3)}\|(C')J')=0 \text{ if } (C)\not\asymp(C')$$

is obvious. $U_q^{(2)}$ is an infinitesimal operator of $U(4)$. So

$$([U](C)J\|U^{(2)}\|[U'](C')J')=0 \text{ if } [U]\not\asymp[U']$$

is seen to be correct as the same reason as above formula. Using these equations we can get the c.f.p. of j-part and tabulate as follows.

j^3 \ j^2				(11) [2] (20) 1	(11) [2] (20) 3	(21) [11] (00) 0	(21) [11] (11) 2
(211) (121)	[21]	(10)	3/2	$\sqrt{\frac{3}{10}}$	$\sqrt{\frac{7}{10}}$	$\sqrt{\frac{5}{6}}$	$\frac{1}{\sqrt{6}}$
		(21)	1/2	-1			1
			5/2	$\sqrt{\frac{7}{15}}$	$-2\sqrt{\frac{2}{15}}$		1
			7/2		1		1
(321)	[111]	(10)	3/2			$-\frac{1}{\sqrt{6}}$	$\sqrt{\frac{5}{6}}$

The charge spin part is simple, therefore it is not necessary to write down. Thus we combine j and charge spin part appropriately so as to make totally antisymmetric by permutation group and get total c.f.p. $((j)^2j:(j)^3)$, $j=3/2$:

j^3 \ j^2				[2] (20) $^1(1)$	[2] (20) $^1(3)$		[11] (00) $^3(0)$	[11] (11) $^3(2)$
[21]	(10)	$^2(3/2)$	$\frac{1}{\sqrt{2}}$	$\sqrt{\frac{3}{10}}$	$\sqrt{\frac{7}{10}}$	$-\frac{1}{\sqrt{2}}$	$\sqrt{\frac{5}{6}}$	$\frac{1}{\sqrt{6}}$
	(21)	$^3(1/2)$		-1				1
		$^2(5/2)$		$\sqrt{\frac{7}{15}}$	$-2\sqrt{\frac{2}{15}}$			1
		$^2(7/2)$			1			1
[111]	(10)	$^4(3/2)$					$-\frac{1}{\sqrt{6}}$	$\sqrt{\frac{5}{6}}$

Similarly we calculate $((21)J\|U^{(3)}\|(21)J')$, $([21](C)J\|U^{(2)}\|[21](C')J')$ so as to coinside the two values which denoted (211) and (121), by changing the phase of $(j)^3$ wave function appropriately. By doing this operation the correct c.f.p. of $(j)^2\rightarrow(j)^3$ is determined as tabulated above and we can enter into the calculation of $(j)^3\rightarrow(j)^4$ smoothly. But in getting the matrix element only it is not necessary to do this correction.

$((21)J\|U^{(3)}\|(21)J')$

J \ J'	1/2	5/2	7/2
1/2	0	$-\sqrt{\frac{15}{14}}$	$\frac{6}{\sqrt{35}}$
5/2	$-\sqrt{\frac{15}{14}}$	$-\frac{3}{7}$	$\frac{6\sqrt{5}}{7}$
7/2	$-\frac{6}{\sqrt{35}}$	$-\frac{6\sqrt{5}}{7}$	$-\frac{2}{7}\sqrt{\frac{33}{10}}$

$([21](C)J\|U^{(3)}\|[21](C')J')$

(C)	(C')	(10)	(21)		
	J \ J'	3/2	1/2	5/2	7/2
(10)	3/2	$\frac{7}{5}$	$\frac{2\sqrt{3}}{5}$	$\frac{6}{5}$	$\frac{4\sqrt{3}}{5}$
(21)	1/2	$-\frac{2\sqrt{3}}{5}$	0	$\frac{\sqrt{21}}{5\sqrt{2}}$	0
	5/2	$-\frac{6}{5}$	$\frac{\sqrt{21}}{5\sqrt{2}}$	$-\frac{\sqrt{3}}{5\sqrt{7}}$	$\frac{12}{5\sqrt{7}}$
	7/2	$\frac{4\sqrt{3}}{5}$	0	$-\frac{12}{5\sqrt{7}}$	$\sqrt{\frac{6}{7}}$

By the same method we obtain the c.f.p. of $(j)^3 \rightarrow (j)^4$, namely:

j^4 \ j^3				(211) (121) [21]					(321) [111]
				(10)		(21)			(10)
				3/2		1/2	5/2	7/2	
(2211) (2121)	[22]	(00)	0	1					
		(11)	2	$\sqrt{\frac{3}{5}}$	$\sqrt{\frac{2}{5}}\,[$	$-\frac{1}{2\sqrt{2}}$	$-\frac{\sqrt{3}}{2\sqrt{2}}$	$\frac{1}{\sqrt{2}}\,]$	
		(22)	2			$-\frac{\sqrt{7}}{2\sqrt{5}}$	$\frac{\sqrt{15}}{2\sqrt{7}}$	$\frac{2}{\sqrt{35}}$	
			4				$\sqrt{\frac{2}{7}}$	$-\sqrt{\frac{5}{7}}$	
(3211) (3121) (1321)	[211]	(11)	2	$-\sqrt{\frac{2}{5}}$	$\sqrt{\frac{3}{5}}\,[$	$-\frac{1}{2\sqrt{2}}$	$-\frac{\sqrt{3}}{2\sqrt{2}}$	$\frac{1}{\sqrt{2}}\,]$	1
		(20)	1	$-\frac{1}{\sqrt{10}}\,[\,1$	$\frac{3}{\sqrt{10}}\,[$	$\frac{\sqrt{5}}{2\sqrt{3}}$	$-\frac{\sqrt{7}}{2\sqrt{3}}$		1
			3	$1\,]$			$\sqrt{\frac{2}{7}}$	$\sqrt{\frac{5}{7}}\,]$	1
(4321)	[1111]	(00)	0						1

Finally we combine this j part with charge spin part by the permutation group, the c.f.p. of $((j)^3, j; (j)^4)$, $j=3/2$ are obtained.

$$
\begin{array}{lll|c|ccc|c}
 & j^4 \backslash & j^3 & \multicolumn{4}{c|}{[21]} & [111] \\
 & & & (10) & \multicolumn{3}{c|}{\overbrace{\hspace{6em}}^{(21)}} & (10) \\
 & & & {}^2(3/2) & {}^2(1/2) & {}^2(5/2) & {}^2(7/2) & {}^4(3/2) \\
\hline
[22] & (00) & {}^1(0) & 1 & & & & \\
 & (11) & {}^1(2) & \sqrt{\frac{3}{5}} & \sqrt{\frac{2}{5}}\Big[-\frac{1}{2\sqrt{2}} & -\frac{\sqrt{3}}{2\sqrt{2}} & \frac{1}{\sqrt{2}}\Big] & \\
 & (22) & {}^1(2) & & -\frac{\sqrt{7}}{2\sqrt{5}} & \frac{\sqrt{15}}{2\sqrt{7}} & \frac{2}{\sqrt{35}} & \\
 & & {}^1(4) & & & \sqrt{\frac{2}{7}} & -\sqrt{\frac{5}{7}} & \\
\hline
[211] & (11) & {}^3(2) & \sqrt{\frac{2}{3}}\Bigg[-\sqrt{\frac{2}{5}} & \sqrt{\frac{3}{5}}\Big[-\frac{1}{2\sqrt{2}} & -\frac{\sqrt{3}}{2\sqrt{2}} & \frac{1}{\sqrt{2}}\Big] & \Big(1 \\
 & (20) & {}^3(1) & -\frac{1}{\sqrt{10}}\Big(1 & \frac{3}{\sqrt{10}}\Big[\frac{\sqrt{5}}{2\sqrt{3}} & -\frac{\sqrt{7}}{2\sqrt{3}} & & \frac{1}{\sqrt{3}}\ 1 \\
 & & {}^3(3) & 1\Big) & & \sqrt{\frac{2}{7}} & \sqrt{\frac{5}{7}}\Big]\Bigg] & 1\Big) \\
\hline
[1111] & (00) & {}^5(0) & & & & & 1
\end{array}
$$

For $j=5/2$ we have only tabulated the necessary formulae and values avoiding the duplication of explanation. For c.f.p. also we omitted the total c.f.p. involving the charge spin part, for symplicity.

$\boxed{j=5/2}$

$n=1$

$[1]=(100)=(5/2)$

$n=2$

$[1]\times[1]=[2]+[11]$

$(100)\times(100)=(200)+(110)+(000)$

$[2]=(200)=(1)+(3)+(5)$

$[11]=(110)+(000)$

$(110)=(2)+(4)$

$n=3$

$[2]\times[1]=[3]+[21]$

$[11]\times[1]=[21]+[111]$

$(200)\times(100)=(300)+(210)+(100)$

$(110)\times(100)=(210)+(111)+(100)$

$[3]=(300)=(3/2)+(5/2)+(7/2)+(9/2)$
$\quad+(11/2)+(15/2)$

$[21]=(210)+(100)$

$[111]=(111)+(100)$

$(210)=(1/2)+(3/2)+(5/2)+2(7/2)$
$\quad+(9/2)+(11/2)+(13/2)$

$(111)=(3/2)+(9/2)$

$n=4$

$[3]\times[1]=[4]+[31]$

$[21]\times[1]=[31]+[22]+[211]$

$[111]\times[1]=[211]+[1111]$

$(300)\times(100)=(400)+(310)+(200)$

$(210)\times(100)=(310)+(220)+(211)$
$\quad+(200)+(110)$

$(111)\times(100)=(211)+(110)$

$[4]=(400)=(0)+2(2)+(3)+2(4)+(5)$
$\quad+2(6)+(7)+(8)+(10)$

$[31]=(310)+(200)$

$[22]=(220)+(110)+(000)$

$[211]=(211)+(200)+(110)$

$[1111]=(110)+(000)$

$(310)=2(1)+2(2)+3(3)+3(4)+3(5)$
$\quad+2(6)+2(7)+(8)+(9)$

$(220)=(0)+2(2)+(3)+2(4)+(5)$
$\quad+2(6)+(8)$

$(211)=(1)+(2)+2(3)+(4)+(5)+(6)+(7)$

$n=5$

$[1111]\times[1]=[2111]+[11111]$

$[11111]=[1]=(100)=(5/2)$

$[2111]=(210)+(111)+(100)$

$((200)\,J\,\|U^{(3)}\|(200)\,J')$

$J \backslash J'$	1	3	5
1	0	$\frac{2\sqrt{6}}{\sqrt{35}}$	0
3	$\frac{2\sqrt{6}}{\sqrt{35}}$	$-\frac{17}{3\sqrt{30}}$	$\frac{5\sqrt{11}}{3\sqrt{21}}$
5	0	$\frac{5\sqrt{11}}{3\sqrt{21}}$	$\frac{\sqrt{143}}{3\sqrt{6}}$

$((110)\,J\,\|U^{(3)}\|(110)\,J')$

$J \backslash J'$	2	4
2	$-\frac{9}{7\sqrt{2}}$	$\frac{5\sqrt{3}}{7}$
4	$\frac{5\sqrt{3}}{7}$	$-\frac{\sqrt{11}}{7\sqrt{2}}$

$([2](200)\,J\,\|U^{(2)}\|(200)\,J')$

$J \backslash J'$	1	3	5
1	$-\frac{8\sqrt{2}}{5\sqrt{7}}$	$\frac{9\sqrt{2}}{5\sqrt{7}}$	0
3	$\frac{9\sqrt{2}}{5\sqrt{7}}$	$-\frac{1}{15}$	$\frac{\sqrt{55}}{3\sqrt{14}}$
5	0	$\frac{\sqrt{55}}{3\sqrt{14}}$	$\frac{\sqrt{13\cdot 22}}{3\sqrt{7}}$

$([11](C)\,J\,\|U^{(2)}\|[11](C')\,J')$

$(C) \backslash (C')$		(000)	(110)	
	$J \backslash J'$	0	2	4
(000)	0	0	$\sqrt{\frac{2}{3}}$	0
(110)	2	$\sqrt{\frac{2}{3}}$	$-\frac{5\sqrt{2}}{7\sqrt{3}}$	$\frac{9}{7\sqrt{2}}$
	4	0	$\frac{9}{7\sqrt{2}}$	$\frac{\sqrt{33}}{7}$

		$j^3 \backslash j^2$	(11) [2] (200) 1	3	5	(21) [11] (000) 0	(110) 2	4
(211) (121) [21]	(100)	5/2	$\frac{1}{\sqrt{7}}$	$\frac{1}{\sqrt{3}}$	$\sqrt{\frac{11}{21}}$	$\frac{\sqrt{7}}{3}$	$\frac{\sqrt{2}}{3}\Big[\sqrt{\frac{5}{14}}$	$\frac{3}{\sqrt{14}}\Big]$
	(210)	1/2		1			1	
		3/2	$-\frac{2}{\sqrt{5}}$	$-\frac{1}{\sqrt{5}}$			$\sqrt{\frac{2}{7}}$	$\sqrt{\frac{5}{7}}$
		5/2	$-\frac{2\sqrt{2}}{\sqrt{35}}$	$\frac{13}{3\sqrt{30}}$	$-\frac{5\sqrt{11}}{3\sqrt{210}}$		$-\frac{3}{\sqrt{14}}$	$\sqrt{\frac{5}{14}}$
		$(7/2)_1$		$-\frac{\sqrt{11}}{3\sqrt{2}}$	$\frac{\sqrt{7}}{3\sqrt{2}}$		$-\sqrt{\frac{11}{14}}$	$\sqrt{\frac{3}{14}}$
		$(7/2)_2$	$-\frac{2}{\sqrt{7}}$	$\frac{1}{\sqrt{6}}$	$\sqrt{\frac{11}{42}}$		$-\sqrt{\frac{3}{14}}$	$-\sqrt{\frac{11}{14}}$
		9/2		$\frac{\sqrt{5}}{3\sqrt{2}}$	$\frac{\sqrt{13}}{3\sqrt{2}}$		$\sqrt{\frac{11}{14}}$	$\sqrt{\frac{3}{14}}$
		11/2		$\frac{\sqrt{13}}{3\sqrt{5}}$	$-\frac{\sqrt{14}}{3\sqrt{3}}$			1
		13/2			1			1
(321) [111]	(100)	5/2				$-\frac{\sqrt{2}}{3}$	$\frac{\sqrt{7}}{3}\Big[\sqrt{\frac{5}{14}}$	$\frac{3}{\sqrt{14}}\Big]$
	(111)	3/2					$-\sqrt{\frac{5}{7}}$	$\sqrt{\frac{2}{7}}$
		9/2					$-\sqrt{\frac{3}{14}}$	$\sqrt{\frac{11}{14}}$

$$((111)\,3/2\,\|U^{(3)}\|(111)\,3/2) = -8/7$$

$$((111)\,3/2\,\|U^{(3)}\|(111)\,9/2) = -20/7\sqrt{6}$$

$((210)\,J\,\|U^{(3)}\|(210)\,J')$

$J \backslash J'$	1/2	3/2	5/2	$(7/2)_1$	$(7/2)_2$	9/2	11/2	13/2
1/2	0	0	$-\frac{2\sqrt{10}}{7}$	$-\frac{8\sqrt{11}}{7\sqrt{15}}$	$\frac{2}{7\sqrt{5}}$	0	0	0
5/2	0	$\frac{2}{7}$	$\frac{5}{7}$	$-\frac{5\sqrt{22}}{21\sqrt{5}}$	$\frac{2\sqrt{10}}{7\sqrt{3}}$	$\frac{\sqrt{55}}{21}$	0	0
5/2	$-\frac{2\sqrt{10}}{7}$	$-\frac{5}{7}$	$-\frac{3}{7}$	$\frac{\sqrt{55}}{21}$	$\frac{5\sqrt{5}}{7\sqrt{3}}$	$\frac{2\sqrt{5}}{21}$	$\frac{\sqrt{65}}{7}$	0
$(7/2)_1$	$\frac{8\sqrt{11}}{7\sqrt{15}}$	$-\frac{5\sqrt{22}}{21\sqrt{5}}$	$-\frac{\sqrt{55}}{21}$	$-\frac{26\sqrt{5}}{21\sqrt{66}}$	$\frac{44}{21\sqrt{10}}$	$-\frac{95\sqrt{5}}{21\sqrt{33}}$	$-\frac{32}{21\sqrt{110}}$	$\frac{10}{3\sqrt{11}}$
$(7/2)_2$	$-\frac{2}{7\sqrt{5}}$	$\frac{2\sqrt{10}}{7\sqrt{3}}$	$-\frac{5\sqrt{5}}{7\sqrt{3}}$	$\frac{44}{21\sqrt{10}}$	$\frac{6\sqrt{11}}{7\sqrt{30}}$	$-\frac{5\sqrt{5}}{21}$	$-\frac{26}{7\sqrt{30}}$	0
9/2	0	$-\frac{\sqrt{55}}{21}$	$\frac{2\sqrt{5}}{21}$	$\frac{95\sqrt{5}}{21\sqrt{33}}$	$\frac{5\sqrt{5}}{21}$	$\frac{17\sqrt{13}}{21\sqrt{33}}$	$\frac{5\sqrt{5}}{3\sqrt{11}}$	$\frac{10\sqrt{2}}{3\sqrt{11}}$
11/2	0	0	$-\frac{\sqrt{65}}{7}$	$-\frac{32}{21\sqrt{110}}$	$-\frac{26}{7\sqrt{30}}$	$-\frac{5\sqrt{5}}{3\sqrt{11}}$	$-\frac{14}{\sqrt{13\cdot 55}}$	$\frac{10\sqrt{2}}{\sqrt{143}}$
13/2	0	0	0	$-\frac{10}{3\sqrt{11}}$	0	$\frac{10\sqrt{2}}{3\sqrt{11}}$	$-\frac{10\sqrt{2}}{\sqrt{143}}$	$\sqrt{\frac{34}{143}}$

$([111](C)\,J\,\|U^{(2)}\|[111](C')\,J')$

$(C) \backslash (C')$		(100)	(111)	
	$J \backslash J'$	5/2	3/2	9/2
(100)	5/2	0	$\frac{2\sqrt{3}}{\sqrt{7}}$	$\frac{3}{\sqrt{7}}$
(111)	3/2	$-\frac{2\sqrt{3}}{\sqrt{7}}$	0	0
	9/2	$\frac{3}{\sqrt{7}}$	0	0

$$([21](100)\,5/2\|U^{2}\|[21](100)\,5/2)=\frac{9}{7}$$
$$(\qquad \text{''} \qquad (210)\,1/2)=2\sqrt{3}/\sqrt{35}$$
$$(\qquad \text{''} \qquad 9/2)=\sqrt{66}/7$$

$([21](C)\,J\|U^{(2)}\|[21](C')\,J')$

(C′)		(100)	(210)			
(C)	J \ J′	$5/2$	$3/2$	$5/2$	$(7/2)_1$	$(7/2)_2$
(210)	$3/2$	$-\frac{4}{7}\sqrt{\frac{3}{5}}$	$\frac{6}{5}\sqrt{\frac{3}{7}}$	$-\frac{\sqrt6}{5}$	$\frac{3\sqrt{22}}{35}$	$-\frac{12\sqrt6}{35}$
	$5/2$	$-\frac{9}{7}\sqrt{\frac{2}{5}}$	$\frac{\sqrt6}{5}$	$-\frac{9}{35}$	$\frac{3\sqrt{33}}{35}$	$\frac{39}{35}$
	$(7/2)_1$	$\frac{2}{7}\sqrt{\frac{66}{5}}$	$\frac{3\sqrt{22}}{35}$	$-\frac{3\sqrt{33}}{35}$	$-\frac{\sqrt2}{35}$	$\frac{2\sqrt{66}}{35}$
	$(7/2)_2$	$\frac{6}{7}\sqrt{\frac{2}{5}}$	$-\frac{12\sqrt6}{35}$	$-\frac{39}{35}$	$\frac{2\sqrt{66}}{35}$	$\frac{3\sqrt2}{35}$

		j^3 \ j^2		(211) (121) [21]												(321) (111)			
				(100)		(210)										(100)		(111)	
				$5/2$		$1/2$	$3/2$	$5/2$	$(7/2)_1$	$(7/2)_2$	$9/2$	$11/2$	$13/2$			$3/2$		$3/2$	$5/2$
(2211) (2121) [22]	(000)	0		1															
	(110)	2	$\frac{2}{\sqrt7}$	1	$\frac{\sqrt3}{\sqrt7}$	$\frac{1}{4}\sqrt{\frac{7}{5}}$	$-\frac{1}{2\sqrt5}$	$-\frac{3}{4}\sqrt{\frac{3}{10}}$	$\frac{1}{2}\sqrt{\frac{11}{10}}$	$\frac{1}{2}\sqrt{\frac{3}{10}}$	$\frac{1}{4}\sqrt{\frac{11}{2}}$								
		4		1			$-\frac{1}{6}\sqrt{\frac{5}{2}}$	$\frac{1}{4}\sqrt{\frac{5}{6}}$	$-\frac{1}{2\sqrt6}$	$\frac{1}{6}\sqrt{\frac{11}{2}}$	$\frac{1}{4}\sqrt{\frac{5}{6}}$	$-\frac{1}{2}\sqrt{\frac{7}{6}}$	$\frac{7}{12}$						
	(220)	0						1											
		$(2)_1$				$-\frac{\sqrt5}{4\sqrt2}$	$\frac{\sqrt7}{2\sqrt{10}}$	$-\frac{9}{8}\sqrt{\frac{3}{35}}$	$\frac{\sqrt{55}}{12\sqrt7}$	$\frac{5\sqrt5}{4\sqrt{21}}$	$-\frac{\sqrt{77}}{24}$								
		$(2)_2$				$-\frac{\sqrt{33}}{4\sqrt{10}}$	$-\frac{\sqrt{33}}{2\sqrt{70}}$	$\frac{1}{8}\sqrt{\frac{11}{35}}$	$\frac{27}{4\sqrt{105}}$	$-\frac{3}{4}\sqrt{\frac{11}{35}}$	$-\frac{9}{8\sqrt{21}}$								
		3				$\frac{1}{\sqrt7}$	$-\frac{3}{2\sqrt{70}}$	$\frac{3}{\sqrt{70}}$	$\frac{1}{6}\sqrt{\frac{11}{14}}$	$\frac{5}{6}\sqrt{\frac{3}{14}}$	$-\frac{1}{3\sqrt{14}}$	$\frac{1}{2}\sqrt{\frac{13}{14}}$							
		$(4)_1$					$\frac{\sqrt{11}}{14\sqrt2}$	$\frac{\sqrt{22}}{7\sqrt3}$	$-\frac{13\sqrt{11}}{14\sqrt{30}}$	$-\frac{9}{14\sqrt{10}}$	$-\frac{19\sqrt2}{7\sqrt{33}}$	$-\frac{13}{2\sqrt{7\cdot11\cdot30}}$	0						
		$(4)_2$					$-\frac{\sqrt{143}}{14\sqrt2}$	$-\frac{\sqrt{143}}{28\sqrt6}$	$-\frac{5\sqrt{65}}{14\sqrt{66}}$	$-\frac{\sqrt{65}}{14\sqrt2}$	$\frac{5\sqrt{13}}{28\sqrt{66}}$	$\frac{3\sqrt5}{2\sqrt{11\cdot13\cdot42}}$	$\frac{7\sqrt5}{4\sqrt{143}}$						
		5						$\frac{1}{2}$	$-\frac{23}{6\sqrt{55}}$	$\frac{1}{2\sqrt{15}}$	$\frac{1}{6}\sqrt{\frac{91}{11}}$	$\frac{1}{\sqrt{110}}$	$-\frac{3}{\sqrt{110}}$						
		$(6)_1$							$\frac{7}{22}\sqrt{\frac{2}{3}}$	$\frac{1}{\sqrt{22}}$	$\frac{5}{11}\sqrt{\frac{7}{3}}$	$-\frac{8}{11}\sqrt{\frac{7}{13}}$	$\frac{9}{11}\sqrt{\frac{7}{39}}$						
		$(6)_2$							$-\frac{17}{6}\sqrt{\frac{39}{3694}}$	$\frac{1}{6}\sqrt{\frac{7\cdot11\cdot21\cdot39}{3694}}$	$\frac{2}{6}\sqrt{\frac{13\cdot42}{3694}}$	$\frac{21\cdot3\sqrt{14}}{6\sqrt{3694}}$	$\frac{30}{6\sqrt{3694}}$						
		8										$-\frac{2}{\sqrt{13}}$	$\frac{3}{\sqrt{13}}$						
(3211) (3121) [211] (1321)	(200)	1	$-\frac{1}{\sqrt7}$	1	$\sqrt{\frac{6}{7}}$		$\frac{1}{2}\sqrt{\frac{7}{5}}$	$-\frac{1}{2}\sqrt{\frac{3}{5}}$	0	$\frac{1}{\sqrt2}$						1			
		3		1		$\frac{1}{4}\sqrt{\frac{3}{2}}$	$\frac{1}{4}\sqrt{\frac{3}{5}}$	$\frac{13}{6\sqrt{15}}$	$\frac{1}{4}\sqrt{\frac{11}{3}}$	$-\frac{1}{4}$	$\frac{5}{6\sqrt3}$	$-\frac{1}{4}\sqrt{\frac{13}{3}}$				1			
		5		1				$-\frac{1}{6}\sqrt{\frac{5}{3}}$	$-\frac{7}{4\sqrt{33}}$	$-\frac{1}{4}$	$\frac{1}{6}\sqrt{\frac{13\cdot35}{33}}$	$\frac{7}{2\sqrt{65}}$	$\frac{7}{4}\sqrt{\frac{3}{22}}$			1			
	(110)	2	$\sqrt{\frac{3}{7}}$	1	$-\frac{2}{\sqrt7}$	$\frac{1}{4}\sqrt{\frac{7}{5}}$	$-\frac{1}{2\sqrt5}$	$-\frac{3}{4}\sqrt{\frac{3}{10}}$	$\frac{1}{2}\sqrt{\frac{11}{10}}$	$\frac{1}{2}\sqrt{\frac{3}{10}}$	$\frac{1}{4}\sqrt{\frac{11}{2}}$				$\frac{\sqrt3}{2}$	1	$-\frac{1}{2}$	$+\frac{2}{\sqrt7}$	$-\sqrt{\frac{3}{7}}$
		4		1			$-\frac{1}{6}\sqrt{\frac{5}{2}}$	$\frac{1}{4}\sqrt{\frac{5}{6}}$	$-\frac{1}{2\sqrt6}$	$\frac{1}{6}\sqrt{\frac{11}{2}}$	$\frac{1}{4}\sqrt{\frac{5}{6}}$	$-\frac{1}{2}\sqrt{\frac{7}{6}}$	$\frac{7}{12}$			1		$-\frac{2\sqrt2}{3\sqrt7}$	$+\frac{\sqrt{55}}{3\sqrt7}$
	(211)	1					$-\frac{1}{2}\sqrt{\frac{1}{5}}$	$-2\sqrt{\frac{3}{55}}$	$-\frac{1}{2}\sqrt{\frac{33}{14}}$	$-\frac{1}{2\sqrt{14}}$								1	
		2				$-\frac{1}{2}\sqrt{\frac{3}{5}}$	$-\frac{3}{2}\sqrt{\frac{3}{35}}$	$\frac{9}{4}\sqrt{\frac{2}{35}}$	$-\frac{11}{12}\sqrt{\frac{6}{11\cdot35}}$	$\frac{9}{4}\sqrt{\frac{2}{35}}$	$\frac{11}{12}\sqrt{\frac{6}{77}}$							$\sqrt{\frac{3}{7}}$	$\frac{2}{\sqrt7}$
		$(3)_1$				$\frac{2\sqrt2}{7}$	$\frac{11}{28\sqrt5}$	$-\frac{3}{7\sqrt5}$	$\frac{\sqrt{11}}{28}$	$\frac{5\sqrt3}{28}$	$-\frac{3}{7}$	$-\frac{3\sqrt{13}}{28}$						1	
		$(3)_2$				$-\frac{\sqrt{33}}{28}$	$\frac{\sqrt{11\cdot15}}{14\sqrt2}$	$\frac{\sqrt{11\cdot15}}{28\sqrt2}$	$-\frac{15}{14\sqrt6}$	$\frac{3\sqrt{11}}{14\sqrt2}$	$-\frac{37}{28\sqrt{6\cdot11}}$	$-\frac{\sqrt{39}}{14\sqrt{22}}$							1
		4					$\frac{11}{12\sqrt{77}}$	$-\frac{11}{6}\sqrt{\frac{3}{77}}$	$-\frac{79}{12}\sqrt{\frac{3}{5\cdot77}}$	$-\frac{11}{12\sqrt{35}}$	$\frac{13}{6}\sqrt{\frac{3}{77}}$	$-\frac{19}{12}\sqrt{\frac{3}{55}}$	$-\frac{39}{6}\sqrt{\frac{2}{5\cdot77}}$					$\frac{\sqrt{35}}{3\sqrt7}$	$\frac{2}{3}\sqrt{\frac{2}{7}}$
		5						$\frac{\sqrt{78}}{6\sqrt7}$	$-\frac{\sqrt{26}}{4\sqrt{15\cdot77}}$	$-\frac{3}{4}\sqrt{\frac{26}{35}}$	$\frac{\sqrt2}{6\sqrt{33}}$	$-\frac{7}{2}\sqrt{\frac{21}{13\cdot55}}$	$\frac{\sqrt{105}}{4\sqrt{143}}$						1
		6							$-\frac{\sqrt{21}}{3\sqrt{11}}$	0	$-\frac{2\sqrt6}{3\sqrt{11}}$	$-\frac{9}{2}\sqrt{\frac{2}{143}}$	$\frac{5}{2}\sqrt{\frac{6}{143}}$						1
		7									$-\frac{3}{\sqrt{66}}$	$\sqrt{\frac{30}{143}}$	$\sqrt{\frac{17}{26}}$						1
(4321) (1111)	(000)	0														1			
	(110)	2													$\frac{1}{2}$	1	$\frac{\sqrt3}{2}$	$+\frac{2}{\sqrt7}$	$-\sqrt{\frac{3}{7}}$
		4														1		$-\frac{2}{3}\sqrt{\frac{2}{7}}$	$+\frac{\sqrt{55}}{3\sqrt7}$

If we continue to calculate the whole c.f.p. of $((j)^4,\ (j):(j)^5)$, it is necessary to coincide the two values of $((C)J\|U^{(3)}\|(C)J')$, $([U](C)J\|U^{(2)}\|[U](C')J')$, separately, each arising from two symmetry types by changing phase or coefficients of linear combinations if they have the same quantum numbers. But; for $((j)^4,\ (j):(j)^5)$, we have only calculated [11111] (100) 5/2 (maximum T only). Therefore we did not such a correction.

$([1111](c)J\|U^{(2)}\|[1111](c')J')$

(c) \ $(c)'$	J \ J'	(000)	(110)	
		0	2	4
(110)	2	$\frac{1}{2\sqrt{6}}$	$-\frac{5}{7\sqrt{6}}$	$\frac{9}{14\sqrt{2}}$
	4	0	$\frac{9}{14\sqrt{2}}$	$\frac{\sqrt{33}}{14}$

j^5 \ j^4	(4321) $[1111]$		
	(000)	(110)	
	0	2	4
$(54321)[11111](100)\,\frac{5}{2}$	$\frac{10\sqrt{2}}{3\sqrt{23}}\,[1]$	$\frac{1}{3}\sqrt{\frac{7}{23}}\Big[\sqrt{\frac{5}{14}}$	$\frac{3}{\sqrt{14}}\Big]$

j^6 \ j^5	(54321) $[11111]$ $(100)\ \frac{5}{2}$
$(654321)[111111](000)\,0$	1

§ 2

The interaction operator may be written generally as

$$Q=\sum_{i>j}Q(i\,j)$$

where

$$Q(i\,j)=T_0^{(p)}(i\,j)(S^{(k)}(i\,j)\cdot L^{(k)}(i\,j))$$

or

$$T_0^{(p)}(i\,j)S_0^{(0)}(i\,j)L_0^{(k)}(i\,j).$$

$S^{(k)}(i\,j)$ is a tensor operator of degree k in the spin space of nucleons i and j. Similarly $L^{(k)}(i\,j)$ operator in a orbital space, and $T^{(p)}(i\,j)$ in a charge space. Here we calculate formulae for the matrix elements of Q in states of a configuration of several closed shells and one unfilled shell, in terms of the basic two nucleons element as J. P. Elliott did.

We consider a set of totally antisymmetric states of N not necessarily equivalent nucleons $\psi(\gamma TM_T JM_J)$ and evaluate for these states the diagonal matrix elements of operator Q. We reform these states by the known fractional parentage reduction to next form;

$$\psi(\gamma TM_T JM_J)=\sum_{\psi''\psi_2}a(\psi,\ \psi''\psi_2)$$
$$\cdot\{\psi'',\ \psi_2(i\,j)\}TM_T JM_J$$

where the ψ'', ψ_2 are antisymmetric states of $(N-2)$ and 2 nucleons respectively and the summation extends over their quantum numbers. The $a(\psi,\ \psi''\psi_2)$ are the known c.f.p.. The notation $\{\psi'',\ \psi_2\}TM_T JM_J$ indicates a state formed by vector coupling ψ'', $\psi_2(i\,j)$ to form resultants $TM_T JM_J$. It is not antisymmetric in the N nucleons. The expectation value of Q in $M_J=J$ is found to be;

$$<Q>=(\psi|Q|\psi)=\frac{N(N-1)}{2}(\psi|Q(i\,j)|\psi)$$
$$=\frac{N(N-1)}{2}\sum_{\psi''\psi_2\psi_2{}^*}a(\psi,\psi''\psi_2)a(\psi,\psi''\psi_2{}^*)$$
$$\times(T''T_2TM_T|T_0^{(p)}|T''T_2{}^*TM_T)$$
$$\times(J''J_2J\,J|J_0^{(k)}|J''J_2{}^*J\,J)$$

where the function $J_0^{(k)}$ is the S and L parts of Q.

For the operator depending on only one nucleon coordinate such as the operator of magnetic moment of nuclei or quadrupole moment, we can get expection values easily using the reduction of $((j)^{n-1},\ j:\ (j)^n)$. But dealing with such a problem is not the aim of this article.

We now specify that the ψ denotes states of the N nucleons belonging to the lowest configuration of the nucleons in j-j-coupling shell model. Such a configuration may be written in the form

$$(n_1j_1)^{A_1}(n_2j_2)^{A_2}\cdots\cdots(n_tj_t)^{A_t}(n\,j)^m$$

where $N=\sum A_t+m$ and $A_t=2(2j_t+1)$.

Each group A_t is in a saturated ${}^1(0)$ state which we denote by χ_t, while m outside nucleons are taken in a state $\chi(\gamma TM_T JM_J)$, each antisymmetric in particles of their own group. A totally antisymmetric state of the whole configuration of N nucleons Ψ is

$$\Psi=\sum_P(-)^pP\chi_1(1\cdots A_1)\cdots$$
$$\cdot\chi_t(\cdots N-m)\chi(\cdots N)\sqrt{\frac{A_1!\cdots A_t!\ m!}{N!}}.$$

Ψ is separable to the next type,

$$\Psi=\{\sum_i a_i-\sum_{i>j}b_{ij}+c-\sum_i d_i\}$$
$$\cdot\sqrt{\frac{A_1!\cdots A_t!\ m!}{N!}},$$

where

$$a_i=\sum_{P(i)}(-)^pP\chi_1\cdots\chi_i(12\cdots)\cdots\chi_t\chi$$
$$b_{ij}=\sum_{P(ij)}(-)^pP\{\chi_1\cdots\chi_i(1\cdots)\cdots$$
$$\cdot\chi_j(2\cdots)\cdots\chi_t\chi-\chi_1\cdots\chi_i(2\cdots)\cdots$$
$$\cdot\chi_j(1\cdots)\cdots\chi_t\chi\}$$
$$c=\sum_{P(m)}(-)^pP\chi_1\chi_2\cdots\chi_t\chi(12\cdots)$$
$$d_i=\sum_{P(im)}(-)^pP\{\chi_1\cdots\chi_i(1\cdots)\cdots\chi_t\chi(2\cdots)$$
$$-\chi_1\cdots\chi_i(2\cdots)\cdots\chi_t\chi(1\cdots)\}.$$

The nucleon numbering is in natural order except for 1 and 2. Permutation sums $P(i)$, $P(ij)$, $P(m)$, $P(im)$ represent summation over the permutation of nucleons excluding 1 and 2, which preserve natural order within each group.

Notation

(All states are normalized and antisymmetric unless otherwise stated.)

$$\chi=(j)^m\gamma TM_T JM_J$$

$$\chi_i=(j)^{A_i 1}(0)$$

Reduction $(j)^m\rightarrow(j)^{m-1}(j)$

$$\chi(1\cdots)=(-)^{m-1}\sum_{\bar{\chi}} a(\chi,\bar{\chi})\{\bar{\chi}(\cdots),{}^2j(1)\}\cdot TM_T JM_J$$

$$\bar{\chi}=(j)^{m-1}\bar{\gamma}\bar{T}\bar{M}_T\bar{J}\bar{M}_J$$

Reduction $(j)^m\rightarrow(j)^{m-2}(j)^2$

$$\chi(12\cdots)=\sum_{\chi''\phi} a(\chi,\chi''\phi)\{\chi''(\cdots),\phi(12)\}\cdot TM_T JM_J$$

$$\chi''=(j)^{m-2}\gamma''T''M_T''J''M_J''$$

$$\phi=(j)^2\gamma_2T_2M_{T2}J_2M_{J2}$$

Reduction $(j_i)^{A_i}\rightarrow(j_i)^{A_i-1}(j_i)$

$$\chi_i(1\cdots)=(-1)^{A_i-1}\{\bar{\chi}_i(\cdots),{}^2j_i(1)\}^1(0)$$

$$\bar{\chi}_i=(j_i)^{A_i-1}\bar{\gamma}_i\,{}^2j_im_im_{ji}$$

Reduction $(j_i)^{A_i}\rightarrow(j^i)^{A_i-2}(j_i)^2$

$$\chi_i(12\cdots)=\sum_{\chi_i''\phi_i} b(\chi_i''\phi_i)\{\chi_i''(\cdots),\ \phi_i(12)\}^1(0)$$

$$\phi_i=(j_i)^2\gamma_2^iT_2^iJ_2^iM_{T_2}^iM_{J_2}^i$$

$$\chi_i''=(j_i)^{A_i-2}\gamma_i''T_2^iJ_2^iM_{T_2}^iM_{J_2}^i$$

$$b(\chi_i''\phi_i)=\sqrt{\frac{2(2T_2^i+1)(2J_2^i+1)}{A_i(A_i-1)}}$$

$\Psi''(R)$ represents the antisymmetric state formed by the coupling of the χ_i and χ''. It is a totally antisymmetric state of the nucleons 3, 4, $\cdots$, N.

$\Psi_i''(R)$ represents a totally antisymmetric state of nucleons 3, 4, $\cdots$, N formed by vector coupling the $\chi_1\cdots\chi_t$ excluding χ_i, with the χ_i'' and χ. $(T_i''\ J_i'')$

*$\bar{\chi}_{ij}$ denotes the vector coupled state of $\bar{\chi}_i$ and $\bar{\chi}_j$.

*$\bar{\Psi}_{ij}$ denotes the vector coupled state of $\bar{\chi}_{ij}$ and χ. $(\bar{T}_{ij}\ \bar{J}_{ij})$

$\bar{\Psi}_{ij}(R)$ represents a totally antisymmetric state of nucleons 3, 4, $\cdots$, N formed by the coupling of $\bar{\Psi}_{ij}$ with the $\chi_1\cdots\chi_t$ excluding χ_i and χ_j.

*ϕ_{ij} denotes the vector coupled state of $\{{}^2j_i\,{}^2j_j\}T_2^{ij}J_2^{ij}$.

$\Phi_{ij}(12)=(1/\sqrt{2})(\phi_{ij}(12)-\phi_{ij}(21))$ is an antisymmetric state of two inequivalent nucleons.

States with a suffix m have, in reference to χ, a similar meaning to those with a suffix i, in reference to χ_i.

After the long calculation similar to the Elliott's paper we can reach the next final form.

$$\begin{aligned}\Psi=&\sum_i\sqrt{\frac{A_i(A_i-1)}{N(N-1)}}\sum_{\chi_i''\phi_i} b(\chi_i''\phi_i)\sum_{T_i''J_i''}\sqrt{\frac{(2T_i''+1)(2J_i''+1)}{(2T+1)(2J+1)(2T_2^i+1)(2J_2^i+1)}}\{\bar{\Psi}_i''(R),\phi_i(12)\}TJ\\&-\sum_{i>i}\sqrt{\frac{A_iA_j}{N(N-1)}}\sum_{\Psi_{ij}\phi_{ij}}\sqrt{\frac{(2\bar{T}_{ij}+1)(2\bar{J}_{ij}+1)}{2(2j_i+1)(2j_j+1)(2T+1)(2J+1)}}\{\Psi_{ij}(R),\ \Phi_{ij}(12)\}TJ\\&+\sqrt{\frac{m(m-1)}{N(N-1)}}\sum_{\chi''\phi} a(\chi,\ \chi''\phi)\{\Psi''(R),\ \phi(12)\}TJ\\&-(-)^m\sum_i\sqrt{\frac{A_im}{N(N-1)}}\sum_{\bar{\chi}} a(\chi\bar{\chi})\frac{1}{\sqrt{(2j_i+1)2\bar{T}+1)(2\bar{J}+1)}}\sum_{\Phi_{im}}\sum_{T_{im}\bar{J}_{im}}\sqrt{(2\bar{T}_{im}+1)(2\bar{J}_{im}+1)}\\&\times U(\bar{T}_{im}\tfrac{1}{2}T\tfrac{1}{2}:\bar{T}T_2^{im})U(\bar{J}_{im}j_iJj:\bar{J}J_2^{im})\{\bar{\Psi}_{im}(R),\ \Phi_{im}(12)\}TJ\ .\end{aligned}$$

Now we will apply the reduced wave function to the general theory and obtain expectation value making use of the table of c.f.p..

§ 3

Among many kinds of operators the vector type operator such as "space exchange magnetic moment" is very interesting case for us to deal with. The operator used in L. Spruch's paper⁷⁾ is

$$\boldsymbol{Q}_{\pi\nu}=\alpha\imath(\mathfrak{L}_\pi\times\mathfrak{L}_\nu)_z\boldsymbol{J}_{\pi\nu}\boldsymbol{P}_{\pi\nu}\ .$$

But as in our scheme if we distinguish proton and neutron by the eigen value of the operator τ_z the magnetic moment operator wil be shown to have the refined form, namely;

$$\boldsymbol{Q}(ij)=-\alpha\boldsymbol{L}_0^{(1)}(ij)\boldsymbol{T}_0^{(1)}(ij)(4\boldsymbol{S}_0^{(0)}(ij)+1)\doteq-\alpha\boldsymbol{T}_0^{(1)}(ij)\boldsymbol{J}_0^{(1)}(ij),$$

where $L_0^{(1)}=J(r_{ij})(\mathfrak{L}_i\times\mathfrak{L}_j)_z, \quad T_0^{(1)}=(\tau^{(i)}\times\tau^{(j)})_z, \quad S_0^{(0)}=(S^{(i)}\times S^{(j)})$.

The expectation value $<Q>$ in one state of *j-j*-coupling model, is reduced to;

$$<Q>=\frac{N(N-1)}{2}\sum_{\psi''\psi_2\psi_2^*}a(\psi,\psi''\psi_2)a(\psi,\psi''\psi_2^*)(\{\psi''\psi_2\}TM_T\,J\,J\,|Q_{12}|\{\psi''\psi_2^*\}TM_T\,J\,J)$$

$$=-\alpha\frac{N(N-1)}{2}\sum_{\psi''\psi_2\psi_2^*}a(\psi,\psi''\psi_2)a(\psi,\psi''\psi_2^*)C^{TM_T}_{TM_T10}\,C^{JJ}_{JJ10}\frac{(T_2\|T^{(1)}\|T_2^*)}{\sqrt{2T_2+1}}$$

$$\times\frac{(J_2\|J^{(1)}\|J_2^*)}{\sqrt{2J_2+1}}U(T'TT_2^*1:T_2T)(U(J''JJ_2^*1:J_2J),$$

where $C^{jm}_{j'm'kq}$ is the same one as the Winger coefficient $(j'm'kq|j'kjm)$.

For ${}_3\mathrm{L}_{i_4}{}^7$ the lowest configuration is assumed $(1s_{1/2})^4(2p_{3/2})^3$, in *j-j*-coupling shell model. The ground state is assumed to be in $[111](10)^4(3/2)$, $M_T=1/2$, $J=3/2$. The contribution from the part (a) and (b) of the reduced wave function are zero, further the contribution from the part (c) is also zero from the fact

$$(T_2\|T^{(1)}\|T_2^*)=\begin{cases}0 & \text{if}\quad T_2=T_2^*\\ -\frac{\sqrt{3}}{2}i & \text{if}\, T_2=1,\ T_2^*=0\ \text{or}\ T_2=0,\ T_2^*=1.\end{cases}$$

Then it is sufficient to evaluate the contribution from the part (d) $<Q>_d$ only.

Evaluation of $<Q>_d$

$$<Q>_d=-\alpha\frac{m}{2}\sum_i A_i\sum_{\bar{\chi}}\frac{a(\chi\bar{\chi})^2}{(2j_i+1)(2\bar{T}+1)(2\bar{J}+1)}\sum_{\Phi_{im}\Phi_{im}^*}\sum_{\bar{T}_{im}\bar{J}_{im}}(2\bar{T}_{im}+1)(2\bar{J}_{im}+1)$$

$$\times U(\bar{T}_{im}\tfrac{1}{2}T\tfrac{1}{2}:\bar{T}T_2^{im})U(\bar{T}^{im}\tfrac{1}{2}T\tfrac{1}{2}:\bar{T}T_2^{im*})U(\bar{T}_{im}TT_2^{im*}1:T_2^{im}T)$$

$$\times U(\bar{J}_{im}j_iJj:\bar{J}J_2^{im})U(\bar{J}_{im}j_iJj:\bar{J}J_2^{im*})U(\bar{J}_{im}JJ_2^{im*}1:J_2^{im}J)$$

$$\times C^{TM_T}_{TM_T10}\,C^{JJ}_{JJ10}\frac{(T_2^{im}\|T^{(1)}\|T_2^{im*})}{\sqrt{2T_2^{im}+1}}\frac{(J_2^{im}\|J^{(1)}\|J_2^{im*})}{\sqrt{2J_2^{im}+1}}$$

$$=-\alpha\sum_i\sum_{\bar{\chi}}a(\chi\bar{\chi})^2\sum_{\Phi_{im}\Phi_{im}^*}C^{TM_T}_{TM_T10}\,C^{JJ}_{JJ10}\frac{\sqrt{2T_2^{im}+1}\sqrt{2J_2^{im}+1}}{2(2j+1)}$$

$$\times(T_2^{im}\|T^{(1)}\|T_2^{im*})(J_2^{im}\|J^{(1)}\|J_2^{im*})U(\bar{T}T\tfrac{1}{2}1::\tfrac{1}{2}T)U(\tfrac{1}{2}T_2^{im}\tfrac{1}{2}1:\tfrac{1}{2}T_2^{im*})$$

$$\times U(\bar{J}Jj1:jJ)U(j_iJ_2^{im}j1:jJ_2^{im*})$$

For the summation $\sum_{\Phi_{im}\Phi_{im}^*}$ in the last equation, it is sufficient to calculate for the next case,

$$\begin{array}{ll|ll} T_2^{im}=0 & J_2^{im}=[2] & T_2^{im}=1 & J_2^{im}=[11]\\ T_2^{im*}=1 & J_2^{im*}=[11] & T_2^{im*}=0 & J_2^{im*}=[2]\end{array}$$

where

$$J_2^{im}[2]=\frac{1}{\sqrt{2}}[\{(1s_{1/2})_1(2p_{3/2})_2\}J_2^{im}+\{(1s_{1/2})_2(2p_{3/2})_1\}J_2^{im}]$$

$$J_2^{im}[11]=\frac{1}{\sqrt{2}}[\{(1s_{1/2})_1(2p_{3/2})_2\}J_2^{im}-\{(1s_{1/2})_2(2p_{3/2})_1\}J_2^{im}].$$

We transform these equations into the scheme of L-S-coupling functions and add these terms separately and finally obtain

$$<Q>_d=-i\alpha\frac{2}{3\sqrt{6}}((1s)_1(2p)_2P\|L^{(1)}\|(1s)_2(2p)_1P)$$

where the last double barred matrix is defined by the relation;

$$(l_1l_2'L_2M_{L2}|L_0^{(1)}|l_1l_2'L_2^*M_{L2})=C^{L_2M_{L2}}_{L_2^*M_{L2}10}\frac{(l_1l_2'L_2\|L^{(1)}\|l_1l_2'L_2^*)}{\sqrt{2L_2+1}}.$$

Then with the expansion

$$L_0^{(1)}=\sum_{k=0}^{\infty}J_k(r_1,r_2)\cdot(x_1y_2-x_2y_1)\cdot P_k(\cos\omega_{12}),$$

the required element $((1s)_1(2p)_2P\|L^{(1)}\|(1s)_2(2p)_1P)$ is expressed as a linear combination of Slater's type integrals; namely

$$\frac{\sqrt{6}}{3i}\left\{-\frac{1}{5}G_2(1s,2p)+G_0(1s,2p)\right\}$$

where

$$G_k(1s,2p)=\iint R_1(1s)R_2(2p)R_1(2p)R_2(1s)r_1^3r_2^3J_k(r_1,r_2)dr_1dr_2,$$

$R(nl)$ is radial part of wave function.

The last required value is

$$<Q>=-\alpha\frac{2}{9}\left\{-\frac{1}{5}G_2(1s,\,2p)+G_0(1s,\,2p)\right\}.$$

For central interaction it is easy to calculate the matrix element and we omitted here how to deal with such a problem. They shall be mentioned in the following paper including another interaction such as "spin-orbit" and "tensor force" interaction.

Conclusion

We showed that in a word it is sufficient to calculate the c.f.p. of the *j-j*-coupling case in order to examine the physical quantities of nuclei in *j-j*-coupling shell model, and the c.f.p. and the Racah's tensor operators play great roles.

The c.f.p. tables of our work are not sufficient, and we think that it is our task in the future to extend to a large extent for $j=7/2$, $9/2,\cdots$. The tables of c.f.p. for these values, calculation of physical quantities, discussion and comparison with experiments are to be left to the next chance.

Acknowledgments

I am indebted to Prof. T. Inui, and A. Amemiya for the opportunity to work on this problem. I also wish to express my hearty thanks to Prof. T. Yamanouchi and T. Ishizu, H. Horie and our Racah's group for their helpful criticism and encouragements throughout of this work. This work has been done by the financial aid of the Educational Ministry in 1952.

References

(1) G. Racah: Phys. Rev. **63** (1943) 367.

(2) G. Racah: "Group Theory and Spectroscopy" (1951); Princeton.

(3) B. H. Flowers: Proc. Roy. Soc. A, **212** (1952) 248.

(4) A. R. Edomonds and B. H. Flowers: Proc. Roy. Soc. **214** (1952) 515.

(5) H. A. Jahn: Proc. Roy. Soc. A, **205** (1951) 192.

(6) J. P. Elliot: unpublished.

(7) L. Spruch: Phys. Rev. **80** (1950) 372.

$U(abcd:ef)=\sqrt{2e+1}\sqrt{2f+1}\,w(abcd:ef)$.

JOURNAL OF THE PHYSICAL SOCIETY OF JAPAN Vol. 8, No. 3, MAY—JUNE, 1953

Thermal Concentration of Carbon Isotopes Using Carbon Monoxide Gas

By Hajime SAKATA, Kazuhisa MATSUDA and Eiichi TAKEDA

Tokyo Institute of Technology, Oh-okayama, Tokyo

(Received February 6, 1953)

Using carbon monoxide as working gas, the concentration of C^{13} by thermal diffusion method was tried. The separation column was a hot wire type and had the length of 5 meters. The separation factor of the column was measured under various pressures and temperatures. The maximum separation factor obtained at the pressure of 53.7 cmHg and the temperature of the hot wire of 1050°K was 5.85. Under these conditions the relaxation time of the column whose both ends closed was about 4.7 hours. The comparison of the results with the theory suggested the existence of the parastic remixing. The measured value of R_T of CO gas was 0.427.

§1. Introduction

The concentration of the heavy isotope of carbon has become a more interesting problem since carbon dating method of Libby[1], et. al.[1] showed the definite role in archaeology. Various methods have been deviced for the concentration of carbon isotopes, such as chemical exchange method, diffusion method, and thermal diffusion method. But the last method is believed the best one for the above purpose.

The concentration of the heavy isotope of carbon by thermal diffusion method was reported by several authors[2]. In all these experiments, methane gas was selected as working gas.

One of us had pointed out that the equally well separation of carbon isotopes would be gotten using carbon monoxide, instead of methane, as operating gas[3]. In this case, the concentration of heavy oxygen isotope O^{18} is also expected. These profits were also described by German authors[2] independently.

In order to confirm these expectations, our experiment was performed on the separation of carbon monoxide gas by a hot wire type column, which will be described in §2. We tried the experiments under various operating conditions and got the character of the column. The experimental procedure and the results will be described in §3. The results obtained will be compared with the theory in §4.

§2. Separation Column

The cross sectional view of the thermal diffusion column used in the present experiment is shown in Fig. 1. The main part of the column which have the length of 5 meters is made from a brass double tube and a platinium centre wire. The inner tube serves as the cold wall and constitutes a water-jacket with the outer tube. The inner diameters of above tubes are 12 mm and 30 mm respectively. Along the axis of the double

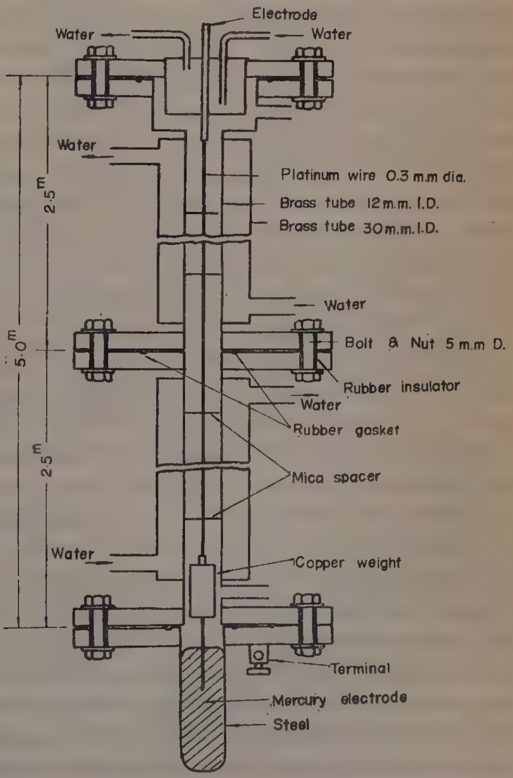

Fig. 1. Cross sectional view of column.

tube, a platinium wire, 0.3 mm in diameter, is suspended from the water-cooled upper electrode. In order to keep the wire at the centre of the tube, mica spacers are fixed to the wire with the intervals of about 50 cm. To prevent the contact of the heating wire with the tube wall, a copper weight is attached to the lower end of the wire and is dipped into the mercury electrode as indicated in Fig. 1. The upper and lower electrodes are insulated from the tube by rubber gaskets. The platinium wire is heated by direct current source.

§ 3. Experimental Procedure and Results

Prior to the operation, we led hydrogen gas in the column and heated the wire to the temperature of about 500°C for about 10 hours. After being out-gassed, the column was evacuated by an oil-diffusion pump.

The carbon monoxide gas used in this experiment was prepared by the following means; formic acid was poured drop into sulpheric acid heated about 100°C. The impurities contained in the evolved carbon monoxide gas, such as carbon dioxide, water vapour and the others, were removed by passing the gas through potassium hydroxide, phosphorus pentoxide and liquid air traps. We measured this purified carbon monoxide gass by a mass spectrometer, and knew that the main impurity was water vapour whose amount was a few percent of $C^{13}O^{16}$, and the other ones were very small. The abundance ratio $C^{13}O^{16}/C^{12}O^{16}$ on this carbon monoxide sample gas was 0.0112±0.0005.

In order to study the performance of the column, the gas was introduced into the column to the suitable pressure by a Taepler pump and operated under various conditions. For these runs, both ends of the column were closed. After the operation, the separated gases were derived from both ends into the reservoirs of 15 cc in capacity, the pressure of which was about 15 cmHg.

Unfortunately, we could not know the temperature of the heating wire directly and the value determined from the pressure variation of gas was not accurate. Therefore we measured the relation between the temperature and electric resistance of the platinum wire previously, and deduced the temperature from the resistance of the wire in the case of operation. The temperature of the cold wall was kept at about 290°K in every runs, and the temperature difference between the inlet and outlet was approximately 3°C.

The analysis of the isotope abundance ratios were made by the second-order focusing mass spectrometer constructed in our laboratory. As the evacuation of the mass spectrometer was carried out by an oil-diffusion pump, there remained small residual ion peaks of 28 and 29 even at the end vacuum with liquid air trap. We measured these peak heights before each run and these values were substructed from the measured peak heights of sample gas. The errors contained in the measurement of the abundance ratios were believed less than ±0.0005.

Table I shows the variation of the separation with the temperature of the hot wire. For these experiments, the pressure was kept at 76.0 cmHg and the operations were continued for 20 hours which was several times of the relaxation time deduced from the theory. These results indicate that the higher the temperature, the larger the separation factor. This tendency agrees qualitatively with the theoretical expectation but the absolute values are smaller than the theoretical ones.

Table I. $C^{13}O^{16}/C^{12}O^{16}$ ratios at both ends of column as a function of temperature of hot wire. Pressure = 76.0 cmHg, and time of operation = 20 hours.

Temp. °K	$\left(\frac{C^{13}O^{16}}{C^{12}O^{16}}\right)^{\text{Top}}$	$\left(\frac{C^{13}O^{16}}{C^{12}O^{16}}\right)^{\text{Bott}}$	Ratio Bott./Top
1050	0.0051	0.0202	3.96
1150	0.0047	0.0211	4.49
1200	0.0045	0.0216	4.80
1300	0.0038	0.0228	6.00

In Table II, the pressure dependence of the separation is given. In these runs the temperature of the hot wire was kept at 1050°K. The time dependence of the separation under various pressures are also given in Table II. These results show the appreciable variation of the separation with the pressure. This pressure dependence of the separation is very useful to test the theory of the column.

Table II. $C^{13}O^{16}/C^{12}O^{16}$ ratios at both ends of column as a function of time at various pressures. $T_2=1050°$ K.

Press. cmHg	Time hour	$\left(\frac{C^{13}O^{16}}{C^{12}O^{16}}\right)_{Top}$	$\left(\frac{C^{13}O^{16}}{C^{12}O^{16}}\right)_{Bott}$	Ratio Bott./Top
30.0	0	0.0112	0.0112	1.00
	5	0.0087	0.0152	1.75
	10	0.0074	0.0165	2.23
	20	0.0067	0.0172	2.57
40.0	5	0.0080	0.0170	2.13
	10	0.0063	0.0189	3.00
	20	0.0052	0.0200	3.85
50.0	5	0.0065	0.0181	2.78
	10	0.0049	0.0206	4.20
	20	0.0040	0.0220	5.50
60.0	5	0.0070	0.0181	2.59
	10	0.0050	0.0203	4.06
	20	0.0040	0.0214	5.04
70.0	5	0.0077	0.0164	2.13
	10	0.0057	0.0185	3.25
	20	0.0048	0.0194	4.04

The separations of the heaviest nuclide oxygen O^{18} from O^{16} under various pressure are shown in Table III. The data listed are the ratio $C^{12}O^{18}/C^{12}O^{16}$ obtained on the samples after the operation of 20 hours when the temperature of the hot wire was 1050°K. The concentration of $C^{12}O^{18}$ is to small to determine the value of the separation factor.

Table III. $C^{12}O^{18}/C^{12}O^{16}$ ratios at both ends of column as a function of pressure. $T_2=1050°$K and time of operation $=20$ hours.

Press. cmHg	$\left(\frac{C^{12}O^{18}}{C^{12}O^{16}}\right)_{Top}$	$\left(\frac{C^{12}O^{18}}{C^{12}O^{16}}\right)_{Bott}$	Ratio Bott./Top
30.0	0.0008	0.0026	3.3
40.0	0.0007	0.0039	5.6
50.0	0.0005	0.0048	9.6
60.0	0.0006	0.0043	7.1
70.0	0.0007	0.0040	5.7

§ 4. Comparision of Theory and Experiment

The separation at equilibrium state is written in the form,

$$q_e=\left(\frac{C_1^B}{1-C_1^B}\right)_e\Big/\left(\frac{C_1^T}{1-C_1^T}\right)_e=\exp(2AL), \tag{1}$$

In our case $\left(\frac{C_1^B}{1-C_1^B}\right)_e$ and $\left(\frac{C_1^T}{1-C_1^T}\right)$ represent the ratios of the equilibrium concentration $C^{13}O^{16}/C^{12}O^{16}$ at the bottom and the top ends of the column respectively. L is the length of the column and A has the following expression

$$A=\frac{H}{2(K_c+K_d)}, \tag{2}$$

where H is the separation term concerning thermal diffusion, K_c is the remixing term due to convection flow and K_d is that due to ordinary diffusion. These terms were given by Takeda[4] as follows,

$$\left.\begin{aligned} H&=2\pi r_1\frac{1+R}{2}\alpha\frac{g\rho^2}{\eta}r_1^3(1-R)^3\frac{h(\theta,R)}{6!},\\ K_c&=2\pi r_1\frac{1+R}{2}\frac{g^2\rho^3}{\eta^2 D}r_1^7(1-R)^7\frac{k_c(\theta,R)}{9!},\\ K_d&=2\pi r_1\frac{1+R}{2}\rho D r_1(1-R)k_d(\theta,R),\end{aligned}\right\} \tag{3}$$

where the following notations are used,

η=coefficient of viscosity,
D=coefficient of ordinary diffusion,
ρ=density,
$\alpha=(D_T/D)\cdot C_1\cdot C_2$,
D_T=thermal diffusion coefficient,
C_1,C_2=concentrations of heavy and light components of gas mixture respectively.

These constants are valued at mean temperature of the column. And

g=acceleration of gravity,
$R=r_2/r_1$,
r_1=radius of cold wall,
r_2=radius of hot wire,
$\theta=T_2/T_1$,
T_1=absolute temperature of cold wall,
T_2=absolute temperature of hot wire,
h,k_c,k_d=functions of θ and R.

Bardeen[5] calculated the time rateof approach to the equilibrium separation. When AL is relatively small, the formula becomes simple. Furthermore, if we assume the concentration of $C^{12}O^{16}$ or $1-C_1$ is almost constant throughout the operation, we can simplify the Bardeen's formula as follows.

$$(C_1^B/1-C_1^B)=(C_1^B/1-C_1^B)_e-B\exp(-t/t_r), \tag{4}$$

$$(C_1^T/1-C_1^T)=(C_1^T/1-C_1^T)_e+B'\exp(-t/t_r), \tag{5}$$

where B and B' are the constants independent of time t, and t_r is the relaxation time.

Using the empirical data listed in Table II, we can determine the constants of the above formulas and calculate the ratios of the equilibrium concentration $C^{13}O^{16}/C^{12}O^{16}$ and t_r at both ends. These values are listed in Table IV. Fig. 2 shows the variation of the con-

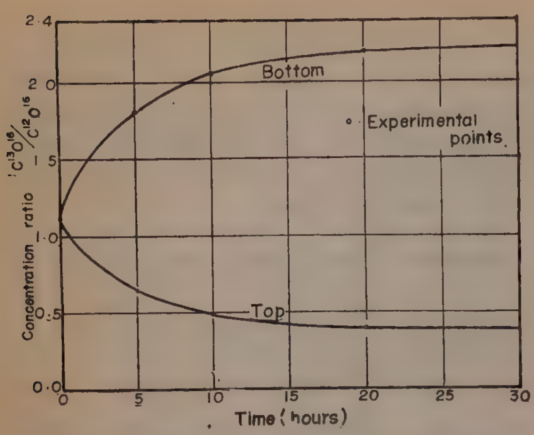

Fig. 2. Varation of concentration with time at both ends of coluum. Pressure=50.0 cmHg and temperature of hot wire=1050°K.

centration with time at a pressure of 50.0 cmHg. The curves are the calculated ones with the constants deduced by the above procedure.

From the ratios of the equilibrium concentration thus obtained, we can determine the empirical values of q_e and then that of AL by Eq. (1) subsequently. These equilibrium values under the various pressures are given in Table IV.

Considering the pressure dependence of H, K_c and K_d, or A, we can rewrite the formula (2) as

$$2AL = \frac{a/p^2}{1+b/p^4}, \qquad (6)$$

where a and b are the constants independent of pressure. If we assume the pressure dependence of this type and use the data of Table IV, we can determine the constants a and b by the method of least square. By inserting the numerical values for a and b in Eq. (6), we get

$$(2AL)_{\text{exp}} = \frac{1.73/p^2}{1+0.248/p^4}, \qquad (7)$$

where we express the pressure by the unit of atomosphere. The curve of this equation is shown in Fig. 3. The fact that all experimental points fall closely on the curve is believed to confirm the theory. The maximum separation factor obtained from this curve is 5.85 at the pressure of 53.7 cmHg.

Table IV. Values of separation at equilibrium state as a function of pressure. T_2=1050°K.

Press. cmHg	$\left(\frac{C^{13}O^{16}}{C^{12}O^{16}}\right)_e$ Top	$\left(\frac{C^{13}O^{16}}{C^{12}O^{16}}\right)_e$ Bott	q_e	$(2AL)_{\text{exp}}$	t_r hour	$(t_r)_{\text{theo}}$ hour
30.0	0.0065	0.0174	2.68	0.986	5.3	5.0
40.0	0.0050	0.0202	4.04	1.40	5.6	5.3
50.0	0.0038	0.0222	5.84	1.76	5.5	4.9
60.0	0.0038	0.0216	5.68	1.73	5.1	4.1
70.0	0.0046	0.0196	4.26	1.45	4.5	3.2

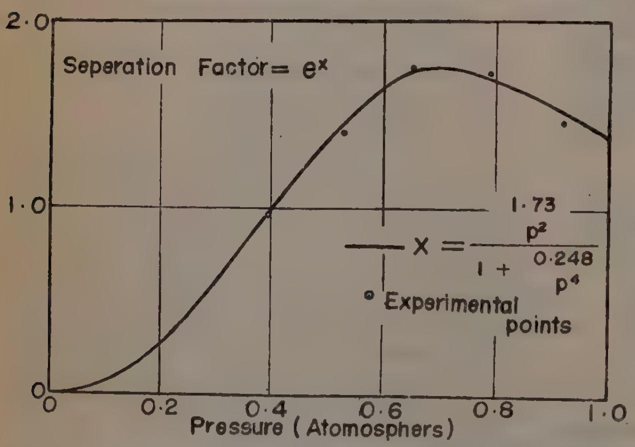

Fig. 3. Graph showing how the separation factor depends upon pressure. Note that separation factor is e^x, where x is the ordinate.

The pressure dependence of Eq. (6) can also be calculated from theoretical equations (2) and (3). In our experiment, the following geometrical values and the temperatures were used,

r_1=6.0mm, r_2=0.15mm L=475cm,
T_1=290°K, T_2=1050°K, T_m=421°K.

T_m represents the mean temperature of the column and was experimentaly determined from the pressure variation of gas. As the values of the gas constants at the temperature, we adopted the following figures,

$\rho=0.8108\times10^{-3}$ g/cm, $\eta=2.378\times10^{-4}$ poise,
$D=0.3845$ cm²/sec, $\alpha=0.007619$.

Here the values of D and α are derived from the theory of Hirschfelder, et. al.[6] Thus we have the following expression,

$$(2AL)_{\text{theo}}=\frac{2.23/p^2}{1+0.276/p^4}\,. \qquad (8)$$

Two equations (7) and (8) are rather different. But, in order to compare these two expressions, we must recall the following two facts. The one is that the value of α derived from the theory is apt to be larger than the experimental one. So the coefficient of numerator of Eq. (8) may be smaller than 2.23. The other is that we must not neglect the another remixing factor, which is called as parastic remixing factor, K_p. This remixing is caused by the existence of the spacers, the deviation from the central position of the hot wire and the longitudinal temperature variations of both walls. Obviously, this factor must have the same pressure dependence as K_c, since both of them are combined in the convection flow. So this factor increase the denominator of the Eq. (8), and the pressure independent term may becomes a little larger than 1.

Thus, we must consider that the most reliable term is the coefficient of $1/p^4$. If we assume this coefficient in Eq. (7) is equal to that in Eq. (8), we can rewrite Eq. (7) as

$$(2AL)_{\text{exp}}=\frac{1.92/p^2}{1.11+0.276/p^4}\,. \qquad (9)$$

According to the above consideration, we must introduce the remixing factor K_p, whose magnitude is 0.11 Kc, besides the terms of K_c and K_d. And then we have the value of α to be 0.00666, which is smaller than the theoretically estimated value, 0.007619.

The theoretical discussions on the third remixing factor K_p have been made⁷⁾, but we cannot know the necessary conditions given by the experiment such as deviation of wire from the central position and azimuthal temperature difference of the column. So the exact estimation of K_p is very difficult.

The relaxation time when both ends are closed was deduced theoretically by Bardeen.⁵⁾ This is expressed by the following equation,

$$(t_r)_{\text{theo}}=\left(\frac{2\mu}{AH}\right)\Big/\left\{1+\left(\frac{\pi}{AL}\right)^2\right\}, \qquad (10)$$

where μ is the mas of the gas per unit length of the column. Using the experimental values of AL and H obtained from Eq. (9), we can calculate the values of the relaxation time by the above formula. These values are listed in the last column of Table IV, and show a fairly good agreement with the values obtained from the experimental curves.

When we adopt 0.00666 as the value of α, the thermal separation ratio R_T can be estimated as

$$R_T=0.427$$

at the temperature of 421°K.

The authors wish to express our sincere thanks to Mr. N. Ono for his assistance. They are also indebted to Dr. T. Kanbara and Mr. S. Shima of Hitachi Ltd. in construction of the mass spectrometer.

References

1) Libby, et. al.: Phys. Rev. **72** (1947) 931.

2) A. O. Nier: Phys. Rev. **57** (1940) 30.
A. O. Nier and J. Bardeen: J. Chem. Phys. **9** (1941) 690.
T. L. Taylor and G. Glockler: J. Chem. Phys. **7** (1939) 530, J. Chem. Phys. **8** (1940) 843.
K. Clusius and G. Dickel: Helv. Phys. Acta. **23** (1950) 103.

3) E. Takeda: Bulletin of Tokyo Institute of Technology **13** (1948) 150.

4) E. Takeda: Bulletin of Tokyo Institute of Technology **13** (1948) 137.

5) J. Bardeen: Phys. Rev. **57** (1940) 35.

6) J. O. Hirschfelder, R. B. Bird and E. L. Spotz: Chem. Rev. **44** (1949) 205.

7) R. C. Jones and W. H. Furry: Rev. Mod. Phys. **18** (1946) 151.

Journal of the Physical Society of Japan Vol. 8, No. 3, May—June, 1953

Secondary Electron Emission of Copper-Beryllium Alloy

The Surface Products of the Alloys and their Secondary Electron Emission Characteristic under Different Oxygen Pressures and Temperatures

By Shigetomo Yoshida, Ikuo Takeda, Yoshitaka Igarashi and Hikaru Arata

Electrical Communication Laboratory, Nippon Telegraph and Telephone Corporation
Musashinoshi, Tokyo, Japan

(Received November 12, 1952)

The surface products of copper-beryllium (0.5, 1.5 and 3.0%) alloys treated under various oxygen pressures and temperatures and their secondary electron emission characteristics are discussed in detail. The results are summarized as follows;

(1) Rapid diffusion of beryllium atoms through copper-beryllium alloy begins at 400°C.

(2) In order to activate copper-beryllium alloys, they must contain beryllium atoms more than 1.5%.

(3) At the activation process temperature must be raised to a desired point at pressure lower than 10^{-4}mm mercury in order to prevent copper from oxidizing, and then oxygen must be added into the tubes to the treatment pressure.

(4) The formation mechanisms of beryllium oxide layers treated at 800°C and below 700°C are different with each other. This difference of treatment temperature is responsible for two different secondary emission characteristics respectively.

§ 1. Introduction

Kollath(1) reported that copper-beryllium and nickel-beryllium alloys treated under appropriate conditions of oxygen pressure and of temperature gave a high secondary electron emission yield. At the earlier stages, the cause of activation was regarded as the change of crystal structure of those alloys under treatment. It was also found that a considerable field strengh(2) was required to obtain saturation of the secondary electron current from those alloys. Moreover it was reported by electron diffraction method(3) that the selective oxidation in those alloys caused a high secondary electron emission yield. The relation between the treatment condition forming the thin oxide layer on the alloy surface and its secondary emission characteristics is, however, not well known. In this paper the surface products on the alloy surface treated under various oxygen pressures and their secondary electron emission characteristics will be discussed in detail.

§ 2. Specimen and Measuring Method

2. 1. Test tubes

Three experimental tubes are shown in Fig. 1. Type (A) tube is used only to examine the surface products formed by the heat treatment at various oxygen pressures. Type (B) tube consists of Fogel type vacuum gauge and of triode parts measuring secondary electron emission. Type (C) tube has the ordinary electron gun and collector parts. The use of shield plates for type (B) and (C) tubes greatly reduces the possibility of contaminating the secondary emission surface, since during treatment process the surface is shielded.

Aquadaq coated on the interior glass wall of type (B) tube is used to remove local charge on the wall and lowers its potential to that of the cathode, availing its secondary emission yield less than unity.

2. 2. Specimen and activation process

Three kinds of copper-beryllium alloys are tested, each contains 0.5, 1.5 and 3.0% beryllium respectively. The surfaces are polished

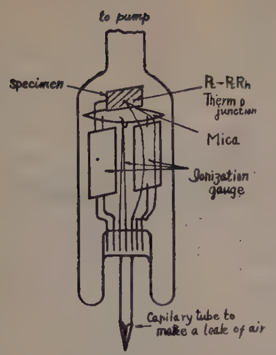

(A) Test tube

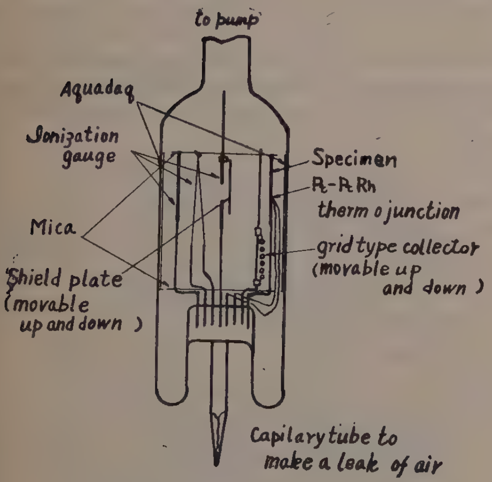
to pump
Aquadaq
Ionization gauge
Mica
Shield plate (movable up and down)
Specimen
Pt-PtRh therm o junction
grid type collector (movable up and down)
Capilary tube to make a leak of air

(B type) Test tube

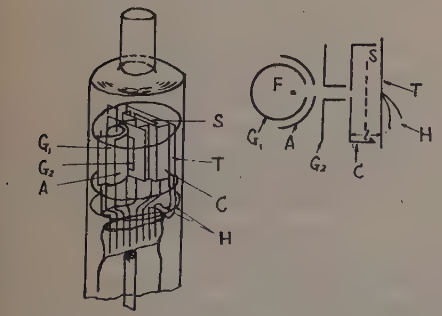

Sketch of (C) type tube

F: Primary filament G_1: Wehnelt grid
A: Anode G_2: Electrode for focusing the beam.
C: Collector S: Shield plate T: Target
H: P_t-P_tR_h thermojunction

Plane figure of (C) type tube

Fig. 1. Three types of test tubes.

with fine chromic oxide powder and washed with distilled water. Before the activation process the test tubes are baked at about 400° C for one hour at a pressure lower than 10^{-4} mm mercury. It is found by electron diffraction method that the surfaces of those alloys are not oxidized during this glass baking process. For the type (A) and (B) tubes, oxygen (air) pressure is controlled by varying the capillary tube diameter opened to atmosphere. In the case of type (C) tube, oxygen is introduced by heating the source contained with potassium dichromate powder which is connected to the evacuating system.

The specimen is heated by means of a high frequency coil.

The heating process in which the sample temperature is raised from the room temperature to the treatment one keeping the pressure at the specified treatment pressure, is applied to both type (A) and (B) tubes. The other heating process in which after raising the sample temperature to the specified temperature at pressure lower than 10^{-4} mm mercury, oxygen is introduced to the desired pressure, is applied to type (C) tube.

§ 3. Results on Copper-Beryllium (0.5 and 3%) Alloys Measured by Type (B) Tubes

3. 1. Surface products and δ max

Temperature-pressure diagrams on the results of three kinds of copper-beryllium alloys are illustrated in Figs. 2, 3 and 4 divided the surface product regions. (As the copper-beryllium 1.5% alloys is measured by type (A) tube, the values of secondary electron emission yield are not illustrated in Fig. 2)

In the case of copper-beryllium 0.5% alloy, growing rate of beryllium oxide may be restricted by the slow diffusion velocity of beryllium atoms through the alloy. So that the beryllium oxide can not cover entirely the surface during our process time and therefore BeO+Cu mixed patterns are obtained at comparatively lower pressures. At a higher pressure, copper is oxidized and BeO+Cu_2O patterns are observed. Boundary between BeO+Cu and BeO+Cu_2O regions is a function of temperature and oxygen pressure. At pressure higher than 10^{-2} mm mercury the growth of cuprous oxide is larger than that of beryllium oxide and consequently cuprous oxide only appears. At temperature lower than 400° C, beryllium atoms can not diffuse through the alloy, so that copper is oxidized at the pressure higher than 10^{-4} mm mercury.

In the case of copper-beryllium 3% alloy, contrary to copper-beryllium 0.5% alloy, cup-

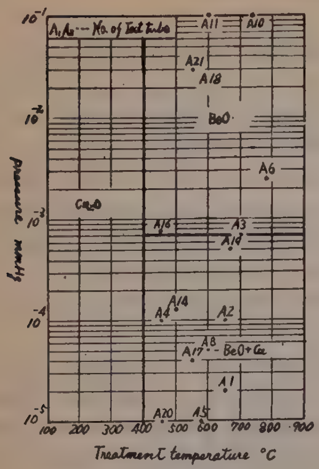

Fig. 2. Temperature-pressure diagram of copper-beryllium (1.5%) alloy.

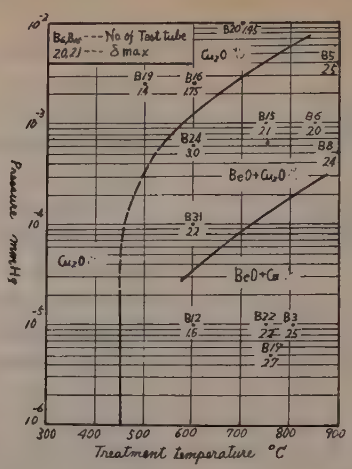

Fig. 3. Temperature-pressure diagram of copper-beryllium (0.5%) alloy.

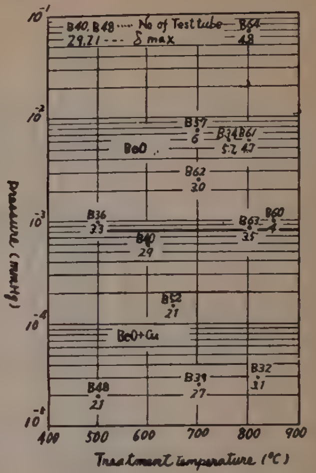

Fig. 4. Temperature-pressure diagram of copper-beryllium (3%) alloy.

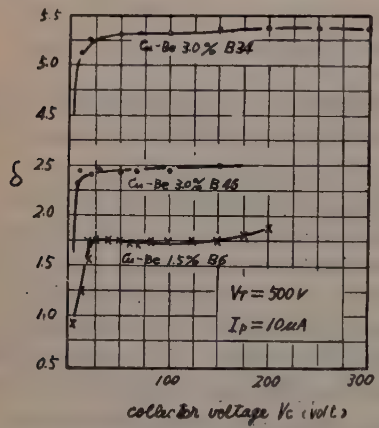

Fig. 5. Saturation curves for copper-beryllium 0.5 and 3% alloys.

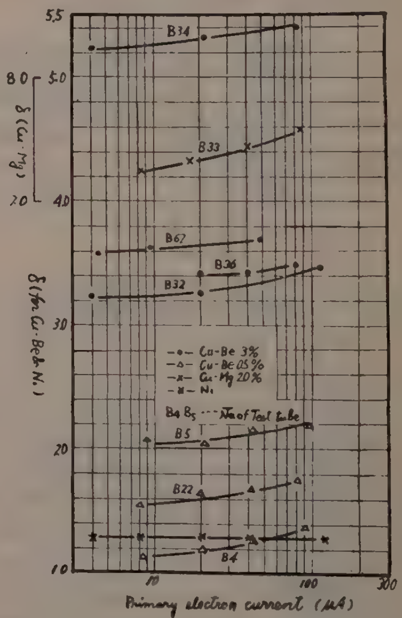

Fig. 6. Secondary emission ratios as a function of primary current density, with a given primary energy ($V_T=500$ V).

rous oxide does not appear except in trace because the rate of diffusion of beryllium atom through the alloy is sufficient at temperature higher than 400° C. The growing velocity of beryllium oxide depends only on the oxygen pressure until the beryllium oxide film has a protective character. At comparatively higher pressure, only beryllium oxide pattern is observed, at lower pressure BeO+Cu mixed patterns are obtained. Boundary between these two regions depends only on pressure and not on temperature except at temperature lower than 400° C.

In the case of copper-beryllium 0.5% alloy, δ max of two regions $BeO+Cu_2O$ and BeO+Cu ranges between 2 and 3. We can not find any difference on δ max between two regions within the limits of experimental accuracy. At pressure higher than 3×10^{-3} mm mercury, cuprous oxide pattern is predominant and consequently δ max becomes 1.5. This value of δ max corresponds to that of ordinary cuprous oxide in bulk.

In the case of copper-beryllium 3% alloy, δ max of BeO+Cu region is also between 2 and 3 and is same as the values of BeO+Cu and $BeO+Cu_2O$ regions of copper-beryllium 0.5% alloy. At 10^{-3} mm mercury and about 800° C, beryllium oxide region appears and

δ max varies from 3 to 5 by increasing the treatment pressure to 10^{-2} mm mercury.

3. 2. Saturation, yield curves due to the primary current density

Some saturation courves of copper-beryllium alloys are shown in Fig. 5.

The yield curves are measured by changing only the primary current density from 5 μA to 100 μA, and shown in Fig. 6. In Fig. 6 datum of nickel is also shown for comparison.

The yield of nickel does not depend on the primary current density. On the contrary, δ of copper-beryllium alloys increases about a few par cent within this range.

3. 3. Yield curves

Some yield curves of those alloys are shown in Fig. 7. In the case of copper-beryllium 0.5% alloy, the value of the primary voltage (V_T max) corresponding δ max of both BeO+Cu_2O and BeO+Cu regions lies between 300 and 400 V, and no difference between two regions is observed as for the character of δ max.

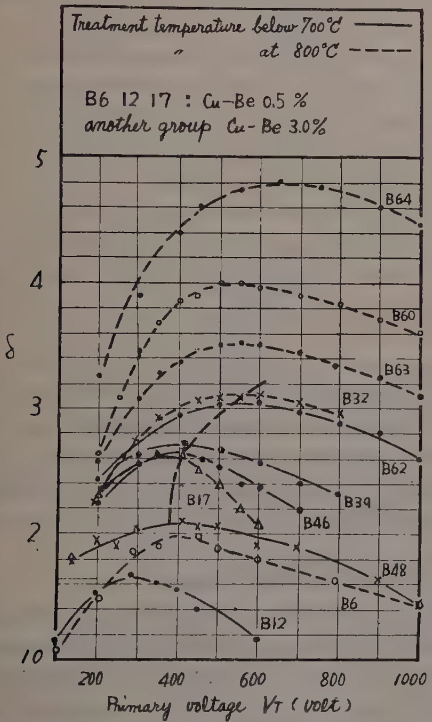

Fig. 7. Yield curves for copper-beryllium 0.5 and 3% alloys.

On the copper-beryllium 3% alloy, V_T max of BeO+Cu region is about 400 V and V_T max of BeO region lies between 400 and 600 V. From these facts it may be concluded that V_T max increases with the increase in the thickness of beryllium oxide layer. Our experiments may be studied on the layer thickness which is thinner than the maximum depth from which secondaries can escape. However, high δ max does not necessarily correspond to high V_T max.

On the point of treatment temperature, the following interesting results are obtained. In Fig. 7 curves of dotted line belong to the specimens at the treatment temperature of about 800° C, and curves of full line belong to the specimens under the treatment lower than 700° C. In the samples treated below 700° C, the shift of V_T max to the higher value always accompanies the increase in δ max. On the contrary, there is no regularity on samples treated about 800° C and V_T max lies at random between 500 and 700 V.

The depth from which secondary electrons can escape will have in average a certain range "d". If the cross section of primary electron decreases with increased primary voltage, primary electron will not create any secondary electrons until at a certain depth, and practically all the secondaries are produced at any point at which the primary energy has dropped down to a certain value. Mean depth "l" at which many secondary electrons are produced may be a function of primary electron voltage. At primary voltage V_T at which d is equal to l, secondary electron emission ratio δ becomes maximum. If the thickness of beryllium oxide layer is t, δ becomes small when $l(V_T)$ is greater than t, for the primary electron loses a great part of energy in the copper-beryllium alloy itself. In the range where $l(V_T)$ is less that t but nearly equal, δ becomes maximum at V_T. Consequently so far as t is less than d, δ max increases with increased t and V_T at which δ becomes δ max is higher. It may be one evidence of the above relationship that with increasing the value of δ max of the specimens treated below 700° C (Fig. 7), V_T max also becomes higher. The reason why the above mentioned relationship does not hold for the specimens treated at about 800° C will be discussed in the latter section.

§ 4. Results on Copper-Beryllium 1.5% Alloy Measured by Type (C) Tube

4. 1. Treatment condition and δ max.

The distributions of δ max are shown in Fig. 8. At a certain treatment condition range, every specimen's δ coincides to the value of 5.

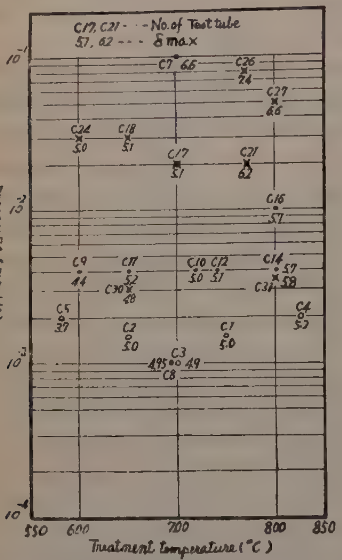

Fig. 8. Pressure-temperature diagram of copper-beryllium 1.5% alloy.

It has been a common sense that the same treatment condition can not necessarily give the same value of δ, so our result obtained may be surprising. The causes may be perhaps due to our special treatment method which raises the specimen temperature to the desired value at pressure lower than 10^{-4} mm mercury, and afterwards introduces oxygen into the tubes to the treatment pressure. Before the protective films of beryllium oxide are formed, copper is easily oxidized and cuprous oxide thus formed may influence the secondary electron emission characteristics. Difficulty of obtaining a fixed value of δ max may be due to a complex degree of initial oxidation of copper. At pressure lower than 10^{-4} mm, mercury copper is not oxidized and only thin layer of beryllium oxide is formed on the surface of alloy. Increasing the oxygen pressure at those state, this thin beryllium oxide film protects the oxidation of copper and consequently copper is not oxidized.

The value of δ max treated at 800° C, increases with the oxygen pressure from 5 to 7. At temperature lower than 700° C, δ max does not depend on the oxygen pressure ranging from 1×10^{-3} mm mercury to 3×10^{-2} mm mercury and lies between 4.9 and 5.1 except a few samples.

4. 2. Yield curves.

The yield characteristics of copper-beryllium 1.5% alloy are very similar to that of copper-beryllium 3% alloy already mentioned. Some yield curves are shown in Fig. 9.

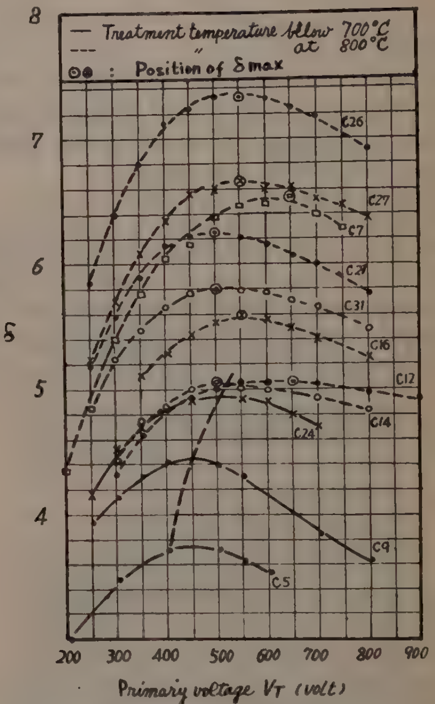

Fig. 9. Yield curves for copper-beryllium 1.5% alloys.

It is found by electron diffraction method that (001) plane of beryllium oxide is parallel to the specimen surface between 650° C and 750° C. This orientation habit of beryllium oxide disappears almost at 800° C.

§ 5. General Discussion

Results of electron diffraction method indicate no difference between the surface products of 1.5 and 3% beryllium-copper alloy. Considering that the oxygen partial pressure is a fifth of the air applicated for (B) type tube, the distributions of δ max are plotted in Fig. 10 schematically together with the results of (C)-type tube.

Until 4×10^{-3} mm mercury, δ max at temperatures between 600° C and 700° C does not depend on the treatment temperature but

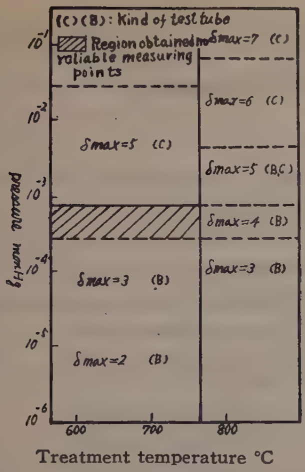

Fig. 10. Change of δ max under various temperatures and pressures.

only on the oxygen pressure. The value of δ max increases from 2 at 2×10^{-3} mm, mercury to 5 at 4×10^{-3} mm mercury. Even increasing the oxygen pressure, δ max remains at 5 between 600° C and 700° C, but δ max at 800° C increases to 7 at 8×10^{-2} mm mercury. Until 4×10^{-3} mm mercury, the growing rate of beryllium oxide layer depends only on the supply of oxygen on account of the easy diffusion of beryllium atoms towards the surface through the thin beryllium oxide layer. At higher oxygen pressure, beryllium oxide layer becomes thicker and diffusion of beryllium atoms through the beryllium oxide stops. At about 800° C, diffusion of beryllium atom becomes again easy on account of the following reason and δ max depends on the supply of oxygen. The reason why diffusion of beryllium atoms stops below 700° C is perhaps due to the forming of so-called Mott's⁴⁾ protective film. The treatment at 800° C breakes this protective oxide film and beryllium atom also can diffuse through the cracking of beryllium oxide layer and secondary layer of beryllium oxide is formed on the orientated beryllium oxide film. This secondary layers of beryllium oxide do not indicate any orientation.

§6. Conclusion

The results are summarized as follows;

(1) Rapid diffusion of beryllium atoms through copper-beryllium alloy begins at 400° C.

(2) In order to activate copper-beryllium atoms more than 1.5%.

(3) Small quantity of copper oxide influences to the secondary electron characteristics. Consequently, at the activation process temperature must be raised to a desired point at pressure lower than 10^{-4} mm mercury in order to prevent copper from oxidizing, and then oxygen must be admitted into the tubes to the treatment pressure.

(4) The formation mechanisms of beryllium oxide layers treated at 800° C and below 700° C are different with each other; at temperatures lower than 700° C a fixed thickness of beryllium oxide layer is formed independent of oxygen pressure, while at 800° C the thickness of beryllium oxide layer increases with oxygen pressure. This difference of treatment temperature is responsible for two different secondary emission characteristics respectively.

In conclusion, the authors wish to express their sincere thanks to Mr. T. Inai and Mr. T. Ichimiya for their encouragements and Dr. K. Hiruma and the members of our laboratory model shop for their kind helps. The authors are indebted to Mr. K. Ono for his electron diffraction tests and valuable discussions.

References

1) R. Kollath: Fernsehn u. Tonfilm 4/5 (1941) 13.

2) T. Arizumi and T. Oshida: J. App. Physics Japan **12** (1943) 269.

3) T. Tokumistu and K. Takeya: J. Institute Elect. Eng. Japan **5** (1944) 424.

4) N. F. Mott and R. W. Gurney: Electronic Processes in Ionic Crystals (1948).

JOURNAL OF THE PHYSICAL SOCIETY OF JAPAN Vol. 8, No. 3, MAY—JUNE, 1953

On the Changes in Contact Potential Difference of a Germanium Rectifier During the Electrical Forming

By Tatsuya NIIMI

Electrical Communication Laboratory, Mitaka, Tokyo

(Read Oct. 31, 1952, Received December 2, 1952)

It has been found experimentally that the change in contact potential difference ΔV_D during the forming process can be determined by observing the variation of a saturation current in the reverse direction with time required for the forming, the values of ΔV_D obtained for three kinds of surfaces ranging from 0.16 V. for a etched surface, from 0.06 V. to 0.07 V. for a cleaved surface, and from 0.04_2 V. to 0.04_6 V. for a surface exposed to nascent hydrogen. The theoretical treatments have been investigated to explain the experimental results, using the idea of Bardeen's surface levels and assuming that the variations in concentration of donor impurities present in the barrier, which had been caused by the thermal diffusion of acceptor impurities from the surface of the semiconductor, would affect the contact potential difference. The qualitative predictions appear to agree with results satisfactorily.

§ 1. Introduction

There are some papers1)2)3)4)5) which have been already published about the electrical forming of germanium rectifiers, in connection with the development of transistors. In most cases, the forming treatments considered involved applications of comparatively large current or voltage in either the forward or reverse direction for times of the order of a second and the resulting forming effects have been interpreted by assuming that the conversion of the conductivity type should occur on the surface of the material by the high local temperature reached during the forming process or that under the forming conditions the temperature and the field are so high that donor or acceptor impurities should move to the surface from the interior of the semiconductor. In this paper, it is reported that the change in height of the potential barrier caused by forming can be estimated experimentally by measuring the saturation current of the static characteristic when a n-type germanium diode is gradually formed by applying a comparatively small d-c voltage in the forward direction. Each of the values of the contact potential difference before or after forming cannot be determined by this method that is quite different from the Benzer's6) in which he determined it by measuring the variation of a saturation current with temperature. The results of several experiments observed by this method are summarized and the equations for the change in contact potential difference are investigated theoretically, assuming that the increasing in contact potential difference during forming would be caused by the diffusion of acceptor impurities or lattice defects into the interior of the semiconductor from the surface proper where they had been initially absorbed or formed and that the diffusion would be facilitated by the high local temperatures reached during the forming process.

§ 2. Experimental Method

The power which was applied to a germanium diode during the forming process in these experiments was comparatively smaller than usual, that is, of the order of about 10–50 milliwatts, obtained by passing a current of 10–30 milliamperes in the forward direction and the static characteristics were observed at every constant intervals after the beginning of the process. During the forming process, it was observed that the resistance of the rectifier in the reverse direction increased rapidly as the forming treatments could be effected, while the forward characteristic was remained almost unchanged and the height in contact potential difference appeared to be changed. Also it was confirmed that the reverse characteristic could be resolved into the three components which Benzer's results had indicated, that is, one component[1] [6] is exponential, rising to a saturation value, the saturation current tails off into the second component, which is essentially linear. The third component rises more rapidly than linearly as the voltage is increased.

The magnitude of a saturation current may be determined by the intercept on the ordinate defined by the intersection with the extention of the second component, as shown in Fig. 1.

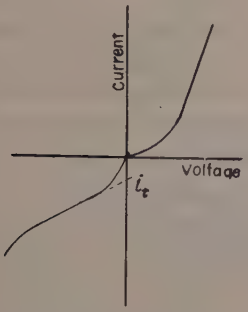

Fig. 1

According to the Bethe's diode theory, the reverse saturation current i_t at time t is given by

$$i_t = j_0 A \exp[-eV_{Dt}/kT], \qquad (1)$$

where V_{Dt} is the contact potential difference at t, j_0 is the thermal current density in the semiconductor, and A is the area of the contact. It was found experimentally that it converged to a constant value i_s with time required for forming, and that a plot of $\log[\log i_t - \log i_s]$ *vs.* t or $\log[-e(V_{Dt}-V_{Ds})/kT]$ *vs.* t becam linear, the relation between i_s and V_{Ds} being given by the same as the eq. (1),

$$i_s = j_0 A \exp[-eV_{Ds}/kT] \qquad (2)$$

then, we have the equation,

$$t/a + \log[-e(V_{Dt}-V_{Ds})/kT]/b = 1 \qquad (3)$$

or

$$V_{Ds}-V_{Dt} = [kT/e]\cdot\exp b\cdot\exp[-t/\tan\theta], \quad (4)$$

where a, b and θ are the intercepts on the abcissa and the ordinate determined by the intersection with the line, and the angle between the line and the ordinate respectively, as shown in Fig. 2. The increased amount of contact potential difference after forming, $\varDelta V_D = V_{Ds} - V_{D0}$ will be given by the equation

$$\varDelta V_D = [kT/e]\cdot\exp b, \qquad (5)$$

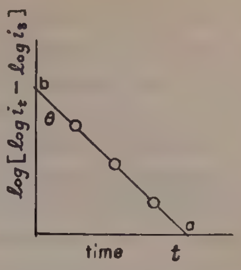

Fig. 2.

putting t equal to 0 in the eq. (4). As b can be determined by the experiment, $\varDelta V_D$ will be calculated by the eq. (5).

§ 3. Experimental Results

The material used in these experiments was obtained from poyllycrystalline ingot of n-type germanium, of which the specific resistance is about 1 Ω-cm and the impurity concentration is $3.0\times10^{15}/\text{cm}^3$, determined by the Hall coefficient measurements. None of the impurities but Zn, which was very faint, could be observed spectroscopically. These ingots were cut to obtain slices of about 1×10^{-1} mm thickness. The slice was, in turn, soldered to a brass base (ohmic contact), and the top surface was chemically etched. The etch showed the grain boundaries clearly so that each experiment could be confined to a single crystal. The point used was 0.12 mm diameter tungsten wire, pointed electrolytically. It was mounted in a micromanipulater by a phosphor-bronze spring that related deflection to applied force. The force applied to the point was about 9.8×10^3 dynes. In all cases, the static characteristic was examined firstly in the reverse direction, and then in the forward at ambient temperature, to avoid the forming effect due to the forward current. Then the forward current was increased to apply a certain forming wattage required for testing. The experiments were performed for three kinds of surfaces, i.e. a cleaved surface, a chemically etched surface, and a surface exposed to nascent hydrogen. A cleaved surface was one of the surfaces obtained when the slice was split open with small pliers, and the etchant for a surface was the mixture of HF, HNO_3 and $Cu(NO_3)_2$[1], and nascent hydrogen was produced by the electrolysis of water containing 10% KOH by weight, into which the surface of a germanium slice was slightly dipped and applied a negative potential to be a cathod. Fig. 3 indicates one of the experimental results obtained when a cleaved surface was treated with a forming power of 20 milliwatts, the curves C_0, C_{10}, C_{20}, etc. corresponding respectively to the static characteristic observed when $t=0$ minutes, 10 min. 20. min. etc. after the beginning of the process and the saturation currents corresponding to each curves were determined by the method previously stated. These values are shown in Table 1. Further observations of the saturation currents showed nearly the same as 40 min. value, determing the value of i_s to be 10 μA. As shown in Fig. 4, a plot of log [log i_t—log i_s]*vs.* t was linear and the value of b was decided 0.96 graphically. According to the eq. (5), we had, at ambient temperature 30° C,

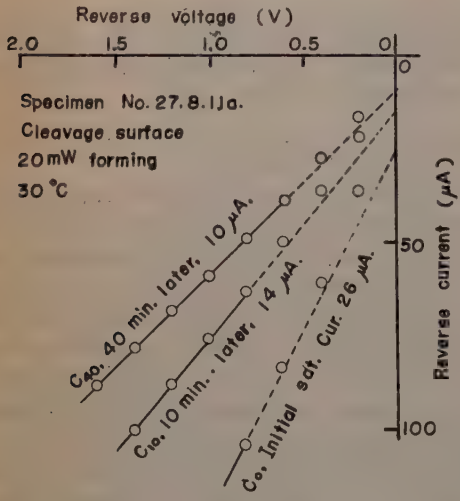

Fig. 3.

$$\Delta V_D=0.07\ V.$$

Then, the surface, on which a cleaved surface experiment had been performed, was in turn, etched with the solution refered already, and the same experiments as those stated above were carried out, showing that for a etched surface

$$\Delta V_D=0.21\ V.$$

at ambient temperature 30 °C., and this was about three times larger than that for a cleaved surface.

Table I.

Time	Sat. Cur. (μA)
Initial	26.0
10 Min. Later	14.0
20 〃	11.0
30 〃	10.3
40 〃	10.0

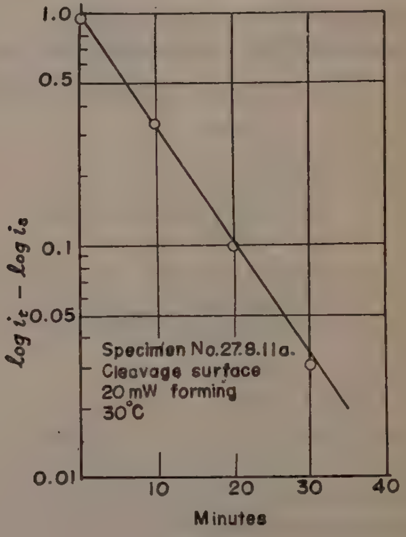

Fig. 4

The etched surface was, then, exposed to nascent hydrogen for an hour and was examined by the same method, and the results showed that the change in contact potential difference decreased to a remarkably smaller value than those observed in two former cases, that is,

$$\Delta V_D=0.04_6\ V.$$

at ambient temperature 31° C.

The values of ΔV_D observed at different ten points on the surfaces treated by the same way varied a little from place to place, ranging from 0.16 V. to 0.21 V. for a etched surface, from 0.06 V. to 0.07 V. for a cleaved surface, and from 0.04_2 V. to 0.04_6 V. for a surface exposed to nascent hydrogen.

The values of ΔV_D appeared to have a close relation with a forming wattage, and to increase with it. One of the experimental results obtained on the same etched surface showed, for example, ΔV_D was about 0.07 V. for a 10 milliwatts forming, 0.20 V. for a 20 milliwatts forming, and 0.22 V. for a 50 milliwatts forming, but no quantitative relations between them could be obtained.

As for the forward current, it was observed to have scarcely changed during the process, or to have sometimes increased at a fraction of a volt, improving a rectifying characteristic.

§ 4. Theoretical Derivations of the Experimental Results

The supposition which is proposed in the present theory to account for the change in contact potential difference is that the forming process would raise the temperature of the contact high enough to cause diffusion of the impurity atoms or lattice defects, which had been initially absorbed or formed on the surface and were considered to act as acceptors, into the n-type germanium, and the variations in concentration of impurities present in the barrier would affect the contact potential difference as the concentration of donor impurities would be reduced by the diffused acceptor impurities. The treatment based on this model involves the change in contact potential difference would have much to do with the change in the reverse current, but few with that in the forward, considering that when the junction is operated in the forward direction, the current is carried chiefly by holes.

According to the Brattain's theory[5] about semiconductor surface phenomena, the potential change V_D across the contact and the concentration of impurity atoms N in the semiconductor, which is assumed uniform, are related by the equation

$$V_D=2\pi e n_s^2/\kappa N\,, \qquad (6)$$

where e is the electronic charge and κ is the dielectric constant of the semiconductor, and by assuming that the surface charge $n_s e$ must equal the charge in the space charge layer $Ne\lambda$, N and n_s are related by the equation

$$n_s=N\lambda \qquad (7)$$

where n_s is the density of surface charges and λ the width of the space charge layer, which will be quoted the λ-layer for simplicity in this paper hereafter.

The material used in the experiment is n-type germanium, of which the concentration of donor impurity atoms N_n may be considered uniform in the bulk material and constant during forming, since it is assumed to make it possible only for the acceptor impurities to diffuse to the interior from the surface. In n-type germanium there may be present acceptor impurity atoms before the forming process, the concentration of which is given by N_a, then the relation between N_n and N_a is shown by

$$N_n \gg N_a\,. \qquad (8)$$

And from the eq. (6) and the eq. (7), the relations

$$V_{D0}=[2\pi e n_{n0}^2/\kappa]\cdot[1/(N_n-N_a)] \qquad (9)$$

$$n_{s0}=N_n\lambda_0 \qquad (10)$$

are given, where V_{D0}, n_{s0} and λ_0 are the values of V_D, n_s and λ respectively before the forming process. For the simplicity of calculation, N_a may be put equal to zero without affecting the physical meanings, because the supposition is that the changes in contact potential should be caused only by the acceptor impurities *diffused*. Then, we have

$$V_{D0}=[2\pi e n_{s0}^2/\kappa]\cdot[1/N_n]\,. \qquad (11)$$

Hence, the reduction in N_n will cause the increase in V_{D0}. The mathematical treatment will be classified into several cases under the physical conditions considered.

(4. 1.) *When the parameters λ and n_s are constant during forming.*

Although the concentration of acceptor impurities in the λ-layer will be increased with time by the thermal diffusion from the surface, the width of λ_0 will be considered unchanged and the density of available surface states n_{s0}, if it is not too large, will be kept constant during the process, provided the concentration of diffused acceptors N_{pt} should be negligibly small compared with N_n. Then, we have

$$\lambda_t=\lambda_0 \qquad (12)$$

$$n_{st}=n_{s0}\,. \qquad (13)$$

The suffix, t, denotes the values at time t after the beginning of the process. As the diffusion of acceptor impurities is assumed to be facilitated by the high local temperatures reached during the forming process, the depth below the surface where they can diffuse will be determined by the temperature distribution caused by a forming current which flows into the surface layer from the point, and raises the temperature high enough to cause diffusion of them. As the current flows into the material deeper and deeper, it will gradually diverge, lowering the temperature it raises. Therefore, the depth where the temperature is so high that the acceptor impurities can diffuse may be assumed to be a constant, μ, at a forming process of such a constant power as in this paper. As the concentration of diffused acceptor impurities will increase with time, the net concentration of impurities present will be decreased or the complete inversion of conductivity type may happen in this μ-layer.

Now, according to the eq. (6), the concentration of impurities and the contact potential difference at time t are related by the equation,

$$V_{Dt}=[2\pi e n_{s0}^2/\kappa]\cdot[1/(N_n-N_{p}t)]\,, \qquad (14)$$

where $N_{p}t$ denotes the concentration of diffused acceptor impurities at time t. Combining the eqs. (11) and (14),

$$V_{Dt}-V_{D0}=[2\pi e n_{s0}^2/\kappa]\cdot[1/(N_n-N_{p}t)-1/N_n]\,. \qquad (15)$$

Using the assumption, $N_n \gg N_{p}t$, we have,

$$\Delta V_{Dt}=V_{Dt}-V_{D0}=[2\pi e n_{s0}^2/\kappa]\cdot[N_{p}t/N_n^2] \qquad (16)$$

Then, n_{p0}, the concentration of impurities on the surface of germanium which would act as acceptors when diffused is assumed to be remained unchanged during forming. This condition will be satisfied when the decrease in n_{p0} due to the diffusion into the interior will be constantly compensated by newly absorbed atoms or newly formed lattice defects on the surface.

The rectifying contact is assumed to be in the plane $\chi=0$, the semiconductor to be along the positive x-axis, and $u(\chi, t)$ to be the amount of acceptor impurities diffused in the μ-layer. According to the assumptions, $u(\chi, t)$ is given by solving the the diffusion equation under the following boundary conditions.

$$\partial u/\partial t=D\cdot\partial^2 u/\partial \chi^2\,, \qquad (17)$$

$$\left.\begin{array}{l}(u)_{\chi=0}=n_{p0}\\ (\partial u/\partial \chi)_{\chi=\mu}=0\\ (u)_{t=0}=0\end{array}\right\} \qquad (18)$$

where D is the diffusion coefficient. Then, we have the solution for $u(\chi, t)$,

$$u(\chi, t)=n_{p0}\Bigg[1-\frac{4}{\pi}\sum_{s=0}^{\infty}\frac{1}{(2s+1)}\times\exp\left(-\frac{D(2s+1)^2\pi^2 t}{4\mu^2}\right)\sin\frac{(2s+1)\pi\chi}{2\mu}\Bigg]. \qquad (19)$$

(4. 11) the case when $\lambda_0 \geqq \mu$.
The total amount diffused into the μ-layer at time t is given by the equation,

$$S=\int_0^{\mu}u(\chi, t)d\chi\,. \qquad (20)$$

Now $N_{p}t$ should be considered equal to the density obtained when the total amount of diffused impurities S would be distributed uniformly into the λ_0-layer, because the potential difference V_D should be considered affected by the density of impurities located in the λ_0-layer, not in the μ-layer. Therefore, we have the relation,

$$N_{pt}=S/\lambda_0 \qquad (21)$$

or

$$N_{nt}=\frac{\mu}{\lambda_0}n_{p0}\Bigg[1-\frac{8}{\pi^2}\sum_{s=0}^{\infty}\frac{1}{(2s+1)^2}\times\exp\left(-\frac{D(2s+1)^2\pi^2 t}{4\mu^2}\right)\Bigg]. \qquad (22)$$

According to the initial assumption, $N_{p}t \ll N_n$, we have the relation

$$\mu n_{p0}/\lambda_0 \ll N_n \qquad (23)$$

(4. 12) the case when $\lambda_0<\mu$.
$N_{p}t$ should be given by the equation,

$$N_{pt}=\int_0^{\lambda_0}u(\chi, t)dt\Big/\int_0^{\lambda_0}dx\,.$$

Calculating the integrals, we have,

$$N_{pt}=n_{p0}\Bigg[1-\left(\frac{\mu}{\lambda_0}\right)\cdot\frac{8}{\pi^2}\sum_{s=0}^{\infty}\frac{1}{(2s+1)^2}\times\left(1-\cos\frac{(2s+1)\pi\lambda_0}{2\mu}\right)\times\exp\left(-\frac{D(2s+1)^2\pi^2 t}{4\mu^2}\right)\Bigg]. \qquad (24)$$

According to the assumption, $N_{pt}\ll N_n$, we have the relation

$$n_{p0}\ll N_n.. \qquad (25)$$

Now, combining the eqs. (16) and (22), we have the relation

$$V_{Dt}-V_{D0}=\frac{2\pi e n_{s0}^2}{\kappa}\cdot\frac{1}{N_n}\cdot\frac{\mu}{\lambda_0}\cdot\frac{n_{p0}}{N_n}\times\Bigg[1-\frac{8}{\pi^2}\sum_{s=0}^{\infty}\frac{1}{(2s+1)^2}\times\exp\left(-\frac{D(2s+1)^2\pi^2 t}{4\mu^2}\right)\Bigg]. \qquad (26)$$

The value of $\Delta V_{Dt}=V_{Dt}-V_{D0}$ will approach to a constant, ΔV_D when time t becomes infinitely large,

$$\Delta V_D=\frac{2\pi e n_{s0}^2}{\kappa}\cdot\frac{1}{N_n}\cdot\frac{\mu}{\lambda_0}\cdot\frac{n_{p0}}{N_n} \qquad (27)$$

and when all the terms but the first in the summation in the eq. (26) can be neglected as small quantities, one finds the relation,

$$V_{Dt}-V_{D0}=\frac{2\pi e n_{s0}^2}{\kappa}\cdot\frac{1}{N_n}\cdot\frac{\mu}{\lambda_0}\cdot\frac{n_{p0}}{N_n}\times\left[1-\frac{8}{\pi^2}\exp\left(-\frac{D\pi^2 t}{4\mu^2}\right)\right], \qquad (28)$$

which indicates that the value of $V_{Dt}-V_{D0}$ varies exponentially with time, agreeing with the experimental results shown by the eq. (4).

(4. 2) *When the parameter λ is not constant but n_{st} is constant.*

In this case, it can be found after the simple calculations that the expression for V_{Dt} will coincide with the eq. (14) and the same discussions as stated in the preceeding section will be valid for this case.

(4. 3) *When parameters λ and n_s are variables.*

In this case, the surface level density, n_{st}, and the width of the space charge layer, λ_s, are related by the equations,

$$n_{st}=(N_n-N_{pt})\cdot\lambda_t \qquad (29)$$

$$n_{s0}=N_n\cdot\lambda_0 . \qquad (30)$$

Putting

$$\lambda_t=\lambda_0+\Delta\lambda , \qquad (31)$$

One can reasonably assume the inequality

$$\Delta\lambda\ll\lambda_0 . \qquad (32)$$

Now, we have the equations, for V_{Dt} and V_{D0},

$$V_{Dt}=[2\pi e n_{st}^2/\kappa]\cdot[1/(N_n-N_{pt})], \qquad (33)$$

$$V_{D0}=[2\pi e n_{s0}^2/\kappa]\cdot[1/N_n] . \qquad (34)$$

The density of available surface states, n_{st}, may be considered to be changed when the acceptor impurities have so much diffused that the order of magnitude of N_{pt} comes to equal that of N_n. Combining the eqs. (29), (30), (33) and (34), we have the equation.

$$V_{Dt}-V_{D0}=\frac{2\pi e}{\kappa}\left[(N_n-N_{pt})(\lambda_0+\Delta\lambda)^2-N_n\cdot\lambda_0^2\right]. \qquad (35)$$

When $\Delta\lambda$ is assumed negligibly small compared with λ_0 for the sake of simplicity, we have,

$$V_{Dt}-V_{D0}=-\frac{2\pi e}{\kappa}\cdot\lambda_0^2\cdot N_{pt}$$

or

$$V_{Dt}-V_{D0}\fallingdotseq-\frac{2\pi e n_{s0}^2}{\kappa}\cdot\frac{1}{N_n}\cdot\frac{N_{pt}}{N_n} . \qquad (36)$$

Contrary to the results in the preceeding section, the decrease in V_{Dt} will occur in this case. The decrease in V_{Dt} during the forming process have been found sometimes when the forming power applied to the contact is too large.

(4. 4) *Comparison with the experiments.*

When $\lambda_0\geqq\mu$, ΔV_D is given by the eq. (27), and the eq. (28) can be written down as follows,

$$V_{Dt}-V_{D0}=\Delta V_D\left[1-\frac{8}{\pi^2}\times\exp\left(-\frac{D\pi^2 t}{4\mu^2}\right)\right]. \qquad (37)$$

This equation is not valid when t equals approximately zero, because the term in the right side of the eq. (37) does not vanish when $t=0$. Therefore, the value of experimental ΔV_D, which can be written $\lim_{t\to0}(V_{Ds}-V_{Dt})$ according to the eq. (4), corresponding to the eq. (37) in this theoretical derivation, comes to differ to a some extent from that of theoretical ΔV_D, which can be determined by the eq. (26). These relations are shown schematically in Fig. 5.

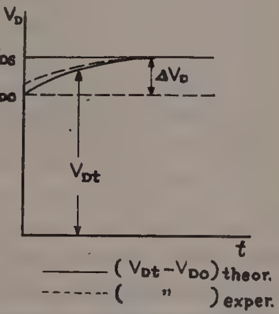

Fig. 5.

Using the eq. (26), we have,

$$(V_{Ds}-V_{Dt})_{\text{theoretical}}=\Delta V_D-(V_{Dt}-V_{D0})$$

$$=\Delta V_D\left[\frac{8}{\pi^2}\sum_{s=0}^{\infty}\frac{1}{(2s+1)^2}\times\exp\left(-\frac{D(2s+1)^2\pi^2 t}{4\mu^2}\right)\right] \qquad (38)$$

and similary, using the eq. (37), we have

$$(V_{Ds}-V_{Dt})_{\text{experimental}}=\Delta V_D\left[\frac{8}{\pi^2}\times\exp\left(-\frac{D\pi^2 t}{4\mu^2}\right)\right]. \qquad (39)$$

Therefore, we have, when $t\to0$,

$$(V_{Ds}-V_{D0})_{\text{theor.}}-(V_{Ds}-V_{D0})_{\text{exper.}}=\Delta V_D\left(1-\frac{8}{\pi^2}\right). \qquad (40)$$

This will give the difference of the observed values and the theoretical for ΔV_D, showing that the values of ΔV_D determined experimentally by the eq. (4), are a little less than those given by the theory.

Considering that the width of the forbidden band, 0.72 V. for germanium, would represent the largest barrier height attainable, and that the Benzer's experiment⁶⁾ indicated the height in contact potential difference in a germanium rectifier was about 0.6 V., and that the maximum value of ΔV_D observed in the above experiments was about 0.2 V., the value of V_{D0} may be expected to range from 0.4 V. to 0.6 V. approximately.

In the case when $N_n \gg n_{p0}$ and $\mu > \lambda_0$, ΔV_{Dt} must be given by combining the eqs. (16) and (24). As the forming proceeds, ΔV_{Dt} will approach to ΔV_D, which can be written down as follows,

$$\Delta V_D = \frac{2\pi e n_{s0}^2}{\kappa} \cdot \frac{1}{N_n} \cdot \frac{n_{p0}}{N_n}. \tag{41}$$

ΔV_D is, therefore, a constant, independent on μ, that is, independent on a forming wattage.

This fact may be verified by indicating the experimental results that ΔV_D seems to be approaching to a constant, taking the value of 0.07 V., 0.20 V. and 0.22 V. respectively when a forming process was performed with applying a wattage of 10 mW, 20 mW, or 50 mW, as stated in section 3.

§ 5. Discussion

Using the ideas of Bardeen's surface states and the diffusion of acceptor impurities into the interior from the surface, due to the local high temperature caused by a forming current, the resulting phenomena of the process could be explained satisfacforily. Though a theory²⁾ that the changes in contact potential difference would be caused by the diffusion of impurity ions from the interior to the surface, due to the field of a forming current, was already discussed, the diffusion of impurities must be considered to be caused from the surface into the interior according to the facts that ΔV_D could be remarkably affected by the surface treatments. The idea that the acceptor impurities absorbed on the surface are assumed to be oxygen atoms was adopted by P. R. Aigrain and others⁷⁾ in their assumption of the existence of a surface layer containing acceptor impurities on n-type germanium to account for the d-c characteristic of a germanium rectifier. Recently, C. S. Fuller⁸⁾ has reported that copper would be a surface acceptor impurity, and it is quite probable that the diffused acceptor impurity atoms in this paper would not be oxygen atoms, but copper ones, because the very thin copper layer has been sometimes formed on the surface of germanium, when it was etched by the mixture solution of HF, HNO_3 and $Cu(NO_3)_2$, probably due to the fact that a copper atom has a larger ionization potential than a germanium. Though the thin layer of copper can be removed away easily by a dilute solution of HNO_3, a very small almost of residuals of copper on the surface would affect the results of the forming, because the ΔV_D for etched surface had the largest value among the three cases examined, and finally, the another consideration which must be taken into account has been presented by R. L. Longini.⁹⁾ In his paper, he has suggested the formation and diffusion of lattice defects would occur on the surface of germanium on the electrical forming of transistor. The high temperature of the contact during forming would cause diffusion of the lattice defects, which would cease to move and would be 'flozen in' at a distance far from the point, where the temperature would not be raised high enough to move. In this case the assumption n_{p0} is constant during forming will be considered most resonable among the three cases. However, it could not be decided clearly in these experiments what the acceptor impurities would be.

In conclusion, the author expresses his sincere thanks to Dr. T. Masaki for his encouragements during the work.

References

1) H. C. Torrey and C. A. Whittmer: Crystal Rectifiers.
2) J. Bardeen and W G. Pfann: Phys. Rev. **77** (1950) 401.
3) L. B. Valdes: Proc. I.R.E. **40** (1952) 445.
4) W. Schockley: Electrons and Holes in Semiconductors.
5) H. K. Henisch: Semiconducting Materials. pp. 37.
6) S. Benzer: Jour. App. Phys. **20** (1949) 804.
7) H. K. Henisch: Semiconducting Materials pp. 95.
8) C. S. Fuller: Phys. Rev. **87** (1952) 526.
9) R. L. Longini: Phys. Rev. **84** (1951) 1254.

JOURNAL OF THE PHYSICAL SOCIETY OF JAPAN Vol. 8, No. 3, MAY—JUNE, 1953

Relationship between Thermionic Emission and Electrical Conductivity of Oxide-Coated Cathodes

By Shin-ichiro NARITA

Kobe Kogyo Corp. Kobe

(Received December 20, 1952)

The relationship between the thermionic emission and the electrical conductivity of both "sintered" and normal oxide-coated cathodes has been investigated.

The "χ" values which obtained from the difference between the work functions and the activation energies of conductivity were much inconsistent between both cathodes. Moreover, in the low temperature range the activation energey of conductivity, smaller than 0.1 ev, was observed.

These results are attributed to the existence of numerous conduction mechanisms in oxide-coating and to the surface formation of barium layer on the oxide-coating particles.

§ 1. Introduction

Inspite of considerable efforts to reveal the mechanism of the thermionic emission of oxide-coated cathode, several difficulties have yet been left unsolved.

The semi-conductor theory seemed hopeful to explain the whole properties in the cathode, and many investigators, e. g. Nishibori & Kawamura[1], Arizumi & the present author[2] and Hanney, MacNair & White[3] studied the relationship between the thermionic emission and the electrical conductivity of oxide-coated cathode to confirm the theoretical prediction.

According to Fowler's theory, the thermionic emission, i, and the electrical conductivity, σ, are given respectively by the following formulae:

$$i=N_e^{1/2}\frac{e(1-\bar{r})}{2\pi m^* h^{3/2}}(2\pi m^* kT)^{5/4}\cdot\exp\{-(\chi+E_0)/kT\}, \tag{1}$$

$$\sigma=N_e^{1/2}ev\{(2\pi m^* kT)^{3/4}/h^{3/4}\}\cdot\exp(-E_0/kT), \tag{2}$$

and therefore we obtain

$$\frac{i}{\sigma}=\frac{1-\bar{r}}{v2\pi m^*}(2\pi m^* kT)^{1/2}\exp(-\chi/kT), \tag{3}$$

where

N_e = the number of excess barium,
v = the mobility of conduction electron,
E_0 = the energy difference between Fermi level and the bottom of the conduction band,
χ = the width of conduction band.
$\bar{r}$ = the reflection coefficient,

and the other symbols have their usual meanings.

Eq. (3) suggests that the emission must be directly proportional to the conductivity at any fixed temperature and $\tilde{\chi}$, the difference between the work function and activation energy of the conductivity at any cathode activity, should be the same within the experimental error.

Moore and Allison[4] have recently pointed out, however, that the proportionality did not give a direct evidence for the cathode being a kind of semiconductor and the other mechanism may be assumed for it.

Vink and Loosjes[5] suggest that the electrical conduction hitherto observed was nothing but that of electron gas through pores existing among oxide particles and the proportionality of emission-conduction held as a matter of course, because the electron gas was formed by the thermionic emission from small oxide crystals, and that the real conduction through the oxide grains should take place only at low temperature.

Another difficulty for applying the semiconductor theory to oxide cathode appears in the difference of thermionic emission-ability between a "normal" cathode and a "sintered" one. (Reference to § 2).

The author has studied the change of thermionic emission of oxide-coated cathodes either with superior or inferior activity by means of barium-sputtering onto their surfaces, and obtained more complicated results than those previously reported, which may be hardly explained by simple semiconductor theory or Vink-Loosjes' one. Now the author will propose a mechanism of emission and conduction of the oxide-coated cathode in order to explain his experimental results. It will be assumed that the surface of oxide particles is covored mono or multiatomically with barium atoms and contact potential barrier exists between two oxide-particles.

§ 2. Experimental Procedure

(*i*) *Preparation of "N" and "S" cathodes*

It has been a well known fact that the thermionic emission of oxide-coated cathode depends much upon the condition of decomposition process of carbonate and the activation process. The cathode decomposed in high gas pressure and at very high temperature during evacuation has always low emission and oxide particles are considered to sinter to have no distinct grain-to-grain boundaries as schematically shown in Fig. 1 (a). These cathodes will be designated as "S" cathode which were prepared actually in this experiment by using barium carbonate, which is more convenient for sintering than barium-strontium carbonate.

The normal cathodes (designated as "N" cathode) of superior activity, decomposed carefully lest the sintering should take place, have distinct grain-to-grain boundary resulting in a rough contact between grains as shown in Fig. 1 (b).

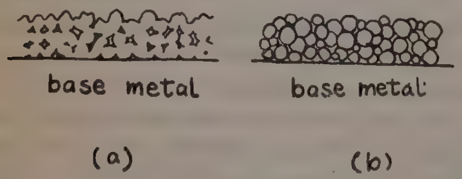

Fig. 1. The structure model of "S" cathode (a) and "N" cathode (b).

The sleeves of both "N" and "S" cathodes are electrolytic nickel of 2.1 mm dia and 3.2 cm long. In the case of "N" cathode (Ba Sr)CO_3 was sprayed on the centre of sleeves to thickness of 0.5 mm, while in the case of "S" cathode the same weight of $BaCO_3$ was coated by cataphoreses. A nickel probe of 0.03 mm dia was imbeded in each coating.

In each case the carbonate was coated only at the centre of the sleeve by a length equal to the anode opening (about 8 mm).

For determing the cathode temperature, a tungsten wire of 0.04 mm dia was welded on the each nickel sleeve and E.M.F. of Ni-W thermocouple was measured.

(*ii*) *Tube construction*

The experimental tubes were designed for studying the differences in characteristics between "N" and "S" cathodes at the various activity obtained by evaporating barium onto their surfaces,

The essential feature of the tube is shown in Fig. 2. "S" and "N" cathodes were mounted inside an anode parallelly to the tube axis and a batalum getter used for the barium source was located in front of the anode opening through which barium atoms were evaporated onto the cathodes. "S" and "N" cathodes were at the equal distances from batalum getter, and a nickel plate, S, prevented the mutual effect of both cathodes.

The tungsten wire, *F*, of 0.1 mm dia before the shield, S, was used to know the amount of evaporated barium by measuring the thermionic emission from it.

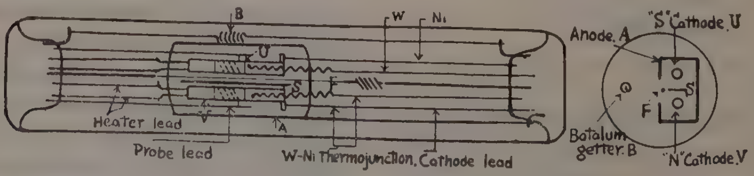

Fig. 2. The experimental tube for measuring the characteristics of "N" and "S" cathodes.

(*iii*) *Exhausting and Measurement*

During the evacuation through the conventional high vacuum system the experimental tube was baked for an hour at about 350°C and then the carbonates of batalum getter and "S" and "N" cathodes were decomposed into oxide, followed by inductive heating of anode and other metal parts and the cleaning of tungsten filament, F. Finally the barium getter was flashed and the tube was sealed off.

Prior to measurement, the "N" and "S" cathodes were aged sufficiently in conventional manner.

The measurements of thermionic emission and electrical conductivity were performed by applying D. C. voltages between anode and cathode, and between probe and sleeve respectively.

The experimental data were taken on three or more tubes and with every tube in every run, consistent results were obtained.

§ 3. M-type Conduction

Vink and Loosjes have reported that they found a small activation energy (less than 0.1 e. v.) of conduction in oxide cathodes. Such a small activation energy of conductivity, however, has never been observed in our previous experiment using electrolytic nickel or MgO-base. Now we have found that it is possible to realize easily such type of conduction (denoted M-type conduction) as shown in Fig. 3 by the method of changing the cathode activity by sputtering barium.

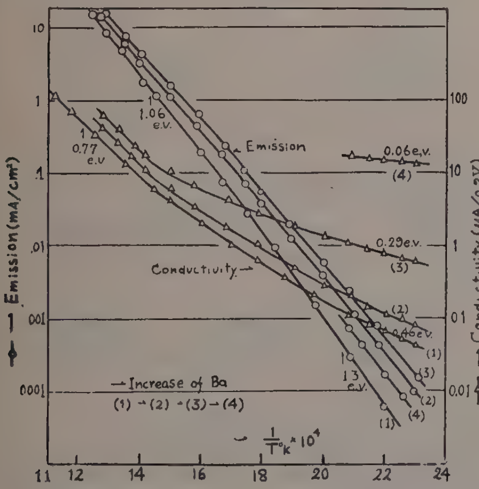

Fig. 3. Logarithmic conduction and emission vs. $1/T$ plots for the cathode, barium sputterd on the surface.

This conduction was, however, so unstable (which has not yet reported to our knowledge by Vink and Loosjes) that the activation energy of less than 0.1 e. v. was impossible to observe beyond 550°K and when the cathode was heated at high temperature its conductivity in low temperature decresed suddenly. This unstability of the conduction is believed to be due to the evaporation of barium from the oxide-coated cathode at high temperature, because the thermionic emission from the detector tungsten filament, F, increased during the process, but ceased to increase, when the conductivity reached its stable state.

Moreover we found the following facts: If barium is evaporated onto the "N" cathode at room temperature, at first M-type conduction does not appear, while after the heat treating above 450°K it becomes observable at room temperature (see Table 1). This may be ascribed to the difficulty in the diffusion of deposited barium into interior at room temperature. Depositing barium onto "S" cathode, on the contrary, M-type conduction is easily observed even at room temperature. The reason for such difference is not clear, but perhaps the deposited barium will break the insulation between probe and nickel sleeve due to the existence of cracks in the "S" cathode coating.

We suppose that M-type conduction may be occured through thin barium layer covering on the oxide- particles, and the properties of barium thin layer must be studied in the next step.

Table I. The change of conductivity of "S" and "N" cathodes with cathode temperature onto which Ba evaporated at room temp.

Conduction Current of M-type (10^{-9} Amp/0.2 V)					
Cathode		"S"		"N"	
Tube No.		1	2	1	2
Initial.	Room temp.	0	0	0	0
Ba. evaporated.	Room temp.	2110	340	0	0
Temp. rise.	Ef=1.0 V.	1320	—	0	0
〃	Ef=2.0 V.	1500	900	4.1	—
〃	Ef=3.0 V.	5500	—	110	—
Temp. lowered.	Room temp.	1600	120	8	80

Ef: heater voltage. (6.3 V normal.)

§ 4. Study of Barium thin Film

An auxiliary experimental tube whose structure is shown in Fig. 4 was prepared in order to make clear the electrical conduction through barium thin layer.

The resistance of the barium thin film on the silica sleeve was measured by applying voltage between electrodes E_1 and E_2 made of nickel films previously sputtered.

The conductivity increased as the amount of deposited barium evaporated from batalum getter, as shown in Fig. 5.

The conduction became measurable beyond the two atomic layers of barium and was approximately of the same order as M-type conduction in oxide-coated cathode and had scarcely temperature dependency (metallic conduction), suggesting that M-type conduction may be a surface conduction through the multiatomic thin film of barium on the surface of the oxide particles.

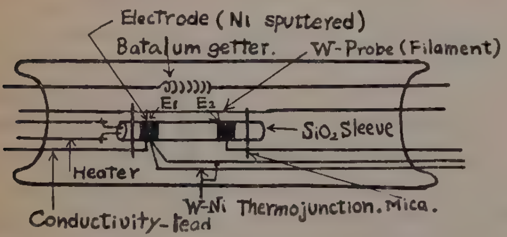

Fig. 4. Experimental tube for measuring the resistance of thin barium film on the silica.

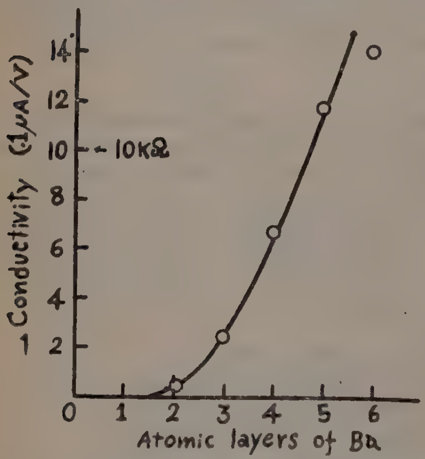

Fig. 5. The increase of conductivity of silica sleeve by deposition of barium.

§ 5. The Characteristics of "N" and "S" Cathodes

(*i*) *The initial state*

In Fig. 6 (a) and (b) the logarithms of the thermionic emission, i, and electrical conductivity, σ, of "N" and "S" cathodes are plotted against $1/T$ and also in Table II the data for the emission, i, and conductivity, σ, at 785°K, work function, $\tilde{\Phi}$, activation energy, $\tilde{E}$, each obtained from the Richardson's plots of i and σ, and the apparent value of the width of conduction band, $\tilde{\chi}=(\tilde{\Phi}-\tilde{E})$, are summerized.

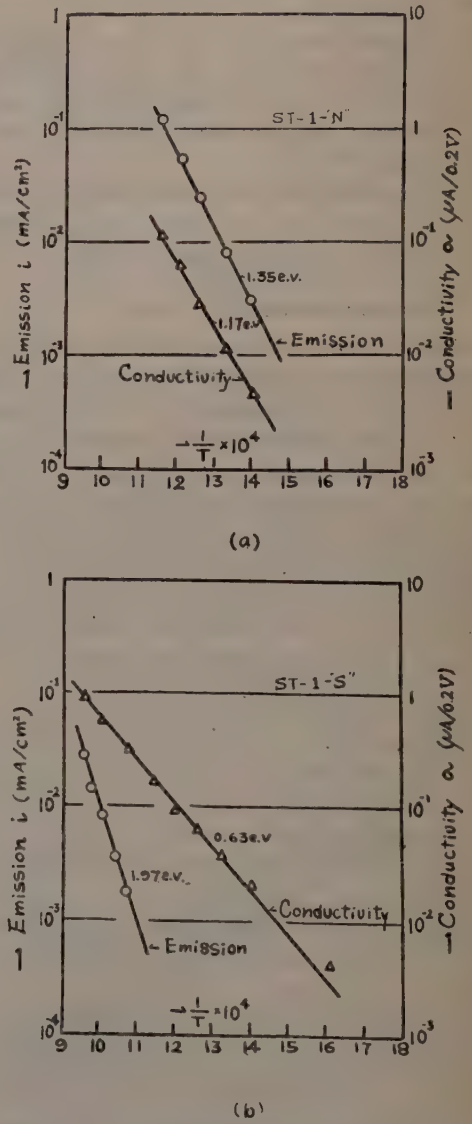

Fig. 6. log i and log $\sigma-1/T$ plots for "N" cathode (a) and "S" cathode (b) at the initial state.

Table II. Data for the initiai states.

Cathode No.	i 10^{-9}A/cm$_2$	σ 10^{-9}A/0.2V	$\tilde{\Phi}$ e.v.	$\tilde{E}$ e.v.	$\tilde{\chi}$ e.v.	Type
1-"N"$^{\Delta}$	2000	25	1.35	1.17	0.18	δ
1-"S"	(2)	65	1.94	0.63	1.31	α
2-"N"	2000	320	1.24	1.07	0.17	δ
2-"S"	40	75	1.80	0.82	0.98	α
3-"S"	2	35	1.81	0.80	1.01	α

Δ: e.g, 1-"S": "S" cathode of tube No. 1.

It is to be noted that the values of "N" cathodes are almost the same order as hitherto reported, while "S" cathodes have lower activation energy and therefore relatively larger electrical conductivity in comparison with "N" cathodes in spite of low emission due to the high work function.

Accordingly the value of $\tilde{\chi}$ in "S" cathode is found to be as large as about 1.0 e. v., while that in "N" cathode is as small as about 0.2 e. v.

(*ii*) *Activation Process*

Both the emission and the conductivity were varied by the evaporation of barium to the cathodes. Similar kinds of data to those in Fig. 6 and Table II, are shown in Fig. 7 (a) and (b) and Table III. The M-type conduction may be considered negligible in these results since the cathode temperature was kept at about 800°K during the evaporation of barium.

In Fig 7 (a) and (b), E_r and C_r mean thermionic emission and electrical conductivity of oxide cathode, being added barium atoms r times (the amount of barium per one evaporation was several atomic layers on the tungsten filament, F.)

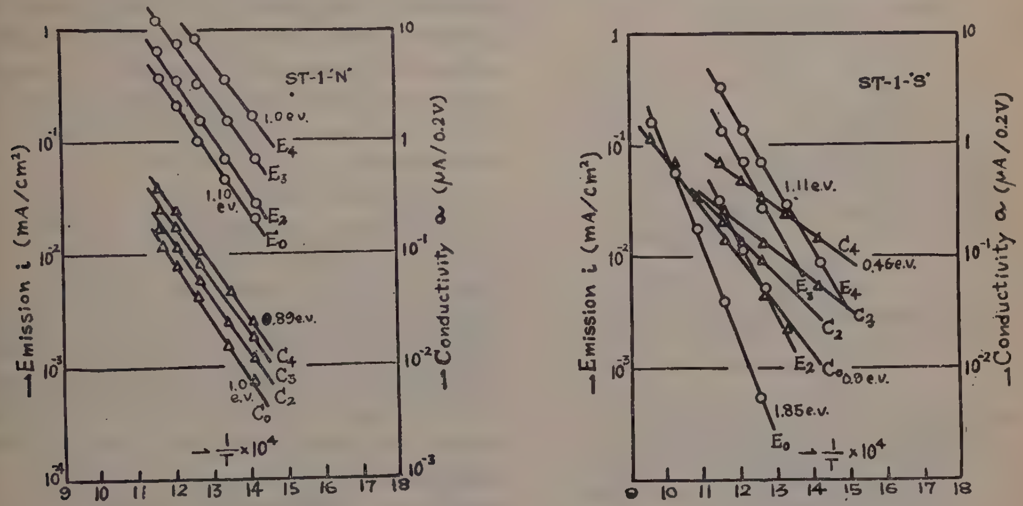

(a) (b)

Fig. 7. The change of emission and conduction by evaporating barium onto the cathodes. (a) "N" cathode, (b) "S" cathode.

Table III. Data on the activation process.

Cathode No.	State §	i 10^{-9}A/cm²	σ 10^{-9}A/0.2V	$\tilde{\phi}$ e.v.	$\tilde{E}$ e.v.	$\tilde{\chi}$ e.v.	Type
1-"N"	0	10000	46	1.10	1.00	0.10	δ
	2	15000	52	1.1	1.0	0.1	δ
	3	32000	75	1.0	0.89	0.11	δ
	4	75000	100	1.0	0.89	0.11	δ
1-"S"	0	55	55	1.87	0.90	0.97	α
	2	480	100	1.65	0·80	0.85	$\alpha-\beta$
	3	2800	150	1.14	0.60	0.54	β
	4	7000	320	1.11	0.46	0.65	β
2-"N"	0	2000	320	1.24	1.07	0.17	δ
	1	16000	740	1.04	0.91	0.13	δ
	2	24000	1700	1.11	0.80	0.31	$\delta-\gamma$
2-"S"	0	40	75	1.80	0.82	0.98	α
	1	2600	260	1.15	0.54	0.61	β
	2	4000	920	1.00	0.37	0.63	β

§ : e.g. 2 : The state after twice times evaporation of Ba onto the cathode surfaces.

In "N" cathode, the emission-conduction proportionality holds with $\tilde{\chi}$ being nearly unvaried, while in "S" cathode the work function and the activation energy of conductivity decrease from about 2.0 e. v. to 1.0 e. v. and from 0.6 e. v. to 0.45 e. v. respectively with $\tilde{\chi}$ being from 1.0 e. v. to 0.55 e. v.

(iii) Deactivation Process

The changes of both emission and conductivity of "N" and "S" cathodes, having been deposited with several ten atomic layers of barium at very low temperature (<550°K), were studied during the evaporation of added barium from the oxide cathodes by heating.

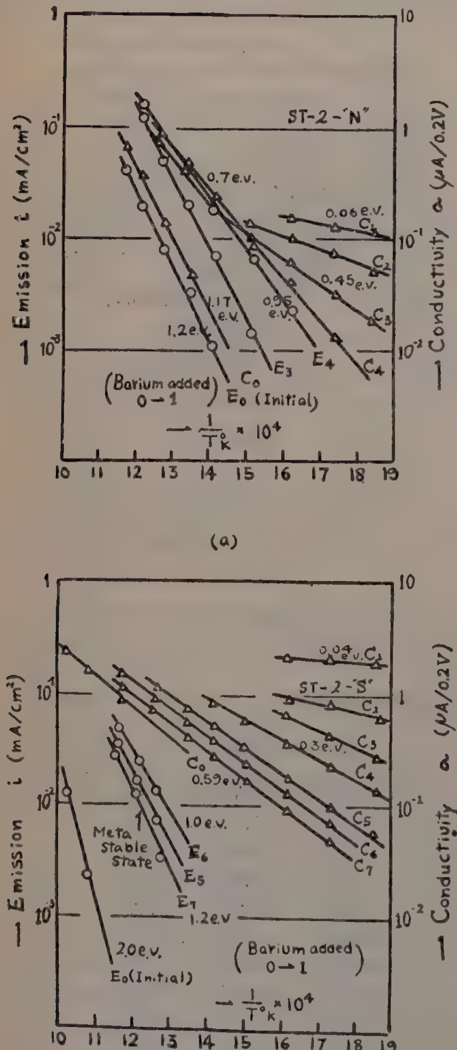

(a)

(b)

Fig. 8. The change of log i and log $\sigma - 1/T$ plots on the process of evaporation of barium from the oxide cathodes by heating up (a) "N" cathode, (b) "S" cathode

The data similar to those on the process of activation are illustrated in Fig. 8 (a) and (b), where E_r and C_r mean the emission and the conductivity of the cathode being heated r times (the temperature of heating is the highest point of measuring temperature.)

In low temperature range both "S" and "N" cathodes had M-type conduction and "S" cathode was more conductive than "N" cathode. The M-type conduction of both cathodes decaeased owing to the evaporation of barium from the cathodes through heating, while the thermionic emission increased, accompanied with the slight decrease of the work function. This may be interpreted as the transition from multilayer to monolayer of the surface barium.

The M-type conduction of "N" cathode changed suddenly to that of high activation energy of 0.7 e. v., while that of "S" cathode changed gradually to the conduction of activation energy of about 0.6 e. v. and its work function of "S" cathode changed to about 1.2 e. v. and the state of "S" cathode was stable upto 1300°K where the work function increased to the initial value. (about 1.7 e. v. ~2.2 e. v.: Reference to Fig. 8 (b))

The metastable state realized in "S" cathode may be considered to correspond to the state in which the oxide particles are covered by monolayer of barium and will be discussed latter.

§ 6. Discussions

In the "N" cathode the emission is proportional to the conduction above 800°K and the semiconductor theory seems, at a glance, to be well applicable.

However, the difference of $\tilde{\chi}$ between "N" and "S" cathode, and the variation of $\tilde{\chi}$ with the activity of "S" cathode, are hardly interpreted by the usual theory. New models for oxide-coated cathode must be introduced to overcome these difficulties. Here we shall propose a following model for oxide-coated cathode. At first we notice the following difference between the N-cathode and S-cathode: In S-cathode coating, we suppose, there is little distinct grain-to-grain boundary, and the contact potential barrier, then we suppose the semiconductor-type conduction through the grains will be predominant in "S" cathode.

In "N" cathode, on the contrary, the height of contact potential barrier between grains will be so large that the electron conduction through pores among oxide-particles may appear at high temperature above 800°K as Vink-Loosjes adovocated. Thus whole resistance of the oxide layer is assumed to connect three kinds of resistances, R_1, R_2 and R_3 in series and parallel as illustrated in Fig. 9.

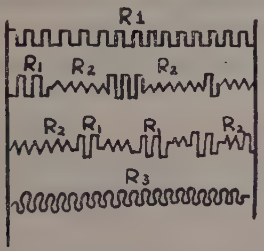

Fig. 9. A schematical diagram of the resistance in the oxide coating

Where R_1 is the resistance through grains, R_3 the resistance of pore-conduction between two grains and R_3 the resistance of M-type conduction. Then the whole resistance R may be given by

$$\frac{1}{R}=\sum_n \frac{1}{a_nR_1+b_nR_2}+\frac{1}{cR_3}. \tag{4}$$

The numerous kinds of measurable conduction are probably due to the difference in values of a_n, b_n and c.

Next two experimental facts, i. e. the variation of $\tilde{\chi}$ with the activity of "S" cathode and the existence of metastable state in emission, described in §5, may give a possibility that a monoatomic layer is formed on the surface of the activated oxide and it reduces the work function. We suppose probably "N" cathode has usually such structure.

§7. The Classification of the Structures of the Oxide Coated Cathodes

From the above discussion, the structures of oxide-coated cathodes would be classified to four different types and their subtypes as illustrated in Fig. 10.

In this paragraph, the following symbols are used.

$\tilde{\varPhi}$ and $\tilde{E}$: the apparent values of the work function and the activation energy respectively.

E_0 and E: the energy difference from the bottom of the conduction band to Fermi level and to donars respectively.

χ: the real width of conduction band.

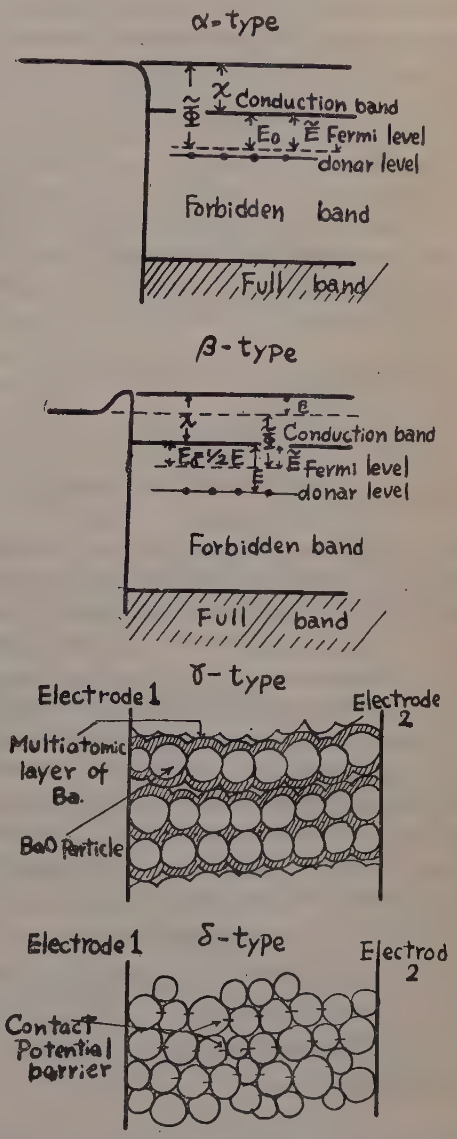

Fig. 10. Schematical energy and structure diagrams for the cathodes of various type.

(i) α-type

This type may be observed at the initial state of "S" cathode before the activation and may be of simple semi-conductor type.

In this type

$$\tilde{\varPhi}=E_0+\chi \quad \text{and} \quad \tilde{E}=E_0$$

where E_0 is greater than $1/2\,E$ since of unactivated state.[6)]

The numerical values of E_0 and χ are probably $0.8\sim1.0$ e. v. and 1.0 e. v. respectively, and then $\tilde{\Phi}=1.8\sim2.0$ e. v. and $\tilde{E}=0.8\sim1.0$ e. v. (Reference to Fig. 6 (b) and Table II.)

(ii) β-type.

The structure of the cathode in this type is considered as a semicondnctor possessing monolayer of barium on the surface and is realized at the activated state of "S" cathode. The work function in this type is lowered due to dipole moment at the surface and the Fermi level locates at the half way between the bottom of conduction band and the donars, for the activity of this cathode is good[6].

As χ is lowered by ε $(=0.45$ e. v.) and the probable value of E is 0.9 e. v., we obtain

$$\tilde{\Phi}=E_0+\chi-\varepsilon=\frac{E}{2}+\chi-\varepsilon=1.0 \text{ e. v.}$$

and $\tilde{E}=\frac{E}{2}=0.45$ e. v.

(Reference to Fig. 7 and Table III.)

(iii) γ-type

When the base metal contains reducing element, e. g. Mg, Si, (the Vink-Loosjes') or when barium is added to the cathode from outer source (the author's) the barium content in the cathode is so large that multiatomic layer of barium may be formed on the surface of oxide-particles through which M-type conduction appears.

In this case the work function is slightly higher than that of monolayer. Its value, ε', may be less than 0.1 e. v. and thus the work function is given by,

$$\tilde{\Phi}=(\chi-\varepsilon)+E_0+\varepsilon'=1.0\sim1.1 \text{ e. v.}$$

and the conduction is of M-type and its activation energy is given by,

$$\tilde{E}=E'=0\sim0.4 \text{ e. v.}$$

(Reference to Fig. 8.)

(iv) δ-type

When the contact potential barrier exist between oxide-particles, as in the case of "N" cathode, the activation energy of the conduction is equal to that of pore conduction which is slightly lower than the work function and it is written

$$\tilde{E}=\tilde{\Phi}-\theta=0.8\sim1.0 \text{ e. v.}$$

and the work function is the same as that of β-type since the activity of these type is usually good. (Reference to Fig. 6, 7 (a) and Tables II and III)

The complicated values of the work function and the activation energy of conductivity obtained in various cathodes shall be put into order by classifying to the four types and their sub-types as tabulated in the last columns of Tables II and III.

§ 8. Conclusion

The relationship between emission and conductivity for both sintered and normal cathodes was obtained at every stage of activity changed by evaporation of barium atoms onto the cathode.

Apparent value of the width of conduction band $\tilde{\chi}$ for "S" cathode known from $\tilde{\Phi}-\tilde{E}$, was very high comparing with that of "N" cathode and it varied with the change of cathode activity. These facts are explained, from the assumption of the existence of electron gas conduction through pores in "N" cathode coating and the effect of monoatomic layer on the cathode surface.

Moreover in the present experiment, the conduction of lower activation energy than 0.1 e. v. as Vink-Loosjes reported appeared in the process of evaporating barium onto cathode at very low temperature.

This conductivity was interpreted as the surface conduction of electron through multiatomic layer of barium on the oxide particles.

The author wishes to express his thanks to Dr. T. Arizumi for his extremely helpful advices and encouragements, and also wishes to express his gratitude to Prof. Y. Uchida for his sincere discussions.

References

1) E. Nishibori and H. Kawamura: Proc. Phys-Math. Soc. Japan **22** (1940) 378.

2) T. Arizumi and S. Narita: J. Phys. Soc. Japan **6** (1951) 15.

3) N. B. Hannay, D. MacNair and A. H. White: J. App. Phys. **7** (1949) 669.

4) G. E. Moore, and H. W. Allison: Phys. Rev. **77** (1950) 246.

5) R. Loosjes and H. J. Vink: Philip. Res. Rep. **4** (1949) 449.

6) T. Arizumi and S. Narita: J. Phys. Soc. Japan **3** (1948) 356.

JOURNAL OF THE PHYSICAL SOCIETY OF JAPAN Vol. 8, No. 3, MAY—JUNE, 1953

Diffusion on the Fermi-Surface and the Conductivity of Metals

By Morikazu TODA

Institute of Physics, Tokyo University of Education

(Received December 23, 1952)

The transport phenomena in metals, such as the electrical and the thermal conductivity, are treated as a kind of the diffusion of electrons on the Fermi-surface. Grüneisen's well-known formula is gained for the electrical conductivity σ, and as for the thermal conductivity κ the expression

$$\kappa=\sigma T\frac{\pi^2}{3}\left(\frac{k}{e}\right)^2\Big/\left\{1+\left(\frac{\theta}{T}\right)^2\left(\frac{K}{q_0}\right)^2\int_0^{\theta/T}\frac{x^3dx}{e^x-e^{-x}}\Big/\int_0^{\theta/T}\frac{x^5dx}{(e^x-1)(1-e^{-x})}\right\}$$

is obtained. In this equation θ denotes the Debye temperature, K and q_0 are the maximum wave numbers of electrons and phonons respectively.

§1. Introduction

The theoretical approach to the transport phenomena in metals is based on the well-known formula called the Bloch's integral equation[1]. The solution of this equation for high temperatures as well as for the lowest temperatures was gained in some cases. Grüneisen thus proposed an interpolation formula for the electrical conductivity σ, which can be written as

$$1/\sigma=A(T/\theta)^5J_5(\theta/T)\,, \qquad (1)$$

and Wilson proposed an interpolation formula for the thermal conductivity κ, which may be written as[2]

$$1/\kappa=B(T/\theta)^3\left\{(K/q_0)^2J_5+(T/\theta)^2\left(\frac{\pi^2}{3}J_5-\frac{1}{6}J_7\right)\right\} \qquad (2)$$

in which

$$A=\frac{\pi^4\theta k^2}{9e^2}B\,,\quad J_n(\theta/T)=\int_0^{\theta/T}\frac{x^n dx}{(e^x-1)(1-e^{-x})}\,.$$

Recently several authors[3] criticized these formulas and effort was made to gain strict formulas for the conductivity. Umeda[3] and Sondheimer[4] solved the Bloch equation in the form of infinite determinants, the results so obtained are, however, in contradiction to the experiments of Berman, MacDonald and others[5], and to the computation of Rhodes[6], who solved the Bloch equation numerically for the electrical conductivity. After Rhodes the Grüneisen's interpolation formula is valid in a few percent error.

On the other hand Koppe[7] suggested a new idea for computing the electrical conductivity of metals. He intended in principle to regard the transition of electronic states by collision with the lattice waves as a kind of diffusion on the Fermi-surface.

In this paper Koppe's idea is extended to include the case of the thermal conductivity, and is simplified making clear the relation of the method to the Bloch's standard integral equations.

§2. Diffusion Equations

If the distorted distribution function for the electrons in metals is written as

$$f=f_0+g(\boldsymbol{k},\varepsilon)\quad (f_0=1/(e^\varepsilon+1),\ \varepsilon=(E-\zeta)/kT) \qquad (3)$$

its change due to collisions with the lattice waves is given by the Bloch's equation which is conveniently written as[1]

$$\left(\frac{\partial g}{\partial t}\right)_c=\int_0^{q_0}B(q)q^2dq\,N_q\int_0^{2\pi}d\varphi\left\{g(\boldsymbol{k}+\boldsymbol{q},\varepsilon+x)\times\frac{e^{\varepsilon+x}+1}{e^\varepsilon+1}+g(\boldsymbol{k}+\boldsymbol{q},\varepsilon-x)e^x\frac{e^{\varepsilon-x}+1}{e^\varepsilon+1}-g(\boldsymbol{k},\varepsilon)\left[\frac{e^\varepsilon+1}{e^{\varepsilon-x}+1}+e^x\frac{e^\varepsilon+1}{e^{\varepsilon+x}+1}\right]\right\}$$

in which the direction of the wave vector $\boldsymbol{k}$ for the electron is taken as the polar axis, and φ denotes the azimuth angle for the lattice wave $\boldsymbol{q}$. Abbreviations

$$\left.\begin{aligned}&x=h\nu/kT,\ N_q=1/(e^x-1)\,,\\&B(q)=\frac{\Omega_0}{8\pi^2(dE/dK)Mu_0q^2}\left|\int u_k{}^*V'u_kd\tau_0\right|^2\end{aligned}\right\} \qquad (5)$$

are used, where u_0 denotes the sound velocity,

K the maximum value for $|\boldsymbol{k}|$, V' being the interaction energy between an electron and a unit displacement of the lattice. In Bethe's notation $\left|\int u_k^* V' u_k d\tau_0\right| = \frac{2}{3} Cq$, and

$$B(q) = \frac{\Omega_0 C^2}{18\pi^2 (dE/dK) M u_0} \,. \tag{6}$$

The external condition is given in terms of the electric field and the temperature gradient in the form

$$\left(\frac{\partial g}{\partial t}\right)_{ext} = -\frac{df_0}{d\varepsilon}\frac{d\varepsilon}{dK}\frac{1}{\hbar} \times \left\{eF - \left(\frac{d\zeta}{dT} + k\varepsilon\right)\frac{dT}{dx}\right\}\cos\Theta \,, \tag{7}$$

where Θ denotes the angle between $\boldsymbol{k}$ and the $\boldsymbol{k}_x$ axis (Fig. 1).

Let us assume the solutions

$$g = -\frac{df_0}{d\varepsilon} F(\Theta, \Phi) \quad \text{or} \quad -\frac{df_0}{d\varepsilon}\varepsilon G(\Theta, \Phi) \tag{8}$$

where F and G depend only slightly on $|\boldsymbol{k}|$ We shall write them if needed as F_k and G_k, which satisfy then

$$-\frac{df_0}{d\varepsilon}\left(\frac{\partial F}{\partial t}\right)_c = \int Bq^2 dq N_q \int d\varphi \times \left\{F_{k+q}(I'_{\varepsilon+x} + I_{\varepsilon-x}) - F_k(I_\varepsilon' + I_\varepsilon)\right\} \,, \tag{9}$$

$$-\frac{df_0}{d\varepsilon}\left(\frac{\partial G}{\partial t}\right)_c = \int Bq^2 dq N_q \int d\varphi \times \left\{G_{k+q}(I'_{\varepsilon+x} + I_{\varepsilon-x}) - G_k(I_\varepsilon' + I_\varepsilon) + \frac{x}{\varepsilon} G_{k+q}(I'_{\varepsilon+x} - I_{\varepsilon-x})\right\} \tag{9'}$$

where

$$I_\varepsilon' = 1/(1+e^{-\varepsilon})(e^{\varepsilon-x}+1) \,,$$
$$I_\varepsilon = 1/(1+e^{-\varepsilon})(e^{\varepsilon}+e^{-x}) \,.$$

Integration with respect to ε is straightforward giving

$$\int_{-\infty}^{\infty} I'_\varepsilon d\varepsilon = \int_{-\infty}^{\infty} I_\varepsilon d\varepsilon = x/(1-e^{-x}) \,.$$

We have then

$$\left(\frac{\partial F}{\partial t}\right)_c = \int \frac{2Bq^2 x dq}{(e^x-1)(1-e^{-x})}\int d\varphi (F_{k+q} - F_k). \tag{10}$$

The right hand side of the above equation (10) for F may be approximated as a kind of diffusion of F if the scattering angle between $\boldsymbol{k}$ and $\boldsymbol{k}+\boldsymbol{q}$ is sufficiently small, that is to say, if

$$q \ll K \,.$$

This condition is evidently satisfied at lowest temperatures where only the small values of $q(\hbar u_0 q \lesssim kT)$ are effective, but is also satisfied if the forward scattering is predominant at all temperatures. Thus we have

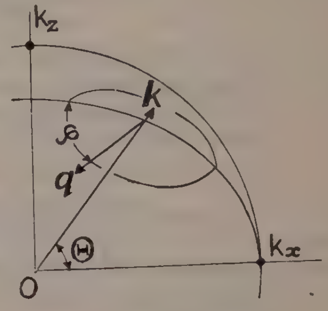

Fig. 1. Fermi-Surface.

$$\left(\frac{\partial F}{\partial t}\right)_c = D\nabla^2 F \tag{11}$$

where ∇^2 denotes the Laplacian operator on the Fermi-sphere:

$$\nabla^2 = \frac{1}{K^2}\left(\frac{1}{\sin\Theta}\frac{\partial}{\partial\Theta}\sin\Theta\frac{\partial}{\partial\Theta} + \frac{1}{\sin^2\Theta}\frac{\partial^2}{\partial\Phi^2}\right) \tag{12}$$

and D is the diffusion constant defined by (see appendix)

$$D = \langle[(\boldsymbol{k}+\boldsymbol{q})_{t+\delta t} - \boldsymbol{k}_t]^2\rangle/4\delta t \,. \tag{13}$$

In this equation the mean square displacement q^2 for the quantity F during a small time interval δt is given immediatly from the above integral as

$$\left\langle \delta t q^2 \frac{2B(q)q^2 x dq}{(e^x-1)(1-e^{-x})} 2\pi \right\rangle .$$

Remembering that $x = \hbar u_0 q/kT$, we have

$$D = \pi\left(\frac{T}{\theta}\right)^5 q_0^5 \int_0^{\theta/T} \frac{B(xq_0T/\theta)x^5 dx}{(e^x-1)(1-e^{-x})} \tag{14}$$

where $\theta = \hbar u_0 q_0/k$ is the Debye temperature. It is easy to verify that for high temperatures we have the well-known relaxation time τ[8]:

$$D = 1/2\tau, \quad 1/\tau = 2\pi K^2 \int_0^\pi P(\theta)(1-\cos\theta)\sin\theta d\theta \,.$$

As to the second term G, we proceed analogously. We have then from Eq. (9')

$$\left(\frac{\partial G}{\partial t}\right)_c = D\nabla^2 G - \alpha G \tag{15}$$

where α is given by

$$\alpha = \int_0^{q_0} Bq^2 dq N_q \int_0^{2\pi} d\varphi \int_{-\infty}^{\infty} \frac{x}{\varepsilon}(I_{\varepsilon-x} - I'_{\varepsilon+x}) d\varepsilon \,. \tag{16}$$

Now in the alteration

$$I_{\varepsilon-x}-I'_{\varepsilon+x}=\frac{1-e^{-\varepsilon}}{e^{x}-e^{-x}}\left\{\left(\frac{1}{e^{-\varepsilon}+1}-\frac{1}{e^{-\varepsilon+x}+1}\right)e^{x}-\left(\frac{1}{e^{-\varepsilon-x}+1}-\frac{1}{e^{-\varepsilon}+1}\right)\right\}$$

the first term in the bracket { } is almost e^{x} for $0<\varepsilon<x$ and the second term -1 for $-x<\varepsilon<0$, and otherwise zero.

Thus we have

$$\alpha\cong 2\pi\left(\frac{T}{\theta}\right)^{3}q_0^{3}\int_0^{\theta/T}\frac{B(xq_0T/\theta)x^3dx}{e^{x}-e^{-x}}$$

where $(1-e^{-\varepsilon})/\varepsilon$ is replaced by 1; the error introduced will be small as $|\varepsilon|$ is limited $(-x<\varepsilon<x)$. The integrand of the last equation diminishes rapidly for $x>1$.

§ 3. Conductivity and the Lorentz number

The conductivity is readily obtained by solving

$$\left(\frac{\partial f}{\partial t}\right)_c+\left(\frac{\partial f}{\partial t}\right)_{ext}=0\ . \tag{18}$$

After integration as to ε we have

$$D\nabla^2F+\left(\frac{d\varepsilon}{dK}\right)\frac{1}{\hbar}\left(eF-\frac{d\zeta}{dT}\frac{dT}{dx}\right)\cos\Theta=0 \tag{19}$$

$$D\nabla^2G-\alpha G-\left(\frac{d\varepsilon}{dK}\right)\frac{k}{\hbar}\frac{dT}{dx}\cos\Theta=0, \tag{19'}$$

or

$$F=\frac{K^2}{2D\hbar}\left(\frac{d\varepsilon}{dK}\right)\left(eF-\frac{d\zeta}{dT}\frac{dT}{dx}\right)\cos\Theta\ , \tag{20}$$

$$G=-\frac{k}{\hbar}\left(\frac{d\varepsilon}{dK}\right)\frac{dT}{dx}\cos\Theta\Big/\left(\frac{2D}{K^2}+\alpha\right)=G_1\cos\Theta. \tag{20'}$$

If the mean free path is defined by

$$l=\frac{K^2}{2D\hbar}\frac{dE}{dK}$$

the electrical condutivity σ is given as

$$\frac{1}{\sigma}=\frac{\hbar K}{e^2nl}=\frac{2\pi\hbar}{e^2K^2}\frac{dK}{dE}q_0^{5}\left(\frac{T}{\theta}\right)^{5}.\times\int_0^{\theta/T}\frac{B(xq_0T/\theta)x^5dx}{(e^{x}-1)(1-e^{-x})} \tag{21}$$

which is essentially the Grüneisen's formula.

The thermal conductivity due to metallic electrons is on the other hand given by

$$\kappa=\frac{nk^2T^2}{\hbar K}\int\varepsilon^2G_1\frac{df_0}{d\varepsilon}d\varepsilon\Big/\frac{dT}{dx}=\frac{\pi^2}{3}\frac{nk^2T}{\hbar K^2}\left(\frac{\partial E}{\partial K}\right)\Big/\left(\frac{2D}{K^2}+\alpha\right)$$

or with the following abbreviations

$$b=\int_0^{\theta/T}\frac{x^3dx}{e^{x}-e^{-x}}\ ,\qquad J_5=\int_0^{\theta/T}\frac{x^5dx}{(e^{x}-1)(1-e^{-x})}\ ,$$

we have, if Bloch's assumption of constant B (Eq. 6) is used,

$$\frac{1}{\kappa}=\frac{3K^2}{2\pi^3\hbar\theta}\frac{1}{k^2}\frac{dE}{dK}\frac{1}{q_0^{5}}\left(\frac{T}{\theta}\right)^2\times\left\{\left(\frac{K}{q_0}\right)^2b+\left(\frac{T}{\theta}\right)^2J_5\right\}\ . \tag{22}$$

The so-called Lorentz number is then

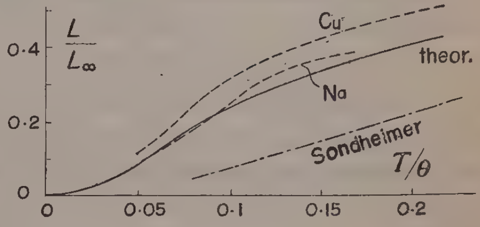

Fig. 2. Comparison with the Experiments on Cu and Na, and with the computation of Sondheimer. $L_\infty=(\pi^2/3)(k/e)^2$.

$$L\equiv\frac{\kappa}{\sigma T}=\frac{\pi^2}{3}\left(\frac{k}{e}\right)^2\Big/\left(1+\frac{\alpha K^2}{2D}\right)=\frac{\pi^2}{3}\left(\frac{k}{e}\right)^2\Big/\left[1+\left(\frac{\theta}{T}\right)^2\left(\frac{K}{q_0}\right)^2\frac{b}{J_5}\right]\ . \tag{23}$$

The experimental results obtained by Berman and MacDonald[5] are to be compared with the above formula. Their results on sodium and cupper are protted against reduced temperature in Fig. 2 for ideally pure metals. The experimental points on these metals run side by side. Theoretical curve of Eq. (23) is given in the figure by a full curve which is seen in qualitative agreement with the experiments. The discrepancy is probably due to the nature of approximation involved in the present method and also to the deviation from the so-called Matthiesen's rule used to extrapolate the experimental results to ideally pure cases. But more serious source of error will be in the Debye model. It is well noticed from both theoretical as well as experimental sides that, in general, the Debye temperature diminishes as the temperature is lowered and this tendency is more and more strengthened as the absolute zero of temperature is approached. If this fact is taken into account much better agreement will be obtained.

Acknowledgement

The author is deeply indepted to the theoretical group for the low temperature physics and especially to Mr. F. Takano for valuable discussion. In conclusion, this work is indepted to the Scientific Research Expenditure of the Ministry of Education.

Appendix

In deriving (14) the fact is used that q is nearly tangential to the Fermi-surface. When q is small the conservation of energy and momenta lead

$$\mu \equiv \cos(q . \nabla E) = \pm \hbar u_0 / (\partial E / \partial K) \ .$$

Let

$$F(\boldsymbol{k}+q) = F(\boldsymbol{k}) + q \cdot \nabla F + \tfrac{1}{2} qq : \nabla\nabla F + \cdots$$

where ∇ denotes the gradient with respect to q; integration of (10) then leads to the expression

$$D = (1-\mu^2)\pi(T/\theta)^5 q_0^5 \int_0^{\theta/T} B x^5 dx / (\mathrm{e}^x - 1)(1 - \mathrm{e}^{-x}).$$

In usual μ is sufficiently small compared to unity.

References

1) See for example A. Sommerfeld and H. Bethe: *Handb. d. Phys.* **24** (1933) 2.

2) A. H. Wilson: Proc. Camb. Phil. Soc. **33** (1937) 371.

3) W. Kroll: Z. Phys. **80** (1933) 50, **81** (1933) 425.

M. Kohler: Z. Phys. **124** (1948) 772, **125** (1949) 679, **126** (1949) 495, K. Umeda et al, Pap. Inst. Phys. Chem. Res. Tokyo **39** (1942) 342, J. Fac. Sci. Hokkaido Univ. (2) **3** (1949) 257, 249.

See also P.G. Klemens, Proc. Phys. Soc. **64** (1951) 681.

4) E. H. Sondheimer: Proc. Roy. Soc. A **203** (1950) 75.

5) D. K. C. MacDonald et al: Proc. Roy. Soc. A **202** (1950) 103, **209** (1951) 368, **211** (1952) 122.

6) P. Rhodes: Proc. Roy. A **202** (1950) 466.

7) H. Koppe: Zeits. f. Naturf. **7a** (1952) 17, 156.

8) N. Mott and H. Jones: *The Theory of the Properties of Metals and Alloys* (1936) Oxford Univ. Press.

JOURNAL OF THE PHYSICAL SOCIETY OF JAPAN Vol. 8, No. 3, MAY—JUNE, 1953

Statistical Mechanics of Surface Tension

By Akira HARASIMA

Tokyo Institute of Technology, Oh-Okayama, Tokyo

(Received January 22, 1953)

It is shown that we can derive by a comparatively simple procedure the formula of surface tension in terms of distribution functions from purely statistical considerations. Surface tension is derived as the increase of free energy which accompanies the increase of unit area of the interface between the liquid and the vapor phases. The expression obtained is the same as MacLellan's:

$$\gamma=\frac{1}{2}\iiiint\frac{d\phi_{12}}{dR_{12}}\frac{x_{12}^2-z_{12}^2}{R_{12}}\rho_s^{(2)}(z,\boldsymbol{R}_{12})dz_1dv_{12},$$

where γ is the surface tension, ϕ_{12} is the intermolecular potential and $\rho_s^{(2)}(z,\boldsymbol{R}_{12})$ is the excess pair density reckoned relative to an arbitrary Gibbs dividing surface. The above expression can be transformed into the form given by Bakker,

$$\gamma=\int(p_N-p_T)dz_1\ ,$$

where

$$p_N(z_1)=kT\rho^{(1)}(z_1)-\frac{1}{2}\iiint dv_{12}\int_{z_1-z_{12}}^{z_1}\frac{d\phi_{12}}{dR_{12}}\frac{z_{12}}{R_{12}}\rho^{(2)}(\zeta,\boldsymbol{R}_{12})d\zeta,$$

$$p_T(z_1)=kT\rho^{(1)}(z_1)-\frac{1}{2}\iiint dv_{12}\frac{d\phi_{12}}{dR_{12}}\frac{x_{12}^2}{R_{12}}\rho^{(2)}(z_1,\boldsymbol{R}_{12})\ .$$

This result coincides with that of Kirkwood and Buff which was derived by calculating stresses directly. The assumption of density discontinuity, which is often made in the theory of surface tension, is examined closely.

§ 1. Introduction

The first attempt to express surface tension in terms of intermolecular forces and distribution functions is due to R. H. Fowler1). He calculated the isothermal work of formation of liquid-vapor interface assuming a mathematical surface of density discontinuity between the two phases. But since the density practically changes continuously near the interface between the liquid and the vapor phases following the equation between singlet and pair densities, it was desirable to formulate a general theory free from Fowler's assumption and this was done by Kirkwood and Buff2).

Kirkwood and Buff developed a general theory of surface tension by calculating the stress transmitted across a strip of unit width, normal to a Gibbs dividing surface, and obtained a formula by which we can calculate the surface tension of a liquid in terms of the intermolecular potential and the moments of distribution functions.

It is the purpose of the present paper to show that, instead of attempting to calculate the stresses, we can obtain surface tension in a form of the surface free energy per unit area of the surface by a comparatively simple calculations.

The author has noticed* that a similar attempt was done by MacLellan3), but the procedure here presented seems to be more simple and straightforward. Further, the relation of the theory with Bakker's interpretation of surface tension is also made clear.

§ 2. Surface Tension as Surface Free Energy Per Unit Area of the Surface

Let us consider a system of N monatomic molecules enclosed in a cubic vessel of edge length a and let the system consist of a liquid film which is stretched parallel to the x-y plane, the other parts (above and under the film) of the vessel being filled with the vapor of the liquid. The thickness of the film, though small compared with the edge length a, is assumed to be sufficiently large, so that in the interior of the film the state of the liquid is the same as that of the liquid in bulk.

---

* The author expresses his thanks to Mr. S. Teramoto who suggested to the author MacLellan's work when the present paper was read at the annual meeting of the Physical Society of Japan.

The Helmholtz free energy F is given by

$$e^{-F/kT}=\frac{1}{N!}\left(\frac{2\pi mkT}{h^2}\right)^{3/2\cdot N}\times\iint\cdots\int_V e^{-\Phi/kT}\prod_{i=1}^{N} d\boldsymbol{r}_i\,, \qquad (1)$$

where $\boldsymbol{r}_i$ is the position vector of the i-th molceule and Φ is the potential energy of the system which we assume to be expressible in the form

$$\Phi=\sum_{i>j}\phi_{ij}\,.$$

Now we shift one of the planes, perpendicular to the x-axis, outward by a length $a\varepsilon$, and simultaneously shift one, perpendicular to the z-axis, inward by a length $a\varepsilon$, this being conducted under isothermal conditions. The volume of the whole system as well as the area of the interface between the vapor and the wall of the vessel are not changed during the procedure and the area of each of the two interfaces between the liquid and the vapor is increased by $a^2\varepsilon$. The free energy F' is then given by

$$e^{-F'/kT}=\frac{1}{N!}\left(\frac{2\pi mkT}{h^2}\right)^{3/2\cdot N}\times\iint\cdots\int_{V'} e^{-\Phi/kT}\prod_{i=1}^{N} d\boldsymbol{r}_i\,. \qquad (2)$$

We now write $\boldsymbol{r}_i=a\boldsymbol{\theta}_i$ in (1) and $x_i=a(1+\varepsilon)\theta_{ix}$, $y=a\theta_{iy}$, $z_i=a(1-\varepsilon)\theta_{iz}$ in (2). Similar procedure was adopted by Born and Green[4] in deriving the equation of state of an assembly of particles. From (1) and (2) we have

$$e^{-F/kT}=\frac{a^{3N}}{N!}\left(\frac{2\pi mkT}{h^2}\right)^{3/2\cdot N}\times\iint\cdots\int e^{-\Phi/kT}\prod_{i=1}^{N} d\theta_{ix}d\theta_{iy}d\theta_{iz}\,, \qquad (3)$$

and

$$e^{-F'/kT}=\frac{a^{3N}}{N!}\left(\frac{2\pi mkT}{h^2}\right)^{3/2\cdot N}\times\iint\cdots\int e^{-\Phi'/kT}\prod_{i=1}^{N} d\theta_{ix}d\theta_{iy}d\theta_{iz}\,. \qquad (4)$$

The domains of θ_{ix}, θ_{iy}, θ_{iz} are the same for (3) and (4). By giving all values θ_{ix}, θ_{iy}, θ_{iz} between 0 and 1, we have all the possible configurations of the system in the two cases respectively. We will compare the integrals in (3) and (4) by comparing the integrands for the same values of θ_{ix}, θ_{iy} and θ_{iz}. Values of Φ and Φ' for the same values of θ_{ix}, θ_{iy} and θ_{iz} are not the same for the two cases. If the distance between the i-th and j-th molecules is

$$R_{ij}=\sqrt{x_{ij}^2+y_{ij}^2+z_{ij}^2}$$

for the system before we shift the planes, the corresponding distance after we have shifted the planes is

$$\sqrt{x_{ij}^2(1+\varepsilon)^2+y_{ij}^2+z_{ij}^2(1-\varepsilon)^2}=R_{ij}+\varepsilon\frac{x_{ij}^3-z_{ij}^3}{R_{ij}}\,.$$

Hence

$$e^{-\Phi'/kT}=e^{-\Phi/kT}\left[1-\frac{1}{kT}\sum\frac{d\phi_{ij}}{dR_{ij}}\varepsilon\,\frac{x_{ij}^3-z_{ij}^2}{R_{ij}}\right],$$

and we have

$$\begin{aligned}e^{-(F'-F)/kT}&=\iint\cdots\int e^{-\Phi/kT}\left[1-\frac{1}{kT}\sum\frac{d\phi_{ij}}{dR_{ij}}\varepsilon\,\frac{x_{ij}^2-z_{ij}^2}{R_{ij}}\right]\prod_{i=1}^{N} d\theta_{ix}d\theta_{iy}d\theta_{iz}\\&\quad\div\iint\cdots\int e^{-\Phi/kT}\prod_{i=1}^{N} d\theta_{ix}d\theta_{iy}d\theta_{iz}\\&=1-\frac{\varepsilon a^2}{2kT}\iiiint\frac{d\phi_{12}}{dR_{12}}\,\frac{x_{12}^2-z_{12}^2}{R_{12}}\,\rho^{(2)}(z_1,\boldsymbol{R}_{12})dz_1dv_{12}\,.\end{aligned}$$

Here $\rho^{(2)}(z_1,\boldsymbol{R}_{12})=\rho^{(2)}(\boldsymbol{r}_1,\boldsymbol{r}_1+\boldsymbol{R}_{12})$ is the pair density which specifies the average number of molecular pairs one member of which is situated in the volume element dv_1 at $\boldsymbol{r}_1$ and the other in dv_{12} at the point $\boldsymbol{R}_{12}$ relative to the point at $\boldsymbol{r}_1$. Since the area between the vapor and the wall of the vessel remains unchanged the effect of the wall on the vapor can be disregarded. Let the integration with respect to z_1 be from the value corresponding to a point in the interior of the liquid film up to the upper wall of the vessel. If we choose the origin of z_1 near the upper surface of the film, then, since

$$\iiint (d\phi_{12}/dR_{12})(x_{12}^2-z_{12}^2)/\boldsymbol{R}_{12}\rho^{(2)}(z_1, \boldsymbol{R}_{12})dv_{12}$$

decreases rapidly as z_1 becomes appreciably different from zero, we can let the limits of z_1 be $-\infty$ and $+\infty$ ($z_1=-\infty$ corresponds to a point in the interior of the liquid). Thus we have for the surface tension γ

$$\gamma=\frac{F'-F}{a^2\varepsilon}=\frac{1}{2}\iiiint \frac{d\phi_{12}}{dR_{12}}(x_{12}^2-z_{12}^2)/R_{12} \times \rho^{(2)}(z_1, \boldsymbol{R}_{12})dz_1 dv_{12}\,. \tag{5}$$

This is the result which MacLellan obtained by a similar but more complicated method. We now define the density $\rho_{\alpha\beta}^{(2)}$, as done in Kirkwood's work, with respect to an arbitrary Gibbs dividing surface in the following manner,

$$\rho_{\alpha\beta}^{(2)}=[1-A(z)]\rho_\alpha^{(2)}+A(z)\rho_\beta^{(2)}\,, \tag{6}$$

where $A(z)=0$ for $z<0$ and $A(z)=1$ for $z\geq 0$, and $\rho_\alpha^{(2)}$ and $\rho_\beta^{(2)}$ are the pair distribution functions in the homogeneous liquid and vapor, respectively. Since $\rho_{\alpha\beta}^{(2)}$ is spherically symmetric with respect to $\boldsymbol{r}_{12}$, we have

$$\frac{1}{2}\iiiint \frac{d\phi_{12}}{dR_{12}}\frac{x_{12}^2-z_{12}^2}{R_{12}}\rho_{\alpha\beta}^{(2)}dz_1 dv_{12}=0\,.$$

Hence, if we put

$$\rho_s^{(2)}(z_1, \boldsymbol{R}_{12})=\rho^{(2)}(z_1,\boldsymbol{R}_{12})-\rho_{\alpha\beta}^{(2)}\,, \tag{7}$$

we have

$$\gamma=\frac{1}{2}\iiiint \frac{d\phi_{12}}{dR_{12}}\frac{x_{12}^2-z_{12}^2}{R_{12}}\rho_s^{(2)}(z_1, \boldsymbol{R}_{12})dz_1 dv_{12}\,, \tag{8}$$

or

$$\left.\begin{aligned}\gamma&=\frac{1}{2}\iiint \frac{d\phi_{12}}{dR_{12}}\frac{x_{12}^2-z_{12}^2}{R_{12}}[\Gamma_s^{(2)}]_0 dv_{12}\,,\\ &\text{where}\\ [\Gamma_s^{(2)}]_0&=\int_{-\infty}^{\infty}\rho_s^{(2)}(z_1, \boldsymbol{R}_{12})dz_1\,.\end{aligned}\right\} \tag{9}$$

§ 3. Comparison of the Present Theory with Those of Bakker and Kirkwood

In Wien-Harms' Handbuch der Experimentalphysik Bakker[5)] explains surface tension to be the result of the breakdown of Pascal's theorem near the interface of the two phases, and he expresses surface tension in the form

$$\gamma=\int (p_N-p_T)dz_1\,, \tag{10}$$

where p_N is the pressure normal to and p_T is that tangential to the interface. The pressure p_N is the same at any point in the system and is equal to the pressure in the interior of the liquid or the vapor.

It is easy to express the equation (8) or (9) in the form of the expression (10). We rewrite the integral contained in (8) or (9) in the following way. Let us put

$$\left.\begin{aligned}I&=\frac{1}{2}\iiint \frac{d\phi_{12}}{dR_{12}}\frac{z_{12}^2}{R_{12}}[\Gamma_s^{(2)}]_0 dv_{12}\,,\\ &\text{where}\\ [\Gamma_s^{(2)}]_0&=\int_{-\infty}^{\infty}\rho_s^{(2)}(z_1, \boldsymbol{R}_{12})dz_1\,.\end{aligned}\right\} \tag{11}$$

Now, we have, generally, for any parameter α

$$\int_{-\infty}^{\infty} f(x)dx=\frac{1}{\alpha}\int_{-\infty}^{\infty}dx\int_{x-\alpha}^{x} f(\zeta)d\zeta\,. \tag{12}$$

Putting $x=z_1$,

$$f(z_1)=\rho_s^{(2)}(z_1, \boldsymbol{R}_{12})=\rho_s^{(2)}(z_1, \boldsymbol{R}_1+\boldsymbol{R}_{12})\,,$$

we have,

$$\int_{-\infty}^{\infty}\rho_s^{(2)}(z_1, \boldsymbol{R}_{12})dz_1=\frac{1}{\alpha}\int_{-\infty}^{\infty}dz_1 \times\int_{z_1-\alpha}^{z_1}\rho_s^{(2)}(\zeta, \boldsymbol{R}_{12})d\zeta\,,$$

so that (11) becomes

$$I=\frac{1}{2}\iiint \frac{d\phi_{12}}{dR_{12}}\frac{z_{12}^2}{R_{12}}dv_{12} \times\left[\frac{1}{\alpha}\int_{-\infty}^{\infty}dz_1\int_{z_1-\alpha}^{z_1}\rho_s^{(2)}(\zeta, \boldsymbol{R}_{12})\,d\zeta\,.\right.$$

The value of the last double integral does not depend on the value of α. If we put $\alpha=z_{12}$, we have

$$I=\frac{1}{2}\iiiint \frac{d\phi_{12}}{dR_{12}}\frac{z_{12}}{R_{12}}dz_1 dv_{12} \times\int_{z_1-z_{12}}^{z_1}\rho_s^{(2)}(\zeta, \boldsymbol{R}_{12})d\zeta\,, \tag{13}$$

and (8) or (9) becomes

$$\gamma=\int_{-\infty}^{\infty}\left[\frac{1}{2}\iiint dv_{12}\frac{d\phi_{12}}{dR_{12}}\frac{x_{12}^2}{R_{12}}\rho_s^{(2)}(z_1, \boldsymbol{R}_{12}) -\frac{1}{2}\iiint dv_{12}\int_{z_1-z_{12}}^{z_1}\frac{\alpha\phi_{12}}{dR_{12}}\frac{z_{12}}{R_{12}}\rho_s^{(2)}(\zeta,\boldsymbol{R}_{12})d\zeta\right]dz_1\,. \tag{14}$$

The formula (14) remains valid if we replace $\rho_s^{(2)}(z_1, \boldsymbol{R}_{12})$ and $\rho_s^{(2)}(\zeta, \boldsymbol{R}_{12})$ by $\rho^{(2)}(z_1, \boldsymbol{R}_{12})$ and $\rho^{(2)}(\zeta, \boldsymbol{R}_{12})$ respectively. Thus if we put

$$p_N(z_1)=kT\rho^{(1)}(z_1)-\frac{1}{2}\iiint dv_{12} \times\int_{z_1-z_{12}}^{z_1}\frac{d\phi_{12}}{dR_{12}}\frac{z_{12}}{R_{12}}\rho^{(2)}(\zeta, \boldsymbol{R}_{12})d\zeta\,, \tag{15}$$

$$p_T(z_1)=kT\rho^{(1)}(z_1)-\frac{1}{2}\iiint dv_{12}\frac{d\phi_{12}}{dR_{12}}\times\frac{x_{12}^2}{R_{12}}\rho^{(2)}(z_1,\boldsymbol{R}_{12})\,, \qquad (16)$$

we have the expression (10) which is the same expression as that given in Bakker's interpretation. We can justify the nondependence of $p_N(z_1)$ upon z_1 as required by Bakker's interpretation in the following way.

From (15), we have

$$\frac{dp_N(z_1)}{dz_1}=kT\frac{d\rho^{(1)}(z_1)}{dz_1}-\frac{1}{2}\iiint dv_{12}\frac{d\phi_{12}}{dR_{12}}\frac{z_{12}}{R_{12}}\times[\rho^{(2)}(z_1,\boldsymbol{R}_{12})-\rho^{(2)}(z_1-z_{12},\boldsymbol{R}_{12})]\,.$$

Since $\rho^{(2)}(z_1-z_{12},\boldsymbol{R}_{12})=\rho^{(2)}(z_1,-\boldsymbol{R}_{12})$, we have

$$\frac{dp_N(z_1)}{dz_1}=kT\frac{d\rho^{(1)}(z_1)}{dz_1}-\iiint dv_{12}\frac{d\phi_{12}}{dR_{12}}\times\frac{z_{12}}{R_{12}}\rho^{(2)}(z_1,\boldsymbol{R}_{12})\,.$$

The right-hand side of this equation vanishes by the integral equation[2)4)] between $\rho^{(1)}$ and $\rho^{(2)}$, so that we have

$$\frac{dp_N(z_1)}{dz_1}=0\,. \qquad (17)$$

which means that $p_N(z_1)$ does not depend upon z_1. In any approximate theory such as that of Tolman[6)] or Hill[7)], constancy of local partial potential is assumed to be the condition for equilibrium. But since the concept of local partial potential is a property of approximate theory when we deal with transition layers which have a thickness only of the same order as that of the distance between molecules, the condition of constancy of p_N, which we have proved to be valid in our strictly statistical theory, may be used in place of the condition of constancy of the local free energy in any approximate theory.

Thus we have derived by a comparatively simple procedure the expression for the surface tension of a liquid as the increase in free energy due to an increase in the surface area. The results coincide with those of Kirkwood and Buff. The pressure p_T given by (16) is just the stress which was calculated by Kirkwood and Buff and we can directly show that the stress across any surface parallel to the interface is given by (15). Since p_N does not depend upon z_1, it is equal to the pressure in the interior of the liquid or of the vapor, that is

$$p_N=kT\cdot\rho_{\alpha\beta}^{(1)}-\frac{1}{6}\iiint R_{12}\frac{d\phi}{dR_{12}}\rho_{\alpha\beta}^{(2)}dv_{12}\,.$$

Thus we find that our results coincide with those of Kirkwood and Buff.

§ 4. Critique on the Assumption of Density Discontinuity at the Surface

As stated in the introduction, Fowler assumed a mathematical surface of density discontinuity when he calculated the isothermal work of formation of liquid-vapor interface. If we calculate the surface tension by the formula (8) assuming the density discontinuity at the surface, we have just the formula which Fowler derived,

$$\gamma=\frac{\pi}{8}\int_0^\infty R^4\frac{d\phi}{dR}\rho^{(2)}(R)dR\,. \qquad (18)$$

We shall now study the nature of this assumption more closely by calculating the normal pressure p_N and the tangential pressure p_T. These pressures can be calculated from Eqs. (15) and (16).

We now assume

$$\left.\begin{array}{lll}\rho^{(1)}(z_1)=\rho_\alpha^{(1)} & & z_1\leqq 0\\ \qquad\quad\;\,=0 & & z_1>0\\ \rho^{(2)}(z_1,\boldsymbol{R}_{12})=\rho_\alpha^{(1)2}g(R) & & z_1<0,\quad z_1+z_{12}<0\\ \qquad\qquad\quad\;=0 & ; & z_1>0 \text{ or } z_1+z_{12}>0\end{array}\right\} \qquad (19)$$

where $g(R)$ is the radial distribution function of the homogeneous liquid phase. From Eqs. (15) and (16), we obtain

$$p_N=p_0+\frac{2\pi}{3}\rho_\alpha^{(1)2}\int_{-z_1}^\infty R^3\frac{d\phi}{dR}g(R)dR-\frac{\pi}{3}\rho_\alpha^{(1)2}z_1^3\int_{-z_1}^\infty\frac{d\phi}{dR}g(R)dR+\pi z_1\rho_\alpha^{(1)2}\times\int_{-z_1}^\infty R^2\frac{d\phi}{dR}g(R)dR\,, \qquad (20)$$

and

$$p_T=p_0+\frac{\pi}{3}\rho_\alpha^{(1)2}\int_{-z_1}^\infty R^3\frac{d\phi}{dR}g(R)dR-\frac{\pi}{6}\rho_\alpha^{(1)2}z_1^3\int_{-z_1}^\infty\frac{d\phi}{dR}g(R)\,dR+\frac{\pi}{2}z_1\rho_\alpha^{(1)2}\times\int_{-z_1}^\infty R^2\frac{d\phi}{dR}g(R)dR\,, \qquad (21)$$

where p_0 is the pressure in the interior of the liquid phase, that is,

$$p_0=kT\rho_\alpha^{(1)}-\frac{2}{3}\pi\rho_\alpha^{(1)2}\int_0^\infty R^3\frac{d\phi}{dR}g(R)dR\,. \qquad (22)$$

From (20) and (21) we see that

$$p_T - p_0 = \tfrac{1}{2}(p_N - p_0) . \tag{23}$$

The expression (20) shows that the calculated normal pressure p_N is far from being constant and at the interface ($z_1=0$), we have

$$p_N = p_0 + \frac{2\pi}{3}\rho_\alpha^{(1)2}\int_0^\infty R^3 \frac{d\phi}{dR} g(R) dR = kT\rho_\alpha^{(1)}$$

which amounts to about 250 atm. at 90°K for argon. Error of the same order of magnitude will be present in the expression (21) for the tangential pressure p_T.

Though the surface tension is expressed as the integral of the difference of p_N and p_T as shown by the formula (10), the writer is of the opinion that we cannot expect that the errors can be cancelled and Fowler's assumption offers a good approximation even if the temperature is low enough. In an approximate theory more careful consideration will have to be given to the condition of equilibrium in the form of constancy of the normal pressure p_N, that is, in the form of (17).

References

1) R. H. Fowler: Proc. Roy. Soc. A **159** (1937) 229.

2) J. G. Kirkwood and F. P. Buff: J. Chem. Phys. **17** (1949) 338.

3) A. G. MacLellan: Proc. Roy. Soc. A **213** (1952) 274.

4) M. Born and H. S. Green: Proc. Roy. Soc. A **188** (1946) 10.

5) G. Bakker: Wien-Harms' Handb. d. Experimentalphysik VI (1928) 383.

6) R. C. Tolman: J. Chem. Phys. **16** (1948) 758.

7) T. L. Hill: J. Chem. Phys. **20** (1952) 141.

JOURNAL OF THE PHYSICAL SOCIETY OF JAPAN Vol. 8, No. 3, MAY—JUNE, 1953

Electrical Resistivity and Thermionic Emission of Silicon

By Leo ESAKI

Kobe Kogyo Corporation, Hyogo-ku, Kobe, Japan

(Received January 26, 1953)

The simultaneous measurements of electrical resistivity and thermionic emission of silicon over the intrinsic temperature range from 1100°C to 1350°C have been carried out by means of heating a small silicon piece directly. The results indicate that the depth of the conduction band, the energy gap between filled and conduction bands and the work function are 3.47 eV, 1.10 eV and 4.02 eV, respectively, and also Richardson's constant 5.6 amp. $\text{cm.}^{-2}\,\text{deg.}^{-2}$

§1. Experimental Procedure

Both electrical resistivity and thermionic emission were simultaneously measured over the temperature range from 1100° C to 1350° C in which silicon behaves as an intrinsic semiconductor. The experiments were carried out by means of heating directly a silicon piece of about $2.4\times0.4\times10\,\text{mm}^3$ in vacuum.[1]

The experimental specimens were pure polycrystalline silicon containing small amounts of some kinds of impurity-aluminium, phosphorus etc.[1] The assembly of the silicon specimen, tungsten whiskers and anodes is illustrated in Fig. 1. Two tantalum ribbons, would around both ends of the silicon, and two tungsten whiskers, pressed in close proximity against the central portion of the specimen, served as leads for heater current and probes for measurement of resistivity. The anode was located in the middle of two whiskers and two auxiliary anodes on both sides. This assembly was sealed in a tube, which was thoroughly evacuated and tipped off at a pressure below 10^{-6} mm Hg after flashing a getter.

The temperature of the silicon was measured by a micro-optical pyrometer under somewhat arbitrary assumption for its spectral emissivity at wave-length of 650 mμ to be 0.4. A possible error due to this uncertainty

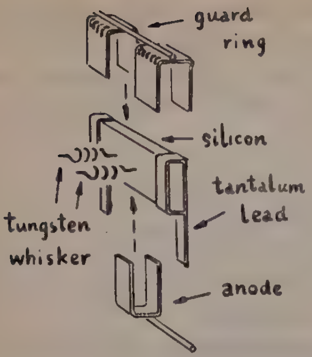

Fig .1. Construction of experimental tube.

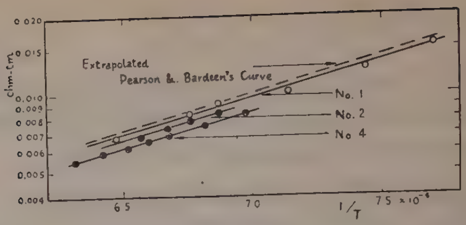

Fig. 2. Log. specific resistivity vs. reciprocal absolute temperature.

will be discussed laterly. The temperature in the neighborhood of the whisker was satisfactorily uniform. All attempts to weld a *Pt-PtRh* thermocouple to the silicon failed, active reaction taking place above 1200° C between platinum and silicon. Tungsten and tantalum were inert with silicon over the entire temperature range.

The silicon, after being subjected to sufficient heating, had a stable thermionic emission, which was measured by the central anode with a simple amplifier of sensitivity 10^{-9} amp. The current-voltage curve of emission gave no indication for the existing of patches. The specific resistivity was simultaneously observed, using a potentiometer. The logarithmic specific resistivity is plotted versus reciprocal temperature in Fig. 2, which is in good agreement with the extrapolation of Pearson and Bardeen's curve indicated with a dotted line.[2] The Richardson's plots of the thermionic emission are also shown in Fig. 3 and the whole data are summarized in Table 1. No remarkable difference was recognized among various specimens.

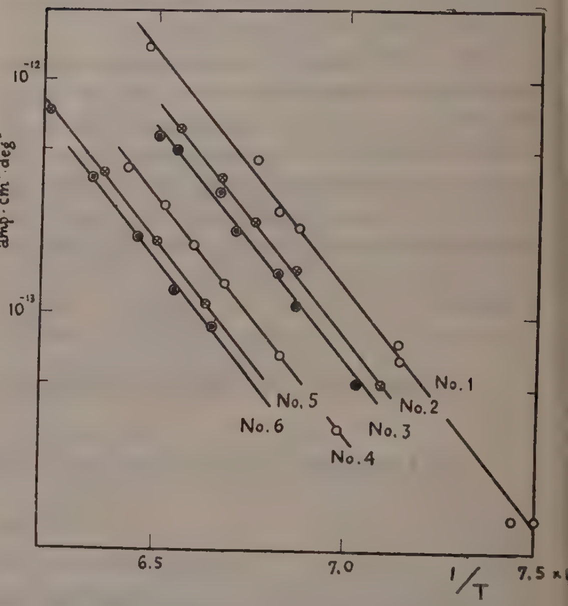

Fig. 3. Richardson's plots of the thermionic emission.

§ 2. Results

The specific resistivity ρ and the thermionic emission current i of an intrinsic semiconductor may be written in the well-known form of[3]

$$\rho = \rho_0 \exp(E_G/2kT)$$

Table I. Data of specific resistivity and thermionic emission.

Specimen	Resistivity		Thermionic Emission	
	Constant (ohm-cm)	Activation energy (eV)	Richardson's const. (amp·cm⁻²·deg⁻²)	Work function (eV)
No. 1	1.1×10^{-4}	0.55	5.5	4.00
No. 2	1.1×10^{-4}	0.55	11.5	4.04
No. 3	—	—	7.0	4.00
No. 4	1.0×10^{-4}	0.55	4.6	4.04
No. 5	—	—	2.5	4.02
No. 6	—	—	2.7	4.04
means	1.1×10^{-4}	0.55	5.6±3.3	4.02±0.02

$$i=e\left(\frac{4\pi mkT^{2}}{h^{3}}\right)\exp\left(\frac{\chi+E_G/2}{kT}\right)$$
$$=AT^{2}\exp(-\varPhi/kT),$$

if the surface roughness factor and transmission coefficient are neglected, where χ is the depth of the conduction band and E_G the energy gap between filled and conduction bands. ρ and the energy gap E_G are experimentally determined as 1.1×10^{-4} ohm-cm and 1.1 eV and also the Richardson's constant A and the work function $\varPhi$ as 5.6 ± 3.3 amp. cm. deg and 4.02 ± 0.02 eV, respectively, giving $\chi=3.47$ eV. Thus the probable energy diagram is as shown in Fig. 4. Assuming that the small value of A in comparison with theoretical one is accounted for by a linear variation with temperature, $\chi(T)=\chi(0)+\alpha T$, as in the case with $E_G(T)=E_G(0)-\beta T$,⁴⁾ α is expected to be the order of 10^{-4} eV/deg.

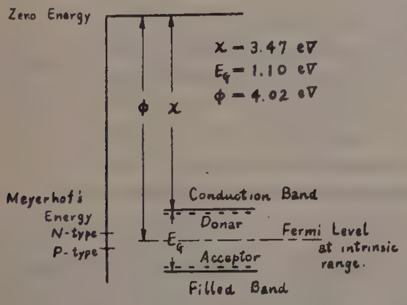

Fig. 4. Schematic energy level diagram for silicon.

Meyerhof determined the work function of silicon by the Kelvin method.⁵⁾ After abrasion in partial vacuum, he obtained the work function 4.12 eV and 3.84 eV for p- and n-type silicon, respectively. The Fermi level determined in the present study is just half-way between those corresponding to Meyerhof's work functions, while the difference of the latter, $4.12-3.84=0.28$ eV, is much smaller than $E_G=1.10$ eV.

§ 3. Estimation of Experimental Error

As the exact spectral emissivity of silicon is unknown, its temperature was measured, assuming the emissivity at 650 mμ to be 0.4. The error in the experimental value will be estimated approximately in the following. Both the emission and the resistivity could be written

$$x=x_0T^{n}\exp(-\varphi/kT),$$

where n is equal to zero for the resistivity, while two for the emission. Rearranging this equation, we get

$$\varphi=-kT\log(x/x_0T^{n})$$
$$x_0=xT^{-n}\exp(-\varphi/kT).$$

Differentials of φ, x_0 and T are

$$\Delta\varphi/\varphi=\Delta T/T^{2}(T+nT^{2}k/\varphi)$$
$$\Delta x_0/x_0=-\Delta T/T^{2}(T+nT+\varphi/k).$$

With the brightness temperature S_λ and the spectral emissivity ε_λ, the true temperature T may be written by Kirchhoff's law

$$1/T-1/S_\lambda=4.55\times10^{-5}\log\varepsilon_\lambda\quad\text{deg}^{-1}.$$

The differentials of ε_λ and T are

$$-\Delta T/T^{2}=4.55\times10^{-5}\Delta\varepsilon_\lambda/\varepsilon_\lambda\,\text{deg}^{-1}.$$

Therefore, we shall find out

$$\Delta\varphi/\varphi=-4.55\times10^{-5}\Delta\varepsilon_\lambda/\varepsilon_\lambda(T+nT^{2}k/\varphi)$$
$$\Delta x_0/x_0=4.55\times10^{-5}\Delta\varepsilon_\lambda/\varepsilon_\lambda(nT+\varphi/k).$$

If the true spectral emissivity is 20% larger or smaller than the assumed one, A and ρ_0 will increase or decrease by about 2.5 amp. cm^{-2} deg^{-2} and 0.13 ohm-cm, while $\varPhi$ and E_G will decrease or increase by about 0.06 eV and 0.015 eV, respectively. Hence the uncertainty of the emissivity has relatively little influence on the results and the discussion in the present paper.

Acknowledgements

The author is indebted to Mr. A. Fujimori for the prepareation of the specimens, and wishes to express his gratitude to Dr. T. Arizumi for his helpful suggestions.

References

1) The present experiment has been carried out, succeeding to the study of "Thermal Treatment of Silicon Rectifiers," Phys. Rev. **89** (1953) 398 by the author. Therefore, the same experimental technique and silicon specimens were availed.

2) G. L. Pearson and J. Bardeen: Phys. Rev. **75** (1949) 865.

3) G. H. Fowler: Proc. Roy. Soc. **140** (1933) 505.

4) See reference (2).

5) W. E. Meyerhof: Phys. Rev. **71** (1947) 727.

JOURNAL OF THE PHYSICAL SOCIETY OF JAPAN Vol. 8, No. 3, MAY—JUNE, 1953

Dynamical Theory of Electron Diffraction for Finite Polyhedral Crystal III.

Fresnel Diffraction Formula*

By Norio KATO

Kobayasi Institute of Physical Research, Kokubunji Tokyo, Japan

(Received February 3, 1953)

Following the first paper of the same title (J. Phys. Soc. Jap. **7** (1952) 397), in which Bethe's dynamical theory of electron diffraction (Ann. d. Phys. Lpz. **87** (1928) 55) was extended to the case of finite polyhedral crystal and the general expressions of wave functions for transmitted and interfracted (=reflected by crystal net plane) wave were obtained, they have been rewritten in a form of the so-called Fresnel diffraction with the purpose that we might have better understanding of electron microscope images of crystallites. From these formulae, it is concluded that the striations due to "*Pendellösung*" are observed in the just-focused images of crystallites in which Bragg reflection occurs while in defocused image they are disturbed in the neighbourhood of a crystal edge by the Fresnel diffraction effect. In a special case where the parameter indicating the deviation from the Bragg condition is very large, the present formulation applies to the phase contrast fringes due to the edge of transparent wedge-shaped substances. The fringes on the vacuum side are expected to be more prominent in the virtual, than in the real, image in accordance with experiment. Some numerical examples of intensity distributions are given for the bright field images of a wedge-shaped crystallite which is out of focus.

§ 1. Introduction

In the first paper[1]* of the same title, the author extended Bethe's dynamical theory of electron diffraction[2] to the case of a finite polyhedral crystal. The general expressions of wave function obtained thereby were rewritten in the second paper[1]** in a Fraunhofer diffraction form more suitable to interprete the fine structure of ordinary electron diffraction patterns. In the present paper, they are further rewritten, this time, in a Fresnel diffraction form so that we may better understand the electron-microscope images.

Consider in Fig. 1 a microscope image on the photographic plate PP′, which, if the effect of aberration and diffraction due to restricted aperture is neglected, may be regarded to be a magnified image of intensity distribution on the plane QQ′ which is conjugate to PP′ with respect to the lens system LL′. The body is in focus if it is on the plane QQ′ and out of focus if it is outside of it. When the body is out of focus its image on PP′ will be accompanied by fringe phenomenon. Actually Boersch discovered the phenomenon[3]. He and later others[4][5] regarded it as a sort of Fresnel fringes and treated it theoretically and compared their results with the fringes observed on the border of collodion film. They considered, however, in their treatments an ideally thin film of opaque or semi-transparent half-plane assuming constant phase shift and certain absorption for the electron wave penetrating the film, explaining the phenomenon only qualitatively. For complete understanding of the phenomenon, especially the fringes due to the edge of a wedge-shaped crystallite, a more thorough treatment is necessary.

On the other hand, when Bragg reflection takes place in a wedge-shaped crystallite, as

---

* The expence of this study was defrayed from the Grant in Aid for Fundamental Scientific Research of the Educational Ministry.

** In the following, the first and the second paper are referred to as Paper I and II respectively.

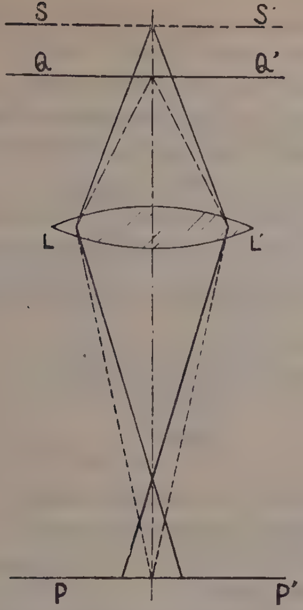

Fig. 1. Focusing of image. This figure illustrates the case of over-focusing of real image. PP′: photographic plate, LL′: lens system, QQ′: the conjugate plane of PP′ concerning to LL′, SS′: specimen.

is the case with MgO or CdO smokes, we observe⁶⁾ regularly spaced striations* superposed on its image. This interfraction (=Bragg reflection) effect was treated by Kossel and Heidenreich and Sturkey in a way which may be regarded generally sufficient but their results are somewhat arbitrary because they based their arguments on Bethe's theory which, as well known, is applicable strictly only to the case of a parallel side crystal of infinite extension and not to the case of the wedge-shaped crystal which, as above said, gives rise to striations. Therefore, the equal-thickness striations in defocused image of crystallite could not be treated by their theory.

The theory we present below will take all these hitherto-not-considered factors into consideration and treat more rigorously the phenomenon of the equal-thickness striations as well as Fresnel fringes**. Although the present theory gives the amplitude distributions on the conjugate plane (QQ′ in Fig. 1) placed near the wedge-shaped crystallite in which Bragg reflection occurs, the case with no Bragg reflection can also be treated by taking the parameter indicative of the deviation from Bragg condition to be very large.

§ 2. Derivation of Fresnel Formulae

When an incident wave, $\varPhi_{\mathrm{I}}=\varPsi_{\mathrm{I}}\exp j(\boldsymbol{K}_{\mathrm{I}}\cdot\boldsymbol{r})$, impinges on a surface S_e of a crystal and the primary and interfracted wave, $\varPhi_0$ and $\varPhi_g$ respectively, leave the crystal from the other surface S_a, their wave functions can be expressed, as given in Paper I, as follows:

$$\left.\begin{aligned}\varPhi_0&=\sum_{i=1,\,2}\varPhi_0^{(i)}(\boldsymbol{r})\\ \varPhi_g&=\sum_{i=1,\,2}\varPhi_g^{(i)}(\boldsymbol{r})\end{aligned}\right\}\quad(1)$$

where

$$\begin{aligned}\varPhi_0^{(i)}=\varPsi_{\mathrm{I}}\iiiint &C_0^{(i)}\exp j(\boldsymbol{K}_{\mathrm{I}}-\boldsymbol{k}_0^{(i)}\cdot\boldsymbol{r}_e)\\ &\times\exp j(\boldsymbol{k}_0^{(i)}-\boldsymbol{K}_0\cdot\boldsymbol{r}_a)\\ &\times\exp j(\boldsymbol{K}_0\cdot\boldsymbol{r})d\boldsymbol{r}_e d\boldsymbol{r}_a d\boldsymbol{t}_e d\boldsymbol{T}_a \qquad (2\mathrm{a})\end{aligned}$$

$$\begin{aligned}\varPhi_g^{(i)}=\varPsi_{\mathrm{I}}\iiiint &C_g^{(i)}\exp j(\boldsymbol{K}_{\mathrm{I}}-\boldsymbol{k}_0^{(i)}\cdot\boldsymbol{r}_e)\\ &\times\exp j(\boldsymbol{k}_g^{(i)}-\boldsymbol{K}_g\cdot\boldsymbol{r}_a)\\ &\times\exp j(\boldsymbol{K}_g\cdot\boldsymbol{r})d\boldsymbol{r}_e d\boldsymbol{r}_a d\boldsymbol{t}_e d\boldsymbol{T}_a\,. \qquad (2\mathrm{b})\end{aligned}$$

Here,

$$\left.\begin{aligned}C_0^{(i)}&=\frac{c^{(1)}c^{(2)}}{c^{(1)}-c^{(2)}}\cdot\frac{(-1)^i}{c^{(i)}}\\ C_g^{(i)}&=\frac{c^{(1)}c^{(2)}}{c^{(1)}-c^{(2)}}\cdot(-1)^i\end{aligned}\right\}\quad(2\mathrm{c})$$

other notations being the same as those explained in Paper I. In the following, we will carry out integration with respect to $\boldsymbol{r}_e$, $\boldsymbol{t}_e$ and $\boldsymbol{T}_a$ under appropriate approximations and rewrite (2a) and (2b) into a form of Fresnel diffraction.

(i) Integrations with respect to $\boldsymbol{r}_e$ and $\boldsymbol{t}_e$.

As was shown in § 2 of Paper II, integration with respect to $\boldsymbol{r}_e$ and $\boldsymbol{t}_e$ can be performed easily by taking account of the fact that the wave length of electrons is very small. (2a) and (2b) become

$$\begin{aligned}\varPhi_0^{(i)}=\overline{C}_0^{(i)}(\nu_a\cdot\boldsymbol{Z}_0)\varPsi_{\mathrm{I}}\iint_{S_a^{(i)}}&\exp j(\boldsymbol{K}_{\mathrm{I}}\cdot\boldsymbol{r}_e)\\ &\times\exp j(\overline{\boldsymbol{k}}_0^{(i)}\cdot\boldsymbol{r}_a-\boldsymbol{r}_e)\\ &\times\exp j(\boldsymbol{K}_0\cdot\boldsymbol{r}-\boldsymbol{r}_a)d\boldsymbol{r}_a d\boldsymbol{K}_0 \qquad (3\mathrm{a})\end{aligned}$$

$$\begin{aligned}\varPhi_g^{(i)}=\overline{C}_g^{(i)}(\nu_a\cdot\boldsymbol{Z}_g)\varPsi_{\mathrm{I}}\iint_{S_a^{(i)}}&\exp j(\boldsymbol{K}_{\mathrm{I}}\cdot\boldsymbol{r}_e)\\ &\times\exp j(\overline{\boldsymbol{k}}_0^{(i)}\cdot\boldsymbol{r}_a-\boldsymbol{r}_e)\exp j(g\cdot\boldsymbol{r}_a)\\ &\times\exp j(\boldsymbol{K}_g\cdot\boldsymbol{r}-\boldsymbol{r}_a)d\boldsymbol{r}_a d\boldsymbol{K}_g\,, \qquad (3\mathrm{b})\end{aligned}$$

---

* In the following descriptions, we call these striations 'equal-thickness striations' since they show contours of equal thickness of a crystallite.

** The effect of absorption can not be fully taken into account in the present paper.

where $\overline{\boldsymbol{k}}_0^{(i)}$ and $\overline{\boldsymbol{k}}_g^{(i)}$ are respectively the wave vector of the primary and interfracted wave in crystal whose wave point is $\overline{D}^{(i)}$ (*cf.* Paper I § 4 (a)). $S_a^{(i)}$ is an integration region with respect to $\boldsymbol{r}_a$ and means the area common to S_a and the projection of S_e on S_a-plane casted in the direction of $\boldsymbol{z}^{(i)}$ which is approximately parallel to $\boldsymbol{K}_{\mathrm{I}}$. (It corresponds to $\Sigma^{(i)*}$ in Fig. II–2a.)

(ii) Integration with respect to $\boldsymbol{K}_0$ or $\boldsymbol{K}_g$.

Integration with respect to $\boldsymbol{K}_0$ or $\boldsymbol{K}_g$ can be expressed by the following form,

$$I=\int \exp j(\boldsymbol{K}\cdot\boldsymbol{r}-\boldsymbol{r}_a)d\boldsymbol{K} \qquad (4)$$

where $\boldsymbol{K}$ indicates $\boldsymbol{K}_0$ or $\boldsymbol{K}_g$. As was shown in § 4 (b) of Paper I, the boundary condition on S_a can be satisfied approximately by taking a superposition of plane waves whose wave vector is nearly equal to $\boldsymbol{K}_{\mathrm{I}}$. Then part of integration with respect to $\boldsymbol{K}$ which lies outside the small region of solid angle Ω shown in Fig. 2 has no contribution to the final results. The integration, therefore, may be calculated correctly by integrating over the whole direction of $\boldsymbol{K}$, after multiplying the integrand by an arbitrary regular function $f(\boldsymbol{K})$ having the following properties:

$f(\boldsymbol{K})=1$ if $\boldsymbol{K}$ lies inside Ω

$f(\boldsymbol{K})\to 0$ if $\boldsymbol{K}$ lies outside Ω.

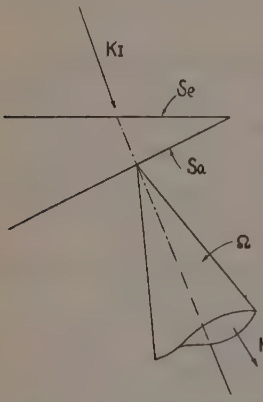

Fig. 2. Integral region of $\boldsymbol{K}$. Ω is the solid angle in which the amplitude function has an appreciable value. See also the text. S_e and S_a are the entrance and exit surface respectively.

Here two cases must be distinguished according as the position of $\boldsymbol{r}$ with respect to S_a varies; (a) $\boldsymbol{r}$ lies on the vacuum side and (b) it lies on the crystal side. They correspond respectively to real and virtual field and are designed by superscript (+) and (−).

Upon taking the direction of $|\boldsymbol{r}-\boldsymbol{r}_a|$ or $|\boldsymbol{r}_a-\boldsymbol{r}|$ as the polar axis for real or virtual field respectively, eq. (4) is rewritten, thus

$$I^{(\pm)}=K^2\int_0^{2\pi}d\varphi\int_0^{\pi}f(\theta)\exp\pm j$$
$$\times(K\cdot|\boldsymbol{r}-\boldsymbol{r}_a|\cos\theta)\cdot\sin\theta d\theta\,. \qquad (5)$$

Applying integration by parts it is transformed into

$$I^{(\pm)}=K^2\cdot\frac{\exp\pm j(K\cdot|\boldsymbol{r}-\boldsymbol{r}_a|}{\pm iK|\boldsymbol{r}-\boldsymbol{r}_a|}$$
$$+K^2O\left(\frac{1}{K^2|\boldsymbol{r}-\boldsymbol{r}_a|^2}\right)\,. \qquad (6)$$

When $K|\boldsymbol{r}-\boldsymbol{r}_a|$ is large enough, $I^{(\pm)}$ may be approximated by the first term. It is to be noted that $I^{(+)}$ and $I^{(-)}$ are conjugate complex to each other.

Substituting from (6), (3a) (3b) can be expressed as follows:

$$\Phi_0^{(i)}=\overline{C}_0^{(i)}(\nu_a\cdot\boldsymbol{K}_0)\Psi_{\mathrm{I}}\exp j(\boldsymbol{K}_{\mathrm{I}}-\overline{\boldsymbol{k}}_0^{(i)}\cdot\boldsymbol{R}_e)$$
$$\times\int_{S_a^{(i)}}\exp j(\overline{\boldsymbol{k}}_0^{(i)}\cdot\boldsymbol{r}_a)\frac{\exp\pm j(K\cdot|\boldsymbol{r}-\boldsymbol{r}_a|)}{\pm i|\boldsymbol{r}-\boldsymbol{r}_a|}d\boldsymbol{r}_a \qquad \text{(7a)}$$

$$\Phi_g^{(i)}=\overline{C}_g^{(i)}(\nu_a\cdot\boldsymbol{K}_g)\Psi_{\mathrm{I}}\exp j(\boldsymbol{K}_{\mathrm{I}}-\overline{\boldsymbol{k}}_0^{(i)}\cdot\boldsymbol{R}_e)$$
$$\times\int_{S_a^{(i)}}\exp j(\overline{\boldsymbol{k}}_g^{(i)}\cdot\boldsymbol{r}_a)\frac{\exp\pm j(K\cdot|\boldsymbol{r}-\boldsymbol{r}_a|)}{\pm i|\boldsymbol{r}-\boldsymbol{r}_a|}d\boldsymbol{r}_a \qquad \text{(7b)}$$

One can see from these formulae the transmitted and interfracted waves are constituted from elementary spherical wavelets according to Huygens' principle. It is, therefore, not difficult to rewrite them in the form of Fraunhofer and Fresnel diffraction formulae following the procedures usual in visible-ray optics[8].

(iii) Fraunhofer diffraction.

Ordinary electron diffraction patterns correspond to $\Phi_g^{(i)}$ in real space at a large distance from the crystal, *i.e.* Fraunhofer diffraction formula. Upon expanding $|\boldsymbol{r}-\boldsymbol{r}_a|$ in the exponential by powers of $1/r$ ($r=|\boldsymbol{r}|$), and neglecting higher terms than the second, (7b) becomes

$$\Phi_g^{(i)}=\overline{C}_g^{(i)}(\nu_a\cdot\boldsymbol{K}_g)\frac{\exp jKr}{ir}\exp j(\boldsymbol{K}_{\mathrm{I}}-\overline{\boldsymbol{k}}_0^{(i)}\cdot\boldsymbol{R}_e)$$
$$\times\Psi_{\mathrm{I}}\int_{S_a^{(i)}}\exp j\,(\overline{\boldsymbol{k}}_g^{(i)}-K\boldsymbol{s}\cdot\boldsymbol{r}_a)d\boldsymbol{r}_a \qquad (8)$$

where $\boldsymbol{s}$ is the unit vector of $\boldsymbol{r}$. By employing the notations used in Paper II, it may be shown that eq. (8) is identical with eq. (II. 15).

(iv) Fresnel diffraction.

In order to discuss electron microscope image, we must know the behaviors of $\Phi_0^{(i)}$ and $\Phi_g^{(i)}$ at a short distance of $|\boldsymbol{r}-\boldsymbol{r}_a|$, *i.e.* Fresnel diffraction formulae. In Fig. 3 (a), Q is an arbitrary point on the conjugate plane of photographic plate, $\boldsymbol{s}_0$ the unit vector in the direction of K_{I}, $\boldsymbol{s}_0^{(i)}$ that in the direction of $\overline{K}_0^{(i)}$. The origin O, is taken at the intersection of S_a and the line $\boldsymbol{s}_0(\mathrm{Q})$*, and $\mathrm{O}^{(i)}$ is defined as that of S_a and the line $\boldsymbol{s}_0^{(i)}(\mathrm{Q})$.

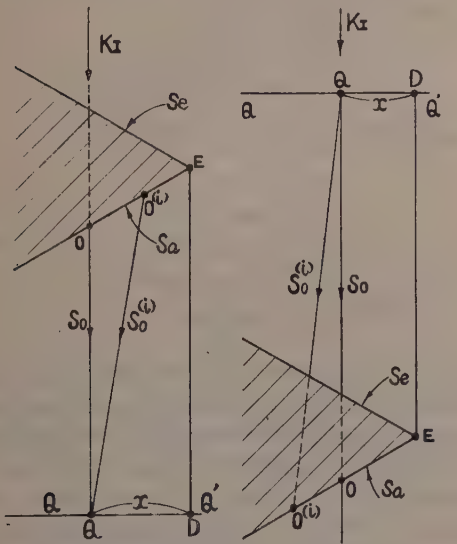

(a) Real image. (b) Virtual image.

Fig. 3. Fresnel diffraction due to half-infinite wedge-shaped crystal. D is the intersection point of the plane QQ′ and the line drawn through the edge E in the direction of K_{I}. This is the origin of coordinate on the plane QQ′. The other notations are explained in the text.

Since the position vectors can be expressed by the following formulae, denoting $\overrightarrow{\mathrm{OO}^{(i)}}$ by $\boldsymbol{r}_0^{(i)}$,

$$\left.\begin{array}{ll} \boldsymbol{R}_e=\boldsymbol{r}_0^{(i)}+\boldsymbol{R}_e^{(i)}, & \boldsymbol{R}_a=\boldsymbol{r}_0^{(i)}+\boldsymbol{R}_a^{(i)} \\ \boldsymbol{r}_e=\boldsymbol{r}_0^{(i)}+\boldsymbol{r}_e^{(i)}, & \boldsymbol{r}_a=\boldsymbol{r}_0^{(i)}+\boldsymbol{r}_a^{(i)} \end{array}\right\} \quad (9)$$

$|\boldsymbol{r}-\boldsymbol{r}_a|=|\boldsymbol{r}^{(i)}-\boldsymbol{r}_a^{(i)}|$ can be expanded as,

$$|\boldsymbol{r}^{(i)}-\boldsymbol{r}_a^{(i)}|=r^{(i)}\Big\{1-\frac{(\boldsymbol{s}_0^{(i)}\cdot\boldsymbol{r}_a^{(i)})}{r^{(i)}} + \frac{1}{2r^{(i)2}}[(r_a^{(i)})^2-(\boldsymbol{s}_0^{(i)}\cdot\boldsymbol{r}_a^{(i)})^2]+\cdots\Big\} \quad (10a)$$

and

$$r^{(i)}=|\boldsymbol{r}-\boldsymbol{r}_0^{(i)}| =r\Big\{1-\frac{(\boldsymbol{s}_0\cdot\boldsymbol{r}_0^{(i)})}{r}+\frac{1}{2r^2}[(r_0^{(i)})^2 -(\boldsymbol{s}_0\cdot\boldsymbol{r}_0^{(i)})^2]+\cdots\Big\} \quad (10b)$$

where $r_a^{(i)}=|\boldsymbol{r}_a^{(i)}|$ and $r_0^{(i)}=|\boldsymbol{r}_0^{(i)}|$. Neglecting the higher terms than the third and using the relation $(\overline{\boldsymbol{k}}_0^{(i)}-K\boldsymbol{s}_0^{(i)}\cdot\boldsymbol{r}_a^{(i)})=0$, the wave function $\Phi_0^{(i)}$ can be rewritten. The wave function $\Phi_g^{(i)}$ in real image can be also obtained in a similar way, by using $\boldsymbol{s}_g$ and $\boldsymbol{s}_g^{(i)}$, which are the unit vector respectively in the direction of $K_{\mathrm{I}}+g$ and $\overline{K}_g^{(i)}$, instead of $\boldsymbol{s}_0$ and $\boldsymbol{s}_0^{(i)}$. In the case of virtual image, the wave function can be obtained by the same procedures, though the position of $\mathrm{O}^{(i)}$ is different from that in the case of real image (*cf.* Fig. 3).

We give below the formulae expressing these cases:

$$\Phi_0^{(i)}(\mathrm{Q})=\frac{\exp\pm jKr}{\pm i}\cdot\Psi_{\mathrm{I}}\cdot D_0^{(i)}\cdot P_0^{(i)}\cdot F_0^{(i)} \quad (11a)$$

$$\Phi_g^{(i)}(\mathrm{Q})=\frac{\exp\pm jKr}{\pm i}\cdot\Psi_{\mathrm{I}}\cdot D_g^{(i)}\cdot P_g^{(i)}\cdot F_g^{(i)} \quad (11b)$$

where

$$\left.\begin{array}{l} D_0^{(i)}=\overline{C}_0^{(i)}\exp j(K_{\mathrm{I}}-\overline{\boldsymbol{k}}_0^{(i)}\cdot\boldsymbol{R}_e^{(i)}) \\ D_g^{(i)}=\overline{C}_g^{(i)}\exp j(K_{\mathrm{I}}-\overline{\boldsymbol{k}}_0^{(i)}\cdot\boldsymbol{R}_e^{(i)}) \end{array}\right\} \quad (12a)$$

$$\left.\begin{array}{l} P_0^{(i)}=\exp j\left(\dfrac{\pm K}{2r}\right)\Big[(r_0^{(i)})^2-(\boldsymbol{s}_0\cdot\boldsymbol{r}_0^{(i)})^2\Big] \\ P_g^{(i)}=\exp j\left(\dfrac{\pm K}{2r}\right)\Big[(r_g^{(i)})^2-(\boldsymbol{s}_g\cdot\boldsymbol{r}_g^{(i)})^2\Big] \end{array}\right\} \quad (12b)$$

$$\left.\begin{array}{l} F_0^{(i)}=\dfrac{(\nu_a\cdot K_{\mathrm{I}})}{r}\displaystyle\int_{S_a^{(i)}}\exp j\left(\frac{\pm K}{2r^{(i)}}\right) \times\Big[(r_a^{(i)})^2-(\boldsymbol{s}_0^{(i)}\cdot\boldsymbol{r}_a^{(i)})^2\Big]d\boldsymbol{r}_a \\ F_g^{(i)}=\dfrac{(\nu_a\cdot K_{\mathrm{I}})}{r}\displaystyle\int_{S_a^{(i)}}\exp j\left(\frac{\pm K}{2r^{(i)}}\right) \times\Big[(r_a^{(i)})^2-(\boldsymbol{s}_g^{(i)}\cdot\boldsymbol{r}_a^{(i)})^2\Big]d\boldsymbol{r}_a \end{array}\right\} \quad (12c)$$

The meaning of the terms D, P and F is as follows:

$D_0^{(i)}$ and $D_g^{(i)}$: the term due to the crystal interfraction.

---

* $\boldsymbol{s}(\mathrm{Q})$ means the line drawn through the point Q, in the direction of $\boldsymbol{s}$.

$P_0^{(i)}$ and $P_g^{(i)}$: the term due to the phase shift between O and $O^{(i)}$, *i.e.* refraction effect.

$F_0^{(i)}$ and $F_g^{(i)}$: the term due to Fresnel diffraction. Further detailed explanations will be given in § 3.

(v) Direct wave.

In the bright field images, the wave that reaches directly to QQ′ and does not pass through the crystal must be taken into account beside $\Phi_0^{(i)}$. This wave is the Fresnel diffraction wave due to the opaque screen of S_a and can be written as follows⁽⁸⁾:

$$\left.\begin{aligned} \Phi^{(t)}(\mathrm{Q}) &= \frac{\exp \pm jKr}{\pm i}\cdot\psi_{\mathrm{I}}\cdot F^{(t)} \\ F^{(t)} &= \frac{(\nu_a\cdot \boldsymbol{K}_{\mathrm{I}})}{r}\int_{S_a^{(t)}} \exp j\left(\frac{\pm K}{2r}\right) \\ &\qquad \times\Big[(\boldsymbol{r}_a)^2-(\boldsymbol{s}_0\cdot \boldsymbol{r}_a)^2\Big]d\boldsymbol{r}_a \end{aligned}\right\} \quad (15)$$

where $S_a^{(t)}$ is the area substracted by S_s from the infinite plane containing S_s.

§ Electron Microscope Images

The electron microscope gives, as explained in § 1, a magnified image of the intensity distribution on QQ′-plane, if the effects of aberration and diffraction due to restricted aperture* are neglected. The wave function on this plane can be expressed by $\{\Phi_0^{(1)}+\Phi_0^{(2)}+\Phi_g^{(1)}+\Phi_g^{(2)}+\Phi^{(t)}\}$ in the most general case where Bragg reflection occurs. A small aperture inserted on the path of electron beam behind the specimen gives rise to a bright field image or a dark field image (depending on its position), by isolating one portion of the waves from the other. The bright field image is composed of the waves $\Phi_0^{(1)}$, $\Phi_0^{(2)}$ and $\Phi^{(t)}$, and the dark field image of the waves $\Phi_g^{(1)}$ and $\Phi_g^{(2)}$.

In the present section, the formulae derived in the previous section are applied to interpretation of electron microscope images of half-infinite wedge-shaped crystal (Fig. 3). The detailed expressions of D, P and F in this case are as follows:

$$\left.\begin{aligned} D_0^{(i)} &= \overline{C}_0^{(i)} \exp j(H^{(i)}\cdot x \pm r\theta_0^{(i)}) \\ D_g^{(i)} &= \overline{C}_g^{(i)} \exp j(H^{(i)}\cdot x \pm r\theta_g^{(i)}) \end{aligned}\right\} \quad (16)$$

$$\left.\begin{aligned} P_0^{(i)} &= \exp j\left(\frac{\pm K}{2r}\right)(r\theta_0^{(i)})^2 \\ P_g^{(i)} &= \exp j\left(\frac{\pm K}{2r}\right)(r\theta_g^{(i)})^2 \end{aligned}\right\} \quad (17)$$

$$\left.\begin{aligned} F_0^{(i)} &= \frac{1\pm i}{2}\left[\left\{\frac{1}{2}+\mathrm{U}(\xi_0^{(i)})\right\} \pm i\left\{\frac{1}{2}+\mathrm{V}(\xi_0^{(i)})\right\}\right] \\ F_g^{(i)} &= \frac{1\pm i}{2}\left[\left\{\frac{1}{2}+\mathrm{U}(\xi_g^{(i)})\right\} \pm i\left\{\frac{1}{2}+\mathrm{V}(\xi_g^{(i)})\right\}\right] \\ F^{(t)} &= \frac{1\pm i}{2}\left[\left\{\frac{1}{2}-\mathrm{U}(\xi)\right\} \pm i\left\{\frac{1}{2}-\mathrm{V}(\xi)\right\}\right] \end{aligned}\right\} \quad (18)$$

where

$$\left.\begin{aligned} \xi &= \sqrt{\frac{2K}{r}}\,x\,, \\ \xi_0^{(i)} &= \sqrt{\frac{2K}{r^{(i)}}}\,(x \pm r\theta_0^{(i)})\,, \\ \xi_g^{(i)} &= \sqrt{\frac{2K}{r^{(i)}}}\,(x \pm r\theta_g^{(i)}) \end{aligned}\right\} \quad (19)$$

$\overline{C}_0^{(i)}$, $\overline{C}_g^{(i)}$ and $H^{(i)}$ are quantities dependent upon the crystal potential on the one hand and on a parameter indicating the deviation from Bragg condition on the other (*cf.* Appendix). $\theta_0^{(i)}$ and $\theta_g^{(i)}$ are the refraction angle of $\Phi_0^{(i)}$- and $\Phi_g^{(i)}$-wave respectively. $x=\mathrm{QD}$ and $r=\mathrm{ED}$ in Fig. 3. In (16), (17), (18) and (19) + and − correspond to the real and virtual image respectively. The function U and V are the so-called Fresnel integral⁸⁾.

(i) Fresnel fringes.

At first, let us consider the effect of defocusing. When Bragg condition is not satisfied in the crystal, $\overline{C}_0^{(i)}$ is either 1 or 0, while $\overline{C}_g^{(i)}$ is always zero. Putting $\overline{C}_0^{(1)}=1$ and $\overline{C}_0^{(2)}=0$, the wave function on QQ′-plane becomes then

bright field:

$$\left.\begin{aligned} \Phi_0 &= \Phi_0^{(1)}+\Phi^{(t)} \\ &= \frac{\exp\pm jKr}{\pm i}\cdot\psi_{\mathrm{I}}[D_0^{(1)}\cdot P_0^{(1)}\cdot F_0^{(1)}(\xi_0^{(1)}) \\ &\qquad +F^{(t)}(\xi)] \end{aligned}\right\} \quad (20a)$$

---

* This effect has been discussed by E. G. Ramberg (J. App. Phys. **20** (1949) 441). He showed that changing the sign of the defocusing does not affect the intensity distribution in the pattern for the opaque edge.

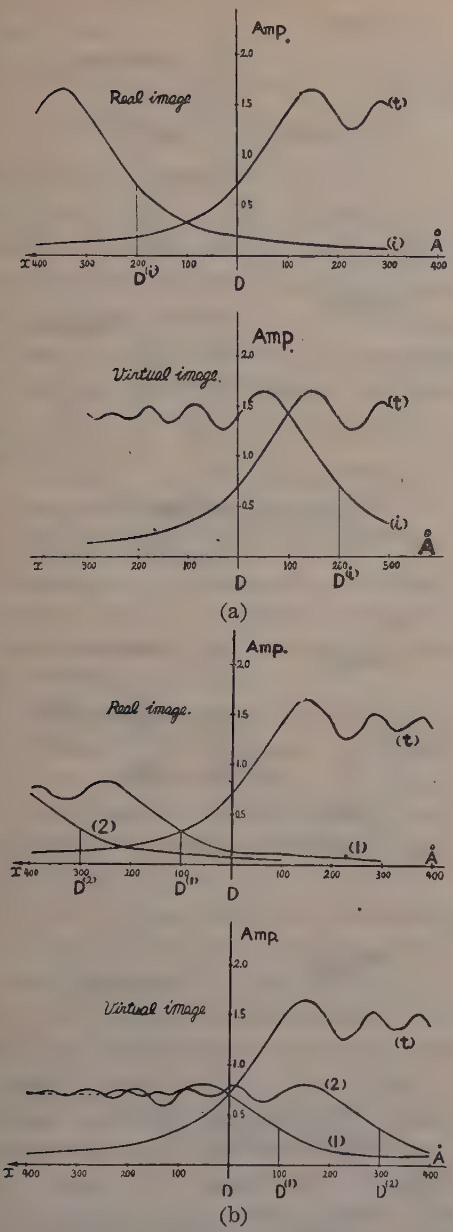

Fig. 4. (a) and (b). Example showing superposition of the amplitudes of the component waves on QQ′-plane. Crystal shape is assumed to be a rectangular wedge. Abscissa represents their amplitude ($\Psi_{\rm I}=1$), the ordinate the variable x shown in Fig. 3. (t) represents the direct wave and (1) and (2) the wave transmitted through the crystal. D and $D^{(i)}$ mean respectively the position where ξ and $\xi_0^{(i)}$, the argument of $F^{(t)}$ and $F_0^{(i)}$, are zero respectively. Adopted numerical values are: $U_{00}\simeq U_{gg}\sim 14\,e.v.$, $|U_{0g}|\sim 7e.v.$, $E=40ke.v.$, which are same as those adopted in describing Fig. 5 of Paper II; $r=50\mu$. (a) Bragg reflection does not occur in crystal ($u=\infty$). (b) Bragg reflection occurs in crystal ($u=0$).

dark field:

$$\Phi_g=0 \ * \qquad (20\mathrm{b})$$

Since the absolute value of $D_0^{(1)}$ and $P_0^{(1)}$ is equal to 1, the amplitude of one of the component wave $\Phi_0^{(1)}$ is determined solely by $F_0^{(1)}$, which is no other than an expression of Fresnel diffraction wave due to the half-infinite-plane screen, as seen from eq. (18). The formula (20a) is similar in form to that obtained previously,** 3)–5) the only difference being that we have here taken into account the following two points: (a) The phase shift of electrons of crystal wave is not constant but variable with x and the degree r of defocusing (*cf.* Fig. 3 and eqs. (16) and (17)). (b) The argument of $F_0^{(1)}$ is different from ξ by $\pm\Delta\xi_0^{(1)}$, meaning that wave is deflected due to refraction effect. The result shows that the degree of overlapping of the crystal wave $\Phi_0^{(1)}$ and the direct wave $\Phi^{(t)}$ increases in the case of virtual image and decreases in the case of real image with increasing degree of defocusing. Fig. 4 (a) shows the amplitude of the component waves overlapped, and Fig. 5 (a) the resnlting intensities.

(ii) Equal-thickness striations in just-focus.

Next, we consider the effect of Bragg reflection on the just-focused image. When r is so small that $r\theta_0^{(i)}$ (or $r\theta_g^{(i)}$) in eqs. (16), (17) and (19), compared with minimum distinguishable length δ, can be neglected, $F_0^{(i)}$ (or $F_g^{(i)}$) and $F^{(t)}$ can be approximated by a function which varies step-wise from zero to unity at D (D is shown in Fig. 4). This is because the arguments of Fresnel integral, ξ and $\xi_0^{(i)}$ (or $\xi_g^{(i)}$), increase so rapidly with x that diffraction effect can not be observed when x is larger than δ. This means that the path of the electron beams is nearly identical with that predicted by geometrical optics when

---

* Actually, the image of crystallite is observed in dark field even when Bragg condition is not satisfied. This is caused by the inelastic scattering which is neglected here.

** Using the present notations, the results of the previous work can be expressed as

$$\Phi_0=\frac{\exp\pm jKr}{\pm i}\cdot\Psi_{\rm I}[Ae^{i\alpha}F_0^{(1)}(\xi)+F^{(t)}(\xi)]$$

where A and α are arbitrary constants ($A<1$).

$|\boldsymbol{r}-\boldsymbol{r}_a|$ is small*. For example, if δ is assumed to be *ca.* 10A and r is less than about 0.2μ such an approximation may be permitted. The intensity at a point Q(x) is then given as follows:

bright field image:

$$I_0(Q)=|D_0^{(1)}+D_0^{(2)}|^2 = \begin{cases} |\Psi_I|^2\left\{1-\dfrac{w^2}{u^2+w^2}\times\sin^2\pi(H^{(1)}-H^{(2)}\cdot x)\right\} & x>0 \\ 1 & x<0 \end{cases} \tag{21a}$$

dark field image:

$$I_g(Q)=|D_g^{(1)}+D_g^{(2)}|^2 = \begin{cases} |\Psi_I|^2\cdot\dfrac{(\nu_e\cdot\boldsymbol{z}_0)}{(\nu_e\cdot\boldsymbol{z}_g)}\cdot\dfrac{w^2}{u^2+w^2}\times\sin^2\pi(H^{(1)}-H^{(2)}\cdot x) & x>0 \\ 0 & x<0 \end{cases} \tag{21b}$$

These formulae show that the equal-thickness striations of the breadth $1/(H^{(1)}-H^{(2)})$ is taking place. The breadth of the striations is therefore determined by the beat between the wave vectors $\overline{K}_0^{(1)}$ and $\overline{K}_0^{(2)}$ (or $\overline{K}_g^{(1)}$ and $\overline{K}_g^{(2)}$). This breadth is different from that of maxima or minima in the intensity distribution on the exit surface S_a, the latter being determined by the beat between $\overline{k}_0^{(1)}$ and $\overline{k}_0^{(2)}$**. However, this difference would be negligible since the quantity involved is so small except when the incident beam is nearly parallel to the crystal surface.

(iii) Effect of defocusing on the striations of equal-thickness.

We now consider the defocused image of a crystallite in which Bragg reflection occurs. In this case, the Fresnel fringes appears superposed on the striations of equal-thickness, and resultant wave will be as follows:

bright field image:

$$\left.\begin{aligned} \Phi_0&=\Phi_0^{(1)}+\Phi_0^{(2)}+\Phi^{(t)} \\ &=\frac{\exp\pm jKr}{\pm i}[D_0^{(1)}\cdot P_0^{(1)}\cdot F_0^{(1)} \\ &\qquad+D_0^{(2)}\cdot P_0^{(2)}\cdot F_0^{(2)}+F^{(t)}] \end{aligned}\right\} \tag{22a}$$

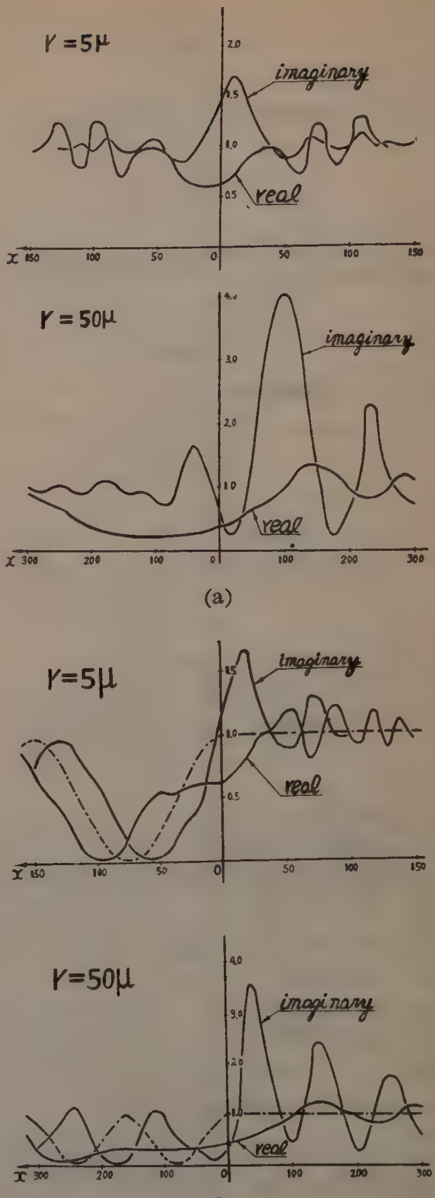

(a)

(b)

Fig. 5. (a) and (b). Intensity distributions on QQ′ plane for two cases, $r=5\mu$ and $r=50\mu$. Numerical values are the same as those adopted in Fig. 4. (a) Bragg reflection does not occur in crystal ($u=\infty$). (b) Bragg reflection occurs in crystal ($u=0$). Dotted line shows the intensity distributions in the case of just focusing.

---

* If r is very small ($Kr\simeq 1$), eqs. (11) and (15) don't hold since the approximations mentioned above can not be permitted. It can be shown, however, by the similar consideration as that in Paper I §4 (b), that the wave propagation can be approximated by geometrical optics.

** The author indebted to Mr. T. Ogawa for pointing out this.

dark field image:

$$\left.\begin{aligned}\Phi_g &= \Phi_g^{(1)} + \Phi_g^{(2)} \\ &= \frac{\exp \pm jKr}{\pm i}[D_g^{(1)}\cdot P_g^{(1)}\cdot F_g^{(1)} \\ &\qquad + D_g^{(2)}\cdot P_g^{(2)}\cdot F_g^{(2)}]\end{aligned}\right\} \quad (22b)$$

The amplitude of each of component wave has the same form as that explained in (i), although its magnitude and phase shift are different according to the degree of departure from the Bragg condition (*cf.* $\overline{C}_0^{(i)}$, $\overline{C}_g^{(i)}$, $H^{(i)}$ in appendix). The behaviors of superposition and numerical results of intensity distribution on QQ′ plane are shown in Fig. 4 (b) and 5 (b).

§ 4. Comparison with experiment

(i) Fresnel diffraction.

According to the foregoing calculations, we should observe, as shown in Fig. 5 (a), the Fresnel fringes on both sides of a crystal edge, in which:

(a) The darkest line appears on the material side of the edge and the brightest line on the vacuum side.

(b) The breadth of the former line is broader than was expected by assuming an ideally thin film³⁾⁴⁾.

(c) The brightest line and the whole fringes on the vacuum side are more prominent for the virtual than for the real images.

(d) This brightest line lies nearer to the edge in the virtual image than was expected by the simple assumption of thin film.

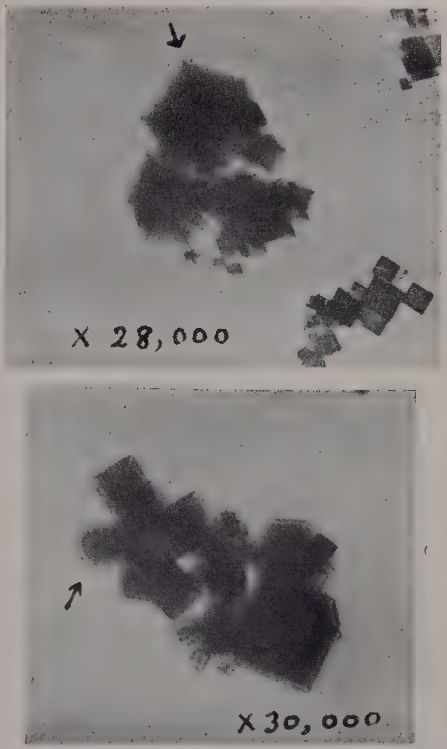

Phot. I. Defocused image of MgO crystal. The arrows show the white and dark line in the case of real (a) and virtual (b) image, respectively. (These photographs are due to the courtesy of Mr. N. Morito and Mr. H. Nagasaki of Hitachi Central Research Laboratory.)

All these describe adequately the observed effects in defocused images that occur in crystal edges and peripheries of collodion films, though the latter may possess not a wedge-shaped but a somewhat rounded edge³⁾⁻⁵⁾. Boersch and others³⁾⁻⁵⁾ simply ascribed the discrepancies between calculation and experiment in their treatments to presumed effects of a prismatic edge, which were not taken into account by them. Our calculation has taken care of them all and their result seems to guarantee their suggestion to a certain degree. A few observed phenomena, however, cannot be explained even by the present theory: For example, it is known⁵⁾ in collodion film that the whole fringes on material side are more prominent in the real than in the virtual images. This may be due to the effect of absorption which is not taken into account in our treatment or to the fact that the peripheries of collodion film is not precisely wedge-shaped as was assumed by us.

(ii) Effect of defocusing on the striations of equal-thickness.

When Bragg reflection occurs in the crystal, we can broadly deduce from our calculation that the equal-thickness striations accompany the Fresnel fringes. This we illustrate in Fig. 5 (b) from which we read readly:

(a) The brightest line takes place on vacuum side of the crystal edge. A dark line takes place between the Fresnel fringes on the vacuum side and the equal-thickness striations on the material side. All of them have similar properties as explained in (a)–(d) in (i).

(b) The spacing of the equal-thickness

striations is almost independent of the degree of defocusing.

The microphotographs of defocused image of crystallites obtained hitherto are not abundant enough to warrant a comparison with our results of calculation. Neverthless, the photographs obtained by Hibi[9] seems to have shown the properties (a)-(d). However, the present theory does not explain the observed fact that the equal-thickness striations tend to be more prominent in the real than in the virtual images. This might be explained if the effect of absorption is taken into consideration in an appropriate manner*.

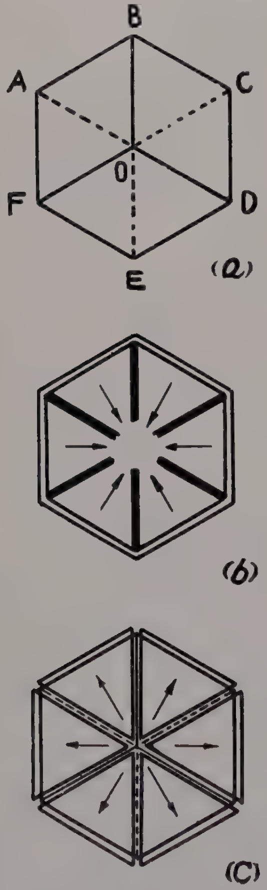

Fig. 6. Dark and bright lines along the edges of defocused image of crystallite. (a) An example of microscope image of crystallite having cubic habit. A body diagonal is perpendicular to the paper. (b) Defocused real image. The arrows show the direction of deflection of penetrating waves due to refraction. Bright lines are expected along the edges AO, BO *etc*. (c) Defocused virtual image. Dark lines are expected along the edges, AO, BO *etc*.

(iii) Bright and dark lines along crystal edges.

It is confirmed that bright and dark lines appear always along the edges in the images of polyhedral crystals such as MgO (Phot. 1.) This fact can be also explained by the refraction effect.

In the real image, the waves transmitted through the portions △ABO and △BCO (in Fig. 6) are deflected inwards to the material side by refraction effect and they overlap each other. Since their phase shifts are likely to be equal, bright lines may be observed along AO, BO *etc*. In the virtual image, on the contrary, the waves transmitted through △ABO, △BCO *etc*, are deflected outwards to the vacuum side, so that the dark lines are expected along AO. BO *etc*. Consequently, if the degree of defocusing is measured accurately, the breadth of the dark and bright line is to be determined by the mean inner potential of crystal.

§ 5. Acknowledgement

It is the author's pleasure to express his sincere thanks to Professor R. Uyeda for his suggestions and valuable advices given throughout this work and to Professor T.

---

* Whereas the absorption effect can not be treated in a satisfactory way at present, it will be permissible to suppose that the amplitude of $\Phi_0^{(i)}$ decreases with increasing x. Since the equal-thickness striations are due to the interference of $\Phi_0^{(1)}$ and $\Phi_0^{(2)}$, they appear clearly where x is so large that the overlapping of $\Phi^{(t)}$ has no effect on them, and simultaneously x is so small that the absorption effect is not conspicuous. Since the overlapping of $\Phi^{(t)}$ with $\Phi_0^{(i)}$ is larger in the virtual image than in the real image, it is reasonablly expected that the striations are more obscure in the virtual image.

Further, the author can point out another reason to explain this fact. It was found in the electron diffraction experiment[10] that the amplitude of $\Phi_g^{(1)}$ is more intensive than that of $\Phi_g^{(2)}$, perhaps this is caused by the absorption effect. (cf. the note added in proof of Paper II) If this is the case, the amplitude of $\Phi_0^{(1)}$ must be more intensive than that of $\Phi_0^{(2)}$[11]. Considering, further, that the refraction angle of $\theta_0^{(2)}$ is larger than that of $\theta_0^{(1)}$, it may be supposed that this amplitude difference between $\Phi_0^{(1)}$ and $\Phi_0^{(2)}$ makes more obscure the striations in the virtual image than in the real image.

Hibi and Mr. N. Morito for their generosities in lending the author many of the interesting microphotographs obtained in their laboratories. Further he wishes to thank Professor T. Ito who very kindly took the trouble of reading through the manuscript before publication and giving the author many valuable advices.

Appendix

Applying the notations defined in Paper I and II, the results of crystal interfraction are given as follows:

(i)

$$\left.\begin{aligned} \overline{C}_0^{(i)} &= (-1)^i \{u+(-1)^i\sqrt{u^2+w^2}\}/2\sqrt{u^2+w^2} \\ \overline{C}_g^{(i)} &= (-1)^i\{U_{g0}/K\}/2\sqrt{u^2+w^2} \end{aligned}\right\} \tag{A1}$$

(cf. eq. (2′) and eq. (II–A2))

(ii)

$$\left.\begin{aligned} \overline{\boldsymbol{k}}_0^{(i)} - \boldsymbol{K}_{\mathrm{I}} &= \left\{\frac{\nu_e}{(\nu_e\cdot\boldsymbol{z}_0)}\right\}\left[\frac{U_{00}}{2K} - \frac{(\nu_e\cdot\boldsymbol{z}_0)}{2(\nu_e\cdot\boldsymbol{z}_g)}\right. \\ &\qquad \left.\times\{u-(-1)^i\sqrt{u^2+w^2}\}\right] \\ \overline{\boldsymbol{K}}_0^{(i)} - \boldsymbol{K}_{\mathrm{I}} &= \left\{\frac{\nu_e}{(\nu_e\cdot\boldsymbol{z}_0)} - \frac{\nu_a}{(\nu_a\cdot\boldsymbol{z}_0)}\right\} \\ &\quad \times\left[\frac{U_{00}}{2K} - \frac{(\nu_e\cdot\boldsymbol{z}_0)}{2(\nu_e\cdot\boldsymbol{z}_g)}\left\{u-(-1)^i\sqrt{u^2+w^2}\right\}\right] \\ \overline{\boldsymbol{K}}_g^{(i)} - \boldsymbol{g} - \boldsymbol{K}_{\mathrm{I}} &= \left\{\frac{\nu_e}{(\nu_e\cdot\boldsymbol{z}_0)}\right\}\left[\frac{U_{00}}{2K} - \frac{(\nu_e\cdot\boldsymbol{z}_0)}{2(\nu_e\cdot\boldsymbol{z}_g)}\right. \\ &\quad \left.\times\left\{u-(-1)^i\sqrt{u^2+w^2}\right\}\right] - \left\{\frac{\nu_a}{(\nu_a\cdot\boldsymbol{z}_g)}\right\}\left[\frac{U_{gg}}{2K}\right. \\ &\qquad \left. + \frac{1}{2}\left\{u+(-1)^i\sqrt{u^2+w^2}\right\}\right] \end{aligned}\right\} \tag{A2}$$

(cf. Appendix of Paper II)

(iii)

$$H^{(i)} = \frac{U_{00}}{K} - \{u-(-1)^i\sqrt{u^2+w^2}\} \tag{A3}$$

(cf. eq. (16))

References

1) N. Kato and R. Uyeda: *Acta Cryst.* **4** (1951) 227, 229.
N. Kato: J. Phys. Soc. Jap. **7** (1952) 397, 406.
2) H. A. Bethe: Ann. d. Phys. Lpz. **87** (1928) 55.
3) H. Boersch: Naturwiss. **28** (1940) 711; Phys. Zeits. **44** (1943) 32.
4) E. Kinder and A. Recknagel: Optik **2** (1947) 346.
5) J. Hillier and E. G. Ramberg: J. App. Phys. **18** (1947) 48.
6) R. D. Heidenreich: Phys. Rev. **62** (1942) 291.
R. D. Heidenreich and L. Sturkey: J. App. Phys. **16** (1945) 97.
E. Kinder: Naturwiss. **31** (1943) 149.
C. E. Hall: J. App. Phys. **19** (1948) 198.
7) W. Kossel: Naturwiss. **31** (1943) 323.
R. D. Heidenreich and L. Sturkey: *ibid.*
8) for example *M. Born: Optik* (1933) p. 154.
9) T. Hibi: *private communication.*
10) G. Honjo and K. Mihama: *Acta Cryst.* **4** (1951) 282.
11) M. V. Laue: *Acta Cryst.* **2** (1949) 106.

JOURNAL OF THE PHYSICAL SOCIETY OF JAPAN Vol. 8, No. 3, MAY—JUNE, 1953

TFD Functions for Non-zero Temperatures and Equations of State Based on Them*

By Kwai UMEDA and Yasuo TOMISHIMA

Department of Physics, Faculty of Science, Okayama University

(Received February 7, 1953)

By means of the Lidiard distribution function for free electron gas, the Thomas-Fermi-Dirac (TFD) equations for non-zero temperatures are derived and integrated numerically for Fe. On the basis of the TFD functions there are given also the equations of state of metals under extremely high pressures.

§ 1. Introduction

The Thomas-Fermi-Dirac (TFD) equations for non-zero temperatures were given previously by Yokota1) in a coarse form by means of the simple Fermi distribution function for free electron gas. In that paper he pointed out that his treatment is rather not self-consistent because account is taken of the effect of exchange energy on the energy expression alone, but not on the distribution function. Recently, the modifications of distribution function by exchange effect were investigated by several authors.2)-7) In particular, Lidiard5) proposed a good variational form, very practical for low temperatures, i.e.

$$f(\boldsymbol{k})=\left(\exp\left[\left(\frac{\hbar^2}{2m}\boldsymbol{k}^2-\zeta\right)\Big/k\tau\right]+1\right)^{-1}, \quad (1)$$

which differs from the simple Fermi form only in the replacement of the temperature T by the modified temperature τ.

In this paper we have refined the Yokota's treatment by substituting the simple Fermi distribution function therein by this Lidiard one.

§ 2. TFD Method for Non-zero Temperatures for General System

According to the usual postulate in the TF method that in each volume-element the inner variation of the potential is neglected and subsequently the electron cloud is approximated by a free electron gas, we get in our case the free energy density at the position of the considered volume-element in an accuracy of Sommerfeld expansion with respect to τ simply by adding to the free energy density for free electron gas given by Lidiard5) (his equation (3)) the potential energy density, as follows

$$f=n\varepsilon_0\left[\frac{3}{5}\left(1+\frac{5}{12}\theta^2\right)-\frac{3}{4}\frac{\varepsilon_j}{\varepsilon_0}\left\{1+\frac{\theta^2}{6}(\ln\theta-1.8207)\right\}-\frac{\pi kT}{\varepsilon_0}\frac{\theta}{2}\right]-en\left(\varPhi+\frac{1}{2}\varphi\right) \quad (2)$$

with $\theta\equiv\pi k\tau/\varepsilon_0$**, $\varepsilon_0\equiv(h^2/8m)(3n/\pi)^{2/3}$=Fermi energy for $T=0$, $\varepsilon_j\equiv e^2(3n/\pi)^{1/3}$=a measure of exchange energy, n=electron density, $\varPhi$=potential due to nucleus, and φ=potential due to electrons.

Minimizing f with respect to τ or θ according to Lidiard5), we have likely the equation determining τ (his eq. (4))

$$\frac{\pi kT}{\varepsilon_0}=\theta-\frac{\varepsilon_j}{\varepsilon_0}\left[\frac{\theta}{2}(\ln\theta-1.8207)+\frac{\theta}{4}\right], \quad (3)$$

which is rewritten in terms of n due to the definitions of ε_0 and ε_j, as

$$\frac{T}{\tau}=1+\frac{1.9468\cdot10^7}{n^{1/3}}\left(\ln\frac{T}{\tau}+\frac{2}{3}\ln n-\ln T-23.688\right). \quad (4)$$

We see that, in contrast to T, τ is not a constant throughout over the volume of the system, but a function of position via the radial dependence of n. This circumstance is the principal difference of our case from the Yokota's.

In thermal equilibrium the total free energy of the system

---

* Published in part preliminarily in Progress Report No. 1 of the Research Group for the Study of Atomic and Molecular Structure of Japan, October 1952, and presented in part at the annual Kyoto meeting of the Physical Society of Japan, October 31, 1952, as well as at the 12th Hiroshima meeting of the Chugoku-Shikoku Branch of the Physical Society of Japan, December 21, 1952.

** In place of x (Lidiard) we have prefered θ reserving x for the TF radial coordinate.

$$F=\int f\,dv \tag{5}$$

must have the minimum value subject to the subsidiary condition that the total number of electrons N is a constant

$$N=\int n\,dv=\text{const.} \tag{6}$$

This requirement is embodied by the variational equation

$$\delta F-\mu'\delta N=0 \tag{7}$$

with δ=functional variation with respect to n, and μ'=Lagrangian multiplier with miuns sign=chemical potential per electron. Using eqs. (2) to (6), we can write eq. (7) explicitly

$$(1+\theta^2/12)\varepsilon_0-(1-\theta^2/12)\varepsilon_J-(\pi kT/6)\theta \\ -e(V+\mu'/e)=0 \tag{8}$$

with $V\equiv\emptyset+\varphi$=total potential.

On the other hand, n is directly related to V by the Poisson equation

$$n=(1/4\pi e)\Delta\varphi=(1/4\pi e)\Delta V \\ =(1/4\pi e)\Delta(V+\mu'/e)\,. \tag{9}$$

Thus, we have three simultaneous equations for three quantities $V+\mu'/e$, τ and n. If we express n in eqs. (8) and (4) in terms of V by eq. (9), we obtain the simultaneous equations determining V with τ as a parameter to be eliminated.

§ 3. Complete TFD Equation for Non-zero Temperatures for Atom

In the case of the sphericallysy mmetrcail compressed atom of atomic number Z, we introduce the TFD function $\psi(x)$, as a function of radial coordinate $x(=r/\mu)$ measured in TF units $\mu\equiv(9\pi^2/128)^{1/3}Z^{-1/3}a_0=0.88534Z^{-1/3}a_0$, on connecting it with $V(r)$ by the relation

$$V(r)+\mu'/e+2me^3/h^2\equiv(Ze/r)\psi(x)\,. \tag{10}$$

Then, eq. (9) is simplified as

$$n=(Z/4\pi\mu^3)(\psi''/x)\,, \tag{11}$$

so that we obtain from eq. (8) our **complete TFD equation for non-zero temperatures**

$$(\psi'')^{2/3}-2\varepsilon x^{1/3}(\psi'')^{1/3}-\tfrac{2}{3}\beta T^2(\tau/T)^2[(2T/\tau \\ -1)x^{4/3}(\psi'')^{-2/3}-2\varepsilon x^{5/3}(\psi'')^{-1}] \\ -x^{-1/3}\psi+\varepsilon^2x^{2/3}=0 \tag{12}$$

with $\varepsilon\equiv(3/32\pi^2)^{1/3}Z^{-2/3}=0.21178Z^{-2/3}$ = TFD parameter, and $\beta\equiv(\pi^2/8)(\mu k/e^2)^2Z^{-2}=0.96992\cdot 10^{-11}Z^{-8/3}(^\circ\mathrm{K})^{-2}$ = Marshak-Bethe parameter, and simultaneously from eq. (4) the equation

$$\frac{T}{\tau}=1+\frac{0.21204}{Z^{2/3}(\psi''/x)^{1/3}}\left(\ln\frac{T}{\tau}+\frac{2}{3}\ln\frac{\psi''}{x} \right. \\ \left. +\frac{4}{3}\ln Z-\ln T+12.983\right). \tag{13}$$

These simultaneous equations must be integrated subject to the boundary condition for the neutral atom of radius $X(=a/\mu)$

$$\psi(0)=1 \quad \text{and} \quad \psi'(X)=\psi(X)/X\,. \tag{14}$$

Eq. (12) yields Marshak-Bethe's[8)] as well as Sakai's[9)] complete TF equation for non-zero temperatures (their eq. (4) and his eq. (23) resp.) when $\tau/T=1$ and $\varepsilon=0$, and the ordinary TFD equation* when $\tau/T=1$ and $T=0$, as is necessary.

Since eq. (12) is an algebraic equation of fifth degree in regards to $(\psi'')^{1/3}$, it is impossible to express ψ'' explicitly in terms of x and ψ, while it is the case for the ordinary TF, ordinary TFD, Marshak-Bethe's TF and Feynmann-Metropolis-Teller's TF (their eq. (17)) equations.

§ 4. Temperature-perturbation TFD Equation for Atom

Treating the temperature-dependent term in eq. (12) as a perturbation, we assume, as done by Feynmann, Metoropolis and Teller[13)] for Marshak-Bethe's TF equation, for $\psi(x)$ such a form expanded up to T^2 as

$$\psi(x)=\psi_0(x)+\beta T^2\psi_1(x)\,. \tag{15}$$

Of course, the unperturbed function $\psi_0(x)$ is a solution of the well-known ordinary TFD equation for $T=0$

$$\psi_0''=x[\varepsilon+(\psi_0/x)^{1/2}]^3\,. \tag{16}$$

The perturbed part $\psi_1(x)$ must, in turn, satisfy our **temperature-perturbation TFD equation**

$$\psi_1''=\left(\frac{x}{\psi_0}\right)^{1/2}\left[\frac{3}{2}\left(\varepsilon+\left(\frac{\psi_0}{x}\right)^{1/2}\right)^2\psi_1+x \right. \\ \left. \times\left\{\frac{\tau}{T}\left(2-\frac{\tau}{T}\right)-2\varepsilon\left(\frac{\tau}{T}\right)^2\left(\varepsilon+\left(\frac{\psi_0}{x}\right)^{1/2}\right)^{-1}\right\}\right] \tag{17}$$

with the boundary condition, the alternate of eq. (14),

$$\psi_1(0)=0\,,\quad \psi_1'(0)=0 \quad \text{and} \\ \psi'(X)=\psi(X)/X\,. \tag{18}$$

Eq. (17) yields the Marshak-Bethe's[8)] temperature-perturbation TF equation (their eq. (8)) when $\tau/T=1$ and $\varepsilon=0$.

Then, in terms of ψ_0 and ψ_1, n can be given explicitly as a function of x

$$n=\frac{Z}{4\pi\mu^3}\left[\Psi_0^3+\beta T^2\left(\frac{x}{\phi_0}\right)^{1/2}\left[\frac{3}{2}\Psi_0^2\frac{\phi_1}{x}\right.\right.$$
$$\left.\left.+\left\{\frac{\tau}{T}\left(2-\frac{\tau}{T}\right)-2\varepsilon\left(\frac{\tau}{T}\right)^2\Psi_0^{-1}\right\}\right]\right] \quad (19)$$

with $$\Psi_0\equiv\varepsilon+(\phi_0/x)^{1/2}. \quad (19a)$$

Substituting this into eq. (4), we have the precise equation for τ in the βT^2-approximation.

In eq. (17) determining the perturbed part ϕ_1, however, τ may be evaluated not by the precise equation mentioned above, but by the unperturbed form of eq. (4) rewritten for the unperturbed electron density n_0 and consequently in terms of ϕ_0, as

$$T/\tau=1+g(x)[\ln(T/\tau)-2\ln g(x)-\ln T+9.8506] \quad (20)$$

with $$g(x)\equiv\varepsilon/[\varepsilon+(\phi_0/x)^{1/2}].$$

The values of ϕ_0 can be taken from the table given recently by Metropolis and Reitz[10)]. In Fig. 1, τ/T is drawn against $x^{1/2}$ in the case of $\phi_0(x)$ of Fe with the initial slope $a_2=-1.6250$ for $T=20000$°K. It is noteworthy that τ/T runs over wide range of x nearly linearly with $x^{1/2}$, as it may be approximated by the formula

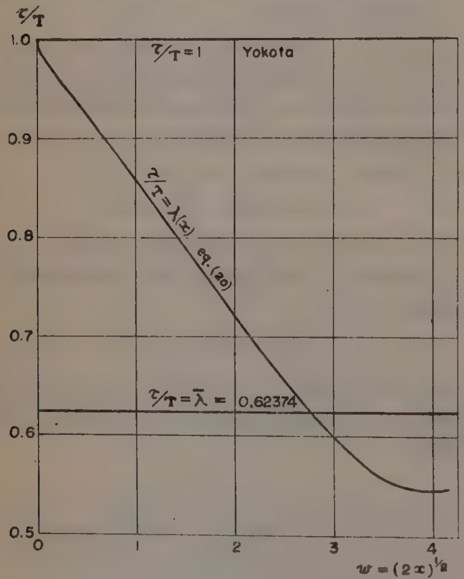

Fig. 1. Modified temperature τ as a function of $x^{1/2}$ according to eq. (20) for Fe, $a_2=-1.6250$, $T=20000$°K.

$$\tau/T=1-\alpha x^{1/2}. \quad (21)$$

Now, it is our principal task to integrate practically eq. (17) on taking account of eqs. (18) and (20).

To initiate the numerical integration routine, $\phi_1(x)$ is first expanded into a semiconvergent power series

$$\phi_1=\sum_{n=0}^{\infty}C_n x^{n/2}. \quad (22)$$

Eq. (18) demands immediately $C_0=C_1=C_2=0$.

If we assume for τ/T about the origin eq. (21), we find, in use of the well-known series expansion for $\phi_0(x)$ about the origin given accurately by Metropolis and Reitz[10)], the following values*

$$\left.\begin{aligned}
C_3&=C_4=C_5=C_6=0,\\
C_7&=4/35,\\
C_8&=-\varepsilon/6,\\
C_9&=(4/63)[-(1/2)a_2+2\varepsilon^2+4\varepsilon\alpha-\alpha^2],\\
C_{10}&=(1/10)[-26/105+\varepsilon a_2-\varepsilon^3-2\varepsilon^2\alpha-\varepsilon\alpha^2],\\
C_{11}&=(4/99)[(3/8)a_2^2-3a_2\varepsilon^2+(211/105)\varepsilon+2\varepsilon^4\\
&\quad+\alpha(-4\varepsilon a_2+4\varepsilon^3)+\alpha^2((1/2)a_2+2\varepsilon^2)],\\
C_{12}&=(1/15)[(44/105)a_2-\varepsilon a_2^2+2\varepsilon^3a_2-(323/\\
&\quad 420)\varepsilon^2-\varepsilon^5+\alpha(3a_2\varepsilon^2-(52/21)\varepsilon-2\varepsilon^4)\\
&\quad+\alpha^2(a_2\varepsilon-\varepsilon^3+2/7)].
\end{aligned}\right\} \quad (23)$$

Similarly, we have further calculated a simplified case with $\tau/T=\bar{\lambda}=$a mean value following from eq. (4) for the mean electron density $\bar{n}$, and then Yokota's case with $\tau/T=1$ (the simple Fermi distribution function). For these $\tau/T=\bar{\lambda}$, we find the following values*

$$\left.\begin{aligned}
C_3&=C_4=C_5=C_6=0,\\
C_7&=(4/35)\bar{\lambda}(2-\bar{\lambda}),\\
C_8&=-(\varepsilon/6)\bar{\lambda}^2\\
C_9&=(2/63)[4\varepsilon^2\bar{\lambda}^2-a_2\bar{\lambda}(2-\bar{\lambda})],\\
C_{10}&=(1/10)[(\varepsilon a_2-\varepsilon^3)\bar{\lambda}^2-(26/105)\bar{\lambda}(2-\bar{\lambda})],\\
C_{11}&=(4/99)[(2\varepsilon^4-3\varepsilon^2a_2+(29/12)\varepsilon)\bar{\lambda}^2\\
&\quad-((57/140)\varepsilon-(3/8)a_2^2)\bar{\lambda}(2-\bar{\lambda})],\\
C_{12}&=(1/15)[(-\varepsilon^5+2\varepsilon^3a_2-(55/84)\varepsilon^2-\varepsilon a_2^2)\bar{\lambda}^2\\
&\quad+((44/105)a_2-(4/35)\varepsilon^2)\bar{\lambda}(2-\bar{\lambda})].
\end{aligned}\right\} \quad (24)$$

In these three cases, i.e. $\tau/T=\lambda(x)$, $\bar{\lambda}$ and 1 resp., we have calculated the values of $\phi_1(x)$ of Fe with $a_2=-1.6250$, -1.6200 and -1.6190 for $T=20000$°K. To any one who may have interest of them we should like

---

* If we put in eqs. (23) $\alpha=\varepsilon=0$ as well as in eqs. (24) $\bar{\lambda}=1$ and $\varepsilon=0$, we get the values of C's for Marshak-Bethe's case given by Feynmann, Metropolis and Teller[13)], provided that there are found unfortunately some discrepancies, as $C_9=-(2/63)a_2$ (in place of $-(4/63)a_2$) as well as $C_{11}=(1/66)a_2^2$ (in place of 0), and added $C_{12}=(44/1575)a_2$.

Table I. Numerical Values for Fe ($Z=26$) at $T=20000°\mathrm{K}$

$M=9.2731\cdot10^{-23}$ g, $\mu=1.6586\cdot10^{-9}$ cm, $\varepsilon=2.4131\cdot10^{-2}$, $\beta=1.6350\cdot10^{-15}(°\mathrm{K})^{-2}$

	$a_2=-1.6250$			$a_2=-1.6200$	$a_2=-1.6190$
τ/T	$\lambda(x)$	$\bar{\lambda}=0.62374$	1	$\bar{\lambda}=0.70603$	$\bar{\lambda}=0.71136$
X	7.7083	7.7087	7.7107	4.3256	4.1628
a (10^{-8} cm)	1.2785	1.2786	1.2789	0.71745	0.69044
$\tau(x)$ (°K)	$1.1029\cdot10^4$	$1.2475\cdot10^4$	$2.0000\cdot10^4$	$1.4121\cdot10^4$	$1.4227\cdot10^4$
$\psi_0(x)$	0.04635	0.04636	0.04637	0.19075	0.20574
$\psi_1(x)$	$6.3553\cdot10^2$	$6.2687\cdot10^2$	$6.0210\cdot10^2$	$4.7088\cdot10$	$3.9900\cdot10$
v (10^{-24} cm³)	8.7537	8.7549	8.7617	1.5469	1.3787
ρ (g/cm³)	10.593	10.592	10.584	59.947	67.261
p (dynes/cm²)	$5.2163\cdot10^{12}$	$5.2293\cdot10^{12}$	$5.2921\cdot10^{12}$	$4.0234\cdot10^{14}$	$5.2363\cdot10^{14}$

to send the tables of the values of $\phi_1(x)$ and $\phi_1'(x)$ thus obtained, Research Note of Department of Physics, Faculty of Science, Okayama University, Okayama, Japan, No. 6, January 31, 1953.

In Table I there are columned only the boundary values which are necessary for the next paragraph.

§ 5. Equations of State of Metals under Extremely High Pressures

On the basis of the TFD functions obtained above it is possible to derive the equations of state of metals under extremely high pressures, as shown by several investigators[11)-14)].

The density ρ is given immediately by the formula

$$\rho=M/v=M/(4/3)\pi a^3=M/(4/3)\pi\mu^3X^3 \quad (25)$$

with M=atomic mass, and v=atomic volume.

The pressure p follows, in turn, from the thermodynamical relation

$$\begin{aligned}p&=-(\partial F/\partial v)_{T,N}=-(1/4\pi a^2)(\partial F/\partial a)_{T,N}\\&=-(1/4\pi a^2)\Big[4\pi a^2[f]_{r=a}+\int_0^a(\partial f/\partial n)\\&\quad\times(\partial n/\partial a)4\pi r^2dr\Big]. \qquad (26)\end{aligned}$$

$\partial f/\partial n$ has been already calculated in the left-hand side of eq. (8), as it is just equal to μ'. Taking account of the relation

$$\partial N/\partial a=4\pi a^2[n]_{r=a}+\int_0^a(\partial n/\partial a)4\pi r^2dr=0, \qquad (27)$$

eq. (26) becomes

$$\begin{aligned}p=[\{&(2/5+\theta^2/12)\varepsilon_0-(1/4)(1-\theta^2/12)\varepsilon_J\\&+(\pi kT/12)\theta\}\cdot n]_{r=a}, \qquad (28)\end{aligned}$$

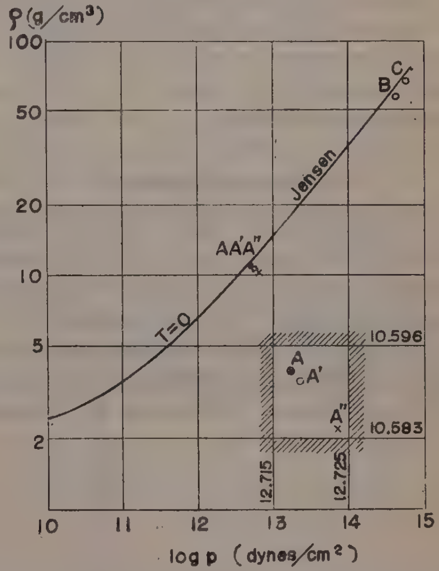

Fig. 2. Density ρ-pressure p diagram for Fe at $T=0$ and $T=20000°$K.

Full line reproduces $T=0$ (Jensen).
A, A′, A′′ correspond to
$T=20000°$K, $a_2=-1.6250$, $\tau/T=\lambda(x)$, $\bar{\lambda}(=0.62374)$, 1 resp.
B correponds to
$T=20000°$K, $a_2=-1.6200$, $\tau/T=\bar{\lambda}(=0.70603)$.
C correponds to
$T=20000°$K, $a_2=-1.6190$, $\tau/T=\bar{\lambda}(=0.71136)$.
Hatched part shows relative positions of A, A′ and A′′ enlarged.

which can be rewritten in terms of ϕ by eq. (11)

$$p=\frac{Z^2e^2}{4\pi\mu^4}\left[\frac{2}{5}\left(\frac{\phi''}{x}\right)^{5/3}-\frac{\varepsilon}{2}\left(\frac{\phi''}{x}\right)^{4/3}+\frac{2}{3}\beta\tau(\tau+T)\left(\frac{\phi''}{x}\right)^{1/3}+\frac{1}{3}\varepsilon\beta\tau^2\right]_{x=X}, \qquad (29)$$

or alternatively in terms of ψ_0 and ψ_1 by eqs. (15) and (19a)

$$p=\frac{Z^2e^2}{4\pi\mu^4}\left[\frac{2}{5}\Psi_0{}^5-\frac{\varepsilon}{2}\Psi_0{}^4+\beta T^2\left\{\frac{\psi_1}{x}\Psi_0{}^3+2\frac{\tau}{T}\Psi_0-\varepsilon\left(\frac{\tau}{T}\right)^2\right\}\right]_{x=X}. \tag{30}$$

In Table I there are columned also the corresponding values of ρ and p, which follow from eqs. (25) and (30) resp. by means of the boundary values given in Table I. The pairs of the values of ρ and p are plotted on the density-pressure diagram given by Jensen[12] in the TFD case for $T=0$°K (his Fig. 2), as shown in Fig. 2. We see that the Yokota's treatment results an overestimation of temperature effect, as Yokota has also expected in the course of discussion with us, and the more the degree of approximation is promoted, the nearer the points come to the curve for $T=0$.

Acknowledgements

We should like to thank Profs. Coulson, Marshak, Metropolis and Teller for sending us reprints which have been of much service to our calculation. We are indebted also to Dr. Yokota at Niigata University and Mr. Suura at Hiroshima University for several clarifying advices. This work is financially supported by the Scientific Research Expenditure of the Ministry of Education granted to one of us (K. U.), a member of the Research Group for the study of Atomic and Molecular Structure.

References

1) I. Yokota: J. Phys. Soc. Jap. **4** (1949) 82.

2) H. Koppe: ZS. f. Naturforsch. **2a** (1947) 429.

3) E. P. Wohlfarth: Phil. Mag. **41** (1950) 534.

4) A. B. Lidiard: Proc. Phys. Soc. A **64** (1951) 814.

5) A. B. Lidiard: Phil. Mag. **42** (1951) 1325.

6) H. Koppe: ZS. f. Naturforsch. **6a** (1951) 517.

7) W. Zimmermann: ZS. f. Phys. **132** (1952) 1.

8) R. E. Marshak & H. A. Bethe: Astrophys. J. **91** (1940) 239.

9) T. Sakai: Proc. Phys. Math. Soc. Jap. **24** (1942) 259.

10) N. Metropolis & J. R. Reitz: J. Chem. Phys. **19** (1951) 555.

11) J. C. Slater & H. M. Krutter: Phys. Rev. **47** (1935) 559.

12) H. Jensen: ZS. f. Phys. **111** (1938) 373.

13) R. P. Feynmann, N. Metropolis & E. Teller: Phys. Rev. **75** (1949) 1561.

14) W. M. Elsasser: Science **113** (1951) 105.

JOURNAL OF THE PHYSICAL SOCIETY OF JAPAN Vol. 8, No. 3, MAY—JUNE, 1953

Low Frequency Coupled Oscillator and its Application to High Polymer Study

By Shigeo IWAYANAGI and Teruo HIDESHIMA

Kinoshita Laboratory, Scientific Research Institute, Tokyo

(Received, November, 27, 1952)

For the study of dynamical properties of high polymers by low frequency oscillations, a simple torsional coupled oscillator was constructed in which two pendulums of the same type having equal frequency (about 1/2 c.p.s.) were coupled to each other through a test material of cylindrical shape. Two modes of oscillations appear in the motion of the oscillator resulting in generating beats under suitable conditions. By observing the beats, it is possible to obtain the shear modulus and the elastic loss of the material through a simple course of calculation. Polymethyl methacrylate was investigated from about −20°C to about 150°C and anomalous absorption ranges were found at about 130°C and at about 20°C, the latter was considered worthy of mention.

§ 1. Introduction

In view of the lack of experimental data by low frequency oscillations for the study of dynamical properties of high polymers, a multiple pendulum oscillator of the frequency of about 1/2 c.p.s. was constructed with the object to investigate the anomalous mechanical dispersion and absorption which occur at so-called second order transition range of temperature. Studies within this temperature range is considered to supply an useful key to uncover the molecular structure of polymers. The position of this range shifts towards higher temperature with the increase of the frequency of oscillations. Hence the use of low frequency has advantage in that the test materials can be chosen of which the position of the temperature range is known in advance by statical experiments and, in particular, if the range is in the neighbourhood of room air temperature for the ease of measurements.

§ 2. Apparatus and Theory

The apparatus used is illustrated in Fig. 1. I and II are two pendulums of the same type, each having a steel rod R fixed to the shaft S which is held by ball bearings Bs. The two shafts are arranged in strict alignment. The period of each pendulum is adjusted by means of a cylindrical brass mass M attached to the bottom of the rod. Dotted lines T show the enclosure of a thermostat. After the pendulums are adjusted to have an equal frequency, the two shafts are firmly coupled to the test piece A through chucks Cs. The test piece is made in a cylindrical form, the

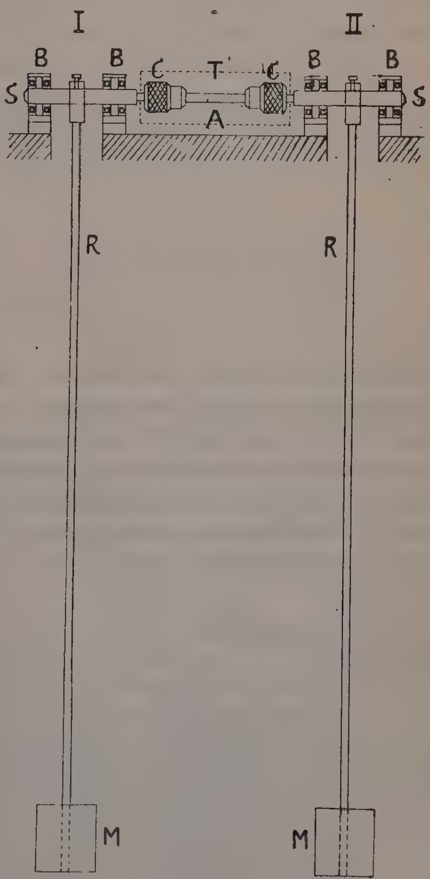

Fig. 1.

length and the radius of which are determined to suit the experimental conditions in every set of observation.

There appear two normal modes of oscillations in the motion of this coupled oscillator. Neglecting the friction of the bearings, they are

$$\omega_1=\sqrt{\frac{Mgh}{I}} \qquad \text{(in phase)} \qquad (1)$$

$$\omega_2=\sqrt{\frac{Mgh+2k}{I}} \qquad \text{(in anti-phase)} \qquad (2)$$

where

- M: the total mass of the pendulum,
- I: the moment, of inertia of the pendulum about the axis of rotation,
- h: the distance between the axis and the center of mass of the pendulum,
- k: the stiffness constant of the test piece,
- g: the gravity constant.

It is assumed that the effect of the inner viscosity of the test piece can be expressed by a complex stiffness

$$k=k'+ik'' \qquad (3)$$

and also that

$$K \gg k' \qquad (4)$$

where $K=Mgh$. (5)

Then $\omega_2=\sqrt{\frac{K}{I}}\left(1+2\frac{k}{K}\right)^{1/2} \fallingdotseq \omega_1\left(1+\frac{k}{K}\right)$

hence

$$\Re(\omega_2)=\omega_1\cdot\left(1+\frac{k'}{K}\right) \fallingdotseq \omega_1 \qquad (6)$$

$$\mathfrak{D}(\omega_2)=\omega_1\cdot\frac{k''}{K}=\Delta_s \qquad (7)$$

Δ_s is the decay factor of oscillations caused by the inner viscosity of the material.

Owing to the condition (4), the frequencies of the two modes of oscillations approach to each other resulting in generating beats. The number of oscillations involved between two successive nodes of beats is given by

$$N=\frac{\omega_1}{\Re(\omega_2)-\omega_1}=\frac{K}{k'}. \qquad (8)$$

Therefore

$$\Delta_s=\frac{\omega_1}{N}\cdot\frac{k''}{k'}. \qquad (9)$$

If the logarithmic decrement δ_s is introduced,

$$\delta_s=\Delta_s/\nu_2 \fallingdotseq \Delta_s/\nu_1 \qquad (10)$$

$$\therefore \frac{k''}{k'}=\frac{G''}{G'}=\frac{N}{2\pi}\delta_s. \qquad (11)$$

On the other hand, the shear modulus of the material is assumed to be related with k' by the formula

$$G'=\frac{2l}{\pi R^4}k' \qquad (12)$$

where

- G', G'': The real and the imaginary part of the shear modulus
- l: the length of the test piece
- R: the radius of the test piece,

$$\therefore G'=\frac{2l}{\pi R^4}\cdot\frac{K}{N}. \qquad (13)$$

By (11) and (13), the shear modulus and the loss factor can be calculated in terms of observable quantities. In actual cases, however, the effect of the frictional resistance of bearings must be considered and the whole analysis is performed as follows. For simplicity, assume that the frictional resistance is made up with fluid and solid frictions obtainable from data of oscillations in phase, the latter being usually negligible.

By reading the successive amplitudes on one side of the swing of one of the coupled pendulums which has been brought into motion under arbitrary conditions, a curve as shown in Fig. 2 is obtained in which a_1 and a_2 are amplitudes of oscillation in phase and in antiphase respectively. If r_1 and r_2 are damping ratios of the corresponding modes, we have

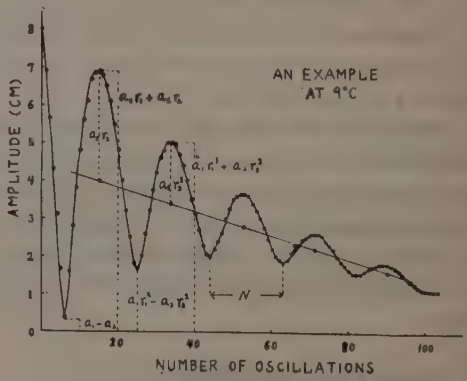

Fig. 2.

$$r_1=\exp\left(-\frac{N}{2}\Delta_1\right) \qquad (14)$$

$$r_2=\exp\left(-\frac{N}{2}\Delta_2\right). \qquad (15)$$

Considering that $\Delta_1 \ll 1$ and $\Delta_2 \ll 1$, it follows

$$2(a_1r_1+a_2r_2)+(a_1-a_2)+(a_1r_1^2-a_2r_2^2)\doteqdot 4a_1r_1\,. \tag{16}$$

From this relation, a_1r_1 and hence a_2r_2 can be obtained. Namely, if the amplitude values of a peak and fore and aft valleys are known, it is possible to calculate the amplitude of the anti-phase mode of oscillation for that peak. A set of points thus obtained gives the logarithmic decrement δ. If δ_B is the logarithmic decrement of oscillation in phase (that is caused by the fluid friction of the bearings),

$$\delta_s=\delta-\delta_B\,. \tag{17}$$

Incidentally, it is clear that the value N is also obtainable from Fig. 2.

In a temperature range where the elastic loss of the material becomes very high, the coupling method cannot be used. In this case, the measuring is performed by firmly arresting one of the pendulums and by observing the period and the rate of decay of the other pendulum before and after the test piece is attached. The shear modulus and the loss are calculated in the usual way.

§ 3. Experimental

Measurements were made mainly on polymethyl methacrylate. Polystyrene and rubber were also investigated for comparison. In the case of polymethyl methacrylate, test pieces which were used up to 100° C and those used above 110° C were cut from two different blocks of the material as a large block was unavailable.* Nevertheless, the two blocks were of the same constitution as proved by the contiguity of observed data in transition from the lower temperature to the higher. All the test pieces were annealed for about ten hours at 100° C～130° C.

In the coupled oscillator method, which could be used up to 110° C, the dimensions of the test piece were so chosen that the number of oscillations N (See Eq. (8)) was 10～20 at the measuring temperature. Two test pieces of $l=9\,cm$, $R=0.3\,cm$ and $l=9\,cm$, $R=0.4\,cm$ satisfied the said condition.

The synchronization of the pendulums was first tested by setting them in parallel motions with equal amplitudes and then by ascertaining there was no perceivable phase difference with the lapse of about 200 oscillations. Coupling of the pendulums to the test piece was made next and the thermostat was set at the measuring temperature and left at least for 0.5～1 hour before the measurements were made. Thermocouples and thermometers were used to read the temperature of the thermostat in which the uniformity of temperature distribution around the test piece was within 1° C.

The accuracy of measurements was about 3% on the shear modulus, about 10% on the loss and ±1° C on the temperature. Above 110° C, the coupled oscillator method failed on account of high elastic loss as stated before. The use of single pendulum method at higher temperatures rendered the measurement on shear modulus less accurate.

§ 4. Results

A typical result of measurements on polymethyl methacrylate made in a temperature range of −20° C～150° C is shown in Fig. 3. The softening temperature is known to exist in the neighbourhood of 100° C. The mechanical dispersion is, therefore, expected to appear thereabout which was evidenced by the results shown in the figure.

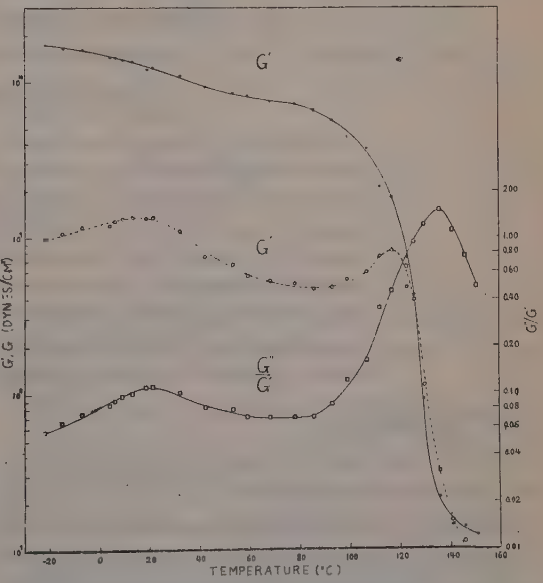

Fig. 3. Temperature dependence of G', G'' and G''/G' at period of oscillation 1.48 *sec.*～1.89 *sec.*

The appearance of another anomalous temperature range in the vicinity of 20° C is worthy of mention. A slight peak of the elastic loss and a steep decrease of the shear modulus with the rise of temperature are noticed in this range. A study on this secondary anomaly is now in progress.

---

* The blocks were manufactured by the Fuji Kasei & Co., Ltd., Tokyo and contained no plasticizer.

In the anomalous range at higher temperature, the freedom of rotation of the main chain is supposed to be released. However, it is doubtful whether the shear modulus increases proportionally with the rise of temperature beyond this range. The position of the anomalies at higher and lower temperature ranges, the height of peaks and other features may depend on the degree of polymerization, the content of plasticizer and etc.. To answer these questions, further investigations are needed.

In conclusion, the authors express their sincere appreciation to Dr. M. Kinoshita, the chief of the laboratory, for his encouragement throughout the study. They also wish to thank for the financial help given by the Scientific Research Fund of the Ministry of Education.

References

Similar ideas are reported in
Le Rolland P.: Physics Abstract Vol. 52, Abs. No. 2765.
Kovacs A.: Physics Abstract Vol. 52, Abs. No. 5023.
But the descriptions in both abstracts are too brief to conjecture the details of neither the apparatus nor the method of analysis.

JOURNAL OF THE PHYSICAL SOCIETY OF JAPAN Vol. 8, No. 3, MAY—JUNE, 1953

Dynamical Study on the Secondary Anomalous Absorption Region of Polymethyl Methacrylate

By Shigeo IWAYANAGI and Teruo HIDESHIMA
Scientific Research Institute, Tokyo

(Received November 27, 1952)

Secondary absorption region of polymethyl methacrylate was studied dynamically. In addition to the absorption region, which corresponds to so-called second order transition or softening temperature, a secondary absorption region was found at lower temperature, its peak being lower and broader. By means of bending and torsional vibrations, frequencies for the maximum absorption were measured at several temperatures. The activation energy of 29 kcal/mol was obtained. The results of the experiment were compared with those obtained electrically by Mead and Fuoss.

§ 1. Introduction

Up to the present, dynamical studies on elastic properties of polymethyl methacrylate were reported by several authors. Alexandrov and Lazurkin[1] demonstrated a remarkable temperature dependence of the strain produced by periodic stresses of various frequencies. Interpreting this temperature and frequency dependence of deformation as a results of a rate process, Eley[2] calculated the Gibbs free energy as well as the heat and the entropy of activation as 39 kcal/mol, 75 kcal/mol and 122 cal/mol °C respectively. In discussions on the nature of this phenomenon, which characterizes nearly all polymers, Buchdahl and Nielsen[3] considered it as a second order transition.

In the accompanying paper[4], the temperature dependence of dynamical rigidity and elastic loss of polymethyl methacrylate measured at a frequency of about 0.5 c.p.s. was stated. There appeared two peaks in elastic loss-temperature curve; one at 120° C and the other at 20°C. It seems that the former corresponds to the phenomenon of elastic dispersion investigated by Alexandrov, Lazurkin and Eley. But of the latter peak, there is so far no report to refer.* In order to elucidate the nature of this anomalous absorption, measurements were made at higher frequencies and within more limited temperature range. Both bending and torsional vibrations were used.

§ 2. Experimental Methods

(1) *Bending vibrations*

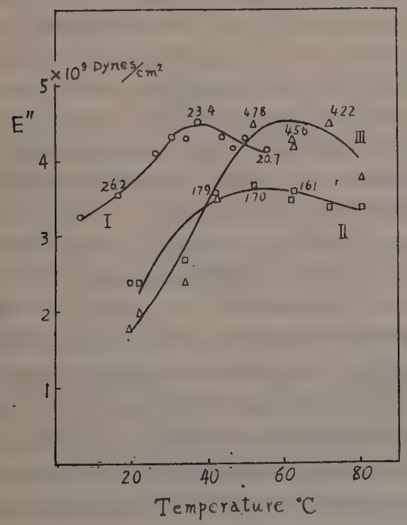

Fig. 1. Imaginary part of dynamic Young's modulus as a function of temperature.

Bending vibrations of a rectangular beam of polymethyl methacrylate clamped at one end were picked up by a magnetic telephone receiver rigidly fixed against a small iron plate cemented at the free end of the beam. The frequency of the fundamental vibrations in the beam of 2 cm in breadth, 0.31 cm in thickness and 20 cm in length was about 20 c.p.s. in the temperature range used. The fundamental vibrations were recorded by an electromagnetic oscillograph. The frequency and the logarithmic decrement were determined at each temperature. The second and the third modes of vibrations were excited by another magnetic telephone receiver. By varying the oscillator frequency, resonance curves were obtained and the resonance frequency and the half value breadth were determined. The whole vibrating system including the telephone receivers was placed in an electrically heating thermostat, the temperature fluctuation remaining within 1° C. Young's modulus E' and the elastic loss E'' were calculated for each mode of vibrations by the following formulas:

$$\left.\begin{aligned} &E'=4\pi^2\frac{\rho}{\kappa^2}\cdot\frac{l^4}{k_n{}^4}\cdot f^2 \\ \text{and}\quad & \\ &\frac{E''}{E'}=\frac{\delta}{\pi}=\frac{\Delta f}{f} \end{aligned}\right\} \qquad (1)$$

where ρ is the density, l the length, κ the radius of gyration of the cross section of the specimen, f the frequency, δ fhe logarithmic decrement and k_n a constant for each mode of vibrations. The half value breadth Δf is defined as the breadth of the peak frequency band between two frequencies at which the amplitudes are equal the $1/\sqrt{2}$ of the peak value.

(2) *Torsional vibrations*

Free torsional vibrations of a cylindrical specimen, vertically fixed at its lower end and loaded at the top, were recorded by the electromagnetic oscillograph as in the case of the bending vibrations. A cylindrical rod of 1 cm in diameter and 2 cm in length gave vibrations of about 16 c.p.s. at 55° C when the moment of inertia of the attached mass was 5.7×10^4 gr. cm². To produce initial pure torsional deformation, two electromagnets were used whereby due care was taken to prevent accompanying bending vibration.

Calculations of the dynamical rigidity G' and the elastic loss G'' were made by the following formulas:

$$\left.\begin{aligned} &G'=\pi I\cdot\frac{l}{R^4}\cdot f^2 \\ \text{and}\quad & \\ &\frac{G''}{G'}=\frac{\delta}{\pi} \end{aligned}\right\} \qquad (2)$$

where R is the radius, l the height of the specimen and I the moment of inertia of the attached mass.

Formulas (1) and (2) are valid only when damping is small as was the case in the present measurements.

§ 3. Experimental Results

Specimens were cut from commercial products of methyl methacrylate made by the Fuji Kasei & Co. Ltd. All the specimens were not from the same block. In Fig. 1, values of the elastic loss E'' obtained by bending vibration measurements are plotted against the temperature and in Fig. 2, those

---

* There are polymers exhibiting two peaks in electric loss-temperature curve (See Reference (5)).

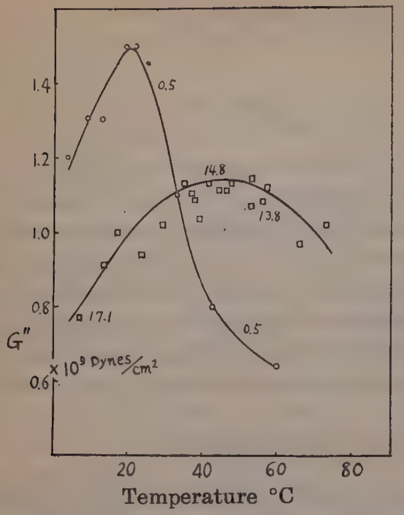

Fig. 2. Imaginary part of dynamic rigidity modulus as a function of temperature.

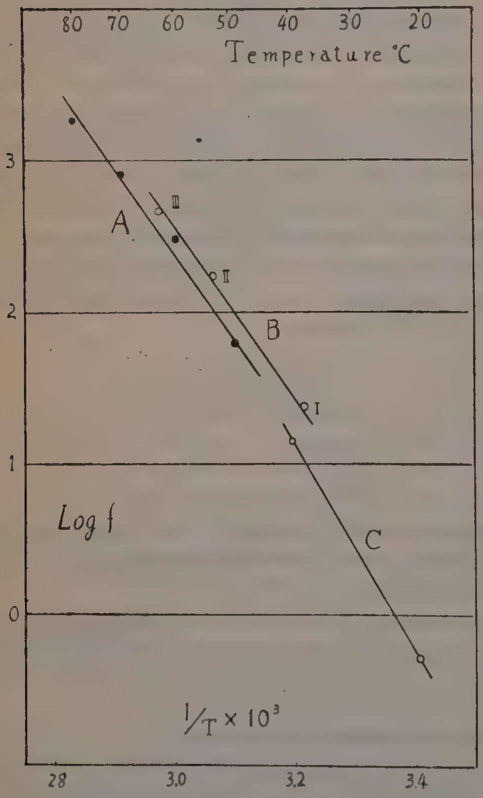

Fig. 3. Dielectric (A) and mechanical (B and C) relaxation. Secondary absorption peaks.

of elastic loss G'' by torsional vibrations together with the results of the 0.5 c.p.s. measurements described in the accompanying paper[4]. The elastic moduli E' and G' measured with E'' and G'' respectively showed montonous decreases with the increasing temperature with no definable inflection points. Owing to these decreases, the measuring frequency of each points varied considerably along each of E'' and G'' curves as shown by the numbers. However, the feature of the frequency-temperature relation at absorption peaks does not seem to have been affected by it. I, II and III in Fig. 1 refer to different modes of vibrations. As expected, when the frequency of vibrations increased, the absorption peak shifted toward a higher temperature region. In the case of G'', the peak became lower and broader as the frequency increased from 0.5 to 14 c.p.s.; in the case of E'', this tendency was not ascertained.

§ 4. Activation Energy and Discussions

Mead and Fuoss[5] determined the dielectric constant ε' and the loss factor ε'' of several polymers at temperatures varying from −70° C to 80° C and at frequencies from 60 to 8000 cycles. For polymethyl methacrylate, they found only one absorption peak (60-cycle loss factor maximum at 50° C). According to the nomenclature by Mead and Fuoss, this electrical absorption peak does not seem to have been caused by the primary absorption but by a secondary one corresponding to the peak found by the mechanical investigation described in the preceding paragraphs. If the electrical measurements were extended up to a higher temperature range, they would have also found the main that is the primary absorption peak.

Using the data of Figs. 1 and 2 values of log f are plotted against reciprocals of the absolute temperature as shown in Fig. 3. The straight lines B and C are by the bending and the torsional vibrations respectively. From the mean inclination of these straight lines, the activation energy of 29 kcal/mol for elastic deformation and the activation entropy of about 60 cal/mol °C were obtained. The straight line A is based upon the result of electrical measurements by Mead and Fuoss and gives a similar value of the activation energy indicating that the same molecular processes are involved in both cases.

In his analytical study of the relation between the rate processes of dipole rotations and the highly elastic deformation in amorphous polar polymers, Tuckett⁶⁾ compared the brittle temperature with the temperature at which the electrical relaxation time becomes *ca* 1 sec.. The two temperatures agree fairly good with polymethyl acrylate, polyvinyl chloride and acetate but not at all so with polymethyl methacrylate. Thus, two absorption bands are expected to exist: one due to rotations in the side group alone, the other due to *C*-*C* bond rotations. It is, therfore, reasonable to assume that the secondary absorption peak found mechanically by the authors at a lower temperature and that found electrically by Mead and Fuoss originate from rotations of the same polar-$COCH_3$ side groups of polymethyl methacrylate. It will be worth making systematical studies on dynamical properties of polymeric esters of methacrylic acid which have longer and/or more bulky side group than methyl group.

The simplest model shown in Fig. 4 would represent the main features of behavior of the polymer under investigation. When a sinusoidal external force of angular frequency ω is impressed upon the model, the rigidity G' and the elastic loss G'' are given by the formulas:

$$\left.\begin{aligned} G' &= G_1+G_2\frac{\omega^2\lambda^2}{1+\omega^2\lambda^2} \\ G'' &= G_2\frac{\omega^2\lambda^2}{1+\omega^2\lambda^2}=\omega\eta \end{aligned}\right\} \qquad (3)$$

where $\lambda=\eta_2/G_2$ is the relaxation time. When a constant external force f_0 is applied, the deformation s is given by the formula:

$$s=\frac{f_0}{G_1+G_2}\left\{1+\frac{G_2}{G_1}(1-e^{-t/\tau})\right\} \qquad (4)$$

where $\tau=\frac{G_1+G_2}{G_1}\lambda$ is the retardation time. In these formulas, G's are assumed to be interchangeable with Young's moduli E's and η's with the longitudinal viscosities ζ's.

Tuckett in his paper⁶⁾ suggested that the "relaxation time" of the Debye theory on dielectrics should correspond to the retardation time and be renamed as "orientation time". This suggestion would explain why the two straight lines *A* and *B* in Fig. 3 do not fall in together. If the retardation time is used instead of the relaxation time, *f* values of the line *B* are diminished by a factor $E_1/(E_1+E_2)$. Tentatively assigning $3\times1.0\times10^{10}$ and $3\times0.7\times10^{10}$ dynes/cm² to the values of E_1 and E_2 respectively*, this factor becomes $1.0/1.7=0.6$ which brings the lines *B* considerably nearer to the line *A*. But at the same time. this correction remove the line *C* further away from the line *A*. In view of the experimental errors, the discrepancy between the lines *B* and *C* together with the difference in their inclinations can not yet be brought into disccussions until further measurements on a larger time scale are carried out.

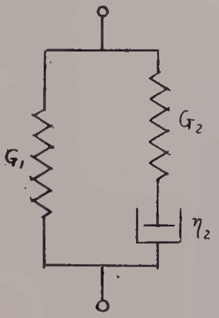

Fig. 4. A model for viscoelastic deformation.

In conclusion, hearty thanks are due to Dr. M. Kinoshita, the chief of the laboratory, for his encouragement in the whole course of the study and also to Mr. K. Shibata for his many useful discussions and to Mr. H. Nakane for his assistance in carrying out the measurements. This study was partially financed by the Scientific Research Fund of the Ministry of Education.

References

1) A. Alexandrov and J. S. Lazurkin: Acta Physicochimica **12** (1940) 647.

2) D. D. Eley: Trans. Faraday Soc. **38** (1942) 299.

3) R. Buchdahl and L. E. Nielsen: J. Appl. Phys. **21** (1950) 482.

4) S. Iwayanagi and T. Hideshima: J. Phys. Soc. Japan **8** (1953) 365.

5) D. J. Mead and R. M. Fuoss: J. Am. Chem. Soc. **64** (1942) 2389.

6) R. F. Tuckett: Trans. Farad. Soc. **40** (1944) 448.

---

* In the G'-temperature curve obtained by the 0.5 c.p.s. experiment, the stationary value of G' at about 30°C gives $G_1=1.0\times10^{10}$ dyne^5/cm^2 and the extreme value at lower temperature side gives $G_1+G_2=1.7\times10^{10}$ dynes/cm^2. The factor 3 is based upon a tentative assumption.

JOURNAL OF THE PHYSICAL SOCIETY OF JAPAN Vol. 8, No. 3, MAY—JUNE, 1953

The Theory Convex Wave Guide Lens

By Tokio SAKURAI

The Electrical Communication Laboratory, Ministry of Telecommunications

(Read October, 5, 1951, Received November 28, 1951)

Wave guide lens is a part of *reflex electromagnetic horn* invented by me which has very sharp directivity over astonishingly wide band of frequencies and posesses excellent properties for microwave repeater uses. The convex wave guide lens is a curved flat wave guide which transforms entering spherical wave into plane wave over infinitely wide band of frequencies. The determination of the form of the curved flat wall of the lens is theoretically discussed and deduced. Formulas, tables, and the designs fitted to production are given for standard type of convex wave guide lens.

§ 1. Introduction

Various lens antennas have been invented by E. Kock in United States of America[1]. Though these antennas have band-width 500 *Mc* in the neighbourhood of 4000 *Mc*, but on account of unevitable quarter wavelength step on lens and the difficulties of wider band impedance matching at the horn throat it seems difficult to expect wider band-width. In order to overcome this imperfection I have invented "*reflex electromagnetic horn*" shown in Fig. 1. The apparatus held at the leg-part of the horn is taken out and shown in Fig. 2. The outlet of rectangular feeding wave guide is to be held on the lower mouth of A_1, and the H_{10} wave transmitted by the rectangular wave guide enters into A_1, passes through A_2 and reaches the joint mouth of A_2 and A_3 hidden behind the sectoral belt B. Since A_1 and A_2 are so bent that the geodesic distances from the lower mouth of A_1 through the tubes A_1 and A_2 to the joint mouth of A_2 and A_3 are all equal with each other and the joint mouth of A_2 and A_3 are of the circular cylindrical form, the same phase surface of the wave passes the joint mouth of A_2 and A_3 and thence travels as circular cylindrical wave through flat wedge tube A_3, W_1, W_2 in order and reaches the *convex wave guide lens* L. The lens L is a tube composed of two flat curved walls very closely confronted with each other and two curved slender side walls. The lens L is held ahead of W_2 and transforms entering circular cylindrical wave into plane wave which enters into the flat horn H held ahead of L. In order to explain the behaviours of the wave hereafter the schematic of the longitudinal section of the reflex electromagnetic horn is shown in Fig. 3. The plane wave entering the horn H is changed into circular cylindrical wave by passing

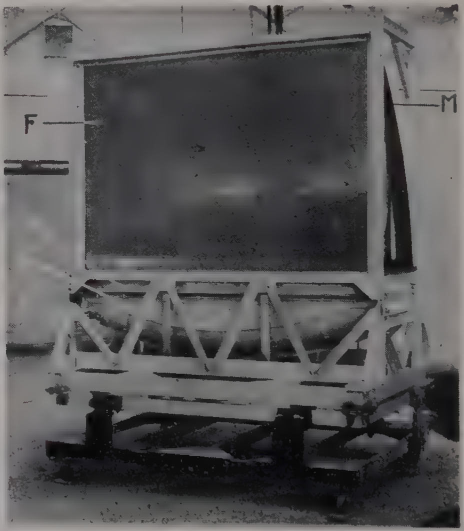

Fig. 1.

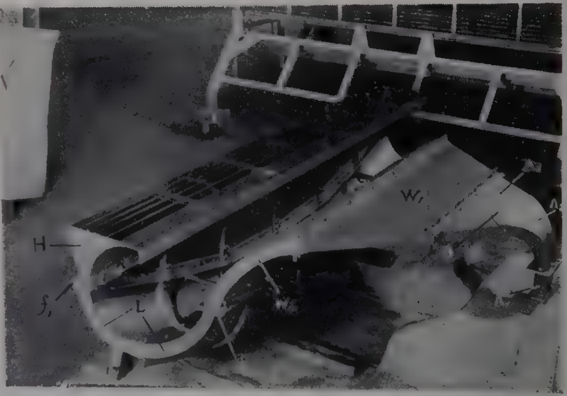

Fig. 2.

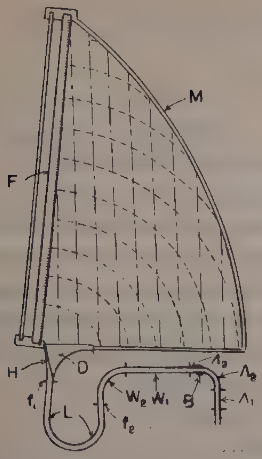

Fig. 3.

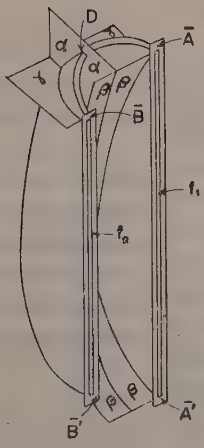

Fig. 4.

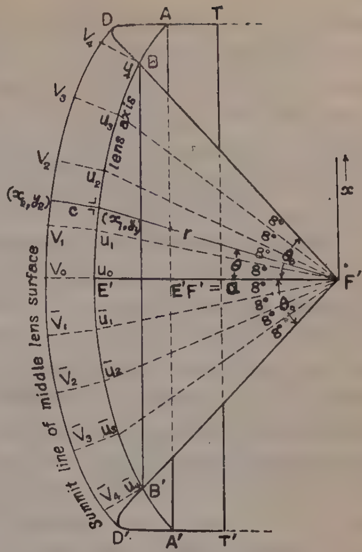

Fig. 5.

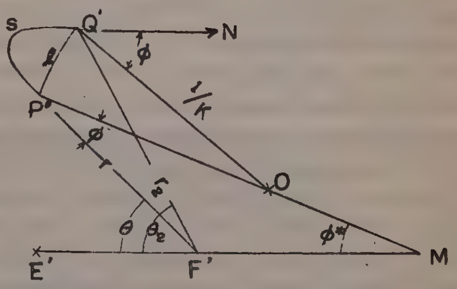

Fig. 6.

through the tapered dielectric lens *D* contained in the horn *H*. The electric field direction of this wave is shown by dotted lines in Fig. 3. This wave is reflected back by parabolic mirror *M* into the plane wave whose electric field direction is shown by chain lines. Since the metallic leaves in the filter *F* placed at the front of the mirror is parallel to the dotted lines, the filter prevents the cylindrical wave from ommission and keep its wave-front form exactly circular, while, since the leaves are nearly perpendicular to the chain lines, the reflected plane wave passes through them with little obstruction. Since reflecting property of the mirror, refracting property of the tapered dielectric lens, and transforming property of the wave form through wave guide lens are independent of frequencies, the reflex electromagnetic horn displays very sharp directivity over an astonishingly wide band of frequencies. Among all requisites hitherto related, the structure and the function of the convex wave guide lens *L* are most important and difficult, hence we shall discuss them hereafter.

§ 2. The Determination of Lens Axis

From the manufacturing point of view it is desirable to make the curved parts of flat confronting wall surfaces of the lens *L* by two curved coaxial cylindrical surfaces with constant radii c_1 and c_2 respectively whose axes are a common slowly curved line on a plane. This line and plane shall be called *lens axis* and *principal plane* respectively. α in Fig. 4 represents the principal plane, and line of the intersection of α and β planes represents the lens axis. The cylindrical surface β in Fig. 4 intersecting perpendicularly with the principal plane α at the lens axis shall be called *axial plane*. The flat wall surfaces of the lens *L* outside the axial plane β are the concentrical curved coaxial cylindrical surfaces just related, while the flat surfaces of the lens *L* inside the axial plane β are two pairs of two confronting parallel planes which are continued with the edges of coaxial curved cylindrical surfaces on the axial plane β on both sides of the principal plane α. The side-walls of the lens *L* are the extensions of the side walls of curved flat wedge tube W_2 along the geodesic lines on the curved flat walls of the lens *L* and continue with side walls of the horn *H*. Fig. 5 is the schematic of the orthogonal projection of the lens L on principal plane α. The orthogonal projections of $\bar{A}, \bar{A}', \bar{B}, \bar{B}'$ on principal plane are expressed by A, A', B, B' in Fig. 5 respectively. Therefore the curve $ABB'A'$ in Fig. 5 expresses the lens axis. The parts of the figure on the left side of the lens axis $ABB'A'$ in Fig. 5 show the orthogonal projections of the middle lens surface (by which we define the surface passing the bisecting points between the confronting curved flat walls of the lens L) on the principal plane. The curve DD' expresses the *summit line of the middle lens surface* of the lens L, while the curves ADB and $A'D'B'$ are the projections of the curved slender side walls of the lens L. If we extend straightly both curves ADB and $A'D'B'$, we get a pair of straight lines BF' and $B'F'$ intersecting at the vertex point F' and another pair of straight lines AT and $A'T'$ which are parallel to the axis of symmetry $F'E'$. The point F' is the orthogonal projection of the center F of the cylindrical wave entering into the lens. Since this wave propagates along geodesic line on the middle lens surface outside the axial plane, we shall first calculates geodesic line on the middle lens surface with the radius c (mean value of c_1 and c_2) whose axis slowly curved with the small curvature k lying on the principal plane. The angular coordinate φ is considered on a plane γ perpendicular to the lens axis in Fig. 4 so that $\varphi=0$ denotes the direction lying on the principal plane directed inside the axial plane. Curvilinear coordinate u is taken along the curved generating line on the curved middle lens surface so that $u=$const. expresses the plane perpendicular to the lens axis and du expresses the line element ds of the generating line when it lies on the axial plane. Then the general line element ds of the middle lens surface is expressed by u, φ-coordinates as follows:

$$(ds)^2=(1-kc\cos\varphi)^2(du)^2+(cd\varphi)^2. \quad (1')$$

Hence the length s of a curve of the curved cylindrical surface is

$$s=\int\sqrt{(1-kc\cos\varphi)^2\left(\frac{du}{d\varphi}\right)^2+c^2d\varphi} \ . \quad (2)$$

If we substitute (2) into Euler-Lagrange's equation in calculus of variation neglecting $kc^2\partial k/\partial u$ as small quantity, we get

$$\frac{d}{d\varphi}\left\{\frac{(1-kc\cos\varphi)^2(du/d\varphi)}{\sqrt{(1-kc\cos\varphi)^2(du/d\varphi)^2+c^2}}\right\}=0\ . \quad (3)$$

Integrating (3) by $d\varphi$ we have

$$du=\frac{\beta c d\varphi}{(1-kc\cos\varphi)\sqrt{(1-kc\cos\varphi)^2-\beta^2}}\ , \quad (4)$$

where β is an integral constant. If by ϕ is expressed the angle of the inclination of the geodesic line with respect to a plane perpendicular to the lens at the intersecting point of the line with the axial plane obtained by integrating (4), there exists

$$\beta=\sin\phi\ . \quad (5)$$

If we expand right-hand side of (4) by binomial theorem and integrate (4) neglecting the quantities of the order of magnitude $(kc)^2$, we get

$$l=[u]_{\varphi=\pi/2}^{\varphi=3\pi/2}=\frac{\beta c}{\sqrt{1-\beta^2}}\int_{\pi/2}^{3\pi/2}\left\{1+\frac{2-\beta^2}{1-\beta^2}\times kc\cos\varphi\right\}d\varphi=\alpha c\left\{\pi-2kc(2+\alpha^2)\right\}\ , \quad (6)$$

where

$$\alpha=\tan\phi\ . \quad (7)$$

If we substitute (4) in (2) and integrate, we have

$$s=[s]_{\pi/2}^{3\pi/2}=\frac{c}{\sqrt{1-\beta^2}}\int_{\pi/2}^{3\pi/2}\left\{1+\frac{kc\beta^2}{1-\beta^2}\cos\phi\right\}d\varphi=c\sqrt{1+\alpha^2}\{\pi-2kc\alpha^2\}\ , \quad (8)$$

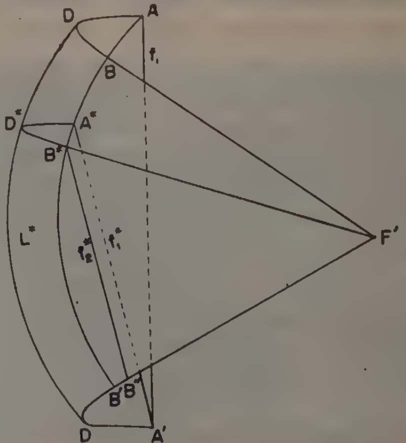

Fig. 7.

which expresses the length of the geodesic line from $\varphi=\pi/2$ to $\varphi=3\pi/2$ along the middle lens surface of the lens L, while l expresses the length of the lens axis between orthogonal projection of both ends of this geodesic line on the principal plane. (*i.e.* $P'Q'$ in Fig. 6.)

We now pick up a wave front which starts from F and travels inclined at an angle θ with the axis FE and reaches the axial plane at the point P, thenceforth propagates along the geodesic line on the curved cylindrical middle surface until the point Q on the axial plane, and afterwards goes towards f_1 perpendicularly to the plane of f_1 in Fig. 4. The orthogonal projection of the path of this wave front on the principal plane is shown in Fig. 6. E', F', P', Q' in Fig. 6 express the projections of E, F, P, Q above related. The point O is the intersection of normals elected at P' and Q' on the lens axis. Hence $OP' = OQ' = 1/k$ approximately. Since the geodesic line is inclined at an angle with the plane orthogonal to the lens axis as already related, it follows that

$$\angle F'P'O = \angle OQ'N = \phi\,, \qquad (9)$$

where $Q'N$ shows the direction parallel to $E'F'$. Since O can approximately be regarded as the center of the curvature of the arc $P'Q'$,

$$\angle P'OQ' = kl\,. \qquad (10)$$

Since $Q'N$ is parallel to $E'F'$, it is evident from Fig. 6 that

$$\theta = 2\phi - kl\,. \qquad (11)$$

Let M be the point of intersection of the elongations of $P'O$ and $F'E'$, and let $\angle E'MP' = \phi^*$, it is clear by Fig. 6 and (11) that

$$\phi^* = (\theta - kl)/2\,. \qquad (12)$$

Let $\angle E'F'Q' = \theta_2$ and $F'Q' = r_2$ as shown in Fig. 6, then the condition that the lengths of every wave paths starting from F via curved middle lens surface to the outlet of the lens L whose orthogonal projection on the principal plane is shown by AA' in Fig. 5 is expressed as follows:

$$r + s + r_2 \cos\theta_2 = \text{const.}\,, \qquad (13)$$

where r expresses the length of $F'P'$ and s expresses the length of the geodesic line from P' to Q' on the middle lens surface. If we regard that the arc $P'Q'$ is circular with its center at O and neglect the quantities of the magnitude $(kl)^2$, we get

$$r_2 \cos\theta_2 = r\cos\theta - l\sin(\theta - \phi + kl/2). \qquad (14)$$

If we substitute (14) in (13) and make use of (11), we have

$$r_2(1+\cos\theta) + s - l\sin(\theta/2) = 2a\,, \qquad (15)$$

where a is a constant. If we substitute (6) in (11) and substitute this result in (7), we get

$$\alpha = \left(\tan\frac{\theta}{2}\right)\left\{1 + \frac{\pi kc}{2}(1+\alpha^2)\right\}. \qquad (16)$$

If we substitute (16) in (6) and (8) and neglect the quantities of the magnitude $(kc)^2$ we have

$$l = \pi c \tan\left(\frac{\theta}{2}\right)\left\{1 + \left(\frac{\pi}{2} - \frac{4}{\pi}\right)kc + \left(\frac{\pi}{2} - \frac{2}{\pi}\right)kc\alpha^2\right\}, \qquad (17)$$

$$s = \pi c \sec\left(\frac{\theta}{2}\right)\left\{1 + \left(\frac{\pi}{2} - \frac{2}{\pi}\right)kc\alpha^2\right\}. \qquad (18)$$

If we substitute (17) and (18) in (15) and neglect the quantities of the magnitude $kc\alpha^2$, we obtain

$$r = \frac{2a}{1+\cos\theta}\left\{\left(1 + \frac{\pi c}{2a}\right) - \frac{\pi c}{2a}\cos\frac{\theta}{2} + \frac{\pi kc^2}{2a}\left(\frac{\pi}{2} - \frac{4}{\pi}\right)\frac{\sin^2(\theta/2)}{\cos(\theta/2)}\right\}. \qquad (19)$$

If we neglect c/a compared with unity, (19) becomes

$$r = 2a/(1+\cos\theta)\,, \qquad (20)$$

which expresses the parabola with its focus at F'. The curvature of (20) is

$$k = (1/2a)\cos^3(\theta/2)\,. \qquad (21)$$

Since the curvature of the curve (19) can approximately be regarded as k given by (21), substituting (21) in (19) we get

$$r = \frac{a}{\cos^2(\theta/2)}\left\{\left(1 + \frac{\pi c}{2a}\right) - \frac{\pi c}{2a}\cos\frac{\theta}{2} + \pi\left(\frac{c}{4a}\right)^2\left(\frac{\pi}{2} - \frac{4}{\pi}\right)\sin^2\theta\right\}, \qquad (22)$$

which is the equation of the lens axis shown by the curve $ABE'B'A'$ in Fig. 5. By putting $\theta = 0$ in (22) we find that a is the length $E'F'$ in Fig. 5.

§ 3. Miscellaneous Consideration

If we choose rectangular x, y-coordinates with its origin at F' and its y-axis on $F'E'$ as shown in Fig. 5, and let by (x_1, y_1) be denoted the coordinates of any U-point on the lens axis $ABB'A'$, there exist the relations

$$x_1 = r\sin\theta\,, \qquad y_1 = r\cos\theta\,. \qquad (23)$$

By (12), (16), (17) and (21) we have

$$\phi^* = \frac{\theta}{2} - \frac{\pi c}{8a}\sin\theta\left\{\cos\frac{\theta}{2} + \frac{c}{a}\left(0.12\sin^2\theta + 0.15\cos^4\frac{\theta}{2}\right)\right\}. \qquad (24)$$

Table 1

θ / c/a	8°		16°		24°		32°	
	x_1/a	y_1/a	x_1/a	y_1/a	x_1/a	y_1/a	x_1/a	y_1/a
0.04	0.13987	0.99525	0.28124	0.98081	0.42565	0.95598	0.57486	0.91991
0.05	0.13987	0.99525	0.28129	0.98101	0.42582	0.95634	0.57523	0.92050
0.06	0.13987	0.99530	0.28135	0.98120	0.42598	0.95671	0.57565	0.92118
0.07	0.13988	0.99530	0.28140	0.98139	0.42614	0.95707	0.57597	0.92169
0.08	0.13988	0.99535	0.28143	0.98149	0.42630	0.95744	0.57634	0.92228
0.09	0.13989	0.99540	0.28146	0.98158	0.42643	0.95771	0.57666	0.92279
0.10	0.13989	0.99540	0.28151	0.98178	0.42659	0.95808	0.57708	0.92347
0.11	0.13989	0.99545	0.28159	0.98206	0.42675	0.95844	0.57745	0.92407
0.12	0.13990	0.99550	0.28162	0.98216	0.42687	0.95872	0.57782	0.92466
0.13	0.13990	0.99555	0.28168	0.98235	0.42708	0.95918	0.57820	0.92525
0.14	0.13991	0.99560	0.28170	0.98245	0.42720	0.95945	0.57851	0.92576
0.15	0.13991	0.99560	0.28176	0.98264	0.42736	0.95981	0.57894	0.92644
0.16	0.13992	0.99565	0.28181	0.98283	0.42757	0.96027	0.57936	0.92712

Table 2

θ / c/a	8°		16°		24°		32°	
	x_2/a	y_2/a	x_2/a	y_2/a	x_2/a	y_2/a	x_2/a	y_2/a
0.04	0.14258	1.03516	0.28664	1.02045	0.43371	0.99516	0.58557	0.95845
0.05	0.14322	1.04513	0.28798	1.03056	0.43583	1.00533	0.58852	0.96870
0.06	0.14387	1.05512	0.28932	1.04067	0.43789	1.01552	0.59148	0.97906
0.07	0.14450	1.06520	0.29062	1.05078	0.43994	1.02570	0.59430	0.98925
0.08	0.14511	1.07518	0.29187	1.06080	0.44193	1.03590	0.59713	0.99953
0.09	0.14572	1.08526	0.29311	1.07082	0.44388	1.04600	0.59988	1.00975
0.10	0.14631	1.09524	0.29436	1.08095	0.44581	1.05621	0.60268	1.02014
0.11	0.14690	1.10523	0.29560	1.09117	0.44774	1.06642	0.60539	1.03046
0.12	0.14747	1.11531	0.29676	1.10120	0.44956	1.07656	0.60807	1.04078
0.13	0.14803	1.12529	0.29793	1.11134	0.45148	1.08687	0.61071	1.05112
0.14	0.14858	1.13537	0.29905	1.12137	0.45324	1.09701	0.61320	1.06139
0.15	0.14911	1.14536	0.30016	1.13150	0.45499	1.10724	0.61582	1.07184
0.16	0.14965	1.15535	0.30131	1.14163	0.45682	1.11757	0.61838	1·08229

If we denote the coordinates of V by (x_2, y_2) which expresses the intersecting point of the summit line of middle lens surface with the normal to the lens axis at U on Fig. 5, since the normal at U is of the length c and inclined at angle ϕ^* with y-axis, there exist

$$x_2=x_1+c\sin\phi^*\,,\quad y_2=y_1+c\cos\phi^*\,. \quad (25)$$

The values of x_1/a, y_1/a; x_2/a, y_2/a are evaluated by using (22), (23), (24) and (25) are given in Table 1 and Table 2 for various ratios of c/a and for $\theta=8°, 16°, 24°, 32°$, from which the coordinates of two set of the points U_1, U_2, U_3, U_4 and the points V_1, V_2, V_3, V_4 in Fig. 5 are determined. It is evident that $x_1/a=0$, $y_1/a=1$; $x_2/a=0$, $y_2/a=1+c/a$ for $\theta=0$ and for any ratio of c/a.

The practical forms of the lens axis $ABB'A'$ is designed by connecting two neighbouring U-points in Fig. 5 by the circular arcs whose radii are all equal to the mean radius of curvature over all range $ABB'A'$. The practical form of the summit line of the middle lens surface DD' is designed by the similar method. This method is theoretically incorrect. But since the curves thus obtained approximate true curves very well, this method is adapted to the practical design of the convex wave guide lens L fitted to mass production.

If v denotes the height from the plane γ orthogonal to the lens axis passing through the point $\overline{B}$ in Fig. 4, v is nearly equal to the value s obtained by integrating (1) with respect to du keeping $d\varphi=0$. Hence

$$v=(1-kc\cos\varphi)u\,, \quad (26)$$

where

$$u=\alpha c\{\varphi^*-2kc(2+\alpha^2)\}\sin^2(\varphi^*/2)\,, \quad (27)$$

which is obtained by integrating (4) with respect to $d\varphi$ from $3\pi/2$ to φ neglecting the quantities of the magnitude $(kc)^2$. φ^* in (27) is combined with φ in (6) by $\varphi^*=(3\pi/2)-\varphi$. Hence $\varphi^*=0, \pi/2, \pi$ express the directions of the points $\overline{B}$, D, $\overline{A}$ viewed from lens axis in Fig. 4 respectively. If we substitute (16), (21) and (27) in (26), we get

$$v=c\varphi^*\left(\tan\frac{\theta_0}{2}\right)\left[1+\frac{\pi c}{4a}\cos\frac{\theta_0}{2}\right.$$
$$+\frac{c}{2a}\cos^3\left(\frac{\theta_0}{2}\right)\sin\varphi^*-\frac{c}{a}\cos\left(\frac{\theta_0}{2}\right)$$
$$\left.\times\left\{2\cos^2\left(\frac{\theta_0}{2}\right)+\sin^2\left(\frac{\theta_0}{2}\right)\right\}\frac{\sin^2(\varphi^*/2)}{\varphi^*}\right], \tag{28}$$

where θ_0 is the angle of inclination of the side walls of wedge tubes W_1 and W_2 with their axes.

The symmetric wave guide lens related above has a fault that reflected wave generated at the lens D in Fig. 3 returns into the throat of the flat wedge tube W_1 and thence travels back into feeding wave guide. This fault can be avoided by asymmetric wave guide lens whose schematic figure corresponding to Fig. 5 in the case of symmetric wave guide lens is shown in Fig. 7. The figure enclosed by $A^*D^*B^*B''D'A'$ represents the orthogonal projection of the middle lens surface of asymmetric lens L^*, and f_1^* and f_2^* are the orthogonal projections of the franges of the lens L^*. Reflected wave generated at the lens D in Fig. 3 passes f_1^* in the same phase and returns back into flat wedge tube W_1 inclined to one side wall of W_1. This wave incident on this wall and reflected towards another side wall of W_1. After the reflection on another side wall of W_1 the wave travels towards the lens L^* and does not enter into the feeding wave guide. The apperatus shown in Fig. 1 and Fig. 2 was manufactured by Model Shop Division in Electrical Communication Laboratory. I express my gratitude who engaged in this task.

Reference

1) H. T. Fris: Microwave Repeater Research, B. S. T. J. **27** (1948) 204.

JOURNAL OF THE PHYSICAL SOCIETY OF JAPAN Vol. 8, No. 3, MAY—JUNE, 1953

Hyperfine Structure of the Spectrum of Gadolinium

By Shigeki SUWA

Institute of Science and Technology, Komaba-machi, Meguro-ku, Tokyo

(Received December 17, 1952)

The hyperfine structures of 32 lines of Gd I and 2 lines of Gd II in the visible region were measured. They could be interpreted as due to the isotope displacement effect of the even isotopes (156, 158 and 160) and the splittings due to the nuclear magnetic moments of the odd isotopes (155 and 157). The ratio of the isotope displacements $\varDelta(158-156)/\varDelta(160-158)=0.97\pm0.06$ was determined. The relative isotope displacement $\varDelta(160-158)$ in some 30 terms of Gd I is tabulated.

§ 1. Introduction

The hyperfine structure (hfs) of the Gd spectrum was first reported by Klinkenberg[1] and was interpreted as due to the isotope shift. Brix and Engler[2] studied the isotope effect in the Gd I spectrum and confirmed that the anomalously large isotope effects in the spectra of Ce, Sm and especially Eu are not due to the $4f^n$-complex but due to anomaly in the nuclear property. The extensive classification of the Gd I and Gd II spectra by Russell[3] has made the study of the hfs of the gadolinium worth while.

In order to investigate the isotope shift in the Gd I spectrum and, if possible, to determine the nuclear spins and the magnetic moments of the odd nuclei Gd^{157} and Gd^{155}, the study of the hfs of Gd in the visible region was undertaken. A brief account of the author's findings was reported previously.[4]

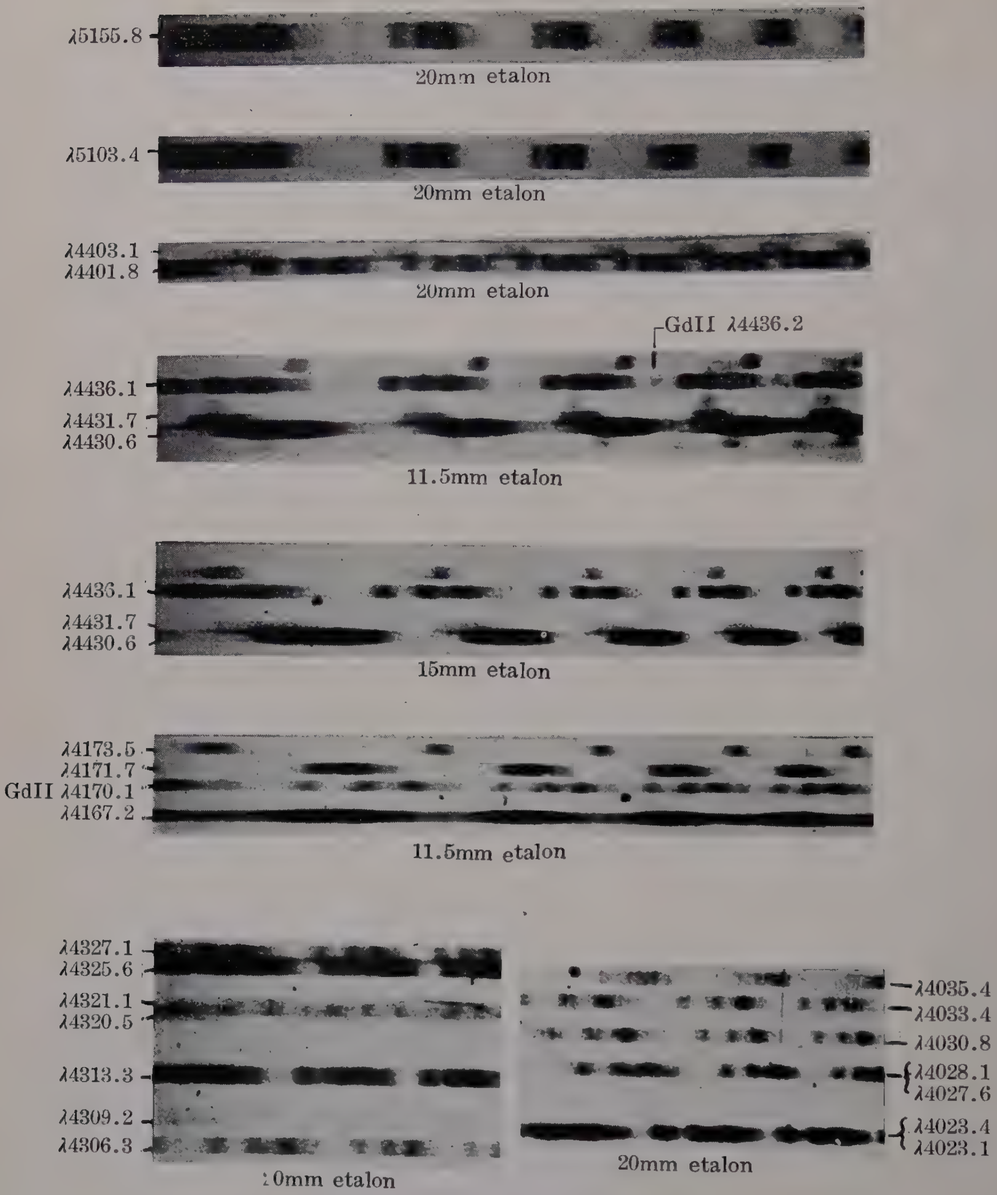

Fig. 1. Enlargement of interference patterns of the spectrum of Gd.

§ 2. Experimental Arrangement

The spectrum was excited by the use of a water-cooled aluminium hollow cathode which was coated with gadolinium oxide of about 20 mg. Neon of a few mm Hg pressure was continuously circulated, the discharging current being 20 to 50 mA. The hfs was examined with a Fabry-Pérot etalon. Interference patterns of some lines are reproduced in Fig. 1.

§ 3. Results

A large number of lines were observed to have hfs which could be interpreted to be due to the displacement effect of the even isotopes (156, 158 and 160) and the splittings caused by the nuclear magnetic moments of the odd isotopes (155 and 157), and they were classified qualitatively into three types. As an example of each of the three types, the hfs of the lines λ4401.8($a^9D_6-y^9F_6$), λ3987.8 ($a^9D_2-z^{11}G_1$) and λ5103.4($a^{11}F_7-z^{11}G_8$) are shown schematically in Fig. 2. λ4401.8 consists of four well resolved components. This type of the hfs will be denoted by type *A*.

Since natural gadolinium is known$^{5)}$ to consist of Gd^{160} (21.8%), Gd^{158} (24.8%), Gd^{157} (15.7%), Gd^{156} (20.6%), Gd^{155} (14.9%) and Gd^{154}(2.2%), the four components were correlated to the isotopes as shown in Fig. 2 (*A*). The Gd^{157} component is superposed on the Gd^{156} component and both of the splittings of Gd^{157} and Gd^{155} are negligibly small in the lines of this type. The line λ3987.8 has a similar structure to that of type *A* except that its fourth (most refrangible) component due to Gd^{155} has a little broadened structure. In the lines having the structure of this type (denoted by *B* in the following), a slight splitting of the Gd^{157} components was also observed. In λ5103.4 and other lines whose structure will be denoted by type *C*, the fourth component appeared as a weak tail broadened continuously from the Gd^{156} component towards higher frequency side and unresolved weak background was observed between the components of Gd^{158} and Gd^{156}. This is shown schematically in Fig. 2 (*C*) and the position of the edge of the tail is also shown.

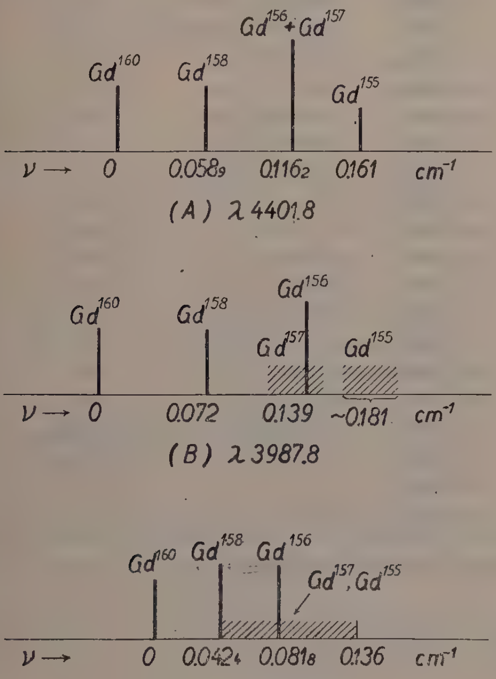

(C) λ 5103.4

Fig. 2. Hfs of Gd I lines λ 4401.8 ($a^9D_6-y^9F_6$), λ3987.8 ($a^9D_2-z^{11}G_1$) and λ5103.4 ($a^{11}F_7-z^{11}G_8$)

In every line the Gd^{154} component could not be detected, being masked by the component of Gd^{155}. Any other type of the hfs (e.g. the structure in which the sign of the isotope displacement was inverted) was not found in the Gd I spectrum.

The hfs of 32 Gd I lines and two Gd II lines that were measured are listed in Table 1 and Table 2 respectively.

For determining the ratio of the isotope displacement $R=\Delta(158-156)/\Delta(160-158)$, the lines of type *C* are most suited, since the density of the components due to Gd^{157} and Gd^{155} is comparatively small in these lines and the disturbing effect of these odd isotopes on the position of Gd^{156} may be assumed to be relatively small. The values of the ratio obtained in some lines are listed in Table 3. The weighted mean of the values in Table 3 gives

$$R=\Delta(158-156)/\Delta(160-158)=0.97\pm0.06\ ,$$

where disturbance of the odd isotopes is roughly taken into account in assigning the limit of uncertainty.

In Table 4 the isotope displacement effect $\Delta(160-158)$ in the Gd I terms that can be derived from Table I is given, where the origin of the displacement is located at the term $4f^75d^26p\ z^{11}G_9$. The displacement effect $\Delta(158-156)$ can be derived from Table 4 by use of the ratio *R*.

From the broadening of the components due to the odd isotopes in the line λ5015.0 and the consideration of their centres of gravity, the magnetic moments of the odd isotopes were estimated as follows:

$$|\mu(\text{Gd}^{157})|=0.3\pm0.2\ \text{nm}$$
$$|\mu(\text{Gd}^{155})|=0.2_5\pm0.15\ \text{nm}\ ,$$

although the signs of the magnetic moments and the spins for both isotopes could not be determined. A detailed discussion of these magnetic moments will be published in the future.

In conclusion the writer wishes to express his sincere thanks to Professor K. Murakawa for helpful consultations throughout the work. He would also like to appreciate the kindness of Professor J. E. Mack who supplied the very pure sample of gadolinium which was used in the present work.

Note added in Proof

After submitting the present paper, the papers of P. Brix (Zeits. f. Phys. **132** (1952) 579) and P. Brix and H. D. Engler (Zeits. f. Phys. **133** (1952)

Table 1. Hfs of the spectrum of Gd I

λ	Combination	Hfs (cm^{-1})					Type**
		Gd^{160}	Gd^{158}	$Gd^{156}+x$*	Gd^{155}		
6114.0	$a\,^9D_6-z\,^9F_6$	0	+0.037	+0.074	+0.118§		*C* (or *B*)
5643.2	$a\,^9D_3-z\,^9F_4$	0	+0.038	+0.073			*C*
5617.9	$a\,^9D_2-z\,^9F_3$	0	+0.037	+0.072	+0.115§		*C*
5307.3	$a^{11}F_5-z^{11}G_5$	0	+0.035	+0.071			*C*
5301.6	$a^{11}F_6-z^{11}G_6$	0	+0.034	+0.069			*C*
5283.0	$a^{11}F_7-z^{11}G_7$	0	+0.040	+0.080			*C*
5251.1	$a^{11}F_8-z^{11}G_8$	0	+0.042	+0.083			*C*
5197.7	$a^{11}F_5-z^{11}G_6$	0	+0.039	+0.076			*C*
5155.8	$a^{11}F_6-z^{11}G_7$	0	$+0.041_1$	$+0.080_5$	+0.129§		*C*
5103.4	$a^{11}F_7-z^{11}G_8$	0	$+0.042_4$	$+0.081_8$	+0.136§		*C*
5015.0	$a^{11}F_8-z^{11}G_9$	0	$+0.043_3$	$+0.085_4$	+0.143§		*C*
4647.6	$a\,^9D_6-z\,^9D_6$	0	+0.047	+0.093	∼+0.130		*B*
4497.1	$a\,^9D_5-z\,^9D_6$	0	+0.047	+0.092	∼+0.130		*B*
4486.8	$a\,^9D_6-y\,^9F_5$	0	$+0.056_0$	$+0.110_0$	+0.154		*A*
4436.1		0	+0.074	+0.143	+0.192	+0.233	*B*
4401.8	$a\,^9D_6-y\,^9F_6$	0	$+0.058_9$	$+0.116_2$	+0.161		*A*
4373.8	$a\,^9D_4-y\,^9F_3$	0	$+0.058_2$	$+0.110_7$	+0.157		*A*
4327.1	$a\,^9D_2-y\,^9F_1$	0	+0.059	+0.113	∼+0.155		*B*
4325.7	$a\,^9D_4-y\,^9F_4$	0	+0.058	+0.112	+0.155		*A*
4306.3	$a\,^9D_2-y\,^9F_2$	0	+0.059	+0.114	∼+0.156		*B*
4266.6	$a\,^9D_5-y\,^9F_6$	0	∼+0.058	∼+0.115			*A*
4260.1	$a\,^9D_4-y\,^9F_5$	0	+0.057	+0.110	∼+0.149		*B* (or *A*)
4225.8	$a\,^9D_6-y\,^9F_7$	0	+0.058	+0.112	∼+0.161		*A*
4100.2	$a\,^9D_5-18_5$	0	+0.065	+0.126	∼+0.171		*B*
4033.4	$a\,^7D_4-x\,^7F_5$	0	+0.061	+0.116	∼+0.160		*B* (or *A*)
4019.7	$a\,^9D_4-z^{11}G_3$	0	+0.066	+0.131	∼+0.186		*B*
4008.3	$a\,^9D_5-z^{11}G_5$	0	+0.079	+0.150	∼+0.207		*B*
4006.9	$a\,^9D_3-z^{11}G_2$	0	+0.066	+0.132	∼+0.181		*B*
3987.8	$a\,^9D_2-z^{11}G_1$	0	+0.072	+0.139	∼+0.181		*B*
3974·8	$a\,^9D_6-z^{11}G_7$	0	+0.087	+0.162	∼+0.223		*B*
3972.7	$a\,^9D_2-z^{11}G_2$	0	+0.067	+0.129			*B*
3969.0	$a\,^9D_3-z^{11}G_3$	0	+0.066	+0.129	∼+0.178		*B*

* x indicates the superposition of the components due to Gd^{157} (and possibly due to Gd^{155} in the case of type *C*).

** See text.

§ The edge on the high frequency side is shown.

Table 2. Hfs of the spectrum of Gd II

λ	Combination	Hfs (cm^{-1})				Type**
		Gd^{160}	Gd^{158}	$Gd^{156}+x$*	Gd^{155}	
4215.0	$a\,^8S_{7/2}-z^{10}F_{9/2}$	0	+0·091	∼+0.174		*B*
4170.1	$a\,^8S_{7/2}-\quad 3_{7/2}$	0	+0.113	+0.211	∼+0.297	*B*

* x indicates the superposition of the components due to Gd^{157}.

** See text.

Table 4. Isotope displacement effect in the terms of Gd I.

Term		$\Delta(\mathrm{Gd}^{160}-\mathrm{Gd}^{158})$* (cm^{-1})
$4f^75d6s^2$	$a\,^9D_6$	0.090
″	$a\,^9D_5$	0.091
″	$a\,^9D_4$	0.091
″	$a\,^9D_3$	0.091
″	$a\,^9D_2$	0.092
$4f^75d^26s$	$a^{11}F_8$	0.043
″	$a^{11}F_7$	0.043
″	$a^{11}F_6$	0.044
″	$a^{11}F_5$	0.049
$4f^75d6s6p$	$z\,^9F_6$	0.053
″	$z\,^9F_4$	0.054
″	$z\,^9F_3$	0.056
$4f^75d6s6p$	$z\,^9D_6$	0.043
$4f^75d^26p$	$z^{11}G_9$	0.000**
″	$z^{11}G_8$	0.001
″	$z^{11}G_7$	0.003
″	$z^{11}G_6$	0.009
″	$z^{11}G_5$	0.013
″	$z^{11}G_3$	0.025
″	$z^{11}G_2$	0.025
″	$z^{11}G_1$	0.020
	$y\,^9F_7$	0.032
	$y\,^9F_6$	0.031
	$y\,^9F_5$	0.034
	$y\,^9F_4$	0.033
	$y\,^9F_3$	0.033
	$y\,^9F_2$	0.033
	$y\,^9F_1$	0.033
	18_5	0.028

* The + sign indicates that the Gd^{160}-level is higher than the Gd^{158}-level.
** assumed.

Table 3.

λ	$\frac{\Delta(158-156)}{\Delta(160-158)}$	λ	$\frac{\Delta(158-156)}{\Delta(160-158)}$
5015.0	0.97	5197.7	0.9_5
5103.4	0.93	5251.1	0.9_7
5155.8	0.96	5283.3	1.0_0
		6114.0	1.0_0

362) appeared. They studied also the isotope effect in the spectra of Gd I and Gd II. Except in λ4008.3, λ3987.8 and λ3974.8, their results agree with those of the present author (within the accuracy of measurement) in the lines which were measured by the present author and the above-mentioned German authors.

References

1) P. F. A. Klinkenberg: Physica **12** (1946) 33.

2) P. Brix u. H. D. Engler: Naturwiss. **38** (1951) 214.

3) H. N. Russell: J. Opt. Soc. Am. **40** (1950) 550.

4) S. Suwa: Phys. Rev. **86** (1952) 247.

5) D. C. Hess, Jr.: Phys. Rev. **74** (1948) 773.

Journal of the Physical Society of Japan Vol. 8, No. 3, May—June, 1953

On Some Regularities in the Isotope Effect in the Spectrum of Lead. Part II.

By Kiyoshi Murakawa

Institute of Science and Technology, Komaba-machi, Meguro-ku, Tokyo

(Received January 28, 1953)

The hyperfine structures of the Pb I lines λλ 5201, 5005, 7228, 4168, 4062, 4020, 3740, 3672, 3573, 4058, 2873, 3683, 3640, 2833 and Pb II lines λλ 6660, 4386.4, 5042.5, 4153 and Pb III line λ 4182.5 were measured, and the ratio of the distances of the adjacent even isotope components $\Delta\nu(206-204)/\Delta\nu(208-206)$ was determined to be 0.905 ± 0.010. The ratio $\Delta\nu(207-206)/\Delta\nu(208-207)$ was found to be constant for all lines (except λ 4062) within experimental error and was found to be 0.615 ±0.008. The anomaly found in the case of λ 4062 is interpreted to be due to a perturbation.

§ 1. Introduction

In a previous paper¹⁾ the author described the regularities existing in the isotope effect in the spectra of heavy elements, and full details concerning the hyperfine structure (hfs) of mercury²⁾, lead³⁾, tungsten⁴⁾ and osmium⁵⁾ spectra were published. The work of reference 3 will be referred to as Part I.* Papers treating the hfs of the lead spectrum from the same point of view as Part I were published by Manning, Anderson and Watson⁶⁾ (to be referred to as MAW) and by Geiger⁷⁾ (to be referred to as GE). MAW used a sample enriched in Pb^{204} and GE used two samples enriched in Pb^{204} and Pb^{207} respectively.

While engaged in the study of the hfs of other spectra, the author obtained plates on which the lead spectrum appeared as impurity lines and on which Pb^{204} component appeared with better resolution than Part I, and this gave the author an opportunity of reviewing the data presented in Part I.

§ 2. Experimental Arrangement

Besides the plates mentioned in § 1, many plates recording the hfs of the lead spectrum were taken. The hollow cathode discharge tube used by the author in 1932⁸⁾ in the study of the lead spectrum (this work will be referred to as MU) was modified so as to be cooled with liquid air. A Fabry-Perot etalon was used for resolving the hfs.

Fig. 1 is a reproduction of some of the interference patterns of the lead spectrum.

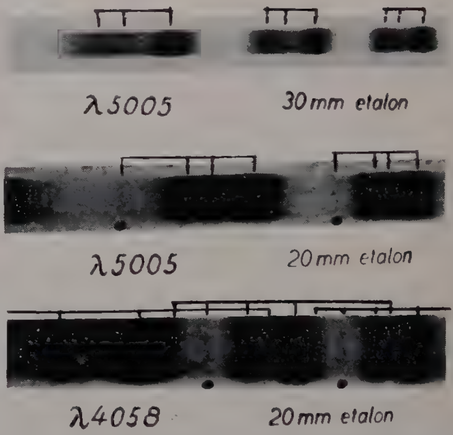

Fig. 1. Enlargement of some interference patterns of the spectrum of lead.

§ 3. Results

We are interested in the ratio of the distances of the neighbouring even isotope components, namely

$$R=\Delta\nu(Pb^{204}—Pb^{206})/\Delta\nu(Pb^{206}—Pb^{208})$$

and the ratio

$$R'=\Delta\nu(Pb^{206}—Pb^{207})/\Delta\nu(Pb^{207}—Pb^{208}) .$$

In order to determine the values of R and R', the hfs of the lines in the visible region and of some lines in the ultra-violet region were measured. Figs. 2–11 show the result of the measurements, the same type of expression as in the case of Part I being used⁹⁾. Under each structure diagram, the transition

---

* Dr. Geiger kindly made the author aware of an error of calculation in Part I. The value of R' of Pb II λ5372 (Fig. 2) should read 0.624 instead of 0.635.

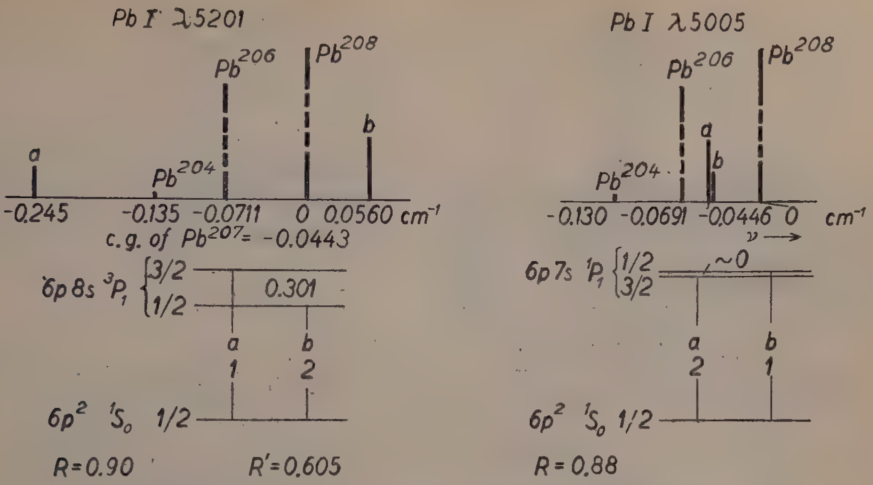

Fig. 2. Hfs of the Pb I lines ending on the term $6p^2$ $^1S_0$.

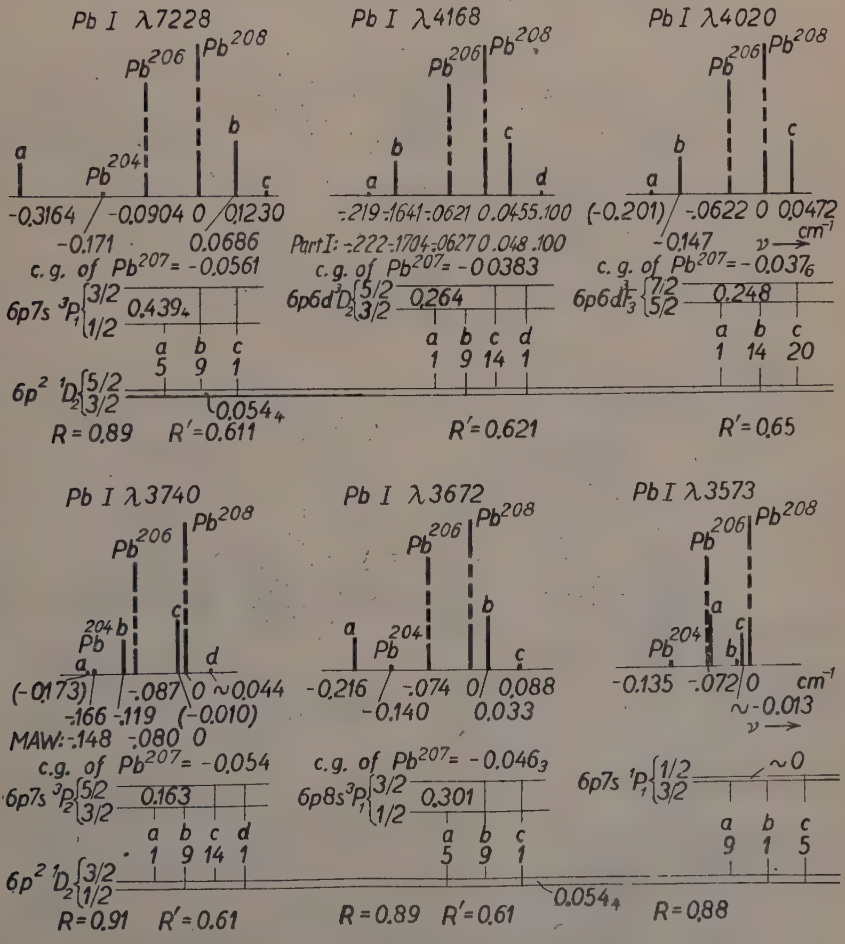

Fig. 3. Hfs of the Pb I lines ending on the term $6p^2$ $^1D_2$.

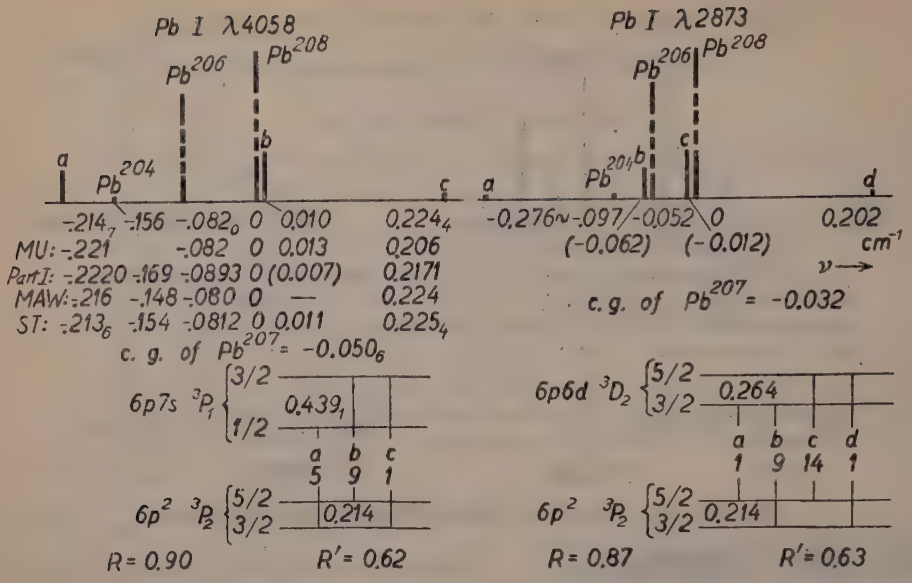

Fig. 4. Hfs of the Pb I lines ending on the term $6p^2\ ^3P_2$.

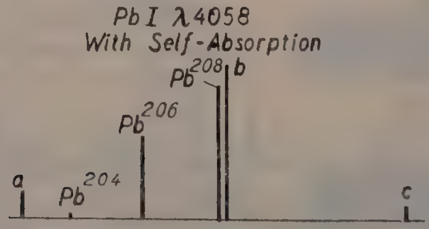

Fig. 5. Modification of the intensity distribution of the hfs of λ4058.

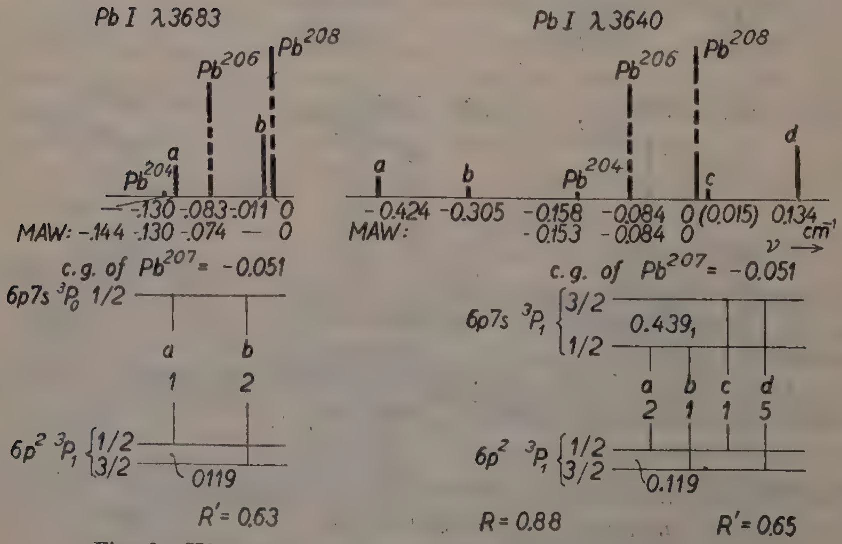

Fig. 6. Hfs of the Pb I lines ending on the term $6p^2\ ^3P_1$.

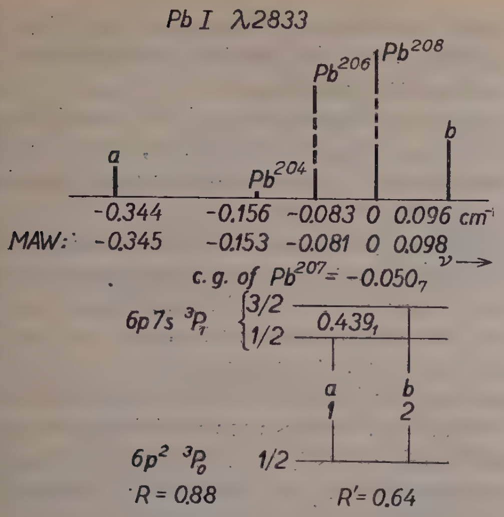

Fig. 7. Hfs of the Pb I line ending on the term $6p^2\ ^3P_0$.

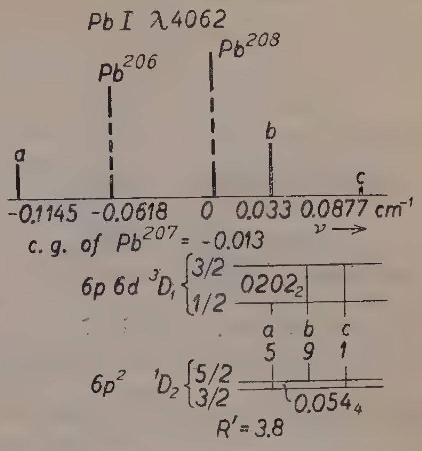

Fig. 8. Hfs of the line Pb I λ4062.

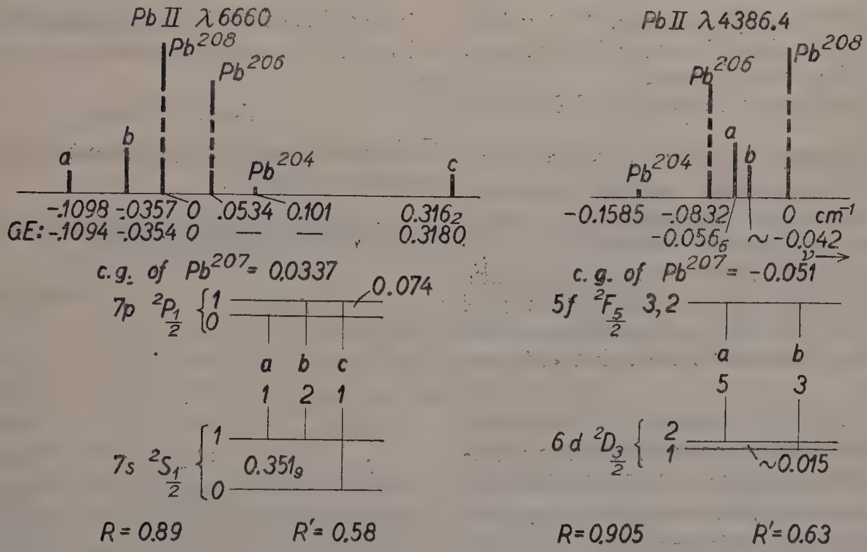

Fig. 9. Hfs of the two Pb II lines.

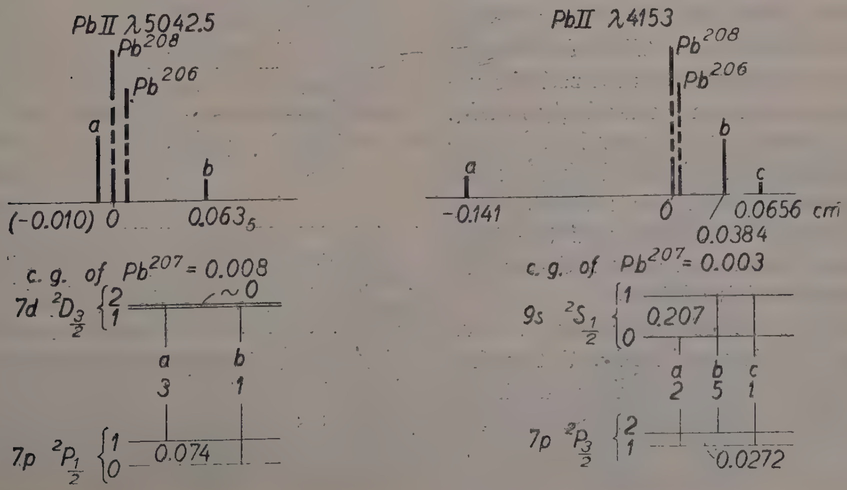

Fig. 10. Hfs of Pb II lines with unresolvable isotope effect.

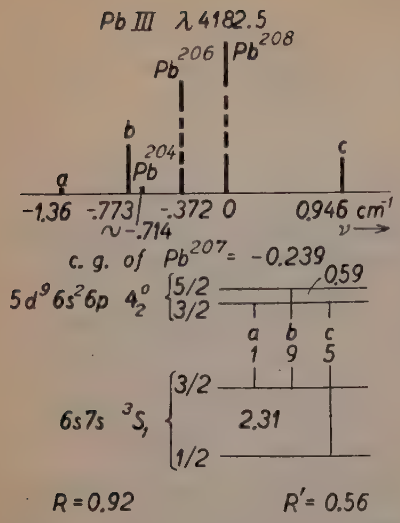

Fig. 11. Hfs of the line Pb III λ4182.5.

scheme for Pb^{207} ($I=1/2$) is given. The values of R and R' are given for each line (where possible) at the bottom space.

Some remarks may be mentioned for some of the lines.

λλ5201 and 5005. These two lines* lie in the region in which the resolving power of the etalon is good, and the accuracy is better than the lines in the violet region.

λλ7228 and 4168. λ4168 was more carefully measured than in Part I. The splitting of the term $p^2\ {}^1D_2$ for Pb^{207} obtained from λ4168 is now in good agreement with that obtained from λ7228.

λ4058. In 1932 MU resolved the component b from the Pb^{208} component. However afterwards when the diameter of tbe hollow cathode was narrowed, fhe resolution disappeared. In the present work many pictures were taken, using zinc hollow cathode which contained lead as an impurity; and the result in 1932 could be reproduced. The hfs given in Part I can now be interpreted as a self-absorption structure, as shown qualitatively in Fig. 5. The component b could now be recognized as an unsymmetrical broadening of the Pb^{208} component,** and the structure was measured, keeping the splitting of the term $p^2\ {}^3P_2$ in mind which splitting had been determined from the hfs of λ2873.

λ2833. The result of the author's own measurement is shown in Fig. 7 together with that of MAW. Both measurements are in good agreement within experimental error.

λ4062. This line has an unusual value of R'. Since the initial term $6p6d\ {}^3D_1$ is only 9 cm^{-1} apart from the term $6p6d\ {}^3F_2$, the anomaly must be due to a perturbation due to the term $6p6d\ {}^3F_2$.

λ5042.5. The splitting of the term $7d\ {}^2D_{3/2}$ in Pb^{207}, if it is not perturbed, should practically vanish. In the present work this has been assumed to be the case.

λ4182.5. In general the hfs components of the Pb III lines are somewhat more diffuse than those of Pb I and Pb II lines. Therefore the measurement of this line has only a poor accuracy. The component a was measured only on plates taken by a 2 mm etalon.

Summing the data presented in the present paper and in Part I, we may assume R to be constant for every Pb line within experimental error and the best value of R seems to be:

$$R=0.905\pm0.010\,.$$

The value of R' is also constant for nearly all the Pb lines and the weighted mean value is

$$R'=0.615\pm0.008\,.$$

This is in complete agreement with the value deduced in Part I.

Table I. Isotope displacement effect in the terms of Pb I.

Term		$\Delta\nu(208-206)$ cm^{-1}
$6p^2$	${}^3P_0$	0.007
	${}^3P_1$	0.006
	${}^3P_2$	0.008
	${}^1D_2$	0.000
	${}^1S_0$	0.003
$6p7s$	${}^3P_0$	0.089
	${}^3P_1$	0.090
	${}^3P_2$	0.087
	${}^1P_1$	0.072
$6p8s$	${}^3P_1$	0.074
$6p6d$	${}^3D_1$	0.062
	${}^3D_2$	0.062
	${}^3F_2$	0.062

---

* Schüler [10] published the hfs of the lead lines λ5005, etc. Unfortunately his data are not accurate enough to be adopted in the discussion of the regularities mentioned in the present work.

** After the manuscript of the present paper had been written, the work of Steudel[12] (to be referred to as ST) appeared. Using a sample that contained only Pb^{208} and Pb^{206} as well as ordinary lead sample, he measured the hfs of λ4058 accurately. The result of his measurement is shown in Fig. 4 of the present paper as ST

Finally we can assume, according to Rosenthal and Breit[11] that the isotope displacement effect is very small for the terms of the configuration $6p^2$. Assuming that in the term $6p^2\ {}^1D_2$ the isotope effect vanishes, isotope displacement effect $\Delta\nu(208\text{–}206)$ in the terms of Pb I are tabulated in Table I. The level for Pb^{208} lies higher than that for Pb^{206}. $\Delta\nu(206\text{–}204)$ can be calculated from Table I by using the value of R.

References

1) K. Murakawa: Phys. Rev. **78** (1950) 480.
2) K. Murakawa and S. Suwa: Jour. Phys. Soc. Japan **5** (1950) 429.
3) K. Murakawa and S. Suwa: Jour. Phys. Soc. Japan **5** (1950) 382.
4) J. A. Vreeland and K. Murakawa: Phys. Rev. **83** (1951) 229.
K. Murakawa: Jour. Phys. Soc. Japan **8** (1953) in press.
5) S. Suwa: Phys. Rev. **83** (1951) 1258.
6) T. E. Manning, C. E. Anderson and W. W. Watson: Phys. Rev. **78** (1950) 417.
7) F. E. Geiger: Doctoral Thesis, University of Wisconsin (1950).
8) K. Murakawa: Sci. Papers Inst. Phys. Chem. Res. **18** (1932) 191.
9) The classification of Pb I, Pb II and Pb III spectra was given by H. Gieseler and W. Grotrian (Zeits. f. Physik **39** (1926) 377), L. T. Earls and R. A. Sawyer (Phys. Rev. **47** (1935) 115) and A. M. Crooker (Canad. Jour. Res. **14** (1936) 115) respectively.
10) H. Schüler u. E. G. Jones: Zeits. f. Physik **75** (1932) 563.
11) J. Rosenthal and G. Breit: Phys. Rev. **41** (1932) 459. G. Breit: Phys. Rev. **42** (1932) 348.
12) A. Steudel: Zeits. f. Physik **133** (1952) 438.

JOURNAL OF THE PHYSICAL SOCIETY OF JAPAN Vol. 8, No. 3, MAY—JUNE, 1953

On Vortex-Equation in Isentropic Flow

By M. Z. v. Krzywoblocki

University of Illinois and
U. S. Naval Ordnance Test Station, China Lake, California

(Received December 13, 1952)

§1. Introduction

Ringleb[1] derived the equation of vortex in an isentropic flow in the hodograph plane. In the present note the author re-derives the equation of vortex in identical flow conditions-which equation differs from that obtained by Ringleb. No attempt was done to reproduce the Ringleb derivation (who cites only the result). The equation of vortex is transformed back onto the physical plane. The Ringleb equation has the form:

$$\psi=C\left[\frac{1}{2}\ln\frac{(1-(1-\alpha w^2)^{1/2})}{(1+(1-\alpha w^2)^{1/2})}+(1-\alpha w^2)^{1/2}\right.$$
$$\left.+\frac{1}{3}(1-\alpha w^2)^{3/2}+\frac{1}{5}(1-\alpha w^2)^{5/2}\right]+C'\ .$$

The way of reasoning is preserved identical to that one in Ringleb's paper.

§2. Derivation of Equations

By means of the well-known transformation of a compressible isentropic flow ($p=\sigma\rho^k$) from the physical $\{x,y\}$-plane onto the hodograph $\{w,\ \theta\}$-plane, under the assumption that the streamfunction ψ in the hodograph plane depends only upon the w-coordinate, Ringleb [*p.* 190] obtained the following equation:

$$w^2(1-\alpha w^2)\psi''+w(1-\beta w^2)\psi'=0, \qquad (1)$$

with

$$\alpha=(2c_0^2)^{-1}(k-1),\ \ \beta=(2c_0^2)^{-1}(k-3),$$
$$\psi'=d\psi/dw, \qquad c_0^2=kRT_0. \qquad (1a)$$

The following relations from Ringleb's paper will be used:

$$\rho_0^{-1}\rho=(1-\alpha w^2)^{1/(k-1)}; \qquad w^2=u^2+v^2;$$
$$\tan\theta=v/u; \qquad (2)$$

$$x_{,w}=w^{-1}\varphi_{,w}\cos\theta-\rho_0\rho^{-1}w^{-1}\psi_{,w}\sin\theta; \qquad (3a)$$

$$x_{,\theta}=w^{-1}\varphi_{,\theta}\cos\theta-\rho_0\rho^{-1}w^{-1}\psi_{,\theta}\sin\theta; \qquad (3b)$$

$$y_{,w}=w^{-1}\varphi_{,w}\sin\theta+\rho_0\rho^{-1}w^{-1}\psi_{,w}\cos\theta; \qquad (3c)$$

$$y_{,\theta}=w^{-1}\varphi_{,\theta}\sin\theta+\rho_0\rho^{-1}w^{-1}\psi_{,\theta}\cos\theta, \qquad (3d)$$

where the symbol φ denotes the potential function. The potential and stream functions are interconnected by the relations (Ringleb, p. 187):

$$\varphi_{,w}=-\rho_0\rho^{-1}(1-c^{-2}w^2)w^{-1}\psi_{,\theta}:\ \varphi_{,\theta}=\rho_0\rho^{-1}w\psi_{,w}, \tag{4}$$

("generalized" Cauchy-Riemann equations). The solution of equation (1) is of the form (Ringleb, p. 190):

$$\psi=C\int\{\exp-\int[(1-\beta w^2)(1-\alpha w^2)^{-1}w^{-1}] \times dw\}dw+C'. \tag{5}$$

By means of elementary methods the sum of the integrals

$$S=\int w^{-1}(\alpha w^2-1)^{-1}dw-\beta\int w(\alpha w^2-1)^{-1}dw, \tag{6}$$

is equal to

$$S=-\ln\{[w^2(\alpha w^2-1)^{-1}](\alpha w^2-1)^{\beta/\alpha}\}^{1/2}=-\ln A. \tag{7}$$

Since $\exp(-\ln A)=A^{-1}$, and $\beta/\alpha=1-2(k-1)^{-1}$, one obtains:

$$\psi=B\int(1-\alpha w^2)^{1/(k-1)}w^{-1}dw+C'; \quad B=(-1)^{1/(1-k)}C. \tag{8}$$

For $\alpha w^2<1$, let us expand the integrand in a series by the use of the binomial theorem and integrate term by term:

$$\psi=B[\ln(w/B)+f_1(w)];\ f_1(w)=-\frac{1}{2}\binom{m}{1}\alpha w^2+\frac{1}{4}\binom{m}{2}(\alpha w^2)^2-\frac{1}{6}\binom{m}{3}(\alpha w^2)^3+\cdots\cdot +(-1)^n(2n)^{-1}\binom{m}{n}(\alpha w^2)^n+\cdots, \tag{9}$$

with $m=(k-1)^{-1}$. Ignoring the lack of physical meaning for $\alpha w^2>1$, let us apply the binomial theorem to the expression $(\alpha w^2)^m(\alpha^{-1}w^{-2}-1)^m$, thus obtaining:

$$\psi=Cf_2(w)+C';\ f_2(w)=(2m)^{-1}(\alpha w^2)^m-\binom{m}{1}[2(m-1)]^{-1}(\alpha w^2)^{m-1}+\cdots +(-1)^m\binom{m}{n}[(2m-n)]^{-1}(\alpha w^2)^{m-n}+\cdots. \tag{10}$$

Analogously like in an incompressible flow ($\psi=B\ln(w/B)$) the expansions (9) and (10) show that ψ possesses singularities ($\psi\to-\infty$) for $w=0$ (9) and ($\psi\to+\infty$) for $w\to\infty$ (10). For an incompressible fluid $\propto$ and f_i ($i=1, 2$) vanish identically. Combining equations (4) and (8) gives the result:

$$\psi_{,w}=B(1-\alpha w^2)^{1/(k-1)}w^{-1},\ \psi_{,\theta}=0 \tag{11a}$$

$$\varphi_{,w}=0;\ \varphi_{,\theta}=B\rho_0\rho^{-1}(1-\alpha w^2)^{1/(k-1)}. \tag{11b}$$

Inserting equation (2) into equation (11b) results in

$$\varphi_{,\theta}=B,\quad \text{or}\quad \varphi=B\theta, \tag{12}$$

with the constant of integration equal to zero by assumption (which can be done without a loss of generality). From the system (3) one obtains

$$x_{,w}=-Bw^{-2}\sin\theta;\ x_{,\theta}=Bw^{-1}\cos\theta, \tag{13a}$$

$$y_{,w}=Bw^{-2}\cos\theta;\ y_{,\theta}=Bw^{-1}\sin\theta. \tag{13b}$$

Following the reasoning in Ringleb's paper (pp. 189 and 191) one can ignore the functions and constants of integration and get

$$x=Bw^{-1}\sin\theta,\quad y=-Bw^{-1}\cos\theta, \tag{14}$$

which implies that

$$r=(x^2+y^2)^{1/2}=Bw^{-1}. \tag{15}$$

Equation (15) jointly with equations (9) and (10) shows that ψ possesses singularities for $r=0$ and $r=+\infty$. Assume on the basis of the physical aspects of the problem in question that $B=\Gamma/(2\pi)$. Then from the expansion (9) and equation (15) one easily derives the formula:

$$\psi=-B(\ln r+f_1(r))+C', \tag{16}$$

$$f_1(r)=\frac{1}{2}\binom{m}{1}\alpha B^2r^{-2}-\frac{1}{4}\binom{m}{2}(\alpha B^2)^2r^{-4}+\cdots -(-1)^n(2n)^{-1}\binom{m}{n}(\alpha B^2)^nr^{-2n}+\cdots. \tag{16a}$$

One can verify equation (16) in more than one way. Inserting equation (15) directly into the integrand of equation (8) one obtains the expression $\psi=-B\int(1-\alpha B^2r^{-2})^{1/(k-1)}r^{-1}dr+C'$, which expanded by use of the binomial theorem and integrated term by term gives again the formula (16). From the equations of continuity and irrotationality in the plane polar coordinates, i. e., from

$$(\rho_0^{-1}\rho r u)_{,r}+(\rho_0^{-1}\rho v)_{,\theta}=0\,;\quad (rv)_{,r}-u_{,\theta}=0, \tag{17}$$

and from the forms of partial derivatives of the potential and stream functions, satisfying (17), i. e., from

$$\psi_{,\theta}=\rho_0^{-1}\rho r u\,;\qquad \psi_{,r}=-\rho_0^{-1}\rho v\,;$$
$$\varphi_{,\theta}=rv\,;\qquad \varphi_{,r}=u, \tag{18}$$

with $u\equiv0$, $v\equiv w$, and with equation (2) one may again easily verify equation (16). For an incompressible fluid $\alpha\equiv0$, and $\psi=-B\ln r+C'$, which is correct. By the D'Alembert ratio test one may verify that the series (16a) is an absolutely convergent one

$$\frac{a_{n+1}}{a_n}=\left|\left(\frac{m-n-1}{n+1}\right)\left(\frac{2n}{2(n+1)}\right)\right.$$
$$\left.\times\alpha B^2r^{-2}\right|\to|\alpha B^2r^{-2}|\ \text{for}\ n\to\infty. \tag{19}$$

To fulfill the condition (19), i. e., $|\alpha B^2r^{-2}|\leqq D<1$, the condition $r^2>\alpha B^2=r_a^2$ must be preserved. Equation (2) implies that ρ vanishes for $r=r_a$ ("limiting circle") and the expression for ψ in terms of r (below equation (16)) implies that the derivative $\psi_{,r}$ vanishes for $r=r_a$. Since for $r\leqq r_a$ the formulas obtained do not have any physical meaning, one may attempt to have such a representation of ψ that ψ vanishes (or is equal to a constant) for $r=r_a$, and that by conventional agreement one has to preserve this value of ψ for $r<r_a$. Without a loss of generality one can assume the value $\psi\equiv0$, for $r=r_a$. To achieve this one may assume the value of C' in equation (16) in such a way that all the terms in (16) vanish for $r=r_a$. If one ignores the physical meaning of the "limiting circle", then the application of the D'Alembert ratio test to equation (10) shows that the series (10) (which has only a mathematical meaning) is an absolutely convergent one for

$$|\alpha w^2|>1,\ \text{or}\ |\alpha B^2r^{-2}|>1,\ \text{for}\ n\to\infty.$$

This implies that $r<r_a$. The "generalized" complex potential (applied by Bergman and others) of the flow in a vortex is

$$F(r,\theta)=\varphi+i\psi=-iB[\ln(r/r_a)+F_1(r)+i\theta], \tag{20}$$

$$F_1(r)=\frac{1}{2}\binom{m}{1}(\alpha B^2r^{-2}-1)-\frac{1}{4}\binom{m}{2}$$
$$\times(\alpha^2B^4r^{-4}-1)+\cdots, \tag{20a}$$

which may be represented by the use of the complex variable notation in the form

$$F(z,\bar z)=\varphi+i\psi=-iB[\ln(z/z_a)+G_1(z,\bar z)], \tag{21}$$

or

$$F(z,\bar z)=(2\pi i)^{-1}\Gamma\ln[(z/z_a)\exp G_1(z,\bar z)], \tag{22}$$

$$G_1(z,\bar z)=\frac{1}{2}\binom{m}{1}[z_a\bar z_a(z\bar z)^{-1}-1]$$
$$-\frac{1}{4}\binom{m}{2}[(z_a\bar z_a)^2(z\bar z)^{-2}-1]+\cdots, \tag{22a}$$

z_a being the constant vector, and $z_a\bar z_a=r_a^2$. When the center of the vortex in an incompressible fluid is located at the origin of the Gaussian plane then $\alpha\equiv z_a\equiv\bar z_a\equiv0$, and the value of the constant C' must be equal to zero, so that $G_1\equiv0$. The complex potential is equal to $(2\pi i)^{-1}\Gamma\ln(z/z_{in})$, with z_{in} being an arbitrarily chosen vector, which is correct. If one ignores the physical meaning of the limiting circle, one may assume the value $C'=0$ in equation (16) and obtain

$$F(z,\bar z)=-iB\ln(z\exp G_1)$$
$$=(2\pi i)^{-1}\Gamma\ln(z\exp G_1), \tag{23}$$

$$G_1(z,\bar z)=\frac{1}{2}\binom{m}{1}(z_a\bar z_a)(z\bar z)^{-1}$$
$$-\frac{1}{4}\binom{m}{2}(z_a\bar z_a)^2(z\bar z)^{-2}+\cdots, \tag{23a}$$

which is in a complete analogy to the incompressible flow: $F=(2\pi i)^{-1}\Gamma\ln z$.

Reference

1) Ringleb, F.: Exakte Lösungen der Differential-gleichungen einer adiabatischen Gasströmung. Z.a. M.M. **20**, 4 (1940), pp. 185-198.

JOURNAL OF THE PHYSICAL SOCIETY OF JAPAN Vol. 8, No. 3, MAY—JUNE, 1953

A New Proof of Lagrange's Theorem in Hydrodynamics

By Hideyuki MASUDA

(Received December 15, 1952)

A new proof of Lagrange's theorem about the persistence of curl vector is given in the light of recent theories of linear partial differential equations. Velocity potential for an arbitrary pressure distribution can be constructed as the Extremal field.

Introduction

Hydrodynamics is a branch of science which was developed at comparatively old times. The author wishes to review the method of derivation of its fundamental theorems, and to make use of the methods of solving linear partial differential equations to the possible maximum extent. It is shown that the Euler equations of motion are equivalent with a linear partial differential equation, whose characteristic curves are the stream lines, from which one can derive the Bernoulli theorem, and the Lagrange theorem, and the velocity potential systematically by considering the behavior of the characteristic curve itself, its infinitesimal neighborhood, and its neighborhood of finite dimension.

§ 1. Equations of Motion

The equations of motion for an ideal fluid are

$$\left.\begin{aligned} u_t+uu_x+vu_y+wu_z&=-P_x/\rho-\Omega_x\\ v_t+uv_x+vv_y+wv_z&=-P_y/\rho-\Omega_y\\ w_t+uw_x+vw_y+ww_z&=-P_z/\rho-\Omega_z \end{aligned}\right\} \tag{1}$$

which are supplemented by the equation of continuity

$$\rho_t+(\rho u)_x+(\rho v)_y+(\rho w)_z=0 \tag{2}$$

where t is the time; x, y, and z are the cartesian coordinates of the physical space; u, v, and w are the velocity components, P, the pressure; Ω the potential of force acting from outside on a unit mass; and the suffices denote differentiation with respect to the variable indicated by the suffices. As is usual, continuity and existence of derivatives for necessary functions are assumed.

If P is given as a function of ρ, as is the case with isentropic mass of fluid, the equations (1) become

$$\left.\begin{aligned} u_t+uu_x+vu_y+wu_z&=-M_x\\ v_t+uv_x+vv_y+wv_z&=-M_y\\ w_t+uw_x+vw_y+ww_z&=-M_z \end{aligned}\right\} \tag{1$'$}$$

where $$M=\int\frac{dP}{\rho}+\Omega\,.$$

These eqations (1′) supplemented by the equation (2) will decide the whole set of field functions. Usual procedure is to solve them from the equation (2). Here we want to take the stand, that we solve at first the equations (1′) for an arbitrary function M, and then try to satisfy the equation (2) by modifying the function M. It is impracticable but at least it is a plausible procedure for theoretical consideration.

§ 2. Theory of Simultaneous Partial Differential Equations with the Same "Hauptteil"[1)]

Because the equations (1′) have the same differential operator

$$\frac{\partial}{\partial t}+u\frac{\partial}{\partial x}+v\frac{\partial}{\partial y}+w\frac{\partial}{\partial z}$$

on the left side, one can easily show that the equations (1′) are equivalent with the linear partial differential equations

$$\varphi_t+u\varphi_x+v\varphi_y+w\varphi_z-M_x\varphi_u-M_y\varphi_v-M_z\varphi_w=0 \tag{3}$$

provided that one does not care for the loss of validity for a very singular case where the solution of the equations (1′) is not covered by any complete integral of the equation (3)

§ 3. Characteristic Equations and their Integration

The characteristic equations for the partial differential equation (3) are

---

Author's address is, Mamada-machi, Tochigi-ken, Japan.

$$\left.\begin{array}{ll} dt/ds=1 & \\ dx/ds=u & du/ds=-M_x \\ dy/ds=v & dv/ds=-M_y \\ dz/ds=w & dw/ds=-M_z \end{array}\right\} \qquad (4)$$

where s is a parameter. By virtue of the first equation, one can replace s with t in the other equations. To recapitulate the theory of differential equations, the solution of the equations (4) will form a five dimensional manifold in (t, x, y, z, u, v, w) space. If one of the characteristic curves has one point in common with the integral of the equation (3), then the whole curve will lie on the same integral. In our case, interest lies in the solutions for u, v, and w, which are to be obtained as the cross section of three independent solutions of the equation (3). As the sought functions u, v, and w are the cross section, the characteristic curve having one point in common with the sought functions u, v, and w is imbedded completely in the sought functions.

The integration of the equations (4) can be carried out quite easily by the Hamilton-Jacobi method. It is obvious that the equations (4) are given by the Hamiltonian

$$H=\tfrac{1}{2}(u^2+v^2+w^2)+M \qquad (5)$$

in a canonical form

$$\left.\begin{array}{lll} \dfrac{dx}{dt}=\dfrac{\partial H}{\partial u} & \dfrac{dy}{dt}=\dfrac{\partial H}{\partial v} & \dfrac{dz}{dt}=\dfrac{\partial H}{\partial w} \\ \dfrac{du}{dt}=-\dfrac{\partial H}{\partial x} & \dfrac{dv}{dt}=-\dfrac{\partial H}{\partial y} & \dfrac{dw}{dt}=-\dfrac{\partial H}{\partial z} \end{array}\right\} \qquad (6)$$

u, v, and w correspod to the moments conjugate to the cordinates x, y, and z.

Consider the Eikonal (action integral),

$$J=\int_\sigma^s(\dot{x}u+\dot{y}v+\dot{z}w-H)dt \qquad (7)$$

between the two points in (t, x, y, z, u, v, w) space,

$$\left.\begin{array}{lllll} \mathrm{A}: & t=\sigma & x(\sigma)=\kappa_1\,, & y(\sigma)=\kappa_2\,, & z(\sigma)=\kappa_3\,, \\ & & u(\sigma)=\pi_1\,, & v(\sigma)=\pi_2\,, & w(\sigma)=\pi_3\,. \\ \mathrm{B}: & t=s & x(s)=q_1\,, & y(s)=q_2\,, & z(s)=q_3\,, \\ & & u(s)=p_1\,, & v(s)=p_2\,, & w(s)=p_3\,. \end{array}\right\} \qquad (8)$$

and we have

$$\left.\begin{array}{ll} J_{q_i}=\partial J/\partial q_i=p_i & J_s=\partial J/\partial s=-H(s) \\ J_{\kappa_\nu}=\partial J/\partial \kappa_\nu=-\pi_\nu & J_\sigma=\partial J/\partial\sigma=H(\sigma) \end{array}\right\} \qquad (9)$$

where

$$J=J(q_i\,,\,\kappa_\nu\,,\,s\,,\,\sigma)\,.$$

Therefore, once we construct the Eikonal for a given function M, we can solve every initial value problem of the equations (4) by solving the relations (9) for the required variables. If we eliminate the coordinates of the point A, we can obtain a complete integral of the partial differential equation (3). As it was pointed out already, our interest is in the behavior of u, v, and w, which can be obtained and discussed more directly from the behavior of the characteristic curves themselves. We do not go into the elimination of the coordinates of the point A.

§ 4. Bernoulli's Theorem

As it is apparent from the appearence of the equations (4), the characteristic curve is exactly what we are accustomed to as the path of fluid element. Corresponding to the energy theorem, we can obtain Bernoulli's theorem. Indeed, consider the variation of H along the path, and

$$\left.\begin{array}{l} \dfrac{dH}{dt}=\sum\dfrac{\partial H}{\partial x}\dfrac{dx}{dt}+\sum\dfrac{\partial H}{\partial u}\dfrac{du}{dt}+\dfrac{\partial H}{\partial t} \\ \quad=\dfrac{\partial H}{\partial t} \end{array}\right\} \qquad (10)$$

If $\partial H/\partial t$ does not depend upon x, y and z, we can integrate the above. Write

$$\frac{\partial H}{\partial t}=-\frac{d}{dt}F(t)$$

and we have an integral along each characteristic curve

$$H+F=\tfrac{1}{2}(u^2+v^2+w^2)+M+F(t). \qquad (11)$$

§ 5. Solution in the Infinitesimal Neiborhood Along a Path of Fluid Motion, and the Proof of Lagrange's Theorem

Next let us consider the fluid motion including the δ-neighborhood around a characteristic curve projected in the four dimensional (x, y, z, t) space. Let the point A: $(\kappa_1\,, \kappa_2\,, \kappa_3\,, \sigma)$ be the starting point at which the velocities are given by $(\pi_1\,, \pi_2\,, \pi_3)$. All the quantities of the second order smallness are neglected. As is familiar in calculus, this approximation is good enough to obtain the behavior of the derivatives of the velocities. Then,

$$\begin{pmatrix}\delta\pi_1\\ \delta\pi_2\\ \delta\pi_3\end{pmatrix}=\begin{pmatrix}u_x & u_y & u_z\\ v_x & v_y & v_z\\ w_x & w_y & w_z\end{pmatrix}_A\begin{pmatrix}\delta\kappa_1\\ \delta\kappa_2\\ \delta\kappa_3\end{pmatrix}$$

where the derivatives of u, v, w, are taken at the point A. In order to simplify notations, write

$$\delta\pi_\nu=\sum_{\mu=1}^{3}\Pi_{\nu\mu}\delta\kappa_\mu$$

$$\begin{pmatrix} u_x & u_y & u_z \\ v_x & v_y & v_z \\ w_x & w_y & w_z \end{pmatrix}_A=\Pi_{\nu\mu}$$

Similarly the velocity field around the point B: (q_1, q_2, q_3, s) are written

$$\delta p_i=\sum_{j=1}^{3}P_{ij}\delta_{qj}$$

$$P_{ij}=\begin{pmatrix} u_x & u_y & u_z \\ v_x & v_y & v_z \\ w_x & w_y & w_z \end{pmatrix}_B$$

where the derivatives are taken at the point B. Now differentiate the equations (9), and

$$\sum_{j=1}^{3}J_{q_iq_j}+\sum_{j=1}^{3}J_{q_i\kappa_\mu}\delta\kappa_\mu=\sum_{j=1}^{3}P_{ij}\delta_{q_j} \qquad (12)$$

$$\sum_{j=1}^{3}J_{\kappa_\nu q_j}\delta_{q_j}+\sum_{\mu=1}^{3}J_{\kappa_\nu\kappa_\mu}\delta\kappa_\mu=-\sum_{\mu=1}^{3}\Pi_{\nu\mu}\delta\kappa_\mu \qquad (13)$$

Our purpose is to obtain P_{ij} as functions of $\Pi_{\mu\nu}$. This can be done by solving the equation (13) for $\delta\kappa_\nu$ and substituting them into (12). In order to avoid useless confusion by multiple suffices, introduce the notatons

$$\begin{aligned} J_{q_iq_j}&=(i,\ j)=(j,\ i)\\ J_{q_i\kappa_\nu}&=(i,\ \nu\rangle=\langle\nu,\ i)\\ J_{\kappa_\nu q_j}&=\langle\nu,\ j)=(j,\ \nu\rangle\\ J_{\kappa_\nu\kappa_\mu}&=\langle\nu,\ \mu\rangle=\langle\mu,\ \nu\rangle \end{aligned}$$

In this notation, the equation (13) are

$$\sum_{j=1}^{3}\langle\nu,\ j)\delta q_j+\sum_{\mu=1}^{3}(\langle\nu,\ \mu\rangle+\Pi_{\nu\mu})\delta\kappa_\mu=0. \quad (14)$$

The simultaneous linear equations (14) for the unknown $\delta\kappa_\mu$ can be solved uniquely, if the determinant

$$\Delta=|\langle\nu,\ \mu\rangle+\Pi_{\nu\mu}|\neq 0\,.$$

When it vanishes, one has the following relation between δq_j independent of the $\delta\kappa_\nu$,

$$\delta_{\kappa_1}\begin{vmatrix} \langle 1,\ 1\rangle+\Pi_{11}, & \langle 1,\ 2\rangle+\Pi_{12}, & \langle 1,\ 3\rangle+\Pi_{13} \\ \langle 2,\ 1\rangle+\Pi_{21}, & \langle 2,\ 2\rangle+\Pi_{22}, & \langle 2,\ 3\rangle+\Pi_{23} \\ \langle 3,\ 1\rangle+\Pi_{31}, & \langle 3,\ 2\rangle+\Pi_{32}, & \langle 3,\ 3\rangle+\Pi_{33} \end{vmatrix}$$

$$=-\begin{vmatrix} \langle 1,\ 1\rangle, & \langle 1,\ 2\rangle+\pi_{12}, & \langle 1,\ 3\rangle+\pi_{12} \\ \langle 2,\ 1\rangle, & \langle 2,\ 2\rangle+\pi_{22}, & \langle 2,\ 3\rangle+\pi_{23} \\ \langle 3,\ 1\rangle, & \langle 3,\ 2\rangle+\pi_{32}, & \langle 3,\ 2\rangle+\pi_{33} \end{vmatrix}\delta q_1$$

$$-\begin{vmatrix} \text{Similar} \\ \text{determinant} \end{vmatrix}\delta q_2-\begin{vmatrix} \text{Similar} \\ \text{determinant} \end{vmatrix}\delta q_3=0$$

The above relation means that the initial three dimensional manifold at A is mapped on a two dimensional surface at the point B. Physically this is converging flow like focus of light rays. Such a point along the path can safely be put outside of discussion. Indeed, the following discussions hold, even if there exists such point in between A and B, provided that the determinant Δ does not vanish at B.

Now let us write the solutions of $\delta\kappa_\nu$ explicitly

$$\delta\kappa_1=\frac{-1}{\Delta}\begin{vmatrix} \sum\langle 1,\ j)\delta q_j & \langle 1,\ 2\rangle+\Pi_{12} & \langle 1,\ 3\rangle+\Pi_{11} \\ \sum\langle 2,\ j)\delta q_j & \langle 1,\ 2\rangle+\Pi_{22} & \langle 2,\ 3\rangle+\Pi_{12} \\ \sum\langle 3,\ j)\delta q_j & \langle 3,\ 2\rangle+\Pi_{23} & \langle 2,\ 3\rangle+\Pi_{33} \end{vmatrix} \qquad (15)$$

Substitute (13) into (12), and one will obtain the following expression easily.

$$\sum_{j=1}^{3}P_{ij}\,\delta q_j=\begin{vmatrix} \sum(i,\ j)\delta q_i & (i,\ 1\rangle & (i,\ 2\rangle & (i,\ 3\rangle \\ \sum(1,\ j)\delta q_j & & & \\ \sum(2,\ j)\delta q_j & & \Delta & \\ \sum(3,\ j)\delta q_j & & & \end{vmatrix}$$

Comparing the coefficient of δq_j's we have

$$P_{ij}=\frac{1}{\Delta}\begin{vmatrix} (i,\ j) & (i,\ 1\rangle & (i,\ 2\rangle & i,\ 3\rangle \\ \langle 1,\ j) & & & \\ \langle 2,\ j) & & \Delta & \\ \langle 3,\ j) & & & \end{vmatrix} \qquad (16)$$

where Δ means the matrix of the determinant expressed by the same letter. Since all the other terms are symmetrical with respect to the change of suffices, if

$$\Pi_{\nu\mu}=\Pi_{\mu\nu}$$

initially, i.e. the initial velocity distribution is representable as a potential flow. Then (P_{ij}) remains symmetrical along the characteristics. If the initial flow covering a finite domain is representable by a velocity potential, then curl expression becomes one of the integral of the characteristics equation, and all the flow inside a finite domain at future time mapped from the former by the integrals (9) can be expressed by a certain potential. One may change the role of equations (12) with that of (13), the same discussion holds vice versa. This is the Lagrange's theorem in hydrodynamics about the persistence of curl vector. Indeed if one furthers the calculation with the help of Laplace's general theorem about the expansion of determinant, one will obtain

$$
\begin{aligned}
&(P_{ij}-P_{ji})\\
&=\frac{1}{2\Delta}(\Pi_{12}-\Pi_{21})\left\{\begin{vmatrix}(i,\ j) & (i,\ 1\rangle & (i,\ 3\rangle\\ \langle 2,\ j) & \langle 2,\ 1\rangle+ & \langle 2,\ 3\rangle+\\ \langle 3,\ j) & \langle 3,\ 1\rangle+ & \langle 3,\ 3\rangle+\end{vmatrix}\right.\\
&\qquad\qquad\left.-\begin{vmatrix}(j,\ i) & \langle j,\ 1) & (j,\ 3)\\ (2,\ i) & \langle 2,\ 1\rangle+ & \langle 2,\ 3\rangle+\\ (3,\ i) & \langle 3,\ 1\rangle+ & \langle 3,\ 3\rangle+\end{vmatrix}\right\}
\end{aligned}
\tag{17}
$$

$+$ Terms obtained by cyclic change of the above.

where $\langle\mu,\ \nu\rangle+=\langle\mu,\ \nu\rangle+\tfrac{1}{2}(\Pi_{\mu\nu}+\Pi_{\nu\mu})$.

§ 6. Construction of Velocity Potential

Suppose that the velocity field in a domain $D(\kappa_\nu)$ at a certain time σ, is given by a potential $\varphi(\kappa_\nu)$, and

$$\pi_\nu=\varphi_{\kappa_\nu}(\kappa_\nu)\,. \tag{18}$$

The velocity potential at a time s, at which time the initial domain is mapped into $D(q_i)$, can be determined as follows.

Substitute the expression (18) into the third of (9), and we have a partial differential equation with respect to the variables κ_ν,

$$J_{\kappa_\nu}(q_i,\ s,\ \kappa_\nu,\ \sigma)=-\varphi_{\kappa_\nu}\,. \tag{19}$$

Integrating the above, we have

$$J(q_i,\ s,\ \kappa_\nu,\ \sigma)=-\varphi(\kappa_\nu)+F(q_i,\ s,\ \sigma) \tag{20}$$

Since $F(q_i,\ s,\ \sigma)$ does not include the initial coordinates, this is exactly the velocity potential looked for. It one expresses the Hamiltonian by means of the derivatives of F, we have.

$$F_s+H(q_i,\ F_{q_i},\ s)=0\,.$$

This is Hamilton's partial differential equation. Following the discussion given in Courant's treatment, one will easily recognize that the field defined by the velocity potential F is an Extremalfeld.[2] As is clearly stated in the reference, an extremal field can be constructed, unless the characteristic curve starting normal to a surface $T(\kappa_\nu,\ \sigma)$ remains on the same surface. The necessary condition for the impossiblity is given by

$$\sum_{\nu=1}^{3}\pi_\nu^2-H=0\,;\qquad \tfrac{1}{2}(\pi_1^2+\pi_2^2+\pi_3^2)=M$$

which are not satisfied in the usual case of fluid motion.

§ 7. Acknowledgement

The author wishes to express his sincere thanks for the encouragement and guidance given by Professor Isao Imai, Tokyo University, ever since the author was a student. He also is indebted to the invariable friendship and encouragements of his classmates at the Tokyo University.

References

1) Courant-Hilbert: Methoden der mathematischen Physik, Bd. II. p. 117.
2) Ibid. p. 102.

JOURNAL OF THE PHYSICAL SOCIETY OF JAPAN Vol. 8, No. 3, MAY—JUNE, 1953

Plane Jet of Gas emitted from a Nozzle with Supersonic Velocity*

By Zirō HASIMOTO

Department of Mathematics and Physics,
Ritumeikan University, Kyoto

(Received January 20, 1953)

When a plane jet of gas issues steadily from a symmetrical nozzle as a parallel supersonic stream into an external medium at rest, its behaviour is governed by the exist velocity as well as by the ratio of exit pressure to pressure in the external medium. As will be seen from Prandtl's photographs, when this pressure ratio is nearly equal to unity, the jet has a periodic character to the first approximation, and its structure can be accounted for by the use of the linear theory due originally to Prandtl. When the pressure ratio departs from unity, however, the quantitative behaviours, such as the wave-length of the jet, cannot be fully explained unless the nonlinear character of the fundamental equation is taken into account.

In the present paper, the fundamental equation for the stream function is considered in the hodograph plane, and the true adiabatic relation is replaced by an approximate adiabatic one so that simple exact solutions may be obtained. Thus, it is shown that, if the exit velocity is not so close to the sonic velocity and the external pressure is not so lower than that at the exit, the jet has, to the present approximation, still a completely periodic structure in the downstream as in the case of the linear theory. An expression is obtained for the wave-length of jet and it is found that the agreement between our theoretical result and Prandtl's experiments is very satisfactory.

§ 1. Introduction

To account for Emden's experiments1) with axially symmetrical jets of gas, Prandtl2) developed a linear theory which assumed slight perturbations about a mean parallel stream with supersonic velocity, and obtained the formulae for the wave-length in both cases of cylindrical and plane jets. Later on, Prandtl3) made experiments on plane supersonic gas jet issuing steadily from a plane slit as a uniform supersonic stream into an external medium at rest. When the ratio of exit pressure to pressure in the external medium is nearly equal to unity, his formula for the wave-length of a plane jet agrees well with experiments unless the exit velocity is so close to the sonic velocity. As the pressure ratio is increased, however, there occur discrepancies between the results of experiments and his linear theory.

Recently, D. C. Pack4) reconsidered Prandtl's formula for the wave-length and concluded that the Mach number on the bounding free streamlines of jet is to be taken as the mean Mach number, in place of the one at the exit as assumed by Prandtl. As a result of such a correction, the pressure ratio stated above becomes effective to some extent and accordingly, the range of applicability of the for, mula might be extended. In fact, it has been ascertained that the modified formula can be applied satisfactorily to the case of experiments on cylindrical jets. In the case of plane jets, Pack's formula accounts for Prandtl's experiments in some cases, while, when the pressure of the external gas at rest is considerably lower than the exit pressure, values of the wave-length given by the modified formula are noticeably smaller than the experimental values. Such discrepancies might be due to the disregard of nonlinearity of the fundamental equation for the velocity potential, when its independent variables are the

---

* Presented at The Eighth International Congress on Theoretical and Applied Mechanics held at Istanbul, Turkey, in 1952.

Cartesian coordinates in the plane of flow. It is therefore desirable to develop a more accurate theoretical analysis than that based upon the linearized equation.

Now we consider the structure of a gas jet issuing with a uniform supersonic speed from a two-dimensional symmetrical nozzle into an external gas at rest whose pressure is lower than the exit one. There develop simple expansion waves at the two rims of the nozzle. The gas close to the nozzle wall flows with uniform velocity, and entering the simple wave region, it is deflected and expanded to the external pressure according to the Prandtl-Meyer expansion law. These two simple waves issuing from the rims interact in the neighbourhood of the axis of symmetry of nozzle, and emerge again as simple waves from the interaction region. There after they reach the bounding free streamilines of the jet and are reflected there. When the pressure in and out of the nozzle are nearly equal, the two simple waves from the rims are approximately independent of each other, and a periodic wavy flow pattern is obtained theoretically. In reality, however, the two simple waves are not independent and the simple waves emerging out of the interaction region have different characters from the initial waves. Therefore, in order to improve the theoretical analysis the problem of the interaction of two simple waves must be solved. But, it is in general rather difficult to treat such problems when the state of gas obeys the adiabatic law, unless numerical or graphical methods are used.

In this paper, the true adiabatic relationship is replaced by an approximate adiabatic one about a certain state of gas, for instance about the state of gas upon exit. Such replacement enables us to obtain a general solution of the fundamental equation for the stream function and also to solve the present problem of jet. The results of the present analysis are much more accurate than those given by the linear theory. Nevertheless, as will be seen in the following, the jet has still a completely periodic structure in the downstream under the condition that the mean velocity exceeds fairly the sonic velocity and the exit pressure in the external gas is not so lower than the exit pressure.

Values of the wave-length obtained by the present analysis are represented graphically against the Mach number associated with the exit uniform flow and the ratio of the pressures above mentioned. Also, the theoretical results are compared with the results of Prandtl's experiments, and a good agreement is found between them.

§ 2. Fundamental Equations

Consider a two-dimensional, steady, irrotational and isentropic flow of a perfect gas. Let Φ, Ψ denote the velocity potential and the stream function respectively, q the magnitude of the flow velocity vector, θ the angle between the flow velocity vector and a fixed direction along which the x-axis is chosen, ρ the density of gas, and c the local velocity of sound. Then we have

$$\Phi_\tau = \chi^2 \Psi_\theta, \qquad \Phi_\theta = \chi^2 \Psi_\tau , \tag{2.1}$$

where

$$\chi = \left(\frac{\rho_0}{\rho}\right)^{1/2} \left(\frac{q^2}{c^2} - 1\right)^{1/4}, \quad \tau = \int_{q*}^{q} \left(\frac{1}{c^2} - \frac{1}{q^2}\right)^{1/2} dq, \tag{2.2}$$

ρ_0, q_* being constants.

When a relationship of changes of state of gas is prescribed, the function χ becomes a definite function of τ. However, in an important case when the changes of state are adiabatic, it is in general impossible to express χ in an explicit form in terms of τ. But, when the range of the state changes is not so wide about a certain given state, the relationship between χ and τ for the case of the true adiabatic law may be approximated, with sufficient accuracy, by

$$\chi = a_0 + a_1 \tau , \tag{2.3}$$

where a_0 and a_1 are constants which are chosen in such a way that Eq. (2.3) may express the equation of the tangent to the true χ–τ curve at a certain point (χ_1, τ_1) in the χ, τ-plane. Once the relation (2.3) is prescribed between χ and τ, then Eqs. (2.1) yield the general solution for Ψ in the form:

$$\Psi = \chi^{-1}\{F(\tau+\theta) + G(\tau-\theta)\}, \tag{2.4}$$

where F and G are arbitrary fucnctions, and the relations between various quantities such as pressure p, density ρ, velocity q and Mach number M can be obtained, by using Imai's method[5], in parametric representation as follows:

$$\frac{q}{q_1}=\frac{t\sin(t_1+\varepsilon)}{t_1\sin(t+\varepsilon)}, \tag{2.5a}$$

$$\frac{p}{p_1}=\frac{\sin(t_1+\varepsilon)\sin(t+\delta)}{\sin(t+\varepsilon)\sin(t_1+\delta)}, \tag{2.5b}$$

$$\frac{\rho}{\rho_1}=\frac{t_1\sin(t+\varepsilon)}{t\sin(t_1+\varepsilon)}\,\frac{\sin(t_1+\varepsilon)-t_1\cos(t_1+\varepsilon)}{\sin(t+\varepsilon)-t\cos(t+\varepsilon)}, \tag{2.5c}$$

$$\frac{p_0}{\rho_1}=a_1{}^2t_1\{1-t_1\cot(t_1+\varepsilon)\}, \tag{2.5d}$$

$$M^2=\frac{q^2}{c^2}=1+\frac{t^2}{\{1-t\cot(t+\varepsilon)\}^2}, \tag{2.5e}$$

with

$$t=\tau+\frac{a_0}{a_1},\qquad t_1=\tau_1+\frac{a_0}{a_1}. \tag{2.6}$$

Here (p_1, ρ_1, q_1) denote a certain given state, τ_1 the corresponding value of τ in this state, and ε, δ are constants of integration, of which ε is found from Eq. (2.5e) by equating the value of M when $\tau=\tau_1$ and that of the state (p_1, ρ_1, q_1), and δ from Eqs. (2.5a, b, c) by letting them satisfy Bernoulli's equation in differential form: $\rho q dq+dp=0$. As to the concrete expressions for determining τ_1, a_0, a_1, ε, δ, reference should be made to a previous paper of the writer⁶⁾.

§ 3. Interaction of Simple Waves in Jet

Suppose that denoting by x, y the Cartesian coordinates in the plane of flow, the two walls of the symmetrical plane nozzle are expressed as

$$x\leqq 0,\qquad y=\pm\tfrac{1}{2}D,$$

where D is the width of the nozzle. Also suppose that the gas flows out from its opening with a constant uniform supersonic velocity q_1, and the jet of escaping gas is separated from the external gas at rest by two surfaces of discontinuity as indicated in Fig. 1.

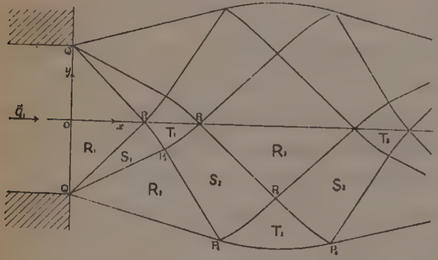

Fig. 1.

When the exit pressure p_1 is higher than the pressure p_2 in the external gas at rest, two simple expansion waves start from the rims Q, Q' and they interact in the neighbourhood of the x-axis. From the interaction region the other simple waves emerge, and they are reflected at the bounding free streamlines. Thus, the situation may be such as indicated in Fig. 1, in which (R_1), (R_2), (R_3) represent regions of constant states, (S_1), (S_2), (S_3) simple wave regions, and (T_1), (T_2) interaction regions in the lower half-part of the x, y-plane. To indicate various quantities of flow in (R_1), (R_2), (R_3), suffices 1, 2, 3 are used respectively. In what follows the state in (R_1) is chosen as the prescribed state (p_1, ρ_1, q_1) mentioned in the previous section.

In order to determine the jet structure, especially its wave-length when it is periodic, we must solve successively the interaction problems in regions (T_1), (T_2) and so on. We begin with the determination of the stream function in (T_1), i. e., the region $P_1P_2P_3$ as indicated in Fig. 1. The arc P_1P_2 (or P_2P_3) is a cross Mach line in region (S_1) (or (S_2)), and is at the same time the boundary curve between (S_1) (or (S_2)) and (T_1). In the τ, θ-plane, regions (S_1) and (S_2) are represented by two straight lines $\tau+\theta=\tau_1$ and $\tau-\theta=\tau_3$ respectively, and region (T_1) is represented by a triangular region $P_1P_2P_3$ as shown in Fig. 2.

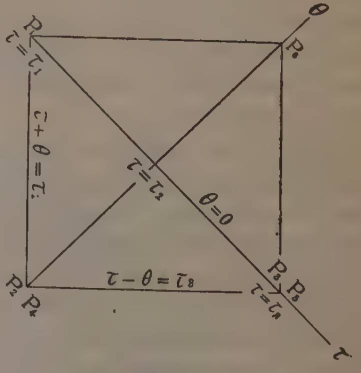

Fig. 2.

When the state of flow in (R_1) and the pressure p_2 are assigned, the states in (S_1) and (R_2) are determined immediately. The general properties as found in another paper of the writer⁷⁾ concerning the cross Mach lines in a simple wave enable us to determine the form of arc P_1P_2 and also the value of Ψ along this arc. Thus, denoting by $\Psi_{P_1P_2}$ the value of Ψ along the arc P_1P_2 we obtain

$$\Psi_{P_1P_2}=\rho_1c_1r_1\left(\frac{\chi_1}{\chi}-1\right),$$

in which $\tau+\theta=\tau_1$ and r_1 denotes the distance between the point P_1 and Q in Fig. 1. Since the x-axis is a particular streamline we assume that $\Psi=0$ along it, namely:

$$\Psi_{P_1P_3}=0.$$

Using the general solution (2.4), the stream function, $\Psi_{(T_1)}$ say, in (T_1), which satisfies the above two conditions, are obtained as follows

$$\Psi_{(T_1)}=\rho_1c_1r_1\frac{a_1\theta}{\chi}. \qquad (3.1)$$

Substitution from Eq. (3.1) into Eqs. (2.1) yields the solution for the velocity potential, $\Phi_{(T_1)}$ say, in (T_1) in the form:

$$\Phi_{(T_1)}=\rho_1c_1r_1a_1\{a_0\tau+\tfrac{1}{2}a_1(\tau^2-\theta^2)\}. \qquad (3.2)$$

Next we proceed to the determination of Ψ and Φ in region (T_2). For this purpose we must first find the value of Ψ along the boundary curve P_4P_5 between (S_2) and (T_2). From the general properties of simple waves we can easily derive the value of Ψ along P_4P_5 as follows:

$$\Psi_{P_4P_5}=\Psi_{P_2P_3}-\rho_2c_2r_2\frac{\chi_2}{\chi}$$

where

$$\chi_2=a_0+a_1\tau_2,$$

r_2 being the distance $\overline{P_2P_4}$ which is equal to the distance $\overline{QP_2}$.

Putting $\tau-\theta=\tau_3$ in Eq. (3.1), we get

$$\Psi_{P_2P_3}=\rho_1c_1r_1\left(1-\frac{\chi_3}{\chi}\right)$$

with

$$\chi_3=a_0+a_1\tau_3.$$

Taking into account that $\rho_1c_1r_1\chi_1=\rho_2c_2r_2\chi_2$ and $\chi_1+\chi_3=2\chi_2$, we get

$$\Psi_{P_4P_5}=\rho_1c_1r_1\left(1-\frac{2\chi_2}{\chi}\right).$$

Moreover it must be

$$\Psi_{P_4P_6}=-\rho_1c_1r_1.$$

With these conditions, the stream function, $\Psi_{(T_2)}$ say, in (T_2) is obtained in the form:

$$\Psi_{(T_2)}=\rho_1c_1r_1\left(1-\frac{2\chi_2}{\chi}\right), \qquad (3.3)$$

which is symmetrical about the τ-axis in the τ, θ-plane. The corresponding velocity potential, $\Phi_{(T_2)}$ say, is given by

$$\Phi_{(T_2)}=2\rho_1c_1r_1a_1(a_0+a_1\tau_2)\theta+\text{constant}. \qquad (3.4)$$

Transformation to the physical x, y-plane can be performed by inserting the expressions for Φ and Ψ obtained above into the relations

$$dx=\frac{\cos\theta}{\rho_0q}d\Phi-\frac{\sin\theta}{\rho q}d\Psi,$$

$$dy=\frac{\sin\theta}{\rho_0q}d\Phi+\frac{\cos\theta}{\rho q}d\Psi,$$

with ρ, ρ_0 and q as given in Eqs. (2.5a, c, d), and then carrying out integrations. As will be seen from the expressions for $\Psi_{(T_2)}$ and $\Phi_{(T_2)}$, the jet has a completely periodic structure in the downstream direction. After some calculations, the wave-length is obtained in the form:

$$\frac{\Lambda}{D}=2\sqrt{M_1^2-1}\,\frac{\sin(t_2+\varepsilon)}{\sin(t_1+\varepsilon)}\times\left\{\cos(t_1-t_2)-\frac{1}{t_1}\sin(t_1-t_2)\right\}, \qquad (3.5)$$

where M_1 is the Mach number of the flow in (R_1), i.e., the Mach number of the flow upon exit, and $t_2=\tau_2+a_0/a_1$. When M_1 is prescribed, the various constants τ_1, a_0, a_1, t_1, ε, δ can be determined. Further, when p_1/p_2 is assigned, the value of t_2 can be determined through Eq. (2.5b). Thus, the value of Λ/D can be ultimately calculated by formula (3.5).

§ 4. Numerical Discussions. Comparison with the Results of the Linear Theory and Experiments

When $p_1=p_2$, we find from Eq. (2.5b) that $t_1=t_2$. Then, formula (3.5) reduces to

$$\frac{\Lambda}{D}=2\sqrt{M_1^2-1}, \qquad (4.1)$$

which is the well-known formula for the wave-length obtained by Prandtl. Table I shows the values of τ_1, a_0, a_1, t_1, ε, δ for the Mach numbers $M_1=\sqrt{2}$, $\sqrt{3}$, 1.85, 2, $\sqrt{5}$ for air whose adiabatic exponent $\gamma=1.4$, where calculations have been made by chosing the constants q_* in τ to be equal to the critical velocity, when $q=c$. Table II gives the values of t_2 for the pressure ratios $p_1/p_2=1.25$, 1.5. Further, the values of Λ/D calculated by formula (3.5) are shown in Table III, where are also given the values of Λ/D calculated by the modified formula due to Pack:

Table I.

M_1	a_0	a_1	τ_1	t_1	ε	δ
$\sqrt{2}$	0.9246	3.6550	0.1637	0.4167	0.2036	−1.0370
$\sqrt{3}$	0.8029	4.0856	0.3273	0.5238	0.1699	−1.0388
1.85	0.6680	4.4626	0.3868	0.5365	0.1495	−1.0303
2	0.4094	5.0695	0.4605	0.5413	0.1258	−1.0126
$\sqrt{5}$	−0.2317	6.3067	0.5701	0.5333	0.0955	−0.9732

Table II.

M_1	t_2	
	$p_1/p_2=1.25$	$p_1/p_2=1.5$
$\sqrt{2}$	0.5184	0.5777
$\sqrt{3}$	0.5972	0.6530
1.85	0.6068	……
2	0.6085	0.6594
$\sqrt{5}$	0.5954	0.6426

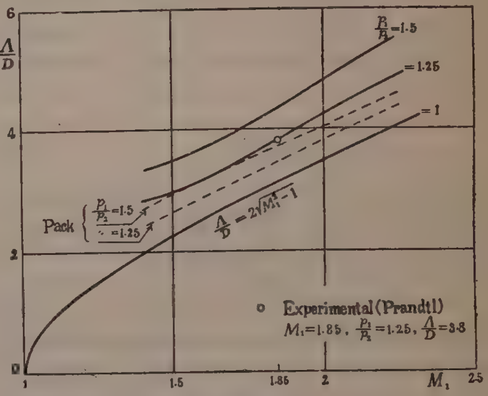

Fig. 3.

Table III.

M_1	Λ/D (formula (3.5))			Λ/D (formula (4.2))	
	$p_1/p_2=1$	$p_1/p_2=1.25$	$p_1/p_2=1.5$	$p_1/p_2=1.25$	$p_1/p_2=1.5$
$\sqrt{2}$	2	2.817	3.325	2.417	2.727
$\sqrt{3}$	2.828	3.491	4.013	3.179	3.454
1.85	3.113	3.806	…..	3.451	…..
2	3.464	4.209	4.792	3.791	4.052
$\sqrt{5}$	4	4.828	5.482	4.314	4.573

$$\frac{\Lambda}{D}=2\sqrt{\overline{M}^2-1}\,, \qquad (4.2)$$

where $\overline{M}$ is the Mach number on the bounding free streamline. Among Prandtl's experiments we find a value of Λ/D equal to 3.8 when $M_1=1.85$, $p_1/p_2=1.25$. In this case, Prandtl's formula (4.1) gives $\Lambda/D=3.113$, and Pack's formula (4.2) gives $\Lambda/D=3.451$, both of which are small compared with Prandtl's experimental value $\Lambda/D=3.8$, while our formula (3.5) gives $\Lambda/D=3.806$, which is in good agreement with the experiment. In Fig. 3, the values of Λ/D are shown graphically as a function of Mach number, M_1, for several values of the pressure ratios p_1/p_2.

§ 5. Conclusion

The structure of a jet issuing steadily with a uniform supersonic velocity into an external gas from a two-dimensional nozzle can be studied satisfactorily by introducing a hypothetical gas obeying an approximate adiabatic relation. Such a relation approximates well the true adiabatic relation, so that the present method of analysis is much more accurate than the linear theory due originally to Prandtl. Nevertheless, as in the case of the linear theory the jet has still a completely periodic structure in the downstream and no singularities occur which might be connected with the appearence of shock waves.

As will be expected from the comparison with a case in Prandtl's experiments, the results of the present analysis may give sufficiently accurate informations about the jet structure, provided that the ratio of the exit pressure to the external pressure is not so greater than unity and the exit velocity is not so close to sonic velocity.

In conclusion, the writer wishes to express his cordial thanks to Professor Dr. S. Tomotika for his kind inspection of the manuscript of the present paper. The writer's thanks are also due to the Ministry of Education for a grant in aid for fundamental scientific research.

References

1) R. Emden: Ann. d. Phys. u. Chem. **69** (1899) 426.

2) L. Prandtl: Phys. Zeits. **5** (1904) 599.

3) L. Prandtl: Phys. Zeits. **8** (1907) 23.

4) D. C. Pack: Quart. J. Mech. and App. Math. **3** (1950) 173.

5) I. Imai: Ooyôsûgaku-Rikigaku (The Applied Mathematics and Mechanics) **1** (1947) 147. (In Japanese.)

6) Z. Hasimoto: Mem. Coll. Sci., Univ. of Kyoto, Ser. A **26** (1950) 193.

7) Z. Hasimoto: J. Phys. Soc. Japan **8** (1953) 248.

JOURNAL OF THE PHYSICAL SOCIETY OF JAPAN Vol. 8, No. 3, MAY—JUNE, 1953

Discontinuous Potential Flow as the Limiting Form of the Viscous Flow for Vanishing Viscosity

By Isao IMAI

Department of Physics, Faculty of Science, University of Tokyo

(Received January 31, 1953)

The asymptotic behaviour of the viscous flow past an obstacle for vanishingly small viscosity is discussed on the basis of Prandtl's boundary layer theory together with Kirchhoff's dead water theory. If the pressure distribution around the obstacle is such that the separation of the boundary layer on the obstacle takes place, then the flow pattern should involve free stream-lines extending from the separation points. From such considerations it is concluded that the asymptotic flow pattern around a smooth obstacle is a discontinuous flow with dead water region of the Kirchhoff type such that the free stream-lines leave the obstacle with a finite curvature equal to that of the obstacle at the separation point.

§ 1. Introduction and Summary

As is well known, exact solution of the Navier-Stokes equations of motion for a viscous fluid is very difficult owing to the non-linearity. For small Reynolds number, the approximate methods due to Stokes and Oseen can be successfully employed. For large Reynolds number, i.e. for vanishingly small viscosity, it will be natural to consider that the limiting form of the flow pattern is the one corresponding to the potential flow of a perfect fluid. But, there are some varieties of possible flow patterns of a perfect fluid: usual irrotational flow and discontinuous flow of the Kirchhoff type, the latter having further indeterminacy corresponding to the arbitrary position of the separation points.

At the Third International Congress for Applied Mechanics, Prandtl [5] expressed the opinion that he believed it to be fairly certain that the viscous flow past a flat plate set perpendicular to the oncoming flow will converge to the Kirchhoff flow as the viscosity tends to zero.

In this paper, combining Prandtl's boundary layer theory with Kirchhoff's discontinuous flow theory, we arrive at the following conclusion. If the continuous potential flow around the given obstacle has such a pressure distribution that the boundary layer separation does not occur, then the said potential flow (plus the boundary layer) is the possible asymptotic flow pattern for vanishing viscosity. Otherwise, the asymptotic flow is given by the discontinuous flow of the Kirchhoff type, where the separation points of the free stream-lines are coincident with those predicted by the boundary layer theory from the pressure distribution given by the same discontinuous flow. In this case, there are two possibilities: one is that the free stream-lines have a finite curvature equal to that of the obstacle at the separation point and the other is that the separation occurs at a corner (if it exists) of the obstacle (just as in the case of a flat plate).

At the suggestion of the present writer, Mr. Kawaguti [3] investigated the discontinuous flow past a circular cylinder with special regard to the nature of the boundary layer. After completion of his work, my attention was called to a very interesting paper of Squire [9], which deals with the same problem as the present paper. His line of thought is quite similar to the present paper, except that he makes use of Southwell-Squire's modification of Oseen's linearized equations of motion for treating the boundary layer. Moreover, he confines himself to the case of a circular cylinder. Therefore, the author believes it to be of some interest to present here the consideration from the more general viewpoints.

It should be finally added that the present consideration is wholly concerned with the purely laminar flow. Actually, there would ineviatably appear turbulent regime for high Reynolds number. Therefore the result of the present paper is mainly of theoretical interest.

§ 2. Three Typical Cases of Asymptotic Flow

Let us consider the uniform flow of a viscous fluid past a fixed obstacle for vanishing viscosity. Putting $\mu=0$, where μ is the coefficient of viscosity, the Navier-Stokes equations of motion reduce to the Euler equations for an inviscid fluid. But, the condition of no slip at the surface of the obstacle cannot be satisfied by the potential flow. However, the condition can be regarded as satisfied if we assume the existence of Prandtl's boundary layer on the surface of the obstacle in the following manner.

In the first place, we consider a flat plate placed parallel to the uniform flow (Fig. 1). Outside the boundary layer and the wake, we can assume that there happens a potential flow, i.e. uniform flow $u=U$, $v=0$. The boundary layer and the wake are of vanishingly small thickness if $\mu=0$. The condition of no slip is obviously satisfied by the boundary layer. Therefore, in this case, the limiting form of the viscous flow past a flat plate is nothing but a potential flow (together with the boundary layer and wake of vanishing thickness).

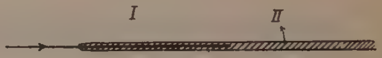

Fig. 1.

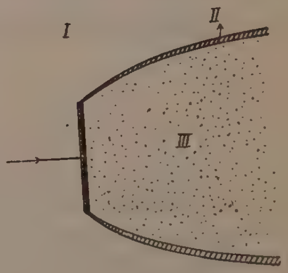

Fig. 2.

In the second place, we consider a flat plate set perpendicular to the oncoming flow (Fig. 2). In this case, the limiting flow for vanishing viscosity may be thought of as consisting of three parts, namely (I) the potential flow, (II) the boundary layer on the front surface of the plate and its extension (discontinuity surface), and (III) the dead water region. This is the well-known flow pattern due to Kirchhoff. The condition of no slip on the surface of the plate is obviously satisfied by taking account of the boundary layer.

As the third typical case, we consider the flow past a circular cylinder (Fig. 3). In this case, we can take a discontinuous flow of the Kirchhoff type as the limiting flow pattern just as for the previous case of a flat plate. But, in this case, the separation points A, A′ are, at first sight, not determinate. Indeed, as Schmieden [6] [7] has proved, we can find a discontinuous flow for any prescribed position of separation point. Thus, there arises

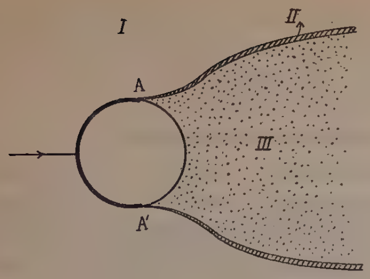

Fig. 3.

a question: what is the limiting form of the viscous flow for vanishing viscosity?

Schmieden has shown that there can be distinguished five cases according to the prescribed position of separation (Fig. 4). Denoting the separation point by the angle α as shown in Fig. 4, we have, with $\theta_1 \doteqdot 55^\circ$, $\theta_2 \doteqdot 120^\circ$,

(i) $\alpha < \theta_1$: the free stream-line cuts the cylinder,
(ii) $\alpha = \theta_1$: the free stream-line has the same curvature as the cylinder at the separation point,
(iii) $\theta_1 < \alpha < \theta_2$: the free stream-line has an infinite curvature at the separation point,
(iv) $\alpha = \theta_2$: the free stream-lines approach each other asymptotically,
(v) $\alpha > \theta_2$: the free stream-lines cut each other.

Accordingly, the range of the angle $\theta_1 \leqq \alpha \leqq \theta_2$ is admissible from the geometrical viewpoint.

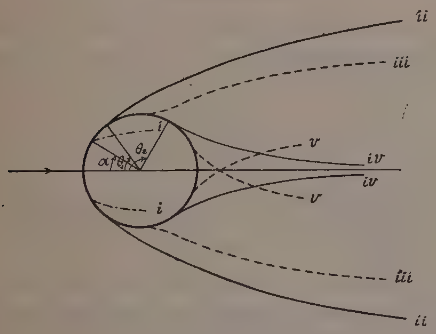

Fig. 4.

Brodetsky [1] adopted the angle $\alpha = \theta_1$ as only permissible, on the ground that it corresponds to a finite curvature. But, the reason seems to be rather arbitrary.

In the following lines, it will be shown that the choice $\alpha = \theta_1$ is well founded from the viewpoint of the boundary layer theory.

§ 3. Potential Flow near the Separation Point

Let us take the separation point A as the origin and the tangent and normal at A to the boundary of the obstacle as the x-axis and y-axis respectively (Fig. 5). Also, let the complex velocity potential of the discontinuous flow be $f(z)$, where $z = x + iy$. Further, we define

$$\Omega = i\log\left(\frac{1}{U}\frac{df}{dz}\right) = \theta + i\log\frac{q}{U}, \tag{1}$$

where q, θ are the magnitude and inclination of the velocity vector and U is the constant velocity along the free stream-line. Then the analytic function $\Omega(z)$ can be expressed in the neighbourhood of A as

$$\Omega = az^m + \cdots, \qquad m > 0 \tag{2}$$

since $\Omega(0) = 0$. On the free stream-line we have $z = re^{i\varphi} = r (>0)$ and $q/U = 1$. Hence

$$\theta = ar^m .$$

Hence, a is real. Next, on the wall of the obstacle, we have $z = re^{\pi i}$. Thus

$$\theta + i\log\frac{q}{U} = ar^m e^{m\pi i} .$$

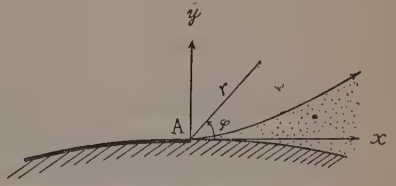

Fig. 5.

Differentiating along the surface of the obstacle, we have near the origin A,

$$\frac{d\theta}{ds} + i\frac{1}{q}\frac{dq}{ds} = -mar^{m-1}e^{m\pi i} ,$$

since $ds = -dr$. Here $d\theta/ds$ is the curvature of the obstacle, which will be assumed to be finite. Thus, taking the real part,

$$\frac{d\theta}{ds} = -mar^{m-1}\cos m\pi .$$

In order that $d\theta/ds$ should remain finite for $r \to 0$, we must have $m = 1/2$ or $m \geqq 1$. Therefore, the expression for Ω near A is in general given by

$$\Omega = az^{1/2} + bz + \ldots , \tag{3}$$

where a, b are real constants. Moreover we have, at A

$$\frac{d\theta}{ds}=b\,, \quad \frac{1}{q}\frac{dq}{ds}=-\frac{a}{2}\frac{1}{r^{1/2}} \quad \text{on the wall} \tag{4}$$

and

$$\frac{d\theta}{ds}=\frac{a}{2}\frac{1}{r^{1/2}}+b\,, \quad q=\text{const}=U \quad \text{on the free stream-line.} \tag{5}$$

(4) and (5) show clearly that at the separation point there takes place, in general, an infinite acceleration, and that the free stream-line has an infinite curvature there. In the particular case ($a=0$) that the velocity gradient at the separation point is zero, the free stream-line has finite curvature there, which is equal to that of the obstacle. This result is in agreement with Schmieden's result for a circular cylinder.

§ 4. Separation of Boundary Layer

In order that the free stream-line may not cut the surface of the cylinder, we must have $a \geqq 0$. (This is a geometrical condition.) But, if $a>0$, we have an infinite deceleration of the potential flow outside the boundary layer at the (prescribed) separation point A. Therefore separation of the boundary layer would be expected upstream of A. This conclusion can be most easily obtained by the well-known method of Pohlhausen [4] or the methods of Wada [11], Hudimoto [2] and Tani [10]. Thus, with the Pohlhausen method, separation takes place for $\Lambda=-12$, where $\Lambda=(\delta^2/\nu)(dq/ds)$, δ and ν being the boundary layer thickness and the kinematic viscosity respectively. Since $\Lambda=-\infty$ at A, separation should occur somewhere upstream of A. Further, with the methods of Wada, Hudimoto and Tani, separation occurs at the value of s given by

$$\frac{1}{q^n}\frac{dq}{ds}\int_0^s q^{n-1}ds=-c\,, \tag{6}$$

where n and c are certain positive constants and s is measured from the forward stagnation point. Since $dq/ds=-\infty$ at A, separation points should naturally lie upstream of A.

Accordingly, the prescribed separation point (as a discontinuous potential flow of the Kirchhoff type) and the separation point of the boundary layer coincide with each other only if $a=0$, so that the velocity gradient vanishes and hence the free stream-line curvature is finite there.

§ 5. Additional Remarks

Southwell and Vaisey [8] have calculated by the relaxation method the discontinuous flow of a perfect fluid past a circular cylinder with finite wake region (Fig. 6). It is clearly seen that the free stream-line has a curvature different from that of the cylinder at the separation point A. Consequently, by the result of the preceding section, it is concluded that the boundary layer separation point must lie further upstream of A and so such a flow pattern cannot be regarded as the limiting form of the viscous flow for vanishing viscosity.

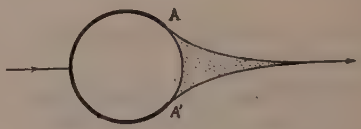

Fig. 6.

Finally, it may be remarked that in the previously mentioned case of a flat plate placed parallel or normal to the undisturbed flow the velocity outside of the boundary layer has no deceleration along the surface of the plate so that separation can take place only at the edge (or edges) of the plate.

References

1) S. Brodetsky: Proc. 2nd Intern. Congr. Appl. Mech. (1926) 527.
2) B. Hudimoto: J. Japan Soc. Aero. **8** (1941) 279.
3) M. Kawaguti: J. Phys. Soc. Japan **8** (1953) 403.
4) E. Pohlhausen: Z. A. M. M. **1** (1921) 252.
5) L. Prandtl: Proc. 3rd Intern. Congr. Appl. Mech. (1930) 42.
6) C. Schmieden: Ing. Arch. **1** (1930) 104.
7) C. Schmieden: Ing. Arch. **3** (1932) 356.
8) R. V. Southwell and G. Vaisey: Phil. Trans. Roy. Soc. A **240** (1946) 117.
9) H. B. Squire: Phil. Mag. **17** (1934) 1150.
10) I. Tani: J. Aeron. Res. Inst. Tokyo Imp. Univ. **199** (1941) 62.
11) K. Wada: Report Aeron. Res. Inst. Tokyo Imp. Univ. **196** (1940).

JOURNAL OF THE PHYSICAL SOCIETY OF JAPAN Vol. 8, No. 3, MAY—JUNE, 1953

Discontinuous Flow past a Circular Cylinder

By Mitutosi KAWAGUTI

Institute of Science and Technology, University of Tokyo

(Received February 2, 1953)

The discontinuous flow past a circular cylinder is studied making use of the theory of discontinuous flow and the boundary-layer theory. The determination of the separation points is carried out by means of an iterative method. It is found that the separation angle which is measured from a forward stagnation point, is approximately equal to 58°. This angle is very close to the smallest one 55° among the angles of separation which can be allowed from the discontinuous flow theory. Thus the flow with separation angles of 55° seems to be the limiting case of the viscous flow past a circular cylinder when the Reynolds number increases indefinitely.

§ 1. Introduction

It is of much theoretical interest to study the limiting behaviour of the flow past an obstacle when the Reynolds number $R(=Ud/\nu)$ becomes infinitely large. The continuous potential flow of perfect fluid is a possible solution, but does not seem to be a real solution of this problem, because the real fluid becomes turbulent, and moreover separates from the surface of the obstacle when the Reynolds number becomes large. If we confine ourselves to the laminar flow, it is highly probable that the discontinuous flow of the Kirchhoff type seems to be a solution of this problem. But when the obstacle has no corner, one cannot find the separation points uniquely from the theory of discontinuous flow only. In this paper, following the procedure suggested by Prof. Imai [1], the discontinuous flow past a circular cylinder is studied making use of the theory of discontinuous flow and the boundary-layer theory.

§ 2. Schmieden's Method of Treating Discontinuous flow

Schmieden [2], [3], [4] studied the discontinuous flow past a circular cylinder and showed that one can determine the flow uniquely if the separation-point is given, and that the angle of separation α(cf. Fig. 1) must lie between 55° and 120°.

Here we shall give the outline of Schmieden's method for convenience.

We consider the uniform flow of a perfect fluid past a circular cylinder, where the undisturbed velocity is 1. We take $z(=x+iy)$-plane as the physical plane, x-axis being the direction of the undisturbed flow. Then we can define the complex velocity potential $w(z)$ as

$$w(z)=\phi+i\psi, \qquad (1)$$

where ϕ is the velocity potential and ψ is the stream function. Next we introduce

$$\zeta=\log\frac{dz}{dw}=-\log q+i\theta, \qquad (2)$$

q, θ being the magnitude and the direction of the velocity respectively.

We consider the mapping of the ζ-plane onto the τ-plane which satisfies the following conditions:

(i) Whole region of the flow is transformed into the upper half of the unit circle of the τ-plane.

(ii) The free stream lines correspond to the diameter of the semi-circle in the τ-plane, so that the separation points to the points $\tau=\pm1$.

(iii) The part of surface of the circular cylinder along which the flow takes place corresponds to the semi-circular arc.

(iv) The stagation points corresponds to the point $\tau=i$.

(v) The point at infinity of the z-plane corresponds to the origin $\tau=0$.

We give schematically the aspect of z-, w-, ζ-, and τ-planes in Fig. 1, using the same letters for the corresponding points.

Then we can easily obtain the relation between w- and τ-plane in the following form

$$w=(1/4)(\tau+1/\tau)^2. \qquad (3)$$

We assume that the transformation between

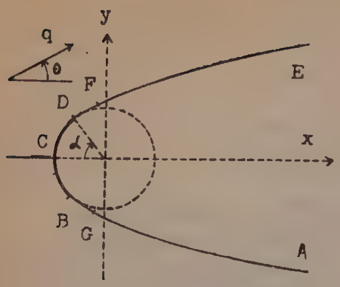

a. z-plane.

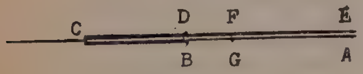

b. w-plane.

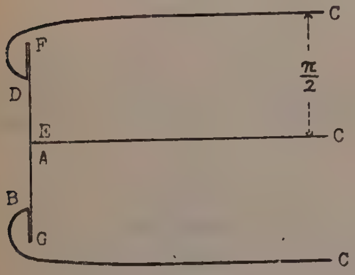

c. ζ-plane.

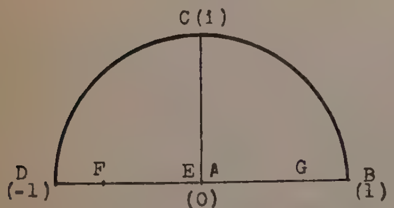

d. τ-plane.

Fig. 1.

ζ-plane and τ-plane can be given by

$$\zeta=\log\left[(\tau+i)/(\tau-i)\right]-i\pi+iZ(\tau). \qquad (4)$$

Here $\log\left[(\tau+i)/(\tau-i)\right]-i\pi$ is the ζ for a flat plate and the singularity corresponding to the separation-point is included in it, so that $Z(\tau)$ is regular and can be expanded in an asending power series of τ in the unit circle of τ-plane, thus:

$$Z(\tau)=\sum_{n=1}^{\infty}a_n\tau^n. \qquad (5)$$

a_n being constants to be determined later. Accordingly (4) takes the form

$$\zeta=\log\left[(\tau+i)/(\tau-i)\right]-i\pi+i\sum_{n=1}^{\infty}a_n\tau^n. \qquad (6)$$

The direction θ_k of the tangent to the contour and the curvature κ_k of the contour in the z-plane are given respectively by

$$\left.\begin{aligned}&\theta_k=\pm\pi/2+\sum_{n=1}^{\infty}a_n\cos n\vartheta,\\ &\tau=\exp i\vartheta,\end{aligned}\right\} \qquad (7)$$

$$\kappa_k=\frac{\exp\left(\sum_{n=1}^{\infty}a_n\sin n\vartheta\right)}{2\sin\vartheta(1+\sin\vartheta)}\sum_{n=1}^{\infty}na_n\sin n\vartheta. \qquad (8)$$

We define the angle of separation α as in Fig. 1. Since the separation points correspond to the points $\tau=\pm1$, we have from (7)

$$\alpha=\pm\sum_{n=1}^{\infty}a_n. \qquad (9)$$

If the angle of separation α is given, we can determine the coefficients a_n by the condition that the curvature as given by (8) should be identical with that of the given contour, together with the condition (9). If the symmetry of the flow with respect to x-axis exists, $a_{2n}(n=1, 2, \ldots)$ become zero. Having obtained a_n we can find the flow from the relations (2), (3) and (6).

§ 3. Iterative Method for Determining the Angle of Separation

(i) We give the angle of separation arbitrarily, and calculate the flow by the method mentioned at the end of § 2.

(ii) Thus we have the velocity distribution on the surface of the circular cylinder. Assuming this to be the velocity outside of the boundary layer, we calculate the angle of separation using the boundary-layer theory.

(iii) If the angle thus obtained is smaller (larger) than the given angle, we take a smaller (larger) angle in (i), and continue (i) to (iii) successively until the angle obtained becomes identical with the given angle, which is the angle of separation looked for.

§ 4. Numerical Results

For simplicity, we approximate the infinite series (5) by a polinomial of the form:

$$Z=a_1\tau+a_3\tau^3+a_5\tau^5+a_7\tau^7. \qquad (10)$$

This approximation gives rise to an error of magnitude of only about 1% for the curvature of the contour κ_k, and so it seems sufficient for the purpose of this paper.

To calculate the angle of separation from the boundary-layer theory, we use Prof. Tani's formula [5] which is given as follows. The value of σ which is defined as

$$\sigma=\frac{0.44}{U^6}\frac{dU}{ds}\int_0^s U^5 ds, \qquad (11)$$

where U is the velocity outside the boundary layer and s is the distance along the surface from the stagnation point, served as the criterion for the separation. Thus $\sigma=-0.084$ corresponds to the separation point.

Table I

α_0	180°	82°	60°	58°	55°
α_1	93.5°	72°	59.3°	57.9°	none

(α_0 is the prescribed angle of separation, and α_1 is the angle of separation obtained from the boundary-layer theory.)

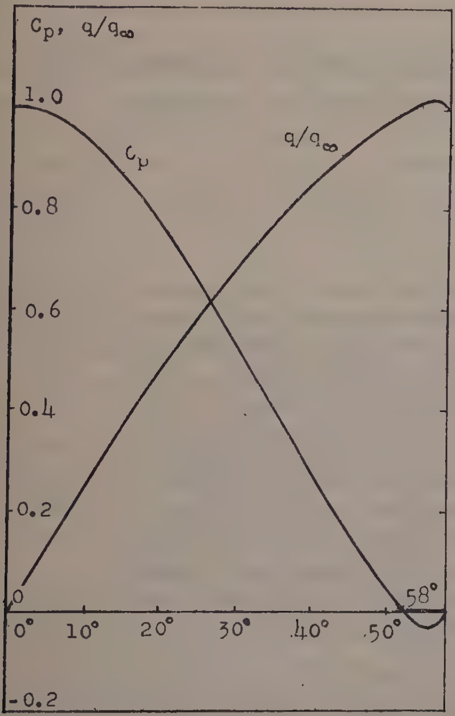

Fig. 2. The velocity and pressure distributions on the surface.

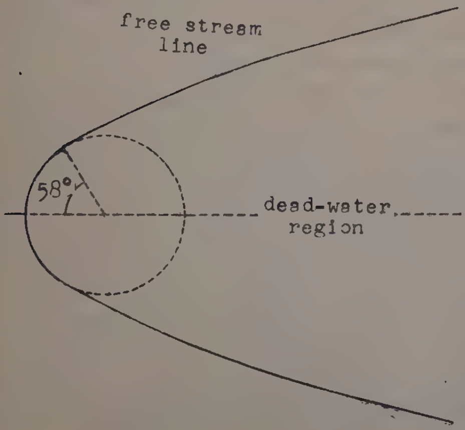

Fig. 3. The free stream lines.

In Table 1, we give the iterated result to determine the separation point, and from this table we can conclude that the angle 58° is the angle of separation from this theory. In Figs. 2 and 3 we give the velocity and pressure distributions on the surface and the free stream lines for this case.

The velocity distribution U for each case has been determined in the following manner. For the case when the prescribed angle is 180°, the velocity distribution for the usual continuous flow was taken. For the cases, 82° and 55°, Schmieden's results were read off from his paper [3]. For the cases 60° and 58° the velocities were calculated following the procedure of § 2, thus obtaining the coefficients a_n's in equation (5) as shown in Table 2. Then, the velocity distributions thus obtained were approximated by polynomials in s, for carrying out the integration (11).

Table 2

α	a_1	a_3	a_5	a_7
58°	0.99041	0.01929	0.00205	0.00054
60°	1.02249	0.02138	0.00257	0.00076

§ 5. Discussion

Thus, we could determine the separation points on the circular cylinder uniquely, so that the whole flow field is determined without recourse to any experimental data. It is very likely that this flow is the limiting flow when the Reynolds numbers R becomes infinitely large.

The calculted angle of separation 58° is fairly different from the experimental value 82°. This discrepancy can be explained from the fact that the pressure in the dead-water region is not equal to, but always smaller than the pressure at infinity as assumed in the discontinuous flow theory.

By the way, it is worthy to note that calculated angle of separation is very close to the smallest one 55° among the angles of separation which can be allowed from the discontinuous flow theory (in this case the stream lines separate smoothly from the cylinder). It is very likely that calculated angle of separation becomes this value 55° when the exact theory of boundary layer is used. In this connection, reference should be made to the preceding paper of Prof. Imai [1].

In conclusion the author wishes to express his sincere thanks to Proffessor I. Imai for his guidance in the course of this work.

References

1) I. Imai: J. Phys. Soc. Japan, **8** (1953) 399.
2) C. Schmieden: Ing. Arch., **1** (1930) 104.
3) C. Schmieden: Ing. Arch., **3** (1932) 356.
4) C. Schmieden: Ing. Arch., **5** (1934) 373.
5) I. Tani: J. Aeron. Res. Inst. Tokyo Imp. Univ. No. 199 (1941).

JOURNAL OF THE PHYSICAL SOCIETY OF JAPAN Vol. 8, No. 3, MAY—JUNE, 1953

Surface Roughening and Oxidation of Galena Cleavage Face in a Vacuum Furnace Under Limited Air Supply

By Hitosi HAGIHARA

Kobayasi Institute of Physical Research, Kokubunzi, Tokyo, Japan

(Read April 29, 1949. Received January 24, 1953)

Surface structures of galena cleavage face heated at reduced air pressures $10^{-2}-10^{-3}$ mm. Hg and at temperatures 100°-600°C. were studied by electron diffraction. Surface roughening commences at 350°C. with the release of sulphur in combination with oxygen. The roughened surface is bounded by the $\{100\}_{PbS}$ facets. Extra structure due presumably to some effect of the enriched lead atoms was also observed. As to the oxidation product, epitaxially oriented lead sulphate ($PbSO_4$) or the suboxide (Pb_2O) crystallites were obtained at temperatures below 400°C. For the latter, the needle like external shape was deduced from the analysis of the diffraction spot. Above 400°C. randomly oriented suboxide or the yellow oxide (PbO) crystallites were observed. With the complete evaporation of the crystal at 600°C. silver powder remained as the residue.

§1. Introduction

Electron diffraction investigation of the surface oxidation of galena (PbS) is of interest both from pure physico-chemical as well as the practical viewpoint. The former interest is concerned with the study of the mechanism of crystal growth of oxides on solid surfaces. The practical interest concerns itself, first, with the importance of the problem to the technical processes for the seperation of sulphide minerals by flotation. In these respects the author already published reports on its oxidation in air or under environments supposed to be realised in crushing and grinding processes of the mineral in its flotation[1)2)3)].

Secondly, in recent years, the importance of the lead sulphide photoconductive cells for the detection of infrared radiations has greatly increased[4)5)]. Their photoconductivity is reported to be largely determined by suitable treatment with oxygen. The PbS deposits are baked in air, in oxygen under reduced pressure, or *in vacuo* in order to produce or increase their photosensitivity. These treatments give rise to an oxidation product on the surface of the PbS crystallites. In this connection, it is stated by Wilman[6)] that $PbO\cdot PbSO_4$ may be formed on the PbS films baked in oxygen at approximately 0.1 mm Hg or heated in air at 350° or 550°C for 10 or 5 min, respectively. The identification of the surface compound was carried out through the analysis of the ring patterns obtained with the oxidised specimens. Doughty *et al.*[7)] have also identified the surface oxidation product on the photoconductive lead sulphide film as lanarkite, $PbO\cdot PbSO_4$, by electron diffraction.

Yamaguti *et al.*[8] studied, from pure physico-chemical interest, the surface oxidation of the etched galena cleavage face at 0.11, 0.2 and 380 mm Hg at temperatures near 600°C for 5 min. They analysed the obtained ring and arc patterns to be due to lead suboxide (Pb_2O), lead yellow oxide (PbO) and the other unidentified lead oxides (Pb_mO_n). The electron diffraction identifications of the surface substances through their ring or arc patterns, however, are often somewhat arbitary in the meaning that their relative intensities are not interpreted unequivocally due to the secondary effects in diffraction. This is particularly so when the pattern is complicated and there are possibilities that the surface coating may be composed of more than one element or compound. The most accurate and detailed informations on the structure and texture of the surface coating are obtained with its single-crystal diffraction patterns. With lead sulphide the single-crystal diffraction patterns of its surface oxidation products are expected to be obtained through the oxidation of the fresh galena cleavage face. The author already reported the formation and orientations of lead sulphate ($PbSO_4$) and the lead basic sulphate ($PbO \cdot PbSO_4$) crystallites on the cleavage face oxidised in air at temperatures below approximately 350°C. At higher temperatures in air the reaction was more complicated, and various kinds of sharp spot patterns, unidentified with the lead compounds of the known structures as yet, were obtained[2)3)].

In the present paper an electron diffraction study of the surface oxidation of galena cleavage face in a vacuum furnace, carried out with the hope of throwing some light on these problems, will be given.

§ 2. Experimental

Fresh galena cleavage face, about 2×2×1 mm in size, was prepared by cleaving its ideally shaped single crystal. It was brought into the silica tube, 5 cm in diameter and 50 cm in length, of a horizontally set electric furnace. After it was evacuated by means of an oil diffusion pump and a cenco hyvac pump to the order of 10^{-4}mm Hg, the furnace was heated to the desired temperature. The transition period required for the temperature elevation of the furnace was controlled to about 30 min in every case. The furnace was kept at the desired stationary temperature for one hour, after which the electric current was cut off. The evacuation continued during the whole heating cycle until the furnace was cooled to the room temperatures. The temperature measurement was carried out with a Pt-PtRh thermo-junction inserted very close to the specimen surface. The air pressure within the furnace was measured by means of the gas discharge within a Geissler tube, calibrated beforehand by a McLeod gauge. The pressure during the heating processes was 10^{-2}—10^{-3} mm Hg.

After the furnace was cooled to the room temperature, air was let into it and the specimen was brought out to be examined by electron diffraction. Its diffraction pattern was obtained with 35-kV-electrons by the reflection method at least at the $\langle 100 \rangle_{PbS}$ and $\langle 110 \rangle_{PbS}$ azimuths. The specimen-plate distance of the apparatus was 30 cm.

The oxidation was carried out at stationary temperatures approximately 100°, 200°, 250°, 300°, 350°, 400°, 425°, 450°, 500°, 550° and 600°C. By spectral analysis Ag, Bi, Cu, Fe, Sb and Zn were detected as the metallic components of the impurities contained in the present galena crystal.

§ 3. Experimental Results and Their Interpretations I. Surface Roughening

Results: With the cleavage faces heated at temperatures below approximately 350°C, Kikuchi lines and bands were observed with electrons at grazing incidence. With the one heated at 100°C, they were observed as distinctly as with the fresh cleavage face. With the specimens heated at temperatures between 200°C and 350°C, they became more and more blurred with the elevation of the heating temperature, and the galena spot pattern, elongated sharply towards the shadow edge, became more and more distinct. However, all the galena patterns obtained with specimens heated at this temperature range showed the appearance of the diffraction of electrons by smooth surfaces. Typical diffraction patterns obtained with specimens heated at 200° and 250°C are represented in Figs. 1 and 2, respectively.

With the specimens heated at 400°C or above, there were observed abrupt changes

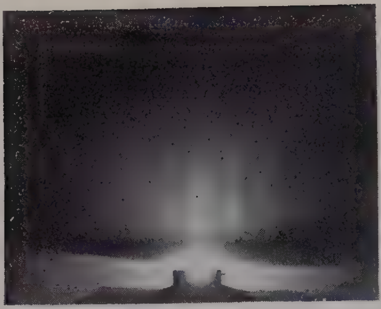

Fig. 1. Galena cleavage face heated in a vacuum furnace at 200°C. for 1 hr. Beam // <110>PbS.

Fig. 2. Galena cleavage face heated in a vacuum furnace at 250°C. for 1 hr. Beam // <100>PbS.

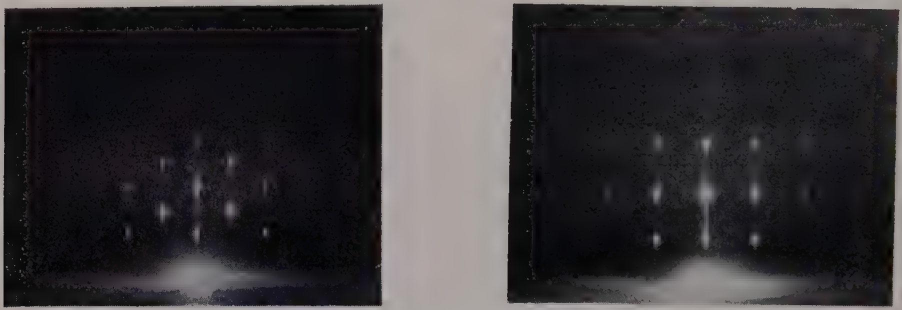

Fig. 3a. Beam // <100>PbS. Fig. 3b. Beam // <110>PbS.

Fig. 3. Galena cleavage face roughened by heat treatment in a vacuum furnace at 400°C. for 1 hr..

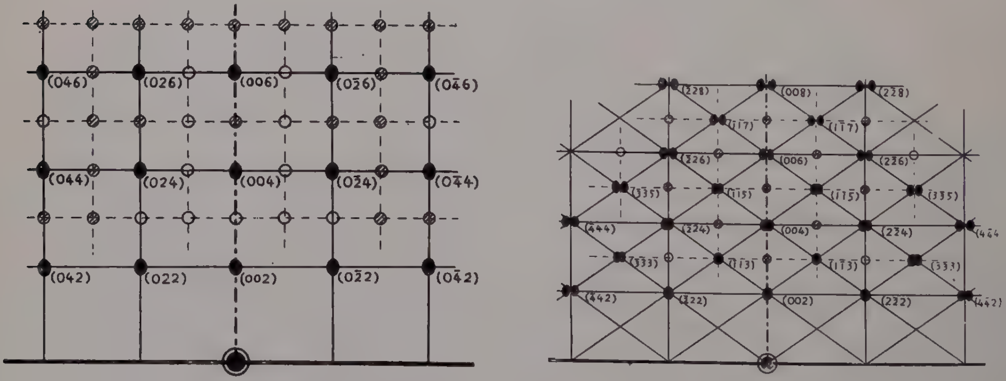

Fig. 4a. Beam // <100>PbS. Fig. 4b. Beam // <110>PbS.

Fig. 4. Extra spots (shaded circles) observed in the diffraction pattern due to roughened galena cleavage face. Plain circles represent those observed extremely weak in intensity and hence somewhat uncertain.

in the features of the diffraction patterns obtained. The pattern showed a transmission type appearance consisting of the regular array of the diffraction spots due to the {100} face of galena. Typical diffraction pattern obtained with a specimen heated at 400°C is represented in Figs. 3a and 3b. In Fig. 3b, where the incidence of electrons is parallel to the face diagonal, it is remarkable that the diffraction spots away from the central spot are replaced by a group of two spots separated horizontally from the place where the normal spot should have been. The separation is larger, the greater the distance of the spot from the spot from the central spot. In Fig. 3a, where the incidence of electrons is parallel to the cube edge, such is not the case.

In addition to the ordinary spot pattern due to the {100} face of galena, weak extra spots were also observed in the diffraction photographs obtained with slightly roughened galena cleavage face. They were observed more distinctly with the <110> than with the <100> azimuth. In both cases the extra spots were diffuse and elongated towards the shadow edge. The positions of these extra spots in the diffraction photographs are shown with shaded circles in Figs. 4a and 4b.

Interpretation of the external shape of the roughened surface from its diffraction patterns: The doubling of spots in Fig. 3b may be interpreted in terms of the intersection of the Ewald sphere of reflection with two spikes drawn out from reciprocal lattice points. The angle between the spikes in the reciprocal lattice may be calculatad readily from the seperations of the pair of spots and their distances from the Ewald sphere. The glancing angle of the electron beam to the crystal surface was calculated from the height of the horizontal edge limiting the lowest boundary of the general background in Fig. 3b. Fig. 5 shows a section of the Ewald sphere cutting through the reciprocal lattice points and spikes drawn to represent the actual geometrical relationships in the present experiment. The angle between the two spikes was found to be approximately 90°; *i.e.*, each spike was found normal to the (100) and (010) faces, respectively.

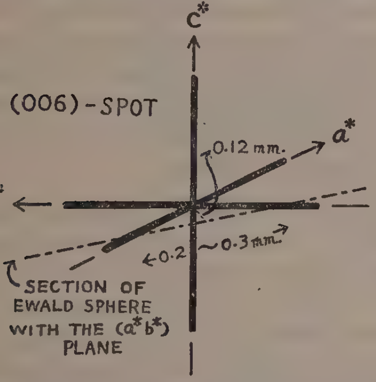

Fig. 5. Reciprocal lattice construction for the explanation of the splitting of diffraction spots in Fig. 3.

The vertical elongation of the diffraction spots as observed nearer to the central spot, where the Ewald sphere cuts almost through the reciprocal lattice points, may be interpreted that the boundary surface is composed also of the (001) facets. The asymmetry in the elongation, *i.e.*, longer in the downward than in the upward direction, may probably be interpreted in terms of the distortion of the crystal as well as refraction effects as discussed by Pashley[9] on electrolytically polished silver crystal. Thus, the diffraction pattern in Fig. 3b, where the incidence of electrons is parallel to the $\langle 110\rangle_{\mathrm{PbS}}$ axes, is interpreted most satisfactorily as due to the diffraction of electrons by projections bounded by the $\{100\}_{\mathrm{PbS}}$ facets.

In Fig. 3a, where the incidence of electrons is parallel to the ⟨100⟩ azimuth, cross-shaped spots are expected to be observed near the central spot where the Ewald sphere cuts the centres of the reciprocal lattice points with spikes. The actual observation, however, showed only vertically elongated spots. This may be interpreted that in the ⟨110⟩ incidence the corners of the projections bounded by the {100} facets were most effective for the diffraction of electrons whereas with the ⟨100⟩ incidence the pattern was due for the most part to the reflection of electrons on the flat (001) facets.

Thus the present analysis has resulted, without contradiction, that the galena cleavage face slightly roughened by heating *in vacuo* is most likely consisting of the minute projections or steps bounded by the {100} facets. The surface state may be similar to, but more sharply edged and cornered than that of the {100} face of rock salt etched slightly by water vapour, the electronmicrograph of which has been shown by Raether in Fig. 47a of his symposium[10].

Interpretation of the extra spots: The extra spots shown with shaded and plain circles in Figs. 4a and 4b are interpreted as due to the diffraction of electrons by a simple cubic array of scattering centres with the edge length of the unit cell same as that of galena and in the identical orientation with the latter. In this interpretation it is assumed that the extra spots are also situated on the positions of the normal galena spots. The extension of this arry on the galena surface is supposed very limited to the order of several unit cells as deduced from the diffuseness of the spots. Its relative abundance as compared with the normal galena arry in the surface layer effective for the diffraction of electrons may also be very scarce, since the extra spots were very weak in intensity as compared with the normal galena spots.

It is only supposed that this array of atoms may be due to some influences of the excess lead atoms remained on the galena surface as the result of the evaporation of sulphur atoms, presumably in the form of sulphur dioxide, from the surface. Lead sulphide has been reported to be provided with an excess of lead by heating in vacuum[11)12)13)14)15)].

§ 4. Experimental Results and Their Interpretations II. Surface Oxidation

Besides the surface roughening above mentioned, the treated cleavage face showed diffraction patterns due to the surface oxidation products in most cases. They were analysed and compared with the single crystal structural data[16)17)] or Debye-Scherrer ring data[18)] on various lead sulphoxides and oxides.*) The result of their identifications is summarised in Fig. 6. In it the abscisse represents the heating temperature of the cleavage face. In the followings detailed explanations on each diffraction pattern and its analysis will be given.

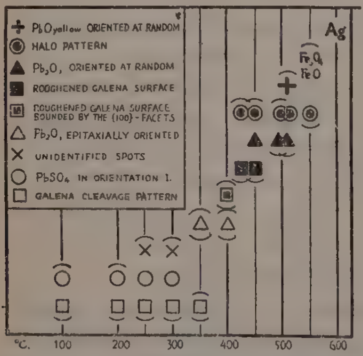

Fig. 6. Summary of the identifications of the surface oxidation products on galena cleavage face heated in a vacuum furnace at pressures $10^{-2}-10^{-3}$ mm. Hg for 1 hr.

Lead sulphate: The formation of lead sulphate, $PbSO_4$, crystallites was confirmed with specimens heated at 100°, 200°, 250° and 300°C. Of them, with specimens heated at temperatures below 250°C, the sulphate pattern was observed faintly on the strong galena cleavage pattern. The sulphate crystallites were oriented with respect to the galena lattice in the manner defined as "orientation I" in the previous works[1)2)3)]. Symbolically, it is written as in Table I.

Table I. "Orientation I" of lead sulphate on galena.

1st direction	$(001)_{PbSO_4}$ // $(001)_{PbS}$
2nd direction	$[100]_{PbSO_4}$ // $[110]_{PbS}$

Detailed considerations of the arrangement of atoms of the sulphate and galena at the interface in this orientation were also given previously[1)2)]. In the present instances "orientation II" of the sulphate crystallites on galena was observed either extremely weakly or was not observed at all.

With the specimen heated at 300°C, comparatively strong ring pattern was observed simultaneously with the spot pattern due to the sulphate crystallites in the above orientation. It was identified best with lead sulphate crystallites in random orientations. Besides these, some weak unidentified spots were also observed. Their identification with those expected from the basic sulphate, $PbSO_4 \cdot PbO$[19)20)], crystallities did not yield any definite conclusions as yet.

Lead suboxide (Pb_2O): Diffraction patterns analysed to be due to the lead suboxide crystallites were obtained with specimens heated at 350°, 400°, 450° and 500°C. Of them those obtained with specimens heated at 350° and 400°C showed the epitaxial orientation of the crystallites with respect to the galena lattice, while the remaining two specimens showed the ring pattern.

(a) *Epitaxially oriented lead suboxide crystallites*;

The diffraction patterns obtained with the specimen heated at 400°C are represented in Figs. 7a and 7b. With the specimen heated at 350°C the sharp spots observed in these figures were more diffuse and elongated downward toward the shadow edge; *i.e.*, all of the diffraction spots were of equal shapes.

The analysis of these patterns resulted that they were due to the diffraction of electrons by a face centred cubic lattice with $a=5.40-5.45$ Å, oriented with respect to the galena

---

*) Their original literatures are conveniently summarised in Wilman's work[6)].

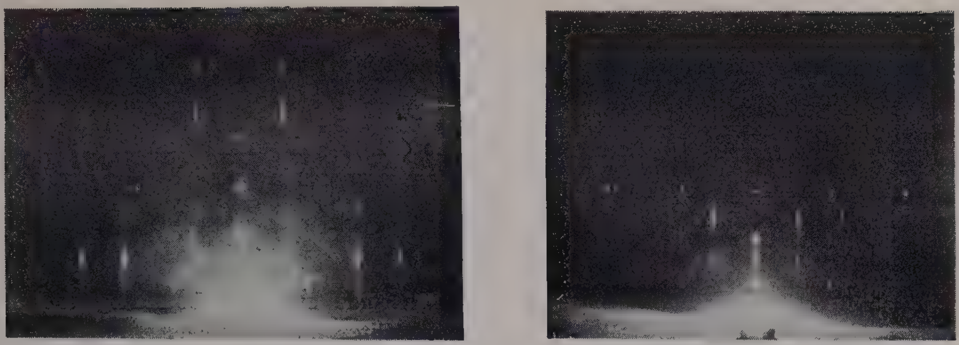

Fig.7a. Beam // <100>$_{PbS}$.

Fig. 7b. Beam // <110>$_{PbS}$.

Fig. 7. Epitaxially oriented lead suboxide (Pb_2O) crystallites on galena cleavage face heated in a vacuum furnace at 400°C. for 1 hr.

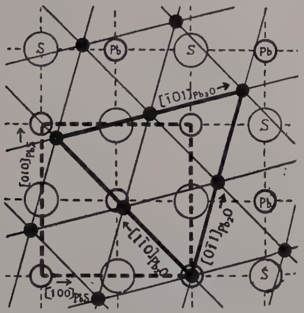

Fig. 8. Arrangement of lead atoms at the interface between the lead suboxide crystallite and the cub face of galena. Lead atoms of both crystals are placed at the common origin.

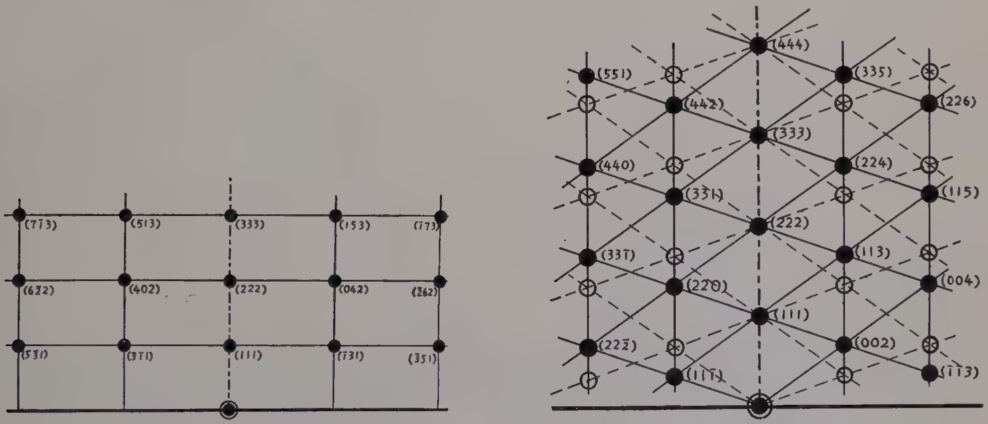

Fig. 9a. Beam ⊥ [1$\bar{1}$0]$_{Pb_2O}$.

Fig. 9b. Black circle: Beam // [1$\bar{1}$0]$_{Pb_2O}$.
White circle: Beam // [$\bar{1}$10]$_{Pb_2O}$.

Fig. 9. Indexing of the diffraction spots as expected from the lead suboxide crystallites on galena when the incidence of electrons is parallel to the latter's face diagonal. (See Fig. 8). Fig. 7b corresponds to the superposition of Figs. 9a and b.

lattice in the manner written symbolically in Table II. Of the lead compounds with known structures lead suboxide, Pb_2O[21], has a cubic face centred array of the lead atoms and its a-axis is 5.38 Å. The agreement between the two is fairly good. Recently, pseudo cubic Pb_3O_4 with a=5.46 Å has been reported[16][*]. However, its structural details are not yet precisely known as to permit the identification of the present cubic lattice with it.

The external shapes of the suboxide

---

[*] T. Katz, M. Siramy and R. Faivre: Compt. rend. **227** (1948) 282.

Table II. Orientation of lead suboxide on galena

1st direction	$(111)_{\mathrm{Pb_2O}}$ // $(001)_{\mathrm{PbS}}$
2nd direction	$[1\bar{1}0]_{\mathrm{Pb_2O}}$ // $[110]_{\mathrm{PbS}}$

crystallites were deduced from considerations of the elongations of the diffraction spots. For the convenience of the following explanations, the arrangement of lead atoms at the interface between the lead suboxide and galena in the above orientation is shown in Fig. 8. The indexing of the diffraction spots in the $\langle 110 \rangle_{\mathrm{PbS}}$ incidence of electrons is shown in Figs. 9a and 9b. The rectangular net pattern in Fig. 9a is expected when the projection of the incident beam on the $(111)_{\mathrm{Pb_2O}}$ face is normal to the $[1\bar{1}0]_{\mathrm{Pb_2O}}$ axis, and the triangular net pattern in Fig. 9b is expected when the projection is parallel to the $[1\bar{1}0]_{\mathrm{Pb_2O}}$ axis.

The diffraction pattern in Fig. 7b shows that the rectangular net pattern is of transmission type, while the diffraction spots constituting the triangular net pattern are elongated considerably towards the shadow edge implying that the pattern is due to the diffraction of electrons by the flat $(111)_{\mathrm{Pb_2O}}$ facets. A possible interpretation of this effect may be that the produced lead suboxide crystallites are elongated like needles along the $\langle 1\bar{1}0 \rangle_{\mathrm{PbS}}$ directions, on which the $[1\bar{1}0]_{\mathrm{Pb_2O}}$ atom row lies in parallel. The vertical elongation of the spots shows that the upper surfaces of the crystallites are bounded by the $(111)_{\mathrm{Pb_2O}}$ facets.

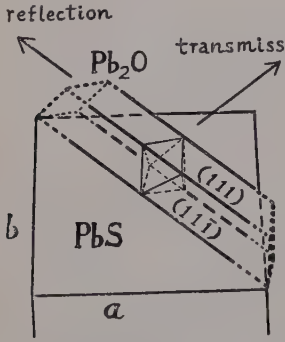

Fig. 10. External shape of the lead suboxide crystallites on galena as deduced from the elongations of the diffraction spots in Fig. 7.

Fig. 11. Lead suboxide (Pb_2O) rings and spots obtained on galena cleavage face heated in a vacuum furnace at 500°C. for 1 hr.

The side surfaces bounding the suboxide crystallites were deduced from the diffraction patterns obtained at the azimuthal setting of the galena face deviated by 1°–2° from the $\langle 110 \rangle_{\mathrm{PbS}}$ incidence. The obtained pattern showed streaks or marked elongations of spots in directions connecting the (111) and (002) spots or the (222) and (113) spots. This means that the side surfaces are also bounded by the octahedral facets. The orientation and the external shapes of the suboxide crystallites on the galena cleavage face thus revealed from their diffraction patterns are depicted in Fig. 10.

Fig. 12. Lead suboxide (Pb_2O) and the yellow oxide (PbO) rings obtained on galena cleavage face heated in a vacuum furnace at 500°C. for 1 hr.

Fig. 13. Iron oxide (Fe_3O_4 and FeO) rings obtained on galena cleavage face heated in a vacuum furnace at 550°C. for 1 hr.

(b) *Halo pattern and the rings due to lead suboxide*;

With specimens heated at 425°C, three haloes were observed superposed on the cross grating pattern due to roughened galena surface. With the one heated at 450°C, ring pattern due to randomly oriented lead suboxide crystallites was also observed superposed on the above pattern. With the specimen heated at 500°C, the crystal surface became matt after the heat treatment and the suboxide rings were predominant in the diffraction photograph. As represented in Fig. 11, regularly arrayed spots of the suboxide were also observed on the rings. The whole pattern showed the transmission type appearance.

The external shapes of the crystallites were not deduced from the present patterns, since they showed no fine structures of the rings. It was only deduced from the sharpness of the rings and spots that the crystallites were fairly large in size to dimensions of more than 100 Å in diameter.

Yellow lead oxide (PbO): With the specimen heated at 500° C, rings due to the other compound than lead suboxide were often obserbed simultaneously with the suboxide rings. Their relative abundance as observed in the diffraction photograph was not constant, but varied considerably even on the same specimen surface. This fact suggested that the surface coatings were composed of the suboxide and the other distinctly different substance distributed non-uniformly over the galena surface. An eample of the diffraction pattern obtained with a specimen heated at 500° C is represented in Fig. 12. The figure shows that the suboxide rings are of whole circles while the present rings are of semicircles meaning that the former may be due to crystallites attached nearer to the edges of the galena surface, while the latter to those distributed heterogeneously over the surface.

The analysis of the latter rings in Fig. 12 is shown in Table III. The observed spacings and intensities of the rings are explained most reasonably, except for the weak 2.64 Å. ring and the very weak and diffuse 2.23–2.13 Å ring, by assuming that the surface is covered with randomly oriented yellow lead oxide, PbO[22], crystallites. The 2.64 Å ring may roughly be identified with the 2.53 Å ring of an iron oxide, Fe_3O_4, the observation of which will be described immediately below.

Table III. Analysis of the ring pattern in Fig. 12.

Spacing in Å (Intensity)	PbO (Halla and Pawlek[22]) Spacing in Å (Intensity)
3.14 (W)	3.08 (S)
2.98 (S)	2.96 (SS)
2.80 (M)	2.76 (M)
2.64 (W)	
2.23 (W, d)	2.37 (M)
2.13	
1.99 (S)	2.01 (S) 1.96 (M)
1.85 (S)	1.85 (S)
1.71 (W)	1.80 (M) 1.72 (S)
1.58 (S)	1.64 (S)
1.52 (S)	1.53 (S) 1.47 (S)
1.37 (W)	1.36 (M)
1.29 (M)	1.29 (S)
1.24 (W)	1.25 (M)
1.20 (M)	1.20 (M) 1.17 (M)
1.15 (W)	1.14 (M) 1.12 (S)
1.07 (M)	1.06 (M)
1.01 (M)	1.02 (M) 0.98 (M)
0.97 (M)	0.97 (M) 0.95 (S)
0.93 (W)	0.93 (M) 0.926 (S)

§ 5. Experimental Results and Their Interpretations. III. Diffraction Patterns Due to Impurities Contained in the Galena Crystal

Rings due to iron oxides: By heat treatment at 550° C galena crystals were reduced considerably in size. The surface was matt and yielded the diffraction pattern consisting of three haloes for the most part. On some portions of the specimen surfaces, however, rings were also observed. They consisted of the semi-circles as represented in Fig. 13. Their analysis resulted, as shown in Table IV, that they were identified best with the rings expected from the mixture of the iron oxides, Fe_3O_4 and FeO, except for the weak 2.00 Å ring. This is almost equal to the 2.01 Å ring of iron, the strongest in it. It is supposed that the iron oxides may have been produced from iron contained in ganela as an impurity presumably in the form of sulphide[23]. Iron might have been enriched on galena surface by the evaporation of lead and sulphur atoms from it, combined with oxygen and coagulated on the roughened surface in patches.

Table IV. Analysis of the ring pattern in Fig. 13.

Spacing in Å (Intensity)	Fe_3O_4*) Spacing in Å (Intensity)	FeO*) Spacing in Å (Intensity)
4.65 (M)	4.85 (0.06)	
2.95 (W)	2.97 (0.28)	
2.57 (S)	2.53 (1.00)	
2.45 (M)	2.42 (0.11)	2.47 (0.50)
2.08 (S)	2.10 (0.32)	2.14 (1.00)
2.00 (W)		
1.76 (M)	1.71 (0.16)	
1.63 (M)	1.61 (0.64)	
1.52 (M)		1.51 (0.60)
1.48 (S)	1.483 (0.80)	
1.30 (M)	1.326 (0.06) 1.279 (0.20)	1.293 (0.15)
1.22 (M)	1.210 (0.05)	12.23 (0.08)

* After Hanawalt, Rinn and Frevel[18].

Metallic silver as residue of evaporation: After the heat treatment at 600° C, the specimen was evaporated completely, except for a very small amount of residual grey powder. Its spectral analysis resulted that its main metallic component was silver. The X-ray Debye-Scherrer rings due to the substance were analysed that it consisted of some crystallites of a face centred cubic structure with $a=4.08$ Å. This is in conformity with the structure of metallic silver, which crystallises in to a face centred cubic structure with $a=4.079$ Å.[16].

§6. Discussion

Galena cleavage face has been found by the present electron diffraction study to loss its ideally flat surface character in a vacuum furnace by heat treatment at temperatures between 350° and 400° C. The analysis of the diffraction spots due to the roughened surface resulted that it consisted of the minute projections or steps bounded by the $\{100\}_{PbS}$ facets. The initiation of this roughening is supposed deeply connected with the commencement of the release atoms from the surface. This supposition is supported from the nature of the surface oxidation products produced on the cleavage face under scanty air supply. At temperatures 300° C or below, lead sulphate was the main oxidation product under such conditions. The sulphate should have been produced on the cleavage face by the reaction, $PbS+2O_2=PbSO_4$, same as that of the activated adsorption of oxygen on galena. At temperatures 350° C or above, lead suboxide or the yellow lead oxide was produced, for the formation of which sulphur should have been driven off from galena surface or the produced sulphate coatings. With sufficient oxygen supply the sulphate may decompose successively into $PbSO_4 \cdot PbO$, $PbSO_4 \cdot 2PbO$, and $PbSO_4 \cdot 3PbO$ until finally into PbO as studied by Schenck[24]. With scanty oxygen supply as in the present experiment the sulphate may have decomposed finally into Pb_2O. Under extremely scanty oxygen supply the Pb-S-O molecules produced on the active portions of the crystal surface, e.g., its corners, edges, steps, or some irregular points where atoms are loosely bound, may be deprived of the S atoms probably in combination with the O atoms. The crystal thus enriched with Pb atoms will finally assume the most stable equilibrium shape bounded by the {100} atomic planes.

The supposition that the evaporation may commence with the release of Pb-S molecules or particles directly from galena lattice may also be possible. However, the extra weak spots observed in the present diffraction study are not explained by this supposition alone. This type of surface roughening is more likely associated with that observed by the heat treatment at temperature above 425° C, which will be explained later. Morton[14] statted from conductivity measurements that with lead sulphide at 350° C in vacuum, sulphur is evaporated out giving a Pb-rich material. The present reduction is in conformity with his result as to the release of sulphur from lead sulphide at this temperature.

The orientations of the crystallites of the surface oxidation products are deeply affected by the degree of the roughening of the underlying crystal surface. At temperatures 400°C or below, the produced sulphate or the suboxide crystallites showed epitaxial orientations with respect to the {100} atomic planes of galena crystal, whereas at 425°C or above the produced suboxide or the yellow oxide crystallites always showed random orientations. At 400°C the ideally flat and perfect cleavage character was found lost by electron diffraction, but the surface was analysed to be bounded by minute {100} facets. These facets should have induced the epitaxial orientation of the growing suboxide crystallites. At 425°C or above, diffraction spots due to the roughened surface did not show marked elongations towards the shadow edge and the suboxide crystallites, when produced, showed random orientations. The ring pattern showed transmission type appearance. At these temperatures the evaporation of galena may have become so severe that atoms may now be torn off even from flat atomic planes making the crystal surface rough in atomic scales. Lead suboxide molecules produced and attached incoherently at the active portions of the roughened surface might have yielded the halo pattern. At approximately 450°C or above, these molecules may condense along crystal edges or at the corners to grow into crystallites in random orientations.

The present results, *i.e.*, the surface roughening of the cleavage face at temperatures above 350°C and the observation of epitaxially oriented lead sulphate crystallites on the cleavage face heated at 100° or 200°C under reduced pressure, throw light on the interpretation of the two halo pattern obtained with the cleavage face baked in open air for several minutes at temperatures below approximately 220°C2)3). The initial temperature elevation of the specimens was carried out rapidly in these cases. The two halo pattern substance may have been produced not through the thermal etching of the cleavage face, but by oxygen molecules arriving so rapidly to the cleavage face as to overcome the mobility of its atoms over the surface, resulting in the formation of incoherent sulphate molecules on its active portions. Under reduced rate of supply of oxygen the growth of the epitaxially oriented crystallites should have been favoured as in the oxidation of metal surfaces discussed by Finch25).

The roughening of the cleavage face at temperatures above 350°C may also explain the rapid growth of the oxidation products on galena heated in open air at these temperatures. The specimen surfaces began to show strong interference colours by the roasting oxidation of galena at approximately 350°C. As stated previously2)3), their diffraction patterns consisted of the very sharp spots indicative of the well grown crystallites.

Yamaguti et al.8) obtained arc and ring patterns with etched galena surface oxidised under reduced atmospheric pressures at temperatures above 550°C. They analysed them to be due to the mixture of lead suboxide, yellow oxide and the other oxides representable as Pb_mO_n. The present study on the cleavage face under scanty air supply has proved the formation of the first two oxides at temperatures approximately 500°C. At temperatures 550°C or above, the effect of the impurities contained in the original galena crystal was observed. However, in no instances were rings to be identified with the other lead oxides detected.

As to the observation of the lead basic sulphate, $PbSO_4 \cdot PbO$, the possible patterns in the present diffraction photographs were the rings or spots obtained superposed on the oriented sulphate pattern at temperatures 250° and 300°C. However, the rings were identified better with the sulphate and the spots were also unable to be identified with the basic sulphate. The basic sulphate, if produced, might have decomposed and changed ultimately into the suboxide by heat treatment as long as one hour. In Wilman's study6) on lead sulphide films, the duration of heating was 5 or 10 minutes.

Part of the present study was carried out at Mitsubishi Mining and Metallurgical Laboratory. The author is grateful to its members, particularly to Mr. K. Suzuki, for the many conveniences offered to him in the course of the present work. He is also grateful to Miss E. Matsudaira for her many assistances throughout this work.

This work was partly supported by the research grant from the Ministry of Education.

References

1) H. Hagihara: Proc. Phys.-Math. Soc. Japan **24** (1942) 762.

2) H. Hagihara: Bull. Kobayasi Inst. Phys. Res. (Tokyo) **1** (1951) 131.

3) H. Hagihara: J. Phys. Chem. **56** (1952) 610.

4) O. Simpson and G. B. B. M. Sutherland: Science **115** (1952) 1.

5) C. J. Milner and B. N. Watts: Research **5** (1952) 267.

6) H. Wilman: Proc. Phys. Soc. (London) **60** (1948) 117.

7) J. Doughty, K. Lark-Horovitz, L. M. Roth and B. Shapiro: Phys. Rev. **79** (1950) 203.
8) T. Yamaguti, M. Sakata and M. Morita: X-Sen (X-Rays) **4** (1945) No. 4, 9.
9) D. W. Pashley: Proc. Phys. Soc. (London) A **64** (1951) 1113.
10) H. Raether: *Ergebn. d. exakt. Naturwiss.* **24** (1951) 54.
11) L. Eisenmann: Ann. d. Phys. **38** (1940) 121.
12) H. Hintenberger: Z. Phys. **119** (1942) 1.
13) H. Hintenberger: Z. Naturforsch. **1** (1946) 13.
14) M. C. Morton: Trans. Faraday Soc. **43** (1947) 194.
15) C. Wagner: J. Chem. Phys. **18** (1950) 62.
16) R. W. G. Wyckoff: *Crystal Structures, Vol. 1*, Interscience, New York, 1948.
17) R. W. G. Wyckoff: *Crystal Structures Vol. 2*, Interscience, New York, 1951.
18) J. D. Hanawalt, H. H. Rinn and L. K. Frevel: Ind. Eng. Chem., Anal. Ed., **10** (1938) 457.
G. L. Clark, J. N. Mrgudich and N. C. Schieltz: Z. anorg. Chem. **229** (1936) 461.
G. L. Clark: *Applied X-Rays.*, McGraw-Hill, New York, 1940, p. 310.
G. L. Clark and R. Rowan: J. Am. Chem. Soc. **63** (1941) 1305.
19) W. E. Richmond and C. W. Wolfe: Am. Mineral. **23** (1938) 799.
20) W. P. Binne: Acta Cryst. **4** (1951) 471.
21) R. W. G. Wyckoff: *The Structure of Crystals.*, Chemical Catalog Co., New York, 1931.
22) Comparisons have been made with the X-ray Debye-Scherrer ring data by F. Halla and F. Pawlek: Z. Phys. Chem. **128** (1927) 49.
23) C. Doelter and H. Leitmeier: *Handbuch der Mineral Chemie* Bd. **4**/1, Theodor Steinkopff, Dresden, 1926. p. 403.
24) R. Schenck: Z. anorg. allgem. Chem. **148** (1925) 351.
25) G. I. Finch: Proc. Phys. Soc. (London) B **63** (1950) 465.

JOURNAL OF THE PHYSICAL SOCIETY OF JAPAN Vol. 8, No. 3, MAY—JUNE, 1953

A Study on Diffusion Pump Oil by the Mass Spectrometer and the Gas Analysis of the Final Vacuum

By Kazuo HISATAKE
Department of Physics, University of Tokyo
and Kazuhisa MATSUDA
Physics Department, Tokyo Institute of Technology

(Received February 6, 1953)

Diffusion pump oil is analysed by the mass spectrometer, especially for the purpose of obtaining some knowledge about the residual gases at the final vacuum when we use oil diffusion pumps. As a sample, we take alkyl-naphtalene and its spectrum is given graphically. The results of our analyses of residual gases confirm the conclusions obtained by Hickman and Blears.

§ 1. Introduction

Some authors [1),2)] have reported on the mass spectra of residual gases when oil diffusion pumps are used. But, as far as we know, there has been no experiment which shows a complete spectrum of such oil. Perhaps this is due to the fact that the oil of this kind is very difficult to treat quantitatively. As the oil is apt to dissociate and to contaminate the walls of the ion source system and the vapor pressure is very sensitive to the temperature. In this paper we undertook this work with the aim to get fundamental data on high vacuum, because even qualitative results are useful in this case. Except the experiments in § 3 and that of the spectrum of residual gases, a special oil source was used as is described in § 2.

The sample is the Lion Diffusion Pump Oil, manufactured by Lion oil and Fat Co. Ltd. Its constituent is pure alkyl-naphtalene, which is comparatively stable against temperature and has fairly low vapor pressure.

The gaseous composition must be made clear near the end vacuum, in order to know the action of ionization gauges on oil vapour, to study the mechanism of formation of CO^+ and H^+ ions and to get a general survey of the background ions in mass spectra. Discussion on these points are given in § 6.

In this experiment the following factors prevent us from obtaining more accurate data of the spectrum: the temperature variation of the ion source, of the oil source and of the connecting glass tubes; the rather long duration of scanning; the small amount of impurity contained in the sample; the inaccuracy caused by the mass spectrometer. Though we took much care upon the stability and the accuracy of above mentioned elements, we could not get such accurate data as in the case of the dissociation of lower mass molecules. But we believe the results are satisfying for our present purposes.

§ 2. Apparatus and Experimental Procedure

The mass spectrometer used has been constructed at Physics Department, Tokyo Institute of Technology and is the second order focusing analyser of sector type magnet, whose ion radius in magnetic field is 20 cm. The whole tube is made of brass and most part of it can be baked by an electric heater. A liquid-air trap is attached to the evacuation tube, and the Lion oil, the same as the sample, is used in the diffusion pump. The working conditions of the mass spectrometer are listed in Table I. In order to take a complete spectrum it is needed to scan the ion accelerating voltage at several strengths of magnetic field. Owing to the voltage discrimination and the electro-static focusing in the ion source, the height of the same ion peak varies with the accelerating voltages applied and the correction factor of this effect on the intensity was measured beforehand by using argon gas.

To introduce the oil vapor into the ion source we used the method shown in Fig. 1. A, B, and C are small vessels in which we put alkyl-naphtalene, D. O. P. and mercury respectively and they were connected with grease-less cocks. The mercury was used for identification of mass number, the ions Hg_{202}^+ and Hg_{202}^{++} being adopted as standard.

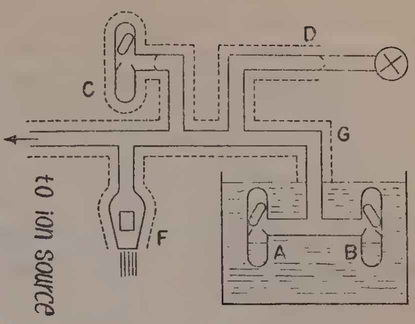

Fig. 1. The Oil source system
……… are heated parts.

D is the inlet for argon, which was used as the test sample and the mass standard. E is the water thermostat to maintain the oil temperature constant. Before the measurement, we filled the trap with liquid-air and kept baking the glass tube G at 250°C, the ion source at 200°C and the analysing tube at 100°C for more than three hours until the ionization gauge F indicated a good vacuum. When no gas was introduced, the vacuum of the analysing tube was about 1×10^{-3} μHg and even under working condition this pressure was not much larger.

Table I. The working conditions of the mass spectrometer.

resolving power	above 100
electron voltage	70 V
catcher voltage	50 V
electron catcher current	40 μA
ion accelerating voltage	variable 1500 V ~700 V
magnetic field strength	at several points
vacuum of the analysing tube	1×10^{-3} μHg
gas flow	$2 \times 10 \mu - l/\text{sec}$
temperature of the ion source	150°C

§ 3. Variation of Ion Yield with the Intensity of Bombarding Electron Current

It is quite natural to suppose that the ratio of ion yield in lower mass region to that in higher mass region varies with the intensity of electron current owing to the second electron impact and to the scarcity of parents molecules fed into the ionizing region. We measured this effect as the preliminary experiment. The result is shown in Fig. 2. The heights of ion peaks at mass numbers of 27, 28, 41 and 219 in residual gases and that of introduced argon for comparison were measured when the intensity of catcher electron current stood at 20 μA, 40 μA, and 200 μA respectively. In Fig. 2 each peak is normalized at 20 μA to show the relative characteristics of ion yield for each mass number. From this result we may conclude that, even in the case of such a long compound as this oil, the ion yield of any molecular weight varies linearly with the intensity of electron current as far as the intensity is low enough. But the fact that the curve for argon in Fig. 2 is not linear with electron current seems to be unreasonable but we consider this may be due to the space charge or some other factors in the ionizing region and it should be linear in the ideal case.

The ion yield of higher mass number does not increase in proportion to electron current, while that of lower mass number increases more than proportionally (, assuming that the curve for argon should be linear). We cannot think the above result depending upon mass number comes from thermal decomposition in the ion -source or on the tungsten filament. Because, in order to test this temperature effect, we found the fact that, with the increase of the temperature of ion source by external heating, the relative yield of high mass number increases, which contradicts the above results.

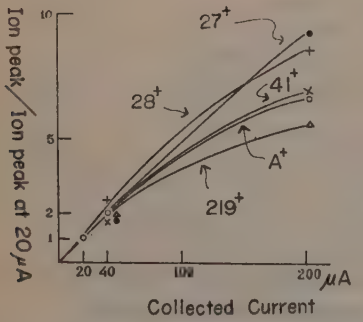

Fig. 2. Relation between collected current and ion peak.

After all the ion yield remains linear within the error of 5 % so long as the catcher current is kept under 40 μA. So we have executed our experiments at the catcher current under 40 μA. The rather different behaviour of the curve for mass number 28 may be caused by the effect discussed in § 6.

§ 4. The Mass Spectrum of Alkyl-Naphtalene

According to the manufacturing company, the alkyl-naphtarene used has the purity of 98.5% and the composition of its main constituent is 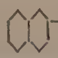 $-C_nH_{2n+1}$ ($n=16$). In this sample, however, small amount of the components with $n=14$ and $n=18$ is contained.

After heat-treating described in § 2, we maintained the temperature of the thermostat E at 79°C and those of the ion source and of the glass tubes G at 150°C during the measurement. Then the vacuum gauge F indicated the pressure of 2×10^{-2} μHg, under which the mean free path of oil vapour and its dissociated ions are much larger than the dimensions of the ionizing region.

Considering the inaccuracy of our experiment, we give the result graphically in Fig. 3. The ordinate represents the relative yield of ions when the ion yield of mass number 141 as 100. Owing to the causes stated in § 1, the relative errors over the entire spectrum are rather large but do not exceed 30 %. In the higher mass region, errors are caused by the deficiency of resolving power and we could not measure small peaks so accurately. As for mass identification, there is little doubt in the region below 219. The lines of mass number 1, 2, 17, 18, 28, 32, and 44 are not shown in Fig. 3, because the ion H^+, H_2^+, HO^+, H_2O^+, CO^+, O_2^+, and CO_2^+ are considered to be produced by other causes. It is to be mentioned that we missed the doubly and triply charged ions. From this spectrum and that of D. O. P. mentioned in § 5 we get the following informations about the dissociation of such a long organic compound by electron impact.

(1) For a long alkyl chain, the yields of ion $C_nH_{2n+1}^+$ and ion $C_nH_{2n-1}^+$ are much larger than their neighbours.

(2) The yield of ions mentioned in (1) increases from $n=1$ to $n=3$ and then decreases gradually as n grows larger. The tendency of (1) and (2) is similar to those of pentane and decane spectra.[3),4)]

(3) The ion yield of the mass number 141 is remarkably large in Fig. 3. The ion is assigned to 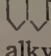 $-CH_2^+$. This is similar to the spectrum of alkyl-benzene[3)4)] where the yield of 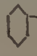 $-CH_2^+$ is very large, because methyl naphtalene ion or methyl benzene ion are

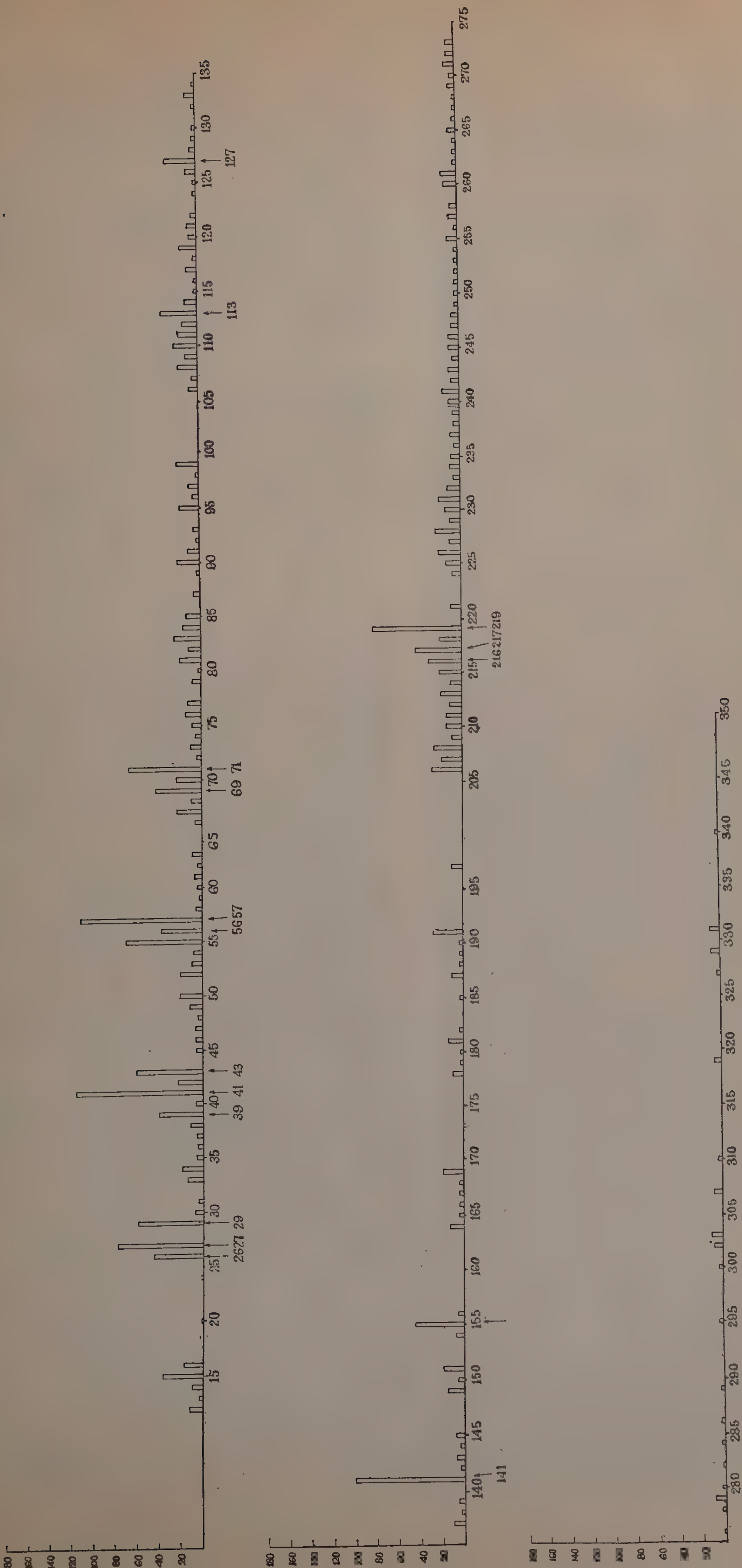

Fig. 3. The Spectrum of Alkyl-Naphtalen

The abscisa represents mass number. The ordinate represents the relative yield of ions in arbitrary scale.

stable.

(4) We are not able to identify the lines of 219 and its neighboures. But these can not be considered as due to contamination as is shown in Table 2.

(5) The ion yield of mass number above 250 are small. To find out the cut-off, we introduce more oil vapour by one handred times more than before, and then lines can be found as far as 380. In the region over 380 there was no ion; that is to say, the mass number 380 is the cut-off of the spectrum which corresponds to the ion 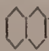$-C_{18}H_{37}^{+}$. However, no paticularly high ion peaks for 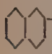$-C_{16}H_{33}$ has been found which is the parent molecule of the main constituent.

§ 5. Discussion on the Back Ground and the Spectrum of D. O. P.

Before the measurement of the spectrum of Fig. 3, we took the mass spectrum of residual gases at end vacuum without the liquid-air trap in order to make a blank test. Then this spectrum was almost ten times less than that of Fig. 3. After the measurement of Fig. 3, we took several lines of the spectrum closing the cock A. The results are given in Table II. These values are larger than those of initial blank data, in spite of using the liquid air trap. We think the larger values in the cases of A and B are caused by the contamination of the oil in the ion source and in the tubes, which cannot be removed immediately even if we close the cock A. Then it is almost certain for Fig. 3 to represent of alkyl-naphtalen itself. As for water vapour, the peak of 18 does not vary with temperature, but after closing the cock we find it decreases to one-fourth of the values in Fig. 3. This seems to mean that the water had been absorbed physically in the oil.

For comparison, we measured the spectrum of D. O. P. 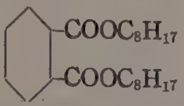

by the same procedure as before. As the sample contained impurities, we could not get a reliable results. Roughly speaking, the spectrum shows not only some lines of Fig. 3, but also several lines which did not appear in alkyl-naphtalene and the percentage of yield in the lower mass region is larger than in the case of alkyl-napntalene. Moreover in the D. O. P. spectrum the limes of higher molecular weight than 270 are very small and those of the parent ions cannot be detected as before.

After all, we can make clear the characteristics of the spectrum of alkyl-naphtalene by comparing with that of D. O. P.

Table II. Relative ion yield of the residual gases

Molecular weight of ion	A	B	C
2	32		25
17	149		22
18	470	114	84
27	79	11	10
28	120	56	46
29	60	12	11
141	100	34	29
219	82	27	23

A is the data in Fig. 3; B is the case when cock A is closed and the glass tubes are kept at 150°C: C is the case when the cock is closed and the glass tubes are at the room temperature, the pressure being $4\times10^{-3}\mu$Hg. All the values of the table represent the relative yields when that of 141 is 100.

§ 6. The Composition of Residual Gases at Final Vacuum

When we took the spectrum of residual gases mentioned in § 5, we did not use the oil source in Fig. 1, and the liquid-air trap. The pressure was 2×10^{-3} μHg. In order to get enough ion current, we increased the electron catcher current to 200 μA. So the errors of this spectrum were larger than the other.

Using the spectrum of alkyl-naphtalene (Fig. 3), we analyse the spectrum of residual gases. Both spectra agree with each other except several lines, allowing the errors of 30%. The result of analysis is given in Table III. From this Table we can see that 60% of residual gases is the vapour from the diffusion pump, 20% water and 6% CO, N_2 and CO_2 and the unknow components amount to 13%. Of course these values does not represent the relative proportion of each gas as it is, because the efficiency of ionization is not always considered equal. The mass numbers of the unknown components are 50, 51, 74, 75, 76, 77, 78, 79, 89, 91, 103, 104, 105, 106 and 115. These are regarded

Table III.

mass number	material	percentage	
2	H	1.0	1%
17	H_2O	5.6	20%
18		14.5	
28	$CO+N_2+CO_2$	4.4	6%
44	CO_2	1.2	
32	O_2	1.1	1%
	Alkyl-naphtalene	59.0	59%
	the others	13.0	13%

as the out-gases from the contamination in our system. In conclusion, we can assert with Hickman[5] and Blears[1]. "The main factor of final vacuum of oil diffusion pumps is the vapour pressure of oil". Although there is another opinion that oil is decomposed thermally in the diffusion pump and the products of decomposition limit the end vacuum, we have found no evidence of such decomposition as far as we use alkyl-naphtalene, because in the background spectrum of residual gases there is no tendency indicating that the ion yield of lower molecular weight is larger comparing with the spectrum of alkyl-naphtalene. If the oil vapour is trapped by liquid-air, the water vapour becomes predominant, though the partial pressure of water is reduced to one-half by liguid-air trap.

As for the formation of CO^+, Blears concluded that carbon monoxide may be formed on any tungsten filament in a vacuum system from water vapour and hydrocarbon vapour. In order to assure his explanation we measured ion peak of 28 both when the filament of the ion gauge F was switched on and off and when the high tention of the gauge was put on and off. The peak was reduced to 50% in five seconds after the filament was switched off, while no effect occured when the high tention was switched off. Though the same procedure was tried for the peaks of 219, 141 and 18, no variation of peak height was found. From the above test Blears' conclusion seems to be correct. But in our case the yield of 28 is smaller than that of Blears' data. OH^+ ion is formed from water vapour, because the yield ratio of 17 to 18 is nearly same as in the case of water spectrum.

§7. Conclusion and Acknowledgement

The mass spectrum of alkyl-naphtalene shows that it is decomposed into various molecular ions of lower mass number by electron impact. But as far as the decomposition is caused only by a single electron impact at the ion source, the spectrum is definite and its characteristics somewhat clear.

Using the spectrum thus obtained, we analysed the residual gases of oil diffusion pump by a different method from those of Hickman and of Blears and reached the same conclusion.

The authors wish to express their sincere thanks to Dr. E. Takeda (Tokyo Institute of Technology) for his encouragement and his kind advices, to Mr. K. Hashimoto and Mr. C. Hayashi (University of Tokyo) for their useful discussions, and to Mr. S. Takao for his preparation of the samples and his information about the chemical data.

References

1) J. Blears: J. Sci. Inst. Vacuum Physics Suppl. (1951) 36.

2) I. Nonaka, S. Hiraswa and K. Tsutsumi: J. Phys. Soc. Japan **6** (1951) 466.

3) Mass Spectral Data. Bureau of Standards (1951).

4) R. Roberts and S. Jonhsen: Anal. Chem. **20** (1948) 690.

5) K. Hickman: J. Franklin Inst. **221** (1936) 383.

Short Notes

J. PHYS. SOC. JAPAN 8 (1953) 422

On the Directivity of Solar Radio Emission from the Sunspots

By Tastuo TAKAKURA

Osaka City University, Osaka Japan

(Received December 15, 1952)

It is said that the solar radio emission has the directivity and the intense radiation is observed when active sunspots are near the central meridian, especially at metre wave region. So it was attempted to investigate numerically the directivities of radio emission at various frequencies.

The intensity of solar radio emission y may be expressed in the first approximation

$$y = Y_0 + Ax_1 + Bx_2$$

where x_1 and x_2 are the relative sunspot number in the central circle zone ($\frac{1}{2}$ dia. circle) and outer-zone, respectively, and Y_0, A and B are constants. The assumed values, y_0, a and b, of Y_0, A and B, respectively, were calculated from the observed daily values of solar radio emission y_i and sunspot relative number x_{1i}, x_{2i}. The ratio of partial regression coefficients, a to b, was inquired severally as the directivities at 3260 mc, 2800 mc, 1200 mc, 600 mc and 200 mc; they were observed severally at our observatory (3260 mc), Canada (2800 mc) and Australia (1200 mc, 600 mc and 200 mc.) in the period from October 1950 to April 1952. These are tabulated in table I.

Though the probable error is comparatively large, the trend can be seen in the table I, that the fraction, a/b, is almost unity at every frequencies in the period when the intensity of emission is weak, and becomes larger than unity according as the average intensity of the emission becomes stronger. Such trend becomes smaller with increasing frequency, and at 2800 mc and 3260 mc the variation of a/b with period is not distinct.

It may be concluded roughly that the "enhanced" radio emission are the superpose of almost nondirective and more directive emission, the directivity or intensity of which becomes larger with decreasing frequency and which disappears at 3000 mc region. As the directive and non directive component cannot be separated in this analysis, it is not clear that the variations of a/b with frequency and period are due to the variation of directivity itself or the variation of intensity ratio of directive to nondirective component, so the directive component may be more directive than the value shown in the Table I.

This analysis is on the directivity of so called "enhanced" radiation, so the directivities of the radio emission of burst and outburst may be outside the scope of this analysis.

I should like in future to investigate the directivities of the circularly polarized emission and of burst and outburst as a method to investigate the mechanism of generation of solar radio emission.

I wish to express my thanks to Prof. Y. Watase for his kind encouragement and critisism and Mr. S. Hayakawa for his helpful advice.

Table I. The variations of partial regression coefficients, a to b with frequencies and with periods. Mean flux y_0 is indicated in the bracket, in the unit 10^{-20} WM^{-2}(c/s)$^{-1}$.

Season frequency	Oct.-Dec. 1950	Jan.-Apr. 1951	May-Aug. 1951	Sep.-Dec. 1951	Jan.-Apr. 1952
3260 mc.	—	—	0.9±0.2 (1.78)	>1* (1.37)	0.9±0.2 (1.16)
2800	1.1±0.2 (0.88)	0.8±0.1 (0.94)	1.1±0.1 (1.20)	1.2±0.2 (0.92)	—
1200	1.5±0.4 (0.41)	1.1±0.3 (0.39)	1.6±0.2 (0.42)	0.9±0.4 (0.39)	—
600	>1*	>1*	2.2±0.8 (0.30)	1.2±0.5 (0.02)	—
200	—	>1*	3.6±2.2 (0.15)	1.3±0.5 (0.09)	—

* As the probable error is large, a/b is meaningless but $a-b>0$ is reasonable.

J. PHYS. SOC. JAPAN 8 (1953) 423~424

Concentration Dependence of the Dielectric Constant of Ionic Solutions

By Makoto MORIYAMA
Electrical Communication Laboratory

(Received December 22, 1952)

Debye1) and Sack2) have already treated concentration dependence of the dielectric constant of dilute ionic solutions qualitatively. Debye considered that the water molecules in the neighborhoods of the ions were saturated by extremely high fields of the ions. Hence, each ion with its surrounding water was replaced by an equivalent empty spherical cavity, the radius of which depended on the distance over which the saturation effect is appreciable. He took the dielectric constant inside the cavity equal to 1. The main contribution to the dielectric lowering came almost entirely from these cavities. According to this conception, he obtained the following Eq. for small concentration:

$$\varepsilon^*=\varepsilon[1-n(4\pi/3)a^3]=\varepsilon(1-\gamma c) \qquad (1)$$

where ε^* denotes the apparent dielectric constant of the solution, ε the dielectric constant of the pure solvent, n the number of ions (=cavities) dissolved per cc, a the radius of each cavity, γ a constant characteristic for the salt and the solvent, and c is the concentration in mols per liter.

Some works regarding this subject have recently been made by Ritson and Hasted3) and Yasumi4). But none of them have discussed it at higher concentration.

We have attempted in this paper to derive qualitatively the dielectric constant-concentration formula at higher concentration in consideration of the interaction of Debye's cavities. With this view, we have made the following assumptions that the cavities has more chances to overlap at random each other with increasing ionic concentration. As the overlapping region ABCD belongs to each cavity in Fig. 1, the number of water molecules saturated by an ion, that is, the effective volume of a cavity will diminish by the volume represented by the shaded lens-shaped region per cavity. Accordingly the depression of dielectric constant with increasing ionic concentration is compensated partly by the overlapping volume. It is easy to show that the volume is proportional to the square of concentration. Assuming that n ions are dissolved in a volume of solution V and that $\overline{v(n)}$ denotes the mean volume of lens-shaped region, the ratio of the volume of it to that of cavity is given by

$$\alpha(n)=\overline{v(n)}/(4\pi a^3/3)\,. \qquad (2)$$

For the effective total volume of cavity δV, we have

$$\delta V=n(4\pi a^3/3)(1-\alpha(n))\,. \qquad (3)$$

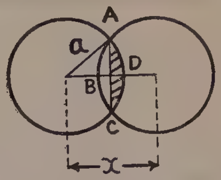

Fig. 1.

According to the assumption mentioned above, we find for the apparent dielectric constant of the ionic solution ε^*

$$\varepsilon^* V=\varepsilon(V-\delta V)\,. \qquad (4)$$

Now using the notation

$$n(4\pi a^3/3)/V=\begin{pmatrix}\text{volume concentra-}\\ \text{tion of cavities}\end{pmatrix}\equiv\gamma c \qquad (5)$$

and introducing Eqs. (2), (3), (5) into (4) gives the Eq.

$$\varepsilon^*=\varepsilon[1-\gamma c(1-\alpha(n))]\,. \qquad (6)$$

To obtain the ratio $\alpha(n)$, we introduce a new function v of x. It denotes the lens-shaped volume when the distance between the centers of two overlapping cavities is x. Then $v(x)$ must have the following values from its definition, that is

$$v(x)\begin{cases}\neq 0 & \text{when} \quad x<2a\\ =0 & \text{when} \quad x\geqq 2a\,.\end{cases} \qquad (7)$$

As we have no information about the probability of overlapping, let us now assume such a simple case that when there is an ion in the volume V/n the probability of finding an ion in the volume v is equal to $v/(V/n)$. Then the probability $dP(x)$, that the center of a cavity enters into the spherical shell which lies between the two concentric spheres having their radii x and $x+dx$ respectively, is given by

$$dP(x)=4\pi x^2dx/(V/n)\,. \qquad (8)$$

Then we can find for the mean lens-shaped volume

$$\overline{v(n)}=\int_0^A v(x)dP(x)\Big/\int_0^A dP(x)\,,$$

where $A=\{(3/4\pi)(V/n)\}^{1/3}$. Using $\int_0^A dP(x)=1$, (7) and (8), we have

$$\overline{v(n)}=\frac{4\pi n}{V}\left(\int_0^{2a}x^2dx\right)\left(\int_0^{2a}v(x)x^2dx\Big/\int_0^{2a}x^2dx\right)$$

$$=\frac{4\pi n}{V}\left(\frac{8a^3}{3}\right)v'\,.$$

In terms of a dimensionless constant λ, "overlapping ratio",

$$\lambda\equiv 8v'\Big/\left(\frac{4\pi a^3}{3}\right)=\frac{9}{4\pi a^6}\int_0^{2a}v(x)x^2dx\,, \qquad (9)$$

$\overline{v(n)}$ and $\alpha(n)$ of (2) are represented by

$$\overline{v(n)}=\gamma c(4\pi a^3/3)\lambda \qquad (10)$$

and

$$\alpha(n)=\gamma c\lambda\ . \qquad (11)$$

We can easily find for the theoretical lens-shaped volume (see Fig. 1)

$$v(x)=\frac{2\pi a^3}{3}\left[1-\frac{3}{4}\left(\frac{x}{a}\right)+\frac{1}{16}\left(\frac{x}{a}\right)^3\right]\ .$$

Substitution of this in (9) gives $\lambda \doteqdot 0.5$, which is able to have values between 0 and 4 for various degrees of overlapping of cavities. Then we have following Eq. for the dielectric constant-concentration formula

$$\varepsilon^*=\varepsilon(1-\gamma c+\lambda\gamma^2c^2) \qquad \lambda\doteqdot 0.5\ . \qquad (12)$$

On the other hand, to determine the numerical values of γ and λ experimentally, we adopt the data on NaCl solution from the paper of Hasted, Ritson and Collie.3) Assuming the dielectric constant of pure water to be 80 at 21.0°C, 84 at 1.5°C, we can find the numerical values for γ and λ as follows:

$$\gamma\doteqdot\begin{cases}0.15\\0.16\end{cases}\quad \lambda=\begin{cases}0.6\\0.39\end{cases}\quad \begin{matrix}\text{at } 21.0°\text{C}\\ \text{at } \ 1.5°\text{C}\ .\end{matrix}$$

Owing to the simplest model, the temperature dependence of λ has not been contained in this treatment. But the theoretical value of λ is in good agreement with the experimental one, notwithstanding the neglect of the change of probability with the temperature and with the ionic interaction. Fig. 2 represents the static dielectric constant of NaCl solution as a function of concentration. Solid curves denote the best fit ones to the experimental data, and dotted curves represent the ones in which λ is theoretical.

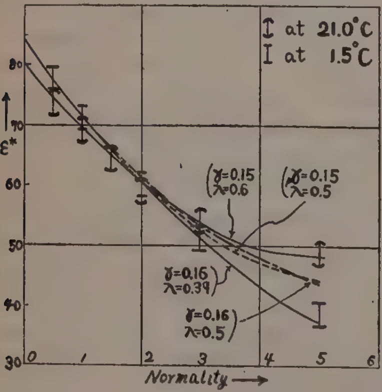

Fig. 2.

Applying Eq. (5) will give us the radius of the equivalent cavity, which is found to be $a\doteqdot 3$A. Taking the opinion of Ritson and Hasted3) into account, this value of a seems probable. In future the dielectric constant of an ionic solutions must be treated quantitatively on the basis of the more refined model. We consider it is important to take account of λ as well as γ for the study of the construction of ionic solutions at higher concentration.

The author is indebted to Dr. S. Yoshida for many valuable discussions, and to Mr. D. Ito and Dr. M. Toda of Tokyo University of Education for many helpful advices and discussions.

References

1) P. Debye: Polar Molecules, p. 109 (1929).
2) H. Sack: Physik. Z., **28** (1927) 199.
3) J. B. Hasted, D. M. Ritson and C. H. Collie: J. Chem. Phys. **16** (1948) 1.
4) M. Yasumi: Bull. Chem. Soc. Japan, **23** (1950) 95.

J. PHYS. SOC. JAPAN 8 (1953) 424~425

A Note on the Theory of the Electron Multiplication in Insulating Crystals

By Hazimu KAWAMURA

Faculty of Science and Engineering,
Osaka City University, Osaka

(Received February 5, 1053)

It has been accepted that the dielectric breakdown of an insulating crystal is caused by the electron multiplication due to the ionization by collision. Under the electric field not so strong, the conduction electrons drift from cathode to anode with zigzag motion. The average energy of this motion is determined by the balance of the energy gain from the field and the loss to the lattice vibrations. Therefore, we can write as

$$d\varepsilon/dt)_E+d\varepsilon/dt)_L=0\ . \qquad (1)$$

If the field is so strong that $d\varepsilon/dt)_E+d\varepsilon/dt)_L=0$ holds for every energy up to ionization potential, the electrons should all attain the ionization energy after few collisions. We shall denote E_H for this critical field. As well known, von Hippel1) considered that E_H is the electric strength of the insulator. Although it is imposible for the average electrons to attain the ionization energy under the field less than E_H, the electron has a chance to be free from collision while it is accelerated from the average energy to the ionization energy, as the deviation from the average behavior. According to Seitz,2) this probability can be given by

$$p=\exp(-\alpha E_H/E)\ , \qquad \alpha\sim 3.8\ , \qquad (2)$$

and the mean range for making an ionization by collision is given by

$$\lambda=(E\varepsilon'/eE^2_H)\exp(\alpha E_H/E), \qquad (3)$$

where E is the applied field and ε' is the mean energy loss due to a collision with the lattice which is about 0.1~1 eV. In the above consideration, only the fluctuation in which the electrons make no collision while they are accelerated to ionization energy is taken into account. But the reasoning, with which Seitz justified the neglection of the effect of electrons which attain the ionization energy after several collisions, does not seem to be so obvious.

Recently, several authors3)4)5) have investigated these problems by taking into account the energy distribution of the conduction electrons under a strong field. They have expanded the distribution function as $f(\boldsymbol{k})=f_0(\varepsilon)+f_1(\varepsilon)k_x/k+\cdots$, and determined $f_0(\varepsilon)$ and $f_1(\varepsilon)$ by the steady state condition, $df/dt)_E+df/dt)_L=0$. They have also introduced $S(\varepsilon)$ which means a current of electrons in $\varepsilon(\boldsymbol{k})$ space. If we assume that the trapping or recombination of the conduction electron can be neglected in the range $0<\varepsilon<\varepsilon_{\text{ion}}$ and also that the secondary electron is generated as soon as the electron reaches the ionization energy, we can consider that $S(\varepsilon)$ is constant fron zero to ε_{ion}, except for the source of electrons at $\varepsilon=0$ and sink at $\varepsilon=\varepsilon_{\text{ion}}$. Because $S(\varepsilon_{\text{ion}})$ is the number of electrons which pass through the ionization energy, it should be the number of ionization by collisions per second. Hence the probability that an electron makes ionization per second is given by $\alpha=S/N$, where N is the density of electrons and given by $\int f(\boldsymbol{k})d\boldsymbol{k}=\int f_0(\varepsilon)d\varepsilon$. Accordingly the mean range of electrons required to make an ionization is

$$\lambda=eE\tau/m\alpha=eE\tau N/mS, \qquad (4)$$

where τ is the collision frequency of electron and phonon, and m is the mass of electron. According to Franz4), we have

$$f_0(\varepsilon)=(3mS/2e^2\varepsilon E^2)\int_\varepsilon^\infty(d\varepsilon'/\tau)\exp\left[\int_\varepsilon^{\varepsilon'}\{(1/\varepsilon'')\times(3F^2(\varepsilon'')/2E^2)-(3/2\varepsilon'')\}d\varepsilon''\right], \qquad (5)$$

where we have assumed that the energies of phonons are sufficiently smaller than the energies of electrons,* and $F(\varepsilon)$ is the field strength for which the relation of the energy balance holds at ε. Therefore, we have $F(\varepsilon)_{\max}=E_H$.

Now we shall confine ourselves in the case of a nonpolar crystal, and assume that the boundary of Brilloun zone almost coincides with the ionization energy. After some approximate calculations, we get

$$\lambda=(cE\sqrt{\varepsilon\varepsilon_{\text{ion}}}/eE_H{}^2)\exp(3E_H{}^2/5E^2), \qquad (6)$$

where c is a constant which is order of 1, and ε is the average energy of electrons. We can see that (3) and (6) resemble so much that it is difficult to see which is better fitted for the experiment. But we believe that the present treatment is a natural extension of the treatment of Seitz2).

References

1) A. von Hippel: Z. S. f. Phys. **68** (1931) 309.
2) F. Seitz: Phys. Rew. **76** (1949) 1376.
3) W. R. Heller: Phys. Rew. **84** (1951) 1130.
4) W. Franz: Z. S. f. Phys. **132** (1952) 285.
5) J. Yamashita and M. Watanabe: Rep. Inst. Sci. & Tech. Univ. Tokyo **6** (1952) 111.

---

* This assumption holds only for the acoustical mode.

J. Phys. Soc. Japan **8** (1953) 425~426

Microwave Spectrum of Methylamine (II)

By Koichi Shimoda and Tetsuji Nishikawa
Department of Physics, Faculty of Science, University of Tokyo

(Received February 18, 1953)

We have measured the microwave spectrum of methylamine in the frequency ranges between 15 and 20 kMc/sec by the second harmonics from a crystal multiplier driven by a klystron, 2K25, and between 24 and 27 kMc/sec by the third harmonics. A source modulation microwave spectrograph with the absorption waveguide-cell of oblate circular cross-section was used. The measured frequencies of the lines are given in Table I, where the marked lines were found by D. R. Lide1) to belong to a series with the first order

Table I. Microwave frequencies of Methylamine Spectrum

Mc/sec	Mc/sec
15146.16±0.03	19013.55±0.04
15252.52±0.08	19110.66±0.03
15357.69±0.03	19724.62±0.03
15397.72±0.04	19776.40±0.07
15824.14±0.04	19776.66±0.07
16088.98±0.05	19776.84±0.07
16089.84±0.05	19919.46±0.04
16410.63±0.04	19933.57±0.05
16661.73±0.04	20076.00±0.04
16670.02±0.05	20243.54±0.06
16681.80±0.06	20243.98±0.10
16742.98±0.03	20325.82±0.06
16947.65±0.05	20547.17±0.06
17042.46±0.04	
17108.99±0.06	

17200.97±0.05	○23873.61±0.04
17237.77±0.10	24889.42±0.06
17238.04±0.06	24889.80±0.06
17263.86±0.08	○25063.65±0.03
17302.03±0.05	○25507.61±0.04
17345.10±0.05	25810.49±0.06
17345.70±0.05	25810.96±0.06
17360.58±0.08	○25861.23±0.05
17361.10±0.10	○26134.72±0.05
17475.66±0.07	○26339.57±0.04
17476.28±0.07	○26487.00±0.04
17585.33±0.08	26493.54±0.04
17660.45±0.10	26493.82±0.04
17849.46±0.04	○26588.65±0.08
17871.76±0.08	○26654.86±0.06
17887.20±0.05	○26695.43±0.03
17913.74±0.03	○26717.89±0.06
18023.18±0.06	○26728.77±0.08
18562.40±0.06	
18680.50±0.06	

Stark-effects. Including the lines which we have reported in the previous note2), we have observed ninety lines and several other lines which are too weak to be accurately measured. The Stark effects of these lines are now being carried out.

References

1) Private communication. We express our thanks to Dr. David R. Lide for his kind informations of his results.

2) K. Shimoda and T. Nishikawa: Journ. Phys. Soc. Japan 8 (1953) 133.

J. Phys. Soc. Japan 8 (1953) 426

New Lines of the Inversion Spectrum of Ammonia

By Tetsuji Nishikawa and Koichi Shimoda

Department of Physics, Faculty of Science, University of Tokyo

(Received February 18, 1953)

Eight lines of the inversion spectrum of ammonia in the frequency range between 15 and 17 kMc/sec were found in cource of investigating methylamine by the source modulation microwave spectrograph. The second harmonics from a crystal multiplier driven by a klystron, 2K25, were used. The measured frequencies of the lines are given in Table I. The calculated frequencies using the empirical formula of Costain1) and their deviations from the observed frequencies are also listed. The correction of the K-type splitting2) on the frequency of 8,3 line is taken as +116.42 Mc/sec. We see that Costain's formula has some systematic errors in the lower frequency region.

Table I. Inversion Spectrum of Ammonia

Assignment J	K	Obs. Freq. Mc/sec	Calc. Freq. Mc/sec	Error Mc/sec
8	3	16455,13±0.04	16460.35	−5.22
10	6	16319.38±0.04	16322.92	−3.54
11	7	15933.32±0.06	15938.51	−4.19
8	2	15639.84±0.06	15642.88	−3.04
12	8	15632.88±0.08	15640.14	−7.26
9	4	15523.96±0.05	15527.93	−3.97
13	9	15412.52±0.06	15422.09	−9.57
8	1	15233.23±0.04	15236.94	−3.71

The frequencies of lines, (8,3), (10,6), (11, 7), (12, 8) and (9,4), show good agreements with the values reported as the lines of deutero-ammonias by H. Lyons and others3). Those frequencies are 16455, 16320, 15935, 15634 and 15524 Mc/sec respectively. Since our sample contains deuterium only in natural abundance, we believe that those should probably be attributed to the undeuterated ammonia.

References

1) C. C. Costain: Phys. Rev. 82 (1951) 108.

2) H. H. Nielsen and D. M. Dennison: Phys. Rev. 72 (1947) 1101.

3) H. Lyons, L. J. Rueger, R. G. Nuckolls, and M. Kessler: Phys. Rev. 81 (1951) 630.

J. Phys. Soc. Japan 8 (1953) 426～427

The 3000 Mc Ion Plasma Noise Radiated from Arc Discharge and Solar Eruption

T. Takakura, K. Baba, K. Nunogaki and H. Mitani

Osaka City University Ohgimachi, Osaka, Japan

(Received February 16, 1953)

It was found that arc discharge in air radiate intense radio noise at the plasma frequency corresponding to their "ion density near the cathode". If "ion plasma oscillation" is able to radiate the intense radio noise, some types of outburst of solar radio noise would be accounted for.

We have observed radiation of 3000 Mc radio noise by d.c. discharge in air whose intensity was found to be equivalent to the thermal emission of 10^6～10^7°K at the current of 0.5 to 5 A, the current range being limited by experimental arrangement. Here, the current density in the vicinity of the cathode is said to be almost constant and independent of varying discharge current. When carbon or mercury electrode was used, exceptionally low noise was observed, corresponding to thermal emission not more than 10^4°K. Measuring relative intensity of 3000 Mc radio noise from d.c. arc discharge with electrodes of various material disclosed that the positive electrode had no significant effect in the intensity of the noise. The radiation electric field of noise was dominantly polarized along the discharge current. The polarity and intensity of the noise was affected little by imposing a magnetic field of 10^3 Gauss along the discharge current. Here, the gyromagnetic field H (gyrofrequency $f=eH/2\pi mc$) at 3000 Mc for electron and copper ion was 10^3 and 10^8 Gauss, respectively.

The shape of electrodes altered the polarity and intensity to some extent, but it seemed that the contribution of electrodes to the radiation of the noise was not essential.

The intensity of the noise decreased usually with decreasing of air pressure near 1 atm.

When mercury drop was used as the negative electrode of the arc discharge, excess noise was not observed at 1 atm; but when the tube was evacuated to a mercury vapor pressure of 0.05mm Hg, excess noise was observed whose intensity changed with increasing discharge current showing a maximum around 1 A. On the other hand, 10Mc radio noise observed at the same time with a shortwave receiver showed monotonous increase.

The electron and ion density near the cathode, estimated from the well known current density[1)] of the copper arc discharge at 1 atm. and mercury arc at "high vacuum", are 10^{14} electrons/cm^3 and 10^{16} ions/cm^3, respectively. Here, the plasma density n (plasma frequency $f=\sqrt{ne^2/\pi m}$) of electron and copper ion at 3000 Mc is 10^{11} electrons/cm^3 and 10^{16} ion/cm^3, respectively. Hereupon it was considerd that the noise was due to the "ion plasma oscillation" near the cathode. However the so called plasma oscillation is usually a "longitudinal oscillation" anddoes not radiate directly any transverse radiowave. The mechanism of production of transverse plasma osillation without any external magnetic field is not yet clear. Further investigation of frequency spectrum and mechanism of the production of noise is under investigation.

If the "ion plasma oscillation" is able to radiate the radio noise by some proper excitation, (without any external strong magnetic field) non-circularly-polarized outbursts of solar radio noise would be accounted for. The dense ion, of the order of 2×10^{14} hydrogen ions per cm^3 (ion plasma density at 3000 Mc) to be found at the solar interior, cannot radiate the radio noise out to the free space, as the electron and ion density is almost equal at the same solar layer and ion plasma noise cannot propagate through the over-dense plasma of the outer layer. However, in the case of eruptions when the dense solar material bursts out and protrudes beyond the outer plasma layer of 10^{11} electrons per cm^3, the 3000Mc ion noise may be radiated out to the free space and may be observed as the outbursts of solar radio emission.

Reference

1) J. D. Cobine: Gaseous Conductors (McGraw-Hill Book Company, 1941)

J. Phys. Soc. Japan 8 (1953) 427~428

On the Structure Loosening of Metal Films deposited from the Vapour

By Yoshibumi Fujiki and Ryōji Suganuma

Department of Physics, University of Kyoto

(Received February 12, 1953)

In the course of study on metal films by the electron diffraction method, the writers noticed that the bismuth film, deposited from the vapour, showed the structural loosening at the temperature appreciably lower than the melting point of bismuth in bulk. Therefore, the writers have tried to investigate how the thickness, the microscopic and the cryatallographic state of the film are correlated with the temperature at which the structure loosening occurs. The material used was Merck's high purity bismuth, and its vapour was deposited in vacuum ($3\times10^{-4}\sim6\times10^{-5}$mm Hg) on a thin glass plate (about 0.1~0.2 mm thickness), which was fastened on a copper plate (2mm thickness).

The local heating of the specimen by electron bombardment was carefully avoided by intermittent irradiation by weak beam and also by continuously changing the part of the specimen irradiated. The temperature of the film was measured by a thermo-couple whose junction was in contact with the surface of the film.

The relation between the temperature, at which the structure loosening occurred, and the mean thickness of the film is shown in Fig. 1. The temperature of the structure loosening approaches the melting point (272°C) when the film becomes thicker than about 3 μ.

The appearance of the surface of the film was examined microscopically. The films, which are thinner than 0.5 μ, co-aggregated when they were heated up to the temperature of the structure loosening and then cooled, but no change was observed for thicker films. The microscopic grain size of the crystal of the surface of the film was about 0.8~1.2 μ in the latter case. The change of the voltage applied on the electron diffraction apparatus from about 45 kV to 70 kV did not change

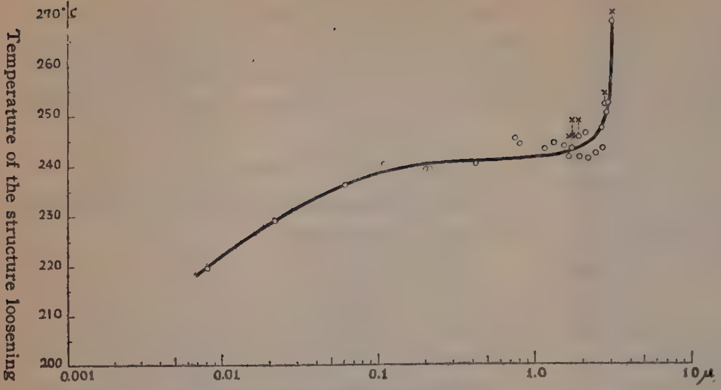

Fig. 1.

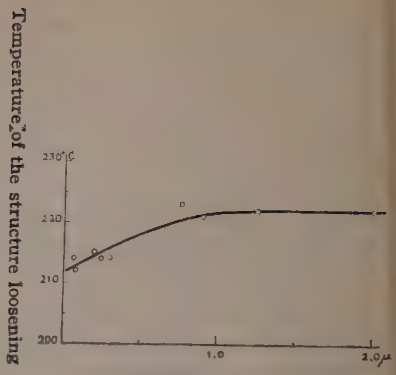

Fig. 2.

the temperature of the structure loosening observed. From these observations it was concluded that microscopic grain size of the surface had little influence on the temperature of the structure loosening and the structure loosening occurred simultaneously to the depth of at least 0.5 μ from the surface.

The specimen prepared as mentioned at the beginning of this note showed the 'one degree orientation' about the axis normal to the surface of the substrate, but the crystallographic plane which tended to lie parallel to the substrate varied as the thickness of the film increased. This relation is shown in Table I. The crystallographic plane which orientated parallel to the substrate varied, however, after the specimen was heated up to the temperature of the structure loosening and then cooled. In every case, it was the (111) plane which orientated predominantly parallel to the substrate after cooling. The temperature of the structure loosening of this film varied little from the value observed in the case of virgin film when the film was thin and somewhat higher when it was thick. The crosses in Fig. 1 show the temperatures of the structure loosening of these specimens.

Table I.

Thickness of the film	*Crystallographic plane parallel to the substrate
0.008 ~ 0.03 μ	(100)+(111)
0.04 ~ 0.5 μ	$(11\bar{1})+(100)$
0.5 ~ 3.1 μ	$(11\bar{1})$

(* Indices are referred to the pseudo-cubic rhombohedral cell with $a=6.56$ Å and $\alpha=87°33'$.)

The evaporation rate of the material and the temperature of the substrate in preparating the specimen were found to have no appreciable influence on the temperature of the structure loosening, or on the grain size of the surface of the film.

Tin films were also examined, and some of the results obtained are shown in Fig. 2. The temperature of the structure loosening was also lower than the melting point (230°C) of tin in bulk.

From these observations it can be concluded that the thickness of the film is the predominant factor that determines the temperature of the structure loosening.

Further investigation about the cause of the structure loosening of the film at the temperature lower than the melting point of the same material is now in progress.

J. Phys. Soc. Japan 8 (1953) 428~429

On the Metastable Phase Change of Ammonium Nitrate

By Kenzo Tanaka and Ikuo Fukuyama
Department of Physics, University of Kyoto

(Received February 12, 1953)

Ammonium nitrate has five stable transitions and in some cases a metastable transition occurs at ordinary pressure. They are shown in the following table.

The conditions for the appearance and disappearance of this metastable transition were studied and it was found that they are related with the maximum temperature reached and the time of the heat-treatment and the water content of the specimen. Fig. 1 shows the result for the condition of appearance of the metastable transition. Each phase of the specimen was determined by the method of X-rays. Curves in Fig. 1 show the relation between the highest temperature of the heat-treatment and the water content of the

(1) Stable transition

Phase	Liquid		I		II		III		IV		V
Trans. Temp.		169°C		125°C		84°C		32°C		−18°C	
Crystal System			Cub.		Tet.		Ortho-rhomb.		Ortho-rhomb.		Hex.

(2) Metastable transition

Phase	II		IV
Trans. Temp.		50°C	

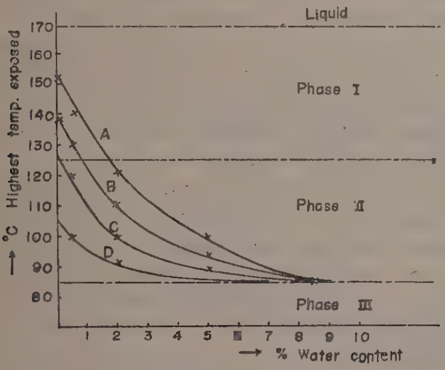

Fig. 1.

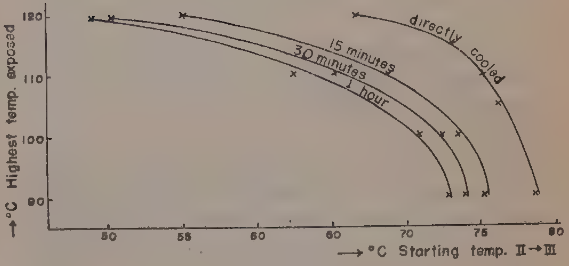

Fig. 2.

specimen, the time of heat-treatment being taken as a parameter. If a specimen is exposed over three minutes at a temperature above the line A, fifteen minutes above the line B, one hour above the line C and six hours above the line D respectively, metastable transition takes place on cooling in each case. The same tendency was also confirmed by the method of dilatometer, thermal analysis and polarization microscope.

Such metastable transition continues to take place for some period after the heat-treatment which is determined by the water content of the specimen. By taking X-ray photographs of a dry specimen in metastable condition at an interval of twenty-four hours, it was found after several days after the heat-treatment that the specimen was inverted to a state of stable phase transition and also that the periods were shorter than this for wet ones. These phenomena seem to be well explained as follows by considering the condition for the formation of nucleus of phase III. When the temperature of the specimen is raised above the range of phase III, the phase II and then phase I appear, but some morecular groups in phase III are still retained which can act as nuclei of phase III when the temperature is lowered. Such molecular groups are gradually destroyed at high temparature and when they are completely destroyed, then phase III does not appear in the course of cooling and phase II goes directly to phase IV whose molecular arrangement is closely similar to that of phase II. The molecular groups are easily destroyed and easily formed by the presence of water by some reason but in dry specimens the formation and destruction of them are not so easy as in wet specimens and so it follows that wet specimens are ersier to go to in and get out from the metastable condition than dry ones. It can then be expected that as the molecular groups or the nuclei of phase III are gradually destroyed in phases II and I, the transition temperature II→III on cooling will be affected by the number of the nuclei retained in higher phases or the temperature and duration of heat treatment to which the specimen was exposed. This supposition was confirmed by a series of experiments shown in Fig. 2. In the figure the curves show the starting temperature of the transition II→III observed by thermal analysis for specimens of the same water content which were heated at various temperatures for different periods. As was expected, the starting temperature is lowered for specimens containing small amount of the nuclei of phase III.

The relation between the molecular groups of phase III and water molecules are now under investigation.

J. Phys. Soc. Japan 8 (1953) 429~431

Field Emission of Crystal Phosphors

By Masayasu Ueta
Department of Physics, University of Kyoto

(Received February 25, 1953)

Gudden and Pohl[1] have found out for the first time the effect of intense electric field upon the luminescence of phosphors through the instantaneous enhancement of afterglows in pre-excited phosphors, and later on Destriau[2] found that phosphors are capable of being excited to emit fluorescences by electric field without pre-excitation by lights. But, detailed studies on its mechanism have not yet been made so far. Recently this method of producing lights has been schemed as a new type of illumination.

The present author has measured the relation between the emission intensity and the depth of activator level, and has thus shown that the first step of emission will be due to the direct excitation of electrons from the impurity centres according to the process analogous to the cold emission of metals.

Benzene solutions of the polystyrene dispersed with fine powders of phosphors are let flow on a brass plate which is acting as one electrode, and the solvent is vaporized gradually. Thus thin film of 1/100∼2/100 mm thickness is made, in which phosphors are uniformly dispersing. Certain insulating oil is inserted between the film and mica (of 4/100 mm thickness), and on the mica is spread salted glycerine or conducting solution to which another electrode is attached. This arrangement is called an electroluminescent cell. It was found that castor oils were most suitable for the insulating oil. Applying the potential difference of 500∼2000 volts, a.c. 60 cycles between the two electrodes, the phosphors were excited with a considerable brightness. Phosphors of ZnS-Cu, Zn_2SiO_3-Mn, Zn_2SiO_4-Be-Mn and $MgAs_2O_6$-Mn were studied. Although all of these are sensitive to the photo- and electron bombardment-excitation, they are not always sensitive to the electric field and $MgAs_2O_6$-Mn cannot be excited.

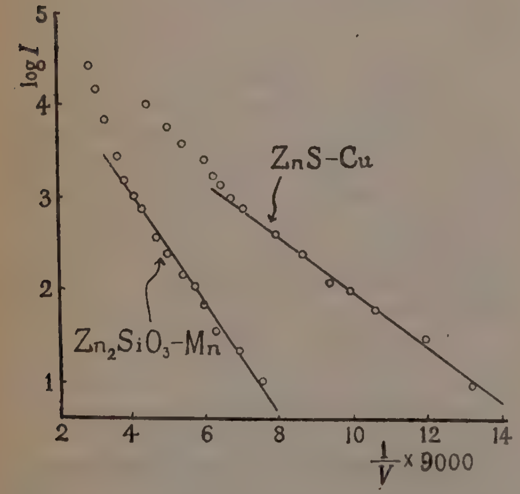

Fig. 1. The relation between applied potential and emission intensity.

The relation between the applied potential V and the emission intensity I for the cases of ZnS-Cu and Zn_2SiO_3-Mn is shown in Fig. 1, and is represented approximately by an formula $I = A\exp(-\phi/V)$, the value of ϕ having been estimated as 1.5 and 0.7 for Zn_2SiO_3-Mn and ZnS-Cu respectively.

The ratio of these two values is approximately 2. The depth of impurity level under the conduction band in these two phosphors was determined through the experiment of excitation by lights, obtaining the values 3.9 ev and 2.7 ev for the minimum values respectively. The fact that the square, or 3/2-power, of the ratio (3.9/2.7) of these energy depths is nearly equal to 2 suggests that the emission process is of Zener's type[3] or of the cold emission type.

There may arise a question that emissions are attributed to the bombardment of electrons extracted from the base metal through the cold emission, and in fact the luminescence due to this process is found in the experiment of Piper and Williams[4]. In our cases, however, it can be proved as follows that such an ambiguity does not occur. The film containing phosphors prepared on the brass plate in which other metals having different work functions such as Mg or Al are embedded, can be excited to emit in uniform brightness. Furthermore, when the half-wave rectified potential is applied, the emission is found to have the equal intensity in the two cases in which metal has the positive and negative potentials respectively.

The above two phosphors can be excited to be luminescent by illumination of ultra-violet light and in crystals conduction electrons are produced during this illumination. Under this condition the potential was applied and the intensity increase was measured. For the case of Zn_2SiO_3-Mn it was found that the increase was of the same amount as the one emitted when the electric field only was applied, and for ZnS-Cu the intensity rather decreased.

From these results it may be concluded that emission of the phosphor in intense electric field is due to the primary electrons ionized directly from impurity centres by the field, and secondary ionization produced by the accelerated primary electrons has no effect in the range of field strength used in the present experiment. Therefore, the relation shown in Fig. 1 is considered to give the electron-exciting probability from the impurity centre by the electric field, assuming that energy distributions of the emission spectrum are not so seriously distorted. At the potential of relatively higher value, emission intensity is found to increase more sharply. This may be due to the effect of secondary ionization.

The photo-exciting emission spectrum of Zn_2SiO_4-Be-Mn is found to be composed of two bands, green and red. The former is assumed to be due to the substitutional Mn^{++} ion, while the latter to the interstitial one. At high temperatures red band is diminished[5]. In the case of the electric field emission, it was found that the green band was predominant. Hence, this analogy in the spectral change suggests that the field emission will be an another method of interpreting the structure of emission centres in phosphors.

In conclusion, the author wishes to express his cordial thanks to Profs. Y. Uchida, T. Muto and J. Yamashita for their encouragements. The author's thanks are also due to Mr. M. Nakamura for his assistance in carrying out the present experiment.

References

1) B. Gudden and R. Pohl: Zeit. Phys. **1** (1920) 365.

2) G. Destriau: Trans. Faraday Soc. **35** (1939) 227, Phil. Mag. **38** (1947) 700.

3) C. H. Zener: Proc. Roy. Soc. A **145** (1934) 523.

4) W. Piper and F. E. Williams: Phys. Rev. **87** (1952) 151.

5) G. R. Fonda and F. Seitz: Preparation and Characteristics of Solid Luminescences (John Wiley, 1948) 406.

J. PHYS. SOC. JAPAN 8 (1953) 431~432

The Temperature Dependence of the Zero Bias Resistance of Cuprous Oxide Rectifiers

By Atuyosi OKAZAKI
Physical Department, Faculty of Science, Kyushu University
By Hiroshi TUBOTA and Hiromichi SUZUKI
The Second Branch of Kyushu University

(Received February 28, 1953)

Billig and Ridout[1] have measured the zero bias resistance R of germanium, silicon and selenium rectifiers and selenium photocells down to the low temperature. From the temperature dependence of the resistance, they have examined the temperature dependence of the diffusion potential V_d, assuming the formula

$$R \propto \exp(V_d/kT) \qquad (1)$$

and found that V_d decreases with decreasing temperatures; for example, in selenium rectifiers the value of V_d is 0.2 V at 70° K, while 0.5 V at room temperature. This fact can not be accounted for by the change of the lattice parameters.[2] Landsberg[3] has recently interpreted the temperature dependence of the zero bias resistance of selenium rectifiers obtained by Billig and Ridout on the assumption of the temperature dependence of the mobility of current carriers.

In the present paper we have done the similar measurement on cuprous oxide rectifiers and interpreted the results on Landsberg's assumption as below.

We applied small d. c. voltages to commercial cuprous oxide rectifiers and measured the currents in both the forward and backward directions, using a K_2-type potentiometer for the measurements of both voltages and currents. Applied voltages were so small that the currents for a given equal voltage in both the forward and backward directions were equal. At very low temperatures, as a difference between the above currents takes place, we adopted the differential resistance from the current-voltage curve. The results are shown in Fig. 1. While only two samples were examined in the very low temperature range by using liquid air, several samples were examined in the temperature range from 0° C to 100° C.

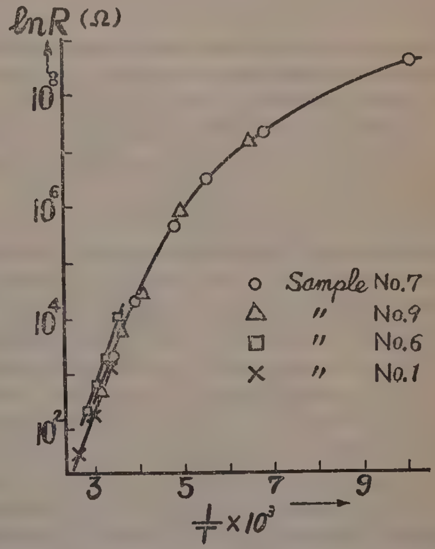

Fig. 1. Temperature dependence of zero bias resistance R.

From the general diffusion theory taking into account image force, Landsberg has deduced the following formula expressing the zero bias resistance R:

$$\frac{1}{R}=\frac{evn(d)}{2(\pi\varepsilon kTb_0^3)^{1/2}}\exp(-V(b_0)/kT), \qquad (2)$$

where the notation introduced by Landsberg are adopted. Equation (2) gives the following rela-

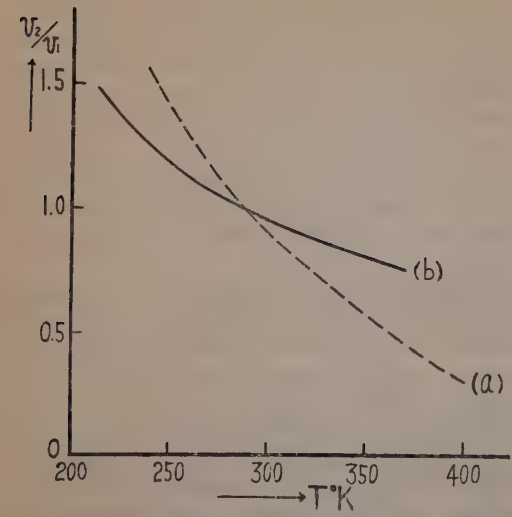

Fig. 2. Temperature dependence of the mobility of current carriers in Cu_2O (a), from zero bias resistance of Cu_2O-rectifier by the authors, and (b), from Hall effect on Cu_2O by Angello.

tion between the zero bias resistances R_1 and R_2 at absolute temperatures T_1 and T_2:

$$\frac{R_2}{R_1} \simeq \frac{v_1}{v_2}\left(\frac{T_1}{T_2}\right)^{1/4} \exp\left[\frac{\beta}{k}\left(\frac{1}{T_2}-\frac{1}{T_1}\right)\right], \quad (3)$$

from which we are able to get the ratio of the mobility v_2 at T_2 to v_1 at T_1.

Assuming reasonable value 0.45 eV for β (which is nearly equal to the potential maximum $V(b_0)$ in the absence of an applied voltage and independent of temperature), we have applied equation (3) to the present results for cuprous oxide rectifiers and 15° C was chosen as the standard temperature T_1. The obtained values of v_2/v_1 are plotted against T in Fig. 2(a). Mobility determinations from Hall effect measurements have been done by S. J. Angello and others.4) According to their results the mobility decreases with increasing temperature in the range from −180° C to 100° C. For the sake of comparison, the mobility-temperature curve obtained from Angello's data is shown in Fig. 2(b).

References

1) E. Billig and M. S. Ridout: Nature **167** (1951) 1028.

2) E. Billig: Proc. Phys. Soc. A **64** (1951) 752.

3) P. T. Landsberg: ibid. B **65** (1952) 397.

4) S. J. Angello: Phys. Rev. **62** (1942) 371; W. Vogt: Ann. d. Phys. **7** (1930) 183; E. Engelhard: ibid **17** (1933) 501; W. Schottky and F. Waibel: Phys. Z. **34** (1933) 858; W. Feldman: Phys. Rev. **64** (1943) 113.

J. Phys. Soc. Japan 8 (1953) 432~434

Chemical Shift of the N^{14} Magnetic Resonance

By Yoshika Masuda and Teinosuke Kanda
Department of Physics, Kobe University

(Received April 20, 1953)

The influence of the chemical compound upon the nuclear magnetic resonance frequency of a nucleus has been previously reported.1)2)3) Such chemical shifts have been observed for some of the nitrogen compounds.2)

We have observed, with a resolution better than 1 part in 10^5, such chemical shifts for N^{14} in aqueous solutions and in organic liquids of several nitrogen compounds.

Experiments were performed with a large permanent magnet made of 110 kgs. NKS-1 steel with a total weight of approximately 1300 kgs. delivering 6200 gauss. This has a gap of 10 cm diameter, 3 cm spacing, the inhomogeneity of the field being less than 0.05 gauss over the entire volume of the sample. The magnetic field is biased linearly by a pair of coils with one milliampere producing a change in field of 0.269 ± 0.010 gauss. To investigate the chemical effect in nitrogen, the autodyne detector at a fixed radiofrequency of 1920 kc, corresponding to a field of 6221 gauss, was employed, and a sweeping magnetic field was superposed upon the permanent field. However, hysteresis of one twentieth of a gauss results when large currents are applied first in one direction and then in the reversed. All resonances were measured in saturated aqueous solutions at room temperature except for $C_6H_5NO_2$, $H_2N\text{-}NH_2\cdot H_2O$, CH_3NO_2, and HNO_3 (liquid at room temperature). No magnetic catalysts were added to the samples. All measurements were made at an identical position in the magnetic field.

We have obtained the results given in Table I. Proctor and Yu2 have shown, within a resolution of a 0.1 kc in the neighborhood of 3300 kc, that the N^{14} resonances of the NO_3^- ion from such compounds as NH_4NO_3, HNO_3, and $Cu(NO_3)_2$ coinside at one frequency. But, in our experiments N^{14} resonance of the NO_3^- ion from $NaNO_3$ and that from HNO_3 do not coincide at one frequency.

We have measured the chemical shift of the nitric acid in various concentrations. Samples were obtained by diluting the anhydrous nitric acid which was prepared by a vacuum distillation from a sulfuric acid solution.

The results are plotted in Fig. 1, where the O-origin was taken at the resonance position of $NaNO_3$ aq. and NH_4NO_3 aq., which had the same

Table I. Chemical shifts of nitrogen compounds to NO_3^-, at room temperature.

	$\Delta H/H$ This research	$\Delta H/H$ Proctor and Yu
NH_4OH(28%)	3.72×10^{-4}	3.64×10^{-4}
NH_4^+ from NH_4NO_3, NH_4SCN	3.46	3.03
$(NH_2)_2CO$	3.46	3.03
$NH_2\text{-}NH_2\cdot H_2O$	3.46	
SCN^- from NH_4SCN, KSCN	1.51	
CN^- from KCN, NaCN	1.12	0.61
HNO_3(100%)	0.52	
$C_6H_5NO_2$	0.17	
NO_3^- from $NaNO_3$, NH_4NO_3	0.00	0.00
CH_3NO_2	0.00	

resonance position and indicating no concentration dependence within experimental error.

There was a chemical shift in the solution of ferric nitrate by the paramagnetism of Fe^{+++}, which was 0.08 gauss in its saturated solution. On the other hand, when we measured the paramagnetic susceptibility of our nitric acid sample by the Quincke method, it was less than one tenth of that of $Fe(NO_3)_3$ saturated solution. Therefore, the concentration shifts among the nitric acid solutions have nothing to do with the paramagnetism by some impurity molecules, such as NO_2.

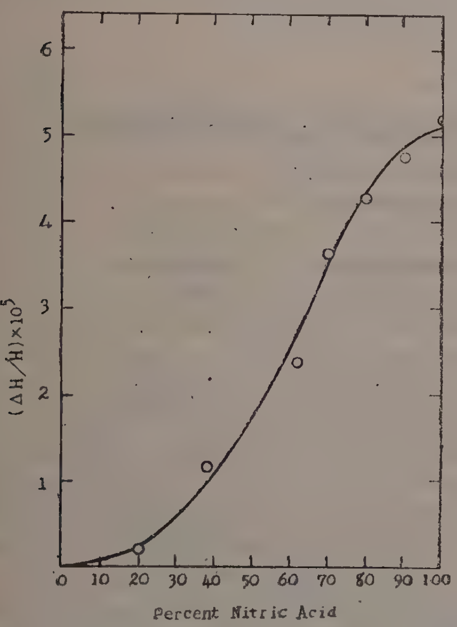

Fig. 1. Chemical shift of N^{14} nuclear magnetic resonance signals of nitric acid dissolved in water from those of $NaNO_3$ aq.

The reason for the dependence on concentration may be said as follows:

(1) The resonance frequency shift exists between NO_3^- ion and HNO_3 molecule, because the nitrogen should experience a different magnetic shielding in the dissociated and molecular state.

(2) In the nitric acid solution, a dissociation equilibrium $HNO_3 \rightleftarrows NO_3^-$ is set up. If the correlation time for the life times, $\tau_{\rm ion}$ and $\tau_{\rm mol}$, of the dissociated and molecular state is extremely shorter than the relaxation time T_2, the nitrogen resonance will be observed at the frequency corresponding to the average shielding for the states and the frequency shifts S measured from the resonance frequency of NO_3^- is given by

$$S=S_{\rm mol}\frac{\tau_{\rm mol}}{\tau_{\rm mol}+\tau_{\rm ion}}\ ,$$

where $S_{\rm mol}$ is the shift of the anhydrous nitric acid molecule.

(3) The apparent degree of the dissociation α is given by

$$\alpha=\frac{\tau_{\rm ion}}{\tau_{\rm mol}+\tau_{\rm ion}}\ .$$

Then,

$$S=S_{\rm mol}(1-\alpha)\ ,$$

α which is given from the measured shift is indicated in Table II. Since changes of concentration will alter the degree of the dissociation, the resonance frequency should be concentration dependent.

(4) There may exist several kinds of molecules $HNO_3\cdot H_2O$, $HNO_3\cdot 2H_2O$, etc. but we regard their shifts from HNO_3 unmeasurably small.

Recently Gutowsky[4] observed that the position of the proton magnetic resonance is concentration dependent in aqueous solutions of electrolytes yielding hydrogen ions. His values of the apparent degrees of dissociation of HNO_3 computed from the proton magnetic resonance shift agree with ours in Table II within experimental error.

The authors wish to express their gratitude to Professor Y. Inoue of the Kobe University who

Table II. Apparent degrees of dissociation α of HNO_3

Concentration %	$(\Delta H/H)_{obs}$	α
20	0.22×10^{-5}	0.96
40	1.04	0.80
60	2.51	0.51
70	3.50	0.31
80	4.33	0.15
90	4.84	0.05

had kindly supplied samples of most of the compounds, especially the anhydrous nitric acid.

References

1) W. C. Dickinson: Phys. Rev. **77** (1950) 736.
2) W. G. Proctor and F. C. Yu: Phys. Rev. **77** (1950) 717.
3) W. D. Knight: Phys. Rev. **76** (1950) 1259.
4) H. S. Gutowsky: private communication. We are indebted to Dr. Cutowsky for sending us a copy of his article prior to publication.

Errata

On the Subsonic Flow of a Compressible Fluid past a Prolate Spheroid

By Kinzō Hida

J. Phys. Soc. Japan **8** (1953) 257-264

p. 257 right column			
line 11 from bottom	orignally	should be read	originally
p. 258 left column			
line 2 from bottom	$(x,\ \omega)$	〃	$(x,\ \tilde{\omega})$
right column			
eq. (4)	$q_1^2=\dfrac{1}{k^2(\zeta^2-\mu^2)}\Big\{\cdots$	〃	$q_1^2=\dfrac{2}{k^2(\zeta^2-\mu^2)}\Big\{\cdots$
eq. (5)	$\bar{\Delta}\Phi_1=0$	〃	$\bar{\Delta}\Phi_0=0$
p. 260 eq. (14c)	$\cdots-\dfrac{1}{2(\zeta^2-1)}\Big(\log\dfrac{\zeta_0+1}{\zeta_0-1}\Big)+\cdots$	〃	$\cdots-\dfrac{1}{2(\zeta_0^2-1)}\Big(\log\dfrac{\zeta_0+1}{\zeta_0-1}\Big)+\cdots$
eq. (16)	$\cdots\int_{\zeta_0}^{\infty}\dfrac{Q^2{}_{2m+1}(\zeta_1)}{(\zeta_1^2-1)}d\zeta_1\Big\}$	〃	$\cdots\int_{\zeta_0}^{\infty}\dfrac{Q^2{}_{2m+1}(\zeta_1)}{(\zeta_1^2-1)^2}d\zeta_1\Big\}$
p. 261 eq. (22)	$\dfrac{P_1^1(\mu)}{14}e^4\Big(\cdots+\dfrac{4277}{1925}e^4+\cdots\Big)$	〃	$\dfrac{P_1^1(\mu)}{14}e^4\Big(\cdots+\dfrac{4777}{1925}e^4+\cdots\Big)$
right column			
line 2 from bottom	$\Big(\dfrac{q^*}{q}\Big)^2$	〃	$\Big(\dfrac{q_*}{q_\infty}\Big)^2$
p. 262 left column			
line 10 from bottom	wnich	〃	which
righ column			
line 9	$^{7()}$	〃	$^{7)}$
p. 263 Table I 3rd column			
line 8	1.25126	〃	1.25216
p. 264 Table II 5th column			
line 3	1.59749	〃	1.09749

JOURNAL OF THE PHYSICAL SOCIETY OF JAPAN Vol. 8, No. 4, JULY—AUGUST, 1953

The Beta-ray Spectra of Co^{60} and Sc^{46}

By Yasukazu YOSHIZAWA

Department of Physics, Faculty of Science, Osaka University

(Received March 18, 1953)

The beta-ray spectra of Co^{60} and Sc^{46} were studied by a semicircular beta-ray spectrometer with the radius of 10 cm. The spectrum of Co^{60} agrees with that of the allowed transition of the Fermi theory from the maximum energy down to about 60 keV. The spectrum of Sc^{46} also agrees with that of the allowed transition from the maximum energy down to 120 keV. For Co^{60} the upward deviation which occurs at the energy less than 60 keV may be due to the effect of the source thickness, but for Sc^{46} the upward deviation at the energy less than 120 keV could not be decisively explained. The maximum energies of Co^{60} and Sc^{46} beta-rays are 316 ± 3 keV and 357 ± 3 keV, respectively.

§ 1. Introduction

Cobalt 60 and Scandium 46 have similar decay schemes. Co^{60}, of which half-life is 5.3 years, emits beta-ray followed by two successive gamma-rays. As it is the most conventional and useful gamma-ray source, gamma-rays have been investigated by many methods. Lind, Brown, and DuMond1) gave the energies of gamma-rays as 1.1715 ± 0.0010 MeV and 1.3316 ± 0.0010 MeV, using a crystal spectometer, and Deutsch and Siegbahn2) and others3)4) measured by beta-ray spectometers. Internal conversion coefficients were measured by Waggoner, Moon, and Roberts,5) Deutsch and Siegbahn2), and Fan6). The angular correlation and the polarization angular correlation between two successive gamma-rays were studied by Brady and Deutsch7), Williams and Wiedenbeck8), and Metzger and Deutsch9). Ni^{60} is even-even nucleus of which the ground state is expected to have zero spin and even parity. According to these results, both gamma-rays are of electric quadrupole radiations, and spins and parities of the ground state, the first and the second excited states of Ni^{60} are 0, 2, 4, res pectively and all even.

On the other hand, the beta-ray spectrum of Co^{60}, which was studied by Deutsch, Elliott, and Roberts10) and others, agreed with that of the allowed transition of the Fermi theory for the high energy part. Deutsch, *et al.*10) and Waggoner, *et al.*11) found the maximum energy of 308 ± 8 keV and 317.8 ± 0.4 keV, respectively. From these results log *ft* value12) is 7.51. Beta-gamma angular correlation was measured by many investigators,13)14)15)16) and they reported that the beta-gamma angular correlation is isotropic.

Sc^{46}, half-life 85 days, decays by negatron emission followed by two successive gamma-rays as like as Co^{60}. The gamma-rays of energies 1.12 MeV and 0.89 MeV were determined by Peacock and Wilkinson,17) Miller and Deutsch,18) Moon, Waggner, and Roberts,19) and Porter and Cook20). The internal conversion coefficients of these gamma-rays were investigated by Peacock and Wilkinson,17) and Moon, *et al.*19) The gamma-gamma angular correlation was measured by Brady and Deutsch,7) and Novey,21) and the gamma-gamma polarization angular correlation was studied by Metzger and Deutsch9). These results shows that both gamma-rays are due to quadrupole transitions, spins of the ground state and the first and the second excited states of Ti^{46} are 0, 2, 4, respectively, and parities of them are all even, as same as for the case of Co^{60}.

The beta-ray spectrum of Sc^{64} was investigated by Peacock and Wilkinson,17) and Miller and Deutsch18) and was found to be that of the allowed transition of the Fermi theory for the high energy part. The maximum energy of the beta-ray is 0.36 Mev17)18) and log *ft* value12) is 6.23. No beta-gamma angular correlation was reported by Novey.21)

Though in the case of Co^{60} the beta-transition to the first excited state has not been found, in the case of Sc^{46} such a transition, having the energy of 1.49 MeV and the intensity of 0.5 percent, has been reported.17)20) Both Co^{60} and Sc^{46} have isometric states of which half-lives are 10.7 min. and 20 sec. and the transition energies between the isomeric states are 59 keV and 180 keV, respectively.

In this experiment we investigated beta-ray spectra of Co^{60} and Sc^{46}, and tried to show whether these spectra fit the allowed transition or the forbidden one down to the low energy part.

§ 2. Apparatus

A conventional semicircular focusing beta-ray spectometer with $\rho = 10$ cm was used. This spectometer has the gathering power of about 0.1 percent and the resolution of about 1.7 percent, which was decided by photo-electric lines of Co^{60} gamma-rays.

Source. We used radioactive samples, Co^{60} and Sc^{46} irradiated at Oak Ridge. Sources are mounted on the collodion films of about 10 $\mu g/cm^2$ which are supported by thin aluminium frames. The thickness of two Co^{60} source are about 30$\mu g/cm^2$ and 100$\mu g/cm^2$ in $CoCl_2$. To make uniform sources, in the former case about forty drops of $CoCl_2$ aq. which have diameters of less than 1 mm are rapidly evaporated with an infra-red lamp, while in the latter case a small part of $CoCl_2$ is deposited on the insuline[22] disolved in diluted acetic acid which is dropped on the collodion film and is evaporated without the lamp. The thickness of Sc^{46} source is about 200 $\mu g/cm^2$ which was made uniform by using insuline as in the case of Co^{60} source. To avoid charging up of the source,[23] a small amount of colloidal carbon was put on the back surface of collodion film in the form of a strip, using insuline, and the film is made somewhat conductive.

Chamber. The spectometer chamber made of aluminium has an aluminium slit at the midway of the electron path and many other aluminium baffles. For the exist slit the counter window is used. There is a lead absorber of about 10 cm between the source and the detector. Baffles and slits were designed, so as to eliminate all electrons which are scattered once at the wall and enter into the detector, except electrons which are scattered at the wall behind the source. In this experiment the wall behind the source is so apart from the source that this effect is negligible. Electrons which enter into the detector after scattered more than once at the wall are negligible in such a chamber as that used in this experiment which is made of aluminium and has many baffles.[24] But for sources accompanied with strong gamma-rays the gamma-ray absorber in the chamber is too small to reduce the background satisfactorily.

Detector. The Geiger-Müller counter filled with alcohol was used for the detector. In the case of the measurement of S^{35} beta-ray spectrum, first we used an end window counter having inner cathode. Absorption effect appeared at the low energy part, though thin window foil and low pressure gas were used. We could eliminate such an effect by adopting side window counter. The absorption effect in the former case may be due to the absorption of electrons by the gas between the counter window and the cathode cylinder of the counter. The effect of the window lattice[25] which suppots the thin window film is negligible, because of the low maximum energy of Co^{60} and Sc^{46} beta-rays. In this experiment the window is the collodion film of 30 $\mu g/cm^2$, and pure alcohol of about 2 cmHg is filled in the counter.

Measurement of the magnetic field. The magnetic field was calibrated by the proton resonance method, in order to know accurate absolute values. We used this method down to about 50 gauss and extrapolated the curve of magnetic field vs. magnetic current to 40 gauss, as the current-field curve is linear from 700 gauss to 50 gauss. The inhomogeneity of the field along the electron path is 0.4 percent. The mean value of the magnetic field along the electron path in the spectrometer was used for the calculation of the momentum of the beta-rays.

§ 3. Results

A. Cobalt 60.

The gamma-ray spectrum was first measured by photo-electron from platinum foil of 20 mg/cm^2 in thickness. In the spectrum the K- and L- photo-electron lines indicate the gamma-rays of 1.17 Mev and 1.33 Mev.

The beta-ray spectrum was studied by two different sources described in the preceding section. The momentum spectra are shown in Fig. 1 and the Kurie plots in Fig. 2. The Kurie plot of the thicker source shows the upward deviation from the straight line at the energy less than 70 keV. In the case of the thinner source, due to the small specific activity of the CoCl$_2$, statistical error in the low energy part is fairly large, so the deviation is not clear. Solid points shown in Fig. 2 are the results corrected for the screening effect.[26]

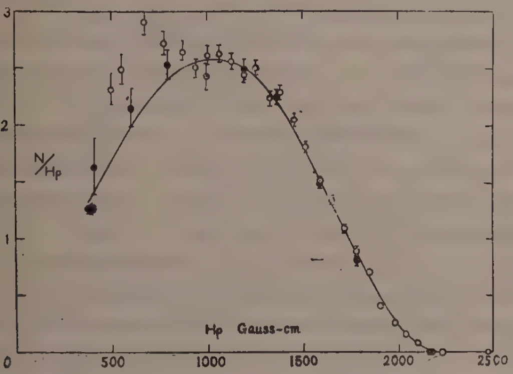

Fig. 1. The momentum of Co^{60} beta-ray. Vacant points show the spectrum from the source of about 100 μg/cm^2, and solid points show the spectrum from that of about 30 μg/cm^2 in thickness.

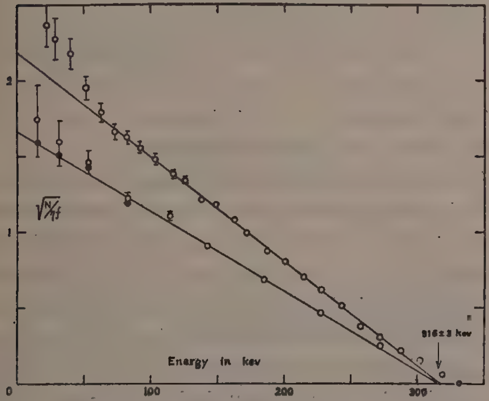

Fig. 2. The Kurie plots of Co^{60} beta-ray spectrum. Upper one shows the plot from the source of about 100 μg/cm^2 and lower one shows the plot from the source of about 30 μg/cm^2 in thickness. Solid points are those corrected by the screening effect.

The both Kurie plots show that the beta-ray spectra from the maximum energy down to 60 keV agree with the allowed spectrum of Fermi theory. In spite of the thin source, there is some upward deviation at the region lower than 60 keV, but it may be the effect of the source thickness or its nonuniformity.

By means of the extrapolation of the straight part of Kurie plots, the maximum energy was decided to be 316±3 Kev.

B. Scandium 46.

The beta-ray spectrum of Sc^{46} was investigated in the same condition at that of Co^{60}, but in this case only one source with the thickness of about 200 μg/cm^2 was used. The momentum spectrum and the Kurie plot are shown in Fig. 3 and Fig. 4, respectively. The vacant points in Fig. 4 are uncorrected Kurie plots, which lie on a straight line from maximum energy down to about 120 Kev. The upward deviation clearly appears from about 120 Kev, though in the case of cobalt spectrum the deviation begins from about 60 Kev.

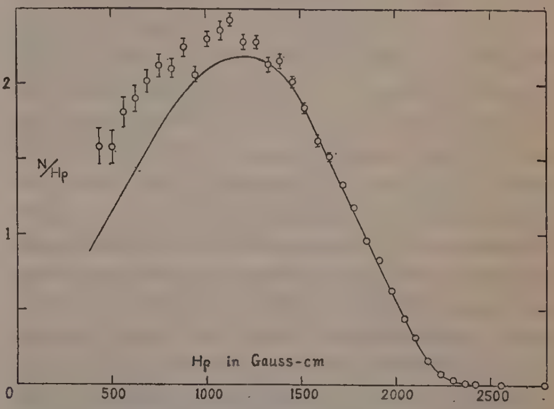

Fig. 3. The momentum spectrum of Sc^{46} beta-ray of which source thickness is about 200 μg/cm^2.

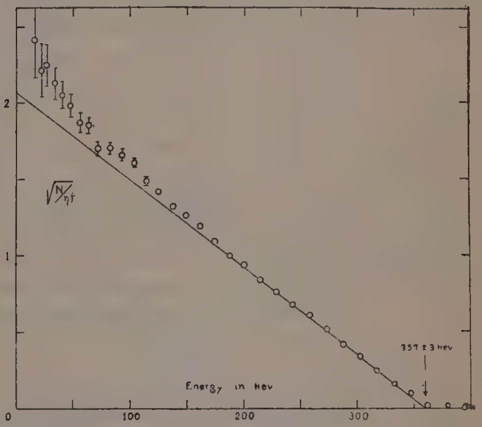

Fig. 4. The Kurie plot of Sc^{46} beta-ray spectrum.

The maximum energy determined from the extrapolation of the straight part of the Kurie plot is 357±3 Kev.

§ 5. Discussion

In the previous experiments[10][17][18] it was reported that the beta-ray spectra of Co^{60} and Sc^{46} have the shape of the allowed transition except for low energy part. The upward deviations from the straight lines in Kurie plots, Figs. 2 and 4, appear at the energy less than 60 Kev and 120 Kev, respectively. According to the result of our measurement of the beta-ray spectrum of S^{35}, there is no effect of chamber scattering and counter absorption in the part higher than 30 Kev. For the Co^{60} spectrum the deviation for energy less than 60 Kev may be due to the effect of source thickness.

For the case of Sc^{46} the upward deviation which clearly appears from about 120 Kev is fairly large in comparison with the case of Co^{60}. We can expect four causes for this deviation. First, it may be the effect of the source thickness. But judging from the thickness of the source, this deviation seems to be too large. Second, Sc^{46} is complex spectra : the second component has the maximum energy of 175±15 Kev, and is about 6 percent of the first component. If the second group is true, it should accompany gamm-ray of about 190 Kev, 1.3 Kev, or 2.2 Mev. But such gamma-rays have not been found. Third, the deviation comes from redioactive impurity : as the sample was measured more than three months after irradiation and the beta-ray of the impurity is about 6 percent of that of Sc^{46}, the impurity must have fairly long life time. As the maximum energy is 175 Kev, only S^{35} is possible in known radioactive isotopes. But we could not analyse chemically whether S^{35} of about 6 percent is contained in the scandium sample. Fourth the deviation is due to true distortion : distortion from the allowed distribution is attributable to the forbidden transition or the linear combination of the interaction. As shown in Fig. 5 a, first forbidden transition $\Delta I=0$ or 1, parity change, can explain such a spectrum, if it is assumed that $|\int\boldsymbol{\sigma}\times\boldsymbol{r}|:|\int\boldsymbol{\alpha}|:(\int\boldsymbol{\sigma}\times\boldsymbol{r}\cdot\int\alpha+c.c.)=1:(10.4)^2:2\cdot10.4$ for the ratio of matrix elements ; that is, the correction factor $C_{IT}=|\int\boldsymbol{\sigma}\times\boldsymbol{r}|^2A_+'+|\int\boldsymbol{\alpha}|^2-[(\int\boldsymbol{\sigma}\times\boldsymbol{r})(\int\boldsymbol{\alpha})+c.c]B$ with these values of nuclear matrix elements makes the Kurie plot straight from the maximum energy down to about 50 Kev, where notations of the Konopinski's paper[27] are used. Such a correction factor can be obtained not only from the tensor interaction but also from the vector and the axial vector interactions, if nuclear matrix elements are appropriately chosen. On the other hand, by the corrections of linear combinations of five invariants for the allowed transition,[28] that is, by using correction factor $C_0=1+0.026/W$, the Kurie plot of Sc^{46} also yields a straight line down to about 50 Kev as shown in Fig. 5 b. Unfortunately, only from this experiment we cannot conclude whether the transition of Sc^{46} is allowed or first forbidden, but it is clear not to be second forbidden.

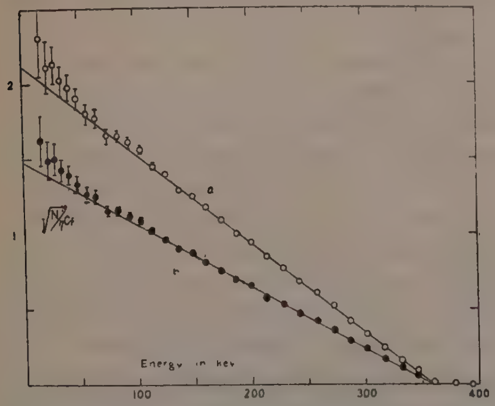

Fig. 5. The corrected Kurie plots of Sc^{46} beta-ray spectrum. The upper line, a, is corrected by the first forbidden factor and the lower line, b, is corrected by the factor of the linear combination of invariants for the allowed transition.

As described in the introduction, the logarithmic comparative half-lives of Co^{60} and Sc^{46}, $\log_{10}ft$, are 7.51 and 6.23[29], respectively. Therefore, Co^{60} and Sc^{46} may be classified as the first forbidden transition, but as values of $\log ft$ of the allowed transition are largely straggled, these classification is not decisive. According to the nuclear shell structure analysis,[30] the ground states of Co^{60} and Sc^{46} are $(f_{7/2}, p_{3/2})$ and $(f_{7/2}, f_{7/2})$, respectively. Both ground states of Ni^{60} and Ti^{46} have zero spin and even parity, and both second excited states have 4 and even. Since both of the initial and the final states have even parity, the allowed or the second forbidden transition for both beta-decays is expected from the shell structure, but the latter is excluded by the allowed shape of the spectra. No beta-gamma angular correlation supports that these spectra are due to the allowed transition or the first forbidden one which has the allowed type spectrum.[31]

By these considerations and our experimental results, the beta-ray decay of Co^{60} is expected to be allowed transition. The large *ft*-value of Co^{60} may be due to the *l*-forbidden[32], and the spin and the parity of the ground state are most probably 5 and even, as reported by Goldhaber and Hill.[33] For Sc^{46} the spectrum shows fairly large deviation in the low energy part, but there are some ambiguities in the experiment as previously described. Besides, even if the deviation is real, it is possible to explain by the linear cambination. Therefore, according to the consideration of the shell structure, the beta-decay of Sc^{46} is probably allowed. The pretty large *ft*-value of Sc^{46} is probably allowed. The pretty large *ft*-value of Sc^{46} may also attributed to the *l*-forbidden, and if so, the spin and the parity of the ground state are 5 and even respectively, differing from Goldhaber and Hill. The beta-transition to the first excited state of Ti^{46} is probably second forbidden, as reported by them.

The author would like to express his thanks to Professor J. Itoh for his kind help and his valuable discussions, and to Dr. S. Nakamura, Tokyo University, for his useful discussions, about this experiment.

References

1) Lind, Brown, and DuMond: Phys. Rev. **76** (1949) 591.
2) M. Deutsch and K. Siegbahn: Ark. f. Fysik **2** (1950) 9.
3) D. E. Alburger: Phys. Rev. **76** (1949) 435.
4) Hornyak, Lauritsen, and Rasmussen: Phys. Rev. **76** (1949) 731.
5) Waggoner, Moon, and Roberts: Phys. Rev. **78** (1950) 295.
6) C. Y. Fan: Phys. Rev. **87** (1952) 252.
7) E. L. Brady and M. Deutsch: Phys. Rev. **78** (1950) 558.
8) A. H. Williams and M. L. Wiedenbeck: Phys. Rev. **78** (1950) 822.
9) F. Metzger and M. Deutsch: Phys. Rev. **78** (1950) 551.
10) Deutsch, Elliott, and Roberts: Phys. Rev. **68** (1945) 193.
11) Waggoner, Moon and Roberts: Phys. Rev. **79** (1950) 236, **80** (1950) 420.
12) A. M. Feingold: Rev. Mod. Phys. **23** (1951) 10.
13) R. L. Garwin: Phys. Rev. **76** (1949) 1876.
14) Allen and Halban: Nature **164** (1950) 538.
15) D. T. Stevenson and M. Deutsch: Phys. Rev. **83** (1951) 1202.
16) T. B. Novey: Phys. Rev. **78** (1950) 66.
17) C. L. Peacock and R. G. Wilkinson: Phys. Rev. **74** (1948) 297.
18) L. C. Miller and M. Deutsch: Phys. Rev. **72** (1947) 527.
19) Moon, Waggoner and Roberts: Phys. Rev. **79** (1950) 905.
20) F. T. Porter and C. S. Cook: Phys. Rev. **81** (1951) 298.
21) T. B. Novey: Phys. Rev. **78** (1950) 66.
22) L. M. Langer: Rev. Sci. Inst. **20** (1950) 216.
23) Braden, Owen, Townsend, Cook, and Shull: Phys. Rev. **74** (1948) 1539.
24) G. E. Owen and C. S. Cook: Rev. Sci. Inst. **20** (1949) 768.
25) Y. Yoshizawa: J. Phys. Soc. Japan **7** (1952) 437.
26) C. Longmire and H. Brown: Phys. Rev. **75** (1949) 267.
27) E. I. Konopinski: Rev. Mod. Phys. **15** (1943) 209.
28) S. R. de Groot and H. A. Tolhoek: Physica XVI (1950) 456.
29) A. M. Freingold: Rev. Mod. Phys. **23** (1951) 10.
30) L. W. Nordheim: Rev. Mod. Phys. **23** (1951) 322.
31) D. L. Falkoff and G. E. Uhlenbeck: Phys. Rev. **79** (1950) 334.
32) L. W. Nordheim: Phys. Rev. **78** (1950) 294.
33) M. Goldhaber and R. D. Hill: Rev. Mod. Phys. **24** (1952) 179.

JOURNAL OF THE PHYSICAL SOCIETY OF JAPAN Vol. 8, No. 4, JULY—AUGUST, 1953

A Study of the Radioactive Decay of RaD by a Spherical Condenser-Type Spectrometer

By Yoshiyuki KOBAYASHI

Department of Physics, Faculty of Science, University of Tokyo

(Received March 30, 1953)

A spherical condenser-type electrostatic spectrometer was constructed, and the spectrum of radioactive decay of RaD was studied with it. For the well-known internal conversion lines due to the 46.7 kev gamma-ray, we obtained the intensity ratios $L_1:M:N=1:0.23\pm0.02:0.06\pm0.01$. In the energy region between 16 and 50 kev, no internal conversion line could be found except those due to the 46.7 kev gamma-ray. Many lines were observed below 16 kev, and most of them were identified as L Auger lines of bismuth. Some of them, i.e., lines at 6.6 or 7.0, 11.0, 15~16 kev may be internal conversion lines. The primary beta-ray seems to have its maximum energy at 16~18 kev. A tentative decay scheme was proposed to explain the result.

§ 1. Introduction

The theory of the spectrometer of this type was first introduced by E. M. Purcell,$^{1)}$ and developed by F. T. Rogers Jr.$^{2)}$. A large apparatus was constructed and examined by C. P. Browne and others in order to measure nuclear reaction energy$^{3)}$.

Advantage of an electrostatic spectrometer is the ease in controlling and measuring the electric field, a merit especially suited for the measurements of low energy particles. Furthermore, a spherical condenser has a property of good directional focusing, so that a large solid angle is available in spite of high resolving power. However, owing to the electrical breakdown and the relativistic spread of the image, mesurements are limited to a relatively low energy region.

The spectrum of RaD was studies as the first application of the apparatus. There have been many studies about the radioactive decay of RaD, but, owing to the difficulties in measuring low energy radiation, many doubts remain about its decay scheme and primary beta-spectra. Many gamma-rays have been reported by various authors$^{4),5),6)}$, but corresponding internal conversion lines have been found only for the 46.7 kev gamma-ray. As for the primary beta-ray, several values from 10 to 40 kev have been reported for its maximum energy, and recent investigations give the value 16~18 kev for it$^{7),8),9)}$. Cranberg reported the existence of an additional beta-spectrum having its maximum energy at about 60 kev$^{10)}$.

We have examined the spectrum from 3 to 50 kev in order to study conversion lines and primary beta-spectra.

§ 2. Apparatus

(*A*) *Theory*

Fig. 1 shows a cross-section of the spectrometer by a plane containing the axis of symmetry. R_1 and R_2 are the radii of the inner and outer spherical surfaces respectively, and ρ is the mean radius. A and F are the positions of the source and the detector respectively.

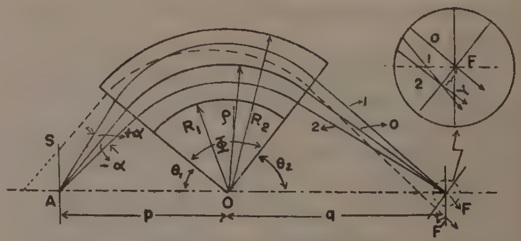

Fig. 1. Schematic cross section of Spherical condenser.

For the non-relativistic case, Purcell obtained the following results:

The velocity dispersion

$$D_v=2\rho(1+q/p). \qquad (1)$$

The spread of the image for a point source

$$Y=-\rho\alpha^2(p^2/q^2+q/p). \qquad (2)$$

The resolving power

$$\Delta=\left|\frac{D_v}{Y}\right|=\frac{1/\alpha^2}{1-p/q+p^2/q^2}\,, \qquad (3)$$

here $p=\rho/\cos\theta_1$, and $q=\rho/\cos\theta_2$. The voltage across the gap

$$V=E(R_2/R_1-R_1/R_2)\doteq 2E/\rho\,, \qquad (4)$$

here, E is the kinetic energy of the particle in ev.

The ratio of the effective solid angle to the whole solid angle, i.e. transmission, ω can be written as

$$\omega=\alpha_0\cos\theta_1\,, \qquad (5)$$

here, α_0 is the maximum available $|\alpha|$. Then Eq. (3) can be written

$$\Delta=\frac{\cos^2\theta_1}{1-p/q+p^2/q^2}\times\frac{1}{\omega^2}\,. \qquad (6)$$

For the incident beam which will just clear the plates, $|\alpha|$ is given by

$$|\alpha|=\frac{\kappa\cos\theta_1}{2}\,,$$

where

$$\kappa=(R_2-R_1)/\rho\,.$$

Consequently, the maximum ω is

$$\omega=\frac{\kappa\cos^2\theta_1}{2}\,. \qquad (7)$$

Eq. (6) is plotted in Fig. 2.

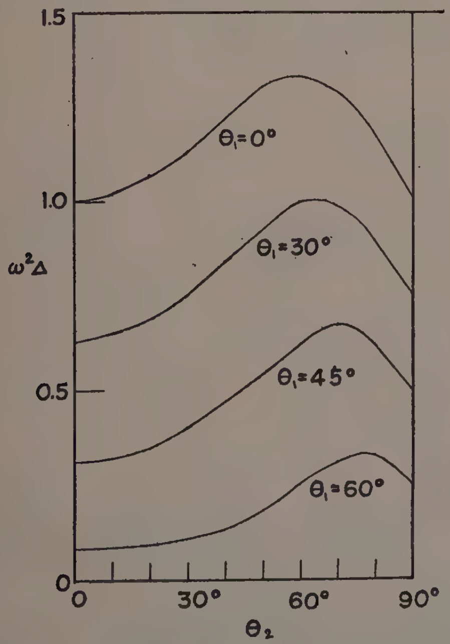

Fig. 2. Relations between transmission and resolving power.

Effect of the finite source width

In a practical case, the spread of the image mentioned above is so small compared with the spread due to the source width, that we can usually neglect the former. We shall consider a circular source having its center at A as shown in Fig. 3 (A). The beam which leaves the point S on the circle in the direction of the arrow will intersect the focal plane, the plane through F and perpendicular to the axis, at point F' on a ellipse shown in Fig. 3 (B). a and b have the values,

$$a=\varepsilon_0\frac{\sin\theta_1\cos\theta_1}{\sin\theta_2\cos\theta_2}\,, \quad \text{and} \quad b=\varepsilon_0\frac{\cos\theta_1}{\cos\theta_2}\,. \qquad (8)$$

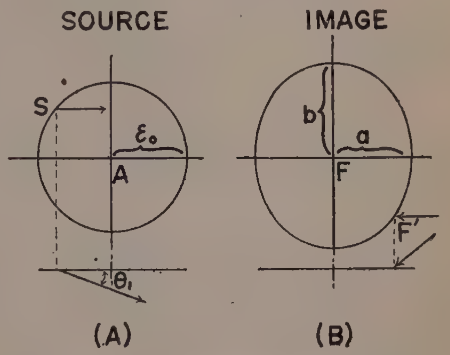

Fig. 3. Diagramatical drawing of source and image.

Then the line profile is given by plotting the area of the ellipse overlapping the circular aperture of the detector *vs*. displacement of the image, which is equivalent to energy. Examples are shown in Fig. 4 for our particular case.

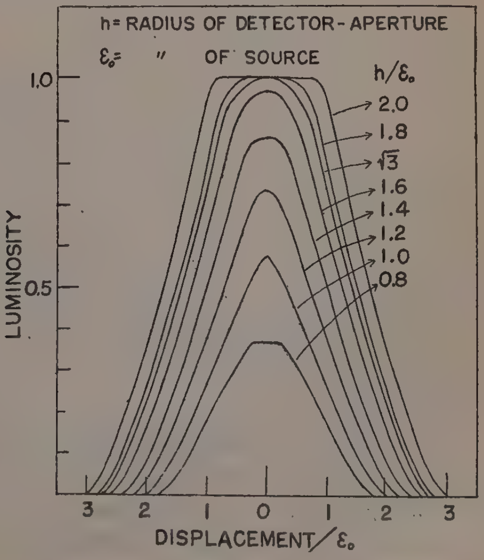

Fig. 4. Calculated line profiles.

Effect of the displacement of the source

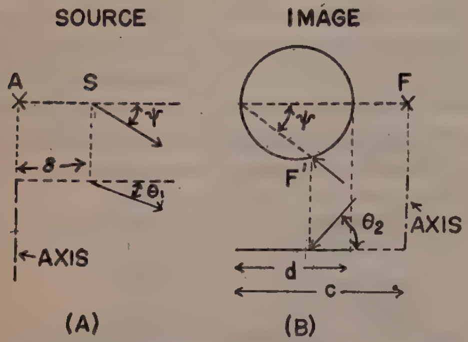

Fig. 5. Diagramatical drawing of source and image when source is displaced.

(a) Displacement perpendicular to the axis:

Fig. 5 shows the positions of the source and the image. The beam which leaves the source S in the direction of the arrow will intersect the focal plane at point F', where c and d are

$$c=\delta \cos\theta_1/\cos\theta_2\,, \qquad \text{and}$$
$$d=\delta(1-\sin\theta_1/\sin\theta_2)\cos\theta_1/\cos\theta_2\,. \qquad (9)$$

When ϕ changes from 0 to 2π; F' will go round the circle twice. Consequently, if the aperture of the detector is small, two peaks will be observed, separated by a distance $2\delta\cos\theta_1\sin\theta_1/\cos\theta_2\sin\theta_2$ from each other.

(b) Displacement along the axis:

When the distance of the source from the center of the spheres is increased by η, we must change the gap voltage to

$$V\left\{1-\frac{\eta}{\rho}\left(\frac{\cos^2\theta_1}{\cos\theta_2}\right)\Big/\left(1+\frac{\cos\theta_1}{\cos\theta_2}\right)\right\}$$

in order to focus the beam at the same point F. In the first approximation, all other equations are found to be valid in this case. Though the second order spread is somewhat different from the normal case, we can usually neglect it, if η is not too large. Moreover, for a certain position of the detector, the second order spread is the same as in the normal case. These considerations are important for our present design.

Relativistic effects:

Using the equations obtained by Sommerfeld for an electron in an atom,[11] we obtain the following results:

The relativistic spread of the image of a point source

$$Y^r/\rho=(k_1\alpha+k_2\alpha^2+\cdots\cdot)\,,$$
$$k_1=\tan\theta_1\cos\gamma\Phi+(1/\gamma)\sin\gamma\Phi+\tan\theta_2\times(\cos\gamma\Phi-\gamma\tan\theta_1\sin\gamma\Phi)\,, \qquad (10)$$

The velocity dispersion

$$Dv=\frac{2\rho}{(1-\beta^2)^2}(1-\cos\gamma\Phi+\gamma\tan\theta_2\sin\gamma\Phi)\,,$$

The energy dispersion

$$De=\frac{(1-\beta^2)(1-\sqrt{1-\beta^2})}{\beta^2}\times Dv\,, \qquad (11)$$

here $\beta=v/c$, and $\gamma^2 \doteqdot 1-\beta^2$.

The gap voltage

$$V^r=\frac{E}{2}\left(\frac{R_2}{R_1}-\frac{R_1}{R_2}\right)\left(1+\frac{1}{1+E/m_0c^2}\right)$$
$$=V\left(1+\frac{1}{1+E/m_0c^2}\right)\Big/2\,, \qquad (12)$$

here, E is the kinetic energy of the particles and V is the gap voltage for the non-relativistic approximation.

For a source of finite width, if α is small, the image is also an ellipse, and its half-axes have the length,

$$a=\varepsilon_0\frac{\sin\theta_1}{\sin\theta_2}(\cos\gamma\Phi-\gamma\tan\theta_2\sin\gamma\Phi)\,,$$
$$\text{and} \qquad b=\varepsilon_0\cos\theta_1/\cos\theta_2\,. \qquad (13)$$

In a higher energy region, however, the spread given by Eq. (10) will deform this image considerably. Eq. (10) and (11) are plotted in Fig. 6 for our present case.

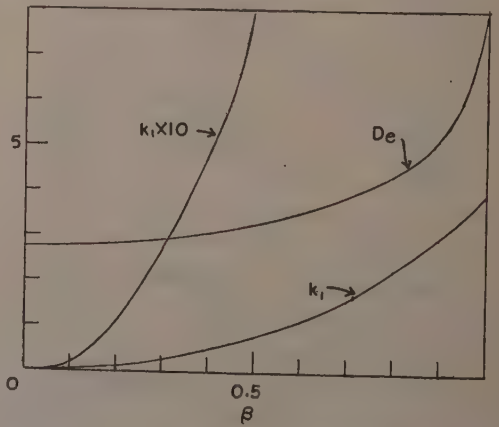

Fig. 6. Spread of the image and energy dispersion in the relativistic region.

The correction to be applied to the peak counting rate of the observed line can be estimated using the above results. In practice, however, owing to the existence of other sources of error, e.g., scattering and absorption, this correction has little meaning. From

Eq. (13), we can see that b does not depend on the energy. Consequently, taking into account the variation of the dispersion with energy, the areas of the observed spectra will give relative intensities immediately. Further, we can estimate the necessary correction from the observed line profile. In a higher energy region, however, it is better to reduce the relativistic effects at the sacrifice of the transmission.

(*B*) *Design and Construction*

In designing the apparatus, the relativistic effect was neglected. Fig. 2 shows that a large $\omega^2\Delta$ is expected for small θ_1, but large θ_1 is more favorable for reducing the absorption and the scattering in the source. It is desired to have the particles entering into the detector with a small angle to the axis. Taking into account these requirements and the ease in machining the parts, we have chosen following parameters,

$$\theta_1=30°, \quad \theta_2=60°, \quad \Phi=90°, \quad R_1=9.5\,cm \quad \text{and} \quad R_2=10.5\,cm\ .$$

In order to use the outer plate as a vacuum chamber, it was grounded instead of supplying voltages symmetrically. This modification is equivalent to a displacement of the source along the axis as discussed briefly above. The apparatus is shown schematically in Fig. 7.

For the ease of work, gun-metal casting was used for the plates. The spherical surfaces were machined by a lathe and the errors were within 0.1 mm around the axis, but somewhat larger along the path of the particles. The latter error is expected to have smaller effect upon the focusing than the former. The inner plate is supported by four glass insulators which can be adjusted without breaking vacuum. It was proved that these supports were quite stable against mechanical shocks to the vacuum chamber. In order to reduce the effects of the fringing fields and the neighbouring metal parts, the grounded slits have been attached to the both ends of the gap. A lead shield at the center of the chamber is supported by a X-shaped metal supporter. To prevent the scattering of particles, the surfaces of the plates have been coated with aquadag, and many serrations of 1 mm both in width and in depth have been grooved on the surface of the chamber just outside the gap.

In our apparatus, ω is calculated to be 3.75×10^{-2}, but in practice it will be reduced to about 3.4×10^{-2} owing to the interruption by the supporters.

(*C*) *High Voltage Supply*

The high voltage was supplied by two high voltage stabilizers, ranging from 1 to 20 kilovolts and from 500 volts to 2 kilovolts respectively. The relative flactuation of the output voltage is within 0.3 per cent. At present the maximum voltage maintainable across the gap without sparking is about 11 kilovolts. The sparking takes place between the inner plate and the slits, spaced about 2 mm. It is believed to be caused by the bad electrical breakdown characteristics of the gun-metal casting. In order to measure higher energy particles we shall have to remove the slits. This will cause some displacement of the position of the image, but the resolving power is expected to remain unchanged as the first approximation.

§ 3. Preliminary Experiments Using Thermal Electrons

Line profiles of the accelerated thermal electrons were examined for adjustment of the apparatus. At first, an electron gun was placed at the geometrically correct position, and the images were examined by a fluorescent screen. A large Helmholtz coil was placed around the spectrometer to cancel the earth's magnetic field, and its current was adjusted until the position of the images did not depend on the accelerating voltages. Next, the fluorescent screen was replaced by a Faraday cage, and the positions of the gun and the detector were adjusted so as to give the most intense and sharp lines. A typical line profile is shown in Fig. 8. The diameter of the detector-aperture was 4 mm, and the electron gun had a cathode of 2 mm in diameter. The expected line width at the half-maximum is 1.1 percent, the observed one is about 1.3 percent, and fairly well coincides with the expected width within the experimental error. E/V was measured to be 4.75 ±0.05 in the non-relativistic region.

§ 4. Preparation of the Source and the Detector

RaD and its daughters in equilibrium were

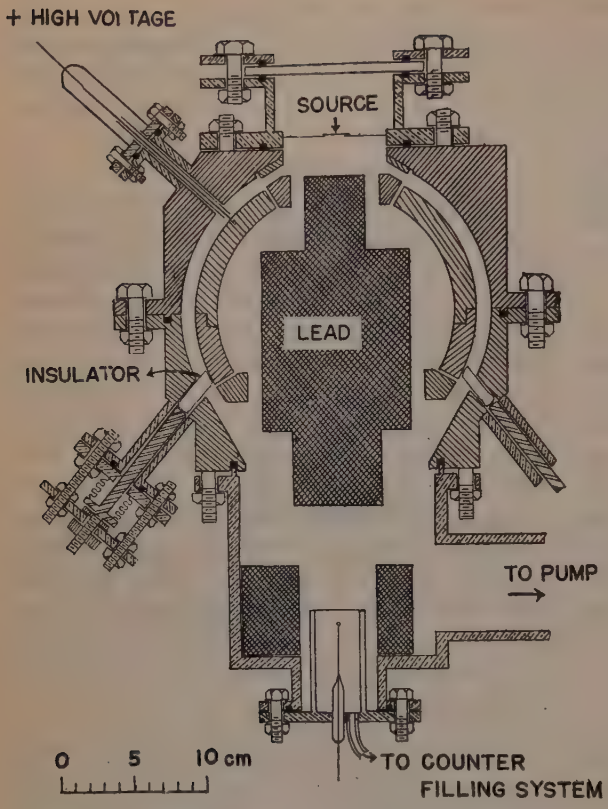

Fig. 7. Vertical cross section of our apparatus.

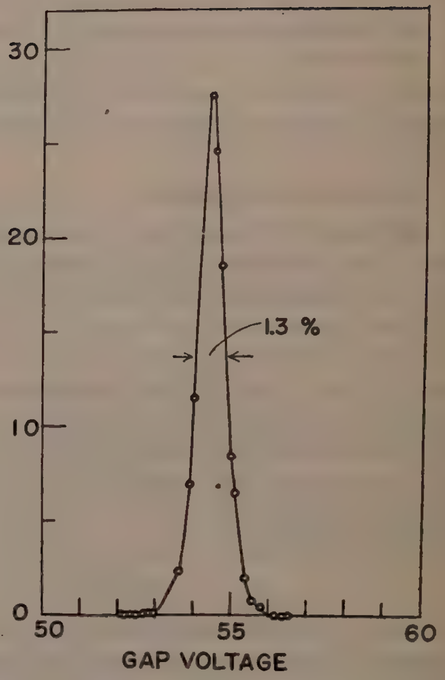

Fig. 8. Observed line profile of accelerated thermal electrons.

collected on a platinum ribbon by electrolysis in 0.1 N HNO_3 solution. Then these deposits were evaporated in a high vacuum using this ribbon as a filament, and were deposited on a zapon film of about 30 $\mu g/cm^2$ in thickness. Though we cannot know the exact thickness of the deposit itself, rough estimation can be made from the fact that there was no visible deposit, but the colour of interference of the film was slightly changed.

The detector was a G-M counter filled with alcohol vapour to about 20 mm Hg. The plateaus were 50∼80 volts with alcohol vapour of 18∼30 mm Hg. Though we obtained a plateau of 50 volts with 10 mm Hg, the operation was quite unstable. As for the efficiency, Langer et al.[12)] reported that with 20 mm Hg the efficiency was 100 percent for electrons of the energy up to at least 150 kev. Consequently, we assume 100 percent efficiency in the higher energy region in our experiments. The counter-window was a zapon film of about 20 $\mu g/cm^2$ (perhaps 15∼20 $\mu g/cm^2$). The diameters of the source and the counter-window were both 6 mm.

§ 5. Results

The results can be devided into three parts: (1) From 16 to 50 kev (conversion lines and additional primary beta-ray), (2) From 4 to 16 kev (primary beta-ray, Auger lines and conversion lines), and (3) From 0 to 8 kev (acceleration). The electrons in this energy region were accelerated by some known electric potentials to get better counter-window transmission.

(1) *From 16 to 50 kev*

The well-known conversion lines due to the 46.7 kev gamma-ray were observed. The result is shown in Fig. 9. The observed breadths at the half-maximum of the L_{I+II}, M, and N conversion lines are 3.7, 3.4, and 3.4 percent respectively. Since the intensity of the L_{II} line is about 9 percent of the L_I line[10)], taking into account the contribution from it, the breadth of the L_I lines alone is estimated to be 3.4 percent. Whereas the

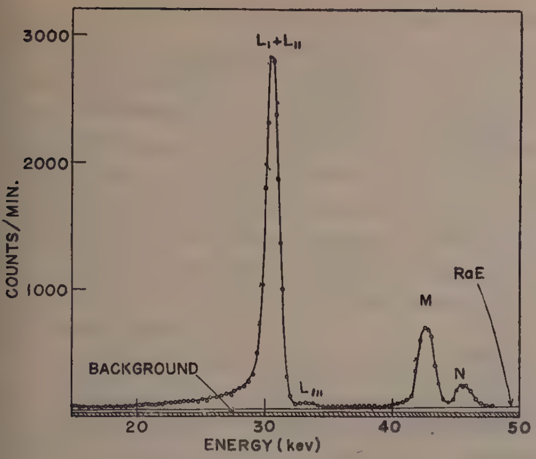

Fig. 9. Conversion lines of RaD.

expected breadth is 1.9 percent in the non-relativistic region. Though the line profiles are somewhat affected by the relativistic spread, the breadths at the half-maximum are expected to be unaffected in the energy region we are concerned. Thus the discrepancies between the observed and expected breadths are mostly attributed to the scattering and the absorption in the source.

The relative counting rates at the peaks of the L_{I+II}, M, and N conversion lines are $1:0.225\pm0.015:0.058\pm0.005$. The contribution of the L_{II} line to the peak counting rate of the L_I line is estimated to be 2.3 percent. The relativistic correction for the ratio $L:M$

Table I. Conversion lines due to the 46.7 kev gamma-ray of RaD

Energy of the line (kev)	Conversion level	Relative intensity			
		Ellis[a)]	Curtiss[b)]	Cranberg[c)]	Present work
30.4	L_I	1.00	1.00	1.00	1.00
31.0	L_{II}	0.04	0.06	0.09 ± 0.015	......
33.3	L_{III}	0.01	....	0.019 ± 0.004	0.01 ± 0.01
42.7	M	0.40	0.50	0.29 ± 0.02	0.23 ± 0.02
45.7	N	0.20	0.20	0.085 ± 0.01	0.06 ± 0.01
46.5	O	......	0.01	0.021 ± 0.007	......

a) C. Ellis: Proc. Camb. Phil. Soc. **21** (1921-23) 121.
b) L. Curtiss: Phys. Rev. **27** (1926) 672.
c) L. Cranberg: Phys. Rev. **77** (1950) 155.

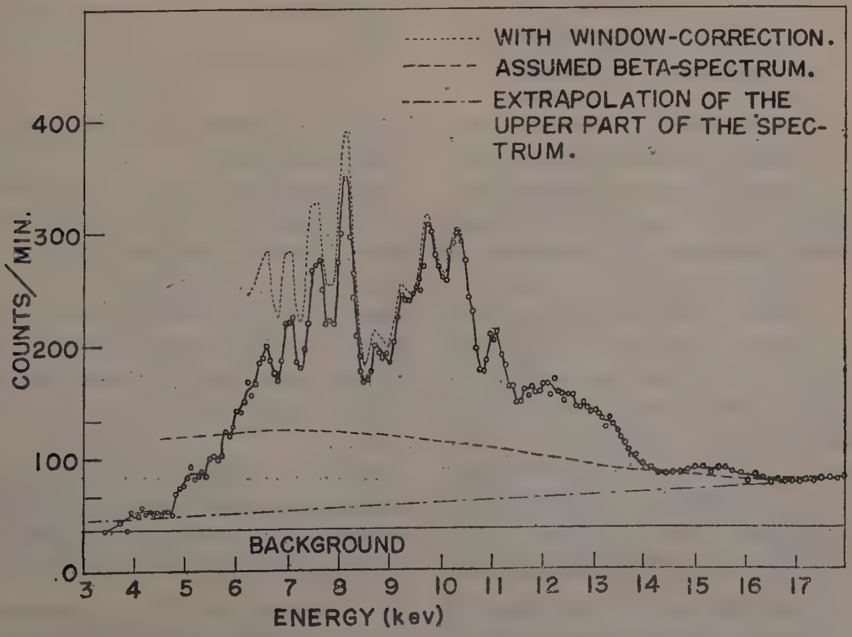

Fig. 10. Auger lines and beta-ray of RaD. The maximum energy of the assumed beta-spectrum is 18.0 kev.

Table II. Auger and conversion lines from RaD

Present work			Robinson and Young[a]		
Energy (kev)	Relative intensity	Transition	Energy (kev)	Relative intensity	Transition
4~5		Conv. line? (7~8 kev)			
5.4		$L_{III}-M_IM_I$			
5.7		$L_{III}-M_IM_{II}$			
6.1?		$L_{III}-M_IM_{III}$			
6.6	4	$L_{III}-M_IM_{IV}$ $L_{III}-M_IM_V$	6.8	2	$L_{\alpha_1}-M_I$
7.0	4~5	$L_{III}-M_{II}M_V$	7.03	2	$L_{\alpha_1}-M_{II}$
7.5	6	$L_{III}-M_{III}M_V$	7.6	3	$L_{\alpha_1}-M_{III}$
8.1	10	$L_{III}-M_{IV}M_V$ $L_{III}-M_VM_V$	8.1 8.2	4 1~2	$L_{\alpha_1}-M_{IV}$ $L_{\alpha_1}-M_V$
8.7	2	$L_{III}-M_IN_{II,III}$	8.75		
9.2	4~5	$L_{II}-M_{II}M_{IV}$ $L_{III}-M_{II}N_V$	9.27		
9.7	7	$L_{II}-M_{III}M_{IV}$ $L_{III}-M_{III}N_V$ $L_{III}-M_VN_I$	9.76	2~3	$L_{\beta_1}-M_{III}$ $L_{\alpha_1}-N$
10.3	7~8	$L_{II}-M_{IV}M_{IV,V}$ $L_{III}-M_{IV}N_V$ $L_{III}-M_VN_{IV,V}$	10.38	5	$L_{\alpha_1}-N$ $L_{\beta_1}-M_{IV,V}$
			10.7	2	$L_{\alpha_1}-O, P$
11.0	4	$L_{II}-M_IN_{IV}$? $L_{III}-M_VO$ Conv. line (27.4 or 15 kev)	11.15	1~2	$L_{\gamma_1}-M_I$
			11.55		
11.7~12.6			12.0	2	$L_{\gamma_1}-M_{III}$ $L_{\beta_1}-N$
12.6~13.5			12.6	3	$L_{\gamma_1}-M_{IV,V}$ $L_{\beta_1}-N$
			13.0	1~2	$L_{\gamma_{6,3}}-M_V$ $L_{\beta_1}-O, P$
			13.6	0~1	$L_{\gamma_4}-M_V$
15.0~16.0		Conv. line (31~32 kev)	16.2	0.1	$L_{\gamma_4}-O$

[a] See reference 14.

is calculated to be about 4 percent. However from the observed line profiles, we can see that the spread due to the scattering and the absorption is larger than the relativistic spread. Besides, the effect of the former on the ratio $L:M$ has a tendency to cancel the effect of the latter. Thus, neglecting these corrections, we have the ratios $L_I:M:N=1:0.23\pm0.02:0.06\pm0.01$. On the other hand, from the areas of these lines, we can obtain the ratios $L_{I+II}:M:N=1:0.19\pm0.02:0.048\pm0.01$. Assuming $L_I:L_{II}=1:0.09$ and taking into account the variations of the dispersion with energy, the ratios turn out to be $L_I:M:N=1:0.22\pm0.02:0.05\pm0.01$. The agreement with the ratios obtained from the peaks is fairly good. The ratio $L_I:L_{III}$ is measured to be $1:0.01\pm0.01$. These results are listed in Table I together with the results obtained by several authors.

No other line could be found in this region. The intensities of any lines relative to the L_I conversion line must be less than 1 percent.

In Fig. 10, the spectrum of RaE was estimated from the total counting rate of the source, using the result reported by Neary[13]. A rough estimation gives the number of conversion electrons as 50±20 per 100 disintegrations.

As for the additional beta-ray reported by Cranberg, we cannot draw any definite conclusion from the observed spectrum, owing to the uncertainly of the RaE contribution.

(2) *From 4 to 16 kev*

The result is shown Fig. 10. Many lines were observed below 14 kev, and almost all the lines could be explained as Auger lines of bismuth. The observed lines and their plausible origins are tabulated in Table II. For the sake of comparison, the result obtained by Robinson and Young[14)] from the study of photoelectrons from bismuth irradiated by the characteristic *X*-rays of silver is also listed. The fact that the lines associated with the L_{III} level are prominent shows a large probability of L_I—L_{III} M Coster-Kronig transition[15),16),17),18)].

As will be discussed later, some of these lines might be conversion lines instead of Auger lines. For example, the line at 6.6 or 7.0 kev may be the conversion line due to the 23.2 kev. gamma-ray[4),6)]. There are some doubts about the line at 11 kev for its energy and intensity as an Auger line. Alternative origin is a gamma-ray of the energy 27.4 kev or 15 kev. A bump at 15~16 kev may be L conversion line due to the 32 kev gamma-ray[4),6)].

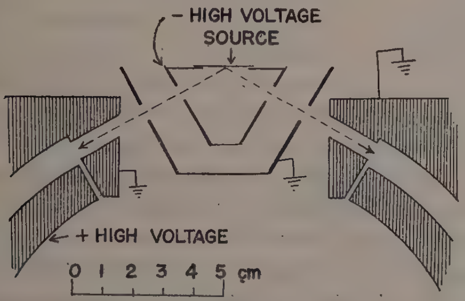

Fig. 11. Schematical drawing of accelerating electrodes.

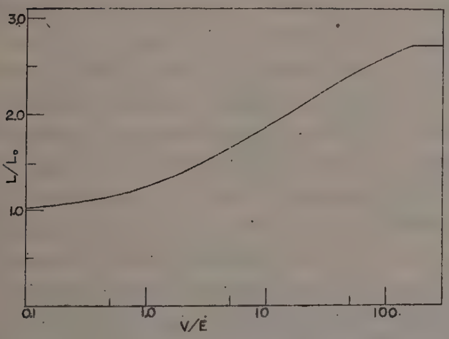

Fig. 12. Plot of the variation of effective solid angle. L_0 is the solid angle for the zero accelerating voltage. V and E are accelerated and initial energy of the particle respectively.

(3) *Acceleration*

Accelerating electrodes are shown in Fig. 11. The effective solid angle varies with accelerating voltage. The correction factor for it has been calculated approximately and the result for our particular case is plotted in Fig. 12.

Fig. 13 and 14 show the observed spectra with constant gap voltage and with constant accelerating voltage respectively. In Fig. 14, the spectrum with constant gap voltage is also plotted for comparison. Owing to the small displacement of the electrodes, the peak counting rate of the L_I conversion line decreased to 2300 counts per minute. Consequently, the correction factor of 2700/2300 must be multiplied to the observed spectra. The spectra in these figures have been already corrected for the variation of the effective solid angle. Further, for the ease of comparison, the spectra in Fig. 14 have been

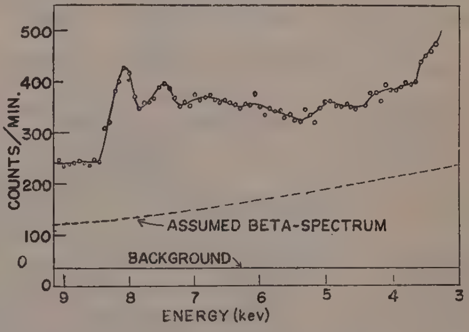

Fig. 13. Spectrum with constant gap voltage, varying accelerating voltage.

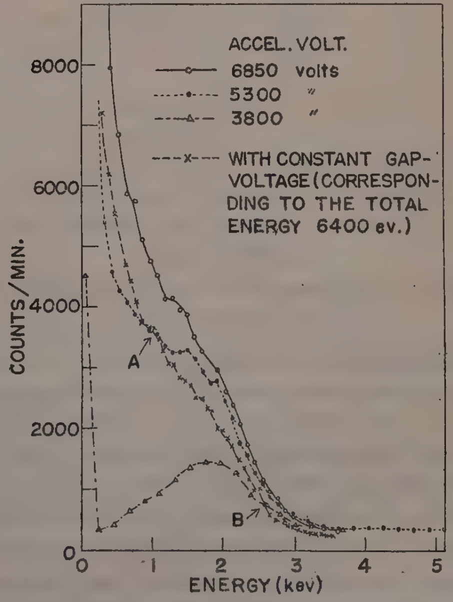

Fig. 14. Spectra with constant accelerating voltage, varying gap voltage.

normalized to the counts per equal energy interval (about 200 ev).

We can see in Fig. 13 bumps at 3.5, 4.0~4.5, and 5.0 kev, which could be seen also in Fig. 10. Though, owing to the decrease of resolving power by the acceleration, the assignment of these lines is rather difficult, they may be attributed to the *M* conversion lines due to the 7.5 kev gamma-ray4),5),6), because Auger lines cannot exist in this region.

In Fig. 14, a large number of electrons below 3 kev are attributed to the delta-ray due to the alpha-particles of polonium. The end point is at 3.0 kev, and coincides with the calculated value, 2.9 kev. In order to confirm its origin, the separated polonium source was studied, and we obtained the similar spectrum except for some bumps. These bumps will be *M* Auger electrons of bismuth.

The points *A* and *B* in Fig. 14 show the validity of the correction factor for the variation of the effective solid angle mentioned above. At these points, the electrons on the constant accelerating voltage curves have the total energy, the sum of the initial energy and the accelerated energy, equal to that of electrons on the constant gap voltage curve plotted by the broken line in the same figure. Thus the correction for the transmission by the counter-window can be neglected, and if the correction for the effective solid angle is correct, the constant accelerating voltage curves must intersect the constant gap voltage curve at these points as is the case in this figure.

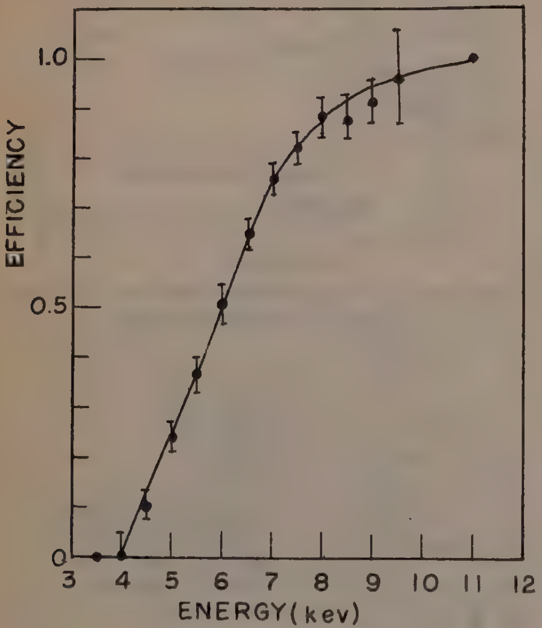

Fig. 15. Transmission of the electrons by the counter-window.

From Fig. 10, 13, 14, and other similar data we could obtain the transmission of the electrons by the counter-window relative to the transmission for 11 kev electrons. The curves obtained from several combinations of these figures coincided with each other within the experimental error. The mean curve is plotted in Fig. 15. At 11 kev we expect at least 90 percent transmission from the results obtained by Saxon19), and by Owen and Cook20).

§ 6. Discussion

On account of the intense Auger electrons, the study of the primary beta-spectrum is very difficult.

We shall assume an allowed spectrum, the intensity of which is equal to the sum of the intensities of the 46.7 kev gamma-ray and conversion lines due to it. Then, as shown in Fig. 10, the maximum energy of the beta-ray cannot exceed 18 kev. The assumption of the allowed spectrum is justified, since its ft value calculated by using 18 kev maximum energy is about 5.5. Though the determination of the lower limit for the maximum energy for this beta-ray is rather indefinite, the examination of the high energy side of the observed spectrum gives 16 kev. These limits coincide with the results reported by several authors7),8),9). Assuming the maximum energy 16~18 kev, we shall examine the part of the spectrum between 5.4 and 16.0 kev. All the *L* Auger lines of bismuth are included in this region. Since the number of the *L* *X*-ray quanta has been reported to be 42~48 percent of the *L* conversion electrons17),21), the number of *L* Auger electrons must be 52~58 percent. The number of the primary beta-particles included in this region is calculated to be 27~33 percent. Whereas the total number of the observed electrons in this region is almost equal to the total number of the assumed beta-particles. Then the observed number of the electrons is larger than the sum of the Auger electrons and the primary beta-particles by about 20~30 percent of the conversion electrons. This

Table III. Gamma-rays of RaD*

Energy (kev)	46.7	42.6	37	31.3	23.2	16.1 (18~19)	7.3
Intensity (quanta per 100 disinteg.)	3.5 (2.8)	0.2	0.2	0.4	~1	~0	~10

* See reference 4) and 6).

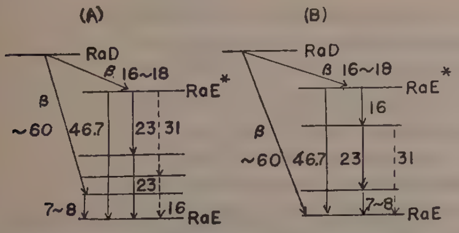

Fig. 16. Assumed decay schemes of RaD.

discrepancy will be attributed to some conversion lines and Auger lines which follow this internal conversions. The gamma-rays so far reported are listed in Table III. Since other gamma-rays (except for the 46.7 kev gamma-ray) and conversion lines due to them are very weak, at least two of the gamma-rays mentioned above must be associated with successive transitions. Thus we can assume two alternative decay schemes as shown in Fig. 16. In both cases, probabilities of these transitions are estimated to be 5~10 percent of that of the transitions going directly to the ground state. The number of the conversion electrons due to the 46.7 kev gamma-ray is considered to be 70 per 100 disintegrations at most[22], and the number of the gamma-quanta except for the 7~8 kev gamma-ray is less than 5 per 100 disintegrations. Thus at least 15 percent of the disintegrations must be an additional beta-transition. Though we failed to reveral the additional beta-spectrum, the existence of rather intense gamma-ray of the energy 7~8 kev implies that the additional beta-ray is followed by this gamma-ray, i.e., the decay scheme (A) in Fig. 16 is more plausible.

In conclusion, the author wishes to express his thanks to Dr. G. Miyamoto and his coworkers for their valuable suggestions, discussions, and encouragement, and especially for their financial aid from their grant in aid from the Ministry of Education. He is grateful also to Mr. G. Iwata and Mr. Y. Nogami for their helpful advice for the publication of these papers, and to Mr. M. Arai for the machining of the spherical surfaces.

References

1) E. M. Purcell: Phys. Rev. **54** (1938) 818.

2) F. T. Rogers Jr.: Rev. Sci. Inst. **22** (1951) 723.

3) C. P. Browne, D. S. Craig and R. M. Williamson: Rev. Sci. Inst. **22** (1951) 952.

4) S. T. Tsien: Phys. Rev. **69** (1946) 38.

5) S. C. Curran, J. Angus and H. L. Cockroft: Phil. Mag. **40** (1949) 36.

6) N. Feather: Nucleonics July (1949) 22.

7) R. C. Bannerman and S. C. Curran: Phys. Rev. **85** (1952) 134.

8) G. M. Insch, J. G. Balfour and S. C. Curran: Phys. Rev. **85** (1952) 805.

9) A. A. Jaffe and S. G. Cohen: Phys. Rev. **86** (1952) 1041.

10) L. Cranberg: Phys. Rev. **77** (1950) 155.

11) Sommerfeld: Atombau und Spektrallinien 5th Edition p. 272.

12) L. M. Langer, J. W. Motz, and H. C. Price Jr.: Phys. Rev. **77** (1950) 788.

13) G. J. Neary: Proc. Roy. Soc. **A 175** (1940) 71.

14) H. R. Robinson and C. L. Young: Proc. Roy. Soc. **A 128** (1930) 92.

15) L. Salgueiro and M. Valadares: Portugaliae Physica **3** (1949) 21.

16) D. Coster and R. De L. Kronig: Physica **2** (1935) 13.

17) B. B. Kinsey: Canad. J. Research **26** (1948) 421.

28) D. K. Butt: Proc. Phys. Soc. **63** (2950) 986.

19) D. Saxon: Phys. Rev. **81** (1951) 639.

20) P. H. Owen and C. S. Cook: Phys. Rev. **86** (1952) 961.

21) H. Lay: Zeits. f. Physik **90** (1934) 533.

22) D. K. Butt and W. D. Brodie: Proc. Phys. Soc. **64** (1951) 791.

JOURNAL OF THE PHYSICAL SOCIETY OF JAPAN Vol. 8, No. 4, JULY—AUGUST, 1953

Heat Transfer in Liquid Helium II through an Extremely Fine Slit

By Tokuzo INOUE

Department of Physics, University of Osaka

(Received February 24, 1953)

Assuming a film of pure superfluid on the wall and introducing a mutual friction somewhat different from that suggested by Gorter, the heat conductivity is calculated on the basis of the two fluid model and internal convection. Our formula of the heat conductivity shows a fairly good agreement with the experiments including the case of very narrow slits. The London-Zilsel's formula is also included as a special case.

In very narrow slits, the heat conductivity approximates to $\langle K\rangle = s_\lambda{}^2 T^{r+1} d/2BT_\lambda$. Here T: absolute temperature, d: slit width, T_λ: transition temperature, s_λ: entropy per gram at T_λ, r: numerical constant 5.5~5.6, B is the quantity concerning with the film and the mutual friction. At the temperature near T_λ, $\langle K\rangle$ is approximately $s_\lambda{}^2/A_1 T_\lambda{}^{2r}\cdot(T_\lambda{}^r - T^r)T^{r+1}$. A_1 is the quantity concerning with the mutual friction. At the intermediate slit width and temperature, $\langle K\rangle$ approximates to the London-Zilsel's formula. B, A_1, and critical velocity are discussed and the numerical values are calculated.

§ 1. Introduction

About ten years ago Keesom[1)] showed experimentally that the heat current in liquid helium II is proportional to (grad $T)^{1/3}$. But recently Meyer and Mellink,[2)] Mellink,[3)] and Keesom and Duyckaerts[4)] have shown that in extremely fine slits (diameter $0.15\mu - 19\mu$) and for sufficiently small heat input the transported heat becomes proportional to the temperature difference.

This results seem to give qualitative support to the general idea, namely the "two fluid" model promoted by Tisza and H. London.

According this idea, F. London and P. R. Zilsel[5)] developped a theory of heat transfer in liquid helium II through a slit (by internal convection).

They got the formula of the mean heat conductivity

$$\langle K\rangle = \frac{Ad^2}{12}, \qquad (1.1)$$

where

d: the diameter of the slit

$A = (\rho s)^2 T/\eta_n$

ρ: total density of the liquid hellium II

s: entropy per gram

T: absolute temperature

η_n: the coefficient of viscosity of the normal component.

Unfortunately, this formula shows only partial agreement with the measurements by Keesom, Meyer and others. Especially in the measurement of heat transfer through a very narrow slit, the discrepancy is remarkable.

Tomita, Nakajima and Usui[6)] have refind the "two fluid model" as a phenomenological theory of liquid helium II by introducing the mutual friction between the superfluid and the normal component as Gorter[7)] had suggested previously. Their theory could show better agreement than that of London and Zilsel in the case of wide slits ($10\mu - 19\mu$). But in very narrow slits, both theories coincide (1.1) and therefore do not agree with experiments.

Assuming a film of pure superfluid on the wall and introducing a mutual friction somewhat different from that suggested by Gortor, the author could get a fairly good agreement with experiments including the case of very narrow slits. The London-Zilsel's formula and Tomita and others's formula are also included as special cases of our formula.

§ 2. Derivation of the Formula

According to the "two fluid" model, liquid helium II is described as consisting of two mutually interpenetrating fluids having densities ρ_n and ρ_s, respectively.

Their macroscopic motion is described by their hydrodynamic velocity field V_n and V_s

respectively.

In the case of the flow through a slit, we assume (See Fig. 1.)

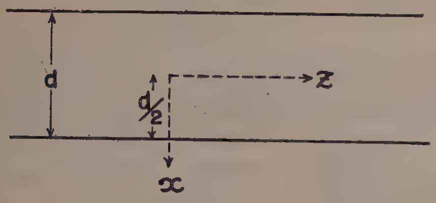

Fig. 1.

$$V_n=(0,\ 0,\ v_n(x)),$$
$$V_s=(0,\ 0,\ v_s(x)). \qquad (2.1)$$

The equations representing the velocity field of the normal fluid are

$$\frac{d^2v_n}{dx^2}=-\frac{\pi}{\eta_n} \qquad \pi=-\frac{dp}{dz} \qquad (2.2)$$

p: pressure in the liquid.

Integrating this, we get

$$v_n=-\frac{1}{2}\frac{\pi}{\eta_n}x^2+c_1x+c_2\ , \qquad (2.3)$$

and c_1 and c_2 are integral constants.

By symmetry, we have

$$c_1=0\ .$$

Next, we assume that there is a film of pure superfluid whose thickness is d_0[8]. Close to this film, we take a small volume of the normal component $A=\Delta x\cdot\Delta y\cdot\Delta z$, and consider the forces working on it. (See Fig. 2.)

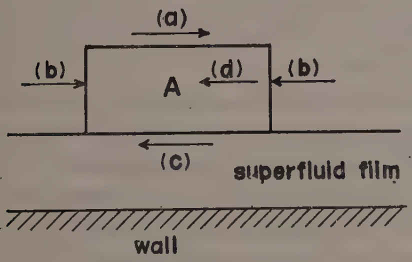

Fig. 2.

(a) the friction in the normal component, that is, the viscosity term;

$$-\eta_n\frac{dv_n}{dx}\Delta y\Delta z\ ,$$

(b) the force caused by the inner pressure difference;

$$p(z)\Delta x\Delta y-p(z+\Delta z)\,\Delta x\Delta y=-\frac{dp}{dz}\Delta x\Delta y\Delta z\ ,$$

(c) the force caused by the mutual friction between the portion (A) and the film of pure superfluid on the surface of (A)*,** (Because the density of the normal component in the film is zero, the density of the superfluid in it is identical with ρ);

$$-B\rho_n\rho v_n\Delta y\Delta z\ ,$$

(d) the force caused by the mutual friction between the two fluids within the volume of A;

$$-A_1\rho_n\rho_s(v_n-v_s)\Delta x\Delta y\Delta z^*.$$

In the stationary flow, we have

$$(a)+(b)+(c)+(d)=0\ .$$

Taking Δx, Δy, Δz sufficiently small, we get

$$B\rho_n\rho v_n=-\eta_n\frac{dv_n}{dx} \text{ at } x=\frac{d}{2}-d_0\ . \qquad (2.4)$$

From (2.3) and (2.4) we get

$$v_n=\frac{\pi d}{2B\rho_n\rho} \text{ at } x=\frac{d}{2}-d_0\ , \qquad (2.5)$$

where $d/2-d_0$ is approximated by $d/2$.

From (2.3) and (2.5) it follows that

$$v_n=\left[\frac{1}{2\eta_n}\left\{\left(\frac{d}{2}\right)^2-x^2\right\}+\frac{d}{2B\rho_n\rho}\right]\pi.$$

Averaging over the cross section of the slit

$$<v_n>=\left[\frac{d^2}{12\eta_n}+\frac{d}{2B\rho_n\rho}\right]\pi \qquad (2.6)$$

According to K. Tomita and others,[6] on the other hand, we have

$$\rho_s\left(\frac{\partial}{\partial t}+V_s\operatorname{grad}\right)V_s+\frac{\rho_s}{\rho}\operatorname{grad}p$$
$$-\rho_s s\operatorname{grad}T-f=0\,,$$

f: mutual friction.

This formula gives in our case

$$v_s=v_n+\frac{\pi-\rho s\theta}{A_1\rho\rho_n} \qquad \theta=-\frac{dT}{dz}\ . \qquad (2.7)$$

The condition of no net mass flow across the cross section is

---

* Gorter[3] suggested the necessity of considering the mutual friction between the normal component and the superfluid and assumed it

$$A_3\rho_n\rho_s(v_n-v_s)^3 \quad (A_3\doteqdot 50\,\mathrm{g}^{-1}\cdot\mathrm{cm}\cdot\mathrm{sec})$$

considering the earlier experimental result that the thermal current is proportional to $(\operatorname{grad} T)^{1/3}$. But by the recent experiments pursuited by Keesom and others in the case of the finer slits and the smaller temperature gradient, thermal current is proportional to grad T. Considering this fact, it is assumed in our case that the term proportional to (v_n-v_s) is eminent than that proportional to $(v_n-v_s)^3$.

** It is assumed that the superfluid film on the wall is at rest.

$$<\rho_n v_n>+<\rho_s v_s>=0. \qquad (2.8)$$

Putting (2.6) and (2.7) into (2.8)

$$\pi=\frac{\rho_s\theta}{A_1\rho_n}\left\{\frac{\rho d^2}{12\eta_n}+\frac{\rho_s}{A_1\rho\rho_n}+\frac{\rho d}{2B\rho_n\rho}\right\}^{-1}. \qquad (2.9)$$

From (2.6) and (2.9), we get

$$<v_n>=\frac{\rho_s s\theta}{A_1\rho_n}\left\{\frac{d^2}{12\eta_n}+\frac{d}{2B\rho_n\rho}\right\} \times\left\{\frac{\rho d^2}{12\eta_n}+\frac{\rho d}{2B\rho_n\rho}+\frac{\rho_s}{A_1\rho\rho_n}\right\}^{-1}$$

According to the idea of London-Zilsel's "internal convection", we represent the heat current density as

$$q=\rho sTV_n.$$

Then the mean heat conductivity becomes

$$\begin{aligned}<K>&=\frac{\rho\rho_s s^2T}{A_1\rho_n}\left\{\frac{d^2}{12\eta_n}+\frac{d}{2B\rho_n\rho}\right\} \times\left\{\frac{\rho d^2}{12\eta_n}+\frac{\rho d}{2B\rho_n\rho}+\frac{\rho_s}{A_1\rho\rho_n}\right\}^{-1}\\ &=\frac{\rho s_\lambda^2(T_\lambda^r-T^r)T^{r+1}}{A_1T_\lambda^{2r}}\left\{\frac{d^2}{12\eta_n}+\frac{dT_\lambda^rT^{-r}}{2B\rho^2}\right\} \times\left\{\frac{\rho d^2}{12\eta_n}+\frac{dT_\lambda^rT^{-r}}{2B\rho}+\frac{T_\lambda^r-T^r}{A_1\rho T^r}\right\}^{-1}\\ &=\gamma\{\alpha_1+\alpha_2\}\{\beta_1+\beta_2+\beta_3\}, \qquad (2.10)\end{aligned}$$

where

$$\frac{\rho_n}{\rho}=\left(\frac{T}{T_\lambda}\right)^r \quad s=s_\lambda\frac{\rho_n}{\rho},$$

T_λ: the transition temperature
s_λ: entropy per gram at $T=T_\lambda$.

§ 3. Comparison with Experiments

At (2.10) the higher the temperature and the larger the diameter of the slit become, the larger get the ratios $\alpha_1:\alpha_2$, $\beta_1:\beta_2$ and $\beta_2:\beta_3$. In particular, when $\alpha_1\gg\alpha_2$, $\beta_1\ll\alpha_3$ and $\beta_2\ll\beta_3$, which means the intermediate scale of the diameter and temperature, the above formula is simplified to

$$<K>=\frac{(\rho s)^2T}{12\eta_n}d^2 \qquad (3.1)$$

This coincides with both London-Zilsel's and Tomita's results. The partial agreement of London-Zilsel's formula with some experiments will be due to the fact that in that case the diameter of the slit and temperature were so arranged that the condition $\alpha_1\gg\alpha_2$, $\beta_1\ll\beta_3$ and $\beta_2\ll\beta_3$ were fulfilled.

In the case of $\alpha_1\ll\alpha_2$, $\beta_1\ll\beta_3$, $\beta_2\ll\beta_3$ we get from (2.10)

$$<K>=\frac{\rho s^2T}{2B\rho_n}d=\frac{s_\lambda^2}{2BT_\lambda^r}T^{r+1}d. \qquad (3.2)$$

Comparison with the measurement by Meyer and Mellink is given in Table 1.

Table I

	T(°K)	$\frac{\Delta\ln<K>\text{exp}}{\Delta\ln T}$	$\frac{<K>\text{exp}}{<K>_L}$	$\frac{<K>\text{exp}}{<K>_{(3\cdot2)}}$
$d=0.3\mu$	1.226	6.4	260	0.96
	1.358	7.5	140	0.94
	1.558	6.0	75	1.06
	1.652		54	1.03
$d=0.5\mu$	1.086	5.0	202	1.09
	1.274	8.3	64	0.85
	1.315	8.3	55	0.88
	1.659		23	1.32

where

$<K>_{\text{exp}}$: measurement values by Meyer and Mellink
$<K>_L$: the values by London-Zilsel's formula
$<K>_{(3.2)}$: the value according to (3.2), which was obtained by using

$s_\lambda=0.403\ \text{cal deg}^{-1}\text{g}^{-1}$, $r=5.6$, $T_\lambda=2.19$

and when

$d=0.3\ \mu$, $B/d=6.6\times10^5\text{g}^{-1}\cdot\text{cm}^3\cdot\text{sec}^{-1}$,
$B=19.8\ \text{g}^{-1}\cdot\text{cm}^4\cdot\text{sec}^{-1}$,
$d=0.5\ \mu$, $B/d=6.7\times10^5\text{g}^{-1}\cdot\text{cm}^3\cdot\text{sec}^{-1}$,
$B=33.5\ \text{g}^{-1}\cdot\text{cm}^4\cdot\text{sec}^{-1}$.

These values of B seem to show their dependence on slit diameter. But as the experementers themselves admit, the width of slit is the most ambiguous among the obtained deta (Meyer and Mellink estimate the probable errer at 20 percent.).

The width were determined from measurements of gas flow through the slits and from optical interference measurements. So they can only give the average width along the slit and the actual width may vary considerably in different parts of the slit.

The better agreement of the formula (3.2) with experiment is due to its temperature dependence $<K>\propto T^{r+1}$ instead of $<K>\propto T^{2r+1}$ in London-Zilsel's formula. In this point the value of B is not eminent.

Using the mean value of B, we further get:

	T(°K)	α_1/α_2
$d=0.3\mu$	1.226	0.003
	1.358	0.005
	1.558	0.011
	1.652	0.022

$d=0.5\mu$	1.086	0.006
	1.274	0.015
	1.315	0.03
	1.659	0.06

§ 4. Determination of A_1

For this purpose, we could hardly find the proper deta. Here we use the measurement by Keesom and Duyckaerts:

$$\text{at } d=9.3\mu,\ T=1.962^\circ$$
$$\langle K\rangle=43.5\ \text{cal/deg.cm.sec}\ .$$

From (2.10), assuming $\beta_1+\beta_2 \gg \beta_3$, we get

$$\langle K\rangle=\frac{s_\lambda^2}{A_1 T_\lambda^{2r}}(T_\lambda^r-T^r)T^{r+1}\ .$$

Then we get for the value of A_1

$$A_1=7.6\times10^4\ \text{g}^{-1}\text{cm}^3\text{sec}^{-1}.$$

Using this value

$$\beta_1=5.2\ \times10^{-4}\ \text{sec}^{-1}$$
$$\beta_2=0.22\times10^{-4}\ \text{〃}$$
$$\beta_3=0.74\times10^{-4}\ \text{〃}$$
$$(\beta_1+\beta_2):\beta_3=5.54:0.74=7.5:1\ .$$

§ 5. Critical Velocity

In order that the condition, which was assumed in § 2,

$$A_1\rho_n\rho_s(v_n-v_s) \gg A_3\rho_n\rho_s(v_n-v_s)^3\ ,$$

is satisfied, using Gorter's value

$$A_3=50\ \text{g}^{-1}\cdot\text{cm}\cdot\text{sec}\ ,$$

we need

$$v_n-v_s \ll 39\ \text{cm}\cdot\text{sec}^{-1}\ . \tag{5.1}$$

The left side of which, in the other hand, can be written as

$$v_n-v_s=\frac{q}{\rho_s sT}=T_\lambda^{2r}q/\rho^2 s_\lambda(T_\lambda^r-T^r)T^{r+1} \tag{5.2}$$

using the condition

$$\rho_n v_n+\rho_s v_s=0\ .$$

From (5.2) and London-Zilsel's Table I, we get the numerous values of (v_n-v_s) and compare them with $q/\text{grad}\,T$, as is shown in Table II.

Table II

$d\times10^4$cm	T°K	$(\bar{q}d/\Delta T)\times10^3$ cal /cm·sec·deg	$\langle v_n-v_s\rangle$ cm/sec
9.3	1.586	15.8	3.3
	〃	15.8	11
	〃	9.5	26
	1.807	72	2.6
	〃	72	4.5
	〃	67	12
	〃	38	16
	1.962	190	2.3
	〃	177	5.6
	〃	133	12
1.75	1.960	11.0	1.2
	〃	11.0	6.7
	〃	10.5	13
	〃	10.3	19
	〃	9.9	33
1.15	1.989	8.2	12
	〃	8.2	35
	〃	7.9	48
	2.170	11.4	11
	〃	10.4	20
	〃	10.2	31
0.75	2.097	8.5	26
	〃	8.5	27
	〃	7.7	43

In the case that the condition (5.1) is satisfied, experimental deta shows

$$q\propto\text{grad}\,T.$$

When (5.1) is not satisfied, the $(v_n-v_s)^3$ term becomes comparable with the (v_n-v_s) term. But even then the above linearity is still valid so long as the condition

$$\frac{1}{2}\rho s_\lambda\left(\frac{\rho}{8}\right)\left(\frac{A_3}{\eta_n^3}\right)^{\frac{1}{2}}\theta d^3\left(\frac{T^r}{T_\lambda^r-T^r}\right)^{\frac{3}{2}} \ll 1\ ,$$

is satisfied.⁶⁾ In other words, (5.1) is the sufficient condition, but not the necessary condition for $q\propto\text{grad}\,T$. It will be due to this and the uncertain values of A_1 and A_3 that q is proportional to grad T in narrow slits even when $\langle v_n-v_s\rangle$ takes comparably large values.

§ 6. Temperature Dependence of Thermal Conductivity

For a very narrow slit, and when the temperature is not much higher than 1°K, we have

$$\alpha_1 \ll \alpha_2,\quad \beta_1+\beta_2 \ll \beta_3,\quad \langle K\rangle\propto T^{r+1}.$$

When the temperature is considerably higher,

$$\alpha_1 \gg \alpha_2,\quad \beta_1+\beta_2 \gg \beta_3,\quad \langle K\rangle\propto T^{2r+1}.$$

When the temperature is near T_λ,

$$\beta_1+\beta_2 \ll \beta_3,\quad \langle K\rangle\propto(T_\lambda^r-T^r)T^{r+1}.$$

The last $\langle K\rangle$ is idependent of d, showing the same temperature dependence as Tomita-Nakajima-Usui's⁶⁾ case of

$$\frac{1}{2}\rho s_\lambda\left(\frac{\rho}{8}\right)\left(\frac{A_3}{\eta_n^3}\right)^{\frac{1}{2}}\theta d^3\left(\frac{T^r}{T_\lambda^r-T^r}\right)^{\frac{3}{2}} \gg 1\ .$$

These results may be compared with

$$\Delta\ln\langle K\rangle_{\text{exp}}/\Delta\ln(T)$$

in the Table II of the London-Zilsel's report,⁵⁾

in which it varies from 12.1 to 3.6.

§ 7. Conclusion

Assuming a film of pure superfluid on the wall of the slit, it was shown that we can get fairly good agreement with the experiments for very narrow slits. Introduction of the (v_n-v_s) term seems to cause better agreement with the fact that in very narrow slits and sufficiently small heat input, the relation $q \propto \mathrm{grad}\, T$ comes in existence at almost all temperatures between T_λ and 1°K.

Concerning the mutual friction, we need further theoretical consideration. More precise experiments, especially near T_λ and 1°K are desirable for investigation of A_1 and B. But perhaps it will be beyond the scope of phenomenological treatment. The molecular treatment may be essential in this point.

In conclusion, the author wishes to express his gratitude to Professor K. Husimi and Professor Y. Nambu for their encouragements, and he also appreciates discussions of Mr. T. Nishiyama, Dr. T. Matsubara, Dr. A. Isihara and Dr. K. Yoshida.

References

1) W. H. Keesom: Helium (Elsevier Publishing Company, Inc. Amsterdam 1942).
2) L. Meyer and T. H. Mellink: Physica **13** (1947) 197.
3) J. H. Mellink: Physica **13** (1947) 180.
4) W. H. Keesom and G. Duyckaerts: Physica **13** (1947) 153.
5) F. London and P. R. Zilsel: Phys. Rev. **74** (1948) 1148.
6) K. Tomita, S. Nakajima and T. Usui: Phys. Rev. **78** (1950) 768.
7) C. J. Gorter: Phys. Rev. **74** (1948) 1544.
8) Allen and Misener: Proc. Roy. Soc. **172** (1939) 467.

JOURNAL OF THE PHYSICAL SOCIETY OF JAPAN Vol. 8, No. 4, JULY—AUGUST, 1953

Electron Diffraction Investigation of the Actions of Aqueous Heavy Metal Salts on Mineral Surfaces

II. Action of Mercuric Sulfate on Galena Cleavage Face

By Ryoitiro SATO

*Mitsubishi Mining and Metallurgical Laboratory,**
Omiya City, Saitama Pref., Japan

(Received March 20, 1953)

The investigation of the actions of aqueous heavy metal salts on mineral surfaces was extended to mercuric sulfate-galena system. Fresh cleavage face of galena was soaked in acidic aqueous mercuric sulfate of low concentrations for 30 min. at room temperatures. The reaction products revealed by electron diffraction were: metacinnabarite (cubic HgS) in random and definite orientation with respect to the substrate, and cinnabar (hexagonal HgS) in a certain epitaxial orientation. Besides, the pattern due to a roughened state of galena cleavage face was observed.

§ 1. Introduction

In order to accumulate data on crystal growth on single crystal surfaces in solid-liquid systems, and to elucidate the mechanism involved in *activation* of sphalerite by heavy metal salts in flotation, the action of aqueous silver nitrate and sulfate on sphalerite cleavage face was dealt with in the previous paper.[1] The study has been extended to many systems,[2][3] in which soluble salts of Cu^{++}, Pb^{++}, Cd^{++}, Ag^{+}, and Hg^{++} are used. As sulfide mineral substrates cleavage faces of sphalerite and galena have been used. Among these systems the one that has lead to the clearest result is mercuric sulfate-galena system. In what follows this system will be dealt with.

---

* Former Taihei Mining and Metallurgical Laboratory.

§ 2. Experimental

Mercuric sulfate was prepared by heating the mixture of mercury (1 part) and concentrated sulfuric acid (1.5 parts) until it became completely dry. When crystal of mercuric sulfate is brought into water, it precipitates yellow basic sulfate of mercury ($HgSO_4 \cdot 2HgO$). Since this would disturb the result of the experiment, the solution was always made tranparent by addition of dilute sulfuric acid. The pH value of the solution was less than 1.

The experimental procedures were almost the same as those in the previous paper.[1]

§ 3. Results

The galena fresh cleavage face was soaked in acidic solution ($pH<1$) of mercuric sulfate of 50 mg/1∼1 g/1 for 30 min. at room temperatures about 15°C. This surface showed no change under naked eye. The electron diffraction pattern obtained from this specimen was generally composed of the following four: (a) the spot pattern due to PbS in the same orientation as the substrate, (b) the Debye-Scherrer rings supposedly due to metacinnabarite (cubic HgS), (c) the spot pattern supposedly due to metacinnabrite, and (d) the spot pattern due to cinnabar (hexagonol HgS). These four kinds of patterns appeared always simultaneously under these experimental conditions, although their relative intensities varied slightly with specimens. The surface state of the specimen was stable in dry air; after being kept in a desiccator for 270 days it yielded almost the same diffraction photograph as immediately after the treatment. Some of the photographs obtained are reproduced in Figs. 1 and 2. In the following these patterns will be interpreted successively.

(a). Galena (PbS) and metacinnabarite (cubic HgS) crystallize both in cubic lattices with almost the same lattice constants (galena: NaCl-type, $a=5.92$ Å[4]); metacinnabarite: ZnS-type, $a=5.84$ Å[4])). Therefore, it is difficult to determine which of them the spot pattern (a) is to be ascribed to. However, all of the spots obtained (the patterns (a), (c), and (d)) only the spots of the pattern (a) were generally elongated towards the shadow edge, and galena cleavage face soaked in acidic water of the same pH value yielded a similar elongated spot pattern. Consequently, this pattern is most likely ascribed to the galena cleavage face in a state slightly roughened by the acidic solution. In Fig. 3 the positions of the spots of the pattern (a) are shown by ×.

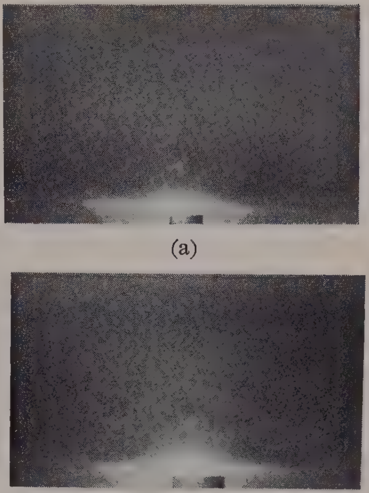
(a)

(b)

Fig. 1. Electron diffraction patterns obtained from galena cleavage face soaked in aqueous mercuric sulfate (50 mg/1, $pH<1$) for 30 min. Beam is parallel to cube edge of galena in (a), and to face diagonal in (b).

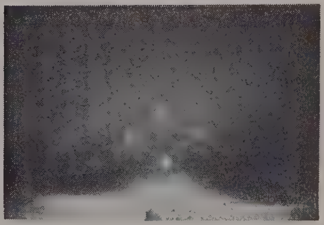

Fig. 2. Electron diffraction pattern obtained from mercuric sulfate-conditioned (50 mg/1, $pH<1$, 30 min.) galena cleavage face. The photograph was taken after the specimen was kept in a a desiccator for 270 days. Beam is parallel to face diagonal of galena.

As will be stated below, in the present system metacinnabarite is supposed to be produced. If so, its simplest orientation with respect to the substrate is the same orientation as that of the latter, yielding the spots at almost the same positions as those of the spots due to the underlying roughened galena. This is supposed to occur actually, although the resolving power of the diffraction camera

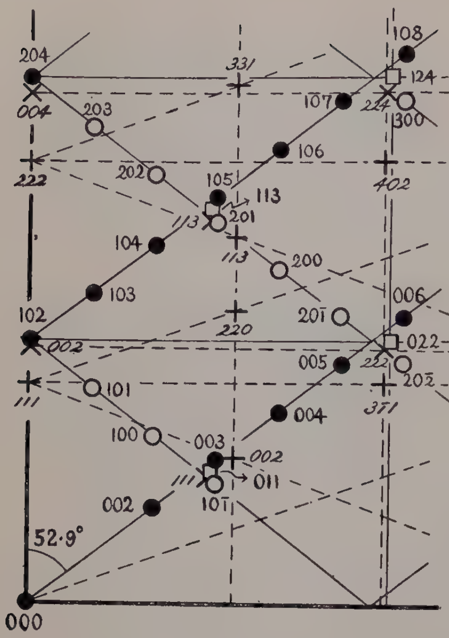

Fig. 3. Indexing of the diffraction spots in Figs. 1 (b) and 2. × : positions of spots due to PbS (pattern (a)). +: positions of spots due to metacinnabarite (pattern (c)). ●, ○, and □: positions of spots due to cinnabar (pattern (d)).

is short in confirming it.

(b). In the Debye-Scherrer rings the (200)-ring is much weaker in intensity than the (111)-ring. From this, these rings are most likely supposed to be due to ZnS-type metacinnabarite, although NaCl-type galena yield the Debye-Scherrer rings with almost the same radii.

(c). Whether the substance resposible for the pattern (c) is either metacinnabarite or galena is again a problem. However, the observation of galena crystallites in an orientation different from that of the substrate would be somewhat incomprehensible for the present experimental conditions. It seems more plausible that the substance is metacinnabarite.

The orientation of metacinnabarite as deduced from the pattern (c) is ;

first direction : $\{111\}_{\text{metacin.}} // \{001\}_{\text{PbS}}$,
second direction : $\langle 110\rangle_{\text{metacin.}} // \langle 110\rangle_{\text{PbS}}$.

In this orientation the plane of metacinnabarite most densely packed by one kind of its constituents is parallel to the cleavage face, and along the ⟨110⟩-direction a good coincidence of the array of the atoms of the produced crystal with that of the substrate exists. In Fig. 3 the positions of the spots of the pattern (c) are shown by +.

(d). Cinnabar crystallizes in a hexagonal structure, with $a=4.16$ Å, $c=9.54$ Å.[4] Two enantiomorphic space groups, D_3^4 and D_3^6, were proposed for the structure. For the former the coordinates are ; Hg : $u00$; $\bar{u}\bar{u}1/3$; $0u\,2/3$, and S: $0v\,1/6$; $v0\,1/2$; $\bar{v}\bar{v}\,5/6$. In the more probable of the suggested arrangements $u=0.33$ and $v=0.21$. If u is exactly 1/3, the mercury atoms are at the points of a rhombohedral lattice. This structure is a slight distortion of the NaCl arrangement. Thus, this lattice can be regarded as pseudo-cubic, with $a=5.76$ Å. The corner angles of its pseudo-cube face are 92.5° and 87.5°.

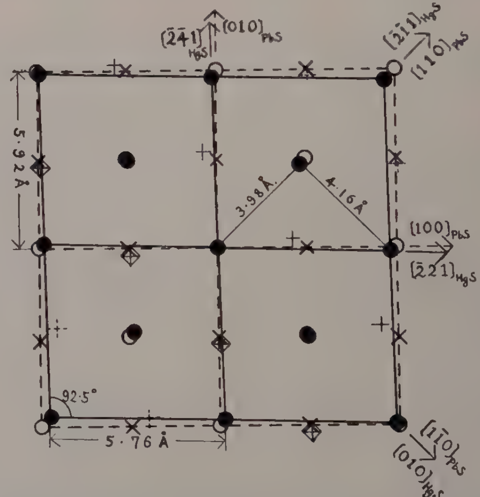

Fig. 4. Geometrical relation between the atomic arrangement of cinnabar and that of galena at the interface. Only one of the four equivalent orientations is shown. The space group of cinnabar is assumed as D_3^4, and the parameters in the coordinates for Hg and S atoms are assumed as $u=1/3$ and $v=0.21$. ●: Hg. +: S of cinnabar at the plane of the paper. ⊕: S of cinnabar about 0.35 Å above the plane of the paper. +: S of cinnabar about 0.35 Å below the plane of the paper. ○: Pb. ×: S of galena.

The analysis of the pattern shows that the pseudo-cube faces of this lattice become parallel to the cleavage face. This orientation can be expressed as follows ;

first direction : $(102)_{\text{cinnabar}} // \{001\}_{\text{PbS}}$,
second direction : $[010]_{\text{cinnabar}} // \langle 110\rangle_{\text{PbS}}$.

These conditions involve four equivalent orientations of cinnabar. The black and white circles and white squares in Fig. 3 designate the positions of the spots due to cinnabar in these four orientations (the spots due to two of them coincide with each other at white squares). The geometrical relation between the atomic arrangement of cinnabar in one of the above orientations and that of the underlying galena at the interface is depicted in Fig. 4.

The remarkable resemblance of the $(102)_{\text{cinnabar}}$-plane with the $(001)_{\text{PbS}}$-plane is supposed to be a cause for this epitaxial orientation.[5]

§ 4. Discussion

An important factor governing the action of aqueous heavy metal salt on sulfide mineral is supposed to be the solubility relation of metal sulfides. Since mercuric sulfide is less soluble than lead sulfide,[6] the production of mercuric sulfide in the present system is well understood according to the metathetical equation: $PbS+HgSO_4=HgS+PbSO_4$. Although cinnabar is more stable than metacinnabarite at ordinary temperatures,[7] mercuric sulfide precipitated from solution seems in general to contain the latter.[7][8] In the present experiment the patterns (b) and (c) are supposed to correspond to metacinnabarite, and the pattern (d) corresponds to cinnabar.

The commonest soluble mercuric salt is mercuric chloride. Electron diffraction investigation of the action of aqueous mercuric chloride on galena cleavage face, however, did not result in the production of mercuric sulfide, but in that of an unknown tetragonal crystal.[3] The marked difference between the results of the two experiments using mercuric sulfate and mercuric chloride requires further detailed study.

From the previous[1] and the present papers it is concluded that the reactions in such solid-liquid systems do not lead to the formation of monomolecular film of sulfide of *activating* metal, as was often supposed, but to the production of its considerably developed crystallites, well accessible by electron diffraction, even at low concentrations. Further, it is interesting to note that the crystallites produced by these reactions take almost complete orientations with respect to the substrates even at room temperatures.

In conclusion the author expresses his sincere thanks to Mr. H. Hagihara for his discussions and encouragement throughout the present work. He is also grateful to the Ministry of Education for the research grant.

References

1) R. Sato: J. Phys. Soc. Jap. **8** (1953) 152.

2) R. Sato: *Research Report of Taihei Mining and Metallugical Laboratory*, No. 1200, 1950, and No. 1250, 1951.

3) R. Sato: *Research Report of Taihei Mining and Metallurgical Laboratory*, No. 1257, 1951.

4) R. W. G. Wyckoff: *Crystal Structures*, Vol. I, Interscience Publishers, Inc., New York, 1951.

5) J. H. van der Merwe: Discussions of the Faraday Society, No. 5 (Crystal Growth) (1949) 201.

6) E. J. Pryor and S. A. Wrobel: Bull. Inst. Mining Met. **60** (1950-51) 201.

7) E. T. Allen, J. L. Crenshaw, and H. E. Merwin: Z. anorg. allgem. Chem. **79** (1913) 125.

8) R. Moltzau and I. M. Kolthoff: J. Phys. Chem. **40** (1936) 637.

Journal of the Physical Society of Japan Vol. 8, No. 4, July—August, 1953

Atomic Distribution in Binary Solid Solutions

IV. The Influence of the Short-Range Order on the Electrical Resistivity of Alloys

By Terutosi MURAKAMI

Institute of Applied Science, Faculty of Engineering, Kyushu University

(Received February 7, 1953)

The temperature dependence of the additional resistivity of binary alloys due to the presence of the short-range order is calculated by means of the pair distribution functions of atoms over crystal lattices, whose analytical expressions are given in the previous parts of this series. The present method used in deriving the expression for the resistivity in alloys is almost similar to the one which has already been developed by Nordheim, who has, however, ignored contribution of the short-range order to the resistance of alloys, and therefore obtained the additional resistivity independent of the temperature. The actual calculation is performed only for simple cubic alloys to avoid computational difficulties. According to the result of calculation, the decrease in the resistivity due to the short-range order becomes appreciable at temperatures immediately above the order-disorder transition point, and, indeed, this contribution decreases the additional resistivity by about 20% compared with the one obtained in the completely random case, even at the temperature 30°C above the critical temperature, if the present theory is applied to the case of Cu_3Au alloy.

§ 1. Introduction

As is well known, the electrons moving through perfectly periodic field are never scattered and, therefore, do not give rise to the electrical resistivity in metals; if the periodicity is disturbed by certain causes such as the thermal vibrations and the presence of foreign atoms in the lattice, then the electrical resistivity appears due to the scattering of electron. And the total resistivity of an alloy may be given as the sum of this resistivity and the ordinary resistivity arising from the thermal vibration of the lattice. Such problem was first treated by Nordheim1),2). He calculated the resistivity of alloys, based on the assumption that the atomic distribution in alloys is completely random, and found that the additional resistance in binary alloys is proportional to the products of the concentrations of atoms of both types. And Mott3) extended Nordheim's method to discuss the substitutional alloys of copper. Muto4) considered the resistivity in the order-disorder alloys, such as Cu_3Au, on the basis of Bragg-Williams' theory, and found the dependence of the resistivity arising from the degree of long-range order. However, no investigation has yet succeeded in treating contribution of short-range order to the resistivity of alloys.

In the present paper, we shall attempt to investigate the resistivity due to the short-range order in alloys, in which the long-range order is absent, with the help of the atomic pair distribution function obtained by means of the statistical method developed in part I5), II6) and III7) of this series*. The present method has some resemblance to Noguti and Nagamiya's8) method for calculating the resistivity of liquid metals from atomic distribution functions, although, unfortunately, their calculation does not agree so successfully with experiments. As the result, it is found that the resistivity of the order-disorder alloys above the critical temperature decreases rather rapidly as the temperature falls in the neighborhood of the critical temperature, and that the presence of local order diminishes appreciably the additional resistivity in the neighborhood of the critical point.

§ 2. Electrical Resistivity Arising from Atomic Disorder in Alloys

Let us consider the binary alloy consisting of N_a A and N_b B atoms distributed over N lattice points, and denote the atomic concentrations of A and B atoms by x_a and x_b respectively. We shall assume that the potential energy of an electron at the point $\boldsymbol{r}$ may be written as the sum of terms arising from each atom:

---

* We will refer these papers merely as I, II and III, respectively.

$$V(\boldsymbol{r})=S_N(\boldsymbol{m})V_m(\boldsymbol{r}-\boldsymbol{m})\,, \qquad (1)$$

where $\boldsymbol{m}=m_1\boldsymbol{a}_1+m_2\boldsymbol{a}_2+m_3\boldsymbol{a}_3$ represents the lattice point specified by a set of integers (m_1, m_2, m_3), $\boldsymbol{a}_1$, $\boldsymbol{a}_2$, and $\boldsymbol{a}_3$ being the primitive translational vectors of the lattice, and $S_N(\boldsymbol{m})$ denote the lattice summation over all points as in the previous papers of this series. Here it is assumed that $V_m(\boldsymbol{r}-\boldsymbol{m})$ vanishes outside the cell $\boldsymbol{m}$. Then the potential $V(\boldsymbol{r})$ is no longer, as in the case of pure metals, a purely periodic function.

We shall divide the potential (1) into a periodic part and a non-periodic part. And here we choose as this periodic potential the average potential $V_0(\boldsymbol{r})$ given by

$$V_0(\boldsymbol{r})=S_N(\boldsymbol{m})\{x_a V_a(\boldsymbol{r}-\boldsymbol{m})+x_b V_b(\boldsymbol{r}-\boldsymbol{m})\}\,, \qquad (2)$$

where $V_a(\boldsymbol{r})$ and $V_b(\boldsymbol{r})$ are the potentials of A and B atoms, respectively. For this periodic potential the eigenfunctions are the Bloch functions given by

$$\psi_k(\boldsymbol{r})=u_k(\boldsymbol{r})\exp\{i\boldsymbol{k}\cdot\boldsymbol{r}\}\,, \qquad (3)$$

where $u_k(\boldsymbol{r})$ has the translational periodicity of the lattice.

The non-periodic part of the potential is given by

$$V'(\boldsymbol{r})=S_N(\boldsymbol{m})V_m(\boldsymbol{r}-\boldsymbol{m})-V_0(\boldsymbol{r})\,, \qquad (4)$$

which we shall consider as the perturbing potential. It is clear from Eqs. (1), (2) and (4) that the average value of the perturbing potential over the eigenfunctions for every state vanishes irrespective of the forms of the eigenfunctions $u_k(\boldsymbol{r})$.

The perturbation causes the transition of electrons from one state to another. As carried out by Nordheim[2], the mean free path of electrons in alloy can be obtained from the calculation of the transition probability. Then, the electrical resistivity arising from the disorder of atoms in alloys obtained from mean free path and the expression for the specific resistivity is given by

$$\rho=\frac{\hbar\Omega_0}{(2\pi)^2e^2n}\frac{KN}{(dE/dK)^2}\int|V'_{\boldsymbol{kk}'}|^2(1-\cos\vartheta)ds\,, \qquad (5)^*$$

where $\Omega_0=(\boldsymbol{a}_1[\boldsymbol{a}_2\boldsymbol{a}_3])$ is the volume of unit cell, ϑ is the angle between to vectors $\boldsymbol{k}$ and $\boldsymbol{k}'$, and ds is the surface element of the Fermi surface, which is assumed to be sphere with the radius K in the $\boldsymbol{k}$-space, and the matrix element $V'_{\boldsymbol{kk}'}$ is given by

$$\begin{aligned}V'_{\boldsymbol{kk}'}&=\int_{N\Omega_0}\psi^*_{\boldsymbol{k}'}V'\psi_{\boldsymbol{k}}d\tau\\&=N^{-1}S_N(\boldsymbol{m})e^{-i(\boldsymbol{k}-\boldsymbol{k}'\cdot\boldsymbol{m})}V'_{\boldsymbol{kk}',m}\,, \qquad (6)\end{aligned}$$

with

$$V'_{\boldsymbol{kk}',m}=\int_{\Omega_0}\psi_{\boldsymbol{k}'}^*V_m'\psi_{\boldsymbol{k}}d\tau_0\,. \qquad (7)$$

In such a system as considered here, $V'_{\boldsymbol{kk},m}$ is given by

$$V'_{\boldsymbol{kk}',a}=x_b\int_{\Omega_0}\psi_{\boldsymbol{k}'}^*(V_a-V_b)\psi_{\boldsymbol{k}}d\tau_0\,, \qquad (8.A)$$

or

$$V'_{\boldsymbol{kk}',b}=x_a\int_{\Omega_0}\psi_{\boldsymbol{k}'}^*(V_b-V_a)\psi_{\boldsymbol{k}}d\tau_0\,, \qquad (8.B)$$

according as the atom at $\boldsymbol{m}$ is A or B.

§ 3. The Relation between Resistivity and Short-Range Order in Alloys

The observable values of resistivity of an alloy may be given as the averaged values of that given by Eq. (5) over all system of statistical ensemble. And, from Eq. (6), we see that this average value of $|V'_{\boldsymbol{kk}'}|^2$ is expressed in the form

$$\begin{aligned}<|V'_{\boldsymbol{kk}'}|^2>&=N^{-2}S_N(\boldsymbol{m})S_N(\boldsymbol{l})\\&\quad\times<V'_{\boldsymbol{kk}',l}\cdot V_{\boldsymbol{kk}',m}>e^{-i(\boldsymbol{k}-\boldsymbol{k}')\cdot(\boldsymbol{l}-\boldsymbol{m})}\,, \qquad (9)\end{aligned}$$

where $< >$ indicates the ensemble average.

Nordheim[1] assumed that the atomic distribution in alloys is completely random. This assumption corresponds to the Bragg-Williams approximation in the statistical-mechanical theory of the order-disorder transformation in alloys. If this assumption were accepted, (9) would become

$$|V'_{\boldsymbol{kk}'}|^2=N^{-1}x_a x_b(V'_{\boldsymbol{kk}',a}-V'_{\boldsymbol{kk}',b})^2\,, \qquad (10)$$

and (5) would become the same expression that Nordheim obtained. It is, however, well known that the short-range order still exists in an alloy above the critical temperature at which the long-range order disappears, and that the assuption of completely random distribution holds only in the sufficiently high temperature region.

---

* cf. Sommerfeld and Bethe[9], Eqs. (43·12) and (43·16), pp. 550–551. In derivation of these equations, Nordheim[2] assumed complete random distribution of atoms, and we shall discuss about this assumption in § 3.

For the system in thermal equilibrium, the average may be taken over all systems of the canonical ensemble. To evaluate this average we shall introduce the distribution function of two atoms $F_{ab}(\boldsymbol{l}, \boldsymbol{m})$ so defined that $x_a x_b F_{ab}(\boldsymbol{l}, \boldsymbol{m})$ be the probability that the A and B atoms occupy simultaneously lattice points $\boldsymbol{l}$ and $\boldsymbol{m}$, respectively. With the help of this function, Eq. (9) is written in the form

$$\begin{aligned}|V'_{kk'}|^2 = N^{-2}[&\underset{\boldsymbol{l}=\boldsymbol{m}}{S(\boldsymbol{l})S(\boldsymbol{m})}(x_a V'^2_{kk',a} - x_b V'^2_{kk',b})\\ &+\underset{\boldsymbol{l}\neq\boldsymbol{m}}{S(\boldsymbol{l})S(\boldsymbol{m})}\cdot\{x_a V'^2_{kk',a} + x_b V'^2_{kk',b}\\ &-x_a x_b (V'_{kk',a} - V'_{kk',b})^2 F_{ab}(\boldsymbol{l}, \boldsymbol{m})\}]\cdot\\ &\times\exp\{-i(\boldsymbol{k}-\boldsymbol{k})\cdot(\boldsymbol{l}-\boldsymbol{m})\}. \qquad (11)\end{aligned}$$

To rewrite (11) in more compact form we shall introduce, instead of $F_{ab}(\boldsymbol{l}, \boldsymbol{m})$, the parameter $\beta(\boldsymbol{l}-\boldsymbol{m})$ defined by

$$F_{ab}(\boldsymbol{l}, \boldsymbol{m}) = 1 - \beta(\boldsymbol{l}-\boldsymbol{m}). \qquad (12)^*$$

Then, we have

$$\begin{aligned}|V'_{kk'}|^2 = &N^{-1} x_a x_b (V_{kk,a} - V_{kk,b})^2\\ &\times[1 + S'_N(\boldsymbol{n})\beta(\boldsymbol{n})\exp\{-i(\boldsymbol{k}-\boldsymbol{k}'\cdot\boldsymbol{n})\}], \qquad (11')\end{aligned}$$

where $S'_N(\boldsymbol{n})$ means the lattice summation excluding the origin, and $\beta(\boldsymbol{n})$ is a kind of order parameter, which vanishes at the completely disordered states. From Eqs. (5) and (11′), the resistivity of an alloy in thermal equilibrium is expressed by

$$\rho = \frac{Q x_a x_b}{4\pi K^2}\int |U_{kk'}|^2 [1 + \Phi(\boldsymbol{k}-\boldsymbol{k}')](1-\cos\vartheta)dS, \qquad (13)$$

where

$$Q = \frac{\hbar\Omega_0}{4\pi e^2 n}\frac{K^3}{(\partial E/\partial K)^2}, \qquad (14)$$

$$U_{kk'} = \int_{\Omega_0} \phi^*_{k'}(V_a - V_b)\phi_k d\tau_0, \qquad (15)$$

and

$$\Phi(\boldsymbol{k}-\boldsymbol{k}') = S'_N(\boldsymbol{n})\beta(\boldsymbol{n})\exp\{-i(\boldsymbol{k}-\boldsymbol{k}'\cdot\boldsymbol{n})\}. \qquad (16)$$

The order parameter $\beta(\boldsymbol{n})$ in Eq. (16) may be obtained from statistical mechanical method developed in the previous parts of this series, according to Eq. (26.2) of II, we have

$$\beta(\boldsymbol{n}) = \frac{C_2}{2(C_2-1)\xi_0(2\pi)^{3/2}}\int\left[\frac{1}{(1/\xi_0)-G(\boldsymbol{k})} - \frac{1}{(C_2/\xi_0)-G(\boldsymbol{k})}\right]\exp(i\boldsymbol{k}\cdot\boldsymbol{n})d\boldsymbol{k}, \qquad (17)$$

where $\xi_0 = \exp(-\Delta\varepsilon/kT) - 1$, and $2\Delta\varepsilon = \varepsilon_{aa} + \varepsilon_{bb} - 2\varepsilon_{ab}$, ε_{aa}, ε_{bb} and ε_{ab} being the interaction energies between an AA, a BB and an AB contact respectively; here $\Delta\varepsilon$ is assumed to be positive, $C_2 = 1/2x_a x_b$, and $\boldsymbol{n}$ and $\boldsymbol{k}$ are a lattice vector and a reciprocal-space vector respectively, defined as

$$\left.\begin{aligned}&\boldsymbol{n} = n_1\boldsymbol{a}_1 + n_2\boldsymbol{a}_2 + n_3\boldsymbol{a}_3\\ \text{and}\\ &\boldsymbol{k} = k_1\boldsymbol{b}_1 + k_2\boldsymbol{b}_2 + k_3\boldsymbol{b}_3,\end{aligned}\right\} \qquad (18)$$

where we have the relations, $(\boldsymbol{a}_i\cdot\boldsymbol{b}_k) = 0$ for $i \neq k$ and $(\boldsymbol{a}_i\cdot\boldsymbol{b}_i) = 1$ for $i = 1, 2, 3$. $G(K)$ is given by one of Eqs. (30) of I for respective lattice structure; e.g.

$$G_{3S}(\boldsymbol{k}) = \sum_{i=1}^{3}\cos k_i \quad \text{for simple cubic,} \qquad (19.1)$$

$$G_{3B}(\boldsymbol{k}) = 4\prod_{i=1}^{3}\cos k_i \quad \text{for body-centered cubic,} \qquad (19.2)$$

$$G_{3D}(\boldsymbol{k}) = 2\sum_{i\neq j}\cos k_i\cdot\cos k_j \quad \text{for face-centered cubic.} \qquad (19.3)$$

On the other hand, Eq. (16) may be written by means of the Fourier inversion as follows:

$$\Phi(\boldsymbol{k}-\boldsymbol{k}') = S'_N(\boldsymbol{n})\beta(\boldsymbol{n})\,e^{-i(\boldsymbol{k}-\boldsymbol{k}'\cdot\boldsymbol{n})} = \Phi'(\boldsymbol{k}-\boldsymbol{k}') - \beta_0, \qquad (20)$$

where

$$\Phi'(\boldsymbol{k}) = S_N(\boldsymbol{n})\beta(\boldsymbol{n})\,e^{-i(\boldsymbol{k}\cdot\boldsymbol{n})} = \Phi_0(\boldsymbol{k})/4x_a x_b, \qquad (21)$$

$$\Phi_0(\boldsymbol{k}) = \frac{\eta_0}{(C_2-1)}\left[\frac{1}{\eta_0 + G(\boldsymbol{k})} - \frac{1}{C_2\eta_0 + G(\boldsymbol{k})}\right], \qquad (22)$$

and

$$\beta_0 = (1/4x_a x_b)(2\pi)^{-3/2}\int_{-\pi}^{\pi}\Phi_0(\boldsymbol{k})d\boldsymbol{k}, \qquad (23)$$

η_0 being used instead of $-1/\xi_0$.

Substituting these formulae into Eq. (12), one has

$$\begin{aligned}\rho = Q(x_a x_b/\pi)&\int_0^{2\pi}\int_0^{\pi}|U_{kk'}|^2\{1 - \beta_0 + \Phi'(K, \theta, \varphi)\}\\ &\times(1-\cos\theta)\sin\theta d\theta d\varphi, \qquad (24)\end{aligned}$$

---

* It is assumed that the correlation function of two atoms at $\boldsymbol{l}$ and $\boldsymbol{m}$ depend only on the difference of the coordinates $\boldsymbol{n} = \boldsymbol{l} - \boldsymbol{m}$.

where the integration over the Fermi-surface is expressed in terms of the spherical coordinates, K, ϑ and φ as shown in Fig. 1, and $\Phi'(K, \theta, \varphi)$ implies the function with the arguments transformed to spherical coordinates.

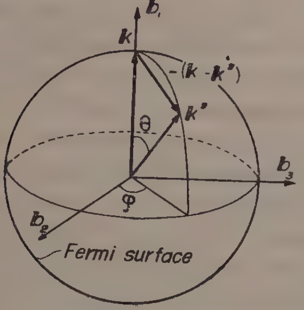

Fig. 1. Spherical coordinates in the reciprocal space.

Here we assume that the scattering is isotropic, as suggested by Seitz[10)]. Then we have

$$\rho=\rho_0[R_a(x_a)-R_b(x_a, T)+R_s(x_a, T)]. \quad (25)$$

where

$$\rho_0=Q|U_{kk'}|^2=\frac{\hbar\Omega_0}{4\pi e^2 n}\frac{K^3}{(dE/dK)}|U_{kk'}|^2, \quad (26)$$

$$R_a(x_a)=4x_a x_b, \quad (27)$$

$$R_b(x_a, T)=4x_a x_b \beta_0=4(2\pi)^{-3/2}\int_{-\pi}^{\pi}\Phi_0(\boldsymbol{k})d\boldsymbol{k}, \quad (28)$$

and

$$R_s(x_a, T)=(1/4\pi)\int_0^{2\pi}\int_0^{\pi}\Phi_0(K, \theta, \varphi) \times(1-\cos\theta)\sin\theta d\theta d\varphi. \quad (29)$$

Here R_b and R_s arise from the presence of short-range order in alloys; the former corresponds to the term giving the uniform background in X-ray scattering, and the latter to the term giving the diffuse maxima*, and both of them are the functions of the temperature and the atomic concentrations.

Since the calculation of R_b and R_s for the case of simple lattice is easier than the one for the other cases, further calculation will be performed only for the simple cubic system, although there exist no real alloys whose crystal structure is simple cubic. For simple cubic crystals, $G(\boldsymbol{k})$ in $\Phi_0(\boldsymbol{k})$ becomes G_{3S} given by Eq. (19.1):

$$G(\boldsymbol{k})=\cos k_1+\cos k_2+\cos k_3, \quad (30)$$

and $G(K, \theta, \varphi)$ becomes

$$G(K, \theta, \varphi)=\cos\{K(1-\cos\theta)\} +\cos\{K\sin\theta\cos\varphi\} +\cos\{K\sin\theta\sin\varphi\}, \quad (31)$$

and, then, R_b defined as (28) may be written in the form

$$R_b=\eta_0(C_2-1)^{-1}\cdot\int_0^{\infty}[I_0(\tau)e^{-\tau}]^3 e^{-(\eta_0-3)\tau}d\tau -\eta_0(C_2-1)^{-1}\cdot\int_0^{\infty}[I_0(\tau)e^{-\tau}]^3 e^{-(C_2\eta_0-3)\tau}d\tau, \quad (32)$$

after the same calculation as in Eq. (31) of II, $I_0(\tau)$ being the zeroth order Bessel function having the purely imaginary argument defined by

$$I_0(\tau)=\sum_{r=0}^{\infty}(\tau/2)^{2r}/(r!)^2. \quad (33)$$

And R_s expressed by (29) is written as follows:

$$R_s=\frac{\eta_0}{4\pi(C_2-1)}\int_0^{2\pi}\int_0^{\pi}\frac{(1-\cos\theta)\sin\theta}{\eta_0+G(K, \theta, \varphi)}d\theta d\varphi -\frac{\eta_0}{4\pi(C_2-1)}\int_0^{2\pi}\int_0^{\pi}\frac{(1-\cos\theta)\sin\theta}{C_2\eta_0+G(K, \theta, \varphi)}d\theta d\varphi. \quad (34)$$

As shown in Table I of II, the present theory as well as Bethe's theory gives the critical temperature T_c, at which the order-disorder transition occurs, by the relation $\exp(-\Delta\varepsilon/kT_c)=1.5$.

§ 4. The Additional Resistivity of Order-Disorder Alloys Immediately above the Critical Temperature

For a binary alloy of monovalent metals, we shall first calculate R_b and R_s in the simple case of 50% concentration with the help of (32) and (34). Then the radius K of the Fermi surface is given by $2\pi(3/8\pi)^{1/3}$. Calculated value of ρ/ρ_0, the ratio of additional resistivity of an alloy with the short-range order to the one in the completely random case, are plotted against $1/T$ in Fig. 2. Then, we have calculated the variation of the resistivity with concentration at $T=1.02T_c$, and show the calculated results in Fig. 3. In real systems, however, this situation may be affected by various other factors such as the lattice distortion and the correlation between the lattice vibration and the short-range order, but it may be concluded that the contribution

---

* cf. III[7)].

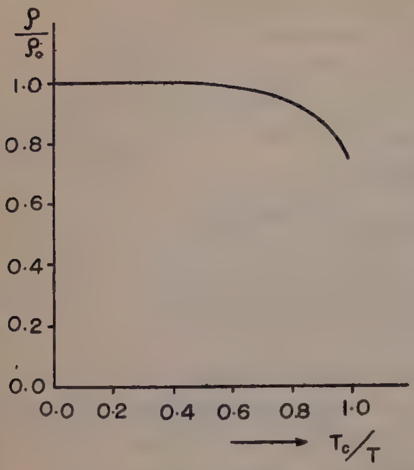

Fig. 2. The temperature dependence of the additional resistivity due to the short-range order.

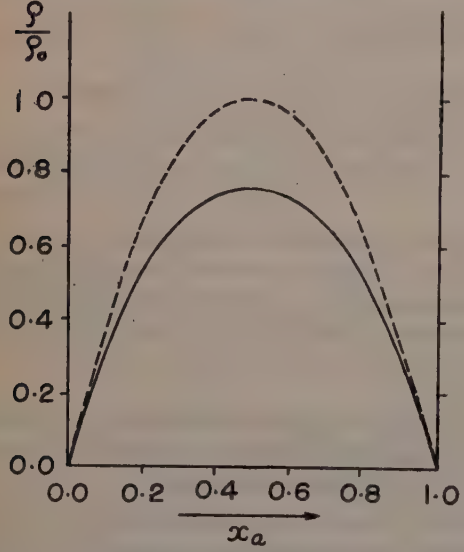

Fig. 3. The change of the additional resistivity of alloys with concentration at $1.02T_c$.
——— the present calculation.
.... Nordheim's calculation, independent of temperature.

of the short-range order to the electrical resistance cannot be ignored even above the critical temperature. Indeed, it is seen that even at temperature as high as 1.04 T_c the effect of short range order decreases the additional resistivity by about 20%, compared with the case of completely disordered alloys considered in Nordheim's theory. Here we may assume that for the alloys, of which the crystal types are not simple cubic, the decreases in the resistivity arising from the presence of the short-range order may be of the same order of the magnitude as in the simple cubic case. Then, the additional resistivity in Cu_3Au may be decreased by about 20% on account of the presence of short-range order, at the temperature 30° C above the critical temperature, T_c=385° C. Although the Fermi-surfaces in alloys of divalent metals cannot be considered as spheres and seem to have so complicated form that the evaluation of the integral (34) over the Fermi-surface will become too difficult, it is expected that alloys of divalent metals may behave differently from ones of monovalent metals as to the temperature dependence of additional resistivity at the neighborhood of the critical temperature.

The author wishes to express his indebtedness to Dr. S. Ono, who suggested this research and provided valuable discussion, and to the Science Research Fund of the National Education Department for its financial aid.

References

1) L. Nordheim: Ann. d. Physik **9** (1931) 607.
2) L. Nordheim: Ann. d. Physik **9** (1931) 641.
3) N. F. Mott: Proc. Camb. Phil. Soc. **32** (1936) 281.
4) T. Muto: Sci. Papers, Inst. Phys. Chem. Res. **30** (1936) 99.
5) T. Murakami: J. Phys. Soc. Japan **7** (1952) 549.
6) T. Murakami: J. Phys. Soc. Japan **8** (1953) 31.
7) T. Murakami: J. Phys. Soc. Japan **8** (1953) 36.
8) T. Noguti and T. Nagamiya: Proc. Phys. Soc. Japan (Nippon Buturi-Gakkai-si) **2** (1947) 23.
9) A. Sommerfeld and H. Bethe: *Handbuch der Physik* 24/2 (Julius Springer, 1933) pp. 540–555.
10) F. Seitz: *Modern Theory of Solids* (MacGrow-Hill, 1940) p. 543.

JOURNAL OF THE PHYSICAL SOCIETY OF JAPAN Vol. 8, No. 4, JULY—AUGUST, 1953

Tables of Integrals Useful for the Calculations of Molecular Energies. III

By Masao KOTANI,
Physics Department, Faculty of Science, University of Tokyo;
Eiichi ISHIGURO,
Physics Department, Faculty of Science, Ochanomizu University;
Katsunori HIJIKATA,
University of Electro-Communications;
Takashi NAKAMURA
Faculty of Science, Hokkaido University,
and Ayao AMEMIYA
Department of Applied Physics, Faculty of Engineering, University of Tokyo

(Received February 28, 1953)

Coulomb, exchange, ionic integrals and one-electron integrals which involve 2s and 2p orbitals have been calculated for homopolar diatomic molecules. Slater type orbitals have been used, with equal values for the exponent δ. Two-center integrals are tabulated as functions of $\alpha=\delta R$ (R: internuclear distance). This work completes the project of tabulation of molecular integrals of which Parts I and II were published in Proc. Phys.-Math. Soc. Japan **20** (1938), **22** (1940), Extra Nos.

§1. Introduction

In 1938–40 Kotani, Amemiya and Simose[1] published Part I and II of this series, which gave the formulae and the auxiliary function tables for the evaluation of the molecular integrals relating to 2s and 2p atomic orbitals. However, these articles were incomplete in the following points: (i) they did not include the formulae for the ionic (or hybrid), kinetic energy and mononuclear integrals; (ii) despite the rather extensive Errata given in Part II, some errors were left unremoved; (iii) numerical values of the molecular integrals were not tabulated except those relating to hydrides molecules. The purpose of the present paper (Part III) is to supplement all these defects. Although works of the same kind* have recently been done by Kopineck[2] and by Araki and Watari,[3] we think that the publication of our results is not superfluous, since it makes this series complete, and since some numerical errors have been found in the papers by the above authors.

In the process of the calculation we have found errors in the foregoing parts of this series, which are listed in Errata at the end of this paper.

§2. Notations and Conventions

The present work is based entirely on the methods and the auxiliary function tables published in Part I and II. The notations and conventions used there will also be employed. We shall now give in the following the list of these notations as well as some new ones. For the sake of convenience, the notations used by Roothaan, Rüdenberg and others[4] will be added.

(1) Units. We shall use the following atomic units: lengths in units of the Bohr radius $a_0=0.5293$ A; energies in units of $e^2/a_0=27.204$ eV.

(2) Atomic orbitals. Let a_α, a_β, ... be the atomic orbitals with their centers at A, and b_γ, b_δ, ... be those with their center at B. Their explicit forms are:

$$a_s(1)=(\delta^5/3\pi)^{1/2}\exp(-\delta r_{a1})r_{a1} \qquad (2s \text{ orbital}),$$

$$a_\sigma(1)=(\delta^5/\pi)^{1/2}\exp(-\delta r_{a1})r_{a1}\cos\theta_{a1} \qquad (2p\sigma \text{ orbital}),$$

---

* Different methods for the evaluation of the ionic integrals have recently been given by Barnett and Coulson and by Brennan and Mulligan (M. P. Barnett and C. A. Coulson, Trans. Roy. Soc. London **243** (1951) 221; R. O. Brennan and J. F. Mulligan, J. Chem. Phys. **20** (1952) 1635.)

$$a_\pi(1)=(\delta^5/\pi)^{1/2}\exp(-\delta r_{a1})r_{a1}\sin\theta_{a1}\cos\varphi_1 \quad (2px \text{ orbital}),$$

$$a_{\pi'}(1)=(\delta^5/\pi)^{1/2}\exp(-\delta r_{a1})r_{a1}\sin\theta_{a1}\sin\varphi_1 \quad (2py \text{ orbital}),$$

$$a_+(1)=(\delta^5/2\pi)^{1/2}\exp(-\delta r_{a1})r_{a1}\sin\theta_{a1}\exp(i\varphi_1) =2^{-1/2}[a_\pi(1)+ia_{\pi'}(1)]\,,$$

$$a_-(1)=(\delta^5/2\pi)^{1/2}\exp(-\delta r_{a1})r_{a1}\sin\theta_{a1}\exp(-i\varphi_1) =2^{-1/2}[a_\pi(1)-ia_{\pi'}(1)].\text{[*]}$$

In the above the coordinate system is chosen as follows: the position of the electron is denoted by P, $r_{a1}=\overline{\mathrm{AP}}$, $r_{b1}=\overline{\mathrm{BP}}$, $\theta_{a1}=\angle\mathrm{BAP}$, $\theta_{b1}=\angle\mathrm{ABP}$.[**]

(3) Integrals

Mononuclear integrals (Table I):

$$J^0{}_{\alpha\beta}=\left(\alpha_a\left|\frac{1}{r_a}\right|\beta_a\right)=\int a_\alpha(1)^*\left(\frac{1}{r_{a1}}\right)a_\beta(1)d\tau,$$

$$T^0{}_{\alpha\beta}=\left(\alpha_a\left|-\frac{1}{2}\Delta\right|\beta_a\right) =\int a_\alpha(1)^*\left(-\frac{1}{2}\Delta\right)a_\beta(1)d\tau,$$

$$D^0{}_{\alpha\beta\gamma\delta}=(\alpha_a\gamma_a;\ \beta_a\delta_a)=\int a_\alpha(1)^*a_\gamma(1)\left(\frac{1}{r_{12}}\right) \times a_\beta(2)^*a_\delta(2)d\tau_1d\tau_2\,.$$

Overlap integrals (Table II):

$$S_{\alpha\beta}=(\alpha_a\,|\,\beta_b)=\int a_\alpha(1)^*b_\beta(1)d\tau\,.$$

Kinetic energy integrals (Table II):

$$T_{\alpha\beta}=\left(\alpha_a\left|-\frac{1}{2}\Delta\right|\beta_b\right)=\int a_\alpha(1)^*\left(-\frac{1}{2}\Delta\right)b_\beta(1)d\tau.$$

Nuclear attraction integrals (Table II):

$$K_{\alpha\beta}=\left(\alpha_a\left|\frac{1}{r_b}\right|\beta_a\right)=\int a_\alpha(1)^*\left(\frac{1}{r_{b1}}\right)a_\beta(1)d\tau\,.$$

Resonance integrals

$$J_{\alpha\beta}=\left(\alpha_b\left|\frac{1}{r_b}\right|\beta_a\right)=\int b_\alpha(1)^*\left(\frac{1}{r_{b1}}\right)a_\beta(1)d\tau\,.\text{[***]}$$

Coulomb integrals (Table II):

$$D_{\alpha\beta\gamma\delta}=(\alpha_a\gamma_a;\ \beta_b\delta_b)=\int a_\alpha(1)^*a_\gamma(1)\left(\frac{1}{r_{12}}\right) \times b_\beta(2)^*b_\delta(2)d\tau_1d\tau_2\,.$$

Exchange integrals (Table III):

$$C_{\alpha\beta\gamma\delta}=(\alpha_a\gamma_b;\ \beta_b\delta_a)=\int a_\alpha(1)^*b_\gamma(1)\left(\frac{1}{r_{12}}\right) \times b_\beta(2)^*a_\delta(2)d\tau_1d\tau_2\,.$$

Ionic integrals (Table III):

$$L_{\alpha\beta\gamma\bar{\delta}}=(\alpha_a\gamma_a;\ \beta_a\delta_b)=\int a_\alpha(1)^*a_\gamma(1)\left(\frac{1}{r_{12}}\right) \times a_\beta(2)^*b_\delta(2)d\tau_1d\tau_2\,.$$

§ 3. Formulae and Numerical Tables

In the following, R=internuclear distance AB; δ=half the effective nuclear charge (see Sec. 2. (2)); $\alpha=\delta R$; $W_\tau{}^\nu(m,n)$ and $G_\tau{}^\nu(m)$ are the auxiliary functions given in Part I and II.

(1) Formulae for kinetic energy.

$$T_{ss}=\delta^2\left\{-\frac{1}{2}S_{ss}+\frac{2J_{ss}}{\delta}-\frac{1}{9}(2\alpha^2+3\alpha+3)e^{-\alpha}\right\},$$

$$T_{s\sigma}=\delta^2\left\{-\frac{1}{2}S_{s\sigma}+\frac{2J_{\sigma s}}{\delta}\right\},$$

$$T_{\sigma\sigma}=\delta^2\left\{-\frac{1}{2}S_{\sigma\sigma}+\frac{2J_{\sigma\sigma}}{\delta}\right\},$$

$$T_{\pi\pi}=\delta^2\left\{-\frac{1}{2}S_{\pi\pi}+\frac{2J_{\pi\pi}}{\delta}\right\}.$$

(2) Formulae for Ionic Integrals

$$L_{sss\bar{s}}=\frac{8\delta}{945}\left(\frac{\delta R}{2}\right)^9[(21W_0(0,4)-70W_0(2,4)+105W_0(4,4))G_0(0)$$
$$+(42W_0(0,3)-140W_0(2,3)+210W_0(3,4))G_0(1)+(-42W_0(0,1)+140W_0(1,2)-210W_0(1,4))G_0(3)$$
$$+(-21W_0(0,0)+70W_0(0,2)-105W_0(0,4))G_0(4)+(60W_2(0,4)-140W_2(2,4))G_2(0)$$
$$+(120W_2(0,3)-280W_2(2,3))G_2(1)+(-120W_2(0,1)+280W_2(1,2))G_2(3)$$

---

[*] The integrals containing the imaginary functions can be easily calculated by the use of the following formulae.

$$X_{\pi\pi}=X_{++}=X_{--}$$

where X means S, K, J or T.

$$X_{\pi\pi\pi\pi}+X_{\pi\pi'\pi\pi'}=2X_{++++}=2X_{+-+-}$$
$$X_{\pi\pi\pi\pi}-X_{\pi\pi'\pi\pi'}=X_{+--+}$$

where X stands for D, C or L.

[**] Araki and Watari used the definition:

$$\theta_{b1}=\pi-\angle\mathrm{ABP}.$$

[***] Araki, Watari and Kopineck defined the J integrals as:

$$J_{\alpha\beta}=\left(\alpha_b\left|\frac{1}{r_a}\right|\beta_a\right)=\int b_\alpha(1)^*\left(\frac{1}{r_{a1}}\right)a_\beta(1)d\tau.$$

$$
\begin{aligned}
&+(-60W_2(0,0)+140W_2(0,2))G_2(4)\\
&+24\{W_4(0,4)G_4(0)+2W_4(0,3)G_4(1)-2W_4(0,1)G_4(3)-W_4(0,0)G_4(4)\}]
\end{aligned}
$$

$$
\begin{aligned}
&\left.\begin{matrix}L_{sss\bar{\sigma}}\\ L_{s\sigma s\bar{s}}\end{matrix}\right\}=\frac{8\sqrt{3}\,\delta}{945}\left(\frac{\delta R}{2}\right)^9[\{(-14W_0(1,4)+70W_0(3,4))G_0(0)+(-28W_0(1,3)+140W_0(3,3))G_0(1)\\
&\quad+(28W_0(1,1)-140W_0(1,3))G_0(3)+(14W_0(0,1)-70W_0(0,3))G_0(4)\}\\
&\pm\{(-63W_1(0,4)+168W_1(2,4)-105W_1(4,4))G_1(0)+(-126W_1(0,3)+336W_1(2,3)-210W_1(3,4))G_1(1)\\
&\quad+(126W_1(0,1)-336W_1(1,2)+210W_1(1,4))G_1(3)+(63W_1(0,0)-168W_1(0,2)+105W_1(0,4))G_1(4)\}\\
&+\{(-10W_2(1,4)-70W_2(3,4))G_2(0)+(-20W_2(1,3)-140W_2(3,3))G_2(1)\\
&\quad+(20W_2(1,1)+140W_2(1,3))G_2(3)+(10W_2(0,1)+70W_2(0,3))G_2(4)\}\\
&\pm42\{(-W_3(0,4)+W_3(2,4))G_3(0)+2(-W_3(0,3)+W_3(2,3))G_3(1)\\
&\quad+2(W_3(0,1)-W_3(1,2))G_3(3)+(W_3(0,0)-W_3(0,2))G_3(4)\}\\
&+24\{W_4(1,4)G_4(0)+2W_4(1,3)G_4(1)-2W_4(1,1)G_4(3)-W_4(0,1)G_4(4)\}]
\end{aligned}
$$

$$
\begin{aligned}
&L_{ss\sigma\bar{s}}=\frac{8\sqrt{3}\,\delta}{945}\left(\frac{\delta R}{2}\right)^9[(21W_0(0,3)-70W_0(2,3)+105W_0(3,4))G_0(0)\\
&\quad+(21W_0(0,2)+21W_0(0,4)-70W_0(2,2)+35W_0(2,4)+105W_0(4,4))G_0(1)\\
&\quad+(-21W_0(0,1)+21W_0(0,3)+70W_0(1,2)-105W_0(1,4)-70W_0(2,3)+105W_0(3,4))G_0(2)\\
&\quad+(-21W_0(0,0)+49W_0(0,2)+70W_0(2,2)-105W_0(0,4)-105W_0(2,4))G_0(3)\\
&\quad+(-21W_0(0,1)+70W_0(1,2)-105W_0(1,4))G_0(4)\\
&\quad+(60W_2(0,3)-140W_2(2,3))G_2(0)+(60W_2(0,2)+60W_2(0,4)-140W_2(2,2)-140W_2(2,4))G_2(1)\\
&\quad+(-60W_2(0,1)+60W_2(0,3)+140W_2(1,2)-140W_2(2,3))G_2(2)\\
&\quad+(-60W_2(0,0)+80W_2(0,2)+140W_2(2,2))G_2(3)+(-60W_2(0,1)+140W_2(1,2))G_2(4)\\
&\quad+24\{W_4(0,3)G_4(0)+(W_4(0,2)+W_4(0,4))G_4(1)+(-W_4(0,1)+W_4(0,3))G_4(2)\\
&\qquad\qquad+(-W_4(0,0)-W_4(0,2))G_4(3)-W_4(0,1)G_4(4)\}]
\end{aligned}
$$

$$
\begin{aligned}
&\left.\begin{matrix}L_{s\sigma\sigma\bar{s}}\\ L_{ss\sigma\bar{\sigma}}\end{matrix}\right\}=\frac{8\delta}{315}\left(\frac{\delta R}{2}\right)^9[\{(-14W_0(1,3)+70W_0(3,3))G_0(0)\\
&\quad+(-14W_0(1,2)-14W_0(1,4)+70W_0(2,3)+70W_0(3,4))G_0(1)\\
&\quad+(14W_0(1,1)-84W_0(1,3)+70W_0(3,3))G_0(2)\\
&\quad+(14W_0(0,1)+14W_0(1,2)-70W_0(0,3)-70W_0(2,3))G_0(3)+(14W_0(1,1)-70W_0(1,3))G_0(4)\}\\
&\pm\{(63W_1(0,3)-168W_1(2,3)+105W_1(3,4))G_1(0)\\
&\quad+(63W_1(0,2)+63W_1(0,4)-168W_1(2,2)-63W_1(2,4)+105W_1(4,4))G_1(1)\\
&\quad+(-63W_1(0,1)+63W_1(0,3)+168W_1(1,2)-105W_1(1,4)-168W_1(2,3)+105W_1(3,4))G_1(2)\\
&\quad+(-63W_1(0,0)+105W_1(0,2)-105W_1(0,4)+168W_1(2,2)-105W_1(2,4))G_1(3)\\
&\quad+(-63W_1(0,1)+168W_1(1,2)-105W_1(1,4))G_1(4)\}\\
&+\{(-10W_2(1,3)-70W_2(3,3))G_2(0)+(-10W_2(1,2)-10W_2(1,4)-70W_2(2,3)-70W_2(3,4))G_2(1)\\
&\quad+(10W_2(1,1)+60W_2(1,3)-70W_2(3,3))G_2(2)\\
&\quad+(10W_2(0,1)+10W_2(1,2)+70W_2(0,3)+70W_2(2,3))G_2(3)+(10W_2(1,1)+70W_2(1,3))G_2(4)\}\\
&\pm42\{(W_3(0,3)-W_3(2,3))G_3(0)+(W_3(0,2)-W_3(2,2)+W_3(0,4)-W_3(2,4))G_3(1)\\
&\quad+(-W_3(0,1)+W_3(1,2)+W_3(0,3)-W_3(2,3))G_3(2)\\
&\quad+(-W_3(0,0)+W_3(2,2))G_3(3)+(-W_3(0,1)+W_3(1,2))G_3(4)\}\\
&+24\{W_4(1,3)G_4(0)+(W_4(1,2)+W_4(1,4))G_4(1)+(-W_4(1,1)+W_4(1,3))G_4(2)\\
&\qquad\qquad+(-W_4(0,1)-W_4(1,2))G_4(3)-W_4(1,1)G_4(4)\}]
\end{aligned}
$$

$$
\begin{aligned}
&L_{s\sigma s\bar{\sigma}}=\frac{8\delta}{315}\left(\frac{\delta R}{2}\right)^9[(-35W_0(0,4)+126W_0(2,4)-35W_0(4,4))G_0(0)\\
&\quad+(-70W_0(0,3)+252W_0(2,3)-70W_0(3,4))G_0(1)+(70W_0(0,1)-252W_0(1,2)+70W_0(1,4))G_0(3)
\end{aligned}
$$

$$
\begin{aligned}
&+(35W_0(0,0)-126W_0(0,2)+35W_0(0,4))G_0(4)\\
&+(-70W_2(0,4)+60W_2(2,4)-70W_2(4,4))G_2(0)+(-140W_2(0,3)+120W_2(2,3)-140W_2(3,4))G_2(1)\\
&+(140W_2(0,1)-120W_2(1,2)+140W_2(1,4))G_2(3)+(70W_2(0,0)-60W_2(0,2)+70W_2(0,4))G_2(4)\\
&+24\{W_4(2,4)G_4(0)+2W_4(2,3)G_4(1)-2W_4(1,2)G_4(3)-W_4(0,2)G_4(4)\}]
\end{aligned}
$$

$$
\begin{aligned}
L_{\sigma s\sigma\bar{s}}=\frac{8\delta}{315}\left(\frac{\delta R}{2}\right)^9&[(21W_0(0,2)-70W_0(2,2)+105W_0(2,4))(G_0(0)-G_0(4))\\
&+(-21W_0(0,0)+70W_0(0,2)-84W_0(0,4)-70W_0(2,4)+105W_0(4,4))G_0(2)\\
&+(42W_0(0,3)-140W_0(2,3)+210W_0(3,4))G_0(1)+(-42W_0(0,1)+140W_0(1,2)-210W_0(1,4))G_0(3)\\
&+(60W_2(0,2)-140W_2(2,2))(G_2(0)-G_2(4))+(120W_2(0,3)-280W_2(2,3))G_2(1)\\
&+(-60W_2(0,0)+140W_2(0,2)+60W_2(0,4)-140W_2(2,4))G_2(2)+(-120W_2(0,1)+280W_2(1,2))G_2(3)\\
&+24\{W_4(0,2)(G_4(0)-G_4(4))+2W_4(0,3)G_4(1)+(-W_4(0,0)+W_4(0,4))G_4(2)-2W_4(0,1)G_4(3)\}]
\end{aligned}
$$

$$
\begin{aligned}
L_{s\sigma\sigma\bar{\sigma}}=\frac{8\sqrt{3}\,\delta}{315}\left(\frac{\delta R}{2}\right)^9&[(-35W_0(0,3)+126W_0(2,3)-35W_0(3,4))G_0(0)\\
&+(35W_0(0,1)-126W_0(1,2)+35W_0(1,4))G_0(4)\\
&+(-35W_0(0,2)+126W_0(2,2)-35W_0(0,4)+91W_0(2,4)-35W_0(4,4))G_0(1)\\
&+(35W_0(0,1)-35W_0(0,3)-126W_0(1,2)+35W_0(1,4)+126W_0(2,3)-35W_0(3,4))G_0(2)\\
&+(35W_0(0,0)-91W_0(0,2)+35W_0(0,4)-126W_0(2,2)+35W_0(2,4))G_0(3)\\
&+(-70W_2(0,3)+60W_2(2,3)-70W_2(3,4))G_2(0)+(70W_2(0,1)-60W_2(1,2)+70W_2(1,4))G_2(4)\\
&+(-70W_2(0,2)+60W_2(2,2)-70W_2(0,4)-10W_2(2,4)-70W_2(4,4))G_2(1)\\
&+(70W_2(0,1)-70W_2(0,3)-60W_2(1,2)+70W_2(1,4)+60W_2(2,3)-70W_2(3,4))G_2(2)\\
&+(70W_2(0,0)+10W_2(0,2)+70W_2(0,4)-60W_2(2,2)+70W_2(2,4))G_2(3)\\
&+24\{W_4(2,3)G_4(0)+(W_4(2,2)+W_4(2,4))G_4(1)+(-W_4(1,2)+W_4(2,3))G_4(2)\\
&\qquad\qquad\qquad\qquad+(-W_4(0,2)-W_4(2,2))G_4(3)-W_4(1,2)G_4(4)\}]
\end{aligned}
$$

$$
\begin{aligned}
\left.\begin{matrix}L_{\sigma s\sigma\bar{\sigma}}\\ L_{\sigma\sigma\sigma\bar{s}}\end{matrix}\right\}=\frac{8\sqrt{3}\,\delta}{315}\left(\frac{\delta R}{2}\right)^9&[\{(-14W_0(1,2)+70W_0(2,3))(G_0(0)-G_0(4))\\
&\quad+(14W_0(0,1)-70W_0(0,3)-14W_0(1,4)+70W_0(3,4))G_0(2)\\
&\quad+(-28W_0(1,3)+140W_0(3,3))G_0(1)+(28W_0(1,1)-140W_0(1,3))G_0(3)\}\\
&\pm\{(-63W_1(0,2)+168W_1(2,2)-105W_1(2,4))(G_1(0)-G_1(4))\\
&\quad+(63W_1(0,0)-168W_1(0,2)+42W_1(0,4)+168W_1(2,4)-105W_1(4,4))G_1(2)\\
&\quad+(-126W_1(0,3)+336W_1(2,3)-210W_1(3,4))G_1(1)\\
&\quad+(126W_1(0,1)-336W_1(1,2)+210W_1(1,4))G_1(3)\}\\
&+\{(-10W_2(1,2)-70W_2(2,3))(G_2(0)-G_2(4))\\
&\quad+(10W_2(0,1)+70W_2(0,3)-10W_2(1,4)-70W_2(3,4))G_2(2)\\
&\quad+(-20W_2(1,3)-140W_2(3,3))G_2(1)+(20W_2(1,1)+140W_2(1,3))G_2(3)\}\\
&\pm 42\{(-W_3(0,2)+W_3(2,2))(G_3(0)-G_3(4))+2(-W_3(0,3)+W_3(2,3))G_3(1)\\
&\quad+(W_3(0,0)-W_3(0,2)-W_3(0,4)+W_3(2,4))G_3(2)+2(W_3(0,1)-W_3(1,2))G_3(3)\}\\
&+24\{W_4(1,2)(G_4(0)-G_4(4))+2W_4(1,3)G_4(1)+(-W_4(0,1)+W_4(1,4))G_4(2)-2W_4(1,1)G_4(3)\}]
\end{aligned}
$$

$$
\begin{aligned}
L_{\sigma\sigma\sigma\bar{\sigma}}=\frac{8\delta}{105}\left(\frac{\delta R}{2}\right)^9&[(-35W_0(0,2)+126W_0(2,2)-35W_0(2,4))(G_0(0)-G_0(4))\\
&+(35W_0(0,0)-126W_0(0,2)+126W_0(2,4)-35W_0(4,4))G_0(2)\\
&+(-70W_0(0,3)+252W_0(2,3)-70W_0(3,4))G_0(1)+(70W_0(0,1)-252W_0(1,2)+70W_0(1,4))G_0(3)\\
&+(-70W_2(0,2)+60W_2(2,2)-70W_2(2,4))(G_2(0)-G_2(4))\\
&+(70W_2(0,0)-60W_2(0,2)+60W_2(2,4)-70W_2(4,4))G_2(2)
\end{aligned}
$$

$$+(-140W_2(0,3)+120W_2(2,3)-140W_2(3,4))G_2(1)+(140W_2(0,1)-120W_2(1,2)+140W_2(1,4))G_2(3)$$
$$+24\{W_4(2,2)(G_4(0)-G_4(4))+2W_4(2,3)G_4(1)+(-W_4(0,2)+W_4(2,4))G_4(2)-2W_4(1,2)G_4(3)\}]$$

$$L_{s\pi s\bar{\pi}}=\frac{8\delta}{315}\left(\frac{\delta R}{2}\right)^9[(7W_0(0,4)-42W_0(2,4)+35W_0(4,4))G_0(0)$$
$$+(14W_0(0,3)-84W_0(2,3)+70W_0(3,4))G_0(1)$$
$$+(-14W_0(0,1)+84W_0(1,2)-70W_0(1,4))G_0(3)+(-7W_0(0,0)+42W_0(0,2)-35W_0(0,4))G_0(4)$$
$$+(5W_2(0,4)+30W_2(2,4)-35W_2(4,4))G_2(0)+(10W_2(0,3)+60W_2(2,3)-70W_2(3,4))G_2(1)$$
$$+(-10W_2(0,1)-60W_2(1,2)+70W_2(1,4))G_2(3)+(-5W_2(0,0)-30W_2(0,2)+35W_2(0,4))G_2(4)$$
$$+12\{(-W_4(0,4)+W_4(2,4))G_4(0)+2(-W_4(0,3)+W_4(2,3))G_4(1)$$
$$+2(W_4(0,1)-W_4(1,2))G_4(3)+(W_4(0,0)-W_4(0,2))G_4(4)\}]$$

$$L_{\pi s\pi\bar{s}}=\frac{4\delta}{315}\left(\frac{\delta R}{2}\right)^9[(-21W_0(0,2)+70W_0(2,2)+21W_0(0,4)-175W_0(2,4)+105W_0(4,4))G_0(0)$$
$$+(21W_0(0,0)-70W_0(0,2)+84W_0(0,4)+70W_0(2,4)-105W_0(4,4))G_0(2)$$
$$+(-21W_0(0,0)+91W_0(0,2)-105W_0(0,4)-70W_0(2,2)+105W_0(2,4))G_0(4)$$
$$+(-60W_2(0,2)+140W_2(2,2)+60W_2(0,4)-140W_2(2,4))G_2(0)$$
$$+(60W_2(0,0)-140W_2(0,2)-60W_2(0,4)+140W_2(2,4))G_2(2)$$
$$+(-60W_2(0,0)+200W_2(0,2)-140W_2(2,2))G_2(4)$$
$$+24\{(-W_4(0,2)+W_4(0,4))G_4(0)+(W_4(0,0)-W_4(0,4))G_4(2)+(-W_4(0,0)+W_4(0,2))G_4(4)\}]$$

$$L_{s\pi\sigma\bar{\pi}}=\frac{8\sqrt{3}\,\delta}{315}\left(\frac{\delta R}{2}\right)^9[(7W_0(0,3)-42W_0(2,3)+35W_0(3,4))G_0(0)$$
$$+(-7W_0(0,1)+42W_0(1,2)-35W_0(1,4))G_0(4)$$
$$+(7W_0(0,2)-42W_0(2,2)+7W_0(0,4)-7W_0(2,4)+35W_0(4,4))G_0(1)$$
$$+(-7W_0(0,1)+42W_0(1,2)+7W_0(0,3)-35W_0(1,4)-42W_0(2,3)+35W_0(3,4))G_0(2)$$
$$+(-7W_0(0,0)+35W_0(0,2)-35W_0(0,4)+42W_0(2,2)-35W_0(2,4))G_0(3)$$
$$+(5W_2(0,3)+30W_2(2,3)-35W_2(3,4))G_2(0)+(-5W_2(0,1)-30W_2(1,2)+35W_2(1,4))G_2(4)$$
$$+(5W_2(0,2)+30W_2(2,2)+5W_2(0,4)-5W_2(2,4)-35W_2(4,4))G_2(1)$$
$$+(-5W_2(0,1)-30W_2(1,2)+5W_2(0,3)+35W_2(1,4)+30W_2(2,3)-35W_2(3,4))G_2(2)$$
$$+(-5W_2(0,0)-35W_2(0,2)+35W_2(0,4)-30W_2(2,2)+35W_2(2,4))G_2(3)$$
$$+12\{(-W_4(0,3)+W_4(2,3))G_4(0)+(-W_4(0,2)-W_4(0,4)+W_4(2,2)+W_4(2,4))G_4(1)$$
$$+(W_4(0,1)-W_4(1,2)-W_4(0,3)+W_4(2,3))G_4(2)+(W_4(0,0)-W_4(2,2))G_4(3)$$
$$+(W_4(0,1)-W_4(1,2))G_4(4)\}]$$

$$\left.\begin{matrix}L_{\pi\sigma\pi\bar{s}}\\ L_{\pi s\pi\bar{\sigma}}\end{matrix}\right\}=\frac{4\sqrt{3}\,\delta}{315}\left(\frac{\delta R}{2}\right)^9[\{(14W_0(1,2)-14W_0(1,4)-70W_0(2,3)+70W_0(3,4))G_0(0)$$
$$+(-14W_0(0,1)+70W_0(0,3)+14W_0(1,4)-70W_0(3,4))G_0(2)$$
$$+(14W_0(0,1)-14W_0(1,2)-70W_0(0,3)+70W_0(2,3))G_0(4)\}$$
$$\pm\{(-63W_1(0,2)+168W_1(2,2)+63W_1(0,4)-273W_1(2,4)+105W_1(4,4))G_1(0)$$
$$+(63W_1(0,0)-168W_1(0,2)+42W_1(0,4)+168W_1(2,4)-105W_1(4,4))G_1(2)$$
$$+(-63W_1(0,0)+231W_1(0,2)-105W_1(0,4)-168W_1(2,2)+105W_1(2,4))G_1(4)\}$$
$$+\{(10W_2(1,2)-10W_2(1,4)+70W_2(2,3)-70W_2(3,4))G_2(0)$$
$$+(-10W_2(0,1)-70W_2(0,3)+10W_2(1,4)+70W_2(3,4))G_2(2)$$
$$+(10W_2(0,1)+70W_2(0,3)-10W_2(1,2)-70W_2(2,3))G_2(4)\}$$
$$\pm42\{(-W_3(0,2)+W_3(2,2)+W_3(0,4)-W_3(2,4))G_3(0)$$
$$+(W_3(0,0)-W_3(0,2)-W_3(0,4)+W_3(2,4))G_3(2)$$

$$\begin{aligned}
&+(-W_3(0,0)+2W_3(0,2)-W_3(2,2))G_3(4)\}\\
&+24\{(-W_4(1,2)+W_4(1,4))G_4(0)+(W_4(0,1)-W_4(1,4))G_4(2)+(-W_4(0,1)+W_4(1,2))G_4(4)\}]
\end{aligned}$$

$$\begin{aligned}
L_{\pi\sigma\pi\bar{\sigma}}=\frac{4\delta}{105}\left(\frac{\delta R}{2}\right)^9&[(35W_0(0,2)-126W_0(2,2)-35W_0(0,4)+161W_0(2,4)-35W_0(4,4))G_0(0)\\
&+(-35W_0(0,0)+126W_0(0,2)-126W_0(2,4)+35W_0(4,4))G_0(2)\\
&+(35W_0(0,0)-161W_0(0,2)+126W_0(2,2)+35W_0(0,4)-35W_0(2,4))G_0(4)\\
&+(70W_2(0,2)-60W_2(2,2)-70W_2(0,4)+130W_2(2,4)-70W_2(4,4))G_2(0)\\
&+(-70W_2(0,0)+60W_2(0,2)-60W_2(2,4)+70W_2(4,4))G_2(2)\\
&+(70W_2(0,0)-130W_2(0,2)+60W_2(2,2)+70W_2(0,4)-70W_2(2,4))G_2(4)\\
&+24\{(-W_4(2,2)+W_4(2,4))G_4(0)+(W_4(0,2)-W_4(2,4))G_4(2)+(-W_4(0,2)+W_4(2,2))G_4(4)\}]
\end{aligned}$$

$$\begin{aligned}
L_{\sigma\pi\sigma\bar{\pi}}=\frac{8\delta}{105}\left(\frac{\delta R}{2}\right)^9&[\{7W_0(0,2)-42W_0(2,2)+35W_0(2,4))(G_0(0)-G_0(4))\\
&+(-7W_0(0,0)+42W_0(0,2)-28W_0(0,4)-42W_0(2,4)+35W_0(4,4))G_0(2)\\
&+(14W_0(0,3)-84W_0(2,3)+70W_0(3,4))G_0(1)+(-14W_0(0,1)+84W_0(1,2)-70W_0(1,4))G_0(3)\\
&+(5W_2(0,2)+30W_2(2,2)-35W_2(2,4))(G_2(0)-G_2(4))\\
&+(-5W_2(0,0)-30W_2(0,2)+40W_2(0,4)+30W_2(2,4)-35W_2(4,4))G_2(2)\\
&+(10W_2(0,3)+60W_2(2,3)-70W_2(3,4))G_2(1)+(-10W_2(0,1)-60W_2(1,2)+70W_2(1,4))G_2(3)\\
&+12\{(-W_4(0,2)+W_4(2,2))(G_4(0)-G_4(4))+2(-W_4(0,3)+W_4(2,3))G_4(1)\\
&+(W_4(0,0)-W_4(0,2)-W_4(0,4)+W_4(2,4))G_4(2)+2(W_4(0,1)-W_4(1,2))G_4(3)\}]
\end{aligned}$$

$$\begin{aligned}
\left.\begin{array}{l}L_{s\pi\pi\bar{s}}\\ L_{\pi ss\bar{\pi}}\end{array}\right\}=\frac{2\delta}{4725}\left(\frac{\delta R}{2}\right)^9&[315\{(W_1{}^1(1,3)-5W_1{}^1(3,3))G_1{}^1(0)+(W_1{}^1(1,2)-5W_1{}^1(2,3))G_1{}^1(1)\\
&\quad+(-W_1{}^1(1,1)+5W_1{}^1(1,3))G_1{}^1(2)+(-W_1{}^1(0,1)+5W_1{}^1(0,3))G_1{}^1(3)\}\\
&\pm25\{(-3W_2{}^1(0,3)+7W_2{}^1(2,3))G_2{}^1(0)+(-3W_2{}^1(0,2)+7W_2{}^1(2,2))G_2{}^1(1)\\
&\quad+(3W_2{}^1(0,1)-7W_2{}^1(1,2))G_2{}^1(2)+(3W_2{}^1(0,0)-7W_2{}^1(0,2))G_2{}^1(3)\}\\
&+35\{W_3{}^1(1,3)G_3{}^1(0)+W_3{}^1(1,2)G_3{}^1(1)-W_3{}^1(1,1)G_3{}^1(2)-W_3{}^1(0,1)G_3{}^1(3)\}\\
&\pm9\{-W_4{}^1(0,3)G_4{}^1(0)-W_4{}^1(0,2)G_4{}^1(1)+W_4{}^1(0,1)G_4{}^1(2)+W_4{}^1(0,0)G_4{}^1(3)\}]
\end{aligned}$$

$$\begin{aligned}
\left.\begin{array}{l}L_{s\pi\pi\bar{\sigma}}\\ L_{\pi\sigma s\bar{\pi}}\end{array}\right\}=\frac{2\sqrt{3}\,\delta}{4725}\left(\frac{\delta R}{2}\right)^9&[315\{(W_1{}^1(0,3)-5W_1{}^1(2,3))G_1{}^1(0)+(W_1{}^1(0,2)-5W_1{}^1(2,2))G_1{}^1(1)\\
&\quad+(-W_1{}^1(0,1)+5W_1{}^1(1,2))G_1{}^1(2)+(-W_1{}^1(0,0)+5W_1{}^1(0,2))G_1{}^1(3)\}\\
&\pm25\{(-3W_2{}^1(1,3)+7W_2{}^1(3,3))G_2{}^1(0)+(-3W_2{}^1(1,2)+7W_2{}^1(2,3))G_2{}^1(1)\\
&\quad+(3W_2{}^1(1,1)-7W_2{}^1(1,3))G_2{}^1(2)+(3W_2{}^1(0,1)-7W_2{}^1(0,3))G_2{}^1(3)\}\\
&+35\{W_3{}^1(0,3)G_3{}^1(0)+W_3{}^1(0,2)G_3{}^1(1)-W_3{}^1(0,1)G_3{}^1(2)-W_3{}^1(0,0)G_3{}^1(3)\}\\
&\pm9\{-W_4{}^1(1,3)G_4{}^1(0)-W_4{}^1(1,2)G_4{}^1(1)+W_4{}^1(1,1)G_4{}^1(2)+W_4{}^1(0,1)G_4{}^1(3)\}]
\end{aligned}$$

$$\begin{aligned}
\left.\begin{array}{l}L_{\pi\pi\sigma\bar{s}}\\ L_{\sigma s\pi\bar{\pi}}\end{array}\right\}=\frac{2\sqrt{3}\,\delta}{4725}\left(\frac{\delta R}{2}\right)^9&[315\{(W_1{}^1(1,2)-5W_1{}^1(2,3))G_1{}^1(0)+(W_1{}^1(1,3)-5W_1{}^1(3,3))G_1{}^1(1)\\
&\quad+(-W_1{}^1(0,1)+5W_1{}^1(0,3))G_1{}^1(2)+(-W_1{}^1(1,1)+5W_1{}^1(1,3))G_1{}^1(3)\}\\
&\pm25\{(-3W_2{}^1(0,2)+7W_2{}^1(2,2))G_2{}^1(0)+(-3W_2{}^1(0,3)+7W_2{}^1(2,3))G_2{}^1(1)\\
&\quad+(3W_2{}^1(0,0)-7W_2{}^1(0,2))G_2{}^1(2)+(3W_2{}^1(0,1)-7W_2{}^1(1,2))G_2{}^1(3)\}\\
&+35\{W_3{}^1(1,2)G_3{}^1(0)+W_3{}^1(1,3)G_3{}^1(1)-W_3{}^1(0,1)G_3{}^1(2)-W_3{}^1(1,1)G_3{}^1(3)\}\\
&\pm9\{-W_4{}^1(0,2)G_4{}^1(0)-W_4{}^1(0,3)G_4{}^1(1)+W_4{}^1(0,0)G_4{}^1(2)+W_4{}^1(0,1)G_4{}^1(3)\}]
\end{aligned}$$

$$\left.\begin{array}{l}L_{\sigma\pi\pi\bar{\sigma}}\\ L_{\pi\sigma\sigma\bar{\pi}}\end{array}\right\}=\frac{2\delta}{1575}\left(\frac{\delta R}{2}\right)^9[315\{(W_1{}^1(0,2)-5W_1{}^1(2,2))G_1{}^1(0)+(W_1{}^1(0,3)-5W_1{}^1(2,3))G_1{}^1(1)$$

$$
\begin{aligned}
&+(-W_1{}^1(0,0)+5W_1{}^1(0,2))G_1{}^1(2)+(-W_1{}^1(0,1)+5W_1{}^1(1,2))G_1{}^1(3)\}\\
&\pm25\{(-3W_2{}^1(1,2)+7W_2{}^1(2,3))G_2{}^1(0)+(-3W_2{}^1(1,3)+7W_2{}^1(3,3))G_2{}^1(1)\\
&\quad+(3W_2{}^1(0,1)-7W_2{}^1(0,3))G_2{}^1(2)+(3W_2{}^1(1,1)-7W_2{}^1(1,3))G_2{}^1(3)\}\\
&+35\{W_3{}^1(0,2)G_3{}^1(0)+W_3{}^1(0,3)W_3{}^1(1)-W_3{}^1(0,0)G_3{}^1(2)-W_3{}^1(0,1)G_3{}^1(3)\}\\
&\pm9\{-W_4{}^1(1,2)G_4{}^1(0)-W_4{}^1(1,3)G_4{}^1(1)+W_4{}^1(0,1)G_4{}^1(2)+W_4{}^1(1,1)G_4{}^1(3)\}]
\end{aligned}
$$

$$
\begin{aligned}
L_{++++}=\frac{2\delta}{105}\left(\frac{\delta R}{2}\right)^9&[(-14W_0(0,2)+14W_0(0,4)+84W_0(2,2)-154W_0(2,4)+70W_0(4,4))G_0(0)\\
&+(14W_0(0,0)-84W_0(0,2)+56W_0(0,4)+84W_0(2,4)-70W_0(4,4))G_0(2)\\
&+(-14W_0(0,0)+98W_0(0,2)-70W_0(0,4)-84W_0(2,2)+70W_0(2,4))G_0(4)\\
&+(-10W_2(0,2)-60W_2(2,2)+10W_2(0,4)+130W_2(2,4)-70W_2(4,4))G_2(0)\\
&+(10W_2(0,0)+60W_2(0,2)-80W_2(0,4)-60W_2(2,4)+70W_2(4,4))G_2(2)\\
&+(-10W_2(0,0)-50W_2(0,2)+60W_2(2,2)+70W_2(0,4)-70W_2(2,4))G_2(4)\\
&+24\{(W_4(0,2)-W_4(2,2)-W_4(0,4)+W_4(2,4))G_4(0)\\
&\quad+(-W_4(0,0)+W_4(0,2)+W_4(0,4)-W_4(2,4))G_4(2)\\
&\quad+(W_4(0,0)-2W_4(0,2)+W_4(2,2))G_4(4)\}]
\end{aligned}
$$

$$
\begin{aligned}
L_{\pi\pi\pi'\bar{\pi}'}\doteq\frac{\delta}{37800}\left(\frac{\delta R}{2}\right)^9&[(-75W_2{}^2(0,2)+525W_2{}^2(2,2))G_2{}^2(0)+(75W_2{}^2(0,0)-525W_2{}^2(0,2))G_2{}^2(2)\\
&\qquad-2W_4{}^2(0,2)G_4{}^2(0)+2W_4{}^2(0,0)G_4{}^2(2)]
\end{aligned}
$$

$$
\left.\begin{array}{l} L_{\pi\pi\pi\bar{\pi}} \\ L_{\pi\pi'\pi\bar{\pi}'} \end{array}\right\}=L_{++++}\pm L_{\pi\pi\pi'\bar{\pi}'}\,,\quad L_{+--+}=2L_{\pi\pi\pi'\bar{\pi}'}\,.
$$

(3) Numerical tables

Tables I–III are our numerical results. We have done our best in order to eliminate errors and misprints from these Tables.* These results were checked by independent recalculations and by making difference tables. It is to be noted that the last figures of ionic integrals may be somewhat uncertain. The auxiliary function tables on which our calculation was based, contained more significant figures than those published in Part I.

The following relations between the two-electron integrals can be used for checking.

$$
\begin{aligned}
3X_{ssss}&=2X_{\pi s\pi s}+X_{\sigma s\sigma s}\\
3X_{sss\sigma}&=2X_{\pi s\pi\sigma}+X_{\sigma s\sigma\sigma}\\
3X_{s\sigma ss}&=2X_{\pi\sigma\pi s}+X_{\sigma\sigma\sigma s}\\
3X_{s\sigma s\sigma}&=2X_{\pi\sigma\pi\sigma}+X_{\sigma\sigma\sigma\sigma}\\
3X_{s\pi s\pi}&=X_{\pi\pi\pi\pi}+X_{\pi\pi'\pi\pi'}+X_{\sigma\pi\sigma\pi}\\
L_{s\pi\sigma\bar{\pi}}&=L_{\pi\sigma s\bar{\pi}}\,,
\end{aligned}
$$

where $X_{\alpha\beta\gamma\delta}$ denotes $D_{\alpha\beta\gamma\delta}$ or $L_{\alpha\beta\gamma\bar{\delta}}$.

Table I

Mononuclear Integrals

$$
J^0{}_{ss}=J^0{}_{\sigma\sigma}=J^0{}_{\pi\pi}=\frac{\delta}{2}\,,\quad T^0{}_{ss}=\frac{\delta^2}{6}\,,\quad T^0{}_{\sigma\sigma}=T^0{}_{\pi\pi}=\frac{\delta^2}{2}
$$

$$
\left.\begin{array}{l}
D^0{}_{ssss}=(s_a s_a\,;\,s_a s_a)\\
D^0{}_{\sigma s\sigma s}=(\sigma_a\sigma_a\,;\,s_a s_a)\\
D^0{}_{\pi s\pi s}=(\pi_a\pi_a\,;\,s_a s_a)
\end{array}\right\}=\frac{93\delta}{256}=0.36328\,1\delta
$$

$$
\left.\begin{array}{l}
D^0{}_{\sigma ss\sigma}=(\sigma_a s_a\,;\,\sigma_a s_a)\\
D^0{}_{\pi ss\pi}=(\pi_a s_a\,;\,\pi_a s_a)
\end{array}\right\}=\frac{185\delta}{2304}=0.08029\,5\delta
$$

$$
\left.\begin{array}{l}
D^0{}_{\sigma\sigma\sigma\sigma}=(\sigma_a\sigma_a\,;\,\sigma_a\sigma_a)\\
D^0{}_{\pi\pi\pi\pi}=(\pi_a\pi_a\,;\,\pi_a\pi_a)
\end{array}\right\}=\frac{4509\delta}{11520}=0.39140\,6\delta
$$

$$
\left.\begin{array}{l}
D^0{}_{\sigma\pi\sigma\pi}=(\sigma_a\sigma_a\,;\,\pi_a\pi_a)\\
D^0{}_{\pi\pi'\pi\pi'}=(\pi_a\pi_a\,;\,\pi_a{}'\pi_a{}')
\end{array}\right\}=\frac{4023\delta}{11520}=0.34921\,8\delta
$$

$$
\left.\begin{array}{l}
D^0{}_{\pi\sigma\sigma\pi}=(\pi_a\sigma_a\,;\,\sigma_a\pi_a)\\
D^0{}_{\pi\pi'\pi'\pi}=(\pi_a\pi_a{}'\,;\,\pi_a\pi_a{}')
\end{array}\right\}=\frac{243\delta}{11520}=0.02109\,4\delta
$$

$$
D^0{}_{++++}=(\pi_a{}^+\pi_a{}^+\,;\,\pi_a{}^+\pi_a{}^+)\;=\frac{4266\delta}{11520}=0.37031\,2\delta
$$

$$
D^0{}_{+--+}=(\pi_a{}^+\pi_a{}^-\,;\,\pi_a{}^-\pi_a{}^+)\;=\frac{486\delta}{11520}=0.04218\,8\delta
$$

---

* Any information about discoveries of errors or misprints in this paper, if they should still exist, would be gratefully acknowledged.

Table II

			2.00	2.25	2.50	2.75	3.00	3.25	3.50	3.75	4.00
S	ss	$(s_a\|s_b)$	0.81501 91	0.77311 98	0.72907 44	0.68356 75	0.63727 45	0.59083 88	0.54485 31	0.49934 40	0.45626 29
	$s\sigma$	$(s_a\|\sigma_b)$	0.46360 61	0.48819 68	0.50353 78	0.51013 88	0.50877 90	0.50042 12	0.48613 11	0.46700 81	0.44413 06
	$\sigma\sigma$	$(\sigma_a\|\sigma_b)$	−0.22555 88	−0.10910 47	−0.00513 03	0.08458 79	0.15931 86	0.21916 52	0.26435 62	0.29755 46	0.31869 21
	$\pi\pi$	$(\pi_a\|\pi_b)$	0.69472 11	0.63601 84	0.57801 52	0.52174 46	0.46799 84	0.41734 78	0.37016 96	0.32667 62	0.28694 50
J/δ	ss	$(s_b\|1/r_b\|s_a)$	0.38345 00	0.35654 58	0.32891 00	0.30116 02	0.27382 89	0.24735 39	0.22207 66	0.19824 72	0.17603 36
	$s\sigma$	$(s_b\|1/r_b\|\sigma_a)$	0.33858 87	0.33801 53	0.33075 52	0.31824 20	0.30181 81	0.28268 53	0.26188 02	0.24026 65	0.21854 05
	σs	$(\sigma_b\|1/r_b\|s_a)$	0.18231 70	0.18968 79	0.19252 92	0.19136 81	0.18683 98	0.17961 51	0.17034 93	0.15964 73	0.14804 35
	$\sigma\sigma$	$(\sigma_b\|1/r_b\|\sigma_a)$	−0.02255 59	0.02882 01	0.07011 43	0.10171 85	0.12446 77	0.13944 58	0.14784 14	0.15084 43	0.14957 77
	$\pi\pi$	$(\pi_b\|1/r_b\|\pi_a)$	0.29322 64	0.26020 43	0.22915 40	0.20044 05	0.17425 47	0.15065 40	0.12959 71	0.11097 44	0.09463 08
T/δ^2	ss	$(s_a\|-\Delta/2\|s_b)$	0.10375 71	0.09377 51	0.08351 01	0.07319 24	0.06306 36	0.05334 65	0.04422 66	0.03584 31	0.02828 75
	$s\sigma$	$(s_a\|-\Delta/2\|\sigma_b)$	0.13283 10	0.13527 75	0.13328 94	0.12766 69	0.11929 00	0.10901 95	0.09763 30	0.08579 05	0.07402 18
	$\sigma\sigma$	$(\sigma_a\|-\Delta/2\|\sigma_b)$	0.06766 76	0.11219 25	0.14279 37	0.16114 32	0.16927 60	0.16930 90	0.16325 46	0.15291 13	0.13980 94
	$\pi\pi$	$(\pi_a\|-\Delta/2\|\pi_b)$	0.23909 23	0.20239 94	0.16930 03	0.14000 87	0.11451 03	0.09263 40	0.07410 94	0.05861 06	0.04578 91
K/δ	ss	$(s_a\|1/r_b\|s_a)$	0.40231 659	0.37910 194	0.35631 564	0.33447 942	0.31391 644	0.29479 502	0.27717 082	0.26102 290	0.24628 196
	$s\sigma$	$(s_a\|1/r_b\|\sigma_a)$	0.16918 040	0.15985 938	0.14866 332	0.13668 253	0.12467 688	0.11313 857	0.10235 734	0.09247 802	0.08354 720
	$\sigma\sigma$	$(\sigma_a\|1/r_b\|\sigma_a)$	0.49266 104	0.46484 106	0.43566 615	0.40655 487	0.37848 210	0.35205 309	0.32759 026	0.30521 377	0.28490 842
	$\pi\pi$	$(\pi_a\|1/r_b\|\pi_a)$	0.35714 437	0.33623 239	0.31664 039	0.29844 169	0.28163 361	0.26616 598	0.25196 110	0.23892 747	0.22696 872
D/δ	$ssss$	$(s_as_a;s_bs_b)$	0.31781 640	0.30755 827	0.29684 265	0.28584 208	0.27471 813	0.26361 675	0.25266 486	0.24196 841	0.23161 175
	σsss	$(s_as_a;s_b\sigma_b)$	0.06599 944	0.06901 680	0.07075 528	0.07132 857	0.07088 286	0.06958 267	0.06759 786	0.06509 295	0.06221 934
	$\sigma\sigma ss$	$(s_a\sigma_a;s_b\sigma_b)$	−0.01788 425	−0.00861 133	−0.00050 739	0.00623 166	0.01172 068	0.01586 120	0.01881 562	0.02073 319	0.02177 975
	$\sigma\sigma\sigma s$	$(s_a\sigma_a;\sigma_b\sigma_b)$	0.05167 952	0.05791 926	0.06310 954	0.06707 607	0.06974 999	0.07115 598	0.07139 184	0.07060 487	0.06896 944
	$\pi s\pi s$	$(s_as_a;\pi_b\pi_b)$	0.31112 883	0.29979 068	0.28816 036	0.27644 745	0.26483 039	0.25345 416	0.24243 067	0.23184 117	0.22173 993
	$\pi\pi ss$	$(s_a\pi_a;s_b\pi_b)$	0.05582 276	0.05108 242	0.04641 958	0.04192 692	0.03767 362	0.03370 679	0.03005 406	0.02672 685	0.02372 380
	$\pi\pi\sigma s$	$(s_a\pi_a;\sigma_b\pi_b)$	0.02121 715	0.02098 328	0.02029 161	0.01925 611	0.01798 430	0.01657 106	0.01509 539	0.01361 959	0.01219 000
	$\pi\pi\sigma\sigma$	$(\sigma_a\pi_a;\sigma_b\pi_b)$	0.00052 538	0.00278 828	0.00449 410	0.00567 371	0.00638 940	0.00671 947	0.00674 629	0.00654 810	0.00619 408
	$\pi\sigma\pi\sigma$	$(\sigma_a\sigma_a;\pi_b\pi_b)$	0.32384 800	0.31529 376	0.30571 957	0.29536 264	0.28447 173	0.27328 606	0.26202 072	0.25085 823	0.23994 532
	$\sigma s\sigma s$	$(s_as_a;\sigma_b\sigma_b)$	0.33119 155	0.32309 347	0.31420 722	0.30463 135	0.29449 362	0.28394 193	0.27313 326	0.26222 288	0.25135 540
	$\pi\sigma\pi s$	$(s_a\sigma_a;\pi_b\pi_b)$	0.07315 940	0.07456 557	0.07457 815	0.07345 482	0.07144 929	0.06879 602	0.06570 088	0.06233 700	0.05884 430
	$\sigma\sigma\sigma\sigma$	$(\sigma_a\sigma_a;\sigma_b\sigma_b)$	0.34587 866	0.33869 289	0.33118 253	0.32316 876	0.31453 738	0.30525 366	0.29535 833	0.28495 218	0.27417 554
	$\pi\pi\pi\pi$	$(\pi_a\pi_a;\pi_b\pi_b)$	0.31666 930	0.30242 770	0.28836 178	0.27468 846	0.26156 118	0.24907 932	0.23729 848	0.22624 042	0.21590 194
	$\pi\pi'\pi\pi'$	$(\pi_a\pi_a;\pi_b'\pi_b')$	0.29286 918	0.28165 057	0.27039 974	0.25929 124	0.24845 825	0.23799 709	0.22797 281	0.21842 486	0.20937 253
	$\pi\pi\pi'\pi'$	$(\pi_a\pi_a';\pi_b\pi_b')$	0.01190 006	0.01038 857	0.00898 102	0.00769 861	0.00655 146	0.00554 111	0.00466 283	0.00390 778	0.00326 471
	$++++$	$(\pi_a^+\pi_a^+;\pi_b^+\pi_b^+)$	0.30476 924	0.29203 914	0.27938 076	0.26698 985	0.25500 971	0.24353 820	0.23263 564	0.22233 264	0.21263 723
	$+--+$	$(\pi_a^+\pi_a^-;\pi_b^-\pi_b^+)$	0.02380 013	0.02077 714	0.01796 203	0.01539 721	0.01310 293	0.01108 222	0.00932 567	0.00781 557	0.00652 941

Table II (Continued)

			4.25	4.50	4.75	5.00	5.25	5.50	6.00	6.50	7.00
S	ss	$(s_a\|s_b)$	0.41448 12	0.37478 98	0.33740 18	0.30245 89	0.27003 81	0.24016 03	0.18788 94	0.14502 13	0.11056 06
	$s\sigma$	$(s_a\|\sigma_b)$	0.41851 36	0.39108 04	0.36264 51	0.33390 50	0.30543 90	0.27771 30	0.22582 89	0.18007 61	0.14114 80
	$\sigma\sigma$	$(\sigma_a\|\sigma_b)$	0.32983 44	0.33257 56	0.32846 03	0.31892 95	0.30528 67	0.28867 93	0.25035 40	0.20998 66	0.17143 38
	$\pi\pi$	$(\pi_a\|\pi_b)$	0.25094 65	0.21856 95	0.18964 34	0.16395 67	0.14127 30	0.12134 31	0.08873 93	0.06420 94	0.04601 96
J/δ	ss	$(s_b\|1/r_b\|s_a)$	0.15553 22	0.13677 95	0.11976 44	0.10443 82	0.09072 47	0.07852 84	0.05825 07	0.04269 14	0.03095 33
	$s\sigma$	$(s_b\|1/r_b\|\sigma_a)$	0.19724 35	0.17677 99	0.15743 54	0.13939 72	0.12277 21	0.10760 30	0.08157 32	0.06088 74	0.04483 81
	σs	$(\sigma_b\|1/r_b\|s_a)$	0.13599 23	0.12386 62	0.11195 96	0.10049 57	0.08963 52	0.07948 56	0.06153 77	0.04678 22	0.03501 06
	$\sigma\sigma$	$(\sigma_b\|1/r_b\|\sigma_a)$	0.14505 69	0.13816 81	0.12966 28	0.12016 01	0.11015 69	0.10004 08	0.08055 94	0.06317 58	0.04848 17
	$\pi\pi$	$(\pi_b\|1/r_b\|\pi_a)$	0.08038 49	0.06804 26	0.05740 76	0.04828 86	0.04050 43	0.03388 61	0.02354 81	0.01622 46	0.01109 46
T/δ^2	ss	$(s_a\|-\Delta/2\|s_b)$	0.02160 62	0.01580 72	0.01086 68	0.00673 79	0.00335 69	0.00064 99	−0.00305 71	−0.00500 21	−0.00573 47
	$s\sigma$	$(s_a\|-\Delta/2\|\sigma_b)$	0.06272 78	0.05219 22	0.04259 65	0.03403 89	0.02655 09	0.02011 47	0.01016 09	0.00352 63	−0.00055 28
	$\sigma\sigma$	$(\sigma_a\|-\Delta/2\|\sigma_b)$	0.12519 65	0.11004 85	0.09509 54	0.08085 54	0.06767 04	0.05574 19	0.03594 19	0.02135 82	0.01124 65
	$\pi\pi$	$(\pi_a\|-\Delta/2\|\pi_b)$	0.03529 65	0.02680 05	0.01999 35	0.01459 89	0.01037 20	0.00710 08	0.00272 66	0.00034 45	−0.00082 07
K/δ	ss	$(s_a\|1/r_b\|s_a)$	0.23285 125	0.22062 132	0.20947 979	0.19931 749	0.19003 208	0.18152 982	0.16654 583	0.15379 589	0.14283 637
	$s\sigma$	$(s_a\|1/r_b\|\sigma_a)$	0.07554 863	0.06842 888	0.06211 509	0.05652 667	0.05158 271	0.04720 632	0.03988 127	0.03407 455	0.02942 027
	$\sigma\sigma$	$(\sigma_a\|1/r_b\|\sigma_a)$	0.26657 500	0.25006 760	0.23521 926	0.22185 876	0.20982 089	0.19895 220	0.18018 170	0.16461 535	0.15153 978
	$\pi\pi$	$(\pi_a\|1/r_b\|\pi_a)$	0.21598 938	0.20589 818	0.19661 005	0.18804 685	0.18013 768	0.17281 864	0.15972 790	0.14838 616	0.13848 467
D/δ	$ssss$	$(s_as_a;s_bs_b)$	0.22165 840	0.21215 256	0.20312 143	0.19457 776	0.18652 246	0.17894 725	0.16517 126	0.15307 930	0.14246 965
	σsss	$(s_as_a;s_b\sigma_b)$	0.05911 033	0.05587 866	0.05261 601	0.04939 405	0.04626 632	0.04327 069	0.03776 438	0.03296 106	0.02884 603
	$\sigma\sigma ss$	$(s_a\sigma_a;s_b\sigma_b)$	0.02212 212	0.02191 727	0.02130 550	0.02040 714	0.01932 160	0.01812 830	0.01564 792	0.01328 383	0.01118 342
	$\sigma\sigma\sigma s$	$(s_a\sigma_a;\sigma_b\sigma_b)$	0.06666 796	0.06387 646	0.06075 484	0.05744 126	0.05404 988	0.05067 103	0.04420 464	0.03837 437	0.03330 030
	$\pi s\pi s$	$(s_as_a;\pi_b\pi_b)$	0.21215 847	0.20310 992	0.19459 312	0.18659 625	0.17910 001	0.17208 011	0.15935 902	0.14820 503	0.13839 708
	$\pi\pi ss$	$(s_a\pi_a;s_b\pi_b)$	0.02103 400	0.01863 993	0.01651 994	0.01465 015	0.01300 603	0.01156 344	0.00919 244	0.00737 395	0.00597 519
	$\pi\pi\sigma s$	$(s_a\pi_a;\sigma_b\pi_b)$	0.01083 877	0.00958 616	0.00844 291	0.00741 253	0.00649 331	0.00567 998	0.00433 987	0.00332 235	0.00255 738
	$\pi\pi\sigma\sigma$	$(\sigma_a\pi_a;\sigma_b\pi_b)$	0.00574 202	0.00523 783	0.00471 629	0.00420 240	0.00371 304	0.00325 868	0.00247 367	0.00185 558	0.00138 527
	$\pi\sigma\pi\sigma$	$(\sigma_a\sigma_a;\pi_b\pi_b)$	0.22939 338	0.21928 137	0.20966 019	0.20055 751	0.19198 259	0.18393 074	0.16933 010	0.15656 897	0.14541 881
	$\sigma s\sigma s$	$(s_as_a;\sigma_b\sigma_b)$	0.24065 824	0.23023 783	0.22017 807	0.21054 077	0.20136 737	0.19268 152	0.17679 573	0.16282 784	0.15061 479
	$\pi\sigma\pi s$	$(s_a\sigma_a;\pi_b\pi_b)$	0.05533 152	0.05187 975	0.04854 659	0.04537 045	0.04237 454	0.03957 051	0.03454 424	0.03025 440	0.02661 890
	$\sigma\sigma\sigma\sigma$	$(\sigma_a\sigma_a;\sigma_b\sigma_b)$	0.26318 797	0.25215 076	0.24121 383	0.23050 729	0.22013 694	0.21018 309	0.19172 699	0.17534 556	0.16100 675
	$\pi\pi\pi\pi$	$(\pi_a\pi_a;\pi_b\pi_b)$	0.20626 226	0.19728 911	0.18894 333	0.18118 229	0.17396 244	0.16724 095	0.15513 146	0.14455 724	0.13526 730
	$\pi\pi'\pi\pi'$	$(\pi_a\pi_a;\pi_b'\pi_b')$	0.20081 977	0.19275 928	0.18517 583	0.17804 896	0.17135 501	0.16506 864	0.15361 550	0.14348 886	0.13450 512
	$\pi\pi\pi'\pi'$	$(\pi_a\pi_a';\pi_b\pi_b')$	0.00272 124	0.00226 492	0.00188 375	0.00156 666	0.00130 372	0.00108 616	0.00075 798	0.00053 419	0.00038 109
	$++++$	$(\pi_a^+\pi_a^+;\pi_b^+\pi_b^+)$	0.20354 102	0.19502 420	0.18705 958	0.17961 563	0.17265 872	0.16615 479	0.15437 348	0.14402 305	0.13488 621
	$+--+$	$(\pi_a^+\pi_a^-;\pi_b^-\pi_b^+)$	0.00544 249	0.00452 983	0.00376 749	0.00313 333	0.00260 744	0.00217 231	0.00151 596	0.00106 838	0.00076 218

			1.00	1.25	1.50	1.75
K/δ	(ss)	$(s_a\|1/r_b\|s_a)$	0.48121 475	0.46584 565	0.44677 378	0.42520 493
	$(s\sigma)$	$(s_a\|1/r_b\|\sigma_a)$	0.15413 395	0.16963 848	0.17599 784	0.17516 501
	$(\sigma\sigma)$	$(\sigma_a\|1/r_b\|\sigma_a)$	0.54895 028	0.54749 101	0.53630 363	0.51723 873
	$(\pi\pi)$	$(\pi_a\|1/r_b\|\pi_a)$	0.44734 698	0.42502 297	0.40200 886	0.37918 803

Table III.

			2.00	2.25	2.50	2.75	3.00
C/δ	$ssss$	$(s_a s_b; s_b s_a)$	0.23816 0	0.21360 3	0.18922 6	0.16559 4	0.14318 2
	σsss	$(\sigma_a s_b; s_b s_a)$	0.15032 7	0.14946 7	0.14454 9	0.13637 7	0.12582 5
	$\sigma\sigma ss$	$(\sigma_a s_b; \sigma_b s_a)$	0.06511 2	0.08110 3	0.09221 2	0.09840 6	0.10008 5
	$\sigma s\sigma s$	$(\sigma_a \sigma_b; s_b s_a)$	−0.03224 9	0.00454 06	0.03293 1	0.05313 9	0.06595 0
	$\sigma ss\sigma$	$(\sigma_a s_b; s_b \sigma_a)$	0.13308 7	0.13661 7	0.13686 8	0.13383 7	0.12784 6
	$\sigma\sigma\sigma s$	$(\sigma_a \sigma_b; \sigma_b s_a)$	−0.00814 18	0.01561 0	0.03721 4	0.05498 3	0.06802 7
	$\sigma\sigma\sigma\sigma$	$(\sigma_a \sigma_b; \sigma_b \sigma_a)$	0.04399 2	0.03937 2	0.04327 1	0.05172 4	0.06140 9
	$\pi\pi ss$	$(\pi_a s_b; \pi_b s_a)$	0.04454 0	0.03828 3	0.03241 6	0.02706 5	0.02229 8
	$\pi s\pi s$	$(\pi_a \pi_b; s_b s_a)$	0.19737 2	0.16977 5	0.14401 5	0.12056 1	0.09967 1
	$\pi ss\pi$	$(\pi_a s_b; s_b \pi_a)$	0.04610 9	0.03986 8	0.03395 4	0.02850 6	0.02361 1
	$\pi\pi\sigma\sigma$	$(\pi_a \sigma_b; \pi_b \sigma_a)$	0.01557 9	0.01746 4	0.01814 4	0.01784 6	0.01682 5
	$\pi\sigma\pi\sigma$	$(\pi_a \pi_b; \sigma_b \sigma_a)$	−0.02402 3	0.00462 08	0.02478 7	0.03753 0	0.04422 9
	$\pi\sigma\sigma\pi$	$(\pi_a \sigma_b; \sigma_b \pi_a)$	0.03917 9	0.03779 8	0.03540 7	0.03229 7	0.02876 5
	$\pi\pi\sigma s$	$(\pi_a \sigma_b; \pi_b s_a)$	0.03158 5	0.02952 3	0.02683 1	0.02379 4	0.02065 0
	$\pi\sigma\pi s$	$(\pi_a \pi_b; \sigma_b s_a)$	0.12432 4	0.11821 5	0.10920 4	0.09835 5	0.08661 8
	$\pi\sigma s\pi$	$(\pi_a s_b; \sigma_b \pi_a)$	0.03752 1	0.03507 6	0.03188 3	0.02827 9	0.02454 7
	$\pi\pi\pi\pi$	$(\pi_a \pi_b; \pi_b \pi_a)$	0.17604 6	0.14537 1	0.11822 7	0.09481 7	0.07507 1
	$\pi\pi\pi'\pi'$	$(\pi_a \pi_b'; \pi_b \pi_a')$	0.00942 94	0.00776 94	0.00630 31	0.00504 13	0.00397 98
	$\pi\pi'\pi\pi'$	$(\pi_a \pi_b; \pi_b' \pi_a')$	0.15718 7	0.12983 3	0.10562 1	0.08473 4	0.06711 2
	$++++$	$(\pi_a^+ \pi_b^+; \pi_b^+ \pi_a^+)$	0.16661 6	0.13760 2	0.11192 4	0.08977 56	0.07109 16
	$+--+$	$(\pi_a^+ \pi_b^-; \pi_b^- \pi_a^+)$	0.01885 9	0.01553 9	0.01260 6	0.01008 3	0.00795 97
L/δ	$sss\bar{s}$	$(s_a s_a; s_a s_b)$	0.28413 40	0.26671 51	0.24860 96	0.23014 07	0.21161 86
	$sss\bar{\sigma}$	$(s_a s_a; s_a \sigma_b)$	0.20466 95	0.21151 17	0.21379 32	0.21200 90	0.20676 13
	$s\sigma s\bar{s}$	$(s_a s_a; \sigma_a s_b)$	0.14972 26	0.15638 37	0.15969 53	0.15991 57	0.15741 10
	$ss\sigma\bar{s}$	$(s_a \sigma_a; s_a s_b)$	0.03296 44	0.03432 27	0.03495 24	0.03489 24	0.03422 06
	$s\sigma\sigma\bar{s}$	$(s_a \sigma_a; \sigma_a s_b)$	0.07065 66	0.06847 17	0.06591 56	0.06297 46	0.05967 25
	$ss\sigma\bar{\sigma}$	$(s_a \sigma_a; s_a \sigma_b)$	−0.00950 15	0.00045 87	0.00891 20	0.01572 95	0.02091 38
	$s\sigma s\bar{\sigma}$	$(s_a s_a; \sigma_a \sigma_b)$	−0.04573 11	−0.00324 87	0.03283 02	0.06214 06	0.08478 61
	$\sigma s\sigma\bar{s}$	$(\sigma_a \sigma_a; s_a s_b)$	0.28774 20	0.27104 57	0.25356 97	0.23560 00	0.21742 67
	$s\sigma\sigma\bar{\sigma}$	$(s_a \sigma_a; \sigma_a \sigma_b)$	0.02734 14	0.03437 69	0.04039 82	0.04511 03	0.04838 50
	$\sigma s\sigma\bar{\sigma}$	$(\sigma_a \sigma_a; s_a \sigma_b)$	0.19706 09	0.20621 57	0.21083 64	0.21123 90	0.20790 71
	$\sigma\sigma\sigma\bar{s}$	$(\sigma_a \sigma_a; \sigma_a s_b)$	0.16154 56	0.16899 73	0.17286 87	0.17339 89	0.17095 15
	$\sigma\sigma\sigma\bar{\sigma}$	$(\sigma_a \sigma_a; \sigma_a \sigma_b)$	−0.05347 86	−0.00664 86	0.03342 54	0.06620 52	0.09169 45
	$s\pi s\bar{\pi}$	$(s_a s_a; \pi_a \pi_b)$	0.23465 02	0.21124 31	0.18858 40	0.16707 17	0.14698 21
	$\pi s\pi\bar{s}$	$(\pi_a \pi_a; s_a s_b)$	0.28232 99	0.26454 97	0.24612 96	0.22741 10	0.20871 46
	$s\pi\pi\bar{s}$	$(s_a \pi_a; \pi_a s_b)$	0.05811 54	0.05339 30	0.04862 51	0.04391 69	0.03935 67
	$\pi ss\bar{\pi}$	$(s_a \pi_a; s_a \pi_b)$	0.05226 56	0.04694 78	0.04177 11	0.03684 11	0.03223 32
	$s\pi\sigma\bar{\pi}$	$(s_a \sigma_a; \pi_a \pi_b)$	0.02981 30	0.02901 33	0.02761 07	0.02578 55	0.02369 69
	$\pi\sigma\pi\bar{s}$	$(\pi_a \pi_a; \sigma_a s_b)$	0.14381 11	0.15007 69	0.15310 86	0.15317 40	0.15064 07
	$\pi s\pi\bar{\sigma}$	$(\pi_a \pi_a; s_a \sigma_b)$	0.20847 38	0.21415 98	0.21527 16	0.21239 35	0.20618 84
	$s\pi\pi\bar{\sigma}$	$(s_a \pi_a; \pi_a \sigma_b)$	0.05367 59	0.05319 75	0.05158 42	0.04910 14	0.04599 92
	$\pi\sigma s\bar{\pi}$	$(s_a \pi_a; \sigma_a \pi_b)$	0.02981 30	0.02901 33	0.02761 07	0.02578 54	0.02369 69
	$\pi\pi\sigma\bar{s}$	$(\sigma_a \pi_a; \pi_a s_b)$	0.00848 16	0.00865 83	0.00862 74	0.00841 86	0.00806 61
	$\sigma s\pi\bar{\pi}$	$(\sigma_a \pi_a; s_a \pi_b)$	0.01314 45	0.01276 12	0.01210 32	0.01125 44	0.01028 98
	$\sigma\pi\pi\bar{\sigma}$	$(\sigma_a \pi_a; \pi_a \sigma_b)$	−0.00014 69	0.00219 39	0.00402 92	0.00537 38	0.00627 20
	$\pi\sigma\sigma\bar{\pi}$	$(\sigma_a \pi_a; \sigma_a \pi_b)$	0.01986 73	0.01870 38	0.01735 34	0.01625 61	0.01435 44
	$\pi\sigma\pi\bar{\sigma}$	$(\pi_a \pi_a; \sigma_a \sigma_b)$	−0.04185 73	−0.00154 87	0.03253 26	0.06010 83	0.08133 18
	$\sigma\pi\sigma\bar{\pi}$	$(\sigma_a \sigma_a; \pi_a \pi_b)$	0.23152 79	0.20932 15	0.18762 18	0.16684 26	0.14728 66
	$\pi\pi\pi\bar{\pi}$	$(\pi_a \pi_a; \pi_a \pi_b)$	0.24848 68	0.22299 70	0.19846 36	0.17529 93	0.15377 86
	$\pi\pi\pi'\bar{\pi}'$	$(\pi_a \pi_a'; \pi_a \pi_b')$	0.01227 54	0.01079 31	0.00939 84	0.00811 30	0.00694 88
	$\pi\pi'\pi\bar{\pi}'$	$(\pi_a \pi_a; \pi_a' \pi_b')$	0.22393 60	0.20141 09	0.17966 68	0.15907 33	0.13988 10
	$++++$	$(\pi_a^+ \pi_a^+; \pi_a^+ \pi_b^+)$	0.23621 14	0.21220 40	0.18906 52	0.16718 63	0.14682 98
	$+--+$	$(\pi_a^+ \pi_a^-; \pi_a^- \pi_b^+)$	0.02455 08	0.02158 62	0.01879 68	0.01622 61	0.01389 76

§ 4. **Errata**

Part I.

page	line	
8	1	$J_{\sigma s} = +\frac{1}{12\sqrt{3}}\delta^5 R^4\{A_0(\delta R)+A_2(\delta R)\}$,
15	8	S_{ah}, J_{ah} and J_{ha} can ......
19	9	$+E_i(-\alpha) = -\int_\alpha^\infty \frac{e^{-x}}{x}dx = C+\log\alpha-\frac{\alpha}{1\cdot 1!}+\frac{\alpha^2}{2\cdot 2!}-\frac{\alpha^3}{3\cdot 3!}+\cdots$,

Table III (Continued)

			3.25	3.50	3.75	4.00	4.25
C/δ	$ssss$	$(s_as_b; s_bs_a)$	0.12236 0	0.10338 2	0.08639 2	0.07143 4	0.05847 0
	σsss	$(\sigma_as_b; s_bs_a)$	0.11375 7	0.10095 6	0.08808 2	0.07565 3	0.06404 4
	$\sigma\sigma ss$	$(\sigma_as_b; \sigma_bs_a)$	0.09794 1	0.09281 6	0.08558 2	0.07705 6	0.06793 8
	$\sigma s\sigma s$	$(\sigma_a\sigma_b; s_bs_a)$	0.07249 0	0.07403 3	0.07185 1	0.06710 4	0.06078 2
	$\sigma ss\sigma$	$(\sigma_as_b; s_b\sigma_a)$	0.11944 3	0.10929 6	0.09809 1	0.08646 6	0.07495 9
	$\sigma\sigma\sigma s$	$(\sigma_a\sigma_b; \sigma_bs_a)$	0.07616 0	0.07972 7	0.07940 9	0.07605 9	0.07055 5
	$\sigma\sigma\sigma\sigma$	$(\sigma_a\sigma_b; \sigma_b\sigma_a)$	0.06994 9	0.07593 1	0.07877 3	0.07850 5	0.07555 0
	$\pi\pi ss$	$(\pi_as_b; \pi_bs_a)$	0.01814 4	0.01459 2	0.01160 8	0.00913 99	0.00712 76
	$\pi s\pi s$	$(\pi_a\pi_b; s_bs_a)$	0.08143 2	0.06579 1	0.05259 7	0.04163 3	0.03264 7
	$\pi ss\pi$	$(\pi_as_b; s_b\pi_a)$	0.01930 9	0.01560 3	0.01246 8	0.00985 84	0.00771 86
	$\pi\pi\sigma\sigma$	$(\pi_a\sigma_b; \pi_b\sigma_a)$	0.01533 0	0.01357 7	0.01173 7	0.00993 60	0.00825 81
	$\pi\sigma\pi\sigma$	$(\pi_a\pi_b; \sigma_b\sigma_a)$	0.04632 9	0.04517 6	0.04192 0	0.03747 6	0.03253 2
	$\pi\sigma\sigma\pi$	$(\pi_a\sigma_b; \sigma_b\pi_a)$	0.02507 4	0.02143 6	0.01800 7	0.01488 8	0.01213 1
	$\pi\pi\sigma s$	$(\pi_a\sigma_b; \pi_bs_a)$	0.01757 9	0.01470 8	0.01211 5	0.00983 84	0.00788 69
	$\pi\sigma\pi s$	$(\pi_a\pi_b; \sigma_bs_a)$	0.07476 7	0.06338 4	0.05286 4	0.04344 1	0.03521 7
	$\pi\sigma s\pi$	$(\pi_as_b; \sigma_b\pi_a)$	0.02090 0	0.01749 1	0.01441 0	0.01170 5	0.00938 58
	$\pi\pi\pi\pi$	$(\pi_a\pi_b; \pi_b\pi_a)$	0.05873 9	0.04546 1	0.03483 2	0.02644 0	0.01989 7
	$\pi\pi\pi'\pi'$	$(\pi_a\pi_b'; \pi_b\pi_a')$	0.00310 44	0.00239 48	0.00182 87	0.00138 33	0.00103 73
	$\pi\pi'\pi\pi'$	$(\pi_a\pi_b; \pi_b'\pi_a')$	0.05253 0	0.04067 2	0.03117 5	0.02367 3	0.01782 2
	$++++$	$(\pi_a^+\pi_b^+; \pi_b^+\pi_a^+)$	0.05563 5	0.04306 7	0.03300 3	0.02505 7	0.01885 9
	$+--+$	$(\pi_a^+\pi_b^-; \pi_b^-\pi_a^+)$	0.00620 87	0.00478 97	0.00365 75	0.00276 67	0.00207 46
L/δ	$sss\bar{s}$	$(s_as_a; s_as_b)$	0.19332 89	0.17552 24	0.15840 89	0.14215 46	0.12688 25
	$sss\bar{\sigma}$	$(s_as_a; s_a\sigma_b)$	0.19870 26	0.18848 49	0.17672 44	0.16397 71	0.15072 46
	$s\sigma s\bar{s}$	$(s_as_a; \sigma_as_b)$	0.15261 15	0.14597 31	0.13794 57	0.12895 07	0.11936 52
	$ss\sigma\bar{s}$	$(s_a\sigma_a; s_as_b)$	0.03303 32	0.03143 53	0.02953 23	0.02742 38	0.02519 92
	$s\sigma\sigma\bar{s}$	$(s_a\sigma_a; \sigma_as_b)$	0.05606 34	0.05222 25	0.04823 55	0.04419 00	0.04016 81
	$ss\sigma\bar{\sigma}$	$(s_a\sigma_a; s_a\sigma_b)$	0.02456 56	0.02684 94	0.02796 47	0.02812 28	0.02752 97
	$s\sigma s\bar{\sigma}$	$(s_as_a; \sigma_a\sigma_b)$	0.10120 58	0.11205 43	0.11810 11	0.12015 33	0.11899 92
	$\sigma s\sigma\bar{s}$	$(\sigma_a\sigma_a; s_as_b)$	0.19933 00	0.18156 83	0.16436 78	0.14791 63	0.13236 06
	$s\sigma\sigma\bar{\sigma}$	$(s_a\sigma_a; \sigma_a\sigma_b)$	0.05023 03	0.05075 40	0.05012 76	0.04855 54	0.04625 00
	$\sigma s\sigma\bar{\sigma}$	$(\sigma_a\sigma_a; s_a\sigma_b)$	0.20142 71	0.19243 01	0.18154 32	0.16935 45	0.15639 00
	$\sigma\sigma\sigma\bar{s}$	$(\sigma_a\sigma_a; \sigma_as_b)$	0.16597 04	0.15893 81	0.15033 97	0.14063 59	0.13024 40
	$\sigma\sigma\sigma\bar{\sigma}$	$(\sigma_a\sigma_a; \sigma_a\sigma_b)$	0.11029 89	0.12269 18	0.12969 88	0.13220 56	0.13108 91
	$s\pi s\bar{\pi}$	$(s_as_a; \pi_a\pi_b)$	0.12848 42	0.11165 94	0.09651 91	0.08302 25	0.07109 11
	$\pi s\pi\bar{s}$	$(\pi_a\pi_a; s_as_b)$	0.19032 84	0.17249 94	0.15542 94	0.13927 38	0.12414 34
	$s\pi\pi\bar{s}$	$(s_a\pi_a; \pi_as_b)$	0.03501 38	0.03093 88	0.02716 55	0.02371 21	0.02058 46
	$\pi ss\bar{\pi}$	$(s_a\pi_a; s_a\pi_b)$	0.02799 51	0.02415 16	0.02070 85	0.01765 71	0.01497 83
	$s\pi\sigma\bar{\pi}$	$(s_a\sigma_a; \pi_a\pi_b)$	0.02147 80	0.01923 40	0.01704 39	0.01496 39	0.01303 03
	$\pi\sigma\pi\bar{s}$	$(\pi_a\pi_a; \sigma_as_b)$	0.14593 20	0.13949 05	0.13174 88	0.12310 81	0.11392 58
	$\pi s\pi\bar{\sigma}$	$(\pi_a\pi_a; s_a\sigma_b)$	0.19734 04	0.18651 23	0.17431 50	0.16128 83	0.14789 19
	$s\pi\pi\bar{\sigma}$	$(s_a\pi_a; \pi_a\sigma_b)$	0.04250 03	0.03879 35	0.03503 22	0.03133 53	0.02779 07
	$\pi\sigma s\bar{\pi}$	$(s_a\pi_a; \sigma_a\pi_b)$	0.02147 80	0.01923 40	0.01704 39	0.01496 39	0.01303 03
	$\pi\pi\sigma\bar{s}$	$(\sigma_a\pi_a; \pi_as_b)$	0.00760 54	0.00707 01	0.00649 01	0.00589 12	0.00529 39
	$\sigma s\pi\bar{\pi}$	$(\sigma_a\pi_a; s_a\pi_b)$	0.00927 16	0.00824 88	0.00725 79	0.00632 40	0.00546 30
	$\sigma\pi\pi\bar{\sigma}$	$(\sigma_a\pi_a; \pi_a\sigma_b)$	0.00678 52	0.00698 11	0.00692 76	0.00668 75	0.00631 57
	$\pi\sigma\sigma\bar{\pi}$	$(\sigma_a\pi_a; \sigma_a\pi_b)$	0.01282 52	0.01133 99	0.00993 24	0.00862 57	0.00743 35
	$\pi\sigma\pi\bar{\sigma}$	$(\pi_a\pi_a; \sigma_a\sigma_b)$	0.09665 93	0.10673 56	0.11230 22	0.11412 72	0.11295 43
	$\sigma\pi\sigma\bar{\pi}$	$(\sigma_a\sigma_a; \pi_a\pi_b)$	0.12915 45	0.11256 02	0.09754 53	0.08409 57	0.07215 52
	$\pi\pi\pi\bar{\pi}$	$(\pi_a\pi_a; \pi_a\pi_b)$	0.13405 89	0.11620 33	0.10020 26	0.08599 39	0.07347 77
	$\pi\pi\pi'\bar{\pi}'$	$(\pi_a\pi_a'; \pi_a\pi_b')$	0.00590 98	0.00499 44	0.00419 66	0.00350 80	0.00291 87
	$\pi\pi'\pi\bar{\pi}'$	$(\pi_a\pi_a; \pi_a'\pi_b')$	0.12223 92	0.10621 46	0.09180 95	0.07897 79	0.06764 04
	$++++$	$(\pi_a^+\pi_a^+; \pi_a^+\pi_b^+)$	0.12814 90	0.11120 90	0.09600 60	0.08248 59	0.07055 90
	$+--+$	$(\pi_a^+\pi_a^-; \pi_a^-\pi_b^+)$	0.01181 97	0.00998 87	0.00839 32	0.00701 60	0.00583 73

page	line	
21	34	cooperation
22	0	M. KOTANI, A. AMEMIYA, T. SIMOSE.
Part II.		
1	11	$L_{\alpha\beta\gamma h}=\iint a_\alpha(1)a_\beta(2)\frac{1}{r_{12}}a_\gamma(1)h(2)d\tau_1d\tau_2$
16	9	$S_{s\sigma}=\frac{1}{12\sqrt{3}}\delta^5R^5\left\{-\frac{1}{5}A_1(\delta R)+A_3(\delta R)\right\}$

Table III (Continued)

			4.50	4.75	5.00	5.25	5.50
C/δ	$ssss$	$(s_a s_b ; s_b s_a)$	0.04739 6	0.03806 5	0.03030 1	0.02391 9	0.01873 0
	σsss	$(\sigma_a s_b ; s_b s_a)$	0.05349 3	0.04412 7	0.03598 2	0.02902 4	0.02317 7
	$\sigma\sigma ss$	$(\sigma_a s_b ; \sigma_b s_a)$	0.05879 0	0.05002 5	0.04192 5	0.03465 2	0.02828 1
	$\sigma s\sigma s$	$(\sigma_a \sigma_b ; s_b s_a)$	0.05368 2	0.04640 4	0.03937 3	0.03286 5	0.02703 6
	$\sigma ss\sigma$	$(\sigma_a s_b ; s_b \sigma_a)$	0.06398 8	0.05384 6	0.04471 5	0.03667 8	0.02974 2
	$\sigma\sigma\sigma s$	$(\sigma_a \sigma_b ; \sigma_b s_a)$	0.06370 8	0.05620 7	0.04859 7	0.04127 1	0.03449 4
	$\sigma\sigma\sigma\sigma$	$(\sigma_a \sigma_b ; \sigma_b \sigma_a)$	0.07052 9	0.06411 6	0.05694 1	0.04953 5	0.04230 5
	$\pi\pi ss$	$(\pi_a s_b ; \pi_b s_a)$	0.00550 84	0.00422 11	0.00320 90	0.00242 14	0.00181 43
	$\pi s\pi s$	$(\pi_a \pi_b ; s_b s_a)$	0.02537 4	0.01955 8	0.01495 6	0.01135 3	0.00855 67
	$\pi ss\pi$	$(\pi_a s_b ; s_b \pi_a)$	0.00598 76	0.00460 46	0.00351 22	0.00265 86	0.00199 79
	$\pi\pi\sigma\sigma$	$(\pi_a \sigma_b ; \pi_b \sigma_a)$	0.00675 26	0.00544 17	0.00432 79	0.00340 13	0.00264 42
	$\pi\sigma\pi\sigma$	$(\pi_a \pi_b ; \sigma_b \sigma_a)$	0.02756 5	0.02288 5	0.01867 0	0.01500 0	0.01188 8
	$\pi\sigma\sigma\pi$	$(\pi_a \sigma_b ; \sigma_b \pi_a)$	0.00975 44	0.00774 85	0.00608 67	0.00473 22	0.00364 41
	$\pi\pi\sigma s$	$(\pi_a \sigma_b ; \pi_b s_a)$	0.00624 78	0.00489 57	0.00379 77	0.00291 86	0.00222 37
	$\pi\sigma\pi s$	$(\pi_a \pi_b ; \sigma_b s_a)$	0.02819 8	0.02232 2	0.01748 5	0.01356 3	0.01042 6
	$\pi\sigma s\pi$	$(\pi_a s_b ; \sigma_b \pi_a)$	0.00743 71	0.00582 90	0.00452 29	0.00347 68	0.00264 97
	$\pi\pi\pi\pi$	$(\pi_a \pi_b ; \pi_b \pi_a)$	0.01485 3	0.01100 4	0.00809 63	0.00591 78	0.00429 89
	$\pi\pi\pi'\pi'$	$(\pi_a \pi_b' ; \pi_b \pi_a')$	0.00077 15	0.00056 955	0.00041 749	0.00030 402	0.00022 004
	$\pi\pi'\pi\pi'$	$(\pi_a \pi_b ; \pi_b' \pi_a')$	0.01331 0	0.00986 53	0.00726 13	0.00530 97	0.00385 89
	$++++$	$(\pi_a^+ \pi_b^+ ; \pi_b^+ \pi_a^+)$	0.01408 1	0.01043 5	0.00767 88	0.00561 37	0.00407 89
	$+--+$	$(\pi_a^+ \pi_b^- ; \pi_b^- \pi_a^+)$	0.00154 31	0.00113 91	0.00083 499	0.00060 805	0.00044 007
L/δ	$sss\bar{s}$	$(s_a s_a ; s_a s_b)$	0.11267 43	0.09957 53	0.08759 86	0.07673 16	0.06694 03
	$sss\bar{\sigma}$	$(s_a s_a ; s_a \sigma_b)$	0.13736 87	0.12423 18	0.11156 20	0.09954 05	0.08829 06
	$s\sigma s\bar{s}$	$(s_a s_a ; \sigma_a s_b)$	0.10951 39	0.09966 64	0.09003 75	0.08079 10	0.07204 61
	$ss\sigma\bar{s}$	$(s_a \sigma_a ; s_a s_b)$	0.02293 48	0.02069 35	0.01852 41	0.01646 24	0.01453 13
	$s\sigma\sigma\bar{s}$	$(s_a \sigma_a ; \sigma_a s_b)$	0.03624 23	0.03247 22	0.02890 38	0.02556 99	0.02249 10
	$ss\sigma\bar{\sigma}$	$(s_a \sigma_a ; s_a \sigma_b)$	0.02637 51	0.02482 60	0.02302 35	0.02108 32	0.01909 61
	$s\sigma s\bar{\sigma}$	$(s_a s_a ; \sigma_a \sigma_b)$	0.11537 06	0.10992 02	0.10321 15	0.09571 53	0.08781 53
	$\sigma s\sigma\bar{s}$	$(\sigma_a \sigma_a ; s_a s_b)$	0.11780 61	0.10431 99	0.09193 41	0.08065 26	0.07045 31
	$s\sigma\sigma\bar{\sigma}$	$(s_a \sigma_a ; \sigma_a \sigma_b)$	0.04341 55	0.04023 60	0.03686 97	0.03344 74	0.03007 14
	$\sigma s\sigma\bar{\sigma}$	$(\sigma_a \sigma_a ; s_a \sigma_b)$	0.14310 01	0.12985 58	0.11695 00	0.10460 28	0.09297 10
	$\sigma\sigma\sigma\bar{s}$	$(\sigma_b \sigma_a ; \sigma_a s_b)$	0.11952 62	0.10878 53	0.09826 38	0.08814 85	0.07857 45
	$\sigma\sigma\sigma\bar{\sigma}$	$(\sigma_a \sigma_a ; \sigma_a \sigma_b)$	0.12717 03	0.12118 60	0.11377 40	0.10546 80	0.09670 36
	$s\pi s\bar{\pi}$	$(s_a s_a ; \pi_a \pi_b)$	0.06062 14	0.05149 55	0.04358 81	0.03677 39	0.03093 03
	$\pi s\pi\bar{s}$	$(\pi_a \pi_a ; s_a s_b)$	0.11010 85	0.09720 30	0.08543 09	0.07477 12	0.06518 39
	$s\pi\pi\bar{s}$	$(s_a \pi_a ; \pi_a s_b)$	0.01777 88	0.01528 28	0.01307 95	0.01114 80	0.00946 54
	$\pi ss\bar{\pi}$	$(s_a \pi_a ; s_a \pi_b)$	0.01264 67	0.01063 23	0.00890 36	0.00742 91	0.00617 83
	$s\pi\sigma\bar{\pi}$	$(s_a \sigma_a ; \pi_a \pi_b)$	0.01126 39	0.00967 37	0.00825 95	0.00701 48	0.00592 94
	$\pi\sigma\pi\bar{s}$	$(\pi_a \pi_a ; \sigma_a s_b)$	0.10450 78	0.09510 69	0.08592 41	0.07711 23	0.06878 18
	$\pi s\pi\bar{\sigma}$	$(\pi_a \pi_a ; s_a \sigma_b)$	0.13450 30	0.12141 98	0.10886 81	0.09700 93	0.08594 52
	$s\pi\pi\sigma$	$(s_a \pi_a ; \pi_a \sigma_b)$	0.02445 91	0.02137 87	0.01856 97	0.01603 83	0.01377 50
	$\pi\sigma s\bar{\pi}$	$(s_a \pi_a ; \sigma_a \pi_b)$	0.01126 39	0.00967 37	0.00825 94	0.00701 48	0.00592 94
	$\pi\pi\sigma\bar{s}$	$(\sigma_a \pi_a ; \pi_a s_b)$	0.00471 44	0.00416 42	0.00365 12	0.00318 00	0.00275 28
	$\sigma s\pi\bar{\pi}$	$(\sigma_a \pi_a ; s_a \pi_b)$	0.00468 33	0.00398 76	0.00337 46	0.00284 03	0.00237 87
	$\sigma\pi\pi\bar{\sigma}$	$(\sigma_a \pi_a ; \pi_a \sigma_b)$	0.00585 90	0.00535 46	0.00483 20	0.00431 31	0.00381 34
	$\pi\sigma\sigma\bar{\pi}$	$(\sigma_a \pi_a ; \sigma_a \pi_b)$	0.00636 16	0.00541 02	0.00457 50	0.00384 88	0.00322 29
	$\pi\sigma\pi\bar{\sigma}$	$(\pi_a \pi_a ; \sigma_a \sigma_b)$	0.10947 07	0.10428 73	0.09793 02	0.09083 90	0.08337 12
	$\sigma\pi\sigma\bar{\pi}$	$(\sigma_a \sigma_a ; \pi_a \pi_b)$	0.06163 85	0.05244 15	0.04444 99	0.03754 62	0.03160 66
	$\pi\pi\pi\bar{\pi}$	$(\pi_a \pi_a ; \pi_a \pi_b)$	0.06253 10	0.05301 80	0.04479 83	0.03773 30	0.03168 84
	$\pi\pi\pi'\bar{\pi}'$	$(\pi_a \pi_a' ; \pi_a \pi_b')$	0.00241 80	0.00199 55	0.00164 11	0.00134 52	0.00109 95
	$\pi\pi'\pi\bar{\pi}'$	$(\pi_a \pi_a ; \pi_a' \pi_b')$	0.05769 49	0.04902 69	0.04151 62	0.03504 26	0.02948 94
	$++++$	$(\pi_a^+ \pi_a^+ ; \pi_a^+ \pi_b^+)$	0.06011 29	0.05102 24	0.04315 73	0.03638 78	0.03058 90
	$+--+$	$(\pi_a^+ \pi_a^- ; \pi_a^- \pi_b^+)$	0.00483 61	0.00399 11	0.00328 22	0.00269 05	0.00219 90

page line

16 11 $J_{s\sigma}=\frac{1}{12\sqrt{3}}\delta^6 R^4\{-A_0(\delta R)+3A_2(\delta R)\}$,

16 14 $+\frac{31}{72}\alpha^3+\frac{29}{252}\alpha^4+\frac{11}{504}\alpha^5+\frac{1}{420}\alpha^6\Big)e^{-2\alpha}\Big\}$,

16 16 $+\frac{13}{336}\alpha^4+\frac{1}{280}\alpha^5\Big)e^{-2\alpha}\Big\}$,

Table III (Continued)

			6.00	6.50	7.00
C/δ	$ssss$	$(s_a s_b; s_b s_a)$	0.01122 9	0.00654 85	0.00372 43
	σsss	$(\sigma_a s_b; s_b s_a)$	0.01437 4	0.00862 31	0.00502 24
	$\sigma\sigma ss$	$(\sigma_a s_b; \sigma_b s_a)$	0.01820 5	0.01126 0	0.00672 80
	$\sigma s\sigma s$	$(\sigma_a\sigma_b; s_b s_a)$	0.01761 0	0.01098 1	0.00659 91
	$\sigma ss\sigma$	$(\sigma_a s_b; s_b\sigma_a)$	0.01895 4	0.01163 7	0.00691 40
	$\sigma\sigma\sigma s$	$(\sigma_a\sigma_b; \sigma_b s_a)$	0.02310 8	0.01475 7	0.00905 20
	$\sigma\sigma\sigma\sigma$	$(\sigma_a\sigma_b; \sigma_b\sigma_a)$	0.02941 0	0.01936 3	0.01218 2
	$\pi\pi ss$	$(\pi_a s_b; \pi_b s_a)$	0.00099 877	0.00053 694	0.00028 260
	$\pi s\pi s$	$(\pi_a\pi_b; s_b s_a)$	0.00476 67	0.00259 26	0.00138 02
	$\pi ss\pi$	$(\pi_a s_b; s_b\pi_a)$	0.00110 59	0.00059 748	0.00031 586
	$\pi\pi\sigma\sigma$	$(\pi_a\sigma_b; \pi_b\sigma_a)$	0.00155 22	0.00088 079	0.00048 538
	$\pi\sigma\pi\sigma$	$(\pi_a\pi_b; \sigma_b\sigma_a)$	0.00720 98	0.00420 15	0.00236 79
	$\pi\sigma\sigma\pi$	$(\pi_a\sigma_b; \sigma_b\pi_a)$	0.00210 57	0.00117 99	0.00064 357
	$\pi\pi\sigma s$	$(\pi_a\sigma_b; \pi_b s_a)$	0.00126 07	0.00069 487	0.00037 363
	$\pi\sigma\pi s$	$(\pi_a\pi_b; \sigma_b s_a)$	0.00601 08	0.00336 48	0.00183 55
	$\pi\sigma s\pi$	$(\pi_a s_b; \sigma_b\pi_a)$	0.00150 30	0.00082 884	0.00044 590
	$\pi\pi\pi\pi$	$(\pi_a\pi_b; \pi_b\pi_a)$	0.00223 05	0.00113 39	0.00056 601
	$\pi\pi\pi'\pi'$	$(\pi_a\pi_b'; \pi_b\pi_a')$	0.00011 332	0.00005 7180	0.00002 8333
	$\pi\pi'\pi\pi'$	$(\pi_a\pi_b; \pi_b'\pi_a')$	0.00200 39	0.00101 95	0.00050 935
	$++++$	$(\pi_a^+\pi_b^+; \pi_b^+\pi_a^+)$	0.00211 72	0.00107 67	0.00053 768
	$+--+$	$(\pi_a^+\pi_b^-; \pi_a^-\pi_b^+)$	0.00022 664	0.00011 436	0.00005 6667
L/δ	$sss\bar{s}$	$(s_a s_a; s_a s_b)$	0.05037 46	0.03739 44	0.02740 88
	$sss\bar{\sigma}$	$(s_a s_a; s_a\sigma_b)$	0.06836 56	0.05196 09	0.03886 41
	$s\sigma s\bar{s}$	$(s_a s_a; \sigma_a s_b)$	0.05634 54	0.04321 35	0.03258 84
	$ss\sigma\bar{s}$	$(s_a\sigma_a; s_a s_b)$	0.01112 92	0.00834 85	0.00615 34
	$s\sigma\sigma\bar{s}$	$(s_a\sigma_a; \sigma_a s_b)$	0.01712 97	0.01280 52	0.00941 81
	$ss\sigma\bar{\sigma}$	$(s_a\sigma_a; s_a\sigma_b)$	0.01523 94	0.01179 97	0.00891 67
	$s\sigma s\bar{\sigma}$	$(s_a s_a; \sigma_a\sigma_b)$	0.07194 09	0.05720 79	0.04440 80
	$\sigma s\sigma\bar{s}$	$(\sigma_a\sigma_a; s_a s_b)$	0.05312 65	0.03949 10	0.02898 33
	$s\sigma\sigma\bar{\sigma}$	$(s_a\sigma_a; \sigma_a\sigma_b)$	0.02374 49	0.01826 02	0.01027 09
	$\sigma s\sigma\bar{\sigma}$	$(\sigma_a\sigma_a; s_a\sigma_b)$	0.07221 36	0.05499 80	0.04118 65
	$\sigma\sigma\sigma\bar{s}$	$(\sigma_a\sigma_a; \sigma_a s_b)$	0.06137 87	0.04700 14	0.03538 14
	$\sigma\sigma\sigma\bar{\sigma}$	$(\sigma_a\sigma_a; \sigma_a\sigma_b)$	0.07908 78	0.06275 69	0.04859 86
	$s\pi s\bar{\pi}$	$(s_a s_a; \pi_a\pi_b)$	0.02169 98	0.01508 59	0.01037 90
	$\pi s\pi\bar{s}$	$(\pi_a\pi_a; s_a s_b)$	0.04899 92	0.03634 61	0.02664 12
	$s\pi\pi\bar{s}$	$(s_a\pi_a; \pi_a s_b)$	0.00675 29	0.00475 80	0.00331 59
	$\pi ss\bar{\pi}$	$(s_a\pi_a; s_a\pi_b)$	0.00423 47	0.00287 23	0.00193 08
	$s\pi\sigma\bar{\pi}$	$(s_a\sigma_a; \pi_a\pi_b)$	0.00418 33	0.00290 90	0.00199 85
	$\pi\sigma\pi\bar{s}$	$(\pi_a\pi_a; \sigma_a s_b)$	0.05382 87	0.04131 95	0.03119 18
	$\pi s\pi\bar{\sigma}$	$(\pi_a\pi_a; s_a\sigma_b)$	0.06644 16	0.05044 23	0.03770 28
	$s\pi\pi\bar{\sigma}$	$(s_a\pi_a; \pi_a\sigma_b)$	0.01003 32	0.00718 85	0.00508 00
	$\pi\sigma s\bar{\pi}$	$(s_a\pi_a; \sigma_a\pi_b)$	0.00418 33	0.00290 90	0.00199 85
	$\pi\pi\sigma\bar{s}$	$(\sigma_a\pi_a; \pi_a s_b)$	0.00202 96	0.00146 87	0.00104 60
	$\sigma s\pi\bar{\pi}$	$(\sigma_a\pi_a; s_a\pi_b)$	0.00164 71	0.00112 39	0.00075 75
	$\sigma\pi\pi\bar{\sigma}$	$(\sigma_a\pi_a; \pi_a\sigma_b)$	0.00291 01	0.00216 27	0.00157 31
	$\pi\sigma\sigma\bar{\pi}$	$(\sigma_a\pi_a; \sigma_a\pi_b)$	0.00223 18	0.00152 38	0.00102 80
	$\pi\sigma\pi\bar{\sigma}$	$(\pi_a\pi_a; \sigma_a\sigma_b)$	0.06836 75	0.05443 34	0.04231 27
	$\sigma\pi\sigma\bar{\pi}$	$(\sigma_a\sigma_a; \pi_a\pi_b)$	0.02221 61	0.01545 17	0.01065 03
	$\pi\pi\pi\bar{\pi}$	$(\pi_a\pi_a; \pi_a\pi_b)$	0.02217 04	0.01536 68	0.00880 74
	$\pi\pi\pi'\bar{\pi}'$	$(\pi_a\pi_a'; \pi_a\pi_b')$	0.00072 87	0.00047 86	0.00031 19
	$\pi\pi'\pi\bar{\pi}'$	$(\pi_a\pi_a; \pi_a'\pi_b')$	0.02071 30	0.01440 95	0.00818 36
	$++++$	$(\pi_a^+\pi_a^+; \pi_a^+\pi_b^+)$	0.02144 17	0.01488 81	0.00849 55
	$+--+$	$(\pi_a^+\pi_a^-; \pi_a^-\pi_b^+)$	0.00145 75	0.00095 72	0.00062 38

page	line	
16	17	$D_{\pi\pi\sigma\sigma}=\delta\left\{+\frac{27}{\alpha^5}-\left(\frac{27}{\alpha^5}+\frac{54}{\alpha^4}+\cdots\cdots\right.\right.$
17	5	$-2W_\tau(1,2)G_\tau(0)G_\tau(3)-2W_\tau(0,2)G_\tau(0)G_\tau(2)\}$,
17	10	$=\left\{\log 2\alpha+C+\sum_{n=1}^{\infty}\frac{(-2\beta)^n}{n\cdot n!}\right\}e^{-(\alpha-\beta)}+[-E_i(-2\alpha)]e^{\alpha-\beta}$, $\beta<0$

Page	line		
25	1	column 6	$\alpha=7.00$
26	21-25		$F_{0,70}$
			$F_{1,00}$
			$F_{1,10}$
			$F_{1,20}$
			$F_{1,30}$
27	14	column 8	$\beta=1.75$
	20	column 2	$\alpha=4.75$
	24-26	column 5	$F_{2,20}$
			$F_{2,30}$
			$F_{3,10}$
	last line	column 5, 7	$F_{3,10}$
28	8	... Promotion of ...	

α		
2.25	A_{12}	1.264 6312 159^{4}
2.50	A_{9}	3.804 0172 439
16.0	A_{4}	9.165 2907 572
0.25	B_{3}	−1.007 4585 827
	B_{7}	−5.603 0294 023^{-2}
3.25	B_{0}	7.923 5586 798^{0}
7.25	B_{7}	−9.528 7535 145^{1}
13.0	B_{0}	3.403 1799 385^{4}
1.25	$f_{0}(4)$	2.565 0435 7
3.50	$f_{0}(8)$	2.452 2870 6
5.00	$f_{1}(13)$	6.427 1740 0
13.00	$f_{0}(2)$	3.780 5926 7
15.00	$f_{0}(2)$	4.526 5079 3
1.00	$-W_{3}^{1}(0,3)$	1.460 90^{0}
	$-W_{3}^{1}(0,4)$	5.088 82
	$-W_{5}^{1}(0,0)$	9.438^{-2}
1.25	$W_{1}^{0}(2,5)$	1.324 1332^{0}
	$-W_{1}^{1}(0,4)$	7.495 629
	$-W_{1}^{1}(1,4)$	1.916 037^{0}
1.50	$W_{4}^{0}(1,2)$	2.257 46
2.00	$W_{0}^{0}(0,0)$	3.596 2173^{-3}
	$W_{2}^{0}(0,2)$	9.962 0775
	$W_{4}^{0}(0,3)$	4.865 82
	$-W_{1}^{1}(2,6)$	4.879 767
2.25	$W_{0}^{0}(0,4)$	9.630 0882
	$W_{3}^{0}(1,4)$	7.971 495
	$W_{4}^{0}(0,2)$	1.358 79
2.5	$W_{2}^{0}(0,4)$	4.990 0641
	$W_{4}^{0}(2,3)$	2.192 38
	$W_{5}^{0}(2.3)$	1.496 9
	$W_{6}^{0}(0,0)$	3.004^{-5}
2.75	$-W_{3}^{1}(2.2)$	1.197 64
	$-W_{5}^{1}(0,0)$	2.713^{-4}
	$W_{2}^{2}(2,2)$	7.001 55
	$W_{4}^{2}(0,0)$	4.336
	$W_{4}^{2}(2,2)$	4.415
3.00	$-W_{2}^{1}(5,5)$	1.854 487^{-2}
	$-W_{4}^{1}(3,3)$	1.568 5^{-3}
	$W_{2}^{2}(0.0)$	2.730 49^{-4}
3.25	$W_{3}^{0}(0,3)$	2.683 656
	$W_{3}^{0}(0,4)$	3.458 295
4.00	$W_{5}^{0}(0,3)$	1.896 0
	$-W_{4}^{1}(0,3)$	2.037 4
4.25	$-W_{2}^{1}(3,4)$	2.959 709
4.75	$W_{3}^{0}(1,2)$	7.095 177
	$W_{3}^{0}(5,5)$	2.928 257
	$-W_{2}^{1}(1,5)$	4.840 338
	$-W_{3}^{1}(4,4)$	1.171 51^{-5}
	$-W_{4}^{1}(0,0)$	1.291 0
5.50	$W_{4}^{0}(0,0)$	6.051 16^{-8}
	$W_{6}^{0}(0,0)$	3.199^{-8}
	$-W_{3}^{1}(0,0)$	1.713 64^{-7}
	$-W_{5}^{1}(0,0)$	2.264^{-7}
	$W_{2}^{2}(0,0)$	1.725 69^{-7}
	$W_{4}^{2}(0,0)$	1.402^{-6}
6.00	$W_{0}^{0}(8,8)$	7.676 2601
6.50	$W_{0}^{0}(8,8)$	1.723 3591
	$W_{2}^{0}(0,1)$	1.768 3024
7.00	$W_{0}^{0}(8,8)$	4.147 5296
3.00	$G_{4}^{1}(3)$	2.094 6913 0
	$G_{4}^{2}(2)$	7.219 0247 3
3.50	$G_{3}^{1}(1)$	−4.904 2330 9
	$G_{3}^{2}(0)$	−15.224 4337 1
4.25	$G_{3}^{1}(0)$	10.432 1328
	$G_{4}^{2}(0)$	29.888 4381

α	β		
2.00	1.00	$F_{3,10}$	1.4426 31
2.00	1.25	$F_{1,39}$	1.2635 04
5.50	3.50	$F_{0,70}$	0.0889 1

Acknowledgement

We are greatly indebted to Dr. H. J. Kopineck, Mr. W. Watari and Prof. G. Araki, whose articles and private communications have been of great help to our work. We are sincerely grateful to Mr. T. Kimura (National Science Museum) who informed us of numerical errors in Parts I and II; to Miss Hama, Miss Mikoshiba, Mr. Fujimoto, Miss Fujita, Miss Komatsu, Miss Iwasaki, Miss Kodaira, Miss Yuminami and Miss Yuasa for the indispensable assistance in the numerical computations or the compilation of the manuscript; to the Bureau of Numerical Calculations for lending us facilities for computation; to the members of the Kotani Laboratory and the Ministry of Education for the financial support.

References

1) Kotani, Amemiya and Simose: Proc. Phys.-Math. Soc. Japan **20**, Extra No. 1 (1938); **22**, Extra No. 1 (1940).

2) Kopineck: Zeits. f. Naturforsch. **5a** (1950) 420; **6a** (1951) 177; **7a** (1952) 785.

3) Araki and Watari: Progress of Theoretical Physics **6** (1951) 961.

4) Parr and Crawford: J. Chem. Phys. **16** (1948) 1049; Roothaan: J. Chem. Phys. **19** (1951) 1445; Rüdenberg, J. Chem. Phys. **19** (1951) 1459.

JOURNAL OF THE PHYSICAL SOCIETY OF JAPAN Vol. 8, No. 4, JULY—AUGUST, 1953

Direct Current Characteristics of the Selenium Rectifier

I. Theory of Rectification

By Masami TOMONO

Hitachi Central Research Laboratory, Kokubunji, Tokyo

(Received July 31, 1952)

On the assumption that the barrier layer of the selenium rectifier has a construction composed of n-type semiconductor, insulating film and p-type semiconductor, the author has offered a new rectification theory. In this theory, the author contrived a structure with which the direction of rectification due to insulating film does not come out to be inverse to the result of experiment, as Wilson's theory.

§ 1. Introduction

Concerning the rectifying properties of metal rectifiers various theories have been offered by several researchers. None of them however could afford a sufficient explanation for the experimental results of the selenium rectifier over a whole range of applied voltage.

Among those theories, for instance, Wilson's theory[1] of the tunnel effect gives an inverse direction of rectification to the experiment. And in the thermal diffusion theory of Mott[2] and Schottky[3], there are many controversies as to follows (1) in the case of forward current, a theoretical relation $j \backsim \exp(\alpha V)$, where j is current and V is applied voltage, gives the value of the constant α remarkably different from the experiment, (2) and as to reverse current it is well known that a far larger current flows, when a comparatively higher voltage is applied. In an attempt to save these inconsistencies, many modifications have been proposed, i. e. the multicontact theory,[4] the theory taking into the influence of image force,[2][5] a combination of above two theories backed by tunnel and thermal diffusion[6] etc., but they provide a solution for only a part of these problems. The author has conducted a series of experiments and researches in order to obtain a theory which may be applied well to the above rectification problems of the selenium rectifier. In the following he will propose a theory and interpret the rectifying phenomena from his viewpoint.

§ 2. Constraction of Barrier Layer

It is a well known fact that a layer of selenides exists between selenium and counter-electrode of the selenium rectifier.[7] Fig. 1 shows the temperature dependence of conductivity of cadmium selenide — one of the above selenides.

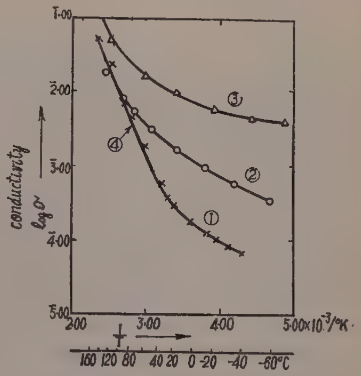

Fig. 1. Conductivity of CdSe with various compositions.

The pure cadmium selenide prepared chemically with a extreme caution shows very small conductivity, but when it is added with cadmium, the conductivity becomes increasingly greater as shown by the curves (1), (2) and (3) in the Figure. This may afford a a direct proof for the fact that cadmium selenide is a n-type semi-conductor.[8]

Mechanical pressures applied on the selenium rectifier causes a marked decrease of resistance, and it will be restored almost to the original value when the pressure is removed.[8] This trend may suggest the existence of electric conduction due to tunnel effect through a insulating film of a barrier layer. It is a well known fact that selenium is a p-type semiconductor.

Basing on the above-mentioned facts, the author has figured out a model for the barrier layer of the selenium rectifier, as shown in Fig. 2.

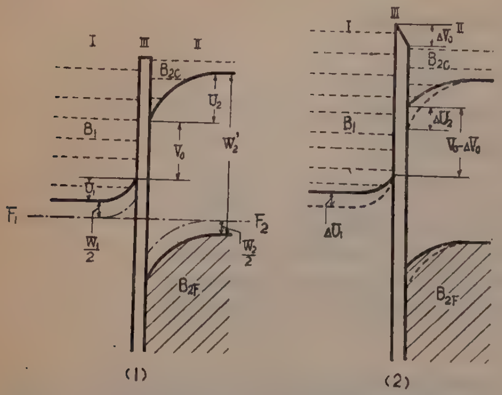

(1) (2)

Fig. 2. Model showing potential distribution of the barrier layer of the selenium rectifier.
(1) The case that the applied voltage is 0.
(2) The case that the voltage, $\varDelta U_1+\varDelta V_0+\varDelta U_2=V$, is applied.

It is assumed that the *n*-type semiconductor (selenide) represented by I and the *p*-type semiconductor (selenium) represented by II make contact with each other across the insulating film represented by III. It is also assumed that free electrons of I, the *n*-type semiconductor, penetrating through III, the insulating film, by the process of the tunnel effect, enter the conduction band of II, the *p*-type semiconductor, thus in this process, in the boundary region of the *p*-type semiconductor excess negative charge is produced and positive holes instantly come on the region to neutralize it moving from the right side through the filled band, resulting in a disappearance of positive carriers in the filled band and negative carriers in the conduction band by the combination of the both. Thus, the current (positive) can flow from II to I. In case that the above process is reversed there will be a current flow in reverse direction.

In the discussion hereafter such a conception will be premised for the sake of simplification that the electric conduction depends solely on electrons in the body of the *n*-type semiconductor and on positive holes in the body of the *p*-type semiconductor. Our rectification theory may be different from Shockley's *p-n* junction theory,[9] for it may have a rectifying mechanism based on the last assumption. By establishing the model as above, it can be considered that semiconductors of I and II produce Schottky's type physical barrier layer[3] on their boundary regions respectively, and the rectification by both insulating film and those physical barriers make unidirectional rectifying characteristics, which makes a difference with the idea[6] given out by Davydow and Dilworth.

On bringing the discussion further, notations appearing hereafter will be defined as follows.

In general:

j: electric current. When electron flows from I to II, the current is assumed to be in positive direction.

V: Applied electromotive force. It should be understood positive when it acts to move the electron in the abovementioned positive direction.

Regarding *n*-type semiconductor:

U_1: diffusion potential of physical barrier layer.

$\varDelta U_1$: voltage applied on physical barrier layer of I when a voltage is applied upon the rectifier.

W_1: activation energy of *n*-type semiconductor.

N_0: number of impurity centers per unit volume.

v_1: mobility of electron.

l_1: thickness of physical barrier layer.

K_1: dielectric constant.

Regarding *p*-type semiconductor:

Except the undermentioned, the same notations as for *n*-type semiconductor are in use, but adding the suffix 2 to each notation.

n_2: number of positive holes per unit volume.

n_2': number of free electrons per unit volume.

N_0': number of inpurity centers per unit volume.

N': number of inpurity centers negatively charged per unit volume.

W_2': width of forbidden region between filled band and conduction band.

Regarding insulating film:

V_0: difference of energy between bottoms of conduction bands of I and II.

$\varDelta V_0$: voltage applied on the insulating film when a voltage applied on the rectifier.

For the quantities other than the above, symbols in common usage will be adopted.

With regard to the relation of the energy bands, an assumption of the energy bands, an assumption is made that the bottom of conduction band of I comes halfway between conduction band and filled band of II as can be seen from Fig. 2. It is easily shown that an equilibrium is attainable in the state shown in the figure.

§ 3. Electron Transmission Coefficient of Insulating Film

To make possible the quantitave consideration regarding rectification, it is essential to determine first an accurate transmission coefficient of electron penetrating through a insulating film.

The author calculated out the transmission coefficient for a rectangular and wedge shaped insulating film illustrated in Fig. 3, not under the WKB approximation method[10] but exact mathematical method. The results will be shown later. As indicated in the Figure, such a case is considered where a free electron having a kinetic energy, E, with 0 potential energy, penetrates perpendicularly into the barrier. In this case, the voltage ΔV_0 is considered to be applied on the insulating film. Quantities dealt with thereby are defined as follows.

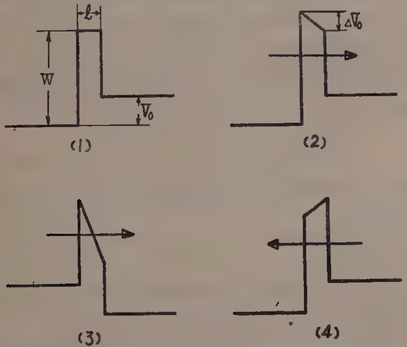

Fig. 3. Potential barrier of insulating film.
(1) Applied voltage is 0.
(2), (3) Applied voltage is positive.
(4) Applied voltage is negative.
The arrow shows the direction of motion of an electron and the magnitude of energy.

$$\kappa^2=8\pi^2 m/h^2\,,$$

where m represents mass of electron

$$\begin{aligned}
&E^{1/2}=\alpha && \\
&(E-W)^{1/2}=\beta && (E>W)\\
&(W-E)^{1/2}=\beta^* && (W>E)\\
&(E-W+\Delta V_0)^{1/2}=\gamma && (E>W-\Delta V_0)\\
&(W-E-\Delta V_0)^{1/2}=\gamma^* && (E<W-\Delta V_0)\\
&(E-V_0+\Delta V_0)^{1/2}=\delta && (E>V_0-\Delta V_0)\\
&2\kappa\beta^3/(3|F|)=\lambda && (E>W)\\
&2\kappa\beta^{*3}/(3|F|)=\lambda^* && (W>E)\\
&2\kappa\gamma^3/(3|F|)=\mu && (E>W-\Delta V_0)\\
&2\kappa\gamma^{*3}/(3|F|)=\mu^* && (W-\Delta V_0>E)\\
&F=\Delta V_0/l &&
\end{aligned}$$

(1) In the case of $\Delta V_0>0$, $E<W-\Delta V_0$ (Fig. 3 (1));

$$\tau=\frac{16\alpha\beta^*\gamma^*\delta\exp(-2\lambda^*)}{(\alpha^2+\beta^{*2})[\{4\pi\kappa/(9F)\}\{I_{2/3}(\mu^*)-I_{-2/3}(\mu^*)\}^2\gamma^{*5}+\{4\pi\kappa/(9F)\}\{I_{1/3}(\mu^*)-I_{-1/3}(\mu^*)\}^2\gamma^{*3}\delta^2]} \tag{1}$$

When μ^* has a sufficiently large value,

$$\tau=\frac{16\alpha\beta^*\gamma^*\delta\exp\{-2(\lambda-\mu^*)\}}{(\alpha^2+\beta^{*2})(\gamma^{*2}+\delta^2)}\,. \tag{2}$$

Where τ is transmission coefficient of electron. In such a special case that $V=0$ and $\mu^*\to\infty$, this formula consists with Nordheim's formula.[11]

(2) In the case of $\Delta V_0>0$, $W-\Delta V_0<E$ (Fig. 3 (2));

$$\tau=\frac{16\alpha\beta^*\gamma\delta\exp(-2\lambda^*)}{(\alpha^2+\beta^{*2})[\{4\pi\kappa/(9F)\}\{J_{2/3}(\mu)-J_{-2/3}(\mu)\}^2\gamma^5+\{4\pi\kappa/(9F)\}\{J_{1/3}(\mu)+J_{-1/3}(\mu)\}^2\gamma^3\delta^2]} \tag{3}$$

In the special case of $\mu\to\infty$, this agrees with Fowler's formula.[12]

(3) In the case of $\Delta V_0>0$ and $E=W-\Delta V_0$;

In this case, the WKB method cannot be used for obtaining τ and according to the author's calculation the following formula is obtained.

$$\tau=\frac{16\alpha\beta^*[\{3^{4/3}/(4\pi)\}\Gamma^2(2/3)(F/\kappa)^{1/3}]\delta\exp(-2\lambda^*)}{(\alpha^2+\beta^{*2})[\{3^{1/3}(\Gamma(\frac{2}{3})/\Gamma(\frac{1}{3}))(F/\kappa)^{1/3}\}^2+\delta^2]} \tag{4}$$

(4) In the case of $\Delta V_0<0$, $W>E$ (Fig. 3 (3)); The case only for large value of μ^* is re-

quired for present purpose, and the result obtained is the same as the formula (2).

§ 4. Electron Current through Insulating Film

In the n-type semiconductor illustrated in Fig. 2 I, number of electrons moving from left to right to strike against a unit area of contacting surface in unit time with the energy of $E\sim E+dE$ is obtained from the following formula[2]

$$2N_0^{1/2}(2\pi mkT/h^6)^{1/4} \times\exp\{-(E+W_1/2+U_1)/(kT)\}dE \quad (5)$$

Next, as to the p-type semiconductor, an assumption that the potential energy of an electron at a distance x from the contacting surface has a value of $-\chi(x)$ measured from a sufficiently distant point, $x\to\infty$, and number of positive holes and electrons in the p-type semiconductor at a sufficiently large distance from the boundary layer can be obtained from the following formulas respectively.

$$\left.\begin{aligned} n_{2\infty}' &= 2(2\pi mkT/h^2)^{9/4}N_0'^{-1/2} \\ &\quad\times\exp\{-(W_2'-W_2/2)/(kT)\} \\ n_{2\infty} &= 2(2\pi mkT/h^2)^{3/4}N_0'^{1/2} \\ &\quad\times\exp\{-W_2/(2kT)\}\,. \end{aligned}\right\} \quad (6)$$

However, at the physical barrier, the functions of the number of free electrons and positive holes vary in many ways according as how the number of excess negative charge depends on a distance x. In spite of this fact, the author assumed that the formula (6) could apply in this case alike for the sake of simplification. Hence the following formula is obtained,

$$\left.\begin{aligned} n_2'(x) &= 2(2\pi mkT/h^2)^{9/4}N_0'^{-1/2} \\ &\quad\times\exp\{-(W_2'-W_2/2-\chi(x))/(kT)\} \\ n_2(x) &= 2(2\pi mkT/h^2)^{3/4}N_0'^{1/2} \\ &\quad\times\exp\{-(W_2/2+\chi(x))/(kT)\} \end{aligned}\right\} \quad (7)$$

As in the case of the formula (5), numbe of electrons moving from right to left to a unit area of the contacting surface with the energy of $E\sim E+dE$ can be formulated as follows,

$$\{2(2\pi mkT)^{7/4}/(h^{9/2}N_0'^{1/2}) \times\exp\{-(W_2'-U_2-W_2/2)/(kT) \times\exp\{-E/(kT)\}dE. \quad (8)$$

By putting the above results together, the number of electrons penetrating through the insulating film in a unit time can be easily obtained.

With regard to the transmission coefficient of insulating film, asymptotic expansion would be used for the Bessel functions of (1) and (3) wherever possible.

(1) Electron current from left to right in the case of

$$\Delta V_0>0,\ V_0>\Delta V_0\,.$$

From the formulas (2) and (5),

$$\begin{aligned} I=eG\int_{V_0-\Delta V_0}^{\infty} &[16E^{1/2}(W-E)^{1/2}(W-\Delta V_0-E)^{1/2} \\ &\times(E-V_0+\Delta V_0)^{1/2}/\{W(W-V_0)\}] \\ &\times\exp[-E/(kT)-\{4\kappa l/(3\Delta V_0)\} \\ &\times\{(W-E)^{3/2}-(W-\Delta V_0-E)^{3/2}\}]dE\,, \end{aligned} \quad (9)$$

where,

$$G=2N_0^{1/2}(2\pi mkT/h^6)^{1/4}\exp\{-(W_1/2+U_1)/(kT)\}. \quad (10)$$

As the integrand of the formula (9) contains expotential function, it is only around such a value of E as making the function maximum that it can contribute to the integration.

Putting

$$E=V_0-\Delta V_0+\varepsilon\,, \quad (11)$$

in the integrand the part necessary for the present purpose is as given below, providing ε is small.

$$(E-V_0+\Delta V_0)^{1/2}\exp[-E/(kT)-\{4\kappa l/(3\Delta V_0)\} \times\{W-E)^{3/2}-(W-\Delta V_0-E)^{3/2}\}],$$

$\varepsilon_{\max}$ or the value of E with which the above function becomes maximum is as follows,

$$\varepsilon_{\max}=\frac{1}{2[1/(kT)-(2\kappa l/\Delta V_0)\{(W-V_0+\Delta V_0)^{1/2}-(W-V_0)^{1/2}\}]}\,. \quad (12)$$

Thus the following formula can be derived by carrying out the integration of the formula (9).

$$\begin{aligned} I=&\frac{32eN_0^{1/2}(2\pi mkT/h^6)^{1/4}\exp\{-(W_1/2+U_1+V_0)/(kT)\}}{2^{1/2}[1/(kT)-(2\kappa l/\Delta V_0)\{(W-V_0+\Delta V_0)^{1/2}-(W-V_0)^{1/2}\}]^{3/2}}\,\frac{(V_0-\Delta V_0)^{1/2}(W-V_0+\Delta V_0)^{1/2}}{W(W-V_0)^{1/2}} \\ &\times\exp[\Delta V_0/(kT)-\{4\kappa l/(3\Delta V_0)\}\{(W-V_0+\Delta V_0)^{3/2}-(W-V_0)^{3/2}\}]\,. \end{aligned} \quad (13)$$

In general, the right side of the formula (12) is positive and the magnitude is in the order of kT. Hence, $\varepsilon_{\max}$ may be considered small enough. In special case that the denominator on the right side diminshes close to 0 the calculation on the above formula becomes imppossible. But in practice, as V approaches this range I grows tremendously. This means that the insulating film turns transparent for electron and mainly the resistance in other part of the rectifier restricts the electric current.

(2) Electron current from left to right in the case of

$$\Delta V_0>0.\ W>\Delta V_0>V_0 .$$

Treatment can be almost the same as the above case, but the calculation should be made on the condition of

$$E=\varepsilon , \tag{14}$$

and ε is small.

$$I=\frac{32eN_0^{1/2}(2\pi mkT/h^6)^{1/4}\exp\{-(W_1/2+U_1)/(kT)\}}{2^{1/2}[1/(kT)-(2\kappa l/\Delta V_0)\{W^{1/2}-(W-\Delta V_0)^{1/2}\}]^{3/2}}\frac{(W-\Delta V_0)^{1/2}(\Delta V_0-V_0)^{1/2}}{W^{1/2}(W-V_0)}$$
$$\times\exp[-\{4\kappa l/(3\Delta V_0)\}\{W^{3/2}-(W-\Delta V_0)^{3/2}\}]. \tag{15}$$

When $\varepsilon_{\max}$ takes a large value the case may be similar to the previous.

(3) Electron current from left to right in the case of

$$\Delta V_0<0,\ W>V_0+|\Delta V_0| .$$

By the treatment almost the same with the formula (13) next formula can be obtained.

$$I=\frac{32eN_0^{1/2}(2\pi mkT/h^6)^{1/4}\exp\{-(W_1/2+U_1+V_0)/(kT)\}}{2^{1/2}[1/(kT)-(2\kappa l/|\Delta V_0|)\{(W-V_0)^{1/2}-(W-V_0-|\Delta V_0|)^{1/2}\}]^{3/2}}\frac{(V_0+|\Delta V_0|)^{1/2}(W-V_0-|\Delta V_0|)^{1/2}}{W(W-V_0)^{1/2}}$$
$$\times\exp[-|\Delta V_0|/(kT)-\{4\kappa l/(3|\Delta V_0|)\}\{(W-V_0)^{3/2}-(W-V_0-|\Delta V_0|)^{3/2}\}] . \tag{16}$$

(4) Electron current in reverse direction, right to left, in the case of

$$\Delta V_0<0,\ W>V_0+|\Delta V_0| .$$

Similarly to the above, the following is obtained.

$$I=\frac{32e(2\pi mkT)^{7/4}\exp\{-(W_2'-U_2-W_2/2)/(kT)\}}{2^{1/2}h^{9/2}N_0'^{1/2}[1/(kT)-(2\kappa l/|\Delta V_0|)\{(W-V_0)^{1/2}-(W-V_0-|\Delta V_0|)^{1/2}\}]^{3/2}}$$
$$\times\frac{(W-V_0-|\Delta V_0|)^{1/2}(V_0+|\Delta V_0|)^{1/2}}{(W-V_0)^{1/2}W}\exp[-\{4\kappa l/(3|\Delta V_0|)\}\{(W-V_0)^{3/2}-(W-V_0-|\Delta V_0|)^{3/2}\}] . \tag{17}$$

(5) Electron current in reverse direction, right to left, in the case of

$$\Delta V_0>0,\ V_0>\Delta V_0 .$$

Similarly to the preceding, the following is obtained.

$$I=\frac{32e(2\pi mkT)^{7/4}\exp\{-(W_2'-U_2-W_2/2)/(kT)\}}{2^{1/2}h^{9/2}N_0'^{1/2}[1/(kT)-(2\kappa l/\Delta V_0)\{(W-V_0+\Delta V_0)^{1/2}-(W-V_0)^{1/2}\}]^{3/2}}$$
$$\times\frac{(W-V_0+\Delta V_0)^{1/2}(V_0-\Delta V_0)^{1/2}}{(W-V_0)^{1/2}W}\exp[-4\kappa l/(3\Delta V_0)\{(W-V_0+\Delta V_0)^{3/2}-(W-V_0)^{3/2}\}]. \tag{18}$$

If necessary, the corresponding formula can be obtained for any other case.

§ 5. Theory of Rectification

Formulae which stand for the rectification of the selenium rectifier can be obtained by combining the above-mentioned several formulae. As to the rectification by insulating film, it is verified that electron is in the forward direction when it moves from the n-type semiconductor (i. e. from left to right), and this theoretically proved direction is consistent with the result of experiment with the selenium rectifier.

It should deserve attention that the direction of rectification is reverse to that based on the conventional conception that the positive hole penetrate through insulating film, which is derived from the simple application by rote of Wilson's theory, concerning the contact between metal and *n*-type semiconductor, to the contact between metal and selenium, *p*-type semiconductor. Thus it results that the physical barrier of the semiconductors and the insulating film unite to contribute to the rectification in the same direction.

(1) Rectification in the case of $V>0, V_0>\varDelta V_0$

In this case, most of the applied voltage is impressed on the insulating film and the effect of physical barrier of the boundary layer is assumed to need practically no consideration. Accordingly,

$$V\approx\varDelta V_0\,.$$

Electron current from left to right is evolved from the formula (13) as follows :

$$I_1=X_1\exp\{-(U_1+V_0+W_1/2)/(kT)\}\exp[V/(kT)-\{4\kappa l/(3V)\}\{(W-V_0+V)^{3/2}-(W-V_0)^{3/2}\}] \tag{19}$$

Where

$$X_1=\frac{32eN_0^{1/2}(2\pi mkT/h^6)^{1/4}(V_0-V)^{1/2}(W-V_0+V)^{1/2}}{2^{1/2}[1/(kT)-(2\kappa l/V)\{W-V_0+V)^{1/2}-(W-V_0)^{1/2}\}]^{3/2}W(W-V_0)^{1/2}}\,. \tag{20}$$

While electron current from right to left is as follows when calculated on the formula (18).

$$I_2=X_1'\exp\{-(W_2'-U_2-W_2/2)/(kT)\}\exp[-\{4\kappa l/(3V)\}\{(W-V_0+V)^{3/2}-(W-V_0)^{3/2}\}]\,. \tag{21}$$

Where

$$X_1'=\frac{32e(2\pi mkT)^{7/4}(W-V_0+V)^{1/2}(V_0-V)^{1/2}}{2^{1/2}h^{9/2}N_0'^{1/2}[1/(kT)-(2\kappa l/V)\{(W-V_0+V)^{1/2}-(W-V_0)^{1/2}\}]^{3/2}(W-V_0)^{1/2}W}\,. \tag{22}$$

Electric current through the rectifier is represented by the next equation

$$j=I_1-I_2\,. \tag{23}$$

By applying the condition of $j=0$, when $V=0$,

$$j=X_1[\exp\{V/(kT)\}-1]\exp[-(U_1+V_0+W_1/2)/(kT)-\{4\kappa l/(3V)\}\{(W-V_0+V)^{3/2}-(W-V_0)^{3/2}\}]\,. \tag{24}$$

(2) Rectification in the case of $V>0,\ W>\varDelta V_0>V_0$,

$$\varDelta U_1\gtrapprox kT\,,\ \varDelta U_2\gtrapprox kT\,.$$

In this case, the voltage applied in the forward direction is larger than the previous case, hence none of $\varDelta V_0$, $\varDelta U_1$, and $\varDelta U_2$ can be ignored.

The relations observed between the current j and the applied voltage, $\varDelta U_1$, $\varDelta U_2$, of each barrier layer are expressed respectively basing on Schttky's formula as follows (3).

$$j=\xi\exp\{-(U_1+W_1/2)/(kT)\}[\exp\{\varDelta U_1/(kT)\}-1] \tag{25}$$

$$=\zeta\exp\{-(U_2+W_2/2)/(kT)\}[\exp\{\varDelta U_2/(kT)\}-1]\,. \tag{26}$$

Where

$$\xi=2ev_1N_0^{1/2}(2\pi mkT/h^2)^{3/4}\{8\pi N_0(U_1-\varDelta U_1)/k_1\}^{1/2} \tag{27}$$

$$\zeta=2ev_2N_0'^{1/2}(2\pi mkT/h^2)^{3/4}\{8\pi N_0'(U_2-\varDelta U_2)/k_2\}^{1/2}\,. \tag{28}$$

The relation between j and $\varDelta V_0$ is turned out to be as follows when U_1 is substituted by $U_1-\varDelta U_1$ in the formula (15)

$$j=X_2\exp\{-(U_1+W_1/2)/(kT)\}\exp\{\varDelta U_1/(kT)\}\exp[-\{4\kappa l/(3\varDelta V_0)\}\{W^{3/2}-(W-\varDelta V_0)^{3/2}\}]\,.$$

Where

$$X_2=\frac{32eN_0^{1/2}(2\pi mkT/h^6)^{1/4}(W-\varDelta V_0)^{1/2}(\varDelta V_0-V_0)^{1/2}}{2^{1/2}[1/(kT)-(2\kappa l/\varDelta V_0)\{W^{1/2}-(W-\varDelta V_0)^{1/2}\}]^{3/2}W^{1/2}(W-V_0)}\,. \tag{30}$$

Obtained the formulas (25) and (26), it is easy to get $\varDelta U_1$ and $\varDelta U_2$ out of these.

By placing

$$Y_1 = -\log \frac{j \exp\{U_1 + W_1/2)/(kT)\}}{X_2[1+(j/\xi)\exp\{(U_1+W_1/2)/(kT)\}} \tag{31}$$

$$\Delta V_0 = 3W/2 - 9Y_1^2/(32\kappa^2 l^2) - \surd\{3W/2 - 9Y_1^2/(32\kappa^2 l^2)\}^2 + \{3W^{3/2}/(2\kappa l)\}(Y_1 - 2W^{1/2}\kappa l) \tag{32}$$

Accordingly, next formula for rectification is derived. However X_2 is taken in this case as practically constant for the sake of convenience.

$$\begin{aligned} V = kT \log [1+(j/\xi)\exp\{U_1+W_1/2)/(kT)\}][1+(j/\zeta)\exp\{(U_2+W_2/2)/(kT)\}] \\ +3W/2 - 9Y_1^2/(32\kappa^2 l^2) - \surd\{3W/2 - 9Y_1^2/(32\kappa^2 l^2)\}^2 + \{3W^{3/2}/(2\kappa l)\}(Y_1 - 2W^{1/2}\kappa l) \end{aligned} \tag{33}$$

(3) Rectification in the case of $V<0$, $W-V_0>|\Delta V_0|$.

When the applied voltage is small, or $V \approx \Delta V_0$, the same formula as (24) can be obtained. And when the obsolute value of V has a certain degree of magnitude, i. e., in the case of $W-V_0>|\Delta V_0|$, $|\Delta U_1| \gtrapprox kT$, $|\Delta U_2| k \gtrapprox T$, the following formula can be obtained by substituting U_1 and U_2 of the formulas (16) and (17) by $U_1 - \Delta U_1$ and $U_2 - \Delta U_2$ respectively,

$$\begin{aligned} j = -X_3[1-\exp\{V/(kT)\}]\exp\{-(U_1+V_0+W_1/2)/(kT)\}\exp\{-\Delta U_2/(kT)\} \\ \times \exp[\{4\kappa l/(3\Delta V_0)\}\{(W-V_0)^{3/2} - (W-V_0+\Delta V_0)^{3/2}\}], \end{aligned} \tag{34}$$

where

$$X_3 = \frac{32eN_0^{1/2}(2\pi mkT/h^6)^{1/4}(V_0-\Delta V_0)^{1/2}(W-V_0+\Delta V_0)^{1/2}}{2^{1/2}[1/(kT)-(2\kappa l/\Delta V_0)\{(W-V_0)^{1/2}-(W-V_0+\Delta V_0)^{1/2}\}]^{3/2} W(W-V_0)^{1/2}}. \tag{35}$$

Although ΔV_0 might be calculated out from formulae (25), (26), and (34) as the function of j by taking X_3 for the constant for the present use, the author effected the calculation graphically for the convenience' sake.

In this way, the value of ΔU_1 and ΔU_2 can easily be obtained, and the result, when formalized, takes the following form.

$$V = \Delta U_1 + \Delta U_2 + \Delta V_0 . \tag{36}$$

(4) Rectification in the case of
$V<0$, $W-V_0>|\Delta V_0|$,
$|\Delta U_1| \gg kT$, and $|\Delta U_2| \gg kT$.

In this case, a large portion of applied voltage is on the physical barrier, and it serves the purpose alike to consider formulae (25), (26) and (34) as the simultaneous equations, resulting to be as follows respectively.

$$\begin{aligned} \Delta U_1 = -\{K_1/(32\pi e^2 v_1^2 N_0^2)\}\{h^2/(2\pi mkT)\}^{3/2} j^2 \\ \times \exp\{(2U_1+W_1)/(kT)\} + U_1 , \end{aligned} \tag{37}$$

$$\begin{aligned} \Delta U_2 = -\{K_2/(32\pi e^2 v_2^2 N_0'^2)\}\{h^2/(2\pi mkT)\}^{3/2} j^2 \\ \times \exp\{(2U_2+W_2)/(kT)\} + U_2 . \end{aligned} \tag{38}$$

By substituting the values of the above in formula (34), an equation concerning ΔV_0 can be obtained. And by solving the equation graphically the value of ΔV_0 is obtained. By substituting these values ΔU_1, ΔU_2, and ΔV_0 in (36) the formula of rectification is obtained.

§ 6. Conclusion

A detailed comparison between the author's theory and the results of experiments is now in progress and the results will be soon published in this journal.

On closing, the author wishes to express his thanks to Dr. R. Miura, Dr. H. Hamada and Dr. K. Yumoto for discussion and advice and Mr. S. Kasashima for help with experiments.

References

1) A. H. Wilson: Proc. Roy. Soc. (A) **136** (1932) 487.

2) N. F. Mott: Proc. Roy. Soc. (A) **171** (1939) 27.

3) W. Schottky: Zeits. f. Phys. **118** (1942) 539.

4) V. A. Johnson, R. N. Smith and H. J. Yearian: J. Appl. Phys. **21** (1950) 283.

5) P. T. Landsberg: Proc. Roy. Soc. (A) **206** (1951) 463, **206** (1951) 477.
E. Billig: Proc. Roy. Soc. (A) **207** (1951) 157.

6) B. Davydov: J. Phys. U.S.S.R. **1** (1939) 167.
C. C. Dilworth: Proc. Phys. Soc. **60** (1948) 315.

7) J. Yamaguchi and S. Katayama: J. Phys. Soc. Jap. **5** (1950) 385.

8) M. Tomono: Unpublished.

9) W. Shockley, G. L. Pearson and J. R. Haynes: Bell System Tech. J. **28** (1949) 344.

10) R. Holm: J. Appl. Phys. **22** (1951) 569.

11) L. Nordheim: Zeits. f. Phys. **75** (1932) 434.

12) R. H. Fowler and L. Nordheim: Proc. Roy. Soc. (A) **119** (1928) 173.

JOURNAL OF THE PHYSICAL SOCIETY OF JAPAN Vol. 8, No. 4, JULY—AUGUST, 1953

On the Capacity of a Discrete Channel. I

Mathematical expression of capacity of a channel which is disturbed by noise in its every one symbol and expressible in one state diagram

By Saburo MUROGA

Electrical Communication Laboratory

(Received October 11, 1952)

This report describes a general and concrete method of calculating the capacity in a noisy channel having one state which Dr. Shannon did not solve analytically. In order to express $H_x(y)$ concisely, the author introduces $H_x(y)$ characteristic equations, the solution of which characterizes the channel capacity, and the capacity problem is solved, considering whether the calculated probabilities of symbols are real or not. Then an analogy between capacity and rank is discussed and the capacity when $H_x(y)$ characteristic equations have no solution is also discussed. Numerical examples and a geometrical representation of capacity are described.

§ Introduction

Information theory has been developed by the great contribution of Dr. C. E. Shannon[1) recently. He introduced not only statistical ideas like entropy used in statistical ideas like entropy used in statistical dynamics, but also originated an idea of channel capacity founded on the statistical structure. In spite of his intuitive insight, he did not seem to get mathematical expression of capacity in general, but only for few special examples as he stated.[2) Since in fact no channel does not contain noise, the analytical expression of the capacity for a noisy channel has very important significance. Taking account of the reality of the calculated symbol probabilities, we treated the mathematical expression of the capacity completely as the greatest value problem and got a perfect formula of the capacity.

§ 1. The Channel Capacity and the Maximum Value Problem

When noise disturbs a channel in every one symbol, the character of the channel can be specified by transition probability p_{ij} in which the symbol j is received at the receiving side for the transmitted symbol i. Then the channel capacity is given by the greatest value of[3)

$$-\sum_{i,j} P_i p_{ij} \log \sum_i P_i p_{ij} + \sum_{i,j} P_i p_{ij} \log p_{ij}\,, \quad (1)$$

where P_i is the probability of use of the transmitted symbol i and the greatest value problem of (1) submits to the condition $\sum P_i = 1$.

The capacity of a noisy channel is specified perfectly by the p_{ij} and this is represented by matrix, i, j element of which is p_{ij}. But this must satisfy the conditions $\sum_j p_{ij} = 1$ and $p_{ij} \geqq 0$. Let us define the matrix $[p_{ij}]$ as *channel matrix*. If channel matrix is given, the statistical properties of a channel are specified and the capacity can be calculated.

Shannon tried to solve (1) as the maximum value problem by the method of Lagrange. Let the inverse matrix of $[p_{sj}]$ be $[h_{st}]$ if it exists. As the relation $\sum h_{st} p_{sj} = \delta_{tj}$ exists,*

$$P_t = \sum_t h_{tt} \exp\Big[-C \sum_s h_{st} + \sum_{s,j} h_{st} p_{sj} \log p_{sj}\Big]\,. \quad (2)^{**}$$

If we substitute (2) into the condition $\sum P_t = 1$, we get capacity C and then, substituting C into (2), we have the probability P_t which specified how to use symbols in order to give maximum transmission rate to this channel.

However these formulae don't express C and P_t explicitly and require heavy labor for their calculation. The author found that Shannon's method can be made complete if we make use of the peculiar property of the channel matrix. Provided that $[p_{ij}]$ is nonsingular, let the cofactor of the element p_{ij} be p_{ij}'. Then:

---

* The order of suffix of h_{st} is different from usual expression.

** C's in formulae at pp. 46 of the reference (1) are opposite and misprinted.

$$\sum_s h_{st}=\sum_s p_{st}'/|p_{ij}|=1 \qquad (3)$$

by the property $\sum_j p_{ij}=1$. Therefore (2) is

$$P_i=\sum_t h_{it}\exp\left[-C+\sum_{s,j}h_{st}p_{sj}\log p_{sj}\right] \qquad (4)$$

and summing on i,

$$\begin{aligned}1&=\sum_t\sum_i h_{it}\exp\left[-C+\sum_{s,j}h_{st}p_{sj}\log p_{sj}\right]\\ &=\sum_t\exp\left[-C+\sum_{s,j}h_{st}p_{sj}\log p_{sj}\right] \qquad (5)\end{aligned}$$

$$\therefore\quad C=\log\left[\sum_t\exp\left\{\sum_{s,j}h_{st}p_{sj}\log p_{sj}\right\}\right]. \qquad (6)$$

Setting

$$X_t\equiv\sum_{s,j}h_{st}p_{sj}\log p_{sj}\,, \qquad (7)$$

(6) is

$$C=\log\left[\sum_t\exp(X_t)\right] \qquad (8)$$

and at last the capacity can be expressed explicitly. Also, (4) is,

$$\begin{aligned}P_i&=\exp(-C)\cdot\sum_t h_{it}\exp(X_t)\\ &=\frac{\exp(-C)}{|p_{ij}|}\cdot\begin{vmatrix}p_{11}, & \cdots\cdots & , p_{1n}\\ \vdots & & \\ \exp(X_1), & \cdots;, & \exp(X_n)\\ \vdots & & \\ p_{n1}, & \cdots\cdots & , p_{nn}\end{vmatrix}\leftarrow\end{aligned}$$

$$(\leftarrow:\text{ the } i \text{ th line}) \qquad (9)$$

This is the probability of use of the symbol at the transmitting side that gives the maximum rate to the channel. Also from (7) and (9) we get

$$H_x(y)=-\sum_t X_t\exp(X_t)/\sum_t\exp(X_t)\,, \qquad (10)$$

that is, the average value of $-X_t$ with the weight of $\exp(X_t)/\sum\exp(X_t)$.

As discussed above, the capacity is expressed in the exact formula. But in a case where the inverse matrix $[h_{st}]$ does not exist, what capacity does the channel have? Moreover, in Shannon's solution the problem of the capacity is treated in the form of the maximum problem, without consideration of the reality of symbol probabilities, but this does not always lead to a correct result. It is due to lack of the condition that P_i is positive, and in fact P_i of (9) may become negative in some cases. Therefore the channel capacity problem must be solved as the greatest value problem, taking account of the reality of symbol probabilities.

Then let us show an example in which treatment as the maximum problem without consideration of the reality of symbol probabilities brings erroneous result.

Misleading example

Let the channel matrix be

$$\begin{bmatrix}\frac12+\delta & \frac14-\delta & \frac14\\ \frac12 & \frac12 & 0\\ \frac12 & 0 & \frac12\end{bmatrix}$$

where $\frac14\geq\delta\geq0$. Then from the above formulae,

$$C=\log\frac12\left[K+\frac2K\right]$$

$$\begin{cases}P_1=\dfrac1\delta\left(\dfrac K2-\dfrac1K\right)\left(K+\dfrac2K\right)^{-1}\\ P_2=\dfrac1\delta\left[\dfrac1{2K}-K\left(\dfrac14-\delta\right)\right]\cdot\left(K+\dfrac2K\right)^{-1}\\ P_3=\dfrac2\delta\left[\dfrac1K\left(\dfrac14+\delta\right)-\dfrac K8\right]\cdot\left(K+\dfrac2K\right)^{-1}\end{cases}$$

where

$$\begin{cases}E\equiv\left(\dfrac12+\delta\right)\log\left(\dfrac12+\delta\right)\\ \qquad+\left(\dfrac14-\delta\right)\log\left(\dfrac14-\delta\right)+\dfrac14\log\dfrac14\,,\\ K\equiv\exp\left[\dfrac1{2\delta}(E+\log 2)\right].\end{cases}$$

If we put $\delta\rightarrow+0$, $E\rightarrow-\frac32\log 2$ and $K\rightarrow+0$. Once K decreases below $\sqrt2$, only P_1 becomes negative and $C\rightarrow\infty$. This is unreasonable.

§ 2. General Treatment of the Capacity Problem

So far we have treated only the case of square channel matrix, but it will be desirable to consider on cases of more general channel matrices. On the other hand, when we have some negative P_i's in calculating the capacity by (8), the calculated value does not express the capacity for the channel. In order to avoid this defect of simple maximizing solution, the capacity problem should be solved, taking account of whether the calculated symbol probabilities are real, in other words, whether all the calculated probabilities are between 0 and 1. But since we have no general method to treat the problem of the greatest value in a given interval, we will solve it in the modification of the simple maximizing solution so that we may be able to calculate the greatest rate of the channel which has the symbols of real probabilities.

In order to treat the problem generally and completely, let us follow a method different from the one tried by Shannon.

Theorem 1: Let solution of $H_x(y)$ characteristic equations[*]

$$\left\{\begin{array}{l} p_{11}X_1+\cdots\cdots+p_{1m}X_m=\sum_j^m p_{1j}\log p_{1j} \\ \vdots \qquad\qquad\qquad\qquad\qquad \vdots \\ p_{n1}X_1+\cdots\cdots+p_{nm}X_m=\sum_j^m p_{nj}\log p_{nj} \end{array}\right. \tag{11}$$

be $X_1, \cdots\cdots, X_m$[**]*. Then the transmission rate of the channel (entropy/symbol) is,*

$$-\sum_{i=1}^m P_i' \log P_i' + \sum_{i=1}^m P_i' X_i\,, \tag{12}$$

and $H_x(y)$ is expressed as

$$-\sum_{i=1}^m P_i' X_i\,, \tag{13}$$

where P_i' is the probability of appearance of the symbol i in the receiving side, for which the relations

$$\left\{\begin{array}{l} p_{11}P_1+\cdots+p_{n1}P_n=P_1' \\ \vdots \qquad\qquad\qquad\quad \vdots \\ p_{1m}P_1+\cdots+p_{nm}P_n=P_m' \end{array}\right. \tag{14}$$

hold.

The proof is simple. Consider the following bilinear form from (11) and (14). Identically,

$$\sum_{i,j} p_{ij}X_jP_i \equiv \sum_{i=1}^m P_i'X_i = \sum_{i=1}^n P_i \sum_{j=1}^m p_{ij}\log p_{ij}\,. \tag{15}$$

We don't require always $m=n$. This corresponds to the relation of Lagrange in linear differential equations. Also using this the rate becomes (12).

m parameters $X_1, \cdots, X_m$ completely determine the rate and $H_x(y)$ with (14).

Now we assume $m=n$ and rank n, which is the case treated by Shannon. First we try to solve it as the simple maximum problem, using the method of Lagrange;

$$U=-\sum P_i' \log P_i' + \sum P_i' X_i + \mu \sum P_i'$$

$$\therefore\ \frac{\partial U}{\partial P_i'} = -(1+\log P_i') + X_i + \mu = 0\,.$$

Multiplying by P_i' and summing over i, $-1+C+\mu=0$.

$$\therefore\ C = X_i - \log P_i'\,.$$

Then,

$$P_i' = \exp(X_i - C)\,. \tag{16}$$

From $\sum P_i'=1$, $C=\log\{\sum \exp(X_i)\}$ and this is identical with (8). P_i' in (16) is always positive. However P_i in (9) is not always positive, as the later example shows. The negative values of P_i's mean that the maximum does not exist in the positive range of P_i's. Therefore some of P_i's must be zero, that is, we need not use these symbols, and the abolition of these symbols is necessary for the greatest transmission rate.

Now let us discuss the case when the P_i's of the first r symbols are positive and the remainders are all zero. Channel matrix without the superfluous symbols is

$$\begin{bmatrix} p_{11}, & \cdots, & p_{1m} \\ \vdots & & \vdots \\ p_{r1}, & \cdots, & p_{rm} \end{bmatrix},\quad r<m\,. \tag{17}$$

According to the theorem 1 we should get the greatest value of (12). Let us set the simultaneous equations

$$\left\{\begin{array}{l} p_{11}S_1+\cdots\cdots+p_{1m}S_m=0 \\ \vdots \qquad\qquad\qquad \vdots \\ p_{r1}S_1+\cdots\cdots+p_{rm}S_m=0 \end{array}\right. \tag{18}$$

and let a set of $m-r$ fundamental solutions of these be $S_1^{(k)}, \cdots, S_m^{(k)}$ $(k=1, \cdots, m-r)$. When we try to get the maximum of (12), we must vary the P_i''s subject to the equations

$$\sum_{i=1}^r p_{ij}P_i = P_j' \qquad (j=1, \cdots, m), \tag{19}$$

corresponding to (14). That is, when we vary $P_1', \cdots, P_m'$ in order to get the maximum, these must not be varied independently of each other, but must be varied so that (19) may be always solved as to the $P_1, \cdots, P_r$. This condition is natural as p_{ij}'s are given and the number of the occurrence of the symbols in the receiving side accumulates according to use of the symbols in the transmitting side. The necessary and sufficient condition for the P_i's to be solved is that the equations

---

[*] Let us call these equations so for want of a better name. The influence of noise is shown by both $H_x(y)$ and $H_y(x)$, the conditional entropies, but more directly by the latter. While Shannon calls $H_x(y)$ equivocation, $H_y(x)$ will be called dissemination or divergence as the transmitted symbols are disseminated or diverge by noise. Then we may call (11) as the dissemination characteristic equations.

[**] We assume the existence of the solution of (11) in § 2 and § 3 when no remark.

$$\begin{cases} P_1'S_1^{(1)}+\cdots+P_m'S_m^{(1)}=0 \\ \vdots \qquad\qquad\qquad \vdots \\ P_1'S_1^{(m-r)}+\cdots+P_m'S_m^{(m-r)}=0 \end{cases} \tag{20}$$

be satisfied.

Let us try to get the maximum of (12) under the constraints (20).

$$U=-\sum_i^m P_i'\log P_i'+\sum_i^m P_i'X_i+\mu\sum_i^m P_i'$$
$$+\nu_1\sum_{i=1}^m P_i'S_i^{(1)}+\cdots+\nu_{m-r}\sum_{i=1}^m P_i'S_i^{(m-r)}.$$

$$\frac{\partial U}{\partial P_i'}=-(1+\log P_i')+X_i+\mu$$
$$+\nu_1 S_i^{(1)}+\cdots+\nu_{m-r}S_i^{(m-r)}.$$

Multiplying by P_i' summing over i, and considering (20), $-1+C+\mu=0$.

$$\therefore\quad P_i'=\exp\left(X_i-C+\sum_j^{m-r}\nu_jS_i^{(j)}\right). \tag{21}$$

Substituting into (20),

$$\sum_{i=1}^m S_i^{(k)}\exp\left(X_i+\sum_j^{m-r}\nu_jS_i^{(j)}\right)=0$$
$$(k=1,\cdots,m-r). \tag{22}$$

From these $m-r$ simultaneous transcendental equations, $m-r$ undecided constants $\nu_1,\cdots,\nu_{m-r}$ are determined. $X_i+\sum\limits_j^{m-r}\nu_jS_i^{(j)}$ $(i=1,\cdots,m)$ is the general solution of (11) (where m is substituted by n and n by r), and the one among general solutions is determined by the constraint (22). Also from $\sum P_i=1$,

$$C=\log\left[\sum_i^m\exp\left(X_i+\sum_j^{m-r}\nu_jS_i^{(j)}\right)\right]. \tag{23}$$

Substituting the constants determined from (22) into this, C can be calculated explicitly. Then if P_i got from P_i' of (21) comes out non-negative, the necessary greatest value is reached.

Theorem 2: The capacity of a channel which has r transmitting symbols, m receiving symbols and channel matrix of rank r, is:

$$C=\log\left[\sum_{i=1}^m\exp\left(X_i+\sum_{j=1}^{m-r}\nu_jS_i^{(j)}\right)\right], \tag{24}$$

where ν_j's are given by the constraint (22), provided that all the P_i's which are solved by substituting the probabilities P_i''s of (21) into (19) are non-negative.

In the above discussion we set P_i's of r symbols as positive and the remainder as zero. But the maximum of the rate, when we omit an arbitrary number of additional symbols out of the above r symbols, must not of course be larger than that of (23).

After all, to explain concrete method of calculating the capacity of a channel, first try to get the maximum rate, using all the transmitting symbols of number n and calculate the P_i's for this maximum. If some of the P_i's come out negative, reduce the number of the transmitting symbols to $n-1$ and then try again calculation for all possible choices of the $n-1$ symbols out of the whole transmitting symbols. If we can find some cases where all the P_i's of the $n-1$ symbols are non-negative, the greatest value of the rate among these cases is the required capacity. But otherwise, reduce number of symbols to be used and continue such trials until all the P_i's become positive at last, that is, the maximum is the capacity. When the number of symbols at the last trial is r, the rates for the cases of the symbols of number less than r cannot exceed the just calculated maximum, the capacity.

Theorem 3: The channel capacity is the greatest value among the maximum values given by (24), provided these give positive values to P_i's. The number of symbols at that time is the greatest one that we can use at this channel, that is, the rate for less number of symbols cannot exceed the just calculated value.

Let us express the set of fundamental solutions of (18) in a concrete form. If we assume that the first r-order determinant is not zero (by replacing the sufixes properly),

$$\begin{cases} S_i^{(1)}=\dfrac{-1}{\begin{vmatrix} p_{11}\cdots p_{1r} \\ \vdots \qquad \vdots \\ p_{r1}\cdots p_{rr}\end{vmatrix}}\cdot\begin{vmatrix} p_{11},\cdots,p_{1r+1},\cdots,p_{1r} \\ \vdots \qquad\qquad\qquad\quad \vdots \\ p_{r1},\cdots,\underset{\substack{\uparrow \\ i\text{-th row}}}{p_{rr+1}},\cdots,p_{rr}\end{vmatrix}, \\ \qquad\qquad\qquad\qquad\qquad\qquad (i=1,\cdots,r) \\ S_{r+1}^{(1)}=1,\ S_{r+2}^{(1)}=0,\ \cdots,\ S_m^{(1)}=0; \\ S_i^{(2)}=\dfrac{-1}{|\ {}''\ |}\cdot\begin{vmatrix} p_{11},\cdots,p_{1r+2},\cdots,p_{1r} \\ \vdots \qquad\qquad\qquad\quad \vdots \end{vmatrix}, \\ \qquad\qquad\qquad\qquad\qquad\qquad (i=1,\cdots,r) \\ S_{r+1}^{(2)}=0,\ S_{r+2}^{(2)}=1,\ S_{r+3}^{(2)}=0,\ \cdots,\ S_m^{(2)}=0; \\ S_i^{(m-r)}=\dfrac{-1}{|\ {}''\ |}\cdot\begin{vmatrix} p_{11},\cdots,p_{1m},\cdots,p_{1r} \\ \vdots \qquad\qquad\qquad\quad \vdots \end{vmatrix}, \\ \qquad\qquad\qquad\qquad\qquad\qquad (i=1,\cdots,r) \\ S_{r+1}^{(m-r)}=0,\ \ldots,\ S_{m-1}^{(m-r)}=0,\ S_m^{(m-r)}=1. \end{cases} \tag{25}$$

As the particular solution of (11) (now m is replaced by n, and n by r), we get

$$\begin{cases} X_i = \dfrac{1}{|\,''\,|} \cdot \begin{vmatrix} p_{11}, \cdots, \sum p_{1j} \log p_{1j}, \cdots, p_{1r} \\ \vdots \qquad\qquad \vdots \qquad\qquad\qquad \vdots \end{vmatrix}, \\ \qquad\qquad\qquad\qquad \nwarrow i\text{-th row} \quad (i=1,\cdots,r) \\ X_{r+1} = \cdots = X_m = 0. \end{cases} \tag{26}$$

The general solution of (*11*) *is the linear combination of* (*25*) *and* (*26*), *but since the relation* (*20*) *holds as for the fundamental solutions, in the expression of* $\sum P_i' X_i$ *a term containing the fundamental solutions vanishes and then we may consider the particular solution of* (*11*) *as the* X_i.

Using the solutions in the forms of (25) and (26), we get

$$\begin{cases} P_i' = \exp\left(X_i - C + \sum_j^{m-r} \nu_j S_i^{(j)}\right) \\ P_{r+1}' = \exp(-C+\nu_1) = -\sum_{i=1}^{r} S_i^{(1)} P_i' \\ \vdots \\ P_m' = \exp(-C+\nu_{m-r}) = -\sum_{i=1}^{r} S_i^{(m-r)} P_i'. \end{cases} \tag{27}$$

and the constraint is

$$\sum_{i=1}^{r} S_i^{(k)} \exp\left(X_i + \sum_j^{m-r} \nu_j S_i^{(j)}\right) + \exp(\nu_k) = 0\,, \qquad (k=1,\ldots,m-r). \tag{28}$$

We calculate C by (28):

Corollary 1 to theorem 2: *In a channel which has* r *transmitting symbols and* m *receiving symbols, we assume* (*by proper rearrangement of symbols*)

$$\begin{vmatrix} p_{11}, & \ldots, & p_{1r} \\ \vdots & & \vdots \\ p_{r1}, & \ldots, & p_{rr} \end{vmatrix} \neq 0\,. \tag{29}$$

Then the channel capacity is

$$C = \log\left[\sum_{i=1}^{r}\left(1 - \sum_{k=1}^{m-r} S_i^{(k)}\right)\exp\left(X_i + \sum_j^{m-r} \nu_j S_i^{(j)}\right)\right], \tag{30}$$

provided all the P_i *'s giving this rate are not negative. Then a set of* P_i *'s is determined uniquely.*

This result can be applied to a case where the maximum of a channel of n transmitting symbols does not exist in the range $P_i \geq 0$ $(i=1,\ldots,n)$ and we search the maximum by setting some of the P_i 's zero. Whichever elements are contained in the condition (29) by rearrangement, the values of C, P_i and P_i' are the same. To explain it concretely, in getting the channel capacity by theorem 3 we should use (30) and examine whether P_i 's got from (27) and (19) are negative or not.

Especially we get from the result of (16),

Corollary 2 to theorem 2: *If the channel matrix is square and non-singular, we get*

$$C = \log\left[\sum_{t=1}^{m} \exp(X_t)\right], \tag{8}$$

provided P_i *'s given by* (*9*) *are not negative. Then* P_i' *'s are given by* (*16*).

From the above discussion we can get the capacity whether the channel matrix be square or not.

§ 3. The Channel Capacity and the Rank of the Channel Matrix

The rank of matrix is defined as the largest order of possible minor determinants which are not zero, and the channel capacity has the analogous properties to the rank. Let us show some simple ones of them.

First, theorem 3 is much analogous to the rank. Let us consider the channel matrix

$$\begin{pmatrix} p_{11}, & \ldots, & p_{1n} \\ \vdots & & \vdots \\ p_{r1}, & \ldots, & p_{rn} \\ p_{r+11}, & \ldots, & p_{r+1n} \\ \vdots & & \vdots \\ p_{n1}, & \ldots, & P_{nn} \end{pmatrix}.$$

Let a channel consisting of the upper half

$$\begin{bmatrix} p_{11}, & \ldots, & p_{1n} \\ \vdots & & \vdots \\ p_{n1}, & \ldots, & p_{nn} \end{bmatrix}$$

have the capacity C_r, provided that all the P_i 's $(i=1,\ldots,r)$ of the transmitting symbols which give the C_r are positive. As to the elements of the lower half

$$\begin{bmatrix} p_{r+11}, & \ldots, & p_{r+1n} \\ \vdots & & \vdots \\ p_{n1}, & \ldots, & p_{nn} \end{bmatrix},$$

we consider all the set satisfying the condition of the transition probability. Then we can divide the set into two subsets. When we try to get the capacity of the whole channel including the lower half matrix which belongs to one subset, some of P_i 's $(i=1,\ldots,n)$ giving the maximum are always negative, whichever transmitting symbols we may abandon to get the maximum. When we don't use all the symbols in the lower half matrix, the channel gets the greatest rate C_r for the first time. The capacity of every channel that includes this subset is C_r indiscriminately. On the contrary every channel that includes the elements of the other subset namely the remainder of the former subset, is larger than C_r, although we cannot show the value of the capacity.

Next let us consider the case where transitions of all the symbols from the transmitting side don't get entangled each other, as shown in Fig. 1. But the capacity of n independent channels, each of which has capacity C_i, is5), as the whole, $C = \log \sum_{i=1}^{r} \exp(C_i)$. Let us consider each dotted box in Fig. 1 as a unit channel C_i. For each unit channel, $C_i = 0$ holds. Then the channel capacity as the whole is $C = \log r$, regardless of the number and the transition probability of the received symbols corresponding to each transmitted symbol.

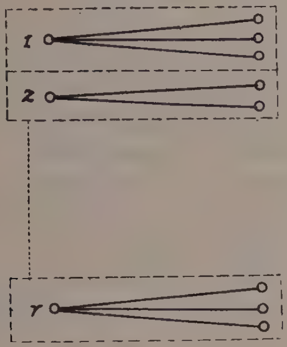

Fig. 1.

It is natural that the capacity gets smaller than $\log r$ as the transmitted symbols become entangled.

$C_r \leq \log r$ holds regardless of the number of the received symbols, where C_r is the capacity of a channel of r transmitting symbols. The capacity of a channel which uses an arbitrary number of symbols besides these r transmitting symbols does not always increase but sometimes remains as it were.

So far we have treated the case where the rank ρ of the channel matrix is equal to n, the number of the transmitting symbols. How is the case* of $\rho \neq n$? In this case we assume again the existence of solution of (11). In the set of fundamental solutions of homogeneous equations

$$\sum_{j=1}^{m} p_{ij} S_j = 0 \qquad (i=1, \ldots, n), \tag{31}$$

there are $m-\rho$ solutions. Then we have $m-\rho$ constraints. We can calculate the particular solution of (11) from ρ equations selected out of (11)6). Replacing r with ρ in theorem 2 and its corollaries, the following results are obtained. Although P_i' 's are determined uniquely now, P_i 's got from these P_i' 's are not determined uniquely and expressible in the form of the particular solution of

$$\sum_{j=1}^{n} p_{ij} P_i = P_j' \qquad (i=1, \ldots, n) \tag{32}$$

plus the general solution of

$$\sum_{j=1}^{n} p_{ij} P_i = 0 \qquad (i=1, \ldots, n). \tag{33}$$

Replacing the symbols properly so that the principal determinant of order r may be not zero, we get

$$\left\{\begin{array}{l} P_i = \dfrac{1}{\begin{vmatrix} p_{11} & \cdots & p_{1\rho} \\ \vdots & & \vdots \\ p_{1\rho} & \cdots & p_{\rho\rho} \end{vmatrix}} \cdot \begin{vmatrix} p_{11}, \ldots, (P_1' - \lambda_1 p_{\rho+11} \cdots - \lambda_{n-\rho} p_{n1}), \ldots, p_{\rho 1} \\ \vdots \qquad\qquad \underset{\nwarrow i\text{-th row}}{\vdots} \qquad\qquad\qquad \end{vmatrix}, \qquad (i=1, \ldots, \rho) \\ P_{\rho+1} = \lambda_1, \ldots, P_n = \lambda_{n-\rho}, \\ \text{where } \lambda_1, \ldots, \lambda_{n-\rho} \text{ are arbitrary constants.} \end{array}\right. \tag{34}$$

If we transmit symbols with the probability P_i given here, we get the same values of P_i' and C, independent of λ_i 's.

We can determine the particular solution from ρ equations out of (16) and the set of fundamental solutions from the simultaneous homogeneous equations which are got by setting the right-hand sides of these ρ equations as zero, and then the capacity from the theorem 2. Therefore we can get the capacity, using a channel constructed only by the coefficients matrix of order ρ corresponding to the above ρ equations. On the other hand the value of the capacity cannot exceed the logarithm of the number of the transmitted symbols, as shown in the above discussion. After all, *when the rank of channel matrix is ρ and the capacity is C, we get an inequality*: $C \leq \log \rho$.

---

* The special case where m the number of receiving symbols is smaller than n is treated here and in § 4.

When the rank ρ of the channel matrix is equal to the number of the transmitting symbols, the capacity depends on the number of receiving symbols as described before, and then,

Theorem 4: *If $\rho = m < n$ (ρ is the rank of the channel matrix). $C = \log \sum_{i=1}^{n} \exp(X_i)$, but P_i 's cannot be determined uniquely, where m is the number of the receiving symbols and n that of the transmitting ones.*

This form is the same to (8) and independent of the number of the transmitting symbols, where we assume the existence of the solution of (11).

§ 4. The Channel Capacity when $H_x(y)$ Characteristic Equations have no Solution

When (11) has no solution, our expression for the properties of a channel in X_i has no significance in itself, but even in this case we can calculate the capacity.

For simplicity let us replace the right sides of (11) by b_i 's:

$$\sum_{j=1}^{m} p_{ij}X_j = b_i \qquad (i=1;\dots,n). \quad (35)$$

The necessary and sufficient condition for the existence of solution of (35) is[4] that, letting a set of fundamental solutions of

$$\left\{\begin{array}{l} p_{11}Q_1 + \dots + p_{n1}Q_n = 0 \\ \vdots \qquad\qquad \vdots \\ p_{1m}Q_1 + \dots + p_{nm}Q_n = 0 \end{array}\right. \quad (36)$$

be $Q_i^{(1)}, \dots, Q_i^{(m-\rho)}$ $(i=1,\dots,n)$, the relations

$$b_1Q_1^{(k)} + \dots + b_nQ_n^{(k)} = 0 \quad (k=1,\dots,n-\rho) \quad (37)$$

should hold. Here ρ is the rank of the channel matrix. If $\rho = n$, these relations are not necessary since the solution always exists.

If the necessary and sufficient condition holds, (11) has solution and we can calculate the capacity because $H_x(y)$ can be expressible in linear combination of P_i' 's. That is the cases which we have discussed so far.

Now let us consider the contrary case where the necessary and sufficient condition (37) does not hold.* The solutions of

$$\sum_{i=1}^{n} p_{ij}P_i = P_j' \quad (38)$$

are

$$P_i = Q_i^{(0)} + \lambda_1 Q_i^{(1)} + \dots + \lambda_{n-\rho} Q_i^{(n-\rho)}, \quad (i=1,\dots,n), \quad (39)$$

where $Q_i^{(0)}$ is a particular solution of (38) and $Q_i^{(1)}, \dots, Q_i^{(n-\rho)}$ are the set of fundamental solutions of (36). Substituting the particular solution into (38) and summing all the equations, we get $\sum Q_i^{(0)} = 1$ from $\sum P_i' = 1$ and since the fundamental solutions satisfy (36), $\sum Q_i^{(k)} = 0$ $(k=1,\dots,n-\rho)$ holds.

On the other hand, the transmission rate

$$\left\{-\sum_{i}^{m} P_i' \log P_i' + \sum_{i}^{n} Q_i^{(0)} b_i\right\} + \left\{\lambda_1 \sum_{i}^{n} b_i Q_i^{(1)} + \dots + \lambda_{n-\rho} \sum_{i}^{n} b_i Q_i^{(n-\rho)}\right\} \quad (40)$$

is divided into two parts. The first { } contains only P_i' 's. The next { } contains only $\lambda_1, \dots, \lambda_{n-\rho}$. To explain in detail, we must vary $P_i', \dots, P_m'$; $\lambda_1, \dots, \lambda_{n-\rho}$ to get the greatest value so that the P_i of (39) may satisfy the relation $1 \geq P_i \geq 0$ $(i=1,\dots,n)$.

In varying P_i', the constraint

$$P_1'R_1^{(k)} + \dots + P_m'R_m^{(k)} = 0 \quad (k=1,\dots,m-\rho) \quad (41)$$

is required and here $R_1^{(k)}, \dots, R_m^{(k)}$ $(k=1,\dots,m-\rho)$ are the set of fundamental solutions of

$$\sum_{j=1}^{m} p_{ij}R_j = 0, \qquad (i=1,\dots,n).$$

Now let us assume that we have got the greatest valne of (40). Then we fix all the P_i' 's and give small displacement to the value of one selected out of λ_i 's**. Being linear combination of λ_i 's, the second term in (40) gets larger for the larger or the smaller value of the λ_i according to the sign of its coefficient

---

* The author is greatly indebted to Assistant Professor H. Takahasi whose advice promoted the accomplishment of the following discussion in this section.

** Variation of λ_i does not vary P_i''s at all, that is, these are independent of one another. But the greatest value of the second term in (40) depends in general on both P_i''s and λ_i's on account of constraints $0 \leq P_i \leq 1$ for the P_i's in (39) where $Q_i^{(0)}$'s are function of P_i''s. Therefore we cannot try to get the greatest values of the first and the second terms independently.

$\sum_k b_k Q_k^{(i)}$. However since a constraint on the λ_i is $0 \leq P_i \leq 1$ for P_i in (39), the value of the λ_i that makes value of (40) greatest is that which places some P_i at the end of its domain, that is, 0 or 1. If $P_i=1$, remaining P_i 's would be zero and the capacity also zero. Excluding this, we find that at least one of P_i 's must be zero. Let us omit this P_i from the channel symbols and number of the transmitting symbols are reduced to $n-1$ and the number of λ_i 's in P_i 's $(i=1, \dots, n-1)$ is $n-1-\rho$, and we see that at least one symbol has zero probability. We continue to omit symbols in the same way until there remains no λ_i. If the rank is preserved at every stage, $n-\rho$ symbols will be omitted but the rank may be lowered in some stages, in which case still more symbols have to be omitted.

To solve the problem, first we omit $n-\rho$ symbols out of all the transmitting symbols and using the particular solution for P_i in (38), we express the transmission rate as a function of P_i', whose greatest value we try to get under the constraints $\sum P_i'=1$ and (41). The greatest value among those for all possible choices of $n-\rho$ symbols is the required capacity, provided that the calculated P_i 's are non-negative*, but we need not take such choice as the rank of channel matrix may be lower than ρ by the omission of $n-\rho$ symbols**. Since such omission of at least $n-\rho$ transmitting symbols results in the coincidence of the rank of channel matrix with the number of the transmitting symbols, $H_x(y)$ characteristic equations has solution and the present case is the same with that in § 2.

Considering the result in § 3 together, we get,

Theorem 5: *For a channel with channel matrix of order ρ, if its $H_x(y)$ characteristic equations have no solution we can reach the greatest transmission rate only by the abolition of at least $n-\rho$ transmitting symbols. If the equations have solution, the probabilities of $n-\rho$ symbols among the transmitting symbols are arbitrary and the probabilities of the other ρ symbols are expressible as linear combinations of those of $n-\rho$ symbols.*

While the present case is the same as that in § 2 after abolition of at least $n-\rho$ symbols, the capacity cannot exceed the logarithm of the number of transmitting symbols. Therefore together with the inequalities in § 3 we can get the following statement.

Theorem 6: *For a channel with the channel matrix of order ρ, an inequality $C \leq \log \rho$ holds irrelevant to whether its $H_x(y)$ characteristic equations have solution or not.*

To refer to the relation with the case of existence of solution of $H_x(y)$ characteristic equations, the second term in (40) vanishes since (37) holds at that time and $H_x(y)$ contains only $-\sum_i^n Q_i^{(0)} b_i$ dependent on P_i' 's.

§ 5. Numerical Examples

Some numerical examples will help to illustrate the significance of the above theory.

Example 1: Consider the simple case where channel matrix is given by

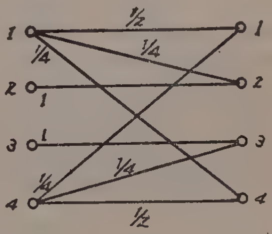

Fig. 2.

$$\begin{pmatrix} \frac{1}{2} & \frac{1}{4} & 0 & \frac{1}{4} \\ 0 & 1 & 0 & 0 \\ 0 & 0 & 1 & 0 \\ \frac{1}{4} & 0 & \frac{1}{4} & \frac{1}{2} \end{pmatrix}.$$

We should use (7), (8) and (9), and examine whether P_i 's are negative or not. $X_1=X_4=-2\log 2$, $X_2=X_3=0$.

$\therefore$ $C=\log 5/2$. Also, $P_1=P_4=2/15$,

$P_2=P_3=11/30$.

All the P_i is positive. The capacity is therefore log 2.5.

Example 2: Consider a rather intricate case where channel matrix is:

$$\begin{pmatrix} \frac{1}{2} & 0 & 0 & \frac{1}{2} \\ \frac{1}{2} & \frac{1}{2} & 0 & 0 \\ 0 & 0 & 1 & 0 \\ \frac{1}{4} & \frac{1}{4} & \frac{1}{4} & \frac{1}{4} \end{pmatrix}$$

---

* If some P_i's are negative, we must abolish more symbols.

** Such choice which brings the omission of more symbols is included in another case.

Calculating directly, we obtain $X_1=4\log 2$, $X_2=X_4=-6\log 2$, $X_3=0$ and $C=\log(17+1/32)$. Then

$$\begin{cases} P_1=P_2=\dfrac{16}{17+1/32}\left(2-\dfrac{1}{512}\right)>0\,, \\ P_3=\dfrac{16}{17+1/32}\left(1+\dfrac{1}{16}-\dfrac{1}{512}\right)>0\,, \\ P_4=\dfrac{16}{17+1/32}\left(\dfrac{1}{128}-4\right)<0\,. \end{cases}$$

That is, P_1, P_2 and P_3 are positive but P_4 negative. So we set $P_4=0$ and channel matrix is

$$\left(\begin{array}{ccc:c} \frac12 & 0 & 0 & \frac12 \\ \frac12 & \frac12 & 0 & 0 \\ 0 & 0 & 1 & 0 \end{array}\right).$$

Also we obtain $S_1^{(1)}=-1$, $S_2^{(1)}=1$, $S_3^{(1)}=0$; $X_1=-2\log 2$, $X_2=X_3=0$. The constraint corresponding to (28) is:

$$-\exp(-2\log 2-\nu)+2\exp(\nu)=0$$

$$\therefore\quad \nu=-\frac{3}{2}\log 2\,.$$

Then

$$\exp(C)=2\exp\left(-2\log 2+\frac{3}{2}\log 2\right)+\exp(0)=1+\sqrt{2}\,.$$

From (27) we get

$$\begin{cases} P_1'=\dfrac{1}{2+\sqrt{2}} \\ P_2'=P_4'=\dfrac{1}{2(2+\sqrt{2})} \\ P_3'=\dfrac{1}{1+\sqrt{2}} \end{cases}$$

and from (9)

$$\begin{cases} P_1=P_2=\dfrac{1}{2+\sqrt{2}} \\ P_3=\dfrac{1}{1+\sqrt{2}}\,. \end{cases}$$

Now all the P_i 's are positive. If we set another symbol zero, the capacity is clearly smaller. Thus we have the capacity

$$C=\log(1+\sqrt{2})\,.$$

Example 3: As an example of the case where the determinant of channel matrix is zero, consider

$$\begin{pmatrix} \frac12 & \frac12 & 0 \\ \frac14 & \frac14 & \frac12 \\ 0 & 0 & 1 \end{pmatrix}.$$

In order to illustrate the description in § 4 we will solve the problem directly.

The fundamental solution of

$$\begin{cases} \frac12 P_1+\frac14 P_2 =P_1' \\ \frac12 P_1+\frac14 P_2 =P_2' \\ \frac12 P_2+P_3=P_3' \end{cases} \tag{42}$$

is $Q_1^{(1)}=1$, $Q_2^{(1)}=-2$, $Q_3^{(1)}=1$ and its particular solution is $Q_1^{(0)}=2P_2'-P_3'$, $Q_2^{(0)}=2P_3'$, $Q_3^{(0)}=0$. From (39), $P_1=2P_2'-P_3'+\lambda$, $P_2=2P_3'-2\lambda$, $P_3=\lambda$. Then from (42) $P_1'=P_2'$ and $P_3'=1-2P_2'$ (from $\sum P_i'=1$). Therefore $P_1=4P_2'-1+\lambda$, $P_2=2-4P_2'-2\lambda$, $P_3=\lambda$. From the conditions $0\leq P_i\leq 1$ and $0\leq P_2'\leq\frac12$ (from $0\leq P_3'=1-2P_2'\leq 1$), the domain of values of P_2' and λ is a black part in Fig. 3.

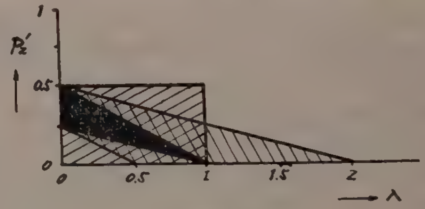

Fig. 3.

The transmission rate is

$$\{-2P_2'\log P_2'-(1-2P_2')\log(1-2P_2')-2(1-P_2')\log 2\}+\{2\lambda\log 2\}\,. \tag{43}$$

The first { } is independent of λ. The next { } is linearly dependent on λ and grows larger as λ increases.

Then the greatest lies on boundary $2P_2'+\lambda=1$. If we try to get the maximum of (43) under this constraint, we get $P_2'=\frac14$, $\lambda=1$; $C=\log 2$; $P_1=P_3=\frac12$, $P_2=0$ and $P_1'=P_4'=\frac14$, $P_3'=\frac12$.

§ 6. Geometrical Representation of the Channel Capacity

Let the channel matrix be square and of order n. We assume that $\boldsymbol{p}_i$ is a vector which has coordinates $(p_{i1},\ldots,p_{in})$ in a vector space of order n. Vertex of $\boldsymbol{p}_n$ is on a hyperplane $x_1+\ldots+x_n=1$ and limited on range $x_i\geq 0$ $(i=1,\ldots,n)$ on its plane. We will call this plane a reference plane. Also since we assume $|p_{ij}|\neq 0$, either two of $\boldsymbol{p}_i$'s do not overlap each other. Then (11) is

$$\left\{\begin{array}{l} \boldsymbol{p}_1\cdot \boldsymbol{X}=\sum\limits_j p_{1j}\log p_{1j}\\ \quad\vdots \qquad\quad \vdots\\ \boldsymbol{p}_n\cdot \boldsymbol{X}=\sum p_{nj}\log p_{nj}\end{array}\right. \qquad (44)$$

where $\boldsymbol{X}$ is a vector of coordinates $(X_1, \ldots, X_n)$. The $\boldsymbol{X}$ satisfying $\boldsymbol{p}_i\cdot\boldsymbol{X}=\sum_j p_{ij}\log p_{ij}$, is on a hyper-plane perpendicular to the $\boldsymbol{p}_i$ as Fig. 4, which passes a point at a distance $\sum_j p_{ij}\log p_{ij}/|\boldsymbol{p}_i|$ from the origin on the vector $\boldsymbol{p}_i$. Then $\boldsymbol{X}$ is an intersection of these n hyper-planes. Seeing (44), all the coordinates of $\boldsymbol{X}$ can not be positive at the same time. We define a vector $\boldsymbol{Y}$ which is determined uniquely by an equation $Y_i=\exp(X_i)$. All the coordinates of $\boldsymbol{Y}$ is always positive. Then channel capacity is given by

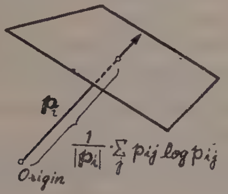

Fig. 4.

$$C=\log(\boldsymbol{Y}\cdot\boldsymbol{I}), \qquad (45)$$

where $\boldsymbol{I}$ has coordinates $(1, \ldots, 1)$. However, whether it expresses the true capacity depends on the signs of P_i 's. Since

$$P_i=\frac{\exp(-C)}{|p_{ij}|}\cdot\begin{vmatrix} p_{11}, \ldots, p_{1n}\\ \vdots \qquad \vdots\\ Y_1, \ldots, Y_n\\ \vdots \qquad \vdots\\ p_{n1}, \ldots, p_{nn}\end{vmatrix}\leftarrow\text{the } i\text{-th line,} \qquad (46)$$

$P_i\geq 0$ requires that $|p_{ij}|$ and the determinant, the second factor in (46) be of opposite sign each other. $|p_{ij}|$ is twice the volume of hyper-pyramid constructed by n vectors $\boldsymbol{p}_1, \ldots, \boldsymbol{p}_n$.[7] The determinant the second factor in (46) is obtained by replacing the i-th line of $|p_{ij}|$ by $Y_1, \ldots, Y_n$ and is twice the volume which $\boldsymbol{p}_1, \ldots, \boldsymbol{p}_{i-1}, \boldsymbol{Y}, \boldsymbol{p}_{i+1}, \ldots, \boldsymbol{p}_n$ construct. Let us move only $\boldsymbol{p}_i$, to consider sign of $|p_{ij}|$. When the sign of $|p_{ij}|$ changes from plus to minus, $\boldsymbol{p}_i$ passes through a hyper-plane $|p_{ij}|=0$ (variables are $p_{i1}, \ldots, p_{in}$). Therefore in order that (46) may not be negative, $\boldsymbol{p}_i$ and $\boldsymbol{Y}$ must be in the opposite sides of the hyper-plane $|p_{ij}|=0$. Similarly, *in order that all the P_i 's may not be negative, $\boldsymbol{Y}$ must be inside or on the hyper-pyramid which $\boldsymbol{p}_1, \ldots, \boldsymbol{p}_n$ construct, and in that case* (45) *gives the capacity.* $\boldsymbol{Y}$ on the hyper-plane $\sum Y_i=$constant, gives always the same capacity. Now if we set $\sum Y_i=1$, $C=0$ holds on this plane (reference plane). If the capacity is not zero, the vertex of $\boldsymbol{Y}$ is on a hyper-plane more distant than this from the origin. However, the distance can not be indefinitely large, since it can not go over $\sum Y_i=n$, where n is the order of the matrix. $\boldsymbol{Y}$ touches $\sum Y_i=n$ only on the point of the vertex of $\boldsymbol{I}$ and does not on other points of this hyper-plane. Also it touches the reference plane only when all the $\boldsymbol{p}_i$'s unite into one vector.

When $\boldsymbol{p}_1, \ldots, \boldsymbol{p}_n$; $\boldsymbol{Y}$ are fixed, a vector $\boldsymbol{P}$ which has coordinates $P_1, \ldots, P_n$ is determined from (46). Then we can state; *the ratio of volume of the hyper-pyramid of $\boldsymbol{p}_1, \ldots, \boldsymbol{p}_n$ to the sum of volumes of n hyper-pyramids of $\boldsymbol{Y}, \boldsymbol{p}_2, \ldots, \boldsymbol{p}_n$; $\boldsymbol{p}_1, \boldsymbol{Y}, \boldsymbol{p}_3, \ldots, \boldsymbol{p}_n$; $\ldots$; $\boldsymbol{p}_1, \ldots, \boldsymbol{Y}$ is* $\exp(C)$. Now using P_i' instead of P_i, $P_i'=Y_i\exp(-C)$ from (16), and $\boldsymbol{P}'=\boldsymbol{Y}\exp(-C)$. Since $\sum P_i'=1$, $\boldsymbol{P}'$ is on the reference plane. Using (46), the sum of volumes of n hyper-pyramids sated above is equal to the volume of the hyper-pyramid wnich $\boldsymbol{p}_1, \ldots, \boldsymbol{p}_n$ construct. An example in a three dimensional space is given in Fig. 5.

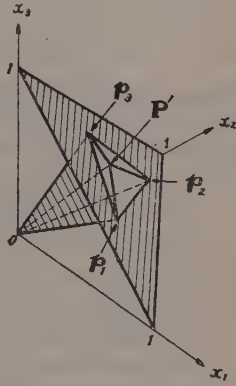

Fig. 5.

Next me assume that $\boldsymbol{P}'$ or $\boldsymbol{Y}$ is not inside the hyper-pyramid of $\boldsymbol{p}_1, \ldots, \boldsymbol{p}_n$, and suppose that we use only r vectors $\boldsymbol{p}_1, \ldots, \boldsymbol{p}_r$. The vectors $\boldsymbol{S}^{(k)}$ $(k=1, \ldots, n-r)$ which are constructed by the set of fundamental solutions $S_1^{(k)}, \ldots, S_n^{(k)}$ $(k=1, \ldots, n-r)$ of

$$\sum_{j=1}^{n} p_{ij}S_j=0 \qquad (i=1, \ldots, r) \quad (47)$$

are on a hyper-plane of (47) and cross one another vertically. A vector $\boldsymbol{X}'$ which has coordinates $X_i+\sum_j^{m-r}\nu_j S_i^{(j)}$ $(i=1, \ldots, n)$ is a general solution of

$$\begin{cases} p_1 \cdot X' = \sum p_{1j} \log p_{1j} \\ \quad\vdots \qquad\qquad \vdots \\ p_r \cdot X' = \sum p_{rj} \log p_{rj} \,. \end{cases}$$

The vertex of vector Y' which has coordinates $\exp(X_i')$ moves along a certain hyper-curve as ν_j 's vary. But the constraint on P_i' 's in the maximum value problem is that the $n-r$ fundamental solution vectors are all vertical to Y', that is, $S^{(k)} \cdot Y' = 0$ $(k=1, \ldots, n-r)$. Then the one satisfying this constraint, out of vectors Y' 's on this hyper-curve, is determined and from its coordinates the capacity is specified.

Acknowledgment

The author acknowledges Dr. K. Maeda, Chief of Research Division, Mr. Z. Kiyasu, Chief of Transmission Research Section, Mr. S. Oshima and also Dr. H. Seki of Radio Research Laboratories, Dr. S. Ikehara of Tokyo Institute of Technology, Assistant Professor H. Takahasi of Tokyo University who discussed on this research and suggested helpful comments. It is a pleasure for the author to express indebtedness to Dr. K. Kunisawa of Tokyo Institute of Technology and Mr. N. Ikeno of his Laboratory for their useful discussions and suggestions in learning Shannon's theory and developing the present theory.

References

1) C. E. Shannon and W. Weaver: The mathematical theory of Communication, 1949, Univ. of Illinois.
2) Symposium of Information Theory, 1950, London, Ministry of Supply, P. 103.
3) P. 45 of (1).
4) A. Duschek: Vorlesungen über Höhere Mathematik II, Springer, Wien 1950 P. 299.
5) P. 47 of (1).
6) P. 63 of (4).
7) O. Schreier und E. Sperner: Einführung in die Analytische Geometrie und Algebra I. 1931 Leipzig. B. G. Teubner. P. 83.

JOURNAL OF THE PHYSICAL SOCIETY OF JAPAN Vol. 8, No. 4, JULY—AUGUST, 1953

Space Charge Effect in the Oxide Cathode Layer (II)

By Takuzo SHINDO

The Electrical Communication Laboratory, Tokyo, Japan

(Received January 26, 1953)

In the previous paper it was pointed out by the writer that the space charge may be formed up in the oxide cathode layer and the Schottky type behavior of the oxide cathode can be well understood as an effect of this space charge. In this paper the theory was extended to the retarding field region and the complete static character of a planar diode was calculated, with some amendment of the theory.

In an accelerating field the static character of the diode depends decisively on the space charge effect in the cathode layer. In a retarding field, however, the space charge has little effect on the static character but the amount of the space charge varies considerably with plate voltages.

§ 1. Introduction

In the previous paper[1]* the writer has pointed out that the space charge may be formed up in the oxide cathode layer and the Schottky type behavior of the oxide cathode can be well understood as an effect of this space charge. Recently D. A. Wright and J. Woods[2] have also proposed similar theory independent of the writer's work. But unfortunately their theory way somewhat restricted and the mathematical treatment was unfavorable in some detail.

In the previous theory the thermal equilibrium of the conduction electron with the donor was neglected, as was remarked in (I), and in this respect the theory should be somewhat amended. In view of the importance of the problem the theory was completely amended and extended so as to include the the retarding field region as well as the accelerating field region and the complete static character of a planar diode was calculated.

---

* This paper will be referred hereafter as (I).

§ 2. Fundamental Equations

As the introduction of the fundamental equations was already discussed in detail in (I), we shall describe here briefly the essential points of the theory.

The electron emmision from an oxide coated cathode follows the well known Fowler-Dushman equation and the emitted current is completely independent of the potential differences between electrodes, if the Schottky effect is neglected. But, on the other hand, the continuity of the current in the oxide layer requires a definite strength of an electric field to act across the oxide layer. This electric field will not in general be in accord with a field which may be produced by the potential differences between the electrodes. Thus, in general, a space charge will be formed up in the oxide layer so as to fit into the continuity equation. In metal cathode, however, owing to its high electron mobility the space charge will provide no essential role, but in semi-conductor the space charge has a remarkable effect.

In line with the above consideration an equation describing the space charge in the cathode layer shall be introduced. We start from one-dimensional diffusion equations:

$$j=en^{-}\mu E_r^{(i)}-eD\frac{dn^{-}}{dx}\,, \tag{2.1}$$

where
- j: the current carried by the conduction electron,
- n^{-}: the density of the conduction electron,
- $E_r^{(i)}$: an electric field in the cathode layer,
- e, μ, D: the charge, mobility and diffusion coefficient of the conduction electron.

An electric field, $E_r^{(i)}$, is composed of an electric field produced by the conduction electrons, E^{-}, and a field produced by the vacant active centers, E^{+}, which are related to the charge densities by the Poisson equations:

$$\left.\begin{aligned}\frac{dE^{-}}{dx}&=\frac{4\pi e}{\kappa}n_0e^{-g(x)}\\ \frac{dE^{+}}{dx}&=-\frac{4\pi e}{\kappa}n_0e^{g(x)}\,,\end{aligned}\right\} \tag{2.2}$$

where κ is the dielectric constant of the oxide, n_0 is the electron density in bulk oxide and a function $g(x)$ determines the electron distribution in the cathode layer*. From an Eq. (2.2) we obtain:

$$E_r^{(i)}=E^{+}+E^{-}=-2N_0\left[\int\sinh g(x)dx+E_0\right], \tag{2.3}$$

where $N_0=\dfrac{4\pi e}{\kappa}n_0$ and E_0 is a constant of integration. Inserting Eq. (2.3) in (2.1) and taking into account a relation

$$n^{-}=n_0e^{-g(x)}\,,$$

the Eq. (2.1) can be regarded as an eqation to determine the electron distribution, in which the current j is an unknown parameter. The parameter, j, is related to the electron density at the cathode surface by an equation

$$j=en^{-}D_0\sqrt{\frac{kT}{2\pi m}}e^{-\chi/kT}=en^{-}\mathit{\Phi}_0\,, \tag{2.4}$$

where k is the Boltzmann constant, T is the cathode temperature in °K, e and m are the charge and mass of the electron, χ is the height of the surface potential barrier and D_0 the mean transmittion coefficent for electrons at the emitting surface.

Thus we obtain an equation for $g(x)$

$$\frac{4\pi}{\kappa}j=-2N_0^2\mu e^{-g(x)}\left[\int\sinh g(x)dx+E_0\right]+\frac{D}{2N_0^2\mu}\frac{dg}{dx}\,. \tag{2.5}$$**

Differentiating with respect to x and introducing a non-dimensional quantity $X=x/l_0$ $\left(l_0=\sqrt{\dfrac{kT}{8\pi n_0e^2}}\right)$, we obtain

---

* Dr. D. A. Wright has kindly pointed out to me that the equation (1.3) in (I) should be written as

$$\left.\begin{aligned}\frac{dE^{-}}{dx}&=N_0(1+f)\\ \frac{dE^{+}}{dx}&=-N_0(1+f)^{-1}\end{aligned}\right\}.$$

** The diffusion coefficient D is related to the mobility μ by the Einstein relation,

$$\mu/D=e/kT\,.$$

$$\left.\begin{aligned}&\ddot{g}-Qe^{g}\dot{g}-\sinh g=0\\&\dot{g}=dg/dX \text{ etc.}\\&Q=\frac{i}{\mu}\sqrt{\frac{8\pi^2 e}{N_0^3\kappa kT}}\,.\end{aligned}\right\}\qquad(2.6)$$

This is an exact differential equation for $g(X)$, which can be solved under appropriate boundary conditions.

The boundary conditions to be imposed on the Eq. (2.6) are

$$\left.\begin{aligned}&g=0 &&\text{at}\quad X=0\\&g=g_l &&\text{at}\quad X=L=l/l_0\,,\end{aligned}\right\}\qquad(2.7)$$

that is; we consider the thickness of the oxide layer to be l and the electron densities at the metal-oxide interface to be

$$n^-=n_0e^{-g_l}\,,$$

and

$$n^-=n_0$$

respectively (see Fig. 1).

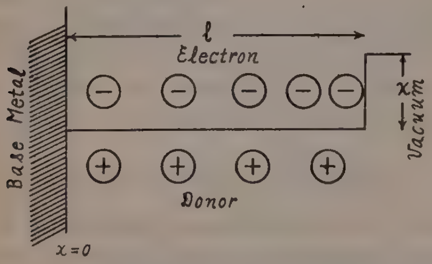

Fig. 1. A simple Model of the Oxide Cathode.

An approximate solution of Eq. (2.6) can be obtained at once by a series expansion

$$g=\sum_n g_n\,,$$

in which g_n is a small quantity of the n-th order. The zeroth order solution g_0 can be written down as follows:

$$\left.\begin{aligned}&g_0=g_l\exp[-\alpha_1(L-X)]\\&\alpha_1=\tfrac{1}{2}(Q\sqrt{Q^2+4})\,,\end{aligned}\right\}\qquad(2.8)$$

provided that a condition $l\gg l_0$ hold. The integration constant, E_0, can be determined from the Eqs. (2.5) and (2.8), and we obtain

$$E_0=I/2N_0^2\mu\,.$$

Thus we can calculate the resultant field in the oxide, $E_r^{(i)}$, by means of the Eqs. (2.8) and (2.3), and the field at cathode surface can be obtained by

$$E_r^{(e)}=\kappa E_r^{(i)}(L)\,,$$

thus, giving

$$\left.\begin{aligned}&E_r^{(e)}=\kappa\left(e^{-g_l}\frac{\Phi_0}{\mu}-\frac{\beta g_l}{\alpha_1}\right)\\&\beta=\sqrt{\frac{8\pi n_0 kT}{\kappa}}\\&\alpha_1=\tfrac{1}{2}(Q+\sqrt{Q^2+4})\\&Q=j/\sigma\beta\,,\quad\sigma=en_0\mu\,.\end{aligned}\right\}\qquad(2.9)$$

On the other hand the emission current, j, is given by

$$j=en_0e^{-g_l}\Phi_0\,.\qquad(2.10)$$

From the Eqs. (2.9) and (2.10) we can calculate the relationship between the field strength, $E_r^{(e)}$, at the cathode surface and the emission current, j, with given value of g_l.

§ 3. Accelerating Field

In the presence of an accelerating field at the cathode surface, the height of surface potential barrier is lowered proportional to $\sqrt{E_r^{(e)}}$ as a result of the Schottky effect. The Eqs. (2.9) and (2.10) should then be replaced by

$$\left.\begin{aligned}&E_r^{(e)}=\kappa\left(e^{-g_l}\frac{\Phi}{\mu}-\frac{\beta g_l}{\alpha_1^*}\right)\\&\alpha_1^*=\tfrac{1}{2}(Q^*+\sqrt{Q^{*2}+4})\\&Q^*=j/\sigma\beta\,,\end{aligned}\right\}\qquad(3.1)$$

and

$$\left.\begin{aligned}&j=en_0e^{-g_l}\Phi\\&\Phi=\Phi_0\exp(4.39/T\cdot\sqrt{E_r^{(e)}})\\&(E_r^{(e)}\text{ in volts/cm.})\,.\end{aligned}\right\}\qquad(3.2)$$

The Eqs. (3.1) and (3.2) are transcendental equations in $E_r^{(e)}$, which can be solved by a self-consistent method.

In order to obtain the static character of a planar diode in an accelerating field, it is desirable to calculate the relationship between $E_r^{(e)}$ and j from the Eqs. (3.1) and (3.2) with given value of T, and then the Langmuir-Child space charge relationship[3)] can be employed.

According to Langmuir-Child theory*, we shall introduce non-dimensional quantities

$$\eta=\frac{V(x)}{V_0}\,,\qquad \xi=\left(\frac{16\pi j}{aV_0^{3/2}}\right)^{1/2}\cdot x=Lx\,,$$

where $V(x)$ is the potential at an arbitrary point x between electrodes, V_0 is given by

$$\tfrac{1}{2}mv_0^2=\tfrac{3}{2}kT=eV_0\,,$$

and a is defined by

---

* Ivey's equation[4)], which was employed by Wright and Woods in their theory, can be deduced from the Langmuir-Child equation.

$$a=v_0/\sqrt{V_0}\,.$$

Then the potential at any point is given by a relation

$$\tfrac{4}{3}(u-2\alpha_1)\sqrt{u+\alpha_1}=\pm\xi+\alpha_2\,, \qquad (3.3)$$

where $u=\sqrt{1+\eta}$, and α_1, α_2 are integration constant. The constant α_1 is related to field strength $E_r{}^{(e)}$, at the cathode surface by a relation:

$$\pm\sqrt{1+\alpha_1}=L/V_0\cdot E_r{}^{(e)}\,. \qquad (3.4)$$

When the cathode is in an accelerating field, the plus sign should be chosen in Eqs. (3.3) and (3.4). The integration constant α_2 is determined by a relation

$$\tfrac{4}{3}(1-2\alpha_1)\sqrt{1+\alpha_1}=\alpha_2\,, \qquad (3.5)$$

if the zero point of the potential is chosen at the cathode surface.

The constants α_1 and α_2 can be determined by the Eqs. (3.4) and (3.5) when the relationship between $E_r{}^{(e)}$ and j is known, which can be calculated by the Eqs. (3.1) and (3.2), for given value of temperature. With these values of constants the plate voltages are determined by Eq. (3.3), in which ξ should be

$\xi=Ld\,.$ (d is a distance between electrodes.)

These calculations are carried out only in a range where the cathode field, $E_r{}^{(e)}$, is positive ($E_r{}^{(e)}\geqq 0$).

§ 4. Retarding Field

When the cathode acts in a retarding field, space charge will be formed up between electrodes and the emission current is limited by a potential hump between electrodes. The fact that the space charge in the cathode layer may act also in the retarding field, can be shown by the following calculations.

According to the well known Fry-Langmuir theory of the space charge conduction, we shall assume that the emitted electron obeys the Maxwellian distribution. Then the space charge between the electrodes can be written down as

$$\rho_\alpha=2e\int_{\sqrt{\frac{2eV}{m}}}^{v_0'}\frac{n(v_0)}{v}dv_0+e\int_{v_0'}^{\infty}\frac{n(v_0)}{v}dv_0\,.$$

$$\rho_\beta=e\int_{v_0'}^{\infty}\frac{n(v_0)}{v}dv_0\,,$$

where ρ_α is a space charge between the cathode and the potential hump whose potential is $-V_m$ (α region), ρ_β is a space charge between the hump and anode (β region), and v_0' is given by

$$v_0'=\left(\frac{2eV_m}{m}\right)^{1/2}.$$

When we adopt the Maxwellian distribution in $n(v_0)$, the integrations are carried out and the field strength at any point is given by the relation:

$$\frac{d\eta}{d\xi}=\left[e^\eta-1\pm\left(e^\eta erf\sqrt{\eta}-\frac{2}{\sqrt{\pi}}\sqrt{\eta}\right)\right]^{1/2}. \qquad (4.1)$$

where ξ and η are non-dimensional quantities:

$$\xi=\frac{x-x_m}{L}\,, \qquad L=\left(\frac{kT}{8\pi ej\sqrt{\frac{\pi m}{2kT}}}\right)^{\frac{1}{2}} \qquad (4.2)$$

x_m is the position of the potential hump, and plus or minus sign corresponds to α or β region respectively. The potential at any point is given by a numerical chart or a graph[5].

In line with above considerations our equations (2.9) and (2.10) should be modified as follows:

$$\left.\begin{aligned} E_r{}^{(e)}&=\kappa\left(e^{-g_l}\frac{\Phi'}{\mu}-\frac{\beta g_l}{\alpha_1'}\right)\\ \beta&=\sqrt{\frac{8\pi n_0 kT}{\kappa}}\\ \alpha_1'&=\tfrac{1}{2}(Q'+\sqrt{Q'^2+4})\\ Q'&=j/\sigma\beta\,, \qquad \sigma=en_0\mu \end{aligned}\right\} \qquad (4.3)$$

and

$$j=en_0e^{-g_l}\Phi' \qquad (\Phi'=\Phi_0e^{-\eta m})\,. \qquad (4.4)$$

The calculations are carried out in following manner. Assuming any value of V_m (or η_m), the cathode field, $E_r{}^{(e)}$, and the current, j, can be calculated by the Eqs. (4.3) and (4.4). On the other hand, Fry-Langmuir theory requires that the cathode field should be euqal to a value given by the equation (4.1) with same value of η_m and j as above. When the value of g_l in Eqs. (4.3) and (4.4) is properly chosen the two values of $E_r{}^{(e)}$ should be coinside. This value of g_l is determined by a trial and error method. The calculations are very tedious but straightfoward. In this manner the static character of the diode was thoroughly calculated in a range of the retarding field. As is shown in Fig. 3, however, the Fry-Langmuir curve does not fit with the Langmuir-Child curve, we have, therefore, shifted the Langmuir-Child curve so as to join smoothly to the Fry-Langmuir curve.

§ 5. Numerical Calculations

We have employed same numerical values as in (I); that is, as the density n_0 of the conduction electrons in thermal equilibrium at 1000° K a value

$$n_0=5\times10^{14}\,\mathrm{cm}^{-3},$$

was chosen. From this value we can calculated the electron densities at various temperature by means of Nijboer formula, taking the energy gap ΔE between the donor level and the bottom of the conduction band to be 0.7 *ev.*. The values of Φ_0 can be computed from Eq. (2.4) taking $D_0=1.0$ and $\chi=0.3$ *ev.*.

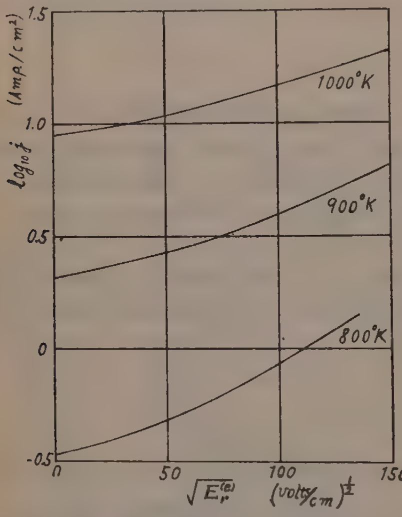

Fig. 2. The Schottky plots of the Oxide Cathode.

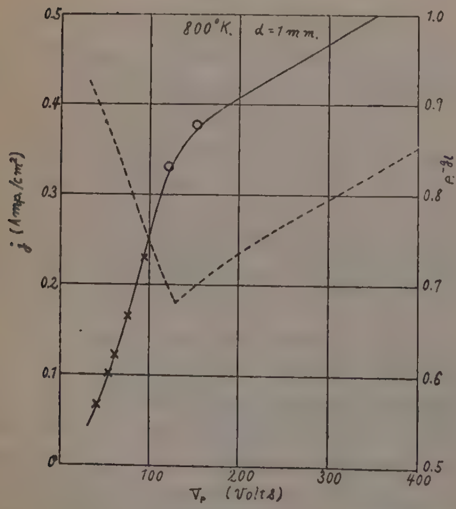

Fig. 3. A Static Character of a Planar Diode.
○ Langmuir-Child. × Fry-Langmuir.

Table I.

g_l	$E_r^{(e)}$ KV/cm	j Amp./cm²	$\log_{10} j$
800° K			
0	9.78	0.870	−0.0607
0.1	7.40	0.733	−0.135
0.2	5.12	0.613	−0.213
0.3	2.85	0.502	−0.300
0.386	0	0.341	−0.467
900° K			
0	19.25	5.79	0.763
0.1	14.16	4.76	0.678
0.2	9.33	3.86	0.587
0.3	4.49	3.02	0.480
0.348	0	2.10	0.322
1000° K			
0	34.28	27.47	1.44
0.22	13.64	16.3	1.21
0.24	11.84	15.5	1.19
0.26	10.00	14.6	1.16
0.28	8.1	13.7	1.14

Table II. (800° K)

A Accelerating Field

V_p volts	j Amp./cm²	g_l	e^{-g_l}
471.6	0.550	0.124	0.887
371.1	0.508	0.178	0.837
275.9	0.457	0.248	0.780
239.1	0.435	0.277	0.758
210.6	0.417	0.300	0.741
189.8	0.402	0.318	0.728
158.6	0.380	0.346	0.708
128.5	0.340	0.386	0.680

B Retarding Field

V_p volts	j Amp./cm²	g_l	e^{-g_l}
118.4	0.319	0.360	0.698
112.3	0.296	0.337	0.714
106.6	0.274	0.313	0.731
101.1	0.254	0.290	0.748
95.8	0.234	0.269	0.764
85.0	0.191	0.231	0.794
71.4	0.155	0.185	0.831
63.3	0.130	0.159	0.853
49.1	0.090	0.120	0.887
37.9	0.062	0.093	0.911

C Fry-Langmuir Theory ($j_0=0.34$ Amp./cm²)

V_p volts	j Amp./cm²
115.2	0.308
107.4	0.278
100.3	0.252
93.7	0.228
87.5	0.206
75.9	0.169
61.7	0.125
53.7	0.102
40.6	0.069

Then for a given cathode temperature, the relation between $E_r^{(e)}$ and j has been calculated by the use of Eqs. (2.9) and (21.0), taking $\mu=100$ cm^2/volts. sec. and $\kappa=10$ as the reasonable values of the mobility μ and dielectric constant κ. These values have been regarded as constants independent of temperature. The results of these calculations are shown in Fig. 2 and in Table I.

Static character of a planar diode was calculated in a scheme described in § 3, taking a distance d between electrodes as 1 mm. and neglecting the potential drop over the oxide layer. Calculated static character at 800° K is shown in Fig. 3 and in Table II–A.

Finally, the static character in a retarding field was calculated according to a scheme of § 4. These calculations have to be carried out also self-consistently. Numerical data at 800° K are shown in Table 2–B and the result in Fig. 3. For comparison, the character calculated by Fry-Langmuir scheme (disregarding the unique relation between $E_r^{(e)}$ and j) is shown by cross marks in Fig. 3, and data in Table 2–C. In this figure, we have shown in broken line the amount of space charge:

$$e^{-g_l}=\frac{\text{(Electron density at the cathod surface)}}{\text{(Electron density in bulk oxide)}}\,.$$

From this result we can conclude that in a retarding field the space charge in the oxide layer can scarcely affect the static character but the amount of the space charge varies considerably with plate voltage.

§ 6. Remarks on Richardson Plot

The work function of hot cathode is usually determined by so called Richardson line method and this method is most commonly used. When the work function is determined by this method, it should be kept in mind that the space charge effect may be superposed on the work function.

The saturation current density, j_0, may be considered to be the value at zero field, as shown in Fig. 3. From the Eq. (2.9), however, the space charge still exists and its amount can be deduced from

$$e^{-g_l}\frac{\Phi_0}{\mu}=\frac{\beta g_l}{\alpha_1}\,.$$

When the value of g_l is small we obtain

$$g_l\equiv g^0=\frac{\Phi_0}{\mu}\Big/\left(\frac{\Phi_0}{\mu}+\frac{\beta}{\alpha_1}\right).$$

Strictly speaking, therefore, the value, g^0, does depend on the cathode temperature. Even if the deviation from Richardson line is small, measured value does not represent the work function, χ, but

$$\chi+g^0\,.$$

We must be carefull, therefore, in the interpretation of work function of the oxide cathode.

§ 7. Conclusions

Space charge equation was calculated in an amended form and the complete static character of a planar diode was calculated, taking into account the space charge effect in the cathode layer.

Static character depends decisively on the space charge effect in the cathode layer when it acts in the accelerating fields. In the retarding fields, it can scarcely affect the static character but its amount varies with the plate voltages.

It should be kept in mind that the value of g^0 may not be separated from the χ value, if we determine the work function of the semi-conductor cathode by the Richordson line method.

The space charge predicted here may have an important role in the problem of value noise and transient phenomenon.

References

1) T. Shindo: Jour. Phys. Soc. Japan **6** (1951) 352.

2) D. A. Wright and J. Woods: Proc. Phys. Soc. B. LXV (1952) 134.

3) H. Rothe and W. Kleen: "Grundlagen und Kennlinien der Elektronenroehren" (1940); Y. Watanabe: "Theory of the Space Charge Conduction". p. 162, (1950) (in Japanese).

4) H. F. Ivey: Phys. Rev. **76** (1949) 554.

5) Y. Watanabe: cit. above (4) p. 113.

JOURNAL OF THE PHYSICAL SOCIETY OF JAPAN Vol. 8, No. 4, JULY—AUGUST, 1953

On the Theory of Diffraction of the Electromagnetic Wave by Mountains

By Koichi FURUTSU

Central Radio Wave Observatory

(Received March 4, 1953)

The equations for the field strength of the diffracted electromagnetic wave by mountains are derived for any polarization of the wave and any positions of the transmitter and receiver, without making important assumption except that the change of the mountain characteristics within the distance of a wave length is sufficiently small. Also, the general equation for the contribution of the field strength of any given picture of wave path which consists of the free space propagation parts and the diffraction or reflection parts by mountains is obtain.

§1. Introduction

Up to the present, the diffracted electromagnetic wave has been calculated either by the method in which the shape of a mountain is assumed to be a sphere or a cylinder, or by Kirchoff's approximation, provided that the mountain is a black body. Although the calculation may be done rigorously in the former within the limits of the assumption, the results may not be available for practical use due to the too idealized forms of the mountain assumed. Also in the latter, the result of the calculation can hardly be accepted unless the definite criterion is given, as will be easily imagined from the fact that the result is independent of the shape and the conductivity of the mountain.

In this paper, these special assumptions as stated above are not introduced, except that the charge of mountain surface characteristics, e.g. radii of curvature, within the distance of a wave length is sufficiently small. Further, the calculations are performed exclusively in the form of vector field formulated by Kemmer[*], which permits us the far simpler calculation than the one in the other method.

§2. Wave Equation and Green's Function of Electromagnetic Field

Using the usual notations, Maxwell's equation can be expressed in the following form:

$$(\mathrm{s}\partial)\begin{pmatrix}0 & 1\\ 1 & 0\end{pmatrix}\begin{pmatrix}jE\\ H\end{pmatrix}-\frac{\omega}{c}\begin{pmatrix}\varepsilon & 0\\ 0 & \mu\end{pmatrix}\begin{pmatrix}jE\\ H\end{pmatrix}=\frac{4\pi}{c}\begin{pmatrix}I_e\\ 0\end{pmatrix}, \tag{2.1}$$

where

$$(\mathrm{s}\partial)=\sum_{i=1}^{3} s_i\partial_i\ , \qquad \partial=j\partial/\partial x_i\ ,$$

$$s_1=\begin{pmatrix}0 & 0 & 0\\ 0 & 0 & j\\ 0 & -j & 0\end{pmatrix}, \qquad s_2=\begin{pmatrix}0 & 0 & -j\\ 0 & 0 & 0\\ j & 0 & 0\end{pmatrix},$$

$$s_3=\begin{pmatrix}0 & j & 0\\ -j & 0 & 0\\ 0 & 0 & 0\end{pmatrix}. \tag{2.2}$$

Introducing Pouli's spin matrices ρ_i's defined by

$$\rho_1=\begin{pmatrix}0 & 1\\ 1 & 0\end{pmatrix}, \qquad \rho_2=\begin{pmatrix}0 & -j\\ j & 0\end{pmatrix}, \qquad \rho_3=\begin{pmatrix}1 & 0\\ 0 & -1\end{pmatrix},$$

then, Eq. (2.1) takes the form

$$[(\gamma\partial)-U/c]\psi(x)=4\pi J(x)\ , \tag{2.3}$$

where

$$\gamma_i=\rho_1 s_1\ , \qquad (x)=(x_1\ , x_3\ , x_3)\ ,$$

$$\psi=\begin{pmatrix}jE\\ \\ E\end{pmatrix}, \qquad J=\begin{pmatrix}\dfrac{I_e}{c}\\ 0\end{pmatrix},$$

$$U=\tfrac{1}{2}\omega\{\varepsilon(1+\rho_3)+\mu(1-\rho_3)\}\ . \tag{2.4}$$[**]

For arbitrary vectors n, m and l, it holds the following lemmata:

$$(ns)(ms)(ls)+(ls)(ms)(ns)=(nm)(ls)+(lm)(ns)\ , \tag{2.5}$$

$$\rho_1{}^2=1\ , \qquad \rho_1\rho_2=j\rho_3\ , \qquad \text{etc.,}$$

$$(ls)(ms)-(ms)(ls)=-j(l\times m\cdot s)\ ,$$

which give the relations for $(nm)=0$

$$(ns)(ms)^2=\{m^2-(ms)^2\}(ns)\ , \qquad (ns)(ms)(ns)=0\ ,$$

$$(ns)^2(ms)^2=(ms)^2(ns)^2\ , \qquad (ns)^4=n^2(ns)^2\ , \tag{2.6}$$

---

[*] Kemmer, Proc. Roy. Soc. (1939).

[**] K. Furutsu, Jour. Phys. Soc. of Japan, Vol. 7, No. 5, p. 458～466, 1952.

and

$$(ns)\{(ns)^2-n^2\}=0\,, \qquad \rho_1\rho_3+\rho_3\rho_1=0\,.$$

From the latter, we find that the eigen values of (ns) are $\pm|n|$ and 0. The formulae (2.6) will be frequently used later.

The Green function $G(x, x')$ of electromagnetic field and its adjoint function $\overline{G}(x', x)$, x' being the coordinate of any point in space, are respectively defined by

$$[\gamma_i\partial_i-U/c]\,G(x\,,\,x')=4\pi\delta(x-x')\,,$$
$$\overline{G}(x', x)[-\gamma_i\overleftarrow{\partial}_i-U/c]=4\pi\delta(x-x')\,, \tag{2.7}$$

with the same boundary condition for both of them. Thus, the solution $\psi(x)$ of (2.3) is given by

$$\psi(x)=\int G(x\,,\,x')J(x')dx'\,,\quad dx'=dx_1'dx_2'dx_3'\,. \tag{2.8}$$

As is easily found from (2.8) or directly from (2.7), the Green functions $G(x\,,\,x')$ and $\overline{G}(x'\,,\,x)$ are matrices having six rows and columns.

For any ψ-vectors ψ' and ψ'', it holds that

$$\psi''(\gamma_i\partial_i-U/c)\psi'-\psi''(-\gamma_i\overleftarrow{\partial}_i-U/c)\psi'$$
$$=\partial_i(\psi''\gamma_i\psi')\,.$$

Hence, integrating the both hand sides in an arbitrary space Σ, we get the following lemma under the assumption that $\psi''\gamma_i\psi'$ is a continuous vector in the space Σ:

$$\int_\Sigma\{\psi''(\gamma_i\partial_i-U/c\psi'-\psi''(-\gamma_i\overleftarrow{\partial}_i-U/c)\psi'\}dv$$
$$=j\int_\sigma\psi''(n_i\gamma_i)\psi'd\sigma\,, \tag{2.9}$$

where the surface integration on the right hand side is performed on the whole surface σ of Σ and n is the outward unit vector normal to σ. When $(\psi''\gamma_i\psi')$'s change discontinuously across any surface, say σ', in the space Σ, then the surface integration on both sides of σ must be added to the right hand side of (2.9). However, in so for as ψ'' and ψ' satisfy the boundary condition of the real electromagnetic field, $(n\gamma)\psi'$, $\psi''(n\gamma)$ and thus also $\psi''(n\gamma)^3\psi'=\psi''(n\gamma)\psi'$ cange continuously across the discontinuous surface σ' of a medium, as is evident from the characteristics of matrices γ_i's. Thus the correction term of (2.9) always vanishes and our following calculations can be done as if $(\psi''\gamma_i\psi')$'s are continuous everywhere.

We now set $\psi'(x)=G(x\,,\,x_2)$ and $\psi''(x)=\overline{G}(x_1\,,\,x)$ in (2.9) and take the space Σ so large that both points x_1 and x_2 are contained in it. Then it follows from (2.7) that

$$\overline{G}(x_1\,,\,x_2)-G(x_1\,,\,x_2)$$
$$=\frac{j}{4\pi}\int_\sigma\overline{G}(x_1\,,\,\sigma)(n\gamma)G(\sigma\,,\,x_2)d\sigma\,. \tag{2.10}$$

The right hand side of (2.10) does not depend on the form of σ, since the left hand side is so. On the other hand, both $\overline{G}(x_1\,,\,x)$ and $G(x\,,\,x_2)$ must be outward propagating wave at $|x_1-x|$, $|x-x_2|\rightarrow\infty$. Hence, if we take σ sufficiently remote from the points x_1 and x_2, the phase term of the right hand side of (2.10) must change with σ. This is consistent with the left hand side only when the right hand side term identically vanishes. Thus,

$$\overline{G}(x_1\,,\,x_2)-G(x_1\,,\,x_2)=0\,. \tag{2.11}$$

The relation (2.11) holds for an arbitrarily changing medium and also for the Green functions G_0 and $\overline{G}_0$ in free space:

$$\overline{G}_0(x_1\,,\,x_2)=G_0(x_1\,,\,x_2)\,. \tag{2.12}$$

We now put $\psi'(x)=G_0(x\,,\,x_2)$, $\psi''(x)=G_0(x_1\,,\,x)$ in (2.9) and take for Σ the whole space bounded by a mountain surface, say σ. Then, using (2.7), we have the equations (Fig. 1)

$$G(x_1\,,\,x_2)=G_0(x_1\,,\,x_2)$$
$$+\frac{j}{4\pi}\int_\sigma G(x_1\,,\,\sigma)(n\gamma)G_0(\sigma\,,\,x_2)d\sigma\,, \tag{2.13}$$

when the points x_1 and x_2 are both in Σ, or

$$0=G_0(x_1\,,\,x_2)$$
$$+\frac{j}{4\pi}\int_\sigma G(x_1\,,\,\sigma)(n\gamma)G_0(\sigma\,,\,x_2)d\sigma\,, \tag{2.14}$$

when the point x_2 is not in Σ.

Taking into account the assumption that the radii of curvature of the mountain surface are sufficiently large compared with the wave length, the integration in (2.13) or (2.14) can be performed by the phase stationary method: As it will be seen later, the phase of $G_0(\sigma', x_2)$ (σ' denotes the coordinate of any point on σ) is proportional to the length of the straight line connecting the points σ' and x_2, and that of $G(x_1\,,\,\sigma')$ is to the length of geodesic line between the points x_2 and σ', which contacts on and slides along the mountain surface σ when the straight line between these points

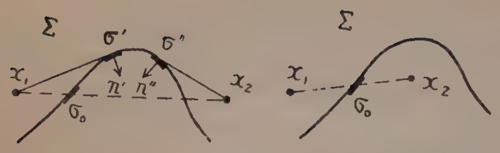

Fig. 1.

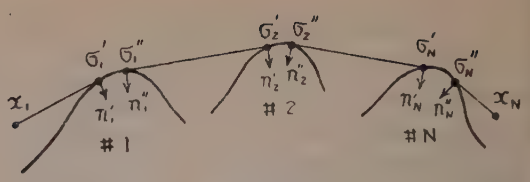

Fig. 2.

is interrupted by the mountain, or proceeds straightly when it is not (Fig. 1). Hence, the value of the surface integral in (2.13) is decisively contributed by the integration on the vicinity of two points σ'' and σ_0 on σ, say respectively σ''-region and σ_0-region shown in Fig. 1, as is evident from the phase stationary method of calculation. On the other hand, the integration value in (2.14) is decisively contributed by the integration on σ_0-region only.

For the integration on the σ_0-region in (2.13), the point x_2 can be considered to be outside of Σ from the point of view of phase stationary method of calculation, and the formula (2.14) can be applied. Thus, the value of this integration is equal to $-G_0(x_1, x_2)$ and is canceled by the first term in the right side of (2.13). Hence,

$$G(x_1, x_2) \simeq \frac{j}{4\pi}\int_{\sigma''} G(x_1, \sigma)(n\gamma) \times G_0(\sigma, x_2)d\sigma . \qquad (2.15)$$

By the similar method of calculation, we have

$$G(x_1, x_2) \simeq -\frac{j}{4\pi}\int_{\sigma'} G_0(x_1, \sigma)(n\gamma) \times G(\sigma, x_2)d\sigma , \qquad (2.16)$$

where σ'-region is shown in Fig. 1.

Since these equations for $G(x_2, x_1)$ hold for any points of x_1 and x_2 which are intervened by a mountain, we can use (2.16) for $G(x_2, \sigma)$ in (2.15), and find

$$G(x_1, x_2) \simeq \left(\frac{1}{4\pi}\right)^2 \int_{\sigma'} d\sigma' \int_{\sigma''} d\sigma'' G(x_1, \sigma')(n'\gamma) G(\sigma', \sigma'')(n''\gamma)G_0(\sigma'', x_2) , \qquad (2.17)$$

where $n(\sigma')$ and $n(\sigma'')$ are respectively denoted by n' and n'' for brevity. The criterion for (2.17) will be rigorously discussed in a later section.

The equation (2.17) can be generalized for the diffracted wave over several mountains, say from the 1-st to the N-th according to the order of mountains over which the wave propagates (Fig. 2):

$$\begin{aligned} G(x_1, x_N) \simeq \prod_{i=1}^{N} \left(\frac{-j}{4\pi}\int_{\sigma_i'} d\sigma_i'\right)\left(\frac{j}{4\pi}\int_{\sigma_i''} d\sigma_i''\right) & \\ \times G_0(x_1, \sigma_1')(n_1'\gamma)G^{(1)}(\sigma_1', \sigma_1'') & \\ \times (n_1''\gamma)G_0(\sigma_1'', \sigma_2')(n_2'\gamma) & \\ \times G^{(2)}(\sigma_2', \sigma_2'')(n_2''\gamma)G_0(\sigma_2'', \sigma_3') & \\ \times \cdots\cdot(n_N''\gamma)G_0(\sigma_N'', x_N) , & \end{aligned} \qquad (2.18)$$

where $G^{(i)}$ is the Green function satisfying the boundary condition in the case in which only the i-th mountain exists, and the regions σ_i' 's and σ_i'' 's are indicated in Fig. 2. The each term in (2.18) closely corresponds to the respective part of the wave path between the points x_1 and x_N, and thus their physical meanings are also evident. As the result, we find that the Green function is exclusively expressed in terms of the respective Green function of each mountain in the vicinity of wave path.

§ 3. General Formulation of Green's Function

We first introduce the following formula:

$$[(\gamma\partial)-U/c][(\gamma\partial)+\{(\gamma\partial)^2-\partial^2 +(\bar{U}/c)(U/c)\}(U/c)^{-1}]=\partial^2-k^2 , \qquad (3.1)$$

where

$$\bar{U}=\rho_1 U \rho_1=\tfrac{1}{2}\omega[\varepsilon(1-\rho_3)+\mu(1+\rho_3)] ,$$
$$k^2=(\bar{U}/c)(U/c)=\varepsilon\mu(\omega/c)^2 . \qquad (3.2)$$

The equation (3.1) is easily verified by the use of the relations

$$\gamma_i U=\bar{U}\gamma_i , \qquad (\gamma\partial)^3=(\gamma\partial)\partial^2 ,$$
$$(U/c)(\gamma\partial)^2(U/c)^{-1}=(\gamma\partial)^2 , \qquad (3.3)$$

which are derived from (2.6). Hence, setting

$$G(x, x')=[(\gamma\partial)+\{(\gamma\partial)^2-\partial^2+k^2\} \times(U/c)^{-1}]\phi(x, x') , \qquad (3.4)$$

then,

$$[(\gamma\partial)-(U/c)]G(x, x')=(\partial^2-k^2)\phi(x, x') . \qquad (3.5)$$

Thus, we find from (2.7)

$$(\partial^2-k^2)\phi(x, x')=4\pi\delta(x-x') . \qquad (3.6)$$

Using (3.6), the expression (3.4) takes the form

$$G(x\,,\,x')=[(\gamma\partial)+(\gamma\partial)^2(U/c)^{-1}]\phi(x\,,\,x')$$
$$-(U/c)^{-1}4\pi\delta(x-x')\,. \qquad (3.7)$$

By the similar method of derivation,

$$G(x\,,\,x')=\phi(x\,,\,x')[-(\gamma\overleftarrow{\partial}')+(U/c)^{-1}(\gamma\overleftarrow{\partial}')^2]$$
$$-(U/c)^{-1}4\pi\delta(x-x')\,. \qquad (3.8)$$

In free space, the solution of (3.6), say ϕ_0, is

$$\phi_0(x_1\,,\,x_2)=e^{-jk|x_1-x_2|}/|x_1-x_2|\,. \qquad (3.9)$$

In the case in which $k|x_1-x_2|\gg 1$,

$$G_0(x_1\,,\,x_2)\simeq\eta(k_{12})\phi_0(x_1\,,\,x_2)\,, \qquad (3.10)$$

where

$$\eta(k_{12})=(\gamma k_{12})+(\gamma k_{12})^2(U/c)^{-1}\,,$$
$$k_{12}=k(x_1-x_2)/|x_1-x_2|\,. \qquad (3.11)$$

To calculate (2.17) or (2.18), it is also necessary to obtain the Green function on each mountain in the vicinity of wave path. In this case, the formulation (3.4) is not convenient, because the solution of (3.6) satisfying the boundary condition on a mountain surface does not generally become a scalar solution but a matrix solution. Hence, it will be necessary to discuss the general formula for the Green function in an arbitrary medium for a while.

We divide a given space into two spaces, say 1-st and 2-nd space, by any surface σ, as is shown in Fig. 3, and denote by $\psi_{k'}^{(1)}$'s and $\psi_{k'}^{(2)}$'s the complete sets of the solutions of

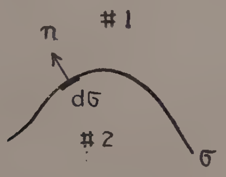

Fig. 3.

$$[(\gamma\partial)-U/c]\psi_{k'}^{(i)}=0\,, \quad (i=1,\,2)\,, \qquad (3.12)$$

satisfying the boundary conditions in the 1-st and 2-nd space, respectively, and by $\overline{\psi}_{k'}^{(1)}$'s and $\overline{\psi}_{k'}^{(2)}$'s the corresponding solutions of

$$\overline{\psi}_{k'}^{(i)}[-(\gamma\overleftarrow{\partial})-U/c]=0\,. \qquad (3.13)$$

Generally, k''s consist of two kinds of suffices. The one discriminates the two kinds of polarization of the wave and the other mainly specifys the phase characteristics, e.g. wave numbers in some two directions (see the later example). Then, putting $\psi''=\overline{\psi}_{k'}$ and $\psi'=\psi_{k''}$ in (2.9) and using (3.12) and (3.13), we find that the value of

$$\int_\sigma \overline{\psi}_{k'}(n\gamma)\psi_{k''}d\sigma \qquad (3.14)$$

is invariant for any deformation of σ in so far as the deformation is performed in the region where the singular points of $\overline{\psi}_{k'}$ and $\psi_{k''}$ do not exist, whether the medium is continuous or not, as is stated in section 2. Further, taking into account the boundary conditions, we have, as in the case of derivation of (2.11),

$$\int_\sigma \overline{\psi}_{k'}^{(1)}(n\gamma)\phi_{k''}^{(1)}d\sigma=\int_\sigma \overline{\psi}_{k'}^{(2)}(n\gamma)\psi_{k''}^{(2)}d\sigma=0\,. \qquad (3.15)$$

Now, we assume that we can suitably find such $\psi_{k'}^{(1)}$'s, $\psi_{k'}^{(2)}$'s and their adjoint solutions which satisfy the conditions

$$\left.\begin{aligned}&\int_\sigma \overline{\psi}_{k'}^{(1)}(n\gamma)\psi_{k''}^{(2)}d\sigma= h_{k'}^{-1}\delta_{k'k''}\,,\\ &\int_\sigma \overline{\psi}_{k'}^{(2)}(n\gamma)\psi_{k''}^{(1)}d\rho= -\overline{h}_{k'}^{-1}\delta_{k'k''}\,.\end{aligned}\right\} \qquad (3.16)$$

Here, $\psi_{k'}^{(i)}$'s are conveniently assumed to be discrete sets of the solutions and n is the unit vector directing from the 2-nd to the 1-st space and normal to the surface σ. Then, $h_{k'}$'s and $\overline{h}_{k'}$'s are the constants independent of the form of the surface σ under the restriction stated above.

On the other hand, any ψ-vector on the surface σ can be expressed in the following form:

$$\psi(\sigma)=\textstyle\sum_{k'}(a_{k'}^{(1)}\psi_{k'}^{(1)}(\sigma)+a_{k'}^{(2)}\psi_{k'}^{(2)}(\sigma))$$
$$+(1-(n)^2\gamma)\xi(\sigma)\,, \qquad (3.17)$$

where $a_{k'}^{(i)}$'s and ξ are respectively the suitable scalars and vector, and the formers take constant values on the given surface σ. The expression (3.17) is derived from the fact that $\psi_{k'}^{(i)}$'s form the complete sets of the solutions of (3.12). The meaning of the term $\xi(\sigma)$ will be made clear later.

In the formula (2.9), we now set $\psi'=\psi$, i.e. the required solution of (2.3), and $\psi''=\overline{\psi}_{k'}^{(1)}$, and take the 1-st space for Σ, then, we find by the use of (2.3) and (3.12)

$$4\pi\int_{(1)} \overline{\psi}_{k'}^{(1)}Jdv=-j\int_\sigma \overline{\psi}_{k'}^{(1)}(n\gamma)\psi d\sigma\,, \qquad (3.18)$$

in which the boundary conditions for $\overline{\psi}_{k'}^{(1)}$ and ψ in the 1-st space are taken into account and thus the surface integral except on the surface σ is dropped by the same reason as in (2.11). Similarly,

$$4\pi\int_{(2)}\overline{\psi}_{k'}^{(2)}Jdv=j\int_{\sigma}\overline{\psi}_{k'}^{(2)}(n\gamma)\psi d\sigma\ . \qquad (3.19)$$

Using the expression (3.17) for ψ on σ and the relations (3.15), (3.16) and (2.6), the equations (3.18) and (3.19) respectively take the forms

$$\left.\begin{aligned}4\pi\int_{(1)}\overline{\psi}_{k'}^{(1)}Jdv&=-jh_{k'}^{-1}a_{k'}^{(2)}\ ,\\ 4\pi\int_{(2)}\overline{\psi}_{k'}^{(2)}Jdv&=-j\overline{h}_{k'}^{-1}a_{k'}^{(1)}\ ,\end{aligned}\right\}\qquad (3.20)$$

from which $a_{k'}^{(i)}$'s are determined. It is to be noticed that $\xi(\sigma)$ does not appear in (3.20). To get $\xi(\sigma)$, we now insert (3.17) into (2.3) and multiply $(1-(n\gamma)^2)$ from the left hand side, then

$$\begin{aligned}(1-(n\gamma)^2)[(\gamma\partial)-U/c]\psi(\sigma)&=\textstyle\sum_{k'}\sum^2{}_{i=1}a_{k'}^{(i)}(1\\ &\quad-(n\gamma)^2)[(\gamma\partial)-U/c]\psi_{k'}^{(i)}(\sigma)+(1-(n\gamma)^2)\\ &\quad\times[(\gamma\partial)-U/c](1-(n\gamma)^2)\xi(\sigma)\\ &=4\pi(1-(n\gamma)^2)J(\sigma)\ ,\end{aligned}$$

where the relations $(n\gamma)^3=(n\gamma)$ and $(1-(n\gamma)^2)(\gamma\partial_n)=0$, ∂_n being the component of ∂ in the direction of the unit vector n, are taken into account for the commutabilities of $a_{k'}^{(i)}$'s and $(1-(n\gamma)^2)[(\gamma\partial)-U/c]$. Hence, using (3.12) and the relation

$$(1-)n\gamma)^2)(\gamma\partial)(1-(n\gamma)^2)=0\ ,$$

which is derived from (2.6), we find

$$\begin{aligned}-(1-(n\gamma)^2)(U/c)(1-(n\gamma)^2)\xi(\sigma)&\\ =4\pi(1-(n\gamma)^2)J(\sigma)\ .&\qquad (3.21)\end{aligned}$$

In the case in which U commutes with $(n\gamma)^2$, Eq. (3.21) takes the form

$$(1-(n\gamma)^2)\xi(\sigma)=-4\pi(1-(n\gamma)^2)(U/c)^{-1}J(\sigma)\ , \qquad (3.22)$$

on account of $(1-(n\gamma)^2)^2=1-(n\gamma)^2$. Now, by the use of (3.20) and (3.22), we have from (3.17)

$$\begin{aligned}\psi(\sigma)=4\pi\Big[\,j\textstyle\sum_{k'}\Big\{&\overline{h}_{k'}\psi_{k'}^{(1)}(\sigma)\int_{(2)}\overline{\psi}_{k'}^{(2)}Jdv\\ &+h_{k'}\psi_{k'}^{(2)}(\sigma)\int_{(1)}\overline{\psi}_{k'}^{(1)}Jdv\Big\}\\ &-(1-(n\gamma)^2)(U/c)^{-1}J(\sigma)\Big].\end{aligned}\qquad (3.23)$$

Hence, the Green function $G(\sigma\ ,\ x)$ becomes

$$\begin{aligned}G(\sigma\ ,\ x)=4\pi\, j\textstyle\sum_{k'}&\begin{cases}\overline{h}_{k'}\psi_{k'}^{(1)}(\sigma)\cdot\overline{\psi}_{k'}^{(2)}(x)\\ \quad\text{for } x \text{ in the 2-nd space}\\ h_{k'}\psi_{k'}^{(2)}(\sigma)\cdot\overline{\psi}_{k'}^{(1)}(x)\\ \quad\text{for } x \text{ in the 1-st space}\end{cases}\\ &-4\pi(1-(n\gamma)^2)(U/c)^{-1}\delta(\sigma-x)\ ,\end{aligned}\qquad (3.24)$$

which gives the value of the Green function on σ.

If we can suitably deform σ so that $\psi_{k'}^{(i)}$'s and $\overline{\psi}_{k'}^{(i)}$'s remain as the complete sets of the solutions satisfying the given boundary conditions, the formula (3.24) can be used on such deformed σ as it is, and thus, by the successive such deformation, we can get the value of the Green function in all space by the use of (3.24), in which $h_{k'}$'s are always constant and do not depend on the form of σ.

The division of a given space into two space and further the conditions of (3.16) are not necessary at least for the formulation of the Green function. Also in the case of the division into several spaces, which will be convenient for a space taking a complicate form, we can use the similar method and get the formulae corresponding to (3.24) for each boundary surface of divided spaces.

§ 4. Green's Function on or Near a Mountain Surface

For the actual calculation, we first introduce the coordinate system $(u_0\ ,\ u_1\ ,\ u_2)$ in which the line element ds is expressed by

$$ds^2=g_0du_0^2+g_1du_1^2+g_2du_2^2\ , \qquad (4.1)$$

and the surface for some constant value of u_0, say $u_0=v_0$, agree with the mountain surface σ considered, and thus u_1 and u_2 are the coordinates parallel to the principal axes of the surface σ, respectively. Hence, the radii of curvature a_1 and a_2 of the surface along the principal axes are respectively given by

$$\left.\begin{aligned}\frac{1}{a_1}&=\frac{1}{\sqrt{g_0}}\Big(\frac{\partial}{\partial u_0}\sqrt{g_1}\Big)\Big/\sqrt{g_1}\\ &=\frac{1}{\sqrt{g_0}}\Big(\frac{\partial}{\partial u_0}g_1\Big)\Big/2g_1\ ,\\ \frac{1}{a_2}&=\frac{1}{\sqrt{g_0}}\Big(\frac{\partial}{\partial u_0}\sqrt{g_2}\Big)\Big/\sqrt{g_2}\\ &=\frac{1}{\sqrt{g_0}}\Big(\frac{\partial}{\partial u_0}g_2\Big)\Big/2g_2\ ,\end{aligned}\right\}\qquad (4.2)$$

where we choose the direction of u_0-axis in the outward direction of the mountain surface. By the suitable transformation of the form

$$\Delta u_0 \to \Delta u_0 + \textstyle\sum_{i=0}^{2} C_{i0}^{0} \Delta u_0 \Delta u_i \,,$$
$$\Delta u_i \to \Delta u_i + \tfrac{1}{2} \textstyle\sum_{k=1}^{2} C_{kk}^{i} \Delta u_k^2 \,, \qquad (i=1,\,2)\,,$$

with

$$\Delta u_i = u_i - v_i \,,\ (i=0,\,1,\,2)\,,$$

we can have the new coordinate system in which, at any given point $u=v$ on the surface σ (Appendix (1)),

$$\left.\begin{aligned} &\left(\frac{\partial}{\partial u_1} g_i\right)_{u=v} = \left(\frac{\partial}{\partial u_2} g_i\right)_{u=v} = 0\,, \\ &\qquad\qquad (i=0,\,1,\,2,)\,, \\ &\left(\frac{\partial}{\partial u_0} g_0\right)_{u=v} = 0\,, \end{aligned}\right\} \qquad (4.3)$$

Hence, new g_1 and g_2 depend only on u_0, and g_0 is constant in the vicinity of the point $u=v$. In the following, we shall restrict our problem to the calculation of the Green function in this range in which the condition (4.3) holds in a good approximation.

Now, we consider the general solution of (3.12) in the case in which the medium characteristics depend only on u_0-axis and its change in the distance of a wave length is sufficiently small, as g_i's are so.

We set

$$\psi = \eta\, e^{-j\phi}\,, \qquad \overline{\psi} = \overline{\eta} e^{+j\phi}\,, \qquad (4.4)$$

and insert (4.4) into Eq. (3.12) and (3.13), then

$$\left.\begin{aligned} &[(\gamma p) - U/c]\eta + (\gamma\partial)\eta = 0\,, \\ &\overline{\eta}[(\gamma p) - U/c] + \overline{\eta}(-\gamma\overleftarrow{\partial}) = 0\,, \end{aligned}\right\} \qquad (4.5)$$

with

$$P_i = \frac{\partial\phi}{\partial x_i}\,.$$

Then, we define η_0, $\overline{\eta}_0$ and ϕ by

$$[(\gamma p) - U/c]\eta_0 = \overline{\eta}_0[(\gamma p) - U/c] = 0\,, \qquad (4.6)$$

or

$$\mathrm{Det}\,[(\gamma p) - U/c] = 0\,,$$

and also $\eta_{\lambda'}(p)$'s and their adjoint vectors $\overline{\eta}_{\lambda'}(p)$'s by

$$[(\gamma p) - U/c]\eta_{\lambda'} = \lambda' \eta_{\lambda'}\,,$$
$$\overline{\eta}_{\lambda'}[(\gamma p) - U/c] = \overline{\eta}_{\lambda'}\lambda'\,, \qquad (4.7)$$

with

$$(\overline{\eta}_{\lambda'}\eta_{\lambda''}) = 0\,, \qquad (\lambda' \neq \lambda'')\,.$$

Hence, η_0 in (4.6) is also contained in $\eta_{\lambda'}$'s, and the eigen value $\lambda'(p)$ for η_0 vanishes only for the value of p satisfying (4.6). We can now set

$$\eta = \textstyle\sum_{\lambda'} \eta_{\lambda'} a_{\lambda'}\,, \qquad \overline{\eta} = \textstyle\sum_{\lambda'} \overline{a}_{\lambda'} \overline{\eta}_{\lambda'}\,, \qquad (4.8)$$

and then, inserting (4.8) into (4.5),

$$\textstyle\sum_{\lambda'} \lambda' \eta_{\lambda'} a_{\lambda'} + (\gamma\partial)\eta = 0\,, \qquad (4.9)$$

which gives, from (4.6) and (4.7),

$$(\overline{\eta}_0(\gamma\partial)\eta) = 0\,, \qquad a_{\lambda'} = -(\overline{\eta}_{\lambda'}(\gamma\partial)\eta)/\lambda'(\overline{\eta}_{\lambda'}\eta_{\lambda})\,,$$
$$(\lambda' \neq 0)\,. \qquad (4.10)$$

Setting,

$$\eta \simeq \eta_0 a_0\,, \qquad (4.11)$$

then, Eq. (4.10) becomes

$$(\overline{\eta}_0(\gamma\partial)(\eta_0 a_0)) = 0\,,$$
$$a_{\lambda'} = -(\overline{\eta}_{\lambda'}(\gamma\partial)(\eta_0 a_0))/\lambda'(\overline{\eta}_{\lambda'}\eta_{\lambda'})\,, \quad (\lambda' \neq 0)\,, \qquad (4.12)$$

which secure the assumption (4.11) conversely. Similarly,

$$((\overline{a}_0\overline{\eta}_0)(\gamma\overleftarrow{\partial})\eta_0) = 0\,,$$
$$\overline{a}_{\lambda'} = ((\overline{a}_0\overline{\eta}_0)(\gamma\overleftarrow{\partial})\eta_{\lambda'})/\lambda'(\overline{\eta}_{\lambda'}\eta_{\lambda'})\,, \quad (\lambda' \neq 0)\,. \qquad (4.13)$$

Eq. (4.12) and (4.13) give

$$\partial_i((\overline{\eta}_0\gamma_i\eta_0)\overline{a}_0 a_0) = 0\,. \qquad (4.14)$$

In the case in which η_0 can be divided into two mutually orthogonal vectors, say η_1 and η_2, the equations for a_0 and $\overline{a}_0$ in (4.12), (4.13) and (4.14) hold for every amplitude of η_ν's, say a_ν's, under the following condition:

$$(\overline{\eta}_\nu(\gamma\partial)\eta_\mu a_\mu) = 0\,, \quad \text{for} \quad \nu \neq \mu(=1,\,2)\,. \qquad (4.15)$$

On the other hand, we find from (3.1)

$$\mathrm{Det}\,((\gamma p) - U/c)\,\mathrm{Det}\,((\gamma p) + \{(\gamma p)^2 - p^2 + k^2\}$$
$$\times (U/c)^{-1}) = (p^2 - k^2)^6\,. \qquad (4.16)$$

Thus, Eq. (4.6) gives

$$p^2 - k^2 = 0\,. \qquad (4.17)$$

Since, using (3.1),

$$((p\gamma) - U/c)((p\gamma) + (p\gamma)^2(U/c)^{-1})$$
$$= (p\gamma)(p^2 - k^2)(U/c)^{-1}\,, \qquad (4.18)$$

we can now set, introducing an arbitrary unit vector n,

$$\left.\begin{aligned} &\eta_0 = \eta_{n,\nu}(p) \equiv ((\gamma p) + (\gamma p)^2(U/c)^{-1})\mathbf{1}_n\mathbf{1}_\nu\,, \\ &\overline{\eta}_0 = \overline{\eta}_{n,\nu} \equiv \overline{\mathbf{1}}_\nu\overline{\mathbf{1}}_n((\gamma p) + (U/c)^{-1}(\gamma p)^2)\,, \end{aligned}\right\}$$
$$(\nu=1,\,2)\,, \qquad (4.19)$$

where

$$\left.\begin{aligned} &(ns)^2\mathbf{1}_n = \overline{\mathbf{1}}_n(ns)^2 = 0\,, \qquad \overline{\mathbf{1}}_n\mathbf{1}_n = 1\,, \\ &\rho_3\mathbf{1}_\nu = (-1)^{\nu+1}\mathbf{1}_\nu\,, \qquad \overline{\mathbf{1}}_\nu\mathbf{1}_\mu = \delta_{\nu\mu}\,, \end{aligned}\right\} \qquad (4.20)$$

viz. $\mathbf{1}_n$ and $\mathbf{1}_n$ are the normalized eigen vectors of (ns) in the subspace of s_i's-matrices, having three components, and $\mathbf{1}_\nu$ and $\overline{\mathbf{1}}_\nu$ are those of ρ_3 having two components. η_0 and $\overline{\eta}_0$ defined in (4.19) satisfy Eq. (4.6) for the value of p satisfying (4.17) on account of (4.18). $\eta_{n,\nu}$'s thus introduced are mutually orthogonal, as is evident from the following lemma:

$$\bar{\eta}_{n,\nu}(p')f(\gamma,\ \rho_3)\eta_{n,\mu}(p'')=0\,, \qquad (\nu\neq\mu)\,, \tag{4.21}$$

where p' and p'' are arbitrary vectors and $f(\gamma,\ \rho_3)$ is an arbitrary function of γ_i's and ρ_3, which also forms a Hermitian matrix with respect to γ_i's independently of ρ_3 and the coefficients implied in $f(\gamma,\ \rho_3)$. The lemma (4.21) is proved as follows: Using (4.19), the left hand side of (4.21) takes the form

$$\bar{\mathbf{1}}_\nu\bar{\mathbf{1}}_n F(\gamma,\ \rho_3)\mathbf{1}_n\mathbf{1}_\mu\,, \qquad (\nu\neq\mu)\,, \tag{4.22}$$

where $F(\gamma,\ \rho_3)$ also has the same characteristics as $f(\gamma,\ \rho_3)$. Taking into account (4.20),

$$\begin{aligned}(4.22)&=\bar{\mathbf{1}}_\nu Sp[F(\gamma,\ \rho_3)(1-(ns)^2)]\mathbf{1}_\mu\\ &=\bar{\mathbf{1}}_\nu Sp[(1-(ns)^2)f(\gamma,\ \rho_3)]\mathbf{1}_\mu\\ &=\tfrac{1}{2}\bar{\mathbf{1}}_\nu Sp[F(\gamma,\ \rho_3)(1-(ns)^2)\\ &\quad+(1-(ns)^2)F(\gamma,\ \rho_3)]\mathbf{1}_\mu\,, \qquad (\nu\neq\mu)\,,\end{aligned} \tag{4.23}$$

where Sp denotes only the spur in the subspace of s_i's matrices. In the case in which $F(\gamma,\ \rho_3)=F(-\gamma,\ \rho_3)$, i.e. when $F(\gamma,\ \rho_3)$ is an even function of γ_i's, then $F(\gamma,\ \rho_3)=F(s,\ \rho_3)$ on account of (2.5). Hence, the spur term in (4.23) does not depend on ρ_1 and thus commutes with ρ_3. Therefore, the right hand side of (4.23) vanishes by the definition of $\mathbf{1}_\nu$'s in (4.20). When $F(\gamma,\ \rho_3)$ is an odd function of γ_i's, the spur in (4.23) does vanish, because $F(\gamma,\ \rho_3)$ is then expressed by the linear combination of the terms of the form

$$\begin{aligned}&(a_1s)(a_2s)(a_3s)\cdots\cdot(a_{2N+1}s)\\ &\quad+(a_{2N+1}s)(a_{2N}s)\cdots\cdot(a_2s)(a_1s)\,,\end{aligned} \tag{4.24}$$

which secure the Hermitian characteristic of $F(\gamma,\ \rho_3)$ with respect to γ_i's independently of the coefficients, and, as is evident from the representations of s_i's (2.2), the transposed matrices of γ_i's are equal to $-\gamma_i$'s, respectively, and thus

$$\begin{aligned}&(a_1s)_{ij}(a_2s)_{jk}\cdots\cdot(a_{2N}s)_{lm}(a_{2N+1}s)_{mi}\\ &\quad=(-1)^{2N+1}(a_{2N+1}s)_{im}(a_{2N}s)_{ml}\cdots\cdot\\ &\qquad\times(a_2s)_{kj}(a_1s)_{ji}\,,\end{aligned}$$

which confirms the vanishing of the spur of the form (4.24). Thus, it follows that the term (4.23) vanishes for arbitrary $F(\gamma,\ \rho_3)$, and thus the lemma (4.21) is verified. Using (4.21), it is evident that the conditions (4.15) also hold for $\eta_{n,\nu}$'s in (4.19).

When g_1 and g_2 depend only on one coordinate, say u_0, as in (4.3), then, we can put

$$\frac{\partial\phi}{\partial u_1}=k_1'\,,\ \frac{\partial\phi}{\partial u_2}=k_2'\,, \qquad (k_1',\ k_2':\ \text{const.})\,, \tag{4.25}$$

which gives from (4.17)

$$\left(\frac{1}{\sqrt{g_0}}\frac{\partial\phi}{\partial u_0}\right)^2=k^2-\left(\frac{k_1'^2}{g_1}+\frac{k_2'^2}{g_2}\right)=k^2-k'^2\,, \tag{4.26}$$

with

$$k'=[0\,,\ k_1'/\sqrt{g_1}\,,\ \ k_2'/\sqrt{g_2}\,]\,.$$

Since $\eta_{\lambda'}$'s and $\bar{\eta}_{\lambda'}$'s then also depend only on u_0 by the definitions (4.7), Eq. (4.14) becomes

$$\frac{1}{\sqrt{g_0g_1g_2}}\frac{\partial}{\partial u_0}(\sqrt{g_1g_2}(\bar{\eta}_{n,\nu}(n\gamma)\eta_{n,\nu})(\bar{a}_{n,\nu}a_{n,\nu}))=0\,, \tag{4.27}$$

with the solution

$$\bar{a}_{n,\nu}a_{n,\nu}=\text{const.}\,/\sqrt{g_1g_2}(\bar{\eta}_{n',\nu}(n\gamma)\eta_{n',\nu})\,, \tag{4.28}$$

where we choose the direction of the unit vector n in that of u_0-axis. Using (4.19) and the method in (4.23), we find

$$\begin{aligned}(\bar{\eta}_{n,\mu}(p')(n\gamma)\eta_{n,\nu}(p'')(&=\bar{\mathbf{1}}_\mu Sp[(1-(ns)^2)\\ &\times((\gamma p')(n\gamma)(\gamma p'')^2(U/c)^{-1}\\ &+(U/c)^{-1}(\gamma p')^2(n\gamma)(\gamma p''))]\mathbf{1}_\nu\,,\end{aligned} \tag{4.29}$$

in which the odd product terms of γ_i's are dropped because of their no contribution. Using the relations (2.5),

$$(1-(ns)^2)(ps)=(ps)(ns)^2-(np)(us)\,. \tag{4.30}$$

Hence, inserting (4.30) into (4.29) and using the cyclic relation in the spur calculation, the spur term in (4.29) becomes

$$\begin{aligned}&(U/c)^{-1}Sp[\{(p's)(ns)(p''s)^2-(np')(ns)^2(p''s)^2\}\\ &\quad+\{(p's)^2(ns)(p''s)-(np'')(p's)^2(ns)^2\}]\,,\end{aligned}$$

which gives, using the the relations (Appendix (2))

$$\begin{aligned}Sp[(as)(bs)]=2(ab)\,,\quad &Sp[(as)(bs)(cs)(ds)]\\ &=(ab)(cd)+(ad)(bc)\,,\end{aligned} \tag{4.31}$$

$$\begin{aligned}(\bar{\eta}_{n,\mu}(p')(n\gamma)\eta_{n,\nu}(p''))&=(\bar{\mathbf{1}}_\mu(U/c)^{-1}\mathbf{1}_\nu)\\ &\times((np'')+(np'))((p'p'')-(np')(np''))\,.\end{aligned} \tag{4.32}$$

Hence, using (4.26),

$$(\bar{\eta}_{n,\mu}(p)(n\gamma)\eta_{n,\nu}(p))=2(k')^2p_n(U/c)_{\nu\nu}{}^{-1}\delta_{\mu\nu}\,,$$

with

$$p_n=\partial\phi/\sqrt{g_0}\,\partial u_0=\pm\sqrt{k^2-k'^2}\,,$$

$$(U/c)_{\mu\nu}=(\bar{\mathbf{1}}_\mu U/c\mathbf{1}_\nu)\,. \tag{4.33}$$

In the case in which U is a Hermitian

matrix, $\bar{a}=a^*$ (complex conjugate of a) and thus, using (4.33), we find from (4.28) that

$$|a_{n,\nu}|=\text{const.}\,(U/c)_{\nu\nu}^{1/2}/(g_1g_2(k^2-k'^2))^{1/4}(k'^2)^{1/2}\,. \tag{4.34}$$

In the vicinity of the position, say $u_0=c$, where

$$(\bar{\eta}_{n,\nu}(n\gamma)\eta_{n,\nu})=0\,, \tag{4.35}$$

Eq. (4.28) takes a infinite value and then Eq. (4.27) is not right. From (4.33), the condition (4.35) means that

$$p_n=0\,. \tag{4.36}$$

Then, instead of (4.4) and (4.8), we set

$$\left.\begin{aligned}&\psi=\eta(u_0)e^{-j(k_1'x_1+k_2'x_2)}\,,\\&\eta(u_0)=\Sigma_{\lambda'}\eta_{\lambda'}(p_0+\partial_n)a_{\lambda'}(u_0)\,,\end{aligned}\right\} \tag{4.37}$$

where

$$p_0=(p)_{u_0=c}=(k')_{u_0=c}=k_0'\,, \tag{4.38}$$

and U implied in $\eta_{\lambda'}(p_0+\partial_n)$ takes the value at $u_0=c$, say U_0. Then inserting (4.37) into (3.12),

$$\Sigma_{\lambda'}((\gamma\cdot k'+\partial_n)+U/c)\eta_{\lambda'}(p_0+\partial_n)a_{\lambda'}(u_0)=0\,. \tag{4.39}$$

For the sufficiently small value of (u_0-c), we can put

$$(\gamma k')+U/c\simeq((\gamma k')+U/c)_{u_0=c}+\Delta H\,, \tag{4.40}$$

where

$$\Delta H=\left\{\frac{\partial}{\partial u_0}((\gamma k')+U/c)\right\}_{u_0=c}(u_0-c)\,.$$

Substituting (4.40) into (4.39) and using (4.38),

$$\begin{aligned}&\Sigma_{\lambda'}[((\gamma\cdot p_0+\partial_n)+U_0/c)\eta_{\lambda'}(p_0+\partial_n)\\&\quad+\Delta H\eta_{\lambda'}(p_0+\partial_n)]a_{\lambda'}=\Sigma_{\lambda'}[\lambda'(p_0+\partial_n)\\&\quad+\Delta H]\eta_{\lambda'}(p_0+\partial_n)a_{\lambda'}=0\,.\end{aligned} \tag{4.41}$$

On the other hand, differentiating the both hand side of (4.7) with respect to p_n, then

$$((\gamma p)-U/c)\frac{\partial}{\partial p_n}\eta_{\lambda'}+(n\gamma)\eta_{\lambda'}=\lambda'\frac{\partial}{\partial p_n}\eta_{\lambda'}+\frac{\partial\lambda'}{\partial p_n}\eta_{\lambda'}\,. \tag{4.42}$$

Hence, when $\eta_{\lambda'}=\eta_{n,\nu}$, i.e. $\lambda'(p_0)=0$, we find, by multiplying $\bar{\eta}_{n,\nu}$ from the left hand side of (4.42) and using (4.35),

$$\begin{aligned}(\partial\lambda'/\partial p_n)_{p=p_0}&=(\bar{\eta}_{n,\nu}(n\gamma)\eta_{n,\nu})_{p=p_0}\\&\quad\times/(\bar{\eta}_{n,\nu}\eta_{n,\nu})_{p=p_0}=0\,.\end{aligned} \tag{4.43}$$

Similarly, by differentiating (4.42) with respect to p_n and using (4.43), we have

$$\begin{aligned}\left(\frac{\partial^2}{\partial p_n{}^2}\lambda'\right)_{p=p_0}&=2\left(\bar{\eta}_{n,\nu}(n\gamma)\frac{\partial}{\partial p_n}\eta_{n,\nu}\right)_{p=p_0}\\&\quad\times\Big/(\bar{\eta}_{n,\nu}\eta_{n,\nu})_{p=p_0}=2\left(\left(\frac{\partial}{\partial p_n}\bar{\eta}_{n,\nu}\right)(n\gamma)\eta_{n,\nu}\right)_{p=p_0}\\&\quad\times\Big/(\bar{\eta}_{n,\nu}\eta_{n,\nu})_{p=p_0}\,,\end{aligned}$$

in which the latter is obtained by exchanging the roles of $\bar{\eta}_{n,\nu}$ and $\eta_{n,\nu}$. Hence,

$$\begin{aligned}\lambda'(p_0+\partial_n)&=\frac{1}{2}\left(\frac{\partial^2}{\partial p_n{}^2}\lambda'\right)_{p=p_0}\partial_n{}^2+O(\partial_n{}^3)\\&\simeq\frac{1}{2}\left\{\frac{\partial}{\partial p_n}(\bar{\eta}_{n,\nu}(n\gamma)\eta_{n,\nu})\right\}_{p=p_0}\\&\quad\times\Big/(\bar{\eta}_{n,\nu}\eta_{n,\nu})\cdot\partial_n{}^2\,.\end{aligned} \tag{4.44}$$

Expanding (4.41) in the ascending powers of ∂_n and taking only the terms of the lowest power with respect to ∂_n and ΔH, respectively, for each term of λ''s, then, Eq. (4.41) becomes

$$\begin{aligned}&\Sigma_{\nu=1}^{2}\left[\frac{1}{2}\left\{\frac{\partial}{\partial p_n}(\bar{\eta}_{n,\nu}(n\gamma)\eta_{n,\nu})\right\}_{p=p_0}\right.\\&\quad\left.\times\Big/(\bar{\eta}_{n,\nu}\eta_{n,\nu})\cdot\partial_n{}^2+\Delta H\right]\eta_{n,\nu}(p_0)a_{n,\nu}(u_0)\\&\quad+\Sigma_{\lambda'\neq 0}\{\lambda'(p_0)+\Delta H\}\eta_{\lambda'}(p_0)a_{\lambda'}(u_0)=0\,.\end{aligned} \tag{4.45}$$

By multiplying $\bar{\eta}_{\lambda'}(p_0)$'s and presupposing $\eta\simeq\eta_{n,\nu}(p_0+\partial_n)a_{n,\nu}$, Eq. (4.45) gives

$$\left.\begin{aligned}&\left[\frac{1}{2}\left\{\frac{\partial}{\partial p_n}(\bar{\eta}_{n,\nu}(n\gamma)\eta_{n,\nu})\right\}_{p=p_0}\partial_n{}^2+(\bar{\eta}_{n,\nu}(p_0)\Delta H\eta_{n,\nu}(p_0)\right]a_{n,\nu}(u_0)=0\,,\\&\frac{1}{2}\left\{\frac{\partial}{\partial p_n}(\bar{\eta}_{n,\mu}(n\gamma)\eta_{n,\mu})\right\}_{p=p_0}\partial_n{}^2a_{n,\mu}(u_0)=0\,,\qquad(\mu\neq\nu)\,,\end{aligned}\right\} \tag{4.46}$$

$$a_{\lambda'}(u_0)\simeq-(\bar{\eta}_{\lambda'}(p_0)\Delta H\eta_{n,\nu}(p_0))/\lambda'(p^0)(\bar{\eta}_{\lambda'}\eta_{\lambda'})_{p=p_0}\cdot a_{n,\nu}(u_0)\,,\qquad(\lambda'\neq 0)\,, \tag{4.47}$$

with

$$(\bar{\eta}_{n,\mu}(p_0)\Delta H\eta_{n,\nu}(p_0))=\left[\bar{\eta}_{n,\mu}\frac{\partial}{\partial u_0}((\gamma k')+U/c)\eta_{n,\nu}\right]_{u_0=c}(u_0-c)\delta_{\mu\nu}\,,$$

which are self-consistent with the assumption in (4.46).

Using (4.33),

$$\frac{1}{2}\left\{\frac{\partial}{\partial p_n}(\bar{\eta}_{n,\nu}(n\gamma)\eta_{,\nu})\right\}_{p=p_0}=(k^2)_{u_0=c}(U/{}_0c)_{\nu\nu}{}^{-1}\,. \tag{4.48}$$

On the other hand, taking into account Eq. (4.6),

$$\left[\bar{\eta}_{n,\mu}\frac{\partial}{\partial u_0}((\gamma k')+U/c)\eta_{n,\nu}\right]_{u_0=c}=\left[\frac{\partial}{\partial u_0}\{\bar{\eta}_{n,\mu}(k')((\gamma k')+U/c)\eta_{n,\nu}(k')\}\right]_{u_0=c}\,, \tag{4.49}$$

which gives, using (4.19) and the relation (4.18),

$$\begin{aligned}&\bar{\mathbf{1}}_\mu\bar{\mathbf{1}}_n\left[\frac{\partial}{\partial u_0}\left(\{(k'\gamma)+(k'\gamma)^2(U/c)^{-1}\}(k'^2-k^2)(k'\gamma)(U/c)^{-1}\right)\right]\mathbf{1}_n\mathbf{1}_\nu\\&=\left(\frac{\partial}{\partial u_0}(k'^2-k^2)\right)_{u_0=c}\bar{\mathbf{1}}_\mu Sp\Big[(1-(ns)^2)((k'\gamma)+(k'\gamma)^2(U/c)^{-1})(k'\gamma)(U/c)^{-1}\Big]_{u_0=c}\mathbf{1}_\nu\,.\end{aligned} \tag{4.50}$$

The spur term in (4.50) becomes, dropping the odd product term of $(k'\gamma)$,

$$(U_0/c)^{-1}Sp[(1-(ns)^2)(k'\gamma)^2]_{u_0=c}=(U_0/c)^{-1}(k'^2)_{u_0=c}\,,\qquad((nk')=0)\,. \tag{4.51}$$

Using (4.26),

$$\left\{\frac{\partial}{\partial u_0}(k'^2-k^2)\right\}_{u_0=c}=-\left(\frac{k_1'^2}{g_1}\frac{\partial g_1/\partial u_0}{g_1}+\frac{k_2'^2}{g_2}\frac{\partial g_2/\partial u_0}{g_2}+\frac{\partial k^2}{\partial u_0}\right)_{u_0=c}\,. \tag{4.52}$$

Since $(k'^2)_{u_0=c}=(k^2)_{u_0=c}$, we can set

$$k_1'=k(c)\sqrt{g_1(c)}\cos\varphi\,,\qquad k_2'=k(c)\sqrt{g_2(c)}\sin\varphi\,. \tag{4.53}$$

Inserting (4.53) into (4.52), the right hand side becomes

$$\begin{aligned}&-2k(c)^2\left(\cos^2\varphi\frac{\partial\sqrt{g_1}}{\partial u_0}\Big/\sqrt{g_1}+\sin^2\varphi\frac{\partial\sqrt{g_2}}{\partial u_0}\Big/\sqrt{g_2}+\frac{\partial k}{\partial u_0}\Big/k\right)_{u_0=c}\\&=-2k(c)^2\left(\cos^2\varphi\frac{\partial}{\partial u_0}(k\sqrt{g_1})/k\sqrt{g_1}+\sin^2\varphi\frac{\partial}{\partial u_0}(k\sqrt{g_2})/k\sqrt{g_2}\right)_{u_0=c}\,.\end{aligned} \tag{4.54}$$

Thus, using (4.49), (4.50), (4.51), (4.52) and (4.54), we have from (4.47)

$$(\bar{\eta}_{n,\mu}(p_0)\Delta H\eta_{n,\nu}(p_0))=-2(k^4)_{u_0=c}(U/c)^{-1}{}_{\nu\nu}\delta_{\nu\mu}a(c,\varphi)^{-1}\sqrt{g_0}(u_0-c)\,, \tag{4.55}$$

where

$$\frac{1}{a(c,\varphi)}=\cos^2\varphi\frac{\partial(k\sqrt{g_1})/\sqrt{g_0}\partial u_0}{k\sqrt{g_1}}+\sin^2\varphi\frac{\partial(k\sqrt{g_2})/\sqrt{g_0}\partial u_0}{k\sqrt{g_2}}\,. \tag{4.56}$$

When k is constant, we find from (4.2) that

$$1/a(c,\varphi)=\cos^2\varphi/a_1(c)+\sin^2\varphi/a_2(c)\,, \tag{4.57}$$

which is the radius of curvature of the surface $u_0=c$ in the direction φ from u_1-axis. Hence, we can interpret $a(c,\varphi)$ as the effective radius of curvature of the surface $u_0=c$ in the direction φ. Using (4.48) and (4.55), the first equation in (4.46) becomes

$$\left[\frac{1}{\sqrt{g_0g_1g_2}}\frac{\partial}{\partial u_0}\sqrt{\frac{g_1g_2}{g_0}}\frac{\partial}{\partial u_0}+2g_0^{3/2}k(c)^2a(c,\varphi)^{-1}(u_0-c)\right]a_{n,\nu}(u_0)=0\,. \tag{4.58}$$

Setting

$$a_{n,\nu}=(g_1g_2)^{-1/4}f\,, \tag{4.59}$$

and inserting (4.59) into (4.58), then,

$$\left[\left(\frac{\partial}{\partial u_0}\right)^2+g_0\{2k^2a^{-1}\sqrt{g_0}(u_0-c)+\epsilon\}\right]f(u_0)=0\,, \tag{4.60}$$

where ϵ consists of the terms proportional to $(\partial(g_1g_2)/\sqrt{g_0}\partial u_0)^2/(g_1g_2)$ or $(\partial^2(g_1g_2)/g_0\partial u_0^2)/(g_1g_2)$ and is thus of the order of magnitude a^{-2} on account of (4.2). Hence, neglecting the terms of larger power than the first power with respect to a^{-1}, the term ϵ vanishes. Then, the general solution of (4.60) is given by

$$f=z^{1/2}(c_1H^{1/3(1)}(\tfrac{2}{3}z^{3/2})+c_2H_{1/8}^{(2)}(\tfrac{2}{3}z^{3/2}))\,, \tag{4.61}$$

with

$$z=(2/ka)^{1/3}k\sqrt{g_0}(u_0-c)\,.$$

We can thus get the general solution of (3.12) in the coordinate system (4.1) in the range of variables in which the conditions (4.3) are satisfied. When both transmitting and receiving points are on or near the mountain surface, the wave propagates nearly along its surface. Hence, then $p_n \sim 0$, and, from (4.36), we can use the approximation in (4.37). In the interior of the mountain, the wave propagates in the inward direction with a sufficiently large incident angle, since k in a mountain, say $k^{(2)}$, takes the larger value compared with the one in air, say $k^{(1)}$. Taking into account that, in the important ranges of k_1' and k_2' in the actual calculation,

$$k'^2 \simeq (k^{(1)})^2 \ll (k^{(2)})^2 ,$$

we can simply set from (4.34)

$$a_{n,\nu} \simeq \text{const.}\, (g_1 g_2)^{-1/4} . \tag{4.62}$$

The solutions stated in the above depend on two parameters k_1' and k_2', since c and φ contained in (4.61) are uniquely determined by k_1' and k_2' from (4.53). Hence, denoting the interior of the mountain by the 2-nd space and the outside space by the 1-st space as in Fig. 3, and $\psi_{k',\nu}$ and $\eta_{n,\nu}$'s satisfying the boundary conditions in the respective space by $\psi_{k',\nu}{}^{(i)}$ and $\eta_{n,\nu}{}^{(i)}$'s, respectively, then, it follows from (4.4), (4.8), (4.19), (4.26), (4.37), (4.59), (4.61) and (4.62) that

$$\left.\begin{aligned} &\psi_{k',\nu}{}^{(1)} \simeq \eta_{n,\nu}{}^{(1)}(k'+\partial_n)e^{-j(k_1'u_1+k_2'u_2)}(g_1g_2)^{-1/4} f(z) , \qquad (u_0 \geqq v_0) , \\ &\psi_{k',\nu}{}^{(2)} \simeq \eta_{n,\nu}{}^{(2)}(k'-nk_n)e^{-j(k_1'u_1+k_2'u_2)}(g_1g_2)^{-1/4} e^{+jk_n\sqrt{g_0}u_0} , \qquad (u_0 \leqq v_0) , \end{aligned}\right\} \tag{4.63}$$

where

$$\left.\begin{aligned} &f(z) = z^{1/2} H_{1/3}{}^{(2)}(\tfrac{2}{3}z^{3/2}) , \qquad z = (2/ka)^{1/3} k^{(1)} \sqrt{g_0}\,(u_0 - c) , \\ &k' = (0 ,\ k_1'/\sqrt{g_1(c)} ,\ k_2'/\sqrt{g_2(c)}\,) , \qquad (k')^2 \simeq (k^{(1)})^2 , \\ \text{and}\quad &k_n = \sqrt{(k^{(2)})^2 - (k')^2} \simeq \sqrt{(k^{(2)})^2 - (k^{(1)})^2} . \end{aligned}\right\} \tag{4.64}$$

In a similar way, we can set

$$\left.\begin{aligned} &\overline{\psi}_{k',\nu}{}^{(1)} \simeq (g_1g_2)^{-1/4} f(z) e^{+j(k_1'u_1+k_2'u_2)} \overline{\eta}_{n,\nu}{}^{(1)}(k'-\overleftarrow{\partial}_n) , \qquad (u_0 \geqq v_0) , \\ &\overline{\psi}_{k',\nu}{}^{(2)} \simeq (g_1g_2) e^{-1/4} e^{+jk_n\sqrt{g_0}u_0} e^{+j(k_1'u_1+k_2'u_2)} \overline{\eta}_{n,\nu}{}^{(2)}(k'-nk_n) , \quad (u_0 \leqq v_0) . \end{aligned}\right\} \tag{4.65}$$

In (4.63) and (4.65), the boundary condition that the wave is an outward propagating wave in the respective space is taken into account. The solutions $\psi_{k',\nu}{}^{(i)}$'s in the other regions, if necessary, must be connected with the ones in (4.63) and (4.65) at the mountain surface σ by the help of the boundary condition. It will be shown later that $\psi_{k',\nu}{}^{(i)}$'s and $\overline{\psi}_{k',\nu}{}^{(i)}$ in (4.63) and (4.65) form the complete sets of solutions of (3.12) and (3.13) satisfying the given boundary conditions, respectively.

Now, using the relations

$$\int_{-\infty}^{\infty} du_1 \int_{-\infty}^{\infty} du_2 e^{-j((k_1'-k_1'')u_1+(k_2'-k_2'')u_2)} = (2\pi)^2 \delta(k_1'-k_1'')\delta(k_2'-k_2'') ,$$

and

$$d\sigma = \sqrt{g_1g_2}\, du_1 du_2 ,$$

we can easily deduce from (4.63) and (4.65) that

$$\begin{aligned} \int \overline{\psi}_{k',\nu}{}^{(1)}(n\gamma)\psi_{k'',\mu}{}^{(2)} d\sigma \simeq & \int_{-\infty}^{\infty} du_1 \int_{-\infty}^{\infty} du_2 e^{-j((k_1'-k_1'')u_1+(k_2'-k_2'')u_2)} \\ & \times f(z)(\overline{\eta}_{n,\nu}{}^{(1)}(k'-\overleftarrow{\partial}_n)(n\gamma)\eta_{n,\mu}{}^{(2)}(k'-nk_n))e^{+jk_n\sqrt{g_0}v_0} , \end{aligned} \tag{4.66}$$

will vanish except in the case $k' = k''$. On the other hand, by the method used in the derivation of (4.32), we find

$$(\overline{\eta}_{n,\nu}{}^{(1)}(k'-\overleftarrow{\partial}_n)(n\gamma)\eta_{n,\mu}{}^{(2)}(k'-nk_n)) = (k')^2[-k_n(U^{(2)}/c)_{\nu\nu}{}^{-1} - (n\overleftarrow{\partial}_n)(U^{(1)}/c)_{\nu\nu}{}^{-1}]\delta_{\nu\mu} . \tag{4.67}$$

Hence, using $(n\partial_n) = j\partial/\sqrt{g_0}\,\partial u_0$, the integration in (4.66) becomes

$$\begin{aligned} \int \overline{\psi}_{k',\nu}{}^{(1)}(n\gamma)\psi_{k'',\mu}{}^{(2)} d\sigma = & -(2\pi)^2(k')^2\{k_n(U^{(2)}/c)_{\nu\nu}{}^{-1} f + j(U^{(1)}/c)_{\nu\nu}{}^{-1}\partial f/\sqrt{g_0}\,\partial u_0\}_{u_0=v_0} e^{jk_n\sqrt{g_0}v_0} \\ & \times \delta_{\nu\mu}\delta(k_1'-k_1'')\delta(k_2'-k_2'') . \end{aligned} \tag{4.68}$$

Hence, the condition (3.16) is satisfied, and we find, using z in (4.64) instead of u_0, that

$$1/h_{k',\nu} = -(2\pi)^2(k^{(1)})^2 k_n (U^{(2)}/c)_{\nu\nu}{}^{-1} e^{jk_n\sqrt{g_0}v_0} \left\{ f - 2^{1/3}\delta\left(\frac{\partial}{\partial z} f\right)_{u_0=v_0} \right\}_{\nu\nu} , \tag{4.69}$$

where
$$\delta=(k^{(1)}U^{(2)}/jk_nU^{(1)})(k^{(1)}a)^{-1/3}\ . \tag{4.70}$$

Now, we can get the explicite formula for $G(x_1, x_2)$ from (3.24) by the use of (4.20), (4.63) and (4.65): Taking into account that
$$h_{k',\nu}=\bar{h}_{k',\nu}\ , \qquad \sum_{\nu=1}{}^{2}\mathbf{1}_\nu\cdot U_{\nu\nu}\cdot\bar{\mathbf{1}}_\nu=U\ ,$$
then, for $(u_0)_{x_1}=v_0>(u_0)_{x_2}$,
$$G(x_1, x_2)\simeq\eta_{n_1}(\overrightarrow{\partial}_1)\cdot S(x_1, x_2)\cdot\bar{\eta}_{n_2}(-\overleftarrow{\partial}_2)\ , \tag{4.71}$$
with
$$S(x_1, x_2)=\frac{-j}{\pi}\int_{-\infty}^{\infty}dk_1'\int_{-\infty}^{\infty}dk_2'(g_1g_2)_{x_1}{}^{-1/4}(g_1g_2)_{x_2}{}^{-1/4}\frac{(U^{(2)}/c)}{(k^{(1)})^2k_n}\frac{f(z_1)e^{jk_n\sqrt{g_0}((u_0)_{x_2}-v_0)}}{\left(f(z_0)-2^{1/3}\delta\dfrac{\partial}{\partial z_0}f(z_0)\right)}e^{-j(k_1'\Delta u_1+k_2'\Delta u_2)}\ , \tag{4.72}$$
where
$$\Delta u_i=(u_i)_{x_2}-(u_i)_{x_1}\ , \qquad z_1=(z)_{x_1}\ , \qquad z_0=(z)_{u_0=v_0}\ ,$$
and $\eta_n(\overrightarrow{\partial})$ and $\bar{\eta}_n(-\overleftarrow{\partial})$ are the ones which are respectively obtained from $\eta_{n,\nu}(\overleftarrow{\partial})$ and $\eta_{n,\nu}(-\overleftarrow{\partial})$ by dropping $\mathbf{1}_\nu$ and $\bar{\mathbf{1}}_\nu$, and take the values $\eta_n{}^{(1)}(\overrightarrow{\partial})$ and $\bar{\eta}_n{}^{(1)}(-\overleftarrow{\partial})$ or $\eta_n{}^{(2)}(\overrightarrow{\partial})$ and $\bar{\eta}_n{}^{(2)}(-\overleftarrow{\partial})$ according as the operations of $\overrightarrow{\partial}$ and $-\overleftarrow{\partial}$ is performed in the 1-st or 2-nd space, respectively. It is evident that, for any small deformation of the surface σ parallel to the mountain surface in the range in which the conditions in (4.3) are valid, our $\psi_{k',\nu}{}^{(i)}$'s and $\bar{\psi}_{k',\nu}{}^{(i)}$'s remain as the complete sets of the solutions satisfying the boundary conditions in the respective deformed spaces. Hence, as is discussed in section 3, the formulae (4.71) and (4.72) are also valid in the case in which the point x_1 or both points x_1 and x_2 exist in the outside space of the mountain in this range.*

Now, using (4.53), we change the variables from k_1' and k_2' to c and φ. Then, by putting $k=k^{(1)}$,
$$dk_1'dk_2'=\left|\frac{\partial(k_1', k_2')}{\partial(c, \varphi)}\right|dcd\varphi\ ,$$
where, using (4.56),
$$\left|\frac{\partial(k_1', k_2')}{\partial(c, \varphi)}\right|=\begin{vmatrix}\dfrac{\partial}{\partial c}(k^{(1)}\sqrt{g_1})\cos\varphi\ , & -k^{(1)}\sqrt{g_1}\sin\varphi\\ \dfrac{\partial}{\partial c}(k^{(1)}\sqrt{g_1})\sin\varphi\ , & +k^{(1)}\sqrt{g_1}\cos\varphi\end{vmatrix}$$
$$=\sqrt{g_0g_1g_2}\,(k^{(1)})^2/a(c, \varphi)\ . \tag{4.73}$$

We must then examine the integration path of c. Since $a(c, \varphi)$ defined in (4.56) is the radius of curvature of the mountain, it is always positive and thus, from the definition of z in (4.64), $z\gtrless0$ according as $u_0\gtrless c$. Hence, for the value of u_0 in the range $u_0<c$, we set $z=|z|e^{j\pi}$. Then, $f(z)$ takes the form
$$f(z)=z^{1/2}\{H_{1/3}{}^{(2)}(\tfrac{2}{3}z^{3/2}j)+e^{\pi/3j}H_{1/3}{}^{(1)}(\tfrac{2}{3}|z|^{3/2}j)\}\ , \tag{4.74}$$
which satisfies the required condition for $f(z)$. Hence, for the integral path of c we must take the line from $-\infty$ to ∞, as in shown in Fig. 4 where the singular points c_s's arise from the denominator of (4.72), i.e. c_s's are the roots of
$$f(z_s)-2^{1/3}\delta\frac{\partial}{\partial z_s}f(z_s)=0\ ,$$
with
$$z_s=(2/k^{(1)}a)^{1/3}k^{(1)}\sqrt{g_0}\,(v_0-c_s)\ . \tag{4.75}$$
On the other hand, for sufficient small values of $(c-v_0)$,
$$k^{(1)}(c)\sqrt{g_i(c)}\simeq k^{(1)}(v_0)\sqrt{g_i(v_0)}+\frac{\partial}{\partial v_0}(k^{(1)}(v_0)\sqrt{g_i(v_0)})(c-v_0)$$
$$=(1+\sqrt{g_0}\,(c-v_0)/a_i(v_0))k^{(1)}(v_0)\sqrt{g_i(v_0)}\ , \qquad (i=1, 2)\ , \tag{4.76}$$

---

* In the latter case, $\bar{\psi}_{k_1,\nu}{}^{(2)}$'s in the range $u_0>v_0$ which are connected with the ones in (4.65) at the mountain surface must be used for the formulation of (4.72). Then, only the term $e^{jk_n\sqrt{g_0}((u_0)_{x_2}-v_0)}$ in (4.72) takes the different form.

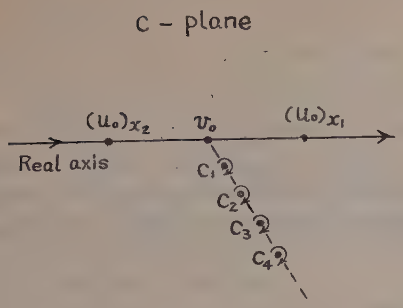

Fig. 4.

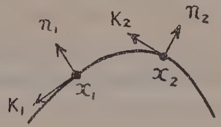

Fig. 5.

with
$$\sqrt{g_0}\,(c-v_0)/a_i(v_0)\ll 1\,,$$
where a_i's are newly defined by
$$\frac{1}{a_i}=\frac{1}{\sqrt{g_0}}\frac{\partial}{\partial u_0}(k^{(1)}\sqrt{g_i})/(k^{(1)}\sqrt{g_i})\,, \tag{4.77}$$
and are thus interpreted as the effective radii of curvature along u_i-axis, respectively, as is evident from (4.2). Using (4.77),
$$\begin{aligned}k_1'\Delta u_1+k_2'\Delta u_2&=k^{(1)}(c)(\sqrt{g_1(c)}\cos\varphi\Delta u_1+\sqrt{g_2(c)}\sin\varphi\Delta u_2\\&\simeq k^{(1)}(v_0)(\sqrt{g_1(v_0)}\cos\varphi\Delta u_1+\sqrt{g_2(v_0)}\sin\varphi\Delta u_2)\\&+k^{(1)}(v_0)(\sqrt{g_1(v_0)}\Delta u_1\cos\varphi/a_1(v_0)+\sqrt{g_2(v_0)}\Delta u_2\sin\varphi/a_2(v_0)\sqrt{g_0}\,(c-v_0)\,.\end{aligned} \tag{4.78}$$
Hence, inserting (4.78) into (4.72), it follows that the exponential term of the integrand on the path of infinitly large lower or upper semi-circle takes the form of $e^{-\text{const.}\,\lambda}$ (const.>0), according as
$$\sqrt{g_1(v_0)}\Delta u_1\cos\varphi/a_1(v_0)+\sqrt{g_2(v_0)}\Delta u_2\sin\varphi/a_2(v_0), \tag{4.79}$$
takes a positive or negative value, respectively. The other term in the integrand in (4.72) for a given real value of φ takes the asymptotic form of const. $e^{-(u_0)_{x_1}-v_0)|\lambda|^{1/2}}$ for $|\lambda|\to\infty$ except on the lines arg. $(\lambda-v_0)=\pi$, $\pm\pi/3$, since the change of $a(c,\varphi)$ is smaller than a itself by a factor of the order of magnitude $1/(k^{(1)}a)$ in the range of c having physical meaning. Thus, we find that the required integration value is equal to the sum of residues at the singular points c_s's or vanishes, according as the value of (4.79) is positive or negative, since the integration value along the path of infinitly large lower or upper simi-circle vanishes, respectively.

Since $f(z_s)$ satisfies (4.75) and Eq. (4.60) or, using (4.75),
$$\frac{\partial^2}{\partial {z_s}^2}f(z_s)+z_s f(z_s)=0\,, \tag{4.80}$$
we find that
$$\frac{\partial}{\partial c_s}\left(f(z_s)-2^{1/3}\delta\frac{\partial}{\partial z_s}f(z_s)\right)=(2^{-1/3}\delta^{-1}+2^{1/3}\delta z_s)f(z_s)(-k^{(1)}\sqrt{g_0}\,(2/k^{(1)}a)^{1/3})\,,$$
which gives, using (4.70),
$$-k^{(1)}\sqrt{g_0}\,(k^{(1)}a)^{-2/3}(k^{(1)}U^{(2)}/jk_nU^{(1)})(\delta^{-2}+2^{2/3}z_s)f(z_s)\,. \tag{4.81}$$
Hence, using (4.73) and (4.78) with (4.75), the integration in (4.72) becomes
$$\begin{aligned}S(x_1\,,\,x_2)=2j\frac{(U^{(1)}/c)}{k^{(1)}}&\frac{{(g_1g_2)_{v_0}}^{1/2}}{{(g_1g_2)_{x_1}}^{1/4}{(g_1g_2)_{x_2}}^{1/4}}\sum_s\int_{\varphi^0}^{\varphi_0+\pi}d\varphi\\\times\frac{f(z_1)}{f(z_s)}&\frac{e^{-jk_nh_2}}{(k^{(1)}a)^{1/3}(\delta^{-2}-2\tau_s)}e^{-jk^{(1)}\{(D_1\cos\varphi+D_2\sin\varphi)+\tau_s(k^{(1)}a)^{1/3}(D_1\cos\varphi/(k^{(1)}a_1)+D_2\sin\varphi/(k^{(1)}a_2))\}}\,,\end{aligned} \tag{4.82}$$

where

$$\left.\begin{array}{l} D_i=\sqrt{g_i(v_0)}\Delta u_i\,, \qquad h_2=\sqrt{g_0}\,(v_0-(u_0)_{x_2})\,, \\ z_1=z_s+(2/k^{(1)}a)^{1/3}(k^{(1)}h_1)=2^{1/3}(k^{(1)}h_1/(k^{(1)}a)^{1/3}-\tau_s)\,, \end{array}\right\} \tag{4.83}$$

with
$$\tau_s=-2^{-1/3}z_s\,, \qquad h_1=\sqrt{g_0}\,((u_0)_{x_1}-v_0)\,,$$
and the range $\varphi_0\leqq\varphi\leqq\varphi_0+\pi$ is defined so that the value of (4.79) is positive definite in it.

We must then perform the integration with respect to φ. In the case in which $|k^{(1)}D_1|$, $|k^{(1)}D_2|\gg 1$, the integrand changes with φ decisively by the first phase term, and the changes due to the other terms can be neglected. Hence, we can use the method of steepest descent or Sattelpunkt Methode: Denoting the root of

$$\frac{\partial}{\partial\varphi}(D_1\cos\varphi+D_2\sin\varphi)=0\,,$$

by φ', then
$$\tan\varphi'=D_2/D_1\,,$$
which gives, in the range $\varphi_0\leqq\varphi'\leqq\varphi_0+\pi$,
$$\cos\varphi'=D_1/D\,, \qquad \sin\varphi'=D_2/D\,, \tag{4.84}$$
with
$$D=\sqrt{D_1^2+D_2^2}\,,$$
because (4.79) is then reduced to, using (4.56) and (4.77),
$$D(\cos^2\varphi'/a_1(v_0)+\sin^2\varphi'/a_2(v_0))=D/a(v_0\,,\,\varphi')\,,$$
which is always positive in the diffraction case. Hence, using (3.2), the integration (4.82) becomes

$$S(x\,,\,x_2)\simeq(\bar{U}^{(1)}/c)^{-1}\frac{(g_1g_2)_{v_0}{}^{1/2}}{(g_1g_2)_{x_1}{}^{1/4}(g_1g_2)_{x_2}{}^{1/4}}(-j)2k^{(1)}\sqrt{\frac{2\pi}{k^{(1)}D}}\,e^{-j(k^{(1)}D-\pi/4)}/(k^{(1)}a)^{1/3}$$
$$\times\sum_s\frac{e^{-jk^{(1)}D\tau_s/(k^{(1)}a)^{2/3}}}{(2\tau_s-1/\delta^2)}\cdot\frac{f(z_1)}{f(z_s)}\cdot e^{-jk_nh_2}\,, \qquad (k^{(1)}D\gg 1)\,. \tag{4.85}$$

In the higher approximation in which the change of the second phase term of the integrand is taken into account, the following term is added to the phase in (4.85):
$$-jk^{(1)}D\,(\tau_s^2/18)(D_1/D)^2(D_2/D)^2(k^{(1)}a)^{2/3}(1/a_1-1/a_2)^2/(k^{(1)})^2\,,$$
whose effect is generally very small compared with the ones due to the other terms and can be neglected. Further, it generally holds in (4.85) that
$$(g_1g_2)_{v_0}{}^{1/2}/(g_1g_2)_{x_1}{}^{1/4}(g_1g_2)_{x_2}{}^{1/4}=1+O(h/a)\simeq1\,, \qquad (h_1\,,\,h_2\ll a_1\,,\,a_2)\,.$$

We now obtain the explicit expression for z_s or τ_s as a function of δ. Since $|\delta|$ is practically less than unity, we may expand z_s in the form of an ascending series of powers of δ: Differentiating the both hand side of (4.75) with respect to δ, then, using (4.80),
$$(z_s'-2^{1/3})f'=2^{1/3}\delta z_s'f''=-2^{1/3}\delta z_sz_s'f\,, \tag{4.86}$$
where
$$z_s'=\partial z_s/\partial\delta\,, \qquad f'=\partial f/\partial z_s\,, \qquad \text{etc.}\,.$$
Denoting the values of z_s's for $\delta=0$ by z_s^0's, respectively, then $f(z_s^0)=0$ from (4.75). Hence, we find from (48.6)
$$(z_s')_{\delta=0}=2^{1/3}\,.$$
Differentiating the both hand side of (4.86) with respect to δ, we have
$$(z_s'')_{\delta=0}=0\,.$$
In a similar way, we get
$$(z_s''')_{\delta=0}=-4z_s^0\,, \qquad (z_s'''')_{\delta=0}=-12\times2^{1/3}\,, \qquad \text{etc.}\,,$$
which gives
$$\left.\begin{array}{l} z_s=z_s^0+2^{1/3}\delta-\frac{2}{3}z_s^0\delta^3-2^{1/3}\frac{1}{2}\delta^4+\cdots\,, \\ \tau_s=\tau_s^0-\delta-\frac{2}{3}\tau_s^0\delta^3+\frac{1}{2}\delta^4\cdots\,, \end{array}\right\} \tag{4.87}$$
or

where
$$\tau_s^0\simeq(1/2)(3\pi(s+3/4))^{2/3}e^{-j\pi/3}\,, \qquad (s=0\,,\,1\,,\,2\,,\,\cdots)\,, \tag{4.88}$$

When both points x_1 and x_2 are in the 1-st space, it is easily deduced that only the factor $e^{-jk_nh_2}$ in (4.85) is replaced by $f(z_2)/f(z_s)$, where z_2 is the one corresponding to z_1 in (4.83).

In the case in which $(k^{(1)}h)/(k^{(1)}a)^{1/3}\gg|\tau_s|$, it follows from (4.83) and (4.64) that

$$f(z)\simeq\sqrt{\frac{3}{\pi}}\,z^{-1/4}e^{-j(2/3\cdot z^{3/2}-5/12\cdot\pi j)}$$

$$\simeq\sqrt{\frac{3}{\pi}}\left(\frac{2}{k^{(1)}}\right)^{1/6}\frac{a^{1/3}}{(2ah)^{1/4}}e^{-jk^{(1)}\left(\frac{1}{3}\frac{(2ah)^{3/2}}{a^2}-\tau_s\frac{(2ah)^{1/2}}{(k^{(1)}a)^{2/3}}\right)+\frac{5}{12}\pi j}, \tag{4.89}$$

with $\frac{1}{2}(k^{(1)}\sqrt{2ah}/(k^{(1)}a)^{2/3})^2 \gg |\tau_s|$.

When both points x_1 and x_2 exist on the mountain surface σ , say the points σ' and σ'', respectively, we find from (4.85), by approaching the points x_1 and x_2 infinitely to the surface σ and using the relation (4.75), that

$$(U^{(1)}/c)^{-1}\frac{\partial}{\partial n'}S(\sigma',\sigma'')=(U^{(2)}/c)^{-1}\frac{\partial}{\partial n''}S(\sigma',\sigma'')=jk_n(U^{(2)}/c)^{-1}S(\sigma',\sigma''). \tag{4.90}$$

Now, using the expression (4.85), the Green function derived from (4.71) takes the form

$$G(x_1,x_2)\simeq\eta_{n_1}(k_1+\partial_n)\cdot S(x_1,x_2)\cdot\eta_{n_2}(k_2-\overleftarrow{\partial}_n), \tag{4.91}$$

where (Fig. 5)

$$k_1=k^{(1)}(\operatorname{grad}D(x,x_2))_{x=x_1},\qquad k_2=-k^{(1)}(\operatorname{grad}D(x_1,x))_{x=x_2},$$

k_1 and k_2 being the vectors with the magnitude $k^{(1)}$ in the direction of the wave path at the points x_1 and x_2, respectively. From (4.19), we get, using (4.20),

$$\left.\begin{aligned}&\eta_{n_1}(k_1+\partial_n)=[(k_1\gamma)+((k_1\gamma)^2+(n_1\gamma)(k_1\gamma)(j\partial/\partial n_1))(U/c)^{-1}]\mathbf{1}_{n_1}\\&\bar{\eta}_{n_2}(k_2-\overleftarrow{\partial}_n)=\bar{\mathbf{1}}_{n_2}[(k_2\gamma)+(U/c)^{-1}((k_2\gamma)^2+(-\overleftarrow{j\partial/\partial n_2})(k_2\gamma)(n_2\gamma))],\end{aligned}\right\} \tag{4.92}$$

with $n_1=n(x_1)$, $n_2=n(x_2)$.

When both points x_1 and x_2 exist on the mountain surface σ , we can use (4.90), and the expression in (4.92) take the simple forms.

In order to get the explicit expression for each component of field, it is convenient to introduce the vectors $\mathbf{1}_{l_1}$ and $\mathbf{1}_{m_1}$ and their adjoint ones besides $\mathbf{1}_{n_1}$ and $\bar{\mathbf{1}}_{n_1}$:

$$\mathbf{1}_{m_1}=((k_1s)/k^{(1)})\mathbf{1}_{n_1},\qquad \mathbf{1}_{l_1}=(n_1s)\mathbf{1}_{m_1}=((n_1s)(k_1s)/k^{(1)})\mathbf{1}_{n_1}, \tag{4.93}$$

which, together with $\mathbf{1}_{n_1}$, form a set of normalized orthogonal vectors, i.e.

$$(\bar{\mathbf{1}}_i\mathbf{1}_j)=\delta_{ij},\qquad (i,j=l_1,m_1,n_1), \tag{4.94}$$

as is easily shown by the relation (2.6) and the method used in (4.23). On the other hand, we can set for the explicit expression of $\mathbf{1}_n$ and $\bar{\mathbf{1}}_n$

$$\mathbf{1}_n=\bar{\mathbf{1}}_n=\begin{pmatrix}n_1\\n_2\\n_3\end{pmatrix} \tag{4.95}$$

with $n=(n_1,n_2,n_3)$, $n^2=1$,

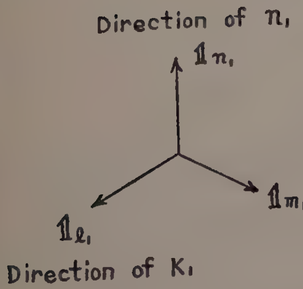

Fig. 6.

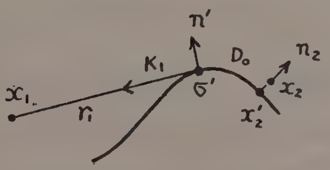

Fig. 7.

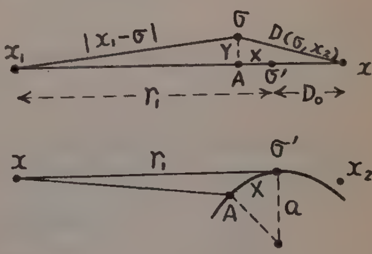

Fig. 8.

which are easily verified by the use of (2.2). Hence, $\mathbf{1}_n$ denotes the unit vector in the spatial direction n in ψ-vector space. Thus, the relations between $\mathbf{1}_{l_1}$, $\mathbf{1}_{m_1}$ and $\mathbf{1}_{n_1}$ can be shown as in Fig. 6, where their phase relations are not taken into account. Using (2.6), we find that $(n_1s)^2$ commutes with $(k_1s)^2$, and thus $\mathbf{1}_{n_1}$ is also the eigen vector of $(k_1s)^2$. Hence,

$$(k_1 s)^2 \mathbf{1}_{n_1} = k_1{}^2 \mathbf{1}_{n_1} . \tag{4.96}$$

Using $\mathbf{1}_l$'s and the relation (4.96), the equations (4.92) become by the help of (3.2)

$$\left.\begin{aligned} &\eta_{n_1}(k_1+\partial_n)=k^{(1)}\mathbf{1}_{m_1}\rho_1+\{\mathbf{1}_{n_1}+\mathbf{1}_l(j\partial/\partial n)/k^{(1)}\}(\bar{U}^{(1)}/c) , \\ &\bar{\eta}_{n_2}(k_2-\overleftarrow{\partial}n)=k^{(1)}\rho_1\bar{\mathbf{1}}_{m_2}+(U^{(1)}/c)\{\bar{\mathbf{1}}_{n_2}+(-j\overleftarrow{\partial}/\partial n)/k^{(1)}\bar{\mathbf{1}}_{l_2}\} , \end{aligned}\right\} \tag{4.97}$$

provided that both points x_1 and x_2 exist in the 1-st space. Hence, for example, taking the element

$$(\bar{\mathbf{1}}_l\bar{\mathbf{1}}_{n_1}G(x_1 , x_2)\ \mathbf{1}_{n_2}\mathbf{1}_l)=(\bar{U}^{(1)}/c)^2 S(x_1 , x_2))_{\rho_3=1} , \tag{4.98}$$

then, the left hand side of (4.98) expresses the normal component of the electric field at the point x_1 produced by the electric dipole current at the point x_2 whose direction is also normal to the surface σ. It may be noted that, using the expression (4.85) for $S(x_1 , x_2)$, the right hand side of (4.98) agree exactly with the one derived by Van der Pole and Bremmer for the diffracted wave by a sphere of radius a, in the same conditions stated in the above.

§ 5. Green's Function at Large Distances from the Mountain

We now consider the case in which one point x_1, say the receiving point, is at a large distance from a mountain and the other point x_2 i.e. the transmitting point is on or near the mountain surface. We can then use the equation (2.16) with the results of section 3. The integration (2.16) is performed in the vicinity of the point σ' shown in Fig. 7, which forms the phase stationary point of the integrand. The change of integrand is almost due to the phase term and the change due to the other terms can be neglected in the range in which the value of the integration is decisively determined. Hence, according to the method of approximation of steepest descent, we can take the values at the point σ' for all the other terms than the phase term. Using the expressions (3.8) and (4.71) for $G_0(x_1 , \sigma)$ and $G(\sigma , x_2)$, respectively, then, the integrand in (2.16) takes the form

$$G_0(x_1 , \sigma)(n\gamma)G(\sigma , x_2)=\phi_0(x_1 , \sigma)\eta(-\overleftarrow{\partial})(n\gamma)\eta_n(\overrightarrow{\partial})\cdot S(\sigma , x_2)\cdot\bar{\eta}_{n_2}(-\overleftarrow{\partial}) , \tag{5.1}$$

whre

$$\eta(\partial)=(\gamma\partial)+(\gamma\partial)^2(U/c)^{-1} , \qquad \eta_n(\partial)=\eta(\partial)\mathbf{1}_n , \qquad \bar{\eta}_n(-\overleftarrow{\partial})=\bar{\mathbf{1}}_n\eta(-\partial) . \tag{5.2}$$

In the vicinity of the point σ', we can put $\overrightarrow{\partial}=k_1+\overrightarrow{\partial}_n$ and $-\overleftarrow{\partial}=k_1-\overleftarrow{\partial}_n$, where, denoting $k^{(1)}$ simply by k,

$$k_1=-k(\operatorname{grad}|x_1-x|)_{x=\sigma'}=k(\operatorname{grad}D(x , x_2))_{x=\sigma'} . \tag{5.3}$$

Hence, the part in (5.1) becomes, neglecting the term of $(\gamma\partial_n)^2$,

$$\begin{aligned} \eta(-\overleftarrow{\partial})(n\gamma)\eta_n(\overrightarrow{\partial})\simeq&[\eta(k_1)-(n\overleftarrow{\partial}_n)\{(n'\gamma)+(U/c)^{-1}((n'\gamma)(k_1\gamma)+(k_1\gamma)(n'\gamma))\}] \\ &\times(n'\gamma)[\eta(k_1)+\{(n'\gamma)+((n'\gamma)(k_1\gamma)+(k_1\gamma)(n'\gamma))(U/c)^{-1}\}(n\overrightarrow{\partial}_n)]\mathbf{1}_{n'} , \end{aligned} \tag{5.4}$$

with

$$n'=n(\sigma') ,$$

which gives, using the relations in (2.6),

$$[-(n\overleftarrow{\partial}_n)\{1+(U/c)^{-1}(k_1\gamma)\}(n'\gamma)^2\eta(k_1)+\eta(k_1)(n'\gamma)^2\{1+(k_1\gamma)(U/c)^{-1}\}(n\overrightarrow{\partial}_n)]\mathbf{1}_{n'} ,$$

where, using the relation (3.2),

$$\begin{aligned} \{1+(U/c)^{-1}(k_1\gamma)\}(n'\gamma)^2\eta(k_1)&=\{1+(U/c)^{-1}(k_1\gamma)\}[(k_1\gamma)(1-(n'\gamma)^2)+(k_1\gamma)^2(U/c)^{-1}(n'\gamma)^2] \\ &=\eta(k_1)(1-(n'\gamma)^2)+\{(k_1\gamma)^2(U/c)^{-1}+((U/c)^{-1}(k_1\gamma)k^2(U/c)^{-1}\}(n'\gamma)^2 \\ &=\eta(k_1)(1-(n'\gamma)^2)+\eta(k_1)(n'\gamma)^2=\eta(k_1) , \end{aligned}$$

and, in a same way,

$$\eta(k_1)(n'\gamma)^2\{1+(k_1\gamma)(U/c)^{-1}\}=\eta(k_1) .$$

Hence, we find from (5.4) that

$$\eta(-\overleftarrow{\partial})(n\gamma)\eta_n(\overrightarrow{\partial})\simeq\eta_{n'}(k_1)\{-(n\overleftarrow{\partial}_n)+(n\overrightarrow{\partial}_n)\} . \tag{5.5}$$

Substituting (5.5) into (5.1), then

$$G_0((x_1, \sigma)(n\gamma)G(\sigma, x_2) \simeq \eta_{n'}(k_1)\cdot\phi_0(x_1, \sigma)\{-(n\overleftarrow{\partial}_n)+(n\overrightarrow{\partial}_n)\}S(\sigma, x_2)\cdot\bar{\eta}_{n_2}(-\overleftarrow{\partial}_2)\,. \tag{5.6}$$

On the other hand, in the vicinity of the point $\sigma=\sigma'$,

$$\left.\begin{aligned} &\phi_0(x, \sigma)\simeq\phi_0(x_1, \sigma')e^{-jk(|x_1-\sigma|-|x_1-\sigma'|)}\,,\\ &S(\sigma, x_2)\simeq\Sigma_l S_l(\sigma', x_2)e^{-jk(1+\tau_l/(ka)^{2/3})(D(\sigma, x_2)-D(\sigma', x_2))}\,, \end{aligned}\right\} \tag{5.7}$$

where S_l denotes the l-th term in the series (4.85). In Fig. 8, the line $\widehat{\sigma A}$ denotes the geodesic line on the mountain surface which is normal to the line $\overline{x_1\sigma'}$, and the length of $\widehat{\sigma A}$ and $\widehat{A\sigma'}$ are respectively denoted by Y and X. Then,

$$\left.\begin{aligned} &|x_1-\sigma|-|x_1-\sigma'|\simeq\frac{1}{2}\frac{Y^2}{r_1}-a\sin\left(\frac{X}{a}\right)\simeq\frac{1}{2}\frac{Y^2}{r_1}-\left(X-\frac{1}{6}\frac{X^3}{a^2}\right),\\ &D(\sigma, x)-D(\sigma', x_2)\simeq\frac{1}{2}\frac{Y^2}{D_0}+X\,, \qquad (D_0\ll a)\,, \end{aligned}\right\} \tag{5.8}$$

Further, for $(n\overrightarrow{\partial}_n)$ in (5.6), we can use the relation (4.90). Hence, taking into account that the direction of n in (2.16) is opposite to that of n in section 4, the integration in (2.16) is reduced to

$$G(x_1,x_2)\simeq\sqrt{\frac{2\pi}{k}}e^{-\pi/4\cdot j}\frac{1}{\sqrt{W}}\Sigma_l\eta_{n'}(k_1)\cdot\phi_0(x_1,\sigma')C_l(\sigma')S_l(\sigma',x_2)\cdot\bar{\eta}_{n_2}(-\overleftarrow{\partial}_2), \tag{5.9}$$

where
$$C_s(\sigma')=\frac{j}{4\pi}\int_{-\infty}^{\infty}dX\left\{k^{(1)}\frac{\partial X}{\partial n}+k_n(U^{(1)}/U^{(2)})\right\}e^{-jk^{(1)}\left(\frac{\tau_s}{(k^{(1)}a)^{2/3}}X+\frac{1}{6a^2}X^3\right)}, \tag{5.10}$$

and
$$\sqrt{\frac{2\pi}{k}}e^{-\pi/4\cdot j}\frac{1}{\sqrt{W}}=\int_{-\infty}^{\infty}dY\,e^{-jk(Y^2/r_1+Y^2/D_0)/2}\,, \tag{5.11}$$

or
$$W=(r_1+D_0)/r_1D_0\,.$$

In (5.10) and (5.11), the phase terms $Y\partial Y/\partial n/r_1^2$ and $(\tau_s/(ka)^{2/3})Y^2/(2D_0)$ are neglected, because they are sufficiently small compared with $\partial X/\partial n$ and $Y^2/(2D_0)$, respectively. Using $\partial X/\partial n=X/a$, the integration in (5.10) can be deformed into

$$C_l(\sigma')=\frac{-1}{4\pi}\left[(k^{(1)}a)^{2/3}\frac{1}{a}\frac{\partial}{\partial\tau_s}+jk_n(U^{(1)}/U^{(2)})\right]\int_{-\infty}^{\infty}e^{-jk^{(1)}((\tau_s/(ka)^{2/3}X+(1/6a^2)X^3)}dX\,,$$

which gives, using (4.70) and (4.83),

$$\frac{1}{4\pi}6^{1/3}(k^{(1)}a)^{1/3}\delta^{-1}\left(2^{1/3}\delta\frac{d}{dz_s}-1\right)\int_{-\infty}^{\infty}e^{-j(-3^{1/3}z_st+t^3)}dt\,,$$

in which

$$\int_{-\infty}^{\infty}=\frac{2}{3}\pi3^{-1/3}z_s^{1/2}\left\{J_{1/3}\left(\frac{2}{3}z_s^{3/2}\right)+J_{-1/3}\left(\frac{2}{3}z_s^{3/2}\right)\right\} \qquad \text{(Airy's integration)*}$$

$$=\frac{2}{3}\pi3^{-1/3}\frac{\sqrt{3}}{2}\{f(z_s)e^{-\pi/6\cdot j}+\bar{f}(z_s)e^{+\pi/6\cdot j}\}\,,$$

where $\bar{f}(z)$ is the one defined in (4.64) and

$$\bar{f}(z)=z^{1/2}H_{1/3}^{(1)}\left(\frac{2}{3}z^{3/2}\right).$$

Hence,
$$C_s(\sigma')=3^{-1/2}2^{-5/3}(ka)^{1/3}\delta^{-1}\left(2^{1/3}\delta\frac{d}{dz_s}-1\right)(f(z_s)e^{-\pi/6\cdot j}+\bar{f}(z_s)e^{+\pi/6\cdot j})\,, \tag{5.12}$$

in which, using the relation (4.75), the term $f(z_s)$ vanishes. Further, by the help of the relation.

$$f(z)\frac{d}{dz}\bar{f}(z)-\bar{f}(z)\frac{d}{dz}f(z)=j6/\pi\,,$$

we have, using (4.75),

$$f(z_s)\left(2^{1/3}\delta\frac{d}{dz_s}-1\right)\bar{f}(z_s)=j(6/\pi)2^{1/3}\delta\,. \tag{5.13}$$

---

* Watson, Theory of Bessel Functions, p. 139, § 6.4.

Hence, substituting (5.13) into (5.12),

$$C_s(\sigma')=je^{\pi/6\cdot j}\frac{\sqrt{3}\,(ka)^{1/3}}{2^{1/3}\pi f(z_s)}. \tag{5.14}$$

Using (5.11), (5.14) and also $\phi_0(x_1,\sigma')=e^{-jkr_1}/r_1$, we find from (5.9) that

$$G(x_1,x_2)\simeq\eta_{n'}(k_1)\cdot\Sigma_l\sqrt{\frac{3}{\pi}}2^{1/6}e^{5/12\cdot\pi j}(ka)^{1/3}\sqrt{\frac{D_0}{k(D_0+r_1)r_1}}S_l(\sigma',x_2)e^{-jkr_1}/f(z_s)\cdot\overline{\eta}_{n_2}(-\overleftarrow{\partial}_2). \tag{5.15}$$

On the other hand, when the point x_1 is sufficiently near the point σ', we have from (4.85) (Fig. 9)

$$S_l(\sigma',x_2)=\sqrt{\frac{D_1+D_0}{D_0}}e^{+jk(1+\tau_s/(ka)^{2/3})D_1}S_l(\sigma_1',x_2). \tag{5.16}$$

Here, σ_1' denotes the point where the vertical line through the point x_1 intersects the mountain surface σ. Hence, inserting (5.16) into (5.15) and taking into account that $r_1\simeq D_1$ and $\eta_{n'}(k_1)\simeq\eta_{n'}(\partial_1)\simeq\eta_{n_1}(\partial_1)$, the expression (5.15) takes the form

$$G(x_1,x_2)\simeq\eta_{n_1}(\overrightarrow{\partial}_1)\cdot\Sigma_s S_s(\sigma_1',x_2)\sqrt{\frac{3}{\pi}}2^{1/6}(ka)^{1/3}\frac{1}{\sqrt{kr_1}}e^{-jk\{(r_1-D_1)-(\tau_s/(ka)^{2/3})\}+5/12\cdot\pi j}f(z_s)^{-1}\cdot\overline{\eta}_{n_2}(-\overleftarrow{\partial}_2), \tag{5.17}$$

which must be equal to (4.71) with the expression (4.85) for $S(x_1,x_2)$. In fact, using $r_1\sim\sqrt{2ah_1}$ and $r_1-D_1\sim(2ah_1)^{3/2}/(3a^2)$, we find from the form for $f(z)$ in (4.80) that they exactly agree with each other.

In the inverse case in which the point x_2 is in the sufficiently large distance from the mountain and the point x_1 is on or near the mountain, the calculation is performed by (2.15) in a same way, and we obtain the equation corresponding to (5.9) as follows (Fig. 10):

$$G(x_1,x_2)\simeq\sqrt{\frac{2\pi}{k}}e^{-\pi/4\cdot j}\frac{1}{\sqrt{W}}\Sigma_s\eta_{n_1}(\overrightarrow{\partial})\cdot S_s(x_1,\sigma'')C_s(\sigma'')\phi_0(\sigma'',x_2)\cdot\overline{\eta}_{n''}(k_2), \tag{5.18}$$

where $C_s(\sigma)$'s are the same as in (5.14) and

$$W=(r_2+D_0)/r_2D_0\,.$$

When both points x_1 and x_2 are in the sufficiently large distance from a mountain (Fig. 11),

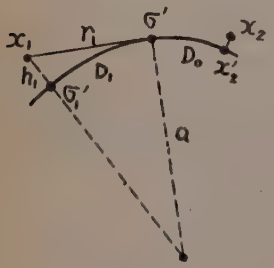

Fig. 9.

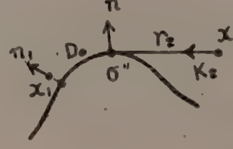

Fig. 10.

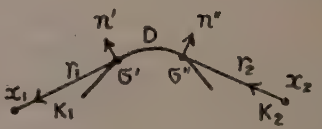

Fig. 11.

we can use (2.17), and it is easily deduced from (5.9) and (5.18) that

$$G(x_1,x_2)\simeq\left(\sqrt{\frac{2\pi}{k}}e^{-\pi/4\cdot j}\right)^2\frac{1}{\sqrt{W}}\Sigma_{s=0}^{\infty}\eta_{n'}(k_1)\cdot\phi_0(x_1,\sigma')C_s(\sigma')S_s(\sigma',\sigma'')C_s(\sigma'')\phi_0(\sigma'',x_2)\cdot\overline{\eta}_{n''}(k_2)\ , \tag{5.19}$$

where W corresponds to the one in (5.11) and defined by

$$\left(\sqrt{\frac{2\pi}{k}}e^{-\pi/4\cdot j}\right)^2\frac{1}{\sqrt{W}}\simeq\int_{-\infty}^{\infty}dY'\int_{-\infty}^{\infty}dY''e^{-jk\{Y'^2/r_1+(Y'-Y'')^2/D+Y''^2/r_2\}/2}, \tag{5.20}$$

or

$$W=(r_1+D+r_2)/r_1Dr_2\,.$$

When the points x_1 and x_2 are sufficiently near the points σ' and σ'', respectively, we can again show that the expression (5.19) agrees exactly with the one obtained from (4.85) by the use of the form of $f(z)$ in (4.89). Conversely, we can get the criterion for the equation (2.17); From the condition in (4.89),

$$\frac{1}{2}(kr_1/(ka)^{2/3})^2\,, \quad \frac{1}{2}(kr_2/(ka)^{2/3})^2 \gg |\tau_s|\,, \tag{5.21}$$

and from the conditions for (4.85), taking into account the condition in (4.76) with $c=c_s$ of (4.75),

$$kD \gg 1\,, \qquad |\tau_s|/(ka)^{2/3} \ll 1\,. \tag{5.22}$$

On the other hand, the magnitude of τ_s for $S_s(\sigma',\sigma'')$'s which can decisively contribute to the value of $G(\sigma',\sigma'')$, are of the order of magnitude or less than $(ka)^{2/3}/(kD)$. Hence, taking into account also the condition $|\tau_s| > 1$, the conditions in (5.21) and (5.22) become

$$\left.\begin{aligned} &\frac{1}{2}(kD)(r_i/a)^2 \gg 1\,, \qquad \frac{1}{2}(kr_i)^2/(ka)^{4/3} \gg 1, \qquad (i=1.2)\,, \\ \text{and} \qquad &kD \gg 1\,, \qquad (ka)^{2/3} \gg 1\,. \end{aligned}\right\} \tag{5.23}$$

We now consider the case in which wave propagates over several mountains. Then, the Green function is given by (2.18). From the above calculations, it is easily deduced that, taking into account the relation in (5.5), the equation corresponding to (5.19) then takes the form (Fig. 2 with the opposite directions of n_i' 's and n_i'' 's)

$$\begin{aligned} G(x_1.x_N) \simeq &\left(\sqrt{\frac{2\pi}{k}}\,e^{-\pi/4\cdot j}\right)^{2N} \frac{1}{\sqrt{W}}\eta_{n_1'}(k_1)\cdot\phi_0(x_1,\sigma_1')C_s(\sigma_1')S_s^{(1)}(\sigma_1',\sigma_1'')C_s(\sigma_1'') \\ &\times\phi_0(\sigma_1'',\sigma_2')\eta_{n_1''n_2'}(k_{12})C_l(\sigma_2')S_l^{(2)}(\sigma_2',\sigma_2'')C_l(\sigma_2'')\phi_0(\sigma_2'',\sigma_3')\eta_{n_2''n_3'}(k_{23})\cdots\cdots \\ &\times C_m(\sigma_N')S_m^{(N)}(\sigma_N',\sigma_N'')C_m(\sigma_N'')\phi_0(\sigma_N'',x_N)\cdot\overline{\eta}_{n_N''}(k_N)\,, \end{aligned} \tag{5.24}$$

where

$$\eta_{n_1''n_2'}(k_{12}) = (\overline{\mathbf{1}}_{n_1''}\eta(k_{12})\mathbf{1}_{n_2'})\,, \quad \text{etc.,} \tag{5.25}$$

$$\begin{aligned} \left(\sqrt{\frac{2\pi}{k}}\,e^{-\pi/4\cdot j}\right)^{2N} \frac{1}{\sqrt{W}} \simeq \Pi_{i=1}^N \int_{-\infty}^{\infty} dY_i' \int_{-\infty}^{\infty} dY_i'' \exp\,[-j(k/2)\{&Y_1'^2/r_1+(Y_1'-Y_1'')^2/D_1 \\ +(Y_1''^2+Y_2'^2-2\cos\theta_{12}Y_1''Y_2')/r_{12}+(Y_2'-Y_2'')^2/D_2&+(Y_2''^2+Y_3'^2-2\cos\theta_{23}Y_2''Y_3')/r_{23} \\ +\cdots\cdots\cdots+(Y_N'-Y_N'')^2/D_N&+Y_N''^2/r_N\}]\,, \end{aligned} \tag{5.26}$$

with

$$\cos\theta_{i,\,i+1} = (n_i'', n_{i+1}')\,,$$

and $S^{(i)}$ is the one belonging to i-th mountain, and the repeated indices are to be so summed. We conveniently introduce the function W defined by

$$\begin{aligned} W\left(\frac{x_1,x_2,x_3,\cdots,x_{n+1},x_n}{\theta_2,\theta_3,\cdots,\theta_{n-1}}\right) = &A_{1,n}+\textstyle\sum_i A_{1,i-1}B_iA_{i+1,n} \qquad (2\leqq i\leqq n-1) \\ &+\textstyle\sum_{i,j}A_{1,i-1}B_iA_{i+1,j-1}B_jA_{j+1,n} \qquad (i+1\leqq j-1) \\ &+\textstyle\sum_{i,j,k}A_{1,i-1}B_iA_{i+1,j-1}B_jA_{j+1,k-1}B_kA_{k-1,n} \qquad (i+1\leqq j-1,\ j+1\leqq k-1) \\ &+\cdots\cdots\cdots\cdots\cdots\cdots\cdots\cdots\cdots\cdots\,, \end{aligned} \tag{5.27}$$

where

$$A_{l,m} = \textstyle\sum_{j=l}^m x_l/\Pi_{i=l}^m x_i\,, \qquad B_l = (\sin\theta_l/x_l)^2. \tag{5.28*}$$

Then, W defined in (5.26) is expressed by

$$W = W(r_1,D_1,r_{12},D_2,r_{23},\cdots,D_N,r_N/0,\theta_{12},0,\theta_{23},\cdots,\theta_{N-1,N},0)\,. \tag{5.29}$$

Hence, in the special case in which all $\theta_{i,i+1}$'s vanish,

$$W = (r_1+D_1+r_{12}+D_2+\cdots+D_N+r_N)/(r_1D_1r_{12}D_2r_{23}\cdots D_Nr_N)\,.$$

On the other hand, using the representations of $\mathbf{1}_n$ and $\overline{\mathbf{1}}_n$ (4.95),

$$\eta_{n_1''n_2'}(k_{12}) = (\overline{\mathbf{1}}_{n_1''}(k_{12}r)+(k_{12}r)^2(U/c)^{-1})\mathbf{1}_{n_2'}) = km_{12}$$

with

$$m_{12} = ((\overline{U}/c)/k)\cos\theta_{12} - j\rho_1\sin\theta_{12}\,, \qquad \theta_{12} = -\theta_{21}\,, \quad \text{etc.,} \tag{5.30}$$

where we count the angle θ_{12} from n_2' to n_1'', etc.. In the vacuum, $(\overline{U}/c)=k$ and then, m_{12} in (5.30) is conveniently expressed by

---

* Appendix (3).

$$m_{12}=e^{-j\rho_1\theta_{12}}\,,\quad \text{etc.}\,. \tag{5.31}$$

Further, using $|\tfrac{2}{3}z_s^{3/2}|\gtrsim 1$,

$$f(z_s)\simeq j2^{5/3}\sqrt{\frac{3}{\pi}}\,e^{-\pi/4\cdot j}\frac{(-1)^s\tau_s^{1/4}\delta e^{j2\pi/3}}{2^{1/4}\sqrt{1-2\tau_s\delta^2}}\,, \tag{5.32}$$

Inserting (5.32) into (5.14),

$$C_s(\sigma)\simeq(-1)^s(ka)^{1/3}\frac{\sqrt{1/\delta^2-2\tau_s}}{2^{7/4}\sqrt{\pi}\,\tau_s^{1/4}}e^{-\pi/4\cdot j}\,. \tag{5.33}$$

Hence, using (4.85) and (5.33),

$$\sum_s 2\pi e^{-\pi/2\cdot j}C_s(\sigma_i{}')S_s{}^{(i)}(\sigma_i{}',\sigma_i{}'')C_s(\sigma_i{}'')=(\overline{U}/c)^{-1}k(ka)^{1/3}(kD)^{-1/2}g(kD/(ka)^{2/3})e^{-j(kD+\pi/4)}\,, \tag{5.34}$$

where

$$g(x)=\frac{\sqrt{\pi}}{2}\sum_{s=0}^{\infty}e^{-j\tau_s x}/\tau_s^{1/2}\,, \tag{5.35}$$

which deponds on the matrix ρ_3 through τ_s 's.

Now, using (5.30), (5.34) and (3.9), the equation (5.24) takes the form

$$\begin{aligned}G(x_1,x_N)\simeq{}&\eta_{n_1}{}'(k_1)\cdot\frac{(ka^{(1)})^{1/3}(ka^{(2)})^{1/3}\cdots(ka^{(N)})^{1/3}}{\sqrt{(kD_1)(kD_2)\cdots(kD_N)}}g(kD_1/(ka^{(1)})^{2/3})m_{12}g(kD_2/(ka^{(2)})^{2/3})m_{23}\\&\times g(kD_3/(ka^{(3)})^{2/3})m_{34}\cdots m_{N-1,N}g(kD_N/(ka^{(N)})^{2/3})\cdot\overline{\eta}_{n_N{}''}(k_N)\\&\times e^{-jk(r_1+D_1+r_{12}+\cdots+D_N+r_N)-jN\pi/4}/(kr_1r_{12}\cdots r_N\sqrt{W})\,.\end{aligned} \tag{5.36}$$

When all $\theta_{i,i+1}$'s vanish and further the first space is the vacuum, then, using the forms (5.29) and (5.31) for W and $m_{i,i+1}$'s, respectively, and also the expressions (4.97) for $\eta_{n_1{}'}(k_1)$ and $\overline{\eta}_{n_N{}''}(k_N)$, the equation (5.36) is reduced to

$$\begin{aligned}G(x_1,x_N)={}&(\rho_1\mathbf{1}_{m_1{}'}+\mathbf{1}_{n_1{}'})\cdot k^2\frac{e^{-jk(r_1+D_1+r_{12}+\ldots+D_N+r_N)-jN\pi/4}}{\sqrt{(kr_1)(kr_{12})(k_{23})\cdots(kr_{N-1,N})\{k(r_1+D_1+r_{12}+\cdots+D_N+r_N)\}}}\\&\times\prod_{i=1}^{N}(ka^{(i)})^{1/3}g(kD_i/(ka^{(i)})^{2/3})\cdot(\rho_1\overline{\mathbf{1}}_{m_N{}''}+\overline{\mathbf{1}}_{n_N{}''})\,,\end{aligned} \tag{5.37}$$

where $a^{(i)}$ is the radius of curvature of the i-th mountain along the wave path, and the function $g(x)$ is defined by (5.33) and its numerical value is shown in Fig. 12, and the unit vectors $\mathbf{1}_n$ and $\mathbf{1}_m$ are defined in (4.93) and (4.95), and their directions are indicated in Fig. 6, and the other notations are shown in Fig. 2. The criterions for (5.37) are given in (5.23), and also exists the one arising from the use of the approximation (5.26). Assuming $r_1, r_N \gg r_{ij}$, the latter will be given by

$$(k/2)(1/r_1+1/r_N)Y_m{}^2\gg 1\,, \tag{5.38}$$

where Y_m is the upper limit for the ranges of $|Y_i|$'s in the integrand of (5.26), in which the profile of the mountains parallel to the wave path can be considered to be invariant.

In the case in which the first space is the vacuum, we find from (2.6), (3.3) and (4.70) that

$$\delta=\left\{\begin{array}{ll}\delta_1\equiv\dfrac{(-j)(\varepsilon+4\pi\sigma/j\omega)}{(ka)^{1/3}\sqrt{\mu(\varepsilon+4\pi\sigma/i\omega)-1}} & \text{for } \rho_3=1,\\[2ex] \delta_2\equiv\dfrac{(-j)\,\mu}{(ka)^{1/3}\sqrt{\mu(\varepsilon+4\pi\sigma/j\omega)-1}} & \text{for } \rho_3=-1,\end{array}\right\} \tag{5.39}$$

Here, ε in (2.1) is replaced by $\varepsilon+4\pi\sigma/j\omega$. The practically important case is the one in which $4\pi\sigma/\omega\ll\varepsilon$ and $\mu\sim1$. Then

$$\delta=-j\nu\,; \tag{5.40}$$

where ν is the pure real number and

$$\nu=\left\{\begin{array}{ll}\dfrac{\varepsilon}{(ka)^{1/3}\sqrt{\varepsilon-1}} & \text{for } \rho_3=1\\[2ex] \dfrac{1}{(ka)^{1/3}\sqrt{\varepsilon-1}} & \text{for } \rho_3=-1\,.\end{array}\right.$$

In Fig. 12, the numerical values of $g(x)$ in (5.35) are given for several values of ν by the use of (4.87) and (4.88).

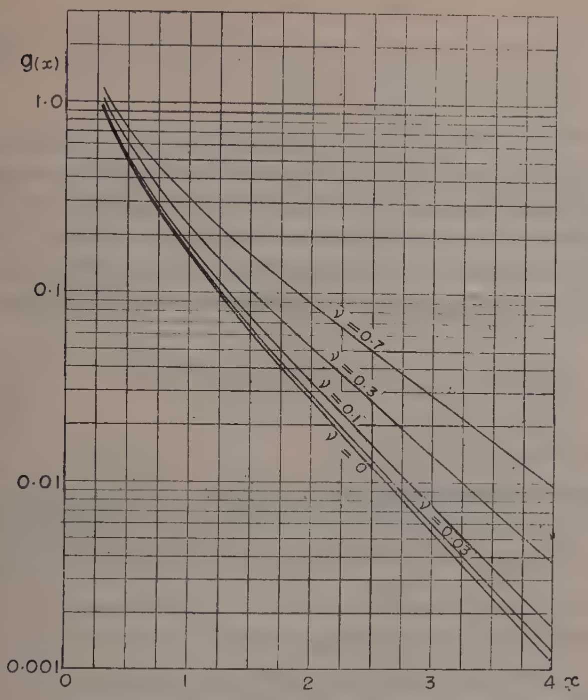

Fig. 12.

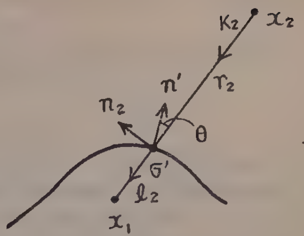

Fig. 13.

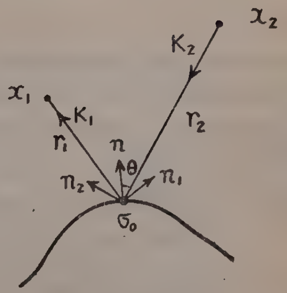

Fig. 14.

The equation (5.37) is considerably simple and may be adapted to practical use. By multiplying the factor $(3/\sqrt{2})\times 10^8$ to (5.37), the field intensity radiated from the dipole with the power 1 KW is given in the unit in which the electric field is measured in μ v/m.

At the end of this section, we may note that the argument $kD/(ka)^{2/3}$ of the function g in (5.37) can be replaced by

$$\int_{\sigma''}^{\sigma'} kdD/(ka)^{2/3} \quad \text{or} \quad kD/(k\bar{a})^{2/3} ,$$

with

$$\bar{a}=\left(D^{-1}\int_{\sigma''}^{\sigma'} a^{-2/3}dD\right)^{-3/2} ,$$

where the integration is performed along the wave path. Hence, when the distance between the points σ' and σ'' is sufficiently large that the change of a alonge the wave path can not be neglected, it is supposed that, taking into account the equation (5.24) and the expressions (5.33) and (4.85), the equation (5.37) also holds to a fairly good approximation by replacing $a^{(i)}$ in the argument of the function g by $\bar{a}^{(i)}$ and the factor $(ka^{(i)})^{1/3}$ by $(ka^{(i)}(\sigma')a^{(i)}(\sigma'')/\bar{a}^{(i)})^{1/3}$, respectively.

§ 6. Reflection by Mountain

The calculation of the field strength of the wave reflected by a mountain may not be necessary for itself. However, for the sake of convenience in the next section, we shall briefly examine the course of the calculation.

Taking any points x' and x_1 respectively inside and outside of the mountain (Fig. 13), then, we have by the similar calculation as in (2.13) and (2.14) (reversing the sign of n),

$$G(x',x_2)=\frac{-j}{4\pi}\int_{\sigma} G(x',\sigma)(n\gamma)G_0(\sigma,x_2)d\sigma , \tag{6.1}$$

$$G(x_1,x_2)=G_0(x_1,x_2)+\frac{j}{4\pi}\int_{\sigma} G_0(x_1,\sigma)(n\gamma)G(\sigma,x_2)d\sigma . \tag{6.2}$$

Substituting (6.1) into (6.2), then

$$G(x_1,x_2)=G_0(x_1,x_2)+\left(\frac{1}{4\pi}\right)^2\int d\sigma'\int d\sigma'' G_0(x_1,\sigma')(n'\gamma)G(\sigma',\sigma'')(n''\gamma)G_0(\sigma'',x_2)\,, \tag{6.3}$$

with $n'=n(\sigma')\,,\quad n''=n(\sigma'')\,.$

The first and the second terms in the right hand side of (6.3) express the direct and reflected waves, respectively. However, we shall now calculate (6.1) and (6.2) separately for convenience's sake. Taking the point x' at an infinitesimal distance from the surface σ, then, the integration value of (6.1) is almost determined by the integration in the vicinity of the phase stationary point σ' shown in Fig. 13. Thus, using the coordinate system introduced in section 4, we can put

$$G_0(\sigma,x_2)\simeq G_0(\sigma',x_2)e^{-jk^{(1)}\left\{\left(\frac{\partial r_2}{\partial u_1}\right)_{\sigma'}\Delta u_1+\left(\frac{\partial r_2}{\partial u_2}\right)_{\sigma'}\Delta u_2\right\}}\,, \tag{6.4}$$

with $\Delta u_i=(u_i)_\sigma-(u_i)_{\sigma'}\,,$

where σ denotes any point on the surface σ in the vicinity of the point σ'. On the other hand, taking into account that we can now use the approximation in (4.34) also for the solution in the 1-st space as in the 2-nd space, we have, by the same method as the one used in deriving the equation (4.72),

$$\begin{aligned}G(x',\sigma)=&-\frac{j}{\pi}\int_{-\infty}^{\infty}dk_1'\int_{-\infty}^{\infty}dk_2'\eta_{n'}{}^{(2)}(k'-n'k_n{}^{(2)})\cdot(g_1g_2)_{x'}{}^{-1/4}(g_1g_2)_\sigma{}^{-1/4}\\&\times\frac{e^{jk_n{}^{(2)}\sqrt{g_0}((u_0)_{x'}-v_0)}}{(k')^2\{k_n{}^{(2)}(U^{(2)}/c)^{-1}+k_n{}^{(1)}(U^{(1)}/c)^{-1}\}}e^{-j(k_1'\Delta u_1'+k_2'\Delta u_2')}\cdot\bar{\eta}_n{}^{(1)}(k'-nk_n{}^{(1)})\,,\end{aligned} \tag{6.5}$$

where $k_n{}^{(i)}=\sqrt{(k^{(i)})^2-(k')^2}\,,\qquad \Delta u_i'=(u_i)_{x'}-(u_i)_\sigma\,.$

Hence, using (6.4) with the expression (3.10) for $G_0(\sigma',x_2)$ and also the relations $d\sigma=\sqrt{g_1g_2}\,du_1du_2$ and $(g_i)_{x'}\sim(g_i)_\sigma$, the integral (6.1) takes the form

$$\begin{aligned}G(x',x_2)\simeq&-\int_{-\infty}^{\infty}dk_1'\int_{-\infty}^{\infty}dk_2'\delta\left(k_1'-k^{(1)}\left(\frac{\partial r_2}{\partial u_1}\right)_{\sigma'}\right)\delta\left(k_2'-k^{(1)}\left(\frac{\partial r_2}{\partial u_2}\right)_{\sigma'}\right)\\&\times e^{-jk^{(1)}\sum^2_{i=1}\left(\frac{\partial r_2}{\partial u_i}\right)_{\sigma'}((u_i)_{x}'-(u_i)_{\sigma}')}\eta_{n'}{}^{(2)}(k'-n'k_n{}^{(2)})\cdot\frac{e^{jk^{(1)}\sqrt{g_0}((u_0)_{x'}-v_0)}}{(k')^2\{k_n{}^{(2)}(U^{(2)}/c)^{-1}+k_n{}^{(1)}(U^{(1)}/c)^{-1}\}}\\&\times\frac{e^{-jk^{(1)}r_2}}{r_2}\cdot\bar{\eta}_{n'}{}^{(1)}(k'-n'k_n{}^{(1)})(n'\gamma)\eta^{(1)}(k_2)\,,\end{aligned}$$

with $k_2=k^{(1)}(\mathrm{grad}\,|x-x_2|)_{x=\sigma'}\,,$

which gives, for $x'\to\sigma'$,

$$\begin{aligned}G(\sigma',x_2)\simeq&-\eta_{n'}{}^{(2)}(k_T-n'k_n{}^{(2)})\cdot k_T{}^{-2}\{k_n{}^{(2)}(U^{(2)}/c)^{-1}+k_n{}^{(1)}(U^{(1)}/c)_{-1}\}^{-1}\\&\times e^{-jk^{(1)}r_2}/r_2\cdot\bar{\eta}_{n'}{}^{(1)}(k_2)(n'\gamma)\eta^{(1)}(k_2)\,,\end{aligned} \tag{6.6}$$

with $k_T=\left[0,\ \frac{1}{\sqrt{g_1}}\frac{\partial r_2}{\partial u_1},\ \frac{1}{\sqrt{g_2}}\frac{\partial r_2}{\partial u_2}\right]_{x=\sigma'}\,.$

Introducing the unit vectors l_2 and n_2 which exist in the incident plane at the point σ' and are respectively parallel and normal to the vector k_2 (Fig. 13), then,

$$n'=n_2\sin\theta-l_2\cos\theta\,,\quad(\theta=\widehat{n'k_2})\,. \tag{6.7}$$

Using (6.7) and the relation (2.6),

$$\bar{\eta}_{n'}{}^{(1)}(k_2)(n'\gamma)\eta^{(1)}(k_2)=-\cos\theta\bar{\eta}_{n'}{}^{(1)}(k_2)(l_2\gamma)\eta^{(1)}(k_2)=-2\cos\theta k^{(1)}\bar{\eta}_{n'}{}^{(1)}(k_2)\,. \tag{6.8}$$

Further, using the vectors introduced in (4.93), we can set

$$\mathbf{1}_{n'}=C_{n_2}\mathbf{1}_{n_2}+C_{m_2}\mathbf{1}_{m_2}+C_{l_2}\mathbf{1}_{l_2}\,, \tag{6.9}$$

where $C_{n_2}=(\overline{\mathbf{1}}_{n_2}\mathbf{1}_{n'})=\sin\theta\ ,\quad C_{m_2}=(\overline{\mathbf{1}}_{m_2}\mathbf{1}_{n'})=0\ ,$ etc. .

Hence, using (6.9) and taking into account $\overline{\mathbf{1}}_{l_2}\eta(k_2)=0$,

$$\overline{\eta}_{n'}(k_2)=\overline{\mathbf{1}}_{n'}\eta(k_2)=\sin\theta\,\overline{\mathbf{1}}_{n_2}\eta(k_2)=\sin\theta\,\overline{\eta}_{n_2}(k_2)\ . \tag{6.10}$$

Using (6.8), (6.9) and the relation $k_T{}^2=\sin^2\theta(k^{(1)})^2$, Eq. (6.6) takes the form

$$G(\sigma',x_2)\simeq\eta_{n'}{}^{(2)}(k_T-n'k_n{}^{(2)})\cdot\frac{2\cot\theta\, e^{-jkr_2}/r_2}{k^{(1)}\{k_n{}^{(2)}(U^{(2)}/c)^{-1}+k_n{}^{(1)}(U^{(1)}/c)^{-1}\}}\cdot\overline{\eta}_{n_2}{}^{(1)}(k_2)\ , \tag{6.11}$$

which, in the special case in which $U^{(1)}=U^{(2)}$, gives, using the relation $k_n{}^{(1)}=\cos\theta k^{(1)}$,

$$G(\sigma',x_2)\sim\eta_{n_2}(k_2)\cdot(\overline{U}/c)^{-1}\cdot\overline{\eta}_{n_2}(k_2)e^{-jkr_2}/r_2\ ,$$

which gives, using the relation $\mathbf{1}_{n_2}\cdot\overline{\mathbf{1}}_{n_2}=1-(n_2s)^2$,

$$\eta(k_2)e^{-jkr_2}/r_2\ ,$$

which is the Green function in free space obtained in (3.10), as is to be so. Conversely, this fact secure the completeness of our sets of solutions $\varphi_{k',\nu}{}^{(i)}$'s and $\overline{\varphi}_{k',\nu}{}^{(i)}$'s defined in section 4.

We then substitute (6.11) into (6.2) and perform the integration. This can be done in a good approximation also by the phase stationary method ; Since, at the phase stationary point σ_0 (Fig. 14), $k_1=k_T+nk_n{}^{(1)}$, we find, using the relation (2.6) and the definition of $\mathbf{1}_n$, that

$$\begin{aligned}\eta^{(1)}(k_1)(n\gamma)\eta_n{}^{(2)}(k_T-nk_n{}^{(2)})&=\eta^{(1)}(k_T+nk_n{}^{(1)})(n\gamma)[(k_T\gamma)-(n\gamma)(k_T\gamma)k_n{}^{(2)}(U^{(2)}/c)^{-1}]\mathbf{1}_n\\&=[\{1+(U^{(1)}/c)^{-1}((n\gamma)k_n{}^{(1)}+(k_T\gamma))\}k_n{}^{(1)}-\{(k_T\gamma)+(n\gamma)k_n{}^{(1)}+(U^{(1)}/c)^{-1}((k_T\gamma)^2+(n\gamma)^2k_n{}^{(1)2})\}\\&\quad\times k_n{}^{(2)}(U^{(2)}/c)^{-1}](n\gamma)^2(k_T\gamma)\mathbf{1}_n=\eta^{(1)}(k_T+nk_n{}^{(1)})\mathbf{1}_nk_n{}^{(1)}-\{(k_T\gamma)^2+(n\gamma)(k_T\gamma)k_n{}^{(1)}+(U^{(1)}/c)^{-1}\\&\quad\times(k_T{}^2+k_n{}^{(1)2})(k_T\gamma)\}k_n{}^{(2)}(U^{(2)}/c)^{-1}\mathbf{1}_n=\eta_n{}^{(1)}(k_T+nk_n{}^{(1)})(U^{(1)}/c)\{k_n{}^{(1)}(U^{(1)}/c)^{-1}-k_n{}^{(2)}(U^{(2)}/c)^{-1}\}.\end{aligned} \tag{6.12}$$

Hence, using (6.11), (6.12) and the relation (6.10), the integration in (6.2), i.e. the reflected wave, say $G_r(x_1,x_2)$, takes the form

$$G_r(x_1,x_2)\simeq\eta_{n_1}{}^{(1)}(k_1)\cdot S\cdot\overline{\eta}_{n_2}{}^{(1)}(k_2)\frac{jk^{(1)}}{2\pi}\int\cos\theta d\sigma e^{-jk^{(1)}(r_1+r_2)}/r_1r_2\ , \tag{6.13}$$

where $S=(\overline{U}/c)^{-1}\{k_n{}^{(1)}(U^{(1)}/c)^{-1}-k_n{}^{(2)}(U^{(2)}/c)^{-1}\}/\{k_n{}^{(1)}(U^{(1)}/c)^{-1}+k_n{}^{(2)}(U^{(2)}/c)^{-1}\}$, (6.14)

and the unit vector n_1 corresponding to n_2 is shown in Fig. 14. After simple calculation, we have

$$\frac{jk}{2\pi}\int\cos\theta d\sigma e^{-jk(r_1+r_2)}/r_1r_2\sim e^{-jk(r_1+r_2)_0}/\sqrt{\operatorname{Det}(r_1+r_2+2r_1r_2/a)_0} \tag{6.15}$$

where $$\frac{1}{a}=\begin{pmatrix}\sec\theta/a_l\ , & (1/a_2-1/a_1)\sin\varphi\cos\varphi\\ (1/a_2-1/a_1)\sin\varphi\cos\varphi\ , & \cos\theta/a_t\end{pmatrix}, \tag{6.16}$$

$$1/a_l=\cos^2\varphi/a_1+\sin^2\varphi/a_2\ ,\quad 1/a_t=\sin^2\varphi/a_1+\cos^2\varphi/a_2\ ,$$

and φ is the similar one defined in section 4, i.e. the angle between the incident plane and u_1-axis.

For the wave reflected by more than two mountains (Fig. 15), the equation corresponding to (6.13) takes the form

$$\begin{aligned}G_r(x_1,x_N)\simeq&\ \eta_{n_1'}(k_1)\cdot S^{(1)}\eta_{n_1''n_2'}(k_{12})S^{(2)}\eta_{n_2''n_3'}(k_{23})S^{(3)}\cdots S^{(N)}\cdot\overline{\eta}_{n_N''}(k_N)\\&\times\Pi_{i=1}{}^{N}\left(\frac{jk}{2\pi}\int\cos\theta_i d\sigma_i\right)e^{-jk(r_1+r_{12}+r_{23}+\cdots+r_N)}/(r_1r_{12}\cdots r_N),\end{aligned} \tag{6.17}$$

where $S^{(i)}$ is the one belonging to the i-th mountain, and n' and n'' correspond to n_1 and n_2 in (6.13), respectively. The integration in (6.17) can be performed without difficulty. Denoting a in (6.16) belonging to the i-th mountain by a_i and the angle between the vectors n_{i+1}' and

n_i'', counting from the former to the latter, by $\theta_{i,i+1}=-\theta_{i+1,i}$ as in section 5, then,

$$\Pi_{i=1}^{N}\left(\frac{jk}{2\pi}\int\cos\theta_i d\sigma_i\right)e^{-jk(r_1+r_{12}+\cdots+r_N)}/(r_1r_{12}\cdots r_N)=e^{-jk(r_1+r_{12}+\cdots+r_N)_0}/\sqrt{\operatorname{Det}(\Delta_{1N})}\,, \tag{6.18}$$

where

$$\begin{aligned}\Delta_{kl}=&\,r_{k-1,l+1}M_{kl}+\textstyle\sum_i r_{k-1,i}r_{i,l+1}(M_{ki}a_i^{-1}M_{il})+\sum_{i<j}r_{k-1,i}r_{i,j}r_{j,l+1}(M_{ki}a_i^{-1}M_{ij}a_j^{-1}M_{jl})\\&+\textstyle\sum_{i<j<m}r_{k-1,i}r_{i,j}r_{j,m}r_{m,l+1}(M_{ki}a_i^{-1}M_{ij}a_j^{-1}M_{jm}a_m^{-1}M_{ml})+\cdots\cdots\cdots\cdots,\end{aligned} \tag{6.19}$$

with

$$\left.\begin{aligned}&r_{i,j}=r_{i,i+1}+r_{i+1,i+2}+\cdots+r_{j-1,j}\,,\qquad (i<j)\,,\\&M_{ij}=\begin{pmatrix}\cos\theta_{ij}\,, & -\sin\theta_{ij}\\ \sin\theta_{ij}\,, & \cos\theta_{ij}\end{pmatrix},\end{aligned}\right\} \tag{6.20}$$

which has the relations

$$M_{ij}=M_{i,i+1}M_{i+1,i+2}\cdots M_{j-1,j}\,,\qquad (i<j)\,, \tag{6.21}$$

and

$$\operatorname{Det}M_{ij}=1\,,$$

with

$$\theta_{ij}=-\theta_{ji}=\theta_{i,i+1}+\theta_{i+1,i+2}+\cdots+\theta_{j-1,j}\,.$$

Hence, in the special case in which the 1-st space is the vacuum, we find, using the forms of $\eta_{n'',n'}$'s in (5.30) and (5.31), that

$$\begin{aligned}G_r(x_1,x_N)\simeq&\,\eta_{1n'}(k_1)\cdot R_1e^{-j\rho_1\theta_{12}}R_2e^{-j\rho_1\theta_{23}}R_3\cdots\\&\times e^{-j\rho_1\theta_{N-1,N}}R_N\cdot\overline{\eta}_{n_N''}(k_N)\,e^{-jk(r_1+r_{12}+\cdots+r_N)_0}/k\sqrt{\operatorname{Det}(\Delta_{1N})}\,,\end{aligned} \tag{6.22}$$

where

$$R=\frac{k_n^{(1)}/k^{(1)}-k_n^{(2)}(U^{(2)}/c)^{-1}}{k_n^{(1)}/k^{(1)}+k_n^{(2)}(U^{(2)}/c)^{-1}}\,. \tag{6.23}$$

The right hand side of (6.22) gives the component which contributes to $G(x_1,x_N)$ by the wave reflected by N mountains, and is right so far as the geometrical optics can be applied to this component.

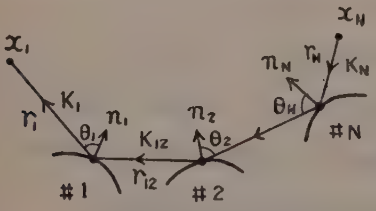

Fig. 15.

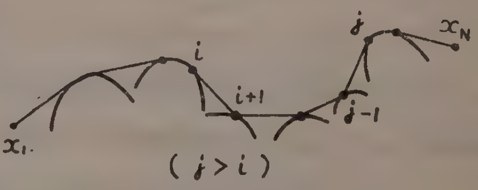

Fig. 16.

§ 7. Field Strength for given Picture of Wave Path

The correspondence between each term in (5.24) or in (6.17) and its corresponding point on the wave path shown in Fig. 2 or in Fig. 15 are very evident. In the following, we shall get the explicit equation for the contribution of the field strength of any given picture of wave path which consists of the free space propagation parts and the diffraction or reflection parts by mountains.

The calculation can be performed in the same way as in section 5 and 6. Using (5.31), the equation corresponding to (5.24) or (6.17) becomes

$$\begin{aligned}G(x_1,x_N)\simeq&\,\eta_{n_1'}(k_1)\cdot R_1e^{-j\rho_1\theta_{12}}R_2e^{-j\rho_1\theta_{23}}R_3\cdots e^{-j\rho_1\theta_{N-1,N}}R_N\cdot\overline{\eta}_{n_N''}(k_N)\\&\times\Pi_{i=1}^{N}\left(\frac{jk}{2\pi}\int d\sigma_i'\right)\frac{e^{-jk(r_1+r_{12}+r_{23}+\cdots+r_{N-1,N}+r_N)}}{kr_1r_{12}\cdots r_{N-1,N}r_N}\,,\end{aligned} \tag{7.1}$$

where

$$R=\left\{\begin{array}{ll} \dfrac{k_n^{(1)}/k^{(1)}-k_n^{(2)}/(U^{(2)}/c)}{k_n^{(1)}/k^{(1)}+k_n^{(2)}/(U^{(2)}/c)} & \text{for reflection} \\ g(k^{(1)}D/(k^{(1)}a)^{2/3})\dfrac{(k^{(1)}a)^{1/3}}{\sqrt{k^{(1)}D}}e^{-j(k^{(1)}D+\pi/4)} & \text{for diffraction,} \end{array}\right\} \tag{7.2}$$

and

$$d\sigma_i'=\left\{\begin{array}{ll} \cos\theta_i\, d\sigma_i & \text{for reflection} \\ \mathrm{d}X_i'\, dY_i'' & \text{for diffraction.} \end{array}\right.$$

For the integration in (7.1), we first consider the simplest case in which reflections occur successively between two mountains, say the i-th mountain, and the j-th mountain as is shown in Fig. 16. Then,
the result of calculation becomes

$$\Pi_{i=1}{}^N\left(\frac{jk}{2\pi}\int d\sigma_i'\right)\frac{e^{-jk(r_1+r_{12}+\cdots+r_{N-1,N}+r_N)}}{r_1r_{12}\cdots r_{N-1,N}r_N}\simeq\frac{e^{-jk(r_1+r_{12}+\cdots+r_{N-1,N}+r_N}}{r_1r_{12}\cdots r_{i-1,i}r_{ij}^e r_{j,j+1}\cdots r_N\sqrt{W(C)}}, \tag{7.3}$$

with

$$r_{ij}^e=\sqrt{\mathrm{Det}\,(\varDelta_{i+1,j-1})}\ , \tag{7.4}$$

where $\varDelta$ is the one defined in section 6 and $W(C)$ is the determinant of the matrix C introduced in Appendix (3) with the matrix elements

$$\left.\begin{array}{l} C_{ij}=C_{ji}=(\overline{m}_{i,i+1}\varDelta_{j-1,i+1}^{-1}m_{j-1,j})\ , \quad (i<j), \\ C_{ii}=r_{i-1,i}^{-1}+(\overline{m}_{i,i+1}\varDelta_{j-1,i+1}^{-1}\{(\varDelta_{j-1,i+1}-\varDelta_{j-1,i+2}M_{i+2,i+1})r_{i,i+1}^{-1}\}m_{i+1,i})\ , \\ C_{jj}=(\overline{m}_{j,j-1}\varDelta_{i+1,j-1}^{-1}\{(\varDelta_{i+1,j-1}-\varDelta_{i+1,j-2}M_{j-2,j-1})r_{j-1,j}^{-1}\}m_{j-1,i})+r_{j,j+1}^{-1}\ , \end{array}\right\} \tag{7.5}$$

with

$$m_{i+1,i}=\overline{m}_{i,i+1}=\begin{pmatrix}\sin\theta_{i,i+1}\\ \cos\theta_{i,i+1}\end{pmatrix},$$

and the other matrix elements are the same as those in section 5 (5.29). Inserting (7.3) into (7.1), then,

$$G(x_1,x_2)\simeq\eta_{n_1'}(k_1)\cdot R_1e^{-j\rho_1\theta_{12}}R_2e^{-j\rho_1\theta_{23}}R_3\cdots e^{-j\rho_1\theta_{N-1,N}}R_N\cdot\overline{\eta}_{n_N''}(k_N) \\ \times\frac{e^{-jk(r_1+r_{12}+\cdots+r_{N-1,N}+r_N)}}{kr_1r_{12}\cdots r_{i-1,i}r_{ij}^e r_{j,j+1}\cdots r_N\sqrt{W(C)}}, \tag{7.6}$$

which is of the same form as the one in (5.36), and thus r_{ij}^e can be interpreted as the effective distance between the i-th and j-th mountains.

The general case in which the successive reflections between pair of two mountains occur any times in the wave path from the transmitting point to the receiving point, can be treated in a same way. It is sufficient to interpret r_{ij}^e and C_{ij} 's defined in (7.4) and (7.5) as the effective distance and matrix elements of C for respective pair of two mountains, and then the equation (7.6) holds as it is.

In conclusion, the author wishes to express his cordial thanks to Mr. T. Yonezawa for his kind reading and discussions to this paper.

Appendix

(1) In the coordinate system in which the line element ds is expressed by

$$ds^2=g_{ij}du_idu_j\ ,$$

g_{ij} 's are transformed in the following way:

$$g_{ij}'=g_{kl}\frac{\partial u_k}{\partial u_i'}\frac{\partial u_l}{\partial u_j'} .$$

Hence, $$\frac{\partial g_{ij}'}{\partial u'_m}=\frac{\partial g_{kl}}{\partial u'_m}\frac{\partial u_k}{\partial u'_i}\frac{\partial u_l}{\partial u'_j}+g_{kl}\frac{\partial^2 u_k}{\partial u'_i\partial u'_m}\frac{\partial u_l}{\partial u_j'}+g_{kl}\frac{\partial u_k}{\partial u'_i}\frac{\partial^2 u_l}{\partial u'_j\partial u'_m} .$$

In the case of the transformation of the form in text,

$$\left(\frac{\partial u_k}{\partial u'_i}\right)_{u'=u=v}=\delta_{ki} , \quad \left(\frac{\partial g_{kl}}{\partial u'_m}\right)_{u'=v}=\left(\frac{\partial g_{kl}}{\partial u_m}\right)_{u=v} , \quad \left(\frac{\partial^2 u_k}{\partial u_l'\partial u_m'}\right)_{u'=v}=C_{im}{}^k=C_{mi}{}^k .$$

Hence, $$\left(\frac{\partial g_{ij}'}{\partial u_m'}\right)_{u'=v}=\left(\frac{\partial g_{ij}}{\partial u_m}\right)_{u=v}+(g_{kj})_{u=v}C_{im}{}^k+(g_{il})_{u=v}C_{jm}{}^l .$$

Further, the number of the equations (4.3) in text is just equal to that of $C_{im}{}^l$'s introduced. Thus, the equations (4.3) in the new coordinate system are secured.

(2) Using the reration (2.6),

$$(as)(bs)\{(as)(bs)-(ab)\}=0 .$$

Hence, the eigen values of $(as)(bs)$ are (ab) or 0. Thus, the spur of $(as)(bs)$ must be a integral multiple of (ab). Taking into account the special case in which $a=b$, it follows that

$$Sp[(as)(bs)]=2(ab) .$$

From (2.6), $$\{(as)(bs)(cs)+(cs)(bs)(as)\}(ds)=(ab)(cs)(ds)+(bc)(as)(ds) ,$$

which gives, taking into account that the transposed matrices of S_i 's are respectively equal to $-S_i$'s, and also using the cyclic relation,

$$Sp[(as)(bs)(cs)(ds)]=\tfrac{1}{2}\{(ab)Sp[(cs)(ds)]+(bc)Sp[(as)(ds)]\}=(ab)(cd)+(bc)(ad) .$$

(3) W defined in (5.27) is the determinant of a matrix of the form

$$W(c)=\begin{vmatrix} C_{11} & C_{12} & 0 & 0 & \cdots \\ C_{21} & C_{22} & C_{23} & 0 & \cdots \\ 0 & C_{32} & C_{33} & C_{34} & \cdots \\ 0 & 0 & C_{43} & C_{44} & \cdots \\ \vdots & \vdots & \vdots & \vdots & \end{vmatrix}=\begin{cases} C_{11}C_{22}\cdots C_{nn}+\sum_i C_{11}C_{22}\cdots C_{i-1,i-1}(-C_{i,i+1}C_{i+1,i}) \\ \quad\times C_{i+2,i+2}\cdots C_{nn}+\sum_{i<j}C_{11}C_{22}\cdots C_{i-1,i-1} \\ \quad\times(-C_{i,i+1}C_{i+1,i})C_{i+2,i+2}\cdots C_{j-1,j-1}(-C_{j,j+1}C_{j+1,j}) \\ \quad C_{j+2,j+2}\cdots C_{nn}+\cdots , \end{cases}$$

with the matrix elements

$$C_{ii}=1/x_{i-1,i}+1/x_{i,i+1} , \quad C_{i,i+1}=C_{i+1,i}=-\cos\theta_{i,i+1}/x_{i,i+1} .$$

JOURNAL OF THE PHYSICAL SOCIETY OF JAPAN Vol. 8, No. 4, JULY—AUGUST, 1953

Measurement of Permittivity of Mixed Barium and Strontium Titanate in 3,000 Mc/s Region

By Hideo IWAYANAGI

Department of Physics, Faculty of Sience, University of Tokyo

(Received April 4, 1953)

The permittivity of ferroelectric substance was measured in a microwave region by two methods, namely, by observing the resonances of a sample inserted either in a water-filled cavity resonator or in a wave guide window. By the two methods its temperature dependence of (Ba: 80%, Sr: 20%)TiO_3, its frequency dependence in a region between 2,200 Mc/s and 3,500 Mc/s, and the permittivities for several constitutions of barium and strontium, were measured. The results indicate the existence of a dispersion in this frequency region.

§ 1. Introduction

Recently, various features of ferroelectric substances, such as barium titanate, have been studied by many investigators. J. G. Powels[1] found that the value of permittivity of barium titanate at 9,450 Mc/s is much smaller than in lower frequency region which leads us to expect a dispersion of the permittivity in a region lower than 9,450 Mc/s. If the frequency where the permittivity falls becomes known, it will contribute much to the study of the ferroelectric mechanism. A. von Hippel[2] published a report in which the frequency dependence of the permittivity of barium titanate was described, and C. Kittel[3] suggested a dispersion at a few kilomegacycles. The author intended to measure the permittivity at 3,000 Mc/s, as the experimental data in this frequency region seemed to be wanting.

The methods of the measurement of the permittivity at microwave region were described by some authors.[4] They are to observe the reflection from or the transmission through the specimen filled in some part of a wave guide. When the permittivity is nearly one thousand or more, its reflection becomes nearly equal to that of a metalic plate necessitating high accuracy of measurement. Another unfavourable point of these methods is that the use of a larger wave length, say 10 cm, requies a larger size of specimen.

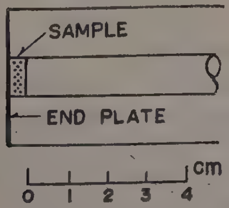

Fig. 1. Cross section of the terminated coaxial cable.

The first attempt by the author was to use the coaxial cable in which a disc of the sample was held between the end plate and the inner conductor as shown in Fig. 1. But it failed, because the calculation of electro-magnetic field near the sample was too difficult to obtain the reliable value of the permittivity. Two improved methods were then adopted as described in section 2 and section 3.

§ 2. Measurement by a Water-Filled Cadity Resonator

Method

The transmission power of a water-filled cavity with the sample fixed on a movable plunger is measured (Fig. 2). The behavior of this resonance curve varies as the thickness of the inserted sample — the first resonant length of the cavity, l_1, and the ratio of power at the second resonant point to the first, P_2/P_1, vary when the thickness becomes nearly equal to $\lambda_g/4$, where λ_g is the wave length for some resonant mode in the sample. It may be thought that the water column acts like an input wave guide to the resonant cavity formed by the ferroelectrics. When the sample is not resonant, l_1, or P_2/P_1 is almost independent of the sample, as the reflection coefficient at the boundary, where the propagation constant has very large discontinuity, is neary -1.

In order to calculate the resonant condition of the sample, we consider the waves which propagate through a wave guide filled with water and ferroelectrics. We assume that all modes except the lowest mode, H_1, are cut off in water* (Fig. 3). When the waves which propagate through water enter the sample, some part is converted into higher modes by the incompleteness of the boundary. Let us assume that the waves perfectly reflected at $z=0$ do not flow out into the water column at $z=d$ except the H_1 mode. The field E at $z=d$ set up by an infinite series of reflected waves is

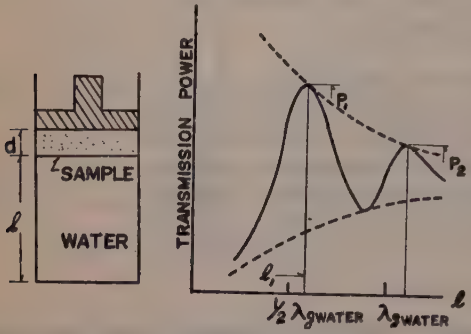

Fig. 2. Transmission Curve.

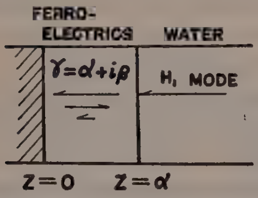

Fig. 3. Wave propagation in a water-filled cavity terminated by a specimen of ferroelectrics.

$$E=1/[1+\exp(-2\gamma d)]\,, \qquad (1)$$

where the first term of the series is taken as unity and γ is the propagation constant to be measured for every mode in the sample. We suppose that $|E|$ will take a maximum value when l_1 or P_2/P_1 abruptly varies. We rewrite Eq. 1 in the form

$$|E|^2=1/[1+\exp(4\alpha d)+2\exp(-2\alpha d)\cos 2\beta d]\,,$$

where $\gamma=\alpha+i\beta$, and put

$$2\alpha d=x \text{ and } \alpha/\beta=k\,. \qquad (2)$$

The above equation becomes

$$f_k(x)\equiv 1/|E|^2$$
$$=1+\exp(-2kx)+2\exp(-kx)\cos x,$$

where k is a parameter. A maximum point of $|E|^2$ or a minimum point of $f_k(x)$ can be obtained from the condition $\partial f_k(x)/\partial x=0$, and we get a relation

$$-k[\exp(-kx)+\cos x]=\sin x\,. \qquad (3)$$

For convenience of calculation, Eq. 3 is written in the form

$$\sin \Delta x=k[\cos \Delta x-\exp(-kx)]\,, \qquad (4)$$

where

$$\Delta x=(2n+1)\pi-x\,. \qquad (4')$$

Fig. 4-a shows the values of

$$\Delta x/x\simeq \Delta x/(2n+1)\pi \text{ vs. } k.$$

When the dielectric loss factor, $\tan\delta$, is large its effect on β, or λ_g, can not be neglected. We write the values

$$\gamma=\alpha+i\beta\,,$$
$$\varepsilon/\varepsilon_0=\varepsilon'-i\varepsilon''=\varepsilon'(1-i\tan\delta)\,, \qquad (5)$$
$$\mu=\mu_0\,,$$

and

$$\gamma=(2\pi i/\lambda)[(\varepsilon/\varepsilon_0)-(\lambda/\lambda_c)^2]^{1/2}$$
$$=(2\pi i/\lambda_{g0})(1-iD)^{1/2}\,, \qquad (6)$$

where λ is the wave length in free space, λ_c is the cut off wave length, $\lambda_{g0}=\lambda/[\varepsilon'-(\lambda/\lambda_c)^2]^{1/2}$ is the corresponding guide wave length for $\varepsilon''=0$, and $D=\tan\delta/[1-(1/\varepsilon')(\lambda/\lambda_c)^2]$. From this complex propagation constant we get the attenuation constant, α, and the phase constant, β

$$\alpha=(-2\pi/\lambda_{g0})Im[(1-iD)^{1/2}]\,,$$
$$\beta=(2\pi/\lambda_{g0})Re[(1-iD)^{1/2}]\,. \qquad (7)$$

If we put

$$(1-iD)^{1/2}=X+iY \text{ and } D=\tan\theta\,;$$

we obtain the convenient forms

$$X=\cos(\theta/2)/(\cos\theta)^{1/2}\,,$$
$$k=\alpha/\beta=-X/Y=\tan(\theta/2)\,, \qquad (8)$$
$$\lambda_g=\lambda_{g0}/X\,.$$

Fig. 4-b shows the curve of X vs. k.

Apparatus

As a large loss in water needs rather a large microwave power, a small magnetron M-60 was used in this experiment. The frequency was about 3,080 Mc/s. The cavity was kept at a constant temperature within the accuracy of ±0.3°C, and the output power was measured by a crystal rectifier and galvanometer. As ε' and $\tan\delta$ of water depend on the temperature, a thermostat was necessary. The block diagram of the measuring system is given in Fig. 5.

---

* This condition is not fully satisfied for a large loss in water.

Cavity Resonator. The construction is shown in Fig. 6. The inner diameter of the cavity is 8.0 mm, and the microwave power is fed from a coaxial line. On moving the plunger, water may flow in and out of the cavity through a small hole in the cavity wall. The plunger is driven by a micrometer, and the accuracy of measuring the resonant length of the cavity was about 2/100 mm.

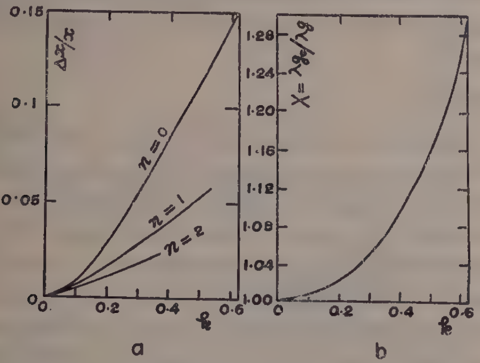

Fig. 4. a) $\Delta x/x$ as a function of k (solution corresponding to Eq. 4).
b) X as a function of k (solution corresponding to Eq. 8).

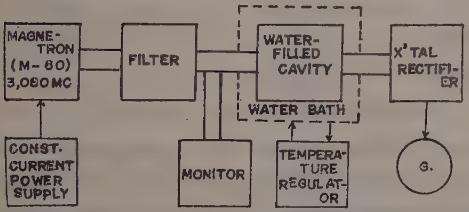

Fig. 5. Block diagram of the measuring system employing the water-filled cavity resonater.

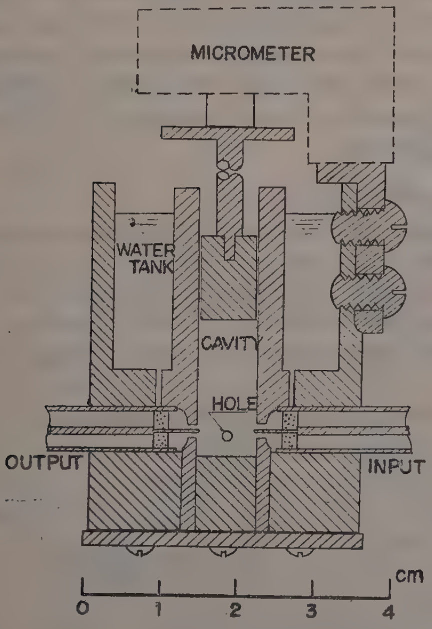

Fig. 6. Construction of the water-filled cavity resonator.

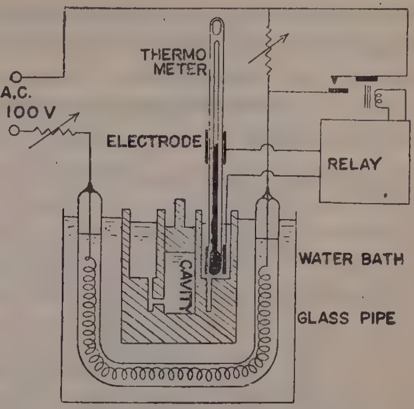

Fig. 7. Relaying system for regulating the temperature.

Temperature Regulator. The current through a heating wire in a water bath is controlled by a relay, and the cavity is put in this water bath (Fig. 7). The relay acts in such a way that if the temperature of the cavity varies, the capacitance between the capillary of the mercury thermometer and the surrounding plate changes altering the frequency of the oscillator. The deviation from a reference frequency is converted into the voltage change, which drives a thyratron tube to operate the relay. It was able to be kept at a constant temperature between the room temperature and 80°C.

Experimental Results (I)

A ceramic mixture of barium titanate: 80% and strontium titanate: 20% was used in this experiment. The observed values of l_1 and P_2/P_1 at 24°C are shown in Fig. 8. The permittivity at 24°C for the wave length of 9.75 cm (3,080 Mc/s) was determined by a graphical method from the observed data. These are

$$\varepsilon'=775\pm15\ ,$$

$$\tan\delta=0.14\pm0.025\ .$$

Similar measurements were carried out at temperatures between 30°C and 80°C in 5°C intervals. The result is plotted in Fig. 9 with data at 1 Mc/s. From the data at 1 Mc/s, it is seen that the sample used here was not favourable because it has a broad peak of ε', and Curie temperature of 75°C was considerably higher than its normal value of about 50°C for a similar material. The author regrets that no measurements were made using a better sample.

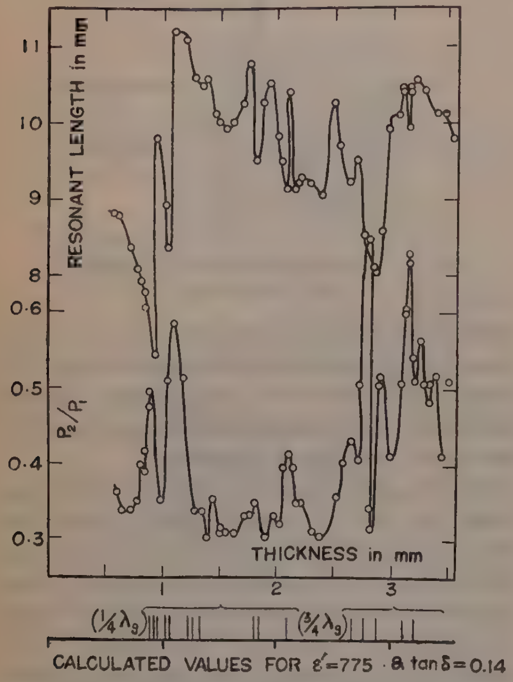

Fig. 8. Data of the measurement of l_1 and P_2/P_1. Their calculated "spectra" are compared with the observed data.

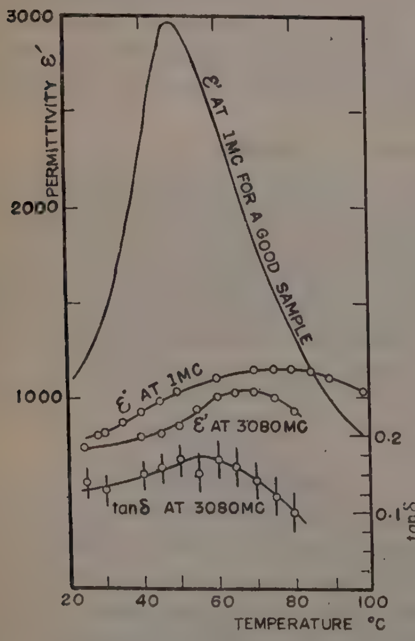

Fig. 9. Temperature dependence of ε' and tan δ of (Ba : 80%, Sr : 20%)TiO$_3$.

§ 3. Measurements by Windows

As the measurement described above took rather a long time to complete one process (a few days), another convenient method was used, though it is not suitable for measuring tan δ.

Method

When the thickness of the dielectrics, which is inserted in the window of a wave guide, becomes about a half wave length or its multiples, the microwave transmission will become maximum. If the specimen is not so much forced out of the window as shown in Fig. 10–c, the deviation of the thickness from $n\lambda_g/2$ is so small that it may be neglected. The deviation which arises due to the existence of the dielectric loss should have been considered, but it was also neglected because of the difficulty of treatment. If the thickness of the specimen and the wave length at a maximum are known, ε' is calculated approximately as follows;

$$\varepsilon' = \lambda^2[(l/2a)^2 + (m/2b)^2 + (n/2d)^2]\,, \qquad (9)$$

where a and b are the dimensions of the rectangular window and d is the thickness of the specimen, and l, m and n are integers depending upon the resonant mode of the specimen. In this measurement various modes appeared, including unexpected modes of $n=0$ (axial electric field types). As it was unable to identify the modes by only one observation for single value of the sample thickness, measurements were repeated for different thicknesses.

Apparatus

The block diagram of the apparatus is shown in Fig. 11. The wave length mas varied between 8.5~14 cm (2,140~3,530 Mc/s) continuously, and modulated with 2,000 c/s. A rectangular cavity (I. D. 5.0×0.9 and stroke

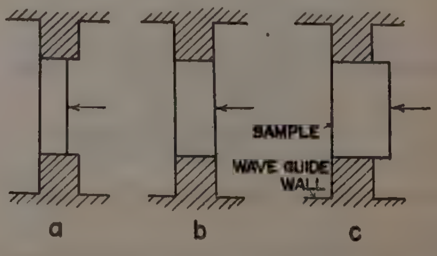

Fig. 10. Three typical situations of the specimen in the window.

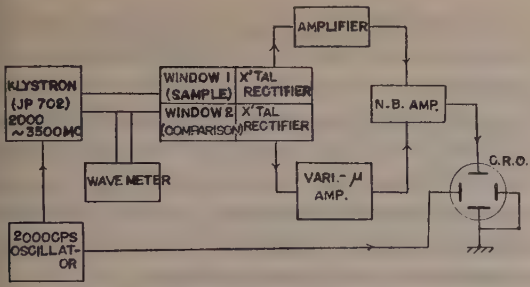

Fig. 11. Block diagram of the apparatus employing the window method.

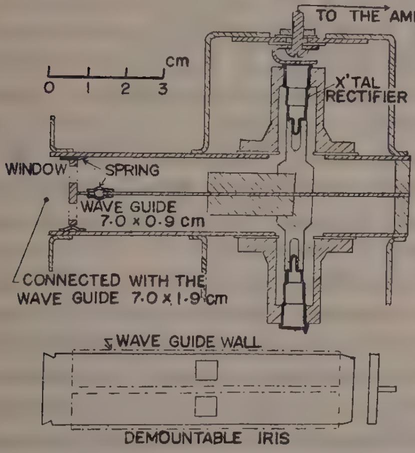

Fig. 12. Construction of the windows and the wide band terminations.

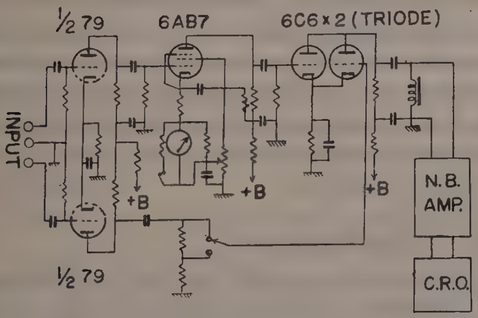

Fig. 13. Balancing amplifier circuit.

of plungers 8, both in cm) was used as an external cavity for klystron, JP–702.

Window and Detecters Two wave guides (I.D. 7.0×0.9 cm each) are piled up, whose frontiers are coupled to a common guide through each window (8.0×4.3 or 5.9×5.9, in mm) (Fig. 12). One of the two windows (window 1) is used for inserting a specimen of the ferroelectrics, while the other (window 2) is used for comparison. The detector was able to measure the transmission power in the wide frequency range used.

Amplifier Each of the two 2,000 c/s outputs is preamplified. After that, the signal from the window 2 is amplified through a variable $-\mu$ tube (6AB7) stage, so that it may balance to the signal from the window 1. The unbalanced output is amplified by a 2,000 c/s tuned amplifier in order to be monitored by a cathode ray oscilloscope. The relative transmission power is known from the cathode current of 6AB7 for balanced output. Fig. 13 shows the circuit.

Experimental Result (II)

The frequency dependence of ε' was measured for a ceramic mixture of barium titanate and strontium titanate (20%) and ZrO_2 (3%). For nine different thickness between 3.42 and 1.72 mm the transmission power was measured

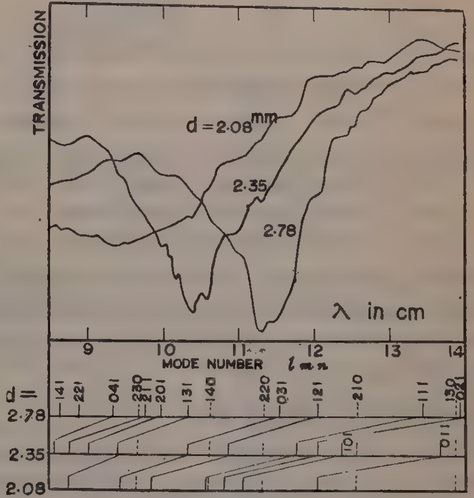

Fig. 14. Some examples of the transmission curves, with their respective modes.

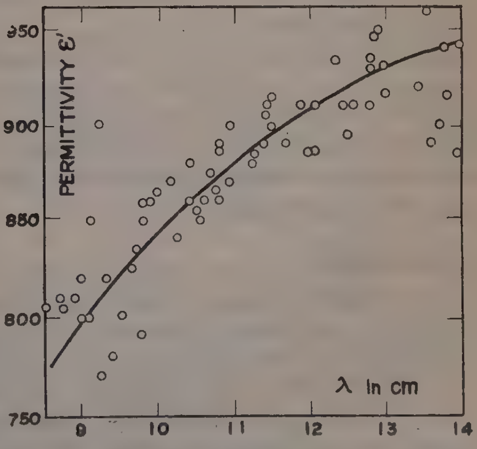

Fig. 15. Frequency dependence of ε' of Ba- and Sr (20%)-TiO_3 at 22°C.

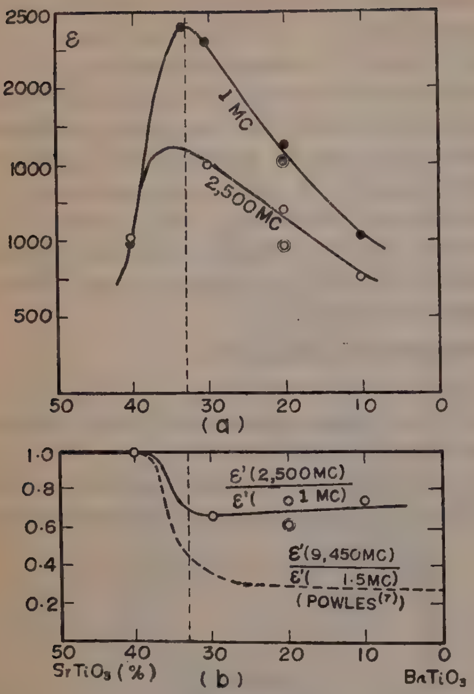

Fig. 16. a) Permittivities for Sr : 10%, 20%, 30%, and 40% at 23°C.
b) ε'(2,500 Mc/s)/ε'(1 Mc/s) and ε'(9,450 Mc/s)/ε'(1.5 Mc/s).

in the range between 2,140 and 3,530 Mc/s. Some examples of observed curves are shown in Fig. 14. Values of ε' obtained from these data plotted in Fig. 15.

Experimental Result (III)

Similar measurements were repeated for samples of barium titanate ceramics mixed with 10, 20, 30 and 40 percent of strontium titanate. For comparison the values at 1 Mc/s were also measured. The results at 23°C for 2,500 Mc/s are plotted in Fig. 16.

Quantitative survey of $\tan\delta$ was not possible. However, it may be said that $\tan\delta$ decreases rapidly when the strontium percentage exceeds 30 percent, since the peaks of the transmission for the 40 percent sample are sharper than those for the 30 percent sample.

§ 4. Discussion

ε' at 3,000 Mc/s is somewhat smaller than the value at much lower frequencies decreasing further with the frequency. According to the curve of ε' in Fig. 20 of von Hippel's paper2), ε' of barium titanate at 3,000 Mc/s is smaller than one half of the d.c. value, and it is shown that the dispersion begins at a few hundred megcycles. In this experiment, however, the ratio of ε' at 3,000 Mc/s to ε' at 1 Mc/s for barium titanate, extrapolated from the values for the ceramic mixtures (Fig. 16–b), is about 0.7 which may lead to a conclusion that the dispersion of the permittivity occurs in the kilomegacycle range. In order to determine the precise dispersion frequency, more experiments are to be performed.

From the curve of the temperature dependence of the permittivity, it is seen that the temperature of the maximum permittivity is slightly lower than that for lower frequencies and the curve of ε' has the character like that of barium titanate at 9,450 Mc/s observed by Powles. Especially in the region above the Curie point, ε decreases nearly in the same order, and it may be thought that ε' begins to decrease at a low frequency region and keep on decreasing.

For several different percentages of constituent strontium titanate a set of similar measurements was made by Powles5) at 9,450 Mc/s. ε'(2,500 Mc/s)/ε'(1 Mc/s) are plotted in Fig. 16–b, with the data of ε'(9,450 Mc/s)/ε'(1.5 Mc/s) by Powles. When the constituent strontium titanate increases to 33 percent approximately the Curie temperature falls to the room temperature. Although the increase of strontium percentage at a given temperature resembles in its result to the increase of temperature at a given percentage of the former, the two processes are essentially different as seen from the behaviors of the curves shown in Figs. 9 and 16–a.

§ 5. Acknowledgement

The author is greatly indebted to Professor K. Shimoda for advice and aid in this work, to Professor S. Sawada for his kindness of preparing the whole samples and to Mr. W. Kinase for discussing the transmission through a window.

References

1) J. G. Powles: Nature **162** (1948) 614.
2) A. von Hippel: Rev. Mod. Phys. **22** (1950) 221.
3) C. Kittel: Phys. Rev. **83** (1951) 458.
4) S. Roberts and A. von Hippel: J. App. Phys. **17** (1946) 610.
W. H. Surber, Jr.: J. App. Phys. **19** (1948) 1130.
J. G. Powles: Nature **161** (1948) 25.
5) J. G. Powles: Nature **162** (1948) 655.

JOURNAL OF THE PHYSICAL SOCIETY OF JAPAN Vol. 8, No. 4, JULY—AUGUST, 1953

Hyperfine Structure of the Spectrum of Al II. Part II

By Shigeki SUWA

Institute of Science and Technology, Komaba, Meguro-ku, Tokyo

(Received April 17, 1953)

As a supplement to the previous work on the anomalous hfs. of the spectrum of Al II, the structure of the multiplet $\lambda3587.4-\lambda3586.5$ (3^3D-4^3F) was studied. The calculated structure of this multiplet was found to be in harmony with that observed by means of interferometers. The triplet separations $\alpha=3^3D_3-3^3D_1$ and $\beta=3^3D_2-3^3D_1$ were found to be $-2.20\,\text{cm}^{-1}$ and $-1.02\,\text{cm}^{-1}$ respectively (the 3^3D term being inverted). The hyperfine energy levels of the n^3D ($n=3,4,5$) series are represented diagramatically (in Fig. 4) in order to show how they depart from the ordinary coupling $\{(\boldsymbol{L}\cdot\boldsymbol{S})\boldsymbol{J}\cdot\boldsymbol{I}\}$ progressively towards the coupling $\{(\boldsymbol{S}\cdot\boldsymbol{I})\boldsymbol{U}\cdot\boldsymbol{L}\}$, as n increases.

§ 1. Introduction

As typical examples of the anomalous hyperfine structure (hfs.), which appears when the gross structure of either term in a transition is very small, the hfs. of the 4^3P-n^3D ($n=4, 5$) and $4^{1,3}F-nG$ ($n=6, 7$) series of Al II were studied previously[1)-4)]. As for the n^3D term series, it was found that in the case of 4^3D[2),4)] the ordinary multiplet character is strongly perturbed and the hfs. largely deviate from Landé's interval rule owing to the fact that the triplet separations are comparable with the hyperfine splittings, and that in the case of 5^3D[1),3)], the triplet separations are smaller than the hyperfine splittings and the inner quantum number J loses its meaning, the total electronic spin **S** coupling first with the nuclear spin **I**, not with orbital angular momentum **L**.

For the sake of completeness it is desirable to investigate the hfs. of the 3^3D term whose triplet separations are somewhat large compared with the hyperfine splittings. The most suitable lines for the study of the 3^3D term would be $\lambda10076-\lambda10122$ (3^3D-4^3P), which were measured by Paschen and Ritschl[5)]. However, since these authors' data seem somewhat insufficient and no photographic plate adequate for this near infrared region is available at present in this country, study of these lines was abandoned and the structure of the multiplet $\lambda3587.4-\lambda3586.5$ (3^3D-4^3F), which was also previously investigated by Paschen[5),6)] with a concave grating, has been reexamined by means of interferometers.

§ 2. The Structure of the Multiplet $\lambda3587.4-\lambda3586.5$ ($3^3D_{3,2,1}-4^3F_{4,3,2}$)—Observed

A water-cooled aluminum hollow cathode discharge tube filled with helium was used as a light source. The structure of the spectrum was examined with a quartz Lummer plate (thickness=4.4 mm) and a Fabry-Pérot etalon with a spacer in the range 1–4 mm.

The result is given in Fig. 1. The accuracy of the indicated positions is $\pm0.02\sim0.03\,\text{cm}^{-1}$. Although no more detailed hfs. than that reported by Paschen could be resolved, intensity estimation in the present work seems to be somewhat more accurate than that of Paschen; the following data are new, as compared with those of Paschen. (1) Each of the three diagonal lines, ${}^3D_1-{}^3F_2$, ${}^3D_2-{}^3F_3$ and ${}^3D_3-{}^3F_4$, is fairly sharp, their breadths being $0.10\sim0.13\,\text{cm}^{-1}$. (2) The line ${}^3D_2-{}^3F_2$ was found to have a broad structure as shown in Fig. 1. Paschen reported that each of ${}^3D_2-{}^3F_2$ and ${}^3D_3-{}^3F_3$ consists of two hyperfine components, but this could not be definitely inferred from our observation, despite that our resolving power (of the order of $0.1\,\text{cm}^{-1}$) is expected to be comparable with that of Paschen's grating. As to the structures of the lines ${}^3D_1-{}^3F_3$, ${}^3D_3-{}^3F_3$ and ${}^3D_2-{}^3F_4$, nothing can be said owing to their weak intensities or owing to nearby situated fringes of other strong components. In Fig. 1 the positions of maximum intensity of these lines are indicated. (3) Paschen's intensities of the off-diagonal transitions relative to those of the diagonal transitions were found to be too strong according to our visual estimation of the intensity. Apart from the above-mentioned facts and that the weak lines $^3D_3-{}^3F_2$ and $^3D_1-{}^3F_4$ which were observed by Paschen could not be detected, our result agrees with that of Paschen within the accuracy of measurement.

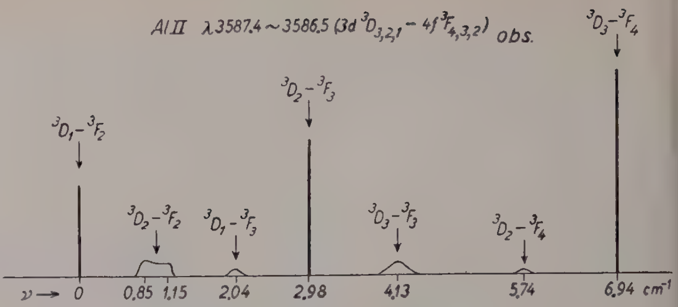

Fig. 1. Observed structure of the multiplet λ 3587.4 − λ 3586.5 ($3^3D_{3,2,1}-4^3F_{4,3,2}$) of Al II.

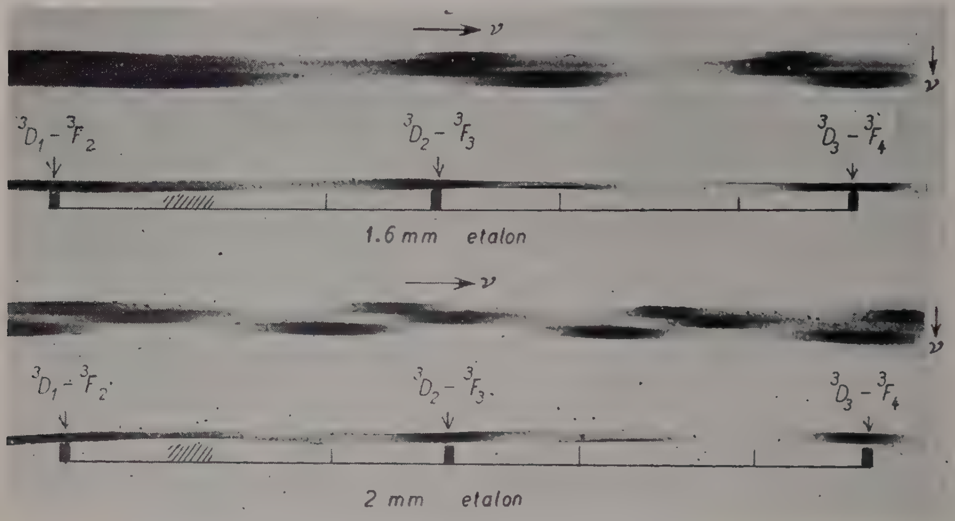

Fig. 2. Reproduction of the interference patterns of Al II λ3587.4 − λ3586.5 (3^3D-4^3F)
The patterns (b) and (d) are extracts which were cut out from the whole pattern in an adequate direction in order to show the entire structure more clearly.

In Fig. 2 reproduction of the interference patterns is shown. Overlapping of different orders of the fringes could be just avoided owing to the dispersion and the narrow slit of the spectrograph. Extracts under the whole patterns in the figure show the whole structure of the multiplet more clearly.

§ 3. The Structure of the Multiplet λ3587.4 − λ3586.5 ($3^3D_{3,2,1}-4^3F_{4,3,2}$)—Calculated

The hfs. of the n^3D term can be expressed in the first approximation by three parameters, α, β and a, as previously described in detail, where $\alpha=H_0(^3D_3)-H_0(^3D_1)$ and $\beta=H_0(^3D_2)-H_0(^3D_1)$ represent the triplet separations of the n^3D term when the hyperfine splitting is neglected. The letter a represents the coupling constant between the nuclear spin $\mathbf{I}$ and the spin $\mathbf{s}$ of the 3s-electron.

Since α and β are large compared with a in the case of 3^3D, the calculation of the hfs. and the corresponding eigen-functions of the 3^3D term was rather easy. Each of the three levels $3^3D_{3,2,1}$ has approximately a normal hfs. and only the deviations from Landé's interval rule must be calculated according to the perturbation theory. Putting $a=0.166\,\mathrm{cm}^{-1}$ as found in Part I* and taking into account the gross and hyperfine structures of the 4^3F term which were determined in Part I, the hfs. of the multiplet 3^3D-4^3F could be calculated. In the calculation the numerical values of α and β were determined so as to make the relative positions of the centers of gravity of the three diagonal transitions $^3D_1-{}^3F_2$, $^3D_2-{}^3F_3$ and $^3D_3-{}^3F_4$ coincide with those which were observed. Thus it was found

$$\alpha=-2.20\,\mathrm{cm}^{-1} \quad \text{and} \quad \beta=-1.02\,\mathrm{cm}^{-1}.$$

The calculated hfs. of each line is shown in

---

* Reference (1) will be referred to as Part I.

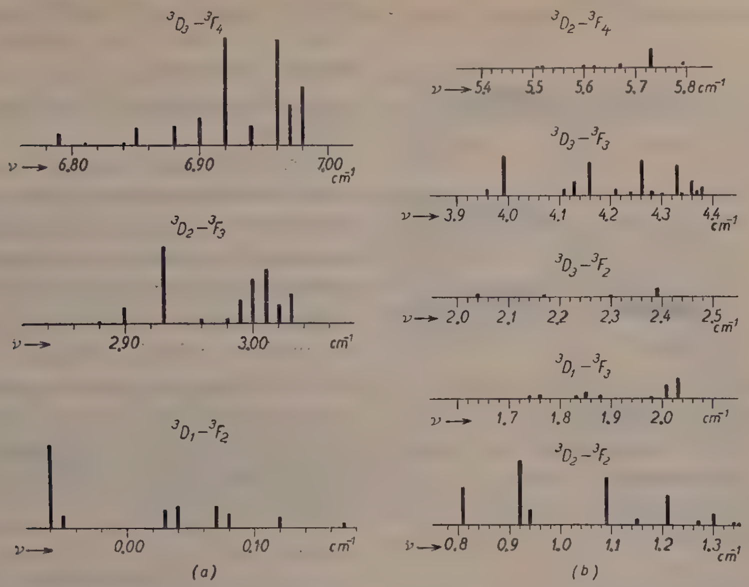

Fig. 3. Calculated hfs. of the multiplet λ 3587.4 − λ 3586.5 (3^3D-4^3F). (a) diagonal transitions (b) nondiagonal and forbidden transitions. Length of a vertical line expresses relative intensity. All the intensities in (b) are expressed with a scale five times larger than that of (a).

Fig. 3. The scales shown under the structure have a common origin which lies at the center of gravity of the hfs. of $3^3D_1-3^3F_2$. (The line $^3D_1-^3F_4$ is omitted since its intensity is very weak compared with those of others and cannot be expressed by the same intensity scale.) Intensity of each hyperfine component was calculated taking into account the first order perturbation in both the 3^3D and 4^3F terms.

Table I gives total relative intensity of each line. The calculated intensities agree at least qualitatively with those which were obtained by eye's estimates. It is noteworthy that the intensity of any of the forbidden transitions $^3D_2-^3F_4$ and $^3D_1-^3F_3$ is larger than that of the transition $^3D_3-^3F_2$.

Table I. Relative intensities of the multiplet $3s3d^3D-3s4f^3F$.

	$^3D_3$	$^3D_2$	$^3D_1$
$^3F_4$	10.0	0.15	0.003
$^3F_3$	1.0	6.0	0.26
$^3F_2$	0.10	1.2	4.5

Table II. Triplet separations of the series n^3D.

n^3D	$\alpha={}^3D_3-{}^3D_1$ (cm⁻¹)	$^3D_3-^3D_2$ (cm⁻¹)	$\beta={}^3D_2-{}^3D_1$ (cm⁻¹)
3^3D	−2.20	−1.18	−1.02
4^3D	−0.70	−0.39	−0.31
5^3D	−0.05	−0.03	−0.02

§ 4. Discussion

Although the observed structure of λ3587.4–λ3586.5 was not sufficient for a critical check on the theoretical calculation and for determining experimentally the hfs. of the 3^3D term, one can see that the observed results described in § 2 does not contradict with the calculated structure when the Doppler broadening of the order of 0.08 cm⁻¹ in the case of our light source and resolving power of the instrument used (of the order of 0.1 cm⁻¹) are taken into account. According to Paschen the 3^3D term has a nearly normal triplet character but the existence of the forbidden lines such as $^3D_2-^3F_4$ and $^3D_1-^3F_3$ are apparent. This was also confirmed in the present work. Keeping in mind that the agreement between theory and observation in the cases of 4^3P-4^3D and 4^3P-5^3D was satisfactory, we may assume that the calculated structure of the 3^3D term will be near the real one. The calculated hyperfine energy levels of 3^3D are diagramatically represented in Fig. 4, together with the structures of 4^3D and 5^3D which were previously studied[1),4)]. The triplet sepa-

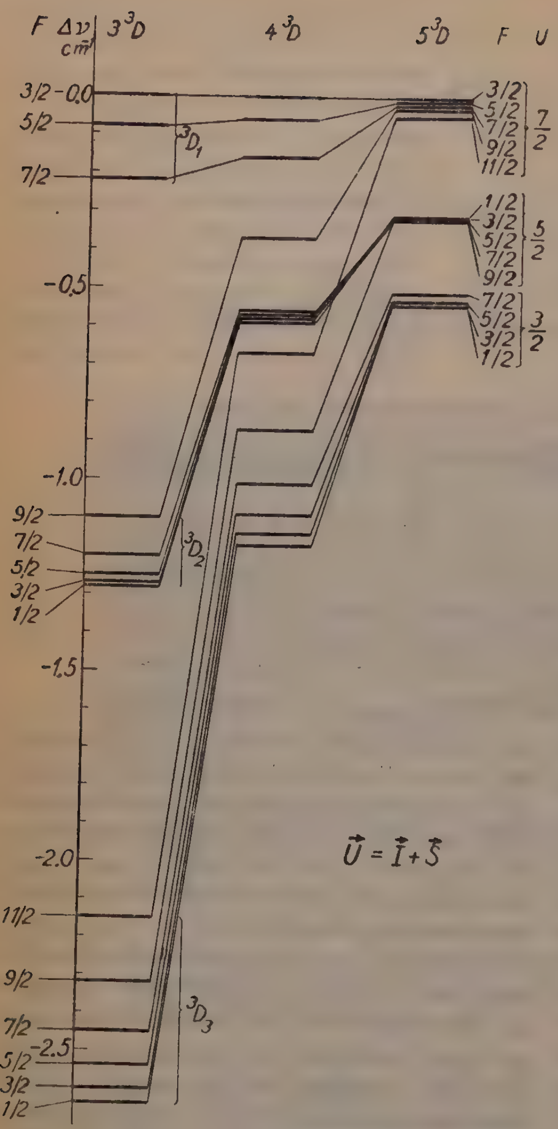

Fig. 4. Diagramatical representation of the hyperfine energy levels of the n^3D series of Al II.

rations of the series n^3D are tabulated in Table II, in which the deepest term of Al II ($3s^2\ ^1S_0$) is assumed to be the origin. The minus sign indicates that the multiplet term is inverted.

As n increases, transition from nearly ordinary coupling state in which the total electronic spin **S** couples first with the orbital angular momentum **L**, making J (**J**=**L**+**S**) a good quantum number, towards another extreme coupling state in which **S** couples first with the nuclear spin **I**, making U (**U**=**S**+**I**) a good quantum number, is apparent in Fig. 4.

In conclusion the writer wishes to express his sincere thanks to Professor K. Murakawa for his valuable discussion and encouragement throughout this work.

References

1) S. Suwa: J. Phys. Soc. Japan **6** (1951) 231.
2) S. Suwa: Phys. Rev. **76** (1949) 874.
3) S. Suwa: Phys. Rev. **78** (1950) 810.
4) S. Suwa: Rep. of the Inst. of Sci. and Tech. **3** (1949) 268 and **4** (1950) 69 (in Japanese).
5) F. Paschen u. R. Ritschl: Ann. d. Phys. [5] **18** (1933) 863.
6) F. Paschen: Sitz. Preuss. Akad. Wiss. **23** (1932) 502.

JOURNAL OF THE PHYSICAL SOCIETY OF JAPAN Vol. 8, No. 4, JULY—AUGUST, 1953

Hyperfine Structure of the Spectrum of Ruthenium

By Kiyoshi MURAKAWA

Institute of Science and Technology, Komaba-machi, Meguro-ku, Tokyo

(Received April 24, 1953)

The hyperfine structure of the spectrum of Ru I was studied, and a displacement effect of the order of 0.015 cm^{-1} between even isotopes having the difference of two neutron numbers was found in the lines corresponding to the transition $5s-5p$. The spins of the odd isotopes were found to be $9/2 \geqq I \geqq 5/2$, the nuclear magnetic moments being negative.

§1. Experimental Arrangements

The spectrum of Ru I was excited by a liquid-air cooled hollow-cathode discharge tube, powdered ruthenium metal being placed in the hollow cathode. The hyperfine structure (hfs) was examined by a Fabry-Pérot etalon.

Fig. 1 shows some reproductions of the interference patterns of the spectrum of Ru I.

§2. Gross Structure of the Spectrum of Ru I

In order to analyse the hfs of the spectrum of Ru I, the gross structure analysis is needed, so a brief account of the literature concerning this will be given here.

The gross multiplet analysis of the spectrum of Ru I was published by Sommer1) and by Meggers and Laporte2), and was extended and revised by Harrison and McNally3). According to their analysis the deepest terms consist of $4d^7 5s\,{}^5F$ and ${}^3F$. Their relative positions are schematically shown in Fig. 2. We may assume that these terms are approximately of LS-coupling type. It is to be noted that the g-value of ${}^3F_4$ published in ref. 3 is 1.284 instead of the theoretical value 1.250, so that some other wave-functions must be superposed to ${}^3F_4$. However the superposition is assumed to be slight in the present work.

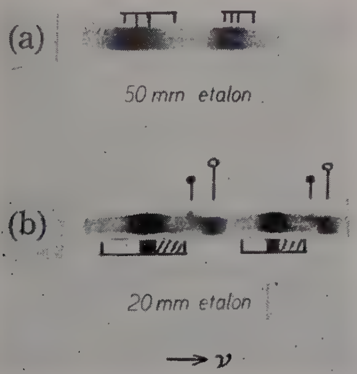

Fig. 1. Enlargements of the interference patterns of the spectrum of Ru I. (a) λ4554.5. (b) λ4361. The components marked with ○ and ● do not belong to this line.

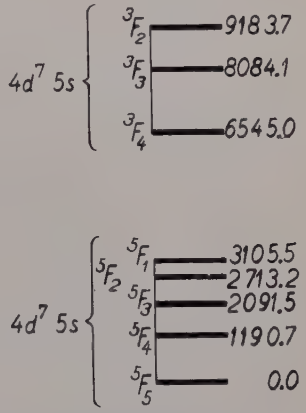

Fig. 2. Deepest terms of Ru I.

§3. Results of Measurements

Natural ruthenium consists of seven isotopes4) as shown in Table I.

Table I. Abundance of the ruthenium isotopes.

Isotope	96	93	99	100	101	102	104
Abundance (%)	5.68	2.22	12.81	12.70	16.98	31.34	18.27

It is expected that the even isotopes 96, 98, 100, 102 and 104 have no nuclear magnetic moment, whereas the odd isotopes 99 and 101 have non-vanishing nuclear magnetic moments.

As shown in Fig. 3 (see also Fig. 1), λ4554 exhibits displacement effect (of the order of 0.015 cm^{-1} per 2 mass units difference) of the even isotopes. The intensity distribution of the components belonging to the odd isotopes

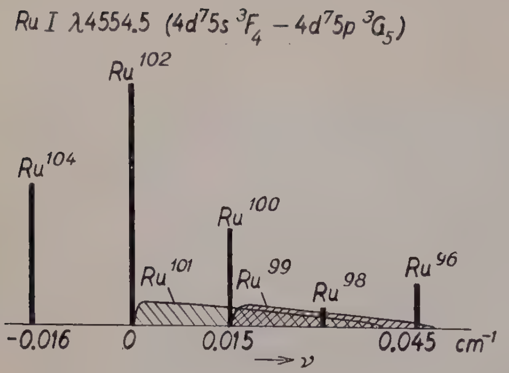

Fig. 3. Hfs of the line Ru I λ4554.5.

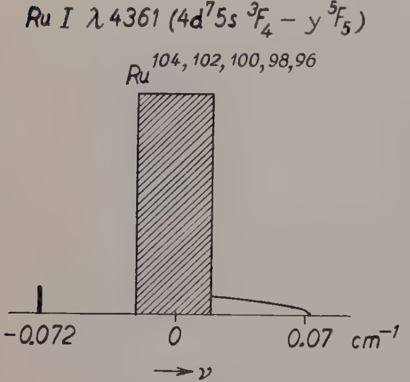

Fig. 4. Hfs of the line Ru I λ4361.

is only qualitatively shown in Fig. 3. Isotope displacement effect of the same order of magnitude was also found in the lines λ4510 ($d^7s^3F_3$—$d^7p^3G_4$) and λ4217 ($d^7s^3F_4$—$d^7p^3G_4$), so the isotope effect of that amount can be ascribed to the transition $5s$—$5p$.

In some lines the hfs due to the odd isotopes could be detected. λ4361 is an example, and the hfs is shown in Fig. 4 (see also Fig.1). The intensity distribution of the hfs components of this and other lines shows that the nuclear magnetic moments of the odd isotopes (Ru^{99} and Ru^{101}) have the same sign and their nuclear spins are $9/2 \geqq I \geqq 5/2$.

The structures of the lines that have $d^7s^3F_4$ as their final term show that in $d^7s^3F_4$ the hyperfine term with the largest F should lie highest. As stated in § 2, the terms d^7s^5F and ^3F are of LS coupling type. If this is assumed, a simple calculation* shows that the nuclear magnetic moments of the odd isotopes are negative.

References

1) L. A. Sommer: Zeits. f. Phys. **37** (1926) 1.

2) W. F. Meggers and O. Laporte: Journ. Washington Acad. Scie. **16** (1926) 143.

3) G. R. Harrison and J. R. McNally, Jr.: Phys. Rev. **58** (1940) 703.

4) H. Ewald, quoted by S. Flügge and J. Mattauch, Ber. d. chem. Ges. **76A** (1943) 1.

---

* $$A(^3F_4) = -\frac{1}{16}a(s) + \frac{393}{504}a_d;$$
$$a_d = 2g\mu_0^2\langle r^{-3}\rangle .$$

JOURNAL OF THE PHYSICAL SOCIETY OF JAPAN Vol. 8, No. 4, JULY—AUGUST, 1953

On the Asymptotic Behaviour of Compressible Fluid Flow at a Great Distance from a Cylinder in the Absence of Circulation

By Isao IMAI

Department of Physics, Faculty of Science, University of Tokyo

(Received February 16, 1953)

In this paper the method of thin-wing-expansion which has been developed by the author is applied to the case of a uniform flow of a compressible fluid past an arbitrary cylinder in the case of the absence of sources, sinks and circulation. The asymptotic expressions for the velocity potential and the stream function at a great distance, r, from the cylinder are determined correctly to the order of $1/r^4$. Hence the velocity can be found exactly to the order of $1/r^5$. This should be compared with Gröbner's result which is correct to the order of $1/r^4$ and is restricted to the case of a cylinder symmetrical with respect to the x-axis. Moreover, the present analysis is far simpler than Gröbner's one in view of the fact that the former requires only some elementary quadratures while the latter the integration of a system of differential equations.

Finally, it is shown that the general expression for the velocity potential is in accord with the author's previous result for flow past a circular cylinder, which is correct to the order of M^6, M being the Mach number.

§ 1. Introduction and Summary

In order to extend the Kutta-Joukowski theorem to the case of compressible fluid, Glauert [2] assumed, in 1928, that the flow at a great distance from a cylinder of arbitrary cross section submerged in a uniform flow can be expressed as:

$$\left.\begin{aligned} q_r&=U\left(\cos\theta+\sum_{n=1}^{\infty}\frac{A_n}{r^n}\right),\\ q_\theta&=-U\left(\sin\theta+\sum_{n=1}^{\infty}\frac{B_n}{r^n}\right),\end{aligned}\right\}\quad(1.1)$$

where (q_r, q_θ) are the component velocities in polar coordinates (r,θ), the undisturbed velocity being of magnitude U and in the direction parallel to the original line $\theta=0$. A_n and B_n are functions of θ only. Glauert himself has found out the functional forms of A_1 and B_1, thus determining the velocity exactly to the order of $1/r$. In 1938, Bateman [1] succeeded in proving the validity of the Kutta-Joukowski theorem in the case of compressible fluid, on the assumption that the velocity potential Φ and the stream function Ψ can be asymptotically expressed in the forms:

$$\Phi=U\Big[r\cos\theta+\{A_0+A_1\log r+A_2(\log r)^2+\cdots\}+\frac{1}{r}\{B_0+B_1\log r+B_2(\log r)^2+\cdots\}+\cdots\Big],\quad(1.2)$$

$$\Psi=U\Big[r\sin\theta+\{C_0+C_1\log r+C_2(\log r)^2+\cdots\}+\frac{1}{r}\{D_0+D_1\log r+D_2(\log r)^2+\cdots\}+\cdots\Big],\quad(1.3)$$

A_n, B_n, C_n, D_n being functions of θ only.

Obviously Bateman's assumption (1.2,3) is more general than Glauert's one (1.1); but the question remains open in what form the asymptotic behaviour of the flow is correctly expressed. In fact, the validity of both (1.1) and (1.2,3) was only assumed, without having been proved mathematically.

By a new method of M^2-expansion proposed by himself, the present writer has shown [5] that the correct expressions for Φ and Ψ are

$$\Phi=U\left\{r\cos\theta+A_0+\frac{1}{r}(B_0+B_1\log r)+O\left(\frac{1}{r^2}\right)\right\},\quad(1.4)$$

$$\Psi=U\left\{r\sin\theta+C_0+C_1\log r+\frac{1}{r}(D_0+D_1\log r)+O\left(\frac{1}{r^2}\right)\right\},\quad(1.5)$$

and that terms of the form $r^{-m}(\log r)^n$ $(m<n)$ do not appear in the expressions (1.2) and (1.3). Therefore, Glauert's assumption is too restricted and Bateman's too general to be in accordance with reality. Further, functional forms of $A_0, B_0, B_1, C_0, C_1, D_0, D_1$ have been explicitly determined by the integration of a system of simultaneous differential equations. Later, he has shown that the same result can be obtained in a much simpler manner by means of the method of thin-wing-expansion [6]. He has further dealt with the flow past an arbitrary cylinder with arbitrary distributions of sources and sinks on its surface and with arbitrary circulation round it, by use of the same method [8]. Thus, it has been found that the correct expressions for $\varPhi$ and $\varPsi$ are

$$\varPhi=U\Big\{r\cos\theta+A_0+A_1\log r+\frac{1}{r}(B_0+B_1\log r)+O\Big(\frac{1}{r^2}\Big)\Big\}, \qquad (1.6)$$

$$\varPsi=U\Big\{r\sin\theta+C_0+C_1\log r+\frac{1}{r}(D_0+D_1\log r)+O\Big(\frac{1}{r^2}\Big)\Big\}, \qquad (1.7)$$

the expressions for the eight functions $A_0, A_1, B_0, B_1, C_0, C_1, D_0, D_1$ being also determined explicitly.

In a paper, which has escaped my attention until quite recently, Gröbner [3] has also tried to extend Glauert's investigation. Adopting Glauert's assumption (1.1) as well as his method of attack, Gröbner endeavoured to find the explicit functional forms of A_n, B_n for higher values of n. However, in the case of flow with circulation, he has already met with difficulty in dealing with the terms of the order of $1/r^2$; indeed he could not determine $B_2(\theta)$ as a periodic function of θ with period 2π, though it should naturally be so. On the basis of this fact, he conceived that in the case of flow with circulation either (i) Glauert's assumption (1.1) is erroneous or (ii) a stationary flow cannot take place. Moreover, it appears that he puts more stress upon the second possibility, which, as is obvious from our result, cannot be the case. Then, confining himself to the case of absence of circulation, Gröbner determined the explicit forms of the six functions A_n, B_n $(n=2,3,4)$, the velocity being thus obtained to the order of $1/r^4$. It must be added, however, that he has given the expressions for A_n and B_n only for the case of a cylinder which is symmetric with respect to the x-axis.

Now, the first approximation of the thin-wing-expansion method mentioned above is effectively equivalent to the well-known linear theory of Prandtl and Glauert, and its application to the case of flow with circulation yields Glauert's result, that is, the asymptotic expression for the velocity which is exact to the order of $1/r$. Also the second approximation yields the present writer's results, (1.6) and (1.7), which are correct to the order of $1/r^2$. In like manner, the approximation proceeds by $O(1/r)$ for each step of successive approximations in applying the thin-wing-expansion method to the flow with circulation. On the other hand, if the same method is applied to the flow without circulation (and without either sources or sinks), it is apparent that the approximation proceeds by $O(1/r^2)$ for each step of successive approximations. Thus the result exact to $O(1/r^2)$ may be obtained already by the first approximation, and the result exact to $O(1/r^4)$ by the second approximation, and so on. Moreover, the method requires only a few simple quadratures, as contrasted to the integration of simultaneous differential equations, which was necessary in Glauert's and Gröbner's investigations. In view of this fact, it may be worth while to apply the method to the flow past a cylinder in the absence of circulation in order to find the asymptotic expressions for $\varPhi$ and $\varPsi$ which are correct to $O(1/r^4)$, the expression for the velocity being thus correct to $O(1/r^5)$. The complication of Gröbner's result may also justify such an analysis as a test for its correctness.

In a previous paper [4], the present writer studied the flow past a circular cylinder and found the expression for the velocity potential $\varPhi$ correct to M^6, M being the Mach number of the undisturbed flow. The term of $1/r$ in that expression has already been shown to be in accordance with the writer's result (1.4) for an arbitrary cylinder [5]. In this paper it will be shown that the term of $1/r^2$ has actually the form predicted by (4.9). It seems that some evidence is thus furnished for the correctness of the general expressions for $\varPhi$ and $\varPsi$, (4.9), (4.10), for an arbitrary cylinder in the case of flow without circulation.

This work was accomplished in 1945 but has been left unpublished.

§ 2. Fundamental Formulae

We consider, in the (x,y) plane, a uniform flow of a compressible fluid past a cylinder of arbitrary cross section. Let the velocity of the undisturbed flow be of magnitude U and in the direction parallel to the x-axis. Then the velocity (u,v) at any point can be expressed as

$$u=\frac{\partial\Phi}{\partial x}=\frac{\rho_\infty}{\rho}\frac{\partial\Psi}{\partial y}\,,\qquad v=\frac{\partial\Phi}{\partial y}=-\frac{\rho_\infty}{\rho}\frac{\partial\Psi}{\partial x}\,,\tag{2.1}$$

where Φ is the velocity potential, Ψ the stream function, ρ the density, and ρ_∞ the density of the undisturbed fluid. Now, the method of thin-wing-expansion [7], [8] gives for the velocity potential Φ and the stream function Ψ

$$\Phi=U(x+\phi)\,,\quad \Psi=U(y+\psi)\,,\tag{2.2}$$

where.

$$\phi=\frac{1}{2}(G+\overline{G})\,,\quad \psi=\frac{\mu}{2i}(G-\overline{G})\,,\tag{2.3}$$

$$G=f(\zeta)+G_2(\zeta,\overline{\zeta})+O(r\varepsilon^3)\,,\tag{2.4}$$

$$G_2=\frac{M^2}{4}\left[\lambda\left(\frac{df}{d\zeta}\right)^2\overline{\zeta}+(1+\lambda)\right.$$
$$\left.\times\left\{2\frac{df}{d\zeta}\overline{f}+\int\left(\frac{d\overline{f}}{d\overline{\zeta}}\right)^2 d\overline{\zeta}\right\}\right]+\mathfrak{F}(\zeta)\,,\tag{2.5}$$

with

$$\zeta=\xi+i\eta\,,\quad \overline{\zeta}=\xi-i\eta\,,\tag{2.6}$$

$$\xi=x\,,\quad \eta=\mu y\,,\tag{2.7}$$

$$\mu=\sqrt{1-M^2}\,,\qquad \lambda=\frac{\gamma+1}{4}\frac{M^2}{1-M^2}\,,\tag{2.8}$$

γ being the ratio of the specific heats of the gas. $f(\zeta)$ and $\mathfrak{F}(\zeta)$ are analytic functions of ζ to be determined from the shape of the cylinder. Further, the functions f and G_2 are of the magnitude $O(r\varepsilon)$ and $O(r\varepsilon^2)$ respectively, where ε is a small quantity and

$$r=\sqrt{x^2+y^2}\ .$$

From (2.3), (2.6) and (2.7), we have

$$\frac{\partial G}{\partial\zeta}=\frac{1}{2}\left(\frac{\partial}{\partial x}-\frac{i}{\mu}\frac{\partial}{\partial y}\right)\left(\phi+\frac{i}{\mu}\psi\right)$$
$$=\frac{1}{2}\left(\frac{\partial\phi}{\partial x}+\frac{1}{\mu^2}\frac{\partial\psi}{\partial y}\right)-\frac{i}{2\mu}\left(\frac{\partial\phi}{\partial y}-\frac{\partial\psi}{\partial x}\right)\,.$$

From (2.1) and (2.2) we have

$$\frac{\partial\phi}{\partial x}=\frac{u}{U}-1,\qquad \frac{\partial\phi}{\partial y}=\frac{v}{U}\,,$$
$$\frac{\partial\psi}{\partial x}=-\frac{\rho}{\rho_\infty}\frac{v}{U}\,,\qquad \frac{\partial\psi}{\partial y}=\frac{\rho}{\rho_\infty}\frac{u}{U}-1.$$

Since u,v,ρ are naturally one-valued and continuous throughout the field of flow, so is $\partial G/\partial\zeta$ too. Also we have

$$u\to U,\ v\to 0,\ \rho\to\rho_\infty\quad\text{as}\quad x,y\to\infty,$$

so that

$$\frac{\partial G}{\partial\zeta}\to 0\quad\text{as}\quad \zeta\to\infty\,.$$

Thus, $\partial G/\partial\zeta$ should satisfy the following two conditions:

(i) $\partial G/\partial\zeta$ is one-valued and continuous throughout the field of flow,

(ii) $\partial G/\partial\zeta\to 0$ as $\zeta\to\infty$.

If the circulation round the cylinder is absent and neither sources nor sinks are present on the surface of the cylinder, the above-mentioned condition (i) may be replaced by the following one:

(i′) G is one-valued and continuous throughout the field of flow.

This may be obvious from the definition of G. Thus, from (2.2) and (2.3), we have

$$G=\phi+\frac{i}{\mu}\psi=\frac{\Phi}{U}-x+\frac{i}{\mu}\left(\frac{\Psi}{U}-y\right),$$

where Φ and Ψ are one-valued and continuous for the assumed type of flow.

§ 3. Complex Velocity Potential

In a recent paper [8] the present writer has investigated the asymptotic behaviour of compressible fluid flow past an arbitrary profile with arbitrary distribution of souces and sinks on its surface and with arbitrary circulation round it. In the present paper we shall confine ourselves to the case of flow without any circulation or distribution of sources and sinks. Owing to this restriction, deeper knowledge would be obtainable about the field of flow by an analysis similar to the previous one.

From (2.4) we have

$$G=f(\zeta)+O(r\varepsilon^2)\,,\tag{3.1}$$

where $f(\zeta)$ is an analytic function of ζ which is assumed to be of the magnitude $O(r\varepsilon)$. Now the conditions (i′) and (ii) require that $f(\zeta)$ should be one-valued and continuous outside the profile and that $df/d\zeta\to 0$ as $\zeta\to\infty$. Hence $f(\zeta)$ should be expansible in a Laurent series as follows:

$$f=\frac{k_1}{\zeta}+\frac{k_2}{\zeta^2}+\cdots, \tag{3.2}$$

where the constant term has been dropped.

Now we have

$$\zeta=\xi+i\eta=x+i\mu y=r(\cos\theta+i\mu\sin\theta), \tag{3.3}$$

and hence

$$O(\zeta)=O(r), \tag{3.4}$$

so that

$$f=O(r^{-1}). \tag{3.5}$$

Remembering that we have assumed $f=O(r\varepsilon)$, we get $O(r^{-1})=O(r\varepsilon)$, and hence

$$\varepsilon=O(r^{-2}). \tag{3.6}$$

Therefore

$$G_2=O(r\varepsilon^2)=O(r^{-3}). \tag{3.7}$$

Thus, it may be seen that the first approximation to G can be expressed in the form:

$$f=\frac{k_1}{\zeta}+\frac{k_2}{\zeta^2}, \tag{3.8}$$

the remainder $k_3/\zeta^3+k_4/\zeta^4+\cdots$ being absorbed in the arbitrary function $\mathfrak{F}(\zeta)$ in the expression (2.5) of $G_2(\zeta,\bar\zeta)$.

We shall next consider G_2. From (2.5) we have

$$G_2(\zeta,\bar\zeta)=H_2(\zeta,\bar\zeta)+\mathfrak{F}(\zeta), \tag{3.9}$$

where

$$H_2(\zeta,\bar\zeta)=\frac{M^2}{4}\Bigg[\lambda\left(\frac{df}{d\zeta}\right)^2\bar\zeta+(1+\lambda)\times\left\{2\frac{df}{d\zeta}\bar f+\int\left(\frac{d\bar f}{d\bar\zeta}\right)^2 d\bar\zeta\right\}\Bigg]. \tag{3.10}$$

Substituting (3.8) into (3.10), we have

$$H_2(\zeta,\bar\zeta)=\frac{M^2}{4}\Bigg[\lambda k_1^2\frac{\bar\zeta}{\zeta^4}-(1+\lambda)\times\left(2k_1\bar k_1\frac{1}{\zeta^2\bar\zeta}+\frac{1}{3}\bar k_1^2\frac{1}{\bar\zeta^3}\right)+4\lambda k_1k_2\frac{\bar\zeta}{\zeta^5}-(1+\lambda)\left(2k_1\bar k_2\frac{1}{\zeta^2\bar\zeta^2}+4\bar k_1k_2\frac{1}{\zeta^3\bar\zeta}+\bar k_1\bar k_2\frac{1}{\bar\zeta^4}\right)\Bigg], \tag{3.11}$$

where terms of the order of magnitude $O(1/r^5)$ have been omitted.

Now the conditions (i′) and (ii) of § 2 require that $G_2(\zeta,\bar\zeta)$ should be one-valued and continuous in the field of flow and that $\partial G_2/\partial\zeta\to 0$ as $\zeta\to\infty$. Since the same conditions are evidently satisfied by $H_2(\zeta,\bar\zeta)$, the analytic function $\mathfrak{F}(\zeta)$ as given by (3.9), should also satisfy them, and hence $\mathfrak{F}(\zeta)$ can be expanded in a Laurent series:

$$\mathfrak{F}(\zeta)=\frac{k_1}{\zeta}+\frac{k_2}{\zeta^2}+\frac{k_3}{\zeta^3}+\cdots.$$

Remembering (3.7), we have to drop the terms $k_1/\zeta+k_2/\zeta^2$ which are, in effect, represented by $f(\zeta)$. Moreover, we can conveniently omit terms of the order of magnitude $O(1/r^5)$. Thus we can write

$$\mathfrak{F}(\zeta)=\frac{k_3}{\zeta^3}+\frac{k_4}{\zeta^4}. \tag{3.12}$$

Substituting (3.8), (3.9), (3.11), (3.12) into (2.4), we finally obtain

$$G=\frac{k_1}{\zeta}+\frac{k_2}{\zeta^2}+\frac{k_3}{\zeta^3}+\frac{k_4}{\zeta^4}+\frac{M^2}{4}\Bigg\{\lambda k_1^2\frac{\bar\zeta}{\zeta^4}-(1+\lambda)\times\left(2k_1\bar k_1\frac{1}{\zeta^2\bar\zeta}+\frac{1}{3}\bar k_1^2\frac{1}{\bar\zeta^3}\right)\Bigg\}+\frac{M^2}{4}\Bigg\{4\lambda k_1k_2\frac{\bar\zeta}{\zeta^5}-(1+\lambda)\left(2k_1\bar k_2\frac{1}{\zeta^2\bar\zeta^2}+4\bar k_1k_2\frac{1}{\zeta^3\bar\zeta}+\overline{k_1k_2}\frac{1}{\bar\zeta^4}\right\}+O\left(\frac{1}{\zeta^5}\right), \tag{3.13}$$

where k_1,k_2,k_3,k_4 are arbitrary complex constants to be determined by the form of the cylinder.

§ 4. Velocity Potential and Stream Function

In the preceding section we have determined the general expression for the complex velocity potential G correctly to the order of $1/r^4$. In this section we shall express the velocity potential and stream function in more explicit forms.

If we put

$$\zeta=te^{i\varphi}=t(\cos\varphi+i\sin\varphi), \tag{4.1}$$

and

$$k_n=h_ne^{i\alpha_n}, \quad n=1,2,3,4, \tag{4.2}$$

then (3.13) can be written as

$$G=\frac{h_1}{t}e^{-i(\varphi-\alpha_1)}+\frac{h_2}{t^2}e^{-i(2\varphi-\alpha_2)}+\frac{h_3}{t^3}e^{-i(3\varphi-\alpha_3)}+\frac{h_4}{t^4}e^{-i(4\varphi-\alpha_4)}+\frac{M^2}{4}\frac{h_1^2}{t^3}\Bigg\{\lambda e^{-i(5\varphi-2\alpha_1)}-(1+\lambda)\times\left(2e^{-i\varphi}+\frac{1}{3}e^{i(3\varphi-2\alpha_1)}\right)\Bigg\}+\frac{M^2}{4}\frac{h_1h_2}{t^4}\times\{4\lambda e^{-i(6\varphi-\alpha_1-\alpha_2)}-(1+\lambda)(2e^{i(\alpha_1-\alpha_2)}+4e^{-i(2\varphi+\alpha_1-\alpha_2)}+e^{i(4\varphi-\alpha_1-\alpha_2)})\}+O\left(\frac{1}{t^5}\right). \tag{4.3}$$

Hence, remembering (2.2) and (2.3), we have

$$
\begin{aligned}
\frac{\Phi}{U}=&\,t\cos\varphi+\frac{h_1}{t}\cos(\varphi-\alpha_1)+\frac{h_2}{t^2}\cos(2\varphi-\alpha_2)+\frac{h_3}{t^3}\cos(3\varphi-\alpha_3)+\frac{h_4}{t^4}\cos(4\varphi-\alpha_4)\\
&+\frac{M^2}{4}\frac{h_1^{\,2}}{t^3}\Big[\lambda\cos(5\varphi-2\alpha_1)-(1+\lambda)\Big\{2\cos\varphi+\frac{1}{3}\cos(3\varphi-2\alpha_1)\Big\}\Big]\\
&+\frac{M^2}{4}\frac{h_1h_2}{t^4}\Big[4\lambda\cos(6\varphi-\alpha_1-\alpha_2)-(1+\lambda)\Big\{2\cos(\alpha_1-\alpha_2)+4\cos(2\varphi+\alpha_1-\alpha_2)\\
&\qquad\qquad\qquad-\cos(4\varphi-\alpha_1-\alpha_2)\Big\}\Big]\\
&+O\Big(\frac{1}{t^5}\Big),
\end{aligned}
\tag{4.4}
$$

and

$$
\begin{aligned}
\frac{\Psi}{\mu U}=&\,\frac{t}{\mu^2}\sin\varphi-\frac{h_1}{t}\sin(\varphi-\alpha_1)-\frac{h_2}{t^2}\sin(2\varphi-\alpha_2)-\frac{h_3}{t^3}\sin(3\varphi-\alpha_3)-\frac{h_4}{t^4}\sin(4\varphi-\alpha_4)\\
&-\frac{M^2}{4}\frac{h_1^{\,2}}{t^3}\Big[\lambda\sin(5\varphi-2\alpha_1)-(1+\lambda)\Big\{2\sin\varphi-\frac{1}{3}\sin(3\varphi-2\alpha_1)\Big\}\Big]\\
&-\frac{M^2}{4}\frac{h_1h_2}{t^4}\Big[4\lambda\sin(6\varphi-\alpha_1-\alpha_2)\\
&\qquad+(1+\lambda)\Big\{2\sin(\alpha_1-\alpha_2)-4\sin(2\varphi+\alpha_1-\alpha_2)+\sin(4\varphi-\alpha_1-\alpha_2)\Big\}\Big]\\
&+O\Big(\frac{1}{t^5}\Big),
\end{aligned}
\tag{4.5}
$$

where h_n and α_n are arbitrary constants depending on the form of the cylinder. The expressions for Φ and Ψ in terms of the polar coordinates (r,θ) have now been found correctly to the order of $1/r^4$. In fact, the relation between the independent variables (t,φ) and (r,θ) can be readily obtained as follows. Thus, by (3.3) and (4.1), we have

$$t\cos\varphi=r\cos\theta\,,\quad t\sin\varphi=\mu r\sin\theta\,, \tag{4.6}$$

whence

$$t^2=r^2(\cos^2\theta+\mu^2\sin^2\theta)=r^2(1-M^2\sin^2\theta)\,, \tag{4.7}$$

and

$$\tan\varphi=\mu\tan\theta\,. \tag{4.8}$$

Of course, we can express Φ and Ψ explicitly in terms of r and θ. Using the relations (4.7) and (4.8), and making elementary transformations, we finally arrive at the result:

$$
\begin{aligned}
\frac{\Phi}{U}=&\,r\cos\theta+\frac{1}{r}\,\frac{a_1\cos\theta+\mu b_1\sin\theta}{N}+\frac{1}{r^2}\Big(\frac{a_{21}}{N}+\frac{a_{22}}{N^2}+\frac{2\mu b_2\sin\theta\cos\theta}{N^2}\Big)\\
&+\frac{1}{r^3}\Big\{\cos\theta\Big(\frac{a_{32}}{N^2}+\frac{a_{33}}{N^3}+\frac{a_{34}}{N^4}\Big)+\mu\sin\theta\Big(\frac{d_{32}}{N^2}+\frac{d_{33}}{N^3}+\frac{d_{34}}{N^4}\Big)\Big\}\\
&+\frac{1}{r^4}\Big\{\Big(\frac{a_{42}}{N^2}+\frac{a_{43}}{N^3}+\frac{a_{44}}{N^4}+\frac{a_{45}}{N^5}\Big)+2\mu\sin\theta\cos\theta\Big(\frac{d_{43}}{N^3}+\frac{d_{44}}{N^4}+\frac{d_{45}}{N^5}\Big)\Big\}\\
&+O\Big(\frac{1}{r^5}\Big),
\end{aligned}
\tag{4.9}
$$

and

$$
\begin{aligned}
\frac{\Psi}{U}=&\,r\sin\theta+\frac{1}{r}\,\frac{\mu b_1\cos\theta-\mu^2a_1\sin\theta}{N}+\frac{1}{r^2}\Big\{\mu\Big(\frac{b_{21}}{N}+\frac{b_{22}}{N^2}\Big)-\frac{2\mu^2a_2\sin\theta\cos\theta}{N^2}\Big\}\\
&+\frac{1}{r^3}\Big\{\mu\cos\theta\Big(\frac{b_{32}}{N^2}+\frac{b_{33}}{N^3}+\frac{b_{34}}{N^4}\Big)-\mu^2\sin\theta\Big(\frac{c_{32}}{N^2}+\frac{c_{33}}{N^3}+\frac{c_{34}}{N^4}\Big)\Big\}\\
&+\frac{1}{r^4}\Big\{\mu\Big(\frac{b_{42}}{N^2}+\frac{b_{43}}{N^3}+\frac{b_{44}}{N^4}+\frac{b_{45}}{N^5}\Big)-2\mu^2\sin\theta\cos\theta\Big(\frac{c_{43}}{N^3}+\frac{c_{44}}{N^4}+\frac{c_{45}}{N^5}\Big)\Big\}\\
&+O\Big(\frac{1}{r^5}\Big),
\end{aligned}
\tag{4.10}
$$

where we have put for brevity

$$N=1-M^2\sin^2\theta\ , \tag{4.11}$$

$$k_n=h_n e^{i\alpha_n}=a_n+ib_n\ , \tag{4.12}$$

$$A_{mn}=a_{mn}+ib_{mn}\ ,\quad B_{mn}=c_{mn}+id_{mn}\ , \tag{4.13}$$

with

$$
\begin{aligned}
A_{21}&=\frac{1+\mu^2}{M^2}k_2\ ,\\
A_{22}&=-\frac{2\mu^2}{M^2}k_2\ ,\\
A_{32}&=\frac{\lambda}{4}\frac{1+10\mu^2+5\mu^4}{M^2}k_1{}^2-\frac{1}{2}(1+\lambda)M^2k_1\overline{k}_1-\frac{1}{12}(1+\lambda)(1+3\mu^2)\overline{k}_1{}^2+\frac{1+3\mu^2}{M^2}k_3\ ,\\
A_{33}&=-\lambda(3+5\mu^2)\frac{\mu^2}{M^2}k_1{}^2+\frac{1}{3}(1+\lambda)\mu^2\overline{k}_1{}^2-4\frac{\mu^2}{M^2}k_3\ ,\\
A_{34}&=4\lambda\frac{\mu^4}{M^2}k_1{}^2\ ,\\
B_{32}&=\frac{\lambda}{4}\frac{5+10\mu^2+\mu^4}{M^2}k_1{}^2-\frac{1}{2}(1+\lambda)M^2k_1\overline{k}_1+\frac{1}{12}(1+\lambda)(3+\mu^2)\overline{k}_1{}^2+\frac{3+\mu^2}{M^2}k_3\ ,\\
B_{33}&=-\lambda(5+3\mu^2)\frac{\mu^2}{M^2}k_1{}^2-\frac{1}{3}(1+\lambda)\mu^2\overline{k}_1{}^2-4\frac{\mu^2}{M^2}k_3\ ,\\
B_{34}&=4\lambda\frac{\mu^4}{M^2}k_1{}^2\ ,\\
A_{42}&=\lambda\frac{1+15\mu^2+15\mu^4+\mu^6}{M^4}k_1k_2-\frac{1}{2}(1+\lambda)M^2k_1\overline{k}_2-(1+\lambda)(1+\mu^2)\overline{k}_1k_2\\
&\quad-\frac{1}{4}(1+\lambda)\frac{1+6\mu^2+\mu^4}{M^2}\overline{k}_1\overline{k}_2+\frac{1+6\mu^2+\mu^4}{M^4}k_4\ ,\\
A_{43}&=-6\lambda\mu^2\frac{3+10\mu^2+3\mu^4}{M^4}k_1k_2+2(1+\lambda)\mu^2\overline{k}_1k_2+2(1+\lambda)(1+\mu^2)\frac{\mu^2}{M^2}\overline{k}_1\overline{k}_2-8(1+\mu^2)\frac{\mu^2}{M^4}k_4\ ,\\
A_{44}&=48\lambda(1+\mu^2)\frac{\mu^4}{M^4}k_1k_2-2(1+\lambda)\frac{\mu^4}{M^2}\overline{k}_1\overline{k}_2+8\frac{\mu^4}{M^4}k_4\ ,\\
A_{45}&=-32\lambda\frac{\mu^6}{M^4}k_1k_2\ ,\\
B_{43}&=\lambda\frac{3+10\mu^2+3\mu^4}{M^2}k_1k_2-(1+\lambda)M^2\overline{k}_1k_2+\frac{1}{2}(1+\lambda)(1+\mu^2)\overline{k}_1\overline{k}_2-2\frac{1+\mu^2}{M^2}k_4\ ,\\
B_{44}&=-16\lambda(1+\mu^2)\frac{\mu^2}{M^2}k_1k_2-(1+\lambda)\mu^2\overline{k}_1\overline{k}_2-4\frac{\mu^2}{M^2}k_4\ ,\\
B_{45}&=16\lambda\frac{\mu^4}{M^2}k_1k_2\ .
\end{aligned}
\tag{4.14}
$$

It may readily be observed that the expressions (4.4) and (4.5) for Φ and Ψ are far simpler than (4.9) and (4.10).

In the above we have found the most general expressions for the velocity potential Φ and the stream function Ψ corresponding to the uniform flow past an arbitrary cylinder in the absence of circulation. If the cylinder has some symmetry in its form, the expressions for Φ and Ψ are considerably simplified. In fact, the following result can be readily obtained.

(i) For a cylinder symmetric with respect to the x-axis

$$\alpha_1=\alpha_2=\alpha_3=\alpha_4=0\quad (\text{if } h_n\neq 0)$$

$$b_{mn}=d_{mn}=0\ .$$

(ii) For a cylinder symmetric with respect to the y-axis

$$\alpha_1=\alpha_3=0\ ,\quad \alpha_2=\alpha_4=\pi/2\quad (\text{if } h_n\neq 0)$$

$$a_{2n}=a_{4n}=b_{3n}=c_{4n}=d_{3n}=0\,.$$

(iii) For a cylinder symmetric with respect to the origin

$$h_2=h_4=0\,,$$

$$a_{2n}=b_{2n}=a_{4n}=b_{4n}=c_{4n}=d_{4n}=0\,.$$

In a previous paper [4], the present writer assumed that if a cylinder of arbitrary cross section is placed in a uniform flow of a compressible fluid the velocity potential at a great distance from the cylinder could, in general, be asymptotically expressed in the form:

$$\Phi=U\left[r\cos\theta+\frac{1}{r}f_1(\theta)+\frac{1}{r^3}f_3(\theta)+\cdots\right].$$

According to the above result, however, this is the case only if the cylinder has a symmetric form with centre of symmetry at the origin. Circular and elliptic cylinders naturally satisfy this condition.

Finally, comparing our analysis with Gröbner's, we may mention as follows. We have determined the asymptotic expressions for Φ and Ψ correctly to the order of $1/r^4$, so that we can at once find the expressions for the velocity correct to the order of $1/r^5$, while Gröbner's result is correct only to the order of $1/r^4$; moreover, it is concerned only with the case of a cylinder symmetrical with respect to the x-axis. Furthermore, our analysis requires only a few simple quadratures, whereas Gröbner's analysis consists essentially in the integration of a system of differential equations.

§ 5. Application to the Flow past a Circular Cylinder

We shall next show some application of the result obtained. In a previous paper [4], the writer has dealt with the flow past a circular cylinder by the method of Janzen and Rayleigh, and has determined the velocity potential correctly to the order of M^6, M being the Mach number of the undisturbed flow. If expressed in a series of descending powers of r, the velocity potential takes the form:

$$\frac{\Phi}{U}=r\cos\theta+\frac{1}{r}f_1(\theta)+\frac{1}{r^3}f_3(\theta)\,, \tag{5.1}$$

where

$$\begin{aligned} f_1(\theta)=\cos\theta&+M^2\left(\frac{13}{12}\cos\theta-\frac{1}{4}\cos3\theta\right)\\ &+M^4\left\{\left(\frac{137}{80}\cos\theta-\frac{19}{48}\cos3\theta+\frac{1}{16}\cos5\theta\right)+\frac{17}{60}(\gamma-1)\cos\theta\right\}\\ &+M^6\left\{\left(\frac{10571}{3360}\cos\theta-\frac{77}{120}\cos3\theta+\frac{25}{192}\cos5\theta-\frac{1}{64}\cos7\theta\right)\right.\\ &\qquad\left.+(\gamma-1)\left(\frac{44}{35}\cos\theta-\frac{17}{240}\cos3\theta\right)+\frac{59}{420}(\gamma-1)^2\cos\theta\right\}+\cdots\,, \end{aligned} \tag{5.2}$$

$$\begin{aligned} f_3(\theta)=M^2&\left(-\frac{1}{2}\cos\theta+\frac{1}{12}\cos3\theta\right)\\ &+M^4\left\{\left(-\frac{4}{3}\cos\theta-\frac{5}{48}\cos3\theta+\frac{1}{16}\cos5\theta\right)\right.\\ &\qquad\left.+(\gamma-1)\left(-\frac{1}{8}\cos\theta-\frac{61}{240}\cos3\theta+\frac{1}{16}\cos5\theta\right)\right\}\\ &+M^6\left\{\left(-\frac{281}{90}\cos\theta-\frac{22291}{20160}\cos3\theta+\frac{109}{192}\cos5\theta-\frac{3}{32}\cos7\theta\right)\right.\\ &\qquad+(\gamma-1)\left(-\frac{163}{240}\cos\theta-\frac{899}{700}\cos3\theta+\frac{97}{240}\cos5\theta-\frac{1}{16}\cos7\theta\right)\\ &\qquad\left.+(\gamma-1)^2\left(-\frac{29}{210}\cos3\theta\right)\right\}+\cdots\,, \end{aligned} \tag{5.3}$$

the radius of the cylinder being taken as 1.

Now, on account of the symmetry property of the cylinder, (4.9) can be written in the form:

$$\frac{\Phi}{U}=r\cos\theta+\frac{1}{r}\,\frac{a_1\cos\theta}{N}+\frac{1}{r^3}\left(\frac{a_{32}}{N^2}+\frac{a_{33}}{N^3}+\frac{a_{34}}{N^4}\right)\cos\theta+\cdots\,, \tag{5.4}$$

where

$$a_{32}=\left\{\frac{\lambda}{4}\,\frac{1+10\mu^2+5\mu^4}{M^2}-\frac{1}{2}(1+\lambda)M^2-\frac{1}{12}(1+\lambda)(1+3\mu^2)\right\}a_1{}^2+\frac{1+3\mu^2}{M^2}a_3\ , \tag{5.5}$$

$$a_{33}=-\left\{\lambda(3+5\mu^2)\frac{\mu^2}{M^2}-\frac{1}{3}(1+\lambda)\mu^2\right\}a_1{}^2-4\frac{\mu^2}{M^2}a_3\ , \tag{5.6}$$

$$a_{34}=4\lambda\frac{\mu^4}{M^2}a_1{}^2\ , \tag{5.7}$$

$$N=1-M^2\sin^2\theta\ , \tag{5.8}$$

$$\mu=\sqrt{1-M^2}\ ,\qquad \lambda=\frac{\gamma+1}{4}\,\frac{M^2}{1-M^2}\ . \tag{5.9}$$

Two constants a_1 and a_3 only remain arbitrary, but it may naturally be expected that they can be determined so that (5.1) may be in perfect agreement with (5.4). To show this, we have only to expand (5.4) in a series of ascending powers of M^2. First, we have from (5.5), (5.6), (5.7)

$$a_{32}=-\left\{\frac{1}{3}-\kappa+\left(\frac{1}{4}+\frac{\kappa}{3}\right)M^2+\frac{\kappa}{12}M^4+\frac{\kappa}{12}M^6\right\}a_1{}^2+\frac{4-3M^2}{M^2}a_3+O(M^8)\ ,$$

$$a_{33}=\frac{1}{3}\left\{1-6\kappa-(1-4\kappa)M^2\right\}a_1{}^2-4\frac{1-M^2}{M^2}a_3\ ,$$

$$a_{34}=\kappa(1-M^2)a_1{}^2\ ,$$

where, for brevity, we have put

$$\kappa=\gamma+1\ .$$

Also, we have from (5.8)

$$1/N=1+M^2\sin^2\theta+M^4\sin^4\theta+M^6\sin^6\theta+O(M^8)\ ,$$
$$1/N^2=1+2M^2\sin^2\theta+3M^4\sin^4\theta+4M^6\sin^6\theta+O(M^8)\ ,$$
$$1/N^3=1+3M^2\sin^2\theta+6M^4\sin^4\theta+10M^6\sin^6\theta+O(M^8)\ ,$$
$$1/N^4=1+4M^2\sin^2\theta+10M^4\sin^4\theta+20M^6\sin^6\theta+O(M^8)\ .$$

Introducing these quantities into (5.4) and carrying out elementary but rather lengthy calculations, it may be shown that (5.4) is in perfect accord with (5.1), if we take

$$a_1=1+\frac{5}{6}M^2+\left\{\frac{13}{16}+\frac{17}{60}(\gamma+1)\right\}M^4+\left\{\frac{97}{120}+\frac{1049}{1680}(\gamma+1)+\frac{59}{420}(\gamma+1)^2\right\}M^6+\cdots\ , \tag{5.10*}$$

$$a_3=\frac{1}{6}M^2+\left\{\frac{83}{360}-\frac{7}{30}(\gamma+1)\right\}M^4+\left\{\frac{6269}{2160}-\frac{13019}{25200}(\gamma+1)-\frac{29}{210}(\gamma+1)^2\right\}M^6+\cdots\ . \tag{5.11}$$

This agreement may be considered as furnishing some evidence for the correctness of our formula (5.4).

References

1) H. Bateman: Proc. Nat. Acad. Sci. U.S.A. **24** (1938) 246.

2) H. Glauert: Proc. Roy. Soc. London A **118** (1928) 113.

3) W. Gröbner: Luftfahrtforschung **20** (1943) 184.

4) I. Imai: Proc. Phys.-Math. Soc. Japan **23** (1941) 180.

5) I. Imai: Proc. Phys.-Math. Soc. Japan **24** (1942) 231.

6) I. Imai: Journ. Phys.-Math. Soc. Japan **17** (1943) 495.

7) I. Imai: Rep. Aeron. Res. Inst. Tokyo Imp. Univ., No. **294** (1944).

8) I. Imai: Sûributurigaku-Kenkyû (Studies in Mathematical Physics) **2** (1952) 67. Iwanami Syoten Publ. (Tokyo).

---

* A numerical error has been discovered in the previous paper [4]. In (9.7) there 3625/1344 should be replaced by 55/21.

JOURNAL OF THE PHYSICAL SOCIETY OF JAPAN Vol. 8, No. 4, JULY—AUGUST, 1953

Sur une Relation entre la Résistance à la Rupture et le Foyer d'Eclatement du Verre*

Par Nobuzo TERAO

Institut de Physique, Faculté des Sciences, Université de Tokyo

(Reçu le 18 Decembre 1952)

The relation between the extent of mirror surface appearing at the starting point of crack produced in glass rod by bending and the applied stress is studied. Two series of experiments are carried out: (a) the load is increased linearly with time, (b) the load is kept constant. There is a tendency that the greater the stress at the moment of rupture, the smaller the mean extent of mirror surface. Under the same condition of stress, however, the marked fluctuations are observed on the extent of mirror as well as on the mode of successive ramifications. For the problems of these fluctuations, statistical theory of fracture is applied. If the probability of the first occurrence of ramification which determines the boundary of the mirror after the crack develops for the distance l from the starting point is denoted by $\mu(l)$, the following relations are proved to hold good.

$$\mu(l)=A(l-l_0)\exp(\alpha f) \qquad \text{when } l>l_0\,,$$
$$\quad =0 \qquad \text{when } l\leqq l_0\,,$$
$$\bar{l}-l_0=C\exp(-\alpha/2\cdot f)\,,$$

where, f being the tensile stress at the starting point of crack, l_0 the minimum extent of the mirror produced under stress f, $\bar{l}$ the mean value of l, and A,C,α, some constants.

§ 1. Introduction

On connaît très bien le fait qu'il existe une variation remarquable parmi les résultats obtenus par l'observation concernant la résistance du verre à la rupture. Au cours des années de 1930 à 1940 M. A. Smekal et ses collègues ont essayé d'expliquer cette variation par rapport au foyer d'éclatement.1)-7) Leur idée fondamentale est en résumé la suivante: Si une baguette de verre, ayant une surface de section "q", se rompt lorsqu'on la tire dans la direction de son axe par une charge L, on définit en général la résistance à la rupture "Z" par

$$Z=L/q\,. \qquad (1)$$

Qu'une matière fragile comme le verre ou le bitume se rompe, on peut voir, au point de départ d'une cassure, ce que nous appelons un foyer d'éclatement ou miroir, c'est-à-dire, une surface sensiblement plane d'un aspect tout particulier.8)-10) La Fig. 1 montre un schéma de la disposition de cette cassure.

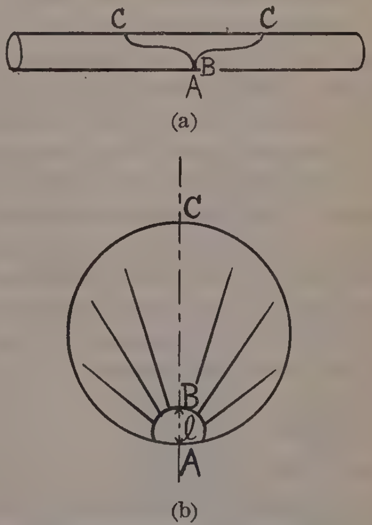

(a)

(b)

Fig. 1. (a) Cassure d'une baguette de verre.
(b) Schéma de la disposition d'une surface de section.
A: Point de départ.
B: Bout du foyer d'éclatement.

Lorsqu'une cassure part du point A comme on le voit dans la Fig. 1 (a), la partie "A B" apparaît d'abord et ensuite se produit la partie "B C" qui s'avance dans deux directions à partir du point "B". La Fig. 1 (b) montre la disposition d'une surface de section. La partie "A B" est ce qu'on appelle le foyer d'éclatement. Supposons maintenant que la partie nommée foyer d'éclatement se développe très lentement, que la vitesse de croissance d'une cassure augmente tout à coup auprès du bord de ce miroir et que la charge L pèse seulement sur la partie qui ne contient pas la surface de section "s" du foyer d'éclatement, la formule qui suit montre la véritable résistance à la rupture "Z_0".

---

* Séance de la Société de Physique, le 1er avril 1952.

$$Z_0=L/(q-s)=Z/(1-s/q)\ . \qquad (2)$$

Pourquoi la valeur "Z" de la formule (1), est-elle très variable, même si on fait des expériences dans les mêmes conditions ? C'est parce que la surface de section du foyer d'éclatement n'est pas constante. Par conséquent, "Z_0" de la deuxieme formule qui remplace la première, doit être la résistance propre à la rupture d'une matière. Voilà l'idée de M. A. Smekal et de ses collègues.

Maintenant examinons leurs résultats d'expérience. La valeur de Z_0 est apparemment moins variable que celle de Z. Il y a tout de même une variation assez grande à propos de Z_0 que nous ne pouvons négliger. En réalité, la vitesse de croissance du foyer d'éclatement n'est jamais si petite et nous croyons qu'il est nécessaire d'examiner à nouveau la signification physique de la formule (2). Ce que nous pouvons affirmer définitivement d'après les résultats obtenus jusqu'ici, c'est que le foyer d'éclatement est d'autant plus petit que l'effort Z est plus grand. La circonstance est commune aux deux cas, soit qu'une cassure se produise par un choc mécanique, soit qu'elle résulte d'un effort thermique.[11] Donc, nous avons fait une recherche plus quantitative selon le conseil de M. M. Hirata sur la relation entre la résistance à la rupture du verre et la grandeur du foyer d'éclatement.

§ 2. Expérience

On fait casser par la flexion une baguette de verre placée horizontalement sur deux appuis cunéiformes à la distance de 100 mm, en disposant une charge au point central de la baguette. Nous avons fait deux séries d'expériences dans les deux conditions suivantes : (a) on impose à l'échantillon une charge qui augmente proportionnellement au temps et (b) on lui impose une charge constante. Nous adoptons ici la distance l entre le point de départ A et le point de bord B (Fig. 1 (b)) comme une dimension représentant la grandeur du foyer d'éclatement à la place de la surface de section s.

(a) : Cas où l'on impose à l'échantillon une charge augmentant proportionnellement au temps. (cas de (I) et (II))

Nous avons placé la charge au milieu de l'échantillon de verre par l'appareil du levier en employant du sable comme dans les essais antérieurs[12],[13] et mesuré le temps entre le commencement de la charge et la rupture soudaine. La diamètre de la bagguette de verre "d" et la vitesse d'augmentation de la charge "r" exprimée par l'effort maximum au point central de l'échantillon, sont dans chaque cas comme il suit :

cas de (I) : $d=4.8\pm0.1\,\text{mm}$, $r=9.50\,\text{kg/cm}^2\cdot\text{sec}$
cas de (II) : $d=5.4\pm0.1\,\text{mm}$, $r=6.98\,\text{kg/cm}^2\cdot\text{sec}$.

La Fig. 2 et la Fig. 3 montrent respectivement la relation entre la grandeur l du foyer d'éclatement et la tension maximum f au point de départ de la cassure dans les cas de (I) et (II).

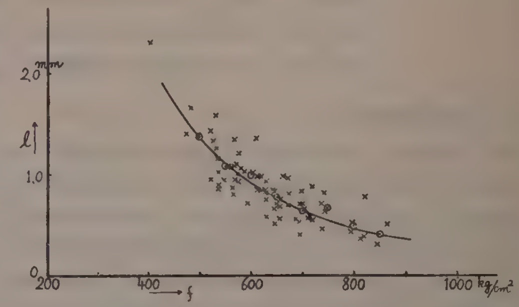

Fig. 2. Relation entre la grandeur l du foyer d'éclatement et la tension f dans le cas (I).

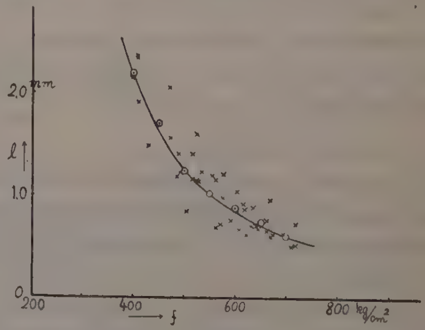

Fig. 3: Relation entre la grandeur l du foyer d'éclatement et la tension f dans le cas (II).

Les figures marquées × montrent chaque valeur obtenue par l'observation et celles marquées ⊙ chaque valeur moyenne $\overline{l}$ de la grandeur du foyer d'éclatement qui prend naissance dans une limite de 50 kg/cm². Il y a une assez grande variation parmi les valeurs obtenues sur *l*, mais en ce qui concerne la valeur moyenne, plus la tension est forte, plus elle a une tendance à être petite, comme nous l'avons dit ci-dessus.

(b) : Cas où l'on impose à l'échantillon une charge constante. (cas de (III) à (VI))

Nous avons mesuré le temps de retard de la rupture *t* dans le cas où l'on maintient l'échantillon sous un effort constant *f*. Les conditions d'expérience dans chaque cas sont :

cas de (III) : $d=5.2\pm0.1$ mm $f=620$ kg/cm²
cas de (IV) : $d=5.0\pm0.1$ mm $f=630$ kg/cm²
cas de (V) : $d=4.6\pm0.1$ mm $f=655$ kg/cm²
cas de (VI) : $d=4.8\pm0.1$ mm $f=660$ kg/cm²

En ce qui concerne le temps de retard, nous avons constaté que le traitement statistique initié par M. M. Hirata est assez satisfaisant.11),13),14) Nous désignerons par *s* la distance entre le point central et celui du départ de la cassure. La Fig. 4 est un exemple précisant les relations entre *s* et *t*, d'un côté de l'autre côté *l* et *t* dans le cas de (III).

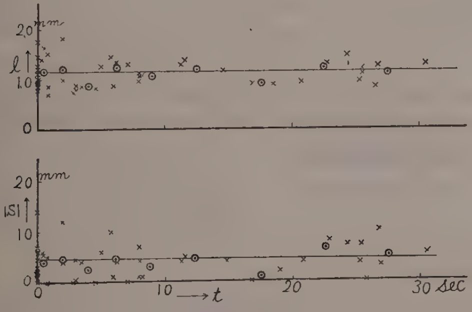

Fig. 4. Relation entre *l*, *s* et le temps de retard de la rupture.

Il y a une assez grande variation entre les valeurs obtenues par l'observation (marquées ×), mais les valeurs moyennes de *l* et *s* sont à peu près constantes (marquées ⊙). D'après ce fait, nous pourrions penser que l'état du verre qui subit un effort ne change pas trop à mesure que le temps passe et que la rupture aura lieu presque dans la même condition d'effort en ce qui concerne le temps et l'effort dont nous rendons compte dans la présente étude.

§ 3. Variation de la Grandeur du Foyer d'Éclatement

Lorsqu'une cassure provenant d'un point de départ se développe dans une étendue à laquelle a été donnée l'énergie de tension élastique, la pointe de cette cassure est une sorte de point singulier sur lequel l'énergie de tension se concentre et c'est au moment où cette pointe se ramifie que se détermine le bord du foyer d'éclatement. On peut donc entrevoir que le traitement statistique de la résistance à la rupture s'appliquera à la variation de la grandeur du foyer d'éclatement de même qu'au problème de la ramification de la cassure.15) Mais, il est nécessaire que l'on amende d'avance la variation systématique due au déplacement du point de départ de la cassure pour traiter l'ensemble de la variation de "*l*" au point de vue statistique. En effect, la Fig. 5 (a) montre une relation entre *l* et *s*, à titre d'exemple, dans le cas de (V), et la relation entre $\bar{l}$, valeur moyenne de *l*, et $1/f(s)$, inverse de la tension au point de départ "*s*" du foyer d'éclatement, est presque linéaire comme on voit dans la Fig. 5 (b) Par la Fig. 5 (b), on convertit chaque valeur de *l* en une grandeur du foyer d'éclatement qui pourrait se produire sous la tension maximum $f(0)$ au point central de l'échantillon.

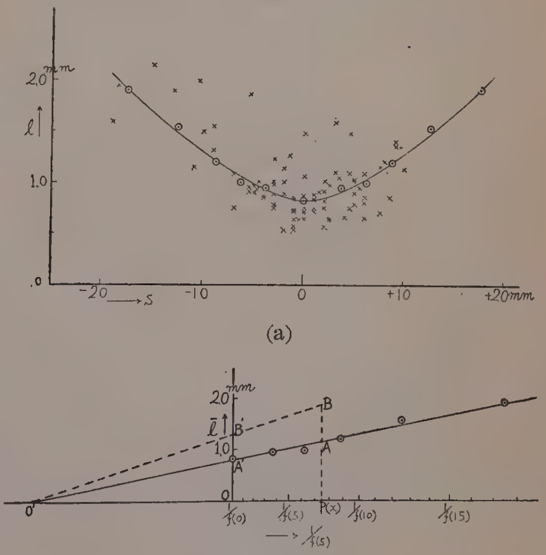

(b)

Fig. 5. (a) Relation entre la grandeur et le point de départ du foyer d'éclatement.
(b) Relation entre la valeur moyenne de la grandeur du foyer d'éclatement et $1/f(s)$.

Désignons par $P(x)$ dans la Fig. 5 (b) le point de $1/f(x)$ qui correspond au point $s=x$. Un foyer d'éclatement de grandeur $l=\mathrm{PA}$

produit au point $s=x$ serait correspondant au foyer d'éclatement de grandeur $l=\text{OA}'$ produit au point $s=0$ sous la tension $f(0)$. Et, le foyer d'éclatement $l=0$ au point $s=x$ correspond aussi à $l=0$ sous la même tension. En conséquence, on pourrait considérer que $l=\text{PB}$ au point $s=x$ correspond approximativement à $l=\text{OB}'$ d'un foyer d'éclatement au point $s=0$. Nous prendrons nos mesures pour que la valeur amendée ainsi soit la grandeur du foyer d'éclatement produit sous la tension $f(0)$. La méthode susdite n'est jamais unique pour l'amendement de "l". Par exemple, les relations entre l et s, l et $1/\sqrt{f}$ ou $\log(l-l_0)$ et f (ce dernier sera expliqué ultérieurement) sont aussi presque linéaires dans les limites d'une si petite valeur de "s" que celle que l'on examine ici et se basant sur ces relations, on peut amender l de la même façon que la précédente. En tous cas, les résultats sont presque les mêmes. Nous adoptons ici la relation entre l et $1/f$. C'est seulement parce que nous possédons la relation de "tension$\propto 1/l$" sur la cassure qui a été provoquée par un effort thermique et qui a beaucoup de ramifications.16)

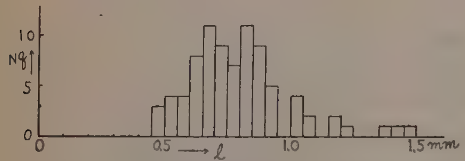

Fig. 6. Distribution de la grandeur du foyer d'éclatement.

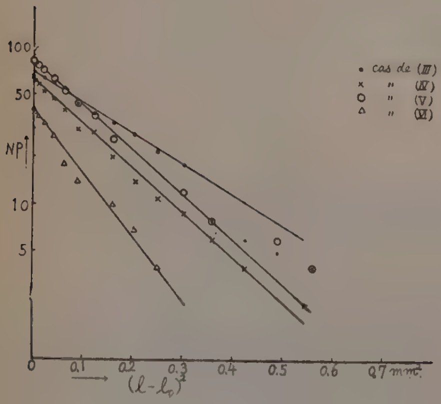

Fig. 7. Relation entre $\log(Np)$ et $(l-l_0)^2$

Désignons par $q(l)dl$ la proportion des échantillons dont la grandeur du foyer d'éclatement est entre l et $l+dl$ et par N le nombre total des échantillons dans chaque cas. La Fig. 6 montre la distribution de "l" obtenu suivant la méthode susdite dans le cas de (V).

Ensuite, désignons par $p(l)$ la proportion des échantillons dont le foyer d'éclatement est plus grand que l. On a

$$p(l)=\int_l^\infty q(l)\,dl\,, \tag{3}$$

$$p(0)=1\,. \tag{4}$$

Les relations entre $\log(Np)$ et $(l-l_0)^2$ sont représentées par les droites de la Fig. 7. Ici, l_0 représente la grandeur du foyer d'éclatement minimum en chaque cas.

De cette relation linéaire,

$$\log p(l)=-(A/2)(l-l_0)^2\,. \tag{5}$$

Ici, A désigne une constante positive. Si nous montrons par $\mu(l)$ la probabilité pour que le foyer d'éclatement se ramifie après s'être développé jusqu'à la distance de l, par la relation suivante :

$$\mu(l)=-dp/p=-d(ln\,p)\,, \tag{6}$$

on a

$$\left.\begin{aligned}\mu(l)&=A(l-l_0) &&\text{pour}\quad l>l_0\,,\\ &=0 &&\text{pour}\quad l\leq l_0\,.\end{aligned}\right\} \tag{7}$$

$\mu(l)$ est une fonction de la tension f comme on voit dans la Fig. 7 et on pourrait la représenter en général

$$\left.\begin{aligned}\mu(l)&=A(l-l_0)F(f) &&\text{pour}\quad l>l_0\,,\\ &=0 &&\text{pour}\quad l\leq l_0\,.\end{aligned}\right\} \tag{8}$$

Par suite

$$p=\exp\left[-\frac{A(l-l_0)^2}{2}F(f)\right], \tag{9}$$

$$q=A(l-l_0)F(f)\exp\left[-\frac{A(l-l_0)^2}{2}F(f)\right]. \tag{10}$$

La valeur moyenne $\bar{l}$ de l est

$$\bar{l}=\int_{l_0}^\infty l\cdot q(l)\,dl\,. \tag{11}$$

En cas de $F(f)=\exp(\alpha f)$, on obtient

$$\bar{l}-l_0=\frac{1}{2}\sqrt{\frac{2\pi}{A}}\exp\left(-\frac{\alpha}{2}f\right)=C\exp\left(-\frac{\alpha}{2}f\right). \tag{12}$$

La Fig. 8 exprime la relation entre $\log(l-l_0)$ et f dans le cas de (I) et (II). De là on peut constater que l'équation (12) est assez satisfaite. Ici, l_0 est de 0.4 mm dans tous les deux.

En ce qui concerne l_0 qui n'a pas paru dans le problème traité antérieurement sur la ramification d'une cassure,[15] on devrait le considérer par rapport au mécanisme de la naissance du foyer d'éclatement. En réalité, plus la tension est grande, plus l_0 a une tendance à être petit et les résultats susdits deviendraient plus complexes.

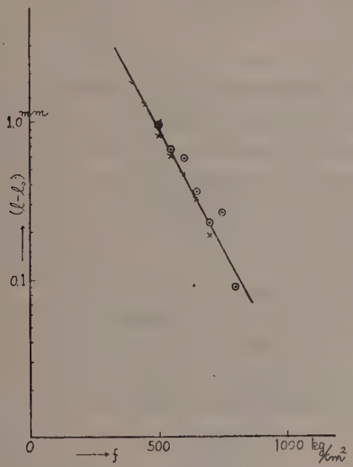

Fig. 8. Relation entre la grandeur moyenne du foyer d'éclatement et la tension.
◉: cas de (I). ×: cas de (II).

Nous tenons à exprimer notre reconnaissance envers M.le Professeur M. Hirata qui a bien voulu nous encourager à poursuivre la présente étude et nous aider de ses conseils.

Bibliographie

1) K. H. H. Müller: Zeits. f. Phys. **69** (1931) 431.

2) G. Apelt: Zeits. f. Phys. **91** (1934) 336.

3) K. Wirtz: Zeits. f. Phys. **93** (1935) 292.

4) A. Smekal: Ergeb. d. Exak. Natw. Bd. **15** (1936) 153.

5) K. Mengelkoch: Zeits. f. Phys. **97** (1935) 46.

6) M. Eichler: Zeits. f. Phys. **98** (1936) 280.

7) G. Schumann: Zeits. f. Phys. **98** (1936) 605.

8) A. Winkelmann, O. Schott: Ann. d. Phys. u. Chem. **51** (1894) 718.

9) Ch. de Fréminville: Rev. de Métallurgie **11** (1914) 971.

10) M. Hirata: J. Appl. Phys. Japan **5** (1936) 386.

11) M. Hirata: *Kikai no Kenkyu* **1** (1949) 182, 231.

12) M. Hirata and N. Terao: J. Appl. Phys. Japan **20** (1951) 234.

13) N. Terao: J. Phys. Soc. Japan **7** (1952) 627.

14) M. Hirata: *Ôyo Tôkei-gaku* (1949) 11.01. Bull. Math. Statis. **3** (1949) 57.

15) N. Terao: J. Appl. Phys. Japan **20** (1951) 109.

16) W. Sasaki: J. Appl. Phys. Japan **17** (1948) 234.

JOURNAL OF THE PHYSICAL SOCIETY OF JAPAN Vol. 8, No. 4, JULY—AUGUST, 1953

Sur la Résistance à la Rupture du Verre
—— L'Influence de l'Humidité*

Par Nobuzo TERAO

Institut de Physique, Faculté des Sciences, Université de Tokyo

(Reçu le 17 mars 1953)

The influence of humidity on the strength of glass strip is studied experimentally. The marked fluctuations are observed on the strength as well as on the extent of mirror surface appearing at the starting point of fracture. By means of statistical analysis, it is found that the probability of breakdown when the load attains the value between f and $f+df$ is expressed by

$$\mu(f)df=a\exp[-(E_0-\beta f)/kT]\cdot df\ .$$

Here, E_0 is the activation energy of glass, βf the energy applied by external loading, T the absolute temperature and k the Boltzmann's constant. For the variation of humidity, β is kept constant, while E_0 decreases with increasing humidity. The effect of humidity is negligible to the extent of mirror, for which the following relation is proved to hold good.

$$\bar{l}-l_0=C\exp(-\alpha/2\cdot f)$$

Here, $\bar{l}$ is the mean extents of mirrors produced by the load f, l_0 the minimum extent of mirror and C, α some constants.

Nous avons étudié jusqu'ici la résistance à la rupture du verre au point de vue statistique en introduisant la probabilité de rupture μ.[1)-3)] D'après les résultats obtenus, on peut exprimer μ par la formule

$$\mu=a\exp[-(E_0-\beta f)/kT]\ , \qquad (1)$$

où E_0 représente l'énergie d'excitation de rupture, f la tension, βf l'énergie donnée par la force extérieure, k la constante de Boltzmann et T la température absolue. Donc, pour la résistance à la rupture, il est nécessaire d'examiner systématiquement comment E_0 et β varient selon les diverses conditions. Ce doit être l'influence du milieu entourant l'échantillon de verre qui est la plus importante après l'influence de la température, recherchée précédemment.[3)] Par exemple, on sait que l'influence de l'humidité est assez remarquable.[4),5)] Cette influence doit se manifester comme une variation de E_0 ou de β. Il y a, de plus, une intime relation entre la résistance à la rupture et le foyer d'éclatement du verre. Pour examiner ces points, nous avons fait les essais suivants.

On met l'échantillon de verre de sodium-chaux, d'une largeur de 10.0 mm et d'une épaisseur de 1.8 mm, sur deux appuis cunéiformes placés à un intervalle de 100 mm et on impose au point central de l'échantillon une charge qui augmente proportionnellement au temps comme précédemment. (La vitesse de la charge employée ici était de 8.89 gr/sec.) Nous avons ainsi mesuré la distribution de la résistance à la rupture dans les cas où l'humidité ambiante était respectivement de 60, 65, 70, 75, 80 et 85 %. La température restait d'environ 25°C. Le nombre total des échantillons était à peu près de 50 dans chaque cas. Malheureusement, comme il était seulement de 9 dans le cas de 85 %, nous avons renoncé dans ce cas à chercher la valeur de μ. La Fig. 1 montre la résistance moyenne à la rupture.

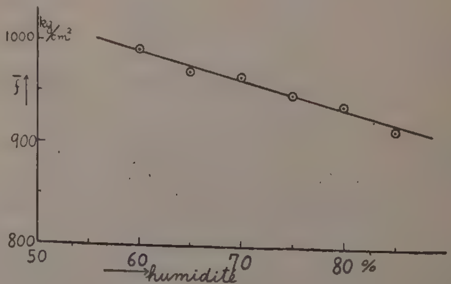

Fig. 1. Résistance moyenne à la rupture.

La relation entre log μ et l'effort f, obtenue par les résultats expérimentaux, manifeste un groupe de droites presque parallèles l'une à l'autre, comme on le voit dans la Fig. 2. La droite la plus haute de la Fig. 2 montre les valeurs de log μ dans le cas où l'on impose la charge sur l'échantillon tout de suite après qu'on l'a trempé dans l'eau. (La résistance moyenne à la rupture, dans ce cas, est de 830 kg/cm².) Ce résultat veut dire que la valeur de β est à peu près constante et que celle de E_0 diminue à mesure que l'humidité s'abaisse. Ici, $\beta=1.84\times10^{-22}\,\text{cm}^3$, si l'on exprime f par l'effort maximum au point central de l'échantillon. La Fig. 3 montre l'énergie d'excitation de rupture E_0 dans le cas où l'on suppose que $a=10^{10}\,\text{sec}^{-1}$.[3),6)]

---

* Séance de la Société de Physique, le 30 oct. 1952.

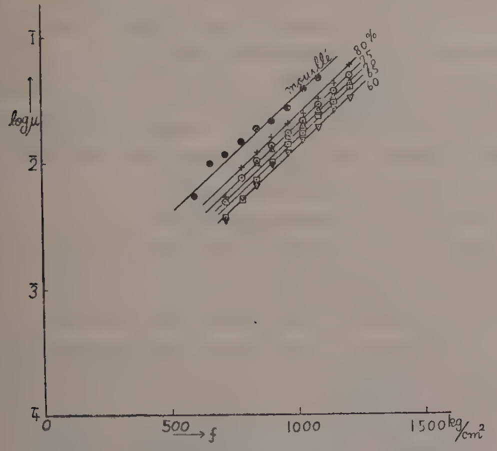

Fig. 2. Relation entre log μ et l'effort.

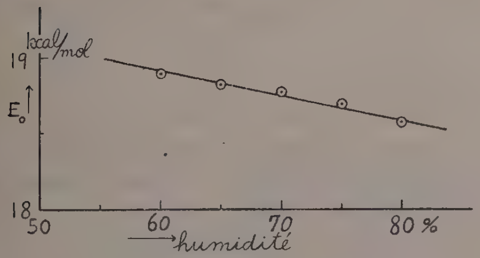

Fig. 3. Énergie d'excitation de rupture.

La Fig. 4 montre un schéma de la disposition de la cassure produite par la rupture susdite. Elle est de la même espèce que la cassure de la baguette de verre que l'on voit dans le mémoire précédent.[7)] La cassure partant du point A se produit la partie BC qui s'avance dans deux directions à partir du point B (Fig. 4 (a), (b)). Ces surfaces de cassure sont montrées dans la Fig. 4 (a′) et la Fig. 4 (b′). La partie AB est plane et appelée le foyer d'éclatement. La Fig. 5 et la Fig. 6 montrent respectivement la relation entre l, représentant la grandeur du foyer d'éclatement et la tension f de rupture au point de départ de la cassure, à titre d'exemple, dans le cas de 80 % et de 65 %.

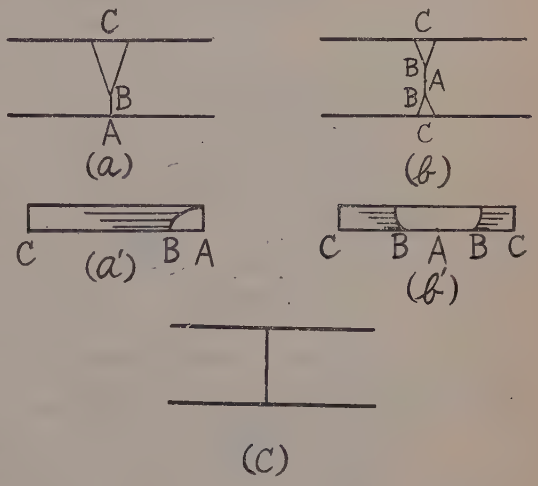

Fig. 4. Schéma de la disposition de la cassure.

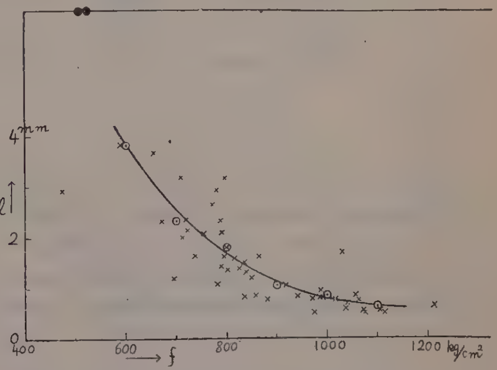

Fig. 5. Relation entre la grandeur l du foyer d'éclatement et la tension f de rupture.
(l'humidité est de 80%)

Ici, les figures marquées × montrent chaque valeur observée et celles marquées ⊙ la valeur moyenne $\bar{l}$ de la grandeur du foyer d'éclatemente qui prend naissance dans une limite de 100 kg/cm². Les figures marquées ● en haut montrent les échantillons qui ne produisent pas de ramification perceptible comme dans la Fig. 4 (c). L'échantillon tend à donner lieu à un foyer d'éclatement plus petit s'il est casse sous une tension plus forte et à produire une cassure plus simple sans sectionnement multiple, si la tension est plus faible. D'après les résultats précédents sur la baguette de verre, il y a la relation approchée suivante entre $\bar{l}$ et la tension f,⁷⁾

$$\bar{l}-l_0=C\exp\left(-\frac{\alpha}{2}f\right), \qquad (2)$$

où l_0 exprime la grandeur la plus petite du foyer d'éclatement, C et α des constantes. La formule (2) reste de même assez convenable pour l'expérience de cette fois-ci (Fig. 7). Ici, l_0 est de 0.4 mm dans tous les cas.

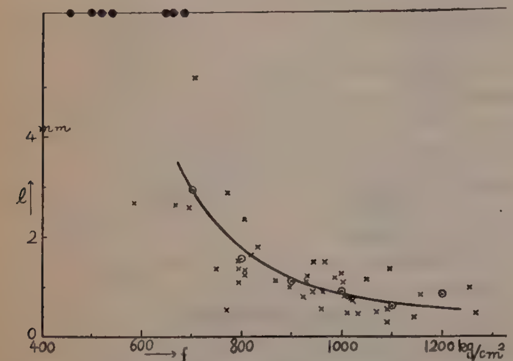

Fig. 6. Relation entre la grandeur l du foyer d'éclatement et la tension f de rupture (l'humidité est de 65%)

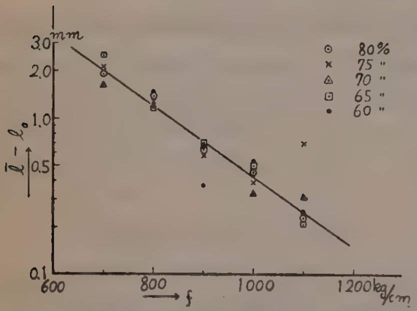

Fig. 7. Relation entre la grandeur moyenne du foyer d'éclatement et la tension.

Quoique la limite de l'humidité traitée ici soit assez étroite, on pourrait dire en conclusion qu'elle n'influe pas beaucoup sur β mais seulement sur E_0. Elle n'a presque aucun effect sur la grandeur du foyer d'éclatement. Mais, de plus, la valeur de E_0, de β et la probabilité de la ramification varient sans doute dans les cas où l'échantillon se trouve dans l'air à une pression plus basse ou dans un autre gaz. Ce serait un problème intéressant à étudier, car il est en relation avec le phénomène d'absorption du gaz par le verre.

Nous tenons à remercier le Professeur M. Hirata pour les conseils bienveillants qu'il nous a donnés au cours de ce travail.

Enfin c,est grâce aux allocations qui nous ont été accordées par le Ministère de l'Instruction Publique que nous avons pu l'effectuer.

Bibliographie

1) M. Hirata: *Kikai no Kenkyu* **1** (1949) 182, 231.

2) M. Hirata: Bull. Math. Stat. **3** (1949) 57.

3) N. Terao: J. Phys. Soc. Japan **7** (1952) 627.

4) T. C. Baker and F. W. Preston: J. Appl. Phys. **17** (1946) 179.

5) N. W. Taylor: J. Appl. Phys. **18** (1947) 943.

6) K. Ômori: J. Eng. Kyushu Univ. **16** (1942) 239.

7) N. Terao: J. Phys. Soc. Japan **8** (1953) 545.

JOURNAL OF THE PHYSICAL SOCIETY OF JAPAN Vol. 8, No. 4, JULY—AUGUST, 1953

Molecular Sound Velocity and Molecular Compressibility of Liquid Mixtures*

By Otohiko NOMOTO

Kobayasi Institute of Physical Research, Kokubunzi, Tokyo

(Received February 9, 1953)

The molecular sound velocity of Rao $R=M/\rho\cdot V^{1/3}$ and the molecular compressibility introduced by Wada** $B=M/\rho\cdot\beta^{-1/7}$ $(=M/\rho^{6/7}\cdot V^{2/7})$, where M means the molecular weight, ρ the density, V the sound velocity and β the adiabatic compressibility, have been computed for 37 mixtures of mutually soluble liquids employing existing ultrasonic velocity data and the number average molecular weights. Although the sound velocity in and the adiabatic compressibility of liquid mixtures are known to be not necessarily monotonous functions of the concentration, exhibiting maxima or minima in some cases, the molecular compressibilities were found to be linear functions of concentration (molar fraction) in most of the liquids examined. The molecular sound velocities were found to be linear functions of the molar fraction in many of the mixtures, but they deviated from straight lines and became concave upwards in mixtures consisting of one heavy component (such as carbon tetrachloride and chloroform) and one light component. Both R and B, however, failed to be linear functions of molar fraction in water-alcohol mixtures, slightly deviating upwards from the straight lines with maxima of deviation in the neighbourhood of the concentrations corresponding to the velocity maxima. A few mixtures showed irregular R- and B-curves. This is presumably attributable to the inaccuracy of velocity data employed.

§ 1. Introduction

It has been pointed out by Rao[1] that the product of molecular volume and the cube root of sound velocity is a temperature independent quantity for each liquid. Now it is customary, to call this quantity

$$R=\frac{M}{\rho}V^{1/3}, \tag{1}$$

the "molecular sound velocity", where M means the molecular weight of the liquid, ρ the density and V the sound velocity in the liquid. It has been further established that there are additivity rules

$$R=\sum_i a_i, \tag{2}$$

(Rao[2]) and

$$R=\sum_i b_i, \tag{3}$$

(Lageman and Corey[3]) where a_i and b_i are the atomic and the bond increments respectively. These rules, however, do not hold true for halogen compounds (Lagemann, Evans and McMillan[4]).

The quantity called "molecular compressibility" (or, more exactly "molecular adiabatic compressibility")

$$B=\frac{M}{\rho}\beta^{-1/7}, \tag{4}$$

has been introduced by Wada***[5] as a quantity independent on temperature for each liquid and obeying additivity rules of the type (3). Here β means the adiabatic compressibility which is to be computed from density and sound velocity by the well-known relation

$$\beta=1/\rho V^2, \tag{5}$$

so that B may also be written as

$$B=\frac{M}{\rho^{\frac{6}{7}}}V^{2/7}. \tag{6}$$

---

* Detailed account of this paper will be published in "Bulletin of the Kobayasi Institute of Physical Research (Vol. 2, No. 3/4 (1952))" in Japanese language, with graphs of ρ, V, β and those of R and B for all the 37 liquid mixtures examined, and with a numerical table of these quantities for all these mixtures and at various concentrations. (The figures and the numerical table are in English.)

** Y. Wada, J. Phys. Soc. Japan **4** (1949) 280.

*** In Wada's notation β in this paper is written as α, and B as A; Wada uses β and B for "isothermal compressibility" and "molecular isothermal compressibility" respectively. This latter quantity is independent of temperature and pressure, according to him.

This indicates that the quantity "molecular compressibility" is only slightly different from Rao's "molecular sound velocity" in spite of the large difference in name. (It may be rather natural to call B as "Wada's molecular sound velocity" in place of "molecular compressibility" but we follow Wada's definition here.) The temperature independence of this quantity follows immediately from that of R because there is a relation

$$B=M^{1/7}R^{6/7}, \qquad (7)$$

between these two quantities.

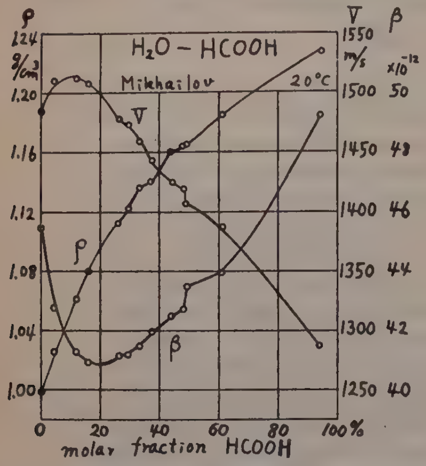

Fig. 1a. Dependence of density, sound velocity and adiabatic compressibility on concentration in water-formic acid mixtures (Mikhailov, 20°C).

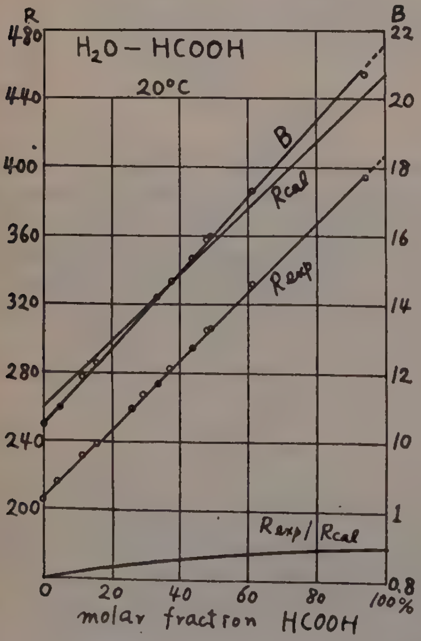

Fig. 1b. Molecular sound velocity and molecular compressibility of mixtures of water and formic acid.

Although there are many papers concerning the molecular sound velocity in liquid and its applications, there are only a few works concerning with the molecular sound velocity in liquid mixtures (Utter and Kling[6], and Iyengar[7]). The former paper is unavailable to the

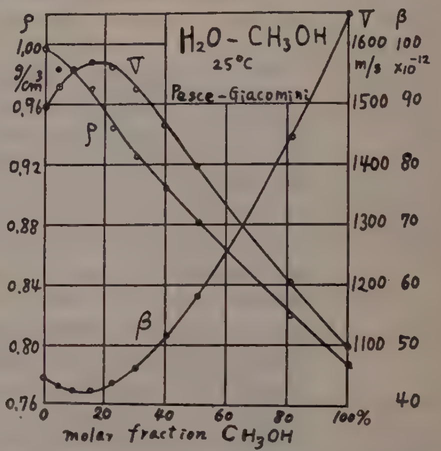

Fig. 2a. Dependence of density, sound velocity and adiabatic compressibility on concentration in water-methanol mixtures (Pesce-Giacomini, 25°C).

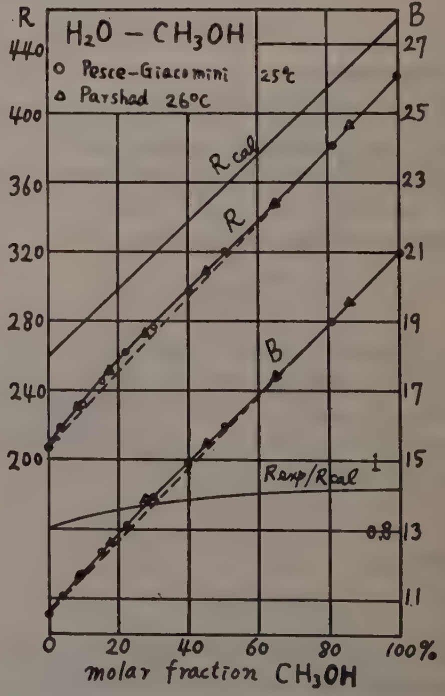

Fig. 2b. Molecular sound velocity and molecular compressibility of mixtures of water and methanol.

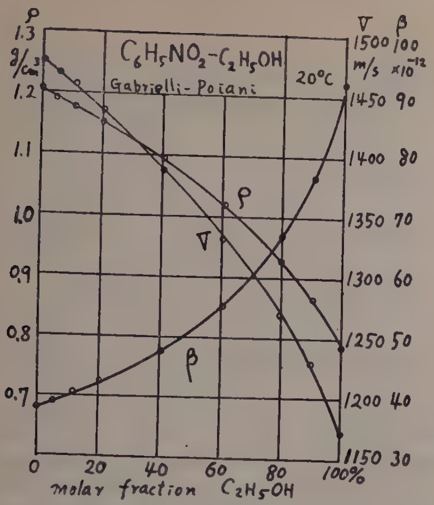

Fig. 3a. Dependence of density, sound velocity and adiabatic compressibility on concentration in nitrobenzene-ethyl alcohol mixtures (Gabrielli-Poiani, ca. 20°C).

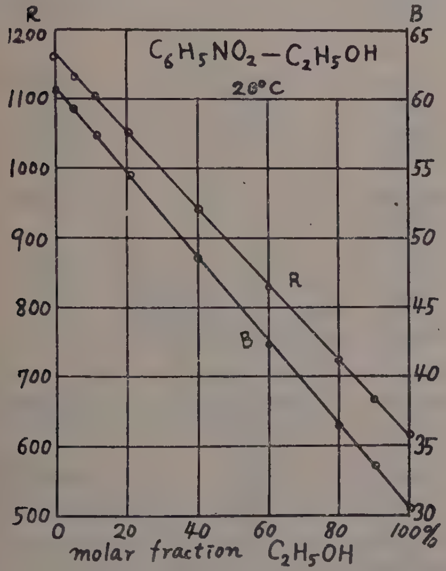

Fig. 3b. Molecular sound velocity and molecular compressibility of mixtures of nitrobenzene and ethyl alcohol.

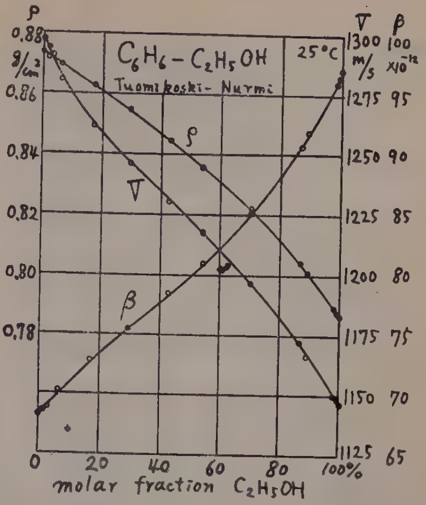

Fig. 4a. Dependence of density, sound velocity and adiabatic compressibility on concentration in benzene-ethyl alcohol mixtures (Tuomikoski-Nurmi, 25°C).

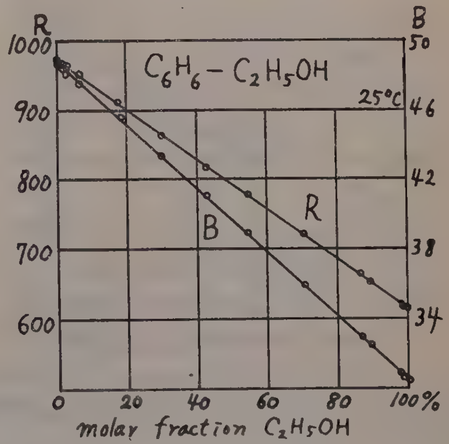

Fig. 4b. Molecular sound velocity and molecular compressibility of mixtures of benzene and ethyl alcohol.

present author as yet, and the second paper deals with the temperature coefficient of molecular sound velocity in some liquid mixtures. The molecular compressibility was only investigated by Wada and in pure liquids only.

In the present article, the molecular sound velocity *R* and the molecular compressibility *B* of liquid mixtures have been computed in dependence on concentration (molar fraction of one of the components) for all the binary mixtures for which the numerical values of the sound (=ultrasonic) velocity and density data were available to the present author (cf. Sette[8]) for tabulation of these data). There are also many papers in which the results are reproduced only in graphical forms, or in which density determinations are lacking. These results could not be employed in the present article. In many of the papers, the concentrations are given in weight percents, and in some cases in volume percents. These require to be transformed into molecular fractions, but many of the calculations have been performed by Sette[8]) and given in his tables. Sette's tables were also of great use in affording many of the data, for which the original papers were

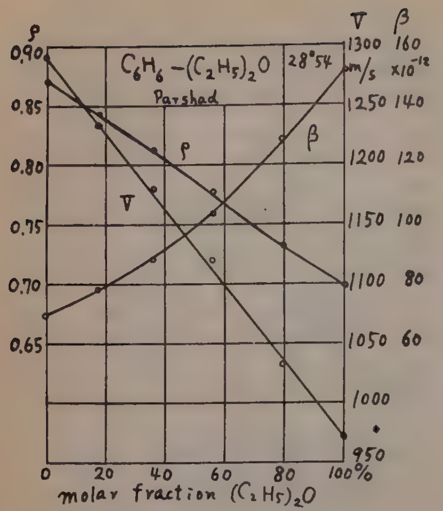

Fig. 5a. Dependence of density, sound velocity and adiabatic compressibility on concentration in benzene-ethyl ether mixtures (Parshad, 28°54).

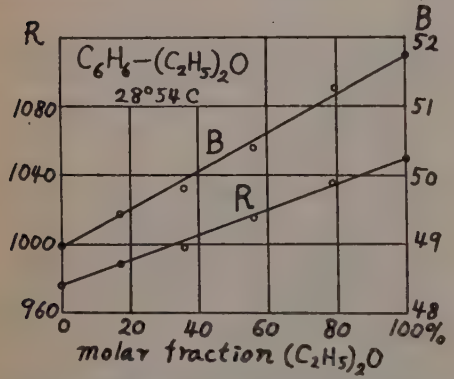

Fig. 5b. Molecular sound velocity and molecular compressibility of mixtures of benzene and ethyl ether.

not available to the present author.

§ 2. Molecular Sound Velocity and Molecular Compressibility in Liquid Mixtures

As is well known, the values of the sound velocity in liquid mixtures depend on concentration in very various manners according to the kinds of the constituent liquids employed. Formally, the mixtures may be classified into 6 groups according to the types of the velocity *vs.* molecular fraction curves: type (I) with maximum of sound velocity and minimum of adiabatic compressibility, type (II) in which the sound velocity is convex upwards and the adiabatic compressibility is concave upwards, type (III) with points of inflection for both sound velocity and adiabatic compressibility, type (IV) where the sound velocity-curve is linear, type (V) in which sound velocity is concave upwards, and type (VI) with minimum of sound velocity. In types (V) and (VI) the adiabatic compressibility sometimes exhibit the

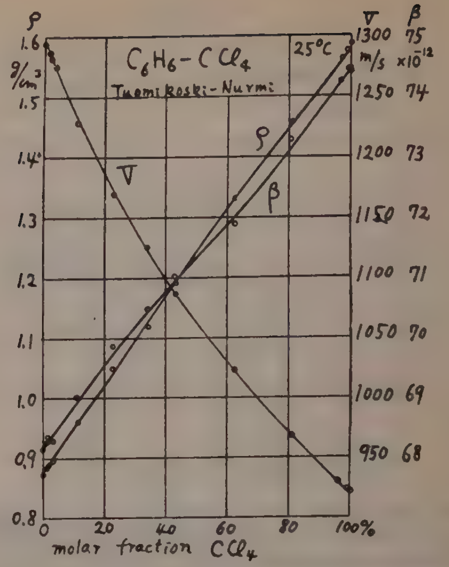

Fig. 6a. Dependence of density, sound velocity and adiabatic compressibility on concentration in benzene-carbon tetrachloride mixtures (Tuomikoski-Nurmi, 25°C).

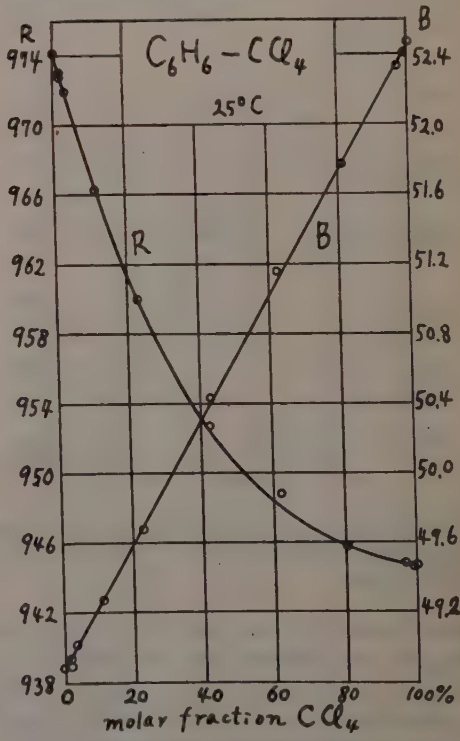

Fig. 6b. Molecular sound velocity and molecular compressibility of mixtures of benzene and carbon tetrachloride.

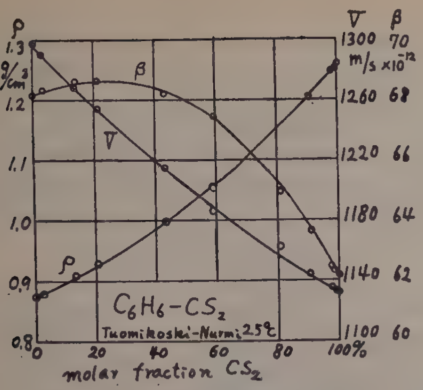

Fig. 7 a. Dependence of density, sound velocity and adiabatic compressibility on concentration in benzene-carbon disulphide mixtures (Tuomikoski-Nurmi, 25°C).

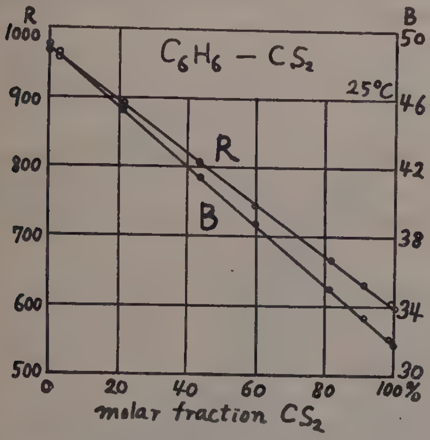

Fig. 7 b. Molecular sound velocity and molecular compressibility of mixtures of benzene and carbon disulphide.

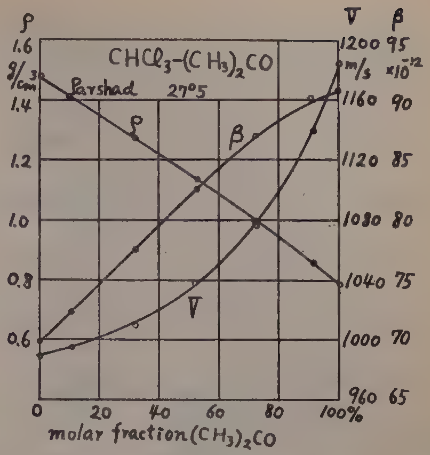

Fig. 8 a. Dependence of density, sound velocity and adiabatic compressibility on concentration in chloroform-acetone mixtures (Parshad, 27°5C).

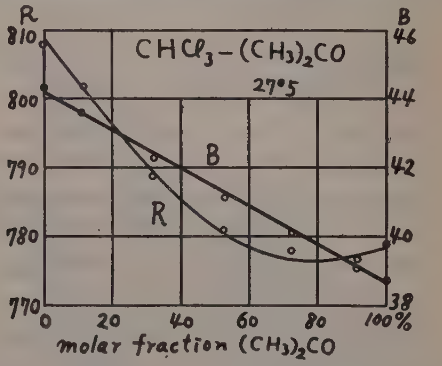

Fig. 8 b. Molecular sound velocity and molecular compressibility of mixtures of chloroform and acetone.

maximum.

The molecular sound velocity and the molecular compressibility, however, were found to be dependent on concentration (molar fraction) in a very regular manner than the sound velocity and the adiabatic compressibility. Table 1 summarizes the result of calculation as to the form of the R *vs.* molar fraction curves and that of the B *vs.* molar fraction curves. Fig. 1 a∼10 b show some representative examples of the dependence of ρ, V, and β, and of R and B on concentration (molar fraction). These figures contain the mixtures belonging to all the 6 groups, above cited.

As is to be seen in the table, many of the mixtures exhibit linear dependence of molecular sound velocity on concentration (molar fraction) with an accuracy of within 0.5 %, which is presumably of the order of accuracy of the experiments. There are, however, mixtures in which R deviate from linear relationships and there is apparently no close connection between this non-linearity and any presumable types of the molecular interactions as the formation of intermolecular compounds, dipole interactions, etc. (Water-alcohols are exceptions; cf. below.)

For example, Fig. 1 b shows a complete linear relationship in the highly interacting water-formic acid mixture. (This mixture was investigated by Mikhailov⁹⁾ and the discontinuous velocity changes at concentrations corresponding to the ratios 1 : 1 and 1 : 2 of numbers of molecules (cf. Fig. 1a) are attributed to the formation of intermolecular compounds. The viscosity data also show irregularities at these concentration.) R_{cal} in the figure indicates the

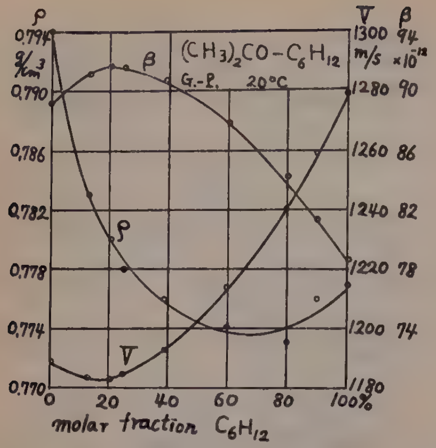

Fig. 9 a. Dependence of density, sound velocity and adiabatic compressibility on concentration in acetone-cyclohexane mixtures (Gabrielli-Poiani, ca. 20°C).

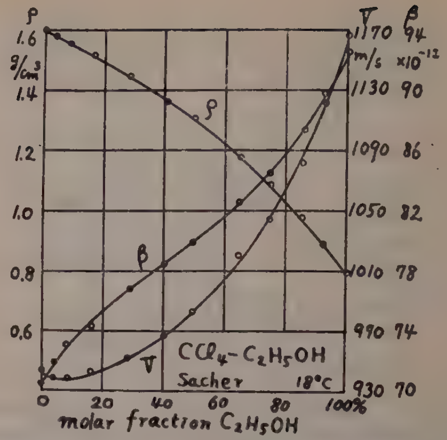

Fig. 10 a. Dependence of density, sound velocity and adiabatic compressibility on concentration in carbon tetrachloride-ethyl alcohol mixtures (Sacher, 18°C).

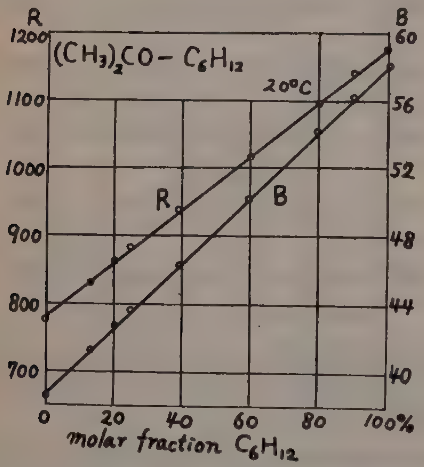

Fig. 9 b. Molecular sound velocity and molecular compressibility of mixtures of acetone and cyclohexane.

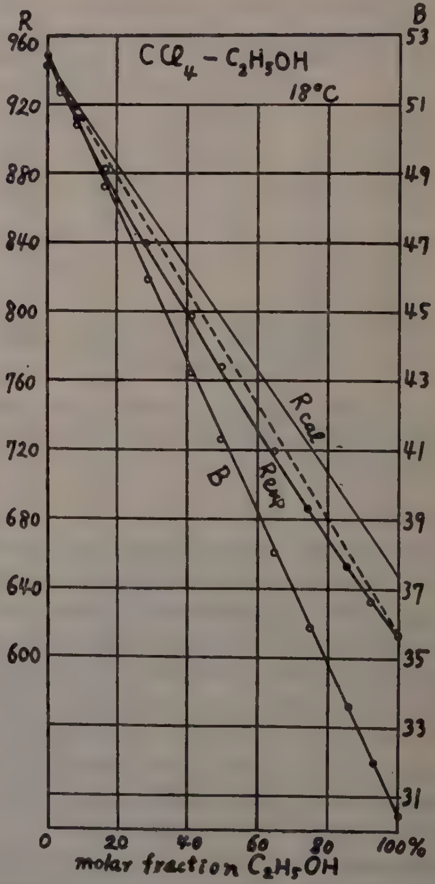

Fig. 10 b. Molecular sound velocity and molecular compressibility of mixtures of carbon tetrachloride and ethyl alcohol.

values computed by employing the additivity rule (2) and employing Rao's values of the atomic increments, while R_{exp} indicates the values obtained from (1) by employing the number average molecular weight for M. The cause of discrepancy between R_{cal} and R_{exp} ($R_{\text{cal}} > R_{\text{exp}}$) in pure liquids is usually attributed to the effect of molecular association (cf. Weissler [23]).

It is observed that the R *vs.* molar fraction curves become concave upwards in mixtures containing one heavy component (such as carbon tetrachloride ($\rho=1.589$ at 25°C) and chloroform ($\rho=1.484$ at 20°C) and one light component. If both are heavy liquids (chloroform-carbon tetrachloride mixtures), the R-curve remains linear. There is no exception for this rule. The deviation from linearity due to this cause (large difference in density

Table I

Types of velocity Curves	Liquid-Mixtures	*R vs.* molar fraction curve	*B vs.* molar fraction curve	Authors of sound velocity data (cf. also Sette (8))
I. With maximum of sound velocity and minimum of adiabatic compressibility	1. water-formic acid	linear	linear	Mikhaïlov (9)
	2. water-acetic acid	linear	linear	Mikhailov (10)
	3. water-acetone	linear	linear	Rao (11)
	4. water-methanol	slightly convex upwards	slightly convex upwards	Pesce-Giacomini (12) Parshad (13)
	5. water-ethanol	〃	〃	Parshad (13)
	6. water-propanol	〃	〃	Parshad (13)
II. Sound velocity is convex upwards and adiab. compress. is concave upwards	7. nitrobenzene-ethanol	linear	linear	Gabrielli-Poiani (14)
	8. nitrobenzene-methanol	linear	linear	Gab.-Poi. (14)
	9. ethanol-aniline	linear	linear	Gab.-Poi. (15)
	10. benzene-acetone	linear	linear	Tuomikoski-Nurmi (16)
III. With points of inflection for sound vel. and adiab. com.	11. benzene-ethanol	linear	linear	Tuomikoski-Nurmi (16)
IV. Sound velocity is linear	12. benzene-ethyl ether	(linear)*	(linear)	Parshad (17)
	13. carbon tetrachloride tetraline	concave upwards	(linear, irregular)	Parthasarathy (18)
	14. nitrobenzene-toluene	(linear)	(linear)	Gabrielli-Poiani (14)
V. Sound velocity is concave upwards	15. benzene-dichloromethane	slightly concave upwards	linear	Tuomikoski-Nurmi (16)
	16. chloroform-benzene	concave upwards	linear	Gabrielli-Poiani (14)
	17. benzene-carbon tetrachloride	concave upwards	linear	Tuomikoski-Nurmi (16)
	18. benzene-chlorobenzene	linear	linear	Tuomikoski-Nurmi (16)
	19. benzene-carbon disulfide	linear	linear	Tuomikoski-Nurmi (16)
	20. benzene-toluene	linear	linear	Gabrielli-Poiani (14)
	21. heptane-benzene	linear	linear	Tuomikoski-Nurmi (16)
	22. heptane-chlorobenzene	linear	linear	Tuomikoski-Nurmi (16)
	23. n. heptane-n. buthanol	linear	linear	Wilson-Richards (19)
	24. heptane-carbon tetrachloride	concave upwards	linear	Tuomikoski-Nurmi (16)
	25. ethyl acetate-carbon tetrachloride	(irregular)	(irregular)	Parthasarathy (18)
	26. carbon disulfide-carbon tetrachloride	linear	linear	Parth. (18)
	27. chloroform-carbon tetrachloride	linear	linear	Gabrielli-Poiani (14)
	28. chloroform-acetone	concave upwards	linear	Parshad (20)
	29. ethanol-ether	linear	linear	Gabrielli-Poiani (15)
	30. methanol-ether	linear	linear	Gab.-Poi. (15)
	31. ethanol-cyclohexane	linear	linear	Gab.-Poi. (15)
	32. nitrobenzene-aniline	linear	linear	Gab.-Poi. (15)
VI. With minimum of sound velocity	33. heptane-ethanol	linear	linear	Tuomikoski-Nurmi (16)
	34. heptane-dichloromethane	linear	linear	Tuomikoski-Nurmi (16)
	35. acetone-cyclohexane	linear	linear	Gabrielli-Poiani (15)
	36. carbon tetra-chloride-ethanol	concave upwards	linear	Sacher (21)
	37. chloroform-ether	concave upwards	(linear)	Parshad (20)

* The word in parentheses, (linear), means that the result is of somewhat greater error (more than 0.5%).

of the constitutive liquids) does not take place for the *B*-curves (cf. Table 1 and Fig. 6 b, 8 b, 10 b).

Fig. 6 b (benzene-carbon tetrachloride mixture, Group V), Fig. 8 (chloroform-acetone, group V mixture), and Fig. 10 b (carbon tetrachloride-ethyl alcohol, group VI mixture) are the examples in which the *R*-curves become concave upwards. In the case of choroform-acetone mixtures, the *R*-curve shows even a minimum (Fig. 8b). The *B*-curves, however are linear in all these cases. Usually the deviation of *R*-curves from linearity in such mixtures is rather slight and Fig. 10 b is an typical example in this respect, while Fig. 6 b and 8 b are rather particular cases in which the deviation from linearity is extremely great.

The other Figures (except Fig. 2 b) show the perfect linearity of both *R vs.* molar fraction and *B vs.* molar fraction curves:

Fig. 1 b. water-formic acid (type I mixture),
Fig. 3 b. nitrobenzene-ethyl alcohol
(type II mixture),
Fig. 4 b. benzene-ethyl alcohol
(type III mixture),
Fig. 5 b. heptane-ethyl ether
(type IV mixture),
Fig. 7 b. benzene-carbon disulphide
(type V mixture), and
Fig. 9 b. acetone-cyclohexane
(type VI mixture).

The only exception are the water-alcohol mixtures (water-methanol, water-ethanol, water-propanol), in which both *R*- and *B*-curves deviate slightly upwards from the straight lines, particularly in the lower concentration regions where the sound velocities exhibit the maxima. Fig. 2 b shows an example of this case (water-methyl alcohol).

This may be explained as due to the decrease in molecular association of water and of alcohol molecules by the mutual interaction of the molecules of water and alcohol, as proposed by Parshad[22]. The values of *R* in water and in alcohol are lower than the ones computed from the additivity rule (2) or (3), and the effect of association is supposed to be the cause of these low values (cf. Weissler[23]). The decrease in association will cause *R* to increase and approach the normal value in greater or less extent.

A few of the mixtures showed irregular behavior of the *R*- and *B*-curves (especially the ethyl acetate—carbon tetrachloride mixture). The reason for this is not clear, but the author is inclined to believe that this is due to the inaccuracy of velocity determinations in these mixtures.

§ 3. Conclusion

Up to the present time, the known properties of molecular sound velocity are mainly of empirical nature and no firm theoretical basis is given to them. As to the molecular compressibility, almost nothing is known. The linear dependence of *B* (and in many cases also of *R*) on molar fraction elucidated above may also be interpreted after a thorough theoretical knowledge of these quantities in pure liquids is obtained. These relationships, however, may be of practical use in computing the sound velocity from known value of the density, or the density from known value of the sound velocity in liquid mixtures except water-alcohol systems. The deviation from linearity of *B*-curve in water-alcohol systems may throw some light in elucidating the molecular interaction in these systems.

References

1) Rama Rao: Indian J. Phys. **14** (1940) 109.
2) Rama Rao: J. Chem. Phys. **9** (1941) 672.
3) R. T. Lagemann and J. E. Corey: J. Chem. Phys. **10** (1942) 759.
4) R. T. Lageman, J. S. Evans and D. R. McMillan, jr.: J. Amer. Chem. Soc. **70** (1948) 2996.
5) Yasaku Wada: J. Phys. Soc. Japan **4** (1949) 280.
6) N. Utter et R. Kling: C. R. **227** (1949) 41.
7) K. S. Iyengar: Proc. Indian Acad. Sci., **35A** (1952) 190.
8) D. Sette: Ricerca Scientifica **19** (1949) 1338.
9) I. G. Mikhailov: C. R. (Doklady) URSS. **31** (1941) 550.
10) I. G. Mikhailov: C. R. (Doklady) URSS. **31** (1941) 324.
11) R. B. Ramachandra Rao: Proc. Indian Acad. Sci. **25A** (1947) 190.
12) B. Pesce e A. Giacomini: Ricerca Scientifica **11** (1940) 619.
13) R. Parshad: Indian J. Phys. **15** (1941) 323.
14) I. Gabrielli et G. Poiani: Colloquium over ultrasonore trillingen. (1951) 234.
15) I. Gabrielli e G. Poiani: Ricerca Scientifica **22** (1952) 1426.
16) P. Tuomikoski and U. Nurmi: Comment. Phys. Math. Helsingf. **10** (1940) 11.
17) R. Parshad: Indian J. Phys. **16** (1942) 1.
18) S. Parthasarathy: Proc. Indian Acad. Sci. **3A** (1936) 297.
19) E. B. Wilson and W. T. Richards: J. Phys. Chem. **36** (1932) 1268.
20) R. Parshad: Indian J. Phys. **16** (1942) 307.
21) K. Sacher: Phys. Zeits. **41** (1940) 360.
22) R. Parshad: J. Acous. Soc. Amer. **20** (1948) 66; J. Chem. Phys. **15** (1947) 418.
23) A. Weissler: J. Chem. Phys. **15** (1947) 210.

Short Notes

J. PHYS. SOC. JAPAN 8 (1953) 561~562

Paramagnetic Resonance Absorption of Mn^{++} Impurity in Salts of Ni^{++}, Co^{++} and Fe^{++}, and Spin-Lattice Relaxation

By Kazuo ŌNO and Izuo HAYASHI

Institute of Science and Technology
University of Tokyo

(Received April 13, 1953)

It is reported by several authors[1] that the manganese ion, when diluted by nonmagnetic ions, shows fine and hyperfine structure in its resonance absorption spectrum and its separated absorption lines are sharp (width of about 10 gauss), owing to the reduction of dipole-dipole interaction between Mn^{++} ions. We, therefore, can observe the detailed structures of absorption lines at room temperature in this case since the spin-lattice coupling of Mn^{++} is expected to be small owing to its zero orbital angular momentum.

For the case of Mn^{++} ion added artificially, as an impurity, to Tutton salts $(R(NH_4)_2(SO_4)_2\cdot 6H_2O)$ of some sorts of magnetic ions i. e., Ni^{++}, Co^{++} and Fe^{++}, we have observed experimentally the similar fine and hyperfine structures due to Mn^{++} as above, whereas, for the case of Mn^{++} added to some salts of Cu^{++} ion ($CuSO_4\cdot 5H_2O$ or $Cu(NH_4)_2(SO_4)_2\cdot 6H_2O$) such detailed structures of the resonance absorption could not be observed in our measurements. The wave length of the microwave used is 3.1 cm.

The observed fine and hyperfine separations are almost the same in any salts mentioned above, but the widths of the absorption lines are somewhat larger than those in salts diluted by nonmagnetic ions. Especially in the case of nickel Tutton salts, the line width of Mn^{++} is found to be rather broad ($\sim$50 gauss) and its intensity is fairly small. That is, integral $\int \frac{\chi''}{\nu} d\nu \doteqdot \int \frac{\chi''}{H} dH$ of Mn^{++} absorption in Ni^{++} Tutton salts is about 15% of that in nonmagnetic salts, although the mentioned integrals $\left[\int \frac{\chi''}{\nu} d\nu \doteqdot \int \frac{\chi''}{H} dH \text{ of } Mn^{++} \text{ absorption}\right]$ in Co^{++} and Fe^{++} Tutton salts are comparable with those in Zn^{++} or Mg^{++} Tutton salts.

Bleaney and others[2] have reported the interesting features of gadolinium ion embedded in neodymium-, cerium- and samarium-ethyl-sulphates, of which absorption lines are as sharp as those in nonmagnetic ions at room temperature, in spite of the fluctuating magnetic field induced by the neighbouring magnetic ions. According to Bleaney et al such situation may be ascribed to the fact that the spin lattice relaxation times of the predominant ions are short compared with the Larmor precession period of gadorinium ion and thus the average local field acting upon Gd^{+++} becomes negligibly small.

The similar interpretation may be valid for our case of the Tutton salts of Co^{++} and Fe^{++} containing Mn^{++} as an impurity. At room temperature, the spin lattice relaxation times of Co^{++} and Fe^{++} are so short that their own absorption lines are too broad to be observed. When cobalt Tutton salt was cooled to 100° K, we have in fact observed the considerable broadening of manganese impurity spectrum. This is consistent with the appreciable appearance of cobalt resonance absorption[3] at this temperature. In case of Cu^{++} salts, in which Mn^{++} impurity lines have not been observed, the spin lattice relaxation time in Cu^{++} will be moderately[4] long, so that we are able to observe the resonance of Cu^{++} at room temperature.

On the other hand, the resonance lines in nickel ions (the line width$\approx$600 gauss) have been actually observed at room temperature although we have been unable to observe the resonance in Co^{++} or Fe^{++} Tutton salts at the mentioned temperature. Although the resonance lines of Mn^{++} impurity in nickel Tutton salts have been observed at room temperature, the appreciable broadening or nallowing of the lines by cooling the salts from 300° K to 100° K could not been observed. These behaviours of nickel Tutton salts containing Mn^{++} impurity are rather complicated as compared with those of Fe^{++} or Co^{++} Tutton salts, and it is doubtful whether the spin lattice relaxation alone is responsible for these behaviours of nickel Tutton salts containing Mn^{++}. In addition, in nickel fluosilicates ($NiSiF_6\cdot 6H_2O$), we could not observe the spectra of Mn^{++} impurity, but the broad line by Ni^{++} ions has been actually observed.

Now, the initial splittings between adjacent levels of the spin triplet of Ni^{++} are $0.75\,\text{cm}^{-1}$ and $1.85\,\text{cm}^{-1}$ in the case of Tutton salts[5] and $0\,\text{cm}^{-1}$ and $0.5\,\text{cm}^{-1}$[6] in the case of fluosilicates, while the initial splitting in Cu^{++} is zero (Kramers degeneracy). It must be noted that the quantum energy of our microwave ($0.33\,\text{cm}^{-1}$) is much smaller than the initial splittings in Ni^{++} Tutton salts, but it is comparable or larger than those in Ni^{++} fluosilicates or salts of Cu^{++}. The origin of appearance of Mn^{++} impurity spectra in nickel Tutton salts, therefore, may be mainly ascribed to the relatively large initial splittings compared with the quantum energy of microwave used.

Our thanks are due to Professor Hiroo Kumagai for his continuous guidance and encouragements throughout this work. We wish to express our appreciation to Professor Toshinosuke Mutō for his cordial discussions.

References

1) B. Bleaney and D. J. E. Ingram: Proc. Roy. Soc. **205** (1951) 336.
H. Kumagai, K. Ōno and I. Hayashi: Phys. Rev. **87** (1952) 374.
I. Hayashi and K. Ōno: J. Phys. Soc. Japan **8** (1953) 270.

2) B. Bleaney ane H. F. D. Scovil: Proc. Phys. Soc. **A 64** (1951) 993.

3) B. Bleaney and D. J. E. Ingram: Proc. Roy. Soc. **208** (1951) 143.

4) D. M. S. Bagguley and J. H. E. Griffith: Proc. Phys. Soc. **A 65** (1952) 594.

5) J. H. E. Griffith and J. Owen: Proc. Roy. Soc. **213** (1952) 459.

6) A. N. Holden, C. Kittel and W. A. Yagar: Phys. Rev. **75** (1949) 1443.
R. P. Penrose and K. W. H. Stevens: Proc. Phys Soc. **A 63** (1950) 36.

J. Phys. Soc. Japan **8** (1953) 562～563

Electron Emission from Mo by Ion Bombardment

By Jun Okano

Department of Physics, Faculty of Science, Osaka University, Osaka, Japan

(Received May 9, 1953)

Secondary electron emission by electron bombardment has been studied experimentary and theoretically by numerous workers, and electron emission from metals by alkali and noble gas ion bombardment has also been studied experimentally. But few experiments have been made with other kinds of ions. In this experiment the author has attempted to measure the total yields for secondary electron emission from a Mo target by various kinds of atomic and molecular ion bombardment.

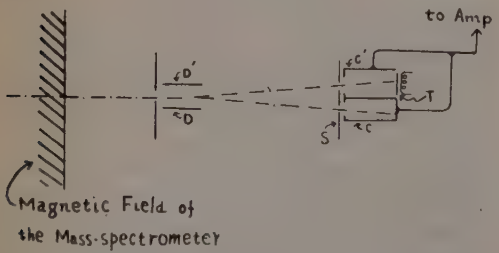

Fig. 1. Schematic diagram of the arrangement of the electrodes near the target. T, target; C, ion collector: C′, electron collector; S, slit; D and D′, deflector electrodes.

A double focussing mass-spectrometer was used, whose central beam radius is 7.0 cm in the electric field and 6.0 cm in the magnetic field. The deflection angle of the ion beam is 90° for each field and the resolving power of this apparatus is about 50. Ion currents at the ion collector are of the order of 1×10^{-11} amp. The target and the collector are shown schematically in Fig. 1.

The target was degassed by the tungsten heater which was placed close to the back of the bombarding surface. Secondary electrons from the target were collected by the electron collector C′ which was connected electrically to the ion collector C. After passing through both fields, ion beams were deflected to the ion collector C or to the target T by the deflecting electrodes D, D′ and the primary ion currents and the secondary electron currents were measured alternately. The yields, which are denoted by γ_1 were obtained from the mean of about ten values for the ratio of the two currents. The pressure remained less than 3×10^{-5} mm Hg during this experiment.

The target was degassed at about 500° C for several hours. By degassing the target, γ decreased by 55% below the initial value, but during one or two hours after degassing it was observed to increase again gradually up to a saturation value. This saturation value was about 25% above the value measured immediately after degassing. The increase of γ after degassing seems to be due to the contamination by the residual gas on the target. The saturation value of γ is constant at 10^{-5} mm Hg and even if the target is exposed to atmospheric pressure during several days, by repeating the degassing process, this saturation value of γ may be obtained reproducibly within a few percent error. In this experiment γ was obtained at the saturation point which may be considered to be for the surface with a little contamination by residual gas, mainly that of hydrocarbons from the diffusion pump.

The relation between γ and ion energy was obtained for A^+ on Mo target in the energy range from 700 eV to 1000 eV. γ increased linearly about 40% from the value at 700 eV up to 1000 eV. For the non-degassed target this increase of γ with the increase of ion energy was larger than that for the degassed target, which is consistent qualitatively with the results obtained by others.[1),2),3),4)]

In Fig. 2, the values of γ of a Mo target for various kinds of ions with 1000 eV energy, were plotted against their mass. There are several interesting points in the results given in Fig. 2. First, γ decreases with increasing mass of ions or molecules. γ for isotopes, Cl^{35} Cl^{37}, K^{39} K^{41} is slightly smaller for heavier isotopes, which seems to be purely a mass effect. This tendency of the γ-mass relation is qualitatively consistent with the results by others.[5),6)] Secondly, for atomic ions the variation of γ with different ions is very similar to that of their ionization potentirl as shown in Fig. 2. From these results it could be inferred that the potential ejection mechanism may play an important role in this case, studied by Oliphant and Moon,⁵⁾ Massey,⁶⁾ Cobas and Lamb,⁷⁾ and Hagstrum.⁸⁾ γ for Si and for N_2 are not the same despite their mass being almost the same, but the molecular ion shows a somewhat larger value than the atomic ion. The same tendency was observed for S and O_2. For a doubly charged A ion the yield per positive ion is 140% larger than that for a singly charged A ion. In this apparatus, doubly charged ions have twice the energy of singly charged ions. If the energy $-\gamma$ curve for A^+ is extrapolated up to 2000 eV, the value of γ for A^+ at 2000 eV is almost equal to that for A^{++} at 1000 eV. But whether the large value for A^{++} is mainly due to the excess energy or due to other effect is not clear. The values of γ for O, OH, OH_2, as well as those for S, SH, SH_2 are very nearly equal as shown in Fig. 2, but the reason for this is unknown.

The experimental error and reproducibility for each γ were less than a few percent. The correction for the reflection of ions at the target was not involved in these data. No correction was made for the ratio of the ion currents reaching the ion collector and the target.

A detailed description of this experiment will be published soon in another paper. The author wishes to express his deep gratitude to Dr. K. Ogata for his guidance and valuable suggestions. Also the author is greatly indebted to Mr. Matsuda and Mr. Hayashi for constructing the amplifier.

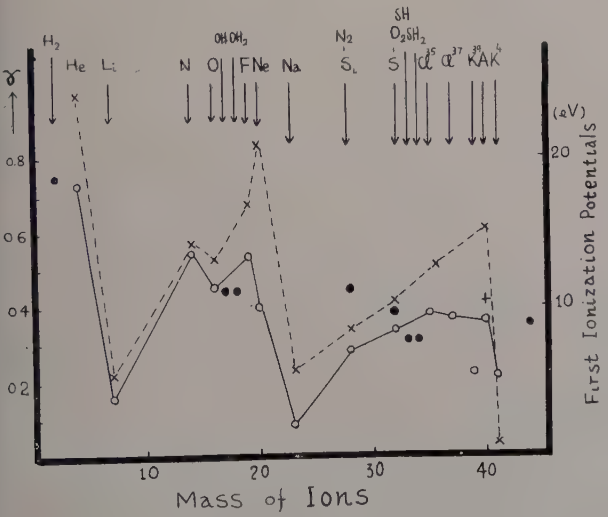

Fig. 2. γ for various kinds of ions. —○—, γ for atomic ions; ●, γ for molecular ions; +, γ for A^{++} ions; ···×···, first ionization potentials of the elements.

Reference

1) H. Healea and E. Chaffee: Phys. Rev. **49** (1936) 925.
2) J. S. Allen: Phys. Rev. **55** (1936) 966.
3) M. Healea and C. Houtermans: Phys. Pev. **58** (1940) 609.
4) W. Ploch and W. Walcher: Zeits. f. Physik **130** (1951) 174.
5) M. L. E. Oliphant and P. B. Moon: Proc. Roy. Soc. (London) **A 127** (1930) 388.
6) H. S. W. Massey: Proc. Cambridge Phil. Soc. **26** (1930) 386.
7) A. Cobas and W. E. Lamb: Phys. Rev. **65** (1944) 327.
8) H. D. Hagstrum: Phys. Rev. **89** (1953) 244.

J. Phys. Soc. Japan **8** (1953) 563~565

High Speed Elongation of Long Test-Piece of Rubber*

By Shin-ichi Hyodo

Department of Physics, Faculty of Science, University of Tokyo

(Received May 23, 1953)

Several types of machine have hitherto been devised by various investigators to measure short time stress strain characteristics of rubber. These machines, however, are not satisfactory for the following points; because of the smallness of the test-pieces used, the absolute displacement of the stretched end is not so large and the elimination of the shape-factor for clamped end is difficult, although the elongation rate can attain a considerably great value. To overcome these difficulties the writer has made an apparatus applying the explosion of gunpowder, as is illustrated in Fig. 1.

A kind of harpoon (H) is fired out which draws a long dumbell test-piece and tears is it off within 0.1 second or so. The length of the narrow part of the test-piece is 32 cm, and its cross section is about 7 mm² in area. The following table gives the composition and curing condition of the five stocks used.

The stress produced is mechanically communicated to a pair of quartz plates and the variations of the electrical potential are recorded on an electromagnetic oscillograph through a D. C. amplifier. The elongation of the test-piece is simultaneously recorded by means of the step-like change of electrical current which is induced by the harpoon cutting each fine cupper wire fixed parallel at regular intervals.

Fig. 2 presents an example of the photograms

---

* Read at the annual meeting of the Physical Society of Japan on Oct. 30, 1952.

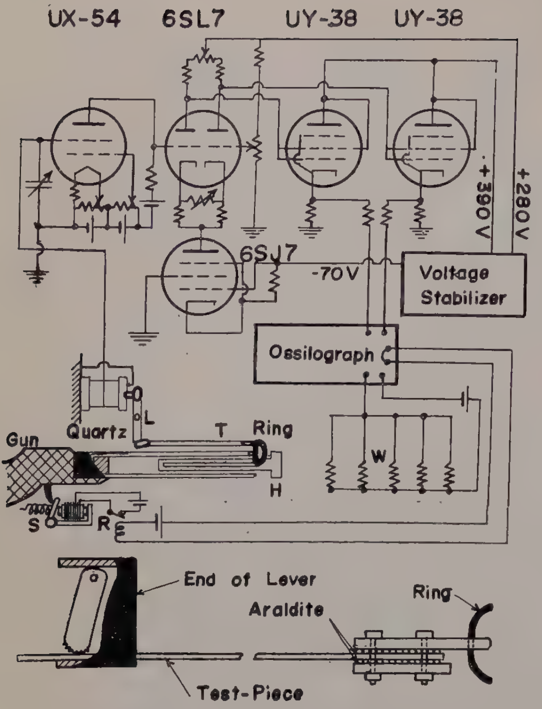

Fig. 1. Apparatus.

H: Harpoon
R: Relay
L: Lever
S: Spring
P: Gunpowder
W: Fine Cupper Wire

Stock No.	I	II	III	IV	V
Hevea	100	100	100	100	100
Channel Black	0	50	50	50	100
Stearic Acid	1	1	1	1	1
Sulphur	1	1	1	1	1
D M	1	1	1	1	1
Phenyl-β-naphtylamine	1	1	1	1	1
Zinc Oxide	5	5	5	5	5
Cure (135°C)	30 min.	20 min.	30 min.	40 min.	30 min.

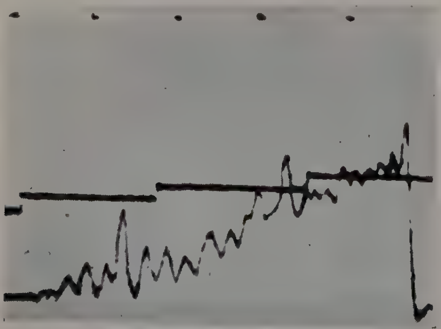

Fig. 2. Photogram.

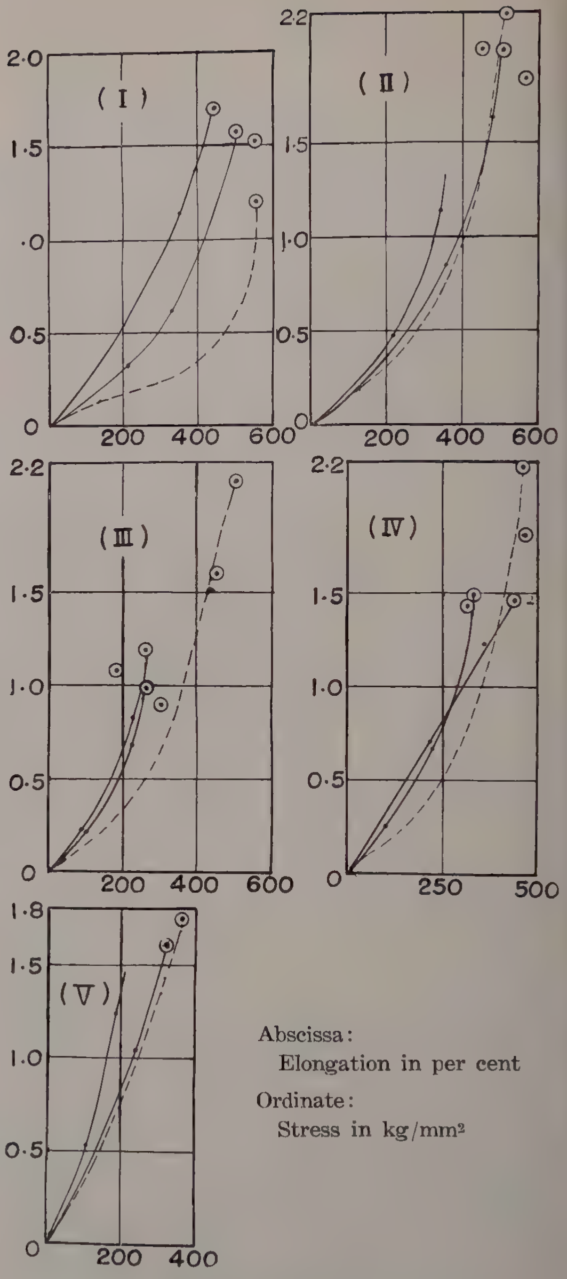

Abscissa:
Elongation in per cent
Ordinate:
Stress in kg/mm²

Fig. 3. High Speed Stress-Strain Curve.
◉: Breaking Point
Each broken line shows the mean value measured statically for five random samples from each stock.

thus obtained. The small oscillations of high frequency superposed in the oscillogram are probably due to the effect of the explosion of gunpowder which is propagated to the oscillograph through both the air and the floor, although the recording table is floated on soft inflated rubber balls.

The mode of these small oscillations, however, is quite independent to the various stages of stretching of the specimen and it seems reasonable to assume that the time mean of these subsidary oscillations is zero, so we can presume the true stress-strain curve by graphical analysis or, more accurately, by K. Takahashi's mathematical method.1)

The stress-strain curves until break for five kinds of stocks are plotted in Fig. 3. It is to be noted that general trend of these curves at high rates of elongation tends to upbend more acutely than at slow rates. This fact seems to contradict with the results reported by D. Villars,2) although his curves were obtained at the stretching rate of 36 %/msec., while the present data at the average rate, 4~12 %/msec. In the present experiment the velocity of the stretching harpoon is about 40 m/sec at first, and about 10~15 m/sec when the test-piece breaks off.

The writer wishes to express his best thanks to Prof. M. Hirata for his helpful guidance and to Dr. H. Tohara of the Railroad Research Institute and Dr. S. Nakano of the Meiji Rubber Manufacturing Company for preparing the specimens.

Reference

1) K. Takahashi: Bullet. Inst. Phys. Chem. Res. **14** (1935) 255.
2) D. Villars: J. Appl. Phys. **21** (1950) 565.

J. PHYS. SOC. JAPAN 8 (1953) 565

Corrections to our paper "On a Non-linear Approximation of the Interatomic Force in Solid"

By Junkichi SOMA and Masamichi OGI
Hokkaido University

(Received March 20, 1953)

The following corrections should be made in our paper which appeared in Vol. 8, No. 1 (1953) of this Journal.

We have got $\bar{x}=(kT/4a^2D)_\varepsilon$ in our paper, but correct calculation shows us $\bar{x}=\frac{3}{2}(kT/4a^2D)_\varepsilon$.1) Then we must multiply the final calculated values of the thermal expansion coefficients by 1.5. This correction diminishes slightly the degree of the agreement between the calculated values and experimental ones.

1) We thank Mr. A. Sugiyama who has suggested us the error in our calculation by his private communication.

J. PHYS. SOC. JAPAN 8 (1953) 565~567

The Influence of Impurity Atoms on Flicker Noise2)

By Yoshio INUISHI & Yang Tsung-Che
Faculty of Engineering, Osaka University

(Received December 11, 1952)

One of the authors has been engaged in the researches on "contact noises" including those from carbon resistors, semiconductor rectifiers and flicker effect in vacuum tubes. We have tried to unify various forms of "contact noises" to one common mechanism in our previous papers.1) 2) That is, they are generated through modulation of the electron current by the density fluctuation of some external "fluctuating agent" at interfaces, e. g. surface Th-atoms in thoriated tungsten cathode, and ionized impurity atoms in blocking layer of semiconductor rectifier. This idea was first proposed by Schottky3) and is generally accepted by recent authors.4) 5)

From this stand-point we can obtain the relation between noise and fluctuating atom density n.1) 2) If the current i through a sample under at applied voltage v is represented by an analytic function of v and fluctuating atom density n,

$$i=f(v,\ n)\,, \qquad (1)$$

then the mean square deviation of i by the fluctuation of n becomes

$$<\Delta i^2>=\left(\frac{\partial f}{\partial n}\right)^2_v\cdot<\Delta n^2> \qquad (2)$$

$$=\left(\frac{\partial f}{\partial n}\right)^2_v\cdot<n>\,, \qquad (3)$$

(3) is deduced from (2) by statistical mechanics when n is canonical ensemble.4) Next, we may give some special form of function $f(v,\ n)$ to (3).

(I) $$i=n^{\alpha}\cdot f(v)\,, \qquad (4)$$

then (3) gives

$$<\Delta i^2>=\alpha^2\cdot i^2\cdot\frac{1}{<n>}\,. \qquad (5)$$

Equation (4) is valid for

(a) barrier in semiconductor rectifier, provided n is the density of ionized impurity atom and $\alpha=\frac{1}{2}$, and

(b) emission from oxide cathode, provided n is excess barium density and $\alpha=\frac{1}{2}$. We may call those noise $1/<n>$ type.

(II) $$i=\exp(\beta\cdot n)\cdot f(v)\,, \qquad (6)$$

in this case, (3) becomes

$$<\Delta i^2>=\beta^2\cdot i^2\cdot<n>\,, \qquad (7)$$

(7) behaves quite oppositely concerning n, and may be called $<n>$ type hereafter. Equation (6) may be valid for the fluctuation of potential barrier shape caused by impurity or absorbed atoms.

We have tried to examine the relations (5) or (7) experimentally for flicker noise at the temperature-saturated diode emission. Two kinds of diodes were used, (i) thoriated tungsten cathode and (ii) barium oxide coated cathode. Three or four tubes of each kind were prepared especially for this purpose by the courtesy of our colleague assistant professor J. Nakai. Apparatus used were CR coupled five stage 6AC7 amplifier with attenuator and filter, operated by batteries and stabilized source, square law type valve voltmeter, and ordinary electronic counting rate meter. All measurements were under temperature limited condition (place voltage 200 v), and noise was reduced to the short circuit noise current $\Delta I_s=\sqrt{<\Delta i^2>}$. First, virgin ThO+W cathodes were flashed and aged increasing their activity from very poor emission to 100 fold value, then again flashed to poor activation. Degrees of Activation were represented quantitatively by the emission current at a definite filament current 2.2 A and denoted by A.

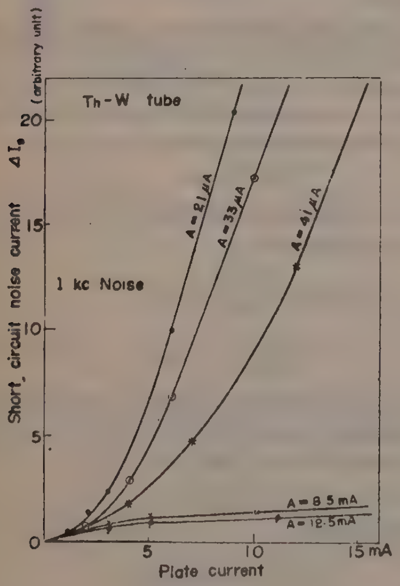

Fig. 1.

Fig. 1. shows the relation between short circuit noise current $\sqrt{<i^2>}$ and plate current i taking the degree of activation A as parameter. The figure shows that the short circuit noise current decreases with increasing degree of activation or surface Th-atom density, and reduced to only shot noise when throughly activated. Here we try to examine this theoretically. As suggested by Schottky,[3] arrival of one Th-atom at surface lowers the work function of its neighbour by its positive charge. Let us denote P, $\phi(n)$ are work function decrement by one Th-ion at its nearest site and by surrounding Th-atoms respectively.

If there are N sites for surface Th-ion, and n of those are occupied, then total emission is

$$i=n\cdot a\cdot e^{+(\phi(n)+P)/kT}+(N-n)ae^{+\phi(n)/kT}, \quad (8)$$

combining (3) & (8), the short circuit noise becomes

$$\left.\begin{aligned}<\Delta i^2>&=i^2\left\{+\frac{\partial\phi/\partial n}{kT}+\frac{(1-b)}{\{n+(N-n)b\}}\right\}^2\cdot<n>,\\ b&=\exp(-P/kT).\end{aligned}\right\} \quad (9)$$

Considering experimental results, the first term in the parenthesis may be neglected unless many Th-atoms appear or disappear simultaneously, then

$$<\Delta i^2>=i^2\cdot\frac{(1-b)^2}{\{n+(N-n)b\}^2}\cdot<n>, \quad (10)$$

thus starting $<\Delta i^2>\doteq 0$ for pure tungsten ($n=0$), there is maximum noise for

$$\left.\begin{aligned}n&=N\cdot\frac{b}{(1-b)},\\ <\Delta i^2>_{\max}&=\frac{i^2(1-b)}{4Nb}.\end{aligned}\right\} \quad (11)$$

passing through the maximum, $<\Delta i^2>$ decreases as

$$<\Delta i^2>\fallingdotseq i^2/n \qquad \text{if } b\ll 1 \quad (12)$$

which belongs to $1/<n>$ type of (5), since we define the degree of activation A as the emission at some define low temperature, A must be approximately proportional to n from (8). So from (12) $<\Delta i^2>$ must be inversely proportional to A but this is not so good contented with experimental results of Fig. 1 quantitatively. In the second place, varying the activity A of BaO-Ni cathode by flashing, the short circuit noise current $\sqrt{<\Delta i^2>}$ was measured under the same plate current as is shown in Fig. 2. Here also A is represented by emission current at a definite low filament current 0.31 A. In this case the emission current is written as a function of excess barium density n,

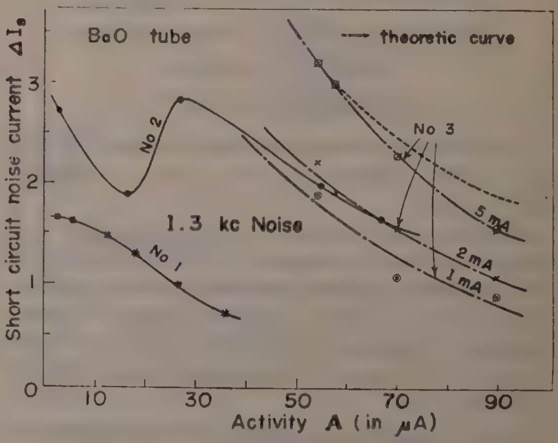

Fig. 2.

$$i=n^{1/2}DaT^{5/4}\exp(-\phi/kT), \quad (13)$$

D: transmission coefficient
ϕ: work function
a: constant

this belongs to equation (4), then

$$<\Delta i^2> = \tfrac{1}{4}\cdot i^2(1/<n>)\,,$$

from (13), activation A defined by us is proportional to $n^{1/2}$, therefore

$$\Delta I_s{}^2 = <\Delta i^2> \propto (i^2/A^2)\,, \qquad (14)$$

This relation is well fitted to the experimental data as shown in Fig. 2. So such a mechanism seems to be correct, but as is mentioned previously, barrier noise generated from interface between Ni and BaO also is expected to obey (14) theoretically.

We are now engaged in the experiment to make clear this point, which will be published in near future.

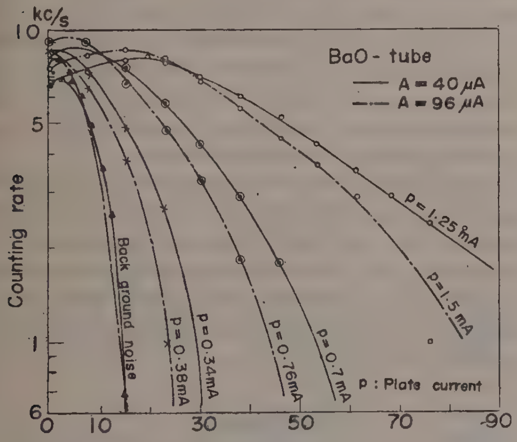

Fig. 3.

Fig. 3 shows the results of pulse size-frequency distribution by counting rate meter. Ordinate shows counting rate of noise pulses which have larger size than the corresponding discriminating voltage (abscissa) at various plate currents P. The shape of distribution are quite similar for Th-W tube. From Fig. 3 we can conclude that flicker noise has nearly Gaussian or Poissonian type distribution and that these results can be explained by the idea of modulation of electron current by some fluctuating agents.

In conclusion, the flicker noise decreases with activity or impurity atom density for both Th-W and BaO-Ni cathode. This may be explained from the theory to some extent.

References

1) Abstract of Meeting of Japanese. Inst. Elec. Eng. Oct. 1950, May 1952.

2) Read Before the annual Meeting of J. P. S. Nov. 1952 (Abstract 1. B. 1).

3) Schottky: Phys. Rev. **28** (1928) 74.

4) Richardson: B. S. T. J, **29** (1950) 117.

5) Du Pré: Phys. Rev. **78** (1950) 615.

J. Phys. Soc. Japan **8** (1953) 567~568

On "the Space Charge Effect" in Dielectric Breakdown of KCl Single Crystals

By Yoshio Inuishi and Tokuo Suita

Faculty of Engineering, Osaka University

(Received March 3, 1953)

In dielectric breakdown of alkalihalide single crystals, space charges play very important rôle as already pointed out by von. Hippel[1] & one of the authors[2].

In alkalihalide this space charge effect masks the intrinsic breakdown voltage, and makes it difficult to compare the experimental values with theoretical ones.

So that we have made several experiments on the mechanism of this effect concerning KCl single crystals[3].

Fig. 1 shows D.C., impulse and H.F. (400 KC) breakdown voltage as a function of temperatures for KCl. As is seen, D.C. value manifests very peculiar behaviour, or strongly temperature dependent having a maximum at 80-100°C, and much larger than other two forms of breakdown voltages at lower temperatures. These effects are to be ascribed to "the space charge effect" in D.C. breakdown. To prove these ideas, superimposed D.C.+impulse voltage was applied under various conditions. Fig. 2 shows the results. From Fig. 2 we can conclude following facts;

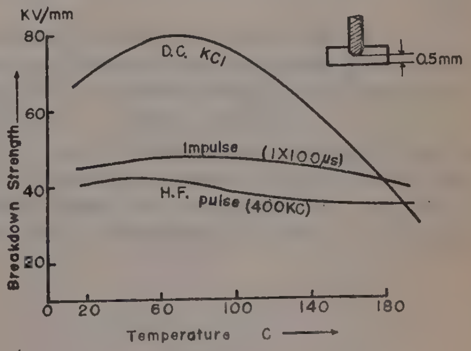

Fig. 1.

(1) Higer temperatures (200°C): breakdown occurs when DC+impulse voltage amounts to a definite value, or no "space charge effect" can be considered in this case. (Fig. 2a)

(2) Lower temperatures: in smaller D.C. values, breakdown occurs when D.C.+impulse amounts to

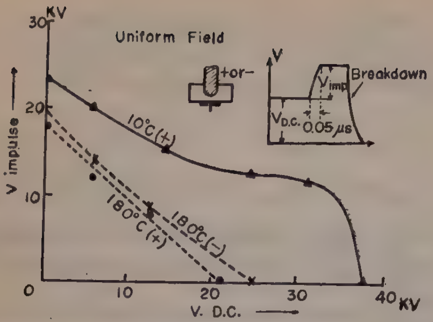

Fig. 2a.

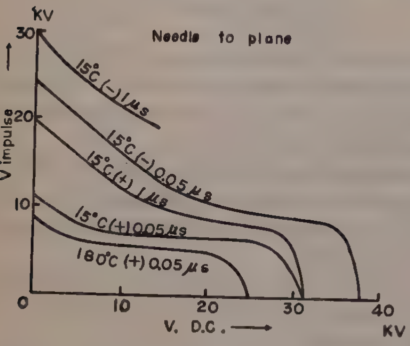

Fig. 2b.

a definite value equal to pure impulse breakdown voltage under the same condition. At higher D.C. voltage superimposed, impulse voltage to cause breakdown becomes considerably larger than the value which is expected from D.C.+impulse= constant.

Finally constant impulse value is required inspite of increasing D.C. superposed voltage near pure D.C. breakdown voltage. These facts may be ascribed to large "space charge effect" by superposed D.C. voltage to increase net breakdown voltage.

(3) Besides D.C. space charge effects, steepness of wave front, or dv/dt at wave front effects impulse breakdown voltage considerably1)3). (Fig. 2b)

(4) D.C. space charge effects become predominant when D.C. superposed voltage reaches to the pure impulse breakdown voltage, as is seen in Fig. 2. Observation of prebreakdown current by amplifier & oscilloscope shows that pulses due to avalanches starts at this D.C. voltage equal to pure impulse breakdown value. Therefore, at higher D.C. voltage "space charge" may be mainly of electronic origin, for instance removal of trapped electrons by higher electron temperature.4) In the second place, we examined the duration of this space charge effect.

D.C. voltage 10KV and 20KV were applied to the sample for 10 minutes, then removed. 4 minutes after removal of D.C. voltage, impulse voltage was applied on the same sample and breakdown voltage was obtained.

The mean value of pure impulse breakdown without D.C. pretreatment were 16KV, and after the D.C. pretreatment this came to 22 KV manifesting long remainning space charge effect.

This long remainning part of space charge effects was found to be readily annihilated by dipping the samples in 180°C oil bath for a few minutes. These facts resemble space charge effects in glass published by Keller3). So that migrated ions or vacancies and shallow traps due to ion migration seem to play important role for long enduring parts of the space charge.

To explain all these phenomena the authors have examined the electron or hole trapping by thus created traps, and it's effects on electron multiplication.3) Also, some imhomogenuity of electronic impurity level in samples seems to be considered. Detailed calculations on these points will soon be published in this journal.

References

1) A. von Hippel et. al.: Phys. Rev. **76** (1949) 127.

2) T. Suita: Tech. Rep. Osaka University, **1** (1951) 4, 51.

3) Y. Inuishi and T. Suita: Read before vernal meeting of J.P.S. May, 1952 (Discharge physics section).

4) H. Fröhlich et al: Proc. Phys. Soc. A **63** (1950) 6.

Errata

On the Changes in Contact Potential Difference of a Germanium Rectifier During the Electrical Forming

By Tatsuya NIIMI

J. PHYS. SOC. JAPAN **8** (1953) 324～330

As the author has erroneously calculated the numerical values of b from the experimental data, the numerical values of ΔV_D should be corrected as follows,

P. 324,	Synopsis,	line 5,	from 0.16 V	should be read	from 0.04_8 V to 0.05_7 V
	〃	line 6	0.06	〃	0.02_2
	〃	line 6	0.07	〃	0.02_5
	〃	line 7	0.04_2	〃	0.01_1
	〃	line 7	0.04_6	〃	0.01_4
P. 325,	L*	line 25	becam	〃	became
〃	R**	line 6	poyllycrystalline	〃	polycrystalline
P. 326,	L	line 17	0.96	〃	log. 0.96
	〃	line 20	0.07	〃	0.02_5
	〃	line 27	0.21	〃	0.05_7
P. 326,	R	line 5	0.04_6	〃	0.01_4
	〃	line 10	0.16	〃	0.04_8
	〃	line 10	02.1	〃	0.05_7
	〃	line 11	0.06	〃	0.02_2
	〃	line 11	0.07	〃	0.02_5
	〃	line 12	0.04_2	〃	0.01_1
	〃	line 12	0.04_6	〃	0.01_4
	〃	line 18	0.07	〃	0.02_5
	〃	line 19	0.20	〃	0.05_2
	〃	line 20	0.22	〃	0.05_6
P. 328,	R	eq. (22)	N_{nt}	〃	N_{pt}
P. 329,	R	line 2	decrease	〃	decreases
P. 330,	L	line 13	0.2	〃	0.05
	〃	line 15	0.4	〃	0.55
	〃	linə 27	0.07	〃	0.02_5
	〃	line 27	0.20	〃	0.05_2
	〃	line 27	0.22	〃	0.05_6

* Left Column, ** Right Column.

PROGRESS OF THEORETICAL PHYSICS

Published by

The Yukawa Hall

with the cooperation of

The Physical Society of Japan

Progress of Theoretical Physics Vol. 9, No. 5, 1953

The Quantum-statistical Theory of Transport Phenomena, II
——On the Theory of Metallic Conductivity ....Hazime MORI....473
Meson-deuteron Rection and Nucleon Isobars
.... Sadahiko MATSUYAMA and Hironari MIYAZAWA....492
The General Theory of the Interaction Representation, II
——General Fields and Interactions
..............Hiroomi UMEZAWA and Yasushi TAKAHASHI....501
The Theory of V-particles .... Ken-ichi ONO....524
On the Structure of the Interaction of the Elementary Particles, IV
——On the Interaction of the Second Kind
..............Susumu KAMEFUCHI and Hiroomi UMEZAWA....529
The Field Theory of Superconductivity ....Abdus SALAM....550
Letters to the Editor:
Remarks on Lévy's Order Potential........T. HAMADA and M. SUGAWARA....555
A Non-local Wave Equation and its Connection with the Dirac Particle
.... T. TAKABAYASHI....557
The Theory of the Structure of Elementary Particles
..............................O. HARA and T. MARUMORI....559
The Theory of the Interaction with Higher Derivatives
.... Y. Katayama....561

Price $ 1.00 per copy
$ 12.00 per year (postage inclusive)
Annual dues for foreign members (individual subscribers)
$ 9.00 (postage inclusive)
〃 for foreign members of the Physical Society of Japan
$ 7.50 (postage inclusive)

Application for members, subscriptions and orders for back numbers should be sent, directly or through book-dealers, to

The Publication Office
in
Yukawa Hall, Kyoto University, Kyoto, Japan

JOURNAL OF THE PHYSICAL SOCIETY OF JAPAN Vol. 8, No. 5, SEP.—OCT., 1953

Energy Spectra of Charged π-mesons Produced in Carbon, Aluminium and Copper at 90° to a 345 MeV Proton Beam

By Senzo TOKUNAGA,
Department of Physics, Saikyo University, Kyoto
Kazunori YUASA,
Department of Physics, Konan University, Kobe
Kiyoshi NISHIKAWA
Department of Physics, Wakayama University, Wakayama
and Taka ISII
Department of Physics, Saikyo University, Kyoto

(Received April 23, 1953)

Energy spectra of charged π-mesons produced in C, Al and Cu bombarded by a 345 MeV proton beam were obtained with nuclear emulsions. The production cross sections of π^+- and π^--mesons from aluminium are $(5.3\pm1.2)\ 10^{-28}\ \mathrm{cm}^2\ \mathrm{ster.}^{-1}$ and $(1.9\pm0.8)\ 10^{-28}\ \mathrm{cm}^2\ \mathrm{ster.}^{-1}$ respectively. In case of copper they are $(1.2\pm0.2)\ 10^{-27}\ \mathrm{cm}^2\ \mathrm{ster.}^{-1}$ and $(3.6\pm1.0)\ 10^{-28}\ \mathrm{cm}^2\ \mathrm{ster.}^{-1}$ respectively. Comparing with the cross section of π-mesons from carbon obtained by Richman et al. it is found that the cross section for charged π-meson production varies roughly as mass number A for small A.

§ 1. Introduction

Since mesons were produced artificially by high energy α-particles at Berkeley in 1948, energy spectra of charged π-mesons in hydrogen, carbon and lead by high energy protons have already been obtained with nuclear emulsion technique.1)2) Also, by means of scintillation counter relative yields of artificially produced π-mesons with energy of 20 MeV, 40 MeV, and 50 MeV in several elements have been investigated.3)4) We have studied, with nuclear emulsions, energy spectra of charged π-mesons produced in carbon, aluminium and copper by 345 MeV protons at 90° to the proton beam. The experiment was planned by Dr. H. Barkas and Prof. R. Sagane as the first experiment of the film programme in the collaboration work between the American and Japanese physicists, and the bombardment of the targetswas done at Berkeley with 345 MeV proton beams from 184 inch cyclotron in autumn of 1950, while the observation of the emulsion was done by us in Japan. As the production cross section of π-mesons from nuclei is closely related to the problem of nucleon-nucleon collisions and nucleon-complex nuclei collision, the energy spectra may throw light on the problem of the process of charged π-meson production.

§ 2. Experimental Detailes

The targets were bombarded by 345 MeV protons from cyclotron. They were metal strips of 1″ in width and about 6″ in length. The plane of the strip was inclined 45° to the median plane of the cyclotron and the proton beam bombarded the strip at an angle of 45° to its normal.

The nuclear emulsion were exposed to mesons in two ways which we will designate the Arrangement A and the Arrangement B. In the former, the plates were inclined at an angle of 15° to the vertical (which had nearly the same direction with that of the moving mesons) as shown in Fig. 1 (a). In the latter the plates were inclined at 45° to the vertical as shown in Fig. 1 (b). In each case the wedge-shaped copper absorber being placed above the plates as shown in Fig. 1, mesons traverse a distance in copper absorber to reach the emulsion. So the range R of meson in copper will be

$R=x\cos 15°$ in Arrangement A
$R=5+x\cos 45°$ in Arrangement B,

where x is the distance in mm measured on the plate from the edge which was uppermost in the exposure to the point at which meson stopped. From the range of meson its energy can be determined. In the plates of the Arrangement A, mesons in entire energy regions are to be recorded, but the background make it impossible to study the lower energy region. So, with the plates of the Arrangement B, mesons with lower energy were investigated.

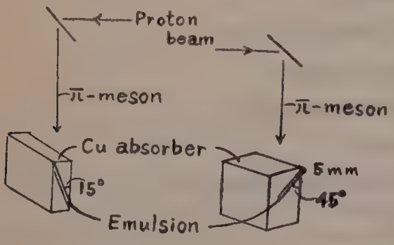

(a) Arrangement A
(b) Arrangement B

Fig. 1. Schematic view of the arrangement.

The relative intensity of the proton beam was determined by measuring C^{11} activity in polystyrene foil which covered the traget.

The backgrounds in the emulsions were extremely numerous and especially in lower energy region. It would probably be due to the tracks of scattered protons, recoil protons by neutrons and neutron induced stars. So, the plates were scanned with binocular microscope with ×90 oil immersion objective and ×5 ocular.

Mesons were recognized by sight by their characteristic scattering and rapid change in grain density. π^+-mesons were identified by $\pi^+-\mu^+$ events, because more than 99 per cents of π^+-mesons decay into μ^+-mesons, while π^--mesons were identified by σ-stars with one or more prongs ; and from the fact that 73 ± 2 per cents of π^--mesons produce stars with one or more prongs,[5)] the number of π^--mesons was obtained by multiplying 1.37 times the number of meson induced stars. Though it was reported that 8.7 per cents of μ-mesons also produce stars, we neglected the effect.

The cross section $d\sigma/dE\,d\Omega$ for the production of mesons per unit solid angle and per unit energy interval at the energy E was calculated from the relation

$$\frac{d\sigma}{dE\,d\Omega}=\frac{NR^2}{nm(dE/dx)_{em}},$$

where N is the number of mesons observed in unit volume of the emulsion when n protons bombarded the target per unit area contained m nuclei per unit volume, R the distance between the target and the point where meson stopped, and $(dE/dx)_{em}$ is the energy loss of meson of energy E per unit length in the emulsion. From the relation we would be able to obtain the energy spectra in each case. But the absolute value of the number of protons being unknown, the cross section for 50 MeV π^+-mesons in carbon was normalised up to the value obtained by Richman et al.

It is necessary to make two corrections for the cross section obtained by the formula mentioned above. One is the correction for the absorption in the copper, because, in our experiment, mesons were counted which stopped in the emulsion after passing through some distance in the absorber of copper. The correction was performed taking the cross section for absorption in copper to be equal to the geometrical cross section of the nucleus ($\pi r^2 A^{2/3}=1.13\times10^{-24}$ cm²). The other is the correction for the decay of the meson in flight between target and emulsions. But the effect being only a few per cents of the number of the observed mesons, we neglected the effect.

§ 3. Results and Discussin

The energy spectra of π-meson production in carbon, aluminium and copper were shown in Fig. 2, 3, 4, 5, 6 and 7. They were all corrected for nuclear absorption taking the absorption cross section equal to the geometrical cross section. In the case of carbon it was not possible to investigate energy regions higher than 60 MeV because of the high background in the emulsion in Arrangement A.

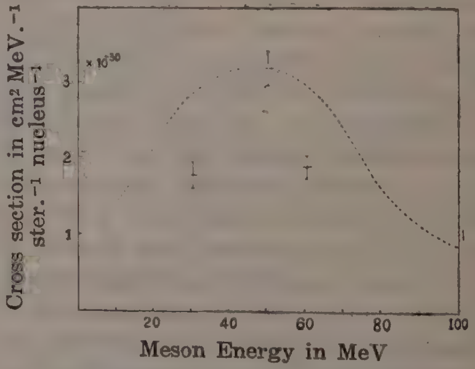

Fig. 2. Energy spectrum of π^+-mesons produced in carbon at 90° from a 345 MeV proton beam (corrected for nuclear absorption). The dotted curve represents Richman's data.

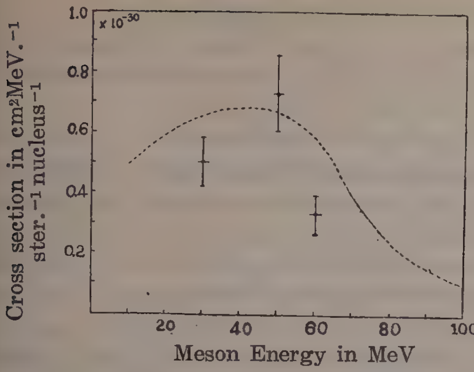

Fig. 3. Energy spectrum of π^--mesons produced in carbon at 90° from a 345 MeV proton beam (corrected for nuclear absorption). The dotted curve represents Richman's data.

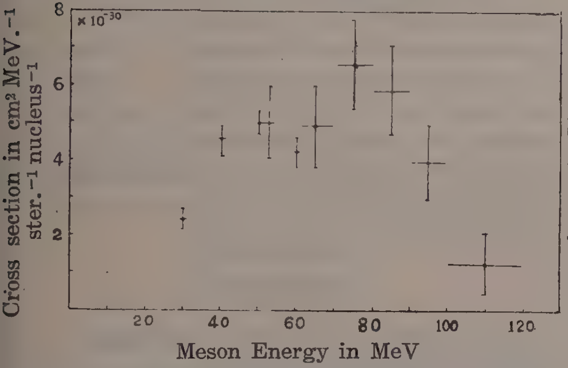

Fig. 4. Energy spectrum of π^+-mesons produced in aluminium at 90° from a 345 MeV proton beam (corrected for nuclear absorption).

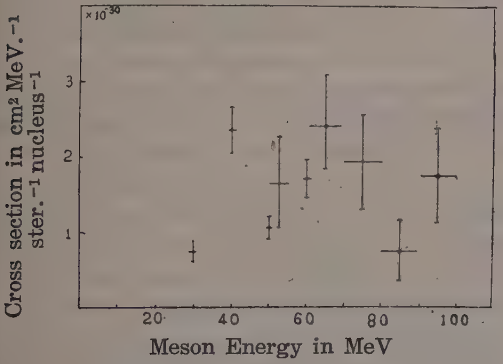

Fig. 5. Energy spectrum of π^--mesons produced in aluminium at 90° from a 345 MeV proton beam (corrected for nuclear absorption).

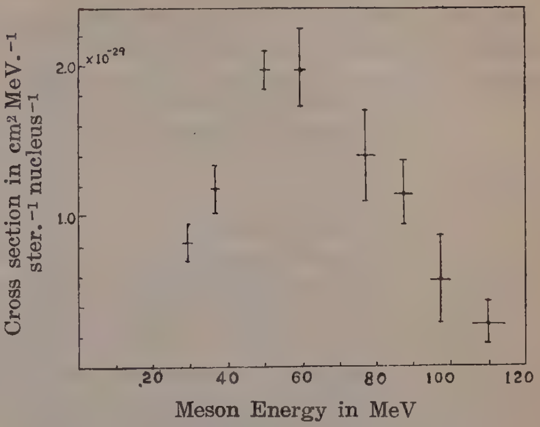

Fig. 6. Energy spectrum of π^+-mesons produced in copper at 90° from a 345 MeV proton beam (corrected for nuclear absorption).

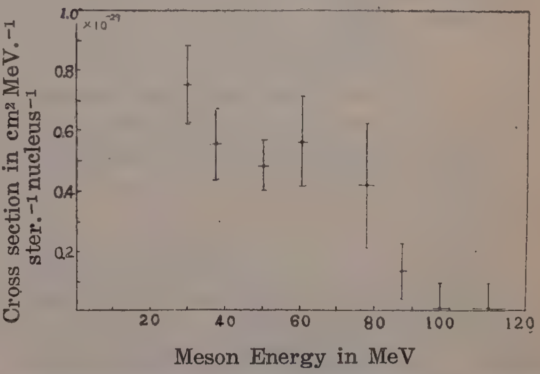

Fig. 7. Energy spectrum of π^--mesons produced in copper at 90° from a 345 MeV proton beam (corrected for nuclear absorption).

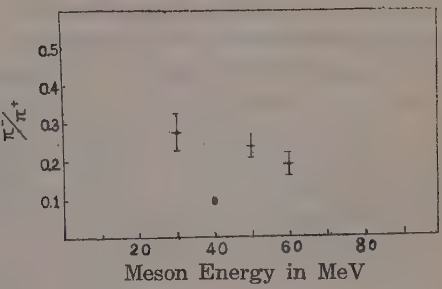

Fig. 8. The ratio of π^-- to π^+-mesons from carbon at 90° to the beam as a function of meson energy.

So the complete energy spectra were not obtained, but in the energy region obtained our results agree with those of Richman's.

The total cross section for π^+ and π^--mesons in aluminium were $(5.3\pm1.2)\times10^{-28}$ cm² ster.$^{-1}$ and $(1.9\pm0.8)\times10^{-28}$ cm² ster.$^{-1}$ From the results the average ratio of π^+ to π^--mesons is 2.8±1.3. Also, the total cross section for π^+- and π^--meson in copper were $(1.2\pm0.2)\times10^{-27}$ cm² ster.$^{-1}$ and $(3.6\pm1.0)\times10^{-28}$ cm² ster.$^{-1}$, and the average ratio of π^+- to π^--mesons is 3.3±1.1. The probable errors shown are only the statistical errors.

In Fig. 8, 9 and 10 each ratio of π^-- to π^+-

mesons was shown in case of carbon, aluminium and copper. The tendency seems to exist that π^-/π^+ decreases as the energy of mesons increases. The fact confirms us that because of the Pauli principle the more π^+-mesons are produced than π^--mesons when high energy protons bombard nuclei as suggested by Chew and Steinberger.⁶⁾

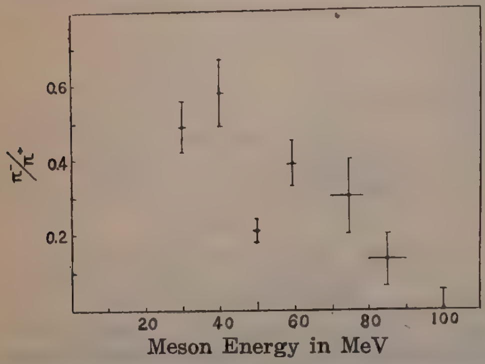

Fig. 9. The ratio of π^-- to π^+-mesons from aluminium at 90° to the beam as a function of meson energy.

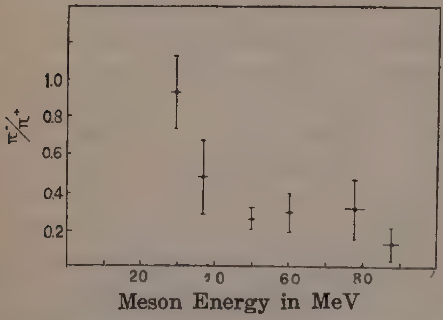

Fig. 10. The ratio of π^-- to π^+-mesons from copper at 90° to the beam as a function of meson energy.

Table I. The relative yields of charged π-mesons by 345 MeV protons

	π^+-meson	π^--meson	A/A_c	$A^{2/3}/A_c^{2/3}$
C	1	1	1	1
Al	2.3±0.7	4.2±2.1	2.25	1.73
Cu	5.2±1.4	8.0±3.2	5.24	3.02

A: mass number
A_c: mass number of carbon

Though the errors are large in our experiment, comparing with the data by Richman et al. for carbon, we see that the cross section for charged π-meson production varies roughly as mass number A for small A as in our experiment. (Table I.) The tendency is nearly the same with the result of Clark,⁴⁾ who obtained the relative yields of 40 MeV charged π-meson in several elements with scintillation counter telescope.

It is a pleasure for the authors to express their gratitude to Dr. W. H. Barkas, Prof. R. Sagane the late Dr. Y. Nishina and the film group of the California Radiation Labaratory, who made this project possible. Thanks are also extended to Dr. H. Tamaki and Prof. K. Kimura for their guidance and encouragement in this work, and to the Brotheren Support Association of Brazil for its financial help.

References

1) C. Richman, M. Weissbluth and H. A. Wilcox: Phys. Rev. **85** (1952) 161.
2) M. M. Block, S. Passman and W. W. Havens: **83** (1951) 167.
3) D. Hamlin, M. Jakobson, J. Meritt and A. Schultz: Phys. Rev. **84** (1951) 857.
4) D. Clark: Phys. Rev. **87** (1952) 157.
5) F. L. Adelman and S. B. Jones: Phys. Rev. **75** (1949) 1468.
6) G. F. Chew and J. L. Steinberger: Phys. Rev. **78** (1950) 497.

JOURNAL OF THE PHYSICAL SOCIETY OF JAPAN Vol. 8, No. 5, SEP.—OCT., 1953

Polarization of Electrons by Scattering, III
Reflection-Transmission Effect

By Norio RYU, Kimio HASHIMOTO and Itaru NONAKA
Department of Physics, Faculty of Science, Kyusyu University, Fukuoka

(Read April 1, 1952, Received April 1, 1953)

With electrons obliquely incident on a foil the intensities of the electrons scattered through a certain angle are different on the reflecting and on the transmitting side because of the plural scattering, and this phenomenon is called the reflection-transmission effect. This effect has been measured experimentally and compared with the calculation which is only a rough estimation. The experimental results obtained are in good agreement with the calculation at energies higher than 80 keV when thin gold foils are used. Since the plural scattering greatly influences the result of electron polarization experiment, the experimental results obtained previously by one of the authors (N.R.) must be corrected from this point of view. It is interesting to compare these corrected values with the theoretical ones obtained by Bartlett and Welton and recently by Mohr considering a nuclear screening by the orbital electrons, and by Bartlett and Watson using the pure Coulomb field. The agreement between experimental results and the corrected theoretical ones is not perfect, but it may be considered to be unavoidable that there are some differences between them, if one takes into account the fact that a small change in the nuclear screening makes a considerable effect on the theoretical values.

§ 1. Introduction

In the scattering of electrons by a thin foil, it is usual that the single scattering is accompanied by the plural and the multiple scatterings. In the scattering experiments, however, it is desirable that the latter two scatterings are so small as they can be neglected. The plural scattering, the existence of which had been pointed out by Goertzel and Cox,[1] is the scattering through a large angle by two succesive deflections of the same order of magnitude, and the multiple scattering is a combination of a number of deflections of small angles.

When electrons make oblique incidence on a foil, the intensities of the electrons scattered through a certain angle are different on the reflecting and on the transmitting side. This phenomenon, which had been observed first by Chase and Cox[2] and had been called the reflection-transmission effect by Shull et. al.,[3] can be estimated theoretically.[1][4] The estimation, however, is rough so long as the diffusion and the variation of intensities of electrons proceeding in a thin foil parallel to its surface can not be determined correctly. An experiment on the reflection-transmission effect have been performed to compare it with the theory to find out the extent of their agreement.

The plural scattering greatly influences the experiment of electron polarization by double scattering, and the corrections for the results of the polarization experiment are obtained provided that the ratio of the plural scattering to the single one is known. It is most interesting from this point of view to compare the experimental results of Ryu[5][6] on the electron polarization after correction for the plural scattering with the theoretical ones of Bartlett and Welton[7] and of Mohr*[8] both of which are obtained correctly considering the nuclear screening by orbital electrons, and also of Bartlett and Watson[9] obtained with the pure Coulomb field.

§ 2. Plural Scattering

Goertzel and Cox,[1] and Ryu[4] have already estimated theoretically the amounts of the plural scattering in a thin foil. We will give a more general discussion of the problem using the method suggested by one of the authors[4] (N. R.).

---

* We are indebted to the private communication from Prof. Mohr for the theoretical values calculated correctly using a nuclear screening by orbital electrons.

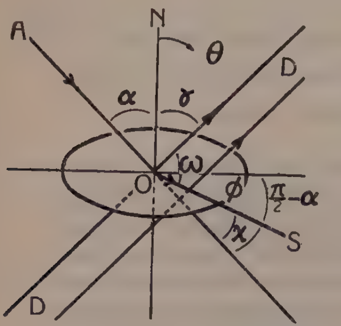

Fig. 1. Directions of scattered electrons.
A: incident electron N: normal to the foil.
D: detector S: scattered electrons in the foil.

The incident electrons are considered to strike the foil along AO in Fig. 1. The electrons which perform the plural scattering will be those which are scattered, for instance, in the direction of OS in the foil, and then take a second deflection at some point on OS into the direction of OD. Then, the ratio r of the number of electrons which reach the detector by plural scattering to that by single scattering is given by

$$r=\frac{4N\cdot F\cdot\Theta\cdot V(\beta_0)}{\Psi(\pi-\alpha-\gamma)}\,, \qquad (1)$$

where N is the number of scatterers in unit volume, α and γ are the angles shown in Fig. 1, and β_0 is the velocity of the incident electrons divided by the light velocity, F, Θ, and Ψ are defined as follows. The differential cross section Φ is in general expressed as

$$\Phi(\chi,\beta_\chi)=\Psi(\chi)V(\beta_0)v(x)\,, \qquad (2)$$

where Ψ is a function of the scattering angle χ, V is a function of β_0, β_χ is the velocity after traversing a distance x in the foil, and $v(x)$ is a function of x which depends on the rate of energy loss of the electron along the path. If we take the intensity of electrons along OS as

$$I(x)=I_0 f(x)\,, \qquad (3)$$

where I_0 is the initial intensity, we can write for F and Θ

$$F=\int_0^x\int_0^{\pi/2} f(x')v(x')\sin\theta\,d\theta\,dx'\,, \qquad (4)$$

and

$$\Theta=\int_0^\pi \Psi(\chi)\Psi(\omega)d\phi\,. \qquad (5)$$

There is no emprical or theoretical expression for $f(x)$, while Θ can be calculated correctly at any angles. The calculation have been worked out in the previous paper[4] under certain assumptions. The separation of Φ as Eq. (2) is possible only when the electron path in the foil is long enough compared with the thickness of the foil. The above calculation, therefore, fails for electrons of low energy and in scattering by a thick foil.

Carrying out the similar calculation on the transmitting side, it is easy to obtain the corresponding ratio t. The reflectiontramsmission effect is, then,

$$R=\frac{1+r}{1+t}\,. \qquad (6)$$

§ 3. Experiments on the Reflection-Transmission Effect

Incident electrons are accelerated by the same accelerator as used in the experiments of the electron polarization.[5][6] The schematic diagram of the scattering chamber is shown in Fig. 2. After passing through several diaphragms (1 mm in diameter) the electrons

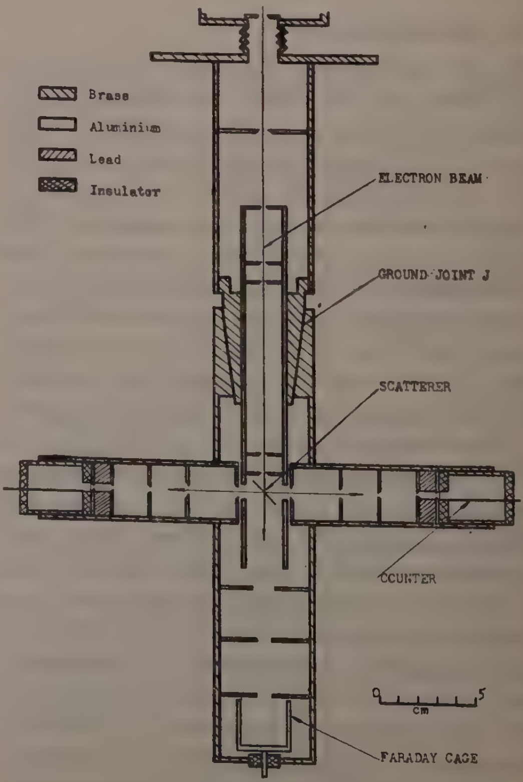

Fig. 2. Shematic diagram of the scattering chamber.

strike the thin foil and those which are deflected through an angle of 90° are detected by two counters set oppositly about the incident beam. The diaphragms and baffles made of aluminium are used to avoid stray electrons. To avoid X-rays the counters are covered with thick lead cylinders. The disturbance from X-rays was found to be negligible in the range of the energies used here. Since the counting system containing diaphragms and baffles is able to be rotated by the ground joint J, the reflection-transmission effect is obtained by two observations one at the position of the counters shown in Fig. 2 and the other at a position rotated through an angle of 180° by ground joint J. It is thus possible to avoid the errors caused by the counting properties of the counters and by the faulty geometry so long as the direction of the incident beam coincide with the axis of the rotation. The number of electrons entering the counters are counted by scale of thirty two recorders.

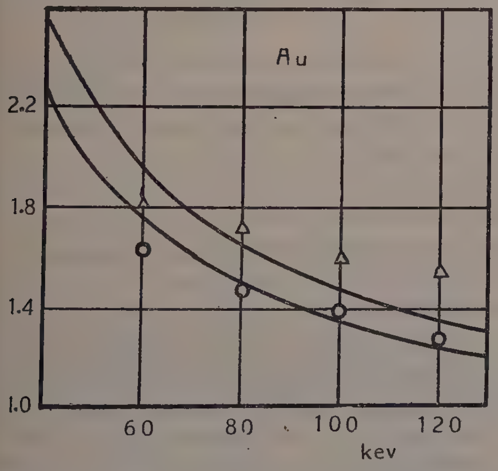

Fig. 3. Reflection-transmission effect of gold foils as a function of incident electron energy. The lower set shows the value for the foil of 5×10^{-6} cm in thickness and the upper ones for 7×10^{-6} cm. Solid curves are calculated values.

With the same gold foil of 5×10^{-6} cm in thickness as in the experiments of the electron polarization,5)6) the reflection-transmission effect shown in Fig. 3 were obtained. The solid line in the figure is the theoretical curve calculated for the foil of the above thickness. The thickness was determined by weighning some area of the foil. Though it seemed that the foils were not so uniform, similar results for four foils were obtained. The experimental results agrees satisfactorily with the theory at energies greater than 80 keV. However, the values at 60 keV are slightly smaller than those of the theory and this tendency increases as the energy is lowered, but the values fluctuate considerably. This phenomenon seems to indicate that the plural scattering at lower energies does not obey the simple mechanism as considered in the calculation and especially that the separation of ϕ as in Eq. (2) is not adequate. We also made a measurement on a gold foil of 7×10^{-6} cm in thickness made by vacuum evapolation. The upper solid line in the figure is the corresponding theoretical curve. The thickness of the foil was determined by the law of $1/4\pi\rho$. The gold foils made by evapalation showed initially large values for the reflection-transmission effect but they became smaller on continuous bombardment by strong beam, while the beaten foils did not show such decrease.

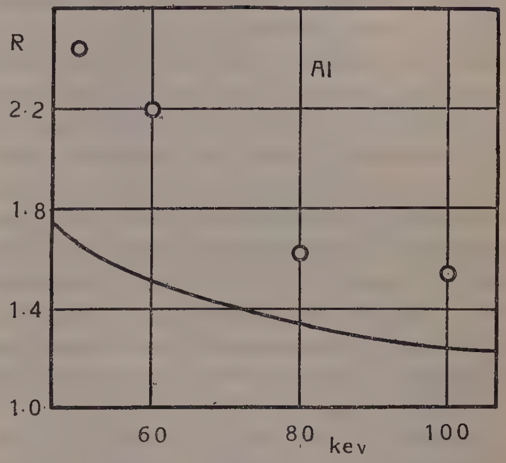

Fig. 4. Reflection-transmission effect of aluminium foils as a function of incident electron energy. Circles are experimental values for a foil of 1.5×10^{-4} cm; solid curve shows calculated values for a foil of 1.5×10^{-4} cm.

The observed values for a aluminium foil of 1.3×10^{-4} cm in thickness made by vacuum evapolation are shown in Fig. 4 together with the corresponding theoretical curve for a foil of 1.5×10^{-4} cm in thickness. The experimental values are very large and fluctuated initially but became smaller on continuous bombardment by a strong beam. The results shown in Fig. 4 is obtained after bombarding the foil by a strong beam for a considerable time.

§ 4. Depolarization of Electrons

It is pointed out frequently that the plural scattering greatly influences the result of the experiment of electron polarization by double scattering. Corrections for this effect for the experimental results of electron polarization obtained recently by one of the authors (N.R.)⁵⁾⁶⁾ were performed using the present experimental results of the reflection-transmission effect, since the same foil was used in the present experiment as in the previous polarization experiment. Since the transmitting side was used in the first foil (polarizer), the correction was negligible, but in the second foil (analyzer) it was not negligible because the beam was incident normally on the foil and the detectors were set on the side of reflection. The intensity of those electrons which suffered plural scatterings in the analyzer and entered into the detectors was calculated theoretically taking account of the magnetic moment of the electrons. In the calculation only the electrons which had scattered through an angle of 90° in the first collision in the analyzer and then scattered in the direction of the detector were considered as an approximation, since most of the electrons which suffered plural scatterings reached the detector after such process. This approximation, however, gives a slighthy larger estimation of the effect. Then, the intensity of such electrons which have scattered by the second foil in the opposit direction to the incident beam is

$$I_1 \propto \Phi_1\Phi_2\Phi_3(1-\delta_1\delta_2)\left\{1-\frac{\delta_3(\delta_1+\delta_2)}{1-\delta_1\delta_2}\right\},$$

where, Φ_1 is the atomic differential cross section of the scattering in the polarizer and Φ_2 and Φ_3 are those of the scatterings in the analyzer, and δ_1^2, δ_2^2 and δ_3^2 are the values of polarization asymmetry* at each angle, respectively. The intensity in the direction of the incident beam is

$$I_2 \propto \Phi_1\Phi_2\Phi_3(1+\delta_1\delta_2)\left\{1-\frac{\delta_3(\delta_1-\delta_2)}{1+\delta_1\delta_2}\right\}.$$

Then, we obtain the asymmetry in the scattering at the analyzer as follows.

$$\frac{I_1}{I_2} \fallingdotseq (1-2\delta_1\delta_2)(1-2\delta_2\delta_3)\,. \qquad (7)$$

According to the theoretical results obtained by Mohr,** the sign of δ_3 is different from those of δ_1 and δ_2, then the term in second parentheses in Eq. (7) express depolarization, but the absolute value of δ_3 is rather small. If we neglect its effect, we obtain

$$\frac{I_1}{I_2} \fallingdotseq (1-2\delta_1\delta_2)\,, \qquad (8)$$

which is equal to the asymmetry in the scattering through an angle of 90° at the analyzer.

We can get the ratio of the plural scattering to the single one by utilizing the experimental values of the reflection-transmission effect obtained in the present experiment, and we can correct the theoretical values of the electron polarization to fit the experimental conditions.

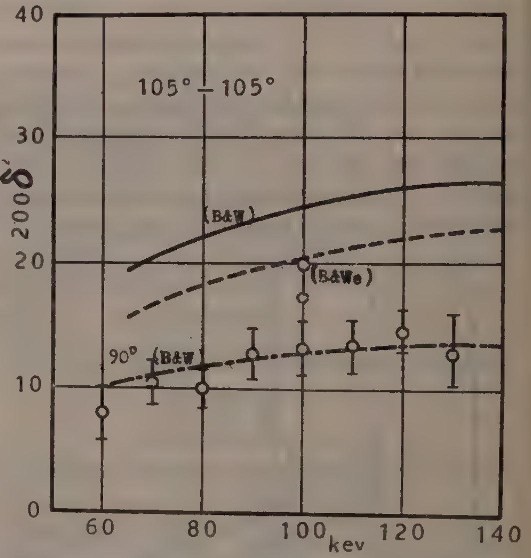

Fig. 5. Polarization asymmetry at an angle of 105° as a function of incident electron energy. (B & W) shows the theoretical curves for 105° and 90° calculated from the table of Bartlett and Watson. (B & We) shows the theoretical value of Bartlett and Welton. Dotted curve is the values corrected for the plural scattering. Circles attached by error symbols are the experimental values of Ryu at 105°.

In Fig. 5 and 6 theoretical values of the polarization asymmetry at 90°, 105° or 120° obtained by Bartlett and Watson,⁹⁾ by Mohr⁸⁾ considering exactly the effect of a nuclear screening by orbital electrons, and by Bartlett and Welton⁷⁾ also considering a screening field are shown together with their corrected values at 105° and 120° as described above, and also with some of the experimental values

---

* In the previous paper (I, II), we called $-2\delta^2$ "the evidence by polarization".

** We are indebted also to Prof. Mohr for the sign of δ.

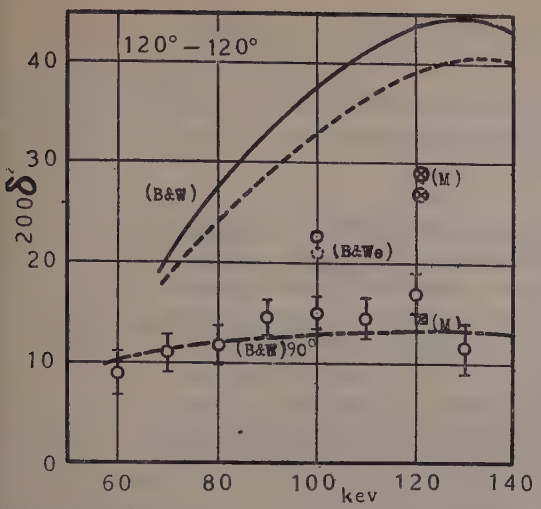

Fig. 6. Polarization asymmetry at an angle of 120° as a function of incident electron energy. (M) shows the theoretical values obtained by Mohr, (B & We) by Bartlett and Welton and (B & W) the theoretical curves calculated from the table of Bartlett and Watson. Dotted curve is the values corrected for the plural scattering. Circles attached by error symbols are the experimental values of Ryu.

at these angles obtained by one of the present authors (N. R.)[5][6] (circles attached by error symbols).

The above corrections due to the plural scattering become smaller as the scattering angle increases, so the corrections at 135° will be considerably smaller than those shown in the figures. It is an interesting fact that the theoretical value of Mohr, and of Bartlett and Welton come near the experimental value, and the effect of the nuclear screening to the theoretical values of the polarization asymmetry is very large.

To see the variation of the polarization asymmetry with angle, the corrected values at angles of 90°, 105°, 120° and 135°, respectively, are calculated from the six experimental values of polarization asymmetry at 100 keV in the previous paper[6] and the values of reflection-transmission effect in the present experiment, by the method of least square. The result are shown in Fig. 7 together with the theoretical values of Bartlett and Watson, and of Bartlett and Welton.

As can be seen in Figs. 5, 6 and 7, the agreement between the experimental values and the theoretical ones is not perfect even if the effect of the plural scattering is corrected for. However, a small correction in the atomic field gives large variations to the theoretical values of the polarization asymmetry, accordingly any perfect agreement can not be expected so long as the screening by orbital electrons is not exactly taken into account.

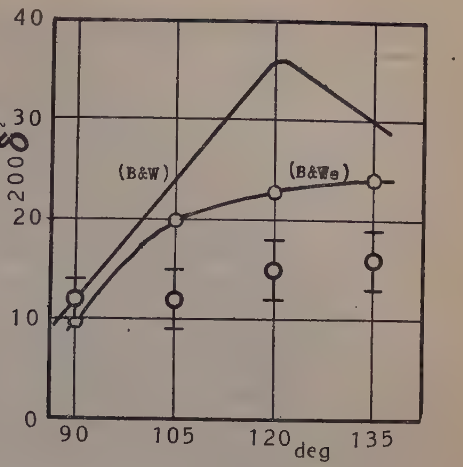

Fig. 7. Polarization asymmetry at 100 keV as a function of angle. (B & W) shows the theoretical curve calculated from the table of Bartlett and Watson and (B & We) the theoretical curve obtained by Bartlett and Welton. Circles attached by error symbols are the calculated values from the experimental results of Ryu by the method of least square.

The authors express their sincere thanks to Prof. C. B. O. Mohr for his kind interest and information about the theoretical values here used, and also to Profs. T. Muto, K. Shinohara and M. Nogami for their useful suggestions. This work has been supported by the Scientific Research Expenditure of the Ministry of Education.

References

1) G. Goertzel and R. T. Cox: Phys. Rev. **63** (1943) 37.

2) C. T. Chase and R. T. Cox: Phys. Rev. **58** (1940) 243.

3) C. G. Shull, C. T. Chase and F. E. Myers: Phys, Rev. **63** (1943) 29.

4) N. Ryu: J. Phys. Soc. Japan **5** (1950) 423.

5) N. Ryu: J. Phys. Soc. Japan **7** (1952) 125.

6) N. Ryu: J. Phys. Soc. Japan **7** (1952) 130.

7) J. H. Bartlett, Jr. and T. A. Welton: Phys. Rev. **59** (1941) 281.

8) C. B. O. Mohr: Proc. Roy. Soc. **A 182** (1943) 189.

9) J. H. Bartlett and R. E. Watson: Proc. American Acad. of Arts and Sci. **74** (1940) 53.

JOURNAL OF THE PHYSICAL SOCIETY OF JAPAN Vol. 8, No. 5, SEP.—OCT., 1953

Experimental Analysis of the Specific Activity

By Yoshio SAJI, Masakatsu SAKISAKA and Kozo MIYAKE

Department of Physics, University of Kyoto

(Received April 16, 1953)

In order to measure the absolute number of β-particles from samples by an end-window G-M counter, the effects of self-absorption and self-scattering of β-rays in samples should be eliminated. Since apparent number of counts of β-rays from samples is generally affected by the effects above mentioned, the curve of the specific activity against the thickness of samples shows a maximum at a certain point and gradually decreases as the thickness of samples increases. We analysed this curve and tried to formulate it in a mathematical form, of which experimental verification in the case of silver samples activated by slow neutrons has been obtained.

§ 1. Introduction

In determining the cross-section for the nuclear reaction, we are often required to obtain some accurate informations concerning the absolute β-counting of thick samples. Since the number of counts of β-particles emitted from thick samples is affected by the effects of both self-absorption and self-scattering, in order to determine the true number of β-particles produced in samples, corrections for these effects are necessary to know.

In our laboratory a method of eliminating these effects has been adopted;[1),2),3)] from the counting data of β-rays from samples of various thickness, we trace a curve of the specific activity, defined as the apparent counts per unit thickness of samples, *versus* the thickness of samples, and extrapolate this curve to a point of zero thickness. From the value of this point, corrections for these effects can be calculated, because the point obtained by this procedure apparently shows a value unsuffering from the effects. This method, however, is very troublesome and the values corresponding to the very thin samples may involve considerable probable errors because of weak intensities of β-rays.

The curve of specific activity shows a maximum at a certain thickness of the sample as shown in Fig. 1. If the curve is expressed by a simple function of thickness, one may be able to calculate the value of the weightless sample from the observed curve.

A few workers[4),5)] have attempted to deduce the function from simple considerations, which, however, resulted to poor agreement with experiments. In the present work, we have tried to analyse the curve of specific activity in more detail, and have compared our result with experiments.

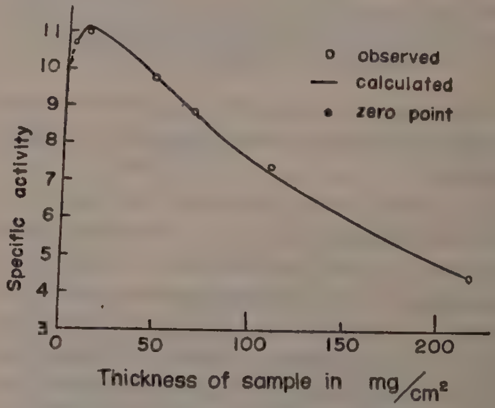

Fig. 1. A curve of specific activity.

§ 2. Preliminary Considerations

The observed number, N, of counts of β-rays emitted from a sample of thickness t is assumed to be

$$N=\int dN=\int_0^t N_0 D(x)A(x)B(x)F(x)dx, \qquad (1)$$

where N_0 is the true number of β-rays produced in unit thickness of the sample, and D, A and B are functions depending upon the distribution of activities, self-absorption and self-backscattering of β-rays respectively, and F is a correction factor for the self-forescattering.

$A(x)$ is easily expressed by

$$A(x)=e^{-\mu x}, \qquad (2)$$

as like as the result of Aten[4)] and Cormar et al[5], and μ means the absorption coefficient of β-rays.

$B(x)$ is considered as follows: Now, there is an active surface A A′ with a backscattere of thickness d as shown in Fig. 2. The rate,

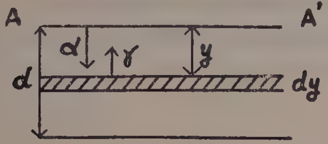

Fig. 2.

α, of β-rays progresses downwards and a fraction, γ, is back-scattered at dy in depth y. Then, the rate of the additional β-rays emitting from the upper surface due to the backscattering at dy is,

$$\alpha\gamma e^{-2\mu y}.$$

Therefore, the total rate of the backscattering is

$$\int_0^d \alpha\gamma e^{-2\mu y}dy=\frac{\alpha\gamma}{2\mu}(1-e^{-2\mu d}).$$

Then, the total rate of β-rays emitted upwards is obtained, by adding unity, as:

$$1+\beta(1-e^{-2\mu d}), \qquad \beta\equiv\frac{\alpha\gamma}{2\mu}.$$

Thus, $B(x)$ in Eq. (1) is represented by

$$B(x)=1+\beta(1-e^{-2\mu(t-x)}). \qquad (3)$$

Finally, the correction factor, $F(x)$, is considered as follows: If a very thin absorber is placed on the sample closely, the apparent count increases rather than in the case of no absorber, due to the effect already known as "forescattering" in the case of the external absorption.[6] The actual correction for such effect will be treated in the following section.

Thus, the function of the specific activity, $S(t)$, is generally represented by

$$S(t)=\frac{N}{t}=\frac{1}{t}\int_0^t N_0D(x)e^{-\mu x}$$
$$\times\{1+\beta(1-e^{-2\mu(t-x)})\}F(x)dx. \qquad (4)$$

§ 3. Experiments

As samples silver discs of various thicknesses and of the same diameter of 21 mm were used. These were activated by slow neutrons in a paraffin pile. The neutrons were produced by $Be(d,n)$ reaction. The thickness of samples was varied from 10.2 mg/cm^2 to 218 mg/cm^2, while silver discs of the same diameter were used as monitors. The samples and monitors were irradiated for five minutes, and after four minutes β-activities produced in the samples and the monitors were measured for seven minutes by the G-M β-counter of end-window type, which had a thin mica window of about 3 mg/cm^2 in thickness and aluminium cathode of 24 mm in diameter. Since, in the present case, β-activities of Ag^{110} with half-life shorter than 30 sec. could be neglected, only those of Ag^{108} with 2.36 min. half-life were counted. The distance from an upper surface of the sample to the sensitive volume of the counter was chosen always as 7.3 mm. This experimental arrangement is shown in Fig. 3. Thus, we obtained a curve of the specific activity *versus* thickness of samples as shown in Fig. 1.

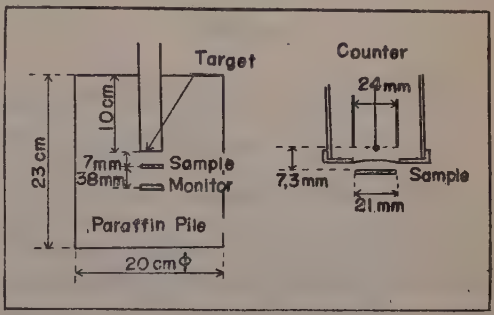

Fig. 3. Arrangement of apparatus.

In the preliminary experiments, we confirmed that the radial distribution of β-activities produced in the sample was uniform, and that the intensities of slow neutrons diffused to forward and backward directions of the sample were similar in our case. But, as the neutrons are absorbed in the sample itself, so the distribution of β-activities might differ with depth. Therefore, during the neutron irradiation the standard sample was covered by silver discs of various thicknesses and of the same diameter on either side and then the β-activities produced in the sample were measured. As a result, we obtained the following expression experimentally:

$$I=\tfrac{1}{2}I_0(e^{-\tau x}+e^{-\tau(t-x)}), \qquad (5)$$

where t is the thickness of the sample, I the intensity of activities at a depth x, I_0 that of zero thickness and τ the absorption coefficient for neutrons. In the present case τ is found to be 0.00202 (mg/cm^2)$^{-1}$. I in Eq. (5) corresponds to $D(x)$ in Eq. (2).

In order to know the self-absorption and the self-forescattering of β-rays in the sample, we closely placed silver discs of various thicknesses and of the fixed diameter, same as that of the sample, on the thinnest sample as absorbers. The result obtained is shown is Fig. 4. From the observed curve, it was found that in the thinner region the apparent counts increased rather than that for zero thickness and reached a maximum at a certain point and then descreased exponentially as the usual absorption curve.

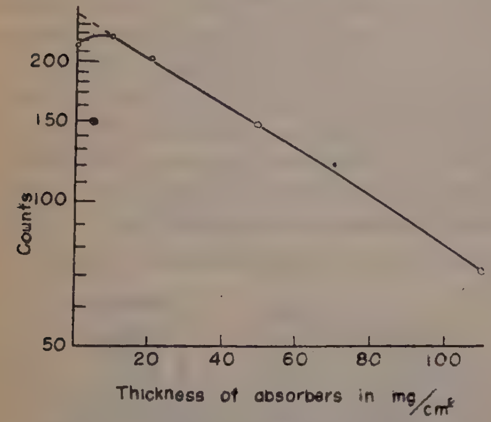

Fig. 4. Apparent absorption curve.

Since, as discussed before, the curve is considered to be composed of both factors $A(x)$ and $F(x)$, it should be formulated by

$$I=I_0A(x)F(x)=I_0F(x)e^{-\mu x}\,. \qquad (6)$$

However, the observed points in the region thicker than the maximum point are found to be precisely on the exponential curve. So we conclude that in that region Eq. (6) should be replaced by

$$I=I_0F(x)e^{-\mu x}=I_0e^{-\mu' x}\,, \qquad (7)$$

where μ' is the apparent absorption coefficient and contains the effect of $F(x)$ implicitly. μ' is found to be $0.0112\ (\mathrm{mg/cm^2})^{-1}$.

Secondly, the curve of the apparent absorption is extrapolated to a point without absorber by the use of the above μ'. The value calculated in the above procedure is larger than the observed zero value and the ratio of the calculated value to the observed value is estimated to be 1.16. Then, the true value for sample of zero thickness should be estimated by considering this ratio.

Finally, we put silver discs of various thicknesses and the same diameter beneath the thinnest sample as backscatteres. The result is shown in Fig. 5. It shows a good agreement with the theoretical equation Eq. (3). In this case we used μ' instead of μ and obtained $\beta=0.367$.

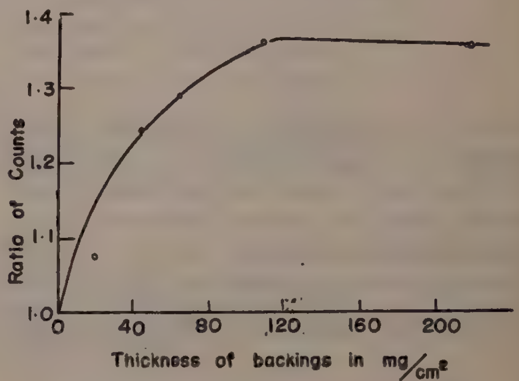

Fig. 5. A curve of backscattering.

Thus, we obtain the formula of $S(t)$ as follows:

$$S(t)=\frac{N(t)}{t}=\frac{1}{t}\,\frac{N_0}{2}\int_0^t[(e^{-\tau x}+e^{-\tau(t-x)})e^{-\mu' x}$$
$$\times\{1+\beta(1-e^{-2\mu'(t-x)})\}]dx\,. \qquad (8)$$

Eq. (8) is found to agree with the experimental value within the error of 3 percent as shown in Fig. 1. But it should be noticed that Eq. (8) should be applied to an only region thicker than $10.2\ \mathrm{mg/cm^2}$ as discussed above. Then, the value for zero thickness will be obtained by

$$N_{0,0}=\lim_{t\to 0}S(t)=\frac{1}{f}\lim_{t\to 0}\frac{1}{t}\,\frac{N_0}{2}\int_0^t[(e^{-\tau x}$$
$$+e^{-\tau(t-x)})e^{-\mu' x}\{1+\beta(1-e^{-2\mu'(t-x)})\}]dx\,, \qquad (9)$$

where f is the correction factor for the self-forescattering and is found to be 1.16 as described before. Adopting this zero value, $S(t)$-curve becomes very smooth in all region shown as the dotted curve in Fig. 1.

§ 4. Discussion

From Eqs. (8) and (9), we can obtain the absolute number of β-particles emitted from a thick sample easily, because, unknown constants *viz* f, τ, μ' and β contained in Eqs. (8)

and (9), are easily obtained experimentally. If these constants are estimated theoretically, the procedure will be more simple. However, it should be noticed that these constants depend on the distance between the sensitive volume of a counter and the upper surface of a sample. In fact, we obtained some different shape of $S(t)$-curve at a different distance as shown in Fig. 6.

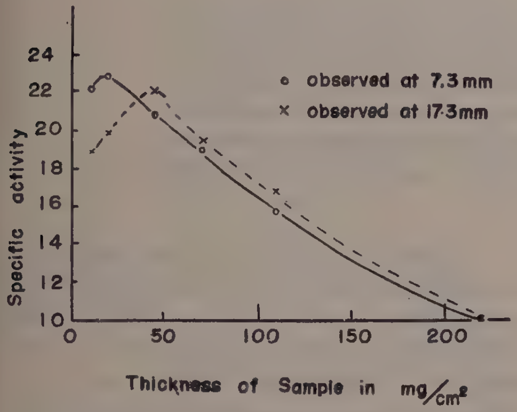

Fig. 6. Curves of specific activity at different distance between a sensitive volume of counter and an upper surface of a sample. Both curves are normalized at the thickest point.

Although some ambiguity is remained in formulations of $F(x)$ and $A(x)$, it is unimportant in the practical procedure of the absolute β-counting, but being of the theoretical interest, we are in progress on this problem.

Acknowledgement

The authors wish to thank Profs. K. Kimura and S. Shimizu and other members of our laboratory for valuable discussions on this work. Particularly, we are indebted to Mr. I. Kumabe and S. Yamashita who assisted us in measurements. This work was supported by the research grant from the Ministry of Education.

References

1) S. Shimizu, Y. Uemura, R. Ishiwari, Y. Saji and J. Muto: Rep. Inst. Chem. Res. Kyoto Univ. **19** (1949) 23.

2) Y. Saji: Saishin-Igaku **5** (1950) 74.

3) S. Shimizu, Y. Saji, S. Yasumi and J. Muto: Mem. Coll. Sci. Univ. of Kyoto, **A 26** (1950) 85.

4) A. H. Aten: Nucleonics **6** No. 1 (1950) 68.

5) C. L. Cormar, San L. Hansand, S. L. Hood, M. P. Plumlee and B. F. Berrete: Nucleonics **8** No. 3 (1951) 19.

6) G. Brownell: Nucleonics **10** No. 6 (1952) 30.

JOURNAL OF THE PHYSICAL SOCIETY OF JAPAN Vol. 8, No. 5, SEP.—OCT., 1953

On the Penetrating Shower originating in Light Element and Heavy Element

By S. HIGASHI, T. KITAMURA, T. KUBOZOE, M. ODA, S. OZAKI and Y. WATASE

Osaka City University

(Received April 13, 1953)

Comparison was made on the penetrating shower originating in carbon and lead. Using the counter hodoscope and the Wilson cloud chamber, the multiplicity of the penetrating shower and the absorption of the shower particle and the secondary event produced by the shower particle were observed. Consequently different energy spectrum at lower energy and its equality at higher energy of the shower particles for different size of the mother nucleus were tentatively concluded and discussed.

§ 1. Introduction

A number of investigations on the penetrating shower have been made by various methods. Recently much efforts were made by many authors in order to investigate the penetrating shower quantitatively. For instance, investigations on the emulsion stars by the Bristol group[1] have offered some knowledges on the shower particles and Frölich, March and Sitte[2] have investigated the penetrating shower with a cloud chamber and counter hodoscope and some rather quantitative conclusions were obtained on the shower particles and the secondary nuclear events. And many studies[3]-[7] have been made comparing the penetrating showers produced on light and heavy element with each other. But our present knowledge is not so conclusive and, at present, we are only able to suppose on the phenomena which occur in the nucleus and little are infered to the "elementary" process occured in the nucleus. In this situation it appears worthwhile to study the shower particles and the secondary events systematically with light and heavy materials. Thus the purpose of this experiment was to know the difference of the penetrating shower originating in carbon and lead producer.

We have investigated the matter using counter hodoscope and a cloud chamber at Mt. Norikura (2740 m) at the summer of 1951. The results are insufficient for the analysis and the discussion on the matter occurring in the nucleus, because the method of our investigation was not suitable for this purpose and the statistics was not so good and, consequently, many possibilities are permissible for the interpretation of the matter. Thus, at most we are able to offer some fragmental knowledges on the penetrating shower.

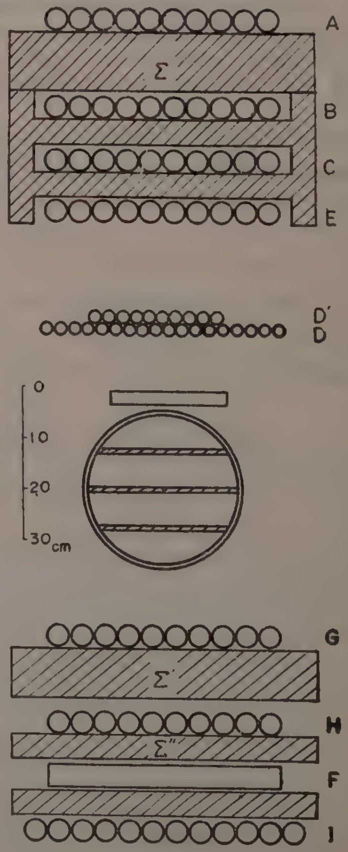

Fig. 1.

§ 2. Experimental Arrangement

Experimental arrangement is shown in Fig. 1. The cloud chamber is of 30 cm diameter and of 10 cm thickness of illuminated region. Three lead plates of 2 cm respectively were set inside. B and C counter trays were of G-M counters of 4 cm dia. and 30 cm length. A, E, G, H and I counter trays were of G-M counters of 4 cm dia. and 40 cm length and D, D′ trays were of G-M counters of 2 cm dia. and 40 cm length. D′ tray was set on D tray parallel or at right angle to axes of D counters. Two air shower trays, each of which was of ten G-M counters, were set 2 m and 4 m apart from the arrangement respectively. The hodoscope was triggered whenever two of eight counters in the middle of B tray, three of C tray and one of two counters in the middle of D tray ($B\geq2$ $C\geq3$ $E\geq1$) were discharged simultaneously and the record was obtained. Resolving time of the coincidence circuits and the hodoscope circuits were about 10 μs and 100 μs respectively. When the hodoscope was triggered and the counters which were upon the cloud chamber were discharged, the cloud chamber was operated.

Σ is the producer of the local shower and carbon or lead was used. In the case of carbon producer, graphite plates of density of 1.6 were piled up by 10 cm, and, in the case of lead producer, thin lead plates were piled up at intervals by 10 cm geometrically, but total amount of lead was 1 cm or 3 cm in the course of the experiment. Σ' was carbon or lead and was 10 cm thickness for both cases. All combinations of carbon and lead were adopted for Σ and Σ'.

Thus, the hodoscope records obtained were interpreted and the penetrating showers were picked up from them. The nature of the shower particle was investigated by the cloud chamber and the hodoscope records of G, H, F and I trays.

§ 3. Definition of the Penetrating Shower

The hodoscope was triggered by ($B\geq2$ $C\geq3$ $E\geq1$). This is in favor of local shower produced in Σ but, of course, all of them are not the penetrating showers. The records were interpreted as the penetrating shower when the following criteria were satisfied.

I) At least two counters in E tray were discharged.

II) When two adjacent counters in F tray were discharged, considerable portion of the records might be explained in terms of knock on electrons and high energy cascade showers. This case was omitted in this work except the case where taking D and D′ trays into account the possibility of those ambiguity was reasonably excluded.

III) The case where terminal counters of any three trays in A, B, C, E and D were discharged were omitted from interpretation.

IV) Considerable portion of the records where two adjacent B counters were discharged was explained by showers produced in the lead layer between B and C trays with particles emitted backward and by other background. Therefore, only the case where three or more of B tray were discharged was taken into account.

V) Some of the records showed complicated events which we could not be sure to what phenomena they corresponded. These records were not used and only the case where probable tracing was possible selected.

Thus, the selected events may correspond to the penetrating shower whose, at least, two secondaries penetrate 10 cm or more lead absorber and three or more secondaries penetrate 5 cm lead absorber and which is produced in Σ. Selection by the criteria, above mentioned, may miss out some of the penetrating showers, especially of small events, but the possibility of picking up the spurious events is expected to be small.

Thus, about 1090 penetrating showers were selected from 7400 records during 260 hours, of which 27 % was extensive air shower, 17% was small shower, probably cascade shower, 33 % was probably the penetrating shower but out of selection 8 % was complicated events, not classified.

A part of the records was interpreted by several ones independently and the selection was made by some different criteria and it is thought to be verified that psychological effect in the analysis of the results is not large and the conclusions are not sensitive to the personal interpretation of the records.

§ 4. Experimental Results

I) Multiplicity of shower particle

This arrangement is not suitable for measurement of the multiplicity of the shower particle, because two or more shower particles entering into one counter cannot be separated and a part of shower particles misses the counter tray and the correction, not so accurate, is needed. But the number of discharged counters in a tray may be used instead of the multiplicity, if the matter is treated relatively and approximately.

For carbon and lead producer the average number of discharged counters in each tray is given in Table I. From this table no difference is seen between carbon and lead producer.

Table I

Producer	Frequency	Average number of discharged counters in		
		E	*D*	*G*
3 cm lead	5.0±0.25/hr	3.7±0.1	2.9±0.1	0.65±0.03
10 cm carbon	3.0±0.15/hr	3.9±0.1	2.7±0.08	0.72±0.03

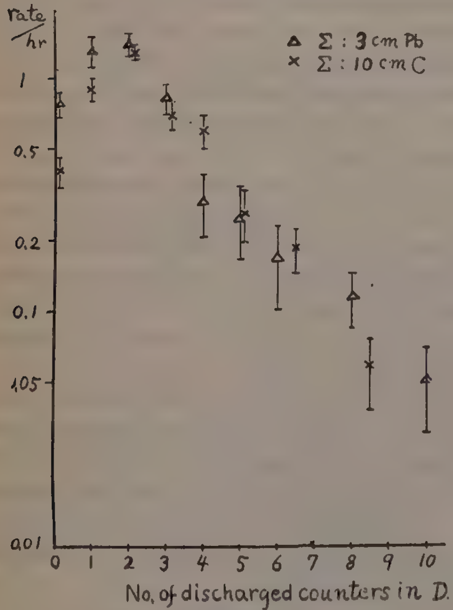

Fig. 2.

An example of the distribution of the number of discharged counters in D tray is shown in Fig. 2 for both elements of the producer and well agreement is concluded. This comparison has been done at sea level with almost the same arrangement and considerable difference has been concluded. But in that case the difference in geometrical condition and ionization loss of shower particles in carbon and lead producer has not been taken into account and we are not sure whether this contrariety of results at sea level and at high altitude is valid or not.

In this arrangement the particle which discharged E, D, G, counters traverse the filter of 10 cm lead and, therefore, the difference between carbon and lead producer might be decreased under the filter. This point will be discussed later.

II) Absorption and collision of the shower particles.

A part of the shower particles entered into the cloud chamber and the pile of the counter trays (G-I) and, then, its nature was observed. When the shower particles were emitted in narrow cone, the observation of the secondary events was difficult and, therefore those case was treated only statistically. From hodoscope records in which path of the shower particle was clear the absorption curves for all combinations of Σ and Σ' (Pb—Pb, Pb—C, C—Pb, C—C) were obtained. The large angle scattering was classified into the absorption. The absorption curves, thus obtained, are shown in Fig. 3. (a) (b). Geometrical corrections which come from missing of the shower particles by the counter tray were done experimentally. From these figures it is presumably

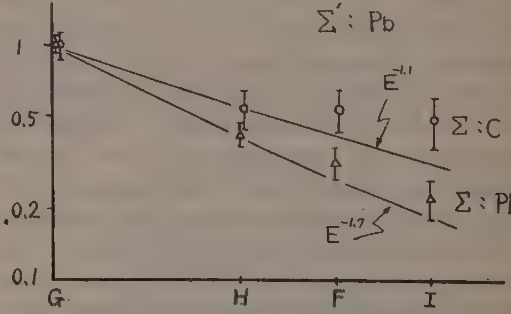

Fig. 3. a)

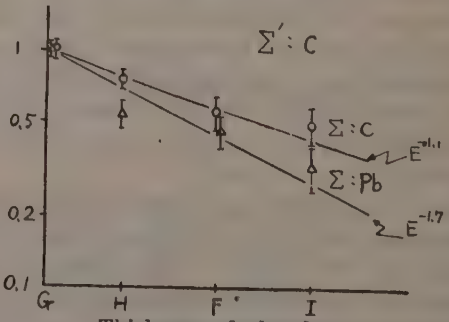

Fig. 3. b)

concluded that the shower particle of carbon initiated penetrating shower is more penetrative than that of lead-initiated penetrating shower. Absorpsion mean free path of the shower particle in the lead absorber for carbon-initiated and lead-initiated penetrating shower is ~260 gr/cm² and ~150 gr/cm² respectively. Absorption of the shower particle is due mainly to ionization loss and to nuclear collision and the rate of absorption depends on its energy. Above result is supposed to show the difference in the average energy of the shower particles in the both cases. If the energy spectrum of the shower particles is known, their rate of absorption may be roughly calculated, using the data of the Bristol group for the absorption due to nuclear disintegration. Two absorption curves are tentatively drawn in the figure for two assumed energy spectrum. Absorption curves of shower particle for different scale of the penetrating shower are shown in Fig. 4 and no difference is concluded from this figure.

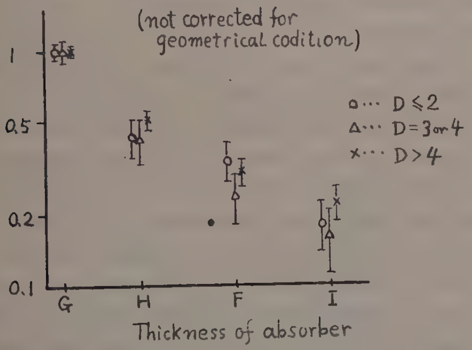

Fig. 4.

This counter arrangement does not serve to observation of the nuclear events which is accompanied by no penetrating particle, so-called Op star.

However, in the cloud chamcer we observed several Op star and s.p.s. produced by the shower particle. Op star was defined by the following conditions, for the events occurred at the second or the third lead plate (Op star at the first lead plete whose all prong ionizing is not distinguished with a electron cascade) all the events whose prong number was ≥3 and the events whose all prong was heavily ionizing or whose ≥1 was scattered by >10° and other was heaving ionizing. In observation 8 " stars " and 2 s.p.s. at the cloud chamber occured in 4200 gr/cm² traversals of the shower particle when Σ was lead and 3 " stars " and 2 s.p.s. were observed in 1500 gr/cm² traversals in the case of carbon Σ. The cloud chamber was too small in order to observe the successive events and, therefore, the statistics is poor.

III) Successive penetrating shower (s. p. s.)

Occasionally a shower particle produced in Σ entered into Σ′ or the lead layer under H tray and appeared to produce two or more penetrating particles. Probability of appearance of these records by chance coincidence were completely negligible and, therefore, these cases were interpreted to be the successive penetrating shower produced by the shower particle. Results are tabulated. In Table II HS_H and HS_S corresponds to the successe penetrating shower whose two or more secondary particles penetrate at least 10 cm lead or 5 cm lead respectively. HS ? is the events which may be the s.p.s. but is not sure. In the column of G, H, F the number of the shower particle entered G, H and F tray respectively in the course of the experiment are given, omitting the case where adjacent counters were discharged and, therefore, the number of the shower particle could not be counted clearly. The number in bracket corresponds to the other data obtained by different criteria of selection of the penetrating shower (p. s.). As seen in Table II, the observed number of the s.p.s. is

Table II

Σ	Σ′	HS_S	HS_H	HS ?	Σ″	HS_S+HS_H	HS ?	G	H	F
Pb	Pb	1	4	1	Pb	1	0	238	67	41
		(1)	(1)	(1)		(0)	(0)	(186)	(62)	(28)
	C	2	4	1	Pb	4	1	142	55	35
		(1)	(4)	(6)		(2)	(2)	(300)	(143)	(71)
C	Pb	1	3	1	Pb	0	0	79	27	23
		(1)	(2)	(6)		(0)	(1)	(219)	(73)	(51)
	C	2	2	1	Pb	2	0	137	69	42
		(4)	(2)	(10)		(4)	(1)	(410)	(215)	(118)

rather small and, therefore, the following conclusions are subject to large statistical uncertainty.

a) Ratio of number of s.p.s. to incident particles should correspond to the probability of production of s.p.s. And this was compared for carbon and lead producer of p.s. with each other, though only the order of magnitude can be compared because of poor statistics. From Table II it is seen that 5/238, 2/186, 6/142, 5/300, 1/67, 0/62, 4/55, 2/143 for lead are to be compared with 4/79, 3/219, 4/137, 6/410, 0/27, 0/73, 2/69, 4/215 for carbon producer respectively. From these comparisons it is presumably concluded that prominent difference do not exist. This fact probably means that the proportion of the shower particle of rather higher energy capable of producing s.p.s. is nearly equal for carbon and lead Σ, though at lower energy different energy spectrum of the shower particle were concluded as mentioned previously and, if this spectrum were valid up to the higher energy, marked difference in s.p.s. should be expected.

b) Probabilities of production of s.p.s were compared for different sized shower. If we express ratio of frequency of the large sized p.s. to the small sized ones by α and the similar ratio of p.s. whose secondary particle produced s.p.s. by β, ratio of probability of production of s.p.s. by the secondary particle of large sized shower to small sized ones is β/α. Thus, if we define the larged sized shower by "discharged $D\geq 2$" or "discharged $D\geq 3$", we obtain 0.63 ± 0.47 or 0.95 ± 0.70 of β/α respectively. Though the statistics is very poor, remarkable dependence of the probability on the size of parent shower is not seen.

c) Ocurrence probability of the s.p.s.. Mean free path of the shower particle for production of the s.p.s. can be calculated from Table II dividing the traversals by the frequency and results are given as follows.

2000∼2500 gr/cm^2 in lead
3000 gr/cm^2 especially for HS_H in lead
500 gr/cm^2 in carbon
700∼1500 gr/cm^2 especially for HS_H in carbon.

Thus the mean free path seems to be roughly 20 times of the geometrical mean free path in lead as well as in carbon.

d) Cross section of producing the s.p.s.

Mean free path given above does not, of course, directly correspond to the cross section of producing the s.p.s because of existence of shower particles whose energy is not sufficient to produce the shower.

The cross section may be estimated by comparing the producing probability of the p.s. in the producer of light and heavy element as is well known.

If the cross section of the s.p.s. by the shower particle is nearly "geometrical", ratio of producing probability of the successive shower in Σ' of lead to carbon is expected to be about 2 and for the very small cross section this ratio is to tend to about 6. This ratio could be estimated from Table II. But it should be noted that the producing probability must not be directly compared because of difference of ionization loss in the secondary producer Σ' of lead and carbon. The true value of the ratio is expected to be between

$$\frac{\text{Freq. of } HS_H+HS_S \text{ originating in lead } \Sigma'/\text{number of incident shower particle}}{\text{Freq. of } HS_H+HS_S \text{ originating in carbon } \Sigma'/\text{number of incident shower particle}}$$

$$\equiv(HS_H+HS_S)Pb/(HS_H+HS_S)_C\approx 0.8\pm0.5 \quad (0.8\pm0.6)$$

and

$$(HS_H+HS_S)Pb/(HS_H)\approx 1.3\pm0.9 \quad (1.4\pm1.1)$$

The ratio seems to be rather smaller than 2. This fact appears to be too curious, because this means that in the nucleus nucleons are packed in nearer distances than "geometrical", but it should be noted that statistical uncertainty is so large. It might be probably supposed that, in reality, the shower particle produces s.p.s. by "geometrical" cross section.

e) Size of the successive penetrating shower. The multiplicity spectrum of the successive penetrating shower represented by the number of discharged counters is compared with that of the primary penetrating shower in Fig. 5.

For the successive shower the discharged counters were counted at 10 cm lead under the secondary producer Σ'.

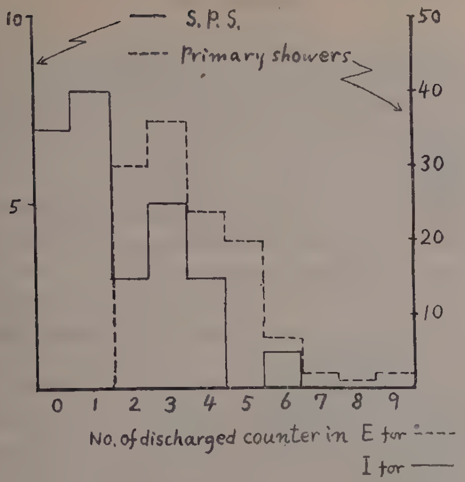

Fig. 5.

§ 5. Conclusions and Discussions

Comparion of multiplicity of penetrating shower for carbon and lead producer has been made by many experimenters but their conclusions are rather conflicting. J. R. Green[3] and W. Y. Chang et al[4] have concluded the agreement of multiplicity of the penetrating shower in light and heavy elements and A. Lovati et al[5], L. Mezzeti et al[6] and W. D. Walker et al[7] have obtained the other conclusion that the multiplicity for heavy element is larger than that for light element.

It this investigation also multiplicity of the penetrating shower was compared for carbon and lead producer. But the following points should be noted. The multiplicity was represented by the number of discharged counters and the observed multiplicity spectrum might be largely different from the real multiplicity spectrum. And the multiplicity was estimated 10 cm or 15 cm lead under the originating point of the penetrating shower and, therefore, we might be guided to erroneous conclusion because of the nuclear disintegrations which might occur in the course of the shower particles. Regarding the first point, expected difference between the real multiplicity spectrum and the observed one was estimated, assuming an angular distribution of the shower particles and taking the geometrical conditions of the counters into consideration. From these consideration it seemed to be improbable that the experimental conditions has struck out the existing disagreement. On the second point a calculation was made on the proportion of the shower particles which has experienced the nuclear interaction before it has traversed the absorbing layer of 10 cm or more lead. The results of Bristol group (IV and VI) were used on the energy distribution of the shower particle and the relation between the number of the shower particles and the energy of the primary particle. Assuming that the cross section of star-production by the shower particle is "geometrical" and considering the geometrical condition of the apparatus and the criteria of selection, it is expected that about 54 % of the shower particle did not cause the nuclear disintegration and was observed 10 cm or more lead under the originating point of the penetrating shower and 10 % or less was the daughter of the nuclear disintegration and the remainder was absorbed in the absorbing layer. Therefore, 5/6 or more of the shower particles observed under the absorbing layer is expected to traverse the absorber free from the nuclear interaction. Thus, the agreement in the multiplicity of the penetrating shower originating in carbon and lead was concluded.

Absorption of the shower particle is due to the nuclear interaction and electromagnetic interaction. If the energy spectrum of the shower particle is given, the latter can be calculated accurately and for the former rough estimation can be made using the results of Bristol group (IV and VI), though accurate results can not be expected. Absorption curves of the shower particles calculated for two different energy spectrum $E^{-1.1}$ and $E^{-1.7}$ are drawn in Fig. 3 (a), (b) assuming that the shower particles are mainly π-mesons and equal proportion of protons are given by the results of Bristol group for both cases. These curves seem to agree with the observed absorption curves for the shower particles originating in carbon and lead respectively. Thus the different energy spectrum of the shower particles originating in carbon and lead might be tentatively concluded at lower energy region (roughly centred around 500 Mev). But at rather higher energy the shower particles produce s.p.s. by, probably, "geometrical" cross section and proportion of those particles in the total shower particle is about 5 %, as the order of magnitude, equally in both cases of carbon-initiated and lead-initiated p.s.

From these conclusions and the conclusion by Walker et al it may be supposed that the comparison of the multiplicity of p.s. in light and heavy element depend on the energy of the shower particles and that if we note the shower particle of rather low energy the multiplicity for the heavy element is larger and if we note the shower particle of, say, 500 Mev or more the multiplicity for the light element is larger and for the shower particle which is capable of producing s.p.s. no difference exists. These supposition may be qualitatively accepted setting some assumptions on the propagation of the shower particles in the nuclear matter and if definite results were obtained along these lines we may be able to know the behavior of the shower particles in the nuclear matter definitely. Thus the conclusions on the matter by the authors, mentioned previously, should be investigated considering the experimental conditions respectively.

References

1) U. Camerini, P. H. Fowler, W. O. Lock and H. Muirhead: Phil. Mag. **41** (1950) 413 (IV).
W. O. Lock, D. H. Perkins and G. Yekutieli: Phil. Mag. **42** (1951) 1241 (VI) and other studies.
2) F. E. Froelich, E. M. Marth and K. Sitte: Physical Review **89** (1952) 504.
3) J. R. Green: Physical Review **80** (1950) 832.
4) W. Y. Chang, G. Castillo and L. Grodzins: Physical Review **84** 1951) 582.
5) A. Lovati, A. Mura, G. Salvini and G. Jagliaferri: Physical Review **77** (1950) 284, Nuovo Ciment **7** (1950) 36.
6) L. Mezzettei and R. Querzoli: Nuovo Ciment **6** (1949) 488, Nuovo Ciment **7** (1950) 470, Physical Review **79** (1950) 168.
7) W. D. Walker, N. M. Duller and J. D. Sorrels: Physical Review **86** (1952) 865.

JOURNAL OF THE PHYSICAL SOCIETY OF JAPAN Vol. 8, No. 5, SEP.—OCT., 1953

Atomic Distribution Functions of Liquids

By Akira HARASIMA
Tokyo Institute of Technology, Oh-Okayama, Meguro, Tokyo

(Received April 25, 1953)

Atomic distribution functions of liquids are treated by the cell method. A correlation between the positions of two atoms in neighboring cells is introduced. By supposing that two atoms, interacting each other, are in an average field due to other atoms, we have derived the form of the first peak of the distribution function. It is shown that we can derive a general law for the temperature dependence of the form of the first peak of the atomic distribution function.

§ 1. The Cell Method

It is well known that the atomic distribution function plays an important rôle in the theory of liquids. If the atomic or molecular distribution function of a liquid is known, we can obtain the equation of state and other thermodynamical properties in terms of the distribution function. Thus it is the most important subject to determine the distribution function of a liquid by the theory of statistical mechanics. Moreover, distribution functions of liquids can be determined by the X-ray scattering technique,[1] so that it is very easy to compare the theoretical results with the experimental ones.

The best method of determining distribution functions would be to solve Kirkwood's integral equation[2] or Born-Green's.[3] But the so-called "superposition approximation" is used in deriving these integral equations, and the theoretical results do not agree well with the experimental ones in low temperature regions. Moreover, it is necessary to resort to numerical calculations to such an extent that the method is not suitable for deriving general conclusions on the behaviors of distribution functions, especially when we inquire how the forms of distribution functions change with temperatures.

Another method which is frequently adopted in the theory of liquid is the "cell method" or "free volume method." In the cell method, each atom is considered to lie in a cell formed by the surrounding atoms and statistical mechanics is applied to this model. Adopting this model we can derive thermodynamical properties of liquids and compare them with experimental data and many theories have been estiblished on this line.

Atomic distribution functions can also be derived by the cell method, and some results were obtained by Wall,[4] Coulson and Rushbrooke,[5] and Harasima.[6] In this model cell centers are assumed to form a regular arrangement and this assumption makes it impossible to discuss the form of the distribution function at a long distance. But it may be used to discuss the shape of the distribution function near its first peak; and it has the advantage of leading to general conclusions, which cannot be derived by the method of solving integral equations numerically.

Though the cell method was at fist somewhat intuitive and the exactitude of approximation was indefinite, the method was made more promising by the work of Korkwood[7] who showed that it is derivable, with a certain approximation, from the fundamental statistical-mechanical basis. Kirkwood's theory was later generalized by Mayer and Careri[8] who showed that the size of the cells and other parameters should be determined in such a way that the value of the free energy of the system may take the minimum value. Thus they made the theory self-consitent in the sence that the pressure of the liquid calculated by the virial theorem coincides with that calculated thermodynamically and the entropy calculated by the kinetic theory coincides with the calculated thermodynamically. Further, Careri[9] showed that the probability distribution function of an atom in the cell is of Gaussian type up to the temperatures approximate to the critical point.

In these theories, however, the correletion of positions of neighboring atoms, each in neighboring cells, are not taken into account. Thus though the chance for two neighboring atoms to come very near to each other should be very small, the fact has not been considered in theories thus far published.

In this paper we wish to develop a theory in which two neighboring atoms, interacting each other, are assumed to be in the field of the mean force from the rest of the liquid, so that the correlation of their positions is taken into account. By this method, we will show that we can derive a general conclusion as to the behavior of the first peak of the distribution function when the temperatured is changed.

§ 2. Calculation of the Distribution Function

We now consider a system composed of N atoms. Let $\Phi(\boldsymbol{r}_1,\boldsymbol{r}_2,\cdots;\boldsymbol{r}_N)$ be the potential energy of the whole system when the atoms are at $\boldsymbol{r}_1,\boldsymbol{r}_2,\cdots,\boldsymbol{r}_N$. Then the mean number of pairs of atoms each in dv at $\boldsymbol{r}$ and dv' at $\boldsymbol{r}'$ is given by $\rho^{(2)}(\boldsymbol{r},\boldsymbol{r}')dvdv'$, where

$$\begin{aligned}\rho^{(2)}(\boldsymbol{r},\boldsymbol{r}')=(N-1)&\iint\cdots\int\exp\\&[-\Phi(\boldsymbol{r},\boldsymbol{r}',\boldsymbol{r}_3,\cdots,\boldsymbol{r}_N)/kT]dv_3dv_4\cdots dv_N\\&\div\iint\cdots\int\exp[-\Phi(\boldsymbol{r}_1,\boldsymbol{r}_2,\boldsymbol{r}_2\cdots,\boldsymbol{r}_N)\\&\times 1/kT]dv_1dv_2dv_3\cdots dv_N\end{aligned}\tag{1}$$

where T is the absolute temperature and k Boltzmann's constant. If we divide $\rho^{(2)}(\boldsymbol{r},\boldsymbol{r}')$ by the mean density ρ we obtain the mean density around any specified atom. We then differentiate the logarithm of $\rho^{(2)}/\rho$ with respect to $\boldsymbol{r}'$. Then, assuming that the potential energy of the whole system can be expressed as a sum of pair potentials, that is, assuming

$$\Phi(\boldsymbol{r}_1,\boldsymbol{r}_2,\cdots,\boldsymbol{r}_N)=\sum_{k<i}\phi(|\boldsymbol{r}_k-\boldsymbol{r}_i|)\,,\tag{2}$$

we have

$$\begin{aligned}kT\nabla_{r'}\log\rho^{(2)}(\boldsymbol{r},\boldsymbol{r}')/\rho=&-\nabla_{r'}\phi(|\boldsymbol{r}'-\boldsymbol{r}|)\\&-\sum_{k=3}^{N}\iint\cdots\int\nabla_{r'}\phi(|\boldsymbol{r}'-\boldsymbol{r}_k|)\exp\\&[-\Phi(\boldsymbol{r},\boldsymbol{r}',\boldsymbol{r}_3,\cdots,\boldsymbol{r}_N)/kT]dv_3\cdots dv_N\\&\div\iint\cdots\int\exp[-\Phi(\boldsymbol{r},\boldsymbol{r}',\boldsymbol{r}_3,\cdots,\boldsymbol{r}_N)\\&\times 1/kT]dv_3\cdots dv_N\,.\end{aligned}\tag{3}$$

The second term on the right side of the above equation is the mean force on an atom at $\boldsymbol{r}'$ when two atoms are fixed at $\boldsymbol{r}$ and $\boldsymbol{r}'$ and other atoms take every possible configurations around these two specified atoms. This mean force depends natually on the position $\boldsymbol{r}$ of the first atom and it is not spherically symmetric around the center O' of the second cell. But, in this preliminary attempt to take the correlation of positions of atoms into consideration, we shall assume that the mean force is of the form spherically symmetric around O'. Then denoting the potential for this mean force by $V(\boldsymbol{r}')$, we have

$$kT\nabla_{\boldsymbol{r}'}\log\rho^{(2)}(\boldsymbol{r},\boldsymbol{r}')/\rho=-\nabla_{\boldsymbol{r}'}\phi(|\boldsymbol{r}'-\boldsymbol{r}|)-\nabla_{\boldsymbol{r}'}V(\boldsymbol{r}')\,.$$

Similarly, we have

$$kT\nabla_{\boldsymbol{r}}\log\rho^{(2)}(\boldsymbol{r},\boldsymbol{r}')/\rho=-\nabla_{\boldsymbol{r}}\phi(|\boldsymbol{r}'-\boldsymbol{r}|)-\nabla_{\boldsymbol{r}}V(\boldsymbol{r})\,.$$

Hence, for the distribution function we have

$$\log\rho^{(2)}(\boldsymbol{r},\boldsymbol{r}')/\rho=-\phi(|\boldsymbol{r}'-\boldsymbol{r}|)/kT \\ -V(r)-V(r')+\text{const}\,,$$

and putting

$$\rho^{(2)}(\boldsymbol{r},\boldsymbol{r}')=\rho\cdot\rho(\boldsymbol{r},\boldsymbol{r}')\,,$$

we have

$$\rho(\boldsymbol{r},\boldsymbol{r}')=C\exp-[\phi(|\boldsymbol{r}'-\boldsymbol{r}|)-V(r)-V(r')]/kT\,. \tag{4}$$

If PdR denotes the probability that the distance between two atoms $|\boldsymbol{r}'-\boldsymbol{r}|=R$ is between R and $R+dR$, we have

$$PdR=A\iint\cdots\int\exp-[\phi(R)-V(r) \\ -V(r')]/kT\,dvdv'\,.$$

Let the two atoms be A and A' and the center of cells O and O'. Putting

$$OO'=a\,,\quad OA=r\,,\quad O'A'=r'\,, \\ AO'=s\,,\quad AA'=R\,,$$

we have

$$dv=(2\pi rs/a)drds\,,\quad dv'=(2\pi Rr'/s)dRdr'\,. \tag{5}$$

Thus we have

$$P=A\int_{a/2}^{3/2a}\int_{|a-s|}^{\infty}\int_{|R-s|}^{\infty}\exp-[\phi(R)-V(r) \\ -V(r')]/kT\cdot(4\pi^2Rr'rs/as)dr'drds\,.$$

If we put

$$\chi(\xi)=\int_{\xi}^{\infty}r\exp[-V(r)/kT]dr=\chi(\xi)\,, \tag{6}$$

we have

$$P=A(4\pi^2R/a)\exp[-\phi(R)/kT] \\ \times\int_{-a/2}^{a/2}\chi(|R-\sigma-a|)\chi(|\sigma|)d\sigma\,.$$

Now, since $\chi(\xi)$ may be assumed to become very small rapidly as ξ increases, we may take the integration interval $(-a/2, a/2)$ to be $(-\infty, \infty)$. Then, we have

$$P=A(4\pi^2R/a)\exp[-\phi(R)/kT] \\ \times\int_{-\infty}^{\infty}\chi(|R-\sigma-a|)\chi(|\sigma|)d\sigma\,. \tag{7}$$

Further in order to simplify our arguments we shall assume that $V(r)$ is of the form

$$V(r)=(1/2)cr^2\,. \tag{8}$$

This means that the atom A' would have a Gaussian distribution if it were in the field of other atoms than A. We can then perform the integration in (7) easily, so that P is given by

$$P=A[4\pi^{5/2}(kT)^{5/2}/ac^{5/2}]R\exp[-\phi(R)/kT] \\ \times\exp[-(c/4kT)(R-a)^2]\,, \tag{9}$$

where A is determined by the condition

$$\int_0^{2a}PdR=1\,.$$

If we assume further that $\exp[-(c/4kT)(R-a)^2]$ decreases very rapidly for larger values of $R-a$, we can expand $\phi(R)$ in a power series of $R-a$. As for the value of a, we may assume it to be equal to the value of R corresponding to the minimum of $\phi(R)$ as can be justified from the experimental distribution functions. Thus, we have

$$P=\{\phi''(a)/2+c/4\}^{1/2}/(\pi kT)^{1/2}\cdot \\ \times\{\exp[-\phi(R)/kT]/\exp[-\phi(a)/kT]\} \\ \times R/a\cdot\exp[-c/4kT(R-a)^2]\,. \tag{10}$$

If the number of atoms in the neighboring cells around an atoms is z, we have

$$4\pi R^2\rho(R)=Pz\,,$$

so that we have for the function

$$y=4\pi R\rho(R)\,, \tag{11}$$

the following expression:

$$y=y_{\max}\exp[-\phi(R)/kT]/\exp[-\phi(a)/kT] \\ \times(1/a)\cdot\exp[-c/4kT(R-a)^2]\,, \tag{12}$$

where

$$y_{\max}=z\{\phi''(a)/2+c/4\}/(\pi kT)^{1/2}\,. \tag{13}$$

§ 3. Dependence of $y_{\max}$ upon the Temperature

The equation (13) shows that, if z and c do not depend on the temperature, then

$$y_{\max}=C/T^{1/2}\,,\qquad C:a\text{ constant}\,. \quad (14)$$

According to the experimental results by Boyd and Wakeham,[10)] z and a do not much vary with temperature in the case of mercury. So we can expect the formula (14) to hold for mercury and this can be confirmed by the distribution functions obtained by Boyd and Wakeham. The $T^{-1/2}$-law can also be derived from the cell model without taking the correlation between neighbouring cells into consideration.[11)] When the potential of the average force on an atom enclosed in a cell is proportional to the square of the distance from the cell center and this potential is independent of the temperature, then it is very easy to derieve $T^{-1/2}$-law for the first peak of the distribution function without taking the correlation into consideration.[6)]

For liquid argon $y_{\max}$ changes with temperature more rapidly than the $T^{-1/2}$-law demands. According to the investigations made by Eisenstein and Gingrich,[12)] the value of z varies with the temperature to a considerable degree. Therefore, we can expect the value of c to vary with temperature considerably, so that the variation of $y_{\max}$ cannot be expressed merely by the $T^{-1/2}$-law.

To obtain a rough estimate of the dependence of $y_{\max}$ on z, we shall estimate the dependence of c on z. As we have already said the fields upon an atom from other atoms than that whose position is to be correlated to the one in question are smeared to give spherically symmetric fields. These smeared filds were calculated by Lennard-Jones and Devonshire;[13)] Prigogine and Raulier;[14)] Prigogine and Garikian;[15)] Hill;[16)] Wentorf, Buehler, Hirschfelder and Curtiss.[17)] Lennard-Jones and Devonshire considered the nearest neighbors only in calculating the field on the atom in the central cell, while others considered the fields from more distant as well as the neighboring atoms. In this paper we shall be satisfied with the field calculated by Lennard-Jones and Devonshire since if we were to use more accurate fields we would have to refine other aspects of the theory.

Let the mutual potential between two atoms be of the form

$$\phi(R)=\phi_0[(a/R)^{12}-2(a/R)^6]\,, \quad (15)$$

then according to Lennard-Jones and Devonshire, the mean potential (smeared potential) due to the neighboring atoms is given by,

$$\psi(r)-\psi(o)=z'\phi_0\{l(y)-2m(y)\}\,, \quad (16)$$

where

$$y=(r/a)^2$$

and

$$l(y)=[1+12y+(25.2)y^2+12y^3+y^4](1-y)^{-10}-1\,,$$
$$m(y)=(1+y)(1-y)^{-4}-1\,.$$

In the equation (16) z' is the number of neighboring atoms which give rise to the field on either of the two central atoms, so that it is given by

$$z'=z-1\,. \quad (17)$$

If we assume that the potential of the mean force $V(r)$ is equal to $\psi(r)-\psi(o)$ which is given by (16), we can obtain $\chi(\xi)$ by (6) and therefore the value of P from (7). In order to let the form of $V(r)$ be of the same form as (8), we shall expand the right side of (16) in powers of y. Thus we have

$$V(r)=\psi(r)-\psi(o)=12z'\phi_0 y\,,$$

so that if we put

$$c=24z'\phi_0/a^2=24(z-1)\phi_0/a^2\,, \quad (18)$$

the form of $V(r)$ will be just of the form of (8). Further, since

$$\phi''(a)=-72\phi_0/a^2\,,$$

we have from (13),

$$y_{\max}=(6\phi_0/\pi ka^2)^{1/2}\{(5+z)/T\}^{1/2}z\,. \quad (19)$$

For argon the constants in the expression of the potential (15) are

$$\phi_0=1.66\times10^{-14}\text{ erg}\,,\qquad a=3.83\times10^{-8}\text{ cm}\,.$$

Substituting these values in (19), we have

$$y_{\max}=1.05\{(5+z)/T\}^{1/2}z\,. \quad (20)$$

This formula shows how $y_{\max}$ depends on the value of z while it is at the same time proportional to $T^{-1/2}$.

Though the result expressed by (20) has been derived by making several approximations, it may be said that the formula will give rough estimates how $y_{\max}$ depends on T and z. Comparison with the experiment of Eisenstein and Gingrich[18] is shown in Table I.

Table I

T	z	$(y_{\max})_{\text{calc.}}$	$(y_{\max})_{\text{obs.}}$
84	11	5.0	3.4
92	7	2.7	2.4
127	6	1.8	1.6
144	4.3	1.2	1.3

From this table we can see that the calculated values of $y_{\max}$ agree with the observed values better than those calculated by $T^{-1/2}$-law.

References

1) F. Zernike and J. A. Prins: Zeits. f. Physik **41** (1927) 181; P. Debye and H. Menke: Physik. Zeits. **31** (1930) 797; R. N. Boyd and H. R. R. Wakeham: J. Chem. Phys. **7** (1939) 958; A. Eisenstein and N. S. Gingrich: Phys. Rev. **62** (1942) 261.

2) J. G. Kirkwood: J. Chem. Phys. **3** (1935) 300; J. G. Kirkwood and E. M. Boggs: J. Chem. Phys. **10** (1942) 394; J. G. Kirkwood, E. K. Maun and B. J. Alder: J. Chem. Phys. **18** (1950) 1040; J. G. Kirkwood, V. A. Lewinson and B. J. Alder: J. Chem. Phys. **20** (1952) 929.

3) M. Born and H. S. Green: Proc. Roy. Soc. **A 188** (1946) 10; A. E. Rodriguez: Proc. Roy. Soc. **A 196** (1949) 73; Revista de la Union Matematica Argentina **V. 14** (1950) 156.

4) C. N. Wall: Phys. Rev. **54** (1938) 1062.

5) C. A. Coulson and G. S. Rushbrooke: Phys. Rev. **56** (1939) 1216.

6) A. Harasima: Proc. Phys.-Math. Soc. Japan **25** (1943) 534; A. Harasima and H. Oguri: Proc. Phys.-Math. Soc. Japan **25** (1943) 425.

7) J. G. Kirkwood: J. Chem. Phys. **18** (1850) 380.

8) J. E. Mayer and G. Careri: J. Chem. Phys. **20** (1952) 1001.

9) G. Careri: J. Chem. Phys. **20** (1952) 1114.

10) R. N. Boyd and H. R. R. Wakeham: loc. cit.

11) A. Harasima and H. Oguri: loc. cit.

12) A. Eisenstein and N. S. Gingrich: loc. cit.

13) J. E. Lennard-Jones and A. F. Devonshire: Proc. Roy. Soc. **A 163** (1937) 53.

14) I. Prigogine and S. Raulier: Physica **9** (1942) 396.

15) I. Prigogine and G. Garikian: J. Chim. Phys. **45** (1948) 273.

16) T. L. Hill: J. Phys. Colloid Chem. **51** (1947) 1219.

17) R. H. Wentorf, R. J. Buehler, J. O. Hirschfelder and C. F. Curtiss: J. Chem. Phys. **18** (1950) 1484.

18) A. Eisenstein and N. S. Gingrich: loc. cit.

JOURNAL OF THE PHYSICAL SOCIETY OF JAPAN Vol. 8, No. 5, SEP.—OCT., 1953

On the Electrical Conductivity of Cuprous Sulfide: A Diffusion Theory

By Isaaki YOKOTA

Department of Physics, Faculty of Science, University of Niigata, Niigata

(Received May 22, 1953)

Mixed electrical conduction of solid cuprous sulfide at the β-phase, a *p*-type semiconductor, is treated theoretically, though phenomenologically, for the case where the current is maintained at a constant intensity, insufficient to electrolize out copper ions. The drift motion of acceptors (vacant copper ion lattice points) may be described with a diffusion equation, which can be linearlized when some physical assumptions are made, and then can easily be integrated under proper initial and boundary conditions. Theoretical expressions for the potential distributions are derived for the process of tending to the limiting stationary state as well as for the stationary state. Expression for the residual potential — a potential which remains after the current has been switched off and decays according as the initial homogeneity is recovered—is derived. *V-I* characteristics for the stationary current are also given. Calculated results are compared with experiments by Miyatani and Suzuki, exhibiting satisfactory agreements.

§ 1. Introduction

Solid ouprous sulfide is a *p*-type semiconductor and exhibits mixed electrical conduction partly ionic and partly electronic, at its *β*-phase (110°–470° C), with the conductivity much depending upon the excess or deficit amount of copper in the specimen.[1] The fact that the electrical conductivity decreases with increasing amount of copper shows that the vacant lattice points of copper-site serve as the acceptors.

Some peculiar behaviors of cuprous sulfide at the *β*-phase, which may be attributed to the drift motion of copper ions, have been observed by Hirahara[1] and Kushida,[2] and recently also by Miyatani and Suzuki.[3]

They have found, for instance, a phenomenon which may be called as voltage creep,[4] when the current was maintained at a constant intensity, insufficient to electrolize out copper ions. When a current is switched in through a specimen of relatively low resistivity, the potential drop between two probes near the anode gradually decreases and tends to a stationary value, while the potential drop between two probes near the cathode gradually increases and tends to another stationary value. This may be interpreted in terms of the drift motion of copper ions towards the cathode driven by the electric force.

When a electric field is applied to a specimen, some of the copper ions in it begin to move towards the cathode. Consequently, the part near the anode becomes more abundant in vacant copper ion lattice points (acceptors), and hence more conductive, while the part near the cathode becomes less abundant in vacant copper ion lattice points, and hence less conductive, as far as the applied voltage is insufficient to electrolize out copper ions at the cathode; and the stationary state is reached when the drift motion of copper ions driven by the electric field is counterbalanced by their back diffusion.

When the current is switched off after the stationary state has been reached, the potential drop through the specimen does not die out instantly, but a part of it remains and decays at first rapidly and then exponentially. This residual potential may be interpreted as caused by the exsistence of internal electric field which drives the holes against the ionic current accompanied by the back diffusion of copper ions, so as to give the null resultant current.

In the followings, a phenomenological theory of mixed conduction shall be given from the above point of view for the case where the current is too weak to electrolize out copper ions, and shall be compared with experiments by Miyatani and Suzuki.

§ 2. Fundamental Equations

The fundamental equations which describe the mixed electrical conduction are the current equation and the diffusion equation of acceptors (or donors). In the present case the acceptors consist of vacant copper ion lattice points. We have[5],[6]

$$I=ep_h n_h E+ep_a n_a E+eD\frac{\partial n_a}{\partial x}\,, \qquad (1)$$

and

$$\frac{\partial n_a}{\partial t}=\frac{\partial}{\partial x}\left(p_a n_a E+D\frac{\partial n_a}{\partial x}\right), \qquad (2)$$

where

I, the current density maintained at a constant value,

p_h, the mobility of holes,

p_a, the mobility of vacant copper ion lattice points,

n_h, the density of holes,

n_a, the density of vacant copper ion lattice points,

E; not the electrostatic field but the gradient of quasi-Fermi level[7] for electrons divided by elementary charge,

and

D; the diffusion coefficient of vacant lattice points of copper ion.

Solving Eq. (1) for E

$$E=\frac{I}{e(p_h n_h+p_a n_a)}-\frac{D}{p_h n_h+p_a n_a}\frac{\partial n_a}{\partial x}\,, \qquad (3)$$

and inserting this into Eq. (2), we have

$$\frac{\partial n_a}{\partial t}=\frac{\partial}{\partial x}\left[D^*\left(\frac{I n_a}{kTp_h n_h}+\frac{\partial n_a}{\partial x}\right)\right], \qquad (4)$$

where

$$D^*=\frac{p_h n_h}{p_h n_h+p_a n_a}D\,, \qquad (5)$$

and the Townsend-Einstien relation

$$D=p_a\frac{kT}{e} \qquad (6)$$

has been used.

Now we assume that the holes are locally in equilibrium with the acceptors. Then the hole density n_h should be a certain function of n_a (and of the temperature T). The mobilities of holes and vacant copper ion lattice points, p_h and p_a, may also depend on n_a (and on T). If these functional relationships are all known, then the diffusion equation (4) can be solved for n_a, at least, in principle, under proper boundary conditions. Substituting the solution thus obtained into Eq. (3) and integrating over the positional coordinate x, we obtain the potential distribution as a function of time and coordinate. In order to carry out the above procedures in practice, we make the following simplified assumptions.

(1) The mobilities of both holes and vacant lattice points are independent of the density of vacant lattice points, as far as the variation of the latter is not so great.

(2) The hole density n_h is proportional to the density of vacant lattice points n_a.

The latter assumption of the proportionality of n_h to n_a seems physically unreasonable except for the special case where the equality $n_h=n_a$ is realized, i.e., the acceptors are completely associated with electrons. As we shall see later, the equality, $n_h=n_a$ seems to be realized in cuprous sulfide at the β-phase; and the proportionality is formally more general than the equality.

If the above assumptions are accepted, we have

$$\frac{n_h}{n_a}=\frac{\bar{n}_h}{\bar{n}_a}\,, \qquad (7)$$

where $\bar{n}_h$ and $\bar{n}_a$ are the respective equilibrium values of n_h and n_a, and Eq. (4) can be reduced to the well known linear diffusion equation

$$\frac{\partial n_a^*}{\partial t}=D^*\frac{\partial^2 n_a^*}{\partial x^2}\,, \qquad (8)$$

with

$$n_a^*=n_a+\frac{eI}{kT\sigma_h}\bar{n}_a x\,, \qquad (9)$$

and

$$D^*=\frac{\sigma_h}{\sigma_h+\sigma_a}D\,, \qquad (10)$$

where

$$\sigma_h=ep_h\bar{n}_h \quad \text{and} \quad \sigma_a=ep_a\bar{n}_a\,, \qquad (11)$$

are hole and ionic conductivities.

The circumstances that the copper ions are neither supplied to nor removed from the specimen can be expressed by the boundary conditions

$$\left(\frac{\partial n_a^*}{\partial x}\right)_{x=0}=\left(\frac{\partial n_a^*}{\partial x}\right)_{x=L}=0\,, \qquad (12)$$

where L is the length of the specimen.

When the current is switched in at the instant $t=0$, the initial condition for n_d^* becomes

$$(n_d^*)_{t=0}=\bar{n}_d\left(1+\frac{eI}{kT\sigma_h}x\right). \qquad (13)$$

The solusion of the diffusion equation (8) under the boundary conditions (12) and the initial condition (13) can easily be obtained as a Fourier series. We have for n_d

$$\frac{n_d}{\bar{n}_d}=1-\frac{eIL}{kT\sigma_h}\left\{\frac{x}{L}-\frac{1}{2}\right.$$
$$+\frac{4}{\pi^2}\sum_{m=0}^{\infty}\frac{1}{(2m+1)^2}e^{-(2m+1)^2\cdot t/\tau}$$
$$\left.\times\cos(2m+1)\pi\frac{x}{L}\right\}, \qquad (14)$$

where

$$\tau=\frac{L^2}{\pi^2 D^*}=\frac{\sigma_h+\sigma_d}{\sigma_h}\frac{L^2}{\pi^2 D}, \qquad (15)$$

has the dimension of time and may be called as the time of diffusion with which one may measure the rate of building up of the stationary distribution.

In the limiting stationary state where the cosine series in Eq. (14) vanishes, we have

$$\frac{n_d}{\bar{n}_d}=1-\frac{eIL}{kT\sigma_h}\left(\frac{x}{L}-\frac{1}{2}\right), \qquad (16)$$

showing that the density of vacant copper ion lattice points decreases linearly along the specimen from the anode to the cathode. Since n_d can never be negative, the inequality

$$\alpha\equiv\frac{eIL}{2kT\sigma_h}<1, \qquad (17)$$

must be satisfied. The inequality (17) indicates the upper limit of the current density for which the present theory can be applied. When the current density is over this limitation, precipitation or pre-precipitation seems to take place at the cathode.[3]

§ 3. Potential Distribution

The expression for the potential drop $V(x)$ from the anode to a point at distance x from the anode can be obtained by integrating Eq. (3) from 0 to x:

$$V(x)=\frac{I}{\sigma_h+\sigma_d}\int_0^x\frac{dx}{(n_d/\bar{n}_d)}$$
$$+\frac{kT}{e}\frac{\sigma_d}{\sigma_h+\sigma_d}\ln\frac{n_d(0)}{n_d(x)}. \qquad (18)$$

The meaning of the first term is obvious: $(\sigma_h+\sigma_d)^{-1}\int_0^x(n_d/\bar{n}_d)^{-1}dx$ is the ohmic resistance. As regards the meaning of the second term, see the next paragraph.

Inserting Eq. (14) into Eq. (18) and carrying out the integration numerically, we can obtain the potential drop at any part of the specimen at any time.

At the instant when the current is switched in, the potential drop through the total length of the specimen is

$$V_i=\frac{IL}{\sigma_h+\sigma_d}, \qquad (19)$$

which we shall call the initial voltage. Sometimes it is more convenient to use the initial voltage instead of the current density. Substituting Eq. (19) into Eq. (14) and (16), we have

$$\frac{n_d}{\bar{n}_d}=1-\frac{\sigma_h+\sigma_d}{\sigma_h}\frac{eV_i}{kT}\left\{\frac{x}{L}-\frac{1}{2}\right.$$
$$+\frac{4}{\pi^2}\sum_{m=0}^{\infty}\frac{1}{(2m+1)^2}e^{-(2m+1)^2\cdot t/\tau}$$
$$\left.\times\cos(2m+1)\pi\frac{x}{L}\right\}, \qquad (14a)$$

for the building up of the stationary state, and

$$\frac{n_d}{\bar{n}_d}=1-\frac{\sigma_h+\sigma_d}{\sigma_h}\frac{eV_i}{kT}\left\{\frac{x}{L}-\frac{1}{2}\right\}, \qquad (16a)$$

for the stationary state. The inequality (17) also can be written as

$$\alpha=\frac{\sigma_h+\sigma_d}{\sigma_h}\frac{eV_i}{2kT}<1. \qquad (17a)$$

For the stationary state, where $n_d/\bar{n}_d$ is given by Eq. (16) or (16a), the integration in (18) can easily be carried out, and we get

$$V(x)=\frac{kT}{e}\ln\frac{1+\dfrac{eIL}{2kT\sigma_h}}{1+\dfrac{eIL}{2kT\sigma_h}\left(1-\dfrac{2x}{L}\right)}, \qquad (20)$$

or

$$V(x)=\frac{kT}{e}\ln\frac{1+\dfrac{\sigma_h+\sigma_d}{\sigma_h}\dfrac{eV_i}{2kT}}{1+\dfrac{\sigma_h+\sigma_d}{\sigma_h}\dfrac{eV_i}{2kT}\left(1-\dfrac{2x}{L}\right)}. \qquad (20a)$$

The $V-I$ characteristics for the stationary current may be obtained by putting $x=L$ in Eq. (20). We find

$$V(x)=\frac{kT}{e}\ln\frac{1+\dfrac{eIL}{2kT\sigma_h}}{1-\dfrac{eIL}{2kT\sigma_h}}, \qquad (21)$$

which shows the non-ohmic characters.

Eq. (20) or (20a) shows that if we plot $\exp(-eV/kT)$ against x for a stationary potential distribution, we should have a straight line, the inclination of which is determined by the numerical value of α defined in Eq. (17) or (17a).

On the ground of the same kind as in the present work, an expression similar to Eq. (20) has been derived by Hebb[6)] for the stationary potential distribution in silver sulfide, a n-type semiconductor with mobile silver ions.

§ 4. Residual Potential

Even when there is no net current in a specimen ($I=0$), there appears a potential gradient as far as inhomogeneity of the density of vacant copper ion lattice points remains in it, as it is easily seen from Eq. (1) or (18). In this case, the diffusion equation and the boundary conditions are the same as Eqs. (8) and (12) except $n_a{}^*$ is replaced by $n_a{}'$:

$$\frac{\partial n_a}{\partial t}=D^*\frac{\partial^2 n_a}{\partial x^2}, \qquad (22)$$

$$\left(\frac{\partial n_a}{\partial x}\right)_{x=0}=\left(\frac{\partial n_a}{\partial x}\right)_{x=L}=0. \qquad (23)$$

And putting $I=0$ in Eq. (18), the potential distribution becomes,

$$V(x)=\frac{\sigma_a}{\sigma_h+\sigma_a}\,\frac{kT}{e}\ln\frac{n_a(o)}{n_a(x)}. \qquad (24)$$

Eq. (24) (or the second term of Eq. (18)) may be interpreted as follow: When there is inhomogeneity of the density of vacant copper ion lattice points in a specimen, there should occur the diffusion of copper ions in it. The diffusion current of copper ions produces an electric field* which drives the holes against the diffusion current so as to give the null resultant current. This electric field, when integrated, gives Eq. (24) (or the second term of Eq. (18)).

The electric field thus produced opposes to the diffusion current. This is the reason why there occurs the apparant diffusion coefficient D^* instead of the true diffusion coefficient D in our diffusion equations.

In such a case as the current is switched off after the stationary potential distribution has been realized, the initial condition for n_a is (see Eq. (16a))

$$\left(\frac{n_a}{\bar{n}_a}\right)_{t=0}=1-\frac{\sigma_h+\sigma_a}{\sigma_h}\,\frac{eV_t}{2kT}\left\{\frac{x}{L}-\frac{1}{2}\right\}, \qquad (25)$$

The solution of the diffusion equation (22) under the boundary conditions (23) and the initial condition (25) may easily be obtained. We get

$$\frac{n_a}{\bar{n}_a}=1+\frac{\sigma_h+\sigma_a}{\sigma_h}\,\frac{eV_t}{kT}\,\frac{4}{\pi^2}\sum_{m=0}^{\infty}\frac{1}{(2m+1)^2}e^{-(2m+1)^2\cdot t/\tau}$$
$$\times\cos(2m+1)\pi\frac{x}{L}. \qquad (26)$$

Inserting Eq. (26) into Eq. (24), we have the expression of residual potential as a function of time and coordinate.

Inserting Eq. (25) into Eq. (24), and comparing with Eq. (20a), we find that the potential at any point of the specimen drops to the fraction $\sigma_a/(\sigma_h+\sigma_a)$ of the stationary value at the instant of switching off.

§ 5. Comparison with Experiments

Now we proceed to the comparison of the present theory with the experiments by Miyatani and Suzuki. The experimental data here adopted are those obtained for a specimen of rather low resistivity (No. 26). The dimension of the specimen is 1.28×7.2×23.2 mm. The current is maintained at 4.07 mA in every case, hence the current density I is 44.1 mA/cm^2.

We start with the comparison concerning residual potential, since it can be computed with less effort. Eq. (26) contains two unknown parameters, $\sigma_a/(\sigma_h+\sigma_a)$ and τ, which need to be determined. (V_t can easily be determined from the initial potential distribution on the probes). The former can, in principle, be determined as the ratio of the residual potential at the instant of switching off to the corresponding stationary value (see § 4). The residual potential, however, decays very rapidly immediately after the switching off, and hence the residual potential value extrapolated to the instant of the switching off should contain considerable inaccuracy. Starting with the value of $\sigma_a/(\sigma_h+\sigma_a)$ roughly estimated as the ratio of the graphically extrapolated initial residual potential to the corresponding stationary value, we determine both $\sigma_d/(\sigma_h+\sigma_d)$ and τ by trials and errors so as to give the best fit with the measured residual potential values. The so determined numerical values of $\sigma_d/(\sigma_h+\sigma_d)$ and τ are tabulated in Table I for four temperatures at which the measurements have been carried out, together with the numerical values of V_t and $\alpha=((\sigma_h+\sigma_d)/\sigma_h)(eV_t/2kT)$.

---

*Strictly speaking, not the electro-static field but the gradient of the quasi-Fermi level.

The calculated decay curves of residual potentials are shown in Fig. 1 together with the corresponding measured values. The number added to each curve denotes the number of the corresponding probe. The ordinate of each curve represents the potential drop between the probe O and the corresponding probe, $V-V_0$. The positions of the probes are indicated on the horizontal line above the figure.

Table I. Numerical values of parameters.

T (°K)	V (mV)	$\frac{\sigma_d}{\sigma_h+\sigma_d}$	τ (sec)	$\alpha=\frac{\sigma_h+\sigma_d}{\sigma_h}\frac{eV_t}{2kT}$
407	27.17	0.052	630	0.405
433	26.75	0.083	390	0.387
456	26.31	0.115	280	0.375
480	25.81	0.150	200	0.364

The changes of the potential drops between the probe O and the others, $V-V_0$, with time after the switching in of the current are calculated according to Eqs. (18) and (14) with the use of the numerical values of parameters tabulated in Table I, and are shown in Fig.

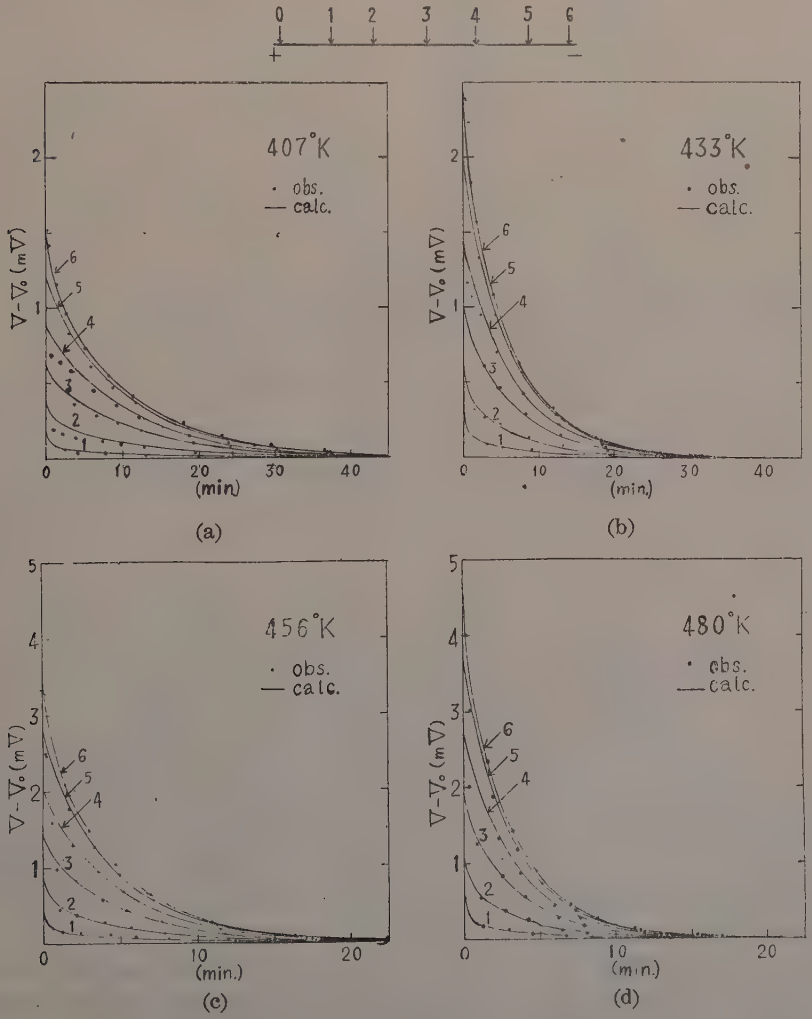

Fig. 1. Comparison of the theoretical curves for decay of residual potential with experiments.

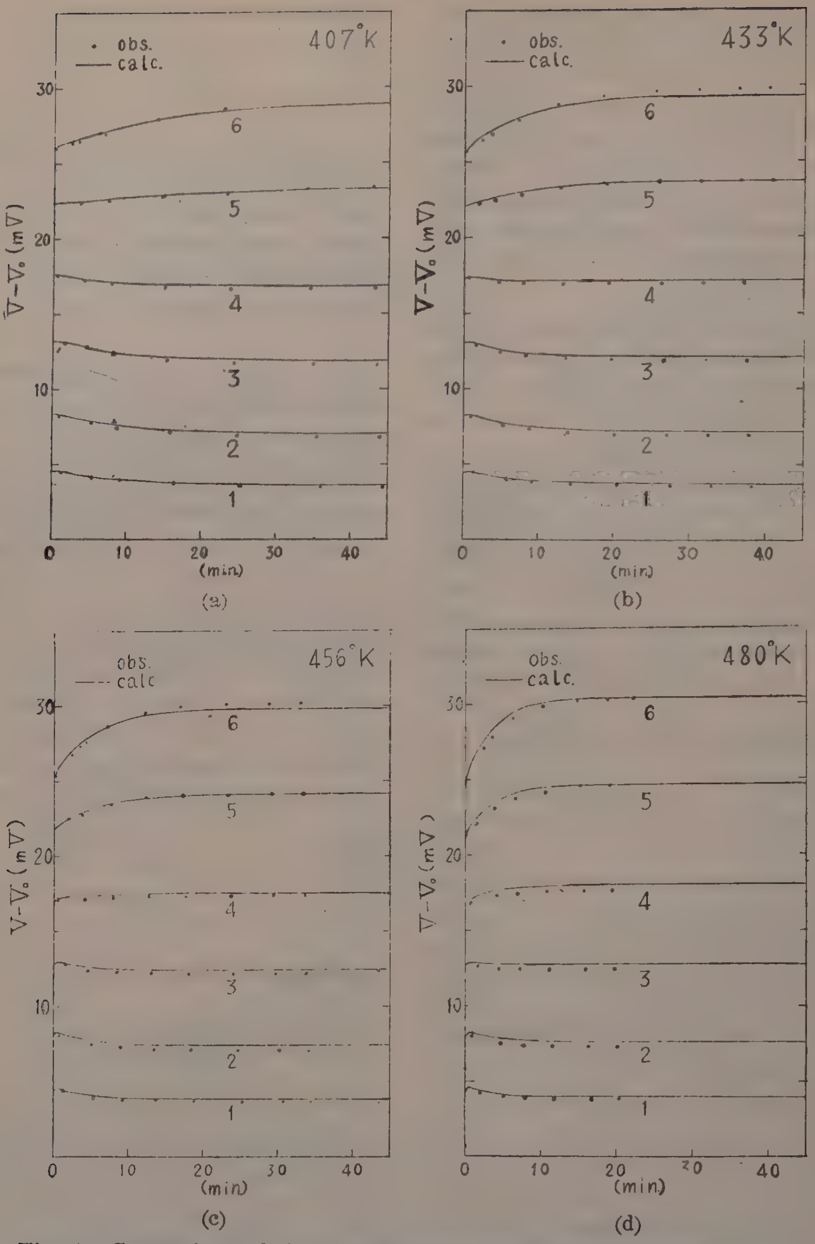

(a) (b) (c) (d)

Fig. 2. Comparison of the theoretical curves for the building up of stationary potential distribution with experiments.

2, together with the corresponding measured values.

The stationary potential distributions are calculated according to Eq. (20a) with the use of the numerical values of parameters tabulate in Table I, and are shown in Fig. 3 together with the corresponding measured values. The dotted lines in the figures represent the respective initial potential distributions.

We see that the numerical values of $\sigma_a/(\sigma_h+\sigma_d)$ and τ, so determined as to give the best fit with the measured residual potentials, yield consistent agreements between theory and experiments to the voltage creep phenomena and to the stationary potential distributions.

The slight discrepancies between calculated and observed values as seen in the figures may be attributed, mainly, to the difference between the boundary conditions assumed in

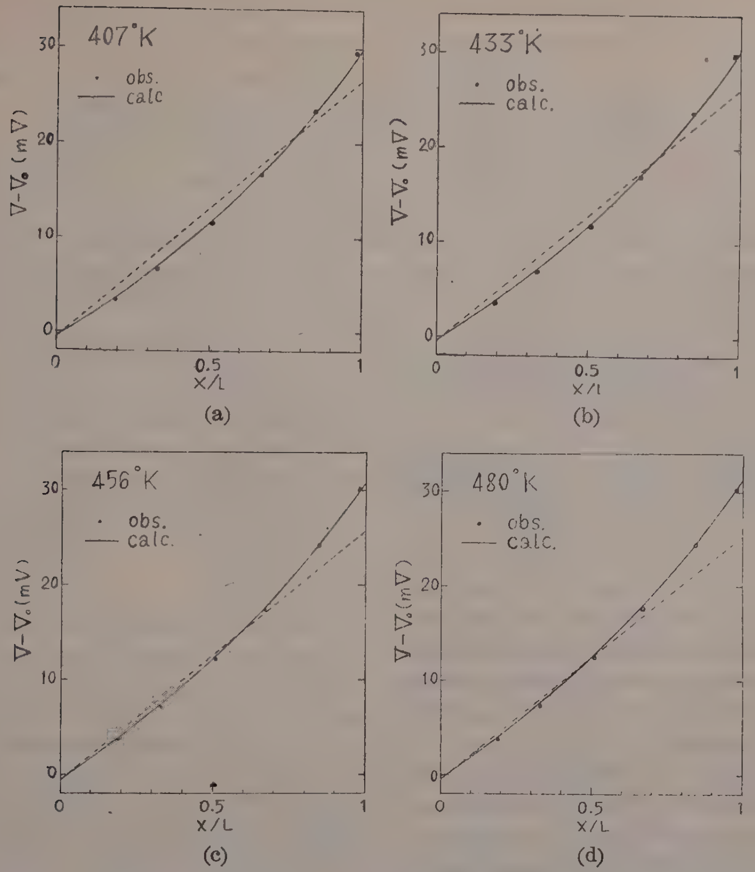

(a) (b)

(c) (d)

Fig. 3. Comparison of the theoretical curves for stationary potential distribution with observed values.

the theory and the experimental terminal conditions in reality.

As for the $V-I$ characteristics for stationary current, the reader should refer to the paper by Miyatani and Suzuki.

§ 6. Discussion

Since the total conductivity, $(\sigma_h+\sigma_d)$, is obtainable from the measured initial voltage V_i by the use of Eq. (11), and since the fraction $\sigma_d/(\sigma_h+\sigma_d)$ can be determined from the residual voltage by the way as described in the preceding paragraph, we can determine the respective values of hole and ionic conductivities. We show σ_h and σ_d at the four temperatures in Table II and in Fig. 4, together with the total conductivity, $\sigma_h+\sigma_d$.

It is seen that the ionic conductivity increases with increasing temperatures, while the hole conductivity slowly decreases, in opposition to the ordinary temperature dependence of hole (or electronic) conductivity in semiconductors.

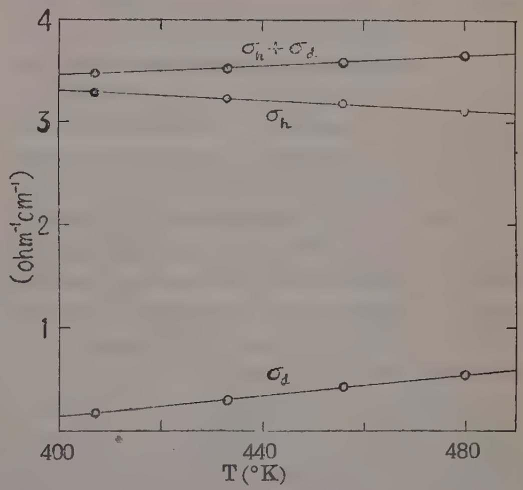

Fig. 4. Temperature dependences of $(\sigma_h+\sigma_\alpha)$, σ_h and σ_α.

This peculiar behavior suggests that in cuprous sulfide at the β-phase the density of holes are independent on temperatures, at least, in approximation. And such temperature in-

Table II. Ionic and hole characteristics.

T (°K)	$\sigma_h+\sigma_d$ (ohm^{-1} cm^{-1})	σ_d (ohm^{-1} cm^{-1})	σ_h (ohm^{-1} cm^{-1})	D (cm^2 sec^{-1})	p_d (cm^2 volt^{-1} sec^{-1})	$\bar{n}_d$ (cm^{-3})	p_h (cm^2 volt^{-1} sec^{-1})
407	3.48	0.18	3.30	0.91×10^{-3}	0.026	4.4×10^{19}	0.46
433	3.54	0.29	3.24	1.53	0.041	4.5	0.45
456	3.59	0.41	3.18	2.20	0.055	4.7	0.44
480	3.66	0.55	3.11	3.21	0.077	4.5	0.43

mean 4.5×10^{19}

dependence of hole density is possible only when acceptors are completely associated with electrons, i.e., when the equality $n_h=n_d$ is realized.

From the time of diffusion τ and $\sigma_d/(\sigma_h+\sigma_d)$, as determined in the preceding paragraph, we can determine the diffusion coefficient D by the use Eq. (15), and further the mobility of vacant copper ion lattice points p_d by the use of the Townsend-Einstein relation, Eq. (6). Furthermore, we can determine the equilibrium density of vacant copper ion lattice points, $\bar{n}_d$, from σ_d and p_d by the use of Eq. (11). These are also tabulated in Table II.

The constancy of $\bar{n}_d$ throughout all the temperatures seems to justify the present theory. It seems that the $\bar{n}_d$ is determined by the atomic ratio of copper and sulfur in the specimen and independent of temperatures, though heat treatment in higher temperatures might bring about the change in $\bar{n}_d$.

In Table II the mobilities of holes are also shown. These are computed under the assumption that $\bar{n}_h$ is equal to $\bar{n}_d$. The average value of $\bar{n}_d$ over the four temperatures is used in computation, instead of the $\bar{n}_d$ values at respective temperatures.

In Fig. 5, p_d is plotted against $1/T$ in semi-logarithmic scale. The measured points are seen to lie on a straight line, from the inclination of which we can deduce the activation energy for the drift motion of copper ions, ΔE. One find

$$\Delta E=0.26\ \text{ev},$$

which is rather smaller than 0.4 ev, previously obtained by Hirahara¹⁾ in the ordinary way of ionic conductivity measurement. The activation energy seems to be dependent on the excess or deficit amount of copper in the specimen.

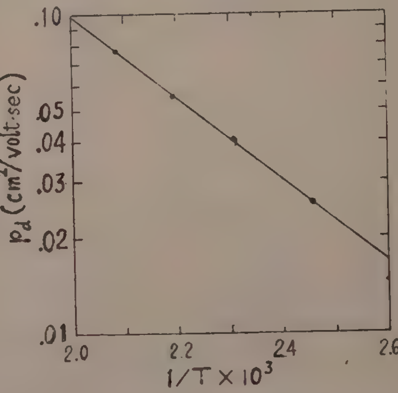

Fig. 5. Temperature dependence of p_d.

The main ideas of the present work have been brought to the author during the discourses with Mr. S. Miyatani and Mr. Y. Suzuki on the subject. The author wishes to express his cordial thanks to them.

References

1) E. Hirahara: J. Phys. Soc. Japan **6** (1951) 422, 428.

2) T. Kushida: J. Sci. Hiroshima Univ. **A 14** (1950) 147.

3) S. Miyatani and Y. Suzuki: J. Phys. Soc. Japan **8** (1953), this issue.

4) Voltage creep phenomena quite similar to those in cuprous sulfide at the β-phase have recently been observed also for cuprous oxide by M. Ono, Memoirs of the Faculty of Engineering, Nagoya Univ., **4** (1952) 57. It appears to the author that the creep phenomena observed by Ono also can be attributed to the drift motion of copper ions, though he has attempted to give an interpretation quite dissimilar to that given in the present work.

5) C. Wagner: Z. Physik. Chem. **B 21** (1933) 25.

6) M. H. Hebb: J. Chem. Phys. **20** (1952) 185.

7) W. Shockley: Electrons and Holes in Semiconductors, Van Nostrand, 1950.

JOURNAL OF THE PHYSICAL SOCIETY OF JAPAN Vol. 8, No. 5, SEP.—OCT., 1953

On the Mechanisms of Aging in Aluminium-Silver Alloys, I

By Ken-ichi HIRANO

Department of Physics, Tokyo Institute of Technology, Oh-okayama,
Meguro-ku, Tokyo, Japan

(Received April 23, 1953)

The Specific Heat-Temperature curves of age-hardened samples of Aluminium-Silver alloy have been obtained by the Nagasaki-Takagi method, the results of which are in good agreement with hardness measurements of Köster and Braumann. A discrete step is observed between two clearly defined stages of aging process, the first of which is attributed to creation of the Guinier-Preston Zone (γ'' phase) and the second of which to precipitation of the γ' phase and its transformation to the γ phase. The phase limits of γ'' and γ' (or γ) phases respectively are determined and shown in the phase diagram. The results are discussed and compared with the measurements of X-ray diffuse diffraction effects.

§ 1. Introduction

Precipitation from supersaturated solid solution is responsible for age-hardening associated with an alloy system in which the solid solubility decreases with decreasing temperature. Because of this, when Al-Ag solid solution (δ phase) is cooled as shown in the phase diagram (Fig. 1), a new phase (γ phase of the composition Ag_2Al) must precipitate to maintain the system in thermal equilibrium.

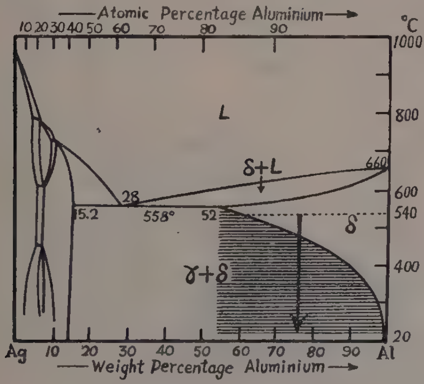

Fig. 1. Phase diagram of Aluminium-Silver system

After annealing the alloy at a temperature above the solvus for sufficient length of time to dissolve the γ phase, the alloy is quenched in water of room temperature to retain supersaturated state, then reheated to an intermediate temperature at which the age-hardening is permitted to occur.

By X-ray diffraction measurements, neither new lines for the precipitates nor any change of lattice parameter due to de-composition of the matrix solid solution has been observed during the low temperature aging (the LT-aging), whilst these are both clearly observed during the high temperature aging (the HT-aging).

In 1938, Guinier1)2)3) and Preston4)5) found independently that streaks developes in Laue photograms during the early stage of the aging in an Al-Cu single crystal, and concluded that within the matrix solid solution there exists a series of Cu-rich parallel plane clusters of very small size, named the Guinier-Preston Zone (P-G zone), whose stability and size being dependent upon temperature and time. Similar diffuse diffraction effects have been observed in an Al-Ag alloy.6) It seems that the question whether there is any actual relation between the LT-aging, that is the creation of the G-P zone, and the HT-aging, that is the precipitation of transient γ' phase and the stable γ phase (both hexagonal), or not has remained open.

If the speciman is reheated at higher temperature, after a heat treatment sufficiently long for the LT-aging had been given beforehand, the recovery of hardness is first observed. This recovery is attributed to dispersion of the G-P zone. But thereafter, hardness increasing follows as the result of the γ' phase precipitation at that temperature. The formation of the G-P zone is accompanied with heat evolution (entropy decreasing process), therefore the above recovery is to be measured as the absorption of heat in specific heat temperature curves.

In this work calorimetric investigations have carried out, which we think are more suitable than X-ray measurement for studing especially the nature of the LT-aging.

§ 2. Measurement of the Specific Heat

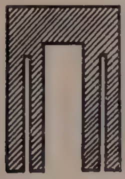

Fig. 2. Specimen used for the specific heat measurement.

The method for specific heat measurement was that of Nagasaki and Takagi(7). The specimen used are cylinders 2 cm in diameter and 3 cm high, the vertical section of which is shown in Fig. 2.

The specific heat was measured while being heated at constant rate of about 2°C per minute. The alloys were prepared from assay silver (99.99% pure) and superpure aluminium (99.99% pure). The metals were melted and cast into a chillmould.

§ 3. Heat Absorption during Dispersion of the G-P Zone

Fig. 3 (a) shows the specific heat vs. temperature curve (S-T curve) for 38.04 wt.% Ag alloy, as quenched from 540°C to water (540°C is chosen as the quenching temperature for all specimens in this work).

Fig. 3 (b) and (c) are the S-T curves for the same specimen after heat treatments of LT-aging, 20°C — 45 hours and 110°C — 110 hours respectively. (d) is for a HT-aging, 330°C — 1 hour. The heat evolution at 50° — 150°C (P in Fig. 3) is clearly to be attributed to formation of the G-P zone during the measurement. Heat absorption at 150° — 190°C (Q) on the other hand is due to the dispersion of the G-P zone(8). The heat evolution (R) is to be regarded as a result of the γ' phase precipitation during the measurement. The decreasing amount of R in (d) shows the existence of considerable amount of the γ' phase prior to the measurement as a result of the HT-aging.

The total amount of P and Q are calculated as follows:

$$P(\text{total})=\int_{50}^{150} p\,dT\,,$$

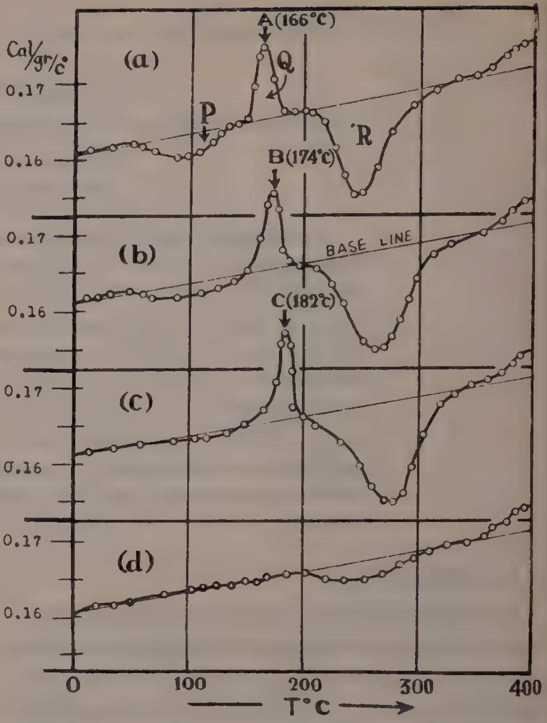

Fig. 3. S-T curves for 38.04 wt.% Ag alloy. The base line is calculated using Neumann-Kopp's law.

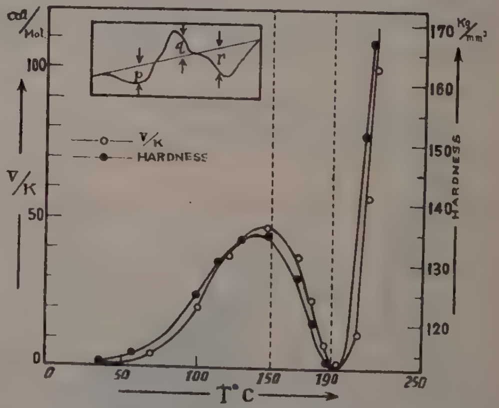

Fig. 4. Amount of Existent G-P zone, corresponding to Fig. 3 (a).

$$Q(\text{total})=\int_{150}^{190} p\,dT\,,$$

If we suppose that the evolved heat is proportional to the volume of the existent G-P zone, then the volume (V) must be

$$V=\begin{cases}(\text{from } 50° \text{ to } 150°\text{C})\ K\displaystyle\int_{50}^{T} p\,dT \\ (\text{from } 150° \text{ to } 190°\text{C})\ K\left[P(\text{total})-\displaystyle\int_{150}^{T} p\,dT\right] \\ \qquad(\text{above } \ 190°\text{C})\ K\displaystyle\int_{190}^{T} r\,dT\,,\end{cases}$$

where K is a suitable constant.

In Fig. 4, V is plotted against temperature, in which the data shown in Fig. 3 (a) have been employed. For comparison, an isochronic hardness-temperature curve (30 minutes after quenching) is also drawn in Fig. 4, after Köster and Braumann's measurement.[9] The close agreement between the two curves strongly supports the assumption of linearity of V vs. hardness. It is seen that the complete recovery as well as the complete disappearance of V do occur at 190°C. From Fig. 3 (a) we get

$$P(\text{total})=48\ \text{cal./mol.}=Q(\text{total})$$
$$V=K[P(\text{total})-Q(\text{total})]=0\ \text{at}\ 190^\circ\text{C}.$$

Furthermore, Fig. 3 shows that the longer the LT-aging process the higher the temperature at which each heat absorption curve attains its maximum (A, B and C in Fig. 3). This means that the G-P zone probably increases its stability with aging time.

§ 4. Nature of the LT-aging

Fig. 5 shows the absorbed heat (Q) vs. aging time (t) curves for 20.25 wt. % Ag alloy subjected to 20° and 160° aging. After sufficiently long aging, the evolution of heat (P) becomes negligible and then whole Q is due to the dispersion of the G-P zones all formed during the aging.

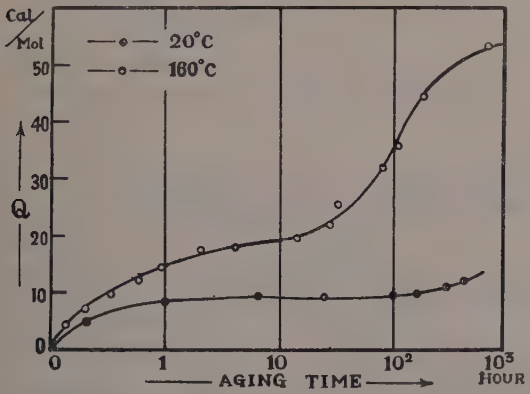

Fig. 5. The absorbed heat vs. aging time curves for 20.25 wt. % Ag alloy.

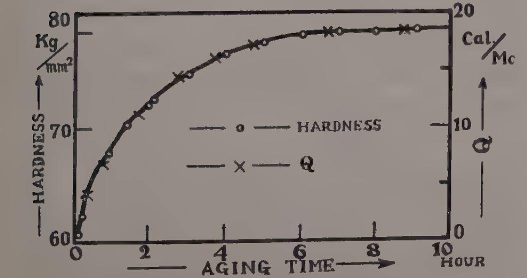

Fig. 6. Detailed Q-t curve and H-t curve at earlier stage of 160°C aging for 20.25% alloy.

Fig. 6 shows a detailed Q-t curve at earlier stage of 160°C aging. The inclination of the Q-t curve agrees fairly well that of the hardness-time curve (H-t curve) obtained by Köster and Braumann.[9] After about 7 hours or more of aging, Q approaches a saturated value Q_s. To find the character of the Q-t curve (or H-t curve), $1/(1-P)$ is plotted against time in Fig. 7, where

$$P=Q/Q_s\ (\text{or}\ P=H/H_s)\,,$$

indicates the degree of aging.

From Fig. 7 we get

$$1/(1-P)=Kt+1\,,$$

or

$$dP/dt=K(1-P)^2\,.$$

It may be concluded that a certain process like a two atomic reaction is operating during formation of the G-P zone.

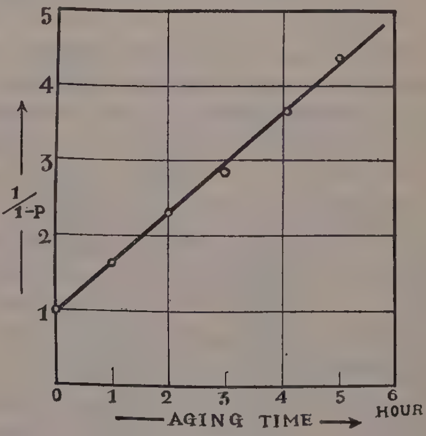

Fig. 7.

Fig. 8 shows the time dependence of T_1, T_2 and T_3; where T_1 is the temperature above which the heat absorption can be detected, that is the upper limit of the stable G-P zone; T_2 is the temperature at which Q attains its maximum, that is a measure of stability of the existent G-P zone; and T_3 is the temperature at which the heat absorption ends itself, which marks the upper limit of the existence range of the G-P zone.

T_2 and T_3 rise up to constant saturated values respectively as aging goes on, while T_1 seems to be independent of aging time and is solely fixed by the composition of the specimen.

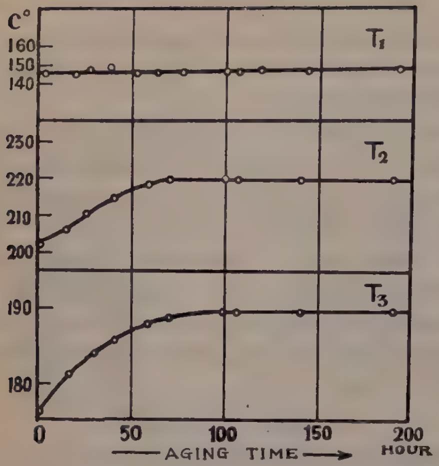

Fig. 8. Dependence of T_1, T_2 and T_3 on the aging time for 20.25 wt.% Ag alloy.

§ 5. Range of the Existence of the G-P Zone. Range of the LT-aging

Fig. 9 shows the *S-T* curves of seven specimens, Ag concentrations of which are respectively 5.25, 10.40, 15.02, 20.25, 25.00, 30.50 and 38.04 wt.%.

A sufficient length of the LT-aging given to each specimen to obtain saturated value of T_2 and T_3. The aging time for each specimen is indicated in Fig. 9.

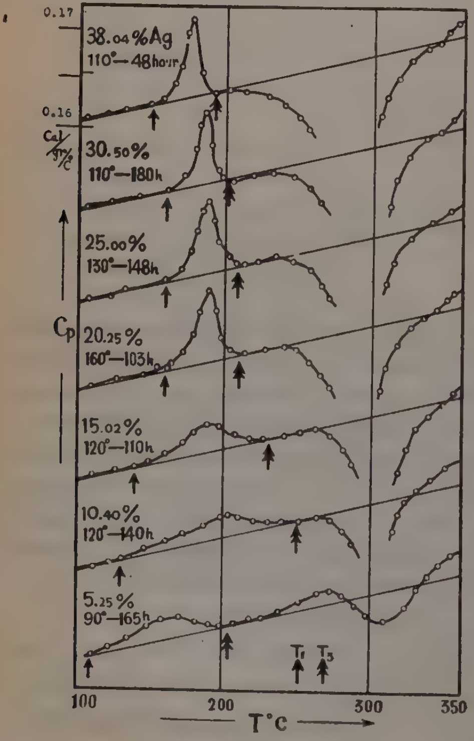

Fig. 9. S-T curves.

In Fig. 10, lines are drawn through these temperatures in the phase diagram. The T_3-line is a boundary of the LT- and the HT-aging. The LT-aging process is impossible in a range above the line, while below it the velocity of the HT-aging is negligibly slow and only the LT-aging can be effective.

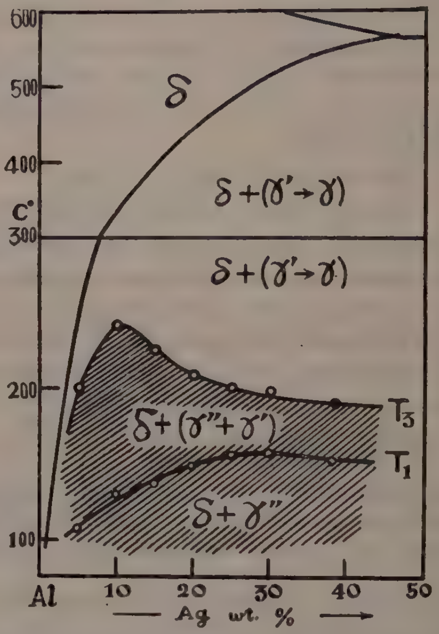

Fig. 10. T_1- and T_3-lines in the phase diagram. The range of LT-aging is denoted by oblique lines.

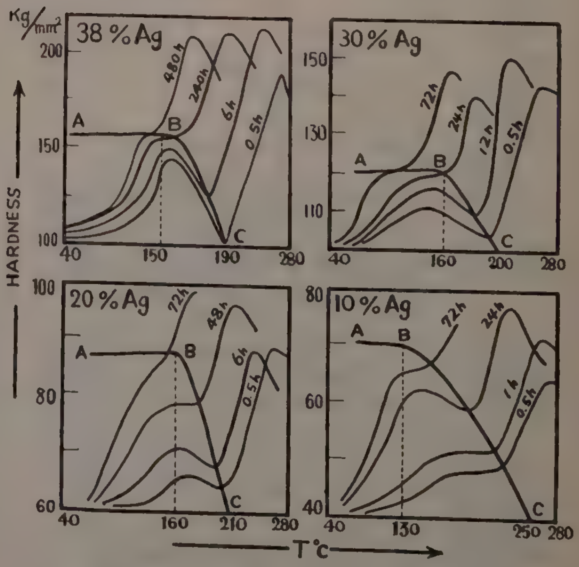

Fig. 11. Isochronic hardness temperature curves after Köster and Braumann.

Fig. 11 shows the isochronic hardness temperature curves drawn after Köster and Braumann's measurements. The two peaks may correspond respectively to the two stages of aging. The curve AC is drawn through the inflexion points between the two peaks. At the point B, the horisontal part (AB) of the AC curve begins to fall nearly vertically toward the point C. The temperatures corresponding to B and C, if named T_1 and T_3 as in Fig. 11, coinside very closely with our T_1 and T_3 obtained in Fig. 9.

The shapes of the age-hardening characteristic of various temperature range are illustrated in Fig. 12.

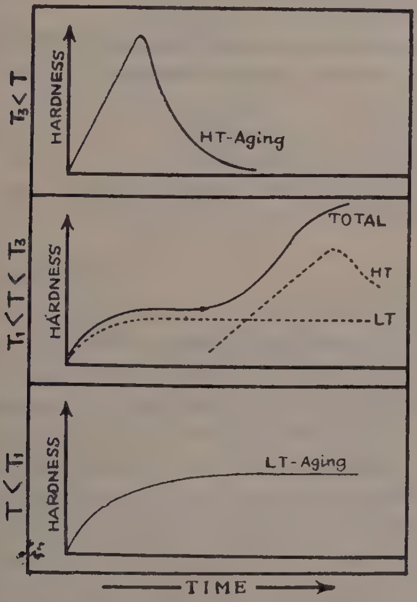

Fig. 12. The characteristic shapes of age-hardening curve for each temperature ranges.

§ 6. Discussion

Mott's theory

Mott[10) has suggested from the standpoint of the dislocation theory, that if the precipitate have not broken away from the matrix, the mean stress σ_i in the matrix is proportional to $G\varepsilon V$, independently of the shape of the G-P zone, where G is the shear modulus, $(1+\varepsilon)r$ is the radius of the solute atom, r being that for the matrix: V is the total volume of the created G-P zone, and if the distance between the precipitates is large ($>100r$), the dislocation can not be set in motion unless the applied stress σ approaches σ_i. On the other hand, the hardness is regarded as the measure of σ_i, therefore the hardness must be proportional to V. This is really supported by the fact that the *Q-t* curve agree very well with the *H-t* curve as shown in Fig. 6.

Interpretations of the results of X-ray measurement

Geisler,[11) based upon his X-ray measurements, concluded that all X-ray effects in early aging are due to the existence of small platelets of the γ' phase, which afterwards can crystallographically grow up to true γ' phase continuously. (Sequence theory)

On the other hand, Guinier and Preston concluded by X-ray measurements, that there exists a discrete step between the LT- and HT-aging. Recently Guinier[12) observed the creation of quasi-spherical platelets in the LT-aging. Ziegler[13) concluded, by the method of reciprocal lattice analysis, the existence of statistically distributed lamella clusters, which are not entirely equal to the γ' phase, though the crystal structure being much like that of the γ' phase.

It seems that Geisler's observation concerns a certain stage of aging somewhat later than Guinier's, and his platelet is rather associated with the HT-aging.

For further determination, a detailed X-ray measurement is desired to see whether Geisler's streaks disappear or not after the recovery of hardness had occured.

We conclude on the bases of our calorimetric and Köster and Braumann's hardness measurements, that there are two discrete processes of aging.

In conclusion, the author is greatly indebted to Professor Yutaka Takagi, whose invaluable discussions have resulted in the publications of this paper, and also to Mr. Hideyo Maniwa and Mr. Makoto Hirabayashi for their kind guidance and encouragement.

NOTE ADDED IN PROOF

Recent work by Köster and Schell* has come to the attension of the author. These investigators also obtained the C_p-T curves of 5, 10, 20, 30 and 38 wt.% alloys, immediately after quenching and after 150°C aging, using the calorimeter of C. Sykes**. Their interpretations are somewhat different from the present investigation, especially for 38 % alloy.

---

* W. Köster, H. A. Schell: Z. Metallkde. **43** (1952) 454.

They obtained larger values for the heat of recovery and smaller values for the heat evolution, P and Q in our notation, at the early stage of the LT-aging. This is because they did not take into account the heat evolution P in the estimation of the total heat of the recovery, which should be given by $(Q-P)$ as shown in our investigation.

For the estimations of the heat absorption and evolution, the relative situation of the base-line versus C_p—T curve exerts an effect to the result and it seems that the base-line of Köster and Schell is chosen rather too low.

References

1) J. Calvet, P. Jacquet, A. Guinier: Compt. rend. **206** (1938) 1972.

2) A. Guinier: Compt. rend. **206** (1938) 1641.

3) A. Guinier: Nature **142** (1938) 569.

4) G. D. Preston: Proc. Roy. Soc. **A 167** (1938) 526.

5) G. D. Preston: Phil. Mag. **26** (1938) 855.

6) C. S. Barett, A. H. Geisler: J. App. Phys. **11** (1940) 733.

7) S. Nagasaki, Y. Takagi: J. App. Phys. Japan **17** (1948) 104.

8) F. W. Jones, P. Leech: Nature **147** (1941) 327.

9) W. Köster, F. Braumann: Z. Metallkde. **43** (1952) 193.

10) N. F. Mott: Imperfections in Nearly Perfect Crystals (Symposium held at Pocono Manor, Oct. 12-14, 1950) p. 175.

11) A. H. Geisler, J. H. Hill: Acta Cryst. **1** (1948) 238.

12) A. Guinier: Z. Metallkde. **43** (1952) 217.

13) G. Ziegler: Z. Metallkde. **43** (1952) 213.

** C. Sykes: Proc. Roy. Soc. London (A) **148** (1935) 422.
C. Sykes, F. W. Jones: J. Inst. Met. **59** (1936) 257.

JOURNAL OF THE PHYSICAL SOCIETY OF JAPAN Vol. 8, No. 5, SEP.—OCT., 1953

Observation of the Grain Boundary in Soap Bubble Raft

Part I. Static Feature of the Grain Boundary

By E. FUKUSHIMA*

Department of Physics, Tokyo Metropolitan University, Tokyo

and A. OOKAWA*

Department of Physics and Chemistry, Gakushuin University,
Mejiro, Tokyo

(Read October 31, 1952; Received April 20, 1953)

The grain boundary is constructed in the soap bubble raft by the procedure of progressively increasing the angle of disorientation between two grains. The grain boundaries observed are classified into three types in respect to the statical transition structure.

At an angle of disorientation $\theta \sim 0°$, the grain boundary (type A) is constituted of the dislocations all on parallel slip planes. At an angle of disorientation $\theta \sim 60°$, the grain boundary (type C) is constituted of two sorts of dislocations each on nonparallel slip planes. At an intermediate angle of disorientation, the grain boundary (type B) is composed of disordered groups of atoms or the diffused holes.

The mechanism of the varying nature of the grain boundary with the angle of disorientation is discussed in the light of the current theory of dislocations, where the stress is laid on the predominance of reactions between the dislocations and the relative shortage of thermal agitation.

§ 1. Introduction

The dislocation model of the grain boundary in poly-crystalline solids has been proposed by Burgers1) and Bragg2) and it has been quantitatively discussed by Shockley-Read3). On the other hand, with regards to the grain boundary viscosity, Kê4) has proposed grain boundaries composed of irregular assembly of atoms or the diffused holes and the problem is attacked theoretically by Mott5) from the stand point that the grain boundary is constituted of molecules in good fit and those in bad fit. In his recent paper on the grain boundary diffusion, Smoluchowski6) is of the opinion that, while the grain boundary between two grains of small orientational difference is constituted of independent dislocations, the constituent dislocations increase in number with increasing disorientation so much that the grain boundary degenerates into thinner layer lattice of high strain.

These characteristics of the grain boundary varying with the angle of disorientation between the grains can be detected with the grain boundary in the soap bubble raft, some observations on which have been reported in our previous short letters7). The varying nature of the grain boundary in the bubble raft is reported independently by Lomer-Nye8). They constructed grain boundaries by attaching two disoriented grains. We have rather taken the procedure of constructing the grain boundary by continuous bending of a formerly single crystalline grain, where one has the advantage of detecting the mechanism of varying nature of the grain boundary.

The experimental apparatus used in constructing the grain boundary and the results of observation on the static feature of the boundary is reported in Part I. The displacement and the deformation of the grain boundaries under shear stress will be reported in Part II.

§ 2. Experimental Apparatus

The procedure of forming the bubble raft is the same as that invented by Bragg-Nye9). The grain boundary is introduced by bending one single crystalline bubble raft. The apparatus used to bend bubble raft consists of two frames, adjustable in desired relative orientation and in desired relative displacement to each other. It is shown schematically in Fig. 1.

The brass bar *abcd* is of 1 mm thickness and of 3 mm breadth, and the length of *ab*,

---

* Member of the Kobayashi Institute of Physical Research.

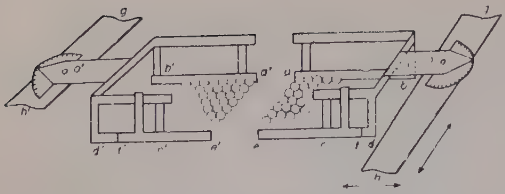

Fig. 1. Sketch of the apparatus used to bend the soap bubble raft.

bd, and *cd* are 50 mm, 40 mm, and 30 mm respectively. The height of the frame is 18 mm. The part *bd* is connected only by the upper bar; this is to set the side *bd* of the bubble raft introduced inside the frame in free surface condition. The bar *ef* hanging on the frame can be shifted horizontally to set the total length *de* adjustable. Two frames *abcdef* and *a′b′c′d′e′f′*, symmetrical to each other, can be set in desired rotational orientation with respect to each rotational centre *o* and *o′*. While the frame *g′h′* attached to *o′* is fixed, the frame *gh* attached to *o* can be shifted back and forth as well as to right and left by micro-manipulator. The frames must be set in proper height in the soap bubble raft, to avoid the unfavourable buckling of the bubbles in contact with the lower bars.

§ 3. Observations

The diamter of the bubbles used is of about 0.95 mm. It is said that the bubble raft composed of bubbles of diameter of about 1 mm resembles the actual metal crystal best[10]. The breadth of the dislocations in these bubble raft is also moderate and favourable for observation.

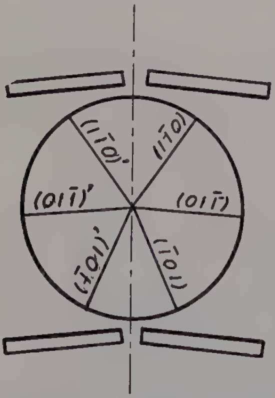

Fig. 2. Assignment of indexes of bubble rafts in each seperate frames.

The frame *abcdef*, adjusted to have the same length *ab* and *ed*, is set in the soap solution such as to locate the lower bars *ab* and *ed* just on surface of the solution. The bubble raft is then introduced inside the frame in regular arrangement to have single crystalline pattern with its $(01\bar{1})$ line parallel to bar *ab* and *de* (see Fig. 2.) The other frame *a′b′c′d′e′f′* is set in the same condition. The two bubble rafts, each in seperate frames with straight free surfaces *ae* and *a′e′*, are brought into contact just as to have *ae* and *a′e′* in one

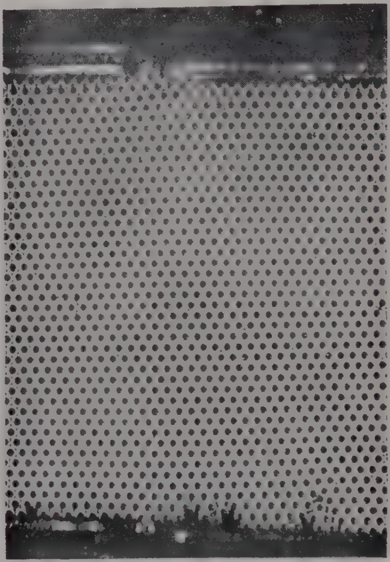

Fig. 3. Composite single crystal at an angle of disorientation $\theta=0°$.

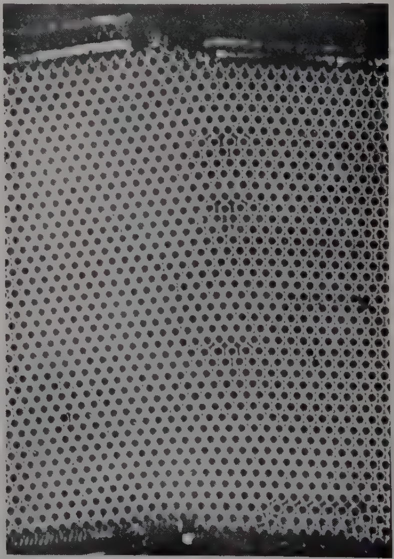

Fig. 4. Grain boundary of type A composed of dislocations all on parallel slip lines, at an angle of disorientation $\theta=8°30'$.

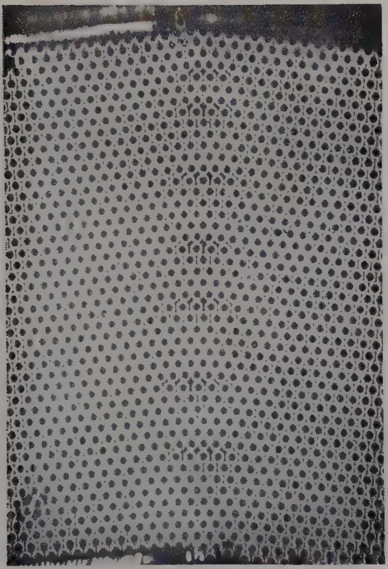

Fig. 5. Typical grain boundary of type A at an angle of disorientation $\theta=13°30'$.

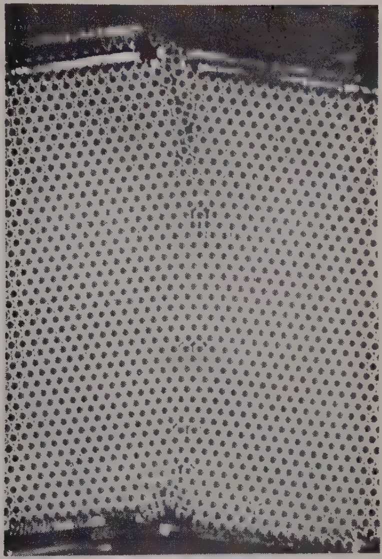

Fig. 6. Grain boundary at an angle of disorientation $\theta=14°$.

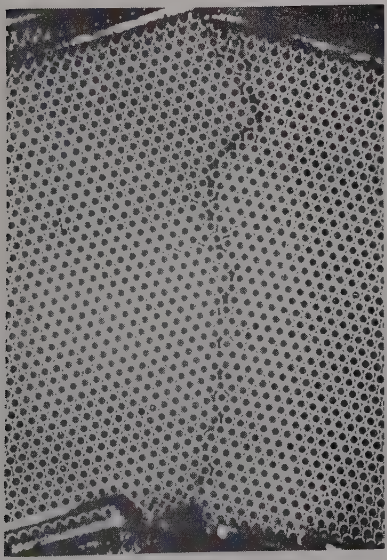

Fig. 7. Grain boundary of type B composed of diffused holes, at an angle of disorientation $\theta=30°30'$.

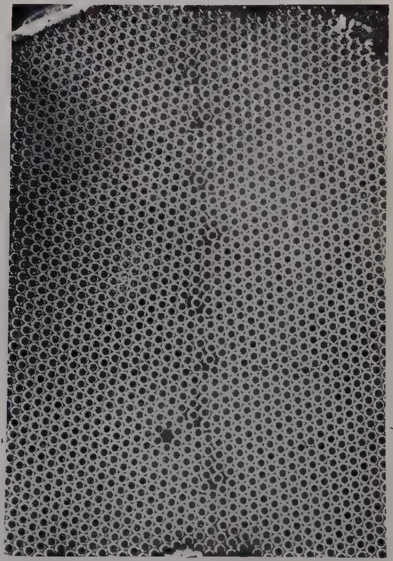

Fig. 8. Grain boundary of type C constituted of two sorts of dislocations each on non-parallel slip lines, at an angle of disorientation $\theta=49°$.

line. Then we have a composite single crystalline bubble raft as shown in Fig. 3.

Two frames *abcdef* and *a′b′c′d′e′f′* are then rotated with *o* and *o′* as rotating centres respectively. To preserve the lines *ae* and *a′e′* in contact, the hanging frames *ef* and *e′f′* are shifted outwards and the frame *abcdef* is shifted leftwards. Fig. 4 shows the stable grain boundary between two grains, the $(01\bar{1})'$ of the left bubble raft and the $(01\bar{1})$ of the right bubble raft forming an angle of disorientation $\theta=8°30'$. It can easily be observed that the grain boundary is constituted of dislocations all on parallel slip lines. This type of grain boundary will be referred to as the grain boundary of type A*.

In the process of bending the single crystalline bubble raft, we have at first bended crystal pattern including three sorts of dislocations distributed at random: the dislocations with Burgers' vectors along $(01\bar{1})$, $(1\bar{1}0)$, and $(\bar{1}01)$. But, as it stands, the annealing proceeds in the form, that the dislocations other than those with Burgers' vector along $(01\bar{1})$ travel away to periphery of the bubble raft and the large scale bending of the lattice dies away progressively. We have in the final state the grain boundary constituted of parallel dislocations as shown in Fig. 4. More typical example of the grain boundary of type A, constituted of parallel dislocations with regular spacing, can be realized by mechanical agitation of the raft portion near the boundary by fine needle. Fig. 5 shows an example corresponding to an angle of disorientation $\theta=13°30'$, where the distortion of the lattice is concentrated locally at or near the dislocations.

For the sake of brevity, we refer by notation $(01\bar{1})'\perp(01\bar{1})$ the dislocation with its Burgers' vector nearly parallel to $(01\bar{1})'$ of the left bubble raft and to $(01\bar{1})$ of the right one.

The angle of disorientation θ between the two bubble rafts was increased in the same procedure as above described. The grain boundary at $\theta=14°$ in continuation to the configuration in Fig. 4 is shown in Fig. 6. It is observed that the grain boundary in the upper part is composed of diffused holes. The grain boundary with diffused holes seems to appear at an angle θ of about 15°. With increasing the angle θ, the whole length of the grain boundary degenerates into diffused holes, as is shown in Fig. 7 at an angle of disorientation $\theta=30°30'$. This type of grain boundary will be referred to as the grain boundary of type B. The grain boundary of type B survives until the angle θ increases to about 40°.

When the angle of disorientation increases to about 50°, the diffused holes disappear and we have in the place again the grain boundary constituted of dislocations. As is shown in Fig. 8 at an angle of disorientation $\theta=49°$, the grain boundary in this case is constituted of two sorts of dislocations, the dislocations $(1\bar{1}0)'\perp(01\bar{1})$ and the dislocations $(01\bar{1})'\perp(1\bar{1}0)$. This type of grain boundary will be referred to as the grain boundary of type C. The two sorts of dislocations in Fig. 8 have centres on nearly straight line. But, in major cases, they are distributed in a zigzag manner and consequently the grain boundary does not appear so sharp as shown in Fig. 8.

Increasing the angle of disorientation further to 60°, we arrive at another perfectly single crystalline bubble raft, where the $(01\bar{1})'$ and $(0\bar{1}1)'$ of the left raft coincides respectively with $(1\bar{1}0)$ and $(01\bar{1})$ of the right raft (Fig. 9.)

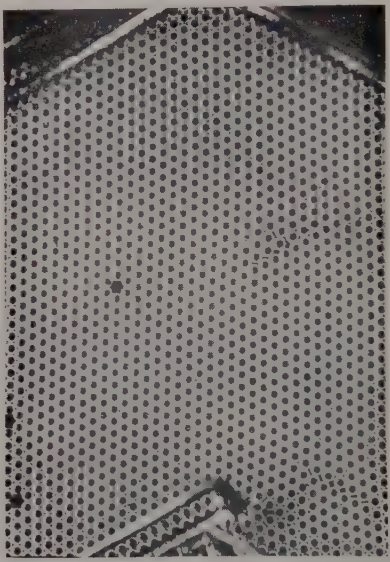

Fig. 9. Composite single crystal at an angle of disorientation $\theta=60°$.

The varying nature of the grain boundary with the angle of disorientation θ is perfectly reversible. With decreasing the angle θ, we have the grain boundary of type C constituted of two sets of dislocations at about 50°, the grain boundary of type B composed of diffused holes at about 40°∼20°, and the grain boundary of type A constituted of parallel dislocations at about 10°.

---

* The nomenclature of each type of the grain boundaries is different from that in our previous short letter7). For the benefit of reference, we insert a table of correspondence:

Nature of the grain boundary	this paper	previous letter
dislocations all on parallel slip planes.	A	B
diffused holes.	B	A
two sets of dislocations, each on non-parallel slip planes.	C	C

§ 4. Discussions

The edge type dislocation observed in the two-dimensional bubble raft is characterized by two excess half lines each with an angle of about 60° to the direction of the slip line[11]. The situation can be represented most conveniently by the notation in Fig. 10, which represents

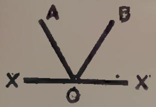

Fig. 10. Slip plane and two excess half lines characterizing the dislocation in the soap bubble raft.

the dislocation located at O on the slip plane XX with its two excess half lines OA and OB.

In the process of building up the grain boundary of type A, composed of parallel dislocations, we observe three sorts of dislocations migrating into the bubble raft from the free surfaces. A dislocation $(\bar{1}01)' \perp (1\bar{1}0)$ and a dislocation $(1\bar{1}0)' \perp (\bar{1}01)$ react, however, to form a dislocation $(01\bar{1})' \perp (01\bar{1})$ according to the dislocation reaction formula

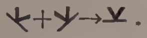 (1)

The dislocation reaction involved can be envisaged as the process of cancelling out of two excess lines, each characterizing the respective dislocations and each directed in opposite directions. So long as the angle of disorientation θ is smaller than 30°, the reaction proceeds towards right, according to the crude criterium

$$\boldsymbol{b}_1^2 + \boldsymbol{b}_2^2 \geqslant \boldsymbol{b}_3^2 \,, \tag{2}$$

between the characteristic Burgers' vectors $\boldsymbol{b}_1$, $\boldsymbol{b}_2$, and $\boldsymbol{b}_3$.

The migration and the reaction of dislocations are shown schematically in Fig. 11. The dislocation AOB introduced at point near *d*

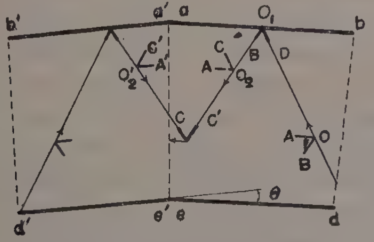

Fig. 11. Dislocation reaction involved in the process of building up the grain boundary of type A, at an angle of disorientation $\theta \sim 0°$.

on the free surface proceeds along $(\bar{1}01)$ until it is transformed to the dislocation AO_2C by reflection at point O_1 on the frame, whereby the remaining dislocation BO_1D does not contribute to any imperfection of the bubble raft inside the frame. Then the dislocation AO_2C proceeds along $(1\bar{1}0)$ until it reacts with the corresponding dislocation $A'O_2'C'$ at the crossing point P to result the dislocation CPC' in accordance with formulae (1) and (2).

In the same way, the process of obtaining a single crystalline pattern at an angle of disorientation $\theta \sim 60°$ is accounted by the process of cancellation between the dislocations constituting the grain boundary and the dislocations introduced by the way of increasing the angle θ. The situation is depictured in Fig. 12. We see that each dislocation intro-

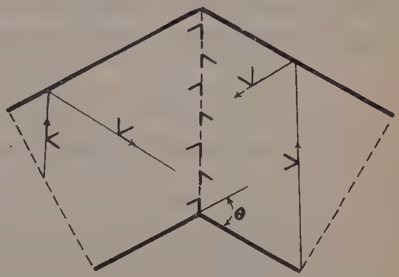

Fig. 12. Cancellation of dislocations in the process of vanishing of the grain boundary of type C, at an angle of disorientation $\theta \sim 60°$.

duced from the free surface is of the same sort and of the opposite sign to one of the dislocations constituting the relevant grain boundary. It is not necessarily provided that the two dislocations cancelling pair-wise are on the same slip plane. As the consequence, it results many excess and missing lines of bubbles nearly parallel to the grain boundary, which are averaged out statistically by the diffusion of bubbles along the grain boundary.

The mechanism of transformation between the grain boundary of type A and that of type C, from the view point of the dislocation structure, can not be visualized, because of the intervening of the grain boundary of type B composed of diffused holes. By the angle of disorientation θ in the neighbourhood of 30°, the degeneration of the dislocation structure into many diffused holes is the consequence of substantial interference between nearby dislocations by large population along the grain boundary. The consequences in respect to the grain boundary energy are discussed by Lomer-Nye[8].

The bubble raft patterns shown in Figs. 3–9 correspond to stable configurations. It is to be noted that, to realize the configurations, we have partly accelerated the annealing process by disturbing the relevant portion of the bubble raft with fine needle. One may be agreeable to the stand point that the bubble raft model simulating to the actual metal crystal corresponds to that at relatively low temperature. The immobility of an accidental vacant site as well as the relative fineness of the grains simulating the annealed polycrystal is sustaining to this view point. In respect to the annealing and/or the activated processes involved in the actual metal crystals, one must appreciate properly the relative shortage of the thermal agitation in the bubble raft model.

References

1) J. M. Burgers: Proc. Phys. Soc. London **52** (1940) 23.

2) W. L. Bragg: Proc. Phys. Soc. London **52** (1940) 54.

3) W. Shockley, W. T. Read: Phys. Rev. **78** (1950) 275.

4) T. S. Kê: Phys. Rev. **73** (1948) 267.

5) N. F. Mott: Proc. Phys. Soc. London **60** (1948) 391.

6) R. Smoluchowski: Phys. Rev. **87** (1952) 482.

7) E. Fukushima. A. Ookawa: J. Phys. Soc. Japan **8** (1953) 129, 280.

8) W. M. Lomer, J. F. Nye: Proc. Roy. Soc. **A 212** (1952) 576.

9) W. L. Bragg, J. F. Nye: Proc. Roy. Soc. **A 190** (1947) 474.

10) W. M. Lomer: Proc. Roy. Soc. **A 196** (1949) 182.

11) F. R. N. Nabarro: Advances in Physics **1** (1952) 271.

12) F. C. Frank: Physica **15** (1949) 131.

JOURNAL OF THE PHYSICAL SOCIETY OF JAPAN Vol. 8, No. 5, SEP.—OCT., 1953

Ferroelectricity versus Antiferroelectricity in the Solid Solutions of $PbZrO_3$ and $PbTiO_3$

By Etsuro SAWAGUCHI*

*Tokyo Institute of Technology, Oh-okayama, Tokyo**

(Received March 17, 1953)

The phase diagram of the solid solutions of $PbZrO_3$-$PbTiO_3$ system has been established by investigating dielectric, dilatometric, calorimetric and structural properties. In Pb(Zr97-Ti3)O_3 four kinds of polymorphic modification have been found, that is, successively, the antiferroelectric, the other antiferroelectric, the ferroelectric and the paraelectric phases. By making use of the phase diagram and of the forced transition which causes a phase change from antiferroelectric phase to ferroelectric one owing to an influence of intense electric field, the free energies of these four states have been compared with one another as functions of temperature and the concentration of the solid solution. It is found that the antiferroelectric phase near the Curie point 230°C in pure $PbZrO_3$ is more stable than the ferroelectric one by only about 4 cal/mole; and with increasing concentration of $PbTiO_3$ the free energy of the ferroelectric phase decreases gradually at an initial rate of 0.5 cal./mole/atomic percent. At the same time the two antiferroelectric phases lose their stability at the rates 5.8 cal./mole/atomic percent and 2.3 cal./mole/atomic percent respectively. The atomic arrangement in the ferroelectric Pb(Zr58-Ti42)O_3 has been examined. The sample of this concentration has the rhombohedral structure $C_{3v}{}^5-R3m$: The displacement of Pb atom relative to Zr or Ti atom is about 0.14 KX along the [111] direction.

§ 1. Introduction

It has been known that both the lead zirconate and the well known ferroelectric barium titanate have the analogous perowskite structure1),2) and that their dielectric constant *vs.* temperature relations3) much resemble each other. But, A. Hoffmann1) have found strange superstructure lines in his Debye-Scherrer photograph of lead zirconate, and in this respect some striking contrasts to the barium titanate have been expected. In the previous papers, by analysing the superstructure4) and by investigating the dielectric properties5),6) of lead zirconate, we have reached the conclusion that lead zirconate is an antiferroelectric rather than ferroelectric. The characteristics observed and supporting the antiferroelectricity in lead zirconate are: 1) In the crystal below the Curie point, there are two kinds of atomic row of the Pb ions, and the atomic displacements, though rather small, in one row are in the opposite direction to that of another row. This is evidently suggesting the existence of the antiparallel set of dipolar orientations in the crystal: 2) An electric bias applied on the $PbZrO_3$ depresses the Curie temperature by a few degrees, and also increases the dielectric constant below the Curie point slightly. These responses to the electric bias can hardly be understood if we regarded the $PbZrO_3$ as ferroelectric, but they can be reasonably explained when we regard it as antiferroelectric.

We have already known the following facts: 1) Near the Curie point and when a very intense electric bias is exerted on the crystal, the phenomenon of the forced transition6) can be observed, which causes a phase transition from the antiferroelectric phase to the ferroelectric one: 2) When the $PbZrO_3$ contains a little Ba or Ti ions,7),8) the ferroelectric phase naturally appears besides the antiferroelectric phase: 3) The antiferroelectric Curie point of $PbZrO_3$ (ca. 230°C) is higher by only 40°C than the paraelectric Curie point near which we might see the phase transition from the paraelectric to the ferroelectric phase provided that there were not the antiferroelectric phase. These all facts have easily been understood by supposing that in $PbZrO_3$

---

* Present address: Electrotechnical Laboratory, Tanashi, Kitatama-gun, Tokyo.

the difference of the free energy between the antiferroelectric phase and the ferroelectric one is very little. In this paper we will estimate quantitatively the difference of the free energy as functions of temperature and of the Ti ion concentrations, and will examine the stability of the antiferroelectric state in the lead zirconate.

There are two methods to estimate the free energies. One of which is to make use of a forced transition. The electrical work required to accomplish the forced transition will give the free energy difference between the two phases. Another method is to utilize the phenomena observed in solid solutions of $PbZrO_3$—$PbTiO_3$. If we know the transition energy and transition temperature of the solid solutions $Pb(Zr-Ti)O_3$ as functions of concentrations, then we can estimate the free energy differences through rather simple reasonings. Synthesis of the above two methods may furnish a reliable information about the free energy relations.

Our second purpose is to complete the phase diagram of the solid solution over the whole range of the concentrations. G. Shirane and A. Takeda⁷⁾ have already determined the phase diagram except in two narrow ranges, namely the range near the pure $PbZrO_3$ and that around the phase boundary separating the rhombohedral ferroelectric phase from the tetragonal ferroelectric phase. We have examined the two regions.

It has been found that there are five phases in all in the solid solution and that in $Pb(Zr97-Ti3)O_3$ four kinds of polymorphic modifications appear, that is, successively, the antiferroelectric, the other antiferroelectric, the ferroelectric and the paraelectric phases. On the phase diagram, we have found that the boundary mentioned above lies at the composition near $Pb(Zr55-Ti45)O_3$.

At last, a tentative explanation about the mechanism for the successive occurence of the five polymorphic modifications in the solid solution shall be given.

§ 2. Preparation of the Sample

In preparing the solid solutions containing less than 5 atomic percent of $PbTiO_3$, special care was taken of the purity of the ZrO_2 chemicals, for we have already known⁵⁾ that the impurities much influence upon the dielectric properties of these solid solutions, especially if the samples near pure $PbZrO_3$ are concerned. We have used the very pure one containing only Ti(0.2 %), Fe(0.05 %), and Si(0.03 %). But because it is very difficult to obtain large amount of ZrO_2 of the highest purity, we could not help using the chemicals of less purity, 98 %, in making the several specimens around $Pb(Zr50-Ti50)O_3$.

The ZrO_2 was throughly mixed with reagent grade PbO, TiO_2, and pressed into the form of a disk and calcined at about 1200°C in a vapour of lead oxide. It was crashed to a fine powder and pressed into the form of a disk, 3 cm in diameter and 0.5 cm thick, and then refired in an electric furnace for 1 hour at maximum temperature 1300°C. The ceramic samples thus obtained were very tight.

§ 3. The Solid Solution Containing a Little Amount of $PbTiO_3$

A) *Dielectric Constant*

The sample of 20 mm² in area and 1 mm thick, with evaporated gold film on both faces, was set in a bath of liquid paraffin which was heated by an electric furnance, and the dielectric constant was measured at 1 Mc./sec. The results are shown as a function of temperature in Fig. 1. In pure $PbZrO_3$, as has been known⁶⁾, only one transition is found at 230°C except a small hump observed just below the Curie point. In $Pb(Zr97-Ti3)O_3$, we have found three anomalous points on heating, i.e., 180°, 202° and 219° C, while two anomalous point on cooling, i.e., 218° and 160°C. With the helps of the X-ray measurement and the phase diagram that will be described in § 3 D and § 7, we are sure that the state Aα appearing in the temperature range up to 180° on heating and below 160°C on cooling is antiferroelectric, undoubtedly of the same kind as was found in pure lead zirconate, and that the state Fα occuring between 202° and 219°C on heating while between 218° and 160°C on cooling is ferroelectric, clearly of the same kind as was found by Shirane and Takeda⁷⁾ in the solid solution around $Pb(Zr85-Ti15)O_3$. To clarify the nature of the new Aβ phase, observed only on heating, between 180° and 200°C is one of the intention of the present study. It turns out that the state is a new type of antiferroelectric, as will be shown in the following section. Though in Pb(Zr97—

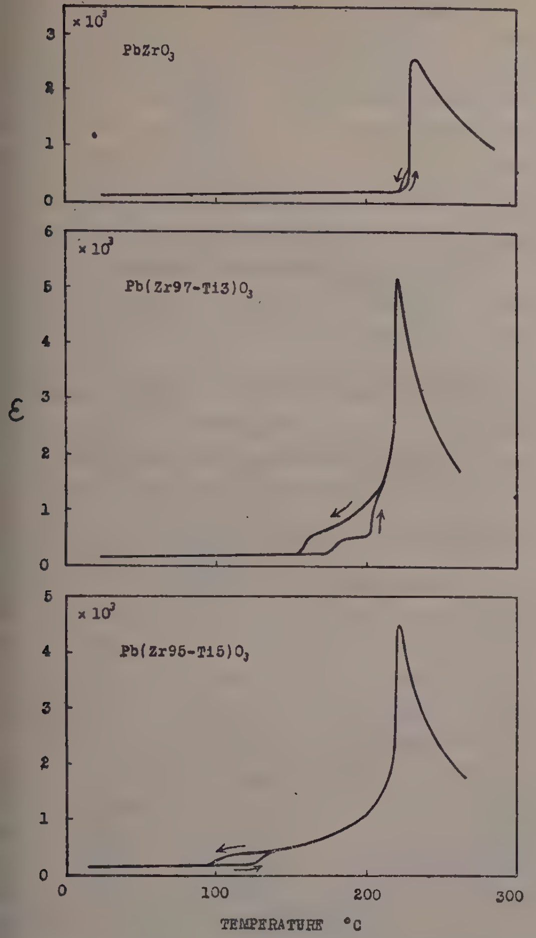

Fig. 1. Dielectric constant as functions of rising and falling temperature, at 1 Mc/sec. (a) $PbZrO_3$, (b) $Pb(Zr97\text{-}Ti3)O_3$, and (c) $Pb(Zr95\text{-}Ti5)O_3$.

Ti3)O_3 there are four polymorphic modifications: Aα, Aβ, Fα and Pα, in Pb(Zr95—Ti5)O_3 Aβ phase is entirely overlaid by Fα phase, thus leaving only Aα, Fα and Pα phases.

The remarkable points observed in the ε-temperature curve are these: 1) Temperature hysteresis at the transition points Aα—Fα or Aβ—Fα are very conspicuous. 2) The peak value of the dielectric constant at the Curie point greatly increases with slight increase of $PbTiO_3$, namely, while it is *ca.* 2.5×10^3 for Aα—Pα transition at 230°C in $PbZrO_3$, it is *ca.* 5×10^3 for Fα—Pα transition at 220°C in Pb(Zr97—Ti3)O_3. Regardless of this remarkable difference of the peak value, the Curie-Weiss constants are nearly invariable, i.e. 1.1—1.5×10^5°K, over the relatively wide concentration range of the solid solution. 3) In contrast to the well known barium titanate, whose dielectric constant varies slowly with varying temperature below the Curie point, the dielectric constant in the ferroelectric state of Pb(Zr95—Ti5)O_3 increases rapidly with temperature.

B) *Thermal Expansion*

Helpful informations may be given from the properties of Pb(Zr97—Ti3)O_3 because the sample reveals the ferroelectric phase as well as the antiferroelectric phase. So the measurements are made mainly on this specimen. The thermal expansion of the ceramic rod, 3 cm in length and 0.5 cm in diameter, was measured with a simple dilatometer. The rate of the temperature variation was about 0.5°—1° C/min. The results $(l-l_0)/l_0$ is shown as a function of temperature in Fig. 2. Corresponding to the anomaly in the ε-temperature curve of Fig. 1, there are three points of anomalous dilatations on heating whereas only two points of anomalous contractions on cooling. The volume expansion coefficients β, and the anomalous volume change $\Delta V/V$ during the transitions are listed in Table I. Very large anomalous expansion observed at Aβ—Fα transition may hinder to some extent the occurrence of the phase transition and hence may be one of the causes for the striking temperature hysteresis.

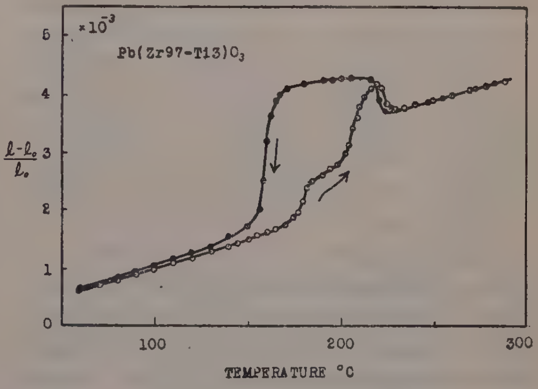

Fig. 2. Linear thermal expansion of Pb(Zr97-Ti3)O_3 at rising and falling temperature.

To examine the temperature hysteresis for Aα—Aβ transition, the heating was stopped at 198°C before the Fα phase appears, then the sample was cooled slowly. The dilatometric curve is shown in Fig. 3. A rather small temperature hysteresis of about 15°C (180°—165°C) was observed in contrast to the remarkable hysteresis of about 40°C at the Aα—Fα transition.

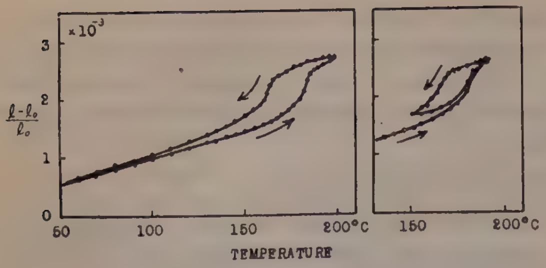

Fig. 3. Temperature hysteresis of the thermal expansion of Pb(Zr97-Ti3)O_3 observed around the $A\alpha-A\beta$ transition point.

Table I. Volume expansion coefficients β, and the anomalous volume change $\Delta V/V$ during the transition. The data listed on the last column are obtained from the X-ray measurement (ref. § 3D).

Phase	Volume expansion coefficient, β	
	(dilato.)	(X-ray)
Aα	2.7×10^{-5}	3.0×10^{-5}
Aβ	5.4 〃	2.7 〃
Fα	0.8 〃	0.7 〃
Pα	2.8 〃	3.0 〃

Phase change	Temp.	Relative volume change, $\Delta V/V$	
		(dilato.)	(X-ray)
Aα→Aβ	180°C	1.8×10^{-3}	0.7×10^{-3}
Aβ→Fα	203	4.5 〃	4.8 〃
Fα→Pα	220	−1.7 〃	−1.0 〃
Fα→Aα (cooling)	160	−7.5 〃	−6.0 〃

C) *Specific Heat*

Using adiabatic calorimeter of Nagasaki-Takagi type[9], the specific heat of Pb(Zr97−Ti3)O_3 powder of about 30 g was measured over the temperature range from 30° to 300°C at the heating rate of about 0.5°C/min. The result is shown in Fig. 4. The anomalous specific heats and the entropy changes are listed in Table II. To estimate the transition energies on cooling, the cooling rate was observed as shown in Fig. 5. While cooling, the temperature of the atomsphere outside the sample was care- fully adjusted to just 9°C lower than that of the sample. Comparing the cooling curve (Fig. 5) with the basic specific heat obtained on heating (Fig. 4), we were able to estimate the anomalous specific heat on cooling. The transition energies thus found are, 270 cal/mole for Pα→Fα at 220°C and 140 cal/mole for Fα→Aα at 160°C. Since the total transition energy (Aα→Pα) estimated for cooling case (270+140=410 cal/mole) is in fair agreement to that obtained by adiabatic calorimeter on heating (100+35+250=385 cal/mole), our method of estimation of the transition energy for cooling case seems to be reliable. Further, the total transition energy is nearly the same as that previously obtained in pure lead zirconate (400[5], and 440 cal/mole[8]). Perhaps this may be because our sample contains a little PbTiO_3 of only 3 atomic percent.

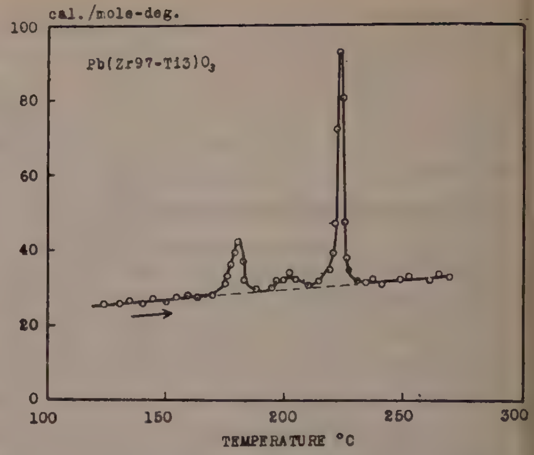

Fig. 4. Specific heat curve of Pb(Zr97-Ti3)O_3 at rising temperature.

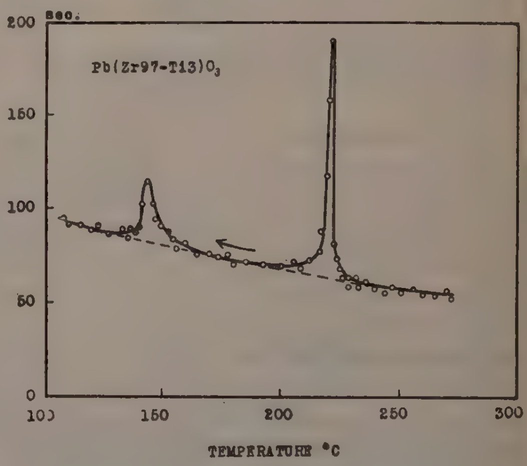

Fig. 5. Cooling rate *vs.* temperature curve of Pb(Zr97-Ti3)O_3.

Table II. The transition energies and the entropy changes observed in Pb(Zr97-Ti3)O_3.

Phase change	Temp.	Energy change (cal/mole)	Entropy change (cal/mole-deg.)
Aα→Aβ	180°C	100	0.22
Aβ→Fα	205	35	0.073
Fα→Pα	220	250	0.51

In the cooling case, as soon as the Fα→Aα

transition starts at 160°C, we have noticed that the temperature of the sample rises, though by only a few degrees. This supercooling suggests that the activated state over which the transition process has to pass may be of high energy.

D) *X-ray Measurement*

Concerning pure lead zirconate we undertook an X-ray study of the temperature change of lattice parameters. The fine powder of lead zirconate was coated over a platinum wire which was used as a standard of lattice dimensions. The Debye-Scherrer photographs were taken in a 50.3 mm camera by the back reflexion method using Cu-Kα radiation. Although it has been found[4] that the true crystal symmetry below the Curie point is slightly orthorhombic, we have for simplicity regarded as if the basic perowskite lattice of the material is tetragonal. The variations of lattice constants and of tetragonality are shown in Figs. 6 and 7 against temperatures. The lattice parameter at 20°C are $a=4.152$ KX, $c=4.101$ KX and $c/a=0.987_7$. As the temperature is raised the axial ratio increases almost linearly towards $c/a=0.993_5$, the value at the Curie point of 230°C, and there it jumps to $c/a=1$. Hence this transition is of the first order. The cell volume as a function of temperature T°C is given as follows:

$$T<230°\mathrm{C} \quad V=70.65\times(1+2.7\times10^{-5}T)\,\mathrm{KX}^3$$

$$T>230°\mathrm{C} \quad V=71.38\times(1+3.3\times10^{-5}(T-230))\,\mathrm{KX}^3$$

The discontinuity of the volume at the transition point is $\Delta V/V=4.1\times10^{-3}$, i.e., 0.29 KX^3 per unit cell. Strictly speaking, the crystal is orthorhombic below the Curie point, because there are faint superstructure lines on the photograph. In the orthorhombic system, we have $a=4.152\times\sqrt{2}=5.872\,\mathrm{KX}$, $b=4.152\times 2\sqrt{2}=11.74\,\mathrm{KX}$ and $c=4.101\times2=8.202\,\mathrm{KX}$.

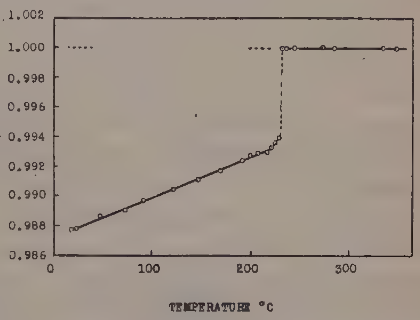

Fig. 7. Axial ratio of $PbZrO_3$ as a function of temperature.

Concerning $Pb(Zr97-Ti3)O_3$ we have examined the crystal forms of the four modifications appearing successively. The experimental procedure is the same as above mentioned. It is found that the Aα phase has the same crystal structure as was found in the pure lead zirconate. Therefore the Aα phase must also be antiferroelectric. The Aβ phase has also the tetragonal structure with $c/a=0.994$ at 190°C, but the arrangement and position of the superstructure lines observed on the photograph are clearly different from those of the Aα phase. The Fα phase has a pseudo-cubic

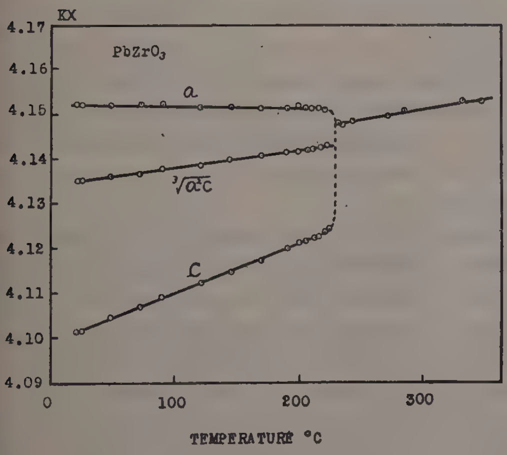

Fig. 6. Lattice constant of $PbZrO_3$ *vs.* temperature curve. Below the Curie point the basic perowskite lattice is assumed, for convenience, as tetragonal.

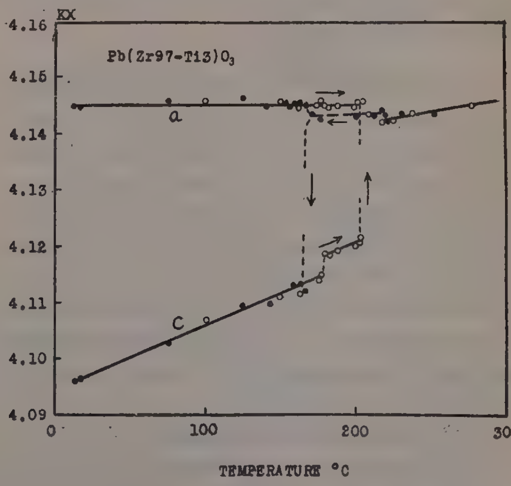

Fig. 8. Lattice constant of $Pb(Zr97-Ti3)O_3$ as a function of temperature.

perowskite structure; recently it has been concluded by Shirane, Hoshino and Suzuki[10][11] that this crystal belongs to the rhombohedral symmetry. Since the Fα phase can display clear *E-D* hysteresis loops, Fα is undoubtedly ferroelectric. The space group, maybe C_{3v}^5, will be given in the following section. The lattice parameter of Pb(Zr97—Ti3)O_3 *vs.* temperature relation and the axial ratio *vs.* temperature curve are shown in Figs. 8 and 9. As a whole, a fair agreement is found between the results of dilatometric measurements and those of X-ray measurements, except for some minute discrepancies concerning the Aβ phase and concerning the Aα→Aβ transition (Table I.). Probably these errors may have been introduced from one or all of the following causes, (1) the temperature range of the Aβ phase is very narrow and the accurate measurement of the thermal expansion coefficient is very difficult; and (2) the experimental conditions, the rate of the temperature variations and the form of the samples, are greatly different in both cases.

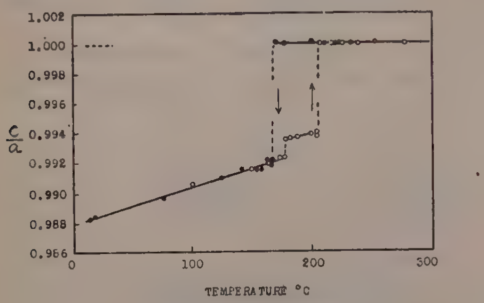

Fig. 9. Axial ratio of Pb(Zr97-Ti3)O_3 at varying temperature.

§ 4. Antiferroelectricity of the Aβ Phase

As stated above, a crystal of the Aβ phase shows superstructure lines, one of the important characteristics of the antiferroelectricity. Further, as shown in Fig. 10 a, the *d.c.* bias of 2 kv/cm increases slightly the dielectric constant of the Aβ phase and lowers the Aβ →Fα transition point (203°C in Pb(Zr97—Ti3) O_3) by about 3°C. Such effects are explainable only if we admit the non-ferroelectricity of the Aβ phase, as already been described in the antiferroelectricity of pure lead zirconate[6]. Since all the experiments performed on the Aβ phase have shown the close resemblances to the antiferroelectric Aα phase, and since there is no evidence at all to deny the anti-ferroelectricity, we may suggest that the Aβ phase is also an antiferroelectric, though of a new kind different from the Aα phase. The detailed structural analysis is, of course, desirable.

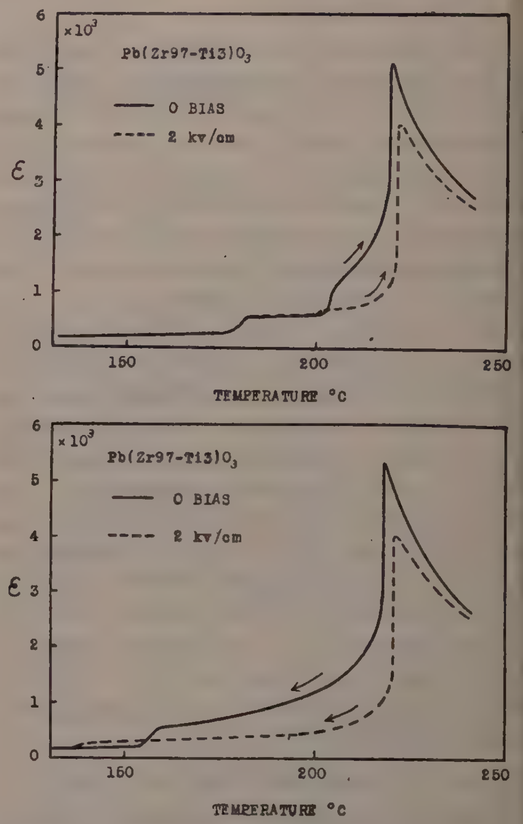

Fig. 10. Effect of biasing *d.c.* field of 2 kv/cm on the dielectric constant of Pb(Zr97-Ti3)O_3, (a) at rising temperature; (b) at falling temperature.

Attention must be paid to the fact that the *E—D* hysteresis loop of Pb(Zr97—Ti3)O_3 on heating displays the ferroelectric character at 195°C if the applied *a. c.* field is higher than 5 kv/cm (Fig. 11). The fact may be mistaken as an evidence of ferroelectricity of the Aβ phase. However, it has been proved that it is not the case. The ferroelectric Fα phase replaces the original Aβ phase under the influence of the strong electric field. We have found that once an intense electric field is applied on the Aβ phase, the dielectric constant *vs.* temperature curve, characteristic of the phase, becomes almost the same as that of the Fα phase under *d. c.* bias (Fig. 11 b, dotted curve), and remains so even after the removal of the applied field. These facts clearly shows that the activation energy for the transition F$\alpha \rightarrow$Aβ is so large that the induced Fα phase in Pb(Zr97—Ti3)O_3 cannot easily return to the original Aβ phase.

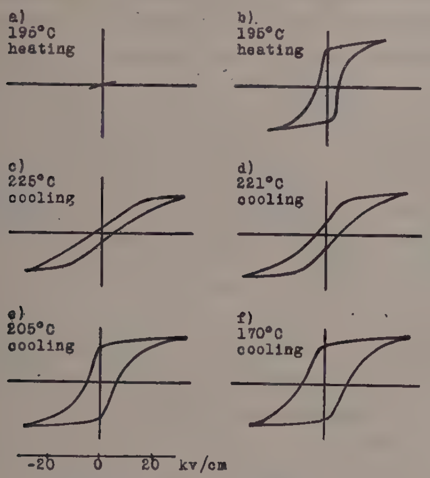

Fig. 11. Hysteresis loops of Pb(Zr97-Ti3)O_3. (a) at 195°C (Aβ phase), (b) at 195°C (Fα phase).

If, on the other hand, the relaxation is shorter than 1/100 sec., the mutual transition between the Aβ and Fα is to be observed on the hysteresis curve. Really, such an hysteresis loop has been found in Pb(Zr99—Ti1)O_3 at temperatures near 217°C. In Fig. 12 b the linear part of the curve ($a\ldots a'$) is corresponding to the Aβ phase, while the outer parts with large polarization ($b\ldots b'$) to the Fα phase. Thus the hysteresis curves, too, powerfully support the non-ferroelectricity of the Aβ phase; for if the Aβ phase were in truth ferroelectric though with very large coercive force, then nothing would prevent the existence of the remanent polarization after the Fα phase was once realized.

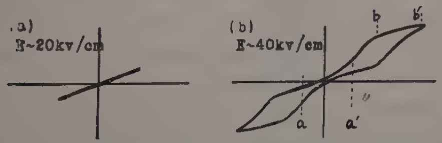

Fig. 12. Hysteresis loops of Pb(Zr99-Ti1)O_3 at 217°C. (a) $E_{max} \sim 20$ kv/cm (Aβ phase), (b) $E_{max} \sim 40$ kv/cm (a—a', Aβ phase; and b—b', Fα phase).

§ 5. Forced Transition

Near the antiferroelectric Curie point, an estimation of the difference of the free energy between the Aα phase and the Fα phase can be furnished by analysing the phenomena of the forced transition. At first we have observed on a cathode-ray oscilloscope the hysteresis loop of pure lead zirconate with steep jumps on both ends (Fig. 13), of which the region AB corresponds to the Aα phase whereas the region CD to the Fα phase. By extrapolating the ferroelectric part CD back to the ordinate axis, and by integrating the area surrounded by the loop ABCF, we can obtain the work done between the state Aα and the Fα. The work per mole, $(Nv/4\pi)\int EdD$, is shown as a function of temperature in Fig. 14, where N is the Avogadro number and v is the volume of the unit cell 71.4 KX^3. Since our experimental condition, *a. c.* field of 50 c.p.s., is rather an adiabatic one, the temperatures T_A and T_F of the states A and F, respectively, should necessarily be not equal. Let the temperature difference $T_A - T_F$ be dT, the arithmetical mean temperature $(T_A+T_F)/2$ be T_m, and the specific heat at constant pressure be C. Then the difference of the free energy between the two phases at the temperature T_m is

$$H_F(T_m)-H_A(T_m)=U_F(T_F)-U_A(T_A)$$
$$-(C_F-C_A)(T_m/2)(dT/2T_m)^2. \qquad (1)$$

The difference of the internal energy $U_F(T_F)-U_A(T_A)$, represented by Fig. 14 is the order 2 cal/mole, while the last term estimated by the caloric data of Pb(Zr97—Ti3)O_3 (Fig. 4), namely $|C_F-C_A|<3$ cal/mole-deg., dT $=$(transition energy)$_{A\alpha\rightarrow F\alpha}$/(specific heat)$\approx 3°$C, and $T_m = 273°+220° \fallingdotseq 500°$K, is only of negligible order 0.01 cal/mole. Therefore the curve of Fig. 14 may practically be regarded as the true difference of the free energy itself. As was expected, it has been proved that the Aα phase in the pure $PbZrO_3$ is by only a few calories per mole more stable than the Fα phase

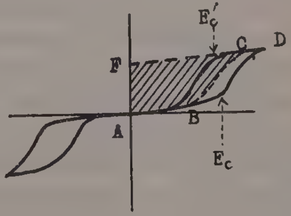

Fig. 13. Hysteresis loop of $PbZrO_3$ that shows the forced transition from the Aα phase (AB) to the Fα phase (CD).

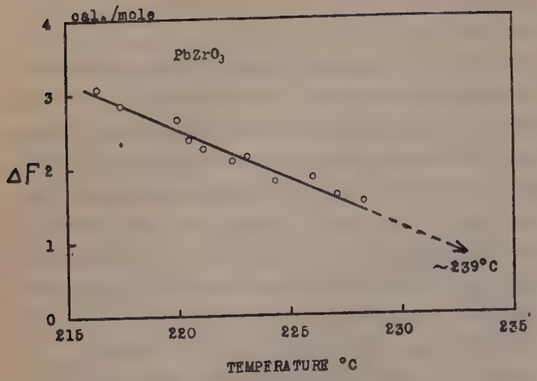

Fig. 14. Free energy difference of $PbZrO_3$ between the Aα phase and the Fα phase.

near the antiferroelectric Curie point. However, because of the following reasons Fig. 14 may be regarded as only representing an approximate magnitude of the difference of the free energies. That is: (1) We have used a tight ceramic sample rather than a single crystal. Since it has been generally known that the behaviour of a ceramic is not merely that of an orientational average of single crystals, and since especially in the *E—D* hysteresis curve a complete saturation of the dielectric polarization is hardly attained in a ceramic, so the free energy difference calculated above may be a bit too small: (2) As shown in Fig. 13, we have observed hysteresis character on the curve. And in the calculation of the free energy difference, we have drawn the curve BC so as to divide the area of the loop into two equal parts. Therefore the curve BC is an approximate curve to the true equilibrium one. In the following section another method will be given, which yields a more accurate result and supports the reasonableness of the above treatment.

The threshold field E_c requisite for the forced transition was estimated from the hysteresis loop and the result is shown in Fig. 15 for $PbZrO_3$ and $Pb(Zr98—Ti2)O_3$. In $PbZrO_3$ E_c decreases with rising temperature with the rate of $dE_c/dT = -1.65$ kv/cm-deg., and the curve if extrapolated intersects the abscissa at about 240°C. The intersection point means that the free energies of the Aα and the Fα should coincide near 240°C, although, in fact, the both phases do not exist at that temperature for they are less stable than the paraelectric phase. In $Pb(Zr98—Ti2)O_3$ there is a distinct kink point at 196°C just corresponding to the Aα→Aβ transition. The curve at temperatures up to 195°C represents the E_c for the Aα→Fα transition while that at temperatures between 195° and 220°C represents the E_c for the Aβ→Fα transition. The slopes calculated are $(dE_c/dT)_{A\alpha\to F\alpha} = -1.37$ kv/cm-deg., and $(dE_c/dT)_{A\beta\to F\alpha} = -0.40$ kv/cm-deg. The intersections of these curves and the abscissa show that in $Pb(Zr98—Ti2)O_3$ the free energy of the Aα and the Fα should coincide at about 211°C and that the free energies of the Aβ and the Fα should coincide at about 245°C.

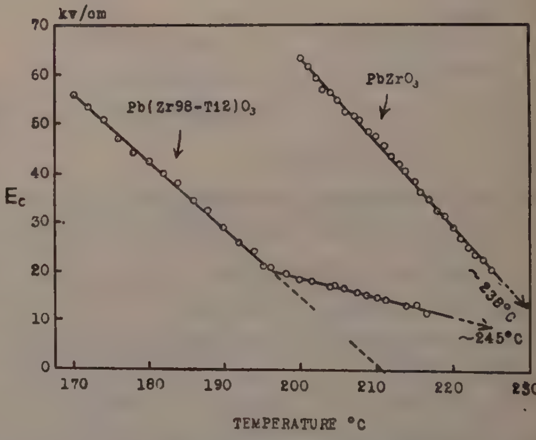

Fig. 15. Threshold field strength for the transition from the antiferroelectric phase to the ferroelectric phase.

A thermodynamical consideration can provide a useful check on our experimental values. If the latent heat is denoted by Q, the ratio of the latent heat of the Aα→Aβ transition to that of the Aβ→Fα transition can be written as follows,

$$\frac{Q_{A\alpha\to A\beta}}{Q_{A\beta\to F\alpha}} = \frac{d(H_{A\alpha}-H_{F\alpha})/dT}{d(H_{A\beta}-H_{F\alpha})/dT} - 1$$

$$= \frac{\frac{d}{dT}\int EdD_{(A\alpha\to F\alpha)}}{\frac{d}{dT}\int EdD_{(A\beta\to F\alpha)}} - 1 . \qquad (2)$$

For simplicity, EdD shall be approximated by $2\pi(P_S+P_m)E_c$, where P_S and P_m denote respectively the spontaneous polarization and the maximum polarization at the E_c of the $F\alpha$ phase. Then,

$$\frac{d}{dT}\int EdD \sim 2\pi(P_s+P_m)E_c \times \left\{\frac{d}{dT}\log(P_s+P_m)+\frac{d}{dT}\log E_c\right\} . \qquad (3)$$

Thus, the right hand side of (2) is

$$\frac{\left\{\frac{1}{P_s+P_m}\cdot\frac{d(P_s+P_m)}{dT}+\frac{1}{E_c}\cdot\frac{dE_c}{dT}\right\}_{A\alpha\to F\alpha}}{\left\{\frac{1}{P_s+P_m}\cdot\frac{d(P_s+P_m)}{dT}+\frac{1}{E_c}\cdot\frac{dE_c}{dT}\right\}_{A\beta\to F\alpha}}-1, \tag{4}$$

where $(1/E_c)(dE_c/dT)$ are −0.069/°C for the Aα→Fα transition and −0.020/°C for the Aβ→Fα transition, at 196°C and at E_c=19 kv/cm. An accurate estimation of $(1/(P_s+P_m))(d(P_s+P_m)/dT)$ of Pb(Zr98—Ti2)O_3 is rather difficult because much intense field must be applied in order to display hysteresis loops with certainly saturated polarizations of the Fα phase. But in Pb(Zr97—Ti3)O_3, because of the high activation energy for the Fα→Aα or the Fα→Aβ transition, the hysteresis loops with ferroelectric character can be easily observed, and the P_s, and P at 20 kv/cm are shown as functions of temperature in Fig. 16. The $(1/(P_s+P))(d(P_s+P)/dT)$ of Pb(Zr97—Ti3)O_3 at 195°C and at 20 kv/cm is of very small value, *ca.* −0.001/°C. If, approximately the same is the case with Pb(Zr98—Ti2)O_3, we can estimate the value of (4), namely the ratio is about 2.3. When this is compared with the direct caloric data obtained in Pb(Zr97—Ti3)O_3 (Fig. 4), $Q_{A\alpha\to A\beta}/Q_{A\beta\to F\alpha}\doteqdot 100/35=2.9$, the agreement between them is satisfactory.

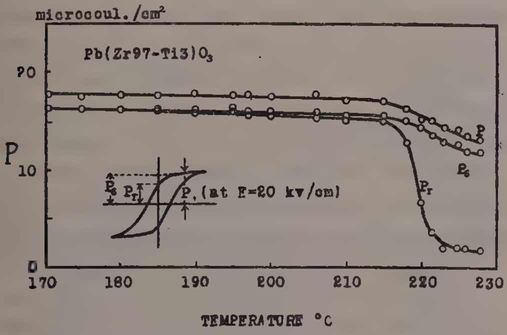

Fig. 16. The spontaneous polarization P_s, the remanence polarization P_r, and the polarization at E=20 kv/cm of Pb(Zr97-Ti3)O_3 are shown as functions of temperature.

In the polycrystalline samples, the forced transition occurs continuously over the region BC of Fig. 13. On the other hand, if we observe the phenomenon using single crystals, we would see that the polarization jumps discontinuously to the spontaneous polarization of the Fα phase just at the E_c of Fig. 13 Then the following relation holds:

$$H_{F\alpha}-H_{A\alpha}=\frac{Nv}{4\pi}\int_{(ABCF)}E\,dD\approx\frac{Nv}{4\pi}E_c\cdot D_s\,, \tag{5}$$

where D_s is the dielectric displacement of a single crystal of the Fα phase. By differentiating the $H_{F\alpha}-H_{A\alpha}$ and $H_{F\alpha}-H_{A\beta}$ with temperature we can obtain the difference of the entropies between the Aα phase and the Aβ phase. The following relation is obtained:

$$D_s=\frac{S_{A\alpha}-S_{A\beta}}{\frac{Nv}{4\pi}\left\{\left(\frac{dE_c}{dT}\right)_{A\alpha\to F\alpha}-\left(\frac{dE_c}{dT}\right)_{A\beta\to F\alpha}\right\}}, \tag{6}$$

At the Aα→Aβ transition point 196°C of Pb(Zr98—Ti2)O_3, it is found from Fig. 15 that $(dE_c/dT)_{A\alpha\to F\alpha}=-1.37$ kv/cm-deg., and $(dE_c/dT)_{A\beta\to F\alpha}=-0.40$ kv/cm.deg. If we assume that the latent heat of the Aα→Aβ transition of Pb(Zr98—Ti2)O_3 is nearly the same as that of Pb(Zr97—Ti3)O_3 (Fig. 4), then the entropy change $S_{A\alpha}\to S_{A\beta}$ of Pb(Zr98—Ti2)O_3 at 196°C is about −0.21 cal/mole.deg. Putting these values and $v=71.2\,KX^3$ in the equation (5), we find that the dielectric displacement of the Fα phase at this temperature is D_s=21 microcoul./cm². Considering that the spontaneous polarization of the Fα phase of a single crystal of Pb(Zr97—Ti3)O_3 should be more than 16 microcoul./cm² obtained from the hysteresis loop of polycrystalline ceramics, (Fig. 16), above result seems to be reasonable.

Theoretically, we will be able to observe not only the forced transition from antiferroelectric to ferroelectric state but also the forced transition from antiferroelectrics to paraelectric[12)] or even from paraelectric to ferroelectric. The hysteresis curve of Pb(Zr97—Ti3)O_3 at 225°C shows the hysteresis character much resembling ferroelectric hysteresis loop (Fig. 11 c). But since the temperature 225°C is higher than the ferroelectric Curie point 219°C, and since the remanent polarization is very small in contrast to the cases below the Curie point, we may suggest that the paraelectric-ferroelectric forced transition is occuring in this case.

§ 6. Solid Solutions Around Pb(Zr55—Ti45)O_3 and Pure $PbZrO_3$

The phase diagram of the $PbZrO_3$—$PbTiO_3$ system has already been investigated[7)] with the exception of two narrow ranges, the one in the neighbourhood of pure lead zirconate and the other around the concentration Pb

(Zr55—Ti45)O_3. These remaining regions have been examined in detail; the phase diagram thus completed is shown in Fig. 17. The phase boundary was determined mainly from the dielectric measurements. As already shown in § 3, a large temperature hysteresis was observed in the Aα—Fα or the Aβ—Fα transition, and we have plotted in Fig. 17 b, the transition points observed for both heating and cooling cases. For the determination of the Aβ—Fα phase boundary, only one point observed in Pb(Zr97—Ti3)O_3 is available, but the forced transition provides a great advantage for our purpose. As is estimated in Fig. 15 the free energies of the Aβ and the Fα in Pb(Zr98—Ti2)O_3 may become the same at 245°C, that gives an hypothetical transition point. Similarly, several such points obtained from the forced transition prove to be useful in the determanation of the phase boundaries. The Aβ phase occupies only a narrow range near the limit of the phase diagram so that it is apt to be overlooked unless very pure ingredients should be used in making the ceramics.

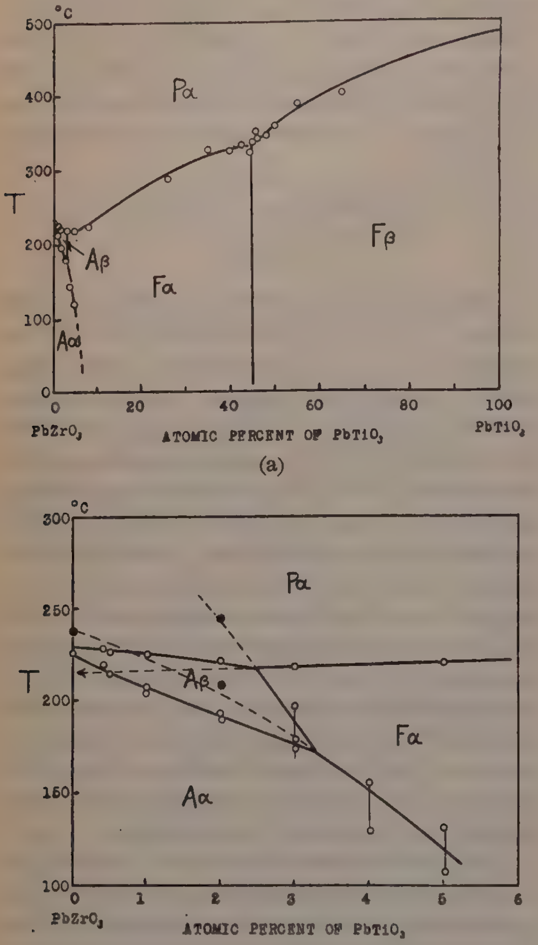

(a)

(b)

Fig. 17. Phase diagram of the $PbZrO_3$-$PbTiO_3$ system; solid circles in Fig. (b) are estimated from Figs. 14 and 15.

It has been suggested by Shirane and Suzuki[11], that on the phase diagram of the solid solution the phase boundary separating the tetragonal ferroelectric state Fβ($PbTiO_3$ side), from the rhombohedral ferroelectric state Fα ($PbZrO_3$ side), lies at room temperature somewhere between Pb(Zr60—Ti40)O_3 and Pb(Zr55—Ti45)O_3. To find the precise position of the boundary, dielectric constants of the eleven samples of solid solutions around Pb(Zr55—Ti45)O_3 have been measured. But at room temperature we could not find any anomaly corresponding to the Fα—Fβ transition. On the other hand the X-ray studies have revealed that the solid solutions with more than 46% of $PbTiO_3$ have tetragonal structure while those with less than 44% of $PbTiO_3$ have rhombohedral structure. The lattice parameters, c/a or α, observed at room temperature are shown as a function of concentration in Fig. 18. Debye-Scherrer photograph of Pb(Zr55—Ti45)O_3 could not be explained as a homogeneous single phase, but consisted of the lines corresponding to the mixtures of the rhombohedral and tetragonal crystals. Moreover the photographs of Pb(Zr55—Ti45)O_3 taken at 100°C and 200°C have shown that with rising temperature, the proportion of the tetragonal structure increases slightly at the expense of that of the rhombohedral structure. On the other hand, the Curie point vs. concentration curve of the eleven

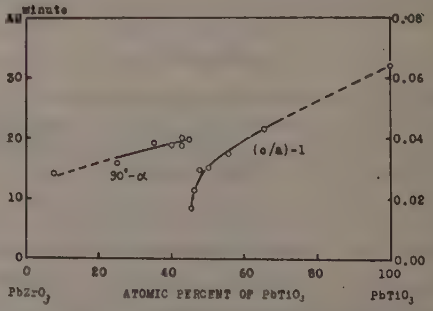

Fig. 18. Axial ratio and angle of distortion of Pb(Zr-Ti)O_3 at room temperature.

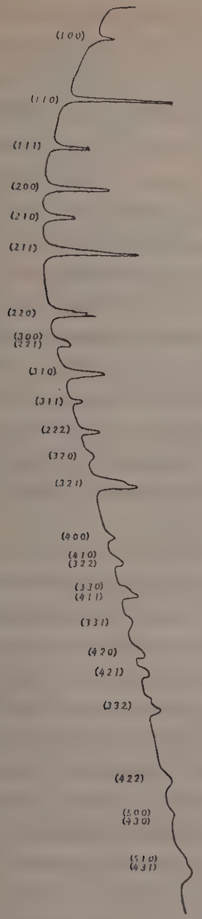

← Fig. 19. Microphotometer curve taken of the powder photograph of Pb(Zr58–Ti42)O_3.

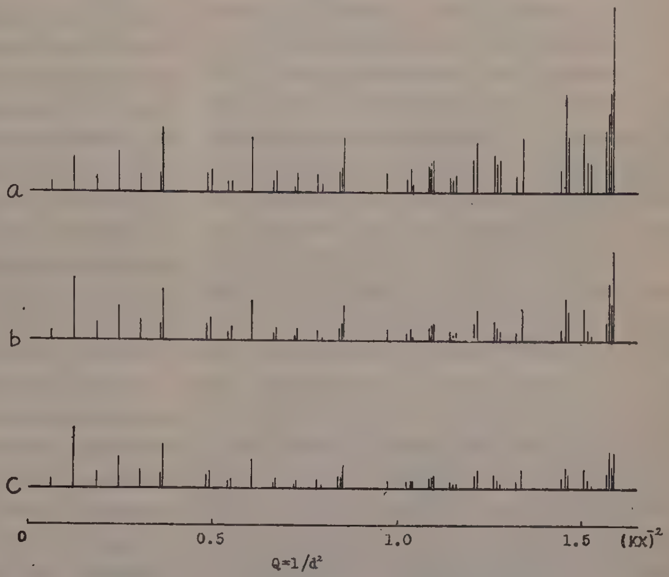

Fig. 20. Calculated line intensities of the X-ray diffraction of Pb(Zr58–Ti42)O_3; correction for the absorption is made by assuming $\mu R=40$. (a) $x=0.04$, (b) $x=0.04$ and $\overline{U}_{Pb}{}^2=0.02$ KX², (c) $x=0.03_5$, $\overline{U}_{Pb}{}^2=0.02$ KX² for [111] direction, $\overline{U}_{Pb}{}^2=0.03$ KX² for $[11\bar{1}]$, $[1\bar{1}1]$ etc., and $\overline{U}_{Zr}{}^2=0.01$ KX².

samples show well defined kink at Pb(Zr55—Ti45)O_3. Hence, it may be concluded that the phase boundary is nearly parallel to the temperature axis. (Fig. 17 a).

Generally speaking, the phase diagram may include two phase regions such as, Aα+Aβ, Aα+Fα etc., but in fact we could not find any region of such kind. The decomposition from one phase into two phases or *vice versa* cannot proceed unless the interchange of the ions should be easy. But it seems that this is not the case, because the activation energy for the interchange of Zr and Ti ions, each closely surrounded by six oxygen atoms, is expected to be extraordinarily high.

§ 7. The Rhombohedral Ferroelectric Structure of the Fα Phase

Concerning the rhombohedral ferroelectric Fα phase the atomic arrangement has been investigated. From the X-ray measurement performed on the Pb(Zr58–Ti42)O_3 the lattice parameter at 20°C has been determined as, $a=4.068$ KX and $\alpha=89°41'$ with a rhombohedral structure. The structural analysis was carried out using the Debye-Scherrer photograph and Cu-$K\alpha$ radiation. The space group is assumed as $C_{3v}{}^5$–$R3m$, the same as is found in barium titanate below −80°C. The microphotometer curve taken of the X-ray photograph is shown in Fig. 19. Owing to the secondary emission from the sample, there is considerable back ground intensity which hinders the accurate analysis. Assuming $C_{3v}{}^5$, we have the following atomic position :

Pb ; 1(a), $(0+x, 0+x, 0+x)$
(Zr–Ti) ; 1(a), $(\frac{1}{2}, \frac{1}{2}, \frac{1}{2})$
3, 0 ; 3(b), $(\frac{1}{2}+y, \frac{1}{2}+y, 0+z)$,
$(\frac{1}{2}+y, 0+z, \frac{1}{2}+y)$,
$(0+z, \frac{1}{2}+y, \frac{1}{2}+y)$,

where x, y, and z each seems to be very small because the distortion of the Fα crystal from the cubic perowskite structure is very small. Since the intensity of the higher order reflection is determined mainly by the relative position of Pb against (Zr—Ti), and since the role of the light oxygen atoms is subordinate, and since there is considerable back ground intensity, it was impossible to determine y or z by using the powder photographs only. So, at first, the analysis was tried under the simplifying assumption that y and z both equal zero.

If we neglected the non-periodic displacement of atoms from the lattice point, for instance, that caused by the thermal vibrations of the atoms or by the difference of the ionic radius between Zr and Ti, it turns out that the observed and the calculated intensities are approximately consistent in the case of $x=0.04$. The calculated intensity diagram is shown in Fig. 20 a. But, as easily be noticed in the back side of the photograph and also of Fig. 20 a, the observed intensity of the reflexions with odd $(h+k+l)$ is generally too weak as compared with the calculated ones. This means that the non-periodic displacement of Pb atoms must be relatively large. Next, the calculations were refined by taking into account the amplitude of the displacement of Pb atoms. The mean-square amplitude of 0.02 KX^2 was found to give considerable improvements (Fig. 20 b). Nevertheless, the calculated intensity of the reflexions $(+h, +k, +l)$, especially those of (h, h, h) is too strong as compared with the observed ones, suggesting that the non-periodic displacement of Pb atoms is not spherically symmetrical but that it is relatively small in the [111] direction.

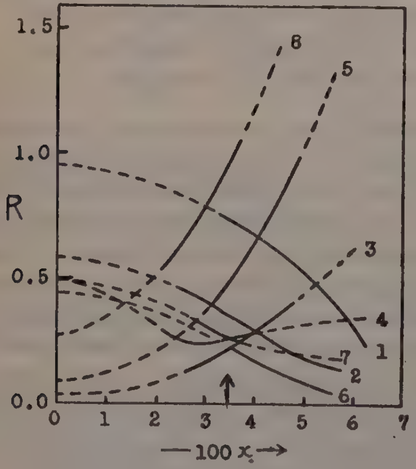

Fig. 21. Calculated ratio of the reflexion intensities of the neighbouring two Debye lines. The solid lines show the range that satisfies the observed conditions.

After several trials it has been concluded that $x=0.03_5$, namely the shift of Pb atoms relative to (Zr—Ti) atoms is 0.14 KX, and the order of the non-periodic displacements is approximatery $\overline{U_{Pb}^2}=0.02$ KX^2 for the [111] direction and $\overline{U_{Pb}^2}=0.03$ KX^2 for the [11$\bar{1}$], [1$\bar{1}$1] etc. The x was determined graphically in Fig. 21, where each curve represents the ratio of the two reflexion intensities calculated as a function of x, and the parts of solid lines are the range which satisfies all the observed conditions. With these values, the calculated intensities are shown in Fig. 20 c. Hence, in other words, the Fα phase has its spontaneous polarization in the [111] direction, as does the trigonal phase of barium titanate.

§ 8. Free Energy Diagram

From the phase diagram we can estimate the temperature where the free energies of the two phases become identical. In pure PbZrO$_3$, these temperatures are 230°C for $H_{A\beta}=H_{P\alpha}$, and 225°C for $H_{A\alpha}=H_{A\beta}$. Further, as was explained with respect to the forced transition in Figs. 14 and 15, the free energies of the Aα phase and the Fα phase coincide at 240°C, and so this temperature must lie on the extrapolation of the phase boundary between the Aα and the Fα. This is really the case, as seen from Fig. 17 b. Similarly, the extrapolation of the phase boundary between the Fα and the Pα intersects the ordinate at 217°C which is to be regarded as a theoretical ferroelectric Curie point if there were not the Aα at all. Remembering that the concentration of PbTiO$_3$ is very small in Pb(Zr97—Ti3)O$_3$ and that the total anomalous energy requisite for the Aα→Pα transition is nearly the same for both pure PbZrO$_3$ and Pb(Zr97—Ti3)O$_3$, we may assume that the internal energy difference between the Fα and the Pα in pure lead zirconate, though in fact we cannot observe the Fα in this case, should be nearly the same as the corresponding transition energy of Pb(Zr97—Ti3)O$_3$. If the above assumption is accepted, thermodynamical relations among all four phases of pure PbZrO$_3$, though in fact two of them are latent, can be calculated and are shown in Table III.

The free energy diagram given by Table III is shown in Fig. 22. For convenience, we have shown the free energy difference relative to the paraelectric Pα phase. Many of the

Table III

Kind of the phase change	T (°C)	Energy change (cal/mole)	Entropy change (cal/mole-deg.)	dT/dx	$dS(dT/dx)$
Aα→Pα	$230>T>225$	400	0.8	–	(−5.8)
Aα→Aβ	225	110	0.22	−16	−3.5
Aβ→Pα	230	290	0.58	− 4	−2.3
Aα→Fα	240	–	–	−19	–
Fα→Pα	217	250	0.51	+1.0	+0.5
Aβ→Fα	–	40	0.08	–	–

observed or the estimated data in Table III can be consistently incorporated in this diagram. Attention must be paid to the fact that the differences of the free energies among Aα-, Aβ-, Fα-, and Pα-phases are very little at temperatures near 230°C. $H_{F\alpha}-H_{A\alpha}$ is about 4 cal/mole and the value is consistent with the approximate value obtained by means of the forced transition in § 4.

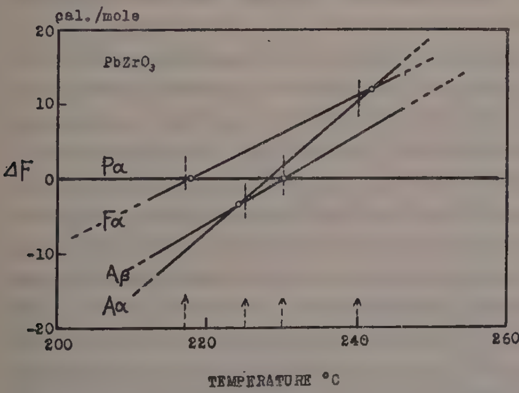

Fig. 22. Free energy diagram of lead zirconate. For the convenience, the differences relative to the Pα phase are shown.

In the solid solution the slope of the free energy curve as well as the intersection point of the two curves may be subject to slight variation with slight increase of the concentration of $PbTiO_3$. If we denote the atomic percent of $PbTiO_3$ by x, the rate of the shift of the transition temperature with x can be estimated from the phase diagram, and the result is shown on the fifth column of Table III. Since both the transition energies and the lattice parameters of pure $PbZrO_3$ and of Pb(Zr97−Ti3)O_3 are found to be nearly the same, it may be assumed that the slope of the free energy curve must also be approximately the same as those given in Fig. 22, so far as x is not too large. With this assumption, the free energy should decrease with the rate of $dS(dT/dx)$ with increasing x. Thus, at temperatures near 230°C, the free energies of solid solutions can be given as follows;

$$\left.\begin{array}{l} H_{A\alpha}=H_{P\alpha}+0.80(T-228)+5.8x \text{ cal/mole} \\ H_{A\beta}=H_{P\alpha}+0.58(T-230)+2.3x \\ H_{F\alpha}=H_{P\alpha}+0.51(T-217)-0.5x \\ \qquad (x \text{ not too large}). \end{array}\right\} \tag{7}$$

It is clearly interpreted that the antiferroelectric phase becomes unstable with increasing $PbTiO_3$, while the ferroelectric phase becomes more favourable under the same condition. But it should be remembered that these free energy equations are available only for small x and at temperatures near 230°C, because we have thus far taken into account neither the difference of the ground level of the normal specific heats of each phase nor the variation of the slope of the free energy curve against x.

§ 9. Conclusion and Discussion

The results may be summarized as follows:

(1) The two gaps of the phase diagram of the solid solution has been filled. There are five phases in all. It is remarkable that Pb(Zr97−Ti3)O_3 reveals four kinds of polymorphic modification including the antiferroelectric, ferroelectric and paraelectric phases.

(2) In respect to pure $PbZrO_3$, the free energies of the antiferroelectric Aα and Aβ as well as that of the latent ferroelectric Fα, have been given as a function of temperature near the Curie point. The free energy diagram shows that the difference of the free energies between the antiferroelectric and the ferroelectric phases is but little. This is the reason why the forced transition can easily be observed under an external electric field. Further, the dependence of the free energy of the solid solution upon small concentration of $PbTiO_3$ has been examined.

(3) The X-ray diffraction lines of the Fα

phase can satisfactorily be explained if we assume the space group C_{3v}^{5} with rhombohedral symmetry; this space group is just that of $BaTiO_3$ at temperatures below −80°C. In $Pb(Zr58-Ti42)O_3$ at room temperature, the displacement of (Zr−Ti) ion relative to Pb ion is about 0.14 KX to the [111] direction.

Now let us a little while meditate upon the role of (Zr−Ti) ion in the polymorphic transformation. As is shown in the phase diagram (Fig. 17 a), the Curie temperature of the tetragonal Fβ phase falls slowly at first with increasing $PbZrO_3$, then begins to fall rather sharply near $Pb(Zr40-Ti60)O_3$ and at last the tetragonal phase entirely disappears at $Pb(Zr55-Ti45)O_3$. On the other hand, in the rhombohedral phase near $Pb(Zr56-Ti44)O_3$, the dependence of the Curie temperature upon the concentration is not remarkable. These facts may be interpreted as follows. With increasing $PbZrO_3$ the tetragonal phase becomes unstable absolutely, and the rhombohedral phase, though it is only a latent metastable one on the $PbTiO_3$ side, begins to replace the tetragonal one. This explanation should be distinguished from the alternative that with increasing $PbZrO_3$ the tetragonal phase does not become unstable while the rhombohedral phase becomes more stable. The former explanation is supported by our X-ray measurement (Fig. 18). With increasing $PbZrO_3$ tetragonality approaches rapidly to unity, while the α is nearly constant about that concentrations.

In the Fα phase, with concentrations approaching pure $PbZrO_3$ the Curie temperature of the Fα phase falls slowly, besides the lattice distortion approaches zero with a gentle slope. These facts mean that the Fα phase becomes unfavourable with increasing $PbZrO_3$, as is told too by the free energy diagram of § 8. On the other hand, the free energies of the Aα and of the Aβ phases decrease somewhat steeply with increasing $PbZrO_3$ (see § 8).

Next step is to consider the reasons why the Fβ and the Fα phases becomes less stable and why the Aα and the Aβ phases become more stable with increasing $PbZrO_3$. For the convenience, we suppose the cubic perowskite type crystal ABX_3, where A, B and X correspond to Pb, (Zr-Ti) and O respectively. It can be supposed, as an approximation, that the variation of the concentration of the solid solution is to alter continuously the polarizability and the ionic radius of B ions. Since the electronic polarizability of the tetravalent ions, such as Zr or Ti, is generally very small, the polarizability of the B ion may be due mainly to the ionic polarizability. And, since the ionic polarizability is closely dependent on the distance between B and X ions, the difference in the dielectric behaviour between $PbZrO_3$ and $PbTiO_3$ seems to be ascribed first of all to the difference of the ionic radii of Zr and Ti rather than that of their electronic palarizabilities. Devonshire(13) has succeeded to explain the ferroelectricity of barium titanate, assuming the potential field acting upon Ti ion as the spherically symmetrical one of the form ar^2+br^4. Since both barium titanate and lead titanate reveal similar tetragonal ferroelectric phases, and since the properties of the solid solution $BaTiO_3-PbTiO_3$(14) has not shown any unexpected anomaly, the Ti ion in the $PbTiO_3$ may also be supposed to be in the spherical potential well. It may be suggested that, with increasing $PbZrO_3$ concentrations, ionic radius of B ion becomes greater and the repulsive force between B and X ions becomes more appreciable, so that the potential on the (Zr−Ti) may no longer be supposed spherical, to such an extent that the potential may become minimum in [100] direction while maximum in [111] direction, and consequently the solid solution may prefer a rhombohedral lattice to a tetragonal one. When the radius of the B ion becomes greater, ionic polarizabilities of B and X ions should become smaller because of the steric hindrance. This may be one of the reasons that the free energy of the Fα phase increases with increasing $PbZrO_3$ concentration (see equation (7)). These explanation may hold also for the case of $BaTiO_3-BaZrO_3$ system(15). Recently, we have found that on the $BaTiO_3$ side of the solid solution, the lowest two transition points of $BaTiO_3$, namely −80°C and 10°C, corresponding to trigonal-orthorhombic transition and to orthorhombic-tetragonal transition respectively, shift to higher temperature with increasing concentration of $BaZrO_3$. Consequently, when the sample contains more than 15 % $BaZrO_3$, neither the tetragonal phase nor the orthorhombic phase appears while the rhombohedral phase extends farther.

In case of a relatively large B ion, namely on the $PbZrO_3$ side of our solid solutions, considerations on the packing of the ions in the crystal may suggest that the ionic polarizability of A ion predominates over that of B or X ions. Through the displacement of A ion relative to the compact BX_3 group a different kind of dipole arrangement may become more stable. Indeed, somewhat large shift of Pb ion has been observed in $PbZrO_3$. Here, some explanetory remarks should be given on the reasons why $PbZrO_3$ has been regarded as antiferroelectric. When merely the packing of ions in the perowskite type crystal is considered, the tolerance factor$^{16)}$ t is usually taken as the measure of the steric hindrance. It has been known$^{2)}$ that $BaZrO_3$ and $SrZrO_3$ has the tolerance factor 0.96 and 0.91 respectively and they are really cubic. On the other hand, $PbZrO_3$ is orthorhombic regardless of the fact that the tolerance factor $t=0.93$ satisfies the cubic condition. The fact evidently means that some interaction other than the steric hindrance may exist and causes the orthorhombic distortion. On the other hand, the most eminent characteristics of $PbZrO_3$ is its very high dielectric constant in comparison with that of $BaZrO_3$ or $SrZrO_3$. The interaction force producing the orthorhombic structure thus seems to be attributed to the very high polarizability of the consituent ions in $PbZrO_3$. Therefore, the antiparallel shifts of Pb ions may be caused mainly by the dipole-dipole interactions analogous to that assumed by Slater$^{17)}$ concerning the origin of the ferroelectricity in barium titanate. Furthermore, it should be remembered that the Takagi theory$^{12)}$ has presented some results favourable to the antiferroelectricity of $PbZrO_3$. That is, not only the shape of the dielectric constant *vs.* temperature curve but also the sense of the effects of applied bias upon the dielectric constant, both expected theoretically, are consistent with those really observed in $PbZrO_3$, even though the crystal structure treated in the theory is much simpler than that of our case. Although the exact conditions to realize the antiferroelectricity in the perowskite structure have not yet been elaborated, we can guess at least that the steric hindrance of more delicate nature is neccessary to explain the occurence of the observed antiferroelectricity, and the suppression of the $BaTiO_3$ type of ferroelectricity.

At last, an interesting observations may be described: As shown in Fig. 10 b, electric bias lowers very much the dielectric constant of $Pb(Zr97—Ti3)O_3$ and also lowers the $F\alpha$—$A\alpha$ transition point by about 20°C. On cooling case, even when the bias was removed at 190°C, nearly the same curve (Fig. 10 b, dotted curve) was observed. The explanation on these effects will be given later.

In conclusion, we wish to express our sincere thanks to Professor Y. Takagi for his advisory discussions and continued encouragement in the course of this research. We are also grateful to Mr. G. Shirane for his helpful advice and discussions, to Mr. Kittaka and Mr. Makita for assistance in the dielectric measurements. This study was helped by the resarch grant from the Ministry of Education.

References

1) A. Hoffmann: Z. Phys. Chem. **B 28** (1935) 65.

2) H. D. Megaw: Proc. Phys. Soc. (London) **58** (1946) 133.

3) S. Roberts: J. Am. Ceram. Soc. **33** (1950) 63.

4) E. Sawaguchi, H. Maniwa and H. Hoshino: Phys. Rev, **83** (1951) 1078.

5) E. Sawaguchi, G. Shirane and Y. Takagi: J. Phys. Soc. Japan **6** (1951) 333.

6) G. Shirane, E. Sawaguchi and Y. Takagi: Phys. Rev. **84** (1951) 476.

7) G. Shirane and A. Takeda: J. Phys. Soc. Japan **7** (1952) 5.
G. Shirane, K. Suzuki and A. Takeda: ibid. **7** (1952) 12.

8) G. Shirane: Phys. Rev. **86** (1952) 219.

9) S. Nagasaki and Y. Takagi: J. Appl. Phys. Japan **17** (1948) 104.

10) G. Shirane and S. Hoshino: Phys. Rev. **86** (1952) 248.

11) G. Shirane and K. Suzuki: J. Phys. Soc. Japan **7** (1952) 333.

12) Y. Takagi: Phys. Rev. **85** (1952) 315.

13) A. F. Devonshire: Phil. Mag. **40** (1949) 1040.

14) G. Shirane and K. Suzuki: J. Phys. Soc. Japan **6** (1951) 274.
G. Shirane and A. Takeda: ibid. **6** (1951) 329.

15) E. Sawaguchi and T. Makita: will be reported shortly.

16) V. M. Goldschmidt: Geochem. Vert. d. Elem. **7** and **8** (1927).

17) J. C. Slater: Phys. Rev. **78** (1950) 748.

JOURNAL OF THE PHYSICAL SOCIETY OF JAPAN Vol. 8, No. 5, SEP.—OCT., 1953

$\sigma\pi$ Interaction in Benzene*)

By Kazuo NIIRA

Physics Department, Tokyo Institute of Technology, Oh-okayama, Tokyo

(Received May 9, 1953)

We have estimated the influence of σ electrons through exchange interaction with π electrons on the lower excited electronic levels of benzene by assuming the approximation of electron pair bonds (epb.) for σ electrons. The result shows an enhancement of excitation energy of every excited level by an amount of a few electron volts, and the shift of ${}^1E_{2g}$ level is the least in favor of Craig's assignment of this level to the observed 6.2 eV band. Discussions for our approximate treatment by the method of epb. are given: (1) A choice of values of one-center atomic integrals between semiempirical and computed values affects the result a little. (2) An error resulted from neglect of two-center molecular integrals over non-adjacent neighbor AO's is found to be negligible. (3) A contribution from three- and four-center integrals to the excitation energy is presumably smaller than 0.1 eV except from a few of them. (4) Neglect of potentials from H atoms and of overlappings between AO's of σ electrons are found to be not so serious. (5) Inclusion of configuration interaction of π electrons would not affect the result much.

As a different approach to the problem, we assume non-localized MO's for σ electrons, tentatively, and compute the $\sigma\pi$ interaction. The result gives a similar conclusion as in the case of epb. approximation.

§ 1. Introduction

Non-empirical calculation of the lower excited electronic levels of benzene, originated by the earlier work of M. G. Mayer and Sklar1) follows the method of antisymmetrized molecular orbitals (ASMO) of π electrons. According to this method, we deal only with $2p\pi$ electrons of each carbon atom, the nodal plane of whose wave function being in the molecular plane, and assume that the other three $2p\sigma$ electrons, the symmetry axes of which are in the molecular plane, contribute mainly to the formation of CC and CH bonds, and they are stable for electronic excitation as compared with π electrons. As to the $\sigma\pi$ interaction, only the coulombic energy is considered, while the exchange energy is completely neglected. In this paper we will show that this neglect of the exchange energy is not legitimate in the quantitative discussion of the excited electronic levels of benzene.

We label carbon and hydrogen atoms in benzene both from 1 to 6 counterclockwise, and choose x_k, y_k and z_k axes with its origin at the k-th carbon atom, where each z_k axis is perpendicular to the molecular plane and y_k axis is directed from the k-carbon atom toward the k-hydrogen atom. For σ electrons we choose sp^3 hybrid orbitals:

$$\left.\begin{aligned}\chi_k^{(1)}&=\frac{1}{\sqrt{3}}S_k-\frac{1}{\sqrt{2}}X_k-\frac{1}{\sqrt{6}}Y_k\,,\\ \chi_k^{(2)}&=\frac{1}{\sqrt{3}}S_k+\frac{1}{\sqrt{2}}X_k-\frac{1}{\sqrt{6}}Y_k\,,\\ \chi_k^{(3)}&=\frac{1}{\sqrt{3}}S_k+\sqrt{\frac{2}{3}}Y_k\,,\end{aligned}\right\}\tag{1}$$

where S_k, X_k and Y_k are $2s$, $2px$ and $2py$ atomic orbitals (AO) of the k-carbon atom, respectively. $\chi_k^{(1)}$ ($\chi_k^{(2)}$) makes a bond (σ bond) together with $\chi_{k+1}^{(2)}(\chi_{k-1}^{(1)})$, and $\chi_k^{(3)}$ makes a bond (CH bond) together with the $1s$ electron of the attached hydrogen atom. Both these kinds of bonds form the skeleton of the benzene molecule. $2p$ orbitals represented by Z_k, the $2pz$ atomic wave function of k-carbon atom, overlap little with each other, and are combined into the molecular orbitals (MO) originally proposed by Hückel2):

$$\left.\begin{aligned}\phi_l(\nu)&=\frac{1}{\sqrt{6N_l}}\sum_{k=1}^{6}\exp(2\pi ilk/6)Z_k(\nu)\,,\\ &\qquad l=0,\pm1,\pm2,3\,,\end{aligned}\right\}\tag{2}$$

---

[*] A preliminary report was given in: J. Chem. Phys. **20** (1952) 1498.

(LCAO approximation). The hamiltonian for the whole π electron system is

$$H_\pi = \sum_{\nu=1}^{6}\left\{T(\nu)+\sum_{k=1}^{6}U_k(\nu)\right\}+\sum_{\mu>\nu=1}^{6}\frac{e^2}{r_{\mu\nu}}, \tag{3}$$

where $T(\nu)$ is the kinetic energy (operator) of ν electron and $U_k(\nu)$ is the mutual potential energy (operator) of ν electron and k-carbon core. The mutual potential energy of π electrons and hydrogen atoms is assumed to be negligible. U_k is written as

$$U_k(\nu) = -\frac{4e^2}{r_{\nu k}} + \sum_{i=1}^{3}\int \frac{e^2}{r_{\mu\nu}}|\chi_k^{(i)}(\mu)|^2 d\tau_\mu\,, \tag{4}$$

where $r_{\nu k}$ is a distance of ν electron from k-carbon nucleus. The second term in (4) gives a coulombic energy between σ and π electrons, and it is usually taken in the form of the penetration integral[1)3)] for practical computations. Z_k is assumed to satisfy the equation

$$(T(\nu)+U_k(\nu))Z_k(\nu) = W_{2p}Z_k(\nu)\,, \tag{5}$$

where W_{2p} is the energy of a $2p$ electron in the valence state of a carbon atom. For Z_k it is usual to assume the Zener function[4)]:

$$Z_k = \sqrt{\frac{\delta^5}{\pi}}\exp(-\delta r) r\cos\theta\,. \tag{6}$$

The whole electronic wave function Ψ for the π electron system is given by an antisymmetrized product of MO's (2) (with suitable spin functions), and the excitation energy of an excited electronic level is given by the difference of the quantity

$$\int \Psi^* H_\pi \Psi d\tau \Big/ \int \Psi^*\Psi d\tau\,,$$

from that of the ground state. Taking the values for 2δ (the effective nuclear charge in a carbon atom for the $2p$ electron) and the CC distance in benzene as 3.18 and 1.39 A, respectively, Mayer and Sklar[1)] made a numerical calculation for several electronic levels of benzene. Further works by London[5)], Parr and Crawford[6)] and Roothaan and Parr[7)] revealed an importance of three- and four-center molecular integrals originally neglected by Mayer and Sklar, and their final result which was consistent with the observed data is shown in the column "ASMO" of Table II. But Craig[8)] pointed out that the configuration interaction (CI) with higher electronic levels of the π electron system influences the electronic levels so much that the above good result was an accidental one, and he expressed his very pessimistic opinion for non-empirical calculation of electronic energy. However, an elaborate calculation by Parr, Craig and Ross[10)] which took into account of CI and all many center molecular integrals showed again a good agreement with experiment (see Table II). But in such a closer calculation as they did, we must investigate the exchange interaction between π and σ electrons and further the effect of hydrogen atoms. Recently, van Dranen[11)] estimated semiquantitatively the effect of σ electrons in the ethylene and benzene molecules, and Altmann[12)] interpreted the absorption spectra of the ethylene molecule by taking into account of $\sigma\pi$ interaction which was derived from the inclusion of valence bond states representing bonds between σ and π electrons.

§ 2. σπ Exchange Energy by the epb. (electron pair bond) Approximation

For the σ electrons we will take the hybrid orbitals (1) and assume electron-pair bonds between $\chi_k^{(1)}$ and $\chi_{k+1}^{(2)}$ (the σ bond) and between $\chi_k^{(3)}$ and h_k, the 1*s* AO of the k-hydrogen atom (the CH bond), respectively. Antisymmetrizing the product of these paired orbitals we obtain the wave function for the system of σ electrons and h_k electrons, and this function belongs to the total symmetric (irreducible) representation (A_{1g}) of the spatial group D_{6h}.[*]

The coulombic part of the $\sigma\pi$ interaction energy is already taken into account in the method of Mayer and Sklar (see Eq. (4)). The coulombic energy between π and 1*s* electrons of hydrogen atoms which is neglected in the method of Mayer and Sklar will be discussed in § 3. The whole exchange energy W' between π electrons and both of σ and h_k electrons, which is a sum of the exchange energy between π electrons and σ bonds ($W(\sigma,\pi)$) and that between π electrons and CH bonds ($W(\mathrm{CH},\pi)$), is computed under the following assumptions:

---

[*] For a proof of this fact, the author owes greatly to Prof. Kotani.

(1) $S_k, X_k Y_k$ and h_k are represented by the Zener functions

$$\left.\begin{aligned} S_k &= \sqrt{\frac{\delta^5}{3\pi}}\exp(-\delta r)r\,, \\ \left.\begin{matrix} X_k \\ Y_k \end{matrix}\right\} &= \sqrt{\frac{\delta^5}{\pi}}\exp(-\delta r)r\sin\theta\left\{\begin{matrix}\cos\varphi\,, \\ \sin\varphi\,,\end{matrix}\right. \\ h_k &= \frac{1}{\sqrt{\pi}}\exp(-r_h)\,, \end{aligned}\right\} \qquad (7)$$

where 2δ is taken as 3.18. For CC and CH distances in benzene we taken 1.39 A and 1.08 A, respectively.

(2) $\chi_1^{(1)}, \chi_2^{(2)}, \cdots ;\ \chi_1^{(3)}, h_1, \cdots$ are assumed to be orthogonal with each other. This does not hold in the actual case, for example,

$$\left.\begin{aligned} &(\chi_1^{(1)},\chi_2^{(2)}) \equiv \int \chi_1^{(1)}\chi_2^{(2)} d\tau = 0.761\,, \\ &(\chi_1^{(3)},\ h_1) = 0.702\,, \qquad (\chi_1^{(3)},\chi_2^{(1)}) = 0.134\,, \\ &(\chi_1^{(1)},\chi_3^{(2)}) = 0.219\,, \qquad (\chi_1^{(1)},\chi_2^{(1)} = 0.133\,, \\ &(\chi_1^{(1)},\ h_1) = 0.145\,, \qquad (\chi_1^{(3)},\ h_2) = 0.074\,. \end{aligned}\right\} \qquad (8)$$

Although most overlap integrals may be neglected, $(\chi_1^{(1)},\chi_2^{(2)})$ and $(\chi_1^{(3)},h_1)$ have considerable values far from to allow us to neglect them entirely, but we can neglect them without any appreciable error on the interaction energy (see § 3).

Taking the Hückel functions ϕ_l's of Eq. (2) for π electrons, the exchange energy $W(\sigma,\pi)$ between π electrons and σ bonds is given by

$$\left.\begin{aligned} W(\sigma,\pi) = &-\frac{1}{2}\sum_l\sum_{i=1}^{6}\left\{\int \phi_l^*(1)\chi_i^{(1)}(1)\frac{e^2}{r_{12}}\phi_l(2)\chi_i^{(1)}(2)d\tau_1 d\tau_2\right. \\ &+\left.\int \phi_l^*(1)\chi_i^{(2)}(1)\frac{e^2}{r_{12}}\phi_l(2)\chi_i^{(2)}(2)d\tau_1 d\tau_2\right\} \\ = &-\frac{1}{2}\sum_l\frac{1}{N_l}\sum_{k=1}^{6}\left\{2(Z_k\chi_1^{(1)}|Z_k\chi_1^{(1)}) + 4\cos\frac{2\pi l}{6}(Z_k\chi_1^{(1)}|Z_{k+1}\chi_1^{(1)})\right. \\ &+\left.4\cos\frac{4\pi l}{6}(Z_k\chi_1^{(1)}|Z_{k+2}\chi_1^{(1)}) + 2(-)^l(Z_k\chi_1^{(1)}|Z_{k+3}\chi_1^{(1)})\right\}\,, \end{aligned}\right\} \qquad (9)$$

where the abbreviation such as

$$(Z_k\chi_1^{(1)}|Z_j\chi_1^{(1)}) \equiv \int Z_k(1)\chi_1^{(1)}(1)\frac{e^2}{r_{12}}Z_j(2)\chi_1^{(1)}(2)d\tau_1 d\tau_2 \qquad (10)$$

is used, and the summation $\sum_l$ extends over all occupied π orbitals in the electronic state under consideration. Similarly, for $W(\text{CH},\pi)$ we have

$$\left.\begin{aligned} W(\text{CH},\pi) = &-\frac{1}{2}\sum_l\sum_{i=1}^{6}\left\{\int \phi_l^*(1)\chi_i^{(3)}(1)\frac{e^2}{r_{12}}\phi_l(2)\chi_i^{(3)}(2)d\tau_1 d\tau_2\right. \\ &+\left.\int \phi_l^*(1)h_i(1)\frac{e^2}{r_{12}}\phi_l(2)h_i(2)d\tau_1 d\tau_2\right\} \\ = &-\frac{1}{2}\sum_l\frac{1}{N_l}\sum_{k=1}^{6}\Big[(Z_k\chi_1^{(3)}|Z_k\chi_1^{(3)}) + (Z_k h_1|Z_k h_1) \\ &+2\cos\frac{2\pi l}{6}\left\{(Z_k\chi_1^{(3)}|Z_{k+1}\chi_1^{(3)}) + (Z_k h_1|Z_{k+1}h_1)\right\} \\ &+2\cos\frac{4\pi l}{6}\left\{(Z_k\chi_1^{(3)}|Z_{k+2}\chi_1^{(3)}) + (Z_k h_1|Z_{k+2}h_1)\right\} \\ &+(-)^l\left\{(Z_k\chi_1^{(3)}|Z_{k+3}\chi_1^{(3)}) + (Z_k h_1|Z_{k+3}h_1)\right\}\Big]\,. \end{aligned}\right\} \qquad (11)$$

In consequence of our assumption of spin pair bonds, both of $W(\sigma,\pi)$ and $W(\text{CH},\pi)$ are determined uniquely by the number of the electrons occupying each π-orbital and independent of both of spatial symmetry type and spin multiplicity of the electronic level. Each term in the right hand side of Eq. (9) is written as

$$
\begin{aligned}
2\sum_{k=1}^{6}(Z_k\chi_1^{(1)}|Z_k\chi_1^{(1)}) &= \frac{2}{3}G_1+4F_2+\frac{4}{3}C_{\pi ss\pi}+\frac{2\sqrt{2}}{3}C_{\pi s\sigma\pi}+\frac{5}{3}C_{\pi\sigma\sigma\pi} \\
&\quad +C_{\pi\pi'\pi'\pi}+\frac{4}{3}C_{\pi ss\pi}^{(2)}+C_{\pi\sigma\sigma\pi}^{(2)}+\frac{5}{3}C_{\pi\pi'\pi'\pi}^{(2)}+2\sqrt{\frac{2}{3}}C_{\pi\sigma s\pi}^{(2)} \\
&\quad +\left\{\frac{2}{3}C_{\pi ss\pi}^{(3)}+\frac{1}{3}C_{\pi\sigma\sigma\pi}^{(3)}+C_{\pi\pi'\pi'\pi}^{(3)}+\frac{2\sqrt{2}}{3}C_{\pi\sigma s\pi}^{(3)}\right\}, \qquad (12.1)
\end{aligned}
$$

$$
\begin{aligned}
2\sum_{k=1}^{6}(Z_k\chi_1^{(1)}|Z_{k+1}\chi_1^{(1)}) &= \frac{4}{3}L_{ss\pi\pi}+\frac{\sqrt{2}}{3}L_{s\sigma\pi\pi}+\frac{\sqrt{2}}{3}L_{\sigma s\pi\pi}+\frac{5}{3}L_{\sigma\sigma\pi\pi}+L_{\pi\pi\pi'\pi'} \\
&\quad +(Z_2\chi_1^{(1)}|Z_3\chi_1^{(1)})+\{(Z_5\chi_1^{(1)}|Z_6\chi_1^{(1)})+(Z_3\chi_1^{(1)}|Z_4\chi_1^{(1)})+(Z_4\chi_1^{(1)}|Z_5\chi_1^{(1)})\}, \qquad (12.2)
\end{aligned}
$$

$$
\begin{aligned}
2\sum_{k=1}^{6}(Z_k\chi_1^{(1)}|Z_{k+2}\chi_1^{(1)}) &= \frac{4}{3}L_{ss\pi\pi}^{(2)}+L_{\sigma\sigma\pi\pi}^{(2)}+\frac{5}{3}L_{\pi\pi\pi'\pi'}^{(2)}+\sqrt{\frac{2}{3}}L_{s\sigma\pi\pi}^{(2)}+\sqrt{\frac{2}{3}}L_{\sigma s\pi\pi}^{(2)} \\
&\quad +\{(Z_2\chi_1^{(1)}|Z_4\chi_1^{(1)}+(Z_6\chi_1^{(1)}|Z_2\chi_1^{(1)}+(Z_3\chi_1^{(1)}|Z_5\chi_1^{(1)})+(Z_4\chi_1^{(1)}|Z_6\chi_1^{(1)})\}, \qquad (12.3)
\end{aligned}
$$

where G_1 and F_2 are the notations for atomic integrals by Slater:

$$
\begin{aligned}
G_1 &= \int S_1(1)Z_1(1)\frac{e^2}{r_{12}}S_1(2)Z_1(2)d\tau_1 d\tau_2\,, \\
F_2 &= \frac{1}{3}\int X_1(1)Z_1(1)\frac{e^2}{r_{12}}X_1(2)Z_1(2)d\tau_1 d\tau_2\,,
\end{aligned}
$$

and $C_{\alpha\beta\gamma\delta}$ and $L_{\alpha\beta\gamma\delta}$ are the notations according to Kotani, Amemiya and Simose[13]:

$$
\left.
\begin{aligned}
C_{\alpha\beta\gamma\delta} &= \int b_\alpha(1)a_\beta(2)\frac{e^2}{r_{12}}a_\gamma(1)b_\delta(2)d\tau_1 d\tau_2 \equiv (b_\alpha a_\gamma|a_\beta b_\delta)\,, \\
L_{\alpha\beta\gamma\delta} &= \int a_\alpha(1)a_\beta(2)\frac{e^2}{r_{12}}a_\gamma(1)b_\delta(2)d\tau_1 d\tau_2 \equiv (a_\alpha a_\gamma|a_\beta b_\delta)\,,
\end{aligned}
\right\} \qquad (13)
$$

where a_α (b_α) is an α type atomic wave function of a- (b-) atom, and superscript (2) ((3)) means that the integral refers to atomic orbitals of C_1 and C_3 (C_4) atoms. The numerical values for $C_{\alpha\beta\gamma\delta}$ and $L_{\alpha\beta\gamma\delta}$ are shown in Table I, where $C_{\alpha\beta\gamma\delta}^{(3)}$ and $L_{\alpha\beta\gamma\delta}^{(3)}$, which are much small, are omitted. For three-center integrals in (12.1–3) we apply Mulliken-Rüdenberg approximation[14] in a slightly modified form, for instance,

$$
\left.
\begin{aligned}
(Z_2\chi_1^{(1)}|Z_3\chi_1^{(1)}) &\sim \frac{S_{12}}{2}\{(Z_2\chi_1^{(1)}|Z_2\chi_1^{(1)})+(Z_3\chi_1^{(1)}|Z_3\chi_1^{(1)})\}\,, \\
S_{12} &= \int Z_1(1)Z_2(1)d\tau_1\,.
\end{aligned}
\right\} \qquad (14)
$$

This approximation, when applied to two-center integrals of the above type ($(Z_6\chi_1^{(1)}|Z_1\chi_1^{(1)})$, for instance), gives no good result, but it serves to estimate the order of magnitude of the integrals. According to this method we find that all terms in the braces in (12.1–3) are much smaller that 0.1 eV and can be neglected for our purpose. Only term to be retained is $(Z_2\chi_1^{(1)}|Z_3\chi_1^{(1)})$. Similarly, the terms in the right hand side of (11) are written as

$$
\begin{aligned}
\sum_{k=1}^{6}(Z_k\chi_1^{(3)})|Z_k\chi_1^{(1)}) &= \frac{1}{3}G_1+2F_2+\frac{1}{3}C_{\pi ss\pi}-\frac{\sqrt{2}}{3}C_{\pi s\sigma\pi}+\frac{1}{6}C_{\pi\sigma\sigma\pi}+\frac{1}{2}C_{\pi\pi'\pi'\pi}^{(2)} \\
&\quad +\frac{1}{3}C_{\pi ss\pi}^{(2)}-\frac{\sqrt{2}}{3}C_{\pi s\sigma\pi}^{(2)}+\frac{1}{2}C_{\pi\sigma\sigma\pi}^{(2)}+\frac{1}{6}C_{\pi\pi'\pi'\pi} \\
&\quad +\left\{\frac{1}{3}C_{\pi ss\pi}^{(3)}-\frac{2\sqrt{2}}{3}C_{\pi s\sigma\pi}^{(3)}+\frac{2}{3}C_{\pi\sigma\sigma\pi}^{(3)}\right\}, \qquad (15.1a)
\end{aligned}
$$

$$
\sum_{k=0}^{6}(Z_k h_1|Z_k h_1) = N_{\pi\pi}+2N_{\pi\pi}^{(2)}+2N_{\pi\pi}^{(3)}+N_{\pi\pi}^{(4)}\,, \qquad (15.1b)
$$

$$\sum_{k=1}^{6}(Z_k\chi_1^{(3)}|Z_{k+1}\chi_1^{(3)})=\frac{2}{3}L_{ss\pi\pi}-\frac{\sqrt{2}}{3}L_{s\sigma\pi\pi}-\frac{\sqrt{2}}{3}L_{\sigma s\pi\pi}+\frac{1}{3}L_{\sigma\sigma\pi\pi}+L_{\pi\pi\pi'\pi'}$$
$$+\{2(Z_2\chi_1^{(3)}|Z_3\chi_1^{(3)})+2(Z_3\chi_1^{(3)}|Z_4\chi_1^{(3)})\}\,, \qquad (15.2a)$$

$$\sum_{k=1}^{6}(Z_kh_1|Z_{k+1}h_1)=2(Z_1h_1|Z_2h_1)+2\{(Z_2h_1|Z_3h_1)+(Z_3h_1|Z_4h_1)\}\,, \qquad (15.2b)$$

$$\sum_{k=1}^{6}(Z_k\chi_1^{(3)}|Z_{k+2}\chi_1^{(3)})=\frac{2}{3}L_{ss\pi\pi}^{(2)}-\sqrt{\frac{2}{3}}L_{s\sigma\pi\pi}^{(2)}-\sqrt{\frac{2}{3}}L_{\sigma s\pi\pi}^{(2)}+L_{\sigma\sigma\pi\pi}^{(2)}+\frac{1}{3}L_{\pi\pi\pi'\pi'}^{(2)}$$
$$+\{2(Z_2\chi_1^{(3)}|Z_4\chi_1^{(3)})+(Z_3\chi_1^{(3)}|Z_5\chi_1^{(3)})+(Z_6\chi_1^{(3)}|Z_2\chi_1^{(3)})\}\,, \qquad (15.3)$$

where the terms in the braces can be neglected and the only three-center integral to be considered is $(Z_1h_1|Z_2h_1)$, the numerical value of which is estimated by the Mulliken-Rüdenberg's method:

$$(Z_1h_1|Z_2h_1)\sim S_{12}/2\cdot\{(Z_1h_1|Z_1h_1)+(Z_2h_1|Z_2h_1)\}\,,$$

and further,

$$N_{\pi\pi}=\int Z_1(1)h_1(1)\frac{e^2}{r_{12}}Z_1(2)h_1(2)d\tau_1d\tau_2\,.$$

The summations in (9) and (11), which are not given explicitly in (12) and (15), for instance $\sum_k(Z_k\chi_1^{(1)}|Z_{k+3}\chi_1^{(1)})$ and $\sum_k(Z_kh_1|Z_{k+2}h_1)$, can be neglected also.

After neglecting the integrals much smaller than 0.1 eV we can compute $W(\sigma,\pi)$ and $W(\mathrm{CH},\pi)$. Numerical values of the molecular integrals shown in Table I are taken from Kotani-Amemiya's table[15] and the table of Kotani, Ishiguro *et al.*[16]. A choice of the values of atomic integral G_1 and F_2 between computed values and semiempirical ones adjusted to obtain agreement with observed atomic spectra of carbon atom[17] gives rather different result for the excitation energies, but we will adopt the latter semiempirical values in our case, for as discussed by Moffitt[18] we would have better results for excitation energies of molecules by making use of empirical values for one-center atomic integrals than by computed ones which should involve some errors for the sake of approximate nature of our nodeless 2*s* function. The difference in the results from the above choice comes from that, if coefficients of $\sum_l\frac{1}{N_l}$, $2\sum\frac{1}{N_l}\cos\frac{4\pi l}{6}$, $2\sum\frac{1}{N_l}\cos\frac{4\pi l}{6}$ and so on in W' are proportional to 1, S_{12}, S_{13} and so on (S_{12} and S_{13} are overlap integrals over AO Z_1 and Z_2, and over Z_1 and Z_3, respectively), W' is common to every configuration of the total π electron system and never contribute to the excitation energy; in the other words, the influence of σ electrons on the excited electronic levels comes from the fact that the ratio of coefficients of $(Z_k\chi_1^{(1)}|Z_k\chi_1^{(1)})$ and $(Z_k\chi_1^{(1)}|Z_{k+1}\chi_1^{(1)})$, for instance, is not equal to the ratio of 1 to S_{12}, as pointed out by van Dranen[11].

Evaluated W''s are shown in Table II, in which we choose as the origin the value for the ground state $0^21^2\text{–}1^2$*

$$W'=-21.88\,\mathrm{eV}(-26.43\,\mathrm{eV},\ \text{if computed } G_1 \text{ and } F_2 \text{ are chosen}).$$

As the energies of higher electron configurations belonging to each specified irreducible representation of D_{6h} are in our case considerably larger than that of the lowest configuration of the same species and our $\sigma\pi$ interaction does not give any contribution to the matrix elements connecting different configurations, we may add our W' directly to the calculated values by Parr, Craig and Ross[10] which have taken into account of CI of π electrons. (We have neglected excited states of σ electrons which would have more important effect than CI of π electrons.) In our evaluation we make use of the values of N_l given by Parr, Craig and Ross:

$$N_0=1.61536\,,\qquad N_1=1.20336\,,$$
$$N_2=0.71890\,,\qquad N_3=0.71890\,.$$

Our result shows that the influence of σ electrons leads to enhance all the excitation energies by an amount of several electron volts, but the effect to the level ${}^1E_{2g}$ is the least, so that the assignment of the observed 6.2 eV band to this level by Craig,[8] would be plausible even when $\sigma\pi$ interaction is included.

§ 3. Discussion on Nonorthogonality and the Effect of Hydrogen Atoms

In § 2 we have assumed the orthogonality

---

* Electronic configuration of the total system of π electrons is specified by the occupied MO's (2).

Table I. Integrals over atomic orbitals (eV).

F_2	0.188^a (0.3042^b)		
G_1	2.18^a (3.4731^b)		
$C_{\pi ss\pi}$	0.3610	$C_{\pi ss\pi}{}^{(2)}$	0.0099
$C_{\pi\sigma\sigma\pi}$	0.5583	$C_{\pi\sigma\sigma\pi}{}^{(2)}$	0.0205
$C_{\pi s\sigma\pi}$	0.4340	$C_{\pi s\sigma\pi}{}^{(2)}$	0.0115
$C_{\pi\pi'\pi'\pi}$	0.0489	$C_{\pi\pi'\pi'\pi}{}^{(2)}$	0.0009
$L_{ss\pi\pi}$	0.6804	$L_{ss\pi\pi}{}^{(2)}$	0.0690
$L_{\sigma\sigma\pi\pi}$	0.3362	$L_{\sigma\sigma\pi\pi}{}^{(2)}$	0.0260
$L_{s\sigma\pi\pi}$	0.5875	$L_{s\sigma\pi\pi}{}^{(2)}$	0.0735
$L_{\sigma s\pi\pi}$	0.2469	$L_{\sigma s\pi\pi}{}^{(2)}$	0.027
$N_{\pi\pi}$	0.7370^c	$N_{\pi\pi}{}^{(2)}$	0.038^d
$(Z_2\chi_1{}^{(1)}\vert Z_3\chi_1{}^{(1)})$	0.1192^e		
$(Z_1h_1\vert Z_2h_1)$	0.1007^e		

a Semiempirical value according to Van Vleck[17].

b Computed value.

c Interpolated from Kotani-Amemiya's table[15].

d Calculated from the table of Kotani, Amemiya and Simose[13].

e Estimated value by Mulliken-Rüdenberg approximation[14].

The other $C_{\alpha\beta\gamma\delta}$ and $L_{\alpha\beta\gamma\delta}$ are obtained by interpolation or extrapolation of the table of Kotani, Ishiguro *et al.*[16].

Table II. Electronic levels of benzene (eV).

	Level	ASMO^a	ASMO$+W'$	ASMO$+$CI^b	ASMO$+$CI$+W'^c$	Observed
Singlets						
	A_{1g}	0.0	0.0 (0.0)^d	0.0	0.0 (0.0)^d	0.0
	A_{2g}	11.1	13.9 (12.8)	12.5	15.3 (14.2)	–
	B_{1u}	7.3	8.7 (8.2)	9.0	10.4 (9.9)	(6.2)^e
	B_{2u}	5.9	7.3 (6.8)	4.4	5.8 (5.3)	4.9
	E_{1u}	9.8	11.2 (10.7)	9.9	11.3 (10.8)	7.0
	E_{2g}	10.9	11.9 (11.1)	7.7	8.7 (7.9)	6.2^f
Triplets						
	A_{1g}	13.6	16.4 (15.3)	14.9	17.7 (16.6)	—
	A_{2g}	11.1	13.9 (12.8)	11.8	14.6 (13.5)	—
	B_{1u}	3.1	4.5 (4.0)	4.1	5.5 (5.0)	3.8
	B_{2u}	5.8	7.2 (6.7)	8.2	9.6 (9.1)	—
	E_{1u}	4.4	5.8 (5.3)	4.7	6.1 (5.6)	—
	E_{2g}	8.3	10.9 (9.9)	6.4	9.0 (8.0)	—

a Calculated values by Roothaan and Parr[7].

b Calculated by Parr, Craig and Ross[10].

c (Value in *b*)$+W'$.

d Values with calculated G_1 and F_2.

e Interpretation before Craig.

f Interpretation by Craig[8].

between AO's of σ electrons. As we have remarked there, although most overlap integrals among σ orbitals and h_k orbitals are smaller than 0.2 and can be neglected, both of $(\chi_1{}^{(1)},\chi_2{}^{(1)})$ and $(\chi_1{}^{(3)},h_1)$ are 0.7 and it would seem improper to neglect them entirely. But, as discussed by Van Vleck,[19] the assumption of orthogonality between AO's does not give any important error for the final result. We will show this in more detail.

We will consider only the following overlap integrals:

$$\left.\begin{aligned} S&=(\chi_1{}^{(1)},\chi_2{}^{(2)})=\int\chi_1{}^{(1)}\chi_2{}^{(2)}d\tau_1\,, \\ T&=(\chi_1{}^{(3)},h_1)=\int\chi_1{}^{(3)}h_1 d\tau_1\,; \end{aligned}\right\} \quad (16)$$

while the other overlap integrals will be neglected. Interaction energy between electrons is given by

$$W=\frac{\int\Psi^*H\Psi d\tau}{\int\Psi^*\Psi d\tau}=\frac{\sum_P U(P)\int\Psi^{0*}HP\Psi^0 d\tau}{\sum_P U(P)\int\Psi^{0*}P\Psi^0 d\tau}=\frac{\sum_P U(P)H(P)}{\sum_P U(P)\Delta(P)}\,, \tag{17}$$

where

$$H=\sum_{\mu>\nu}\frac{e^2}{r_{\mu\nu}}$$

is the interaction between electrons (operator), and Ψ is the wave function for the whole molecule and is given by antisymmetrizing Ψ^0, the product of wave functions of π and σ electrons. And further, P means a permutation operator for electrons, and $U(P)$ is a matrix of an irreducible representation of the symmetry group. When we label π electrons from 1 to 6, σ electrons from 7 to 24, and 1*s* electrons of hydrogen atoms from 25 to 30, respectively, the interaction energy W' between σ and π electrons is obtained from the following H', the part of H above:

$$H'=H'_{78}+H'_{9,10}+\cdots\,,$$

$$H'_{78}=\sum_{i=1}^{6}\left(\frac{e^2}{r_{i7}}+\frac{e^2}{r_{i8}}\right)\equiv\sum_{i=1}^{6}H'^{(i)}_{78}\ . \tag{18}$$

Then,

$$W'=\frac{\sum_P\sum_i\{U(P)H'^{(i)}_{78}(P)+U(P)H'^{(i)}_{9,10}(P)+\cdots\}}{\sum_P U(P)\Delta(P)}\ . \tag{19}$$

Due to our assumption of electron pair bonds for σ electrons, we are concerned only in the diagonal element of $U(P)$, whose row and column correspond to give

$$\left.\begin{array}{lll} U(P)=1 & \text{for} & P=1,\ (78),\ (9,10)\ \text{etc.}\,, \\ U(P)=-1/2 & \text{for} & P=(17),\ (18)\ \text{etc.}\,, \end{array}\right\} \tag{20}$$

therefore $U(P)$ can be treated as one dimensional. As π orbitals are mutually orthogonal and overlap integrals other than S and T are neglected, it is only necessary to take into account of the higher order permutations which can be written as products of P in (20) and transpositions between electrons in an electron pair bond (for instance, such transpositions as (78) and (9,10)). Then it can be shown that

$$\sum_P U(P)\Delta(P)\doteq(1+S^2)^6(1+T^2)^6\ . \tag{21}$$

The proof of (21) is as follows. For a permutation $P^{(l)}$ written as a product of l transpositions, each of these transposes electrons in a σ bond, $\Delta(P)$ is given as

$$\Delta(P)=S^{2l}\ .$$

There are $\binom{6}{l}$ different $P^{(l)}$'s, which give the same $\Delta(P)$. The same it true for permutations concerning electrons in CH bonds. As $U(P^{(l)})$ is unity, as mentioned above, we get finally

$$\sum_P U(P)\Delta(P)=\sum_{l,m=0}^{6}\binom{6}{l}S^{2l}\times\binom{6}{m}T^{2m}=(1+S^2)^6(1+T^2)^6\ .$$

Next, nonvanishing terms $H'^{(i)}_{78}(P)$ in the numerator of (19) are the following types:

$$\left.\begin{array}{ll} H'^{(i)}_{78}(1)=(\phi_i^2|\chi_1^{(1)2})+(\phi_i^2|\chi_2^{(2)2})\,, & U(1)=1\,, \\ H'^{(i)}_{78}((i7))=(\phi_i\chi_1^{(1)}|\phi_i\chi_1^{(1)})\,, & U((i7))=-\frac{1}{2}\,, \\ H'^{(i)}_{78}((i8))=(\phi_i\chi_2^{(2)}|\phi_i\chi_2^{(2)})\,, & U((i8))=-\frac{1}{2}\,, \\ H'^{(i)}_{78}((78))=2S(\phi_i^2|\chi_1^{(1)}\chi_2^{(2)})\,, & U((78))=1\,, \\ \left.\begin{array}{l} H'^{(i)}_{78}((i7)(78)) \\ H'^{(i)}_{78}((78)(i7)) \end{array}\right\}=S(\phi_i\chi_1^{(1)}|\phi_i\chi_2^{(2)})\,, & \begin{array}{l} U((i7)(78))=-\frac{1}{2}\,, \\ U((78)(i7))=-\frac{1}{2}\,, \end{array} \end{array}\right\} . \tag{22}$$

where notations such as

$$(\phi_i^2|\chi_1^{(1)2})=\int|\phi_i(1)|^2\frac{e^2}{r_{12}}|\chi_1^{(1)}(2)|^2 d\tau_1 d\tau_2\ ,$$

$$(\phi_l\chi_1^{(1)}|\phi_l\chi_2^{(2)})=\int\phi_l^*(1)\chi_1^{(1)}(1)\frac{e^2}{r_{12}}\phi_l(2)\chi_2^{(2)*}(2)d\tau_1 d\tau_2\ ,$$

are used. In W' appears each of these terms multiplied by

$$\sum_{l=0}^{5}\sum_{m=0}^{6}\binom{5}{l}\binom{6}{m}S^{2l}T^{2m}=(1+S^2)^5(1+T^2)^6\ ,$$

for every permutation which consists of the one of the permutations in (22) and tranpositions of electrons in each electron pair bond gives the above term; therefore

$$\begin{aligned}
W'=&\frac{\sum_l\sum_i\{(\phi_l^2|\chi_i^{(1)2})+(\phi_l^2|\chi_{i+1}^{(2)2})\}}{1+S^2}+\frac{\sum_l\sum_i\{(\phi_l^2|\chi_i^{(3)2})+(\phi_l^2|h_i^2)\}}{1+T^2}\\
&+\frac{2S}{1+S^2}\sum_l\sum_i(\phi_l^2|\chi_i^{(1)}\chi_{i+1}^{(2)})+\frac{2T}{1+T^2}\sum_l\sum_i(\phi_l^2|\chi_i^{(3)}h_i)\\
&-\frac{1}{2}\frac{1}{1+S^2}\sum_l\sum_i\{(\phi_l\chi_i^{(1)}|\phi_l\chi_i^{(1)})+(\phi_l\chi_{i+1}^{(2)}|\phi_l\chi_{i+1}^{(2)})\}\\
&-\frac{1}{2}\frac{1}{1+T^2}\sum_l\sum_i\{(\phi_l\chi_i^{(3)}|\phi_l\chi_i^{(3)})+(\phi_l h_i|\phi_l h_i)\}\\
&-\frac{S}{1+S^2}\sum_l\sum_i(\phi_l\chi_i^{(1)}|\phi_l\chi_{i+1}^{(2)})-\frac{T}{1+T^2}\sum_l\sum_i(\phi_l\chi_i^{(3)}|\phi_l h_i)\\
=&\sum_l\sum_i\{(\phi_l^2|\chi_i^{(1)2})+(\phi_l^2|\chi_i^{(2)2})+(\phi_l^2|\chi_i^{(3)2})+(\phi_l^2|h_i^2)\}\\
&-\frac{1}{2}\sum_l\sum_i\{(\phi_l\chi_i^{(1)}|\phi_l\chi_i^{(1)})+(\phi_l\chi_i^{(2)}|\phi_l\chi_i^{(2)})+\phi_l\chi_i^{(3)}|\phi_l\chi_i^{(3)}+(\phi_l h_i|\phi_l h_i)\}\\
&+w_{\sigma c}+w_{\tau c}+w_{\sigma e}+w_{\tau e}\ ,
\end{aligned}\tag{23}$$

$$\left.\begin{aligned}
w_{\sigma c}=&-\frac{S}{1+S^2}\sum_l\sum_i\{S(\phi_l^2|\chi_i^{(1)2})+S(\phi_l^2|\chi_i^{(2)2})-2(\phi_l^2|\chi_i^{(1)}\chi_i^{(2)})\}\ ,\\
w_{\tau c}=&-\frac{T}{1+T^2}\sum_l\sum_i\{(T(\phi_l^2|\chi_i^{(3)2})+T(\phi_l^2|h_i^2)-2(\phi_l^2|\chi_i^{(3)}h_i)\}\ ,\\
w_{\sigma e}=&\frac{1}{2}\frac{S}{1+S^2}\sum_l\sum_i\{S(\phi_l\chi_i^{(1)}|\phi_l\chi_i^{(1)})+S(\phi_l\chi_i^{(2)}|\phi_l\chi_i^{(2)})-2(\phi_l\chi_i^{(1)}|\phi_l\chi_{i+1}^{(2)})\}\ ,\\
w_{\tau e}=&\frac{1}{2}\frac{T}{1+T^2}\sum_l\sum_i\{T(\phi_l\chi_i^{(3)}|\phi_l\chi_i^{(3)})+T(\phi_l h_i|\phi_l h_i)-2(\phi_l\chi_i^{(3)}|\phi_l h_i)\}\ .
\end{aligned}\right\}\tag{23a}$$

The terms in (23a) give the approximate correction for nonorthogonality, but they are not so large as anticipated from the fact that

$$\frac{S}{1+S^2}=0.479\ ,\qquad \frac{T}{1+T^2}=0.470\ ,$$

and Mulliken-Rüdenberg approximation such as

$$(\phi_l^2|\chi_i^{(1)}\chi_{i+1}^{(2)})\sim S/2\cdot\{(\phi_l^2|\chi_i^{(1)2})+(\phi_l^2|\chi_i^{(2)2})\}\ ,$$

is fairly well applicable. The term $(\phi_l^2|h_i^2)$ in (23) stands for the coulombic energy between π electrons and 1s electrons of hydrogen atoms, and the coulombic attraction from hydrogen nuclei must be included in (23) to give the total contribution w_{hc} from hydrogen atoms:

$$w_{hc}=\sum_l\sum_i(\phi_l^2|h_i^2)-\sum_l\sum_i\int|\phi_l(1)|^2\frac{e^2}{r_{hi}}d\tau_1\ .\tag{23b}$$

By expanding ϕ_l the right hand sides of (23a, b) are written as, for instance,

$$\begin{aligned}\sum_l\sum_i(\phi_l^2|h_i^2)=\sum_l\frac{1}{N_l}\sum_k\Big\{&(Z_k^2|h_1^2)+2\cos\frac{2\pi l}{6}(Z_kZ_{k+1}|h_1^2)+\cos\frac{4\pi l}{6}(Z_kZ_{k+2}|h_1^2)\\&+(-)^l(Z_kZ_{k+3}|h_1^2)\Big\}\ .\end{aligned}$$

Then we compute coefficients of $\sum_l 1/N_l$ etc. as shown in Table II I, where Mulliken-Rüdenberg's method is used for the estimation of three-center integrals. For the ground state $0^2 1^2 - 1^2$, the sum of (23a, b) is -0.76 eV ($+0.835$ eV), if we choose for F_2 and G_1 the semi-empirical (computed) values. And we find that these terms representing the effect of non-orthogonality and of hydrogen atoms cancel with each other and contribute to the excitation energy of the molecule at most in the order of 0.1 eV.

Table III. Corrections for nonorthogonality and the effect of hydrogen atoms (eV).

	Coefficient of			
	$\sum_l 1/N_l$	$\sum_l 2\cos\frac{2\pi l}{6}\Big/N_l$	$\sum_l 2\cos\frac{4\pi l}{6}\Big/N_l$	$\sum_l \frac{(-)^l}{N_l}$
W_{hc}	-0.803	-0.209	—	—
$W_{\sigma c}$	0.984	0.226	-0.010	-0.004
$W_{\tau c}$	0.313	0.084	—	—
$W_{\sigma e}$	-0.41 (-0.171)*	-0.143	-0.08	—
$W_{\tau e}$	-0.20 (-0.081)	-0.034	—	—
sum	-0.11 ($+0.24$)	-0.076	-0.09	-0.004

* With computed values for F_2 and G_1.

§ 4. Calculation by MO Approximation for σ Electrons

In § 2 we took the assumption of epb. for σ electrons. To proceed further step, we should consider excited electronic states of the system of σ electrons altogether, but it would be a very complicated many body problem hardly to be handled. As a different approach to the problem, we will assume non-localized MO's for σ electrons, tentatively. Some justification for it is found in the recent works by Coulson, March and Altmann[20] and by March[21] which show that the charge distribution of σ electrons in benzene extends considerably over the molecule and is not localized near each nucleus. In the latter work MO's which are similar to those in the present paper are assumed for σ electrons.

We start by assuming the following symmetry orbitals for σ electrons:

$$\sigma_k = \frac{1}{\sqrt{2N_\sigma}}(\chi_k^{(1)} + \chi_{k+1}^{(2)}), \qquad k = 1, 2, \cdots, 6, \tag{24.1}$$

$$\tau_k = \frac{1}{\sqrt{2N_\tau}}(\chi_k^{(3)} + \lambda h_k), \qquad (\lambda > 0), \tag{24.2}$$

where

$$N_\sigma = 1 + \int \chi_k^{(1)} \chi_{k+1}^{(2)} d\tau_1 = 1 + S,$$

$$N_\tau = \frac{1+\lambda^2}{2} + \lambda \int \chi_k h_k d\tau_1 = \frac{1+\lambda^2}{2} + \lambda T.$$

There are also other symmetry orbitals such as $\frac{1}{\sqrt{2(1-S)}}(\chi_k^{(1)} - \chi_{k+1}^{(2)})$ and $\frac{1}{\sqrt{1+\mu^2-2\mu T}}(\chi_k^{(3)} - \mu h_k)$, but as these are considered to corresponds presumably to higher excited states, we will not take into account of them. λ, which should be determined by the condition of minimizing the total energy of the molecule, is left as a parameter giving a polarity of the CH bond. Assuming that 24 electrons occupy the symmetry orbitals (24), we have a closed shell configuration for the system of σ electrons, and we can make use of any orthonormol set constructed from (24) for calculating the electronic energy.

We form LCAO MO from (24):

$$\phi_l^\sigma = \frac{1}{\sqrt{6L_l}} \sum_{k=1}^{6} \exp(2\pi i k l/6) \sigma_k, \tag{25.1}$$

$$\psi_l{}^\tau = \frac{1}{\sqrt{6M_l}} \sum_{k=1}^{6} \exp(2\pi ikl/6)\tau_k\,, \qquad l=0,\pm1,\pm2,3\,. \tag{25.2}$$

L_l and M_l are normalization factors, for instance:

$$L_l = 1+2\cos\frac{2\pi l}{6}(\sigma_1,\sigma_2)+2\cos\frac{4\pi l}{6}(\sigma_1,\sigma_3)+(-)^l(\sigma_1,\sigma_4)\,.$$

$\psi_l{}^\sigma$ and $\psi_l{}^\tau$ belong to the irreducible representations of D_{6h}:

$$\psi_0{}^\sigma,\psi_0{}^\tau \subset A_{1g}\,, \qquad \psi_{\pm1}{}^\sigma,\psi_{\pm1}{}^\tau \subset E_{1u}\,,$$
$$\psi_{\pm2}{}^\sigma,\psi_{\pm2}{}^\tau \subset E_{2g}\,, \qquad \psi_3{}^\sigma \subset B_{2u}\,, \quad \psi_3{}^\tau \subset B_{1u}\,.$$

From $\psi_l{}^\sigma$ and $\psi_l{}^\tau$ we construct the orthonormal set of functions:

$$\left.\begin{aligned}
&\psi_1 = c_1(\psi_0{}^\sigma+\psi_0{}^\tau)\,, && \psi_9 = c_9\,(\psi_2{}^\sigma+\psi_2{}^\tau)\,,\\
&\psi_2 = c_2(\psi_0{}^\sigma-\psi_0{}^\tau)\,, && \psi_{10} = c_{10}(\psi_2{}^\sigma-\psi_2{}^\tau)\,,\\
&\psi_3 = \psi_3{}^\sigma\,, && \psi_{11} = c_9\,(\psi_{-2}{}^\sigma+\psi_{-2}{}^\tau)\,,\\
&\psi_4 = \psi_3{}^\tau\,, && \psi_{12} = c_{10}(\psi_{-2}{}^\sigma-\psi_{-2}{}^\tau)\,,\\
&\psi_5 = c_5(\psi_1{}^\sigma+\psi_1{}^\tau)\,, &&\\
&\psi_6 = c_6(\psi_1{}^\sigma-\psi_1{}^\tau)\,, &&\\
&\psi_7 = c_5(\psi_{-1}{}^\sigma+\psi_{-1}{}^\tau)\,, &&\\
&\psi_8 = c_6(\psi_{-1}{}^\sigma+\psi_{-1}{}^\tau)\,, &&
\end{aligned}\right\} \tag{26}$$

where c_i is a normalization factor. Or, inserting (25) into (26), we can rewrite (26) as

$$\left.\begin{aligned}
&\psi_i = \sum_{j=1}^{12} U_{ij}\omega_j\,, \qquad (i=1,2,\cdots,12)\,,\\
&(\omega_1,\cdots,\omega_6) \equiv (\sigma_1,\cdots,\sigma_6)\,,\\
&(\omega_7,\cdots,\omega_{12}) \equiv (\tau_1,\cdots,\tau_6)\,.
\end{aligned}\right\} \tag{27}$$

Assuming the configuration for σ electrons in which each MO of (27) is occupied by two electrons we obtain the energy of $\sigma\pi$ interaction (inclusive of the effect of hydrogen atoms) as

$$\left.\begin{aligned}
W &= \sum_l \sum_{i=1}^{12} \left\{2\int |\phi_l(1)|^2 \frac{e^2}{r_{12}} |\psi_i(2)|^2 d\tau_1 d\tau_2 - \int \phi_l{}^*(1)\psi_i(1) \frac{e^2}{r_{12}} \phi_l(2)\psi_i{}^*(2) d\tau_1 d\tau_2\right\}\\
&\qquad\qquad - \sum_l \sum_{k=1}^{6} \int |\phi_l(1)|^2 \frac{e^2}{r_{hk}} d\tau_1\,,\\
&= \sum_l \sum_i \sum_j \sum_h U_{ij}{}^* U_{ih} \left\{2\int |\phi_l(1)|^2 \frac{e^2}{r_{12}} \omega_j(2)\omega_h{}^*(2) d\tau_1 d\tau_2 - \int \phi_l{}^*(1)\omega_j(1) \frac{e^2}{r_{12}} \phi_l(2)\omega_h{}^*(2) d\tau_1 d\tau_2\right\}\\
&\qquad\qquad - \sum_l \sum_{k=1}^{6} \int |\phi_l(1)|^2 \frac{e^2}{r_{hk}} d\tau_1\,,
\end{aligned}\right\} \tag{28}$$

where $\sum_l$ extends over MO's ϕ_l occupied by π electrons, and r_{hk} is the distance from H_k nucleus. If we write as

$$\sum_i U_{ij}{}^* U_{ih} = \delta_{jh} + Q_{jh}\,, \qquad \delta_{jh} = \begin{cases} 0, & j \neq h\,,\\ 1, & j = h\,, \end{cases} \tag{29}$$

every Q_{jh} is real and

$$\left.\begin{aligned}
&Q_{11} = Q_{22} = \cdots = Q_{66}\,,\\
&Q_{77} = Q_{88} = \cdots = Q_{12,\,12}\,,\\
&Q_{jh} = Q_{hj}{}^* = Q_{hj}\,.
\end{aligned}\right\} \tag{30}$$

Then (28) is rewritten as

$$W = \sum_{s=1}^{5} (w_c{}^{(s)} + w_e{}^{(s)})\,, \tag{31}$$

$$w_c{}^{(1)} = 2(1+Q_{11}) \sum_l \sum_{j=1}^{6} (\phi_l{}^2|\sigma_j{}^2)\,, \tag{32.1a}$$

$$w_e{}^{(1)} = -(1+Q_{11}) \sum_l \sum_j (\phi_l\sigma_j|\phi_l\sigma_j)\,, \tag{32.1b}$$

$$w_c^{(2)}=2(1+Q_{77})\sum_l\sum_j(\phi_l^2|\tau_j^2)-\sum_l\sum_k\int|\phi_l|^2\frac{e^2}{r_{hk}}d\tau_1\,, \tag{32.2a}$$

$$w_e^{(2)}=-(1+Q_{77})\sum_l\sum_j(\phi_l\tau_j|\phi_l\tau_j)\,, \tag{32.2b}$$

$$w_c^{(3)}=2\sum_l\sum_{j\neq k}\sum Q_{jk}(\phi_l^2|\sigma_j\sigma_k)\,, \tag{32.3a}$$

$$w_e^{(3)}=-\sum_l\sum_{j\neq k}\sum Q_{jk}(\phi_l\sigma_j|\phi_l\sigma_k)\,, \tag{32.3b}$$

$$w_c^{(4)}=2\sum_l\sum_{j\neq k}\sum Q_{jk}(\phi_l^2|\tau_j\tau_k)\,, \tag{32.4a}$$

$$w_e^{(4)}=-\sum_l\sum_{j\neq k}\sum Q_{jk}(\phi_l\tau_j|\phi_l\tau_k)\,, \tag{32.4b}$$

$$w_c^{(5)}=4\sum_l\sum_j\sum_k Q_{jk}(\phi_l^2|\sigma_j\tau_k)\,, \tag{32.5a}$$

$$w_e^{(5)}=-2\sum_l\sum_j\sum_k Q_{jk}R_e(\phi_l\sigma_j|\phi_l\tau_k)\,, \tag{32.5b}$$

where the abbreviation such as

$$(\phi_l\sigma_j|\phi_l\sigma_k)=\int\phi_l^*(1)\sigma_j(1)\frac{e^2}{r_{12}}\phi_l(2)\sigma_k^*(2)d\tau_1d\tau_2\,,$$

is used. As the integrals in (32.3a–5b) depend only on $|j-k|$ etc., and

$$\sum_j Q_{j,j+\alpha}=\sum_j Q_{j-\alpha,j}\,,\qquad \alpha=1,\ 2\,,$$

we can write as, for instance,

$$w_c^{(3)}=4\sum_l\left\{(\sum_j Q_{j,j+1})(\phi_l^2|\sigma_1\sigma_2)+\sum_j Q_{j,j+2}(\phi_l^2|\sigma_1\sigma_3)+\tfrac{1}{2}\sum_j Q_{j,j+3}(\phi_l^2|\sigma_1\sigma_4)\right\}, \tag{33a}$$

$$w_e^{(3)}=-2\sum_l\left\{\sum_j Q_{j,j+1}(\phi_l\sigma_1|\phi_l\sigma_2)+\sum_j Q_{j,j+2}(\phi_l\sigma_1|\phi_l\sigma_3)+\tfrac{1}{2}\sum_j Q_{j,j+3}(\phi_l\sigma_1|\phi_l\sigma_4)\right\}. \tag{33b}$$

When we add the above $\sigma\pi$ interaction energy W to the energy of the system of π electrons given in the previous works, we must subtract from (28) the third term in (4) which stands for the mutual potential energy between σ and π electrons. Then, W', the correction due to "$\sigma\pi$ interaction", is

$$W'=W-\sum_l\sum_{j=1}^{6}\sum_{\alpha=1}^{3}(\phi_l^2|\chi_j^{(\alpha)2})=w_c^{(1)\prime}+w_c^{(2)\prime}+\sum_{j=3}^{5}w_c^{(j)}+\sum_{j=3}^{5}w_e^{(j)}\,, \tag{34}$$

$$w_c^{(1)\prime}=w_c^{(1)}-\sum_l\sum_j\{(\phi_l^2|\chi_j^{(1)2})+(\phi_l^2|\chi_j^{(2)2})\}\,, \tag{35.1}$$

$$w_c^{(2)\prime}=w_c^{(2)}-\sum_l\sum_j(\phi_l^2|\chi_j^{(3)2})\,. \tag{35.2}$$

Inserting (24) in (34) we obtain the final formulas such as

$$\begin{aligned}w_c^{(1)\prime}=&-\frac{1}{1+S}\sum_l\sum_j\{S(\phi_l^2|\chi_j^{(1)2})+S(\phi_l^2|\chi_{j+1}^{(2)2})-2(\phi_l^2|\chi_j^{(1)}\chi_{j+1}^{(2)})\}\\&+\frac{Q_{11}}{1+S}\sum_l\sum_j\{(\phi_l^2|\chi_j^{(1)2})+(\phi_l^2|\chi_{j+1}^{(2)2})+2(\phi_l^2|\chi_j^{(1)}\chi_{j+1}^{(2)})\}\,,\end{aligned} \tag{36.1}$$

$$\begin{aligned}w_e^{(1)\prime}=&-\frac{(1+Q_{11})}{2(1+S)}\sum_l\sum_j\{(\phi_l\chi_j^{(1)}|\phi_l\chi_j^{(1)})+(\phi_l\chi_j^{(2)}|\phi_l\chi_j^{(2)})\}\\&-(1+Q_{11})\frac{1}{1+S}Re\sum_l\sum_j(\phi_l\chi_j^{(1)}|\phi_l\chi_{j+1}^{(2)})\,,\end{aligned} \tag{36.2}$$

and so on.

Values of many molecular integrals (two-center) are taken from the table of Kotani, Ishiguro *et al.*[16]. Coulomb integrals $D_{\alpha\beta\gamma\delta}$ are not so small even for those over C_1 and C_4 atoms that we evaluate them by the table of Kotani, Amemiya and Simose[13]. Values of the effective nuclear charge of carbon atom and of nuclear distances are chosen as the same as in § 2. For three- and four-center integrals except these already involved in the penetration integrals in the previous works where the London's approximation[5] was used, the Mulliken-Rüdenberg approximation is applied. This would be a considerably better method for coulombic integrals. For the exchange integrals which are estimated as the order of magnitude of 0.1 eV, the same approximation as in § 2 is applied. Q_{ij}'s are evaluated for the two values of λ, i.e. 0.5 and 1 (Table IV). The final result for W_c' and W_e is shown in Table V, where

$$W' = W_c' + W_e$$

$$W_c' = w_c^{(1)\prime} + w_c^{(2)\prime} + \sum_{j=3}^{5} w_c^{(j)} ,$$

$$W_e = \sum_{j=1}^{5} w_e^{(j)} .$$

Table IV. Values of Q_{ij} .

	$\lambda=0.5$	$\lambda=1$		$\lambda=0.5$	$\lambda=1$
Q_{11}	0.086	0.095	$\sum_{i=7}^{12} Q_{i,i+1}$	-0.514	-0.481
Q_{77}	0.067	0.076	$\sum_{i} Q_{i,i+2}$	2.168	2.204
$\sum_{j=1}^{6} Q_{j,j+1}$	-0.464	-0.442	$\sum_{i} Q_{i,i+3}$	-0.257	-0.241
$\sum_{j} Q_{j,j+2}$	1.821	1.843	$\sum_{j=1}^{6} Q_{j,j+6}$	-0.130	-0.191
$\sum_{j} Q_{j,j+3}$	-0.252	-0.221			

Table V. Contribution of $\sigma\pi$ interaction energy to the excitation energy of benzene by MO for σ electrons (eV).

	W_c'	W_e	W'
$\lambda=0.5$			
Singlets			
A_{1g}	126.03	-27.38^a $(-30.91)^b$	98.65^a $(95.12)^b$
A_{2g}	-1.04	2.75 (1.89)	1.71 (0.85)
B_{1u}, B_{2u}, E_{1u}	-0.41	1.40 (0.96)	0.99 (0.55)
E_{2g}	-0.44	1.33 (0.73)	0.89 (0.29)
Triplets			
A_{1g}, A_{2g}	-1.04	2.75 (1.89)	1.71 (0.85)
B_{1u}, B_{2u}, E_{1u}	-0.41	1.40 (0.96)	0.99 (0.55)
E_{2g}	-1.16	2.92 (2.13)	1.76 (0.97)
$\lambda=1$			
Singlets			
A_{1g}	111.45	-27.51^a $(-30.35)^b$	83.94^a $(81.10)^b$
A_{2g}	-0.66	2.79 (2.10)	2.13 (1.44)
B_{1u}, B_{2u}, E_{1u}	-0.24	1.40 (1.05)	1.16 (0.81)
E_{2g}	-0.24	1.35 (0.87)	1.11 (0.63)
Triplets			
A_{1g}, A_{2g}	-0.66	2.79 (2.10)	2.13 (1.44)
B_{1u}, B_{2u}, E_{1u}	-0.24	1.40 (1.05)	1.16 (0.81)
E_{2g}	-0.80	2.96 (2.32)	2.16 (1.52)

Values for excited levels are shown relative to the values of the ground state.

[a] With empirical values for G_1 and F_2.

[b] With computed values for G_1 and F_2.

As seen from Table V, the contribution of W_c' to the excitation energy is relatively small owing to the good approximate nature of Mulliken-Rüdenberg approximation for two-center coulombic integrals. The electronic levels of benzene corrected by W' of Table V are analogous to those in § 2, which would give the correct order of magnitude.

The author expresses his sincere thanks to Professor M. Kotani of the University of Tokyo and Associate Professor E. Ishiguro of the Ochanomizu University for their valuable discussions and encouragement. He thanks also cordially the member of Kotani Laboratory for the communication of the unpublished useful table, without which this work would not have been accomplished. He is also indebted to the Ministry of Education for its research grant.

References

1) M. G. Mayer and A. L. Sklar: J. Chem. Phys. **6** (1938) 645.
2) E. Hückel: ZS. f. Physik **70** (1931) 204.
3) A. L. Sklar and R. H. Lydden: J. Chem. Phys. **7** (1939) 374.
4) C. Zener: Phys. Rev. **36** (1930) 51.
5) A. London: J. Chem. Phys. **13** (1945) 396.
6) R. G. Parr and B. L. Crawford: ibid. **17** (1949) 726.
7) C. C. J. Roothaan and R. G. Parr: ibid. **17** (1949) 1001.
8) D. P. Craig: Proc. Roy. Soc. **A 200** (1950) 401.
9) D. P. Craig: ibid. **A 200** (1950) 474.
10) R. G. Parr, D. P. Craig and I. G. Ross: J. Chem. Phys. **18** (1950) 1561.
11) J. van Dranen: Thesis, University of Amsterdam (1951).
12) S. L. Altmann: Proc. Roy. Soc. **A 210** (1952) 327.
13) M. Kotani, A. Amemiya and T. Simose: Proc. Phys.-Math. Soc. Japan **20** (1938) Extra No. 1.
14) R. S. Mulliken: J. Chim. Physique **46** (1949) 500, 521.
K. Rüdenberg: J. Chem. Phys. **19** (1951) 1432.
15) M. Kotani and A. Amemiya: Proc. Phys.-Math. Soc. Japan **22** (1940) Extra number.
16) M. Kotani, E. Ishiguro. K. Hijikata, T. Nakamura, and A. Amemiya: J. Phys. Soc. Japan **8** (1953) 463.
17) J. H. Van Vleck: J. Chem. Phys. **2** (1934) 297.
18) W. Moffitt: Proc. Roy. Soc. **A 210** (1951) 224.
19) J. H. Van Vleck: Phys. Rev. **49** (1936) 232.
20) C. A. Coulson, N. H. March and S. L. Altmann: Proc. Nat. Acad. Sci. **38** (1952) 372.
21) N. H. March: Acta Crys. **5** (1952) 187.

JOURNAL OF THE PHYSICAL SOCIETY OF JAPAN Vol. 8, No. 5, SEP.—OCT., 1953

The Direct Current associated with Microwave Gas Discharge between Coaxial Cylinders, III

By Kenji MITANI
Yoshida College, University of Kyoto

(Received May 12, 1953)

The author has found in his experiment that the microwave power in the region of glow discharge does not change the electron states but only controls the discharge area. In this point, the microwave discharge and the normal d.c. discharge are very alike.

§ 1. Introduction

When the high power microwave is introduced into the coaxial type cavity resonator, the gas discharge takes place at the loop of the microwave electric field and the glow appears thereabout. In a previous paper¹⁾, the author has discussed the relation between the length of this glow and the microwave power. At that time the author has assumed that the microwave discharge starts at a certain definite value of electric field and this value is kept constant where discharge continues and thus the microwave power only controls the length of glow.

In order to verify whether this assumption is correct or not, it is necessary to measure the microwave potential between the central wire and the outer cylinder of the cavity resonator, but it is very difficult to measure directly. So the author has intended to verify the fitness of this assumption indirectly, namely, to measure the electron states (the electron temperatures and the electron densities) corresponding to various glow lengths.

For this purpose, the author interpreted the central wire and the outer cylinder of the cavity resonator as two probes of the double probe method[2)] and has applied the d.c. potential between them, and these are of course electrically isolated except that the isolation is broken only by gas discharge as reported in another previous paper[3)]. To determine the electron temperature, the author has modified the method of Johnson and Malter[2)] and applied it.

And the electron density has been determined from the saturation part of probe current that is spacecharge-limited electron current and the electron temperature.

In this way the author has been able to verify the above-mentioned assumption is correct.

§ 2. Experimental Method and Results

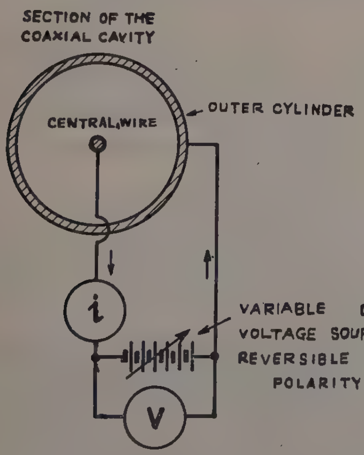
SECTION OF THE COAXIAL CAVITY
CENTRAL WIRE
OUTER CYLINDER
i
VARIABLE D.C. VOLTAGE SOURCE REVERSIBLE IN POLARITY
V

Fig. 1. Diagram of the experiment.

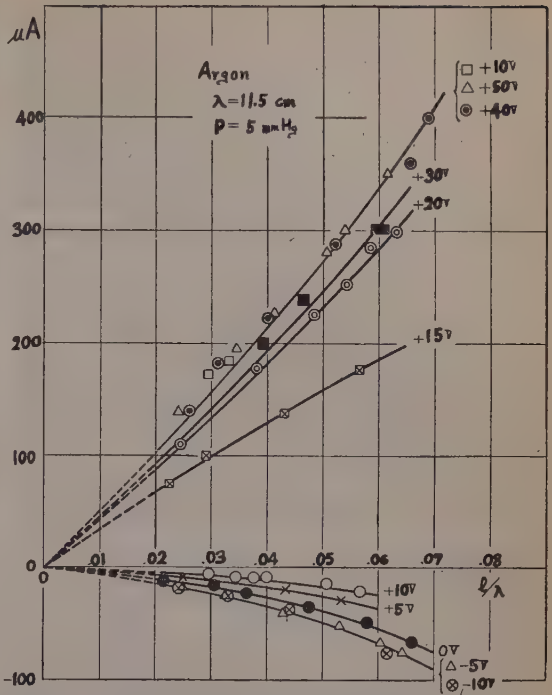

Fig. 2. Probe current i vs. the glow length l/λ for various applied d.c. potentials.

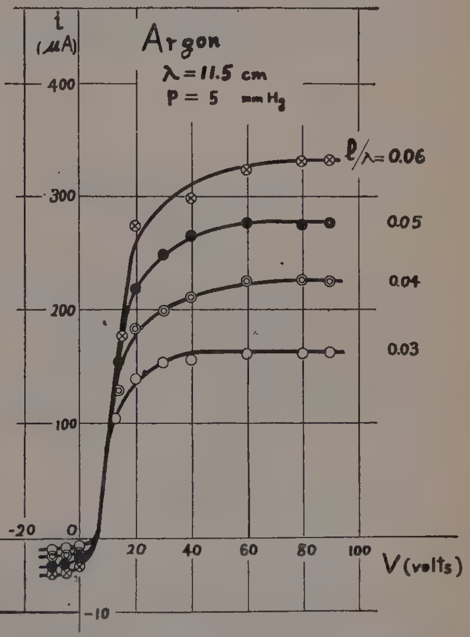

Fig. 3. Probe current i vs. the applied d.c. potential for various glow length l/λ.

The apparatus used in this experiment is the same as that reported in the preceding paper[3)] except that we have used this timea power divider instead of an attenuator. The experiment was performed at a wave length $\lambda = 11.5$ cm with argon at pressure $p = 5$ mmHg.

For the purpose of using the central wire and the outer cylinder of the coaxial resonator cavity as double probe electrodes, we have applied the d.c. voltage which can be changed in polarity and in magnitude as shown in Fig. 1. The voltage is considered positive or negative according to the sign of the voltage of outer cylinder against the central wire and the current is taken positive in the direction from the central wire to the outer cylinder along the outer circuit.

Fig. 2 shows experimental curves of the probe current i versus the glow length l/λ for various d. c. potentials, while in Fig. 3 are shown experimental curves of the probe current i plotted against the applied d.c. potential for various glow lengths l/λ (viz. the various microwave powers). These curves have the typical form of probe current with saturation.

§ 3. Discussions

Though the author intends to discuss in a subsequent paper in detail the mechanism of probe current when the double probe method is applied to the researches on microwave discharge, here the author will report about the modification of the method of Johnson and Malter[2] by which he has tried to determine the electron temperature and the experimental results.

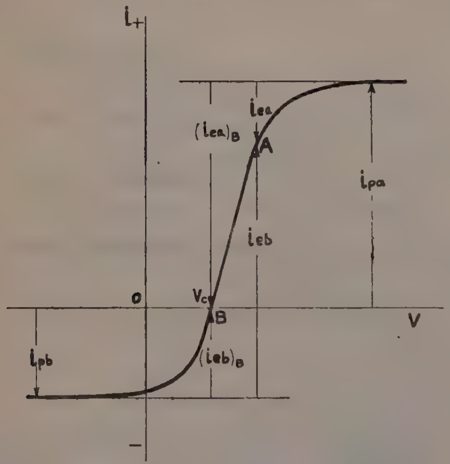

Fig. 4. Probe current characteristic of the double probe method.

Fig. 4 shows the probe current i.e. the voltage-current characteristic obtained from Fig. 3. In this figure, i_{pa} is the value of the positive ion current flowing to the central wire and i_{pb} that flowing to the outer cylinder. These are respectively the saturation currents to both electrodes[4]. The electron currents on any point A of probe current are given by i_{ea} and i_{eb}, of which the former is flowing to the central wire and the latter to the outer cylinder. The probe current i is given by these currents as follows,

$$i=i_{pa}-i_{ea}=i_{eb}-i_{pb}\,. \qquad (1)$$

When the electrons follow the Maxwellian distribution, i_{ea} and i_{eb} are given by:

$$\left.\begin{aligned} i_{ea}&=2\pi alj_{oa}\exp(-\phi V_a)\,,\\ i_{eb}&=2\pi blj_{ob}\exp(-\phi V_b)\,, \end{aligned}\right\} \qquad (2)$$

where the potentials V_a and V_b represent respectively the voltages of the existing plasma with respect to the central wire and the outer cylinder (Fig. 5). b is the radius of the cylinder and a that of the ion sheath around the central wire. j_{oa} and j_{ob} are respectively the electron space current densities in the plasma which occur in the neighbourhood of the central wire and the outer cylinder.

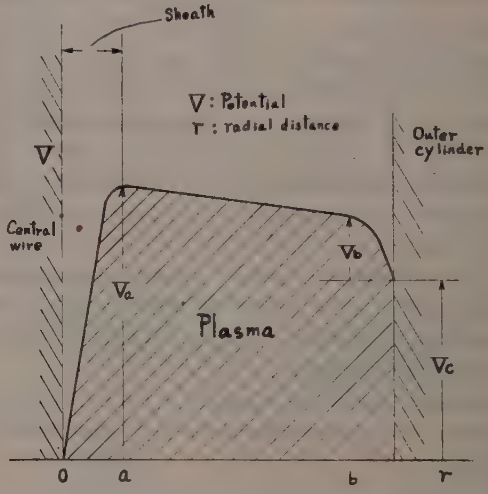

Fig. 5. Potential distribution in the plasma for the double probe method.

Also ϕ is given by

$$\phi=e/kT_e=11{,}600/T_e\,, \qquad (3)$$

where e is the electron charge, k the Boltzmann's constant, and T_e the electron temperature.

Now we pay attention to the point B in Fig. 4 where the probe current is zero. The conditions for the probe current being zero follow from (1) and (2):

$$\left.\begin{aligned} &i_{pa}=(i_{ea})_B=2\pi alj_{oa}\exp(-\phi V_a')\,,\\ \text{and}\quad &i_{pb}=(i_{eb})_B=2\pi blj_{ob}\exp(-\phi V_b')\,, \end{aligned}\right\} \qquad (4)$$

where $(i_{ea})_B$ and $(i_{eb})_B$ are the electron currents corresponding to the point B, and V_a' and V_b' are the corresponding plasma voltages against the central wire and the outer cylinder respectively. From eq. (4),

$$V_b'-V_a'=(kT_e/e)\cdot\ln(j_{ob}i_{pa}b/j_{oa}i_{pb}a) \qquad (5)$$

is derived.

Now, if we assume that the plasma is uniformly distributed along the radial direction, we can put

$$j_{ob}/j_{oa}=1\,. \qquad (6)$$

And also we can neglect the small potential difference which may occur between two regions of plasma existing near both electrodes, and thus the probe potential V_c which corresponds zero probe current can be represented by

$$V_c=V_b'-V_a'\,. \qquad (7)$$

From (6) and (7), eq. (5) becomes

$$V_c=(kT_e/e)\ln(i_{pa}b/i_{pb}a)\,. \qquad (8)$$

This is nothing but the equation which Kojima and Takayama[5)6)] have derived by the method which is slightly from that of the author. From this equation, we can determine the electron temperature. In this paper we put always the ion sheath radius $a=0.02$ cm for various l/λ.

The electron density n can be determined in the following manner. If we make the voltage of the outer cylinder against the central wire strongly negative, then the probe current becomes the spacecharge-limited electron current i_-. From Fig. 4, this current is equal to the total positive ion current, i.e.

$$i_-=i_{pa}+i_{pb}\,. \qquad (9)$$

On the other hand, this current is given as follows[7)],

$$i_-=2\pi alen\sqrt{k/2\pi m}\cdot\sqrt{T_e}\,, \qquad (10)$$

or

$$j_-=i_-/2\pi al=en\sqrt{k/2\pi m}\cdot\sqrt{T_e}\,, \qquad (10')$$

where n is the electron density at the radial distance $r=a$ and m the electron mass. From the electron temperature and (10′), we can determine the electron density.

Table I gives the data as obtained from Fig. 2 which are necessary to calculate the electron temperature and the electron density. In this table, we must notice that the space-charge-limited electron current density j_- is nearly constant in spite of different values of l/λ.

Table II gives the electron temperature and the electron density obtained from eqs. (6), (10′) and the foregoing table.

Table I. The data necessary to calculate the electron temperature and the electron density.

l/λ	0.03	0.04	0.05	0.06
a (cm)	0.02	0.02	0.02	0.02
b (cm)	1.25	1.25	1.25	1.25
i_a (μA)	170	227	285	340
i_b (μA)	2.0	3.3	5.0	6.8
i_- (μA)	172	230	290	347
j_- (μA/cm^2)	3.98	3.98	4.03	3.98
V_c (volts)	12.0	11.6	11.3	11.0

Table II. The electron temperature and the electron density for various l/λ.

l/λ	0.03	0.04	0.05	0.06
T_e (°K)	16,200	16,100	16,000	16,000
n (cm^{-3})	1.24×10^9	1.24×10^9	1.28×10^9	1.26×10^9

§ 4. Conclusion

Table II shows that the electron temperature and the electron density are nearly constant against various l/λ or various microwave powers. So we can say that the microwave power in the region of glow discharge does not change the electron states but only controls the length of glow (discharge area). This character also appears in the d.c. gas discharge. In Loeb's book[8)] we read, 'This discharge is in the region of normal cathode fall, and we might expect the potential V across the tube to remain constant as current increases and hence as the glow area increases'. Thus, from our experiment, at least in the region of the glow discharge, we can say that in this character the microwave and the normal d.c. discharge are very alike but not in the discharge mechanism.

In conclusion, the author wishes to express his sincere appreciation to Professors K. Honda and S. Kojima for their helpful suggestions and also to thank Professor I. Takahashi for his encouragement to this work and discussions of the results. He is also indebted to H. Kudo who devoted his efforts to the experiment.

References

1) K. Mitani: J. Phys. Soc. Japan **7** (1952) 637.

2) E. O. Johnson and L. Malter: Phys. Rev. **80** (1950) 58.

3) K. Mitani: J. Phys. Soc. Japan **7** (1952) 634.

4) L. B. Loeb: *Fundamental Process of Electrical Discharge in Gases* (John Wiley and Sohns, Inc., New York, (1939), first edition, p. 238.

5) S. Kojima and K. Takayama: J. Phys. Soc. Japan **4** (1949) 349.

6) S. Kojima (private communication).

7) L. B. Loeb: loc. cit. p. 243.

8) L. B. Loeb: loc. cit. p. 606.

Journal of the Physical Society of Japan Vol. 8, No. 5, Sep.—Oct., 1953

The Rotational Structure of the Band Spectrum of S_2 Molecule. Part I.

By Katumi Ikenoue

Department of Physics, Faculty of Science, University of Tokyo

(Received July 7, 1953)

The band spectrum of the S_2 molecule has been studied in the region from 3700 A to 4500 A. The following values of the rotational constants have been obtained.

$$B_e''=0.2962\ \text{cm}^{-1},\qquad \alpha_e''=0.00163\ \text{cm}^{-1},$$
$$D_e''=-0.000023\ \text{cm}^{-1},\qquad \beta_e''=-0.0000003\ \text{cm}^{-1},$$
$$\gamma''=-0.035\ \text{cm}^{-1}.$$

§ 1. Introduction

It is well known that the sulphur molecules emit a well-developed band spectrum which lies chiefly in the visible and the neighboring region of the ultraviolet and infra-red. It formed the subject of a large number of investigations and its structure was fairly well known. Nevertheless it presents still a number of problems which admits of being further studied. Especially the strong rotational perturbations produced in the upper state of the bands have not been studied up to the present.

The structure of the band spectrum of sulphur is in many ways analogous to that of the spectrum of the oxygen molecule. Consequently it will be reasonable to admit that the main bands of S_2 are due to the transition $^3\Sigma_u^-\rightarrow{}^3\Sigma_g^-$ (ground state), and the angular momentum of S^{32} nucleous is zero. These have already been verified by many investigators,[1),2),3)] and are assumed in the present work.

The arrangement of the wave-lengths of the band-heads is shown in Table I. Of these, the bands marked with (†) were analysed by M. Naudé and A. Christy,[3)] those marked with (††) by E. Olsson,[3)] and the remainders are left uninvestigated up to the present. The analysis of some of them, shown by Gothic letters, belongs to the scope of the present research.

It is to be remarked that other faint bands appear in the neighborhood of some intense band-head, which is marked with (∗) in the

Table I.

v'' v'	0	1	2	3	4	5	6	7	8
0					3469	3555	3644*	**3737,3***	**3834,6***
1			3260	3336††	3417††	3500	3586	3676	
2		3144	3216††	3291††	3369††	3451		3622	3713
3	3033	3101	3171††	3244††	3320				
4	2997	3063	3132	3203					
5	2960	3024	3091	3161					
6	2926	2989	3055						
7	2892	2954							
8	2860†	2920†							
9	2829	2888†							
10	2799	2857†							

v'' v'	9	10	11	12	13	14	15	16	
0	**3936,9***	**4043,5***	4155*	4272	4394	4522			
1		3973	4080	4193	4310	4434	4563	4700	
2	**3809,0**	**3908,4**	4012		4234	**4353,4**	**4479,6**	4610	

Table II

(0–7) band λ 3737.3A

K	ν (cm^{-1})					
	R_1	R_2	R_3	P_1	P_2	P_3
81			26407.30			26336.07
79			26.20			56.79
77		26439.01	45.09			76.93
75		56.89	63.01		26390.43	96.56
73		74.23	80.43		26409.50	26415.71
71		91.10	97.38		28.10	34.40
69	26510.77	26507.49	26513.86	26450.93	46.24	52.62
67	28.00	23.39	29.83	69.28	63.92	70.37
65	44.13	38.84	45.36	86.89	81.17	87.73
63	59.50	53.86	60.49	26503.84	98.01	26504.69
61	74.22	68.47	75.21	20.19	26514.46	21.25
59	88.32	82.67	89.52	35.99	30.50	37.44
57	26601.87	96.46	26603.46	51.28	46.14	53.22
55	14.94	26609.87	17.03	66.10	61.41	68.68
53	27.52	22.91	30.25	80.44	76.31	83.76
51	39.62	35.57	43.10	94.37	90.83	98.47
49	51.33	47.85	55.56	26607.92	26604.98	26612.85
47	62.64	59.76	67.69	21.07	18.76	
45	73.56	71.31		33.83	32.16	
43	84.06	82.45		46.15	45.19	
41	94.14			58.09		
39	26703.84			69.68		
37	13.18			80.93		
35	22.18			91.82		

(0–8) band λ 3834.6 A

K	ν (cm^{-1})					
	R_1	R_2	R_3	P_1	P_2	P_3
81			25737.86			
79			56.67			25686.88
77		25768.61	74.70		25700.48	25706.56
75		86.02	92.17		19.56	25.71
73		25802.90	25809.12		38.16	44.39
71		19.29	25.59	25759.72	56.29	62.60
69	25838.55	35.20	41.57	78.71	73.96	80.34
67	55.31	50.63	57.08	96.60	91.15	97.63
65	71.00	65.61	72.17	25813.75	25807.93	25814.55
63	85.91	80.18	86.88	30.26	24.33	31.10
61	25900.22	94.36	25901.20	46.19	40.35	47.26
59	13.92	25908.15	15.13	61.60	55.98	63.04
57	27.09	21.54	28.71	76.49	71.24	78.47
55	39.77	34.59	41.86	90.93	86.15	93.52
53	51.99	47.28	54.73	25904.92	25900.69	25908.25
51	63.76	59.61	67.23	18.49	14.89	22.63
49	75.12	71.58	79.38	31.70	28.71	36.65
47	86.09	83.16	91.16	44.52	42.16	50.31
45	96.67	94.40		56.95	55.26	
43	26006.88	26005.26		68.98		
41	16.69			80.66		
39	26.14			90.98		
37	35.23			26002.96		
35	43.98					

above table, as pointed out by A. Fowler and W. M. Vaidya.[4] These weak bands can be expected to produce the perturbation on the main band. These will be treated in Part II of the present report.

§ 2. Experimental Procedure

A fused quartz tube of conventional design

(0-9) band λ 3936.9 A

K	ν (cm^{-1})					
	R_1	R_2	R_3	P_1	P_2	P_3
81			25054.81		24996.39	24982.06
79		25085.89	73.82		25016.09	25002.59
77		25103.40	92.17		35.26	22.36
75		20.38	25109.75		53.93	41.60
73		36.83	26.79		72·09	60.34
71		52.77	43.31		89.77	78.57
69		68.26	59.32		25107.01	96.32
67	25188.04	83.28	74.87	25129.32	23.79	25113.63
65	25203.28	97.84	89.97	46.04	40.18	30.51
63	17.81	25212.01	25204.64	62.15	56.18	47.01
61	31.72	25.82	18.92	77.67	71.80	63.12
59	45.03	39.23	32.82	92.71	87.05	78.87
57	57.85	52.26	46.36	25207.26	25201.94	94.26
55	70.17	64.93	59.54	21.31	16.49	25209.31
53	82.00	77.26		34.93	30.66	
51	93.41	89.21		48.16	44.48	
49	25304.43	25300.83		61.01	57.94	
47	15.06	12.07		73.49	71.06	
45	25.32	22.97		85.58	83.84	
43	35.21	33.53		97.32	96.26	
41	44.75	43.74		25308.72	25308.33	
39	53.93			19.77		
37	62.77			30.51		
35	71.30			40.95		

(0-10) band λ 4043.5 A

K	ν (cm^{-1})					
	R_1	R_2	R_3	P_1	P_2	P_3
83			24397.37			24324.62
81			24415.81		24338.39	44.59
79		24427.32	33.60		57.51	63.81
77		44.26	50.63		76.13	82.49
75		60.70	67.14		94.24	24400.68
73		76.64	83.14		24411.91	18.41
71		92.11	98.68		29.12	35.68
69	24510.55	24507.12	24513.76	24450.71	45.87	52.51
67	26.45	21.69	28.40	67.74	62.20	68.94
65	41.29	35.83	42.64	84.04	78.16	85.00
63	55.42	49.60	56.51	99.76	93.76	24500.72
61	68.91	62.99	70.03	24514.87	24508.98	16.07
59	81.84	76.01	83.17	29.51	23.83	31.08
57	94.29	88.67	95.99	43.70	38.36	45.77
55	24606.28	24601.01	24608.49	57.44	52.56	60.13
53	17.82	13.00	20.64	70.75	66.40	74.16
51	28.92	24.64	32.47	83.65	79.90	87.88
49	39.60	35.93	43.98	96.17	93.05	24601.26
47	49.93	46.89	55.16	24608.34	24605.88	
45	59.90	57.53		20.16	18.40	
43	69.52	67.84		31.62	30.56	
41	78.77			42.73		
39	87.67			53.52		
37	96.24			63.98		
35	24704.51			74.15		
33	12.45					

with cylindrical nickel electrodes and a capillary of 7 mm inner diameter, was used for the discharge tube. The sulphur was introduced into the tube in the form of H_2S, which was dried over P_2O_5 and was frozen with a liquid air trap before the introduction into the tube. In the discharge tube the H_2S is dissociatted, giving sulphur and hydrogen. The

Table III

(2-9) band λ 3809.0 A

K	ν (cm^{-1})					
	R_1	R_2	R_3	P_1	P_2	P_3
65			26030.81			25974.88
63			46.79			92.27
61			61.96		25981.70	26008.91
59		26049.10	76.38		99.14	24.89
57		64.34	90.16		26015.71	40.28
55		78.69	26103.34		31.56	55.14
53		92.34	15.99	26055.34	46.72	69.50
51	26113.84	26105.28	28.14	70.63	61.22	83.35
49	26.91	17.56	39.75	85.08	75.05	96.70
47	39.14	29.16	50.90	98.77	88.25	26109.54
45	50.62	40.16	61.54	26111.76	26100.85	21.89
43	61.40	50.55	71.68	24.11	12.88	33.74
41	71.54	60.37	81.31	35.82	24.35	45.12
39	81.03	69.65	90.49	46.93	35.30	56.03
37	89.91	78.38	99.17	57.47	45.73	66.47
35	98.22	86.57	26207.38	67.46	55.62	76.47
33	26205.98	94.24	15.19	76.88	65.03	86.08
31	13.19	26201.44	22.58	85.76	73.97	95.27
29	19.83	08.14	29.53	94.06	82.40	26204.05
27	25.91	14.36		26201.86	90.36	
25	31.45	20.09		09.14	97.87	
23	36.47	25.36		15.90	26204.91	
21	41.02	30·18		22.20	11.57	
19	45.08			28.01		

(2-10) band λ 3908.4 A

K	ν (cm^{-1})					
	R_1	R_2	R_3	P_1	P_2	P_3
65			25369.02			25313.10
63			84.60			30.06
61			99.37			46.31
59			25413.41			61.90
57			26.79			76.91
55		25414.70	39.61		25367.56	91.43
53		27.98	51.92		82.38	25405.44
51		40.61	63.74	25406.02	96.53	18.97
49	25461.96	52.56	75.07	20.11	25410.06	32.00
47	73.84	63.87	85.88	33.49	22.95	44.53
45	85.04	74.58	96.22	46.18	35.27	56.58
43	95.53	84.71	25506.10	58.23	47.02	68.18
41	25505.39	94.26	15.50	69.68	58.23	79.31
39	14.63	25503.27	24.43	80.55	68.93	89.97
37	23.29	11.76	32.87	90.85	79.12	25500.18
35	31.37	19.74	40.89	25500.60	88.80	09.97
33	38.90	27.20	48.46	09.81	97.97	19.34
31	45.91	34.18	55.61	18.47	25506.69	28.30
29	52.35	40.70	62.41	26.58	14.95	37.01
27	58.26	46.74		34.21	22.74	
25	63.66	52.29		41.33	30.07	
23	68.53	57.41		47.95	36.98	
21	72.91			54.10		
19	76.80			59.80		

other end of the tube was connected to a second liquid air trap, in which the sulphur and H_2S were frozen out again. This trap in turn was connected to an oil diffusion pump which was kept running while the discharge was going on. The pressure of the sulphur in the discharge tube could be regulated by controlling the flow of H_2S by means of a

(2-14) band λ 4353.4 A

K	ν (cm^{-1})					
	R_1	R_2	R_3	P_1	P_2	P_3
69						22689.46
67			22763.57			22706.31
65			78.28			22.36
63			92.19			37.65
61			22805.34		22724.29	52.30
59		22789.77	17.86		39.80	66.37
57		22803.13	29.77		54.50	79.91
55		15.67	41.14		68.54	92.94
53		27.55	52.02		81.93	22805.55
51		38.79	62.47	22804.30	94.71	17.71
49	22858.94	49.44	72.49	17.10	22806.93	29.43
47	69.61	59.52	82.07	29.24	18.59	40.72
45	79.61	69.03	91.22	40.74	29.72	51.58
43	88.96	78.01	99.92	51.65	40.33	61.98
41	97.71	86.47	22908.18	62.00	50.43	71.97
39	22905.89	94.41	16.13	71·81	60.07	
37	13.54	22901.89		81.10	69.25	
35	20.68	08.92		89.91	77.99	
33	27.33	15.51		98.22	86.29	
31	33.49	21.66		22906.06	94.18	
29	39.14	27.39		13.38	22901.65	
27	44.28	32.67		20.22	08.68	
25	48.96			26.63	15.27	

(2-15) band λ 4479.6 A

K	ν (cm^{-1})					
	R_1	R_2	R_3	P_1	P_2	P_3
67			22130.76			22073.49
65			45.05			89.12
63			58.55			22104.02
61			71.31			18.26
59		22155.19	83.41		22105.22	31.92
57		68.16	94.93		19.53	45.05
55		80.33	22205.92		33.19	57.74
53		91.85	16.48		46.23	70.00
51		22202.77	26.61	22168.35	58.69	81.83
49	22222.67	13.10	36.31	80.84	70.59	93.25
47	33.03	22.86	45.59	92.66	81.93	22204.24
45	42.72	32.07	54.46	22203.84	92.76	14.82
43	51.76	40.75	62.91	14.46	22203.06	24.97
41	60.23	48.92	70.92	24.51	12.90	34.71
39	68.14	56.62	78.51	34.05	22.26	44.06
37	75.54	63.82	85.73	43.10	31.17	53.02
35	82.44	70.60	92.54	51.66	39.66	61.62
33	88.87	76.95	99.00	59.76	47.72	69.87
31	94.81	82.89		67.37	55.40	
29	22300.26	88.40		74.49	62.67	
27	05.23	93.52		81.17	69.54	
25	09.73	98.24		87.40	76.02	
23	13.79	22302.55		93.20	82.10	
21	17.42	06.48		98.59	87.87	

stopcock connected to a capillary tube inserted between the discharge tube and the primary liquid air trap, and by removing slowly the liquid air reservoir. Thus the spectrum of S_2 was obtained with great intensity by excitation with an ordinary 5 KW leakage transformer with currents of about 300 mA.

The H_2S was prepared with utmost care, and the absence of impurities was checked by means of Hilger E1 spectrograph preceding the exposure with the grating spectrograph of high dispersion.

Table IV

K	$\Delta_2F_3''(K)-\Delta_2F_2''(K)$		$\Delta_2F_2''(K)-\Delta_2F_1''(K)$		K	$\Delta_2F_3''(K)-\Delta_2F_2''(K)$		$\Delta_2F_2''(K)-\Delta_2F_1''(K)$	
	$v'=0$	$v'=2$	$v'=0$	$v'=2$		$v'=0$	$v'=2$	$v'=0$	$v'=2$
80	0.08				50	0.07	0.06	0.08	0.08
78	0.07				48	0.06	0.07	0.07	0.07
76	0.07				46		0.07	0.07	0.07
74	0.07				44		0.08	0.07	0.07
72	0.07				42		0.08		0.08
70	0.07				30		0.08		0.09
68	0.07		0.08		38		0.08		0.09
66	0.07		0.08		36		0.09		0.09
64	0.07		0.06		34		0.09		0.09
62	0.07		0.08		32		0.09		0.10
60	0.07	0.07	0.07		30		0.10		0.12
58	0.07	0.07	0.07		28				0.11
56	0.07	0.08	0.07		26				0.13
54	0.07	0.07	0.07		24				0.14
52	0.07	0.07	0.07		22				0.15

Table V

v''	B_v''	B_v''(cal)$-B_v''$(obs)	D_v''	D_v''(cal)$-D_v''$(obs)
7	0.2840	−0.0001	−0.000027	−0.000002
8	0.2823	0.0000	−0.000026	0.000000
9	0.2806	+0.0001	−0.000024	+0.000002
10	0.2790	0.0000	−0.000025	+0.000001
14	0.2725	0.0000	−0.000027	0.000000
15	0.2710	−0.0001	−0.000029	−0.000001

The photographs of the bands in the region between 3700 A and 4500 A used for the analysis were taken in the third order of the 21-ft. concave grating, giving a dispersion of 0.8 A per mm. A Wratten filter or a SK3 glass plate of 1 cm thickness was used in order to cut off the 4th and 5th order spectra, and the second order spectrum, longer than 5500 A in wave-length, had no effect on the blue-sensitive plate specially prepared for our purpose. The time of exposure was about 3 hours.

The accuracy of the wave number of each spectral line measured is about 0.03 cm^{-1}.

§ 3. Results

The bands due to S_2 are very numerous, and there is practically no region of the spectrum in which overlapping does not occur. Thus the rotational analysis should be performed by noticing and depending upon the line intensity. It was noticed that as to the strong bands in this region, for examples (0–7), (0–8), (0–9) and (0–10), three pairs of the series of the strong lines could be recognised at the region some twenty angstroms apart from the band-head, and the pair R_3 and P_3 is regularly situated far away from head and so the pair R_1 and P_1 is far near to the head, which is the weakest of them.

Table II gives the wave number of the four bands $v'=0$, and Table III gives the wave number of the four bands $v'=2$.

The combination differences $\Delta_2F_i'(K)=R_i(K)-P_i(K)$ should agree for the bands (0–7), (0–8), (0–9), (0–10) and for the bands (2–9), (2–10), (2–14), (2–15); and also the values of $\Delta_2F_i''(K)=R_i(K-1)-P_i(K+1)$ should agree for the bands (0–9), (2–9) and (0–10), (2–10). These agreements were satisfactory within the limits of the experimental errors in all cases, since the maximum deviation is 0.02 cm^{-1}.

The values of $\Delta_2F_3''(K)-\Delta_2F_2''(K)$ and $\Delta_2F_2''(K)-\Delta_2F_1''(K)$ are tabulated in Table IV. These differences are equal to $-2\gamma''$ for the large number of K, as has been shown by Kramers.

The rotational perturbations could not be recognised in the lower state as shown by

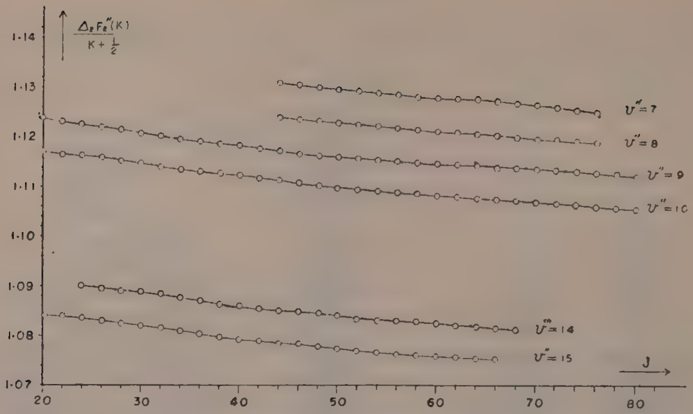

Fig. 1. Plot of the combination differences for the lower electronic state showing no perturbation.

Fig. 1.

The rotational constants B_v'' and D_v'' for each band were calculated with the least-square method and are shown in Table V. From these values the equilibrium constants B_e'' and D_e'' are obtained again with the least-square method, as

$$B_e''=0.2962\ \text{cm}^{-1}, \qquad \alpha_e''=0.00163\ \text{cm}^{-1},$$
$$D_e''=-0.000023\ \text{cm}^{-1}, \quad \beta_e''=-0.0000003\ \text{cm}^{-1},$$

and from these B_v'' and D_v'' can be calculated. The differences $B_v''(\text{cal.})-B_v''(\text{obs.})$ and $D_v''(\text{cal.})-D_v''(\text{obs.})$ are also given in Table V.

For the moment of inertia and internuclear distance for the lower state the following values were obtained;

$$I_e''=94.77\times10^{-40}\ \text{g.cm}^2, \quad r_e''=1.887\times10^{-8}\ \text{cm}.$$

The author has pleassure in recording his indebtedness to Prof. T. Tanaka and Prof. Z. Koana for the guidance and encouragement shown during the course of this work.

References

1) Rene Maeder: Helv. physica Acta **XXI** (1948) 411.

2) M. Naudé and A. Christy: P. R. **37** (1931) 490.

3) E. Olsson: Z. P. **100** (1936) 656.

4) A. Fowler and W. M. Vaidya: P. R. S. **132** (1931) 310.

JOURNAL OF THE PHYSICAL SOCIETY OF JAPAN Vol. 8, No. 5, SEP.—OCT., 1953

On the Flow of a Viscous Fluid past an Inclined Elliptic Cylinder at Small Reynolds Numbers

By Hidenori HASIMOTO

Department of Physics, Faculty of Science, University of Tokyo

(Received April 4, 1953; Read April 3, 1952)

The steady flow of a viscous fluid past an elliptic cylinder set at an arbitrarily given angle to the uniform flow, is discussed on the basis of Oseen's linearized equation of motion, using elliptic coordinates. New fundamental solutions for the stream function are obtained. The expansion formulae for the lift and drag in powers of Reynolds numbers are obtained, which coincide perfectly with Imai's formulae obtained by a new expansion method using complex variables.

§ 1. Introduction and Summary

The steady flow of a viscous fluid past an elliptic cylinder has been discussed by several authors on the basis of Oseen's linearized equation of motion, since Harrison's study1) in 1924. Recently, Tomotika and Aoi2) have obtained the formulae correct to R^4) for the drag on an elliptic cylinder whose major axis is either parallel or perpendicular to the undisturbed flow, where R is the Reynolds number.

On the other hand, asymmetric flow when the elliptic cylinder is set at an arbitrarily given angle α to the uniform flow has hitherto been left untouched except the works of Meksyn3) and Lewis4). Lewis has shown that Meksyn's solution is erroneous on account of an infinite circulation, and has given a formal method to give a correct solution on the basis of modified Oseen's approximation (due to Southwell and Squire5)). Explicit solution by his method, however, seems to be difficult. Recently, Imai6) developed a very elegant method applicable to arbitrarily shaped cylinder on the basis of Reynolds number expansion using complex variables, and obtained the expansion formulae for the lift and drag experienced by an elliptic cylinder, at an arbitrary angle of attack.

In this paper, we treat the same problem using elliptic coordinates and Mathieu functions. In § 3 we introduce new fundamental solutions of Oseen's equation, which made our attack successful. In § 4 we show the formal method of determining the stream function, and in § 5 we obtain the expansion formulae for the lift and drag in powers of Reynolds number to the order of the second approximation, which coincide perfectly with Imai's formulae.

The author wishes to express his cordial gratitude to Professor I. Imai for his continual guidance throughout this work. The author's gratitude is also due to Professor S. Tomotika, Mr. T. Aoi and Mr. H. Yosinobu of the University of Kyoto for their kind suggestions.

§ 2. Fundamental Equation and Its Solutions

Using a stream function Ψ, the Navier-Stokes equation for the two-dimensional steady motion of an incompressible viscous fluid is expressed as follows;

$$\Delta\Delta\Psi=-\frac{1}{\nu}\frac{\partial(\Psi,\Delta\Psi)}{\partial(x,y)}, \qquad (2.1)$$

where $\Delta=\partial^2/\partial x^2+\partial^2/\partial y^2$, and ν is the kinematic viscosity.

Let us assume that a cylindrical obstacle is placed in a uniform flow of velocity U streaming parallel to the x-axis. Writing

$$\Psi=Uy+\psi, \qquad (2.2)$$

and using the Oseen approximation which neglects terms of the second order in ψ, i.e. $-\dfrac{1}{\nu}\dfrac{\partial(\psi,\Delta\psi)}{\partial(x,y)}$, we obtain

$$\Delta\left(\Delta-2k\frac{\partial}{\partial x}\right)\psi=0, \qquad (2.3)$$

where

$$2k=U/\nu. \qquad (2.4)$$

The solution of (2.3) can be written in the form

$$\psi=\psi_1+\psi_2, \qquad (2.5)$$

where

$$\Delta\psi_1=0, \qquad (2.6)$$

$$(\Delta-k^2)(e^{-kx}\psi_2)=0. \qquad (2.7)$$

According to Filon,7) the solutions satifying (2.6), (2.7) and the condition at infinity are

$$\left.\begin{aligned}\phi_1&=A_0\log r+B_0\theta+\sum_{n=1}^{\infty}r^{-n}(A_n\cos n\theta+B_n\sin n\theta)\,,\\ \phi_2&=a_0e^{kx}K_0(kr)+b_0\int_0^{\theta}kr[K_1(kr)+K_0(kr)]e^{kr\cos\theta}d\theta\\ &\quad+e^{kx}\sum_{n=1}^{\infty}K_n(kr)(a_n\cos n\theta+b_n\sin n\theta)\,,\end{aligned}\right\}\tag{2.8}$$

where

$$b_0=-B_0\,,\qquad x=r\cos\theta\,,\qquad y=r\sin\theta\,,\tag{2.8$'$}$$

and $K_n(kr)$ is the modified Bessel function of order n which tends to zero when $kr\to\infty$. Then the lift L and drag D experienced by the cylinder are respectively given by

$$L=2\pi\rho UA_0=\rho U\Gamma\,,\tag{2.9}$$

$$D=2\pi\rho UB_0=\rho Um\,,\tag{2.10}$$

where ρ is the density of the fluid, m and Γ are respectively the inward flow in the wake and the circulation in the clockwise sence round a large circle surrounding the cylinder. (2.8′) is the condition for Ψ to be one-valued and continuous in the field of flow.

§ 3. Elliptic Cylinder

Introducing elliptic coordinates ξ,η, related with x,y by the equation

$$x+iy=ce^{-i\alpha}\cosh(\xi+i\eta)\,,\tag{3.1}$$

$$\left.\begin{aligned}x&=c(\cos\alpha\cosh\xi\cos\eta+\sin\alpha\sinh\xi\sin\eta)\,,\\ y&=c(\cos\alpha\sinh\xi\sin\eta-\sin\alpha\cosh\xi\cos\eta)\,,\end{aligned}\right\}\tag{3.1$'$}$$

we obtain from (2.6) and (2.7),

$$\left(\frac{\partial^2}{\partial\xi^2}+\frac{\partial^2}{\partial\eta^2}\right)\phi_1=0\,,\tag{3.2}$$

$$\left\{\frac{\partial^2}{\partial\xi^2}+\frac{\partial^2}{\partial\eta^2}-k^2c^2(\cosh^2\xi-\cos^2\eta)\right\}(e^{-kx}\phi_2)=0\,.\tag{3.3}$$

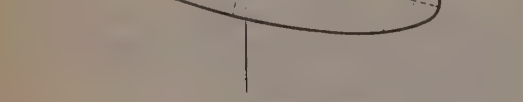

Fig. 1. Elliptic cylinder.

The surface of the elliptic cylinder is given by $\xi=\xi_0$, the angle of incidence between the uniform flow and the major axis of the ellipse is α.

If we take

$$\sigma=\exp(-\xi_0)\,,\qquad c=2\sigma\,,\tag{3.3}$$

the half lengths of the major and minor axes are respectively given by

$$a=c\cosh\xi_0=1+\sigma^2\,,\tag{3.4}$$

$$b=c\sinh\xi_0=1-\sigma^2\,.\tag{3.5}$$

Making $\xi\to\infty$ in (3.1) we see

$$\xi\sim\log r\qquad\text{or}\qquad r^{-n}=e^{-n\xi}\,,\tag{3.6}$$

$$\eta\sim\theta+\alpha\,.\tag{3.7}$$

Therefore, taking account of (2.8), we may take as the general solutions satisfying (3.2), (3.3) and the condition at infinity,

$$\left.\begin{aligned}\phi_1&=A_0\xi+B_0\eta+\sum_{n=1}^{\infty}\frac{1}{n}e^{-n(\xi-\xi_0)}(A_n\cos n\eta+B_n\sin n\eta)\,,\\ \phi_2&=\sum_{n=0}^{\infty}[a_nF_n(\xi,\eta)+b_nG_n(\xi,\eta)]\,,\end{aligned}\right\}\tag{3.8}$$

where

$$F_n(\xi,\eta)=e^{kx}FEK_n(\xi)ce_n(\eta)\,,\tag{3.9}$$

$$G_n(\xi,\eta)=\int_{\eta_0}^{\eta}\left(\frac{\partial}{\partial\xi}-2k\frac{\partial x}{\partial\xi}\right)F_n(\xi,\eta)d\eta-\int_{\xi}^{\infty}\left\{\frac{\partial}{\partial\eta_0}-2k\frac{\partial x(\xi,\eta_0)}{\partial\eta_0}\right\}F_n(\xi,\eta_0)d\xi\ . \tag{3.10}$$

(See Appendix. I).

$ce_n(\eta)$ are proper solutions of the Mathieu equation[8)][9)]

$$\left\{\frac{d^2}{d\eta^2}+(\lambda_n+k^2c^2\cos^2\eta)\right\}ce_n(\eta)=0\ , \tag{3.11}$$

which are periodic and even in η:

$$ce_{2n}(\eta)=(-1)^n\sum_{p=0}^{\infty}a_{2p}{}^{2n}\cos 2p\eta\ , \qquad ce_{2n+1}(\eta)=(-1)^n\sum_{p=0}^{\infty}a_{2p+1}{}^{2n+1}\cos(2p+1)\eta\ , \tag{3.12}$$

$FEK_n(\xi)$ are solutions of the associated Mathieu equation, corresponding to the characteristic values λ_n's of (3.11):

$$\left\{\frac{d^2}{d\xi^2}-(\lambda_n+k^2c^2\cosh^2\xi)\right\}FEK_n(\xi)=0\ , \tag{3.13}$$

and tend to zero as ξ tends to infinity. According to Mclachlan[9)] and Aoi,[10)] they can be expressed in series of products of the modified Bessel functions;

$$\left.\begin{aligned} FEK_{2n}(\xi)&=\frac{1}{A_0{}^{(2n)}}\sum_{p=0}^{\infty}A_{2p}{}^{(2n)}I_p(v_1)K_p(v_2)\ ,\\ FEK_{2n+1}(\xi)&=\frac{1}{B_1{}^{(2n+1)}}\sum_{p=0}^{\infty}B_{2p+1}{}^{(2n+1)}[I_p(v_1)K_{p+1}(v_2)-I_{p+1}(v_1)K_p(v_2)]\ , \end{aligned}\right\} \tag{3.14}$$

where $A_{2p}{}^{(2n)}=(-1)^{n+p}a_{2p}{}^{(2n)}$, $B_{2p+1}{}^{(2n+1)}=(-1)^{n+p}a_{2p+1}{}^{(2n+1)}$, $v_1=\frac{1}{2}kce^{-\xi}$, $v_2=\frac{1}{2}kce^{\xi}$.

Taking into account (2.8), (3.6) and (3.7) we see that the lift L and the drag D experienced by the elliptic cylinder are expressed by (2.9) and (2.10) using the same A_0 and B_0. The condition of one-valuedness corresponding to (2.8′) will be mentioned in § 4 and Appendix II. Circulation at $\xi=\infty$ takes a finite value $2\pi B_0$ (See Appendix III).

§ 4. Determination of the Constants in the Stream Function from the Boundary Conditions

The constants a_n, b_n, A_n and B_n in Ψ have to be determined from the following boundary conditions:

i) Ψ is one-valued and continuous in the field of flow.

ii) $u=v=0$ on the surface of the cylinder, or in terms of normal and tangential velocities

$$u_n=h\frac{\partial\Psi}{\partial\eta}=0\ , \qquad u_s=-h\frac{\partial\Psi}{\partial\xi}=0 \quad \text{at} \quad \xi=\xi_0\ , \tag{4.1}$$

where $h^{-2}=c^2(\cosh^2\xi-\cos^2\eta)$

iii) $u=\dfrac{\partial\Psi}{\partial y}\to U$ and $v=-\dfrac{\partial\Psi}{\partial x}\to 0$ as $x,y\to\infty$.

The condition iii) is already satisfied by taking

$$\Psi=Uy+\phi_1+\phi_2\ , \tag{4.2}$$

given by (3.8), (3.9) and (3.10).

Using the relations

$$\left.\begin{aligned} \frac{\partial F_n}{\partial\xi}&=e^{kx}\left[FEK_n'(\xi)+k\frac{\partial x}{\partial\xi}FEK_n(\xi)\right]ce_n(\eta)\ ,\\ \frac{\partial G_n}{\partial\xi}&=e^{kx}FEK_n(\xi)\left[k\frac{\partial x}{\partial\eta}ce_n(\eta)-ce_n'(\eta)\right] \qquad \text{etc.}\ , \end{aligned}\right\} \tag{4.3}$$

(see Appendix I.5)
and (3.8), (3.9) and (4.2), the condition (4.1) becomes

$$0=U\left(\frac{\partial y}{\partial\xi}\right)_{\xi=\xi_0}+A_0-\sum_{n=1}^{\infty}(A_n\cos n\eta+B_n\sin n\eta)+\sum_{n=0}^{\infty}\frac{\partial}{\partial\xi}[a_nF_n+b_nG_n]_{\xi=\xi_0}\ , \tag{4.4}$$

$$0=U\left(\frac{\partial y}{\partial \eta}\right)_{\xi=\xi_0}+B_0-\sum_{n=1}^{\infty}(A_n \sin n\eta-B_n \cos n\eta)+\sum_{n=0}^{\infty}\frac{\partial}{\partial \eta}[a_nF_n+b_nG_n]_{\xi=\xi_0}\,, \tag{4.5}$$

Making Fourier expansions

$$\left.\begin{aligned}\left(\frac{\partial F_n}{\partial \xi}\right)_{\xi=\xi_0}&=X_{n0}+\sum_{m=1}^{\infty}(X_{nm}\cos m\eta+\overline{X}_{nm}\sin m\eta)\,,\\ \left(\frac{\partial G_n}{\partial \xi}\right)_{\xi=\xi_0}&=\Xi_{n0}+\sum_{m=1}^{\infty}(\Xi_{nm}\cos m\eta+\overline{\Xi}_{nm}\sin m\eta)\,,\\ \left(\frac{\partial F_n}{\partial \eta}\right)_{\xi=\xi_0}&=\sum_{m=1}^{\infty}(Y_{nm}\cos m\eta+\overline{Y}_{nm}\sin m\eta)\,.\\ \left(\frac{\partial G_n}{\partial \eta}\right)_{\xi=\xi_0}&=H_{n0}+\sum_{m=1}^{\infty}(H_{nm}\cos m\eta+\overline{H}_{nm}\sin m\eta)\,,\end{aligned}\right\} \tag{4.6}$$

and equating to zero the constant terms and the coefficients of $\cos m\eta$ and $\sin m\eta$ in (4.4) (4.5), we get

$$A_0+\sum_{n=0}^{\infty}(a_nX_{n0}+b_n\Xi_{n0})=0\,, \tag{4.7$_0$}$$

$$-A_m+\sum_{n=0}^{\infty}(a_nX_{nm}+b_n\Xi_{nm})=U\delta_{1m}(1-\sigma^2)\sin\alpha\,, \tag{4.7$_c$}$$

$$-B_m+\sum_{n=0}^{\infty}(a_n\overline{X}_{nm}+b_n\overline{\Xi}_{nm})=-U\delta_{1m}(1+\sigma^2)\cos\alpha\,, \tag{4.7$_s$}$$

$$B_0+\sum_{n=0}^{\infty}b_nH_{n0}=0\,, \tag{4.8$_0$}$$

$$B_m+\sum_{n=0}^{\infty}(a_nY_{nm}+b_nH_{nm})=-U\delta_{1m}(1-\sigma^2)\cos\alpha\,, \tag{4.8$_c$}$$

$$-A_m+\sum_{n=0}^{\infty}(a_n\overline{Y}_{nm}+b_n\overline{H}_{nm})=-U\delta_{1m}(1+\sigma^2)\sin\alpha, \tag{4.8$_s$}$$

where, $\delta_{11}=1$, $\delta_{1m}=0(m\neq 1)$.

We see easily that (4.8$_0$) is the necessary and sufficient condition for i) to be satisfied, in view of the fact that the only non-periodic part of Ψ is $[B_0+\sum_{n=0}^{\infty}b_nH_{n0}]\eta$ (see Appendix II).

Subtracting (4.8$_s$) from (4.7$_c$), and adding (4.7$_s$) to (4.8$_c$), we obtain a system of linear algebraic equations for a_m's and a_n's,

$$2U\delta_{1m}\sin\alpha=\sum_{n=0}^{\infty}(a_nP_{nm}+b_n\overline{P}_{nm})\,, \tag{4.9}$$

$$-2U\delta_{1m}\cos\alpha=\sum_{n=0}^{\infty}(a_nQ_{nm}+b_n\overline{Q}_{nm})\,,\qquad (m=1,2,\cdots)\,, \tag{4.10}$$

where

$$P_{nm}=X_{nm}-\overline{Y}_{nm}\,,\qquad \overline{P}_{nm}=\Xi_{nm}-\overline{H}_{nm}\,, \tag{4.9$'$}$$

$$Q_{nm}=\overline{X}_{nm}+Y_{nm}\,,\qquad \overline{Q}_{nm}=\overline{\Xi}_{nm}+H_{nm}\,. \tag{4.10$'$}$$

After determining the values of a_n's and b_n's from (4.9) and (4.10), A_n's and B_n's are given by (4.7) and (4.8); especially

$$A_0=-\sum_{n=0}^{\infty}(a_nX_{n0}+b_n\Xi_{n0})\,, \tag{4.7$'$}$$

$$B_0=-\sum_{n=0}^{\infty}b_nH_{n0}\,. \tag{4.8$'$}$$

§ 5. Expansion Formulae for the Lift and Drag at Small Reynolds Numbers

In § 4 we have shown a formal method for determining the stream function. The values of the drag and lift may also be found numerically for any given σ, α and Reynolds number

$$R=2aU/\nu=2(1+\sigma^2)U/\nu=4ka=4k(1+\sigma^2)\,. \tag{5.1}$$

However, the work is very laborious, and comparison with other results is not easy. It will therefore be desirable to derive formulae expressed in powers of R or k, considering that the Oseen approximation itself already assumes R to be small.

Assuming k to be small it is easily found that the coefficients of a_n and b_n in (4.9) and (4.10) can be expanded as follows: (see Appendix IV)

$$\left.\begin{aligned}
&P_{01}=k\cos\alpha[2s-(1+\sigma^2)]+k^3p_{01}+O(k^5)\,,\\
&\overline{P}_{01}=k\sin\alpha[2s+(1-\sigma^2)]+k^3\overline{p}_{01}+O(k^5)\,,\\
&Q_{01}=k\sin\alpha[2s-(1-\sigma^2)]+k^3q_{01}+O(k^5)\,,\\
&\overline{Q}_{01}=-k\cos\alpha[2s+(1+\sigma^2)]+k^3\overline{q}_{01}+O(k^5)\,,\\
&\begin{Bmatrix}P_{11},\overline{P}_{11},\,Q_{11},\,\overline{Q}_{11}\\ P_{13},\overline{P}_{13},\,Q_{13},\,\overline{Q}_{13}\end{Bmatrix}=k\times\begin{Bmatrix}p_{11},\overline{p}_{11},q_{11},\overline{q}_{11}\\ p_{13},\overline{p}_{13},q_{13},\overline{q}_{13}\end{Bmatrix}+O(k^3)\,,\\
&\begin{Bmatrix}P_{21},\overline{P}_{21},\,Q_{21},\,\overline{Q}_{21}\\ P_{23},\overline{P}_{23},\,Q_{23},\,\overline{Q}_{23}\end{Bmatrix}=\frac{1}{k}\times\begin{Bmatrix}p_{21},\overline{p}_{21},q_{21},\overline{q}_{21}\\ p_{23},\overline{p}_{23},q_{23},\overline{q}_{23}\end{Bmatrix}+O(k)\\
&\qquad\qquad\qquad\qquad=\frac{-2}{k}\begin{Bmatrix}\sigma^2\cos\alpha,\sigma^2\sin\alpha,\sigma^2\sin\alpha,-\sigma^2\cos\alpha\\ -\cos\alpha,-\sin\alpha,-\sin\alpha,\cos\alpha\end{Bmatrix}+O(k)\,,\\
&\{P_{03},\overline{P}_{03},\,Q_{03},\,\overline{Q}_{03}\}=k^3\times\{p_{03},\overline{p}_{03},q_{03},\overline{q}_{03}\}+O(k^5)\,,\\
&\{P_{02},\overline{P}_{02},\,Q_{02},\,\overline{Q}_{02}\}=k^2\times\{p_{02},\overline{p}_{02},q_{02},\overline{q}_{02}\}+O(k^4)\,,\\
&\{P_{12},\overline{P}_{12},\,Q_{12},\,\overline{Q}_{12}\}=\{\cos a,\,\sin\alpha,\,\sin\alpha,-\cos\alpha\}+O(k^2)\,,\\
&\{P_{22},\overline{P}_{22},\,Q_{22},\,\overline{Q}_{22}\}=O(1)\,,\\
&\cdots
\end{aligned}\right\} \tag{5.2}$$

where

$$s=-\gamma-\log(k/2)\,,\qquad \gamma=0.5772\cdots(\text{Euler's const.}) \tag{5.2$'$}$$

Thus, from (4.9) and (4.10) we may expand $a_0,a_1\cdots$, $b_0,b_1\cdots$ as:

$$\left.\begin{aligned}
&a_0=k^{-1}\overline{\alpha}+k\alpha_0+O(k^2)\,, && b_0=k^{-1}\overline{\beta}+k\beta_0+O(k^3)\,,\\
&a_1=\qquad\quad k\alpha_1+O(k^2)\,, && b_1=\qquad\quad k\beta_1+O(k^3)\,,\\
&a_2=\qquad\qquad\quad k^3\alpha_2+O(k^5)\,, && b_2=\qquad\qquad\quad k^3\beta_2+O(k^5)\,,\\
&\cdots && \cdots\\
&a_n=O(k^{2n-1})\,, && b_n=O(k^{2n-1})\,.
\end{aligned}\right\} \tag{5.3}$$

The coefficients X_{n0},Ξ_{n0},H_{n0} in (4.7′) and (4.8′) are expanded as:

$$\left.\begin{aligned}
&X_{00}=-\left[1-\frac{k^2}{2}\{2(1-\sigma^4)s-\sigma^2\cos2\alpha\}\right]+O(k^4)\,,\\
&X_{10}=-\sigma^2\cos\alpha+O(k^2),\\
&\cdots\\
&\Xi_{00}=O(k^3)\,,\qquad \Xi_{10}=(1-\sigma^2)\sin\alpha+O(k^2)\,,\\
&\cdots\\
&H_{00}=-\left(1+\frac{\sigma^2k^2}{2}\cos2\alpha\right)+O(k^3)\,,\qquad H_{10}=-\cos\alpha+O(k^2)\,.\\
&\cdots
\end{aligned}\right\} \tag{5.4}$$

Using (5.2) and (5.3), A_0 and B_0 are expressed as

$$\left.\begin{aligned}
A_0&=a_0+O(k)\\
&=k^{-1}\bar{\alpha}\left[1+k^2\left\{\frac{\alpha_0}{\bar{\alpha}}+\sigma^2\frac{\alpha_1}{\bar{\alpha}}\cos\alpha-(1-\sigma^2)\frac{\beta_1}{\bar{\alpha}}\sin\alpha\right.\right.\\
&\qquad\qquad\left.\left.-(1-\sigma^4)s+\frac{\sigma^2}{2}\cos 2\alpha\right\}\right]+O(k^3)\,,\\
B_0&=b_0+O(k)\\
&=k^{-1}\bar{\beta}\left[1+k^2\left\{\frac{\beta_0}{\bar{\beta}}+\frac{\beta_1}{\bar{\beta}}\cos\alpha+\frac{\sigma^2}{2}\cos 2\alpha\right\}\right]+O(k^3)\,.
\end{aligned}\right\}\qquad(5.5)$$

Introducing (5.3) into (4.9) and (4.10) we obtain for the first approximation (taking only the terms $m=1$ and $n=0$):

$$\left.\begin{aligned}
&\bar{\alpha}[2s-(1+\sigma^2)]\cos\alpha+\bar{\beta}[2s+(1-\sigma^2)]\sin\alpha=2U\sin\alpha\,,\\
&\bar{\alpha}[2s-(1-\sigma^2)]\sin\alpha-\bar{\beta}[2s+(1+\sigma^2)]\cos\alpha=-2U\cos\alpha\,,
\end{aligned}\right\}\qquad(5.6)$$

which can be solved for $\bar{\alpha}$ and $\bar{\beta}$, giving

$$\bar{\alpha}=\frac{2\sigma^2U\sin 2\alpha}{D_1}\,,\qquad \bar{\beta}=\frac{2U[2s-(1+\sigma^2\cos 2\alpha)]}{D_1}\,,\qquad(5.7)$$

where

$$D_1=4s^2-(1+2\sigma^2\cos 2\alpha+\sigma^4)\,.\qquad(5.7')$$

Then from (5.5), (2.9), (2.10) and (5.1), we obtain for the lift and drag coefficients C_L and C_D

$$C_L=L/(\tfrac{1}{2}\rho U^2\cdot 2a)=\frac{16\pi}{R}\frac{\sigma^2\sin 2\alpha}{D_1}\,,\qquad C_D=D/(\tfrac{1}{2}\rho U^2\cdot 2a)=\frac{16\pi}{R}\frac{2s-(1+\sigma^2\cos 2\alpha)}{D_1}\qquad(5.8)$$

We now proceed to the second approximation. A system of linear algebraic linear equations for α_0, α_1, α_2, β_0, β_1 and β_2 is obtained by equating the terms of the magnitude $O(k^2)$ in (4.9) and (4.10) (taking $m=1,2,3$, $n=0,1,2$):

$$\left.\begin{aligned}
&\alpha_0[2s-(1+\sigma^2)]\cos\alpha+\beta_0[2s+(1-\sigma^2)]\sin\alpha=-\bar{\alpha}p_{01}-\bar{\beta}\bar{p}_{01}-\sum_{n=1}^{2}(\alpha_np_{n1}+\beta_n\bar{p}_{n1})\,,\\
&\alpha_0[2s-(1-\sigma^2)]\sin\alpha-\beta_0[2s+(1+\sigma^2)]\cos\alpha=-\bar{\alpha}q_{01}-\bar{\beta}\bar{q}_{01}-\sum_{n=1}^{2}(\alpha_nq_{n1}+\beta_n\bar{q}_{n1})\,,
\end{aligned}\right\}\qquad(5.9_0)$$

$$\left.\begin{aligned}
&\alpha_1\cos\alpha+\beta_1\sin\alpha=-\bar{\alpha}p_{02}-\bar{\beta}\bar{p}_{02}\,,\\
&\alpha_1\sin\alpha-\beta_1\cos\alpha=-\bar{\alpha}q_{02}-\bar{\beta}\bar{q}_{02}\,,
\end{aligned}\right\}\qquad(5.9_1)$$

$$\left.\begin{aligned}
&2\alpha_2\cos\alpha+2\beta_2\sin\alpha=-\bar{\alpha}p_{03}-\bar{\beta}\bar{p}_{03}-\alpha_1p_{13}-\beta_1\bar{p}_{13}\,,\\
&2\alpha_2\sin\alpha-2\beta_2\cos\alpha=-\bar{\alpha}q_{03}-\bar{\beta}\bar{q}_{03}-\alpha_1q_{13}-\beta_1\bar{q}_{13}\,.
\end{aligned}\right\}\qquad(5.9_2)$$

Solving (5.9) successively from (5.9_1) to (5.9_0) we obtain

$$\begin{aligned}
\alpha_1=&-(\bar{\alpha}/4)[4s(2\sigma^2+1)\cos\alpha-\{(4\sigma^2+1)\cos\alpha+\sigma^4\cos 3\alpha\}]\\
&-(\bar{\beta}/4)[4s\sin\alpha\qquad\qquad-\{(4\sigma^2-1)\sin\alpha+\sigma^4\sin 3\alpha\}]\,,\\
\beta_1=&-(\bar{\alpha}/4)[4s(2\sigma^2-1)\sin\alpha-\{(4\sigma^2-1)\sin\alpha+\sigma^4\sin 3\alpha\}]\\
&-(\bar{\beta}/4)[4s\cos\alpha\qquad\qquad+\{(4\sigma^2+1)\cos\alpha+\sigma^4\cos 3\alpha\}]\,,\\
\alpha_2=&\ \ (\bar{\alpha}/96)[12s\{2\sigma^4+(\sigma^4+\sigma^2+1)\cos 2\alpha\}-\{12\sigma^4+12\sigma^2\\
&\qquad\qquad+(3\sigma^6+12\sigma^4+3\sigma^2+4)\cos 2\alpha+4\sigma^6\cos\alpha\}]\\
&-(\bar{\beta}/96)[12s(\sigma^4-\sigma^2-1)\sin 2\alpha+\{(3\sigma^6+12\sigma^4-3\sigma^2-4)\sin 2\alpha+4\sigma^6\sin 4\alpha\}]\,,\\
\beta_2=&\ \ (\bar{\alpha}/96)[12s(\sigma^4+\sigma^2-1)\sin 2\alpha-\{(3\sigma^6-12\sigma^4-3\sigma^2+4)\sin 2\alpha-4\sigma^6\sin 4\alpha\}]\\
&+(\bar{\beta}/96)[12s(\sigma^4-\sigma^2+1)\cos 2\alpha-\{12\sigma^4-12\sigma^2+(3\sigma^6-12\sigma^4+3\sigma^2-4)\cos 2\alpha-4\sigma^6\cos 4\alpha\}]\,,\\
\alpha_0=&-(\bar{\alpha}/D_1)[s^3(4\sigma^2+2\cos 2\alpha)+(s^2/2)\{2\sigma^4-4\sigma^2+5+(2\sigma^6-\sigma^4+4\sigma^2-1)\cos 2\alpha+\sigma^4\cos 4\alpha\}\\
&\quad-(s/24)\{9\sigma^8-24\sigma^6-6\sigma^4-36\sigma^2+63+(12\sigma^6-60\sigma^4+52\sigma^2-12)\cos 2\alpha\\
&\qquad\qquad+(12\sigma^4-12\sigma^2)\cos 4\alpha\}
\end{aligned}$$

$$\left.\begin{aligned}
&\quad -(1/48)\{21\sigma^8-30\sigma^6+18\sigma^4-30\sigma^2-33+(5\sigma^{10}-6\sigma^8+51\sigma^6-60\sigma^4-31\sigma^2-6)\cos 2\alpha\\
&\qquad\qquad +(2\sigma^8-6\sigma^6+20\sigma^4-6\sigma^2)\cos 4\alpha+3\sigma^6\cos 6\alpha\}],\\
&-(\overline{\beta}/D_1)[2s^3\sin 2\alpha-(s^2/2)\{(\sigma^4-2\sigma^2-1)\sin 2\alpha-\sigma^4\sin 4\alpha\}\\
&\quad +(s/12)\{(12\sigma^6-6\sigma^4+4\sigma^2-6)\sin 2\alpha-(\sigma^8-3\sigma^4+6\sigma^2)\sin 4\alpha\}\\
&\quad -(1/48)\{(5\sigma^{10}-6\sigma^8+9\sigma^6-11\sigma^2+6)\sin 2\alpha\\
&\qquad\qquad +(2\sigma^8-6\sigma^6+10\sigma^4+6\sigma^2)\sin 4\alpha+3\sigma^6\sin 6\alpha\}],\\
\beta_0=&-(\overline{\alpha}/D_1)[2s^3\sin 2\alpha+(s^2/2)\{(2\sigma^6+\sigma^4-1)\sin 2\alpha+\sigma^4\sin 4\alpha\}\\
&\quad -(s/12)\{(12\sigma^6+6\sigma^4-28\sigma^2+6)\sin 2\alpha+(\sigma^8-3\sigma^4+6\sigma^2)\sin 4\alpha\}\\
&\quad -(1/48)\{(\sigma^{10}+6\sigma^8+9\sigma^6-7\sigma^2-6)\sin 2\alpha\\
&\qquad\qquad -(2\sigma^8-6\sigma^6-14\sigma^4+6\sigma^2)\sin 4\alpha+3\sigma^6\sin 6\alpha\}],\\
&+(\overline{\beta}/D_1)[2s^3\cos 2\alpha-(s^2/2)\{2\sigma^4-4\sigma^2-1-(\sigma^4+2\sigma^2+1)\cos 2\alpha-\sigma^4\cos 4\alpha\}\\
&\quad -(s/24)\{3\sigma^8+18\sigma^4-12\sigma^2-15+(12\sigma^6-12\sigma^4+4\sigma^2-12)\cos 2\alpha-(2\sigma^8+12\sigma^2)\cos 4\alpha\}\\
&\quad +(1/48)\{9\sigma^8+30\sigma^6+30\sigma^4+30\sigma^2-9+(\sigma^{10}+6\sigma^8+27\sigma^6+60\sigma^4+13\sigma^2+6)\cos 2\alpha\\
&\qquad\qquad -(2\sigma^8-6\sigma^6-16\sigma^4-6\sigma^2)\cos 4\alpha+3\sigma^6\cos 6\alpha\}].
\end{aligned}\right\}\tag{5.10}$$

Substituting (5.7) and (5.10) into (5.5), the lift and drag coefficients correct to the order of $O(R^2)$ are

$$\left.\begin{aligned}
C_L=&\frac{16\pi}{R}\frac{\sigma^2\sin 2\alpha}{D_1}\Bigg\{1-\frac{R^2}{16(1+\sigma^2)^2}\Bigg[2s^2+\frac{s}{2}(\sigma^4+1+2\sigma^2\cos 2\alpha)+\frac{1}{6}\{4+(\sigma^6-3\sigma^2)\cos 2\alpha\}\\
&\qquad +\frac{1}{D_1}\Bigg[\frac{s}{4}(\sigma^8-4\sigma^4+13+8\sigma^2\cos 2\alpha+2\sigma^4\cos 4\alpha)\\
&\qquad +\frac{1}{6}\{3\sigma^8+9\sigma^4+6+(\sigma^{10}+6\sigma^6+13\sigma^2)\cos 2\alpha+(\sigma^8+\sigma^4)\cos 4\alpha\}\Bigg]\Bigg]\Bigg\},\\
C_D=&\frac{16\pi}{R}\frac{1}{D_1}\Bigg\{2s-(1+\sigma^2\cos 2\alpha)-\frac{R^2}{16(1+\sigma^2)^2}\Bigg[s^2+\frac{s}{2}(2\sigma^4-1-2\sigma^2\cos 2\alpha-\sigma^4\cos 4\alpha)\\
&\qquad +\frac{1}{48}\{3\sigma^8-36\sigma^4+15-(24\sigma^6-8\sigma^2)\cos 2\alpha-(4\sigma^8-18\sigma^4)\cos 4\alpha\}\\
&\qquad +\frac{1}{D_1}\Bigg[\frac{s}{12}\{9\sigma^8+36\sigma^4-15+(\sigma^{10}+33\sigma^6-11\sigma^2)\cos 2\alpha\\
&\qquad\qquad +(4\sigma^8-14\sigma^4)\cos 4\alpha-3\sigma^6\cos 6\alpha\}\\
&\qquad +\frac{1}{24}\{\sigma^{12}-33\sigma^8-11\sigma^4+15-(12\sigma^{10}+56\sigma^6-26\sigma^2)\cos 2\alpha\\
&\qquad\qquad -(2\sigma^{12}+10\sigma^8)\cos 4\alpha-(2\sigma^{10}-4\sigma^6)\cos 6\alpha\}\Bigg]\Bigg]\Bigg\},
\end{aligned}\right\}\tag{5.11}$$

which coincide perfectly with Imai's results obtained by a new method, with Tomotika and Aoi's results for $\alpha=0$ and $\alpha=\pi/2$, and also with Tomotika and Yosinobu's results for $\alpha=0$.

Appendices

I. Non-periodic Solution of (2.7) and (3.3): $G_n(\xi,\eta)$

(2.7) or (3.3) is equivalent to

$$(\partial^2/\partial x^2+\partial^2/\partial y^2)F=2k\partial F/\partial x\,,\tag{I.1}$$

or

$$(\partial^2/\partial\xi^2+\partial^2/\partial\eta^2)F=2k(\partial x/\partial\xi\cdot\partial F/\partial\xi+\partial x/\partial\eta\cdot\partial F/\partial\eta)\,,\tag{I.2}$$

where

$$\partial x/\partial\xi=\partial y/\partial\eta\,,\quad \partial x/\partial\eta=-\partial y/\partial\xi\,.\tag{I.3}$$

Consider

$$G(\xi,\eta)=\int_{\eta_0}^{\eta}\left(\frac{\partial}{\partial\xi}-2k\frac{\partial x}{\partial\xi}\right)F(\xi,\eta)d\eta-\int_{\xi}^{\infty}\left\{\frac{\partial}{\partial\eta_0}-2k\frac{\partial x(\xi,\eta_0)}{\partial\eta_0}\right\}F(\xi,\eta_0)d\xi\,, \tag{I.4}$$

then, using (I.2) and (I.3)

$$\begin{aligned}\frac{\partial G}{\partial\xi}&=\int_{\eta_0}^{\eta}\left(\frac{\partial^2}{\partial\xi^2}-2k\frac{\partial^2 x}{\partial\xi^2}-2k\frac{\partial x}{\partial\xi}\frac{\partial}{\partial\xi}\right)F(\xi,\eta)d\eta+\frac{\partial}{\partial\eta_0}F(\xi,\eta_0)-2k\frac{\partial x(\xi,\eta_0)}{\partial\eta_0}F(\xi,\eta_0)\\&=\int_{\eta_0}^{\eta}\left(-\frac{\partial^2}{\partial\eta^2}+2k\frac{\partial^2 x}{\partial\eta^2}+2k\frac{\partial x}{\partial\eta}\cdot\frac{\partial}{\partial\eta}\right)F(\xi,\eta)d\eta+\left(\frac{\partial}{\partial\eta_0}-2k\frac{\partial x(\xi,\eta_0)}{\partial\eta_0}\right)F(\xi,\eta_0)\\&=-\left(\frac{\partial}{\partial\eta}-2k\frac{\partial x}{\partial\eta}\right)F(\xi,\eta)\,,\end{aligned} \tag{I.5}$$

$$\frac{\partial G}{\partial\eta}=\left(\frac{\partial}{\partial\xi}-2k\frac{\partial x}{\partial\xi}\right)F(\xi,\eta)\,. \tag{I.6}$$

Thus,

$$\partial^2G/\partial\xi^2+\partial^2G/\partial\eta^2=2k(-\partial x/\partial\xi\cdot\partial F/\partial\eta+\partial x/\partial\eta\cdot\partial F/\partial\xi)=2k(\partial x/\partial\xi\cdot\partial G/\partial\xi+\partial x/\partial\eta\cdot\partial G/\partial\eta)\,. \tag{I.7}$$

Taking $F_n=e^{kx}FEK_n(\xi)ce_n(\eta)$ as $F(\xi,\eta)$, it is seen that $G_n(\xi,\eta)$ given by (3.10) satisfies (1.7).

II. One-valuedness of Ψ

Since $F_n(\xi,\eta)$ and $\partial\xi/\partial x$ are continuous and periodic in η, $\partial G_n/\partial\eta=(\partial/\partial\xi-2k\partial x/\partial\xi)F_n(\xi,\eta)$ can be expanded in Fourier series ;

$$W_n(\xi)+\text{terms of }\cos n\eta\text{ and }\sin n\eta\,. \tag{II.1}$$

Thus non-periodic part of $G_n(\xi,\eta)$ in η is given by $W_n(\xi)\eta$, where

$$\begin{aligned}2\pi W_n(\xi)&=\int_0^{2\pi}\frac{\partial}{\partial\eta}G_n(\xi,\eta)d\eta=\int_0^{2\pi}\left[FEK_n'(\xi)-k\frac{\partial x}{\partial\xi}FEK_n(\xi)\right]e^{kx}ce_n(\eta)d\eta\\&=FEK_n'(\xi)\tau_n(\xi)-FEK_n(\xi)\tau_n'(\xi)\,,\end{aligned} \tag{II.2}$$

with

$$\tau_n(\xi)=\int_0^{2\pi}e^{kx}ce_n(\eta)d\eta\,. \tag{II.3}$$

Using $x_{\xi\xi}=-x_{\eta\eta}$, $x_\xi^2+x_\eta^2=c^2(\cosh^2\xi-\cos^2\eta)$, integration by parts and (3.11) we obtain

$$\begin{aligned}\left[\frac{d^2}{d\xi^2}-(\lambda_n+k^2c^2\cosh^2\xi)\right]\tau_n(\xi)&=-e^{kx}[kce_n(\eta)x_\eta-ce_n'(\eta)]_0^{2\pi}\\&\quad-\int_0^{2\pi}e^{kx}[ce_n''(\eta)+(\lambda_n+k^2c^2\cos^2\eta)ee_n(\eta)]d\eta=0\,.\end{aligned} \tag{II.4}$$

We see that $\tau_n(\xi)$ satisfies the same differential equation (3.13) as $FEK_n(\xi)$ with the same characteristic value λ_n. Thus, $2\pi W_n(\xi)$ defined by (II.2) is the Wronskian of (3.13), and is a constant $2\pi W_n$ independent of ξ, as easily proved. From (4.6), we see

$$W_n=H_{n0}\,, \tag{II.5}$$

which shows that (4.8_0) is the condition for one-valuedness of Ψ corresponding to (2.8′).

III. Circulation at a Great Distance from the Cylinder

This is given by

$$\Gamma_\infty=\lim_{\xi\to\infty}\int_0^{2\pi}\frac{\partial\Psi}{\partial\xi}d\eta\,. \tag{III.1}$$

It is easily seen that

i) contribution from $Uy+\phi_1$ is $2\pi A_0$,
ii) contribution from ϕ_2 is 0.

Thus

$$\Gamma_\infty=2\pi A_0\,. \tag{III.2}$$

ii) is proved as follows. Making $\xi\to\infty$ and taking account of (3.6), (3.7) and (3.1′) we obtain

$$FEK_n(\xi)=K_n(kr)[1+O(r^{-1})]=\sqrt{\frac{\pi}{2kr}}e^{-kr}[1+O(r^{-1})]\,.$$

$$FEK_n'(\xi)=krK_n'(kr)[1+O(r^{-1})]=-\sqrt{\frac{\pi kr}{2}}e^{-kr}[1+O(r^{-1})]\,,$$

$$x=r\cos(\eta-\alpha)+O(1)\,,$$

$$\partial x/\partial\xi=r\cos(\eta-\alpha)+O(1)\,.$$

Consider

$$\int_0^{2\pi}\frac{\partial F_n}{\partial\xi}d\eta=\int_0^{2\pi}\left[FEK_n'(\xi)+k\frac{\partial x}{\partial\xi}FEK_n(\xi)\right]e^{kx}ce_n(\eta)\,,$$

We divide the integration interval as $0\to(\alpha-\varepsilon)$, $(\alpha-\varepsilon)\to(\alpha+\varepsilon)$, $(\alpha+\varepsilon)\to2\pi$. On account of exponential factor $\exp[-k(r-x)]$ which tends to $\exp[-kr\{1-\cos(\eta-\alpha)\}]$ the first and the third integrals vanish as $\xi\to\infty$, ε being kept at a small fixed value. Introducing new variable $\theta=(\sqrt{kr/2})(\eta-\alpha)$ the second integral reduces to

$$\int\frac{\sqrt{2}}{\sqrt{kr}}\,d\theta\exp(-\theta^2)\sqrt{\frac{\pi kr}{2}}\left(1-\cos\frac{\sqrt{2}\,\theta}{\sqrt{kr}}\right)ce_n(\alpha)[1+O(r^{-1})+O(\varepsilon)],$$

which tends to 0 as $r\to\infty$ and $\varepsilon\to0$. $\int_0^{2\pi}\frac{\partial G_n}{\partial\xi}d\eta=\int_0^{2\pi}\left[k\frac{\partial x}{\partial\eta}ce_n(\eta)-ce_n'(\eta)\right]e^{kx}FEK_n(\xi)$ tends to 0 more rapidly as easily proved.

IV. Coefficients of a_n, b_n

We have used expressions of $a_{2r}^{(2n)}, A_{2r}^{(2n)}$, etc expanded in powers of k,[8)9)] and [11)]

$$\begin{aligned}
FEK_0(\xi_0)&=s+(k^2/4)[s(\sigma^4+1)+\sigma^4-1]+\cdots\,,\\
FEK_1(\xi_0)&=(1/k)[1-(k^2/8)\{4s(\sigma^4+1)-\sigma^4+2\}+\cdots]\,,\\
FEK_2(\xi_0)&=(2/k^2)[1+(k^2/12)(\sigma^4-3)+\cdots]\,,\\
FEK_0'(\xi_0)&=-1-(k^2/4)\{2s(\sigma^2-1)-(\sigma^4+1)\}+\cdots\,,\\
FEK_1'(\xi_0)&=-(1/k)[1-(k^2/8)\{4s(\sigma^2-1)-3\sigma^4+4\sigma^2+2\}+\cdots]\,,\\
FEK_2'(\xi_0)&=-(4/k^2)[1+(k^2/6)\sigma^4+\cdots]\,.
\end{aligned}$$

After some straightforward calculations we get

$$\begin{aligned}
&p_{01}=-(1/8)[s(6\sigma^6-10\sigma^2-12-4\sigma^2\cos2\alpha)-\sigma^6+5\sigma^4+\sigma^2-5+(2\sigma^4+2\sigma^2)\cos2\alpha]\cos\alpha\,,\\
&\bar{p}_{01}=-(1/8)[s(2\sigma^6-6\sigma^2-4-4\sigma^2\cos2a)-\sigma^6+3\sigma^4+\sigma^2-3+(2\sigma^4-2\sigma^2)\cos2\alpha]\sin\alpha\,,\\
&q_{01}=(1/8)[s(6\sigma^6-10\sigma^2+12+4\sigma^2\cos2\alpha)-\sigma^6-5\sigma^4+\sigma^2+5+(2\sigma^4-2\sigma^2)\cos2\alpha]\sin\alpha\,,\\
&\bar{q}_{01}=-(1/8)[s(2\sigma^6-6\sigma^2+4+4\sigma^2\cos2\alpha)-\sigma^6-3\sigma^4+\sigma^2+3+(2\sigma^4+2\sigma^2)\cos2\alpha]\cos\alpha\,,\\
&p_{11}=-(1/4)[4s+3\sigma^4-2\sigma^2-2+(\sigma^4-1)\cos2\alpha]\,,\qquad \bar{p}_{11}=-(1/4)(\sigma^4-3)\sin2\alpha\,,\\
&q_{11}=(1/4)(\sigma^4+1)\sin2\alpha\,,\qquad \bar{q}_{11}=-(1/4)[4s-\sigma^4+2\sigma^2+2+(\sigma^4+3)\cos2\alpha]\,,\\
&p_{13}=(1/4)(3\sigma^2+2\cos2\alpha)\,,\qquad \bar{p}_{13}=q_{13}=(1/2)\sin2\alpha\,,\qquad \bar{q}_{13}=-(1/4)(\sigma^2+2\cos2\alpha)\,,\\
&p_{03}=(1/24)[3s(6\sigma^4+12\sigma^2-2+4\cos2\alpha)+\sigma^6-9\sigma^4-9\sigma^2+1-2(\sigma^6+1)\cos2\alpha]\cos\alpha\,,\\
&\bar{p}_{03}=(1/24)[3s(2\sigma^4+4\sigma^2+2+4\cos2\alpha)-\sigma^6-9\sigma^4+9\sigma^2+1-2(\sigma^6-1)\cos2\alpha]\sin\alpha\,,\\
&q_{03}=-(1/24)[3s(6\sigma^4-12\sigma^2-2-4\cos2\alpha)-\sigma^6-9\sigma^4+9\sigma^2+1-2(\sigma^6-1)\cos2\alpha]\sin\alpha\,,\\
&\bar{q}_{03}=(1/24)[3s(2\sigma^4-4\sigma^2+2-4\cos2\alpha)+\sigma^6-9\sigma^4-9\sigma^2+1-2(\sigma^6+1)\cos2\alpha]\cos\alpha\,,\\
&p_{02}=(1/4)[4s(2\sigma^2+\cos2\alpha)-4\sigma^2-(\sigma^4+1)\cos2\alpha]\,,\\
&\bar{p}_{02}=(1/4)[4s-\sigma^4+1]\sin2\alpha\,,\\
&q_{02}=(1/4)[4s+\sigma^4-1]\sin2\alpha\,,\\
&\bar{q}_{02}=-(1/4)[4s\cos2\alpha+4\sigma^2+(\sigma^4+1)\cos2\alpha]\,.
\end{aligned}$$

References

1) W. J. Harrison: Trans. Cambr. Phil. Soc. **23** (1924) 71.

2) S. Tomotika and T. Aoi: Quart. J. Mech. a. Appl. Math. **6** (1953).

3) D. Meksyn: Proc. Roy. Soc. **A 162** (1937) 232.

4) T. Lewis: Quart. J. Math. **9** (1938) 21.

5) R. V. Southwell and H. B. Squire: Phil. Trans. **A 232** (1934) 27.

6) I. Imai: to be published.

7) L. N. G. Filon: Proc. Roy. Soc. **A 113** (1926) 7.

8) Whittaker and Watson: Modern Analysis 4th ed. 411.

9) N. W. McLachlan: Theory and Application of Mathieu Functions (1947) 248.

10) T. Aoi: to be published.

11) S. Tomotika and H. Yosinobu: Mem. Coll. Sci. Univ. Kyoto **27** (1953).

Journal of the Physical Society of Japan Vol. 8, No. 5, Sep.—Oct., 1953

On the Propagation and Structure of the Blast Wave, I

By Akira Sakurai

Tokyo Electrical Engineering College

(Received April 24, 1953)

Concerning blast waves with front surfaces of plane, cylindrical and spherical shape, the propagation velocity U and the distribution of hydrodynamical quantities are discussed. The solutions are constructed in the form of power series in $(C/U)^2$, where C is the sound velocity of undisturbed fluid. Especially R, the distance of shock front from the charge, is represented as,

$$\left(\frac{C}{U}\right)^2\left(\frac{R_0}{R}\right)^{\alpha+1}=J_0\left[1+\lambda_1\left(\frac{C}{U}\right)^2+\frac{1}{2}\lambda_2\left(\frac{C}{U}\right)^4+\cdots\cdots\right],$$

where R_0 is the characteristic length related to the energy of explosion, J_0 and λ_i are constants, and $\alpha=0,1,2$ correspond to plane, cylindrical and spherical case, respectively. In this paper the first approximations for $\alpha=0,1$ are discussed (The case $\alpha=2$ has been discussed by G. I. Taylor). The solution is obtained numerically for the case of the adiabatic index $\gamma=1.4$. The approximate solution is also considered. Using these solutions, J_0 is found to be:

α \ γ	1.2	1.3	1.4	1.667
0	3.02	2.15	1.70	1.14
1	1.55	1.10	0.88	0.59

The second approximation will appear in part II to be published subsequently.

§ 1. Introduction

In this paper we shall deal with the blast waves of plane, cylindrical and spherical front surfaces with particular consideration of the propagation velocity of their front and the distribution of hydrodynamical quantities in them.

Immediately after the explosion, the front of the blast wave is surrounded by the surfaces of the shock wave. This shock front propagates with decreasing velocity, so that the distribution of hydrodynamical quantities behind the front is continuously changing in form. Of course, the decrease of the velocity of shock front occurs also in the case of plane waves owing to dissipation effect of shock waves which is related to the increase of entropy of fluid elements passed by the shock wave. Therefore, we must treat the flow with variable entropy bounded by the shock wave, although the viscosity and thermal conductivity are assumed to be negligible in the flow behind the shock front.

When the velocity of front is almost constant or is not so large as the velocity of sound, the change in entropy is negligible. For such cases, various investigations have appeared concerning the waves of finite amplitude. (See bibliographies in references[1,2])

But in the blast wave, especially in the neighbourhood of the charge, we must consider the change in entropy. Kirkwood and Brinkley[3,4] established a differential equation to find the change of the peak pressure at the shock front, introducing a semiemprical formula for the energy equation. This theory is applicable to either gas or liquid but gives little information about the structure of blast wave. In the spherical case, Guderley[5] found a particular set of solutions with some parameters. In these solutions, the only interesting case which satisfies the boundary condition of our present problem is the same as the solution which has been found by Taylor[6]. This solution corresponds to the approximation valid for the case when the velocity of shock front is so large that the ratio $(c/U)^2$ can be neglected, where c and U are the velocity of sound and shock front respectively.

In this paper, we construct the solution in the form of a power series in $(c/U)^2$ so as to imply Taylor's solution as the first approximation for the case of spherical wave. § 2, § 3 deal with a fundamental system of equations and the similarity principle and in § 4 is presented the solution in the form of power series in $(c/U)^2$ while § 5 gives its first approximation which corresponds to Taylor's solution.

In part II to be published subsequently, we shall treat the second approximation and compare the results with available experimental data.

§ 2. Fundamental Equations

In the interior of the blast wave, we have the following equations under the assumption that the change in the state of each element of fluid is adiabatic with the exponent γ

$$\frac{Du}{Dt}=-\frac{1}{\rho}\frac{\partial p}{\partial r}\,, \tag{1}$$

$$\frac{D\rho}{Dt}=-\rho\left(\frac{\partial u}{\partial r}+\frac{\alpha u}{r}\right), \tag{2}$$

$$\frac{Dp\rho^{-\gamma}}{Dt}=0\,, \tag{3}$$

where u is the particle velocity, p is the pressure, ρ is the density, t is the position of the fluid element. The coefficient α takes on the values,

$\alpha=0$ for a plane wave,
$\alpha=1$ for a cylindrical wave,
$\alpha=2$ for a spherical wave,

and the expression D/Dt denotes

$$\frac{D}{Dt}=\frac{\partial}{\partial t}+u\frac{\partial}{\partial r}\,.$$

Using the equation (2), the equation (3) transforms into

$$\frac{Dp}{Dt}=-\gamma p\left(\frac{\partial u}{\partial r}+\frac{\alpha u}{r}\right). \tag{4}$$

If the position of the shock front is given by R as a function of time t, the propagation velocity of the shock front U is given by

$$\frac{dR}{dt}=U\,.$$

At the shock front $(r=R)$, we have the Rankine-Hugoniot conditions,

$$\left.\begin{aligned}
(u)_{r=R}&=\frac{2}{\gamma+1}\,\frac{U^2-C^2}{U}\,,\\
(p)_{r=R}&=p_0\left\{\frac{2\gamma}{\gamma+1}\left(\frac{U}{C}\right)^2-\frac{\gamma-1}{\gamma+1}\right\},\\
(\rho)_{r=R}&=\rho_0\frac{\gamma+1}{\gamma-1}\Big/\left\{\frac{2}{\gamma-1}\left(\frac{C}{U}\right)^2+1\right\},
\end{aligned}\right\} \tag{5}$$

where p_0 and ρ_0 are respectively the pressure and density of the undisturbed atomsphere and C is the sound velocity which is equal to $(\gamma p_0/\rho_0)^{1/2}$.

The energy carried by the blast wave is equal to the energy supplied by the explosive and thus remains constant. Therefore we have

$$E_\alpha=\int_0^R\left\{\frac{1}{2}u^2+\frac{1}{\gamma-1}\left(\frac{p}{\rho}-\frac{p_0}{\rho_0}\right)\right\}\rho r^\alpha dr\,,$$
$$\alpha=0,\ 1,\ 2,$$

where the constant E_α expresses the explosion energy per unit area of the surface of the shock front when R equals unity. Considering the relation

$$\int_0^R\frac{\rho}{\rho_0}r^\alpha dr=\frac{R^{\alpha+1}}{\alpha+1}\,,$$

which results from the Lagrangian equation of continuity, the above equation transforms into

$$E_\alpha=\int_0^R\left(\frac{1}{2}\rho u^2+\frac{1}{\gamma-1}p\right)r^\alpha dr-\frac{p_0}{\gamma-1}\,\frac{R^{\alpha+1}}{\alpha+1}\,. \tag{6}$$

To determine u, p, ρ as functions of r and t, and R as function of t only, we shall use the system of four equations (1), (2), (4), (6) and the system of boundary conditions (5).

§ 3. Transformation of the Fundamental Equations
The Principle of Similarity

In place of r, t, we introduce new independent variables x, y defind by

$$r/R=x\,,\quad (C/U)^2=y\,, \tag{7}$$

and express the quantities u, p, ρ in the following form:

$$\left.\begin{aligned}
u&=U\cdot f(x,y)\,,\\
p&=p_0(U/C)^2\,g(x,y)=p_0\,g(x,y)/y\,,\\
\rho&=\rho_0\cdot h(x,y)\,,
\end{aligned}\right\} \tag{8}$$

where f, g, h, are non-dimensional new variables. Using (7), (8) we have

$$\left.\begin{aligned}
\frac{\partial}{\partial r}&=\frac{1}{R}\cdot\frac{\partial}{\partial x}\,,\\
\frac{D}{Dt}&=\frac{U}{R}\left\{(f-x)\frac{\partial}{\partial x}+\lambda y\frac{\partial}{\partial y}\right\},
\end{aligned}\right\} \tag{9}$$

where $\lambda = R(dy/dR)/y$ and λ is a function of y only.

We substitute (7), (8), (9) into the fundamental equations (1), (2), (4), (6) and boundary conditions (5). Then (1), (2), (4) become

$$\left.\begin{aligned}
&h\left\{-\frac{1}{2}\lambda f+(f-x)\frac{\partial f}{\partial x}+\lambda y\frac{\partial f}{\partial y}\right\}=-\frac{1}{\gamma}\frac{\partial g}{\partial x},\\
&(f-x)\frac{\partial h}{\partial x}+\lambda y\frac{\partial h}{\partial y}=-h\left(\frac{\partial f}{\partial x}+\frac{\alpha f}{x}\right),\\
&-\lambda g+(f-x)\frac{\partial g}{\partial x}+\lambda y\frac{\partial g}{\partial y}=-\gamma g\left(\frac{\partial f}{\partial x}+\frac{\alpha f}{x}\right),
\end{aligned}\right\} \tag{10}$$

(6) gives

$$y\left(\frac{R_0}{R}\right)^{\alpha+1}=\int_0^1\left(\frac{\gamma}{2}hf^2+\frac{1}{\gamma-1}g\right)\times x^\alpha dx-\frac{y}{(\alpha+1)(\gamma-1)}, \tag{11}$$

where

$$R_0=(E_\alpha/p_0)^{1/(\alpha+1)}. \tag{12}$$

Also, (5) become

$$\left.\begin{aligned}
&f(1,y)=\{2/(\gamma+1)\}(1-y),\\
&g(1,y)=2\gamma/(\gamma+1)-\{(\gamma+1)/(\gamma-1)\}y,\\
&h(1,y)=\{(\gamma+1)/(\gamma-1)\}/\{1+(2/(\gamma-1))\cdot y\}.
\end{aligned}\right\} \tag{13}$$

To find the expression for λ we differentiate the equation (11) with respect to y and put,

$$\int_0^1\left(\frac{\gamma}{2}h\,f^2+\frac{g}{\gamma-1}\right)x^\alpha dx=J. \tag{14}$$

Thus

$$\lambda=\frac{(\alpha+1)J-y/(\gamma-1)}{J-y(dJ/dy)}, \tag{15}$$

The similarity principle for the explosion phenomena[2] is clearly represented in the above non-dimensional form of the fundamental system of equations, especially in the expression (12).

§ 4. Construction of Solutions in Power Series of y

While the shock waves are strong, the velocity U is large compared with C and y is considered to be small there, so that the quantities f, g, h, can be expanded in rapidly convergent series of powers of y such as,

$$\left.\begin{aligned}
&f=f^{(0)}+yf^{(1)}+y^2f^{(2)}+\dots\dots,\\
&g=g^{(0)}+yg^{(1)}+y^2g^{(2)}+\dots\dots,\\
&h=h^{(0)}+yh^{(1)}+y^2h^{(2)}+\dots\dots,
\end{aligned}\right\} \tag{16}$$

where $f^{(i)}$, $g^{(i)}$, $h^{(i)}$ $(i=0,\ 1,\ 2,\ \dots\dots)$ are all functions of x only.

Inserting (16) in the expression (14), we have

$$J=J_0(1+\sigma_1y+\sigma_2y^2+\dots\dots), \tag{17}$$

where,

$$\left.\begin{aligned}
&J_0=\int_0^1\left(\frac{\gamma}{2}h^{(0)}f^{(0)2}+\frac{1}{\gamma-1}g^{(0)}\right)x^\alpha dx,\\
&\sigma_1J_0=\int_0^1\left(\gamma f^{(0)}h^{(0)}f^{(1)}+\frac{\gamma}{2}f^{(0)2}h^{(1)}+\frac{1}{\gamma-1}g^{(1)}\right)x^\alpha dx,\\
&\sigma_2J_0=\int_0^1\left(\gamma f^{(0)}h^{(0)}f^{(2)}+\frac{\gamma}{2}f^{(0)2}h^{(2)}+\frac{1}{\gamma-1}g^{(2)}\right)x^\alpha dx+\frac{\gamma}{2}\int_0^1(h^{(0)}f^{(1)2}+2h^{(1)}f^{(1)}f^{(0)})x^\alpha dx,\\
&\dots\dots\dots\dots\dots\dots\dots\dots\dots\dots\dots\dots
\end{aligned}\right\} \tag{18}$$

Using (17) the equation (11) becomes

$$y\left(\frac{R_0}{R}\right)^{\alpha+1}=J_0\left[1+\left\{\sigma_1-\frac{1}{J_0(\alpha+1)(\gamma-1)}\right\}y+\sigma_2y^2+\dots\dots\right], \tag{19}$$

or in view of (7),

$$\left(\frac{C}{U}\right)^2\left(\frac{R_0}{R}\right)^{\alpha+1}=J_0\left[1+\left\{\sigma_1-\frac{1}{J_0(\alpha+1)(\gamma-1)}\right\}\left(\frac{C}{U}\right)^2+\sigma_2\left(\frac{C}{U}\right)^4+\dots\dots\right]. \tag{20}$$

This is the equation in the form of power series in $(C/U)^2$ which gives the relation between the propagation velocity U and the position of shock front R, if we know the quantities J_0, σ_i.

λ is also expanded by (15) and (17) as

$$\lambda=(\alpha+1)\left[1+\left\{\sigma_1-\frac{1}{J_0(\alpha+1)(\gamma-1)}\right\}y+2\sigma_2y^2+\dots\dots\right]. \tag{21}$$

If we use, for simplicity, the expressions

$$\left.\begin{aligned} \sigma_1-\frac{1}{J_0(\alpha+1)(\gamma-1)}&=\lambda_1\,, \\ 2\sigma_2 \qquad\qquad &=\lambda_2\,, \\ \cdots\cdots\cdots\cdots&\cdots, \end{aligned}\right\} \tag{22}$$

the equation (21) becomes

$$\lambda=(\alpha+1)(1+\lambda_1 y+\lambda_2 y^2+\ldots\ldots\ ). \tag{23}$$

Now, substituting (16) and (23) in (10) and comparing the coefficients of the same powers of y on both sides of (10) we get the following system of equations:
For zeroth power of y,

$$\left.\begin{aligned} (f^{(0)}-x)h^{(0)}f_x^{(0)}+g_x^{(0)}/\gamma&=(\alpha+1)f^{(0)}h^{(0)}/2\,, \\ h^{(0)}f_x^{(0)}+(f^{(0)}-x)h_x^{(0)}&=-\alpha f^{(0)}h^{(0)}/x \\ \gamma g^{(0)}f_x^{(0)}+(f^{(0)}-x)g_x^{(0)}&=g^{(0)}(\alpha+1-\alpha\gamma f^{(0)}/x)\,. \end{aligned}\right\} \tag{24}$$

For the first power of y,

$$\left.\begin{aligned} h^{(0)}(f^{(0)}-x)f_x^{(1)}+g_x^{(1)}/\gamma&=-\{(\alpha+1)/2+f_x^{(0)}\}h^{(0)}f^{(1)} \\ &\quad+\{(\alpha+1)f^{(0)}/2+(x-f^{(0)})f_x^{(0)}\}h^{(1)}+(\alpha+1)\lambda_1 f^{(0)}h^{(0)}/2\,, \\ h^{(0)}f_x^{(1)}+(f^{(0)}-x)h_x^{(1)}&=-(h_x^{(0)}+\alpha h^{(0)}/x)f^{(1)}-(f_x^{(0)}+\alpha f^{(0)}/x+\alpha+1)h^{(1)}\,, \\ \gamma g^{(0)}f_x^{(1)}+(f^{(0)}-x)g_x^{(1)}&=-(g_x^{(0)}+\alpha\gamma g^{(0)}/x)f^{(1)}-\gamma(f_x^{(0)}+\alpha f^{(0)}/x)g^{(1)}+(\alpha+1)\lambda_1 g^{(0)}\,. \end{aligned}\right\} \tag{25}$$

Substituting (16) into (13), we have, in a similar manner,

$$f^{(0)}(1)=\frac{2}{\gamma+1}\,,\qquad g^{(0)}(1)=\frac{2\gamma}{\gamma+1}\,,\qquad h^{(0)}(1)=\frac{\gamma+1}{\gamma-1}\,; \tag{26}$$

$$f^{(1)}(1)=-\frac{2}{\gamma+1}\,,\qquad g^{(1)}(1)=-\frac{\gamma-1}{\gamma+1}\,,\qquad h^{(1)}(1)=-\frac{2(\gamma+1)}{(\gamma-1)^2}\,; \tag{27}$$

$$\cdots\cdots\cdots\cdots\cdots\cdots\cdots\cdots\cdots\cdots\cdots\cdots$$

The first step of the solution of the problem is then to solve the system of non-linear equations (24) about $f^{(0)}$, $g^{(0)}$, $h^{(0)}$ with the boundary conditions (26) and insert this solution to the first equation of (18). Then we have the first approximation to the structure and velocity of the blast wave in the forms

$$\begin{aligned} &u=Uf^{(0)}(x)\,,\quad p=p_0(U/C)^2g^{(0)}(x)\,, \\ &\rho=\rho_0 h^{(0)}(x)\,,\quad (C/U)^2(R_0/R)^{\alpha+1}=J_0\,. \end{aligned} \tag{28}$$

For $\alpha=2$, this step is nothing other than the case of Taylor's theory and the above equations are the same as Taylor's except for the difference in symbols.

The second step is somewhat complicated. Substituting the first approximations $f^{(0)}$, $g^{(0)}$, $h^{(0)}$ in the equation (25), we have a system of linear inhomogeneous differential equations. But these equations involve an undetermined parameter λ_1 which is related to σ_1 by the relation (22). The solutions $f^{(1)}$, $g^{(1)}$, $h^{(1)}$ to be obtained then include λ_1 in a linear form. Inserting these solutions to the right side of the second equation of (18), we have an equation to determine λ_1. Using this λ_1, $f^{(1)}$, $g^{(1)}$, $h^{(1)}$ are determined finally. This fact presents inconvenience in solving the equations by a numerical method. At any rate, in this step, we have the second approximation to the structure and velocity of the blast wave in the forms,

$$\left.\begin{aligned} u&=U[f^{(0)}+(C/U)^2f^{(1)}+O((C/U)^4)]\,, \\ p&=p_0(U/C)^2[g^{(0)}+(C/U)^2g^{(1)}+O((C/U)^4)]\,, \\ \rho&=\rho_0[h^{(0)}+(C/U)^2h^{(1)}+O((c/U)^4)]\,, \\ (C/U)^2(R_0/R)^{\alpha+1}&=J_0[1+\lambda_1(C/U)^2+O((C/U)^4)]. \end{aligned}\right\} \tag{29}$$

The procedure of the third and the following steps are the same in principle as the second step.

§ 5. The First Approximation

The equations (24) are written in the forms,

$$(f^{(0)}-x)h^{(0)}f_x^{(0)}+g_x^{(0)}/\gamma=(\alpha+1)f^{(0)}h^{(0)}/2\,, \tag{30}$$

$$h_x^{(0)}/h^{(0)}=(f_x^{(0)}+\alpha f^{(0)}/x)/(x-f^{(0)})\,, \tag{31}$$

$$g_x^{(0)}/g^{(0)}=(\gamma f_x^{(0)}+\alpha\gamma f^{(0)}/x-\alpha-1)/(x-f^{(0)})\,, \tag{32}$$

By (32), (30) is transformed into,

$$f_x^{(0)}=\frac{(\alpha+1)/\gamma-\alpha f^{(0)}/x+(\alpha+1)h^{(0)}(x-f^{(0)})f^{(0)}/2g^{(0)}}{1-h^{(0)}(x-f^{(0)})^2/g^{(0)}}\,, \tag{33}$$

For the case $\alpha=2$, Taylor solved equations (31)—(33) with boundary conditions (26), first numerically, and then using the knowledge of this solution he found the approximate solution. For the cases $\alpha=0$ and 1 we shall follow his method. But it will be worth while to notice that the equations (31) and (32) have an intermediate integral. The operation $(\gamma-1)\times(31)$—(32) gives,

$$(\gamma-1)h_x^{(0)}/h^{(0)}-g_x^{(0)}/g^{(0)}=(1-f_x^{(0)})/(x-f^{(0)})+\alpha/x\,.$$

Integrating this equation and inserting the condition (26) to determine the integration constant, we have a relation,*

$$g^{(0)}(x-f^{(0)})h^{(0)-(\gamma-1)}x^{\alpha}=\{2\gamma/(\gamma+1)\}\{(\gamma-1)/(\gamma+1)\}^{\gamma}\,. \tag{34}$$

By (34), we can reduce the three equations (31)—(33) and boundary conditions (26) to the following two equations:

$$f_x^{(0)}=\left(\frac{\alpha+1}{\gamma}-\frac{\alpha f^{(0)}}{x}+\frac{\alpha+1}{2}Df^{(0)}\right)\Big/\{1-(x-f^{(0)})D\}\,, \tag{35}$$

$$\frac{D_x}{D}=\left\{\alpha+2-\gamma f_x^{(0)}-\frac{\alpha(\gamma-1)}{x}f^{(0)}\right\}\Big/(x-f^{(0)})\,, \tag{36}$$

and boundary conditions.

$$f^{(0)}(1)=2/(\gamma+1)\,,\quad D(1)=(\gamma+1)/2\gamma\,, \tag{37}$$

where

$$D=h^{(0)}(x-f^{(0)})/g^{(0)}\,. \tag{38}$$

For $\gamma=1.4$, (35) and (36) were integrated numerically with the initial value (37). This was done by the Runge-Kutta method in intervals from $x=1$ to $x=0.92$ for $\alpha=0$ and $x=0.88$ for $\alpha=1$, taking the interval of one step of numerical integration as 0.02 in both cases. In the remaining part of intervals, the Levy method was applied where the interval of one step was also 0.02 until $x=0.4$ for $\alpha=0$ and $x=0.6$ for $\alpha=1$ and then it was taken as 0.1 until $x=0$ for $\alpha=0$ and $x=0.4$ for $\alpha=1$. Using the values of $f^{(0)}$ and $f_x^{(0)}$ obtained from the above mentioned procedure, $g^{(0)}$ and $h^{(0)}$ were found by numerical integrations of the relations (31) and (32). These results are shown in Table I for $\alpha=0$ and in Table II for $\alpha=1$ and plotted in Fig. 1, where the results for the case $\alpha=2$ reproduced from Taylor's paper are also presented.

Now we constract approximate solutions as Taylor has done. That is, the solution of $f^{(0)}$ is assumed to be of the form,

$$f^{(0)}=x/\gamma+Ax^n\,, \tag{39}$$

and the constants A and n are determined by the values of $f^{(0)}$ and $f_x^{(0)}$ at $x=1$ which are given by the boundary condition (26) and the equation (33) for $f_x^{(0)}$. Thus we have,

$$A=\frac{1}{\gamma}\frac{\gamma-1}{\gamma+1}\,,\qquad n=\frac{(2-\alpha)\gamma^2+(3\alpha+1)\gamma-1}{\gamma^2-1}\,, \tag{40}$$

from the values

$$f^{(0)}(1)=\frac{2}{\gamma+1}\,,\qquad f_x^{(0)}=\frac{(3-\alpha)\gamma+3(\alpha+1)}{(\gamma+1)^2}\,.$$

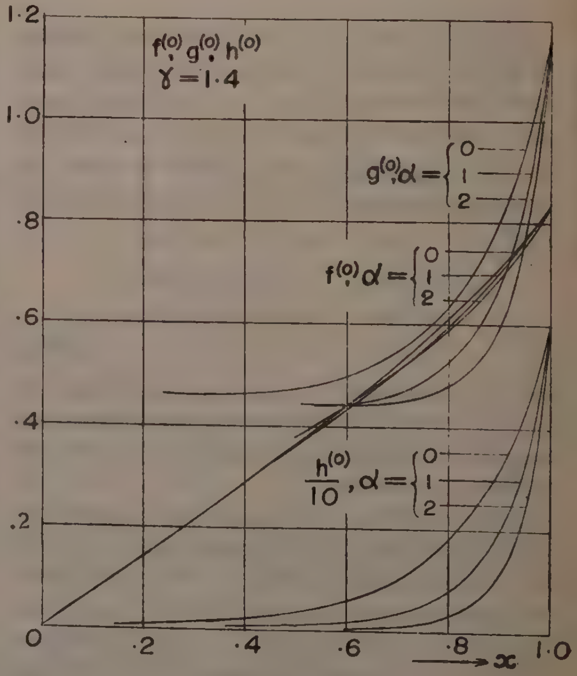

Fig. 1.

---

* In the case of equations (25) for the second approximation there also exists an intermediate integral somewhat similar to (34).

Table I.

Calculations for $\gamma=1.4$, $\alpha=0$: numerical and approximate solutions.

	numerical			approximate		
x	$f^{(0)}$	$g^{(0)}$	$h^{(0)}$	$f^{(0)}$	$g^{(0)}$	$h^{(0)}$
1.00	0.8333	1.167	6.000	0.8333	1.167	6.000
0.98	0.8086	1.070	5.183	0.8087	1.071	5.186
0.96	0.7844	0.987	4.508	0.7848	0.991	4.518
0.94	0.7607	0.917	3.945	0.7616	0.923	3.961
0.92	0.7376	0.856	3.472	0.7390	0.865	3.494
0.90	0.7151	0.804	3.071	0.7170	0.815	3.096
0.88	0.6931	0.756	2.729	—	—	—
0.86	0.6717	0.720	2.435	—	—	—
0.84	0.6509	0.686	2.181	—	—	—
0.82	0.6307	0.656	1.960	—	—	—
0.80	0.6110	0.631	1.766	0.6151	0.647	1.785
0.78	0.5917	0.608	1.595	—	—	—
0.76	0.5730	0.588	1.443	—	—	—
0.74	0.5547	0.571	1.308	—	—	—
0.72	0.5369	0.555	1.187	—	—	—
0.70	0.5194	0.542	1.079	0.5239	0.556	1.080
0.68	0.5023	0.530	0.980	—	—	—
0.66	0.4855	0.520	0.891	—	—	—
0.64	0.4691	0.511	0.811	—	—	—
0.62	0.4529	0.503	0.736	—	—	—
0.60	0.4370	0.496	0.669	0.4405	0.504	0.658
0.58	0.4213	0.490	0.607	—	—	—
0.56	0.4058	0.484	0.549	—	—	—
0.54	0.3904	0.480	0.497	—	—	—
0.52	0.3753	0.476	0.448	—	—	—
0.50	0.3602	0.472	0.403	0.3624	0.473	0.389
0.48	0.3453	0.469	0.362	—	—	—
0.46	0.3305	0.467	0.323	—	—	—
0.44	0.3158	0.465	0.288	—	—	—
0.42	0.3012	0.463	0.255	—	—	—
0.40	0.2866	0.461	0.225	0.2877	0.456	0.214
0.30	0.215	0.456	0.107	0.2148	0.447	0.102
0.20	0.143	0.455	0.039	0.1430	0.443	0.037
0.10	0.072	0.455	0.006	0.0714	0.442	0.006
0.00	0.000	0.455	0.000	0.0000	0.442	0.000

If we substitute (39) with the values (40) into (31) and (32) these equations can easily be integrated to give,

$$g^{(0)}=\frac{2\gamma}{\gamma+1}\left(\frac{\gamma+1-x^{n-1}}{\gamma}\right)^{-\frac{2\gamma^2+(3\alpha+1)\gamma-(\alpha+1)}{(1-\alpha)\gamma+3\alpha+1}}, \tag{41}$$

$$h^{(0)}=\frac{\gamma+1}{\gamma-1}x^{\frac{\alpha+1}{\gamma-1}}\left(\frac{\gamma+1-x^{n-1}}{\gamma}\right)^{-\frac{2(2\alpha+1+\gamma)}{(1-\alpha)\gamma+3\alpha+1}}, \tag{42}$$

where we have used the boundary condition (26) to determine the integration constants.

Table II.

Calculations for $\gamma=1.4$, $\alpha=1$: numerical and approximate solutions.

	numerical			approximate		
x	$f^{(0)}$	$g^{(0)}$	$h^{(0)}$	$f^{(0)}$	$g^{(0)}$	$h^{(0)}$
1.00	0.8333	1.167	6.000	0.8333	1.167	6.000
0.98	0.8035	1.009	4.578	0.8037	1.011	4.584
0.96	0.7750	0.890	3.575	0.7758	0.895	3.590
0.94	0.7479	0.799	2.845	0.7494	0.807	2.862
0.92	0.7223	0.728	2.300	0.7245	0.739	2.317
0.90	0.6980	0.673	1.884	0.7008	0.685	1.898
0.88	0.6749	0.629	1.560	0.6783	0.641	1.570
0.86	0.6531	0.593	1.303	0.6568	0.605	1.309
0.84	0.6322	0.564	1.095	0.6362	0.576	1.098
0.82	0.6124	0.541	0.926	0.6164	0.551	0.925
0.80	0.5934	0.522	0.786	0.5973	0.531	0.783
0.78	0.5751	0·506	0.670	—	—	—
0.76	0.5574	0.493	0.572	—	—	—
0.74	0.5404	0.482	0.488	—	—	—
0.72	0.5238	0.474	0.417	—	—	—
0.70	0.5076	0.466	0.356	0.5104	0.468	0.347
0.68	0.4917	0.460	0.304	—	—	—
0.66	0.4762	0.455	0.258	—	—	—
0.64	0.4608	0.451	0.219	—	—	—
0.62	0.4457	0.448	0.186	—	—	—
0.60	0.4308	0.445	0.157	0.4322	0.441	0.153
0.50	0.360	0.438	0.061	0.3582	0.429	0.058
0.40	0.288	0.435	0.019	0.2859	0.425	0.019
0.30	—	—	—	0.2143	0.424	0.005
0.20	—	—	—	0.1429	0.424	0.001
0.10	—	—	—	0.0714	0.424	0.000
0.00	—	—	—	0.0000	0.424	0.000

Table III

γ \ α	0	1	2 (Taylor)
1.2	3.024	1.547	1.031
1.3	2.147	1.102	0.755
1.4	1.696 (1.701)	0.877 (0.880)	0.596
1.667	1.137	0.585	0.404

Taking $\gamma=1.2$, 1.3, 1.4, 1.667, values of $f^{(0)}$, $g^{(0)}$, $h^{(0)}$ for $\alpha=0$, 1 were calculated from the above approximate solutions (39), (41), (42). To compare them with the numerical solutions, values for the case $\gamma=1.4$ are presented in Table I and II. There are comparatively good agreement between them as in the case $\alpha=2$. For the cases $\gamma=1.2$, 1.3, 1.667, only graphs of the values are plotted in Figs. 2–7.

Using the above values of $f^{(0)}$, $g^{(0)}$, $h^{(0)}$, the values of J_0 given by the integral (18) are calculated numerically and shown in Table III and plotted in Fig. 8 where the case $\alpha=2$ is also presented.

The numbers in the brackets for the $\gamma=1.4$ represent the values obtained from the approximate solution.

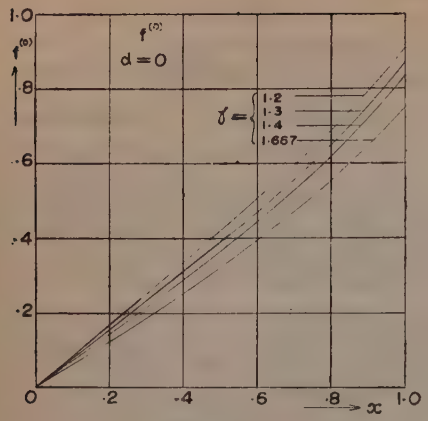

Fig. 2.

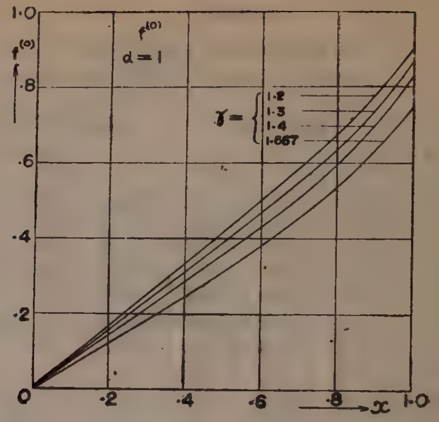

Fig. 3.

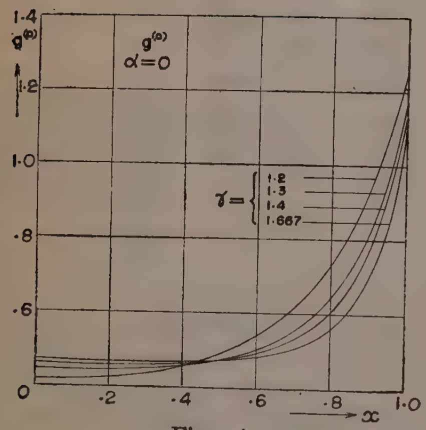

Fig. 4.

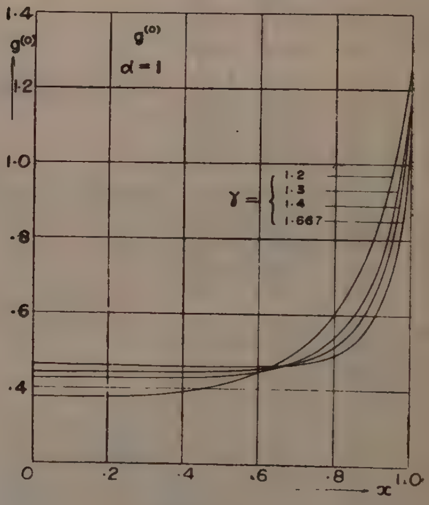

Fig. 5.

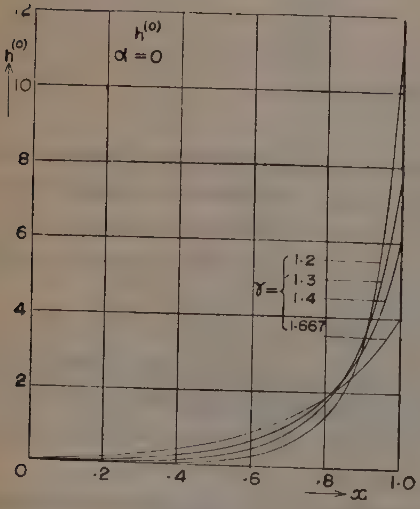

Fig. 6.

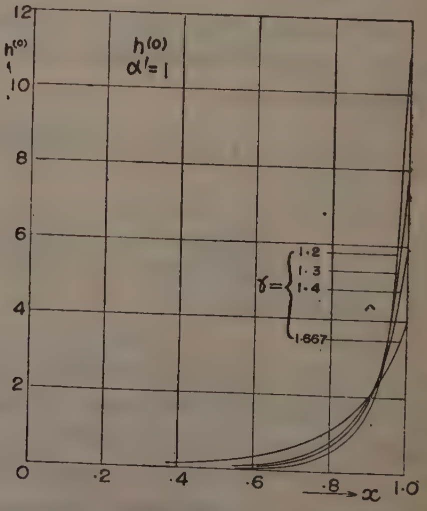

Fig. 7.

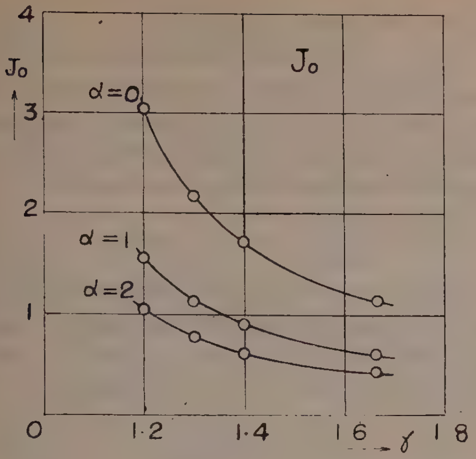

Fig. 8.

In conclusion the author wishes to express his gratitude to Professor I. Imai for his guidance and encouragement and to Dr. T. Murata for giving valuable discussions.

References

1) Courant-Friedrichs: Supersonic flow and shock waves (1948).
2) R. H. Cole: Underwater explosions (1948).
3) J. G. Kirkwood and S. R. Brinkley: Phys. Rev. **71** (1947) 606.
4) J. G. Kirkwood and S. R. Brinkley: Phys. Rev. **72** (1947) 1107.
5) G. Guderley: Luftfahrtforschung, 19, No. 9.
6) G. I. Taylor: Proc. Roy. Soc. London, **A 201** (1950) 159.

JOURNAL OF THE PHYSICAL SOCIETY OF JAPAN Vol. 8, No. 5, SEP.—OCT., 1953

On the Definition of Stress in the Finite Deformation Theory[*]

By Yoshimaru YOSHIMURA

Institute of Science and Technology, University of Tokyo

(Received November 21, 1952)

In the present paper, three kinds of stresses, i.e. the stress tensor, the true and nominal stress in the finite deformation theory being considered, taking orthogonal curvilinear coordinates as the independent variables, the interrelations of each stress are obtained. The equilibrium equations corresponding to each definition of stress are given in the form convenient to the statical and dynamical problems respectively. The tensorial equation is more simple formally, but not so substancially.

§ 1. Introduction

In the theory of finite deformation for elastic or plastic solids, strain and stress can not be defined uniquely. There exist many theories[1] according to their different definitions. Especially in the plastic body, the matter is more complicated because of the necessity of taking the strain path into consideration. It may be said to be attributed to the way of treating of stress and strain that many theories existing at present is not satisfactory for the practical utility, although they are all reasonable theoretically. Moreover, whatever kind of stress may be used in the theory, its relation with the actual stress, which is the basis of the experimental stress-strain law, must be known to us.

The present paper, as a preliminary study concerning this problem, deals with some kinds of strees, defined reasonably in the Lagrangean method, and their interrelations, and furthermore derives the equilibrium equations, corresponding to these definitions of stress, in curvilinear coordinates system.

§ 2. Definition of Stress

According to the Lagrangean method, we suppose that the coordinates (curvilinear coordinate in general) are fixed to every material point under deformation. Therefore, assuming that the material point which is at $\boldsymbol{r}^0(\boldsymbol{u}^i)$, when in the unstrained state, is displaced to the position $\boldsymbol{r}(\boldsymbol{u}^i)$ by the deformation, the base vectors in the unstrained and strained state are given by

---

[*] Presented to the Eighth International Congress on Theoretical and Applied Mechanics, Istanbul, 1952.

$$g_i^0=\frac{\partial r^0}{\partial u^i}\,, \qquad g_i=\frac{\partial r}{\partial u^i}\,, \tag{1}$$

and the metric fundamental tensors by

$$g_{ij}^0=g_i^0\cdot g_j^0\,, \qquad g_{ij}=g_i\cdot g_j \tag{2}$$

respectively. If any curvilinear coordinates orthogonal in the unstrained state are used $g_{ij}^0=0$ $(i\neq j)$.

When either the displacement or the coordinates, with respect to any reference frame which may generally be different in the strained and unstrained state, is given, it will be easy to obtain the relation between g_i and g_i^0, and hence to derive the analytical expression of the quantity

$$e_{ij}=g_{ij}-g_{ij}^0$$

which is usually defined as strain. But it may be useless from the practical view point to write out the expression of strain nonlinear regarding displacement.

Denoting the reciprocal systems of g_i^0 and g_i by g_0^i and g^i, we have

$$g_0^i=\frac{g_{i+1}^0\times g_{i+2}^0}{\sqrt{g^0}}\,; \qquad g^i=\frac{g_{i+1}\times g_{i+2}}{\sqrt{g}} \tag{3}$$

in which $i+1$ and $i+2$ represent the values smaller by 3 than themselves, when they exceed 3, and

$$\sqrt{g^0}=[g_1^0g_2^0g_3^0]\,, \qquad \sqrt{g}=[g_1g_2g_3] \tag{4}$$

$$g^0=|g_{ij}^0|\,, \qquad g=|g_{ij}|\,. \tag{5}$$

Then the contravariant components of the metric tensors are given by

$$g_0^{ij}=\frac{G_0^{ij}}{g_0}=g_0^i\cdot g_0^j\,, \quad g^{ij}=\frac{G^{ij}}{g}=g^i\cdot g^j\,, \tag{6}$$

where G_0^{ij}, G^{ij} denote the minor determinants of g^0, g with respect to the elements g_0^{ij}, g^{ij} respectively.

The stress can be defined in different ways according to the magnitude and direction of the surface on which it acts, and to the direction in which it is resolved. But it will be natural to take the direction of the surface coincident with the vector g^i, and the direction of the compoent with g_i. Even when it will be so determined, and yet there remains the freedom of considering, as the stress, the so-called nominal stress, the true stress and the tensorial stress. At first, the stress tensor in the strained state is defined by

$$S=\sum S^{ij}g_ig_j\,, \tag{7}$$

accordingly the stress vector S^i acting on the unit area of the surface of which normal have the direction g^i (or, equivalently, which is parallel to g_{i+1} and g_{i+2}) is given by

$$S^i=\frac{g^i}{\sqrt{g^{ii}}}\cdot S=\sum_j\frac{1}{\sqrt{g^{ii}}}S^{ij}g_j \tag{8}$$

In the next, denoting the true stress vector acting on the unit area of the surface which have the direction g^i by σ^i, and its components on g_j-direction by σ^{ij}, we have

$$\sigma^i=\sum_j\sigma^{ij}\frac{g_j}{\sqrt{g_{jj}}}\,. \tag{9}$$

Since obviously

$$S^i=\sigma^i\,, \tag{10}$$

the relation between stress tensor S^{ij} and true stress is described by the formula

$$S^{ij}=\sqrt{\frac{g^{ii}}{g_{jj}}}\sigma^{ij}\,. \tag{10}$$

It must be remarked that the quantity σ^{ij} is not a tensor, though the tensorial notation is used conveniently.

Since the nominal stress σ_0 is related to unit area in the unstrained state, while the true stress σ to the unit area in the strained state, it follows that

$$\sigma^i|g_{i+1}\times g_{i+2}|du^{i+1}du^{i+2}=\sigma_0^i|g_{i+1}^0\times g_{i+2}^0|du^{i+1}du^{i+2}$$

or

$$\sqrt{gg^{ii}}\sigma^i=\sqrt{g^0g_0^{ii}}\sigma_0^i\,. \tag{11}$$

As we can put

$$\sigma_0^i=\sum_j\sigma_0^{ij}\frac{g_j}{\sqrt{g_{jj}}}\,, \tag{12}$$

the same relation as Eq. (11)

$$\sqrt{gg^{ii}}\sigma^{ij}=\sqrt{g^0g_0^{ii}}\sigma_0^{ij}\,, \tag{13}$$

is obtained also as to the components. Consequently its relation with the stress tensor S^{ij} is obtained as

$$S^{ij}=\sqrt{\frac{g^0g_0^{ii}}{gg_{jj}}}\sigma_0^{ij}\,; \tag{14}$$

from Eq. (10).

We can take the tensor density

$$X^{ij}=\sqrt{g}S^{ij}\,, \tag{15}$$

in place of S^{ij}. And in this case, it follows that

$$X^{ij}=\sqrt{\frac{gg^{ii}}{g_{jj}}}\sigma^{ij}=\sqrt{\frac{g^0g_0^{ii}}{g_{jj}}}\sigma_0^{ij}\,. \tag{16}$$

Denoting the extension of $\boldsymbol{g}_i^0$-axis by ε_i, and the angle between $\boldsymbol{g}_i, \boldsymbol{g}_j$, by γ_{ij}, we have

$$\left.\begin{aligned} g_{ii}&=g_{ii}^0(1+\varepsilon_i)^2 \\ g_{ij}&=\sqrt{g_{ii}^0 g_{jj}^0}(1+\varepsilon_i)(1+\varepsilon_j)\cos\gamma_{ij} \\ G^{ii}&=g^0{}_{i+1,\,i+1}g^0{}_{i+2,\,i+2}(1+\varepsilon_{i+1})^2(1+\varepsilon_{i+2})^2 \\ &\qquad\times\sin^2\gamma_{i+1,\,i+2} \end{aligned}\right\} \tag{17}$$

therefore

$$\left.\begin{aligned} X^{11}&=\sqrt{\frac{g_{22}^0 g_{33}^0}{g_{11}^0}}\,\frac{(1+\varepsilon_2)(1+\varepsilon_3)}{1+\varepsilon_1}\sin\gamma_{23}\sigma^{11} \\ &=\sqrt{\frac{g_{22}^0 g_{33}^0}{g_{11}^0}}\,\frac{\sigma_0^{11}}{1+\varepsilon_1}\,,\cdots \\ X^{12}&=\sqrt{g_{33}^0}\,(1+\varepsilon_3)\sin\gamma_{23}\sigma^{12} \\ &=\frac{\sqrt{g_{33}^0}}{1+\varepsilon_2}\sigma_0^{12},\cdots\cdot \\ X^{21}&=\sqrt{g_{33}^0}\,(1+\varepsilon_3)\sin\gamma_{31}\sigma^{21} \\ &=\frac{\sqrt{g_{33}^0}}{1+\varepsilon_1}\sigma_0^{21},\cdots\cdot \end{aligned}\right\} \tag{18}$$

The relation among X^{ij}, σ^{ij} and σ_0^{ij} and that among X^{ji}, σ^{ji} and σ_0^{ji} is not same in general. X^{ij}, σ_0^{ij} agrees with the difinition of stress by *R.* Kappus in the rectangular Cartesian coordinates.

Since g is expressed in terms of ε's and γ's as

$$\begin{aligned} g=g_{11}^0 g_{22}^0 g_{33}^0&(1+\varepsilon_1)^2(1+\varepsilon_2)^2(1+\varepsilon_3)^2 \\ &\times[1+2\sin\gamma_{12}\sin\gamma_{23}\sin\gamma_{31}-\sin^2\gamma_{23} \\ &-\sin^2\gamma_{31}-\sin^2\gamma_{12}] \end{aligned} \tag{19}$$

the relation between S^{ij} and X^{ij} (Eq. (15)), and consequently the relation among S^{ij}, σ^{ij} and σ_0^{ij} (Eqs. (10) and (14)) is very complicated except when the deformation is equivoluminal.

The expression of the elastic or plastic law varies according as which of the above definitions of stress is used. This problem is not decided unless the strain definition and the experimental stress-strain relation would be treated in a coherent way.

From the equilibrium condition of moment

$$\sum_i[\boldsymbol{g}_i du^i\times\sigma^i\sqrt{g g^{ii}}\,du^{i+1}dn^{i+2}]=0\,,$$

we have

$$\sum_{i,j}\sigma^{ij}\sqrt{\frac{g g^{ii}}{g_{jj}}}[\boldsymbol{g}_i\times\boldsymbol{g}_j]du^1du^2du^3=0\,,$$

therefore

$$\sigma^{ij}\sqrt{\frac{g g^{ii}}{g_{jj}}}-\sigma^{ji}\sqrt{\frac{g g^{jj}}{g_{ii}}}=0\,. \tag{20}$$

or

$$S^{ij}=S^{ji}\,,\qquad X^{ij}=X^{ji}\,. \tag{21}$$

Hence the symmetry relation is satisfied for S^{ij} and X^{ij}, but not for σ^{ij} and σ_0^{ij}. Therefore σ^{ij} is to be considered as the $\boldsymbol{g}_j$-component of the stress vector on the surface parallel to $\boldsymbol{g}^i$ and it must not be permitted to interchange the direction of the surface and that of the component. As we have

$$\sigma^{12}\sin\gamma_{23}=\sigma^{21}\sin\gamma_{31}\,,\cdots\cdot \tag{22}$$

$$\frac{\sigma_0^{12}}{1+\varepsilon_2}=\frac{\sigma_0^{21}}{1+\varepsilon_1}\,,\cdots\cdot \tag{23}$$

form Eq. (17), it follows the symmetry relation

$$\sigma^{12}=\sigma^{21} \tag{22'}$$

for the shearing stress in the case of plane strain, or the mean shearing stress taken over the plate thickness in the case of plane stress.

The above mentioned is about the contravariant component S^{ij}, X^{ij}, and the covariant or mixed component will be treated similarly.

§ 3. Equation of Equilibrium

It is not reasonable to assume vanishing of the divergence of tensor as the equilibrium condition. It prescribes the equilibrium of the stress existing actually in the material. Since the actual stress vector, exerting on the surface u^i of the volume element (u^i, u^i+du^i) in the strained state, is

$$\sigma^i|\boldsymbol{g}_{i+1}\times\boldsymbol{g}_{i+2}|du^{i+1}du^{i+2}$$

and that exerting on the surface u^i+du^i is

$$\begin{aligned} &\sigma^i|\boldsymbol{g}_{i+1}\times\boldsymbol{g}_{i+2}|du^{i+1}du^{i+2}+ \\ &\qquad+\frac{\partial}{\partial u^i}\{\sigma^i|\boldsymbol{g}_{i+1}\times\boldsymbol{g}_{i+2}|du^{i+1}du^{i+2}\}du^i \end{aligned}$$

the equilibrium equation is given by

$$\sum_i\frac{\partial}{\partial u^i}\{\sigma^i|\boldsymbol{g}_{i+1}\times\boldsymbol{g}_{i+2}|\}+\rho\boldsymbol{Z}[\boldsymbol{g}_1\boldsymbol{g}_2\boldsymbol{g}_3]=0\,, \tag{24}$$

or by means of Eqs. (3), (4) and (6), by

$$\sum_i\frac{\partial}{\partial u^i}\{\sigma^i\sqrt{g g^{ii}}\}+\sqrt{g}\,\rho\boldsymbol{Z}=0\,, \tag{24'}$$

where ρ denotes the density in the strained state, $\boldsymbol{Z}$ the sum of the external force per unit mass and the inertia force. Resolving the external force on $\boldsymbol{g}_i$-direction:

$$\boldsymbol{Z}=\sum_i Z^i\frac{\boldsymbol{g}_i}{\sqrt{g^{ii}}}\,. \tag{25}$$

Eq. (24) becomes, by means of (9),

$$\sum_{i,j}\left\{\frac{\partial}{\partial u^i}\left[\sigma^{ij}\sqrt{\frac{gg^{ii}}{g_{jj}}}\boldsymbol{g}_j\right]-\sqrt{g}\,\rho\frac{Z^j}{\sqrt{g_{jj}}}\boldsymbol{g}_j\right\}=0. \tag{26}$$

Accordingly, by virtue of

$$\frac{\partial \boldsymbol{g}_i}{\partial u^j}=\frac{\partial \boldsymbol{g}_j}{\partial u^i}=\Gamma_{ij}{}^k\boldsymbol{g}_k \tag{27}$$

$$\Gamma_{ij}{}^k=\Gamma_{ji}{}^k=\frac{1}{2}\sum_s g^{ks}\left(\frac{\partial g_{si}}{\partial u^j}+\frac{\partial g_{sj}}{\partial u^i}-\frac{\partial g_{ij}}{\partial u^s}\right). \tag{28}$$

Eq. (26) is written in the form

$$\sum_{i,j,k}\boldsymbol{g}_k\left\{\frac{\partial}{\partial u^i}\left[\sigma^{ik}\sqrt{\frac{gg^{ii}}{g_{kk}}}\right]\right.$$
$$\left.+\sigma^{ij}\sqrt{\frac{gg^{ii}}{g_{jj}}}\Gamma_{ij}{}^k+\sqrt{g}\,\rho\frac{Z^k}{\sqrt{g_{kk}}}\right\}=0\,. \tag{29}$$

So that the equilibrium equation with respect to the direction of $\boldsymbol{g}_k$ is given by

$$\sum_{i,j}\left\{\frac{\partial}{\partial u^i}\left[\sigma^{ik}\sqrt{\frac{gg^{ii}}{g_{kk}}}\right]\right.$$
$$\left.+\sigma^{ij}\sqrt{\frac{gg^{ii}}{g_{jj}}}\Gamma_{ij}{}^k+\sqrt{g}\,\rho\frac{Z^k}{\sqrt{g_{kk}}}\right\}=0. \tag{30}$$

As against to the true stress expression of the equilibrium equation (30), the expression by means of the stress tensor is written, by Eq. (10) or (15), as

$$\sum_{i,j}\left\{\frac{\partial(\sqrt{g}\,S^{ik})}{\partial u^i}+\sqrt{g}\,S^{ij}\Gamma_{ij}{}^k\right.$$
$$\left.+\sqrt{g}\,\rho\frac{Z^k}{\sqrt{g_{kk}}}\right\}=0 \tag{31}$$

or

$$\sum_{i,j}\left\{\frac{\partial X^{ik}}{\partial u^i}+X^{ij}\Gamma_{ij}{}^k+\sqrt{g}\,\rho\frac{Z^k}{\sqrt{g^{kk}}}\right\}=0, \tag{32}$$

which expresses the divergence of tensor.

The above equations, which is refered to the $\boldsymbol{g}_i$-direction regarding both the stress and the equilibrium of forces, is much simpler than the equation, which is refered to the $\boldsymbol{g}_i{}^0$-direction about the equilibrium of forces, as was derived formerly by R. Kappus in the case of rectangular Cartesian coordinate system in the unstrained state.

From the formal comparison among Eqs. (30), (31) and (32), it will be supposed that when the stress tensor is used, the equation seems to become simple apparently, only the terms, which exhibit the effect of the curvature change by deformation, being introduced into the equation; while when the true or nominal stress is used, the terms exhibiting the effect of extension and the change of sectional area is introduced (into the equation) besides the curvature change. But it will not be so necessarily, as will be seen from the following example.

Considering, as an example, the plane strain case

$$g_{33}=g_{33}{}^0\ \ (\varepsilon_3=0),\ \ g_{13},\ g_{23}=0\,,$$
$$G^{11}=gg^{11}=g_{22}\,,\quad G^{22}=gg^{22}=g_{11}\,.$$

Equs. (30) and (32) is respectively written as

$$\left.\begin{aligned}
&\frac{\partial\sigma^{11}}{\partial u^1}\sqrt{g_{22}}+\frac{\partial\sigma^{21}}{\partial u^2}\sqrt{g_{11}}+\sigma^{11}\left(\sqrt{g_{22}}\Gamma_{11}{}^1+\sqrt{g_{11}}\frac{\partial}{\partial u^1}\sqrt{\frac{g_{22}}{g_{11}}}\right)\\
&\qquad\qquad+2\sigma^{12}\sqrt{g_{11}}\Gamma_{12}{}^1+\sigma^{22}\frac{g_{11}}{\sqrt{g_{22}}}\Gamma_{22}{}^1+\sqrt{g}\,\rho Z^1=0\\
&\frac{\partial\sigma^{22}}{\partial u^2}\sqrt{g_{11}}+\frac{\partial\sigma^{12}}{\partial u^1}\sqrt{g_{22}}+\sigma^{22}\left(\sqrt{g_{11}}\Gamma_{22}{}^2+\sqrt{g_{22}}\frac{\partial}{\partial u^2}\sqrt{\frac{g_{11}}{g_{22}}}\right)\\
&\qquad\qquad+2\sigma^{12}\sqrt{g_{22}}\,\Gamma_{12}{}^2+\sigma^{22}\frac{g_{22}}{\sqrt{g_{11}}}\Gamma_{11}{}^2+\sqrt{g}\,\rho Z^2=0
\end{aligned}\right\} \tag{33}$$

$$\left.\begin{aligned}
&\frac{\partial X^{11}}{\partial u^1}+\frac{\partial X^{12}}{\partial u^2}+X^{11}\Gamma_{11}{}^1+2X^{12}\Gamma_{12}{}^1+X^{22}\Gamma_{22}{}^1+\rho\sqrt{g_{22}}Z^1=0\\
&\frac{\partial X^{12}}{\partial u^1}+\frac{\partial X^{22}}{\partial u^2}+X^{11}\Gamma_{11}{}^2+2X^{12}\Gamma_{12}{}^2+X^{22}\Gamma_{22}{}^2+\rho\sqrt{g_{11}}Z^2=0
\end{aligned}\right\} \tag{34}$$

where

$$\begin{aligned}
&\Gamma_{11}{}^1=\frac{1}{2g}\left(g_{22}\frac{\partial g_{11}}{\partial u^1}-2g_{12}\frac{\partial g_{12}}{\partial u^1}+g_{12}\frac{\partial g_{11}}{\partial u^2}\right)\\
&\Gamma_{12}{}^1=\Gamma_{12}{}^1=\frac{1}{2g}\left(g_{22}\frac{\partial g_{11}}{\partial u^2}-g_{12}\frac{\partial g_{22}}{\partial n^1}\right)
\end{aligned}$$

$$\left.\begin{aligned}
\Gamma_{22}{}^{1}&=\frac{1}{2g}\left(2g_{22}\frac{\partial g_{12}}{\partial u^2}-g_{22}\frac{\partial g_{22}}{\partial u^1}-g_{12}\frac{\partial g_{22}}{\partial u^2}\right)\\
\Gamma_{11}{}^{2}&=\frac{1}{2g}\left(-g_{12}\frac{\partial g_{11}}{\partial u^1}+2g_{11}\frac{\partial g_{12}}{\partial u^1}-g_{11}\frac{\partial g_{11}}{\partial u^2}\right)\\
\Gamma_{12}{}^{2}&=\Gamma_{21}{}^{2}=\frac{1}{2g}\left(-g_{12}\frac{\partial g_{11}}{\partial u^2}+g_{11}\frac{\partial g_{22}}{\partial u^1}\right)\\
\Gamma_{22}{}^{2}&=\frac{1}{2g}\left(-2g_{12}\frac{\partial g_{12}}{\partial u^2}+g_{12}\frac{\partial g_{22}}{\partial u^1}+g_{11}\frac{\partial g_{22}}{\partial u^2}\right)
\end{aligned}\right\}\qquad(35)$$

Taking $u^1=\text{const}$, $u^2=\text{const}$ as the principal direction of the stress ($g_{12}=0$, σ^{12}, $X^{12}=0$), the equilibrium equations is simplified as follows:

$$\left.\begin{aligned}
&\frac{\partial\sigma^{11}}{\partial u^1}+(\sigma^{11}-\sigma^{22})\frac{\partial g_{22}/\partial u^1}{2g_{22}}+\sqrt{g_{11}}\rho Z^1=0\\
&\frac{\partial\sigma^{22}}{\partial u^2}+(\sigma^{22}-\sigma^{11})\frac{\partial g_{11}/\partial u^2}{2g_{11}}+\sqrt{g_{22}}\rho Z^2=0
\end{aligned}\right\}\qquad(36)$$

$$\left.\begin{aligned}
&\frac{\partial X^{11}}{\partial u^1}+X^{11}\frac{\partial g_{11}/\partial u^1}{2g_{11}}-X^{22}\frac{\partial g_{22}/\partial u^1}{2g_{11}}+\rho\sqrt{g_{22}}Z^1=0\\
&\frac{\partial X^{22}}{\partial u^2}-X^{11}\frac{\partial g_{11}/\partial u^2}{2g_{22}}+X^{22}\frac{\partial g_{22}/\partial u^2}{2g_{22}}+\rho\sqrt{g_{11}}Z^2=0
\end{aligned}\right\}\qquad(37)$$

Consequently, it is hard to say which of the equations is substancially more simple. In the case of plane stress, we should make use of $(t\sigma^{ij})$, (tX^{ij}) (t: plate thickness) in place of σ^{ij}, X^{ij} in Eqs. (36) and (37) respectively.

In contrast to the case of statical equilibrium above mentioned, for the purpose of treating of the dynamical problem it will be convenient to consider the equilibrium of forces in the $\boldsymbol{g}_i{}^0$-direction. Introducing the displacement $\boldsymbol{w}$ by

$$\boldsymbol{r}=\boldsymbol{r}^0+\boldsymbol{w}\qquad(38)$$

$$\boldsymbol{w}=v^i\boldsymbol{g}_i{}^0\,,\qquad v^i=\frac{w^i}{\sqrt{g^0{}_{ii}}}\qquad(39)$$

we have

$$\boldsymbol{g}_j=\sum_k\left[\delta_j{}^k+\frac{\partial v^k}{\partial u^j}+\sum_h v^h\Gamma_{hj}{}^{0k}\right]\boldsymbol{g}_k{}^0\qquad(40)$$

where $\Gamma_{ij}{}^{0k}$ indicates the expression $\Gamma_{ij}{}^k$ in which g_{ij} is replaced by $g_{ij}{}^0$. Applying Eq. (40) to Eq. (9), and substituting σ^i represented by $\boldsymbol{g}_j{}^0$ into (24), we obtain the equation of motion

$$\sum_{i,j,k,h}\left\{\frac{\partial}{\partial u^i}\left[X^{ij}\left(\delta_j{}^a+\frac{\partial v^a}{\partial u^j}+v^h\Gamma_{hj}{}^{0a}\right)\right]\right.$$
$$+X^{ij}\left(\delta_j{}^k+\frac{\partial v^k}{\partial u^j}+v^h\Gamma_{hj}{}^{0k}\right)\Gamma_{ki}{}^{0a}$$

$$\left.+\rho_0\sqrt{g_0}\left(Z_0{}^a\frac{1}{\sqrt{g_{aa}{}^0}}-\frac{\partial^2 v^a}{\partial t^2}\right)\right\}=0$$
$$(a=1,2,3)\qquad(41)$$

where $Z_0{}^a$ denotes the $g_a{}^0$-component of the external force. Eq. (41), when expressed in the rectangular Cartesian coordinates, becomes the following equation obtained by R. Kappus:

$$\frac{\partial}{\partial x}[X^{11}(1+u_x)+X^{12}u_y+X^{13}u_z]$$
$$+\frac{\partial}{\partial y}[X^{21}(1+u_x)+X^{22}u_y+X^{23}u_z]$$
$$+\frac{\partial}{\partial z}[X^{31}(1+u_x)+X^{32}u_y+X^{32}u_z]$$
$$+\rho_0\left(Z_0-\frac{\partial^2 u}{\partial t^2}\right)=0,\quad\text{etc.}\qquad(42)$$

References

1) F. D. Murnaghan: Amer. J. Math. **59** (1937) 235-260.
M. A. Biot: Phil. Mag. **27** (1939) 449-452, 468-469.
R. Kappus, Z. A. M. M. **19** (1939) 271-285, 344-361.
A. E. Green and W. Zerna: Phil. Mag. 7th. s. **41** (1950) 313-336.
2) R. Kappus: ibid.

JOURNAL OF THE PHYSICAL SOCIETY OF JAPAN Vol. 8, No. 5, SEP.—OCT., 1953

Measurement of the Net Thermal Conductivity of Fibrous Substances

By Yosomatsu TAKAMURA

The Nara Women's University

(Received November 17, 1952)

When a steady flow of heat is established in a plate, composed of fibres under very intense pressure, a relation between the apparent thermal conductivity of it (K_c) and the net thermal conductivity of the fibres (K_f) is given approximately as follows

$$\frac{d}{K_c}=\frac{m/\rho}{K_f}+\frac{1}{K_g}\left(d-\frac{m}{\rho}\right),$$

where d is the thickness of the plate, K_g the thermal conductivity of occluded air, m the mass per unit area of the plate and ρ the net density of the fibrous subtance.

The experimental results for glass wool and cotton were found to be explained nearly by this relation.

§ 1. Principle

It seems resonable to assume that a plate consisting of a fibrous substance compressed uniformly between parallel plane plates be equivalent to a system of thin layers of the same material as the fibre and that of air pilled up alternately, as far as the heat conduction in the direction perpendicular to the plate concerns. When the plate is sufficiently large in comparison with its thickness, we shall have

$$\frac{d}{K_c}=\frac{d_f}{K_f}+\frac{d_g}{K_g}\ , \qquad (1)$$

neglecting the edge effect, where K_f, K_g and K_c are the net thermal conductivity of the fibre, the conductivity of air and the effective conductivity of the composite plate with the thickness d respectively, while d_f and d_g, the total sum of the thickness of layers of the fibre and that of air respectively.

Now, let ρ be the net density of the fibrous substance and m the mass per unit area of the plate, then we have

$$\frac{d}{K_c}=\frac{m/\rho}{K_f}+\frac{1}{K_g}\left(d-\frac{m}{\rho}\right). \qquad (2)$$

Since K_f and K_g are constant and m/ρ can also be kept constant for various values of d, a linear relation will hold between d/K_c and $d-(m/\rho)$. So, we can estimate the values of K_f and K_g from the diagram plotted d/K_c versus $d-(m/\rho)$.

§ 2. Experiments

As for the measurement of thermal conductivity of a sample the usual method of comparison was adopted as in the previous investigations,[1] namely the specimen under consideration and a standard substance were interposed between two vessels of different temperatures as shown in Fig. 1. To minimize the edge effect for heat flow, the sample and standard plates of sufficiently large diameter were employed.[2] Four pairs of thermo-couples of copper-constantan were used to measure the temperatures at necessary points. A certain amount of the fibrous substance was made in to a form of circular flat disc, about 25 cm. in diameter, and then it was kept in a

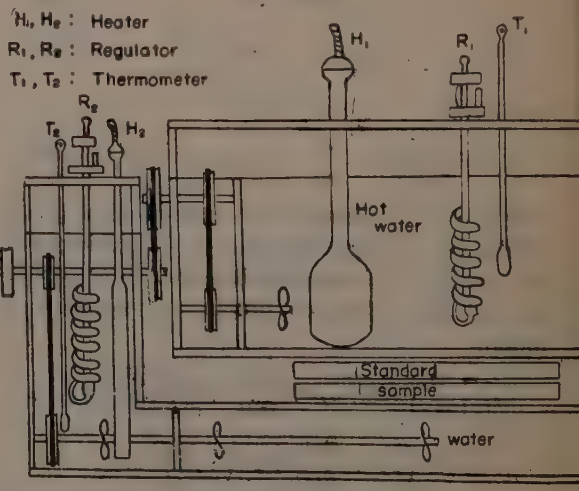

Fig. 1. Experimental appratus.

vessel as shown in Fig. 2. In this figure, *ab* and *cd* are copper plates, while *ef* is a circular ring of rubber, the hight of which being adjustable within a certain extent. Ebonite was chosen as the standard substance, its thermal conductivity being assumed as 0.000380.[3)]

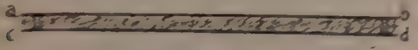

Fig. 2. Vessel for the sample of fibre under test.

(a) *Glass wool*

Some preliminary experiments were carried out for glass wools whose thermal conductivities had already be known, for the pupose of testifying the adequacy of eq. (2). Two lumps of glass wool of different sorts were examined. Each of them, weighing 100.6 grams and 71.9 grams respectively, was compressed in to a form of plate. The area of its flat face was kept constant, 452 cm², while its thickness was varied step by step from 1.61 cm. to 0.70 cm. Using the densities of the glass wools $\rho=2.48$ and 2.46 measured by means of pycnometer, the observed values of d/K_e and $d-m/\rho$ are plotted in Fig. 3. This graph seems to show that there is a linear relation between d/K_e and $d-(m/\rho)$ for each specimen within experimental errors. From the points of interseption of these straight lines with the d/K_e axis it may be found that K_f. But as the points of the interseption in the present case lie very near the origin, errors of estimation of the values may happen to be fairly large. So, the approximate upper and lower values of K_f are obtained respectively from the lower and upper interceptes of the lines drawn passing through the scattered points, thus

$$K_{\text{glass}}(\text{upper})\fallingdotseq 1.7\times10^{-3}$$
$$\fallingdotseq 2\times10^{-3}\ (\text{cal. deg.}^{-1}\ \text{cm.}^{-1}\ \text{sec.}^{-1})$$
$$K_{\text{glass}}(\text{lower})\fallingdotseq 4.2\times10^{-4}$$
$$\fallingdotseq 4\times10^{-4}\ (\text{cal. deg.}^{-1}\ \text{cm.}^{-1}\ \text{sec.}^{-1})$$

Thus, taking the approximate middle value $K_{\text{glass}}(\text{middle})\fallingdotseq 1\times10^{-3}$ as a intermediate one between these values, we may accepted it as consistent in the order of magnitude.[4)] On the otherhand the thermal conductivity of occluded air, K_{air} was estimated from the inclinations of the lines in Fig. 3 as 1.9×10^{-4} and 1.2×10^{-4} (cal. deg.$^{-1}$ cm.$^{-1}$ sec.$^{-1}$) showing right order of magnitude.*

(b) *Cotton*

As a typical fibrous substance, cotton was investigated by the same apparatus. Its net density was found by the method of Yosida and Takei as 1.590.[5)] The results of the experiments for thermal conductivity are plotted in Fig. 4. An approximately linear relation hold also between d/K_e and $d-(m/\rho)$, although somewhat large irregularity is observed in the region of lower density. As in the previous case, the approximate upper and lower values of the net thermal conductivity of the cotton

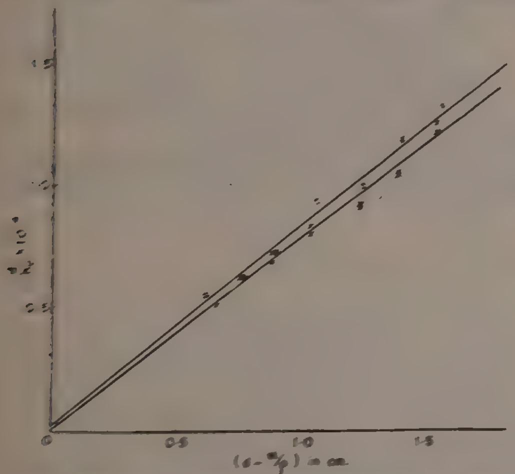

Fig. 3. The graph of d/K_e versus $d-(m/\rho)$ of glass wool.

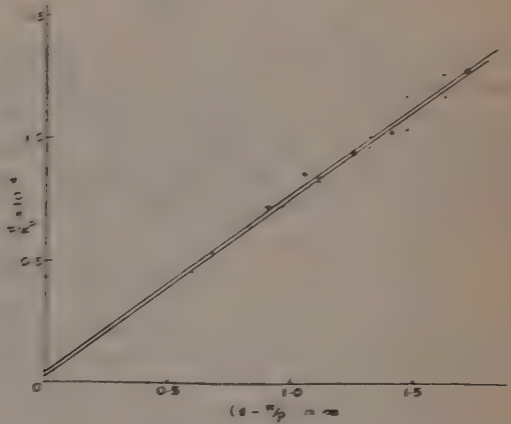

Fig. 4. The graph of d/K_e versus $d-(m/\rho)$ of cotton.
-·- plot for cotton of 30.62 grams,
-+- plot for that of 46.17 grams.

---

* The generally accepted value of the ordinary air is 0.0000574.

wool, K_f, and that the occluded air, K_g, thus obtained respectively are:

$$K_{\rm cotton}(\text{upper}) \fallingdotseq 4.0\times10^{-4} \fallingdotseq 4\times10^{-4} \quad (\text{cal. deg.}^{-1}\,\text{cm.}^{-1}\,\text{sec.}^{-1})$$

$$K_{\rm cotton}(\text{lower}) \fallingdotseq 1.2\times10^{-4} \fallingdotseq 1\times10^{-4} \quad (\text{cal. deg.}^{-1}\,\text{cm.}^{-1}\,\text{sec.}^{-1})$$

$$K_{\rm air} \fallingdotseq 1.4\times10^{-4} \fallingdotseq 1\times10^{-4} \quad (\text{cal. deg.}^{-1}\,\text{cm.}^{-1}\,\text{sec.}^{-1})$$

The approximate middle value $K_{\rm cotton}$(midle) $\fallingdotseq 3\times10^{-4}$ and $K_{\rm air} \fallingdotseq 1\times10^{-4}$ may give an order of magnitude of the net conductivity of cotton wool and the conductivity of occluded air respectively.

§ 3. Remarks

C. Matano has also investigated the same problem[6)7)] as the present one. For the apperent conductivity of a plate composed of two substances 1 and 2, he has derived two extreme values K_p and K_s by assuming two kinds of models, (a) and (b). In the model (a) each substance is assumed to make the form of columns arranged perpendicular to the face of the plate,

$$K_p = K_2 + (K_1 - K_2)w\,, \qquad \text{(i)}$$

while in the model (b) the substances 1 and 2 are pilled up alternately, each parallel to the face of the plate,

$$\frac{1}{K_s} = \frac{1}{K_2} - \left(\frac{1}{K_2} - \frac{1}{K_1}\right)w\,. \qquad \text{(ii)}$$

In these expressions, K_1 and K_2 are thermal conductivities of 1 and 2, K_p and K_s, the apperent thermal conductivities in the direction perpendicular to the plate in the models respectively and w, the "impenetrability" of the substance 1 in the plate. Here, impenetrability means the ratio of the volume occupied by the substance 1 to the whole volume of the plate. Replacing K_1, K_2 and K_s by K_f, K_g add K_e the formula (ii) will be writen as

$$\frac{1}{K_e} = \frac{1}{K_g} - \left(\frac{1}{K_g} - \frac{1}{K_f}\right)w\,. \qquad (3)$$

This is essentially the same as formula (2).

Now, C. Matano has claimed that his experimental results were explained more satisfactarily by model (a) than the model (b). By closer examination of the data given by him together with that of several investigators for rayon fibre, however, it seems more probable that the relation (ii) may hold good, especially for the case of intense compression. Namely, when a lump of fibres is compressed into the form of plate, each fibre shows a tendency to be arranged almost parallel to the plate. And in our case, an observation of the sample by microscope is also comfirmed this conjecture.

References

1) Y. Takamura: Proc. of the Phys.-Math. Soc. of Japan **18** (1936) 280: Loc. cit. **18** (1936) 491.

2) Guthrie: The flat disc method; Phil. Mag. **37** (1869) 468; T. Preston, Theory of heat, chap. VII, p. 653.

3) Landolt-Börnstein: Physikalische-chemische Tabelle.

4) Landolt-Börnstein: Loc. cit. crown glass (0.00163), mirror glass (0.00179); Y. Takamura: loc. cit. window glass (0.00164).

5) U. Yoshida and B. Takei: Memoirs of College of Science, Kyoto University, **A 15** (1932) 1.

6) C. Matano: Oyo Butsuri (in Japanese), **11** (1942) 351; Loc. cit. **11** (1942) 578.

7) C. Matano: Physics of Fibres (in Japanese), 1642, pp. 64-103.

Short Notes

J. PHYS. SOC. JAPAN 8 (1953) 677～678

On the Magnetization of Magnesium Ferrite

By Nobuhiko SAKAMOTO, Takashi ASAHI
and Syôhei MIYAHARA

*Department of Physics, Faculty of Science,
Hokkaido University*

(Received April 13, 1953)

It is well known that the magnetic property of ferrites are explained by the theory of "ferrimagnetism" introduced by L. Néel1). Perfectly inversed ferrites, in which all of the divalent cations lie at the 8f positions surrounded tetrahedrally by oxygens, must show the bulk saturation magnetization due to the magnetic moments of the divalent ions. (We assume 16c–8f interaction be strong.) In the case of Mg-ferrite, if it were perfectly inversed, it would show no ferro (or ferri) magnetism; if Mg ions lie both at 8f and 16c positions, however, the difference of magnetizations of 8f and 16c sublattices does not vanish. Of some ferrites one can control the distribution of cations by appropriate heat treatments2); and the Mg-ferrite is of particular interst, because it may be easily influenced by the heat treatment. L. Néel supposed that the ionic arrangement of the ferrite at high temperature is determined by the following chemical equilibrium condition3):—

$$\frac{x(1+x)}{(1-x)^2}=\exp\left(-\frac{\theta}{T}\right),$$

where x means the fractional number of Mg ions on 8f sublattices and may be given from the measurement of saturation magnetization μ of the sample.

$\mu=10\,\mu_B x$, μ: magnetization per mol
μ_B: the Bohr magneton

We made a study concerning the change of magnetization of Mg-ferrite after various heat treatments. Samples are prepared by the chemical method. $MgFe_2O_4$ are precipitated by the reaction:

$$MgSO_4+Fe_2(SO_4)_3+8KOH =MgFe_2O_4+4K_2SO_4+4H_2O,$$

then dried at 100°C, pressed by 10 ton/cm² and sintered at 1100°C; from this we cut eight samples. Heat treatments of the samples are shown in Table I. The saturations magnetizations are measured at room temperature by the pendulum magnetometer.4) Then, again the following heat treatments are made and the magnetizations are measured.

Table I.

Sample		μ
(a)	1 hour 1100°C r.c. from 1100°C	1.63
(b)	1 hour 1100°C r.c. from 1100°C	1.63
(c)	1 hour 1100°C s.c. to 750°C r.c. from 750°C	1.49
(d)	1 hour 1100°C s.c. to 500°C r.c. from 500°C	1.39
(e)	1 hour 1100°C s.c. to 400°C r.c. from 400°C	1.15
(f)	1 hour 1100°C s.c. to 300°C r.c. from 300°C	1.08
(g)	1 hour 1100°C s.c. to room temperatures	1.06
(h)	1 hour 1100°C s.c. to room temperatures	1.06

r.c. rapidly cooled (quenched)
s.c. slowly cooled by the rate of 30° C/hour

Table II.

T_q	T
1100°C	620°C
750°C	530°C
600°C	480°C
500°C	460°C
400°C	360°C
300°C	340°C

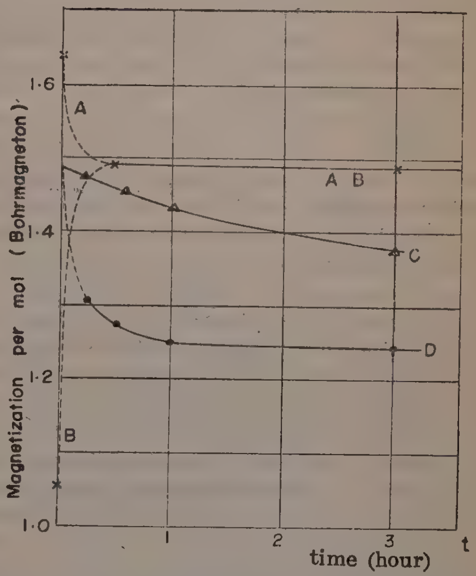

Fig. 1. The relation between the magnetization and time of tempering. The magnetization are mesured at room temperature.

(1) Two samples ((a) quenched from 1100°C and (g) slowly cooled to room temperatures) are tempered at 750°C for ½ hour and quenched, and (b) and (h) are tempered at 750°C for 3 hours and quenched. The results are shown in Fig. I, curves A and B.

(2) One of the sample is tempered at 750°C for 3 hours and quenched and again tempered at 300°C for 5 honrs and quenched. Any change in magneti-

zation could not be observed.

(3) Four samples are tempered at 750°C for 3 hours and quenched and again tempered at 350°C for 10 minutes, 30 minutes, 1 hour and 3 hours respectively and quenched from each stage of tempering. (Fig. I, curve C).

(4) Three samples are tempered at 750°C for 3 hours and quenched and again tempered at 500°C for 30 minutes, 1 hour and 3 hours respectively and quenched from each stage of tempering. (Fig. I, curve D).

From above experiments we can recognize that the samples slowly cooled from 1100°C by the rate of 30°C/hour are in thermal equilibrrium so long as the temperature are above 750°C, but they thought to be not in equilibrium below 750°C. The heat treatment at 500°C shows, however, that they reach the thermal equilibrium after tempering for an hour or more. Of cours, even if these samples are cooled rapidly, the ionic arrangement at room temperature does not correspond to that of the tempered state, for Mg ions may still move during cooling process. Therefor we take the values of saturation magnetization of the samples, which are rapidly cooled from the temperatures above 600°C, for ordinate and the tempered temperatures for absissa, and the curve is extrapolated to the room temperature. The value thus obtained, $\mu=0.18$, would be aproximately equal to that of the magnetization in thermal equilibrium at room temperature. From this and Néel's equation we obtain $\theta=1150°\mathrm{K}$. Using this value of θ we can estimate the relation between the quenching temperatures T_q in Table I and the characteristic temperature T responsible to Néel's equation. The relation obtained is shown in Table II. We think the results are reasonable from the point of view of the rate process.

We are now dealing with the saturation magnetization of $\mathrm{MgO \cdot ZnO \cdot Fe_4O_8}$ from the same idea, we can show the results in near future.

A part of the expense of this research has been defrayed from the Scientific Research Expenditure of the Educational Ministry in Japan.

References

1) L. Néel: Ann. Physiques XII **3** (1948) 137.
2) Gorter: Nature **165** (1950) 798.
3) L. Néel: C. R. **230** (1950) 190.
4) C. R. Domenicali: Rev. Sci. Inst. **21** (1950) 321.

J. Phys. Soc. Japan 8 (1953) 678~680

Resolving Power of the Scintillation Counter for Energy Measurement of Relativistic Particles

By Yujiro Koh

Faculty of Science and Engineering, Osaka City University

(Received April 18, 1953)

Reduction in the resolving power of energy measurement with the scintillation counter is caused by the following: (1) the output fluctuation of photomultiplier tube on account of too small a number ν of photons entering its window; (2) wide variation of energy dissipation itself in scintillator even for monoenergetic incident particles when the average range is larger than the thickness of the scintillator, etc.. Cause (1) can be made smaller by increasing ν in proportion to $\sqrt{\nu}/\nu$, but, the fluctuation by (2), which is the same phenomenon as the so-called straggling, cannot be reduced and causes a serious disadvantage in the measurement of ionization loss by the scintillation counter especially for the penetrating cosmic particles. Here, the effect of this undesirable phenomenon on the accuracy of the scintillation technique was investigated, to begin with, by the use of cosmic μ-mesons.

The straggling was studied systematically by Williams1) in 1929 by means of photographic plate for penetrating beta-particles. But in his studies the condition was complicated because of the relatively large energy loss in the absorber. Recently, the fluctuation of the output pulse of the cosmic μ-meson was observed by AgCl crystal counter (Hereford2)) and also by scintillation counter using anthracene crystal (Bowen and Roser3)). These results were compared with the theoretical fluctuation of the ionization loss in detectors (Landau4) and Symon5)).

As the unavoibable imperfection of the crystal will make light outputs more or less smaller, the liquid scintillator (5 gr/li p-terphenyl xylene solution) was used here. Fig. 1 shows the apparatus schematically. Only the light flashs caused by the narrow μ-meson beam (whose zenith angle is smaller than 7°) with their momentum larger than 430 Mev were registered, selected by G.M. counter telescope combined with 25 cm Pb. As the specific collision loss in liquid absorber does not change appreciably by the density effect6) for such high energy range, the average dissipated energy in the scintillator between the beaker's bottom and the window of the RCA 5819 photomultiplier tube, which looks down-ward, will be constant within 2.5%, for 90% of registered particles with various energies; and the relatively large fluctuation of output pulses, as shown in Fig. 2, does not come from the inhomogeneity of the incident energies. As the ordinary method used for proportional registering of pulse of ~0.1 μsec duration by the cathode ray oscilloscope was not yet available for us, the proportional pulse-lengthener of Dewan Allen type[7] has been reformed in such a manner that the input of 0.7 μ sec duration can be lengthened faithfully to the output of 1 sec duration, in order to be recorded in the automatic pen-recorder. The pulse-form of the circuits was occasionally checked by the oscilloscope and the mercury switch pulser[8] at several important points as shown in Fig. 1. The fluctuation of high voltage source for 5819 was less than 0.1%.

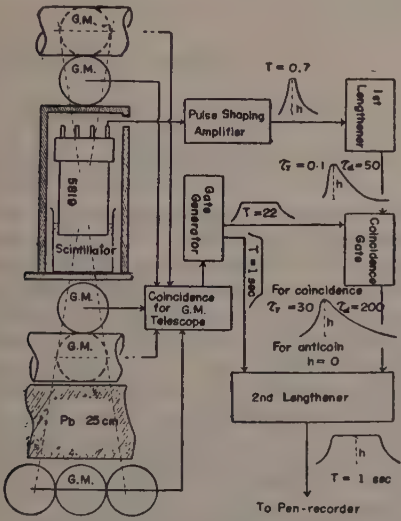

Fig. 1. Schematic diagram of the apparatus for the observation of the scintillation pulse height. T and τ in μ sec, unless indicated otherwise.

The results obtained, for two cases of scintillator thickness x=3.7 cm and 8.7 cm, are shown in Fig. 2 and the Table. The smooth curves, which show the theoretical[4)5)] values calculated under the assumption that the output pulse is proportional to the dissipated energy in the detector, are normalized at point A, so that it may agree with the experimental histogram at the most probable pulse height for x=3.7 cm. The similarity of the histogram to the theoretical curve seems to be satisfactory in general shape. But, (1) for x=8.7 cm the histogram displaces as a whole to the direction of smaller pulse, showing the considerable absorption of emitted light and (2) in each histogram smaller pulses are more frequent than expected from the theory, which may be attributed perhaps to defects in the complicated recording system adoped, including the friction of the pen-recorder, but these are not yet examined in detail. As the theory seems to be adequate in so far as the absorption is not important, one can estimate the relative half-width $R_{\frac{1}{2}}$ for monoenergetic incidence from the shape of the curve;[3)4)5)]

$$R_{1/2}=5.05\ \xi/E_{prob}$$

$$\xi=\pi(r_0)^2(nx)2mc^2/\beta^2 \qquad r_0=e^2/mc^2$$

n=number of electrons in unit cube

E_{prob}=most probable energy dissipation

In a case, where the density effect is dominant,

$$E_{prob}=\xi\ \ln\frac{2.9\ mv^2\ \xi}{nh^2e^2/\pi m}$$

$$R_{1/2}=2.19/[\log_{10}(5.8\,\pi^2 r_0 m^2c^2/h^2)+\log_{10}x$$

$$=2.19/[8.44+\log_{10}x] \qquad (x \text{ in cm})$$

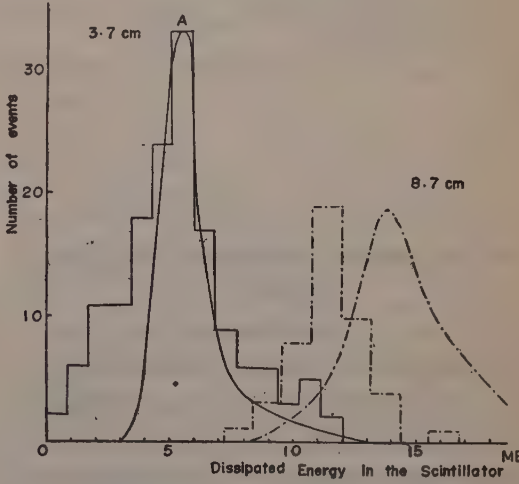

Fig. 2. Distribution of the scintillation pulse height for two scintillator width 3.7 cm and 8.7 cm. The smooth curves show the results of theoretical calculation normalized at point A.

As $R_{\frac{1}{2}}$ decreases very slowly with x and is independent on the phosphor material, it is not practical to increase x in order to obtain large resolving power, as shown in the Table.

Table. Comparison of Observed and Calculated Values

Scintillator Width in cm	Calculated Most Probable Energy Loss		Observed Most Probable Pulse Height	Relative Half Width	
	in Mev	in ratio	in ratio	Calcu.	Obser.
3.7	5.6	1	1	0.243	0.2~0.5
8.7	13.8	2.4	2.0	0.234	0.2~0.3

In conclusion, the author wishes to express his sincere thanks to prof. Y. Watase for his encouragement and to Dr. S. Ohba of the Fuji Film Company, Mr. S. Sakuyama of the Osaka Gas Company

and Miss H. Namba of the Tokyo University for their kindness in getting valuable phosphor substances.

References

1) E. J. Williams: Proc. Roy. Soc. London **A 125** (1929) 420.

2) F. L. Hereford: Phys. Rev. **74** (1948) 574.

3) T. Bowen and F. X. Roser: Phys. Rev. **83** (1951) 689 L; **85** (1952) 992.

4) L. Landau: J. Phys. U.S.S.R. **8** (1944) 201.

5) K. R. Symon: Dissertation, Harvard University (1948).

6) O. Halpern and H. Hall: Phys. Rev. **57** (1940) 459; **73** (1948) 477.

7) J. T. Dewan and K. W. Allen: Rev. Sci. Inst. **21** (1950) 823.

8) R. L. Garwin: Rev. Sci. Inst. **21** (1950) 903.

J. Phys. Soc. Japan 8 (1953) 680~681

On the Electric Conductivity of Cuprous Sulfide:

Experiment

By Shin-ya Miyatani and Yasumasa Suzuki

Department of Physics, University of Niigata

(Received April 21, 1953)

It has heen observed that cuprous sulfide has both ionic and hole-conductivity in the β-phase range (110°C–470°C)¹⁾. We have measured the building up and decay of the potential differences between probes when the current is switched on and off. From these data we can calculate the mobility and density of lattice defects separately by the theory given by I. Yokota²⁾.

The specimens are prepared from samples obtained by a direct reaction (at 600°C) of materials sealed in a vacuum hard glass tube or by melting so reacted samples. Single crystals (e.g. 5×7×20 mm) can be cut out from recrystalized samples. (They have no special property different from polycrystals as far as the behaviors of defects are concerned.) The method of measurements is the one which is usually used for the studies of this sort (probes — rotary switch — potentiometer). Platinum foils are used as electrodes and seven nichrome springs (platinum-pointed) as probes and specimen is put in a vacuum (10^{-3} mmHg) furnace.

When the current is switched on, the copper ions (defects) drift toward the cathode (anode) and a stationary state is realized when the drift by the field and the back-diffusion cancel each other and so ionic current decays out (Fig. 1).

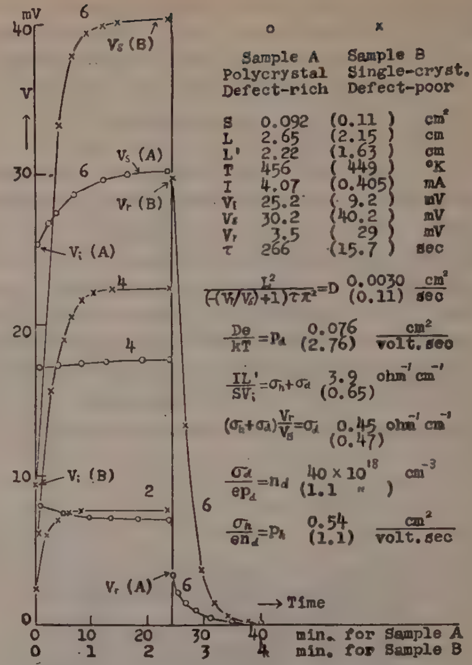

Fig. 1. The potential differences between the probe 0 (nearest to anode) and 2, 4 or 6 (nearest to cathode) vs. time. Two typical cases are illustrated (the values in parentheses are of sample B), where S, area of cross section of the specimen, L, total length, L′, distance between probes 0 and 6, T, temperature, I, current intensity, V_i, initial potential drop, V_S, stationary potential drop, V_r, residual potential difference at the moment of switching off, τ, time constant of building up or decay, D, diffusion coefficient of defect, p_d, defect mobility, σ_d, defect conductivity, σ_h, hole conductivity, n_d, defect density, and p_h is hole mobility (assuming $n_d=n_h$).

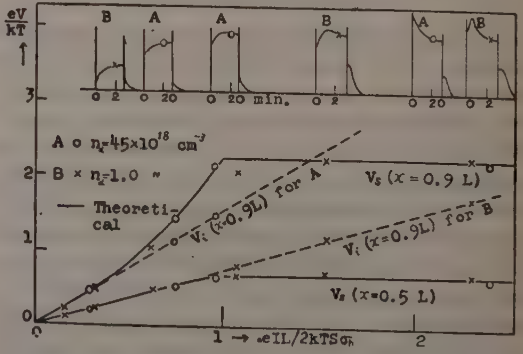

Fig. 2. V–I characteristics for the initial and stationary states. Upper curves illustrate the building up and decay of potential ($x=0.9$ L) for different current intensities corresponding to respective abscissa³⁾.

When the current becomes large (accurately speaking, $eIL/2kTS\sigma_h$ becomes larger than 1), precipitation (or pre-precipitation) seems to take place at the cathode and the potential drop through the total length of the specimen begins to decrease after taking a maximum. If the current is sufficiently large, decreasing only appears and the precipitation seems to continue until the limiting distribution is almost realized (i.e.

$$eV_S(x)/kT = -\log(1-x/L),$$

where x is distance from the anode) (Fig. 2).

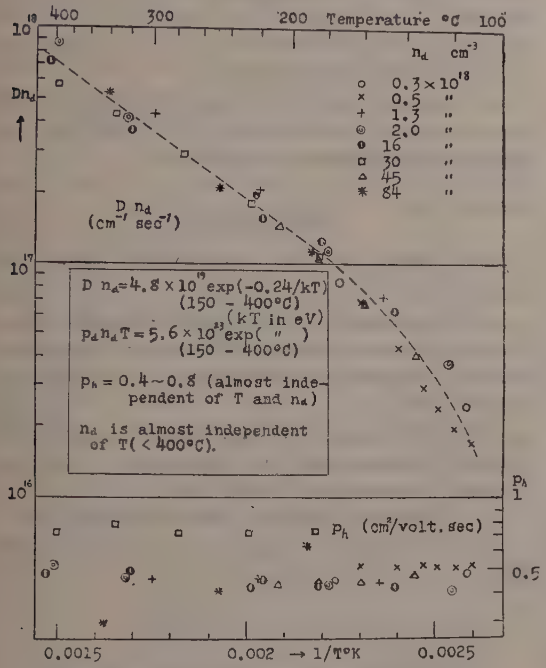

Fig. 3. Dn_d and p_h vs. $1/T$.

D, p_d, n_d and p_h are calculated (Fig. 1) for various samples (Fig. 3). We shall mention two facts as a justification for Yokota's theory: (1) When the recrystalized sample is heat-treated (e.g. at 450°C for 1 hr.) the copper precipitates on the surface of the specimen and the difference of defect number (n_dSL) between before and after the treatment agrees roughly with the number of precipitated copper atoms estimated by weighing the dust-like precipitate. (2) When two different samples are brought into contact at the β-phase temperature, the diffusion of copper takes place and the differences of n_dSL between before and after the contact are roughly equal with each other.

From these data (Fig. 3), defects seem to move like nearly free particles (mean free path inversely proportional to n_d), while hole mobility is almost constant. (Full paper will be published in J. Faculty of Sci. Niigata Univ. Ser. 1.)

References

1) E. Hirahara: J. Phys. Soc. Japan **6** (1951) 422.

2) I. Yokota: J. Phys. Soc. Japan **8** (1953) 595.

3) T. Kushida: J. Sci. Hiroshima Univ. **A 14** (1950) 147.

J. PHYS. SOC. JAPAN **8** (1953) 681~682

On Photographic Chemical Development

By Shintaro SUGAI and Jiro FURUICHI

Department of Physics, Faculty of Science, Hokkaido University

(Received April 23, 1953)

Recently Uryu¹⁾ has measured the relation between temperature and the velocity of the chemical activity involved in the first stage of the development of photographic dry plates. He used a certain commercial dry plate and metol developer and got 0.66 e.v. for the activation energy. This value agrees very well with the value of the activation energy for ionic conductivity of silver bromide²⁾.

Uryu then stated his belief that Gurney-Mott's theory for chemical development³⁾ is probably correct.

However, there is no certain knowledge available on the correct values of the activation energies for other mechanisms which seem proper for this reaction⁴⁾ and for ionic conductivity of the small grains in the photographic emulsions which perhaps differ from that of bulk crystals⁵⁾. Furthermore, commercial dry plates generally contain silver iodide, which has inflence upon the value of ionic conductivity. Therefore, it can not be affirmed from Uryu's data alone that Gurney-Mott's theory is correct.

Using five dry plates, in which silver iodide was contained in various proportions, and metol developer, the present authors observed the activation energy by a method measures the relation between temperature and the duration of development needed for the progress of the reaction from $D=0.1$ to $D=0.4$, where D means diffuse blackness. Within this range the rate of image coagulation is in fact about linear to the duration of the development. Thus it seems that the reaction is in progress at all developing nucleii.

For example, the relation between D and the duration of the development for a commercial dry plate is shown in Fig. 1. We can get immediately from Fig. 1 the relation between temprature T and the desired duration of development P, and the activation energy U for this plate. This relation for some plates are shown in Fig. 2. Table I shows U of all the observed plates.

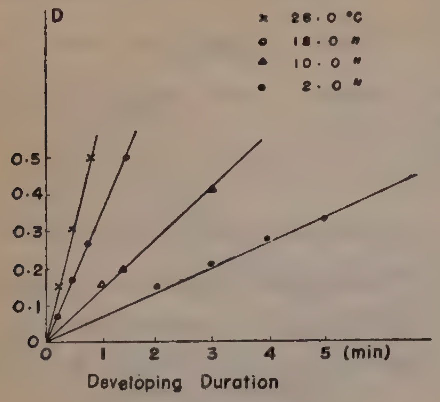

Fig. 1.

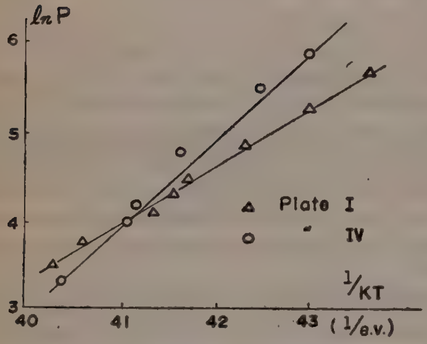

Plate I; Silver iodide content 0 Mol %
IV; 40 Mol %
(Exposure on two plates is considerably different)

Fig. 2.

Table I.

Plate	Silver iodide content Mol %	U e.v.
I	0	0.62±0.02
II	2.5	0.63±0.02
III	7	0.66±0.02
IV	40	0.91±0.02
V	commercial*	0.64±0.02

* Fuji A. I.

The above exhibited results indicate clearly; (1) that U for a pure silver bromide emulsion is smaller than the activation energy for ionic conductivity of silver bromide crystal; and (2) that as the proportion of content of silver iodide glows the greater the activation energy becomes. The former fact is perhaps in fabour of Gurney-Mott's theory in view of some published experimental findings on ionic conductivity of small grains⁵⁾. From the later, it can't be said certainly that ionic conductivity plays a role in the development, because we have no correct data available on variation of ionic conductivity of silver bromide caused by the inclusion of iodine ion in the emulsion. However, it is well known that the photographic sensitivity of silver halide emulsion depends upon the content of silver iodide⁶⁾.

Thus, if results can be obtained, similar to the above described, in a study of ionic conductivity of small grains in dry plates from its direct measurement, or from indirect ones through study of the effect of temperature on high intensity reciprocity law failure⁷⁾, then our results may be considered to be of some values as experimental proof of Gurney-Mott's theory.

The authors wish to thank Mr. Mizuki for supplying the experimental dry plates and for giving the suggestion to this work.

References

1) T. Uryu: J. Soc. Sci. Photo. Japan **14** (1951) 4.
2) W. Lehfeldt: Z. f. Physik. **85** (1933) 717.
3) N. F. Mott and R. W. Gurney: Electronic Processes in Ionic Crystals (1940). Proc. Roy. Soc. **A 164** (1938) 151.
4) T. H. James: J. Chem. Phys. **11** (1943) 338.
5) E. Mizuki and J. Yamashita: Nippon Butsuri Gakukai-shi **7** (1952) 196.
6) E. Mizuki: Kagaku Butsuri **1** (1949) 49.
7) J. H. Webb: J. Opt. Soc. America **32** (1942) 299.

J. PHYS. SOC. JAPAN 8 (1953) 682~683

The Straggling of Fast Electrons

By Seizaburo KAGEYAMA and Kazuaki NISHIMURA
Physical Institute, Tokyo University of Education
and Yoshio ONAI
Radiological Department, Japanese Foundation for Cancer Research

(Received May 14, 1953)

In the experiment to investigate the energy loss of electrons passing through matter, which is described in the previous paper,¹⁾ the results for the most probable energy loss were in good accordance with the Landau theory²⁾ within the experimental errors. However, the energy loss distribution curves calculated were considerably narrower than those obtained experimentally. The results agreed with the observations of several authors³⁾.

In order to complement this discrepancy, Blunck and Leisegang⁴⁾ have refined Landau's theory introducing the second order terms in the quantum mechanical "resonance" energy transfer. According to them, the probability that charged particles passing through thin layer of thickness R will lose energy $Q \sim Q+dQ$ is given by the following formula

$$W(Q)dQ=\sum_{\nu=1}^{4}\frac{C_\nu\gamma_\nu}{\sqrt{\gamma_\nu^2+b^2}}\exp\left[-\frac{(\lambda-\lambda_\nu)^2}{\gamma_\nu^2+b^2}\right]d\lambda$$

$$b^2=\frac{2\cdot\overline{K_r^2}}{a^2R}, \qquad a=154\frac{Z}{A}\cdot\frac{\rho}{\beta^2} \quad \text{(Kev/cm)}$$

where Z, A, β and ρ are the atomic number, atomic weight, v/c and density of material, respectively. $\overline{K_r^2}$ is the second moment of the energy transfer due to resonance collisions. λ is the universal dimension-less parameter and $C_\nu, \gamma_\nu, \lambda_\nu$ are constant given by them.

The effect of the second order corrections on the most probable energy loss is less than the experimental error, but the effect on the distribution curve is appreciable and gives a much larger spread than Landau's curve except when $b^2 \ll 3$. When $b^2 \ll 3$, the Blunck-Leisegang distribution curve reduces completely to the Landau's curve. Taking into account of this fact, the previous experimental results were compared with the B-L curves.

In Fig. 1 is shown a representative experimental result of 1414 K-conversion electrons passing through 12 mg/cm² of Al. The ordinate gives the relative intensity in arbitrary unit and the abscissae λ value or Q in Kev. The relation between λ and Q is given in B-L's paper. The data employed in constructing the theoretical distribution curve are summarized in Table 1 and are corrected for the additional effect of the wall of the Rn glass tube and mica window of the counter. In the figure, it is seen that the peak shift due to the second order term is small. There is a small discrepancy between the theoretical curve and the experimental points in the tail region. This may, however, mainly be attributed to an improper correction for K-conversion electrons of weak 1379 Kev γ-rays. The half-value widths of the distribution curves were tabulated in Table 2 together with the observed. The experimental results were in good agreement with the B-L calculations.

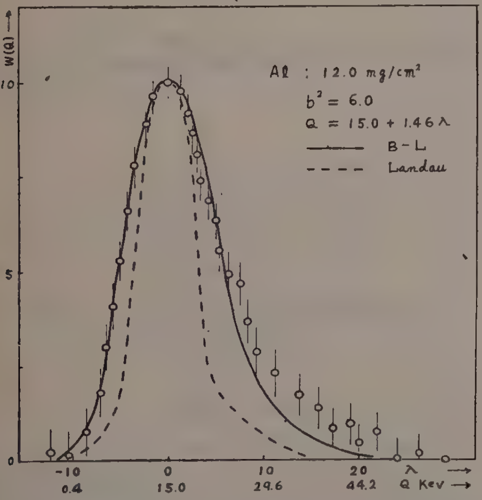

Fig. 1. Energy distribution curve of 1414 Kev conversion electron passing through Al foil (12.0 mg/cm²).

.... Landau's theory

—— Blunck and Leisegang theory.

Table 1. Data employed in constructing the energy distribution curves

Element	ρR (mg/cm²)	aR (Kev)	$R\overline{K}$ (Kev)	$\overline{K_r^2}$ [(Kev)²/cm]	b^2	$dQ/d\lambda$ (Kev)
Al	12.0	0.965	16.25	4.75a	6.0	1.46
Cu	12.8	0.976	16.12	12.2a	11.8	1.47
In	14.7	1.05	17.41	26.6a	22.4	1.55
Pb	18.1	1.20	15.71	51.9a	39.3	1.70

$\overline{K}$ is the average energy loss per unit path length.

Table 2. Comparison of half-value width (Kev)

Element	Calculated values		Observed values
	Landau	B-L	
Al	10.2	16.4	16.4
Cu	10.6	17.9	16.9
In	14.2	19.8	20.1
Pb	15.3	23.8	24.8

In conclusion, the authors wish to express their thanks to Prof. Mitsuo Miwa for his valuable discussion and helpful suggestions. This work was supported by the Scientific Research Expenditure of the Ministry of Education.

References

1) S. Kageyama and K. Nishimura: J. Phys. Soc. Japan **7** (1952) 292.

2) L. Landau: J. Phys. (U.S.S.R) **8** (1944) 201.

3. J. J. L. Chen and S. D. Warshaw: Phys. Rev. **84** (1951) 355.

P. Rothwell: Proc. Phys. Soc. B. **64** (1951) 911.

4) O. Blunck and S. Leisegang: ZS. fur Phys. **128** (1950) 500.

J. Phys. Soc. Japan 8 (1953) 684~685

Beta-Spectrum of Ni^{63}

By Yoshiyuki Kobayashi, Goro Miyamoto
and Shigeru Mori

Department of Physics, Faculty of Science,
University of Tokyo

(Received May 15, 1953)

The beta-spectrum of Ni^{63} was studied by several authors1),2),3), and the values 63 and 67 kev were obtained for its maximum energy, but definite conclusion about its shape has not been drawn.

The spectrum was studied here by a spherical condenser-type electrostatic spectro meter4). Sources were prepared by electrolysis in an ammoniacal solution. Since the sources were considerably thick owing to the low specific activity of the sample supplied by Oak Ridge, several sources different in thickness were used for the measurements. The counter-window was a zapon film of 27 μg/cm^2 in thickness, and its diameter was equivalent to 3.4 percent resolution.

The resulting Fermi plots with correction factor a5), which is the correction factor for the transition $\Delta j=2$ (parity change yes), are shown in Fig. 1. The end-point energy was determined to be 61.5±1 kev. The energy scale was calibrated by the conversion lines of RaD. Both the allowed and a-type Fermi plots are shown in Fig. 2 for comparison. A good agreement can be seen between the observed spectrum and the theoretical a-type spectrum. The correction for the counter-window absorption was estimated from the result obtained by Saxon6) for a 50 μg/cm^2 Nylon film. A measurement with a source of 4 μg/cm^2 in thickness prepared by evaporation onto a 80 μg/cm^2 zapon film also showed the same feature as in Fig. 2, though the statistical error was considerably large.

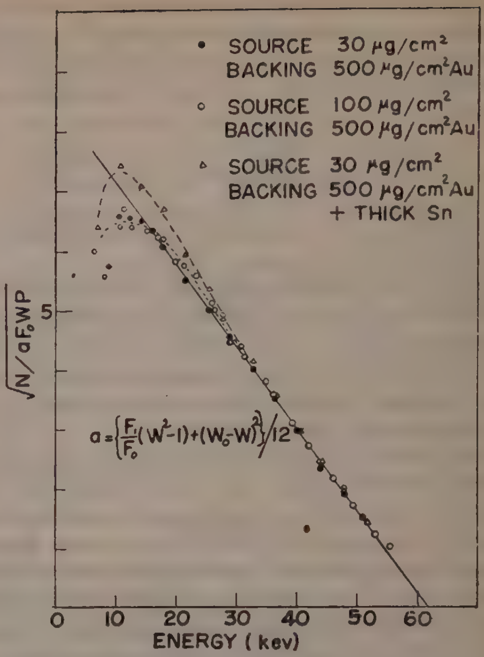

Fig. 1. Fermi plots of beta-spectrum of Ni^{63} corrected by a correction factor. Results for different source- and backing-thicknesses are shown.

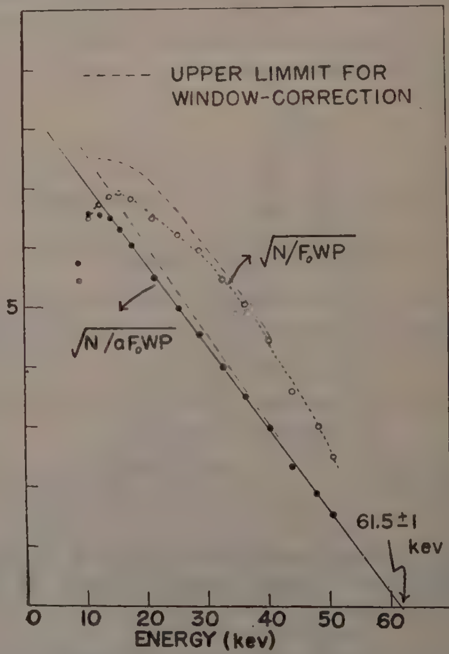

Fig. 2. Allowed and a-type Fermi plots of Ni^{63}. The thickness of source and backing are 30 μg/cm^2 and 500 μg/cm^2 respectively.

In order to confirm these results, the low energy region of the spectrum was studied by accelerating the beta-particles before the entrance to the gap of the spectrometer4). Fig. 3 shows the spectrum obtained with fixed gap voltage, the accelerating voltage being varied. The window absorption can be neglected perfectly in this case. The spectrum shown in Fig. 3 is already corrected for the variation of the effective solid angle due to acceleration4). The agreement between the observed spectrum and the theoretical a-type spectrum is very good except for the extremely low energy region. A peak at the origin of the abscissa is due to the cold emission from the accelerating electrode. A steep drop below 4 kev might be attributed either to the rearrangement of the orbital electrons7) or to the screening effect. There is, however, no adequate theory about the screening in such a low energy region. The contributions from K Auger electrons from Ni^{59} may be neglected, because the intensity of the K X-ray from it was reported to be about 1/1200 of the intensity of the beta-ray of Ni^{63}[2].

The value of $\log ft$ is calculated to be 4.3 for the half life of 60 years[8] (5.0 for 300 years[9]). Where f is given by[5]

$$\left.\begin{aligned} f&=\int aF_0(Z,W)(W^2-1)^{1/2}W(W_0-W)^2dW\,,\\ &\text{and}\\ a&=\left(\frac{1}{12}K^2L_0+\frac{3}{4}L_1\right)\\ &=\frac{1}{12}\left\{\frac{F_1}{F_0}(W^2-1)+(W_0-W)^2\right\}\,. \end{aligned}\right\} \quad (1)$$

This value of $\log ft$ is smaller by about 3 than those of other a-type beta-emitters. Further, according to the nuclear shell model, the beta-spectrum of Ni^{63} must be an l-forbidden spectrum ($\Delta j=1$, $\Delta l=2$, and parity change no)[10], which has an allowed shape.

To explain these discrepancies, further investigations and discussions are now in progress.

The anthors wish to express their thanks to Dr. M. Umezawa for his helpful discussions.

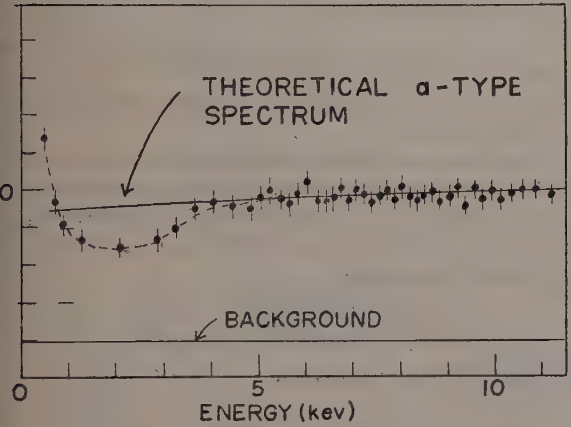

Fig. 3. Low energy part of the beta-spectrum of Ni^{63}.

References

1) H. W. Wilson and S. C. Curran: Phil. Mag. **40** (1949) 631.
2) H. W. Wilson: Phys. Rev. **79** (1950) 1032.
3) A. R. Brosi, C. J. Borkowski, E. E. Conn, and J. C. Griess Jr.: Phys. Rev. **81** (1951) 391.
4) Y. Kobayashi: Journ. Phys. Soc. Jap. **8** (1953) 440.
5) E. J. Konopinski and G. E. Uhlenbeck: Phys. Rev. **60** (1941) 308.
6) D. Saxon: Phys. Rev. **81** (1951) 639.
7) H. M. Schwartz: Phys. Rev. **86** (1952) 195.
8) H. W. Wilson: Phys. Rev. **82** (1951) 548.
9) G. T. Seaborg and I. Perlman: Rev. Mod. Phys. **20** (1948) 585.
10) M. G. Mayer, S. A. Moszkowski and L. W. Nordheim: Rev. Mod. Phys. **23** (1951) 315.

J. Phys. Soc. Japan 8 (1953) 685~686

Excess and Defect Kikuchi-bands

By Yoshiro KAINUMA
Physical Institute, Nagoya University, Nagoya

(Received May 22, 1953)

The theory of Kikuchi-pattern presented by the author[1], in which he improved Laue's theory of Kikuchi-pattern[2], gives only excess (black) Kikuchi-bands. But many investigators have observed defect (white) bands as well as excess ones. The experimental conditions for their appearance are summarised as follows.

(A) In the case of *transmission* of the electrons with nearly normal incidence through a crystal film[3][4], excess bands are observed, provided that the wavelength of electrons is small and the crystal is thin. When the wavelength of electrons λ or the thickness of crystals D is increased, the part of pattern near the incident spot turns into defect. And the defect part extends outwards with the further increase of λ or D.

(B) In the case of *reflection* on a crystal surfaces[5], excess bands are observed when the angle ϕ is small, ϕ being the angle between the incident beam and the surface (Fig. 1). When ϕ is increased, the part of the pattern with small $\bar{\phi}$, $\bar{\phi}$ being the angle illustrated in Fig. 1, turns into defect. And the defect part extends to larger $\bar{\phi}$ with the further increase of ϕ.

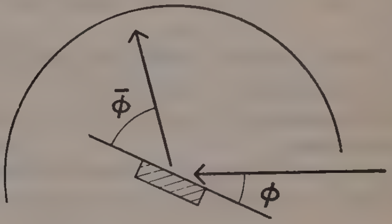

Fig. 1.

Recently Pfister, who observed defect bands, explained his experimental results[4] by taking into account the effect of absorption of electrons in Laue's theory of Kikuchi-pattern.

In this note we take into account the effect of absorption in the author's theory by adopting the complex potential[6] $V^r(\boldsymbol{r})+iV^i(\boldsymbol{r})$, where $V^r(\boldsymbol{r})$ is the ordinary real potential. We expand $V^r(\boldsymbol{r})$ and $V^i(\boldsymbol{r})$ in Fourier series

$$V^r(\boldsymbol{r})=\sum_{\boldsymbol{h}} V_{\boldsymbol{h}}{}^r \exp(-2\pi i\boldsymbol{h}\cdot\boldsymbol{r})$$

and

$$V^i(\boldsymbol{r})=\sum_{\boldsymbol{h}} V_{\boldsymbol{h}}{}^i \exp(-2\pi i\boldsymbol{h}\cdot\boldsymbol{r})\,,$$

and assumed the following conditions for the coefficients.

(1) $V_0{}^i<0$. This is necessary for $V^i(r)$ to represent absorption.

(2) $V_H{}^r V_{-H}{}^i + V_{-H}{}^r V_H{}^i > 0$. This is likely to be the case for low indices H, because the general features of $V^r(r)$ and $V^i(r)$ are supposed to be not very different.

The result of the calculation performed under the above mentioned assumptions on symmetrical bands is summarised as follows.

(A) In tne case of *transmission*, excess bands are expected similarly as in the case of no absorption, if λD is small. When λD is increased, we have the critical angle $\bar{\theta}_c{}^{(-)}$ given by the relation

$$\cos \bar{\theta}_c{}^{(-)} = \{1 - |V_H{}^i| / |V_0{}^i| \sqrt{1+W^2}\} \cos \theta ,$$

where θ is the angle of incidence (Fig. 2) and W is the Bethe's parameter⁷⁾ representing the deviation from Bragg condition. For $\bar{\theta} > \bar{\theta}_c{}^{(-)}$ excess bands remain excess, while for $\bar{\theta} < \bar{\theta}_c{}^{(-)}$ they chang into defect, where $\bar{\theta}$ is illustrated in Fig. 2.

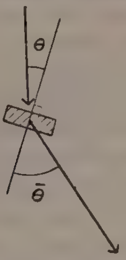

Fig. 2.

(B) In the case of *reflection*, excess bands are expected for $\bar{\phi} > \phi$, and they change into defect for $\bar{\phi} < \phi$.

The above mentioned results agree well with the foregoing experimental observations.

A full account of this work is being prepared for publication.

It is a great pleasure to thank Professor R. Uyeda for his guidance and encouragement.

References

1) Y. Kainuma: To be submitted to Acta Crystallographica.
2) M. v. Laue: Ann. Phys. Lpz. **23** (1935) 705.
3) K. Shinohara and K. Matsukawa: Sc. Pap. Inst. Phys. Chem. Res. **21** (1933) 21.
4) H. Boersch: Phys. Z. **38** (1937) 1000.
H. Pfister: Z. Naturforschg. **7a** (1952) 499.
R. Uyeda, Y. Fukano and T. Ichinokawa: Unpublished.
5) Alam, D. W. Pashley and M. Blackman: Private communication.
6) K, Moliére: Ann. Phys. Lpz. **34** (1939) 461.
K. Kohra: J. Phys. Soc. Jap. **5** (1950) 272.
G. Honjo, K. Kanbe and K. Mihama: Unpublished.
7) H. Bethe: Ann. Phys. Lpz. **87** (1928) 55.

J. Phys. Soc. Japan **8** (1953) 686~687

On Isihara-Hayashida's Theory of the Second Virial Coefficient for Rigid Convex Molecules

By Taro Kihara
Department of Physics, University of Tokyo
(This note is sent from the University of Wisconsin, U.S.A.)

(Received May 26, 1953)

Isihara and Hayashida¹⁾ derived a general formula of the second virial coefficient, B, for rigid convex molecules:

$$B = v + \frac{1}{4\pi} \rho s ,$$

or

$$B = 4vf , \qquad f \equiv \frac{1}{4}\left(1 + \frac{1}{4\pi} \frac{\rho s}{v}\right) .$$

Here v and s are the volume and the surface area of the convex moiecule and ρ is the integral of the supporting function, H, with respect to the entire orientations (θ, φ),

$$\rho = \int H d\omega = \int\int H(\theta, \varphi) \sin \theta d\theta d\varphi .$$

The value $f-1$ indicates deviation from rigid sphere behavier.

They also calculated the values of v, s, and ρ for several particular convex bodies and tabulated the results²⁾. Some parts of their calculations, however, are in error and will be corrected here.

Eq. (10) should be

$$d\omega = \frac{1}{\sqrt{3}} \frac{x+y+z}{(x^2+y^2+z^2)^{1/2}} \frac{dS}{x^2+y^2+z^2} \tag{10}$$

instead of their expression

$$d\omega = \frac{dS}{x^2+y^2+z^2} .$$

Consequently, Eqs. (11) and (12) should be corrected as

$$\frac{4}{\sqrt{3}} \int_{\Delta BCD} \frac{(x+y+z)^2}{(x^2+y^2+z^2)^2} dS$$
$$= \frac{24}{\sqrt{3}} \int_{\Delta BGL} \frac{r dr d\theta}{(\frac{1}{3}+r^2)^2} = 12\sqrt{2} \tan^{-1}\sqrt{2} ,$$

and

$$\rho = 6 \tan^{-1}\sqrt{2} . \tag{12}$$

The f-value for the regular tetrahedron is, therefore,

$$f = \frac{1}{4}\left(\frac{9\sqrt{6}}{\pi} \tan^{-1}\sqrt{2} + 1\right) = 1.926 \tag{13}$$

instead of their value 5/2.

As regards regular octahedron, Eqs (15), (16), and (18) should also be corrected as

shape	sphere	cube	regular tetrahedron	regular octahedron	circular cylinder	circular disk	line segment
size	radius 1	side 1	side 1	side 1	length l radius a	radius 1	length 1
v	$4\pi/3$	1	$\sqrt{2}/12$	$\sqrt{2}/3$	$\pi a^2 l$	0	0
s	4π	6	$\sqrt{3}$	$2\sqrt{3}$	$2\pi a(a+l)$	2π	0
ρ	4π	3π	$6\tan^{-1}\sqrt{2}$	$12\cot^{-1}\sqrt{2}$	$\pi(\pi a+l)$	π^2	π
f	1	1.375	1.926	1.330	$\dfrac{\pi a^2+(\pi+3)al+l^2}{8al}$	—	—

$$6\int_{PQRS}\frac{z^2}{(x^2+y^2+z^2)^2}dS$$

$$=48\int_{\Delta ALS}\frac{rdrd\theta}{(r^2+1)^2}=12\sqrt{2}\cot^{-1}\sqrt{2}, \quad (15)$$

$$\rho=12\cot^{-1}\sqrt{2}\ , \quad (16)$$

and

$$f=\frac{1}{4}\left(\frac{9\sqrt{6}}{\pi}\cot^{-1}\sqrt{2}+1\right)=1.330. \quad (18)$$

As a result, their table must be replaced by the table given here. (s for the sphere and ρ for the cylinder were miswritten!)

It is to be noted that these values of ρ can be obtained without any integral calculation. The simplest way is to use the relation

$$\rho=\frac{1}{2}\sum_{i=1}^{N}(\pi-\alpha_i)l_i\ ,$$

which holds for any convex polyhedron. Here l_1, $l_2, \ldots, l_N$ indicate the length of the edges and α_i is the angle of the i-th edge. (Details will be published later.)

Their result for the ellipsoid of revolution with the eccentricity ϵ seems to be right except that Eq. (25) should be

$$f=1+\frac{1}{15}\epsilon^4+\frac{1}{15}\epsilon^6+\ldots, \quad (25)$$

as I have already noticed3).

References

1) A. Isihara and T. Hayashida: J. Phys. Soc. Japan **6** (1951) 40.

2) Isihara and Hayashida: J. Phys. Soc. Japan **6** (1951) 46.

3) T. Kihara: J. Phys. Soc. Japan **6** (1951) 289.

PROGRESS OF THEORETICAL PHYSICS

Published by

The Yukawa Hall

with the cooperation of

The Physical Society of Japan

Progress of Theoretical Physics Vol. 9, No. 6, 1953

On the Interaction of Additive Electrons with the Polarization in Ionic Crystals, I....Yutaka Toyozawa, Teturo Inui and Yasutada Uemura....563
On the Inelastic Collision between Molecules, III ——Rotational Transitions in H_2-gas——............Kazuo Takayanagi and Tadashi Kishimoto....578
On the Convergence of the Perturbation Method in the Quantum Field Theory ....Ryôyû Utiyama....593
Scattering Problem in the Intermediate-coupling Theory, I .....Ziro Maki, Masatomo Sato and Sin-itiro Tomonaga....607
On the Quantum Theory of Fields...........................Dominique Rivier....633
On the Origin of the Anisotropy Energy of $CuCl_2 \cdot 2H_2O$ ....Toru Moriya and Kei Yosida....663
Letters to the Editor:
On the Evaluation of the Operator Function log $(e^y e^x)$.....I. Fujiwara....676

On the Electronic Polaron State……………………Y. TOYOZAWA….677
A Note on the Elastic Frequency Distribution Function of Crystal
……………………………………S. HUZINAGA….678
Numerical Work on the Fluctuation Problem of Electron Cascades
………………A. RAMAKRISHNAN and P. M. Mathews….679
On the Separability of Dirac Equation ………………T. TAKABAYASI….681
On the D State Probability of Deuteron …………………S. MACHIDA….683
On the Families of Spinor Fields …………S. ÔNEDA and H. UMEZAWA….685

Progress of Theoretical Physics Vol. 10, No. 1, 1953

Deuteron Stripping Reaction……………………………Shiro YOSHIDA…. 1
Statistical Mechanics of General Brownian Motions Underlying Irreversible Processes ……………………………Tsunenobu YAMAMOTO…. 11
Ionization of Gas by Electrons…………Julian K. KNIPP, Tetsuo EGUCHI, Masato OHTA and Shozo NAGATA…. 24
Theory of the Interactions with Higher Derivatives and its Application to the Non-local Interaction……………………Yasuhisa KATAYAMA…. 31
On the Interaction of Additive Electrons with the Polarization in Ionic Crystals, II………Yutaka TOYOZAWA, Teturo INUI and Yasutada UEMURA…. 57
A Tentative Interpretation of Bickford's Observation of the Resonance Absorption in Magnetic below its Transition Point……Takeo NAGAMIYA ……. 72
Theory of Normal Modes of Vibration of Crystal …………Sadaaki YANAGAWA…. 83
Statistical Theory of Hindered Rotation in Molecular Crystals, II ——Quantum Effects ……………………………Tutô NAKAMURA…. 95

Letters to the Editor:

Perturbation Theory of Relativistic Eigenvalue Problem ……………………N. MUGIBAYASHI and M. NAMIKI….108
New Description of Field——Classical Field——.Y. TAKANO and I. SUZUKI….110
Some Comments on the Theory of V-particle…………………K. ONO….111
The β-γ Angular Correlation of Sb^{124}……..M. MORITA and M. YAMADA….111
Theory of Rearrangement Collisions ………Y. FUJIMOTO, S. HAYAKAWA and K. NISHIJIMA….113
On the Conservation of Heavy Particles O. HARA, T. MARUMORI, Y. OHNUKI and H. SHIMODAIRA….114
The Statistical Quantum Mechanics of Time-dependent Phenomena and Viscosity ……………………………T. SASAKAWA….116
Interaction between Spin Waves and Conduction Electrons….A. KONDOH….117
'Quantum Condition' in the Phase-space Representation of Quantum Mechanics……………………………T. TAKABAYASI….119
Equivalence between the Formulation of Quantum Mechanics in terms of Quantum Potential and the One in terms of Markoff-like Process ……………………………T. TAKABAYASI….121
Subsidiary Conditions in the Phase-space Representation of Quantum Mechanics……………………………T. TAKABAYASI….122

Price $1.00 pea copy
$12.00 per year (postage inclusive)
Annual dues for foreign members (individual subscribers)
$ 9.00 (postage inclusive)
〃 for foreign members of the Physical Society of Japan
$ 7.50 (postage inclusive)

Application for members, subscriptions and orders for back mumbers should be sent, directly or through book-dealers, to

The Publication Office
in
Yukawa Hall, Kyoto University, Kyoto, Japan

JOURNAL OF THE PHYSICAL SOCIETY OF JAPAN Vol. 8, No. 6, Nov.—Dec., 1953

On the Disintegration of RaB

By Seizaburo KAGEYAMA

Physical Institute, Tokyo University of Education

(Received May 14, 1953)

The disintegration of RaB was studied by a β-ray spectrometer, with coincidence counter techniques. The β-ray spectrum of RaB obtained was complex, consisting of two components with end point energies 590±10 and 650±10 Kev.

This results was also confirmed by coincidence measurements between the internal conversion electrons of the 242, 295 and 350 Kev γ-rays of RaC and the β-rays of RaB, using a pair of 180° focussing spectrometers.

The relative intensities of the two β-ray groups obtained 5:4 was in accord with the excitation probabilities given by Ellis, and also with the transition probabilities calculated from the γ-ray intensities obtained by Muller et al.

Judging from these experimental results, the level scheme proposed by Ellis seems to be more plausible than that of Stern.

§ 1. Introduction

The β-ray spectrum of RaB was first studied by Gurney[1], who obtained a value of about 650 Kev for the end point energy. Ellis and Skinner[2] have proposed the level scheme of RaC shown in Fig. 1 (a), on the basis of the observed energies and intensities of internal conversion electrons. Ellis[3] later revised it, on the basis of results of photoelectric measurements of γ-ray intensities and further gave the excitation probability of each level, as shown in Fig. 1 (b). Nothing was definitely mentioned by him however concerning the correlation between the 650 Kev β-ray group and the excited levels of RaC, though the spin assignments and the excitation probabilities given by Ellis indicate that the 295 (or 350) Kev excited level of RaC is fed by the 650 Kev β-ray group and also suggest the presence of another β-ray group to directly feed the 350 (or 295) Kev excited level. Therefore, we should have a complex β-ray spectrum composed of two components differing in energy only to the extent of about 57 Kev and possessing approximately the same intensities.

Moreover, Latyshev[4] has suggested the presence of a hard component of about 720 Kev, from the analysis of the β-ray spectrum of RaB and RaC.

On the other hand, according to the disintegration scheme proposed by Stern[5] and shown in Fig. 1 (c), we should have a single β-ray spectrum having an end point energy of 650 Kev.

Recently, Muller, Hoyt, Klein and DuMond[6] have confirmed the energy relation expected to occur between the 295, 242 and 53 Kev γ-rays, by precise measurements of these γ-ray energies, and this supports Stern's scheme, but their assertion seems also to be applicable to Ellis' scheme.

Leaving out the common problem on the level schemes of 1 (b) and 1 (c), which will be discussed later, there is a questionable point in this latter scheme, that is, if we adopt it, the probability of the transition from the 56 Kev excited level to the ground state should be very large and a strong L_1 conversion line corresponding to this transition should be found, be it only an electric dipole transition. However, no trace of such

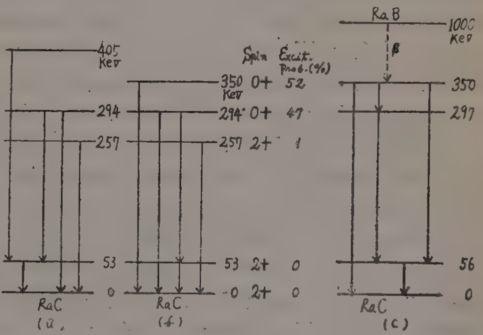

Fig. 1. Decay schemes for RaB.
(a) Ellis and Skinner, (b) Ellis, (b) Stern.

a conversion line is to be found in the spectra obtained either by Gurney or by Ellis et al.

The direct investigation of the disintegration scheme of RaB is hampered by the shortness of its life time and by the superposition of the powerful β-rays of its daughter product RaC. Therefore, in order to look into the discrepancies described above, we resorted to β-γ and γ-γ coincidence measurements, using a pair of 180° focusssing spectrometers.

§ 2. Experimental Arrangement and procedure

In order to investigate the structure of the β-ray spectrum of RaB and to obtain some information on the relative intensities of its components, the β-ray spectra of RaB and RaC were re-examined with the same magnetic focussing spectrometer and experimental procedures as described in the previous papers⁽⁷⁾. As source for the β-rays, Rn sealed in a glass ampule, with a thickness of about 2.7 mg/cm² was used. Similar G–M tubes, having mica windows of about 0.3 mg/cm² thickness and working in coincidence, were employed as a detector.

At first, by mounting the source in the spectrometer described just above (herein-after to be designated as M_1), the coincidence rates between the internal conversion electrons focussed by M_1 and primary β-rays emitted backwards through the mica window of about 1 mg/cm² in thickness are measured as a function of the Al absorber thickness interposed in front of the β-ray counter. Upon considering the sensitivity of this arrangement, which will be discussed in the next section, M_1 was soon after reconstructed to have a focussing radius of 6 cm. A single G–M counter (herein-after to be designated as the M_1-counter) of the same size as in the above experiment was used as a detector for the focussed electrons, and β-particles penetrating the mica window and the Al absorber were counted by a G–M tube of end window type (β-counter) having a mica window of 3 mg/cm².

Individual G–M tube pulses were counted alternately by a 512-scaling circuit and the coincidence rates continuously by a 16-scaling circuit. By suitably selecting the RC constant of the Rossi circuit and the grid bias of the mixer valve, the over-all circuit resolving time could be varied from 1 to 0.1 micro-second.

When the chance and cosmic coincidence rates are subtracted from the observed rates, the resultant rates should represent the coincidence rates between the β-particles of RaB and the internal conversion electrons of the RaC γ-rays. However, with the finite resolving time of the electrical circuit, in addition to the coincidence rates sought, there exist various true coincidence rates between the conversion electrons examined and the β-rays of RaC, between the β-rays of RaB and RaC detected in each other counter, etc. These contributions may be calculated as will be seen in § 5, and are found to be small compared with the coincidence rates sought. However, even these, excepting the coincidences related to conversion electrons, have been completely eliminated by the use of the offset method⁽⁸⁾ as explained below.

β-ray spectra taken on M_1 are shown in Fig. 3a. In the figure, position (1) represents the obtained conversion electron peak and (2) is the offset point. The total counting rates of the M_1-counter, at the exciting current corresponding to the positions (1) and (2), and of the β-counter may be expressed as follows,

$$\left.\begin{aligned} N_1 &= n_{1c}+n_{1\beta}+n_{1\beta}'+n_{1\gamma}+n_{1\gamma}' , \\ N_2 &= n_{2\beta}+n_{2\beta}'+n_{2\gamma}+n_{2\gamma}' , \\ N_\beta &= n_\beta+n_\beta'+n_\gamma+n_\gamma' , \\ &(n_{1\gamma}\equiv n_{2\gamma} , \quad n_{1\gamma}'\equiv n_{2\gamma}') , \end{aligned}\right\} \quad (1)$$

where numerical subscripts refer to the positions of the M_1-counter in the spectrum. n_{1c}, $n_{1\beta}$ and $n_{1\beta}'$ are the partial rates at the position (1), due to conversion electrons, and the continuous β-rays of RaB and RaC respectively. $n_{1\gamma}$ and $n_{1\gamma}'$ are the partial rates due to the γ-rays of RaC and RaC′ respectively. Analogous values are represented in the case of position (2) by $n_{2\beta}$, $n_{2\beta}'$, $n_{2\gamma}$ and $n_{2\gamma}'$, while n_β, n_β', n_γ, and n_γ' are the values for the β-counter. Now, let us represent by $n_{1\beta}$–n_β', etc. the true coincidence rates between the β-rays of RaB recorded by the M_1-counter and the β-rays of RaC counted by the β-counter etc. Then, the true coincidences expected for the position (1) may be given as follows,

$$\left.\begin{array}{lllll} n_{1e}-n_{\beta} & n_{1\beta}-n_{\beta}' & n_{1\beta}'-n_{\beta} & n_{1\gamma}-n_{\beta} & n_{1\gamma}'-n_{\beta} \\ n_{1e}-n_{\beta}' & n_{1\beta}-n_{\gamma} & n_{1\beta}'-n_{\gamma} & n_{1\gamma}-n_{\beta}' & n_{1\gamma}'-n_{\beta}' \\ n_{1e}-n_{\gamma} & n_{1\beta}-n_{\gamma}' & n_{1\beta}'-n_{\gamma}' & n_{1\gamma}-n_{\gamma} & n_{1\gamma}'-n_{\gamma} \\ n_{1e}-n_{\gamma}' & & & n_{1\gamma}-n_{\gamma}' & n_{1\gamma}'-n_{\gamma}' \end{array}\right\} \tag{2}$$

Except for the first column, similar coincidences may be expected for position (2).

Let us now assume that a small increase of the exciting current (position (2)) does not change the partial rates due to the continuous β-rays of RaB and RaC. We may then write

$$n_{1\beta}=n_{2\beta}\,,\quad n_{1\beta}'=n_{2\beta}'$$

and the difference of the true coincidence rates for the two positions would then be represented by the terms given in the first column of expression (2). The contributions of $n_{1e}-n_{\gamma}$, $n_{1e}-n_{\gamma}'$ coincidences among the remaining true coincidences were experimentally obtained by the interposition of a thick Pb absorber in front of the β-counter and were found to be negligibly small. The magnitude of the remaining $n_{1e}-n_{\beta}'$ can be theoretically calculated and so can the coincidence between β-rays of RaB and RaC (§ 5), and its contribution is found to be also very small.

For the purpose of determining more precisely the end point energy of each spectrum of RaB, and of obtaining the momentum distribution curve of each β-ray spectrum which feeds the three intense γ-rays and also to investigate the correlations between these γ-rays, we replaced the Al absorber used in the experiment described above by a second spectrometer (M_2 in Fig. 2). This spectrometer has a vacuum chamber 3 cm deep and a fixed focussing radius of 4 cm. A G–M counter employed for this spectrometer was of a type similar to that used for M_1. For measuring the γ-γ coincidence the resolving power of the M_2 spectrometer must necessarily be high and the same may be said M_1, but this does not apply for the β–γ coincidence. This point will be further discussed in next section, but it may be mentioned here that this fact permitted us to change the available solid angle of the focussed beam by modifying the width of the baffle system according to the aim.

The magnetic field of each spectrometer was independently adjusted by separate exciting coils. The M_1 field, however, suffered a large disturbance from the M_2 field. Therefore, we usually measured the β-ray spectrum on M_1 with a fixed exciting current on M_2. The absolute counting rates of conversion electrons on M_1 are not influenced by the superposition the M_2 field.

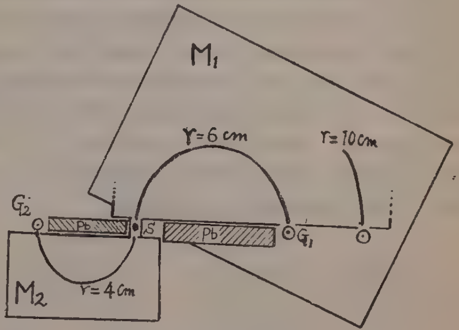

Fig. 2. Experimental arrangement of a pair of spectrometers.

In addition to the coincidence rates sought between the β-rays of RaB and conversion electrons, and between conversion electron groups, there again are various coincidences between the β-rays of RaB and that of RaC, etc. just as in the experiment described above. By the use of the offset method already described, these contributions were again completely eliminated. That is, the coincidence measurements were alternately performed at the positions (1,4) and (2,4) for γ–β coincidences, and (1,3) (1,4) (2,3) and (2,4) for γ–γ coincidences (Fig. 3). The former figures in the brackets correspond to the positions of the M_1-counter in the β-ray spectrum and the latter those concerned with the M_2 counter.

The intensity of Rn source used in these experiments was about 0.02 mC.

The time lag occurring between the entrance of the particle into the G–M counter and the potential drop of the wire has been experimentally and theoretically examined by many authors⁽⁹⁾. Rotblat⁽¹⁰⁾ found the average differences in time lag to be of the same order of magnitude as the time lag itself, and to be about 1 microsecond in ordinary G–M tubes. On the other hand, Mandeville and Scherb⁽¹¹⁾, Ticho⁽¹²⁾, Hartob, Muller and Verster⁽¹³⁾ have shown that the genuine coincidences were not varied by the reduction of the resolving time down to the order of magnitued of 10^{-8} second.

However, the time lag is obviously dependent upon the size of the counter, the nature and pressure of the contained gas, and the value of the leak resistance. Therefore, when the G–M tube is used with an electrical circuit of short resolving time, the variation of the genuine coincidences must be examined as a function of the time constant of the circuit. We have examined this, using the coincidences between the conversion electrons of the 350 Kev γ-rays and β-rays of RaB and varying the time constant from 1 to 0.1 microsecond. We found absolutely no variation of the genuine coincidence.

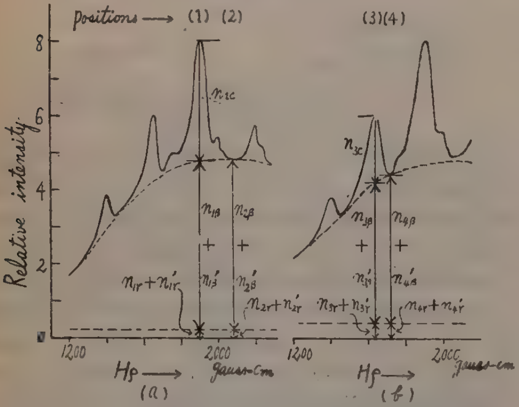

Fig. 3. β-ray spectrum obtained on each spectrometer.

§ 3. The Sensitivity of the β–γ and γ–γ Coincidence Experiments[14)]

Fig. 3 shows a part of the spectrum obtained by the spectrometers M_1 and M_2 respectively. From these data, we may discuss the sensitivity of the β–γ and γ–γ coincidence measurements by the use of a pair of fixed focussing spectrometers.

For the positions (1,2,3 and 4), the total counting rates are given by the expression (1) except for the last one. This last must be replaced by the next two expressions.

$$\left.\begin{aligned} N_3 &= n_{3c}+n_{3\beta}+n'_{3\beta}+n_{3\gamma}+n'_{3\gamma} \\ N_4 &= \qquad\ \ n_{4\beta}+n'_{4\beta}+n_{4\gamma}+n'_{4\gamma} \\ &(n_{3\gamma}\equiv n_{4\gamma},\quad n'_{3\gamma}\equiv n'_{4\gamma}) \end{aligned}\right\} \quad (3)$$

where the notations on the right have similar meanings as in Ex. (1).

Let us first consider the β–γ coincidence. Let ω_1 be the fraction of the conversion electrons of groups 1 collected by the M_1-counter at the position (1). ω_4 the fraction of the continuous β-spectrum of RaB collected by the M_2-counter at the position (4), and N_0 the rate of disintegration of RaB per unit time.

Then the β–γ coincidence rates may be expressed as follows

$$C_g = N_0\omega_1\omega_4 = n_{1c}n_{4\beta}/N_0 . \qquad (4)$$

The chance coincidence is given by the usual formula, $C_c = 2\tau N_1 N_4$. The ratio of the true to the chance coincidence rates, therefore, is given by

$$\frac{C_g}{C_c} = \frac{1}{2\tau N_0} \cdot \frac{n_{1c}}{N_1} \cdot \frac{n_{4\beta}}{N_4} .$$

From this formula, it evidently follows that:

(1) From the first factor: In order to obtain true coincidence rates comparable to the chance coincidences, it is necessary to use an electrical circuit having a very short resolving time constant and a weak source.

(2) To increase the second factor, we must use a spectrometer for M_1 which has a fairly high resolving power, not however at the expense of the counting rates of n_{1c}. For this reason, M_1 was reconstructed to have a focussing radius of 6 cm.

(3) From the third factor: We see that high resolving power is not needed for M_2, in contrast to the case of M_1.

In the case of the γ–γ coincidence measurements, the last factor of the above formula is replaced by n_{3c}/N_3. In this case, in addition to the coincidence rates between the conversion electron groups, there exist the true electron-β coincidence rates discussed just above. The total true coincidence rates, at the positions (1,3), may be given as follows:

$$C'_g = (n_{1c}n_{3c} + n_{1\beta}n_{3c} + n_{1c}n_{3\beta})/N_0 .$$

In order to obtain the γ–γ coincidence rates comparable to the β–γ coincidences, we are therefore required to have a predominant conversion peak collected by M_2.

§ 4. Experimental Results

The β-ray spectra of RaB and RaC obtained are in complete agreement with that obtained in previous experiments[7)].

A Fermi plot of the spectra is shown in Fig. 4a. The lower energy part and the 650 Kev region are also shown respectively in Fig. 4b and 4c in an enlarged scale.

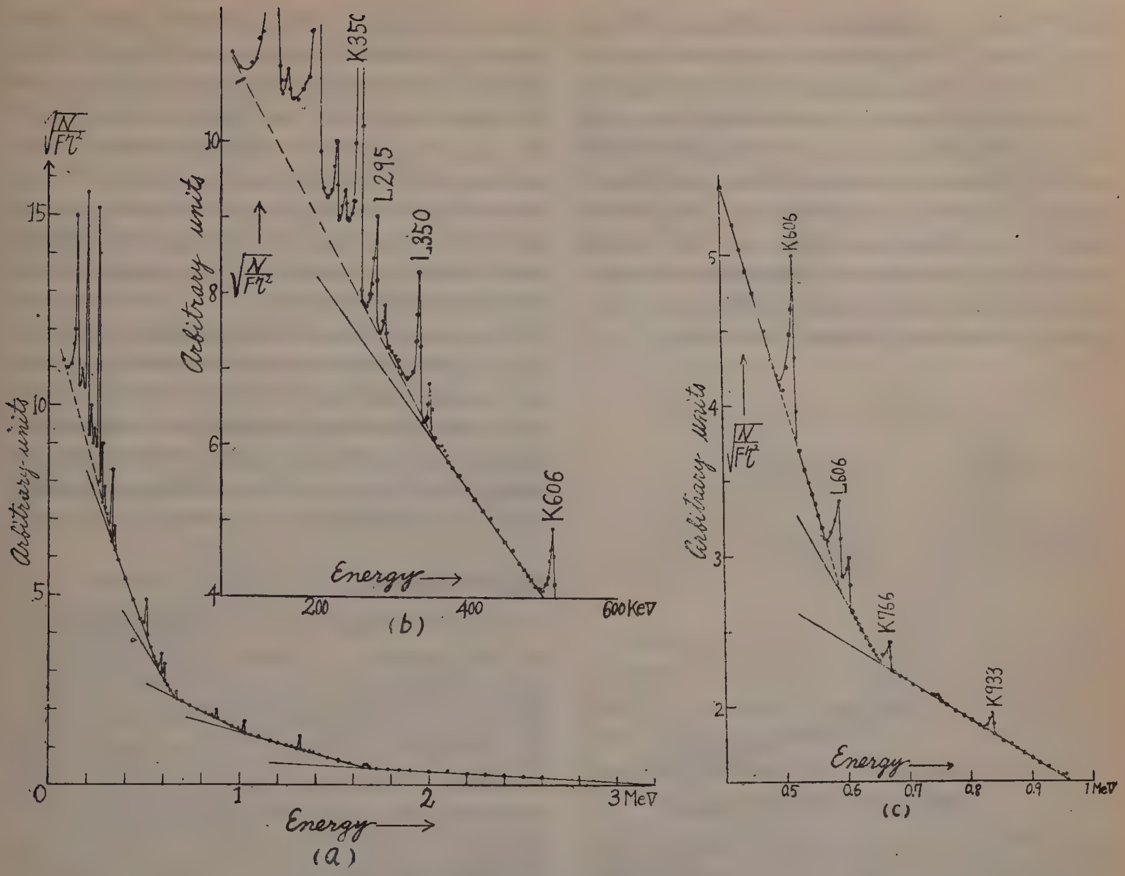

Fig. 4.
(a) Fermi plot of the β-ray spectra of RaB and RaC. (b) shows the lower energy part (c) shows the 650 KeV region in enlarged scale respectively.

The subtraction of the various components was done in the usual manner assuming that an allowed shape is applied to each. In this way six β-ray groups could be resolved. Their end point energies were found to be 360 ± 20, 590 ± 10, 650 ± 10, 1000 ± 30, 1650 ± 50 and 3200 ± 100 Kev respectively. The relative intensities of the six components were obtained by reconstructing the momentum distribution of each component and comparing their areas. These were 35 : 200 : 160 : 70 : 200 :80. The error in the intensity determination was about 15% for each component.

Two groups of higher energy, 3200 and 1650 Kev, unmistakably belong to RaC and their end point energies are in good agreement with the results obtained by Latyshev et al.⁴⁾ The 1000 Kev group probably also belongs to RaC. The relative intensity of the sum of the 1000 and 1650 Kev components and the 3200 Kev component is also in excellent agreement with Latyshev's results.

The actual presence of the softest 360 Kev component is doubtful. It may be explained by the superposition of the internal conversion electrons of the 242, 295 and 350 Kev γ-rays straying out of the glass ampule and the backscattered electrons. Indeed, the corresponding end point energy was found to move toward the higher energy side when a thicker glass ampule was used. A 720 Kev β-group, suggested by Latyshev was not distinguished in our experiment.

The two β-ray groups of 590 and 650 Kev end point energies unmistakably belong to RaB. The end point energy of the harder component is in excellent agreement with the result obtained by Gurney. The intensity ratio of the two groups was in agreement with the excitation probability given by Ellis within the experimental error.

The absorption curves of coincidence rates between conversion electrons of 295 and 350 Kev γ-rays, and β-rays of RaB are shown in

Fig. 5, with normalization at 21 mg/cm² for both curves. The dotted curve shows the absorption of β-rays recorded by the β-counter.

The end points 210±10 and 230±10 mg/cm² correspond to the maximum energy of 590±20 and 650±20 Kev, calculated from the range-energy relation obtained by Katz and Penfold[15]. However, the true to chance coincidence ratios for the presence of energetically predominant β-rays of RaC are very small for the end parts of the curves.

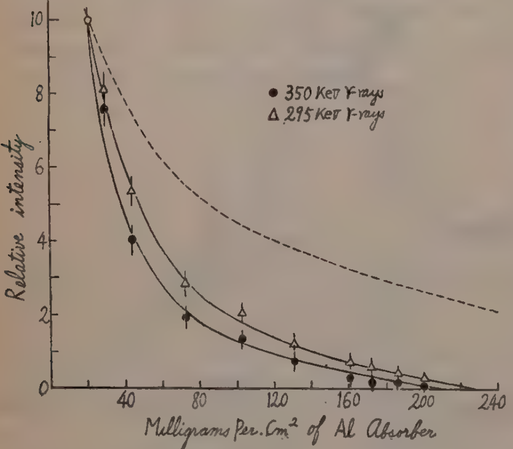

Fig. 5. The absorption of the coincidence rates between β-rays of RaB and internal conversion electrons as a function of the Al absorber interposed in front of β-ray counter. The dotted curve shows the absorption of β-rays of RaB and RaC recorded by the β-counter.

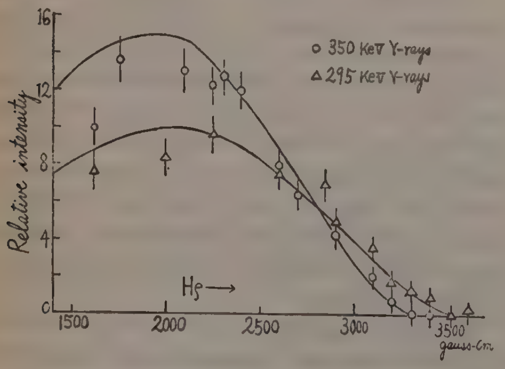

Fig. 6. Conversion electron-β-ray coincidences as taken on a pair of spectrometers. The two curves show the two component of the β-ray spectrum of RaB derived from the analysis of the Fermi plot (Fig. 4).

The momentum distributions of the β-ray groups feeding the 295 and 350 Kev γ-rays are shown in Fig. 6 respectively. Each spectrum roughly agrees with that derived from an analysis of the Fermi plot. The same experiment was repeated using K conversion electrons of the 242 Kev γ-rays. In this case, however, the experimental error was larger compared with the former cases, because of the small counting rates of the conversion electrons. But it seems reasonable to conclude that these γ-rays are related to the hard component of the β-rays as is expected from Fig. 1 (b).

The γ–γ coincidence was measured between the K conversion electrons of 295 and 350, and between 242 and 350 Kev γ-rays. The experimental results showed no correlation between these three intense γ-rays, but the experimental errors were very large compared with that described just above.

§ 5. Discussion

From the ft-value, the β-disintegration of RaC is thought to belong to the first forbidden change $\Delta I=1$ and parity change yes. Therefore, the splitting of the Fermi plot into straight lines may not necessarily be significant, since some spectra do not show a simple Fermi distribution. However, the condition that the correction factor for forbiddenness reduces to a constant is given by Konopinski[16] as

$$Z \gg 1.6 W_0^{3/2}$$

where W_0 is the maximum total energy of the ejected electrons in a unit of m_0c^2. This condition is roughly satisfied in the case of RaC. Therefore, we may assume that the allowed form is applicable to each β-ray spectrum of RaC as a first approximation.

The energy differences between the two β-ray components, 590 and 650 Kev, and the spurious component 360 Kev were accidentally in accordance with the 242 and 295 Kev γ-rays within experimental error. However, in the γ–γ coincidence experiment, there was found no correlation between three intense γ-rays. The origins of the appearance of this spurious group are discussed in the previous section, and moreover it may also be explained by the correction term of the forbidden shape.

The observation of the 590 Kev β-ray component from the Fermi plot was rendered very difficult by the small energy difference between the two β-ray groups. Moreover, superposition of the L and M internal conversion electrons of the 606 Kev γ-rays at about 590 Kev and the K electrons of 766 Kev γ-rays at about 670 Kev would have made it even more difficult. Indeed when the spectrometer was of poor resolving power, the soft component was completely masked by the hard group. However, coincidence measurements both with and without the M_2 spectrometer have clearly shown the presence of the two components of the β-rays, and the energy difference at their end points was in agreement with that of the excited levels. The relative intensities of the two components obtained accord with the excitation probabilities given by Ellis. They are also in good agreement with the transition probabilities for the sum of 242 and 295 Kev, and for 350 Kev, calculated from the γ-ray intensities obtained by Muller et al, and from α_k's described below.

The magnitude of the coincidence rates between the conversion electrons of RaC and the β-rays of the same not eliminated by the offset method may be obtained from the following considerations.

The probability that RaC will disintegrate in the time interval between t and $t+dt$, measured from the moment of disintegration of the RaB atom, is $\lambda e^{-\lambda t}dt$, λ being the disintegration constant of RaC. Hence, the rates of expected genuine coincidence, when the duration of the impulses of the conversion electrons is τ, is given by

$$C_g''=C_{\max}\int_0^{\tau}\lambda e^{-\lambda t}dt=C_{\max}(1-e^{-\lambda\tau}),$$

where $C_{\max}$ is the maximum rate of coincidence, which can be experimentally obtained with a circuit having an infinitely long resolving time, and is given by $C_{\max}=n_{1c}n_{4\beta}'/N_0$. The effect of the intrinsic time lag of the counter was neglected in the above integration, since its influence is very small. Thus

$$C_g''=n_{1c}n_{4\beta}'(1-e^{-\lambda\tau})/N_0 .$$

Comparing this expression with Ex. (4), the contribution in question is completely neglected in our cases.

Ellis has assumed that the three intense γ-rays of RaC arise from electric quadrupole transitions, having a strong admixture of magnetic dipole radiation. However, by the use of the relative intensities of the internal conversion lines described in the previous paper[7) and that of the γ-rays obtained by Muller et al.[6), α_k's are given to be (0.49 ± 0.04), (0.20 ± 0.016) and (0.125 ± 0.01) for the 242, 295 and 350 Kev γ-rays, respectively, α_k of 606 Kev γ-rays of RaC′ being taken as 0.006. From a comparison of these values with the theoretical one calculated by Hulme et al.[17) (Table 1), it may not be unreasonable to assign a pure $M1$ radiation for the 242 Kev γ-rays.

Table 1. α_k for γ-rays of RaC

γ-rays in Kev	Experiment	α_k Theoretical	
		E2	M2
242	0.49 ± 0.04	0.15	0.48
295	0.20 ± 0.016	0.083	0.28
350	0.125 ± 0.01	0.052	0.19

According to the ft-value calculated by Feingold[18), the β-decay of RaB assuredly belongs to the allowed transition. The ground state of RaB has zero spin and even parity, since it is a nucleus of even-even type. If Fermi selection rules are applied to this case, the angular momentum assignments given by Ellis [Fig. 1 (b)] seems to be reasonable. However, if the 242 Kev γ-rays were a $M1$ radiation, the assignment of spin 1 and even parity should be given to the 53 Kev excited state. Then, in contradiction with experimental results, we may expect strong β-rays decaying directly to this level, since it becomes an allowed one. The absence of a corresponding β-ray group, however, rules out such an assignment and demands such a transition to be forbidden at least twice more than the observed transitions. The assignment of spin 2 and even parity given by Ellis satisfies these requirements. This discrepancy was theoretically explained by Hulme et al[17).

On the other hand, if the Gamow-Teller selection rules are applied, the angular momental of 1, 1, 3 (or 2), 3 and 3 are given to the five levels respectively, beginning from the top level. In this case, the β-decay from the ground state of RaC to the first excited state of RaC′ should be of $\Delta I=2$ type and have a parity change. This conclusion is in accord with the selection rules for the first forbidden transitions claimed by Nordheim[19).

However, the ground state of ThC differing by two neutrons from RaC has even parity and spin 2. Therefore, RaC becomes an exception to the theoretical requirement, and the explanation of the absence of the 56 Kev γ-rays corresponding to a transition between 350 and 295 Kev excited levels is not given by this assignment.

From the level scheme proposed by Stern, we may expect a strong 56 Kev transition from the 56 Kev level to the ground state. For the γ-rays too soft to be converted in the K-shell, the internal conversion coefficient of the L_1 shall would be large, even if it were an El transition20). Moreover, we have reason to believe that it should be an M1 or E2 transition17). As a result, we may expect strong L_1 conversion electrons for such a transition. However, this has not yet been observed.

From these facts, we come to the conclusion that the disintegration scheme proposed by Ellis is more reasonable than that by Stern. However, the level scheme of neither one satisfactorily explains the absence of the 297 Kev γ-rays, corresponding to the transition from 350 to 53 Kev excited state in the former and from the 297 Kev excited state to the ground state in the latter. The discrimination of those γ-rays from the 295 Kev γ-rays differing in energy by only 2 Kev could not be performed in our experiment. However, no contributions to the K conversion electrons of the 295 Kev γ-rays attributable to such γ-rays could be found by us. There was no difference in the energy distribution of K conversion lines among the 242, 295 and 350 Kev γ-rays.

In conclusion, the author wishes to express his deep appreciation of the encouragement accorded him by Prof. Yoshio Fujioka, and his indebtedness to Prof. Mitsuo Miwa for his valuable suggestions and discussions. Thanks are also due to the Japanese Foundation for Cancer Research for the supply of radon through the kindness of Dr. K. Tsukamoto and Mr. Y. Onai and also to the Ministry of Education for finantial support.

References

1) R. W. Gurney: Proc. Roy. Soc. **A109** (1925) 540.

2) C. D. Ellis and H. W. B. Skinner: Proc. Roy. Soc. **A105** (1924) 165.

3) C. D. Ellis: Inter. Conf. Phys. **1** (1934) 43.

4) C. D. Latyshev: Rev. Mod. Phys. **19** (1947) 132.

5) M. O. Stern: Rev. Mod. Phys. **21** (1949) 316.

6) Muller, Hoyt, Klein and DuMond: Phys. Rev. **88** (1952) 775.

7) M. Miwa and S. Kageyama: J. Phys. Soc. Japan **5** (1950) 416, S. Kageyama, ibid **6** (1951) 285.

8) C. M. Fowler and R. G. Shreffler: Rev. Mod. Phys. **21** (1950) 740.

9) C. G. Montgomery and D. D. Montgomery: Phys. Rev. **57** (1940) 1030.

10) J. Rotblat: Proc. Roy. Soc. **A177** (1941) 260.

11) C. E. Mandeville and M. Scherb: Phys. Rev. **73** (1948) 90.

12) H. K. Ticho: Rev. Sci. Inst. **18** (1947) 281.

13) Hartog, Muller and Verster: Physica **13** (1947) 251.

14) N. Feather: Proc. Cam. Phil. Soc. **36** (1940) 224.

15) L. Katz and A. S. Penfold: Rev. Mod. Phys. **24** (1952) 28.

16) E. J. Konopinski: Rev. Mod. Phys. **15** (1943) 209.

17) Hulme, Mott, Oppenheimer and Taylor: Proc. Roy. Soc. **A155** (1936) 315.

18) A. M. Feingold: Rev. Mod. Phys. **23** (1951) 10.

19) L. W. Nordheim: Rev. Mod. Phys. **23** (1951) 322.

20) Gellman, Griffith and Stanley: Phys. Rev. **80** (1950) 866, ibid **85** (1952) 944; J. B. Fisk: Proc. Roy. Soc. **A143** (1934) 674.

JOURNAL OF THE PHYSICAL SOCIETY OF JAPAN Vol. 8, No. 6, NOV.—DEC., 1953

Thermodynamical Analysis of Life

I. Thermodynamics of transient phenomena

By Motoyosi SUGITA

Hitotubasi University, Kunitati, Tokyo and
Kobayasi Institute of Physical Research, Kokubunzi, Tokyo

(Received April 9, 1953)

The idea of the quasi-static change is based on the local equilibrium. It will be generalized on the base of molecular kinetics. Let us consider the quasi-chemical reaction of the type

$$\sum \nu_{js} A_j \rightarrow \sum \nu_{ks} A_k\,,$$

the rate of this reaction be $\dot{q}_s$ and the distribution function of A_l be n_l. Then

$$\dot{G} = \sum_l u_l \dot{n}_l = -\sum_s \left(\sum_j \nu_{js}\mu_j - \sum \nu_{ks}\mu_k\right)\dot{q}_s\,,$$

where μ_l is the chemical potential of A_l and G is Gibbs' free energy. In the transient state some of $\dot{q}_s s$ are yet very small and they are called the *second coordinate*. Then

$$\sum \nu_{js}\mu_j - \sum \nu_{ks}\mu_k \doteqdot 0\,,$$

on the coordinate. This is the generalization of the *local equilibrium*. Then the product term of G is the *small quantity of higher order* and may be neglected. Then it may be expressed by finite number of $\dot{q}_s$, which can not be neglected and is called the *first coordinate*. Such change of state, which is expressed by the *finite* parameter, is called *generalized quasistatic* one. In the following the living system is assumed to be in such state. Here

$$\left(\sum \nu_{js}\mu_j - \sum \nu_{ks}\mu_k\right)\dot{q}_s\,,$$

of the first coordinate is the heat from the *virtual heat source*, which is the fundamental idea of this paper. Thermodynamics can not be applied to the first coordinate, but we can assume the empirical relation between q_s and the *field of chemical potential*, which can be introduced thermodynamically. Thermodynamical analysis of the phenomena of life is igven in the following.

§ 1. Introduction

The author of this paper is studying the thermodynamics of the irreversible phenomena[1] since 1933 basing on the ideas of the *generalized quasi-static change* and of the *virtual heat source*. Afterwards the theory is applied to many transient phenomena like thermoelectricity[2], gasdynamical phenomena[3], diffusion[4], dielectric loss and dispersion[5], elastic relaxation[6], biochemical reactions[7], metastability and condensation[8]. The results are summarized at first in his work, *New lecture on Thermodynamics*[9] and afterwards in his dissertation, *Thermodynamics of the Transient Phenomena*[10].

The writer's interest is now concentrated on the thermodynamical analysis of life and he has introduced the idea of the *field of chemical potential* and that of the *entropy interaction*[7]. But the *foundation* of the analysis requires the generalization of the idea of the quasi-static change on the base of molecular statistics and also of the new principle, like the maximum principle of the transient phenomena, which has been discussed in the Bulletin of the Kobayasi Institute[11].

In this paper the theory published in Japanese is summarized and the thermodynamical analysis of life is extended further. The method of study is quasi-thermodynamical[12][13][14], which is partly phenomenological and partly statistical. The rigorous method of the statistics might be desirable, but the transient phenomena is very complicated to be treated by the *orthodox* method , especially in the living system.

§ 2. Generalized Quasistatic Process

Thermodynamical quantities are logically defined with regard to the quasi-static change. But in the irreversible or transient phenomena the *local equilibrium* is valid. Local value of temperature and other quantities are thus defined in the transient state. Many authors hesitate, however, in defining the entropy in this manner.

In the generalized quasistatic change, introduced by the author[3][9], the local equilibrium is valid and the physical state is defined by the characteristic functions like

$$\text{(i)}\quad p=f(v,\ T),\qquad \text{(ii)}\quad u=g(v,\ T), \tag{2.1}$$

in which p is the pressure, v the specific volume, T the absolute temperature, u the internal energy, and the functional forms of f and g are assumed to have the same form of the ordinary one. Then the entropy of the "small part" must be defined in the ordinary manner, so that

$$ds=\frac{du+p\,dv}{T}\,. \tag{2.2}$$

Such procedure is taken by many authors in their study of the transient phenomena[15], but the *logical foundation* was somewhat obscure. It is now quite clear from the assumption (i) and (ii) and the local value of the entropy in the transient state is now clearly defined.

The assumption (i) and (ii) are, however, not always valid in any case. For instance in the relaxation phenomena[6] the characteristic equation must have somewhat different form. The generalization on the base of molecular statistics will be described in § 4.

§ 3. Virtual Heat Source

$-dW$ be the work done by the external force and dQ_a the heat flows out of the external system. Then

$$du=dQ_a-dW \quad\text{or}\quad dQ_a=du+dW\,. \tag{3.1}$$

The author has introduced the quantity

$$dQ=du+p\,dv\,, \tag{3.2}$$

basing on the assumption (i) and (ii), where u and p have the ordinary functional form. Then

$$dQ-dQ_a=p\,dv-dW=\delta A\,, \tag{3.3}$$

where δA is the work done against the dissipative force[2][3]. The quantity $dQ-dQ_a$ is called the heat from the *virtual heat source*[4]. The quantity

$$dQ=dQ_a+\delta A\,, \tag{3.4}$$

was called "reversible Wärme" in his previous work[1], but the quantity plays an important role in the irreversible phenomena and therefore the name is not adequate.

From the equation (2.2)

$$dS=dQ/T\,, \tag{3.5}$$

having the same form as in equilibrium state. Let us consider that the reservoir has the same temperature and it's state changes quasi-statically. Then the entropy change of the reservoir is

$$dS_a=-dQ_a/T\,, \tag{3.6}$$

where dQ_a is the heat income to the small part having the entropy change of (3.5). Therefore

$$dS_a+dS=\frac{dQ-dQ_a}{T}=\frac{\delta A}{T}>0\,, \tag{3.7}$$

where $dQ-dQ_a$ is the heat from the virtual heat source. Detailed discussion is omitted, for it has already been discussed previously[6][9].

The equation like (3.4) appears also in the work of Tolman and Fine[16]. The form was, however, adopted already by many authors[17] in their treatment of the irreversible change*, but the *logical base* was not clear. The idea of the *virtual heat source* was introduced in 1933[1] and it is very convenient either in the theory of the transient phenomena or in education[9]. The entanglement of the idea of *heat* in school and college will be put aside and the *logics* will be clear and transparent. The idea will be founded on the base of the molecular statistics in § 4 and § 7.

§ 4. Equilibrium Condition of the Second Coordinates

Let us assume that the partition function of the total system is known. Then the timely change of Gibb's free energy G is

$$\dot G=\sum_i \mu_i \dot n_i\,, \tag{4.1}$$

where

$$\mu_i=\frac{\partial G}{\partial n_i} \tag{4.2}$$

is the chemical potential and n_i is the parameter of the microscopic state i, which is the state in μ-space. Electronic states may also be included in them. If we can consider n_i the number of molecules of i state, them μ_i must be the mean value of the n_i molecules, although the system is in the transient state.

---

* "Puissance d'irréversibilité" of de Donder may be the same idea.

Let us consider the following generalized chemical reaction

$$\sum_j \nu_{js} A_j \rightarrow \sum_k \nu_{ks} A_k \,, \tag{4.3}$$

where A_i's are the symbol of substances and ν_{is}'s are integers, and the rate of this reaction be $\dot{q}_s$. Then $\dot{n}_i$ can be written in the form

$$\dot{n}_i = \sum \Gamma_{is} \dot{q}_s \,, \tag{4.4}$$

where Γ_{is}'s are constants, which can be expressed by ν_{js}'s. For instance there is chemical flow of a substance from j to i, and from i to k in the living body, so that the change of the substance in i state must be

$$\dot{n}_i = \sum \dot{q}_{ji} - \sum \dot{q}_{ik} \,, \tag{4.4$'$}$$

where $\dot{q}_{ji}$ is the rate of flow from j to i (see part III).

From (4.1) and (4.4) we can get

$$\dot{G} = \sum (\sum \Gamma_{is} \mu_i) \dot{q}_s \,. \tag{4.5}$$

The chemical reaction of (4.3) is the type of generalized character, so that the collision of two molecules A and B can be represented by

$$A + B \rightarrow C + D. \tag{4,3$'$}$$

Then the rate of this reaction is

$$\dot{q}_s \propto (n_A n_B - n_C n_D) \,, \tag{4.6}$$

where the suffix specifies the reaction of (4.3′) and n_A is the distribution function of the molecules in the state A. Therefore $\dot{n}_A = -\sum \dot{q}_s$ and

$$\sum_i \Gamma_{is} \mu_i = -(\mu_A + \mu_B) + \mu_C + \mu_D \,. \tag{4.7}$$

In the case of ideal gas $\mu_A \propto kT \log n_A$, so that

$$\sum \Gamma_{is} \mu_i \propto (-\log n_A n_B + \log n_C n_D) \,, \tag{4.7$'$}$$

and

$$\dot{q}_s \propto \{ e^{(\mu_A + \mu_B)/kT} - e^{(\mu_C + \mu_D)/kT} \} \,. \tag{4.6$'$}$$

$\dot{q}_s$ of (4.6′) corresponds to the relation (5.2) of **§ 5.**

If we take (4.3) into account,

$$\sum \Gamma_{is} \mu_i = -\sum \nu_{js} \mu_j + \sum \nu_{ks} \mu_k = -\Delta \mu_s . \tag{4.7$''$}$$

Then

$$\dot{G} = -\sum \Delta \mu_s \dot{q}_s = -\sum (\sum \nu_{js} \mu_j - \sum \nu_{ks} \mu_k) \dot{q}_k \,, \tag{4.5$'$}$$

Therefore $\dot{G}/kT$ may be considered as $\dot{H}$ of Boltzmann's *H*-function in the case of the isothermal change. It will be discussed in **§ 7.**

In the equilibrium state the condition of the *detailed balance* is represented by the equations

$$\dot{q}_s = 0 \text{ and } \sum_j \nu_{js} \mu_j - \sum_k \nu_{ks} \mu_k = 0 \,. \tag{4.8}$$

The last one of (4.8) is the condition of the chemical equilibrium. The steady state is, however, not the equilibrium, so that $\dot{q}_s \neq 0$. If the distribution of n_i is in the steady state, then

$$\dot{n}_i = \sum \Gamma_{is} \dot{q}_s = 0 \,, \quad \dot{q}_s \neq 0 \,. \tag{4.9}$$

(4.9) corresponds to the balance of the chemical substances in our body in the steady state (see part III).

We must notice here a remarkable fact, that some of the $\dot{q}_s$s have very small values in the transient state and (4.8) is approximately valid for them. Then the products $\Delta \mu_s \dot{q}_s$ must be the *small quantity of higher order*, so that the terms of those products in (4.5′) may be neglected. These coordinates, $\dot{q}_s$, are called the *second coordinate*, which are negligible in (4.5′). The chemical *equilibrium* is maintained on these coordinates, although the total system is in the transient state. Then $\dot{G}$ is expressed by the *finite terms*, in which $\dot{q}_s$ is not so small. These coordinates, which can not be neglected, are called the *first coordinate*[11]. It is ordinarily believed, that the system in the transient state must have *infinite* number of parameters. But the equilibrium conditions are maintained on the second coordinates of infinite number, and the system in the transient state is expressed by the first coordinates of the finite number.

Equilibrium of the second coordinates is unconsciously maintained by many authors. For instance, the equilibrium between the activated state and the normal state is assumed in Eyring's theory of the rate processes. This is an example of the equilibrium of the second coordinate, which is the extension of the idea of the local equilibrium. We will call the change of states in the transient phenomena the *generalized quasi-static change* too, which is expressed by the finite numbers of the first coordinates. Then $\sum_s \Delta \mu_s \dot{q}_s$ of the first coordinates is the heat from the *virtual heat source* of **§ 3.** It will be discussed in **§ 8.**

The above consideration is the foundation of the thermodynamics of the transient phenomena and of life. It is ordinarily said that thermodynamics can be applied only to the equilibrium states, In the preceding work[1][9] it is shown that the principle can be applied to the local equilibrium, but now it is clear that the principle is valid on the *second coordinate* of the irreversible system and the equilibrium condition of (4.8) is useful as it will be shown in § **6**.

Thermodynamics is no longer applicable to the first coordinate. But the *idea of the ch. p.* (chemical potential) can be extended to such a system and the kinetic relation $\dot{q}_s$ of the first coordinates and the *field of ch. p.*[5][8][10] may be obtained, if we assume the value of the *kinetic quantities*, which can not be determined thermodynamically. It is discussed in § **5**.

§ 5. Field of Chemical Potential

In regard to the first coordinates it is ordinarily assumed that $\dot{q}_s$ is proportional to $\Delta\mu_s=\sum\nu_{js}\mu_j-\sum\nu_{ks}\mu_k$. It is, however, only true when $\dot{q}_s$ is very small.

From the theory of ordinary thermodynamics it is known that

$$\left.\begin{array}{l}\dot{q}_s>0,\ \text{if}\ \sum\nu_{js}\mu_j>\sum\nu_{ks}\mu_k\\ \dot{q}_s=0,\ \text{if}\ \sum\nu_{js}\mu_j=\sum\nu_{ks}\mu_k\\ \dot{q}_s<0,\ \text{if}\ \sum\nu_{js}\mu_j<\sum\nu_{ks}\mu_k\end{array}\right\}\qquad(5.1)$$

Some authors like Ostwald, Jouguet and de Donder have intended to extend (5.1) quantitatively and got the quasi-thermodynamical relation of the chemical rate:

$$\dot{q}_s=\frac{1}{Rs}\{e^{\Sigma\nu_{js}\mu_j/kT}-e^{\Sigma\nu_{ks}\mu_k/kT}\},\qquad(5.2)$$

where R_s is called the chemical resistance. The bracket, { }, of (5.2) is the *field of ch. p.* (chemical potential), which is the quantity of the thermodynamical nature. Such quantity is called the *circumstance of the equilibrium theory*. But R_s is no longer the thermodynamical quantity, which is called the *kinetic circumstance* or the *circumstance of the theory of rate processes*[7][10]. Its value can be estimated in some cases by the kinetic theory of the rate processes but in general it is not easy. So that we will not go further[10] in the detail of the kinetic circumstance and take the empirical value of R_s. Such phenomenological method is adopted by many authors, like Onsager, Meixner[15] and others. Ordinarily we are content with the empirical values of the diffusion constant, the heat conductivity and others.

R_s has the relation to the reaction constants k_s and k_s' in the following way,

$$k_s=\frac{1}{R_s}e^{\Sigma\nu_{js}\chi_j/kT},\qquad k_s'=\frac{1}{R_s}e^{\Sigma\nu_{ks}\chi_k/kT},\qquad(5.3)$$

where χ_j is the enthalpy and is expressed by

$$\mu_i=\chi_i+kT\log a_i,\qquad(5.4)$$

where a_i is the activity.

This method is very rough but it is powerful to analyse the transient phenomena. This phenomena are very important but are remaining in darkness. Life is also an instance of the transient phenomena. The theoretical base of this method is founded in this paper. For instance the ch, p. in the transient state is obtained by the "cut off method" which is described in § **6**.

On the other hand, there is the misunderstanding concerning the rate of reaction and the field of ch. p.. The mixture of $2H_2+O_2$, for instance, has large chemical stress but the rate of combustion is negligibly small in ordinary temperature. Such system has large chemical resistance R_s and is called *frozen*. The coordinate having large stress and large R_s is called the frozen one. The need for the common sense in this theory is not uncommon and these people including biologists seem to feel *paradoxical aspect*[7]. This is due to the misunderstanding concerning the relation between the field or the stress of ch. p. and the kinetic circumstance.

(5.1) shows the *reversal* of the field, which is very important in the molecular kinetics of condensation, as is shown by (6.8), or of crystal formation as well as in biology[10]. For instance the field of growth of snow flakes must turn in the field of destruction, if the super-saturation of the vapour disappears. The field of growth in our body may also turn in that of destruction, which is determined by a_k or c_k of (5.4). These quantities are depending on the supply of matter, as is shown in the crystal growth of snow flakes. In our body, the supply is maintained by the production of the substances by anabolism. There is close analogy between the social phenomena and construction and destruction in our body, which will be discussed later (see part III).

§ 6. Cut Off Method and Chemical Potential

In stead of the rigorous method of Mayer, Frenkel's method[14] is rough and quasi-thermodynamical, but is very convenient. It will give us valuable information to the treatment of the living system. Let (n) be the symbol of the cluster of n molecules, Z_n the number of the cluster (n) in unit volume and S_M the mixing entropy of the system of single molecules and clusters (2), (3) .... (n). Then

$$G=\sum \mu_k' Z_k - TS_M \,, \qquad (6.1)$$

where

$$\mu_k' = k\mu_0 + \alpha k^{2/3} \,, \qquad (6.2)$$

and μ_0 is the ch. p. of a molecule in the liquid state and $\alpha k^{2/3}$ is the surface energy of (k). If the system is the ideal mixture,

$$S_M = -k \sum Z_k \log c_k \,, \quad c_k = Z_k / \sum Z_k \,, \qquad (6.3)$$

where Z_1 is the number of single molecules. Frenkel derived the following relation from (6.1), (6.3) and $\sum k Z_k = const$

$$\mu_k = \mu_k' + kT \log c_k = k\mu_1 \,. \qquad (6.4)$$

Then

$$c_k = e^{-k\xi} e^{-\alpha k^{2/3}} \,, \quad \xi = (\mu_0 - \mu_1)/kT \,, \qquad (6.5)$$

where $\mu_1 = \mu_1'$ is the ch. p. of the single molecule. In supersaturated state $\xi < 0$, so that $e^{-k\xi}$ must diverge for large value of k. Therefore Frenkel introduced the *upper limit* of k and *cut off* the terms corresponding to the higher numbers of k. The method is generalized in the following[18].

μ_k of (6.4) is the ch. p. of (n) in the system and the relation to the total system (i.e. super-saturation) is expressed by $kT \log c_k$. In the living system the calculation of S_M is hardly possible, but we can take formally the activity a_k in stead of c_k into consideration. Then

$$\mu_k = \mu_k' + kT \log a_k \,, \qquad (6.6)$$

is the ch. p. of a part k of the living system, in which the character of life is expressed by a_k, on the other hand μ_k' is the ch. p., in which the inter-relation to the total system is neglected. It is clear that the clusters and snow flakes have large *negative entropy* and their growth seems to be the *reversed course* from the point of thermodynamics. But the negative entropy comes from $kT \log c_k$ or $kT \log a_k$ and the reversed course is by no mean contrary to thermodynamics, if we take S_M into consideration.

(6.4) means the equilibrium of the cluster (k) and (1)

$$(k) \rightleftarrows k(1) \,, \qquad (6.7)$$

where (1) represents the single molecule. Total system is, however, in the transient state, so that (6.7) represents the equilibrium of the second coordinate. Therefore we can get Frenkel's equation (6.5) from the *equilibrium condition* of the second coordinate. In this manner Frenkel's method is generalized in the transient phenomena[18], in which q_s of the first coordinate is not zero. Becker and Döring considered the main reaction of the cluster growth, i.e.

$$(k)+(1) \rightarrow (k+1) \,.$$

Their equation of $\dot{q}_s$ is modified in the form[10],

$$\dot{q}_{k,k+1} = \frac{1}{R_c} \{ e^{(\mu_k + \mu_1)/kT} - e^{\mu_{k+1}/kT} \} \,, \qquad (6.8)$$

where

$$R_c = const \; e^{\mu'_k/kT} \,, \qquad (6.9)$$

is the chemical resistance*. (6.8) is very convenient in many cases. $k=M$ be the upper limit of the clusters. Then $\log c_{M+1} \rightarrow \infty$ and $\mu_M + \mu_1 \gg \mu_{M+1}$. Therefore the field or the stress of $(M)+(1) \rightarrow (M+1)$ is very large. But R_c is also very large. Therefore $\dot{q}_{k,k+1}$ is very small and the system is staying in the vapour state as if it were in the stable equilibrium. This is the reason for the *metastability* or the frozen phenomena. For the small value of $k<M$, μ_k has approximately the equilibrium value of (6.4) and R_c of (6.9) is far smaller, for μ_k' is very small. Then either $(1/R_c)e^{(\mu_k+\mu_1)/kT}$ or $(1/R_c)e^{\mu_{k+1}/kT}$, which is called the molecular condensation or vaporization respectively, is far greater than $\dot{q}_{k,k+1}$. The latter is the net value of the molecular processes. Then the balance of the molecular condensation and vaporization is

$$\mu_k + \mu_1 \doteqdot \mu_{k+1} \,, \qquad (6.10)$$

although $\dot{q}_{k,k+1} \not\doteqdot 0$. Such *equilibrium* is always assumed in the kinetic theory of rate processes, like that of Eyring. Though the first coordinate is not in the equilibrium, the freedom of the second coordinate is staying before the neck M with resistance R_c. The consideration is very important for the thermodynamical analysis of life.

Now let us take small interval τ into account, which is larger than the time of the molecular process but smaller than the ordinary magnitude of macrophysics. Such consideration is always necessary for those, who are studying statistical mechanics of the transient phenomena. We can choose τ so small that $\dot q_s\tau$ is very small in regard to the first coordinate. Then the point in the phase space representing the transient state is staying in the interval τ in a *limited region* of the phase space. Then quasi-Brownian motion of this point in the region is seen in this interval. Though the microscopic transition of (6.7), which is the second coodinate, is very frequent in τ, the centre of quasi-Brownian motion can hardly displace in this time interval. Let us take the region into account and *cut off* the other part of the space. The partition function of the transient system can be calculated in this manner with respect to this region. The "cut off" method of Frenkel is thus generalized and logically founded. The chemical potential of the living system can also be defined in this manner[8][18].

---

* *Const* of (6.9) is $\dfrac{c_1^2}{Z_1 W_I O_k}$, where W_I is probability of condensation per unit area and O_k is the surface area of (k).

§ 7. Blotzmann's *H*-Theorem and Virtual Heat Source

Whether the idea of the virtual heat source described in § 3 is reasonable or not will be discussed here, considering diffusion for instance[4][19].

Let us consider a section perpendicular to the diffusion current and the number of the sectional surface be j. The thickness of the part between j and $j+1$ be Δx_j. Then there is frequent transition of molecules in Δx_j, which corresponds to the local equilibrium, and the transition is nearly balanced. But the transitions between far separated parts are very rare, so that we can neglect such transitions in the time interval τ introduced in § 6. The part of the phase space which is combined by such transitions may be *cut off* from our consideration. Then the number of complexion of the system[4][10] is

$$W=\prod_j\frac{\{(n_{1j}+n_{2j})\Delta x_j\}!}{(n_{1j}\Delta x_j)!\,(n_{2j}\Delta x_j)!}. \tag{7.1}$$

Then

$$G=\sum_j(n_{1j}\mu_{1j}+n_{2j}\mu_{2j})\Delta x_j, \tag{7.2}$$

where

$$\mu_{ij}=\frac{\partial G}{\partial(n_{ij}\Delta x_j)}. \tag{7.3}$$

From (7.2)

$$\dot G=-T\dot S=\sum_j(n_{1j}\mu_{1j}+n_{2j}\mu_{2j})\Delta x_j, \tag{7.4}$$

is derived easily and it can be transformed in the following form[4][19]

$$\dot G=\sum_j\sum_i J_{ij}\,\mathrm{grad}\,\mu_{ij}\Delta x_j, \tag{7.4'}$$

where J_{ij} is the diffusion current of the component i. (7.4′) represents the heat[4] from the *virtual heat source*, which is due to the diffusing particles against the frictional resistance. The field driving the particles is $-\mathrm{grad}\,\mu_{ij}$ of (7.4′), which shows that the heat is equal to $T\dot S$ of the system in the isothermal diffusion. The idea of the virtual heat source is then *reasonable* and gives us many useful results.[19]

(7.4) or (7.4′) can also be derived[18] from (4.5′). The transition (s) in Δx_j corresponds $\dot q_{is}$ of the second coordinate of the component i and can be neglected. Let us consider between the parts Δx_j and Δx_{j+1}. Then q_{is} of the first coordinate is the vector quantity with various angle to the sectional surface. Then the field

$$\overrightarrow{\Delta\mu_i}=-\mathrm{grad}\,\mu_{ij}\Delta\boldsymbol{r}_j,$$

is also a vector and

$$\dot q_{is}\Delta\boldsymbol{r}=(\dot q_{is})_x\Delta x_j,$$

where $(\dot q_{is})_x$ denotes the x component of the vector. Then $\Delta\mu_i=-\mathrm{grad}\,\mu_{ij}\Delta x_j$ has the common value for various vectors of the transitions between j and $j+1$. Then we have

$$\sum_{is}\overrightarrow{\Delta\mu_i}\dot q_{is}=\sum_i\Delta\mu_i\sum_s(\dot q_{is})_x, \tag{7.5}$$

and $\sum_s(\dot q_{is})_x$ is equal to the diffusion current J_{ij}, so that (4.5′) is

$$\sum_j\Big(\sum_i J_{ij}\,\mathrm{grad}\,\mu_{ij}\Delta x_j\Big), \tag{7.6}$$

which is equal to (7.4′). (4.5′) can be interpreted as $\dot H$ of Boltzmann's *H*-function in the isothermal change and its mean value is expressed by the macroscopic variables like J_{ij}, which is the so-called *dissipation function*[18]. The field of ch. p. like $-\mathrm{grad}\,\mu$ is not the *real field* of force but the field of statistical nature. But our method takes the field as if it were the real force, and calculates the dissipative work done by this force.

Those who are studying thermodynamics of the irreversible processes assert that the dissipation function is *positive definite*. It must be founded on the base of the molecular statistics and Boltzmann's H-theorem.

In classical thermodynamics the variables like entropy and temperature are defined with regard to the equilibrium state, and in the irreversible phenomena it is believed that we can not define the thermodynamical variables and the number of variables defining the irreversible change must be *infinitely* large. But in our generalized quasi-static change the second coordinates are in its equilibrium state and the system is defined by the *finite* number of variables of the first coordinate. Now we have shown that the number of variables are very few, if we sum up q_s having the same $\Delta\mu_s$ in common as its factor in (7.5), and also that $kT\dot{H}$ is expressed by those *macroscopic* variables, which are observable. In the equilibrium state the number of variables are decreased. For instance the diffusion current vanishes, so that $\dot{n}_1=0$, $\dot{n}_2=0$ and μ_{10} and μ_{20} have constant values. Therefore in the quasi-static change

$$\dot{G}=\dot{n}_1\mu_{10}+\dot{n}_2\mu_{20}\ ,$$

and the variable besides p and T is only n_1/n_2 or the concentration. On the contrary the number of variables increases, if the state is far from the equilibrium. Therefore the theory can be uniformly developed from the equilibrium to the transient state.

(to be continued)

References

(from 1) to 11) are the works of M. Sugita).

1) Thermodynamik der nicht reversiblen Erscheinungen: Proc. Phys. Math. Soc. Japan **15** No. 1 (1933).

2) On Clausius' Inequality and Thermoelectricity (in Japanese): Kaisi of Phys. Math. Soc. Japan **16** No. 1 (1942).

3) Thermodynamics of Gas Flow (in Japanese): Ooyo Buturi **11** No. 3 (1942).

4) On the Mixing Entropy (in Japanese): Kaisi of Phys. Soc. Japan **4** No. 4 (1949).

5) Theory of Dielectrics under Alternating Field (in Japanese): Busseiron Kenkyu No. 10, 11, 12 (1948).

6) Thermodynamische Betrachtung über die mechanische Eigenschaft der amorphen Substanzen, Proc. Phys. Math. Soc. Japan **25** No. 6 (1943).

7) Thermodynamical Method in Biology, Annals of the Hitotubasi Academy, 1950.

8) On the metastability and the Origin of Life (in Japanese), Kagaku **18** No. 5 (1948).

9) Neturikigaku Sinko (1942), Tizin Syokan, Tokyo.

10) Katoteki Gensyo no Neturikigaku (1950) Iwanamisyoten, Tokyo.

11) Sugita, Maximum Principle in Transient Phenomena and its Application to Biology, Bulletin of the Kobayashi Institute **1** No. 2 (1950).

12) Volmer, Kinetik der Phasenbildung 1938; Becker u. Döring, Ann. der Phys. **24** (1935) 719 and so on.

13) Wagner: Ann. der Phys. **3** (1929) 627 and so on.

14) Frenkel: Jour. Chem. Phys. **7** (1939) 200.

15) For instance Meixner, Ann. d. Phys. **39** (1941) 333.

16) Tolman and Fine: Rev. Mod. Phys. **20** (1948) 51.

17) Busemann: Gasdynamik, Hand. d. Exp. Phys. IV Teil **1** S. 351.

18) Sugita: Boltzmann's H-Theorem and Dissipation Function, Bulletin of the Kobayasi Institute **2** No. 3 (1952).

19) N. Saito and M. Sugita; Journal Phys. Soc. Japan **7** No. 6 (1952).

JOURNAL OF THE PHYSICAL SOCIETY OF JAPAN Vol. 8, No. 6, Nov.—Dec., 1953

Thermodynamical Analysis of Life
II. On the Maximum Principle of Transient Phenomena

By Motoyosi SUGITA

Hitotubasi University, Kunitati, Tokyo and
Kobayasi Institute of Physical Research, Kokubunzi, Tokyo

(Received April 23, 1953)

In transient phenomena, nature seems to prefer the pass of the maximum rate of reaction. The principle is called by Lord Rayleigh *the principle of the least dissipation of energy*. The other aspect of this principle is the equilibrium of the *second coordinate*. It is a very important law of nature and might be called the *fourth law of thermodynamics*. The most important meaning of this principle is seen in the application to the bio-physics. Foundation of this principle is endeavoured in the following.

§ 1. Introduction

It is well known that many laws of nature are expressed by the maximum or minimum principle and the laws of dynamics, electrodynamics, thermodynamics and statistical mechanics are derived using the principle of variation. But in regard to the latter two, the principle is used to determine the equilibrium state. In regard to the transient state of the irreversible change the use of the maximum principle is tried by Lord Kelvin[1] and Lord Rayleigh but it is not yet well developed. In this paper the principle is clarified and generalized, especially in relation to biology[2].

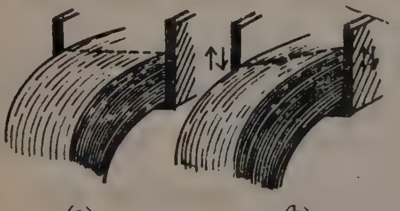

(a) (b)

Fig. 1.

At first let us take some instances of this principle into consideration.

§ 2. Maximum Principle and Joule's Heat

Let us consider two equipotential surfaces A and B. R be the resistance between A and B and i the current. If i is constant, then the current between A and B must take the distribution, so that the Joule's heat Ri^2 is minimum. Such principle is called by Lord Rayleigh *the principle of the least dissipation of energy*. On the other hand, if we take the potential difference V_A-V_B constant, Joule's heat $(V_A-V_B)^2/R$ must be maximum, so that the energy of the battery might be discharged as soon as possible, because R must take the minimum value for this distribution of current.

It can be considered, that Joule's heat is given by the *virtual heat source* described in the preceding report[3]. Then the local production of entropy must be Q/T, where Q is Joule's heat. Therefore the production of entropy due to Joule's heat must be minimum, when i is constant, and maximum, when V_A-V_B is constant. In the latter case the rate of increase of the entropy as well as the rate of decrease of f.e. (free energy) of the total system is maximum.

§ 3. Water Height of River

There is no difference in the water heights of the water flowing between both sides of the river, as water tends to equalize the surface. But there is a difference along the flow, for water must equalize the surface against the resistance of the stream. Let us call the difference of the heights or the rate of flow the *first coordinate*, and those, which can be equalized, the *second coordinate*. In the figure 1 (b) the second coordinate is not yet equalized. Then the surface must be equalized and the state (b) will return to (a). Then the rate of flow, which is the first coordinate, might be maximum, and there is the equilibrium in the second coordinate, though the system is in *transient state*. This is a very important fact for the study of the transient phenomena.

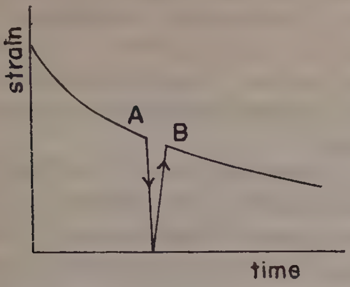

Fig. 2. Relaxation of Strain.

In the case of electric current the deviation from the equilibrium distribution of the current corresponds to the second coordinate. If so, the equipotential surface A or B is no more equipotential, and the deviation of the potential on A or B corresponds to the deviation of the level of the river banks. They are also the second coordinates. The maximum principle can be also considered to be the *principle of the equilibrium of the second coordinate*.

§ 4. The Maximum Principle in Gas Theory

The maximum principle is used in calculating the heat conductivity and the coefficient of viscosity in gas theory. The distribution function is so determined in the case of heat conduction, that the temperature difference disappears as soon as possible. In this case there is *reaction coordinate,* which can never be stabilized and must be the first coordinate. But there is *local equilibrium,* which corresponds to the second coordinate. In this respect Hasizume$^{4)}$ said that "the molecular motion which is realized and is also obeying Boltzmann's equation and the supplementary condition is that, in which the local production of entropy must be maximum."

This is, however, not the conclusion of *the second law* of thermodynamics, for this law requires only that the system, which is not in equilibrium, must reach the equilibrium state sooner or later. The *process* or the *rate* of reaction to equilibrium is not the problem of the second law and *the new principle* is required, which might be the graviest one in nature. So that the author is going to call the maximum or minimum principle the *fourth law of thermodynamics*.

It is well known that the first and the second law must be complemented by some other principle in the transient phenomena, for instance the reciprocal relation of Onsager or of the idea of the generalized quasi-static change and the field of ch. p. (chemical potential) described in the preceding report$^{3)}$. These principles might be, however, summarised by the maximum principle.

§ 5. Onsager's Reciprocal Relation

Lord Kelvin derived the reciprocal relation for the coefficient of electric current J_e and heat current J_t, which can be written in the form

$$\left.\begin{aligned} J_e&=A_{ee}E-\frac{A_{et}}{T}\operatorname{grad}T \\ J_t&=A_{te}E-\frac{A_{tt}}{T}\operatorname{grad}T\,, \end{aligned}\right\} \tag{4.1}$$

where E is electric force, A_{ee}, A_{et}, A_{te}, A_{tt} are the constants. Then the reciprocal relation is

$$A_{te}=A_{et}\,. \tag{4.2}$$

But there is a question in the application of the second law, which is discussed in my work* "New Lecture on Thermodynamics, 1943, Tokyo (in Japanese)."

The general theory of Onsager is based on the theory of fluctuation. Let $\alpha_1, \alpha_2, \cdots, \alpha_n$ be the parameters or the *gross variables* of a system and $\alpha_{10}, \alpha_{20}, \cdots, \alpha_{n0}$ be the equilibrium values. Then the entropy of the system is $S(\alpha_1, \alpha_2, \cdots, \alpha_n)$ and $S_0(\alpha_{10}, \alpha_{20}, \cdots, \alpha_{n0})$ respectively. If the state is nearly in equilibrium,

$$S'=S-S_0=\sum\tfrac{1}{2}A_{ik}\alpha_i'\alpha_k' \tag{4.3}$$

where $\alpha_i'=\alpha_i-\alpha_{i0}$. Therefore

$$\dot{S}'=\dot{S}=\sum A_{ik}\alpha_i'\alpha_k'=\sum X_k\alpha_k' \tag{4.4}$$

where

$$X_k=\sum_i A_{ik}\alpha_i' \tag{4.5}$$

is generalized force to put the deviation α_k back to α_{k0}. Using the principle of microscopic reversibility Onsager has shown that

$$\dot{S}=\tfrac{1}{2}\sum B_{ik}\dot{\alpha}_i'\dot{\alpha}_k'\,, \tag{4.6}$$

where

---

* Derivation of the relation from the theory of thermoelectricity was delivered at the aniversary meeting of Physico-Mathematical Society of Japan in 1943.

$$B_{ik}=B_{ki}\,, \qquad (4.7)$$

and also that $\dot{S}/2$ corresponds to the dissipation function Φ of Lord Rayleigh. Therefore

$$X_k=\frac{\partial \Phi}{\partial \dot{\alpha}_k'}=\Sigma B_{ik}\dot{\alpha}_i'\,. \qquad (4.8)$$

The most important result of Onsager is that the reciprocal relation can be derived from the maximum principle,

$$\dot{S}(\alpha_i',\dot{\alpha}_i')-\Phi(\dot{\alpha}_i',\dot{\alpha}_k')=\max\,. \qquad (4.9)$$

Therefore the entropy of the system increases as soon as possible, if the reciprocal relation is valid. This is a fact to show the fourth law, but there is a restriction that S can be written in the quadratic form. Of this restriction we will return later.

§ 6. Condition of the Detailed Balance

Let $n_i(X)$ be the distribution function of a microscopic state of X. In the preceding report[3] it is written, that

$$\dot{n}_i(X)=\Sigma\Gamma_{is}(X)\dot{q}_s(X)\,, \qquad (5.1)$$

where $\dot{q}_s(X)$ is the rate of reaction of quasi-chemical changes from j to i or from i to k. $\dot{n}_i(X)$ corresponds to $[\dot{n}_i(X)]_{\text{coll}}$ of the gas theory and (5.1) is generalized Boltzmann's equation. In the detailed balance $\dot{q}_s(X)=0$. In the steady state $\dot{q}_s(X)$ is not always zero but $\dot{n}_i(X)=0$. (See part III).

If Boltzmann's H-function is written in the form

$$H=\Sigma n_i(X)(\log n_i(X)-1)\,, \qquad (5.2)$$

then

$$\dot{H}=\Sigma_i\dot{n}(X)\log n_i(X)$$
$$=\Sigma(\Sigma\Gamma_{is}(X)\log n_i(X))\dot{q}_s(X)\,. \qquad (5.3)$$

Put

$$-k\Sigma\Gamma_{is}(X)\log n_i(X)=\Delta\mu_s(X) \qquad (5.4)$$

and

$$-k\dot{H}=\dot{S}\,, \qquad (5.5)$$

then

$$dS=\Sigma\Delta\mu_s(X)dq_s(X) \qquad (5.6)$$

and

$$\frac{\Delta\mu_s}{T}=\frac{\partial S}{\partial q_s}\,, \qquad (5.7)$$

where q_s is not the macroscopic variable but the *gross variable*. The condition of the detailed balance is then

$$\dot{q}_s(X)=0\,,\quad \Delta\mu_s(X)=0 \qquad (5.8)$$

$\dot{q}_s(X)=0$ shows, however, the balance of two reversed reactions, like a chemical reaction and it's reversed reaction or molecular vaporization and condensation. Therefore there must be frequent microscopic transitions, and only the *net value* of these reactions must be zero. Such transitions may be considered as quasi-Brownian motion in the phase space.*

In the preceding paper it is shown that (5.8) is also *valid for the second coordinates* in transient state. Therefore quasi-Brownian motion is maintained in a *limited region of the phase space*, and the centre of the motion will shift slowly, corresponding to the change of the first coordinate. We have considered small time interval τ, in which $\dot{q}_s\tau$ is very small, where $\dot{q}_s$ is the first coordinate. Then the microscopic state of the system changes very frequently but will return to its initial state in this time interval. The fact might correspond to the microscopic reversibility. In this time-interval the system will reach *nearly every point* in the limited domain in the space and quasi-ergodic hypothesis might be fulfilled in this domain. On this logical base the "cut off method" was proposed[3] to get the partition function in transient state. The assumption of the *equilibrium of the second coordinate* might be an expression of the *fourth law* or the maximum principle.

§ 7. The Field of Chemical Potential

X_k of (4.5) can be interpreted like the field of force, which must arise as the result of the deviation from the equilibrium state. From (4.4) and (5.6) $\Delta\mu_s(X)$ corresponds to X_k of (4.5). But in general the relation of $\dot{q}_s$ and $\Delta\mu_s(X)$ is not simple. In the preceding paper it is shown that

$$\dot{q}_s=\frac{1}{R_s}\left\{e^{\Sigma\nu_{is}\mu_i/kT}-e^{\Sigma\nu_{js}\mu_j/kT}\right\}\,, \qquad (6.1)$$

where $\dot{q}_s$ is the rate of the quasi-chemical reaction

$$\Sigma\nu_{is}A_i\rightarrow\Sigma\nu_{js}A_j\,. \qquad (6.2)$$

Then

$$\Delta\mu_s=\Sigma\nu_{is}\mu_i-\Sigma\nu_{js}\mu_j\,. \qquad (6.3)$$

Let us consider the isothermal change, in which

---

* Such idea is also described by Yamamoto, Busseiron Kenkyu **57** (1952) 66.

$$\dot{S}=\sum\frac{\Delta\mu_s}{T}\dot{q}_s$$

$$=\sum\frac{\Delta\mu_s}{R_sT}\left\{e^{\sum\nu_{is}\mu_i/kT}-e^{\sum\nu_{js}\mu_j/kT}\right\}, \tag{6.4}$$

which can not be written in the quadratic form. If the system is, however, nearly in the thermodynamical equilibrium, the equation (6.1) or (6.4) may be simplified. Let

$$\mu_i=\chi_i+kT\log a_i \tag{6.5}$$

where χ_i is the enthalpy and a_i the activity of the component i, then

$$\dot{q}_s=\frac{1}{R_s}\left\{\prod_i(a_i)^{\nu_{is}}e^{\sum\nu_{is}\chi_i/kT}-\prod_j(a_j)^{\nu_{js}}e^{\sum\nu_{js}\chi_j/kT}\right\}$$

$$=k_s\Pi(a_i)^{\nu_{is}}-k_s'\Pi(a_j)^{\nu_{js}},$$

where

$$k_s=\frac{1}{R_s}e^{\sum\nu_{is}\chi_i/kT}, \quad k_s'=\frac{1}{R_s}e^{\sum\nu_{js}\chi_j/kT}$$

are the reaction constants.

Then

$$\dot{q}_s=k_s\Pi(a_i)^{\nu_{is}}\left\{1-e^{-\Delta\mu_s/kT}\right\}$$

$$=-k_s\Pi(a_i)^{\nu_{is}}\sum_{n=1}^{\infty}\frac{1}{n!}\left(\frac{-\Delta\mu_s}{kT}\right)^n \tag{6.1$'$}$$

or

$$\sum_{n=1}^{\infty}\frac{-1}{n!}\left(\frac{-\Delta\mu_s}{kT}\right)^n=\frac{\dot{q}_s}{k_s\Pi(a_i)^{\nu_{is}}}, \tag{6.1$''$}$$

which can be also expanded in the form

$$\frac{\Delta\mu_s}{kT}=\sum C_{sh}\left(\frac{\dot{q}_s}{k_s\Pi(a_i)^{\nu_{is}}}\right)^h, \tag{6.6}$$

where C_{sh} is the constant. On the other hand following expansion

$$\Pi(a_i)^{\nu_{is}}=\Pi(a_{i0})^{\nu_{is}}+\sum K_n\dot{q}_s^n \tag{6.7}$$

might be obtained, if a_{i0} is the equilibrium value and K_n is the constant. Then (6.4) can be written in the form*

$$\dot{S}=k\sum_s C_{s1}\frac{\dot{q}_s^2}{k_s\Pi(a_i)^{\nu_{is}}}+k\sum_s C_{s2}\frac{\dot{q}_s^3}{[k_s\Pi(a_i)^{\nu_{is}}]^2}+\cdots$$

$$=k\sum C_{s1}\frac{\dot{q}_s^2}{k_s\Pi(a_{i0})^{\nu_{is}}}+O(\dot{q}_s^3), \tag{6.4$'$}$$

which can be written in the quadratic form like (4.4), if the terms of the higher order of $\dot{q}_s$ is neglected and $\dot{q}_s$ is transformed in α_k' by

$$\dot{q}_s=\sum\gamma_{ks}\dot{\alpha}_k', \tag{6.8}$$

where γ_{ks}s are constants. Then the reciprocal relation of the coefficient of $\dot{\alpha}_i'\dot{\alpha}_k'$ is easily derived.

It is clear that (6.4′) is the local production of entropy and $T\dot{S}$ is the heat from the virtual heat source[3]. $\dot{q}_s$ of (6.1′) must be the first coordinate and (6.7) means the equilibrium of the second coordinate. Therefore the above derivation of the reciprocal relation might be based on the equilibrium of the second coordinate.

If we take the second term of (6.4′) into consideration and transform $\dot{q}_s$ by (6.8), then the symmetrical relation can be obtained concerning the coefficient of $\alpha_i'\alpha_j'\alpha_k'$. This derivation is, however, restricted on the isothermal change.

§ 8. Other Facts Concerning this Principle[5]

(i) In the theory of rate processes transportations in by-path is neglected. For instance Becker and Döring[6] took only the process $(n)+(1)\rightarrow(n+1)$ into consideration in their theory of cluster formation, where (n) is the cluster of n molecules. In Volmer's theory of crystal growth[7] the main route is taken into consideration, which is the diagonal path in the net-work of the circuit model. This is the ordinary method of the theory of rate processes like that of Eyring[8]. It might be said, that nature prefers the path with the maximum rate of the increase of entropy or decrease of the free energy, and that nature does not take by-paths.

(ii) There is cascade principle[5] (Stufenregel von Ostwald). In the super-saturated vapour under freezing temperature, for instance, super-cooled droplets are frequently formed, which are unstable but have small free energy of activation. Then the droplets freeze and become the nucleus of condensation. It seems queer, because usually we expect the formation of ice under freezing temperature. So that nature seems to prefer to detour to promote the rate of access to the equilibrium.

(iii) There is natural selection in nature. For instance, ice nucleus will grow in supersaturated vapour under freezing temperature, when it is once formed, and the super-cooled droplets vaporize and disappear. On the electrode of discharged battery some crystallits of large size of $PbSO_4$ will grow and the crystallits of smaller size become smaller. The rate of minimizing of unequilibrium might be accelerated by this natural selection. Natural selection in the living world might be also an instance of the maximum principle.

---

* Whether $\dot{S}$ of (6.4′) is maximum or not is not yet clear.

(iv) Crystallit of snow flakes must have small entropy or large N.E. (negative entropy). But the condensation of the supersaturated vapour is promoted by the N.E. and the rate of discharge of supersaturation must be accelerated. The curious form of snow flakes is destroyed on the earth, evaporating from the nib, and then it will become ordinary ice block. We can notice also the detour of natural phenomena.

The local increase of N.E. seems to be paradoxical for those, who have scarcely the knowledge of the theory of rate processes or of transient phenomena.

(v) Strain of some polymer has large time of relaxation and it relaxes very slowly. The strain may vanish if external force is applied (at the point A of Fig. 2). But the recovering is only superficial, for the strain will appear again, when the force is removed (at the point B). The superficial recovering might be due to new strain by the applied force, which has small time of relaxation and vanishes soon if the applied force is removed. The new strain might be considered as the second coordinate and it is superposed on the strain of the first coordinate with large relaxation time. It is not for certain, however, whether the vanishing of the strain of the second coordinate will promote the rate of relaxation of the first coordinate.

Such recovery of the disturbance is also seen in the living organism.

§ 9. Conclusion

The maximum principle of the transient phenomena might be a very important law of nature. The second law asserts the necessity, that the orderliness must be destroyed to molecular chaos, but does not assert in what rate the chaos is attained and what is the process to the equilibrium. Therefore a new principle must be indispensable, which can not be described logically now but may be summarized in the form, that "the second coordinate changes to promote the reaction rate of the first coordinate." In many cases the equilibrium of the second coordinate is maintained, but in some cases the equilibrium is disturbed by the reaction of the first coordinate and the relaxation oscillation is excited by the coupling of the first and the second coordinate. Creaking noise may be an instance of such oscillation. Pulsating reaction of the first coordinate can be seen also in the living system.

The first coordinate is not the space coordinate, but it will take detour like the cascade principle. The zigzag form of thunder lightning is the visual instance of the reaction coordinate. Of course, there is no will or intention for nature to *prefer the most optimum path,* which must be taken by natural *necessity*. But the path seems to be very curious, and by-path seems rather to be the main route frequently. Such illusion is clarified by this principle, and the aspect that nature prefers to take the path *on purpose* will be explained on the base of natural *necessity*. The formation of the activated complex with large N.E. is the result of the necessity, that the N.E. accelerates the rate of the first coordinate. Such phenomena have great importance in biology.

Deviation from the real path of the first coordinate corresponds to the *fluctuation of the second coordinate*. Therefore it might be difficult to select by-path by the fluctuation, and nature seems to select the optimum path. Large deviation will produce *excess heat loss*, so that the optimum path will be taken according to the maximum or minimum principle of the transient phenomena.

Important meaning of this principle concerning the living system will be described in the following paper. The work is supported by the research grant of the Ministry of Education.

References

1) Lord Kevin: Proc. Roy. Soc. Edinburgh (1854), Collected Papers I. pp. 237-241.

2) M. Sugita: Maximum Principle in Transient Phenomena and its Application to Biophysics. Bull. Kobayasi Institute **1** (1951) 88.

3) M. Sugita: Thermodynamical Analysis of

Life I.
4) M. Hasizume: Busseiron-Kenkyu (in Japanese) **29** (1950) 1.
5) M. Sugita: Thermodynamical Method in Biology. Annals. of the Hitotubasi Academy, Supplement **1** (1951).
6) R. Becker und W. Döring: Ann. d. Physik **24** (1953) S. 719.
7) M. Volmer: Kinetik der Phasenbildung (1938).
8) Glasstone, Laidler and Eyring: The Theory of Rate Processes (1941).

JOURNAL OF THE PHYSICAL SOCIETY OF JAPAN Vol. 8, No. 6, NOV.—DEC., 1953

Thermodynamical Analysis of Life
III. Mathematical Analysis of Metabolism

By Motoyosi SUGITA

Hitotubasi University, Kunitati, Tokyo and
Kobayasi Institute of Physical Research, Kokubunzi, Tokyo

(Received April 23, 1953)

Living organism is the open system, in which chemical substances are taken from the external system and excreted. Let the free energy taken and excreted be Z_1 and Z_2 respectively, then the change of the free energy of the organism is

$$\dot{G}_k = Z_1 - Z_2 - D, \tag{4.5}$$

where D is the free energy used to maintain life or for external work W. G_a be the free energy of the external system, then $-\dot{G}_a = Z_1 - Z_2$ and the second law may by written in the form

$$\dot{G}_a + \dot{G}_k = -D < 0. \tag{4.8}$$

On the other hand $\dot{G}_k$ can be written in the form

$$\dot{G}_k = R - D_r, \tag{5.7}$$

where

$$R = Z_1 - Z_2 - W - D_f, \quad D_r = D - W - D_f \tag{5.6}$$

and D_f is the energy loss in our body. This is the fundamental equation of thermodynamics of life. R is the repair of free energy of the organism and D_r is its depreciation.

§ 1. Introduction

Conservation of matter and energy is the universal law of nature and the living organism can not be the exception of this law. But physicists and biologists hesitate to rely upon the second law of thermodynamics, for the steadiness of orderliness of the organism with N. E. (negative entropy) seems to be contrary1)2) to the law. The steadiness is, however, apparent as it is shown in this report. On the other hand our body is the *open system* in transient state, so that thermodynamics might hardly be applicable to such system. In the preceding paper3) the equilibrium of the second coordinate in transient state is explained and the "cut off method" is introduced to evaluate the partition function. The theory of transient phenomena3) is to be extended to the living system and the mathematical analysis of the metabolic turnover will be given in the following. There is no difficulty in the treatment of the open system, although biologists hesitate to treat it thermodynamically.

§ 2. Hydrodynamical Model of the System4)

Let us consider the potential energy of the water of a pool and its water passage (see Fig. 3), which is P_R and P respectively, H_i be the water height at a point of the passage and m_i be the quantity of water at the point. Then $P = \sum m_i H_i$ and

$$\dot{P} = \sum H_i \dot{m}_i. \tag{2.1}$$

Let $J_{i-1,i}$ be the quantity of flow $i-1$ to i, then

$$\dot{m}_i=J_{i-1,i}-J_{i,i+1} . \qquad (2.2)$$

Therefore

$$\begin{aligned}\dot{P}&=\sum H_i(J_{i-1,i}-J_{i,i+1})\\&=-\sum \Delta H_i J_{i-1,i}+P_0J_0-P_NJ_N , \qquad (2.3)\end{aligned}$$

where

$$\Delta H_i=H_{i-1}-H_i ,$$

$i=0$ corresponds to the upper end of the passage connecting to the pool and $i=N$ is the lowest end, where $H_N=0$, $P_N=0$. Then P_0J_0 must be the energy flowing out of the pool in unit time, for the passage is an open system. Therefore

$$-\dot{P}_R=P_0J_0 , \qquad (2.5)$$

and

$$\dot{P}_R+\dot{P}=-\sum \Delta H_i J_{i-1,i}<0 , \qquad (2.6)$$

where $\sum \Delta H_i J_{i-1,i}$ is the energy dissipated in the passage, which corresponds to the local production of entropy. Then P_0J_0 corresponds to the entropy flow, if we compare the flow with that of heat. Equations of the types (2.3), (2.5) and (2.6) are also obtained in the living organism, through which chemical substances flow and which is the typical open system.

§ 3. Flow of Chemical Substances

The living organism is the flow of chemical sabstances, which is taken out of the organism and then excreted. There is, however, two sorts of flow, i.e. anabolism and catabolism. Let $n_i(X)$ be the quantity of X in the state i, where X is the chemical element like C, H, N and i means the state of the chemical combination. Then

$$\dot{n}_i(X)=\sum_j J_{ji}(X)-\sum_k J_{ik}(X) . \qquad (3.1)$$

Let $\mu_i(X)$ be the ch. p. of X in the state i. Then the rate of an anabolism and catabolism may be defined in the following way.

i) if $\mu_i(X)>\mu_j(X)$, $J_{ji}(X)$ is called the rate of *anabolism*. Let us write it $Q_{ji}(X)$.

ii) if $\mu_i(X)>\mu_k(X)$, $J_{ik}(X)$ is called the rate of *catabolism*. Let us write it $q_{ik}(X)$. Therefore

$$\dot{n}_i(X)=\sum_j Q_{ji}(X)-\sum_l Q_{il}(X)-\sum_k q_{ik}(X)+\sum_m q_{mi}(X). \qquad (3.2)$$

To simplify this, let us take only $j=i-1$ into consideration. Therefore the flow of the anabolism does not shoot in branches (see Fig. 1). Our body is built of such net-work of the chemical flow. In the steady state $\dot{n}_i(X)=0$ and

$$Q_{i-1,i}(X)-Q_{i,i+1}(X)-\sum_k q_{ik}(X)+\sum_m q_{mi}(X)=0 . \qquad (3.3)$$

The combination of $Q_{i-1,i}(X)$ and $q_{ik}(X)$ shows the circulation of the chemical substance in our body, which is called the chemical cycle. For instance, there is ATP⇄ADP or the cycle of citric acid. (see Fig. 2) Therefore the living organism is a *gear* or *net-work* of the chemical cycle and is also the self-maintaining system.

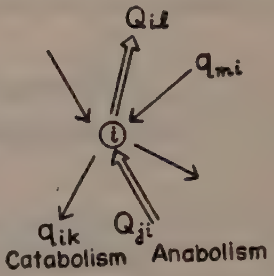

Fig. 1.

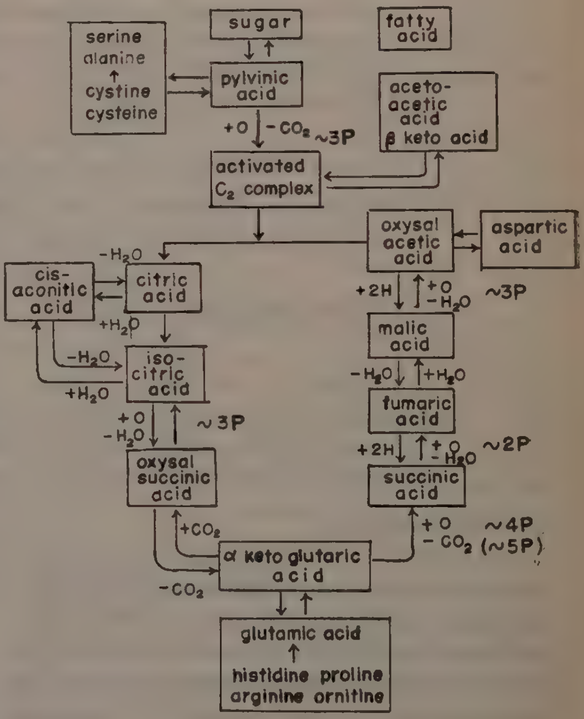

Fig. 2. Cycle of citric acid.

§ 4. Thermodynamics of the Open System

Let G_k be Gibbs' F. E. (free energy) of the living organism. Then

$$\dot{G}_k=\sum_{i,X}\dot{n}_i(X)\mu_i(X)\,, \qquad (4.1)$$

where

$$\mu_i(X)=\partial G_k/\partial n_i(X)\,. \qquad (4.2)$$

F. E. of transient state may be derived from the partition function evaluated by the "cut off method", which is described in the preceding paper[3]. From (3.2) and (4.1)

$$\begin{aligned}\dot{G}_k=&\sum \mu_i(X)(Q_{i-1,i}(X)-Q_{i,i+1}(X))\\ &-\sum\mu_i(X)(\sum q_{ik}(X)-\sum q_{mi}(X))\\ =&\sum_{i,X}(\mu_i(X)-\mu_{i-1}(X))Q_{i-1,i}(X))\\ &-\sum_{j,k,X}(\mu_i(X)-\mu_k(X))q_{ik}(X)+Z_1-Z_2\,,\end{aligned} \qquad (4.3)$$

where

$$\left.\begin{aligned}Z_1&=\sum \mu_i(X)J_{ai}(X)\\ \text{and}\quad Z_2&=\sum \mu_k(X)J_{ka}(X)\,,\end{aligned}\right\} \qquad (4.4)$$

is the free energy taken out of the organism and excreted respectively and $J_{ai}(X)$ or $J_{ka}(X)$ is the rate of the chemical flow. (4.3) can be written in the form,

$$\dot{G}_k=Z_1-Z_2-D\,, \qquad (4.5)$$

where

$$\begin{aligned}-D=&\sum_{i,X}(\mu_i(X)-\sum\mu_{i-1}(X))Q_{i-1,i}(X)\\ &-\sum_{i,k,X}(\mu_i(X)-\mu_k(X))q_{ik}(X)\,. \end{aligned}\qquad (4.6)$$

D is the F. E. consumed in our body to maintain life, in which the external work is also included. (4.5) is the reasonable consequence from the point of biology.

Let G_a be the F. E. of the external system, then

$$-\dot{G}_a=Z_1-Z_2\,. \qquad (4.7)$$

Therefore

$$\dot{G}_a+\dot{G}_k=-D<0\,, \qquad (4.8)$$

because $-D$ is equal to $kT\dot{H}$ of Boltzmann's H-function and then D is positive definite. From (4.8) F. E. of the total system, G_a+G_k, decreases according to the second law, which is also valid in the living organism. There is no difficulty in the application of the second law, if we take the total system into consideration. But the general conclusion of the second law is not quantitative as it is shown by (4.8). We must go into detail of D on the base of biochemical knowledge and molecular statistics, if we want the quantitative result, which is not the simple conclusion of the second law. General conclusion of (4.8) is, however, a very important step of the analysis. The second law is valid notwithstanding the rate or the process of the decreasing of F. E. or the increasing of the entropy of the total system. How much complex the phenomena of life is, the tendency of the decreasing of F. E, is yet unchanged. Therefore we can obtain the concrete step to proceed to the next step.

§ 5. Balance of Free Energy

Let the first term of D, which corresponds to the anabolism, be R. Then

$$\sum_{i,X}(\mu_i(X)-\mu_{i-1}(X))Q_{i-1,i}(X)=R\,.$$

R is combined with the rate of the catabolism, which releases energy. Our body is a sort of power source and the out put of power is used partly to the chemical work of the synthesis, which is against the tendency of the ordinary chemical reaction, for the compound or system with large ch. p. or small positive entropy is produced in the anabolism. The model of Fig. 3 will explain the circumstance. Let the F. E. liberated for the pump action of Fig. 3 be P and the energy loss be D_f'. Then

$$-R+P=D_f'\,. \qquad (5.2)$$

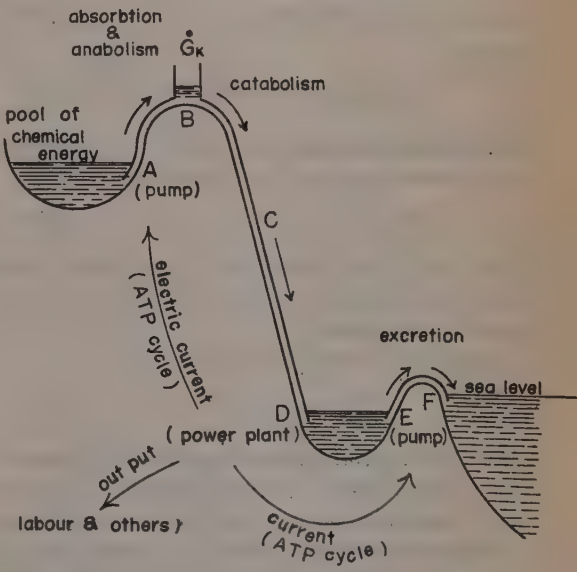

Fig. 3. Model of hydroelectric plant with pump at A.

The out put of power is partly fed back into the chemical work of the anabolism, R, and

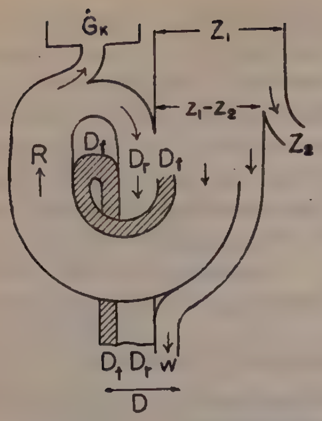

Fig. 4. Balance of free energy.

partly used in the work to take free energy from the external system and to excrete, i.e. Z_1, Z_2, or in the work of muscle. Let the part be Q, the work be W and the energy loss be D_f''. Then

$$-W+Q=D_f''. \qquad (5.3)$$

The second term of D of (4.6) may be writtern in the form

$$\Sigma(\mu_i(X)-\mu_k(X))q_{ik}(X)=P+Q+D_r\,,$$

where D_r is the loss of F. E. due to catabolism. Then

$$\begin{aligned} D&=-R+P+Q+D_r \\ &=D_f+W+D_r\,, \end{aligned} \qquad (5.4)$$

where

$$D_f=D_f'+D_f''. \qquad (5.5)$$

The relation between Z_1-Z_2, R, D_f, W and D_r is shown in Fig. 4. Therefore

$$R=Z_1-Z_2-W-D_f. \qquad (5.6)$$

If $D_f=0$, Z_1-Z_2 must turn into power, and the internal and external work, $R+W$, is done by the power.

From (4.5), (5.6) and (5.4)

$$\dot{G}_k=R-D_r. \qquad (5.7)$$

This is the *fundamental equation of metabolism*. Steadiness of the orderliness of our body was the question of physicists. Some of them[1)2)] declared, that the destruction is delayed or frozen in. But such opinion is against the experimental fact of metabolic turnover. D_r of (5.7) shows destruction of N. E. of the orderly system, for the main part of F. E. of our body must be due to N. E.. The steadiness is only *apparent*, for the orderliness is destructed in every moment and also reconstructed. The reconstruction, which is represented by R, seems to be the *reversed course*, for positive entropy decreases against our common sense. It is, however, clear that the reaction producing N. E. is due to the pump action of Fig. 3, and the power is transmitted by ATP-cycle instead of the electric current of the model. The reaction ATP→ADP is combined with many synthetic reactions, and the reversed reaction ADP→ATP is combined with those like fermentation, which releases energy (see Fig. 5). We have considered the gear of the chemical cycle. The energy released does not disperse in heat but is transferred as energy quantum of 15∼20 kT, which is the order of energy of ADP→ATP. The transfer of such quantum will distrub the polymers of the living organism more violently than the thermal motion, which is the order of kT. The destruction of N. E. or D_r might be due to such disturbance. If so, R and D_r is not independent quantities, for the result of the vivid anabolism will be vivid destruction due to the energy transfer.

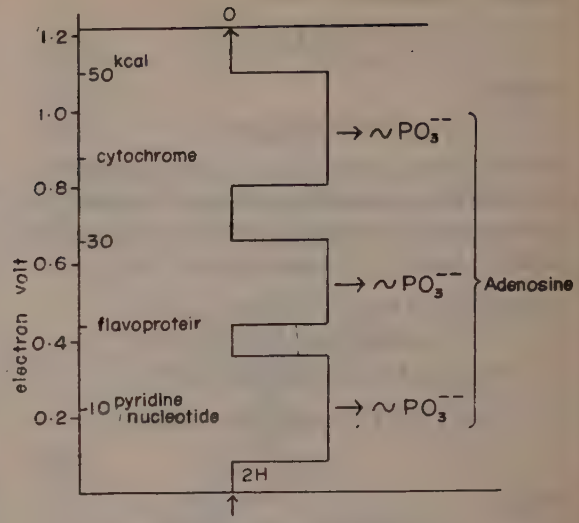

(Transfer of energy by Lippmann)

Fig. 5.

There might be no turnover of protein in the spermatozoon. If so, R=0 and

$$\dot{G}_k=-D_r. \qquad (5.8)$$

Then the N. E. of spermatozoon will be sooner or later destroyed. It is said that there is the protein like acto-myosin in spermatozoon, which absorbs, for instance, glucose from the external system and transfers the energy released to ADP→ATP. The motion of the spermatozoon is due to the periodic contraction of the protein molecule under the action of ATP. The protein is the chemical apparatus of the energy transfer. The function of the protein can not be repaired but might be depreciated by the energy transfer.

Generally, in the steady state $\dot{G}_k=0$ and

$$R=D_r \tag{5.9}$$

is the balance of free energy, which can be written in the form

$$(\mu_i(X)-\mu_{i-1}(X))Q_{i-1,i}(X)=\sum{}'(\mu_i(X)-\mu_k(X))q_{ik}(X), \tag{5.9'}$$

where

$$\sum{}'(\mu_i(X)-\mu_k(X))q_{ik}(X)=\sum(\mu_i(X)-\mu_k(X)q_{ik}(X)-P-Q\,.$$

The ch. p. is not $\mu_i(X)$ of the meat or the giblets on the market, but the value in the living state, so that it is not easy to know the value. But the use of the maximum principle⁵⁾ gives us the method⁶⁾ to estimate the ch. p. in the living state, which will be described in the following paper.

§ 6. Conclusion

(5.7) is the very important result of biophysics. It will be applied to many problems of biophysics.

This equation can be also applied to a part of the living organism, where Z_1, Z_2 is the exchange of F. E. with other parts of the organism or the external world. From (5.6), R might be proportional to the surface area, if it is applied to a cell, for Z_1-Z_2 must be proportional to the surface. In the multicellular organism R must diminish also, if the organism grows. D_r might be proportional to the volume, for N. E. of every part will be destroyed by the catabolism. So that growth of the organism must be sooner or later saturated and then senility will appear.

Detailed discussion will be given in the next report. The work is supported by the research grant from the Ministry of Education.

(to be continued)

References

1) E. Schrödinger: What is Life.

2) L. Brillouin: American Scientist **37** No. 4 (1949); **38** No. 4 (1950).

3) M. Sugita: Thermodynamical Analysis of Life I and II.

4) M. Sugita: Bullet. Kobayasi Institute **2** Nos. 3∼4 (1952)

5) M. Sugita: Bullet. Kobayasi Institute **1** No. 2 (1951).

6) M. Sugita: Thermodynamical Analysis of Life II.

JOURNAL OF THE PHYSICAL SOCIETY OF JAPAN Vol. 8, No. 6, NOV.—DEC., 1953

On Mayer's Theory of Dilute Ionic Solutions

By Eijiro HAGA

Department of Physics, Faculty of Science,
University of Niigata, Niigata

(Received July 10, 1953)

Explicit expressions for the logarithms of activily coefficient of dilute ionic solutions right up to $c^{3/2}$ and for the osmotic pressure right up to $c^{5/2}$ are calculated according to Mayer's theory by the use of Fourier transformation. The two prototypes which Mayer supposed, by his rough evaluations, to lead to the terms of higher order are proved to be included in the present approximation. The results of calculations are compared with the existing theories. Calculated osmotic coefficients for 1-1 electrolytes are compared with experimental values, yielding to mean ionic diameters values which are more reasonable than in Debye-Huckel's theory.

§ 1. Introduction

In a recent paper Mayer[1)] has published a theory of dilute ionic solutions in which he has shown how to calculate the virial development expression of the osmotic pressure in terms of the potentials of average forces between ionic pairs at infinite dilution. In this paragraph we summarize his method briefly.

We consider a dilute ionic solution composed of σ species of ions labelled as $1,2,\cdots,\sigma$ and a solvent. Let $U_n(\boldsymbol{r}_1,\boldsymbol{r}_2,\cdots,\boldsymbol{r}_n)$ be the potential of average force of n ions in the solution at infinite dilution. Then U_n can be expressed in the form

$$\left.\begin{aligned} &U_n=\sum_{n\geq i\geq j\geq 1} u(r_{ij}) \\ &\text{with} \\ &u(r_{ij})=\frac{z_i z_j e^2}{D r_{ij}}+u^*(r_{ij})\,, \end{aligned}\right\} \quad (1)$$

where z_i the integral charge of i-th ion, D the dielectric constant of the solvent, e the electronic charge, and $u^*(r_{ij})$ is the repulsive potential due to overlaping which has a extremely large positive value at sufficiently small r_{ij}. For the simplicity of calculation we assume for all pairs of ions that

$$\begin{aligned} u^*(r_{ij})&=\infty\,, & r_{ij}&<a\,, \\ &=0\,, & r_{ij}&>a\,, \end{aligned}$$

where a means the average diameter of ions.

In evaluating the logarithm of activity coefficient and the osmotic pressure we assume for $u(r_{ij})$ the form

$$u(r_{ij})=\frac{z_i z_j e^2}{D r_{ij}}e^{-\alpha r_{ij}}+u^*(r_{ij})\,,$$

instead of Eq. (1), so that the integral calculations should be convergent, and after carrying out integrations take the limiting values when α approaches to zero.

Now we put

$$\lambda=\frac{4\pi e^2}{DkT}\,, \qquad g(r)=\frac{e^{-\alpha r}}{4\pi r}\,,$$

$$k^*(r_{ij})=e^{-u^*(r_{ij})/kT}-1\,,$$

then we have for $f_{ij}=\exp[-u(r_{ij})/kT]-1$

$$f_{ij}=k^*(r_{ij})+\sum_{s\geq 1}[-\lambda z_i z_j g(r_{ij})]^s[k^*(r_{ij})+1]/s\,!\,.$$

For our simplified form of $u^*(r_{ij})$, we have

$$\begin{aligned} k^*(r_{ij})&=-1\,, & 0\leqq r_{ij}&\leqq a\,, \\ &=0\,, & a<r_{ij}&<\infty\,. \end{aligned}$$

We define S as

$$S=\sum_{n}(\Sigma n_i\geq 2)B_n C^n\,,$$

with

$$B_n=\frac{1}{\prod_i n_i\,!}\iint\cdots\int\Sigma\,\Pi\, f_{ij}d\boldsymbol{r}_1 d\boldsymbol{r}_2\cdots d\boldsymbol{r}_{n-1}\,, \quad (3)$$

and

$$C^n=c_1^{n_1}c_2^{n_2}\cdots c_\sigma^{n_\sigma}\,,$$

where c_i denotes the number of the i-th species in cm³.

Then the logarithm of activity coefficient γ_i of the i-th species, the osmotic pressure P of the solution, and the mean activity coefficient $\gamma_\pm$ can be expressed in terms of S as follows:

$$-\log\gamma_i=\frac{\partial S}{\partial c_i}\,, \quad (4)$$

$$P/kT=\sum_{i=1}^{\sigma}c_i+S-\sum_{i=1}^{\sigma}c_i\frac{\partial S}{\partial c_i}\,, \quad (5)$$

$$\log \gamma_\pm = \frac{1}{c}\sum_{i=1}^{\sigma} c_i \log \gamma_i\,, \quad \left(c=\sum_{i=1}^{\sigma} c_i\right) \tag{6}$$

The integrand of B_n is a sum of products. In forming the sum S, Mayer has chosen the way in which one first sums over all members belonging to a given type of product, which he has called "prototype," and then sums over all types. He has shown*, for any prototype (t,m)1) that, in the limit $\alpha \to 0$,

$$\sum_{n} B_{m+n}^{(tm)} c^{m+n} = B_m^{(t)} c^m\,, \tag{7}$$

where

$$B_m^{(t)} = (-\lambda)^{\nu}\left[\prod_i z_i^{\nu_i}\right]\frac{A_{tm}}{m\,!} I_m^{(t)} \tag{8}$$

with

$$m\,! = m_1\,!\, m_2\,! \cdots m_\sigma\,!\,.$$

In the above expression for $B_m^{(t)}$, $I_m^{(t)}$ is the integral of single product corresponding to the prototype (t,m), in which $g(r)$ is replaced by

$$q(r) = e^{-\kappa r}/4\pi r\,, \tag{9}$$

where κ is the Debye-Huckel κ:

$$\kappa^2 = \lambda \sum_i z_i^2 c_i\,. \tag{10}$$

§ 2. Integrations

Now we evaluate the contribution to the sum S from the following types of product:

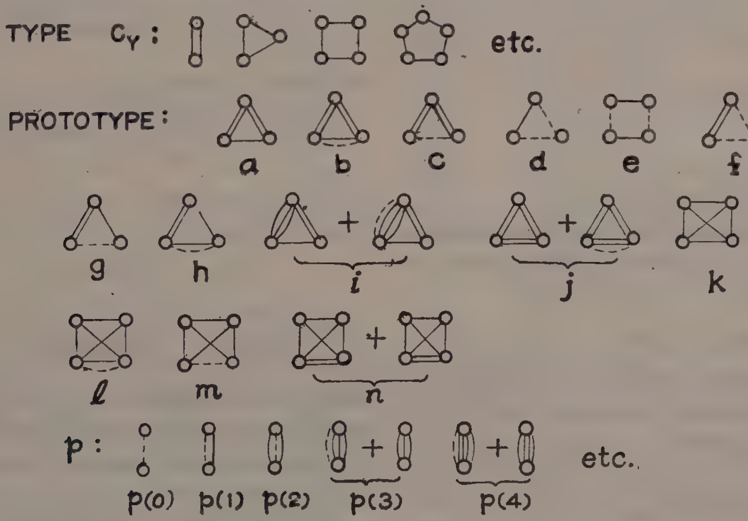

Fig. 1.

In the above graphs, the small circles represent ions, and full and broken lines connecting them represent q (g for the type c) and k bonds** respectively. Now we proceed to evaluate B_n and I's corresponding to the above prototypes.

(1) *Type* c_y

If we denote the Fourier transform of $g(r)$ by $\chi_1(t)$, we have

$$\chi_1(t) = \int e^{i(tr)} g(r)\, dr = \frac{1}{t^2+\alpha^2}\,. \tag{11}$$

Now put

$$q_n(r_{ij}) = \iint \cdots \int g(r_{i1}) g(r_{12}) \times \cdots g(r_{nj})\, dr_1 dr_2 \cdots dr_n\,, \tag{12}$$

then we can easily find the explicit expression for $q_n(r_{ij})$ by the inverse Fourier transformation:

$$q_n(r_{ij}) = \frac{1}{(2\pi)^3}\int e^{-i(tr_{ij})}[\chi_1(t)]^{n+1} dt = \frac{1}{2\pi^2 r_{ij}}\int_0^\infty \frac{t \sin t r_{ij}}{(t^2+\alpha^2)^{n+1}} dt\,. \tag{12a}$$

Now $B_n^{(c_y)}$ can be expressed in terms of q_n by the equation

$$B_n^{(c_y)} = \frac{1}{\prod n_i\,!}\prod_i (-\lambda z_i^2)^{n_i} q_{n-1}(r=0)\,.$$

Multiplying the above expression by the factor $\frac{1}{2}(n-1)!\,c^n$ and suming over all possible sets of n with $n=\sum n_i \geqq 2$, we have the contribution to the sum S from the type c_y:

---

* As regards to the definitions of ν_i and A_{tm}, see the Mayer's paper.

** For the meaning of q (g) and k bonds, see Mayer's paper.

$$S^{(c_y)}=\sum_{n\geq 2} B_n^{(c_y)}c^n=\sum_{n\geq 2}\frac{1}{2n}\times\left[n!\prod_i\frac{(-\lambda z_i^2 c_i)^{n_i}}{n_i!}\right]q_{n-1}(r=0)$$

$$=\sum_{n\geq 2}\frac{1}{2n}(-\kappa^2)^n q_{n-1}(r=0)$$

$$=\sum_{n\geq 2}\frac{(-\kappa^2)^n}{4\pi^2 n}\int_0^\infty\frac{t^2}{(t^2+\alpha^2)^n}dt\,.$$

Differentiating the above expression with respect to κ^2 and taking the limit $\alpha\to 0$, we have $\partial S^{(c_y)}/\partial\kappa^2=\kappa/8\pi$. Integrating this equation with respect to κ^2, we have $S^{(c_y)}=\kappa^3/12\pi$. From Eqs. (4), (5) and (6), we finally find that

$$-\log\gamma_i^{(c_y)}=\frac{\lambda z_i^2\kappa}{8\pi}\,, \tag{13}$$

$$P^{(c_y)}/kT=c-\frac{\kappa^3}{24\pi}\,, \tag{14}$$

$$-\log\gamma_\pm^{(c_y)}=\frac{\kappa^2}{8\pi c}\,, \tag{15}$$

in agreement with Mayer's results which has been obtained by the method, essentially the same as ours.

(2) *Prototype a, b and c*

For the evaluation of the prototype a, we construct the Fourier transform $\chi_2(t)$ of $q^2(r)$. It is easy to see that

$$\chi_2(t)=\int e^{i(tr)}q^2(r)dr=\frac{1}{4\pi t}\operatorname{arctg}\frac{t}{2\kappa}\,. \tag{16}$$

Now let us call the graph shown in the Fig. 2 type A. Corresponding to type A we have the integral

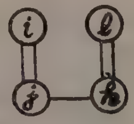

Fig. 2.

$$I^{(a)}(r_{il})=\iint q^2(r_{ij})q(r_{jk})\times q^2(r_{kl})dr_j dr_k\,, \tag{17}$$

which can be evaluated in terms of $\chi_1(t)$ and $\chi_2(t)$ by the inverse Fourier transformation:

$$I^{(a)}(r_{il})=\frac{1}{(2\pi)^3}\iiint e^{-i(tr_{il})}\chi_1(t)[\chi_2(t)]^2 dt$$

$$=\frac{1}{32\pi^4}\int_0^\infty\frac{\sin tr_{il}}{tr_{il}}\frac{1}{t^2+\kappa^2}\operatorname{arctg}^2\frac{t}{2\kappa}dt\,. \tag{17a}$$

We have the integral $I^{(a)}$ corresponding to the prototype a as the limit $r_{il}\to 0$ of the expression (17a):

$$I^{(a)}=\frac{1}{16\pi^4\kappa}\int_0^{\pi/2}\frac{\theta^2}{1+4\tan^2\theta}\sec^2\theta d\theta\,.$$

Carrying out the numerical integration, we obtain

$$I^{(a)}=0.000259\frac{1}{\kappa}\,.$$

From Eqs. (7) and (8) we have

$$S^{(a)}=\sum_{n=3} B_n c^n=-0.000032\frac{1}{\kappa}\times\left[\lambda^2\sum_{i=1}^{\sigma}(z_i^4 c_i)\right]\left[\lambda^{3/2}\sum_{i=1}^{\sigma}(z_i^3 c_i)\right]^2.$$

Now we define κ_n as

$$\kappa_{n-2}^2=\lambda^{n/2}\sum_i c_i z_i^n\,, \tag{18}$$

κ_0 being Debye-Hückel's κ. Then we have

$$S^{(a)}=-0.000032\frac{\kappa_1^4\kappa_2^2}{\kappa}$$

and finally we find that

$$-\log\gamma_i^{(a)}=\frac{\partial S^{(a)}}{\partial c_i}=-0.000032\left(-\frac{\lambda z_i^2}{2}\frac{\kappa_1^4\kappa_2^2}{\kappa^3}+2\lambda^{3/2}z_i^3\frac{\kappa_1^2\kappa_2^2}{\kappa}+\lambda^2 z_i^4\frac{\kappa_1^4}{\kappa}\right) \tag{19}$$

$$P^{(a)}/kT=0.000032\frac{\kappa_1^4\kappa_2^2}{\kappa} \tag{20}$$

$$-\log\gamma_\pm^{(a)}=-0.000080\frac{\kappa_1^4\kappa_2^2}{c\kappa}\,. \tag{21}$$

Next, we evaluate the contribution of the prototype b to the osmotic pressure. At first we integrate with respect to the ion ⓙ over the entire space by the use of $\chi_2(t)$, and then we integrate with respect to the ion ⓘ inside the sphere of radius a which has the ion ⓚ as its centre. (See Fig. 2) Thus we have the integral $I^{(b)}$ corresponding to the prototype b:

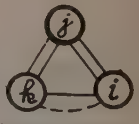

Fig. 3.

$$I^{(b)}=-\frac{1}{32\pi^4}\frac{1}{\kappa}\int_0^{\kappa a}e^{-r}dr\int_0^\infty\frac{\sin tr}{t}\operatorname{arctg}^2\frac{t}{2}dt.$$

It is easy to see that

$$\lim_{\kappa\to 0}I^{(b)}=-\frac{a}{32\pi^4}\lim_{\kappa\to 0}e^{-\kappa a}\int_0^\infty\frac{\sin\kappa at}{t}\times\operatorname{arctg}^2\frac{t}{2}=0\,.$$

Hence, $I^{(b)}$ is of the higher order than c^0 and the contribution of this prototype to the osmotic pressure is of the higher order than c^3.

By the same method as in the above, it is easily seen that the contribution of the prototype c to the osmotic pressure is of the higher order than c^3.

(3) *Prototype d and e*

At first we construct the Fourier transform $\chi_3(t)$ of $k^*(r)$. We have

$$\chi_3(t)=\int e^{i(rt)}k^*(r)d\mathbf{r}$$
$$=\frac{4\pi}{t^3}(ta\cos ta-\sin ta).$$

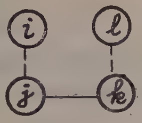

Fig. 4.

We define the integral $I^{(d)}(r_{il})$ as

$$I^{(d)}(r_{il})=\iint k^*(r_{ij})q(r_{jk})k^*(r_{kl})d\mathbf{r}_j d\mathbf{r}_k\,.$$

in which the integrations are carried out with respect to the ions ⓙ and ⓚ, with the ions ⓘ and ⓛ being fixed. It is easily seen that

$$I^{(d)}(r_{il})=\frac{8}{r_{il}}\int_0^\infty\frac{\sin tr_{il}}{t^5(t^2+\kappa^2)}(ta\cos ta-\sin ta)^2dt,$$

by the use of $\chi_1(t)$ and $\chi_3(t)$. The integral $I^{(d)}$ corresponding to the prototype d can be obtained as the limit $r_{il}\to 0$ of the above expression:

$$I^{(d)}=8\int_0^\infty\frac{1}{t^4(t^2+\kappa^2)}(ta\cos ta-\sin ta)^2dt\,,$$

which is finite at the limit $\kappa\to 0$. Hence, $I^{(d)}$ is of the order c^0 and the contribution of this prototype to the osmotic pressure is of the order c^3.

The integral $I^{(e)}$ corresponding to the prototype e is obtained if we multiply $I(r_{il})$ by the factor $e^{-\kappa r_{il}}/4\pi r_{il}$ and integrate with respect to $\mathbf{r}_l$ over the entire space:

$$I^{(e)}=8\int_0^\infty\frac{1}{t^4}\cdot\frac{1}{(t^2+\kappa^2)^2}(ta\cos ta-\sin ta)^2dt\,.$$

Since $\kappa^2I^{(e)}$ is finite at the limit $\kappa\to 0$, the contribution of this prototype to the osmotic pressure is the order c^3.

(4) *Prototype f*

We define the integral $I^{(f)}(r_{il})$ as

$$I^{(f)}(r_{il})=\iint k^*(r_{ij})$$
$$\times q(r_{jk})^2k^*(r_{kl})d\mathbf{r}_jd\mathbf{r}_k\,.$$

It is easily seen that

$$I^{(f)}(r_{il})=\frac{2}{\pi}\frac{1}{r_{il}}\int_0^\infty\frac{\sin tr_{il}}{t^6}$$
$$(ta\cos ta-\sin ta)^2\operatorname{arctg}\frac{t}{2\kappa}dt\,,$$

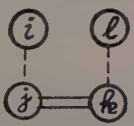

Fig. 5.

by the use of $\chi_2(t)$ and $\chi_3(t)$. The integral $I^{(f)}$ corresponding to the prototype f is obtained as the limit $r_{il}\to 0$ of the above expression:

$$I^{(f)}=\frac{2}{\pi}\int_0^\infty\frac{1}{t^5}(ta\cos ta-\sin ta)^2$$
$$\times\operatorname{arctg}\frac{t}{2\kappa}dt\,,$$

which is finite at the limit $\kappa\to 0$. Hence the contribution of this prototype to the osmotic pressure is of the order c^3.

(5) *Prototype g, h and i*

At first we integrate with respect to the ion ⓙ over the entire space, with the ions ⓘ and ⓚ being fixed, and then we integrate with respect to the ion ⓚ inside the sphere of radius a, and we have

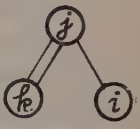

Fig. 6.

$$I^{(g)}=-\frac{1}{2\pi^2}\frac{1}{\kappa^3}\int_0^{\kappa a}rdr\int_0^\infty\frac{\sin tr}{t^2+1}\operatorname{arctg}\frac{t}{2}dt\,.$$

Hence we have

$$\lim_{\kappa\to 0}|I^{(g)}|=\frac{1}{2\pi^2}\lim_{\kappa\to 0}\frac{1}{3\kappa^2}\kappa a\int_0^\infty\frac{\sin\kappa at}{t^2+1}\operatorname{arctg}\frac{t}{2}dt$$
$$=\frac{a^2}{6\pi^2}\int_0^\infty\frac{t}{t^2+1}\operatorname{arctg}\frac{t}{2}dt=\infty\,.$$

We can show that $\kappa^\varepsilon|I^{(g)}|$ tends to zero at the limit $\kappa\to 0$, where $\mathcal{E}$ is any positive number:

$$\lim_{\kappa\to 0}\kappa^\varepsilon|I^{(g)}|<\lim_{\kappa\to 0}\frac{1}{4\pi}\frac{1}{\kappa^{3-\varepsilon}}\int_0^{\kappa a}rdr\int_0^\infty\frac{\sin tr}{t^2+1}dt$$
$$=\lim_{\kappa\to 0}\frac{1}{4(3-\mathcal{E})\pi}\frac{a}{\kappa^{1-\varepsilon}}\int_0^\infty\frac{\sin\kappa at}{t^2+1}dt$$
$$=\frac{a}{8(3-\mathcal{E})\pi}\lim_{\kappa\to 0}\frac{1}{\kappa^{1-\varepsilon}}\Big\{e^{-\kappa a}E_i(\kappa a)$$
$$-e^{\kappa a}E_i(-\kappa a)\Big\}$$
$$=-\frac{a^2}{4(3-\mathcal{E})\pi}\lim_{\kappa\to 0}\kappa^\varepsilon\log\kappa a=0\,.$$

Hence we can conclude that $I^{(g)}$ is of the order $\log c$ and the contribution of this type to the osmotic pressure is of the order $c^3\log c$.

By the same method as in the above, we conclude that the integral $I^{(h)}$ and $I^{(i)}$ corresponding to the prototypes h and i respectively is of the order $\log c$.

(6) *Prototype j*

At first we define the integral $K(r_{ik})$ as

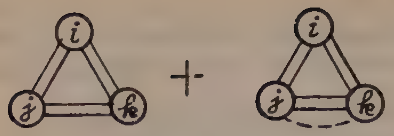

Fig. 7.

$$K(r_{jk})=\int q^2(r_{ji})q^2(r_{ik})d\boldsymbol{r}_i$$

$$=\frac{1}{(2\pi)^3}\int e^{-i(\boldsymbol{t}\boldsymbol{r}_{ik})}[\chi_2(t)]^2 d\boldsymbol{t}=\frac{L(r_{jk})}{32\pi^4 r_{jk}}\,,$$

$$L(r_{jk})=\int_0^\infty \frac{\sin\sigma x}{x}\,\mathrm{arctg}^2 x dx \qquad (\sigma=2\kappa r_{jk})$$

It is easily shown that

$$\int_{-\infty}^\infty \frac{x\sin\sigma x}{(a^2+x^2)(b^2+x^2)}dx=\frac{\pi}{a^2-b^2}(e^{-b\sigma}-e^{-a\sigma})\ .$$

If we integrate the both sides of the above expression with respect to a and b from zero to unity, we have

$$\int_0^\infty \frac{\sin\sigma x}{x}\,\mathrm{arctg}^2 x dx$$

$$=\frac{\pi}{2}\iint_S \frac{e^{-\sigma b}-e^{-\sigma a}}{a^2-b^2}da\,db-\frac{\pi^3}{8}\,,$$

where the integral domain S is the square of the side length unity. (See Fig. 8)

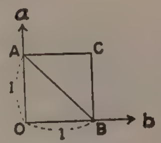

Fig. 8.

Transforming the integral variables from a, b to ξ, η, where $\xi=a+b$, $\eta=a-b$ we have

$$M(\sigma)\equiv\iint_S \frac{e^{-\sigma b}-e^{-\sigma a}}{a^2-b^2}da\,db$$

$$=\frac{1}{2}\iint_S \frac{e^{-\sigma/2\cdot\xi}}{\xi\eta}(e^{\sigma/2\cdot\eta}-e^{-\sigma/2\cdot\eta})d\xi d\eta\ .$$

Now we divide the integral domain S into S_{0AB} and S_{ABC}. At S_{0AB}, we integrate, at first, with respect to η from $-\xi$ to ξ and then with respect to ξ from zero to unity. At S_{ABC}, we integrate, at first, with respect to η from $-(2-\xi)$ to $(2-\xi)$ and then with respect to ξ from 1 to 2. After the elementary calculation, we have

$$M(\sigma)_{0AB}=2\sum_{n,m=0}^{\infty}\frac{(-1)^m(\kappa r)^{2n+m+1}}{n!\,(2n+1)!\,(2n+1)(2n+m+1)}$$

and

$$M(\sigma)_{ABC}=\sum_{k,l,m,n=0}^{\infty}$$

$$\times\frac{(-1)^k 2^{k-l}(\kappa r)^{k+m+2n+1}}{k!\,m!\,(2n+1)!\,(2n+1)(l+m+2n+2)}\ .$$

It is seen that $M(\sigma)$ is a power series of κr which begins from the first power of κ. If we integrate $K(r_{jk})$ with respect to the ion ⓚ outside the sphere of radius a, we have the integral $I^{(j)}$ corresponding to the prototype j:

$$I^{(j)}=\frac{1}{138\pi^5}\int_a^\infty \frac{e^{-2\kappa r}}{r}\left(\frac{\pi}{2}M(\kappa r)-\frac{\pi^3}{8}\right)dr\ .$$

Differentiating n times of the both sides of the equality

$$\int_a^\infty e^{-2\kappa r}dr=e^{-2\kappa a}/2\kappa\ ,$$

we see that the term of the lowest order with respect of κ in

$$\int_a^\infty e^{-2\kappa r}(\kappa r)^{n+1}/r dr$$

is of the order κ^0. It is also seen that

$$\int_a^\infty e^{-2\kappa r}/r dr=-\gamma-\log 2\kappa a+2\kappa a-+\cdots,$$

where γ is Euler's constant. Hence, we see that $I^{(j)}$ consists of the term independent of κ, the term of the order of $\log 2\kappa a$, and the powers of κ equal to and higher than the contribution of this prototype to the osmotic pressure is of the order $c^3\log c$.

(7) *Prototype k, l, m and n*

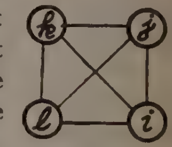

Fig. 9.

We evaluate the order of the contribution of the prototype k to the osmotic pressure. For this purpose, we, at first, carry out the integrations with respect to the ions ⓙ and ⓚ with the ion ⓘ and ⓛ being fixed. (See Fig. 9) Since $\boldsymbol{r}_{ij}=\boldsymbol{r}_{lj}-\boldsymbol{r}_{li}$, $\boldsymbol{r}_{ik}=\boldsymbol{r}_{lk}+\boldsymbol{r}_{il}$, and $\boldsymbol{r}_{il}$ is a constant vector we can consider the bonds lj and ik to be functions of $\boldsymbol{r}_{lj}$ and $\boldsymbol{r}_{lk}$, respectively. The integrations with respect to the ions ⓙ and ⓚ can be carried out by the use of Fourier transformation. We construct the characteristic function $\chi(\boldsymbol{r}_{il},\boldsymbol{t})$ with respect to the bonds ij and lj:

$$\chi(\boldsymbol{r}_{il},\boldsymbol{t})=\int e^{i(\boldsymbol{t}\boldsymbol{r}_{ij})}q(r_{ij})q(r_{jl})d\boldsymbol{r}_j$$

$$=\frac{1}{(2\pi)^3}\int\frac{e^{-i(\boldsymbol{y}\boldsymbol{r}_{il})}}{(\boldsymbol{y}+\boldsymbol{t})^2+\kappa^2}\cdot\frac{d\boldsymbol{y}}{y^2+\kappa^2}\,,$$

where we have used the inverse Fourier transformation by the use of the characteristic functions of the two factors which contain $\boldsymbol{r}_{ij}$ and $\boldsymbol{r}_{jl}$. In the same way, we can construct the characteristic function with respect to the bonds kl and ki:

$$\chi'(r_{il},t)=\int e^{i(\mathbf{t}\mathbf{r}_{kl})}q(r_{kl})q(r_{ki})d\mathbf{r}_k$$

$$\doteq e^{i(\mathbf{t}\mathbf{r}_{il})}\int e^{-i(\mathbf{t}\mathbf{r}_{ik})}q(r_{kl})q(r_{ki})d\mathbf{r}_k$$

$$=\frac{e^{i(\mathbf{t}\mathbf{r}_{il})}}{(2\pi)^3}\int\frac{e^{i(\mathbf{z}\mathbf{r}_{il})}}{(\mathbf{z}+\mathbf{t})^2+\kappa^2}\frac{d\mathbf{z}}{z^2+\kappa^2}\,.$$

Hence, we have the integral $I^{(k)}$ corresponding to the prototype k:

$$I^{(k)}=\iiint q(r_{il})q(r_{kl})q(r_{ki})q(r_{jk})\times q(r_{ij})q(r_{lj})d\mathbf{r}_l d\mathbf{r}_k d\mathbf{r}_j$$

$$=\frac{1}{(2\pi)^9\kappa^3}\iiint\frac{1}{(\mathbf{x}+\mathbf{y})^2+1}\frac{1}{(\mathbf{y}-\mathbf{z})^2+1}\times\frac{1}{(\mathbf{z}+\mathbf{x})^2+1}\frac{1}{x^2+1}\frac{1}{y^2+1}\frac{1}{z^2+1}d\mathbf{x}d\mathbf{y}d\mathbf{z}$$

or

$$=\frac{1}{(2\pi)^9\kappa^3}\int_0^\infty re^{-r}dr\iiint_\infty\frac{d\mathbf{x}}{x^2+1}\iiint_\infty\frac{e^{-i(\mathbf{y}\mathbf{r})}}{(\mathbf{x}+\mathbf{y})^2+1}\times\frac{d\mathbf{y}}{y^2+1}\iiint_\infty\frac{e^{i(\mathbf{z}\mathbf{r})}}{(\mathbf{z}+\mathbf{x})^2+1}\frac{d\mathbf{z}}{z^2+1}\,.$$

We see that the contribution of the prototype k to the osmotic pressure is of the order $c^{5/2}$.

The integral $I^{(l)}$ for the prototype l is the same as $I^{(k)}$ except the upper limit of integration with respect to r is replaced by κa instead of ∞ in $I^{(k)}$, and we see that $\kappa^2 I^{(l)}$ tends to zero when κ approaches to zero. Hence, $I^{(l)}$ is of the higher order than κ^{-2} and the contribution of the prototype l to the osmotic pressure is of the order higher than c^3.

For the prototype m, we have

$$I^{(m)}=-\frac{2}{(2\pi)^8}\frac{1}{\kappa^4}\int_0^{\kappa a}r^2dr\iiint_\infty\frac{d\mathbf{x}}{x^2+1}\times\iiint_\infty\frac{e^{-i(\mathbf{y}\mathbf{r})}}{(\mathbf{x}+\mathbf{y})^2+1}\frac{d\mathbf{y}}{y^2+1}\iiint_\infty\frac{e^{i(\mathbf{z}\mathbf{r})}}{(\mathbf{z}+\mathbf{x})^2+1}\frac{d\mathbf{z}}{z^2+1}$$

where $\kappa^2 I^{(m)}$ tends to zero when κ approaches to zero. Hence the contribution of the prototype m to the osmotic pressure is of order higher than c^3.

For the prototype n, we have

$$I^{(n)}=-\frac{1}{2(2\pi)^{10}}\frac{1}{\kappa^2}\int_{\kappa a}^\infty e^{-2r}dr\iiint_\infty\frac{d\mathbf{x}}{x^2+1}\times\iiint_\infty\frac{e^{-i(\mathbf{y}\mathbf{r})}}{(\mathbf{x}+\mathbf{y})^2+1}\frac{d\mathbf{y}}{y^2+1}\iiint_\infty\frac{e^{i(\mathbf{z}\mathbf{r})}}{(\mathbf{z}+\mathbf{x})^2+1}\frac{d\mathbf{z}}{z^2+1}$$

Hence, $I^{(n)}$ is of the order κ^2 and the contribution of the prototype n to the osmotic pressure is of the order c^3.

(8) *The calculation of the prototype k*

As the contribution of the prototype k to the osmotic pressure is of the order $c^{5/2}$, it becomes necessary to obtain the explicit expressions for the contribution of this prototype osmotic pressure and to the activity coefficient.

At first we consider the integral

$$I^{(k)}(r_{ik})=\iint q(r_{ij})q(r_{jk})q(r_{kl})q(r_{li})q(r_{jl})d\mathbf{r}_j d\mathbf{r}_l$$

corresponding to the type B shown in Fig. 10. Then the integral $I^{(k)}$ corresponding to the prototype k can be expressed in terms of $J(r_{ik})$ by the integral:

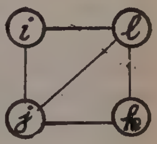

Fig. 10.

$$I^{(k)}=\int J(r_{ik})q(r_{ik})d\mathbf{r}_k$$

As it is impossible to evaluate the integral $I^{(k)}(r_{ik})$ exactly, we evaluate it by means of the following approximate way.

We see that $I^{(k)}(0)$ is equal to $I^{(a)}(0)$ given by the Eq. (17a). We see also that $I^{(k)}(r_{ik})$ integrated with respect to $\mathbf{r}_k$ gives

$$\bar{I}^{(k)}=\int I^{(k)}(r_{ik})d\mathbf{r}_k=\int q(r_{jl})[q_1(r_{jl})]^2d\mathbf{r}_l$$

where $q_1(r_{jl})$ is given by the Eq. (12a) with $n=1$:

$$q_1(r_{jl})=\frac{1}{2\pi^2 r_{jl}}\int_0^\infty\frac{t\sin tr_{jl}}{(t^2+\kappa^2)^2}dt=\frac{e^{-\kappa r}}{8\pi\kappa}\,.$$

Inserting this expression into the above, we have

$$\bar{I}^{(k)}=\frac{1}{576\pi^2}\frac{1}{\kappa^4}=0.000176\frac{1}{\kappa^4}\,. \qquad (22)$$

We adopt, as the approximate expression for $I^{(k)}(r_{ik})$, $I^{(a)}(r_{ik})$ multiplied by the facter

$$(e^{-\kappa r_{ik}}-e^{-2\kappa r_{ik}})/\kappa r_{ik}$$

which are equal to 1 at $r_{ik}=0$:

$$J(r_{ik})=\frac{1}{32\pi^4}\frac{e^{-\kappa r_{ik}}-e^{-2\kappa r_{ik}}}{\kappa r_{ik}}\times\int_0^\infty\frac{\sin tr_{ik}}{tr_{ik}}\frac{1}{t^2+\kappa^2}\operatorname{arctg}^2\frac{t}{2\kappa}dt\,. \qquad (22a)$$

The above integral with respect to t have appeared in the type A of Fig. 2. (See Eq. (17a)) Let us consider the type A. (See Fig. 2) At very large r_{il}, the main contribution to the integral $I^{(a)}(r_{il})$ corresponding to the type A comes out when the ion ⓙ is near the ion ⓘ and at same time the ion ⓚ near the ion ⓛ. And so $I^{(a)}(r_{il})$ behaves like $e^{-\kappa r_{il}}$, at very large r_{il}. Hence, $J(r_{ik})$ at large r_{ik} consists of the part which behaves like $e^{-2\kappa r_{ik}}$ and the part which behaves like $e^{-3\kappa r_{ik}}$. Now let us consider the type B. At large r_{ik}, the main contribution to the exact integral $I^{(k)}(r_{ik})$ corresponding to the type B comes out when (1) the ions ⓙ and ⓛ are near the ion ⓘ or the ion ⓚ and when (2) one of the ions ⓙ and ⓛ are near the ion ⓘ and at same time the other near the ion ⓚ. Hence, at large r_{ik}, $I^{(k)}(r_{ik})$ consists of the term which behaves like $e^{-2\kappa r_{ik}}$ and the term which behaves like $e^{-3\kappa r_{ik}}$. Hence the approximate expression $J(r_{ik})$ gives a good approximation for large r_{ik}, and, of course, gives the exact value at $r_{ik}=0$ and, when integrated with respect to $\mathbf{r}_k$, gives

$$\bar{J}=\int J(r_{ik})d\mathbf{r}_k=\frac{1}{4\pi^3\kappa^4}\int_0^{\pi/2}\left\{\frac{1}{(1+4\tan^2\theta)^2}-\frac{1}{3}\right.$$
$$\left.\times\left(\frac{1}{1+4\tan^2\theta}-\frac{1}{4(1+\tan^2\theta)}\right)\right\}\theta^2\sec^2\theta d\theta$$

which is shown to be equal to

$$\bar{J}=0.000155\frac{1}{\kappa^4}$$

by the numerical integration. This is approximately equal to the exact value given by the Eq. (22). Thus we may use the approximate expression (22a) for $I^{(k)}(r_{ik})$ without serious errors. When this approximate expression is used, the integral $I^{(k)}$ can easily evaluated and we have

$$I^{(k)}=\int_0^\infty J(r_{ik})q(r_{ik})4\pi r_{ik}^2 dr_{ik}$$
$$=\frac{1}{32\pi^4\kappa}\int_0^\infty\frac{1}{t}\,\frac{1}{t^2+\kappa^2}\operatorname{arctg}^2\frac{t}{2\kappa}dt$$
$$\times\int_0^\infty\frac{\sin tr_{ik}}{r_{ik}}(e^{-2\kappa r_{ik}}-e^{-3\kappa r_{ik}})\,dr_{ik}$$
$$=\frac{1}{32\pi^4\kappa^3}\int_0^{\pi/2}\left\{\frac{1}{\tan\theta}\,\frac{\theta^3(1+\tan^2\theta)}{1+4\tan^2\theta}\right.$$
$$\left.-\frac{1}{\tan\theta}\,\frac{\theta^2(1+\tan^2\theta)}{1+4\tan^2\theta}\operatorname{arctg}\left(\frac{2}{3}\tan\theta\right)\right\}d\theta,$$

which is shown to be equal to

$$I^{(k)}=0.000013\frac{1}{\kappa^3},$$

by the numerical integration.

From Eqs. (7) and (8) we have

$$S^{(k)}=0.00000054\frac{\kappa_1^8}{\kappa^3}$$

and finally we find

$$-\log\gamma_i^{(k)}=0.00000054\left(-\frac{3}{2}\lambda z_i^2\frac{\kappa_1^8}{\kappa^5}\right.$$
$$\left.+\frac{4\kappa_1^6}{\kappa^3}\lambda^{3/2}z_i^3\right)\qquad(23)$$

$$P^{(k)}/kT=-0.00000081\frac{\kappa_1^8}{\kappa^3}\qquad(24)$$

$$-\log\gamma_{\pm}^{(k)}=0.00000135\frac{\kappa_1^8}{c\kappa^3}\qquad(25)$$

(9) *Prototype p*

It is easy to see that the contribution to the sum S from the prototype $p(0)$ becomes

$$S_0=\Sigma\frac{c_ic_j}{1+\delta(i,j)}\int k^*(r_{ij})d\mathbf{r}_i=-\frac{2\pi}{3}a^3c^2\,.$$

As for the contribution from the prototype $p(1)$, we have

$$S_1=\Sigma\frac{c_ic_j}{1+\delta(i,j)}\int(-\lambda z_iz_jq(r_{ij}))k^*(r_{ij})d\mathbf{r}_i$$
$$=\lambda\Sigma\frac{z_iz_jc_ic_j}{1+\delta(i,j)}\int_0^a q(r_{ij})d\mathbf{r}_i$$

which is equal to zero because of the neutrality of the solution, since

$$\Sigma\frac{z_iz_jc_ic_j}{1+\delta(i,j)}=\frac{1}{2}\left(\sum_{i=1}^{\sigma}z_ic_i\right)^2=0.$$

The contribution from the prototype $p(2)$ becomes

$$S_2=\Sigma\frac{c_ic_j}{1+\delta(i,j)}\int\frac{1}{2!}(-\lambda z_iz_jq(r_{ij}))^2k^*(r_{ij})d\mathbf{r}_i$$
$$=-\frac{\kappa^3}{16}(1-e^{-\kappa a})=-\frac{\kappa^4a}{16\pi}+\frac{\kappa^5a^2}{32\pi}-+\cdots.$$

To evaluate the contribution from the prototype $p(n)$ $(n\geqq3)$, we consider the integral

$$S_n^{ij}=\frac{4\pi c_ic_j}{1+\delta(i,j)}\left(-\frac{\lambda z_iz_j}{4\pi}\right)^n\frac{1}{n!}\int_a^\infty\frac{e^{-n\kappa r}}{r^{n-2}}dr$$
$$=\frac{4\pi c_ic_j}{(1+\delta(i,j))}\left(-\frac{\lambda z_iz_j}{4\pi}\right)^n\frac{(n\kappa)^{n-3}}{n!}\int_{n\kappa a}^\infty\frac{e^{-\kappa}}{x^{n-2}}dx,$$
$$(n\geqq3)\,.$$

For $n=3$, we have

$$S_3^{ij}=\frac{4\pi c_ic_j}{1+\delta(i,j)}\left(-\frac{\lambda z_iz_j}{4\pi}\right)^3\frac{1}{3!}(-E_i(-3\chi a)),$$

where $E_i(x)$ is exponential integral of the argument. Since the exponential integral can be expanded into the power series of the argument as

$$-E_i(-x)=\int_x^\infty \frac{e^{-t}}{t}dt=-\gamma-\log x+x-\frac{1}{2}\frac{1}{2!}x^2+-\cdots$$

where γ is the Euler's constant, we have

$$S_3{}^{ij}=\frac{4\pi c_i c_j}{1+\delta(i,j)}\left(-\frac{\lambda z_i z_j}{4\pi}\right)^3\frac{1}{3!}\times(-\gamma-\log 3\kappa a+3\kappa a)$$

in our approximation.

In a similar way we obtain, for $n=4$,

$$S_4{}^{ij}=\frac{4\pi c_i c_j}{1+\delta(i,j)}\left(-\frac{\lambda z_i z_j}{4\pi}\right)^4\frac{1}{4!}\times\left(\frac{1}{a}+4\kappa(-1+\gamma+\log 4\kappa a)\right).$$

For $n\geq 5$, we obtain

$$S_n{}^{ij}=\frac{4\pi c_i c_j}{1+\delta(i,j)}\left(-\frac{\lambda z_i z_j}{4\pi}\right)^n\frac{1}{n!}\times\left(\frac{1}{(n-3)a^{n-3}}-\frac{n}{n-4}\kappa\frac{1}{a^{n-4}}\right).$$

Summing up all the expressions S_0, S_2 and $S_n{}^{ij}$ ($n\geq 3$, $\sigma\geq i\geq j\geq 1$) we have the contribution to the sum S from the prototype p:

$$S^{(p)}=S_0+S_2+\sum_{\sigma\geq i\geq j\geq 1}\sum_{n=3}^{\infty}S_n{}^{ij}=-\frac{2\pi}{3}a^3c^2-\frac{\kappa^4 a}{16\pi}+\frac{\kappa^5 a^2}{32\pi}+\frac{\kappa_1{}^4}{192\pi^2}(\gamma+\log 3\kappa a-3\kappa a)$$
$$+\frac{\kappa\kappa_2{}^4}{768\pi^3}(-1+\gamma+\log 4\kappa a)+2\pi a^3\sum_{n=4}^{\infty}\frac{(-)^n}{n!\,(n-3)}\frac{\kappa_{n-2}{}^4}{(4\pi a)^n}+\frac{1}{2}a^3\kappa\sum_{n=4}^{\infty}\frac{(-)^n}{n!\,(n-3)}\frac{\kappa_{n-1}{}^4}{(4\pi a)^n}$$

and finally we find that

$$-\log\gamma_i{}^{(p)}=-\frac{4\pi}{3}a^3c-\frac{\kappa^2 a}{8\pi}\lambda z_i{}^2+\frac{5\kappa^3 a^2}{64\pi}\lambda z_i{}^2+\frac{\kappa_1{}^2\lambda^{3/2}z_i{}^3}{96\pi^2}(\gamma+\log 3\kappa a-3\kappa a)$$
$$+\frac{\kappa_1{}^4}{192\pi^2}\left(\frac{\lambda z_i{}^2}{2\kappa^2}-\frac{3a}{2\kappa}\lambda z_i{}^2\right)+\frac{1}{768\pi^3}\left(\frac{\kappa_2{}^4}{2\kappa}\lambda z_i{}^2+2\kappa\kappa_2{}^2\lambda^2 z_i{}^4\right)(-1+\gamma+\log 4\kappa a)$$
$$+\frac{1}{1536\pi^3}\frac{\kappa_2{}^4}{\kappa}\lambda z_i{}^2+4\pi a^3\sum_{n=4}^{\infty}\frac{(-)^n}{n!\,(n-3)}\frac{\kappa_{n-2}{}^2}{(4\pi a)^n}\lambda^{n/2}z_i{}^n$$
$$+a^3\kappa\sum_{n=4}^{\infty}\frac{(-)^n}{n!\,(n-3)}\frac{\kappa_{n-1}{}^2}{(4\pi a)^n}\lambda^{(n+1)/2}z_i{}^{n+1}+\frac{a^3}{4\kappa}\lambda z_i{}^2\sum_{n=4}^{\infty}\frac{(-)^n}{n!\,(n-3)}\frac{\kappa_{n-1}{}^4}{(4\kappa a)^n} \tag{26}$$

$$P^{(p)}/kT=\frac{2\pi}{3}a^3c^2+\frac{\kappa^4 a}{16\pi}-\frac{3\kappa^5 a^2}{64\pi}-\frac{\kappa_1{}^4}{192\pi^2}\left(\frac{1}{2}+\gamma+\log 3\kappa a-\frac{9}{2}\kappa a\right)$$
$$-\frac{\kappa\kappa_2{}^4}{512\pi^3}\left(-\frac{2}{3}+\gamma+\log 4\kappa a\right)-2\pi a^3\sum_{n=4}^{\infty}\frac{(-)^n}{n!\,(n-3)}\frac{\kappa_{n-2}{}^4}{(4\pi a)^n}$$
$$-\frac{3}{4}a^3\kappa\sum_{n=4}^{\infty}\frac{(-)^n}{n!\,(n-3)}\frac{\kappa_{n-1}{}^4}{(4\pi a)^n} \tag{27}$$

$$-\log\gamma_\pm{}^{(p)}=\frac{1}{c}\left[-\frac{4\pi}{3}a^3c^2-\frac{\kappa^4 a}{8\pi}+\frac{5\kappa^5 a^2}{64\pi}+\frac{\kappa_1{}^4}{96\pi^2}\left(\frac{1}{4}+\gamma+\log 3\kappa a-\frac{15}{4}\kappa a\right)\right.$$
$$+\frac{5\kappa\kappa_2{}^4}{1536\pi^3}\left(-\frac{4}{5}+\gamma+\log 4\kappa a\right)+4\pi a^3\sum_{n=4}^{\infty}\frac{(-)^n\kappa_{n-2}{}^4}{n!(n-3)(4\pi a)^n}$$
$$\left.+\frac{5}{4}a^3\kappa\sum_{n=4}^{\infty}\frac{(-)^n}{n!\,(n-3)}\frac{\kappa_{n-1}{}^4}{(4\pi a)^n}\right. \tag{28}$$

§ 3. Discussion and Comparism with Experiments

In the preceding paragraphs we have succeeded to find the osmotic pressure expression for dilute ionic solutions which is right up to $c^{5/2}$. In this paragraph, we will compare the theoretical expression for the osmotic coefficient, g, of the 1–1 ionic solutions, derived by us, with that in the existing theories and with experiments.

It is easily seen that $\kappa_n{}^2$ with odd n becomes zero and $\kappa_n{}^2$ with even n becomes $\lambda^{n/2}c$ for 1–1 ionic solutions. Hence we have for the osmotic coefficient of 1–1 ionic solutions

$$I-g=\frac{1}{c}\left[\frac{\kappa^3}{24\pi}-\frac{2\pi}{3}a^3c^2-\frac{\kappa^4 a}{16\pi}+\frac{3\kappa^5a^2}{64\pi}\right.$$

$$\left.+\frac{\kappa\kappa_2{}^4}{512\pi^3}\left(-\frac{2}{3}+\gamma+\log 4\kappa a\right)\right]+A'c-B'c^{3/2}\,, \tag{29}$$

where

$$A'=2\pi a^3\sum_{n=2}^{\infty}\frac{1}{(2n)\,!\,(2n-3)}\left(\frac{\lambda}{4\pi a}\right)^{2n}$$

and

$$B'=\frac{3}{4}a^3\lambda^{3/2}\sum_{n=2}^{\infty}\frac{1}{(2n+1)\,!\,(2n-2)}\left(\frac{\lambda}{4\pi a}\right)^{2n+1}.$$

The first term in the above expression for $1-g$, which has been originated from the prototype c_y (cycles), gives the well-known Debye-Hückel's limiting law line; and the second term, which has come out of the prototype $p(0)$, corresponds to the second virial coefficient for the non-interacting rigid sphere molecules with diameter a.

Now, according to the Debye-Hückel's second approximation⁽²⁾, which takes into account the finiteness of ionic diameters,

$$1-g=\frac{\kappa^3}{24\pi c}\left(1-\frac{3}{2}\kappa a+\frac{9}{5}(\kappa a)^2+\cdots\right). \tag{30}$$

Comparing our Eq. (29) with Eq. (30), we see that the first and the third terms in Eq. (29) perfectly coincide with the first and the second terms in Eq. (30), respectively, and the fourth term in Eq. (29) is 5/8 of the third term in Eq. (30). We see also that the former contains the second and other terms which are not contained in the latter.

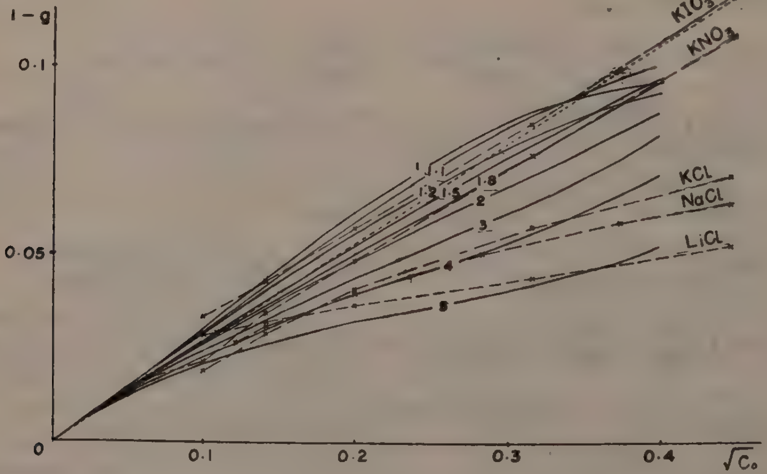

Fig. 11. Comparison of the calculated and experimental osmotic coefficients for 1-1 ionic solutions. ———, calculated according to Eq. (29) for several values of mean ionic diameters; the figures added to the curves are respective mean ionic diameters in Angstrom unit. --------, Debye-Hückel's limiting line. — — × — — experimental osmotic coefficient determined from freezing point data.

For the purpose of the comparison of Eq. (29) with experiments, we replace c by mol number per litre, c_0, $c=c_0N_0/1000$, where N_0 is Avogadro's number, $N_0=6.0228\times10^{23}$. We take $T=273$°K, at which the dielectric constant of water D is $D=88.23$; hence, we have $\lambda=87.164\times10^{-8}$. And we express the ionic diameter a by Angstrom unit, $a=10^{-8}x$. Then Eq. (29) becomes

$$1-g=0.2649c_0{}^{1/2}+A_0c_0+B_0c_0{}^{3/2}+0.5778c_0{}^{3/2}\log_{10}c_0 \tag{31}$$

where

$$A_0=-0.001262x^3-0.09105x+A\,,$$

$$B_0=0.01565x^2-0.09115+1.1557\log_{10}x-B\,,$$

$$A=0.003785x^3\sum_{n=2}^{\infty}\frac{1}{(2n)\,!\,(2n-3)}(6.9363/x)^{2n}\,,$$

$$B=0.009024x^3\sum_{n=2}^{\infty}\frac{1}{(2n+1)\,!\,(2n-2)}\times(6.9363/x)^{2n+1}\,.$$

In Fig. 11 $1-g$ is plotted against $\sqrt{c_0}$ according to Eq. (31) for several values.

The experimental osmotic coefficient can most accurately be determined as the ratio of the freezing point depression ΔT to its value for ideal solution, $\overline{\Delta T}$. The latter is 1.859° per mole per litre for aqueous solutions. The g values thus determined from freezing point data are also shown in Fig. 11 for several 1–1 ionic solutions. It is seen that experimental g values for one species of ionic solution lie nearly on one of the theoretical curves. The ionic diameters a so determined as to give the best fits with experimental g values are tabulated in Table I. The a values which have been determined according to Debye-Hückel's second approximation and those which have been determined according to the theory of Bjerrum and Gronwall-La Ma-Sandved are also shown in Table I. It is seen that our a values are more reasonable than those of Debye-Hückel's second approximation and nearly the same as those of the theory of Bjerrum and others.

Table I. Values of a in Ångstrom unit.

	KaCl	NaCl	LiCl	KNO_3	KIO_3
Debye-Hückel	3.40	4.02	—	0.43	0.03
Bjerrum	3.40	4.02	—	1.57	1.33
Gronwall-La Mer-Sandved	3.40	4.02	—	1.40	1.25
Mayer	3.6	4.0	4.7	1.8	1.2

In conclusion the author wishes to express his cordial thanks to Dr. Kubo, University of Tokyo, for his suggestion of the problem, and to Mr. Yokota for his helpful advices throughout this work.

References

1) J. E. Mayer: J. Chem. Phys. **18** (1950) 1426.
2) Fowler and Guggenheim: Statistical Thermodynamics, Cambridge 1939.

JOURNAL OF THE PHYSICAL SOCIETY OF JAPAN Vol. 8, No. 6, Nov.—Dec., 1953

Studies on the Cs_3Sb Photo-Cathode

By Toshimichi SAKATA
The Electrical Communication Laboratory

(Received April 13, 1953)

Spectral and energy distributions for external photoelectrons ejected from Cs_3Sb photo-cathodes were determined by the method of interchangeable emitters. Precautions were taken to secure electrically uniform surfaces.

The energy distribution had an usual form for $h\nu=2.14$, 2.27, 2.84 3.06, 3.39 and 3.96 ev. The results indicated that Cs_3Sb were semiconductors with a small values of $\delta=0.2\sim0.3$ ev. Here δ is the energy difference between the Fermi level and the top of the occupied band of energy states. The photoelectric work function (φ') was found about 1.8 ± 0.1 ev. The work function obtained from the contact potential techniques were about $1.5\sim1.6$ ev. On the other hand, the thermionic work function was found about $1.3\sim1.5$ ev, using Richardson's formula. Typical values of m1)2) [parameter depending both on the form of occupied band and on the energy dependence of the photo-electric excitation probability] obtained both from energy and spectral measurements were 1. Thermoelectric measurements showed that all samples were P type.

§ 1. Introduction

It has been known for many years that photoelectric layers of Cs_3Sb are extremely sensitive photoelectrically. At optimum sensitized condition, these layers can be considered as an intermetallic compound Cs_3Sb.

The detailed electronic state of the substance, however, are not clear at present. The surface photoeffect in metals has so far been calculated by using Sommerfeld's assumption of completely free electrons within the metal. In the case of semiconductors, however, it is assumed that the energy bands are completely filled and the free electron theory is no longer adequate. Following Apker and his collaborators¹⁾, we suppose that the number of electrons N(E) dE emitted with a given energy E by light is proportional to the numbers of electrons with an equivalent energy ϵ within the material and proportional to the transition probability P. When the electrons emitted come from states in the upper edge of a filled band, we can use the fact that the density of states near the upper edge is known to be const. $\times(\epsilon_0-\epsilon)^{1/2}d\epsilon$, where ϵ_0 is the highest energy in the band. They further assumed that the probability P is proportional to the velocity of the "hole" created by the removal of the electrons.

The foregoing discussion is useful for discussing energy and spectral data for Cs_3Sb photo-cathodes. In the work reported here, photoelectric emission, contact potential and thermoelectric measurements have been made on several Cs_3Sb photo-cathodes, in order to obtain further information concerning the energy level structure.

§ 2. Fundamental Formulas

Simplifying assumptions made in reference¹⁾ led to the following expression for the current-voltage characteristic at 0°K

$$(I/I_s)\,Y=\int_{E}^{E_m'} N(\nu,E)\,dE \propto q(\nu)(h\nu-\varphi')^{m+2}$$

$$\times[(m+2)(1-v')^{m+1}-(m+1)(1-v')^{m+2}] \quad (1)$$

where

$$v'=(V_s-V)/(V_s-V_0')$$

E : Kinetic energy of the photoelectron

$E'm$: the maximum energies from a semiconductor

m : parameter depending both on the form of occupied band and on the energy dependence of the photoelectric excitation probability.

q : slowly varying function of ν

Y : the photoelectric yild

S : the probability of excitation from the state ϵ to the state $(\epsilon+h\nu)$.

If S is proportional to the velocity of the hole formed in the filled band by the transition, $m=1$.

The value of m can be found from the plots which best fit the experimental curves. An independent value may be obtained from the spectral distribution.

§ 3. Experimental Details

Fig. 1 shows the construction of the phototubes used in this work. A is the emitter support (Mo wire 0.7 mm in diameter) with interchangeable emitters (B_1, B_2), hanging on it, and D is the quartz window that admits the radiation. The inside of the glass sphere is coated with a conducting layer of Ag, which serves as the collector. The glass spheres were 60 mm in diameter and these emitters $4\times5\ mm^2$ in diameter. Two evaporation chambers were mounted in a side tube. The thin films of Sn were formed onto the Mo plate (B_2) in Fig. 1 by evaporating Sn from the tungsten spiral (2).

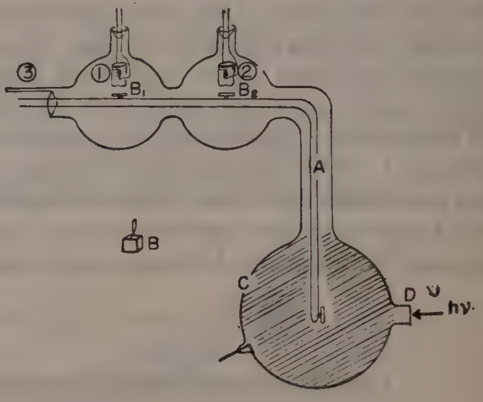

Fig. 1. Typical experimental tube for measuring contact potential and energy distribution of the photoelectrons.

The thin films of Cs_3Sb were formed on the B_1 (Mo plate) in another chamber. The first step in the preparation of Cs_3Sb is to produce a layer of Sb. The next step in the process is the introduction of Cs into the phototube through (3) in Fig. 1.

After the baking process is completed, the completed phototube is sealed off from the pumping system. It is also well known fact that the Cs introduced in the tube in the second process above mentioned escapes to all directions and condenses on the colder parts of the glass wall or else upon a conducting metallic coating such as Sn previously deposited. Such a metallic emitter is named "Sn–Cs" layer. Spectral sensitivity of the Sn—Cs layer is surprisingly different from that of the Sn in the region of visible ray (see Fig. 4.)

But it is evident that this Sn—Cs layer shows metallic characters. [See section 4 (A)]

The collector C, (Ag films), is found to be similarly photosensitive in the visible region, although pure Ag metal is known to respond only to ultraviolet radiation. This fact may be correctly attributed to the deposition of Cs atoms on the collector.

It may be possible to evaporate the adsorbed Cs atoms on the glass wall (Collector) by heating. But these heating processes were avoided, because it may occur, by heating of Cs, the deposition of excess Cs atoms on the surface of the Cs_3Sb photo-cathodes. Radiation sources for energy measurements were high pressure Hg discharges (250 watt).

The desired spectral lines were isolated with a quartz monochromator. Intensities were constant within 0.3%. On the emitter, the area of spot of light were 0.8~1.2 mm^2.

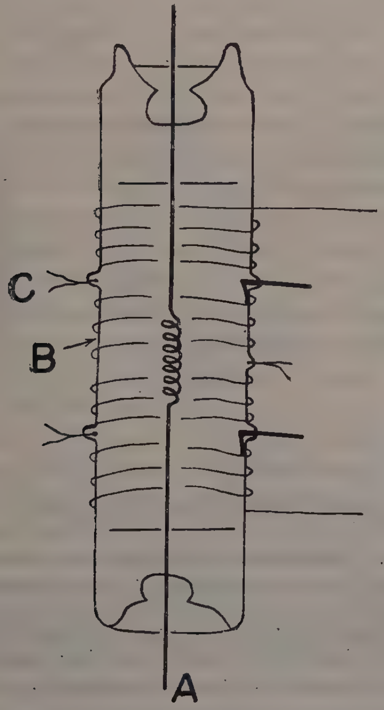

Fig. 2. Experimental tube for the measurement of conductivity and thermionic emission.

For spectral measurements, a tungsten (standard) lamp a high pressure Hg discharge lamp were used as the light source. Intensities were determined with a $(Sb+B_i)-(Sb)$ thermopile (2.8Ω, 3 mm^2).

Currents were measured with a UX-54A electrometer tube with a $5\times10^{10}\Omega$ grid resistor and a sensitivity of 1 mm per 0.1 mV. Next, thermoelectric measurements on Cs_3Sb were done, and these results were compared with the foregoing results based on the photoelectric measurement. All of the experiments were made in tubes with a central anode and two conductivity strips of Mo, encompassing the photo-cathodes. For this purpose tubes as shown in Fig. 2 were adopted, in which A and B were plate and cathode respectively. C is Cu-constantan thermocouple 0.03 mm in diameter welded in the glass bulb. By mounting three thermocouple in the cathode, they were able to make simultaneous measurements of the conductivity and thermionic emission of the cathode. Thus, precaution were taken to observe the exact value of temperature of the cathode. The cathode is heated by means of direct current in the coil placed around the tube (diameter 27 cm and 125 cm long).

The temperature of cathodes is variable from room temperature up to 120°C with accuracy±0.5°C. After considerable experimenting, the following technique of measurements (conductivity and thermionic emission) was developed:

(1) Heater power was raised to an amount sufficient to maintain the temperature 371° K. During the measurements, three thermocouple indicated the same value of mV.

(2) Heater power was then reduced to zero, and hence the cathode was cooled to room temperature (At least fourty minutes was allowed for cooling).

(3) The measurement of thermionic emission were performed with the well known method, using the UX-54A amplifier.

The thermo-electromotive force of Cs_3Sb was measured using the UX-54A amplifier. The construction of experimental tube was quite same as described in the previous paper.[3)-4)]

§ 4. Discussion of Results

(A) *Metallic Emitter*

In Fig. 3 are shown the current-voltage curves for the Sn—Cs metal at room temperature for the $h\nu=2.84$; 3.06 and 3.39 ev.

In this case the Sn–Cs metallic emitters were used to determine the stopping potential V_0 at 0°K by Du Bridge's method.

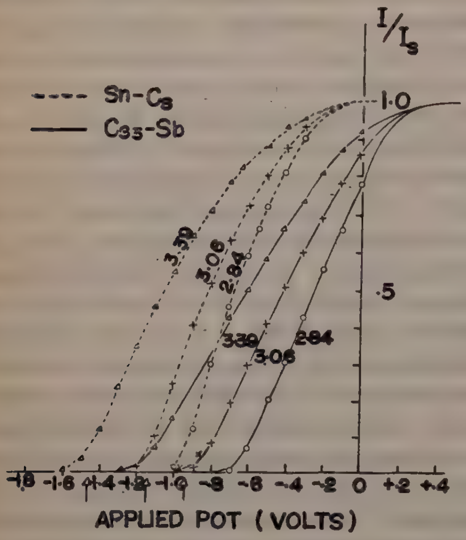

Fig. 3. Current-voltage characteristics for Cs_3Sb and for a metallic emitter Sn-Cs. The arrow marks V_0, "the stopping potential for 0°K." Currents are normalized at $V=3$ volts. To avoid confusion, only a few of the experimental points are given.

This reference point, $V_0=(\varphi_c-h\nu)/e$, corresponding to the coincident Fermi levels of the emitters, is marked by an arrow for various values of $h\nu$. Here φ_c is the work function of the collector. The values of V_0 are shown in Table I.

Table I.

$h\nu$ (ev)	V_0 (v)	φ_c (ev)
2.84	−0.95	1.90
3.06	−1.15	1.91
3.39	−1.49	1.89

Fig. 4 shows the current-voltage curves plotted on a parabolic scale. Currents were normalized at V=3.0 volt, a point definitely on the saturation line.

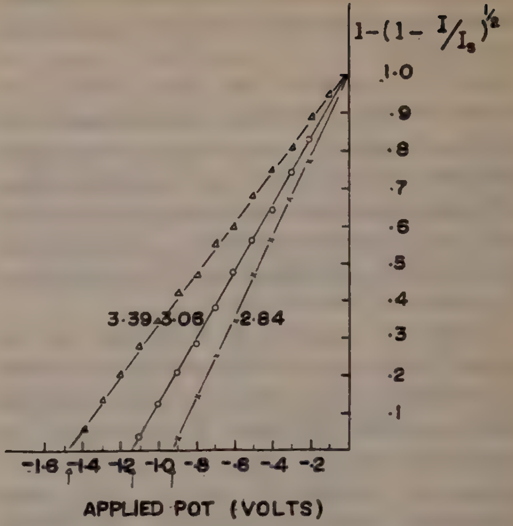

Fig. 4. Current-voltage data for 2.84, 3.06 and 3.39 ev. plotted on a parabolic scale. The lower arrows show values of V_0 determined from Du Bridge's analysis.

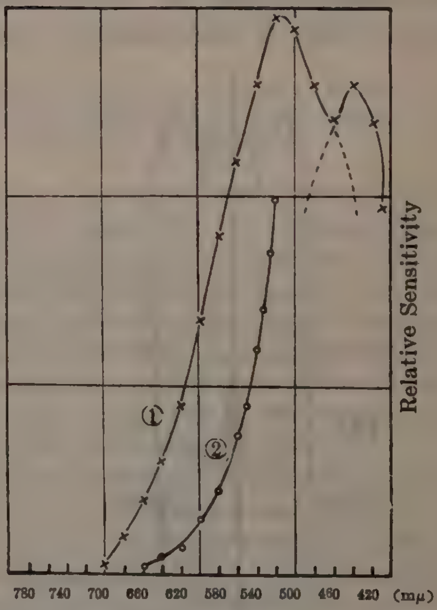

Fig. 5. Photoelectric emission from Sn-Cs. In Curve 1 the corresponding photo-currents (×) are plotted for the light source. In curve 2 the photo-currents (○) are shown as calculated for an ideal light source radiating equal amounts of energy at every wavelength.

Saturation points determined by this extrapolation process were $V_s=0$. The value of $\phi[\phi=h\nu-e(V_s-V_0)]$ determined from Einstein relation, was 1.90±0.01 (ev). Fig. 5 shows the spectral distribution of photoelectron from these representative Sn–Cs emitters. In Fig. 5, one notices that the photoelectrons emerge in two groups. The first may be called the Cs–group, since these photoelectrons behave as though ejected in normal fashion from the Cs film, whereas the second may be termed Sn–group. Fig. 6 shows the Fowler plot for normal incidence for T=300°K. The work function determined from Fig. 6 was

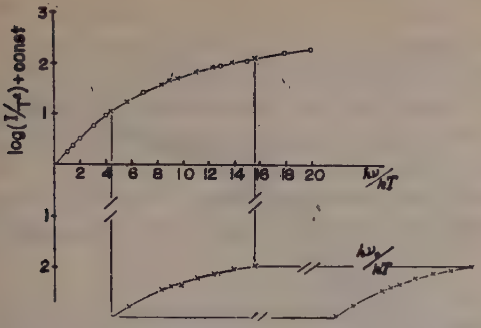

Fig. 6. Fowler plot for normal incidence for T 300°K

$$\phi=1.87\pm0.03\,(\text{ev})\,.$$

The results above mentioned show that the methods of Fowler and Du Bridge give consistent values for the work function of Sn—Cs film. Thus it is evident that $\phi=\phi_c=1.90$ ev. Other values of $h\nu=3.96$ ev gave the same result for ϕ_c.

(*B*) *Cs_3Sb emitter*

Fig. 3 shows Current-voltage characteristics for Cs_3Sb and for a typical metal Sn—Cs having the work function, $\varphi=1.90$ ev. The curves for Cs_3Sb had a saturation point Vs, which determines the condition of zero field between emitter and collecter, is indicated at $+0.4$ volt. Current-voltage characterristics faild to show clear-cut saturation points. One way to minimize this difficulty is to illminate the emitter with low light intensity for several waveslengths. ($h\nu=2.84$, 3.06 and 3.39 electron-volt.) Fig. 7 shows the lower portions of characteristics analogous to those in Fig. 3, except that the ordinate scale is expanded by a factor of 10.

At these levels a measurable fraction of the photo-current may be due to stray radiation scattered from the emitter to the collector and then to the emitter support. Hence the curves (after correction for reverse currents) represent upper limit to the current from the Cs_3Sb. The curve for Cs_3Sb approaches the axis tangentially and falls to unmeasurable values at point $V_0\sim-1.2$, -0.9 and -0.7 volt respectively for $h\nu=3.39$, 3.06 and 2.84 ev. Thus as compared with Sn—Cs metals of the work function $\varphi=1.9$ ev, the Cs_3Sb emitted very few electrons having energies within a range $\delta=e(V_0'-V)\sim0.3$ ev of the Einstein maximum $h\nu-\varphi$. This range

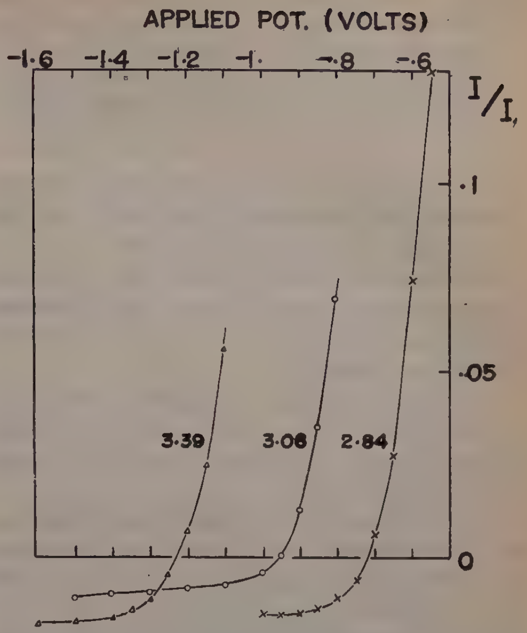

Fig. 7. Lower portions of curves like those in Fig. 3 (Cs_3Sb). The ordinates for $h\nu=2.84$, 3.06 and 3.39 ev are expanded by a factor of ten in the inset to show the behaviour of the expotential temperature "Tails" in the presence of reverse currents.

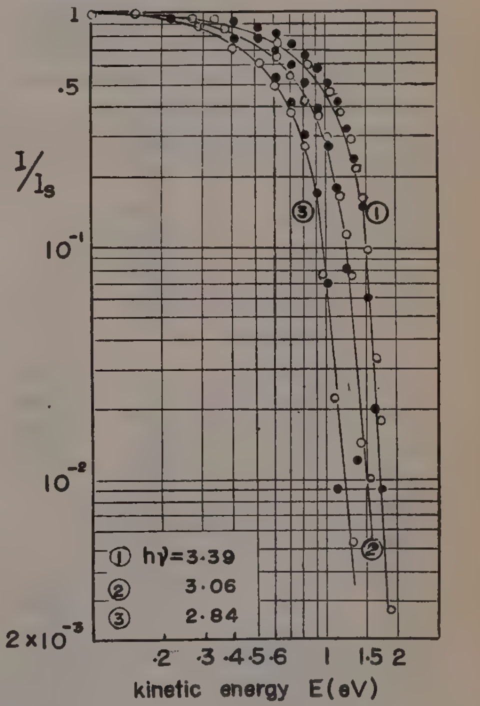

Fig. 8. In this figure, open and filled symbols show logarithmic plots of current vs. kinetic energy for Cs_3Sb at room temperature. The solid line is computed from the Equation (1) using $m=1$, $\delta\sim0.3$ ev.
○: Tube No. 1; ●: Tube No. 2.

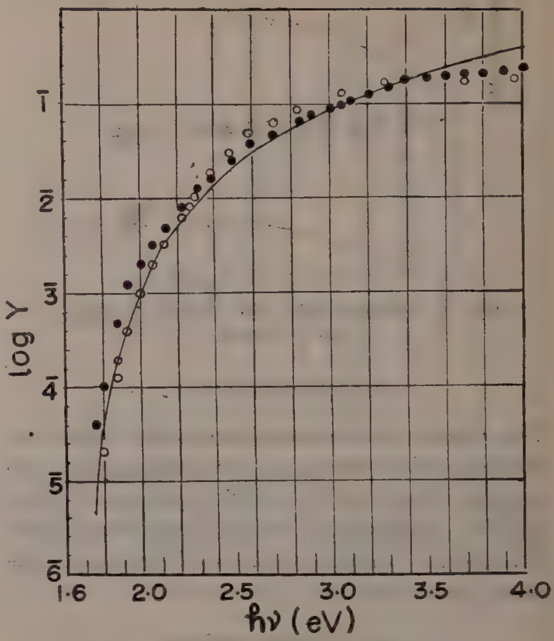

Fig. 9. Spectral distribution of the yield from the Cs_3Sb. The smooth solid line is calculated from the relation $Y=(1/2.8)\times10^{-1}(h\nu-1.7)^3$. Filled symbols are the results reported for Cs_3Sb by Apker, Taft and Dickey[5]. The open symbols shows the magnitude of the observed value.

was correlated with the forbidden energy interval lying between Fermi level μ and the top of the occupied band of Cs_3Sb.

Another tests made at $h\nu=3.96$, 2.27 and 2.14 ev gave the same results. Fig. 8 shows the logarithmic plots of current *vs.* kinetic energy for Cs_3Sb.

The solid curves are calculated from Eq. (1) with $m=1$. When $m=1$ and $\delta=0.30$, this relation leads to characteristics like those observed for Cs_3Sb.

Fig. 9 shows the spectral distribution of the photoelectric yield Y near the threshold for Cs_3Sb. Here, the value of Y at $h\nu=3.39$ ev are adjusted to coincide with Apker et al's[5]. The spectral distribution of the yield can be described approximately by the relation $Y=C\times10^{-1}(h\nu-\varphi')^3$ (electrons/quantum),

Table II. Photoelectric yield (Y) from the Cs_3Sb.

$h\nu$		Apker Taft and Dickey (Log Y)		(Calc.) $Y=C\times10^{-1}(h\nu-\varphi')^3$ (Log Y)		(Obs.) (Log Y)	
ev				electrons/quantum			
4		$\bar{1}.4$		$\bar{1}.62$	$\varphi'=1.7$ ev.	$\bar{1}.25$	
3.9		$\bar{1}.3_8$		$\bar{1}.58$	$C=1/2.8$	—	
3.8		$\bar{1}.3_3$		$\bar{1}.52$		—	
3.7		$\bar{1}.3_1$		$\bar{1}.45$		$\bar{1}.23$	
3.6	3.39	$\bar{1}.3$	$\bar{1}.2_3$	$\bar{1}.39$	$\bar{1}.23$	—	$\bar{1}.23$
3.5	3.3	$\bar{1}.2_8$	$\bar{1}.2$	$\bar{1}.32$	$\bar{1}.18$	—	—
	3.2		$\bar{1}.1$		$\bar{1}.08$		—
	3.06		$\bar{1}.0$		$\bar{2}.93$		$\bar{1}.10$
2.84	3.0	$\bar{2}.8_2$	$\bar{2}.9_2$	$\bar{2}.73$	$\bar{2}.89$	$\bar{2}.96$	—
2.7	2.9	$\bar{2}.7$	$\bar{2}.8_8$	$\bar{2}.56$	$\bar{2}.78$	$\bar{2}.80$	—
2.58		$\bar{2}.6$		$\bar{2}.38$		$\bar{2}.70$	
2.48		$\bar{2}.4$		$\bar{2}.23$		$\bar{2}.52$	
2.38		$\bar{2}.2_7$		$\bar{2}.04$		$\bar{2}.24$	
2.29		$\bar{2}.1$		$\bar{3}.88$		$\bar{2}.02$	
2.27	2.21	$\bar{2}.0$	$\bar{3}.9$	$\bar{3}.83$	$\bar{3}.70$	$\bar{3}.96$	$\bar{3}.80$
	2.13		$\bar{3}.7$		$\bar{3}.46$		$\bar{3}.54$
	2.06		$\bar{3}.5$		$\bar{3}.26$		$\bar{3}.31$
	2.0		$\bar{3}.3$		$\bar{4}.98$		$\bar{3}.00$
	1.93		$\bar{3}.1$		$\bar{4}.56$		$\bar{4}.60$
	1.87		$\bar{4}.7$		$\bar{4}.23$		$\bar{4}.18$
	1.8		$\bar{4}.0$		$\bar{5}.60$		$\bar{5}.32$
	1.76		$\bar{5}.6$		$\bar{6}.85$		

where $h\nu < 3.60$ ev. Here φ' is the photoelectric threshold energy and C is a constant dependent on samples. Thus both the energy and spectral distributions are indicative of the same energy structure.

By the above experimental formula the quantum yield Y is calculated for every wave-length, of which values are shown in Table II.

(C) Thermoelectric measurements

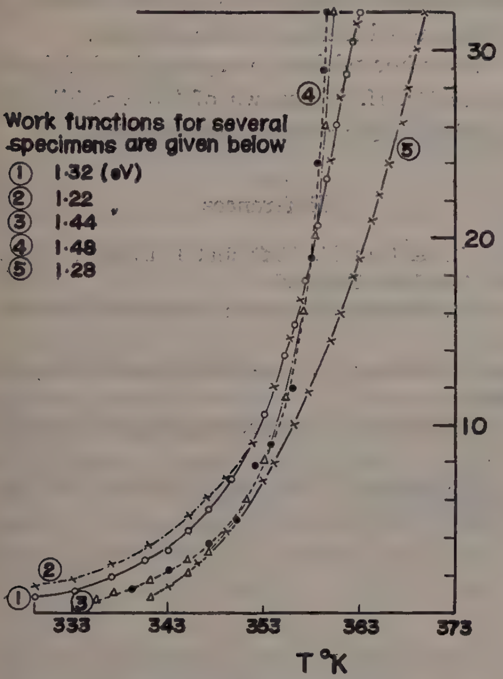

Fig. 10. Thermionic emission vs. temperature curves for Cs_3Sb photo-cathodes.

Table III.

φ (ev)	$\Delta E/2$ (ev)
1.2_0	0.30
1.2_2	0.28
1.3_2	0.26
1.4_4	0.27
1.4_8	0.25

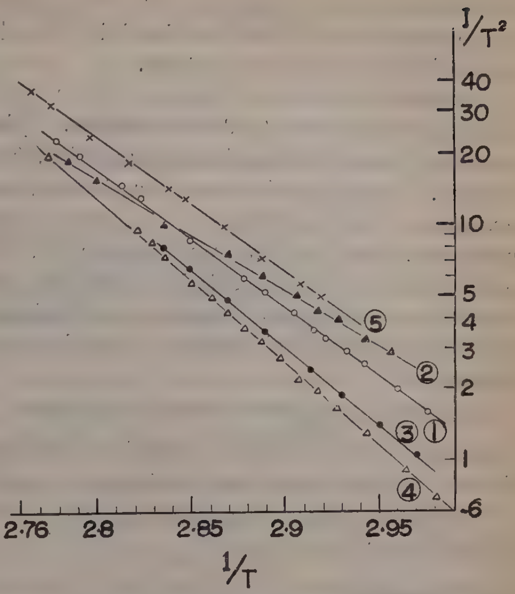

Fig. 11. Richardson plots for Cs_3Sb photo-cathodes.

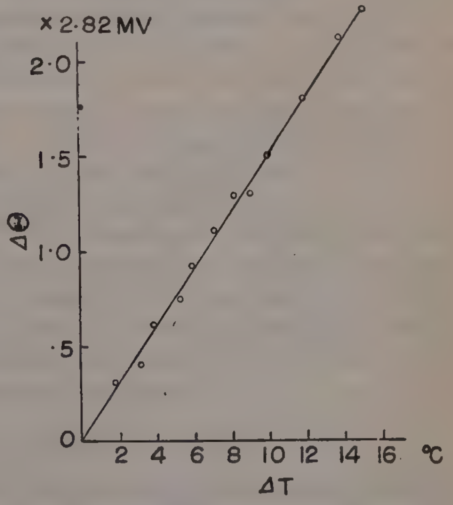

Fig. 12. The relation between the T.E.M.F $\Delta\Theta$ and any temperature difference ΔT.

The saturated thermionic emission from the photo-cathode was determined as a function of temperature, and Richardson plots were made. These results are shown in Fig. 10 and Fig. 11. The thermionic work function determined from the slope of these curves for various samples ranged from 1.2_2 to 1.4_8 ev. The activation energies $\Delta E/2$ of their conductivities measured at the same time respectively. These values were shown in Table III. As previously[3)-4)] indicated the sign of thermo-electromotive force showed the P-type semiconductor for Cs_3Sb photo-cathodes. The relation between ΔT and $\Delta\Theta$ (thermal electromotive force) were linear over the range of ΔT (temperature difference) from 0° to 15°C. The typical results are shown in Fig. 12. From the gradients of these straight lines, $d\Theta/dT$ can be obtained. The warmer electrode was always negative, indicating positive charge carriers. The activation energy $\Delta E/2$ of the conductivity simultaneously were 0.24 and 0.26 ev.

Thermo-electromotive force at room temperature has values 0.42∼0.44 ev/deg. The chemical potential thus had values of 0.18∼0.19 ev. The atomic concentration n_b of acceptors was estimated at room temperatures, these values were always 5×10^{19} $\sim10^{20}$ per cm^3. The relation between the number n_b of impurity atoms in unit volume and the number n of electron holes in unit volume is

$$n=n_b^{1/2}[2\cdot(2\pi mkT)^{3/2}/h^3]^{1/2}\exp(-\Delta E/2kT),$$

where ΔE is the energy separation between the top of filled band and the impurity level.

The values of n were consequently $4.8\times10^{15}\sim10^{16}$ per cm^3.

§ 5. Summary

The following points are suggested by the experimental results.

(1) In spherical phototubes with interchangeable emitters, the energy and the spectral distributions of Cs_3Sb are indicative of the same energy structure ($m=1$, $\delta\sim0.3$ ev). It was very difficult t find definite stopping potentials corresponding to upper edges of occupied band in Cs_3Sb.

The work function thus found for Cs_3Sb was $1.4_6\sim1.5$ ev. Within the experimental uncertainties the Cs_3Sb was a semiconductor with $\delta\sim0.3$ ev.

(2) The spectral distribution of the quantum yield near threshold can be described approximately by the relation

$$Y=C\times10^{-1}(h\nu-\phi')^3,$$

consistent with the values $m=1$. Here ϕ' is the photoelectric threshold and C is constant depending on specimens.

(3) The thermionic emission and conductivity results appear to be capable of interpretation by a semiconductor picture as a P type semiconductor.

(4) The sign of the thermoelectromotive force indicates positively charged carriers in agreement with these above concept.

The author wishes to express his indebtedness to Dr. H. Miyasawa of Tokyo-Shibaura Electric Co. for numerous discussions.

References

1) L. Apker; E. Taft and J. Dickey: Phys. Rev. **74** (1948) 1562-1474.

2) E. Taft and L. Apker: Phys Rev. **75** (1949) 1181.

3) T. Sakata: J. Phys. Soc. Japan **8** (1953) 125 (No. 1).

4) T. Sakata: J. Phys. Soc. Japan **8** (1953) 272 (No. 2).

5) E. Apker, E. Taft and J. Dickey: J.O.S.A. **43** (1953) 78.

JOURNAL OF THE PHYSICAL SOCIETY OF JAPAN Vol. 8, No. 6, NOV.—DEC., 1953

Statistical Time Lag and Electron Avalanche in Dielectric Breakdown of Mica II

Hazimu KAWAMURA and Masami ONUKI

Faculty of Science and Engineering, Osaka City University

(Received June 1, 1953)

The sizes of electron avalanches were measured by noise pulses just before the disruption on mica. Because the breakdown does not occure at the instant of the application of the transient over voltage, owing to the statistical time lag, we can count the number of the noise pulses during the interval from the instant of the application of the voltage to the instant of the disruption, which were about 10^{-2} sec. in our experiment. Measuring the distribution of the noise pulses at once, we have estimated the avalanche size just sufficient to cause the disruption to be 10^8 electrons.

§ 1. Introduction

When in an insulator the applied electric field becomes very strong and an accidental free electron has a chance to be accelerated up to the ionization energy, in spite of the friction due to collisions with phonons, the valence electrons can be ejected into the conduction band and the electron avalanche is generated. A great deal of energy is dissipated in a minute portion of the solid as the consequence of the drift of the avalanche electrons under the strong electric field, finally bringing the solid to disruption.

If λ is the mean range of the electron for making an ionization by collision under a strong electric field, the mean avalanche size after path L is given by

$$\bar{n}=\exp(L/\lambda)\,. \qquad (1)$$

And the probability that the avalanche size is greater than n is given by[1]

$$P(n)=\exp(-n/\bar{n})\,. \qquad (2)$$

If ν_0 electrons are supplied at the cathode per second, the frequency, with which the avalanches whose sizes are greater than n are generated, is given by

$$\nu(n)=\nu_0\exp(-n/\bar{n})\,, \quad \bar{n}=\exp(d/\lambda)\,. \qquad (3)$$

where d is the thickness of the solid.

If we assume that the breakdown of the solid occurs by a single avalanche which is greater than n_0, the mean frequency with which the disruption occurs will be

$$\nu(n_0)=\nu_0\exp(-n_0/\bar{n})\,. \qquad (4)$$

and hence the mean statistical time lag of the breakdown will be given by

$$\tau=1/\nu(n_0)=(1/\nu_0)\exp(n_0/\bar{n})\,. \qquad (5)$$

In the previous report[2] we measured the statistical time lag τ for constant over-voltages on one hand, and the distribution of the noise puls due toes the electron avalanche generated under the pre-breakdown voltage on the other. In order to compare τ, n and ν_0, we must employ the values of those parameters at the same field strength. The values of n and ν_0 at the same over-voltage fields where the measurements of the statistical time lag τ were made, are obtained by extrapolating the experimental values. We put these values in (5), and n_0 is found to be 10^8, the minimum avalanche size required for the breakdown of the solid. This value for n_0 seems to be reasonable according to the estimation by Seitz[3]. But the procedure adopted there had a serious fault that the measurements under the transient over-voltages and the d. c. applications of pre-breakdown voltages were combined.

In the present experiment we have measured the distribution of the avalanche sizes generated between the instant of application of a slight over-voltage and the following disruption. Thus we can employ τ, ν_0 and n which are measured simultaneously, for the estimation of n_0.

§ 2. Experimental Method

The measuring equipment is shown in Fig. 1. The top flatted single pulse of the width 1/120 sec. is applied to the grid of T-305 whose grid bias is kept at the cut-off voltage. Hence we can obtain a pulse voltage at the plate load resistance ($8\,\mathrm{m}\Omega$), which is applied on the specimen. The pulse voltage is adjusted beforehand, so as to be slightly higher than the breakdown voltage of the specimen, and that the statistical time lag is slightly less than 1/120 sec. The avalanche pulses during this time interval are counted by three countors having discriminators of different bias voltages, after being amplified by a feed-back linear amplifier whose gain is 80 db for 300 kc~2 mc. The time lag of the breakdown is measured by an oscilloscope which displays a linearly rising pulse continuing from the time of voltage application to the consequently occuring disruption, as in the previous report[2)]. The gate circuit attached to the discriminators is opened by a top flatted pulse which continues during the above time interval, and thus we can count the number of the avalanche pulses generated during the statistical time lag. In order to prevent the over-counts at the instants of opening and closing of the gate, the rise and fall of the gate pulse are made to be smooth and the response of the amplifier is cut off below 200 kc. Nevertheless, the natural counts of about 2~5, when the applied pulse voltage is around 2 KV, have not been removed.

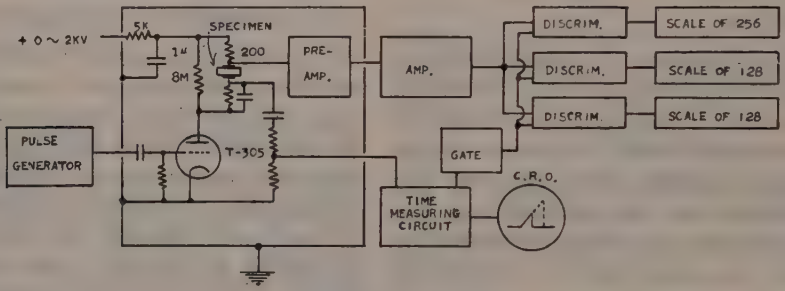

Fig. 1.

On the entering in experiment, the pulse voltage applications on the specimen were tried for many times raising the applied voltage slowly until the breakdown occured with a large time lag. Thus we measured the time lag τ and the number of avalanche pulses of three different sizes simultaneously. As it was difficult to drive a mechanical countor because the rate of generation of pulses was as large as 10^4 1/sec., the neon lamps of scale of 256 and 128 countors, which had been switched off until then, were employed to record the number of pulses. The bias voltages of the discriminatos were respectively 13, 22 and 34 V, so that each countor could record the avalanche pulses whose sizes were greater 8.2×10^7, 1.4×10^8 2.2×10^8 correspondingly. Thus we obtained the distribution of the sizes of the avalanche pulses.

Biotite was used as the specimen, because its breakdown strength is about 4×10^6 V/cm —twice as small as that of muscovite (8×10^6 V/cm)—and therefore its breakdown voltages being less than 2 KV, as the thickness of the specimens are $2\sim4\times10^{-4}$ cm. The processing of the specimens were the same as in the previous report[3)]. The electrodes were vacuum evaporated aluminium films upon the both surfaces of the specimen, which was inserted between steel balls and coated with paraffin.

§ 3. Result and Discussion

The results are shown in Fig. 2. Since the breakdown voltages were small (less than 2 KV), the Schoenfeld noise[4)] due to the sudden discharge between the electrode and the specimen was negligible. This fact was confirmed by using a relatively thick specimen. We have obtained n from the slope of the line and ν_0 from the point of intersection of the line with the ordinate. Substitution of these values and that of τ, which were simultaneously measured, into (5) determines n_0 as shown in Table I. The values in the last column are estimated ones on the assumption that n_0 is proportional to the thickness of the specimen. It amounts to 10^{12} for the specimen of 1 cm thick.

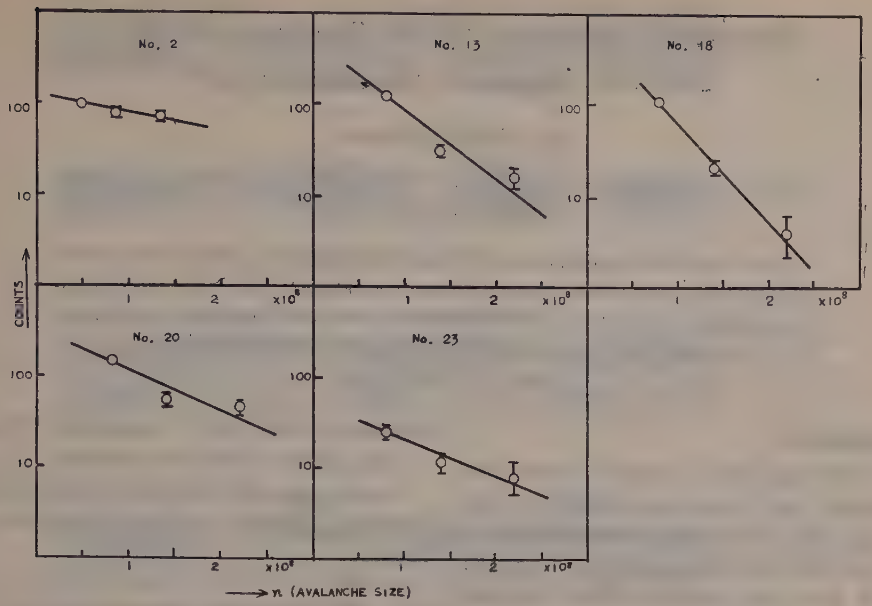

Fig. 2.

Table I.

No.	thickness (in cm)	applied voltage (in KV)	applied field (in V/cm)	ν_0 (in sec^{-1})	$\bar{n}$	τ (in sec)	n_0	n_0 (es)
9	3.2×10^{-4}	1.75	5.5×10^{6}	2.0×10^{4}	2.0×10^{7}	6.5×10^{-3}	9×10^{8}	3×10^{8}
13	2.9	1.8	6.2	6.2	6.0	7.9	4	3
18	3.3	2.0	6.0	8.7	4.2	7.8	3	3
20	3.3	2.0	6.0	3.7	11	7.5	6	3
23	4.4	2.0	4.5	0.6	13	7.0	5	4

The merit of the present investigation compared with the last consists in the simultaneous measurement of ν_0, n and τ. But in the present case the number of the counts is very few and hence large statistical errors as shown in Fig. 2 are unavoidable.

For muscovite, we have seen that ν_0 is less than that for biotite by about an order of magnitude, although the measurement cannot be said absolutely reliable because of the small count number. It is made clear, however, from our experiment⁵⁾ that the conductivity of muscovite is also less than that of biotite by about an order of magnitude at the same field strength. Therefore it seems reasonable to assume that the number of starting electrons for avalanche is proportional to the number of conduction electrons, and we may ascribe the remarkably large statistical time lag of mica²⁾⁶⁾ to its poor conductivity. Such is a typical solid for which the simple electron avalanche theory of breakdown can be applied. If the density of conduction electrons is so high that the interactions among themselves can no longer be neglected, it will be insufficient to take only a single avalanche into consideration and a more complicated theory, taking account of the interactions among electrons, such as proposed by Fröhlich⁷⁾ Heller⁸⁾ and Franz⁹⁾, will be necessary.

References

1) W. H. Furry: Phys. Rev. **52** (1937) 569; R. A. Wijsmann: Phys. Rev. **75** (1949) 833.
2) H. Kawamura, M. Onuki and H. Okura: Jour. Phys. Soc. Japan **7** (1952) 528.
3) F. Seitz: Phys. Rev. **76** (1949) 1376.
4) H. Schoenfeld: Ann. d. Phys. **19** (1934) 733.
5) Unpublished.
6) R. Striegel: Wiss. Veroeff. Siem. Werk. **18** (1939) 101.
7) H. Fröhlich: Proc. Roy. Soc. **A188** (1947) 521.
8) W. R. Heller: Phys. Rev. **84** (1951) 1130.
9) W. Franz: Z. Physik **132** (1952) 285

JOURNAL OF THE PHYSICAL SOCIETY OF JAPAN Vol. 8, No. 6, Nov.—Dec., 1953

Hyperfine Structure of the Spectrum of Zr I and the Magnetic Moment of Zr^{91}

By Shigeki SUWA

Institute of Science and Technology, Komaba-machi, Meguro-ku, Tokyo

(Received July 2, 1953)

The hfs of the spectrum of Zr I was investigated, natural zirconium sample being used; and in some lines the hfs of Zr^{91} was observed. The magnetic moment of Zr^{91} calculated from the measured splittings in the line $\lambda 4687.80$ $(4d^3 5s\,{}^5F_5 - 4d^3 5p\,{}^5G_6)$ and other lines is

$\mu(Zr^{91}) = -1.3 \pm 0.3$ nm..

§1. Introduction

Using a Zr^{91}-enriched sample, Arroe and Mack[1)] studied the hyperfine structure (hfs) of Zr I, and determined the nuclear spin 5/2 of Zr^{91}. In order to determine the magnetic moment of Zr^{91}, the present author studied the hfs of Zr I, using natural zirconium; and the hfs of Zr^{91} in some lines were observed. In the meantime, Arroe's paper[2)] describing among other things the details of his investigation on the enriched Zr^{91} isotope was published. Arroe's data, being considered more accurate than ours, were utilized in the preliminary estimation[3)]* of the magnetic moment of Zr^{91}. In the present work the magnetic moment of Zr^{91} was recalculated based upon our own observation.

§2. Experimental Arrangement

The spectrum was excited in a liquid-air cooled hollow cathode discharge tube, and the hfs was examined with a Fabry-Pérot etalon. Reproduction of some of the interference patterns is given in Fig. 1.

§3. Experimental Results

Natural zirconium is known to consist of five isotopes[4)], namely Zr^{90} (51.46%), Zr^{91} (11.23%), Zr^{92} (17.11%), Zr^{94} (17.40%) and Zr^{96} (2.80%). As usual, the strongest component of each line can be ascribed to the even isotopes and the weak satellites to the odd isotope, Zr^{91}. The result of measurements is shown schematically in Fig. 2.

In lines having $d^3 s a^5 F_4$ as the final level the splittings due to Zr^{91} were so small that the measurement was less accurate than in others. The hfs of the lines $\lambda\lambda 4687.80$ and 4227.76 were measured most accurately (within $\pm 0.002\,\mathrm{cm}^{-1}$), especially the position of the head of the flag pattern.

As to the displacement effect of the even isotopes, details will be published in the future.

§4. The Magnetic Moment of Zr^{91}

The magnetic moment $\mu(Zr^{91})$ was calculated from the hfs of the line $\lambda 4687.80 (4d^3 5s\, a^5F_5 - 4d^3 5p y^5G_6)$ by the following procedure. Since the final level a^5F_5 contains one 5s-electron while the initial level y^5G_6 contains none, a^5F_5 must have a larger splitting of Zr^{91} than y^5G_6. The complete hfs pattern cannot be resolved, but center of gravity considerations show that the over-all width of the splitting is given by

$$\Delta = \frac{55}{2}\left[A(a^5F_5) - \frac{7}{6}A(y^5G_6)\right], \qquad (1)$$

where $A(a^5F_5)$ and $A(y^5G_6)$ are interval factors. As to the quadrupole moment effect, even if we assume $|Q| = 1\times 10^{-24}\,\mathrm{cm}^2$, the contribution will be of the order of $0.001\,\mathrm{cm}^{-1}$ and can be neglected. Δ obtained from the measurement is given in Table I (column 3).

The interval factors appearing in (1) can be expressed in terms of coupling constants of individual electrons under the assumption of LS coupling. Necessary formulas are summarized in appendix. The coupling constants are given by the usual formulas:

$$a(s) = \frac{Z_i(s) Z_0 F(1-\delta)}{117.8} \cdot \frac{dn^*/dn}{n^{*3}} \cdot \frac{\mu}{I}\ (\mathrm{cm}^{-1}) \qquad (2)$$

---

* In reference (3) an error occurred in a numerical value: $a(5s)$ for Zr^{91} should read $-0.064\,\mathrm{cm}^{-1}$ instead of $-0.078\,\mathrm{cm}^{-1}$, while the value $\mu = -1.1$ nm. remains unchanged.

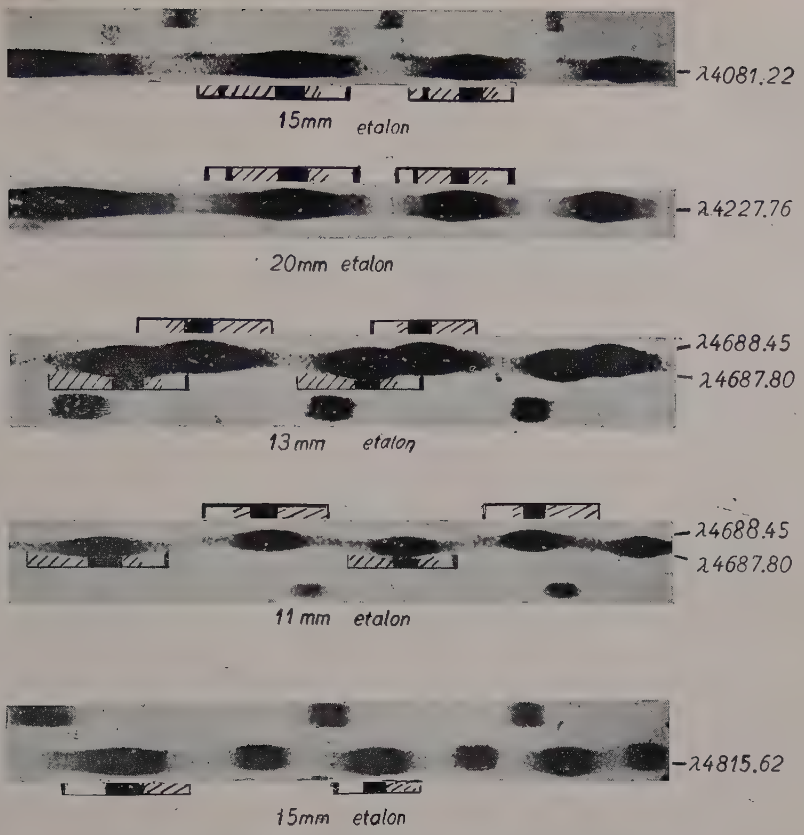

Fig. 1. Interference patterns of the spectrum of Zr I.

Table I.

(Δ = Over-all width of the Zr^{91}-components)

λ	Combination	$\Delta_{\text{obs.}}$ (cm^{-1})*	$\Delta_{\text{calc.}}$ (cm^{-1})	μ (nm.)
4687.80	$d^3s\,^5F_5 - d^3p\,^5G_6$	-0.190	$0.377\ \mu/I$	-1.26
4227.76	〃 $-d^3p\,^5F_5$	-0.199	0.390 〃	-1.28
4081.22	〃 $-d^3p\,^5D_4$	-0.20_5	0.434 〃	-1.1_8
4710.08	$d^3s\,^5F_4 - d^3p\,^5G_5$	-0.13_5	0.254 〃	-1.3_2
4239.31	〃 $-d^3p\,^5F_4$	-0.15_0	0.290 〃	-1.3_0
4072.71	〃 $-d^3p\,^5D_3$	-0.15_7	0.319 〃	-1.2_3
4815.62	$d^3s\,^5F_1 - d_3p\,^5G_2$	$+0.131$	-0.246 〃	-1.33
4688.45	$d^2s^2\,^3F_4 - d^2spz\,^3G_5$	$+0.209$	-0.476 〃 **	-1.10
5623.56	$d^2s^2\,^3P_0 - d^2spz\,^3S_1$	$+0.170$ §	-0.475 〃 **	-0.90

* The + sign indicates that the strongest component lies on the high frequency side.

** For these lines $a(s) = 0.19\ \mu/I\ \text{cm}^{-1}$ was assumed.

§ Data taken from reference (1) and (2).

$$a(p) = \frac{\zeta_p}{1836\,Z_i(p)} \cdot \frac{\mu}{I}\ (\text{cm}^{-1}),$$

$$a(d) = \frac{\zeta_d}{1836\,Z_i(d)} \cdot \frac{\mu}{I}\ (\text{cm}^{-1}),$$

Relativity correction factors except for $a(s)$ and $a''(p)$ can be neglected. Substituting $n^{*3}/(dn^*/dn) = 2.7$, $Z_i(s) = 40$, $Z_0 = 1$, $F = 1.18$, $\delta = 0.02$, $\zeta_{5p} = 433\ \text{cm}^{-1}$, $Z_i(p) = 36$, $\zeta_{4d} = 290\ \text{cm}^{-1}$ and $Z_i(d) = 30$ in the above formulas, one obtains:

$$a(5s) = 0.145\mu/I,\ a(5p) = 0.0066\mu/I,$$
$$a(4d) = 0.0053\mu/I,\ \Delta = 0.377\mu/I.$$

Comparing this with the observed value $\Delta = -0.190\ \text{cm}^{-1}$, one obtains ($I = 5/2$):

$$\mu = -1.26\ \text{nm.}.$$

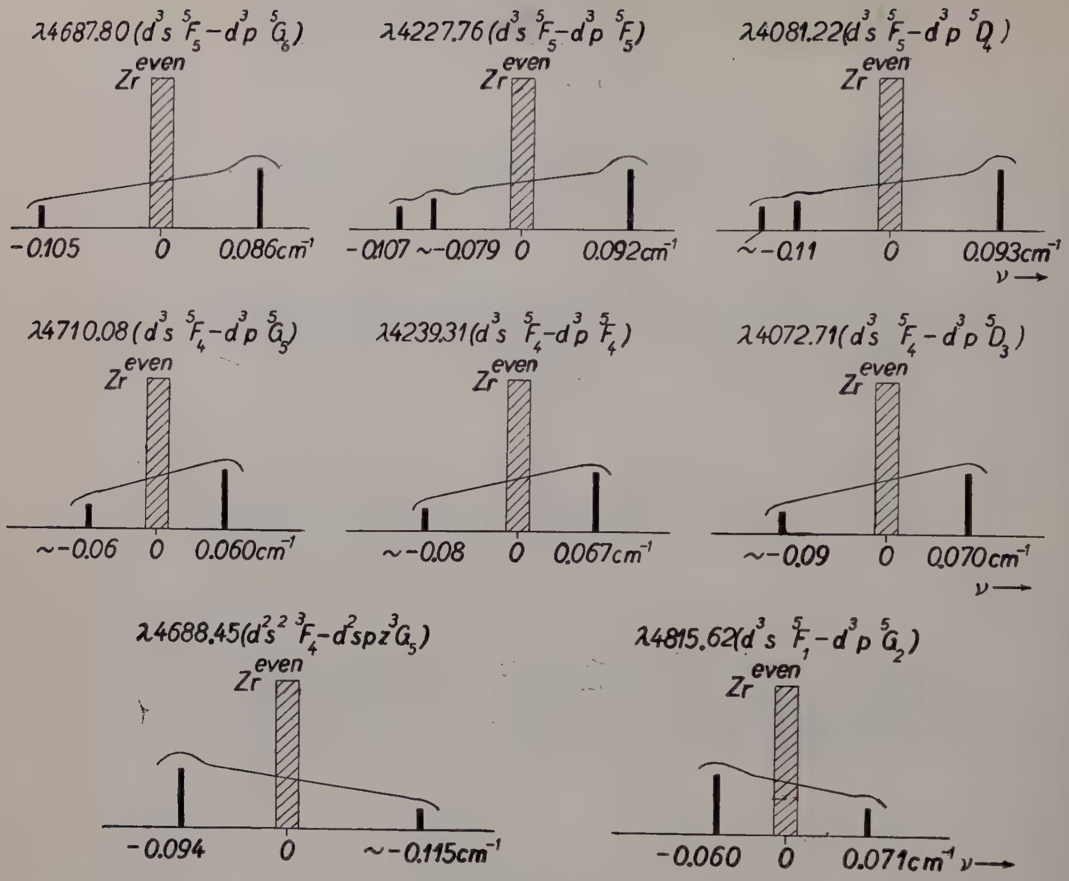

Fig. 2. Hfs of the spectrum of Zr I.

Summarizing the considerations given in the next paragraph, the limits of uncertainty are taken to be ±0.3 nm. and we might, therefore, consider

$$\underline{\mu = -1.3 \pm 0.3 \text{ nm.}}$$

the best value that can be obtained by optical means.

It may be noted that according to the nuclear shell scheme, Zr^{91} ($N=51$) has one $4d_{5/2}$ neutron outside the completed shells comprising 50 neutrons. The negative value of $\mu(Zr^{91})$ together with the nuclear spin of 5/2 comfirms this structure.

The value of μ having been determined, the numerical values of the interval factors can be calculated to be $A(a^5F_5) = -0.0090$ cm^{-1} and $A(y^5G_6) = -0.0018$ cm^{-1}, resulting in the total separations $\sum(a^5F_5) = -0.247$ cm^{-1} and $\sum(y^5G_6) = -0.059$ cm^{-1}.

Similar calculations of μ were carried out for other lines whose hfs were measured, and the results are presented in Table I. (See also Table V.)

§ 5. Accuracy of Calculation

(a) Accuracy regarding the *LS* coupling assumption.

In the literatures[5),6)] it is shown that in the case of *LS* coupling the configuration interactions between corresponding quintet terms (^5G, ^5F and ^5D) arising from d^3p and d^2sp vanish.

The classification of the spectrum of Zr I[7)] shows that departure from *LS* coupling is very small for the lowest odd as well as even quintets. Each of the initial and final levels of λ4687 has the highest J value in the respective quintet; therefore, the value of $\mu(Zr^{91})$ determined from the hfs of this line should be the most reliable in Table I. The fact that the values determined from other lines agree well with that of λ4687 seems to show that the *LS* coupling approximation is

Table II. The magnetic coupling matrix elements for the *p*-electron in $m_l^{m_s}$ scheme.

$$(1^+|B_z|1^+) = -(-1^-|B_z|-1^-) = \frac{3}{2}\,a'(p)$$

$$(0^+|B_z|0^+) = -(\ 0^-|B_z|\ 0^-) = \frac{1}{3}\,a'(p) + \frac{1}{6}\,a''(p) + \frac{4}{3}\,a'''(p)$$

$$(1^-|B_z|1^-) = -(-1^+|B_z|-1^+) = \frac{1}{6}\,a'(p) + \frac{1}{3}\,a''(p) - \frac{4}{3}\,a'''(p)$$

$$(0^+|B_z|1^-) = -(\ 0^-|B_z|-1^+) = \frac{\sqrt{2}}{6}\,a'(p) - \frac{\sqrt{2}}{6}\,a''(p) - \frac{\sqrt{2}}{3}\,a'''(p)$$

Table III. The magnetic coupling matrix elements for the *d*-electron in $m_l^{m_s}$ scheme.

$$(2^+|B_z|2^+) = -(-2^-|B_z|-2^-) = \frac{5}{2}\,a'(d)$$

$$(1^+|B_z|1^+) = -(-1^-|B_z|-1^-) = \frac{6}{5}\,a'(d) + \frac{3}{10}\,a''(d) + \frac{8}{5}\,a'''(d)$$

$$(0^+|B_z|0^+) = -(\ 0^-|B_z|\ 0^-) = \frac{3}{10}\,a'(d) + \frac{1}{5}\,a''(d) + \frac{12}{5}\,a'''(d)$$

$$(2^-|B_z|2^-) = -(-2^+|B_z|-2^+) = \frac{3}{10}\,a'(d) + \frac{6}{5}\,a''(d) - \frac{8}{5}\,a'''(d)$$

$$(1^-|B_z|1^-) = -(-1^+|B_z|-1^+) = \frac{1}{5}\,a'(d) + \frac{3}{10}\,a''(d) - \frac{12}{5}\,a'''(d)$$

$$(1^+|B_z|2^-) = -(-1^-|B_z|-2^+) = \frac{3}{5}\,a'(d) - \frac{3}{5}\,a''(d) - \frac{6}{5}\,a'''(d)$$

$$(0^+|B_z|1^-) = -(\ 0^-|B_z|-1^+) = \frac{\sqrt{6}}{10}\,a'(d) - \frac{\sqrt{6}}{10}\,a''(d) - \frac{\sqrt{6}}{5}\,a'''(d)$$

sufficient for our purpose*.

(b) Accuracy of the numerical values of the coupling constants.

The largest error in evaluating μ comes from the error of $n^{*3}/(dn^*/dn)$ in the Goudsmit-Fermi-Segrè formula (2). However the error for this quantity does not seem to exceed ±0.2 (8%). Errors from other causes are smaller and negligible.

(c) Accuracy consideration in analogy with other spectra.

According to Arroe[2)], the optically determined $\mu(\mathrm{Mo}^{95})$ is about 20% larger than the nuclear induction value. This appears to show that to the μ-values determined by optical means an uncertainty of about 20% should be assigned in this region of the periodic table.

In conclusion the writer wishes to express his sincere thanks to Professor K. Murakawa for his kind advice and encouragement throughout this work.

Appendix: Interval Factors of Some *LS* Coupling Terms Arising from the d^3s-, d^3p- and d^2sp-Configurations.

---

* In Table I the lines λλ4688.45 and 5623.56 are included for the purpose of comparison. In these lines the calculation of the interval factors was less accurate, since three ^3G and two ^3S terms arise from the d^2sp-configuration and furthermore configuration interaction must be taken into account. The calculation was carried out under the simple assumption that $z\,^3G$ and $z\,^3S$ converge to the limits $d^2s\,^4F$ and $d^2s\,^4P$ of Zr II respectively. The latter assignment is different from that of Kiess and Kiess[7)] while the former is identical with that of Kiess and Kiess. It can easily be shown that the above-mentioned assumption regarding the parent terms of $z\,^3G$ and $z\,^3S$ will probably result in diminishing the magnitudes of the final μ-values for both lines. The result given in Table I corresponds to this expectation. In view of the fact that the μ-values for these lines are in fair agreement with those calculated from other lines, our assignments seem to be good approximation. (If one assumes $d^2s\,^2P$ as the parent of $z\,^3S$ according to Kiess, a quite different value of $\mu(=+2.3)$ is obtained

Table IV. Interval factor formulas in *LS* coupling.

$d^3s\,{}^5F$

$$A(5)=\frac{1}{10}a(s)+\frac{1}{10}[8a'(d)+a''(d)+8a'''(d)]\approx\frac{1}{10}a(s)+\frac{22}{35}a(d)$$

$$A(4)=\frac{7}{80}a(s)+\frac{1}{80}[67a'(d)+6a''(d)+44a'''(d)]\approx\frac{7}{80}a(s)+\frac{179}{280}a(d)$$

$$A(3)=\frac{1}{16}a(s)+\frac{1}{400}[341a'(d)+34a''(d)+68a'''(d)]\approx\frac{1}{16}a(s)+\frac{197}{280}a(d)$$

$$A(2)=0+\frac{1}{50}[41a'(d)+9a''(d)-32a'''(d)]\approx0+\frac{32}{35}a(d)$$

$$A(1)=-\frac{1}{4}a(s)+\frac{1}{100}[59a'(d)+66a''(d)-368a'''(d)]\approx-\frac{1}{4}a(s)+\frac{64}{35}a(d)$$

$d^3s\,{}^3F$

$$A(4)=-\frac{1}{16}a(s)+\frac{1}{240}[221a'(d)+34a''(d)+188a'''(d)]\approx-\frac{1}{16}a(s)+\frac{131}{168}a(d)$$

$$A(3)=-\frac{1}{48}a(s)+\frac{1}{240}[199a'(d)+46a''(d)-28a'''(d)]\approx-\frac{1}{48}a(s)+\frac{149}{168}a(d)$$

$$A(2)=\frac{1}{12}a(s)+\frac{1}{60}[29a'(d)+26a''(d)-128a'''(d)]\approx\frac{1}{12}a(s)+\frac{26}{21}a(d)$$

$d^3p\,{}^5G$

$$A(6)=\frac{2}{3}a'(d)+\frac{1}{12}a''(d)+\frac{2}{3}a'''(d)+\frac{1}{4}a'(p)\approx\frac{11}{21}a(d)+\frac{2}{15}a(p)$$

$$A(5)\approx\frac{23}{42}a(d)+\frac{14}{75}a(p);\qquad A(4)\approx\frac{957}{1568}a(d)+\frac{1403}{5600}a(p)$$

$$A(3)\approx\frac{3569}{4704}a(d)+\frac{657}{3360}a(p);\qquad A(2)\approx\frac{170}{147}a(d)+\frac{23}{42}a(p)$$

$d^3p\,{}^5F$

$$A(5)=\frac{1}{40}[31a'(d)+3a''(d)+32a'''(d)]+\frac{1}{40}[5a'(p)+a''(p)+8a'''(p)]\approx\frac{4}{7}a(d)+\frac{1}{10}a(p)$$

$$A(4)\approx\frac{395}{672}a(d)+\frac{17}{480}a(p);\qquad A(3)\approx\frac{753}{1150}a(d)-\frac{3}{160}a(p)$$

$$A(2)\approx\frac{179}{210}a(d)-\frac{1}{15}a(p);\qquad A(1)\approx\frac{358}{210}a(d)-\frac{2}{15}a(p)$$

$d^3p\,{}^5D$

$$A(4)=\frac{1}{4200}[4021a'(d)+354a''(d)+4208a'''(d)]+\frac{1}{504}[4a'(p)-25a''(p)+160a'''(p)]\approx\frac{508}{735}a(d)-\frac{19}{105}a(p)$$

$$A(3)\approx\frac{472}{735}a(d)-\frac{16}{105}a(p);\qquad A(2)\approx\frac{89}{147}a(d)-\frac{1}{420}a(p)$$

$$A(1)\approx\frac{61}{105}a(d)-\frac{7}{60}a(p);\qquad A(0)=0$$

$d^2s({}^4F)p\,{}^3G$

$$A(5)=\frac{1}{12}a(s)+\frac{1}{150}[103a'(d)+12a''(d)+34a'''(d)]+\frac{1}{20}[2a'(p)+a''(p)-4a'''(p)]\approx\frac{1}{12}a(s)+\frac{121}{210}a(d)+\frac{11}{50}a(p)$$

$$A(4)\approx\frac{1}{48}a(s)+\frac{2449}{3360}a(d)+\frac{179}{800}a(p);\qquad A(3)\approx-\frac{5}{48}a(s)+\frac{4687}{4704}a(d)+\frac{59}{224}a(p)$$

$d^2s(^4P)p\,^3S$

$$A(1)=\frac{5}{12}a(s)+\frac{1}{6}[7a'(d)-2a''(d)+16a'''(d)]-\frac{1}{36}[10a'(p)-a''(p)+16a'''(p)]\approx\frac{5}{12}a(s)$$

$d^2s(^2P)p\,^3S$

$$A(1)=-\frac{1}{6}a(s)+\frac{2}{15}[7a'(d)-2a''(d)+16a'''(d)]+\frac{1}{18}[10a'(p)-a''(p)+16a'''(p)]\approx-\frac{1}{6}a(s)$$

Table V. Interval factors calculated for Zr^{91}. (assuming $\mu=1.26$ nm.)

Levels	A (cm^{-1})	Levels	A (cm^{-1})
Even		Odd	
$d^3s\,^5F_5$	-0.0090	$d^3p\,^5F_5$	-0.0019
″ $^5F_4$	-0.0081	″ $^5F_4$	-0.0017
″ $^5F_3$	-0.0064	″ $^5F_3$	-0.0017
″ $^5F_2$	-0.0024	″ $^5F_2$	-0.0020
″ $^5F_1$	$+0.0133$	″ $^5F_1$	-0.0041
Odd			
$d^3p\,^5G_6$	-0.0018	$d^3p\,^5D_4$	-0.0012
″ $^5G_5$	-0.0021	″ $^5D_3$	-0.0012
″ $^5G_4$	-0.0024	″ $^5D_2$	-0.0016
″ $^5G_3$	-0.0027	″ $^5D_1$	-0.0012
″ $^5G_2$	-0.0049	″ $^5D_0$	0

Since calculation of the transformation matrices from *jj* to *LS* coupling for the above-mentioned configurations does not seem feasible, the method applied by Crawford⁸⁾ extending the procedure of Breit and Wills⁹⁾ in deriving the formulas for d^3s configuration was not adopted. Instead, a procedure analogous to that used by Schmidt in evaluating the quadrupole moment of Ta^{181} ¹⁰⁾ was used.

The matrix elements of the operator B_z representing the magnetic interaction between the nucleus and the single *l*-electron are expressed in terms of $a'(l)$, $a''(l)$ and $a'''(l)$ as shown in Tables II and III in the $m_l m_s$ representation. (Notations of various quantities are hereafter adopted from the work of Breit and Wills.)

Using these matrix elements and the *LS* eigenfunction of each level written as a sum of the antisymmetrized products of the $m_l m_s$ functions of individual electrons¹¹⁾, one obtains the formulas of the interval factors. The result is given in Table IV. Of the odd terms only terms necessary for the present work are included in the table.

Neglecting relativity correction, we can put:

$$a'(p)\approx\frac{8}{15}a(p),\qquad a''(p)\approx\frac{8}{3}a(p),$$

$$a'''(p)\approx-\frac{1}{6}a(p),$$

$$a'(d)\approx\frac{24}{35}a(d),\qquad a''(d)\approx\frac{8}{5}a(d),$$

$$a'''(d)\approx-\frac{1}{10}a(d),$$

$$a(p)=\frac{\zeta_p}{1836\,Z_i(p)}\cdot\frac{\mu}{I},\quad a(d)=\frac{\zeta_d}{1836\,Z_i(d)}\cdot\frac{\mu}{I}.$$

Finally, using these formulas and the value $\mu=-1.26$ nm., the interval factors for Zr^{91} were calculated. The result is shown in Table V.

References

1) O. H. Arroe and J. E. Mack: Phys. Rev. **76** (1949) 873.

2) O. H. Arroe: *Studier over Spektralliniers Struktur med Anvendelse af Koncentrerede Isotoper* (Diss. Copenhagen, 1951).

3) S. Suwa: Phys. Rev. **86** (1952) 247.

4) J. R. White and A. E. Cameron: Phys Rev. **74** (1948) 991.

5) C. W. Ufford: Phys. Rev. **44** (1933) 732.

6) F. Rohrlich: Phys. Rev. **74** (1948) 1381.

7) C. C. Kiess and H. K. Kiess: Jour. Res. Bur. Stand. **6** (1931) 621.

8) M. F. Crawford: Phys. Rev. **47** (1935) 768.

9) G. Breit and L. A. Wills: Phys. Rev. **44** (1933) 470.

10) T. Schmidt: Zeits. f. Physik **121** (1943) 63.

11) E. U. Condon and G. H. Shortley: *Theory of Atomic Spectra* (Cambridge, 1935).

JOURNAL OF THE PHYSICAL SOCIETY OF JAPAN Vol. 8, No. 6, NOV.—DEC., 1953

An Approximate Study on the Detached Shock Wave in front of a Circular Cylinder and a Sphere

By Kinzo HIDA

Department of Applied Physics, Faculty of Engineering,
Naniwa University

(Received May 18, 1953)

In this paper is given an approximate analysis for the detached shock wave in front of a circular cylinder and a sphere moving with supersonic speed. Assuming the flow behind the detached shock wave to be similar to the rotational flow of an incompressible fluid, we can determine various quantities relating to the shock in such a way that the shock conditions may be satisfied in the neighbourhood of the nose of the shock wave. It is found that the vorticity correction does not alter the non-dimensional curvature of the shock at the nose but makes its location further away from the body than in the case without vorticity. Our theoretical result is compared with some experiments and a fairly good agreement is found between them.

§ 1. Introduction and Summary

The flow containing the detached shock wave in front of a body moving with a speed higher than that of sound has been treated by many authors. In particular K. Tamada1) and T. Kawamura2) attacked the problem by assuming that the flow behind the shock wave can be replaced by the irrotational flow of an incompressible fluid and making it to satisfy the usual shock conditions in the neighbourhood of the normal portion of the shock wave, the shape of which is also assumed with some parameters. They applied such an approximate method with success to the detached shock wave in front of a circular cylinder, a sphere and a finite wedge. But, actually the entropy of fluid particle increases appreciably when it passes through the shock wave and therefore the flow behind the curved shock wave is necessarily vortical.

In the present paper we shall discuss the effect of the vorticity upon the location of the shock wave as well as its curvature. However, the fluid is still assumed to be incompressible and moreover both the thermal conductivity and the viscosity of the fluid are neglected as usual.

The vortical flow past a circular cylinder and a sphere is approximately expressed in terms of the stream function, Ψ, near the obstacle and the symmetrical axis which is a part of the particular stream line $\Psi=0$. Besides the usual two shock conditions, namely the conditions for the deflection angle of the stream line on passing through the shock wave and the magnitude of the velocity immediately behind the shock wave, one more condition is considered which arises from the entropy change. Calculations are made consistently by neglecting the higher order terms than ε^3, where ε is the angular position on the shock wave as indicated in Fig. 1.

It is found that the vorticity correction does not alter the non-dimensional curvature of the shock at its nose which is referred to the reciprocal of its distance from the centre of the body, while it makes the location of the shock further away from the body than in the case without vorticity. A fairly good agreement is found between our theoretical results and some experiments3),4),5) provided that the velocity of the body is not too small.

On the other hand, C. C. Lin and S. I. Rubinov6) and J. Dugundji7) have developed analyses for the same problem by using the power series expansion of the coordinates with its origin at the stagnation point as well as at the nose of the shock. Although their analyses seem to be rigorous, agreement between their theoretical results and various experiments are not so satisfactory. Recently T. Kawamura8) has obtained the good results by the method of series expansion in coordinates, but he has taken as shock conditions some higher order one (equation (12) in his paper) in place of the lower order condition (formula (7.30) in reference 6).

§ 2. Shock Conditions

Taking the coordinate system fixed to an obstacle, we consider a uniform flow with a supersonic speed past the body. Let it be assumed that in passing through the oblique shock wave inclined at an angle β to the direction of the uniform flow at infinity upstream, the flow is deflected by an angle δ. Then, the Mach numbers M_1, M_2, pressures p_1, p_2 and densities ρ_1, ρ_2 on both sides of the shock wave are connected by the following relations:

$$\frac{1}{\tan\delta}=\left(\frac{\gamma+1}{2}\frac{M_1^2}{M_1^2\sin^2\beta-1}-1\right)\tan\beta\,, \tag{1}$$

$$\left(\frac{1}{M_1^2\sin^2\beta}+\frac{\gamma-1}{2}\right)\left(\frac{1}{M_2^2\sin^2(\beta-\delta)}+\frac{\gamma-1}{2}\right)=\left(\frac{\gamma+1}{2}\right)^2, \tag{2}$$

$$\frac{p_2}{p_1}=\frac{2\gamma}{\gamma+1}\left(M_1^2\sin^2\beta-\frac{\gamma-1}{2\gamma}\right), \tag{3}$$

$$\frac{\rho_1}{\rho_2}=\frac{2}{\gamma+1}\left(\frac{1}{M_1^2\sin^2\beta}+\frac{\gamma-1}{2}\right). \tag{4}$$

Here suffixes 1,2 refer respectively to values in front of and immediately behind the shock wave and γ denotes the adiabatic gas constant.

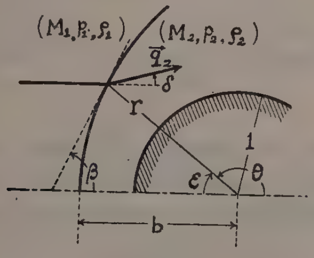

Fig. 1.

In the first place we assume that in polar coordinates as indicated in Fig. 1, the shape of the shock in the neighbourhood of its nose is expressed by

$$r=b(1+\lambda\varepsilon^2+O(\varepsilon^4))\,,\quad \varepsilon=\pi-\theta \tag{5}$$

where b, λ are constants to be determined which are connected with the curvature, $1/R$, of the shock at its nose by

$$\frac{1}{R}=\frac{1-2\lambda}{b}\,. \tag{6}$$

Then, (1) is rewritten in an alternative form as

$$\tan\delta=\frac{(1-2\lambda)(M_1^2-1)}{1+\frac{\gamma-1}{2}M_1^2}\varepsilon+O(\varepsilon^3)\,, \tag{7}$$

while (2) is replaced by the following relation giving the magnitude of the fluid velocity, q_2, just behind the shock wave:

$$\left(\frac{q_2}{a_s}\right)^2=\frac{4}{(\gamma+1)^2M_1^2}\left\{\left(1+\frac{\gamma-1}{2}M_1^2\right)+\frac{(1-2\lambda)^2(1+\gamma M_1^4)}{1+\frac{\gamma-1}{2}M_1^2}\varepsilon^2+O(\varepsilon^4)\right\}, \tag{8}$$

where a_s is the sonic speed at the stagnation point. In deriving this equation use has been made of Bernoulli's equation. The increase of entropy, ΔS, of the unit mass of fluid when it passes through the shock, is found from (3), (4) to be

$$\frac{\Delta S}{\mathfrak{R}}=\log\left(\frac{2\gamma M_1^2}{\gamma+1}-\frac{\gamma-1}{\gamma+1}\right)^{\frac{1}{\gamma-1}}\times\left(\frac{\gamma-1}{\gamma+1}+\frac{2}{\gamma+1}\frac{1}{M_1^2}\right)^{\frac{\gamma}{\gamma-1}}-\frac{\gamma(1-2\lambda)^2(M_1^2-1)^2}{\left(1+\frac{\gamma-1}{2}M_1^2\right)\left\{2\gamma M_1^2-(\gamma-1)\right\}}\varepsilon^2+O(\varepsilon^4), \tag{9}$$

where $\mathfrak{R}$ is the gas constant.

On the other hand, for a steady rotational flow of a compressible fluid we have

$$-\frac{dS}{dn}=\frac{\gamma\mathfrak{R}}{a^2}(\boldsymbol{q}\times\operatorname{rot}\boldsymbol{q})\cdot\boldsymbol{n}\,, \tag{10}$$

where $\boldsymbol{n}$ denotes the unit vector normal to the stream line and a is the sonic speed at the point under consideration.

Now, if we make an assumption that the flow behind the shock wave can be replaced by that of an incompressible fluid, the stream function Ψ for the floweis given by

$$\frac{d\Psi}{dn}=q(r\sin\theta)^{\kappa}\,, \tag{11}$$

where κ is a constant to be taken zero for two-dimensional cases and unity for axisymmetrical cases.

Then, taking account of the relation:

$$\left(\frac{dS}{d\Psi}\right)_2=\frac{d(\Delta S)/d\varepsilon}{d\Psi_2/d\varepsilon}\,,$$

and inserting (9), (10) and (11) in this relation, we have finally

$$\frac{d\Psi_2}{d\varepsilon}(\mathrm{rot}\,\boldsymbol{q})_2=-\frac{4(1-2\lambda)^2(M_1{}^2-1)^2}{(\gamma+1)^2M_1{}^2\left(1+\frac{\gamma-1}{2}M_1{}^2\right)}\times a_s{}^2b^{\kappa}\varepsilon^{1+\kappa}+O(\varepsilon^{3+\kappa})\,. \quad (12)$$

Here the suffix 2 has the same meaning as before, and the vectorial notation, rot $\boldsymbol{q}$, is conveniently used for its (scalar) component normal to the meridian plane. The condition (12) as well as (7), (8) provide the shock conditions to be used hereafter in this paper.

§ 3. Detached Shock Wave in front of a Circular Cylinder

As is well known, the vorticity of the two-dimensional flow of an incompressible inviscid fluid is expressed in terms of the stream function Ψ as

$$\mathrm{rot}\,\boldsymbol{q}=-\left\{\frac{1}{r}\frac{\partial}{\partial r}\left(r\frac{\partial\Psi}{\partial r}\right)+\frac{1}{r^2}\frac{\partial^2\Psi}{\partial\theta^2}\right\}, \quad (13)$$

and is a function of Ψ only. On account of the symmetry of the flow, we can put the vorticity distribution for smaller values of Ψ in the form:

$$\mathrm{rot}\,\boldsymbol{q}=-k\Psi+O(\Psi^3)\,, \quad (14)$$

where k is a constant to be determined later. From (13) and (14), we get

$$\frac{1}{r}\frac{\partial}{\partial r}\left(r\frac{\partial\Psi}{\partial r}\right)+\frac{1}{r^2}\frac{\partial^2\Psi}{\partial\theta^2}=k\Psi+O(\Psi^3)\,. \quad (15)$$

Neglecting the terms higher than Ψ^3, we obtain a linear differential equation of Helmholtz type and its particular solutions are given in terms of the modified Bessl functions I_n, K_n, by

$$\begin{matrix} I_n(\sqrt{k}r) \\ K_n(\sqrt{k}r) \end{matrix}\cdot\sin n\theta\,.$$

For simplicity, we take the radius of a circular cylinder to be unity and make use of the boundary condition on the surface of the body. Then, with arbitrary constants A_n's the general solution of (15) is given by

$$\Psi=\sum_{n=1}^{\infty}A_n\{K_n(\sqrt{k})I_n(\sqrt{k}r)-I_n(\sqrt{k})K_n(\sqrt{k}r)\}\sin n\theta\,,$$

and if we retain only the first term corresponding to $n=1$, we have

$$\Psi=U\{K_1(\sqrt{k})I_1(\sqrt{k}r)-I_1(\sqrt{k})K_1(\sqrt{k}r)\}\sin\theta\,, \quad (16)$$

where U is a new indeterminate constant.

It is easily shown that the following relations hold at the position immediately behind the shock wave:

$$\left.\begin{aligned}
&\frac{\Psi_2}{U}=F\varepsilon+O(\varepsilon^3)\,,\\
&\tan\delta=\left(\frac{b}{F}\frac{\partial F}{\partial b}-1\right)\varepsilon+O(\varepsilon^3)\,,\\
&\left(\frac{q_2}{U}\right)^2=\left(\frac{F}{b}\right)^2\left[1+\left\{\left(\frac{b}{F}\frac{\partial F}{\partial b}-1\right)^2\right.\right.\\
&\qquad\left.\left.+2(1+\lambda)\left(\frac{b}{F}\frac{\partial F}{\partial b}-1\right)\right\}\varepsilon^2+O(\varepsilon^4)\right],\\
&(\mathrm{rot}\,\boldsymbol{q})_2=-kUF\varepsilon+O(\varepsilon^3)\,;
\end{aligned}\right\} \quad (17)$$

with

$$F=K_1(\sqrt{k})I_1(\sqrt{k}b)-I_1(\sqrt{k})K_1(\sqrt{k}b). \quad (18)$$

Substituting (17) into (7), (8), (12) and comparing the terms of the same order on both sides, we have, to the second order of ε,

$$\left.\begin{aligned}
&\frac{(1-2\lambda)(M_1{}^2-1)}{1+\frac{\gamma-1}{2}M_1{}^2}=\frac{b}{F}\frac{\partial F}{\partial b}-1\,,\\
&\frac{4\left(1+\frac{\gamma-1}{2}M_1{}^2\right)}{(\gamma+1)^2M_1{}^2}=\left(\frac{F}{b}\right)^2\left(\frac{U}{a_s}\right)^2,\\
&\frac{4(1-2\lambda)^2(1+\gamma M_1{}^4)}{(\gamma+1)^2M_1{}^2\left(1+\frac{\gamma-1}{2}M_1{}^2\right)}=\left(\frac{b}{F}\frac{\partial F}{\partial b}-1\right)\\
&\qquad\times\left\{(1+2\lambda)+\frac{b}{F}\frac{\partial F}{\partial b}\right\}\left(\frac{F}{b}\right)^2\left(\frac{U}{a_s}\right)^2,\\
&\frac{4(1-2\lambda)^2(M_1{}^2-1)}{(\gamma+1)^2M_1{}^2\left(1+\frac{\gamma-1}{2}M_1{}^2\right)}=kF^2\left(\frac{U}{a_s}\right)^2.
\end{aligned}\right\} \quad (19)$$

These four equations are sufficient to determine four unknown constants b, λ, k, U/a_s.

For example we can easily find that

$$1-2\lambda=\frac{3(M_1{}^2-1)}{3M_1{}^2-1}\,, \quad (20)$$

$$kb^2=\frac{3(M_1{}^2-1)^2}{(3M_1{}^2-1)\left(1+\frac{\gamma-1}{2}M_1{}^2\right)}\equiv C. \quad (21)$$

According to (6), (20) gives the ratio of the distance, b, of the shock wave from the centre of the cylinder to the radius of curvature, R, of the shock at its nose, and it is interesting to note that this value is exactly equal to that given by Tamada[1] who obtained it by assuming that the flow behind the shock wave is incompressible and irrotational. (Of course, the third condition (12) is superfluous in this case.) This implies that the vorticity correction has no influence at all upon the non-dimensional curvature of the shock.

Since the constant $C(=kb^2)$ defined in (21) is found to be comparatively small, we can expand the modified Bessel functions in (18) in power series of their moduli. Then, neglecting higher order terms, we have approximately

$$F=\frac{1}{2}\left(b-\frac{1}{b}\right)+k\left\{-\frac{b}{4}\log b+\frac{1}{16}b\left(b^2-\frac{1}{b^2}\right)\right\}.$$

Using this, we get from (19) a transcendental equation for determining b as:

$$C(C^2-2C+8)b^4+4(C^2-2C-4)b^2$$
$$-4C^3b^2\log b-C^2(2+C)=0. \quad (22)$$

For any given value of M_1 (and consequently of C), the value of b is estimated numerically from (22) and consequently k from (21). Taking the air for which $\gamma=1.40$ as an example, the non-dimensional distance of the shock wave from the stagnation point as referred to the diameter of the circular cylinder is given in Fig. 2 for various values of M_1. In this figure the corresponding curve for the case without vorticity is also shown by a dotted-line curve for comparison.

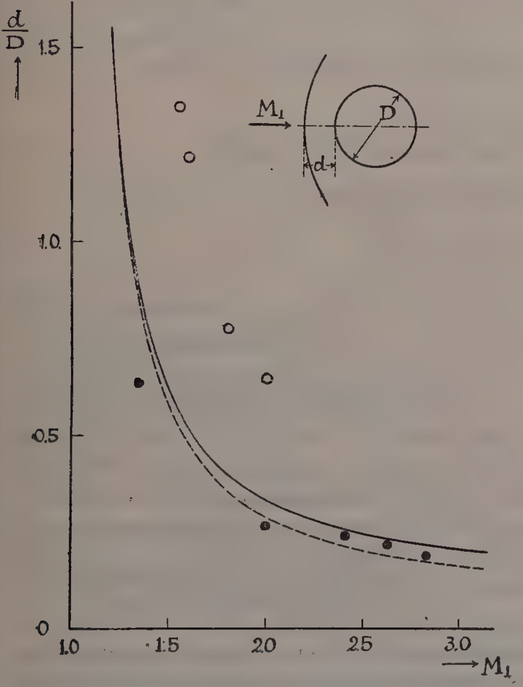

Fig. 2. Case of a Circular Cylinder
——— Present Theory
– – – – Irrotational Case (Tamada[1])
● (Sugimoto[3]) } Experimental Values
○ (Alperin[5]) }

It will clearly be seen that the vorticity in the flow has the effect of moving the location of the shock wave further away from the obstacle than in the case of irrotational flow. For larger values of M_1, Sugimoto's experiments seem to justify this result, while the contrary is found for smaller values of M_1. But the recent experiments carried out by Alperin, who had tested deliberately the end effect of a cylinder as well as tunnel wall interference, gave much larger values than Sugimoto's for $M_1 < 2.00$.

Following him, the reciprocal of the distance of the shock wave from the centre of a circular cylinder to its nose are shown in Fig. 3.

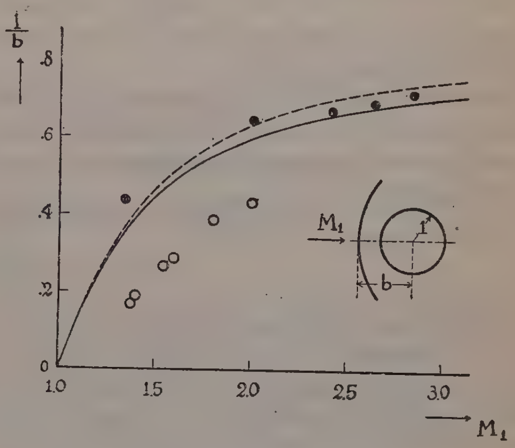

Fig. 3. $1/b$ vs. M_1
——— Present Theory
– – – – Irrotational Case (Tamada[1])
● (Sugimoto[3]) } Experimental Values
○ (Alperin[5]) }

The reason why such large discrepancies between these two series of experiments do appear is not clear and is left to future detailed studies, both theoretical and experimental.

§ 4. Detached Shock Wave in front of a Sphere

Next we shall apply the same method as in § 3 to the detached shock wave in front of a sphere. For axisymmetrical flows the vorticity component normal to the meridian plane is expressed in terms of Stokes' stream function, Ψ, as

$$\operatorname{rot} q=-\frac{1}{r\sin\theta}\left\{\frac{\partial^2}{\partial r^2}+\frac{1}{r^2}\sin\theta\frac{\partial}{\partial\theta}\times\left(\frac{1}{\sin\theta}\frac{\partial}{\partial\theta}\right)\right\}\Psi, \quad (23)$$

and in this case $\operatorname{rot} q/r\sin\theta$ is a function of Ψ only, which we assume to be constant as a first approximation. Let U, k be two indeterminate constants and we can get the fundamental equation for Ψ in the form:

$$\frac{\partial^2\Psi}{\partial r^2}+\frac{1}{r^2}(1-\mu^2)\frac{\partial^2\Psi}{\partial\mu^2}=\frac{kU}{2}r^2(1-\mu^2), \quad (24)$$

with

$$\mu=\cos\theta .$$

The solution of this inhomogeneous linear differential equation subject to the boundary condition on the surface of the sphere, radius of which is taken to be unity, is given by

$$\Psi=\frac{U}{2}\left\{\left(r^2-\frac{1}{r}\right)+\frac{k}{10}\left(r^4-\frac{1}{r}\right)\right\}(1-\mu^2). \quad (25)$$

Here, we have retained only the first term corresponding to $n=1$.

Starting from (25) and proceeding as in the last section, we have the following four equations as the shock conditions:

$$\left.\begin{aligned}
&\frac{(1-2\lambda)(M_1^2-1)}{1+\frac{\gamma-1}{2}M_1^2}=\frac{b}{2G}\frac{\partial G}{\partial b}-1,\\
&\frac{4\left(1+\frac{\gamma-1}{2}M_1^2\right)}{(\gamma+1)^2M_1^2}=\frac{G^2}{b^4}\left(\frac{U}{a_s}\right)^2,\\
&\frac{4(1-2\lambda)^2(1+\gamma M_1^4)}{(\gamma+1)^2M_1^2\left(1+\frac{\gamma-1}{2}M_1^2\right)}=\left(\frac{b}{2G}\frac{\partial G}{\partial b}-1\right)\\
&\qquad\times\left\{(1+4\lambda)+\frac{b}{2G}\frac{\partial G}{\partial b}\right\}\frac{G^2}{b^4}\left(\frac{U}{a_s}\right)^2,\\
&\frac{4(1-2\lambda)^2(M_1^2-1)^2}{(\gamma+1)^2M_1^2\left(1+\frac{\gamma-1}{2}M_1^2\right)}=\frac{1}{2}kG\left(\frac{U}{a_s}\right)^2,
\end{aligned}\right\} \quad (27)$$

where we have put for simplicity

$$G=\left(b^2-\frac{1}{b}\right)+\frac{k}{10}\left(b^4-\frac{1}{b}\right). \quad (27)$$

These suffice to determine four constants b, λ, k, U/a_s.

In the first place, we obtain, for the nondimensional curvature of the shock,

$$1-2\lambda=\frac{2(M_1^2-1)}{2M_1^2-1}. \quad (28)$$

This value coincides with the value in the irrotational case[1] as in the case of a circular cylinder, and shows that the vorticity has not any effect upon the shape of the shock wave.

Next, we can find the distance, b, of the shock wave from the centre of the sphere by solving the following algebraic equation of fifth order:

$$2C(C-5)b^6+5(3-C)(1+C)b^3+3C^2=0, \quad (29)$$

with

$$C=\frac{2(M_1^2-1)^2}{(2M_1^2-1)\left(1+\frac{\gamma-1}{2}M_1^2\right)}. \quad (30)$$

Taking the air for which $\gamma=1.40$, the curve of d/D, where $d=b-D/2$, plotted against M_1 is shown in Fig. 4 by a thick-line curve.

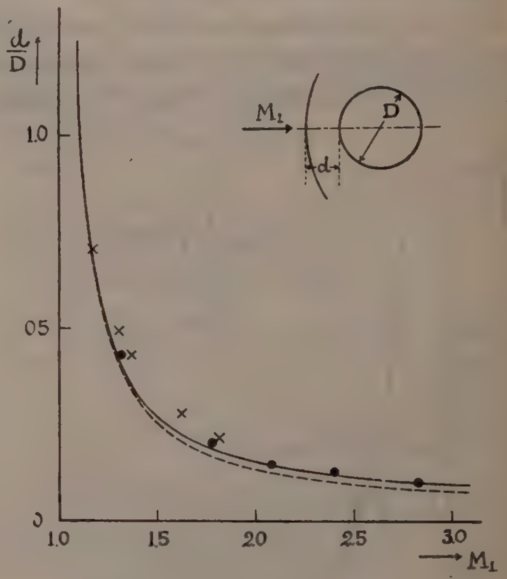

Fig. 4. Case of a Sphere

——— Present Theory

– – – – Irrotational Case (Tamada[1])

● (Sugimoto[3]) } Experimental Values

× (Heberle, Wood and Gooderum[4]) } Experimental Values

Comparison of this curve with the corresponding curve for the irrotational case[1] (shown by a dotted-line curve in Fig. 4) implies that the effect of vorticity is to move the location of the shock wave a little further away from the body. Our theoretical values are in excellent agreement with Sugimoto's experimental values, although for smaller values of M_1 our values deviate somewhat from Heberle, Wood and Gooderum's experimental values[4].

Lastly, the constant k as multiplied by b^3

is given by

$$kb^2=\frac{6C^2}{(3-C)(1+C)}\,. \tag{31}$$

The value of kb^2 becomes infinite when C tends to 3, i.e. when M_1 tends to 3.300 approximately. This shows that there may perhaps be a limit for the validity of our analysis, but as is easily seen from (29), b has no singularity at this value of M_1.

In conclusion, the author wishes to express his cordial thanks to Prof. S. Tomotika for his continual guidance throughout this work and especially for his kind inspection of the manuscript. The author's thanks are also due to Dr. K. Tamada and Dr. T. Kawamura for their useful suggestions and discussions. The author is greatly indebted to the Ministry of Education for a grant in aid for fundamental scientific research.

References

1) K. Tamada: Unpublished.

2) T. Kawamura: Mem. Coll. Sci. Kyoto Univ. **26** (1950) 207.

3) M. Sugimoto: Giken-Zappo No. 355 (1944) (in Japanese).

4) J. W. Heberle, G. P. Wood and P. B. Gooderum: N.A.C.A. Tech. Note 2100 (1950).

5) M. Alperin: Progress Rep. No. 4-44 Jet Propul. Lab. C.I.T. (1950).

6) C. C. Lin and S. I. Rubinov: Journ. Math. Phys. **27** (1948) 105.

7) J. Dugundji: Journ. Aeron. Sci. **15** (1948) 699.

8) T. Kawamura: Journ. Phys. Soc. Japan **7** (1952) 486.

JOURNAL OF THE PHYSICAL SOCIETY OF JAPAN Vol. 8, No. 6, NOV.—DEC., 1953

The "Independent Scalars" In Homogeneous Turbulence In Compressible Media

By M. Z. v. KRZYWOBLOCKI

§ 1. Introduction

Coburn[1] furnished a method for the construction of independent scalars in various types of homogeneous turbulence in incompressible fluids. By definition, these scalars must satisfy, in addition to other conditions, continuity relations identically, that is, these tensors must have zero divergence. Briefly, they are solenoidal tensors. But, as was proved by the author in many of his papers, the tensors in the theory of turbulence in compressible media are not any longer solenoidal, and their divergence must be equal "identically" to some given function. The present note discusses the changes which must be introduced into Coburn's paper in order to obtain a generalization of his method of the construction of independent scalars for homogeneous turbulence in compressible media. The author pressumes that the reader is perfectly acquainted with Coburn's paper; however, the reader is warned to have a copy of that paper right next to him during the reading of the present note. Consequently, only the items absolutely necessary from Coburn's paper will be cited which will be marked by (C). In order to facilitate a comparison, the same numbering of sections and equations will be used as in (C).

§ 2. The Independent Scalars in Isotropic Turbulence in Compressible Media

Preserving the notation used by Coburn, one can easily notice that the correlation tensors in a compressible medium have the same form (2.1C) as in an incompressible fluid, with A, B, C, D, E, F in (2.1C) being scalar functions of r and the time t. These tensors satisfy the following continuity relations

(2.2)

$$R^{\lambda},_{\lambda}=F_1(r,t)=P^0\,;\quad R^{\lambda\mu},_{\lambda}=F_2(r,t)\xi^{\lambda}=P^{\lambda}\,;$$
$$R^{\lambda\mu\alpha},_{\alpha}=F_3(r,t)\xi^{\lambda}\xi^{\mu}+F_4(r,t)g^{\lambda\mu}=P^{\lambda\mu}\,,$$

where F_i's ($i=1$ to 4) are given scalar functions of r and t. The relation (2.2) furnishes a first order differential equation for A. Hence R^{λ} does not depend upon an independent scalar but depends upon F_1. Further, we notice that (2.2) determines a correlation vector and a correlation tensor of the second order equal to P^{λ} and $P^{\lambda\mu}$, respectively. Thus, both $R^{\lambda\mu}$ and $R^{\lambda\mu\alpha}$ depend upon one independent scalar and F_i's (2, 3, 4). Below, we shall determine expressions for R^{λ}, $R^{\lambda\mu}$, $R^{\lambda\mu\alpha}$ which depend upon single independent scalars and F_i's respectively.

First, we consider the tensor $R^{\lambda\mu}$. Equation (2.3C) preserves its form, but others are subject to changes:

$$\overline{R}^{\mu\alpha}=e^{\alpha\gamma\rho}\overline{S}_{\gamma\cdot}{}^{\mu}{}_{,\rho}+g^{\mu\alpha}\int rF_2dr\,; \tag{2.4}$$

and

$$\overline{R}^{\mu\alpha}=[\int rF_2dr-(2C+rdc/dr)]g^{\mu\alpha}+r^{-1}(dc/dr)\xi^{\alpha}\xi^{\mu}\,,$$

with

$$(\partial/\partial\xi^{\alpha}\int rF_2dr)g^{\mu\alpha}=\xi^{\mu}F_2\,.$$

The above expression furnishes a second order correlation tensor which depends upon a single scalar C and known scalar F_2, and for which the continuity relation (2.2) is identically satisfied.

The following changes occur in the third order correlation tensor, $R^{\lambda\mu\alpha}$:

$$\overline{R}^{\lambda\mu\nu}=e^{\nu\gamma\rho}\overline{S}_{\gamma\cdot}{}^{\lambda\mu}{}_{,\rho}+\tfrac{1}{2}(\xi^{\lambda}g^{\mu\nu}+\xi^{\mu}g^{\lambda\nu})\int rF_3dr+\xi^{\nu}g^{\lambda\mu}r^{-3}\int r^2(F_4-\int rF_3dr)dr\,, \tag{2.7}$$

and

$$\overline{R}^{\lambda\mu\nu}=2(r^{-1}dE/dr)\xi^{\lambda}\xi^{\mu}\xi^{\nu}-(3E+rdE/dr-\tfrac{1}{2}\int rF_3dr)(\xi^{\lambda}g^{\mu\nu}+\xi^{\mu}g^{\lambda\nu})+(2E+r^{-3}\int r^2(F_4-\int rF_3dr)dr)\xi^{\nu}g^{\lambda\mu}\,. \tag{2.9}$$

The correlation tensor of the first order is simply given by the formula:

$$\overline{R}^{\alpha}=\xi^{\alpha}r^{-3}\int r^2F_1dr\,\cdot \tag{2.10}$$

It is easily verified that it satisfies identically (2.2). Since there are no essential differences in the reasoning, we shall not discuss the independent scalar in turbulence with axial symmetry in compressible media (§ 3C).

§ 4. The Theory of Correlation Tensors which Depend Upon Independent Scalars

In this Section there are some changes:

a. The General Problem. We consider the following problem: given the arbitrary correlation tensors $R^{\lambda}(\xi^{\gamma})$; $R^{\lambda\mu}(\xi^{\gamma})$; $R^{(\lambda\mu\alpha)}(\xi^{\gamma})$, the independent fields ξ^{λ}, j^{λ}, i^{λ}, respectively, and known tensors of the order zero, one or two, respectively, in the independent field ξ^{λ}, j^{λ}, i^{λ}, respectively,

$$P^{0}{}_{(\xi)}=F_{1(\xi)}(r,t);\quad P^{\lambda}{}_{(\xi)}=F_{2(\xi)}(r,t)\xi^{\lambda};$$
$$P^{\lambda\mu}{}_{(\xi)}=F_{3(\xi)}\xi^{\lambda}\xi^{\mu}+F_{4(\xi)}g^{\lambda\mu};$$
$$P^{0}{}_{(j)}=F_{1(j)}(r,t);\quad P^{\lambda}{}_{(j)}=F_{2(j)}(r,t)j^{\lambda};$$
$$P^{\lambda\mu}{}_{(j)}=F_{3(j)}j^{\lambda}j^{\mu}+F_{4(j)}g^{\lambda\mu};$$

etc.; to determine associated tensors $\overline{R}^{\lambda}(\xi^{\gamma})$, $\overline{R}^{\lambda\mu}(\xi^{\gamma})$, $\overline{R}^{\lambda\mu\alpha}(\xi^{\gamma})$, such that:

(1) $\overline{R}^{\lambda}$ is a linear function of $\overline{P}^{0}{}_{(\xi)}=\xi^{\lambda}\overline{F}_{1(\xi)}$ ($\overline{F}_{1(\xi)}$ being some function of $F_{1(\xi)}$) and of R^{λ} and its first derivatives......(as in 1.C):

(2) The divergence of $\overline{R}^{\lambda}$, $\overline{R}^{\lambda\mu}$, $\overline{R}^{\lambda\mu\alpha}$, is identically equal to $P^{0}{}_{(\xi)}$, $P^{\lambda}{}_{(\xi)}$, $P^{\lambda\mu}{}_{(\xi)}$, in the field, $\{\xi^{\lambda}\}$, to $P^{0}{}_{(j)}$, $P^{\lambda}{}_{(j)}$, etc., in the field $\{j^{\lambda}\}$, etc., respectively:

(3) like in (3C), (4) like in (4C).

(5) The desired tensors $\overline{R}^{\lambda}$, $\overline{R}^{\lambda\mu}$, $\overline{R}^{\lambda\mu\alpha}$ are determined by

$$\overline{R}^{\alpha}=e^{\alpha\gamma\rho}\overline{S}_{\gamma,\rho}+\xi^{\alpha}r^{-3}\int r^2F_{1(\xi)}dr\,, \tag{4.4}$$

with analogous formulas for ${}'\overline{R}^{\alpha}$ and ${}''\overline{R}^{\alpha}$ (instead of ξ^{α} insert j^{α} and i^{α}, respectively; instead of $F_{1(\xi)}$, insert $F_{1(j)}$ and $F_{1(i)}$, respectively;

$$\overline{R}^{\mu\alpha}=e^{\alpha\gamma\rho}\overline{S}_{\gamma\cdot}{}^{\mu}{}_{,\rho}+g^{\mu\alpha}\int rF_{2(\xi)}dr,\ \text{etc.}; \tag{4.5}$$

$$\overline{R}^{\lambda\mu\alpha}=e^{\alpha\gamma\rho}S_{\gamma\cdot}{}^{\lambda\mu}{}_{,\rho}+(\tfrac{1}{2}\int rF_{3(\xi)}dr)\times(\xi^{\lambda}g^{\mu\alpha}+\xi^{\mu}g^{\lambda\alpha})+r^{-3}\int r^2(F_{4(\xi)}-\int rF_{3(\xi)}dr)\times dr\xi^{\alpha}g^{\lambda\mu}\,,\quad \text{etc.} \tag{4.6}$$

The section (6) in (a) and the part (b) remain unchanged, except the section (5) in (b) which should read:

(5) It should be noted that the divergences of the tensors $\overline{R}^{\lambda}$, $\overline{R}^{\lambda\mu}$, $\overline{R}^{\lambda\mu\alpha}$, etc., are equal to $P^{0}{}_{(\xi)}$, $P^{\lambda}{}_{(\xi)}$, etc., respectively, by virtue of (4.4) through (4.6).

§ 5. Proof of the Results

In general, Coburn's proof remains valid in the present case with a few changes here and there. First, consider the vector $\overline{R}^{\lambda}$. This vector is a general linear combination of R^{λ} and its derivatives with respect to ξ^{λ}, and of $\overline{P}^{0}{}_{(\xi)}=\xi^{\lambda}\overline{F}_{1(\xi)}$, etc.. Hence, we may write

$$\overline{R}^{\lambda}=\xi^{\lambda}r^{-3}\int r^2F_{1(\xi)}dr+j^{\lambda}r^{-3}\int r^2F_{1(j)}dr+\ldots\ldots\ \text{(like in 5.1.C)}; \tag{5.1}$$

$$\overline{R}^{\lambda}=\xi^{\lambda}r^{-3}\int r^2F_{1(\xi)}dr+\ldots\quad \text{(5.3C)}, \tag{5.3}$$
$${}'\overline{R}^{\lambda}=j^{\lambda}r^{-3}\int r^2F_{1(j)}dr+\ldots\quad \text{(5.3C)}.$$

Notice, that the third term in (5.3C) should read: $+D\xi^\lambda R^\alpha{}_{,\alpha}+\ldots\ldots$ Forming the divergence of the first vector in (5.3) we obtain:

$$\overline{R}^\lambda{}_{,\lambda}=F_{1(\xi)}(r,t)+\ldots\ldots \qquad (5.4) \quad (5.4C).$$

Hence, the condition that the divergence of $\overline{R}^\lambda$ is identically equal to $F_{1(\xi)}$ for arbitrary R^λ, ξ^λ, implies that.......... The remaining part of Coburn's reasoning remains valid. Thus we obtain:

$$(5.7) \quad \overline{R}^\lambda=-2R^\lambda-\xi^\alpha R^\lambda{}_{,\alpha} +\xi^\lambda(R^\alpha{}_{,\alpha}+r^{-3}\int r^2F_{1(\xi)}dr).$$

$$(5.8) \quad '\overline{R}^\lambda=j^\alpha\, 'R^\lambda{}_{,\alpha}-j^\lambda('R^\alpha{}_{,\alpha}-r^{-3}\int r^2F_{1(j)}dr).$$

By carrying out a similar analysis, one may show that the only possible second order tensor is

$$(5.9) \quad \overline{R}^{\mu\alpha}=g^{\mu\alpha}\int rF_{2(\xi)}dr+\ldots\ldots \quad (5.9C),$$

$$(5.10) \quad \overline{R}^{\mu\alpha}=g^{\mu\alpha}\int rF_{2(j)}dr+\ldots\ldots \quad (5.10C).$$

The remaining part of Coburn's proof may be easily adjusted to the present case of a compressible medium.

§ 6. The Symmetry of $\overline{R}^{\mu\alpha}$

The only change is in

$$(6.1) \quad \overline{R}^{\mu\alpha}=g^{\mu\alpha}\int rF_{2(j)}dr+\ldots\ldots \quad (6.1C).$$

Reference

1) Coburn, N.: The "Independent Scalars" In Homogeneous Turbulence. Am. Jour. Math. 74, 2 (Apr. 1952), 296-306.

Journal of the Physical Society of Japan Vol. 8, No. 6, Nov.—Dec., 1953

Numerical Solution of the Navier-Stokes Equations for the Flow around a Circular Cylinder at Reynolds Number 40

By Mitutosi Kawaguti

Institute of Science and Technology, University of Tokyo

(Received July 10, 1953)

The steady two-dimensional flow around a circular cylinder submerged in a viscous fluid for the case $R=40$ is investigated, integrating numerically the exact Navier-Stokes equations. The main results are as follows. (i) The steady flow solution exists even for the Reynolds number as high as 40. Moreover, it seems that the solution goes over smoothly to the solution of the Kirchhoff discontinuous flow theory which seems to be the limiting flow for the case $R\to\infty$. (ii) The flow pattern and the coefficients of pressure and drag are in good agreement with the experimental data.

§ 1. Introduction and Summary

It is well known that the flow around an obstacle submerged in a viscous fluid can be treated successfully with the Stokes or the Oseen approximation to the Navier-Stokes equations, when the Reynolds number of the flow is sufficiently low. On the other hand, it has been shown experimentally [9], [13], that above some critical Reynolds number the flow becomes unstable and periodic and transforms into the flow with so-called von Kármán's vortex street. But unfortunately, Stokes's and Oseen's approximations become worse as the Reynolds number is increased, so that we must grapple with the exact Navier-Stokes equations in order to investigate the flow near the critical Reynolds number.

For such an intermediate flow régime, very few works have been reported as far as the author is aware: i.e. Thom's numerical solutions for the flow past a circular cylinder for $R=10$ and 20 [13], R being the Reynolds number, and the author's approximate solutions for the flow past a circular cylinder [5] and a sphere [6] by the Galelkin method, and the numerical solution for a sphere when $R=20$ [7]. Although Galelkin's method gave fairly good results, these do not seem to be sufficient to elucidate the problem of the critical Reynolds number. For such a discussion, it seems that there is no appropriate method other than the numerical one.

It is a well-known experimental fact that the flow past a circular cylinder becomes unstable and there appears von Kármán's vortex street, when the Reynolds number of the flow exceeds about 40 [9]. However, it seems natural to expect that even above the critical Reynolds number the steady flow solution would exist, which becomes unstable and gives rise to the von Kármán vortex street by the effect of the small disturbance which is hidden in the uniform flow.

In this paper, the flow around a circular cylinder submerged in a viscous fluid for the case $R=40$ is investigated, integrating numerically the exact Navier-Stokes equations. It is found that even for this Reynolds number there is a steady solution in accordance with our anticipation.

In § 2, equations of motion, boundary conditions, and transformation of the physical plane into an appropriate plane are stated. In § 3, reduction of differential equations and boundary conditions into finite difference equations and conditions is carried out. In § 4, the numerical procedure is shortly explained, some modification of Thom's method being also shown. In § 5, the results obtained are shown together with a number of figures, some of which are compared with experimental data. In § 6. the accuracy of the results is discussed, and in § 7, some discussions and conclusions are given.

The main results obtained are as follows:

(i) The steady flow solution exists even for the Reynolds number as high as 40. Moreover, it seems that the solution goes over smoothly to the solution of the discontinuous flow theory which seems to be the limiting flow for the case $R\to\infty$ [4], [8].

(ii) The flow pattern and the coefficients of pressure and drag are in accord with the experimental data. It seems that the results may have some relation with Kovasznay's estimation that von Kármán's vortex street arises from the instability of the laminar wake [9].

§ 2. Equations of Motion and Boundary Conditions

In this paper, all the quantities are expressed non-dimensionally, so that we consider a circular cylinder of radius 1 which is submerged in a viscous fluid streaming with general velocity 1 in the direction of the positive x-axis.

Then the equations of motion for two-dimensional flow can be written as,

$$\frac{\partial(\Psi,\zeta)}{\partial(x,y)}+\frac{2}{R}\Delta\zeta=0\,, \tag{2.1}$$

and

$$\zeta=-\Delta\Psi, \tag{2.2}$$

where

$$\Delta=\frac{\partial^2}{\partial x^2}+\frac{\partial^2}{\partial y^2}\,, \tag{2.3}$$

and x, y are the cartesian coordinates of the physical plane, Ψ is the stream function, ζ is the vorticity, and $R=2/\nu$ is the Reynolds number defined as (uniform velocity)×(diameter)÷(kinematic viscosity), ν being the kinematic viscosity.

For the convenience of numerical computation, we introduce the disturbance stream function ϕ defined as

$$\Psi=y+\phi\,. \tag{2.4}$$

ϕ is finite throughout the flow region. Then the equations (2.1) and (2.2) become

$$\frac{\partial(\phi,\zeta)}{\partial(x,y)}-\frac{\partial\zeta}{\partial x}+\frac{2}{R}\Delta\zeta=0\,, \tag{2.5}$$

and

$$\zeta=-\Delta\phi\,. \tag{2.6}$$

Boundary conditions are then expressed as

(a) $\phi=\dfrac{\partial\phi}{\partial r}=-\sin\theta$, on the surface of the cylinder $(r=1)$, (2.7)

and

(b) $\dfrac{\partial\phi}{\partial r}=\dfrac{1}{r}\dfrac{\partial\phi}{\partial\theta}\to 0$, as $r\to\infty$, (2.8)

where r and θ are the polar coordinates of the physical plane.

We next introduce the transformation;

$$X=1/r\,,\quad Y=(2/\pi)\theta\,. \tag{2.9}$$

Since the flow is symmetrical with respect to the x-axis, we have only to consider the upper half of the (x, y)-plane. With transformation (2.9), the upper half flow region

($\infty \geqq r \geqq 1$, $\pi \geqq \theta \geqq 0$) is transformed into a finite rectangular region of the (X, Y)-plane ($1 \geqq X \geqq 0$, $2 \geqq Y \geqq 0$), (cf. Fig. 1).

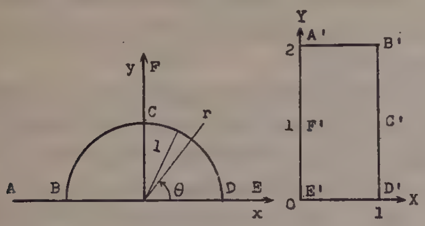

Fig. 1.

Then (2.5) and (2.6) become

$$-\frac{2X^3}{\pi}\frac{\partial(\psi,\zeta)}{\partial(X,Y)}+X^2\frac{\partial\zeta}{\partial X}\cos\frac{\pi Y}{2}+\frac{2X}{\pi}\frac{\partial\zeta}{\partial Y}\sin\frac{\pi Y}{2}+\frac{2}{R}\left\{X^4\Delta\zeta-\left(X^4-\frac{4X^2}{\pi^2}\right)\times\frac{\partial^2\zeta}{\partial Y^2}+X^3\frac{\partial\zeta}{\partial X}\right\}=0\,, \tag{2.10}$$

and

$$\zeta=-X^4\Delta\psi+\left(X^4-\frac{4X^2}{\pi^2}\right)\frac{\partial^2\psi}{\partial Y^2}-X^3\frac{\partial\psi}{\partial X}\,. \tag{2.11}$$

§ 3. Reduction to Finite Difference Relations

For the numerical integration, we must divide the whole region into meshes, and find the relations between one point and its neighbouring points for the equations of motion and the boundary conditions.

First, we divide all points into three sorts: (i) ordinary points, (ii) surface points, and (iii) infinity points.

(i) *Ordinary points.* (cf. Fig. 2)

We obtain the following relation neglecting the terms of order $O(n^4)$,

$$f_0=f_M-(n^2/4)\Delta f\,, \tag{3.1}$$

where f is any function of the point, and n is the distance between the mesh points, and suffix M indicates the average value of the four neighbouring points and 0 indicates the value at the point 0.

For f, we take ψ and ζ, and for $\Delta\psi$ and $\Delta\zeta$, we take the expressions obtained from (2.10) and (2.11), and finally we replace the differentials by the differences. Thus we obtain following two relations which take the place of the differential equations (2.10) and (2.11):

$$\left(\frac{1}{2}+\frac{2}{X^2\pi^2}\right)\psi_0=\psi_M+\frac{n^2}{4X^4}\zeta_0$$

$$-\left(\frac{1}{4}-\frac{1}{X^2\pi^2}\right)(\psi_1+\psi_3)+\frac{n}{8X}(\psi_2-\psi_4)\,, \tag{3.2}$$

and

$$\left(\frac{1}{2}+\frac{2}{X^2\pi^2}\right)\zeta_0=\zeta_M-\left(\frac{1}{4}-\frac{1}{X^2\pi^2}\right)(\zeta_1+\zeta_3)+\frac{n}{8X}(\zeta_2-\zeta_4)+\frac{R}{16\pi X}\{(\psi_2-\psi_4)(\zeta_1-\zeta_3)-(\psi_1-\psi_3)(\zeta_2-\zeta_4)\}+\frac{Rn}{16X^2}(\zeta_2-\zeta_4)\cos\frac{\pi Y}{2}-\frac{Rn}{8\pi X^3}(\zeta_1-\zeta_3)\sin\frac{\pi Y}{2}\,, \tag{3.3}$$

where suffixes 1, 2, 3, 4 indicate that the values at the points 1, 2, 3, 4 in Fig. 2 should be taken. Here, it must be noticed that ψ and ζ are 0 at the points $Y=0$ and 2, because of the symmetry of flow with respect to the x-axis.

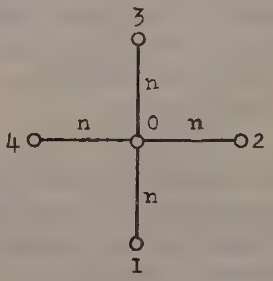

Fig. 2.

(ii) *Surface points.*

For the points on the surface of the cylinder, ($r=1$ or $X=1$), we use the relation (2.11) with the boundary conditions (2.7). Thus we have for $X=1$,

$$\psi=-\sin(\pi Y/2)\,, \tag{3.4}$$

and

$$\zeta=-\frac{\partial^2\psi}{\partial X^2}-\frac{4}{\pi^2}\frac{\partial^2\psi}{\partial Y^2}-\frac{\partial\psi}{\partial X}\,. \tag{3.5}$$

The values of $\partial^2\psi/\partial Y^2$ and $\partial\psi/\partial X$ on the surface are easily calculated as

$$(\partial^2\psi/\partial Y^2)_{X=1}=(\pi^2/4)\sin(\pi Y/2)\,, \tag{3.6}$$

and

$$(\partial\psi/\partial X)_{X=1}=\sin(\pi Y/2)\,, \tag{3.7}$$

and $\partial^2\psi/\partial X^2$ can be expressed as the following limiting form:

$$\left(\frac{\partial^2\psi}{\partial X^2}\right)_{X=1}=\lim_{X\to 1}\left\{\frac{2}{(1-X)^2}(\psi-\psi_{X=1})+\frac{2}{(1-X)}\left(\frac{\partial\psi}{\partial X}\right)_{X=1}\right\}. \tag{3.8}$$

Then if we take X as 0.9 as we shall do in this paper, (3.8) becomes

$$\left(\frac{\partial^2\psi}{\partial X^2}\right)_{X=1}=200\psi_{X=0.9}+220\sin\frac{\pi Y}{2}\ . \tag{3.8$'$}$$

Introducing the values (3.6), (3.7) and (3.8′) into (3.5), we finally obtain the relation for the surface points as:

$$\zeta_{X=1}=-200\psi_{X=0.9}-222\sin(\pi Y/2)\ . \tag{3.9}$$

(iii) *Infinity points.*

For the points corresponding to the infinity of the physical plane ($r=\infty$ or $X=0$), we use the result of Imai's investigation concerning the asymptotic behaviour of viscous flow far from a submerged cylinder [3]. According to this, ψ can be expressed asymptotically as

$$\psi=-\frac{C_D}{2}\left(1-\frac{Y}{2}\right), \tag{3.10}$$

when r tends to infinity, where C_D is the drag coefficient of the cylinder which can be calculated, as we shall see in §5, from the values of ψ and ζ on the surface. One more relation is naturally that

$$\zeta=0\ . \tag{3.11}$$

Of course, relations (3.10) and (3.11) satisfy the boundary conditions (2.8) at infinity.

Now we have all the relations necessary for the numerical integration.

§4. Procedure of Computation

We take the mesh constant to be 0.1 for X and Y, so we have 232 mesh points for the half flow region. In this manner, we have smaller meshes near the surface and bigger ones far from the surface in the physical plane; this is suitable for the study of the flow, since large variations of ψ and ζ seem to be restricted near the surface of the cylinder.

Numerical integration of (2.10) and (2.11) are carried out by an iterative procedure according to following steps:

(i) We assume appropriate values for ψ and ζ on all the mesh points. These may be conveniently obtained by some method.

(ii) Then, ζ's on the line $X=0.1$ are corrected using the relation (3.3) with the values of ζ on the lines $X=0$ and 0.2, and the values of ψ on the lines $X=0$, 0.1, and 0.2. This procedure consists in solving 19 simultaneous equations for the ζ's on the line $X=0.1$.

(iii) Using the values of ζ on the line $X=0.1$ corrected by (ii), together with the values of ψ on the lines $X=0$ and 0.2, we can obtain the values of ψ on the line $X=0.1$, from the relation (3.2) in the same manner as (ii).

(iv) Repeating the analogous procedure as done in (ii) and (iii), we can correct the values of ψ and ζ on the lines from $X=0.2$ to $X=0.9$, where the already corrected values of ψ and ζ must be substituted for the values assumed in (i).

(v) Then the values of ζ on the surface ($X=1$) can be corrected by the formula (3.9).

(vi) Lastly, we calculate the drag coefficient from the values of ζ on the surface. Then we get the values of ψ on the line $X=0$ by the formula (3.10).

The procedure from (ii) to (vi) makes one cycle of the iterative calculation.

When we calculate the ζ values, we assume that positive ζ value does not occur except in the wake. Thus if any positive value is obtained for ζ, it is replaced by 0. This assumption corresponds to the fact that positive ζ values are negligibly small as can be confirmed by the discussion of accuracy in §6. This is also suggested from the numerical investigation of the flow past a sphere [7].

Because of the strong variation of ζ along the lines $X=0.1$ and 0.2, we cannot correctly replace the differential by the difference for the points $(X, Y)=(0.1, 0.1)$ and $(0.2, 0.1)$. Therefore following procedure is introduced, based on physical consideration: if $\zeta=0$ along the line $X=i$, $Y\geqq j$, then along the line $X=i-0.1$, $Y\geqq j-0.1$, ζ is taken as 0. (Otherwise, the calculated values of ζ will oscillate strongly, which seems unnatural.)

We take the starting values from the author's calculation by the Galelkin method [5], as:

$$\begin{aligned}\psi=&-(2.2377r^{-1}-1.4701r^{-3}+0.2271r^{-5}\\&\qquad+0.0053r^{-7})\sin\theta\\&-(1.2267-2.8618r^{-2}+2.0435r^{-4}\\&\qquad-0.4084r^{-6})\sin 2\theta\ ,\end{aligned} \tag{4.1}$$

$$\begin{aligned}\zeta=&-(11.7608r^{-5}-5.4504r^{-7}-0.2544r^{-9})\sin\theta\\&-(4.9068r^{-2}-24.5220r^{-6}+13.0688r^{-8})\sin 2\theta.\end{aligned} \tag{4.2}$$

The iterative procedure from (ii) to (vi) was carried out about 65 cycles, keeping five digits for most points, and six digits for the values of ψ at the points near the surface of the cylinder. But calculated values of ψ and ζ at each point and the value of the drag coefficient C_D are fairly strongly oscillating and their convergence is rather slow as can be seen from Fig. 3, where the variation of the calculated drag coefficient for each cycle is shown as the typical example. The variations of ψ and ζ at each point show the analogous features.

To secure more rapid convergence of the iteration process, we then extrapolate the values of ψ and ζ at each step of approximation to find the final values, assuming that the extremum value decreases as the geometric progression.

Then, the iterative procedures have been carried out 10 times. It will be seen from the behaviour of the drag coefficient (cf. Fig. 3) that the process of extrapolation yields satisfactory results. Thus, the difference between the values of successive approximation for the ψ and ζ does not exceed 0.3% of the maximum values for the last 4 cycles.

Therefore we may safely take the final result of calculation as a sufficiently good approximation.

The numerical integration in this study took about one year and a half with twenty working hours every week, with a considerable amount of labour and endurance.

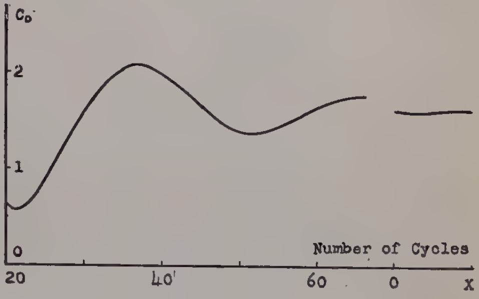

Fig. 3. Variation of drag coefficient.

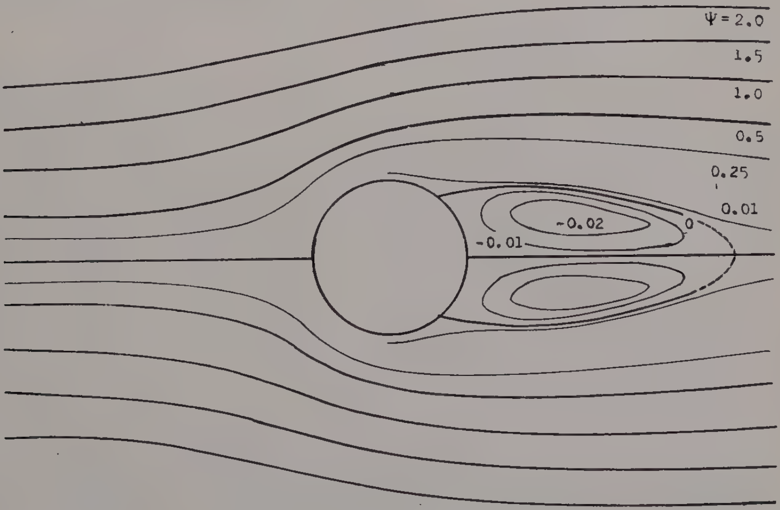

Fig. 4. Flow pattern ($R=40$).

§ 5. Results

By use of the numerical results obtained, we can closely investigate the viscous flow around a circular cylinder at the Reynolds number of 40.

(i) *Flow pattern.*

The flow pattern calculated from the values of ψ is shown in Fig. 4, together with the experimental one ($R=33.5$) which was obtained by F. Homann by means of the ultra-microscopic photography (Fig. 4a) [2]. A long

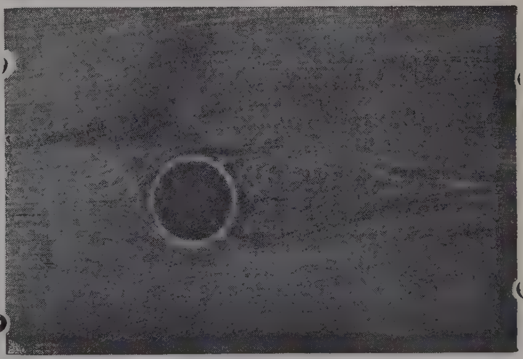

Fig. 4a. Flow pattern ($R=33.5$) F. Homann [2].

standing vortex region is seen distinctly in the theoretical flow pattern. The dotted part of the stream line $\Psi=0$ which limits the wake region has been drawn by guess, because of the shortage of data near that region. As regards the separation points and long standing vortex region, the resemblance between the theoretical and experimental flow patterns is striking, considering that the standing vortex region elongates as the Reynolds number increases.

(ii) *Vorticity distribution.*

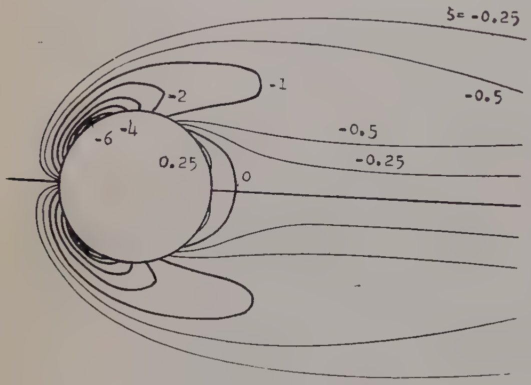

Fig. 5. Equivorticity lines.

In Fig. 5, the equivorticity lines are shown for the whole region.

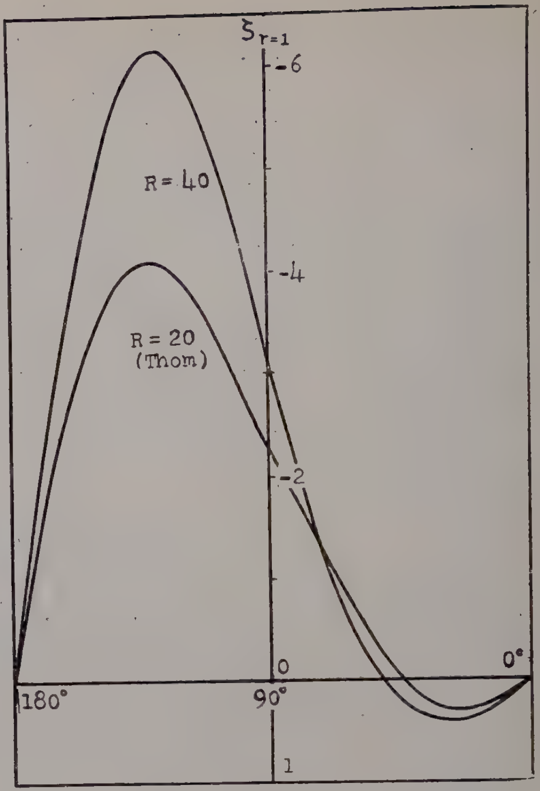

Fig. 6. Vorticity distribution over the surface.

In Fig. 6, the vorticity distribution over the surface of the cylinder is shown for the cases $R=40$ and $R=20$, the latter being taken from the numerical investigation of Thom [13].

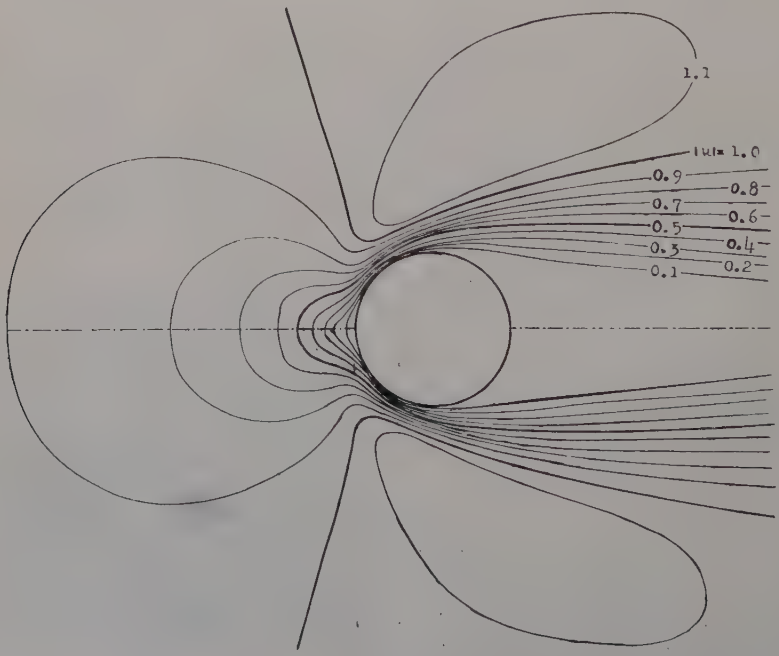

Fig. 7. Velocity distribution.

(iii) *Velocity distribution.*

In Fig. 7, the velocity distribution over the whole flow region is shown. The velocity has been calculated from the values of the stream function by means of numerical differentiation using differences as high as 6th order.

In Fig. 8, the velocity distribution in the wake is shown. We can compare the data at the point $x=4$ with the one experimentally obtained by Kovasznay ($R=34$, with laminar wake) [9]. The agreement is fairly good.

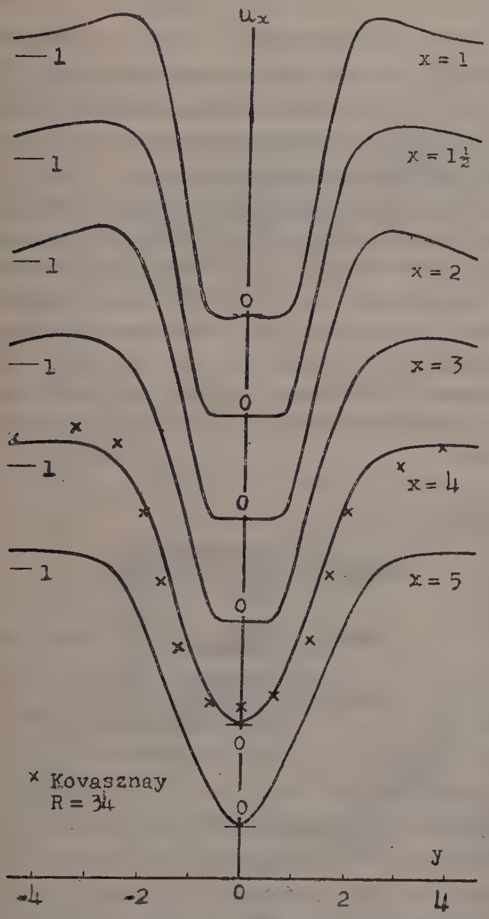

Fig. 8. Velocity distribution in the wake.

In Fig. 9, the velocity distribution along the x-axis is shown, where $|u|$ is the magnitude of velocity, and u_x is the x-component of the velocity.

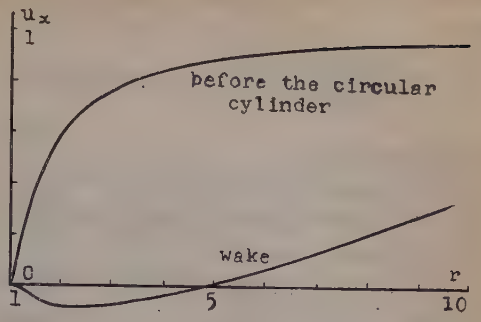

Fig. 9. Velocity distribution along the x-axis.

(iv) *Pressure and drag on the cylinder.*

The Navier-Stokes equations of motion can be written as,

$$\frac{\partial p}{\partial r}=\frac{2}{R}\left(\Delta u-\frac{u}{r^2}-\frac{2}{r^2}\frac{\partial v}{\partial \theta}\right)-\left(u\frac{\partial u}{\partial r}+\frac{v}{r}\frac{\partial u}{\partial \theta}-\frac{v^2}{r}\right), \qquad (5.1)$$

$$\frac{1}{r}\frac{\partial p}{\partial \theta}=\frac{2}{R}\left(\Delta v+\frac{2}{r^2}\frac{\partial u}{\partial \theta}-\frac{v}{r^2}\right)-\left(u\frac{\partial v}{\partial r}+\frac{v}{r}\frac{\partial v}{\partial \theta}+\frac{uv}{r}\right), \qquad (5.2)$$

where u and v are the r and θ components of the velocity, respectively, and p is the pressure.

To obtain the pressure $p(r, \theta)$ at the point (r, θ), first we seek for the value $p(1, \pi)$ using the equation (5.1) together with the relations

$$u=\frac{1}{r}\frac{\partial \Psi}{\partial \theta}, \qquad v=-\frac{\partial \Psi}{\partial r}, \qquad \zeta=-\Delta\Psi, \qquad (5.3)$$

and

$$v=0 \qquad \text{along the } x\text{-axis.} \qquad (5.4)$$

Then the equation (5.1) becomes, along the negative x-axis,

$$\frac{\partial p}{\partial r}=-\frac{2}{R}\frac{1}{r}\frac{\partial \zeta}{\partial \theta}-\frac{1}{2}\frac{\partial}{\partial r}\left(\frac{1}{r}\frac{\partial \Psi}{\partial \theta}\right)^2. \qquad (5.5)$$

Integrating (5.5), we have

$$p(1, \pi)-p(\infty, \pi)=\frac{2}{R}\int_1^\infty \frac{1}{r}\frac{\partial \zeta}{\partial \theta}\,dr+\left[\frac{1}{2}u^2\right]_1^\infty. \qquad (5.6)$$

The first term on the right hand side of (5.6) can be integrated numerically using the data of ζ on the line $Y=1.9$. Thus

$$\frac{2}{R}\int_1^\infty \frac{1}{r}\frac{\partial \zeta}{\partial \theta}\,dr=0.0713\,. \qquad (5.7)$$

The second term is clearly equal to ½, since

$$u(1, \pi)=0, \qquad u(\infty, \pi)=1.$$

Then we have

$$p(1, \pi)-p(\infty, \pi)=0.5713. \qquad (5.8)$$

Next, we seek for the pressure $p(1, \theta)$ on the surface of the cylinder. From (5.2) we have

$$\frac{\partial p}{\partial \theta}=-\frac{2}{R}\left(\frac{\partial^3 \Psi}{\partial r^3}+\frac{\partial^2 \Psi}{\partial r^2}\right), \quad \text{on the surface.} \tag{5.9}$$

On the other hand,

$$\begin{aligned}\frac{\partial \zeta}{\partial r}&=-\left(\frac{\partial^3 \Psi}{\partial r^3}+\frac{\partial^2 \Psi}{\partial r^2}-\frac{\partial \Psi}{\partial r}+\frac{\partial^3 \Psi}{\partial r \partial \theta^2}-\frac{\partial^2 \Psi}{\partial \theta^2}\right)\\&=-\left(\frac{\partial^3 \Psi}{\partial r^3}+\frac{\partial^2 \Psi}{\partial r^2}\right), \quad \text{on the surface.}\end{aligned} \tag{5.10}$$

Combining (5.9) and (5.10), we obtain

$$\frac{\partial p}{\partial \theta}=\frac{2}{R}\frac{\partial \zeta}{\partial r}, \tag{5.11}$$

and integrating it, we have

$$p(1,\theta)=\frac{2}{R}\int_{\pi}^{\theta}\left[\frac{\partial \zeta}{\partial r}\right]_{r=1} d\theta+p(1,\pi). \tag{5.12}$$

From (5.12) and (5.8), we have the pressure distribution over the surface. In Fig. 10, the pressure distribution over the surface of the circular cylinder is given in the form of pressure coefficient defined as

$$C_p=(p-p_\infty)/(\tfrac{1}{2}\rho U^2).$$

Comparison with Thom's experimental investigation [13] is made, and the coincidence is seen to be very good.

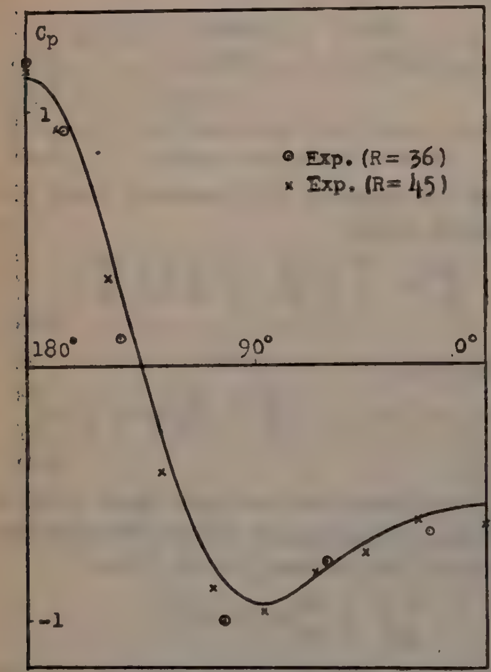

Fig 10. Pressure distribution over the surface.

The drag experienced by the cylinder can be expressed using the values of the pressure and vorticity as

$$D=-2\int_0^{\pi} p(1,\theta)\cos\theta\, d\theta-\frac{4}{R}\int_0^{\pi}\zeta_{r=1}\sin\theta\, d\theta. \tag{5.13}$$

The first and second terms in (5.13) represent the pressure drag and the frictional drag respectively. They were calculated by means of numerical integration using differences as high as 6th. The results are

$$C_{D_p}=1.0528\,, \tag{5.14}$$

$$C_{D_f}=0.5649\,, \tag{5.15}$$

and

$$C_D=1.6177\,, \tag{5.16}$$

where C_D is the drag coefficient which is defined as the ratio of drag to $(\frac{1}{2}\rho U^2 S)$, and C_{D_p} and C_{D_f} are the pressure and frictional drag coefficients respectively.

Fig. 11 gives the calculated drag coefficient together with some other theoretical and experimental results. The coincidence between our theoretical result and the experimental results is very good, but this cannot be overestimated, in view of the fact that the experiments have been carried out with the flow with periodic nature, for the régime $R=40$.

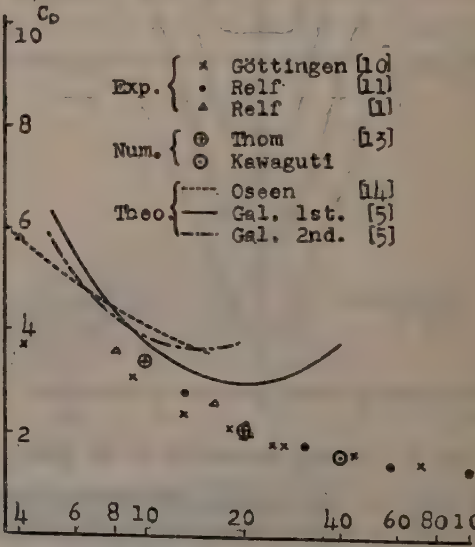

Fig. 11. Drag coefficient

(v) *Some special lines characteristic of the flow.*

In Fig. 12, some special lines characteristic of the flow are shown:

(a) The zero stream line ($\Psi=0$) for $R=40$.

(a′) The zero stream line ($\Psi=0$) for $R=20$

(Thom [13]).

(b) The maximum vorticity line which is defined as the locus of the maximum vorticity point on each concentric circle r=constant: this line may be considered as approximately representing the line along which the vorticity is carried away.

(c) The equi-velocity line: $|v|=1$.

(d) The free stream line in the discontinuous flow theory. This stream line is reproduced from Schmieden's paper [12]. This flow has recently been shown to be the limiting solution of the equations of motion for the viscous fluid when the Reynolds number increases indefinitely [4], [8].

It may be conjectured that the lines (a), (b), and (c) would coalesce into one and the same line (d), when the Reynolds number of the flow is increased indefinitely.

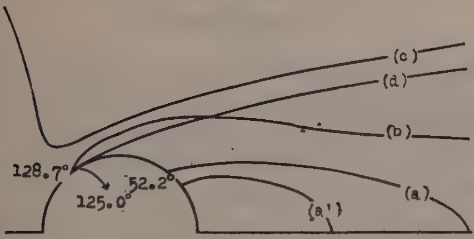

Fig. 12. Some special lines.

§ 6. Estimation of the Accuracy

The accuracy of the present investigation is estimated as follows:

(a) *The equation* (2.11). The right hand side of (2.11) is calculated from the data of ψ, by numerical differentiation, and compared with the known value of ζ at each point. The difference of these may be considered as some measure of the inaccuracy of the calculation. This amounts at most to 0.1267, where the maximum value of $|\zeta|$ is 6.1498.

(b) *The equation* (2.10). The equation (2.10) can be written as

$$F \equiv A+B=0\,, \tag{6.1}$$

where

$$A=-\frac{2X^3}{\pi}\frac{\partial(\psi,\zeta)}{\partial(X,Y)}+X^2\frac{\partial\zeta}{\partial X}\cos\frac{\pi Y}{2}$$

$$+\frac{2X}{\pi}\frac{\partial\zeta}{\partial Y}\sin\frac{\pi Y}{2}\,,$$

$$B=\frac{2}{R}\left\{X^4\Delta\zeta-\left(X^4-\frac{4X^2}{\pi^2}\right)\frac{\partial^2\zeta}{\partial Y^2}+X^3\frac{\partial\zeta}{\partial X}\right\}, \tag{6.2}$$

i.e., A and B are the inertia and friction term of the equation respectively. We have calculated A and B separately by means of numerical differentiation. The maximum value of F thus obtained is 0.2201, whereas the maximum value of A and B is 2.2378. It should be remarked that one or even two of significant digital places are lost when we calculate the differential of the values of A and B, and that rather low accuracy is restricted only near the line (b) of Fig. 12, where the gradient of ζ is very large and the differential cannot be given correctly even by means of numerical differentiation. With these estimation of accuracy, it may be allowed to conclude that our solution has fairly good accuracy.

§ 7. Discussions

We can conclude the existence of the solution of the Navier-Stokes equations of motion as well as the validity of these equations even in the case $R=40$, which is the critical Reynolds number for the existence of steady flow according to Kovasznay [9]. This conclusion is reached from the fact that our procedure of numerical integration of these equations converges with good accuracy, and that the results obtained are in good agreement with the experimental results concerning the flows with laminar wake near $R=40$.

The agreement of our results and experimental ones regarding the flow pattern, pressure and drag coefficients and so on, shows that our solution is smoothly connected to the flow with Reynolds number less than 40. The ratio C_{Dp}/C_D is 0.65, whereas it is constant and is ½ from Oseen's approximate theory [14]. This discrepancy shows that Oseen's theory can no longer be used as a good approximation for the flow near the critical Reynolds number.

On the other hand, the resemblance between the lines (a), (b), and (c) in Fig. 12 obtained from this study, and the stream line (d) in Fig. 12 obtained from the discontinuous flow theory combined with boundary layer theory [4], [8], which is believed to be the limiting laminar flow for infinite Reynolds number, suggests that the laminar flow solution of the Navier-Stokes equations exists for any Reynolds number. This is in striking contrast with the experimental result of the existence of the critical Reynolds number about 40. Thus the origin of the occurrence of von Kármán's vortex street must be seeked for in a different way.

As to the origin of periodicity of the flow, Kovasznay states thus [9]: "The vortices develop some distance down stream within the Reynolds number range 40 to 160, and are not shed directly from the cylinder. Consequently the phenomenon can properly be considered as an instability of the laminar wake, that develops up to an amplitude limit, but dies out becoming turbulent, at least in this low Reynolds number range." The result of this paper is not sufficient for the confirmation of Kovasznay's idea, but it seems to the author that it furnishes a starting point for the theoretical investigation of this interesting and important phenomenon of instability.

In Appendix, the numerical values for ψ (Table I), and ζ (Table II) at the mesh points are given for convenience.

In conclusion the author wishes to express his hearty gratitude to Professor Isao Imai for his kind suggestion and discussion in the course of this work.

Appendix

Table I. Calculated values of $-\psi$.

Y \ X	0.0	0.1	0.2	0.3	0.4	0.5	0.6	0.7	0.8	0.9	1.0
0.0	0	0	0	0	0	0	0	0	0	0	0
0.1	.768	.863	.719	.535	.416	.334	.2750	.2317	.1992	.17466	.15643
0.2	.728	1.089	1.145	.970	.786	.643	.5359	.4545	.3923	.34476	.30902
0.3	.688	1.109	1.280	1.237	1.074	.908	.7705	.6604	.5736	.50597	.45399
0.4	.647	1.071	1.278	1.337	1.258	1.114	.9690	.8429	.7385	.65427	.58779
0.5	.607	1.020	1.226	1.332	1.335	1.248	1.1227	.9959	.8822	.78595	.70711
0.6	.566	.964	1.160	1.278	1.333	1.310	1.2249	1.1136	1.0005	.89760	.80902
0.7	.526	.905	1.089	1.208	1.286	1.311	1.2741	1.1916	1.0895	.98621	.89101
0.8	.485	.844	1.016	1.132	1.218	1.271	1.2764	1.2294	1.1468	1.04942	.95106
0.9	.445	.781	.942	1.053	1.140	1.207	1.2420	1.2294	1.1716	1.08566	.98769
1.0	.404	.717	.866	.972	1.057	1.129	1.1815	1.1969	1.1649	1.09426	1.00000
1.1	.364	.650	.788	.887	.969	1.041	1.1027	1.1377	1.1290	1.07540	.98769
1.2	.324	.582	.708	.800	.877	.947	1.0105	1.0572	1.0670	1.03009	.95106
1.3	.283	.513	.625	.709	.781	.846	.9077	.9595	.9821	.95997	.89101
1.4	.243	.442	.540	.615	.670	.739	.7961	.8478	.8776	.86726	.80902
1.5	.202	.371	.454	.518	.574	.626	.6766	.7244	.7565	.75455	.70711
1.6	.162	.298	.365	.418	.465	.508	.5502	.5913	.6217	.62474	.58779
1.7	.121	.224	.275	.316	.352	.385	.4181	.4505	.4759	.48100	.45399
1.8	.081	.150	.184	.212	.236	.259	.2814	.3037	.3219	.32664	.30902
1.9	.040	.075	.092	.106	.118	.130	.1415	.1529	.1623	.16512	.15643
2.0	0	0	0	0	0	0	0	0	0	0	0

Table II. Calculated values of $-\zeta$.

$Y \backslash X$	0.0	0.1	0.2	0.3	0.4	0.5	0.6	0.7	0.8	0.9	1.0
0.0	0	0	0	0	0	0	0	0	0	0	0
0.1	0	.260	.495	.353	.261	.185	.118	.050	−.023	−.107	−.203
0.2	0	.084	.512	.667	.528	.384	.252	.120	−.020	−.176	−.350
0.3	0	.023	.251	.736	.788	.624	.435	.244	.044	−.171	−.408
0.4	0	.005	.095	.493	.924	.904	.705	.463	.204	−.069	−.366
0.5	0	.001	.027	.241	.769	1.111	1.043	.798	.489	.151	−.212
0.6	0	0	.006	.090	.473	1.068	1.328	1.210	.901	.514	.082
0.7	0	0	.001	.028	.233	.805	1.408	1.587	1.401	1.024	.562
0.8	0	0	0	.007	.096	.506	1.257	1.820	1.913	1.662	1.251
0.9	0	0	0	.001	.032	.275	.974	1.846	2.339	2.368	2.135
1.0	0	0	0	0	.009	.130	.678	1.689	2.604	3.052	3.148
1.1	0	0	0	0	.003	.052	.430	1.425	2.677	3.621	4.187
1.2	0	0	0	0	0	.016	.251	1.128	2.574	4.000	5.117
1.3	0	0	0	0	0	.005	.135	.849	2.342	4.146	5.810
1.4	0	0	0	0	0	0	.064	.612	2.028	4.048	6.150
1.5	0	0	0	0	0	0	.026	.428	1.678	3.724	6.068
1.6	0	0	0	0	0	0	.006	.287	1.318	3.206	5.540
1.7	0	0	0	0	0	0	0	.185	.968	2.533	4.586
1.8	0	0	0	0	0	0	0	.109	.633	1.749	3.274
1.9	0	0	0	0	0	0	0	.051	.313	.892	1.705
2.0	0	0	0	0	0	0	0	0	0	0	0

References

1) L. Bairstow, B. M. Cave, and F. D. Lang: Phil. Trans. Roy. Soc. London. **223** (1923) 420.

2) F. Homann: Forschung auf den Gebiete des Ingenieurwesens. **7** (1936) 1.

3) I. Imai: Proc. Roy. Soc. London. **A 208** (1951) 487.

4) I. Imai: J. Phys. Soc. Japan. **8** (1953) 399.

5) Kawaguti, M.: Rep. Inst. Sci. Technol. Tokyo. **2** (1948) 33 (in Japanese).

6) M. Kawaguti: Rep. Inst. Sci. Technol. Tokyo **2** (1948) 66 (in Japanese).

7) M. Kawaguti: Rep. Inst. Sci. Technol. Tokyo **4** (1950) 154 (in Japanese).

8) M. Kawaguti: J. Phys. Soc. Japan **8** (1953) 403.

9) L. S. G. Kovasznay: Proc. Roy. Soc. London **A 198** (1949) 174.

10) L. Prandtl: Ergebnisse der Aerodynamischen Versuchsanstalt zu Göttingen. **2** (1923).

11) E. F. Relf: A.R.C.R. & M. No. 102 (1914).

12) C. Schmieden: Ing. Arch. **1** (1930) 104.

13) A. Thom: Proc. Roy. Soc. London. **A 141** (1933) 651.

14) S. Tomotika and T. Aoi: Quart. J. Mech. Appl. Math. **3** (1950) 140.

JOURNAL OF THE PHYSICAL SOCIETY OF JAPAN Vol. 8, No. 6, NOV.—DEC., 1953

Oriented Overgrowth of Primary Oxide on α-Fe

By Ryoitiro SATO

Mitsubishi Mining and Metallurgical Laboratory,
Omiya City, Saitama Pref., Japan

(Received March 20, 1953)

Electron diffraction investigation of the primary oxide of iron (γ-Fe_2O_3 or Fe_3O_4) produced on the α-Fe layer, which was deposited on oxidized zincblende cleavage face by evaporation, showed that the orientation of the oxide with respect to α-Fe was:

$\{100\}_{\mathrm{oxide}}//\{100\}_{\mathrm{Fe}}$, $\langle 110\rangle_{\mathrm{oxide}}//\langle 100\rangle_{\mathrm{Fe}}$.

§ 1. Introduction

Concerning the crystalline orientation of the primary oxide with respect to α-Fe, Nelson[1)] found the incompletely defined condition: $[\sqrt{2}10]_{\mathrm{oxide}}//[111]_{\mathrm{Fe}}$. According to Iimori[2)], the oxide in this case is most likely γ-Fe_2O_3, although γ-Fe_2O_3 and Fe_3O_4 (both cubic) yield electron diffrac tion patterns virtually indistinguishable. As the completely defined orientation relation has been arrived at during the course of electron diffraction investigation of thin iron films, the result will be reported in the following.

§ 2. Evaporation of α-Fe onto Oxidized Zincblende Cleavage Face

When zincblende cleavage face is heated in air at red heat, zinc oxide is produced with the particular crystalline orientation[3-7)]:

1st direction : $(103)_{\mathrm{ZnO}}//(110)_{\mathrm{ZnS}}$,
2nd direction : $[010]_{\mathrm{ZnO}}//[1\bar{1}0]_{\mathrm{ZnS}}$.

Onto such a zinc oxide layer kept at about 400°C thin layer of iron, 500~1000 Å thick, was deposited by evaporation *in vacuo* (~10^{-3} mm Hg). The thickness of the deposited layer was estimated from the amount of the speck of iron to be evaporated. After the specimen was cooled to the room temperature, air was let into the evaporation apparatus, and the specimen was brought into the electron diffraction camera* to be inspected by electrons.

The diffraction photographs obtained from such a specimen are reproduced in Fig. 1. The diffraction spots are analyzed to be due to α-Fe (body centred cubic, a=2.86Å[10)]) and to its cubic primary oxide. The spots due to the latter are much weaker in intensity than those due to the former. This result is in harmony with the statement by König[9)] that the iron film formed by evaporation *in vacuo* consists of α-Fe alone, spart from the inevitable slight oxidation of α-Fe to its cubic primary oxide. The indexing of the diffraction spots due to α-Fe in Fig. 1 is shown in Fig. 2. From this it is found that the α-Fe crystallites take two equivalent orientations with respect to the substrate[11)]:

1st directions : $(112)_{\mathrm{Fe}}//(103)_{\mathrm{ZnO}}//(110)_{\mathrm{ZnS}}$,
2nd directions : $[\bar{1}\bar{1}1]_{\mathrm{Fe}}$ and
$[11\bar{1}]_{\mathrm{Fe}}//[010]_{\mathrm{ZnO}}//[110]_{\mathrm{ZnS}}$.

§ 3. Orientation of the Cubic Oxide with Respect to α-Fe

When the residual air during the process of evaporation was not so scanty as compared with that in the case of the preceding section, the oxidation of the deposited α-Fe proceeded to a considerable extent. Such an oxidized specimen was inspected by electrons with many azimuths. The diffraction photographs obtained with two of these azimuths are reproduced in Fig. 3. The calculated spacings corresponding to the diffraction spots in these photographs are presented in Table I. In

Table I. Analysis of spacings of cubic oxide.

$d_{\mathrm{obs.}}$ (Å)	*hkl*	$h^2+k^2+l^2$	$a_{\mathrm{obs.}}$ (Å)
2.96	220	8	8.38
2.51	311	11	8.33
2.10	400	16	8.40
1.72	422	24	8.43
1.61	333, 511	27	8.38
1.48	440	32	8.37
1.28	533	43	8.38
1.19	444	48	8.34
			$a_{\mathrm{obs.}}$ (mean) =8.38

---

* The diffraction camera was the same as that in the previous work[8)].

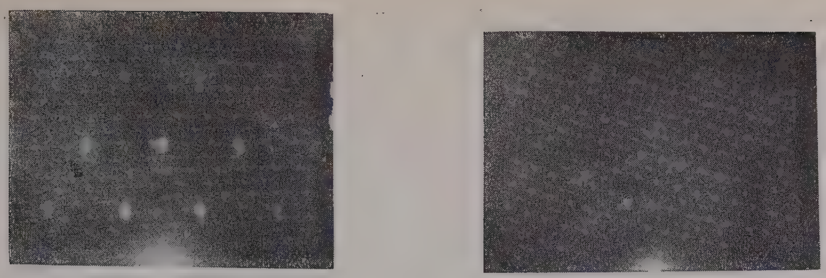

(a) (b)

Fig. 1. Electron diffraction photographs obtained from α-Fe film, 1000 Å thick, deposited onto zinc oxide layer at 400°C. (a) $\alpha=0°$, and (b) $\alpha=90°$, where α is the azimuth of the electron beam, *i.e.*, the angle between the incident beam and the $[1\bar{1}0]_{Fe}$-direction ($//[00\bar{1}]_{ZnS}$). Besides the diffraction spots due to α-Fe weaker ones due to primary oxide are seen.

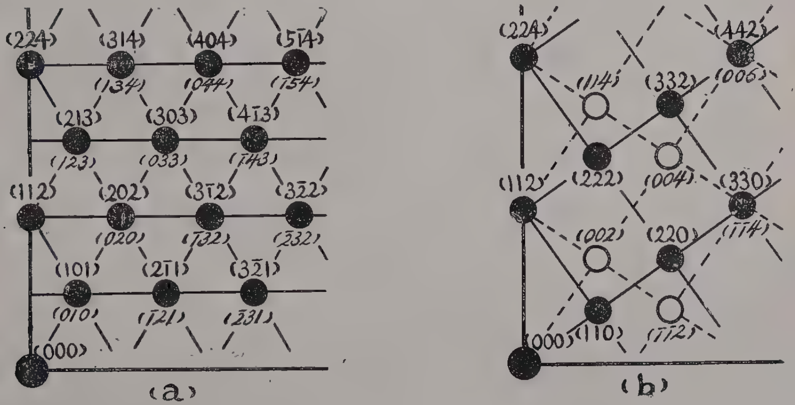

Fig. 2. Indexing of the diffraction spots due to α-Fe in Fig. 1. (a) and (b) correspond to Fig. 1 (a) and Fig. 1 (b), respectively.

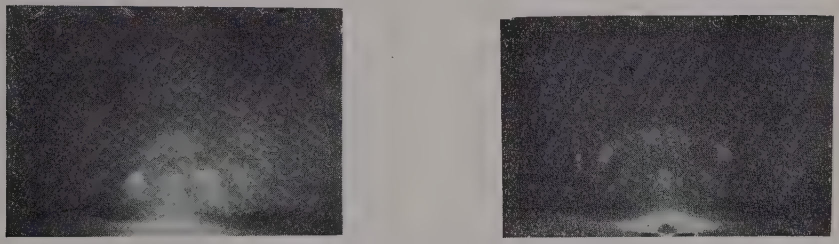

(a) (b)

Fig. 3. Electron diffraction photographs obtained from cubic oxide produced on α-Fe layer, 500 Å thick, deposited onto zinc oxide layer at 400°C. (a) $\alpha=0°$, and (b) $\alpha=90°$, where α is the azimuth of the electron beam as in Fig. 1 and in Table II.

these photographs no spot due to α-Fe was observed. The lattice constant of the cubic oxidation product as shown in Table I ($a_{obs.}$(mean)=8.38Å) is in a close agreement with that of γ-Fe_2O_3 (a=8.30Å[10]) and with that of Fe_3O_4 (a=8.374Å[10]). The electron diffraction method can hardly discriminate these two oxides from each other.

The fact that the cubic oxide (γ-Fe_2O_3 or Fe_3O_4) yields the diffraction patterns consisting of spots indicates that the oxide crystallites show some preferred orientation with respect to the α-Fe crystallites. From the arcings of the diffraction spots, however, it is known that this preferred orientation involves some tolerance. By comparing the sharpnesses of the spots in Figs. 1 and 3, the oxide crystallites are supposed to be more minute than the α-Fe crystallites.

The simplest condition, which defines the relative orientation completely and is consistent with that given by Nelson is :

$$\{100\}_{\text{oxide}} // \{100\}_{\text{Fe}} ,$$
$$\langle 110\rangle_{\text{oxide}} // \langle 100\rangle_{\text{Fe}} .$$

If this condition is assumed, six orientations of the oxide are to arise, since three are possible for one orientation of α-Fe. The calculation shows that all of the spots of $\{440\}_{\text{oxide}}$- and $\{400\}_{\text{oxide}}$-reflections, as expected from these six orientations, should appear corresponding to $\phi_{\text{calc.}}$ shown in the second and the fourth columns of Table II, respectively.

Table II. $\{440\}_{\text{oxide}}$- and $\{400\}_{\text{oxide}}$-reflections.

α	$\{440\}_{\text{oxide}}$		$\{400\}_{\text{oxide}}$	
	$\phi_{\text{calc.}}$	$\phi_{\text{obs.}}$	$\phi_{\text{calc.}}$	$\phi_{\text{obs.}}$
0.0°	9.7° 35.3° 85.2°	9° (25°) 35°	35.3° 54.7°	35° 55°
8.5°*	85.2°	—		—
19.8°	25.7°	(8°) 26°		
31.5°*		—	73.2°	—
50.8°	65.9°	(5°) (54°) 67°	65.9°	67°
60.0°	54.7°	(0°) 55° (70°)		
64.5°*	71.1°	—		—
78.8°	60.5°	(0°) 61°		(29°)
90.0°		(0°)	30.0°	30°

α: azimuth of the electron beam, *i.e.*, the angle between the incident beam and the $[1\bar{1}0]_{\text{Fe}}$ direction ($//[00\bar{1}]_{\text{ZnS}}$).

ϕ: angle on the photographic plate between the centre line and the radius from the central spot to the intensity maximum of the spot under consideration.

* With these azimuths diffraction photographs were not taken.

The observed positions of the $\{440\}_{\text{oxide}}$- and the $\{400\}_{\text{oxide}}$-spots correspond to $\phi_{\text{obs.}}$ in the third and the last columns, respectively.

In Table II the values in parentheses in the columns of $\phi_{\text{obs.}}$ do not agree with those in the columns of $\phi_{\text{calc.}}$. All of them, however, can be explained as resulting from the situation that the intensity regions of the spots are quite extended, because of the tolerance in the orientations of the oxide and of the minuteness of its crystallites, and therefore the spots are to be observed with considerable range of the azimuth of the incident beam. Further, Table II shows that the spots whose $\phi_{\text{calc.}}$ are near to 90° cannot be observed actually. However, this is well understood as a nature of electron diffraction reflection method. Apart from these two points, the values of $\phi_{\text{obs.}}$ are in good agreement with those of $\phi_{\text{calc.}}$. Also with the reflections other than $\{440\}_{\text{oxide}}$ and $\{400\}_{\text{oxide}}$ the agreement of $\phi_{\text{obs.}}$ with $\phi_{\text{calc.}}$ is almost complete.

Thus, it has been confirmed that the above simple orientation of the oxide with respect to α-Fe is the case, and that all of the possible orientations, six in all in this case, actually occur.

§ 4. Discussion

As was mentioned in the preceding section, the analysis of the electron diffraction patterns could not determine whether the cubic oxide responsible for Fig. 3 was either γ-Fe_2O_3 or Fe_3O_4. In this connection the specimen of Fig. 1 was heated in air at 250°C for 10 min. According to Iimori[2] the oxidation product under this condition is γ-Fe_2O_3. The diffraction patterns obtained from this heated specimen were similar to those of Fig. 3, though with more diffuse feature. This result indicates that of the two cubic oxides at least γ-Fe_2O_3 takes the above simple orientation with respect to α-Fe. Accordingly, in the following discussion the cubic oxide taking the above orientation will be assumed as γ-Fe_2O_3, although it remains possible that the cubic oxide in the case of Fig. 3 is Fe_3O_4.

In the structure of γ-Fe_2O_3 it is supposed that magnetite (Fe_3O_4) of spinel structure and iron oxide form solid solution[10]. The manner of rearrangement of Fe atoms during the process of the oxidation of α-Fe to γ-Fe_2O_3 would be far more complicated than in the case, for example, of oxidation of barium to barium oxide[12]. However, as is seen in Fig. 4, the arrangement of the Fe atoms on the basal plane of γ-Fe_2O_3 shows some approximate coincidence with that of α-Fe in the present relative orientation. The misfit of half the face diagonal of the cube face of γ-Fe_2O_3 ($\sqrt{2}/2\times8.30Å=5.87Å$) relative to twice the cube edge of α-Fe ($2\times2.86Å=5.72Å$) is +2.6%. This approximate coincidence may be a cause for the present relativ eorientation.

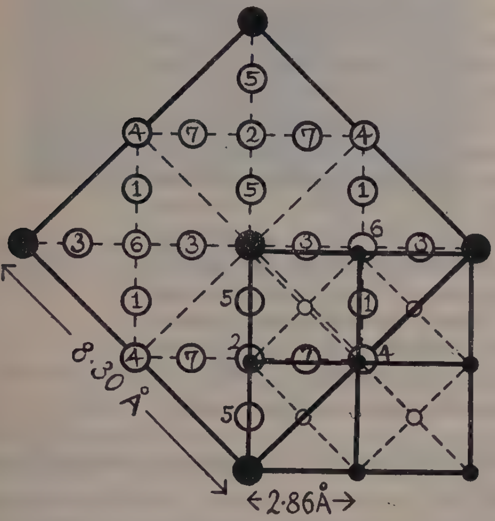

Fig. 4. Projection of the Fe atoms of γ-Fe_2O_3 and of α-Fe to their basal planes, which lie parallel to each other in the present relative orientation. Although the arrangement of the Fe atoms of γ-Fe_2O_3 has not been determined definitely, it is supposed to be very similar to that of spinel type magnetic (Fe_3O_4)10). Therefore, in drawing the figure, it is assumed to be of spinel type. Large black circle: Fe atom of γ-Fe_2O_3 on the basal plane. Large white circle to which a number n is attached: Fe atom of γ-Fe_2O_3, whose distance above the basal plane is $n/8$ in fractional parts of the cube edge. Small black circle: Fe atom of α-Fe on the basal plane. Small white circle: Fe atom of α-Fe, whose distance above the basal plane is half the cube edge.

In the direction perpendicular to the plane of the paper of Fig. 4 there is another approximate coincidence of the cube edge of γ-Fe_2O_3 (8.30Å) with three times the cube edge of α-Fe ($3\times2.86Å=8.58Å$). The misfit of the former relative to the latter is −3.3%. However, this seems not to be a primary cause for the present orientation; if this be so, the cubic lattice of γ-Fe_2O_3 should be oriented parallel to that of α-Fe.

In conclusion the author wishes to express his sincere thanks to Mr. H. Hagihara of Kobayasi Institute of Physical Research for his discussions and encouragement throughout the work.

References

1) H. R. Nelson: J. Chem. Phys. **5** (1937) 252.

2) T. Iimori: Nature **140** (1937) 278; Sci. Pap. I.P.C.R. **34** (1937) 60.

3) T. Yamaguti: Paoc. Phys. -Math. Soc. Jap. **17** (1935) 443.

4) G. Aminoff and B. Broomé: Kgl. Svenska Vetenskapsakad. Hand. **16** (1938) 3.

5) R. Uyeda, S. Takagi, and H. Hagihara: Proc. Phys. -Math. Soc. Jap. **23** (1941) 1049.

6) D. M. Evans. and H. Wilman: Proc. Phys. Soc. A **63** (1950) 298.

7) R. Sato: J. Phys. Soc. Jap. **6** (1951) 528.

8) R. Sato: J. Phys. Soc. Jap. **8** (1953) 152.

9) H. Köig: Z. Metallk. **43** (1952) 26.

10) R. W. G. Wyckoff: *Crystal Structures*, Vols. I and II, Interscience Publishers, Inc., New York, 1951.

11) R. Sato: Read at the Annual Meeting of Phys. Soc. Jap., November, 5, 1950.

12) W. G. Burgers and J.J.A.P. van Amstel: Physica **3** (1936) 1057.

JOURNAL OF THE PHYSICAL SOCIETY OF JAPAN Vol. 8, No. 6. NOV.—DEC., 1953

Study on the Intensity Anomaly of Electron Diffraction Powder Patterns from Minute Silver Crystallites

By Kazuo KIMOTO

Faculty of Science, Nagoya University, Nagoya, Japan

(Received April 2, 1953)

Electron diffraction powder patterns from extremely minute crystallites of evaporated silver show a peculiar intensity anomaly: the most remarkable part of it is that the ratio of the integral intensity of the (200)-reflection to that of the (111)-reflection is far smaller than the one calculated, and the former reflection is much broader than the latter. The anomaly can be ascribed to a stacking disorder in the (111)-plane in the minute silver crystallites. The calculated line profiles can be made to coincide with the observed ones, if the following parameters are adequately determined: α, the probability with which the stacking fault occurs; L_1 and L_2, the dimensions of the crystallites parallel and perpendicular respectively to the (111)-plane of the crystallite; and $\sqrt{\langle u^2\rangle_{AV.}}$, the amount of the average lattice distortion due to small inhomogeneous lattice distortions in the crystallites. For example they turned out to be, for one specimen, $\alpha=0.84$, $L_1=20$ Å, $L_2=47$ Å; for another specimen, $\alpha=0.70$, $L_1=14$ Å, $L_2=33$ Å and $\sqrt{\langle u^2\rangle_{AV}}=0.14$ Å.

§ 1. Introduction

It was reported by Germer and White[1] that the electron diffraction powder patterns from minute crystallites of copper evaporated in *vacuo* show an anomalous intensity distribution: *i.e.* the ratio of the integral intensity of the (200)-reflection to that of the (111)-reflection is much smaller than the one calculated. He ascribed this phenomenon to the smallness of copper crystallites; but the result of his calculation, which was obtained by applying the scattering formula of gas molecules, could not account for the integral intensity, if the particle size is so chosen that the calculated breadth of the diffraction ring is fitted with that observed.

A similar intensity anomaly was also observed by the author in the case of silver, gold and nickel; and the anomaly of silver was studied in detail in this experiment. To study this anomaly the accuracy of intensity measurement were improved by using an electron diffraction camera provided with a rotating sector; and in interpreting the observed intensity curve the idea of stacking disorder was introduced. The calculated intensity curves showed a good agreement with those observed, if the parameters representing the crystal size and the degree of stacking disorder are chosen adequately by trials.

§ 2. Experimental Procedure

The specimens of small silver crystallites were prepared on supporting Formvar films by two methods: vacuum evaporation and evaporation in nitrogen gas. In the former method crystallites of about 14 Å are obtained, when the calculated thickness of deposited silver is about 3 Å. In the latter method, the crystal size can be controlled by changing the heating temperature of the tungsten filament and the gas pressure; crystallites of about 20 Å are obtained when the temperature is about 1900°C and the pressure about 1 mm Hg. The deposit was made on both sides of the supporting film, in the first method, to increase the intensity of the diffraction pattern due to silver. The randomness of orientation of crystallites in these samples were confirmed by taking diffraction photographs with inclined incidence, the angle of which amounts sometimes up to 60°.

Transmission photographs of the specimens prepared as mentioned above and those of the supporting Formvar film only were taken by an electron diffraction camera provided with a rotating sector[2]. The applied sector was always of the type $\theta=cr$, where θ is the angle of the aperture, r the radius and c a constant. The specimen-to-plate distance of the camera was 30 cms; and the accelerating voltage was about 50 KV. An example of photographs due to a composite film (silver on Formvar) and that of Formvar alone are reproduced in Fig. 1 a and b.

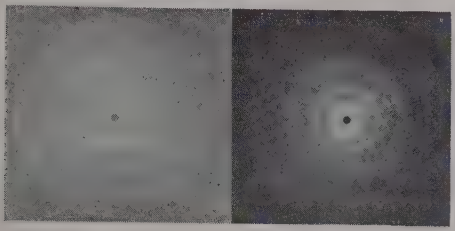
(a) (b)

Fig. 1. Electron diffraction photographs obtained by using a rotating sector.
(a) Silver on Formvar.
(b) Formvar alone.

The darkness of the pattern was measured with a Riken B-type microphotomer which was improved so that a plate can be rotated in order to avoid fluctuations in the microphotometer curve due to coarseness of the photographic emulsion. In Fig. 2 a and b microphotometer records of Fig. 1 a and b respectively are reproduced.

Fig. 2. Microphotometer records of electron diffraction patterns.
(a) Silver on Formvar (corresponding to Fig. 1a.)
(b) Formvar alone (corresponding to Fig. 1b.)

The relationship between the darkness of the plate and the intensity of the electron beam was determined by the method described by Ino[2] which is almost the identical with that previously reported by Karle[3]. In Fig. 3 a and b the intensity curves corresponding to Fig. 2 a and b respectively are shown. A smooth background curve was drawn, as shown in the figure, to exclude the background intensity.

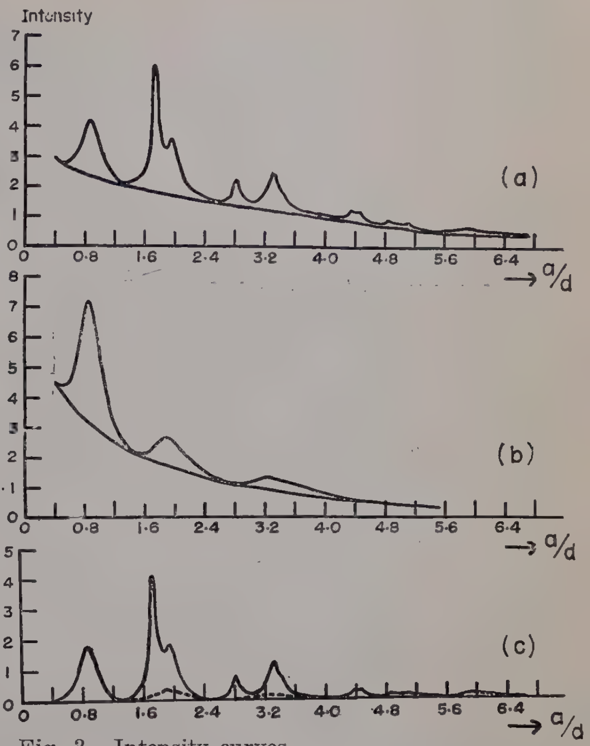

Fig. 3. Intensity curves.
(a) Silver on Formvar (corresponding to Fig. 2a).
(b) Formvar alone (corresponding to Fig. 2b).
(c) Intensity curves, background subtracted, to obtain the intensity caused by silver alone. Numerical values of the abscissa are expressed in terms of $a/d=\sqrt{h^2+k^2+l^2}$, where a and d being respectively the lattice constant and the spacing of the reflecting plane. The ordinate is expressed in arbitrary scale.

To obtain the intensity caused by silver alone from that of the composite (Fig. 3a), the part due to Formvar must be subtracted. Since the first halo in the composite pattern is due to Formvar alone, this procedure is carried out in Fig. 3c by normalizing the Formvar intensity so that the first halo coincides to each other. The result of the subtraction is shown in Fig. 4b; curves a and c are examples from other silver specimens.

To obtain the integral intensity of each reflection, the (111)- and the (200)-reflection, which overlap in Fig. 4, were analysed by assuming the symmetrical shape of the (111)-reflection. As an example the analysed curves are shown in Fig. 4b by dotted curves.

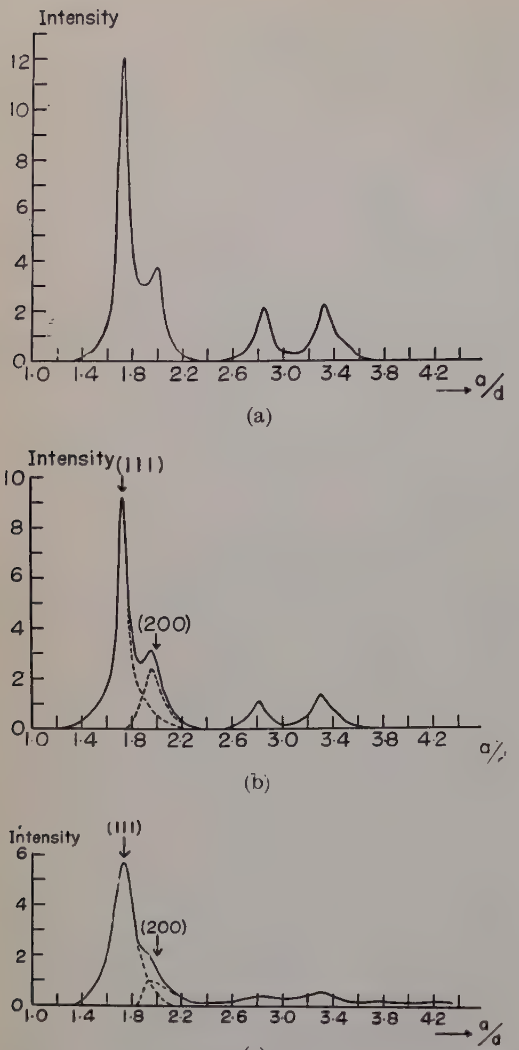

Eig. 4. Intensity curves of silver.
Curve (b) corresponds to the sample of Fig. 1a: (a) and (c) are curves from other samples. Curves (a) and (b) are obtained from samples of silver smoke produced in nitrogen, curve (c) from a sample produced by vacuum evaporation. The scale of the abscissa and the ordinate is the same as in Fig. 3.

§ 3. Experimental Results

As a measure for the intensity anomaly the measured values of the integral intensity and the half-breadth of each diffraction ring are listed in the first three lines of the Table I. The intensity of the (111)-reflection of each pattern is normalized as unity and the half-breadth is expressed in terms of a/d. In the fourth line of the Table theoretical values of the integral intensity for silver, calculated from the f-values of James and Brindley[4] and corrected for the thermal agitation at room temperature (27°C, in summer), are listed. In the last column of the Table the apparent particle size, calculated from the half-breadth of the (111)-reflection by Scherrer's formula, is given.

In Fig. 4a the integral intensity is normal, but in Fig. 4b and 4c the (200)-reflection and the (220)-reflection are much weaker than the theoretical. It is also concluded from the results of many other experiments, which are not reproduced here, that this tendency is getting stronger as the crystallites become smaller. It is also seen from the Table I that the width of the (200)-reflection is broader than that of the (111)-reflection. The shape of the (200)-reflection, shown by the dotted curve in Fig. 4b and 4c, is not symmetrical but has a long tail towards the right side.

In Fig. 4a the peak of the (200)-reflection is in the normal position; but in Fig. 4b it is shifted towards the left side, and in Fig. 4c this tendency is also evident, although this can not be seen before the analysis of the (111)- and the (200)-reflection.

§ 4. Interpretation of the Pattern

An anomalous intensity in electron diffraction powder patterns is often due to the

Table I.

	(111)		(200)		(220)		(311) + (222)		
	Intensity	Half-Breadth	Intensity	Half-Breadth	Intensity	Half-Breadth	Intensity	Half-Breadth	Grain size
Fig. 4a	1.00	0.10	0.43	0.16	0.22	0.14	0.28	0.16	46 Å
Fig. 4b	1.00	0.10	0.36	0.17	0.14	0.16	0.23	0.20	46 Å
Fig. 4c	1.00	0.20	0.19	0.26	0.13	0.36	0.17	0.32	22 Å
Theoretical Intensity	1.00		0.43		0.22		0.24		
Fig. 6a	1.00	0.14	0.38	0.20	0.19	0.20	0.22	0.21	29 Å
Fig. 6b	1.00	0.21	0.26	0.25	0.16	0.29	0.21	0.33	19 Å
Fig. 7	1.00	0.19	0.24	0.27	0.12	0.29	0.15	0.30	20 Å

dynamical effect[5], or the absorption of the electron beam by the sample[6], or the external form of the crystals[7], or the preferred orientation of the specimen.

The dynamical and the absorption effect can not explain the anomalous intensity observed here, because the anomaly should be more serious when the crystals are larger, but the present anomaly is getting more remarkable as the crystals become smaller. The effect of the external form of crystals also cannot explain the observed anomaly because, even though it can affect the shape of the line profile, it cannot change the integral intensity. Finally it is not the effect of the preferred orientation, what was proved by the experiment mentioned in § 2. Thus the cause of the anomaly must be looked for from another point of view.

It may be suggested that the stacking fault parallel to the (111)-plane of the crystal may be the cause of the anomaly.

In order to treat this problem it is convenient to choose the hexagonal axes $\boldsymbol{a}_1'$, $\boldsymbol{a}_2'$ and $\boldsymbol{a}_3'$ in the crystal instead of the cubic axes $\boldsymbol{a}_1$, $\boldsymbol{a}_2$ and $\boldsymbol{a}_3$, where $\boldsymbol{a}_1'$, $\boldsymbol{a}_2'$ and $\boldsymbol{a}_3'$ have $[\bar{1}10]$, $[0\bar{1}1]$ and $[111]$ directions respectively represented in terms of the cubic axes. Then the Miller's indices of the new hexagonal axis $(h'k'l')$ are related to those of the cubic axis (hkl) by

$$h'=\tfrac{1}{2}(k-h),\ k'=\tfrac{1}{2}(l-k),\ l'=\tfrac{2}{3}(h+k+l)\ .$$

If the stacking fault is distributed at random parallel to the (111)-plane (or the basal plane) in the crystal of the cubic (or the hexagonal) close packed structure, the intensity regions corresponding to $(h'-k')$ which are not divisible by three, are strung out along the $\boldsymbol{a}_3'^*$-axis in the reciprocal lattice space (normal to the plane of faulting) and the intensity regions corresponding to the other indices remain unaltered. (See Wilson[8].) For example eight reflections which contribute to the {111}-ring are divided into two groups: namely the one group which contains the (111)- and the $(\bar{1}\bar{1}\bar{1})$-reflection, or the (00.2)- and the $(00.\bar{2})$-reflection in the hexagonal indices; and the other group which contains the $(\bar{1}11)$-, $(1\bar{1}\bar{1})$-; $(1\bar{1}1)$-, $(\bar{1}1\bar{1})$-; and the $(11\bar{1})$-, $(\bar{1}\bar{1}1)$-reflection, corresponding respectively to the (10.2/3)-, $(\bar{1}1.2/3)$- and the $(0\bar{1}.2/3)$-type reflections in the hexagonal indices. The intensity regions of the first group are not affected by the stacking faults; but those of the second group are elongated by the faults. Six reflections which contribute to the {200}-ring are all affected by the faults.

Thus the intensity regions, when the stacking faults exist in the crystal, can be constructed around the reciprocal lattice points. To obtain a rough picture of the powder pattern produced by such intensity regions, let us rotate the reciprocal lattice around the $\boldsymbol{a}_3'^*$-axis, by which the intensity regions turn to the annular ones. The upper half of Fig. 5 shows a section of such intensity regions by a plane containing the rotation axis $\boldsymbol{a}_3'^*$. The shaded areas indicate the elongated intensity regions and the open ones the unaffected. The cubic index of each reciprocal lattice point is given in the figure. The intensity of each reflection in the powder

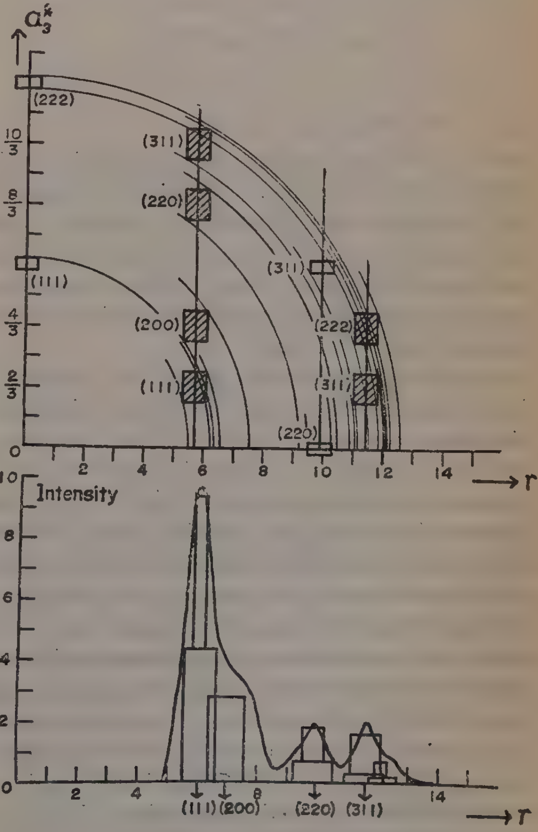

Fig. 5. Schematic representation of the intensity distribution in the reciprocal lattice space when the stacking fault exists in the crystal; and resulting profile of the powder pattern.

pattern can be easily derived from the upper figure as shown by the block diagrams in the lower half of Fig. 5. The width of the blocks can be determined from the upper figure and the height of the blocks is determined so that their area is proportional to the theoretical values of the integral intensity, taking into account the multiplicity of each reflection. These figures, though they are purely schematic, illustrate to some extent the characteristic tendency of the observed anomaly. To treat the problem quantitatively the formula given by Wilson[8] is available. The important terms of the Wilson's formula which gives the intensity distribution mentioned above are as follows:

$$
\begin{aligned}
I_0=\frac{\sin^2 n_1\pi h'}{\sin^2\pi h'}\cdot\frac{\sin^2 n_2\pi k'}{\sin^2\pi k'}\times\Bigg[&\frac{1+2K}{3}\cdot\frac{\sin^2 n_3\pi l'}{\sin^2\pi/2\cdot l'}\\
&+(1-K)Q_e\left\{\frac{2n_3(1-\rho_e^2)}{1-2\rho_e\cos\pi l'+\rho_e^2}+2\cdot\frac{2\rho_e^2-\rho_e(1+\rho_e^2)\cos\pi l'}{(1-2\rho_e\cos\pi l'+\rho_e^2)^2}\right.\\
&+(1-K)Q_0\left\{\frac{2n_3(1-\rho_0^2)}{1-2\rho_0\cos\pi l'+\rho_0^2}+2\cdot\frac{2\rho_0^2-\rho_0(1+\rho_0^2)\cos\pi l'}{(1-2\rho_0\cos\pi l'+\rho_0^2)^2}\right\}\Bigg]
\end{aligned}
\qquad (1)
$$

where h', k', l' being the Miller's indices of the hexagonal form; n_1, n_2 and n_3 being the numbers of unit cells in the direction of axes of the hexagonal structure;

$$
\begin{aligned}
Q_e&=\{1-(1-\alpha)/\sqrt{4-8\alpha+\alpha^2}\}/3\\
Q_0&=\{1+(1-\alpha)/\sqrt{4-8\alpha+\alpha^2}\}/3\\
\rho_e&=\{-\alpha+\sqrt{4-8\alpha+\alpha^2}\}/2\\
\rho_0&=-\{\alpha+\sqrt{4-8\alpha+\alpha^2}\}/2\\
K&=\cos 2\pi(h'-k')/3
\end{aligned}
$$

and α is the probability with which the fault occurs. The formula (1) holds if α is not in the immediate neighbourhood of unity. The probability α is zero when a crystal has an ordinary hexagonal close packed structure and equal to unity when a crystal has a face centred cubic structure.

In studying the anomaly of the intensity it is desirable to discuss the precise shape of the each reflection rather than just the breadth or the integral intensity. The intensity distribution given in (1) can be converted into the line profile of the powder pattern by using the method similar to that of Warren[9] which he used in the structure determination of amorphous graphite. To make the quantitative comparison with the experiment, line profiles $I(a/d)$ were calculated numerically by this method for a set of values α, L_1* and n_3. Then a correction for the thermal agitation was made, neglecting the anisotoropy of the crystal although it has lost cubic symmetry.

$$I=I_0 e^{-2M} \qquad (2)$$

where M being the ordinary Debye temperature factor. The profiles thus obtained were compared with the intensity curves obtained experimentally corresponding to Fig. 4b and 4c; and the parameters were improved by the trial and error method. The results are shown in Fig. 6a and 6b as dotted curves.

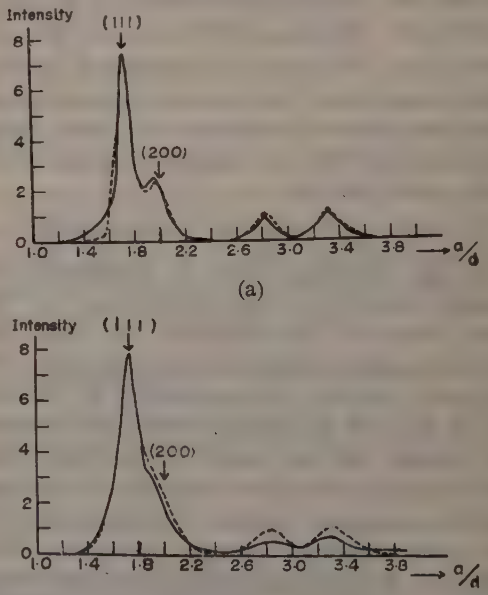

(a)

(b)

Fig. 6. Comparison between the experimental and the calculated intensity curves. The full line represents the experimental curve, the broken line the calculated. Fig. 6a corresponds to Fig. 4b and Fig. 6b corresponds to Fig. 4c.

---

* The quantity L_1 has the significance of a particle dimension in the (111)-plane of a crystal. See reference (9).

The integral intensity and the breadth of the thus calculated curves are listed in the fifth and sixth line of the Table I. In these calculations three parameters α, L_1 and n_3 were determined as in the Table II.

Table II.

	α	L_1	n_3 (or L_2)
Fig. 6a	0.84	20 Å	10 (47 Å)
Fig. 6b	0.70	14 Å	7 (33 Å)

In Fig. 6a the calculated intensity agrees with the experimental value far better than with the ordinary theoretical. As for the shift of the peak of the (200)-reflection the agreement is satisfactory. In Fig. 6b, though the main features of the intensity anomaly is explained by the dotted curve, the calculated curve lies somewhat higher than the experimental in larger scattering angles. This discrepancy can not be eliminated by changing α, L_1 or n_3.

It may be natural to suppose that a crystal, condensed from a vapor phase, would be in a quenched state having a small inhomogeneous lattice distortion; and it is likely that such a tendency would be more prominent as a crystal becomes smaller. This lattice distortion causes the effect of the so-called "frozen heat motions"; then the intensity becomes, neglecting again the anisotoropy of the crystal,

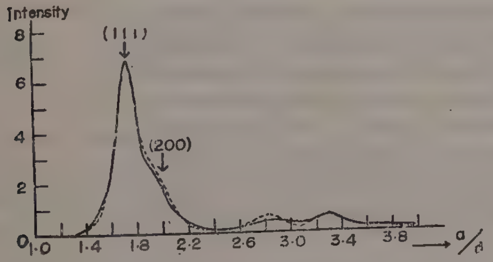

Fig. 7. The broken line represents the calculated intensity curve when the small inhomogeneous lattice distorsion is considered. $\sqrt{\langle u^2\rangle_{AV.}}=0.14$ Å

$$I=I_0e^{-2M-2M'} \qquad (3)$$

$$M'=8\pi^2\langle u^2\rangle_{AV.}\sin^2\theta/\lambda^2$$

where $\sqrt{\langle u^2\rangle_{AV.}}$ is the projection of the root mean square displacement of atoms in the direction perpendicular to the reflecting net plane due to the frozen heat motions. The best fit for the case of Fig. 6b is obtained when $\sqrt{\langle u^2\rangle_{AV.}}$ is taken to be 0.14Å. This value corresponds nearly to 600°K, the equivalent temperature of the frozen heat motions. The resulting profile is shown in Fig. 7 by the dotted one and the integral intensity is listed in the last line of the Table I.

§ 5. Discussions

In this study it is attempted to interpret the intensity anomaly of electron diffraction powder patterns from minute silver crystallites on the assumption that the stacking fault is distributed at random in the crystals.

It must be remembered, however, that some inadequate points remain in the adopted model. In Wilson's idea[8)], upon which the present analysis is based, it is assumed that n_3, the number of unit cells along the a_3'-axis (in the hexagonal structure), is large enough to permit the statistical treatment. In this case, however, n_3 turned out to be only about ten. In calculating the line profile it is also assumed that the shape of the intensity region in the reciprocal lattice space is cylindrical.

It is also pointed out by Warren and Averbach[10)] that, if too high a background curve is drawn, the effect of the apparent frozen heat motions arises. The author cannot insist on it that the frozen heat motions actually exist, because in the case of the present study, there can be no definite criterion how to exclude the background intensity in high angle region of scattering.

No comment has been made so far on the pattern of Fig. 4a. Though the integral intensity of it is normal, the line width is abnormal suggesting that a small amount of faults exists. Since, because α is near unity in this case, the approximate formula (1) can not be used, the author has abandoned the attempt of numerical calculation because the expectation on the degree of agreement seemed not to justify the labour to carry it out.

§ 6. Acknowledgement

The author expresses his best thanks to Prof. R. Uyeda for his continual guidance and encouragement throughout this work. He is indebted to Mr. T. Ino for the loan of the sector camera and for his valuable discussions; also to Mr. T. Fukazu for his assistance in some stages of this experiment. The financial aid for this research has been furnished by the Ministry of Education in a Grant in Aid of Scientific Research.

References

1) L. H. Germer and A. H. White: Phys. Rev. **60** (1941) 447.
2) T. Ino: Jour. Phys. Soc. Japan **8** (1953) 92.
3) I. L. Karle and J. Karle: Jour. Chem. Phys. **18** (1950) 957.
4) International Tables for the Determination of Crystal Structures. Vol. 2, p. 572.
5) M. Blackman: Proc. Roy. Soc. **A 173** (1939) 68.
6) L. H. Germer and A. H. White: Jour. Chem. Phys. **9** (1941) 492.
7) R. W. James: The Optical Principles of the Diffraction of X-Rays. G. Bell and Sons Ltd. (1950) p. 531.
A. R. Stokes and A. J. C. Wilson: Proc. Camb. Phil. Soc. **38** (1942) 313.
8) A. J. C. Wilson: Proc. Roy. Soc. **A 180** (1942) 277.
9) B. E. Warren: Phys. Rev. **59** (1941) 693.
B. E. Warren and B. L. Averbach: Jour. App. Phys. **21** (1950) 595.
10) B. E. Warren and B. L. Averbach: Imperfections in Nearly Perfect Crystals. (1952) p. 152.

JOURNAL OF THE PHYSICAL SOCIETY OF JAPAN Vol. 8, No. 6, Nov.—Dec., 1953

An Investiagtion of Thermocouple Psychrometer, I

By Suekichi KAWATA and Yoshirō ŌMORI

Department of Applied Physics, Faculty of Engineering,
Kyōto University

(Received May 9, 1953)

Properties and use of thermocouple psychrometers consisted of fine wires of constantan and manganin have been studied. In Part I various effects on psychrometric measurements have been examined experimentally such as transference of heat through wires and also through air between dry- and wet-junctions, ventilation, lag of indication, and conditions have been shown to avoid misleading causes. The thermocouple psychrometer is of rapid response owing to its small thermal capacity, and its wet-junction is cooled sufficiently by slight ventilation mostly due to its small size which makes effect of radiation on wet-junction small.

§ 1. Introduction

For psychrometric determination of humidity in air it is generally accepted to use the following formula

$$p=p_m'-AP(\theta-\theta_m')\,, \qquad (1)$$

where θ and θ_m' are respectively temperature of dry- and wet-bulbs in °C, and P is atomospheric pressure, p and p_m' are respectively water vapour pressure in question and saturation pressure at θ_m' all in mm Hg, and A is the so-called psychrometer constant. This formula can be derived from the condition of thermal equilibrium of a wet-bulb. We may put $Q_a=\kappa_a(\theta-\theta_m')$ for the rate of transfer of heat by conduction and convection from surrounding air, $Q_r=\kappa_r(\theta-\theta_m')$ for that by radiation and $Q_c=\kappa_c(\theta-\theta_m')$ for that by conduction through the stem of the wet-bulb thermometer, where κ_a, κ_r and κ_c are constants of proportionality. Again we may take the latent heat lost by evaporation of water from the wet-bulb $Q'=\gamma L(D_m-D)$ where D_m and D are respectively absolute saturation humidity at θ_m' and absolute humidity in the air, L is the latent heat of vaporisation of water and γ is a constant of proportionality. Thus, if we neglect the sensible heat used in raising temperature of water vapour evaporated from the wet-bulb, we have for the condition of equilibrium

$$\gamma L(D_m - D) = (\kappa_a + \kappa_r + \kappa_c)(\theta - \theta_m'), \qquad (2)$$

and by making use of the relation

$$D = 0.622\rho \frac{p}{P}, \qquad (3)$$

where ρ is the density of the air at θ and P, we obtain

$$p - p_m' = -\frac{(\kappa_a + \kappa_r + \kappa_c)}{0.622\rho\gamma L} P(\theta - \theta_m'). \qquad (4)$$

Again, if conduction of heat through the stem is excluded by some means, the relation will be written as

$$p = p_m' - \frac{\kappa_a}{0.622\rho\gamma L}\left(1 + \frac{\kappa_r}{\kappa_a}\right) P(\theta - \theta_m'), \quad (5)$$

which will be made identical with (1) by putting

$$A = A_a(1 + (\kappa_r/\kappa_a)) \text{ and } A_a = \kappa_a/0.622\rho\gamma L. \qquad (6)$$

The factor $(1+(\kappa_r/\kappa_a))$ shows effect of radiation on the wet-bulb. Now, it is well known that temperature of a wet-bulb is effected by ventilation. The temperature is decreased to some extent with increasing speed of wind, then becoming nearly constant with sufficient ventilation. The wet-bulb temperature in the last state is taken as standard in a sense for psychrometric measurement and used for θ_m' in formula (1). In unventilated condition, depression of temperature of a wet-bulb from that of a dry-bulb frequently shows only 70–80% of that under sufficient ventilation, and it is not very unusual that formula (1) gives relative humidity differing 10% or more from a correct value. With an Assmann aspriation psychrometer which is widely used as a standard psychrometer, relative humidity is calculated by using wet-bulb temperature under a wind of 2.5 m/sec in Sprung's formula. But frequently it may be inconvenient or difficult to pass a wind of 2.5 m/sec over a wet-bulb. To get rid of necessity of ventilation of such high speed and minimize lag of indication experienced with a mercury-in-glass thermometer, use of thermometers of other sorts has been tried. Excellent characteristics are expected especially for a fine wire thermocouple thermometer, but so far as we know the most detailed work about it has been that performed by Powell[1)] referring to Kettenacker's theory[2)] and we have intended to advance the researches furthermore.

§ 2. Manufacture of Thermocouple Psychrometers and Procedure of Measurements

As thermocouple wires we have used well-annealed constantan and manganin wires of diameter of about 0.1, 0.2, 0.3 and 0.6 mm, and made butt-jointed junctions with silver solder. In the case of wires of 0.1 mm junctions were difficult to make and they lumped larger rather than those made of wires of 0.2 or 0.3 mm. A junction corresponding to a wet-bulb was covered with a fine cotton thread washed in alcohol and in boiling water, and was moistened with a small quantity of distilled water. Care was taken to use water cooled nearly to expected wet-bulb temperature and to wait a time till thermal equilibrium was established. For measurements of humidity two sets of thermocouples were used, one being consisted of wet- and dry-junctions differentially connected and the other making a separate dry thermocouple, and thermoelectromotive forces were measured with a precision type potentiometer of Yokogawa Seisakusho with the smallest scale of 0.5 μV and galvanometers of R-B, R-C and sometimes M-E type of Shimadzu Seisakusho. The necessity of such a high precision potentiometer and a sensitive galvanometer and indirect reading of temperature are the weak points of a thermocouple psychrometer. Calibration of thermocouples was performed with a mercury-in-glass thermometer graduated to 0.1°C tested with special care at the Ōsaka Meteorological Observatory.

§ 3. Experiments about Influences on the Indication of Thermocouple Psychrometers

(i) *Effect of conduction of heat through wires.*

Owing to conduction of heat, distribution of temperature on a wire about a wet-junction appears as shown in Fig. 1. So, in order to prevent the junction from being warmed by this cause, it must be situated at distances more than a and b in the figure from the ends of the moistened thread. To know the necessary lengths a and b, which may be assumed nearly equal in the present case since wires of nearly equal thermal conductivity and size are used, we took two

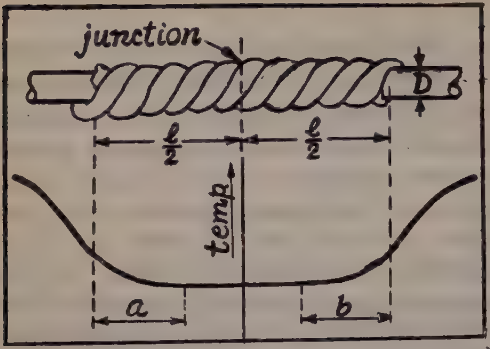

Fig. 1. Distribution of temperature along a thermocouple wire about a wet-junction.

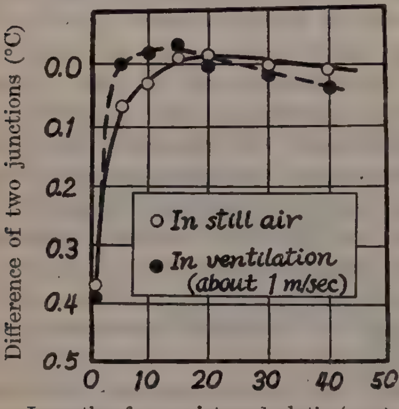

Length of a moistened cloth (mm)

Fig. 2. Variation of temperature of a wet-junction with length of a moistened covering.
Diameter of the wire: 0.1 mm.
Thickness of the covering: 0.15 mm.

differentially connected wet-junctions, having covered one of them (taken as standard) with a thread to sufficient length—in reality, 5 cm on each side of the junction—and the other (test junction) to various lengths, and measured difference of their temperature. Fig. 2 shows one of the results with a wire of 0.1 mm covered with a thin thread. The thickness of the covering was estimated with a comparator as 0.15 mm. The necessary minimum length of the wet covering is determined from the point where the difference of temperature, indicated by the ordinate, becomes zero. Thus, with a wind of 1 m/sec it is found to be 5 mm in total length, but without ventilation it should be more than 13 mm and yet there is possibility that the standard junction may have not been cooled sufficiently. Summary of results for wires of 0.2 and 0.3 mm and also for a covering 0.4 mm thick is shown in Table I. The figures shown in ( ) are values for a wire of 0.1 mm with a covering of 0.4 mm made of a thicker thread and indicate that a longer covering is necessary with thicker threads. In the following experiments the thinner thread was used always whenever no remarks are made. Next, we should be cautious so that a dry-junction may not be cooled by a moistened part. This effect was examined as follows. One junction (reference junction) was kept at constant temperature by immersing it in a mixture of ice and water, and the other junction (test junction) was placed in the air. A thread was wrapped on the wire near the test junction, and was moved at various places thus varying the distance of the end of the moistened thread from the junction. Fig. 3 gives one of the results showing a relation of depression of temperature of a dry-junction and distance between

Table I. Minimum length of a wet-covering necessary to avoid effect of conduction of heat through a wire.

Diameter of wire	0.1 mm	0.2	0.3
With ventilation	About 5 (10) mm	20	20
Without ventilation	13 (20)	23	25

Figures out of ( ) are for a covering of 0.15 mm thickness and those in ( ) are for that of 0.4 mm thickness.

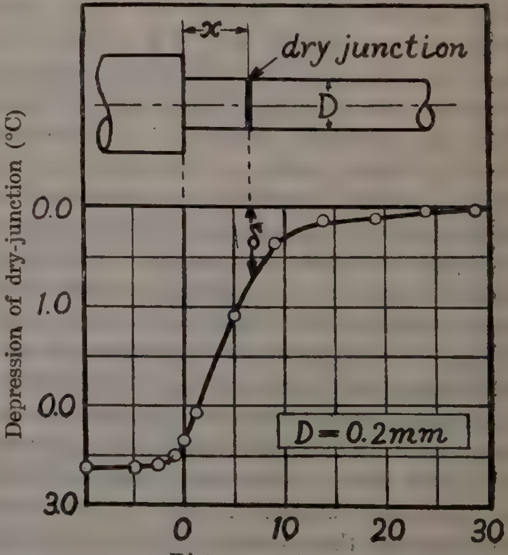

Distance x (mm)

Fig. 3. Depression of temperature of a dry-junction when a wet-covering is moved at various places near the junction. (In still air.)

the junction and the nearer end of a wet covering. Since the thermocouple consists of wires of nearly equal thermal conductivity and thickness, and the junction is only slightly thicker than wires themselves when they are more than 0.2 mm thick, we may regard it as a single wire of uniform thickness. Then, if we call temperature of the junction θ, temperature of the air θ_0 (The condition that the air near the junction is of uniform temperature will not hold strictly, but it may be assumed approximately.), temperature of the end of the moistened thread θ', conductivity of the wire λ, diameter D, coefficient of heat-transfer between the wire and the surrounding air α, then depression of temperature δ of the junction will be found, by solving the equation

$$\frac{d^2\theta}{dx^2}=\frac{4\alpha}{\lambda D}(\theta-\theta_0)\,, \qquad (7)$$

as

$$\delta=(\theta_0-\theta)=(\theta_0-\theta')e^{-2\sqrt{\frac{\alpha}{\lambda D}}\cdot x} \qquad (8)$$

From this a linear relation will be expected between $\log\left|\frac{\delta}{\theta_0-\theta'}\right|$ and x. This seems to be ascertained by Fig. 4, and values of x are shown in Table II where δ becomes 1% of $\theta_0-\theta'$ for wires of 0.1 mm (In this case the above assumption made for calculation may be questionable), 0.2 mm and 0.6 mm. The necessary separation will be estimated approximately in this way. Thus it will not be a difficult matter to make the effect of conduction of heat sufficiently small by adequate selection of length of a moistened thread and distance between two junctions according to required accuracy and conditions of measurements.

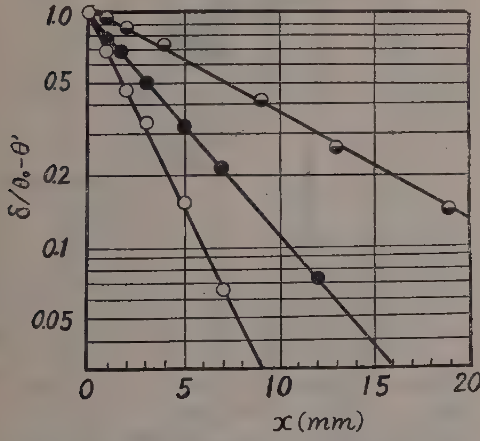

Fig. 4. Relation between $\delta/(\theta_0-\theta')$ and x.
○: 0.1 mm; ●: 0.2 mm; ◒: 0.6 mm

Table II. Minimum length of a wire between a dry-junction and the nearer end of a wet-covering necessary to avoid cooling effect through the wire.

Diameter of wire	Length which makes $\frac{\delta}{\theta_0-\theta'}=\frac{1}{100}$
0.1 mm	About 12 mm
0.2	22
0.6	46

(ii) *Effect of ventilation.*

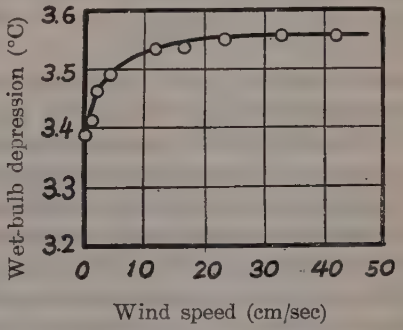

Fig. 5. Relation between depression of temperature of a wet-junction and speed of a wind. Diameter of the wire = 0.1 mm; thickness of the wet-covering = 0.15 mm; temp. of the dry-junction = 11.5°C.

A thermocouple covered with a moistened thread to 2 cm on each side of a junction was attached vertically to a horizontal arm which was made to rotate about a vertical axis fixed in a glass desiccator maintained at constant humidity. Fig. 5 shows the relation between the depression of temperature of the wet-junction and the speed of wind in a certain condition of the air for a wire of 0.1 mm. It will be seen that the temperature of the wet-junction experiences maximum depression by a wind of about 20 cm/sec, and that it stands about 0.15°C higher when ventilation is not made. Examinations for wires of 0.2 and 0.3 mm have shown similar results. Next, by making use of the data of Fig. 5 a relation was obtained between speed of a wind and "degree of depression of temperature" of a wet-junction, which means the ratio

$$\frac{\text{actual depression of temperature}}{\text{maximum depression of temperature}}\,,$$

as shown by the full line in Fig. 6. The dotted curve in the figure is drawn by the results of Powell[1] with a mercury-in-glass thermometer where speed of a wind is shown in ( ). It will be seen that a wind of more than 3 m/sec, i.e., ten times faster than the case of the thermocouple psychrometer, has to be passed to get maximum depression of wet-bulb temperature. That the wet-junction of a thermocouple psychrometer undergoes maximum depression by a very slow wind is one of the merits of this psychrometer, and the error will be relatively small even when it is used in a place where only very weak ventilation is possible or ventilation is wholly impossible, and the error accompanied then may be estimated approximately. Here we would like to add some remarks. The change of depression of wet-bulb temperature with ventilation is inferred to be due almost to the effect of radiation. That wet-bulb temperature has arrived at the state of maximum depression indicates only that the effect of radiation (κ_r/κ_a) has nearly ceased to alter with wind velocity. In this state effect of radiation may have become fairly smaller indeed, but may not be said negligibly small. It may be noticed that change of temperature of a wet-bulb due to change of 1% of κ_r/κ_a will be within limits of error in ordinary measurements owing to accuracy of a thermometer and unsteadiness of temperature and humidity of air.

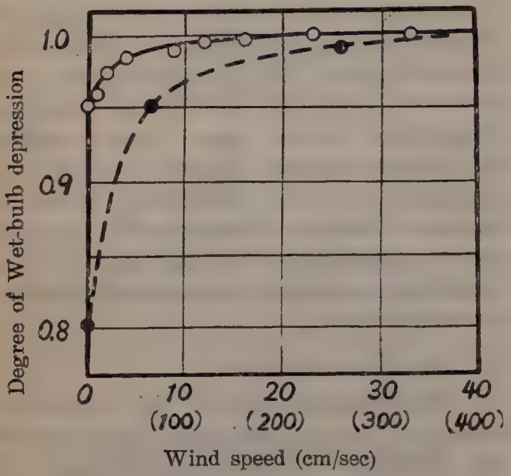

Fig. 6. Relation between degree of depression of temperature of a wet-bulb and speed of a wind.
○ Wet-junction of a thermocouple (Diameter of the wire=0.1 mm; thichness of wet-covering=0.15 mm; dry-bulb temp.=11.5°C.).
● Wet-bulb of a mercury-in-glass thermometer, plotted by the data of R. W. Powell, wind speed being indicated in ( ).

(iii) *Effect of transference of heat through air between dry- and wet-junctions.*

To measure humidity in a narrow space it may be often wanted to place dry- and wet-bulbs close together, but then there may be fear of cooling of the dry-junction by the air surrounding the wet-junction. This effect of transference of heat through air was studied in the following manner. A test dry-junction was put at various positions about a wet-junction, the both parts of wires being held horizontally. Fig. 7 (A similar figure has been shown by Powell[1].) shows curves

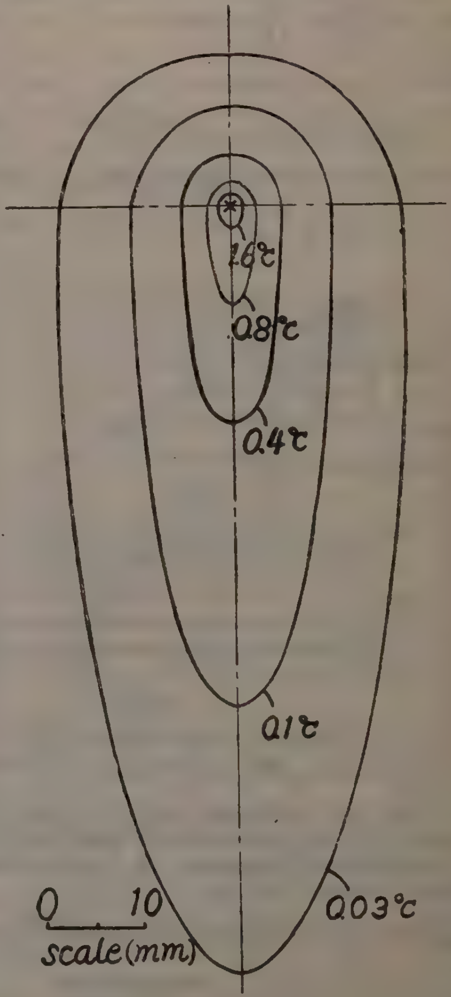

Fig. 7. Curves of equal depression of temperature of a dry-junction placed near a wet-junction (indicated by ×) in still air.

of equal depression of temperature of the dry-junction in still air. The mark × indicates the position of the wet-junction and numerals given to individual curves show depression of temperature relative to the normal dry-bulb temperature. Actually the curves may not be exact as the observed points are not numerous but general features may be represented. From the curves it will be seen that distance of two isothermal air layers about the wet-junction is nearly equal at the upper and horizontal sides, but is much larger at the lower side due to downward stream of cooled air about the wet surface. In this way necessary distance to separate the two junctions will be found in still air. However, further experiments show that in ventilated conditions the dry-junction may be brought at a windward position about 2 mm from the wet-junction without appreciable cooling. Special care should be taken for multiply-connected thermocouples used to raise sensitivity of thermocouple psychrometer to arrange in proper situation. It is often stated that owing to the small size the thermocouple psychrometer may be used for measurement of humidity in a narrow space, but there is a question about this expression. For, so far as there is a wet-bulb, water vapour will evaporate from it until saturation is reached, and naturally the humidity of the space will increase if there is no wind to carry the vapour away from there. Again, when a wet-bulb is placed near a wall, free convection will be prevented in some degrees, and humidity will be increased locally. Fig. 8 shows the results that temperature of a wet-junction was raised when it was put in various distances above (○) and below (◒) a horizontal metal plate and also sideways a vertical plate (●)

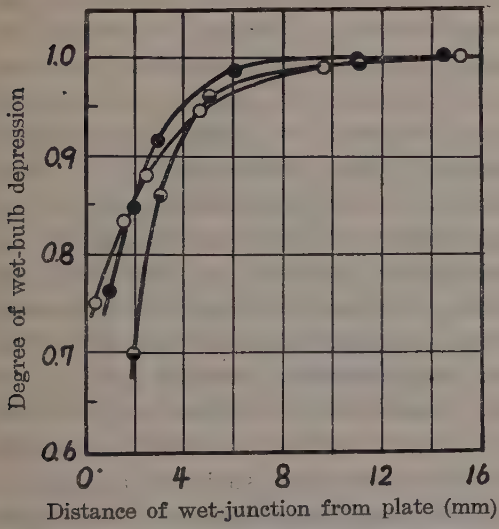

Fig. 8. Relation of degree of depression of a wet-junction placed in various positions near a metal plate. (In still air.)

(iv) *Lag of indication of temperature.*

Since the thermal capacity of this thermocouple psychrometer is far smaller than an ordinary mercury-in-glass thermometer, it is very useful to know rapid change of humidity. Lag of indication of temperature is mainly due to a wet-bulb, and we investigated it by the following procedure. Both junctions of a thermocouple were made as wet-junctions, and one of them (reference junction) was always exposed to the air, while the other (test junction) was covered with a small glass cap initially and was uncovered suddenly after a while. Thus change of electromotive force between two wet-junctions was examined with an electromagnetic oscillograph of Yokogawa Seisakusho using a vibrator of F-type. Fig. 9 shows an example of the oscillograms. The electromotive force or the temperature difference seems to vary exponentially. Then, taking the temperature at time t as θ, the initial temperature of the test junction as θ_1 and the final temperature or the reference temperature as θ_2, and assuming the relation

$$-\frac{d\theta}{dt}=\frac{1}{k}(\theta-\theta_2), \qquad (9)$$

we will have

$$\frac{\theta-\theta_2}{\theta_1-\theta_2}=e^{-t/k}, \qquad (10)$$

where k represents the lag constant or the time during which θ will become so that $(\theta-\theta_2)/(\theta_1-\theta_2)=1/e$. Fig 10 shows some results under various conditions. The curves a, b, c and d are purposely shifted somewhat to the right to avoid confusion. In ventilated conditions linear relations seem to hold between $\log\left|\frac{\theta-\theta_2}{\theta_1-\theta_2}\right|$ and t as expected from (10), but the curve b in an unventilated condition shows an irregular course affected by slight disturbances of the air. The horizontal

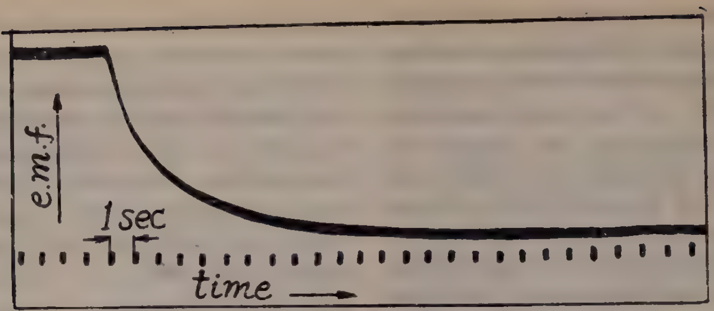

Fig. 9. Oscillogram showing lag of indication of a wet-junction.

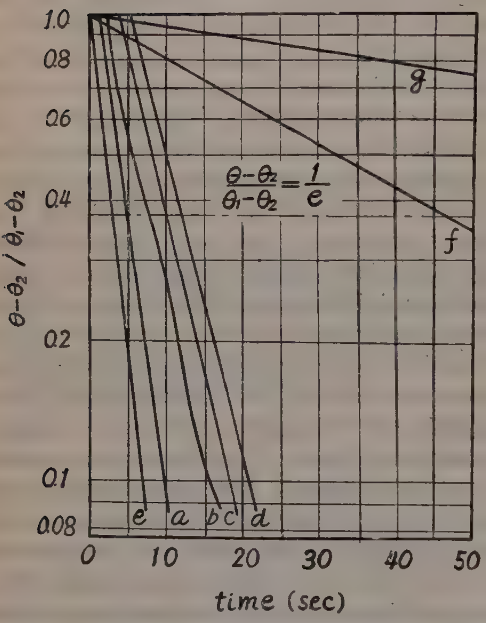

Fig. 10. Curves showing lag of indication of temperature of wet-junctions in various conditions.

- a. Wire of 0.1 mm, thinner thread, with slight ventilation.
- b. Wire of 0.1 mm, thinner thread, in still air.
- c. Wire of 0.1 mm, thicker thread, with slight ventilation.
- d. Wire of 0.3 mm, thinner thread, with slight ventilation. (For the curves a, b, c and d the air about the test junction was varied from 8°C, 100% R.H. to 8°C, 50%.)
- e. Wire of 0.1 mm, thinner thread, with slight ventilation. (The air was varied from 35°C, 100% R.H. to 8°C, 55% R.H.)
- f. Wet-bulb of a mercury-in-glass thermometer, with wind of 1 m/sec.
- g. Wet-bulb of a mercury-in-glass thermometer, in still air.

chain line indicates the line $(\theta-\theta_2)/\theta_1-\theta_2)=1/e$. For a wire of 0.1 mm under slight ventilation (curve a) $k\doteqdot4$ sec, and for a wire of 0.3 mm (curve d) $k\doteqdot7$ sec. It may be seen that k will increase with diameter of a wire and thickness of a moistened cloth, and will decrease by ventilation. Moreover, it seems to decrease with the amount of change of either temperature or humidity. For comparison test was made about a wet-bulb of a mercury-in-glass thermometer, and k was found to be about 50 sec even under a wind of 1 m/sec as shown by the curve f.

(v) *Effect of radiation.*

Lastly we must consider effect of radiation on the wet-junction from surrounding air and other substances. This has an intimate connection with the effect of ventilation described in (ii). Ideally it is desirable to make the effect as small as possible. But with a mercury-in-glass thermometer the effect seems to be very large unless a wind of very high velocity is used. For example the experiments of Skinner[3] and Yamamoto and Yamamoto[4] seem to indicate that the amount of heat transferred to a wet-bulb by conduction and convection through still air and that transferred by radiation may be of the same order. And yet it is difficult to calculate the magnitude with sufficient accuracy to apply for actual measurements. To minimize the effect experimentally it is advisable to provide a wet-bulb with a small metal tube whose inner surface is polished and outer surface is covered with a moistened cloth. The device has, however, some difficult points in practice such as complexity of the instrument, introduction of a large amount of moisture in the space especially in the cylinder without good ventilation. But it is inferred that the effect of radiation will decrease when the size of a wet-bulb decreases. If we denote coefficient of transfer of heat due to convection and conduction through air by h_a and that due to radiation by h_r, κ_r/κ_a is equal to h_r/h_a and the correction term for psychrometer constant by radiation becomes $1+(h_r/h_a)$, in which h_r is independent of wind velocity and also of size of a wet-bulb, but h_a depends on the both factors, and increases with increase of wind velocity and with decrease of size of a wet-bulb. The functional relations may be illustrated, for instance, by Hilpert's researches about heat transfer on circular cylinders⁵⁾, and it will be infered that the wet-junction of the thermocouple psychrometer will be cooled sufficiently by slight ventilation mostly due to its small size, which makes h_r/h_a small. The details will be discussed in a forth-coming Part II.

In conclusion, we wish to express our cordial thanks to the Ministry of Education for a grant-in-aid to the present research.

References

1) R. W. Powell: Proc. Phys. Soc. London **48** (1936) 406.

2) L. Kettenacker: Zeits. f. Instrumentenkunde **52** (1932) 319.

3) S. Skinner: Proc. Phys. Soc. London **34** (1922) lxii.

4) G. Yamamoto and A. Yamamoto: Ōyobtsuri (Jour. App. Phys. Japan, in Japanese) **16** (1947) 100.

5) E. R. G. Eckert, "Introduction to the Transfer of Heat and Mass," McGraw-Hill Co., 1950, p. 144.

JOURNAL OF THE PHYSICAL SOCIETY OF JAPAN Vol. 8, No. 6, NOV.—DEC., 1953

Fine Structure Due to Refraction Effect in Electron Diffraction Pattern of Powder Sample

Part I. Fine Structure given by Magnesium and Cadmium Oxide Smoke having a Fibrous Orientation

By Goro HONJO

Tokyo Institute of Technology, Oh-okayama, Tokyo

(Received June 16, 1953)

Fine structures due to refraction effect in electron diffraction patterns of cubic magnesium and cadmium oxides are studied when the sample have a fibrous orientation around [001] axis and the electron incidence is nearly perpendicular to the axis. In the case of magnesium oxide, most of the reflexions split into doublets corresponding to the ordinary refraction effect due to a mean inner potential of about 15~16 volts; (002) reflexion, however, splits into quartet corresponding to the double refraction effect, which was formerly pointed out by Sturkey, the separation of which is also in accordance with the theoretical expectation. The intensities of the two spots corresponding to a double refraction are found to be remarkably different; the spot of larger deviation is weaker than that of smaller deviation. In the case of cadmium oxide, though the fine structures of the fibrous reflexion are less apparent than in the case of magnesium oxide, it is noted the fact that the (111) reflexion splits only into doublet showing anomalously small separation, although well separated quartet according to a large double refraction effect is expected. The doublet, however, is to be considered as the two inner spots of the quartet, while the outer two are inappreciably weak on account of a much exaggerated intensity difference between the doubly refracted electron rays than that of (002) for magnesium oxide.

§ 1. Introduction

The higher resolution attainable by recent electron diffraction cameras has revealed in Debye-Scherrer rings fine structures due to the refraction of electrons at surfaces of powder particles. This was noted at first for magnesium oxide and cadmium oxide smokes[1]. The present author[2] as well as Cowley and Rees[3] have discussed the effect in some details according to the simple theory of the refraction of electrons, in which a crystal is assumed to have a constant refractive index μ for electrons given by

$$\mu=\sqrt{(E+V_0)/E}=1+\delta_0, \quad \delta_0=V_0/2E, \tag{1}$$

where E is the accelerating potential for the electrons, V_0 is the mean inner potential of the crystal and δ_0 is the unit increment of the refractive index, which is of the order of 10^{-4} for E of $3\sim5\times10^4$ volts, since V_0 is of the order of 10 volts for most of crystals.

Sturkey[4] has pointed out an effect that the fine structure should be further duplicated by the double refraction effect as expected from the dynamical theory of electron diffraction[5]. According to this theory the refractive index of a crystal depends not only on the mean inner potential V_0 but also on the coefficient V_h of Fourier expansion of the periodic inner potential of the crystal, which is given by the relation

$$V_h=\frac{e}{\pi|\boldsymbol{h}|^2v}\sum_j(Z_j-f_j)\cdot\exp-2\pi i(\boldsymbol{h}\cdot\boldsymbol{r}_j), \tag{2}$$

where e is the electronic charge, v, the volume of the unit cell of the crystal, Z_j, f_j and $\boldsymbol{r}_j$ are the atomic number, the atom form factor and the position of the j-th atom in the cell respectively and $\boldsymbol{h}$ is the reciprocal lattice vector corresponding to the Fourier coefficient. Sturkey has concluded that, when a reflexion due to $\boldsymbol{h}(h_1h_2h_3)$ net plane takes place, the refractive index of the crystal should be given by

$$\mu^{(1),(2)}=1+\delta_0\pm\delta_h, \tag{3}$$

where superscripts (1) and (2) correspond to + and − signs respectively and

$$\delta_h = |V_h|/2E \ .$$

The two values $\delta_0 \pm \delta_h$ of the unit increment of the refractive index correspond to a double refraction effect. Kato⁶⁾ has developed a more rigorous theory than that given by Sturkey, by extending Bethe's dynamical theory of electron diffraction. The experimental observation for the double refraction effect, however, seems to be insufficient yet.

The present author has performed observations for the fine structure of diffraction spots due to refraction effect and reported some results in a brief communication⁷⁾. In the following papers a fuller description will be given. In Part I, we will discuss the fine structures due to smoke samples of magnesium and cadmium oxide having a fibrous orientation, which are of interest because they correspond to a case of simple geometrical condition and show an illustrative example of the double refraction effect. In Part II, a detailed study of the fine structure due to individual crystallites of magnesium and cadmium oxide will be given.

§ 2. Experimentals

In the most part of our observations a diffraction camera of conventional type, with single focussing coil and a specimen-plate distance of 15 cm, was utilized, but a comparatively high resolution was attained by reducing the size of electron source as small as possible, which was effected by depositing a very small amount of barium and strontium oxides on the tip of a fine platinum hair pin filament.

Smoke samples of magnesium and cadmium oxide prepared as usual by igniting the metals in atmospheric air, were deposited on a flat surface such as a cleavage face of a crystal. The sample were examined by the reflexion method. It was found that the smoke particles show a fibrous orientation having [001] axis perpendicular to the underlying surface, especially when the amount of the deposit was reduced. This may be due to the fact that the crystallites of cubic form bounded by {100} planes settle down on the substrate like dice on a flat table. Examples of diffraction patterns which show distinguished structures due to the orientation are reproduced in Fig. 1a and 3.

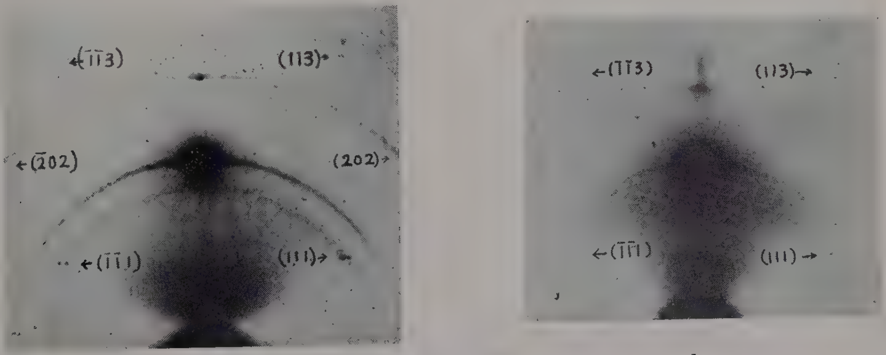

(a) (b)

Fig. 1.

(a) Fibrous pattern due to MgO smoke particles of cubic shape deposited on a flat substrate.

(b) Pattern due to the same sample after metallic shadowing.

§ 3. Structures of Reflexion Spots in the Fibrous Pattern

(a) Magnesium Oxide

It may be seen that the (111) and (113) reflexions of magnesium oxide (Fig. 1a) are doublets split in the horizontal direction, whereas (202) is singlet. Such a splitting into doublet was found generally in other reflextions of indices (h, h, l) and $(2h, h, l)$ with $h \neq 0$. The (004) and (006) reflexions were also respectively composed of two well-defined spots split horizontally to both sides from their proper positions on the vertical central line (Fig. 2a). The (002) reflexion was found to be a quartet extended in the horizontal direction as shown in Fig. 2b.

b) Cadmium Oxide

It may be seen in Fig. 3 that the fibrous reflexions of cadmium oxide show generally elongations in horizontal direction. Though the fine details of the reflexions were in general less distinct than in the case for magnesium oxide, we could found certain structure suggesting splitting into doublet of (111), (113) and (115) reflexions.

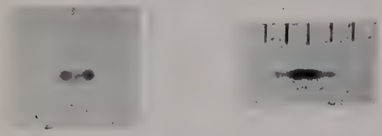
(a) (b)

Fig. 2. (a) (004) doublet and (b) (002) quartet due to smoke sample of MgO having [001] orientation. (The central streak in the (004) doublet is the mirror reflexion of the substrate surface).

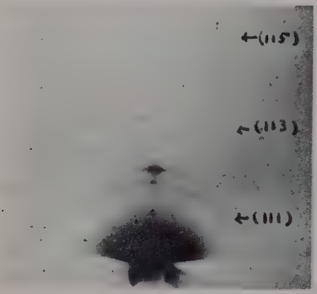

Fig. 3. Fibrous pattern due to CdO smoke. (The two strong spots in the vicinity of (115) are due to substrate.)

§4. Discussion on the Observation for Magnesium Oxide

(i) A General Remark[2)]

When refraction effects in powder pattern are concerned, we are to consider in general only the cases where the electron beam have comparatively large glancing angles to the boundary surfaces of the particles, since otherwise the cross sections of the surfaces against the electron beam become so small that the intensities of refracted reflexions are inappreciably weak. Compared with the glancing angles, Bragg angles for electrons are very small, being of the order of 10^{-2} radians, so that in calculating the deviation of reflexion spot from the position expected when there were no refraction effect, we may approximately assume the electron rays of the reflexion to be parallel to the reflecting net plane.

The crystallite which gives rise to a reflexion assumes in general such an orientation that the plane of electron incidence containing the normal of the reflecting net plane crosses the corresponding Debye ring at the point of the reflexion. When there is no specified orientation of the sample crystallites, the reflecting crystallite may take arbitrary azimuth around the normal, so that we encounter certain difficulties in observing definite fine structures of the refraction effect and in knowing the azimuth of the crystallite participating in the observed reflexion (See Part II). In this respect the sample of the fibrous orientation gives a particular case showing such a simple and definite fine structures as mentioned above since the geometrical condition of the crystallites participating in reflexions is simple as is seen in the followings.

(ii) Reflexions other than (00*l*)

It may be easily seen that (h,h,l), $(2h,h,l)$ and $(h,0,l)$ reflexions of our diffraction pattern come only from the crystallites which assume respectively [110], [120] and [010] axes nearly parallel to the electron beam. Then it is expected, as shown in Fig. 4, that, by the ordinary refraction effect, (h,h,l) splits horizontally into doublet, $(2h,h,l)$, similarly into triplet composed of two deviated and one undeviated spot and $(h0l)$ does not show any splitting. In our observation the undeviated spot in $(2h,h,l)$ reflexions are hardly detected and unsplit (202) is found to be weak when compared to other reflexions. This may be due to the absorption of

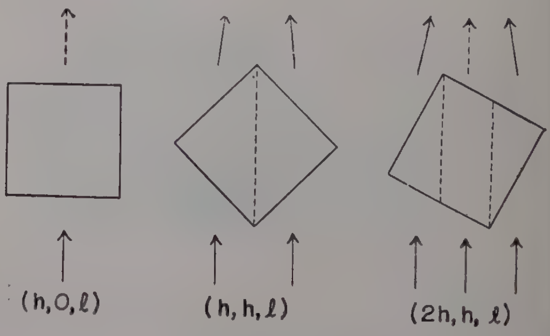

Fig. 4.

electrons because of the longer paths through the crystallites.

The correspondence between the observed fine structure and the above geometry can be visualized when we apply the method of metallic shadowing to the diffraction sample7) which is used in common practice of the electronmicroscopy. As the result of shadowing, the surfaces of the crystallites facing to the source of the metallic vapour are covered with the deposited metal and the member of the doublet due to the surfaces are extinguished as shown in Fig. 1b.

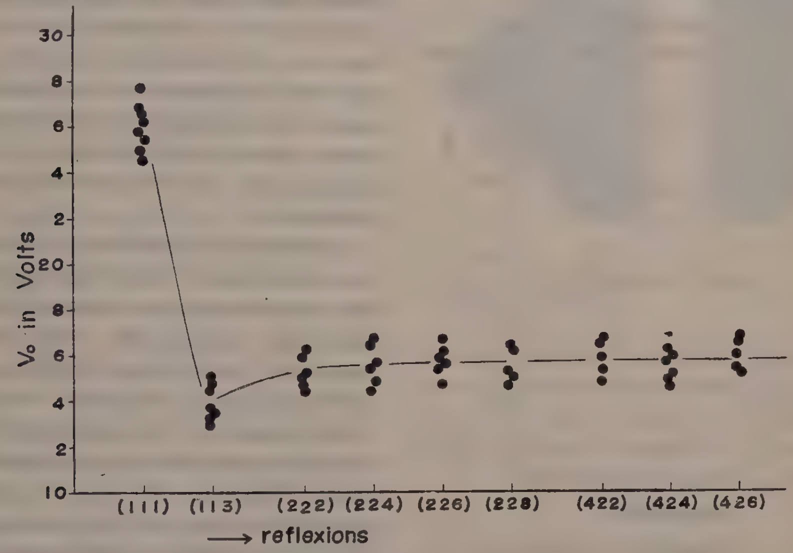

Fig. 5. Mean inner potential V_0 of MgO obtained from fibrous reflexions (h, h, l) and $(2h, h, l)$.

A simple calculation according to the above approximation shows that the angular deviations, α, of (h,h,l) and $(2h,h,l)$ reflexions from the position expected without the refraction effect are given respectively by

$$\left.\begin{aligned} &\alpha=2\delta_0 \\ \text{and}\qquad &\alpha=2.5\delta_0\,. \end{aligned}\right\} \qquad (4)$$

Utilizing these relations the value of the mean inner potential is calculated from the observed separations between the two spots in the doublets of the various reflexions and plotted in Fig. 5. Though we can not claim higher accuracies than 2 volts the values due to higher order reflexions suggest a value about 15~16 volts for the mean inner potential. The values due to (111) and (113) are anomalously high and low respectively. This may be explained by the dynamical theory of the electron diffraction as an anomaly due to simultaneous occurrence of the other strong reflexion as discussed previously by Miyake and the present author8).

(iii) (004) and (006) reflexions

The $(00l)$ reflexions due to the fibrous sample come from an assembly of crystallites assuming arbitrary azimuths around the fibre axis. A reflexion, due to a crystallite having an azimuth defined as shown in Fig. 6, will deviate from the central line by an amount

$$\alpha=2\delta_0 \sec\varphi\,. \qquad (5)$$

Therefore the spots due to the assembly of crystallites may be elongated according to continuous values of φ.

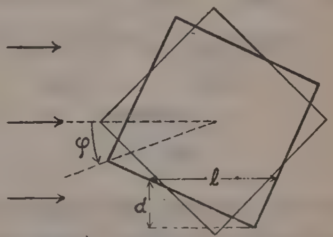

Fig. 6.

The observed spots, however, are fairly sharp which seems to contradict the above relation. This fact can be elucidated as follows. For simplicity we define a critical path length l such that the electrons pass through the crystallite without any absorption or with complete absorption, respectively, if the path length is shorter or longer than l. In accordance with the fact that the undeviated central spot was not observed, edges of the cubic crystallites in the sample may be considered to be longer than l. Then the effective cross section for the electrons suffering the deviation (5) may be proportional to

$$d=l/2\cdot\cos 2\varphi\ .$$

(Fig. 6). α and d are plotted against φ in Fig. 7. This shows that a half of the total intensity of the deviated reflexions comes from the crystallites in the range of φ from 0° to 15°, the corresponding range of α being from $2\delta_0$ to $2.3\delta_0$. It is known then that the most of the deviated reflexions are concentrated within a narrow range extremely close to the minimum deviation resulting in a sharp spot as observed. Assuming that the positions of spots correspond to those of the minimum deviation, the mean inner potential is calculated from the observed separations of (004) and (006) doublets and the results are plotted in Fig. 8. They correspond to about 15 volts.

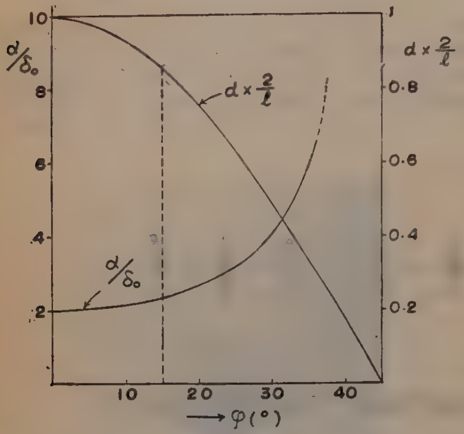

Fig. 7.

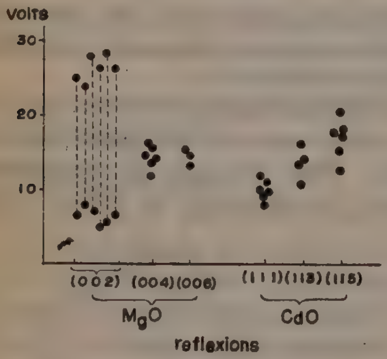

Fig. 8.

(iv) (002) Reflexion

Since the geometrical condition for (002) reflexion is quite similar to that for (004) and (006), the splitting into quartet of the reflexion is naturally considered to correspond to the double refraction effect. It was found that, by the metallic shadowing, the two spots of (002) quartet in the side of the vertical central line opposite to the source of metallic vapour are extinguished simultaneously with the one spot of (004) or (006) doublet of the same side[7].

Assuming the positions of spots as above, we can calculate then $V_0 \pm |V_{002}|$ respectively from the separations between the outer two spots and that of the inner two spots, as plotted in Fig. 8, from which we obtain 16 ~17 volts for V_0 and 8~11 volts for V_{002}.

The values of V_h calculated from (2) utilizing the known atom form factors are tabulated in Table I. It may be seen that the observed values of $|V_{002}|$ show reasonable agreement with the calculated value.

Table I. V_h in volts (calculated).

reflexion	MgO	CdO
(002)	7.66	13.75
(004)	3.48	6.60
(006)	1.87	3.44
(111)	1.25	9.67
(113)	0.29	4.89

(v) Summary

Though the double refraction effect was found only in the (002) reflexion, the observation for magnesium oxide is quite in accordance with the theory, since the splitting due to the double refraction is expected to be proportional to $|V_h|$ and this quantity is comparatively small for reflexions other than (002), so that they are naturally considered as unresolved quartet.

§ 5. Discussion of Observation for Cadmium Oxide

The (111), (113) and (115) reflexions show structures suggesting splitting into doublet as if they correspond to the ordinary refraction effect due to the mean inner potentials as plotted in Fig. 8. Though our observation was in general less successful for cadmium oxide, it is a notable fact that the (111) reflexion splits only into doublet without any indication into quartet, since a quartet of well separated doubly refracted spots is expected on account of the large value of V_h for this reflexion (Table 1), so that the observation seems to contradict to the theoretical reasoning of the double refraction effect. It may be noted, however, that the value about 10 volts for the mean inner potential obtained from this reflexion is anomalously small since this is expected to be about 20 volts for cadmium oxide[4)].

Here, we take notice of the fact that the intensities of the two outer components of the (002) quartet of magnesium oxide are remarkably weaker than those of the inner two (Fig. 2b). This fact suggests an explanation for the above contradiction. When we suppose that such an intensity difference between the doubly refracted electron rays is more exaggerated in the case of cadmium oxide, the observed (111) doublet of cadmium oxide may be interpreted to be the two inner spots of the quartet due to the double refraction, while the outer two of larger deviations are inappreciably weak. Then the separation of the observed two spots corresponds not to V_0 but to $V_0 - V_{(111)}$, whose numerical value, about 10 volts, is in agreement with the observation. It should be mentioned here that a similar fact is experienced in Debye-Scherrer pattern of cadmium oxide: the (111) ring of this crystal shows doubling quite similar to the (111) ring of magnesium oxide[1)], but the separation of the double ring of the former is too small if we assume for it the ordinary refaction effect (Fig. 9). The intensity difference between the doubly refracted electron rays suggests an anomalous absorption effect, on which we will give a more detailed observation and discussion in Part II.

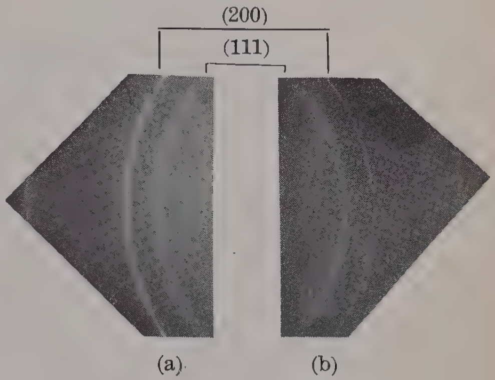

Fig. 9. Debye-Scherrer pattern of (a) MgO and (b) CdO.

References

1) L. Sturkey & L. K. Frevel: Phys. Rev. **68** (1945) 56.
J. Hillier & R. F. Baker: Phys. Rev. **68** (1945) 98.
2) G. Honjo: J. Phys. Soc. Jap. **2** (1947) 133.
3) J. M. Cowley & A. L. G. Rees: Proc. Phys. Soc. **59** (1947) 287.
4) L. Sturkey: Phys. Rev. **73** (1948) 183.
5) H. A. Bethe: Ann. d. Phys. **87** (1928) 55.
6) N. Kato: Proc. Jap. Acad. **25** (1949) 41: J. Phys. Soc. Jap. **7** (1952) 397, 407.
N. Kato & R. Uyeda: Acta Cryst. **4** (1951) 227.
7) G. Honjo & K. Mihama: Acta Cryst. **4** (1951) 282.
8) S. Miyake & G. Honjo: Nature **165** (1950) 644.

JOURNAL OF THE PHYSICAL SOCIETY OF JAPAN Vol. 8, No. 6, NOV.—DEC., 1953

Studies in Glass-Cleaning Procedures by Static Friction Measurement

By Koreo KINOSITA

Department of Physics and Chemistry, Gakushuin University, Mejiro, Tokyo

(Received Jun. 20, 1953)

Static friction of cleaned glass surfaces was accurately measured, with the aim of establishing a practical scale for the cleanness of the surface and comparing the power of various cleaning procedures. The coefficient of static friction μ of a cleaned glass surface is characteristic of the cleaning procedure adopted. Samples prepared by one and the same procedure yield the same value of μ within a few per cent., if close attention is paid to the practice of treatment. Some practical problems on the technique of cleaning, preservation of cleaned samples, *etc*. are dealt with. The relation between μ and the nature of the surface is briefly discussed in conclusion.

§ 1. Introduction

Those who engage in the experimental study of the nature of solid surfaces are acquainted with the difficulty of preparing a clean surface. Many ambiguities seem to have arisen out of the obscurity of the preparation of samples. The present work aims to contribute something to this point.

In the course of our studies on the *physical cleaning of surfaces*¹⁾, we found it necessary to establish a method of expressing the cleanness of solid surfaces, such as those of glass, in some quantitative manner. What the word cleanness means is very complicated. One could probably define a perfectly clean surface without difficulty, but what he demands for a gradation of cleanness would be rather ambiguous and dependent on his standpoint. It is, however, outside of our scope at present to formulate the general definition of the gradation of cleanness ; what we want is a practical or conventional scale, and, for this purpose, it seems to be one of the most adequate schemes to express the cleanness in terms of the coefficient of static friction of the surface. The well-known fact2) that clean solid faces adhere to each other and show extraordinarily large friction suggests that the measurement of friction would provide a valuable scale for the cleanness of surfaces.

A number of trials on this line have been published in this country, including the present author's preliminary study3). We described there an experiment to compare the power of several kinds of glass-cleaning procedures by measuring the static friction of the cleaned samples by means of the *method of inclination*, with somewhat detailed discussions on the precision of the measurement. The result was insufficient, though promissing, owing to the limitation of the precision. In this respect, Dobashi's4) and Kuroda and his collaborators'5) works are none the better.

In the present work, we achieved a considerable improvement in the precision of the friction measurement by adopting a device of the type originally used by Hardy2) with some modifications ; and this enabled us to carry out the above described scheme with far better accuracy, as well as further detailed studies on the surface-cleaning procedures.

§ 2. Measurement of Static Friction

The device is illustrated in Fig. 1. The table of the instrument has a rectangular opening, in which a graduated glass plate *G* is fixed ; this serves, in combination with an inclined mirror *M*, in facilitating the observation of the movement of the slider. The sliding members consist of a glass plate *Pl* (4×5cm.) fixed on *G* and a curved slider *Sl* (a small watch-glass of 6.5 cm. radius of curvature) weighted with lead. A three-leg clamp fixed on *Sl* has an arm of the inverse U-type, to which two silk threads are attached.

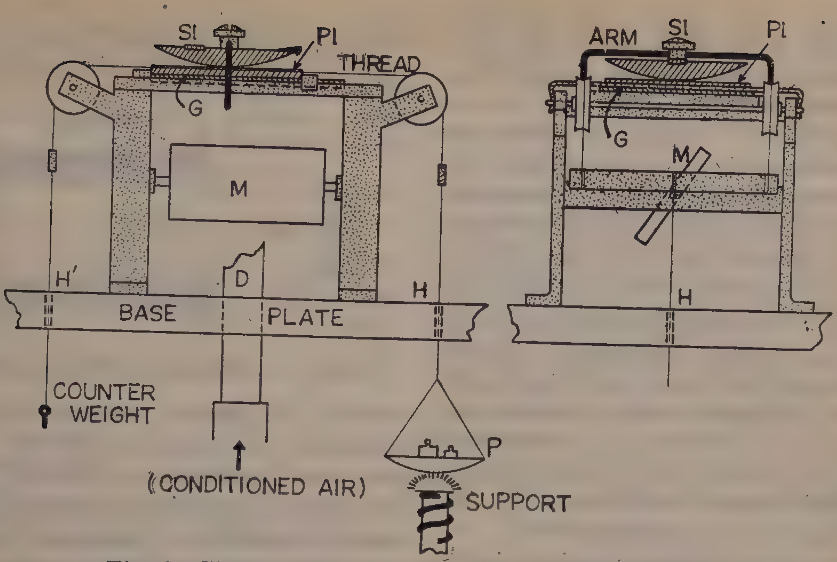

Fig. 1. The device for the measurement of static friction.
Sl and *Pl*: sliding members. *G*: graduated glass plate. *M*: inclined mirror.
H and *H'*: small holes. *P*: pan. *D*: duct for conditioned air.

The height of these knots and of pulleys was finely adjusted to give a horizontal pull just in the plane of contact of *Pl* and *Sl*, so as to avoid the "rocking"2) of the latter. The pull was given by applying poises on a pan *P*, which is furnished with a movable support. A vertical thread leads through *H'* to a counter-weight, which compensates the weight of the pan and the pulley friction.

The tangential force was applied by slowly withdrawing the support from the pan. The weight of the poises p which is just enough to bring about the forward movement of the slider divided by the total weight w of the slider gives the coefficient of static friction μ: $\mu = p/w$. w was 26g. on the average; accurate value was measured for each slider. Detailed discussion on the method of measurement will be given in a forthcoming paper*.

The instrument was set on a steel base plate, and was enclosed in a bell jar. In most cases, the chamber was filled with unconditioned air (50–80% R.H.), but dry or moist air could be introduced through a duct *D*, if necessary. The conditioned air was pushed in with a slight pressure, and leaked away through *H* and *H'*.

The plates, pieces of ordinary window pane, and the watch-glass sliders were of the same make respectively, but both were not of common constitution. We made it a rule to clean the pair of plate and slider to be investigated in one and the same process.

§ 3. Cleaning Procedures and Their Characteristic μ's

3-1. Cleaning Procedures

Five kinds of glass-cleaning techniques, *finger-tip-wash*, *chromic-sulphuric acid treatment*, *hydrofluoric acid treatment*, *surface gliding discharge treatment* and *flaming* are discussed in this paper**. Details of the standard practice of each method in our laboratory are as follows.

A. *Finger-Tip-Wash* (*F. T. W.*): The sample is at first washed with soap and water, and then rubbed all over under a vigorous flow of tap-water with a finger-tip previously cleaned. The well-known "clinging state"6) is reached in a few minutes, but, for obtaining consistent results, rubbing should be continued for about 15 minutes. The sample is then rinsed with distilled water, and desiccated by the *alcohol-warm-bath* (*A. W. B.*) *method* which is to be described later. Possible creep out of contaminants from the hand supporting the sample can be reduced to a minimum by holding the edges of the back surface with finger-tips. Sharp edges of the front face, which is to be cleaned, seem to hinder the creep-over of contaminants effectively.

---

* "Static Friction of Glass. Part I" which will be published in this Journal.

** A brief note on the usual manner of cleaning lenses and other optical parts in optical shops was given elsewhere3).

British workers2)6) look like to have a peculiar affection to this simple technique.

B. Chromic-Sulphuric Acid Treatment: This is the standard glass-cleaning technique in chemical laboratories. Our procedure is as follows: (1) washing with soap and water, (2) soaking in the concentrated sulphuric acid solution of potassium bichromate at room temperature for 20 hours, (3) *F. T. W.* (for 15 minutes), (4) rinsing with a vigorous flow of tap-water for 20 hours, (5) abbreviated *F. T. W.* (for a few minutes), and (6) rinsing with distilled water. The sample is then dried by the *A. W. B.* method.

Often, the *F. T. W.* after soaking in the oxidizing solution was reduced to an *abbr. F. T. W.*, and the *abbr. F. T. W.* after rinsing with tap-water omitted. This simplified treatment shall be called *Treatment B′*.

C. Hydrofluoric Acid Treatment: After applying *abbr. F. T. W.*, the sample is soaked in a 0.1% solution of commercial hydrofluoric acid at room temperature for about 5 minutes. *Abbr. F. T. W.* is applied again, and, after being rinsed with tap-water for an hour, the sample is rinsed with distilled water and dried. Prescriptions for time and concentration given above is not authoritative; over-treatment should be avoided carefully.

D. Surface Gliding Discharge Treatment: The fact that the surface gliding discharge on a glass surface cleans up the latter was found by Baker7), and later discussed by the present author1). An effective cleaning method as it is, the difficulty of obtaining a uniformly cleaned surface has been the obstruction to its practical application. This was overcome by the following technique. The sample is placed face to face on another similar piece, both after having undergone *abbr. F. T. W.* and subsequent desiccation by the *A. W. B. method*. Tin foil electrodes of the form illustrated in Fig. 2 are inserted between these, and high tension is applied.

If adequate high tension source is used, hissing streamers will run all over the narrow gap between the glass surfaces, which will clean up the latter in about 5 minutes. Occasional grown-up sparks will bridge over the projections P_1 and P_2, or P_1' and P_2', keeping clear of the narrow gap, thus securing the uniformity of the surface cleaning action. The surface must not be exposed to streamers too long; otherwise, numerous microscopic grooves and pits will form over the surface, resulting macroscopically in a fogged appearance, apparently like that of a sample overtreated with hydrofluoric acid solution (see § 4-2).

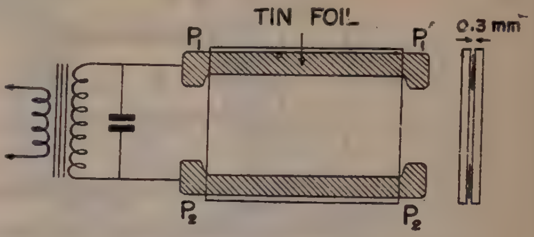

Fig. 2. Surface gliding discharge treatment.

E. Flaming: After *abbr. F. T. W.*, the sample is dried and passed over a high-temperature, tall flame of an ordinary gas-burner for glass work. The surface exposed to the flame is known to be cleaned up7). In our practice, the plate was passed horizontally crossing the upper, hottest part of the flame as many as ten times, each time staying about a second in the flame.

Two sliding members, the plate and the slider, were treated as similarly as possible in the cleaning as well as in the drying process.

Desiccation is one of the most difficult processes in these experiments. We tried a number of methods3), among which the following one, the *alcohol-warm-bath method*, proved to be most successful. Plates and sliders, as they are wet, are inserted into the middle tube of a large Soxhlet's extractor specially constructed for this purpose. An all-glass carrier was used for supporting the samples. On heating the solvent reservoir, the distilled, hot alcohol fills the middle tube gradually, until it reaches the top level of the siphon tube and flows down rapidly back to the reservoir. After repeating this cycle once more, the samples are taken out. They are dry in a minute.

3-2. Characteristic μ's

The coefficient of static friction between two clean glass faces, the plate and the slider, depends not only on the chemical constitution of the two, as was pointed out by Hardy[2)], but on the cleaning procedure adopted*. Characteristic values of the coefficient of static friction μ_A, μ_B, μ_C, μ_D and μ_E for the five cleaning procedures described above are given in Table I.

Table I. Characteristic μ's for *Treatments A—E.*

Treatment	Charact. μ	No. of pairs of samples
A. Finger-Tip-Wash	0.903	22
B. Chromic-Sulphuric Acid Treatment	0.935	27
C. Hydrofluoric Acid Treatment	0.908	5
D. Surface Gliding Discharge Treatment	0.990	17
E. Flaming	0.981	5

The measurement of the coefficient of static friction was repeated five times for each pair of plate and slider, and their mean value was adopted as the coefficient of static friction of the pair. This was the case throughout the course of our study. The numerical value given in the table is the mean of the coefficient of static friction as determined in the above process of as many pairs of samples as jotted in the third column of the table.

The relative standard deviation of the repeated measurements of μ for a pair was less than one per cent. The relative standard deviation of μ among the pairs prepared by one and the same cleaning procedure was a little larger. (one or two per cent**.).

On examining Table I and some other supplementary data, we can make the following remarks:

1. Cleaning procedures described in § 3-1, including the finger-tip-wash, are powerful enough to raise the coefficient of static friction to $\mu > 0.9$ from that of ordinary (naturally contaminated) glass pieces, $\mu \sim 0.3$.

2. The delicate differences of the surface cleaning action of various procedures show themselves in the static friction measurement.

3. The *physical* cleaning techniques, *D* and *E*, seem to be superior to the other three, so far as it is admitted that an increase in μ always implies an increase in the grade of cleanness (See § 6).

The fact that we could have got the laboratory techniques of preparing samples which yield the same value of μ within a few per cent. was the foundation of a series of experimental studies on the static friction of glass later developed in this laboratory, which will be published in this Journal. It must be noted, however, that this degree of reproducibility is only attained when utmost attention is paid to keep every detail of the cleaning practice identical. Thus, for instance, μ_B is affected by the degree of freshness of chromic-sulphuric mixture, the quality of the stock sulphuric acid***, the quality of tap-water and so on. Consequently, too much stress should not be laid on the absolute values of characteristic μ's given in Table I *etc.*

§ 4. Notes on Cleaning and Desiccating Procedures

This section will deal with some details of cleaning and desiccating procedures, which will complement the last section.

4-1. The Effect of Rubbing the Face in *Treatment B*

Treatment A, the finger-tip-wash, is rather of mechanical or physical nature in contrast to *Treatment B* and *C*, which are essentially chemical. The latter two, however, include in our way of doing finger-tip-wash before and after the purely chemical processes. It is desirable to distinguish the effect of mechanically rubbing the face in these *Treatments*.

Treatment B includes six steps (1)—(6), as was previously described. These were modified in three gradations as follows:

Treatment B′: (3) reduced to an *abbr. F. T. W.*; (5) omitted.

Treatment B″: (3) and (5) omitted.

Treatment B‴: (1), (3) and (5) omitted.

Five pairs of samples were prepared by respective procedures. The result of the measurement of the characteristic μ's for these *Treatments* is given in Table II.

We find from these data that each of the steps (1), (3) and (5) does contribute a definite amount to the increase of μ, or the cleanness.

It would be worthy of note that the popular

---

* The surface roughness has not so much to do with the coefficient of static friction. See Hardy[2)] *et al.*

** The reproducibility of μ_C was inferior.

*** Sulphuric aid for industrial use was used throughout this work. If chemically pure sulphuric acid is used, μ_B gets larger.

Table II. Characteristic μ's for *Treatments B, B′, B″, and B‴*.

Treatment	B	B′	B″	B‴
Charact. μ	0.936	0.932	0.916	0.889

chromic-acid treatment is, if one omits washing with soap and water and *F.T.W.* in its process, inferior to *Treatment A*, the thorough finger-tip-wash. The contribution of the step (1) suggests that there usually are contaminants on glass surfaces which are not decomposed with ease by the powerful oxidizing agent. The contributions of the steps (3) and (5) show the difficulty of perfect rinsing*, a familiar fact to chemists.

4-2. Effect of Over-Exposure in *Treatment D*

As was noticed in § 3-1, a sample over-exposed to streamers in *Treatment D* appears cloudy, complicated microscopic irregularities forming over the surface (Fig. 3). It is of interest to see whether the coefficient of static friction is affected by the presence of these irregularities. Four pairs of plates and sliders were cleaned by the regular *Treatment D* (exposure 5 minutes). Other four, prepared at the same time, were over-exposed (*Treatment D′*, exposure 20 minutes). The latter had cloudy appearance. μ's for these eight pairs of samples were found to be identical within the experimental error, as shown in Table III. This might be regarded as an example which illustrates that the surface roughness has not so much to do with the static friction.

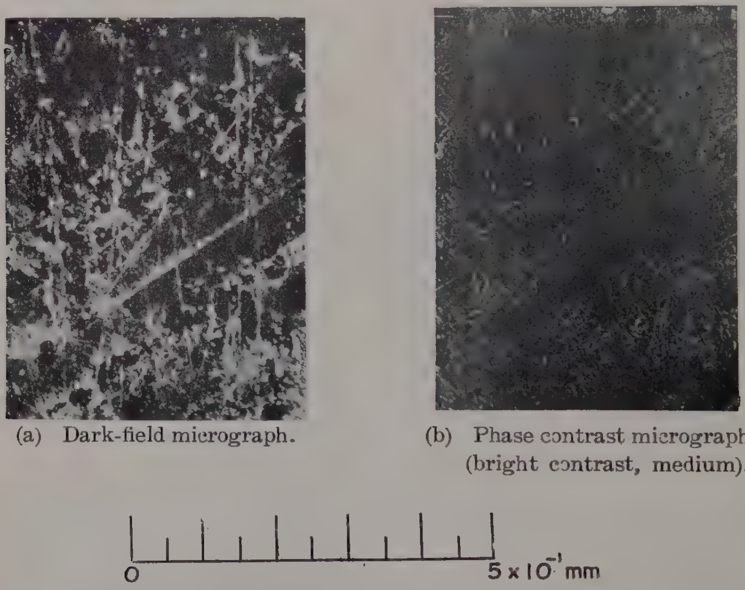
(a) Dark-field micrograph.

(b) Phase contrast micrograph (bright contrast, medium).

Fig. 3. Microscopic irregularities of a sample over-exposed to streamers. Photographed by S. Saito of this laboratory.

Table III. The effect of over-exposure in *Treatment D*.

Sample No.	Treat. D (Exp. 5 min.)	Sample No.	Treat. D′ (Exp. 20 min.)
1	0.990	5	0.991
2	0.989	6	0.991
3	0.992	7	0.987
4	0.987	8	0.986
Av.	0.989	Av.	0.989

4-3. Notes on Desiccation

In our experiments, the samples were always desiccated by the *alcohol-warm-bath* (*A. W. B.*) *method*.(§ 3-1) This desiccation process itself is expected to have a surface-cleaning action, and it may have contributed a certain amount to the increase of μ. Thus, the characteristic μ's given in Table I *etc.*

---

* Rinsing should not be continued too long; if the samples stand in water, be it moving or still water, for two or more days, the coefficient of static friction is lowered.

may possibly be dependent on the method of desiccation.

In order to investigate the cleaning action of the *A. W. B. method*, untreated, naturally contaminated samples were placed in the Soxhlet's extractor, and washed with distilled, hot alcohol in the usual manner three times over. Table IV gives μ's in the original state and those after the treatment, for four pairs of plates and sliders. Thus it was found that, for untreated (contaminated) samples, the A. W. B. method increases μ by *ca.* 0.3.

Table IV. Cleaning Action of *Alcohol-Warm-Bath Method.*

Sample No.	Before A.W.B.	After A.W.B.	Difference
1	0.271	0.588	0.317
2	0.353	0.612	0.259
3	0.292	0.588	0.296
4	0.327	0.613	0.286

Next, we investigated the effect of drying processes on the characteristic μ's in combination with cleaning procedures. Ten pairs of plates and sliders were prepared at the same time by *Treatment B′* and five were dried by the *A. W. B. method*, the rest by passing a clean, dry air current through the glass vessel in which they were stored (Fig 4). Table V gives the characteristic μ for each group, together with the result of the similar experiment for *Treatment A* (the finger-tip-wash). The *alcohol-warm-bath method* increases μ more than the dry air method does, as it would have been expected, but the difference is rather small.

Table V. Influence of the method of desiccation on the characteristic μ's of *Treatments B′* and *A*.

	Treat. B′	Treat. A
A.W.B. Method	0.933	0.903
Dry Air Method	0.925	0.880

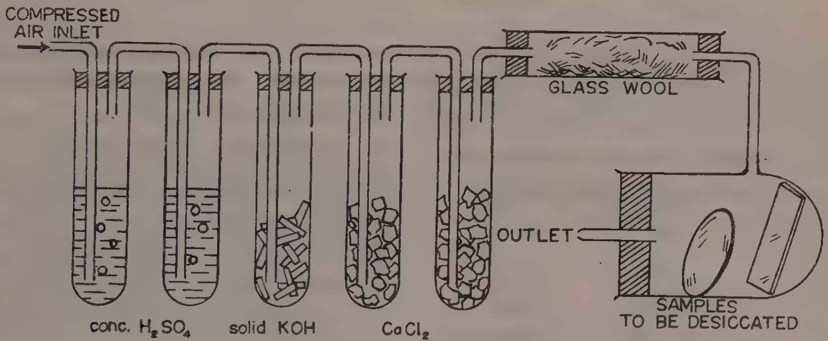

Fig. 4. Desiccation by means of a clean, dry air current.

For the sake of the study of cleaning procedures, the dry air method is preferable in that the things are simpler. However, it takes scores of minutes, and needs troublesome precautions for obtaining consistent results. For this reason, the *A. W. B. method* was used throughout the course of our study.

§ 5. On the Preservation of Cleaned Samples

It must be a matter of concern of the experimental workers in this field how long a cleaned sample can be kept without altering its surface conditions.

Macaulay[8)] reported that the power of seizure of freshly cleaved mica faces was lost much more rapidly if the faces were placed upward than if they were placed vertically. If placed with the cleaved faces downward, they retained their power of seizure for two days or longer. He concluded from these experiments that the contamination is deposited by simple settling from the air of greasy matter. Our following experiment is akin to his.

Three pairs of plates and sliders were prepared by *Treatment B*. One of them was placed with cleaned faces upward, another vertical, and the last downward. The first and the last were placed on the round tops of turned-over clean watch-glasses, and the second in a clean glass cylinder. All these were placed on a table in the laboratory. Fig. 5 shows the lowering of μ of these samples with the lapse of time. The result

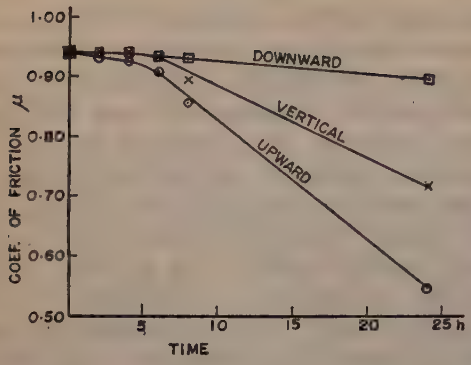

Fig. 5. Lowering of μ with the lapse of time of cleaned samples stored with their surfaces upward, vertical and downward.

supports Macaulay's view.

Table VI illustrates the change of μ when the samples were kept in a clean desiccator. They were placed, as before, on the round tops of turned-over clean watch-glasses, with the surfaces to be investigated upward. This way of supporting is recommended. Table VII gives the results when the samples were stored in the friction measuring apparatus*.

It can be concluded from these data that, if adequate precautions are taken, cleaned samples can be stored as long as scores of hours practically without altering their friction coefficients. Confirmation of this point contributed much to the efficiency of our subsequent laboratory work.

Table VI. Lowering of μ with the lapse of time. Samples stored in a clean desiccator.

Sample No.	0 hr.	5 hr.	10 hr.	25 hr.	30 hr.	40 hr.	45 hr.
1	0.936					0.934	
2	0.938	0.936	0·934	0.934	0.900		
3	0.916				0.916		
4	0.918						0.910

Nos. 1 and 2 were cleaned by *Treat. B*, Nos. 3 and 4 by the same method but that the period of soaking in the oxidizing agent was reduced. Remarkable lowering of μ of No.2 is presumably due to frequent handling for measurements.

Table VII. Lowering of μ with the lapse of time. Samples stored in the measuring chamber.

Sample No.	0 hr.	24 hr.
1	0.933	0.932
2	0.933	0.932
3	0.934	0.933
4	0.936	0.935

§ 6. Discussion on the Relation between μ and the Nature of Surfaces

We have assumed thus far that the cleanness of a glass surface can be expressed in terms of its coefficient of static friction, a larger μ corresponding to a cleanness of higher grade. In general, this would be the case: an increase of μ of a sample from 0.3 to 0.9 no doubt means a remarkable improvement in the cleanness. But as to whether the delicate differences in characteristic μ's given in Table I *et al.* represent the differences in the grade of cleanness, there is room for investigation.

A glass surface exposed to air is covered with various heterogeneous matter, *e.g.* H_2O-, CO_2- and other gas-molecules, and in most cases some organic molecules habitually called the "greasy matter". At least the greater part of the adsorbed molecules which are in direct contact with glass are believed to be chemically combined with the atomic network of the glass. It is conceivable that some gas molecules travel more or less into the network; it may also happen that the "grease" molecules, as a whole or partly, anchor themselves in the cracks or pits on the surface. On the other hand, atoms which are the constituents of the network of glass, especially those of alkali metals, may depart from their original sites toward the surface to form more stable compounds with the heterogeneous molecules. Accordingly, there is expected a gradual change of composition from that of pure glass to that of the adsorbed, heterogeneous layer. It is difficult to suppose a "surface" of glass in the strict sense of the word in these circumstances.

Thus, a thoroughgoing cleaning of a glass surface seems to be necessarily accompanied with destruction and removal of glass itself to more or less extent. The order of the magnitude of characteristic μ's would presumably correspond to the order of the intensity of destructive action of respective cleaning procedures. The destructive actions of various cleaning procedures, however, are supposed to be different not only in quantitative gradation but in nature. For instance, the chromic-sulphuric acid will hardly damage the SiO_2 framework, thus leaving a skeleton layer of silicate on the surface, whereas the surface gliding discharge treatment will destroy the latter, as was pointed out elsewhere1)9) (see also § 4-2.). The real state of things is so complicated that we can scarcely inspect any details at the present stage. But it would be certain that a surface which has a very high μ is abundant with the atoms whose bonds are freshly broken off. Most of these free bonds will be occupied by gas molecules in a moment, but the activity of the surface is expected to be different from what it was and what it will be after a long time.

---

* Small holes H and H' in the base plate (Fig. 1) were kept open.

It is believed that there is practically no greasy matter remaining on the surface, even in the case of the finger-tip-wash for which the characteristic μ is lowest**. But the water-, and probably the carbon dioxide- and other gas-, molecules are adsorbed on the cleaned surface, and their influence on μ, at least that of water, cannot be neglected.

The coefficient of static friction of a clean glass surface is independent of the atmospheric humidity, so far as it remains in the range 50—80% R.H. It rises, however, when the moisture of the air in the measuring chamber approaches saturation, and remarkably lowers when extremely dry (Table VIII).

Table VIII. Change of μ according to the variation of atmospheric humidity.

Treat. \ Humidity	Ordinary Condition	Very damp	Very dry
Treat. A	0.90	0.99	0.70
Treat. B′	0.93	0.99	0.70
Treat. D	0.99	1.00	0.73

In this experiment, a gentle current of conditioned air was let in through the duct D (Fig. 1) into the chamber. The coefficient of static friction μ increased or decreased rather gradually, and it took scores of minutes until the equilibrium value was reached. These final values are given in the table. The change of μ (equilibrium value) with the variation of humidity was entirely reversible and reproducible, showing that the effect was due to the physical adsorption of water vapour on the glass surface. It is believed, however, that the glass surface still retains chemisorbed water even in the "extremely dry" state, which is supposed to be responsible for the rather low values of μ in this state. The numerical value of μ in the case of 100% R.H. is nearly equal to the value of μ in the case when the surfaces are wet with extra-pure liquid water. The results here described seem to be contradictory to those obtained by former workers.2)10)11)12) Details of this interesting adsorption effect will be reported in the near future.

It is worthy of note that the 100% R.H. values of μ_A, μ_B' and μ_D differ by far the smaller among themselves than they do in ordinary atmospheric conditions. This suggests that the differences in the latter case are at least partly due to the differences in the amount of water adsorbed on respective samples at ordinary humidities. Razouk and Salem's recent work13) is suggestive in this respect.

The greater part of the experimental work was carried out in the period 1948–1949 at the Department of Applied Physics, Faculty of Engineering, University of Nagoya, the author's former post. The author wishes to express his cordial thanks to the late Mr. Koichi Miura for his assistance in experiments, whose skill and patience were invaluable. Thanks are due to my colleague Prof. Akiya Ookawa for useful discussions. The work was financially supported by the Scientific Research Expenditure of the Department of Education.

References

1) K. Kinosita, M. Sumi and T. Owaki: J. Phys. Soc. Japan 4 (1949) 30.

2) W. B. Hardy and J. K. Hardy: Phil. Mag.

** This view is supported by the S-spectrum test, developed in our previous work1).

38 (1919) 32. See also N. K. Adam, *The Physics and Chemistry of Surfaces*, Oxford, 1938, p. 219 *ff*.
3) K. Kinosita and J. Maki: J. Appl. Phys. Japan **18** (1949) 260.
4) S. Dobashi: J. Japan. Ceram. Ass. **50** (1942) 448.
5) T. Kuroda, T. Noda and R. Uyeda: J. Appl. Phys. Japan **17** (1948) 331.
6) Lord Rayleigh: Phil. Mag. **35** (1918) 157.
7) T. J. Baker: Phil. Mag. **44** (1922) 752.
8) J. M. Macaulay: J. Roy. Tech. Coll. Glasgow **3** (1935) 353; N. K. Adam, *loc. cit.*, p. 174.
9) K. Kinosita: J. Illumin. Engin. Inst. **34** (1950) 164.
10) W. B. Hardy and I. Doubleday: Proc. Roy. Soc. **A 104** (1923) 34.
11) J. Sameshima and M. Miyake: Bull. Chem. Soc. Japan **12** (1937) 96; J. Sameshima and Y. Tsubuku: *ibid.* **12** (1937) 127; T. Isemura, *ibid.* **14** (1939) 270, 297.
12) R. H. Savage: J. Appl. Phys. **19** (1948) 1.
13) R. I. Razouk and A. S. Salem: J. Phys. Colloid Chem. **52** (1948) 1208.

Short Notes

J. PHYS. SOC. JAPAN **8** (1953) 790

On the Coefficient of Restitution

By Etujiro TAKEDA

Department of Physics, Faculty of Liberal Arts, Ibaraki University

(Received May 8, 1953)

The coefficient of restitution between two solid spheres of the same material was measured by means of falling pendulum. Fig. 1 shows the schematic diagram of the apparatus. Two solid spheres A, B, both 3 cm in diameter, were suspended by a cotton thread about one meter long respectively from 0_1 anp 0_2 whose distance was so adjusted that the two spheres should be just in contact at the vertical position of the pendulum. Next, the sphere A was lifted up with a looped thread to the position A_1 whose subtending angle θ_1 with the vertical was determined by a telescope. By cutting off the looped thread with a Bunsen burner, the sphere A was let fall and collide with the other sphere B. The angle θ_2 which B was brought up by the impact, was observed by the other telescope.

By assuming the law of conservation of momentum and the Newtonian law of restitution y was obtained from the following relation,

$$y=2\sqrt{\frac{1-\cos\theta_2}{1-\cos\theta_1}}\left(1+\frac{Tc}{4m}\right)-1$$

where m being the mass of sphere A, B; T, the period of the pendulum and c, the damping factor.

The experimental results for each pairs of glass, ivory, copper and lead are shown in Fig. 2, in which the abscissa indicate the impacting velocity. They indicate that the coefficient of restitution varies with the impact velocity, and that the variation is dominant at the region of lower velocity, especially, for the material with the smaller coefficient of restitution. It is generally recognized, independently of the kind of material, that the coefficient tends to unity as the velocity approaches to zero, while in the region of large velocity of impact the coefficient versus velocity curve becomes a straight line with small inclination. Namely, the empirical formula for the coefficient of restitution may be assumed to be $y=e^{-\alpha u^n}$, where α is a constant characteristic for the material, u, the impact velocity and n, the fraction about 1/3 ~1/5 respectively.

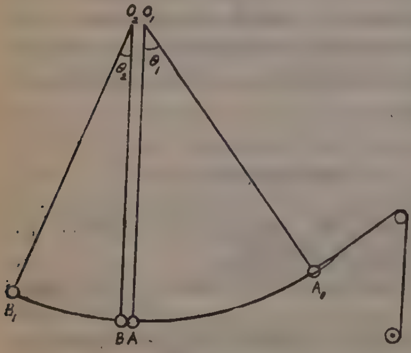

Fig. 1.

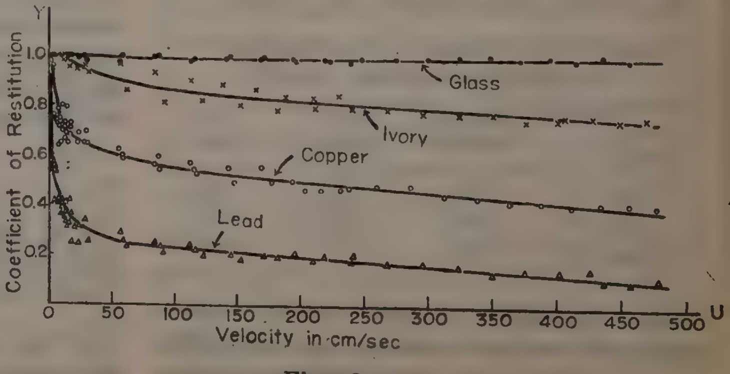

Fig. 2.

J. PHYS. SOC. JAPAN (1953) 8 791~792

On the Effective Mass of the Conduction Electron in Germanium

Wataru SASAKI and Mituko KUNO
Electrotechnical Labolatory, Tokyo

(Received May 13, 1953)

The effective mass of the conduction electron in germanium is reported to be about 1/4 of the free electron mass from data on the variation of carrier concentration with temperature and relations between Hall mobility and resistivity[1]).

Another estimation is possible from Hall and thermoelectric measurements.

If the *effective mass model* for the energy band is accepted, the charge carrier concentration n, provided they are not degenerated, and Hall coefficient R are related by

$$n=\beta/|R|, \qquad (1)$$

and the thermoelectric power ϵ and the energy difference ζ between the bottom of conduction band and the Fermi potential for the conduction electrons are related by

$$|\epsilon|=\frac{k}{e}\left(\frac{\zeta}{kT}+\gamma\right). \qquad (2)$$

β and γ in the above equations are factors determined by the scattering processes of conduction electrons, whereon some informations are available from Hall mobility versus temperature plots. n and ζ are related by

$$n=\frac{2g(2\pi m^*kT)^{3/2}}{h^3}\exp\left(-\frac{\zeta}{kT}\right), \qquad (3)$$

where g is the degeneracy of the energy band except for spins, and m^* the effective mass of the conduction electron.

Measurements have been carried out on n-type specimens cut out from single crystals which were grown in graphite cruicibles from molten germanium by slow cooling. Rods of about 1×1 mm section and 15 mm length were cut out from the single crystals. The homogeniety of specimens was tested by probing potential distribution along the rod axis under constant current, and only homogeneous parts of the rods were used as specimens.

Some of the Hall mobility measurements are shown in Fig. 1. The straight line shows

$$\mu=2500(T/300)^{-3/2} \quad (\text{in cm}^2/\text{v. sec}).$$

The fact that all the experimental points are found on this straight line in the higher temperature range shows that scattering processes involved are mostly those where mean free paths are the same for the electrons possessing different velocities. The factors in Eqs. (1) and (2) for this range are estimated as follows:

$$\beta=7.37\times10^{-18}\,\text{coul}^{-1}, \quad \gamma=2.00.$$

We can then calculate the thermoelectric power from the Hall measurement and above three equations, which are combined in the following equation, if proper values are fitted for the effective mass and degeneration factor.

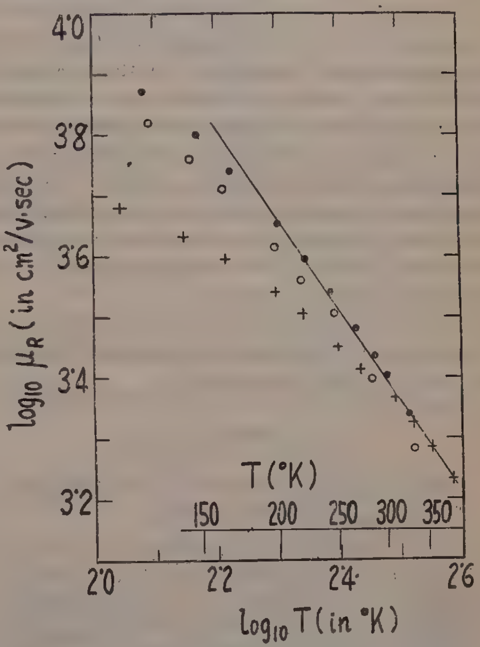

Fig. 1. The Hall mobility versus temperature plot for three specimens with different resistivities.

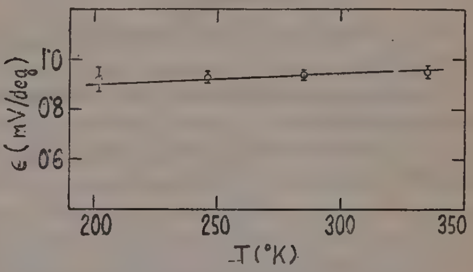

Fig. 2. The temperature dependence of thermoelectric power.

$$|\epsilon|=0.086\,[2.31(\log_{10}|R|+\tfrac{3}{2}\log_{10}T)-5.34 +2.31\log_{10}g(m^*/m)^{3/2}] \quad (\text{in mV/deg}). \qquad (4)$$

Fig. 2 shows one of the thermoelectric measurements. Though errors are involved in thermoelectric measurement, they can be estimated by using a proper device[2]). The vertical lines attached to the experimental points indicate the limit of probable maximum error. The curve in the figure, which is calculated from the Hall measurement by use of Eq. (4) with $g^{2/3}(m^*/m)=1.30$ is well fitted with experiment over the temperature range where μ_R varies as $T^{-3/2}$.

If this agreement is considered as the verification for the *effective mass model*, we can assign the $g^{2/3}(m^*/m)$ value so that the thermoelectric and Hall measurements may be combined in Eq. (4). The $g^{2/3}(m^*/m)$ values thus obtained, taking into account the experimental errors, are shown in Table I for three specimens with resistivity and Hall data. While $g^{2/3}(m^*/m)$ values for the two specimens with lower resistivities agree within the experimental errors, that for the specimen of the highest resistivity differs from the others. These results do not agree with another estimation by Debye and Conwell in the case of $g=1$. If these inconsistent values are due to the rather complicated structure of the conduction band, which was suggested probable from the magnetoresistance effects3), the equations used by our analysis should be improved.

The authors wish to represent their sincere thanks to M. Hatoyama, M. Sibuya, and M. Kikuti for their valuable discussions.

Table I.

ρ	R	$g^{2/3}(m^*/m)$
at 300°K		
2.8 Ωcm	6.7×10^3 cm³/coul	3.0 ± 0.9
0.60* 〃	1.52×10^3 〃	1.3 ± 0.2
0.082 〃	1.67×10^2 〃	1.5 ± 0.3

* Fig. 2 shows the result for this specimen.

References

1) P. P. Debye and E. M. Conwell: Phys. Rev. **87** (1952) 1131.
2) W. Sasaki and M. Kuno: Bul. Electrotech. Lab. **17** (1953) 169.
3) G. L. Pearson and H. Suhl: Phys. Rev. **83** (1951) 768.

J. Phys. Soc. Japan 8 (1953) 792~793

A Note on the Hydrogen Bond

Kenji Nukasawa
Research Institute of Applied Electricity
University of Hokkaido
Jiro Tanaka and Saburo Nagakura
Institute of Science and Technology
University of Tokyo

(Received June 19, 1953)

It has been customary to seek the source of the energy in the hydrogen bond to the electrostatic interaction. However, the possibility that a sort of quantum-mechanical resonance might exist so as to stabilize the whole system, has not been excluded altogether.1)2) Unfortunately any comprehensive theory based on the latter mechanism has not yet successfully been constructed because of its complicated nature. In this note, we wish to present an approximate method, from somewhat new angle, in which the concept of resonance is introduced implicitly. Our basic procedure consists of the combination of molecular orbital theory and perturbation theory,3)4) which has been found useful in the analysis of dipole moments and ultraviolet absorption spectra and other observations on some conjugated systems.4)5)

The phenomena that the localized molecular orbitals migrate, are usually limited to the π bonds, because the perturbing exchange energies are not large between σ bonds. However, the hydrogen bond is an exception to this tendency; in spite of its σ bond character, bond H–X can couple with the non-bonding σ orbital of an atom Y, σ_y (Fig. 1). The reason for this resides in the character of the H atom, that is, spherical symmetry of 1*s* orbital *h*, non-existence of any electron pair which would repel σ_y, and smallness in the electronegativity scale of the orbital *h*. These circumstances enable the overlap of the two orbitals *h* and σ to become sufficiently large, before the effective exchange repulsion sets in. In fact, O···H distance in ice is expected to be about 1.8 A, where the overlap integral would become as large as *ca.* 0.18 if the tetrahedral hybridization for the lone pair orbital σ_y be assumed.

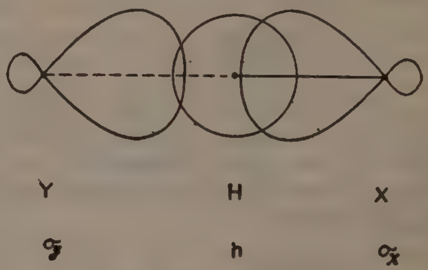

Fig. 1.

In order to solve strictly the energy relation in the system Y···H—X, it is necessary to perform the calculation, taking all of the mutual interactions of possible configurations in the 3-orbital 4-electron problem. Such a procedure would be laborious but not perspective. Taking allowance for the fact that the interaction between Y and H—X would be small, we therefore take an approximate method in which the following three effects might be estimated separately;

(a) attractive energy due to permanent, induced and instantaneous multipoles, (b) attractive energy due to delocalization of the orbital σ_y, and (c) repulsive energy due to exchange force between σ_y and h. Factor (a) has been often estimated semi-empirically to be several kcal/mole. Our task is to calculate factors (b) and (c). Although quantitative calculations have not been finished, we wish to report some qualitative observations on factor (b).

According to the perturbation theory, the energy of delocalization of orbital σ_y becomes

$$\Delta\varepsilon = \frac{2\delta^2}{M_{HX}-I_Y} \qquad (1)$$

where M_{HX}, I_Y and δ are the electron affinity of the vacant orbital H$-$X, the ionization potential of the occupied orbital Y and the perturbing exchange energy between the two orbitals, respectively. It is evident from Eq. (1), that the larger stability would result, the larger the M_{HX}, the smaller the I_Y or the larger the δ. Preliminary examinations show that in the actual cases δ and $M_{HX}-I_Y$ become of the orders of -1 and -10 e.v., respectively, therefore the delocalization energy could easily amount to several kcal/mole.

Most of the experimental facts which have been attributed to the inductive effect, can be explained equally well from the above-mentioned viewpoint: e.g., the red shift of the ultraviolet absorption band in phenol and others,6)7) the increase in the stabilizing energy of Y$\cdots$H due to the conjugation with π bonds,8)9) etc. Further there exist some observations which would be explained more clearly through this non-localization theory. For instance, the shifts in the infrared absorption bands observed in the system H—Y$\cdots$H—X can be interpreted as the changes in the bond orders. Thus, the vacant level of H—X into which electrons migrate is of anti-bonding type, therefore the delocalization lowers the bond order of H—X and shifs the absorption band to the side of longer wave-lenths, while it scarcely shifts the absorption band of H—Y, since its bond order remains unchanged.10)

The authors wish to thank Professor K. Higasi of Hokkaido University for his kind interest and encouragement. Their thanks are also due to Professor Y. Kakiuchi of Tokyo University for his valuable discussions.

The expence of the present work was defrayed in part from the Scientific Research Expenditure of the Ministry of Education.

References

1) R. S. Mulliken: J. Phys. Chem. **56** (1952) 801.
2) C. A. Coulson: "Valence" Oxford Univ. Press (1952) p. 303.
3) M. J. S. Dewar: J. Am. Chem. Soc. **74** (1952) 3341.
4) K. Nukasawa: Busseiron Kenkyu (1952) July 1 (in Japanese); J. Phys. Soc. Japan **8** (1953) 132.
5) S. Nagakura and J. Tanaka: Unpublished work.
6) S. Nagakura and H. Baba: J. Am. Chem. Soc. **74** (1952) 5693.
7) S. Nagakura: J. Chem. Soc. Japan **74** (1953) 153 (in Japanese).
8) M. Tsuboi: Bull. Chem. Soc. Japan **25** (1952) 385.
9) L. Pauling: "The Nature of the Chemical Bond" Cornell Univ. Press (1940) p. 316.
10) F. A. Smith and E. C. Creitz: J. Research of National Bureau of Standards **46** No. 2 (1951) 145.

J. Phys. Soc. Japan **8** (1953) 793～795

The Hall Effect in Cs_3Sb Photo-Cathode

By Toshimichi Sakata

The Electrical Communication Laboratory
Tokyo, Japan

(Received June 23, 1953)

As mentioned in the previous report,1-2) the sign of thermo-electromotive force (T.E.M.F) showed P-type semiconductivity for Cs_3Sb photo-cathodes. Recently the influence of excess Cs were discussed by several investigators.3-4) The purpose of this paper is to give data on the Hall effect and conductivity of Cs_3Sb which contribute to confirm further quantitative results.

The present experiment measures the Hall effect by using the a.c. system (800-cps). Use of a.c. method minimizes electrolytic effects and transverse voltages caused by thermo-electric effects. An a.c. method also simplifies the problem of amplifying small Hall voltages, and it avoids the troublesome drifts of long time constant common in d.c. systems. Several a.c. methods have been recently proposed.5-6)

The probe balance circuit is shown in Fig. 1. The voltage across the transformer T is applied to an R-C phase shift circuit. Since one of the grids of the tube (6SN7) is connected to one of these Hall probes, balancing out any probe-to-probe voltage resulting from the inevitable inexact positioning of the probes requires merely that the other grid of the tube be externally adjusted to the corresponding potential. Having roughly adjusted, small out-of-balance voltage remaining adjusted with fine balance potentiometer (R_3, R_4)

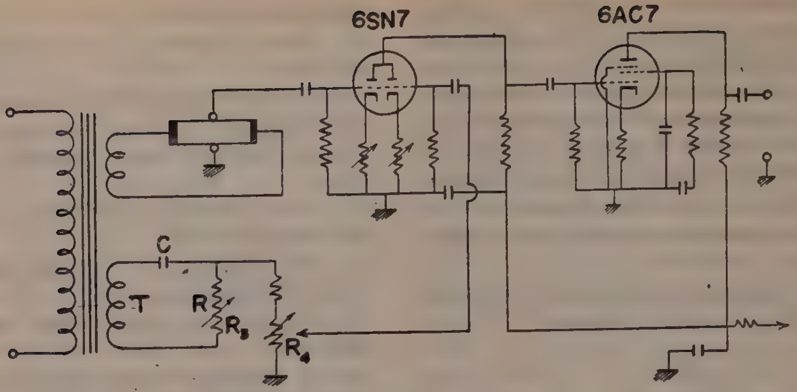

Fig. 1. Probe balance circuit.

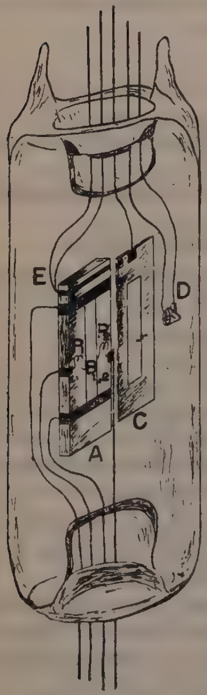

Fig. 2.

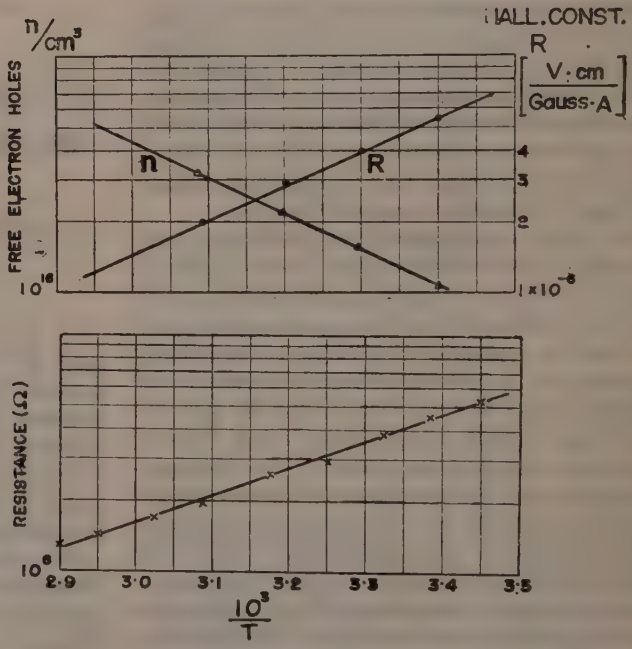

Fig. 3.

until the amplifier output falls to zero under conditions of zero magnetic field. The output of the pre-amplifier feeds into a low noise a.c. amplifier containing low and high pass filters.

The construction of experimental vacuum tube is shown in Fig. 2. In this figure, A and C are plain glass plate and cupper plate respectively. Sb film of adequate thickness was deposited (10^{-4} cm) on the surface of A from the anode coil in D. C was used to prevent unfavorable condensing of Sb atoms on the glass wall. Fine W wires (diameter 0.15 mm) are used as the measuring proves of Hall potential. Fine W wires (B_1, B_2) are pressed to A with W springs (P_1, P_2) to prevent B_1, Cs_3Sb and B_2 from the loose contact. E is copper-constantan thermo-junction 0.08 mm in diameter welded behind the A. Conductivities were measured also by using a.c. system, and the data were found to be reproducible. The resistance measurements were made by measuring the a.c. voltage across the sample and through a standard resistance in series with the sample with an a.c. voltmeter. Typical data are presented in Fig. 3.

The measured Hall voltage was directly proportional to the magnetic field, for fields up to 7,000 gauss; and it was directly proportional to the applied voltage, for voltages from 0.65 to 30 volts. Typical data are presented in Fig. 4 and 5. As shown in Fig. 3, there is a linear relation between $\log R$ or $\log n$ and $1/T$. The gradient of this line gives an activation energy of the sample, and its values are same order as the values obtained from the linearity between log σ and $1/T$.

From the above results of the measurements on the conductivity and Hall effect, it may be calculated that the numbers n of free electron excited into impurity levels and the numbers n_b of impurity centers. Values so calculated are given in Table I. With the present measurement, it is reasonable to assume that ΔE(0.4~0.6 ev) obtained from the electrical conductivity data must be due to impurities. More detailed consideration is unwarranted, since our Hall effect data were checked only in two samples. We are now constructing a detector in the amplifier output to obtain the polarity of the Hall voltage. Details will be reported later.

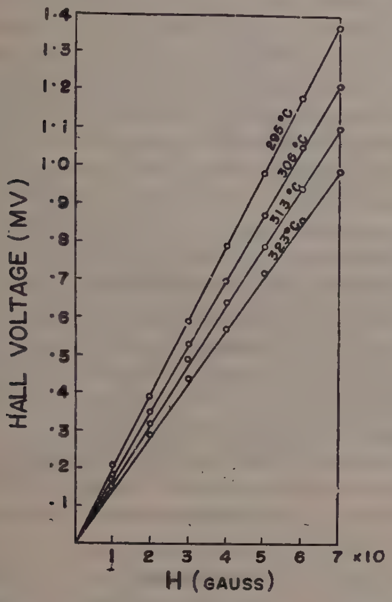

Fig. 4.

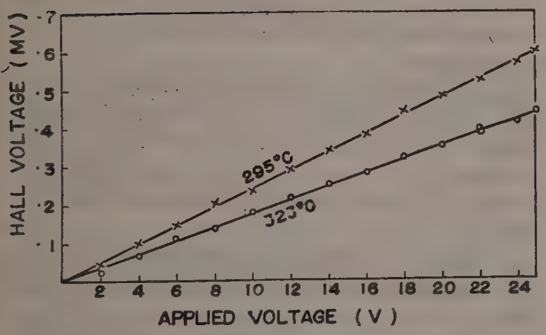

Fig. 5.

Table I.

T	n	n_b	$\Delta E/2$	ζ(chemical Pot.)
294	1.18×10^{16}	9×10^{20}	0.24	~0.21
306	1.61	〃		〃
313	2.31	〃		〃
323	3.45	〃		〃

References

1) T. Sakata: J. Phys. Soc. Japan **1** (1953) 125.
2) T. Sakata: J. Phys. Soc. Japan **2** (1953) 272.
3) P. G. Borzyak: Zhur. Tekh. Fiz **20** (1950) 923; See chem. Abstract **45** (1951) 437.
4) E. Taft and L. Apker; J.O.S.A. **2** (1953) 81.
5) J. J. Donogue and W. P. Eatherly: Rev. Sci. Instr. **22** (1951) 513.
6) E. M. Pell and R. L. Sproull: Rev. Sci. Instr. **23** (1952) 548.

J. PHYS. SOC. JAPAN **8** (1953) 795~796

Injection of Positive Holes in the Alkali Halide Crystal

By Yōichi UCHIDA and Yoshio NAKAI
Department of Physics, Faculty of Science, University of Kyotō

(Received July 14, 1953)

So far, the V-centre has been produced by heating the crystal in the presence of halogen vapour[1], or by irradiating it with X-rays[2], or by bombarding it with electrons. Information concerning properties of this centre was increased recently by many workers[3]. Seitz[4] and Nagamiya[5] proposed some models to explain experimental facts on their disposal.

Although the detail is not yet conclusive, it is generally accepted that this centre is electron-deficient and the positive hole generated in the crystal in some ways might play an important role. A strong support to this speculation will be given by the following experiment. As is shown schematically in Fig. 1, a piece of KI crystal C($5\times4\times15$ mm^3) was mounted on a graphite support S. A top of platinum wire P(~0.3 mm in diameter, ~3.5 mm in length) was forced to press the crystal by means of two clamping metal sheets H, insulated mutually by an ebonite block E.

The whole system was introduced into a furnace F and heated at a temperature of about 500°C, the platinum wire having been found to penetrate and stick tightly to the crystal at a depth of about 1~2 mm as shown in Fig. 1, (b).

Next, when a D. C. voltage 250 v was applied between the anode P and the cathode S, yellow colour was observed to emerge from the anode, spread, and arrive at the cathode within 30 seconds, accompaning a current of ∼0.1 ma. (ionic current included).

Our Beckman DU spectrophotometer revealed that this colouration is due to the presence of a characteristic absorption shown by curve A in Fig. 2. Curve A corresponds to a colouration made at a temperature of 520°C and voltage of 250 v, while curve B to the V-absorption produced by heating the KI crystal in the presence of iodine vapour in our laboratory1)6).

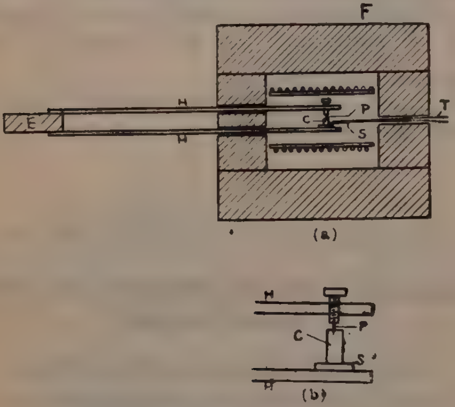

Fig. 1. Colouring Equipment.

E: ebonite insulator, H: metallic holder, F: furnace, C: crystal, P: platinum electrode, S: graphite support, T: thermocouple.

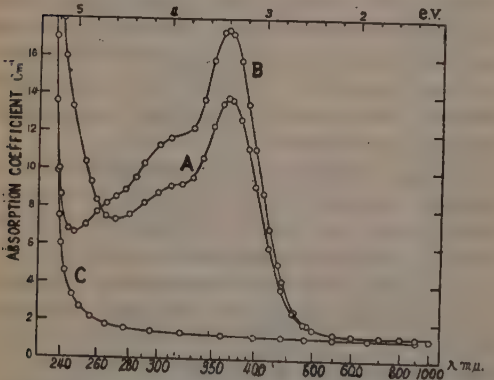

Fig. 2. Absorption curves of V-centres in KI.

A: coloured by the pointed anode, at 520°C, and 250 volt. B: coloured by heating in the iodine vapour. C: original colourless KI crystal. All curves were measured at room temperature using air as blank.

It will be seen that the general appearance of both curves are identical except the position of small hump7) of the curve B in the tail part of the first fundamental absorption band. Thus, it may be concluded that V-centres were produced by our experimental procedures.

One of the best-known methods to produce F-centres is to push electrons in the crystal at an elevated temperature from a pointed cathode. F-centres will then emerge from the pointed cathode and migrate to the anode. Just the same thing but reverse in signs has occurred in our experimental method to produce V-centres. Our interpretation is as follows: By electrolysis, halogen atoms are first produced at the surface of the sealed anode where the intimate contact of the halogen atoms with crystal is effective to originate positive holes. These holes drift towards the cathode and eventually are trapped to form V-certres. The conclusion is this: The positive holes can be injected into the alkali halide crystals.

A further verification in support of the intimate connection between holes and V-centres will be given as follows. First, V-centres were introduced from the pointed anode as mentioned above. When the V-colouration reached at the flat cathode, and signs of electrodes were interchanged, the V-colour was observed to disappear from the (new) anode side, leaving an increasing clear region behind the colour. As soon as the V-colour was nearly exhausted, the growth of F-colour was observed to emerge from the (new) cathode.

All the facts mentioned above suggest directly the role of positive holes in V-centres, details of which will be published in the near future.

References

1) Mollwo, E: Ann. Phys. (5) **29** (1937) 394.

2) Molnar, J. P.: Thesis, M.I.T. (1940). We are deeply indebted to Dr. J. P. Molnar for copies of this paper.

3) Alexander, J. and E. E. Schneider: Nature, **164** (1949) 653. Casler, R., P. Pringsheim and P. Yuster: J. Chem. Phys. **18** (1950) 887, 1564. Dorendorf, H.: Zeits. f. Phys. **129** (1951) 317. Dutton, D., and R. Maurer: Phys. Rev. **90** (1953) 126.

4) Seitz, F.: Phys. Rev. **79** (1950) 529.

5) Nagamiya, T.: J. Phys. Soc. Japan **7** (1952) 358.

6) Uchida, Y. and Y. Nakai: To be published.

7) The nature of this peak is not ascertained. Cf. Reference (6).

J. PHYS. SOC. JAPAN 8 (1953) 797~798

Dielectric Breakdown of Thin Alumina Film

By Hazimu KAWAMURA and Kazuko AZUMA

Faculty of Science and Engineering,
Osaka City University

(Received August 6, 1953)

If the dielectric breakdown is caused by electron avalanche due to the ionizations by collisions, it can be expected that the breakdown strength becomes very large when the thickness of the specimen is made as small as the mean free path of the free electron, just as in the case of spark discharge in gas. This fact was confirmed for mica and alumina[1] and explained theoretically by Fröhlich.[2]

If the mean range for ionization by collision is λ, the mean avalanche size after path d is $n = \exp(d/\lambda)$. If d is the thickness of the specimen, n becomes the mean size of the avalanches which have started at the cathode. As it may be assumed that the breakdown occurs when the avalanche size exceeds some critical value which is proportional to the thickness of the specimen, we have the relation

$$n_0 d = \exp(d/\lambda) , \qquad (1)$$

where n_0 is the critical avalanche size for the specimen of 1 cm thick, which is about 10^{12} according to the estimation of Seitz.[3] On the other hand, λ is given by[3][4]

$$\lambda = E(e/m)\tau^2 \exp(\alpha E_H/E) , \quad \alpha = 3.8, \qquad (2)$$

where E is the applied field, τ the relaxation time for the drift of the electron and E_H the breakdown field according to Hippel's criterion. From (1) and (2) we have

$$\log(d/E) = (\alpha E_H/E) + \log[(e/m)\tau^2 \log(n_0 d)] . \qquad (3)$$

Therefore, if we plot $\log(d/E)$ v.s. $1/E$, we get a straight line whose slope and the intersection with the ordinate give αE_H and $\log[(e/m)\tau^2\log(n_0 d)]$. From the latter we can estimate τ and mobility $(\mu = e\tau/m)$ of the electron.

The specimens employed were thin films of alumina of 100~2000 Å thick made by the anodic oxidations of aluminium films evaporated on glass plates. The thickness of the film was determined from its electric capacitance. The rectangular pulses of 30 microseconds with the P.R.T. of 100 1/sec. were applied on the specimen. Increasing slowly the pulse height, the pulse voltage at the instant of the disruption was read on the oscilloscope. The measurements were done at 373°K, 300°K and 198°K. The results are shown in fig. 1 and table I. The values of τ and μ shown respectively in the second and third columns of the table seem to be reasonable. If the interaction between the electron and the lattice is polar, the temperature dependency of τ is expressed as

$$1/\tau = (1/\tau_0)(2n+1) , \text{ where } n = 1/[\exp(\Theta/T) - 1] .$$

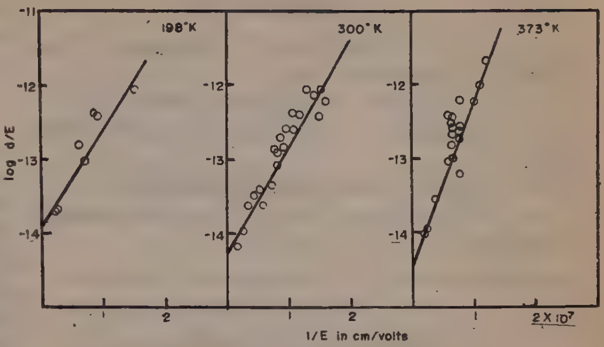

Fig. 1.

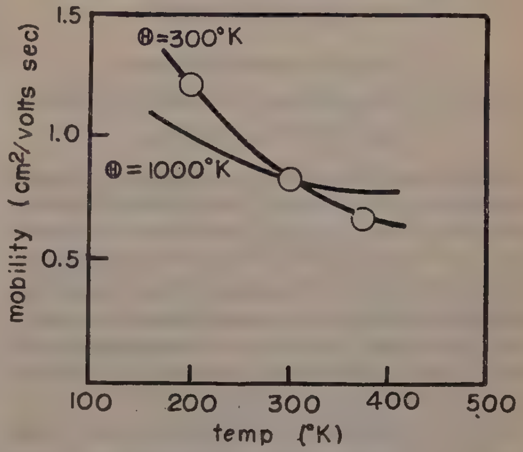

Fig. 2. ◉ experimental points
— theoretical curve

Table I.

temp (°K)	τ (sec)	μ (cm² /V. sec)	αE_H (V./cm)	E_H (V./cm)	α
198	6.9×10^{-16}	1.21	3.1×10^7	1.36×10^7	2.3
300	4.7×10^{-16}	0.83	3.3×10^7	1.62×10^7	2.1
373	3.8×10^{-16}	0.67	5.1×10^7	1.85×10^7	2.8

Assuming the Debye temperature Θ to be 300°K, we have a good agreement between experimental points and the theoretical curve as shown in fig. 2. Putting the experimental value of τ_0 into the expression $E = (\sqrt{mk\Theta}/\tau_0 e) \log(\gamma\sqrt{2n+1})$, $(\gamma \sim 3)$, we have the 5th column of the table. Finally we get α by comparing E_H with αE_H obtained by the slope of the lines in fig. 1, as shown in the last column of the table.

References

1) A. E. W. Austin and S. Whitehead: Proc. Roy. Soc. **A176** (1940) 33.
P. D. Lomer: Nature **166** (1950) 191.

2) H. Fröhlich: Proc. Roy. Soc. **A178** (1941) 493.

3) F. Seitz: Phys. Rev. **76** (1949) 1376.

4) H. Kawamura: Jour. Phys. Soc. Japan **8** (1953) 424.

J. PHYS. SOC. JAPAN **8** (1953) 798

Internal Friction of Metal Crystals Due to Vacancy Pairs

By Ryukiti Robert HASIGUTI

Faculty of Engineering, University of Tokyo

(Received July 10, 1953)

When a metal crystal is subjected to a plastic deformation, many atomic vacancies and interstitials are formed, of which mechanisms of formation were considered in terms of dislocations by various authors.1) It is accepted that a moving jog of screw dislocation leaves behind it either a line of vacancies or a line of interstitials according to the sign.2) Now the discussion in this short note will be focussed on vacancies.

A line of vacancies will dissociate into single vacancies and pairs of vacancies by thermal vibration. On account of unusual stability of vacancy pairs3), they will be formed preferentially. There are other sources of vacancy pairs: e. g. combination of two single vacancies produced in various ways during plastic deformation. Thus it is considered that a deformed metal crystal contains a fairly high density of vacancy pairs, if the temperature is not too high for vacancy pairs to remain without diffusing out of the crystal.

When an atom is removed from a lattice point to form a vacant site, the surrounding atoms of the vacancy are considered to be redistributed to regain energy.3) This redistribution of atoms may tend to decrease slightly the radius of vacancy, producing a stress field around it. The strain around a vacancy may be very small, if a vacancy is created in an otherwise perfect crystal. But the strain will be considerable, when a vacancy is in a stress field due to other sources. This can be explained by the fact that the potential energy curve for an atom neighboring to a vacancy is not so steep for a displacement towards the vacancy as it is for the displacement against the vacancy.

Strain around a vacancy pair would be larger than that around a single vacancy. It must be anisotropic, because the displacement of atoms should be larger in the direction perpendicular to pair axis. This anisotropy will be larger, when the pair is in a stress field due to other sources.

If this picture of strain around a vacancy pair is correct, it is possible that vacancy pairs act as a source of internal friction, just as zinc atom pairs do in copper zinc solid solution.4) The axes of vacancy pairs will tend to align parallel to tension axis and perpendicular to compression axis. Vibrational external stress will cause rotational vibrations of vacancy pairs around the axes perpendicular to the pair axes, if the vibrational frequency of external stress is appropriate. Because of the small value of activation energy of migration of vacancy pairs3), this kind of pair vibration is very likely.

The internal friction of cold-worked copper crystals is about ten times larger than that of cold-worked aluminum crystals6). It has been repeatedly pointed out1)2) that vacancies produced during plastic deformation will diffuse out in a few minutes at room temperature in the case of aluminum, while some of them will remain in the case of copper. Thus the difference in internal friction between copper and aluminum may be at least partly explained in terms of vacancy pair. The internal friction of cold-worked copper crystal decreases when the specimen is kept at room temperature for hours, while its hardness does not change. This may also be explained at least partly in terms of vacancy pairs, because it is easier for them to diffuse out than dislocations which increase hardness of the crystal.

Interstitial pairs may also be responsible for the internal friction. There is also a possibility that single vacancies and single interstitials will contribute to the internal friction, when the applied stress is inhomogeneous.

A detailed numerical calculation on the vacancy pair mechanism of internal friction will be published later.

References

1) See, for example, F. Seitz: Supplement to Phil. Mag. **1** (1952) 43.

2) See, for example,: N. F. Mott, Proc. Phys. Soc. B **64** (1951) 729.

3) J. H. Bartlett and G. J. Dienes: Phys. Rev. **89** (1953) 848.

4) C. Zener: Phys. Rev. **71** (1947) 34.

5) R. R. Hasiguti and T. Hirai: J. Appl. Phys. **22** (1951) 1084.

6) R. R. Hasiguti, T. Hirai and G. Kamoshita: To be published.

J. Phys. Soc. Japan 8 (1953) 799

Note on the Theory of Transport Phenomena in Polyatomic Gases

By Akira Isihara
Department of Physics, Faculty of Science, University of Tokyo

(Received March 2, 1953)

Transport phenomena in a classical gas with internal degrees of freedom are treated by Uhlenbeck and Wang1). We have treated the quantum mechanical case.

We thus start with the Boltzmann's equation:

$$Df_i=\frac{\partial f_i}{\partial t}+\boldsymbol{\nu}\cdot\frac{\partial f_i}{\partial x}+\boldsymbol{X}\cdot\frac{\partial f_i}{\partial \boldsymbol{\nu}}$$

$$=-\sum_{jkl}\int\{f_if_j(1+\theta f_k')(1+\theta f_l')$$

$$-f_i'f_j'(1+\theta f_k)(1+\theta f_l)\}gw_{ij}^{kl}(\vartheta,g)d\Omega d\phi_j \quad (1)$$

with the following auxiliary equations:

$$f_i^{(0)}=1\bigg/\frac{1}{A_i}\exp\tau^2-\theta\ ;\quad \tau^2=\frac{m}{2kT}V^2=c^2V^2\ , \quad (2)$$

$$\boldsymbol{V}=\boldsymbol{\nu}-\boldsymbol{u};\quad \varepsilon_i=E_i/kT;\quad A_i=A\exp(-\varepsilon_i), \quad (3)$$

$$\boldsymbol{\xi}=c^{1/2}(\boldsymbol{\nu}-\boldsymbol{u})=c^{1/2}\boldsymbol{V}\ , \quad (4)$$

$$n=\sum_i\int f_i^{(0)}d\phi=G\frac{(2\pi mkT)^{3/2}}{h^3}F^*_{1/2}(A)\ , \quad (5)$$

$$F^*_s(A)=\sum g_iF_s(A_i)\ , \quad (6)$$

$$U=U_k+U_i\ , \quad (7)$$

$$U_k=\frac{3kT}{\rho}G\frac{(2\pi mkT)^{3/2}}{h^3}F^*_{3/2}(A)\ , \quad (8)$$

$$U_i=\frac{kT}{m}\frac{H_{1/2}(A)}{F^*_{1/2}}\ ;\quad H_{1/2}(A)=\sum g_i\varepsilon_iF_{1/2}(A_i)\ , \quad (9)$$

$$p=\frac{2}{3}\rho U_k\ . \quad (10)$$

Here, U_k and U_i correspond to the kinetic and internal energies respectively. The other notations are similar to the previous articles and we may omit the explanations1)2).

To solve Eq. (1), we must replace the time derivative appeared in the left hand side by derivatives with respect to coordinate and temperature. For this purpose, the equations of continuity:

$$\frac{d\rho}{dt}+\rho\frac{\partial \boldsymbol{u}}{\partial \boldsymbol{x}}=0\ , \quad (11)$$

$$\rho\frac{dU}{dt}+\frac{\partial \boldsymbol{q}}{\partial \boldsymbol{x}}=-p\frac{\partial \boldsymbol{u}}{\partial \boldsymbol{x}}\ , \quad (12)$$

and the first law of thermodynamics are useful.

Thus, for example, we obtain the following expressions:

$$\frac{d\log T}{dt}=-\frac{2}{3}\left(1-\frac{c_i}{c_v}\right)\frac{\partial \boldsymbol{u}}{\partial \boldsymbol{x}}\ , \quad (13)$$

$$\frac{\partial\log p}{\partial \boldsymbol{x}}-\frac{5}{2}\frac{\partial\log T}{\partial \boldsymbol{x}}=\frac{nkT}{p}\left(\frac{\partial\log A}{\partial \boldsymbol{x}}+\bar{\varepsilon}_i\frac{\partial\log T}{\partial \boldsymbol{x}}\right), \quad (14)$$

$$\frac{d\log A}{dt}=\left(\frac{2}{3}\bar{\varepsilon}_i-\frac{2}{3}\frac{c_i}{c_v}\bar{\varepsilon}_i-\frac{c_i}{c_v}\right)\frac{\partial \boldsymbol{u}}{\partial \boldsymbol{x}}\ , \quad (15)$$

$$\bar{\varepsilon}_i=mU_i\ , \quad (16)$$

and using these equations, we can easily calculate the reduced form of Eq. (1):

$$Df_i^{(0)}=\frac{f_i^{(0)2}e^{\tau^2}}{A_i}\left\{2\left(\boldsymbol{\xi}\boldsymbol{\xi}-\frac{\tau^2}{3}\boldsymbol{1}\right):\frac{\partial}{\partial \boldsymbol{x}}\boldsymbol{u}\right.$$

$$+\frac{c_i}{c_v}\left(\frac{2}{3}\tau^2+\frac{2(\bar{\varepsilon}_i-\varepsilon_i)c_v}{3c_i}-1\right)\frac{\partial \boldsymbol{u}}{\partial \boldsymbol{x}}$$

$$+\frac{\boldsymbol{\xi}}{c^{1/2}}\cdot\left(\tau^2-\frac{5}{2}\frac{p}{nkT}\right)\frac{\partial\log T}{\partial \boldsymbol{x}}$$

$$\left.+\frac{\boldsymbol{\xi}}{c^{1/2}}\cdot(\bar{\varepsilon}_i-\varepsilon_i)\frac{\partial\log T}{\partial \boldsymbol{x}}\right\}\ , \quad (17)$$

which corresponds to Uhlenbeck's Eq. (10)1).

References

1) C. S. Wang Chang and G. E. Uhlenbeck, U. S. Navy Department, Contract NOrd 7924, July, 1951.

2) A. Isihara: J. Phys. Soc. Japan **5** (1950) 213; 217.

J. Phys. Soc. Japan 8 (1953) 799~801

Some Particular Solutions of Compressible Flow Equations for Arbitrary Pressure-Density Relation

By Isao Imai
Department of Physics, Faculty of Science, University of Tokyo

(Received July 9, 1953)

In a recent paper [3] entitled "On Vortex-Equation in Isentropic Flow" v. Krzywoblocki has considered a particular solution of the hodograph equation for an adiabatic gas flow which corresponds to the flow due to a point vortex. The problem had already been treated as a particular example by Ringleb in his famous paper on the hodograph method in the compressible flow theory [4]. v. Krzywoblocki states that his result differs from that obtained by Ringleb.

The object of this short note is firstly to remark that the difference can be traced back to the fact that Ringleb has assumed the value of the adiabatic index k to be 1.4, without stating so explicitly. The second and main object is to remark that the formulae giving the analogous flow patterns as well as the flow around a semi-infinite plate have already been obtained by the present writer for a compressible fluid with arbitrary pressure-density relation [2].

According to the writer's paper, the hodograph equations can be written as

$$\frac{\partial \Phi}{\partial q}=q\frac{d}{dq}\left(\frac{\rho_0}{q\rho}\right)\frac{\partial \Psi}{\partial \theta}, \quad \frac{\partial \Phi}{\partial \theta}=q\frac{\rho_0}{\rho}\frac{\partial \Psi}{\partial q} \tag{1}$$

or

$$\frac{\partial \Phi}{\partial \theta}=\frac{\partial \Psi}{\partial t}, \quad \frac{\partial \Phi}{\partial t}=-K\frac{\partial \Psi}{\partial \theta} \tag{2}$$

with

$$t=\int\frac{\rho}{\rho_0}\frac{dq}{q}, \tag{3}$$

$$K=-q^2\frac{\rho_0}{\rho}\frac{d}{dq}\left(\frac{\rho_0}{q\rho}\right)=q\frac{d^2}{dt^2}\left(\frac{1}{q}\right)$$
$$=\left(1-\frac{q^2}{c^2}\right)\left(\frac{\rho_0}{\rho}\right)^2, \quad c^2=\frac{dp}{d\rho}. \tag{4}$$

Here Φ is the velocity potential, Ψ is the stream function, q and θ are the magnitude and direction of the velocity, c is the local sound velocity, p is the pressure, ρ is the density, and ρ_0 is the stagnation density.

Ψ and Φ satisfying (1) and the corresponding cartesian coordinates (x,y) of the physical plane were obtained in the forms:

$$\Psi=A_0\Psi_{00}+B_0\Psi_{01}+\sum(A_n\Psi_{nc}+B_n\Psi_{ns}),$$
$$\Phi=A_0\Phi_{00}+B_0\Phi_{01}+\sum(A_n\Phi_{nc}+B_n\Phi_{ns}),$$
$$x=A_0x_{00}+B_0x_{01}+\sum(A_nx_{nc}+B_nx_{ns}),$$
$$y=A_0y_{00}+B_0y_{01}+\sum(A_ny_{nc}+B_ny_{ns}),$$

where A_n, B_n are arbitrary constants, $\Psi_{00}=Q_0(q)$, $\Psi_{01}=Q_0(q)\theta$, $\Psi_{nc}=Q_n(q)\cos n\theta$, $\Psi_{ns}=Q_n(q)\sin n\theta$, $(n\neq 0)$. Expressions for Φ_{nc}, Φ_{ns}, x_{nc}, $\cdots$, y_{ns} were also given. For $n=0$ and $n=1$, particularly simple expressions have been obtained. Thus, after some transformations, the result of the paper can be rewritten as follows.

For $n=0$

$$\Psi=t, \quad \Phi=\theta, \quad x+iy=-i\frac{1}{q}e^{i\theta}. \tag{5}$$

$$\Psi=\theta, \quad \Phi=-\int K dt, \quad x+iy=\frac{\rho_0}{q\rho}e^{i\theta}. \tag{6}$$

$$\Psi=t\theta, \quad \Phi=\frac{1}{2}\theta^2-\int Kt dt,$$
$$x+iy=\frac{1}{q}e^{i\theta}\left(-i\theta+1+\frac{\rho_0}{\rho}t\right). \tag{7}$$

For $n=1$

$$\Psi=\frac{1}{q}\cos\theta, \quad \Phi=-\frac{\rho_0}{q\rho}\sin\theta,$$
$$x+iy=\frac{i}{2}\frac{\rho_0}{\rho q^2}e^{2i\theta}-\frac{i}{2}\int\frac{\rho_0}{\rho}\frac{dq}{qc^2}. \tag{8}$$

$$\Psi=\frac{p}{q}\cos\theta, \quad \Phi=-\left(\frac{\rho_0}{\rho}\frac{p}{q}+\rho_0 q\right)\sin\theta,$$
$$x+iy=\frac{i}{2}\left(\frac{\rho_0}{2}+\frac{\rho_0}{\rho}\frac{p}{q^2}\right)e^{2i\theta}-\frac{\rho_0}{2}(\theta+i\log q)$$
$$-\frac{i}{2}\int\frac{\rho_0}{\rho}\frac{p}{qc^2}dq. \tag{9}$$

The above are the solutions corresponding to Ψ_{nc}. Those corresponding to Ψ_{ns} are naturally obtained by substituting $\theta+\pi/2$ for θ in the above solutions.

The set of solutions (5) represents the flow due to a point vortex, which has been treated by Ringleb and v. Krzywoblocki. For the adiabatic flow

$$\frac{\rho}{\rho_0}=(1-\alpha q^2)^{1/(k-1)}, \quad \alpha=\frac{k-1}{2c_0^2}.$$

Hence

$$t=\int(1-\alpha q^2)^{1/(k-1)}\frac{dq}{q}.$$

Ringleb's solution (p. 190)

$$\Psi=C\left[\frac{1}{2}\log\frac{1-W}{1+W}+W+\frac{1}{3}W^3+\frac{1}{5}W^3\right]+C',$$

where $W=(1-\alpha q^2)^{1/2}$, is readily found to have been obtained on the assumption $k=1.4$.

The flow around a semi-infinite plate treated by Ringleb corresponds to the set of solutions (8). His formula (24)

$$\int\frac{\rho_0}{\rho}\frac{dq}{qc^2}=-\frac{1}{c_0^2}\left[\frac{1}{2}\log\frac{1+W}{1-W}-\frac{1}{W}\right.$$
$$\left.-\frac{1}{3}\frac{1}{W^3}-\frac{1}{5}\frac{1}{W^5}\right]$$

could not be obtained without the assumption $k=1.4$, which is not stated explicitly in his paper.

Finally, combination of (8) and (9) such that

$$\Psi=\frac{p-p_1}{q}\cos\theta, \quad \Phi=-\left(\frac{\rho_0}{\rho}\frac{p-p_1}{q}+\rho_0 q\right)\sin\theta$$
$$x+iy=\frac{i}{2}\left(\frac{\rho_0}{2}+\frac{\rho_0}{\rho}\frac{p-p_1}{q^2}\right)e^{2i\theta}$$
$$-\frac{\rho_0}{2}(\theta+i\log q)-\frac{i}{2}\int\frac{\rho_0}{\rho}\frac{p-p_1}{qc^2}dq \tag{10}$$

gives the flow (at rest at infinity and having *U*-shaped stream-lines) along two parallel semi-infinite plates and a free stream-line, the pressure on the free stream-line being $p=p_1$. In fact, the stream-line $\Psi=0$ is given by $\theta=\pm\pi/2$ and $p=p_1$. The flow of this type has been considered in detail by Hasimoto [1]. The form of the free stream-line is given by putting $p=p_1$ in (10). Thus

$$x+iy=\frac{\rho_0}{2}\left(\frac{i}{2}e^{2i\theta}-\theta\right)+\text{const}. \tag{11}$$

Therefore, the form of the free stream-line is not affected by the compressibility of the gas for any arbitrary pressure-density relation, remaining the same as that for an incompressible fluid. This conclusion has been reached by Hasimoto under the special assumption $p\propto\rho^{1\cdot 4}$.

References

1) Z. Hasimoto: Sûributurigaku-Kenkyû (Studies in Mathematical Physics) **2** (1952) 141. (In Japanese)

2) I. Imai: Ooyôsûgaku-Rikigaku (Applied Mathematics and Mechanics) **1** (1947) 147. (In Japanese)

3) M. Z. v. Krzywoblocki: J. Phys. Soc. Japan **8** (1953) 387.

4) F. Ringleb: Z.A.M.M. **20** (1940) 185.

J. Phys. Soc. Japan **8** (1953) 801~802

An Unusual Star

S. Nakagawa, H. Huzita
and K. Okudaira

Department of Physics,
Rikkyo University, Tokyo

(Received July 3, 1953)

Ilford G5 400 μ emulsions imbedded in a paraffin block, which is shown in Fig. 1 had been exposed for about one hour above 20 km high by mean of balloons in August 1952. We observed 35 big stars ($\geqslant 7$ prongs) and 187 small stars ($7 >$ star size $\geqslant 3$) in the emulsion of volume 6.13 cc. The grain densities of some gray prongs (5 min $>$ grain density $>$ 1.5 min) were found to be increasing or decreasing with the distance from the stars. All the prongs of big stars and some from small stars had increasing densities, while five prongs from small stars, decreasing. This seems to show that the latter were produced by the star-inducing particles.

Measuring the multiple scattering angles along these prongs and the energy balance of these stars, we concluded that the four were produced by protons. The one, showing somewhat larger scattering, could not be produced by a proton considering the energy balance, and this event might be interpreted as the capture of a heavy meson. This is shown in Fig. 2.

Track (1) is 2.9 mm long and the grain density decreases from the star about 3.8 to 3.2 times minimum to the emulsion surface grain counts were taken in a layer between 110 and 13 microns from the emulsion air surface. The inhomogeneity of the plate was examined by measuring the grain densities of 13 tracks near this track ($3\times 3\,\text{mm}^2$ area), but the abnormal change of grain density was not found within experimental limit.

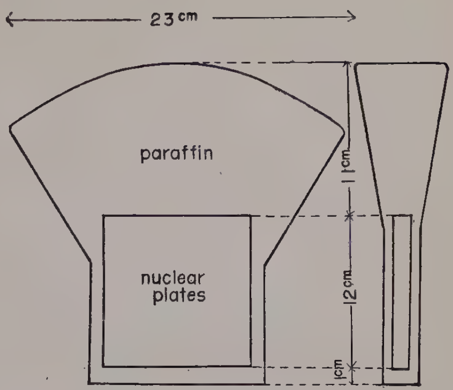

Fig. 1. Schematic arrangement of G5 plates and a paraffin block.

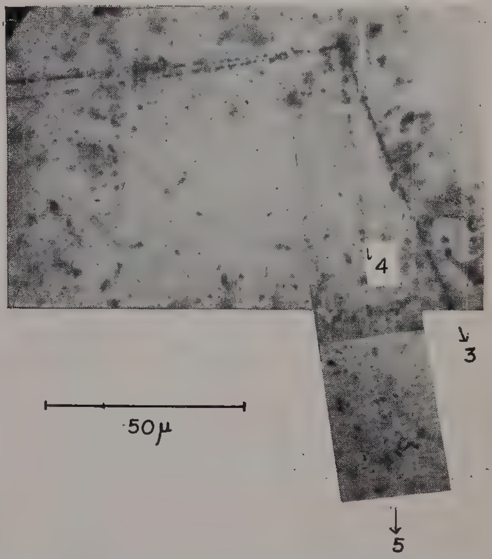

Fig. 2. An event which is interpreted as a star due to the nuclear interaction of a heavy meson.

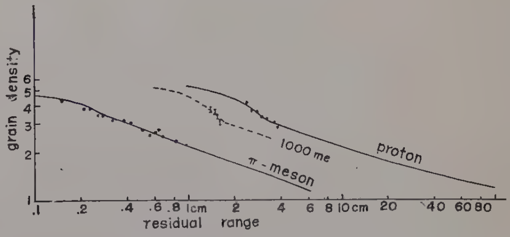

Fig. 3. Grain density versus range curves. Solid line shows Goldschmidt-Clermont's data.

We also selected tracks in this emulsion which had nearly same grain density as track (1) and examined the variation in their grain density. In Fig. 3 the single proton track 1.6 cm long and μ-meson track 1 cm long were plotted to compare with the data of Goldschmidt-Clermont.[1] Although the variation of grain density is rather steeper at 3~5 times minimum, our data shows good agreement with his. All the tracks which were determined from the scattering angle measurement as the proton showed nearly same trend of the variation. The observed density of the track (1) is also plotted on the curve of 1000 me particle which is obtained tentatively by the mass ratio displacement from the proton burve.

Multiple scattering angles along the track (1) were also measured segmentally, but the variation of the angle was not certainly determined, from the data 0.24°±0.05 to 0.20°±0.05. However, since the variation of grain density is clear, the track (1) is considered to be produced by the incident particle. The mass estimated from the scattering angle is 1400±400 me. Both measurement shows that the star was produced by a heavy meson.

The track (2) is 600 μ long and goes to the backing glass plate and the track (3) is 4.6 mm long and stops in the emulsion. Measurements of scattering angle versus grain density or range of track, show that both tracks are produced by the proton. The energy of the former is about 90 MeV and that of the latter is about 33 MeV. The track (4) is 54μ and (5) is 220μ long and both go to the backing glass plate. The grain density along the former track is about 3.9 times minimum and along the latter is about minimum. As the scattering angle cannot be measured with these short tracks, the masses of the particles are not certain. The track (6) stopped in the emulsion is 2.7μ long and is interpreted as that produced by a recoil nucleus.

If we assume the incident particle be a proton, its energy is estimated to be about 90 MeV. With such an assumption, however, the emission of particles of track (2), (3), (4) and (5) is energitically impossible. Alternatively the lower limit of the mass of the incident particle may be estimated from the energy balance between incident and outgoing particles. Assuming the track (4) is produced by a proton of about 88 MeV energy, track (5) by a π-meson of about the rest energy, the lower limit of the mass of particle produced track (1) is estimated to be about 860 me using only the data of charged particles.

It may be concluded that the event is an example of the nuclear interaction of a heavy meson with a nucleus in the emulsion. Such an event has been reported by Fry and Lord[2] in the case of the nuclear capture of a slow negative τ- or κ-meson.

The author is grateful to Professor O. Minakawa of Kobe University and the member of the High Altitude Meteorological Observatory for the cooperation in flying balloons. This experiment was supported by the Scientific Research Expenditure of the Ministry of Education.

References

1) Y. Goldschmidt-Clermont, Bulletin du centre de Physique nuclearire de l'universite libre de Bruxelles. No. 14 (1950).

2) W. F. Fry and J. J. Lord: Phys. Rev. **87** (1952) 533.

J. Phys. Soc. Japan **8** (1953) 802~803

Paramagnetic Resonance in the Nickel Sulphate Heptahydrate

By Kazuo Ōno

Institute of Science and Technology,
University of Tokyo

(Received July 25, 1953)

The behaviour of the Ni^{++} ion $[(3d)^8\,{}^3F]$ under influence of crystalline field was investigated theoretically by Schlapp and Penney[1]. A cubic field splits the F state into two orbital triplets and a singlet. The singlet lies lowest and the triplets are of the order of 10000 cm^{-1} higher in energy. When the combined effects of the rhombic crystalline field and the spin-orbit coupling are included, the lowest orbital singlet which has three fold degeneracy due to the spin ($S=1$) undergoes a further small splittings of the order of 1 cm^{-1}. When a magnetic field is applied, the spin triplet is described by the Hamiltonian

$$H=DS_z^2+E(S_x^2-S_y^2)+g\beta \boldsymbol{HS}\,.$$

According to the experimental results of Penrose and Stevens[2], Griffiths and Owen[3] and others[4]

$$|D|=0.32\,\mathrm{cm}^{-1},\ E=0\,\mathrm{cm}^{-1},\ g=2.29 \quad \text{for } NiSiF_6\cdot 6H_2O\ ^{2)}$$

$$D=-2.24\,\mathrm{cm}^{-1},\ E=-0.38\,\mathrm{cm}^{-1},\ g=2.25 \quad \text{for } Ni(NH_4)_2SO_4\cdot 6H_2O\ ^{3)}.$$

There is no paramagnetic resonance experiment in $NiSO_4\cdot 7H_2O$, due to its rather large initial splittings, although measurements of static susceptibility in this salt have been obtained by many authers[5]. We have recently succeeded to accomplish a magnetron harmonic generater described by Klein et al in R.S.I. (1952)[6]. Using this oscillator, we can observe the resonance absorption lines in $NiSO_4\cdot 7H_2O$ at $\lambda=0.54$ cm and $\lambda=0.65\,\mathrm{cm}^{-1}$. That is; 0.54 cm wave-length is sixth and 0.65 cm wave-length is fifth harmonics of 3.24 cm wave-length generated by the magnetron (peak power≒50 kW. mean power≒100 watts).

The magnetic field used is up to about 25000 gauss.

The magnetic fields corresponding to the observed peaks in a-b plane are shown in Fig. 1 and the line width is about 1500 gauss. Full and dotted lines in the figure are those obtained using $\lambda=0.54$ cm and $\lambda=0.65$ cm respectively. Using the results in Fig. 1 and other experimental data, it is found that $g=2.2_0$, $D=-3.5_6\,\mathrm{cm}^{-1}$, $E=-1.5_0\,\mathrm{cm}^{-1}$, the splittings between adjacent lebels when $H=0$ are $|D-E|=2.0_6\,\mathrm{cm}^{-1}$ and $|2E|=3.0_0\,\mathrm{cm}^{-1}$.

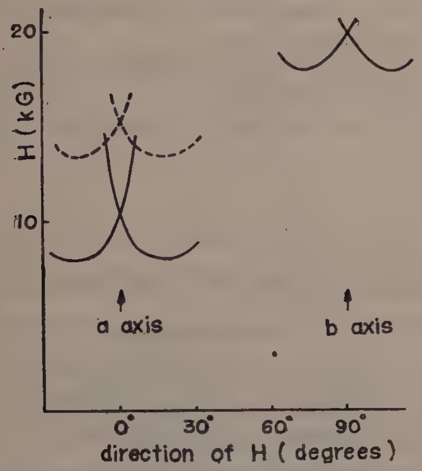

Fig. 1. The position H of absorption lines of $NiSO_4 \cdot 7H_2O$ in a—b plane. Full and dotted lines are respectively obtained at $\lambda=0.54$ cm and $\lambda=0.65$ cm.

$NiSO_4 \cdot 7H_2O$ (rhombic; a:b:c=0.9815:1:0.5656)[7] contains four inequivalent ions in a unit cell.[8] The direction cosines of the rhombic axes of the crystalline field for each of these four ions refered to the crystal axes (a b c) are found from the present measurements to be as follows:

$z_1 \doteqdot z_2$: (0.95, 0.31, 0) $z_3 \doteqdot z_4$: (0.95, −0.31, 0)

y_1: (−0.31, 0.95, 0.09) y_2: (−0.31, 0.95, −0.09)

y_3: (0.31, 5.95, 0.09) y_4: (0.31, 0.95, −0.09)

There may be errors of several percent in the experimental values of D, E and g and more than ten percent in the direction cosines of crystalline field.

A comparison can be made between the magnitudes of magnetic anisotropy in static susceptibility and the values calculated from the present measurements. Using the formulae derived by Griffiths and Owen[3] and adapting $\lambda=-280\,\mathrm{cm}^{-1}$ (λ: coefficient of L. S. coupling), we can obtain the results in Tab. I. The agreement of observed values and calculated ones are fairly good.

Table I. Comparison of the experimental and calculated values of the anisotropy (per mol).

	$(x_a-x_b)\times10^6$ (e.m.u)	$(x_a-x_c)\times10^6$ (e.m.u)	$(x_c-x_b)\times10^6$ (e.m.u.)
calculated values	1.7	0.6	1.1
observed values	1.69	0.49	1.20

Thanks are due to Professor Hiroo Kumagai for his continuous guidence and encouragement throughout this work.

References

1) R. Schlap and W. G. Penney: Phys. Rev. **42** (1932) 666.

2) R. P. Penrose and K. W. H. Stevens: Proc. Phys. Soc. **A63** (1950) 29.

3) J. H. E. Griffiths and J. Owen; Proc. Roy. Soc. **A213** (1952) 473.

4) Holden et al: Phys. Rev. **75** (1949) 1443.

5) K. S. Krishnan et al: Phil. Trans. **A232** (1933) 99.

B. C. Guha: Proc. Roy. Soc. **A206** (1951) 353.

6) J. A. Klein et al: R. S. I. **23** (1952) 78.

7) Groth: Chemische Krystallographie II, 434.

8) C. A. Beevers and C. M. Schwarkz: Z. Krist. **A91** (1935) 157.

J. Phys. Soc. Japan **8** (1953) 803~804

An Improvement in High Speed Expansion of Counter-Controlled Cloud Chamber

By Isao Kita

Department of Physics, Kobe University

(Received August 12, 1953)

When a cloud chamber is controlled by Geiger counters, it is necessary to complete expansions in a very short time after the event triggering the counter system has occured. The expansion valve for a cloud chamber usually consists of an electro-magnet holding a valve disk against a self-sealing gasket[1], and the pulse from the counter system acts to decrease the field in the magnet, allowing the valve disk to be pushed open by the air pressure inside. While air escapes through the valve opening, the cloud chamber is expanding. Hence the following time delays have to be considered. First, there is the decay time, t_1, of the field in the holding magnet. t_1 depends on the electrical constants and on the structure of the magnet. Secondly t_2 will designate the time during which air flows through the valve opening, while the valve disk is in motion and thereafter. Of course the aerodynamic resistance of the air duct determines t_2 and hence it depends on the size of the valve opening and the structure of the cloud chamber.

To reduce t_1, Shutt and Whittemore[2] employed double expansion valves and showed that the delay time of the *first* valve opening could be made very short as 0.001 sec. and the power consumption of the magnet small. But the structure of the valve is somewhat complicated and in the case of the larger valve opening of the same type as 10 cm in diameter, the opening of the *main* valve is delayed about 0.015 sec.[3] For a expansion valve of usual electromagnet type used at this laboratory, however, it appeared very useful to improve the electrical circuit in the following way. The circuit diagram is shown in Fig. 1.

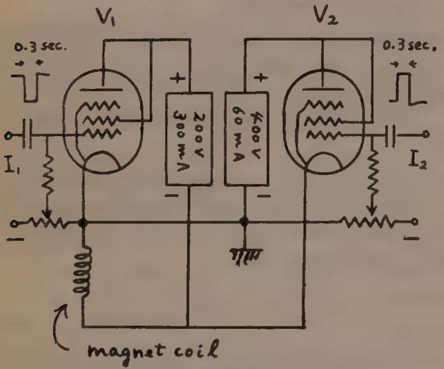

Fig. 1. The circuit diagram of expansion electro-magnet.

While the cloud chamber is compressed, V_1 is conductive and V_2 cut off, and the magnet holds the valve disk against the inner air pressure. When the counter system is triggered, the negative square pulse is applied to I_1 and at the same time the positive square pulse to I_2. Hence V_2 turns to be conductive and V_1 cut off and the inverse voltage is applied across the coil of the magnet. The current through the coil of magnet is, therefore, decreased very fast to the opposite sign. To the contrary when V_2 is not in operation the current decays to zero more slowly than in the former case. Hence, the decay time t_1 can be considerably shorter than that without the inverse voltage.

The value opening of the cloud chamber used by the author was 60 mm in diameter and the power consumption 4.9 watts. It was found experimentally that the decay time, t_1, of the field in the magnet was 0.004 sec. when this method was adopted, while it was 0.014 sec. when the inverse voltage was not applied, and it appeared very useful to adopt this simple method for completing the expansion in a short time.

References

1) W. R. Chang and J. R. Winckler: Rev. Sci. Inst. **20** (1949) 276.
2) R. P. Shutt and W. L. Whittmore: Rev. Sci. Inst. **21** (1950) 643.
3) Cosmic Ray Group of Osaka City Univ.

J. Phys. Soc. Japan 8 (1953) 804~805

Polarization of Electrons by Scattering, IV

By Norio Ryu
Department of Physics, Faculty of Science,
Kyusyu University, Fukuoka

(Received August 22, 1953)

In the previous papers (Parts I[1] and II[2]) the author have reported the results of experiments on the electron polarization by double scattering carried out at angles larger than 90° using thin gold foils of 5×10^{-6} cm in thickness. The results showed the existence of the polarization effect clearly agreeing with the experiment of Shull *et al.*, but contradicted with those of Dymond[4] and Thomson[5]. It seems probable that the contradiction between these experiments is due mostly to plural scattering in the foil. Although our experimental results show the similar tendency predicted by the theories[6], the amounts of the polarization asymmetry are even smaller than anyone of the theoretical values which depend, however, considerably on the nuclear screening by ordital electrons. It is considered, therefore, to be important to try again the polarization experiments more accurately at some conditions. So investigations were carried out at some conditions used in the previous experiment, and at a higher energy or at an other angle (135°).

The apparatus was newly designed to make an improvement in the geometory of scattering chambers and to avoid a disturbance from X-rays at higher energy. The experimental procedure was quite similar as used in Parts I and II, i.e., the intensities of the scattered electrons from the second foil (analizer) were detected simultaneously by G. M. counters in the direction of the incident beam and in the opposit direction, and then the analyzing chamber was rotated through an angle of 180° together with the counters and the scattered electrons were measured again. On detecting the scattered electrons, the use of two counters separated by a hole in coincidence at each detector was very favourable to avoid the effects of X-rays and stray electrons; while the measured intensities were far less than the case of single counter even when the beam was so strong as to damage the foil, because the scattering at the aluminium window (10^{-3} cm) of the front counter was very large at the energy region used here. Some results so obtained are shown in Table I of which statistical errors are rather large by the reason mentioned above. We used also a single counter as the detector to give good statistics. In the experiments of 120°-120° the backgrounds of X-rays, which have to be corected in the results, were 0.3, 2 and 22 per cent of the detected intensities at energies of 100, 120 and 140 keV, respectively. The results are shown in Table I and they show a good agreement with the previous ones except at 140 keV where a new result was obtained. In the previous experiments, the fact that some results at 130 keV showed a little smaller values than the ones at 120 keV was probably due to the incompleteness in correcting the effect of X-rays.

Table I. Values of $-200\delta^2$ at 120°-120°.

energy (keV)	coincidence method	single counter method		previous results
100	13±4	14.0±1.3	13.5±1.6	15.0±1.6
110	—	—	—	14.5±1.9
120	18±6	17.8±0.8	17.9±1.4	16.9±2.0
130	—	—	—	11.6±2.3
140	—	18.9±1.5	—	—

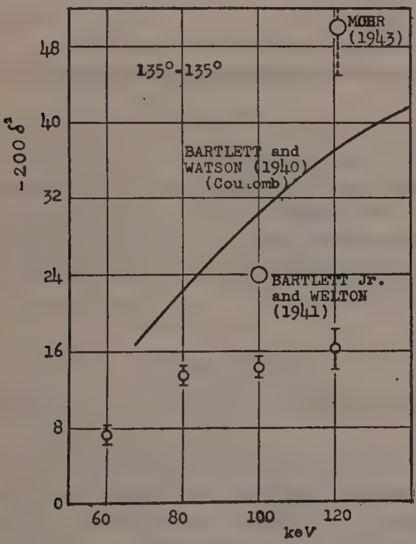

Fig. 1. Values of $-200\,\delta^2$ in the experiment of 135°—135° as a function of the energy of electrons. Small circles show the experimental results and large ones the theoretical values.

The results of 135°-135° are shown in Table II and in Fig. 1 together with the values predicted by a theory. The backgrounds of X-rays were 0.2, 1.5 and 14 per cent of the detected intensities at 80, 100 and 120 keV, respectively. The general features of these results that the values are smaller than any theoretical ones are similar to those at other angles, and there is no considerable change of the values themselves compared with those at other angles. The correction from the plural scattering is very small in this case, amounting to a few per cent, because of the large scattering angle.

Table II. Values of $-200\,\delta^2$ at 135°-135°.

energy (keV)	experiment	theory* (Coulomb)
60	7.3±1.0	—
80	13.5±1.0	23
100	14.3±1.1	31
120	16.2±2.1	37

* The theoretical values are rough estimation from the theory of Bartlett and Waston.

Sources of errors of the results in Tables I and II caused by X-rays and others may be discussed similarly as in Parts I and II, but there is no other discussion than those which the present author have already made an attempt in Parts I, II and III.7)

The author wishes to express his sincere thanks to Prof. I. Nonaka for his kind guidance, and also to Mr. T. Ide for his assistance in measurements.

References

1) N. Ryu: J. Phys. Soc. Japan **7** (1952) 125.

2) N. Ryu: J. Phys. Soc. Japan **7** (1952) 130.

3) C. G. Shull, C. T. Chase and F. E. Myers: Phys. Rev. **63** (1943) 29.

4) E. G. Dymond: Proc. Roy. Soc. **A 136** (1932) 638; *ibid.* **A 145** (1934) 657.

5) G. P. Thomson: Phil. Mag. **17** (1934) 1058.

6) N. F. Mott: Proc. Roy. Soc. **A 124** (1929) 425; *ibid.* **A 135** (1932) 429; J. H. Bartlett and R. E. Watson: Phys. Rev. **56** (1939) 612; J. H. Bartlett and R. E. Watson: American Acad. of Arts and Sci. **74** (1940) 53; J. H. Bartlett, Jr. and T. A. Welton: Phys. Rev. **59** (1941) 281; H. S. W. Massey and C. B. O. Mohr: Proc. Roy. Soc. **A 177** (1941) 341; C. B. O. Mohr: Proc. Roy. Soc. A **182** (1943) 189.

7) N. Ryu, K. Hashimoto and I. Nonaka: J. Phys. Soc. Japan **8** (1953) 575.

J. Phys. Soc. Japan 8 (1953) 806

Damage as an Initial Stage of Fatigue Fracture

By Takeo Yokobori

Institute of Science and Technology, University of Tokyo

(Received October 8, 1953)

It has been understood from previous studies[1][2] that the number of repeated cycles to fatigue fracture is essentially statistical in nature, after the repitition of some certain number of cycles. Initial stage of fatigue fracture is required to be studied to get detailed knowledge upon the related probability in these statistical phenomena. The so-called damage seems to be available for this purpose. The term of damage[3] mentioned above usually means that the endurance limit of the specimen subjected to a constant applied stress range for some certain repeated cycles becomes less than that of the virgin specimen. On the other hand, the endurance limit of the specimen unloaded immediately before damaged shows in general higher value than that of the virgin specimen.

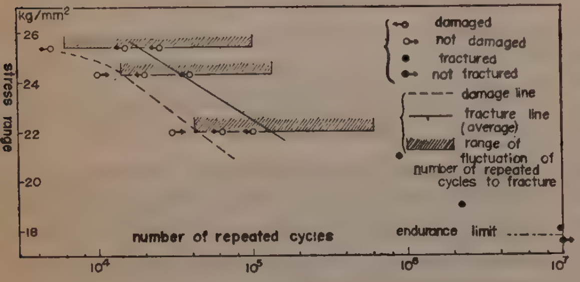

Fig. 1.

In this note, as the continuations of the previous experiments[2] upon the fluctuations of the number of repeated cycles to fracture, damage line, that is, the relation between the stress range and the number of repeated cycles to damage was experimentally determined. Damage was found to occur near the lower boundary of fluctuation range of number of cycles to fracture as shown in Fig. 1. It is also understood that the fluctuation of the number of cycles to damage is very much smaller than that to fracture. It justifies the assumption made in the previous analysis.[2] These results seem to support the view that after damage occurred the phenomenon of fatigue fracture becomes one of an essentially statistical nature.

The variation of hardness with the number of repeated cycles is shown in Fig. 2. From this and the previous experiments[1], damage seems to occur roughly near the stage when strain hardening has saturated.

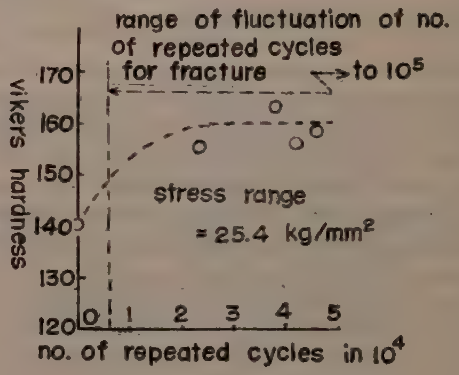

Fig. 2.

The author wishes to express his hearty thanks to Prof. M. Hirata for kind guidance, to Prof. F. Nakanisi for kindness for the experiments in this Institute and to Mr. K. Amino for help with experiments.

References

1) T. Yokobori: J. Phys. Soc. Japan **6** (1951) 81.
2) T. Yokobori: Ibid. **8** (1953) 265.
3) Battelle Memorial Institute, Prevention of the Failure of Metals under Repeated Stress, John Wiley & Sons. (1941) 188.

CONTENTS

(Vol. 8)

No. 1

Tetsuo WAKATSUKI: On the Capture Scattering of Fast Neutrons 1
Junkichi SOMA and Masamichi OGI: On a Non-linear Approximation of the Interatomic Force in Solid 6
Kyozaburo KAMBE, Ichiro NAKADA and Hidetosi TAKAHASI: Hysteresis Loops of Ceramic Barium Titanate at Higher Frequencies I 9
Kyozaburo KAMBE: Hysteresis Loops of Ceramic Barium Titanate at Higher Frequencies II 15
Shoichi MATSUDA: On the Superlattice Formation in Ternary Alloys 20
Nobuhiko KUNITOMI: Internal Friction of Field-Cooled Ferromagnetic Substances (II) 65-Permalloy and Perminvar 26
Terutosi MURAKAMI: Atomic Distribution in Binary Solid Solutions II. Modified Theory for the Case of Nearly Equal Concentrations 31
Terutosi MURAKAMI: Atomic Distribution in Binary Solid Solutions III. Diffuse Scattering of X-ray by Binary Alloys 36
Takashi ITOH, Kimio OHNO and Masao KOTANI: On the Valence Theory of the Methyl Radical 41
Yuichi IKEDA: On Verwey-Overbeek's Theory of the Interaction Force between Two Colloidal Particles 49
Shoji KOJIMA, Kazuo TAKAYAMA and Akira SHIMAUCHI: Probe Measurement for High Frequency Discharge III 55
Hirosi YOSIMOTO: Oscillatory Phenomena of Arc in Hot Cathode Discharge Tube I. Experimentals 59
Hirosi YOSIMOTO: Oscillatory Phenomena of Arc in Hot Cathode Discharge Tube II. Theoretical 69
Kōzō ISHIGURO and Toshio KATO: The Reflection and Transmission of a Multilayer Film 77
Hirosi SATO: Experimental Study of the Spectrum of Isotropic Turbulence III 82
Tetsuya ARIZUMI and Shun-ichi MAEKAWA: The Evolution of Gas from Nickel Plate 87
Tadashi INO: An Electron Diffraction Camera with a Rotating Sector 92
Ryozi UYEDA and Yoshikazu SUGIURA: A Flow-Meter in Vacuum Technique 99
Takeo YOKOBORI: Failure and Fracture of Metals from the Standpoint of the Stochastic Theory 104
Takeo YOKOBORI: Ductility Transition and Cold Brittleness 107
Takeo HAYASHI, Yoshihide ISHIZAKI and Isao KUMABE: The Half-Life of ThC' 110
Goro HONJO: Electron Diffraction Studies on Oxide Films formed on Metals and Alloys II 113
Yasuo TORIKAI and Katsuo NEGISHI: The Application of the Phase Method in Visualizing Ultrasonic Waves 119

No. 2

Isao KITA and Osamu MINAKAWA: On the Nuclear Interactions of Cosmic Ray Shower Particles in Lead 139
Takehiko OGUCHI: Statistical Theory of Rotational Phase Transition II 142
Yoshinobu SEKI: A New Type of Striation Observed in Electron-Micrographs of Sericite 149
Ryoitiro SATO: Electron Diffraction Investigation of the Actions of Aqueous Heavy Metal Salts on Mineral Surface I. Action of Silver Nitrate and Sulfate on Sphalerite Cleavage Face 152
Jitsuo TERADA: Crystal Structure of the Ba, Sr and Ca Triple Carbonate 158
Sigeru NAGAHARA: The Scattering of Slow Electrons by the Diatomic Molecules I. General Theory 165
Hisao MIYAZAWA: Photoelectric Emission and Energy Structure of Cs_3Sb 169
Hideya GAMO: The Faraday Rotation of Waves in a Circular Waveguide 176

Masaki HIRASHIMA: Motion of Electrons in Retarding-Field Tubes under Optimum Receiving Conditions 182
Shoji KIMURA: On Mechanisms of Mercury Vapour Arc Discharge I 193
Shoji KIMURA: On Mechanisms of Mercury Vapour Arc Discharge II 200
Shoji KIMURA: On Mechanisms of Mercury Vapour Arc Discharge III 207
Kiyoshi MURAKAWA: Hyperfine Structure of the Spectrum of Mg I 213
Kiyoshi MURAKAWA: Hyperfine Structure of the Spectrum of Tungsten 215
Koreo KINOSITA: Numerical Evaluation of the Intensity Curve of a Multiple-Beam Fizeau Fringe 219
Kikusaburo OSADA: Ultraviolet Absorption Spectra of Glasses Containing Ti, and Heavy Metals 226
Goro KUWABARA: On the Fatigue of Ag-Cs Photoelectric Tubes 229
Yasuo TORIKAI: Transmission of Ultrasonic Waves through a Plane Plate made of Viscoelastic Material Immersed in a Liquid medium 234
Kō TAMADA: On the Detachment of Shock Wave from the Leading Edge of a Finite Wedge 242
Zirō HASIMOTO: A Note on Cross Mach Lines in Simple Waves in the Plane Super-Sonic Flow 248
Zirō HASIMOTO: On the Limiting Line in a Simple Wave 251
Shōichi WAKIYA: A Spherical Obstacle in the Flow of a Viscous Fluid through a Tube 254
Kinzo HIDA: On the Subsonic Flow of a Compressible Fluid past a Prolate Spheroid 257
Takeo YOKOBORI: Fatigue Fracture from the Standpoint of the Stochastic Theory .. 265

No. 3

Shoji KOJIMA and Shizuko OGAWA: Proton Magnetic Resonance Absorption in Cetyl Alcohol 283
Junkichi ITOH, Riichiro KUSAKA, Yukio YAMAGATA, Ryoiti KIRIYAMA, Hideko IBAMOTO, Teinosuke KANDA and Yoshitaka MASUDA: Nuclear Magnetic Resonance Experiment on the Single Crystal of $K_2HgCl_4 \cdot H_2O$ and $K_2SnCl_4 \cdot H_2O$. Part I .. 287
Junkichi ITOH, Riichiro KUSAKA, Yukio YAMAGATA, Ryoiti KIRIYAMA and Hideko IBAMOTO: Nuclear Magnetic Resonance Experiment on the Single Crystals of $K_2HgCl_4 \cdot H_2O$ and $K_2SnCl_4 \cdot H_2O$. II The Resonance absorption due to four proton system and the revised determination of their crystal structures 293
Sadaaki YANAGAWA: Mathematical Formations of Physical Quantities for j-j-coupling Nuclear Shell Model 302
Hajime SAKATA, Kazuhisa MATSUDA and Eiichi TAKEDA: Thermal Concentration of Carbon Isotopes Using Carbon Monoxide Gas 313
Shigetomo YOSHIDA, Ikuo TAKEDA, Yoshitaka IGARASHI and Hikaru ARATA: Secondary Electron Emission of Copper-beryllium Alloy 318
Tatsuya NIIMI: On the Changes in Contact Potential Difference of a Germanium Rectifier During the Electrical Forming 324
Shin-ichiro NARITA: Relationship between Thermionic Emission and Electrical Conductivity of Oxide-Coated Cathodes 331
Morikazu TODA: Diffusion on the Fermi-Surface and the Conductivity of Metals.... 339
Akira HARASIMA: Statistical Mechanics of Surface Tension 343
Leo ESAKI: Electrical Resistivity and Thermionic Emission of Silicon 347
Norio KATO: Dynamical Theory of Electron Diffraction for Finite Polyhedral Crystal III. Fresnel diffraction formula 350
Kwai UMEDA and Yasuo TOMISHIMA: TFD Functions for Non-zero Temperatures and Equations of State Based on Them 360
Shigeo IWAYANAGI and Teruo HIDESHIMA: Low Frequency Coupled Oscillator and its Application to High Polymer Study 365
Shigeo IWAYANAGI and Teruo HIDESHIMA: Dynamical Study on the Secondary Anomalous Absorption Region of Polymethyl Methacrylate 268
Tokio SAKURAI: The Theory Convex Wave Guide Lens 372
Shigeki SUWA: Hyperfine Structure of the Spectrum of Gadolimium 377
Kiyoshi MURAKAWA: On Some Regularities in the Isotope Effect in the Spectrum of Lead. Part II 382

M. Z. v. KRZYWOBLOCKI: On Vortex-Equation in Isentropic Flow 387
Hideyuki MASUDA: A New Proof of Lagrange's Theorem in Hydrodynamics 390
Zirō HASIMOTO: Plane Jet of Gas emitted from a Nozzle with Supersonic Velocity .. 394
Isao IMAI: Discontinuous Potential Flow as the Limiting Form of the Viscous Flow for Vanishing Viscosity 399
Mitutosi KAWAGUTI: Discontinuous Flow past a Circular Cylinder 403
Hitosi HAGIHARA: Surface Roughening and Oxidation of Galena Cleavage Face in a Vacuum Furnace Under Limited Air Supply 406
Kazuo HISATAKE and Kazuhisa MATSUDA: A Study on Diffusion Pump Oil by the Mass Spectrometer and the Gas Analysis of the Final Vacuum 416

No. 4

Yasukazu YOSHIZAWA: The Beta-ray Spectra of Co^{60} and Sc^{46} 435
Yoshiyuki KOBAYASHI: A Study of the Radioactive Decay of RaD by a Spherical Condenser-Type Spectrometer 440
Tokuzo INOUE: Heat Transfer in Liquid Helium II through an Extremely Fine Slit 450
Ryoitiro SATO: Electron Diffraction Investigation of the Actions of Aqueous Hervy Metal salts on Mineral surfaces II. Action of Mercuric Sulfate on Galena Cleavage Face 454
Terutosi MURAKAMI: Atomic Distribution in Binary Solid Solutions IV. The Influence of the Short-Range Order on the Electrical Resistivity of Alloys 458
Masao KOTANI, Eiichi ISHIGURO, Katsunori HIJIKATA, Takashi NAKAMURA and Ayao AMEMIYA: Tables of Integrals Useful for Calculations of Molecular Energies. III 463
Masami TOMONO: Direct current Characteristics of the Selenium Rectifier I. Theory of Rectification 477
Saburo MUROGA: On the Capacity of a Discrete Channel. I Mathematical expression of capacity of a channel which is disturbed by noise in its every one symbol and expressible in one state diagram 484
Takuzo SHINDO: Space Charge Effect in the Oxide Cathode Layer II 494
Koichi FURUTSU: On the Theory of Diffraction of the Electromagnetic Wave by Mountains 500
Hideo IWAYANAGI: Measurement of Permittivity of Mixed Barium and Strontium Titanate in 3,000 Mc/s Region 525
Shigeki SUWA: Hyperfine Structure of the Spectrum of Al II. Part II 531
Kiyoshi MURAKAWA: Hyperfine Structure of the Spectrum of Ruthenium 535
Isao IMAI: On the Asymptotic Behaviour of Compressible Fluid Flow at a Great Distance from a Cylinder in the Absence of Circulation 537
Nobuzo TERAO: Sur une Relation entre la Résistance a la Rupture et le Foyer d'Eclatement du Verre 545
Nobuzo TERAO: Sur la Résistance a la Rupture du Verre —— L'Influence de l'Humidité 550
Otohiko NOMOTO: Molecular Sound Velocity and Molecular Compressibility of Liquid Mixtures 553

No. 5

Senzo TOKUNAGA, Kazunori YUASA, Kiyoshi NISHIKAWA and Taka ISII: Energy Spectra of Charged π-mesons Produced in Carbon, Aluminium and Copper at 90° to a 345 MeV Proton Beam 571
Norio RYU, Kimio HASHIMOTO and Itaru NONAKA: Polarization of Electrons by Scattering, III. Reflection-Transmission Effect 575
Yoshio SAJI, Masakatsu SAKISAKA and Kozo MIYAKE: Experimental Analysis of the Specific Activity 580
S. HIGASHI, T. KITAMURA, T. KUBOZOE, M. ODA, S. OZAKI and Y. WATASE: On the Penetrating Shower Originating in Light Element and Heavy Element 584
Akira HARASIMA: Atomic Distribution Functions of Liquids 590
Isaaki YOKOTA: On the Electrical Conductivity of Cuprous Sulfide: A Diffusion Theory 595
Ken-ichi HIRANO: On the Mechanisms of Aging in Aluminium-Silver Alloys, I 603

E. Fukushima and A. Ookawa: Observation of the Grain Boundary in Soap Bubble Raft. Part I. Static Feature of the Grain Boundary 609
Etsuro Sawaguchi: Ferroelectricity versus Antiferroelectricity in the Solid Solutions of $PbZrO_3$ and $PbTiO_3$ 615
Kazuo Niira: $\sigma\pi$ Interaction in Benzene 630
Kenji Mitani: The Direct Current associated with Microwave Gas Discharge between Coaxial Cylinders, III 642
Katumi Ikenoue: The Rotational Structure of the Band Spectrum of S_2 Molecule Part I 646
Hidenori Hasimoto: On the Flow of a Viscous Fluid past an Inclined Elliptic Cylinder at Small Reynolds Numbers 653
Akira Sakurai: On the Propagation and Structure of the Blast Wave, I 662
Yoshimaru Yosimura: On the Definition of Stress in the Finite Deformation Theory 669
Yosomatsu Takamura: Measurement of the Net Thermal Conductivity of Fibrous Substances 674

No. 6

Seizaburo Kageyama: On the Disintegration of RaB 689
Motoyosi Sugita: Thermodynamical Analysis of Life I. Thermodynamics of transient phenomena 697
Motoyosi Sugita: Thermodynamical Analysis of Life II. On the Maximum Principle of Transient Phenomena 704
Motoyosi Sugita: Thermodynamical Analysis of Life III. Mathematical Analysis of Metabolism 709
Eijiro Haga: On Mayer's Theory of Dilute Ionic Solutions 714
Toshimichi Sakata: Studies on the Cs_3Sb Photo-Cathode 723
Hazimu Kawamura and Masami Onuki: Statistical Time Lag and Electron Avalanche in Dielectric Breakdown of Maica II 731
Shigeki Suwa: Hyperfine Structure of the Spectrum of Zr I and the Magnetic Moment of Zr^{91} 734
Kinzo Hida: An Approximate Study on the Detached Shock Wave in front of a Circular Cylinder and a Sphere 740
M. Z. v. Krzywoblocki: The "Independent Scalars" in Homogeneous Turbulence in Compressible Media 745
Mitutosi Kawaguti: Numerical Solution of the Navier-Stokes Equations for the Flow around a Circular Cylinder at Reynolds Number 40 747
Ryoitiro Sato: Oriented Overgrowth of Primary Oxide on α-Fe 758
Kazuo Kimoto: Study on the Intensity Anomaly of Electron Diffraction Powder Patterns from Minute Silver Crystallites 762
Suekichi Kawata and Yoshirō Omori: An Investigation of Thermocouple Psychrometer I 768
Goro Honjo: Fine Structure due to Refraction Effect in Electron Diffraction Pattern of Powder Sample Part I. Fine Structure given by Magnesium and Cadmium Oxide Smoke having a Fibrous Orientation 776
Koreo Kinosita: Studies in Glass-Cleaning Procedures by Static Friction Measurement 782

SHORT NOTES

No. 1

Toshimichi Sakata: Some Experimental Studies of the Conductivity and Thermo-Electromotive Force of Cs_3Sb Photo-Cathodes 125
Tokuo Suita: Directional Dielectric Breakdown in Single Crystals 126
Yoshio Inuishi: On the Temperature Dependence of Contact Noise 128
E. Fukushima and A. Ookawa: The Transition Structure of the Grain Boundary observed in Soap Bubble Raft 129
Osamu Tukizi: On the Frequency of Scintillation Fading of Microwaves 130

Koichi SHIMODE: Length of Coherent Microwaves Generated by an Electronic Oscillator 131

Kenji NUKASAWA: On the Contribution of the Mutual Perturbation of the Localized Molecular Orbitals to the Charge Distribution 132

Koichi SHIMODA and Tetsuji NISHIKAWA: Microwave Spectrum of Methylamine I.. 133

Mitio HATOYAMA, Wataru SASAKI and Zensho ISHII: Silicocarbon-Thermal Decomposition Product of Silicone Resin 134

Yoshiyuki KOBAYASHI and Goro MIYAMOTO: Spherical Condenser Type Spectrometer 135

No. 2

Kozo ISHIGURO: The Change of the Refractive index of Semi-conducting Film irradiated by Intense Light 269

Izuo HAYASHI and Kazuo ÔNO: Fine and Hyper-fine Structure of Paramagnetic Resonance Spectra in Several Diluted Manganese Salts 270

Hiroshi FUJITA: Diffusion accompanied with Absorption of the Langmuir Type 271

Toshimichi SAKATA: Some Experimental Studies of the Conductivity and Thermo-electromotive Force of Cs$_3$Sb Photo-Cathodes II 272

Yoshiyuki KOBAYASHI and Gorō MIYAMOTO: Auger and Conversion Lines from RaD 273

Chiyoe YAMANAKA and Tokuo SUITA: Electronic Conductivities of Solids in Strong Electric Fields I 274

Chiyoe YAMANAKA and Tokuo SUITA: Electron Avalanche in Liquids at Strong Electric Fields 277

Seiichi KONDO and Masaru MATSUMOTO: Color-centers of KCl-KBr Mixed Crystals in Visible Region 279

E. FUKUSHIMA and A. OOKAWA: On the Dynamical Behaviour of the Grain Boundary in Bubble Raft under Shear Stress 280

No. 3

Tatsuo TAKAKURA: On the Directivity of Solar Radio Emission from the Sunspots.. 422

Makoto MORIYAMA: Concentration Dependence of the Dielectric Constant of Ionic Solutions 423

Hazimu KAWAMURA: A Note on the Theory of the Electron Multiplication in Insulating Crystals 424

Koichi SHIMODA and Tetsuji NISHIKAWA: Microwave Spectrum of Methylamine II 425

Tetsuji NISHIKAWA and Koichi SHIMODA: New Lines of the Inversion Spectrum of Ammonia 426

T. TAKAKURA, K. BABA, K. NUNOGAKI and H. MITANI: The 3000Mc Ion Plasma Noise Radiated from Arc Discharge and Solar Eruption 426

Yoshibume FUJIKI and Ryōichi SUGANUMA: On the Structure Loosening of Metal Films deposited from the Vapour 427

Kenzo TANAKA and Ikuo FUKUYAMA: On the Metastable Phase Change of Ammonium Nitrate 428

Masayasu UETA: Field Emission of Crystal Phosphors 429

Atuyosi OKAZAKI, Hirosi TUBOTA and Hiromichi SUZUKI: The Temperature Dependence of the Zero Bias Resistance of Cuprous Oxide Rectifiers 431

Yoshika MASUDA and Teinosuke KANDA: Chemical Shift of the N^{14} Magnetic Resonance 432

No. 4

Kazuo ŌNO and Izuo HAYASHI: Paramagnetic Resonance Absorption of Mn^{++} Impurity in Salts of Ni^{++}, Co^{++} and Fe^{++}, and Spin-Lattice Relaxation 561

Jun OKANO: Electron Emission from Mo by Ion Bombardment 562

Shin-ichi HYODO: High Speed Elongation of Long Test-Piece of Rubber 563

Junkichi SOMA and Masamichi OGI: Corrections to our paper "On a Non-linear Approximation of the Interatomic Force in Solid" 565

Yoshio INUISHI and Yang Tsung-che: The Influence of Impurity Atoms on Flicker Noise 565

Yoshio INUISHI and Tokuo SUITA: On the Space Charge Effect in Dielectric Breakdown of KCl Single Crystals 567

No. 5

Nobuhiko SAKAMOTO, Takashi ASAHI and Syôhei MIYAHARA: On the Magnetization of Magnesium Ferrite 677
Yujiro KOH: Resolving Power of the Scintillation Counter for Energy Measurement of Relativistic Particles 678
Shinya MIYATANI and Yasumasa SUZUKI: On the Electric Conductivity of Cuprous Sulfide; Experiment 680
Shintaro SUGAI and Jiro FURUICHI: On the Photographic Chemical Development .. 681
Seizaburo KAGEYAMA and Kazuaki NISHIMURA: The Straggling of Fast Electrons .. 682
Yoshiyuki KOBAYASHI, Goro MIYAMOTO and Shigeru MORI: Beta-Spectrum of Ni^{63}. 684
Yoshiro KAINUMA: Excess and Defect Kikuchi-bands 685
Taro KIHARA: On Ishihara-Hayashida's Theory of the Second Virial Coefficient for Rigid Convex Molecules 686

No. 6

Etujiro TAKEDA: On the Coefficient of Resititution 790
Wataru SASAKI and Mituko KUNO: On the Effective Mass of the Conduction Electron in Germanium 791
Kenji NUKASAWA, Jiro TANAKA and Saburo NAGAKURA: A Note on the Hydrogen Bond 792
Toshimichi SAKATA: The Hall Effect in Cs_3Sb Photo-Cathode 793
Yoichi UCHIDA and Yoshio NAKAI: Injection of Positive Holes in the Alkali Halide Crystal 795
Hazimu KAWAMURA and Kazuko AZUMA: Dielectric Breakdown of Thin Alumina Film 797
Ryukiti Robert HASIGUTI: Internal Friction of Metal Crystals Due to Vacancy .. 798
Akira ISIHARA: Note on the Theory of Transport Phenomena in Polyatomic Gases 799
Isao IMAI: Some Particular Solutions of Compressible Flow Equations for Arbitrary Pressure-Density Relation 799
S. NAKAGAWA, H. HUZITA and K. OKUDAIRA: An Unusual Star 801
Kazuo ONO: Paramagnetic Resonance in the Nickel Sulphate Heptahydrate 802
Isao KITA: An Improvement in High Speed Expansion of Counter-Controlled Cloud Chamber 803
Norio RYU: Polarization of Electrons by Scattering, IV 804
Takeo YOKOBORI: Damage as an Initial Stage of Fatigue Fracture 806

Errata

Syohei MIYAHAKA and Tadayasu MITUI: Effect of Magnetic Field on Precipitation of Ferromagnetic Phase 137
Nobuzo TERAO: Un Traitment Statistique de la Résistance à la Rupture du Verre —— Sur l'Influence de la Temperature 137
Tadashi INO: An Electron Diffraction Camera with a Rotating Sector 282
Kinzō HIDA: On the Subsonic Flow of a Compressible Fluid past a Prolate Spheroid 432
Tatsuya NIIMI: On the Changes in Contact Potential Difference of a Germanium Rectifier During the Electrical Forming 569

AUTHOR INDEX TO Vol. 8

AMEMIYA Ayao;
M. KOTANI, E. ISHIGURO K. HIJIKATA, T. NAKAMURA and ———: Tables of Integrals Useful for the Calculations of Molecular Energies. III 463
ARATA Hikaru;
S. YOSHIDA, I. TAKEDA, Y. IGARASHI and ———: Secondary Electron Emission of Copper-beryllium Alloy 318
ARIZUMI Tetsuya;
—— and S. MAEKAWA: The Evolution of Gas from Nickel Plate 87
ASAHI Takashi;
N. SAKAMOTO, ——— and S. MIYAHARA: On the Magnetization of Magnesium Ferrite 677
AZUMA Kazuo;
H. KAWAMURA and ———: Dielectric Breakdown of Thin Alumina Film....
BABA Kōzaburo;
T. TAKAKURA, ———, K. NUNOGAKI and H. MITANI: The 3000 Mc Ion Plasma Noise Radiated from Arc Discharge and Sólar Eruption............ 426
ESAKI Leo: Electrical Resistivity and Thermionic Emission of Silicon 347
FUJIKI Yoshibumi;
——— and R. SUGANUMA: On the Structure Loosening of Metal Films deposited from the Vapour 427
FUJITA Hiroshi: Diffusion accompanied with Absorption of the Langmuir Type 271
FUKUSHIMA Einosuke;
—— and A. OOKAWA: The Transition Structure of the Grain Boundary observed in Soap Bubble Raft 129
——— and A. OOKAWA: On the Dynamical Behaviour of the Grain Boundary in Bubble Raft under Shear Stress...... 280
——— and A. OOKAWA: Observation of the Grain Boundary in Soap Bubble Raft. Part I. Static Feature of the Grain Boundary 609
FUKUYAMA Ikuo;
K. TANAKA and ———: On the Metastable Phase Change of Ammonium Nitrate...... 428
FURUICHI Jiro;
S. SUGAI and ———: On the Photographic Chemical Development.......... 681
FURUTSU Koichi: On the Theory of Diffraction of the Electromagnetic Wave by Mountains 500
GAMO Hideya: The Faraday Rotation of Waves in a Circular Waveguide 176
HAGA Eijiro: On Mayer's Theory of Dilute Ionic Solutions ....
HAGIHARA Hitosi: Surface Roughening and Oxidation of Galena Cleavage Face in a Vacuum Furnace Under Limited Air Supply 406
HARASIMA Akira: Statistical Mechanics of Surface Tension 343
———: Atomic Distribution Functions of Liquids 590
HASHIMOTO Kimio;
N. RYU, ——— and I. NONAKA: Polarization of Electrons by Scattering, III. Reflection-Transmission Effect...... 575
HASIGUTI Ryukiti: Internal Friction of Metal Crystals Due to Vacancy 798
HASIMOTO Hidenori: On the Flow of a Viscous Fluid past an Inclined Elliptic Cylinder at Small Reynolds Numbers...... 653
HASIMOTO Zirō: A Note on Cross Mach Lines in Simple Waves in the Plane Supersonic Flow 248
———: On the Limiting Line in a Simple Wave 251
———: Plane Jet of Gas emitted from a Nozzle with Supersonic Velocity .. 394
HATOYAMA Mitio;
———, W. SASAKI and Z. ISHII: Silicocarbon-Thermal Deconposition Product of Silicone Resin 134

HAYASHI Izuo;
——— and K. ŌNO; Fine and Hyper-fine Structure of Paramagnetic Resonance Spectra in Several Diluted Manganese Salts 270
K. ŌNO and ———: Paramagnetic Resonance Absorption of Mn^{++} Impurity in Salts of Ni^{++}, Co^{++} and Fe^{++}, and Spin-Lattice Relaxation........... 561
HAYASHI Takeo;
———, Y. ISHIZAKI and I. KUMABE: The Half-Life of ThC' 110
HIDA Kinzo: On the Subsonic Flow of a Compressible Fluid past a Prolate Spheroid 257
———; (errata) On the Subsonic Flow of a Compressible Fluid past a Prolate Spheroid.. 432
———: An Approximate Study on the Detached Shock Wave in Front of a Circular Cylinder and a Sphere.. 740
HIDESHIMA Teruo;
S. IWAYANAGI and ———: Low Frequency Coupled Oscillator and its Application to High Polymer Study 365
S. IWAYANAGI and ———: Dynamical Study on the Secondary Anomalous Absorption Region of Polymethyl Methacrylate 368
HIGASHI Sigeru;
———, T. KITAMURA, T. KUBOZOE, M. ODA, S. OZAKI and Y. WATASE: On the Penetrating Shower Originating in Light Element and Heavy Element 584
HIJIKATA Katsunori;
M. KOTANI, E. ISHIGURO, ———, T. NAKAMURA and A. AMEMIYA: Tables of Integrals Useful for the Calculations of Molecular Energies. III 463
HIRANO Ken-ichi: On the Mechanisms of Aging in Aluminium-Silver Alloys, I 603
HIRASHIMA Masaki: Motion of Electrons in Retarding-Field Tubes under Optimum Receiving Conditions 182
HISATAKE Kazuo;
——— and K. MATSUDA: A Study on Diffusion Pump Oil by the Mass Spectrometer and the Gas Analysis of the Final Vacuum.................. 416
HONJO Goro: Fine Structure due to Refraction Effect in Electron Diffraction Pattern of Powder Sample Part I. Fine Structure given by Magnesium and Cadmium Oxide Smoke having a Fibrous Orientation 776
———: Electron Diffraction Studies on Oxide Films formed on Metals and Alloys II 113
HUZITA Humiaki;
S. NAKAGAWA, ——— and K. OKUDAIRA: An Unusual Star 801
HYODO Shin-ichi: High Speed Elongation of Long Test-Piece of Rubber 563
IBAMOTO Hideko;
J. ITOH, R. KUSAKA, Y. YAMAGATA, R. KIRIYAMA, ———, T. KANDA and Y. MASUDA: Nuclear Magnetic Resonance Experiment on the Single Crystal of $K_2HgCl_4 \cdot H_2O$ and $K_2SnCl_4 \cdot H_2O$. Part I......................... 287
J. ITOH, R. KUSAKA, Y. YAMAGATA, R. KIRIYAMA and ———: Nuclear Magnetic Resonance Experiment on the Single Crystals of $K_2HgCl_4 \cdot H_2O$ and the $K_2SnCl_4 \cdot H_2O$. II The Resonance absorption due to four proton system and the revised determination of their crystal structures 293
IGARASHI Yoshitaka;
S. YOSHIDA, I. TAKEDA, ——— and H. ARATA:: Secondary Electron Emission of Copper-beryllium Alloy 318
IKEDA Yuichi: On Verwey-Overbeek's Theory of the Interaction Force Between Two Colloidal Particles 49
IKENOUE Katsumi: The Rotational Structure of the Band Spectrum of S_2 Molecule Part I 646
IMAI Isao: Discontinuous Potential Flow as the Limiting Form of the Viscous Flow for Vanishing Viscosity 399
———: On the Asymptotic Behaviour of Compressible Fluid Flow at a Great Distance from a Cylinder in the Absence of Circulation 537
IMAI Isao: Some Particular Solutions of Compressible Flow Equations for Arbitrary Pressure-Density Relation 799

INO Tadashi: An Electron Diffraction Camera with a Rotating Sector 92
———: (errata) An Electron Diffraction Camera with a Rotating Sector 282
INOUE Tokuzo: Heat Transfer in Liquid Helium II through an Extremely Fine Slit 450
INUISHI Yoshio;
  ——— and T. YANG: The Influence of Impurity Atoms on Flicker Noise .. 565
  ——— and T. SUITA: On the Space Charge Effect in Dielectric Breakdown of KCl Single Crystals 567
  ———: On the Temperature Dependence of Contact Noise 128
ISHIGURO Eiichi;
  M. KOTANI, ———, K. HIJIKATA, T. NAKAMURA and A. AMEMIYA: Tables of Integrals Useful for the Calculations of Molecular Energies. III 463
ISHIGURO Kōzō;
  ——— and T. KATO: The Reflection and Transmission of a Multilayer Film 77
  ———: The Change of the Refractive index of Semi-conducting Film irradiated by Intense Light 269
ISHII Zensho;
  M. HATOYAMA, W. SASAKI and ———: Silicocarbon-Thermal Deconposition Product of Silicone Resin 134
ISIHARA Akira: Note on the Theory of Transport Phenomena in Polyatomic Gases 799
ISII Taka;
  S. TOKUNAGA, K. YUASA, K. NISHIKAWA and ———: Energy Spectra of Charged π-mesons Produced in Carbon, Aluminium and Copper at 90° to a 345 MeV Proton Beam 571
ISHIZAKI Yoshihide;
  T. HAYASHI, ——— and I. KUMABE: The Half-Life of ThC' 110
ITOH Junkichi;
  ———, R. KUSAKA, Y. YAMAGATA, R. KIRIYAMA, H. IBAMOTO, T. KANDA and Y. MASUDA: Nuclear Magnetic Resonance Experiment on the Single Crystal of $K_2HgCl_4\cdot H_2O$ and $K_2SnCl_4\cdot H_2O$. Part I 287
  ———, R. KUSAKA, Y. YAMAGATA, R. KIRIYAMA and H. IBAMOTO: Nuclear Magnetic Resonance Experiment on the Single Crystals of $K_2HgCl_4\cdot H_2O$ and $K_2SnCl_4\cdot H_2O$. II The Resonance absorption due to four proton system and the revised determination of their crystal structures 293
ITOH Takashi;
  ——— K. OHNO and M. KOTANI: On the Valence Theory of the Methyl Radical 41
IWAYANAGI Hideo: Measurement of Permittivity of Mixed Barium and Strontium Titanate in 3,000 Mc/s Region 525
IWAYANAGI Shigeo;
  ——— and T. HIDESHIMA: Low Frequency Coupled Oscillator and its Application to High Polymer Study 365
  ——— and T. HIDESHIMA: Dynamical Study on the Secondary Anomalous Absorption Segion of Polymethyl Methacrylate 368
KAGEYAMA Seizaburo;
  ——— and K. NISHIMURA: The Straggling of Fast Electrons 682
  ———: On the Disintegration of RaB 689
KAINUMA Yoshiro: Excess and Defect Kikuchi-bands 685
KAMBA Kyozaburo;
  ———, I. NAKADA and H. TAKAHASI: Hysteresis Loops of Ceramic Barium Titanate at Higher Frequencies. I 9
  ———: Hysteresis Loops of Ceramic Barium Titanate at Higher Frequencies II 15
KANDA Teinosuke;
  J. ITOH, R. KUSAKA, Y. YAMAGATA, R. KIRIYAMA, H. IBAMOTO, ——— and Y. MASUDA: Nucler Magnetic Resonance Experiment on the Single Crystal of $K_2HgCl_4\cdot H_2O$ and $K_2SnCl_4\cdot H_2O$. Part I 287
  Y. MASUDA and ———: Chemical Shift of the N^{14} Magnetic Resonance 432

Kato Norio: Dynamical Theory of Electron Diffraction for Finite Polyhedral Crystal III. Fresnel diffraction formula 350

Kato Toshio;

K. Ishiguro and ———: The Reflection and Transmission of a Multilayer Film 77

Kawaguti Mitutosi: Discontinuous Flow past a Circular Cylinder.......... 403

———: Numerical Solution of the Navier-Stokes Equations for the Flow around a Circular Cylinder at Reynolds Number 40.......... 747

Kawamura Hazimu: A Note on the Theory of the Electron Multiplication in Insulating Crystals 424

——— and K. Azuma: Dielectric Breakdown of Thin Alumina Film.......... 797

——— and M. Onuki: Statistical Time Lag and Electron Avalanche in Dielectric Breakdown of Mica II 731

Kawata Suekichi;

——— and Y. Omori: An Investigation of Thermocouple Psychrometer, I..

Kihara Taro: On Ishihara-Hayashida's Theory of the Second Virial Coefficient for Rigid Convex Molecules 686

Kimoto Kazuo: Study on the Intensity Anomaly of Electron Diffraction Powder Patterns from Minute Silver Crystallites 762

Kimura Shoji: On Mechanisms of Mercury Vapour Arc Discharge I.......... 193

———: On Mechanisms of Mercury Vapour Arc Discharge II 200

———: On Mechanisms of Mercury Vapour Arc Discharge III 207

Kinosita Koreo: Numerical Evaluation of the Intensity Curve of a Multiple Beam Fizeau Fringe 219

———: Studies in Glass-Cleaning Procedures by Static Friction Measurement 782

Kiriyama Ryoiti;

J. Itoh, R. Kusaka, Y. Yamagata, ———, H. Ibamoto, T. Kanda and Y. Masuda: Nuclear Magnetic Resonance Experiment on the Single Crystal of $K_2HgCl_4 \cdot H_2O$ and $K_2SnCl_4 \cdot H_2O$. Part I 287

J. Itoh, R. Kusaka, Y. Yamagata, ——— and H. Ibamoto: Nuclear Magnetic Resonance Experiment on the Single Crystals of $K_2HgCl_4 \cdot H_2O$ and $K_2SnCl_4 \cdot H_2O$. II The Resonance absorption due to four proton system and the revised determination of their crystal structures.......... 293

Kita Isao;

——— and O. Minakawa: On the Nuclear Interactions of Cosmic Ray Shower Particles in Lead.......... 139

———: An Improvement in High Speed Expansion of Counter-Controlled Cloud Chamber 803

Kitamura Takashi;

S. Higashi, ———, T. Kubozoe, M. Oda, S. Ozaki and Y. Watase: On the Penetrating Shower Originating in Light Element and Heavy Element 584

Kobayashi Yoshiyuki: A Study of the Radioactive Decay of RaD by a Spherical Condenser-type Spectrometer 440

——— and G. Miyamoto: Spherical Condenser Type Spectro-meter 135

——— and G. Miyamoto: Auger and Conversion Lines from RaD 273

———, G. Miyamoto and S. Mori: Beta-Spectrum of Ni^{63} 684

Koh Yujiro: Resolving Power of the Scintillation Counter for Energy Measurement of Relativistic Particles.......... 678

Kojima Shoji;

———, K. Takayama and A. Shimauchi: Probe Measurement for High Frequency Discharge III 55

——— and S. Ogawa: Proton Magnetic Resonance Absorption in Cetyl Alcohol 283

Kondo Sei-ichi;

——— and M. Matsumoto: Color-centers of KCl-KBr Mixed Crystals in Visible Region 279

Kotani Masao;

T. Itoh, K. Ohno and ———: On the Velence Theory of the Methyl Radical 14

———, E. Ishiguro, K. Hijikata, T. Nakamura and A. Amemiya: Tables of Integrals Useful for the Calculations of Molecular Energies. III 463

Krzywoblocki M. Z. v.: On Vortex-Equation in Isentropic Flow 387

———: The "Independent Scalars" in Homogeneous Turbulence in Compressible Media 745

Kubozoe Tadayoshi;

S. Higashi, T. Kitamura, ———, M. Oda, S. Ozaki and Y. Watase: On the Penetrating Shower Originating in Light Element and Heavy Element.. 584

Kumabe Isao;

T. Hayashi, Y. Ishizaki and ———: The Half-Life of ThC' 110

Kunitomi Nobuhiko: Internal Friction of Field-Cooled Ferromagnetic Substances (II) 65-Permalloy and Perminvar 26

Kuno Mituko;

W. Sasaki and ———: On the Effective Mass of the Conduction Electron in Germanium 791

Kusaka Riichiro;

J. Itoh, ———, Y. Yamagata, R. Kiriyama, H. Ibamoto, T. Kanda and Y. Masuda: Nuclear Magnetic Resonance Experiment on the Single Crystal of $K_2HgCl_4\cdot H_2O$ and $K_2SnCl_4\cdot H_2O$. Part I 287

J. Itoh, ———, Y. Yamagata, R. Kiriyama and H. Ibamoto: Nuclear Magnetic Resonance Experiment on the Single Crystals of $K_2HgCl_4\cdot H_2O$ and $K_2SnCl_4\cdot H_2O$. II The Resonance absorption due to four proton system and the revised determination of their crystal structures 293

Kuwabara Goro: On the Fatigure of Ag-Cs Photoelectric Tubes 229

Maekawa Shun-ichi;

T. Arizumi and ———: The Evolution of Gas from Nickel Plate 87

Masuda Hideyuki: A New Proof of Lagrange's Theorem in Hydrodynamics 390

Masuda Yoshika;

——— and T. Kanda: Chemical Shift of the N^{14} Magnetic Resonance...... 432

Masuda Yoshitaka:

J. Itoh, R. Kusaka, Y. Yamagata, R. Kiriyama, H. Ibamoto, T. Kanda and ———: Nuclear Magnetic Resonance Experiment on the Single Crystal of $K_2HgCl_4\cdot H_2O$ and $K_2SnCl_4\cdot H_2O$. Part I 287

Matsumoto Masaru;

S. Kondo and ———: Color-Centers of KCl-KBr Mixed Crystals in Visible Region 279

Matsuda Kazuhisa;

H. Sakata, ——— and E. Takeda: Thermal Concentration of Carbon Isotopes Using Carbon Monoxide Gas 313

K. Hisatake and ———: A Study on Diffusion Pump Oil by the Mass Spectrometer and the Gas Analysis of the Final Vacuum 416

Matsuda Shoichi: On the Superlattice Formation in Ternary Alloys 20

Minakawa Osamu;

I. Kita and ———: On the Nuclear Interactions of Cosmic Ray Shower Particles in Lead 139

Mitani Hichiro;

T. Takakura, K. Baba, K. Nunogaki and ———: The 3000 Mc Ion Plasma Noise Radiated from Arc Discharge and Solar Eruption 426

Mitani Kenji: The Direct Current associated with Microwave Gas Discharge between Coaxial Cylinders, III 642

Mitui Tadayasu;

S. Miyahara and ———: (Errata) Effect of Magnetic Field on Precipitation of Ferromagnetic Phase 137

Miyahara Shōhei;

N. Sakamoto, T. Asahi and ———: On the Magnetization of Magnesium Ferrite 677

——— and T. Mitui: (Errata) Effect of Magnetic Field on Precipitation of Ferromagnetic Phase 137

MIYAKE Kozo;
  Y. SAJI, M. SAKISAKA and ———: Experimental Analysis of the Specific Activity 580
MIYAMOTO Goro;
  Y. KOBAYASHI and ———: Spherical Condenser Type Spectrometer 135
  Y. KOBAYASHI and ———: Auger and Conversion Lines from RaD 273
  Y. KOBAYASHI, ——— and S. MORI: Beta-Spectrum of Ni^{63} 684
MIYATANI Shin-ya;
  ——— and Y. SUZUKI: On the Electric Conductivity of Cuprous Sulfide; Fxperiment 680
MIYAZAWA Hisao: Photoelectric Emission and Energy Structure of Cs_3Sb 169
MORI Shigeru;
  Y. KOBAYASHI, G. MIYAMOTO and ———: Beta-Spectrum of Ni^{63} 684
MORIYAMA Makoto: Concentration Dependence of the Dielectric Constant of Ionic Solutions 423
MURAKAMI Terutosi: Atomic Distribution in Binary Solid Solutions II. Modified Theory for the Case of Nearly Equal Concentrations 31
  ———: Atomic Distribution in Binary Solid Solutions III. Diffuse Scattering of X-rays by Binary Alloys 36
  ———: Atomic Distribution in Binary Solid Solutions IV. The Influence of the Short-Range Order on the Electrical Resistivity of Alloys 458
MURAKAWA Kiyoshi: Hyperfine Structure of the Spectrum of Mg I 213
  ———: Hyperfine Structure of the Spectrum of Tungsten 215
  ———: On Some Refularities in the Isotope Effect in the Spectrum of Lead. Part II 382
  ———: Hyperfine Structure of the Spectrum of Ruthenium 535
MUROGA Saburo: On the Capacity of a Discrete Channel. I Mathematical expression of capacity of a channel which is disturbed by noise in its every one symbol and expressible in one state diagram 484
NAGAHARA Sigeru: The Scattering of Slow Electrons by the Diatomic Molecules. I. General Theory 165
NAGAKURA Saburo;
  K. NUKASAWA, J. TANAKA and ———: A Note on the Hydrogen Bond 792
NAKADA Ichiro;
  K. KAMBE, ——— and H. TAKAHASI: Hystresis Loops of Ceramic Barium Titanate at Higher Frequencies I 9
NAKAGAWA Shigeo;
  ———, H. HUZITA and K. OKUDAIRA: An Unusual Star 801
NAKAI Yoshio;
  Y. UCHIDA and ———: Injection of Positive Holde in the Alkali Halide Crystal 795
NAKAMURA Takashi;
  M. KOTANI, E. ISHIGURO, K. HIJIKATA, ——— and A. AMEMIYA: Tables of Integrals Useful for the Calculations of Molecular Energies. III 463
NARITA Shin-ichiro: Relationship between Thermionic Emission and Electrical conductivity of Oxide-Coated Cathodes 331
NEGISHI Katsuo;
  Y. TORIKAI and ———: The Application of the Phase Method in Visualizing Ultrasonic Waves 119
NIIMI Tatsuya: On the Changes in Contact Potential Difference of a Germanium Rectifier During the Electrical Forming 324
  ———: (Errata) On the Changes in Contact Potential Difference of a Germanium Rectifier During the Electrical Forming 569
NIIRA Kazuo: $\sigma\pi$ Interaction in Benzene 630
NISHIKAWA Kiyoshi;
  S. TOKUNAGA, K. YUASA, ——— and T. ISII: Energy Spectra of Charged π-mesons Produced in Carbon, Aluminium and Copper at 90° to a 345 MeV Proton Beam 571

NISHIKAWA Tetsuji;
K. SHIMODA and ———: Microwave Spectrum of Methylamine I 133
K. SHIMODA and ———: Microwave Spectrum of Methylamine II 425
——— and K. SHIMODA: New Lines of the Inversion Spectrum of Ammonia 426
NISHIMURA Kazuaki;
S. KAGEYAMA and ———: The Straggling of Fast Electrons 682
NOMOTO Otohiko: Molecular Sound Velocity and Molecular Compressibility of Liquid Mixtures 553
NONAKA Itaru;
N. RYU, K, HASHIMOTO and ———: Polarization of Electrons by Scattering, III. Reflection-Transmission Effect 575
NUKASAWA Kenji: On the Contribution of the Mutual Perturbation of the Localized Molecular Orbitals to the Charge Distribution 132
———, J. TANAKA and S. NAGAKURA: A Note on the Hydrogen Bond...... 792
NUNOGAKI Kan-ichi;
T. TAKAKURA, K. BABA, ——— and H. MITANI: The 3000 Mc Ion Plasma Noise Radiated from Arc Discharge and Solar Eruption 426
ODA Minoru;
S. HIGASHI, T. KITAMURA, T. KUBOZOE, ———, S. OZAKI and Y. WATASE: On the Penetrating Shower Originating in Light Element and Heavy Element 584
OGAWA Shizuko;
S. KOJIMA and ———: Proton Magnetic Resonance Absorption in Cetyl Alcohol 283
OGI Masamichi;
J. SOMA and ———: On a Non-linear Approximation of the Interatomic Force in Solid 6
J. SOMA and ———: Corrections to our paper "On a Non-linear Approximation of the Interatomic Force in Solid" 565
OGUCHI Takehiko: Statistical Theory of Rotational Phase Transition II 142
OHNO Kimio;
T. ITOH, ——— and M. KOTANI: On the Valence Theory of the Methyl Radical 41
OKANO Jun: Electron Emission from Mo by Ion Bombardment 562
OKAZAKI Atuyosi;
———, H. TUBOTA and H. SUZUKI: The Temperature Dependence of the Zero Bias Resistance of Cuprous Oxide Rectifiers 431
OKUDAIRA Kiyoshi;
S. NAKAGAWA, H. HUZITA and ———: An Unusual Star 799
OMORI Yoshirō;
S. KAWATA and ———: An Investigation of Thermocouple Psychrometer, I 768
ŌNO Kazuo;
I. HAYASHI and ———: Fine and Hyper-fine Structure of Paramagnetic Resonance Spectra in Several Diluted Manganese Salts 270
——— and I. HAYASHI: Paramagnetic Resonance Absorption of Mn^{++} Impurity in Salts of Ni^{++}, Co^{++} and Fe^{++}, and Spin-Lattice Relaxation 561
———: Paramagnetic Resonance in the Nickel Sulphate Heptahydrate 802
ONUKI Masami;
H. KAWAMURA and ———: Statistical Time Lag and Electron Avalanche in Dielectric Breakdown of Mica II 731
OOKAWA Akiya;
E. FUKUSHIMA and ———: The Transition Structure of the Grain Boundary observed in Soap Bubble Raft 129
E. FUKUSHIMA and ———: On the Dynamical Behaviour of the Grain Boundary in Bubble Raft under Shear Stress 280
E. FUKUSHIMA and ———: Observation of the Grain Boundary in Soap Bubble Raft. Part I. Stativ Feature of the Grain Boundary 609

OSADA Kikusaburo: Ultraviolet Absorption Spectra of Glasses Containing Ti, and Heavy Metals 226

OZAKI Seinosuke;
  S. HIGASHI, T. KITAMURA, T. KUBOZOE, M. ODA, ——— and Y. WATASE: On the Penetrating Shower Originating in Light Element and Heavy Element 584

RYU Norio;
  ———, K. HASHIMOTO and I. NONAKA: Polarization of Electrons by Scattering, III. Reflection-Transmission Effect 575
  ———: Polarization of Electrons by Scattering, IV 804

SAJI Yoshio;
  ———, M. SAKISAKA and K. MIYAKE: Experimental Analysis of the Specific Activity 580

SAKAMOTO Nobuhiko;
  ———, T. ASAHI and S. MIYAHARA: On the Magnetization of Magnesium Ferrite 677

SAKATA Hajime;
  ———, K. MATSUDA and E. TAKEDA: Thermal Concentration of Carbon Isotopes Using Carbon Monoxide Gas 313

SAKATA Toshimichi: Some Experimental Studies of the Conductivity and Thermo-electromotive Force of Cs_3Sb Phot-Cathodes 125
  ———: Some Experimental Studies of the Conductivity and Thermo-electromotive Force of Cs_3Sb Photo-Cathodes II 272
  ———: Studies on the Cs_3Sb Photo-Cathode 732
  ———: The Hall Effect in Cs_3Sb Photo-Cathode 793

SAKISAKA Masakatsu;
  Y. SAJI, ——— and K. MIYAKE: Experimental Analysis of the Specific Activity 580

SAKURAI Akira: On the Propagation and Structure of the Blast Wave, I 662

SAKURAI Tokio: The Theory Convex Wave Guide Lens 372

SASAKI Wataru;
  M. HATOYAMA, ——— and Z. ISHII: Silicocarbon-Thermal Deconposition Product of Silicone Resin 134
  ——— and M. KUNO: On the Effective Mass of the Conduction Electron in Germanium 791

SATO Hiroshi: Experimental Study of the Spectrum of Isotropic Turbulence III 82

SATO Ryoitiro: Electron Diffraction Investigation of the Actions of Aqueous Heavy Metal Salts on Mineral Surfaces I. Action of Silver Nitrate and Sulfate on Sphalerite Cleavage Face 152
  ———: Electron Diffraction Investigation of the Actions of Queous Heavy Metal Salts on Mineral Surfaces II. Action of Mercuric Sulfate on Galena Cleavage Face 454
  ———: Oriented Overgrowth of Primary Oxide on α: Fe 758

SAWAGUCHI Etsuro: Ferroelectricity versus Antiferroelectricity in the Solid Solutions of $PbZrO_3$ and $PbTiO_3$ 615

SEKI Yoshinabu: A New Type of Striation Observed in Electron-Micrographs of Sericite 149

SHIMAUCHI Akira;
  S. KOJIMA, K. TAKAYAMA and ———: Probe Measurement for High Frequency Discharge III 55

SHIMODA Koichi: Length of Coherent Microwaves Generated by an Electric Oscillator 131
  ——— and T. NISHIKAWA: Microwave Spectrum of Methylamine I 133
  ——— and T. NISHIKAWA: Microwave Spectrum of Methylamine II 425
  T. NISHIKAWA and ———: New Lines of the Inversion Spectrum of Ammonia 426

SHINDO Takuzo: Space Charge Effect in the Oxide Cathode Layer II 494

SOMA Junkichi;
  ——— and M. OGI: On a Non-linear Approximation of the Interatomic Force in Solid 6

——— and M. OGI: Corrections to our paper "On a Non-linear Approximation of the Interatomic Force in Solid" 565

SUGAI Shintaro;
——— and J. FURUICHI: On the Photographic Chemical Development 681

SUGANUMA Ryōji;
Y. FUJIKI and ———: On the Structure Loosening of Metal Films deposited from the Vapour 427

SUGITA Motoyosi: Thermodynamical Analysis of Life II. On the Maximum Principle of Transient Phenomena 697
———: Thermodynamical Analysis of Life III. Mathematical Analysis of Metabolism 704
———: Thermodynamical Analysis of Life I. Thermodynamics of transient phenomena 709

SUGIURA Yoshikazu;
R. UYEDA and ———: A Flow-Meter in Vacuum Technique 99

SUITA Tokuo;
C. YAMANAKA and ———: Electron Avalanche in Liquids at Strong Electric Fields 277
Y. INUISHI and ———: On the Space Charge Effect in Dielectric Breakdown of KCl Single Crystals 567
———: Directional Dielectric Breakdown in Single Crystals 126
C. YAMANAKA and ———: Electric Conductivities of Solids in Strong Electric Fields I 274

SUWA Shigeki: Hyperfine Structure of the Spectrum of Gadolimium 377
———: Hyperfine Structure of the Spectrum of Al II. Part II 531
———: Hyperfine Structure of the Spectrum of Zr I and the Magnetic Moment of Zr^{91} 734

SUZUKI Hiromichi;
A. OKAZAKI, H. TUBOTA and ———: The Temperature Dependence of the Zero Bias Resistance of Cuprous Oxide Rectifiers 431

SUZUKI Yasumasa;
S. MIYATANI and ———: On the Electric Conductivity of Cuprous Sulfide; Experiment 680

TAKAHASI Hidetosi;
K. KAMBE, I. NAKADA and ———: Hysteresis Loops of Ceramic Barium Titanate at Higher Frequencies I 9

TAKAKURA Tatsuo;
———, K. BABA, K. NUNOGAKI and H. MITANI: The 3000 Mc Ion Plasma Noise Radiated from Arc Discharge and Solar Eruption 426
———: On the Directivity of Solar Radio Emission from the Sunspots 422

TAKAMURA Yosomatsu: Measurement of the Net Thermal Conductivity of Fibrous Substances 674

TAKAYAMA Kazuo;
S. KOJIMA, ——— and A. SHIMAUCHI: Probe Measurement for High Frequency Discharge III 55

TAKEDA Eiichi;
H. SAKETA, K. MATSUDA and ———: Thermal Concentration of Carbon Isotopes Using Carbon Monoxide Gas 313

TAKEDA Etujirō: On the Coefficient of Restitution 790

TAKEDA Ikuo;
S. YOSHIDA, ———, Y. IGARASHI and H. ARATA: Secondary Electron Emission of Copper-beryllium Alloy 318

TAMADA Kō: On the Detachment of Shock Wave from the Leading Edge of a Finite Wedge 242

TANAKA Kenzo;
——— and I. FUKUYAMA: On the Metastable Phase Change of Ammonium Nitrate 428

TANAKA Jiro;
K. NUKASAWA, ——— and S. NAGAKURA: A Note on the Hydrogen Bond..
TERADA Jitsuo: Crystal Structure of the Ba, Sr and Ca Triple Carbonate ... 158
TERAO Nobuzo: (Errata) Un Traitment Statistique de la Résistance à la Rupture du Verre—Sur l'Influence de la Température ... 137
———: Sur une Relation entre la Résistance à la Rupture et le Foyer d'Eclatement du Verre ... 545
———: Sur la Résistance à la Rupture du Verre—L'Influence de l'Humidité ... 550
TODA Morikazu: Diffusion on the Fermi-Surface and the Conductivity of Metals ... 339
TOKUNAGA Senzo;
———, K. YUASA, K. NISHIKAWA and T. ISII: Energy Spectra of Charged π-mesons Produced in Carbon, Aluminium and Copper at 90° to a 345 MeV Proton Beam ... 571
TOMISHIMA Yasuo;
K. UMEDA and ———: TFD Functions for Non-zero Temperatures and Equations of State Based on Them ... 360
TOMONO Masami: Direct current Characteristics of the Selenium Rectifier I. Theory of Rectification ... 477
TORIKAI Yasuo;
——— and K. NEGISHI: The Application of the Phase Method in Visualizing Ultrasonic Waves ... 119
———: Transmission of Ultrasonic Waves through a Plane Plate made of Viscoelastic Material Immersed in a Liquid Medium ... 234
TUBOTA Hirosi;
A. OKAZAKI, ——— and H. SUZUKI: The Temperature Dependence of the Zero Bias Resistance of Cuprous Oxide Rectifiers ... 431
TUKIZI Osamu: On the Frequency of Scintillation Fading of Microwaves ... 130
UCHIDA Yōichi;
——— and Y. NAKAI: Injection of Positive Holes in the Alkali Halide Crystal 795
UETA Masayasu: Field Emission of Crystal Phosphors ... 429
UMEDA Kwai;
——— and Y. TOMISHIMA: TFD Functions for Non-zero Temperatures and Equations of State Based on Them ... 360
UYEDA Ryozi;
——— and Y. SUGIURA: A Flow-Meter in Vacuum Technique ... 99
WAKATSUKI Tetsuo: On the Capture Scattering of Fast Neutrons ... 1
WAKIYA Shōichi: A Spherical Obstacle in the Flow of a Viscous Fluid through A Tube ... 254
WATASE Yuzuru;
S. HIGASHI, T. KITAMURA, T. KUBOZOE, M. ODA, S. OZAKI and ———: On the Penetrating Shower Originating in Light Element and Heavy Element 584
YAMAGATA Yukio;
J. ITOH, R. KUSAKA, ———, R. KIRIYAMA, H. IBAMOTO, T. KANDA and Y. MASUDA: Nuclear Magnetic Resonance Experiment on the Single Crystal of $K_2HgCl_4 \cdot H_2O$ and $K_2SnCl_4 \cdot H_2O$. Part I. ... 287
J. ITOH, R. KUSAKA, ———, R. KIRIYAMA and H. IBAMOTO: Nuclear Magnetic Resonance Experiment on the Single Crystals of $K_2HgCl_4 \cdot H_2O$ and $K_2SnCl_4 \cdot H_2O$. II The Resonance absorption due to four proton system and the revised determination of their crystal structures ... 293
YAMANAKA Chiyoe;
——— and T. SUITA: Electric Conductivities of Solids in Strong Electric Fields I ... 274
——— and T. SUITA: Electron Avalanche in Liquids at Strong Electric Fields 277
YANAGAWA Sadaaki: Mathematical Formulations of Physical Quantities for j-j-coupling Nuclear Shell Model ... 302
YANG Tsung-che;
Y. INUISHI and ———: The Influence of Impurity Atoms on Flicker Noise · 565

YOKOBORI Takeo: Failure and Fracture of Metals from the Standpoint of the Stochastic Theory 104
———: Ductility Transition and Cold Brittleness 107
———: Fatigue Fracture from the Standpoint of the Stochastic Theory 265
———: Damage as an Initial Stage of Fatigue Fracture 806
YOKOTA Isaaki: On the Electrical Conductivity of Cuprous Sulfide: A Diffusion Theory 595
YOSHIDA Shigetomo;
———, I. TAKEDA, Y. IGARASHI and H. ARATA: Secondary Electron Emission of Copper-beryllium Alloy 318
YOSHIMURA Yoshimaru: On the Definition of Stress in the Finite Deformation Theory 669
YOSHIZAWA Yasukazu: The Beta-ray Spectra of Co^{60} and Sc^{46} 435
YOSIMOTO Hirosi: Oscillatory Phenomena of Arc in Hot Cathode Discharge Tube I. Experimentals 59
———: Oscillatory Phenomena of Arc in Hot Cathode Discharge Tube II. Theoretical 69
YUASA Kazunori;
S. TOKUNAGA, ———, K. NISHIKAWA and T. ISII: Energy Spectra of Charged π-mesons Produced in Carbon, Aluminium and Copper at 90° to a 345 MeV Proton Beam 571

PROGRESS OF THEORETICAL PHYSICS

Published by

The Yukawa Hall

with the cooperation of

The Physical Society of Japan

Progress of Theoretical Physics　　Vol. 10, No. 2, 1953

On the Constants of Motion for the Case of Non-localized Interactions ....Yôrô ÔNO....125

On the Equivalence of the Particle Formalism and the Wave Formalism of Meson, II ——Case of Interacting Meson and Nucleon Fields—— ....Zensuke TOKUOKA....137

Antiferromagnetism. The Kagomé Ising Net ....Kenzi KANO and Shigeo NAYA....158

Miscellanea in Elementary Quantum Mechanics, III ....Kôdi HUSIMI and Masuhiko ÔTUKA....173

On Gauge Invariance in Electrodynamics and the Self-energy Problem of the Photon....Osamu HARA and Hisaichiro OKONOGI....191

On the Effects of Excited States of Nucleons upon Static Nuclear Potential in Symmetrical Pseudoscalar Meson Theory, I ——Derivation of Nuclear Potential and Qualitative Conclusions—— ..Tokuji MATSUMOTO, Tetuo HAMADA and Masao SUGAWARA....199

A Speculation on V-spin....D. C. PEASLEE....227

Letters to the Editor:

- On the Solution of the Equation of Motion....H. KITA....231
- On the Theory of β-decay....Y. TANIKAWA and K. SAEKI....232
- On the Spin-lattice Relaxation at Extremely Low Temperature ....K. SUGIHARA....234
- Nonlinear Pseudoscalar Meson Theory....F. CAP....235
- Angular Distribution of the Deuteron Photodisintegration at Moderate Energies....A. SUGIE and S. YOSHIDA....236
- Cloud Chamber Study of Nuclear Interactions in Lead and Carbon of Secondaries emitted in Cosmic Ray Penerating Showers....I. KITA and O. MINAKAWA....237
- The Absolute Intensity of Cosmic Rays at Geomagnetic Latitude 25°N....Y. KITAMURA and O. MINAKAWA....239
- The π-nucleon Scattering and the Damping Effect ....K. HASEGAWA and S. AZUMA....240
- Note on the Finite Nuclear Size Effect in Beta-decay ....M. YAMADA....241

Price　　$ 1.00 per copy
$12.00 per year (postage inclusive)

Annual dues for foreign members (individual subscribers)
$ 9.00 (postage inclusive)

〃　for foreign members of the Physical Society of Japan
$ 7.50 (postage inclusive)

Application for members, subscriptions and orders for back mumbers should be sent, directly or through book-dealers, to

The Publication Office
in
Yukawa Hall, Kyoto University, Kyoto, Japan